

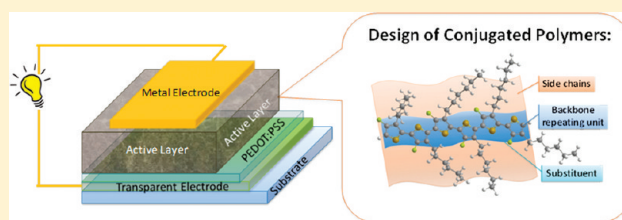
Rational Design of High Performance Conjugated Polymers for Organic Solar Cells

Huaxing Zhou,[†] Liqiang Yang,[‡] and Wei You^{*,†,‡}

[†]Department of Chemistry, University of North Carolina at Chapel Hill, Chapel Hill, North Carolina 27599-3290, United States

[‡]Curriculum in Applied Sciences and Engineering, University of North Carolina at Chapel Hill, Chapel Hill, North Carolina 27599-3287, United States

ABSTRACT: The research on the polymer-based solar cells (PSCs) has attracted an increasing amount of attention in recent years because PSCs pose potential advantages over mainstream inorganic-based solar cells, such as significantly reduced material/fabrication costs, flexible substrates, and light weight of finished solar cells. The research community has made great progress in the field of bulk heterojunction (BHJ) polymer solar cells since its inception in 1995. The power conversion efficiency (PCE), a key parameter to assess the performance of solar cells, has increased from 1% in the 1990s to over 8% just recently. These great advances are mainly fueled by the development of conjugated polymers used as the electron-donating materials in BHJ solar cells. In this Perspective, we first briefly review the progress on the design of conjugated polymers for polymer solar cells in the past 16 years. Since a conjugated polymer can be arbitrarily divided into three constituting components—the conjugated backbone, the side chains, and the substituents—we then focus on the rational design of conjugated polymers by separately discussing the influence of each component on the physical and photovoltaic (PV) properties of these polymers. Special attention is paid to the design of donor–acceptor type low-band-gap polymers because this approach is prevailing in the literature with its unique features. In doing so, we strive to extract useful rules for the rational design of conjugated polymers with predictable properties. We conclude by proposing future research opportunities to achieve even higher PCEs for PSCs.



1. INTRODUCTION

1.1. Background. Polymer solar cells (PSC) have attracted an increasing amount of attention in the research community due to the potential advantages of PSC over inorganic-based solar cells, including low cost, light weight, and fast/cheap roll-to-roll production.^{1–7} Typically, p-type semiconductor (i.e., electron DONOR, such as conjugated polymers) and n-type semiconductor (i.e., electron ACCEPTOR, such as fullerene derivatives) are blended in a bulk heterojunction (BHJ) configuration as the core component for PSC.³ The interpenetrated network of BHJ offers two advantages: (a) it minimizes the traveling distance of excitons (electron–hole pair generated upon light absorption) to the DONOR/ACCEPTOR (D/A) interface and concurrently maximizes the D/A interfacial area, thereby ensuring the exciton dissociation at the D/A interface to generate maximum free charge carriers; (b) it offers charge transport pathways to facilitate the charge collection at electrodes, completing the conversion of the photon energy to electrical energy (i.e., photovoltaic effect). In a complete BHJ solar cell, the active layer is sandwiched between a transparent anode (typically tin-doped indium oxide, ITO) and a metal cathode (Figure 1). Additionally, a thin layer of poly(3,4-ethylenedioxythiophene)–poly(styrenesulfonate) (PEDOT:PSS) is generally applied in between the ITO and the active layer to improve the electrical contact between the ITO and the active layer and to adjust energy levels.⁸

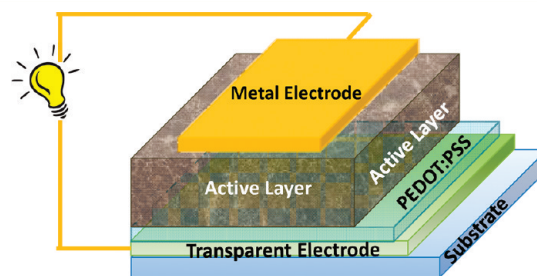


Figure 1. Schematic illustration of the structure of a typical bulk heterojunction polymer solar cell device.

The power conversion efficiency (PCE) of polymer solar cells has improved rapidly from below 1% to over 8% in the past 16 years.⁹ This impressive accomplishment is mainly achieved by the molecular engineering of the structure of conjugated polymers (as the DONOR materials),^{10–12} assisted by limited successes in derivatizing the fullerenes (as the electron ACCEPTOR).^{12–18}

Because of the limited solubility of buckminsterfullerene (C₆₀) in common organic solvents, a fullerene derivative, [6,6]-phenyl-C₆₁-butyric acid methyl ester (PC₆₁BM), has been used as

Received: July 18, 2011

Revised: November 11, 2011

Published: January 11, 2012

a standard and efficient ACCEPTOR material in PSC. The photoinduced charge transfer from the conjugated polymer to PC₆₁BM occurs quantitatively on the picosecond time scale with exciton dissociation rate near unity,³ a unique feature inherited from the original C60.¹⁹ Although some other high performance fullerene derivatives have also been developed over the years,^{12–18,20} the relatively cheap and commercially available PC₆₁BM is still widely applied as the standard ACCEPTOR material. In recent years, PC₇₁BM, a C₇₀ analogue of PC₆₁BM, was used in some research groups to increase PCE because of its better light absorption in the visible region.¹⁵ *In this Perspective, we will focus on the rational design of conjugated polymers under the assumption that PC₆₁BM/PC₇₁BM is used as the electron ACCEPTOR.* The seemingly narrow topic of conjugated polymer-based solar cells in fact covers a much wider range of active research thrusts, ranging from materials synthesis, physical chemistry (e.g., exciton behavior and morphological study of active layers), to device physics and involves multiple disciplines (chemistry, physics, and engineering). Therefore, interested readers should refer to other related reviews to grasp a more comprehensive picture of the extremely active and productive field of polymer solar cells.^{10,12,21–33} Finally, to avoid confusion, donor and acceptor are generally referred to as building units for the design of polymers, while DONOR and ACCEPTOR with all letters capitalized are reserved to represent the DONOR polymer and ACCEPTOR (e.g., fullerene) in the BHJ blend, respectively.

1.2. A Brief History of the Development of Conjugated Polymers for Polymer Solar Cells. The rather short history of BHJ solar cells can be roughly divided into three phases from the perspective of the conjugated backbones of DONOR polymers. Phase one centered on poly(phenylene vinylene)s (PPV), such as poly[2-methoxy-5-(2'-ethylhexyloxy)-1,4-phenylenevinylene] (MEH-PPV) and poly[2-methoxy-5-(3',7'-dimethyloctyloxy)-1,4-phenylenevinylene] (MDMO-PPV). Power conversion efficiency as high as 3.3% was achieved in PPV-based BHJ solar cells with PC₆₁BM as the ACCEPTOR material, mainly through the application of chlorinated solvents to tune active layer morphologies.^{34,35} A high open-circuit voltages (V_{oc}) up to 0.82 V was obtained as a result of the relatively low highest-occupied molecular orbital (HOMO) energy level of –5.4 eV of MDMO-PPV; however, the large band gap of MDMO-PPV limited the short-circuit current density (J_{sc}) to 5–6 mA/cm². Therefore, in phase two, a smaller-band-gap polymer, regioregular poly(3-hexylthiophene) (rr-P3HT), was thoroughly investigated.²⁷ P3HT-based BHJ devices provide a noticeably higher current density (over 10 mA/cm²), attributed to its lower band gap (1.9 eV) as well as to its increased π -stacking and crystallinity which yields a higher hole mobility.^{36–38} Upon optimization of the active layer morphology via thermal³⁸ or solvent annealing,³⁹ an impressive PCE of 5% was achieved.^{27,40} Unfortunately, the high HOMO (–5.1 eV) energy level of P3HT has restricted the V_{oc} to ~0.6 V in its related BHJ solar cells with PC₆₁BM as the ACCEPTOR, which consequently limits the overall efficiency.

Presently in phase three, numerous polymer backbones have been reported. High V_{oc} over 1 V,^{41–43} high J_{sc} over 17.3 mA/cm²,⁵ and fill factor (FF) over 70%^{44,45} have been demonstrated in different polymer-based BHJ solar cells. If all these impressive values could be combined in one polymer solar cell, it would give a PCE as high as 12%! However, due to the interplay of polymer properties such as energy levels and band gap and their correlation with V_{oc} and J_{sc} , highest V_{oc} and highest J_{sc} cannot be concurrently obtained.⁴⁶ In order to achieve the highest possible PCE, one needs to carefully balance

the V_{oc} and J_{sc} via judicious control over physical properties of a conjugated polymer (i.e., in pursuit of “ideal polymers”).

1.3. Required Properties for Ideal Polymers. To design ideal polymers as the DONOR in polymer-based BHJ solar cells with high PCE ($PCE = V_{oc} \times J_{sc} \times FF/P_{in}$), the following issues need to be carefully addressed.

a. Open-Circuit Voltage (V_{oc}). V_{oc} is tightly correlated with the energy level difference between the HOMO of the DONOR polymer and the LUMO of the ACCEPTOR (e.g., PC₆₁BM).⁴⁷ In theory, polymers with low-lying HOMO levels would exhibit higher V_{oc} . However, the HOMO level of the DONOR polymer cannot go too low. This is because generally a minimum energy difference of ~0.3 eV between the LUMO energy levels of the DONOR polymer and the ACCEPTOR is required to facilitate efficient exciton splitting and charge dissociation. When PC₆₁BM with a LUMO level of –4.2 eV is used as the ACCEPTOR, the lowest possible LUMO level of the DONOR polymer would be near –3.9 eV. Continuously lowering the HOMO level of the DONOR polymer would inevitably enlarge the band gap of the polymer, diminishing the light absorbing ability of the DONOR polymer (thereby a low J_{sc}). The origin of V_{oc} is still under intense debate, and recent data indicate that V_{oc} is decided by a couple of other factors besides just the HOMO level of the polymer.^{48,49} Furthermore, bulkiness of side chains, interchain distances, and morphology of active layer have also been demonstrated to have a noticeable effect on the V_{oc} .⁵⁰

b. Short-Circuit Current (J_{sc}). The theoretical upper limit for J_{sc} of any excitonic solar cell is decided by the number of excitons created during solar illumination. Ideally, the absorption of the active layer should be compatible with the solar spectrum to maximize the exciton generation. Since PC₆₁BM has a poor absorption in the visible and near-IR region where most of the solar flux is located, the DONOR polymer has to serve as the main light absorber. Roughly 70% of the sunlight energy is distributed in the wavelength region from 380 to 900 nm;⁵¹ hence, an ideal polymer should have a broad and strong absorption in this range, which requires the polymer band gap to be 1.4–1.5 eV. A narrower band gap polymer could absorb more light, which would increase the J_{sc} ; however, continuing to lower the band gap would require an increase of the HOMO level of the DONOR polymer (since the LUMO level cannot be lower than –3.9 eV with PC₆₁BM as the ACCEPTOR for efficient exciton splitting and charge dissociation)²¹ and would reduce the V_{oc} .

If one assumes a fill factor of 0.65, an external quantum efficiency of 65%, and an optimal morphology, one can approximate the overall PCE from the optical band gap and the LUMO/HOMO of the DONOR polymer in a polymer:PC₆₁BM BHJ solar cell (Figure 2).⁴⁷ It is clearly seen that a PCE of 10% can be achieved by an “ideal” polymer with an optimal band gap of 1.5 eV and a HOMO level around –5.4 eV.

Though the experimentally determined V_{oc} can be very close to the predicted value based on the measured HOMO level of the polymer, the actual J_{sc} extracted from a polymer solar cell is usually significantly lower than the theoretical J_{sc} due to a number of loss mechanisms (e.g., monomolecular or bimolecular recombination) during the charge generation, transport, and extraction.^{22,51} Thus a few other desirable features need to be included to mitigate these losses, such as high molecular weight, high charge mobility, and optimized active layer morphology, all of which will help improve the actual J_{sc} .

c. Fill factor (FF). From a semiconductor photovoltaic device point of view, a high FF requires a small series resistance (R_s) and a large shunt resistance (R_{sh}),⁵² both of which are

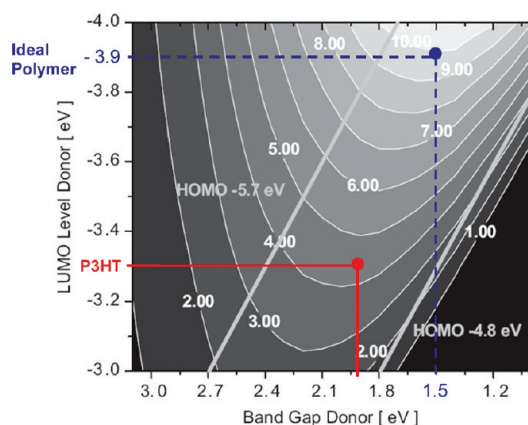


Figure 2. Calculated energy-conversion efficiency of P3HT and an “ideal” polymer, assuming *FF* and *IPCE* at 65%. Reprinted with permission from ref 47. Copyright 2006 Wiley-VCH Verlag GmbH & Co. KGaA.

significantly impacted by the morphology of the polymer/fullerene blend. Thus, the morphology of the active layer should be optimized to promote charge separation and favorable transport of photogenerated charges in order to maximize the *FF* and the attainable J_{sc} .

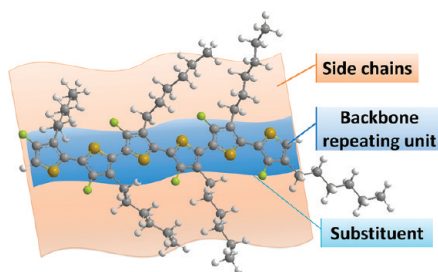
Finally, besides high PCE, solution processability (offered by side chains) and long-term stability of polymer solar cells (related with both materials and encapsulation) are of equal importance for future application and commercialization.

In short, the properties desired for a high performance polymer are (1) good solubility, (2) high molecular weight, (3) HOMO level around -5.4 eV, (4) LUMO level around -3.9 eV, (5) high hole mobility, (6) optimal morphology, and (7) long-term stability.

2. MOLECULAR ENGINEERING OF CONJUGATED POLYMERS FOR POLYMER SOLAR CELLS

2.1. Structural Features of Conjugated Polymers: A Bird's Eye View. A typical conjugated polymer used as the electron DONOR in polymer solar cells is illustrated in Scheme 1.

Scheme 1. Illustration of a Typical Conjugated Polymer for Polymer Solar Cells



Generally, a conjugated polymer can be arbitrarily divided into three constituting components: the conjugated backbone, the side chains, and the substituents. The conjugated backbone is the most important component because it dictates most of the PSC-related physical properties of the conjugated polymer, such as energy levels, band gap, and inter/intra molecular interactions. Hundreds of different backbones have been reported so far;^{10–12} however, the design of polymer backbones has been quite empirical. As a result, the discovery of high performance polymers is

rather serendipitous. Therefore, the rational design of conjugated backbone (i.e., the repeating units) is of utmost importance in the further development of polymer solar cells.

On the other hand, side chains play a crucial role in improving the molecular weight, solubility, and processability of conjugated polymers. Furthermore, these side chains can adjust intermolecular interactions and allow proper mixing with PC₆₁BM to form the desired morphology. However, these insulating side chains also dilute the chromophore density and disturb π -stacking of polymer backbones, which could thwart the light absorption and charge transport. In addition, improper attachment of side chains may introduce steric hindrance and twist the conjugated backbone, which could lead to a large band gap, low charge carrier mobility, and poor photovoltaic properties. Finally, there are increasing evidence showing that the shape and length of side chains have noticeable impact on the photovoltaic properties of conjugated polymers.

Lastly, substituents (such as F and CN) are generally used as fine-tuning methods to tweak the physical properties of conjugated polymers, particularly the electronic properties (energy levels, band gap, mobility, etc.). Since photovoltaic properties of conjugated polymers are very sensitive toward their electronic properties, sometimes substituents can have important influence on the photovoltaic performance of related conjugated polymers.

2.2. Rational Design of Conjugated Polymer Backbones. All reported conjugated backbones for PSC can be arbitrarily classified into a few categories based on the constitution of the repeating unit, namely (a) homopolymer, (b) donor–acceptor polymer, (c) quinoid polymer, and (d) other types of polymers, as shown in Figure 3.

The repeating unit of the homopolymer usually consists of a single aromatic unit or fused aromatics. The physical properties of these polymers are largely determined by the intrinsic properties of the constituting single or fused aromatics, with appreciable contribution from steric hindrance between these repeating units. Thus, most of the homopolymers have large band gaps (>1.9 eV), which limit the light absorption of these materials. In addition, very often the aforementioned steric hindrance forces the adjacent repeating units off the desired coplanarity of these units, negatively impacting the band gap and the crystallinity of the polymer, thereby diminishing photovoltaic properties of related BHJ devices.^{40,53,54} The best polymer of this type is the regioregular P3HT with PCE over 5% after thorough optimizations.^{27,38,40}

On the other hand, it is fairly easy to construct low-band-gap polymers with tunable energy levels via the donor–acceptor (D–A) approach. The repeating unit of D–A polymers comprises of an electron-rich “donor” moiety and an electron-deficient “acceptor” moiety. The internal charge transfer between the “donor” and the “acceptor” moieties leads to the observed low band gap.⁵⁵ This strategy was first proposed in 1993^{56,57} and best illustrated by Tour et al. by using a copolymer of 3,4-aminothiophene and 3,4-nitrothiophene to reach a band gap of 1.0 eV, as shown in Figure 3.⁵⁸ The internal charge transfer (ICT) intrinsic with the D–A structure leads to more desirable double-bond characteristic between repeating units. Therefore, the conjugated backbone adopts a more planar configuration to facilitate the π -electrons delocalization along the conjugated backbone, leading to a smaller band gap. One unique feature of the D–A polymers is that the HOMO and LUMO energy levels are largely localized on the donor moiety and the acceptor moiety, respectively (though HOMO is more delocalized along the D–A structure).^{33,59} This feature offers an important advantage of *individually* tuning the band gap and energy levels of the conjugated polymer. For example, a smaller band gap can

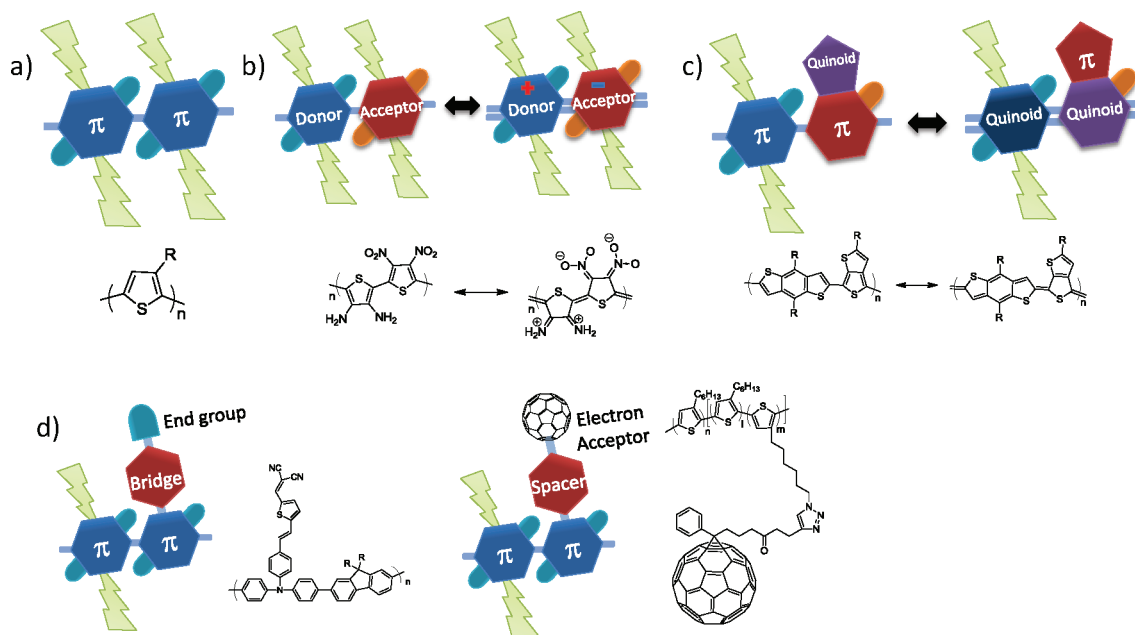


Figure 3. Different types of conjugated polymers with representative structures: (a) homopolymer; (b) donor–acceptor polymer; (c) quinoid polymer; (d) other types.

be obtained by copolymerizing a more electron-rich donor moiety and a more electron-deficient acceptor moiety, whereas the HOMO and LUMO levels can also be adjusted by varying the electron-donating ability of the donor moiety and the electron affinity of the acceptor moiety.⁵⁹ Most of the conjugated polymers for PSC reported so far are based on this D–A concept, with several of them showing over 7% efficiency in their BHJ cells.^{45,60–63}

“Quinoid” polymers employ a different approach to effectively lower the band gap. Typically two aromatic units are fused in a particular geometry to take advantage of the larger value of resonance energy of the first aromatic unit (e.g., benzene, 1.56 eV) over the second unit (e.g., thiophene, 1.26 eV), so that the second aromatic unit (e.g., thiophene) tends to dearomatize to adopt a quinoid structure. Since the quinoid resonance form is lower in energy than the aromatic form, stabilizing the quinoid form will effectively reduce the band gap of related conjugated polymers. Figure 4 shows a few successful

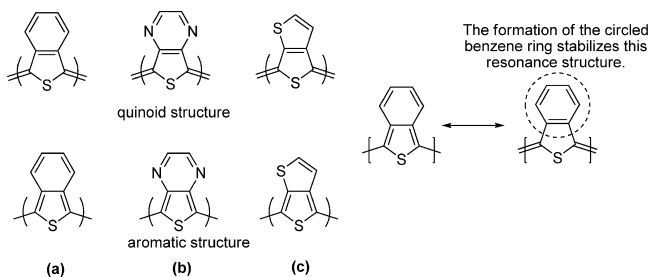


Figure 4. Aromatic and quinoid forms of poly(benzo[*c*]thiophene) (a), poly(thieno[3,4-*b*]pyrazine) (b), and poly(thieno[3,4-*b*]thiophene) (c). Reprinted with permission from ref 7. Copyright 2010 American Chemical Society.

examples, including poly(benzo[*c*]thiophene) ($E_g = 1.1$ eV),⁶⁴ poly(thieno[3,4-*b*]pyrazine) ($E_g = 0.95$ eV),⁶⁵ and poly(thieno[3,4-*b*]thiophene) ($E_g = 0.8–0.9$ eV).^{66,67} The major drawback of these fused systems lies in their relatively high-lying HOMO energy levels, which explains that low-band-gap copolymers synthesized by

alternating these prequinoid monomers with other aromatic rings such as thiophenes and fluorenes showed low V_{oc} in BHJ solar cells.^{68–73} Further engineering the substituents on these conjugated backbone can lower the HOMO levels,^{74–77} thereby leading to impressive efficiency numbers (over 7%).^{74,78}

Rather than inserting electron-deficient acceptor moieties into the conjugated backbone to lower the band gap, the bridge polymer attaches them as the pendant groups to the backbone, aiming to optimize the absorption and conserve/promote the isotropic charge transport without any interruption by these acceptor moieties.^{79,80} There are only a few examples of these bridge polymers with limited success.^{79–81} One challenge for this type of polymers is the understanding and control of the active layer morphology.

The so-called “double-cable” approach was designed with the hope of “building in” well-defined nanostructure/morphology, rather than going through an arduous struggle in controlling the morphology in typical BHJ cells of polymer/fullerene blends. This “double-cable” design covalently links electron acceptors such as fullerenes (ACCEPTOR cable) to electron DONORS such as the conjugated backbones (DONOR cable). The advantages of this design include (i) a larger DONOR–ACCEPTOR interfacial area when compared with a typical BHJ structure, (ii) absence of undesirable large phase separation, (iii) relatively stable morphology, and (iv) variation of the chemical structures of the DONOR and the ACCEPTOR and length of the spacer between them, allowing to fine-tune the electronic interaction among the double-cable components.^{82,83} Several materials of this “double-cable” design have been demonstrated in polymer solar cells.^{84–89} However, the PCE of such devices is still at a very low level, likely due to fast recombination of opposite charges, ineffective interchain charge transport, and low ACCEPTOR content.^{90,91}

Because of the aforementioned advantages, the versatility in design, and the popularity of the D–A polymers, we will focus on the design of donor–acceptor polymers in this Perspective.

2.3. A “Weak Donor–Strong Acceptor” Approach toward Ideal Polymers. As discussed in section 1.3, the ideal

conjugated polymer for BHJ solar cells should have a low-lying HOMO energy level to ensure a high V_{oc} and a narrow band gap to maximize the J_{sc} . Because the D–A polymers offer the unique feature of almost independently tuning the energy levels and the band gap, a “weak donor–strong acceptor” strategy has been proposed to maintain a low HOMO energy level via the “weak donor” and to result a narrow band gap by employing a “strong acceptor” via ICT (Figure 5).⁵⁹ In addition, the charge

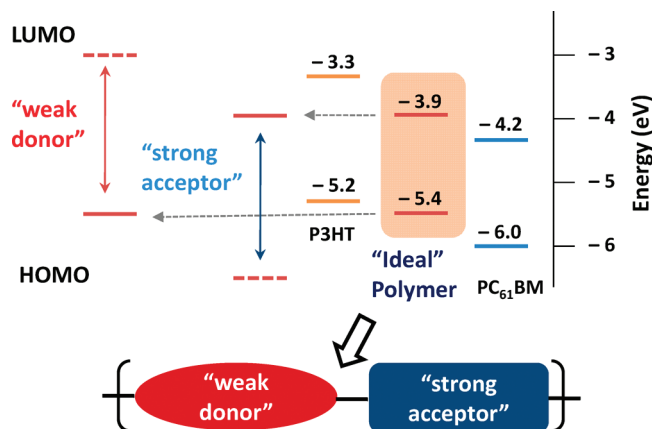


Figure 5. “Weak donor–strong acceptor” concept and energy levels. Adapted with permission from ref 59. Copyright 2010 American Chemical Society.

mobility, molecular interaction, and stability of a conjugated polymer can also be optimized by appropriate backbone design.

In the following sections, we will categorize various electron-donating units and electron-accepting units from the literature based on their structural features. The goals are to (a) summarize structure–property relationships of these units, and (b) identify principles that can facilitate future designs.

2.3.1. Selection of Donor Units. To design a suitable donor unit, first and foremost is to control its electron-donating ability, which has a large impact on the HOMO level and the band gap of conjugated polymers. Fused conjugated units are generally employed, since an appropriate fusion of a few single aromatic units can not only tune the electronic properties but also impact the charge mobility and intermolecular interactions of related conjugated polymers.

2.3.1.1. Fused Three Rings: Control over the Energy Levels. Figure 6a summarizes a few fused conjugated units with three rings. For example, fluorene is one of the most popular donor units used in D–A polymers for PSC due to a few notable features of the polyfluorenes, such as good thermal and chemical stability, high charge carrier mobility, and high absorption coefficients. In addition, the synthesis and alkylation of fluorene unit are readily accessible.^{95–98} Furthermore, the central fused five-membered ring structure of the fluorene eliminates the otherwise severe steric hindrance of adjacent benzene units. Also, the alkyl chains are usually anchored on the 9-position of the fluorene, which does not add any

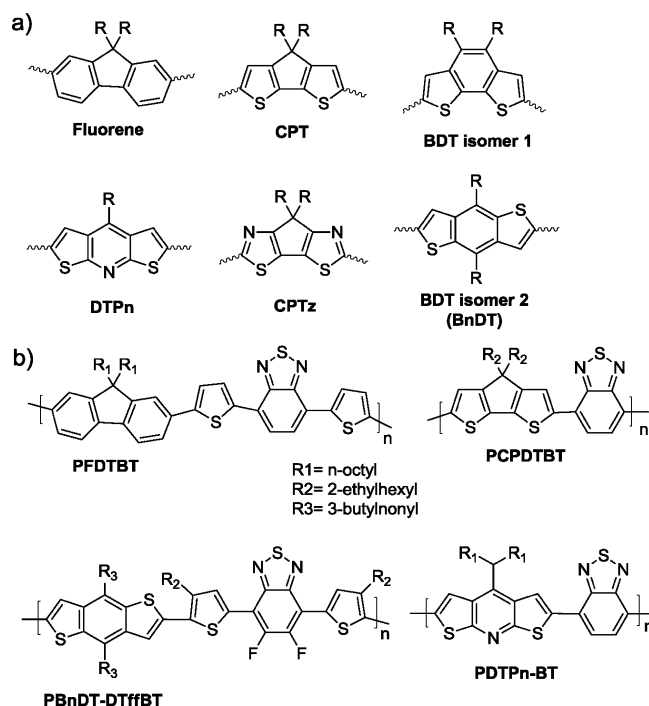


Figure 6. (a) Examples of fused-three-ring donor units. (b) Chemical structures of related copolymers.

additional steric hindrance. All these lead to a planar backbone of fluorene-related conjugated polymers, improving the intermolecular interaction and stacking of conjugated polymers.

Electronically, the fluorene unit is a very weak electron donor because of the relatively electron-deficient benzene units.⁹⁹ Therefore, most fluorene-based conjugated polymers have low HOMO levels around -5.5 eV.^{74,100–103} As a result, V_{oc} of polyfluorene-based BHJ solar cells are generally around 1 V (Table 1).^{100,102} However, these polymers usually have relatively large band gaps, which are not ideal for efficient light harvesting. To address this band-gap challenge, the thiophene analogue of the fluorene, cyclopentadithiophene (CPT) unit by fusing two thiophene units, was developed.¹⁰⁴ The CPT unit is much more electron-rich than the fluorene; thus, the ICT between the CPT donor unit and the acceptor unit is much stronger, leading to a significantly decreased band gap of related polymers (e.g., 1.4 eV).^{104–106} The J_{sc} of CPT-based polymers can reach up to ~ 17 mA/cm² by optimizing the morphology with additives, which is among the highest J_{sc} in polymer solar cells.^{5,93} Unfortunately, the electron-rich nature of the CPT raises the HOMO of CPT-based polymers to around -5.2 eV; therefore, a small V_{oc} is generally observed (0.5–0.6 V).

Comparison between the fluorene and the CPT leads to the conclusion that a weak donor with electron-donating ability in between CPT and fluorene would be desirable toward the ideal polymer of both a low HOMO energy level and a narrow band gap. One natural choice is to fuse the benzene unit and the thiophene unit, such as the BDT unit (and its isomers). Both

Table 1. Summary of Band Gaps, HOMO Levels, and Photovoltaic Properties of Conjugated Polymers in Figure 6b

polymer	band gap (eV)	HOMO (eV)	V_{oc} (V)	J_{sc} (mA/cm ²)	FF	PCE (%)	ref
PFDTBT	1.9	-5.7	1.04	4.66	0.46	2.2	92
PCPDTBT	1.4	-5.3	0.62	16.2	0.55	5.5	93
PBnDT-DTfBT	1.7	-5.5	0.91	12.91	0.61	7.2	61
PDTPh-BT	2.1	-5.6	0.31	0.75	0.37	0.09	94

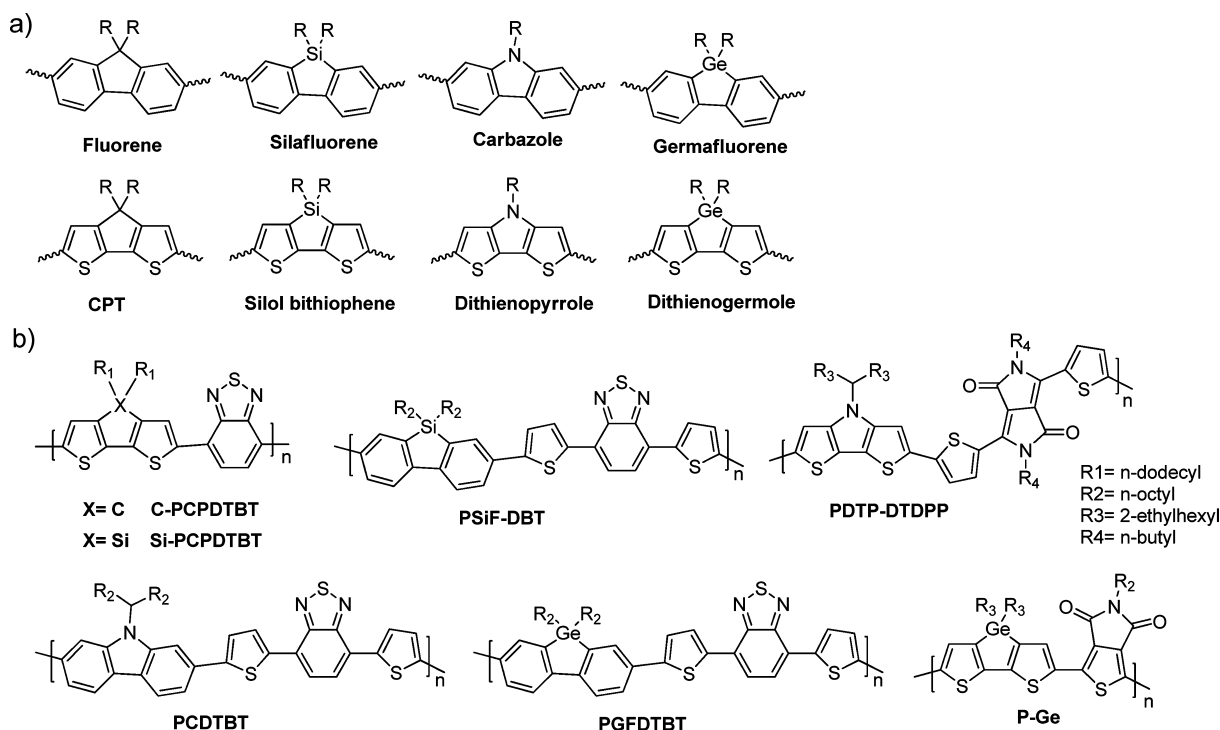


Figure 7. (a) Structures of donor units fused by bridging atoms. (b) Chemical structures of related copolymers.

Table 2. Summary of Band Gaps, HOMO Levels, and Photovoltaic Properties of Conjugated Polymers in Figure 7b

polymer	band gap (eV)	HOMO (eV)	V_{oc} (V)	J_{sc} (mA/cm ²)	FF	PCE (%)	ref
Si-PCPDTBT	1.4	−5.3	0.57	17.3	0.61	5.9	5
C-PCPDTBT	1.3	−5.3	0.37	15.5	0.48	2.7	5
PSiF-DBT	1.82	−5.4	0.90	9.5	0.51	5.4	109
PDTP-DTDP	1.13	−4.90	0.38	14.87	0.48	2.7	110
PCDTBT	1.9	−5.5	0.88	10.6	0.66	6.1	4
PGFDTBT	1.8	−5.6	0.79	6.9	0.51	2.8	111
P-Ge	1.69	−5.6	0.85	12.6	0.68	7.3	62

BDT isomers have a benzo core in the center and two flanking thiophene rings. BDT units offer two advantages: the necessary alkylation (to improve the solubility of resulting polymers) can be fulfilled on the center benzene ring, and the two flanking thiophene units render much less steric hindrance with adjacent acceptor units, leading to a more planar backbone. The differences of the isomers are on the linking position of these three subunits and symmetry of the molecule (to be discussed later in section 2.3.1.4). Both of the isomers exhibit weaker electron-donating ability compared with that of the CPT. Therefore, the HOMO levels of some BDT-based polymers are closer to the ideal HOMO energy level.^{6,45,61,107} Together with a relatively narrow band gap, a few BDT-based polymers have demonstrated PCE over 6% in their BHJ cells.^{45,61,107} Particularly, BHJ PV devices based on PBnDT-DTfBT has been shown with a V_{oc} around 0.9 V and a J_{sc} over 12 mA/cm², leading to a PCE over 7%.⁶¹

Further decreasing of electron-donating ability of the donor unit can be realized by changing the benzo unit to the pyridine unit or switching thiophene units to thiazole units as exemplified in Figure 6. Polymers based on both of the units show significantly decreased HOMO levels.^{94,108} However, dithienopyridine (DTPn)-based polymers exhibit decreased V_{oc} along with decreased J_{sc} due to their larger band gaps. Possible

reasons are non-ideal polymer–PC₆₁BM interaction and poor exciton dissociations.⁹⁴

Further tuning of the electron-donating ability and other physical properties of these donor units can be achieved via modifying specific atoms of the donor units (Figure 7 and Table 2).

Replacing the center (the only sp³) carbon atom of the CPT unit with silicon has been thoroughly studied by Brabec and co-workers.^{112,113} Since carbon and silicon have similar electron negativity and outer layer electronic structure (s²p²), CPT and silol dithiophene have a similar electron-donating ability. This explains the fact that HOMO levels and band gaps of the Si-bridged polymer (Si-PCPDTBT) and the C-bridged polymer (PCPDTBT) are nearly identical. However, the larger silicon atom and the longer C–Si bond modify the geometry of the fused dithiophene unit, allowing a better stacking of the polymer backbone. This helps improve hole and electron mobilities of Si-PCPDTBT/PC₇₁BM blend, a factor of 2–3 higher than those of the PCPDTBT/PC₇₁BM blend. Further indication for the better stacking of Si-PCPDTBT can be found from the absorption spectra of polymer thin films. In spite of similar band gaps between Si-PCPDTBT and PCPDTBT, a strong aggregation peak is present around 750 nm in the case of Si-PCPDTBT. This is confirmed by grazing incidence X-ray study (Figure 8). A pronounced diffraction peak at 5.2° (17 Å), typical for alkyl chains separating the backbones, and a weak

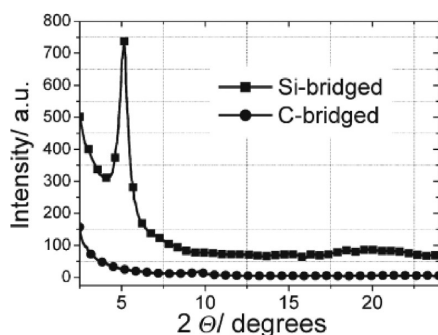


Figure 8. Diffractometry images of films of pristine silicon-bridged (squares) and carbon-bridged polymer deposited on quartz substrates. Reprinted with permission from ref 112. Copyright 2010 Wiley-VCH Verlag GmbH & Co. KGaA.

peak at around 20° corresponding to the backbone π - π stacking are observed in thin films of Si-PCPDTBT. These data support a much ordered stacking of backbone and side chains of Si-PCPDTBT. Importantly, this enhanced aggregation reduces the formation of charge-transfer complexes¹¹⁴ and increases the formation of free charge carriers. Thus, this seemingly small change from carbon to silicon leads to pronounced increases on both the V_{oc} (from 0.37 to 0.57 V) and the J_{sc} (from 15.5 to 17.3 mA/cm²) under the same processing condition, with a PCE of 5.9% achieved for Si-PCPDTBT (vs 2.7% for PCPDTBT).⁵

However, changing the bridging atom of the fluorene from carbon to silicon has a strong effect on the electron-donating ability and energy levels of related polymers (PFDTBT vs PSiF-DBT).¹⁰⁹ Furthermore, silafluorene-based polymers have higher electroluminescent efficiency, thermal stability, and slightly larger hole mobility.¹¹⁵ Therefore, a larger J_{sc} has been demonstrated with a little drop on V_{oc} , and a PCE over 5% has been realized for a silafluorene-based polymer.¹⁰⁹

On the other hand, pyrrole is much more electron-rich than the cyclopentadiene (the center structural unit of the CPT). By replacing the bridging carbon atom of the CPT unit with a nitrogen atom, the resulting dithienopyrrole unit should have a stronger electron-donating ability than that of the CPT.¹¹⁶ This leads to a more pronounced ICT between the dithienopyrrole and the acceptor unit; therefore, a decreased band gap is generally observed for dithienopyrrole-based polymer when compared with those of CPT-based D-A polymers. The FET mobility of dithienopyrrole-based polymers is slightly increased due to an enhanced polymer chain planarity and chain-chain interaction.¹¹⁷ However, because of the electron-rich nature of the dithienopyrrole, the HOMO levels of dithienopyrrole-based polymers are elevated to around 5.0 eV,^{110,116,118} which would lead to significantly decreased V_{oc} and environmental instability of related solar cells. In addition, since only one side chain is allowed on the N atom, a long and bulky alkyl chain is required to render reasonable solubility in common organic solvents. In general, these long and bulky side chains have negative impacts on the PV properties (further discussion will be provided in section 2.5.2). Nevertheless, a high J_{sc} of 14.87 mA/cm² and a respectable total efficiency of 2.7% were demonstrated for a dithienopyrrole-based polymer in its BHJ solar cells with PC₇₁BM, despite a V_{oc} of just 0.4 V.¹¹⁰

However, substituting the center carbon in the fluorene unit with a nitrogen (i.e., converting the fluorene into the carbazole) received more success for a number of reasons. First, since

fluorene unit itself is relatively electron-deficient (compared with the CPT), the addition of an electron-donating nitrogen would slightly increase the electron density of the resulted carbazole unit. Therefore, the HOMO energy levels of carbazole-based D-A polymers would increase, closer to the ideal HOMO level (Figure 5). Second, the polycarbazoles have been successfully used in polymer LED¹¹⁹ and FET,¹²⁰ demonstrating excellent p-type transport properties. Third, the carbazole unit is fully aromatic and not too electron rich, offering a decent chemical and environmental stability.¹²¹ Therefore, it is not surprising that a carbazole-based polymer (PCDTBT) has been demonstrated with a V_{oc} of 0.88 V, a J_{sc} of 10.6 mA/cm², and an impressive FF around 66%, leading to an overall PCE over 6% in its BHJ cells with PC₇₁BM.⁴

Other heteroatoms have also been explored as the bridging atoms (Figure 7). For example, germafluorene-containing polymers have been reported.¹¹¹ Germanium is in the same group (group 14 on the periodic table) with C and Si, but with a larger radius. The optical band gap and the HOMO level of polygermafluorene are similar to those of poly(silafluorene)s, indicating a similar electron-donating ability of the germafluorene. Interestingly, polymers based on germafluorene do not show as good PV performance as poly(silafluorene)s, largely because of a decreased V_{oc} in spite of lower HOMO levels than these of poly(silafluorene)s. Similarly, dithienogermole with Ge as the bridging atom was also reported by Amb et al.⁶² Similar energy levels and band gaps were reported for silol-dithiophene- and dithienogermole-based copolymers. Both copolymers exhibit great photovoltaic properties with PCEs over 6% in inverted BHJ solar cells with PC₇₁BM as the acceptor.

2.3.1.2. High Level of Fusion: Ladder Type Donors. Inspired by the success of fused three rings, high level of fusion of the aromatic units on the conjugated backbone has also been actively explored because it can facilitate π -electron delocalization to increase the effective conjugation length, offering an effective method to reduce the band gap, in addition to controlling energy levels (Figure 9).^{122,123} Moreover, the resulting coplanar geometries and rigid structures can suppress the rotational disorder around interannular single bonds and lower the reorganization energy, which in turn can enhance the charge mobility.^{124–126} This high level of fusion can be achieved by either covalently fastening adjacent aromatic units in the backbone (i.e., ladder type) or by fusing three or more aromatic units into an enlarged conjugated π unit. However, excessively strong interchain π - π stacking interactions arising from this high degree of coplanarity could make the conjugated polymers insoluble and unprocessable.¹²⁷

For example, the poly(fluorene) and the poly(CPT) discussed above can be considered as fused poly(phenylene) and poly(thiophene), respectively. Besides the benefits such as band gap reduction and charge mobility enhancement, the symmetry of these alkylated fused thiophene units eliminates any possible regioregularity issue of poly(3-alkylthiophene)s, which could decrease effective π -conjugation of the conjugated backbone.^{53,54}

The higher level of fusion can help increase environment stability of related polymers and fix possible isomerization of conjugated polymer backbones. For example, in the poly(phenylenevinylene) (PPV), the photo-oxidation via [2 + 2] cycloaddition of excited-state singlet oxygen and vinylene group would result in an irreversible chain scission with consequent reduction of the conjugation length and a blue-shifted absorption.^{130,131} To address the issue of the easy oxidation of the vinyl linkage, Song et al. cyclized the vinylene group with

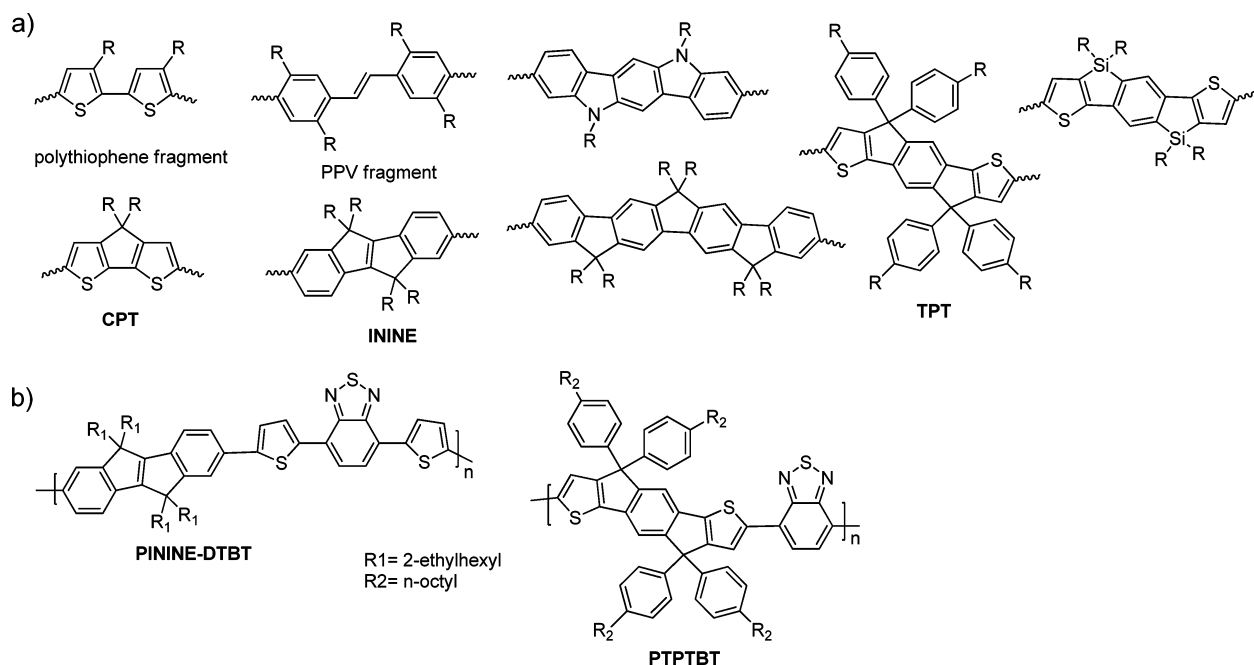


Figure 9. (a) Chemical structures of ladder-type donor units. (b) Chemical structures of related copolymers.

Table 3. Summary of Band Gaps, HOMO Levels, and Photovoltaic Properties of Conjugated Polymers in Figure 9b

polymer	band gap (eV)	HOMO (eV)	V_{oc} (V)	J_{sc} (mA/cm ²)	FF	PCE (%)	ref
PININE-DTBT	1.84	−5.45	0.47	5.93	0.43	1.88	128
PTPTBT	1.57	−5.36	0.85	11.2	0.67	6.41	129

adjacent benzene units using two 5-membered rings with carbon as the bridge.¹²⁸ This conversion of PPV into ININE copolymers would prevent backbone scission by singlet oxygen. Thus, polymers containing ININE show significantly enhanced UV–vis and PL stability after irradiation with white light in air.

More ladder-type donor units by fusing three or more adjacent units have been developed (Figure 9).^{43,132–138} In addition to the advantages mentioned above for these fused systems, these ladder-type systems may additionally lead to broader, more intense absorption bands which will result in enhanced solar light harvesting. Furthermore, for every repeating unit in the ladder-type donor containing polymers, there are more positions to attach solubilizing chains, which may provide a better solution processability of the related polymers.⁴³ Some typical ladder-type donor units are summarized in Figure 9. All the constructing subunits are just benzene and thiophene rings. With different bridging atoms, the electronic properties of these ladder-type donors can be adjusted as discussed above. The highest PCE over 6% with a high V_{oc} of 0.85 V has been achieved by a conjugated polymer containing ladder-type donor unit TPT with a low HOMO level of 5.36 eV (Table 3).¹²⁹

2.3.1.3. High Level of Fusion: Fused Conjugation over Three or More Aromatic Units. Another method to achieve the high level of fusion is to fuse three or more aromatic units into an enlarged conjugated unit with extended π -conjugation (Figure 10). Similar to ladder type systems, these extended π -conjugation systems feature enforced planarity and more effective π -electron delocalization, which can lead to broader light absorption and improve π – π interactions between polymer chains in thin solid films to enhance the charge carrier mobility.¹⁴⁰ In addition, the HOMO energy levels of

related polymers can be tuned through adjusting the fused aromatic moieties within these polycyclics.

For example, replacing the benzene core of benzodithiophene (BDT isomer 1) with a more electron-deficient naphthalene core leads to the naphthalenedithiophene (NDT isomer 1). NDT-based polymers exhibit both small band gaps and low HOMO levels.¹⁴¹ Noticeably, a NDT-based polymer (PNDT-DTPyT) exhibited a large J_{sc} of 14.16 mA/cm² and a decent V_{oc} of 0.71 V, with a PCE of 6% in its BHJ solar cells (Table 4).¹⁰⁷ To further decrease the electron-donating ability of the donor unit for a deeper HOMO level, dithienoquinoline (QDT) with a more electron-deficient quinoxaline core was designed. Indeed, QDT-based polymers exhibited enhanced V_{oc} , but smaller J_{sc} in related BHJ solar cells due to decreased HOMO levels but concomitantly larger band gaps when compared with those of NDT analogues.^{46,107,141} In another example, quadrathienonaphthalene (QTN) with an even larger pancake-like π -conjugation prompts better electron delocalization, molecular interaction, and hole mobility. Therefore, the QTN-based polymers exhibit smaller band gaps and slightly decreased HOMO levels. The homopolymer of QTN has a band gap of 2.0 eV, and an efficiency over 2% was demonstrated.¹³⁹

Besides cyclic extension of the conjugation, linear extension on the donor unit has also been explored to adjust energy levels and enhance molecular interaction and charge mobility. However, there are only a few reported cases due to synthetic difficulties of these units (structures on the second row of Figure 10a).^{142–146} Further, it is quite a challenge to attach solubilizing chains on these linearly extended aromatic systems. Nevertheless, some unique properties of this type of donor units do exist. For example, these donor units have very stiff backbones, long

Table 4. Summary of Band Gaps, HOMO Levels, and Photovoltaic Properties of Conjugated Polymers in Figure 10b

polymer	band gap (eV)	HOMO (eV)	V_{oc} (V) exp	J_{sc} (mA/cm ²)	FF	PCE (%)	ref
PNDT-DTPyT	1.53	−5.36	0.71	14.16	0.62	6.2	107
PQDT-DTPyT	1.56	−5.50	0.75	13.49	0.55	5.6	107
HMPQTN	2.00	−5.39	0.72	5.69	0.50	2.06	139

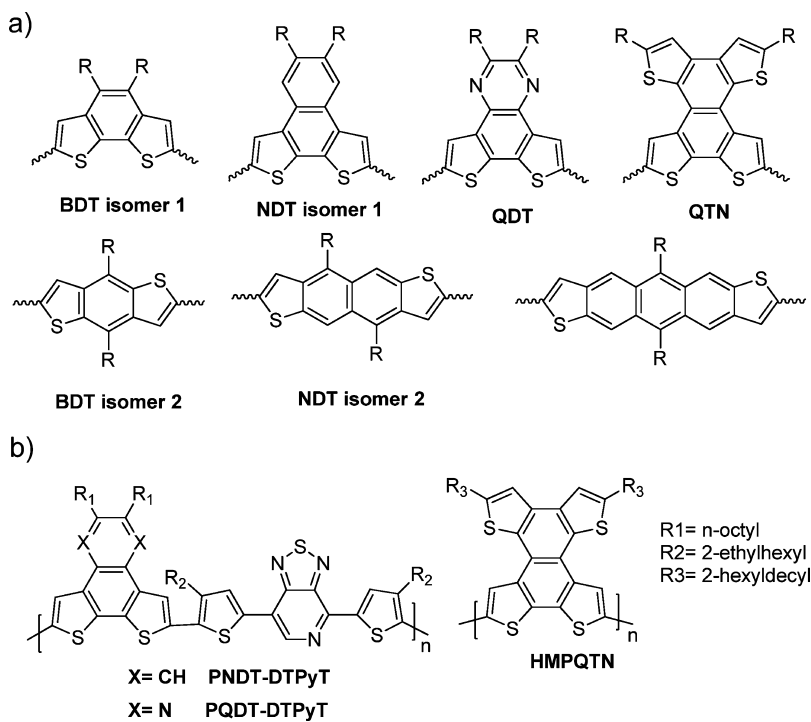


Figure 10. (a) Chemical structures of polyaromatic donor units. (b) Chemical structures of related copolymers.

effective π -conjugation length, good environment stability, and moderate electron-donating properties. They usually have strong π -stacking, which allows effective overlap of π -orbitals; thus, they are good candidates for OFET applications with excellent charge carrier mobilities. These high mobilities also render related polymers promising candidates for PSC. In addition, the distance between side chains can be adjusted by varying the number of (unalkylated) fused aromatics between alkylated ones, which allows tuning of the intercalation of PC₆₁BM.^{147,148}

Interestingly, sometimes unfused rings offer additional advantages, especially when these unfused additional aromatic units are pendant to the conjugated backbone, without introducing steric hindrance to the backbones.^{6,149} Figure 11

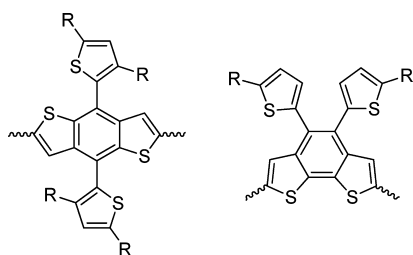


Figure 11. Chemical structures of donor units with aromatic side chains.

provides two such examples where these pendant thiophene units are not coplanar with the conjugated donor units on the

polymer main chain. However, these pendant thiophene units would prohibit excessive π -stacking of polymer backbones; thus, they can be used to adjust molecular interaction and active layer morphology. Reduced π -stacking would also lead to better solubility of the conjugated polymers. Unlike these insulating alkyl chains, these aromatic rings can potentially help the charge transport. In addition, polymers containing these unfused rings exhibit significantly increased V_{oc} in BHJ solar cells.^{6,149} The same enhancement has also been reported in small molecule solar cells and systematically studied.⁴⁸

2.3.1.4. Symmetry of Donor Units. As already alluded in the previous discussion, fused aromatics often lead to isomers. In this scenario, symmetry of the molecule plays an important role. Recent studies have indicated that symmetry of the monomers and the related curvature of the polymer chains have large impacts on HOMO levels and charge mobility of conjugated polymers.

A comprehensive investigation on the impact of the symmetry was recently completed with the linear- and angular-shaped naphthodithiophenes (NDTs) (Figure 12).^{150,151} Takimiya et al. discovered that NDTs of angular shapes (NDT3 and NDT4) showed lower HOMO levels and larger band gaps than their linear counterparts (NDT1 and NDT2).¹⁵¹ Interestingly, when it comes to the mobility, NDTs of centrosymmetry (NDT1, NDT3, and NDT4) have enhanced mobilities than that of the NDT of axis symmetry (NDT2). Further, NDT4 with sulfur atoms facing outward presumably has a larger intermolecular orbital overlap through sulfur-involved nonbonding contact than that of NDT3 with sulfur atoms embedded in the bay region, which explains the observed higher mobility of NDT4.

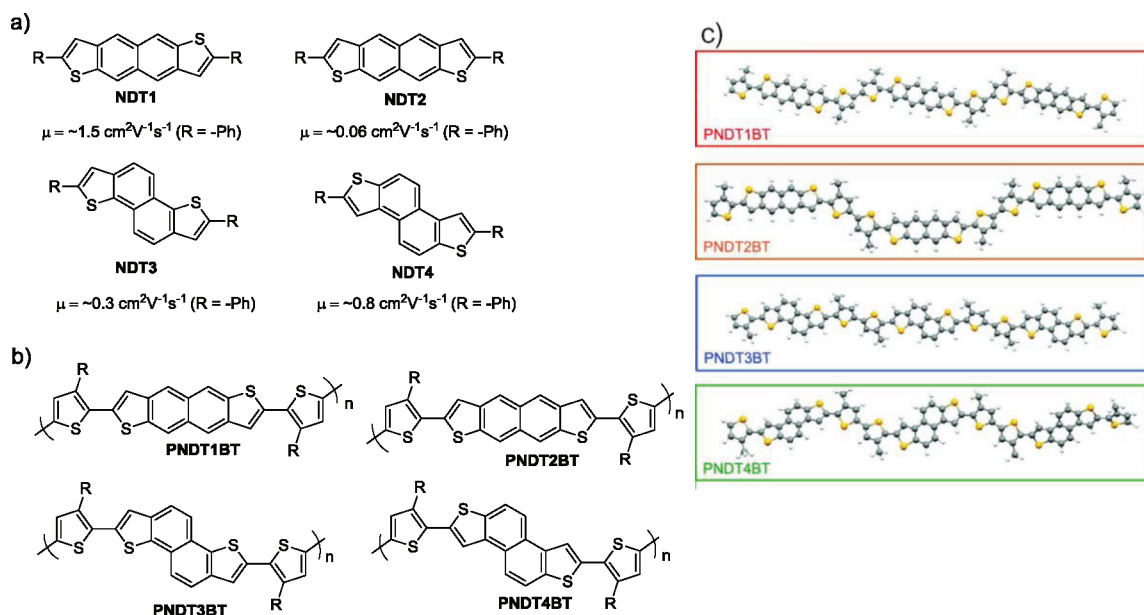


Figure 12. (a) Four isomeric naphthodithiophenes: naphtho[2,3-*b*:6,7-*b'*]dithiophene (NDT1), naphtho[2,3-*b*:7,6-*b'*]dithiophene (NDT2), naphtho[1,2-*b*:5,6-*b'*]dithiophene (NDT3), and naphtho[2,1-*b*:6,5-*b'*]dithiophene (NDT4). (b) Chemical structures of the naphthodithiophene-based semiconducting polymers. (c) Optimized backbone structures of the polymers PNDT1BT, PNDT2BT, PNDT3BT, and PNDT4BT. The side chains were replaced with methyl groups to simplify the calculation. Reprinted with permission from refs 150 and 151. Copyright 2011 American Chemical Society.

Lower HOMO levels are also observed in polymers containing angular-shaped NDTs. In addition, stacking of polymer chains is much stronger in polymers containing NDTs of centrosymmetry than in polymers with NDTs of axis symmetry. However, the mobility of polymers are affected by other factors than just the shape and symmetry of the donor unit (NDT).¹⁵⁰ A different mobility rank was summarized for these polymers containing NDT and two thiophene units (PNDT3BT > PNDT4BT > PNDT1BT > PNDT2BT). This difference in mobility rank between the polymers and NDT molecules can be related to the curvature of the backbone of these polymers. As shown in Figure 12, though NDT1 has a linear shape and NDT3 has an angular shape, the PNDT3BT could adopt a pseudostraight-shaped backbone (rather than a zigzag-shaped one in the case of PNDT1BT), which would lead to an effective packing of PNDT3BT into most highly ordered structure among all these four polymers, thereby the highest mobility. Similar results were reported by Müllen and co-workers, who also studied the impact of the shapes and curvature of the molecules on mobilities.^{152,153}

To conclude this discussion on the donor units, Figure 13 shows an empirical electron-donating ability trend of representative donor units. This donor unit trend is based on the comparison of oxidation potentials and band gaps of polymers with identical acceptor units. Due to the influences of other factors, such as steric hindrance and significant differences on π -stacking, this trend may vary. Generally, a “weak donor” with moderate electron donating ability is needed to create polymers with ideal HOMO levels around -5.4 eV . High mobility, proper intermolecular interaction, enhanced π -electron delocalization, and bonding geometry also need to be taken into consideration in order to design high performance conjugated polymers.

2.3.2. Design of Acceptor Units. Similar to the donor units, the acceptor units are of equal importance in controlling the energy levels and band gaps of conjugated polymers. However,

compared with the great variety of donor units reported (e.g., a few successful examples discussed in previous section), the design and synthesis of functional acceptors only received moderate success. Nevertheless, several novel acceptor units have been developed, which contributed significantly to the enhanced photovoltaic performance of related polymers.

Perhaps the most commonly employed acceptor unit is the 2,1,3-benzothiadiazole (BT). Because of its strong electron-accepting ability and commercial availability, BT has been very popular in constructing low-band-gap conjugated polymers.^{93,104,154} Moreover, these two N atoms in the thiadiazole ring could possibly form hydrogen bonding with adjacent units (e.g., the hydrogen atom on the thiophene ring), leading to a more planar backbone. With all these good features, many polymers with a BT acceptor unit have shown low band gaps and good photovoltaic properties.^{5,104,154} The best example comes from a conjugated polymer copolymerizing dithienosilole (Si-PCPDTBT) with the BT unit, which exhibited a band gap of 1.37 eV and thereby a J_{sc} of 17.3 mA/cm^2 , with a PCE up to 5.9% in its BHJ devices.⁵

Adding one thienyl group on both sides of the BT converts BT into di-2-thienyl-2,1,3-benzothiadiazole (DTBT) (Figure 14),^{4,41,42,109,155–157} which has a few more advantages when compared with the original BT unit. First, the two flanking thienyl units relieve the otherwise possibly severe steric hindrance between the BT unit and donor aromatic units (especially when benzene based aromatics are used).¹²⁸ Thus, the synthesized donor–acceptor polymers adopt more planar structures, thereby reducing the band gap by enhancing the D–A conjugation. In addition, a more planar conjugated backbone facilitates the chain–chain interactions among polymers in the solid state, improving the charge carrier (usually hole) mobility. Second, while the electron-accepting BT unit maintains the low band gap, the two electron-rich, flanking thienyl units would help improve the hole mobility, since thiophene-based polymers (such as P3HT) have shown noticeably high hole mobility.¹⁵⁸ Third, the

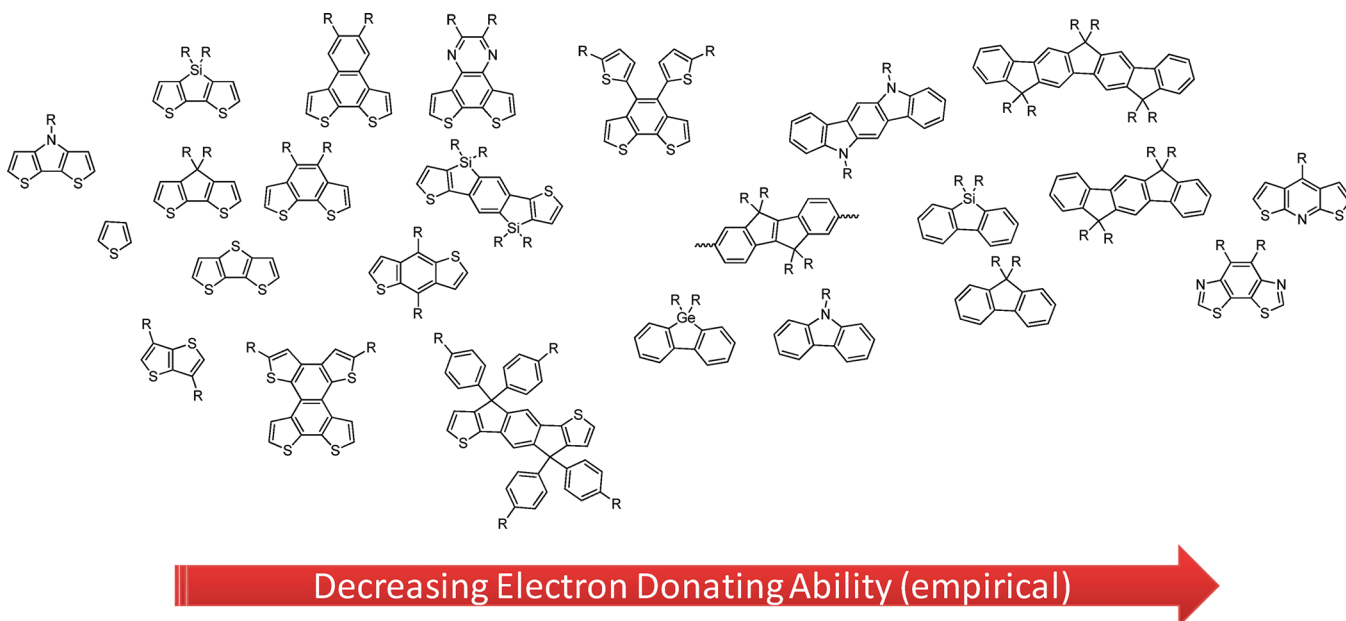


Figure 13. An empirical chart showing the relative electron-donating ability of various donor units.

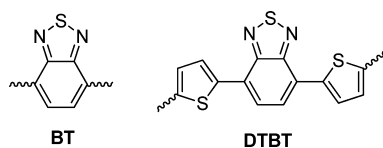


Figure 14. Chemical structures of BT and DTBT acceptor units.

BT unit has limited positions for addition of solubilizing chains or substituents, and attaching these units would likely introduce steric hindrance. To this end, these flanking thienyl units can provide more possible positions for further modification of electronic properties and solubility of conjugated polymers, with minimal steric hindrance involved if properly introduced.¹⁵⁹ However, due to the electron-rich nature of these thienyl units, in some cases, the two flanking thienyl units slightly increase the HOMO levels of the conjugated polymers when compared with BT-based polymers.^{128,132}

Similar to the design of donor units (Figure 7), the electron affinity of acceptors can also be fine-tuned by varying specific atoms. Figure 15 lists a series of such units which can be treated as structurally related with the BT. For example, replacing the sulfur atom of the BT unit with a nitrogen atom, the electron-accepting ability of the triazole is significantly reduced when compared with that of the BT. It is because the lone pair on the middle nitrogen atom of the triazole unit is more basic than the lone pairs on the sulfur of the BT and is more easily donated into the triazole ring, making it relatively electron-rich when compared with the original BT. Thus, conjugated polymers incorporating triazole unit usually show a larger band gap around 2.0 eV (Table 5).⁴⁵ On the other hand, the electron-accepting ability of the quinoxaline (Qx) is in between the triazole and BT. One advantage of Qx is that it can be alkylated to improve the solubility of conjugated polymers without introducing steric hindrance.¹⁶⁰ In addition, alkylated benzo units can be introduced to the periphery of the Qx instead of alkyl chains, which provides additional control to adjust molecular interactions and may increase V_{oc} and charge mobility.^{161,162} Benzoxadiazole (BX), the oxygen containing analogue to the BT unit, has very similar electron-accepting

ability to that of BT. Thus, polymers containing the BX unit have very similar HOMO and LUMO levels to those of BT-based analogues. Interestingly, these BX-based polymers usually do not perform as well as these BT-based analogues, possibly due to lower mobilities of these BX-containing polymers.^{106,156,163} Lastly, the selenium analogue of the BT unit, 2,1,3-benzoselenadiazole (BSe), demonstrates many interesting properties in photoelectronic devices.^{160,164} In general, BSe-based polymers exhibit smaller band gaps and lower HOMO and LUMO levels (from CV).^{69,165,166} However, the photovoltaic properties of BSe-based polymers are restricted by the weak absorption of the active layer and the imbalance in the hole and electron transport of the active layer which may result from bad morphology.

In most of the high performance D–A conjugated polymers reported, close to ideal HOMO energy levels were achieved (e.g., -5.4 eV), which lead to an observed open-circuit voltage (V_{oc}) as high as 0.92 V.^{6,45,61} However, very often the band gaps of these materials are still larger than the proposed 1.5 eV of ideal polymers, resulting in mediocre short-circuit currents (J_{sc}). In order to further improve the efficiency, a smaller band gap is needed to achieve a higher J_{sc} while the low HOMO energy level should still be maintained (for a high V_{oc}). According to the proposed approach of “weak donor–strong acceptor”, one should incorporate “strong acceptors” with large electron deficiency in the conjugated backbone to lower the LUMO levels, thereby decreasing the band gap of related polymers. We will elaborate on this concept by discussing several such strong acceptors.

One such example is the dithienylthiadiazolo[3,4-*c*]pyridine (DTPyT), which differs from the original DTBT by only one atom (Figure 16). Compared with benzene, pyridine is π -electron deficient. Therefore by replacing the benzene in the BT unit with pyridine, the new acceptor, thiadiazolo[3,4-*c*]pyridine (PyT), would be one such stronger acceptor. Polymers incorporating DTPyT unit were first reported by Leclerc et al.,¹⁵⁶ and their PV performances were then enhanced up to 6.3% by You et al. (Table 6)¹⁰⁷ by copolymerizing with “weak donors” to adjust energy levels and attaching solubilizing chains

Table 5. Summary of Band Gaps, HOMO/LUMO Levels, and Photovoltaic Properties of Conjugated Polymers in Figure 15b

polymer	band gap (eV)	HOMO (eV)	LUMO (eV)	V_{oc} (V) exp	J_{sc} (mA/cm ²)	FF	PCE (%)	ref
PBnDT-HTAZ	1.98	−5.29	−2.87	0.70	11.14	0.55	4.30	45
PCDTQx	2.02	−5.46	−3.42	0.95	3.0	0.56	1.8	156
PCDTBT	1.88	−5.45	−3.60	0.86	6.8	0.56	3.6	156
PCDTBX	1.87	−5.47	−3.65	0.96	3.7	0.60	2.4	156
H11	1.52	−4.88	−3.33	0.55	1.05	0.32	0.18	69

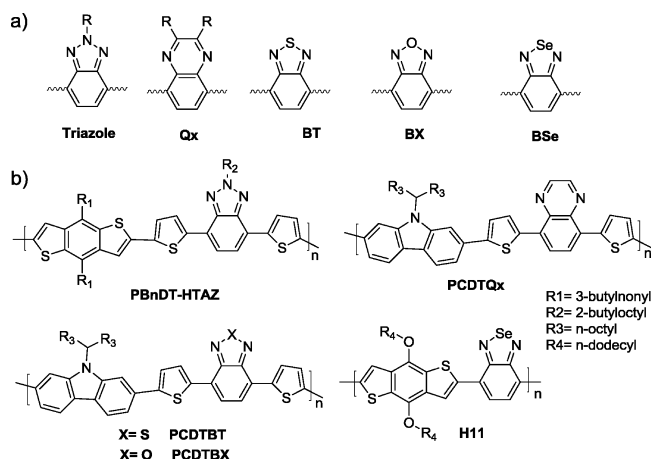


Figure 15. (a) Chemical structures of triazole, Qx, BT, Bx and BSe units. (b) Chemical structures of related copolymers.

to improve the molecular weight and the film morphology. All the DTPyT-containing polymers reported by You and co-workers showed noticeably reduced LUMO levels, slightly reduced HOMO levels, and thus smaller band gaps than those of their DTBT counterparts. The smaller band gap significantly improves the observed J_{sc} of the related BHJ devices, while the low HOMO energy level maintains the high V_{oc} . Therefore all three polymers (PNDT-DTPyT, PQDT-DTPyT, and PBnDT-DTPyT) achieved high efficiency numbers in their BHJ devices, demonstrating the great utility of DTPyT acceptor moiety in designing high performance solar cell materials.

Similarly, tetrazine (Tz) which has a very high electron affinity has also been used as a strong acceptor to construct low-band-gap polymers with over 5% efficiency achieved.¹⁶⁷ When incorporated into D–A conjugated polymers, both HOMO and LUMO levels of Tz-based copolymers are lower than those of BT-based copolymers, indicating a stronger electron affinity of the Tz unit. Interestingly, the Tz unit shows more impact on HOMO levels than on LUMO levels, which is different from most acceptor units. This results in slightly broader band gaps of Tz-based polymers when compared with these of BT-based polymers.

Isoindigo is a symmetrical and perfect planar π -conjugated molecule consisting of two indolin-2-one units, which are strongly electron withdrawing.^{168,170,171} A few conjugated polymers based on isoindigo units possess near-ideal low HOMO levels around −5.4 eV and low LUMO levels around −3.9 eV. However, relatively low PCE up to 3% was obtained, with a large V_{oc} of 0.9 V but a low J_{sc} around 5 mA/cm².¹⁶⁸ Further improvement can be anticipated by choosing proper donor units and side chains as well as by improving the active layer morphology.

Structurally similar to isoindigo, pyrrolo[3,4-*c*]pyrrole-1,4-dione (DPP) has also been used in a number of D–A conjugated polymers in the past 3 years.^{1,44,118,169,172–176} Low

band gaps around 1.3 eV are generally obtained, which is beneficial for J_{sc} ; however, HOMO levels of DPP-based polymers are significantly elevated when compared with those of their analogues with other acceptors, possibly due to these two flanking electron-donating thienyl units. Nevertheless, efficiency numbers as high as 5.5% were reported for DPP-based polymers.^{169,176}

The thieno[3,4-*c*]pyrrole-4,6-dione (TPD) unit was recently intensively explored. The symmetric and planar structure of TPD could improve the electron delocalization, enhancing the polymer chain–chain interactions and increasing the hole mobility. Similar to DPP and isoindigo, electron-withdrawing amide groups render TPD a strong acceptor. It was first incorporated in BnDT-based copolymers by Leclerc and co-workers.¹⁷⁷ The resultant copolymer not only has a small band gap (thereby a potentially high J_{sc}), also maintains a low HOMO energy level of −5.56 eV. Therefore a high V_{oc} of 0.85 V was achieved in the BHJ device with PC₇₁BM as the acceptor. Along with a J_{sc} of 9.81 mA/cm² and a FF of 0.66, a PCE of ~5.5% was obtained. It is particularly worth mentioning that Leclerc et al. obtained these impressive values from devices with an active area of 1.0 cm². Achieving high efficiencies on devices of large area is advantageous for real world application of PSC because efficiencies obtained on areas smaller than 0.2–0.3 cm² may become strongly substrate size-dependent, in addition to the possible overestimation of the J_{sc} from a very small area device. Similar polymers with identical conjugated backbone but having different solubilizing chains were independently reported by Jen's group and Xie's group with PCEs varying from 3.42% to 4.79% after certain optimization.^{178,179} Fréchet and co-workers later did a detailed study on the impact of these side chains on the TPD–BDT copolymer.¹⁸⁰ PCEs up to 6.8% were reported just by varying the side chains of the conjugated backbone. More recently, TPD-based polymers of efficiency as high as 7.3% were reported by Amb et al. and Tao and co-workers.^{60,62,63,181} In their studies, the TPD acceptor was copolymerized with fused bithiophene with different bridging atoms. All of these copolymers exhibit high PCEs over 6% in BHJ solar cells, which indicates a great potential of TPD unit in constructing novel materials for PSC.

However, acceptors should not be too electron withdrawing. As discussed earlier, the LUMO of the conjugated polymer should be at least 0.3 eV larger than the LUMO of the n-type material to facilitate efficient exciton dissociation. Too strong an acceptor in the D–A polymer would lead to too low a LUMO level and the inability to split excitons at the interface between the polymer and fullerenes. Thus, no photocurrent or extremely small J_{sc} would be observed. Several examples include benzo[1,2-*c*:4,5-*c'*]bis([1,2,5]thiadiazole) (BBTD),¹⁸² [1,2,5]-thiadiazolo[3,4-*g*]quinoxaline,^{183,184} pyrazino[2,3-*g*]quinoxaline,¹⁸⁵ and [1,2,5]thiadiazole[3,4-*d*]pyridazine.¹⁸⁶

2.4. Substituents. Though the energy levels and band gap of a conjugated polymer are mainly determined by the selection of conjugated aromatic units (e.g., D and A in D–A polymers),

Table 6. Summary of Band Gaps, HOMO/LUMO Levels, and Photovoltaic Properties of Conjugated Polymers in Figure 16b

polymer	band gap (eV)	HOMO (eV)	LUMO (eV)	V_{oc} (V) exp	J_{sc} (mA/cm ²)	FF	PCE (%)	ref
PBnDT-DTPyT	1.51	−5.47	−3.44	0.85	12.78	0.58	6.3	107
PCPDTTz	1.68	−5.34	−3.48	0.75	12.2	0.59	5.4	167
PTI-1	1.60	−5.85	−3.88	0.89	5.4	0.63	3.0	168
PDPPTPT	1.53	−5.35	−3.53	0.80	10.3	0.65	5.5	169
P-Ge	1.69	−5.6	NA	0.85	12.6	0.68	7.3	62

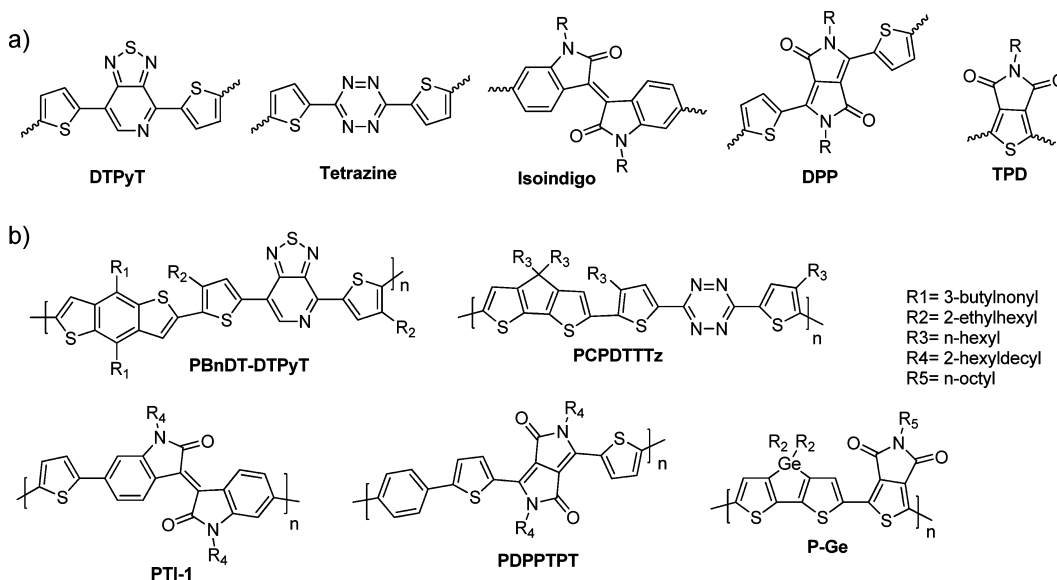
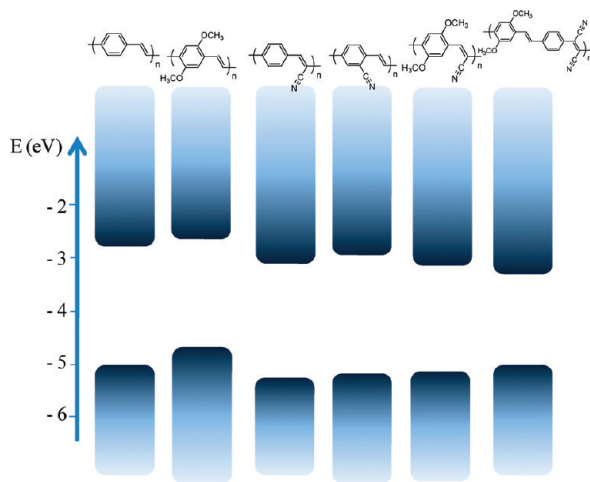


Figure 16. (a) Chemical structures of some “strong acceptor” units. (b) Chemical structures of related copolymers.

substituents can be used to further tune energy levels, band gaps, molecular interaction, and even morphology.

Using archetypical PPV as the model polymer, the substituent effect on conjugated polymers was systematically studied by Bredas and Heeger with the valence effective Hamiltonian (VEH) method (Figure 17).¹⁸⁷ Attaching

Figure 17. HOMO and LUMO of the compound investigated, relative to the work functions of calcium and aluminum.¹⁸⁷

electron-donating methoxy groups to the benzene unit of the PPV would raise the HOMO energy level when compared with the original PPV (with similar LUMO level). This effect was also observed experimentally.¹⁸⁸ When switching to the electron-withdrawing group (such as cyano), stabilization on

both HOMO and LUMO levels would be expected. However, calculations found that the band gaps of the cyano PPVs would be larger than that of PPV because of the asymmetry in the stabilization of the HOMO and LUMO levels by the cyano substituent. Furthermore, the position of the cyano (either on the phenylene or on the vinylene) affects the energy levels and band gap. When cyano was added on the vinylene, the calculated LUMO level was noticeably lower than that of the analogue with cyano on the phenylene, with less difference on the HOMO energy levels. The authors attributed this effect to the different number of π -electrons on the vinylene and phenylene. Since vinylene unit only has two π -electrons whereas phenylene unit has six, substitution on the vinylene would introduce a relatively larger perturbation to the conjugated backbone, further lowering the LUMO level. All these results presented above indicate that electron-donating substituents (such as methoxy) would have a more significant impact on the HOMO level, while electron-withdrawing ones (such as cyano) would affect more strongly on the LUMO level. Therefore, by attaching both methoxy group and cyano group on the phenylene and the vinylene part of PPV, respectively, the resulting polymer exhibited a similar HOMO level with that of the methoxy PPV and a similar LUMO with that of the cyano PPV, leading to a significantly decreased band gap.¹⁸⁹ This result is in good agreement with the proposed “weak donor–strong acceptor” strategy to design ideal polymers.⁵⁹

Another interesting substituent is the fluorine. Fluorine is the smallest electron-withdrawing group with a van der Waals radius of 1.35 Å and a Pauling electronegativity of 4.0. Fluorinated organic molecules exhibit a series of unique features such as great thermal and oxidative stability,¹⁹⁰ elevated resistance to degradation,¹⁹¹ enhanced hydrophobicity, and

high lipophobicity in perfluorinated substances.¹⁹² In addition, these fluorine atoms often have a great influence on inter- and intramolecular interactions via C–F···H, F···S, and C–F··· π_F interactions.^{191,193} Applying fluorine substitution in the D–A polymers was investigated by You and co-workers in two recent studies.^{45,61} In one report, they added two fluorine atoms to the commonly employed benzothiadiazole (BT), converting BT into fluorinated benzothiadiazole (ffBT) (Figure 18).⁶¹ The

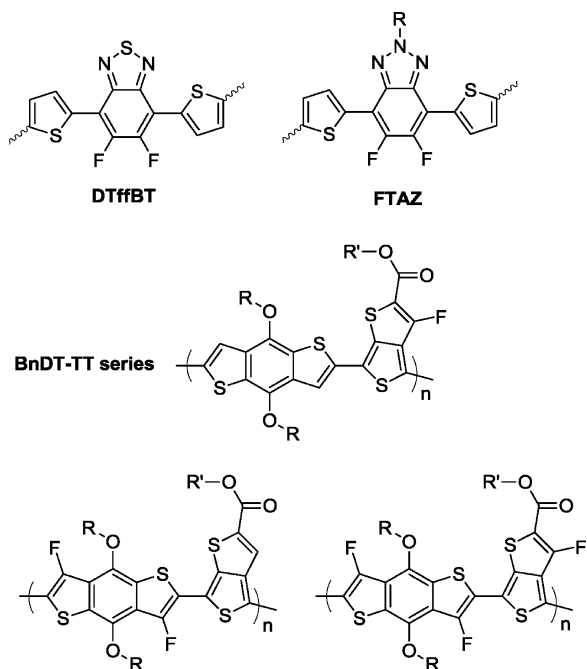


Figure 18. Chemical structures of fluorine atom containing acceptor units and conjugated polymers.

ffBT-based polymer showed decreased HOMO and LUMO levels but a similar band gap when compared with those of its nonfluorinated analogue. Preliminary PV tests on BHJ devices demonstrated both increased V_{oc} (0.91 V) and J_{sc} (12.9 mA/cm²). Together with an also enhanced fill factor of 0.61, an impressive PCE of 7.2% was thus obtained without special treatments. In another related study, BnDT-based copolymers (PBnDT-FTAZ) with 5,6-difluoro-2H-benzo[d][1,2,3]triazole (FTAZ) as the acceptor unit was synthesized.⁴⁵ This polymer exhibited a medium band gap of 2.0 eV when compared with that of the DTBT-based polymer due to the weaker electron affinity of the FTAZ unit. Surprisingly, in spite of a band gap of ~2.0 eV, the J_{sc} of PBnDT-FTAZ based BHJ solar cells could reach over 12 mA/cm² (depending upon the thickness of the active layer), which can be explained by the high molecular weight and the large hole mobility of PBnDT-FTAZ. The BHJ devices based on PBnDT-FTAZ consistently showed a higher FF and J_{sc} than those of devices based on the polymers without fluorine substituents (PBnDT-HTAZ) at comparable thicknesses. A peak PCE of 7.1% was obtained in BHJ devices of PBnDT-FTAZ:PC₆₁BM without annealing or any additives. Remarkably, PBnDT-FTAZ:PC₆₁BM solar cells can still achieve over 6% efficiency even at an unprecedented thickness of 1 μ m (of the active layer).

Besides the study on the fluorine substituent effect in D–A polymers, the fluorine atom has also been applied in quinoid polymers. For example, Yu and co-workers studied a series of polymers based on fluorinated thienothiophene (TT).^{74,78,194,195} As expected, the substitution of electron-withdrawing fluorine

onto the polymer backbone reduced the HOMO energy levels of polymers when compared with the nonfluorinated analogues. Furthermore, this structural modification optimized the polymers' spectral coverage of absorption and their hole mobility as well as their miscibility with PC₇₁BM. All these contributed to an enhanced polymer solar cell performance up to 7.4%, which is one of the highest efficiencies within the literature reports.^{74,78} Further, using the original conjugated backbone (BnDT-TT) as the subject of study, Son et al. showed that the incorporation of the fluorine onto various positions of the polymer backbone significantly affected the performance of related solar cells (Figure 18).⁷⁶ Depending upon which hydrogen of the conjugated backbone is substituted by the fluorine, PCE of corresponding BHJ devices can vary from 2.3% to 7.2%. They also observed that fluorination of the BnDT unit lowered both the HOMO and LUMO levels of the conjugated polymer but widened the band gap. Finally, perfluorination of the polymer backbone led to a poor compatibility of the polymer with PC₇₁BM; thus, poor solar cell performance was observed. In addition, the authors found that perfluorination of the polymer backbone resulted in poor photochemical stability against singlet oxygen attack.⁷⁶ These interesting effects of substituents on physical properties of conjugated polymers are still under active investigation.

2.5. Side Chains. For conjugated polymers used in organic solar cells, solubilizing side chains are required to allow solution processability, which is the key feature for future low-cost mass production of these flexible solar cells. Without solubilizing chains, the conjugated backbone would adopt a more planar structure, thereby facilitating the chain–chain interactions among polymers and leading to unprocessable “bricks”. In addition to imparting the solubility to conjugated polymers, side chains have been discovered to play important roles in certain key properties of conjugated polymers, such as molecular weight, inter- and intramolecular interactions, charge transport, and active layer morphology.⁵⁰ In this section, these recently emerged understandings of the side-chain effect will be discussed, followed by the suggested guidelines of designing solubilizing chains.

2.5.1. Position. It is well-known that decorating the polymer backbone with side chains can effectively improve the solubility of the polymer, which is a crucial prerequisite toward achieving high molecular weight of the resulting conjugated polymer. However, substituting the small hydrogen atoms on these aromatic units with rather big alkyl or alkoxy chains often result in significant steric hindrance between these aromatic units on the conjugated backbone. For example, a computational simulation revealed that severe steric hindrance introduced by these alkyl/alkoxy chains on the DTBT would lead to a twisted conjugated backbone in polymers incorporating the substituted DTBT.¹⁹⁶ Therefore, the hole mobilities of the polymers incorporating such substituted DTBT were noticeably lower than that of the polymer with unsubstituted DTBT, which accounted for a smaller J_{sc} in the former case.¹⁹⁶ In an earlier study, the homopolymers of alkylated DTBT were prepared by Jayakannan et al. by varying alkyl chains on either 3- or 4-positions of the thienyl groups.¹⁹⁷ Though relatively high molecular weight polymers were obtained, the steric hindrance introduced by these alkyl chains in these polymers led to much larger band gaps than that of the homopolymer of unsubstituted DTBT.¹⁹⁸ Later, Wang et al. synthesized a series of internal donor–acceptor type of copolymers containing benzothiadiazole (BT) and four thiophenes incorporating side

chains on different position as shown in Figure 19.¹⁹⁹ Despite identical alkyl side chains, the positions where these alkyl side

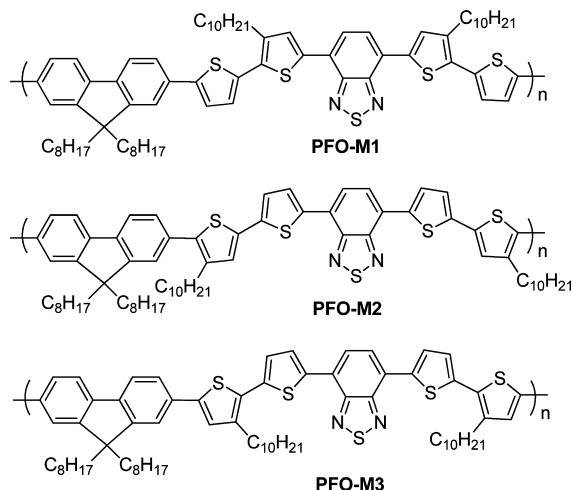


Figure 19. Chemical structures of PFO-M1, PFO-M2, and PFO-M3.

chains are attached to different thiophene rings have significant influence on the physical properties and photovoltaic performance of resulting polymers. Positioning these alkyl chains close to the fluorene renders large steric hindrance during polymerization, which results in a significantly lower molecular weight of PFO-M2 and consequently a poor PV performance of related BHJ cells when compared with 1.82% for PFO-M1 and 2.63% for PFO-M3 based BHJ solar cells.

Most recently, You and co-workers systematically investigated what effect the side-chain positions had on the optical, electrochemical, and photovoltaic properties of conjugated polymers using PBDT-DTBT as the model polymer (Figure 20).¹⁵⁹

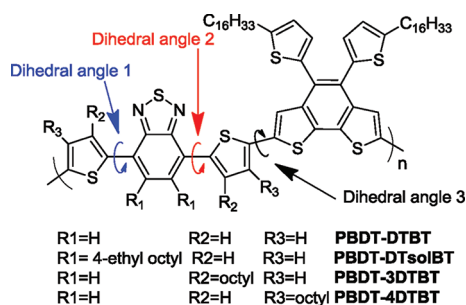


Figure 20. Chemical structures of PBDT-DTBT, PBDT-4DTBT, PBDT-3DTBT, and PBDT-DTsolBT. Reprinted with permission from ref 159. Copyright 2010 American Chemical Society.

These three polymers with alkyl chains attached on DTBT have similar molecular weights (much higher than that of PBDT-DTBT without alkyl chains on DTBT), thereby minimizing the potential complication from the influence of different molecular weights. Thus, all observed differences in properties (optical, electrochemical, and photovoltaic) can be ascribed to the difference in where these side chains were placed. They quantitatively measured the steric hindrance introduced by these alkyl chains by calculating the dihedral angles between two thiophene groups with the center BT unit as well as with the donor BDT. There is only a slight increase of the dihedral angle between the 4-substituted thiophene group and the BDT unit in PBDT-4DTBT when compared with the original PBDT-DTBT,

indicating a minimum steric hindrance introduced by the 4DTBT. Moreover, the DFT calculation showed that the electron density is delocalized in the HOMO of PBDT-4DTBT, similar to that of PBDT-DTBT. This results in an almost negligible difference between the HOMO energy level of PBDT-DTBT and that of PBDT-4DTBT. On the other hand, moving these alkyl chains away from the vicinity of BDT unit in the case of PBDT-3DTBT and PBDT-DTsolBT decreases the steric hindrance between substituted DTBT and BDT unit, recovering small numbers on the dihedral angle 3. However, greater steric hindrance is formed between the thienyl groups and the center BT unit, as shown by a dramatic numerical increase in the dihedral angles 1 and 2. This severe steric hindrance essentially breaks the conjugation at the linkages between these thienyl groups and the BT, thereby rendering large band gaps for these two polymers (2.21 eV for PBDT-3DTBT and 2.48 eV for PBDT-DTsolBT).

The thorough investigation of this library of structurally related polymers clearly indicates that attaching alkyl chains on the 4-positions of these thienyl groups (i.e., 4DTBT) only introduces minimum steric hindrance into the related D–A polymer. Therefore, PBDT-4DTBT maintains almost identical band gap and energy levels when compared with those of PBDT-DTBT. However, these additional side chains offer a high molecular weight and excellent solubility of PBDT-4DTBT, the latter leading to a more uniform mixture with PC₆₁BM with better control on the film morphology. All these features of PBDT-4DTBT contribute to a noticeably enhanced efficiency (up to 2.2%) of PBDT-4DTBT-based BHJ cells, significantly higher than that of PBDT-DTBT-based devices (0.7%).

2.5.2. Shape and Length. Even when the side chains are “properly” anchored on the conjugated backbone, the length and shape of these side chains also have a noticeable (sometimes substantial) impact on the properties of resulting conjugated polymers. Gadisa et al. completed a comparative investigation on the photovoltaic properties of BHJ devices based on a series of poly(3-alkylthiophene)s of butyl (P3BT), pentyl (P3PT), and hexyl (P3HT).²⁰⁰ FF of 0.529, 0.624, and 0.675 were obtained from solar cells based on P3BT:PC₆₁BM (1:0.8), P3PT:PC₆₁BM (1:1), and P3HT:PC₆₁BM (1:1), respectively. Bipolar measurements made by field-effect transistors showed a decrease in the hole mobility and an increase in the electron mobility with increasing alkyl chain length, which is attributed to the an increase in the degree of phase separation. The longer side chains facilitate the clustering of PC₆₁BM molecules and establish fast electron-percolation pathways, leading to improved electron mobility. Since holes and electrons exhibit well-balanced mobilities in the case of P3HT:PC₆₁BM, a better fill factor was observed.

In another study, Egbe et al. grafted different side chains to the backbone of a series of anthracene-containing poly(*p*-phenyleneethynylene)-*alt*-poly(*p*-phenylenevinylene) (PPE–PPV) copolymers to tune the π – π stacking ability of the materials (Figure 21).²⁰¹ Polymers with octyloxy substitution close to the AnE units (*ab*, *ad*, *ae*) arrange in a stacked manner, whereas asymmetric (*cc*) or branched side chain substitution (*bb*, *ba*) near the AnE unit yields less organized or even amorphous polymers. The best performance of 3.14% was achieved from BHJ devices based on *ab* ANE-PV which shows both stacking ability and biggest π – π stacking distance of 0.386 nm as opposed to 0.380 nm for the other polymers in this series. Lower efficiency values were obtained for the BHJ devices based on amorphous polymers *ba* and *bb*, due to a high miscibility of components in the active layer resulting in insufficient percolation paths for the

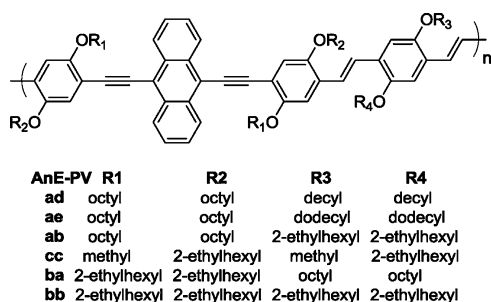


Figure 21. Chemical structures of PPE-PPV with different alkyl side chains. Reprinted with permission from ref 201. Copyright 2010 American Chemical Society.

photogenerated charges. Moreover, BHJ devices based on *ad* and *ae* with higher side chain density (number of carbons) exhibited lower photovoltages and fill factors and thus lower photovoltaic performance when compared with those of *ab* based BHJ devices. The authors believed that high density side chains dilute the concentration of the light absorbing conjugated species per volume unit and reduce the amount of light absorbed by the active layer. High density side chains also reduce the interfacial area between the DONOR polymer and the PC₆₁BM, leading to a strong phase separation and concomitant poor PV performance. Finally, a large V_{oc} change from ~ 0.65 V to ~ 0.90 V was observed, which is likely influenced by the shape and size of these side chains. However, the relationship between the V_{oc} and the side chains (shape and size) was not further investigated in the report.

The first quantitative analysis of the influence from the size of these side chains on photovoltaic properties of polymer–fullerene solar cells was carried out by You and co-workers.⁵⁰ In their report, six polymers with an identical polymer backbone (PNDT-DTBT) but different side chains (i.e., size and branching) were synthesized and investigated (Figure 22a). In good solvent and at high temperature, all polymer chains are completely solvated with minimum intermolecular interactions, which leads to almost identical UV–vis absorptions due to the

identical backbone of PNDT-DTBT. However, BHJ solar cells employ the polymer:PC₆₁BM blend at the solid state where the intermolecular interactions (i.e., between polymers and between the polymer and the PC₆₁BM molecules) play a crucial role. Since these seemingly subtle differences in the polymer structures (size and branching of these side chains) affect the intermolecular interactions in the solid state, the observed V_{oc} and J_{sc} of these polymer-based BHJ devices can vary as much as 100%. Consequently, the overall efficiency of these solar cells has shown a significant variation as much as 2.5-fold (from 1.20% to 3.36%). More importantly, the observed V_{oc} change was quantitatively correlated with a pre-exponential dark current term, J_{so} , which accounts for the intermolecular interactions in the polymer/PC₆₁BM blends. There is excellent agreement between the experimentally observed V_{oc} values and the calculated ones using the following theoretical equation (Table 7), a clear indication of the viability and effectiveness of this simulation for V_{oc} :

$$V_{oc} \approx \frac{nkT}{q} \ln \left(\frac{J_{sc}}{J_{so}} \right) + \frac{\Delta E_{DA}}{2q}$$

where q is the fundamental charge, n is the diode ideality factor, and ΔE_{DA} is the energy difference between the LUMO level of the ACCEPTOR and the HOMO level of the DONOR.

Specifically, the polymer with the long and branched side chains (C10,6–C6,2) displayed the highest V_{oc} of 0.81 V in its BHJ cells. As the long branched chains were systematically converted to short linear chains—until the extreme of the polymer C8–C8—the measured V_{oc} gradually decreased to a minimum of 0.41 V (Table 7). From the XRD spectrum, the very weak (010) peak intensity in the C10,6–C6,2 polymer indicates a weak π -overlapping among individual conjugated polymer chains which results in weak intermolecular interaction (Figure 22b). This weak intermolecular interaction leads to a small J_{so} that is beneficial to the V_{oc} (see above equation). On the other hand, short and straight side chains would promote the

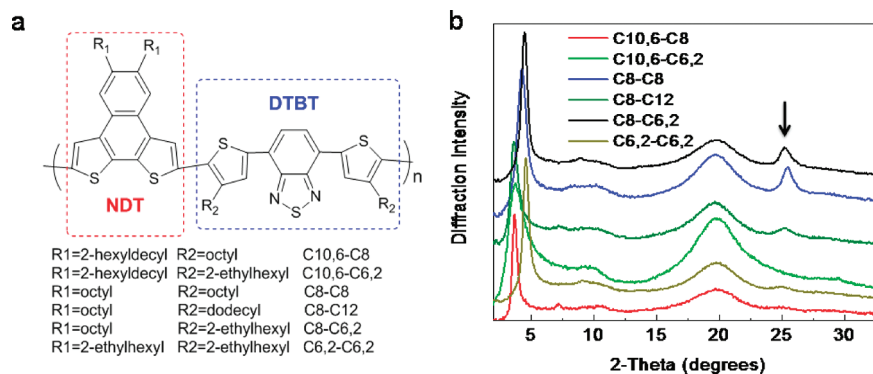


Figure 22. (a) Chemical structures of six polymers based on the PNDT-DTBT backbone. (b) XRD spectra of conjugated polymers:PC₆₁BM (1:1) blends in thin films (arrows indicating (010) peaks).⁵⁰

Table 7. Measured and Calculated Performance Parameters for All Devices of PNDT-DTBT Series⁵⁰

polymer	J_{so} (mA/cm ²)	HOMO (eV)	V_{oc} (V) cal	V_{oc} (V) exp	J_{sc} (mA/cm ²)	FF	PCE (%)
C10,6–C8	148	−5.32	0.60	0.59	7.98	0.46	2.17
C10,6–C6,2	3.38	−5.33	0.83	0.81	5.62	0.44	2.01
C8–C8	399	−5.13	0.39	0.41	6.97	0.42	1.20
C8–C12	254	−5.27	0.53	0.52	5.88	0.42	1.28
C8–C6,2	68.8	−5.30	0.60	0.59	10.93	0.46	3.00
C6,2–C6,2	22.6	−5.34	0.70	0.69	10.67	0.46	3.36

intermolecular interaction, as confirmed by the highly intense (010) peak. This improved intermolecular interaction (represented by a large J_{so}) renders a small optical band gap and better charge transport, which should increase the J_{sc} (though at the expense of V_{oc}). The short and branched side chains (C6,2–C6,2) strike a desirable balance between V_{oc} and J_{sc} to reach the optimum efficiency via an appropriate J_{so} . Therefore the C6,2-C6,2 polymer based BHJ cells exhibited the highest efficiency of 3.36% in this study with a V_{oc} of 0.69 V and a J_{sc} of 10.67 mA/cm².

A similar impact of these side chains has also been observed by Yu and co-workers on a series of low-band-gap polymers with identical conjugated backbone of poly(thieno[3,4-*b*]-thiophene–benzodithiophene) (Figure 23).^{74,194,202} The first

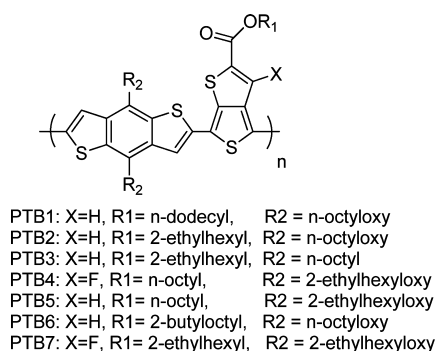


Figure 23. Chemical structures of polymers PTB1–PTB7.²⁰²

six polymers (PTB1 to PTB6) have similar weight-averaged molecular weights between 19.3 and 25.0 kg/mol with a relatively narrow polydispersity index (PDI) between 1.25 and 1.50, indicating that the changes in monomer structures did not lead to significant changes in the polymerization reaction. A clear relationship between properties and structure was observed from the careful study of these six polymers. Generally, the branched side chain grafted polymers (PTB2 through PTB6) show larger V_{oc} in their related BHJ devices than that of PTB1 with only straight side chains, partly due to lower HOMO energy levels of these polymers of branched side chains. However, too bulky side chains reduce the miscibility of polymer with PC₆₁BM, leading to excessive phase separation between polymer chains and PC₆₁BM molecules and thereby reducing the interfacial areas for charge separation in PTB5- or PTB6-based solar cells. The related smaller currents lead to the diminished solar cell performances in the case of PTB5 or PTB6.

To further understand the effect of side chains on the performance of solar cells based on the PTB series, both GIWAXS and GISAXS were employed to investigate the film morphology of these six polymers and their blends with PC₆₁BM/PC₇₁BM, along with PTB7 which shows an impressive efficiency as high as 7.4% of its BHJ cells.²⁰² Both the π – π stacking interactions in the polymer domains and PC₆₁BM/PC₇₁BM incorporation into these domains are very sensitive to the structure of the side chains attached to the TT or the BnDT subunits of the PTB polymers. The branched side chains attached on the BnDT unit cause an increase in the π – π stacking spacing in thin films and a decrease in the efficiency of related BHJ devices, while the branched side chain attached on the TT unit does not interfere with the π – π stacking spacing in the film and enhances the device efficiency. On the other hand, linear alkyl side chains occupy less space than branched alkyl

side chains, resulting in a π – π stacking distance of 3.65 Å for PTB1 vs 3.89 Å for PTB5. A striking relationship between the fill factor (*FF*) of related BHJ devices and the π – π stacking distances of the seven PTB polymers was also revealed, which indicates that a closer π – π stacking distance in the polymer film gives a larger *FF* of its corresponding BHJ device. This behavior was ascribed to the fact that the PTB polymers with the strongest π – π stacking should have the most crystalline polymer domains and bind most strongly to the anode interfacial layer, facilitating electronic communication across the interface.

The studies on PTB polymers also reveal that devices based on the fluorinated polymers (PTB4 and PTB7) show larger V_{oc} than those of other PTB polymers, mainly because the electron-withdrawing nature of these fluorine atoms leads to observed lower HOMO energy levels of PTB4 and PTB7. Moreover, the comparison of PTB2 and PTB3 discloses that replacing the octyloxy side chains with octyl side chains improves the V_{oc} of related BHJ devices from 0.6 V of PTB2 to 0.74 V in the case of PTB3. These alkoxy groups anchored on BnDT ring are strongly electron-donating, which can raise the HOMO energy level of resulting polymers and lead to the observed reduction in V_{oc} . The differences between alkyl chains and alkoxy side chains will be further discussed in the next section.

2.5.3. Alkoxy vs Alkyl. Compared with alkyl groups, alkoxy groups are more electron-donating, which usually raise up the HOMO energy level of related conjugated polymers when they are attached with alkoxy side chains. Shi et al. studied a series of poly(thiophene)s with alkoxy side chains.²⁰³ Table 8 compares

Table 8. Optical and Electronic Properties of P3HT, P3DOT, and POT-*co*-DOT

polymer	λ_{max} (nm)		E_g^{opt} (eV)	HOMO (eV)	LUMO (eV)
	CHCl ₃ soln	film			
P3HT	425	514	1.92	−4.75	−2.83
P3DOT	565	624	1.60	−4.47	−2.87
POT- <i>co</i> -DOT	538	621	1.64	−4.55	−2.91

the optical and electronic properties of regioregular P3HT, regioregular poly(3-decyloxythiophene-2,5-diyl) (P3DOT), and regioregular copolymer poly(3-octylthiophene-2,5-diyl-*co*-3-decyloxythiophene-2,5-diyl) (POT-*co*-DOT). P3DOT demonstrates an optical absorption maximum at longer wavelength than that of the P3HT. This can be attributed to both the electron-donating effect of the alkoxy group and the more coplanar backbone of the P3DOT than that of the P3HT (because of the smaller size of O than that of CH₂). It is not surprising that when the alkyl chains are only partially replaced by alkoxy groups in the case of POT-*co*-DOT, the HOMO energy level and band gap of this regioregular copolymer are in between those of P3DOT and P3HT. Similar effect of the electron-donating alkoxy group was also reported by Hou et al. on conjugated polymers with benzo-[1,2-*b*:3,4-*b'*]dithiophene (BnDT) and 4,7-dithiophen-2,1,3-benzothiadiazole (DTBT) units.²⁰⁴

When the steric hindrance is not a primary concern, employing alkyl chains rather than alkoxy chains will lower the HOMO energy level of resulting polymers and increase the V_{oc} of related BHJ solar cells. This was best illustrated by the studies on PBDTTT series (structures shown in Figure 24).^{74,205} The HOMO level of the original PBDTTT-E was successfully reduced by replacing the alkoxy group on the carbonyl of the

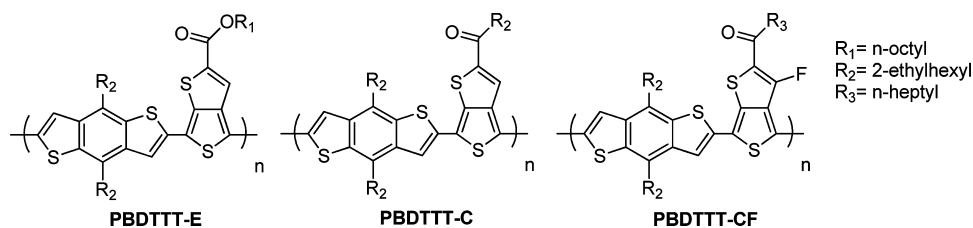


Figure 24. Chemical structures of PBDTTT-E, PBDTTT-C and PBDTTT-CF.⁷⁴ Reprinted with permission from ref 74. Copyright 2009 Nature Publishing Group.

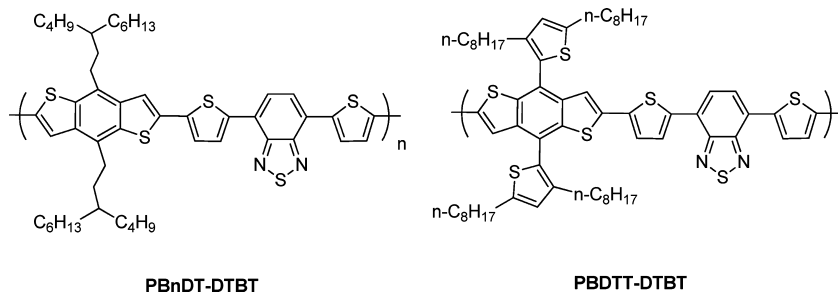


Figure 25. Chemical structures of PBnDT-DTBT and PBDTT-DTBT.

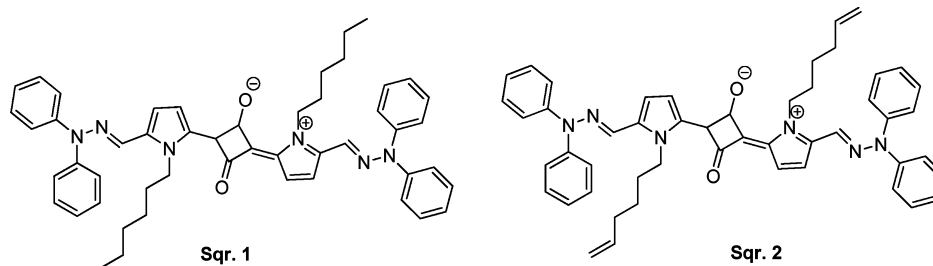


Figure 26. Chemical structures of squaraine 1 and squaraine 2.²⁰⁷

thieno[3,4-*b*]thiophene unit with an alkyl side chain (hereafter referred to as PBDTTT-C). Because of its low HOMO level, a V_{oc} of 0.70 V was obtained in the device based on PBDTTT-C, 0.12 V higher than that of the PBDTTT-E/PC₇₁BM-based device. Interestingly, the substitution of the alkoxy by the alkyl group almost has no influence on the band gap for this kind of polymer, implying a complete delocalization of electronic states in low-band-gap polymers based on quinoid structures. Therefore, devices based on PBDTTT-C maintain a high J_{sc} of 14.7 mA/cm², with an overall PCE reaching 6.58%. Further structural modification was accomplished by substituting the hydrogen atom on the thienothiophene with a fluorine (as discussed in section 2.4), which converted the PBDTTT-C into PBDTTT-CF. As expected, the introduction of fluorine further lowered both the HOMO and LUMO levels, resulting in a similar band gap when compared with those of other PBDTTT-based polymers. Thus, the V_{oc} of devices based on PBDTTT-CF can be further increased to 0.76 V. Combined with a high J_{sc} and a fill factor (FF), a very impressive average PCE of 7.38% was achieved in the PBDTTT-CF-based BHJ cells.⁷⁴ The highest measured PCE is 7.73%, which is the highest efficiency value for polymer solar cells as reported in the literature.

2.5.4. Other Side Chains. Adding additional aromatic units (not fused) to the conjugated backbone as part of the side chains has also been explored. For example, Yang and co-workers incorporated additional thienylene units to the original PBnDT-DTBT (Figure 25).⁶ The resulting polymer PBDTT-

DTBT-based solar cells exhibited a high V_{oc} of 0.92 V and a high J_{sc} of 10.7 mA/cm², which are almost 0.1 V and 3 mA/cm² larger than those of PBnDT-DTBT-based solar cells.²⁰⁶ Consequently, the overall efficiency increased from 3.85% of PBnDT-DTBT-based devices to 5.66% of PBDTT-based ones. Interestingly, since both PBDTT-DTBT and PBnDT-DTBT exhibited similar HOMO levels and band gaps, the improved V_{oc} and J_{sc} of PBDTT-DTBT-based devices cannot be simply attributed to a lower HOMO level or a smaller band gap introduced by these thienylene groups. It is plausible that these side chains with bulky thienylene groups decrease the intermolecular interaction between polymer and fullerene derivatives, leading to an enhanced V_{oc} . Also, it is likely that an improved carrier transport introduced by these thienylene groups helps increase the J_{sc} .

Lastly, Bangis et al. reported characterization of BHJ solar cells based on two new squaraine dyes, substituted at the pyrrolic nitrogen with *n*-hexyl (squaraine 1) or *n*-hexenyl (squaraine 2) chains (Figure 26).²⁰⁷ Squaraine 2-based devices invariably outperform those based on hexyl-substituted squaraine 1. This performance improvement predominantly arises from the J_{sc} enhancement. To further understand the property differences between squaraine 1 and squaraine 2, the crystal structures of these two dyes were investigated. The data reveal that the *n*-alkenyl substituent affords a more compact solid-state structure, enhancing charge mobility (thin film transistor hole mobility is increased by ~ 5 times) and hence increasing J_{sc} .

Although this report investigated only the side-chain effect on small molecules, it implies a new structural strategy of conjugated polymer to enhance charge transport efficiency via noncovalent alkenyl–phenyl contacts by incorporating alkenyl side chains to the polymer backbone.

3. OUTLOOK AND CHALLENGES

3.1. Maximum Efficiency Reachable with Polymer: Fullerene BHJ Solar Cell. Tremendous progress has been made in the past 16 years in the field of polymer solar cells, particularly in the design and synthesis of novel conjugated polymers as discussed in previous sections. The record high efficiency has been constantly updated in the past 3 years by the synergistic efforts between the academic researchers (e.g., design and synthesis of new polymers) and companies (e.g., device optimizations). Furthermore, the design and synthesis of these novel polymers would not have been possible without a deeper understanding of the governing physical principles,^{33,208,209} device physics,^{31,51,210} and morphology investigation and control.^{211–216} As a result of the synergy in the community (including both academia and companies), the J_{sc} can reach as high as 17.3 mA/cm²,^{5,217} the highest V_{oc} obtained has been over 1 V,^{41–43} and the highest obtained FF has breached 70%.^{44,45} If we could achieve all these impressive values with one system, this champion BHJ solar cell would offer an unprecedented value of 12%! This is the bright future of the exciting field of polymer solar cells and also the goal that numerous researchers strive for. Unfortunately, all these high values are obtained from different polymer-based BHJ systems, partly due to an intrinsic “tug of war” between J_{sc} and V_{oc} as elaborated on in section 1.3⁵⁹ and experimentally demonstrated.⁴⁶ A more rigorous model calculation on the ultimate performance of polymer:fullerene BHJ cells was recently accomplished by Blom and co-workers (ref 218 and references therein). They predicted a maximum power efficiency of 11.7% for single junction cells and 14.1% for tandem structures. This is very encouraging, and the community is steadily approaching these numbers: for example, a new record high efficiency of 9.2% for organic solar cells has been recently reported.⁹

3.2. Even Higher Efficiency Possible? However, if polymer solar cells (and organic solar cells in general) intend to compete with other thin film PV technologies (such as CIGS or CdTe) as a viable economic solution for renewable energy future, higher efficiencies (15–20%) will be strongly desirable if not required. For example, flexible thin film solar cells based on copper indium gallium (di)selenide (CIGS) can reach an energy conversion efficiency as high as 18.7%,²¹⁹ and the efficiency of mass-produced CIGS thin film modules has breached 13%.²²⁰ Can polymer (organic) solar cells achieve similar performances? To answer this challenge, one has to analyze the J_{sc} , V_{oc} , and FF individually, since these three parameters ultimately decide the efficiency of any solar cells. To facilitate the discussion and related recommendations, we collected roughly 200 data sets from different polymer/fullerene BHJ systems in the literature reports and plotted the J_{sc} versus the band gap of the polymer (Figure 27) and V_{oc} versus the HOMO energy level of the polymer (Figure 28). To make the analysis meaningful, we averaged all the experimental values in related intervals in both figures.

• J_{sc} : Figure 27 clearly shows that a smaller band gap favors a higher short-circuit current. However, this trend reaches its maximum around 1.3 eV. Polymers with even smaller band gap than 1.3 eV fail to offer more current as expected from their absorption extending into the near-IR. Two possible reasons

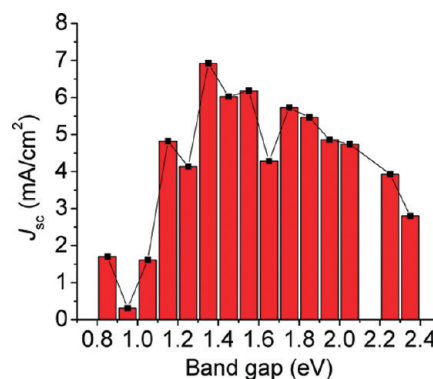


Figure 27. E_g vs J_{sc} plot. A total of ~200 data points were taken and summarized with 0.1 eV interval, e.g., 0.80–0.89, 0.90–0.99 eV.

account for this observation. The first is related with the energy levels of these polymers having extremely small band gaps. Often a very strong acceptor (such as benzobisthiadiazole) was paired with a strong donor to achieve the small band gap via the donor–acceptor low-band-gap approach; however, these strong acceptors could lower the LUMO level below -3.9 eV, leading to an inefficient exciton dissociation when PC₆₁BM was used as the electron ACCEPTOR in the BHJ solar cells. The second is the usually small full width at half-maximum (FWHM) of these conjugated polymers, normally on the order of 200 nm. Thus, continuously shifting the absorption of the polymer toward the IR end of the solar spectrum would inevitably diminish its ability to absorb the light in the visible region. In addition, these near-IR/IR absorbing polymers usually have low absorption coefficients, which exacerbate the light harvesting. On the basis of these analyses, we identify a few potential directions worth of further research:

a. Choosing appropriate structural units in D–A polymers: In order to achieve a narrow band gap, a strong electron-accepting structural unit is required in donor–acceptor copolymers. However, one should develop appropriate “strong” acceptors such that they would bring the LUMO level close to but not lower than the ideal LUMO level (Figure 5). As discussed in section 2.3.2 which is focused on the design of acceptors, the relative easier approach is to fine-tune existing acceptors by attaching substituents (e.g., changing DTBT to DTfBT⁶¹) or changing specific atoms (e.g., switching DTBT to DTPyT¹⁰⁷). A better approach—though more challenging—is to envision new designs of chemical structures. For example, one can certainly benefit from a close look at dyes and pigments since a number of the recently developed “strong” acceptors were adapted from existing dyes. Equally important in achieving a narrow band gap is the fine-tuning of HOMO levels of these electron-donating structural units, which certainly require deliberation. As indicated in section 2.3.1 which is dedicated to the design of donors, polyaromatic units with fused aromatic rings offer noticeable advantages as donor moieties. The rigid and planar structures of these fused aromatics usually lead to strong π -interactions, which help improve the hole mobility and decrease the band gap of related conjugated polymers in the solid state. However, appropriate side chains need to be carefully selected to maintain the beneficial polymer–polymer interactions and polymer–PCBM interactions, while still providing enough solubility to the polymer (for high molecular weight and easy processability).

b. Increasing FWHM: Two possible solutions have emerged to increase the FWHM, both of which used random copolymerization to bring more than two monomers into the

conjugated backbone, though in a slightly different manner. Liang et al. incorporated the pre-quinoid unit of thieno[3,4-*b*]-thiophene (TT) into the polythiophene backbone, basically introducing the low-band-gap character of the TT into the backbone.²² Depending upon the feed ratio of the TT vs thiophene, the band gap and the energy level of the random copolymer can be tuned. In an earlier report, Li and co-workers added another conjugated oligomer (bithienylenevinylene) to the 3-position of the thiophene and polymerized this modified thiophene unit with 3-hexylthiophene and unsubstituted thiophene monomers in a random manner into the biTV-PT.²²¹ These conjugated side chains add strong absorption from 350 to 480 nm, thereby leading to a broad absorption spectrum from 350 to 650 nm of these copolymers. Both reports did obtain better performance from these random copolymers than that of the benchmark P3HT in their studies, though the obtained efficiency numbers are still noticeably lower than that of the optimized P3HT-based cell (~5%). Nevertheless, considering the effective broadening of the absorption by these approaches, further investigation is still warranted.

c. Making n-type material absorb: Alternatively, one can employ electron-accepting materials that absorb the complementary part of the solar spectrum in regard to the absorption of the electron-donating polymers, thereby broadening the light harvesting of the active layer. The most successful example is the PC₇₁BM, whose lesser symmetry (compared with PC₆₁BM) renders a much enhanced absorption from 300 to 600 nm.¹⁵ This strong absorption in the UV–vis region by the PC₇₁BM effectively complements the main absorption in the visible to NIR region by these narrow-band-gap polymers (600 to 900 nm), offered by these narrow-band-gap polymers, thereby leading to an appreciable increase (20% or more) in the J_{sc} of related solar cells when compared with that of PC₆₁BM-based ones. Almost all reported polymer/PCBM-based solar cells with over 7% efficiency have used PC₇₁BM,^{60,62,74,78} with only few exceptions.^{45,61} A more elegant solution comes from the design and synthesis of electron-accepting polymers with tunable absorption. Though these polymer:polymer solar cells have not reached high efficiency (highest around 2.5%²²²) as polymer:fullerene solar cells, the full tunability (e.g., energy level and band gap) of these electron-accepting polymers offers a viable approach toward not only a higher J_{sc} but also a high V_{oc} in these all polymer solar cells.

d. Improving EQE: In contrast to the internal quantum efficiency (IQE) which already reached 100% in some recent reports,⁴ the external quantum efficiency (EQE) remains relatively low (50%–80%), even in these highly efficient polymers/fullerene BHJ solar cells. For example, the highest reported J_{sc} of 17.3 mA/cm² could have been 30 mA/cm² based on its band gap of 1.3 eV, if the EQE were 100% instead of the observed ~55%.⁵ This is mainly due to the low mobility of charge carriers in these polymer:fullerene blends and the intrinsically disordered morphology of the BHJ cells, which limits the optimal film thickness of the active layer to less than 200 nm. A thicker film would be able to harvest all the light within the film absorption; however, the generated charges after dissociating these excitons would not be able to transverse the thick film and reach the individual electrode before various recombination mechanisms kick in to annihilate these energy carrying charges. Thus further improving the carrier mobilities (both holes and electrons), controlling the morphology, and finding methods to slow down or even eliminate charge recombination should be among research priorities.

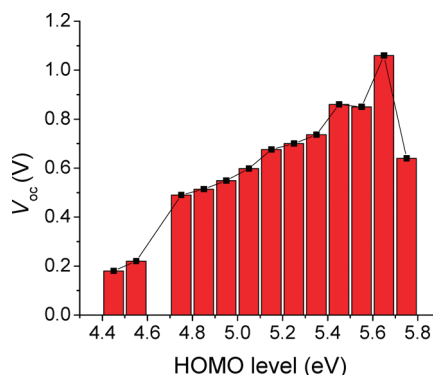


Figure 28. HOMO vs V_{oc} plot. A total of ~200 data points were taken and summarized with 0.1 eV interval, e.g., 4.40–4.49, 4.50–4.59 eV. Please note that all HOMO energy levels should be negative. In the Y axis, the “–” sign was omitted for clarity.

• V_{oc} : A similar trend has been observed for V_{oc} vs HOMO level (Figure 28). The open-circuit voltage increases as the HOMO energy level lowers, reaching the maximum of 1.02 V around a HOMO level of –5.56 eV, and then drops.¹⁰² This observation is not surprising since after years of investigation, it is generally accepted that the V_{oc} is proportional to the difference between the HOMO of the DONOR and the LUMO of the ACCEPTOR, though recent advances in understanding the origin of the V_{oc} have provided further insights.^{48–50,223} Thus, a lower HOMO energy level (but not too low) is desirable. As shown in earlier discussion (e.g., section 2.3.1), polyaromatic units with flanking thiophene units are good candidates of such “weak” donors to offer appropriate HOMO levels in D–A conjugated polymers. This is because the electron-donating ability of those units can be fine-tuned by varying fused aromatic units and/or attaching substituents. Moreover, thiophene units are less likely to have steric hindrance with adjacent units than benzene would have. Therefore, having thiophenes as the finish for these polyaromatic units can lead to a more planar backbone with better conjugation. But is achieving a V_{oc} of 1.1 V indeed applaudable? If we took –4.2 eV as the LUMO of the PC₆₁BM, we would still have lost 0.4 eV from the energy difference ($E_{LUMO(ACCEPTOR)} - E_{HOMO(DONOR)}$) which was not converted to the V_{oc} . This loss of 0.4 eV or more is typically observed in polymer solar cells. If we consider another source of the voltage loss, the empirical 0.3 eV between the LUMOs of the DONOR polymer and the fullerene, we have lost ~0.7 eV altogether, which could have doubled the V_{oc} if all contributed to the V_{oc} ! Therefore, much more work needs to be done on two possible fronts:

a. Further understanding the origin of V_{oc} and searching for new acceptors: First, is the empirical 0.3 eV required for effective exciton splitting at the interface really necessary? With a recently developed new π -electron ACCEPTOR (D99'BF),²²⁴ Heeger and Wudl showed that a V_{oc} of 1.2 V could be obtained from the P3HT/D99'BF BHJ solar cell,²²⁵ as opposed to the usually obtained 0.6 V in the case of P3HT/PC₆₁BM solar cells. More importantly, these authors demonstrated that electron transfer could still occur even with only 0.12 eV in the LUMOs offset. Apparently, the exciton binding energy could be as small as 0.1 eV (at least in the case of P3HT). This exciting discovery points to a potential further increase on the V_{oc} via designing non-fullerene-based acceptors. However, even in this successful demonstration, a loss of over 0.5 eV was still observed since the difference between the LUMO of D99'BF and the HOMO of

P3HT was 1.78 eV. This leads to the second question: can we minimize the commonly observed loss of 0.4–0.6 eV from the energy level difference between $E_{\text{LUMO(ACCEPTOR)}}$ and $E_{\text{HOMO(DONOR)}}$? There have been some suggestions that reducing the electron–phonon coupling of these excitons thereby smaller Stokes shift would help diminish this loss mechanism.²²⁶ This would call for well-ordered polymers with delocalized excitons. Further, recent advances in further understanding of the V_{oc} suggest that reducing the electronic coupling between the polymer and the fullerene would increase the V_{oc} .^{48–50,223} Nevertheless, there is still a lot to be done to determine a clearer structure–property relationship regarding the V_{oc} so the synthetic chemists will know how to design better materials (both electron-donating and electron-accepting materials).

b. Engineering the fullerene: Alternatively, before we find new acceptors that can replace the fullerene on all fronts, we can still modify the structure of this fascinating group of molecules to raise up their LUMO energy levels in order to gain a higher V_{oc} . There have been successful examples such as trimetallic nitride endohedral fullerenes (TNEFs, in particular $\text{Lu}_3\text{N@C80}$),¹³ indene- C_{60} bisadduct (ICBA),¹⁶ among others.²²⁷ The V_{oc} of related P3HT:modified fullerene BHJ cells can be increased as much as 0.26 V¹⁶ when compared with P3HT/ PC_{61}BM cells because of the raised LUMO energy level of the modified fullerene.

- **FF:** Unlike silicon solar cell or even dye-sensitized solar cells, both of which give high fill factors (75%–80% or higher), the polymer solar cells usually only offer a fill factor around 60%. The fill factor is ultimately determined by the series resistance (R_{s}) and the shunt resistance (R_{sh}) of the devices. Because of the low charge carrier mobilities (especially holes) and the disordered nature of the BHJ film, BHJ solar cells usually have a relatively high R_{s} and relatively low R_{sh} . In order to get a high FF, one would require to achieve both a low R_{s} and a high R_{sh} . Research efforts are needed to reach a balanced and rapid charge transport (holes vs electrons), to optimize and control the film morphology into more ordered structure, and to improve all electric contacts.

- **Morphology:** The full potential of any conjugated polymer for solar cells can only be realized with an optimized morphology. Though there is a general consensus regarding what defines a preferred morphology (i.e., interpenetrating network at nanometer scale), the “ideal” morphology could vary from one polymer/fullerene system to the other. How to control the morphology poses an even bigger challenge, though considerable progress has been made,²²⁸ particularly the annealing (via thermal or solvent) and the discovery of processing additives.^{211,213,216} The interactions between DONOR polymers, between DONOR polymer and fullerene ACCEPTORS and between fullerene ACCEPTORS all contribute to the formation of the morphology in a thin film. First, the interaction between DONOR polymers is dominated by the π – π interaction among conjugated backbones, which can bring polymer backbones close enough to form stacked polymer clusters. This stacking is beneficial for charge transport between polymer chains. However, too strong π – π interactions can lead to the formation of large polymer-rich domains, resulting in a low hole mobility across the entire film due to multiple crosses over grain boundaries. In addition to the conjugated backbone, the side chains can also impact the intermolecular interaction as discussed in section 2.5. Therefore, both conjugated backbone and side chains need to be carefully designed in order to control the polymer–polymer interaction such that these

polymers can form desired “channels” to facilitate the charge transport. Second, the polymer–fullerene interactions and their contribution to the morphology are even more complicated. Progress has been made, though. For example, McGehee and co-workers showed that fullerene derivatives were intercalated between the polymer side chains in some polymer:fullerene blends.^{147,148,229} This intercalation is important in determining the optimal polymer:fullerene ratio. For example, in blends where intercalation occurs, fullerenes must fill all available space between the polymer side chains prior to the formation of a pure electron-transporting fullerene phase. This intercalation would also affect some important device characteristics such as mobility, light absorption, photoluminescence, and recombination due to the intimate mixing of the polymer DONORS and fullerene ACCEPTORS in the intercalated phase. In short, we are still in the early stage of fully understanding the morphology of polymer:fullerene blends in thin films. Further development of analytical tools to unveil the “true” morphology of highly efficient BHJ systems, and novel approaches to render the ideal morphology (via chemical design or physical methods), should remain on the top of research priorities.

3.3. Other Pertinent Issues. Though the constitution of the active layer (i.e., polymer and fullerene or other ACCEPTORS) ultimately determine the maximum efficiency achievable with the BHJ cell, one still needs to solve a number of other issues before reaching the full potential of any given cell. Listed below are a few other active research fronts:

- **Interfaces:** The interface between organic active layers and these two contact electrodes (cathode and anode) needs to be optimized to facilitate the charge collection and minimize any loss.^{230,231} Metal oxides recently emerged as versatile interface modifiers, such as NiO ,²³² MoO_3 ,^{233–235} and WO_3 ,^{236,237} as the hole transport layer and TiO_x ,^{37,238} and ZnO ,^{239–242} as the electron transport layer.

- **Device engineering:** Progress has been made in the inverted cells (to increase the air stability),²⁴³ applying light trapping for better light harvesting,²⁴⁴ and using tandem structure²⁴⁵ to increase the overall efficiency of polymer solar cells.

In addition, to achieve the commercial viability, the community still needs to work on the following issues:

- **Transparent contact electrode (TCO):** ITO has been the standard TCO for polymer solar cells. However, the physical nature (brittleness) and the high price associated with ITO prevent a large-scale production of polymer solar cells based on this particular material. Carbon nanotubes, graphenes,^{246–254} and metal nanowires^{255,256} have been proposed, and respectable results have been obtained.

- **Stability:** Significant progress has been made; for example, Konarka has shown a lifetime of 3 years for their polymer solar cells.²⁵⁷

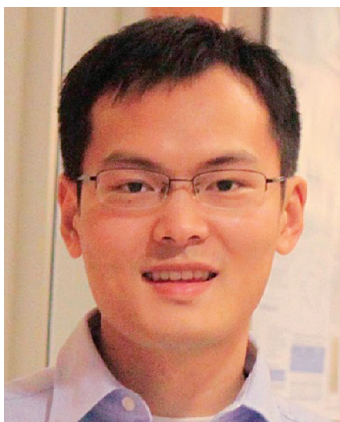
All these challenges (also opportunities) compose the major part of the rather long wish list for the research community of polymer (organic) solar cells. This is a tall order; however, if we could achieve these goals via collaborative efforts, the payoff would be huge—single junction polymer solar cells with 15% efficiency would be within reach (for example, a band gap of 1.3 eV with an EQE of 80%, a V_{oc} of 0.8 V, and a FF of 0.75)!

■ AUTHOR INFORMATION

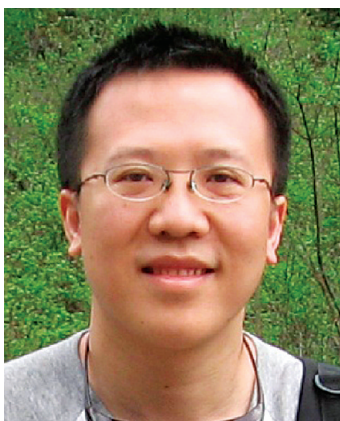
Corresponding Author

*E-mail: wyou@unc.edu.

BIOGRAPHIES



Huaxing Zhou obtained his B.S. degree in polymer chemistry from the University of Science and Technology of China in 2007. He recently received his Ph.D. degree from the department of Chemistry at the University of North Carolina at Chapel Hill under the direction of Prof. Wei You (2011). His Ph.D. research was focused on the rational design of conjugated polymers for organic solar cells. He is currently a postdoctoral fellow in the research group of Prof. Jeremiah A. Johnson at Massachusetts Institute of Technology.



Liqiang Yang is currently a PhD candidate under the guidance of Prof. Wei You at the University of North Carolina at Chapel Hill. He received his B.S. degree in material sciences and engineering at Xi'an Jiaotong University in 2004 and obtained an M.S. degree in material engineering at the University of Wisconsin–Milwaukee in 2007. His current research focus is the fundamental understanding the structure–properties relationships of novel polymers for organic solar cells.



Wei You was born in a small village outside of Chuzhou in Anhui Province of China and grew up in Hefei, the provincial capital of

Anhui. After receiving a B.S. degree in Polymer Chemistry from University of Science and Technology of China in 1999, he attended the graduate program of chemistry at the University of Chicago, where he obtained his Ph.D. in 2004 under the guidance of Professor Luping Yu. He then moved west and finished his postdoctoral training at Stanford University in 2006 with Professor Zhenan Bao. In July 2006, he joined the University of North Carolina at Chapel Hill as an Assistant Professor in Chemistry. Professor You's research interests focus on the development of novel multifunctional materials for a variety of applications, including organic solar cells, molecular electronics, and spintronics.

■ ACKNOWLEDGMENTS

The authors want to thank past and present members of the You group (Dr. Shengqiang Xiao, Dr. Paul G. Hoertz, Dr. Samuel C. Price, Andrew Stuart, Rycel Uy, Wentao Li, among others) for their contributions. We gratefully acknowledge financial support (past and present) from the University of North Carolina at Chapel Hill, a DuPont Young Professor Award, Office of Naval Research (Grants N000140911016 and N000141110235), and a NSF CAREER Award (DMR-0954280).

■ REFERENCES

- (1) Bijleveld, J. C.; Zoombelt, A. P.; Mathijssen, S. G. J.; Wienk, M. M.; Turbiez, M.; de Leeuw, D. M.; Janssen, R. A. J. *J. Am. Chem. Soc.* **2009**, *131* (46), 16616–16617.
- (2) Lewis, N. S. *Science (Washington, DC, U. S.)* **2007**, *315* (5813), 798–801.
- (3) Yu, G.; Gao, J.; Hummelen, J. C.; Wudl, F.; Heeger, A. J. *Science (Washington, DC, U. S.)* **1995**, *270* (5243), 1789–1791.
- (4) Park, S. H.; Roy, A.; Beaupre, S.; Cho, S.; Coates, N.; Moon, J. S.; Moses, D.; Leclerc, M.; Lee, K.; Heeger, A. J. *Nature Photonics* **2009**, *3* (5), 297–302.
- (5) Coffin, R. C.; Peet, J.; Rogers, J.; Bazan, G. C. *Nature Chem.* **2009**, *1* (8), 657–661.
- (6) Huo, L.; Hou, J.; Zhang, S.; Chen, H.-Y.; Yang, Y. *Angew. Chem., Int. Ed.* **2010**, *49* (8), 1500–1503.
- (7) Xiao, S.; Price, S. C.; Zhou, H.; You, W. *ACS Symp. Ser.* **2010**, *1034*, 71–80.
- (8) Kirchmeyer, S.; Reuter, K. J. *Mater. Chem.* **2005**, *15* (21), 2077–2088.
- (9) Service, R. F. *Science (Washington, DC, U. S.)* **2011**, *332* (6027), 293.
- (10) Cheng, Y.-J.; Yang, S.-H.; Hsu, C.-S. *Chem. Rev. (Washington, DC, U. S.)* **2009**, *109* (11), 5868–5923.
- (11) Chen, J.; Cao, Y. *Acc. Chem. Res.* **2009**, *42* (11), 1709–1718.
- (12) Facchetti, A. *Chem. Mater.* **2010**, *23* (3), 733–758.
- (13) Ross, R. B.; Cardona, C. M.; Guldi, D. M.; Sankaranarayanan, S. G.; Reese, M. O.; Kopidakis, N.; Peet, J.; Walker, B.; Bazan, G. C.; Van Keuren, E.; Holloway, B. C.; Drees, M. *Nature Mater.* **2009**, *8* (3), 208–212.
- (14) Lenes, M.; Wetzelaer, G.-J. A. H.; Kooistra, F. B.; Veenstra, S. C.; Hummelen, J. C.; Blom, P. W. M. *Adv. Mater.* **2008**, *20* (11), 2116–2119.
- (15) Wienk, M. M.; Kroon, J. M.; Verhees, W. J. H.; Knol, J.; Hummelen, J. C.; van Hal, P. A.; Janssen, R. A. J. *Angew. Chem., Int. Ed.* **2003**, *42* (29), 3371–3375.
- (16) He, Y.; Chen, H.-Y.; Hou, J.; Li, Y. *J. Am. Chem. Soc.* **2010**, *132* (4), 1377–1382.
- (17) Zhao, G.; He, Y.; Li, Y. *Adv. Mater.* **2010**, *22* (39), 4355–4358.
- (18) Matsuo, Y.; Sato, Y.; Niinomi, T.; Soga, I.; Tanaka, H.; Nakamura, E. *J. Am. Chem. Soc.* **2009**, *131* (44), 16048–16050.
- (19) Sariciftci, N. S.; Smilowitz, L.; Heeger, A. J.; Wudl, F. *Science (Washington, DC, U. S.)* **1992**, *258* (5087), 1474–1476.

- (20) Murata, M.; Morinaka, Y.; Murata, Y.; Yoshikawa, O.; Sagawa, T.; Yoshikawa, S. *Chem. Commun. (Cambridge, U. K.)* **2011**, 47 (26), 7335–7337.
- (21) Thompson, B. C.; Fréchet, J. M. J. *Angew. Chem., Int. Ed.* **2008**, 47 (1), 58–77.
- (22) Kroon, R.; Lenes, M.; Hummelen, J. C.; Blom, P. W. M.; de Boer, B. *Polym. Rev. (Philadelphia, PA, U. S.)* **2008**, 48 (3), 531–582.
- (23) Kippelen, B.; Bredas, J.-L. *Energy Environ. Sci.* **2009**, 2 (3), 251–261.
- (24) Helgesen, M.; Sondergaard, R.; Krebs, F. C. *J. Mater. Chem.* **2010**, 20 (1), 36–60.
- (25) Delgado, J. L.; Bouit, P.-A.; Filippone, S.; Herranz, M. A.; Martin, N. *Chem. Commun. (Cambridge, U. K.)* **2010**, 46 (27), 4853–4865.
- (26) Heeger, A. J. *Chem. Soc. Rev.* **2010**, 39 (7), 2354–2371.
- (27) Dennler, G.; Scharber, M. C.; Brabec, C. J. *Adv. Mater.* **2009**, 21 (13), 1323–1338.
- (28) Günes, S.; Neugebauer, H.; Sariciftci, N. S. *Chem. Rev. (Washington, DC, U. S.)* **2007**, 107 (4), 1324–1338.
- (29) Hains, A. W.; Liang, Z.; Woodhouse, M. A.; Gregg, B. A. *Chem. Rev. (Washington, DC, U. S.)* **2010**, 110 (11), 6689–6735.
- (30) Po, R.; Maggini, M.; Camaioni, N. *J. Phys. Chem. C* **2009**, 114 (2), 695–706.
- (31) Blom, P. W. M.; Mihailescu, V. D.; Koster, L. J. A.; Markov, D. E. *Adv. Mater.* **2007**, 19 (12), 1551–1566.
- (32) Krebs, F. C.; Tromholt, T.; Jorgensen, M. *Nanoscale* **2010**, 2 (6), 873–886.
- (33) Brédas, J.-L.; Norton, J. E.; Cornil, J.; Coropceanu, V. *Acc. Chem. Res.* **2009**, 42 (11), 1691–1699.
- (34) Shaheen, S. E.; Brabec, C. J.; Sariciftci, N. S.; Padinger, F.; Fromherz, T.; Hummelen, J. C. *Appl. Phys. Lett.* **2001**, 78 (6), 841–843.
- (35) Brabec, C. J.; Shaheen, S. E.; Winder, C.; Sariciftci, N. S.; Denk, P. *Appl. Phys. Lett.* **2002**, 80 (7), 1288–1290.
- (36) Reyes-Reyes, M.; Kim, K.; Carroll, D. L. *Appl. Phys. Lett.* **2005**, 87 (8), 3–6.
- (37) Kim, J. Y.; Kim, S. H.; Lee, H. H.; Lee, K.; Ma, W. L.; Gong, X.; Heeger, A. J. *Adv. Mater.* **2006**, 18 (5), 572–576.
- (38) Ma, W. L.; Yang, C. Y.; Gong, X.; Lee, K.; Heeger, A. J. *Adv. Funct. Mater.* **2005**, 15 (10), 1617–1622.
- (39) Li, G.; Shrotriya, V.; Huang, J. S.; Yao, Y.; Moriarty, T.; Emery, K.; Yang, Y. *Nature Mater.* **2005**, 4 (11), 864–868.
- (40) Kim, Y.; Cook, S.; Tuladhar, S. M.; Choulis, S. A.; Nelson, J.; Durrant, J. R.; Bradley, D. D. C.; Giles, M.; McCulloch, I.; Ha, C.-S.; Ree, M. *Nature Mater.* **2006**, 5 (3), 197–203.
- (41) Gadisa, A.; Mammo, W.; Andersson, L. M.; Admassie, S.; Zhang, F.; Andersson, M. R.; Inganäs, O. *Adv. Funct. Mater.* **2007**, 17 (18), 3836–3842.
- (42) Zhang, F.; Jørgensen, K. G.; Björström, C.; Svensson, M.; Andersson, M. R.; Sundström, V.; Magnusson, K.; Moons, E.; Yartsev, A.; Inganäs, O. *Adv. Funct. Mater.* **2006**, 16 (5), 667–674.
- (43) Zheng, Q.; Jung, B. J.; Sun, J.; Katz, H. E. *J. Am. Chem. Soc.* **2010**, 132 (15), 5394–5404.
- (44) Zoombelt, A. P.; Mathijssen, S. G. J.; Turbiez, M. G. R.; Wienk, M. M.; Janssen, R. A. J. *J. Mater. Chem.* **2010**, 20 (11), 2240–2246.
- (45) Price, S. C.; Stuart, A. C.; Yang, L.; Zhou, H.; You, W. *J. Am. Chem. Soc.* **2011**, 133 (12), 4625–4631.
- (46) Zhou, H.; Yang, L.; Liu, S.; You, W. *Macromolecules* **2010**, 43 (24), 10390–10396.
- (47) Scharber, M. C.; Mühlbacher, D.; Koppe, M.; Denk, P.; Waldauf, C.; Heeger, A. J.; Brabec, C. J. *Adv. Mater.* **2006**, 18 (6), 789–794.
- (48) Perez, M. D.; Borek, C.; Forrest, S. R.; Thompson, M. E. *J. Am. Chem. Soc.* **2009**, 131 (26), 9281–9286.
- (49) Vandewal, K.; Tvingstedt, K.; Gadisa, A.; Inganäs, O.; Manca, J. V. *Nature Mater.* **2009**, 8 (11), 904–909.
- (50) Yang, L.; Zhou, H.; You, W. *J. Phys. Chem. C* **2010**, 114 (39), 16793–16800.
- (51) Moliton, A.; Nunzi, J.-M. *Polym. Int.* **2006**, 55 (6), 583–600.
- (52) <http://www.pveducation.org/pvcdrom/>.
- (53) Mauer, R.; Kastler, M.; Laquai, F. *Adv. Funct. Mater.* **2010**, 20 (13), 2085–2092.
- (54) Kim, Y.; Nelson, J.; Durrant, J. R.; Bradley, D. D. C.; Heo, K.; Park, J.; Kim, H.; McCulloch, I.; Heeney, M.; Ree, M.; Ha, C.-S. *Soft Matter* **2007**, 3 (1), 117–121.
- (55) Roncali, J. *Chem. Rev. (Washington, DC, U. S.)* **1997**, 97 (1), 173–205.
- (56) Havinga, E. E.; ten Hoeve, W.; Wynberg, H. *Synth. Met.* **1993**, 55 (1), 299–306.
- (57) Ajayaghosh, A. *Chem. Soc. Rev.* **2003**, 32 (4), 181–191.
- (58) Zhang, Q. T.; Tour, J. M. *J. Am. Chem. Soc.* **1998**, 120 (22), 5355–5362.
- (59) Zhou, H.; Yang, L.; Stoneking, S.; You, W. *ACS Appl. Mater. Interfaces* **2010**, 2 (5), 1377–1383.
- (60) Chu, T.-Y.; Lu, J.; Beaupré, S.; Zhang, Y.; Pouliot, J.-R. m.; Wakim, S.; Zhou, J.; Leclerc, M.; Li, Z.; Ding, J.; Tao, Y. *J. Am. Chem. Soc.* **2011**, 133 (12), 4250–4253.
- (61) Zhou, H.; Yang, L.; Stuart, A. C.; Price, S. C.; Liu, S.; You, W. *Angew. Chem., Int. Ed.* **2011**, 50 (13), 2995–2998.
- (62) Amb, C. M.; Chen, S.; Graham, K. R.; Subbiah, J.; Small, C. E.; So, F.; Reynolds, J. R. *J. Am. Chem. Soc.* **2011**, 133 (26), 10062–10065.
- (63) Su, M.-S.; Kuo, C.-Y.; Yuan, M.-C.; Jeng, U. S.; Su, C.-J.; Wei, K.-H. *Adv. Mater.* **2011**, 23 (29), 3315–3319.
- (64) Wudl, F.; Kobayashi, M.; Heeger, A. J. *J. Org. Chem.* **1984**, 49 (18), 3382–3384.
- (65) Pomerantz, M.; Chaloner, B.; Harding, L. O.; Tseng, J. J.; Pomerantz, W. J. *J. Chem. Soc., Chem. Commun.* **1992**, 22, 1672–1673.
- (66) Hong, S. Y.; Marynick, D. S. *Macromolecules* **1992**, 25 (18), 4652–4657.
- (67) Sotzing, G. A.; Lee, K. H. *Macromolecules* **2002**, 35 (19), 7281–7286.
- (68) Qin, Y.; Kim, J. Y.; Frisbie, C. D.; Hillmyer, M. A. *Macromolecules* **2008**, 41 (15), 5563–5570.
- (69) Hou, J. H.; Park, M. H.; Zhang, S. Q.; Yao, Y.; Chen, L. M.; Li, J. H.; Yang, Y. *Macromolecules* **2008**, 41 (16), 6012–6018.
- (70) Wienk, M. M.; Turbiez, M. G. R.; Struijk, M. P.; Fonrodona, M.; Janssen, R. A. J. *Appl. Phys. Lett.* **2006**, 88 (15), 153511–153513.
- (71) Zhang, F.; Mammo, W.; Andersson, L. M.; Admassie, S.; Andersson, M. R.; Inganäs, O. *Adv. Mater.* **2006**, 18 (16), 2169–2173.
- (72) Liang, Y. Y.; Xiao, S. Q.; Feng, D. Q.; Yu, L. P. *J. Phys. Chem. C* **2008**, 112 (21), 7866–7871.
- (73) Kleinhenz, N.; Yang, L.; Zhou, H.; Price, S. C.; You, W. *Macromolecules* **2011**, 44 (4), 872–877.
- (74) Chen, H.-Y.; Hou, J.; Zhang, S.; Liang, Y.; Yang, G.; Yang, Y.; Yu, L.; Wu, Y.; Li, G. *Nature Photonics* **2009**, 3 (11), 649–653.
- (75) Huang, Y.; Hou, L.; Zhang, S.; Guo, X.; Han, C. C.; Li, Y.; Hou, J. *Chem. Commun. (Cambridge, U. K.)* **2011**, 47 (31), 8904–8906.
- (76) Son, H. J.; Wang, W.; Xu, T.; Liang, Y.; Wu, Y.; Li, G.; Yu, L. *J. Am. Chem. Soc.* **2011**, 133 (6), 1885–1894.
- (77) He, F.; Wang, W.; Chen, W.; Xu, T.; Darling, S. B.; Strzalka, J.; Liu, Y.; Yu, L. *J. Am. Chem. Soc.* **2011**, 133 (10), 3284–3287.
- (78) Liang, Y.; Xu, Z.; Xia, J.; Tsai, S.-T.; Wu, Y.; Li, G.; Ray, C.; Yu, L. *Adv. Mater.* **2010**, 22 (20), E135–E138.
- (79) Li, Y.; Zou, Y. *Adv. Mater.* **2008**, 20 (15), 2952–2958.
- (80) Huang, F.; Chen, K.-S.; Yip, H.-L.; Hau, S. K.; Acton, O.; Zhang, Y.; Luo, J.; Jen, A. K. Y. *J. Am. Chem. Soc.* **2009**, 131 (39), 13886–13887.
- (81) Duan, C.; Chen, K.-S.; Huang, F.; Yip, H.-L.; Liu, S.; Zhang, J.; Jen, A. K. Y.; Cao, Y. *Chem. Mater.* **2010**, 22 (23), 6444–6452.
- (82) Cravino, A.; Sariciftci, N. S. *J. Mater. Chem.* **2002**, 12 (7), 1931–1943.
- (83) Giacalone, F.; Martín, N. *Chem. Rev. (Washington, DC, U. S.)* **2006**, 106 (12), 5136–5190.
- (84) Ramos, A. M.; Rispens, M. T.; van Duren, J. K. J.; Hummelen, J. C.; Janssen, R. A. J. *J. Am. Chem. Soc.* **2001**, 123 (27), 6714–6715.
- (85) Yang, C.; Li, H.; Sun, Q.; Qiao, J.; Li, Y.; Li, Y.; Zhu, D. *Sol. Energy Mater. Sol. Cells* **2005**, 85 (2), 241–249.

- (86) Tan, Z. a.; Hou, J.; He, Y.; Zhou, E.; Yang, C.; Li, Y. *Macromolecules* **2007**, *40* (6), 1868–1873.
- (87) Martín, N.; Sánchez, L.; Herranz, M. a. Á.; Illescas, B.; Guldi, D. M. *Acc. Chem. Res.* **2007**, *40* (10), 1015–1024.
- (88) Hirayama, D.; Takimiya, K.; Aso, Y.; Otsubo, T.; Hasobe, T.; Yamada, H.; Imahori, H.; Fukuzumi, S.; Sakata, Y. *J. Am. Chem. Soc.* **2002**, *124* (4), 532–533.
- (89) Miyanishi, S.; Zhang, Y.; Tajima, K.; Hashimoto, K. *Chem. Commun. (Cambridge, U. K.)* **2010**, *46* (36), 6723–6725.
- (90) Cravino, A.; Sariciftci, N. S. *Nature Mater.* **2003**, *2* (6), 360–361.
- (91) Roncali, J. *Adv. Energy Mater.* **2011**, *1* (2), 147–160.
- (92) Svensson, M.; Zhang, F.; Veenstra, S. C.; Verhees, W. J. H.; Hummelen, J. C.; Kroon, J. M.; Inganäs, O.; Andersson, M. R. *Adv. Mater.* **2003**, *15* (12), 988–991.
- (93) Peet, J.; Kim, J. Y.; Coates, N. E.; Ma, W. L.; Moses, D.; Heeger, A. J.; Bazan, G. C. *Nature Mater.* **2007**, *6* (7), 497–500.
- (94) Price, S. C.; Stuart, A. C.; You, W. *Macromolecules* **2010**, *43* (2), 797–804.
- (95) Svensson, M. *Synth. Met.* **2003**, *135–136*, 137–138.
- (96) Hsu, S. L.-C.; Lin, Y.-C.; Lee, R.-F.; Sivakumar, C.; Chen, J.-S.; Chou, W.-Y. *J. Polym. Sci., Part A: Polym. Chem.* **2009**, *47* (20), 5336–5343.
- (97) Kreyenschmidt, M.; Klaerner, G.; Fuhrer, T.; Ashenurst, J.; Karg, S.; Chen, W. D.; Lee, V. Y.; Scott, J. C.; Miller, R. D. *Macromolecules* **1998**, *31* (4), 1099–1103.
- (98) Yohannes, T.; Zhang, F.; Svensson, M.; Hummelen, J. C.; Andersson, M. R.; Inganäs, O. *Thin Solid Films* **2004**, *449* (1–2), 152–157.
- (99) Inganäs, O.; Zhang, F.; Andersson, M. R. *Acc. Chem. Res.* **2009**, *42* (11), 1731–1739.
- (100) Yang, R.; Tian, R.; Yan, J.; Zhang, Y.; Yang, J.; Hou, Q.; Yang, W.; Zhang, C.; Cao, Y. *Macromolecules* **2005**, *38* (2), 244–253.
- (101) Janietz, S.; Krueger, H.; Schleiermacher, H.-F.; Würfel, U.; Niggemann, M. *Macromol. Chem. Phys.* **2009**, *210* (18), 1493–1503.
- (102) Li, W.; Qin, R.; Zhou, Y.; Andersson, M.; Li, F.; Zhang, C.; Li, B.; Liu, Z.; Bo, Z.; Zhang, F. *Polymer* **2010**, *51* (14), 3031–3038.
- (103) Zhou, E.; Cong, J.; Yamakawa, S.; Wei, Q.; Nakamura, M.; Tajima, K.; Yang, C.; Hashimoto, K. *Macromolecules* **2010**, *43* (6), 2873–2879.
- (104) Mühlbacher, D.; Scharber, M.; Morana, M.; Zhu, Z.; Waller, D.; Gaudiana, R.; Brabec, C. *Adv. Mater.* **2006**, *18* (21), 2884–2889.
- (105) Moulé, A. J.; Tsami, A.; Bünnagel, T. W.; Forster, M.; Kronenberg, N. M.; Scharber, M.; Koppe, M.; Morana, M.; Brabec, C. J.; Meerholz, K.; Scherf, U. *Chem. Mater.* **2008**, *20* (12), 4045–4050.
- (106) Bijleveld, J. C.; Shahid, J.; Gilot, J.; Wienk, M. M.; Janssen, R. A. J. *Adv. Funct. Mater.* **2009**, *19* (20), 3262–3270.
- (107) Zhou, H.; Yang, L.; Price, S. C.; Knight, K. J.; You, W. *Angew. Chem., Int. Ed.* **2010**, *49* (43), 7992–7995.
- (108) Kudla, C. J.; Dolfen, D.; Schottler, K. J.; Koenen, J.-M.; Breusov, D.; Allard, S.; Scherf, U. *Macromolecules* **2010**, *43* (18), 7864–7867.
- (109) Wang, E.; Wang, L.; Lan, L.; Luo, C.; Zhuang, W.; Peng, J.; Cao, Y. *Appl. Phys. Lett.* **2008**, *92* (3), 033307–033310.
- (110) Zhou, E.; Wei, Q.; Yamakawa, S.; Zhang, Y.; Tajima, K.; Yang, C.; Hashimoto, K. *Macromolecules* **2009**, *42* (2), 821–826.
- (111) Allard, N.; Aich, R. d. B.; Gendron, D.; Boudreault, P.-L. T.; Tessier, C.; Alem, S.; Tse, S.-C.; Tao, Y.; Leclerc, M. *Macromolecules* **2010**, *43* (5), 2328–2333.
- (112) Scharber, M. C.; Koppe, M.; Gao, J.; Cordella, F.; Loi, M. A.; Denk, P.; Morana, M.; Egelhaaf, H.-J.; Forberich, K.; Dennler, G.; Gaudiana, R.; Waller, D.; Zhu, Z.; Shi, X.; Brabec, C. J. *Adv. Mater.* **2010**, *22* (3), 367–370.
- (113) Morana, M.; Azimi, H.; Dennler, G.; Egelhaaf, H.-J.; Scharber, M.; Forberich, K.; Hauch, J.; Gaudiana, R.; Waller, D.; Zhu, Z.; Hingerl, K.; van Bavel, S. S.; Loos, J.; Brabec, C. J. *Adv. Funct. Mater.* **2010**, *20* (7), 1180–1188.
- (114) Veldman, D.; ipek, O. z.; Meskers, S. C. J.; Sweelssen, J. r.; Koetse, M. M.; Veenstra, S. C.; Kroon, J. M.; Bavel, S. S. v.; Loos, J.; Janssen, R. A. J. *J. Am. Chem. Soc.* **2008**, *130* (24), 7721–7735.
- (115) Boudreault, P.-L. T.; Michaud, A.; Leclerc, M. *Macromol. Rapid Commun.* **2007**, *28* (22), 2176–2179.
- (116) Zhou, E.; Nakamura, M.; Nishizawa, T.; Zhang, Y.; Wei, Q.; Tajima, K.; Yang, C.; Hashimoto, K. *Macromolecules* **2008**, *41* (22), 8302–8305.
- (117) Liu, J.; Zhang, R.; Sauvè, G. v.; Kowalewski, T.; McCullough, R. D. *J. Am. Chem. Soc.* **2008**, *130* (39), 13167–13176.
- (118) Zhou, E.; Yamakawa, S.; Tajima, K.; Yang, C.; Hashimoto, K. *Chem. Mater.* **2009**, *21* (17), 4055–4061.
- (119) Morin, J.-F.; Leclerc, M.; Adès, D.; Siove, A. *Macromol. Rapid Commun.* **2005**, *26* (10), 761–778.
- (120) Drolet, N.; Morin, J. F.; Leclerc, N.; Wakim, S.; Tao, Y.; Leclerc, M. *Adv. Funct. Mater.* **2005**, *15* (10), 1671–1682.
- (121) Blouin, N.; Leclerc, M. *Acc. Chem. Res.* **2008**, *41* (9), 1110–1119.
- (122) Chen, C.-P.; Chan, S.-H.; Chao, T.-C.; Ting, C.; Ko, B.-T. *J. Am. Chem. Soc.* **2008**, *130* (38), 12828–12833.
- (123) Roncali, J. *Macromol. Rapid Commun.* **2007**, *28* (17), 1761–1775.
- (124) Brédas, J. L.; Calbert, J. P.; da Silva Filho, D. A.; Cornil, J. *Proc. Natl. Acad. Sci. U. S. A.* **2002**, *99* (9), 5804–5809.
- (125) Ando, S.; Nishida, J.-i.; Tada, H.; Inoue, Y.; Tokito, S.; Yamashita, Y. *J. Am. Chem. Soc.* **2005**, *127* (15), 5336–5337.
- (126) Baek, N. S.; Hau, S. K.; Yip, H.-L.; Acton, O.; Chen, K.-S.; Jen, A. K. Y. *Chem. Mater.* **2008**, *20* (18), 5734–5736.
- (127) Wu, J.-S.; Cheng, Y.-J.; Dubosc, M.; Hsieh, C.-H.; Chang, C.-Y.; Hsu, C.-S. *Chem. Commun. (Cambridge, U. K.)* **2010**, *46* (19), 3259–3261.
- (128) Song, S.; Jin, Y.; Kim, S. H.; Moon, J.; Kim, K.; Kim, J. Y.; Park, S. H.; Lee, K.; Suh, H. *Macromolecules* **2008**, *41* (20), 7296–7305.
- (129) Chen, Y.-C.; Yu, C.-Y.; Fan, Y.-L.; Hung, L.-L.; Chen, C.-P.; Ting, C. *Chem. Commun. (Cambridge, U. K.)* **2010**, *46* (35), 6503–6505.
- (130) Hale, G. D.; Oldenburg, S. J.; Halas, N. J. *Appl. Phys. Lett.* **1997**, *71* (11), 1483–1485.
- (131) Cumpston, B. H.; Jensen, K. F. *Synth. Met.* **1995**, *73* (3), 195–199.
- (132) Wang, J.-Y.; Hau, S. K.; Yip, H.-L.; Davies, J. A.; Chen, K.-S.; Zhang, Y.; Sun, Y.; Jen, A. K. Y. *Chem. Mater.* **2011**, *23* (3), 765–767.
- (133) Chen, C. H.; Cheng, Y. J.; Dubosc, M.; Hsieh, C. H.; Chu, C. C.; Hsu, C. S. *Chem.—Asian J.* **2010**, *5* (12), 2483–92.
- (134) Xia, Y.; Su, X.; He, Z.; Ren, X.; Wu, H.; Cao, Y.; Fan, D. *Macromol. Rapid Commun.* **2010**, *31* (14), 1287–1292.
- (135) Lee, T. W.; Kang, N. S.; Yu, J. W.; Hoang, M. H.; Kim, K. H.; Jin, J.-I.; Choi, D. H. *J. Polym. Sci., Part A: Polym. Chem.* **2010**, *48* (24), 5921–5929.
- (136) Zhou, E.; Yamakawa, S.; Zhang, Y.; Tajima, K.; Yang, C.; Hashimoto, K. *J. Mater. Chem.* **2009**, *19* (41), 7730–7737.
- (137) Lu, J.; Liang, F.; Drolet, N.; Ding, J.; Tao, Y.; Movileanu, R. *Chem. Commun. (Cambridge, U. K.)* **2008**, *44* (42), 5315–5317.
- (138) Yu, C.-Y.; Chen, C.-P.; Chan, S.-H.; Hwang, G.-W.; Ting, C. *Chem. Mater.* **2009**, *21* (14), 3262–3269.
- (139) Xiao, S.; Stuart, A. C.; Liu, S.; Zhou, H.; You, W. *Adv. Funct. Mater.* **2010**, *20* (4), 635–643.
- (140) Coropceanu, V.; Kwon, O.; Wex, B.; Kaafarani, B. R.; Gruhn, N. E.; Durivage, J. C.; Neckers, D. C.; Brédas, J.-L. *Chem.—Eur. J.* **2006**, *12* (7), 2073–2080.
- (141) Xiao, S.; Zhou, H.; You, W. *Macromolecules* **2008**, *41* (15), 5688–5696.
- (142) Osaka, I.; Abe, T.; Shinamura, S.; Miyazaki, E.; Takimiya, K. *J. Am. Chem. Soc.* **2010**, *132* (14), 5000–5001.
- (143) Laquindanum, J. G.; Katz, H. E.; Lovinger, A. J. *J. Am. Chem. Soc.* **1998**, *120* (4), 664–672.
- (144) Jiang, Y.; Okamoto, T.; Becerril, H. A.; Hong, S.; Tang, M. L.; Mayer, A. C.; Parmer, J. E.; McGehee, M. D.; Bao, Z. *Macromolecules* **2010**, *43* (15), 6361–6367.

- (145) Umeda, R.; Fukuda, H.; Miki, K.; Rahman, S. M. A.; Sonoda, M.; Tobe, Y. C. R. *Chim.* **2009**, *12* (3–4), 378–384.
- (146) Loser, S.; Bruns, C. J.; Miyauchi, H.; Ortiz, R. O. P.; Facchetti, A.; Stupp, S. I.; Marks, T. J. *J. Am. Chem. Soc.* **2011**, *133* (21), 8142–8145.
- (147) Mayer, A. C.; Toney, M. F.; Scully, S. R.; Rivnay, J.; Brabec, C. J.; Scharber, M.; Koppe, M.; Heeney, M.; McCulloch, I.; McGehee, M. D. *Adv. Funct. Mater.* **2009**, *19* (8), 1173–1179.
- (148) Cates, N. C.; Gysel, R.; Dahl, J. E. P.; Sellinger, A.; McGehee, M. D. *Chem. Mater.* **2010**, *22* (11), 3543–3548.
- (149) Xiao, S.; Stuart, A. C.; Liu, S.; You, W. *ACS Appl. Mater. Interfaces* **2009**, *1* (7), 1613–1621.
- (150) Osaka, I.; Abe, T.; Shinamura, S.; Takimiya, K. *J. Am. Chem. Soc.* **2011**, *133* (17), 6852–6860.
- (151) Shinamura, S.; Osaka, I.; Miyazaki, E.; Nakao, A.; Yamagishi, M.; Takeya, J.; Takimiya, K. *J. Am. Chem. Soc.* **2011**, *133* (13), 5024–5035.
- (152) Rieger, R.; Beckmann, D.; Pisula, W.; Steffen, W.; Kastler, M.; Müllen, K. *Adv. Mater.* **2010**, *22* (1), 83–86.
- (153) Rieger, R.; Beckmann, D.; Mavrinskiy, A.; Kastler, M.; Müllen, K. *Chem. Mater.* **2010**, *22* (18), 5314–5318.
- (154) Hou, J.; Chen, H.-Y.; Zhang, S.; Li, G.; Yang, Y. *J. Am. Chem. Soc.* **2008**, *130* (48), 16144–16145.
- (155) Blouin, N.; Michaud, A.; Leclerc, M. *Adv. Mater.* **2007**, *19* (17), 2295–2300.
- (156) Blouin, N.; Michaud, A.; Gendron, D.; Wakim, S.; Blair, E.; Neagu-Plesu, R.; Belletete, M.; Durocher, G.; Tao, Y.; Leclerc, M. *J. Am. Chem. Soc.* **2008**, *130* (2), 732–742.
- (157) Slooff, L. H.; Veenstra, S. C.; Kroon, J. M.; Moet, D. J. D.; Sweelssen, J.; Koetse, M. M. *Appl. Phys. Lett.* **2007**, *90* (14), 143506.
- (158) Kline, R. J.; McGehee, M. D.; Kadnikova, E. N.; Liu, J.; Fréchet, J. M. J.; Toney, M. F. *Macromolecules* **2005**, *38* (8), 3312–3319.
- (159) Zhou, H.; Yang, L.; Xiao, S.; Liu, S.; You, W. *Macromolecules* **2010**, *43* (2), 811–820.
- (160) Wang, X.; Perzon, E.; Mammo, W.; Oswald, F.; Admassie, S.; Persson, N.-K.; Langa, F.; Andersson, M. R.; Inganäs, O. *Thin Solid Films* **2006**, *511–512* (1), 576–580.
- (161) Tsai, J.-H.; Chueh, C.-C.; Lai, M.-H.; Wang, C.-F.; Chen, W.-C.; Ko, B.-T.; Ting, C. *Macromolecules* **2009**, *42* (6), 1897–1905.
- (162) Lee, J.-Y.; Shin, W.-S.; Haw, J.-R.; Moon, D.-K. *J. Mater. Chem.* **2009**, *19* (28), 4938–4945.
- (163) Padhy, H.; Huang, J.-H.; Sahu, D.; Patra, D.; Kekuda, D.; Chu, C.-W.; Lin, H.-C. *J. Polym. Sci., Part A: Polym. Chem.* **2010**, *48* (21), 4823–4834.
- (164) Yang, R.; Tian, R.; Hou, Q.; Yang, W.; Cao, Y. *Macromolecules* **2003**, *36* (20), 7453–7460.
- (165) Hou, J.; Chen, T. L.; Zhang, S.; Yang, Y. *J. Phys. Chem. C* **2009**, *113* (4), 1601–1605.
- (166) Jung, I. H.; Kim, H.; Park, M.-J.; Kim, B.; Park, J.-H.; Jeong, E.; Woo, H. Y.; Yoo, S.; Shim, H.-K. *J. Polym. Sci., Part A: Polym. Chem.* **2010**, *48* (6), 1423–1432.
- (167) Li, Z.; Ding, J.; Song, N.; Lu, J.; Tao, Y. *J. Am. Chem. Soc.* **2010**, *132* (38), 13160–13161.
- (168) Wang, E.; Ma, Z.; Zhang, Z.; Henriksson, P.; Inganäs, O.; Zhang, F.; Andersson, M. R. *Chem. Commun. (Cambridge, U. K.)* **2011**, *47* (17), 4908–4910.
- (169) Bijleveld, J. C.; Gevaerts, V. S.; Di, N. D.; Turbiez, M.; Mathijssen, S. G. J.; de, L. D. M.; Wienk, M. M.; Janssen, R. A. J. *Adv. Mater.* **2010**, *22* (35), E242–E246.
- (170) Liu, B.; Zou, Y.; Peng, B.; Zhao, B.; Huang, K.; He, Y.; Pan, C. *Polym. Chem.* **2011**, *2* (5), 1156–1162.
- (171) Mei, J.; Graham, K. R.; Stalder, R.; Reynolds, J. R. *Org. Lett.* **2010**, *12* (4), 660–663.
- (172) Wienk, M. M.; Turbiez, M.; Gilot, J.; Janssen, R. A. J. *Adv. Mater.* **2008**, *20* (13), 2556–2560.
- (173) Zou, Y.; Gendron, D.; Badrou-Aïch, R. d.; Najari, A.; Tao, Y.; Leclerc, M. *Macromolecules* **2009**, *42* (8), 2891–2894.
- (174) Huo, L.; Hou, J.; Chen, H.-Y.; Zhang, S.; Jiang, Y.; Chen, T. L.; Yang, Y. *Macromolecules* **2009**, *42* (17), 6564–6571.
- (175) Woo, C. H.; Beaujuge, P. M.; Holcombe, T. W.; Lee, O. P.; Frechet, J. M. J. *J. Am. Chem. Soc.* **2010**, *132* (44), 15547–15549.
- (176) Bronstein, H.; Chen, Z.; Ashraf, R. S.; Zhang, W.; Du, J.; Durrant, J. R.; Shukla, T. P.; Song, K.; Watkins, S. E.; Geerts, Y.; Wienk, M. M.; Janssen, R. A. J.; Anthopoulos, T.; Sirringhaus, H.; Heeney, M.; McCulloch, I. *J. Am. Chem. Soc.* **2011**, *133* (10), 3272–3275.
- (177) Zou, Y.; Najari, A.; Berrouard, P.; Beaupre, S.; Reda, A. B.; Tao, Y.; Leclerc, M. *J. Am. Chem. Soc.* **2010**, *132* (15), 5330–5331.
- (178) Zhang, Y.; Hau, S. K.; Yip, H.-L.; Sun, Y.; Acton, O.; Jen, A. K. Y. *Chem. Mater.* **2010**, *22* (9), 2696–2698.
- (179) Zhang, G.; Fu, Y.; Zhang, Q.; Xie, Z. *Chem. Commun. (Cambridge, U. K.)* **2010**, *46* (27), 4997–4999.
- (180) Piliago, C.; Holcombe, T. W.; Douglas, J. D.; Woo, C. H.; Beaujuge, P. M.; Frechet, J. M. J. *J. Am. Chem. Soc.* **2010**, *132* (22), 7595–7597.
- (181) Li, Z.; Tsang, S.-W.; Du, X.; Scoles, L.; Robertson, G.; Zhang, Y.; Toll, F.; Tao, Y.; Lu, J.; Ding, J. *Adv. Funct. Mater.* **2011**, *21* (17), 3331–3336.
- (182) Bundgaard, E.; Krebs, F. C. *Macromolecules* **2006**, *39* (8), 2823–2831.
- (183) Perzon, E.; Wang, X.; Zhang, F.; Mammo, W.; Delgado, J. L.; de la Cruz, P.; Inganäs, O.; Langa, F.; Andersson, M. R. *Synth. Met.* **2005**, *154* (1–3), 53–56.
- (184) Wang, X.; Perzon, E.; Delgado, J. L.; de la Cruz, P.; Zhang, F.; Langa, F.; Andersson, M.; Inganäs, O. *Appl. Phys. Lett.* **2004**, *85* (21), 5081–5083.
- (185) Zhang, F.; Bijleveld, J.; Perzon, E.; Tvingstedt, K.; Barrau, S.; Inganäs, O.; Andersson, M. R. *J. Mater. Chem.* **2008**, *18* (45), 5468–5474.
- (186) Gendron, D.; Morin, P.-O.; Najari, A.; Leclerc, M. *Macromol. Rapid Commun.* **2010**, *31* (12), 1090–1094.
- (187) Brédas, J. L.; Heeger, A. J. *Chem. Phys. Lett.* **1994**, *217* (5–6), 507–512.
- (188) Helbig, M.; Hörhold, H.-H. *Makromol. Chem.* **1993**, *194* (6), 1607–1618.
- (189) Greenham, N. C.; Moratti, S. C.; Bradley, D. D. C.; Friend, R. H.; Holmes, A. B. *Nature (London, U. K.)* **1993**, *365* (6447), 628–630.
- (190) Wong, S.; Ma, H.; Jen, A. K. Y.; Barto, R.; Frank, C. W. *Macromolecules* **2003**, *36* (21), 8001–8007.
- (191) Reichenbacher, K.; Suss, H. I.; Hulliger, J. *Chem. Soc. Rev.* **2005**, *34* (1), 22–30.
- (192) Pagliaro, M.; Ciriminna, R. *J. Mater. Chem.* **2005**, *15* (47), 4981–4991.
- (193) Wang, Y.; Parkin, S. R.; Gierschner, J.; Watson, M. D. *Org. Lett.* **2008**, *10* (15), 3307–3310.
- (194) Liang, Y.; Feng, D.; Wu, Y.; Tsai, S.-T.; Li, G.; Ray, C.; Yu, L. *J. Am. Chem. Soc.* **2009**, *131* (22), 7792–7799.
- (195) Liang, Y.; Yu, L. *Acc. Chem. Res.* **2010**, *43* (9), 1227–1236.
- (196) Cho, S.; Seo, J. H.; Kim, S. H.; Song, S.; Jin, Y.; Lee, K.; Suh, H.; Heeger, A. J. *Appl. Phys. Lett.* **2008**, *93* (26), 263301–263303.
- (197) Jayakannan, M.; Van Hal, P. A.; Janssen, R. A. J. *J. Polym. Sci., Part A: Polym. Chem.* **2002**, *40* (2), 251–261.
- (198) Karikomi, M.; Kitamura, C.; Tanaka, S.; Yamashita, Y. *J. Am. Chem. Soc.* **2002**, *117* (25), 6791–6792.
- (199) Wang, E.; Wang, M.; Wang, L.; Duan, C.; Zhang, J.; Cai, W.; He, C.; Wu, H.; Cao, Y. *Macromolecules* **2009**, *42* (13), 4410–4415.
- (200) Gadisa, A.; Oosterbaan, W. D.; Vandewal, K.; Bolsée, J.-C.; Bertho, S.; D’Haen, J.; Lutsen, L.; Vanderzande, D.; Manca, J. V. *Adv. Funct. Mater.* **2009**, *19* (20), 3300–3306.
- (201) Egbe, D. A. M.; Türk, S.; Rathgeber, S.; Kühnlenz, F.; Jadhav, R.; Wild, A.; Birkner, E.; Adam, G.; Pivrikas, A.; Cimrova, V.; Knör, G. n.; Sariciftci, N. S.; Hoppe, H. *Macromolecules* **2010**, *43* (3), 1261–1269.

- (202) Szarko, J. M.; Guo, J.; Liang, Y.; Lee, B.; Rolczynski, B. S.; Strzalka, J.; Xu, T.; Loser, S.; Marks, T. J.; Yu, L.; Chen, L. X. *Adv. Mater.* **2010**, *22* (48), 5468–5472.
- (203) Shi, C. J.; Yao, Y.; Yang, Y.; Pei, Q. B. *J. Am. Chem. Soc.* **2006**, *128* (27), 8980–8986.
- (204) Hou, J.; Chen, H.-Y.; Zhang, S.; Yang, Y. *J. Phys. Chem. C* **2009**, *113* (50), 21202–21207.
- (205) Hou, J.; Chen, H.-Y.; Zhang, S.; Chen, R. L.; Yang, Y.; Wu, Y.; Li, G. *J. Am. Chem. Soc.* **2009**, *131* (43), 15586–15587.
- (206) Price, S. C.; Stuart, A. C.; You, W. *Macromolecules* **2010**, *43* (10), 4609–4612.
- (207) Bagnis, D.; Beverina, L.; Huang, H.; Silvestri, F.; Yao, Y.; Yan, H.; Pagani, G. A.; Marks, T. J.; Facchetti, A. *J. Am. Chem. Soc.* **2010**, *132* (12), 4074–4075.
- (208) Clarke, T. M.; Durrant, J. R. *Chem. Rev. (Washington, DC, U. S.)* **2010**, *110* (11), 6736–6767.
- (209) Zhu, X. Y.; Yang, Q.; Muntwiler, M. *Acc. Chem. Res.* **2009**, *42* (11), 1779–1787.
- (210) Deibel, C.; Dyakonov, V. *Rep. Prog. Phys.* **2010**, *73* (9), 096401.
- (211) Peet, J.; Heeger, A. J.; Bazan, G. C. *Acc. Chem. Res.* **2009**, *42* (11), 1700–1708.
- (212) Peet, J.; Senatore, M. L.; Heeger, A. J.; Bazan, G. C. *Adv. Mater.* **2009**, *21* (14–15), 1521–1527.
- (213) Moulé, A. J.; Meerholz, K. *Adv. Funct. Mater.* **2009**, *19* (19), 3028–3036.
- (214) van Bavel, S.; Veenstra, S.; Loos, J. *Macromol. Rapid Commun.* **2010**, *31* (21), 1835–1845.
- (215) Groves, C.; Reid, O. G.; Ginger, D. S. *Acc. Chem. Res.* **2010**, *43* (5), 612–620.
- (216) Chen, L.-M.; Hong, Z.; Li, G.; Yang, Y. *Adv. Mater.* **2009**, *21* (14–15), 1434–1449.
- (217) Huo, L.; Zhang, S.; Guo, X.; Xu, F.; Li, Y.; Hou, J. *Angew. Chem., Int. Ed.* **2011**, *50* (41), 9697–9702.
- (218) Kotlarski, J. D.; Blom, P. W. M. *Appl. Phys. Lett.* **2011**, *98* (5), 053301–053303.
- (219) <http://www.flisom.ch/>.
- (220) <http://www.q-cells.com/en/index.html>.
- (221) Hou, J.; Tan, Z. a.; Yan, Y.; He, Y.; Yang, C.; Li, Y. *J. Am. Chem. Soc.* **2006**, *128* (14), 4911–4916.
- (222) Zhou, E.; Cong, J.; Wei, Q.; Tajima, K.; Yang, C.; Hashimoto, K. *Angew. Chem., Int. Ed.* **2011**, *50* (12), 2799–2803.
- (223) Schlenker, C. W.; Thompson, M. E. *Chem. Commun. (Cambridge, U. K.)* **2011**, 47 (13), 3702–3716.
- (224) Brunetti, F. G.; Gong, X.; Tong, M.; Heeger, A. J.; Wudl, F. *Angew. Chem., Int. Ed.* **2010**, *49* (3), 532–536.
- (225) Gong, X.; Tong, M.; Brunetti, F. G.; Seo, J.; Sun, Y.; Moses, D.; Wudl, F.; Heeger, A. J. *Adv. Mater.* **2011**, *23* (20), 2272–2277.
- (226) Street, R. A. *Appl. Phys. Lett.* **2008**, *93* (13), 133308–133311.
- (227) Varotto, A.; Treat, N. D.; Jo, J.; Shuttle, C. G.; Batará, N. A.; Brunetti, F. G.; Seo, J. H.; Chabinyc, M. L.; Hawker, C. J.; Heeger, A. J.; Wudl, F. *Angew. Chem., Int. Ed.* **2011**, *50* (22), 5166–5169.
- (228) Brabec, C. J.; Heeney, M.; McCulloch, I.; Nelson, J. *Chem. Soc. Rev.* **2011**, *40* (3), 1185–1199.
- (229) Cates, N. C.; Gysel, R.; Bailey, Z.; Miller, C. E.; Toney, M. F.; Heeney, M.; McCulloch, I.; McGehee, M. D. *Nano Lett.* **2009**, *9* (12), 4153–4157.
- (230) Steim, R.; Kogler, F. R.; Brabec, C. J. *J. Mater. Chem.* **2010**, *20* (13), 2499–2512.
- (231) Chen, L.-M.; Xu, Z.; Hong, Z.; Yang, Y. *J. Mater. Chem.* **2010**, *20* (13), 2575–2598.
- (232) Irwin, M. D.; Buchholz, D. B.; Hains, A. W.; Chang, R. P. H.; Marks, T. J. *Proc. Natl. Acad. Sci. U. S. A.* **2008**, *105* (8), 2783–2787.
- (233) Sun, Y.; Takacs, C. J.; Cowan, S. R.; Seo, J. H.; Gong, X.; Roy, A.; Heeger, A. J. *Adv. Mater.* **2011**, *23* (19), 2226–2230.
- (234) Subbiah, J.; Kim, D. Y.; Hartel, M.; So, F. *Appl. Phys. Lett.* **2010**, *96* (6), 063303–063306.
- (235) Kröger, M.; Hamwi, S.; Meyer, J.; Riedl, T.; Kowalsky, W.; Kahn, A. *Appl. Phys. Lett.* **2009**, *95* (12), 123301–123304.
- (236) Tao, C.; Ruan, S. P.; Xie, G. H.; Kong, X. Z.; Shen, L.; Meng, F. X.; Liu, C. X.; Zhang, X. D.; Dong, W.; Chen, W. Y. *Appl. Phys. Lett.* **2009**, *94* (4), 043311–043314.
- (237) Meyer, J.; Kroger, M.; Hamwi, S.; Gnam, F.; Riedl, T.; Kowalsky, W.; Kahn, A. *Appl. Phys. Lett.* **2010**, *96* (19), 193302–193305.
- (238) Hayakawa, A.; Yoshikawa, O.; Fujieda, T.; Uehara, K.; Yoshikawaa, S. *Appl. Phys. Lett.* **2007**, *90* (16), 163517–163520.
- (239) Sun, Y.; Seo, J. H.; Takacs, C. J.; Seifert, J.; Heeger, A. J. *Adv. Mater.* **2011**, *23* (14), 1679–1683.
- (240) Yip, H.-L.; Hau, S. K.; Baek, N. S.; Ma, H.; Jen, A. K. Y. *Adv. Mater.* **2008**, *20* (12), 2376–2382.
- (241) Bulliard, X.; Ihn, S.-G.; Yun, S.; Kim, Y.; Choi, D.; Choi, J.-Y.; Kim, M.; Sim, M.; Park, J.-H.; Choi, W.; Cho, K. *Adv. Funct. Mater.* **2010**, *20* (24), 4381–4387.
- (242) Chang, C.-Y.; Wu, C.-E.; Chen, S.-Y.; Cui, C.; Cheng, Y.-J.; Hsu, C.-S.; Wang, Y.-L.; Li, Y. *Angew. Chem., Int. Ed.* **2011**, *50* (40), 9386–9390.
- (243) Ameri, T.; Dennler, G.; Waldauf, C.; Azimi, H.; Seemann, A.; Forberich, K.; Hauch, J.; Scharber, M.; Hingerl, K.; Brabec, C. J. *Adv. Funct. Mater.* **2010**, *20* (10), 1592–1598.
- (244) Ko, D.-H.; Tumbleston, J. R.; Zhang, L.; Williams, S.; DeSimone, J. M.; Lopez, R.; Samulski, E. T. *Nano Lett.* **2009**, *9* (7), 2742–2746.
- (245) Hadipour, A.; de Boer, B.; Blom, P. W. M. *Adv. Funct. Mater.* **2008**, *18* (2), 169–181.
- (246) Hu, L.; Hecht, D. S.; Grüner, G. *Nano Lett.* **2004**, *4* (12), 2513–2517.
- (247) Wu, Z.; Chen, Z.; Du, X.; Logan, J. M.; Sippel, J.; Nikolou, M.; Kamaras, K.; Reynolds, J. R.; Tanner, D. B.; Hebard, A. F.; Rinzler, A. G. *Science (Washington, DC, U. S.)* **2004**, *305* (5688), 1273–1276.
- (248) Zhang, M.; Fang, S.; Zakhidov, A. A.; Lee, S. B.; Aliev, A. E.; Williams, C. D.; Atkinson, K. R.; Baughman, R. H. *Science (Washington, DC, U. S.)* **2005**, *309* (5738), 1215–1219.
- (249) Li, J.; Hu, L.; Wang, L.; Zhou, Y.; Grüner, G.; Marks, T. J. *Nano Lett.* **2006**, *6* (11), 2472–2477.
- (250) Miller, A. J.; Hatton, R. A.; Silva, S. R. P. *Appl. Phys. Lett.* **2006**, *89* (13), 133117–133120.
- (251) Rowell, M. W.; Topinka, M. A.; McGehee, M. D.; Prall, H.-J.; Dennler, G.; Sariciftci, N. S.; Hu, L.; Gruner, G. *Appl. Phys. Lett.* **2006**, *88* (23), 233506–233509.
- (252) Eda, G.; Fanchini, G.; Chhowalla, M. *Nature Nanotechnol.* **2008**, *3* (5), 270–274.
- (253) Kim, K. S.; Zhao, Y.; Jang, H.; Lee, S. Y.; Kim, J. M.; Kim, K. S.; Ahn, J.-H.; Kim, P.; Choi, J.-Y.; Hong, B. H. *Nature (London, U. K.)* **2009**, *457* (7230), 706–710.
- (254) Gomez De Arco, L.; Zhang, Y.; Schlenker, C. W.; Ryu, K.; Thompson, M. E.; Zhou, C. *ACS Nano* **2010**, *4* (5), 2865–2873.
- (255) Gaynor, W.; Burkhard, G. F.; McGehee, M. D.; Peumans, P. *Adv. Mater.* **2011**, *23* (26), 2905–2910.
- (256) Yang, L.; Zhang, T.; Zhou, H.; Price, S. C.; Wiley, B. J.; You, W. *ACS Appl. Mater. Interfaces* **2011**, *3* (10), 4075–4084.
- (257) <http://www.konarka.com/>.

Synthesis, Properties, and Processing of New Siloxane-Substituted Poly(*p*-xylylene) via CVD

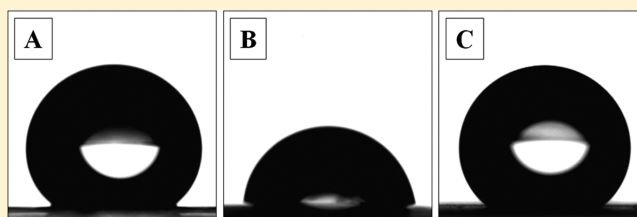
Anna K. Bier, Michael Bognitzki, Alexander Schmidt, and Andreas Greiner*

Fachbereich Chemie und Wissenschaftliches Zentrum für Materialwissenschaften, Philipps-Universität Marburg, Hans-Meerwein Strasse, D-35032, Marburg, Germany

Emanuela Gallo, Patrick Klack, and Bernhard Schartel

6.35 Flammenschutz von Polymeren, BAM Federal Institute for Materials Research and Testing, Unter den Eichen 87, 12205 Berlin, Germany

ABSTRACT: The synthesis of a disiloxane-functionalized [2.2]paracyclophane and its polymerization to the corresponding siloxane-substituted poly(*p*-xylylene) via chemical vapor deposition (CVD) has been described. Because of the enhanced solubility of the siloxane substituted poly(*p*-xylylene) analysis of the molecular structure by NMR, molecular weight, and polydispersity by gel permeation chromatography (GPC), and processing by film casting as well as nanofiber formation by electrospinning was possible. Structural isomers were found by NMR which was expected due to the isomeric mixture of the precursor. High molecular weights at moderate polydispersities were found by GPC which was unexpected for a vapor phase deposition polymerization. The amorphous morphology in combination with a low glass transition temperature led to high elongation at break for the siloxane substituted poly(*p*-xylylene). Significant difference for the wetting versus water was found for as-deposited films, solution cast films, and nanofibers obtained by electrospinning with contact angles up to 135° close to superhydrophobic behavior.



1. INTRODUCTION

Poly(*p*-xylylene)s (PPXs) form an important class of polymers which is in use as barrier coatings for packaging, medical, automotive, aerospace, and electronic applications.¹ The most important features are their biocompatibility, excellent insulation properties (in terms of the high dielectric constant), low dissipation factor, and high chemical and thermal stability, including excellent moisture barrier properties.²

In the technical process PPXs (trade name parylene) are obtained via chemical vapor deposition (CVD) using the so-called Gorham process.³ The vaporization of [2.2]paracyclophanes, followed by pyrolysis of these precursors at temperatures between 500 and 700 °C under reduced pressure yields quinodimethanes, which polymerize spontaneously on nearly any solid substrate at ambient temperatures.⁴ The final product of this process is a highly conformal pinhole free coating (coating thickness >0.7 μm⁵) of PPX on the given substrate. The main advantages of this process are solvent and initiator-free products, no side products, quantitative yields, and mild reaction temperatures.^{6,7} Although four precursors are commercially available the overall number of suitable precursors is limited and thereby the full potential of this interesting class of polymers with its unique combined process of polymerization and film formation cannot be fully exploited. Major limitations for new precursors are their volatility and the thermal stability of attached substituents.⁸ PPX derivatives from

[2.2]paracyclophanes equipped with iodine, bromine, ethyl, aminomethyl, cyano groups or different degrees of fluorination attracted some attention but were never commercialized.⁹

In the past few years, mainly surface techniques provided an easily applicable tool for changing the properties of inert PPX films. Plasma or (photo)chemical treatment hydrophilized the PPX surface by not well-defined functionalization, and these treatments were often accompanied by a loss of the characteristic optical and mechanical properties of the PPXs.¹⁰ Grafting techniques offer another easy access to surface functionalization but all benefits of the CVD process are lost by usage of catalysts and solvents.¹¹ Copolymerization of different functionalized [2.2]paracyclophanes or other vinylic copolymers led to either inhomogeneous films, undesired side reactions, or high contents of starting materials present in the obtained films.^{12–18}

For example film compositions using a monofunctionalized [2.2]paracyclophane can be changed by temperature controlled deposition, even a separated deposition of completely functionalized and unfunctionalized PPX is possible.^{3,13} Pyrolysis of monofunctionalized [2.2]paracyclophanes often does not lead to desired compositions of 50:50 e. g. for

Received: September 21, 2011

Revised: November 27, 2011

Published: December 27, 2011

poly(alkynyl-*p*-xylylene-*co-p*-xylylene) a composition of 80 to 20 for functionalized to unfunctionalized units was found.^{14,15} Easily different gradient copolymers can be formed¹⁶ but a copolymerization basically faces the same problems known for monofunctionalized [2.2]paracyclophanes used as starting materials in the CVD process because at least two different quinodimethanes (reactive species) with different deposition properties are present in the gaseous phase.

Using acrylic comonomers in CVD often leads to high amounts of unreacted acrylates deposited as liquid in the deposition chamber which have to be removed by annealing.¹⁷ Also the proper control of the film composition is hardly achieved¹⁷ or a gradient film can be formed instead.¹⁸ To avoid these problems often droplets of acrylic comonomer (low vapor pressure) are placed in the deposition chamber and a PPX film is polymerized on this substrate to form a surface functionalized film.¹⁹

Recently, the synthesis of various monofunctionalized [2.2]paracyclophanes has been successfully accomplished. Subsequent CVD led to a reactive coating material to which biomolecules or dyes could be attached.^{16,20} In these cases composition and homogeneity of the obtained film were often not well-defined or differed from the expected composition.^{14,15,21} Another tool for changing the surface properties was the growth of PPX nanorods by setting an angle of 15° (oblique angle) between the monomer flow and the substrate, which has been further developed to a powerful tool for engineered PPX films with unidirectional wetting properties.^{22,23} The field could surely be further developed with advanced PPX derivatives by CVD and by better characterization of molecular properties like molecular configuration, molecular weight, and polydispersity. Improved mechanical properties would be of importance for numerous coating applications typically for PPX coatings, e.g., stent coatings.

We wondered, whether the mechanical properties with respect to a drastic increase in strain at break could be achieved by bulky substituents at the PPX backbone. Our concept was to use siloxane substituents at the phenylene moieties, which otherwise also provide high inertness to bases and acids, insulation, and high thermal stability. Furthermore, it is expected, that siloxane substituents would hydrophobize PPX which has been shown previously for other materials, e.g., inorganic surfaces.²⁴ Another important outcome of such bulky substituents could be enhanced solubility of the resulting PPX derivatives, which could give chance for molecular weight analysis by GPC, which has not been done to for CVD-based PPX to the best of our knowledge. Although film formation indicate enhanced molecular weight of Gorham-type PPX the unusual polymerization of a solid-state type polymerization in combination with vapor deposition of a gaseous monomer raises interesting questions with respect to molecular chain growth, chain length, and molecular chain length distribution.

2. EXPERIMENTAL PART

2.1. Materials. Methyltriphenylphosphonium bromide (Fisher Scientific, 98%), sodium hydrogen carbonate (Fisher Scientific) magnesium sulfate (Acros, 97%), *n*-butyllithium (Sigma-Aldrich, 2.5 M solution in hexane), *s*-butyllithium (Sigma-Aldrich, 1.4 M solution in cyclohexane), propylene carbonate (Sigma-Aldrich, 99%), hydrochloric acid 37% (VWR, AnalaR Normapur), xylene (VWR, isomeric mixture, 98%), (Pt(0)-1,3-divinyl-1,1,3,3-tetramethylsiloxane complex (Karstedt catalyst) (Heraeus GmbH, 20% Pt in xylene), sodium chloride (Carl Roth), chloroform-*d*₁ (CDCl₃) (C. Roth, 99.8 atom % D) were

used as obtained. Tri-*o*-tolylphosphine was synthesized according to the literature.²⁵ THF, DMF, diethyl ether, and cyclohexane (BASF) were dried over phosphorus pentoxide and distilled prior to use. Hexane, toluene, and ethanol (BASF) were distilled prior to use.

2.2. Analytical Techniques. ¹H (400 MHz), ¹³C (100 MHz), and ²⁹Si NMR (100 MHz), ¹H,¹³C-HSQC, and ¹H,¹H-COSY spectra were recorded on a Bruker DRX 400 or Avance 300 A, respectively, at room temperature with CDCl₃ as solvent.

GPC analysis was performed with 5–10 mg of polymer (directly after pyrolysis) in 10 mL chloroform with toluene as the internal standard. The flow rate was 0.5 mL/min, and the setup included a Knauer Smartline 1000 pump, three SDV columns (pore size 1000; 100 000; 1 000 000 Å) from PSS and a Knauer Refractive Index Detector (RI 2300). Calibration was performed by using linear polystyrene purchased from PSS.

GC/MS measurements were done with a QP5050 A instrument from Shimadzu with a 30 m FS-SE-54-CB-0.25 column, electron ionization unit and helium as carrier gas. A program from 100 to 280 °C with a heating rate of 10 °C and an additional 20 min at 280 °C was chosen. The injection temperature was 300 °C and the interface temperature was maintained at 230 °C.

Mechanical properties were determined using a Zwick Roell BT-FRO.STN.D14 equipped with a KAF-TC load sensor. The samples were prepared with a Rayran manual press using a dogbone cutter ISO 5272-1BB. For cyclic measurements, grip-to-grip separation of 20 mm, test speed of 10 mm/min, and preload of 0.1 N was used. Elongation was 100% for each of the 25 cycles with 20 s between them. For elongation to break, a grip-to-grip separation of 20 mm, test speed of 25 mm/min, a starting speed of 1 mm/min and a preload of 0.1 N were used.

For differential scanning calorimetry (DSC), a 821 DSC module from Mettler calibrated with indium and zinc standards was used. Then, 10–15 mg of the sample was placed into a sealed aluminum pan and heated/cooled under nitrogen with a heating/cooling rate of 20 K/min. The glass transition temperature was taken at the inflection point of the observed shift of the baseline of the second heating run.

Thermogravimetric analysis was performed by means of a 851 TG module from Mettler under nitrogen atmosphere (flow rate: 50 mL/min), 10–12 mg of the sample was placed in an alumina crucible which was heated to 800 °C at a rate of 10 °C/min. Thermogravimetric analysis under synthetic air or nitrogen respectively with a flow of 30 mL/min and a temperature range between 25 and 900 °C were accomplished with a TGA 209 F1 from Netsch coupled with an IR Tensor 27 (4000–600 cm⁻¹) from Bruker and a mass spectrometer QMS 403C Aeolos from Netzsch (range: 0 to 140 *m/z*). In an alumina crucible 10 mg of the polymer was heated at a rate of 10 °C/min.

For static contact angle measurements the contact angle measurement System G10 from Krüss equipped with a CCD video camera module was used. For evaluation, 5–10 values were measured at different points of the sample surface.

Electrospinning of a 2.9 wt % solution of siloxane modified PPX, pyrolyzed at 500 °C in chloroform, led, due to the low conductivity, to fiber production with a narrow spinning area. The addition of 5 wt % of benzyltributylammonium bromide led to a broader spinning area. The best results were obtained using a high voltage (15 to 20 kV) of the cathode and with no voltage applied to the collector electrode at an electrode distance of 15 cm. The temperature was 18 °C, and the air humidity was 45%.

For IR measurements, an UMA 600 from Digilab with an ATR unit from Pike Miracle with diamond as the top plate was used.

SEM images were taken on a 7500F SEM from Jeol.

2.3. Precursor Synthesis. *Synthesis of 4,12-Diformyl[2.2]-paracyclophane (2).* A 2 L three-necked, round-bottom flask equipped with a dropping funnel and an argon inlet was filled with 46.13 g (126.00 mmol, 1.00 equiv) of **1** dissolved in 1.2 L of THF. The solution was stirred under argon at –65 °C then 300 mL (420.00 mmol, 3.33 equiv) of *s*-butyllithium solution (1.4 M) in cyclohexane was added dropwise. The solution immediately turned

orange. After stirring for 2 h at $-65\text{ }^{\circ}\text{C}$, 48.5 mL (630 mmol, 15 equiv) of dimethylformamide were added dropwise, and the solution was stirred without cooling for 1 h. The solution was washed three times with 400 mL of brine, twice with 400 mL of saturated sodium hydrogen carbonate solution and dried over magnesium sulfate. The solvent was removed under reduced pressure at $60\text{ }^{\circ}\text{C}$. The raw product was recrystallized from toluene to yield 26.64 g (108.00 mmol, 80%) of colorless crystals.

^1H NMR (300 MHz, CDCl_3): δ (ppm) = 9.93 (s, 2H), 7.04 (d, 2H, $J = 2.0$ Hz), 6.62 (2H, dd, $J = 2.0$ Hz, $J = 7.8$ Hz), 6.52 (d, 2H, $J = 7.8$ Hz), 4.17–4.08 (m, 2H), 3.32–3.24 (m, 2H), 3.19–3.10 (m, 2H), 3.05–2.96 (m, 2H).

^{13}C NMR (75 MHz, CDCl_3): δ (ppm) = 191.9, 142.9, 140.5, 136.9, 136.5, 135.2, 34.3, 32.8.

Mp: $166\text{ }^{\circ}\text{C}$.

IR: ν (cm^{-1}) = 3019, 2930, 2855, 2750, 1672, 1589, 1552, 1485, 1399, 1277, 1219, 1183, 1134, 946, 868, 791, 721, 651, 618.

MS (EI, m/e): $M^+ = 264$, $M^+/2 = 132$, 99%.

Synthesis of 4,12-Divinyl[2.2]paracyclophane (3). In a three necked, round-bottom flask equipped with dropping funnel, cooler and an argon inlet, a suspension of 88.38 g (247.4 mmol, 3.8 equiv) of methyltriphenylphosphonium bromide in 1.2 L of THF was cooled to $0\text{ }^{\circ}\text{C}$. Then 100 mL (250.0 mmol, 3.8 equiv) of *n*-butyllithium in hexane was added dropwise, and the temperature was maintained between 0 and $5\text{ }^{\circ}\text{C}$. After 2 h an orange solution was obtained and the solid was nearly dissolved. Then 17.19 g (65.10 mmol, 1.00 equiv) of **2** was added in portions, and the temperature increased slightly (3 – $5\text{ }^{\circ}\text{C}$). At room temperature, the solution was stirred for 2 h. Then the reaction was stopped by adding 500 mL of hydrochloric acid (5%) dropwise. The organic phase was separated, and the aqueous phase was diluted with brine and extracted with three portions of THF. The combined organic layers were washed with a saturated sodium chloride solution and a saturated sodium hydrogen carbonate solution. Afterward, the solution was dried over magnesium sulfate and the solvent was completely removed under reduced pressure at $60\text{ }^{\circ}\text{C}$. The solid containing phosphonium salt was extracted with hexane (4 times 600 mL). After evaporation of the solvent, the raw product was recrystallized from ethanol to yield 13.73 g (52.73 mmol, 81%) of colorless crystals.

^1H NMR (300 MHz, CDCl_3): δ (ppm) = 6.83–6.62 (m, 6H), 3.37 (dd, 2H, $J = 7.7$ Hz, $J = 1.8$ Hz), 5.57 (dd, 2H, $J = 17.3$ Hz, $J = 1.3$ Hz), 5.29 (dd, 2H, $J = 10.8$ Hz, $J = 1.3$ Hz), 3.46–3.34 (m, 2H), 3.16–3.06 (m, 2H), 3.00–2.90 (m, 2H), 2.83–2.72 (m, 2H).

^{13}C NMR (75 MHz, CDCl_3): δ (ppm) = 139.4, 137.7, 137.5, 135.3, 133.4, 130.1, 129.3, 114.3, 34.2, 33.0.

Mp: $178\text{ }^{\circ}\text{C}$.

IR: ν (cm^{-1}) = 3041, 2936, 2891, 2852, 1896, 1580, 1533, 1474, 1450, 1389, 1188, 1028, 827, 646.

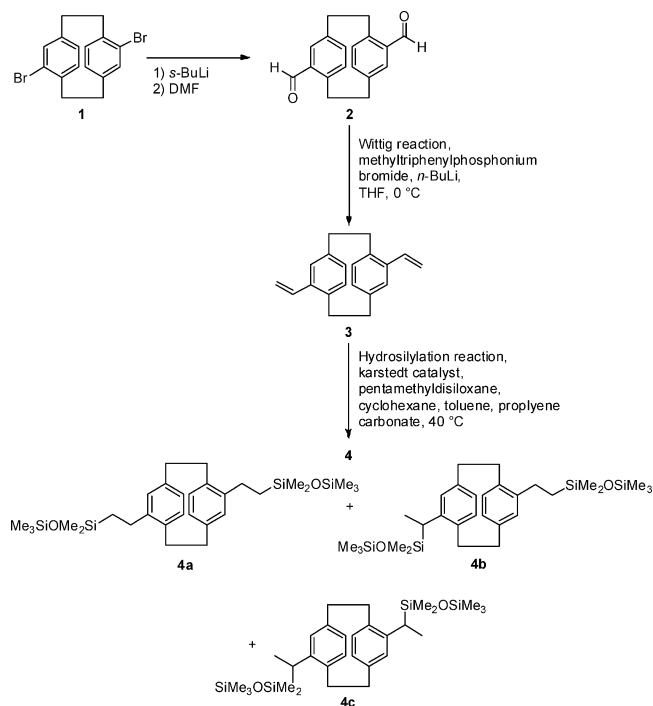
MS (EI, m/e): $M^+ = 260$, $M^+/2 = 130$, 99%.

Synthesis of the Siloxane-Modified [2.2]Paracyclophane (4). A suspension of 4.00 g (15.38 mmol) of **3** in toluene, cyclohexane and pentamethyldisiloxane was added with 5 mL of a solution of 4.2 mL of Karstedt-catalyst in 22 mL of propylene carbonate. The light yellow suspension turned bright orange and then yellow again after 10 min, as the solid dissolved slowly. A GC/MS measurement showed quantitative conversion. The product was obtained as black oil, and propylene carbonate was removed via steam-distillation. The obtained black oil was purified by column chromatography (hexane:Et₂O, 10:1) to yield 7.53 g (85%) of colorless oil, which crystallized slowly within a few days. The product contained three different constitutional isomers with amounts of 56% (**4a**), 35% (**4b**), and 9% (**4c**), respectively (Scheme 1).

^1H NMR (300 MHz, CDCl_3): δ (ppm) = 6.59–6.56 (m, 0.8H), 6.49–6.44 (m, 1H), 6.37–6.24 (m, 2.2H), 6.17–6.07 (m, 2H), 3.42–3.27 (m, 2H), 3.09–2.93 (m, 4.1H), 2.83–2.59 (m, 3.4H), 2.39–2.25 (m, 2H), 1.43–1.40 (m, 2.0H), 0.77–0.64 (m, 2.5H), 0.17–(–0.15) (m, 30H).

^{13}C NMR (75 MHz, CDCl_3): δ (ppm) = 144.4, 142.4, 139.7, 139.3, 139.1, 138.9, 136.7, 136.7, 136.5, 133.8, 133.7, 133.7, 133.6, 133.5, 133.4, 133.0, 129.6, 129.1, 127.6, 127.6, 126.3, 126.2, 124.9, 34.0, 34.0,

Scheme 1. Synthesis of the Siloxane-Modified [2.2]Paracyclophane 4 Starting with 4,12-Dibromo[2.2]paracyclophane 1



33.9, 33.6, 33.5, 32.9, 27.8, 27.8, 27.0, 19.1, 19.0, 12.5, 12.4, 2.1, 1.8, 0.3, 0.3, –1.6, –1.9.

^{29}Si NMR (CDCl_3): δ (ppm) = 7.12, 7.10, 5.60.

MS (EI, m/e): $M^+ = 557$ (M^+), 263 ($\text{Me}_3\text{SiOSiMe}_2\text{C}_8\text{H}_7^+$), 147 ($\text{Me}_3\text{SiOMe}_2^+$), 133 ($\text{Me}_3\text{SiOSiMe}_2^+$).

Mp: $42\text{ }^{\circ}\text{C}$.

IR: ν (cm^{-1}) = 2951, 2901, 2857, 1589, 1438, 1408, 1251, 1173, 1048, 867, 833, 802, 779, 752, 684.

Anal. Calcd for $\text{C}_{30}\text{H}_{52}\text{Si}_4\text{O}_2$: C, 64.68; H, 9.41; Si, 20.17. Found: C, 64.45; H, 9.46; Si, 20.57.

2.4. Polymer Synthesis (5). The siloxane-containing polymer was obtained via CVD in a custom built apparatus with 3 heating zones, each with a diameter of 5.5 cm and a length of 35 cm. The working pressure was between 1.8 and 2.2×10^{-3} mbar. Precursor **4** (0.50 g) was sublimed at $135\text{ }^{\circ}\text{C}$ (heating zone 1) and the vapor was led through a quartz glass tube maintained between 420 and $580\text{ }^{\circ}\text{C}$ (heating zone 2) where the corresponding quinodimethanes formed, heating zone 3 was set to $300\text{ }^{\circ}\text{C}$. In the deposition chamber, a borosilicate glass chamber with a cooling jacket, the reactive monomer gas polymerized spontaneously to form the desired siloxane containing polymer on the chamber walls, which were maintained at $0\text{ }^{\circ}\text{C}$. For GPC measurements the polymer was used without further purification. For thermo analysis, mechanical and NMR measurements the polymer was dissolved in chloroform, precipitated in methanol and then dried for 48 h at 15 mbar and $60\text{ }^{\circ}\text{C}$.

2.5. Characterization of 5e. Yield: 100% substance in deposition chamber, 69% after reprecipitation in methanol

IR: ν (cm^{-1}) = 2955 (m), 1497 (w), 1447 (w), 1413 (w), 1252 (s), 1169 (w), 1047 (s), 833 (s), 802 (s), 785 (m), 687 (w), 631 (w).

^1H NMR (300 MHz, CDCl_3): δ (ppm) = 7.36–6.64 (m, 3H), 3.05–2.41 (m, 5.6H), 1.37 (bs, 0.9H), 0.89 (bs, 1.3H), 0.29 to –0.17 (m, 15H).

^{13}C NMR (100 MHz, CDCl_3): δ (ppm) = 143.4, 142.9, 140.1, 136.89, 129.2, 129.0, 128.6, 127.2, 125.8, 124.4, 38.0, 37.8, 35.6, 34.9, 34.1, 26.2, 20.5, 15.9, 2.1, 1.9, 0.3, –0.9.

$T_{50\%} = 444\text{ }^{\circ}\text{C}$, $T_g = -10.4\text{ }^{\circ}\text{C}$, $M_n = 620\,000$, $M_p = 1\,176\,000$, $M_w = 1\,314\,000$, $D = 2.11$.

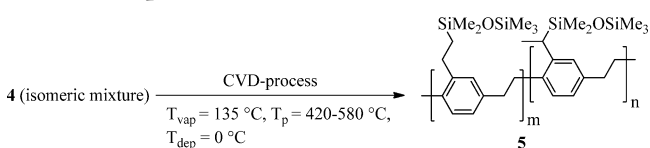
Anal. Calcd (5f): C, 64.68; H, 9.41; Si, 20.17. Found: C, 64.02; H, 9.15; Si, 19.93; N, 0.12.

3. RESULTS AND DISCUSSION

3.1. Synthesis of the Siloxane-Modified [2.2]Paracyclophane. The precursor **4** was synthesized by a three-step procedure according to Scheme 1. 4,12-Dibromo[2.2]paracyclophane **1** was reacted with *s*-BuLi and DMF to form the corresponding 4,12-diformyl[2.2]paracyclophane **2**, which was converted to 4,12-divinyl[2.2]paracyclophane **3** by the Wittig reaction. The siloxane substituted precursor **4** was obtained as a product mixture (isomers **4a**, **4b**, **4c**) by hydrosilylation reaction.

3.2. Polymer Synthesis. The siloxane-substituted PPX **5** was synthesized according to the Gorham procedure by pyrolysis of **4** (isomeric mixture) at different pyrolysis temperatures (Scheme 2). In contrast to most of the known

Scheme 2. Synthesis of Siloxane-Modified PPX **5 by CVD at Various Temperatures**



PPXs obtained by the Gorham process, **5** showed excellent solubility in organic solvents like toluene, THF, and chloroform, which allowed work-up by reprecipitation and analysis in solution. The yield after pyrolysis was nearly quantitative, but work-up of the raw product by reprecipitation showed a maximum yield for **5e** at 500 °C (Figure 1).

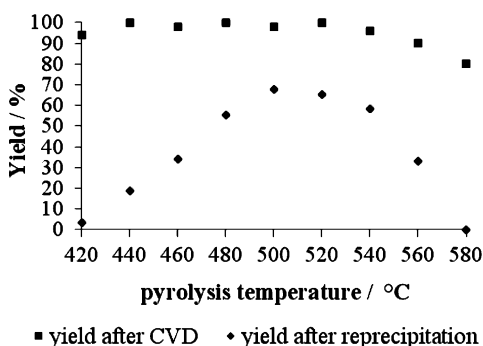


Figure 1. Yield of **5a–i** depending on different deposition temperatures T_p between 420 and 580 °C directly after pyrolysis and after work up procedure (dissolving in chloroform and reprecipitation in methanol).

All further analytical data, with the exception of the GPC analysis, refer to **5e**. Analysis of the filtrate of **5e** by MALDI-TOF proved that the raw product was mainly contaminated by unreacted **4** and cyclic trimer of **5**. The IR spectra of **5e** showed strong signals at 1250 cm^{-1} (Si-CH₃) and 1050 cm^{-1} (Si-O-Si) indicating siloxane moieties, which was confirmed also by ^{29}Si NMR spectra showing signals at 7.75, 7.56, and 6.84 ppm (Figure 2). ^1H and ^{13}C NMR spectra of **5e** display the substitution pattern of the isomeric mixture of **4** (Figure 3, 4). The broad ^1H NMR signals and the multiple ^{13}C NMR signals also indicate a head-to-head, a head-to-tail and a tail-to-tail connection within the polymer.

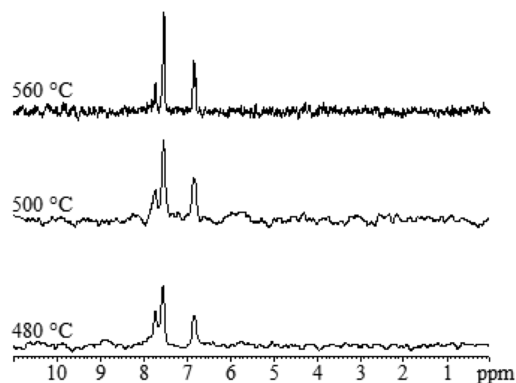


Figure 2. ^{29}Si NMR spectra of **5d**, **5e**, and **5h**.

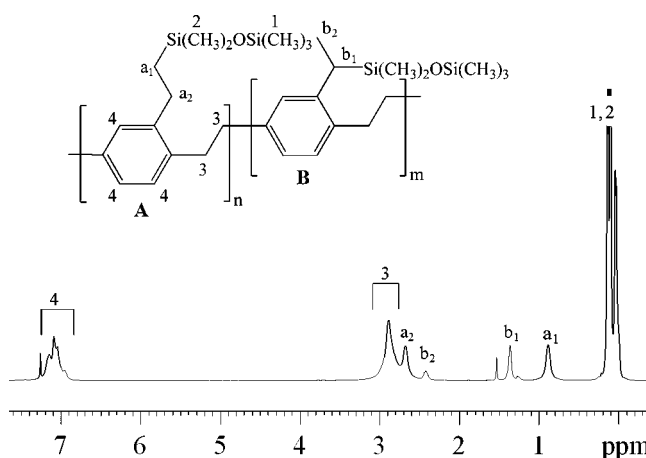


Figure 3. ^1H NMR spectrum (300 MHz, CDCl_3) of **5e**. Numbers show hydrogen signals belonging to both possible structure elements (A, B). Letters show signals only belonging to one structure element.

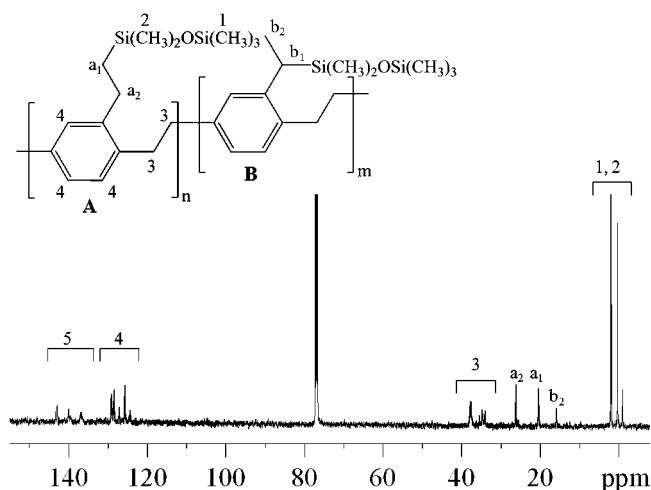


Figure 4. ^{13}C NMR spectrum (100 MHz, CDCl_3) of **5e**.

^1H , ^1H -COSY and HSQC NMR were employed for further structural characterization and showed the presence of segment A and segment B deriving from the isomeric mixture of the precursor (Figure 5, 6).

5 showed very high molecular weights with relatively polydispersities between 1.3 and 3.0 (Table 1). The peak molecular weight went through a maximum in correlation with the pyrolysis temperature, where **5e** showed the highest and **5i**

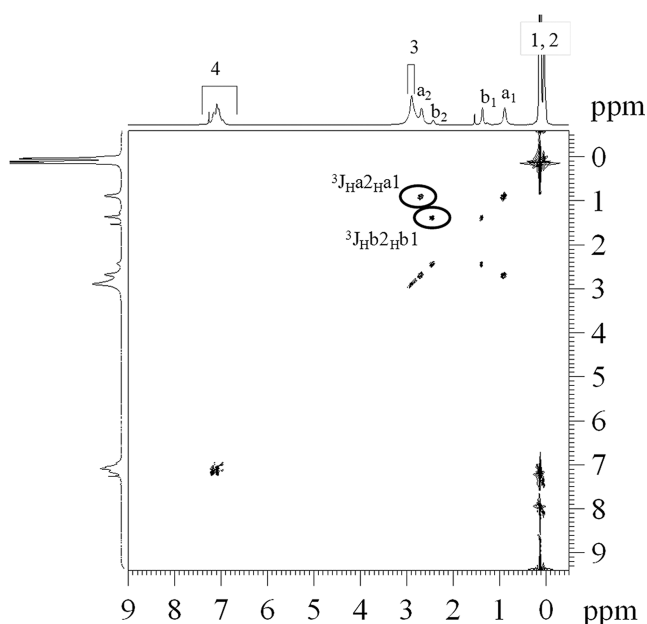


Figure 5. ^1H , ^1H -COSY spectrum of **5e**.

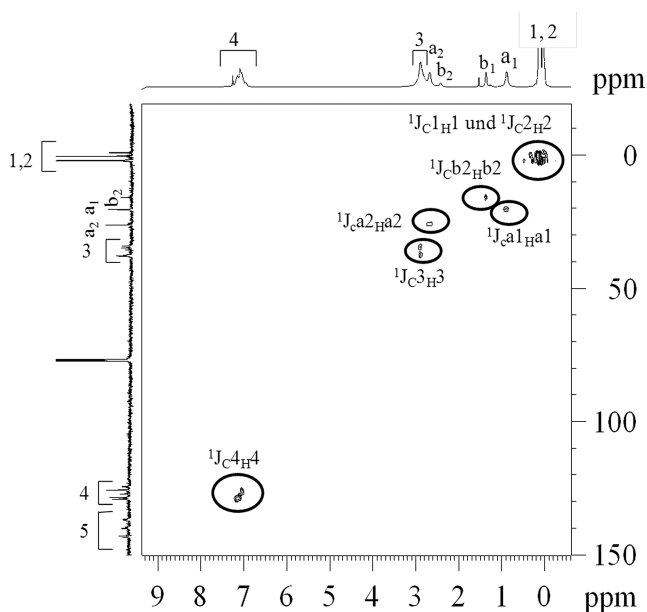


Figure 6. ^1H , ^{13}C -HSQC spectrum of **5e**.

the lowest peak molecular weight. The GPC traces of **5e** and **5i** showed slight shoulders (Figure 7).

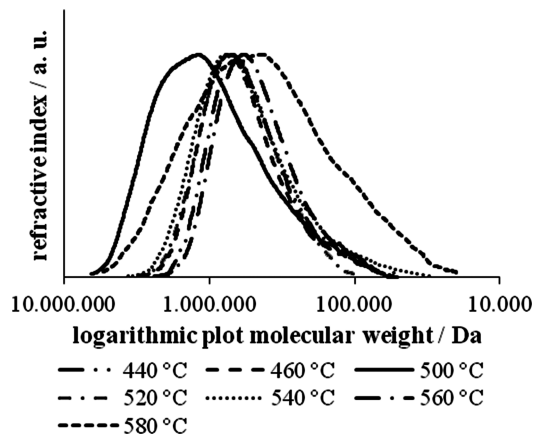


Figure 7. GPC traces of **5** pyrolyzed at different temperatures between 440 and 580 °C. The calibration curve was obtained by retention times of polystyrene standards with toluene as the internal standard.

The physical appearance of **5e** was like a soft colorless amorphous material, which was confirmed by DSC measurement where only a glass transition temperature (T_g) was detected at -10 °C. In comparison, the monochloro-substituted PPX is a crystalline polymer with a T_g of 80 °C.²⁶ No crystalline melting temperature was detected by DSC prior to thermal decomposition, which was found to be by TGA above 400 °C with a 5% weight loss at 442 °C. The IR spectrum of the degradation products showed typical signals at 3800 and 2364 cm^{-1} , which indicate water and carbon dioxide, and the presence of silicon is verified by Si–H, Si–CH₃, and Si–O–Si vibration (2128, 1257, 1061, and 694 cm^{-1}). Signals at 3015, 2960, 1600, 914, and 845 cm^{-1} reveal the presence of aromatic and aliphatic moieties (Figure 8). The mass spectrum also showed the presence of water (m/z 18) and CO₂ (m/z 22 and 44) as well as ion series for $[\text{C}_n\text{H}_{2n+3}\text{Si}]^+$ with m/z 45, 59, and 73 and $[\text{C}_n\text{H}_{2n+3}\text{SiO}]^+$ with m/z 75 and 89 indicating the cleavage of the Si–O–Si bond and formation of trialkylsilanol and trialkylsilane groups during decomposition. Also characteristic signals for aliphatic groups (m/z 39, 52) as well as benzene and benzyl groups (m/z 78, 103, 105, 117, 133) were detected. On the basis of these results the degradation model depicted in Scheme 3 is suggested. According to the bond dissociation energy values, the Si–C bond with 76 kcal/mol was the first bond cleaved leading to alkyl disiloxane groups. Then a cleavage of the backbone C–C bond (83 kcal/mol) led to a formation of benzene and benzyl fragments, and cleavage of the strongest Si–O bond (110 kcal/mol) led to trialkylsilane and trialkylsilanol groups.

Table 1. GPC Results of **5b–i** Including Number Averaged Molecular Weight (M_n), Weight-Averaged Molecular Weight (M_w), Molecular Weight at Peak Top (M_p), and Polydispersity (PD)

sample	$T_{\text{pyrolysis}}/\text{°C}$	pressure/mbar	M_n/Da	M_w/Da	M_p	PD
b	440	2.4×10^{-3}	393 000	602 000	698 000	1.53
c	460	3.2×10^{-3}	453 000	696 000	734 000	1.54
d	480	3.2×10^{-3}	801 000	1 243 000	1 292 000	1.29
e	500	2.2×10^{-3}	622 000	1 314 000	1 176 000	2.11
f	520	3.4×10^{-3}	508 000	715 000	716 000	1.41
g	540	1.8×10^{-3}	389 000	704 000	740 000	1.81
h	560	1.8×10^{-3}	385 000	555 000	578 000	1.44
i	580	1.8×10^{-3}	233 000	711 000	440 000	3.04

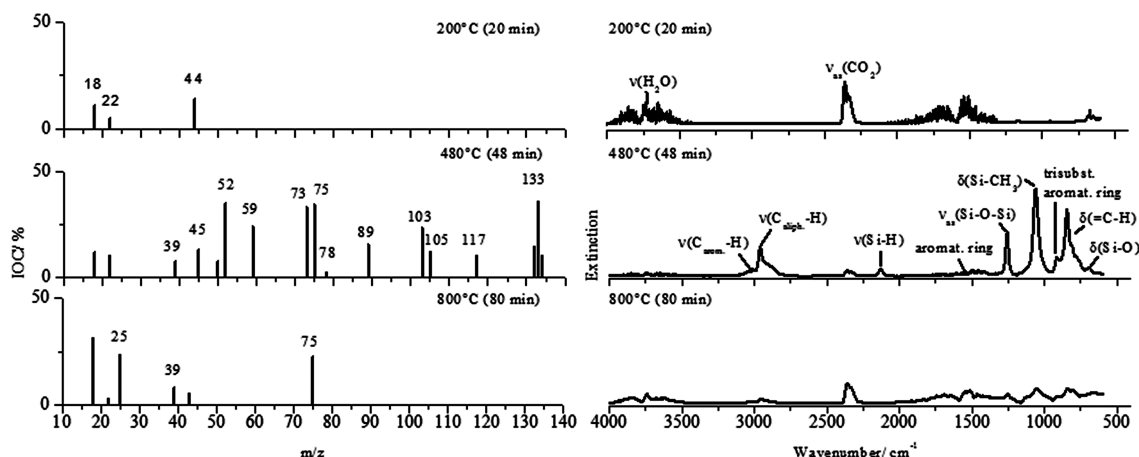
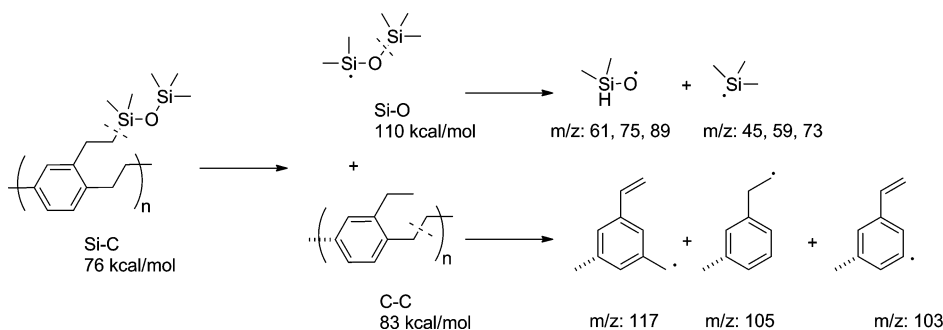


Figure 8. Release of gaseous products analyzed by IR and MS from **5e** maintained at different temperatures.

Scheme 3. Decomposition Model and Mass Fragments for Siloxane-Modified Polymer **5e** from Degradation Studies



The soft nature of **5e** was confirmed by stress–strain experiments at 20 °C, which showed an average Young's modulus of 0.02 GPa (Table 2). Compared to technically used

Table 2. Average Values for Mechanical Measurements of **5e**

	Young's modulus/GPa	maximum force/MPa	elongation at break/%
average value	0.0202	32.0	469
standard deviation/%	16.7	13.6	7.5

monochloro-substituted PPX with an elongation at break of 200% the average elongation at break of **5e** is 470%.²⁵ Cyclic measurements showed that the polymer remained elongated by 10% after elongation to 100% but in the following cycles the polymer nearly maintained its shape (Figure 9).

Significant differences in the wetting behavior of water on different surfaces of **5e** were found by contact angle measurements. The as-deposited film of **5e** (135°, attention: contaminated by precursor and trimer) as well as the electrospun sample (135°) of **5e** showed significantly larger contact angles of water as compared to the solution cast film (103°) (Figure 10). The difference in contact angle is most likely due to more structured surfaces of the as-deposited film and the electrospun sample (Figure 11). For comparison unsubstituted PPX (81°) and monochloro-substituted PPX (90°) have significantly lower contact angles,^{9d} but structured PPX films showed exceptional wetting behavior.^{22,23}

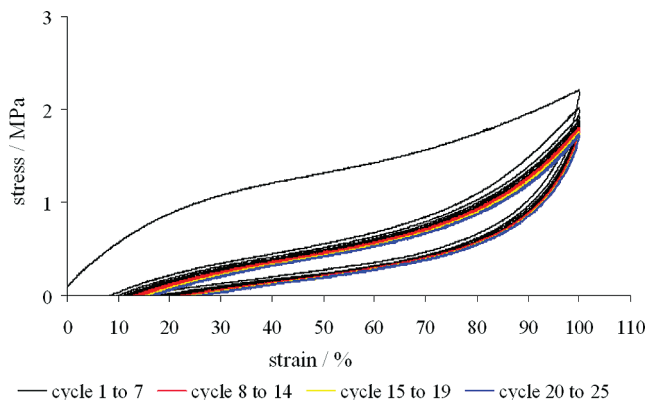


Figure 9. Cyclic stress–strain tests of **5e**, which was elongated to double its size 25 times with a rate of 25 mm/min and a break of 20 s between each cycle.

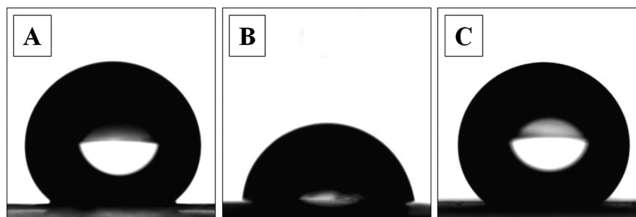


Figure 10. Contact angles on different surface morphologies of **5e**: (A) film as-deposited, (B) solvent-casted film, and (C) electrospun fiber mat.

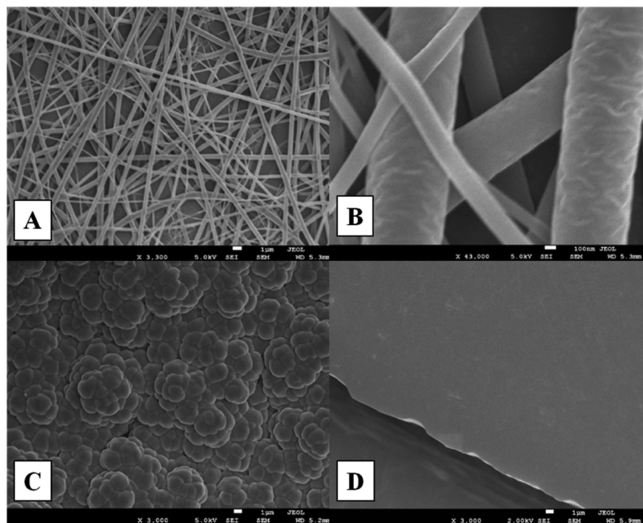


Figure 11. (A and B) SEM images of electrospun **5e** obtained from CH_3Cl (2.9 w%): solution A, magnification 3.3000; solution B, magnification 10.000. (C) SEM image with magnification of 3.000, film surface **5e** deposited horizontally to the monomer flow at 0 °C directly after pyrolysis. (D) SEM image with magnification of 3.000, film surface of solvent casted-film of **5e**.

4. CONCLUSIONS

PPX with siloxane substituents can be prepared by the technically well established Gorham process with [2.2]paracyclophanes as precursors. In contrast to other PPXs obtained by the Gorham process the siloxane substituted PPX **5** is soluble in organic solvents at ambient temperatures, which allowed analysis by NMR techniques and by GPC. Very high molecular weights were found for **5**, which is surprising as the reaction is heterogeneous by vapor deposition of the monomer on a solid polymer. The solubility of **5** and the relatively low polydispersities also indicate no cross-linkings and, if at all, a low degree long chain branching, which was a matter of debate for many decades.

Not unexpectedly, **5** is an amorphous polymer with a low glass transition temperature, which is most likely due to the bulky and flexible siloxane substituents and the isomeric substitution pattern of the precursor. Somewhat surprisingly, the contact angle did not increase as expected from siloxane substituents but enhanced hydrophobicity could be found with electrospun nanofiber surfaces of **5e**. Nevertheless, **5e** and related PPX derivatives could show interesting wetting behavior with structured PPX films similar to the work of Demirel et al. by shadowing growth mentioned before.

AUTHOR INFORMATION

Corresponding Author

*E-mail: greiner@staff.uni-marburg.de.

ACKNOWLEDGMENTS

The authors thank Deutsche Forschungsgemeinschaft for financial support and Specialty Coating Systems for [2.2]paracyclophane (Parylene N).

REFERENCES

- (1) Xylylene Polymers. *Kirk-Othmer Encyclopedia of Chemical Technology* [Online]; Wiley & Sons: Posted March 14, 2008.
- (2) Greiner, A.; Mang, S.; Schäfer, O.; Simon, P. *Acta Polym.* **1997**, *48*, 1–15.
- (3) Gorham, W. F. *J. Polym. Sci., Part A: Polym. Chem.* **1966**, *4* (12), 3027–3039.
- (4) Wintermantel, E.; Ha, S.-W. *Medizintechnik mit biokompatiblen Werkstoffen und Verfahren*; 3rd ed.; Springer: Berlin/Heidelberg, Germany, 2002.
- (5) Hanefeld, P.; Sittner, F.; Ensinger, W.; Greiner, A. *e-Polym.* **2006**, *26*, 1–6.
- (6) Simon, P.; Mang, S.; Hasenhiindl, A.; Gronski, W.; Greiner, A. *Macromolecules* **1998**, *31*, 8775–8780.
- (7) Alf, M. E.; Asatekin, A.; Barr, M. C.; Baxamusa, S. H.; Chelawat, H.; Ozyaydin-Ince, G.; Petruczuk, C. D.; Sreenivasan, R.; Tenhaeff, W. E.; Trujillo, N. J.; Vaddiraju, S.; Xu, J.; Gleason, K. K. *Adv. Mater.* **2010**, *22* (18), 1993–2027.
- (8) Fink, J. K. *High Performance Polymers*; William Andrew: Norwich, 2008.
- (9) Santayana, G. *WBF Draft* **1999**, 1863–1952.
- (10) Senkevich, J. J.; Yang, G.-R.; Lu, T.-M. *Colloids Surf., A* **2003**, *216* (1–3), 167–173. Meng, E.; Li, P.-Y.; Tai, Y.-C. *J. Microeng. Microeng.* **2008**, *18* (4), 1–13. Herrera-Alonso, M.; McCarthy, T. J. *Langmuir* **2004**, *20* (21), 9184–9189. Pruden, K. G.; Sinclair, K.; Beaudoin, S. J. *Polym. Sci., Part A: Polym. Chem.* **2003**, *41*, 1486–1496.
- (11) Wahjudi, P. N.; Oh, J. H.; Salman, S. O.; Seabold, J. A.; Rodger, D. C.; Tai, Y.-C.; Thompson, M. E. *J. Biomed. Mater. Res., Part A* **2009**, *89A* (1), 206–214. Lahann, J.; Langer, R. *Macromol. Rapid Commun.* **2001**, *22* (12), 968–971. Jiang, X.; Chen, H.-Y.; Galvan, G.; Yoshida, M.; Lahann, J. *Adv. Funct. Mater.* **2008**, *18* (1), 27–35.
- (12) Pu, H.; Wang, Y.; Yang, Z. *Mater. Lett.* **2007**, *61* (13), 2718–2722.
- (13) Gorham, W. F. Para-Xylylene Copolymers. U.S. Patent 3,288,728, Nov. 24, 1966.
- (14) Senkevich, J. J.; Woods, B. W.; McMahon, J. J.; Wang, P. I. *Chem. Vap. Deposition* **2007**, *13* (1), 55–59.
- (15) Lahann, J.; Klee, D.; Pluester, W.; Hoecker, H. *Biomater.* **2001**, *22*, 817–826. Lahann, J.; Klee, D.; Höcker, H. *Macromol. Rapid Commun.* **1998**, *19* (9), 441–444. Elkasabi, Y.; Yoshida, M.; Nandivada, H.; Chen, H.-Y.; Lahann, J. *Macromol. Rapid Commun.* **2008**, *29*, 855–870.
- (16) Elkasabi, Y.; Lahann, J. *Macromol. Rapid Commun.* **2009**, *30* (1), 57–63. Chen, H.-Y.; Lahann, J. *Langmuir* **2011**, *27* (1), 34–48.
- (17) Gaynor, J. F. Polymeric Thin Films by Chemical Vapor Deposition for the Microelectronics Industry. Ph.D. Thesis, Virginia Polytechnic Institute and State University: Blacksburg, VA, October 1995.
- (18) Gaynor, J. F.; Desu, S. B.; Senkevich, J. J. *Macromolecules* **1995**, *28*, 7343–7348.
- (19) Bobrowski, M.; Skurski, P.; Freza, S. *Chem. Phys.* **2011**, *382* (1), 20–26. Naddaka, M.; Asen, F.; Freza, S.; Bobrowski, M.; Skurski, P.; Laux, E.; Charmet, J.; Keppner, H.; Bauer, M.; Lellouche, J.-P. *J. Polym. Sci., Part A: Polym. Chem.* **2011**, *49* (13), 2952–2958.
- (20) Elkasabi, Y.; Lahann, J. *Methods Mol. Biol.* **2011**, *671*, 261–279. Chen, H.-Y.; Lahann, J. *Langmuir* **2011**, *27* (1), 34–48.
- (21) Elkasabi, Y.; Lahann, J.; Krebsbach, P. H. *Biomaterials* **2011**, *32* (7), 1809–1815. Senkevich, J. J.; Woods, B. W.; McMahon, J. J.; Wang, P. I. *Chem. Vap. Deposition* **2007**, *13* (1), 55–59. Lahann, J.; Klee, D.; Höcker, H. *Macromol. Rapid Commun.* **1998**, *19* (9), 441–444.
- (22) Demirel, M. C.; Boduroglu, S.; Cetinkaya, M.; Lakhtakia, A. *Langmuir* **2007**, *23* (11), 5861–5863. Cetinkaya, M.; Boduroglu, S.; Demirel, M. C. *Polymer* **2007**, *48*, 4130–4134.
- (23) Malvadkar, N. A.; Hancock, M. J.; Sekeroglu, K.; Dressick, W. J.; Demirel, M. C. *Nat. Mater.* **2010**, *9*, 1023–1028.
- (24) Heck, R. F.; Ziegler, C. B. *J. Org. Chem.* **1978**, *43*, 2941–2946.
- (25) Krumpfer, J. W.; McCarthy, T. J. *Langmuir* **2011**, *27*, 11514–11519.
- (26) Greiner, A. Poly(p-xylylene)s (Structure, Properties, and Applications). In *The Polymeric Materials Encyclopedia*; Salamone, J. C., Ed.; CRC Press: New York, 1996; Vol. 9, pp 7171–7180.

Computational Studies on Isospecific Polymerization of 1-Hexene Catalyzed by Cationic Rare Earth Metal Alkyl Complex Bearing a C₃/iPr-trisox Ligand

Xiaohui Kang,[†] Yuming Song,[†] Yi Luo,^{*,†} Gang Li,[‡] Zhaomin Hou,^{*,†,§} and Jingping Qu^{*,†}

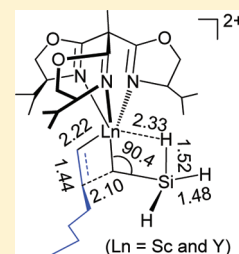
[†]State Key Laboratory of Fine Chemicals, School of Pharmaceutical Science and Technology, Dalian University of Technology, Dalian 116024, China

[‡]School of Chemical Engineering, Dalian University of Technology, Dalian 116024, China

[§]Organometallic Chemistry Laboratory, RIKEN Advanced Science Institute, 2-1 Hirosawa, Wako, Saitama 351-0198, Japan

Supporting Information

ABSTRACT: 1-Hexene polymerization catalyzed by dicationic rare earth metal alkyl species $[\text{Ln}(\text{iPr-trisox})(\text{CH}_2\text{SiMe}_3)]^{2+}$ (Ln = Sc and Y; trisox = trisoxazoline) has been computationally studied by using QM/MM approach. It has been found that the initiation of 1-hexene polymerization kinetically prefers 1,2-insertion (free energy barrier of 17.23 kcal/mol) to 2,1-insertion (free energy barrier of 20.05 kcal/mol). Such a preference of 1,2-insertion has been also found for chain propagation stage. The isotactic polymerization was computed to be more kinetically preferable in comparison with syndiotactic manner, and the dicationic system resulted in lower insertion free energy barrier and more stable insertion product in comparison with the monocationic system. The stereoselectivity was found to follow chain-end mechanism, and the isospecific insertion of 1-hexene is mainly controlled by kinetics. In addition, the current computational results, for the first time, indicate that the higher activity of Sc species toward 1-hexene polymerization in comparison with the Y analogue could be ascribed to lower insertion barrier, easier generation of the active species, and its larger chemical hardness.



INTRODUCTION

Poly(1-hexene) as an important long-chain poly(α -olefin) is a pectinate polymer with special properties. It can be used as oil additive, which is suitable for lowering setting point, lowering dynamic viscosity, and limiting shear tension of paraffin oils under transportation and storage conditions. Generally, the microstructure of synthetic polymer has significant influences on its physical and chemical properties, and hence for certain usage. Therefore, the synthesis of poly(1-hexene) with certain microstructure has attracted more and more interests. In this context, group 4 and late transition metal complexes have been widely used as precatalysts.^{1,2} For example, *ansa*-zirconium catalysts,^{2a} zirconium and rhodium heterobimetallic complexes,^{2b} and chiral $[N,N,N]$ -ligated titanium/zirconium catalysts^{2g} have been reported for 1-hexene polymerization. These catalysts have C₁ or C₂ symmetric feature and show excellent isospecific control in 1-hexene polymerization. However, catalyst systems showing both high activity and stereoselectivity for 1-hexene polymerization remained rare.^{2b,j} The zirconium amine bis(phenoxide) complexes have been reported to be highly active precatalysts for 1-hexene polymerization, whereas the polymers obtained were atactic in spite of the C₁ symmetric feature of the ancillary ligand.^{2d} Kol and his co-workers reported a Ti diamine bis(phenolate) catalyst showing high activity toward 1-hexene polymerization, but the polymer obtained had low-to-medium degree of isospecificity.^{2e} Therefore, studies on the search for highly active and stereoselective

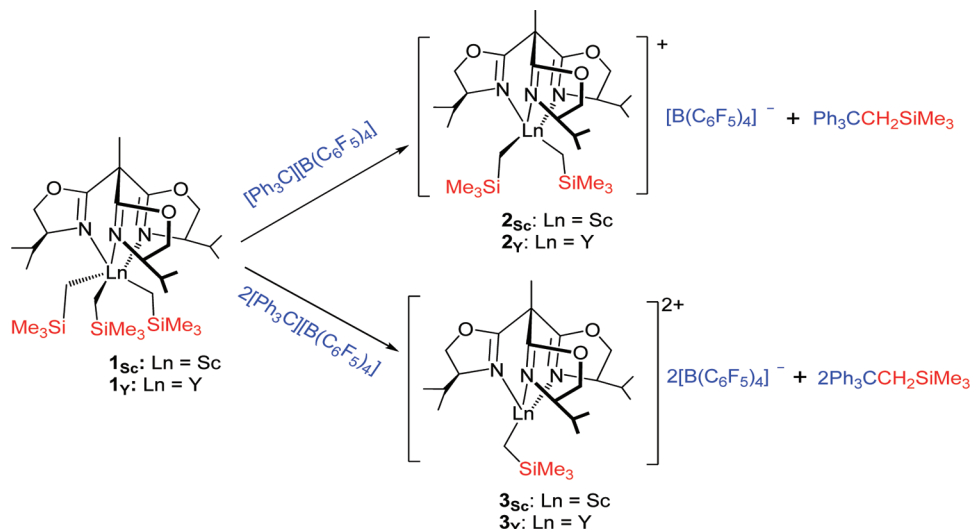
catalysts for 1-hexene polymerization are of much interest and importance.

Recently, cationic rare earth alkyl complexes have been reported to act as a new family of polymerization catalysts.³ For example, the cationic half-sandwich scandium alkyl species, such as $[(\text{C}_5\text{Me}_4\text{SiMe}_3)\text{Sc}(\text{CH}_2\text{SiMe}_3)]^+$, showed excellent activity and selectivity for the polymerization and copolymerization of a wide range of olefins, such as syndiospecific polymerization and copolymerization of styrene with ethylene, dienes and other olefins.⁴ However, this catalyst showed no stereoselectivity for the polymerization of 1-hexene, yielding poly(1-hexene) in both 1,2- and 2,1-fashions.⁵ The cationic scandium alkyl species bearing a neutral 1,4,7-trithiacyclononane ligand, $[\text{Sc}([9]\text{aneS}_3)(\text{CH}_2\text{SiMe}_3)_2]^+$, was also reported to polymerize 1-hexene but without showing stereoselectivity.⁶ Gade et al. reported that a series of cationic rare-earth metal alkyl species, such as those of **2**_{Sc} (**2**_Y) and **3**_{Sc} (**3**_Y) shown in Scheme 1, bearing a C₃-chiral trisoxazoline (trisox) ancillary ligand could be generated by the reaction of a trialkyl complex $\text{Ln}(\text{iPr-trisox})(\text{CH}_2\text{SiMe}_3)_3$, such as **1**_{Sc} (**1**_Y), with 1 and 2 equiv of a borate compound $[\text{Ph}_3\text{C}][\text{B}(\text{C}_6\text{F}_5)_4]$ as an activator, respectively (Scheme 1).⁷ Among these species, the dicationic Sc alkyl species showed extremely high activity ($36200 \text{ kg mol}^{-1} \text{ h}^{-1}$) and isoselectivity toward the polymerization of 1-hexene.

Received: October 31, 2011

Revised: December 20, 2011

Published: January 9, 2012

Scheme 1. Generation of Cationic Rare Earth Metal Alkyl Species Bearing C₃-Chiral Trisoxazoline Ancillary Ligand

However, other dicationic rare-earth metal alkyl species showed rather low or no activity,^{7c} and all of the monocationic species showed lower activity in comparison with their corresponding dicationic analogues. However, the related mechanism and factors governing the activity and regio- and stereoselectivity remain unclear.

Numerous computational studies^{8–11} have been widely and successfully conducted to investigate the mechanism of various olefin polymerizations catalyzed by group 4 and late transition metal complexes. In this context, studies on α -alkenes have almost been limited to propylene possibly due to the bulky substituent of higher alkenes. A palladium-catalyzed polymerization of propylene has been computationally explored.^{10a} It was found that 2,1-insertion is more favorable than 1,2-insertion in the palladium catalyst system, and the insertion barrier of propylene was higher than that of ethylene. However, the polymerization of propylene catalyzed by a series of Ti complexes featuring fluorine-containing phenoxy-imine chelate ligands was computationally found to occur exclusively via 1,2-insertion at the initial stage and 2,1-insertion as the principal mode in the chain propagation.^{10h} Caporaso et al. reported a more general picture of the enantioselectivity in the process of chain transfer to monomer during propylene polymerization.¹⁰ⁱ

In comparison with computational studies on the polymerization of propylene and other olefins, the polymerization of 1-hexene has received much less attention.⁸ Carpentier et al. optimized a variety of possible cationic zirconium species, which was used in the stereospecific polymerization of 1-hexene.^{11a} The first determination of empirical and computed ¹²C/¹³C kinetic isotope effects for metallocene-catalyzed polymerization of propylene as a model of the 1-hexene was also reported.^{11b} Thomson and co-workers studied the quantitative effects of ion pair and sterics on chain propagation kinetics in 1-hexene polymerization catalyzed by mixed Cp'/ArO ligated complexes.^{11d} They found that the Ti-based catalyst exhibiting unusually high reactivity has lower ion-pair separation energy in toluene in comparison with the Zr analogue. Extensive theoretical studies on the mechanism of olefin polymerization by late and group 4 transition metal complexes effectively promoted the design and development of homogeneous transition metal catalyst.

In contrast, computational studies on the mechanism of olefin polymerization catalyzed by rare-earth metal catalysts have been much less explored despite recent progress.^{12,13} Recently, Maron

et al. conducted a series of computational studies on the syndio-specific polymerization of styrene by single-component ansa-lanthanidocenes,^{12l,n} the polymerization of conjugated dienes by cationic species $[\text{Cp}^*\text{ScR}]^+$, and the copolymerization of conjugated dienes with olefins (including 1-hexene) by a hemilanthanidocene $[(\text{Cp}^*)(\text{BH}_4)\text{LnR}]$.^{12k,m} A computational study on styrene polymerization catalyzed by *ansa*-bis(indenyl) allyl rare earth complexes was reported by Carpentier and co-workers. The results suggested a favorable secondary insertion of styrene during both chain initiation and propagation stages.^{12o} Mountford et al. performed a DFT study on the ligand binding ability in $\text{Ln}(\text{L})(\text{CH}_2\text{SiMe}_3)_3$ ($\text{Ln} = \text{Sc}$ or Y ; $\text{R} = \text{Me}$ or CH_2SiMe_3 ; $\text{L} = \text{Me}_3[9]\text{aneN}_3$ or $[9]\text{aneS}_3$) complexes. They found that the electron-deficient base-free dialkyl cations $[\text{Ln}(\text{L})(\text{CH}_2\text{SiMe}_3)_2]^+$ were usually stabilized by a β -Si–C agostic interaction.^{12a} During our computational studies on rare earth metal complexes,¹³ we have also carried out a series of theoretical calculations on olefin polymerization catalyzed by cationic rare earth metal complexes in combination with experimental studies.^{12b–e} We recently found that the mechanism of styrene–ethylene copolymerization catalyzed by a cationic half-sandwich scandium alkyl species is different from that involved in group 4 catalyst systems.^{12f} In spite of these recent achievements in this field, an in-depth study on 1-hexene polymerization catalyzed by a rare earth metal catalyst has not been reported previously.

In this paper, we report a QM/MM (quantum mechanics/molecular mechanics) study on the mechanism of 1-hexene polymerization catalyzed by the dicationic alkyl complex $[\text{Sc}(\text{iPr-trisox})(\text{CH}_2\text{SiMe}_3)]^{2+}$. The catalytic activity of this cationic species has also been computationally compared with its Y analogue. There are three purposes in this study. The first is to clarify whether the 1-hexene insertion preferably adopts a 1,2-insertion or 2,1-insertion manner in the chain initiation and propagation stages. The second is to find out the reason why such kind of catalyst system produced isotactic poly(1-hexene). The third is to computationally clarify the origins of the higher activity of dicationic active species in comparison with the monocationic ones and the higher activity of Sc species compared to Y analogue. We hope that the results reported here would be helpful for better understanding of the polymerization

mechanism of 1-hexene and for the development of new rare-earth metal polymerization catalysts.

■ COMPUTATIONAL DETAILS

The dicationic scandium alkyl species $[\text{Sc}(\text{iPr-trisox})-(\text{CH}_2\text{SiH}_3)]^{2+}(\mathbf{3}_{\text{Sc}}')$ (Figure 1) was used for modeling the initial

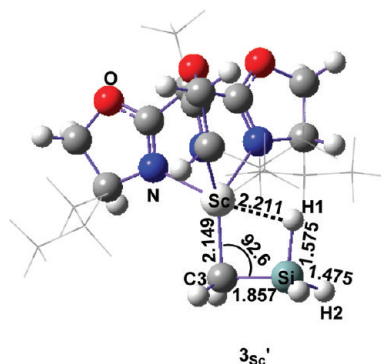


Figure 1. Optimized cationic species $\mathbf{3}_{\text{Sc}}'$ showing a β -Si-H agostic interaction as suggested by the $\text{Sc}\cdots\text{H1}$ distance of 2.211 Å, Si-H1 bond length of 1.575 Å, and Sc-C3-Si angle of 92.6°. The similar geometrical feature, viz. β -Si-C agostic interaction, was also observed in real structure $[\text{Sc}(\text{iPr-trisox})(\text{CH}_2\text{SiMe}_3)]^{2+}(\mathbf{3}_{\text{Sc}})$, see Figure S-3 in Supporting Information).

catalytic species in the computations. The QM/MM calculations were carried out with ONIOM(B3LYP:UFF) approach,¹⁴ as implanted in Gaussian 09 program.¹⁵ In the ONIOM(B3LYP:UFF) calculations, one methyl and three isopropyl groups of the ancillary ligand are placed in the outside layer treated by the universe force field (UFF)¹⁶ for saving computational time and consideration of steric effects. The other atoms, including those in the monomer molecules, constitute the inner layer. During the calculations on the generation of ion pair and its separation, the species $[\text{Ln}(\text{iPr-trisox})(\text{CH}_2\text{SiMe}_3)]^{2+}$ (Ln = Sc and Y) and counterion $[\text{B}(\text{C}_6\text{F}_5)_4]^-$ were adopted. The ONIOM-(B3LYP:UFF) method was used for geometry optimization and subsequent analytic frequency calculation. The treatment of $[\text{Ln}(\text{iPr-trisox})(\text{CH}_2\text{SiMe}_3)]^{2+}$ species for the ONIOM calculation is same as that described above. As to the part of $[\text{B}(\text{C}_6\text{F}_5)_4]^-$ anion, the B atom and the $-\text{C}_6\text{F}_5$ group interacting directly with the metal atom are included in the inner layer. While the remained three $-\text{C}_6\text{F}_5$ groups are placed in the outside layer. The ONIOM energy of the whole system is calculated as

$$E(\text{ONIOM}) = E(\text{high-level, inner layer}) + E(\text{low-level, real}) \\ - E(\text{low-level, inner layer})$$

where the $E(\text{high-level, inner layer})$ is the energy of the inner layer calculated with the high-level method (B3LYP), $E(\text{low-level, real})$ is the energy of the whole system calculated with the low-level method (UFF force field), and $E(\text{low-level, inner layer})$ is the energy of the inner layer calculated with the low-level method. For the B3LYP calculation, the 6-31G* basis set was used for C, H, N, O, B, and F atoms, and the Sc, Y and Si atoms were treated by the Stuttgart/Dresden effective core potential (ECP) and the associated basis sets.¹⁷ In the Stuttgart/Dresden ECP used in this study, the most inner 10 electrons of Si and Sc and the most inner 28 electrons of Y are included in the core, respectively. The 4 valence electrons of Si atom and 11 valence electrons of Sc and Y atoms were treated by the optimized basis sets, viz. (4s4p)/[2s2p] for Si, (8s7p6d1f)/[6s5p3d1f] for Sc, and (8s7p6d)/[6s5p3d] for Y, respectively. The basis set for Sc atom contains one f-polarization function with exponent of 0.27. One f-polarization function (exponent of 0.84) and one d-polarization function (exponent of 0.45) were augmented for Y and Si, respectively. Normal-coordinate analyses were performed to

verify the geometrically optimized stationary points and to obtain the thermodynamic data. In the present study, the complexation energy was defined as the energy difference in free energy between a π -complex and separated species. The more negative the complexation energy, the more favorable the formation of a π -complex. Insertion barriers were calculated as the difference between the transition state and the most stable structures (separated species or π -complex). Reaction energies were calculated as the energy difference between the insertion product and the energy sum of isolated monomer and active species. All optimizations were carried out in the gas phase without any symmetry constraint. Energy profiles were described by relative free-energies obtained from gas-phase ONIOM calculations (ΔG , kcal/mol).

The basis set superposition error (BSSE) correction was included in the calculation of interaction energy between the active species and 1-hexene motif. For estimation of BSSE, single point calculations were performed for the ONIOM-optimized geometries. To estimate the changes in enthalpy during the formation of ion pair and their separation via the coordination of olefin, single-point energy calculations were also performed on optimized ONIOM geometries. In such single-point calculations, the larger basis set 6-31+G** was used for nonmetal atoms, and the basis sets for metal atoms are same as those in geometry optimizations. The enthalpy correction obtained from analytic frequency calculation was added to the single-point energy to estimate enthalpy change. Such single-point calculations were also performed for some structures to obtain chemical hardness.

■ RESULTS AND DISCUSSION

1. Regioselectivity in the Insertion Reaction of 1-Hexene.

For d^0 -metal complex catalyst, the insertion reaction of alkenes was proposed to follow the Cossee-Arlman mechanism,¹⁸ in which the olefin initially approaches the metal center to form a π -complex and then the reaction proceeds via a four-center transition state (TS) leading to the insertion product (Scheme 2a). This general mechanism is also suitable for hexene insertions into the $\text{Sc}-\text{CH}_2\text{SiH}_3$ bond of $\mathbf{3}_{\text{Sc}}'$. The hexene polymerization, however, has some differences from ethylene polymerization. Two C atoms of the ethylene are equivalent when inserting the metal-alkyl (M-R) bond, while the insertion of a hexene into the M-R bond can adopt two manners with two enantiofaces,¹⁹ viz. 1,2-insertion (primary insertion with *re*- and *si*-faces in the transition state, respectively) and 2,1-insertion (secondary insertion with *re*- and *si*-faces in the transition state, respectively) because of the existence of an *n*-butyl group (Scheme 2b). Therefore, the issue of regioselectivity appears in the polymerization of an α -olefin.

In the present paper, we investigated in detail the regioselectivity of 1-hexene polymerization. Considering that the regioselectivity is determined by an insertion TS structure, four TSs for the insertion of 1-hexene into $\text{Sc}-\text{CH}_2\text{SiH}_3$ bond of $\mathbf{3}_{\text{Sc}}'$ have been located with respect to 1,2-*si*-, 1,2-*re*-, 2,1-*si*-, and 2,1-*re*-insertion manners, respectively. It was found that free energies (relative to the energy sum of $\mathbf{3}_{\text{Sc}}'$ and 1-hexene) of these TSs are 18.70, 19.51, 25.07, and 30.19 kcal/mol for 1,2-*si*-, 1,2-*re*-, 2,1-*si*-, and 2,1-*re*-insertion manners, respectively (see Figure S-4 in Supporting Information). This result indicates that the 1,2-*si*-insertion TS is most stable among these four TSs and that the 2,1-*si*-insertion TS is more stable than 2,1-*re*-insertion TS. Therefore, the 1,2-*si*-insertion pattern was considered in the following, and the 2,1-*si*-insertion manner was also investigated for comparison. The computed energy profiles for 1,2- and 2,1-insertion of 1-hexene into the $\text{Sc}-\text{CH}_2\text{SiH}_3$ bond of $\mathbf{3}_{\text{Sc}}'$ are shown in Figure 2. As shown in this figure, the free energies are relative to the energy sum of active species $\mathbf{3}_{\text{Sc}}'$ and **m** (monomer, 1-hexene). The 1,2-insertion starts with the formation of complex $\text{C}_{12\text{Sc}}$ and proceeds via a

Scheme 2. (a) Cossee–Arlman Mechanism for Alkene Insertion into a Metal–Alkyl Bond and (b) Four Possible Transition States for the Insertion of a Hexene into the M–R Bond

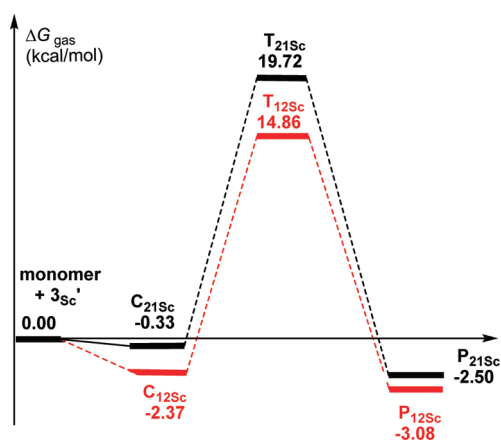
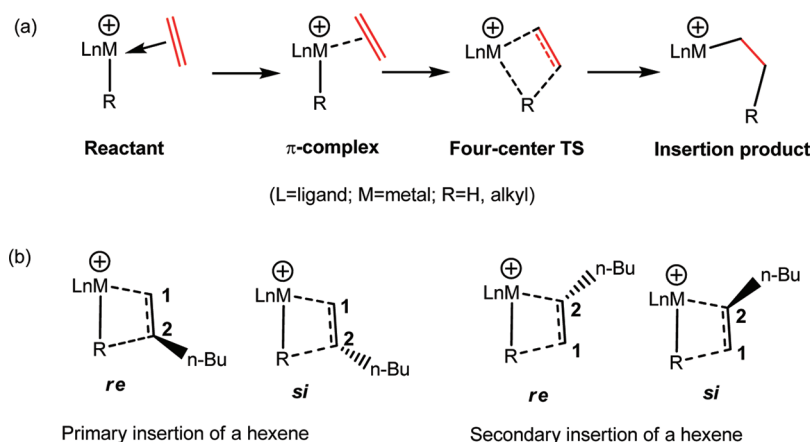


Figure 2. Computed energy profiles (energy in kcal/mol) for 1,2- and 2,1-insertion of 1-hexene at the chain initiation stage.

four-center transition state $\text{T}_{12\text{Sc}}$, leading to the insertion product $\text{P}_{12\text{Sc}}$. The $\text{C}_{12\text{Sc}}$ is lower in free energy than the energy sum of $3\text{Sc}^{\cdot\cdot}$ and **m** by -2.37 kcal/mol. This insertion process, which overcomes a free energy barrier of 17.23 kcal/mol, is exergonic by -3.08 kcal/mol. However, the 2,1-insertion needs to overcome a free-energy barrier of 20.05 kcal/mol and is exergonic by -2.50 kcal/mol. Both the prereaction complex ($\text{C}_{21\text{Sc}}$) and transition state ($\text{T}_{21\text{Sc}}$) for 2,1-insertion are higher in energy than those for 1,2-insertion by 2.04 and 4.86 kcal/mol, respectively. The 1,2-insertion product $\text{P}_{12\text{Sc}}$ is also slightly stable than the 2,1-insertion product $\text{P}_{21\text{Sc}}$. Single-point calculations at the level of B3LYP were also performed on the optimized stationary points involved in Figure 2. In the single-point calculations, the basis set 6-311+G** was used for C, H, O, and N atoms and the basis set for Sc and Si atoms are same as that in geometry optimizations. The results show that the insertion free energy barrier for 1,2-insertion is smaller than that for 2,1-insertion by 6.12 kcal/mol, and the $\text{P}_{12\text{Sc}}$ is more stable than $\text{P}_{21\text{Sc}}$ by 3.39 kcal/mol (see Figure S-1 in Supporting Information). To corroborate this result, the MPW1K functional has been also utilized to compute the energy profile. The MPW1K functional developed by Truhlar's group was suggested to be an efficient method for predicting reaction energy and barrier heights and was comparable to multi-reference methods.²⁰ The MPW1K calculations also indicate the preference of 1,2-insertion over 2,1 insertion (see Figure S-2

in Supporting Information). These results suggest that the 1,2-insertion is both kinetically and energetically more favorable than the 2,1-insertion at the chain initiation stage. To elucidate the origin of the kinetic preference for such a regioselectivity, we further analyzed the energies and geometries of $\text{T}_{12\text{Sc}}$ and $\text{T}_{21\text{Sc}}$. An analysis of energy (electronic energy, ΔE_{TS}) decomposition of $\text{T}_{12\text{Sc}}$ and $\text{T}_{21\text{Sc}}$ was performed. The energies of the fragments $\text{Sc}(\text{iPr-trisox})(\text{CH}_2\text{SiH}_3)^{2+}$ (**A**) and 1-hexene (**B**) in the geometry they have in the two TSs were evaluated in single-point calculations. Such single-point energies of the fragments and the energy (corrected by BSSE) of TS were used to estimate the interaction energy ΔE_{int} . These energies, together with the energy of the respective fragments in their optimal geometry, allow for the estimation of the deformation energies of the two fragments, $\Delta E_{\text{def}}(\text{A})$ and $\Delta E_{\text{def}}(\text{B})$. As the energy of the TS, ΔE_{TS} , is evaluated with respect to the energy of the two separated fragments, the relation $\Delta E_{\text{TS}} = \Delta E_{\text{int}} + \Delta E_{\text{def}}(\text{A}) + \Delta E_{\text{def}}(\text{B})$ holds. The following components were found for $\text{T}_{12\text{Sc}}$: $\Delta E_{\text{int}} = -37.21$ kcal/mol; $\Delta E_{\text{def}}(\text{A}) = 18.83$ kcal/mol; $\Delta E_{\text{def}}(\text{B}) = 25.10$ kcal/mol; and therefore $\Delta E_{\text{TS}} = 6.72$ kcal/mol. While the following components were found for $\text{T}_{21\text{Sc}}$: $\Delta E_{\text{int}} = -28.08$ kcal/mol; $\Delta E_{\text{def}}(\text{A}) = 20.08$ kcal/mol; $\Delta E_{\text{def}}(\text{B}) = 20.71$ kcal/mol; and therefore $\Delta E_{\text{TS}} = 12.71$ kcal/mol. The ΔE_{TS} value of 12.71 kcal/mol for $\text{T}_{21\text{Sc}}$ is larger than that for $\text{T}_{12\text{Sc}}$ by 5.99 kcal/mol. It is obvious that the total ΔE_{def} of 43.93 kcal/mol in $\text{T}_{12\text{Sc}}$ is larger than that (40.79 kcal/mol) in $\text{T}_{21\text{Sc}}$. However, the increased deformation energy could be compensated by the favorable ΔE_{int} (-37.21 kcal/mol) in $\text{T}_{12\text{Sc}}$, and resulted in lower ΔE_{TS} (6.72 kcal/mol) for $\text{T}_{12\text{Sc}}$ in comparison with that (12.71 kcal/mol) for $\text{T}_{21\text{Sc}}$. Therefore, the more favorable interaction of **A** with **B** in $\text{T}_{12\text{Sc}}$ could account for more stability of $\text{T}_{12\text{Sc}}$ in comparison with $\text{T}_{21\text{Sc}}$. Structurally, in $\text{T}_{21\text{Sc}}$ (Figure 3), a repulsive interaction between the ancillary ligand and the $\text{CH}_3(\text{CH}_2)_3$ group of 1-hexene moiety could exist, which destabilized $\text{T}_{21\text{Sc}}$, whereas such an interaction is absent in $\text{T}_{12\text{Sc}}$. The $\text{C1}=\text{C2}$ bond length of 1-hexene moiety is 1.440 Å in $\text{T}_{12\text{Sc}}$ and 1.425 Å in $\text{T}_{21\text{Sc}}$, suggesting that the $\text{C1}=\text{C2}$ double bond was more activated in the former. The $\text{T}_{12\text{Sc}}$ has a shorter $\text{Sc}-\text{C1}$ (2.218 Å) bond length than the $\text{Sc}-\text{C2}$ (2.268 Å) in $\text{T}_{21\text{Sc}}$, which suggests that the 1-hexene moiety interacts with the metal center more tightly in $\text{T}_{12\text{Sc}}$ compared with $\text{T}_{21\text{Sc}}$. This is in line with the analysis of energy decomposition described above. The geometrical character associated with the β -Si–H agostic interactions in $\text{T}_{12\text{Sc}}$ (2.331 Å for $\text{Sc}\cdots\text{H1}$, 1.524 Å for

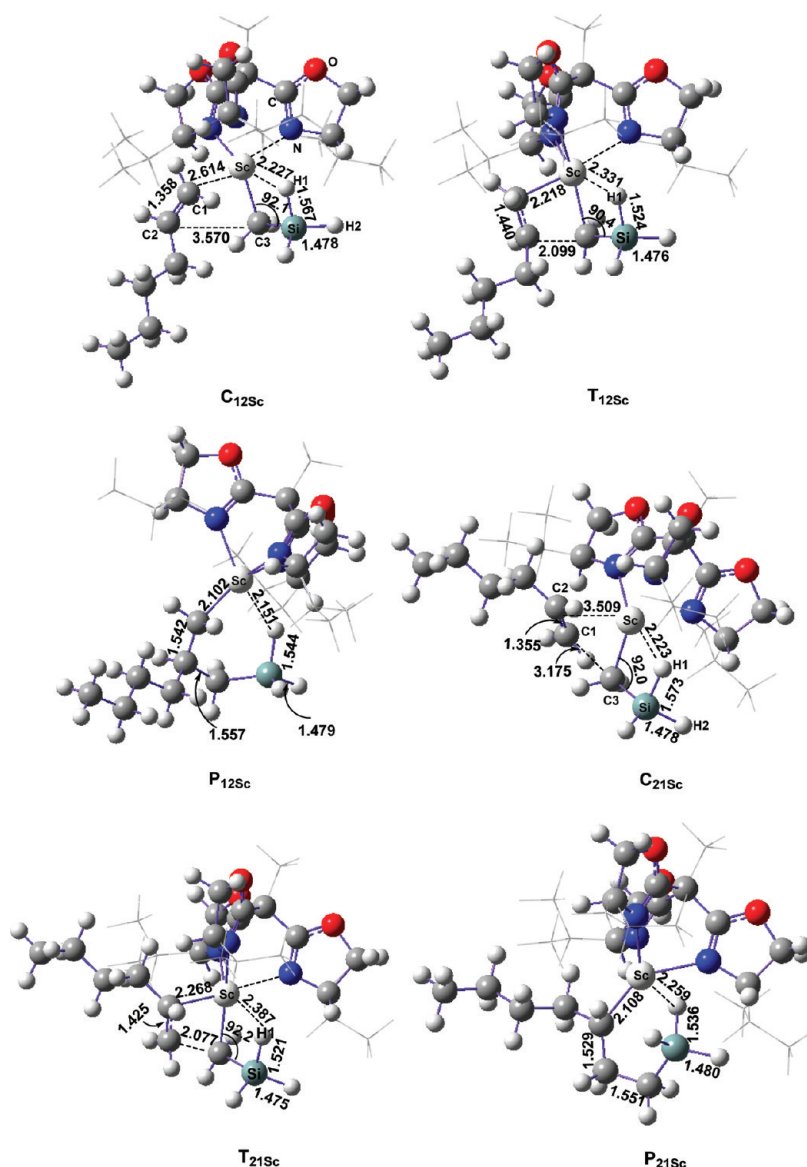


Figure 3. Geometric structures (distance in Å and angle in deg) involved in the energy profiles of 1,2- and 2,1-insertion of 1-hexene at the chain initiation stage.

Si...H1 and 90.4° for the Sc-CH₂-Si angle) and that in T_{21Sc} (2.387 Å for Sc-H1, 1.521 Å for Si-H1 and 92.2° for the Sc-CH₂-Si angle) indicates the shorter Sc...H1 distance and smaller Sc-CH₂-Si angle in T_{12Sc}. This suggests that such an agostic interaction in T_{12Sc} is stronger than that in T_{21Sc} and may also account for the more stability of T_{12Sc}. The similar geometrical feature was also observed when using the real structure of active species [Sc(*i*Pr-trisox)(CH₂SiMe₃)]²⁺ (see Figure S-5 in Supporting Information for more details).

To further access the regioselectivity in the chain propagation stage, the insertion of monomer into the Sc-CH₂ bond of P_{12Sc} was also investigated. As the insertion of the first monomer does, both 1,2- and 2,1-insertions of the incoming monomer into the Sc-C bond of P_{12Sc} were calculated, and the energy profiles are shown in Figure 4. As shown in this figure, the 1,2-insertion of the second monomer starts with the formation of complex C_{1212Iso} (stereoselectivity discussed below, *vide infra*), which is slightly lower in free energy than the energy sum of separated P_{12Sc} and *m* by 1.03 kcal/mol. This insertion

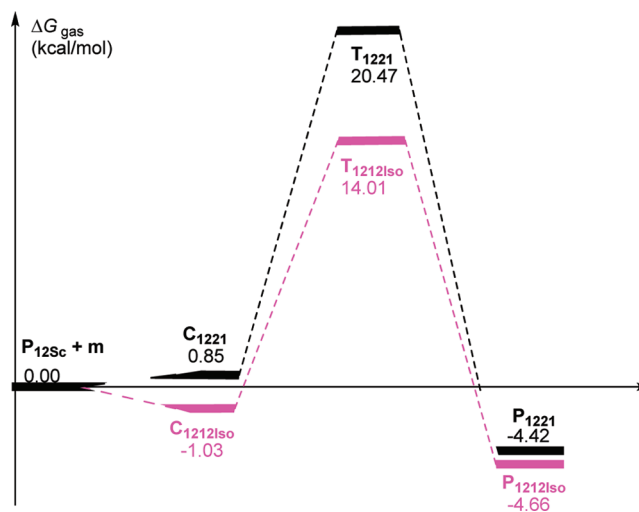


Figure 4. Computed energy profiles (energy in kcal/mol) for 1,2- and 2,1-insertion processes of 1-hexene at the chain propagation stage.

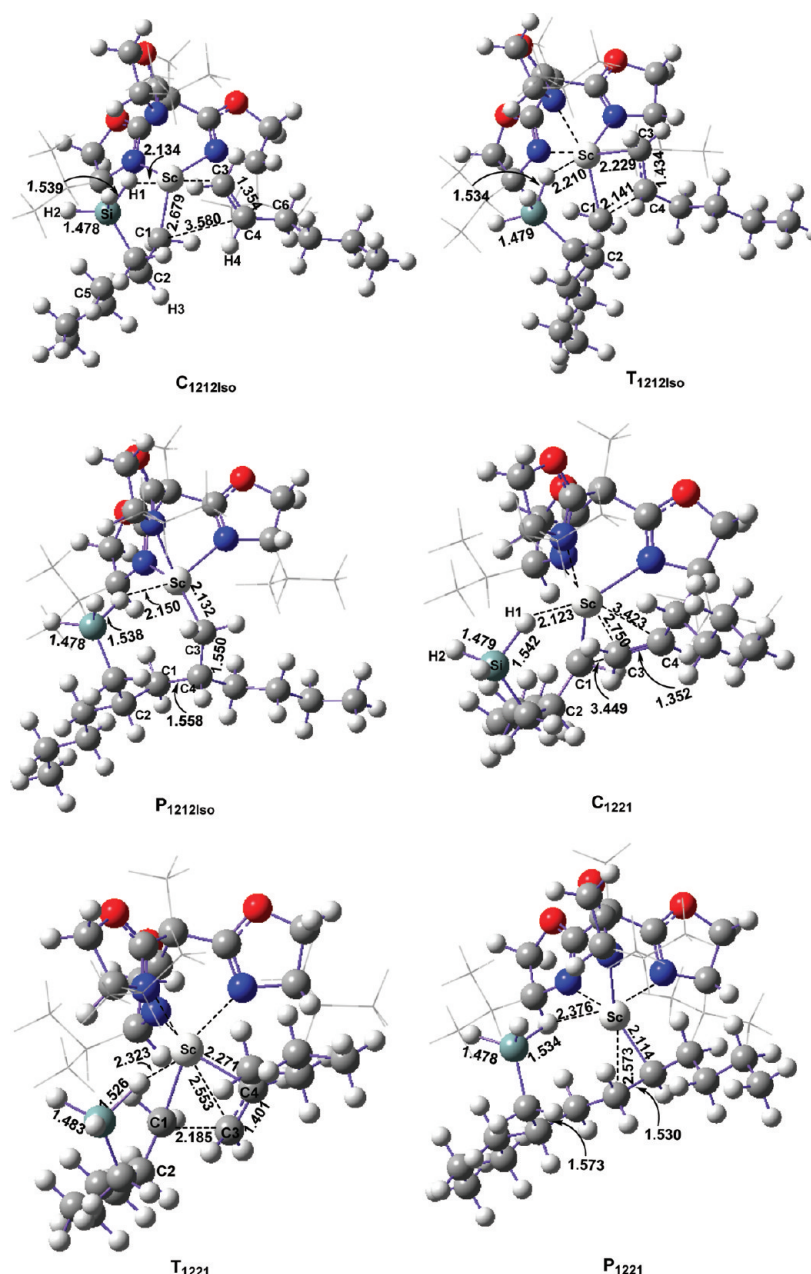


Figure 5. Geometric structures (distance in Å) involved in the energy profiles of 1,2- and 2,1-insertions of 1-hexene at the chain propagation stage.

process, which overcomes an energy barrier of 15.04 kcal/mol, is exergonic by 4.66 kcal/mol. Whereas, the 2,1-insertion process, which goes through prereaction complex C_{1221} and transition state T_{1221} leading to insertion product P_{1221} , is kinetically less favorable in comparison with 1,2-insertion reaction. This is suggested by the higher insertion energy barrier of 20.47 kcal/mol for 2,1-insertion (15.04 kcal/mol for 1,2-insertion, Figure 4). However, the energetic superiority of 1,2-insertion manner is so slight since the relative free energies of for C_{1221} (0.85 kcal/mol) and P_{1221} (−4.42 kcal/mol) and are close to those for $C_{1212Iso}$ (−1.03 kcal/mol) and $P_{1212Iso}$ (−4.66 kcal/mol), respectively. To elucidate the origin of the kinetic preference of 1,2-insertion, we further analyzed the structures and energies of $T_{1212Iso}$ and T_{1221} . As shown in Figure 5, the Sc–C3 distance of 2.229 Å and C1⋯C4 contact of 2.141 Å in $T_{1212Iso}$ are shorter than the corresponding interatomic distances in T_{1221} (Sc–C4 distance of 2.271 and C1⋯C3 contact of 2.185 Å). This indicates that the

1-hexene moiety binds more tightly to the metal center of $T_{1212Iso}$ in comparison with that of T_{1221} . A further analysis of energy decomposition of $T_{1212Iso}$ and T_{1221} has also been carried out. The decomposition scheme is similar to that for T_{12Sc} and T_{21Sc} (*vide ante*). The interaction energies ΔE_{int} between P_{12Sc} and 1-hexene moieties in $T_{1212Iso}$ and in T_{1221} are −35.16 and −24.98 kcal/mol, respectively, which could partly offset the unfavorable item ΔE_{def} (total deformation energy, 42.04 kcal/mol for $T_{1212Iso}$ and 36.40 kcal/mol for T_{1221}). Therefore, the ΔE_{TS} (−35.16 + 42.04 = 6.88 kcal/mol) obtained for $T_{1212Iso}$ is lower than that (−24.98 + 36.40 = 11.42 kcal/mol) for T_{1221} . Like the case of T_{12Sc} and T_{21Sc} , the less stability of T_{1221} is mainly due to the weaker interaction between P_{12Sc} and 1-hexene moiety. Furthermore, taking a closer look at the structures of $T_{1212Iso}$ and T_{1221} , one may find that there are significant interactions between Sc and a H atom of SiH_3 in the preinserted CH_2SiH_3 group, as suggested by the Sc⋯H distances (2.210 Å in $T_{1212Iso}$

and 2.323 Å in T_{1221}), the elongated Si–H bond lengths (1.534 Å in $T_{1212\text{Iso}}$ and 1.526 Å in T_{1221}) compared with the normal Si–H contact of 1.48 Å, and the more negative NBO charges (−0.33 in $T_{1212\text{Iso}}$ and −0.31 in T_{1221}) on the H atom interacting with Sc atom (Figure 5). In comparison with T_{1221} , $T_{1212\text{Iso}}$ has a shorter Sc···H distance (2.210 Å), longer Si–H bond length (1.534 Å), and more negative NBO charge (−0.33). As a whole, these geometrical and electronic features could account for the more stability of $T_{1212\text{Iso}}$.

2. Stereoselectivity in the 1-Hexene Polymerization.

To computationally interpret the stereoselectivity of 1-hexene polymerization observed experimentally, it is necessary to conduct calculations for both *iso*- and *syndio*-specific manners. The coordination of 1-hexene in 1,2-*si* and 1,2-*re* manner to the metal center of $P_{12\text{Sc}}$ could lead to the *iso*- and *syndio*-tactic polymers, respectively. Figure 6 shows the computed energy

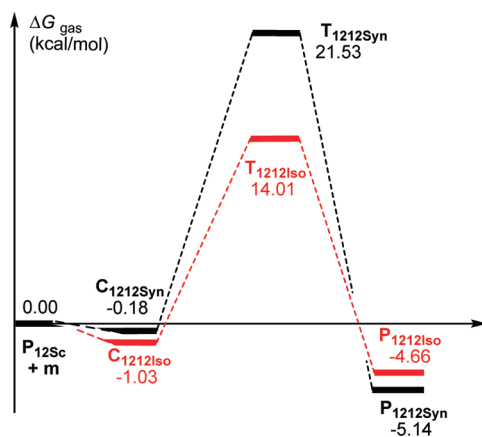


Figure 6. Computed energy profiles (energy in kcal/mol) for isotactic and syndiotactic insertion processes of 1-hexene.

profile for *re*-coordination of 1-hexene to the metal center of $P_{12\text{Sc}}$ and subsequent insertion process. Since $C_{1212\text{Iso}}$ shows the *si*-coordination fashion of 1-hexene (Figure 5) and the resulting product $P_{1212\text{Iso}}$ is isotactic, the energy profile for the process of $C_{1212\text{Iso}} \rightarrow T_{1212\text{Iso}} \rightarrow P_{1212\text{Iso}}$ (Figure 4) is also included in Figure 6 for comparison. As shown in this figure, the isospecific insertion of 1-hexene starts with its *si*-coordination to metal center (formation of $C_{1212\text{Iso}}$), and goes through a transition state $T_{1212\text{Iso}}$ leading to corresponding product $P_{1212\text{Iso}}$. However, the syndiospecific insertion occurs through the *re*-coordination of monomer to the metal center and then proceeds via a transition state $T_{1212\text{Syn}}$ to give insertion product $P_{1212\text{Syn}}$. In comparison, the lower insertion free-energy barrier of 15.04 kcal/mol for $T_{1212\text{Iso}}$ lends kinetic advantage to isotactic polymerization over syndiotactic polymerization, which has a higher insertion energy barrier of 21.71 kcal/mol (Figure 6). The syndiospecific product and the isospecific enantiomer are almost isoenergetic (energy difference of 0.48 kcal/mol, Figure 6). That is to say, the microstructure of polymer is mainly controlled by kinetics. In this sense, the current computational results are in agreement with the isoselectivity observed experimentally.

For better understanding of the origin of isospecific polymerization, the structure characters of some stationary points have been analyzed. In $C_{1212\text{Iso}}$, the 1-hexene moiety interacts with the metal center via *si*-coordination, which gives rise to isospecific product $P_{1212\text{Iso}}$ with *R*-configuration (refer to the chiral C4 atom, see Figure 5). Such a *si*-coordination manner

could avoid the repulsive interaction between the polymer chain and the $(\text{CH}_2)_3\text{CH}_3$ group of the coordinated 1-hexene moiety (see $C_{1212\text{Iso}}$ and $T_{1212\text{Iso}}$ in Figure 5). While, the *re*-coordination of the incoming monomer resulted in significant repulsion between the polymer chain and the $(\text{CH}_2)_3\text{CH}_3$ group of the coordinated 1-hexene moiety (see $C_{1212\text{Syn}}$ and $T_{1212\text{Syn}}$ in Figure 7). Such repulsion could destabilize $T_{1212\text{Syn}}$.

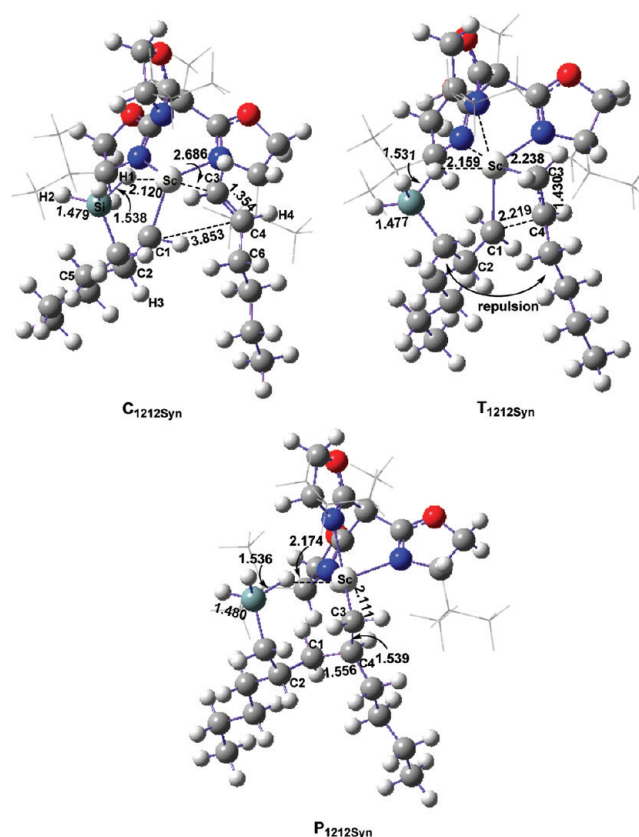


Figure 7. Geometric structures (distance in Å) involved in the energy profile of the syndiotactic insertion process.

The *re*-coordination manner could lead to syndiotactic product $P_{1212\text{Syn}}$ with *S*-configuration (refer to the chiral C4 atom). It is therefore concluded that the steric effects of the growing chain-end could be the main factor governing the stereoselectivity in this system.

3. Activity Comparison of Dicationic and Monocationic Species. Experimental studies have shown that the dicationic species $[\text{Sc}(\text{iPr-trisox})(\text{CH}_2\text{SiMe}_3)]^{2+}$ has higher activity for 1-hexene polymerization than the monocationic analogue $[\text{Sc}(\text{iPr-trisox})(\text{CH}_2\text{SiMe}_3)]^+$ by 3 orders of magnitude.^{7a} For comparison, calculations on $[\text{Sc}(\text{iPr-trisox})(\text{CH}_2\text{SiH}_3)]^+$ (2_{Sc}) modeling the monocation of 2_{Sc} has been also performed. The computed energy profile is shown in Figure 8. The energy profile for 3_{Sc} -involved process $C_{12\text{Sc}} \rightarrow T_{12\text{Sc}} \rightarrow P_{12\text{Sc}}$ is also included in this figure for convenience in discussion. Insertion processes catalyzed by monocationic 2_{Sc} and dicationic 3_{Sc} start with the formations of prereaction complexes C_{MC} and $C_{12\text{Sc}}$ and then goes through four-center transition states T_{MC} and $T_{12\text{Sc}}$ to give the insertion products P_{MC} and $P_{12\text{Sc}}$ respectively. The coordination complex C_{12} (complexation energy of −2.37 kcal/mol) is more stable than C_{MC} (complexation energy of 7.42 kcal/mol). The complex C_{MC} is higher in free energy by 7.42 kcal/mol in comparison

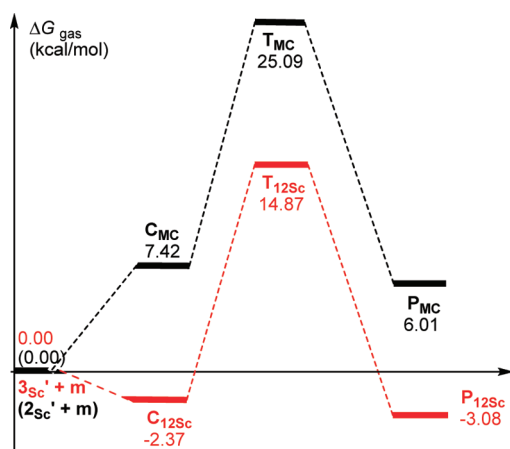


Figure 8. Computed energy profiles (energy in kcal/mol) for 1-hexene polymerization catalyzed by dication ($3_{sc'}$) and monocation ($2_{sc'}$) species at the chain initiation stage.

with separated species ($2_{sc'} + m$). The higher relative free energy of 7.42 kcal/mol for C_{MC} could be due to overestimation of translational entropy in gas-phase. The insertion process catalyzed by $3_{sc'}$ has a lower free-energy barrier of 17.24 kcal/mol and is exergonic by -3.08 kcal/mol. This process is both kinetically and energetically favorable than the $2_{sc'}$ -catalyzed one (free-energy barrier of 25.09 kcal/mol and endergonic by 6.01 kcal/mol). In the $2_{sc'}$ -catalyzed process, the

endergonic feature and the insertion energy barrier of 25.09 kcal/mol, which is higher than that (~ 20 kcal/mol) for the usual olefin insertion reaction, could add better understanding to the fact that the monocationic species has a very low activity toward 1-hexene polymerization.^{7a}

Geometrically, the two alkyl groups of $2_{sc'}$ (Figure 9) make their respective metal centers more crowded in comparison with $3_{sc'}$ (Figure 1) having one alkyl group. Such a situation sterically hampered the binding of 1-hexene moiety to the metal center of $2_{sc'}$, which accounts for the less stabilities of C_{MC} and T_{MC} in comparison with C_{12Sc} and T_{12Sc} , respectively. To further access the origin of the higher activity of $3_{sc'}$, the analyses of energy and electronic character have also been performed. The interaction energy ΔE_{int} between 1-hexene moiety and the active species $(iPr\text{-}trisox)Sc(CH_2SiH_3)_2^{2+}$ in T_{12Sc} and $(iPr\text{-}trisox)Sc(CH_2SiH_3)_2^+$ in T_{MC} were computed to be -37.21 and -23.37 kcal/mol, respectively. The sum of deformation energy ΔE_{def} of the active species and the 1-hexene moiety were computed to be 43.93 and 38.28 kcal/mol for T_{12Sc} and in T_{MC} , respectively. The energy of TS (ΔE_{TS}) could be obtained for T_{12Sc} ($-37.21 + 43.93 = 6.72$ kcal/mol) and T_{MC} ($-23.37 + 38.28 = 14.91$ kcal/mol), respectively. Therefore, the less stability of T_{MC} could be due to the weaker interaction between the $(iPr\text{-}trisox)Sc(CH_2SiH_3)_2^+$ species and the 1-hexene moiety in T_{MC} . To get more insights on the different activities of the monocationic and dicationic species, the frontier orbital energies of the related cations were also analyzed on the basis of their optimized geometries. The dication

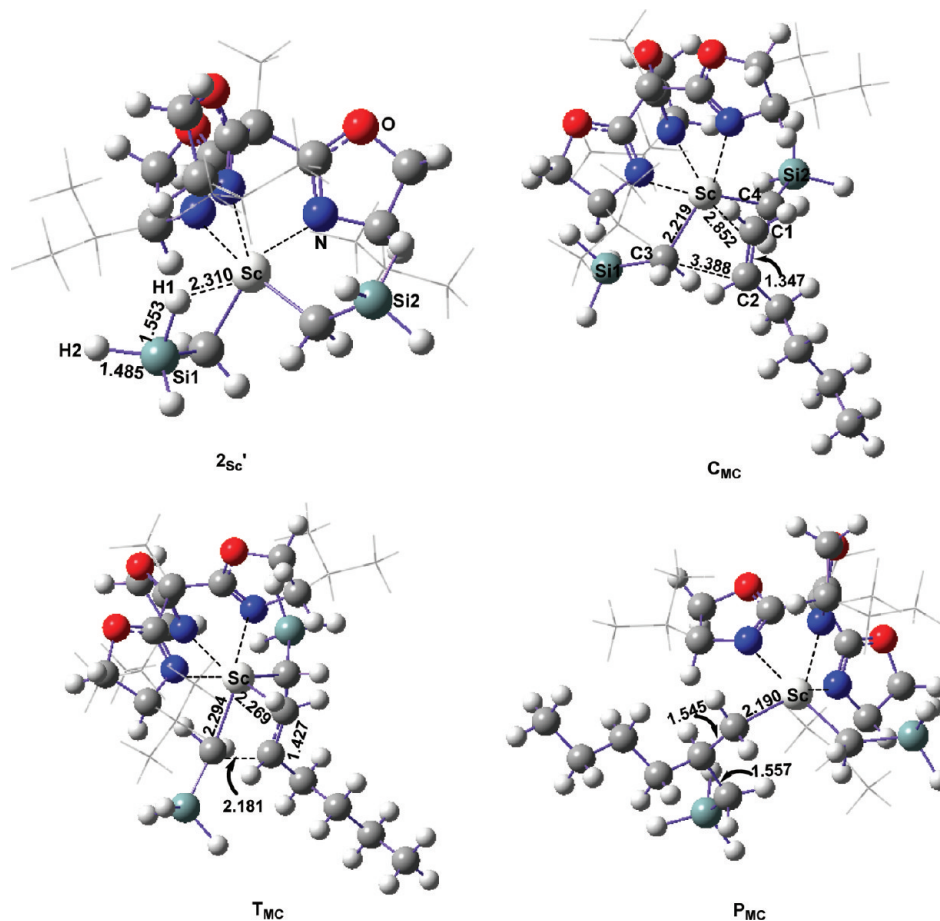


Figure 9. Geometric structures (distance in Å) involved in the energy profiles of 1-hexene polymerization catalyzed by monocation $2_{sc'}$ species at the chain initiation stage.

of 3_{Sc} is more electron-deficient and is a stronger Lewis acid with bigger chemical hardness (computed to be 2.847 eV, derived from the energies of frontier orbitals) compared to monocation of 2_{Sc} (chemical hardness of 2.603 eV), which could account for the higher reactivity of dication toward electron-rich olefin. Our calculations also show that the LUMO energies of the cations of 3_{Sc} and 2_{Sc} are -0.3112 au and -0.1718 au, respectively, and the HOMO energy of 1-hexene is -0.2591 au. By comparison, the HOMO energy of 1-hexene is closer to the LUMO energy of the dication, suggesting that 1-hexene is easier to react with the dication in comparison with the monocationic analogue.

4. Activity Comparison of $(i\text{Pr-trisox})\text{Sc}(\text{CH}_2\text{SiMe}_3)^{2+}$ with $(i\text{Pr-trisox})\text{Y}(\text{CH}_2\text{SiMe}_3)^{2+}$ Species. It was experimentally found that the Sc active species possesses significantly higher catalytic activity toward 1-hexene polymerization compared with the Y analogue. This motivated us to computationally elucidate the origin of the difference in activity. The computed energy profile for the reaction of 1-hexene with 3_{Y} (the Y analogue of 3_{Sc}) and the related structures are shown in Figure 10 and 11, respectively. For a comparison, the

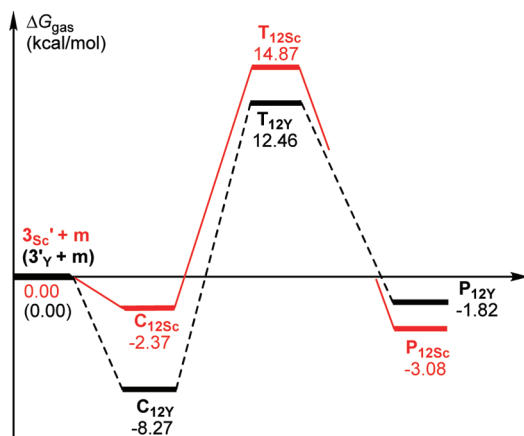


Figure 10. Computed energy profiles (energy in kcal/mol) for 1-hexene polymerization catalyzed by 3_{Sc} and 3_{Y} species at the chain initiation stage.

corresponding energy profile for 3_{Sc} -containing system is also included in this figure. Like 3_{Sc} , the structure of 3_{Y} (Figure 11) also shows a β -Si–H agostic interaction as suggested by the $\text{Y}\cdots\text{H1}$ distance of 2.309 Å, the Si–H1 bond length of 1.590 Å, and the $\text{Y}-\text{C3}-\text{Si}$ angle of 92.8° . As shown in Figure 10, the complexation energy of $\text{C}_{12\text{Y}}$ (-8.27 kcal/mol) is lower than that of $\text{C}_{12\text{Sc}}$ (-2.37 kcal/mol). The insertion energy barrier of 20.73 kcal/mol for 3_{Y} assisted insertion reaction is larger than that (17.24 kcal/mol) for 3_{Sc} -involved reaction. The insertion product $\text{P}_{12\text{Y}}$ is also slightly less stable than $\text{P}_{12\text{Sc}}$ by 1.26 kcal/mol. However, the relative energy (12.46 kcal/mol) of 3_{Y} -involved insertion transition state ($\text{T}_{12\text{Y}}$) is slightly lower than that (14.87 kcal/mol) of $\text{T}_{12\text{Sc}}$. The energy profile shown in Figure 10 indicates that the larger insertion barrier for 3_{Y} reaction system is mainly due to the lower $\text{C}_{12\text{Y}}$ in energy in comparison with 3_{Sc} -containing system. The chemical hardness of $(i\text{Pr-trisox})\text{Sc}(\text{CH}_2\text{SiMe}_3)^{2+}$ and $(i\text{Pr-trisox})\text{Y}(\text{CH}_2\text{SiMe}_3)^{2+}$ were computed to be 2.847 and 2.751 eV, respectively, suggesting a stronger Lewis acidity and hence higher reactivity of the former toward olefin in comparison with the later.

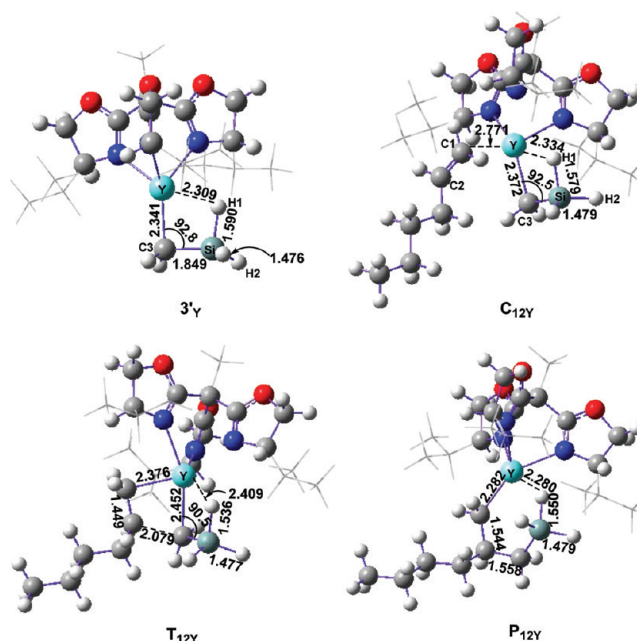
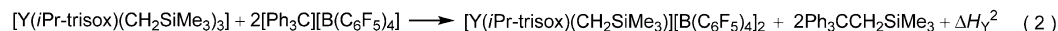
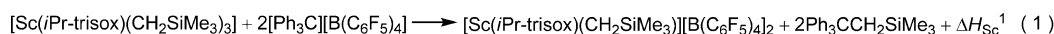


Figure 11. Geometric structures (distance in Å and angle in degree) involved in the energy profiles of 1-hexene polymerization catalyzed by 3_{Sc} and 3_{Y} species at the chain initiation stage.

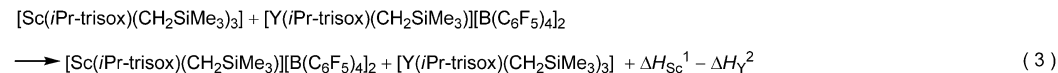
To cast a light on the reason for the stability of $\text{C}_{12\text{Y}}$, energy decomposition analyses of $\text{C}_{12\text{Sc}}$ and $\text{C}_{12\text{Y}}$ (electronic energy, ΔE) were carried out in a similar manner described above. The complex $\text{C}_{12\text{Sc}}$ (or $\text{C}_{12\text{Y}}$) can be divided into two fragments, viz. 3_{Sc} (or 3_{Y}) species and 1-hexene moiety. The following information was obtained for $\text{C}_{12\text{Sc}}$: $\Delta E_{\text{int}} = -23.22$ kcal/mol, $\Delta E_{\text{def}}(3_{\text{Sc}}) = 8.79$ kcal/mol, $\Delta E_{\text{def}}(1\text{-hexene}) = 2.51$ kcal/mol; and therefore $\Delta E(\text{C}_{12\text{Sc}}) = -23.22 + 8.79 + 2.51 = -11.92$ kcal/mol. While the following components were obtained for $\text{C}_{12\text{Y}}$: $\Delta E_{\text{int}} = -25.10$ kcal/mol; $\Delta E_{\text{def}}(3_{\text{Y}}) = 5.65$ kcal/mol; $\Delta E_{\text{def}}(1\text{-hexene}) = 2.51$ kcal/mol; and therefore $\Delta E(\text{C}_{12\text{Y}}) = -25.10 + 5.65 + 2.51 = -16.94$ kcal/mol, which is lower than that (-11.92 kcal/mol) of $\text{C}_{12\text{Sc}}$. It is obvious that the lower ΔE_{int} for $\text{C}_{12\text{Y}}$ and less deformation energy of $\Delta E_{\text{def}}(3_{\text{Y}})$ account for the more stability of $\text{C}_{12\text{Y}}$ in comparison with $\text{C}_{12\text{Sc}}$.

Although the 3_{Y} assisted insertion of 1-hexene is less favorable both kinetically and energetically than the 3_{Sc} involved process, such low superiorities are hard to explain well the large difference in activity between the Sc active species and its Y analogue. This drove us to further access the formations of the two kinds of active species and their interactions with counterion, respectively.

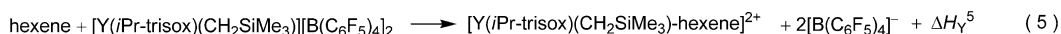
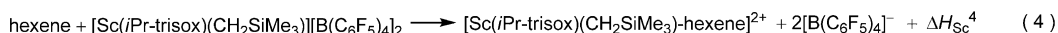
According to experimental findings,^{7a} the reaction of the trialkyl precursor $[(i\text{Pr-trisox})\text{Ln}(\text{CH}_2\text{SiMe}_3)_3]$ ($\text{Ln} = \text{Sc}, \text{Y}$) with 2 equiv of the borate compound $[\text{Ph}_3\text{C}][\text{B}(\text{C}_6\text{F}_5)_4]$ gives rise to 1 equiv of the contact ion-pair $[\text{Ln}(i\text{Pr-trisox})(\text{CH}_2\text{SiMe}_3)]-[\text{B}(\text{C}_6\text{F}_5)_4]_2$ and 2 equiv of $\text{Ph}_3\text{CCH}_2\text{SiMe}_3$, as illustrated by reactions 1 and 2 in Scheme 3. The optimized structures of the contact ion-pairs are shown in Figure 12. As shown in this figure, the counterions coordinate to the metal atom Sc (or Y) via three F atoms, viz. F1 and F2 atom in one counterion and F3 atom in another one (Figure 12). We assume that the reaction enthalpies of reactions 1 and 2 are ΔH_{Sc}^1 and ΔH_{Y}^2 (Scheme 3), respectively. Let (1) minus (2) give (3), and the reaction enthalpy of (3) is therefore $\Delta H_{\text{Sc}}^1 - \Delta H_{\text{Y}}^2$. Let $\Delta H^3 = \Delta H_{\text{Sc}}^1 - \Delta H_{\text{Y}}^2$. According to the calculated enthalpies based on optimized structures of $[(i\text{Pr-trisox})\text{Ln}(\text{CH}_2\text{SiMe}_3)_3]$ and

Scheme 3. Formation Process of Active Species $[\text{Ln}(\text{iPr-trisox})(\text{CH}_2\text{SiMe}_3)][\text{B}(\text{C}_6\text{F}_5)_4]_2$ ($\text{Ln} = \text{Sc}$ and Y) and the Separation of Ion Pairs via Hexene Coordination


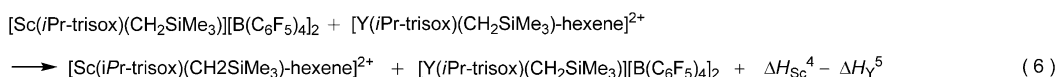
(1) – (2):



$$\Delta H^3 = \Delta H_{\text{Sc}}^1 - \Delta H_{\text{Y}}^2 = -5.96 \text{ kcal/mol}$$



(4) – (5):



$$\Delta H^6 = \Delta H_{\text{Sc}}^4 - \Delta H_{\text{Y}}^5 = -6.00 \text{ kcal/mol}$$

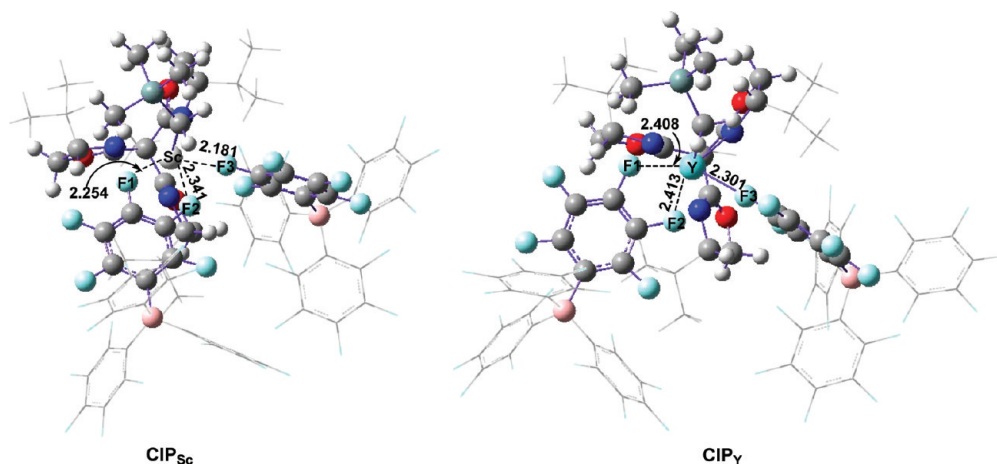


Figure 12. Optimized structures for contact ion-pair $[\text{Ln}(\text{iPr-trisox})(\text{CH}_2\text{SiMe}_3)][\text{B}(\text{C}_6\text{F}_5)_4]_2$ (CIP_{Sc} , $\text{Ln} = \text{Sc}$; CIP_{Y} , $\text{Ln} = \text{Y}$).

$[\text{Ln}(\text{iPr-trisox})(\text{CH}_2\text{SiMe}_3)][\text{B}(\text{C}_6\text{F}_5)_4]_2$ ($\text{Ln} = \text{Sc}$, Y) shown in eq 3, the reaction enthalpy of (3), viz. $\Delta H^3 = \Delta H_{\text{Sc}}^1 - \Delta H_{\text{Y}}^2$, was computed to be -5.96 kcal/mol . The negative value of ΔH^3 suggests that eq 1 is more exothermic (or less endothermic) than eq 2. That is to say, it is thermodynamically easier for Sc trialkyl precursor to be activated by $[\text{Ph}_3\text{C}][\text{B}(\text{C}_6\text{F}_5)_4]$ and to give corresponding active species in comparison with the Y trialkyl complex. This could account for the higher activity of Sc species compared with Y analogue. Similarly, the difference in the enthalpies required for the reactions of hexene with the contacted ion pairs (CIP_{Sc} or CIP_{Y} in Figure 12) leading to the anion and hexene-complexed cation, as shown in eqs 4 and 5 in Scheme 3, could be also computed. We assume that the reaction enthalpies of (4) and (5) are ΔH_{Sc}^4 and ΔH_{Y}^5 (Scheme 3), respectively. Let (4) minus (5) give (6), and the reaction enthalpy of (6) is therefore $\Delta H_{\text{Sc}}^4 - \Delta H_{\text{Y}}^5$. Let $\Delta H^6 = \Delta H_{\text{Sc}}^4 - \Delta H_{\text{Y}}^5$. In eqs 4–6, the $[\text{Sc}(\text{iPr-trisox})(\text{CH}_2\text{SiMe}_3)\text{-hexene}]^{2+}$ is actually the $\text{C}_{12\text{Sc}}$ shown in Figure 3, and the $[\text{Y}(\text{iPr-trisox})(\text{CH}_2\text{SiMe}_3)\text{-hexene}]^{2+}$ is actually the $\text{C}_{12\text{Y}}$ shown in Figure 11. Like eq 3,

according to the calculated enthalpies of optimized structures, the reaction enthalpy of (6), viz. $\Delta H^6 = \Delta H_{\text{Sc}}^4 - \Delta H_{\text{Y}}^5$, was computed to be -6.00 kcal/mol . The negative value of ΔH^6 illustrates that the two anions of ion pair CIP_{Sc} is easier to be replaced by hexene to coordinate to the metal center in comparison with that of ion pair CIP_{Y} . This result could also account for the higher activity of Sc system in comparison with Y analogue.

CONCLUSION

We have computationally studied the regio- and stereo-selectivity of the polymerization of 1-hexene catalyzed by the dicationic rare-earth metal complexes $[(\text{iPr-trisox})\text{Ln}(\text{CH}_2\text{SiMe}_3)]^{2+}$ ($\text{Ln} = \text{Sc}$ and Y). At both chain initiation and propagation stages, 1,2-insertion has been found to be kinetically favorable over 2,1-insertion. The kinetic priority of 1,2-insertion pattern is mainly due to the absence of repulsive interaction between the ancillary ligand and the $\text{CH}_3(\text{CH}_2)_3$ group of 1-hexene moiety in the insertion transition state and the resulting stronger binding between the metal center and the

1-hexene motif. The stereoselectivity has been found to follow chain-end mechanism, and the iso-specific insertion of 1-hexene observed experimentally is mainly controlled by kinetics. The insertion reaction catalyzed by dicationic active species is easier than that by monocationic species both kinetically and energetically, which is in agreement with the higher activity of the dicationic species observed experimentally. The features of frontier molecular orbitals of the two kinds of species could also account for their different activities. The origin of difference in activity between the scandium active species and its yttrium analogue has been also computationally investigated. It has been found that the scandium-catalyzed insertion reaction has kinetic preference over the yttrium-catalyzed reaction and that the generation of scandium active species is easier compared with that of yttrium analogue. These results could help understand better the higher activity of the scandium complex than its yttrium analogue and develop rare earth polymerization catalysts.

■ ASSOCIATED CONTENT

■ Supporting Information

Figures giving the energy profiles of 1,2- and 2,1-insertion process computed at the levels of B3LYP and MPW1K, optimized structures with CH_2SiMe_3 group, and tables giving the optimized Cartesian coordinates, total energies, and the imaginary frequencies of TSs. This material is available free of charge via the Internet at <http://pubs.acs.org>.

■ AUTHOR INFORMATION

Corresponding Author

*E-mail: luoyi@dlut.edu.cn (Y.L.); honz@riken.jp (Z.H.); qujp@dlut.edu.cn (J.Q.).

■ ACKNOWLEDGMENTS

This work was partly supported by the National Natural Science Foundation of China (No. 21028001, 21174023, 21137001, 20806012). Y.L. thanks the SEM Scientific Research Funding for ROCS. Z.H. acknowledges financial support from China's Thousand Talents Program. The authors also thank RICC (RIKEN Integrated Cluster of Clusters) and the Network and Information Center of Dalian University of Technology for computational resources.

■ REFERENCES

- (1) Recent reviews: (a) Gibson, V. C.; Spitzmesser, S. K. *Chem. Rev.* **2003**, *103*, 283–315. (b) Bochmann, M. *J. Organomet. Chem.* **2004**, *689*, 3982–3998. (c) Park, S.; Han, Y.; Kim, S. K.; Lee, J.; Kim, H. K.; Do, Y. *J. Organomet. Chem.* **2004**, *689*, 4263–4276. (d) Bolton, P. D.; Mountford, P. *Adv. Synth. Catal.* **2005**, *347*, 355–366. (e) Domski, G. J.; Rose, J. M.; Coates, G. W.; Bolig, A. D.; Brookhart, M. *Prog. Polym. Sci.* **2007**, *32*, 30–92. (f) Takeuchi, D. *Dalton Trans.* **2010**, *39*, 311–328.
- (2) (a) Babu, G. N.; Newmark, R. A. *Macromolecules* **1994**, *27*, 3383–3388. (b) Yamaguchi, Y.; Suzuki, N.; Mise, T.; Wakatsuki, Y. *Organometallics* **1999**, *18*, 996–1001. (c) Tshuva, E. Y.; Goldberg, I.; Kol, M. *J. Am. Chem. Soc.* **2000**, *122*, 10706–10707. (d) Groysman, S.; Goldberg, I.; Kol, M.; Genizi, E.; Goldschmidz, Z. *Inorg. Chim. Acta* **2003**, *345*, 137–144. (e) Segal, S.; Goldberg, I.; Kol, M. *Organometallics* **2005**, *24*, 200–202. (f) Vijayakrishna, K.; Sundararajan, G. *Polymer* **2006**, *47*, 3363–3371. (g) Sudhakar, P.; Sundararajan, G. *J. Polym. Sci., Part A: Polym. Chem.* **2006**, *44*, 4006–4014. (h) Sudhakar, P. *J. Polym. Sci., Part A: Polym. Chem.* **2007**, *45*, 5470–5479. (i) Domski, G. J.; Lobkovsky, E. B.; Coates, G. W. *Macromolecules* **2007**, *40*, 3510–3513. (j) Ishii, A.; Toda, T.; Nakata, N.; Matsuo, T. *J. Am. Chem. Soc.* **2009**, *131*, 13566–13567. (k) Cohen, A.; Kopilov, J.; Lamberti, M.; Venditto, V.; Kol, M. *Macromolecules* **2010**, *43*, 1689–1691.
- (3) Selected reviews: (a) Nishiura, M.; Hou, Z. *Nat. Chem.* **2010**, *2*, 257–268. (b) Rodrigues, A. S.; Carpentier, J. F. *Coord. Chem. Rev.* **2008**, *252*, 2137–2154. (c) Li, X.; Hou, Z. *Coord. Chem. Rev.* **2008**, *252*, 1842–1869. (d) Zeimentz, P. M.; Arndt, S.; Elvidge, B. R.; Okuda, J. *Chem. Rev.* **2006**, *106*, 2404–2433. (e) Kretscher, W. P.; Meetsma, A.; Hessen, B.; Schmalz, T.; Sadaf, Q.; Kempe, R. *Chem. A. Eur. J.* **2006**, *12*, 8969–8978. (f) Hou, Z.; Wakatsuki, Y. *Coord. Chem. Rev.* **2002**, *231*, 1–22. (g) Evans, W. J.; Davis, B. L. *Chem. Rev.* **2002**, *102*, 2119–2136. (h) Marques, M.; Sella, A.; Takats, J. *Chem. Rev.* **2002**, *102*, 2137–2160. (i) Chen, E. Y. X.; Marks, T. J. *Chem. Rev.* **2000**, *100*, 1391–1434.
- (4) (a) Luo, Y.; Baldamus, J.; Hou, Z. *J. Am. Chem. Soc.* **2004**, *126*, 13910–13911. (b) Zhang, L.; Luo, Y.; Hou, Z. *J. Am. Chem. Soc.* **2005**, *127*, 14562–14563. (c) Li, X.; Hou, Z. *Macromolecules* **2005**, *38*, 6767–6769. (d) Li, X. F.; Baldamus, J.; Nishiura, M.; Tardif, O.; Hou, Z. M. *Angew. Chem., Int. Ed.* **2006**, *45*, 8184–8188. (e) Li, X. F.; Nishiura, M.; Mori, K.; Mashiko, T.; Hou, Z. M. *Chem. Commun.* **2007**, 4137–4139. (f) Yu, N.; Nishiura, M.; Li, X. F.; Xi, Z. F.; Hou, Z. M. *Chem. Asian J.* **2008**, *3*, 1406–1414. (g) Zhang, H.; Luo, Y.; Hou, Z. *Macromolecules* **2008**, *41*, 1064–1066. (h) Li, X.; Nishiura, M.; Hu, L.; Mori, K.; Hou, Z. *J. Am. Chem. Soc.* **2009**, *131*, 13870–13882. (i) Li, X.; Hou, Z. *Macromolecules* **2010**, *43*, 8904–8909. (j) Pan, L.; Zhang, K.; Nishiura, M.; Hou, Z. *Macromolecules* **2010**, *43*, 9591–9593. (k) Guo, F.; Nishiura, M.; Koshino, H.; Hou, Z. *Macromolecules* **2011**, *44*, 6335–6344. (l) Guo, F.; Nishiura, M.; Koshino, H.; Hou, Z. *Macromolecules* **2011**, *44*, 2400–2403. (m) Pan, L.; Zhang, K.; Nishiura, M.; Hou, Z. *Angew. Chem., Int. Ed.* **2011**, DOI: 10.1002/anie.201104011.
- (5) (a) Luo, Y. J.; Hou, Z. *Stud. Surf. Sci. Catal.* **2006**, *161*, 95–104. (b) Hou, Z.; Luo, Y. J.; Li, X. *J. Organomet. Chem.* **2006**, *691*, 3114–3121.
- (6) Tredget, C. S.; Bonnet, F.; Cowley, A. R.; Mountford, P. *Chem. Commun.* **2005**, 3301–3303.
- (7) (a) Ward, B. D.; Bellemin-Laponnaz, S.; Gade, L. H. *Angew. Chem., Int. Ed.* **2005**, *44*, 1668–1671. (b) Lukešová, L.; Ward, B. D.; Bellemin-Laponnaz, S.; Wade, P. H.; Gade, L. H. *Dalton Trans.* **2007**, 920–922. (c) Lukešová, L.; Ward, B. D.; Bellemin-Laponnaz, S.; Wade, P. H.; Gade, L. H. *Organometallics* **2007**, *26*, 4652–4657. (d) Ward, B. D.; Lukešová, L.; Wade, P. H.; Bellemin-Laponnaz, S.; Gade, L. H. *Eur. J. Inorg. Chem.* **2009**, 866–871.
- (8) Reviews, see: (a) Rappe, A. K.; Skiff, W. M.; Casewit, C. J. *Chem. Rev.* **2000**, *100*, 1435–1456. (b) Niu, S.; Hall, M. B. *Chem. Rev.* **2000**, *100*, 353–406. (c) Michalak, A.; Ziegler, T. In *Computational Modeling of Homogeneous Catalysis*; Feliu, M.; Agusti, L., Eds.; Kluwer: Dordrecht, The Netherlands, 2002; Vol. 25, pp 57–78. (d) Tobisch, S. *Acc. Chem. Res.* **2002**, *35*, 96–104. (e) Bo, C.; Maseras, F. *Dalton Trans.* **2008**, 2911–2919. (f) Mandal, S. K.; Roesky, H. W. *Acc. Chem. Res.* **2010**, *43*, 248–259.
- (9) Examples, see: (a) Woo, T. K.; Ziegler, T. *Organometallics* **1994**, *13*, 2252–2261. (b) Xu, Z.; Vanka, K.; Firman, T.; Michalak, A.; Zurek, E.; Zhu, C.; Ziegler, T. *Organometallics* **2002**, *21*, 2444–2453. (c) Flisak, Z.; Ziegler, T. *Macromolecules* **2005**, *38*, 9865–9872. (d) Margl, P.; Deng, L.; Ziegler, T. *J. Am. Chem. Soc.* **1998**, *120*, 5517–5525. (e) Froese, R. D. J.; Musaev, D. G.; Morokuma, K. *Organometallics* **1999**, *18*, 373–379. (f) Froese, R. D. J.; Musaev, D. G.; Matsubara, T.; Morokuma, K. *J. Am. Chem. Soc.* **1997**, *119*, 7190–7196. (g) Musaev, D. G.; Froese, R. D. J.; Svensson, M.; Morokuma, K. *J. Am. Chem. Soc.* **1997**, *119*, 367–374. (h) Froese, R. D. J.; Musaev, D. G.; Morokuma, K. *J. Am. Chem. Soc.* **1998**, *120*, 1581–1587. (i) Yoshida, T.; Koga, N.; Morokuma, K. *Organometallics* **1996**, *15*, 766–777. (j) Margl, P.; Deng, L.; Ziegler, T. *Organometallics* **1998**, *17*, 933–946. (k) Deng, L.; Margl, P.; Ziegler, T. *J. Am. Chem. Soc.* **1997**, *119*, 1094–1100. (l) Tobisch, S.; Bogel, H.; Taube, R. *Organometallics* **1998**, *17*, 1177–1196. (m) Tobisch, S. *J. Am. Chem. Soc.* **2004**, *126*, 259–272. (n) Lanza, G.; Fragala, I. L.; Marks, T. J. *Organometallics* **2001**, *20*, 4006–4017. (o) Lanza, G.; Fragala, I. L.; Marks, T. J.

- Organometallics* **2002**, *21*, 5594–5612. (p) Novaro, O.; Blaisten-Barojas, E.; Clementi, E.; Giunchi, G.; Ruiz-Vizcaya, M. E. *J. Chem. Phys.* **1978**, *68*, 2337–2351. (q) Fujimoto, H.; Yamasaki, T.; Mizutani, H.; Koga, N. *J. Am. Chem. Soc.* **1985**, *107*, 6157–6161. (r) Kawamura-Kuribayashi, H.; Koga, N.; Morokuma, K. *J. Am. Chem. Soc.* **1992**, *114*, 2359–2366. (s) Koga, N.; Yoshida, T.; Morokuma, K. *Organometallics* **1993**, *12*, 2777–2787. (t) Weiss, H.; Ehrig, M.; Ahlrichs, R. *J. Am. Chem. Soc.* **1994**, *116*, 4919–4928. (u) Bierwagen, E. P.; Bercaw, J. E.; Goddard, W. A. *J. Am. Chem. Soc.* **1994**, *116*, 1481–1489. (v) Linnolahti, M.; Pakkanen, T. A. *Macromolecules* **2000**, *33*, 9205–9214. (w) Motta, A.; Fragala, I. L.; Marks, T. J. *J. Am. Chem. Soc.* **2008**, *130*, 16533–16546. (x) Yang, S. Y.; Ziegler, T. *Organometallics* **2006**, *25*, 887–900. (y) Guerra, G.; Corradini, P.; Cavallo, L. *Macromolecules* **2005**, *38*, 3973–3976. (z) Zhang, Y.; Ning, Y.; Caporaso, L.; Cavallo, L.; Chen, E. Y. X. *J. Am. Chem. Soc.* **2010**, *132*, 2695–2709.
- (10) (a) Michalak, A.; Ziegler, T. *Organometallics* **1999**, *18*, 3998–4004. (b) Michalak, A.; Ziegler, T. *J. Am. Chem. Soc.* **2002**, *124*, 7519–7528. (c) Michalak, A.; Ziegler, T. *Kinet. Catal.* **2006**, *47*, 310–325. (d) Liu, Y.; Zhang, M.; Drew, M. G. B.; Yang, Z.; Liu, Y. *J. Mol. Struct.: THEOCHEM* **2005**, *726*, 277–283. (e) Yang, Z.; Liu, Y.; Liu, Y. *Chinese J. Struct. Chem.* **2005**, *24*, 723–728. (f) Liu, Y.; Liu, Y.; Drew, M. G. B. *Struct. Chem.* **2010**, *21*, 21–28. (g) Moscardi, G.; Resconi, L. *Organometallics* **2001**, *20*, 1918–1931. (h) Mitani, M.; Furuyama, R.; Mohri, J.; Saito, J.; Ishii, S.; Terao, H.; Nakano, T.; Tanaka, H.; Fujita, T. *J. Am. Chem. Soc.* **2003**, *125*, 4293–4305. (i) Borrelli, M.; Busico, V.; Cipullo, R.; Ronca, S. *Macromolecules* **2003**, *36*, 8171–8177. (j) Saßmannshausen, J. *Dalton Trans.* **2009**, 8993–8999. (k) Lee, J. W.; Jo, W. H. *J. Organomet. Chem.* **2009**, *694*, 3076–3083. (l) Caporaso, L.; Rosa, C. D.; Talarico, G. *J. Polym. Sci., Part A: Polym. Chem.* **2010**, *48*, 699–708.
- (11) (a) Kirillov, E.; Lavanant, L.; Thomas, C.; Roisnel, T.; Chi, Y.; Carpentier, J. F. *Chem.—Eur. J.* **2007**, *13*, 923–935. (b) Landis, C. R.; Rosaen, K. A.; Uddin, J. *J. Am. Chem. Soc.* **2002**, *124*, 12062–12063. (c) Zuccaccia, C.; Busico, V.; Cipullo, R.; Talarico, G.; Froese, R. D. J.; Vosejka, P. C.; Hustad, P. D.; Macchioni, A. *Organometallics* **2009**, *28*, 5445–5458. (d) Manz, T. A.; Sharma, S.; Phomphrai, K.; Novstrup, K. A.; Fenwick, A. E.; Fanwick, P. E.; Medvedev, G. A.; Abu-Omar, M. M.; Delgass, W. N.; Thomson, K. T.; Caruthers, J. M. *Organometallics* **2008**, *27*, 5504–5520. (e) Manz, T. A.; Phomphrai, K.; Sharma, G. S.; Haq, J.; Novstrup, K. A.; Thomson, K. T.; Delgass, W. N.; Caruthers, J. M.; Abu-Omar, M. M. *J. Am. Chem. Soc.* **2007**, *129*, 3776–3777.
- (12) (a) Tredget, C. S.; Clot, E.; Mountford, P. *Organometallics* **2008**, *27*, 3458–3473. (b) Zhang, L.; Suzuki, T.; Luo, Y.; Nishiura, M.; Hou, Z. *Angew. Chem., Int. Ed.* **2007**, *46*, 1909–1913. (c) Li, X.; Nishiura, M.; Hu, L.; Mori, K.; Hou, Z. *J. Am. Chem. Soc.* **2009**, *131*, 13870–13882. (d) Zhang, L.; Luo, Y.; Hou, Z. *J. Am. Chem. Soc.* **2005**, *127*, 14562–14563. (e) Luo, Y.; Hou, Z. *Organometallics* **2006**, *25*, 6162–6165. (f) Luo, Y.; Luo, Y.; Qu, J.; Hou, Z. *Organometallics* **2011**, *30*, 2908–2919. (g) Du, G.; Wei, Y.; Ai, L.; Chen, Y.; Xu, Q.; Liu, X.; Zhang, S.; Hou, Z.; Li, X. *Organometallics* **2011**, *30*, 160–170. (h) Liu, J.; Ling, J.; Shen, Z. *J. Mol. Cat. A Chem.* **2009**, *300*, 59–64. (i) Paoluccia, G.; Bortoluzia, M.; Napolib, M.; Longob, P.; Bertolasic, V. *J. Mol. Cat. A Chem.* **2010**, *317*, 54–60. (j) Ling, J.; Shen, J.; Hogen-Esch, T. E. *Polymer* **2009**, *50*, 3575–3581. (k) Perrin, L.; Bonnet, F.; Visseaux, M.; Maron, L. *Chem. Commun.* **2010**, *46*, 2965–2967. (l) Perrin, L.; Sarazin, Y.; Kirillov, E.; Carpentier, J. F.; Maron, L. *Chem.—Eur. J.* **2009**, *15*, 3773–3783. (m) Perrin, L.; Bonnet, F.; Chenal, T.; Visseaux, M.; Maron, L. *Chem.—Eur. J.* **2010**, *16*, 11376–11385. (n) Perrin, L.; Kirillov, E.; Carpentier, J. F.; Maron, L. *Macromolecules* **2010**, *43*, 6330–6336. (o) Annunziata, L.; Rodrigues, A. S.; Kirillov, E.; Sarazin, Y.; Okuda, J.; Perrin, L.; Maron, L.; Carpentier, J. F. *Macromolecules* **2011**, *44*, 3312–3322.
- (13) Selected examples: (a) Luo, Y.; Selvam, P.; Endou, A.; Kubo, M.; Miyamoto, A. *J. Am. Chem. Soc.* **2003**, *125*, 16210–16212. (b) Luo, Y.; Selvam, P.; Ito, Y.; Takami, S.; Kubo, M.; Imamura, A.; Miyamoto, A. *Organometallics* **2003**, *22*, 2181–2183. (c) Luo, Y.; Baldamus, J.; Tardif, O.; Hou, Z. *Organometallics* **2005**, *24*, 4362–4366. (d) Luo, Y.; Hou, Z. *Organometallics* **2007**, *26*, 2941–2944.
- (e) Luo, Y.; Hou, Z. *Int. J. Quantum Chem.* **2007**, *107*, 374–381. (f) Luo, Y.; Hou, Z. *J. Phys. Chem. C* **2008**, *112*, 635–638.
- (14) (a) Svensson, M.; Humbel, S.; Froese, R. D. J.; Matsubara, T.; Sieber, S.; Morokuma, K. *J. Phys. Chem.* **1996**, *100*, 19357–19363. (b) Maseras, F.; Morokuma, K. *J. Comput. Chem.* **1995**, *16*, 1170–1179. (c) Vreven, T.; Morokuma, K. *J. Comput. Chem.* **2000**, *21*, 1419–1432.
- (15) Frisch, M. J.; Trucks, G. W.; Schlegel, H. B.; Scuseria, G. E.; Robb, M. A.; Cheeseman, J. R.; Scalmani, G.; Barone, V.; Mennucci, B.; Petersson, G. A.; Nakatsuji, H.; Caricato, M.; Li, X.; Hratchian, H. P.; Izmaylov, A. F.; Bloino, J.; Zheng, G.; Sonnenberg, J. L.; Hada, M.; Ehara, M.; Toyota, K.; Fukuda, R.; Hasegawa, J.; Ishida, M.; Nakajima, T.; Honda, Y.; Kitao, O.; Nakai, H.; Vreven, T.; Montgomery, J. A.; Jr.; Peralta, J. E.; Ogliaro, F.; Bearpark, M.; Heyd, J. J.; Brothers, E.; Kudin, K. N.; Staroverov, V. N.; Kobayashi, R.; Normand, J.; Raghavachari, K.; Rendell, A.; Burant, J. C.; Iyengar, S. S.; Tomasi, J.; Cossi, M.; Rega, N.; Millam, J. M.; Klene, M.; Knox, J. E.; Cross, J. B.; Bakken, V.; Adamo, C.; Jaramillo, J.; Gomperts, R.; Stratmann, R. E.; Yazyev, O.; Austin, A. J.; Cammi, R.; Pomelli, C.; Ochterski, J. W.; Martin, R. L.; Morokuma, K.; Zakrzewski, V. G.; Voth, G. A.; Salvador, P.; Dannenberg, J. J.; Dapprich, S.; Daniels, A. D.; Farkas, O.; Foresman, J. B.; Ortiz, J. V.; Cioslowski, J.; Fox, D. J. *Gaussian 09, Revision A.02*; Gaussian, Inc.: Wallingford CT, 2009.
- (16) Rappé, A. K.; Casewit, C. J.; Colwell, K. S.; Goddard, W. A. III; Skiff, W. M. *J. Am. Chem. Soc.* **1992**, *114*, 10024–10035.
- (17) (a) Dolg, M.; Wedig, U.; Stoll, H.; Preuss, H. *J. Chem. Phys.* **1987**, *86*, 866–872. (b) Schwerdtfeger, P.; Dolg, M.; Schwarz, W. H. E.; Bowmaker, G. A.; Boyd, P. D. W. *J. Chem. Phys.* **1989**, *91*, 1762–1774. (c) Dolg, M.; Stoll, H.; Savin, A.; Preuss, H. *Theor. Chim. Acta.* **1989**, *75*, 173–194. (d) Andrae, D.; Haeussermann, U.; Dolg, M.; Stoll, H.; Preuss, H. *Theor. Chim. Acta.* **1990**, *77*, 123–141. (e) Dolg, M.; Stoll, H.; Preuss, H. *Theor. Chim. Acta.* **1993**, *85*, 441–450. (f) Bergner, A.; Dolg, M.; Kuechle, W.; Stoll, H.; Preuss, H. *Mol. Phys.* **1993**, *80*, 1431–1441.
- (18) (a) Cossée, P. *J. Catal.* **1964**, *3*, 80–88. (b) Arlman, E. J. *J. Catal.* **1964**, *3*, 89–98. (c) Arlman, E. J.; Cossée, P. *J. Catal.* **1964**, *3*, 99–104. (d) Brookhart, M.; Green, M. L. H. *J. Organomet. Chem.* **1983**, *250*, 395–408. (e) Grubbs, R.; Coates, G. W. *Acc. Chem. Res.* **1996**, *29*, 85–93. (f) Fan, L.; Harrison, D.; Woo, T. K.; Ziegler, T. *Organometallics* **1995**, *14*, 2018–2026.
- (19) Resconi, L.; Cavallo, L.; Fait, A.; Piemontesi, F. *Chem. Rev.* **2000**, *100*, 1253–1345.
- (20) Lynch, B. J.; Truhlar, D. G. *J. Phys. Chem. A* **2003**, *107*, 3898–3906.

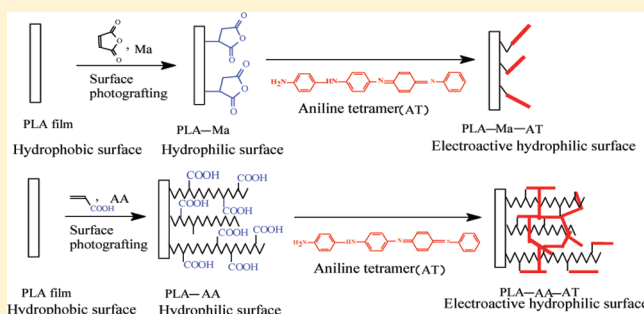
Electroactive Hydrophilic Polylactide Surface by Covalent Modification with Tetraaniline

Baolin Guo, Anna Finne-Wistrand, and Ann-Christine Albertsson*

Department of Fibre and Polymer Technology, School of Chemical Science and Engineering, KTH Royal Institute of Technology, SE-100 44 Stockholm, Sweden

Supporting Information

ABSTRACT: Covalent surface functionalization is presented as a versatile tool to increase the hydrophilicity and to introduce the electroactivity of polyester films. Acrylic acid and maleic anhydride were photografted onto a polylactide (PLA) surface with a “grafting from” method to increase the surface wettability, and the subsequent coupling of conductive aniline oligomer was used to introduce electroactivity to the PLA surface. The photopolymerization of maleic anhydride and acrylic acid and the coupling of aniline tetramer (AT) were characterized by FT-IR, UV, and TGA. The surface morphology of the PLA surface before and after modification was examined by scanning electron microscopy (SEM) and atomic force microscopy (AFM). A medium hydrophilic surface of PLA was achieved by surface modification with maleic anhydride, acrylic acid, and AT. An electrically conductive surface was obtained after grafting with AT, and the conductivity increased with increasing AT content on the surface. The hydrophilic and electroactive surface of polyesters while retaining their bulk properties offers new possibilities in biomedical applications, such as bone, cartilage, neural, and cardiovascular tissue engineering.



INTRODUCTION

The performance of polymeric materials depends greatly on the surface properties of the biomaterials because most biological reactions occur between a polymeric implant and the host tissue.^{1–3} The development of biomaterials for tissue regeneration applications requires the construction of a suitable surface that can induce a specific cellular response and regulate the formation of new tissue. The most widely used biomaterials in tissue engineering are polyesters such as polylactide (PLA), polycaprolactone (PCL), etc., because of their excellent biocompatibility, degradability, and mechanical properties.^{4–6} However, the hydrophilicity of PLA is not appropriate for cell attachment on its surface; the PLA surface lacks chemically modifiable side-chain groups, and PLA is a biologically inert polymeric biomaterial that is not able to induce cell adhesion and tissue formation.^{7,8} To improve the host–implant interaction of biomaterials, various modifications of PLA have been studied,^{8–10} such as copolymerization with other functional and hydrophilic monomers^{11–13} or blending of PLA with other materials.^{14,15} However, copolymerization and blending changes the bulk properties of PLA, and this is considered to be a drawback in many applications. Therefore, surface modification of the PLA has been the subject of attention. Among the techniques employed for surface modification of biodegradable polymers, photografting is a useful tool with the advantages of low cost of operation, mild reaction conditions, and a permanent alteration of the surface

chemistry.^{16,17} Photografting employs a much lower energy than γ or electron beam irradiation, and this reduces the risk of possible degradation of the polymer. Poly(acrylic acid) (PAA) has been covalently grafted onto the surface of degradable biomaterials including PLA and PCL by photografting.^{18,19} PLA has a much more hydrophilic surface after grafting with AA or maleic anhydride, and the rate of degradation of PLA was enhanced as a result of the hydrophilic surface.^{20,21} More importantly, the surface with functional groups could be used for the further covalent immobilization of bioactive molecules, such as gelatin, heparin, and nerve growth factor or vascular endothelium growth factor,² which could enhance cell adhesion and further regulate the cell behavior.

Conducting polymers such as polyaniline and polypyrrole have been shown to regulate the behavior of a series of cells (neural, cardiac, fibroblast, and endothelial cells) by electrical stimulation, including cell adhesion, spreading, proliferation, differentiation, and DNA synthesis.^{22–24} To take advantage of conducting polymers, polypyrrole was coated onto electrospun poly(lactic-co-glycolic acid) nanofibers²⁵ and PLA and PCL nanofibers²⁶ by in situ solution polymerization of pyrrole. However, the interaction between the polypyrrole and substrate is weak due to the noncovalent deposition. Another severe

Received: November 15, 2011

Revised: December 16, 2011

Published: December 28, 2011

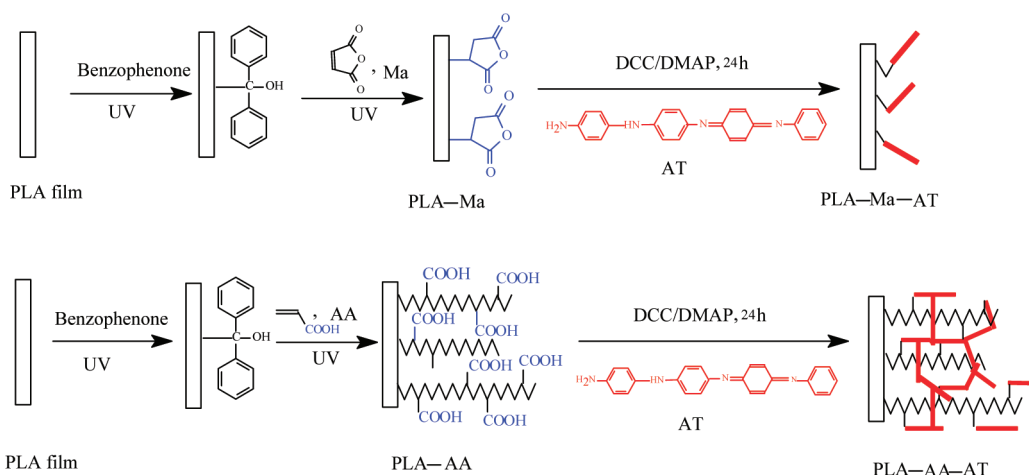


Figure 1. Surface grafting of polylactide (PLA) films with aniline tetramer (AT).

limitation of the conducting polymers used in tissue engineering is their nondegradability. In contrast, aniline oligomers such as aniline trimer, aniline tetramer, and aniline pentamer have a well-defined structure, good biocompatibility, and an electroactivity similar to that of polyaniline, together with specific end groups which offers possibilities for further extensive modification.^{27,28} In addition, the aniline oligomers would be consumed by macrophages, and subsequently cleared by the kidney,^{29,30} which eliminates the need for a second surgical removal of the materials. Our group have designed and synthesized a series of linear (diblock³¹ and triblock³²), star-shaped,³³ hyperbranched,³⁴ and cross-linked^{35,36} degradable and electrically conducting polymers and hydrogels and porous tubular scaffolds³⁷ based on PLA, PCL, and aniline oligomers, and we have found that macromolecular architecture is a useful tool to tune the properties of these polymers. All these studies have focused on the bulk properties of the materials.

The goal of the present work is to functionalize the PLA film with aniline oligomer to create a conductive and hydrophilic surface by covalent surface modification. We hypothesize that a moderately hydrophilic PLA surface would have a better interaction with the host tissue and that the electrically conductive PLA surface could be used to induce specific cellular responses to tune and control the formation of new tissue. A covalent modification with AT is preferred rather than noncovalent modification because of its superior environmental stability. First, we introduce maleic anhydride and acrylic acid which contain carboxyl groups to the surface of the PLA film by photografting. Second, we attach the electroactive aniline tetramer to these pendant carboxyl groups by a coupling reaction. The hydrophilic and electroactive surface of PLA films together with the bulk properties of PLA, such as its good mechanical properties, has a great potential in tissue engineering applications.

EXPERIMENTAL SECTION

Materials. Polylactide (PLA) with a molecular weight of 200 000 was bought from Nature Works Co. Ltd. Acrylic acid (AA, Aldrich) was distilled under reduced pressure before use. Maleic anhydride (Ma), *N*-phenyl-1,4-phenylenediamine, ammonium persulfate ((NH₄)₂S₂O₈), phenylhydrazine, ammonium hydroxide (NH₄OH), hydrochloric acid (HCl), *N,N'*-dicyclohexylcarbodiimide (DCC), 4-(dimethylamino)pyridine (DMAP), ethanol (EtOH), and dimethyl sulfoxide (DMSO, dried with molecular sieve) were all purchased from Aldrich and used without further purification.

Aniline tetramer (AT) was synthesized according to ref 38. ¹H NMR (400 MHz, DMSO-*d*₆): 8.36 (s, 1H), 7.23 (t, 2H), 7.07 (s, 4H), 7.04–6.96 (m, 5H), 6.91–6.82 (m, 2H), 6.83–6.79 (m, 2H), 6.62–6.60 (m, 2H), 5.54 (s, 2H). These data agree with the literature.³⁸

Preparation of PLA Films. PLA films were fabricated by a solution-casting method. 1.2 g of PLA was dissolved in 20 mL of CHCl₃, and the solution was poured into a silanized Petri dish. The Petri dish was covered and then placed in a horizontal position. CHCl₃ was allowed to evaporate at room temperature for 1 week. The PLA film was then peeled from the Petri dish and dried in a vacuum oven. The thickness of the film was determined by a thickness meter (Mitutoyo Corp., Japan) at five different points, and an average value was taken as the film thickness. The PLA film after drying was cut into 2 × 2 cm squares with a thickness of about 108 μm.

Synthesis of PLA-Ma and PLA-AA. PLA films were washed in ethanol and then immersed in a 5% w/w solution of benzophenone in ethanol. The solution was purged with nitrogen for 10 min, and it was then placed under the UV lamp (Osram Ultra-Vitalux 300 W lamp) to activate the PLA film. The distance between the sample and lamp was 50 cm. After irradiation for 20 min, the PLA films were washed many times in ethanol to remove the unbonded benzophenone. The films were finally dried in a vacuum oven for 24 h.

The benzophenone-activated PLA films were soaked in 10% w/w maleic anhydride (Ma) solution in ethanol and purged with nitrogen for 10 min. The mixture was then placed under a UV lamp (Osram Ultra-Vitalux 300 W lamp) to initiate the reaction. After 5 h, the films were taken from the solution and extensively washed with ethanol to remove unreacted maleic anhydride. The sample was finally dried in a vacuum oven for 48 h. The reaction route is shown in Figure 1.

Acrylic acid (AA) was photografted to PLA film by a procedure similar to that used for the preparation of PLA-Ma sample. The samples were coded as PLA-AA2h, PLA-AA3.5 h, and PLA-AA5h, which means that the samples were respectively grafted with AA for 2, 3.5, and 5 h.

Synthesis of PLA-Ma-AT and PLA-AA-AT. PLA-Ma-AT and PLA-AA-AT were prepared by a coupling reaction between the carboxyl group of Ma or AA and amino group of AT with DCC as water condensing agent and DMAP as catalyst. In general, 80 mg of AT, 112 mg of DCC, and 66.5 mg of DMAP were dissolved in a dry DMSO solution; the PLA-Ma or PLA-AA film sample was then put into the mixture, and the vial was sealed. The vial was then put on a mini-shaker with a shaking speed of 50 rpm at room temperature. The reaction was allowed to proceed for 24 h. The PLA films after grafting with AT were washed first with DMSO to remove the unreacted AT and then with an excess of ethanol to remove the DMSO. The PLA-Ma-AT and the PLA-AA-AT were finally dried in a vacuum oven for 24 h. The synthesis pathway is shown in Figure 1.

For comparison, benzophenone-activated PLA film exposed to UV in the absence of maleic anhydride or acrylic acid for 0, 2, 3.5, and 5 h

were prepared in the same way as that of PLA-Ma and PLA-AA samples. The PLA-Ma and PLA-AA samples after incubation in DMSO for 24 h were also prepared as control samples for water contact angle test and scanning electron microscope observations.

Characterization. FT-IR spectra of AT, PLA, PLA-Ma, PLA-Ma-AT, PLA-AA, and PLA-AA-AT were recorded using a Perkin Elmer Spectrum 2000 spectrometer (Perkin-Elmer Instrument, Inc.) equipped with an attenuated total reflectance (ATR) crystal accessory (Golden Gate). Each spectrum was recorded as the average of 16 scans at a resolution of 2 cm^{-1} for wavenumbers between 4000 and 600 cm^{-1} with a correction for atmospheric water and carbon dioxide. The data obtained were evaluated using the Perkin Elmer Instrument v3.02 software.

The wettability of the PLA films before and after grafting was evaluated by determining the contact angle of water using a contact angle and surface tension meter (KSV instruments Ltd.). A drop of Milli-Q water was placed on the surface of the sample, and images of the water drop were recorded by a digital camera. Contact angle data were obtained by analyzing the images with KSV software. The average contact angle of each sample was obtained from five measurements at different points on the samples.

The morphology of the PLA films and modified PLA films mounted on metal stubs was observed using a field emission scanning electron microscope (FE-SEM, S-4800, Hitachi, Japan).

The surface topography of the PLA, PLA-Ma, PLA-Ma-AT, PLA-AA, and PLA-AA-AT was examined with a Nanoscope III atomic force microscope (AFM) (Digital Instrument Inc.) in the contact mode with a scanning area of $5.0\text{ }\mu\text{m}$. The average roughness of the PLA surface before and after modification was obtained directly from the AFM images.

The UV-vis spectra of AT, PLA-AA-AT and HCl-doped AT, HCl-doped PLA-AA-AT were recorded with a UV-vis spectrophotometer (UV-2401) using 1,4-dioxane as solvent.

A thermogravimetric analysis (TGA) (Mettler) of the PLA and PLA-AA-AT samples was carried out to determine the thermal stability of the polymers. TGA tests were conducted under a nitrogen atmosphere (nitrogen flow rate 50 mL/min) with a heating rate of $10\text{ }^{\circ}\text{C/min}$ from 50 to $800\text{ }^{\circ}\text{C}$.

The PLA-Ma-AT and PLA-AA-AT samples were cut into $1 \times 1\text{ cm}$ squares and immersed in 1 mol/L HCl for 5 min. They were first dried in air and then dried in a vacuum oven for 48 h. The electrical conductivity of these films was determined by the Van Der Pauw four-probe technique (potentiostat, Solartron, SI 1287).

RESULTS AND DISCUSSION

The hydrophobicity and lack of recognition site for cells on the surface are the disadvantages of polyesters such as PLA and PCL for use in tissue engineering. Surface modification and functionalization are useful tools to overcome these drawbacks while maintaining the bulk properties of the polyesters, such as good biocompatibility, good degradability, and good mechanical strength. In this work, a two-step surface functionalization strategy on PLA films is presented to increase the hydrophilicity of the materials and to introduce conductive aniline oligomers onto the PLA surface to regulate the cell behavior in a later stage. The carboxyl groups ($-\text{COOH}$) from maleic anhydride (Ma) and acrylic acid (AA) were first grafted onto PLA film by photografting. These $-\text{COOH}$ groups were subsequently covalently coupled with the amino group ($-\text{NH}_2$) of a conductive aniline tetramer segment. The synthesis route is shown in Figure 1, and the PLA film after modification was characterized by FT-IR and UV spectrum analysis.

Surface Covalent Grafting of PLA Films with Aniline Tetramer. FT-IR spectra were used to verify the grafting of the PLA films. The FT-IR spectra of PLA, PLA-Ma, and PLA-Ma-AT are shown in Figure 2 as curves a, b, and c, respectively. Pure PLA showed an absorbance peak at 1747 cm^{-1}

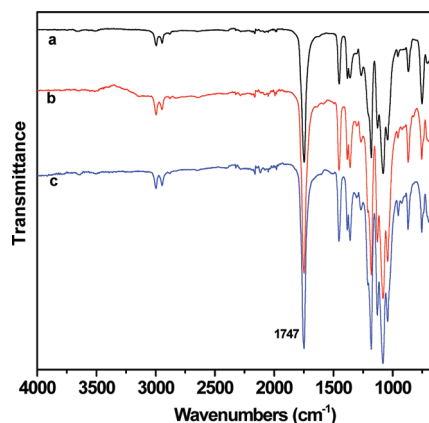


Figure 2. FT-IR spectra of (a) PLA (polylactide), (b) PLA-Ma (polylactide–maleic anhydride), and (c) PLA-Ma-AT (polylactide–maleic anhydride–aniline tetramer).

corresponding to the ester group in the PLA main chain. Maleic anhydride cannot homopolymerize on the PLA surface due to the steric hindrance. Therefore, Ma only forms a monomeric layer on the PLA surface, and a low intensity of the peaks relating to the succinic anhydride groups is expected. There are no peaks corresponding to anhydride functionality appearing between 1830 and 1740 cm^{-1} in curve b. This implies that the anhydride groups are not present on the PLA surface because the anhydride groups are not very stable, and they may hydrolyze during the film grafting and purification with ethanol. A broad $\text{C}=\text{O}$ peak at 1640 cm^{-1} is present in curve b, indicating that Ma was chemically grafted onto the PLA surface.³ The peak at 1640 cm^{-1} is weak because only a small amount of Ma was chemically attached to the PLA surface. Compared to curve b, curve c of PLA-Ma-AT showed two new peaks at 1602 and 1507 cm^{-1} , which correspond respectively to the quinoid ring and benzenoid ring in AT. This indicated that AT was grafted onto the Ma through the coupling reaction between the carboxyl group of Ma and the amino group of AT, as shown in Figure 1.

Compared to the monolayer of carboxyl group from PLA-Ma, the carboxyl polymer brush has a much higher bonding capacity because of the high concentration of carboxyl group at the brush interface. To increase the amount of conductive AT segment on the PLA surface, AA was grafted to PLA films, and PLA-AA samples were synthesized as shown in Figure 1. AA would homopolymerize during the UV irradiation and longer flexible PAA chain was formed, and a large quantity of $-\text{COOH}$ groups was introduced onto the PLA film surface. This was confirmed by the FT-IR spectra, as shown in Figure 3. Curves a, b, c, d, and e show the IR spectra of PLA, PLA-AA, AT, PLA-AA2h-AT, and PLA-AA5h-AT, respectively. Compared to curve a, curve b shows that a new peak at 1720 cm^{-1} corresponding to acid group ($-\text{COOH}$) of acrylic acid forms a shoulder peak with that of PLA at 1747 cm^{-1} , indicating that AA was grafted to the PLA film.^{17,21} In curve c of AT, the amine group ($-\text{NH}_2$) showed two characteristic peaks at 3367 and 3192 cm^{-1} , but in curve d of PLA-AA2h-AT, these two peaks changed into a single broad peak at about 3320 cm^{-1} corresponding to $-\text{NH}-$, indicating that the coupling reaction between the amine group of AT and the carboxyl group of PAA had taken place. In addition, a new peak at 1650 cm^{-1} is assigned to the amide group formed in the coupling reaction of $-\text{COOH}$ group of PAA and $-\text{NH}_2$ group of AT. The new

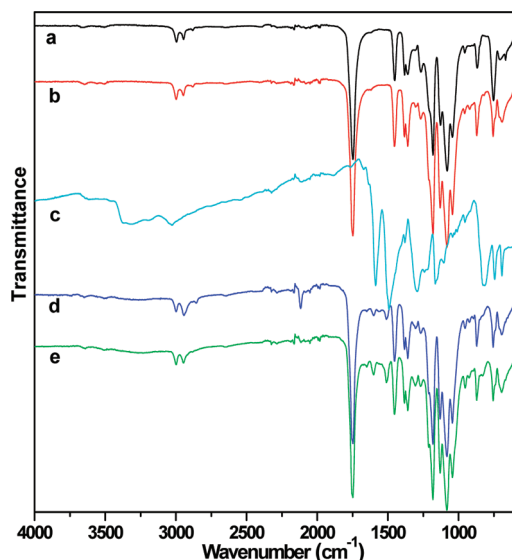


Figure 3. FT-IR spectra of (a) PLA (polylactide), (b) PLA-AA (polylactide-acrylic acid), (c) pure AT (aniline tetramer), (d) PLA-AA2h-AT, and (e) PLA-AA5h-AT.

peaks at 1600 and 1504 cm^{-1} present in curve d, but not in curve b, are attributed to the quinoid ring and benzenoid ring of AT, respectively. The absorption intensities of these peaks are much stronger than those in PLA-Ma-AT, indicating that a larger amount of AT was grafted onto the PLA surface. The peaks at 1650, 1600, and 1510 cm^{-1} in curve e of PLA-AA5h-AT showed a much stronger intensity than in curve d of PLA-AA2h-AT, indicating that the amount of AT grafted onto the PLA surface increased with increasing grafting time of AA to PLA films.

The PLA-AA5h-AT film was dissolved in 1,4-dioxane, and the UV-vis absorption spectrum was recorded as shown in Figure 4. Curve a for AT shows two absorption peaks at 545

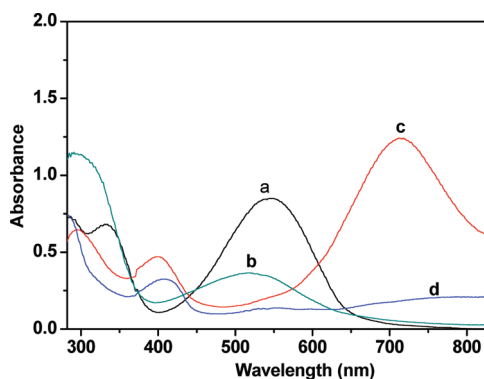


Figure 4. UV-vis spectra of polymers in 1,4-dioxane: (a) AT, (b) PLA-AA5h-AT, (c) HCl-doped AT, and (d) HCl-doped PLA-AA5h-AT.

and 332 nm, corresponding respectively to the characteristic absorption of the excitonic transition from the benzenoid to the quinoid ring and to the $\pi-\pi^*$ transition of the benzenoid ring. In curve b for PLA-AA5h-AT, the absorption of the benzenoid ring shows a hypsochromic shift from 332 to 301 nm, probably because the PAA chains disturb the extent of conjugation between the adjacent phenyl rings in the AT segment.³⁹ In addition, the quinoid ring absorption underwent a blue shift

from 545 to 520 nm, and the ratio of the absorption intensity of the quinoid to the benzenoid ring of PLA-AA5h-AT was less than that of AT. This is because the amide group ($-\text{CO}-\text{NH}-$) is an electron-withdrawing group compared to the amino group of AT, and this reduces the electron density of the quinoid ring. These data indicate that the coupling reaction between $-\text{COOH}$ and $-\text{NH}_2$ had taken place.³³ The HCl-doped AT, as shown in curve c, showed two new absorption peaks at 402 and 712 nm, but the HCl-doped PLA-AA5h-AT showed only one new absorption peak at 402 nm ascribed to the formation of delocalized polarons.⁴⁰ This result is consistent with our previous work.⁴¹ These data indicate that the electroactivity of the AT segment was retained after grafting onto the PLA-AA surface.

The amount of AT grafted onto the PLA films was also determined. The AT grafting yield and extent of grafting were calculated by the following equations:

$$\text{grafting yield} = (W_g - W_0)/W_0 \times 100\%$$

$$\text{extent of grafting} = (W_g - W_0)/S$$

where W_g and W_0 represent the weights of the film before and after grafting with AT, and S is the surface area of the PLA film. The results of AT grafting yield and extent of grafting of PLA films are listed in Table 1. The AA grafting yield of PLA-AA2h,

Table 1. Extent of Grafting and Grafting Yield of AT on the PLA Films

sample name	extent of grafting ($\mu\text{g}/\text{cm}^2$)	grafting yield (%)
PLA-Ma-AT	380	2.3
PLA-AA2h-AT	1010	5.7
PLA-AA3.5h-AT	1740	9.9
PLA-AA5h-AT	1850	10.6

PLA-AA3.5h, and PLA-AA5h were 1.0%, 1.6%, and 1.9%, respectively, and they increased with increasing grafting time of AA on PLA surface. The AT grafting yield of PLA-Ma-AT was 2.3%, and the extent of grafting of AT was 380 $\mu\text{g}/\text{cm}^2$. The PLA-Ma film after grafting with AT was purple in color, indicating that AT was attached to the PLA-Ma surface. The AT grafting yield and extent of grafting of PLA-AA2h-AT were much greater than that of PLA-Ma-AT. For PLA-AA-AT samples, the AT grafting yield and extent of grafting increased with increasing AA grafting time on the PLA film; i.e., the amount of AT grafted onto the PLA-AA surface increased with increasing AA amount on the PLA film. However, the increase was slow after 3.5 h grafting of AA. Therefore, the grafting time of AA was set as 5 h in this work.

Thermal Properties of the Polymers. The AT grafting yield on the PLA surface was also confirmed by TGA, as shown in Figure 5. The PLA showed one degradation stage between 80 and 350 $^{\circ}\text{C}$ in a nitrogen atmosphere. The slight weight loss between 80 and 150 $^{\circ}\text{C}$ may be attributed to a loss of the solvent and moisture entrapped in the polymer. However, the PLA-AA-AT samples showed a two-step degradation process. The first degradation occurred between 50 and 360 $^{\circ}\text{C}$, which indicates a higher thermal stability than pure PLA, probably due to the better thermal stability of the grafted AT. The second degradation process took place between 360 and 600 $^{\circ}\text{C}$, and this is attributed to a degradation of the AT segment. The second degradation stage of PLA-AA5h-AT was used to determine the AT content in the PLA film because the PLA

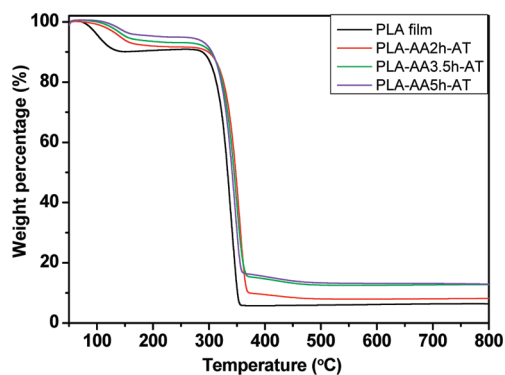


Figure 5. TGA curves of the PLA, PLA-AA2h-AT, PLA-AA3.5h-AT, and PLA-AA5h-AT.

was completely degraded in the first degradation stage. The AT contents determined from the TGA curves agree with the AT grafting yield results shown in Table 1. This further confirmed that the AT segment was successfully grafted onto the PLA-AA surface.

Wettability of the PLA Surfaces after Modification.

The surface hydrophilicity, surface charge, surface energy, and surface roughness have great effect on the cell adhesion on the materials.^{42–44} Moderate surface hydrophilicity has been shown to be important for cell attachment and cell adhesion.^{44,45} The wettability of the PLA surface before and after modification was assessed by determining the contact angle of water, and the results are shown in Figure 6. The contact angle of water on the

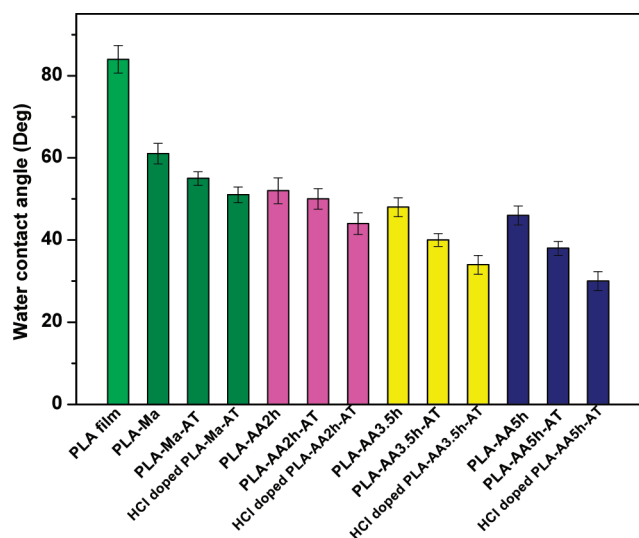


Figure 6. Contact angles of water on the polymer films.

pure PLA surface was about 84°, which is quite hydrophobic. The values of contact angle on the benzophenone activated PLA film exposed to UV in the absence of maleic anhydride or acrylic acid for 0, 2, 3.5, and 5 h were 82°, 81°, 77°, and 76°, respectively. They decreased slightly compared to that of PLA, and these results are consistent with earlier published results.¹⁷ The contact angle of water on PLA-Ma was 61° as a result of the hydrophilic carboxyl group introduced onto the PLA surface. The PLA-AA exhibited a lower contact angle than PLA, and it decreased with increasing grafting time of AA (Figure 6). However, the contact angle was almost stable for PLA-AA3.5 h and PLA-AA5h samples. The contact angles of PLA-Ma, PLA-

AA2h, PLA-AA3.5 h, and PLA-AA5h after incubation in DMSO for 24 h were 59°, 56°, 51°, and 46°, respectively. These values were somewhat higher or similar to those of PLA-Ma, PLA-AA2h, PLA-AA3.5 h, and PLA-AA5h, which were 61°, 52°, 48°, and 46°, respectively (Figure 6). The PLA-Ma-AT and PLA-AA-AT sample showed lower contact angle than the corresponding PLA-Ma and PLA-AA samples, probably because the unreacted –COOH groups on the PLA surface doped the AT segment and formed a self-doped polymer.^{39,46} The hydrophilicity increased due to the self-doped AT segments. The contact angle of PLA-AA-AT also decreased with increasing AA grafting time because the AT segment has a greater chance to become covalently attached to the larger quantity of –COOH groups. The contact angle of water on the HCl-doped PLA-Ma-AT and PLA-AA-AT was much less than on the corresponding PLA-Ma-AT and PLA-AA-AT because HCl is a strong acid compared to AA and the doped AT form increased sharply.^{39,46} The values of the contact angle of water on the (HCl-doped) PLA-Ma-AT and (HCl-doped) PLA-AA-AT were between 58 and 30°, which is much more hydrophilic than pristine PLA, and this will improve the cell attachment on these modified PLA surfaces.^{44,45}

Electrical Conductivity of the AT-Modified PLA Films.

The electrical conductivity of the PLA films grafted with AT doped with 1 mol/L HCl are listed in Table 2. The

Table 2. Electrical Conductivity of the Films

sample name	conductivity (S/cm)
PLA-Ma-AT	4.36×10^{-8}
PLA-AA2h-AT	1.01×10^{-7}
PLA-AA3.5h-AT	5.57×10^{-7}
PLA-AA5h-AT	6.43×10^{-7}

conductivity of PLA-Ma-AT was about 4.36×10^{-8} S/cm, probably due to the quite low AT grafting yield on the PLA-Ma surface. The conductivity of PLA-AA-AT samples was between 1.01×10^{-7} and 6.43×10^{-7} S/cm, and it increased with increasing AT grafting yield on the PLA surface. This is because the AT segment formed a condensed layer and an intricate conductive network with increasing grafting yield of AT. This conductivity was comparably low because the AT layer on the PLA surface was thin. However, this conductivity value may be sufficient for biomedical applications, since the microcurrent in the human body is quite low.⁴⁷ In addition, electroactive polymers with a relatively low conductivity due to the low content of aniline oligomers in the materials can enhance cell adhesion and differentiation without electrical stimulation.^{48,49} The AT layer on the PLA surface has direct contact with the host tissue when it is transplanted into human body, and this electroactive layer may improve the cell adhesion and could be used to tune the cellular activity in a later stage. The role of the AT-modified PLA films in adjusting cell functions will be explored in the future.

Morphology of the Films. The morphology of biomaterials is very important for biomedical applications. The morphology of the PLA films before and after photografting was examined by SEM, as shown in Figure 7. The pure PLA film showed a rather flat and smooth surface (Figure 7a). Benzophenone-activated PLA film exposed to UV in the absence of Ma or AA for 0, 2, 3.5, and 5 h also showed a smooth surface (see Figure 1 in the Supporting Information). The surface of Ma-grafted PLA films in Figure 7b is slightly

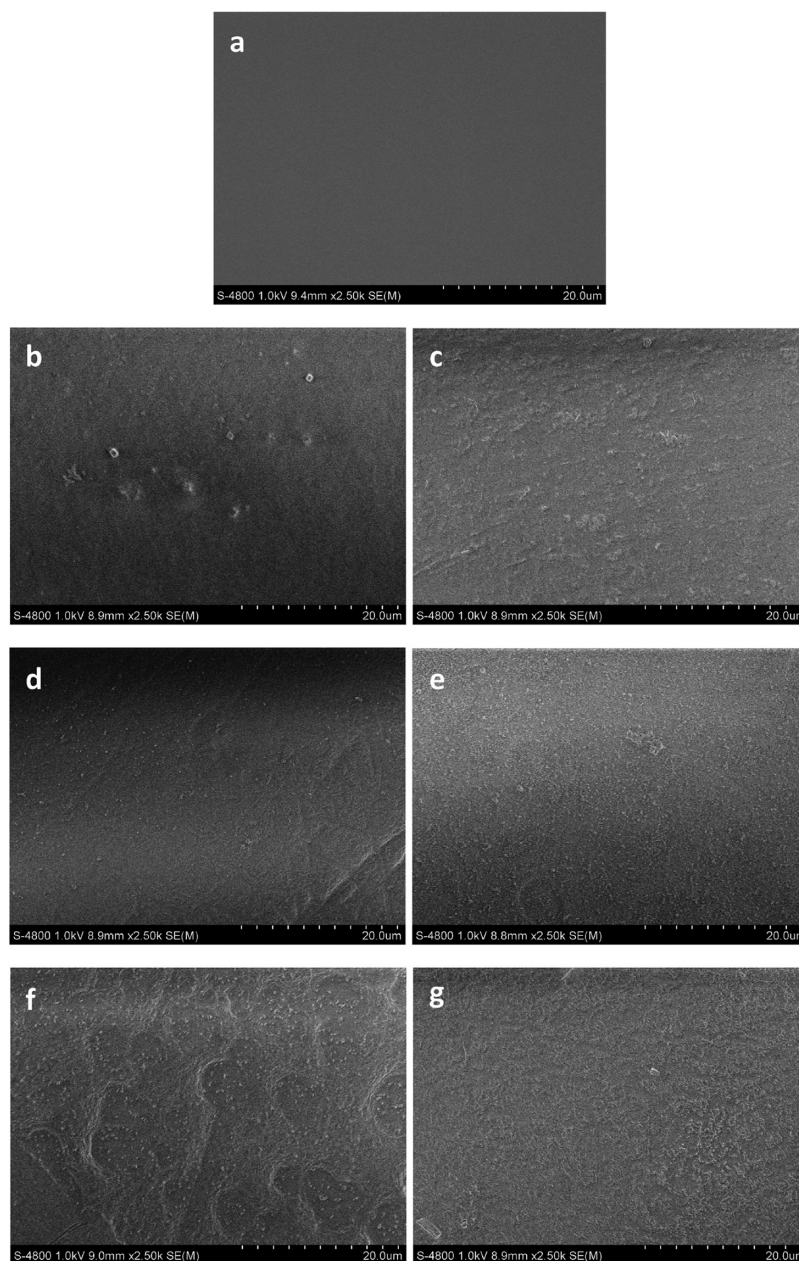


Figure 7. Representative SEM images of the surfaces: (a) PLA, (b) PLA-Ma, (c) PLA-Ma-AT, (d) PLA-AA2h, (e) PLA-AA2h-AT, (f) PLA-AA5h, and (g) PLA-AA5h-AT.

rougher than that of the PLA film. Figure 7d for PLA-AA2h and Figure 7f for PLA-AA5h show that AA segments totally covered the PLA surface. Especially in Figure 7f, the AA segment formed a dense AA layer, and the small round dots are probably attributed to the grafted AA brushes and increase with increasing grafting time of AA compared to Figure 7d. There is no hill appearing on the surface of PLA-Ma and PLA-AA after incubation in DMSO for 24 h (see Figure 2 in the Supporting Information). PLA-Ma-AT (Figure 7c) exhibited a rougher morphology than PLA-Ma in Figure 7b, and some small hills appeared. The PLA-AA2h-AT and PLA-AA5h-AT images in Figure 7e,g show that a condensed AT layer was formed on the PLA-AA surface. Some small dots on the PLA-AA-AT surface probably correspond to the aggregates of AT segments after grafting on the AA brushed, since AT segment would gather together due to their strong interaction between the AT

moiety. The AT layer could be doped by acid and provided a conductive surface. These surface changes were also confirmed by AFM observations. For example, the AFM image in Figure 8a for PLA film showed a smooth surface with a roughness of 3 nm. The PLA-Ma (Figure 8b) and PLA-Ma-AT (Figure 8c) images both showed a slightly rougher surface with a roughness of 8 and 17 nm, respectively. These roughness increases indicate that the Ma was successfully grafted onto PLA films and that AT was subsequently attached onto the PLA-Ma. AFM images of PLA-AA5h and PLA-AA5h-AT are shown in Figure 8d,e. The surface of PLA-AA5h with a roughness of 32 nm is much rougher than that of PLA-Ma, indicating that the grafting yield of AA increased dramatically compared to that of PLA-Ma. The roughness of PLA-AA5h-AT is 26 nm, which is higher than that of PLA-Ma-AT but slightly lower than that of PLA-AA5h. This may be because the strong interactions between the

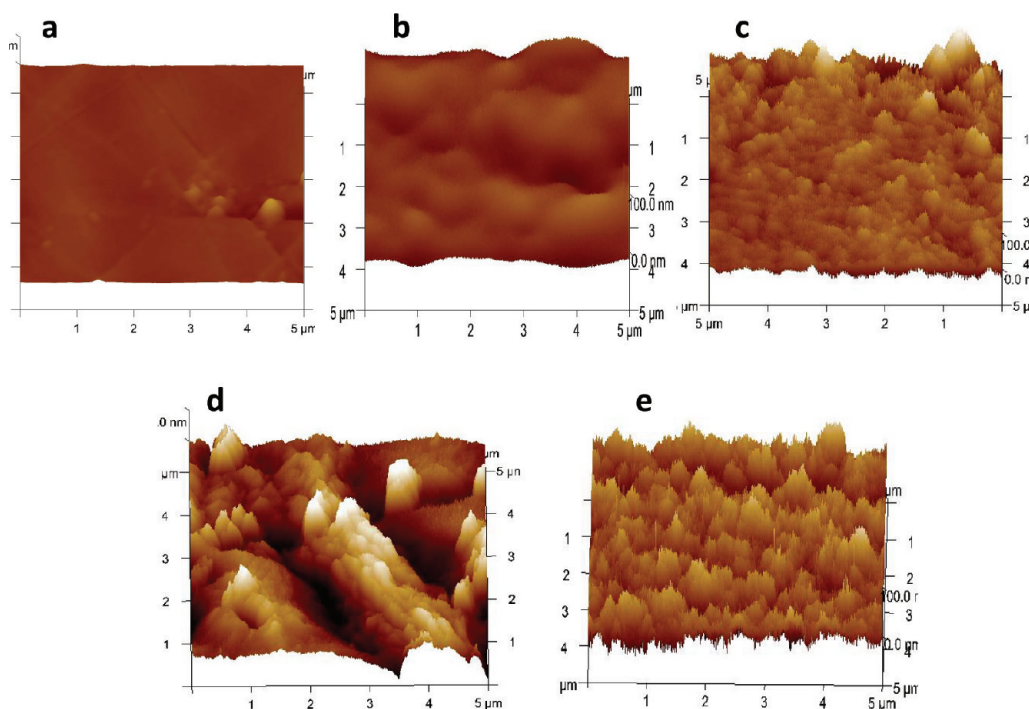


Figure 8. Representative AFM images of PLA surface before and after modification: (a) pristine PLA film, (b) PLA-Ma, (c) PLA-Ma-AT, (d) PLA-AAsh, and (e) PLA-AAsh-AT.

AT segment grafted on PAA chain make the molecular brushes entangle with each other, and a denser surface with a lower roughness is consequently formed. These results are consistent with the SEM images in Figure 7 and FT-IR spectra in Figure 3 and AT grafting yield data in Table 1.

We have demonstrated a versatile method for the covalent surface functionalization of polyester films to create a conducting hydrophilic surface. Different polyesters such as polycaprolactone, poly(1,5-dioxepan-2-one), poly(trimethylene carbonate), and their copolymers with different degradation, mechanical, and thermal properties can be used as substrate films. In addition, different aniline oligomers such as aniline trimer, aniline tetramer, and aniline pentamer, etc., with different electrical conductivities can be employed for coupling to the polyester surface. Therefore, this versatile technique will lead to a library of materials exhibiting a tunable conductivity and hydrophilic surface through the choice of the suitable substrates and aniline oligomers. This could meet the requirement for a particular biomedical application.

CONCLUSIONS

An electroactive and hydrophilic polylactide (PLA) surface was successfully developed by the photografting of acrylic acid (AA) and maleic anhydride (Ma) onto PLA film and subsequent coupling with conductive aniline tetramer (AT). The contact angle of water on the PLA film after grafting and coupling reaction with AT decreased sharply, indicating that a more hydrophilic surface was obtained. The UV grafting and coupling reaction between the carboxyl group of AA (or Ma) and the amino group of AT was confirmed by FT-IR, UV, TGA, and grafting yield determination. The grafting yield of AT on the PLA surface increased with increasing time of grafting of AA onto the PLA films. The conductivity of the PLA surface after coupling with AT is in the range of a semiconductor, and the conductivity increased with the increasing AT grafting yield on

the PLA films. The roughness of the PLA surfaces after modification increased dramatically, as demonstrated by SEM and AFM observations. These PLA films with a moderate hydrophilic and electroactive surface will find application in tissue regeneration.

ASSOCIATED CONTENT

Supporting Information

SEM images of benzophenone activated PLA film exposed to UV in the absence of Ma or AA for 0, 2, 3.5, and 5 h and SEM images of PLA-Ma and PLA-AA samples after incubation in DMSO for 24 h. This material is available free of charge via the Internet at <http://pubs.acs.org>.

AUTHOR INFORMATION

Corresponding Author

*Tel +46-8-790 8274; Fax +46-8-20 84 77; e-mail aila@polymer.kth.se.

ACKNOWLEDGMENTS

The authors are grateful to the China Scholarship Council (CSC) and The Royal Institute of Technology (KTH) for financial support for this work. We thank Robertus Wahyu Nayan Nugroho for AFM measurement.

REFERENCES

- (1) Elbert, D. L.; Hubbell, J. A. *Annu. Rev. Mater. Sci.* **1996**, *26*, 365–394.
- (2) Goddard, J. M.; Hotchkiss, J. H. *Prog. Polym. Sci.* **2007**, *32*, 698–725.
- (3) Edlund, U.; Kallrot, M.; Albertsson, A. C. *J. Am. Chem. Soc.* **2005**, *127*, 8865–8871.
- (4) Hubbell, J. A. *Bio-Technology* **1995**, *13*, S65–S76.
- (5) Nair, L. S.; Laurencin, C. T. *Prog. Polym. Sci.* **2007**, *32*, 762–798.
- (6) Albertsson, A. C.; Varma, I. K. *Biomacromolecules* **2003**, *4*, 1466–1486.

- (7) Jiao, Y. P.; Cui, F. Z. *Biomed. Mater.* **2007**, *2*, R24–R37.
- (8) Rasal, R. M.; Janorkar, A. V.; Hirt, D. E. *Prog. Polym. Sci.* **2010**, *35*, 338–356.
- (9) Xu, F. J.; Yang, X. C.; Li, C. Y.; Yang, W. T. *Macromolecules* **2011**, *44*, 2371–2377.
- (10) Oh, J. K. *Soft Matter* **2011**, *7*, 5096–5108.
- (11) Wan, Y. Q.; Chen, W. N.; Yang, J.; Bei, J. Z.; Wang, S. G. *Biomaterials* **2003**, *24*, 2195–2203.
- (12) Deng, C.; Chen, X. S.; Sun, J.; Lu, T. C.; Wang, W. S.; Jing, X. B. *J. Polym. Sci., Part A: Polym. Chem.* **2007**, *45*, 3218–3230.
- (13) Spasova, M.; Mespouille, L.; Coulembier, O.; Paneva, D.; Manolova, N.; Rashkov, I.; et al. *Biomacromolecules* **2009**, *10*, 1217–1223.
- (14) Cai, Q.; Yang, J. A.; Bei, J. Z.; Wang, S. G. *Biomaterials* **2002**, *23*, 4483–4492.
- (15) Wan, Y.; Wu, H.; Yu, A. X.; Wen, D. J. *Biomacromolecules* **2006**, *7*, 1362–1372.
- (16) Deng, J. P.; Wang, L. F.; Liu, L. Y.; Yang, W. T. *Prog. Polym. Sci.* **2009**, *34*, 156–193.
- (17) Janorkar, A. V.; Metters, A. T.; Hirt, D. E. *Macromolecules* **2004**, *37*, 9151–9159.
- (18) Rasal, R. M.; Bohannon, B. G.; Hirt, D. E. *J. Biomed. Mater. Res., Part B* **2008**, *85B*, 564–572.
- (19) Janorkar, A. V.; Proulx, S. E.; Metters, A. T.; Hirt, D. E. *J. Polym. Sci., Part A: Polym. Chem.* **2006**, *44*, 6534–6543.
- (20) Hoglund, A.; Hakkarainen, M.; Edlund, U.; Albertsson, A. C. *Langmuir* **2010**, *26*, 378–383.
- (21) Kallrot, M.; Edlund, U.; Albertsson, A. C. *Biomacromolecules* **2007**, *8*, 2492–2496.
- (22) Wong, J. Y.; Langer, R.; Ingber, D. E. *Proc. Natl. Acad. Sci. U. S. A.* **1994**, *91*, 3201–3204.
- (23) Shi, G. X.; Zhang, Z.; Rouabhia, M. *Biomaterials* **2008**, *29*, 3792–3798.
- (24) Gumus, A.; Califano, J. P.; Wan, A. M. D.; Huynh, J.; Reinhart-King, C. A.; Malliaras, G. G. *Soft Matter* **2010**, *6*, 5138–5142.
- (25) Lee, J. Y.; Bashur, C. A.; Goldstein, A. S.; Schmidt, C. E. *Biomaterials* **2009**, *30*, 4325–4335.
- (26) Xie, J. W.; MacEwan, M. R.; Willerth, S. M.; Li, X. R.; Moran, D. W.; Sakiyama-Elbert, S. E.; et al. *Adv. Funct. Mater.* **2009**, *19*, 2312–2318.
- (27) Wei, Z. X.; Faul, C. F. J. *Macromol. Rapid Commun.* **2008**, *29*, 280–292.
- (28) Udeh, C. U.; Fey, N.; Faul, C. F. J. *J. Mater. Chem.* **2011**, *21*, 18137–18153.
- (29) Rivers, T. J.; Hudson, T. W.; Schmidt, C. E. *Adv. Funct. Mater.* **2002**, *12*, 33–37.
- (30) Green, T. R.; Fisher, J.; Matthews, J. B.; Stone, M. H.; Ingham, E. *J. Biomed. Mater. Res.* **2000**, *53*, 490–497.
- (31) Guo, B. L.; Finne-Wistrand, A.; Albertsson, A. C. *Macromolecules* **2011**, *44*, 5227–5236.
- (32) Guo, B. L.; Finne-Wistrand, A.; Albertsson, A. C. *Chem. Mater.* **2011**, *23*, 4045–4055.
- (33) Guo, B. L.; Finne-Wistrand, A.; Albertsson, A. C. *Biomacromolecules* **2010**, *11*, 855–863.
- (34) Guo, B. L.; Finne-Wistrand, A.; Albertsson, A. C. *Macromolecules* **2010**, *43*, 4472–4480.
- (35) Guo, B. L.; Finne-Wistrand, A.; Albertsson, A. C. *J. Polym. Sci., Part A: Polym. Chem.* **2011**, *49*, 2097–2105.
- (36) Guo, B. L.; Finne-Wistrand, A.; Albertsson, A. C. *Biomacromolecules* **2011**, *12*, 2601–2609.
- (37) Guo, B. L.; Sun, Y.; Finne-Wistrand, A.; Mustafa, K.; Albertsson, A. C. *Acta Biomater.* **2012**, *8*, 144–153.
- (38) Rozalska, I.; Kulyk, P.; Kulszewicz-Bajer, I. *New J. Chem.* **2004**, *28*, 1235–1243.
- (39) Chan, H. S. O.; Ng, S. C.; Sim, W. S.; Tan, K. L.; Tan, B. T. G. *Macromolecules* **1992**, *25*, 6029–6034.
- (40) Xia, Y. N.; Wiesinger, J. M.; Macdiarmid, A. G.; Epstein, A. J. *Chem. Mater.* **1995**, *7*, 443–445.
- (41) Guo, B. L.; Finne-Wistrand, A.; Albertsson, A. C. *Chem. Mater.* **2011**, *23*, 1254–1262.
- (42) Reuveny, S.; Mizrahi, A.; Kotler, M.; Freeman, A. *Biotechnol. Bioeng.* **1983**, *25*, 469–480.
- (43) Denbraber, E. T.; Deruijter, J. E.; Smits, H. T. J.; Ginsel, L. A.; Vonrecum, A. F.; Jansen, J. A. *J. Biomed. Mater. Res.* **1995**, *29*, 511–518.
- (44) Lampin, M.; WarocquierClerout, R.; Legris, C.; Degrange, M.; SigotLuizard, M. F. *J. Biomed. Mater. Res.* **1997**, *36*, 99–108.
- (45) Vanwachem, P. B.; Hogt, A. H.; Beugeling, T.; Feijen, J.; Bantjes, A.; Detmers, J. P.; et al. *Biomaterials* **1987**, *8*, 323–328.
- (46) Kim, S. C.; Whitten, J.; Kumar, J.; Bruno, F. F.; Samuelson, L. A. *Macromol. Res.* **2009**, *17*, 631–637.
- (47) Niple, J. C.; Daigle, J. P.; Zaffanella, L. E.; Sullivan, T.; Kavet, R. *Bioelectromagnetics* **2004**, *25*, 369–373.
- (48) Hu, J.; Huang, L. H.; Zhuang, X. L.; Zhang, P. B.; Lang, L.; Chen, X. S.; et al. *Biomacromolecules* **2008**, *9*, 2637–2644.
- (49) Liu, Y. D.; Hu, J.; Zhuang, X. L.; Zhang, P. B. A.; Chen, X. S.; Wei, Y.; et al. *Macromol. Biosci.* **2011**, *11*, 806–813.

Modifying the Hydrophilic–Hydrophobic Interface of PEG-*b*-PCL To Increase Micelle Stability: Preparation of PEG-*b*-PBO-*b*-PCL Triblock Copolymers, Micelle Formation, and Hydrolysis Kinetics

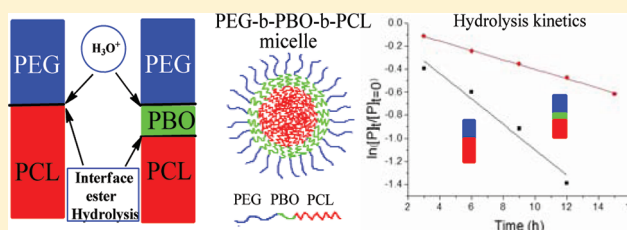
Xiaobo Zhu,[†] Michael Fryd,[†] Benjamin D. Tran,[‡] Marc A. Ilies,[‡] and Bradford B. Wayland^{*,†}

[†]Department of Chemistry, Temple University, Philadelphia, Pennsylvania 19122, United States

[‡]Department of Pharmaceutical Sciences, School of Pharmacy, Temple University, Philadelphia, Pennsylvania 19140, United States

S Supporting Information

ABSTRACT: A set of PEG-*b*-PBO-*b*-PCL triblock copolymers were prepared for comparative studies of micelle formation and relative stability compared to the parent PEG-*b*-PCL diblock copolymers. Block copolymers that were characterized by ¹H NMR and GPC were self-assembled in water by nanoprecipitation from organic solvents. Spherical micelles produced in near-quantitative yield were characterized by dynamic light scattering (DLS) and transmission electron microscopy (TEM). The initial step in degradation of the block copolymers assembled in spherical micelles is shown by GPC and ¹H NMR in acidic media to occur by hydrolysis of the interface ester group which cleaves the PCL segment in the core from the -PBOPEG and -PEG segments. Kinetics of hydrolysis of the ester groups that bind the hydrophobic PCL segment with either PEG or PBO units were followed by ¹H NMR and demonstrate that the triblock has a reduced rate of hydrolysis. Inserting a short block of PBO between the PEG and PCL segments provides increased protection from hydrolysis for the ester group at the hydrophilic–hydrophobic interface.



INTRODUCTION

Amphiphilic diblock copolymers self-assemble into a variety of supramolecular aggregate structures including core–shell micelles,^{1–5} filomicelles,^{6–8} and polymersomes^{9–11} that are finding applications as drug and gene delivery systems.^{12–16} In particular, micelles formed from block copolymers that contain poly(ethylene glycol) (PEG) and poly(ϵ -caprolactone) (PCL) segments are widely applied in the design of drug delivery systems because the hydrophilic PEG block is biocompatible and the hydrophobic PCL block is biodegradable.^{17–21} The PEG-*b*-PCL block copolymers that were designed for drug delivery have a hydrolytically sensitive ester^{22–25} link between the hydrophilic and hydrophobic segments. This ester group is normally located at the aqueous/hydrophobic interface in core–shell micelles and thus is readily accessed for reactions with the aqueous medium. Hydrolysis of the interface ester leads to shedding of the PEG block and destabilization of the micelle.^{26–29} This paper reports on an initial effort to tune the stability of micelles by moving the hydrolytically accessible ester linkage away from the core–shell interface. This is achieved by inserting a short nonbiodegradable hydrophobic segment of poly(1,2-butylene oxide) (PBO) between the PCL core and PEG corona. Our working hypothesis is that the rate of PEG shedding can be retarded by separating the interface between the biodegradable PCL and nondegradable PEG blocks from the hydrophilic–hydrophobic interface and thus extends micelle stability without affecting the self-assembly process. This article reports on the preparation of low-polydispersity

PEG-*b*-PCL diblock and PEG-*b*-PBO-*b*-PCL triblock polymers that self-assemble into spherical micelles. Kinetics of acid-catalyzed hydrolysis of the interface ester groups are shown to occur substantially slower in the triblock copolymer micelles when compared to micelles of the parent diblock copolymer.

RESULTS AND DISCUSSION

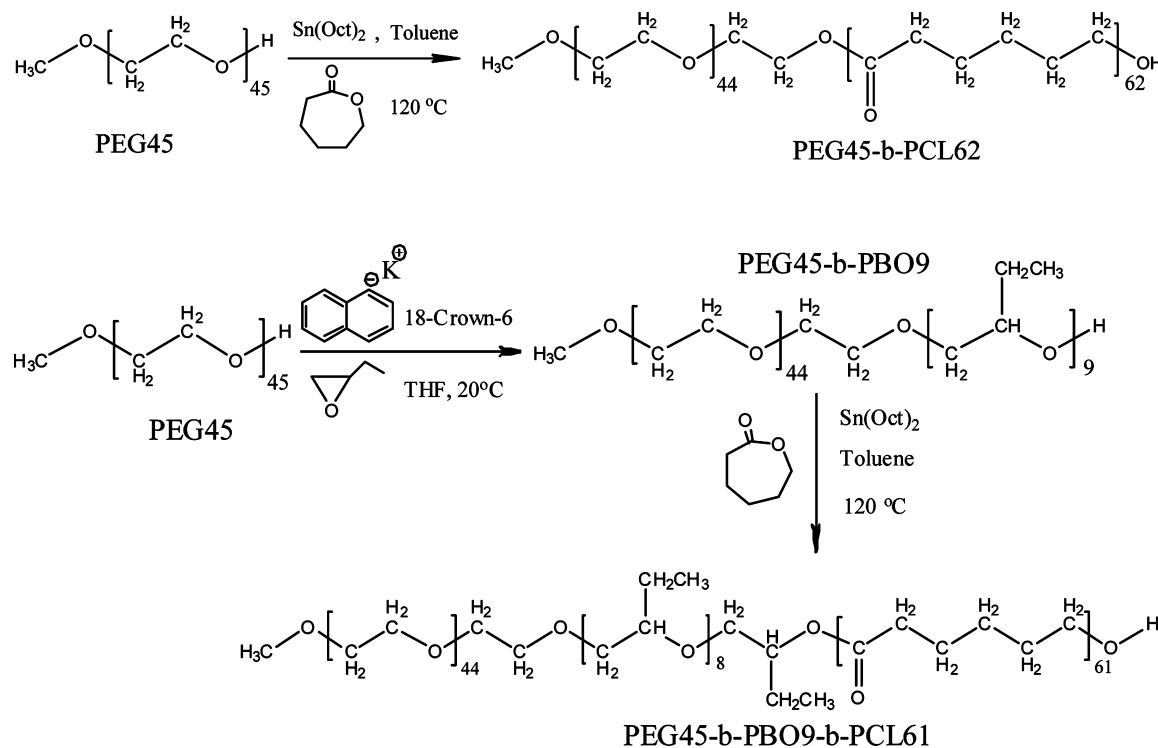
Synthesis and Characterization of PEG45-*b*-PCL62 and PEG45-*b*-PBO9-*b*-PCL61 Block Copolymers. The block copolymers of PEG45-*b*-PCL62 and PEG45-*b*-PBO9-*b*-PCL61 were synthesized as shown in Scheme 1. Molecular weights of the polymers were determined by ¹H NMR analysis (Table 1 and Figure S2), and the molecular weight distribution was evaluated by GPC (Figure S1). Amphiphilic block copolymer PEG45-*b*-PCL62 (PDI = 1.08) was synthesized utilizing methoxy poly(ethylene glycol) as the macroinitiator for the controlled ring-opening polymerization (ROP) of ϵ -caprolactone (CL) in the presence of stannous octoate (Sn(Oct)₂) as a catalyst.^{14,21} The labeled NMR spectrum is shown in Figure S2. The degree of polymerization (DP) of CL was evaluated to be 62 by comparing the integration of signals at 3.62 ppm for CH₂ of PEG (labeled b) and triplet at 2.30 ppm for CH₂ of PCL (labeled d). Copolymer was synthesized by

Received: November 18, 2011

Revised: December 22, 2011

Published: January 10, 2012



Scheme 1. Synthesis of PEG45-*b*-PCL62 and PEG45-*b*-PBO9-*b*-PCL61 Block CopolymersTable 1. Synthetic Results for PEG45-*b*-PCL62 and PEG45-*b*-PBO9-*b*-PCL61 Block Copolymers

sample	$M_n(\text{theory})^a$	$M_n(\text{NMR})^b$	$W(\text{PEG})^c$	PDI^d
PEG45- <i>b</i> -PBO9	2830	2650	0.76	1.08
PEG45- <i>b</i> -PBO9-PCL61	9260	9610	0.21	1.10
PEG45- <i>b</i> -PCL62	8600	9080	0.22	1.08

^aNumber-average molecular weight of block copolymers based on a standard conversion of 36.0 (3.0)% for each monomer polymerization.

^bNumber-average molecular weight of block copolymers determined by integration of ^1H NMR resonances unique to each segment.

^cWeight fraction of PEG in the block copolymers based on the M_n from ^1H NMR. ^dPolydispersity (M_w/M_n) evaluated by GPC.

terminating the reaction at only moderate CL conversion (36.0 (3.0)%) to ensure narrow molecular weight distributions.

The triblock copolymer of PEG45-*b*-PBO9-PCL61 ($\text{PDI} = 1.10$) was analogously synthesized by ROP of CL with PEG45-*b*-PBO9 as macroinitiator and $\text{Sn}(\text{Oct})_2$ as catalyst. Synthesis of PEG45-*b*-PBO9 ($\text{PDI} = 1.08$) was accomplished by anionic polymerization of 1,2-butylene oxide (BO) with PEG as a macroinitiator.^{30–33} The DP of the PBO was determined by comparing the integration of signals at 3.62 ppm for CH_2 of PEG (labeled b) and triplet at 0.93 ppm for CH_3 of BO methyl group (labeled e).

Preparation and Characterization of PEG45-*b*-PCL62 and PEG45-*b*-PBO9-*b*-PCL61 Block Copolymer Micelles. Samples of 1.0 mg/mL of PEG45-*b*-PCL62 and PEG45-*b*-PBO9-PCL61 copolymer micelles were prepared by adding water to a stock solution of polymer in acetone under vigorous stirring.^{24,34} Results from dynamic light scattering (DLS) studies for these micelle solutions are shown in Figure 1. The single monomodal particle distributions are indicative of highly efficient micelle formation and provide that the average micelle sizes of 22 nm for PEG45-*b*-PBO9-*b*-PCL61 and 18 nm for PEG45-*b*-PCL62. The slightly larger average size for the

triblock copolymer from the DLS is consistent with the larger hydrophobic–hydrophilic ratio. TEM images of the micelles from diblock and triblock copolymers revealed only spherically shaped particles with average sizes comparable to those obtained by DLS (Figure 1). Neither DLS nor TEM observations produced evidence for larger particles such as filomicelles and polymerosomes even at concentrations of polymer higher than the 1.0 mg/mL used in this study. Selective formation of spherical micelles probably results from the strong self-assembling property of the PCL hydrophobic core. Both the di- and triblock copolymer micelles have similar size and narrow size distributions, which justifies comparing results of acid catalyzed hydrolysis studies.

Acid-Catalyzed Degradation of PEG45-*b*-PCL62 and PEG45-*b*-PBO9-*b*-PCL61 Block Copolymer Micelles. The hydrolytic degradation of PEG45-*b*-PCL62 and PEG45-*b*-PBO9-*b*-PCL61 block copolymer micelles was evaluated in aqueous HCl ($\text{pH} = 1.0$) at 25 °C by terminating the hydrolysis with NaOH at 3.0 h time intervals and extracting the polymeric materials with CH_2Cl_2 for ^1H NMR and GPC studies. GPC traces for the polymer products from degradation of PEG45-*b*-PCL62 micelles in water at a series of time intervals are shown in Figure 2A,B. The GPC results clearly show that the PEG45-*b*-PCL62 diblock copolymer is cleaved into two individual polymer units with the low-molecular-weight peak occurring precisely at the same position as the pure PEG block shown in Figure S1. The average molecular weight decreased and the width increased regularly for the PEG45-*b*-PCL62 diblock copolymer GPC peak as the relative intensity of peak for PEG increased with the time of degradation.

The ^1H NMR chemical shift of the unique CH_2 group that is connected to the hydrophilic–hydrophobic interface ester group (Scheme 2) occurs at 4.23 ppm in the PEG-*b*-PCL block copolymer and shifts to 3.62 ppm when the interface ester group hydrolyzes and the PEG segment cleaves off. The

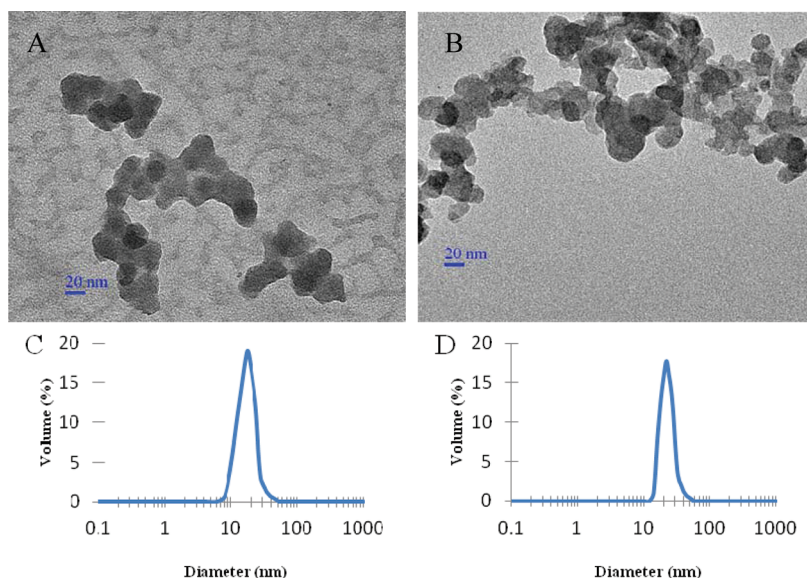


Figure 1. TEM images of PEG45-*b*-PCL62 (A) and PEG45-*b*-PBO9-*b*-PCL61 (B) micelles. Size distribution of PEG45-*b*-PCL62 (C) and PEG45-*b*-PBO9-*b*-PCL61 (D) micelles determined by DLS.

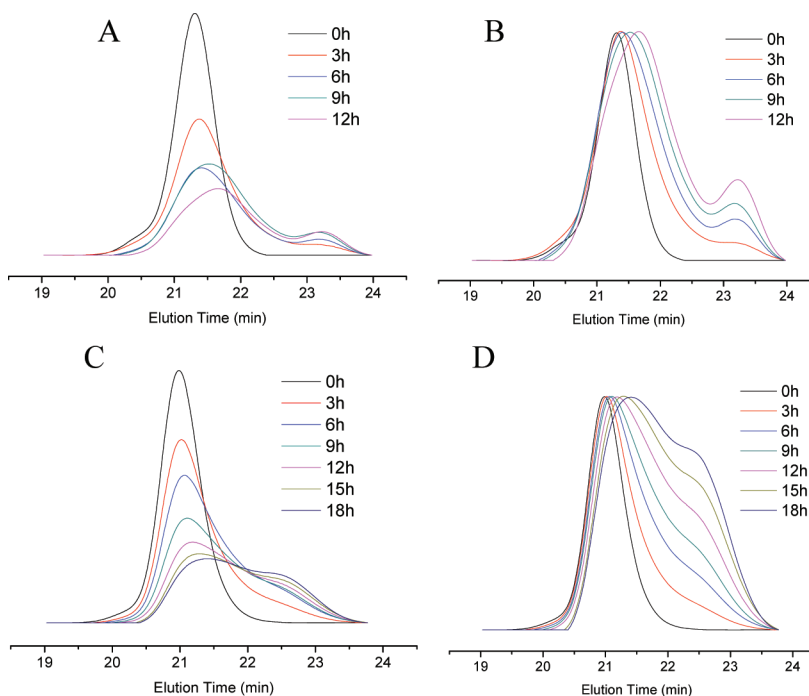


Figure 2. GPC traces for degradation products of PEG45-*b*-PCL62 micelles before normalization of block copolymer peak (A), after normalization (B), PEG45-*b*-PBO9-*b*-PCL61 micelles before normalization (C), and after normalization (D).

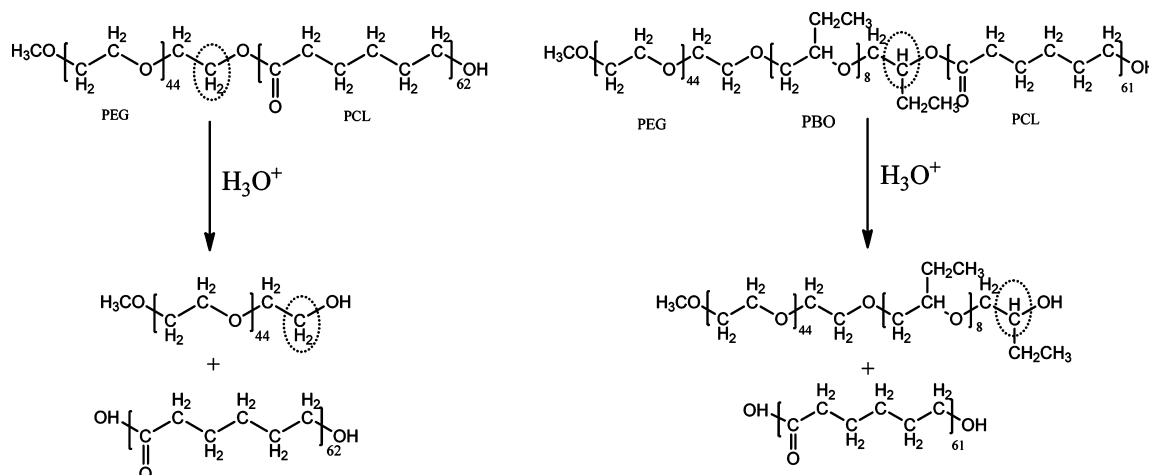
peak intensity of this special CH₂ group relative to the intensity of the end methyl group of PEG, which is set as constant, was monitored by the time evolution of the ¹H NMR (Figure S3). The ¹H NMR peak intensity of the CH₂ group decreases with time as hydrolysis proceeds.

Results from DLS and TEM studies show that diblock copolymers of PEG45-*b*-PCL62 self-assemble into narrowly size distributed micelles with a core-shell structure. The hydrophilic corona permits relatively facile access of water to the junction between the hydrophilic and hydrophobic polymer segments. The ester group at the hydrophilic-hydrophobic interface is exposed to the aqueous solution for hydrolysis. The initial event for acid-catalyzed ester hydrolysis is observed to

occur exclusively at the unique interface ester group as shown by appearance of the PEG homopolymer segment on the GPC traces and a decrease of ¹H NMR peak intensity of the CH₂ group that connects to ester group at the junction of the PEG-PCL on ¹H NMR traces. These observations are in agreement with the results of previous hydrolytic degradation studies of PEG-*b*-PCL which concluded that an initial stage of interfacial erosion was followed by bulk degradation in the micellar core.^{24,27,35,36}

Short segments of hydrophobic and hydrolytically stable PBO were inserted between the PEG and PCL blocks as a strategy to tune access of water to the interface ester linkage and thus alter the rate of hydrolysis and ultimately the micelle

Scheme 2. Hydrolysis of the Interface Ester Groups in Spherical Micelles



stability. The working hypothesis is that water can only freely reach the PEG–PBO junction in the triblock copolymer micelles and thus access by water to the ester group at the PBO–PCL interface will be retarded by the insulating PBO segment.

The GPC and ^1H NMR results for the interface ester hydrolysis of the PEG45-*b*-PBO9-*b*-PCL61 triblock copolymer micelles (Figure 2C,D and Figure S3) are analogous with those for the PEG45-*b*-PCL62 diblock copolymer micelles. The GPC results show that the PEG45-*b*-PBO9-*b*-PCL61 triblock copolymer micelle is cleaved into two individual polymer units with the low-molecular-weight peak occurring at the same position as the PEG45-*b*-PBO9 block shown in Figure S1. The average molecular weight decreased and the width of the distribution increased regularly for the PEG45-*b*-PBO9-*b*-PCL61 triblock copolymer GPC peak as the relative peak intensity of PEG45-*b*-PBO9 increased with the time of hydrolysis.

The time evolution of the ^1H NMR for the triblock copolymer micelle ester hydrolysis products is shown in Figure S3(B). The ^1H NMR intensity of the unique CH group (Scheme 2) bonded to the ester group at the PEGPBO–PCL junction decreases with time relative to the end methyl group of PEG as hydrolysis proceeds, which is very similar to results for the PEG45-*b*-PCL62 diblock copolymer. However, the rate of the disappearance of the CH ^1H NMR resonance resulting from the interface ester hydrolysis for the triblock copolymer micelle proceeds slowly relative to that of the diblock copolymer micelle.

Kinetic Comparison of Acid Hydrolysis of PEG45-*b*-PCL62 and PEG45-*b*-PBO9-*b*-PCL61 Block Copolymer Micelles. Quantitative comparison of the rate for acid-catalyzed ($\text{pH} = 1.0$) hydrolysis of the ester group at the PEG–PCL and PEGPBO–PCL junctions were obtained by following the time evolution of the ^1H NMR. First-order kinetic plots for the intact di- and triblock copolymers as a function of time are shown in Figure 3. The kinetic plots demonstrate that the rate of interface ester hydrolysis for the PEG45-*b*-PCL62 diblock copolymer micelles (0.11 h^{-1}) is faster than that of the PEG45-*b*-PBO9-*b*-PCL61 triblock copolymer micelles (0.041 h^{-1}). The half-life of the interface ester for diblock copolymer micelles is 6.3 h compared to a 16.9 h half-life for triblock copolymer micelles. Insertion of a short hydrophobic PBO segment between PEG and PCL is thus observed to provide

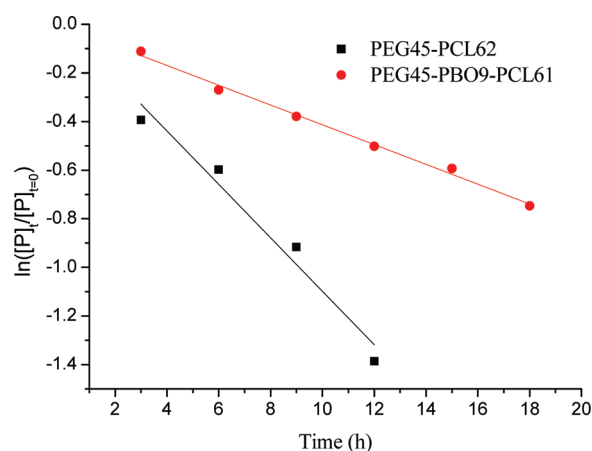


Figure 3. First-order kinetic plots for the acid-catalyzed hydrolysis of interface ester groups that occur at the PEG–PCL and PEGPBO–PCL junctions. $[\text{P}]_t$ is defined as the relative molar concentration of the intact block copolymer at time t .

increased kinetic stability for the PEG-*b*-PBO-*b*-PCL triblock copolymer micelles relative to the PEG-*b*-PCL diblock copolymer micelles. Systematic variation of the chemical nature and size of the spacer segments in a series of triblock copolymers is currently being used to evaluate their influence on micelle formation and stability.

CONCLUSIONS

Narrow polydispersity PEG45-*b*-PBO9-*b*-PCL61 triblock and PEG45-*b*-PCL62 diblock copolymers were prepared for comparative studies of micelle formation and relative stability in acidic media. DLS results indicate that both polymers form near-quantitative yields of micelles that are shown to be spherical by TEM. GPC and ^1H NMR results for the degradation of block copolymer spherical micelles proved that the initial hydrolysis of the micelles occurs at the interface ester group that binds the PCL segment with PBOPEG or PEG segments. Kinetics of hydrolysis of this unique ester group was followed by ^1H NMR and showed that insertion of a short chain PBO segment between the nondegradable PEG block and the biodegradable PCL units reduced the rate of hydrolysis of the interface ester group for the diblock copolymer micelle by a factor of 2.7, which is attributed to the PBO segment

providing a kinetic barrier for water to reach the ester group at the PEGPBO–PCL junction.

■ EXPERIMENTAL SECTION

Materials. Tetrahydrofuran (THF) and toluene were distilled just prior to use. Methoxy poly(ethylene glycol) (PEG, $M_n = 2000$, $M_w/M_n = 1.06$) was purified by precipitating from petroleum ether prior to use. ϵ -Caprolactone (CL) was dried by CaH_2 and distilled under vacuum. 1,2-Butylene oxide (BO) was also dried by CaH_2 and distilled before use. 18-Crown-6 ether (18C6) and stannous octoate ($\text{Sn}(\text{Oct})_2$) were used as received. Potassium naphthalenide–THF solution (0.89 M) was prepared by mixing of naphthalene (3.0 g), potassium (0.92 g), and THF (26 mL). All chemicals were purchased from Sigma-Aldrich.

Characterization. ^1H NMR spectra were obtained using Bruker 400 and 500 MHz spectrometers with CDCl_3 as solvent and internal standard. Gel permeation chromatography (GPC) measurements were carried out on a Shimadzu LC-20AV liquid chromatography system equipped with PolarGel-M 300×7.5 mm column and SPD-20AV UV/vis detector. DMF was used as the eluent at a flow rate of 1.0 mL/min at 50 °C. Calibration was based on polystyrene standards.

Synthesis of PEG45-*b*-PBO9 Diblock Copolymer. Dried PEG (8.0 g, 4.0 mmol) was dissolved in 80 mL of anhydrous THF in a 250 mL dry flask under an inert atmosphere. Potassium naphthalenide (9.0 mL, 0.89 M in THF) and 18C6 (1.5 g, 5.7 mmol)–THF solution were added into the solution via syringe. After stirring the mixture for 15 min while the dark green color persisted, BO (10 mL, 0.12 mol) was added into the reaction mixture via syringe. The solution was stirred for 1 h at room temperature, the reaction was terminated by the adding of HCl (0.80 mL, 12.2 M), and the green solution became colorless again. The undissolved inorganic salt was removed by filtration, and the PEG-*b*-PBO block copolymer was precipitated from petroleum ether. The white precipitates were recovered by filtration, redissolved in toluene, and precipitated from the petroleum ether again. The precipitates were collected and dried under vacuum at 40 °C for 48 h.

Synthesis of PEG45-*b*-PBO9-*b*-PCL61 Triblock Copolymer. Dried PEG45-*b*-PBO9 (0.90 g, 0.34 mmol) was dissolved in dry toluene (16 mL) in a 50 mL dry flask under an inert atmosphere. CL (6 mL, 0.054 mol) and $\text{Sn}(\text{Oct})_2$ (0.02 g) were added into the solution via syringe. The mixture was gently refluxed under nitrogen for at 120 °C. After stirring the solution for 5 h, excess cold methanol was poured into the solution to terminate and precipitate the product. The white precipitate was collected by filtration, redissolved in dichloromethane, and precipitated from the methanol again. The precipitate was collected and dried under vacuum at 40 °C for 48 h.

Micelle Preparation and Characterization. The nanoprecipitation method was used to prepare the PEG45-*b*-PCL62 and PEG45-*b*-PBO9-PCL61 micelles. Polymer stock solutions (10 mg/mL) of PEG45-PCL62 and PEG45-PBO9-PCL61 were prepared in acetone. Polymer stock solutions (0.8 mL) were introduced into vials, and filtered deionized water (8 mL) was subsequently added to the stirred polymer solutions at the rate of 1.0 mL/min. The remaining acetone in resulting micelle suspensions was removed at room temperature under a flow of nitrogen, applied for 36 h. The near-quantitative yield of micelle suspensions were filtered through a PVDF 100 nm pore size membrane filter to ensure removal of occasional small quantities of nondispersed polymer aggregates.

Dynamic Light Scattering (DLS). Hydrodynamic diameter of micelles was measured by a Zetasizer Nano ZS (Malvern Instruments, Westborough, MA) at 25 °C, using 1 cm polystyrene cuvettes. The mean diameter was obtained from the instrument's DTS software using the volume reading.

Transmission Electron Microscopes (TEM). Micelle morphology was evaluated by a JEOL JEM-1400 TEM operating at an acceleration voltage of 80 kV. The 1.0 mg/mL of micelle solution was diluted by a factor of 10 to reduce the aggregation during sample drying process. One drop of micelle solution was deposited on carbon-coated copper grid (Ted Pella Inc., Redding, CA). The droplet was

then blotted and allowed to evaporate under ambient conditions.^{37,38} The average diameters of the spherical micelles were analyzed by a digital micrograph.

Degradation of PEG45-*b*-PCL62 and PEG45-*b*-PBO9-*b*-PCL61 Block Copolymer Micelles. The hydrolytic degradation of PEG45-PCL62 and PEG45-*b*-PBO9-*b*-PCL61 micelles was studied in HCl (pH = 1.0) at 25 °C. The acid-catalyzed degradation experiment was done in a series of vials. In each 5 mL vial, 0.7 mL of micelle suspension (1.0 mg/mL) was added. Subsequently, 0.7 mL of HCl (2 M) solution was added into the vials. The reactions were terminated by adding 1.4 mL of NaOH (1 M) solution every 3 h. The final degradation products were extracted from water solution by CH_2Cl_2 for ^1H NMR and GPC evaluation.

■ ASSOCIATED CONTENT

Supporting Information

Experimental details on preparation of PEG45-*b*-PCL62 diblock copolymer; GPC traces and ^1H NMR spectra for PEG-*b*-PCL, PEG-*b*-PBO, and PEG-*b*-PBO-*b*-PCL block copolymers; ^1H NMR time evolution of ester hydrolysis for di- and triblock copolymers. This material is available free of charge via the Internet at <http://pubs.acs.org>.

■ AUTHOR INFORMATION

Corresponding Author

*E-mail: bwayland@temple.edu.

■ ACKNOWLEDGMENTS

Partial support of this research by NSF (CHE 0809395) and funding of a JEOL JEM-1400 TEM by the NSF (CHE-0923077) are gratefully acknowledged. The authors are also grateful to Dr. Hongwen Zhou for TEM experiments.

■ REFERENCES

- (1) Kang, N.; Perron, M.-È.; Prud'homme, R. E.; Zhang, Y.; Gaucher, G.; Leroux, J.-C. *Nano Lett.* **2005**, *5*, 315–319.
- (2) Hayward, R. C.; Pochan, D. J. *Macromolecules* **2010**, *43*, 3577–3584.
- (3) Cameron, N. S.; Corbierre, M. K.; Eisenberg, A. *Can. J. Chem.* **1999**, *77*, 1311–1326.
- (4) Discher, B. M.; Won, Y.-Y.; Ege, D. S.; Lee, J. C.-M.; Bates, F. S.; Discher, D. E.; Hammer, D. A. *Science* **1999**, *284*, 1143–1146.
- (5) Zhang, X.; Cheng, J.; Wang, Q.; Zhong, Z.; Zhuo, R. *Macromolecules* **2010**, *43*, 6671–6677.
- (6) Cai, S.; Vijayan, K.; Cheng, D.; Lima, E.; Discher, D. *Pharm. Res.* **2007**, *24*, 2099–2109.
- (7) Christian, D. A.; Cai, S.; Garbuzenko, O. B.; Harada, T.; Zajac, A. L.; Minko, T.; Discher, D. E. *Mol. Pharmaceutics* **2009**, *6*, 1343–1352.
- (8) Shuvaev, V. V.; Ilies, M. A.; Simone, E.; Zaitsev, S.; Kim, Y.; Cai, S. S.; Mahmud, A.; Dziubla, T.; Muro, S.; Discher, D. E.; Muzykantov, V. R. *ACS Nano* **2011**, *5*, 6991–6999.
- (9) Pang, Z.; Lu, W.; Gao, H.; Hu, K.; Chen, J.; Zhang, C.; Gao, X.; Jiang, X.; Zhu, C. *J. Controlled Release* **2008**, *128*, 120–127.
- (10) Hvasanov, D.; Wiedenmann, J.; Braet, F.; Thordarson, P. *Chem. Commun.* **2011**, *47*, 6314–6316.
- (11) Christian, D. A.; Cai, S.; Bowen, D. M.; Kim, Y.; Pajeroski, J. D.; Discher, D. E. *Eur. J. Pharm. Biopharm.* **2009**, *71*, 463–474.
- (12) Benahmed, A.; Ranger, M.; Leroux, J.-C. *Pharm. Res.* **2001**, *18*, 323–328.
- (13) Studer, P.; Limal, D.; Breton, P.; Riess, G. *Bioconjugate Chem.* **2004**, *16*, 223–229.
- (14) Master, A. M.; Rodriguez, M. E.; Kenney, M. E.; Oleinick, N. L.; Gupta, A. S. *J. Pharm. Sci.* **2010**, *99*, 2386–2398.
- (15) Kagaya, H.; Oba, M.; Miura, Y.; Koyama, H.; Ishii, T.; Shimada, T.; Takato, T.; Kataoka, K.; Miyata, T. *Gene Ther.* **2012**, *19*, 61–69.
- (16) Rameez, S.; Alosta, H.; Palmer, A. F. *Bioconjugate Chem.* **2008**, *19*, 1025–1032.

- (17) Jette, K.; Law, D.; Schmitt, E.; Kwon, G. *Pharm. Res.* **2004**, *21*, 1184–1191.
- (18) Forrest, M. L.; Zhao, A.; Won, C.-Y.; Malick, A. W.; Kwon, G. S. *J. Controlled Release* **2006**, *116*, 139–149.
- (19) Gan, Z.; Jim, T. F.; Li, M.; Yuer, Z.; Wang, S.; Wu, C. *Macromolecules* **1999**, *32*, 590–594.
- (20) Nie, T.; Zhao, Y.; Xie, Z.; Wu, C. *Macromolecules* **2003**, *36*, 8825–8829.
- (21) Meier, M. A. R.; Aerts, S. N. H.; Staal, B. B. P.; Rasa, M.; Schubert, U. S. *Macromol. Rapid Commun.* **2005**, *26*, 1918–1924.
- (22) Cuong, N.-V.; Jiang, J.-L.; Li, Y.-L.; Chen, J.-R.; Jwo, S.-C.; Hsieh, M.-F. *Cancers* **2010**, *3*, 61–78.
- (23) Ge, H.; Hu, Y.; Jiang, X.; Cheng, D.; Yuan, Y.; Bi, H.; Yang, C. *J. Pharm. Sci.* **2002**, *91*, 1463–1473.
- (24) Hu, Y.; Zhang, L.; Cao, Y.; Ge, H.; Jiang, X.; Yang, C. *Biomacromolecules* **2004**, *5*, 1756–1762.
- (25) Cuong, N.-V.; Hsieh, M.-F.; Chen, Y.-T.; Liao, I. *J. Appl. Polym. Sci.* **2010**, *117*, 3694–3703.
- (26) Ahmed, F.; Discher, D. E. *J. Controlled Release* **2004**, *96*, 37–53.
- (27) Shen, C.; Guo, S.; Lu, C. *Polym. Adv. Technol.* **2008**, *19*, 66–72.
- (28) Carstens, M. G.; van Nostrum, C. F.; Verrijck, R.; de Leede, L. G. J.; Crommelin, D. J. A.; Hennink, W. E. *J. Pharm. Sci.* **2008**, *97*, 506–518.
- (29) Shen, C.; Guo, S.; Lu, C. *Polym. Degrad. Stab.* **2007**, *92*, 1891–1898.
- (30) Nagasaki, Y.; Kutsuna, T.; Iijima, M.; Kato, M.; Kataoka, K.; Kitano, S.; Kadoma, Y. *Bioconjugate Chem.* **1995**, *6*, 231–233.
- (31) Park, S.-J.; Kang, S.-G.; Fryd, M.; Saven, J. G.; Park, S.-J. *J. Am. Chem. Soc.* **2010**, *132*, 9931–9933.
- (32) Ding, J.; Price, C.; Booth, C. *Eur. Polym. J.* **1991**, *27*, 891–894.
- (33) Wu, J.; Thio, Y. S.; Bates, F. S. *J. Polym. Sci., Part B: Polym. Phys.* **2005**, *43*, 1950–1965.
- (34) Giacomelli, C.; Borsali, R. *Macromol. Symp.* **2006**, *245–246*, 147–153.
- (35) Jiang, Z.; Zhu, Z.; Liu, C.; Hu, Y.; Wu, W.; Jiang, X. *Polymer* **2008**, *49*, 5513–5519.
- (36) Zweers, M. L. T.; Engbers, G. H. M.; Grijpma, D. W.; Feijen, J. *J. Controlled Release* **2004**, *100*, 347–356.
- (37) Fairley, N.; Hoang, B.; Allen, C. *Biomacromolecules* **2008**, *9*, 2283–2291.
- (38) Luo, L.; Tam, J.; Maysinger, D.; Eisenberg, A. *Bioconjugate Chem.* **2002**, *13*, 1259–1265.

Surfactant-Free Polymerization Forming Switchable Latexes That Can Be Aggregated and Redispersed by CO₂ Removal and Then Readdition

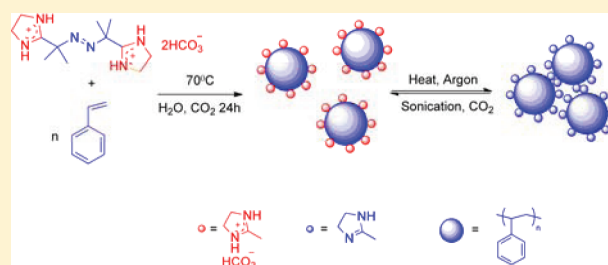
Xin Su,[†] Philip G. Jessop,^{*,†} and Michael F. Cunningham^{*,†,‡}

[†]Department of Chemistry, Queen's University, 90 Bader Lane, Kingston, Ontario, Canada K7L 3N6

[‡]Department of Chemical Engineering, Queen's University, 19 Division Street, Kingston, Ontario, Canada K7L 3N6

S Supporting Information

ABSTRACT: Polystyrene latexes prepared using the bicarbonate salt of initiator 2,2'-azobis[2-(2-imidazolin-2-yl)propane] via surfactant-free emulsion polymerization can be aggregated using only argon and gentle heat and redispersed using carbon dioxide and sonication. The bicarbonate and hydrochloride salts of the initiator have similar thermal decomposition behavior, but only the bicarbonate salt of 2,2'-azobis[2-(2-imidazolin-2-yl)propane] can be switchable between ionic and nonionic forms by addition and removal of CO₂. Measurements of particle size and zeta potential were used to study the aggregation and redispersion of the latexes. The latex is aggregated by heating and bubbling with argon to remove CO₂ and convert the active cyclic amidinium groups to their neutral form. When treated with sonication and bubbling with CO₂, the aggregated polystyrene latex can be redispersed successfully, as evidenced by restoration of the original latex particle size and zeta potential from the large aggregated polymer particles. This is the simplest method to date to prepare a redispersible latex stabilized by CO₂.



INTRODUCTION

The development of redispersible polymer latexes is of significant interest from both scientific and industrial perspectives.^{1–3} Emulsion polymerization is extensively used industrially to synthesize polymer latexes. While some applications such as coatings and adhesives require the latex be preserved in colloidal form, many other applications involve aggregation of the latex to give a polymer resin. There is also demand for redispersible powders that are stored and delivered as a dry powder but are then redispersed in water for final use. Many industrial uses of polymer latexes therefore require control of aggregation and redispersion processes.

Unfortunately, the current aggregation methods are not ideal. The common approach for aggregating latexes generally involves addition of large amounts of salts, acids, or bases to destabilize and aggregate the polymer latexes,⁴ but the subsequent washing of the latex is often ineffective in completely removing the surfactant and added salts. Furthermore, it is not usually possible to redisperse the aggregated particles. Switchable surfactants may offer an alternative solution to these problems; they have surface activity which can be reversibly changed using a trigger stimulus. Switchable surfactants triggered by the addition of acid,⁵ redox reagents,^{6–12} or even light¹³ have been reported. However, these materials are not suitable for the preparation of switchable polymer latexes, for reasons of cost, environmental impact, or, in the case of photochemical methods, by the opacity of polymer latexes.

CO₂ is an inexpensive, benign, and effective trigger for switchable surfactants and switchable latexes. Our group prepared surfactants consisting of long-chain alkyl amidine compounds that can be reversibly switched “on” and “off” by addition and removal of CO₂.^{14–16} Amidine groups react with dissolved CO₂ in the continuous water phase to produce the corresponding cationic amidinium bicarbonate.¹⁷ Bubbling argon (or any nonacidic gas) through the amidinium bicarbonate solutions reverses the reaction, releasing CO₂. In the absence of CO₂ or any other acidic trigger, these amidine compounds do not stabilize emulsions or suspensions. We previously showed that these surfactants were effective in preparing stable polystyrene (PS) latexes via emulsion polymerization.^{14,18,19} Importantly, both the surfactant and the initiator were amidinium bicarbonate salts, so that all of the amidinium groups in the resulting latexes were switchable. The latexes were readily aggregated¹⁸ by removal of CO₂ in order to convert all of the amidinium groups to neutral amidine groups and could also be effectively redispersed by reintroducing CO₂ to switch the surfactant back “on”.¹⁹

Zhu's group²⁰ also reported a switchable latex that contained amidine groups and was prepared via surfactant-free emulsion polymerization (SFEP). It had switching ability because of a switchable comonomer (2-methyl-1-(4-vinylbenzyl)-1,4,5,6-tet-

Received: November 22, 2011

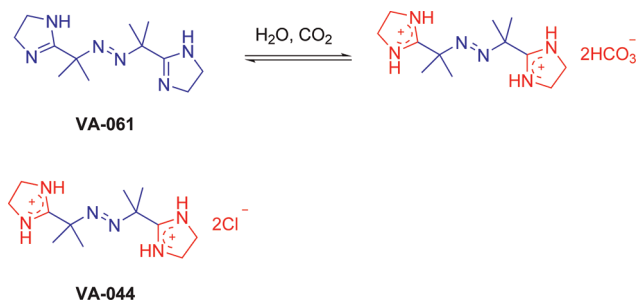
Revised: December 22, 2011

Published: January 11, 2012

rahydropyrimidinium bicarbonate), which contained amidinium groups. Aggregation of the latexes required caustic addition, probably because the initiator was a hydrochloride salt rather than a bicarbonate salt and therefore could not be switched to neutral by the removal of CO₂. Redispersion was achieved by sonication and sparging with CO₂. A surfactant-free process for preparing switchable latexes has distinct advantages.²¹ Because the colloidal stability of latex is provided by amidine groups that are covalently bound to the surface of the polymer particle, surfactant migration and leaching in the final product are eliminated. Furthermore, the high utilization efficiency of stabilizing moieties minimizes surfactant demand and reduces cost.

The most valuable important process would be one that uses only commercially available materials. In this article we present the preparation of switchable PS latexes via an SFEP process that uses only the commercially available 2,2'-azobis[2-(2-imidazolin-2-yl)propane] as a CO₂-triggered switchable initiator. This azo-based free radical initiator contains cyclic amidine groups and is slightly soluble in water in its neutral form. The cyclic amidine groups of the initiator react with CO₂ in water to produce the corresponding water-soluble bicarbonate salt (Scheme 1). Electrostatic stabilization of the

Scheme 1. Structures of the Initiators VA-044 and VA-061 and the Switchable Behavior of VA-061 Based on CO₂^a



^aBlue represents the neutral and hydrophobic; red represents charged and hydrophilic.

latex particles is achieved with the amidinium moieties from the initiators that comprise the polymer chain ends.

EXPERIMENTAL SECTION

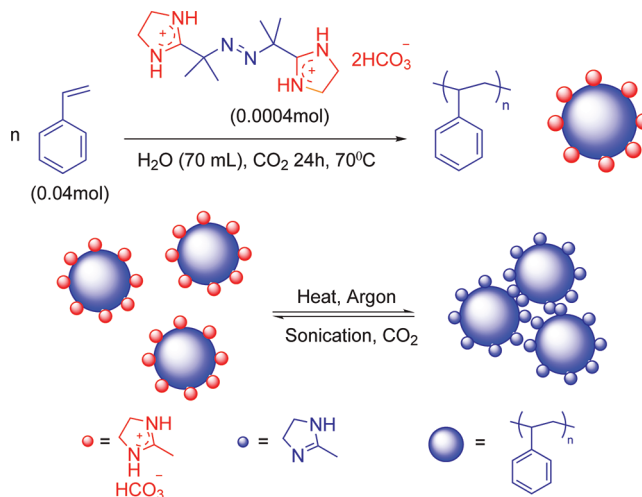
Materials. CO₂ (Praxair, Medical grade) and argon (Praxair, 99.998%) were used as received. 2,2'-Azobis[2-(2-imidazolin-2-yl)propane] (VA-061) and 2,2'-azobis[2-(2-imidazolin-2-yl)propane] dihydrochloride (VA-044) were purchased from Wako Pure Chemical Industries Ltd. Styrene (99%), dimethyl sulfoxide (DMSO), methanol-*d*₄, and D₂O were purchased from Aldrich. Inhibitor removal columns (Aldrich) were used to purify the monomers.

Preparation of Switchable PS Latex. Carbonated water was prepared by bubbling CO₂ for 30 min via a needle through deionized water in a round-bottom flask. Emulsion polymerization reactions were carried out in 100 mL round-bottomed flasks equipped with a stir bar and a condenser. The typical SFEP reaction conditions are as follows: Under a CO₂ atmosphere, deionized water (60 mL) and styrene (4.16 g, 0.04 mol) were added to the reactor. After 15 min of stirring, the system attained temperature equilibrium at 70 °C. VA-061 (0.10 g, 0.0004 mol) was added to 10 mL of carbonated water and sonicated to dissolve the initiator. The initiator aqueous solution was then added to the flask, and polymerization was carried out for 24 h under a CO₂ atmosphere (Scheme 2).

Switching Behavior of PS Latex. PS latexes prepared as described above were destabilized by continuous bubbling of argon

(0.5–1 h) through the latex at 65 °C via a needle while the sample was stirred. The polymer particles were then left to settle under gravity. In redispersing the coagulated PS particles into the same solution or into deionized water, the mixture was bubbled with CO₂ for several minutes, followed by sonication using a 100 W sonicator bath (Scheme 2).

Scheme 2. Preparation of Switchable Polystyrene and Reversible Aggregation and Redispersion of Polystyrene Latex Triggered by Removal and Addition of CO₂^a



^aBlue represents neutral and hydrophobic; red represents charged and hydrophilic.

Measurements. The conversion was measured by gravimetry. During polymerization, 1–2 g samples of the reaction mixture withdrawn from the reactor were first exposed to air, quenched in an ice/water bath, and then vacuum-dried without heating for determination of the monomer conversion.

Particle size was determined using a Malvern Mastersizer 2000 (size range of 50 nm to 2000 μm) equipped with a Hydro2000S optical unit and/or a Zetasizer Nano ZS (size range of 0.6 nm to 6.0 μm). The choice of instrument depended on the particle size of the sample. The particle sizes of the latex samples were typically at the lower end of the particle size range for the Mastersizer 2000, so the Zetasizer Nano ZS was used. However, after destabilization, the particle size fell at or above the upper end of the Zetasizer Nano ZS size range, necessitating the use of the Mastersizer 2000. Z-average and volume average particle diameters were measured by a Zetasizer Nano ZS and Mastersizer 2000, respectively. SEM images were acquired using a Hitachi S-5200 185 scanning electron microscope.

Zeta potentials were determined using the Zetasizer Nano ZS. Latex samples were diluted with distilled water presaturated with carbon dioxide, and measurements were taken using a disposable capillary cuvette.

The conductivity of VA-044 and VA-061 solutions was measured using a Jenway model 470 portable conductivity meter at 25 ± 0.5 °C.

The decomposition kinetics of VA-061 and VA-044 were studied under argon or CO₂ with methanol-*d*₄ or D₂O as a solvent and DMSO as an internal standard. The concentration of initiator at different times was determined from the ¹H NMR spectra on a Bruker Avance-400 instrument.

RESULTS AND DISCUSSION

Initiator Behavior. The initiators VA-044 and VA-061 have similar structures, but VA-044 is a dihydrochloride while VA-061 is a neutral compound (Scheme 1). The conductivity of VA-044 and VA-061 (14 mM) in water was determined at 25 ± 0.5 °C for two cycles of alternating CO₂ and argon bubbling.

Continuous bubbling of CO₂ ensures that the solution remains saturated with CO₂. The purpose of bubbling argon is to accelerate the removal of CO₂ and consequent neutralization of the bicarbonate salts. The results are shown in Figure 1. The

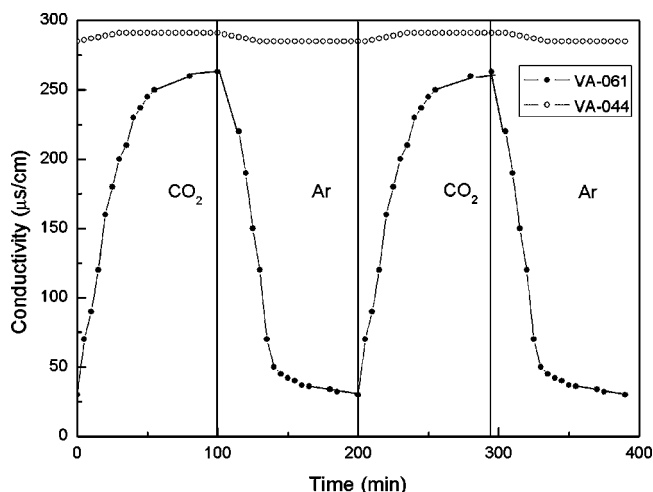


Figure 1. Conductivity of aqueous solutions of VA-044 and VA-061 (14 mM) at 25 ± 0.5 °C as a function of time during two cycles of sparging with CO₂ followed by argon.

conductivity of the VA-061 solution increased from 26 to 252 μS/cm after CO₂ bubbling for 50 min. It decreased to its initial value upon bubbling with argon. VA-061, an unprotonated amidine, is converted to a bicarbonate salt in the presence of CO₂ and water. From Figure 1, it is apparent that the aqueous solution of VA-044 has no significant switchability, though its conductivity does appear to increase very slightly in the presence of CO₂ and decrease in the presence of argon. The conductivity remains at a high, nearly constant value, between 261 and 289 μS/cm.

The decomposition kinetics of both initiators under different atmospheres were measured. VA-044 has been previously used to prepare PS latexes via surfactant-free emulsion polymerization.²² We therefore anticipated that VA-061 under CO₂ could be used during surfactant-free emulsion polymerization. The rate constants of VA-061 decomposition under CO₂ were estimated from NMR investigations and compared with results from VA-061 under argon and VA-044 under argon. DMSO was chosen as an internal standard in order to measure the exact concentrations of initiators during decomposition. According to ¹H NMR data, during decomposition, the concentrations of initiator at different times can be obtained from the ratio of the peak areas for initiator and DMSO (Supporting Information).

In the ideal case, the initiator decomposition is a first-order process,²³ so there is a relationship between decomposition rate constant and concentration of initiator

$$-\ln \frac{[I]_t}{[I]_0} = k_d t \quad (1)$$

where k_d is the decomposition rate constant of the dimension time⁻¹ at a certain temperature; $[I]_0$ and $[I]_t$ are separately the concentrations of initiator at zero time and any time t during the decomposition reaction. A graph showing $-\ln([I]_t/[I]_0)$ as a function of the decomposition time was linear for at least two half-lives, except that the experiment at the lowest temperature

was monitored for 1 half-life (Supporting Information). The rate constant k_d can be calculated from the slope of the straight line. After the decomposition of an initiator reacted under different temperatures, several straight lines were formed, and k_d at different temperatures was obtained. According to the Arrhenius equation²³

$$\ln k_d = -\frac{E_d}{RT} + \ln A_d \quad (2)$$

the activation energy and pre-exponential factor can be calculated from a plot of $\ln k_d$ as a function of $1/T$ (Supporting Information).

Table 1 shows the results of the decomposition experiments and the published data from Wako Pure Chemical Industries

Table 1. Decomposition Kinetics of VA-061 and VA-044 in Different Atmospheres and Solvents^a

initiator	solvent	atmosphere	$E_d \times 10^5$ J/mol	$A_d \times 10^{13}$ s ⁻¹	$T_{10 \text{ h half-life}}$ °C
VA-044	D ₂ O	argon	1.07	1.22	43
VA-061	CD ₃ OD	argon	1.15	1.30	60
VA-061	D ₂ O	CO ₂	1.07	1.11	42
VA-044 ^b	H ₂ O	^c	1.08	1.21	44
VA-061 ^b	CH ₃ OH	^c	1.14	1.29	61

^a E_d : activation energy; A_d : pre-exponential factor; $T_{10 \text{ h half-life}}$: 10 h half-life decomposition temperature. ^bThe data from the web site of Wako Pure Chemical Industries, Ltd.²⁴ ^cPresumably air.

Ltd.²⁴ The data reported and measured are almost the same. The results for VA-044 under argon and VA-061 under CO₂ show similar decomposition rate parameters, including activation energy, pre-exponential factor, and the 10 h half-life decomposition temperature. VA-044 and VA-061 bicarbonate salt have similar molecular structure except for the anionic counterion. However, the neutral VA-061 under argon has a significantly higher 10 h half-life decomposition temperature.

Synthesis of Switchable PS Latex. SFEP of styrene with the bicarbonate salt of VA-061 was performed under CO₂. Amidine groups within the initiator react with dissolved CO₂ in the water phase to produce charged amidinium bicarbonate groups which become the polymer chain ends and provide sufficient charge to make the PS latex colloidal stable. We used styrene-to-initiator molar ratios of 50, 100, or 200 to observe the effect on particle size and zeta potential. The particle size and zeta potential were observed to vary only slightly over the range of monomer-to-initiator ratios used. A typical monomer conversion curve is shown in Figure 2. The curve shows the standard shape associated with standard surfactant-free emulsion polymerization. Absence of surfactant leads to a slower polymerization rate than for conventional emulsion polymerization, but high conversions are achieved.²¹

Switching Behavior of the PS Latex. If the amidinium group from the initiator is covalently bound to the particle surface instead of being adsorbed physically, the stabilization of particles in the latex should be more effective and the switching more reversible.²⁵ In order to evaluate this hypothesis, we subjected the initial stable latex to different treatments to promote aggregation or redispersion. Excellent switching behavior from the initiator-derived, covalently bound amidine groups was observed. Photographs of the latexes at various stages of treatment are shown in Figure 3, as are the particle

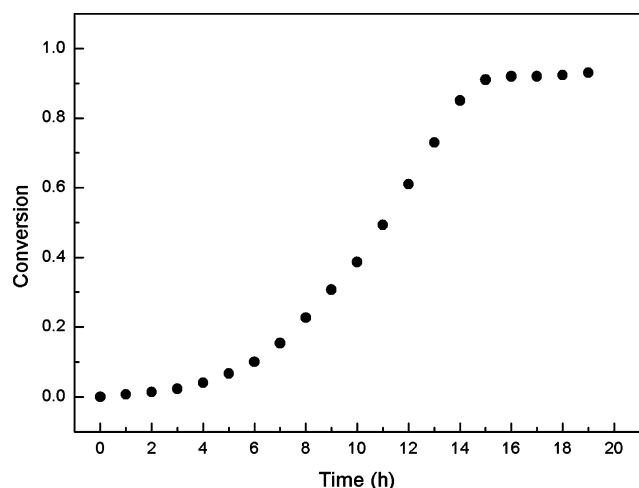


Figure 2. Conversion curve for the surfactant-free emulsion polymerization of styrene using VA-061 as initiator. Weight ratio of styrene:VA-061:water = 4.16:0.11:70; molar ratio between styrene and VA-061 is 100:1. Temperature = 70 °C.

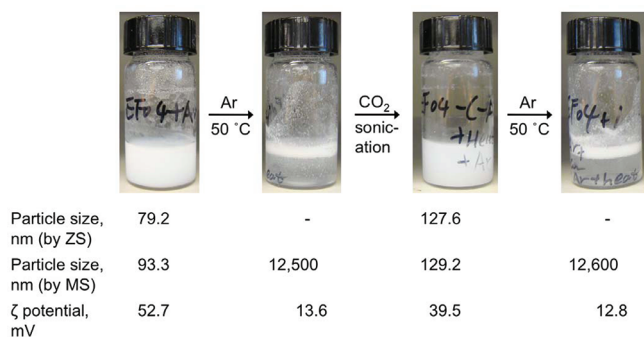


Figure 3. Reversible aggregation/redispersion behavior of PS latex. Photograph of original PS latex (prepared using 4.16 g of styrene, 0.11 g of VA-061, and 70 g of water); latex treated with argon with flow rate of 90 mL/min at 50 °C for 1 h; later, latex was treated with CO₂ with flow rate of 90 mL/min at room temperature and sonication for 15 min; finally, latex was treated with argon with flow rate of 90 mL/min at 50 °C for 1 h again. Particle sizes and zeta potentials in each stage are shown; z-average and volume-average particle diameters were obtained by a Zetasizer Nano ZS and a Mastersizer, respectively.

size, PDI and zeta potential of the PS latexes after each processing step. The zeta potential of the original latex was 52.7 mV, a high value suggesting that many of the charged cyclic amidine groups are located at or near the surface of the latex particles. It is likely that some amidine groups will remain in the aqueous phase, for example as the end groups on water-soluble oligoradicals. The colloids are cationically stabilized, but the reaction between amidine and carbonated water is reversible. Bubbling argon through the latex solution reversed the reaction, releasing CO₂, switching the amidine groups to their neutral forms and therefore breaking the stability of the latex. The zeta potential dropped to 13.6 mV after bubbling with argon. Although the zeta potential decreased significantly when argon was bubbled at room temperature, particle aggregation was quite slow. However when the latex was heated to 50 °C, aggregation was rapid and a white aggregated latex quickly formed. (The decomposition of the bicarbonate salts of amidines to their neutral form is an endothermic reaction.^{14,17}) The mean size of the aggregates formed from destabilization of

the latex was 125 μm, measured by static light scattering, and as shown in Figure 3. Figure 3 also shows the precipitate is floating. The reason is the formation of relatively stable foams after bubbling with argon. The surface of the polymer latex particle becomes hydrophobic; aggregated latex particles are then adsorbed at the argon–water interface and stabilize the aqueous foams. The aggregated particles settle after standing for several hours. In order to redisperse the aggregated latex, CO₂ was again bubbled through the water/aggregate mixture. The zeta potential returned to 33.1 mV, but there was no visible evidence that the white aggregated latex was redispersed. However, if sonication was used for several minutes with CO₂ bubbling, the PS suspension was redispersed and the precipitate disappeared. The particle size of the redispersed latex was 129 nm (compared to 79.2 nm for the original latex), and the zeta potential is 39.5 mV. To test the repeatability of the aggregation/redispersion cycle, we again treated the redispersed latex using heat and argon. The particles were successfully aggregated again. The particle size increased to 126 μm, and the zeta potential decreased to 12.8 mV. When the second redispersion was accomplished with sonication and CO₂, the results were comparable to those of the first redispersion (125 nm, 40.8 mV).

To allow better visualization of the initial latex particle size distribution compared to the aggregated and redispersed size distributions, we show the data measured with the Mastersizer 2000 under different situations. Figure 4 shows the particle size

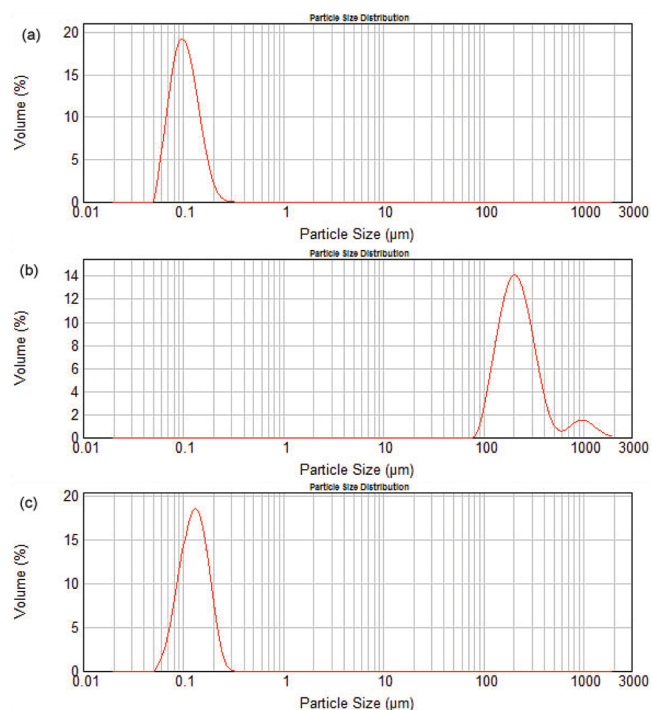


Figure 4. Graphs of volume average particle diameters of (a) original, (b) aggregated, and (c) redispersed PS latex measured by a Mastersizer. (a) Original PS latexes (prepared using 4.16 g of styrene, 0.11 g of VA-061, and 70 g of water). (b) Aggregated latex was treated with argon with flow rate of 90 mL/min at 50 °C for 1 h. (c) Redispersed latex was treated with CO₂ with flow rate of 90 mL/min at room temperature and sonication for 15 min.

distributions of the original latex, the aggregated latex, and the redispersed latex. After aggregation, the particle diameter is increased dramatically. The diameters of original and

redispersed latex are very similar, indicating the redispersion was successfully achieved using CO₂-triggered switchable materials.

The original and aggregated PS latexes were observed by scanning electron microscopy. Figure 5a is the SEM image of

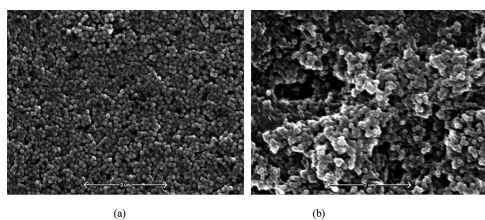


Figure 5. SEM images of (a) the original and (b) the aggregated polystyrene latexes. (a) In the original latex, the molar ratio between styrene and VA-061 is 100:1. (b) Aggregated latex was treated with argon with a flow rate of 90 mL/min at 50 °C for 1 h.

the original PS particles that have been obtained from SFEP. The mean particle size is about 100 nm, agreeing with the data from the Mastersizer from which the diameter is 93.3 nm. Figure 5b reveals the presence of aggregates, showing latex particles gather together to form clusters, consistent with the data from the Mastersizer.

The above results show that the aggregation and redispersion of the latex are reversible, repeatable, and controlled. The key factors are the covalent binding of the amidine groups and the lack of HCl salts in the system. Amidine groups in the latex, resulting from the initiator, can be switched between charged and uncharged states using CO₂ as the trigger. The latex is aggregated when CO₂ is removed, suggesting that colloidal stability is poor as a result of the decreasing surface charge. On the other hand, the latex can be redispersed when CO₂ is passed into the water/PS aggregated mixture, and the amidine group is reprotonated. But restoration of the charge is not sufficient to achieve redispersion; the ultrasonication treatment added some necessary energy to the system, presumably to overcome the free energy required to increase the interfacial area between the two phases and finely disperse one phase into the other.²⁶

CONCLUSION

Stimuli-responsive polymer latexes were successfully prepared with only commercially available reagents by surfactant-free emulsion polymerization using styrene as monomer and VA-061 as a switchable initiator. An important factor is that the amidine groups are covalently bound on the surface of the polymer latex. The latex can switch between aggregated and dispersed states using CO₂ as a trigger without the addition of salts, acids, or bases. The latex is aggregated by heating and bubbling with argon to remove CO₂ and convert the active cyclic amidinium groups to their neutral form. When treated with sonication and bubbling with CO₂, the aggregated polystyrene latex can be redispersed successfully, as shown by recovery of the original latex particle size and zeta potential from the large aggregated polymer particles.

ASSOCIATED CONTENT

Supporting Information

¹H NMR spectra of D₂O solution of VA-061 and DMSO under CO₂ at different times; graphs for calculating k_d , E_d , and A_d .

This material is available free of charge via the Internet at <http://pubs.acs.org>.

AUTHOR INFORMATION

Corresponding Author

*E-mail: michael.cunningham@chee.queensu.ca (M.F.C.), jessop@chem.queensu.ca (P.G.J.).

ACKNOWLEDGMENTS

We thank the Xerox Research Center of Canada for continued support and advice and the National Sciences and Engineering Research Council, the Ontario Research Chairs Program (Cunningham), and the Canada Research Chairs Program (Jessop) for financial support.

REFERENCES

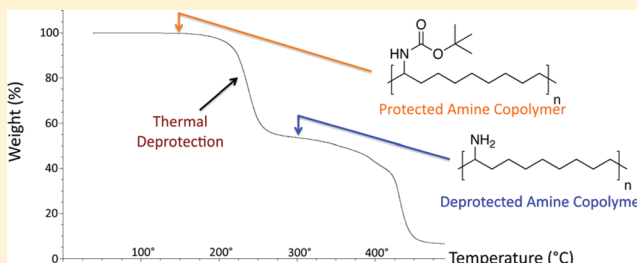
- (1) Du Chesne, A.; Bojkova, A.; Gapinski, J.; Seip, D.; Fischery, P. *J. Colloid Interface Sci.* **2000**, *224*, 91–98.
- (2) Fujii, S.; Kakigi, Y.; Suzaki, M.; Yusa, S.; Muraoka, M.; Nakamura, Y. *J. Polym. Sci., Part A: Polym. Chem.* **2009**, *47*, 3431–3433.
- (3) Wang, J.; Sun, L.; Mpoukouvalas, K.; Lienkamp, K.; Lieberwirth, I.; Fassbender, B.; Bonaccorso, E.; Brunklaus, G.; Muehlebach, A.; Beierlein, T.; Tilch, R.; Butt, H.-J.; Wegner, G. *Adv. Mater.* **2009**, *21*, 1137–1141.
- (4) Hsu, J.; Liu, B. *J. Phys. Chem. B* **1998**, *102*, 334–337.
- (5) Malcolm, A. S.; Dexter, A. F.; Middelberg, A. P. *J. Soft Matter* **2006**, *2*, 1057–1066.
- (6) Saji, T.; Hoshino, K.; Aoyagui, S. *J. Am. Chem. Soc.* **1985**, *107*, 6865–6868.
- (7) Anton, P.; Koeberle, P.; Laschewsky, A. *Prog. Colloid Polym. Sci.* **1992**, *89*, 56–59.
- (8) Datwani, S. S.; Truskett, V. N.; Rosslee, C. A.; Abbott, N. L.; Stebe, K. *J. Langmuir* **2003**, *19*, 8292–8301.
- (9) Aydogan, N.; Abbott, N. L. *Langmuir* **2001**, *17*, 5703–5706.
- (10) Cheng, Z.; Ren, B.; Gao, M.; Liu, X.; Tong, Z. *Macromolecules* **2007**, *40*, 7638–7643.
- (11) Tsuchiya, K.; Orihara, Y.; Kondo, Y.; Yoshino, N.; Ohkubo, T.; Sakai, H.; Abe, M. *J. Am. Chem. Soc.* **2004**, *126*, 12282–12283.
- (12) Ghosh, S.; Irvin, K.; Thayumanavan, S. *Langmuir* **2007**, *23*, 7916–7919.
- (13) Minkenberg, C. B.; Florusse, L.; Eelkema, R.; Koper, G. J. M.; van Esch, J. H. *J. Am. Chem. Soc.* **2009**, *131*, 11274–11275.
- (14) Liu, Y.; Jessop, P. G.; Cunningham, M.; Eckert, C. A.; Liotta, C. L. *Science* **2006**, *313*, 958–960.
- (15) Harjani, J. R.; Liang, C.; Jessop, P. G. *J. Org. Chem.* **2011**, *76*, 1683–1691.
- (16) Arthur, T.; Harjani, J.; Phan, L.; Jessop, P. G.; Hodson, P. V. *Green Chem.* **2011**, DOI: 10.1039/c1gc15620a.
- (17) Heldebrant, D. J.; Jessop, P. G.; Thomas, C. A.; Eckert, C. A.; Liotta, C. L. *J. Org. Chem.* **2005**, *70*, 5335–5338.
- (18) Mihara, M.; Cunningham, M. F.; Jessop, P. G. *Macromolecules* **2011**, *44*, 3688–3693.
- (19) Fowler, C. I.; Muchemu, C.; Miller, R. E.; Phan, L.; Cunningham, M. F.; Jessop, P. G. *Macromolecules* **2011**, *44*, 2501–2509.
- (20) Zhang, Q.; Wang, W.; Lu, Y.; Li, B.; Zhu, S. *Macromolecules* **2011**, *44*, 6539–6545.
- (21) Mahdavian, A.; Abdollahi, M. *Polymer* **2004**, *45* (10), 3233–3239.
- (22) Sakota, K.; Okaya, T. *J. Appl. Polym. Sci.* **1976**, *20*, 1725–1733.
- (23) Turcsányi, B. *Polym. Bull.* **1993**, *30* (3), 297–303.
- (24) Wako Pure Chemical Industries Ltd. (a) <http://www.wako-chem.co.jp/specialty/waterazo/VA-044.htm>; (b) <http://www.wako-chem.co.jp/specialty/waterazo/VA-061.htm> (accessed Nov 2011).
- (25) Ceska, G. W. *J. Appl. Polym. Sci.* **1974**, *18*, 2493–2499.
- (26) Delmas, T.; Piroux, H.; Couffin, A.; Texier, I.; Vinet, F.; Poulin, P.; Cates, M. E.; Bibette, J. *Langmuir* **2011**, *27*, 1683–1692.

Synthesis and Thermal Characterization of Precision Poly(ethylene-co-vinyl Amine) Copolymers

James K. Leonard, Yuying Wei, and Kenneth B. Wagener*

The George and Josephine Butler Polymer Research Laboratory, Department of Chemistry, University of Florida, Gainesville, Florida 32611, United States

ABSTRACT: A structural investigation of linear ethylene-co-vinyl amine (EVAm) copolymers having a primary amine branch on every 9th, 15th, 19th, or 21st carbon along the ethylene backbone has been completed using step polymerization chemistry. Acyclic diene metathesis (ADMET) polymerization has been used with symmetrical α,ω dienes containing protected amine groups to afford polymers with exact primary structures and constant methylene run lengths between branches. The effects of subtle structural changes such as the ethylene run lengths between amine branches can be observed and used to correlate structure property relationships. NMR and FT-IR techniques are used to characterize and verify the excellent structural control this synthetic approach provides over traditional chain polymerization techniques. Thermal decomposition of these copolymers is shown to additionally support polymer structure while differential scanning calorimetry demonstrates crystallinity in the polymers with an amine on every 15th and 21st carbon, whereas the polymer with an amine on every ninth carbon is amorphous. Variations of the physical and spectral properties are discussed as a consequence of the amine branch spacing, protection, and saturation of the ethylene backbone.



INTRODUCTION

Ethylene-co-vinyl amine polymers (PEVAm) have several desirable characteristics and numerous commercial applications. The primary amine functionality along the ethylene backbone is a highly reactive site that can be utilized for derivatization and cross-linking. In the protonated form, the cationic charge density of the ammonium ion makes it useful in ionomer applications.¹ In addition, the ability of amines to chelate allow them to form complexes with various metal ions^{2,3} and to serve as support scaffolds for enzymes.⁴ Considering the many potential applications of these materials, it is important to have an understanding of their primary structure's relationship to physical properties. However, structure–property information of this type has not been readily available or even known.

The lack of fundamental studies can be attributed partly to synthetic difficulties, which have also limited the applications of PEVAm. The copolymerization of ethylene with vinyl amine type monomers is a difficult task due to both the large reactivity ratio disparity of the two vinyl monomers and the tendency of the vinyl amine to act as an efficient chain-transfer agent during radical and cationic polymerization.⁵ The simplest precursor monomer for synthesis of polyvinylamine (PVAm), vinyl amine, does not exist in the free state because it tautomerizes to the acetaldehyde imine.⁵ This monomer lability necessitates the synthesis of PVAm indirectly from an intermediate polymer, a synthetic approach similar to that used with poly(vinyl alcohol) (PVA).⁵

Although PVAm has been synthesized in numerous ways,^{6–8} preparation of PVAm via radical chemistry with minimal structural defects and reasonably high molecular weights has

involved two main precursors: *tert*-butyl *N*-vinylcarbamate (TBNVC)⁹ and vinylformamide (VFA) monomers.^{10,11} BASF, the largest commercial producer of PVAm, has utilized vinylformamide (VFA) with the subsequent hydrolysis of its amide side chains to make PVAm.

Of all the potential copolymers that can be made with vinylamine, those with ethylene as the comonomer are of particular interest. Poly(ethylene-co-vinyl amine) (PEVAm) polymers, with ethylene:vinylamine molar ratios of at least 1:1, are ideal for use as flocculants in water clarification. The molar ratio of these copolymers is modified by monomer addition under high-pressure conditions via radical chemistry. The ideal ethylene:vinylamine ratio in these materials is 2:1 to 4:1.¹² Within this preferred range, the desired physical and chemical properties imparted by the amine units are preserved, while the cost of the polymers is markedly lowered by the presence of the more economical ethylene units.¹²

Other than the usual backbone defects elicited by the radical chain polymerization of these materials, irregularities encountered in PEVAm materials come from both the acid and base hydrolysis of the poly(*N*-vinylformamide). Acid hydrolysis can proceed via transiently formed amidine rings, but is unable to surpass the 80% level due to repulsions among the protonated amine side chains.¹¹ Basic hydrolysis can be carried out completely, but Spange¹⁰ and Bortel¹¹ have both observed the

Received: October 6, 2011

Revised: November 30, 2011

Published: December 19, 2011

elimination of ammonia as noted by elemental analysis and the perceptible smell during the hydrolysis.

By taking advantage of step polymerization chemistry offered by acyclic diene metathesis (ADMET), our research group has been able to avoid the random nature of addition polymerizations, as well as the unwanted side reactions often observed in radical polymerizations of vinyl monomers. This mild polymerization chemistry also avoids the defects usually imparted by catalysts during chain propagation processes. These defects, in either small or large amounts, can have profound effects on the macromolecule's material behavior and thermal response.

Both Breitenkamp¹³ and Masuda¹⁴ have utilized ring-opening metathesis polymerization (ROMP) to prepare amine-functionalized polymers. Herein, we report the synthesis and thermal characterization of a family of four linear EVAm copolymers with amine branches precisely spaced along the polyethylene backbone at intervals of every 9th, 15th, 19th, or 21st carbon. Their preparation has been accomplished using ADMET chemistry, which assures that the branches are set at specific, not random, intervals along the backbone, generating polymers incapable of being made by other methodologies.^{15–21} Primary structural analysis has been achieved by ¹H and ¹³C NMR and FT-IR techniques, and detailed calorimetry data are presented to demonstrate the morphological differences arising from the combined effects of branch frequency and the regular distribution of amine branches.

■ EXPERIMENTAL SECTION

Materials. Reagents and chemicals were used as received from Aldrich Chemical Co. unless otherwise noted. Diethyl ether and THF were used as dry solvents from the Aldrich keg system and dried over 4 Å sieves. The second generation Grubbs catalyst (tricyclohexylphosphine[1,3-bis(2,4,6-trimethylphenyl)-4,5-dihydroimidazol-2-ylidene][benzylidene]ruthenium(IV) dichloride) was synthesized and used as previously described by Grubbs et al.²²

Instrumentation and Analysis. ¹H NMR and ¹³C NMR spectra were recorded on a Varian Associates Mercury 300 spectrometer. Chemical shifts for ¹H and ¹³C NMR were referenced to residual signals from CDCl₃ (¹H = 7.24 ppm and ¹³C = 77.23 ppm) with 0.03% v/v TMS as an internal reference. High resolution mass spectra (HRMS) were obtained on a Finnegan 4500 gas chromatograph/mass spectrometer using the chemical ionization mode. IR data was obtained using a Perkin-Elmer Spectrum One FT-IR outfitted with a LiTaO₃ detector, measurements were automatically corrected for water and carbon dioxide. FT-IR polymer samples were prepared by solution-casting a thin film from THF onto a KBr salt plate.

Gel permeation chromatography (GPC) of polymers was performed at 40 °C using a Waters Associates GPCV2000 liquid chromatography system with an internal differential refractive index detector (DRI) and two Waters Styragel HR-4E columns (10 μm PD, 7.8 ID, 300 mm length) using HPLC grade tetrahydrofuran as the mobile phase at a flow rate of 1.0 mL/min. Injection volumes of 220.5 μL were made at 0.05–0.07 w/v sample concentrations. Retention times were calibrated against a minimum of nine narrow molecular weight polystyrene standards purchased from Polymer Laboratories (Amherst, MA).

Solid-State NMR (SS-NMR) spectra were performed at the Max Planck Institute for Polymer Research (MPIP) in Mainz, Germany using a Bruker DSX 7.05 T instrument at 21.7 MHz for ¹⁵N employing a magic angle spinning (MAS) frequency of 10 kHz. The ¹⁵N cross-polarization from ¹H was conducted using a contact angle of 7 ms and a high-power ¹H decoupling two-pulse phase modulation (TPPM) of 100 kHz. The ¹⁵N spectra were referenced to the ¹⁵NO₃ in ¹⁵N-enriched NH₄NO₃. All spectra were acquired from a 4 mm rotor at room temperature. Because of the low natural abundance of nitrogen-15 (0.37%),

long time scans from these nonlabeled materials were conducted in order to achieve good signal-to-noise ratios.

Differential scanning calorimetry (DSC) was performed on a TA Instruments Q1000 equipped with a liquid nitrogen cooling accessory and calibrated using sapphire and high purity indium metal. All samples were prepared in hermetically sealed pans (4–7 mg/sample) and were referenced to an empty pan. A scan rate of 10 °C per minute was used. Melting temperatures were taken as the peak of the melting transition, glass transition temperatures as the midpoint of a step change in heat capacity. Thermal experiments were conducted as follows: samples were heated through the melt to erase thermal history, followed by cooling at 10 °C per minute to –150 °C, and then heated through the melt at 10 °C per minute. Data reported reflects this second heating scan.

Premonomer Amine Diene Synthesis. Magnesium (4.89 g, 0.20 mol) was added to a 500 mL three-necked flask equipped with a reflux condenser and an addition funnel. The reaction vessel was backfilled three times with Ar and flame-dried after each backfill. Dry THF (100 mL) was added, followed by the addition of 5-bromo-1-pentene (25.0 g, 0.17 mol) dropwise via syringe. The solution was refluxed for 2 h to completely form the Grignard. Ethyl formate (5.64 g, 0.076 mol) in 30 mL THF was added dropwise to the cooled mixture (0 °C), and the solution was allowed to warm slowly to room temperature and then refluxed for 21 h. Hydrochloric acid (1M, 100 mL) was added, and the solution was extracted with ether (3 × 25 mL), washed with 1 M HCl (1 × 30 mL), and washed with brine (3 × 20 mL). The solution was dried over MgSO₄, followed by evaporation of the solvent to yield 14.18 g of the crude alcohol.

To a 500 mL round-bottom flask equipped with an addition funnel were added pyridinium chlorochromate (PCC) (26.0 g, 0.12 mol), Celite (equal weight to crude alcohol), and methylene chloride (100 mL) followed by the addition of the crude alcohol (1 equiv). The reaction was stirred for 4 h at room temperature, diethyl ether (200 mL) was added, and the mixture was filtered through a pad of silica gel. Solvent evaporation yielded 13.0 g of the crude ketone.

To a 500 mL round-bottom flask was added the crude ketone, dry methanol (225 mL), ammonium acetate (60 g, 0.78 mol), sodium cyanoborohydride NaCNBH₃ (25 g, 0.40 mol), and a spatula tip of crushed 4 Å molecular sieves; the mixture was refluxed for 48 h under N₂. The crushed molecular sieves were filtered via Büchner filtration and deionized water (200 mL) was added to the filtrate, followed by extraction with diethyl ether (3 × 50 mL). The organic layer was washed with 1 M NaOH (2 × 50 mL) and brine (2 × 30 mL) and dried over MgSO₄. The solution was concentrated to a brown viscous oil, which was purified by flash column chromatography using a 3:1:1 (hexane:ethyl acetate:methanol) mobile phase yielding 9.28 g of the desired 3,3NH₂ product for an overall yield of 73%.

1-Undec-10-enyl-dodec-11-enylamine (3,3NH₂). ¹H NMR (300 MHz, CDCl₃): δ 1.15–1.70 (m, 8H), 2.01–2.15 (br, 4H), 2.65–2.76 (br, 1H), 4.90–5.10 (m, 4H), 5.75–5.90 (m, 2H). ¹³C NMR (75 MHz, CDCl₃): δ 25.87, 34.29, 37.84, 51.45, 114.95, 139.19.

Heptadeca-1,16-dien-9-amine (6,6NH₂). This premonomer was in limited supply and is extremely valuable so it was used *in situ* to directly make the Boc-protected monomer.

Tricosa-1,22-dien-12-amine (9,9NH₂). The 9,9NH₂ was synthesized as described above using 11-bromo-1-undecene (25.0 g, 0.106 mol) instead of 5-bromo-1-pentene. After purification, a final yield of 48% (13.0 g) was obtained. ¹H NMR (300 MHz, CDCl₃): δ 1.15–1.45 (br, 32H), 2.05 (q, 4H), 2.65–2.75 (br, 1H), 4.88–5.05 (m, 4H), 5.72–5.38 (m, 2H). ¹³C NMR (75 MHz, CDCl₃): δ 26.39, 29.20, 29.41, 29.76, 29.84, 29.90, 30.07, 34.08, 38.02, 51.50, 114.36, 139.50.

1-Dec-9-enyl-undec-10-enylamine (8,8NH₂). Synthesis was performed using a modified procedure by Zantour and co-workers.³⁹ To a 500 mL three-neck round-bottom flask equipped with a reflux condenser and an addition funnel was added 10-undecenyl chloride (20.27 g, 100 mmol) and dry diethyl ether (150 mL). The solution was cooled to 0 °C, and triethylamine (18.21 g, 180 mmol) was added dropwise, instantly forming white triethylammonium chloride salts. The reaction mixture was warmed to room temperature and stirred for 24 h, followed by Büchner filtration of the salts and evaporation to yield

the liquid intermediate β -lactone. Deionized water (100 mL) and NaOH (8.80 g, 2.10 mol) were added, and the mixture was refluxed for 12 h. The solution was acidified with 1 M HCl and extracted with diethyl ether (3 \times 50 mL). The combined organic layers were washed with 1 M HCl (2 \times 20 mL) and brine (2 \times 20 mL). After drying over MgSO_4 and recrystallizing from MeOH, 13.15 g of the pure ketone was obtained. The ketone was converted to the amine using the same methodology as described with the 3,3 NH_2 and 9,9 NH_2 syntheses. The overall yield for the two steps was 58%. ^1H NMR (300 MHz, CDCl_3): δ 1.18–1.62 (br, 28H), 2.04 (q, 4H), 2.80–2.94 (m, br, 1H), 4.03–4.54 (br, 2H), 4.88–5.07 (m, 4H), 5.71–5.91 (m, 2H). ^{13}C NMR (75 MHz, CDCl_3): δ 26.52, 29.34, 29.54, 29.88, 30.01, 30.20, 34.21, 38.18, 41.61, 114.46, 139.50.

General Fmoc Protection of the Amine Dienes. To a dry 500 mL round-bottom flask were added 150 mL of dry THF, 50 mL of dry pyridine, and Fmoc-Cl (1.0 g, 3.90 mmol) under argon. Then, 9,9 NH_2 (1 g, 3.25 mmol) was slowly added over 0.5 h and the reaction was allowed to stir at room temperature for an additional 2 h. After 2 h, 100 mL of ether was added to the reaction and it was extracted with 1 M HCl (2 \times 50 mL) and brine (2 \times 50 mL). The protected amine solution was dried over MgSO_4 followed by rotary evaporation to yield the 9,9 NHFmoc product. The 9,9 NHFmoc was purified via column chromatography using ethyl acetate:hexane (3:2).

(9H-Fluoren-9-yl)methyl Henicosa-1,20-dien-11-ylcarbamate (9,9 NHFmoc). ^1H NMR (300 MHz, CDCl_3): δ 7.75 (d, 2H), 7.61 (d, 2H), 7.40 (t, 2H), 7.28 (t, 2H), 5.82 (m, 2H), 4.94 (m, 4H), 4.40 (d, 2H), 4.23 (t, 1H), 2.04 (m, 4H), 1.15–1.45 (br, 28H). EI/HRMS [$M + 1$]: calcd for $\text{C}_{36}\text{H}_{51}\text{NO}_2$, 530.3998; found, 530.4006.

General Boc Protection of the Amine Dienes. To a dry 500 mL round-bottom flask was charged 150 mL dry THF and the appropriate amine (2.5 g) under argon. A syringe was used to add the Boc anhydride (1 M in THF, 1 equiv) over 15 min at room temperature. The reaction was allowed to stir for 24 h and was monitored by TLC (ethyl acetate:hexane, 1:19) for disappearance of the starting material amine. At the end of the 24 h reaction period, 100 mL of ether was added and the solution was extracted with water (1 \times 50 mL), NaHCO_3 (2 \times 50 mL), and brine (2 \times 50 mL). The washed solution was dried over MgSO_4 followed by rotary evaporation to yield the Boc protected product. The monomer was purified via column chromatography using ethyl acetate:hexane (1:19).

***tert*-Butyl Undeca-1,10-dien-6-ylcarbamate 3,3 NHBoc (1).** Monomer is a colorless oil. ^1H NMR (300 MHz, CDCl_3): δ 1.20–1.46 (br, m, 8H), 1.48 (s, 9H), 2.01 (m, 4H), 3.52 (br, 1H), 4.22 (br, d, 1H), 4.93 (m, 4H), 5.76 (m, 2H). ^{13}C NMR (75 MHz, CDCl_3): δ 25.33, 27.60, 28.62, 33.79, 35.25, 50.57, 79.00, 114.78, 138.83, 155.89. FT-IR (KBr pellet): 3348, 3077, 2978, 2934, 2860, 1814, 1692, 1641, 1522, 1457, 1443, 1416, 1391, 1366, 1284, 1249, 1174, 1120, 1056, 1026, 944, 910, 868, 773, 637 cm^{-1} . ESI/HRMS [$2M + 1$]: calcd for $\text{C}_{16}\text{H}_{29}\text{NO}_2$, 535.4469; found, 535.4463. Anal. Calcd for CHNO : C, 71.86; H, 10.93; N, 5.24. Found: C, 71.91; H, 11.06; N, 5.23.

***tert*-Butyl Heptadeca-1,16-dien-9-ylcarbamate 6,6 NHBoc (2).** Monomer is a waxy white solid that melts at 38 $^\circ\text{C}$. ^1H NMR (300 MHz, CDCl_3): δ 1.23–1.40 (br, m, 8H), 1.41 (s, 9H), 2.01 (q, 4H), 3.50 (br, 1H), 4.20 (br, d, 1H), 4.91 (m, 4H), 5.78 (m, 2H). ^{13}C NMR (75 MHz, CDCl_3): δ 26.01, 28.65, 29.05, 29.27, 29.63, 33.97, 35.79, 50.83, 79.00, 114.37, 139.35, 155.92. FT-IR (KBr pellet): 3444, 3346, 3077, 2977, 2928, 2856, 1821, 1703, 1693, 1641, 1522, 1455, 1441, 1415, 1390, 1365, 1248, 1174, 1092, 1057, 993, 909, 869, 778, 750, 725, 636, 555 cm^{-1} . EI/HRMS [$2M + 1$]: calcd for $\text{C}_{22}\text{H}_{41}\text{NO}_2$, 703.6347; found, 703.6327. Anal. Calcd for CHNO : C, 75.16; H, 11.75; N, 3.98. Found: C, 75.26; H, 11.99; N, 3.93.

***tert*-Butyl Henicosa-1,20-dien-11-ylcarbamate 8,8 NHBoc (3).** Monomer is a waxy white solid that melts at 43 $^\circ\text{C}$. ^1H NMR (300 MHz, CDCl_3): δ 1.21–1.41 (br, m, 28H), 1.42 (s, 9H), 2.01 (q, 4H), 3.50 (br, 1H), 4.20 (br, d, 1H), 4.93 (m, 4H), 5.80 (m, 2H). ^{13}C NMR (75 MHz, CDCl_3): δ 26.06, 28.67, 29.14, 29.33, 29.64, 29.76, 29.80, 34.02, 35.82, 50.87, 78.95, 114.31, 139.42, 155.94. FT-IR (KBr pellet): 3348, 3077, 2977, 2926, 2855, 1701, 1641, 1503, 1456, 1390, 1365, 1245, 1173, 1046, 993, 909, 865, 723, 640 cm^{-1} . EI/HRMS [$2M + 1$]: calcd for $\text{C}_{26}\text{H}_{49}\text{NO}_2$, 815.7599; found, 815.7466. Anal. Calcd for

CHNO : C, 76.60; H, 12.11; N, 3.44. Found: C, 76.58; H, 12.26; N, 3.47.

***tert*-Butyl Tricosa-1,22-dien-12-ylcarbamate 9,9 NHBoc (4).** Monomer is a waxy white solid that melts at 46 $^\circ\text{C}$. ^1H NMR (300 MHz, CDCl_3): δ 1.22–1.40 (br, m, 32H), 1.41 (s, 9H), 2.01 (q, 4H), 3.49 (br, 1H), 4.20 (br, d, 1H), 4.91 (m, 4H), 5.78 (m, 2H). ^{13}C NMR (75 MHz, CDCl_3): δ 26.07, 27.63, 28.66, 29.15, 29.34, 29.68, 29.74, 29.80, 34.02, 35.84, 50.90, 78.95, 114.30, 139.43, 155.94. FT-IR (KBr pellet): 3446, 3349, 3077, 2977, 2927, 2855, 1820, 1705, 1641, 1503, 1456, 1415, 1390, 1365, 1247, 1174, 1049, 992, 909, 867, 780, 750, 722, 636, 552, 464 cm^{-1} . EI/HRMS [$2M + 1$]: calcd for $\text{C}_{28}\text{H}_{53}\text{NO}_2$, 871.8225; found, 871.8195. Anal. Calcd for CHNO : C, 77.18; H, 12.26; N, 3.21. Found: C, 77.24; H, 12.27; N, 3.25.

General ADMET Polymerization Procedure for Symmetrical Boc Amine Monomers. Monomer was transferred into a dry 25 mL Schlenk tube equipped with a stir bar and glass stopcock and dried by heating the vessel in an oil bath at 50 $^\circ\text{C}$ under full vacuum (10^{-3} mmHg) for 24 h. After 24 h, the reaction vessel was backfilled with argon and first-generation Grubbs' Ru catalyst (200:1/monomer-catalyst) was added. The full vacuum was placed back on the polymerization reaction after 0.5 h. Additional catalyst was added 60 h into the polymerization to ensure maximum possible couplings. The polymerization reaction was monitored closely by ^1H NMR to confirm that no remaining terminal olefin was present. Upon completion, the reaction was quenched by opening the flask and adding 25 mL of toluene and 1 mL of ethyl vinyl ether. The polymer was purified by precipitation of the polymer solution into 1.5 L of cold methanol. The polymer was then filtered and dried for characterization.

Polymerization of *tert*-Butyl Undeca-1,10-dien-6-ylcarbamate 3,3 NHBoc (5). ^1H NMR (300 MHz, CDCl_3): δ 1.18–1.48 (br, 17H), 1.92 (br, 4H), 3.48 (br, 1H), 4.26 (br, 1H), 5.24–5.40 (br, 2H). ^{13}C NMR (75 MHz, CDCl_3): δ 26.01, 27.26, 28.63, 29.18, 29.85, 32.64, 35.31, 50.63, 78.92, 129.95, 130.43, 155.88. FT-IR (KBr pellet): 3443, 3341, 2977, 2931, 2857, 2248, 1691, 1523, 1456, 1391, 1365, 1248, 1174, 1056, 968, 912, 867, 779, 734, 647, 462 cm^{-1} .

Polymerization of *tert*-Butyl Heptadeca-1,16-dien-9-ylcarbamate 6,6 NHBoc (6). ^1H NMR (300 MHz, CDCl_3): δ 1.26 (br, 14H), 1.41 (s, 9H), 1.96 (br, 4H), 3.49 (br, 1H), 4.21 (br, 1H), 5.28–5.537 (br, 2H). ^{13}C NMR (75 MHz, CDCl_3): δ 26.04, 27.39, 28.64, 29.03, 29.25, 29.33, 29.47, 29.67, 29.90, 32.76, 33.95, 35.79, 50.85, 78.91, 130.03, 130.49, 155.93. FT-IR (KBr pellet): 3445, 3344, 2977, 2927, 2855, 1692, 1525, 1456, 1390, 1365, 1248, 1174, 1090, 1013, 967, 909, 867, 778, 728, 646, 463 cm^{-1} .

Polymerization of *tert*-Butyl Henicosa-1,20-dien-11-ylcarbamate 8,8 NHBoc (7). ^1H NMR (300 MHz, CDCl_3): δ 1.21–1.40 (br, m, 28H), 1.41 (s, 9H), 1.91–1.99 (br, 4H), 3.49 (br, 1H), 4.22 (br, d, 1H), 5.29–5.39 (br, 2H). ^{13}C NMR (75 MHz, CDCl_3): δ 26.10, 27.44, 28.67, 29.37, 29.70, 29.81, 29.88, 29.98, 32.82, 35.85, 50.93, 78.95, 130.53, 155.93. FT-IR (KBr pellet): 3443, 3344, 2975, 2927, 2854, 1691, 1523, 1456, 1390, 1365, 1247, 1174, 1093, 1019, 967, 914, 864, 778, 724, 645, 464 cm^{-1} .

Polymerization of *tert*-butyl tricosa-1,22-dien-12-ylcarbamate 9,9 NHBoc (8). ^1H NMR (300 MHz, CDCl_3): δ 1.21–1.41 (br, m, 32H), 1.42 (s, 9H), 2.01 (br, 4H), 3.49 (br, 1H), 4.21 (br, d, 1H), 5.30–5.38 (br, 2H). ^{13}C NMR (75 MHz, CDCl_3): δ 26.10, 27.45, 28.67, 29.42, 29.55, 29.74, 29.81, 29.84, 29.90, 30.00, 32.84, 35.84, 50.92, 78.93, 130.10, 130.56, 155.94. FT-IR (KBr pellet): 3445, 3346, 3136, 2975, 2925, 2854, 2248, 1693, 1523, 1456, 1390, 1365, 1247, 1174, 1097, 1048, 1024, 966, 910, 865, 778, 723, 647, 463 cm^{-1} .

Hydrogenation of Unsaturated ADMET Polymers. The crude polymer solution was transferred to a Parr Bomb glass sleeve and diluted to \sim 200 mL with toluene. Argon was bubbled through the solution for 30 min, after which a spatula tip of Wilkinson's catalyst ($\text{RhCl}(\text{PPh}_3)_3$) was added to the solution and the sleeve was sealed inside a Parr Bomb equipped with a mechanical stirrer and temperature control. The vessel was purged three times with 600 psi hydrogen gas, then filled to 600 psi with hydrogen gas and left for 4 days at room temperature. Upon depressurization, argon was bubbled through the crude reaction mixture for 30 min. The solution was concentrated to \sim 50 mL and slowly dripped into 1 L of cold

methanol. The precipitated polymer was filtered and dried for characterization.

Polysat3,3NHBoc (9). ^1H NMR (300 MHz, CDCl_3): δ 1.23 (br, 16H), 1.41 (s, 9H), 3.48 (br, 1H), 4.21 (br, d, 1H). ^{13}C NMR (75 MHz, CDCl_3): δ 14.24, 22.82, 25.72, 26.09, 27.89, 28.66, 29.79, 29.91, 32.03, 35.85, 50.90, 78.95, 155.95. FT-IR (KBr pellet): 3446, 3342, 3134, 2928, 2855, 2248, 1692, 1524, 1456, 1390, 1365, 1248, 1175, 1098, 1048, 1020, 909, 865, 802, 733, 667, 647, 556, 463 cm^{-1} .

Polysat6,6NHBoc (10). ^1H NMR (300 MHz, CDCl_3): δ 1.22 (br, 24H), 1.41 (br, s, 13H), 3.49 (br, 1H), 4.21 (br, d, 1H). ^{13}C NMR (75 MHz, CDCl_3): δ 14.33, 22.89, 26.10, 28.67, 29.48, 29.86, 29.91, 32.10, 35.84, 50.92, 78.94, 155.95. FT-IR (KBr pellet): 3446, 3346, 3137, 2977, 2924, 2854, 2249, 1695, 1525, 1456, 1390, 1365, 1247, 1175, 1060, 1013, 909, 866, 778, 734, 646, 465 cm^{-1} .

Polysat8,8NHBoc (11). ^1H NMR (300 MHz, CDCl_3): δ 1.21–1.41 (br, m, 36H), 1.42 (s, 9H), 3.49 (br, 1H), 4.21 (br, d, 1H). ^{13}C NMR (75 MHz, CDCl_3): δ 14.32, 22.88, 26.06, 28.64, 29.83, 29.89, 32.10, 35.80, 50.87, 78.92, 155.93. FT-IR (KBr pellet): 3445, 3348, 3135, 2925, 2854, 2248, 1693, 1526, 1457, 1390, 1365, 1248, 1175, 1096, 1019, 909, 865, 801, 732, 647, 464 cm^{-1} .

Polysat9,9NHBoc (12). ^1H NMR (300 MHz, CDCl_3): δ 1.15–1.34 (br, 40H), 1.41 (s, 9H), 3.49 (br, 1H), 4.21 (br, d, 1H). ^{13}C NMR (75 MHz, CDCl_3): δ 14.33, 22.90, 26.08, 28.66, 29.56, 29.84, 29.94, 32.13, 35.82, 50.88, 78.92, 155.93. FT-IR (KBr pellet): 3446, 3346, 3136, 2925, 2854, 1696, 1523, 1465, 1457, 1390, 1365, 1248, 1175, 1058, 1019, 866, 783, 753, 721, 650, 462 cm^{-1} .

Removal of the Boc Protection Group from the Polymers.

Each saturated, protected polymer was readily dissolved in THF and transferred to a 10 mL screw-cap vial. The solution was rotovapped with rapid spinning to create a thin film along the walls of the vials. The vial was attached to a vacuum vial adapter and placed under high vacuum (10^{-3} mmHg) for 1 day to dry. After the polymer was dry, the vial was submerged in 275 $^{\circ}\text{C}$ sand in an aluminum foil lined heating mantle and left under heat and vacuum for 2 h. Upon submersion into the hot sand, each polymer began to slowly melt and then bubble. Each sample melted and went from a light beige color to a dark brown color within the first 5 min of heating under vacuum.

RESULTS AND DISCUSSION

Polymer Design and Synthesis. The preparation of linear, precisely branched, ethylene-*co*-vinyl amine (EVAm) polymers requires the synthesis of a symmetrically branched α,ω -diene monomer for the ADMET reaction. In light of the recent successes of other groups performing ROMP on free amines,^{13,14} and with the development of more nitrogen tolerant metathesis catalysts,²³ an initial attempt was made to polymerize the free amine diene. However, the reaction was unsuccessful due to the tendency of the amine to facilitate catalyst decomposition. As a result, a protection strategy was required to polymerize the amine dienes.

Use of the 9-fluorenyl carbamate (Fmoc) group as an amine protection strategy was previously developed in our group by Leonard et al.²⁴ for the synthesis of amino acid containing polyolefins. Because of the ease with which the Fmoc group is removed under mild basic conditions, this same methodology was attempted for EVAm. The synthesis of the 9,9NHFmoc monomer was readily accomplished by protecting the corresponding amine diene with 9-fluorenylmethyl chloroformate (Fmoc-Cl) to yield a white fluffy powder with a sharp melting point. However, polymerization of this monomer in THF led to the formation of dimers and trimers almost immediately upon addition of catalyst, as observed by the precipitation of these oligomers from solution (Figure 1). Attempts to characterize these oligomers failed due to lack of solubility in any known solvent.

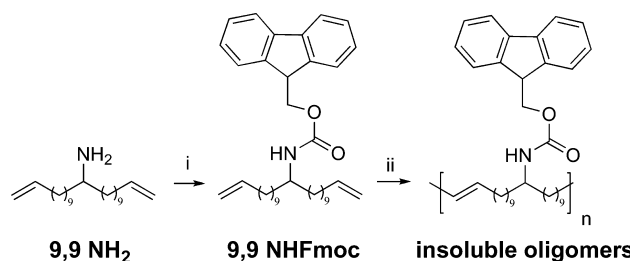


Figure 1. Initial protection strategy for amine monomers: (i) FmocCl, DMAP, THF; (ii) first-generation Grubbs' catalyst.

As an alternative protection strategy, the *tert*-butyl oxycarbonyl (Boc) group was employed, because it can be readily removed using acid or heat. Figure 2 details the synthetic approach employed to conduct the metathesis polymerization, hydrogenation, and deprotection. Monomer 1 is a colorless viscous oil while monomers 2, 3, and 4 are white crystalline solids that melt at 38, 43, and 46 $^{\circ}\text{C}$, respectively. As a result, all four monomers can be polymerized neat in the melt with no solvent. The ADMET polymerization of the Boc-protected monomers proceeded normally under vacuum. The molecular weight and thermal data for the unsaturated polymers are presented in Table 1. Subsequent hydrogenation was performed in toluene with Wilkinson's catalyst under hydrogen pressure in a Parr reactor. These hydrogenations were done at room temperature; there was no spectroscopic evidence that any Boc protection groups were removed during this step.

Structural Analysis with ^{13}C and ^1H NMR and IR.

Primary structural analysis by ^1H - and ^{13}C NMR revealed the kind of pristine primary structure that can be obtained when using ADMET polymerizations and hydrogenation reactions.^{17,25,26} Confirmation of the branch precision and knowledge of methylene run lengths between branches allows confident determination of molar ratios of ethylene and vinyl amine. These proton and carbon spectra are the best techniques to determine primary structure of monomer, unsaturated polymer, and saturated polymer.

The proton spectra in Figure 3 shows the clean and complete transformation of the 9,9 monomer (4) to unsaturated polymer (8) and then to the saturated polymer (12). The resonances from the terminal olefins of 4, at roughly 4.8 and 5.8 ppm, condense to one peak, at 5.3 ppm in 8, while the chemical shifts of the other peaks are maintained and slightly broadened. From the unsaturated (8) to saturated polymer (12), the internal olefin and its alpha proton peak at 2.0 ppm are completely removed from the sample through the hydrogenation step. The hydrogenation of the unsaturated polymer also leads to the formation of methyl end groups resonating at 0.9 ppm. The final hydrogenated polymer (12) shows five proton shifts relating to the polymer: (1) methyl end groups at 0.8 ppm; (2) backbone protons at 1.23 ppm; (3) nine Boc group protons at 1.41 ppm; (4) proton on the carbon with the amine branch at 3.48 ppm; (5) carbamate nitrogen's proton at 4.21 ppm.

The same trends are observed in the carbon spectra of the corresponding 6,6 molecules (2, 6, 10), shown in Figure 4. The terminal olefin resonances at 130 and 156 ppm in 2 are condensed to an internal olefin peak in 6, (two peaks due to *cis/trans* isomers). This internal olefin peak is then eliminated from the sample upon hydrogenation.

Compound structure and purity was also confirmed with FT-IR throughout the EVAm copolymer synthesis. The analysis for all of these copolymers is essentially identical due to the

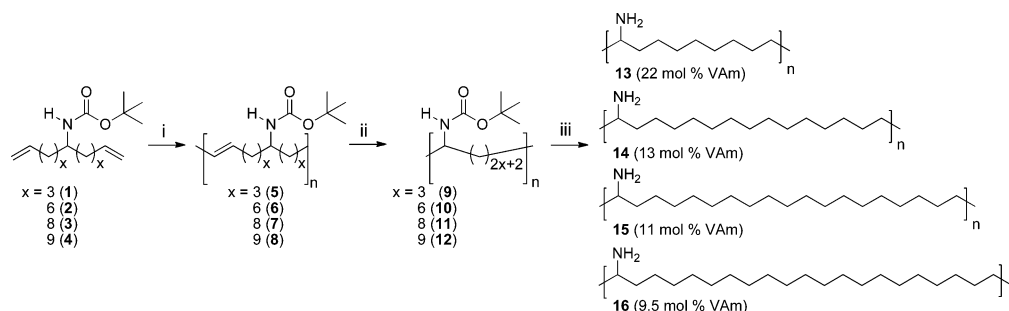


Figure 2. Ethylene-*co*-vinyl amine copolymer synthesis: (i) first-generation Grubbs' catalyst; (ii) H₂ (600 psi), RhCl(PPh₃)₃, toluene, room temperature; (iii) 250 °C under vacuum.

Table 1. Molecular Weight and Thermal Data for Unsaturated Ethylene Vinyl Amine Copolymers:

polymer	mol % vinylamine ^a	<i>T</i> _g ^b (°C)	<i>M</i> _w ^c	PDI ^c	<i>D</i> _p ^c
5	22	19.1	7.4	1.45	21
6	13	−5.4	11.4	1.43	25
7	10.5	−8.5	14.7	1.99	20
8	9.5	−24.2	13.3	1.67	20

^aCalculated from theoretical repeat unit, confirmed by NMR. ^b10 °C/min scan rate, values determined from second scan data. ^cReported in kg/mol and performed in THF at 40 °C with calibration vs polystyrene standards.

identical functional groups contained in each material. The polymerization was verified by the coalescence of two absorbance bands from α -olefins in monomers at 991 and 908 cm^{−1} into a single band at 967 cm^{−1} indicating a mostly *trans* 1,2-disubstituted olefin and successful polymerization.²⁷ The elimination of the olefinic band at 967 cm^{−1} corresponding to the out-of-plane C–H bend confirms complete hydrogenation of the ethylene backbone. Strong absorbance bands present at 2925 and 2854 cm^{−1} for these copolymers

correspond to the asymmetric and symmetric methylene C–H stretching motions of the backbone carbons. The carbonyl stretch of the Boc's carbamate functionality is observed at 1692 cm^{−1} with additional carbamyl bands at 1524 and 1248 cm^{−1}. Scissoring bands from the methylene C–H vibrations are also readily observed at 1457 cm^{−1}.

Thermal Analysis. Thermal gravimetric analysis (TGA) and differential scanning calorimetry (DSC) were performed on each of the three groups of polymer samples: the unsaturated protected, the saturated protected, and the saturated deprotected polymers. Table 2 summarizes the thermal properties exhibited while Figures 5, 6, 7, 10, and 11 show thermograms which detail the decomposition, glass transition, and melting points of these materials. It is apparent from this thermal data that the molar ratio of incorporated vinyl amine has a dramatic effect on the material behavior.

The decomposition traces of both the unsaturated and saturated protected amine polymers (Figure 5) are predictable. Yamamoto²⁸ and Ahn²⁹ have shown in their research that the Boc group can be removed thermally at about 175 °C.^{28,29} A sharp loss in weight occurs at this temperature for each of the

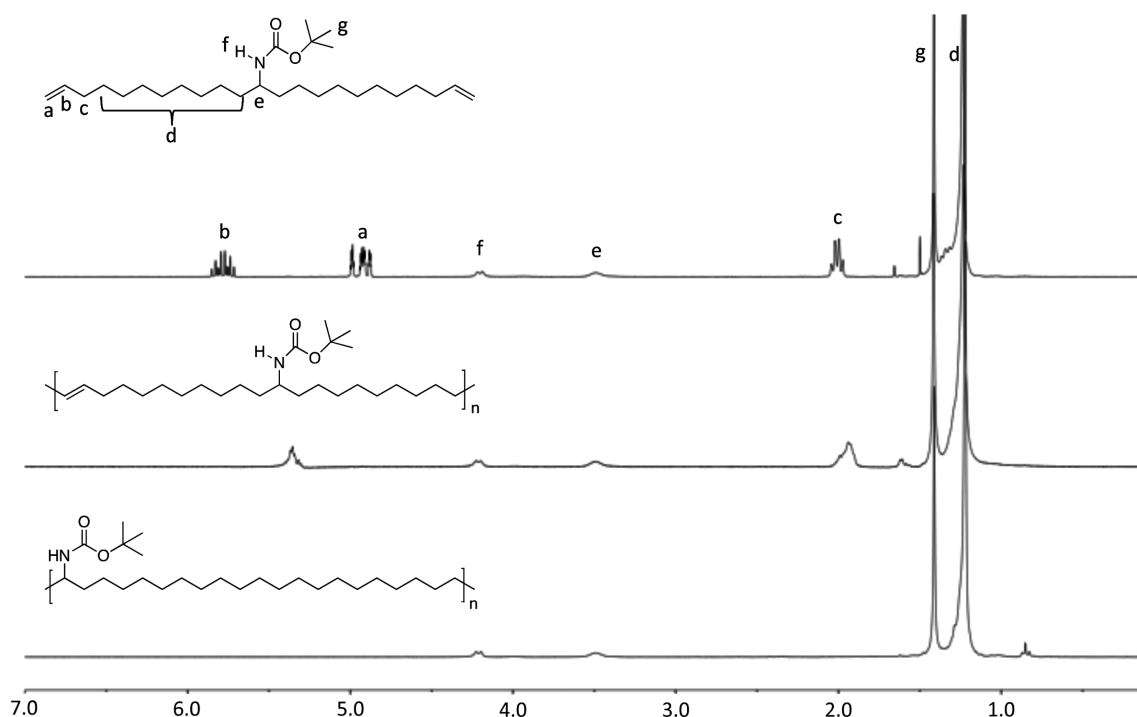


Figure 3. Progression of monomer to polymer monitored by ¹H NMR.

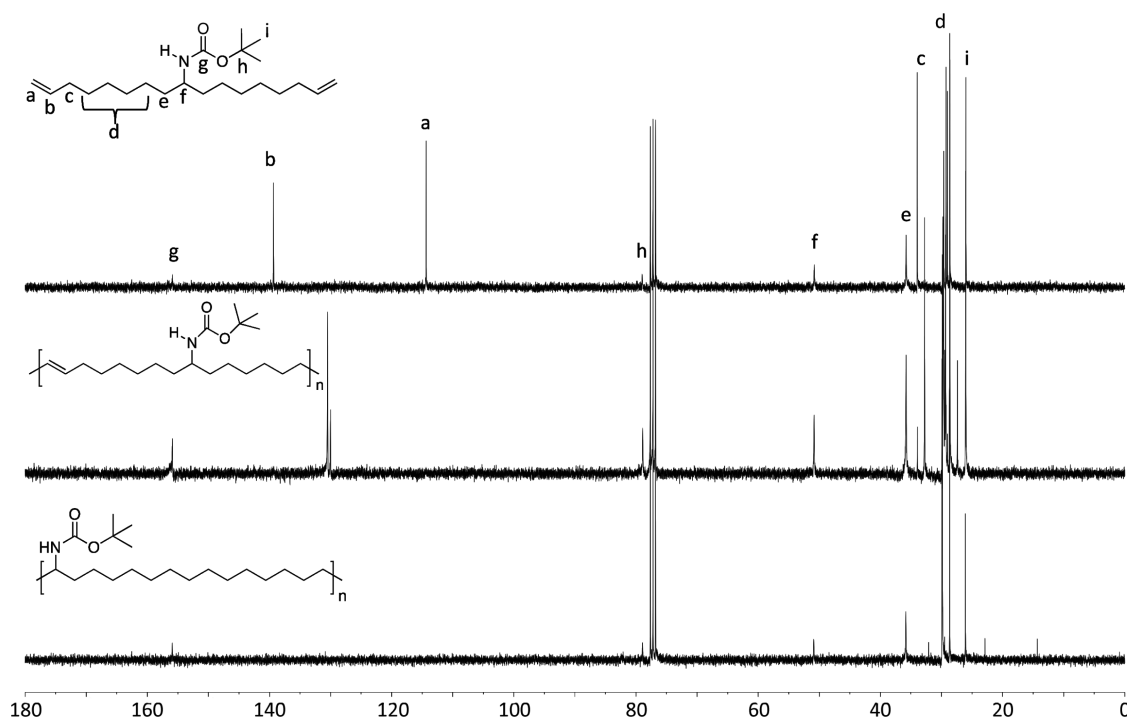


Figure 4. Progression of monomer to polymer monitored by ^{13}C NMR.

Table 2. Thermal Data for the Protected and Deprotected Polymers

polymer	mol % vinylamine ^a	T_g^b (°C)	T_m^b (°C)
9	22	4	N/A
10	13	2	N/A
11	10.5	−8	N/A
12	9.5	2	N/A
13	22	10	N/A
14	13	N/A	49
16	9.5	N/A	44

^aCalculated from theoretical repeat unit, confirmed by NMR. ^b10 °C/min scan rate, values determined from second scan data.

eight protected polymers; the shoulder or plateau area of each curve represents the stable deprotected amine polymer. The percent weight losses experimentally observed in these decomposition curves were 45, 32, 29, and 25% as measured to the inflection point of the plateau. These percent weight

losses correspond to the Boc protection group being cleaved from the amine releasing carbon dioxide and isobutene from each repeat unit. The calculated predictive weight losses of 42, 31, 26, and 25% are in excellent agreement with these experimental values. The TGA traces for both the unsaturated and saturated polymer families are nearly identical which prove that the addition of hydrogen to the internal alkene has a minimal net effect on the weight loss. It can be determined from these weight loss profiles that the thermally deprotected polymer is stable and exists over a 100° range, indicating that these materials are excellent candidates for a single thermal deprotection step.

Figure 6 shows the DSC data (second heating scan) for the series of unsaturated and saturated protected polymers. All four unsaturated polymers are amorphous, but the T_g 's are consistent with ADMET sequenced materials.²⁷ Amorphous sequenced copolymers occur as a consequence of steric congestion along the polymer backbone, thus preventing the ethylene run lengths between branches to crystallize. The

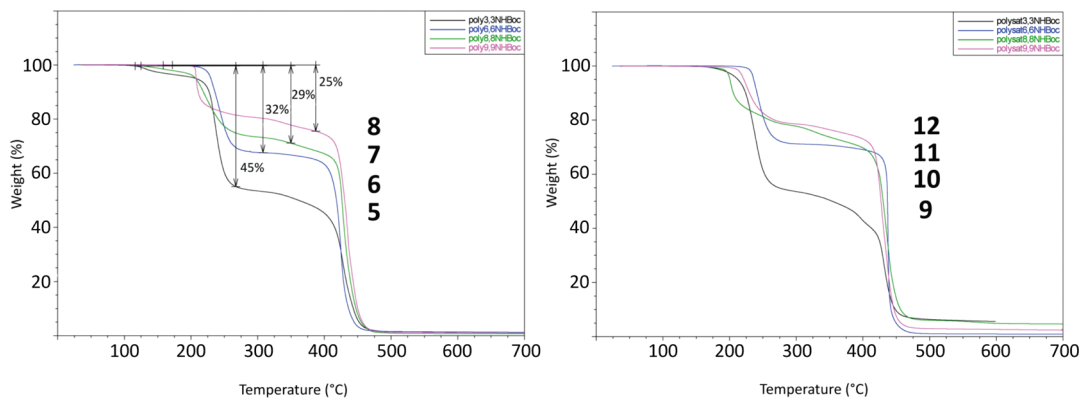


Figure 5. TGA traces for (left) unsaturated protected polymers (right) saturated protected polymers.

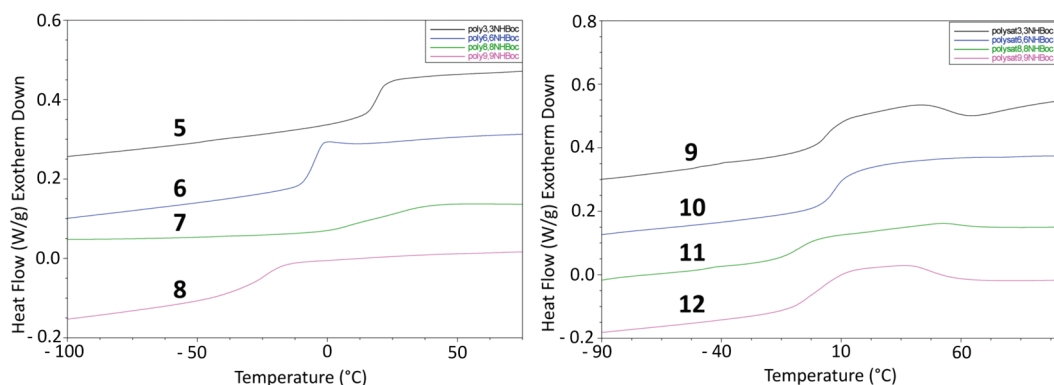


Figure 6. DSC of ADMET (left) unsaturated protected polymers (right) saturated protected polymers.

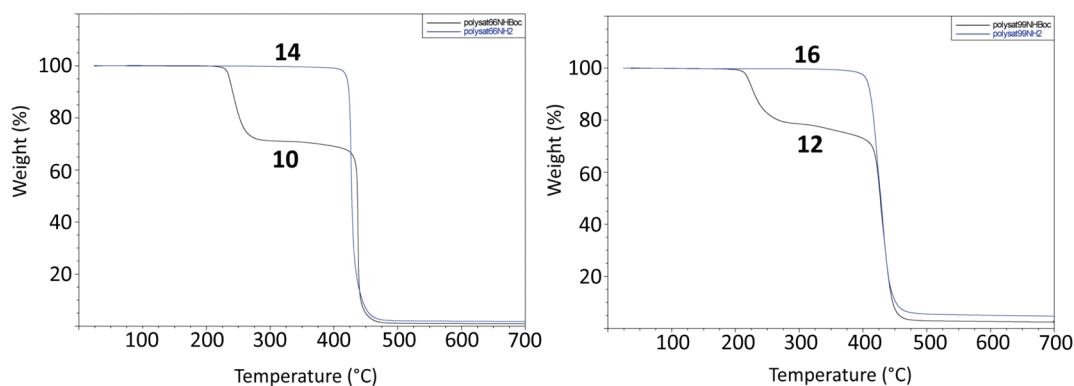


Figure 7. TGA traces of (left) polysat6,6NHBoc (10) and polysat6,6NH₂ (14) (right) polysat9,9NHBoc (12), and polysat9,9NH₂ (16) polymers.

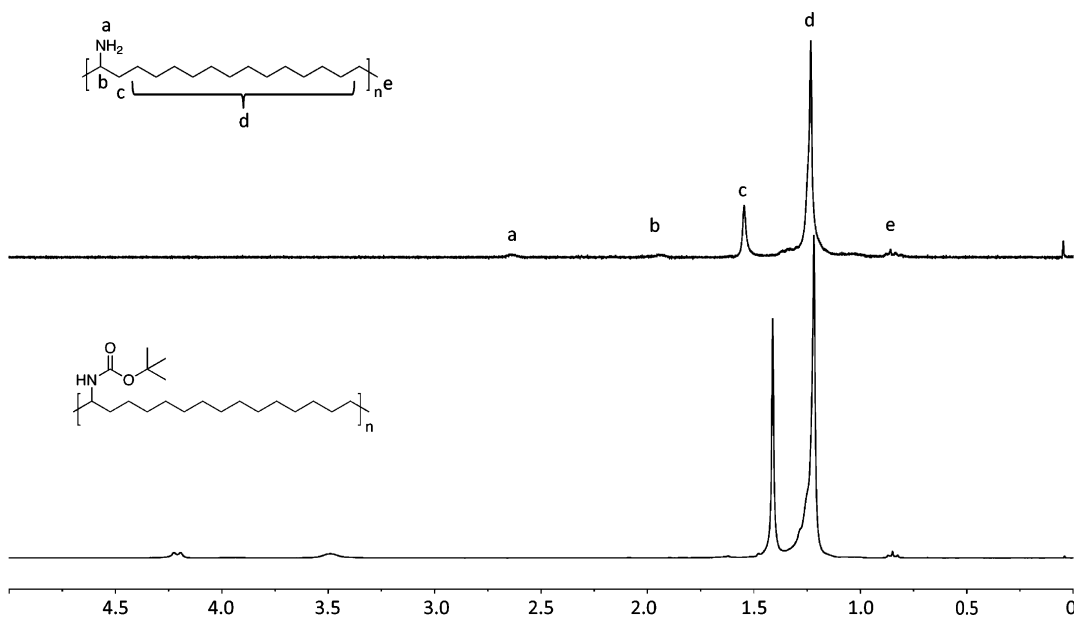


Figure 8. ¹H NMR of (top) polysat6,6NH₂ (14) and (bottom) polysat6,6NHBoc (10).

tert-butyl carbamate protection group explains the general trend of a decreasing T_g with decreasing branch frequency, since it allows for hydrogen bonding with other such protecting groups. This hydrogen bonding allows branches to become associated with each other to form a physically cross-linked structure. As the number of H-bond cross-links decreases in the compounds 5, 6, 7, and 8, the polymer chain has greater flexibility and a lower T_g . The DSC traces for the saturated protected polymers

each shows a complicated transition, which resembles the start of a T_g but then appears to lead directly into a melt. The general trend observed in precision polymers previously synthesized in this group demonstrates that increasing the pendant branch frequency yields materials with less and less crystalline character, until a critical threshold is met and the material becomes amorphous.^{15,25,26} This threshold is not obvious in the present data, because the polymer with the

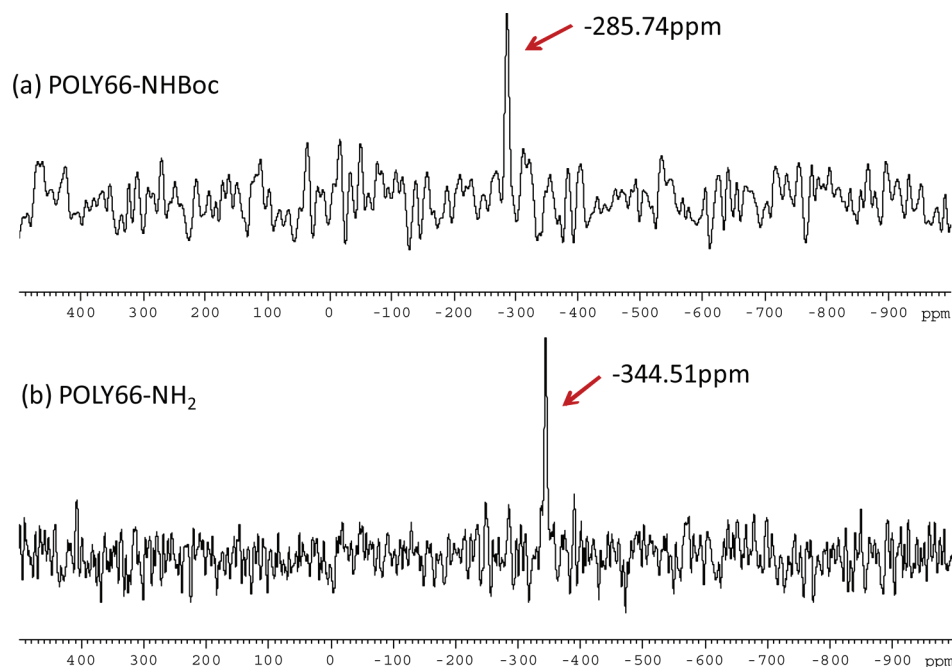


Figure 9. ^{15}N CP/MAS spectra of (a) protected precision polymer POLY-NHBoc, and (b) deprotected precision polymer POLY66-NH₂.

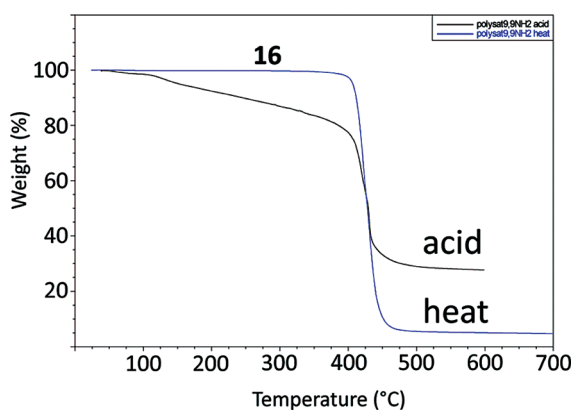


Figure 10. TGA traces of polysat9,9NH₂ polymers deprotected from heat and acid.

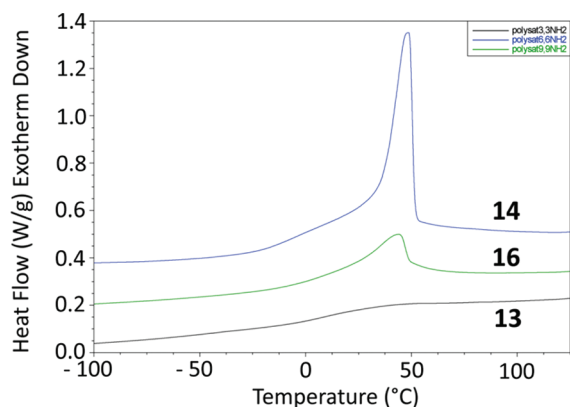


Figure 11. DSC of the deprotected amine branch every 9th, 15th, and 21st carbon on polymer.

most closely spaced pendant groups (every ninth carbon, 9) exhibits a melt peak. Additional work on polymers with more

frequent branches is needed to determine if the trend holds for precision PEVAm.

Deprotection Strategy. Initial attempts to deprotect these polymers were carried out in solution with hydrochloric acid. The protected polymer was readily dissolved in a minimum amount of a 1:1 THF/dioxane solvent mixture, and 10 vol equiv of 4 M HCl in dioxane were added at room temperature. Within minutes, a dark brown polymer started to precipitate onto the sides of the round-bottom flask. After 1 h the solution was extracted with ether, but no polymer was obtained upon rotary evaporation of the organic layer. Multiple attempts to remove the polymer remaining on the walls of the flask were unsuccessful due to lack of solubility. The polymer was finally removed from the flask by physically scraping it from the sides, placing the dark brown scrapings into a vial, and drying them.

It is believed that the negligibly soluble polymer on the flask walls was the ammonium chloride salt of the amine. Upon protic acid deprotection in solution, the corresponding ammonium salt branches are attracted to each other and likely cluster together tightly with the polymer backbone coil around them, thus preventing any further solvation of the material.

In order to prevent this strong ionic aggregation, the thermal degradation information gathered from the TGA thermograms shown in Figure 5 was advantageously used. To employ this deprotection technique, the polymer was cast as a thin film in a 10 mL vial and placed in a 275 °C sand bath under vacuum. For each of these materials, the protected, tan-colored polymer films turned dark brown within minutes upon heating with bubbles, presumed to be carbon dioxide and isobutene, eliminated from the viscous melted polymer. Since this deprotection is performed under vacuum, the isobutene is removed upon elimination with no further need of purification. Figure 7 shows the overlapping TGA traces of the saturated protected 6,6 polymer and 9,9 polymer with their respective deprotected counterparts. The weight loss corresponding to the Boc group no longer exists in the TGA trace from the polymer recovered from the vial. These thermally deprotected polymers,

like the chemically deprotected ones, have negligible solubility in all solvents tested. However, a small amount of the deprotected 6,6 saturated polymer dissolved in CDCl_3 , and the corresponding ^1H NMR spectra are shown in Figure 8. No ^{13}C NMR spectra was observed due to this lack of copolymer solubility.

To better elucidate both the protected and deprotected 6,6 amine polymer's chemical structures and demonstrate the success of synthesis, natural-abundance ^{15}N solid state NMR (SS-NMR) spectra were collected at Max Planck Institute for Polymer Research in Mainz, Germany. The SS-NMR spectroscopy when coupled with cross-polarization magic angle spinning (CP-MAS) provides excellent sensitivity and narrow line widths. Moreover, this technology also eliminates possible errors arising from the partial solubility of the deprotected precision amine polymer samples.

Compared to commonly seen ^{13}C SS-NMR, ^{15}N CP-MAS NMR offers generally simple and readily interpretable ^{15}N spectra in terms of probing a polymer's structure. Figure 9 shows the spectra of both a protected and deprotected ADMET amine polymer: POLY66- NH_2 (**14**) and POLY66-NHBoc (**10**), each of which exhibits a single resonance at -344.51 ppm and -285.74 ppm, respectively. The signal at -344.51 ppm in Figure 9b falls within the resonance range of primary amine NH_2 groups^{30–32} and can be readily assigned to the amine groups on the deprotected POLY66- NH_2 (**14**) side chains. Considering the single peak at -285.74 ppm from the protected sample as shown in Figure 9a, this peak should be the only nitrogen resonance arising from the amide groups in POLY66-NHBoc (**10**), if the deprotection step is successful, which is indeed the case herein. It is known that amide isotropic chemical shifts are highly sensitive to both hydrogen bonds and protonation at the carbonyl oxygen.³³ The single resonance at -285.74 ppm in Figure 9a is quite close to the reported ^{15}N isotropic chemical shifts from amides and urethanes.^{34–36} The introduction of the electron-withdrawing Boc group causes the nitrogen nuclei in POLY66-NHBoc (**10**) to shift downfield exhibiting a significantly more positive chemical shift.

In short, ^{15}N solid-state NMR analysis has demonstrated that the deprotection step is successful based on the significant isotropic chemical shift changes between the protected and deprotected precision polymers. The synthetic route employed in this study is applicable to offer precise amine polymers.

Figure 10 contains the TGA traces of both the saturated 9,9 polymer (**16**) deprotected by heat and (**16**) deprotected by acid. These overlapping thermograms demonstrate the biggest advantages of thermal over acid deprotection—solvent and counterion contamination. The weight loss on the acid deprotected polymer begins below 100°C , and this weight loss continues until the main chain decomposes at 400°C . However, the thermally deprotected polymer shows no solvent contamination or other impurity associated weight loss upon TGA analysis and is immediately ready for further analysis.

The final deprotected polymers with amine groups on every 15th, and 21st carbon polymers exhibit crystallinity. The DSC traces in Figure 11 show that the polymer with an amine on every 15th carbon (**14**) has a sharp melt at 49°C , whereas **16** (an amine on every 21st carbon) has a broader melt at 44°C . Although the every 15th polymer exhibits a sharper melting point than the 21st material, we believe the hydrogen bonding of the branches may induce different chain packing and alter the crystallinity of this material relative to the other

copolymers. This is contrary to the trend observed in the series of precision ethylene copolymers prepared in our laboratory, in which the melting points usually increase as the number of CH_2 groups between branches increases.²⁶ In previous polymer families made in our group,²⁵ the polymer substituted on every ninth carbon is amorphous. This trend is upheld for the PEVAm materials, Figure 11, as the polymer with an amine branch on every ninth carbon appears completely amorphous. Unfortunately, a lack of copolymer with an amine on every 19th carbon prevented thermal analysis for this material.

CONCLUSIONS

Reported for the first time, a family of four sequenced copolymers of ethylene with vinyl amine has been prepared with predetermined comonomer ratios. Although metathesis catalysts are evolving to become more tolerant of amine and nitrogen functionality, the amine functionalized dienes synthesized here must be protected prior to ADMET polymerization. The Boc protected monomers provided soluble polymers while the Fmoc protected analogues did not. These polymers possess exact ethylene run lengths between pendant primary amine branches on every 9th, 15th, 19th, or 21st carbon along the backbone. Spectroscopic analysis via NMR and FT-IR affirms the microstructural control achieved via metathesis polymerization. The pristine nature of these copolymers' primary structures imparts marked effects on thermal behavior. Mass losses observed by TGA verify that the thermal deprotection reactions yielded the expected amine copolymers. Both thermal and chemical deprotection approaches yielded minimally soluble product but the thermal approach provided less contamination to the sample. Although this poor solubility of the deprotected PEVAm polymer hampered characterization efforts, a combination of ^{15}N solid-state NMR, ^1H NMR, and TGA confirmed quantitative deprotection. The polymers with an amine branch on every 15th and 21st carbon were shown to be crystalline, whereas the polymer with an amine on every ninth carbon is amorphous.

AUTHOR INFORMATION

Corresponding Author

*E-mail: wagener@chem.ufl.edu.

ACKNOWLEDGMENTS

The authors would like to thank the National Science Foundation (Grant No. DMR-0703261) for funding. Additional thanks is owed to Dr. Robert Graf and Professor Hans Spiess of the Max Planck Institute for Polymer Research in Mainz, Germany, for use of their Solid-State NMR instrumentation. Generous support from the Army Research Office and Materia Inc. for the development and acquisition of catalysts is also acknowledged.

REFERENCES

- (1) Robeson, L. M.; Kuphal, J. A.; Vratsanos, M. S. *J. Appl. Polym. Sci.* **1996**, *61*, 1561–1569.
- (2) Kobayashi, S.; Hiroishi, K.; Tokunoh, M.; Saegusa, T. *Macromolecules* **1987**, *20*, 1496–1500.
- (3) Kobayashi, S.; Suh, K. D.; Shirokura, Y. *Macromolecules* **1989**, *22*, 2363–2366.
- (4) Martel, B.; Pollet, A.; Morcellet, M. *Macromolecules* **1994**, *27*, 5258–5262.
- (5) Noro, K. *Polyvinyl Alcohol* **1973**, 91–120.

- (6) Jones, G. D.; Zomlefer, J.; Hawkins, K. J. *Org. Chem.* **1944**, *9*, 500–512.
- (7) Maki, Y.; Mori, H.; Endo, T. *Macromol. Chem. Phys.* **2007**, *208*, 2589–2599.
- (8) Reynolds, D. D.; Kenyon, W. O. *J. Am. Chem. Soc.* **1947**, *69*, 911–915.
- (9) Fischer, T.; Heitz, W. *Macromol. Chem. Phys.* **1994**, *195*, 679–687.
- (10) Madl, A.; Spange, S. *Macromol. Symp.* **2000**, *161*, 149–157.
- (11) Witek, E.; Pazdro, M.; Bortel, E. J. *Macromol. Sci., Part A: Pure Appl. Chem.* **2007**, *44*, 503–507.
- (12) Wingard, R. E.; Larson, E. R. U.S. Patent 4,255,548, March 10, 1980.
- (13) Breitenkamp, R. B.; Ou, Z.; Breitenkamp, K.; Muthukumar, M.; Emrick, T. *Macromolecules* **2007**, *40*, 7617–7624.
- (14) Sutthasupa, S. S., F.; Masuda, T. *Macromolecules* **2009**, *42*, 1519–1525.
- (15) Baughman, T. W.; Chan, C. D.; Winey, K. I.; Wagener, K. B. *Macromolecules* **2007**, *40*, 6564–6571.
- (16) Baughman, T. W.; van der Aa, E.; Wagener, K. B. *Macromolecules* **2006**, *39*, 7015–7021.
- (17) Boz, E.; Wagener, K. B.; Ghosal, A.; Fu, R. Q.; Alamo, R. G. *Macromolecules* **2006**, *39*, 4437–4447.
- (18) Gomez, F. J.; Wagener, K. B. *J. Organomet. Chem.* **1999**, *592*, 271–277.
- (19) Hopkins, T. E.; Pawlow, J. H.; Koren, D. L.; Deters, K. S.; Solivan, S. M.; Davis, J. A.; Gomez, F. J.; Wagener, K. B. *Macromolecules* **2001**, *34*, 7920–7922.
- (20) Hopkins, T. E.; Wagener, K. B. *Macromolecules* **2003**, *36*, 2206–2214.
- (21) Watson, M. D.; Wagener, K. B. *Macromolecules* **2000**, *33*, 8963–8970.
- (22) Scholl, M.; Ding, S.; Lee, C. W.; Grubbs, R. H. *Org. Lett.* **1999**, *1*, 953–956.
- (23) Vieira, E. M.; Snapper, M. L.; Hoveyda, A. H. *J. Am. Chem. Soc.* **2011**, *133*.
- (24) Leonard, J. K.; Hopkins, T. E.; Chaffin, K.; Wagener, K. B. *Macromolecular Chemistry And Physics* **2008**, *209*, 1485–1494.
- (25) Baughman, T. W.; Sworen, J. C.; Wagener, K. B. *Macromolecules* **2006**, *39*, 5028–5036.
- (26) Sworen, J. C.; Smith, J. A.; Berg, J. M.; Wagener, K. B. *J. Am. Chem. Soc.* **2004**, *126*, 11238–11246.
- (27) Baughman, T. W.; Wagener, K. B. *Recent Advances in ADMET Polymerization*; Springer Verlag: Berlin and Heidelberg, Germany, 2005.
- (28) Yamamoto, T.; Yoshizawa, M.; Mahmut, A.; Abe, M.; Kuroda, S.; Imase, T.; Sasaki, S. *J. Polym. Sci., Part A: Polym. Chem.* **2005**, *43*, 6223–6232.
- (29) Ahn, K. D.; Lee, Y. H.; Koo, D. I. *Polymer* **1992**, *33*, 4851–4856.
- (30) Bottot, R. E.; Coxon, B. *J. Am. Chem. Soc.* **1983**, *105*, 1021–1028.
- (31) Rao, Y.; Kemp, T. F.; Trudeau, M.; Smith, M. E.; Antonelli, D. M. *J. Am. Chem. Soc.* **2008**, *130*, 15726–15731.
- (32) Schwab, M. G.; Fassbender, B.; Spiess, H. W.; Thomas, A.; Feng, X.; Mullen, K. *J. Am. Chem. Soc.* **2009**, *131*, 7216–7217.
- (33) Andreis, M.; Koenig, J. L. *Adv. Polym. Sci.* **1995**, *124*, 192–237.
- (34) Duff, D. W.; Maciel, G. E. *Macromolecules* **1990**, *23*, 4367–4371.
- (35) Facelli, J. C.; Purmire, R. J.; Grant, D. M. *J. Am. Chem. Soc.* **1996**, *118*, 5488–5489.
- (36) Levy, G. C.; Lichter, R. L. *Nitrogen-15 Nuclear Magnetic Resonance Spectroscopy*; J. Wiley: New York, 1979.

Precision Ionomers: Synthesis and Thermal/Mechanical Characterization

Brian S. Aitken,[†] C. Francisco Buitrago,[‡] Jason D. Heffley,[†] Minjae Lee,[§] Harry W. Gibson,[§] Karen I. Winey,^{‡,⊥} and Kenneth B. Wagener^{*,†}

[†]George and Josephine Butler Polymer Research Laboratory, Department of Chemistry, University of Florida, Gainesville, Florida 32611, United States

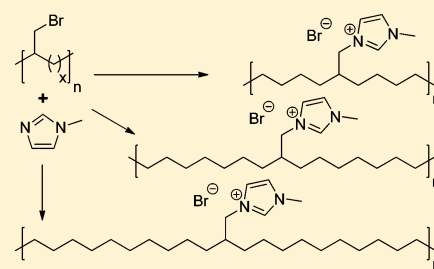
[‡]Department of Chemical and Biomolecular Engineering, University of Pennsylvania, Philadelphia, Pennsylvania 19104, United States

[§]Department of Chemistry, Virginia Polytechnic Institute & State University, Blacksburg, Virginia 24061, United States

[⊥]Department of Materials Science and Engineering, University of Pennsylvania, Philadelphia, Pennsylvania 19104, United States

S Supporting Information

ABSTRACT: Six perfectly regioregular polyethylene (PE)-based ionomers containing 1-methylimidazolium bromide groups on exactly every 9th, 15th, or 21st carbon (precision ionomers) and two regiorandom analogues have been synthesized and characterized via dynamic mechanical analysis (DMA) and differential scanning calorimetry (DSC). Because these materials were synthesized by a postpolymerization functionalization route, their number-average molecular weights (M_n s) and polydispersity indices (PDIs) could be accurately calculated based on measurements of the preionized polymers; M_n s range from 36 to 53 kDa with PDIs all close to 2. Thermal gravimetric analysis (TGA) indicates stability up to 250 °C, and DSC measurements indicate that crystallinity is a function of the polymer backbone spacer length. T_m s range from ~80 to 106 °C, with longer spacer lengths inducing semicrystallinity. DSC measured glass transition temperatures (T_g s) range from -1.6 to 26.8 °C and appear to be dependent on both spacer length and crystallinity. DMA data loosely mirror the DSC results, but with transitions occurring at lower temperatures that we attribute to differences in the thermal history and/or the different heating ramp rates used.



INTRODUCTION

Ionomers comprise a class of polymers containing a relatively low concentration of pendant ionic groups. At a global production rate of about 300 million pounds/year, they are of great commercial importance and find use in a range of applications as ion transport membranes, electromechanical devices, thermoplastic elastomers, adhesives, and other uses.¹ Moreover, while polyanions are by far the more common derivatives, recently there has been considerable interest in polycations, which are the focus of this paper, due to their potential applicability in anion exchange membrane fuel cells² and mechanical actuators.³ Ionic polymers are often prepared via polymerization of acryloyl- or vinyl-functionalized ionic liquids or by ionization of electrically neutral polymers.^{1–17} Countless studies have been and continue to be conducted in efforts to understand and control ionomer morphology. With some exceptions, such as regularly sequenced polyurethane,^{18–20} polysiloxane,^{21,22} and poly(ethylene oxide)^{23,24} based ionomers, most current synthetic approaches yield a random (or pseudorandom) distribution of ionic groups along a polymer backbone (type A of Figure 1); thus, the impact of perfect regioregularity on ionomer morphology and performance in various applications remains largely unexplored due to a lack of synthetic methodology.^{1,25}

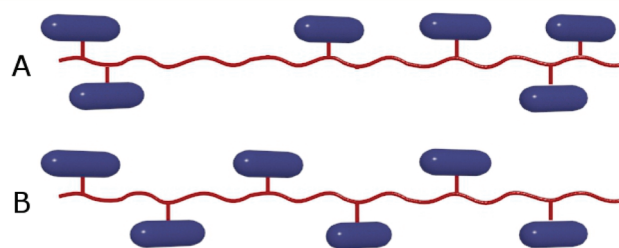


Figure 1. General architectures of regiorandom ionomers (A) and precision ionomers (B).

We recently reported the synthesis of an ionomer and an ionene (in which the ionic group is in the main chain of the polymer) by acyclic diene metathesis polymerization (ADMET) of α,ω -diene-functionalized ionic liquids.²⁶ This method, for the first time, provided access to a polyolefin-based precision ionomer (type B of Figure 1); an imidazolium hexafluorophosphate group was located on each and every 21st carbon along a linear polyolefin backbone. Synthesis of these materials by ADMET proved quite challenging due to

Received: October 13, 2011

Revised: November 28, 2011

Published: January 6, 2012

difficulties in achieving the very high monomer purity required for the reaction and the extremely high viscosities encountered after oligomerization. Later attempts to prepare a library of ionomers containing functionality spaced at shorter intervals for a structure property study were hampered by the same issues as were discussed in the original report; however, difficulties were exacerbated further by the greater ion content. Additionally, due to the incompatibility of ionic liquids with hydrocarbons, we found it impossible to produce regiorandom materials by copolymerization with linear hydrocarbon dienes, which is the usual method in our laboratory.²⁷ Thus, no comparisons between regioregular and regiorandom analogues were possible. Furthermore, because the polymers were produced by ADMET, thereby containing one alkene per repeat unit, we intended to enhance crystallinity by saturating the double bonds. However, the polymers were soluble only in DMSO, and quantitative hydrogenation using Wilkinson's catalyst proved impossible. Finally, as is often the case for ionomers, measurement of their molecular weights proved impossible by any means due to aggregation even in hot electrolyte solutions.

In the present report, we have overcome all of the aforementioned difficulties by preparing regioregular primary bromide-functionalized polymers and their regiorandom analogues via ADMET. This was followed by hydrogenation of the alkene residuals in the soluble neutral polymers and finally quantitative quaternization using excess 1-methylimidazole. The set of eight ionomers was characterized via NMR, DSC, TGA, DMA, and molecular weights were calculated based on GPC measurements of the precursor primary bromide functional polymers.

■ EXPERIMENTAL SECTION

Materials and Instrumentation. All materials were purchased from Aldrich and used as received, unless noted otherwise. Dry solvents were obtained from an MBraun solvent purification system. The 1,9-decadiene was dried and purified via a potassium mirror distillation and stored over activated molecular sieves. Grubbs' first-generation ruthenium catalyst, bis(tricyclohexylphosphine)benzylidene ruthenium(IV) dichloride, was a generous gift from Materia, Inc. Proton and ¹³C NMR spectra were acquired on a Varian Mercury 300 MHz spectrometer. Differential scanning calorimetry (DSC) data were obtained on a TA Instruments Q1000 from -60 to 220 °C at a typical scan rate of 10 °C/min under a He purge. Dynamic mechanical analysis (DMA) was performed with a Rheometrics Solids Analyzer (RSAII) at a frequency of 0.16 Hz and a maximum strain set to 3% under nitrogen purge. A static load of 100 gmF was applied initially and was then adjusted to 125% of each measured dynamic load. This adjusted static load was necessary to prevent sample buckling. Mechanical data were collected starting at -50.0 °C and every 20 s thereafter, while the temperature increased at a rate of 3.0 °C/min. The DMA samples were films pressed from a mold at ~10 °C higher than the maximum thermal transition reported by DSC. The film dimensions based on the mold were approximately 53 mm long, 6 mm wide, and 0.3 mm thick; exact dimensions for each polymer deviated slightly but were accurately measured and used in DMA calculations. Gel permeation chromatography (GPC) was performed at 40 °C using a Waters Associates GPCV2000 liquid chromatography system with an internal differential refractive index detector and two Waters Styragel HR-5E columns (10 μm PD, 7.8 mm i.d., 300 mm length) using HPLC grade THF as the mobile phase at a flow rate of 1.0 mL/min.

Monomer Synthesis. Synthesis of 1–3 and 6 has been previously described by our group.^{28,29} Synthesis of 4 and 5 from 1 and 2 was carried out using a procedure identical to that used in the preparation of 6 from 3.²⁹

6-(Bromomethyl)undeca-1,10-diene (4) (x = 3). ¹H NMR (300 MHz, CDCl₃), δ (ppm): 1.30–1.45 (m, 8H), 1.63 (p, 1H), 2.05 (q,

4H), 3.45 (d, 2H), 4.91–5.10 (m, 4H), 5.65–5.90 (m, 2H). ¹³C NMR (75 MHz, CDCl₃), δ (ppm): 26.1, 32.5, 34.1, 39.50, 39.55, 114.8, 138.8.

9-(Bromomethyl)deptadeca-1,16-diene (5) (x = 6). ¹H NMR (300 MHz, CDCl₃), δ (ppm): 1.18–1.50 (m, 20H), 1.61 (p, 1H), 2.06 (q, 4H), 3.45 (d, 2H), 4.90–5.05 (m, 4H), 5.73–5.90 (m, 2H). ¹³C NMR (75 MHz, CDCl₃), δ (ppm): 26.7, 29.1, 29.3, 29.8, 32.8, 34.0, 39.7, 39.8, 114.4, 139.3.

Polymerization of Monomers 4–6. A typical synthesis of P1–P4 is given. 3.00 g (7.25 mmol) of 6 was added to a custom-built flat-bottomed mechanically stirred reactor designed to continuously spread the polymerization matrix as a thin film. The vessel was evacuated overnight to remove dissolved oxygen and then purged with argon, and 59 mg (72 μmol, 1 mol %) of Grubbs' first-generation catalyst was carefully added under a strong flow of argon. A cycle of evacuation and refilling with argon was repeated three times before a final evacuation. The reaction mixture was then heated to 40 °C and stirred at 350 rpm for 24 h under vacuum, at which point the vessel was cooled to room temperature, refilled with argon, and 10 mL of dry degassed toluene was added to dissolve the polymer (P3). After dissolution, 1 mL of dry degassed ethyl vinyl ether (EVE) was added, and stirring was continued for 1 h at room temperature under argon. After 1 h the EVE was evaporated *in vacuo*, and the polymer solution was left to stir open to air for 24 h to facilitate decomposition of the ethereal ruthenium alkylidene into ruthenium oxide, as indicated by a change in color from pale red-brown to black. The solution was concentrated to ~5 mL by passing air over its surface under gentle heating, and finally it was passed through a short plug of silica (approximately 2 cm in diameter × 6 cm tall) using toluene as eluent to remove the ruthenium species. The column fractions were concentrated to ~10 mL of clear, very pale yellow solution, which was precipitated into 400 mL of methanol to yield a bright white tacky gum. The gum was dried under vacuum overnight and then coalesced into a clear colorless gum (2.54 g, 91%) over a period of a few days.

P1 (x = 3). ¹H NMR (300 MHz, CDCl₃), δ (ppm): 1.24–1.50 (m, 8H), 1.58–1.70 (m, 1H), 2.0–2.18 (m, 4H), 3.44 (d, 2H), 5.29–5.40 (m, 2H). ¹³C NMR (75 MHz, CDCl₃), δ (ppm): 25.9, 26.9, 29.6, 32.3, 32.4, 33.9, 39.5, 39.6, 129.8, 130.4. GPC (THF, light scattering detector, PS standards): M_n = 26 kDa, PDI = 2.0.

P2 (x = 6). ¹H NMR (300 MHz, CDCl₃), δ (ppm): 1.16–1.50 (m, 20H), 1.55–1.63 (m, 1H), 2.0–2.12 (m, 4H), 3.45 (d, 2H), 5.31–5.40 (m, 2H). ¹³C NMR (75 MHz, CDCl₃), δ (ppm): 26.7, 27.4, 29.1–29.3 (broad overlapping signals), 29.8, 33.8, 34.0, 39.7, 39.8, 129.5, 130.0. GPC (THF, light scattering detector, PS standards): M_n = 31 kDa, PDI = 1.9.

P3 (x = 9). ¹H NMR (300 MHz, CDCl₃), δ (ppm): 1.20–1.44 (m, 32H), 1.55–1.64 (m, 1H), 1.90–2.05 (m, 4H), 3.43 (d, 2H), 5.33–5.42 (m, 2H). ¹³C NMR (75 MHz, CDCl₃), δ (ppm): 26.8, 27.7, 29.1–29.8, (broad overlapping signals), 29.9, 33.8, 34.0, 39.7, 39.9, 129.5, 130.0. GPC (THF, light scattering detector, PS standards): M_n = 40 kDa, PDI = 2.0.

P4 (Random Copolymer Analogous to P3). ¹H NMR (300 MHz, CDCl₃), δ (ppm): 1.20–1.40 (m, 20H), 1.54–1.64 (m, 1H), 1.90–2.11 (m, 10H), 3.43 (d, 2H), 5.30–5.45 (m, 5H). ¹³C NMR (75 MHz, CDCl₃), δ (ppm): 26.0, 26.4, 27.7, 27.8, 29.0–29.9 (broad overlapping signals), 33.5, 33.6, 39.70, 39.75, 39.80, 39.85, 39.9, 129.5, 129.9, 130.2, 130.3, 130.5, 131.0. GPC (THF, light scattering detector, PS standards): M_n = 33 kDa, PDI = 2.0.

Hydrogenation Conditions for Synthesis of P5–P8. A typical procedure for hydrogenation of P1–P4 is given. One gram of P3 was dissolved in 50 mL of dry degassed toluene and sparged with argon for 30 min to remove oxygen. The solution was transferred to a Parr bomb hydrogenation apparatus charged with 30 mg of Wilkinson's catalyst. The bomb was charged to 400 psi with hydrogen gas, and the gas was released via a needle valve. The sequence of pressurization and release of hydrogen was repeated three times to remove oxygen. The bomb was then charged to 800 psi, heated to 50 °C, and left to stir for 48 h, at which point a small sample was removed for NMR. After collecting ¹H NMR (acquisition time of 1 h) to ensure complete loss of residual olefin signals and indicate reaction completion, the reactor

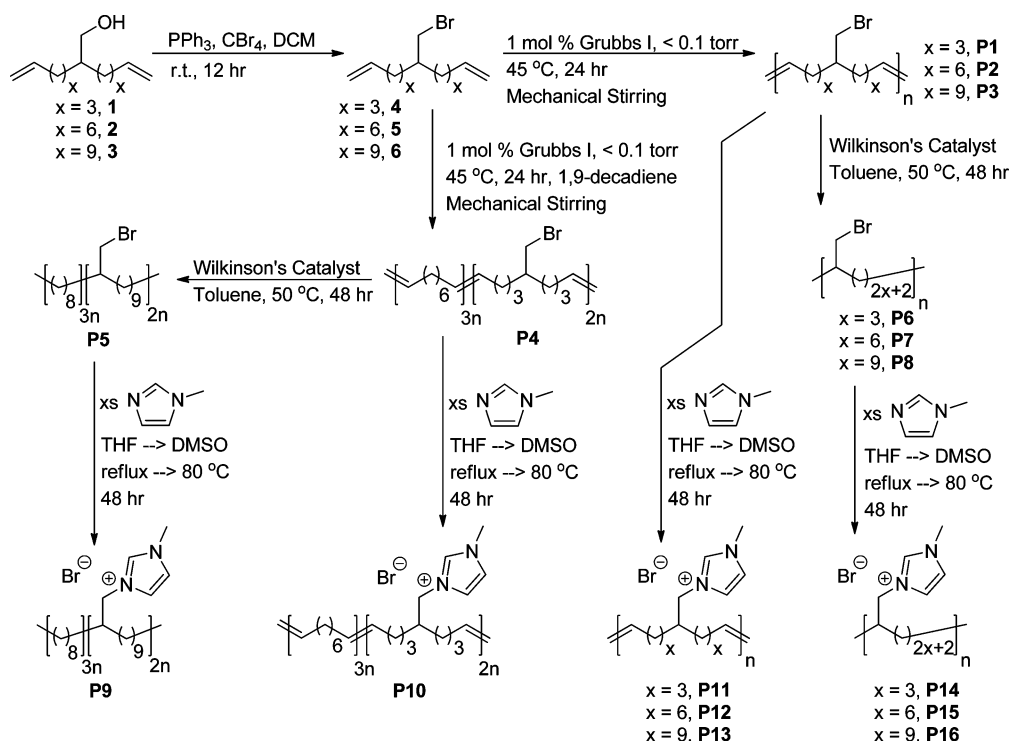


Figure 2. Synthesis of six precision ionomers and two regiorandom analogues.

was opened and the mixture was stirred under a slow stream of pressurized air for 24 h to facilitate decomposition of Wilkinson's catalyst into rhodium oxide. The concentrated solution of **P8** was passed through a short plug of silica and ultimately precipitated into methanol in a manner similar to that used for the removal of ruthenium from **P1**–**P4**. After precipitation and drying *in vacuo*, 963 mg (96%) of white gum was obtained.

P5 (Random Copolymer Analogous to P8). ^1H NMR (300 MHz, CDCl_3), δ (ppm): 1.10–1.40 (m, 40H), 1.57–1.68 (m, 1H), 3.44 (d, 2H). ^{13}C NMR (75 MHz, CDCl_3), δ (ppm): 25.9, 26.7, 29.0–29.6 (broad overlapping signals), 33.9, 34.0, 39.6, 39.7, 39.9. GPC (THF, light scattering detector, PS standards): $M_n = 35$ kDa, PDI = 2.0.

P6 (x = 3). ^1H NMR (300 MHz, CDCl_3), δ (ppm): 1.20–1.50 (m, 16H), 1.60–1.70 (m, 1H), 3.45 (d, 2H). ^{13}C NMR (75 MHz, CDCl_3), δ (ppm): 25.8, 29.6, 29.9, 33.9, 39.5, 39.6. GPC (THF, light scattering detector, PS standards): $M_n = 28$ kDa, PDI = 2.1.

P7 (x = 6). ^1H NMR (300 MHz, CDCl_3), δ (ppm): 1.14–1.49 (m, 28H), 1.57–1.63 (m, 1H), 3.44 (d, 2H). ^{13}C NMR (75 MHz, CDCl_3), δ (ppm): 26.6, 29.1–29.6 (broad overlapping signals), 34.0, 39.7, 39.8. GPC (THF, light scattering detector, PS standards): $M_n = 35$ kDa, PDI = 2.0.

P8 (x = 9). ^1H NMR (300 MHz, CDCl_3), δ (ppm): 1.18–1.44 (m, 40H), 1.55–1.65 (m, 1H), 3.43 (d, 2H). ^{13}C NMR (75 MHz, CDCl_3), δ (ppm): 26.7, 29.1–29.6 (broad overlapping signals), 34.0, 39.7, 39.9. GPC (THF, light scattering detector, PS standards): $M_n = 44$ kDa, PDI = 2.0.

Quaternization of 1° Br Polymers To Produce Ionomers P9–P16. Typical quaternization reaction conditions for synthesis of **P9**–**P16** are given. To a 50 mL round-bottom flask charged with 1 g of **P3** dissolved in 15 mL of anhydrous THF was added 2 mL of 1-methylimidazole. The flask was equipped with a Vigreux column, and the entire reaction vessel was purged with argon for 30 min. The mixture was then heated at reflux for 4 h, the THF was evaporated *in vacuo*, and 15 mL of dry DMSO was added. The reaction was heated at 80 °C for 40 h, at which time the DMSO and excess 1-methylimidazole were removed by vacuum distillation. The polymer was then rigorously dried by heating at 80 °C under high vacuum (<20 mTorr) for 2 days, followed by continued application of vacuum at

room temperature for 1 week to give 1.05 g (87%) of **P13**. To avoid water sorption, all polymers were stored under vacuum.

P9 (Random Copolymer Analogous to P16). ^1H NMR (300 MHz, $\text{DMSO}-d_6$), δ (ppm): 1.20 (bs, 32H), 1.84 (bs, 1H), 3.86 (bs, 3H), 4.05 (bs, 2H), 7.75 (bs, 2H), 9.24 (bs, 1H). ^{13}C NMR (75 MHz, $\text{DMSO}-d_6$), δ (ppm): 26.1, 29.0–31.0 (broad multiplet), 36.5, 38.5, 53.1, 123.5, 124.3, 137.6. GPC (THF, light scattering detector, PS standards, calcd from data for **P5**): $M_n = 42$ kDa, PDI = 2.0. Anal. Calcd $\text{C}_{26}\text{H}_{49}\text{BrN}_2$: C, 66.50; H, 10.52; Br, 17.02; N, 5.97. Found: C, 65.89; H, 10.86; N, 6.22.

P10 (Random Copolymer Analogous to P13). ^1H NMR (300 MHz, $\text{DMSO}-d_6$), δ (ppm): 1.21 (bs, 20H), 1.89 (bs, 11H), 3.87 (bs, 3H), 4.12 (bs, 2H), 5.31 (bs, 5H), 7.77 (bs, 2H), 9.29 (bs, 1H). ^{13}C NMR (75 MHz, $\text{DMSO}-d_6$), δ (ppm): 26.0, 27.3, 29.0–31.0 (broad multiplet), 32.7, 36.5, 38.2, 53.0, 123.4, 124.3, 130.0–131.5 (multiplet), 137.5. GPC (THF, light scattering detector, PS standards, calcd from data for **P4**): $M_n = 40$ kDa, PDI = 2.0. Anal. Calcd $\text{C}_{26}\text{H}_{44}\text{BrN}_2$: C, 67.22; H, 9.55; Br, 17.20; N, 6.03. Found: C, 66.57; H, 10.03; N, 6.31.

P11 (x = 3). ^1H NMR (300 MHz, $\text{DMSO}-d_6$), δ (ppm): 1.23 (m, 8H), 1.89 (m, 5H), 3.87 (s, 3H), 4.08 (d, 2H), 5.34 (m, 2H), 7.78 (s, 1H), 7.82 (s, 1H), 9.33 (s, 1H). ^{13}C NMR (75 MHz, $\text{DMSO}-d_6$), δ (ppm): 26.1, 30.3, 32.8, 36.5, 38.2, 52.9, 123.5, 124.2, 130.3, 130.7, 137.5. GPC (THF, light scattering detector, PS standards, calcd from data for **P1**): $M_n = 36$ kDa, PDI = 2.0. Anal. Calcd $\text{C}_{14}\text{H}_{23}\text{BrN}_2$: C, 56.19; H, 7.75; Br, 26.70; N, 9.36. Found: C, 56.28; H, 7.85; N, 9.31.

P12 (x = 6). ^1H NMR (300 MHz, $\text{DMSO}-d_6$), δ (ppm): 1.20 (s, 20H), 1.90 (s, 5H), 3.86 (s, 3H), 4.07 (d, 2H), 5.34 (s, 2H), 7.75 (s, 1H), 7.79 (s, 1H), 9.25 (s, 1H). ^{13}C NMR (75 MHz, $\text{DMSO}-d_6$), δ (ppm): 26.1, 27.3, 29.2, 29.8, 30.8, 32.7, 36.5, 38.4, 53.1, 123.4, 124.2, 130.2, 130.7, 137.5. GPC (THF, light scattering detector, PS standards, calcd from data for **P2**): $M_n = 40$ kDa, PDI = 1.9. Anal. Calcd $\text{C}_{20}\text{H}_{35}\text{BrN}_2$: C, 62.65; H, 9.20; Br, 20.84; N, 7.31. Found: C, 62.3; H, 9.17; N, 7.82.

P13 (x = 9). ^1H NMR (300 MHz, $\text{DMSO}-d_6$), δ (ppm): 1.19 (s, 32H), 1.90 (m, 5H), 3.86 (s, 3H), 4.07 (d, 2H), 5.31 (m, 2H), 7.75 (s, 1H), 7.78 (s, 1H), 9.28 (s, 1H). ^{13}C NMR (75 MHz, $\text{DMSO}-d_6$), δ (ppm): 26.0, 27.3, 29.3, 29.6, 29.7, 29.8, 29.9, 30.7, 32.7, 36.5, 38.4, 53.1, 123.4, 124.3, 130.2, 130.7, 137.5. GPC (THF, light scattering

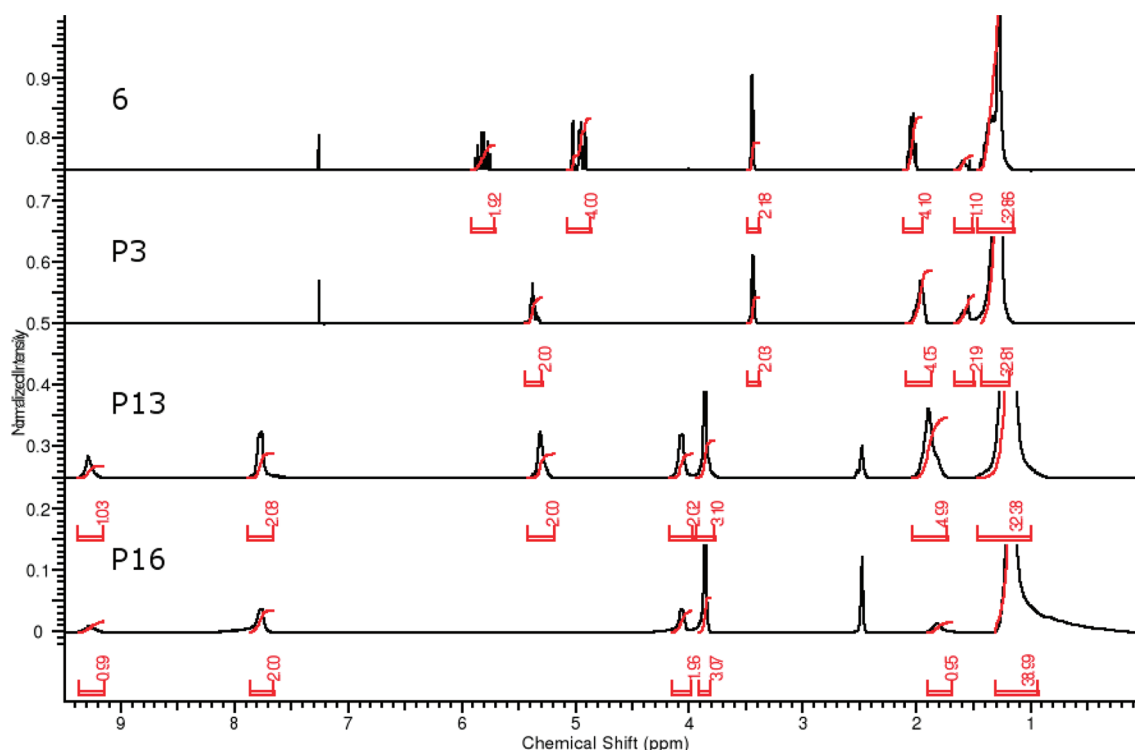


Figure 3. ^1H NMR spectra of monomer **6** and its corresponding polymers **P3** (after polymerization), **P13** (after quaternization), and **P16** (after hydrogenation of **P3** to afford **P8** followed by quaternization), showing complete conversion in all postpolymerization modifications.

detector, PS standards, calcd from data for **P3**): $M_n = 49$ kDa, PDI = 2.0. Anal. Calcd $\text{C}_{26}\text{H}_{47}\text{BrN}_2$: C, 66.79; H, 10.13; Br, 17.09; N, 5.99. Found: C, 66.41; H, 10.2; N, 6.21.

P14 ($x = 3$). ^1H NMR (300 MHz, $\text{DMSO}-d_6$), δ (ppm): 1.19 (s, 16H), 1.83 (s, 1H), 3.87 (s, 3H), 4.08 (d, 2H), 7.77 (s, 1H), 7.80 (s, 1H), 9.30 (s, 1H). ^{13}C NMR (75 MHz, $\text{DMSO}-d_6$), δ (ppm): 25.1, 28.5, 28.9, 29.7, 35.4, 37.3, 51.9, 122.3, 123.1, 136.4. GPC (THF, light scattering detector, PS standards, calcd from data for **P6**): $M_n = 38$ kDa, PDI = 2.1. Anal. Calcd $\text{C}_{14}\text{H}_{23}\text{BrN}_2$: C, 55.81; H, 8.36; Br, 26.52; N, 9.30. Found: C, 55.62; H, 8.37; N, 9.41.

P15 ($x = 6$). ^1H NMR (300 MHz, $\text{DMSO}-d_6$), δ (ppm): 1.20 (s, 28H), 1.83 (s, 1H), 3.86 (s, 3H), 4.06 (d, 2H), 7.75 (s, 1H), 7.78 (s, 1H), 9.25 (s, 1H). ^{13}C NMR (75 MHz, $\text{DMSO}-d_6$), δ (ppm): 26.1, 29.6, 29.7, 29.8, 29.9, 30.7, 36.5, 38.4, 53.1, 123.4, 124.3, 137.5. GPC (THF, light scattering detector, PS standards, calcd from data for **P7**): $M_n = 44$ kDa, PDI = 2.0. Anal. Calcd $\text{C}_{20}\text{H}_{37}\text{BrN}_2$: C, 62.32; H, 9.68; Br, 20.73; N, 7.27. Found: C, 61.95; H, 9.94; N, 7.46.

P16 ($x = 9$). ^1H NMR (300 MHz, $\text{DMSO}-d_6$), δ (ppm): 1.20 (s, 40H), 1.83 (s, 1H), 3.86 (s, 3H), 4.06 (d, 2H), 7.75 (s, 2H), 9.26 (s, 1H). ^{13}C NMR (75 MHz, $\text{DMSO}-d_6$), δ (ppm): 25.9, 29.6, 29.7, 29.80, 29.86, 29.9, 30.5, 30.5, 30.7, 36.5, 38.3, 53.1, 123.4, 124.3, 137.5. GPC (THF, light scattering detector, PS standards, calcd from data for **P8**): $M_n = 53$ kDa, PDI = 2.0. Anal. Calcd $\text{C}_{26}\text{H}_{49}\text{BrN}_2$: C, 66.50; H, 10.52; Br, 17.02; N, 5.97. Found: C, 66.21; H, 10.63; N, 6.24.

RESULTS AND DISCUSSION

Synthesis, NMR, and GPC. Synthesis of the six precision ionomers and two regiorandom analogues, according to Figure 2, began with preparation of dieneols **1**, **2**, and **3** via a previously published protocol in three steps from commercially available materials, requiring only one purification by column chromatography.²⁸ Appel bromination to afford bromomethyl-diene monomers **4**, **5**, and **6** was carried out in quantitative yield, and purification required only passage of the crude reaction mixture through a short plug of silica to remove excess reagents and the POPh_3 byproduct, followed by removal of the

bromoform byproduct *in vacuo*. Polymerization of diene monomers **4**, **5**, and **6** was easily completed in 24 h with 1 mol % of Grubbs' first-generation catalyst under high vacuum using a vacuum-bearing equipped overhead mechanical stirring reactor to aid in the necessary removal of the ethylene condensate. Polymerizations were quenched using ethyl vinyl ether (EVE) in degassed toluene to remove the ruthenium alkylidene end groups; excess EVE was then removed *in vacuo* to prevent its cationic polymerization. Similar to a published protocol,³⁰ the target polymer solutions were stirred open to air for 24 h to allow for decomposition of the ethereal ruthenium alkylidene into ruthenium oxide. Subsequently, purification was achieved simply by passing the crude polymerization products through a plug of silica using toluene as eluent; ruthenium oxide hardly moves in this eluent while the relatively nonpolar polymers rapidly elute. One gram samples of each polymer were exhaustively hydrogenated using Wilkinson's catalyst in toluene, and subsequent removal of the catalyst was achieved in a fashion similar to that for the Grubbs' catalyst. A random copolymer (**P4**) containing an identical functional group frequency as **P3** was also prepared by copolymerizing **4** with 1,9-decadiene at a prescribed ratio, and its hydrogenation product (**P5**), which is analogous to regioregular **P8**, was prepared and isolated. GPC of **P1**–**P8** was carried out to analyze their M_n s and PDIs. Exact values can be found in the Experimental Section; they ranged from $M_n = 26$ to 44 kDa, and all PDIs approached 2.

After isolation of the primary bromide-functionalized polyolefins, they were exhaustively reacted with excess 1-methylimidazole to afford the desired ionomers **P9**–**P16** using a procedure loosely based on the preparation of imidazolium chloride-based ionomers from poly(vinyl chloride) reported by Wang and co-workers.^{11,31} It should be noted that in their report toluene was chosen as the quaternization solvent, but

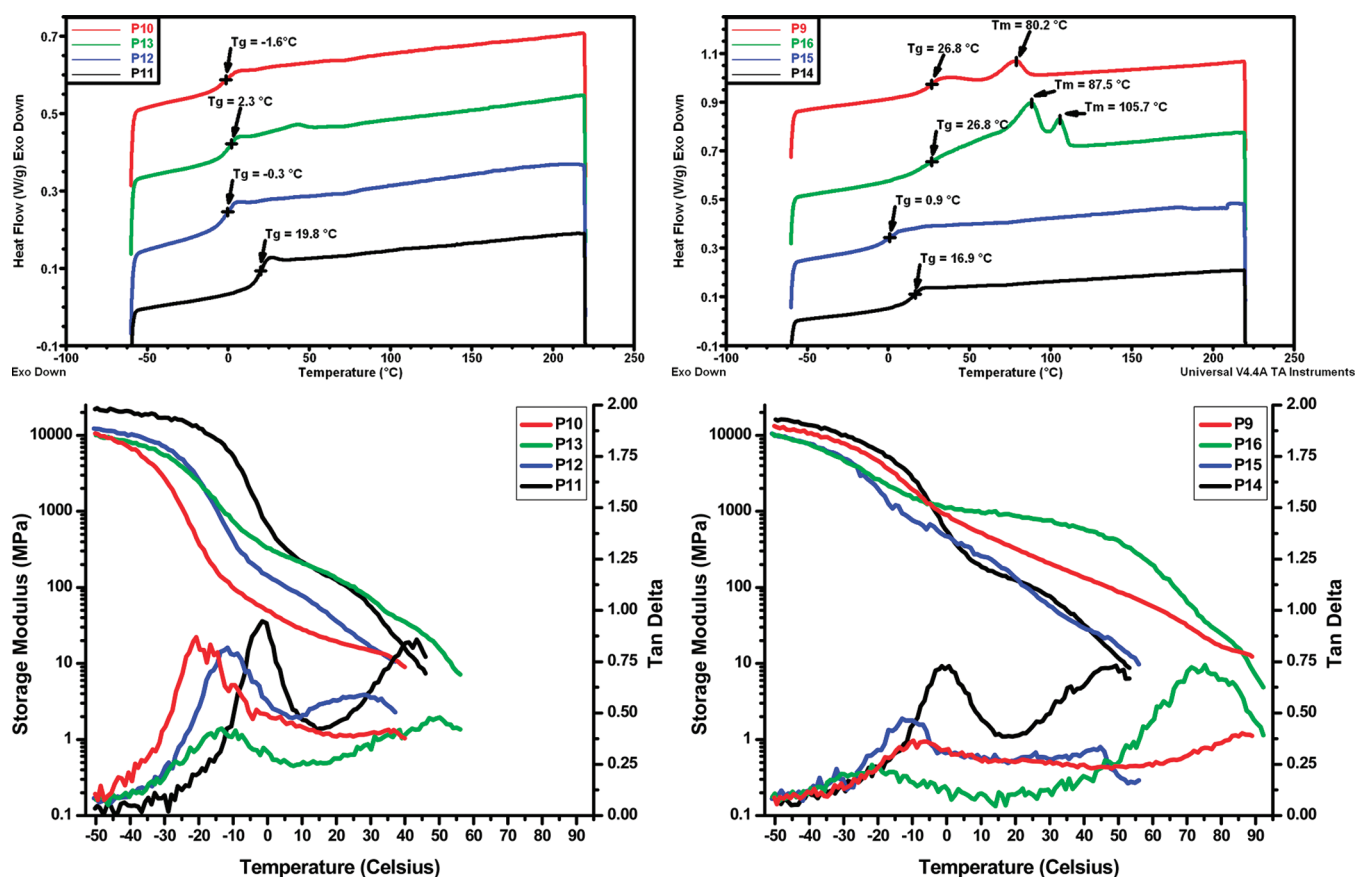


Figure 4. Top: DSC thermograms (second heat) of unsaturated ionomers (left) and saturated ionomers (right). Bottom: DMA thermograms of unsaturated ionomers (left) and saturated ionomers (right). Loss moduli are plotted along with storage moduli and tan delta in Figures S9–S16.

because its low polarity makes it a poor solvent for S_N2 chemistry, their conversion yields were quite low (not an issue for their target application). Using excess 1-methylimidazole, the quaternization reactions reported here were initiated in THF, the most polar solvent capable of dissolving the polymers. After only a few minutes at reflux, gelatinous precipitates were observed due to ionomer formation. The reactions were continued for 4–6 h, at which point the solvent was exchanged for DMSO due to its higher efficacy for S_N2 reactions and because, from our earlier work, we expected these ionomers to be soluble only in highly polar media.²⁶ The reactions were continued at 80 °C for an additional 40 h (approximate), at which point the DMSO and excess 1-methylimidazole were removed *in vacuo*. Complete removal of the 1-methylimidazole proved somewhat challenging due to the formation of extremely tough polymer glasses near the completion of distillation. Therefore, flasks containing the ionomers as relatively thin films adhered to the walls were placed under very high vacuum ($<10^{-2}$ mmHg) at 80 °C for 48 h and then at room temperature for 1 week. After this period, no 1-methylimidazole was visible by ^1H NMR even after 1 h spectral acquisition times (in fact, none was visible after the 48 h heating period). It should be noted that all postpolymerization modifications in this work were achieved with 100% conversion. However, isolated yields for P1–P16 were closer to 90% in most cases due to losses during purification and transfers of the polymers, especially during solvent distillation following the quaternization reactions, in which some ionomer was left as a difficult-to-remove film on the distillation head. Finally, elemental analysis was carried out on P9–P16 to be

sure of their purities, and their molecular weights were calculated based on measurements carried out on P1–P8 by assuming total conversion during the quaternization step. M_n s ranged from 36 to 53 kDa with PDIs all close to 2.

Analysis of the NMR spectra shown in Figure 3 and elemental analyses demonstrate that complete conversion during all postpolymerization steps was in fact achieved. Starting at the top and working down, terminal alkene signals for monomer 6 are clearly visible at approximately 5.0 and 5.7 ppm. After polymerization, the spectrum for P3 shows complete conversion of the terminal alkenes to internal alkenes, as indicated by total disappearance of the aforementioned signals and the appearance of a new one at ~ 5.4 ppm. In the next spectrum for ionomer P13, there are three new signals with correct integrations: two in the aryl region and one at about 3.9 ppm. Additionally, the pendant methylene group has shifted downfield from 3.4 to 4.1 ppm, with total disappearance of the signal at 3.4 ppm. In the last spectrum for saturated ionomer P16, we see a total disappearance of the alkene signals and shifting of the once allylic protons (at ~ 1.8 ppm in P13) into the large aliphatic signal near 1.1 ppm. The remaining signal near 1.8 ppm corresponds to the only tertiary proton and careful inspection shows that its movement can be traced through the entire synthesis as well.

Thermal Characterization (TGA, DSC, and DMA). Ionomers P9–P16 were characterized by TGA to assess their thermal stability, DSC to determine the presence of crystallinity, and DMA in an effort to understand the impact of regioregularity and spacer length on the glass transitions. TGA under nitrogen indicated excellent stability for these

materials; the onset of weight loss occurs beyond 250 °C for all ionomers. DSC thermograms are shown at the top of Figure 4. All data are for the second heating ramp in a heat–cool–heat–cool cycle and were collected at a 10 °C/min ramp rate. Cooling curves can be found in the Supporting Information (Figures SII–SI8) but were omitted here for clarity and because only the heating cycles of DSC are comparable to DMA measurements. As can be seen, unsaturated ionomers **P10–P13** are amorphous, with the possible exception of **P13** which shows a shallow ill-defined signal near 45 °C. Because attempts to enhance the size of this signal by annealing at various temperatures above the T_g were unsuccessful, we have tentatively assigned the observed transition to the temperature overshoot effect. This is in contrast to our earlier report of an identical ionomer structure with a PF_6^- counterion; in that case, a well-defined T_m was clear along with a cold crystallization exotherm during heating cycles.²⁶ The saturated derivatives **P14** and **P15** exhibit thermal data nearly identical to their two unsaturated analogues **P11** and **P12**. They are completely amorphous due to their higher ion content and short PE backbone run lengths, which prevent PE crystallization, and T_g s in the set of four decrease with decreasing ion content (as the length of the flexible PE chain segments increase). Unlike the aforementioned set of four, stark differences exist between the remaining two pairs of ionomers, **P10** vs **P9** and **P13** vs **P16**. The saturated analogues exhibit semicrystallinity. This is not surprising since most of the saturated polymers synthesized by our group are semicrystalline when functionality is placed on every 21st carbon, a sufficiently long PE run length to allow for lamella formation.^{25,27,32–34} What is surprising is the occurrence of two melting points in the precision ionomer **P16**, both higher than the one in its random analogue **P9**; both of the corresponding T_g s are also clearly visible in the cooling traces for **P16** (Figure SI8). On the basis of earlier work on ADMET polymers, one would expect precision PE-based materials with large pendant groups (like those here) to exhibit well-defined but somewhat smaller lamellar thicknesses, giving rise to very sharp but lower T_m s relative to random copolymer analogues.^{33–37} In contrast, due to the statistical incorporation of comonomers, random copolymers exhibit a distribution in the length of defect free polymer segments (ion depleted regions in this case), the longer of which give rise to thicker lamellae of varying sizes and therefore higher but broader T_m s.^{33–35,37} The lack of such behavior in these materials may indicate that their crystallites are more structurally complex than simple $-\text{CH}_2-$ segments. Alternatively, this may be the result of enhanced ordering in **P16** due to its regioregularity, leading to a different morphology all together, as was previously observed in acid-functionalized ADMET polymers and their partially neutralized derivatives.^{25,34} We are currently carrying out X-ray scattering measurements, which will shed light on the morphologies of these materials.

DMA thermograms of melt-pressed ionomer films, shown at the bottom of Figure 4, were acquired at a relatively low frequency (0.16 Hz) and ramp rate (3 °C/min) using an instrument-controlled dynamic force set to maintain a strain of <3%, with mechanical data collected at 20 s intervals. Ionomers can exhibit two glass transitions in DMA, the matrix and cluster T_g s. The lower matrix T_g pertains to the polymer segments for the ionic aggregates and is comparable to the T_g expected for the corresponding homopolymer and is also detected by DSC. Adjacent to the ionic aggregates, the polymer segments have restricted mobility and this is the origin of the higher cluster T_g .

Both the matrix and cluster T_g s, as well as plateau regions, are visible in the sample runs. The mechanical relaxations occurred at significantly lower temperatures than the corresponding transitions observed during DSC, as one might expect for the different thermal histories prior to testing and the slower heating rate of the DMA experiments. Although the DMA-measured matrix T_g s in the unsaturated materials (**P10–P13**) roughly corresponded to their DSC-measured T_g s, the discrepancy between DMA and DSC results in the saturated materials (**P9** and **P14–P16**) was larger. While the DSC T_g s, measured immediately after recrystallization at 10 °C/min, increased substantially upon hydrogenation and subsequent generation of crystallinity in **P9** and **P16**, their DMA matrix T_g s were less systematic. The reason for this discrepancy is not yet clear. Interestingly, the cluster T_g s in **P9** and **P16** increased substantially relative to their unsaturated analogues, presumably due to the semicrystallinity of the former which tends to retard motion. Unfortunately, because of the film geometry of the DMA experiments imposed by the limited quantity of materials, mechanical properties at higher temperatures were unattainable.

CONCLUSIONS

A synthetic strategy based on ADMET polymerization of symmetric 1° bromide functional monomers followed by postpolymerization quaternization with 1-methylimidazole has allowed for the preparation of perfectly regioregular polyolefin-based precision ionomers, with complete control of the spacer lengths separating the pendant ionic groups ensured by the monomer structure. A set of six precision ionomers containing 1-methylimidazolium bromide groups on exactly every 9th, 15th, or 21st carbon and two regiorandom analogues were characterized via TGA, DSC, and DMA. TGA indicates that these materials have excellent thermal stabilities; the onset of weight loss occurs above 250 °C in all ionomers. DSC shows that these materials exhibit relatively low T_g s, ranging from –1.6 to 26.8 °C, with an apparent dependence on both spacer length and the presence of crystallinity. Two of the ionomers with longer spacer lengths are semicrystalline, with T_m s of 80.2, 87.5, and 105.7 °C, while the remaining six ionomers do not exhibit crystallinity due to insufficiently long backbone polymethylene run lengths to allow for lamella formation and/or the presence of kinks due to backbone alkenes. Interestingly, the precision ionomer **P16** exhibits two T_m s, both higher than the T_m observed for regiorandom **P9**, despite the fact that **P9** contains some longer PE backbone sequences due to its statistical copolymer architecture. This anomalous thermal data suggests that **P16** may exhibit a different morphology due to its regioregularity, as has been observed for precision acid-functionalized PEs and their partially neutralized ionomer derivatives. Furthermore, such morphological differences, if they indeed exist, suggest this material's potential applicability as an ion transporting thermoplastic. DMA data were collected from melt-pressed films of these materials and indicate T_g s somewhat different from the DSC results (second heat), perhaps due to differences in the heating rate or the crystallinity that may arise from the distinct thermal histories inherent in the two methods. Variable temperature X-ray scattering studies are currently underway on these materials to explore their fascinating hierarchical morphologies.

■ ASSOCIATED CONTENT

■ Supporting Information

DSC and DMA thermograms. This material is available free of charge via the Internet at <http://pubs.acs.org>.

■ AUTHOR INFORMATION

Corresponding Author

*E-mail: wagener@chem.ufl.edu.

■ ACKNOWLEDGMENTS

B.S.A., J.D.H., and K.B.W. acknowledge financial support from the U.S. Army Research Office (W911NF-09-1-0290) and the National Science Foundation (DMR 0703261). C.F.B. and K.I.W. acknowledge support from the National Science Foundation (DMR 11-03858). M.L. and H.W.G. acknowledge support from U.S. Army Research Office (W911NF-07-1-0452, Ionic Liquids in Electro-Active Devices (ILEAD) MURI).

■ REFERENCES

- (1) Grady, B. P. *Polym. Eng. Sci.* **2008**, *48*, 1029.
- (2) Lin, B.; Qiu, L.; Lu, J.; Yan, F. *Chem. Mater.* **2010**, *22*, 6718.
- (3) Green, M. D.; Long, T. E. *Polym. Rev.* **2009**, *49*, 291.
- (4) Ohno, H.; Ito, K. *Chem. Lett.* **1998**, *27*, 751.
- (5) Hirao, M.; Ito-Akita, K.; Ohno, H. *Polym. Adv. Technol.* **2000**, *11*, 534.
- (6) Ohno, H. *Electrochim. Acta* **2001**, *46*, 1407.
- (7) Yoshizawa, M.; Ohno, H. *Electrochim. Acta* **2001**, *46*, 1723.
- (8) Yoshizawa, M.; Ogihara, W.; Ohno, H. *Polym. Adv. Technol.* **2002**, *13*, 589.
- (9) Ohno, H.; Yoshizawa, M.; Ogihara, W. *Electrochim. Acta* **2004**, *50*, 255.
- (10) Ogihara, W.; Washiro, S.; Nakajima, H.; Ohno, H. *Electrochim. Acta* **2006**, *51*, 2614.
- (11) Shu, Y.; Chen, X.-W.; Wang, J.-H. *Talanta* **2010**, *81*, 637.
- (12) Brown, R. H.; Duncan, A. J.; Choi, J.-H.; Park, J. K.; Wu, T.; Leo, D. J.; Winey, K. I.; Moore, R. B.; Long, T. E. *Macromolecules* **2010**, *43*, 790.
- (13) Chen, H.; Elabd, Y. A. *Macromolecules* **2009**, *42*, 3368.
- (14) Sugimura, R.; Qiao, K.; Tomida, D.; Yokoyama, C. *Catal. Commun.* **2007**, *8*, 770.
- (15) Mathis, A.; Zheng, Y.-L.; Galin, J.-C. *Polymer* **1991**, *32*, 3080.
- (16) Mathis, A.; Zheng, Y.-L.; Galin, J.-C. *Makromol. Chem., Rapid Commun.* **1986**, *7*, 333.
- (17) Lee, M.; Choi, U. H.; Colby, R. H.; Gibson, H. W. *Chem. Mater.* **2010**, *22*, 5814.
- (18) Williams, C. E.; Russell, T. P.; Jerome, R.; Horrión, J. *Macromolecules* **1986**, *19*, 2877.
- (19) Ding, Y. S.; Register, R. A.; Yang, C.-z.; Cooper, S. L. *Polymer* **1989**, *30*, 1204.
- (20) Ding, Y. S.; Register, R. A.; Yang, C.-z.; Cooper, S. L. *Polymer* **1989**, *30*, 1213.
- (21) Batra, A.; Cohen, C.; Kim, H.; Winey, K. I.; Ando, N.; Gruner, S. M. *Macromolecules* **2006**, *39*, 1630.
- (22) Batra, A.; Cohen, C.; Duncan, T. M. *Macromolecules* **2006**, *39*, 426.
- (23) Dou, S.; Zhang, S.; Klein, R. J.; Runt, J.; Colby, R. H. *Chem. Mater.* **2006**, *18*, 4288.
- (24) Wang, W.; Tudryn, G. J.; Colby, R. H.; Winey, K. I. *J. Am. Chem. Soc.* **2011**, *133*, 10826.
- (25) Seitz, M. E.; Chan, C. D.; Oppen, K. L.; Baughman, T. W.; Wagener, K. B.; Winey, K. I. *J. Am. Chem. Soc.* **2010**, *132*, 8165.
- (26) Aitken, B. S.; Lee, M.; Hunley, M. T.; Gibson, H. W.; Wagener, K. B. *Macromolecules* **2010**, *43*, 1699.
- (27) Baughman, T. W.; Wagener, K. B. Recent Advances in ADMET Polymerization. In *Metathesis Polymerization*; Buchmeiser, M., Ed.;

Advances in Polymer Science; Springer-Verlag GmbH: Berlin, Germany, 2005; Vol. 176, pp 1–42.

(28) Smith, J. A.; Brzezinska, K. R.; Valenti, D. J.; Wagener, K. B. *Macromolecules* **2000**, *33*, 3781.

(29) Sworen, J. C.; Smith, J. A.; Berg, J. M.; Wagener, K. B. *J. Am. Chem. Soc.* **2004**, *126*, 11238.

(30) Knight, D. W.; Morgan, I. R.; Proctor, A. J. *Tetrahedron Lett.* **2010**, *51*, 638.

(31) Chen, M.-L.; Zhao, Y.-N.; Zhang, D.-W.; Tian, Y.; Wang, J.-H. *J. Anal. At. Spectrom.* **2010**, *25*, 1688.

(32) Lehman, S. E.; Wagener, K. B. ADMET Polymerization. In *Handbook of Metathesis*; Grubbs, R. H., Ed.; Wiley-VCH: Weinheim, Germany, 2003; Vol. 3, pp 283–353.

(33) Oppen, K. L.; Wagener, K. B. *J. Polym. Sci., Part A: Polym. Chem.* **2011**, *49*, 821.

(34) Baughman, T. W.; Chan, C. D.; Winey, K. I.; Wagener, K. B. *Macromolecules* **2007**, *40*, 6564.

(35) Hosoda, S.; Nozue, Y.; Kawashima, Y.; Suita, K.; Seno, S.; Nagamatsu, T.; Wagener, K. B.; Inci, B.; Zuluaga, F.; Rojas, G.; Leonard, J. K. *Macromolecules* **2011**, *44*, 313.

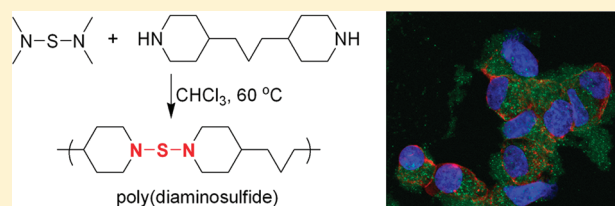
(36) Rojas, G.; Inci, B.; Wei, Y.; Wagener, K. B. *J. Am. Chem. Soc.* **2009**, *131*, 17376.

(37) Hosoda, S.; Nozue, Y.; Kawashima, Y.; Utsumi, S.; Nagamatsu, T.; Wagener, K.; Berda, E.; Rojas, G.; Baughman, T.; Leonard, J. *Macromol. Symp.* **2009**, *282*, 50.

Synthesis of the First Poly(diaminosulfide)s and an Investigation of Their Applications as Drug Delivery Vehicles

Jun Yoo,[†] Sheetal R. D'Mello,[‡] Tyler Graf,[†] Aliasger K. Salem,[‡] and Ned B. Bowden^{*,†}[†]Department of Chemistry, University of Iowa, Iowa City, Iowa 52242, United States[‡]College of Pharmacy, University of Iowa, Iowa City, Iowa 52242, United States

ABSTRACT: This paper reports the first examples of poly(diaminosulfide)s that were synthesized by the reaction of a sulfur transfer reagent and several secondary diamines. The diaminosulfide group has the general structure of $R_2N-S-NR_2$, and although it has been used in the synthesis of small molecules, it has never been utilized in the synthesis of macromolecules until this report. A series of poly(diaminosulfide)s were synthesized at elevated temperatures, and the molecular weights of the polymers were as high as $12\,400\text{ g mol}^{-1}$ with conversions for the polymerization reaction up to 99%. The rate constants for the transamination reactions that lead to the polymers were measured in several solvents to provide an understanding of the reaction conditions necessary to polymerize the monomers. The degradation of diaminosulfides was studied in D_2O , C_6D_6 , CD_3OD , $CDCl_3$, and $DMSO-d_6/D_2O$ to demonstrate that they were very stable in organic solvents but degraded within hours under aqueous conditions. These results clearly demonstrated that diaminosulfides are very stable in organic solvents under ambient conditions. Poly(diaminosulfide)s have sufficient stabilities to be useful for many applications. The ability of these polymers to function as drug delivery vehicles was studied by the fabrication of nanoparticles of a water-insoluble poly(diaminosulfide) with a dye. The microparticles were readily absorbed into human embryonic 293 cells and possessed no measurable toxicity toward these same cells.



■ INTRODUCTION

The integration of new functional groups into polymer chemistry opens new avenues for research and possible commercial applications. For instance, the development of well-defined carbene catalysts based on Mo, W, and Ru in the 1980s and 1990s increased the types and complexities of polymers that could be synthesized and the problems in macromolecular science that could be addressed.^{1–12} These catalysts led to the development of living ring-opening metathesis polymerization (ROMP) and acyclic diene metathesis (ADMET) polymerization, which were significant reasons the Nobel Prize was awarded to Schrock, Grubbs, and Chauvin in 2005.^{13–22} The use of “click” chemistry is another example, and its use has increased the complexity of the structure of macromolecules and has found widespread applications in polymer science.^{23–25} In a recent example by the Hawker group published in 2010, polymers were synthesized for the first time with a functional group that was a precursor to ketenes and provided a simple route to synthesize cross-linked polyethylene to systematically study its materials properties.^{26,27} From these examples and more, it is clear that when new functional groups are integrated into macromolecules, new applications are developed that take advantage of their unique reactivities.

In this article we report the first examples of polymers that utilize diaminosulfide functional groups along their backbones. The diaminosulfide functional group has the general structure of $R_2N-S-NR_2$ as shown in Figure 1. Small molecules with

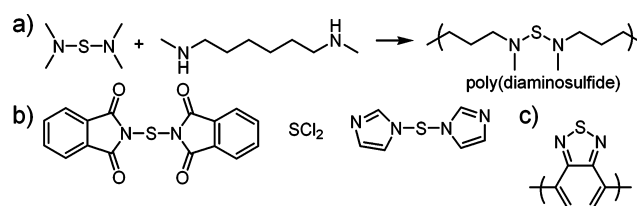


Figure 1. (a) A polymerization to yield a poly(diaminosulfide). (b) Sulfur transfer reagents that are commonly used in small molecule synthesis. (c) A polymer of a benzo[1,2,5]thiadiazole.

this functional group have been synthesized using sulfur transfer reagents such as those molecules shown in Figure 1b.^{28–30} The most prominent applications of small molecules with diaminosulfides have been in the chemical industry for the high-temperature vulcanization of rubber and in the construction of polymers with benzo[1,2,5]thiadiazoles along the backbone (Figure 1c).³¹ Polymers that incorporate benzo[1,2,5]thiadiazoles have found uses as semiconductors, fluorophores, and photoactive components in organic solar cells due to their interesting electro-optical properties.^{32–40} These polymers link the monomers through carbon–carbon bonds as shown in Figure 1c rather than through the nitrogen or sulfur atoms as in poly(diaminosulfide)s. Surprisingly, no

Received: October 15, 2011

Revised: December 9, 2011

Published: January 6, 2012

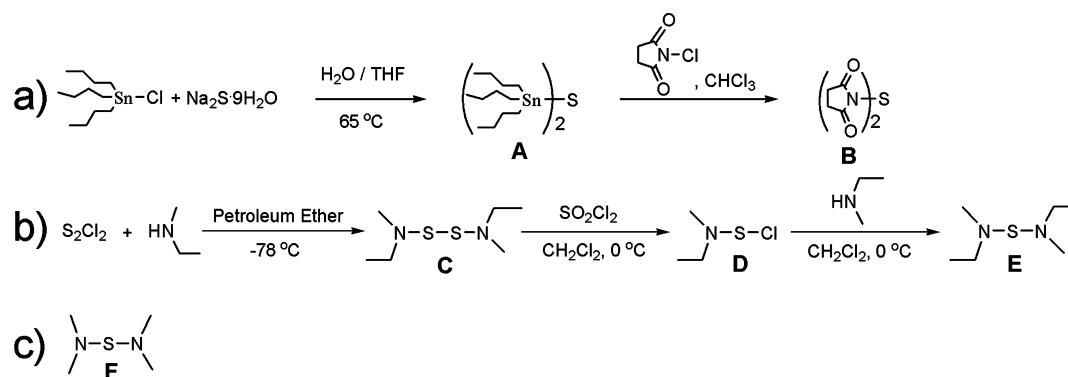


Figure 2. Synthesis of two sets of sulfur transfer reagents. (a) The synthesis of a dithiosuccinimide. (b) The synthesis of a diaminosulfide in two steps. Molecules C and E were purified by distillation. (c) Molecule F was synthesized using the same procedure as molecule E.

one has used diaminosulfides to bond monomers together as shown in Figure 1a, and these polymers are the focus of this report.

An important characteristic of the diaminosulfide group is that it is based on inorganic atoms (one sulfur and two nitrogens). Most functional groups that are used to synthesize polymers are based on organic functional groups such as esters, amides, anhydrides, acetals, cyclic olefins, vinyl groups, carbonates, urethanes, and epoxides. Although many monomers are known to possess inorganic functional groups, it is uncommon that an inorganic functional group is transformed in the polymerization reaction and used to link monomers together as shown in Figure 1a. Most inorganic functional groups found in monomers or polymers are not transformed during the polymerization reaction. Three notable examples of inorganic functional groups that have been polymerized include the polymerization of thiols into poly(disulfides), the polymerization of cyclic phosphazenes into poly(phosphazenes), and the polymerization of cyclic siloxanes into poly(siloxanes).^{41–50} Inorganic functional groups are interesting targets for polymer synthesis because they can be expected to have new reactivities that differ from those of organic functional groups and they have the potential to act as ligands for metals.^{51–54} The use of inorganic functional group transformations in the synthesis of polymers is understudied and represents a potentially rich source of functional group diversity in macromolecular science.

One part of our motivation to synthesize polymers through the polymerization of diaminosulfides was based on the chemical properties of this functional group in small molecule synthesis. These polymers are structurally related to polythiazyl (SN)_x which was first synthesized in 1953 from S₂N₂.^{55–59} This polymer is electrically conducting at room temperature and superconducting at low temperatures.⁵⁵ In prior work by others, molecules with diaminosulfides were stable and readily isolated by traditional methods (distillation or chromatography).^{28,29,60–63} In addition, some examples of the synthesis of molecules containing diaminosulfides proceeded with isolated yields of 80% or higher. Although promising, these results do not predict immediate success in a step-growth polymerization. In these polymerizations, the degree of polymerization, X_n , is related to the fractional monomer conversion, P , by the equation $X_n = 1/(1 - P)$.⁶⁴ Thus, to synthesize poly(diaminosulfide)s with modest to high molecular weights via a step-growth polymerization, the yield of the coupling reaction must be >95%.

To illustrate a possible application of poly(diaminosulfides), we completed initial experiments to investigate the application of a poly(diaminosulfide)s as a delivery vehicle for drugs. Many drugs suffer from poor bioavailability, poor water solubility, short serum circulation lifetimes, and inadequate mechanisms to enter cells or have serious side effects that limit the amount of drug that can be administered. To overcome these and more limitations, drugs are often condensed with synthetic, biodegradable polymers into nanoparticle delivery vehicles that are administered to patients.^{65–73} The polymer protects the drugs from degradation in the bloodstream and allows their delivery to tumors by the enhanced permeation and retention effect where they can be taken into cancer cells. The polymers used in this field degrade slowly in the bloodstream but have a rapid rate of degradation when taken into the acidic compartments of cells—the endosome and lysosome—where they release their cargo.^{74–77} It is critically important that the polymer be biodegradable such that it will not accumulate within the body and cause a toxic response.^{78,79} In this article, some of the characteristics of poly(diaminosulfides) as drug delivery vehicles were investigated, including the stabilities of diaminosulfides in water under basic, acidic, and neutral conditions, whether nanoparticles fabricated from these polymers were internalized by cells, and whether any *in vitro* toxicity was observed from the nanoparticles. These studies are meant to illustrate an interesting application of poly(diaminosulfide)s in medicine.

We report the synthesis of a small molecule that is a highly successful sulfur transfer reagent and how this molecule can be used to synthesize the first poly(diaminosulfide)s reported in the literature. Some of the key, initial studies of a diaminosulfide in numerous solvents are reported to demonstrate their stabilities and, by extension, the stabilities of poly(diaminosulfide)s. Finally, one example of a poly(diaminosulfide) was fabricated into microparticles and studied for their ability to be internalized by human embryonic kidney-293 (HEK-293) cells and whether they showed any toxicity toward these cells.

RESULTS AND DISCUSSION

Synthesis and Reactions of Sulfur Transfer Reagents.

We hypothesized that poly(diaminosulfide)s could be synthesized by reacting secondary diamines with a sulfur transfer reagent as shown in Figure 1a. Many secondary diamines were commercially available or easily synthesized, so the challenge in the polymerization was to develop a useful sulfur transfer

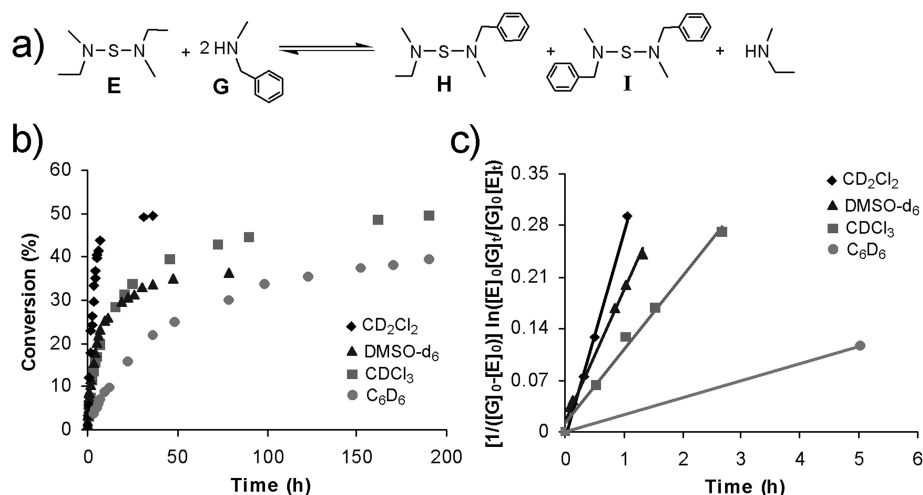


Figure 3. Kinetics of transamination reactions. (a) The reaction that was studied in a sealed NMR tube. (b) The conversion of the transamination reactions as a function of time. The conversion was defined as the sum of the S–N(CH₂)Bn bonds divided by the sum of all of the S–N bonds for molecules E, H, and I. (c) The plot of the initial data points used to find the rate constants for the reaction in each solvent. More data points were used to find the rate constant for the experiment in C₆D₆, but they are not shown here.

reagent. Although SCl₂ is used in the synthesis of small molecules with diaminosulfides, its use has several drawbacks.^{80–85} This molecule has a low boiling point (59 °C), must be handled under inert atmospheres, is challenging to purify, reacts with multiple functional groups such as alcohols and alkenes, and releases HCl. Because of these limitations, we have not pursued the synthesis or use of SCl₂.

Two different sulfur transfer reagents were studied (Figure 2). Molecule B was initially explored as a sulfur transfer reagent based on the rapid reactions of thiosuccinimides with amines.^{86,87} Although the synthesis of B was straightforward and did not require any chromatography, its purification was challenging because of its poor solubility in many solvents. Molecule B was mostly insoluble in benzene, chloroform, DMSO, and methylene chloride. Molecule B was cleaned by washing the crude product with hexanes, and an isolated yield of 69% was obtained. To increase the purity of molecule B, it was recrystallized from methanol. Replacement of *N*-chlorosuccinimide with *N*-chlorophthalimide in the second step yielded a diphthalimide sulfur transfer reagent that also possessed limited solubility in organic solvents.

Although B was partially soluble in DMSO, it was not used to synthesize polymers for several reasons. First, the synthesis of B had poor atom efficiency. The addition of one sulfur (atomic weight: 32 g mol^{−1}) to yield a diaminosulfide functional group along the backbone of a polymer would require the use of 2 equiv of tributyltin chloride (MW: 326 g mol^{−1}) and 2 equiv of *N*-chlorosuccinimide (MW: 134 g mol^{−1}). Thus, significant amounts of waste were produced in the synthesis of molecule B. Second, the poor solubility of molecule B made it challenging to use in solvents that dissolve many polymers. Furthermore, it decomposed when heated in CDCl₃ and DMSO-*d*₆.

A second sulfur transfer reagent was synthesized (molecule E in Figure 2) based on a literature procedure. In the first step, an excess of ethylmethylamine was reacted with sulfur chloride at −78 °C. Reactions run at 0 °C had unidentified side products, but the reaction at −78 °C yielded molecule C in high purity. Molecule C could be carried onto the next step without purification, or it could be purified by distillation. In the second step, C reacted with SO₂Cl₂ to yield D that was not isolated.

Rather, D was slowly added to ethylmethylamine to yield the sulfur transfer reagent E. This procedure was followed to synthesize F using dimethylamine in both steps. Both E and F were readily purified by distillation and yielded clean products as shown by ¹H and ¹³C NMR spectroscopy and high-resolution mass spectrometry. Because no chromatography was necessary for the synthesis of E or F, these reactions could be scaled up to yield large amounts of product in a short period of time.

Kinetics of Transamination Reactions. To synthesize polymers via transamination reactions between molecule E and secondary diamines, the second-order kinetics of the reaction between molecule E and benzylmethylamine was studied in four solvents (Figure 3). Benzylmethylamine was chosen for these reactions because of the easily identified benzylic CH₂ group that shifted downfield in the ¹H NMR spectra when proceeding from benzylmethylamine to H to I.

The reactions between molecule E and 2 mol equiv of benzylmethylamine were studied, and the rate constants were measured in CD₂Cl₂ (7.81 × 10^{−5} M^{−1} s^{−1}), DMSO-*d*₆ (4.89 × 10^{−5} M^{−1} s^{−1}), CDCl₃ (2.79 × 10^{−5} M^{−1} s^{−1}), and C₆D₆ (5.47 × 10^{−6} M^{−1} s^{−1}). The rate constants were found using the data points for conversions of less than 10% using the assumption that the reaction was irreversible. Although the reaction was reversible, this assumption has been commonly used to find rate constants for reversible reactions at low conversions.⁸⁸ It is important to note that the ethylmethylamine (boiling point = 36 °C) remained in the sealed NMR tube.

Although the reaction was most rapid in CD₂Cl₂ and reached equilibrium in 14 h, small amounts of unidentified side products were visible. The presence of side products made methylene chloride a poor choice for the polymerization. The reaction in CDCl₃ took 8 days to reach equilibrium, and the reaction in C₆D₆ did not reach equilibrium after 8 days. Despite the slow rates for reactions in these solvents, the reactions were clean and no side products were observed. The reaction in DMSO-*d*₆ also did not show any side products after 3 days, but this reaction reached 37% conversion and did not proceed any further. The final conversion was less than 50% because molecule I had limited solubility in DMSO-*d*₆ due to the apolar structure of molecule I and the polar structure of DMSO-*d*₆.

The ^1H NMR spectra of this reaction in $\text{DMSO}-d_6$ showed a lower than expected concentration of molecule I even after 3 days.

The reaction between molecule E and benzylmethylamine only reached 51% conversion in 17 h when completed at 40°C in an uncapped NMR tube, despite the low boiling point of ethylmethylamine. Prolonged reaction times resulted in a slow increase in conversion, but this reaction was judged to be too slow. Molecule F was synthesized for the polymerization reactions because of the low boiling point of dimethylamine (boiling point 7°C) which would make it simple to remove from a reaction.

Reactions between molecule F and benzylmethylamine were studied in CDCl_3 , $\text{DMSO}-d_6$, and C_6D_6 in vented reaction vessels to allow dimethylamine to boil off (Figure 4 and Table

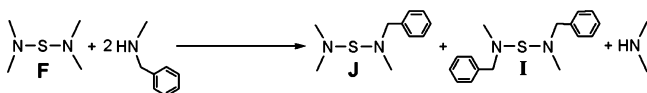


Figure 4. A transamination reaction with dimethylamine as the leaving group.

Table 1. Transamination Reactions of Molecule F and Benzylmethylamine

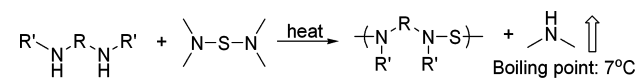
entry	solvent	temp ($^\circ\text{C}$)	reaction time (h)	conv ^a (%)
1	CDCl_3	50	24	39
2	CDCl_3	50	72	93
3	$\text{DMSO}-d_6$	50	73	84
4	C_6D_6	50	24	41
5	C_6D_6	50	72	84
6	C_6D_6	85	24	>97

^aThe conversion was defined as the sum of the $\text{S}-\text{N}(\text{CH}_3)\text{Bn}$ bonds divided by all of the $\text{S}-\text{N}$ bonds in molecules F, J, and I.

1). Each of the reactions in Table 1 did not show any impurities by ^1H NMR spectroscopy even when heated to 85°C for extended periods of time. The conversions for the reactions were high for each solvent for reactions at 50°C but went to quantitative conversions for reactions in C_6D_6 at 85°C .

Synthesis of Poly(diaminosulfide)s. Poly(diaminosulfide)s were synthesized by reaction of secondary diamines and molecule F at elevated temperatures (Scheme 1

Scheme 1. Polymerization of Diamines with the Sulfur Transfer Reagent



and Table 2). These polymerizations were run for 24 to 96 h, and the resulting polymers were characterized by GPC against polystyrene standards, ^1H NMR spectroscopy, and ^{13}C NMR spectroscopy.

The polymers in entries 1, 2, 5, and 6 had high molecular weights and degrees of polymerization. The degrees of polymerization were determined by two methods using the molecular weight measured by GPC and by end-group analysis in the ^1H NMR spectra of the polymers. These values for the degree of polymerization agreed with each other and demonstrated that these reactions cleanly proceeded to high

conversions. The polymerization with piperazine (entry 7) yielded an insoluble polymer in all solvents.

The polymer synthesized in entries 3 and 4 had limited stability. When this polymer was precipitated into methanol and water, it rapidly degraded as shown by the presence of numerous, unidentified peaks in the ^1H NMR spectra. To isolate the polymer with minimal degradation, benzene was removed under vacuum after the polymerization was complete, and the polymer was characterized without further purification. The GPC and ^1H NMR spectra were consistent with the indicated polymer. We believe that the internal, tertiary amine reacts with the diaminosulfide through an intramolecular reaction and was the source of the instability of this polymer.

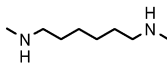
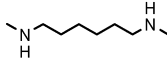
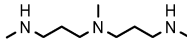
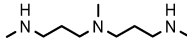

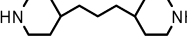

The polymer shown in entry 6 was characterized by elemental analysis to provide further evidence that it possessed the indicated composition. The calculated weight composition of the repeat unit was carbon (64.95%), hydrogen (10.06%), nitrogen (11.65%), and sulfur (13.34%). The measured weight composition of the polymer was carbon (64.70%), hydrogen (9.97%), nitrogen (11.76%), and sulfur (13.44%). The agreement between the calculated and measured elemental compositions provided strong evidence that there was only one sulfur atom bridging between the nitrogens.

Stability of Diaminosulfides in Organic Solvents and in Water. Although numerous small molecules possessing diaminosulfide functional groups have been synthesized, no report on their long-term stabilities in organic solvents or water have been published. The stability of this functional group was investigated to estimate the stabilities of poly(diaminosulfide)s for future work. Molecule E and an internal standard of diethylene glycol dimethyl ether were added to CDCl_3 , $\text{DMSO}-d_6/\text{D}_2\text{O}$ (10/1 by volume), and C_6D_6 and allowed to sit at room temperature in capped NMR tubes (Figure 5). Periodic ^1H NMR spectra were collected to determine the percent decomposition by the mole ratio of molecule E to the ether. After 32 days the amount of decomposition ranged from no detectable decomposition in C_6D_6 to 38% decomposition in $\text{DMSO}-d_6/\text{D}_2\text{O}$. Because molecule E was not soluble in methanol, the stability of molecule K was studied in CD_3OD . After 32 days, 15% of molecule K degraded.

These results demonstrated that the diaminosulfide functional group was stable in apolar, aprotic solvents but that it very slowly degraded in polar, protic solvents. The rate of degradation was slow enough that polymers with diaminosulfide functional groups are expected to have reasonable stabilities in these solvents, and this stability was observed for the prepared poly(diaminosulfide)s. The polymers were synthesized in benzene and chloroform at elevated temperatures and isolated by precipitation into methanol. Despite these conditions, the polymers possessed high degrees of polymerization.

To further explore the stability of the diaminosulfide functional group, molecule L was synthesized and studied in water (Figure 6). Molecule L and an internal standard of *tert*-butanol were added to D_2O with 9 mol equiv of acetic acid (acidic conditions), 9 mol equiv of KOH (basic conditions), or no additional acid or base (neutral conditions). The rate constants for the decomposition of this molecule were $1.29 \times 10^{-4} \text{ s}^{-1}$ under neutral pH conditions and $9.88 \times 10^{-5} \text{ s}^{-1}$ under basic conditions. Under acidic conditions, molecule L completely degraded by the time the first ^1H NMR spectrum was obtained so only a lower limit of the rate constant was calculated ($1.70 \times 10^{-2} \text{ s}^{-1}$).

Table 2. Synthesis of Poly(diaminosulfide)s

Entry	Diamine	Solvent	Temperature (°C)	Reaction time (h)	M_n^a (g mol ⁻¹)	PDI ^a	Yield (%)	DP ^b (%)	DP ^c (%)
1		C ₆ H ₆	85	24	5,600	3.7	75	98	99
2		C ₆ H ₆	85	48	5,200	3.4	97	98	99
3		C ₆ H ₆	85	72	810	1.6	97	87	97
4		C ₆ H ₆	85	96	1,600	1.6	89	93	98
5		CHCl ₃	60	72	12,400	6.6	88	99	98
6		CHCl ₃	60	96	7,200	3.3	95	98	98
^d 7		C ₆ H ₆	85						

^aThe M_n and PDI were measured using size exclusion chromatography versus polystyrene standards. ^bThe degree of polymerization were based on the values for M_n measured by GPC. ^cThe degree of polymerization were based on ¹H NMR spectra. ^dThe polymer was insoluble.

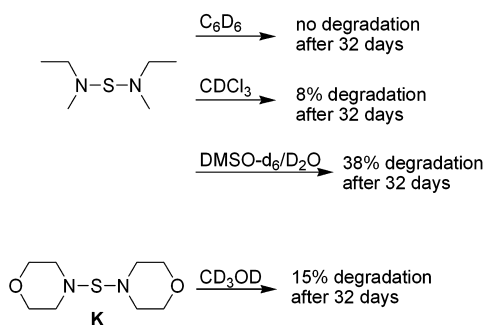


Figure 5. Stability of two molecules were studied at room temperature in organic solvents including DMSO-*d*₆/D₂O (10/1 v/v).

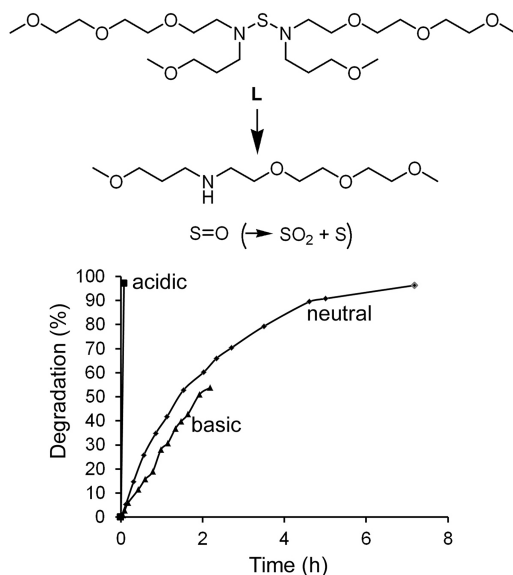


Figure 6. Degradation of molecule L was studied in D₂O under acidic (with acetic acid), neutral, and basic (with KOH) conditions. The amount of the diaminosulfide that degraded as a function of time was plotted.

The only product of degradation determined by ¹H NMR spectroscopy was the secondary diamine used in the synthesis of molecule L. From prior work by others, it was known that diaminosulfides react in water to form sulfur monoxide, which possessed a half-life of seconds and decomposed to release SO₂ and elemental sulfur.^{89,90}

Fabrication of Microparticles from a Poly(diaminosulfide) and Their Uptake into Cells. Synthetic polymers are widely used in drug delivery. In this field a polymer and drug are fabricated into nano- to micrometer sized particles and delivered to the body. Most of the polymers used in this field are based on polyesters—although other polymers are under investigation—because of the need to have the polymer degrade *in vivo* before it accumulates in the body and provokes a toxic response. Polyesters are widely used because they degrade in the body under neutral or acidic conditions without the need for enzymes. This observation of the role of polyesters in drug delivery and the degradation of diaminosulfides in water led us to speculate that poly(diaminosulfide)s may be useful as drug delivery vehicles. The diaminosulfide functional group degrades several orders of magnitude faster than ester bonds under acidic conditions, and they possess reasonable stabilities in water under neutral conditions.⁹¹ Some of the first key experiments to demonstrate the ability of poly(diaminosulfide)s to function as drug delivery vehicles are described here, and more results will be published in subsequent articles.

A polymer with the structure of entry 6 in Table 2 was used to fabricate microparticles that were studied as potential drug delivery vehicles (Figure 7). The microparticles were prepared according to a water/oil/water double emulsion-solvent evaporation method using poly(vinyl alcohol) as a surfactant. Briefly, the poly(diaminosulfide) was insoluble in water, and it was added to dichloromethane with a dye (FITC-dextran). A surfactant solution of water with 1 wt % poly(vinyl alcohol) was added to the dichloromethane and sonicated to produce the particles. This solution was diluted with more water and poly(vinyl alcohol) and further sonicated. After removal of the dichloromethane by evaporation, the microparticles were

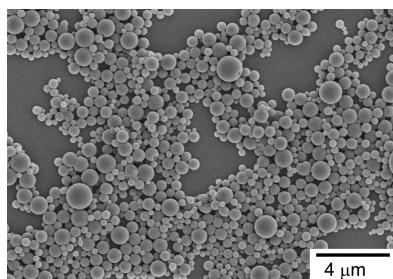


Figure 7. SEM micrographs of microparticles fabricated from the polymer shown in entry 6 of Table 2.

filtered and isolated. The particles were spherical in shape and possessed a smooth, nonporous surface. The z-average particle size determined by dynamic light scattering was 660 nm and consistent with the SEM micrograph shown in Figure 7. The surface charge determined to be -11.6 ± 0.8 mV.

Microparticles were fabricated and loaded with fluorescein isothiolate-dextran (FITC-dextran) to appear green under optical microscopy. These microparticles were incubated with HEK-293 cells at 37 °C for 24 h to study if they were internalized into the cells. After 24 h, the cells were washed with PBS buffer twice to remove any microparticles not internalized into cells. The cells were then fixed with paraformaldehyde and stained with 4',6-diamidino-2-phenylindole (DAPI) and phalloidin as described in the Experimental Section. The results in Figure 8 clearly demonstrated that the

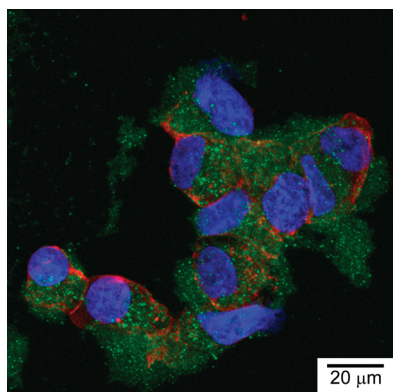


Figure 8. A laser scanning microscopic image is shown of HEK-293 cells that were exposed to microparticles loaded with FITC-dextran (green) for 24 h and then washed to remove microparticles that were not internalized into the cells. The nuclei of the cells were stained blue by DAPI, and the cytoplasm/cell membranes were stained red by phalloidin. This image clearly shows that the microparticles were internalized into the cells.

microparticles were internalized into the HEK-293 cells. In this image, the microparticles were green, the nucleus was blue (due to the DAPI stain), and the cytoplasm/cell membrane was red (due to the phalloidin stain). In control experiments with cells not exposed to the microparticles and not treated with phalloidin or DAPI, the cells did not fluoresce green. Thus, it is clear that there was no autofluorescence from the cells and that the observed green fluorescence within the cells was due to the uptake of the fluorescently labeled dextran loaded particles. This result demonstrates that these microparticles have potential as new drug delivery vehicles.

The cell viability of HEK-293 cells was investigated to determine whether the microparticles derived from poly-(diaminosulfide)s were toxic. The toxicity of microparticles fabricated from the polymer with the structure shown in entry 6 of Table 2 was studied via a MTS assay that is widely accepted as one method to determine cell viability in the presence of foreign molecules.^{92,93} Briefly, the MTS assay measures the mitochondrial activity of the cells and is used as an indication of the cell growth and viability. In living cells the MTS reagent (a yellow, water-soluble tetrazolium salt) is cleaved by the mitochondrial enzyme dehydrogenase (NADH-dependent reduction of the tetrazolium ring in MTS) to generate a water-soluble purple product called formazan. The concentration of formazan can be measured, and in this way, the relationship between the cell number and the amount of formazan generated is established since the absorbance is directly proportional to the number of viable cells. Damaged or dead cells exhibit a reduced or diminished enzyme activity and therefore less or no formazan production. Here, the incubation period of 24 h ensured the exposure of the cells to the different treatments in their exponential growth phase. Figure 9 shows

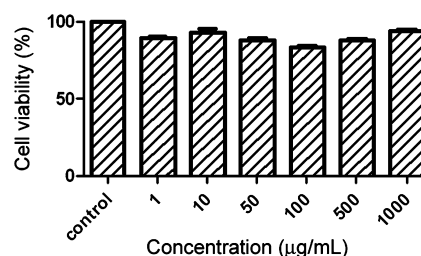


Figure 9. Cell viabilities of HEK-293 cells incubated with increasing concentrations of poly(diaminosulfide)-based microparticles.

the cell viability as a function of the concentration of microparticles and demonstrates excellent biocompatibility of these novel polymeric microparticles in HEK-293 cells. Microparticles in the concentration range of 1–1000 μg/mL had no adverse effect on cell viability. Even high concentrations of the microparticles did not reduce cell viability with cell survival rates greater than 85% for all the concentrations tested.

CONCLUSIONS

This paper described the first synthesis of poly-(diaminosulfide)s from two simple starting materials. The sulfur transfer reagent used in the synthesis was readily synthesized in two steps, and because it was purified by distillation rather than column chromatography, large quantities could be synthesized in only a few days. These polymers have many of the right properties to be used as synthetic polymers for different applications. For instance, we investigated the stabilities of diaminosulfides in different solvents so that future applications of poly(diaminosulfide)s could be envisioned. This functional group was very stable in organic solvents and not prone to oxidation; in fact, no evidence of oxidation of the sulfur was observed in any sample. One exciting application of these polymers as drug delivery vehicles was explored, and the results were very promising. A poly(diaminosulfide) was readily fabricated into nanoparticles that were absorbed into cells. These nanoparticles were also nontoxic toward HEK-293 cells. These results were promising, but more work is needed to investigate the advantages poly(diaminosulfide)s may possess

over polymers used in drug delivery. We propose a general label of poly(NSN) for any poly(diaminosulfide) to emphasize the functional group used in their synthesis and found in their backbones. Poly(NSN) can be used to describe a general family of polymers in the same way that the terms polystyrenes and polyacrylates are used.

One significant characteristic of diaminosulfides is that they are based on an inorganic functional group. Their structures differentiate them from the numerous organic functional groups used in the synthesis of most polymers. We believe that by working with inorganic functional groups with reactivities that differ from those of organic functional groups, new opportunities in macromolecular science will be realized.

EXPERIMENTAL SECTION

Materials. Sodium sulfide nonahydrate ($\text{Na}_2\text{S}\cdot 9\text{H}_2\text{O}$), tributyltin chloride, *N*-chlorosuccinimide, sulfur monochloride, *N*-ethylmethylaniline, *N*-benzylmethylaniline, *N,N'*-dimethyl-1,6-hexanediamine, *N,N'*-bis[3-(methylamino)propyl]methylaniline, 4,4'-trimethylenedipiperidine, *N,N'*-di-*sec*-butyl-*p*-phenylenediamine, dimethylamine, *p*-toluenesulfonyl chloride, and 3-methoxypropylamine were purchased from Aldrich or Acros Organics at their highest purity and used as received. FITC (fluorescein isothiocyanate)-dextran (M_w 20 kDa) and Mowiol (poly(vinyl alcohol), PVA, $\text{av } M_w \sim 67\text{K}$, 86.7–88.7% hydrolyzed) was obtained from Sigma-Aldrich (Sigma Chemical Co., St. Louis, MO). Deionized distilled water produced by Barnstead Nanopure Diamond Water purification Systems (Dubuque, IA) was used throughout. All other solvents including petroleum ether (39–56 °C) were reagent grade and purchased from Fisher Scientific. Because dimethylamine is a gas at room temperature, it was condensed inside a graduate cylinder in a –78 °C bath before use. Piperazine (99%) was purchased from Aldrich and was purified by sublimation under vacuum at 130 °C. Genduran silica gel 60 (230–400 mesh) and Basic Alumina Brockman Activity I (60–325 mesh) were purchased from Fisher Scientific were used for all column chromatography.

Dulbecco's Modified Eagle Medium (DMEM, with high glucose 1X and 4 mM L-glutamine), Trypsin-EDTA (0.25%, 1X solution), and Dulbecco's phosphate buffered saline (PBS) were purchased from Gibco (Invitrogen, NY). Fetal bovine serum (FBS) was obtained from Atlanta Biologicals (Lawrenceville, GA). Gentamycin sulfate (50 mg/mL) was purchased from Mediatech Inc. (Manassas, VA). MTS cell growth assay reagent (Cell Titer 96 Aqueous One Solution cell proliferation assay) was purchased from Promega Corp, Madison, WI. The HEK-293 cell lines were obtained from the American Type Culture Collection (ATCC, Manassas, VA).

Characterization. ^1H and ^{13}C NMR spectra were recorded on a Bruker DPX 300 at 300 and 75 MHz, respectively. CDCl_3 was used as the NMR solvent with tetramethylsilane (TMS) as an internal standard. Size-exclusion chromatography (SEC) was performed using tetrahydrofuran as the mobile phase (1.00 mL min^{-1}) at 25 °C. A Shimadzu LC-10AT HPLC pump and one Varian column (PLgel 5 μm MIXED-D) were used in series. A Shimadzu RID-10A refractive index detector and a Shimadzu SCL-10A system controller were used to measure molecular weights of polymers based on a polystyrene standard calibration curve.

Bis(tributyltin) Sulfide (Molecule A). This molecule was prepared according to a literature procedure.⁹⁴ A solution of sodium sulfide nonahydrate ($\text{Na}_2\text{S}\cdot 9\text{H}_2\text{O}$) (42.0 g, 175 mmol) in deionized water (34.8 mL) was prepared. This solution was added to a solution of tributyltin chloride (28.5 g, 87.4 mmol) in THF (174 mL). Extra deionized water (17.4 mL) was used to transfer the $\text{Na}_2\text{S}\cdot 9\text{H}_2\text{O}$ to the flask. The mixture was reacted at 65 °C for 5 h. After cooling the reaction, the organic layer was evaporated. The residue was extracted with Et_2O . The extract was dried over anhydrous magnesium sulfate and evaporated to give a colorless oil (21.8 g, 81% yield). ^1H NMR (CDCl_3): δ 0.91 (t, 18H, $J = 7.2$ Hz), 1.08 (m, 12H), 1.34 (m, 12H), 1.55 (m, 12H). ^{13}C NMR (CDCl_3): δ 13.66, 15.85, 27.17, 28.68.

Bis(succinimide) Sulfide (Molecule B).⁹⁴ *N*-Chlorosuccinimide (2.22 g, 16.6 mmol) was slowly added to a solution of molecule A (5.08 g, 8.30 mmol) in CHCl_3 (22 mL) at 0 °C and stirred. After 1.7 h, the ice bath was removed and the reaction was stirred for 8 h. A yellow solid stuck to the walls of the flask. The yellow organic phase was decanted. The yellow solid was washed with hexanes and dried under vacuum to give a crude yellow solid (1.30 g, 69% yield). ^1H NMR ($\text{DMSO}-d_6$): δ 2.57 (s, 8H). ^{13}C NMR ($\text{DMSO}-d_6$): δ 29.55, 179.47.

***N,N'*-Dithio(bisethylmethylaniline) (Molecule C).**⁹⁵ A solution of *N*-ethylmethylaniline (10.5 g, 178 mmol) in petroleum ether (400 mL) was cooled to –78 °C for 30 min. To this solution, sulfur monochloride (6.00 g, 44.4 mmol) was added dropwise for 10 min. The solution was stirred for 20 min at –78 °C and another 35 min at room temperature. The mixture was washed with a saturated NaCl solution in water. The organic layer was dried over anhydrous magnesium sulfate and evaporated to give a yellow–green oil (7.00 g). The product was isolated by vacuum distillation at 30–35 °C to yield a colorless oil (6.20 g, 78% yield). ^1H NMR (CDCl_3): δ 1.14 (t, 6H, $J = 7.2$ Hz), 2.64 (s, 6H), 2.69 (q, 4H, $J = 7.1$ Hz). ^{13}C NMR (CDCl_3): δ 13.81, 46.28, 53.54. HRMS calcd for $\text{C}_6\text{H}_{16}\text{N}_2\text{S}_2$: 180.0755. Found: 180.0759.

***N*-Ethylmethanysulfonyl Chloride (Molecule D).**⁹⁶ A solution of molecule C (4.81 g, 26.7 mmol) in CH_2Cl_2 (70 mL) was precooled to 0 °C for 40 min under N_2 . Sulfuryl chloride (3.96 g, 29.4 mmol) was added dropwise to the solution for 17 min under N_2 . The reaction was stirred for 30 min at 0 °C and another 50 min at room temperature to give a crude product (6.70 g, 53.4 mmol), which was used *in situ* for the preparation of molecule E.

Bis(*N*-ethylmethyl) Sulfide (Molecule E).⁹⁶ A solution of molecule D (6.70 g, 53.4 mmol) in CH_2Cl_2 (40 mL) was slowly added to a solution of *N*-ethylmethylaniline (7.89 g, 13.3 mmol) in CH_2Cl_2 (60 mL) at 0 °C under N_2 and stirred for 1 h. The reaction was washed with a saturated NaCl solution in water. The organic phase was dried over anhydrous magnesium sulfate and evaporated to give a yellow–green oil (4.22 g). The product was purified by distillation under vacuum at room temperature to yield a colorless oil (2.53 g, 32% yield). ^1H NMR (CDCl_3): δ 1.14 (t, 6H, $J = 7.2$ Hz), 2.95 (s, 6H), 3.11 (q, 4H, $J = 7.1$ Hz). ^{13}C NMR (CDCl_3): δ 14.24, 46.29, 54.89. HRMS calcd for $\text{C}_6\text{H}_{16}\text{N}_2\text{S}$: 148.1034. Found: 148.1033.

***N,N'*-Dithiobisdimethylamine.**⁹⁵ A solution of dimethylamine (8.01 g, 178 mmol) in anhydrous ether (400 mL) was cooled to –78 °C for 44 min. Sulfur monochloride (6.00 g, 44.4 mmol) was added dropwise to the solution for 14 min. The solution was stirred for 30 min at –78 °C and another 30 min at room temperature. The mixture was washed with a saturated NaCl solution in water. The organic layer was dried over anhydrous magnesium sulfate and evaporated to give a colorless oil (6.66 g, 99% yield), which could be used directly for the preparation of molecule F without further purification. ^1H NMR (CDCl_3): δ 2.63 (s, 12H). ^{13}C NMR (CDCl_3): δ 48.31. HRMS calcd for $\text{C}_4\text{H}_{12}\text{N}_2\text{S}_2$: 152.0442. Found: 152.0444.

***N*-Dimethylsulfonyl Chloride.**⁹⁶ A solution of *N,N'*-dithiobisdimethylamine (6.03 g, 39.6 mmol) in anhydrous Et_2O (50 mL) was cooled to 0 °C for 1 h under N_2 . Sulfuryl chloride (5.88 g, 43.6 mmol) was added dropwise to the solution under N_2 . The reaction was stirred for 36 min at 0 °C and another 50 min at room temperature to give a crude product (8.84 g, 79.2 mmol), which was used *in situ* for the preparation of molecule F.

Bis(*N,N'*-dimethyl) Sulfide (Molecule F).⁹⁶ A solution of *N*-dimethylsulfonyl chloride (8.84 g, 79.2 mmol) in anhydrous Et_2O (50 mL) was slowly added to a solution of dimethylamine (17.9 g, 39.6 mmol) in anhydrous Et_2O (75 mL) at –5 °C under N_2 and stirred for 1.2 h. The reaction was washed with saturated aqueous NaCl. The organic phase was dried over anhydrous magnesium sulfate, and the solvent was removed after freezing the product at –5 °C to give yellow–green oil (7.0 g). Further purification was achieved by distillation under vacuum at 30 °C to yield a colorless oil (4.39 g, 46% yield). ^1H NMR (CDCl_3): δ 3.02 (s). ^{13}C NMR (CDCl_3): δ 49.69. HRMS calcd for $\text{C}_4\text{H}_{12}\text{N}_2\text{S}$: 120.0721. Found: 120.0719.

Bis(*N,N'*-(3-methoxypropyl)(triethylene glycol monomethyl ether) sulfide) (Molecule L). In a flask was added *N*-(3-

methoxypropyl(triethylene glycol monomethyl ether)) (2.27 g, 9.64 mmol) and 3.6 mL of benzene. Next, molecule F (0.503 g, 4.18 mmol) was added, and the flask was connected to a reflux condenser and heated to 85 °C for 48 h. The benzene was removed under vacuum. The product was cleaned by chromatography on basic alumina oxide using ethyl acetate. The product was a clear oil (1.54 g, 73% yield). ¹H NMR (CDCl₃): δ 1.81 (p, 2H, *J* = 6 Hz), 3.12 (t, 2H, *J* = 7.2 Hz) 3.2–3.4 (m, 10H), 3.5–3.7 (m, 10H). ¹³C NMR (CDCl₃): δ 29.06, 54.83, 57.53, 58.56, 59.02, 70.13, 70.28, 70.45, 70.56, 70.64, 71.95. HRMS calcd for C₂₂H₄₈N₂O₈S: 500.3131. Found: 500.3125.

Entry 1, Table 2. Molecule F (0.942 g, 7.83 mmol) was reacted with *N,N'*-dimethyl-1,6-hexanediamine (1.13 g, 7.83 mmol) in refluxing benzene (11 mL) at 85 °C for 24 h. After evaporating the solvent, the polymer was precipitated into methanol (10 mL). The polymer was dried under vacuum to yield a brown oil (1.02 g, 75% yield). ¹H NMR (CDCl₃): δ 1.29 (m, 4H), 1.54 (m, 4H), 2.94 (s, 6H), 3.07 (t, 4H, *J* = 7.2 Hz). ¹³C NMR (CDCl₃): δ 26.88, 28.86, 46.90, 61.05.

Entry 3, Table 2. Molecule F (0.186 g, 1.55 mmol) was reacted with *N,N'*-bis[3-(methylamino)propyl]methylamine (0.268 g, 1.55 mmol) in refluxing benzene (1.4 mL) at 85 °C for 72 h. The benzene was removed under vacuum. When the polymer was redissolved in 4 mL of CH₃OH and precipitated into 9 mL of water, the polymer decomposed to unknown products, and the ¹H NMR spectrum became too complicated to assign the peaks. Therefore, after the polymerization was complete the polymer was dried under vacuum to yield a brown oil (0.310 g, 97% yield) that was used without further purification. ¹H NMR (CDCl₃): δ 1.71(m, 4H), 2.21 (s, 3H), 2.32 (t, 4H, *J* = 7.5 Hz), 2.95 (s, 6H), 3.12 (t, 4H *J* = 7.1 Hz). ¹³C NMR (CDCl₃): δ 25.59, 42.43, 46.90, 55.38, 59.01.

Entry 5, Table 2. Molecule F (0.186 g, 1.55 mmol) was reacted with 4,4'-trimethylenedipiperidine (0.326 g, 1.55 mmol) in CHCl₃ (1.6 mL) at 60 °C for 72 h. After evaporating the solvent and redissolving it in CH₂Cl₂ (4 mL), the polymer was precipitated into methanol (8 mL) to give a white-yellow powder (0.330 g, 88% yield). ¹H NMR (CDCl₃): δ 1.22(m, 12H), 1.59 (m, 4H), 3.08 (t, 4H, *J* = 11.0 Hz), 3.44 (m, 4H). ¹³C NMR (CDCl₃): δ 23.68, 34.02, 34.96, 36.72, 58.57.

Reactions of Molecule E and *N*-Benzylmethylamine (Figure 3). Molecule E (46.3 mg, 312 μmol) was dissolved in 1.35 mL of CD₂Cl₂, and 1 mL (34.4 mg, 232 μmol) of the solution was transferred to a NMR tube. After the addition of *N*-benzylmethylamine (56.3 mg, 464 μmol) and sealing the NMR tube with a rubber septum, ¹H NMR spectra were continually recorded for 3 days. The reaction was monitored by conversion of the benzyl hydrogens in *N*-benzylmethylamine at 3.71 ppm to the benzyl hydrogens in molecule H at 4.31 ppm and in molecule I at 4.38 ppm.

The same procedure was also followed for the kinetics in CDCl₃. The conversion from molecule E to molecules H and I was monitored by comparing the benzyl peak (3.74 ppm) of *N*-benzylmethylamine with the benzyl peak (4.32 ppm) of molecule H and the benzyl peak (4.38 ppm) of molecule I for 10 days.

For the kinetics in DMSO-*d*₆, molecule E (51.3 mg, 345 μmol) was dissolved in 1.49 mL of DMSO-*d*₆, from which 1 mL (34.4 mg, 232 μmol) was added to an NMR tube. After adding *N*-benzylmethylamine (56.3 mg, 464 μmol) and sealing the NMR tube with a rubber septum, the reaction was monitored by ¹H NMR spectroscopy for 5 days. The conversion was observed by comparing the benzyl hydrogens in *N*-benzylmethylamine at 3.63 ppm with the benzyl hydrogens in molecule H at 4.29 ppm and in molecule I at 4.36 ppm.

For the kinetics in C₆D₆, molecule E (49.4 mg, 333 μmol) was dissolved in 1.44 mL of C₆D₆ and 1 mL (34.4 mg, 232 μmol) was added to an NMR tube, followed by the addition of *N*-benzylmethylamine (56.3 mg, 464 μmol) and sealing the NMR tube with a rubber septum. The conversion from molecule E to molecules H and I was monitored by comparing the benzyl hydrogens in *N*-benzylmethylamine at 3.62 ppm with the benzyl hydrogens in molecule H at 4.34 ppm and in molecule I at 4.36 ppm.

Transamination Reaction of Molecule F and *N*-Benzylmethylamine (Table 1). *N*-Benzylmethylamine (153 mg, 1.26 mmol) was added to a solution of molecule F (75.8 mg, 631 μmol) in 1.26 mL

of CDCl₃. After connecting a condenser to the flask, the mixture was reacted at 50 °C, and the reaction was monitored by ¹H NMR spectroscopy every 24 h showing 9% conversion to J and 88% conversion to I after 72 h.

The same procedure was followed for the reaction of molecule F (88.3 mg, 735 μmol) and *N*-benzylmethylamine (178 mg, 1.47 mmol) in 1.47 mL of DMSO-*d*₆ showing 13% conversion to J and 77% conversion to I after 72 h. The reaction of molecule F (82.3 mg, 685 μmol) and *N*-benzylmethylamine (166 mg, 1.37 mmol) in 1.37 mL of C₆D₆ showed 17% conversion to J and 75% conversion to I after 72 h.

Molecule F (89.9 mg, 748 μmol) and *N*-benzylmethylamine (181 mg, 1.50 mmol) were reacted in 1.5 mL of benzene at 85 °C showing 3% conversion to J and 97% conversion to I after 24 h.

Stability of Molecule E in Organic Solvents. The stability of molecule E was studied in CDCl₃, DMSO-*d*₆/D₂O (10/1 v/v), and C₆D₆ following the same procedure. Molecule E (34.4 mg, 2.32 × 10^{−4} mol) was added to an NMR tube with 1 mL of solvent. Next, diethylene glycol dimethyl ether (31.2 mg, 2.32 × 10^{−4} mol) was added. The NMR tube was capped, and ¹H NMR spectra were periodically collected. The amount of decomposition was determined by the difference in ratio of the peaks due to molecule E and the ether measured on days 1 and 32.

Stability of Molecule L in D₂O. Molecule L (31.4 mg, 6.27 × 10^{−5} mol) was added to an NMR tube. A 1 mL solution in D₂O of *tert*-butanol (5.96 mg, 6.27 × 10^{−5} mol) and acetic acid (30.3 mg, 5.02 × 10^{−4} mol) was added to the NMR tube, and it was vigorously shaken. The first ¹H NMR spectrum after 271 s showed no evidence of molecule L and showed the secondary amine as the only degradation product.

The same procedure was followed except that no acetic acid was added (the neutral conditions). The decomposition of molecule L was followed by ¹H NMR spectroscopy. The same procedure was followed except that no acetic acid was added and KOH (9 mol equiv) was added (the basic conditions). The decomposition of molecule L was followed by ¹H NMR spectroscopy.

Formulation of Microparticles. Microparticles were fabricated from the polymer in entry 6 of Table 2 using a double emulsion-solvent evaporation method that is widely used for the encapsulation of hydrophilic drugs. The surfactant solution (1 wt % PVA in water, internal water phase or W₁) was added to the polymer solution (in dichloromethane, oil phase or O) under microtip probe sonication for 30 s (10 W energy output, Fisher Scientific sonic dismembrator Model 100) to form the first emulsion (W₁/O). This was then immediately added to the second PVA solution (in water, external water phase or W₂) and further sonicated at the same speed for another 30 s to form the second emulsion (W₁/O/W₂). These processes were carried out under an ice bath. The final emulsion was then added to aqueous PVA solution under magnetic agitation and stirred at room temperature and under atmospheric pressure until complete evaporation of dichloromethane. The microparticles were collected by centrifugation at 8500 rpm for 10 min (Fischer Scientific Accuspin 400), washed twice with water, and freeze-dried for 48 h (FreezeZone 4.5, Labconco). The FITC-dextran loaded microparticles were prepared in the same manner by dissolving FITC-dextran in the internal water phase used in making the primary emulsion.

Determination of Particle Size (Hydrodynamic Diameter) and Size Distribution. Particle size and particle size distribution of microparticles were analyzed at a concentration of approximately 1 mg particles/1 mL of deionized water. Appropriate dilution of the particle suspension is necessary in order to avoid multiscattering events. The measurements were carried out on microparticle suspensions using a Zetasizer Nano-ZS (Malvern Instruments). The particle size and size distribution by intensity were measured by dynamic light scattering (He–Ne laser with a fixed wavelength of 633 nm, 173° backscatter at 25 °C) in 10 mm diameter cells.

Measurement of Surface Charge. The zeta potential of microparticles was analyzed by dispersing the microparticles in deionized distilled water at a concentration of 1 mg/mL using folded capillary cells. Sample dilution is often necessary in order to eliminate particle interactions. Zeta potential is an indicator of the charge on the

surface of the microparticles. The surface charge measurements of the blank microparticles were performed using the electrophoretic laser scattering method (Laser Doppler Microelectrophoresis, He–Ne laser 633 nm at 25 °C).

Scanning Electron Microscopy (SEM). The shape and the surface morphology of the microparticles were studied using a scanning electron microscope. The particles were mounted on silicon wafers which were placed on aluminum specimen stubs using adhesive carbon tape. The mount was then coated by ion sputtering (K550 Emitech sputter coater, set at 10 mA for 2.5 min) with conductive gold and examined using a Hitachi Model S-4800 SEM, operated at 4 kV accelerating voltage.

Cell Culture. The cells were maintained in DMEM supplemented with 10 vol % FBS and gentamycin at a concentration 50 µg/mL in a humidified incubator (Sanyo Scientific Autoflow, IR direct heat CO₂ incubator) at 37 °C containing 95% air and 5% CO₂. The cells were plated and grown as a monolayer in 75 cm² polystyrene cell culture flasks (Corning Inc., Corning, NY) and subcultured (subcultivation ratio of 1:4) after 80–90% confluence was achieved. Cell lines were started from frozen stocks, and the medium was changed every 2–3 days. The passages used for the experiment were between 4 and 15.

Investigation of FITC-Dextran Loaded Microparticle Uptake by HEK-293 Cells Using Confocal Microscopy. To determine the qualitative *in vitro* intracellular uptake of microparticles, cells were plated at a density of 50 000 cells/well in a clear, flat-bottom, 8-chambered glass slide with cover (Lab-Tek, Nunc, NY) that were previously coated with 0.1 wt % poly(L-lysine). The cells were allowed to attach overnight, and the next day the cell culture medium was removed and the cells were treated with an aliquot of a suspension of FITC-dextran loaded microparticles in medium and further incubated at 37 °C for 24 h. The experiment was terminated by removing the particulate suspension and washing the cell monolayer two times with PBS in order to remove particles not internalized by the cells. The cells were then fixed with 4 vol % paraformaldehyde, followed by permeabilization of cells with 0.2 wt % Triton X-100 (Sigma, Sigma-Aldrich, St. Louis, MO). The cells were later treated with phalloidin and finally mounted with Vectashield, Hardset mounted medium with DAPI (H-1500, Vector Laboratories, Inc., Burlingame, CA). The cells were washed with PBS during every step in the process. Cellular uptake of FITC-dextran loaded microparticles and their intracellular distribution was visualized by confocal microscopy (Carl Zeiss LSM 710, 60× oil objective lens) by using DAPI, FITC, and phalloidin filters equipped with Zen 2009 imaging software.

Evaluation of the Cytotoxicity of Microparticles Incubated in HEK-293 Cells. The *in vitro* cytotoxicity of blank nanoparticles was examined by a colorimetric MTS assay. A stock suspension of microparticles was prepared by dispersing freeze-dried particles in an appropriate volume of cell culture medium. To obtain different test concentrations (1–1000 µg/mL), serial dilutions from the stock microparticle suspension were prepared with the medium. On the first day of the experiment, confluent cells were seeded in clear polystyrene, flat bottom, 96-well plates (Costar, Corning Inc., Corning, NY) at a density of 10 000 cells/well and allowed to attach overnight in the incubator. Next day, the cells were exposed to the polymer by replacing the culture medium with different dilutions of stock suspensions and further incubating for 24 h. On the last day of the experiment, the treatments were removed and fresh medium was added along with 20 µL of MTS reagent. The plate was incubated at 37 °C in a humidified, 5% CO₂ atmosphere for 4 h. To measure the amount of soluble formazan produced by the reduction of MTS reagent by viable cells, the plate was read by Spectramax 384 Plus (Softmax Pro, Molecular Devices, Sunnyvale, CA) at a wavelength of 490 nm. The absorbance readings were recorded and quantitated for the colorimetric assay and the cell viability was expressed by the following equation:

$$\text{cell viability(\%)} = \frac{[\text{absorbance intensity of cells treated with MP}]/[\text{absorbance intensity of cells without any treatment (control)}]}{\times 100}$$

The cytotoxic effect of different treatments was calculated as a percentage of cell growth with respect to the control. Values are expressed as mean ± SEM for each microparticle concentration (*n* = 6).

AUTHOR INFORMATION

Corresponding Author

*E-mail: ned-bowden@uiowa.edu; Tel: (319) 335-1198.

ACKNOWLEDGMENTS

N.B.B. gratefully thanks the NSF for generous funding (CHE-0848162). A.K.S. gratefully acknowledges support from the American Cancer Society (RSG-09-015-01-CDD), the National Cancer Institute at the National Institutes of Health (1R21CA13345-01/1R21CA128414-01A2/UI Mayo Clinic Lymphoma SPORE), and the Pharmaceutical Research and Manufacturers of America (PhRMA) Foundation. A.K.S. thanks the Core Microscopy Research Facility for use of imaging equipment.

REFERENCES

- (1) Chauvin, Y. *Angew. Chem., Int. Ed.* **2006**, *45*, 3741.
- (2) Schrock, R. R. *Angew. Chem., Int. Ed.* **2006**, *45*, 3748.
- (3) Grubbs, R. H. *Angew. Chem., Int. Ed.* **2006**, *45*, 3760.
- (4) Connon, S. J.; Blechert, S. *Angew. Chem., Int. Ed.* **2003**, *42*, 1900.
- (5) Fuerstner, A. *Angew. Chem., Int. Ed.* **2000**, *39*, 3012.
- (6) Garber, S. B.; Kingsbury, J. S.; Gray, B. L.; Hoveyda, A. H. *J. Am. Chem. Soc.* **2000**, *122*, 8168.
- (7) Grubbs, R. H.; Chang, S. *Tetrahedron* **1998**, *54*, 4413.
- (8) Schrock, R. R.; Murdzek, J. S.; Bazan, G. C.; Robbins, J.; DiMare, M.; O'Regan, M. *J. Am. Chem. Soc.* **1990**, *112*, 3875.
- (9) Schwab, P.; France, M. B.; Ziller, J. W.; Grubbs, R. H. *Angew. Chem., Int. Ed.* **1995**, *34*, 2039.
- (10) Schwab, P.; Grubbs, R. H.; Ziller, J. W. *J. Am. Chem. Soc.* **1996**, *118*, 100.
- (11) Trnka, T. M.; Grubbs, R. H. *Acc. Chem. Res.* **2001**, *34*, 18.
- (12) Wilkes, J. S.; Zaworotko, M. J. *J. Chem. Soc., Chem. Commun.* **1992**, 965.
- (13) Bielawski, C. W.; Grubbs, R. H. *Prog. Polym. Sci.* **2007**, *32*, 1.
- (14) Buchmeiser, M. R. *Chem. Rev.* **2000**, *100*, 1565.
- (15) Lynn, D. M.; Kanaoka, S.; Grubbs, R. H. *J. Am. Chem. Soc.* **1996**, *118*, 784.
- (16) Trnka, T. M.; Morgan, J. P.; Sanford, M. S.; Wilhelm, T. E.; Scholl, M.; Choi, T.-L.; Ding, S.; Day, M. W.; Grubbs, R. H. *J. Am. Chem. Soc.* **2003**, *125*, 2546.
- (17) Weskamp, T.; Kohl, F. J.; Hieringer, W.; Gleich, D.; Herrmann, W. A. *Angew. Chem., Int. Ed.* **1999**, *38*, 2416.
- (18) Weskamp, T.; Schattenmann, W. C.; Spiegler, M.; Herrmann, W. A. *Angew. Chem., Int. Ed.* **1998**, *37*, 2490.
- (19) Baughman, T. W.; Wagener, K. B. *Adv. Polym. Sci.* **2005**, *176*, 1.
- (20) Smith, D. W. Jr.; Wagener, K. B. *Macromolecules* **1993**, *26*, 1633.
- (21) Smith, J. A.; Brzezinska, K. R.; Valenti, D. J.; Wagener, K. B. *Macromolecules* **2000**, *33*, 3781.
- (22) Sworen, J. C.; Smith, J. A.; Berg, J. M.; Wagener, K. B. *J. Am. Chem. Soc.* **2004**, *126*, 11238.
- (23) Ayres, N. *Polym. Rev.* **2011**, *51*, 138.
- (24) Braunecker, W. A.; Matyjaszewski, K. *Prog. Polym. Sci.* **2007**, *32*, 93.
- (25) Matyjaszewski, K.; Xia, J. *Chem. Rev.* **2001**, *101*, 2921.
- (26) Leibfarth, F. A.; Kang, M.; Ham, M.; Kim, J.; Campos, L. M.; Gupta, N.; Moon, B.; Hawker, C. J. *Nature Chem.* **2010**, *2*, 207.

- (27) Leibfarth, F. A.; Schneider, Y.; Lynd, N. A.; Schultz, A.; Moon, B.; Kramer, E. J.; Bazan, G. C.; Hawker, C. J. *J. Am. Chem. Soc.* **2010**, *132*, 14706.
- (28) Harpp, D. N.; Gringras, M.; Aida, T.; Chan, T. H. *Synthesis* **1987**, *12*, 1122.
- (29) Huang, N.-Z.; Lakshmikantham, M. V.; Cava, M. P. *J. Org. Chem.* **1987**, *52*, 169.
- (30) Harpp, D. N.; Steliou, K.; Chan, T. H. *J. Am. Chem. Soc.* **1978**, *100*, 1222.
- (31) Losev, Y. P.; Paushkin, Y. M. *J. Appl. Polym. Sci.* **1992**, *45*, 1517.
- (32) Chen, C.-H.; Lin, J. T.; Yeh, M.-C. *P. Org. Lett.* **2006**, *8*, 2233.
- (33) Hou, J.; Park, M.-H.; Zhang, S.; Yao, Y.; Chen, L.-M.; Li, J.-H.; Yang, Y. *Macromolecules* **2008**, *41*, 6012.
- (34) Mishra, S. P.; Palai, A. K.; Srivastava, R.; Kamalasanan, M. N.; Patri, M. J. *Polym. Sci., Part A: Polym. Chem.* **2009**, *47*, 6514.
- (35) Wang, E.; Wang, M.; Wang, L.; Duan, C.; Zhang, J.; Cai, W.; He, C.; Wu, H.; Cao, Y. *Macromolecules* **2009**, *42*, 4410.
- (36) Woo, C. H.; Holcombe, T. W.; Unruh, D. A.; Sellinger, A.; Frechet, J. M. J. *Chem. Mater.* **2010**, *22*, 1673.
- (37) Bundgaard, E.; Krebs, F. C. *Macromolecules* **2006**, *39*, 2823.
- (38) Hennrich, G.; Sonnenschein, H.; Resch-Genger, U. *J. Am. Chem. Soc.* **1999**, *121*, 5073.
- (39) Karikomi, M.; Kitamura, C.; Tanaka, S.; Yamashita, Y. *J. Am. Chem. Soc.* **1995**, *117*, 6791.
- (40) Thomas, K. R. J.; Lin, J. T.; Velusamy, M.; Tao, Y.-T.; Chuen, C.-H. *Adv. Funct. Mater.* **2004**, *14*, 83.
- (41) Drake, C. S.; Aissaoui, A.; Agyros, O.; Serginson, J. M.; Monnery, B. D.; Thanou, M.; Steinke, J. H. G.; Miller, A. D. *Mol. Pharmaceutics* **2010**, *7*, 2040.
- (42) Ou, M.; Xu, R.; Sun, S. H.; Bull, D. A.; Kim, S. W. *Biomaterials* **2009**, *30*, 5804.
- (43) Brochon, C.; Mingotaud, A. F.; Schappacher, M.; Soum, A. *Macromolecules* **2007**, *40*, 3547.
- (44) Chojnowski, J.; Cypriak, M.; Fortuniak, W.; Scibiorek, M.; Rozga-Wijas, K. *Macromolecules* **2003**, *36*, 3890.
- (45) Dworak, D. P.; Soucek, M. D. *Macromolecules* **2004**, *37*, 9402.
- (46) Pibre, G.; Chaumont, P.; Fleury, E.; Cassagnau, P. *Polymer* **2008**, *49*, 234.
- (47) Ragheb, R. T.; Riffle, J. S. *Polymer* **2008**, *49*, 5397.
- (48) Allcock, H. R.; de, D. C. R.; Prange, R.; Laredo, W. R. *Macromolecules* **2001**, *34*, 2757.
- (49) Chaplin, A. B.; Harrison, J. A.; Dyson, P. J. *Inorg. Chem.* **2005**, *44*, 8407.
- (50) Luten, J.; van, N. C. F.; De, S. S. C.; Hennink, W. E. J. *Controlled Release* **2008**, *126*, 97.
- (51) Gates, D. P. *Annu. Rep. Prog. Chem., Sect. A: Inorg. Chem.* **2005**, *101*, 452.
- (52) Gates, D. P. *Ann. Rep. Prog. Chem., Sect. A: Inorg. Chem.* **2009**, *105*, 397.
- (53) Rivard, E. *Ann. Rep. Prog. Chem., Sect. A: Inorg. Chem.* **2010**, *106*, 391.
- (54) Rivard, E. *Ann. Rep. Prog. Chem., Sect. A: Inorg. Chem.* **2011**, *107*, 319.
- (55) Banister, A. J.; Gorrell, I. B. *Adv. Mater.* **1998**, *10*, 1415.
- (56) Kanazawa, H.; Stejny, J.; Keller, A. J. *Mater. Sci.* **1990**, *25*, 3838.
- (57) Kurmaev, E. Z.; Poteryaev, A. I.; Anisimov, V. I.; Karla, I.; Moewes, A.; Schneider, B.; Neumann, M.; Ederer, D. L.; Lyubovskaya, R. N. *Physica C* **1999**, *321*, 191.
- (58) Larsson, S. *Faraday Discuss.* **2006**, *131*, 69.
- (59) Rawson, J. M.; Longridge, J. J. *Chem. Soc. Rev.* **1997**, *26*, 53.
- (60) Armitage, D. A.; Clark, M. J.; White, A. M. *J. Chem. Soc. C* **1971**, *18*, 3141.
- (61) Kapanda, C. N.; Muccioli, G. G.; Labar, G.; Poupaert, J. H.; Lambert, D. M. *J. Med. Chem.* **2009**, *52*, 7310.
- (62) Sun, R.; Zhang, Y.; Chen, L.; Li, Y.; Li, Q.; Song, H.; Huang, R.; Bi, F.; Wang, Q. *J. Agric. Food Chem.* **2009**, *57*, 3661.
- (63) Zhao, Q.; Ou, X.; Huang, Z.; Bi, F.; Huang, R.; Wang, Q. *J. Agric. Food Chem.* **2008**, *56*, 10799.
- (64) Odian, G. G. *Principles of Polymerization*; Wiley: New York, 1991.
- (65) Anderson, D. G.; Nurdick, J. A.; Langer, R. *Science* **2004**, *305*, 1923.
- (66) Cao, J.; Langer, R. *Nano Lett.* **2010**, *10*, 3223.
- (67) Fox, M. E.; Szoka, F. C.; Frechet, J. M. J. *Acc. Chem. Res.* **2009**, *42*, 1141.
- (68) Le Garrec, D.; Ranger, M.; Leroux, J.-C. *Am. J. Drug Delivery* **2004**, *2*, 15.
- (69) Thierry, B. *Curr. Drug Delivery* **2009**, *6*, 391.
- (70) Agarwal, A.; MacKey, M. A.; El-Sayed, M. A.; Bellamkonda, R. V. *ACS Nano* **2011**, *5*, 4919.
- (71) Hirsjarvi, S.; Passirani, C.; Benoit, J.-P. *Curr. Drug Discovery Technol.* **2011**, *8*, 188.
- (72) Malam, Y.; Lim, E. J.; Seifalian, A. M. *Curr. Med. Chem.* **2011**, *18*, 1067.
- (73) Wang, M.; Thanou, M. *Pharmacol. Res.* **2010**, *62*, 90.
- (74) Arima, H.; Motoyama, K. *Sensors* **2009**, *9*, 6346.
- (75) Meng, H. X.; Xia, T.; Zhao, Y.-L.; Tamaoi, F.; Stoddart, J. F.; Zink, J. I.; Nel, A. E. *J. Am. Chem. Soc.* **2010**, *132*, 12690.
- (76) Mohanad, M.; Dixon, A. S.; Lim, C. S. *Ther. Delivery* **2010**, *1*, 169.
- (77) Oh, K. T.; Yin, H.; Lee, E. S.; Bae, Y. H. *J. Mater. Chem.* **2007**, *17*, 3987.
- (78) Kohane, D. S.; Langer, R. *Chem. Sci.* **2010**, *1*, 441.
- (79) Kroeze, R. J.; Helder, M. N.; Govaert, L. E.; Smit, T. H. *Materials* **2009**, *2*, 833.
- (80) Banister, A. J.; Bricklebank, N.; Clegg, W.; Elsegood, M. R. J.; Gregory, C. I.; Lavender, I.; Rawson, J. M.; Tanner, B. K. *J. Chem. Soc., Chem. Commun.* **1995**, 679.
- (81) Cooper, D. L.; Cunningham, T. P.; Gerratt, J.; Karadakov, P. B.; Raimondi, M. J. *Am. Chem. Soc.* **1994**, *116*, 4414.
- (82) Derbesy, G.; Harpp, D. N. *Tetrahedron Lett.* **1994**, *35*, 5381.
- (83) Harpp, D. N.; Steliou, K.; Chan, T. H. *J. Am. Chem. Soc.* **1978**, *100*, 1222.
- (84) Kuhn, N.; Bohnen, H.; Fahl, J.; Blaaser, D.; Boese, R. *Chem. Ber.* **1996**, *129*, 1579.
- (85) Weinstock, L. M.; Davis, P.; Handelsman, B.; Tull, R. J. *J. Org. Chem.* **1967**, *32*, 2823.
- (86) Refvik, M. D.; Schwan, A. L. *J. Org. Chem.* **1996**, *61*, 4232.
- (87) Bowman, W. R.; Clark, D. N.; Marmon, R. J. *Tetrahedron Lett.* **1991**, *32*, 6441.
- (88) Anslyn, E. V.; Dougherty, D. A. *Modern Physical Organic Chemistry*; University Science Books: Sausalito, CA, 2006.
- (89) Grainger, R. S.; Patel, B.; Kariuki, B. M.; Male, L.; Spencer, N. J. *Am. Chem. Soc.* **2011**, *133*, 5843.
- (90) Schenk, P. W.; Steudel, R. *Inorganic Sulfur Chemistry*; Elsevier: Amsterdam, 1968.
- (91) Wolfenden, R.; Yuan, Y. *J. Am. Chem. Soc.* **2011**, *133*, 13821.
- (92) Mosmann, T. J. *Immunol. Methods* **1983**, *65*, 55.
- (93) Cory, A. H.; Owen, T. C.; Barltrop, J. A.; Cory, J. G. *Cancer Commun.* **1991**, *3*, 207.
- (94) Harpp, D. N.; Gringras, M.; Aida, T.; Chan, T. H. *Synthesis* **1987**, *12*, 1122.
- (95) Kapanda, C. N.; Muccioli, G. G.; Labar, G.; Poupaert, J. H.; Lambert, D. M. *J. Med. Chem.* **2009**, *52*, 7310.
- (96) Sun, R.; Zhang, Y.; Chen, L.; Li, Y.; Li, Q.; Song, H.; Huang, R.; Bi, F.; Wang, Q. *J. Agric. Food Chem.* **2009**, *57*, 3661.

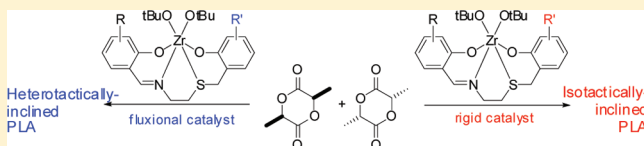
Ring-Opening Polymerization of Lactide with Zr Complexes of {ONSO} Ligands: From Heterotactically Inclined to Isotactically Inclined Poly(lactic acid)

Ayellet Stopper,[†] Jun Okuda,[‡] and Moshe Kol^{†,*}

[†]School of Chemistry, Raymond and Beverly Sackler Faculty of Exact Sciences, Tel Aviv University, Ramat Aviv, Tel Aviv 69978, Israel

[‡]Institute of Inorganic Chemistry, RWTH Aachen University, Landoltweg 1, D-52056 Aachen, Germany

ABSTRACT: Six members of a new family of {ONSO}-type ligands—the tetradentate-dianionic imine-thiobis(phenolate) ligands—were prepared by a two-step synthesis. Their [{ONSO}Zr(O^tBu)₂] complexes formed as single diastereomers with different degrees of fluxionality that depended on the substitution pattern of the two phenolate rings. The complexes were active in polymerization of L-lactide and *rac*-lactide. The tacticity of the poly(lactic acid) prepared from *rac*-lactide changed gradually from heterotactically inclined through atactic to isotactically inclined. The most flexible complex and the most rigid complex gave the highest degrees of heterotacticity and isotacticity, respectively.



INTRODUCTION

Poly(lactic acid) (PLA) is a biodegradable polyester derived from annually renewable resources, which finds applications as a commodity plastic and in biomedicine.¹ The physical properties and degradation tendency of PLA depend strongly on the microstructure of the polymer chains, and, in particular, on their stereochemistry.² The most common method of producing PLA is the ring-opening polymerization (ROP) of lactide, the cyclic dimer of lactic acid.³ Lactide includes two stereogenic centers, which are not altered in the polymerization process by catalysts operating by the coordination–insertion mechanism. The tacticity of the obtained PLA thus depends on the constitution of the monomer and on the selectivity of the catalyst.^{2a,4} Polymerization of the homochiral lactides, L-lactide and D-lactide yields the isotactic enantiomeric polymers poly(L-lactic acid), PLLA, and poly(D-lactic acid), PDLA, respectively, having a melting point of 180 °C, irrespective of the catalyst employed. For *rac*-lactide, the character of the catalyst plays a crucial role. Non selective catalysts, like the industrially employed tin octoate, give rise to atactic PLA, whereas selective catalysts may favor consecutive insertions of either the same or the opposite lactide enantiomer, with formation of isotactic or heterotactic PLA, respectively. Isolelective catalysts are relatively scarce and may operate by either the chain-end or enantiomorph-site control mechanism. Most of the isolelective catalysts reported to date are based on aluminum complexes, which feature a low activity.^{5,6} A racemic mixture of the isotactic PLLA and PDLA crystallizes as a stereocomplex whose melting point is 50 °C above that of the homochiral polymers, so an isolelective catalyst that can yield a stereocomplex PLA or its stereoblock analogues from *rac*-lactide is highly desirable.⁷ Heteroselective catalysts are more abundant.⁸ Suitable such catalysts should be devoid of permanent chirality that may favor a specific enantiomer.

Indeed, two types of heteroselective catalysts that have emerged recently are the rigid C_s-symmetric catalysts operating by the chain-end control mechanism⁹ and the fluxional-chiral catalysts that may operate by the dynamic enantiomorph-site control mechanism and are proposed to invert chirality between consecutive insertions of enantiomeric lactide monomers.^{10,11} Herein, we introduce semirigid catalysts for lactide polymerization based on zirconium complexes of newly designed imine–thiobis(phenolate) ligands.¹² We demonstrate that by stepwise adjustment of the ligand character, the tacticity of the PLA produced from *rac*-lactide may be gradually shifted from heterotactically inclined to isotactically inclined.

RESULTS AND DISCUSSION

Ligand Design. Since fluxional-chiral catalysts often induce heterotacticity and rigid-chiral catalysts possibly induce isotacticity, we were intrigued by the possibility of merging these two facets in the form of semirigid complexes, i.e., complexes containing a rigid segment and a flexible segment. A possible way of achieving semirigidity is by designing a sequential tetradentate dianionic ligand that features an internal rigid anchor and an internal flexible anchor. In addition, it is preferred that the complex fluctuation would interconvert between enantiomers rather than diastereomers (so as to avoid a possible bias toward a specific lactide enantiomer by a given catalyst molecule). Therefore, upon binding to a metal, the rigid donor should be nonstereogenic and the flexible donor should be stereogenic. Suitable candidates for these distinct roles are the imine donor that typically orients its neighboring

Received: October 18, 2011

Revised: December 12, 2011

Published: January 6, 2012

donors in a *meridional* arrangement,¹³ and the thio donor that typically orients its neighboring donors in a *facial* arrangement,¹⁴ respectively. The peripheral anionic arms were chosen to be of the phenolate type, because their steric and electronic

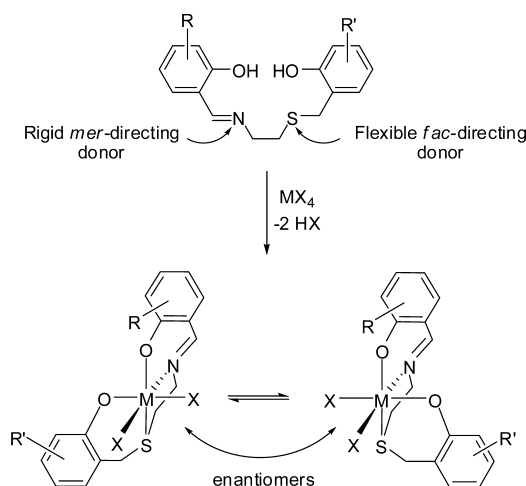


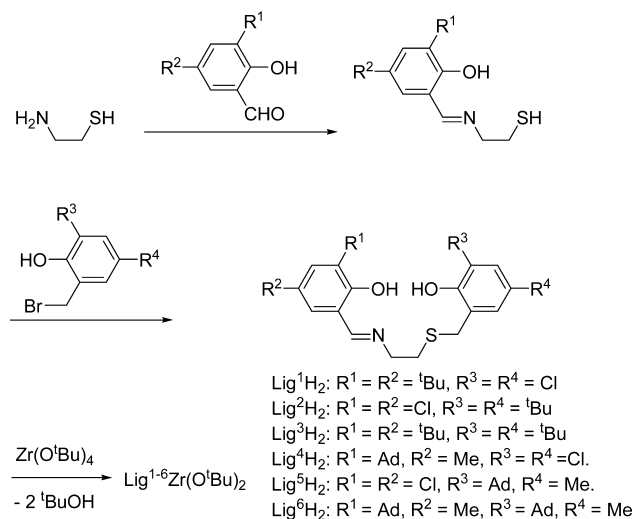
Figure 1. {ONSO} ligand design and proposed structure of semirigid octahedral complexes.

character may be accurately modified by substitutions (Figure 1).

Ligands and Complexes Synthesis and Characterization. Six imine-thiobis(phenolate) ligand precursors were targeted for this exploratory work. They include different combinations of bulky alkyl groups and electron withdrawing chloro groups in the *ortho* and *para* positions of the two phenol rings. As one of the phenol rings is bound to the flexible donor and the other is bound to the rigid donor, the placement of the substituents may play different roles on the degree of fluxionality of the corresponding complexes and on their activity in lactide polymerization. To investigate this possibility, the targeted ligands included the isomeric pairs Lig¹H₂/Lig²H₂ and Lig⁴H₂/Lig⁵H₂ having inversely linked substituted phenols. The ligands were prepared in moderate yields by a two step synthesis starting from 2-aminoethanethiol: condensation of the amine functionality with the appropriate salicylaldehyde,¹⁵ followed by nucleophilic reaction of the thiol functionality with the given bromomethyl phenol. The six {ONSO}H₂ ligand precursors were reacted with 1 equiv of Zr(O^tBu)₄ yielding the corresponding [{ONSO}Zr(O^tBu)₂] complexes in high to quantitative yields, as described in Scheme 1.

¹H NMR characterization of the complexes revealed that they had all formed as single diastereomers, and supported their mononuclear structures. As expected, the complexes were fluxional. Having a C₁-symmetry on the slow-exchange regime, and an average C_s-symmetry of the fast-exchange regime, the geometry of these complexes is consistent with the proposed *meridional* (imine)/*facial* (thio) wrapping of the {ONSO} ligand around the octahedral metal center (Figure 1). Variable temperature NMR experiments revealed that the barriers for interconversion ranged from ΔG^\ddagger of 13.3 to >19.0 kcal/mol. Bulkier substituents led to higher rigidity, especially if they were located in the *ortho* position of the flexible-segment phenol. For example, Lig³Zr(O^tBu)₂ having two *tert*-butyl groups on both phenol arms exhibited a ΔG^\ddagger of 17.1 kcal/mol. Replacing the two *tert*-butyl groups on the rigid-side phenol with chloro

Scheme 1. Synthesis of the {ONSO} Ligand Precursors and their Zirconium Complexes



groups led to a mild decrease of the interconversion barrier to ΔG^\ddagger = 15.6 kcal/mol (Lig²Zr(O^tBu)₂), while the analogous replacement on the flexible-side phenol led to a more pronounced decrease of the interconversion barrier to ΔG^\ddagger = 13.3 kcal/mol (Lig¹Zr(O^tBu)₂). The same trend was found for the complexes of the three other ligands, Lig^{4–6}Zr(O^tBu)₂ having interconversion barriers of ΔG^\ddagger = 15.5, 17.7, and >19.0 kcal/mol, respectively, with the highest barrier found for the most crowded complex, containing *ortho*-adamantyl groups on both phenolate rings (Figure 2).

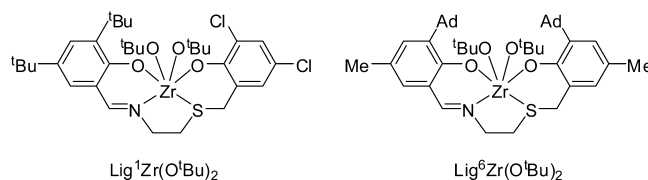


Figure 2. The most fluxional complex (Lig¹Zr(O^tBu)₂; ΔG^\ddagger = 13.3 kcal/mol) and the most rigid complex (Lig⁶Zr(O^tBu)₂; ΔG^\ddagger > 19.0 kcal/mol) described in this work.

Lactide Polymerization. The performance of these [{ONSO}Zr(O^tBu)₂] complexes in polymerization of L-lactide and *rac*-lactide was investigated. The complexes exhibited high catalytic activities in the polymerization of both monomers at 140 °C. As may be appreciated from Tables 1 and 2, high conversions of monomer to polymer were usually obtained within a few minutes, and in certain cases almost complete conversions were attained (entries 1 and 3 in Tables 1 and 2). The complex of the bulkiest {ONSO} ligand—Lig⁶Zr(O^tBu)₂ seemed to be somewhat slower requiring longer times to reach high conversions of both L-lactide and *rac*-lactide. For L-lactide, the molecular weight distributions were relatively narrow (PDI as low as 1.10) which seems to support a living polymerization, however, in several polymerizations, the molecular weights were higher than calculated based on a single growing polymer chain for each catalyst molecule. For example, Lig¹Zr(O^tBu)₂ led to PLLA with M_n = 72 600 g mol^{−1} whereas the calculated molecular weight for 87% conversion of 300 equiv of L-lactide is $M_{n,calc}$ = 37 500 g mol^{−1}. This is consistent with partial activation of the catalyst. Slightly broader molecular weight

Table 1. Polymerization of L-Lactide at 140 °C

entry	initiator ^a	L-lactide (g)	time (min)	PLA obtained (g)	convn	M_n^b (g mol ⁻¹)	$M_{n,calc}^c$ (g mol ⁻¹)	PDI
1	Lig ¹ Zr(O- <i>tert</i> -Bu) ₂	0.62	15	0.54	0.87	72 600	37 500	1.10
2	Lig ² Zr(O- <i>tert</i> -Bu) ₂	0.58	14	0.18	0.31	22 300	13 400	1.12
3	Lig ³ Zr(O- <i>tert</i> -Bu) ₂	0.60	10	0.55	0.92	49 200	39 700	1.39
4	Lig ⁴ Zr(O- <i>tert</i> -Bu) ₂	0.58	13	0.41	0.71	20 300	30 600	1.16
5	Lig ⁵ Zr(O- <i>tert</i> -Bu) ₂	0.58	6	0.40	0.69	23 000	30 000	1.47
6	Lig ⁶ Zr(O- <i>tert</i> -Bu) ₂	0.49	54	0.28	0.57	29 100	24 500	1.17

^a10 mg of catalyst were employed. ^bCorrection parameter $0.58 \times M_n$ polystyrene standards. ^ccalculated from $144.13 \times (LA/I) \times$ conversion of monomer.

Table 2. Polymerization of *rac*-Lactide at 140 °C

entry	initiator ^a	<i>rac</i> -lactide (g)	time (min)	PLA obtained (g)	convn	M_n^b (g mol ⁻¹)	$M_{n,calc}^c$ (g mol ⁻¹)	PDI	P_r/P_m^d
1	Lig ¹ Zr(O- <i>tert</i> -Bu) ₂	0.62	6	0.58	0.92	16 300	39 500	1.55	0.63/0.37
2	Lig ² Zr(O- <i>tert</i> -Bu) ₂	0.61	5	0.46	0.75	17 700	32 500	1.38	0.58/0.42
3	Lig ³ Zr(O- <i>tert</i> -Bu) ₂	0.63	7	0.61	0.97	20 300	42 000	1.57	0.50/0.50
4	Lig ⁴ Zr(O- <i>tert</i> -Bu) ₂	0.58	8	0.42	0.72	9500	31 000	1.44	0.50/0.50
5	Lig ⁵ Zr(O- <i>tert</i> -Bu) ₂	0.58	6	0.41	0.70	7000	30 000	1.44	0.50/0.50
6	Lig ⁶ Zr(O- <i>tert</i> -Bu) ₂	0.52	18	0.32	0.61	20 300	26 500	1.34	0.55/0.45

^a10 mg of catalyst were employed. ^bCorrection parameter $0.58 \times M_n$ polystyrene standards. ^cCalculated from $144.13 \times (LA/I) \times$ conversion of monomer. ^d P_r and P_m are the probability for heterotactic and isotactic enchainment calculated from homonuclear decoupled ¹H NMR spectrum.

Table 3. Polymerization of *rac*-Lactide at 70 °C in Toluene

entry	initiator ^a	<i>rac</i> -lactide (g)	PLA obtained (g)	convn	M_n^b (g mol ⁻¹)	$M_{n,calc}^c$ (g mol ⁻¹)	PDI	P_r/P_m^d
1	Lig ¹ Zr(O- <i>tert</i> -Bu) ₂	0.64	0.63	0.98	8500	42 000	1.45	0.72/0.28
2	Lig ² Zr(O- <i>tert</i> -Bu) ₂	0.59	0.51	0.87	14 700	37 500	1.50	0.65/0.35
3	Lig ³ Zr(O- <i>tert</i> -Bu) ₂	0.62	0.50	0.81	21 300	35 000	1.70	0.50/0.50
4	Lig ⁴ Zr(O- <i>tert</i> -Bu) ₂	0.57	0.40	0.70	11 200	30 000	1.42	0.50/0.50
5	Lig ⁵ Zr(O- <i>tert</i> -Bu) ₂	0.59	0.44	0.75	8700	32 500	1.56	0.38/0.62
6	Lig ⁶ Zr(O- <i>tert</i> -Bu) ₂	0.56	0.09	0.18	18 000	8000	1.17	0.33/0.67

^a10 mg of catalyst and 5 mL of toluene were employed. Polymerization time was 20 h. ^bCorrection parameter $0.58 \times M_n$ polystyrene standards. ^cCalculated from $144.13 \times (LA/I) \times$ conversion of monomer. ^d P_r and P_m are the probability for heterotactic and isotactic enchainment calculated from homonuclear decoupled ¹H NMR spectrum.

distributions and lower molecular weights were found for polymerizations of *rac*-lactide with these catalysts at 140 °C, and the molecular weights of the PLA did not exceed the calculated values (Table 2). The solution polymerizations of *rac*-lactide were pursued for 20 h (Table 3). Most catalysts, except for Lig⁶Zr(O^{*t*}Bu)₂, exhibited high conversions after that period. The molecular weights and molecular weight distributions were generally in line with the values obtained for the polymerizations run in the melt. The polymerization of *rac*-lactide versus time by Lig²Zr(O^{*t*}Bu)₂ in toluene-*d*₈ at 90 °C was monitored by ¹H NMR spectroscopy. Following an induction period of a few minutes (that may be caused by catalyst activation as well as monomer dissolution), the polymerization was found to be first order with respect to lactide up to a conversion of 88% (8 h), as evident from a linear relationship of $\ln([lactide]_{t=0}/[lactide]_t)$ versus time (Figure 3).

We found that the microstructure of the PLA obtained in the polymerization of *rac*-lactide could be gradually shifted by variation of the phenolate substituents. Significantly, the character of the substituents on the flexible segment phenol played a major role, and the character of the substituents on the rigid segment phenol played a minor role, in parallel to their effects on the fluxionality of the complexes. This phenomenon, clearly observable in the homodecoupled ¹H NMR spectra of the PLA was more apparent for the solution polymerizations run at 70 °C. The most flexible complex—Lig¹Zr(O^{*t*}Bu)₂—which includes chloro substituents on the flexible segment

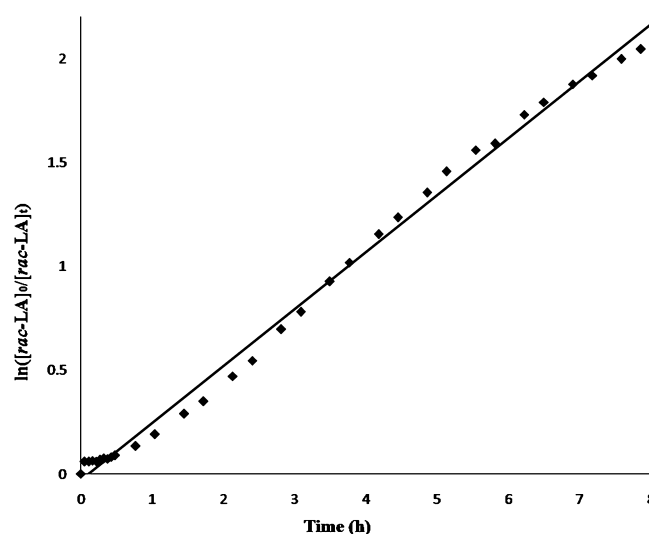


Figure 3. Semilogarithmic plot of *rac*-LA conversion versus time employing Lig²Zr(O^{*t*}Bu)₂ in toluene-*d*₈ at 90 °C. $[rac-LA]_{t=0} = 0.34$ M. $[rac-LA]_{t=0} : [Zr] = 80$. $r^2 = 0.994$.

phenol and *tert*-butyl substituents on the rigid segment phenol led to PLA having the highest degree of heterotacticity, with $P_r = 0.72$ at 70 °C. The degree of heterotacticity was diminished to $P_r = 0.63$ at 140 °C. Lig⁴Zr(O^{*t*}Bu)₂, the analogous complex

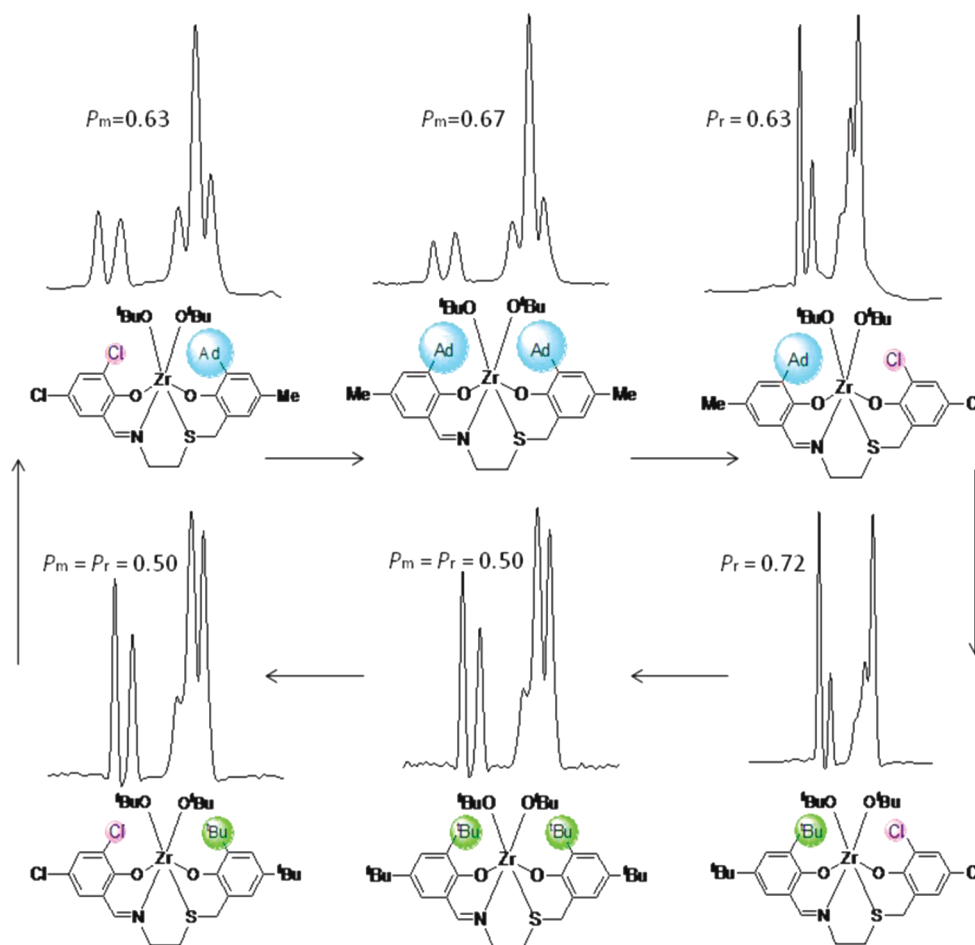


Figure 4. Homo-decoupled ^1H NMR of the polymer samples prepared from catalysts $\text{Lig}^{1-6}\text{Zr}(\text{O}^t\text{Bu})_2$ at 70°C in toluene.

which includes chloro substituents on the flexible segment phenol and an *o*-adamantyl substituent on the rigid segment phenol led to PLA with a slightly lower heterotacticity of $P_r = 0.65$ at 70°C and $P_r = 0.58$ at 140°C . $\text{Lig}^2\text{Zr}(\text{O}^t\text{Bu})_2$ and $\text{Lig}^3\text{Zr}(\text{O}^t\text{Bu})_2$, the two complexes featuring *tert*-butyl groups on the flexible segment phenol, yielded atactic PLA at both 70°C and at 140°C . Most unusually, $\text{Lig}^5\text{Zr}(\text{O}^t\text{Bu})_2$ and $\text{Lig}^6\text{Zr}(\text{O}^t\text{Bu})_2$, the two complexes featuring the bulky 1-adamantyl *ortho*-substituent on the flexible segment phenol led to clear isoselective polymerization at 70°C , which was more apparent for the more rigid of the two— $\text{Lig}^6\text{Zr}(\text{O}^t\text{Bu})_2$ that yielded PLA with $P_m = 0.67$. The isoselectivity was reduced for the two complexes at 140°C . The transition between tacticity types can be clearly appreciated in the homodecoupled ^1H NMR spectra of the corresponding polymers in Figure 4. Notably, reverse tacticity induction could be attained by merely inverting the substitution patterns on the two different phenol arms, as apparent for the isomer pair $\text{Lig}^4\text{Zr}(\text{O}^t\text{Bu})_2$ ($P_r = 0.63$) and $\text{Lig}^5\text{Zr}(\text{O}^t\text{Bu})_2$ ($P_m = 0.63$). To our knowledge, the only precedence for reversal of tacticity of PLA in *rac*-lactide polymerization upon a change of the substitution pattern of a given ligand bound to a given metal involved Salan and related ligands bound to aluminum.¹⁶ While the tacticities reported herein are not exceptionally high, the ability to manipulate them by ligand modifications, and the relatively high catalytic activities indicate that such design motifs may be important for future stereoselective catalysts.

CONCLUSIONS

In summary, zirconium complexes of tetradentate ligands that combine a rigid segment and a flexible segment were described. These tailor-made complexes exhibited broad ranges of steric congestion on each of the different phenol arms that was manifested in their degree of fluxionality. Notably, the substitution pattern on the phenolate rings was shown to play equivalent roles in the degree of fluxionality of the complexes and in their tendencies to insert the same or the opposite lactide enantiomer, i.e., their tendency to form isotactic or heterotactic PLA from *rac*-lactide. It still needs to be established whether the reversal of stereoselectivity is a direct consequence of the change of ligand substitution pattern, or results from the change of complex fluxionality. Current efforts in our groups include the development of rigid analogues of the above systems aiming at catalysts of higher isoselectivity based on the findings introduced herein.

EXPERIMENTAL SECTION

General Information. All reactions with air- and/or water sensitive compounds were carried out under dry nitrogen atmosphere in a glovebox. Ether was purified by distillation under dry argon atmosphere from purple Na/benzophenone solution. Pentane was washed with $\text{HNO}_3/\text{H}_2\text{SO}_4$ prior to distillation from Na/benzophenone/tetraglyme. Toluene was refluxed over Na and distilled. 3,5-Dichloro-2-hydroxybenzaldehyde, 3,5-di-*tert*-butyl-2-hydroxybenzaldehyde, 2-aminoethanethiol, triethylamine, and $\text{Zr}(\text{tert}-\text{butoxide})_4$ were purchased from Aldrich and used as received. D-Lactide and L-lactide were obtained by Purac and used as received, *rac*-lactide was prepared

by mixing equal molar amounts of L-lactide and D-lactide and crystallizing from toluene. 3-Adamantyl-2-hydroxy-5-methylbenzaldehyde,¹⁷ 2-(bromomethyl)-4,6-dichlorophenol,¹⁸ 2-(bromomethyl)-4,6-di-*tert*-butylphenol,¹⁸ and 2-(bromomethyl)-4-methyl-6-adamantylphenol¹⁹ were synthesized according to published procedures.

All NMR data were recorded on a Bruker Avance-400 spectrometer. C₆D₆ (impurities in benzene-*d*₆ at δ 7.15, and ¹³C chemical shift of benzene at δ 128.70 were used as reference) and C₇D₈ (impurities in toluene-*d*₈ at δ 2.09, 6.98, 7.00, 7.09) were used as NMR solvents for the metal complexes. CDCl₃ was used as NMR solvent for the PLA samples (chemical shift of TMS at δ 0.00 as reference). Elemental analyses were performed in the microanalytical laboratory at the Hebrew University of Jerusalem. PLA molecular weights were determined by gel permeation chromatography (GPC) using TSKgel GMHHR-M and TSKgel G 3000 HHR columns set on a Jasco instrument equipped with a refractive index detector. Molecular weight determination was carried out relative to polystyrene standards using THF (high-performance liquid chromatography grade, distilled and filtered under vacuum prior to use) as the eluting solvent.

Synthesis of 2-(Mercaptoethylimino)methyl-4,6-di-*tert*-butylphenol. 2-Aminoethanethiol (0.88 g, 11.4 mmol) was added to a solution of 3,5-di-*tert*-butyl-2-hydroxybenzaldehyde (2.68 g, 11.4 mmol) in benzene and refluxed for 2 h. The solvent was evaporated yielding a yellow solid (3.14 g, 93%). MS(APPI): calcd for C₁₇H₂₇NOS, 293.5; found, 294.1.

Synthesis of Lig¹H₂. A solution of 2-(bromomethyl)-4,6-dichlorophenol (1.40 g, 5.5 mmol) in THF (20 mL) was added dropwise to a solution of 2-(mercaptoethylimino)methyl-4,6-di-*tert*-butylphenol (1.61 g, 5.5 mmol) and triethylamine (0.75 mL) in THF (20 mL) and stirred for 2 h. The solid that had formed was filtered out, the solvent was removed under vacuum. The crude product was purified by flash chromatography over Silica gel 60 with a mixture of petroleum ether/dichloromethane in increasing polarity as eluent. The pure product was obtained as a yellow solid in a final yield of 40%. ¹H NMR (400 MHz, CDCl₃): δ 8.32 (s, 1H, NCH), 7.39 (d, 1H, *J* = 2.4 Hz, ArH), 7.23 (d, 1H, *J* = 2.4 Hz, ArH), 7.15 (d, 1H, *J* = 2.4 Hz, ArH), 7.09 (d, 1H, *J* = 2.4 Hz, ArH), 3.76 (s, 2H, ArCH₂S), 3.74 (t, 2H, *J* = 6.7 Hz, CH₂), 2.80 (t, 2H, *J* = 6.7 Hz, CH₂), 1.44 (s, 9H, C(CH₃)₃), 1.31 (s, 9H, C(CH₃)₃). ¹³C NMR (100.66 MHz, CDCl₃): δ 167.3 (CN), 158.1 (C), 148.6 (C), 140.2 (C), 136.8 (C), 129.1 (CH), 127.7 (CH), 127.3 (C), 127.2 (CH), 126.1 (CH), 125.3 (C), 121.1 (C), 117.7 (C), 59.2 (CH₂), 35.1 (C), 34.2 (C), 32.6 (CH₂), 31.5 (CH₃), 31.3 (CH₂), 29.5 (CH₃). MS(APPI): calcd for C₃₂H₄₉NO₂S, 511.8; found, 534.3 (MNa⁺). Anal. Calcd for C₂₄H₃₁Cl₂NO₂S: C, 61.53; H, 6.67; N, 2.99. Found: C, 61.95; H, 6.65; N, 2.82.

Synthesis of 2-(Mercaptoethylimino)methyl-4-methyl-6-adamantylphenol. 2-Aminoethanethiol (0.30 g, 3.88 mmol) was added to a solution of 3-adamantyl-2-hydroxy-5-methylbenzaldehyde (1.05 g, 3.88 mmol) in benzene and refluxed for 2 h. The solvent was removed under reduced pressure yielding a yellow solid (0.91 g, 71%). MS(APPI): calcd for C₂₀H₂₇NOS, 329.5; found, 330.1.

Synthesis of Lig²H₂. A solution of 2-(bromomethyl)-4,6-dichlorophenol (0.60 g, 2.3 mmol) in THF (20 mL) was added dropwise to a solution of 2-(mercaptoethylimino)methyl-4-methyl-6-adamantylphenol (0.76 g, 2.3 mmol) and triethylamine (0.32 mL) in THF (20 mL) and stirred for 2 h. The reaction mixture was worked up as described above for Lig¹H₂ giving Lig²H₂ in a final yield of 50%. ¹H NMR (400 MHz, CDCl₃): δ 8.28 (s, 1H, NCH), 7.25 (d, 1H, *J* = 2.3 Hz, ArH), 7.16 (d, 1H, *J* = 2.4 Hz, ArH), 7.08 (d, 1H, *J* = 1.9 Hz, ArH), 6.90 (d, 1H, *J* = 3.3 Hz, ArH), 3.75 (s, 2H, ArCH₂S), 3.75 (t, 2H, *J* = 8.3 Hz, CH₂), 2.80 (t, 2H, *J* = 6.7 Hz, CH₂), 2.28 (s, 3H, ArCH₃), 2.16 (bs, 6H, adamantyl), 2.07 (bs, 3H, adamantyl), 1.78 (m, 6H, adamantyl). ¹³C NMR (100.66 MHz, CDCl₃): δ 167.7 (CN), 159.1 (C), 149.3 (C), 138.2 (C), 131.5 (CH), 130.3 (CH), 129.8 (CH), 128.5 (CH), 127.8 (C), 127.5 (C), 126.0 (C), 121.8 (C), 118.9 (C), 59.9 (CH₂), 41.0 (CH₂), 37.9 (CH₂), 37.7 (C), 33.1 (CH₂), 32.0 (CH₂), 29.8 (CH), 21.4 (CH₃). MS(ESI): calcd for C₂₇H₃₁Cl₂NO₂S, 504.5; found, 504.2. Anal. Calcd for C₂₇H₃₁Cl₂NO₂S: C, 64.28; H, 6.19; N, 2.78. Found: C, 63.14; H, 5.89; N, 2.51.

Synthesis of 2-(Mercaptoethylimino)methyl-4,6-dichlorophenol. 2-Aminoethanethiol (0.99 g, 12.9 mmol) was added to a solution of 3,5-dichloro-2-hydroxybenzaldehyde (2.46 g, 12.9 mmol) in ethanol and stirred for 2 h at room temperature. The solvent was removed under reduced pressure yielding a yellow solid (2.88 g, 89%). MS(APPI): calcd for C₉H₉Cl₂NOS, 250.1; found, 250.0.

Synthesis of Lig³H₂. A solution of 2-(bromomethyl)-4,6-di-*tert*-butylphenol (1.52 g, 5.1 mmol) in THF (20 mL) was added dropwise to a solution of 2-(mercaptoethylimino)methyl-4,6-dichlorophenol (1.27 g, 5.1 mmol) and triethylamine (0.70 mL) in THF (20 mL) and stirred for 2 h. The reaction mixture was worked up as described above for Lig¹H₂ giving Lig³H₂ in a final yield of 53%. ¹H NMR (400 MHz, CDCl₃): δ 8.18 (s, 1H, NCH), 7.41 (d, 1H, *J* = 2.5 Hz, ArH), 7.28 (d, 1H, *J* = 2.4 Hz, ArH), 7.13 (d, 1H, *J* = 2.5 Hz, ArH), 6.92 (d, 1H, *J* = 2.7 Hz, ArH), 3.83 (s, 2H, ArCH₂S), 3.68 (t, 2H, *J* = 6.4 Hz, CH₂), 2.74 (t, 2H, *J* = 6.6 Hz, CH₂), 1.42 (s, 9H, C(CH₃)₃), 1.28 (s, 9H, C(CH₃)₃). ¹³C NMR (100.66 MHz, CDCl₃): δ 164.5 (CN), 156.6 (C), 151.9 (C), 142.5 (C), 137.3 (C), 132.4 (CH), 129.1 (CH), 125.3 (CH), 123.9 (CH), 122.9 (C), 122.7 (C), 121.4 (C), 119.3 (CH), 58.1 (CH₂), 34.9 (C), 34.4 (CH₂), 34.2 (C), 31.6 (CH₃), 31.3 (CH₂), 29.8 (CH₃). MS(APPI): calcd for C₂₄H₃₁Cl₂NO₂S, 468.5; found, 506.2 (MK⁺). Anal. Calcd for C₂₄H₃₁Cl₂NO₂S: C, 61.53; H, 6.67; N, 2.99. Found: C, 60.94; H, 6.58; N, 2.69.

Synthesis of Lig⁴H₂. A solution of 2-(bromomethyl)-4,6-di-*tert*-butylphenol (1.46 g, 4.9 mmol) in THF (20 mL) was added dropwise to a solution of 2-(mercaptoethylimino)methyl-4,6-di-*tert*-butylphenol (1.43 g, 4.9 mmol) and triethylamine (0.68 mL) in THF (20 mL) and stirred for 2 h. The reaction mixture was worked up as described above for Lig¹H₂ giving Lig⁴H₂ in a final yield of 30%. ¹H NMR (400 MHz, CDCl₃): δ 8.28 (s, 1H, NCH), 7.38 (d, 1H, *J* = 2.0 Hz, ArH), 7.27 (d, 1H, *J* = 2.1 Hz, ArH), 7.06 (d, 1H, *J* = 1.9 Hz, ArH), 6.95 (d, 1H, *J* = 2.0 Hz, ArH), 3.85 (s, 2H, ArCH₂S), 3.67 (t, 2H, *J* = 6.7 Hz, CH₂), 2.72 (t, 2H, *J* = 6.6 Hz, CH₂), 1.43 (s, 9H, C(CH₃)₃), 1.42 (s, 9H, C(CH₃)₃), 1.30 (s, 9H, C(CH₃)₃), 1.27 (s, 9H, C(CH₃)₃). ¹³C NMR (100.66 MHz, CDCl₃): δ 167.2 (CN), 158.0 (C), 152.0 (C), 142.3 (C), 140.2 (C), 137.2 (C), 136.8 (C), 127.2 (CH), 125.9 (CH), 125.3 (CH), 123.8 (CH), 121.6 (C), 117.7 (C), 59.2 (CH₂), 35.0 (CH₂), 34.5 (CH₂), 34.2 (C), 34.1 (C), 31.6 (CH₃), 31.5 (CH₃), 31.3 (C), 29.8 (CH₃), 29.4 (CH₃), 29.3 (C). MS(APPI): calcd for C₃₂H₄₉NO₂S, 511.8; found, 534.3 (MNa⁺). Anal. Calcd for C₃₂H₄₉NO₂S: C, 75.10; H, 9.65; N, 2.74. Found: C, 75.26; H, 9.36; N, 2.44.

Synthesis of Lig⁵H₂. A solution of 2-(bromomethyl)-4-methyl-6-adamantylphenol (1.00 g, 3.0 mmol) in THF (20 mL) was added dropwise to a solution of 2-(mercaptoethylimino)methyl-4,6-dichlorophenol (0.75 g, 3.0 mmol) and triethylamine (0.42 mL) in THF (20 mL) and stirred for 2 h. The reaction mixture was worked up as described above for Lig¹H₂ giving Lig⁵H₂ in a final yield of 31%. ¹H NMR (400 MHz, CDCl₃): δ 8.15 (s, 1H, NCH), 7.41 (d, 1H, *J* = 2.4 Hz, ArH), 7.14 (d, 1H, *J* = 2.4 Hz, ArH), 6.99 (d, 1H, *J* = 1.6 Hz, ArH), 6.73 (s, 1H, ArH), 3.78 (s, 2H, ArCH₂S), 3.66 (t, 2H, *J* = 6.3 Hz, CH₂), 2.74 (t, 2H, *J* = 6.5 Hz, CH₂), 2.24 (s, 3H, ArCH₃), 2.12 (bs, 6H, adamantyl), 2.07 (bs, 3H, adamantyl), 1.77 (bs, 6H, adamantyl). ¹³C NMR (100.66 MHz, CDCl₃): δ 165.3 (CN), 157.3 (C), 152.9 (C), 138.9 (C), 133.1 (CH), 129.9 (C), 129.8 (CH), 129.4 (CH), 128.4 (CH), 123.7 (C), 123.4 (C), 122.8 (C), 120.1 (C), 58.7 (CH₂), 41.4 (CH₂), 37.8 (CH₂), 37.6 (C), 34.8 (CH₂), 32.1 (CH₂), 29.8 (CH), 21.5 (CH₃). MS(APPI): calcd for C₂₇H₃₁Cl₂NO₂S, 504.5; found, 526.1 (MNa⁺). Anal. Calcd for C₂₇H₃₁Cl₂NO₂S: C, 64.28; H, 6.19; N, 2.78. Found: C, 63.83; H, 6.11; N, 2.74.

Synthesis of Lig⁶H₂. A solution of 2-(bromomethyl)-4-methyl-6-adamantylphenol (0.93 g, 2.8 mmol) in THF (20 mL) was added dropwise to a solution of 2-(mercaptoethylimino)methyl-4-methyl-6-adamantylphenol (0.91 g, 2.8 mmol) and triethylamine (0.38 mL) in THF (20 mL) and stirred for 2 h. The reaction mixture was worked up as described above for Lig¹H₂ giving Lig⁶H₂ in a final yield of 20%. ¹H NMR (400 MHz, CDCl₃): δ 8.23 (s, 1H, NCH), 7.08 (d, 1H, *J* = 2.0 Hz, ArH), 6.98 (d, 1H, *J* = 1.9 Hz, ArH), 6.88 (d, 1H, *J* = 1.8 Hz, ArH), 6.76 (d, *J* = 1.7, 1H, ArH), 3.77 (s, 2H, ArCH₂S), 3.64 (t, 2H, *J* = 6.4 Hz, CH₂), 2.72 (t, 2H, *J* = 6.6 Hz, CH₂), 2.28 (s, 3H, ArCH₃), 2.24 (s, 3H, ArCH₃), 2.17 (m, 6H, adamantyl), 2.13 (m, 6H,

adamantyl), 2.07 (bs, 6H, adamantyl), 1.77 (bs, 12H, adamantyl). ^{13}C NMR (100.66 MHz, CDCl_3): δ 167.8 (CN), 159.1 (C), 153.1 (C), 138.8 (C), 138.2 (C), 131.5 (CH), 130.2 (CH), 129.7 (C), 129.6 (CH), 128.2 (CH), 127.5 (C), 122.9 (C), 118.9 (C), 59.9 (CH_2), 41.3 (CH_2), 41.0 (CH_2), 37.9 (CH_2), 37.8 (CH_2), 37.7 (C), 37.6 (C), 34.9 (CH_2), 32.1 (CH_2), 29.8 (CH), 29.8 (CH), 21.5 (CH_3), 21.4 (CH_3). MS(APPI): calcd for $\text{C}_{38}\text{H}_{49}\text{NO}_2\text{S}$, 583.9; found, 606.3 (MNa^+). Anal. Calcd for $\text{C}_{38}\text{H}_{49}\text{NO}_2\text{S}$: C, 78.17; H, 8.46; N, 2.40. Found: C, 77.89; H, 8.16; N, 2.12.

Synthesis of $\text{Lig}^1\text{Zr}(\text{O-tert-Bu})_2$. Lig^1H_2 (47 mg, 0.10 mmol) was dissolved in ca. 2 mL of ether and was added dropwise to a solution of $\text{Zr}(\text{O}^i\text{Bu})_4$ (38 mg, 0.10 mmol) at room temperature. The solution was stirred for 2 h after which the solvent was removed under vacuum and the resulting yellow solid was washed with pentane (49 mg, 70%). ^1H NMR (400 MHz, C_6D_6): δ 7.71 (d, 1H, $J = 1.8$ Hz, ArH), 7.29 (d, 1H, $J = 1.8$ Hz, ArH), 7.24 (s, 1H, NCH), 6.94 (d, 1H, $J = 2.0$ Hz, ArH), 6.63 (d, $J = 2.4$, 1H, ArH), 3.50 (bs, 2H, CH_2), 2.85 (bs, 2H, CH_2), 1.91 (m, 2H, CH_2), 1.75 (s, 9H, $\text{C}(\text{CH}_3)_3$), 1.29 (s, 27H, $\text{C}(\text{CH}_3)_3$). ^{13}C NMR (100.66 MHz, C_6D_6): δ 167.8 (CN), 160.7 (C), 158.4 (C), 139.1 (C), 138.6 (C), 129.7 (CH), 129.6 (CH), 128.5 (CH), 128.1 (CH), 124.9 (C), 123.4 (C), 122.1 (C), 119.8 (C), 59.2 (CH_2), 35.5 (CH_2), 34.5 (CH_2), 33.9 (C), 32.5 (CH_3), 31.3 (CH_3), 31.1 (C), 29.7 (CH_3). Anal. Calcd for $\text{C}_{32}\text{H}_{47}\text{Cl}_2\text{NO}_4\text{SZr}$: C, 54.60; H, 6.73; N, 1.99. Found: C, 53.82; H, 6.43; N, 1.75.

Synthesis of $\text{Lig}^2\text{Zr}(\text{O-tert-Bu})_2$. Lig^2H_2 (34 mg, 0.07 mmol) was dissolved in ca. 2 mL of ether and was added dropwise to a solution of $\text{Zr}(\text{O}^i\text{Bu})_4$ (26 mg, 0.07 mmol) at room temperature. The solution was stirred for 2 h after which the solvent was removed under vacuum, yielding a yellow solid quantitatively (55 mg). ^1H NMR (400 MHz, C_6D_6): δ 7.34 (s, 1H, ArH), 7.30 (s, 1H, ArH), 7.28 (s, 1H, NCH), 6.65 (s, 1H, ArH), 6.63 (s, 1H, ArH), 3.68 (d, 1H, $J = 11.7$, CH), 3.08 (d, 1H, $J = 12.6$, CH), 3.02 (m, 1H, CH), 2.69 (m, 1H, CH), 2.47 (s, 3H, ArCH_3), 2.22 (m, 6H, adamantyl), 2.01 (m, 6H, adamantyl), 1.92 (m, 1H, CH), 1.86 (m, 3H, adamantyl), 1.67 (m, 1H, CH), 1.38 (s, 9H, $\text{C}(\text{CH}_3)_3$), 1.25 (s, 9H, $\text{C}(\text{CH}_3)_3$). ^{13}C NMR (100.66 MHz, C_6D_6): δ 167.7 (CN), 139.9 (C), 139.4 (C), 134.5 (CH), 132.5 (CH), 130.4 (CH), 126.6 (C), 125.8 (C), 124.0 (C), 123.5 (C), 120.3 (C), 59.7 (CH_2), 41.2 (CH_2), 38.0 (CH_2), 37.4 (C), 35.2 (CH_2), 33.4 (CH_3), 31.6 (CH_2), 30.1 (CH), 21.2 (CH_3). Anal. Calcd for $\text{C}_{35}\text{H}_{47}\text{Cl}_2\text{NO}_4\text{SZr}$: C, 56.81; H, 6.40; N, 1.89. Found: C, 56.98; H, 6.41; N, 1.85.

Synthesis of $\text{Lig}^3\text{Zr}(\text{O-tert-Bu})_2$. Lig^3H_2 (46 mg, 0.09 mmol) was dissolved in ca. 2 mL of ether and was added dropwise to a solution of $\text{Zr}(\text{O}^i\text{Bu})_4$ (37 mg, 0.09 mmol) at room temperature. The solution was stirred for 2 h after which the solvent was removed under vacuum, resulting in a yellow solid (62 mg, 90%). ^1H NMR (400 MHz, C_6D_6): δ 7.57 (d, 1H, $J = 2.5$ Hz, ArH), 7.40 (d, 1H, $J = 2.7$ Hz, ArH), 6.95 (d, 1H, $J = 2.4$ Hz, ArH), 6.69 (s, 1H, NCH), 6.52 (d, $J = 2.7$, 1H, ArH), 4.31 (d, 1H, $J = 12.2$, CH), 3.67 (m, 1H, CH), 3.56 (d, 1H, $J = 12.5$, CH), 2.11 (m, 3H, CH, CH_2), 1.63 (s, 9H, $\text{C}(\text{CH}_3)_3$), 1.58 (s, 9H, $\text{C}(\text{CH}_3)_3$), 1.38 (s, 9H, $\text{C}(\text{CH}_3)_3$), 1.23 (s, 9H, $\text{C}(\text{CH}_3)_3$). ^{13}C NMR (100.66 MHz, C_6D_6): δ 165.9 (CN), 159.8 (C), 159.5 (C), 139.4 (C), 137.0 (C), 133.9 (CH), 130.3 (CH), 126.5 (C), 126.3 (CH), 124.1 (CH), 123.1 (C), 121.4 (C), 119.6 (C), 76.9 (C), 60.0 (CH_2), 35.9 (CH_2), 35.3 (CH_2), 34.0 (C), 32.5 (CH_3), 31.7 (CH_3), 30.5 (C), 29.7 (CH_3). Anal. Calcd for $\text{C}_{32}\text{H}_{47}\text{Cl}_2\text{NO}_4\text{SZr}$: C, 54.60; H, 6.73; N, 1.99. Found: C, 54.90; H, 6.68; N, 1.70.

Synthesis of $\text{Lig}^4\text{Zr}(\text{O-tert-Bu})_2$. Lig^4H_2 (42 mg, 0.08 mmol) was dissolved in ca. 2 mL of ether and was added dropwise to a solution of $\text{Zr}(\text{O}^i\text{Bu})_4$ (32 mg, 0.08 mmol) at room temperature. The solution was stirred for 2 h after which the solvent was removed under vacuum and the resulting yellow solid was washed with pentane affording the product quantitatively (63 mg). ^1H NMR (400 MHz, C_6D_6): δ 7.69 (d, 1H, $J = 2.5$ Hz, ArH), 7.54 (d, 1H, $J = 2.2$ Hz, ArH), 7.23 (s, 1H, NCH), 6.93 (d, 1H, $J = 2.4$ Hz, ArH), 6.89 (d, $J = 2.4$, 1H, ArH), 4.25 (d, 1H, $J = 12.7$, CH), 3.58 (d, 1H, $J = 13.3$, CH), 3.47 (m, 1H, CH), 2.50 (m, 1H, CH), 2.25 (m, 2H, CH_2), 1.78 (s, 9H, $\text{C}(\text{CH}_3)_3$), 1.61 (s, 9H, $\text{C}(\text{CH}_3)_3$), 1.37 (s, 9H, $\text{C}(\text{CH}_3)_3$), 1.35 (s, 18H, $\text{C}(\text{CH}_3)_3$), 1.31 (s, 9H, $\text{C}(\text{CH}_3)_3$). ^{13}C NMR (100.66 MHz, C_6D_6): δ 167.8 (CN), 160.9 (C), 139.2 (C), 138.9 (C), 138.6 (C), 138.1 (C), 130.3 (CH),

126.4 (CH), 124.7 (CH), 123.1 (CH), 121.1 (C), 76.9 (C), 75.8 (C), 60.1 (CH_2), 36.7 (CH_2), 36.3 (CH_2), 35.9 (C), 34.7 (C), 33.6 (CH_3), 32.4 (CH_3), 32.0 (CH_3), 31.9 (C), 31.6 (C), 30.6 (CH_3). Anal. Calcd for $\text{C}_{40}\text{H}_{65}\text{NO}_4\text{SZr}$: C, 64.29; H, 8.77; N, 1.87. Found: C, 63.36; H, 8.59; N, 1.54.

Synthesis of $\text{Lig}^5\text{Zr}(\text{O-tert-Bu})_2$. Lig^5H_2 (49 mg, 0.10 mmol) was dissolved in ca. 2 mL of ether and was added dropwise to a solution of $\text{Zr}(\text{O}^i\text{Bu})_4$ (38 mg, 0.10 mmol) at room temperature. The solution was stirred for 2 h after which the solvent was removed under vacuum, giving a yellow solid quantitatively (76 mg). ^1H NMR (400 MHz, C_6D_6): δ 7.33 (d, 1H, $J = 2.5$ Hz, ArH), 7.07 (d, 1H, $J = 2.4$ Hz, ArH), 6.86 (s, 1H, NCH), 6.61 (d, 1H, $J = 2.6$ Hz, ArH), 6.50 (d, 1H, $J = 1.8$, ArH), 3.89 (d, 1H, $J = 13.9$, CH), 3.36 (d, 1H, $J = 13.9$, CH), 3.08 (m, 1H, CH), 2.40 (m, 1H, CH), 2.24 (s, 3H, ArCH_3), 2.14 (m, 6H, adamantyl), 1.86 (m, 6H, adamantyl), 1.70 (m, 3H, adamantyl), 1.54 (s, 9H, $\text{C}(\text{CH}_3)_3$), 1.45 (m, 1H, CH), 1.22 (m, 1H, CH), 1.14 (s, 9H, $\text{C}(\text{CH}_3)_3$). ^{13}C NMR (100.66 MHz, C_6D_6): δ 164.0 (CN), 160.9 (C), 139.0 (C), 134.5 (CH), 131.7 (CH), 129.4 (CH), 126.9 (C), 125.4 (C), 123.9 (C), 121.4 (C), 120.9 (C), 77.2 (C), 76.2 (C), 61.3 (CH_2), 41.2 (CH_2), 37.7 (CH_2), 37.5 (C), 36.5 (CH_2), 33.3 (CH_3), 33.2 (CH_3), 31.8 (CH_2), 30.1 (CH), 21.4 (CH_3). Anal. Calcd for $\text{C}_{35}\text{H}_{47}\text{Cl}_2\text{NO}_4\text{SZr-Et}_2\text{O}$: C, 57.54; H, 7.06; N, 1.72. Found: C, 57.60; H, 6.61; N, 1.64.

Synthesis of $\text{Lig}^6\text{Zr}(\text{O-tert-Bu})_2$. Lig^6H_2 (34 mg, 0.06 mmol) was dissolved in ca. 2 mL of ether and was added dropwise to a solution of $\text{Zr}(\text{O}^i\text{Bu})_4$ (22 mg, 0.06 mmol) at room temperature. The solution was stirred for 2 h after which the solvent was removed under vacuum, giving a yellow solid quantitatively (55 mg). ^1H NMR (400 MHz, C_6D_6): δ 7.33 (s, 1H, NCH), 7.26 (d, 1H, $J = 2.2$ Hz, ArH), 7.15 (s, 1H, ArH), 6.58 (d, 2H, $J = 1.8$ Hz, ArH), 4.05 (d, 1H, $J = 13.7$, CH), 3.48 (d, 1H, $J = 13.7$, CH), 3.11 (m, 1H, CH), 2.57 (m, 2H, CH), 2.48 (bs, 6H, adamantyl), 2.40 (m, 1H, CH), 2.31 (s, 3H, ArCH_3), 2.26 (m, 6H, adamantyl), 2.15 (s, 3H, ArCH_3), 2.10 (m, 3H, adamantyl), 1.85 (m, 12H, adamantyl), 1.64 (m, 3H, adamantyl), 1.55 (s, 9H, $\text{C}(\text{CH}_3)_3$), 1.16 (s, 9H, $\text{C}(\text{CH}_3)_3$). ^{13}C NMR (100.66 MHz, C_6D_6): δ 166.5 (CN), 161.7 (C), 161.1 (C), 139.8 (C), 139.1 (C), 134.2 (CH), 132.7 (CH), 129.4 (CH), 128.9 (CH), 126.3 (C), 124.6 (C), 123.7 (C), 120.9 (C), 76.0 (C), 75.5 (C), 61.5 (CH_2), 41.8 (CH_2), 41.6 (CH_2), 38.2 (C), 38.0 (CH_2), 37.9 (CH_2), 37.7 (C), 36.6 (CH_2), 33.7 (CH_3), 33.3 (CH_3), 32.0 (CH_2), 30.1 (CH), 30.0 (CH), 21.4 (CH_3), 21.1 (CH_3). Anal. Calcd for $\text{C}_{46}\text{H}_{65}\text{NO}_4\text{SZr}$: C, 67.43; H, 8.00; N, 1.71. Found: C, 67.48; H, 7.52; N, 1.25.

General Polymerization Procedure. Bulk polymerizations of L-lactide and rac-lactide were carried out by heating the monomer and the catalyst in a closed glass vessel to 140 °C for a period of time by which the melt had become viscous. Here, 10 mg of catalyst and a 300:1 lactide to catalyst molar ratio were employed for all polymerizations. The polymerization runs were terminated by the addition of 1 mL of methanol. The reaction mixture was dissolved in dichloromethane, followed by removal of the volatiles under reduced pressure. The resulting polymer was purified by stirring with excess of methanol overnight to remove any unreacted monomer, filtered, and dried under vacuum for 2 h. ^1H NMR analysis of the PLA samples obtained by polymerization of L-lactide (400 MHz, CDCl_3) indicated that no epimerization occurred during the polymerization, and that the polymer was isotactic, as was evident from a quartet (5.16 ppm) and a doublet (1.58 ppm) in a ratio of 1:3.

Solution polymerization runs of rac-lactide in 5 mL of toluene were carried out at 70 °C employing 10 mg of catalyst and a 300:1 lactide to catalyst molar ratio. After 20 h the reaction was terminated by the addition of 1 mL of methanol and the volatiles were removed under vacuum. The resulting polymer was purified by stirring with excess of methanol overnight to remove any unreacted monomer, filtered, and dried under vacuum for 2 h. The homonuclear-decoupled ^1H NMR spectrum of the PLA samples (400 MHz, CDCl_3) of the methine region was consistent with the formation of chains that are predominantly heterotactic, isotactic or atactic estimated from the relative intensities of the *rmr* (δ 5.23 ppm) and the *mrm* (δ 5.16 ppm) tetrads for heterotactic sequences and the *mmm* (δ 5.17 ppm) tetrad for isotactic sequences vs other tetrads (*rmr* δ 5.23 ppm, *mrm* δ 5.16

ppm, *rmm/mmr* δ 5.22 and 5.18 ppm, *mmm* δ 5.17 ppm).^{20–22} Molecular weight determination and PDI analysis were done by GPC measurements.

AUTHOR INFORMATION

Corresponding Author

*E-mail: moshekol@post.tau.ac.il.

Author Contributions

The manuscript was written through contributions of all authors.

ACKNOWLEDGMENTS

We thank the German Israeli Foundation (G.I.F.) and the Britain-Israel Research and Academic Exchange Partnership (BIRAX) foundation for funding. We thank Purac for a generous gift of D- and L-lactide.

REFERENCES

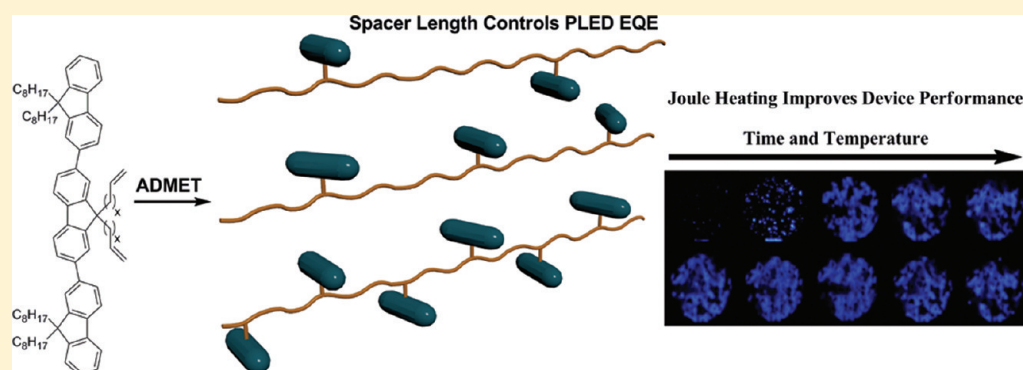
- (1) (a) Drumright, R. E.; Gruber, P. R.; Henton, D. E. *Adv. Mater.* **2000**, *12*, 1841. (b) Auras, R.; Harte, B.; Selke, S. *Macromol. Biosci.* **2004**, *4835*. (c) Albertsson, A. C.; Varma, I. K. *Biomacromolecules* **2003**, *4*, 1466.
- (2) (a) Stanford, M. J.; Dove, A. P. *Chem. Soc. Rev.* **2010**, *39*, 486. (b) Becker, J. M.; Pounder, R. J.; Dove, A. P. *Macromol. Rapid Commun.* **2010**, *31*, 1923.
- (3) (a) Dechy-Cabaret, O.; Martin-Vaca, B.; Bourissou, D. *Chem. Rev.* **2004**, *104*, 6147. (b) Platel, R. H.; Hodgson, L. M.; Williams, C. K. *Polym. Rev.* **2008**, *48*, 11.
- (4) (a) Thomas, C. M. *Chem. Soc. Rev.* **2010**, *39*, 165. (b) Dijkstra, P. J.; Du, H.; Feijen, J. *Polym. Chem.* **2011**, *2*, 520.
- (5) (a) Spassky, N.; Wisniewski, M.; Pluta, C.; Le Borgne, A. *Macromol. Chem. Phys.* **1996**, *197*, 2627. (b) Ovitt, T. M.; Coates, G. W. *J. Polym. Sci., A: Polym. Chem.* **2000**, *38*, 4686. (c) Ovitt, T. M.; Coates, G. W. *J. Am. Chem. Soc.* **2002**, *124*, 1316. (d) Zhong, Z.; Dijkstra, P. J.; Feijen, J. *Angew. Chem., Int. Ed.* **2002**, *41*, 4510. (e) Majerska, K.; Duda, A. *J. Am. Chem. Soc.* **2004**, *126*, 1026. (f) Chisholm, M. H.; Patmore, N. J.; Zhou, Z. *Chem. Commun.* **2005**, 127. (g) Hormnirun, P.; Marshall, E. L.; Gibson, V. C.; Pugh, R. I.; White, A. J. P. *Proc. Natl. Acad. Sci. U.S.A.* **2006**, *103*, 15343. (h) Nomura, N.; Ishii, R.; Yamamoto, Y.; Kondo, T. *Chem.—Eur. J.* **2007**, *13*, 4433. (i) Pang, X.; Du, H.; Chen, X.; Wang, X.; Jing, X. *Chem.—Eur. J.* **2008**, *14*, 3126. (j) Bouyahyi, M.; Grunova, E.; Marquet, N.; Kirillov, E.; Thomas, C. M.; Roisnel, T.; Carpentier, J. —F. *Organometallics* **2008**, *27*, 5815. (k) Darensbourg, D. J.; Karoonnirun, O. *Organometallics* **2010**, *29*, 5627.
- (6) For nonaluminum based catalytic systems showing isoselectivity bias, see: (a) Douglas, A. F.; Patrick, B. O.; Mehrkhodavandi, P. *Angew. Chem., Int. Ed.* **2008**, *47*, 2290. (b) Buffet, J. C.; Okuda, J.; Arnold, P. L. *Inorg. Chem.* **2010**, *49*, 419. (c) Arnold, P. A.; Buffet, J.; Blaudeck, R. P.; Sujecki, S.; Blake, A. J.; Wilson, C. *Angew. Chem., Int. Ed.* **2008**, *47*, 6033. (d) Jensen, T. R.; Breyfogle, L. E.; Hillmyer, M. A.; Tolman, W. B. *Chem. Commun.* **2004**, 2504. (e) Whitelaw, E. L.; Davidson, M. G.; Jones, M. D. *Chem. Commun.* **2011**, 10004. (f) Dove, A. P.; Li, H.; Pratt, R. C.; Lohmeijer, B. G. G.; Culkin, D. A.; Waymouth, R. M.; Hedrick, J. L. *Chem. Commun.* **2006**, 2881. (g) Zhang, L.; Nederberg, F.; Messman, J. M.; Pratt, R. C.; Hedrick, J. L.; Wade, C. G. *J. Am. Chem. Soc.* **2007**, *129*, 12610.
- (7) (a) Ikada, Y.; Jamshidi, K.; Tsuji, H.; Hyon, S. *Macromolecules* **1987**, *20*, 906. (b) Fukushima, K.; Kimura, Y. *Polym. Int.* **2006**, *55*, 626.
- (8) (a) Cheng, M.; Attygalle, A. B.; Lobkovsky, E. B.; Coates, G. W. *J. Am. Chem. Soc.* **1999**, *121*, 11583. (b) Chisholm, M. H.; Gallucci, J.; Phomphrai, K. *Chem. Commun.* **2003**, 48. (c) Pietrangelo, A.; Knight, S. C.; Gupta, A. K.; Yao, L. J.; Hillmyer, M. A.; Tolman, W. B. *J. Am. Chem. Soc.* **2010**, *132*, 11649.
- (9) (a) Amgoune, A.; Thomas, C. M.; Roisnel, T.; Carpentier, J. —F. *Chem.—Eur. J.* **2006**, *12*, 169. (b) Bouyahyi, M.; Ajellal, N.; Kirillov, E.; Thomas, C. M.; Carpentier, J. —F. *Chem.—Eur. J.* **2011**, *17*, 1872.
- (c) Liu, X.; Shang, X.; Tang, T.; Hu, N.; Pei, F.; Cui, D.; Chen, X.; Jing, X. *Organometallics* **2007**, *26*, 2747. (d) Clark, L.; Cushion, M. G.; Dyer, H. E.; Schwarz, A. D.; Duchateau, R.; Mountford, P. *Chem. Commun.* **2010**, 273.
- (10) (a) Ma, H.; Spaniol, T. P.; Okuda, J. *Angew. Chem., Int. Ed.* **2006**, *45*, 7818. (b) Ma, H.; Spaniol, T. P.; Okuda, J. *Inorg. Chem.* **2008**, *47*, 3328. (c) Chmura, A. J.; Chuck, C. J.; Davidson, M. G.; Jones, M. D.; Lunn, M. D.; Bull, S. D.; Mahon, M. F. *Angew. Chem., Int. Ed.* **2007**, *46*, 2280. (d) Chmura, A. J.; Davidson, M. G.; Frankis, C. J.; Jones, M. D.; Lunn, M. D. *Chem. Commun.* **2008**, 1293.
- (11) (a) Zelikoff, A. L.; Kopilov, J.; Goldberg, I.; Coates, G. W.; Kol, M. *Chem. Commun.* **2009**, 6804. (b) Sergeeva, E.; Kopilov, J.; Goldberg, I.; Kol, M. *Inorg. Chem.* **2010**, *49*, 3977.
- (12) For a report on different{OSNO} ligands, see: Meppelder, G.-J. M.; Fan, H.-T.; Spaniol, T. P.; Okuda, J. *Inorg. Chem.* **2009**, *48*, 7378.
- (13) (a) Yeor, A.; Gendler, S.; Groysman, S.; Goldberg, I.; Kol, M. *Inorg. Chem. Commun.* **2004**, *7*, 280. (b) Press, K.; Cohen, A.; Goldberg, I.; Venditto, V.; Mazzeo, M.; Kol, M. *Angew. Chem., Int. Ed.* **2011**, *50*, 3591.
- (14) Cohen, A.; Yeor, A.; Goldberg, I.; Kol, M. *Inorg. Chem.* **2007**, *46*, 8114.
- (15) The intermediate thio-imine monophenolate derivatives formed as a mixture, presumably with the phenol-substituted 5-membered heterocycle thiazolidine, and were reacted without purification.
- (16) For Al-Salan and related systems which revert tacticity preference upon changing of ligand substituents, see: (a) Hormnirun, P.; Marshall, E. L.; Gibson, V. C.; White, A. J. P.; Williams, D. J. *J. Am. Chem. Soc.* **2004**, *126*, 2689. (b) Hormnirun, P.; Marshall, E. L.; Gibson, V. C.; Pugh, R. I.; White, A. J. P. *Proc. Natl. Acad. Sci. U.S.A.* **2006**, *103*, 15343. (c) Du, H.; Velders, A. H.; Dijkstra, P. J.; Sun, J.; Zhong, Z.; Chen, X.; Feijen, J. *Chem.—Eur. J.* **2009**, *15*, 9836. (d) Tang, Z.; Gibson, V. C. *Eur. Polym. J.* **2007**, *43*, 150.
- (17) Bryliakov, K. P.; Talsi, E. *Eur. J. Org. Chem.* **2008**, 3369.
- (18) Gendler, S.; Zelikoff, A. L.; Kopilov, J.; Goldberg, I.; Kol, M. *J. Am. Chem. Soc.* **2008**, *130*, 2144.
- (19) Cohen, A.; Kopilov, J.; Goldberg, I.; Kol, M. *Organometallics* **2009**, *28*, 1391.
- (20) Thakur, K. A. M.; Kean, R. T.; Hall, E. S.; Doscotch, M. A.; Munson, E. S. *Anal. Chem.* **1997**, *69*, 4303.
- (21) Thakur, K. A. M.; Kean, R. T.; Hall, E. S.; Kolstad, J. J.; Lindgren, T. A.; Doscotch, M. A.; Siepmann, I.; Munson, E. S. *Macromolecules* **1997**, *30*, 2422.
- (22) Chamberlain, B. M.; Cheng, M.; Moore, D. R.; Ovitt, T. M.; Lobkovsky, E. B.; Coates, G. W. *J. Am. Chem. Soc.* **2001**, *123*, 3229.

Perfectly Regioregular Electroactive Polyolefins: Impact of Inter-Chromophore Distance on PLED EQE

Brian S. Aitken, Patrick M. Wieruszewski, Kenneth R. Graham, John R. Reynolds,* and Kenneth B. Wagener*

The George and Josephine Butler Polymer Research Laboratory, Department of Chemistry, Center for Macromolecular Science and Engineering, University of Florida, Gainesville, Florida 32611-7200, United States

S Supporting Information



ABSTRACT: Acyclic diene metathesis polymerization (ADMET) was used to synthesize a series of perfectly regioregular polyolefins, in which the number of backbone atoms between pendant terfluorene groups was precisely controlled at 8, 14, or 20 carbons. Analogous random copolymers containing identical chromophore densities were also synthesized to study the impact of regioregularity on the performance of this class of materials in polymer light emitting diodes (PLEDs). Additionally, the backbone alkene remnants of ADMET were saturated to generate materials with somewhat different ordering. These saturated derivatives led to improvements in PLED external quantum efficiencies (EQEs) over their unsaturated analogues in most cases, with a large improvement in one material. Charge mobility, as manifested in current density during PLED characterization, and relative solid-state fluorescence quantum yield (Φ_F) also exhibit reasonable dependencies, with longer distances between electroactive groups yielding lower PLED current densities and higher Φ_F . Regioregularity has the opposite effect, giving rise to higher current densities and lower Φ_F as compared to regiorandom analogues.

■ INTRODUCTION

As global economic development occurs, the demand for cheap, energy-efficient displays and lighting continues to increase,^{1–3} placing higher demands on our understanding of design parameters for fabrication of high performance polymer light emitting diodes (PLEDs). These devices can be processed from solution by, for example, ink jet printing or spin coating, as opposed to the costly processes requiring high temperature, ultra clean conditions and high vacuum needed in inorganic LED and small molecule OLED construction. Thus, PLEDs afford a low cost option for the fabrication of large and or flexible displays such as television screens, computer monitors, and large emissive lighting surfaces.^{4–10}

However, even state-of-the-art PLEDs currently suffer from lower performance compared to their inorganic and molecular counterparts.^{3,9–24} Figure 1 shows that the design of efficient PLEDs necessitates a balance of hole and electron mobilities, which must also be sufficiently high, to ensure that charge recombination occurs near the center of the emissive layer of the device.^{22,25–31} For those based on emission from singlet

excitons, high fluorescence quantum yields (Φ_F) are required as well. However, attaining high performance in both parameters for one material is quite challenging. Highly ordered organic semiconductors tend to exhibit increased charge mobility over their amorphous counterparts,^{27,32–38} but ordering may simultaneously reduce Φ_F by enhancing quenching mechanisms via increased energy migration and formation of non emissive complexes.^{39–47}

Donor–donor energy migration (DDEM, also referred to as homo resonance energy transfer), a process closely related to Förster resonance energy transfer (FRET) but between chemically identical species,^{48–57} enhances quenching in fluorescent materials by allowing excited state energy to migrate via adjacent identical fluorophores to either dark complexes (static quenching) or to fluorophores which have a greater propensity to undergo dynamic quenching as a result of

Received: October 30, 2011

Revised: November 30, 2011

Published: January 6, 2012



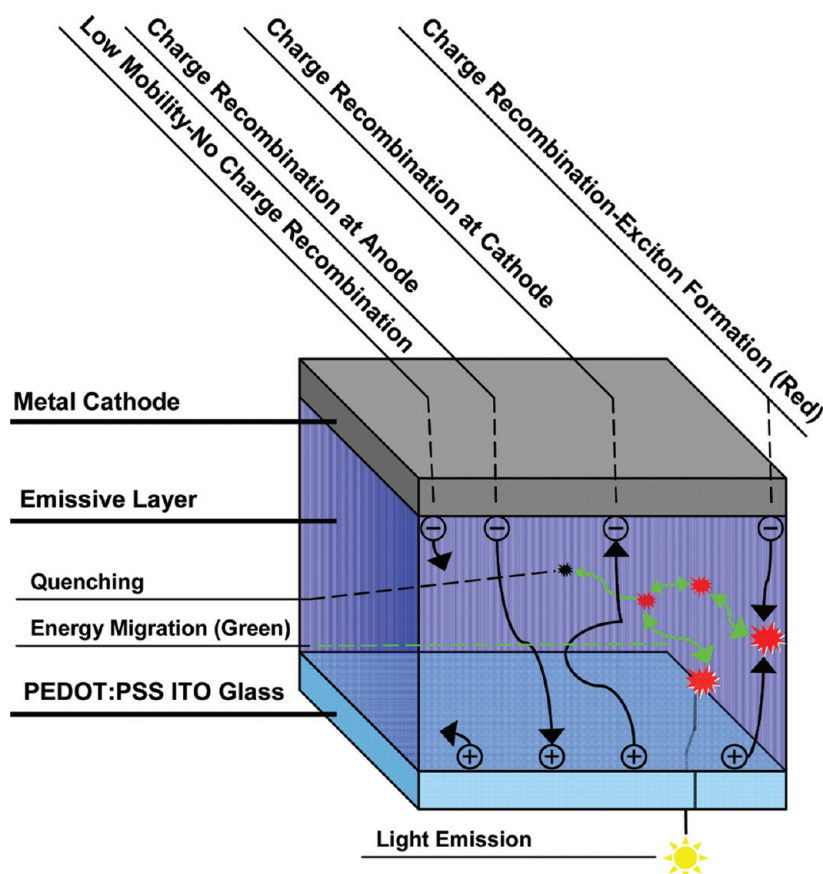


Figure 1. Schematic of the various processes leading to quenching or light emission that may occur in a PLED.

their microenvironments;^{58–62} the latter is referred to as partial donor–donor energy migration (PDDEM).^{63–68} The rate of resonance energy transfer (RET) is dependent on, among other variables, the distance between energy donor and energy acceptor to the inverse sixth power.^{66,69,70} Therefore, increasing the intermolecular distance between the fluorophores of interest is advantageous if one wishes to reduce the effects of RET. Particularly, in PLEDs and OLEDs, *unintentional* RET is disadvantageous as it reduces the device's external quantum efficiency (EQE) by enhancing the effects of both self-quenching and quenching due to impurities such as residual transition metal catalysts. However, the immediate solution of increasing the distance between chromophores may be deleterious to device performance, since charge mobility will simultaneously drop. The obvious question is “how distant should chromophores be to limit quenching while, still allowing for sufficiently high charge mobility for exciton generation?” One might attempt to approach the problem theoretically, however calculation of the resulting changes in DDEM, PDDEM, and FRET rates upon variation of the aforementioned distance, and ultimately the corresponding changes in Φ_F , requires knowledge of the geometric attitude of the donor with respect to the acceptor for calculation of the orientational factor (κ^2) in the Förster treatment.^{55–57,66–71} This parameter is extremely difficult or even impossible to predict for materials of the general type presented here, particularly in the solid state, where orientational randomization is quite slow and precludes the oft used approximation of $\kappa^2 = 2/3$, which is valid for small molecules in solution.^{55–57,66–68,70,71} Furthermore, estimation of the variation in charge mobility, which will invariably result from such structural changes, is impossible at

the current level of theory, and charge injection rates remain an additional theoretical problem.⁷² Therefore, an empirical structure–property study to assess the impact of chromophore–chromophore distance variation on PLED performance is necessary.

To determine the effects of chromophore separation on device parameters, we have prepared a set of perfectly regioregular electroactive polyolefins with carefully controlled average chromophore–chromophore distances. As shown in Figure 2A, regioregular electroactive polyolefins comprise a

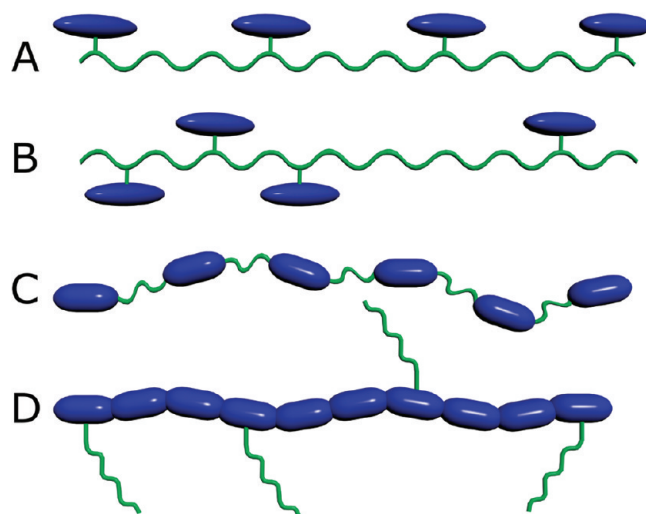
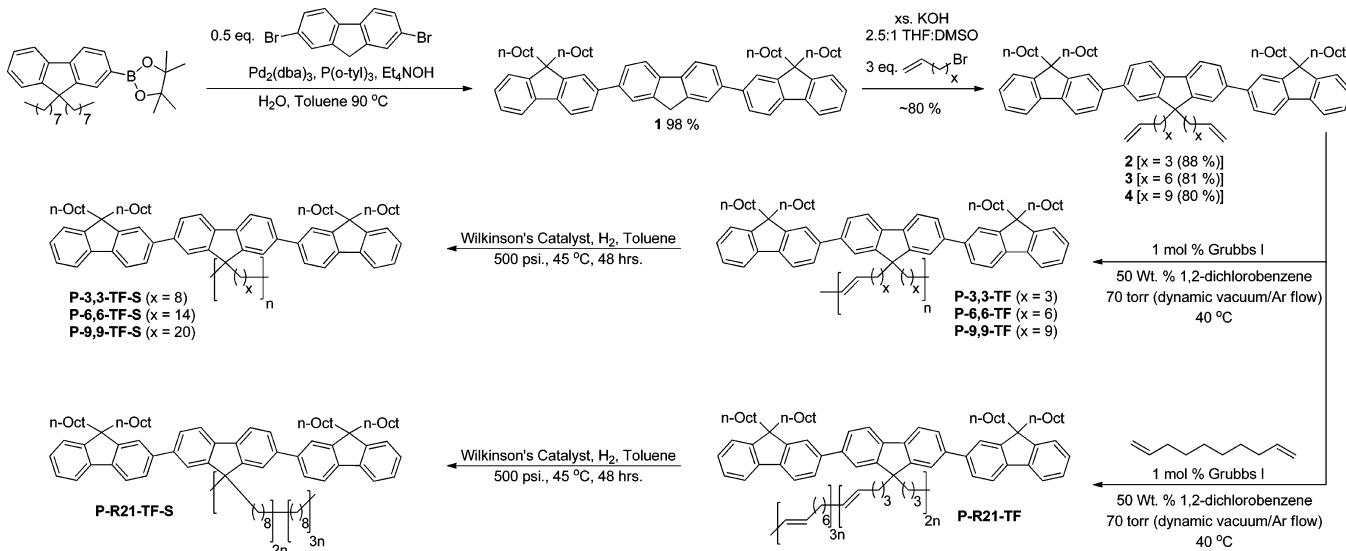


Figure 2. Architecture of polymeric electroactive materials.

Scheme 1. Synthetic Approach to Regioregular Electroactive Polyolefins and Two Regiorandom Analogues



class of materials in which the active pendant group occurs at exactly defined backbone run length intervals (spacer lengths).^{73,74} These regioregular materials are analogous to previously reported vinyl type or regiorandom polymers containing pendant electroactive moieties (Figure 2B).^{75–93} Similar to main chain π -functional materials (Figure 2C),^{94–98} pendant π -functional polymers offer the opportunity for inclusion of various electroactive units, which may serve their purposes cooperatively (e.g., various chromophores for white emission, emissive units and charge transporters, etc.)^{84,92,93} and thus afford an interesting and relatively new avenue for exploration into optoelectronic materials, as compared to conjugated polymers (Figure 2D).

Good control over the average distance between chromophores can be accomplished via acyclic diene metathesis polymerization (ADMET) of symmetric α,ω -diene functionalized chromophores followed by alkene hydrogenation or, as was demonstrated in our earlier work, by post polymerization coupling of chromophore fragments to regioregular borylated polyolefins.^{73,74} In the work reported here, terfluorenylidenes were placed pendant to fully linear polyethylene at exactly defined spacer lengths via the former method. We have found that polymers with longer spacer lengths exhibit higher PLED performance, despite yielding reduced current densities at identical device driving voltages. Furthermore, analogous regiorandom polymers exhibit enhanced relative solid-state Φ_F , presumably due to relatively reduced ordering and therefore less quenching. However, they also exhibit somewhat lower charge mobilities, as manifested in reduced PLED current densities, also resulting from their disorder. The concepts demonstrated here may also prove useful in the design of polymers for other Φ_F dependent devices such as scintillation detectors^{99–101} and luminescent solar concentrators.^{102–106}

EXPERIMENTAL SECTION

Materials and Instrumentation. All materials were purchased from Aldrich and used as received, unless noted otherwise. Absorption spectra were measured with a PerkinElmer Lambda 25 UV–vis spectrometer. Photoluminescence spectra were obtained using a Horiba Jobin Yvon Fluorolog-3 fluorimeter.

Synthesis. Synthesis of these materials was briefly described elsewhere;⁷³ however, due to length constraints, characterization was

limited to differential scanning calorimetry and gel permeation chromatography of the polymers. Complete characterization of all materials, including NMR, mass spectrometric data, and elemental analysis is now fully divulged in the Supporting Information for this article.

Device Fabrication and Characterization. PLEDs were fabricated with a device architecture of glass/ITO/PEDOT:PSS/polymer/LiF/Al. Prepatterned indium tin oxide (ITO) coated glass (25 mm \times 25 mm) was used with either a 12 or 20 Ω/\square resistance. ITO-coated glass was cleaned by sequential sonication in sodium dodecyl sulfate solution, 18.2 M Ω MilliQ water, acetone, and 2-propanol. Immediately following 2-propanol sonication, substrates were blown dry with nitrogen and exposed to oxygen plasma for 20 min. Under a particle free hood, substrates were spun cast with PEDOT:PSS (Baytron P VP Al 4083 which was filtered through 0.45 μ m nylon filters) at 5000 rpm for 45 s, then annealed for 20 min at 130 °C in an Ar filled glovebox with H₂O and O₂ concentrations of less than 0.1 ppm. In the glovebox, active layer solutions were prepared at 15 mg/mL concentrations in anhydrous and deoxygenated chlorobenzene and spun cast onto the PEDOT:PSS coated substrates for 60 s at 1000 rpm. Cathodes consisting of 1 nm LiF and 100 nm Al were thermally deposited on the substrates at a pressure of 1×10^{-6} mbar through shadowmasks defining 8 pixels/substrate, each with an area of 0.071 cm². Electroluminescence spectra were collected using an ISA SPEX Triax 180 spectrograph, maintained at \sim 140 K, with a Keithley 2400 sourcemeter driving the device at a constant current. Radiant emittance and current density data were acquired using a custom written LabVIEW program coupled with a calibrated UDT Instruments silicon diode and a Keithley 2400 sourcemeter. Luminance data were collected using a Konica CS-100 minolta chromameter with the device at a constant voltage bias.

RESULTS AND DISCUSSION

Synthesis and Physical Characterization. Perfectly regioregular polymers of the general architecture shown in Figure 2A may be synthesized in at least one of two ways. In our first report, we described a general method which allows for Suzuki coupling of aryl groups to regioregular borylated fluorene functionalized polyolefins.⁷⁴ However, this method was limited to polymers with no more than one electroactive group on every 21st polymer backbone carbon. This limitation was the result of solubility issues stemming from ionization of the polymer during the Suzuki coupling step. As shown in Scheme 1, this problem has been alleviated by reversing the

order of synthesis from post polymerization modification for installation of the chromophore to polymerization of fully functionalized monomers. The latter method allows for increased chromophore density, and materials containing chromophores on exactly every 21st, 15th, and ninth carbon have been prepared (though presumably, these numbers could be raised or lowered further via known synthetic protocols^{107–109}). Furthermore, the choice of terfluorenylidenes as the active species allows for hydrogenation of the residual backbone olefin after ADMET, thus providing a handle on material morphology, which is known to dramatically change upon olefin hydrogenation in similar polymers.¹¹⁰ The regioregularity of these polymers, as opposed to the regiorandom materials produced in various copolymerizations, and the distribution of chromophore densities over a reasonable range, provides good control over the average distance between electroactive groups in a set of materials. Their interchromophore distances as well as any potential aggregates' sizes and shapes should exhibit greater homogeneity (reduced polydispersity in distance/size/shape) than in analogous random copolymers, as previously observed in other systems containing interactive pendant groups.^{111,112} Although the synthesis of the polymers in this work was reported previously,⁷³ the design rationale and issues encountered during their preparation were not provided in detail, thus a more thorough discussion can be found in the Supporting Information.

Characterization of the polymers by gel permeation chromatography (GPC), differential scanning calorimetry (DSC), polarized optical microscopy, and atomic force microscopy (AFM) was carried out. The GPC and DSC data, were reported previously⁷³ and can also be found in the Supporting Information. Molecular weights were high in all cases ($M_n = 21\text{--}65$ kDa), although P-3,3-TF (21 kDa) and P-3,3-TF-S (22 kDa) exhibited somewhat lower M_n and PDI due to a cyclization issue also discussed in the Supporting Information. No melting transitions were detected during DSC experiments up to 200 °C at various scan rates ranging from 1 to 20 °C/min, and no birefringence was observed under polarized light microscopy. To further probe morphology, AFM measurements were carried out on spun cast polymer films; however, we again observed no unique features in any polymer. Instead, AFM indicated only very flat surfaces with root mean squared surface roughnesses around 0.3 nm (see Supporting Information for micrographs).

UV–Vis Characterization. To assess whether or not control over Φ_F in this system was achieved, thin films with nearly identical optical densities ($\pm 5\%$) were prepared by spin coating onto glass substrates from dilute solutions of each polymer in chloroform. Using identical instrument parameters, the front face fluorescence spectra of each film was then measured and corrected for the small changes in optical density of each sample (see Figure 3). Each measurement was carried out in duplicate after rotating the substrate 90°, and two films were prepared for each polymer (total of four measurements each).

Except for P-9,9-TF-S, it is evident that the relative Φ_F increases as the spacer between each fluorophore increases in length, and that regiorandom analogues also exhibit increased Φ_F . Both increases in Φ_F are presumably due to reduced $\pi\text{--}\pi$ interaction, which is known to systematically vary as a function of copolymer composition in regiorandom pendant π -functional materials;^{87–90} reduced $\pi\text{--}\pi$ interactions lead to

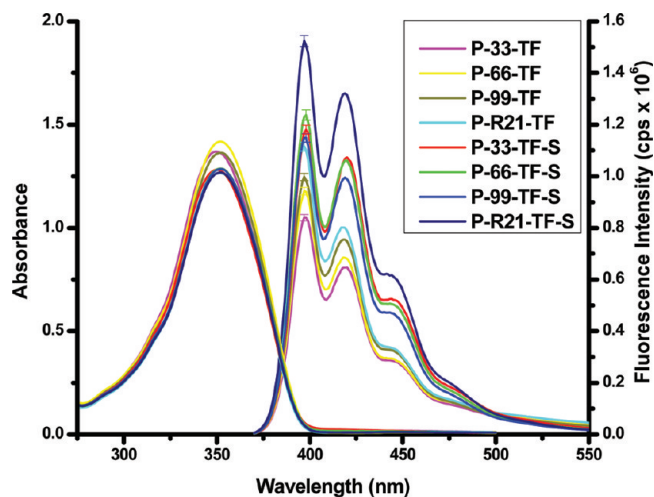


Figure 3. Solid-state absorbance and front-face fluorescence spectra (corrected for optical density at excitation = 350 nm). Error bars are 95% confidence intervals for the corrected fluorescence intensity at λ_{max} . All data points used to create the plots were averaged over four trials.

decreased energy migration and quenching. Furthermore, as evidence against the possibility of method error or false results due to various levels of residual transition metal catalyst contamination, we carried out similar comparative fluorescence measurements in chloroform solution; all polymers exhibited identical fluorescence intensities and therefore identical Φ_F (see Figure 4).

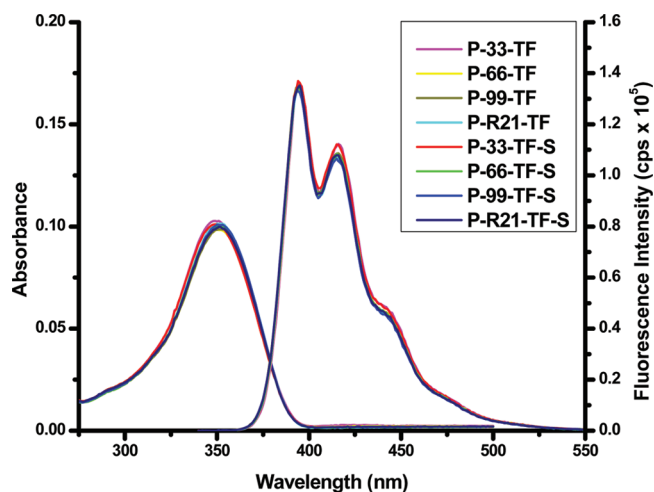


Figure 4. Chloroform solution absorbance and fluorescence spectra (corrected for optical density at excitation = 350 nm) for all polymers.

Careful examination of the data will show that P-9,9-TF-S is the only polymer which does not fit the aforementioned spacer length trend; indeed, it has the lowest Φ_F of the backbone-saturated polymers. This is perhaps the result of a unique morphology relative to the other materials. However, as previously discussed, we have been unable to directly observe any morphological features by AFM or optical microscopy in any of these materials.

PLED Fabrication and Characterization. Having demonstrated systematic control of solid-state Φ_F through polymer backbone run length variation, we were motivated to prepare relatively simple PLEDs using a Glass/ITO/PEDOT:PSS/

ActiveLayer/LiF/Al architecture. Electroluminescence spectra, radiant emittance, current density, and luminance data were collected for each device, and EQEs were calculated.

As shown in Figure 5, all devices exhibited similar but subtly different electroluminescence spectra. This is to be expected

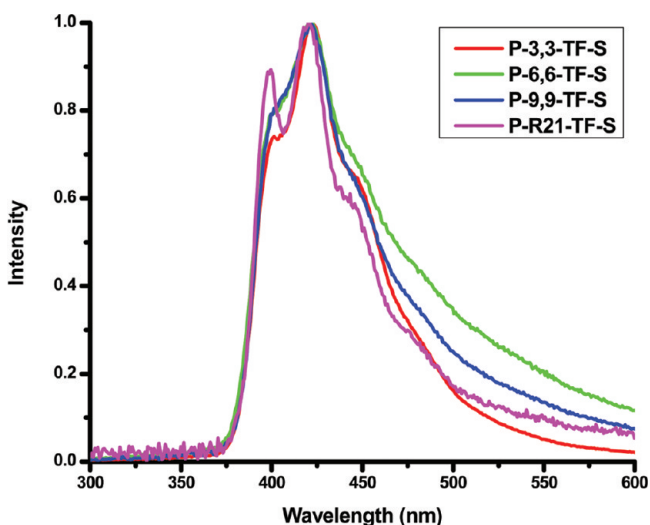


Figure 5. Normalized electroluminescent spectra of saturated polymers.

since each polymer contains identical chromophores but differing degrees of interaction between them. On the other hand, device performance varies greatly. Figures 6 and 7 show

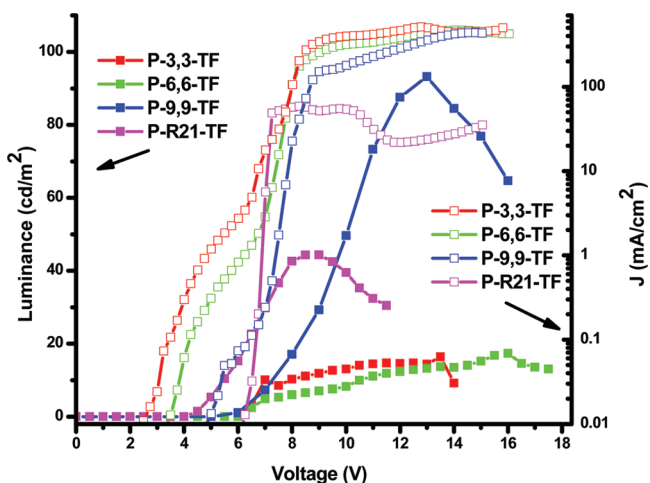


Figure 6. Luminance and current density vs driving voltage for devices fabricated from unsaturated polymers.

the current density and luminance as a function of applied voltage for devices fabricated from unsaturated and saturated polymers, respectively. These data are from single devices; however, device reproducibility is excellent as indicated by averaged EQE data shown in Figure 8. Examination of the current density plots for each device reveals an interesting trend; as the polymer backbone run length separating pendant chromophores increases, current density at identical driving voltages decreases. This is presumably due to reduced charge mobilities resulting from lower chromophore densities and longer hopping distances. Furthermore, regiorandom P-R21-TF, which is an analogue of P-9,9-TF, exhibits a somewhat

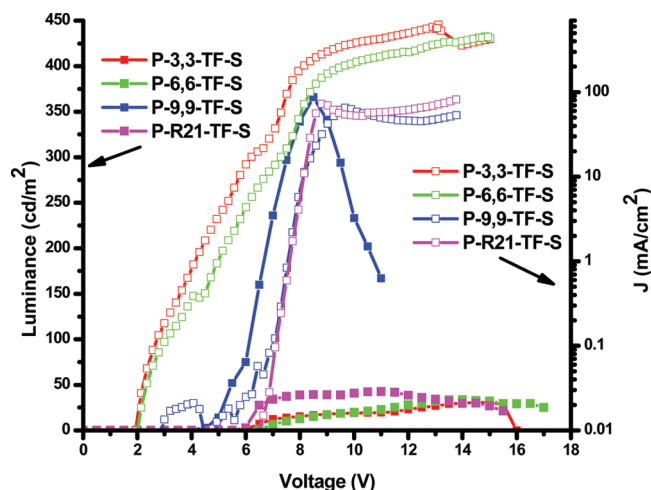


Figure 7. Luminance and current density vs driving voltage for devices fabricated from saturated polymers.

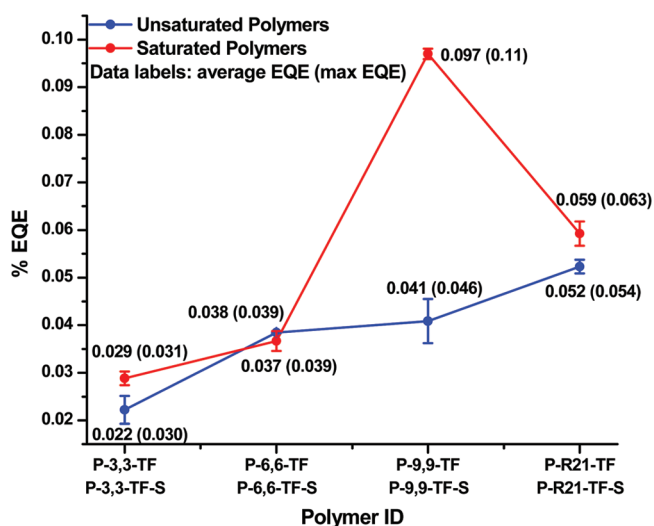


Figure 8. Average EQEs measured from eight pixels per polymer (error bars represent a full standard deviation).

lower current density. One might attribute this difference to reduced charge mobility resulting from reduced ordering in the regiorandom polymer; however, P-R21-TF and P-9,9-TF-S devices show nearly identical current densities, although the latter is somewhat special in its characteristics, as will be discussed below.

In contrast with the current density and solid-state Φ_F data, which shows general spacer length effects, device luminance output is somewhat less systematic. Instead, P-3,3-TF, P-3,3-TF-S, P-6,6-TF, and P-6,6-TF-S show similar luminance (<35 cd/m^2), P-R21-TF and P-R21-TF-S show some improvement (max of 43, 45 cd/m^2 respectively), while P-9,9-TF and P-9,9-TF-S show far greater luminosity (max of 93, 366 cd/m^2 respectively). Finally, EQEs have been calculated and are shown in Figure 8. Again, a general trend emerges, with longer backbone run lengths resulting in improved EQEs, thus it can be concluded that *lower chromophore densities* are actually *beneficial* to the efficiency of this class of materials in PLEDs. Additionally, for all polymers except P-9,9-TF-S, device EQE was only slightly effected by backbone saturation; however in P-9,9-TF-S, saturation led to an over 2-fold improvement in EQE. Much like the fluorescence and PLED luminance measure-

ments, in which P-9,9-TF-S was an outlier, such an improvement indicates again that morphological changes may have occurred as a result of backbone saturation in this polymer and that such changes play an important role in its performance. Furthermore, electrode surface texturization, which will be discussed below, provides additional evidence for morphological differences between the materials studied here.

Having demonstrated systematic control of PLED EQE via spacer length variation, it is important to discuss two anomalous observations: emergence of gold coloration on the aluminum electrode surface of *only* P-9,9-TF-S devices, indicative of morphological changes leading to surface texturization, as well as temporal and spatial modulation of PLED pixel luminosity. As expected, vacuum-deposited aluminum electrodes for all other devices were bright silver in color (see Figure 9). Here again, the morphological differences

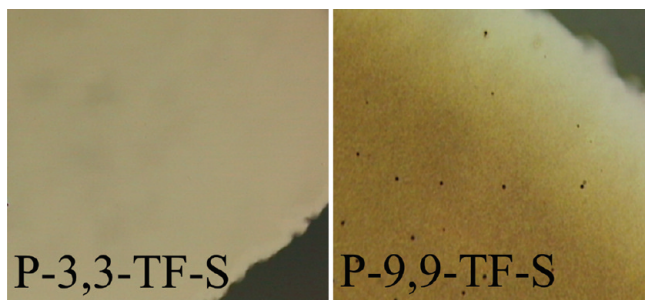


Figure 9. Optical microscope images of electrode surfaces on P-9,9-TF-S and, as a representative image, P-3,3-TF-S devices.

in P-9,9-TF-S are highlighted by the occurrence of electrode surface coloration/texturization; however, attempts to elucidate the nature of this phenomenon via AFM of the electrode have proven quite challenging.

The observation of spatial and temporal fluctuation of PLED luminosity (see Figure 10) is somewhat less puzzling. Since the

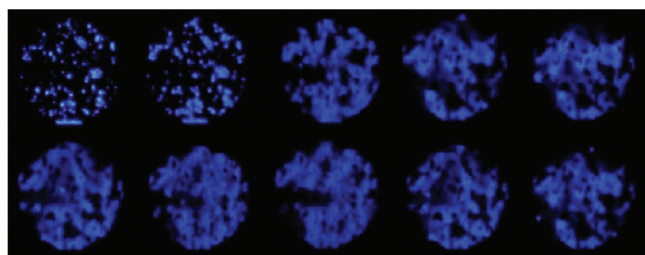


Figure 10. Sequence of time lapsed photographs of P-9,9-TF-S pixel at a constant driving voltage of 13 V beginning at device turn on (top left) and ending 22.5 s later (bottom right).

T_g s of these materials are relatively low (22–50 °C, see Supporting Information), we believe the fluctuation results from Joule heating, which has been demonstrated to raise the temperature of PLEDs by several tens of degrees,^{113–115} thus providing the polymer chains with sufficient thermal energy to undergo long-range segmental motion. This would allow microdomains to temporarily attain a highly emissive morphology before temporarily changing to a darker one. Furthermore, overall luminance increases over the first few seconds of device operation before reaching a plateau, indicating that Joule heating is, in this case, beneficial to device performance. The luminosity fluctuation continues until the

device is turned off or is driven to burn out at high voltage biases. Annealing at 80 °C (well above polymer T_g s) before carrying out measurements makes no difference in EQE or the occurrence of the luminosity fluctuation. We are currently investigating the possibility of utilizing the residual backbone alkenes in the unsaturated polymers for cross-linking, as this would reduce the segmental motion hypothesized as the cause of this optical phenomenon.

CONCLUSIONS

We have synthesized and characterized a series of six perfectly regioregular electroactive polyolefins and two regiorandom analogues. Differential scanning calorimetry and polarized optical microscopy illustrate that these materials are amorphous. They exhibit *spacer length dependent* solid-state Φ_F , PLED current densities (presumably resulting from spacer length dependent charge mobilities), and PLED EQEs. In summary, longer spacer lengths result in higher Φ_F , lower charge mobility (as manifested in PLED current density), and higher PLED EQE. Furthermore, by comparing the four P-9,9 and P-R21 derivatives, we found that regioregularity reduces solid-state Φ_F . Interpretation of current densities in the set of four is less straightforward; charge mobility was improved by regioregularity in the unsaturated pair but not in the saturated pair (which we believe is a special case due to suspected morphological differences in P-9,9-TF-S). While the PLED performance of this series of polymers leaves much to be desired, we believe the general trends which they exhibit will be useful in the design of new electroactive materials based on pendant π -functional architectures, and their direct application in other Φ_F dependent devices such as scintillation detectors or luminescent solar concentrators may prove more valuable.

ASSOCIATED CONTENT

Supporting Information

Synthesis discussion, detailed experimental data, and AFM images. This material is available free of charge via the Internet at <http://pubs.acs.org>.

AUTHOR INFORMATION

Corresponding Author

*E-mail: (J.R.R.) Reynolds@chem.ufl.edu; (K.B.W.) Wagener@chem.ufl.edu.

ACKNOWLEDGMENTS

B.S.A and K.B.W gratefully acknowledge financial support from the National Science Foundation (DMR 0703261). P.M.W., K.R.G., and J.R.R gratefully acknowledge financial support from the U.S. Army (W31P4Q-08-1-0003). The views and conclusions contained in this document are those of the authors and should not be interpreted as representing the official policies, either expressed or implied, of the U.S. Army, the National Science Foundation, or the U.S. Government.

REFERENCES

- (1) Energy Savings Potential of Solid State Lighting in General Illumination Applications; Building Technologies Program, Office of Energy Efficiency and Renewable Energy, U.S. Department of Energy: Washington, DC, November, 2003.
- (2) Organic Light Emitting Diodes (OLEDs) for General Illumination Update 2002; Optoelectronics Industry Development Association: Washington, DC, August, 2002.

- (3) Crawford, M. H. *IEEE J. Sel. Top. Quantum. Electron.* **2009**, *15*, 1028.
- (4) Carlise, J. R.; Wang, X.-Y.; Weck, M. *Macromolecules* **2005**, *38*, 9000.
- (5) Schulz, G. L.; Chen, X.; Chen, S.-A.; Holdcroft, S. *Macromolecules* **2006**, *39*, 9157.
- (6) Evans, N. R.; Sudha Devi, L.; Mak, C. S. K.; Watkins, S. E.; Pasqu, S. I.; Köhler, A.; Friend, R. H.; Williams, C. K.; Holmes, A. B. *J. Am. Chem. Soc.* **2006**, *128*, 6647.
- (7) Friend, R. H.; Gymer, R. W.; Holmes, A. B.; Burroughes, J. H.; Marks, R. N.; Taliani, C.; Bradley, D. D. C.; Dos Santos, D. A.; Brédas, J. L.; Lögdlund, M.; Salaneck, W. R. *Nature* **1999**, *397*, 121.
- (8) Heeger, A. J. *Angew. Chem., Int. Ed.* **2001**, *40*, 2591.
- (9) Sessolo, M.; Bolink, H. J. *Adv. Mater.* **2011**, *23*, 1829.
- (10) Forrest, S. R. *Nature* **2004**, *428*, 911.
- (11) Wu, H.; Huang, F.; Mo, Y.; Yang, W.; Wang, D.; Peng, J.; Cao, Y. *Adv. Mater.* **2004**, *16*, 1826.
- (12) Chen, G.; Craven, M.; Kim, A.; Munkholm, A.; Watanabe, S.; Camras, M.; Götz, W.; Steranka, F. *Phys. Status Solidi A* **2008**, *205*, 1086.
- (13) Huang, W.-S.; Wu, Y.-H.; Lin, H.-C.; Lin, J. T. *Polym. Chem.* **2010**, *1*, 494.
- (14) Gong, X.; Robinson, M. R.; Ostrowski, J. C.; Moses, D.; Bazan, G. C.; Heeger, A. J. *Adv. Mater.* **2002**, *14*, 581.
- (15) Deng, L.; Furuta, P. T.; Garon, S.; Li, J.; Kavulak, D.; Thompson, M. E.; Fréchet, J. M. J. *Chem. Mater.* **2005**, *18*, 386.
- (16) Cao, Y.; Parker, I. D.; Yu, G.; Zhang, C.; Heeger, A. J. *Nature* **1999**, *397*, 414.
- (17) Krames, M. R.; Ochiali-Holcomb, M.; Höffler, G. E.; Carter-Coman, C.; Chen, E. I.; Tan, I.-H.; Grillot, P.; Gardner, N. F.; Chui, H. C.; Huang, J.-W.; Stockman, S. A.; Kish, F. A.; Craford, M. G.; Tan, T. S.; Kocot, C. P.; Hueschen, M.; Posselt, J.; Loh, B.; Sasser, G.; Collins, D. *Appl. Phys. Lett.* **1999**, *75*, 2365.
- (18) Krames, M. R.; Shchekin, O. B.; Mueller-Mach, R.; Mueller, G. O.; Zhou, L.; Harbers, G.; Craford, M. G. *J. Disp. Technol.* **2007**, *3*, 160.
- (19) Kabra, D.; Lu, L. P.; Song, M. H.; Snaith, H. J.; Friend, R. H. *Adv. Mater.* **2010**, *22*, 3194.
- (20) Hyunkoo, L.; Insun, P.; Jeonghun, K.; Yoon, D. Y.; Changhee, L. *Appl. Phys. Lett.* **2010**, *96*, 153306.
- (21) Lu, H.-H.; Ma, Y.-S.; Yang, N.-J.; Lin, G.-H.; Wu, Y.-C.; Chen, S.-A. *J. Am. Chem. Soc.* **2011**, *133*, 9634.
- (22) Hung, L. S.; Chen, C. H. *Mater. Sci. Eng., R* **2002**, *39*, 143.
- (23) Huang, F.; Zhang, Y.; Liu, M. S.; Jen, A. K. Y. *Adv. Funct. Mater.* **2009**, *19*, 2457.
- (24) This set of references is not intended to be a complete list of record breaking LEDs. Some of the highest performance LEDs have been referenced for comparison. Some reports containing similar comparative statements have also been referenced irrespective of the reported device performance therein.
- (25) Armstrong, N. R.; Wang, W.; Alloway, D. M.; Placencia, D.; Ratcliff, E.; Brumbach, M. *Macromol. Rapid Commun.* **2009**, *30*, 717.
- (26) Redecker, M.; Bradley, D. D. C.; Inbasekaran, M.; Woo, E. P. *Appl. Phys. Lett.* **1998**, *73*, 1565.
- (27) Liu, C.-Y.; Chen, S.-A. *Macromol. Rapid Commun.* **2007**, *28*, 1743.
- (28) Monkman, A. P.; Rothe, C.; King, S. M. *Proc. IEEE* **2009**, *97*, 1597.
- (29) Ma, H.; Liu, M. S.; Jen, A. K. Y. *Polym. Int.* **2009**, *58*, 594.
- (30) Gao, H.; Zhang, H.; Mo, R.; Sun, S.; Su, Z.-M.; Wang, Y. *Synth. Met.* **2009**, *159*, 1767.
- (31) Tessler, N. *Appl. Phys. Lett.* **2000**, *77*, 1897.
- (32) van Bavel, S.; Veenstra, S.; Loos, J. *Macromol. Rapid Commun.* **2010**, *31*, 1835.
- (33) Chen, M.-C.; Hung, W.-C.; Su, A.-C.; Chen, S.-H.; Chen, S.-A. *J. Phys. Chem. B* **2009**, *113*, 11124.
- (34) Sirringhaus, H.; Brown, P. J.; Friend, R. H.; Nielsen, M. M.; Bechgaard, K.; Langeveld-Voss, B. M. W.; Spiering, A. J. H.; Janssen, R. A. J.; Meijer, E. W.; Herwig, P.; de Leeuw, D. M. *Nature* **1999**, *401*, 685.
- (35) Yang, X.; Loos, J.; Veenstra, S. C.; Verhees, W. J. H.; Wienk, M. M.; Kroon, J. M.; Michels, M. A. J.; Janssen, R. A. J. *Nano Lett.* **2005**, *5*, 579.
- (36) Sworakowski, J.; Janus, K.; Nespurek, S.; Vala, M. *IEEE Tran. Dielectr. Electr. Insul* **2006**, *13*, 1001.
- (37) Silinsh, E. A. *Organic molecular crystals: their electronic states*; Springer-Verlag: Berlin, 1980.
- (38) Silinsh, E. A.; Capek, V. *Organic molecular crystals: interaction, localization, and transport phenomena*; American Institute of Physics: New York, 1994.
- (39) Vu, T. T.; Badre, S.; Dumas-Verdes, C. c.; Vachon, J.-J.; Julien, C.; Audebert, P.; Senotrusova, E. Y.; Schmidt, E. Y.; Trofimov, B. A.; Pansu, R. B.; Clavier, G.; Meallet-Renault, R. *J. Phys. Chem. C* **2009**, *113*, 11844.
- (40) Mikroyannidis, J. A.; Fenenko, L.; Adachi, C. *J. Phys. Chem. B* **2006**, *110*, 20317.
- (41) Chen, C.-T. *Chem. Mater.* **2004**, *16*, 4389.
- (42) Tong, H.; Hong, Y.; Dong, Y.; Ren, Y.; Haussler, M.; Lam, J. W. Y.; Wong, K. S.; Tang, B. Z. *J. Phys. Chem. B* **2007**, *111*, 2000.
- (43) Birks, J. B. *Photophysics of aromatic molecules*; Wiley-Interscience: London, 1970.
- (44) Liang, Z.-Q.; Li, Y.-X.; Yang, J.-X.; Ren, Y.; Tao, X.-T. *Tetrahedron Lett.* **2011**, *52*, 1329.
- (45) Liu, Y.; Tao, X.; Wang, F.; Dang, X.; Zou, D.; Ren, Y.; Jiang, M. *Org. Electron.* **2009**, *10*, 1082.
- (46) Levschin, V. L. *Z. Phys.* **1927**, *43*, 230.
- (47) Rabinowitch, E.; Epstein, L. F. *J. Am. Chem. Soc.* **1941**, *63*, 69.
- (48) Jablonski, A. *Acta Phys. Pol., A* **1955**, *14*, 295.
- (49) Knox, R. S. *Physica* **1968**, *39*, 361.
- (50) Bojarski, P.; Kulak, L.; Bojarski, C.; Kowski, A. *J. Fluoresc.* **1995**, *5*, 307.
- (51) Gochanour, C. R.; Fayer, M. D. *J. Phys. Chem.* **1981**, *85*, 1989.
- (52) Gaviola, E.; Pringsheim, P. *Z. Phys.* **1924**, *24*, 24.
- (53) Weber, G. *Trans. Faraday Soc.* **1954**, *50*, 552.
- (54) Kowski, A.; Bojarski, P.; Kubicki, A.; Bojarski, C. *J. Lumin.* **1991**, *50*, 61.
- (55) Johansson, L. B. Å.; Peter, E.; Westlund, P. O. *J. Chem. Phys.* **1996**, *105*, 10896.
- (56) Håkansson, P.; Isaksson, M.; Westlund, P.-O.; Johansson, L. B. A. *J. Phys. Chem. B* **2004**, *108*, 17243.
- (57) Isaksson, M.; Hägglöf, P.; Håkansson, P.; Ny, T.; Johansson, L. B. A. *Phys. Chem. Chem. Phys.* **2007**, *9*, 3914.
- (58) Bojarski, C.; Grabowska, J.; Kulak, L.; Kuśba, J. *J. Fluoresc.* **1991**, *1*, 183.
- (59) Twardowski, R.; Bauer, R. K. *Chem. Phys. Lett.* **1982**, *93*, 56.
- (60) Baumann, J.; Fayer, M. D. *J. Chem. Phys.* **1986**, *85*, 4087.
- (61) Huber, D. L. *Phys. Rev. B* **1979**, *20*, 2307.
- (62) Burshtein, A. I. *Zh. Eksp. Teor. Fiz.* **1972**, *62*, 1695.
- (63) Kalinin, S.; Johansson, L. B.-Å. *J. Fluoresc.* **2004**, *14*, 681.
- (64) Kalinin, S. V.; Molotkovsky, J. G.; Johansson, L. B.-Å. *Spectrochim. Acta, Part A* **2002**, *58*, 1087.
- (65) Kalinin, S.; Molotkovsky, J. G.; Johansson, L. B.-Å. *J. Phys. Chem. B* **2003**, *107*, 3318.
- (66) Opanasyuk, O.; Johansson, L. B.-Å. *Phys. Chem. Chem. Phys.* **2010**, *12*, 7758.
- (67) Norlin, N.; Westlund, P. O.; Johansson, L. B.-Å. *J. Fluoresc.* **2009**, *19*, 837.
- (68) Norlin, N.; Håkansson, P.; Westlund, P. O.; Johansson, L. B.-Å. *Phys. Chem. Chem. Phys.* **2008**, *10*, 6962.
- (69) Forster, T. *Mod. Quantum Chem., Lect. Istanbul Int. Summer Sch.* **1965**, 93.
- (70) Jares-Erijman, E. A.; Jovin, T. M. *Nat. Biotechnol.* **2003**, *21*, 1387.
- (71) van der Meer, B. W.; Coker, G.; Chen, S.-Y. S., *Resonance energy transfer: theory and data*; VCH: New York, 1994.
- (72) Troisi, A. *Adv. Polym. Sci.* **2010**, *223*, 259.

- (73) Aitken, B. A.; Mei, J.; Graham, K. R.; Reynolds, J. R.; Wagener, K. B. *Polym. Prepr.* **2011**, *52*, 467.
- (74) Mei, J.; Aitken, B. S.; Graham, K. R.; Wagener, K. B.; Reynolds, J. R. *Macromolecules* **2010**, *43*, 5909.
- (75) Nantalaksakul, A.; Krishnamoorthy, K.; Thayumanavan, S. *Macromolecules* **2010**, *43*, 37.
- (76) Park, J. H.; Yun, C.; Park, M. H.; Do, Y.; Yoo, S.; Lee, M. H. *Macromolecules* **2009**, *42*, 6840.
- (77) Sugiyama, K.; Hirao, A.; Hsu, J.-C.; Tung, Y.-C.; Chen, W.-C. *Macromolecules* **2009**, *42*, 4053.
- (78) Hsu, J.-C.; Chen, Y.; Kakuchi, T.; Chen, W.-C. *Macromolecules* **2011**, *44*, 5168.
- (79) Hu, Z.; Reichmanis, E. *J. Polym. Sci., Part A: Polym. Chem.* **2011**, *49*, 1155.
- (80) Kang, B.-G.; Kang, N.-G.; Lee, J.-S. *Macromolecules* **2010**, *43*, 8400.
- (81) Hsu, J.-C.; Sugiyama, K.; Chiu, Y.-C.; Hirao, A.; Chen, W.-C. *Macromolecules* **2010**, *43*, 7151.
- (82) Naga, N.; Sakai, H.; Usui, C.; Tomoda, H. *J. Polym. Sci., Part A: Polym. Chem.* **2010**, *48*, 3542.
- (83) Liu, C.-L.; Hsu, J.-C.; Chen, W.-C.; Sugiyama, K.; Hirao, A. *ACS Appl. Mater. Interfaces* **2009**, *1*, 1974.
- (84) Furuta, P. T.; Deng, L.; Garona, S.; Thompson, M. E.; Fréchet, J. M. J. *J. Am. Chem. Soc.* **2004**, *126*, 15388.
- (85) Park, M. H.; Park, J. H.; Do, Y.; Lee, M. H. *Polymer* **2010**, *51*, 4735.
- (86) Park, J. H.; Yun, C.; Koh, T.-W.; Do, Y.; Yoo, S.; Lee, M. H. *J. Mater. Chem.* **2011**, *21*, 5422.
- (87) Anderson, R. A.; Reid, R. F.; Soutar, I. *Eur. Polym. J.* **1980**, *16*, 945.
- (88) McNally, I.; Reid, R. F.; Rutherford, H.; Soutar, I. *Eur. Polym. J.* **1979**, *15*, 723.
- (89) Anderson, R. A.; Reid, R. F.; Soutar, I. *Eur. Polym. J.* **1979**, *15*, 925.
- (90) Reid, R. F.; Soutar, I. *J. Polym. Sci., Polym. Phys. Ed.* **1978**, *16*, 231.
- (91) Moad, G.; Chen, M.; Häussler, M.; Postma, A.; Rizzardo, E.; Thang, S. H. *Polym. Chem.* **2011**, *2*, 492.
- (92) Sommer, M.; Lang, A. S.; Thelakkat, M. *Angew. Chem., Int. Ed.* **2008**, *47*, 7901.
- (93) Lindner, S. M.; Hüttner, S.; Chiche, A.; Thelakkat, M.; Krausch, G. *Angew. Chem., Int. Ed.* **2006**, *45*, 3364.
- (94) Hong, Y.; Miller, L. L. *Chem. Mater.* **1995**, *7*, 1999.
- (95) Iacono, S. T.; Budy, S. M.; Moody, J. D.; Smith, R. C.; Smith, D. W. *Macromolecules* **2008**, *41*, 7490.
- (96) Asai, K.; Konishi, G.-I.; Sumi, K.; Mizuno, K. *J. Organomet. Chem.* **2010**, *696*, 1236.
- (97) Hargadon, M. T.; Davey, E. A.; McIntyre, T. B.; Gnanamgari, D.; Wynne, C. M.; Swift, R. C.; Zimbalist, J. R.; Fredericks, B. L.; Nicastro, A. J.; Goodson, F. E. *Macromolecules* **2008**, *41*, 741.
- (98) Guimard, N. K. E.; Sessler, J. L.; Schmidt, C. E. *Macromolecules* **2009**, *42*, 502.
- (99) Quaranta, A.; Carturan, S.; Marchi, T.; Cinausero, M.; Scian, C.; Kravchuk, V. L.; Degerlier, M.; Gramegna, F.; Poggi, M.; Maggioni, G. *Opt. Mater.* **2010**, *32*, 1317.
- (100) Adadurov, A. F.; Yelyseev, D. A.; Titskaya, V. D.; Lebedev, V. N.; Zhmurin, P. N. *Radiat. Meas.* **2011**, *46*, 498.
- (101) Kosfeld, R.; Masch, K. Luminescence of Thin Plastic Scintillators. In *Multicomponent Polymer Systems*; Platzner, N. A. J., Ed.; ACS: Washington, DC, 1971; Vol. 99, pp 581–588.
- (102) Amanda, C.; Rahul, B.; Daniel, F.; Ye, X.; Ngai, C.; Liberato, M.; Andreas, B. S.; Jana, Q.; Michael, D.; Keith, B. Luminescent Solar Concentrators. In *Nanotechnology for Photovoltaics*; Tsakalakos, L., Ed.; CRC Press: Boca Raton, FL, 2010; pp 323–349.
- (103) Fara, V. L.; Grigorescu, R.; Dimofte, C. Transparent Insulation and Superwindows. In *Optimum efficiency of fluorescent solar concentrators*; Optical Materials Technology for Energy Efficiency and Solar Energy Conversion XI: Selective Materials, Concentrators and Reflectors; SPIE: Toulouse-Labege, France, 1992; pp 306–312.
- (104) Fisher, B.; Biddle, J. *Sol. Energy Mater. Sol. Cells* **2011**, *95*, 1741.
- (105) Mansour, A. F.; Killa, H. M. A.; Abd El-Wanees, S.; El-Sayed, M. Y. *Polym. Test.* **2005**, *24*, 519.
- (106) Rowan, B. C.; Wilson, L. R.; Richards, B. S. *IEEE J. Sel. Top. Quantum Electron.* **2008**, *14*, 1312.
- (107) Zuluaga, F.; Inci, B.; Nozue, Y.; Hosoda, S.; Wagener, K. B. *Macromolecules* **2009**, *42*, 4953.
- (108) Baughman, T. W.; Sworen, J. C.; Wagener, K. B. *Macromolecules* **2006**, *39*, 5028.
- (109) Inci, B.; Wagener, K. B. *J. Am. Chem. Soc.* **2011**, *133*, 11872.
- (110) Berda, E. B.; Wagener, K. B. *Macromolecules* **2008**, *41*, 5116.
- (111) Baughman, T. W.; Chan, C. D.; Winey, K. I.; Wagener, K. B. *Macromolecules* **2007**, *40*, 6564.
- (112) Seitz, M. E.; Chan, C. D.; Oppen, K. L.; Baughman, T. W.; Wagener, K. B.; Winey, K. I. *J. Am. Chem. Soc.* **2010**, *132*, 8165.
- (113) Zhou, X.; He, J.; Liao, L. S.; Lu, M.; Ding, X. M.; Hou, X. Y.; Zhang, X. M.; He, X. Q.; Lee, S. T. *Adv. Mater.* **2000**, *12*, 265.
- (114) Tessler, N.; Harrison, N. T.; Thomas, D. S.; Friend, R. H. *Appl. Phys. Lett.* **1998**, *73*, 732.
- (115) Choi, S. H.; Lee, T. I.; Baik, H. K.; Roh, H. H.; Kwon, O.; Suh, D. h. *Appl. Phys. Lett.* **2008**, *93*, 183301.

Polymer Library Comprising Fluorene and Carbazole Homo- and Copolymers for Selective Single-Walled Carbon Nanotubes Extraction

Fabien Lemasson,[†] Nicolas Berton,[†] Jana Tittmann,[†] Frank Hennrich,[†] Manfred M. Kappes,^{*,†,‡,§} and Marcel Mayor^{*,†,§,⊥}

[†]Institute for Nanotechnology (INT), Karlsruhe Institute of Technology (KIT), 76021 Karlsruhe, Germany

[‡]Institute of Physical Chemistry, Karlsruhe Institute of Technology, 76021 Karlsruhe, Germany

[§]DFG Center for Functional Nanostructures, 76028 Karlsruhe, Germany

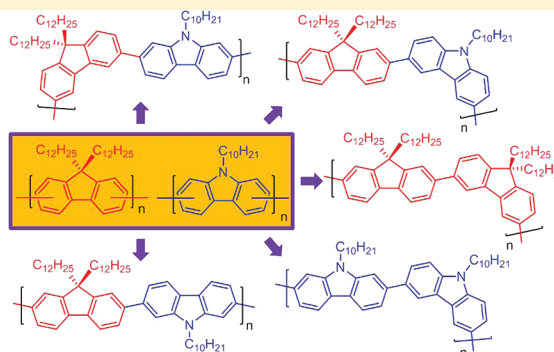
[⊥]Department of Chemistry, University of Basel, 4003 Basel, Switzerland

S Supporting Information

structural variations
polymer library

SWNTs
sorting

structure-property
relationship



ABSTRACT: To date, (n, m) single-walled carbon nanotubes (SWNTs) cannot be selectively synthesized. Therefore, postprocessing of SWNTs including solubilization and sorting is necessary for further applications. Toward this goal, we have synthesized a polymer library consisting of fluorene- and carbazole-based homo- and copolymers. Variations of the connection of these aromatics together with the incorporation of further conjugated monomers give access to a broad diversity of polymers. Their ability to selectively wrap specific (n, m) species is investigated toward HiPco SWNTs raw material which contains more than 40 (n, m) species. Absorption and fluorescence spectroscopies were used to analyze SWNTs/polymer suspensions. These results provide evidence for selective SWNTs/polymer interactions and allow a more detailed assessment of polymer structure–property relationships, thus paving the way toward custom synthesis of polymers for single (n, m) SWNTs extraction.

INTRODUCTION

Single-walled carbon nanotubes (SWNTs) exhibit unique physical and mechanical properties, making them excellent candidates for applications in the fields of optics, electronics, high-strength fibers, and electrolytes.¹ The corresponding raw materials are produced in bulk scale using several different processes including chemical vapor deposition (CVD), laser vaporization, or arc discharge. However, all these methods are not selective in terms of electronic structure type (metallic or semiconducting) or chiral angle (n, m) .² Despite many efforts in this direction, selective synthetic methods yielding monodisperse (n, m) SWNT samples are still not available. As their physical properties are mainly dictated by their chiral angle, postprocessing including sorting of SWNTs is needed to tackle fundamental issues as well as for applications in electronics, optoelectronics, and photonics.³

Any postprocessing approach requires the preparation of SWNT suspensions, either using covalent or noncovalent

functionalization.⁴ The former approach induces defects on the SWNT sidewalls which degrade their physical properties. In the latter approach, the SWNT intrinsic properties remain mainly unchanged due to the preservation of the sp^2 -carbon hybridization of their backbone. This approach was chosen to solubilize SWNTs for enrichment and sorting and several methods were developed for this purpose, which include DNA wrapping followed by ion-exchange chromatography,⁵ solubilization using detergents followed by either dielectrophoresis,⁶ density gradient centrifugation⁷ or nonlinear density gradient centrifugation,⁸ dispersion with small molecules,⁹ or polymer wrapping.¹⁰ Recently, several types of conjugated polymers have been shown to be selective toward a few (n, m) species like poly(9,9-dialkyl-2,7-fluorene) for large chiral angles (close to

Received: August 19, 2011

Revised: December 16, 2011

Published: December 29, 2011



armchair: $\theta \geq 25^\circ$)^{10a,c,h,i} or poly(*N*-decyl-2,7-carbazole) for lower chiral angles (typically $10^\circ \leq \theta \leq 20^\circ$).^{10b} At the same time they also exhibit strong selectivity toward semiconducting SWNTs. This approach is of great interest due to the relatively cheap availability of these materials and due to the perspectives for further improvement thanks to the great variety of structural modifications possible with these types of structures.

Despite numerous studies comprising experimental probes as well as molecular modeling of polymer/SWNT interactions, the reasons for selective solubilization of SWNTs are not fully understood.^{10–12} In order to investigate the correlation between the polymer structures and its SWNT dispersing features, a systematic variation of the polymers structure is desirable. Here we have therefore investigated a small polymer library comprising homo- and copolymers based on 9,9-didodecylfluorene and *N*-alkylcarbazole units connected either in the 2,7 or 3,6 position. The selectivity of these polymers was investigated toward HiPco SWNTs as this material contains more than 40 different (*n*, *m*) tube types ranging from 0.7 to 1.3 nm diameter.¹³ Despite a wide range of parameters able to influence the polymer/SWNT interactions, significant information based on polymeric structural aspect was identified. Although many variables are still not identified, the structural diversity of the library allows to get more insight into specific interactions of polymer/SWNTs and hopefully paves the way toward custom sorting of single (*n*, *m*) species.

■ RESULTS AND DISCUSSION

Synthesis of Monomers and Polymers. The library comprises four families which include 23 homo- and copolymers stemming from (i) 9,9-didodecyl-2,7-fluorenyl, (ii) 9,9-didodecyl-3,6-fluorenyl, (iii) *N*-alkyl-2,7-carbazolyl, and (iv) *N*-alkyl-3,6-carbazolyl. Additionally, combinations of the aforementioned subunits either with available dihaloareomatics or with themselves completed the collection of copolymers. An overview of the library is given in Table 1. All these conjugated polymers were synthesized by Suzuki coupling, except for polymer **P5** which was synthesized by Yamamoto coupling and polymer **P9** which was assembled by Kumada coupling (Scheme 3). Details of synthetic procedures for monomers and polymers are given in the Supporting Information. The synthesis of several polymers presented in this study has already been reported, namely polymers **P1**,¹⁴ **P7**,^{10b} and **P15–P20**.^{10f}

Yamamoto and Kumada couplings required dihaloareomatics as building blocks, whereas Suzuki cross-coupling required boronic esters and a building block comprising two halides or pseudohalides. Diboronic esters **2**,¹⁵ **4**,^{10b} and **6**¹⁶ were used in this study to access the diversity of the library. They were synthesized by palladium-catalyzed Miyaura borylation of their corresponding dibromides **1**, **3**, and **5**, respectively (Scheme 1). Monoboronic ester **12** (Scheme 2) was synthesized by monolithiation of dibromide **11**¹⁷ followed by quenching with isopropoxy-pinacolborane, yielding monomer **12** in 37% yield. The synthesis of 3,6-dibromofluorene **9** was shortened from five to three steps¹⁸ by starting from the commercially available phenanthrenequinone to access 3,6-dibromo-9,9-didodecylfluorene **10** after alkylation (Scheme 2). Direct reduction of ketone **8** using either hydrazine hydrate¹⁹ or polysiloxane in combination with tris(pentafluorophenyl)borane afforded 3,6-dibromofluorene in good yields. Reduction of ketone **8** using magnesium in dry methanol yields the alcohol.²⁰ Other haloaromatics were commercially available or synthesized according to the literature (see Supporting Information).

For convenience, the yields and molecular weights of the polymers described in this article are summarized in Table 2. Diboronic ester **2**, which displays a 2,7-fluorenyl moiety, was used to synthesize a large part of the library and was reacted in a Suzuki coupling with 11 comonomers to access a variety of polymers. Thus, reaction with its parents 2,7-dibromo-9,9-didodecylfluorene **1** yielded poly(9,9-didodecylfluorene-2,7-diyl) **P1**, in very good yield (99%). Copolymer **P2**, featuring a 2,7 and a 3,6 fluorenyl moiety, was obtained by reaction of diboronic ester **2** with dibromide **10** in very good yield (99%). Strictly alternating copolymers **P6** and **P10**, in which a 2,7 and 3,6 carbazolyl moiety is installed, were synthesized from dibromide **3** and **11** in 98% and 94% yield, respectively. Electron-withdrawing groups such as BTD (benzo-2,1,3-thiadiazole) and anthraquinone were also introduced via their corresponding 4,7-dibromo-2,1,3-benzothiadiazole and 1,5-dichloroanthraquinone to yield polymers **P13** and **P15** in 96% and 80% yields, respectively. Finally, a series of five polyaromatics comonomers were reacted with diboronic ester **2**, namely 1,4-dibromonaphthalene, 1,5-bis(trifluoromethylsulfonyloxy)naphthalene, 1,5-dibromoanthracene, 2,6-dibromoanthracene, and 9,10-dibromoanthracene to access polymers **P23** (90%), **P17** (95%), **P19** (88%), **P21** (94%), and **P22** (88%), respectively.

Diboronic ester **4**, displaying a 2,7-carbazolyl moiety, was also reacted in a Suzuki coupling with various (pseudo)haloareomatics to access a large diversity of polymers. Reaction with its parent dibromide **3** yielded poly(*N*-decyl-2,7-carbazole) in **P7** in 76% yield. Polymers **P3** and **P11**, which display a 3,6-fluorenyl and carbazolyl moieties, were obtained from dibromide **10** and **11** in 94 and 89% yield, respectively. The reddish polymer **P14** was synthesized from dibromide **5** in 29% yield. The low yield might be attributed to the low solubility of this polymer. Finally, reaction of diboronic ester **4** with 1,5-dichloroanthraquinone, 1,5-bis(trifluoromethylsulfonyloxy)naphthalene, and 1,5-dibromoanthracene allowed the synthesis of polymers **P16** (39%), **P18** (97%), and **P20** (79%), respectively.

Diboronic ester **6** was reacted first with dibromide **10** to access polymer **P4** (87%) which allowed the introduction of a BTD moiety to a 3,6-fluorenyl moiety. Moreover, the low solubility of polymer **P14** led us to increase the number of carbon atoms in the *N*-alkyl side chain. Thus, diboronic ester **6** was reacted with carbazole **7**, which displays a branched 2-hexyldecyl chain at the carbazole nitrogen atom, to give the reddish polymer **P8** in 76% yield.

Finally, three homopolymers were obtained as follow. A Suzuki coupling of the bifunctional carbazole **12** yielded poly(*N*-decylcarbazole-3,6-diyl) **P12**, and homopolymer **P5** was obtained via Yamamoto homocoupling of its corresponding dibromide **10**. As previously observed for similar 3,6-linked structures, it should be noticed that ¹H NMR spectrum and SEC data of **P5** and **P12** point at the presence of cyclic oligomers within the polymer sample.^{18,21} The first attempt to synthesize polymer **P9** was performed via a Yamamoto coupling of dibromide **7** which yielded high molecular weight polymer **P9** barely soluble in toluene (see Supporting Information). As further investigation of the polymers takes place in toluene, the polymers should be soluble in this solvent. Therefore, dibromide **7** was engaged in a Kumada coupling to yield a lower molecular weight polymer **P9** ($M_n = 1189 \text{ g mol}^{-1}$) which exhibits much higher solubility in common organic solvents including toluene.

Preparation of Polymer/SWNT Dispersions. Dispersions of SWNTs were obtained by sonicating pristine HiPco SWNTs in toluene with an excess of the polymer under investigation.

Table 1. Overview of the Conjugated Polymers Library^a

<div> <div>Boronic (pseudo) esters</div> <div>aryl halides</div> </div>	<div> <div> <chem>C12H25</chem> <chem>C12H25</chem> </div> <div>PinB</div> <div> <chem>C12H25</chem> <chem>C12H25</chem> </div> <div>BPin</div> </div> <div>2</div>	<div> <div> <chem>C10H21</chem> </div> <div>PinB</div> <div> <chem>C10H21</chem> </div> <div>BPin</div> </div> <div>4</div>	<div> <div> <chem>N</chem> <chem>S</chem> <chem>N</chem> </div> <div>Bpin</div> <div> <chem>N</chem> <chem>S</chem> <chem>N</chem> </div> <div>Bpin</div> </div> <div>6</div>	Homo-coupling
<div> <chem>C12H25</chem> <chem>C12H25</chem> </div> <div>Br</div> <div> <chem>C12H25</chem> <chem>C12H25</chem> </div> <div>1</div>	<div> <chem>C12H25</chem> <chem>C12H25</chem> </div> <div>P1</div>			
<div> <chem>C12H25</chem> <chem>C12H25</chem> </div> <div>Br</div> <div> <chem>C12H25</chem> <chem>C12H25</chem> </div> <div>10</div>	<div> <chem>C12H25</chem> <chem>C12H25</chem> </div> <div>P2</div>	<div> <chem>C10H21</chem> <chem>C12H25</chem> </div> <div>P3</div>	<div> <chem>C12H25</chem> <chem>C12H25</chem> </div> <div>P4</div>	<div> <chem>C12H25</chem> <chem>C12H25</chem> </div> <div>P5</div>
<div> <chem>C10H21</chem> </div> <div>Br</div> <div> <chem>C10H21</chem> </div> <div>3</div>	<div> <chem>C12H25</chem> <chem>C12H25</chem> </div> <div>P6</div>	<div> <chem>C10H21</chem> </div> <div>P7</div>		
<div> <chem>C8H17</chem> <chem>C8H13</chem> </div> <div>Br</div> <div> <chem>C8H17</chem> <chem>C8H13</chem> </div> <div>7</div>			<div> <chem>C8H17</chem> <chem>C8H13</chem> </div> <div>P8</div>	<div> <chem>C8H17</chem> <chem>C8H13</chem> </div> <div>P9</div>
<div> <chem>C10H21</chem> </div> <div>Br</div> <div> <chem>C10H21</chem> </div> <div>11</div>	<div> <chem>C12H25</chem> <chem>C12H25</chem> </div> <div>P10</div>	<div> <chem>C10H21</chem> </div> <div>P11</div>		<div> <chem>C10H21</chem> </div> <div>P12*</div>
<div> <chem>N</chem> <chem>S</chem> <chem>N</chem> </div> <div>Br</div> <div> <chem>N</chem> <chem>S</chem> <chem>N</chem> </div> <div>5</div>	<div> <chem>C12H25</chem> <chem>C12H25</chem> </div> <div>P13</div>	<div> <chem>C10H21</chem> </div> <div>P14</div>		<div> Polymer P12 was synthesized from bifunctional carbazole 12. </div>
<div> <chem>Cl</chem> <chem>O</chem> <chem>Cl</chem> </div> <div> <chem>Cl</chem> <chem>O</chem> <chem>Cl</chem> </div>	<div> <chem>C12H25</chem> <chem>C12H25</chem> </div> <div>P15</div>	<div> <chem>C10H21</chem> </div> <div>P16</div>		
<div> <chem>OTf</chem> </div>	<div> <chem>C12H25</chem> <chem>C12H25</chem> </div> <div>P17</div>	<div> <chem>C10H21</chem> </div> <div>P18</div>		
<div> <chem>Br</chem> </div>	<div> <chem>C12H25</chem> <chem>C12H25</chem> </div> <div>P19</div>	<div> <chem>C10H21</chem> </div> <div>P20</div>		
<div> <chem>Br</chem> </div>	<div> <chem>C12H25</chem> <chem>C12H25</chem> </div> <div>P21</div>			
<div> <chem>Br</chem> </div>	<div> <chem>C12H25</chem> <chem>C12H25</chem> </div> <div>P22</div>			
<div> <chem>Br</chem> </div>	<div> <chem>C12H25</chem> <chem>C12H25</chem> </div> <div>P23</div>			

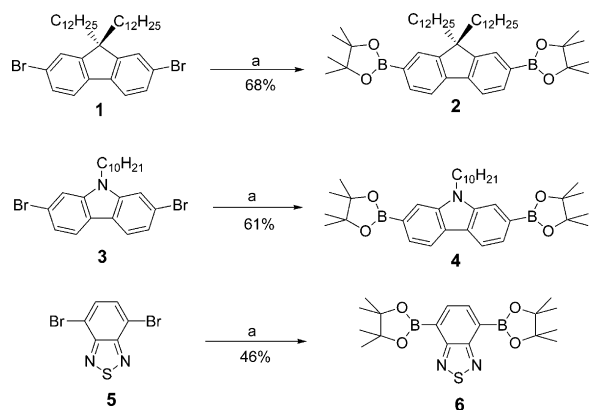
^aPolymers dispersing SWNTs are shaded in green (good), light green (medium), and yellow (poor dispersing properties). Pale red shading indicates that the corresponding suspension was not stable.

Typically, ~1 mg of HiPco SWNTs was added to a solution of 50 mg of the investigated polymer in toluene (15 mL), and the suspension was sonicated for 1 h. Following an established procedure, centrifugation with a mild centripetal acceleration (10 000 rpm, 10 min) was applied to remove large bundles of nanotubes and remaining catalyst particles. A density gradient centrifugation (DGC) was applied to remove the excess polymer and to investigate the possibility of further enrichment.^{10f} The dispersions were analyzed by absorption and photoluminescence–excitation spectroscopy (PLE), allowing the identification and quantification of semiconducting SWNT species (see also Supporting Information).^{13,22}

Dispersing Properties. All recorded PL maps (Figure 1 and Figures S3, S4, S6, and S7) were translated into normalized (see Supporting Information for details concerning the normalizing

procedure) chiral angle (θ) vs diameter (\varnothing) maps in order to visualize the composition of the SWNTs dispersion (Figure 2). The SWNT distribution in HiPco material is represented by sodium cholate dispersions in D₂O, assuming that all SWNT are equally well dispersed in this surfactant. Relative intensity maps of each polymer suspension are also presented in order to allow facile comparison to the original nonuniform distribution of SWNTs in the HiPco material (Figure 3). Relative intensity maps represent the ratio between normalized PL maps and the normalized HiPco SWNTs suspended in D₂O using sodium cholate (i.e., if a polymer disperses all SWNTs equally well, then the relative intensity map would contain only circles with the same diameter). We note that the accuracy of such relative intensity maps is likely to be lower in regions of higher diameters due to the correspondingly low amount of SWNTs present.

Scheme 1. Synthesis of Boronic Esters 2, 4, and 6 Used for the Synthesis of the Polymer Library^a



^aReagents and conditions: (a) $\text{PdCl}_2(\text{dppf})$, bis(pinacolato)diboron, dioxane, 80 °C, overnight.

For most of the polymers, the DGC did not allow a significant enrichment of the dispersions and similar PL maps were obtained before and after DGC. Figure 2 presents the chiral angle (θ) vs diameter (ϕ) maps of these suspensions, and Figure 3 contains their corresponding relative intensities (versus sodium cholate as described in the previous paragraph). However, we observed a clear enhancement of the selectivity caused by DGC for three copolymers comprising a 9,9-didodecyl-2,7-fluorenyl subunit (**P6**, **P13**, and **P23**). The corresponding chiral angle (θ) vs diameter (ϕ) maps obtained from PL maps before and after DGC treatment are presented in Figure 4.

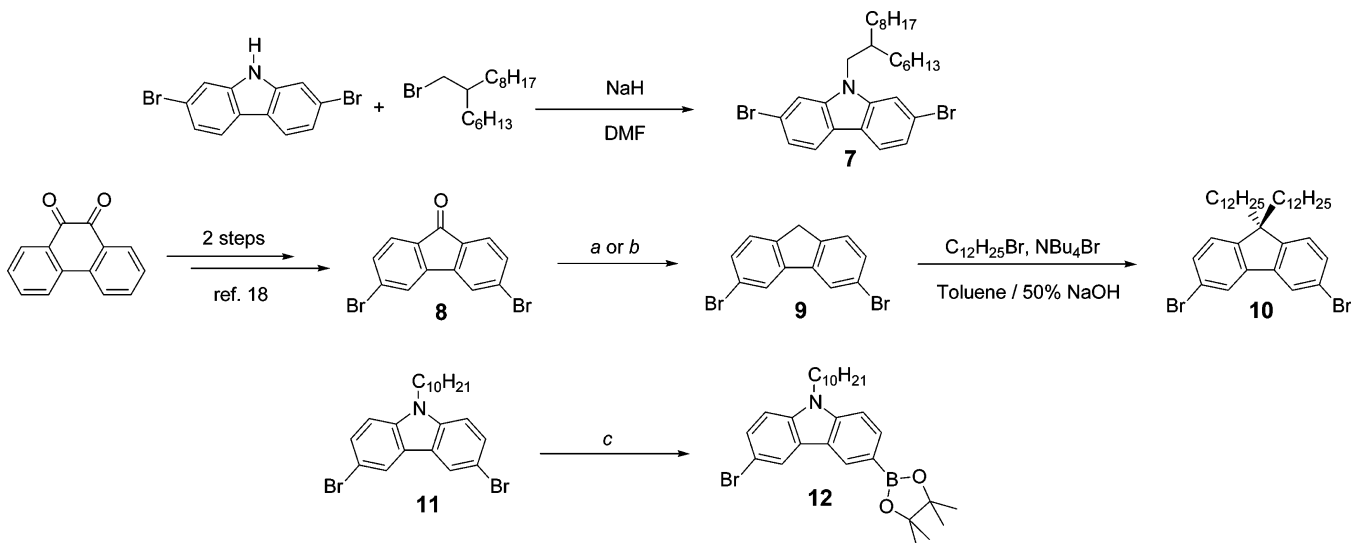
In order to get a qualitative estimate of the SWNT dispersion efficiency of HiPco tubes for each polymer (i.e., how many SWNTs from the parent HiPco mixture are suspended by a polymer regardless to the (n , m) indice), the sum of the intensities of all PL maps peaks attributed to SWNTs (before DGC) was considered. This estimation does not consider any difference in quantum yields of each SWNT as the data required to provide an analysis considering individual quantum yields for each (polymer-wrapped) SWNT type are not available until

now. Thus, the polymers were classified into three categories according to the amount of SWNT (in mg/L) which was dispersed (cf. Table S1 in Supporting Information and related color code in Table 1). Note that this qualitative estimation depends on the parent composition of HiPco tubes. Having a polymer which exclusively selects a (n , m) species which has a low concentration in the starting raw material would lead to a low concentration in the polymer/SWNT suspension. Moreover, this estimation fits fairly well with the absorption spectra of the suspensions displayed in Figure S2. Because of a low signal-to-noise ratio, the absorption spectra of low concentrated suspensions were not displayed.

Finally, some of the reported polymers formed unstable suspensions with SWNTs and precipitation occurred within a few minutes or hours. These polymers, namely **P2–P5**, **P10**, **P14**, and **P20**, were not investigated further.

Polymers Containing a 2,7-Fluorene Moiety. As previously mentioned, poly(2,7-dialkylfluorene)s are known to be extremely selective toward close-to-armchair SWNTs ($\theta > 25^\circ$) and poly(9,9-didodecylfluorene-2,7-diyl) **P1** was found to behave similarly (Figure 2). It should be noticed that the length of the alkyl chains at the C-bridging atom has an influence on the diameter distribution which shifts toward higher diameter tubes. Indeed, the main species in the polymer **P1**/SWNT dispersion is the (7, 6) species, while in comparable conditions (dispersions of HiPco SWNTs in toluene) poly(9,9-dioctylfluorene-2,7-diyl) was reported to mainly disperse the (8, 6) species having a slightly larger diameter.^{10b,c,h} Also, poly(9,9-dihexylfluorene-2,7-diyl) mainly disperses (8, 7) and (9, 7) SWNTs species under similar conditions.^{10c,e} Thus, our results confirm that the diameter of the dispersed nanotubes is inversely proportional to the alkyl chain length, whereas the θ -selectivity is not affected by alkyl chain length variations. This pronounced effect of the length of the alkyl chains of poly(9,9-dialkylfluorene-2,7-diyl) on the diameter selectivity, though not fully understood, is consistent with the predominance of CH/ π interactions between the alkyl chains and the zigzag bonds of the fused hexagons on the nanotubes walls as has recently been suggested by molecular dynamics simulations.^{10b,12} However,

Scheme 2. Synthesis of Monomers 7, 10, and 11^a



^aReagents and conditions: (a) hydrazine monohydrate, KOH, triethylene glycol, 80 °C to reflux, 68%;¹⁹ (b) $\text{B}(\text{C}_6\text{F}_5)_3$, poly(triethoxysilane), CH_2Cl_2 , RT, 67%; (c) $n\text{-BuLi}$, isopropoxypinacolborane, THF, -78°C to RT, 37%.

Scheme 3. Overview of the Polymerization Procedures Used in This Study

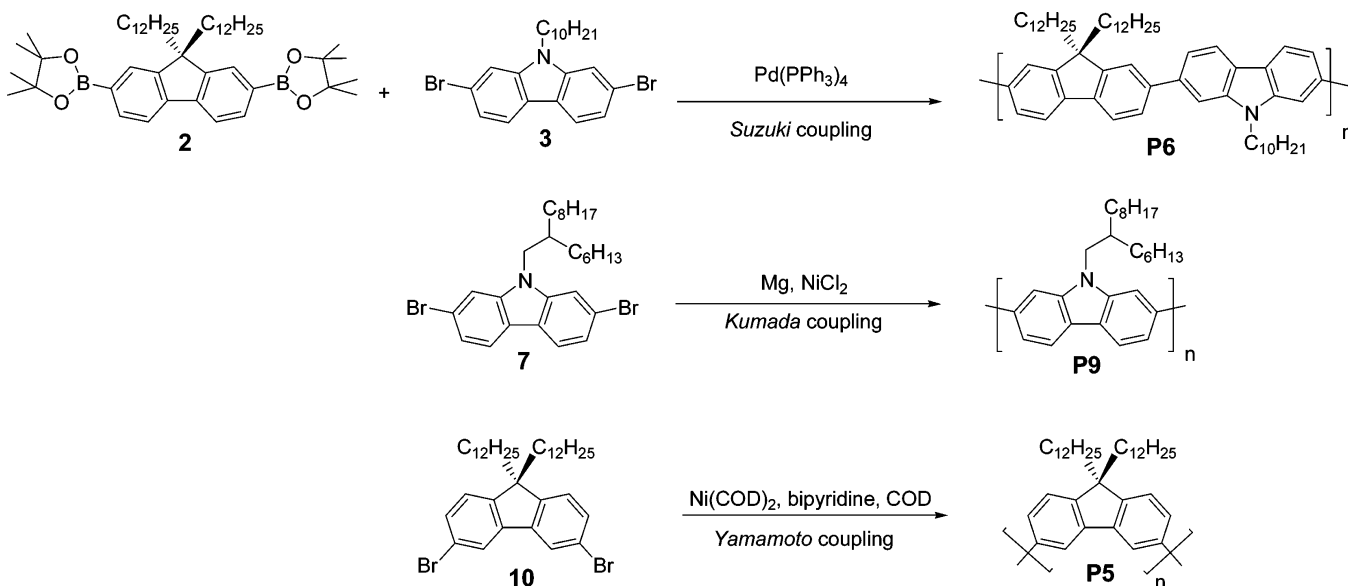


Table 2. Summary of the Synthesis of the Polymers Presented in Table 1 and Used in This Study, Including Yield, Number-Average Molecular Weight, Weight-Average Molecular Weight, and Polydispersity Index

polymer	yield (%)	M_n (Da)	M_w (Da)	PDI	ref
P1	99	12878	53510	4.2	14b
P2	99	8608	14136	1.6	
P3	94	5471	8404	1.5	
P4	87	2350	4760	2.0	
P5	83	11920	66990	5.6	
P6	98	18840	58620	3.1	
P7	20 ^a (76)	3402 ^b	5333 ^b	1.6 ^b	10b
P8	76	17510	50490	2.9	
P9	87 ^c	1189 ^c	1987 ^c	1.7 ^c	
P10	94	10722	19125	1.6	
P11	89	4461	6912	1.6	
P12	98	3035	4552	1.5	
P13	96	29000	58000	2.0	
P14	16 ^a (29)	2250 ^e	2450 ^e	1.1 ^e	
P15	80	11861	25764	2.2	10f
P16	39	2390	3245	1.4	10f
P17	95	59735	220990	3.7	10f
P18	97	23278	133480	5.7	10f
P19	88	21165	51175	2.4	10f
P20	24 ^a (79)	6900 ^e	16800 ^e	2.4 ^e	10f
P21	94	12364	29632	2.4	
P22	38 ^d (88)	17100	24000	1.4	
P23	90	16800	29200	1.7	

^aFraction stemming from Soxhlet extraction with toluene. The percentage in parentheses corresponds to the total yield which comprises a further extraction with chloroform. ^bValue given for the toluene fraction. ^cSynthesized by Kumada coupling. ^dValue given for the chloroform fraction. The percentage in parentheses corresponds to the total yield which comprises a further extraction with toluene. ^eValue given for the toluene fraction which was not fully soluble in THF—the solvent in which the SEC measurement was performed.

it can be noticed that the relative intensities of P1/SWNT dispersion presented in Figure 2 suggests a less pronounced selectivity toward $\theta > 25^\circ$ for $\Phi > 0.95$ nm. Besides its sorting

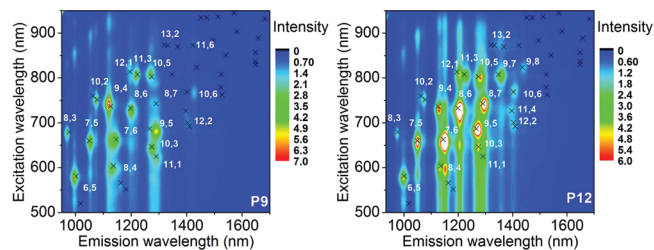


Figure 1. Representative PLE maps of HiPco SWNTs suspensions prepared from polymers P9 and P12 in toluene which allow the identification of each semiconducting (n, m) species. These maps are translated into θ/Φ maps allowing an overview of diameter and chiral index selectivity (Figure 2).

properties, polymer P1 is also estimated to have good dispersion efficiency (cf. Table S1).

Changing the selectivity of poly(2,7-fluorene) can be achieved by introduction of aromatic moieties in the polymer main chain. Indeed, polymer P19 exhibits strong diameter selectivity toward SWNTs having $\Phi > 0.95$ nm, which corresponds to a minor fraction in the starting HiPco material (Figures 2 and 3).^{10f} In contrast, there is no significant chiral angle selectivity: the dispersed SWNTs chiral angles θ range from close to zigzag (12, 1) to armchair (8, 7). Despite the dispersion of only a minor fraction of HiPco nanotubes, polymer P19 yields high concentrations of SWNTs in suspension with regards to the other polymers; i.e., it disperses very efficiently large diameter SWNTs (cf. Table S1). Similar but not so pronounced selectivity properties were observed for polymer P15 having an electron-poor 1,5-anthraquinone moiety in the polymer backbone (Figure 2). Its relative intensity map indicates affinity for high diameter SWNTs (Figure 3). However, the dispersion ability of polymer P15 is much lower than that of polymer P19. Noteworthy is that SWNTs with $\theta < 10^\circ$ were not selected. Introduction of a 1,5-naphthyl moiety as in polymer P17 did not lead to pronounced diameter selectivity. Structural selectivity is directed toward close-to-armchair SWNTs motifs (Figures 2 and 3). The dispersion ability of P17 is also reduced compared with polymer P19. The anthracene connectivity of polymer P19 was varied from 1,5 to 2,6 and 9,10 positions leading to

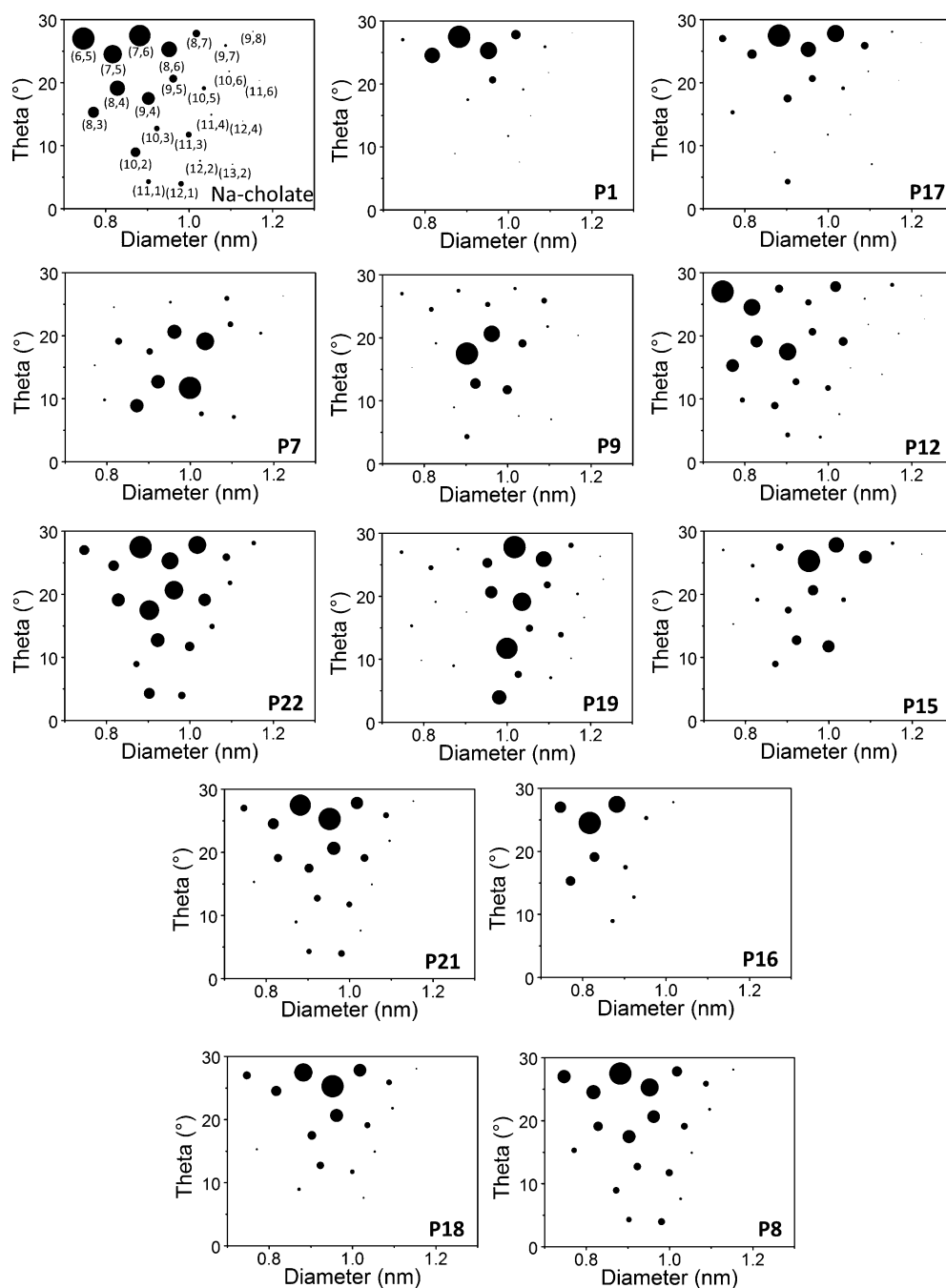


Figure 2. Normalized θ/\varnothing maps of HiPco SWNTs dispersed in aqueous solution using sodium cholate compared to HiPco SWNTs dispersed in toluene using the polymers of this study (after DGC) (see Table 1). Within an individual θ/\varnothing map, the circles areas are proportional to the concentration of the corresponding SWNT species in this dispersion. In the sodium cholate map (top left), the circles are assigned to the (n, m) indices of the corresponding SWNT.

polymers **P21** and **P22**, respectively. Neither of these two polymers is efficient at dispersing SWNTs having $\varnothing < 0.85$ nm (Figures 2 and 3). The suspension stemming from polymer **P22** is relatively more concentrated in low chiral index SWNTs compared to polymer **P21**/SWNTs dispersions. However, polymer **P22** exhibits poor overall solubilizing properties compared with polymer **P21**. Neither of them exhibits a diameter selectivity as pronounced as observed with the parent polymer **P19**.

Polymers Containing a 3,6-Fluorene Moiety. One major observation of these results stems from the family of polymers containing 3,6-fluorenyl units. Whereas polymers derived from 9,9-dialkyl-2,7-fluorene units show good to outstanding dispersing

properties and high wrapping selectivity, all homologous polymers containing 9,9-dialkyl-3,6-fluorenes, namely **P2–P5**, yield unstable suspensions with SWNTs precipitating within minutes. Such behavior demonstrates that the 3,6-connectivity prevents SWNTs dispersion, which can in turn be attributed to an unfavorable polymer conformation that does not enable efficient wrapping of the nanotubes. An analogous unfavorable conformation has been proposed in the case of foldamers which are able to reversibly suspend and release SWNTs by adopting a different conformation by tuning solvent polarity.²³

Polymers Containing a 2,7-Carbazole Moiety. While poly(9,9-didodecylfluorene-2,7-diyl) **P1** exhibits selectivity

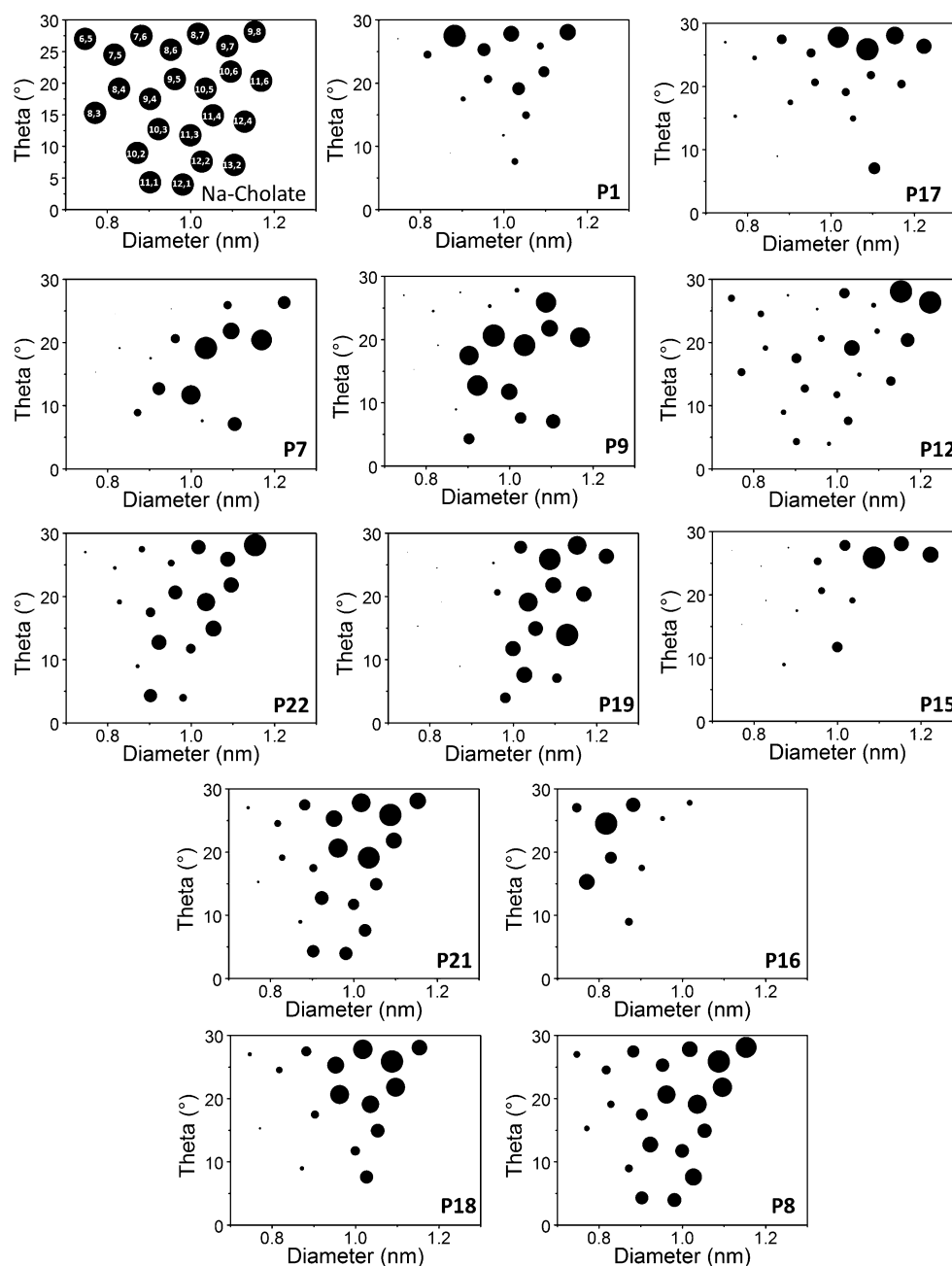


Figure 3. θ/\varnothing maps presenting normalized relative intensities of HiPco SWNTs dispersed in toluene using the polymers of this study (after DGC). Intensities are relative to those of the same (n, m) SWNT species in sodium cholate/water dispersion.

toward high chiral angle SWNTs, its structural proxy poly(*N*-decylcarbazole-2,7-diyl) **P7** exhibits selectivity for lower chiral angles, namely between $10^\circ < \theta < 20^\circ$, making both polymers nicely complementary.^{10b} Another noticeable difference is the dispersing efficiency which was estimated to be 5 times lower in the case of polymer **P7** compared to polymer **P1**. This can be attributed to the single linear alkyl chain attached at the N atom of the carbazole moiety. A way to increase its dispersing efficiency is to introduce a branched alkyl chain at the N atom, yielding poly(*N*-2-hexyldecylcarbazole-2,7-diyl) **P9**. Indeed, the dispersing efficiency is then estimated to increase by a factor of 2. Polymer **P9** exhibits selectivity features relatively similar to those of its parent poly(2,7-carbazole) **P7** despite the increased bulkiness of the side chain (Figures 1–3). Note that polymer **P7** disperses mainly the (11, 3) and (10, 5) species, while polymer

P9 selects preferentially (9, 4) and (9, 5) SWNTs, which represents a slight shift toward smaller diameters and higher θ values (around 20°). Thus, as observed for poly(9,9-dialkylfluorene)s, the nature of the alkyl chain only slightly influences the selectivity. As previously postulated and simulated, the selectivity for lower chiral indices may arise from the sp^2 hybridization of the N-bridging atom which reduces the steric hindrance at this position, thus allowing a tighter complex with the SWNT than the poly(9,9-dialkyl-2,7-fluorene)s which have a sterically more demanding sp^3 -hybridized C-bridging atom.^{10b}

The low solubility of copolymer **P14** did not allow us to test its dispersing properties toward SWNTs (*vide supra*). The introduction of a branched alkyl chain at the N atom of the carbazole moiety afforded the more soluble polymer **P8**, and its dispersing properties toward HiPco SWNTs were tested.

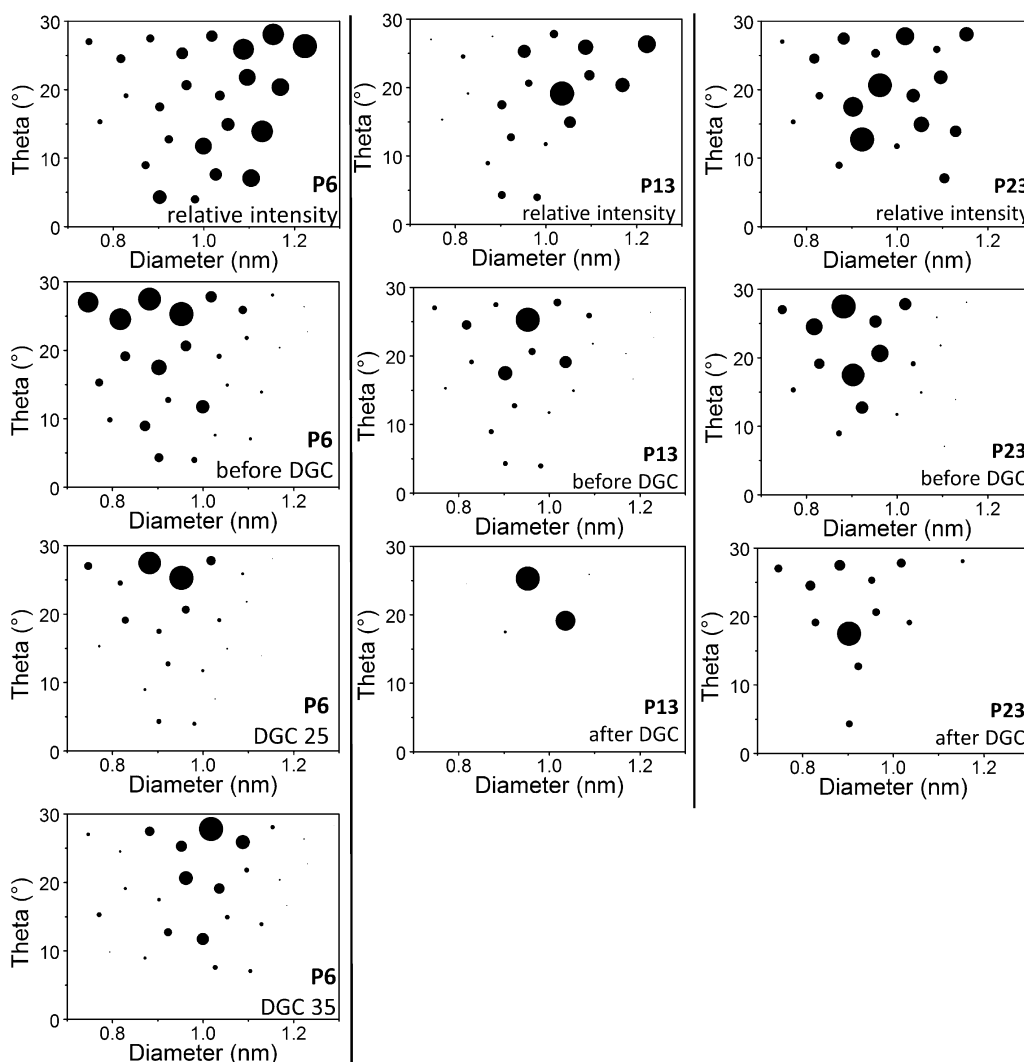


Figure 4. Normalized θ/ϕ maps of HiPco SWNTs dispersed in toluene using polymers **P6**, **P13**, and **P23** before DGC (second row). First row: normalized relative intensity θ/ϕ maps corresponding to the second row. Third and fourth row: normalized θ/ϕ maps after DGC. In the case of polymer **P6**, DGC fractions 25 and 35 are presented due to an inhomogeneous enrichment along the DGC tube, in contrast to suspensions arising from polymers **P13** and **P23** which exhibit homogeneous enrichment.

P8 was found to disperse most SWNTs species, regardless of the diameter and chiral angle, with the (7, 6) and (8, 6) nanotubes dominating the distribution (Figure 2). The θ/ϕ map representing the relative intensities of SWNTs dispersed by polymer **P8** shows a tendency to suspend SWNTs of higher diameter regardless of the chiral angle (Figure 3). Furthermore, polymer **P8** exhibits high dispersion efficiency.

Copolymers **P16** and **P18** which contain a 2,7-carbazole moiety do not exhibit the same trend and their selectivity is mainly driven by the 1,5-linked anthraquinone and naphthalene groups respectively, as previously reported.^{10f} Indeed, polymer **P16** is selective toward small diameter SWNTs having $\phi < 0.9$ nm (Figures 2 and 3) but shows extremely low dispersing efficiency. Polymer **P18** dominantly disperses high chiral indices $\theta > 25^\circ$ with only a minor fraction of $\theta < 25^\circ$. Part of this effect may also be attributable to the HiPco SWNT distribution as shown by the related relative intensity θ/ϕ map (Figure 3). Even though polymer **P18** yields higher concentration of SWNTs than polymer **P16**, it is not an efficient dispersing agent.

Polymers Containing a 3,6-Carbazole. As shown in Figures 1 and 2, poly(*N*-decylcarbazole-3,6-diyl) **P12** is able to

disperse SWNTs, in contrast to its poly(3,6-fluorene) homologue **P5**. However, no strong selectivity was observed as **P12** disperses most of the nanotubes species initially present and exhibits a θ/ϕ map similar to the one obtained for sodium cholate aqueous dispersions. The corresponding relative intensity θ/ϕ map confirms this behavior while also underlining that large diameter SWNTs are well dispersed. Moreover, polymer **P12** shows excellent dispersing efficiency (cf. Table S1). The other mixed polymeric structures **P10** and **P11**, both having a 3,6-linked carbazole subunit in their backbone, yielded unstable suspensions of SWNTs, thus showing behavior similar to their 3,6-fluorene homologues **P2** and **P3**. It should be pointed out that **P11**/SWNTs suspensions are slightly more stable and precipitated within a few hours instead of minutes, thus allowing fluorescence measurements to be recorded. Although the intensity was relatively low, the PL map indicated selectivity toward $\theta \geq 15^\circ$ and diameters ≥ 0.9 nm (Figure S7).

Enhancement Induced by DGC: Polymers P6, P13, and P23. In most cases the polymer wrapping is not that uniform that further fractionation by DGC is possible. However, in the case of the polymers **P6**, **P13**, and **P23**, besides their

intrinsic wrapping selectivity (*vide infra*), a clear enhancement caused by DGC treatment was observed (Figure 4). Copolymer **P6**, which possesses strictly alternating 2,7-linked fluorene and carbazole moieties, is an interesting example of a combination of wrapping selectivities. Given the complementary selectivity of poly(9,9-dialkylfluorene-2,7-diyl) and poly(*N*-alkylcarbazole-2,7-diyl) toward high- and low-chiral angle SWNTs, respectively, it was expected that **P6** would combine both properties. Indeed, as evidenced from the θ/\emptyset map of **P6**/SWNT dispersion in toluene before DGC (Figure 4), the dispersion of a wide range of SWNTs was observed. This tendency is slightly attenuated in the relative intensity θ/\emptyset map which shows the preferential solubilization of higher diameter SWNTs together with the absence of θ sorting (Figure 4). Moreover, the dispersion efficiency of polymer **P6** is high. Interestingly, a post-DGC inhomogeneous enrichment effect was found in this system by harvesting/analyzing discrete fractions within the density gradient. In particular, DGC fraction 25 was enriched with SWNTs having $\theta \geq 25^\circ$, mainly the (7, 6) and (8, 6) species, whereas DGC fraction 35 showed diameter-selective features with $\emptyset \geq 1.0$ nm. The corresponding evolution of the SWNTs distribution—reflecting characteristic buoyant density differences—was further confirmed by absorbance spectrometry (Figure S5). Thus, the nanotubes having the biggest diameter move to higher (= lower density) regions within the density gradient than do smaller nanotubes. The opposite trend has been observed for aqueous dispersions of SWNTs using sodium cholate, where DGC-induced diameter sorting results in smaller-diameter SWNTs settling out at higher points in the centrifuge tube.^{4a} This indicates that in the case of **P6** the polymer coating strongly influences the density of the polymer/SWNT complexes. Note that in most other cases of polymer/SWNTs dispersions studied here we did not find analogous enrichment effects via DGC, possibly because of nonuniform coating of the polymer on the SWNT.^{10f} In contrast, the coating density of polymer **P6** on SWNTs might be relatively uniform for each single (*n*, *m*) species and vary significantly from one species to another, leading to the differentiation of the buoyant coefficients for polymer/SWNTs complexes, depending upon diameter/(*n*, *m*) characteristics.

BTD-containing copolymer **P13** showed reduced dispersion efficiency compared to copolymer **P8**. Copolymer **P13** leads to a suspension in which (8, 6) nanotubes are predominant, with a noticeable amount of (9, 4) and (10, 5) as well as other tubes (Figure 4). In this case, applying DGC to the dispersion resulted in a highly enriched suspension of (8, 6) and (10, 5) tubes. All other species, in particular the (9, 4) tube, were efficiently removed during the DGC step. An opposite trend was observed by replacing the electron-deficient BTD unit in copolymer **P13** by a naphthalene unit in polymer **P23**. Polymer **P23** did not show significant sorting properties before DGC. However, the relative intensity map indicates the preferential dispersion of smaller diameter SWNTs (Figure 4). Moreover, after DGC treatment the relative amount of the (9, 4) tubes dramatically increased compared to the other tubes, which might indicate specific interactions between polymer **P23** and the (9, 4) tube. It is worth noting that energy transfer is observed in the case of the low-band-gap polymer **P13** (Figure S6). Indeed, we attributed the PL signals observed at excitation wavelength around 500 nm (corresponding to the absorption onset of polymer **P13**, Figure S8) with emission wavelength at around 1200 and 1280 nm, corresponding to the (8, 6) and (10, 5) tubes to energy transfers from the polymer to the corresponding tubes.²⁴

Further features stemming from similar energy transfer were not observed, probably due to the PL analysis window which is out of the absorption region of the described polymers.

CONCLUSION

We have synthesized a polymer library comprising conjugated homopolymers and strictly alternating copolymers based on fluorene and carbazole groups in which their connectivity was varied in either 2,7- or 3,6-positions. The selectivity of these polymers toward specific (*n*, *m*) SWNTs was investigated with HiPco material containing more than 40 different nanotube species. The dispersing properties were estimated from optical absorption spectra and from photoluminescence intensities, allowing to classify the polymers into three categories depending upon their dispersing efficiency. An indirect correlation between dispersing efficiency and selectivity is observed due to somewhat inhomogeneous distribution of (*n*, *m*) species in the raw material. Exceptions are polymer **P19**, which shows high concentrated suspensions despite the low “availability” of SWNTs having $\emptyset > 0.95$ nm in raw HiPco material, and polymers **P16**, **P18**, and **P22**, which show low dispersion efficiency despite selecting tubes of high availability.

The trends observed in the SWNTs dispersing features with this polymer library can be summarized as follows: (a) In contrast to the stable suspensions formed with 2,7-connected fluorenyl and/or carbazolyl, SWNTs dispersions derived from polymers containing 3,6-connected building blocks exhibited rapid precipitation of the SWNTs, with the noticeable exception of poly(*N*-decyl-3,6-carbazole) **P12** which efficiently disperses all (*n*, *m*) SWNTs species. (b) While poly(9,9-didodecylfluorene-2,7-diyl) **P1** is selective toward high chiral angle-SWNTs ($\theta > 20^\circ$), poly(*N*-alkyl-2,7-carbazole) **P7** and **P9** show a strong preference toward SWNTs with $10^\circ < \theta < 20^\circ$. Interestingly, this trend was not affected by the increased bulkiness of the *N*-alkyl side chain of poly(2,7-carbazole), which confirms that the sp^2 hybridization at the N atom may be the origin of the difference in selectivity with poly(9,9-dialkyl-2,7-fluorene). However, the dispersing efficiency was strongly improved, which can be attributed to the enhanced solubility of the polymer. (c) The behavior of alternating fluorene- and carbazole-based copolymers toward SWNTs can be tuned via the chemical nature and connectivity of the subunits. In particular, efficient diameter sorting is achieved by introducing 1,5-linked anthracene units (polymer **P19**). (d) Although in most cases DGC has no impact on the selectivity, DGC-induced separation of SWNTs was observed for some of the copolymers comprising 9,9-didodecylfluorene-2,7-diyl subunits. In particular, DGC fraction-dependent SWNT compositions were observed for copolymers **P6**, **P13**, and **P23**.

This study provides valuable information on structure–property relationships of conjugated homo- and copolymers featuring 2,7- and 3,6-fluorenyl and carbazolyl building blocks—in particular, as pertaining to their interactions with semiconducting SWNTs. Fine tuning of comonomers allowed a high degree of enrichment in terms of (*n*, *m*) species as well as in terms of diameters. Ultimately, we expect such studies to pave the way toward custom polymer design for comprehensive direct extraction of single species of SWNTs corresponding to the requirements for specific applications in electronics, optoelectronics, or photonics.

In spite of the systematic structural variation within the (co)polymer libraries of this and other recent studies, clear design rules for a polymer to be able to enrich a particular (*n*, *m*)

SWNT species still remain to be established. On the experimental side, we are currently investigating structural aspects like the peripheral alkyl chain or the backbone composition of the polymer in further detail. At the same time we hope that our present study will stimulate further computational modeling of polymer wrapping of semiconducting (and metallic) SWNTs.

■ ASSOCIATED CONTENT

■ Supporting Information

Experimental section containing synthetic procedures and characterization of monomers and polymers, description of the preparation and characterization of polymer/SWNTs dispersions, and additional PL maps. This material is available free of charge via the Internet at <http://pubs.acs.org>.

■ AUTHOR INFORMATION

Corresponding Author

*E-mail: marcel.mayor@unibas.ch (M.M.); manfred.kappes@kit.edu (M.M.K.).

■ ACKNOWLEDGMENTS

We thank Peter Gerstel and Christopher Barner-Kowollik for size exclusion chromatography measurements. We also acknowledge ongoing generous support by the DFG Center for Functional Nanostructures (CFN), by the Helmholtz Programme POF NanoMikro, by the Karlsruhe Institute of Technology (KIT), and by the University of Basel.

■ REFERENCES

- (1) (a) Reich, S.; Thomsen, C.; Maultzsch, J. *Carbon Nanotubes: Basic Concepts and Physical Properties*; Wiley-VCH: Weinheim, 2004. (b) O'Connell, M. J. *Carbon Nanotubes: Properties and Applications*; CRC Press Taylor & Francis Group: Boca Raton, FL, 2006. (c) Ajayan, P. M. *Chem. Rev.* **1999**, *99*, 1787–1799. (d) Moniruzzaman, M.; Winey, K. I. *Macromolecules* **2006**, *39*, S194–S205. (e) Ryu, S.; Lee, Y.; Hwang, J.-W.; Hong, S.; Kim, C.; Park, T. G.; Lee, H.; Hong, S. H. *Adv. Mater.* **2011**, *23*, 1971–1975.
- (2) Joselevich, E.; Dai, H.; Lui, J.; Hata, K.; Windle, A. H. In *Carbon Nanotubes*; Jorio, A.; Dresselhaus, G.; Dresselhaus, M. S., Eds.; Topics in Applied Physics, Vol. 111; Springer: Berlin, 2008; pp 101–104.
- (3) (a) Martel, R. *ACS Nano* **2008**, *2*, 2195–2199. (b) Adam, E.; Aguirre, C. M.; Marty, L.; St-Antoine, B. C.; Meunier, F.; Desjardins, P.; Ménard, D.; Martel, R. *Nano Lett.* **2008**, *8*, 2351–2355. (c) Cao, Q.; Kim, H. S.; Pimparkar, N.; Kulkarni, J. P.; Wang, C.; Shim, M.; Roy, K.; Alam, M. A.; Rogers, J. A. *Nature* **2008**, *454*, 495–500. (d) Xia, F.; Steiner, M.; Lin, Y. M.; Avouris, P. *Nature Nanotechnol.* **2008**, *3*, 609–613. (e) Holt, J. M.; Ferguson, A. J.; Kopidakis, N.; Larsen, B. A.; Bult, J.; Rumbles, G.; Blackburn, J. L. *Nano Lett.* **2010**, *10*, 4627–4633.
- (4) (a) Hersam, M. C. *Nature Nanotechnol.* **2008**, *3*, 387–394. (b) Komatsu, N.; Wang, F. *Materials* **2010**, *3*, 3818–3844.
- (5) (a) Tu, X.; Manohar, S.; Jagota, A.; Zheng, M. *Nature* **2009**, *460*, 250–253. (b) Zheng, M.; Semke, E. D. *J. Am. Chem. Soc.* **2007**, *129*, 6084–6085.
- (6) Krupke, R.; Hennrich, F.; von Loehneysen, H.; Kappes, M. M. *Science* **2003**, *301*, 344–347.
- (7) Arnold, M. S.; Green, A. A.; Hulvat, J. F.; Stupp, S. I.; Hersam, M. C. *Nature Nanotechnol.* **2006**, *1*, 60–65.
- (8) Gosh, S.; Bachilo, S. M.; Weisman, R. B. *Nature Nanotechnol.* **2010**, *5*, 443–450.
- (9) (a) Peng, X.; Komatsu, N.; Bhattacharya, S.; Shimawaki, T.; Aonuma, S.; Kimura, T.; Asuka, A. *Nature Nanotechnol.* **2007**, *2*, 361–365. (b) Wang, F.; Matsuda, K.; Mustafizur Rahman, A. F. M.; Peng, X.; Kimura, T.; Komatsu, N. *J. Am. Chem. Soc.* **2010**, *132*, 10876–10881. (c) Rahman, A. S. F. M.; Wang, F.; Matsuda, K.; Kimura, T.; Komatsu, N. *Chem. Sci.* **2011**, *2*, 862–867. (d) Marquis, R.; Greco, C.; Sadokierska, I.; Lebedkin, S.; Kappes, M. M.; Michel, T.; Alvarez, L.; Sauvajol, J.-L.; Meunier, S.; Mioskowski, C. *Nano Lett.* **2008**, *8*, 1830–1835.
- (10) (a) Stürzl, N.; Hennrich, F.; Lebedkin, S.; Kappes, M. M. *J. Phys. Chem. C* **2009**, *113*, 14628–14632. (b) Lemasson, F. A.; Strunk, T.; Gerstel, P.; Hennrich, F.; Lebedkin, S.; Barner-Kowollik, C.; Wenzel, W.; Kappes, M. M.; Mayor, M. J. *Am. Chem. Soc.* **2011**, *133*, 652–655. (c) Hwang, J.-Y.; Nish, A.; Doig, J.; Douven, S.; Chen, C. W.; Chen, L.-C.; Nicholas, R. J. *J. Am. Chem. Soc.* **2008**, *130*, 3543–3553. (d) Cheng, F.; Imin, P.; Maunders, C.; Botton, G.; Adronov, A. *Macromolecules* **2008**, *41*, 2304–2308. (e) Nish, A.; Hwang, J.-Y.; Doig, J.; Nicholas, R. J. *Nature Nanotechnol.* **2007**, *2*, 640–646. (f) Berton, N.; Lemasson, F.; Tittmann, J.; Stürzl, N.; Hennrich, F.; Kappes, M. M.; Mayor, M. *Chem. Mater.* **2011**, *23*, 2237–2249. (g) Ozawa, H.; Fujigaya, T.; Song, S.; Suh, H.; Nakashima, N. *Chem. Lett.* **2011**, *40*, 470–472. (h) Chen, F.; Wang, B.; Chen, Y.; Li, L.-J. *Nano Lett.* **2007**, *7*, 3013–3017. (i) Wang, W. Z.; Li, W. F.; Pan, X. Y.; Li, C. M.; Li, L.-J.; Mu, Y. G.; Rogers, J. A.; Chan-Park, M. B. *Adv. Funct. Mater.* **2011**, *21*, 1643–1651.
- (11) Star, A.; Stoddart, J. F.; Steuerman, D.; Diehl, M.; Boukai, A.; Wong, E. W.; Yang, X.; Chung, S. W.; Choi, H.; Heath, J. R. *Angew. Chem., Int. Ed.* **2001**, *40*, 1721–1725. Kang, Y. K.; Lee, O. S.; Deria, P.; Kim, S. H.; Park, T. H.; Bonnell, D. A.; Saven, J. G.; Therien, M. J. *Nano Lett.* **2009**, *9*, 1414–1418. Caddeo, C.; Melis, C.; Colombo, L.; Mattoni, A. *J. Phys. Chem. C* **2010**, *114*, 21109–21113.
- (12) (a) Ozawa, H.; Fujigaya, T.; Niidome, Y.; Hotta, N.; Fujiki, M.; Nakashima, N. *J. Am. Chem. Soc.* **2011**, *133*, 2651–2657. (b) Gao, J.; Loi, M. A.; de Carvalho, E. J. F.; dos Santos, M. C. *ACS Nano* **2011**, *5*, 3993–3999.
- (13) Bachilo, S. M.; Strano, S. M.; Kittrell, C.; Hauge, R. H.; Smalley, R. E.; Weisman, R. B. *Science* **2002**, *298*, 2361–2366.
- (14) (a) Teetsov, J.; Fox, M. A. *J. Mater. Chem.* **1999**, *9*, 2117–2122. (b) Lemasson, F.; Tittmann, J.; Hennrich, F.; Stürzl, N.; Malik, S.; Kappes, M. M.; Mayor, M. *Chem. Commun.* **2011**, *47*, 7428–7430.
- (15) Utsa, H.; Facchetti, A.; Marks, T. J. *Org. Lett.* **2008**, *10*, 1385–1388.
- (16) Zhang, M.; Tsao, H. N.; Pisula, W.; Yang, C.; Mishra, A. K.; Müllen, K. *J. Am. Chem. Soc.* **2007**, *129*, 3472–3473.
- (17) Zhang, Z.-B.; Fujiki, M.; Tang, H.-Z.; Motonaga, M.; Torimitsu, K. *Macromolecules* **2002**, *35*, 1988–1990.
- (18) Fomina, N.; Hogen-Esch, T. E. *Macromolecules* **2008**, *41*, 3765–3768.
- (19) During this study, the following publication appeared where ketone **8** was reduced using hydrazine monohydrate: Song, Y.; Xu, W.; Zhu, D. *Tetrahedron Lett.* **2010**, *51*, 4894–4897.
- (20) Khurana, J. M.; Bansal, K.; Pandey, R. R. *Monatsh. Chem.* **2003**, *134*, 1365–1371.
- (21) Ostrauskaite, J.; Strohriegel, P. *Macromol. Chem. Phys.* **2003**, *204*, 1713–1718.
- (22) Weisman, R. B.; Bachilo, S. M. *Nano Lett.* **2003**, *3*, 1235–1238. Lebedkin, S.; Hennrich, F.; Kiowski, O.; Kappes, M. M. *Phys. Rev. B* **2008**, *77*, 165429.
- (23) Zhang, Z.; Che, Y.; Smaldone, R. A.; Xu, M.; Bunes, B. R.; Moore, J. S.; Zang, L. *J. Am. Chem. Soc.* **2010**, *132*, 14113–14117.
- (24) Berton, N.; Lemasson, F.; Hennrich, F.; Kappes, M. M.; Mayor, M. Manuscript submitted.

The Use of Piers–Rubinsztajn Conditions for the Placement of Triarylamine Pendant to Silicone Polymers

Michael J. Gretton,[†] Brett A. Kamino,[†] Michael A. Brook,[§] and Timothy P. Bender^{*,†,‡}

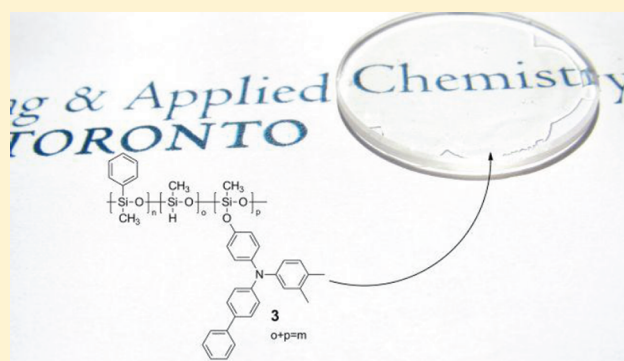
[†]Department of Chemical Engineering and Applied Chemistry, University of Toronto, 200 College St., Toronto, Ontario, Canada M5S 3E5

[‡]Department of Chemistry, University of Toronto, 80 St. George St., Toronto, Ontario, Canada M5S 3H6

[§]Department of Chemistry and Chemical Biology, McMaster University, 1280 Main St., Hamilton, Ontario, Canada L8S 4M1

S Supporting Information

ABSTRACT: The use of Piers–Rubinsztajn conditions was explored for the synthesis of silicone polymers bearing pendant triarylamine functionality. We have found that up to 60% of the hydride groups of a silicone copolymer can be successfully substituted with a triarylamine moiety, without metathesis or redistribution of the silicone. The resulting polymers are hydrolytically stable. The functionalization procedure is straightforward, conducted under ambient conditions with a simple one-step work-up, and avoids the use of a metal-based catalyst. The resulting phenylated triarylamine–silicone hybrid polymer was characterized by optical absorption and fluorescence spectroscopy, CV, and differential scanning calorimetry. The hybrids maintain the physical appearance of a silicone polymer while adopting the photophysical and electrochemical characteristics of the triarylamine.



INTRODUCTION

Triarylamine are a well-known class of organic hole-transporting materials (HTMs).^{1,2} Often, as small molecules, HTMs are incorporated in organic electronic devices as thin films using vacuum deposition techniques. However, solution processing methods, such as inkjet printing, hold particular advantages in the production of uniform layers across large areas.³ Incorporating a triarylamine into the structure of a flexible polymer is recognized to provide better film-forming properties and allows for facile, cost-effective solution processing methods to be used.^{4,5} For example, a polymeric version of a fluorinated triphenyldiamine, made by polymerization of a constituent vinyl group, showed similar or better performance in an organic light-emitting diode (OLED) than the small-molecule analogue.⁶ In addition to the direct polymerization of vinyl-containing triarylamine,^{7,8} a postpolymerization grafting technique has been used to form triarylamine-containing polymers.⁹ Most commonly this technique has involved hydrosilylation of vinyl,^{10–13} allyl,^{12–23} or ethynyl^{24,25} groups attached to a triarylamine or carbazole derivative with silanes (Si–H) using hexachloroplatinate(IV) hydrate or other Pt- or Ru-based catalysts.^{3,25,26,28} For example, Belfield et al. and the groups of Moerner and Siegel and co-workers have attached *N*-allylcarbazoles and an allyl-functionalized triarylamine, respectively, to poly(methylhydro)siloxane using hydrosilylation to synthesize new photorefractive polymers.^{28,9,27} The former group found the resulting polymer to be soluble in a broad range of solvents including CH₂Cl₂,

CHCl₃, CH₃CN, THF, and DMF. The latter group noted the speed and versatility of this methodology when both nonlinear optical (NLO) and hole-transporting moieties were grafted to the same chain.⁹ The incorporation of a triarylamine pendant to poly(methylhydrosiloxane) was also found to produce a silicone–triarylamine hybrid polymer with hole-transporting properties comparable to the respective small molecule.²⁸ Similar results were observed for polymers containing the related carbazole group.⁹ Another method for the formation of pendant triarylamine silicone polymers involves the use of organometallic reagents, such as Grignard or halolithium triarylamine, which are reacted with chloro- or alkoxy silanes; however, these reactions are known to create byproducts.²⁹ It is presumed that if the metal species remains in the final polymer, it will result in charge trapping, unbalanced carrier transport, or nonradiative recombination, all of which are generally detrimental to performance of organic electronic devices.^{30–32} Regardless of the method, there is a clear and demonstrated desire to form silicone polymers with pendant triarylamine functionality, and the utility of such polymers has been demonstrated.

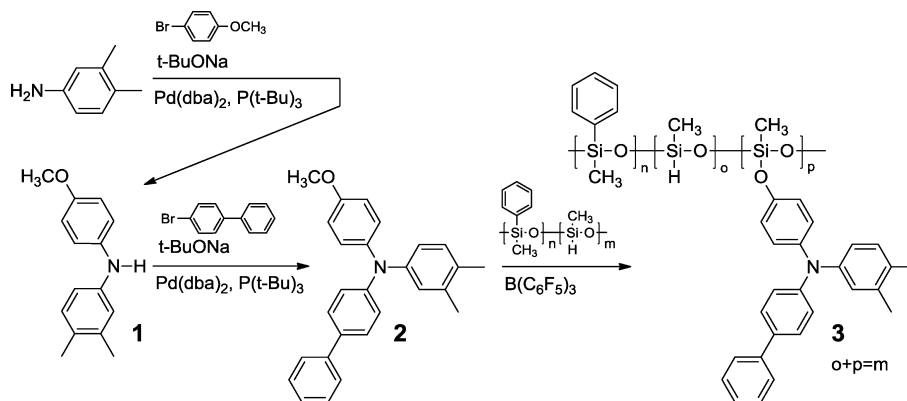
Recently, we have demonstrated the applicability of Piers–Rubinsztajn (P–R) conditions^{33–40} in the functionalization of triarylamine with simple and discrete oligosiloxanes.⁴¹ The

Received: September 7, 2011

Revised: November 25, 2011

Published: December 28, 2011

Scheme 1. Synthesis of Triarylamine **2** Followed by Grafting onto Silicone Polymer under Piers–Rubinsztajn Conditions To Produce Silicone–Triarylamine Hybrid Polymer **3**



procedure uses the strong Lewis acid tris(pentafluorophenyl)-borane (BCF) to effect the reaction under mild conditions. It was previously known that BCF selectively activates Si–H bonds to coupling with Si–OH,³⁹ Si–O–alkyl,^{40,42} and aryl–OH⁴³ groups.^{44–46} We have shown that BCF can also do the same in the presence of a Lewis basic triarylamine substrate containing arylmethoxy groups, the result of which is the formation of an Si–O–triarylamine bond with the elimination of CH₄ as a byproduct. Given the utility outlined above for silicone–triarylamine hybrid polymers, it was of interest to see whether P–R conditions can be extended past the use of simple small discrete silicone fragments and be applicable to the preparation of silicone–triarylamine hybrid polymers whereby the triarylamine is in a position pendant to the polymer main chain. Therefore, in this article, we describe the application of P–R conditions to install a model triarylamine pendant to a siloxane copolymer and compare the physical properties of the triarylamine moiety before and after grafting to the silicone.

RESULTS AND DISCUSSION

The synthetic route used to construct the model triarylamine **2** is outlined in Scheme 1. The synthesis of **2** was accomplished by reaction of 3,4-dimethylaniline with 4-bromoanisole to form the intermediate diarylamine (**1**) under standard Buchwald–Hartwig coupling conditions.^{47,48} Further reaction of **1** with 4-bromobiphenyl, again under standard conditions, gave the model triarylamine **2** in good yield and purity. Triarylamine **2** contains the reactive arylmethoxy unit that is necessary for participation in the P–R coupling reaction. It also contains both 3,4-dimethylphenyl and biphenyl molecular fragments. These were chosen because of their presence in the triarylamine bis(3,4-dimethylphenyl)-(1-biphenyl)amine, whose electronic properties, including oxidation potential and charge carrier mobility, are known.⁴⁹

A silicone polymer was then selected for reaction with the triarylamine **2**. The silicone selected was HPM-502 of Gelest Inc., a silicone copolymer of moderate viscosity containing both methyl–hydride (45–50%) and methyl–phenyl units with a hydride terminus. A silicone polymer containing phenyl units was chosen to ensure compatibility/cosolubility of the silicone polymer and the triarylamine at ambient temperatures in toluene (the solvent of choice for P–R reactions on triarylamines). Furthermore, qualitatively the presence of phenyl units should ensure the polymer adopts a largely extended uncoiled conformation in solution,⁵⁰ thus making the

hydride functionality available for reaction. By comparison, poly(dimethylsiloxane) is expected to adopt a coiled conformation in toluene solution owing to its unfavorable χ -parameter (0.802).⁵¹ If we extend this to the structurally related methyl–hydride/dimethylsiloxane copolymer, the hydride groups would potentially be unavailable for reaction due to a likely coiled conformation in solution.

Initial reaction of HPM-502 with 1.1 equiv of triarylamine **2** (relative to hydride) at a solution concentration of 25 wt % resulted in incorporation of only 53% of the triarylamine into the polymer, leaving 40% of the original hydrides (Si–H) remaining in the polymer (i.e., 60% reacted, run 1, Table 1).

Table 1. Summary of Reactions of Silicone Copolymer with Triarylamine **2** under Piers–Rubinsztajn Conditions

run	temp (°C)	wt % solids (±1%)	mol equiv triarylamine (±0.02)	% conv of triarylamine	% conv of Si–H
1	rt	25	1.1	53	60
2	rt	25	0.9	69	62
3	rt	20	0.9	60	54
4	rt	15	0.9	44	39
5	55	25	0.9	66	60
6	80	25	0.9	66	59
7	rt	25	0.6	82	48
8	rt	25	0.55	100	53
9	rt	25	0.55	100	53
10	rt	25	0.55	100	54
11	rt	25	0.55	100	56
12	rt	25	0.55	100	56

The percent incorporation of the triarylamine in the polymer was calculated based on comparison of areas of the resolved polymer and triarylamine peaks in a GPC chromatogram (extracted from a PDA chromatogram at a wavelength specific for the triarylamine chromophore, 330 nm) with the assumption of similar molar absorptivities of free and pendant triarylamine moiety. Chromatograms of the product **3** and HPM-502 are given in the Supporting Information (Figure S1). The initial polymer, HPM-502, had an apparent molecular weight of $M_n = 1390$ (PDI = 2.39, relative to polystyrene standards). After functionalization to given polymer **3**, a moderate increase to $M_n = 2700$ (PDI = 2.73) was seen. The Gaussian appearance of the polymer traces suggest that no metathesis or other redistribution of the silicone occurred. The

presence of residual Si–H groups was confirmed by FTIR spectroscopy showing the distinctive Si–H stretch around 2160 cm^{-1} ,²⁷ as illustrated in Figure 1. Decreasing the amount of

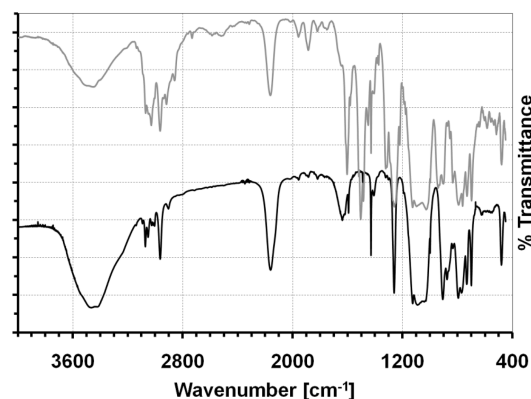


Figure 1. Representative FTIR transmission spectra of starting siloxane copolymer HPM-502 (bottom, black) and polymer 3 (top, gray).

triarylamine **2** used to 0.9 equiv resulted in a similar result: 60% of the hydride functionality was converted (run 2, Table 1). Continued use of 0.9 equiv of triarylamine **2**, but decreasing the concentration of the reaction solution from 25 to 20 wt % and then 15 wt %, resulted in 54 and 39% of the hydride functionality reacting, respectively (runs 3 and 4, Table 1). Again, by maintaining 0.9 equiv of triarylamine **2** but increasing the temperature to 55 and 80 °C, respectively, and while maintaining a concentration of 25 wt % resulted in ~60% of the hydride functionality reacting (runs 5 and 6, Table 1). The conclusions from these initial experiments are that there is a ceiling above which no further reaction of the hydride occurs. The ceiling occurs at ~60% conversion and is independent of temperature and the amount of triarylamine **2** present and decreases on decreasing the concentration of the reaction. We concluded that the cause of this observation must be steric in nature whereby the reaction is hindered once a neighboring hydride, or a series of neighbors, has been substituted with the triarylamine. This occurs even though toluene is a good solvent for the base silicone, the triarylamine, and, presumably, a silicone–triarylamine hybrid polymer.

Polymer **3** is a highly viscous oil or glassy solid in appearance even when it contains residual triarylamine. Its physical state makes removal of residual triarylamine problematic using techniques such as selective precipitation, solvent extraction, or chromatography on silica or alumina. Therefore, we preferred to develop reaction conditions under which the triarylamine is quantitatively incorporated into the hybrid polymer **3**. Given the observed ceiling of 60% conversion of hydride groups, we initially tried reacting 0.6 equiv of triarylamine **2** (run 7, Table 1). However, we observed only 82% conversion of the triarylamine. A small reduction to 0.55 equiv of triarylamine resulted in its complete incorporation into the polymer (run 8, Table 1). The only purification that was necessary was removal of the BCF catalyst by treatment of the reaction mixture with a small amount of alumina for a short period of time. Filtration followed by removal of the toluene by rotary evaporation gave the final polymer **3**. We found that prolonged stirring of the solution (overnight) in the presence of alumina resulted in the partial hydrolysis of the triarylamine from the silicone polymer, presumably due to the presence of trace amounts of water

adsorbed on the alumina surface or present in the toluene. These conditions were subsequently replicated four times with equivalent results (runs 9–12, Table 1).

Having polymer **3** free of residual triarylamine in hand, its basic physical properties were determined. The electrochemical properties of **2** and **3** were compared by cyclic voltammetry, the results of which are illustrated in Figure 2. In each case the

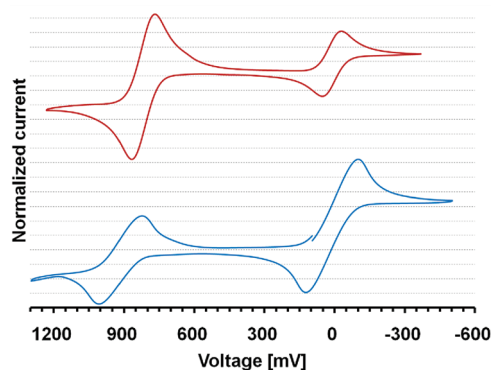


Figure 2. Cyclic voltammogram of triarylamine **2** (red) and polymer **3** (blue); second cycles only are shown, corrected to the known reference value for decamethylferrocene standard (−0.012 V).

voltammograms were acquired using the same technique as we have previously published which involves the use of an internal standard of decamethylferrocene.⁵³ The reversible oxidation of the triarylamine moiety pendant to the silicone copolymer occurs at higher half-wave potential (967 mV) than that of parent triarylamine (807 mV), behavior similar to that previously observed for oligosilicone-functionalized triarylamines.⁴⁷

DSC experiments were performed on triarylamine **2** and polymer **3**. The samples were first heated to ~275 °C under an inert atmosphere followed by flash freezing to ~−75 °C. For polymer **3** on second heating a glass transition temperature (T_g) was found at ~−60 °C and a second found at ~20 °C (Figure 3). The first T_g is the range expected for a silicone

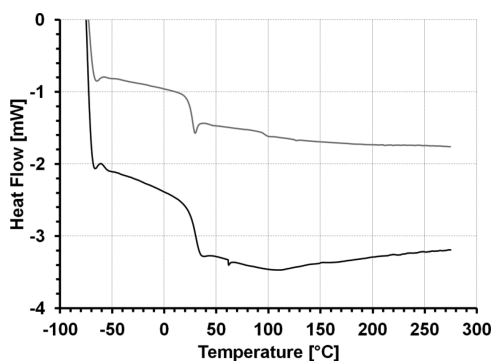


Figure 3. DSC traces for polymer **3** (black) and parent triarylamine **2** (gray). DSC traces collected on second heating.

polymer while the second is in the range expected for a pure triarylamine.⁵³ Indeed, DSC confirms that the T_g for triarylamine **2** to be ~25 °C (Figure 3). A small melt transition is also observed for polymer **3** at ~62 °C. While melt transition is well below that observed for pure triarylamine **2** (~100 °C), its presence and the presence of a T_g in the range expected for

pure triarylamine would suggest the possibility of aggregation of the triarylamine moieties in the solid state.

In order to examine whether aggregation of the triarylamine moieties occurs in polymer 3, UV-vis absorbance and fluorescence emission spectroscopy were conducted on triarylamine 2 and polymer 3 (Figure 4). In each case the

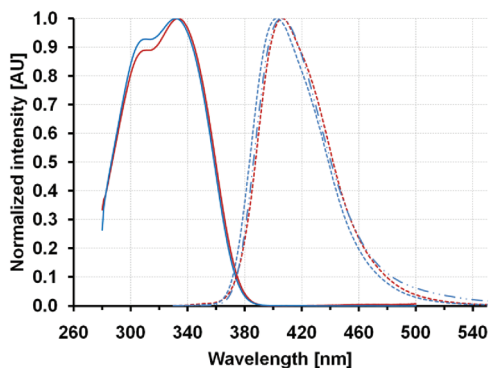


Figure 4. Overlay of UV-vis absorption and fluorescence emission spectra for triarylamine (2, red) and polymer 3 in both solution (dashed blue) and solid state (dash-dotted blue).

characteristic absorption of the triarylamine was seen (334 nm for triarylamine 2 and 333 nm for polymer 3). Similarly, ordinary fluorescence spectra were observed with Stokes shifts of 73 and 71 nm for 2 and 3, respectively, in toluene solution. A fluorescence spectrum obtained on a solid-state sample of polymer 3 showed a nearly identical emission spectrum to the solution sample, albeit with a slightly larger Stokes shift. In an attempt to force aggregation in solution, we compared the fluorescence spectrum of polymer 3 in pure toluene to that in a series of solvent mixtures with increasing proportions of hexamethyldisiloxane (HMDS, a nonsolvent for the triarylamine). As can be seen in Figure 5, the emission maximum

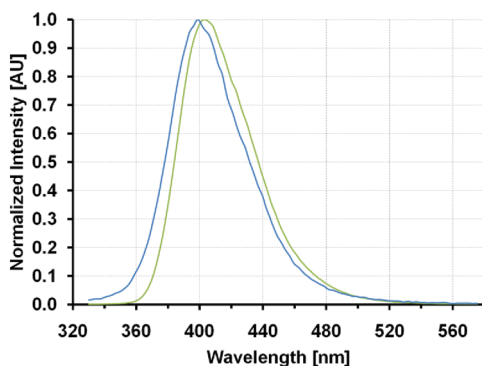


Figure 5. Overlay of fluorescence emission spectra of polymer (3) in toluene solution (green) and 99:1 (v/v) hexamethyldisiloxane:toluene (blue).

underwent a small hypsochromic shift, but no additional shoulders or structure was seen in the spectrum. The rather ordinary photophysical behavior of polymer 3 in both solution and solid state indicates that if aggregation of the triarylamine does occur (as suggested by the DSC thermogram), it does not result in energy transfer on excitation and emission from an excimer or aggregate.^{54,55} Finally, the hydrolytic stability of 3 was evaluated using FTIR spectroscopy on a thin film of polymer 3 exposed to air at rt over a 1 month period. This was

compared to the same treated with acidic standard alumina over a 2 day period in solution (conditions mentioned above which results in hydrolysis). The thin film exposed to air showed no change in the FTIR spectrum between 4000 and 4500 cm^{-1} over time, whereas the alumina-treated sample developed an absorbance band at 3546 cm^{-1} , which is attributable to the stretch of an Si-OH bond formed on hydrolysis (Supporting Information, Figure S2). The absence of a 3546 cm^{-1} stretch for the thin film indicates polymer 3 is hydrolytically stable over the period of 1 month.

CONCLUSION

In conclusion, Piers-Rubinsztajn conditions were found to be useful in functionalizing a phenylmethyl-methylhydride silicone copolymer with a triarylamine leading to the formation of a silicone-triarylamine hybrid polymer. The reaction requires very low concentration of the BCF catalyst; work-up is clean and straightforward. No redistribution or metathesis of the silicone polymer was observed, and the polymer showed excellent hydrolytic stability in air. We did observe a ceiling whereby only 60% of the hydride functionality present in the silicone polymer could be reacted under these conditions. The hybrid silicone-triarylamine hybrid polymer displayed comparable electronic and optical properties to the parent triarylamine as determined from CV and optical absorption and fluorescence spectroscopy. We can therefore conclude that Piers-Rubinsztajn conditions are suitable to prepare polymers of this class that have a demonstrated utility in the field where we do not believe the residual hydride functionality would be a problem.

EXPERIMENTAL SECTION

Materials and Syntheses. Toluene was purified using a PureSolv solvent purification system prior to use. Tris(pentafluorophenyl)-borane, montmorillonite K10 clay, and tetrabutylammonium perchlorate were obtained from Sigma-Aldrich and used without further purification. HPM-502 (methylhydrosiloxane-phenylmethylsiloxane copolymer, 45–50 mol % MeHSiO, hydride-terminated) was purchased from Gelest Inc. (Morrisville, PA) and used without further purification. All other solvents were 99% or higher purity from Caledon Laboratories Ltd. (Brockville, ON, Canada), as was chromatographic silica gel 60 (50–100 μm). Deuterated chloroform (CDCl_3) was purchased from Cambridge Isotopes and used without further purification.

Characterization Techniques. Melting points are uncorrected. Triarylamine syntheses were monitored by TLC on SilicaPlate 250 μm thick silica gel with F-254 indicator, using 1:1 (v/v) cyclohexane:toluene as eluent and visualizing using 254 and 365 nm UV light. Polymer functionalization was monitored by gel permeation chromatography (GPC) using Waters Styragel HR 4E THF and Styragel HR SW THF columns in series, 5 μm particle size, THF eluent at a flow rate of 1.0 mL/min at 30 $^{\circ}\text{C}$; a photodiode array (254–800 nm) in “MaxPlot” mode was used for detection. Chromatograms were uncorrected by individual compounds’ molar absorptivities. All NMR spectra were collected on a Varian Mercury 400 spectrometer in CDCl_3 . Chemical shifts are reported in parts per million referenced relative to tetramethylsilane internal standard. Coupling constants (J) are reported in hertz. High-resolution mass spectroscopy was taken with an AB/Sciex QStar mass spectrometer. Samples were introduced with an ESI source in solution (50:50 methanol and water) via an HPLC pump. Cyclic voltammetry (CV) was performed with a Bioanalytical Systems C3 electrochemical cell setup. The working electrode was a 1 mm platinum disk with a platinum wire used as a counter electrode. The reference electrode was Ag/AgCl saturated salt solution. All electrochemistry was done in “Spectro” grade dichloromethane from Caledon Laboratories with

(Bu)₄NClO₄ as a supporting electrolyte. Decamethylferrocene was added to the solutions as an internal reference. All DSC half-wave potentials are reported from the second scan and corrected by the internal reference (−0.012 V vs Ag/AgCl₂).⁵⁶ Fourier transform infrared (FTIR) spectra were recorded on KBr plates using a Perkin-Elmer Spectrum 100 spectrometer from 4000 to 400 cm^{−1}. Solution spectroscopy was performed in quartz cuvettes with 1.0 cm path length. Optical absorption measurements were conducted using a Perkin-Elmer Lambda 1050 UV/vis/NIR spectrometer. Fluorescence measurements were conducted using a Perkin-Elmer F555 spectrofluorometer. Polymer films were drop-cast onto quartz disks and dried overnight at 80 °C under vacuum before fluorescence measurements were taken. Spectra were processed using Spekwin 32 (all types), Perkin-Elmer UV Winlab (UV–vis), or FL WinLab (fluorescence) software. Differential scanning calorimetry was performed with a TA Instruments 2920 DSC with a refrigerated cooling system, using Al hermetic pans. Tests were performed under a blanket of nitrogen.

N-(3,4-Dimethylphenyl)-4-anisidine (1). The synthesis procedure is similar to that previously reported,⁵³ using Buchwald–Hartwig reaction conditions, washing crude product with 1.0 M HCl(aq) and NaHCO₃, and substituting silica gel and montmorillonite K10 clay for alumina and acidic benonite clay. Recrystallization from *n*-heptane yielded white needles (46%); mp 99–101 °C. ¹H NMR (400 MHz, CDCl₃): δ 7.02 (2H, d, *J* = 8.9 Hz), 6.98 (1H, d, *J* = 8.2 Hz), 6.84 (2H, d, *J* = 8.9 Hz), 6.75 (1H, d, *J* = 2.2 Hz), 6.70 (1H, dd, *J*₁ = 8.8 Hz, *J*₂ = 2.4 Hz), 5.34 (1H, br s), 3.79 (3H, s), 2.20 (3H, s), 2.19 (3H, s). ¹³C NMR (100 MHz, CDCl₃): δ = 155.3, 143.4, 137.3, 137.3, 130.7, 127.9, 121.5, 118.6, 115.0, 114.6, 55.1, 20.0, 19.0. HRMS (ESI, [M + H]⁺) calcd for C₁₅H₁₈NO *m/z* = 228.1388; found 228.1377.

N-(3,4-Dimethylphenyl)-N-(4-methoxyphenyl)biphenyl-4-amine (2). The synthesis procedure is similar to that previously reported,⁵⁷ using a bis(dibenzylideneacetone)palladium(0) and tri-*tert*-butylphosphine catalyst system and using silica gel with montmorillonite K10 clay in purification. Excess 4-bromobiphenyl was distilled off at elevated temperature. Product was recrystallized from *n*-heptane as fluffy white powder (48%); mp 134–136 °C. ¹H NMR (400 MHz, CDCl₃): δ 7.60–7.56 (2H, m), 7.47–7.39 (4H, m), 7.30 (1H, t, *J* = 7.4 Hz), 7.12 (2H, d, *J* = 8.8 Hz), 7.05 (3H, d, *J* = 8.8 Hz), 6.95 (1H, d, *J* = 2.1 Hz), 6.91–6.84 (3H, m), 3.83 (3H, s), 2.25 (3H, s), 2.21 (3H, s). ¹³C NMR (100 MHz): δ 156.0, 147.9, 145.6, 140.8, 137.5, 133.4, 131.1, 130.3, 128.7, 127.5, 127.0, 126.5, 125.5, 121.8, 121.6, 114.7, 55.5, 19.9, 19.1. HRMS (ESI, [M + H]⁺) calcd for C₂₇H₂₆NO *m/z* = 380.2014; found 379.2025. UV–vis (nm) 311.1, 333.2. Fluorescence (nm) 406.2; CV oxidation (mV) 795 vs Ag/AgCl.

Poly[methyl-N-(3,4-dimethylphenyl)-N-(4-biphenyl)-N-(4-phenyloxy)siloxane-co-phenylmethylsiloxane-co-methylhydrosiloxane] (3). *N*-4-Anisyl-*N*-3',4'-xylyl-4-biphenylamine (600 mg, 1.53 mmol), methylhydrosiloxane–phenylmethylsiloxane copolymer (458 mg, 2.78 ± 0.08 mmol of Si–H), and 3.06 mL of anhydrous toluene were loaded into a 4 dram vial with stir bar. The vial was heated to the reaction temperature if not rt. 115 μL of 0.025 g/mL tris(pentafluorophenyl)borane in anhydrous toluene was then injected, resulting in vigorous bubbling within seconds to <4 min after catalyst addition. Catalyst loading was either 0.25 or 0.50 mol % relative to triarylamine R–O–Ar groups. *Caution: an exotherm and flammable gas evolution are associated with this reaction, which should be accounted for in larger scale experiments.* Stirring was continued for 20–30 min after bubbling was no longer visible, after which 600 mg of basic standard alumina was added, stirred for 20–30 s, and the mixture filtered through 0.22 μm PTFE. Overnight stirring with silica or alumina, in ambient conditions or at elevated temperature, was found to result in more extensive decomposition and so was avoided. ¹H NMR of the purified product showed no detectable toluene after drying overnight at 80 °C under vacuum. UV–vis (nm) 310.7, 331.4. Fluorescence (nm) 402.3 (toluene solution), 406.0 (film). CV oxidation (mV) 891 vs Ag/AgCl. *T*_g (°C) 27.8 (second heating curve in DSC).

■ ASSOCIATED CONTENT

■ Supporting Information

GPC data for silicone HPM-502 and polymer 3; ¹H and ¹³C NMR for compounds 1 and 2 and polymer 3. This material is available free of charge via the Internet at <http://pubs.acs.org>.

■ AUTHOR INFORMATION

Corresponding Author

*E-mail: tim.bender@utoronto.ca.

■ ACKNOWLEDGMENTS

We thank the Natural Sciences and Engineering Research Council of Canada (NSERC) for their support through the Discovery Grant Program (T.P.B.) and an NSERC-CREATE fellowship (M.J.G.) as well as the Ontario Graduate Scholarship program and the Bert Wasmund Fellowship (University of Toronto) for assistance (B.A.K.). Mohsen Soleimani Kheibari and Prof. Mitchell A. Winnik (Department of Chemistry, University of Toronto) are acknowledged for assistance in acquiring the DSC data.

■ REFERENCES

- (1) Shirota, Y.; Kageyama, H. *Chem. Rev.* **2007**, *107*, 953–1010.
- (2) Klenkler, R. A.; Voloshin, G. J. *Phys. Chem. C* **2011**, *115* (34), 16777–16781.
- (3) Igarashi, T. EP 2 083 013 (A1). Filed Oct 31, 2007.
- (4) Bellmann, E.; Jabbour, G. E.; Grubbs, R. H.; Peyghambarian, N. *Chem. Mater.* **2000**, *12*, 1349–1353.
- (5) Nuyken, O.; Jungermann, S.; Wiederhorn, V.; Bacher, E.; Meerholz, K. *Monatsh. Chem.* **2006**, *137*, 811–824.
- (6) Shaheen, S. E.; Jabbour, G. E.; Kippelen, B.; Peyghambarian, N.; Anderson, J. D.; Marder, S. R.; Armstrong, N. R.; Bellmann, E.; Grubbs, R. H. *Appl. Phys. Lett.* **1999**, *74* (21), 3212–3214.
- (7) Lindner, S. M.; Thelakkat, M. *Macromolecules* **2004**, *37* (24), 8832–8835.
- (8) Sommer, M.; Lindner, S. M.; Thelakkat, M. *Adv. Funct. Mater.* **2007**, *17* (9), 1493–1500.
- (9) Bratcher, M. S.; DeClue, M. S.; Grunnet-Jepsen, A.; Wright, D.; Smith, B. R.; Moerner, W. E.; Siegel, J. S. *J. Am. Chem. Soc.* **1998**, *120*, 9680–9681.
- (10) Ushakov, N. V.; Pritula, N. A.; Rebrov, A. I. *Russ. Chem. Bull.* **1993**, *42* (8), 1372–1376.
- (11) Chen, K.-B.; Chang, Y.-P.; Yang, S.-H.; Hsu, C.-S. *Thin Solid Films* **2006**, *514*, 103–109.
- (12) Witker, D.; Suzuki, T. WO2009/089031 (A1). Filed Jan 8, 2009.
- (13) Mochizuki, A.; Kondo, T.; Li, S.; Froelich, J. D.; Chae, H.-S. WO2010/045263 (A3). Filed Oct 13, 2009.
- (14) Strohriegel, P. *Makromol. Chem., Rapid Commun.* **1986**, *7*, 771–775.
- (15) Bisberg, J.; Cumming, W. J.; Gaudiana, R. A.; Hutchinson, K. D.; Ingwall, R. T.; Kolb, E. S.; Mehta, P. G.; Minns, R. A.; Petersen, C. P. *Macromolecules* **1995**, *28*, 386–389.
- (16) Chun, H.; Moon, I. K.; Shin, D.-H.; Kim, N. *Chem. Mater.* **2001**, *13*, 2813–2817.
- (17) Lee, S. H.; Jahng, W. S.; Park, K. H.; Kim, N.; Joo, W.-J.; Choi, D. H. *Macromol. Res.* **2003**, *11* (6), 431–436.
- (18) Moon, I. K.; Oh, J.-W.; Kim, N. *J. Photochem. Photobiol., A* **2008**, *194*, 327–332.
- (19) Moon, I. K.; Oh, J.-W.; Kim, N. *J. Photochem. Photobiol., A* **2008**, *194*, 351–355.
- (20) Moon, I. K.; Choi, C.-S.; Kim, N. *J. Photochem. Photobiol., A* **2009**, *202*, 57–62.
- (21) Yang, X.; Froelich, J. D.; Chae, H. S.; Li, S.; Mochizuki, A.; Jabbour, G. E. *Adv. Funct. Mater.* **2009**, *19*, 2623–2629.
- (22) Lin, Y. C.; Chen, C. T. *Org. Lett.* **2009**, *11* (21), 4858–4861.

- (23) Moon, I. K.; Oh, J.-W.; Lee, C. K.; Kim, N. *Opt. Mater.* **2010**, *32*, 436–442.
- (24) Lee, T.; Song, K. H.; Jung, I.; Kang, Y.; Lee, S.-H.; Kang, S. O.; Ko, J. *J. Organomet. Chem.* **2006**, *691*, 1887–1896.
- (25) Lu, P.; Lam, J. W. Y.; Liu, J.; Jim, C. K. W.; Yuan, W.; Chan, C. Y. K.; Xie, N.; Hu, Q.; Cheuk, K. K. L.; Tang, B. Z. *Macromolecules* **2011**, *44* (15), 5977–5986.
- (26) Waehner, J.; Marciniak, B.; Pawluć, P. *Eur. J. Org. Chem.* **2007**, 2975–2980. Synthetic routes other than hydrosilylation continue to be used, such as this Ru-catalyzed silylative coupling, but based on a literature search, this technique is still less common than hydrosilylation.
- (27) Belfield, K. D.; Chinna, C.; Najjar, O. *Macromolecules* **1998**, *31*, 2918–2924.
- (28) Wright, D.; Gubler, U.; Moerner, W. E.; DeClue, M. S.; Siegel, J. S. *J. Phys. Chem. B* **2003**, *107*, 4732–4737.
- (29) Tachikawa, M.; Takei, K. US 5,994,573. Nov 30, 1999.
- (30) Kang, S. H.; Crisp, T.; Kymissis, I.; Bulović, V. *Appl. Phys. Lett.* **2004**, *85* (20), 4666–4668.
- (31) Choi, J.-S.; Cho, Y. S.; Yook, J. Y.; Suh, D. H. *Polym. Adv. Technol.* **2010**, *21*, 780–783.
- (32) Kuik, M.; Nicolai, H. T.; Lenes, M.; Wetzelaer, G.-J. A. H.; Lu, M. T.; Blom, P. W. M. *Appl. Phys. Lett.* **2011**, *98*, 093301:1–3. Trap creation can also occur by evaporation or diffusion of metal contact material in, e.g., field effect transistors. See, for example: Koehler, M.; Biaggio, I.; da Luz, M. G. E. *Phys. Rev.* **2008**, *78*, 153312:1–4.
- (33) Parks, D. J.; Piers, W. E. *J. Am. Chem. Soc.* **1996**, *118*, 9440–9441.
- (34) Blackwell, J. M.; Foster, K. L.; Beck, V. H.; Piers, W. E. *J. Org. Chem.* **1999**, *64*, 4887–4892.
- (35) Parks, D. J.; Blackwell, J. M.; Piers, W. E. *J. Org. Chem.* **2000**, *65*, 3090–3098.
- (36) Gevorgyan, V.; Rubin, M.; Benson, S.; Liu, J.-X.; Yamamoto, Y. *J. Org. Chem.* **2000**, *65* (19), 6179–6186.
- (37) Gevorgyan, V.; Rubin, M.; Liu, J.-X.; Yamamoto, Y. *J. Org. Chem.* **2001**, *66*, 1672–1675.
- (38) Blackwell, J. M.; Morrison, D. J.; Piers, W. E. *Tetrahedron* **2002**, *58*, 8247–8254.
- (39) Piers, W. E. The chemistry of perfluoroaryl boranes. In *Advances in Organometallic Chemistry*; West, R., Hill, A. F., Eds.; Elsevier Academic Press: San Diego, 2005; Vol. 52, pp 1–46.
- (40) Chojnowski, J.; Rubinsztajn, S.; Cella, J. A.; Fortuniak, W.; Cypriak, M.; Kurjata, J.; Kazmierski, K. *Organometallics* **2005**, *24*, 6077–6084.
- (41) Kamino, B. A.; Grande, J. B.; Brook, M. A.; Bender, T. P. *Org. Lett.* **2011**, *13* (1), 154–157.
- (42) Thompson, D. B.; Brook, M. A. *J. Am. Chem. Soc.* **2008**, *130*, 32–33.
- (43) Cella, J.; Rubinsztajn, S. *Macromolecules* **2008**, *41* (19), 6965–6971.
- (44) Rubinsztajn, S.; Cella, J. A. *Macromolecules* **2005**, *38* (4), 1061–1063.
- (45) Chojnowski, J.; Fortuniak, W.; Kurjata, J.; Rubinsztajn, S.; Cella, J. A. *Macromolecules* **2006**, *39*, 3802–3807.
- (46) Brook, M. A.; Grande, J. B.; Ganachaud, F. *Adv. Polym. Sci.* **2011**, *235*, 161–183.
- (47) Hartwig, J. F.; Kawatsura, M.; Hauck, S. I.; Shaughnessy, K. H.; Alcazar Roman, L. M. *J. Org. Chem.* **1999**, *64*, 5575–5580.
- (48) Jiang, L.; Stephan, B. L. Palladium-Catalyzed Aromatic Carbon-Nitrogen Bond Formation. *Metal-Catalyzed Cross-Coupling Reactions*, 2nd ed.; de Meijere, A., Diederich, F., Eds.; Wiley-VCH: New York, 2004; Chapter 13.
- (49) Klenkler, R. A.; Xu, G.; Graham, J. F.; Popvic, Z. D. *Appl. Phys. Lett.* **2006**, *88*, 102101–1:3.
- (50) Morariu, S.; Brunchi, C. E.; Cazacu, M.; Bercea, M. *J. Chem. Eng. Data* **2011**, *56*, 1468–1475.
- (51) Summers, W. R.; Tewari, Y. B.; Schreiber, H. P. *Macromolecules* **1972**, *5*, 12–16.
- (52) Bratcher, M. S.; DeClue, M. S.; Grunnet-Jepsen, A.; Wright, D.; Smith, B. R.; Moerner, W. E.; Siegel, J. S. *J. Am. Chem. Soc.* **1998**, *120*, 9680–9681.
- (53) Bender, T. P.; Graham, J. F.; Duff, J. M. *Chem. Mater.* **2001**, *13*, 4105–4111.
- (54) Halkyard, C. E.; Rampey, M. E.; Kloppenburg, L.; Studer-Martinez, S. L.; Bunz, U. H. F. *Macromolecules* **1998**, *31* (25), 8655–8659.
- (55) Prieto, I.; Teetsov, J.; Fox, M. A.; Vanden Bout, D. A.; Bard, A. J. *J. Phys. Chem. A* **2001**, *105*, 520–523.
- (56) Noviandri, I.; Brown, K. N.; Fleming, D. S.; Gulyas, P. T.; Lay, P. A.; Masters, A. F.; Phillips, L. *J. Phys. Chem. B* **1999**, *103*, 6713–6722.
- (57) Monguchi, Y.; Kitamoto, K.; Ikawa, T.; Maegawa, T.; Sajiki, H. *Adv. Synth. Catal.* **2008**, *350*, 2767–2777.

Members of CMY Color Space: Cyan and Magenta Colored Polymers Based on Oxadiazole Acceptor Unit

Merve İçli Özkut,^{†,‡} Melek Pamuk Algi,[§] Zahide Öztaş,[§] Fatih Algi,[§] Ahmet M. Önal,^{*,†} and Atilla Cihaner^{*,‡}[†]Department of Chemistry, Middle East Technical University, TR-06531 Ankara, Turkey[‡]Department of Chemistry, Yüzüncü Yıl University, TR-65080 Van, Turkey[§]Laboratory of Organic Materials (LOM), Çanakkale Onsekiz Mart University, TR-17100 Çanakkale, Turkey[‡]Atılım Optoelectronic Materials and Solar Energy Laboratory (ATOMSEL), Atılım University, TR-06836 Ankara, Turkey

S Supporting Information

ABSTRACT: In this study, three novel oxadiazole-based polymers were synthesized and their electrochemical and optical properties were investigated. The polymers were found to have both p- and n-type doping properties accompanied by electrochromic response. Two polymer films exhibit cyan and magenta colors, which constitute two legs of CMY color spaces, in their neutral states and they are soluble in common-organic solvents. According to the color mixing theory, all colors in the visible spectrum including black color can be obtained by using these polymers with a yellow colored electrochromic polymer. Among these polymers, the polymer bearing propyldioxythiophene donor units has some superior properties like high stability (it retains 94% of its electroactivity after 2000 cycles), solubility, and high coloration efficiency (230 cm²/C), whereas as expected ethylenedioxythiophene containing one has the lowest band gap as 1.08 eV.



■ INTRODUCTION

In spite of the fact that the earliest electrochromic materials are mostly based on inorganic oxides (tungsten, iridium and nickel oxides, etc.), the use of organic compounds (i.e., viologens, phthalocyanines, and organic π -conjugated polymers), has opened new avenues as well as myriad of applications such as smart windows,¹ displays,² mirrors,³ camouflage materials,⁴ and electrochromic devices.⁵ In particular, polymer electrochromes (PECs),^{6,7} based on organic π -conjugated materials, have been envisioned as one of the most useful next generation electrochromes for high performance innovative devices, since they can show high redox stability, long cycle life, multicolors with the same material, high optical contrast ratio, low response time, and low operation voltage.^{8–10} Furthermore, PECs can easily be processed, if they are soluble.

Colors are important parameters for the PECs, among them red–green–blue (RGB) and cyan–magenta–yellow and “key” black (CMYK) colors are important since by mixing two of these colors, any colors in the visible spectrum can be obtained according to the color mixing theory.¹¹ In order to obtain desired colors, many methodologies have been investigated and among them, donor–acceptor–donor (D–A–D) method developed by Havinga et al.¹² is the most widely and efficiently used one. By using a D–A–D approach, blue,^{13,14} green^{13,15–18} and black^{19–21} colored polymers in their neutral states have been synthesized whereas CMY colors remain elusive. Very recently, two novel yellow colored soluble polymers have been synthesized,^{22,23} however, still there has been inadequate attention

on the synthesis of magenta and cyan colored polymers. Reynolds and his group synthesized a new cyan–blue colored polymer having optical band gap and transmittance change around 1.6 eV and 41.7%, respectively.²⁴ However, this polymer was very unstable; i.e., it lost 20% of its electroactivity after 20 cycles between its redox states. Derivatives of poly(3,4-propylenedioxythiophene) have strong magenta color and also poly(4-(2-ethylhexyloxy)-3-methoxy-2-(3,4-dimethoxythiophen-2-yl)-thiophene) has magenta colors in their neutral states.¹¹

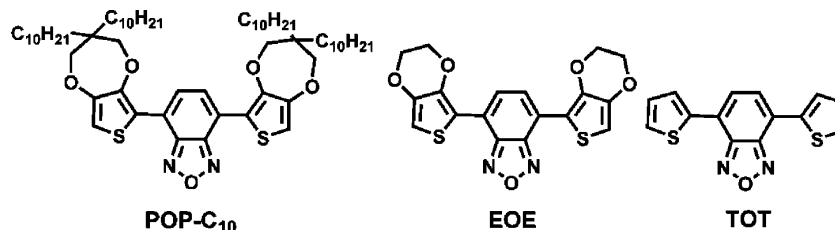
Recently, in our group color tuning has been achieved via changing the acceptor units in the polymeric structure by keeping the donor groups same.¹³ In this study, the aim is not only to synthesize cyan and magenta colored PECs, which are rare in the literature, but also to adjust the color of polymers by changing the donor units. Furthermore, via applying the color mixing theory to these polymers obtaining all color in the visible spectrum was the second target of this study.

For this aim, three novel monomers called as 4,7-bis(3,3-didecyl-3,4-dihydro-6-methyl-2H-thieno[3,4-*b*][1,4]dioxepin-8-yl)benzo[*c*][1,2,5]oxadiazole (POP-C₁₀), 4-(2,3-dihydrothieno[3,4-*b*][1,4]dioxin-5-yl)-7-(2,3-dihydrothieno[3,4-*b*][1,4]dioxin-7-yl)benzo[*c*][1,2,5]oxadiazole (EOE) (Scheme 1), and 4,7-di(thiophen-2-yl)benzo[*c*][1,2,5]oxadiazole (TOT) (Scheme 1) and the optical and electrochemical properties of

Received: October 18, 2011

Revised: December 8, 2011

Published: December 27, 2011

Scheme 1. Chemical Structure of POP-C₁₀, EOE, and TOT

their corresponding polymers, namely poly(4,7-bis(3,3-didecyl-3,4-dihydro-6-methyl-2H-thieno[3,4-*b*][1,4]dioxepin-8-yl)benzo[*c*][1,2,5]oxadiazole) (P(POP-C₁₀)), poly(4-(2,3-dihydrothieno[3,4-*b*][1,4]dioxin-5-yl)-7-(2,3-dihydrothieno[3,4-*b*][1,4]dioxin-7-yl)benzo[*c*][1,2,5]oxadiazole) (P(EOE)), and poly(4,7-di(thiophen-2-yl)benzo[*c*][1,2,5]oxadiazole) (P(TOT)), were investigated.

RESULTS AND DISCUSSION

Three novel monomers, POP-C₁₀, EOE, and TOT, having the same acceptor unit as benzo[*c*][1,2,5]oxadiazole and different donor units as 3,3-didecyl-3,4-dihydro-2H-thieno[3,4-*b*][1,4]dioxepine, 3,4-ethylenedioxythiophene, and thiophene were synthesized via a Stille coupling reaction.²⁵ Their characterizations were done based on ¹H, ¹³C NMR and FTIR measurements (see Supporting Information, Figures S1–S7).

First, in order to investigate the effect of donor units on the redox behavior, electrochemical properties of the monomers were examined. EOE and TOT were dissolved in acetonitrile (ACN) containing 0.1 M tetrabutylammonium hexafluorophosphate (TBAH) and POP-C₁₀ dissolved in dichloromethane (DCM): ACN (5: 95 by volume) containing 0.1 M TBAH since POP-C₁₀ is insoluble in ACN. POP-C₁₀, EOE, and TOT showed irreversible oxidation peaks at 1.09, 1.01, and 1.36 V, respectively (Figure 1 and Table 1). This is an expected result and it is in accordance with our previous results.¹³

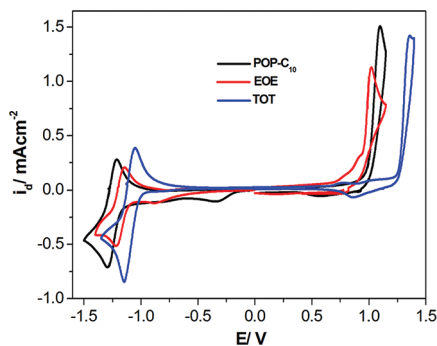


Figure 1. Cyclic voltammograms of 5.0×10^{-3} M of EOE and 3.5×10^{-3} M of TOT in 0.1 M TBAH/ACN, and 1.5×10^{-3} M of POP-C₁₀ in 0.1 M TBAH/DCM:ACN (5: 95 v/v) at a scan rate of 100 mV/s vs Ag/AgCl.

According to the D–A–D method as the donor group is changed, the HOMO level will also change, without any appreciable change in the LUMO level. From this point of the view, since the acceptor groups are same, the reduction half peak potential values ($E_{m,1/2}^{red}$) should be almost same for the three monomers. The results are in accordance with the theory for POP-C₁₀ and EOE, that is, their $E_{m,1/2}^{red}$ values are very

Table 1. Electrochemical and Optical Properties of P(POP-C₁₀), P(EOE), and P(TOT) as Well as Electrochemical Properties of Their Monomers

polymers	$E_{m,a}^{ox}$ (V)	$E_{m,1/2}^{red}$ (V)	$E_{p,1/2}^{ox}$ (V)	$E_{p,1/2}^{ox}$ (V)	$E_{p,1/2}^{red}$ (eV)	E_g^{SPEL} (eV)
P(POP-C ₁₀)	1.09	−1.3	0.60	−1.3	1.48	1.40
P(EOE)	1.01	−1.2	0.20	−1.24	1.08	1.27
P(TOT)	1.36	−1.1	1.33	−1.06	1.62	1.48

similar. In contrast to this general expectation, sometimes LUMO level could also be affected from the donor unit,²⁶ as it was observed in the TOT, i.e., it exhibits somehow lower $E_{m,1/2}^{red}$ value during cathodic scan.

Then, electrochemical polymerization of the monomers were carried out in ACN solution containing 0.1 M TBAH for EOE and TOT and in a mixture of DCM and ACN solution containing 0.1 M TBAH for POP-C₁₀ since P(POP-C₁₀) was soluble in DCM. During the repetitive anodic scans, a new reversible redox couple appeared, which is a characteristic sign of a conducting polymer film formation on the electrode surface. Also, as the number of the cycles increases, the current density of the redox couple was intensified, confirming the formation of the electroactive polymer on the working electrode surface with increasing film thickness (Figure 2).

Next, the polymer films were scanned both anodically and cathodically to determine their electrochemical properties. As it was reported earlier, selenadiazole, thiadiazole and triazole containing counterparts of P(POP-C₁₀) did not show n-doping property¹³ most probably due to the steric effect of long alkyl chains in the polymer structure. However, in the case of P(POP-C₁₀) a pseudo reversible peak was observed at about −1.5 V during the cathodic scan indicating that P(POP-C₁₀) is not only p-dopable but also n-dopable (Figure 3). The presence of n-doping property in P(POP-C₁₀) in contrast to its selenadiazole, thiadiazole and triazole containing counterparts can be explained in terms of the electronegativity differences between the heteroatoms of these monomers. Since oxygen atom has the highest electronegativity among the others (i.e., N, S, and Se), it can be concluded that the best acceptor groups between them is the benzo[*c*][1,2,5]oxadiazole and the electronegativity of heteroatom is more effective than the steric effect of the alkyl chains. An inspection of Figure 3 reveals that oxidation potentials of the polymers show similar behaviors with the monomers; that is, the oxidation potentials of the polymers depend on the electron density of the donor units.

In order to investigate the redox process during p-doping process, the behaviors of P(POP-C₁₀), P(EOE), and P(TOT) polymer were investigated in monomer free electrolyte solutions at different scan rates. A linear increase in the peak currents as a function of the scan rates confirmed well-adhered electroactive polymer film on the electrode surface as well as nondiffusional redox process (see Supporting Information, Figures S8–S10).

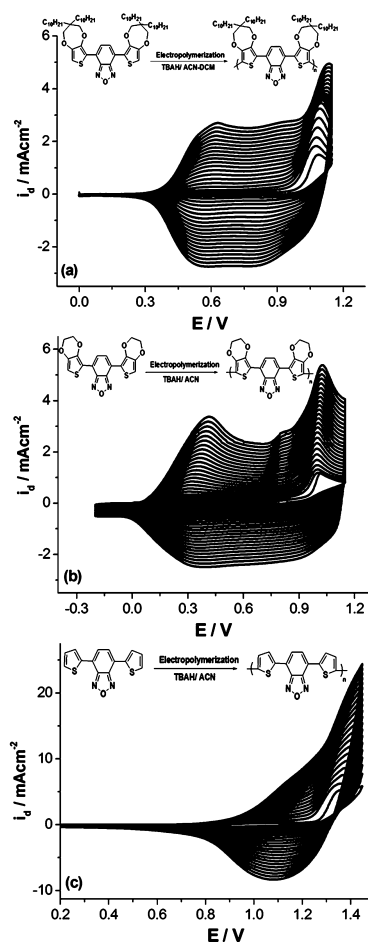


Figure 2. Repetitive cyclic voltammograms (CVs) of (a) 1.5×10^{-3} M POP-C₁₀ in 0.1 M TBAH–DCM/ACN (5:95 v/v), (b) 5.0×10^{-3} M of EOE, and (c) 1.5×10^{-2} M of TOT in 0.1 M TBAH/ACN at a scan rate of 100 mV/s by potential scanning to get P(POP-C₁₀), P(EOE), and P(TOT), respectively.

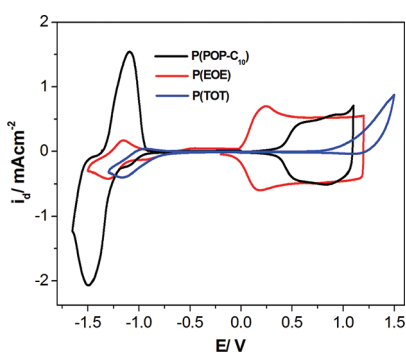


Figure 3. CVs of P(POP-C₁₀), P(EOE), and P(TOT) in 0.1 M TBAH/ACN electrolyte solution at a scan rate of 100 mV/s vs Ag/AgCl.

Spectroelectrochemical behaviors of these polymers during p- and n-doping were also investigated (Figure 4). P(POP-C₁₀), P(EOE), and P(TOT) polymers have two absorption bands having maxima around 400 and 697 nm; 420 and 775 nm; and 345 and 560 nm, respectively. These bands had been diminished for P(POP-C₁₀), and reached a minimum value for P(EOE), and P(TOT) upon oxidation and formation of new

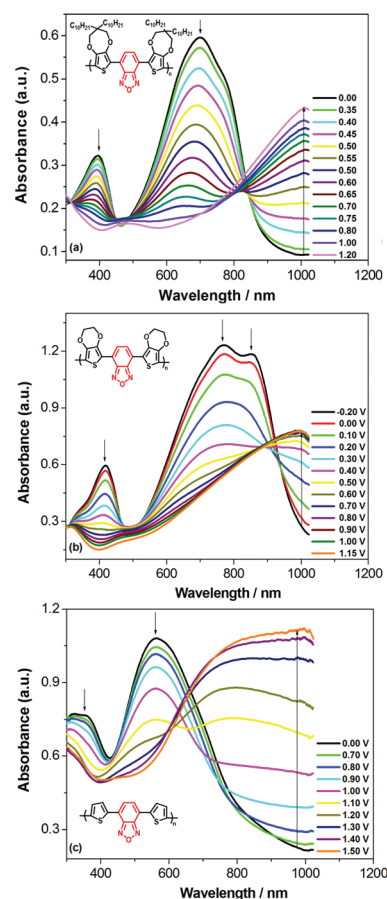


Figure 4. Spectroelectrochemical behaviors of (a) P(POP-C₁₀), (b) P(EOE), and (c) P(TOT) on ITO in 0.1 M TBAH/ACN at various applied potentials during p-doping.

bands observed beyond 900, 1000, and 750 nm, respectively, showing the formation of the charge carriers. The optical band gap (E_g^{SPEL}) of P(POP-C₁₀), P(EOE), and P(TOT) were calculated as 1.40, 1.27, and 1.48 eV, respectively, from spectroelectrochemical data. These data are in agreement with those were obtained from electrochemically (E_g^{CV}) obtained ones (Table 1).

The optical contrasts, switching time and coloration efficiency of P(POP-C₁₀) were found to be 38%, 0.9 s and 230 cm²/C for 697 nm, respectively; those of P(EOE) were calculated to be 23%, 1 s and 199 cm²/C at 775 nm, respectively; also, those for P(TOT) were found as 19%, 2.4 s and 75 cm²/C for 560 nm, respectively, at 95% of optical contrast (see Supporting Information, Figures S11–S13).

Since the reduction peaks observed in the cyclic voltammogram of polymer films might also be due to the monomers trapped inside the polymer or a reduction process taking place on the polymer backbone, using electrochemical analysis alone is not enough to prove if the process taking place during the cathodic scan is n-doping or not. Therefore, to find further support for the n-doping process, formation of the charge carriers upon reduction should be observed with the optical data. Upon reduction, formation of new species observed with spectroelectrochemical data confirming electrochemical data of P(POP-C₁₀), P(EOE), and P(TOT) polymers that n-doping process taking place for these polymers (Figure 5).

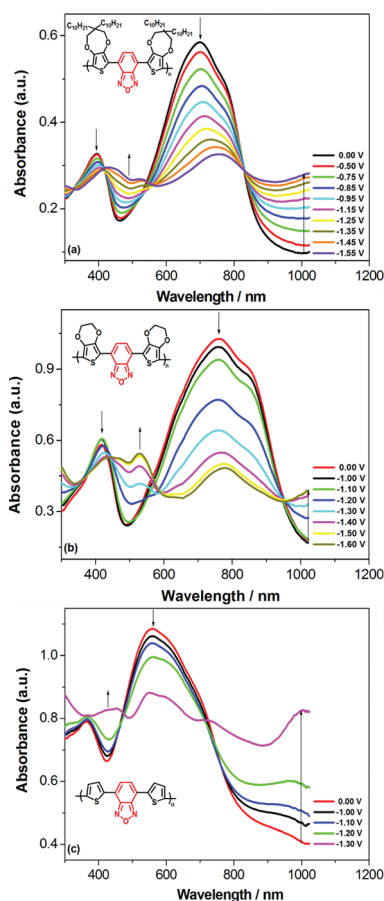


Figure 5. Spectroelectrochemical behaviors of (a) **P(POP-C₁₀)**, (b) **P(EOE)**, and (c) **P(TOT)** on ITO in 0.1 M TBAH/ACN at various applied potentials during n-doping.

P(EOE), **P(POP-C₁₀)**, and **P(TOT)** have greenish-blue, cyan and magenta color in their neutral states, upon oxidation their colors changed to light gray, transmissive gray and light navy, respectively. Also, during n-doping process the colors of **P(EOE)**, **P(POP-C₁₀)**, and **P(TOT)** are light brown, brown, and dark gray, respectively. Colorimetric experiment results have been tabulated in Table 2. It can be seen from the colorimetric results that color tuning can be achieved between greenish-blue region to magenta region of the visible spectrum via changing the donor units.

According to color mixing theory L^* is the parameter of the lightness (it is between 0 and 100, that is, between black and white). Whereas, a^* is the parameter of the red-green balance and b^* is the parameter of yellow-blue balance.¹¹ From this point of the view, it can be concluded that **P(EOE)** is more close to green color due to its more negative a^* value (−30.58) as compared to b^* value (−0.73). In contrast to this, since a^* and b^* values are almost similar for **P(POP-C₁₀)**, the polymer has cyan color. **P(TOT)** contains highly positive a^* value, that is, it has more red balance, however, since yellow balance is not enough the color of the polymer is magenta instead of red. If the b^* value were more negative, magenta color would be more intense (Table 2).

Since stability is a crucially important property for any material to be amenable for use in applications, the stability of the polymer films was investigated under ambient conditions (without purging with inert gas). Although, **P(POP-C₁₀)** and

P(EOE) are very stable, **P(TOT)** is very unstable since **P(POP-C₁₀)** and **P(EOE)** retained 94% and 90% of their electroactivities after 2000 cycles, respectively (Figure S14, Supporting Information), **P(TOT)** lost 45% of its electroactivity after 200 cycles. These data confirms that adding 3,4-ethylenedioxythiophene and 3,4-propylenedioxythiophene units instead of thiophene to the polymeric structure increases stability of the polymer films.¹³

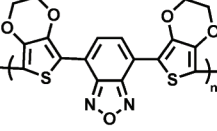

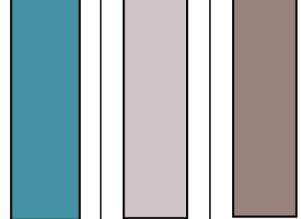
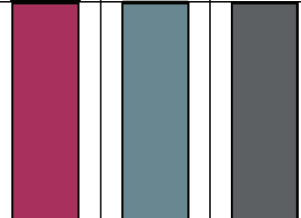
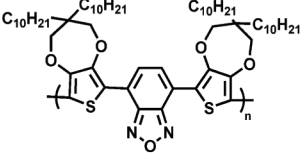
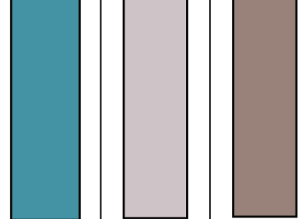
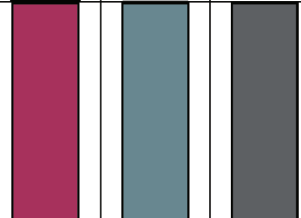
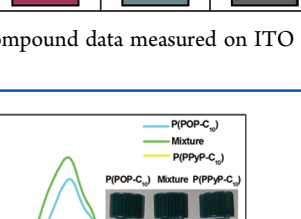
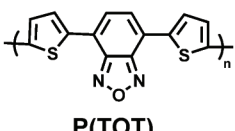
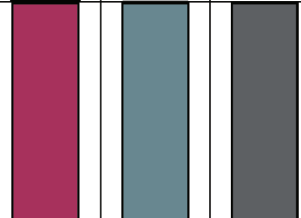
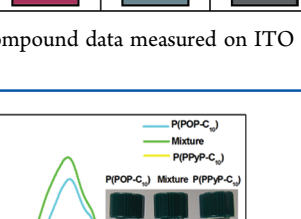
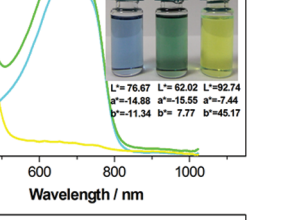
P(POP-C₁₀) and **P(TOT)** are soluble in common organic solvents such as chloroform, and tetrahydrofuran (THF) and partially soluble in dichloromethane. In order to obtained large quantities, **P(POP-C₁₀)** was also synthesized chemically, and optical and electrochemical properties of polymer was investigated (Figure S15, Supporting Information). Chemically obtained polymer has similar properties with electrochemically obtained one, just a 15 nm red shift was observed in optical behavior. In order to determine molecular weight of **P(POP-C₁₀)** GPC measurements had been done. HPLC grade of THF was used as a solvent for this study. M_w value was found as 5867 with a polydispersity index of 2.08. **P(POP-C₁₀)** had average number of 6 repeating trimeric units bearing 18 heterocyclic units (Figure S16, Supporting Information). GPC analysis was also done for electrochemically obtained **P(TOT)** at the same conditions with **P(POP-C₁₀)** and the results are as followings: $M_n = 1485$; $M_w = 8450$; $M_z = 19402$; $HI = 5.7$). The higher heterogeneity index and M_w value obtained for **P(TOT)** when compared to **P(POP-C₁₀)** can be explained in terms of different polymerization methods utilized in their synthesis, that is, in general electrochemical polymerization yielded high HI index products.

In order to obtain any color in the visible spectrum, three subtractive colors; that is, RGB or CMY colors and “key” black colors are needed in theory. Since the polymers are nonemitting systems, it should be possible to obtain, for example, blue via mixing cyan and magenta.¹¹

In Figure 6, some members of RGB and CMYK color spaces can be seen.^{11,13,23,27–29} RGB and black colors were obtained via using cyan colored **P(POP-C₁₀)**, magenta colored **P(TOT)** and yellow colored **P(PPyP-C₁₀)**²³ (poly(3,3-didecyl-6-(1-(3,3-didecyl-3,4-dihydro-2H-thieno[3,4-*b*][1,4]dioxepin-6-yl)pyren-6-yl)-3,4-dihydro-2H-thieno[3,4-*b*][1,4]-dioxepine)).

Figure 7 shows how to obtain a third color, via using color mixing theory, from the polymers containing CMY colors. The explanation of the results is very reasonable for the color mixing theory. For example, in order to obtain green color, at least two absorption bands were needed; that is, the polymer should absorb red and blue light (absorptions around 400 and 700 nm were needed) at the same time.^{17,18,30} **P(POP-C₁₀)** showed two absorption bands at these wavelengths actually; however, the intensity of the band around 400 nm was not enough to obtain green color. Then, via mixing **P(POP-C₁₀)** polymer with a polymer absorbing the red region of visible spectrum (a yellow polymer, **P(PPyP-C₁₀)**), green color was obtained (Figure 7a). Also, red and blue colors can be obtained via using CMY color space according to the same theory (see Figure S17, Supporting Information). In order to obtain black color, the whole visible spectrum should be absorbed by the material; however, it is not an easy task to obtain such as this kind of compound. In literature, copolymerization had been applied to obtain black color PECs.^{19–21} Actually, the color mixing theory is a viable route to obtain black color. During this study, the black color was obtained via mixing cyan, magenta and yellow colored

Table 2. Colorimetric Data for P(EOE), P(POP-C₁₀), and P(TOT) Polymers on ITO According to CIE (The Commission Internationale de l'Éclairage-International Commission on Illumination) Method Developed in 1976

Polymers	Colorimetric results				Colors of Polymers		
		Neut.	Ox.	Red.	Neut.	Ox.	Red.
 P(EOE)	L*	64.99	76.17	65.27			
	a*	-30.58	1.02	10.24			
	b*	-0.73	-8.76	6.33			
 P(POP-C₁₀)	L*	59.96	82.12	59.89			
	a*	-19.69	3.93	6.46			
	b*	-16.02	-0.71	7.95			
 P(TOT)	L*	42.82 [‡]	57.65	44.19			
	a*	51.52 [‡]	-8.76	-0.13			
	b*	0.72 [‡]	-8.09	-2.40			

[‡]These data are measured in the THF solution different from the others polymers' conditions, for this compound data measured on ITO are $L^* = 38.19$, $a^* = 11.63$, and $b^* = -25.95$.

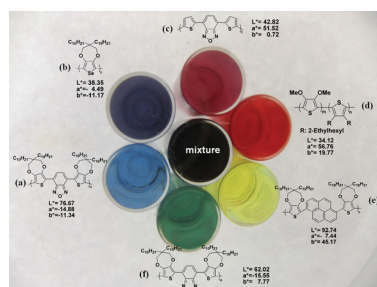


Figure 6. Representation of CMYK and RGB color spaces from the polymer solutions: (a) P(POP-C₁₀); (b) PProDOS-C₁₀ (poly(3,3-didecyl-3,4-dihydro-2H-selenopheno[3,4-b][1,4]dioxepine));^{27,28} (c) P(TOT); (d) ECP-Red (poly(3,4-di(2-ethylhexyloxy)thiophene-co-3,4-di(methoxy)thiophene));^{11,29} (e) P(PPyP-C₁₀) (poly(3,3-didecyl-6-(1-(3,3-didecyl-3,4-dihydro-2H-thieno[3,4-b][1,4]dioxepin-6-yl)pyren-6-yl)-3,4-dihydro-2H-thieno[3,4-b][1,4]dioxepine));²³ (f) P(PSeP-C₁₀) (poly(4,7-bis(3,3-didecyl-3,4-dihydro-2H-thieno[3,4-b][1,4]dioxepin-6-yl)-2,1,3-benzoselenadiazole))¹³ in CHCl₃.

polymers (Figure 7a). As a result RGB colors and also black color can be acquired by using color mixing theory from CMY colors or vice versa.

It can be seen from the colorimetric measurements results that the negative a^* value (-15.55) of the cyan and yellow colored polymer mixtures determine the green color of the solution however due to its somehow positive b^* value mixture contains yellow balance in it (Figure 7a). For the cyan, magenta, and yellow mixture, as expected L^* value is

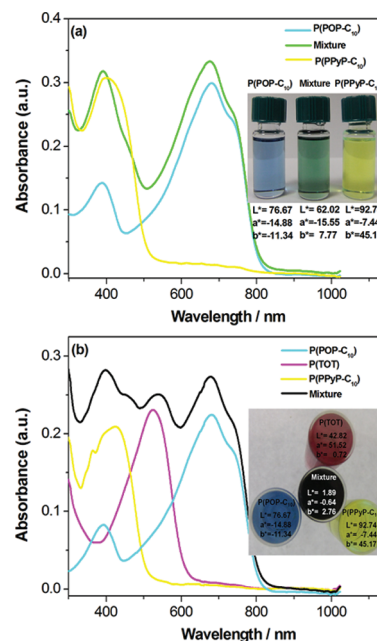


Figure 7. Obtaining (a) green color (absorption spectrum of cyan colored P(POP-C₁₀), yellow colored P(PPyP-C₁₀),²³ and their mixtures having a green color) and (b) black color (absorption spectrum of cyan colored P(POP-C₁₀), magenta colored P(TOT), yellow colored P(PPyP-C₁₀), and their mixtures having black color) according to color mixing theory.

very close to zero, however, it contains a few yellow parameter in it (Figure 7b).

■ CONCLUSIONS

Three novel monomers, POP-C₁₀, EOE, and TOT, and their corresponding polymers, P(POP-C₁₀), P(EOE), and P(TOT), were synthesized and their optical and electrochemical properties were investigated. Cyan colored P(POP-C₁₀) and magenta colored P(TOT) are very precious polymers since they are not only soluble, i.e. processable, but also one leg of the CMY color space. Via using these polymers and applying the color mixing theory, all colors in the visible spectrum were obtained. All these polymer have both p- and n-type doping properties, so they are potential candidates on the applications of electrochromic devices. Also, color tuning is achieved in the range of greenish-blue to magenta region of the visible spectrum via keeping constant acceptor units and just changing the donor units in the polymer structure.

■ ASSOCIATED CONTENT

■ Supporting Information

Experimental procedures, ¹H and ¹³C NMR and FTIR of monomers, some optical, electrochemical data of polymers, and GPC of one of the polymer. This material is available free of charge via the Internet at <http://pubs.acs.org>.

■ AUTHOR INFORMATION

Corresponding Author

*(A.M.Ö.) Telephone: +903122103188. Fax: +903122103200. E-mail: aonal@metu.edu.tr. (A.C.) Fax: +903125868091. Telephone: +903125868304. E-mail: cihaner@atilim.edu.tr.

■ ACKNOWLEDGMENTS

We want to express our thanks to the Scientific and Technical Research Council of Turkey (TUBITAK-110T564), European Cooperation in Science and Technology (COST-108T959), Atılım University (ATU-ALP-1011-02 and ATU-BAP-1011-01) and The Turkish Academy of Sciences (TUBA) for their financial supports.

■ REFERENCES

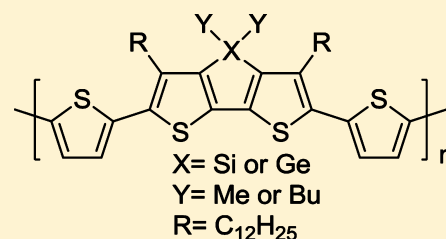
- (1) Pennisi, A.; Simone, F.; Barletta, G.; Di Marco, G.; Lanza, L. *Electrochim. Acta* **1999**, *44*, 3237.
- (2) Bange, K.; Gambke, T. *Adv. Mater.* **1990**, *2*, 10.
- (3) Rosseinsky, D. R.; Mortimer, R. J. *Adv. Mater.* **2001**, *13*, 783.
- (4) Beaupré, S.; Breton, A.-C.; Dumas, J.; Leclerc, M. *Chem. Mater.* **2009**, *21*, 1504.
- (5) Meng, H.; Tucker, D.; Chaffins, S.; Chen, Y.; Helgeson, R.; Dunn, B.; Wudl, F. *Adv. Mater.* **2003**, *15*, 146.
- (6) Beaujuge, P. M.; Reynolds, J. R. *Chem. Rev.* **2010**, *110*, 268.
- (7) Amb, C. M.; Dyer, A. L.; Reynolds, J. R. *Chem. Mater.* **2011**, *23*, 397.
- (8) Buckley, D. N.; Burke, L. D.; Mukahy, J. K. *J. Chem. Soc., Faraday Trans. 1* **1976**, *72*, 1896.
- (9) Burke, L. D.; Thomey, T. A. M.; Whelan, D. P. *J. Electroanal. Chem.* **1980**, *107*, 201.
- (10) Dautremont-Smith, W. C. *Displays* **1982**, *3*, 3.
- (11) Dyer, A. L.; Thompson, E. J.; Reynolds, J. R. *Appl. Mater. Interfaces* **2011**, *3*, 1787.
- (12) Havinga, E. E.; Ten Hoeve, W.; Wynberg, H. *Polym. Bull.* **1992**, *29*, 119.
- (13) İçli, M.; Pamuk, M.; Algi, F.; Önal, A. M.; Cihaner, A. *Chem. Mater.* **2010**, *22*, 4034.
- (14) Amb, C. M.; Beaujuge, P.; Reynolds, J. R. *Adv. Mater.* **2010**, *22*, 724.
- (15) Sonmez, G.; Sonmez, H. B.; Shen, C. K. F.; Jost, R. W.; Rubin, Y.; Wudl, F. *Macromolecules* **2005**, *38*, 669.
- (16) Durmus, A.; Gunbas, G.; Camurlu, P.; Toppare, L. *Chem. Commun.* **2007**, *31*, 3246.
- (17) Beaujuge, P. M.; Ellinger, S.; Reynolds, J. R. *Adv. Mater.* **2008**, *20*, 2772.
- (18) Cihaner, A.; Algi, F. *Adv. Funct. Mater.* **2008**, *18*, 3583.
- (19) Beaujuge, P. M.; Ellinger, S.; Reynolds, J. R. *Nat. Mater.* **2008**, *7*, 795.
- (20) İçli, M.; Pamuk, M.; Algi, F.; Önal, A. M.; Cihaner, A. *Org. Electron.* **2010**, *11*, 1255.
- (21) Öktem, G.; Balan, A.; Baran, D.; Toppare, L. *Chem. Commun.* **2011**, *47*, 3933.
- (22) Amb, C. M.; Kerszulis, J. A.; Thompson, E. J.; Dyer, A. L.; Reynolds, J. R. *Poly. Chem.* **2011**, *2*, 812.
- (23) İçli-Özkut, M.; Öztaş, Z.; Algi, F.; Cihaner, A. *Org. Elec.* **2011**, *12*, 1505.
- (24) Beaujuge, P. M.; Vasilyeva, S. V.; Ellinger, S.; McCarley, T. D.; Reynolds, J. R. *Macromolecules* **2009**, *42*, 3694.
- (25) Shin, W. S.; Kim, M.; Jin, S.; Shim, Y.; Lee, J.; Lee, J. W.; Gal, Y. *Mol. Cryst. Liq. Cryst.* **2006**, *444*, 129.
- (26) Kaya, E.; Balan, A.; Baran, D.; Cirpan, A.; Toppare, L. *Org. Electron.* **2011**, *12*, 202.
- (27) İçli-Özkut, M.; Atak, S.; Önal, A. M.; Cihaner, A. *J. Mater. Chem.* **2011**, *21*, 5268.
- (28) Atak, S.; İçli-Özkut, M.; Önal, A. M.; Cihaner, A. *J. Polym. Sci., Part A: Polym. Chem.* **2011**, *49*, 4398.
- (29) Dyer, A. L.; Craig, M. R.; Babiarez, J. E.; Kiyak, K.; Reynolds, J. R. *Macromolecules* **2010**, *43*, 4460.
- (30) Gunbas, G.; Durmus, A.; Toppare, L. *Adv. Funct. Mater.* **2008**, *18*, 2026.

Comparative Optoelectronic Study between Copolymers of Peripherally Alkylated Dithienosilole and Dithienogermole

Zhuping Fei,[†] Youngju Kim,[‡] Jeremy Smith,[§] Ester Buchaca Domingo,[⊥] Natalie Stingelin,[⊥] Martyn A. McLachlan,[⊥] Kigook Song,[‡] Thomas D. Anthopoulos,[§] and Martin Heeney^{*,†}[†]Department of Chemistry and Centre for Plastic Electronics, Imperial College London, London SW7 2AZ, U.K.[‡]Materials Research Center for Information Display, Kyung Hee University, Yongin, Gyeonggi-do 446-701, Korea[§]Department of Physics & Centre for Plastic Electronics, Imperial College London, London SW7 2AZ, U.K.[⊥]Department of Materials & Centre for Plastic Electronics, Imperial College London, London SW7 2AZ, U.K.

S Supporting Information

ABSTRACT: Here we report a simple methodology for the synthesis of dithienosilole and dithienogermole monomers in which the necessary solubilizing long chain alkyl groups are incorporated into the peripheral 3,5-positions of the fused ring. We report four novel monomers in which methyl or butyl groups are attached to the bridging Si and Ge atom. Copolymers with bithiophene were synthesized by a Stille polymerization in high molecular weight. We report the optical, electrical, electrochemical and morphological properties of the resulting polymers. We find that the nature of the bridging heteroatom (Si or Ge) has only a minor influence on these properties, whereas the nature of the alkyl chain attached to the bridging atom is found to have a much larger effect.



■ INTRODUCTION

Semiconducting polymers have attracted much attention for their interesting optoelectronic properties in a number of applications. Many conjugated building blocks have been investigated in polymer backbones, and in particular much attention has focused upon building blocks in which the aromatic units are forced to be coplanar by the use of bridging heteroatoms.¹ In addition to ensuring full delocalization between the coplanar aromatics, the bridging heteroatom plays an important role, both in modifying the electronic properties of the system and in serving as a point of attachment for the solubilizing side chains typically required to ensure processability. Understanding the optoelectronic and morphological effects of systematically changing the heteroatom within one group of the periodic table has been the focus of much research, particularly within group 14 (C, Si, Ge).^{2–10} For example the replacement of 9,9-dialkylfluorene with 9,9-dialkylsilfluorene has resulted in copolymers that show enhanced photoluminescence emission stability¹¹ and improved photovoltaic efficiency in blends with PCBM.³ The improved device efficiency was attributed to a reduction in optical band gap, increased hole carrier mobility and a higher ionization potential of the silfluorene polymer over the fluorene polymer. These changes in electronic properties can be related to both the interaction of the low lying σ^* orbitals of the Si atom with the π^* orbitals of the conjugated carbon framework which can have a stabilizing effect on LUMO,¹² as well as to the lengthening of the C–Si bond in comparison to the C–C bond. In bridged aromatics this can have the effect of increasing the distance between adjacent sp^2 hybridized carbon

atoms and therefore reducing the strength of the interaction between them.

Furthermore, copolymers containing alkylated dithienosiloles (DTS) units have demonstrated improved performance over their carbon-bridged analogues (cyclopentadithiophene, CDT), with FET mobilities up to 0.08 cm²/(V s)^{8,13} and solar cell power conversion efficiencies up to 7.3%⁴ reported. Several studies have demonstrated the DTS containing polymers exhibit smaller band gaps than the carbon-bridged analogues which has been attributed to the stabilizing effects on the LUMO described above.^{14–16} In addition to the electronic effects, copolymers of DTS have been found to be more crystalline in the solid state, compared to the analogous CDT copolymers which were amorphous. This has been attributed to the longer carbon–silicon bond in DTS, which results in a reduction of intermolecular steric hindrance between the alkyl groups on the bridging Si and adjacent comonomer units and allows better packing in the solid state.^{15,16}

Despite this interest in silicon bridged aromatics, there has been less work on germanium containing polymers. Germanium sits below silicon in the periodic table and typical C–Ge bonds are slightly longer than a C–Si bond (1.96 versus 1.88 Å, respectively^{17,18}), possibly reducing intermolecular steric hindrance further. Germafluorene containing polymers were recently reported by Leclerc¹⁹ and Huang²⁰ and showed encouraging optoelectronic properties in solar and electro-

Received: October 24, 2011

Revised: December 8, 2011

Published: December 22, 2011

luminescent devices. Very recently, several copolymers containing dithienogermole (DTG) have been reported by Ohshita,²¹ Reynolds,²² Leclerc,²³ and our group²⁴ and exhibit promising properties. For example the copolymer between 4,4'-bis(2-ethylhexyl)dithieno[3,2-*b*:2',3'-*d*]germole and 2,1,3-benzothiadiazole (BT) exhibits a FET mobility up to 0.11 cm²/(V s),²⁴ while the copolymer with *N*-octylthieno[3,4-*C*]pyrrole-4,6-dione (TPD) had solar cell power conversion efficiencies up to 7.3%,²² higher than the analogous DTS polymer in comparative studies.

In all of the cases reported to date, the required long chain alkyl solubilizing groups have been directly attached to the bridging Ge atom. This introduces some additional synthetic complexity because the required long chain dialkyldichlorogermans are not commercially available, and their synthesis is rather tedious. In this paper we report a different approach to afford soluble polymer materials. Rather than include the long chain solubilizing groups on the bridging heteroatom, we instead move them onto adjacent thiophene rings (Figure 1) in

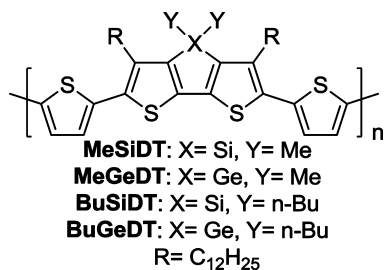


Figure 1. Structures of polymers **MeSiDT**, **MeGeDT**, **BuSiDT**, and **BuGeDT**.

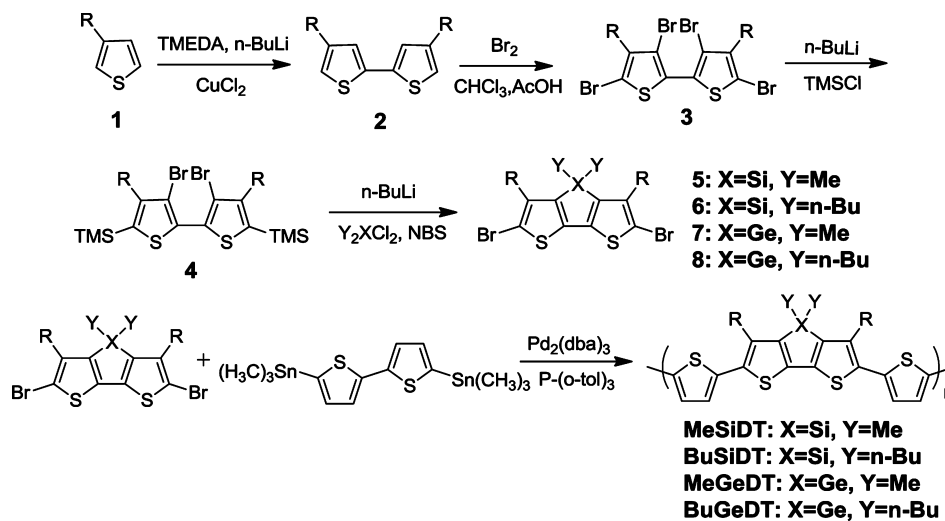
the peripheral 3,5-positions. This now allows the use of commercially available short chain dialkyldichlorogermans and silanes to readily introduce the silyl and germyl bridging groups, such that we can systematically investigate the electronic effects of the different heteroatoms. Furthermore, we can also vary the alkyl group on the heteroatom as a second tool to potentially control molecular packing and polymer solubility. In this study we investigate methyl and more sterically demanding butyl groups on the heteroatom, and copolymerize the resulting

dithienosiloles and dithienogermoles with 2,2'-bithiophene to afford four novel polymers **MeSiDT**, **MeGeDT**, **BuSiDT**, and **BuGeDT** (Figure 1) whose optoelectronic properties we report here.

RESULTS AND DISCUSSION

Synthesis and Characterization of Monomers and Polymers. The synthetic route to the monomers and polymers is shown in Scheme 1, and begins with commercially available 3-dodecylthiophene (**1**). This was selectively lithiated in the less hindered 5 position by treatment with a preformed TMEDA/*n*-BuLi complex. The resulting anion was oxidatively dimerized by treatment with CuCl₂ to afford the tail-to-tail coupled dimer (**2**) in 57% yield.²⁵ This was exhaustively brominated in all the free aromatic positions by reaction with bromine in a chloroform/acetic acid mixture in an 87% yield%. The more reactive 5,5'-positions were then cleanly lithiated by treatment with *n*-BuLi and protected as trimethylsilyl groups to afford **5** in 89% yield. This important intermediate was readily made on a 30 g scale. The 3,3'-positions could then be readily dilithiated by treatment with *n*-BuLi at -78 °C. This dianion appeared stable at cryogenic temperatures with no competing rearrangements by silyl group migration observed.^{26,27} Treatment of this dianion with dialkyldichlorosilane or dialkyldichlorogermans afforded the respective dithienosiloles or dithienogermoles in good yields. Purification was complicated by the tendency of the trimethylsilyl groups to protodesilylate, especially during flash chromatography. We therefore developed a protocol in which the crude heterocycles were rapidly filtered through silica, and the resultant mixtures containing dithienosilole (or germole) with 2, 1, or 0 trimethylsilyl groups were brominated directly with an excess of NBS to give the final monomers **5**, **6**, **7**, and **8** in yields of 69–81%. Here we found that short reaction times were necessary (2 h). On one occasion when the reaction was left overnight, some cleavage of the bridging (Ge) heteroatom was observed. The monomers were polymerized by Stille cross coupling with 5,5'-bis-(trimethylstannyl)-2,2'-bithiophene under microwave heating conditions similar to those previously reported.²⁸ After precipitation and solvent extraction to remove lower weight oligomers and catalyst residues, the polymers were obtained as dark-red solids in yields of 55–89%. The structure and purity of

Scheme 1. Synthetic Route to Monomers and Polymers



the polymers was confirmed by ^1H NMR (see Supporting Information) and elemental analysis. The two butyl-bridged polymers gave well resolved ^1H NMR spectra in CDCl_3 at room temperature, whereas the methyl-bridged polymers only gave well resolved spectra in $\text{C}_2\text{D}_2\text{Cl}_4$ at 130°C due to line broadening by aggregation at lower temperatures.

The molecular weights and the polydispersities (PDI) of obtained polymers were determined by gel permeation chromatography (GPC) in chlorobenzene at 80°C against polystyrene standards. The GPC elution curves of polymers are shown in Figure 2. All the polymers displayed a monomodal

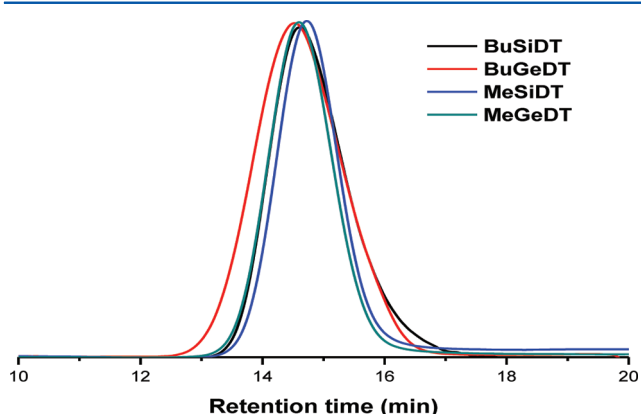


Figure 2. GPC elution traces of BuSiDT, BuGeDT, MeSiDT, and MeGeDT.

molecular weight distribution as expected for a polycondensation reaction, with reasonable molecular weights and polydispersities (PDI) around 2 (see Table 1). The nature of

Table 1. Molecular Weight and Polydispersity of BuSiDT, BuGeDT, MeSiDT, and MeGeDT

polymers	M_n^a (kDa)	P_n^b	M_w (kDa)	P_w^c	polydispersity
MeSiDT	35	48	57	79	1.6
MeGeDT	41	53	68	89	1.7
BuSiDT	26	32	59	73	2.3
BuGeDT	38	45	83	97	2.2

^aDetermined by SEC and reported as their polystyrene equivalents.

^bThe number of repeat units calculated by M_n . ^cThe number of repeat units calculated by M_w .

the alkyl group on the heteroatom had a significant influence on the solubility of the polymer. BuSiDT and BuGeDT were readily dissolved in THF, CHCl_3 and chlorobenzene, whereas MeSiDT and MeGeDT could only be dissolved in hot chlorobenzene or 1, 2-dichlorobenzene. This explains the slightly narrower PDI for the two methyl bridged polymers, since low molecular weight material was removed by chloroform extraction (Soxhlet) prior to subsequent extraction into chlorobenzene and precipitation. In the case of the butyl bridged polymers, all material was soluble in chloroform.

Thermal Properties. The thermal properties of the polymers were evaluated by differential scanning calorimetry (DSC) under nitrogen. The DSC curves of these polymers are shown in Figure 3. All polymers show evidence of crystallinity in these curves. BuSiDT and BuGeDT each exhibit a single endothermic melting peak at 216 and 225°C respectively in the heating cycle, and a single exothermic crystallization peak at $\sim 195^\circ\text{C}$ in the cooling cycle. These temperatures are much

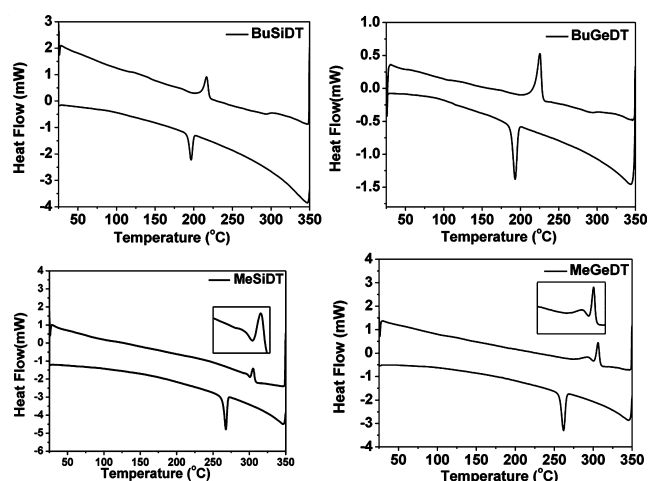


Figure 3. DSC heating and cooling traces (second cycle) of BuSiDT, BuGeDT, MeSiDT, and MeGeDT at a scanning speed of $10^\circ\text{C}/\text{min}$ under N_2 (endo up).

above the typical temperature range expected for dodecyl side chain melting, and we ascribe them to backbone melting and crystallization, respectively. Changing the central bridging group from butyl to methyl causes a significant increase in the observed melting peaks, and also uncovers a second thermal transition just before the backbone melting. Thus, MeSiDT exhibits two endothermic peaks at 296 and 305°C and a single exothermic peak at 268°C , and MeGeDT has a slightly more pronounced first endothermic peak at 292°C and a backbone melt at 306°C , with a crystallization peak at 262°C . The nature of the first transition is unclear, but it may correspond to the formation of a mesophase before backbone melting. In addition to raising the melting point, changing the bridging alkyl chain has a clear influence on the crystallization enthalpy, which the Me-bridged polymers exhibiting significantly higher values than the Bu-bridged (ca. 9.3 J/g vs ca. 5.3 J/g) suggesting that the methyl substituted polymers have a closer packing in the solid state. It is apparent therefore that while the length of the alkyl chain on the heteroatom has a significant effect on the thermal behavior, the nature of the heteroatom itself has very minor influence on thermal behavior.

Optical Properties. The UV–visible absorption and PL spectra of the polymers in chlorobenzene solution and as spin coated films are shown in Figure 4 and the data is summarized in Table 2. In solution, BuSiDT and BuGeDT exhibit nearly identical absorption spectra, with a maximum at 508 and 509 nm , whereas MeSiDT and MeGeDT exhibit broad spectra with maximum at 559 and 548 nm , respectively. Heating the solutions of MeSiDT and MeGeDT resulted in a significant narrowing of their spectra and a blue shift of λ_{max} to 501 and 510 nm , although longer wavelength shoulders remain visible. The red-shift (58 and 37 nm) of absorption maximum of MeSiDT and MeGeDT from hot solution to cold solution indicated there was strong π – π interaction between the polymers' backbones even in solution. The absorption maximum in the solid state of BuSiDT, BuGeDT, MeSiDT and MeGeDT are 558 , 558 , 586 , and 579 nm , respectively. The red-shift of the absorption maximum from the solution to solid state of all polymers indicated there is strong aggregation between the polymers' backbones in the solid state. In addition the red-shift of the absorption maximum from BuSiDT (BuGeDT) to MeSiDT (MeGeDT) indicated that the

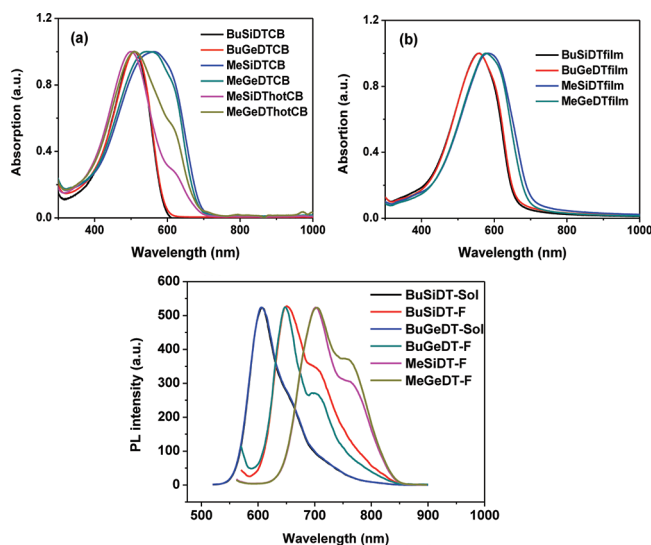


Figure 4. The UV-vis absorption spectra of **BuSiDT**, **BuGeDT**, **MeSiDT** and **MeGeDT** (a) in chlorobenzene solution (b) as spun cast films. (c) PL spectra of **BuSiDT** and **BuGeDT** both in chlorobenzene solution and thin film, **MeSiDT** and **MeGeDT** in thin films.

polymers with methyl groups attached have a stronger interaction between the backbones than the polymers with the butyl group attached, suggesting that the bridging alkyl group can be used effectively to tune solid state packing. The absorption onsets of **BuSiDT**, **BuGeDT**, **MeSiDT**, and **MeGeDT** in the solid state are 653, 655, 696, and 686 nm, which corresponds to an optical band gap of 1.90, 1.89, 1.78, and 1.81 eV respectively.

The emission spectra of **BuSiDT** and **BuGeDT** chlorobenzene solution, and **BuSiDT**, **BuGeDT**, **MeSiDT**, and **MeGeDT** as thin films are shown in Figure 3c. Both **BuSiDT** and **BuGeDT** exhibit a red emission with a maximum at 604 nm in solution corresponding to a large Stokes shift of 96 nm. Such large shifts have been observed in other silole-based polymers, and may be related to excimer emission.²⁹ In thin films, the maximum emission is red-shifted to approximately 650 nm. The emission spectra of **MeSiDT** and **MeGeDT** in chlorobenzene solution were not tested due to their tendency to aggregate in solution. In thin films **MeSiDT** and **MeGeDT** exhibit a red emission with a maximum at around 700 nm. The red-shift of the emission maximum from **BuSiDT** (**BuGeDT**) to **MeSiDT** (**MeGeDT**) in films further indicated that the polymers with methyl groups attached have a stronger interaction between the backbones than the polymers with the butyl group attached.

Electrochemical Properties. Cyclic voltammograms of the polymer thin films are shown in Figure 5, and the electro-

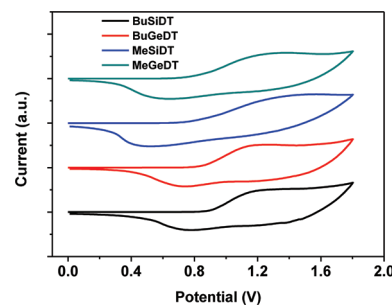


Figure 5. Cyclic voltammograms of **BuSiDT**, **BuGeDT**, **MeSiDT**, and **MeGeDT** as thin films in 0.1 M Bu_4NPF_6 solution in acetonitrile at a scan rate of 0.1 V s^{-1} .

chemical data is summarized in Table 2. All four polymers show quasi-reversible oxidation peaks, but reduction peaks were not observed. The HOMO energy levels of **BuSiDT**, **BuGeDT**, **MeSiDT**, and **MeGeDT** determined by the oxidation onset were -5.34 , -5.29 , -5.25 , and -5.22 eV. The Si-containing polymers consistently have a slightly higher oxidation potential than the analogous Ge-containing polymers. This is in agreement with previous theoretical results on germole and silole oligomers,¹⁸ as well as with recent reports which found DTG-containing polymers to have slightly higher HOMO levels than the corresponding DTS polymer.²² The LUMO could not be measured directly by CV, so was estimated to be -3.44 , -3.40 , -3.47 , and -3.41 eV, respectively, by subtracting the optical band gap from the electrochemical oxidation.

Thin Film Morphology. The ordering of thin films of **BuSiDT**, **BuGeDT**, **MeSiDT**, and **MeGeDT** was investigated by wide-angle X-ray scattering (WAXS). Films were prepared by drop casting hot chlorobenzene solutions onto 100°C glass substrates, followed by annealing at 140°C for 20 min. As shown in Figure 6, in agreement with the DSC data, all films displayed evidence of crystallinity with clear diffraction peaks observed in all cases. The nature of the alkyl group on the bridging heteroatom had the clearest influence of film morphology. Thus, **BuSiDT** and **BuGeDT** films showed similar behavior, with pronounced peaks at 3.92 and 3.85 deg (2θ) corresponding to a d -spacing of 22.5 and 22.9 Å. No obvious peaks corresponding to a π - π stacking distance were observed. The lamellar spacings are similar to those reported for a polymer of similar molecular structure except that the bridging group is sulfur (i.e., Figure 1, $\text{X} = \text{S}$). This polymer (**P2TDC10FT3**), which has decyl side chains instead of the

Table 2. Physical Properties of **MeSiDT**, **MeGeDT**, **BuSiDT**, and **BuGeDT**

polymers	T_m, T_c^a ($^\circ\text{C}$)	ΔH (T_c) (J/g)	$\lambda_{\text{abs max}}^b$ (sol) (nm)	$\lambda_{\text{abs max}}^b$ (film) (nm)	$\lambda_{\text{abs onset}}^b$ (film) (nm)	E_{gap}^c (eV)	$\lambda_{\text{em max}}^d$ (sol) (nm)	$\lambda_{\text{em max}}^d$ (film) (nm)	HOMO ^e (eV)	LUMO ^f (eV)
MeSiDT	296 and 305, 268	9.3	559 (501 ^b)	586	696	1.78	<i>d</i>	701, 758	-5.25	-3.47
MeGeDT	292 and 306, 262	9.1	548 (510 ^b)	579	686	1.81	<i>d</i>	706, 760	-5.22	-3.41
BuSiDT	216, 196	5.3	508	558	653	1.90	604	652, 699	-5.34	-3.44
BuGeDT	225, 193	5.2	509	558	655	1.89	604	649, 698	-5.29	-3.40

^aMelting temperature (T_m) and crystallization temperature (T_c) determined by DSC. ^bUV-vis data from hot chlorobenzene solution. ^cOptical band gap estimated from the low energy band edge in the optical spectrum. ^dNot measured. ^eHOMO level estimated from cyclic voltammetry (CV).

^fLUMO = HOMO + E_{gap}

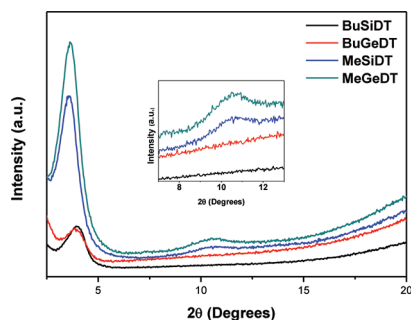


Figure 6. X-ray diffraction patterns of BuSiDT, BuGeDT, MeSiDT, and MeGeDT films.

dodecyl reported here, had a d -spacing of 24.8 Å and is reported to pack in a lamellar type morphology.³⁰ In analogy to this and other thiophene polymers,³¹ this is suggestive of a lamellar type ordering where the majority of the polymers have an edge on orientation on the substrate, with the π - π stacking direction parallel to the substrate. Reducing the size of the bridging substituent results in an increase of d -spacing, with MeSiDT and MeGeDT exhibiting peaks at 3.55 and 3.62 degree (2θ) corresponding to d -spacings of 24.9 and 24.4 Å. Both polymers also show weak higher order peaks at 10.50 deg (2θ) (8.4 Å), suggesting improved ordering compared to butyl-bridged polymers. The increase in lamellar distance upon reducing the size of the bridging group may be related to a reduction in the tilt angle of the dodecyl side chains due to a reduction in steric strain between the alkyl substituents on the bridging atom.

OFET Performance. The charge transport behavior of the polymers was investigated in bottom-gate, top-contact transistor devices. All transistors were fabricated at the same time to reduce process variations. Bottom gate devices used heavily doped Si²⁺ substrates as the gate electrode and a 400 nm thermally oxidized SiO₂ layer as the gate dielectric. The SiO₂ layer was treated with octyltrichlorosilane (OTS) before use in order to both passivate the surface and promote edge on alignment of the polymers. Polymers thin films were fabricated by spin coating, followed by thermal annealing before Au source/drain electrodes were deposited by shadow masking. All of the polymers exhibited typical p-type semiconducting behavior. The performance data of MeSiDT, MeGeDT, BuSiDT, and BuGeDT are outlined in Table 3. Comparison between the various polymers was complicated by difficulties in forming homogeneous films. MeSiDT and BuSiDT formed smooth films after spin coating and annealing (150 °C) which showed reproducible electrical characteristics with little hysteresis between the forward and reverse sweeps. However films of MeGeDT and BuGeDT demonstrated poor reproducibility and high hysteresis after annealing at 150 °C. This could be solved by annealing at 200 °C for 20 min, but at this temperature films of MeSiDT and BuSiDT dewetted, preventing measurement. The reasons behind this difference in

film forming and wetting behavior are not clear, but nevertheless working devices with low hysteresis could be obtained in all cases. The saturated and linear charge carrier mobilities were rather low in all cases, on the order of 10⁻⁴ cm²/(V s). Figure 7 shows the typical transfer and output

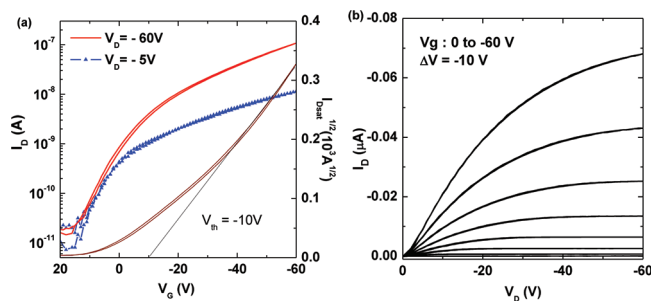


Figure 7. Representative transfer (a) and output (b) characteristics of bottom-gate, top-contact organic field-effect transistor (OFET) of MeSiDT (transistor channel = 50 μm, transistor width = 1000 μm).

characteristics of an OFET device based on MeSiDT, which was the best performing polymer with a saturated mobility of 8.0×10^{-4} . Increasing the length of the bridging group as in BuSiDT resulted in a reduction of saturated mobility to 1.3×10^{-4} cm²/(V s), which we believe is reasonable to attribute to the reduced ordering over MeSiDT. However, the same trend was not observed for the Ge bridged polymers, with MeGeDT and BuGeDT having similar mobility after annealing at 200 °C, around 3×10^{-4} cm²/vs. Because of the wetting difficulties with the germanium bridged polymers in the bottom gate device architecture, top gate, bottom contact devices were also fabricated for MeGeDT and BuGeDT. Here the semiconductor was coated onto glass substrates prepatterned with Au source drain electrodes. The substrate in this case was less hydrophobic than the OTS treated SiO₂ of the bottom gate devices, and smooth films were formed after annealing at 150 °C. Following deposition of the dielectric (Cytop) and gate electrode, working devices were obtained which displayed low hysteresis (see Supporting Information). In this configuration differences in the mobility were observed depending on the length of the alkyl bridge, with MeGeDT exhibiting linear and saturated mobilities of 1.7×10^{-4} cm²/(V s), while BuGeDT was lower, around 4×10^{-5} cm²/(V s) for both the linear and saturated regimes.

In conclusion it would appear that there are not significant differences in the transistor performance of the Si or Ge bridged polymers for identical side chain lengths. Increasing the length of the side chain on the bridging heteroatom does appear to result in a reduction in device performance. In all cases the observed mobilities are rather low, and are comparable to the analogous polymer bridged with a sulfur group (P2TDC10FT3).³⁰ In agreement with earlier studies, the low mobility may be a result of the packing pattern of the dodecyl side chains on the DTS or DTG monomer, since they

Table 3. OFET Device Performance of MeSiDT, MeGeDT, BuSiDT, and BuGeDT in Bottom Gate, Top Contact Devices

polymers	annealing temperature (°C)	μ_{lin} (cm ² /(V s))	μ_{sat} (cm ² /(V s))	V_T (V)	I_{on}/I_{off}
MeSiDT	150	3.8×10^{-4}	8.0×10^{-4}	-10.0	7.4×10^3
MeGeDT	200	1.7×10^{-4}	3.2×10^{-4}	-11.0	4.4×10^3
BuSiDT	150	6.4×10^{-5}	1.3×10^{-4}	-7.2	2.4×10^3
BuGeDT	200	1.3×10^{-4}	4.0×10^{-4}	-8.3	3.2×10^2

are both are positioned on the same side of the polymer backbone resulting in a lack of C_2 rotational symmetry.^{32,33} This has been observed to result in a less dense lamellar packing due to a lack of side chain interdigitation and reduced transistor performance.³²

CONCLUSIONS

In summary, we have reported a straightforward methodology for the synthesis of fused dithienosilole or dithienogermole monomers in which the required solubilizing side chains are attached in the peripheral 3,3'-positions of the heterocycle. Such an approach allows the use of simple commercially available dialkyl-dichloro-silanes and -germanes for the construction of the fused ring. We have reported the synthesis and characterization of a four series of Si- or Ge-containing bithiophene copolymers. High molecular weight soluble polymers were obtained by the Stille coupling reaction in all cases. The optical, electrical, electrochemical, and morphological properties of the polymers are reported. We find that the nature of the bridging atom (Si or Ge) only has a minor influence on these properties. However, the nature of the alkyl substituent attached to the bridging Si or Ge atom has a much greater influence and can be used as an additional tool to control polymer packing, crystallinity, and optoelectronic properties. Further tuning of the polymer properties by variation of the comonomer unit is currently under investigation in our laboratories.

EXPERIMENTAL SECTION

General Data. All reactions were carried out in oven-dried glassware using reagents and chemicals as commercially supplied from Aldrich and Acros unless otherwise noted. Syringes which were used to transfer reagents or solvents were purged with Ar prior to use. ^1H and ^{13}C NMR spectra were recorded on Bruker AV-400 (400 MHz) spectrometers. Chemical shifts are quoted in parts per million (ppm), referenced to the residual solvent peak, 7.26 ppm (^1H NMR) and 77.0 ppm (^{13}C NMR) for CDCl_3 and coupling constants (J) are given in Hertz (Hz). **Number-average (M_n) and weight-average (M_w)** were determined by Agilent Technologies 1200 series GPC running in chlorobenzene at 80 °C, using two PL mixed B columns in series, and calibrated against narrow polydispersity polystyrene standards. **Micro-wave experiments** were performed in a Biotage initiator V 2.3 in constant heating mode. **Electron ionization mass spectrometry** was performed with a Waters Micromass AutoSpec Premier, coupled to an Agilent 6890 gas chromatograph for GC-MS measurements. **UV-vis spectra** were recorded on a UV-1601 Shimadzu UV-vis spectrometer. **Flash chromatography (FC)** was performed on silica gel (Merck Kieselgel 60 grade 40–63 μm F₂₅₄) using flash techniques. **Analytical thin layer chromatography (TLC)** was performed on Merck Kieselgel 60 F₂₅₄ aluminum sheets and visualization was effected with UV fluorescence (254 and 365 nm). **Cyclic voltammetry (CV)** was carried out with a standard three-electrode cell in a 0.1 M tetrabutylammonium hexafluorophosphate ((TBA)PF₆) solution in acetonitrile at room temperature with a scanning rate of 0.1 V s⁻¹. A Pt wire working electrode, a Pt mesh counter electrode, and an Ag wire reference electrode were used. The oxidation potentials were calibrated with a standard ferrocene/ferrocenium (FOC) redox system as the standard (assuming the energy level of FOC is 4.8 e V below vacuum) for estimating the HOMO energy level of polymers. The polymer films were prepared by dipping the platinum working electrode into the polymer solution in chloroform or chlorobenzene, and drying on a hot plate. **X-ray diffraction (XRD) measurements** were carried out with a Panalytical X'Pert-pro MRD diffractometer equipped with a nickel-filtered Cu K α source and X'Celerator detector, using current $I = 40$ mA and accelerating voltage $V = 40$ kV. Samples were prepared by drop casting.

OFET (Organic Field Effect Transistors) Device Fabrication.

Bottom-gate, top-contact devices were fabricated on highly doped p type Si wafer with 400 nm SiO₂ dielectric layer. The SiO₂ dielectric was treated with octyltrichlorosilane (OTS) prior to deposition of the semiconductor. Polymer films were spin-casted from hot chlorobenzene with 1000 rpm and annealed at 150 °C for 20 min. 60 nm Au source/drain electrodes were deposited by vacuum sublimation through shadow masks. Channel width and length of the transistors were 1 mm and 50 μm , respectively. V_G was varied from 10 to -60 V in 1 V steps V_D set at -5 or -6 V (linear) and -60 V (saturation).

Electrical characterization was carried out in N₂ at atmospheric pressure using a Keithley 4200 semiconductor parameter analyzer. Using standard semiconductor models,³⁴ the field effect mobility was determined from transfer characteristics in the saturation regime using the following equation:

$$\mu = \left(\frac{\partial \sqrt{I_D}}{\partial V_G} \right)^2 \frac{2L}{WC_i}$$

Here μ is the field-effect mobility, I_D is the drain current in the saturation regime, V_G is the voltage applied to the gate terminal of the OFET, L and W are the OFET channel length and width, respectively, and C_i is the geometrical capacitance of the gate dielectric.

Synthesis of Monomers and Polymers. **4,4'-Bis(dodecyl)-2,2'-bithiophene (2).** In a slight modification of the published procedure,²⁵ dry TMEDA (55 mL, 196.7 mmol) and THF (80 mL) were charged to a 250 mL 3-neck round bottomed flask and the mixture was cooled to -30 °C. 2.5 M *n*-BuLi in hexane (86.5 mL, 216.4 mmol) was added via a syringe slowly and the temperature was kept below -30 °C. 3-Dodecylthiophene (1) (49.6 g, 196.7 mmol) and dry THF (300 mL) were charged to a 500 mL 3-neck round bottomed flask at room temperature and the cooled *n*-BuLi/TMEDA mixture was introduced in portions into the solution over 15 min via cannula. After the addition was complete, the reaction mixture was heated to reflux for 1 h, then cooled to -40 °C. Anhydrous copper(II) chloride (29.1 g, 216.4 mmol) was added. The mixture was allowed to warm to room temperature by removing the cold-bath and stirring overnight. Upon completion of the reaction (TLC controlled), 37% HCl (70 mL) and water (200 mL) were added. The aqueous layer was extracted with ether (3 \times 200 mL). The combined organic phases were washed with 5% Na₂SO₃ solution, followed by water (3 \times 150 mL), dried over Na₂SO₄ and concentrated *in vacuo*. The crude product was collected by vacuum filtration through a pad of silica gel eluting with warm hexane (60 °C). The filtrate was concentrated *in vacuo*. Recrystallization from acetone afforded the bithiophene (2) as a pale yellow solid (28.2 g, 57%). ^1H NMR (CDCl_3 , 400 MHz), δ (ppm): 6.98 (s, 2H), 6.76 (d, $J = 1.2$ Hz, 2H), 2.56 (t, $J = 7.5$ Hz, 4H), 1.63–1.58 (m, 4H), 1.31–1.26 (m, 36H), 0.88 (t, $J = 6.8$ Hz, 6H). ^{13}C NMR (CDCl_3 , 100 MHz), δ (ppm): 144.0, 137.4, 124.8, 118.7, 31.9, 30.4, 29.7, 29.6, 29.5, 29.4, 29.3, 22.7, 14.1. GC-MS (EI): $m/z = 502$ (M^+).

3,3',5,5'-Tetrabromo-4,4'-bis(dodecyl)-2,2'-bithiophene (3). To the stirring mixture of 4,4'-bis(dodecyl)-2,2'-bithiophene (27.0 g, 53.8 mmol) dissolved in acetic acid (50 mL) and chloroform (200 mL) was added liquid Br₂ (11.4 mL, 221.6 mmol) in the absence of light and the solution was stirred at ambient temperature for 2 h. The reaction mixture was then heated to 70 °C and stirred overnight. Upon completion of the reaction (TLC indicated), the mixture was quenched by addition of 5% Na₂SO₃ solution, followed by extraction with CH₂Cl₂ (2 \times 100 mL). The combined organic layer was washed with water (3 \times 200 mL), dried over MgSO₄ and concentrated *in vacuo*. Recrystallization from acetone yielded tetrabromo bithiophene (3) as a pale yellow solid (38.2 g, 87%). ^1H NMR (CDCl_3 , 400 MHz), δ (ppm): 2.66 (t, $J = 7.8$ Hz, 4H), 1.56–1.52 (m, 4H), 1.37–1.27 (m, 36H), 0.88 (t, $J = 6.8$ Hz, 6H). ^{13}C NMR (CDCl_3 , 100 MHz), δ (ppm): 141.5, 128.6, 114.6, 111.1, 31.9, 30.4, 29.7, 29.7, 29.6, 29.4, 28.6, 22.7, 14.1. GC-MS (EI): $m/z = 818$.

3,3'-Dibromo-5,5'-bis(trimethylsilyl)-4,4'-bis(dodecyl)-2,2'-bithiophene (4). To a solution of 3,3',5,5'-tetrabromo-4,4'-bis(dodecyl)-2,2'-bithiophene (38.2 g, 46.7 mmol) in dry THF (800 mL) was added 2.5 M *n*-BuLi in hexane (39.6 mL, 99.0 mmol) dropwise at -78 °C. The

mixture was stirred for a further 20 min at this temperature, followed by addition of chlorotrimethylsilane (14.3 mL, 113.3 mmol) in one portion. The mixture was allowed to warm to ambient temperature. Solvent was removed *in vacuo*. Column chromatography using hexane as eluent gave TMS-protected bithiophene (**4**) as a pale yellow oil (33.4 g, 89%). ¹H NMR (CDCl₃, 400 MHz), δ (ppm): 2.67 (t, *J* = 8.3 Hz, 4H), 1.58–1.54 (m, 4H), 1.32–1.30 (m, 36H), 0.88 (t, *J* = 6.8 Hz, 6H), 0.35 (s, 18H). ¹³C NMR (CDCl₃, 100 MHz), δ (ppm): 149.5, 135.3, 134.0, 116.6, 32.0, 31.9, 30.8, 30.0, 29.7, 29.6, 29.4, 22.7, 14.2, 0.2. MS (EI) *m/z* = 804 (M⁺).

3,5-Didodecyl-2,6-dibromo-4,4'-dimethyldithieno[3,2-b:2',3'-d]-silole (5). 2.5 M *n*-BuLi in hexane (6.2 mL, 15.4 mmol) was added dropwise to a solution of (**4**) (5.9 g, 7.3 mmol) in THF (20 mL) at –78 °C. After stirring for 15 min at this temperature, dichlorodimethylsilane (1.1 mL, 8.8 mmol) was added in one portion. The mixture was allowed to warm to room temperature with further stirring for 0.5 h, followed by treatment with water (50 mL) and extraction with hexane (3 × 50 mL). The combined organics were dried over MgSO₄ and concentrated under reduced pressure. The residue was purified by column chromatography from hexane to afford a pale yellow oil.

To the resulting oil dissolved in THF (40 mL) was added NBS (2.6 g, 14.6 mmol) in one portion followed by stirring for 2 h at room temperature in the absence of light. Upon completion of the reaction (TLC controlled), an aqueous solution of Na₂SO₃ (40 mL) was added to quench this reaction. The aqueous layer was extracted with hexane (3 × 50 mL). The combined organics were dried over MgSO₄ and concentrated under reduced pressure. Purification by column chromatography using hexane afforded title compound (**5**) as a pale yellow oil (4.2 g, 80%). ¹H NMR (CDCl₃, 400 MHz), δ (ppm): 2.56 (t, *J* = 8.4 Hz, 4H), 1.58–1.52 (m, 4H), 1.34–1.26 (m, 36H), 0.88 (t, *J* = 7.7 Hz, 6H), 0.44 (s, 6H). ¹³C NMR (CDCl₃, 100 MHz), δ (ppm): 147.0, 145.0, 141.5, 108.1, 32.0, 30.3, 30.3, 29.7, 29.7, 29.6, 29.5, 29.4, 22.7, 14.2, –3.2. HRMS (EI): calcd for C₃₄H₅₆Br₂S₂Si, 714.1959; found, 714.1945.

3,5-Didodecyl-2,6-dibromo-4,4'-di-*n*-butyldithieno[3,2-b:2',3'-d]-silole (6). 2.5 M *n*-BuLi in hexane (6.7 mL, 16.7 mmol) was added dropwise to a solution of (**4**) (6.1 g, 7.6 mmol) in THF (40 mL) at –78 °C. After stirring for 15 min at –78 °C, di-*n*-butyldichlorosilane (2.0 mL, 9.1 mmol) was added in one portion. The mixture was allowed to warm to room temperature with a further stirring for 0.5 h, followed by treatment with water (50 mL) and extraction with hexane (3 × 50 mL). The combined organic phases were dried over MgSO₄ and concentrated *in vacuo*. Column chromatography using hexane afforded a pale yellow oil.

To the resulting oil dissolved in THF (40 mL) was added NBS (2.7 g, 15.2 mmol) in one portion. The mixture was stirred for 2 h at room temperature in the absence of light. The reaction was quenched by treatment of Na₂SO₃(aq) (40 mL), extracted with hexane (3 × 50 mL). The combined organic layer was dried over MgSO₄ and concentrated *in vacuo*. Column chromatography using hexane afforded the title compound (**6**) as a pale yellow oil (4.4 g, 73%). ¹H NMR (CDCl₃, 400 MHz), δ (ppm): 2.57 (t, *J* = 7.9 Hz, 4H), 1.59–1.52 (m, 4H), 1.45–1.16 (m, 44H), 1.03–0.95 (m, 4H), 0.89 (t, *J* = 6.8 Hz, 6H), 0.83 (t, *J* = 7.1 Hz, 6H). ¹³C NMR (CDCl₃, 100 MHz), δ (ppm): 147.6, 145.0, 140.3, 108.1, 32.0, 30.6, 30.2, 29.7, 29.7, 29.6, 29.6, 29.5, 29.4, 25.9, 22.7, 14.2, 13.6, 12.5. HRMS (EI): calcd for C₄₀H₆₈Br₂S₂Si, 798.2898; found, 798.2888.

3,5-Didodecyl-2,6-dibromo-4,4'-dimethyldithieno[3,2-b:2',3'-d]-germole (7). A 2.5 M sample of *n*-BuLi in hexane (4.4 mL, 10.9 mmol) was added dropwise to a solution of (**4**) (4.0 g, 5.0 mmol) in THF (15 mL) at –78 °C. After the reaction was stirred for 20 min at this temperature, dichlorodimethylgermane (0.63 mL, 5.5 mmol) was added in one portion. The mixture was allowed to warm to room temperature with a further stirring for 0.5 h, followed by treatment with water (50 mL) and extraction with hexane (3 × 50 mL). The combined organic layer was dried over MgSO₄ and concentrated under reduced pressure. Column chromatography using hexane afforded a pale yellow oil.

To the resulting oil dissolved in THF (30 mL) was added NBS (1.8 g, 10.0 mmol) in one portion. The mixture was stirred for 2 h at room temperature in the absence of light. Upon completion of the reaction (TLC indicated), the mixture was quenched by treatment with an aqueous solution of Na₂SO₃ (40 mL). The aqueous layer was extracted with hexane (3 × 50 mL). The combined organic layer was dried over MgSO₄ and concentrated *in vacuo*. Column chromatography using hexane afforded title compound (**7**) as a pale yellow oil (2.6 g, 69%). ¹H NMR (CDCl₃, 400 MHz), δ (ppm): 2.59 (t, *J* = 7.7 Hz, 4H), 1.59–1.54 (m, 4H), 1.36–1.29 (m, 36H), 0.91 (t, *J* = 7.1 Hz, 6H), 0.70 (s, 6H). ¹³C NMR (CDCl₃, 100 MHz), δ (ppm): 144.6, 144.6, 142.4, 107.9, 32.0, 30.5, 30.3, 29.8, 29.7, 29.7, 29.6, 29.5, 29.5, 22.8, 14.2, –2.1. HRMS (EI): calcd for C₃₄H₅₆Br₂S₂Ge, 760.1402; found, 760.1391.

3,5-Didodecyl-2,6-dibromo-4,4'-di-*n*-butyldithieno[3,2-b:2',3'-d]-germole (8). A 2.5 M sample of *n*-BuLi in hexane (6.8 mL, 17.0 mmol) was added dropwise to a solution of (**4**) (6.2 g, 7.7 mmol) in THF (30 mL) at –78 °C. After stirring for 20 min at –78 °C, di-*n*-butyldichlorogermane (2.0 mL, 9.3 mmol) was added in one portion. The mixture was allowed to warm to room temperature with a further stirring for 0.5 h, followed by treatment with water (50 mL) and extraction with hexane (3 × 50 mL). The combined organic phases were dried over MgSO₄ and concentrated *in vacuo*. Column chromatography using hexane afforded a pale yellow oil.

To the resulting oil in THF (40 mL) was added NBS (2.7 g, 15.2 mmol) in one portion at ambient temperature, followed by a further stirring for 1 h at room temperature in the absence of light. Upon completion of the reaction (TLC indicated), the mixture was quenched by treatment with an aqueous solution of Na₂SO₃ (40 mL). The aqueous layer was extracted with hexane (3 × 50 mL). The combined organic phases were dried over MgSO₄ and concentrated *in vacuo*. Column chromatography using hexane yielded title compound (**8**) as a pale yellow oil (5.3 g, 81%). ¹H NMR (CDCl₃, 400 MHz), δ (ppm): 2.55 (t, *J* = 8.1 Hz, 4H), 1.57–1.53 (m, 4H), 1.28–1.21 (m, 48H), 0.89 (t, *J* = 6.8 Hz, 6H), 0.83 (t, *J* = 7.1 Hz, 6H). ¹³C NMR (CDCl₃, 100 MHz), δ (ppm): 145.0, 144.7, 141.3, 107.7, 32.0, 30.8, 30.2, 29.7, 29.7, 29.6, 29.4, 27.4, 26.1, 22.7, 14.9, 14.2, 13.6. HRMS (EI): calcd for C₄₀H₆₈Br₂S₂Ge, 844.2341; found, 844.2338.

Poly(3,5-didodecyl)-4,4'-dimethyldithieno[3,2-b:2',3'-d]silole)-2,6-diyl-alt-(2,2'-bithiophene)-5,5'-diyl (MeSiDT). To an oven-dried 5 mL high pressure microwave reactor tube equipped with a sealed septum was added the following reagents in a sequential fashion: compound (**5**) (297.4 mg, 0.42 mmol), 5,5'-bis(trimethylstannyl)-2,2'-bithiophene (204.1 mg, 0.42 mmol), Pd₂(dba)₃ (7.6 mg, 0.0084 mmol) and P-(*o*-tol)₃ (10.1 mg, 0.033 mmol). The tube was sealed and flushed with Ar, then degassed chlorobenzene (2.5 mL) was added. The mixture was thoroughly degassed under Ar, and then the argon inlet was removed. The tube was subjected to the following conditions in a microwave reactor: 120 °C for 5 min, 140 °C for 5 min and 180 °C for 50 min. After cooling to room temperature, the polymer was precipitated into methanol (100 mL), and filtered through a Soxhlet thimble. The polymer was extracted using Soxhlet apparatus with methanol, acetone, hexane, chloroform and chlorobenzene. The chlorobenzene solution was concentrated *in vacuo* and precipitation was induced in methanol. Vacuum filtration followed by drying under vacuum afforded MeSiDT as a dark-red solid (165 mg, 55%). ¹H NMR (1,1,2,2-tetrachloroethane-*d*₂, 130 °C, 400 MHz), δ (ppm): 7.20 (broad, 2H), 7.11 (broad, 2H), 2.88 (broad, 4H), 1.78 (broad, 4H), 1.52–1.38 (broad, 36H), 0.97 (broad, 6H), 0.63 (broad, 6H). Anal. Calcd: (C₄₂H₆₀SiS₄)_n: C, 69.94; H, 8.38. Found: C, 69.51; H, 8.14.

Poly(3,5-didodecyl)-4,4'-di-*n*-butyldithieno[3,2-b:2',3'-d]silole)-2,6-diyl-alt-(2,2'-bithiophene)-5,5'-diyl (BuSiDT). Compound (**6**) (286.5 mg, 0.36 mmol), 5,5'-bis(trimethylstannyl)-2,2'-bithiophene (176.6 mg, 0.36 mmol), Pd₂(dba)₃ (6.6 mg, 0.0072 mmol), and P-(*o*-tol)₃ (8.7 mg, 0.029 mmol) were reacted following the procedure reported for MeSiDT. The polymer was extracted using Soxhlet apparatus with methanol, acetone, hexane and chloroform. The chloroform solution was concentrated *in vacuo* and precipitation was induced in methanol. Vacuum filtration followed by drying under

vacuum yielded **BuSiDT** as a dark-red solid (203 mg, 71%). ^1H NMR (CDCl_3 , 400 MHz), δ (ppm): 7.14 (broad, 2H), 7.06 (broad, 2H), 2.82 (broad, 4H), 1.67 (broad, 4H), 1.48–1.29 (broad, 44H), 1.06 (broad, 4H), 0.88 (broad, 12H). Anal. Calcd: ($\text{C}_{48}\text{H}_{72}\text{SiS}_4$) $_n$: C, 71.58; H, 9.01. Found: C, 71.23; H, 9.10.

Poly(3,5-didodecyl)-4,4'-dimethyldithieno[3,2-b:2',3'-d]germole)-2,6-diyl-alt-(2,2'-bithiophene)-5,5'-diyl (MeGeDT). Compound **7** (230.7 mg, 0.30 mmol), $5,5'$ -bis(trimethylstannyl)-2,2'-bithiophene (149.0 mg, 0.42 mmol), $\text{Pd}_2(\text{dba})_3$ (5.5 mg, 0.006 mmol), and $\text{P}-(o\text{-tol})_3$ (7.3 mg, 0.024 mmol) were reacted following the procedure for **MeSiDT** to afford **MeGeDT** as a dark-red solid (195 mg, 84%). ^1H NMR (1,1,2,2-tetrachloroethane- d_4 , 130 °C, 400 MHz), δ (ppm): 7.19 (broad, 2H), 7.11 (broad, 2H), 2.89 (broad, 4H), 1.78 (broad, 4H), 1.50–1.38 (broad, 36H), 0.97 (broad, 6H), 0.63 (broad, 6H). Anal. Calcd: ($\text{C}_{42}\text{H}_{60}\text{GeS}_4$) $_n$: C, 65.88; H, 7.90. Found: C, 65.31; H, 7.78.

Poly(3,5-didodecyl)-4,4'-di-n-butylthieno[3,2-b:2',3'-d]germole)-2,6-diyl-alt-(2,2'-bithiophene)-5,5'-diyl (BuGeDT). Compound **8** (484.5 mg, 0.57 mmol), $5,5'$ -bis(trimethylstannyl)-2,2'-bithiophene (281.8 mg, 0.57 mmol), $\text{Pd}_2(\text{dba})_3$ (10.5 mg, 0.011 mmol) and $\text{P}-(o\text{-tol})_3$ (13.9 mg, 0.046 mmol) were reacted following the method reported for **BuSiDT** to afford **BuGeDT** as a dark-red solid (430 mg, 89%). ^1H NMR (CDCl_3 , 400 MHz), δ (ppm): 7.15 (broad, 2H), 7.06 (broad, 2H), 2.82 (broad, 4H), 1.67 (broad, 4H), 1.56–1.29 (broad, 48H), 0.88 (broad, 12H). Anal. Calcd: ($\text{C}_{48}\text{H}_{72}\text{GeS}_4$) $_n$: C, 67.83; H, 8.54. Found: C, 67.23; H, 8.80.

■ ASSOCIATED CONTENT

■ Supporting Information

Top gate transistor data and transfer and output plots and ^1H and ^{13}C NMR spectra. This material is available free of charge via the Internet at <http://pubs.acs.org>.

■ AUTHOR INFORMATION

Corresponding Author

*E-mail: m.heeney@imperial.ac.uk.

■ ACKNOWLEDGMENTS

This work was carried out in part under work supported by EPSRC Grants EP/F056648/2, EP/G060738/1, EP/I002936/1 and Dutch Polymer Institute Grant 678, with support from the International Collaborative Research Program of Gyeonggi-do, Korea.

■ REFERENCES

- (1) Cheng, Y. J.; Yang, S. H.; Hsu, C. S. *Chem. Rev.* **2009**, *109*, 5868.
- (2) Hou, J.; Chen, H.-Y.; Zhang, S.; Li, G.; Yang, Y. *J. Am. Chem. Soc.* **2008**, *130*, 16144.
- (3) Wang, E. G.; Wang, L.; Lan, L. F.; Luo, C.; Zhuang, W. L.; Peng, J. B.; Cao, Y. *Appl. Phys. Lett.* **2008**, *92*, 033307.
- (4) Chu, T.-Y.; Lu, J.; Beaupré, S.; Zhang, Y.; Pouliot, J.-R.; Wakim, S.; Zhou, J.; Leclerc, M.; Li, Z.; Ding, J.; Tao, Y. *J. Am. Chem. Soc.* **2011**, *133*, 4250.
- (5) Ding, J.; Song, N.; Li, Z. *Chem. Commun.* **2010**, *46*, 8668.
- (6) Ashraf, R. S.; Chen, Z. Y.; Leem, D. S.; Bronstein, H.; Zhang, W. M.; Schroeder, B.; Geerts, Y.; Smith, J.; Watkins, S.; Anthopoulos, T. D.; Sirringhaus, H.; de Mello, J. C.; Heeney, M.; McCulloch, I. *Chem. Mater.* **2011**, *23*, 768.
- (7) Wang, J.-Y.; Hau, S. K.; Yip, H.-L.; Davies, J. A.; Chen, K.-S.; Zhang, Y.; Sun, Y.; Jen, A. K. Y. *Chem. Mater.* **2011**, *23*, 765.
- (8) Lu, G.; Usta, H.; Risko, C.; Wang, L.; Facchetti, A.; Ratner, M. A.; Marks, T. J. *J. Am. Chem. Soc.* **2008**, *130*, 7670.
- (9) Zhang, M.; Fan, H.; Guo, X.; He, Y.; Zhang, Z.; Min, J.; Zhang, J.; Zhao, G.; Zhan, X.; Li, Y. *Macromolecules* **2010**, *43*, 5706.
- (10) Hong, Y.-R.; Wong, H.-K.; Moh, L. C. H.; Tan, H.-S.; Chen, Z.-K. *Chem. Commun.* **2011**, *47*, 4920.
- (11) Chan, K. L.; McKiernan, M. J.; Towns, C. R.; Holmes, A. B. *J. Am. Chem. Soc.* **2005**, *127*, 7662.
- (12) Ohshita, J. *Macromol. Chem. Phys.* **2009**, *210*, 1360.
- (13) Usta, H.; Lu, G.; Facchetti, A.; Marks, T. J. *J. Am. Chem. Soc.* **2006**, *128*, 9034.
- (14) Morana, M.; Azimi, H.; Dennler, G.; Egelhaaf, H.-J.; Scharber, M.; Forberich, K.; Hauch, J.; Gaudiana, R.; Waller, D.; Zhu, Z.; Hingerl, K.; van Bavel, S. S.; Loos, J.; Brabec, C. J. *Adv. Funct. Mater.* **2010**, *20*, 1180.
- (15) Chen, H. Y.; Hou, J. H.; Hayden, A. E.; Yang, H.; Houk, K. N.; Yang, Y. *Adv. Mater.* **2010**, *22*, 371.
- (16) Scharber, M. C.; Koppe, M.; Gao, J.; Cordella, F.; Loi, M. A.; Denk, P.; Morana, M.; Egelhaaf, H.-J.; Forberich, K.; Dennler, G.; Gaudiana, R.; Waller, D.; Zhu, Z.; Shi, X.; Brabec, C. J. *Adv. Mater.* **2010**, *22*, 367.
- (17) Karnezis, A.; O'Hair, R. A. J.; White, J. M. *Organometallics* **2009**, *28*, 6480.
- (18) Yamaguchi, S.; Itami, Y.; Tamao, K. *Organometallics* **1998**, *17*, 4910.
- (19) Allard, N.; Aich, R. B.; Gendron, D.; Boudreault, P.-L. T.; Tessier, C.; Alem, S.; Tse, S.-C.; Tao, Y.; Leclerc, M. *Macromolecules* **2010**, *43*, 2328.
- (20) Chen, R.; Zhu, R.; Zheng, C.; Liu, S.; Fan, Q.; Huang, W. *Sci. China Ser. B: Chem.* **2009**, *52*, 212.
- (21) Ohshita, J.; Hwang, Y.-M.; Mizumo, T.; Yoshida, H.; Ooyama, Y.; Harima, Y.; Kunugi, Y. *Organometallics* **2011**, *30*, 3233.
- (22) Amb, C. M.; Chen, S.; Graham, K. R.; Subbiah, J.; Small, C. E.; So, F.; Reynolds, J. R. *J. Am. Chem. Soc.* **2011**, *133*, 10062.
- (23) Gendron, D.; Morin, P.-O.; Berrouard, P.; Allard, N.; Aich, R. B.; Garon, C. N.; Tao, Y.; Leclerc, M. *Macromolecules* **2011**, *44*, 7188.
- (24) Fei, Z.; Kim, J. S.; Smith, J.; Domingo, E. B.; Anthopoulos, T. D.; Stingelin, N.; Watkins, S. E.; Kim, J.-S.; Heeney, M. *J. Mater. Chem.* **2011**, *21*, 16257.
- (25) Zagorska, M.; Krische, B. *Polymer* **1990**, *31*, 1379.
- (26) Al-Hashimi, M.; Labram, J. G.; Watkins, S.; Motevalli, M.; Anthopoulos, T. D.; Heeney, M. *Org. Lett.* **2010**, *12*, 5478.
- (27) Getmanenko, Y. A.; Tongwa, P.; Timofeeva, T. V.; Marder, S. R. *Org. Lett.* **2010**, *12*, 2136.
- (28) Tierney, S.; Heeney, M.; McCulloch, I. *Synth. Met.* **2005**, *148*, 195.
- (29) Huang, H.; Youn, J.; Ortiz, R. P.; Zheng, Y.; Facchetti, A.; Marks, T. *Chem. Mater.* **2011**, *23*, 2185.
- (30) He, M.; Li, J.; Sorensen, M. L.; Zhang, F.; Hancock, R. R.; Fong, H. H.; Pozdin, V. A.; Smilgies, D.-M.; Malliaras, G. J. *Am. Chem. Soc.* **2009**, *131*, 11930.
- (31) Salleo, A.; Kline, R. J.; DeLongchamp, D. M.; Chanbiny, M. L. *Adv. Mater.* **2010**, *22*, 3812.
- (32) He, M.; Li, J.; Tandia, A.; Sorensen, M.; Zhang, F.; Fong, H. H.; Pozdin, V. A.; Smilgies, D.-M.; Malliaras, G. G. *Chem. Mater.* **2010**, *22*, 2770.
- (33) McCulloch, I.; Heeney, M.; Bailey, C.; Genevicius, K.; MacDonald, I.; Shkunov, M.; Sparrowe, D.; Tierney, S.; Wagner, R.; Zhang, W.; Chabinyc, M. L.; Kline, R. J.; McGehee, M. D.; Toney, M. F. *Nat. Mater.* **2006**, *5*, 328.
- (34) Zaumseil, J.; Sirringhaus, H. *Chem. Rev.* **2007**, *107*, 1296.

Donor–Acceptor Conjugated Polymers Based on *p*- and *o*-Benzodifuranone and Thiophene Derivatives: Electrochemical Preparation and Optical and Electronic Properties

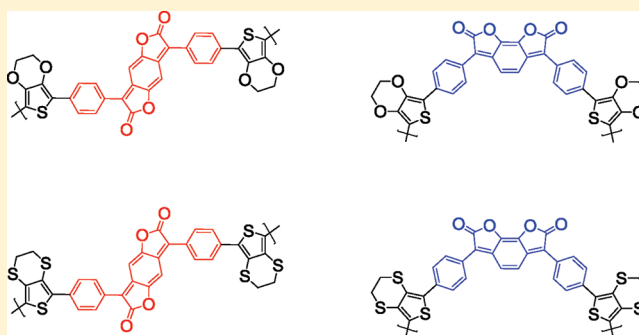
Kai Zhang,[†] Bernd Tieke,^{*,†} John C. Forgie,[‡] Filipe Vilela,[‡] and Peter J. Skabara[‡]

[†]Department of Chemistry, University of Cologne, Luxemburger Str. 116, D-50939 Cologne, Germany

[‡]WestCHEM, Department of Pure and Applied Chemistry, University of Strathclyde, Glasgow G1 1XL, United Kingdom

S Supporting Information

ABSTRACT: A series of π -conjugated polymers consisting of bis-EDOT or bis-EDTT units and *p*- or *o*-diphenylbenzodifuranones have been prepared electrochemically. The monomers and polymers were investigated using UV/vis absorption spectroscopy and cyclic voltammetry. The monomers were synthesized from 3,4-ethylenedioxythien-2-yl or 3,4-ethylenedithiathien-2-yl trimethylstannane and 3,7-bis(4-bromophenyl)benzo[1,2-*b*:4,5-*b'*]-difuran-2,6-dione or 3,6-bis(4-bromophenyl)benzo[1,2-*b*:6,5-*b'*]-difuran-2,7-dione using Stille coupling. The polymers exhibit broad absorption bands, and strong donor–acceptor characteristics with very small band gaps (in a range from 0.40 to 1.20 eV). Electrochemically grown polymer thin films exhibit reversible behavior under oxidative and reductive conditions. Under reduction, the polymer films show color changes from dark to almost transparent.



■ INTRODUCTION

The incorporation of chromophores in π -conjugated polymer chains, which are highly absorbing and emitting in the visible and near-infrared region, has been widely used for the design of new polymers for electronic applications. Potentially useful chromophores can be found among the various organic colorants, especially in the field of so-called “high-performance pigments” developed in the past three decades.¹ Among these pigments are 2,5-diketopyrrolo[3,4-*c*]pyrrole (DPP) derivatives, which were commercialized in the 1980s.² In recent years, a growing number of polymer chemists and physicists became interested in DPPs since it was shown that DPP-containing polymers exhibit light-emitting³ and photovoltaic properties.⁴ Very recently, Janssen et al. demonstrated the utility of thiophene-2-yl-DPP-containing conjugated polymers for application in photovoltaic devices exhibiting a power conversion efficiency up to 5.5%.⁵ Another interesting chromophore with a related structure, benzodifuranone (Scheme 1), has attracted our interest very recently.

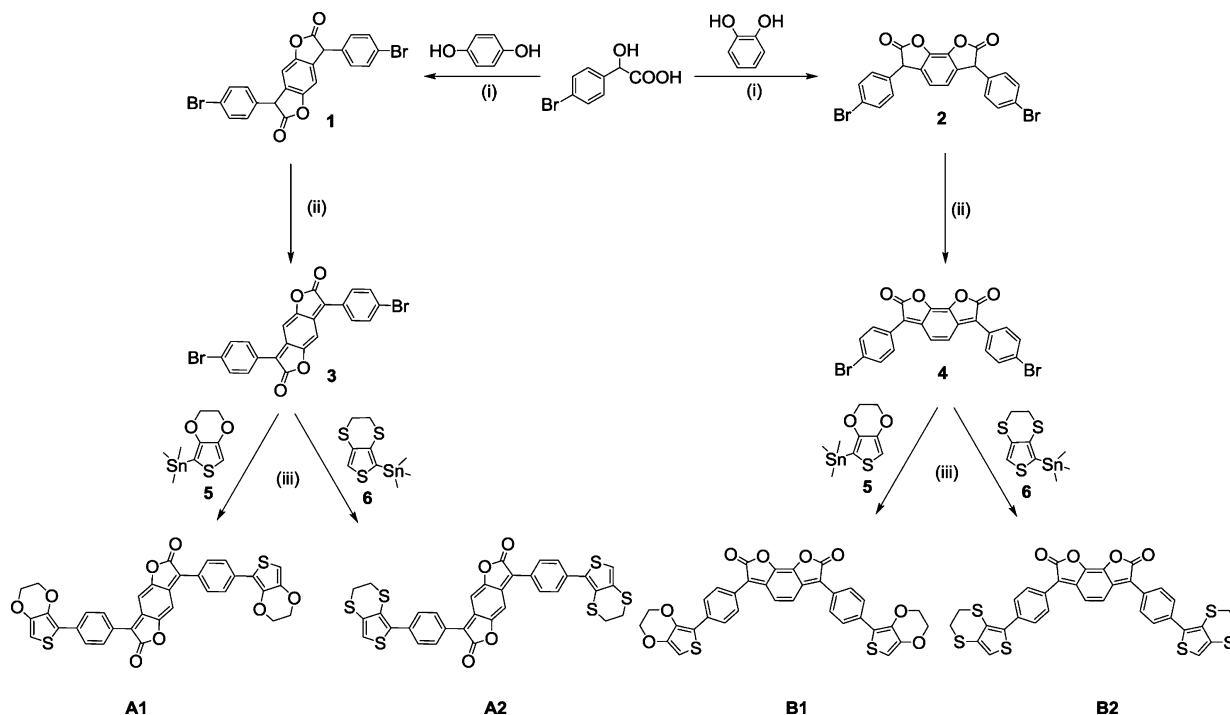
The benzodifuranone chromophore belongs to a class of currently used dyes and chromophores, which have been developed in the past 30 years.⁶ Because of their deep color and high brightness of shape, they were commercialized as disperse dyes for textiles, especially for polyesters. Depending on the substitution pattern, benzodifuranones exhibit red to blue colors⁷ and exhibit strong solvatochromism in organic solvents.⁸ Benzodifuranones are prepared upon condensation of 1,4- or 1,2-dihydroxybenzene with derivatives of mandelic acid.⁹

The final deep color originates from the quinoid structure of the central core unit, which is obtained upon oxidation of the benzene unit with chloranil. The broad absorption in the visible region of the spectrum, combined with a high color depth, renders benzodifuranones interesting as building blocks for novel π -conjugated polymers suitable for electronic applications. In a first report it has been shown that low-band-gap polymers can be prepared from dibromobenzodifuranone derivatives via Stille and Suzuki coupling reactions.¹⁰ In another study, benzodipyrrolidone-based conjugated polymers following a similar synthetic route have been reported very recently.¹¹ As an alternative way to synthesize such polymers we have chosen the electrochemical polymerization of benzodifuranones functionalized by EDOT or EDTT units at both ends of the molecules because their low oxidation potential enables electrochemical coupling¹² and because thiophene-based compounds are known for their role in organic semiconductor materials.¹³ In the present work, we describe the synthesis of π -conjugated polymers with benzodifuranone chromophores in the main chain via electrochemical coupling. Synthesis, optical, electrochemical, and electronic properties of the polymers will be described. It is demonstrated that the polymers exhibit interesting redox behavior and can be cathodically reduced with high reversibility.

Received: October 26, 2011

Revised: December 16, 2011

Published: December 23, 2011

Scheme 1. Synthetic Route to Monomers A1, A2, B1, and B2^a

^aReagents and conditions: (i) 1,2,4-trichlorobenzene, 200 °C, 12 h; (ii) nitrobenzene, 200 °C, 2 h; (iii) tetrakis(triphenylphosphine)palladium(0), DMF, microwave, 1 h.

■ EXPERIMENTAL SECTION

Materials. 3,4-Ethylenedioxythien-2-yl trimethylstannane and 3,4-ethylenedithiathien-2-yl trimethylstannane were synthesized according to literature procedures¹⁴ (see also Supporting Information). All other chemicals and solvents were purchased from commercial sources and used without further purification. Air- and/or water-sensitive reactions were conducted under nitrogen using dry solvents. Microwave-assisted syntheses were carried out using a Biotage Initiator Sixty EXP microwave system.

Physical Measurements. ^1H NMR spectra were recorded on a Bruker DPX instrument at 400 and 100 MHz; chemical shifts are given in parts per million. Elemental analyses were obtained on a Perkin-Elmer 2400 elemental analyzer. Absorption spectra were measured on a Unicam UV 300 spectrophotometer.

Electrochemistry. Dichloromethane (DCM) (HPLC grade, Acros), acetonitrile (HPLC grade, Aldrich) and tetra-*n*-butylammonium hexafluorophosphate (TBAPF₆, electrochemical grade, Fluka) were used as received. Electrochemical measurements were performed on a CH Instruments 660A electrochemical workstation using anhydrous dichloromethane or acetonitrile as the solvent, silver wire as the pseudo reference electrode, and platinum wire and glassy carbon as the counter and working electrodes, respectively. Electrochemical data were referenced to the ferrocene/ferrocenium redox couple using metalocene as an internal standard. All solutions were degassed (Ar) and contained monomer substrates in concentration of ca. 1×10^{-3} M, together with TBAPF₆ (0.1 M) as the supporting electrolyte. Spectroelectrochemical experiments were conducted on ITO glass. The gel electrolyte was prepared according to a literature procedure.¹⁵ The electrolyte contains 70 wt % of acetonitrile, 20 wt % of propylene carbonate, 7 wt % of PMMA (M_w : 50 000 Da), and 3 wt % of tetra-butylammonium hexafluorophosphate. HOMO and LUMO levels were calculated according to the literature.¹⁶

Synthesis. 3,7-Bis(4-bromophenyl)benzo[1,2-b:4,5-b']difuran-2,6-dione (**3**). Using a Dean–Stark apparatus, hydroquinone (0.60 g, 5.41 mmol) and 4-bromomandelic acid (2.5 g 10.82 mmol) were dissolved in 1,2,4-trichlorobenzene (25 mL) and stirred at 200 °C for 12 h. After cooling to 60 °C, nitrobenzene (2.2 mL) was added, and the mixture

was stirred at 200 °C for another hour. After cooling to room temperature, 50 mL of methanol was added. A precipitate formed, which was filtered off, washed with methanol, and dried in air. Compound **3** was obtained as a dark green solid (1.75 g, 65%), which was only sparingly soluble in common organic solvents at room temperature. However, the product showed high solubility at temperatures above 100 °C (mp above 300 °C). Anal. Calculated for $C_{22}H_{10}Br_2O_4$: C, 53.05%; H, 2.02%. Found: C, 52.80%; H, 2.08%. UV/vis (dichloromethane): λ_{max} at 483 nm.

3,7-Bis(4-(2,3-dihydrothieno[3,4-*b*][1,4]dioxin-5-yl)phenyl)benzo[1,2-*b*:4,5-*b'*]difuran-2,6-dione (A1). In a vial, 200 mg (0.40 mmol) of 3,7-bis(4-bromophenyl)benzo[1,2-*b*:4,5-*b'*]difuran-2,6-dione (3), 305 mg (1.00 mmol) of 3,4-ethylenedioxythien-2-yl trimethylstannane, and 14 mg (0.012 mmol) of tetrakis(triphenylphosphine)palladium(0) were dissolved in 5 mL of dry DMF and stirred for 5 min. The mixture was degassed and heated in the microwave synthesizer at 160 °C for 1 h. After cooling, the mixture was diluted with 50 mL of DCM and washed with 50 mL of brine and 50 mL of water. The organic layer was separated, dried over magnesium sulfate, and evaporated. The dark product was recrystallized from DCM/methanol. Yield: 196 mg (79%). ¹H NMR (400 MHz, CDCl₃): δ = 7.87 (d, aromatic, 8H), 6.96 (s, EDOT aromatic H, 2H), 6.41 (s, aromatic, 1H), 4.33 (m, EDOT-CH₂, 8H). UV/vis (dichloromethane): 298, 391, 590 nm. ε(590) = 63 580 L mol⁻¹ cm⁻¹.

3,7-Bis(4-(2,3-dihydrothieno[3,4-*b*][1,4]dithien-5-yl)phenyl)-benzo[1,2-*b*:4,5-*b'*]difuran-2,6-dione (A2). The same procedure as described for compound **A1** was used except that 3,4-ethylenedioxythien-2-yl trimethylstannane was replaced by 3,4-ethylenedithiathien-2-yl trimethylstannane. A dark solid (200 mg, 89%) was obtained. ¹H NMR (400 MHz, CDCl₃): δ = 7.85 (d, aromatic, 8H), 6.69 (s, EDTT aromatic H, 2H), 7.09 (s, aromatic, 1H), 3.24 (m, EDTT-CH₂, 8H). UV/vis (dichloromethane): 306, 502 nm. ε(502) = 79 220 L mol⁻¹ cm⁻¹.

3,6-Bis(4-bromophenyl)benzo[1,2-b:6,5-b']difuran-2,7-dione (4). Using a Dean–Stark apparatus, 1,2-dihydroxybenzene (1.20 g, 10.82 mmol) and 4-bromomandelic acid (5.0 g 21.64 mmol) were dissolved in 1,2,4-trichlorobenzene (30 mL) and stirred at 200 °C for 5 h. After cooling to 60 °C, nitrobenzene (5.0 mL) was added, and the mixture was stirred for another hour at 200 °C. After cooling to room

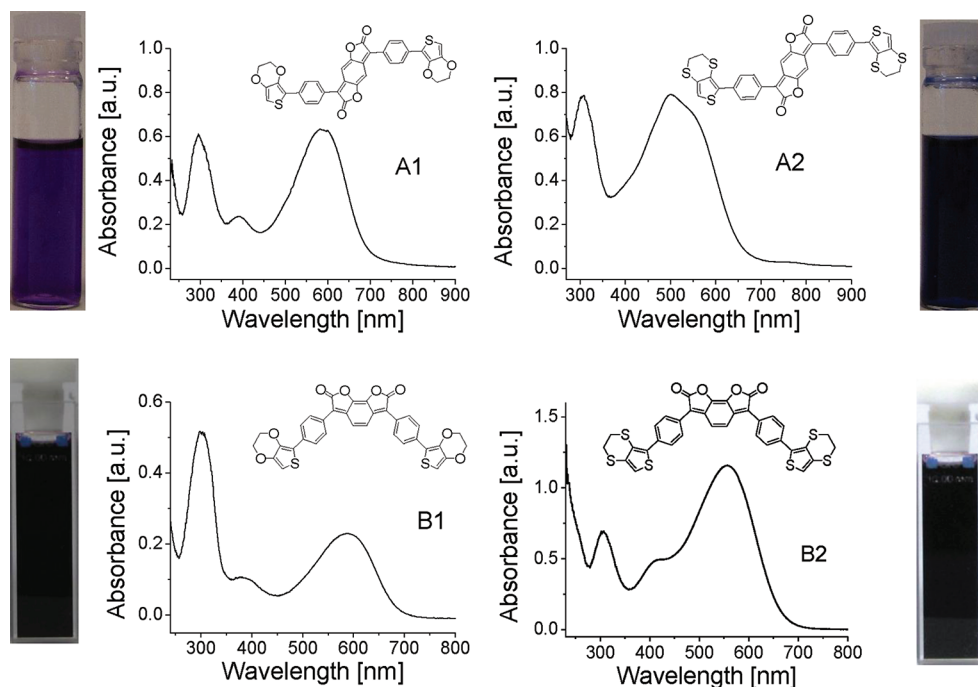


Figure 1. UV/vis absorption spectra of monomers A1, A2, B1, and B2 in dichloromethane solution.

Table 1. Optical and Electrochemical Data for Monomers^a

	UV (nm)	HOMO–LUMO gap/opt (eV)	onset of oxidation (V)	HOMO (eV)	onset of reduction (V)	LUMO (eV)	HOMO–LUMO gap (eV)
A1	298, 391, 590	1.81	+0.83	−5.63	−0.50	−4.30	1.33
A2	306, 502	1.88	+0.82	−5.62	−0.47	−4.33	1.29
B1	302, 588	1.80	+0.45	−5.25	−0.80	−4.00	1.25
B2	307, 407, 558	1.86	+0.85	−5.65	−0.41	−4.39	1.26

^aAbsorption spectra were taken in dichloromethane solutions. All redox potentials are referenced to the ferrocene/ferrocenium redox couple. HOMO–LUMO gap according to the equation¹⁶ $-E_{\text{LUMO}} = E_{\text{onset}(\text{red})} + 4.8 \text{ eV}$ and $-E_{\text{HOMO}} = E_{\text{onset}(\text{ox})} + 4.8 \text{ eV}$, where $E_{\text{onset}(\text{ox})}$ and $E_{\text{onset}(\text{red})}$ are the onset potentials for the oxidation and reduction processes vs ferrocene.

temperature, 50 mL of methanol was added. The solid formed was filtered off, washed with methanol, and dried in air. Compound **4** was obtained as a dark red solid (3.28 g, 61%). ¹H NMR (400 MHz, CDCl₃): δ = 7.85 (d, aromatic, 4H), 7.47 (d, aromatic, 4H), 7.16 (d, aromatic, 2H). (mp over 300 °C). Anal. Calculated for C₂₂H₁₀Br₂O₄: C, 53.05%; H, 2.02%. Found: C, 52.10%; H, 2.09%. UV/vis (dichloromethane): λ_{max} at 493 nm.

3,6-Bis(4-(2,3-dihydrothieno[3,4-b][1,4]dioxin-5-yl)phenyl)benzo[1,2-b:6,5-b']difuran-2,7-dione (B1). The same procedure as described for compound A1 was used. A dark solid (93 mg, 82%) was obtained. ¹H NMR (400 MHz, CDCl₃): δ = 7.88 (d, aromatic, 8H), 6.98 (s, EDOT aromatic H, 2H), 7.29 (s, aromatic, 1H), 4.34 (m, EDOT-CH₂, 8H). UV/vis (dichloromethane): 302, 588 nm. $\epsilon(588)$ = 23 080 L mol^{−1} cm^{−1}.

3,6-Bis(4-(2,3-dihydrothieno[3,4-b][1,4]dithien-5-yl)phenyl)benzo[1,2-b:6,5-b']difuran-2,7-dione (B2). The same procedure as described for compound A1 was followed except that compound **3** was replaced by **4**. A dark solid (120 mg, 86%) was obtained. ¹H NMR (400 MHz, CDCl₃): δ = 7.84 (d, aromatic, 8H), 7.44 (s, EDTT aromatic H, 2H), 7.09 (s, aromatic, 1H), 3.27 (m, EDTT-CH₂, 8H). UV/vis (dichloromethane): 307, 407, 558 nm. $\epsilon(558)$ = 115 560 L mol^{−1} cm^{−1}.

RESULTS AND DISCUSSION

Synthesis. The starting compounds **1–4** and key compounds A1, A2, B1, and B2 containing *para*- and *ortho*-benzodifuranone units were synthesized as shown in Scheme 1. In general, the synthesis of the starting compounds **3** and **4** required the

condensation of 1 equiv of *p*-bromomandelic acid with 0.5 equiv of hydroquinone or 1,2-dihydroxybenzene, respectively, leading to a double cyclization to benzodihydrofuranones **1** and **2**. A Dean–Stark apparatus was used for the removal of water as a byproduct, favoring the double cyclization into **1** and **2**. **1** and **2** were not isolated but directly oxidized with nitrobenzene. This resulted in the conjugated system of benzodifuranone in 65% yield for *para*- (**3**) and 61% for the *ortho*-isomer (**4**). The low solubility of benzodifuranone **3** in common solvents at room temperature could be overcome upon heating to temperatures above 100 °C. This allowed us to use the monomer for further synthetic procedures.

The 3,4-ethylenedioxythiophene (EDOT) and 3,4-ethylenedithiathiophene (EDTT) substituted monomers A1, A2, B1, and B2 were synthesized upon a microwave-assisted Stille coupling of **3** and **4** with 3,4-ethylenedioxythien-2-yl trimethylstannane (**5**) and 3,4-ethylenedithiathien-2-yl trimethylstannane (**6**) using Pd(PPh₃)₄ as the catalyst and DMF as the solvent. The coupling gave high yields of 79, 89, 82, and 86% for A1, A2, B1, and B2, respectively. The four monomers are dark bluish solids being slightly up to moderately soluble in common solvents such as chloroform, dichloromethane, DMF, THF, and toluene, for example.

The ¹H NMR spectra of A1, A2, B1, and B2 displayed all the expected resonances with no discernible peaks corresponding

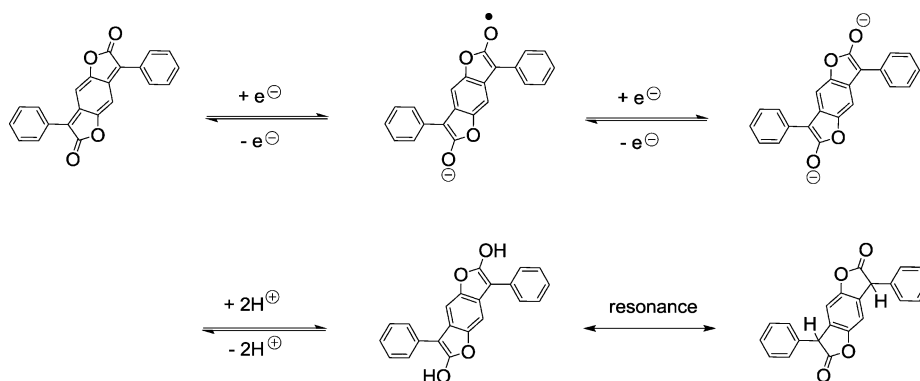


Figure 2. A suggested reduction mechanism for *p*-benzodifuranone monomers.

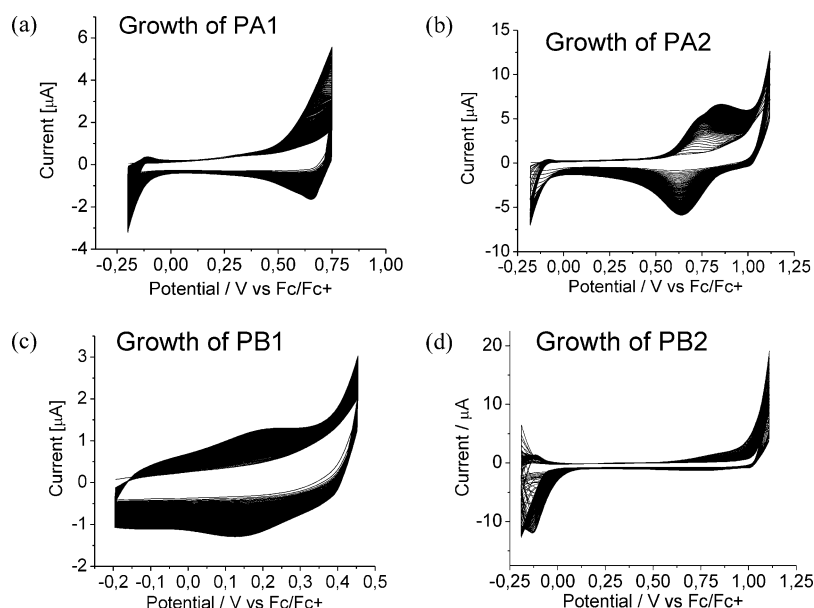


Figure 3. Growth of PA1 (a), PA2 (b), PB1 (c), and PB2 (d) by cyclic voltammetry in dichloromethane using a carbon working electrode, Ag wire pseudoreference electrode. Supporting electrolyte: 0.1 M TBAPF₆. Scan rate: 100 mV s⁻¹; *T* = 20 °C.

to impurities (see Supporting Information). Significantly, the singlet signal at about 7.0 ppm can be ascribed to the thiophene unit in the EDOT and EDTT substituents. The two multiplet signals with a chemical shift of about 4.34 ppm are typical for the ethylene bridge of the EDOT unit. The two multiplet signals at about 3.37 ppm are typical for the ethylene bridge of the EDTT unit and are similar to those reported in the literature.^{14b} Unfortunately, the solubility in solvents such as chloroform-*d* or dimethyl-*d* sulfoxide was not high enough to measure ¹³C NMR spectra for further structural characterization.

UV/vis Absorption of Monomers. In the UV/vis absorption spectra of A1, A2, B1, and B2, a large bathochromic shift is introduced upon the addition of EDOT and EDTT to the conjugated system. Compared with their starting compounds 3 and 4, the shifts are 154 nm for A1, 64 nm for A2, 95 nm for B1, and 65 nm for B2. The spectra are displayed in Figure 1. In dichloromethane A1 exhibits an absorption maximum at 590 nm, A2 at 502 nm, B1 at 588 nm, and B2 at 558 nm (Table 1). The bathochromic shifts result from a combination of two phenomena: (i) an extension in conjugation through the thiophene units and (ii) a push–pull donor–acceptor interaction between the electron-rich thiophenes and the carbonyls of the furanone units. Interestingly, the EDTT-sub-

stituted monomers A2 and B2 are not shifted bathochromically as largely as the EDOT-substituted monomers A1 and B1. The reason could be a larger electron-withdrawing effect caused by sulfur in the EDTT unit compared to oxygen in the EDOT units. Alternatively, it is well-known that conjugated compounds incorporating EDOT and EDTT units provide planar and twisted geometries, respectively. Therefore, it can be assumed that there is a lower degree of conjugation in the EDTT-containing compounds. From the absorption edge of the monomers (about 690 nm) similar optical HOMO–LUMO gaps between 1.80 and 1.90 eV (Table 1) can be determined.

Electrochemistry. *Cyclic Voltammograms of Monomers.* The electrochemistry of compounds A1, A2, B1, and B2 was studied using cyclic voltammetry in dichloromethane solution. The electrochemical details are given in the Experimental Section, the cyclic voltammograms of the monomers are shown in the Supporting Information, and the electrochemical data are compiled in Table 1. For the *para*-substituted compound A1, the oxidative cycle exhibits an irreversible peak at +0.91 V. The reductive cycle shows two reversible waves at −0.61/−0.55 and −0.94/−0.88 V. A2 shows an irreversible oxidation peak at +0.84 V and two reversible cationic waves at −0.61/−0.55 and −0.93/−0.87 V. The *ortho*-substituted analogue B1 shows an irreversible oxidation peak at +0.65 V and two reversible

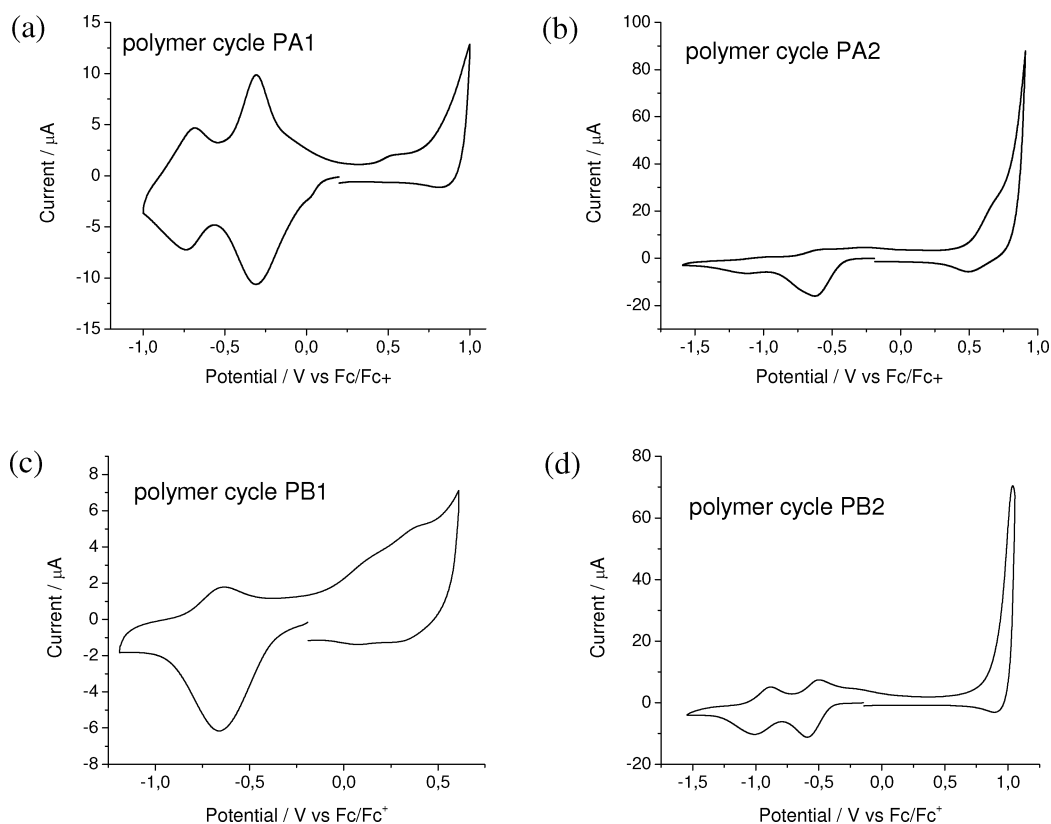


Figure 4. Cyclic voltammograms of PA1 (a), PA2 (b), PB1 (c), and PB2 (d) as thin films deposited on a glassy carbon electrode. Solvent: 0.1 M TBAPF₆/acetonitrile. Potential calculated versus ferrocene. Scan rate: 100 mV s⁻¹; *T* = 20 °C.

reductive waves at $-0.93/-0.86$ and $-1.22/-1.18$ V. **B2** undergoes an irreversible oxidation at +1.00 V, and the reduction shows two reversible waves at $-0.55/-0.49$ and $-0.87/-0.82$ V. Within this monomer series, a high stability of the anion radical and dianion showing reversible reductive waves was observed. The driving force for facile and stable reduction is the aromatization of the core benzene ring in the four benzodifuranone monomers. This represents a strong acceptor character of the benzodifuranone unit. A suggested reduction mechanism for the *p*-benzodifuranone is shown in Figure 2. It also should be noted that the four monomers show narrow band gaps in the range from 1.25 to 1.33 eV.

Electropolymerization. The four monomers were electropolymerized at the anode using the same cell as for the cyclic voltammetry experiments. Repetitive cycling over the oxidation range of the materials produced the desired polymers, which were deposited as thin films on the working electrode. The polymer growth plots for the series are displayed in Figure 3. Whereas **A1**, **A2**, and **B1** polymerized readily, **B2** required more cycles (120 cycles for **B2**, 60 cycles for **A1**, **A2**, and **B1**) of continuous scanning between -0.20 and $+1.10$ V before a satisfactory film was obtained. It should be noted that the electropolymerization of thiophenes, especially for EDTTs, at relatively low oxidation potentials can lead to oligomeric products rather than to long chain polymers. This could be the reason for the slow growth rate of **B2**. In comparison with **B2**, the EDTT-substituted **A2** exhibited much better growth characteristics. In this case the angled structure of **B2** could be sterically unfavorable for polymer growth in comparison with the rodlike structure of **A2**. For all compounds, a plot of scan rate vs current gives a linear fit (see Supporting Information),

confirming the stability of adhered films and that charge transport through the film is not diffusion limited.

Cyclic Voltammograms of Polymers. The cyclic voltammetric response of the four polymers was studied using films of the polymers on a glassy carbon working electrode in monomer-free acetonitrile vs Ag/AgCl. The CV diagrams of **PA1** (a), **PA2** (b), **PB1** (c), and **PB2** (d) are shown in Figure 4, and the electrochemical data are listed in Table 2. The four polymers

Table 2. Optical and Electrochemical Data for Polymers^a

	UV (nm)	onset of oxidation (V)	HOMO (eV)	onset of reduction (V)	LUMO (eV)	HOMO– LUMO gap (eV)
PA1	589	+0.41	−5.21	0.03	−4.77	0.44
PA2	348, 417	+0.50	−5.30	−0.41	−4.39	0.91
PB1	515, 587	−0.01	−4.79	−0.37	−4.43	0.36
PB2	530	+0.87	−5.67	−0.41	−4.39	1.28

^aAbsorption spectra were taken from thin films.

show a quasi-reversible oxidative and two reductive waves, although the reduction process for **PB1** was represented by a broad single peak. The higher stability under reductive conditions, compared with the less stable oxidation processes, was similar to the behavior of the monomers. Good reversibility for reduction processes was observed for polymers **PA1** and **PB2**. The difference between the onsets of the oxidation and reduction potentials of conjugated polymers normally represents the electrochemical band gap of the semiconductor. From cyclic voltammetry, small electrochemical band gaps are inferred for all four polymers (0.44, 0.91, 0.36, and 1.28 eV for **PA1**, **PA2**, **PB1**, and **PB2**, respectively). The polymers containing

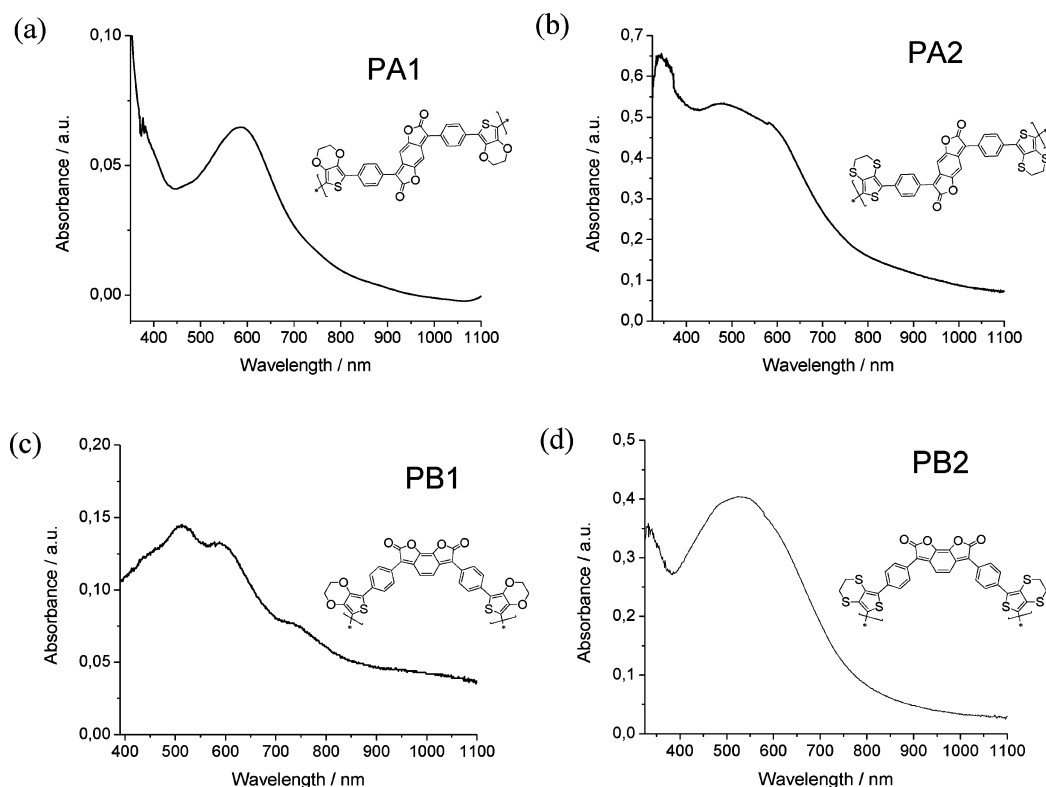


Figure 5. UV/vis absorption spectra of monomers **PA1**, **PA2**, **PB1**, and **PB2** as thin films.

EDOT-substituted benzodifuranone show smaller electrochemical band gaps and lower oxidation potentials than the EDTT analogues, but the reduction onsets were very similar throughout the series. This could be caused by more planar structures of the polymer main chains due to the oxygen–sulfur interaction between adjacent EDOT units.¹⁷ EDTT does not provide this advantage for planarity, and in fact there is normally a significant twist between the thiophene units.^{17,18} In a comparison, the electrochemical HOMO–LUMO gap of **PB2** (1.28 eV) is similar to the value found for monomer **B2** (1.26 eV). Again, the reason could be that the polymer chain of **PA2** is not fully conjugated due to the expected twists between EDTT units in the polymer chain. The narrow HOMO–LUMO gaps arise from localized donor and acceptor sites within the polymer chain through the bithiophene units and the benzodifuranones, respectively. This is similar to our previous work, where even in conjugated polythiophenes containing strongly redox-active components the donor and acceptor units can exhibit independent electroactivity.¹⁹

Spectroelectrochemistry. The absorption spectra of the four polymers were taken from thin films on ITO-coated glass substrates. The spectra are displayed in Figure 5, and the absorption data are listed in Table 2. The UV/vis absorption spectra of the polymers show very broad bands with no clear edges so that optical band gaps could not be calculated with a satisfactory degree of confidence; the four polymers showed very broad shoulders ranging from about 680 to 750 nm. However, the optical band gap of the polymer, determined from the onset of the longest wavelength absorption band, is estimated to be wider than the electrochemically determined value. The discrepancy in HOMO–LUMO gap values determined by the two different methods, cyclic voltammetry and absorption spectroscopy, is explained by the following. Absorption spectroscopy reveals the band gap as the energy corresponding to the

π – π^* transition, and this is normally represented by the longest wavelength absorption band. The π – π^* transition arises from the conjugated chain of the polymer, and the length and planarity of this chain dictate the position of this band. Cyclic voltammetry, on the other hand, provides information on the HOMO and LUMO energy levels. In simple structures, particularly in homopolymers, the optical band gap and the HOMO–LUMO gap are the same, since the redox processes involve electrons being extracted from or injected into the conjugated polymer chain. In more complex structures, in which the redox sites are discrete parts of the polymer, the sites of oxidation and reduction are localized and the conjugated segment may not extend over both these components. Therefore, the association between the donor–acceptor sites is no longer representative of the effective conjugation length of the polymer. In such cases, the HOMO–LUMO and band gap values are not the same and must be considered as separate properties of the polymer. In our case, the bithiophene units within the polymers and the benzodifuranone heterocycles act as localized donor and acceptor redox entities, and this explains the differences observed in the data relating to the “HOMO–LUMO” gap.

Because of the high stability under reduction, it was of great interest to study the spectroelectrochemical properties for this series of polymers. For this study, the polymer films were grown on ITO-coated glass substrates, and the electronic absorption spectra were taken with a gel electrolyte. 3-D absorption spectroelectrochemical plots for **PA1**, **PA2**, **PB1**, and **PB2** are shown in Figure 6.

The absorption of **PA1** did not change much until a potential of -1.0 V was reached. From -1.0 to -1.3 V a large drop in absorbance was observed, which could point to the reduction from mono- to dianion involving a break in the conjugated system. Starting at -1.0 V, the film becomes more transparent. For **PA2**, it can be seen that the change in the absorption

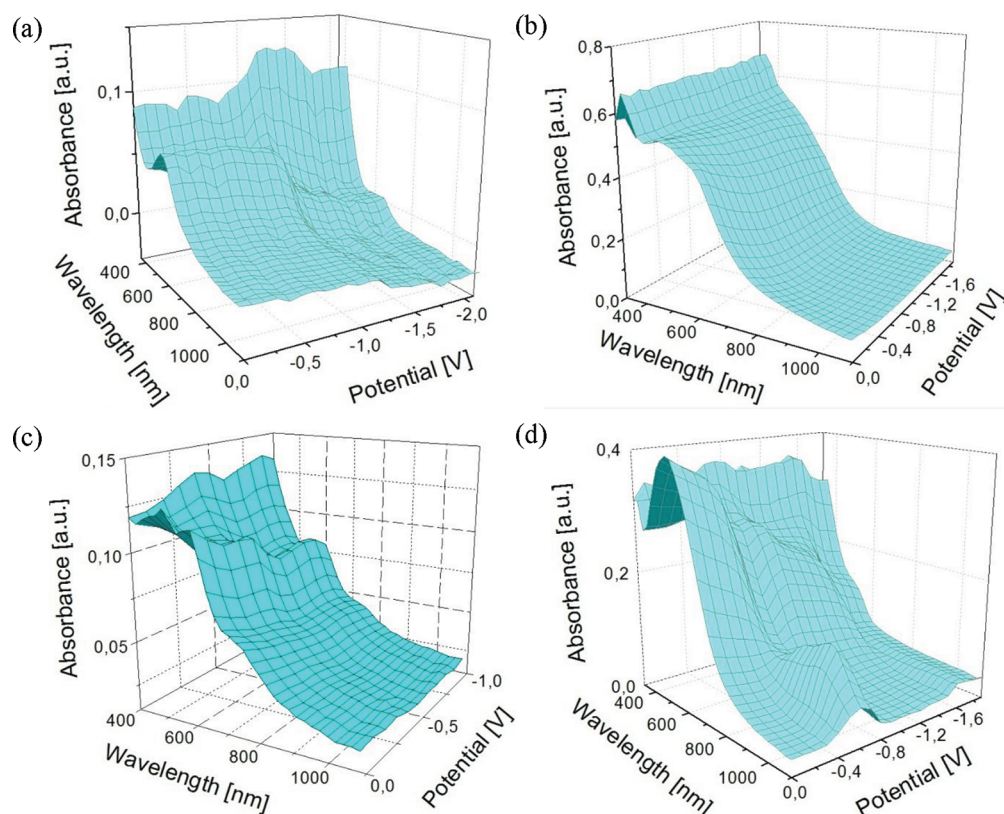


Figure 6. 3-D absorption spectroelectrochemical plots for **PA1**, **PA2**, **PB1**, and **PB2** as thin films on ITO in gel electrolyte. Ag wire pseudoreference electrode. Potential calculated versus ferrocene. Scan rate: 100 mV s^{-1} ; $T = 20^\circ \text{C}$.

spectra takes place during the first 10 measurements until a potential of -0.7 V is reached. This is just past the first reduction peak in the CV. By taking it to -1.9 V , there is only little more change in the absorption which corresponds to the fact that the second reduction peak was smaller compared to the first one. The color change was only small; the film turned from a dark to a lighter purple/brown color. The 3D plot of **PB1** shows that there is a drop in the absorption at -0.5 V as the polymer goes from a purple color to a more transparent film. The spectroelectrochemistry of **PB2** shows that at the first reduction peak down to -0.8 V a decrease in intensity of the $\pi-\pi^*$ band occurs, and a new band ranging from 770 nm into the near-IR forms, which might originate from the formation of a radical anion in the polymer chain. This peak diminishes at -1.0 V , and with the formation of a dianion (second reductive wave) there is a continuous drop in the $\pi-\pi^*$ transition toward -1.9 V . The color of the film changed from dark purple to a light orange, transparent color. For this series of polymers, 2-D electronic absorption spectra are shown in the Supporting Information.

CONCLUSIONS

In summary, we have presented the synthetic route and the key properties of a series of electropolymerizable monomers containing *p*- and *o*-diphenylbenzodifuranones. We also have synthesized the first polymers based on EDOT or EDTT and *p*- or *o*-benzodifuranone units electrochemically. The polymers exhibit broad absorption bands, and very small HOMO–LUMO gaps (about 0.40 eV for **PA1** and **PB1**). Interesting electrochromic properties were found under oxidative and reductive conditions. Under reduction, the polymers showed

color changes from dark to almost transparent. Because of their reversibility in oxidation and reduction processes, **PA1**, **PA2**, **PB1**, and **PB2** might be useful for electronic applications. Further studies to optimize film formation and conductivity of these materials are underway.

ASSOCIATED CONTENT

Supporting Information

UV/vis absorption spectra and ^1H NMR spectra of some key compounds, cyclic voltammograms of monomers **A1**, **A2**, **B1**, and **B2**, scan rate studies of polymers **PA1**, **PA2**, **PB1**, and **PB2**, and 2-D electronic absorption plots for polymers **PA1**, **PA2**, **PB1**, and **PB2**. This material is available free of charge via the Internet at <http://pubs.acs.org>.

AUTHOR INFORMATION

Corresponding Author

*E-mail: tieke@uni-koeln.de.

ACKNOWLEDGMENTS

Financial support by BASF Schweiz AG, Basle, Switzerland, is gratefully acknowledged. Drs. M. Düggeli and P. Hayoz from BASF are kindly thanked for helpful discussions.

REFERENCES

- (1) Hao, Z.; Iqbal, A. *Chem. Soc. Rev.* **1997**, *26*, 203.
- (2) (a) Iqbal, A.; Jost, M.; Kirchmayr, R.; Pfenniger, J.; Rochat, A.; Wallquist, O. *Bull. Soc. Chim. Belg.* **1988**, *97*, 615. (b) Iqbal, A.; Cassar, L.; Rochat, A. C.; Pfenniger, J.; Wallquist, O. J. *Coat. Technol.* **1988**, *60*, 37.
- (3) (a) Beyerlein, T.; Tieke, B. *Macromol. Rapid Commun.* **2000**, *21*, 182. (b) Beyerlein, T.; Tieke, B.; Forero-Lenger, S.; Brütting, W. *Synth.*

- Met.* **2002**, *130*, 115. (c) Smet, M.; Mellen, B.; Dehaen, W. *Tetrahedron Lett.* **2001**, *42*. (d) Cao, D.; Liu, Q.; Zeng, W.; Han, S.; Peng, J.; Liu, S. *J. Polym. Sci., Part A: Polym. Chem.* **2006**, *44*, 2395. (e) Zhu, Y.; Rabindranath, A. R.; Beyerlein, T.; Tieke, B. *Macromolecules* **2007**, *40*, 6981. (f) Zhang, K.; Tieke, B. *Macromolecules* **2008**, *41*, 7287. (g) Tieke, B.; Rabindranath, A. R.; Zhang, K.; Zhu, Y. *Beilstein J. Org. Chem.* **2010**, *6*, 830.
- (4) (a) Kanimozhi, C.; Baljaru, D.; Sharma, G. D.; Patil, S. J. *Phys. Chem. B* **2010**, *114*, 3095. (b) Qiao, Z.; Peng, J.; Jin, Y.; Liu, Q.; Weng, J.; He, Z.; Han, S.; Cao, D. *Polymer* **2010**, *51*, 1016. (c) Woo, C. H.; Beaujuge, P. M.; Holcombe, T. W.; Lee, O. P.; Fréchet, J. M. J. *J. Am. Chem. Soc.* **2010**, *132*, 15547.
- (5) Bijleveld, J. C.; Gevaerts, V. S.; Nuzzo, D. D.; Turbiez, M.; Mathijssen, S. G. J.; de Leeuw, D. M.; Wienk, M. M.; Janssen, R. A. J. *Adv. Mater.* **2010**, *22*, E242.
- (6) Annen, O.; Egli, R.; Henzi, B.; Jacob, H.; Matzinger, P. *Rev. Prog. Color.* **1987**, *17*, 72.
- (7) Greenhalgh, C. W.; Carey, J. L.; Hall, N.; Newton, D. F. *J. Soc. Dyes Colour* **1994**, *110*, 178.
- (8) Gorman, A. A.; Huuttings, M. G.; Wood, P. H. *J. Am. Chem. Soc.* **1996**, *118*, 8497.
- (9) (a) Greenhalgh, C. W.; Carey, J. L.; Newton, D. F. *Dyes Pigm.* **1980**, *1*, 103. (b) ICI EP023080, 1979. (c) ICI BP2068402, 1980. (d) ICI BP2101988, 1981. (e) ICI BP2103231, 1982. (f) Hallas, G.; Yoon, C. *Dyes Pigm.* **2001**, *48*, 107.
- (10) Zhang, K.; Tieke, B. *Macromolecules* **2011**, *44*, 4596.
- (11) Cui, W.; Yuen, J.; Wudl, F. *Macromolecules* **2011**, *44*, 7869.
- (12) (a) Pozo Gonzalo, C.; Khan, T.; McDouall, J. J. W.; Skabara, P. J.; Roberts, D. M.; Light, M. E.; Coles, S. J.; Hursthouse, M. B.; Neugebauer, H.; Cravino, A.; Sariciftci, N. S. *J. Mater. Chem.* **2002**, *12*, 500. (b) Turbiez, M.; Frère, P.; Allain, M.; Gallego-Planas, N.; Roncali, J. *Macromolecules* **2005**, *38*, 6806.
- (13) Skabara, P. J. In *Handbook of Thiophene-Based Materials*, 1st ed.; John Wiley & Sons: New York, 2009.
- (14) (a) Wang, C.; Schindler, J. L.; Kannewurf, C. R.; Kanatzidis, M. G. *Chem. Mater.* **1995**, *7*, 58. (b) Pang, H.; Skabara, P. J.; Crouch, D. J.; Duffy, W.; Heeney, M.; McCulloch, I.; Coles, S. J.; Horton, P. N.; Hursthouse, M. B. *Macromolecules* **2007**, *40*, 6585.
- (15) Schwendeman, I.; Hickman, R.; Sonmez, G.; Schottland, P.; Zong, K.; Welsh, D. W.; Reynolds, J. R. *Chem. Mater.* **2002**, *14*, 3118.
- (16) Bredas, J. L.; Silbey, R.; Boudreau, D. S.; Chance, R. R. *J. Am. Chem. Soc.* **1983**, *105*, 6555.
- (17) Spencer, H. J.; Skabara, P. J.; Giles, M.; McCulloch, I.; Coles, S. J.; Hursthouse, M. B. *J. Mater. Chem.* **2005**, *15*, 4783.
- (18) McEntee, G. J.; Skabara, P. J.; Vilela, F.; Tierney, S.; Samuel, I. D. W.; Gambino, S.; Coles, S. J.; Hursthouse, M. B.; Harrington, R. W.; Clegg, W. *Chem. Mater.* **2010**, *22*, 3000.
- (19) Berridge, R.; Skabara, P. J.; Pozo-Gonzalo, C.; Kanibolotsky, A.; Lohr, J.; McDouall, J. J. W.; McInnes, E. J. L.; Wolowska, J.; Winder, C.; Sariciftci, N. S.; Harrington, R. W.; Clegg, W. *J. Phys. Chem. B* **2006**, *110*, 3140.

Synthesis and Properties of Oxygen-Linked *N*-Phenylcarbazole Dendrimers

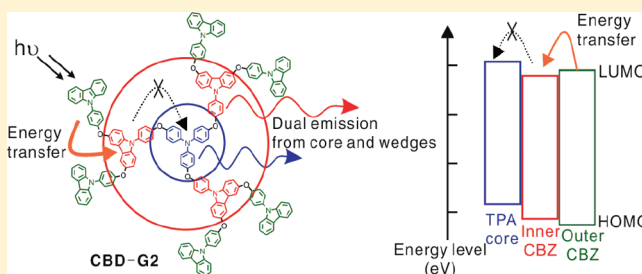
Chung-Chieh Lee,[†] Man-kit Leung,^{*,†,‡} Pei-Yu Lee,^{||} Tien-Lung Chiu,^{||} Jiun-Haw Lee,[§] Chun Liu,[†] and Pi-Tai Chou^{*,†}

[†]Department of Chemistry, [‡]Institute of Polymer Science and Engineering, and [§]Graduate Institute of Photonics & Optoelectronics and Department of Electrical Engineering, National Taiwan University, 1 Roosevelt Road, Section 4, Taipei 106, Taiwan, R.O.C.

^{||}Department of Photonics Engineering, Yuan Ze University, Taoyuan 32003, Taiwan

S Supporting Information

ABSTRACT: A series of novel oxygen-linked *N*-phenylcarbazole (NPC) dendritic wedges (3–5) and triphenylamine-centered dendrimers (CBD-G0 to -G2) have been synthesized and extensively studied. The aryl–oxygen–aryl (Ar–O–Ar) linkages were established on 3,6-positions of carbazole and 4-position of *N*-phenyl group. UV–vis spectra revealed that the Ar–O–Ar linkage would break down the π conjugation and make NPC units manifest their individual absorption moiety. Both steady-state luminescence and fluorescence decay dynamics at room temperature and 77 K in tetrahydrofuran suggested that the transfer of energy from the carbazole wedges to the triphenylamine (TPA) core operates in CBD-G1, so that the luminescence mainly arises from the core unit. The quenching of the emission from carbazole wedges by the TPA core becomes less effective as the generation develops into CBD-G2. The oxidation potential of the NPC derivatives clearly revealed the mesomeric electron-donating effect of the oxygen atom and inductive electron-withdrawing effect of the carbazole unit. The potential gradient could be established on those triphenylamine-centered dendrimers (CBD-G1 and CBD-G2), such that the outer layer is electron-poor and the inner layer is electron-rich. It is remarkable that the HOMO level of the NPC dendrimers is as high as -5.17 eV and triplet energy level is kept above 2.85 eV. These levels of HOMO and triplet energy, together with good thermal stability and compatibility of solution processing, make NPC dendrimers ideal host materials for blue triplet emitters. Using CBD-G2 as the host material, the FIrpic-doped solution-processed light-emitting diodes were fabricated, and maximum luminous efficiency could be achieved at a record high of 24.7 cd/A at 484 cd/m².



INTRODUCTION

The advance of the architecture for constructing dendritic molecules has attracted considerable attention during the past two decades.¹ The availability nowadays of a large variety of dendrons with well-defined branches allows ample materials of intriguing supramolecular properties for light harvesting, exciton harvesting, electronic potential gradient, and molecular recognition to be prepared. Applications including drug delivery,² organic electronics,³ and homogeneous catalysis⁴ have been reported. The maturity of synthetic architecture also allows chemists to explore the manipulation of the relationships between molecular structures and energy levels, one of the most important topics in current chemistry.

Carbazole-based (CB) dendrimers have emerged as a new and attractive family of advanced materials. Because of the interesting photo- and electrochemistries, as well as distinguished electronic properties of the carbazole unit, the CB dendrons and dendrimers have been utilized in nanocomposites,⁵ efficient light-harvesting antennae,⁶ phosphorescent iridium(III) dendrimers,⁷ and fluorescent dendritic emitters⁸ for organic light-emitting diode (OLED). Besides, the CB dendrimers hold promise as hole-transporting⁹ and

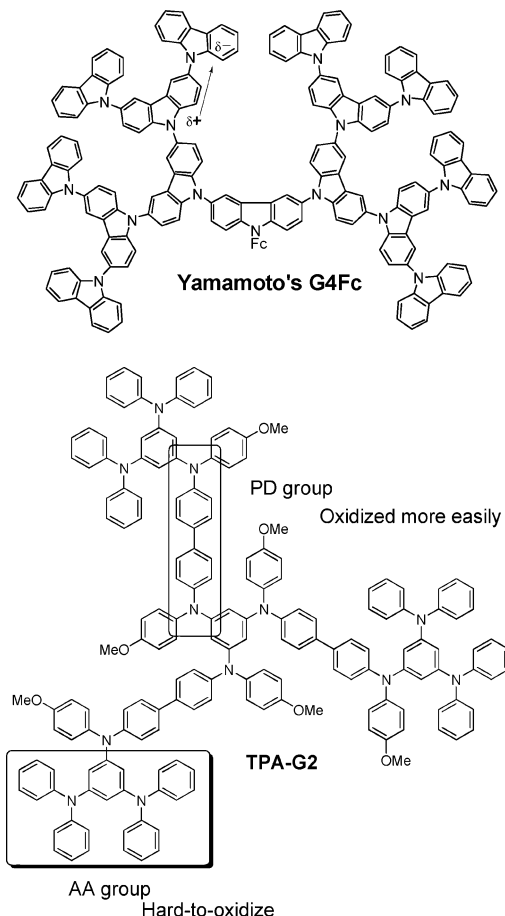
host¹⁰ materials of OLEDs. The CB dendrimers could be categorized into two classes from the structural point of view: The first class contains the carbazole units tethered to the saturated C–C chains.⁵ The carbazole units therefore function independently so that their original physical properties such as electrochemical oxidation potential and/or photophysical properties would be maintained. The second class has the carbazole units chained through π -conjugation to form dendritic wedges.¹¹ Usually, this type of conjugated dendrimer demonstrates fascinating optoelectronic properties that are different from the carbazole monomer unit. Recently, explorations about formation of the potential or redox gradient have been reported.¹² For examples, Yamamoto and Albrecht reported the synthesis of *N*-linked rigid dendritic carbazoles G4Fc and discovered the accumulative π -polarization substituent effect of the carbazole unit producing a potential gradient in the carbazole dendron such that the outer layer becomes electron-rich while the inner layers are electron-

Received: November 3, 2011

Revised: December 3, 2011

Published: December 22, 2011

poor.^{12a} Blackstock and Selby reported redox-active polyarylamine dendrimer **TPA-G2**, which exhibits contrary oxidation gradients.^{12b} The core, phenylenediamino (PD) group, is more easily oxidized than the periphery, triarylamino (AA) group.



As for our continuing efforts in arylamine derivatives,¹³ *N*-phenylcarbazole (NPC) is another interesting monomeric unit that can be used to construct the CB dendrimer.^{8c,e,14} Although NPC and *N*-H-carbazole belong to the same family of heterocyclic compounds and exhibit similar photophysical¹⁵ and electrochemical¹⁶ properties, pure NPC-based dendrimers are seldom reported.¹⁷ Most carbazole-based dendrimers have been prepared through the formation of C–N linkages, coupling the nitrogen atom of an external carbazole unit to the activated C3 and C6 sites of an inner carbazole moiety. In the past decade, copper-catalyzed Ullmann condensations have been extensively used for diaryl ether synthesis.¹⁸ Therefore, we are interested in extending our study to the novel oxygen-linked CB dendrimer **CBD-G2** and its derivatives listed in Scheme 1. We foresee that these compounds may possess intriguing oxidation potential gradient in the designated structure. However, achieving the C–O coupling at the C3 and C6 site of carbazole moiety is challenging. We have thus developed a novel synthetic approach for building up our Ar–O–Ar linkage, instead of using the commonly adopted Ar–N–Ar linkage to construct the molecular framework. We are also interested in exploring whether the novel C–O–C linkage would bring any interesting effects on the physical properties of the NPC units.

RESULTS AND DISCUSSION

Preparation of the Carbazole–Oxy–Carbazole Dendritic Wedge. In our strategy, we adopted the coupling reaction of **1** with **2** to construct the dendron. To optimize the reaction conditions, coupling **1** with phenol was first attempted under different CuI promoted C–O coupling conditions to give **3**.¹⁹ Table 1 summarizes the results in which only under the condition of CuI/*N,N*-dimethylglycine hydrochloride^{19a} and (DMGlyHCl)/1,4-dioxane did the reaction give a satisfactory yield of **3** after prolonged heating for 72 h (entry 5). Other ligands such as 2-(hydroxymethyl)-2-methylpropane-1,3-diol (TrisOH),^{19b} ethyl 2-oxacyclohexanecarboxylate (CYCOEt),^{19c} and *trans*-*N,N'*-dimethylcyclohexyldiamine (DMCHDA)^{19d} were found to be less effective. In order to increase the reaction efficiency, microwave (MW) irradiation (200 W, open vessel), which has proved to be a practical synthetic tool,²⁰ was adopted to accelerate the C–O coupling reaction. Under this condition, the reaction time could be significantly reduced to 4 h with the yield maintained at 45% (entry 6). The single crystal of **3** was grown by slow evaporation from acetonitrile solution, and its structure was supported by X-ray crystallographic analysis (Figure S-2).

However, the C–O coupling reaction of **1** with **2** was found to be sluggish under similar conditions (entry 7), so that higher reaction temperature was required to facilitate the process. This may be due to the inductive electron-withdrawing properties of the carbazole group^{12a} that reduce the nucleophilic properties of the phenol unit. After several attempts under various conditions, we discovered that the coupling reactions could be conducted in dipolar aprotic solvents at 150 °C by application of microwave (MW) irradiation (entries 8–11). The disubstituted product **4** was obtained in moderate yields. The deiodo product **5** could also be isolated (31%) as a side product. Deprotection of **4** was performed by demethylation in the presence of pyridinium chloride in NMP under MW irradiation²¹ for 7 h to give the key dendritic wedge **6** in 86% yield.

Synthesis of the CBD-G0, CBD-G1, and CBD-G2. Tris(4-bromophenyl)amine (**7**)²² was employed as the precursor of the electron-rich TPA core in the syntheses of **CBD-G0**, **CBD-G1**, and **CBD-G2** (Scheme 2). By applying our MW-assisted Ullmann condensation protocol to the present synthesis, **8** could be smoothly coupled with phenol in benzonitrile at 150 °C to give **CBD-G0** (57%). Similar conditions could be applied to **2**, giving **CBD-G1** a 59% yield. The de-bromo disubstituted product **9** (24%) could also be incidentally isolated. This reaction yield of **CBD-G1** is surprisingly high, considering that three C–O couplings proceed in one step.

By employing the same strategy, **CBD-G2** could be prepared from **6** and **7** in 31% yield. Although the yield is as not amazingly high as that of **CBD-G1**, it is still acceptable because the procedure allows ones to prepare the desired **CBD-G2** in one pot. Furthermore, **CBD-G2** could be purified conveniently by liquid column chromatography. The structures of **CBD-G1** and **CBD-G2** were verified with ¹H and ¹³C spectroscopy, elemental analysis, and mass spectroscopy. In the gel-permeation chromatography (GPC), the purity and monodispersity of dendrimers were clearly confirmed (Figure 1).

Photophysical Properties. Pertinent photophysical data for **3**, **4**, **5**, **8**, **CBD-G0**, **CBD-G1**, and **CBD-G2**, including their UV–vis absorption properties, as well as the PL behavior, were

Chemical structures of the synthesized compounds are shown. The structures are labeled 1 through 9, and their maximum absorption wavelengths (λ_{max}) are provided.

1 λ_{max} : 304, 356 nm

2 R = H
8 R = Me (λ_{max} : 293, 341 nm)

3 λ_{max} : 304, 356 nm

4 R = Me
6 R = H
 λ_{max} : 304, 361 nm

5 λ_{max} : 292, 341 nm

9 λ_{max} : 292, 340 nm

CBD-G0 λ_{max} : 303 nm

CBD-G1 λ_{max} : 292, 340 nm

CBD-G2 λ_{max} : 292, 340 nm

Chemical reaction scheme showing the Ullmann condensation of compound **1** (2,6-diiodo-N-(4-methoxyphenyl)carbazole) with an aryl alcohol (ArOH) to form a bis-ether derivative. The reaction is catalyzed by Pd(PPh₃)₄ and CuI in NMP at 100 °C for 24 h.

^a1 (0.5 M, 1 equiv), phenol (2.4 equiv), CuI (20 mol %), ligand (40 mol %), Cs₂CO₃ (4 equiv), solvent (0.77 M). ^b1 (0.5 M, 1 equiv), 2 (2.4 equiv), CuI (20 mol %), DMGlyHCl (60 mol %), Cs₂CO₃ (3 equiv), solvent (0.77 M). ^cIsolated yield. ^dNo reaction.

UV-vis Absorption Behavior. The solution UV-vis spectra shown in Figures 2 and 3 were collected in THF (Uvasol spectral grade) at the concentration of $\sim 1 \times 10^{-5}$ M. The UV-

NPC shows two absorption bands at 292 and 340 nm, assigned as $S_0 \rightarrow S_2$ and $S_0 \rightarrow S_1$, respectively.²³ Characteristic

Scheme 2. Synthesis of the CBD-G0 through Our Modified Ullman Coupling Conditions

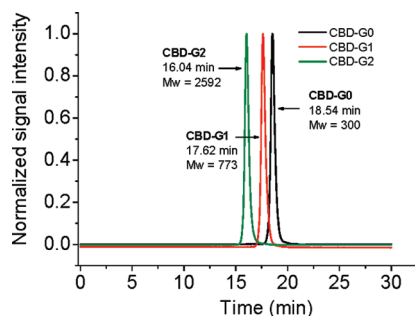
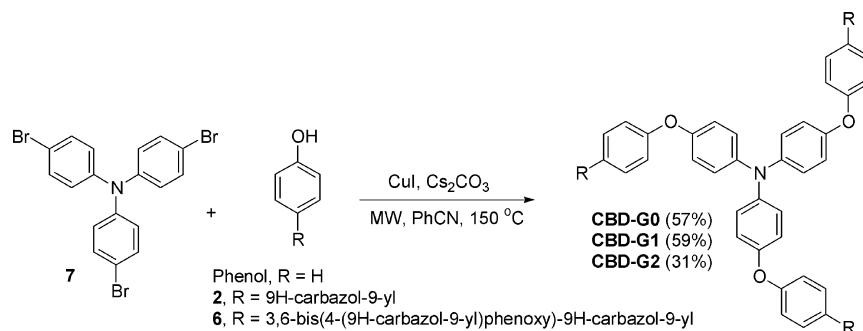


Figure 1. GPC analyses for the dendrimers CBD-G0 to CBD-G2.

fine structures were observed in both bands (Figure 2). 9-(4-Methoxyphenyl)-9H-carbazole (**8**) shows similar spectral behavior with the absorption only slightly red-shifted to 293 and 341 nm, indicating that the electronic perturbations arising from the methoxy substituent on the *N*-phenyl ring are minimal.^{15b}

On the other hand, when aryloxy substituents are introduced at the C3- and C6-positions of the carbazole ring, electronic perturbation becomes so significant that **3** exhibits the absorption maxima red-shifted substantially to 304 and 356 nm, respectively, along with the disappearance of the fine vibronic structures. As extending the NPC from **3**, the dendron **4** exhibits four sets of UV–vis absorption. The bands peaking at $\lambda_{\text{max}} = 292$ and 341 nm are attributed to the absorption arising

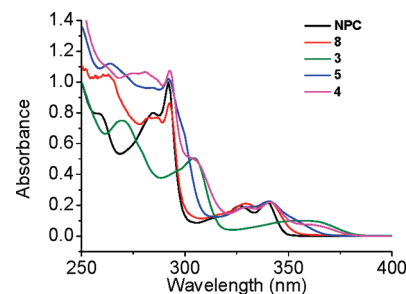
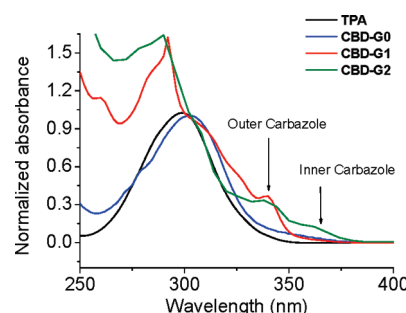
Figure 2. Absorption spectra of NPC, **3**–**5**, and **8** in THF. For details of the absorptivity in terms of extinction coefficient, please see Table 2.

Figure 3. Absorption spectra of TPA, CBD-G0, CBD-G1, and CBD-G2 in THF. See Table 2 for the corresponding absorption extinction coefficient.

Table 2. Photophysical Data for NPC Derivatives

	UV absorption ^a			fluorescence ^a			phosphorescence ^a	
	λ_{abs}^c ($\epsilon \times 10^{-4}$)	λ_{onset}^c	λ_{max}^c	τ^d	QY ^b		$\lambda_{0,0}^c$	T ₁ level ^e
NPC	292 (1.93)	340 (0.40)	348	347	6.44 (7.57) ^{15c}	0.29	409	3.03
8	293 (1.79)	341 (0.41)	352	356	6.18	0.25	411	3.02
3	304 (2.15)	356 (0.42)	381	387	4.25	0.21	437	2.86
4	292 (6.35)	341 (1.30)	380	386	4.19	0.19	438	2.85
	304 (2.80) ^f	361 (0.50) ^f						
5	292 (4.11)	341 (0.89)	367	372	4.59	0.22	425	2.92
	300 (2.28) ^f	352 (0.44) ^f						
TPA	299 (2.13)		340	358	2.31 (2.19) ²⁵	0.07	414	3.00
CBD-G0	303 (3.48)		375	389	1.86	0.06	433	2.85
CBD-G1	292 (8.80)	340 (2.07)	375	392 ^g	2.14	0.11	434	2.86
	302 (4.70) ^f			355 ^g	0.23 ^h			
CBD-G2	292 (21.1)	340 (4.25)	379	385	2.1 (32%)	0.14	435	2.85
	302 (13.1) ^f	362 (1.70) ^f			4.2 (68%)			

^aMeasured in THF. ^bQuantum yield (QY): Quantified in THF against coumarin 1 (QY: 0.85) as standard.²⁴ The value obtained by this method would be within 30% accuracy. ^cWavelength (nm). ^dMeasured in THF at 298 K, nanosecond (ns). ^eT₁ level (eV) = 1240.8/ $\lambda_{0,0}$ (nm). ^fBroad shoulders. ^g392 nm: major emission band, 355 nm: very minor emission band. ^hMonitored at 350 nm.

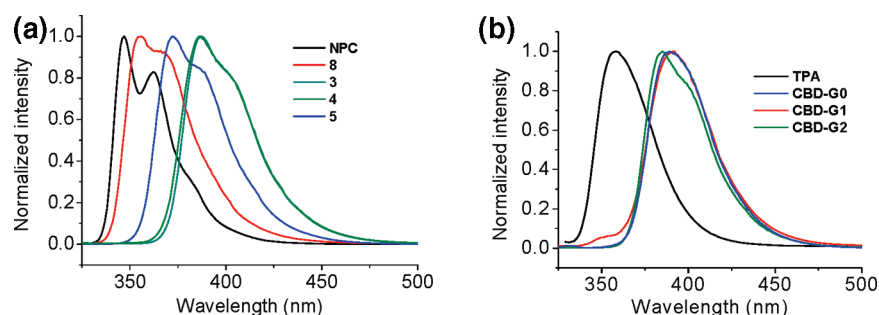


Figure 4. (a) Solution fluorescence spectra of NPC, 3–5, and 8 at room temperature. (b) Solution fluorescence spectra of TPA and CBD-G0 to CBD-G2 for comparison. The emission spectra are normalized at each peak wavelength. The excitation wavelength is selected at the peak wavelength of the lowest absorption band.

Table 3. Pertinent Data of Lifetime, k_{ISC} , and $\Delta E_{\text{S1-T1}}$ for the Titled Compounds

	$\tau(298\text{ K})^a$	$\tau(77\text{ K})^b$	$\tau(77\text{ K})/\tau(298\text{ K})$	k_{ISC}^c	$\lambda_{0,0}(\text{S1})^d$	$\lambda_{0,0}(\text{T1})^d$	$\Delta E_{\text{S1-T1}}^e$
NPC	6.44	8.10	1.26	7.8	342	409	4790
8	6.18	8.51	1.38	7.7	346	411	4570
3	4.25	5.87	1.38	12	369	437	4220
4	4.19	5.43	1.30	14	366	438	4490
5	4.59	5.63	1.23	13	355	425	4640
TPA	2.31	2.98	1.29	31	337	414	5520
CBD-G0	1.86	2.05	1.10	46	367	433	4150
CBD-G1	2.14 ^f	2.84 ^f	1.33	30	367	434	4210
CBD-G2	3.53 ^g	4.85 ^g	1.37	11	366	435	4330

^aMeasured in THF at 298 K, nanosecond (ns). ^bMeasured in THF at 77 K, nanosecond (ns). ^cDerived from eq 4; units: $\times 10^7\text{ s}^{-1}$. ^dWavelength (nm). ^eDerived from the reciprocal of low-temperature (77 K) fluorescence $\lambda_{0,0}$ (obtained from the crossing-point of the normalized absorption and fluorescence spectra) and phosphorescence $\lambda_{0,0}$, wavenumber (cm^{-1}) at 77 K. ^fMonitored at 380 nm. ^gThe weighted average of two components.

from the outer NPC units that possess similar chromophores with 8, while the bands peaking at $\lambda_{\text{max}} = 304$ and 361 nm are attributed to the absorption arising from the inner NPC unit analogous with 3. The half-dendron 5 demonstrates an absorption spectrum slightly different from that of 4; the inner monosubstituted carbazole displays the shoulder bands at $\lambda_{\text{max}} = 300$ and 352 nm. The degree of red shifts is apparently lower in comparison to that of 3 and 4, manifesting a lesser perturbation of the mono aryloxy (5) than that of the dual aryloxy (3, 4) substitution.

Figure 3 depicts the UV–vis absorption spectra of TPA, CBD-G0, CBD-G1, and CBD-G2. CBD-G0 has the absorption peaking at 303 nm. The λ_{max} is slightly red-shifted from that of TPA. In addition, a small shoulder is observed at 350 nm with a broad tail extending to 375 nm. The spectrum of CBD-G1 consists of a shoulder band at 302 nm ascribed to the TPA moiety as well as the bands at $\lambda_{\text{max}} = 292$ and 340 nm originating from the NPC chromophore. As the generation grows to CBD-G2, the contribution of dendron 4 could be clearly observed so that the spectrum comprises the absorption band at $\lambda_{\text{max}} = 340$ nm for the outer carbazole units analogous with 8 and the bands at $\lambda_{\text{max}} = 362$ nm for the inner carbazole units similar to that of 4. The well overlaying of the above spectra implicates that the conformations of the Ar–O–Ar linkage²⁵ and the *N*-phenyl group²⁶ are twisted so that the electronic coupling between the NPC units is broken down. In these situations, all carbazole groups are decoupled and behave essentially as independent chromophores. Therefore, the transitions of the core TPA as well as the carbazole groups at the inner or outer site can be assigned unambiguously.

Photoluminescence (PL) Studies. Room temperature fluorescence (FL) emission in degassed THF (Figure 4 and

Table 2), low-temperature fluorescence and phosphorescence (Ph) at 77 K in degassed THF (Uvasol spectral grade) glass (Figures 7 and 8), and their associated relaxation dynamics (Table 3) were performed to shed light on the effects of the dendrons on the PL properties of the dendrimers. The quantum yields were quantified in THF against coumarin 1 (QY: 0.85) as a standard according to the protocol published elsewhere^{24a,b} and announced by Jobin-Yvon Ltd. (Horiba Scientific).^{24c} Although the QY being measured by this method is not as accurate as that obtained by an absolute method using an integrating sphere, this approach has been widely used due to the fact that the relative trends of the QY changes are still reliable for a fair comparison. The spectra were collected within the concentration range of 1×10^{-6} – 5×10^{-6} M, in which a linear fluorescence response to the concentration was obtained (Figure S-6). The observation of the linear response indicated that the interferences arising from the self-quenching and self-absorption problems are negligible in this concentration range.

Room Temperature FL Behavior. Introduction of the aryloxy substituents onto either the TPA or the NPC cores leads to the perturbation on their fluorescence spectra. NPC, the reference compound, emits at 347 nm with vibronic fine structures being observed. The quantum yield (QY) was found to be 0.29 in THF (298 K), which is higher than that of the carbazole dendrons 3 (0.21) and 4 (0.19). Red-shifts in the emission spectra are observed in moving from the least aryloxy-substituted 8 at $\lambda_{\text{max}} = 356$ nm (Figure 4a) to the dendron 4 at $\lambda_{\text{max}} = 386$ nm, along with decreasing quantum yield. The trend of the bathochromic shifts is parallel to the red shifts in their UV spectra. The preservation of the vibronic fine patterns, regardless of the significant red shift of the spectra, signifies that all the emission of the dendrons originates from the rigid

carbazole units. The decreasing of the QY as well as the spectral red shifts may due to the electronic perturbations arising from the electron-donating aryloxy substituent on the carbazole ring. On the other hand, the aryloxy substituent might also introduce the loose-bolt and free-rotor effects²⁷—the torsional motion of which, in part, might induce the additional radiationless deactivation pathway and hence quench the emission. Not until the low-temperature fluorescence lifetime measurements have been carried out, we are unable to identify the importance of the loose-bolt and free-rotor effects on the quantum yield. This issue will be discussed in the later section regarding relaxation dynamics in the 77 K solid matrix. It is also noteworthy that the emission spectra of **3** and **4** well overlay with each other, indicating that the luminescence is mainly arising from the inner carbazole fluorophore. Also, evidenced by the absorption spectrum, the outer carbazole units on **4** do not cause significant perturbation to electronic structures of the inner carbazole unit (*vide supra*). Therefore, the lack of emission from outer carbazole units indicates that the outer carbazole units, upon excitation, must undergo fast energy transfer to the inner carbazole units, giving rise to the observed emission.

The dendrimers **CBD-G0**, **CBD-G1**, and **CBD-G2** also display red-shifted emission spectra at $\lambda_{\text{max}} \sim 390$ nm in comparison with that of **TPA** (358 nm) (Figure 4b). As for **CBD-G0**, since no NPC unit involves in the framework, the emission originating from the intact tri-*para*-phenoxy-substituted **TPA** unit is unambiguous. As for **CBD-G1**, first of all, the spectral profile and peak wavelength (390 nm) of the major emission band are nearly identical with that of **CBD-G0**. Thus, both **CBD-G0** and **CBD-G1** may share the same origin of the emission from the core tri-*para*-aryloxy-substituted **TPA** unit. This viewpoint is further supported by nearly the same emission lifetime of 1.9 and 2.1 ns for **CBD-G0** and **CBD-G1**, respectively. However, as shown in Figure 4b, we notice that for **CBD-G1**, a minor, short wavelength emission maximized at ~ 350 nm cannot be ignored. We tentatively assign this emission to the outer mono aryloxy-substituted NPC unit (see Scheme 1) due to its similar spectral profile and peak position with respect to that of **8**. However, upon monitoring at 350 nm, the emission decay time is measured to be 230 ps, which is much faster than the lifetime of 6.2 ns for **8**. Since the 350 nm emission overlaps with the absorption tail of **CBD-G0** (Figure 3), it is thus reasonable to propose the occurrence of energy transfer from the outer mono aryloxy-substituted NPC unit to the core tri-*para*-aryloxy-substituted **TPA** moiety for **CBD-G1**.

The energy transfer phenomenon was further investigated by using a model system of **8** and **CBD-G0** in polystyrene (PS) (Figure 5). As mentioned before, compound **8** shows characteristic absorption peaking at 330 and 345 nm. When the film of **8** in PS (10 wt %) was irradiated at 321 nm, strong PL at 355 and 370 nm were recorded. However, mixing **CBD-G0** (4 wt %) into the **8** (10 wt %)-PS blend led to significant fluorescent quenching at 355 and 370 nm. Instead, a new emission band from **CBD-G0** was clearly observed. The emission from **8** was completely quenched when the amount of **CBD-G0** was increased to 8 wt %. To further confirm the energy transfer phenomenon, excitation spectra of the blends were collected by monitoring the fluorescence at 392 nm. The observation of the corresponding signals at 330 and 345 nm, the signature of **8**, strongly supports the energy transfer mechanism, in which **8** would have the photoenergy absorbed

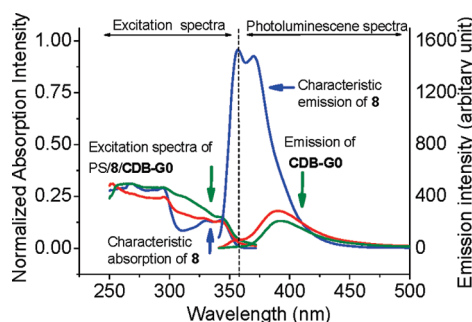


Figure 5. Study of the energy transfer phenomenon from **8** to **CBD-G0** in polystyrene: (a) The blue lines show the absorption and emission of **8** in PS. (b) The red lines show the emission and the excitation spectra of the thin-film **8-CBD-G0-PS** (10:4:100 by weight). (c) The green lines show the emission and the excitation spectra of the thin-film **8-CBD-G0-PS** (10:8:100 by weight).

and transferred to **CBD-G0** and finally contributed to the emission at 392 nm.

Another question to be addressed is the possibility of having self-quenching between the carbazole side-arms on **CBD-G1**, which might also reduce of the FL intensity of carbazole part. Although the linear response of the fluorescence intensity versus the concentration of **8** in the QY measurements indicated that the intermolecular self-quenching phenomenon is not particularly serious in highly diluted conditions, it is still difficult to justify if the self-quenching would occur when three carbazole side-arms being grouped with the **TPA** core in a close distance. Therefore, fluorescence experiments with various doping concentration **8** in PS thin films were adopted to probe this problem. In these measurements, front-face detection was adopted to reduce the interference arising from the self-absorption phenomenon.^{24d} Figure 6 shows the fluorescence

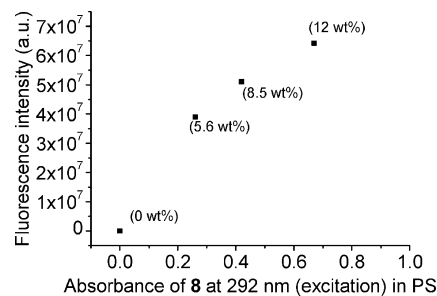


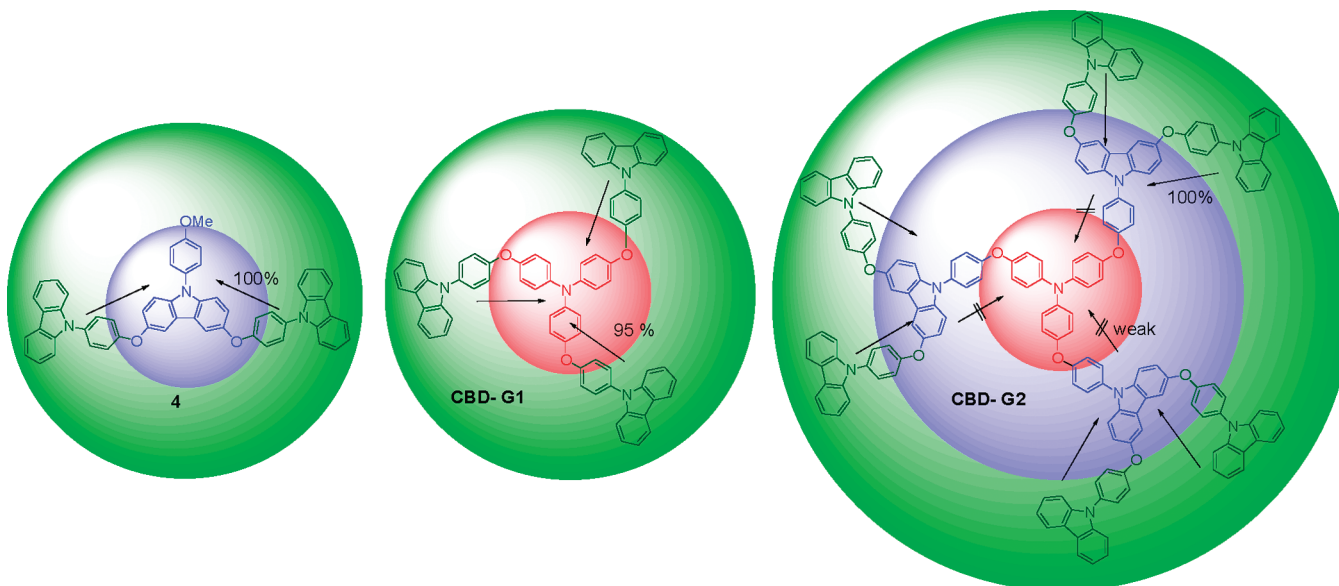
Figure 6. Study of the fluorescence self-quenching phenomenon of **8** in PS at various doping levels. The samples were excited at 292 nm, with the emission intensity being traced at 330 nm.

response of the films with different doping weight ratios of **8** in PS. One can easily to perceive that the self-quenching problem is insignificant even with high doping weight ratio up to 12%.

On the basis of the results discussed above, and by assuming that the energy-transfer mechanism is the major pathway that leads to the fluorescence decay, we take the lifetime of 230 ps (350 nm band in **CBD-G1**) and 6.2 ns (for **8**) to be the time scale of energy transfer for NPC and energy-transfer-free NPC moiety; the efficiency of energy transfer ET (%) can thus be estimated from the expression

$$\text{ET (\%)} = \frac{k_{\text{ET}}}{k_{\text{ET}} + k_{\text{f}}} \quad (1)$$

Scheme 3. Energy Transfer Pathways of Three Representative Dendron and Dendrimers



where k_{ET} is the energy transfer rate constant and k_f is the fluorescence decay rate constant with no energy transfer process involved, which are $(230 \text{ ps})^{-1}$ and $(6.2 \text{ ns})^{-1}$, respectively. As a result, ET (%) for the mono aryloxy-substituted NPC unit to the core tri-*para*-aryloxy-substituted TPA moiety in **CBD-G1** is estimated to be only $\sim 96\%$. For dendron **4**, due to the lack of emission from the outer carbazole units, ET is expected to be complete (100%) from the outer carbazole units to the inner carbazole units; in other words, the k_{ET} for **CBD-G1** is presumably much slower than that of **4**, an ultrafast one.

However, the rational explanations behind these observations have not yet been completely disclosed. Therefore, it is necessary to collect more evidence in order to outline the mechanisms. One possibility leading to the major difference between mono-aryloxy NPC \rightarrow tri-aryloxy TPA (in **CBD-G1**) and mono-aryloxy NPC \rightarrow triaryloxy NPC (in **4**) may lie in that the former has relatively poor spectral overlap between energy donor (emission of mono-aryloxy NPC) and energy acceptor (absorption of tri-aryloxy TPA), as shown in Figures 3 and 4b. This is a fundamental requirement for having either the Dexter energy transfer or the Förster resonance energy transfer. A more clear-cut picture will be provided in a later discussion on the basis of the HOMO–LUMO diagram.

For the largest generation dendrimer **CBD-G2**, as shown in Figure 4b, the spectral coverage of emission is nearly the same as that of **CBD-G0** or **CBD-G1**. However, unlike the structureless emission profile in **CBD-G0** and **CBD-G1**, the emission regains certain vibronic profile similar to that observed in the dendrons **3** or **4**. Moreover, the fluorescence decay, obtained by excitation at 299 nm, cannot be well fitted by a single-exponential component. Instead, the decay is fitted by the combination of two single-exponential decay components, indicating the existence of dual emissions. The lifetimes are fitted to be 2.1 ns (32%) and 4.2 ns (68%), which, within experimental error, well correlate with the lifetime of **CBD-G1** core and dendron **3** (or **4**), respectively. This, together with the aforementioned results for all dendrons, **CBD-G0** and **CBD-G1**, leads us to the following conclusion about the dual emission behavior of **CBD-G2**: (1) Similar to that of **4**, energy

transfer from the outmost mono-aryloxy NPC to the inner tri-aryloxy NPC units with unity efficiency does occur. (2) The energy transfer from the inner tri-aryloxy NPC units to the core tri-aryloxy TPA is sluggish so that emissions from the inner tri-aryloxy NPC units and the core tri-aryloxy TPA could be simultaneously observed.

Of course, ineffective energy transfer in the latter case is understandable due to the facts that (1) the core tri-aryloxy TPA and the inner tri-aryloxy NPC units are electronically decoupled (*vide supra*) and (2) both units have nearly identical S_0/S_1 gap (Figures 2–4) so that the overlap between their absorption (either acceptor) and emission (either donor) is minimal. According to these reasons, one may perceive that each excited-state relaxation can be treated independently, giving dual emission covering nearly the same spectral range.

This hypothesis could also explain for the observation of the high percentage weight for the longer lifetime carbazole emission ($\tau = 4.2 \text{ ns}$): Dendron **4** and **CBD-G0** have nearly identical extinction coefficients of 3.1×10^4 and $3.5 \times 10^4 \text{ M}^{-1} \text{ cm}^{-1}$ at 299 nm but very different fluorescence quantum yields of 0.19 and 0.06, respectively. On the basis of extinction coefficient of the dendron and the 3-fold symmetry of **CBD-G2**, one might expect that around 70% of photons should be harvested by the three dendritic branches on **CBD-G2**, while about 30% of photons would be captured by the TPA core. If each S_1 -state relaxation can be treated independently, and by taking the QY factor into account, the contribution from the carbazole dendrons in the emission intensity should be around 90%. Although one may expect to see some discrepancy based on this qualitative model, the observation of nearly 70% contribution from the longer lifetime carbazole clearly supports that the energy transfer from carbazole dendron to the core TPA must be minimal.

To sum up in brief, Scheme 3 depicts the energy transfer pathways of three representative cases: dendron **4** and dendrimers **CBD-G1** and **CBD-G2**.

Low-Temperature FL and Ph Properties. NPC derivatives are commonly used as the phosphorescent host materials for OLEDs.^{10b,28} To further explore the steady-state emission behavior of the dendrimers, especially the triplet state energy

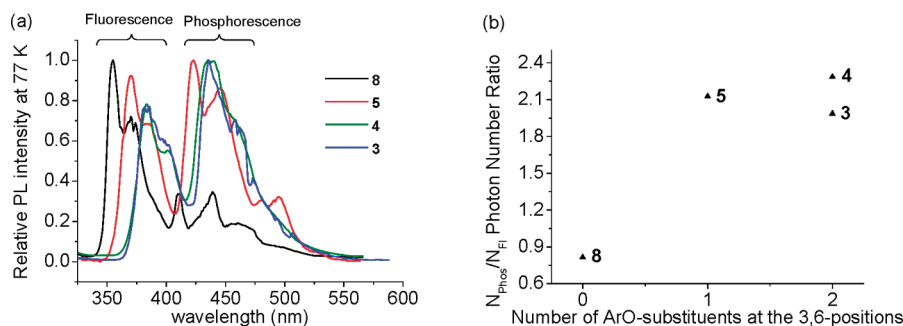


Figure 7. Low-temperature PL behavior of 3–5 and 8: (a) Steady state photoluminescence spectra being collected in THF glass at 77 K. (b) Correlation between $N_{\text{phos}}/N_{\text{fl}}$ value and the number of ArO substituents on the carbazole unit.

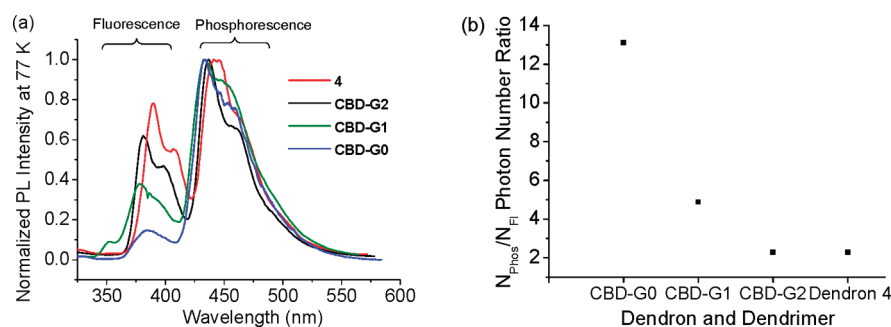


Figure 8. Low-temperature PL behavior of CBD-G0, CBD-G1, CBD-G2, and dendron 4: (a) Steady state photoluminescence spectra being collected in THF glass at 77 K. (b) Correlation between $N_{\text{phos}}/N_{\text{fl}}$ value and the generation of the dendrimers.

for the later application, low-temperature (LT) steady-state PL spectra of 3–5 and 8 and CBD-G0, CBD-G1, and CBD-G2 in the organic glass of THF (Uvasol spectral grade) at 77 K were collected and shown in Figures 7 and 8. The low-temperature steady-state PL experiments were carried out using Hitachi F-4500 spectrofluorometer equipped with a quartz Dewar flask setup for handling the measurements in liquid nitrogen. The data were collected at the fluorescence and phosphorescence modes, respectively, in degassed THF glass. When the spectra were collected at the fluorescence mode, both phosphorescence and fluorescence emissions could be simultaneously observed. The spectra of the phosphorescence part are identical with their spectra measured in the phosphorescence mode, signifying that these signals really originate from the phosphorescence. A similar phenomenon in solid matrix has been reported by Bonesi and Erra-Balsells for carbazole.^{15c} The observation of the phosphorescent signals attracted us to systematically explore this phenomenon, and the related data are summarized in Table 2.

ArO Substituent Effects on the Phosphorescence Emission. Most of them exhibit phosphorescence at the region of 410–440 nm, corresponding to triplet state energy of 3.03–2.81 eV. Introduction of the ArO substituents at the C3 and C6 positions leads to a small red-shift effect on the triplet state emission. The first band of the phosphorescence emission of 8, 5, and 4 is therefore recorded as 411, 425, and 441 nm, respectively. It is worth to emphasize here the phosphorescence emissions of 3 and 4 are very similar and well-overlapping with each others, indicating that the inner carbazole core is the key phosphor in these cases. According to the above data, we conclude that the dendrons and the corresponding dendrimers possess substantially high energy for their lowest lying triplet state and therefore are suitable host materials for blue-light triplet emitters that would be discussed in later sections.

Intensity Ratio for the Phosphorescence versus Fluorescence. The intensity ratio reported in Figures 7 and 8 were estimated based on the integration of the spectral signals and denoted as $N_{\text{phos}}/N_{\text{fl}}$. As shown in Figure 7b, the least aryloxy-substituted 8 shows strong fluorescence over the phosphorescence emission at 77 K with the $N_{\text{phos}}/N_{\text{fl}}$ value of 0.81 was found. When one ArO substituent is introduced at the C3 position to form 5, the intensity ratio for phosphorescence versus fluorescence was significantly enhanced to $N_{\text{phos}}/N_{\text{fl}} = 2.1$. When two ArO substituents are introduced onto the carbazole ring, the relative intensity of $N_{\text{phos}}/N_{\text{fl}} = 2.3$ was obtained for 4. Compound 3 also shows a value of $N_{\text{phos}}/N_{\text{fl}} = 2.0$, indicating that aryloxy substituent effects are salient features in the presence system.

On the other hand, the dendrimers exhibit photophysical behaviors that are different from the dendritic wedges. Although CBD-G0 shows PL in a similar region, the observed relative phosphorescence intensity is much stronger, and hence a substantially larger $N_{\text{phos}}/N_{\text{fl}}$ value of 13.1 was recorded (Figure 8a). When three NPC units are introduced in CBD-G1, the $N_{\text{phos}}/N_{\text{fl}}$ value drops significantly to 4.9. Since this value is still far larger than that of 2.3 for dendron 8, we therefore believe that the emission from the TPA core might be overwhelming in this case. This is consistent with the early conclusion about the NPC → TPA energy transfer process in CBD-G1. In CBD-G2, the $N_{\text{phos}}/N_{\text{fl}}$ value of 2.3 is nearly identical to that of 4 ($N_{\text{phos}}/N_{\text{fl}} = 2.3$) (Figure 8). It is again consistent with our previous suggestion that the carbazole dendrons on CBD-G2 is the major group responsible for the observed emission behavior.

Although the above systematic analyses revealed the ratiometric phosphorescence/fluorescence changes of the compounds, any justifications or conclusions simply attributed to the structural change are not immediately obvious. Many

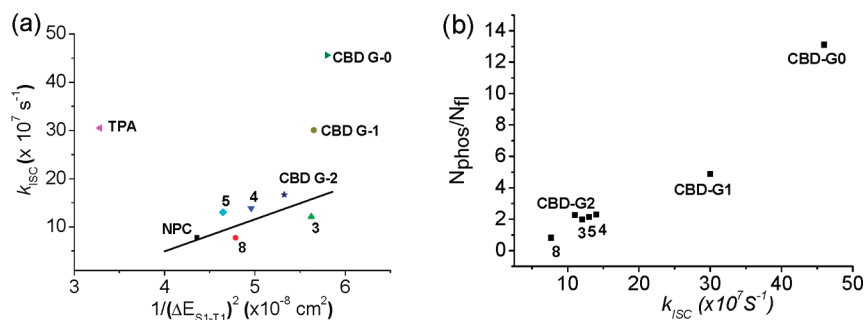


Figure 9. Correlation analysis about k_{ISC} : (a) Plot of k_{ISC} as a function of $1/(\Delta E_{\text{S1-T1}})^2$. (b) Plot of $N_{\text{phos}}/N_{\text{fl}}$ against k_{ISC} .

parameters about the fluorescence and the intersystem crossing (ISC) process may vary as a result of the variances of the singlet–triplet energy gap. Therefore, further understanding about the relaxation dynamics becomes essential for our study.

Time-Resolved PL Spectroscopy and the Associated Relaxation Dynamics. To elucidate the correlation between the ratiometric phosphorescence/fluorescence changes and the ISC ($S_1 \rightarrow T_n$) rate constants among the titled dendrons and/or dendrimers, their fluorescence properties were characterized by time-resolved PL spectroscopy.^{15c,d,27a,b}

Pertinent data measured in THF at 77 K are summarized in Table 3. Among the titled compounds studied, the longest lifetime $\tau = 8.51$ ns ($\lambda_{\text{fl max}} = 356$ nm) was obtained for carbazole **8**. Having the aryloxy substituents at the C3 and/or C6-positions, carbazole dendrons **3**, **4**, and **5** show similar fluorescence lifetime of $\tau = 5.87$, 5.43 , and 5.63 ns, respectively. As for the dendrimers, **CBD-G0** exhibits the shortest fluorescence decay time of $\tau_f = 2.05$ ns.

By assuming that the intermolecular quenching processes are insignificant in highly diluted solutions, the equations that could be used to estimate the overall deactivation rate in S_1 , i.e. k_{obs} , and the corresponding fluorescence quantum yield can be expressed as

$$k_{\text{obs}} = k_f + k_{\text{ISC}} + k_{\text{nr}}(T) = \frac{1}{\tau_{\text{obs}}} \quad (2)$$

$$\Phi_f(T) = \frac{k_f}{k_f + k_{\text{ISC}} + k_{\text{nr}}(T)} = \frac{k_f}{k_{\text{obs}}} \quad (3)$$

The radiative decay rate constant, k_f , is an intrinsic property, which is proportional to the square of the transition moment and is thus independent of the temperature. A similar standpoint can be applied for k_{ISC} if $S_1 \rightarrow T_1$ is the only intersystem crossing channel. Assuming that the thermally activated deactivation process $k_{\text{nr}}(T)$ in eqs 2 and 3 is drastically suppressed in the 77 K THF solid matrix and can thus be neglected, k_{ISC} could be deduced as

$$k_{\text{ISC}} = k_{(77\text{K})} - k_f = \frac{1}{\tau_{(77\text{K})}} - \frac{\Phi_f(298\text{K})}{\tau_{(298\text{K})}} \quad (4)$$

Knowing the lifetime in 77 and 298 K, together with fluorescence QY estimated at 298 K, the values of k_{ISC} among the titled compounds are listed in Table 3.

As one can see in Table 3, the fluorescence lifetimes for all dendrons and dendrimers at 77 K increase. The ratio of $\tau(77\text{K})/\tau(298\text{K})$ falls into a range of 1.10–1.38, dependent on the chemical structure. This observation is consistent with our assumption that the thermally activated deactivation process is

suppressed at low temperature in an organic glass, which leads to a longer lifetime. Among the data we collected, the $\tau(77\text{K})/\tau(298\text{K}) = 1.26$ for **NPC**, which serves as a reference molecule, is recorded. Since the carbazole unit is relatively rigid, and only the *N*-phenyl ring is allowed to rotate freely in **NPC**, we therefore suggest that the thermally activated deactivation process may arise from the free rotation of the phenyl unit. Further introduction of RO groups to the carbazole ring might also lead to some enhancement of the $\tau(77\text{K})/\tau(298\text{K})$ value even though the change is not that remarkable. For example, **3** and **8** actually show a higher value of $\tau(77\text{K})/\tau(298\text{K}) = 1.38$.

Although **CBD-G1** exhibits slightly slower decay time of $\tau = 2.84$ ns than that of **CBD-G0**, this value is much shorter than that of **8**. The $\tau(77\text{K})/\tau(298\text{K})$ value of 1.33 for **CBD-G1** is close to that of **3** and **8**, revealing that similar extents of the loose-bolt and free rotor effects are operating in **CBD-G1**.

CBD-G2 exhibits a decay time constant of $\tau = 5.4$ ns (79%) and 2.8 ns (21%), which well correlate with the lifetime of dendron **4** and **CBD-G1**, respectively. Both results are consistent with the resulting trend at 298 K and are in good agreement with the dual emission hypothesis. Again, this observation supports the argument that energy transfer from the outmost mono-aryloxy NPC to the inner tri-aryloxy NPC units may be more efficient than energy transfer from inner triaryloxy NPC units to TPA core (**CBD-G2**) so that dual emission could be observed.

Theoretical Implications. Under the assumption that the intersystem crossing takes place solely via the $S_1 \rightarrow T_1$ pathway, the corresponding rate constant, k_{ISC} , could thus be expressed as

$$k_{\text{ISC}} \propto \frac{\langle \Psi_{T_1} | H_{\text{SO}} | \Psi_{S_1} \rangle^2}{(\Delta E_{S_1-T_1})^2} \quad (5)$$

where H_{SO} is the Hamiltonian for spin–orbit coupling (SOC) and $\Delta E_{S_1-T_1}$ is the energy difference between S_1 and T_1 states due to the difference in electron correlation energy,^{27d} which can be calculated by the gap of the first vibronic peak energy between fluorescence and phosphorescence (see Table 3). For compounds having the same type of fluorophore, their SOC term should be similar and hence their k_{ISC} should be inversely proportional to $(\Delta E_{S_1-T_1})^2$. We then made an attempt by plotting the k_{ISC} value as a function of $1/(\Delta E_{S_1-T_1})^2$. First, as shown in Figure 9, the plotted data of the carbazole dendrons **3–5**, **8**, **NPC**, and **CBD-G2** are lined up to give a linear correlation. Knowing that the slope should be proportional to spin–orbit coupling constant expressed in eq 5, the linear correspondence of the carbazole dendrons and **CBD-G2** indicates that this family of compounds may have a similar

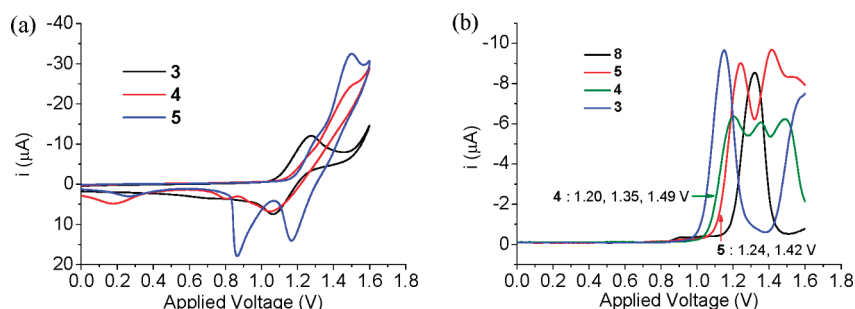


Figure 10. Electrochemical study of the dendrons: (a) Cyclic voltammograms of 3–5. (b) Differential pulse voltammograms of 3–5, 8. Solvent: CH_2Cl_2 .

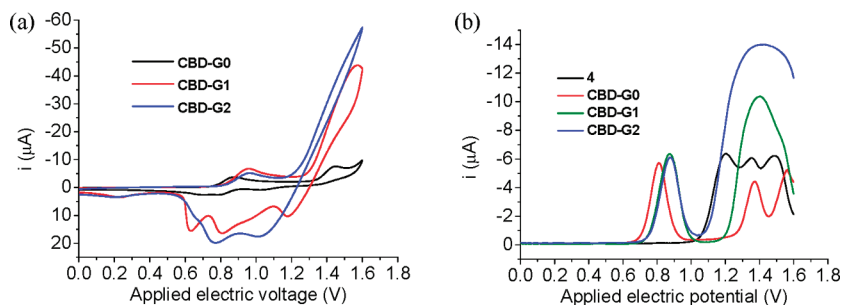


Figure 11. Electrochemical behavior of the dendrimers: (a) Cyclic voltammograms of CBD-G0, CBD-G1 and CBD-G2. (b) Differential pulse voltammograms of CBD-G0, CBD-G1, CBD-G2, and 4 for comparison. Solvent: CH_2Cl_2 .

Table 4. Thermal and Electrochemical Data for *N*-Phenylcarbazole Derivatives

	thermal analysis ^a (°C)		E_{onset} (V) (CV) ^c		E^{ox} (V) (DPV) ^c		energy level (eV)		
	T_g	T_d	E_1	E_2	E_{pa1}	$E_{1/2}$ ^d	HOMO ^e	E_g^f	LUMO ^g
NPC			1.32		1.38	1.41	−5.68	3.57	−2.11
8			1.26		1.31	1.34	−5.61	3.53	−2.08
3	86	378	1.08		1.15	1.18	−5.45	3.25	−2.20
5	65	351	1.18	1.28	1.24	1.27	−5.54	3.38	−2.16
4	129	505	1.14	1.21	1.20	1.23	−5.50	3.27	−2.23
TPA			1.01		1.07	1.10	−5.37	3.65	−1.72
CBD-G0	— ^b	314	0.76	1.34	0.81	0.84	−5.11	3.31	−1.80
CBD-G1	129	571	0.82	1.28	0.87	0.90	−5.17		
CBD-G2	198	617	0.82	1.22	0.87	0.90	−5.17		

^aScan rate: 10 deg/min. ^bNo T_g observed, $T_c = 108$ °C. ^cIn CH_2Cl_2 with Bu_4NClO_4 (0.1 M) as supporting electrolyte vs Ag/AgCl. ^d $E_{1/2} = E_{\text{pa1}} + \Delta E/2$, where $\Delta E = 0.05$ V. ^eHOMO = $-(E_{1/2} - 0.53) - 4.8$ (eV). ^fBand gap = $1240.8/\text{absorption } \lambda_{\text{onset}}$ (nm). ^gLUMO = HOMO + band gap (eV).

SOC term and their emissions mainly originate from the NPC chromophore.

On the other hand, slower k_{ISC} rate was obtained with the generation growth of dendrimers. The k_{ISC} of CBD-G0, CBD-G1, and CBD-G2 vary dramatically even their $\Delta E_{\text{S}_1-\text{T}_1}$ values are confined within a narrow range of 4150–4350 cm^{-1} , indicating that CBD-G0, CBD-G1, and CBD-G2 should possess a very different SOC term. This result implies that very different intersystem crossing and relaxation mechanisms are operating in these compounds; this picture is consistent with our previous conclusion being shown in Scheme 3.

It is noteworthy to point out that the value of $N_{\text{phos}}/N_{\text{fl}}$ being obtained in the last section is positively correlated to the k_{ISC} value (Figure 9b). This relationship clearly explains for the fact that higher intersystem crossing rate from S_1 to T_1 would lead to stronger the relative phosphorescence emission in the low-temperature PL experiments.

Electrochemical Oxidation Properties. The electrochemical properties were studied by cyclic voltammetry (CV)

and differential pulse voltammetry (DPV).²⁹ The HOMO values are determined from the estimated $E_{1/2}$ with respect to ferrocene (Fc). Selected CV and DPV diagrams are displayed in Figures 10 and 11. Pertinent data of the oxidation potentials (versus Ag/AgCl couple) are summarized in Table 4.

The first point to note from the electrochemistry about the dendrons is that there appears to be a trend for the first wave shifting to less positive potentials when more ArO substituents are introduced to the carbazole unit (Figure 10). NPC displayed irreversible oxidation wave that is attributed to the oxidation of the carbazole ring with the onset voltage at 1.32 V. The irreversibility is arising from the oxidative NPC dimerization.³⁰ Because of the π -electron-donating ability of the MeO group, 8 shows lower onset oxidation voltage at 1.26 V, which is about 0.06 V earlier than that of NPC. When the π -electron donating PhO substituents were introduced at the C3 and C6 positions of 3, further destabilization on the HOMO occurs so that the CV wave exhibits a reversible pattern with the onset oxidation at 1.08 V, which coincides with the

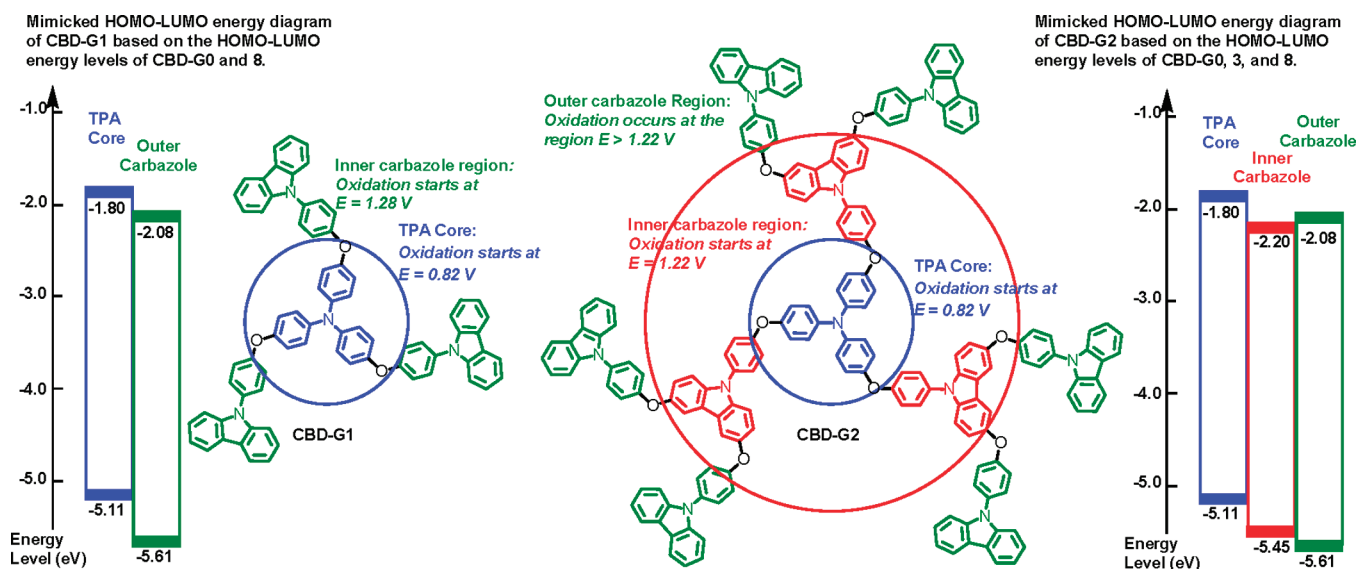


Figure 12. Distribution of the oxidation potential and mimicked energy diagrams of CBD-G1 and CBD-G2.

reported result of 9-ethyl-3,6-dimethoxy-9*H*-carbazole.^{16a} An explanation for the shift to the less oxidative potential is that the electron density on the carbazole unit would be substantially enriched due to the presence of the PhO substituents. On the other hand, irreversible oxidations were observed for **4** and **5**, with the onsets at 1.14 and 1.18 V, respectively. It is necessary to point out that the oxidation potential of **3** is lower than that of **4** by 0.06 V, reflecting the fact that the outer carbazole units on **4** are more electron-withdrawing than the phenyl substituent on **3**. This is consistent with the Yamamoto's conclusion on **G4Fc**,^{12a} in which the carbazole units are electron-withdrawing through inductive or π -polarization effects.

The irreversible oxidative process on the NPCs was also examined by DPV method and could be partially resolved. From the DPV (see Figure 10b), it was estimated that the first oxidation of **8** was at ~ 1.31 V while that of **3** was at ~ 1.15 V. On the other hand, **5** demonstrates two waves peaking at 1.24 and 1.42 V. The first wave is assigned to the electrochemical oxidation of the inner 3-ArO-substituted carbazole while the second wave is assigned to the outer one. Dendron **4** shows three waves peaking at 1.20, 1.35, and 1.49 V that are reasonably attributed to the oxidations of the inner carbazole as well as two outer carbazoles, respectively.

The second group of molecules worthy to compare with is **CBD-G0**, **CBD-G1**, and **CBD-G2**. Unlike **CBD-G0** that has the simple electrochemical oxidation behavior, the electrochemical properties of **CBD-G1** and **CBD-G2** are intricate by integration of the dendritic wedges to the TPA core. The waves could only be partially resolved even by DPV methods (Figure 11b).

First of all, two oxidation processes onset at 0.76, and 1.34 V are respectively observed in the CV of **CBD-G0**. The first oxidation process is reversible with the onset lower than that of TPA by 0.25 V, implying that **CBD-G0** is more electron-rich due to the presence of the π -donating ArO substituents. The $E_{1/2}$ of 0.84 V was recorded accordingly. On the other hand, the second oxidation is irreversible with the onset at 1.34 V, which might be due to the oxidation of the radical cation (**CBD-G0^{•+}**) to dication (**CBD-G0²⁺**), giving rise to the quinoidal forms.³¹

On the other hand, both cyclic voltammograms of **CBD-G1** and **CBD-G2** exhibit two oxidation waves: one corresponds to the TPA core oxidation while the other is relevant to the oxidation of the carbazole dendron (Figure 11a). Both of the first waves of **CBD-G1** and **CBD-G2** are reversible and have the $E_{1/2}$ appearing at 0.90 V. They are unambiguously assigned to the single electron oxidation of the TPA core. However, the $E_{1/2}$ value is higher than that of **CBD-G0**, supporting the assumption that the dendritic wedge is electron-withdrawing as elaborated in the early sections.

The second set of irreversible oxidation for **CBD-G1** and **CBD-G2** onsets at 1.28 and 1.22 V, respectively. Although the waves are complicated and could only be partially resolved even by DPV methods (Figure 11b), we believe that they are corresponding to the oxidation of the NPC dendrons due to the close E_{onset} values of the **CBD-G1**, **CBD-G2**, **4**, and **5**. Close examination revealed that the E_{onset} of **CBD-G2** is almost identical to the E_{onset} of **4**. This result implies that the dendritic wedge oxidation would not be repelled by cation formed on the TPA⁺ core in the first oxidation. In addition, the E_{onset} of **CBD-G2** is slightly lower than those of **CBD-G1**. This is reasonable due to the electron rich environment of the inner carbazole of the **CBD-G2**.

Summarizing the above electrochemistry results, we conclude that the central core of **CBD-G2** is the most electron-rich, the inner-carbazole units form the second electron-rich interlayer, while the outmost carbazoles construct the least electron-rich shell (Figure 12). Therefore, both **CBD-G1** and **CBD-G2** possess oxidation potential gradients such that the outer layer is electron-poor and the inner layer is electron-rich. This result is similar to the phenylazomethine dendrimers,³² but opposite to the dendrimers with pure *N*-H-carbazole backbone.^{12a}

Estimation of the HOMO–LUMO Levels. The HOMO levels of the compounds were estimated according to the $E_{1/2}$ values obtained from the DPV experiments. Herein the HOMO levels were calculated on the basis of the equation of $\text{HOMO} = -(E_{1/2} - 0.53) - 4.8$ (eV). For simple compounds such as **3**–**5**, **8**, NPC, TPA, and **CBD-G0**, their LUMO levels could be estimated directly from the equation of $\text{LUMO} = \text{HOMO} + \text{band gap (eV)}$, provided that the corresponding optical band gaps could be easily obtained from the UV–vis absorption

experiments. However, due to the multichromophoric behavior of the dendrimers of **CBD-G1** and **CBD-G2**, evaluation of their electronic levels is relatively complicated. Fortunately, our early results elucidated that the subgroups in each shell of the dendrimers are only weakly coupled so that they can be considered as electronically isolated subgroups. Therefore, we were able to build their energy level diagrams respectively, as shown in Figure 12, based on the HOMO–LUMO values of **CBD-G0**, **3**, and **8**. From the diagram one can easily perceive that the HOMO of **CBD-G1** and **CBD-G2** are located at the TPA core, while the corresponding LUMO falls onto the carbazole units.

On the basis of these HOMO–LUMO diagrams, our energy transfer mechanism proposed in Scheme 3 could be explained: (1) Transfer of the energy from the outer carbazole to the inner carbazole in **CBD-G2** is exothermic. In addition, while the LUMO level of the inner carbazole is lower than the outer one, the HOMO level of the inner carbazole is higher than that of the outer one. This type of HOMO–LUMO alignment would be beneficial for the Dexter energy transfer mechanisms, and therefore fast energy transfer is allowed to occur in this case. This explanation could also be applicable to the dendron **4** due to the fact that all subgroups could be treated as electronically isolated ones. (2) On the other hand, the energy transfer process from the outer carbazole to the core TPA in **CBD-G1** would be relatively slow in comparison to the first one. In this case, although energy transfer process is still exothermic due to the fact that the energy gap of the outer carbazole is larger than that of the core TPA unit, the LUMO energy level of the core TPA is higher than that of the outer carbazole by 0.28 eV (+27 kJ). The endothermic alignment of the LUMO energy levels would slow down the energy transfer process. This could help to understand why residual emission from the outer carbazole could be observed in the PL spectrum of **CBD-G1** in Figure 4b. (3) Energy transfer from the inner carbazole of **CBD-G2** to the core TPA unit is unfavorable. The energy transfer process is slightly endothermic by 0.06 eV (+6 kJ). In addition, the LUMO energy level alignment is endothermic by 0.4 eV (+39 kJ). These two factors prohibit any effective energy transfer from the inner carbazole to the core TPA. On the other hand, the reverse energy transfer from the core TPA to the inner carbazole is also unfavorable due to the endothermic alignment of the HOMO by 0.34 eV (+33 kJ). This would lead to the observation of the dual-emission phenomenon.

It is noteworthy to point out the interesting LUMO energy-level features in **CBD-G2**; either the LUMO of the outer-shell carbazole units or the central TPA core would have higher LUMO energy levels in comparison to the LUMO of the inner-shell carbazole units. This feature would play important role in the electroluminescence behavior that would be discussed in the later sections.

Thermal Properties of the Carbazole Dendrons and Dendrimers. All O-linked-NPC shows high thermal stability in the TGA analysis (Figure 13). In particular, **CBD-G1** and **CBD-G2** can stand for high temperature up to 500 °C or above under nitrogen atmosphere. Except **CBD-G0**, the dendritic NPCs form amorphous organic glass. No crystallization takes place from the corresponding amorphous glasses when heated after T_g . This is a key criterion to fabricate thermally stable thin film materials for optoelectronic applications.

Performance of NPC Derivatives as Host in the Phosphorescent OLED. According to the results above, the NPC-based dendrimers **CBD-G1** and **CBD-G2** possess high

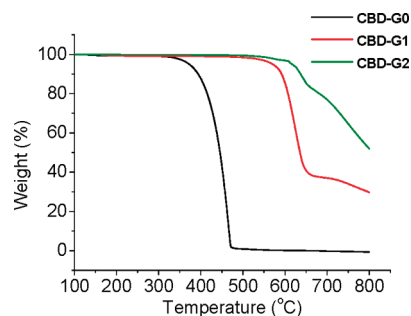


Figure 13. Thermal gravimetric analyses of **CBD-G0** to **CBD-G2**.

HOMO levels, which matches the Fermi level of PEDOT:PSS (−5.1 eV).³³ The hole injection between the interfaces of PEDOT/host would become more efficient. More importantly, the triplet energy of **CBD-G1** and **CBD-G2** is higher than that of FIrPic measured to be ~2.75 eV. Therefore, the reverse energy transfer from the triplet emitter to host³⁴ would be prohibited. Along with their good thermal stability, **CBD-G1** and **CBD-G2** are potential candidates of solution-processable dendritic hosts for blue-electrophosphorescent device. To evaluate the performance of **CBD-G1** and **CBD-G2** as host materials, a device consisting of ITO (100 nm)/Host-FIrPic (10 wt %) (40 nm)/TAZ (50 nm)/LiF (1.2 nm)/Al (120 nm) was employed for the preliminary study (Figure 14). The maximum luminous efficiency of **CBD-G2** could be achieved up to 24.7 cd/A at 484 cd/m². It is quite appealing that the **CBD-G2** device could maintain good luminous efficiency at such high brightness. Another comparable result^{10b} was reported in pure carbazole-based conjugated dendritic host at lower brightness. As a reference, small molecule **3** has also been applied as host material for FIrPic by thermal deposition processes. However, only ~2 cd/A maximum luminous efficiency could be obtained on the multilayer devices.

The fluorescence quantum yield of triphenylamine is smaller than that of *N*-phenylcarbazole due to its less rigid structure. This also indicates faster nonradiative deactivation processes and shorter lifetime of singlet state in triphenylamine. In light of this viewpoint, triphenylamine should be a poor candidate for host materials since those fast nonradiative deactivation processes would compete with the energy transfer process and lower the efficiency of singlet-state harvesting. The singlet excited state is mainly populated on the TPA core in **CBD-G1** and on the inner tri-aryloxy NPC units in **CBD-G2** (vide supra). Therefore, the high luminous efficiency of **CBD-G2** could be attributed to two combination factors. On the one hand, the singlet-state harvesting is facilitated via energy transfer from the inner tri-aryloxy NPC units to the triplet emitters. On the other hand, as evidenced by both CV and DPV data (vide supra), HOMO of **CBD-G2** is strictly located at the TPA core, whereas LUMO is mainly confined at the inner NPC sites. The spatial separation of HOMO and LUMO energy level may, in part, lead to high efficiency of the device performance.³⁵

CONCLUSION

In summary, a series of novel oxygen-linked *N*-phenylcarbazole (NPC) dendritic wedges (**3–5**) and triphenylamine-centered dendrimers (**CBD-G0** to **-G2**) have been synthesized and extensively studied. The analyses of UV–vis spectra revealed that the Ar–O–Ar linkage would break down the π

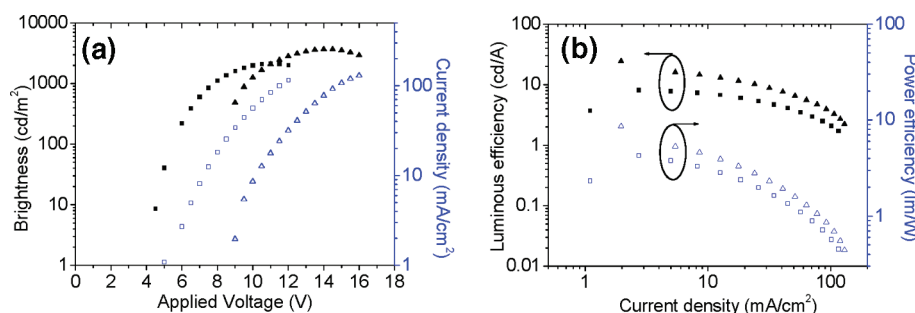


Figure 14. (a) Brightness and current density versus applied voltage characteristics for CBD-G1 (squares) and CBD-G2 (triangles). (b) Luminous and power efficiency versus current density for CBD-G1 (squares) and CBD-G2 (triangles).

conjugation and make NPC units manifest their individual absorption peaks. The PL properties were fully characterized by luminescence spectroscopy at both room temperature and 77 K in THF. The results reveal the operation of energy transfer between NPC and core TPA as well as the NPCs between different generations. As a result, the origin of emission in both singlet and triplet manifolds can be ascribed to two categories, namely the TPA, CBD-G0, and CBD-G1 from the TPA moiety and the rest of titled compounds from NPC chromophore. Note that CBD-G2 may possess both but keen on the major NPC moiety. From the measurement of the oxidation potential of the NPC derivatives, the mesomeric electron-donating effect of the oxygen atom and inductive electron-withdrawing effect of the carbazole unit were revealed. The potential gradient could be established on those triphenylamine-centered dendrimers (CBD-G1 and CBD-G2) such that the outer layer is electron-poor and the inner layer is electron-rich. Standing on these intriguing physical properties, using CBD-G2 as the host material, the FIrpic-based electrophosphorescent devices were successfully fabricated and the maximum luminous efficiency could be achieved up to a record high of 24.7 cd/A at 484 cd/m².

EXPERIMENTAL SECTION

General Procedure of Microwave-Assisted Synthesis. The reaction flask was charged with corresponding aryl halides (1 equiv), aryl phenols (2.4 equiv for wedges and 3.6 equiv for dendrimers), copper iodide (0.2 equiv), *N,N*-dimethylglycine hydrochloride (0.6 equiv), Cs₂CO₃ (3 equiv for wedges and 4 equiv for dendrimers), and benzonitrile (0.77 M). The reaction mixtures were then put into microwave reactor and reacted at 200 W, open vessel, 150 °C, for 4 h. The reaction mixture was quenched with water and extracted with CH₂Cl₂. The organic layer was separated and dried over anhydrous MgSO₄. The solution was filtered through Celite and distilled under vacuum to remove the high polar solvent. The crude product was purified thorough chromatography.

9,9'-(4,4'-(9-(4-Methoxyphenyl)-9H-carbazole-3,6-diyl)bis(oxy)bis(4,1-phenylene))bis(9H-carbazole) (4). Elution: hexane/CH₂Cl₂ = 1/1; white solid; yield 49%; mp 145 °C, *T*_g = 129 °C, *T*_d = 505 °C. ¹H NMR (400 MHz, CD₂Cl₂): δ 8.14 (d, *J* = 7.7 Hz, 2H), 7.91 (d, *J* = 2.3 Hz, 2H), 7.54–7.49 (m, 6H), 7.42–7.38 (m, 10H), 7.32–7.22 (m, 6H), 7.17 (d, *J* = 8.9 Hz, 2H), 3.93 (s, 3H). ¹³C NMR (100 MHz, CD₂Cl₂): δ 159.78, 159.15, 150.16, 141.77, 139.74, 132.23, 130.51, 129.11, 128.98, 126.47, 124.11, 123.67, 120.73, 120.30, 118.90, 115.78, 112.33, 111.70, 110.23, 56.21. HRMS (FAB) calcd for C₅₅H₃₇N₃O₃ 787.2835 (M⁺), obsd 787.2823. Anal. Calcd for C₅₅H₃₇N₃O₃: C, 83.84; H, 4.73; N, 5.33. Found: C, 83.63; H, 4.74; N, 5.21.

Tris(4-phenoxyphenyl)amine (CBD-G0). Elution: hexane/CH₂Cl₂ = 2/1; white solid; yield 57%; mp 131 °C, *T*_c = 108 °C, *T*_d = 373 °C. ¹H NMR (400 MHz, CD₂Cl₂): δ 7.33 (t, *J* = 8.0 Hz, 6H), 7.10–7.06 (m, 9H), 7.01 (d, *J* = 8.0 Hz, 6H), 6.93 (d, *J* = 8.9 Hz, 6H).

¹³C NMR (100 MHz, CD₂Cl₂): δ 158.39, 152.81, 144.35, 130.27, 125.69, 123.50, 120.63, 118.82. HRMS (EI) calcd for C₃₆H₂₇NO₃ 521.1991 (M⁺), obsd 521.1990. Anal. Calcd for C₃₆H₂₇NO₃: C, 82.90; H, 5.22; N, 2.69. Found: C, 83.04; H, 4.93; N, 2.63.

Tris(4-(4-(9H-carbazol-9-yl)phenoxy)phenyl)amine (CBD-G1). Elution: hexane/CH₂Cl₂ = 2/1; white solid; yield 59%; mp 176 °C, *T*_g = 129 °C, *T*_d = 571 °C. ¹H NMR (400 MHz, CD₂Cl₂): δ 8.15 (d, *J* = 8.0 Hz, 6H), 7.53 (d, *J* = 8.7 Hz, 6H), 7.44–7.38 (m, 12H), 7.30–7.25 (m, 12H), 7.21 (d, *J* = 8.9 Hz, 6H), 7.11 (d, *J* = 8.9 Hz, 6H). ¹³C NMR (100 MHz, CD₂Cl₂): δ 157.75, 152.48, 144.75, 141.73, 132.83, 129.17, 126.49, 125.92, 123.72, 121.14, 120.76, 120.38, 119.76, 110.21. HRMS (FAB) calcd for C₇₂H₄₈N₄O₃ 1016.3726 (M⁺), obsd 1016.3730. Anal. Calcd for C₇₂H₄₈N₄O₃: C, 85.02; H, 4.76; N, 5.51. Found: C, 85.19; H, 4.78; N, 5.32.

Tris(4-(4-(3,6-bis(4-(9H-carbazol-9-yl)phenoxy)-9H-carbazol-9-yl)phenoxy)phenyl)amine (CBD-G2). Elution: hexane/CH₂Cl₂ = 1/1; white solid; yield 31%; mp 231–233 °C, *T*_g = 198 °C, *T*_d = 617 °C. ¹H NMR (400 MHz, CD₂Cl₂): δ 8.13 (d, *J* = 7.8 Hz, 12H), 7.90 (d, *J* = 2.3 Hz, 6H), 7.58 (d, *J* = 2.1 Hz, 6H), 7.29–7.44 (m, 18H), 7.41–7.36 (m, 24H), 7.32–7.20 (m, 42H), 7.12 (d, *J* = 9.0 Hz, 6H). ¹³C NMR (200 MHz, CD₂Cl₂): δ 159.05, 157.96, 152.38, 150.33, 144.79, 141.74, 139.47, 132.61, 132.28, 129.10, 126.46, 125.94, 124.27, 123.66, 121.21, 120.73, 120.31, 119.85, 118.93, 112.36, 111.66, 110.20. MS (MALDI) calcd for ¹³CC₁₇₉H₁₁₄N₁₀O₉ 2559.9 (M⁺), obsd 2559.2. Anal. Calcd for C₁₈₀H₁₁₄N₁₀O₉: C, 84.42; H, 4.49; N, 5.47. Found: C, 84.64; H, 4.44; N, 5.25.

ASSOCIATED CONTENT

Supporting Information

Experimental section, UV–vis and PL spectra, NMR spectra, crystal structure, cif file, and several additional data. This material is available free of charge via the Internet at <http://pubs.acs.org>.

AUTHOR INFORMATION

Corresponding Author

*Phone +886-2-3366-1673, Fax +886-2-23636359, e-mail mkleung@ntu.edu.tw (M.-k.L.). Phone 886-2-3366-3894, Fax 886-2-2369-5208, e-mail chop@ntu.edu.tw (P.-T.C.).

ACKNOWLEDGMENTS

The present work was supported by the Ministry of Education and National Taiwan University, Academia Sinica Thematic Project, National Science Council of Taiwan (NSC-98-2119-M-002-006-MY3, NSC-98-2221-E-002-038-MY3, NSC-99-2218-E-155-003, NSC-99-2221-E-155-092, and NSC-99-2622-E-155-010-CC3).

REFERENCES

- (a) Astruc, D.; Boisselier, E.; Ornelas, C. *Chem. Rev.* **2010**, *110*, 1857. (b) Caminade, A.-M.; Majoral, J.-P. *Chem. Soc. Rev.* **2010**, *39*,

2034. (c) Franc, G.; Kakkar, A. K. *Chem. Soc. Rev.* **2010**, 39, 1536. (d) Newkome, G. R.; Shreiner, C. *Chem. Rev.* **2010**, 110, 6338.
- (2) (a) Li, Y.; Hou, T. *Curr. Med. Chem.* **2010**, 17, 4482. (b) Mintzer, M. A.; Grinstaff, M. W. *Chem. Soc. Rev.* **2011**, 40, 173. (c) Roeglin, L.; Lempens, E. H. M.; Meijer, E. W. *Angew. Chem., Int. Ed.* **2011**, 50, 102.
- (3) (a) Percec, V.; Glodde, M.; Bera, T. K.; Miura, Y.; Shiyonovskaya, I.; Singer, K. D.; Balagurusamy, V. S. K.; Heiney, P. A.; Schnell, I.; Rapp, A.; Spiess, H. W.; Hudson, S. D.; Duan, H. *Nature* **2002**, 419, 384. (b) Lo, S.-C.; Burn, P. L. *Chem. Rev.* **2007**, 107, 1097.
- (4) (a) Astruc, D.; Chardac, F. *Chem. Rev.* **2001**, 101, 2991. (b) Astruc, D. *Tetrahedron: Asymmetry* **2010**, 21, 1041. (c) Astruc, D.; Ornelas, C.; Diallo, A. K.; Ruiz, J. *Molecules* **2010**, 15, 4947.
- (5) (a) Taranekar, P.; Park, J.-Y.; Patton, D.; Fulghum, T.; Ramon, G. J.; Advincula, R. *Adv. Mater.* **2006**, 18, 2461. (b) Kaewtong, C.; Jiang, G.; Felipe, M. J.; Pulpoka, B.; Advincula, R. *ACS Nano* **2008**, 2, 1533. (c) Park, Y.; Taranekar, P.; Park, J. Y.; Baba, A.; Fulghum, T.; Ponnappati, R.; Advincula, R. C. *Adv. Funct. Mater.* **2008**, 18, 2071. (d) Jiang, G.; Ponnappati, R.; Pernites, R.; Grande, C. D.; Felipe, M. J.; Foster, E.; Advincula, R. *Langmuir* **2010**, 26, 17629. (e) Kaewtong, C.; Jiang, G.; Ponnappati, R.; Pulpoka, B.; Advincula, R. *Soft Matter* **2010**, 6, 5316.
- (6) (a) Loiseau, F.; Campagna, S.; Hameurlaine, A.; Dehaen, W. J. *Am. Chem. Soc.* **2005**, 127, 11352. (b) Li, S.; Zhu, W.; Xu, Z.; Pan, J.; Tian, H. *Tetrahedron* **2006**, 62, 5035. (c) Xu, T. H.; Lu, R.; Qiu, X. P.; Liu, X. L.; Xue, P. C.; Tan, C. H.; Bao, C. Y.; Zhao, Y. Y. *Eur. J. Org. Chem.* **2006**, 4014. (d) Kwon, T.-H.; Kim, M. K.; Kwon, J.; Shin, D.-Y.; Park, S. J.; Lee, C.-L.; Kim, J.-J.; Hong, J.-I. *Chem. Mater.* **2007**, 19, 3673. (e) Xu, T.; Lu, R.; Liu, X.; Zheng, X.; Qiu, X.; Zhao, Y. *Org. Lett.* **2007**, 9, 797. (f) Xu, T.; Lu, R.; Liu, X.; Chen, P.; Qiu, X.; Zhao, Y. *Eur. J. Org. Chem.* **2008**, 1065.
- (7) (a) Namdas, E. B.; Ruseckas, A.; Samuel, I. D. W.; Lo, S.-C.; Burn, P. L. *Appl. Phys. Lett.* **2005**, 86, 091104. (b) Lo, S.-C.; Namdas, E. B.; Shipley, C. P.; Markham, J. P. J.; Anthopolous, T. D.; Burn, P. L.; Samuel, I. D. W. *Org. Electron.* **2006**, 7, 85. (c) Ding, J.; Gao, J.; Cheng, Y.; Xie, Z.; Wang, L.; Ma, D.; Jing, X.; Wang, F. *Adv. Funct. Mater.* **2006**, 16, 575. (d) Jung, K. M.; Kim, K. H.; Jin, J.-I.; Cho, M. J.; Choi, D. H. *J. Polym. Sci., Part A: Polym. Chem.* **2008**, 46, 7517. (e) Ding, J.; Lü, J.; Cheng, Y.; Xie, Z.; Wang, L.; Jing, X.; Wang, F. *Adv. Funct. Mater.* **2008**, 18, 2754. (f) Knights, K. A.; Stevenson, S. G.; Shipley, C. P.; Lo, S.-C.; Olsen, S.; Harding, R. E.; Gambino, S.; Burn, P. L.; Samuel, I. D. W. *J. Mater. Chem.* **2008**, 18, 2121. (g) Liu, Q.-D.; Lu, J.; Ding, J.; Tao, Y. *Macromol. Chem. Phys.* **2008**, 209, 1931. (h) Ding, J.; Lü, J.; Cheng, Y.; Xie, Z.; Wang, L.; Jing, X.; Wang, F. *J. Organomet. Chem.* **2009**, 694, 2700. (i) Ding, J.; Wang, B.; Yue, Z.; Yao, B.; Xie, Z.; Cheng, Y.; Wang, L.; Jing, X.; Wang, F. *Angew. Chem., Int. Ed.* **2009**, 48, 6664. (j) Iguchi, N.; Pu, Y.-J.; Nakayama, K.-i.; Yokoyama, M.; Kido, J. *Org. Electron.* **2009**, 10, 465. (k) Jung, K. M.; Lee, T. W.; Kim, K. H.; Cho, M. J.; Jin, J.-I.; Choi, D. H. *Chem. Lett.* **2009**, 38, 314. (l) Kim, H.-J.; Kim, M.-J.; Park, H.-D.; Lee, J.-H.; Noh, S. T.; Lee, Y.-C.; Kim, J.-J. *Synth. Met.* **2010**, 160, 1994.
- (8) (a) Pan, J.; Zhu, W.; Li, S.; Zeng, W.; Cao, Y.; Tian, H. *Polymer* **2005**, 46, 7658. (b) Lu, J.; Xia, P. F.; Lo, P. K.; Tao, Y.; Wong, M. S. *Chem. Mater.* **2006**, 18, 6194. (c) Liu, Q.-D.; Lu, J.; Ding, J.; Day, M.; Tao, Y.; Barrios, P.; Stupak, J.; Chan, K.; Li, J.; Chi, Y. *Adv. Funct. Mater.* **2007**, 17, 1028. (d) Adhikari, R. M.; Duan, L.; Hou, L.; Qiu, Y.; Neckers, D. C.; Shah, B. K. *Chem. Mater.* **2009**, 21, 4638. (e) Zhang, H.; Wang, S.; Li, Y.; Zhang, B.; Du, C.; Wan, X.; Chen, Y. *Tetrahedron* **2009**, 65, 4455. (f) Zhao, Z.; Li, J.-H.; Chen, X.; Wang, X.; Lu, P.; Yang, Y. *J. Org. Chem.* **2009**, 74, 383. (g) Jin, H.; Xu, Y.; Shen, Z.; Zou, D.; Wang, D.; Zhang, W.; Fan, X.; Zhou, Q. *Macromolecules* **2010**, 43, 8468. (h) Zhao, Z.-H.; Jin, H.; Zhang, Y.-X.; Shen, Z.; Zou, D.-C.; Fan, X.-H. *Macromolecules* **2011**, 44, 1405.
- (9) (a) Du, P.; Zhu, W.-H.; Xie, Y.-Q.; Zhao, F.; Ku, C.-F.; Cao, Y.; Chang, C.-P.; Tian, H. *Macromolecules* **2004**, 37, 4387. (b) Kimoto, A.; Cho, J.-S.; Higuchi, M.; Yamamoto, K. *Macromol. Symp.* **2004**, 209, 51. (c) Kimoto, A.; Cho, J.-S.; Ito, K.; Aoki, D.; Miyake, T.; Yamamoto, K. *Macromol. Rapid Commun.* **2005**, 26, 597. (d) Albrecht, K.; Yamamoto, K. *J. Photopolym. Sci. Technol.* **2006**, 19, 175. (e) Promarak, V.; Ichikawa, M.; Meunmart, D.; Sudyoasuk, T.; Saengsuwan, S.; Keawin, T. *Tetrahedron Lett.* **2006**, 47, 8949. (f) Promarak, V.; Ichikawa, M.; Sudyoasuk, T.; Saengsuwan, S.; Jungstittiwong, S.; Keawin, T. *Synth. Met.* **2007**, 157, 17. (g) Albrecht, K.; Kasai, Y.; Kimoto, A.; Yamamoto, K. *Macromolecules* **2008**, 41, 3793. (h) Promarak, V.; Ichikawa, M.; Sudyoasuk, T.; Saengsuwan, S.; Jungstittiwong, S.; Keawin, T. *Thin Solid Films* **2008**, 516, 2881. (i) Usluer, O.; Demic, S.; Egbe, D. A. M.; Birkner, E.; Tozlu, C.; Pivrikas, A.; Ramil, A. M.; Sariciftci, N. S. *Adv. Funct. Mater.* **2010**, 20, 4152.
- (10) (a) Tsai, M.-H.; Hong, Y.-H.; Chang, C.-H.; Su, H.-C.; Wu, C.-C.; Matoliukstyte, A.; Simokaitiene, J.; Grigalevicius, S.; Grazulevicius, J. V.; Hsu, C.-P. *Adv. Mater.* **2007**, 19, 862. (b) Ding, J.; Zhang, B.; Lü, J.; Xie, Z.; Wang, L.; Jing, X.; Wang, F. *Adv. Mater.* **2009**, 21, 4983. (c) Yang, J.; Ye, T.; Zhang, Q.; Ma, D. *Macromol. Chem. Phys.* **2010**, 211, 1969. (d) Soh, M. S.; Santamaria, S. A. G.; Williams, E. L.; Perez-Morales, M.; Bolink, H. J.; Sellinger, A. J. *Polym. Sci., Part B: Polym. Phys.* **2011**, 49, 531. (e) Yang, J.; Ye, T.; Ma, D.; Zhang, Q. *Synth. Met.* **2011**, 161, 330.
- (11) (a) Hameurlaine, A.; Dehaen, W. *Tetrahedron Lett.* **2003**, 44, 957. (b) Kimoto, A.; Cho, J.-S.; Higuchi, M.; Yamamoto, K. *Chem. Lett.* **2003**, 32, 674. (c) McClenaghan, N. D.; Passalacqua, R.; Loiseau, F.; Campagna, S.; Verheyde, B.; Hameurlaine, A.; Dehaen, W. *J. Am. Chem. Soc.* **2003**, 125, 5356.
- (12) (a) Albrecht, K.; Yamamoto, K. *J. Am. Chem. Soc.* **2009**, 131, 2244. (b) Selby, T. D.; Blackstock, S. C. *J. Am. Chem. Soc.* **1998**, 120, 12155. (c) Xu, Z.; Moore, J. S. *Acta Polym.* **1994**, 45, 83. (d) Tada, T.; Nozaki, D.; Kondo, M.; Yoshizawa, K. *J. Phys. Chem. B* **2003**, 107, 14204. (e) Wang, J.; Yan, J.; Tang, Z.; Xiao, Q.; Ma, Y.; Pei, J. *J. Am. Chem. Soc.* **2008**, 130, 9952. (f) Bronk, K.; Thayumanavan, S. *J. Org. Chem.* **2003**, 68, 5559. (g) Holzapfel, M.; Lambert, C. *J. Phys. Chem. C* **2008**, 112, 1227. (h) Lambert, C.; Schelter, J.; Fiebig, T.; Mank, D.; Trifonov, A. *J. Am. Chem. Soc.* **2005**, 127, 10600.
- (13) (a) Lin, K.-R.; Chien, Y.-H. C.; Chang, C.-C.; Hsieh, K.-H.; Leung, M.-k. *Macromolecules* **2008**, 41, 4158. (b) Chiang, C. C.; Chen, H.-C.; Lee, C.-s.; Leung, M.-k.; Lin, K.-R.; Hsieh, K.-H. *Chem. Mater.* **2008**, 20, 540. (c) Leung, M.-k.; Chang, C.-C.; Wu, M.-H.; Chuang, K.-H.; Lee, J.-H.; Shieh, S.-J.; Lin, S.-C.; Chiu, C.-F. *Org. Lett.* **2006**, 8, 2623. (d) Chien, C.-H.; Leung, M.-k.; Su, J.-K.; Li, G.-H.; Liu, Y.-H.; Wang, Y. *J. Org. Chem.* **2004**, 69, 1866. (e) Leung, M.-k.; Chou, M.-Y.; Su, Y. O.; Chiang, C. L.; Chen, H.-L.; Yang, C. F.; Yang, C.-C.; Lin, C.-C.; Chen, H.-T. *Org. Lett.* **2003**, 5, 839.
- (14) Wong, K.-T.; Lin, Y.-H.; Wu, H.-H.; Fungo, F. *Org. Lett.* **2007**, 9, 4531.
- (15) (a) Mo, Y.; Bai, F.; Wang, Z. *J. Photochem. Photobiol. A* **1995**, 92, 25. (b) Zaion, S. M.; Hashim, R.; Taylor, A. G.; Phillips, D. *J. Mol. Struct.: THEOCHEM* **1997**, 401, 287. (c) Bonesi, S. M.; Erra-Balsells, R. *J. Lumin.* **2001**, 93, 51. (d) De, A. K.; Ganguly, T. *J. Lumin.* **2001**, 92, 255.
- (16) (a) Ambrose, J. F.; Carpenter, L. L.; Nelson, R. F. *J. Electrochem. Soc.* **1975**, 122, 876. (b) Lamm, V. W.; Pragst, F.; Jugelt, W. *J. Prakt. Chem.* **1975**, 317, 995. (c) Desbene-Monvernay, A.; Lacaze, P. C.; Dubois, J. E. *J. Electroanal. Chem.* **1981**, 129, 229.
- (17) (a) Zhu, Z.; Moore, J. S. *Macromolecules* **2000**, 33, 801. (b) Zhu, Z.; Moore, J. S. *J. Org. Chem.* **2000**, 65, 116. (c) Feng, G.-L.; Ji, S.-J.; Lai, W.-Y.; Huang, W. *Synlett* **2006**, 2841.
- (18) (a) Monnier, F.; Taillefer, M. *Angew. Chem., Int. Ed.* **2008**, 47, 3096. (b) Monnier, F.; Taillefer, M. *Angew. Chem., Int. Ed.* **2009**, 48, 6954. (c) Das, P.; Sharma, D.; Kumar, M.; Singh, B. *Curr. Org. Chem.* **2010**, 14, 754. (d) Niu, J.; Zhou, H.; Li, Z.; Xu, J.; Hu, S. *J. Org. Chem.* **2008**, 73, 7814. (e) Xia, N.; Taillefer, M. *Chem.—Eur. J.* **2008**, 14, 6037. (f) Jammi, S.; Sakthivel, S.; Rout, L.; Mukherjee, T.; Mandal, S.; Mitra, R.; Saha, P.; Punniyamurthy, T. *J. Org. Chem.* **2009**, 74, 1971. (g) Larsson, P.-F.; Correa, A.; Carril, M.; Norrby, P.-O.; Bolm, C. *Angew. Chem., Int. Ed.* **2009**, 48, 5691. (h) Naidu, A. B.; Jaseer, E. A.; Sekar, G. *J. Org. Chem.* **2009**, 74, 3675. (i) Sreedhar, B.; Arundhati, R.; Reddy, P. L.; Kantam, M. L. *J. Org. Chem.* **2009**, 74, 7951. (j) Zhang, Q.; Wang, D.; Wang, X.; Ding, K. *J. Org. Chem.* **2009**, 74, 7187.
- (19) (a) Ma, D.; Cai, Q. *Org. Lett.* **2003**, 5, 3799. (b) Chen, Y.-J.; Chen, H.-H. *Org. Lett.* **2006**, 8, 5609. (c) Lv, X.; Bao, W. *J. Org. Chem.*

2007, 72, 3863. (d) Jogdand, N. R.; Shingate, B. B.; Shingare, M. S. *Tetrahedron Lett.* **2009**, 50, 4019.

(20) (a) Loupy, A. *Microwaves in Organic Synthesis*, 2nd ed.; Wiley-VCH: Weinheim, 2006. (b) Kappe, C. O.; Dallinger, D.; Murphree, S. S. *Practical Microwave Synthesis for Organic Chemists*; Wiley-VCH: Weinheim, 2009. (c) He, H.; Wu, Y.-J. *Tetrahedron Lett.* **2003**, 44, 3445. (d) Zhu, X.-H.; Chen, G.; Ma, Y.; Song, H.-C.; Xu, Z.-L.; Wan, Y.-Q. *Chin. J. Chem.* **2007**, 25, 546.

(21) (a) Lamba, M. S.; Makrandi, J. K. *J. Chem. Res.* **2007**, 585. (b) Mason, J. J.; Janosik, T.; Bergman, J. *Synthesis* **2009**, 3642.

(22) Cao, X.; Wen, Y.; Guo, Y.; Yu, G.; Liu, Y.; Yang, L.-M. *Dyes Pigm.* **2010**, 84, 203.

(23) Sarkar, A.; Chakravorti, S. *J. Lumin.* **1998**, 78, 205.

(24) (a) Rusalov, M.; Druzhinin, S.; Uzhinov, B. *J. Fluoresc.* **2004**, 14, 193. (b) Williams, A. T. R.; Winfield, S. A.; Miller, J. N. *Analyst* **1983**, 108, 1067. (c) For standard procedure announced by Jobin-Yvon Ltd, see "A Guide to Recording Fluorescence Quantum Yields" at <http://www.jobinyvon.com/usadivisions/Fluorescence/applications/quantumyieldstrad.pdf>. (d) For the procedure and setup for the front face detection announced by Jobin-Yvon Ltd, see http://www.horiba.com/fileadmin/uploads/Scientific/Documents/Fluorescence/Small_Samples_FL-6.pdf.

(25) Berlman, I. B. *Handbook of Fluorescence Spectra of Aromatic Molecules*, 2nd ed.; Academic Press: New York, 1971.

(26) (a) Rettig, W.; Zander, M. *Chem. Phys. Lett.* **1982**, 87, 229. (b) Galievsky, V. A.; Druzhinin, S. I.; Demeter, A.; Mayer, P.; Kovalenko, S. A.; Senyushkina, T. A.; Zachariasse, K. A. *J. Phys. Chem. A* **2010**, 114, 12622.

(27) (a) Lakowicz, J. R. *Principles of Fluorescence Spectroscopy*, 2nd ed.; Springer: New York, 1999. (b) Chou, P. T.; Chen, Y. C.; Yu, W. S.; Chou, Y. H.; Wei, C. Y.; Cheng, Y. M. *J. Phys. Chem. A* **2001**, 105, 1731. (c) Turro, N. J.; Ramamurthy, V.; Scaiano, J. C. *Modern Molecular Photochemistry of Organic Molecules*; University Science: Sausalito, CA, 2005. (d) Turro, N. J. *Modern Molecular Photochemistry*; University Sciences: Sausalito, CA, 1991; p 170. (e) McGlynn, S. P.; Azumi, T.; Kinoshita, M. *Molecular Spectroscopy of the Triplet State*; Prentice-Hall: Englewood Cliffs, NJ, 1969.

(28) (a) Marsal, P.; Avilov, I.; da Silva Filho, D. A.; Brédas, J. L.; Beljonne, D. *Chem. Phys. Lett.* **2004**, 392, 521. (b) Shih, P.-I.; Chiang, C.-L.; Dixit, A. K.; Chen, C.-K.; Yuan, M.-C.; Lee, R.-Y.; Chen, C.-T.; Diau, E. W.-G.; Shu, C.-F. *Org. Lett.* **2006**, 8, 2799. (c) Sapochak, L. S.; Padmaperuma, A. B.; Cai, X.; Male, J. L.; Burrows, P. E. *J. Phys. Chem. C* **2008**, 112, 7989. (d) Cosimbescu, L.; Koech, P.; Polikarpov, E.; Swensen, J.; Von Ruden, A.; Rainbolt, J. E.; Padmaperuma, A. *Dig. Tech. Pap.—Soc. Inf. Disp. Int. Symp.* **2010**, 41, 1887.

(29) Bard, A. J.; Faulkner, L. R. *Electrochemical Methods*, 2nd ed.; Wiley: New York, 2001.

(30) (a) Heinze, J.; Hinkelmann, K.; Dietrich, M.; Mortensen, J. *Ber. Bunsen-Ges. Phys. Chem.* **1985**, 89, 1225. (b) Oyama, M.; Matsui, J. *Bull. Chem. Soc. Jpn.* **2004**, 77, 953.

(31) (a) Wu, X.; Davis, A. P.; Lambert, P. C.; Kraig Steffen, L.; Toy, O.; Fry, A. J. *Tetrahedron* **2009**, 65, 2408. (b) Amthor, S.; Noller, B.; Lambert, C. *Chem. Phys.* **2005**, 316, 141. (c) Sreenath, K.; Thomas, T. G.; Gopidas, K. R. *Org. Lett.* **2011**, 13, 1134.

(32) (a) Higuchi, M.; Shiki, S.; Ariga, K.; Yamamoto, K. *J. Am. Chem. Soc.* **2001**, 123, 4414. (b) Yamamoto, K.; Higuchi, M.; Shiki, S.; Tsuruta, M.; Chiba, H. *Nature* **2002**, 415, 509. (c) Yamamoto, K.; Imaoka, T. *Bull. Chem. Soc. Jpn.* **2006**, 79, 511.

(33) Brunner, K.; van Dijken, A.; Börner, H.; Bastiaansen, J. J. A. M.; Kiggen, N. M. M.; Langeveld, B. M. W. *J. Am. Chem. Soc.* **2004**, 126, 6035.

(34) (a) Holmes, R. J.; Forrest, S. R.; Tung, Y.-J.; Kwong, R. C.; Brown, J. J.; Garon, S.; Thompson, M. E. *Appl. Phys. Lett.* **2003**, 82, 2422. (b) Sudhakar, M.; Djurovich, P. I.; Hogen-Esch, T. E.; Thompson, M. E. *J. Am. Chem. Soc.* **2003**, 125, 7796.

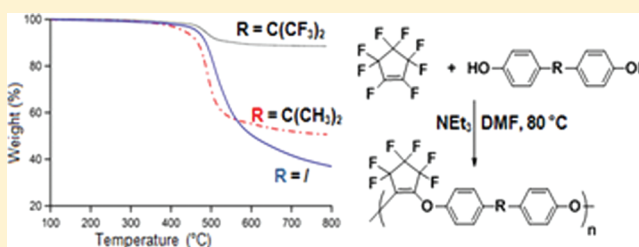
(35) (a) Fan, C.; Chen, Y.; Jiang, Z.; Yang, C.; Zhong, C.; Qin, J.; Ma, D. *J. Mater. Chem.* **2010**, 20, 3232. (b) Ge, Z.; Hayakawa, T.; Ando, S.; Ueda, M.; Akiike, T.; Miyamoto, H.; Kajita, T.; Kakimoto, M.-a. *Org. Lett.* **2008**, 10, 421. (c) Ge, Z.; Hayakawa, T.; Ando, S.;

Ueda, M.; Akiike, T.; Miyamoto, H.; Kajita, T.; Kakimoto, M.-a. *Chem. Mater.* **2008**, 20, 2532. (d) Ge, Z.; Hayakawa, T.; Ando, S.; Ueda, M.; Akiike, T.; Miyamoto, H.; Kajita, T.; Kakimoto, M.-a. *Adv. Funct. Mater.* **2008**, 18, 584.

Perfluorocyclopentenyl (PFCP) Aryl Ether Polymers via Polycondensation of Octafluorocyclopentene with Bisphenols

Jean-Marc Cracowski,[†] Babloo Sharma,[‡] Dakarai K. Brown,[†] Kenneth Christensen,[†] Benjamin R. Lund,[‡] and Dennis W. Smith, Jr.*[‡][†]Department of Chemistry, School of Material Science and Engineering and Center for Optical Materials Science and Engineering Technologies (COMSET), Clemson University, Clemson, South Carolina 29634, United States[‡]Department of Chemistry and The Alan G. MacDiarmid NanoTech Institute, The University of Texas at Dallas, Richardson, Texas 75080, United States

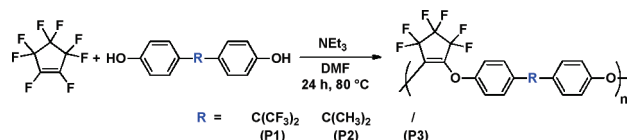
ABSTRACT: A unique class of aromatic ether polymers containing perfluorocyclopentenyl (PFCP) enchainment was prepared from the simple step growth polycondensation of commercial bisphenols and octafluorocyclopentene (OFCP) in the presence of triethylamine. Model studies indicate that the second addition/elimination on OFCP is fast and polycondensation results in linear homopolymers and copolymers without side products. The synthesis of bis(heptafluorocyclopentenyl) aryl ether monomers and their condensation with bisphenols further led to PFCP copolymers with alternating structures. This new class of semifluorinated polymers exhibit surprisingly high crystallinity in some cases and excellent thermal stability.



INTRODUCTION

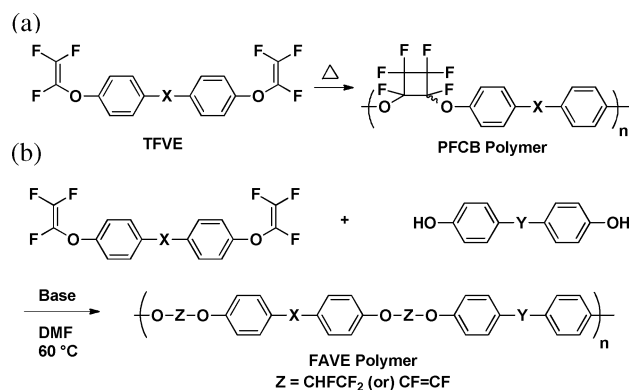
Fluoropolymers exhibit outstanding thermal stability, chemical resistance, unique surface properties, low refractive index, and low dielectric constant.^{1–5} Despite their general limited solution and melt processability, emerging technologies continue to drive the incorporation of fluorine into new polymeric systems due to their unique combination of properties. Here we report the polycondensation of commercial octafluorocyclopentene (OFCP) and commercial bisphenols to give a new class of semifluorinated aromatic ether polymers (Scheme 1).

Scheme 1. Perfluorocyclopentenyl (PFCP) Aryl Ether Polymer Synthesis



Although, by far, the largest volume of fluoropolymers are accessed by chain growth polymerization of fluorine-containing olefins, step growth mechanisms have also been established. In particular, Babb and co-workers⁶ at Dow Chemical introduced a new class of semifluorinated perfluorocyclobutyl (PFCB) aryl ether polymers prepared from thermal cyclopolymerization of aromatic trifluorovinyl ether (TFVE) monomers (Scheme 2a). These PFCB polymers, investigated as potential dielectric resins for integrated circuits at Dow and later for next generation optical applications by others,⁵ are uniquely amorphous due to their stereorandomness and exhibit excellent

Scheme 2. (a) Synthesis of PFCB Polymer and (b) FAVE Polymer from TFVE Monomers



processability, high thermal stability, and tunable optical properties.^{5,8}

More recently, a new class of semifluorinated polymer was developed from the nucleophilic addition of bisphenols and aromatic TFVE monomers to give fluorinated arylene vinylene ether (FAVE) polymers (Scheme 2b).^{9–11} The new FAVE polymers exhibit similar advantageous properties to PFCB while offering more cost-effective functional diversity since both aromatic TFVE monomers and functional bisphenols are commercially available or easily prepared. Further, FAVE

Received: November 7, 2011

Revised: December 1, 2011

Published: December 22, 2011



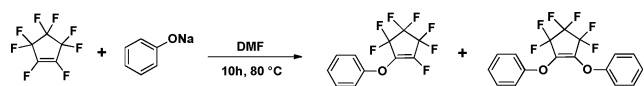
polymers containing fluorinated vinyl groups are found to be potentially reactive and thermally cross-linkable.

Octafluorocyclopentene (OFCP) is a readily available perfluorocyclic olefin with unique chemistry. Many studies have been reported on the reaction of OFCP with nucleophiles, such as phenoxides,^{12–15} arenethiolates,¹⁶ amines,^{17–19} enolates, phosphonium ylides,²⁰ and organolithium reagents.^{20–22} Many other examples include OFCP derivatives for photochromic applications.^{23–25} There are very few examples of polymers of perfluorocyclopentene by traditional chain growth mechanisms. This perfluorocyclic olefin does not homopolymerize under radical conditions,²⁶ and radical copolymerizations with styrene and vinyl acetate lead to copolymers with a very low molar ratio of perfluorocyclopentene.²⁷ Nevertheless, copolymerization with electron-rich monomers like vinyl ethers leads to alternating copolymers.^{26,27} Step growth polymerization of OFCP with bis(silyl) ethers was reported, but the resulting polymers exhibited low molecular weight.²⁸ To our knowledge, the polycondensation of bisphenols with perfluorocycloolefins has not been previously reported.

RESULTS AND DISCUSSION

Prior to polycondensation, a model reaction was performed using OFCP and sodium phenoxide (Scheme 3). Interestingly,

Scheme 3. Model Reaction between OFCP and Sodium Phenoxide



75% of the clean product mixture was the bis adduct as determined by ¹⁹F NMR spectroscopy, most likely due to increased solubility of the monoadduct (Figure 1).

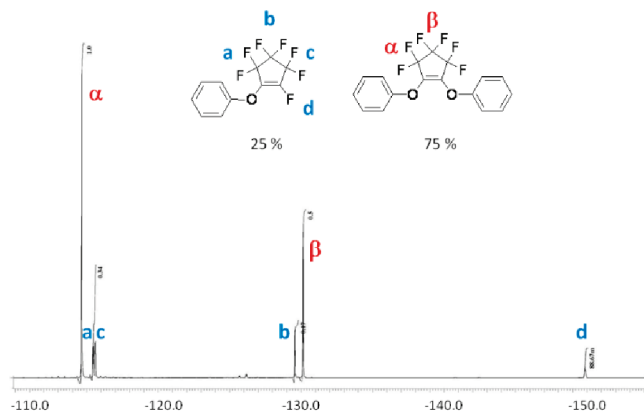


Figure 1. ¹⁹F NMR spectrum of the model reaction product mixture.

Polycondensation was attempted using the sodium salt of bis(hydroxyphenyl)hexafluoroisopropylidene (Bisphenol AF) and OFCP in DMF at 80 °C for 10 h. Low-molecular-weight oligomers were obtained. Thus, an alternative method was explored using triethylamine as the base (Scheme 1) to afford perfluorocyclopentenyl (PFCP) aryl ether homopolymer **P1** of number-average molecular weight and PDI of 9100 g mol⁻¹ and 2.5, respectively (Table 1).

Moreover, homopolymer **P1** was determined to be hydroxytelechelic by the absence of ¹⁹F NMR signals centered at -149 ppm representative of the fluoroolefin (Figure 2b).

Table 1. PFCP Polymers Molecular Weight, Polydispersity Index (PDI), Thermal Properties, and Yield of Polymerization

PFCP	<i>M_n</i>	<i>M_w</i>	PDI ^a	<i>T_g</i> (°C) ^b	<i>T_{15%}</i> (°C) ^c	yield (wt %)
homopolymer P1	9100	22900	2.5	124	483	70
homopolymer P2	9600	11100	1.1	89	432	54
homopolymer P3	15450	29800	1.9	105	460	90
P3-co-P1 ^d	5900	9300	1.5	94	325	74
copolymer (M1-alt-BP)	8400	14500	1.7	98	310	69
copolymer (M2-alt-6F)	2000	3000	1.5	68	224	51

^aGPC in THF using polystyrene as standard after precipitation in methanol. ^bDSC (heating rate 10 °C/min) in a nitrogen atmosphere. ^cTGA (heating rate 10 °C/min) in a nitrogen atmosphere. ^d0.49/0.51 molar ratio of monomer 1/2 in copolymer as determined by ¹⁹F NMR spectroscopy.

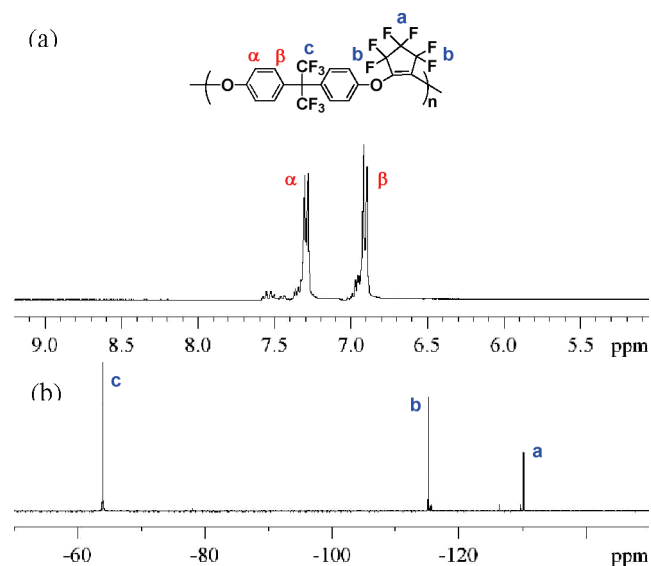


Figure 2. (a) ¹H NMR and (b) ¹⁹F NMR of PFCP aryl ether homopolymer **P1**.

In the ¹H NMR spectrum (Figure 2a), there are two signals representing aromatic (6.9 and 7.3 ppm) protons, as expected. These signals (dd, *J* = 8.8 Hz) indicate a symmetric environment around both ether linkages of the PFCP rings and support an addition–elimination reaction which leaves the double bond of the PFCP ring intact. Further, ¹⁹F NMR shows three clean signals, corresponding to three unique fluorine atoms in symmetrical environments, as expected (Figure 2b). A PFCP end-capped polymer was also prepared by the addition of an excess of OFCP at the end of the reaction.

PFCP aryl ether homopolymer **P2** was prepared from Bisphenol A via the same methodology as **P1** (Scheme 1). For homopolymer **P2**, the number-average molecular weight and PDI were 9600 and 1.15 after 24 h reaction time (Table 1). Homopolymer **P2** was characterized by ¹H NMR and ¹⁹F NMR spectroscopy and, as before, exhibited a clean addition–elimination polycondensation (Figure 3). ¹H NMR shows symmetric aromatic groups and a clean singlet for the methyl protons (1.57 ppm). ¹⁹F NMR shows only two resonances corresponding to the PFCP ring substituted in a symmetrical fashion.

PFCP aryl ether homopolymer **P3** was prepared from biphenol under similar conditions (Scheme 1). **P3** shows a

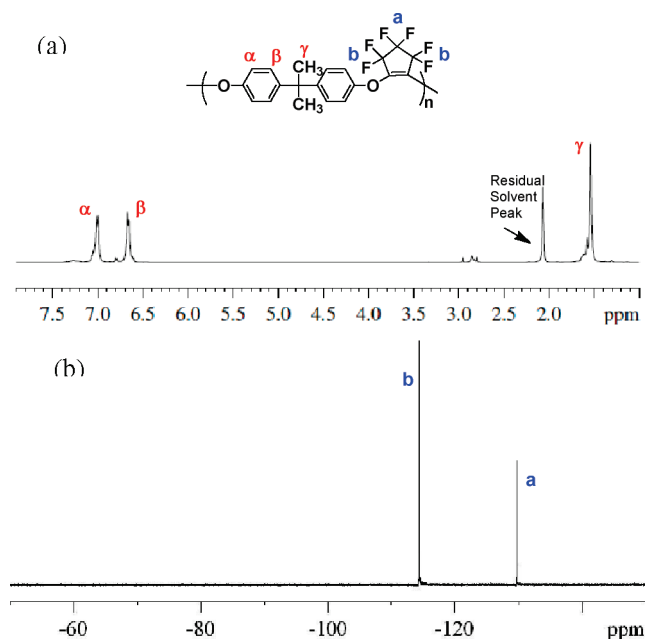


Figure 3. (a) ^1H NMR and (b) ^{19}F NMR of PFCP aryl ether homopolymer **P2**.

higher number-average molecular weight of 15 450, with a PDI of 1.9 (Table 1), relative to the above-mentioned homopolymers (**P1** and **P2**), with clean and well-integrated signals in ^1H NMR and ^{19}F NMR spectroscopy (Figure 4).

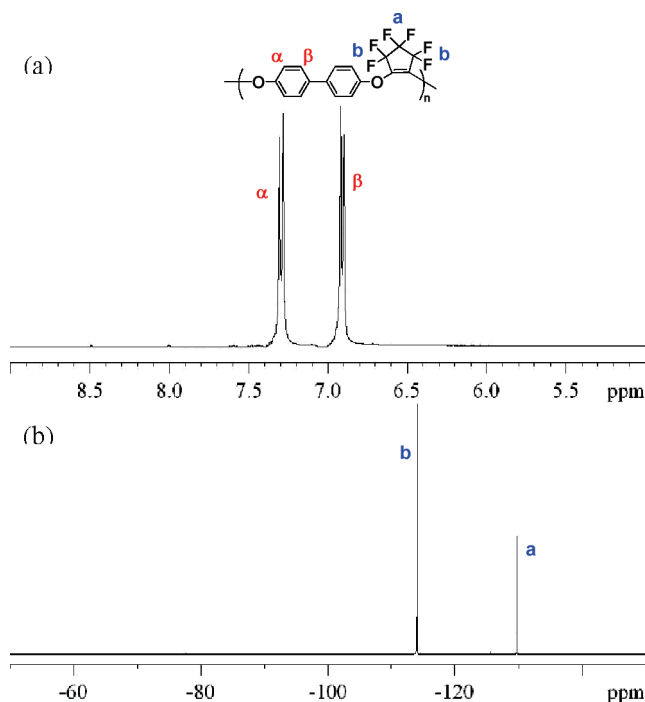


Figure 4. ^1H NMR and ^{19}F NMR of PFCP aryl ether homopolymer **P3**.

^1H and ^{19}F NMR spectra show no evidence of chiral carbon atoms within the cyclopentene ring as would be expected in the case of an addition rather than an addition–elimination reaction. PFCP homopolymers (**P1**, **P2**, and **P3**) show absorption in the ultraviolet spectrum (λ_{max} 210 nm for **P1**, **P2** and 260 nm for **P3**) with no corresponding fluorescence.

Thermal analysis of these polymers shows unexpected properties (Table 1). **P1** exhibits a glass transition temperature (T_g) of 124 $^\circ\text{C}$, as determined by DSC, and a polymorphic crystallization and melting at ca. 218 and 250 $^\circ\text{C}$, respectively (Figure 5a). The decomposition temperature (T_d) at 5% weight

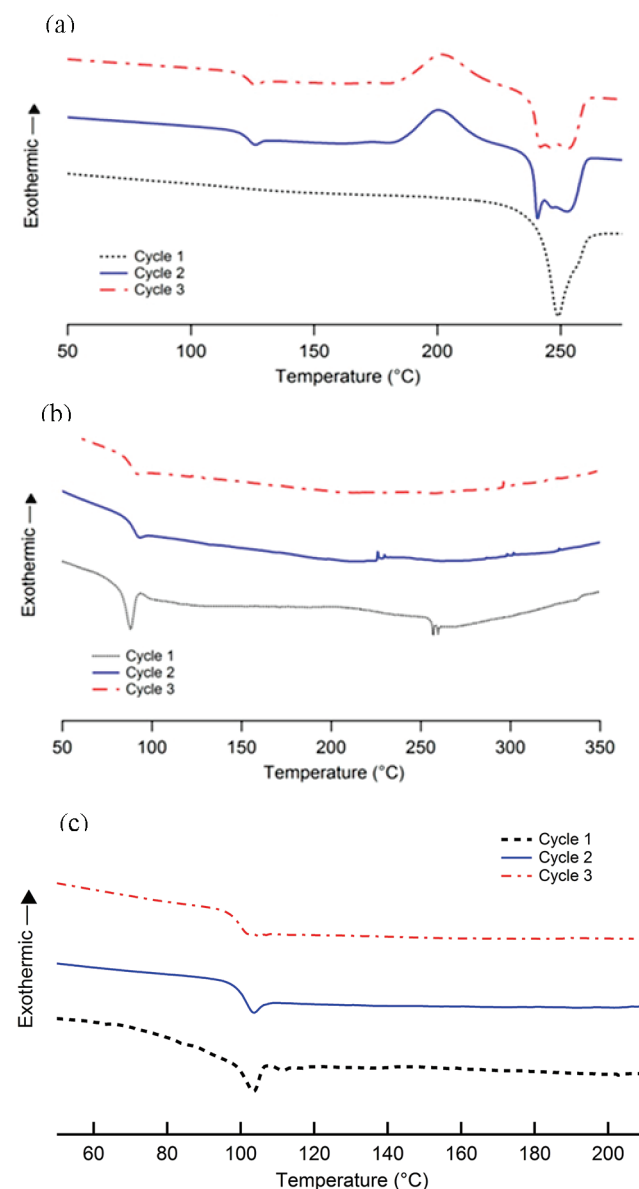


Figure 5. DSC thermograms of PFCP aryl ether homopolymer (a) **P1**, (b) **P2**, and (c) **P3**.

loss determined by thermogravimetric analysis (TGA) under N_2 was 483 $^\circ\text{C}$ for **P1** with a number-average molecular weight of 9100 (Figure 6). Remarkably, homopolymer **P1** exhibited an exceptional char yield of greater than 85% up to 800 $^\circ\text{C}$.

DSC thermograms for **P2** exhibited a glass transition temperature of 89 $^\circ\text{C}$. However, unlike **P1**, PFCP polymer **P2** does not show crystallinity under these conditions (Figure 5b), presumably due to the decreased fluorine content as analogously observed for the 6F-PFCB polymer.²⁹ TGA analysis under a N_2 atmosphere shows that the decomposition temperature (T_d) at 5% weight loss exceeds 430 $^\circ\text{C}$ (Figure 6).

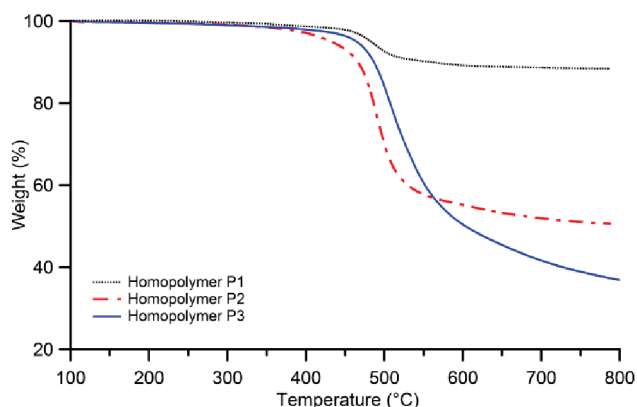
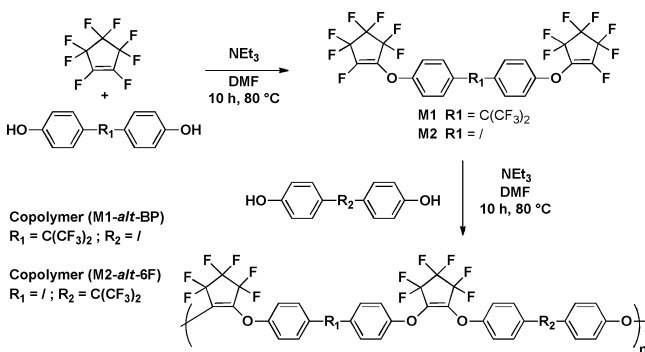


Figure 6. TGA thermograms of PFCP aryl ether homopolymers **P1**, **P2**, and **P3**.

PFCP aryl ether homopolymer **P3** exhibited an endothermic transition determined by DSC of 105 °C (Figure 5c). Like **P2** and unlike **P1**, **P3** does not show crystallinity or melting behavior under these conditions (Figure 5c). This higher molecular weight homopolymer **P3** gave decomposition temperature of 460 °C (T_d at 5% weight loss, Figure 6).

A random PFCP copolymer was also prepared in one step with bisphenols and OFCP (Table 1). Reactions of variable bisphenols with a slight excess of OFCP led to novel bis-(heptafluorocyclopentenyl) aryl ether monomers (**M1**, **M2**) and their step growth polymerization with other bisphenols afforded PFCP copolymers with alternating arylene ether structures (Scheme 4).

Scheme 4. Bis-(heptafluorocyclopentenyl) Aryl Ether Monomers Synthesis and Polymerization



As seen earlier, biphenol gave higher molecular weight than Bisphenol AF during polymerization with OFCP (**P3** vs **P1**). This may be due to the electron-withdrawing effect of the CF_3 groups decreasing its nucleophilicity compared to biphenol. Likewise, alternating copolymers of **6F** containing monomer **M1** gave the highest molecular weight for identical copolymer structures of different monomers (Table 1). This method demonstrates a modular approach to alternating copolymers from monomers of variable reactivity. Further, because of its higher molecular weight, copolymer **M1-alt-BP** exhibits more robust thermal properties than copolymer **M2-alt-6F**.

CONCLUSION

We have developed a step growth polymerization of bisphenols with OFCP toward synthesis of a new class of perfluorocyclopentenyl (PFCP) aryl ether polymers from commercial

feedstocks. PFCP polymers can be easily modified and functionalized by using bisphenols with different spacer functional groups. PFCP polymers exhibited very interesting thermal properties with variable T_g depending upon the chosen bisphenol. These polymers were obtained in good yields and show high thermal stabilities under N_2 with T_d at 5% weight loss ranging from 432 to 483 °C for homopolymers and 224 to 325 °C for copolymers. This new family of semifluorinated aryl ether polymers can easily have phenolic or perfluorocyclopentenyl terminal groups depending on the stoichiometry of the reactants. Further, PFCP polymers contain main chain vinyl ether groups for postpolymerization modification and potential cross-linking.

EXPERIMENTAL SECTION

Chemical Reagents. Octafluorocyclopentene (99%) was purchased from Synquest Laboratories and used as received. Bis-(hydroxyphenyl)hexafluoroisopropylidene (Bisphenol AF) and 4,4'-biphenol were donated by Tetramer Technologies, L.L.C., Pendleton, SC. Deuterated solvents were purchased from Mallinckrodt Chemicals Inc. All other chemicals and solvents (analytical grade) were purchased from Sigma-Aldrich and used as received unless otherwise stated.

Instrumentation. **M1** and **M2** and copolymers were characterized on a JEOL ECX-300 MHz NMR spectrometer via ^1H , ^{19}F , and proton-fluorine decoupled ^{13}C spectroscopy. **P1**, **P2**, and **P3** were characterized on a Bruker 400 MHz NMR spectrometer via ^1H , proton decoupled ^{19}F , and proton decoupled ^{13}C spectroscopy. Chemical shifts were measured in ppm (δ) with reference to internal tetramethylsilane (0 ppm), deuterated chloroform (77 ppm)/deuterated tetrahydrofuran (25.3 ppm)/deuterated acetone (29.8 ppm), and trichlorofluoromethane (0 ppm) for ^1H , ^{13}C , and ^{19}F NMR, respectively. For coupled spectra, values are reported from the center of the pattern. Attenuated total reflectance Fourier transform infrared (ATR-FTIR) analyses of neat samples were performed on a Thermo-Nicolet Magna 550 FTIR spectrophotometer with a high endurance diamond ATR attachment. Ultraviolet–visible absorption and fluorescence spectroscopy were measured in THF on an Agilent 8453 UV–vis spectroscopy system and Perkin-Elmer LS 50 B luminescence spectrometer, respectively. Differential scanning calorimetry (DSC) analysis was performed on a Mettler Toledo DSC 1 system in nitrogen at a heating rate of 10 °C/min. The glass transition temperature (T_g) was obtained from a second heating cycle using Star E version 10.0 software suite. Thermal gravimetric analysis (TGA) was performed on a Mettler-Toledo TGA/DSC 1 LF instrument in nitrogen at a heating rate of 10 °C/min up to 800 °C. Molecular weights for polymers **P1**, **P2** and **P3** were measured by size exclusion chromatography (SEC) analysis on a Viscotek VE 3580 system equipped with a Viscogel column (GMHHR-M), connected to a refractive index (RI) detector. GPC solvent/sample module (GPCmax) was used with HPLC grade THF as the eluent and calibration was based on polystyrene standards. For copolymers, gel permeation chromatography (GPC) data were collected in THF from a Waters 2690 Alliance System with photodiode array detection. GPC samples were eluted in series through Polymer Laboratories PLGel 5 mm Mixed-D and Mixed-E columns at 35 °C. Molecular weights were obtained using polystyrene as a standard (Polymer Laboratories Easical PS-2).

Synthesis of PFCP Aryl Ether Homopolymer P1. In a 25 mL Schlenk tube equipped with a magnetic stirrer was added 1.00 g (2.97 mmol) of Bisphenol AF, 0.662 g (6.54 mmol) of triethylamine, and 10 mL of DMF. The solution was degassed with nitrogen for 10 min, and 0.631 g (2.97 mmol) of octafluorocyclopentene was added via syringe; the Schlenk flask was heated slowly to 80 °C for 24 h. The polymer was then precipitated in 100 mL of methanol, filtered, washed several times with methanol, and dried under vacuum at 50 °C for 24 h, giving 1.1 g of a white powder (yield = 74%). ^1H NMR (400 MHz, $\text{THF}-d_8$, δ): 6.91 (dm, $^3J_{\text{H-2(H-1)}} = 8.80$ Hz, 4H), 7.32 (dm, $^3J_{\text{H-1(H-2)}} = 8.80$ Hz, 4H). ^{19}F NMR (376 MHz, $\text{THF}-d_8$, δ): −63.85 (6F), −115.13 (4F), −130.17 (2F). ^{13}C NMR (100 MHz, $\text{THF}-d_8$, δ):

64.6, 110.8 (PFCP, CF₂), 113.8 (PFCP, CF₂), 117.5, 125.2, 130.8, 132.7, 134.9 (PFCP, C=C), 155.2. FTIR (ν , cm⁻¹): 3150 and 3063 (H-C=C), 1274 (C-O), 1151 (C-F), 780 and 658 (C-F).

Synthesis of PFCP Aryl Ether Homopolymer P2. Homopolymer P2 was synthesized using the same method as P1, except it was precipitated in a 0.5/0.5 volume ratio of water/methanol and washed several times with a solution of 0.5/0.5 volume ratio of water/methanol, giving a white powder after drying (yield = 90%). ¹H NMR (400 MHz, acetone-d₆, δ): 1.51 (dm, 6H), 6.69 (dm, ³J_{H-2(H-1)} = 8.91 Hz, 4H), 7.08 (dm, ³J_{H-1(H-2)} = 8.91 Hz, 4H). ¹⁹F NMR (376 MHz, acetone-d₆, δ): -114.20 (4F), -129.71 (2F). ¹³C NMR (100 MHz, THF-d₈, δ): 31.0, 42.7, 110.6 (PFCP, CF₂), 114.1 (PFCP, CF₂), 117.1, 128.5, 134.8 (PFCP, C=C), 147.8, 153.0. FTIR (ν , cm⁻¹): 3130 and 3065 (H-C=C), 1272 (C-O), 1142 (C-F), 782 and 654 (C-F).

Synthesis of PFCP Aryl Ether Homopolymer P3. Homopolymer P3 was synthesized using the same method as P2, except the reaction time was 36 h, giving a white powder after drying (yield = 50%). ¹H NMR (400 MHz, acetone-d₆, δ): 6.92 (dm, ³J_{H-2(H-1)} = 8.58 Hz, 4H), 7.31 (dm, ³J_{H-1(H-2)} = 8.58 Hz, 4H). ¹⁹F NMR (376 MHz, acetone-d₆, δ): -113.89 (4F), -129.60 (2F). ¹³C NMR (100 MHz, acetone-d₆, δ): 110.5 (PFCP, CF₂), 114.0 (PFCP, CF₂), 118.5, 128.8, 135.0 (PFCP, C=C), 137.7, 154.5. FTIR (ν , cm⁻¹): 3151 and 3070 (H-C=C), 2941 (C-H), 1270 (C-O), 1150 (C-F), 780 and 653 (C-F).

Synthesis of P3-co-P1. In a 25 mL Schlenk tube equipped with a magnetic stirrer was added 0.793 g (2.36 mmol) of Bisphenol AF, 0.439 g (2.36 mmol) of biphenol, 1.052 g (10.39 mmol) of triethylamine, and 10 mL of DMF. The solution was degassed with argon for 10 min, and 0.631 g (2.97 mmol) of octafluorocyclopentene was added via syringe; the Schlenk flask was heated at 80 °C for 10 h. The dissolved polymer was then precipitated in 100 mL of 0.5/0.5 volume ratio of water/methanol and washed several times with a solution of 0.5/0.5 volume ratio of water/methanol and dried under vacuum at 50 °C for 24 h, giving 1.7 g of a white powder (yield = 74%). ¹H NMR (300 MHz, acetone-d₆, δ): 7.15 (m). ¹⁹F NMR (282 MHz, acetone-d₆, δ): -64.44 (m, 3F), -115.21 (m, 4F), -130.61 (m, 2F). FTIR (ν , cm⁻¹): 3150 and 3075 (H-C=C), 1273 (C-O), 1150 (C-F), 787 and 661 (C-F).

Synthesis of M1. To a 50 mL round-bottom flask equipped with a magnetic stirrer were introduced 2.00 g (5.95 mmol) of Bisphenol AF, 2.77 g (13.1 mmol) of triethylamine, and 20 mL of DMF, and the solution was degassed with argon for 10 min. 2.775 g (13.09 mmol) of octafluorocyclopentene was then introduced with a syringe, and the solution was heated slowly to 80 °C for 10 h. The solvent was then removed, and the crude product was isolated by column chromatography in dichloromethane (R_f = 0.93) to give 3.1 g of a colorless oil (yield = 65%). ¹H NMR (300 MHz, CDCl₃, δ): 7.19 (d, ³J_{H-1(H-2)} = 8.58 Hz, 4H), 7.43 (d, ³J_{H-1(H-2)} = 8.58 Hz, 4H). ¹⁹F NMR (282 MHz, CDCl₃, δ): -63.91 (s, 6F), -115.32 (d, ³J_{F1(F-2)} = 9.84 Hz, 4F), -115.65 (d, ³J_{F-1(F-2)} = 13.11 Hz, 4F), -129.39 (s, 4F), -146.61 (s, 2F). ¹³C NMR (75 MHz, CDCl₃, δ): 67.4, 105.5, 109.1, 111.1, 112.0, 118.3, 123.9, 131.3, 131.7, 138.0, 154.1. FTIR (ν , cm⁻¹): 3150 and 3075 (H-C=C), 1270 (C-O), 1160 (C-F), 783 and 665 (C-F). GC-MS (*m/z*) [M + H]⁺: 720.4 Elemental analysis: Calcd (Found) C = 41.69 (41.62), H = 1.12 (1.03), F = 52.75 (53.03).

Synthesis of M2. M2 was synthesized and isolated with the same method as described for M1 (R_f = 0.86 in dichloromethane) to give a white solid (yield = 69%). ¹H NMR (300 MHz, CDCl₃, δ): 7.25 (dm, ³J_{H-1(H-2)} = 8.61 Hz, 4H), 7.59 (d, ³J_{H-1(H-2)} = 8.61 Hz, 4H). ¹⁹F NMR (282 MHz, CDCl₃, δ): -115.32 (m, 4F), -115.36 (m, 4F), -129.36 (s, 4F), -148.85 (s, 2F). ¹³C NMR (75 MHz, CDCl₃, δ): 104.3, 111.4, 114.1, 118.1, 122.2, 130.2, 131.2, 131.9, 153.9. FTIR (ν , cm⁻¹): 3133 and 3074 (H-C=C), 1272 (C-O), 1145 (C-F), 787 (C-F). GC-MS (*m/z*) [M + H]⁺: 570.3 Elemental analysis: Calcd (Found) C = 46.33 (46.36), H = 1.41 (1.36), F = 46.64 (46.70).

Synthesis of Copolymer (M1-alt-BP). To a 25 mL Schlenk tube equipped with a magnetic stirrer was added 0.500 g (0.694 mmol) of M1, 0.129 g (0.694 mmol) of biphenol, 0.155 g (1.53 mmol) of triethylamine, and 5 mL of DMF. The solution was degassed with argon for 10 min, and the Schlenk tube was heated slowly to 80 °C for

10 h under stirring. The dissolved polymer was then precipitated in 100 mL of 0.5/0.5 volume ratio of water/methanol and washed several times with a solution of 0.5/0.5 volume ratio of water/methanol, giving a white powder after drying (yield = 51%). ¹H NMR (300 MHz, acetone-d₆, δ): 6.88 (m, 8H), 7.15 (m, 4H), 7.35 (m, 4H). ¹⁹F NMR (282 MHz, acetone-d₆, δ): -64.45 (m, 3F), -115.02 (m, 4F), -130.6 (m, 2F). FTIR (ν , cm⁻¹): 315 and 3090 (H-C=C), 2941 (C-H), 1265 (C-O), 1150 (C-F), 790 and 658 (C-F).

Synthesis of Copolymer (M2-alt-6F). The copolymer was prepared using the same method as copolymer M1-alt-BP, giving a white powder after drying (yield = 69%). ¹H NMR (300 MHz, acetone-d₆, δ): 6.72 to 7.19 (m, 8H), 7.26 to 7.45 (m, 8H). ¹⁹F NMR (282 MHz, acetone-d₆, δ): -64.18 (m, 3F), -115.37 (m, 4F), -130.54 (m, 2F). FTIR (ν , cm⁻¹): 3130 and 3103 (H-C=C), 2960 (C-H), 1263 (C-O), 1145 (C-F), 785 (C-F).

AUTHOR INFORMATION

Corresponding Author

*E-mail: dwsmith@utdallas.edu.

ACKNOWLEDGMENTS

The authors thank Defense Advanced Research Projects Agency (DARPA) for funding and Tetramer Technology LLC for the gift of bisphenols. We also thank the Robert A. Welch Foundation (Grant AT-0041), Intel Corporation, and The University of Texas at Dallas for partial support.

REFERENCES

- (1) Banks, R. E.; Smart, B. E.; Tatlow, J. *Organo-fluorine Chemistry: Principles and Commercial Applications*; Plenum Press: New York, 1994.
- (2) Scheirs, J. *Modern Fluoropolymers: High Performance Polymers for Diverse Applications*; Wiley: New York, 1997.
- (3) Hougham, G. G.; Cassidy, P. E.; Johns, K.; Davidson, T. *Fluoropolymers: Synthesis*; Plenum Pub Corp.: New York, 1999.
- (4) Ameduri, B.; Boutevin, B. *Well-Architected Fluoropolymers: Synthesis, Properties and Applications*; Elsevier Science: San Diego, 2004.
- (5) For a review see: Iacono, S. T.; Budy, S. M.; Jin, J.; Smith, D. W. Jr. *J. Polym. Sci., Part A: Polym. Chem.* **2007**, *45*, 5705.
- (6) Babb, D. A.; Ezzell, B. R.; Clement, K. S.; Richey, W. F.; Kennedy, A. P. *J. Polym. Sci., Part A: Polym. Chem.* **1993**, *31*, 3465.
- (7) Andrew, T. L.; Swager, T. M. *Macromolecules* **2011**, *44*, 2276.
- (8) Smith, D. W.; Chen, S.; Kumar, S. M.; Ballato, J.; Topping, C.; Shah, H. V.; Foulger, S. H. *Adv. Mater.* **2002**, *14*, 1585.
- (9) Iacono, S. T.; Budy, S. M.; Ewald, D.; Smith, D. W. Jr. *Chem. Commun.* **2006**, 4844.
- (10) Iacono, S. T.; Budy, S. M.; Moody, J. D.; Smith, R. C.; Smith, D. W. Jr. *Macromolecules* **2008**, *41*, 7490.
- (11) Moody, J. D.; VanDerveer, D.; Smith, D. W.; Iacono, S. T. *Org. Biomol. Chem.* **2011**, *9*, 4842.
- (12) Lindner, P. E.; Lemal, D. M. *J. Org. Chem.* **1996**, *61*, 5109.
- (13) Bayliff, A. E.; Bryce, M. R.; Chambers, R. D. *J. Chem. Soc., Perkin Trans. 1* **1987**, 763.
- (14) Stockel, R. F.; Beachem, M. T.; Megson, F. H. *J. Org. Chem.* **1965**, *30*, 1629.
- (15) Stockel, R. F.; Beachem, M. T.; Megson, F. H. *Can. J. Chem.* **1964**, *42*, 2880.
- (16) Matsui, M.; Tsuge, M.; Funabiki, K.; Shibata, K.; Muramatsu, H.; Hirota, K.; Hosoda, M.; Tai, K.; Shiozaki, H.; Kim, M.; Nakatsu, K. *J. Fluorine Chem.* **1999**, *97*, 207.
- (17) McBee, E. T.; Turner, J. J.; Morton, C. J.; Stefani, A. P. *J. Org. Chem.* **1965**, *30*, 3698.
- (18) Cullen, W. R.; Dhaliwal, P. S. *Can. J. Chem.* **1967**, *45*, 719.
- (19) Mir, Q. C.; Guo, C. Y.; Kirchmeier, R. L.; Shreeve, J. n. M. *J. Org. Chem.* **1994**, *59*, 173.
- (20) Yamada, S.; Ishii, E.; Konno, T.; Ishihara, T. *Org. Biomol. Chem.* **2007**, *5*, 1442.

- (21) Park, J. D.; Bertino, C. D.; Nakata, B. T. *J. Org. Chem.* **1969**, *34*, 1490.
- (22) Yamada, S.; Konno, T.; Ishihara, T.; Yamanaka, H. *J. Fluorine Chem.* **2005**, *126*, 125.
- (23) Irie, M.; Sakemura, K.; Okinaka, M.; Uchida, K. *J. Org. Chem.* **1995**, *60*, 8305.
- (24) Wigglesworth, T. J.; Sud, D.; Norsten, T. B.; Lekhi, V. S.; Branda, N. R. *J. Am. Chem. Soc.* **2005**, *127*, 7272.
- (25) Malval, J.-P.; Gosse, I.; Morand, J.-P.; Lapouyade, R. *J. Am. Chem. Soc.* **2002**, *124*, 904.
- (26) Beale, J. H.; Schwartz, N. N.; Mantell, G. J. *J. Polym. Sci., Polym. Lett. Ed.* **1978**, *16*, 67.
- (27) Nishida, S.; Nishida, H.; Endo, T. *J. Polym. Sci., Part A: Polym. Chem.* **2002**, *40*, 1151.
- (28) Farnham, W. B.; Nappa, M. J. Reaction of Perfluoroolefins with Bis(silyl) Ethers to Produce Fluorinated Compounds. U.S. Patent 5,457,215, 1995.
- (29) Smith, D. W.; Jin, J.; Shah, H. V.; Xie, Y.; DesMarteau, D. D. *Polymer* **2004**, *45*, 5755.

Influence of the Alkyl Substituents Spacing on the Solar Cell Performance of Benzodithiophene Semiconducting Polymers

Prakash Sista,[†] Bofei Xue,[§] Mitchell Wilson,[§] Natalie Holmes,[§] Ruvini S. Kularatne,[†] Hien Nguyen,[†] Paul C. Dastoor,[§] Warwick Belcher,[§] Katelyn Poole,[‡] Benjamin G. Janesko,[‡] Michael C. Biewer,[†] and Mihaela C. Stefan^{*,†}

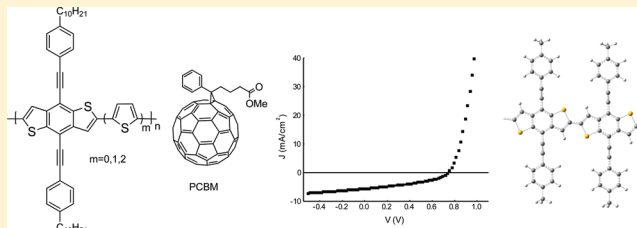
[†]Department of Chemistry, University of Texas at Dallas, 800 West Campbell Road, Richardson, Texas 75080, United States

[‡]Department of Chemistry, Texas Christian University, 2800 S. University Drive, Fort Worth, Texas 76129, United States

[§]Centre for Organic Electronics, The University of Newcastle, University Drive, Callaghan NSW 2308, Australia

Supporting Information

ABSTRACT: Three semiconducting polymers containing benzodithiophene with decylphenylethynyl substituents have been synthesized for which the spacing between alkyl substituents has been systematically increased by introduction of thiophene and bithiophene units in the backbone of the polymer. As the spacing between the side chains increased, an increase of the weight ratio of polymer to fullerene acceptor was required for achieving the highest power conversion efficiency of bulk heterojunction solar cells. The spacing between the side chains of the polymers was estimated from DFT calculations. The TMAFM analysis of polymer PCBM blends showed that the smooth films exhibited the highest solar cell performance.



Semiconducting polymers are gaining favor as alternatives for inorganic semiconductors because they are easily processable, can be used on flexible substrates, and they are inexpensive.^{1–4} Semiconducting polymers have extended π -electron delocalization, large absorption in the UV–vis region of the solar spectrum, and possess reasonable charge carrier mobilities. As such, they are now being used in numerous organic electronics applications, such as organic field effect transistors (OFETs),^{5,6} organic light-emitting diodes (OLEDs),^{7,8} and organic photovoltaics (OPVs).^{2,9} Blends of semiconducting polymers with the soluble electron acceptor [6,6]-phenyl-C₆₁-butyric acid methyl ester (PCBM) have been shown to function as the active layer in bulk heterojunction solar cells. Of these semiconducting polymers, regioregular poly(3-hexylthiophene) (rr-P3HT) is the most used in bulk heterojunction solar cells with PCBM. The reported efficiencies of organic solar cells with blended P3HT donor and PCBM acceptor have reached up to 5%.^{10,11} These relatively high efficiencies were achieved by morphological control of the P3HT–PCBM blend film with variations in solvent, composition of the blend, film thickness, and annealing conditions used.^{10–14}

Despite its advantages, P3HT suffers from a poor matching of its absorption spectrum with the solar emission spectrum resulting in the polymer only collecting a maximum of ~20% of the solar photons.¹ This has led to the development of new semiconducting polymers with lower band-gaps and good charge mobilities.^{15–26} One of the most explored building blocks are the fused-ring thiophenes.^{25–43} The application of

fused-ring monomers planarizes the polymer backbone, enabling efficient π -stacking and higher charge carrier mobilities. Furthermore, using symmetrical fused-ring monomers also avoids the need to control regioregularity. Benzodithiophene is one of the most used fused-ring building blocks.^{25–41} Donor–acceptor polymers containing benzodithiophene have been reported to give power conversion efficiencies higher than 7%.^{36,44–46} The process to optimize the efficiency from a benzodithiophene-containing polymer remains the same as for P3HT. For example, as with P3HT, the blend composition is one of the most critical parameters that needs to be optimized to generate the highest performance of the polymer in bulk heterojunction solar cells with PCBM.^{10,47–49}

McCulloch and co-workers first proposed the idea of intercalation of PCBM between the side chains of a semiconducting polymer when the spacing between the side chains is sufficiently large.⁵⁰ McGehee and co-workers further studied intercalation in both amorphous and semicrystalline semiconducting polymer/fullerene blends using X-ray diffraction and photoluminescence quenching studies.^{51–53} McGehee and co-workers demonstrated that PC₆₁BM and PC₇₁BM acceptors intercalate into the available open spaces between the side chains of the polymer before forming the pure electron transporting PCBM phase.^{51–53} As a result, when intercalation

Received: November 12, 2011

Revised: December 20, 2011

Published: January 9, 2012



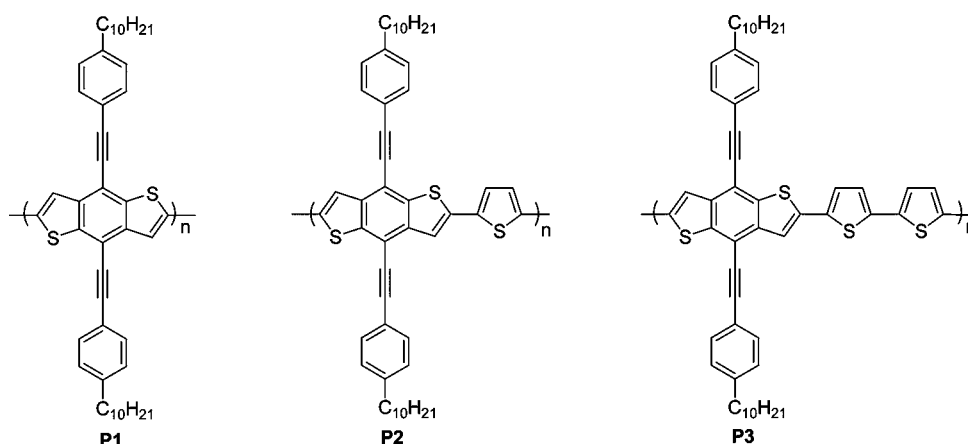


Figure 1. Homopolymer and alternating copolymers containing benzodithiophene with decyl phenylethynyl substituents: **P1** = poly{4,8-bis(4-decylphenylethynyl)benzo[1,2-*b*:4,5-*b'*]dithiophene}, **P2** = poly{4,8-bis(4-decylphenylethynyl)benzo[1,2-*b*:4,5-*b'*]dithiophene-*alt*-thiophene}, and **P3** = poly{4,8-bis(4-decylphenylethynyl)benzo[1,2-*b*:4,5-*b'*]dithiophene-*alt*-bithiophene}.

Table 1. Optoelectronic Properties and Molecular Weights of the Synthesized Polymers

polymer	M_n (g/mol)	PDI	$\lambda_{\max,L}$ (nm)	$\lambda_{\max,S}$ (nm)	HOMO ^a (eV)	LUMO ^a (eV)	E_g^a (eV)
P1	23400	3.0	363, 520	366, 525	−5.10	−3.05	1.95
P2	16000	1.7	368, 529	376, 540	−5.21	−3.18	2.03
P3	8060	2.6	388, 512	380, 520	−5.26	−2.96	2.30

^aHOMO and LUMO levels obtained from cyclic voltammetry measurements using a nonaqueous Ag/Ag⁺ electrode.

occurs, a correspondingly higher level of fullerene loading is necessary to generate the optimal phase separation for an efficient bulk heterojunction solar cell.^{52,53} For example, optimum blend ratios of 1:3 to 1:4 were observed for polymers that allow intercalation, as compared to 1:1 for polymers that do not allow intercalation.^{52,53}

Previously, we have reported the optoelectronic properties of a benzodithiophene semiconducting polymer with decylphenylethynyl substituents.^{54–57} In this report we vary the spacing between the side chains of benzodithiophene by introducing thiophene and bithiophene units as spacers in order to systematically study intercalation effects of the PCBM acceptor. The phenylethynyl groups on which the side chains are attached are rigid and expected to maintain a constant spacing between the phenyl groups of the three polymers. We have tested these three semiconducting polymers as donors in bulk heterojunction solar cells with PCBM acceptor to study the correlation of the distance between side chains and the amount of PCBM required to achieve the optimum power conversion efficiency. Investigation of the polymer/PCBM blends by atomic force microscopy (TMAFM) and X-ray diffraction (XRD) was employed to aid in interpretation of the photovoltaic response of the blends.

RESULTS AND DISCUSSION

Three semiconducting polymers containing benzodithiophene with decylphenylethynyl substituents were synthesized. Homopolymer poly{4,8-bis(4-decylphenylethynyl)benzo[1,2-*b*:4,5-*b'*]dithiophene} (**P1**)⁵⁷ and two alternating copolymers with thiophene and bithiophene were synthesized and tested in bulk heterojunction polymer:PCBM solar cells. Alternating copolymers poly{4,8-bis(4-decylphenylethynyl)benzo[1,2-*b*:4,5-*b'*]dithiophene-*alt*-thiophene} (**P2**) and poly{4,8-bis(4-decylphenylethynyl)benzo[1,2-*b*:4,5-*b'*]dithiophene-*alt*-bithiophene} (**P3**) were synthesized by Stille coupling polymerization of 2,6-

(trimethyltin)-4,8-bis(4-decylphenylethynyl)benzo[1,2-*b*:4,5-*b'*]dithiophene with the corresponding dibromo monomers (Figure 1).^{54–57} By synthesizing alternating dibromo monomers with thiophene and bithiophene, we are able to generate a systematic increase of the spacing between the decyl side chains of the polymer. Consequently, we were able to directly investigate the influence of the spacing between the decyl side chains on the loading with PCBM acceptor in bulk heterojunction solar cells. The syntheses of polymers **P1–P3** are reported in the Supporting Information. Bulk heterojunction solar cells were fabricated at different ratios between the polymers and PCBM, and the experimental results have been interpreted in correlation with the morphology of the blends.

The number-average molecular weight and polydispersity index of the synthesized polymers were measured using size-exclusion chromatography (SEC) (Table 1). The three polymers display a broad polydispersity index due to the nonliving nature of Stille coupling polymerization. The polymers were purified by consecutive extractions with methanol, diethyl ether, hexane, and chloroform. The final polymer was obtained by evaporation of the chloroform extract. Polymers **P2** and **P3** have a lower solubility as compared to homopolymer **P1**. As the number of thiophene units increased, the solubility of the polymers decreases, and hence the soluble fraction of polymer collected from the chloroform extraction has a correspondingly lower molecular weight.

The UV–vis absorbance spectra of polymers **P1–P3** were measured in chloroform solution as well as in thin films (Table 1 and Supporting Information). The three polymers display two absorption maxima in solution (**P1**: 363 and 520 nm; **P2**: 368 and 531 nm; **P3**: 388 and 512 nm). The absorption band in the visible region is assigned to the benzodithiophene backbone, while the band in the UV region is due to the 1,4-bis(phenylethynyl)benzene substituents. The intensity of benzodithiophene and (phenylethynyl)benzene bands correlates well with their relative ratio in the repeating units. A red

Table 2. Photovoltaic Properties of Poly{4,8-bis(4-decylphenylethynyl)benzo[1,2-*b*:4,5-*b'*]dithiophene} (P1) in Solar Cell Devices^a

[P1]:[PCBM]	V_{oc} (V)	J_{sc} (mA/cm ²)	FF	η (%)	film thickness (nm)
3:1	0.66 (0.73)	1.03 (1.10)	0.26 (0.26)	0.18 (0.20)	61.9
2:1	0.74 (0.80)	1.75 (1.96)	0.25 (0.25)	0.33 (0.39)	68.9
1:1	0.75 (0.75)	5.72 (5.83)	0.39 (0.39)	1.67 (1.72)	51.9
1:2	0.72 (0.73)	5.41 (5.66)	0.41 (0.42)	1.62 (1.74)	60.2
1:3	0.70 (0.71)	4.73 (4.83)	0.39 (0.39)	1.29 (1.33)	57.5
1:4	0.70 (0.70)	4.58 (4.58)	0.42 (0.44)	1.36 (1.40)	57.7
1:5	0.71 (0.72)	4.06 (4.18)	0.41 (0.43)	1.17 (1.28)	67.0

^aThe data in the table represent average values while the numbers in parentheses are the highest measured values.

Table 3. Photovoltaic Properties of Poly{4,8-bis(4-decylphenylethynyl)benzo[1,2-*b*:4,5-*b'*]dithiophene-*alt*-thiophene} (P2) in Solar Cell Devices^a

[P2]:[PCBM]	V_{oc} (V)	J_{sc} (mA/cm ²)	FF	η (%)	film thickness (nm)
3:1	0.61 (0.66)	0.40 (0.44)	0.24 (0.24)	0.06 (0.07)	45.3
2:1	0.70 (0.74)	0.97 (1.10)	0.24 (0.24)	0.16 (0.19)	44.7
1:1	0.71 (0.73)	1.80 (1.99)	0.31 (0.31)	0.39 (0.44)	52.0
1:2	0.73 (0.76)	2.04 (2.23)	0.39 (0.40)	0.62 (0.68)	45.6
1:3	0.77 (0.80)	2.11 (2.18)	0.42 (0.43)	0.69 (0.74)	59.0
1:4	0.81 (0.83)	2.10 (2.22)	0.46 (0.47)	0.79 (0.86)	55.6
1:5	0.80 (0.82)	2.09 (1.80)	0.47 (0.58)	0.79 (0.86)	61.0
1:7	0.80 (0.80)	1.97 (2.10)	0.48 (0.47)	0.75 (0.80)	52.5
1:10	0.71 (0.73)	1.84 (1.82)	0.48 (0.51)	0.62 (0.67)	50.6

^aThe data in the table represent average values while the numbers in parentheses are the highest measured values.

Table 4. Photovoltaic Properties of Poly{4,8-bis(4-decylphenylethynyl)benzo[1,2-*b*:4,5-*b'*]dithiophene-*alt*-bithiophene} (P3) in Solar Cell Devices^a

[P3]:[PCBM]	V_{oc} (V)	J_{sc} (mA/cm ²)	FF	η (%)	film thickness (nm)
3:1	0.12 (0.12)	0.82 (0.84)	0.26 (0.26)	0.02 (0.03)	43.1
2:1	0.18 (0.18)	1.52 (1.56)	0.26 (0.26)	0.07 (0.07)	35.3
1:1	0.35 (0.37)	2.52 (2.54)	0.28 (0.28)	0.25 (0.26)	40.8
1:2	0.34 (0.36)	2.79 (2.95)	0.29 (0.29)	0.28 (0.29)	41.6
1:3	0.49 (0.50)	3.02 (3.07)	0.33 (0.33)	0.48 (0.51)	48.1
1:4	0.47 (0.48)	2.94 (3.02)	0.32 (0.32)	0.44 (0.46)	46.1
1:5	0.57 (0.57)	3.00 (3.10)	0.38 (0.38)	0.65 (0.67)	44.8
1:6	0.53 (0.51)	3.42 (1.93)	0.29 (0.29)	0.51 (0.58)	50.0
1:7	0.62 (0.63)	2.98 (3.09)	0.39 (0.39)	0.71 (0.75)	43.4
1:8	0.58 (0.61)	3.05 (3.11)	0.35 (0.37)	0.62 (0.70)	39.9

^aThe data in the table represent average values while the numbers in parentheses are the highest measured values.

shift of 5–20 nm was observed for the thin films of the copolymers drop-casted from chloroform solutions, suggesting that the polymers have a rigid-rod conformation in the solid state.^{40,62}

The highest occupied molecular orbital (HOMO) and lowest unoccupied molecular orbital (LUMO) energy levels of the polymers **P1**–**P3** were determined by cyclic voltammetry (CV) using a Ag/Ag⁺ nonaqueous reference electrode. The HOMO and LUMO levels show little change across the series; however, a small systematic increase in band gap from **P1**–**P3** is observed.

The photovoltaic properties of polymers **P1**–**P3** were investigated in bulk heterojunction solar cells with PCBM as an electron acceptor. The solar cells were fabricated using a conventional device structure: ITO/PEDOT:PSS/polymer:PCBM/Ca/Al. In our earlier publication, we reported a power conversion efficiency (PCE) of 1.05% for the homopolymer **P1**, which was obtained for 1:1 weight ratio from a dichlorobenzene solution. In this study chloroform was

used as a solvent for blend preparation due to the better solubility of the polymers. The conditions for polymer **P1** were optimized in chloroform at a 1:1 weight ratio of polymer to PCBM for blend concentrations ranging from 5 to 30 mg/mL (see Table S1, Supporting Information). A maximum PCE of 1.67% was measured for a blend concentration of 15 mg/mL. The polymer/PCBM blends for the subsequent full investigation were prepared in chloroform maintaining the total blend concentration at 15 mg/mL in order to achieve comparable thicknesses of the active layer.

In order to determine the optimum blending ratio, homopolymer **P1** was tested in bulk heterojunction solar cells at [P1]:[PCBM] weight ratios ranging from 3:1 to 1:5 (Table 2). Although the highest PCE of 1.67% was achieved at 1:1 weight ratio, similar PCEs were measured for both the 1:1 and 1:2 blends, indicating that the highest efficiency may lie at a ratio between 1:1 and 1:2. The solar cells with blends of 3:1 and 2:1 display very low efficiencies (Table 2), suggesting that these blend ratios may lie below the percolation threshold for

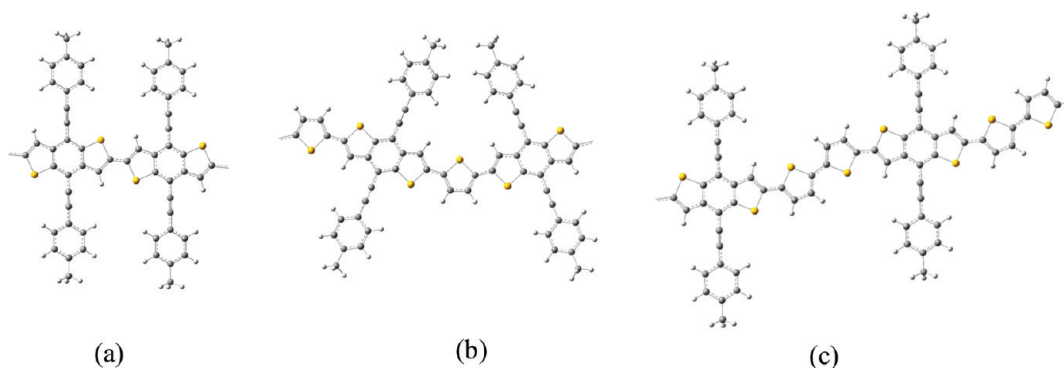


Figure 2. Lowest energy conformations for the chains that mimic polymers: (a) **P1**; (b) **P2**; (c) **P3**.

PCBM and preventing effective electron transport within these devices. This hypothesis is supported by the observed large decrease in J_{sc} for these devices, while V_{oc} is largely unaffected. The performance of solar cell devices decreases with further increase in the PCBM concentration with blends of 1:3, 1:4, and 1:5 having lower PCEs as compared to the 1:1 and 1:2 ratios.

The copolymer with thiophene (**P2**) was tested in bulk heterojunction solar cells at 15 mg/mL blend concentration and at weight ratios [**P2**]:[PCBM] ranging from 3:1 to 1:10 (Table 3). A maximum PCE of 0.79% was measured at both the 1:4 and 1:5 weight ratios.

The copolymer with bithiophene (**P3**) was tested at 10 mg/mL blend concentration at weight ratios [**P3**]:[PCBM] ranging from 3:1 to 1:8. A lower blend concentration was chosen due to the lower solubility of the polymer in chloroform, and so, accordingly, the spin conditions were adjusted to obtain an active layer thickness for **P3** comparable to those obtained for **P1** and **P2**. A maximum PCE of 0.71% was measured at 1:7 ratio for the **P3** blend devices (Table 4).

There are two observations that can be made as the polymer component in the blend devices is varied from **P1** to **P3**. First, the maximum PCE decreases for the series from **P1** to **P3** (as illustrated by the I – V curves for the best measured solar cell devices shown in the Supporting Information). Second, the PCBM loading required to maximize device performance increases systematically through the series from **P1** to **P3**.

Recent seminal work by McGehee and co-workers has demonstrated that intercalation of PCBM between the lamellar side chains of semiconducting polymers plays a key role in determining OPV device performance.⁵² In particular, they showed that for nonintercalated BHJ systems (such as P3HT:PCBM) the polymer:PCBM blend ratio optimizes at 1:1, whereas for intercalated systems (such as MDMO-PPV:PCBM) the optimum ratio is 1:4.⁵¹ For the polymers **P1** to **P3**, we see that the optimum PCBM loading increases systematically with distance between the decyl side chains, with optimum ratios of 1:1, 1:4, and 1:7 for **P1**, **P2**, and **P3**, respectively. Whereas the optimum ratio of 1:1 for the **P1**:PCBM blend indicates a nonintercalated system, the larger PCBM loading required for optimal device performance with copolymer **P2** suggests that PCBM now intercalates between the alkyl side chains. Moreover, the further increase in the required ratio of polymer **P3** to PCBM correlates well with the increased spacing between the alkyl chains and is consistent with the trend observed for polymers **P1** and **P2**. Comparing the solar cell performance of polymers **P2** and **P3**, we observe that the excess loading of PCBM required to achieve the best

performance doubles, suggesting that **P3** can intercalate twice as many PCBM molecules as **P2**.

Thin film XRD studies were performed on the pristine polymers to investigate the self-assembly of the polymers in thin films (Supporting Information). The polymers were dissolved in chloroform, and thin films were spin-cast onto a SiO₂ substrate. The three polymers **P1**–**P3** all show a single lamellar packing peak around $2\theta = 3.91^\circ$ (d -spacing of 22.6 Å) and a π -stacking peak around $2\theta = 20.4^\circ$ (d -spacing of 4.4 Å). Lamellar spacings of 16–20 Å have previously been reported for poly{4,5-bis(2-ethoxy)benzo[2,1-*b*:4,5-*b'*]dithiophene-2,7-diyl-*alt*-5,5'-dithienyl-4,4'-dihexyl,2,2'-bithiazole-2,2'-diyl}⁶³ and poly{4,8-bis(2-ethylhexyloxy)benzo[1,2-*b*:4,5-*b'*]dithiophene-2,6-diyl-*alt*-3-fluoro-2-[(2-ethylhexyl)carbonyl]thieno[3,4-*b*]thiophenediyl}.⁶⁴ The larger lamellar spacing observed for the three polymers in this study is likely due to the longer decylphenylethynyl side chains. However, the polymers appear to be semicrystalline with only a single (100) reflection observed.

Thin film XRD was also performed on the blends of **P1**–**P3** with PCBM at weight ratios of [**P**]:[PCBM] 1:1. The XRD pattern at 1:1 weight ratio [**P**]:[PCBM] for polymers **P2** and **P3** were compared with the XRD pattern of the blends that gave the highest PCE (Supporting Information). The sample preparation technique was similar to that of pristine polymer films. The lamellar packing peak of the blends is observed at 22.6 Å, which is the same as that for the pristine polymers. In addition, no peaks corresponding to pure PCBM are observed in the XRD patterns of the blends, consistent with many reports in the literature.^{63,65} While the McGehee group observed an increase in the lamellar packing distance in blends as compared to pristine pBTTT polymer due to the interdigitation of the alkyl substituents,⁵³ for blends of **P1**–**P3** with PCBM the lamellar packing distance is identical to the lamellar packing distance in the pristine polymers. We speculate that unlike the pBTTT system (which shows ordered crystalline behavior with sharp X-ray reflections up to (400)) the three polymer systems here are much less crystalline and exhibit a lack of interdigitation between the alkyl chains. As such, it is possible for the PCBM to intercalate between the polymer side chains without influencing the solid-state packing of the polymers **P1**–**P3** as probed by XRD. Indeed, the polymers can locally order even in the presence of PCBM,⁶⁵ and we even observe a slight increase in crystallinity with all three polymers exhibiting a faint (200) reflection upon addition of PCBM. Thus, the semicrystalline nature of polymers **P1**–**P3** means that (as noted by McGehee et al. for the MDMO–PPV system⁵¹) direct detection of intercalation of PCBM using XRD

is challenging since we also cannot simply measure the change in lattice spacing. Alternatively, it is also possible that PCBM intercalates between the polymers side chains in the amorphous polymer region.

Further support for the intercalation of PCBM was sought by using molecular modeling of polymers **P1**–**P3** to quantify the side-chain spacings in these polymers. The calculated lowest energy structures of isolated polymer chains are shown in Figure 2. In all cases, the lowest energy conformations have all intramonomer S–C–C–S dihedral angles of $\sim 180^\circ$. Calculated side-chain spacings are presented in Table 5. The calculated

Table 5. Estimated Spacing between the Side Chains of the Polymers **P1**–**P3** and the Weight Ratios Used in the Best Performing Solar Cells

polymer	[P]:[PCBM]	spacing (nm)
P1	1:1	0.85
P2	1:4	0.47, 1.96
P3	1:7	1.62

side-chain spacing in **P1** is 0.85 nm vs the 0.7 nm calculated width of an isolated C_{60} and suggests that polymer **P1** cannot have significant PCBM intercalation; consistent with the 1:1 [**P1**]:[PCBM] ratio in the best performing solar cells. The

lowest energy conformation of **P2** has a bent benzodithiophene–thiophene repeat unit yielding two different side-chain spacings. The larger of the two spacings (1.96 nm) could reasonably allow PCBM intercalation, which again is consistent with the observed optimum [**P2**]:[PCBM] ratio of 1:4. The calculated side-chain spacing of polymer **P3** is 1.62 nm, which is again large enough to allow PCBM intercalation. With the bithiophene repeating unit, the side-chain spacing is the same on both sides of the polymer backbone. Thus, PCBM can intercalate on either side of **P3**, while it is limited to intercalation on only one side of **P2**. This difference is in excellent agreement with the larger PCBM loading ([**P3**]:[PCBM] = 1:7) observed for **P3** for highest PCE compared to **P2**. Therefore, molecular modeling and the polymer:PCBM ratios observed for optimal device performance are entirely consistent with the hypothesis that **P1** does not intercalate PCBM in the blend film, whereas **P2** intercalates one PCBM molecule per monomer unit and **P3** intercalates two PCBM molecules per monomer unit.

TMAFM analysis was used to investigate the surface morphology of the polymer/PCBM blends. TMAFM images were recorded for the polymer/PCBM blends at 3:1, 1:1, 1:4, and 1:7 weight ratios (Supporting Information). For polymers **P2** and **P3** the surface morphology of 1:1 weight ratio [**P**]:[PCBM] was compared with the morphology of the blends that

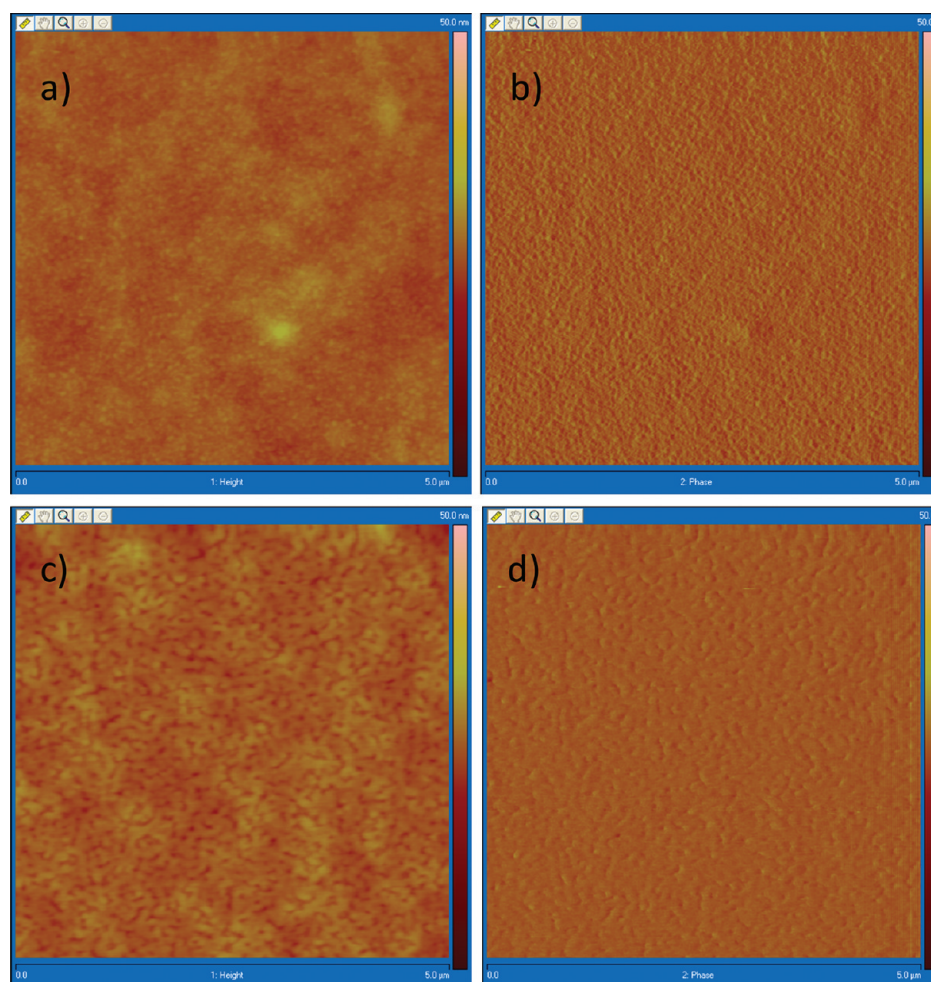


Figure 3. 5 $\mu\text{m} \times 5 \mu\text{m}$ TMAFM images of **P1**/PCBM blends: (a, b) height and phase images of 1:1 blend; (c, d) height and phase images of 1:4 blend.

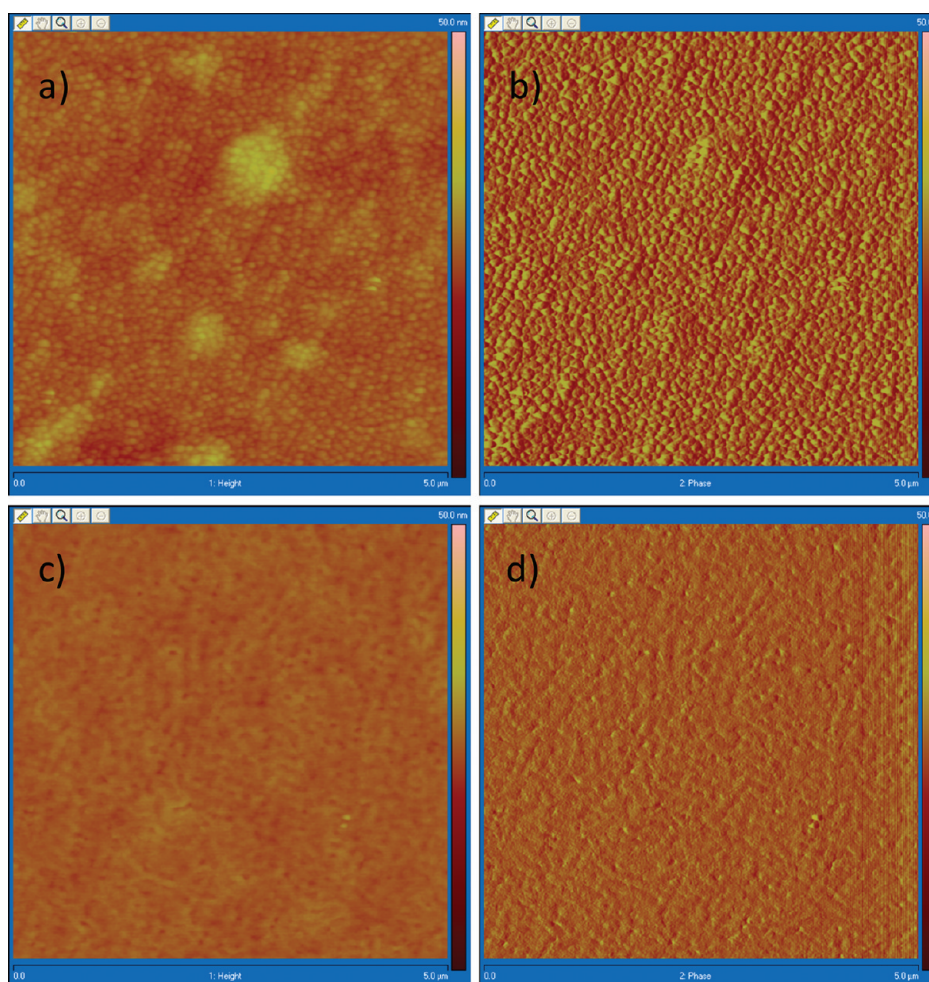


Figure 4. $5\ \mu\text{m} \times 5\ \mu\text{m}$ TMAFM images of **P2**/PCBM blends: (a, b) height and phase images of 1:1 blend; (c, d) height and phase images of 1:4 blend.

gave the highest PCE. The highest PCE was measured at a weight ratio of 1:1 for polymer **P1**, 1:4 for polymer **P2**, and 1:7 for polymer **P3**. All the TMAFM images obtained at the other ratios are shown in the Supporting Information.

Figure 3 shows the surface morphology of the blends of **P1** and PCBM at weight ratios of 1:1 and 1:4. The TMAFM images of the 1:1 blends show a more uniform surface morphology (rms roughness = 1.14 nm), indicating a uniform blending of the donor polymer and PCBM acceptor. By contrast, the TMAFM image of the 1:4 blend displays a granular morphology (rms roughness = 1.40 nm) with some large domains formed by the phase separation of the donor polymer and PCBM acceptor. This observation is in agreement with our previously published data for polymer **P1** which showed that the highest PCE was obtained for a smooth surface morphology of the blend.⁵⁷

The TMAFM images obtained at 1:1 and 1:4 **P2**/PCBM weight ratios are shown in Figure 4. The TMAFM image of the 1:1 blend clearly shows a more granular and a rougher surface morphology (rms roughness = 1.80 nm). By contrast, the TMAFM image of the 1:4 blend displays a smoother surface morphology (rms roughness = 0.805 nm). The image obtained at 1:7 ratio (Supporting Information) shows a rougher surface morphology (rms roughness = 0.866 nm) as compared to that of the 1:4 blend, indicating the aggregation of excess PCBM to form larger domains. Consistent with the data obtained for

polymer **P1**, the best performing blends for polymer **P2** also show a smooth surface morphology.

For polymer **P3**, the TMAFM images obtained at **P3**/PCBM weight ratios 1:1 and 1:7 are shown in Figure 5. The TMAFM image of the 1:1 blend shows significant phase separation and a rough surface morphology (rms roughness = 1.88 nm). By contrast, the best PCE was measured for the 1:7 blend, which displays a smooth surface morphology (rms roughness = 0.875 nm), again indicating uniform blending between the polymer **P3** and PCBM acceptor.

Thus, the surface morphology of the different polymer blends also exhibits a phase segregation behavior that is consistent with the proposed intercalation model. We have observed that for all the polymers/PCBM blends the highest PCEs were measured for the films that have smoothest surface morphologies and least phase segregation despite the fact that the PCBM loading is increasing as we go from **P1** to **P3**. The increasing intercalation of PCBM between the polymer side chains from **P1** to **P3** allows the blend system to accommodate increasing PCBM concentration without a corresponding increase in PCBM aggregation.

Finally, the observation that the optimum PCE decreases from **P1** to **P3** is also consistent with increased PCBM intercalation between the polymer side chains. Previous work on ternary blend systems has shown that decreasing the separation across donor–acceptor (D–A) interfaces results in

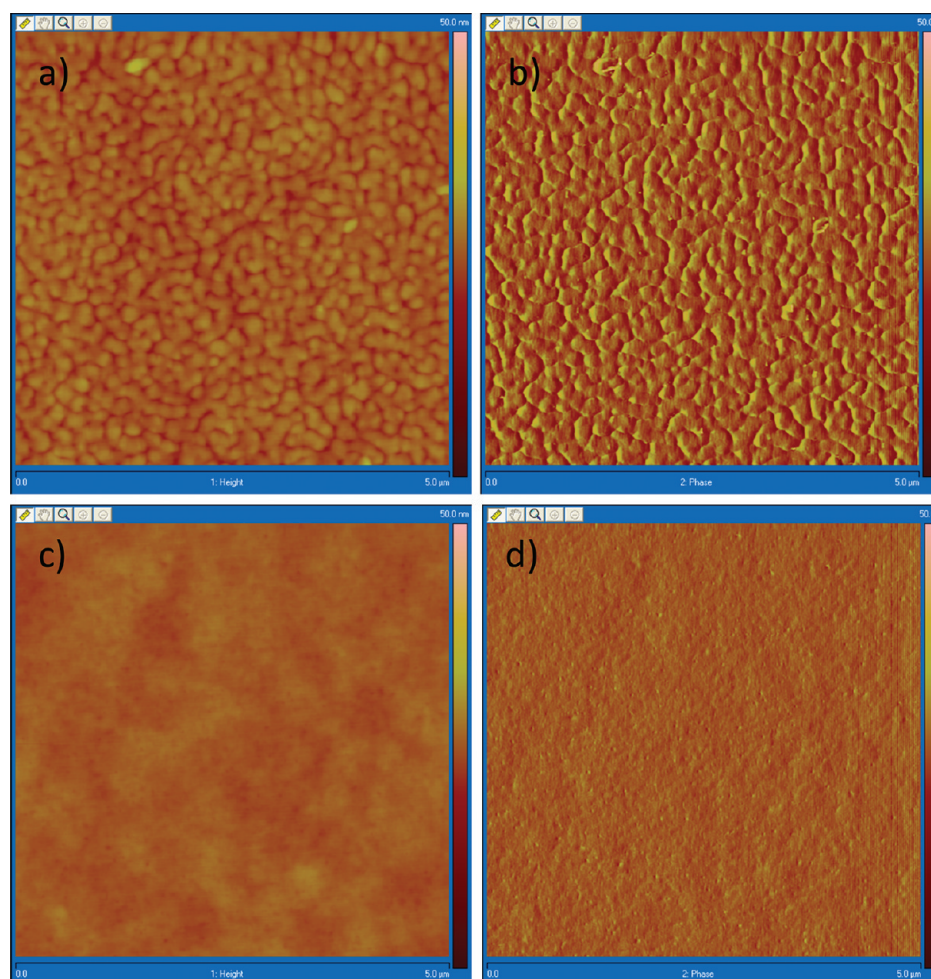


Figure 5. 5 $\mu\text{m} \times 5 \mu\text{m}$ TMAFM images of **P3**/PCBM blends: (a, b) height and phase images of 1:1 blend; (c, d) height and phase images of 1:7 blend.

increased recombination.⁶⁶ As such, geminate recombination is likely to be more prevalent in intercalated blends (such as **P2** and **P3**) as opposed to nonintercalated blends (such as **P1**). Indeed, such a mechanism was also recently proposed as an explanation for the higher efficiency of the P3HT:PCBM system vis a vis the MDMO-PPV:PCBM system.⁵¹

CONCLUSION

We have synthesized three semiconducting polymers containing benzodithiophene with decylphenylethynyl substituents. The spacing between the alkyl substituents of the polymers is systematically increased by the introduction of thiophene and bithiophene units as spacers in the backbone of the polymers. The weight ratio [P]:[PCBM] for the devices that displayed the optimal PCE value in bulk heterojunction solar cells is 1:1 for **P1**, 1:4 for **P2**, and 1:7 for **P3**. The amount of PCBM required for achieving highest PCE increases with spacing providing evidence that PCBM does intercalate between the side chains of the polymers when the spacing is large enough and that the number of intercalated PCBM molecules per monomer unit in the optimal blend ratio is 0, 1, and 2 for **P1**, **P2**, and **P3**, respectively. XRD patterns of thin films of pristine polymers revealed that the lamellar packing distance is 22.6 Å and the π -stacking distance is 4.4 Å. No difference was observed between the XRD patterns of the pristine polymers and that of the blends, indicating that there is no influence of blending with

PCBM on the solid state packing of the semicrystalline polymers as probed by XRD. DFT calculations on the polymers reveal that the spacing between the alkyl chains on the side chain increases with the addition of each thiophene unit and that no intercalation of PCBM is possible in **P1** films, while **P2** and **P3** can indeed intercalate one and two PCBM molecules per monomer unit, respectively. TMAFM images of the blend films show that the devices with the highest efficiencies correspond to the blend ratios that give the smoothest films, consistent with the hypothesis that intercalation increases across the series **P1**, **P2**, and **P3**.

EXPERIMENTAL SECTION

Materials. All commercial chemicals were purchased from Aldrich Chemical Co., Inc., and were used without further purification, unless otherwise noted. All reactions were conducted under nitrogen. The polymerization glassware and syringes were dried at 120 °C for at least 24 h before use and cooled under a nitrogen atmosphere. Tetrahydrofuran (THF) was dried over sodium/benzophenone ketyl and freshly distilled prior to use.

Analysis. ¹H NMR spectra of the synthesized monomers were recorded on a JEOL-Delta 270 MHz spectrometer at 25 °C. ¹H NMR spectra of the polymers were recorded on a Varian Inova 500 MHz spectrometer at 30 °C. ¹H NMR data are reported in parts per million as chemical shift relative to tetramethylsilane (TMS) as the internal standard. Spectra were recorded in CDCl₃.

GC/MS was performed on an Agilent 6890-5973 GC-MS workstation. The GC column was a Hewlett-Packard fused silica capillary column cross-linked with 5% phenylmethylsiloxane. Helium was the carrier gas (1 mL/min). The following conditions were used for all GC/MS analyses: injector and detector temperature, 250 °C; initial temperature, 70 °C; temperature ramp, 10 °C/min; final temperature, 280 °C.

The UV-vis spectra of polymer solutions in chloroform solvent were carried out in 1 cm cuvettes using an Agilent 8453 UV-vis spectrometer. Thin films of polymer were obtained by evaporation of chloroform from polymer solutions of 5 mg/mL concentration on glass microscope slides.

Molecular weights of the synthesized polymers were measured by size exclusion chromatography (SEC) analysis on a Viscotek VE 3580 system equipped with Viscogel columns (GMHHR-M), connected to a refractive index (RI) detector. A GPC solvent/sample module (GPCmax) was used with HPLC grade THF as the eluent and calibration was based on polystyrene standards. Running conditions for SEC analysis were as follows: flow rate = 1.0 mL/min, injector volume = 100 μ L, detector temperature = 30 °C, column temperature = 35 °C. All the polymer samples were dissolved in THF and the solutions were filtered through PTFE filters (0.45 μ m) prior to injection.

Cyclic Voltammetry. Electrochemical grade tetrabutylammonium perchlorate (TBAP) was used as the electrolyte without further purification. Acetonitrile (low water 99.9% grade) was distilled over calcium hydride (CaH₂). Electrochemical experiments were performed using a BAS CV-50W voltammetric analyzer (Bioanalytical Systems, Inc.). The electrochemical cell was comprised of a platinum electrode, a platinum wire auxiliary electrode, and an Ag/AgCl reference electrode. Acetonitrile solutions containing 0.1 M tetrabutylammonium perchlorate were placed in a cell and purged with argon. A drop of the polymer dissolved in chloroform was placed on top of the platinum electrode. The solvent was evaporated in air. The film was immersed in the electrochemical cell containing the electrolyte prior to measurements. All electrochemical shifts were standardized to the ferrocene redox couple at 0.471 V.

TMAFM (Tapping Mode Atomic Force Microscopy). TMAFM studies were carried out on a VEECO dimension 5000 scanning probe microscope with a hybrid xyz head equipped with NanoScope Software run in tapping mode. TMAFM images were obtained using silicon cantilevers with nominal spring constant of 42 N/m and nominal resonance frequency of 300 kHz (OTESPa). Image analysis software Nanoscope 7.30 was used for surface imaging and image analysis. All TMAFM measurements were conducted under ambient conditions. All cantilever oscillation amplitude was equal to ca. 375 mV, and all images were acquired at 2 Hz scan frequency. Sample scan area was 5 μ m. In order to prepare the samples for TMAFM, glass substrates were precleaned and exposed to UV/ozone for 15 min to make the surface hydrophilic. 130 μ L of PEDOT:PSS (Clevios) was spin-coated onto the substrates at a spin rate of 4000 rpm and an acceleration of 1740 rpm/s. The substrates were then annealed at 150 °C for 10 min under a nitrogen atmosphere. Blends of polymer and PCBM at varying weight ratios (w/w) were prepared such that the total blend concentration was always 15 mg/mL. These blends were spin-cast on top of the PEDOT:PSS layer at a spin rate of 2000 rpm and an acceleration of 1740 rpm/s.

Preparation of Solar Cell Devices. OLED-grade glass slides were purchased with prepatterned ITO electrodes from Luminescence Technology Corp. (Taiwan). The slides were cleaned with deionized water, acetone, and isopropanol successively by sonication for 20 min each and then ashed for 10 min in an oxygen plasma prior to use. Immediately following plasma treatment, a 40 nm layer of poly(3,4-ethylenedioxythiophene):poly(styrenesulfonate) (PEDOT:PSS) was spin-coated onto the substrate (4000 min⁻¹, 1740 min⁻¹ s⁻¹, 90 s) followed by annealing at 120 °C for 20 min under nitrogen. The PCBM/polymer blend was prepared in chloroform, at the required weight ratio of polymer and PCBM, with a constant total concentration. This blend was then spin-cast (2000 min⁻¹, 1740 min⁻¹ s⁻¹, 60 s) onto the PEDOT-PSS/substrate. Finally, a cathode

consisting of calcium (10 nm) and aluminum (100 nm) were thermally evaporated at a rate of \sim 2.5 Å/s through a shadow mask to define solar cell active areas.

IV testing was carried out under a controlled N₂ atmosphere using a Keithley 236, model 9160 power source interfaced with LabView software. The solar simulator used was a Thermo Oriel equipped with a 300 W xenon lamp; the intensity of the light was calibrated to 100 mW cm⁻² with a NREL certified Hamamatsu silicon photodiode. The active area of the devices was 0.1 cm². The active layer film thickness was measured using a Veeco Dektak VIII profilometer.

Computation. All calculations used the Gaussian 09 electronic structure program.⁵⁸ Calculations model isolated, infinite, periodic, quasi-one-dimensional (1D) polymer chains, using generalized Kohn-Sham density functional theory with the B3LYP^{59,60} exchange-correlation functional and the 6-31G(d)⁶¹ basis set. The 4-decylphenylethynyl substituents used experimentally were replaced with 4-methylphenylethynyl groups to save computational time. Calculations treated several reasonable conformations of each (benzodithiophene)-(thiophene)_n system. Results are presented for the lowest energy conformations. Calculated side-chain spacings are reported as the distance between the methyl carbons of the 4-methylphenylethynyl substituents.

■ ASSOCIATED CONTENT

● Supporting Information

Experimental procedures for the synthesis of polymers, liquid and solid state UV-vis spectra of polymers, TMAFM images of blends, XRD of pristine polymers and blends, minimized energy conformations calculated by DFT. This material is available free of charge via the Internet at <http://pubs.acs.org>.

■ AUTHOR INFORMATION

Corresponding Author

*E-mail: mci071000@utdallas.edu.

■ ACKNOWLEDGMENTS

Mihaela C. Stefan gratefully acknowledges financial support from NSF (Career DMR-0956116).

■ REFERENCES

- (1) Perepichka, I. F.; Perepichka, D. F., Eds.; *Handbook of Thiophene-Based Materials: Applications in Organic Electronics and Photonics*; Wiley: West Sussex, 2009.
- (2) Brabec, C. J.; Dyakonov, V.; Parisi, J.; Sariciftci, N. S., Eds.; *Organic Photovoltaics: Concepts and Realization*; Springer-Verlag: Heidelberg, 2003.
- (3) Sun, S.-S.; Dalton, L. R., Eds.; *Introduction to Organic Electronic and Optoelectronic Materials and Devices*; CRC Press: Boca Raton, FL, 2008.
- (4) Skotheim, T. A.; Reynolds, J., Eds.; *Handbook of Conducting Polymers*; CRC Press: Boca Raton, FL, 2006.
- (5) Horowitz, G. *Adv. Mater.* **1998**, *10*, 365.
- (6) Bao, Z.; Locklin, J., Eds.; *Organic Field-Effect Transistors*; CRC Press: Boca Raton, FL, 2007.
- (7) Burroughes, J. H.; Bradley, D. D. C.; Brown, A. R.; Marks, R. N.; Mackay, K.; Friend, R. H.; Burns, P. L.; Holmes, A. B. *Nature* **1990**, *347*, 539.
- (8) Mullen, K.; Scherf, U. *Organic Light Emitting Devices: Synthesis, Properties and Applications*; Wiley-VCH: New York, 2006.
- (9) Brabec, C.; Dyakonov, V.; Scherf, U., Eds.; *Organic Photovoltaics: Materials, Device Physics, and Manufacturing Technologies*; Springer-Verlag: Heidelberg, 2008.
- (10) Ma, W.; Yang, C.; Gong, X.; Lee, K.; Heeger, A. J. *Adv. Funct. Mater.* **2005**, *15*, 1617.
- (11) Reyes-Reyes, M.; Kim, K.; Dewald, J.; Lopez-Sandoval, R.; Avadhanula, A.; Curran, S.; Carroll, D. L. *Org. Lett.* **2005**, *7*, 5749.

- (12) Peet, J.; Senatore, M. L.; Heeger, A. J.; Bazan, G. C. *Adv. Mater.* **2009**, *21*, 1395.
- (13) Chen, F.-C.; Ko, C.-J.; Wu, J.-L.; Chen, W.-C. *Sol. Energy Mater. Sol. Cells* **2010**, *94*, 2426.
- (14) Watts, B.; Belcher, W. J.; Thomsen, L.; Ade, H.; Dastoor, P. C. *Macromolecules* **2009**, *42*, 8392. He, M.; Qiu, F.; Lin, Z. *J. Mater. Chem.* **2011**, *21*, 17039. He, M.; Han, W.; Ge, J.; Yang, Y.; Qiu, F.; Lin, Z. *Energy Environ. Sci.* **2011**, *4*, 2894. He, M.; Han, W.; Ge, J.; Yu, W.; Yang, Y.; Qiu, F.; Lin, Z. *Nanoscale* **2011**, *3*, 3159. He, M.; Zhao, L.; Wang, J.; Han, W.; Yang, Y.; Qiu, F.; Lin, Z. *ACS Nano* **2010**, *4*, 3241.
- (15) Scharber, M. C.; Mühlbacher, D.; Koppe, M.; Denk, P.; Waldauf, C.; Heeger, A. J.; Brabec, C. J. *Adv. Mater.* **2006**, *18*, 789.
- (16) Soci, C.; Hwang, I.-W.; Moses, D.; Zhu, Z.; Waller, D.; Gaudiana, R.; Brabec, C. J.; Heeger, A. J. *Adv. Funct. Mater.* **2007**, *17*, 632.
- (17) Svensson, M.; Zhang, F.; Veenstra, S. C.; Verhees, W. J. H.; Hummelen, J. C.; Kroon, J. M.; Inganäs, O.; Andersson, M. R. *Adv. Mater.* **2003**, *15*, 988.
- (18) Winder, C.; Sariciftci, N. S. *J. Mater. Chem.* **2004**, *14*, 1077.
- (19) Zhang, G.; Fu, Y.; Xie, Z.; Zhang, Q. *Polymer* **2011**, *52*, 415.
- (20) Chen, J.; Cao, Y. *Acc. Chem. Res.* **2009**, *42*, 1709.
- (21) Wang, E.; Wang, L.; Lan, L.; Luo, C.; Zhuang, W.; Peng, J.; Cao, Y. *Appl. Phys. Lett.* **2008**, *92*, 033307.
- (22) Wang, E.; Wang, M.; Wang, L.; Duan, C.; Zhang, J.; Cai, W.; He, C.; Wu, H.; Cao, Y. *Macromolecules* **2009**, *42*, 4410.
- (23) Xia, Y.; Deng, X.; Wang, L.; Li, X.; Zhu, X.; Cao, Y. *Macromol. Rapid Commun.* **2006**, *27*, 1260.
- (24) Zhou, Q.; Hou, Q.; Zheng, L.; Deng, X.; Yu, G.; Cao, Y. *Appl. Phys. Lett.* **2004**, *84*, 1653.
- (25) Hou, J.; Chen, H.-Y.; Zhang, S.; Li, G.; Yang, Y. *J. Am. Chem. Soc.* **2008**, *130*, 16144.
- (26) Hou, J.; Chen, H.-Y.; Zhang, S.; Chen, R. L.; Yang, Y.; Wu, Y.; Li, G. *J. Am. Chem. Soc.* **2009**, *131*, 15586.
- (27) Liang, Y.; Wu, Y.; Feng, D.; Tsai, S.-T.; Son, H.-J.; Li, G.; Yu, L. *J. Am. Chem. Soc.* **2009**, *131*, 56.
- (28) Pan, H.; Li, Y.; Wu, Y.; Liu, P.; Ong, B. S.; Zhu, S.; Xu, G. *Chem. Mater.* **2006**, *18*, 3237.
- (29) Pan, H.; Li, Y.; Wu, Y.; Liu, P.; Ong, B. S.; Zhu, S.; Xu, G. *J. Am. Chem. Soc.* **2007**, *129*, 4112.
- (30) Wang, Y.; Parkin, S. R.; Watson, M. D. *Org. Lett.* **2008**, *10*, 4421.
- (31) Hou, J.; Chen, H.-Y.; Zhang, S.; Yang, Y. *J. Phys. Chem. C* **2009**, *113*, 21202.
- (32) Hou, J.; Park, M.-H.; Zhang, S.; Yao, Y.; Chen, L.-M.; Li, J.-H.; Yang, Y. *Macromolecules* **2008**, *41*, 6012.
- (33) Pan, H.; Wu, Y.; Li, Y.; Liu, P.; Ong, B. S.; Zhu, S.; Xu, G. *Adv. Funct. Mater.* **2007**, *17*, 3574.
- (34) Chen, J.; Shi, M.-M.; Hu, X.-L.; Wang, M.; Chen, H.-Z. *Polymer* **2010**, *51*, 2897.
- (35) Zhang, Y.; Hau, S. K.; Yip, H.-L.; Sun, Y.; Acton, O.; Jen, A. K. Y. *Chem. Mater.* **2010**, *22*, 2696.
- (36) Price, S. C.; Stuart, A. C.; Yang, L.; Zhou, H.; You, W. *J. Am. Chem. Soc.* **2011**, *133*, 4625.
- (37) Huo, L.; Hou, J.; Zhang, S.; Chen, H.-Y.; Yang, Y. *Angew. Chem., Int. Ed.* **2010**, *49*, 1500.
- (38) Zhang, G.; Fu, Y.; Zhang, Q.; Xie, Z. *Chem. Commun.* **2010**, *46*, 4997.
- (39) Beaujuge, P. M.; Subbiah, J.; Choudhury, K. R.; Ellinger, S.; McCarley, T. D.; So, F.; Reynolds, J. R. *Chem. Mater.* **2010**, *22*, 2093.
- (40) Zou, Y.; Najari, A.; Berrouard, P.; Beaupre, S.; Reda Aich, B.; Tao, Y.; Leclerc, M. *J. Am. Chem. Soc.* **2010**, *132*, 5330.
- (41) Liang, Y.; Yu, L. *Acc. Chem. Res.* **2010**, *43*, 1227.
- (42) Piliago, C.; Holcombe, T. W.; Douglas, J. D.; Woo, C. H.; Beaujuge, P. M.; Frechet, J. M. J. *J. Am. Chem. Soc.* **2010**, *132*, 7595.
- (43) Guo, X.; Xin, H.; Kim, F. S.; Liyanage, A. D. T.; Jenekhe, S. A.; Watson, M. D. *Macromolecules* **2011**, *44*, 269.
- (44) Liang, Y.; Xu, Z.; Xia, J.; Tsai, S.-T.; Wu, Y.; Li, G.; Ray, C.; Yu, L. *Adv. Mater.* **2010**, *22*, E135.
- (45) Chen, H.-Y.; Hou, J.; Zhang, S.; Liang, Y.; Yang, G.; Yang, Y.; Yu, L.; Wu, Y.; Li, G. *Nature Photonics* **2009**, *3*, 649.
- (46) Son, H. J.; Wang, W.; Xu, T.; Liang, Y.; Wu, Y.; Li, G.; Yu, L. *J. Am. Chem. Soc.* **2011**, *133*, 1885.
- (47) Krebs, F. C. *Sol. Energy Mater. Sol. Cells* **2009**, *93*, 394.
- (48) Hoppe, H.; Sariciftci, N. S. *J. Mater. Chem.* **2006**, *16*, 45.
- (49) Mayer, A. C.; Scully, S. R.; Hardin, B. E.; Rowell, M. W.; McGehee, M. D. *Mater. Today* **2007**, *10*, 28.
- (50) Koppe, M.; Scharber, M.; Brabec, C.; Duffy, W.; Heeney, M.; McCulloch, I. *Adv. Funct. Mater.* **2007**, *17*, 1371.
- (51) Cates, N. C.; Gysel, R.; Dahl, J. E. P.; Sellinger, A.; McGehee, M. D. *Chem. Mater.* **2010**, *22*, 3543.
- (52) Cates, N. C.; Gysel, R.; Beiley, Z.; Miller, C. E.; Toney, M. F.; Heeney, M.; McCulloch, I.; McGehee, M. D. *Nano Lett.* **2009**, *9*, 4153.
- (53) Mayer, A. C.; Toney, M. F.; Scully, S. R.; Rivnay, J.; Brabec, C. J.; Scharber, M.; Koppe, M.; Heeney, M.; McCulloch, I.; McGehee, M. D. *Adv. Funct. Mater.* **2009**, *19*, 1173.
- (54) Hundt, N.; Palaniappan, K.; Servello, J.; Dei, D. K.; Stefan, M. C.; Biewer, M. C. *Org. Lett.* **2009**, *11*, 4422.
- (55) Sista, P.; Bhatt, M. P.; McCarty, A. R.; Nguyen, H.; Hao, J.; Biewer, M. C.; Stefan, M. C. *J. Polym. Sci., Part A: Polym. Chem.* **2011**, *49*, 2292.
- (56) Sista, P.; Hao, J.; Elkassih, S.; Sheina, E. E.; Biewer, M. C.; Janesko, B. G.; Stefan, M. C. *J. Polym. Sci., Part A: Polym. Chem.* **2011**, *49*, 4172.
- (57) Sista, P.; Nguyen, H.; Murphy, J. W.; Hao, J.; Dei, D. K.; Palaniappan, K.; Servello, J.; Kularatne, R. S.; Gnade, B. E.; Xue, B.; Dastoor, P. C.; Biewer, M. C.; Stefan, M. C. *Macromolecules* **2010**, *43*, 8063.
- (58) Frisch, M. J.; Trucks, G. W.; Schlegel, H. B.; Scuseria, G. E.; Robb, M. A.; Cheeseman, J. R.; Scalmani, G.; Barone, V.; Mennucci, B.; Petersson, G. A.; Nakatsuji, H.; Caricato, M.; Li, X.; Hratchian, H. P.; Izmaylov, A. F.; Bloino, J.; Zheng, G.; Sonnenberg, J. L.; Hada, J. L.; Ehara, M.; Toyota, K.; Fukuda, R.; Hasegawa, J.; Ishida, M.; Nakajima, T.; Honda, Y.; Kitao, O.; Nakai, H.; Vreven, T.; Montgomery, J. A.; Peralta, J. E.; Ogliaro, F.; Bearpark, M.; Heyd, J. J.; Brothers, E.; Kudin, K. N.; Staroverov, V. N.; Keith, T.; Kobayashi, R.; Normand, J.; Raghavachari, K.; Rendell, A.; Burant, J. C.; Iyengar, S. S.; Tomasi, J.; Cossi, M.; Rega, N.; Millam, J. M.; Klene, M.; Knox, J. E.; Cross, J. B.; Bakken, V.; Adamo, C.; Jaramillo, J.; Gomperts, R.; Stratmann, R. E.; Yazyev, O.; Austin, A. J.; Cammi, R.; Pomelli, C.; Ochterski, J. W.; Martin, R. L.; Morokuma, K.; Zakrzewski, V. G.; Voth, G. A.; Salvador, P.; Dannenberg, J. J.; Dapprich, S.; Daniels, A. D.; Farkas, O.; Foresman, J. B.; Ortiz, J. V.; Cioslowski, J.; Fox, D. J. *Gaussian Inc.*, Wallingford, CT, 2010.
- (59) Becke, A. D. *J. Chem. Phys.* **1993**, *98*, 5648.
- (60) Stephens, P. J.; Devlin, F. J.; Chabalowski, C. F.; Frisch, M. J. *J. Phys. Chem.* **1994**, *98*, 11623.
- (61) Hehre, W. J.; Ditchfield, R.; Pople, J. A. *J. Chem. Phys.* **1972**, *56*, 2257.
- (62) Brown, P. J.; Thomas, D. S.; Kohler, A.; Wilson, J. S.; Kim, J.-S.; Ramsdale, C. M.; Sirringhaus, H.; Friend, R. H. *Phys. Rev. B: Condens. Matter Mater. Phys.* **2003**, *67*, 064203/1.
- (63) Fan, H.; Zhang, M.; Guo, X.; Li, Y.; Zhan, X. *ACS Appl. Mater. Interfaces* **2011**, *3*, 3646.
- (64) Chen, W.; Xu, T.; He, F.; Wang, W.; Wang, C.; Strzalka, J.; Liu, Y.; Wen, J.; Miller, D. J.; Chen, J.; Hong, K.; Yu, L.; Darling, S. B. *Nano Lett.* **2011**, *11*, 3707.
- (65) Vanlaeke, P.; Swinnen, A.; Haeldermans, I.; Vanhoyland, G.; Aernouts, T.; Cheyins, D.; Deibel, C.; D'Haen, J.; Heremans, P.; Poortmans, J.; Manca, J. V. *Sol. Energy Mater. Sol. Cells* **2006**, *90*, 2150.
- (66) Cooling, N.; Burke, K. B.; Zhou, X.; Lind, S. J.; Gordon, K. C.; Jones, T. W.; Dastoor, P. C.; Belcher, W. J. *Sol. Energy Mater. Sol. Cells* **2011**, *95*, 1767.

Redox-Active Macrocyclic and Linear Oligo-Carbosiloxanes Prepared via Hydrosilylation from 1,3-Divinyl-1,3-Dimethyl-1,3-Diferrocenyldisiloxane

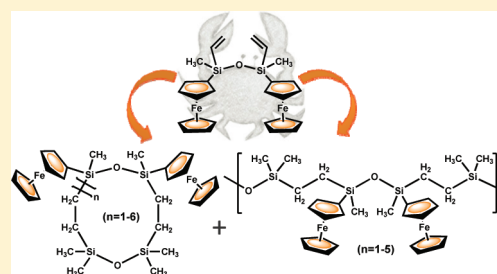
Sonia Bruña,[†] Ana M^a González-Vadillo,[†] Daniel Nieto,[†] César J. Pastor,[‡] and Isabel Cuadrado^{*,†}

[†]Departamento de Química Inorgánica, Facultad de Ciencias, Universidad Autónoma de Madrid, Cantoblanco, 28049, Madrid, Spain

[‡]Servicio Interdepartamental de Investigación (SIDI), Universidad Autónoma de Madrid, Madrid, Spain

S Supporting Information

ABSTRACT: A series of novel, precisely defined, redox-active macrocyclic and linear co-oligocarbosiloxanes containing pendant ferrocenyl moieties attached to the carbosiloxane backbones, have been synthesized via hydrosilylation reactions of the bifunctional 1,3-divinyl-1,3-dimethyl-1,3-diferrocenyldisiloxane $[(CH_2=CH)(Fc)MeSi]_2O$ (**6**) ($Fc = (\eta^5-C_5H_4)Fe-(\eta^5-C_5H_5)$). Specifically, **6** was reacted with 1,1,3,3-tetramethyldisiloxane, in the presence of Karstedt's catalyst, to afford both the cyclic species **7**, **8** and **9_n** ($n = 3-6$) and several linear co-oligomeric carbosiloxanes **10** and **11_n** ($n = 2-5$), containing a backbone in which the $-Me_2Si-O-SiMe_2-$ moiety and the ferrocenyldisiloxane unit $-MeFcSi-O-SiFcMe-$ are alternately linked by $-(CH_2)_2-$ bridges. Ferrocenyl cyclocarbosiloxanes **7** and **8**, as well as linear **10**, were isolated by column chromatography. The crude reaction mixtures, as well as pure macrocycles and oligocarbosiloxanes have been thoroughly characterized by elemental analysis, multinuclear (1H , ^{13}C , ^{29}Si) NMR spectroscopy, FT-IR and MALDI-TOF mass spectrometry, to establish their chemical structures and chain-end functionalities. The molecular structure of **7**, in solid state, has been determined by single-crystal X-ray analysis. Cyclocarbosiloxane **7** shows a bent arrangement of the ferrocenyl-substituted disiloxane linkage ($Si-O-Si$ angle of $144.05(16)^\circ$). The electrochemical behavior of **7-11_n** has been examined by cyclic (CV) and square wave (SWV) voltammetries, in dichloromethane solution using $[PF_6]^-$ and $[B(C_6F_5)_4]^-$, as supporting electrolyte anions of different coordinating ability. Macrocycles **7** and **8** and oligomer **10** show two well-resolved oxidation waves, which suggests significant interaction between neighboring ferrocenyl redox centers linked by the $Si-O-Si$ bridge. The linear oligomer **11_n**, containing the higher number of pendant ferrocenyl moieties, undergoes oxidative precipitation yielding electroactive films on platinum electrode surfaces.



INTRODUCTION

The chemistry of ferrocene-containing macromolecules continues to attract considerable scientific and technical interest in various areas of research because of their unique electrochemical, magnetic and catalytic properties and great potential as functional materials.¹⁻⁵ Many synthetic strategies have been devised, enabling access to a wide variety of ferrocene-based macromolecular systems including polymers, dendrimers and nanostructured materials. Our group has a long-standing interest in ferrocene-containing macromolecules, dendrimers and polymers.⁶⁻⁹ Among the various synthetic approaches we have developed to prepare such ferrocene-containing structures, hydrosilylation reactions that exploit the reactivity of $Si-H$ multifunctionalized carbosilanes and siloxanes toward suitable alkenyl-functionalized ferrocenes, have proven to be particularly useful and versatile.^{7,8} Hydrosilylation is one of the most important laboratory and industrial method to form $Si-C$ bonds,¹⁰ although its use for the introduction of organometallic moieties into macromolecular structures has been much less explored. For instance, some recent examples of ferrocenyl-containing silicon-based polymers prepared via hydrosilylation

reactions have been reported by Manners et al.,¹¹ Pannell et al.,¹² Sheridan et al.,¹³ Frey et al.,¹⁴ and by our own group.⁷

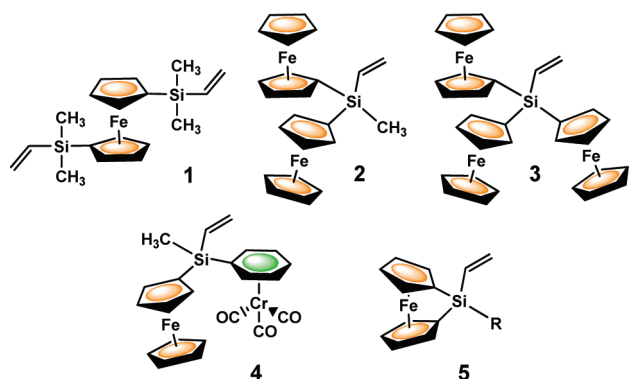
Within this context, we have described synthetic methods for obtaining a variety of ferrocene molecules containing vinylsilyl or allylsilyl functionalities.⁶⁻⁸ In fact, vinylsilanes constitute a versatile class of functional molecules of potentially wide applicability in modern organosilicon chemistry. In particular, the hydrosilylation reactions of vinylsilanes and silylhydrides,¹⁰ as well as silylative coupling and cross-metathesis of vinyl silanes,¹⁵ are well-established routes for the synthesis of well-defined novel organosilicon compounds. In the same way, vinylsilyl-functionalized ferrocenes are valuable reactive molecules which offer interesting possibilities in organometallic synthesis. To the best of our knowledge, relatively few ferrocenyl-containing vinylsilanes have been reported so far and examples of such compounds (**1-5**) are shown in Scheme 1. All of them represent useful reagents for further synthesis

Received: November 16, 2011

Revised: December 13, 2011

Published: January 3, 2012

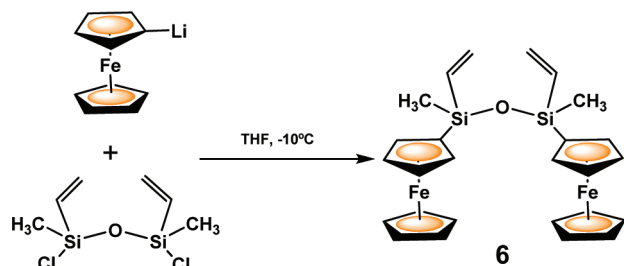
Scheme 1. Ferrocenyl Derivatives with Reactive Vinylsilyl Groups



and chemical transformations. For instance, we have prepared and characterized vinylsilyl-functionalized compounds 1–4, and we have used them successfully as reactive precursors for the construction of homo- and heterometallic dendritic and polymeric structures, via hydrosilylation reactions.^{6–8} Likewise, Pannell and co-workers have recently established that 1,1'-bis(dimethylvinylsilyl)ferrocene (1) acts as an efficient monomer for the synthesis of remarkable ferrocenylene copolymers and carbosiloxane-bridged sila[1]-ferrocenophanes.¹² Very recently, Müller et al. also used compound 1 as monomer in hydroboration reactions for the synthesis of hyperbranched ferrocene-containing poly(boro)-carbosilanes.¹⁶ In addition, the interesting chemical behavior of 1 in ruthenium-catalyzed silylative coupling cyclization reactions has been investigated by Marciniec and co-workers.¹⁷ On the other hand, Manners and co-workers have prepared and characterized vinylsilyl-bridged[1]ferrocenophane (5), and studied its ability to undergo ring-opening polymerization (ROP), allowing the synthesis of interesting examples of polyferrocenylsilanes containing pendant reactive Si–vinyl groups.¹¹

During the course of our research on the chemistry of vinylsilyl-functionalized organometallic molecules, the bifunctional compound 1,3-divinyl-1,3-dimethyl-1,3-diferrocenyldisiloxane, $[(\text{CH}_2=\text{CH})(\text{Fc})\text{MeSi}]_2\text{O}$ (6) (Scheme 2) was

Scheme 2. Preparation of Vinylsilylferrocenyl-Functionalized Disiloxane 6



obtained and electrochemically studied.¹⁸ In this work we focus our attention on the platinum-catalyzed hydrosilylation reactions of 6 with the bis(silylhydride) 1,1,3,3-tetramethyldisiloxane, which leads to the formation of structurally new types of ferrocenyl-containing macrocyclic and linear oligocarbosi-oxanes. The electrochemical behavior of the novel oligocarbosi-oxanes has been studied, especially regarding the electronic communication between the redox-active ferrocenyl moieties

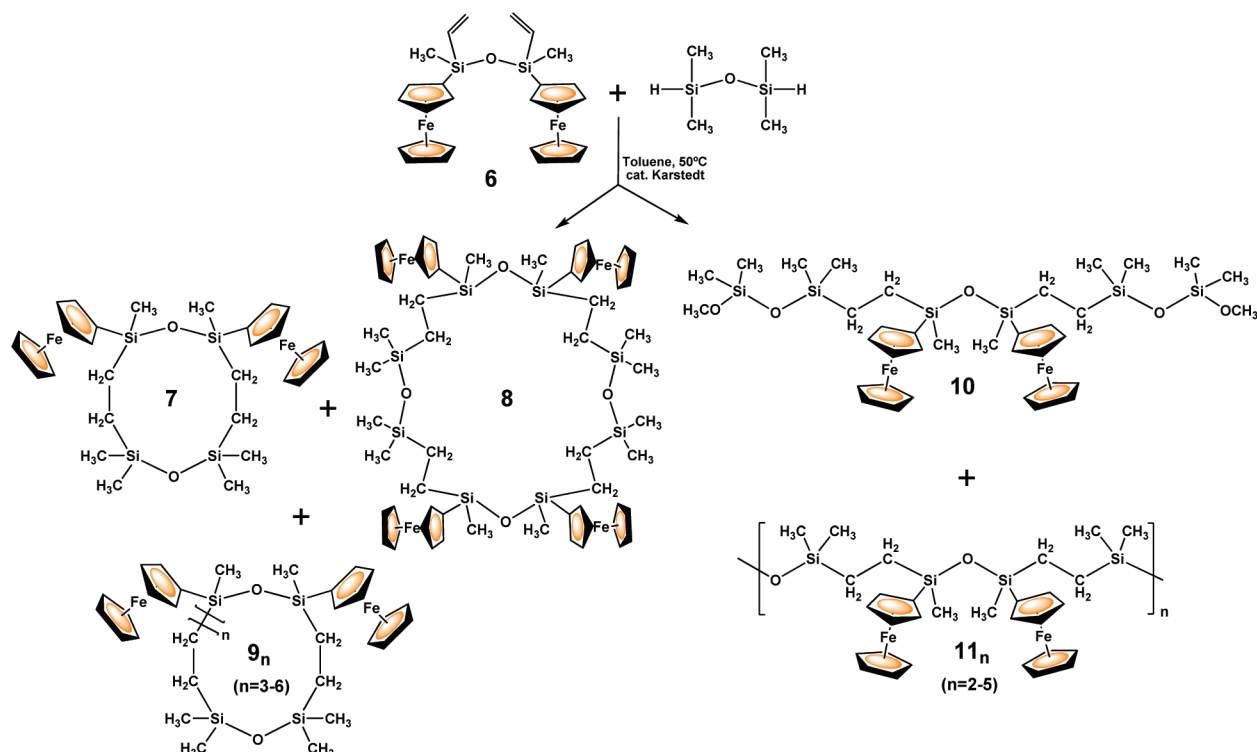
linked through the three atom Si–O–Si bridge. It is noteworthy to mention that silicon-containing ferrocenyl macrocycles are very interesting organometallic molecules because of their unique properties and structures that differ from their linear analogues.¹⁹ However, examples of these molecules are extremely rare, mainly due to the difficulty in their preparation. Remarkable cyclic oligoferrocenyldisiloxanes have been reported by Manners and co-workers,^{19a–c} Köhler and co-workers,^{19d} and Pannell and co-workers.^{19e} Herein we report the formation of the first examples of redox-active macrocyclic carbosiloxanes from the hydrosilylation of the divinylsilyl monomer 6.

RESULTS AND DISCUSSION

The main objective of this research was to study the reactivity of diferrocenyldisiloxane 6, since this bifunctional molecule with two Si–CH=CH₂ groups, able to undergo hydrosilylation reactions, could be of interest for the construction of polymeric structures of higher nuclearity. The key monomer 6 was successfully synthesized via the salt elimination reaction of ferrocenyllithium and 1,3-divinyl-1,3-dimethyl-1,3-dichlorodisiloxane, in THF at low temperature,¹⁸ as shown in Scheme 2.

The hydrosilylation reactivity of difunctional organosilicon monomers containing Si–vinyl bonds toward bis(silylhydrides) is well documented in the literature,¹⁰ and has become a valuable synthetic approach for obtaining different organo-silicon polymers. Thus, polycarbosi-oxanes, with both Si–C and Si–O–Si bonds in the main backbones, are an interesting type of polymers since they have shown intermediate properties between those of polymethylsiloxanes, polycarbosi-oxanes and saturated hydrocarbons.²⁰ Leading studies in this field were carried out in 1994 by Dvornic and co-workers,^{21,22} who have studied the Karstedt's catalyst catalyzed reaction between 1,3-divinyl-1,1,3,3-tetramethyldisiloxane and 1,1,3,3-tetramethyldisiloxane, and succeeded in obtaining remarkable examples of polycarbosi-oxanes $-\text{[Me}_2\text{Si-O-SiMe}_2\text{-(CH}_2\text{)}_2\text{]}_n-$, the first hybrid silicones with a high molecular weight. More recently, the kinetics and mechanism of this reaction have been revised in detail by the same group.²³ Dvornic and co-workers effected the hydrosilylation polymerization between $[\text{Me}_2\text{SiH}]_2\text{O}$ and $[(\text{CH}_2=\text{CH})\text{Me}_2\text{Si}]_2\text{O}$ in different conditions (in bulk and with diluted and concentrated solutions) and in all cases found truly high molecular weight linear polycarbosi-oxanes (ranging from 21950 to 75900). It was with this first intention in mind that we studied the reaction of divinylsilyl 6 with bis(silyl hydrides), with the formation of ferrocenyl–carbosiloxane polymeric species as our first target.

Hydrosilylation of 6 with $[\text{Me}_2\text{SiH}]_2\text{O}$: Synthesis and Characterization of Ferrocenyl–Carbosiloxane Macrocycles 7, 8, and 9_n and Linear Oligocarbosi-oxanes 10 and 11_n. The hydrosilylation reaction of 6 with 1,1,3,3-tetramethyldisiloxane (Scheme 3), was performed in toluene solution in the presence of Karstedt's catalyst (bis-(divinyltetramethyldisiloxane)platinum(0) in xylene), following approximately the same reaction conditions used by Dvornic et al. for the synthesis of high molecular weight polycarbosi-oxanes.²¹ Specifically, we used both more diluted and concentrated toluene solutions, and reaction temperature, time, catalyst concentration and reactants amounts were varied (see Table 1). In addition, in reaction no. 4 (Table 1) the “one monomer deficient method”,²⁴ was used. This consists of incremental additions of portions of the bis(silylhydride) monomer to the reaction mixture which contained the

Scheme 3. Synthesis of Cyclic and Linear Oligo-Carbosiloxanes with Pendant Ferrocenyl Units^a

^aThe $-\text{OCH}_3$ end groups of **10** are due to the use of MeOH as terminated agent.

Table 1. Hydrosilylation Reaction of **6** with $[\text{Me}_2\text{SiH}]_2\text{O}$ Using Karstedt's Catalyst

no.	6 (mM)	$[\text{Me}_2\text{SiH}]_2\text{O}$ (mM)	catalyst (mM)	time (h)	temp (°C)
1	43.9	43.9	5.17	24	45–50
2	43.9	43.9	5.17	24	70–75
3	127	127	22.4	24	45–50
4	190	190	33.6	72	50–55
5	1900	1425	299	24	50–55

difunctional ferrocenyl monomer **6**. In spite of the variety of conditions used, all the reactions tested afforded the same results (described below). In all cases, the reaction solutions remained homogeneous mixtures during the entire period of reaction; only darkening in the color of the reaction mixture was observed. After appropriate reaction times, analysis of the reaction mixture by ^1H NMR confirmed the disappearance of the $\text{Si}-\text{CH}=\text{CH}_2$ protons in the range δ 5.8–6.4 ppm and the appearance of a set of new resonances at δ 0.5–0.9 ppm corresponding to new hydrosilylated products with CH_2-CH_2 linkages, indicating quantitative transformation of the vinyl and $\text{Si}-\text{H}$ reactive groups.

It is noteworthy that the MALDI-TOF mass spectrometry is one of the most useful tools for the characterization of polymers and oligomers, since it has the advantage of obtaining specific information about the composition of macrocyclic oligomers and copolymers, sequence distribution, end-groups nature, and molecular mass distributions.^{25–27} In particular, MALDI-TOF MS has been successfully used for the study of macrocyclic oligoferrocenes.²⁶ For this reason, the crude reaction mixtures from hydrosilylation of **6** with dihydrosilanes, as well as pure macrocycles and co-oligomers described below, have been thoroughly characterized by MALDI-TOF

mass spectrometry in order to establish the chemical structure of the oligomer repeat units and chain-end functionalities.

The MALDI-TOF mass spectrum of the crude product from hydrosilylation of **6** with $[\text{Me}_2\text{SiH}]_2\text{O}$ (see Figure S1 in Supporting Information), exhibits several peaks from m/z 660.1 to m/z 3965.2, corresponding to different hydrosilylated oligomeric products. The major species are cyclic oligomers ranging from 1 to 6 repeat units. In addition the presence of other oligomers can be noticed. Although peaks at higher m/z values are not observed in this spectrum, the formation of higher molecular weight species cannot be ruled out, since the MALDI-TOF technique tends to show considerable molecular weight discrimination for polydisperse samples.²⁷ The mixture of the reaction products was then dissolved in a small amount of CH_2Cl_2 and precipitated into methanol. The oily residue thus obtained was found to be highly soluble in hexane and was subsequently subjected to column chromatography (silica gel, 3 cm \times 12 cm), from which several bands were separated. The first band (eluted with hexane/ CH_2Cl_2 100:10) was found to contain a mixture of the cyclic species **7**, **8**, and **9_n** (see Figure 1A) whereas the successive band (eluted with hexane/ CH_2Cl_2 100:50) contained a mixture of linear co-oligomers **10** and **11_n** (see Figure 1B) with a backbone consisting of alternating $-\text{MeFcSi}-\text{O}-\text{SiFcMe}-$ and $-\text{Me}_2\text{Si}-\text{O}-\text{SiMe}_2-$ units linked by $-(\text{CH}_2)_2-$ bridges (Scheme 3). As we used MeOH as terminated agent, the MALDI-TOF spectra of these latter fractions showed a different shift corresponding to the formation of the end groups ($-\text{OCH}_3$, $-\text{OH}$), thus confirming the presence of linear species (see below).

A close analysis of the MALDI-TOF spectra of the cyclic and linear oligomer mixtures (Figure 1, parts A and B) revealed the perfect alternating structure of the oligomers, which is caused by the hydrosilylation reaction itself. Thus, the

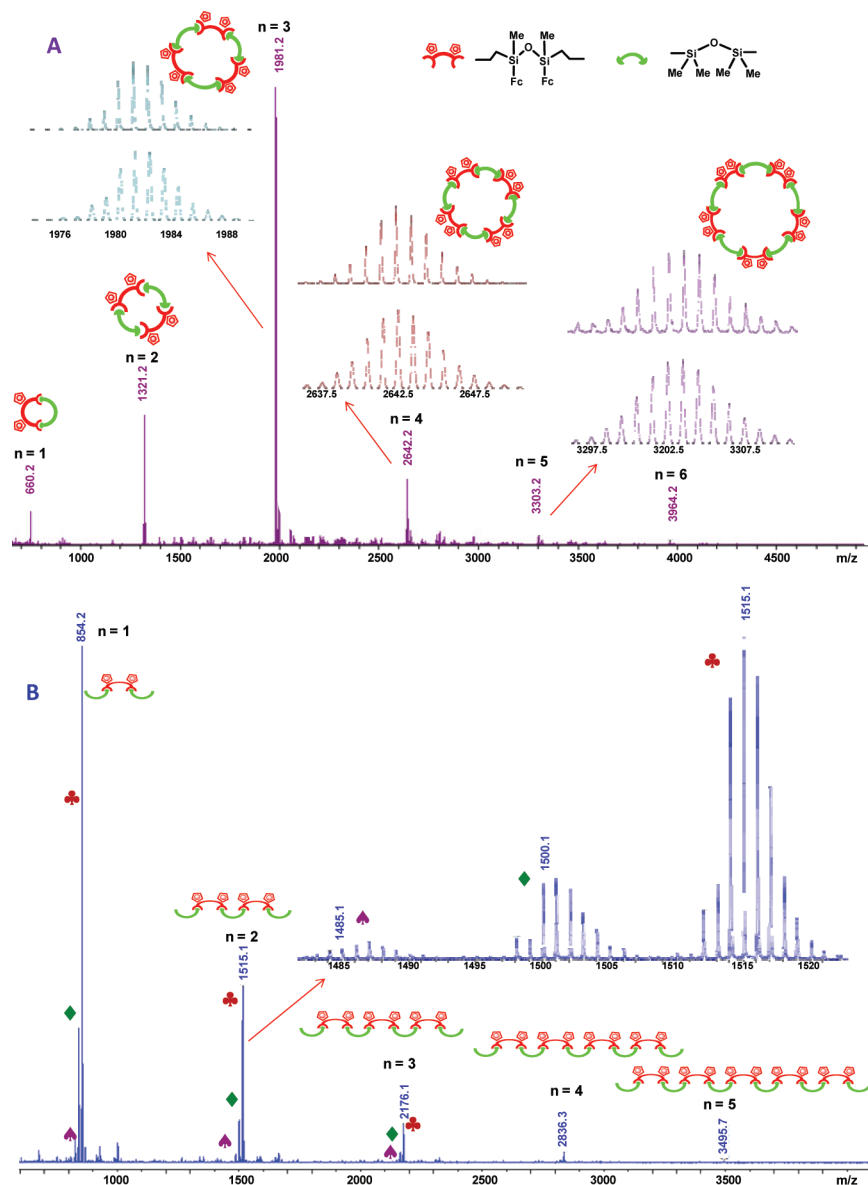


Figure 1. MALDI-TOF mass spectrum: (A) the mixture of cyclic reaction products resulting from the hydrosilylation of **6** and 1,1,3,3-tetramethyldisiloxane (the insets show the experimental and calculated isotopic patterns); (B) mixture of linear oligomers from the same reaction (the inset corresponds to an enlargement of the peak of **11**₂ with different ending groups, $-\text{CH}_3$, $-\text{OH}$, $-\text{OCH}_3$).

oligomers (cyclic and linear) were formed on the well-known fact that compound **6** and hydride terminated disiloxane entities copolymerize by hydrosilylation reaction to yield co-oligomers with a regular sequence of the type $(-\text{ABABAB}-)$. In the MALDI-TOF spectrum of the mixture of cyclic species **7**, **8** and **9**_{*n*} (with $n = 3-6$) shown in Figure 1A, the interval between peaks ($m/z = 660$) corresponds to the fragment mass of one tetramethyldisiloxane monomer and one di(ferrocenylmethyl)disiloxane monomer. Their isotopic masses agree well with that of the calculated ones, confirming their precisely defined cyclic structure. In addition, oligomers with different end groups were observed in the MALDI-TOF spectrum of the linear oligocarbosiloxane mixture, as can be seen in Figure 1B. In the enlargement of this figure, one can clearly note that the intervals between main, middle and minor peaks are all m/z 15, which can be assigned to a $-\text{CH}_3$ unit. These differences can be attributed to the different terminal monomer patterns during the polymerization process. Termination

A: the ends of the polymer chain are different, being $-\text{OH}$ and $-\text{OCH}_3$ respectively. Termination B: both ends terminate with $-\text{OCH}_3$. Termination C: both ends terminate with $-\text{OH}$. In Figure 1B, the corresponding peaks of the linear oligomer ending in $-\text{OH}$ and $-\text{OCH}_3$ are tagged with \blacklozenge ($m/z = 840, 1500, 2160, 2820$ and 3480), in two $-\text{OCH}_3$ with a \bullet ($m/z = 855, 1515, 2175, 2835$ and 3495), and fragments with two terminal $-\text{OH}$ units were labeled as a $*$ ($m/z = 825, 1485, 2145, 2805$ and 3465). The fact that the co-oligomers end in $-\text{OCH}_3$ or $-\text{OH}$ units provides unambiguous evidence that the two terminal monomers in the selected comonomer chain must be two siloxane ($\text{SiMe}_2\text{OSiMe}_2$) moieties. In other words, the series observed revealed a formula with n units of $-\text{MeFcSi}-\text{O}-\text{SiFcMe}-$ and $n + 1$ units of $-\text{Me}_2\text{Si}-\text{O}-\text{SiMe}_2-$. All these peaks correlate well with the calculated ones (see Figures S19–S22, Supporting Information).

A second careful column chromatography on silica gel (2 cm \times 15 cm), of the mixture containing macrocyclic products

allowed us to separate and isolate spectroscopically and analytically pure ferrocenyl-carbosiloxane macrocycles **7** (eluted with hexane/ CH_2Cl_2 100:5) and **8** (with hexane/ CH_2Cl_2 100:15) in 20% and 9% yields, respectively. Unfortunately, pure samples of ferrocenyl-macrocycles **9_n** ($n = 3-6$) could not be isolated, so far, although its existence is fully supported by the MALDI-TOF mass spectrometric study. Finally, a third careful column chromatography on silica gel (2 cm \times 15 cm), was carried out in order to try a separation of the linear oligomers. In this case the linear co-oligocarbosiloxane **10** (with both sides terminated in $-\text{OCH}_3$ groups) was successfully separated (with hexane/ CH_2Cl_2 100:40) in 6% yield, but no more pure linear oligomers could have been isolated so far. Once separated, the pure macrocyclic dimer **7**, trimer **8**, and the linear oligomer **10** were isolated as crystalline yellow-orange solids, and were thoroughly characterized by elemental analysis, multinuclear (^1H , ^{13}C , ^{29}Si) NMR spectroscopy and MALDI-TOF mass spectrometry.

Figure 2 shows the ^1H NMR spectra of pure macrocycle **7** and linear co-oligomer **10** together with their divinylidisiloxane

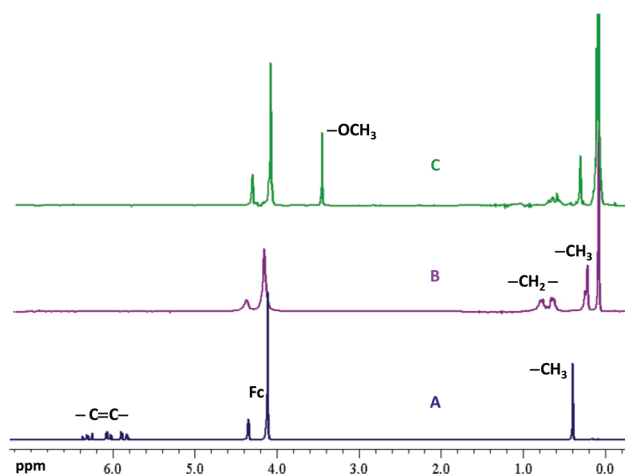


Figure 2. Comparison of the ^1H NMR spectra (in CDCl_3): (A) bis(vinylsilylferrocenyl) disiloxane monomer **6**; (B) cyclocarbosiloxane **7**; (C) linear oligocarbosiloxane **10**.

precursor **6**. Comparison of ^1H NMR spectra in CDCl_3 for **6** (Figure 2A), macrocycles **7** (Figure 2B) and **8** (see Figure S6, Supporting Information), and co-oligomer **10** (Figure 2C), reveals that the signals for the terminal vinyl protons at δ 6.38, 6.06, and 5.90 ppm disappeared after the hydrosilylation reaction, while new signals in the range δ 0.5 and 0.9 ppm are observed as a consequence of the formation of new $-\text{CH}_2-\text{CH}_2-$ linkages. This is in good agreement with the no existence of vinyl sp^2 carbon signals at δ 131.9 and 138.7 ppm in the ^{13}C NMR spectra of **7**, **8** and **10**, and the presence of new sp^3 resonances around δ 9 ppm. In addition, the total absence of $\text{Si}-\text{H}$ and $\text{Si}-\text{CH}=\text{CH}_2$ resonances, corresponding to end reactive functionalities, agrees with the cyclic structures of compounds **7** and **8**. Likewise, on the basis of the ^1H NMR spectra obtained for **7**, **8**, and **10**, it was determined that addition of $\text{Si}-\text{H}$ to vinyl-groups of **6** occurred according to the anti-Markownikov rule, so that the obtained cyclic molecules **7** and **8**, and linear **10** are truly β -addition products. In the case of the ^1H NMR of the linear co-oligomers mixture **11_n**, two significant resonances from terminal groups can be observed, one at δ 3.46 ppm assignable to the $-\text{OCH}_3$ end groups, and

other, less intense, at δ 3.49 ppm of the $-\text{OH}$ ends (see Figure S12, Supporting Information). This last peak disappeared when some drops of D_2O were added to the NMR tube. Signals at δ 3.46 and 49.7 ppm were observed in the ^1H NMR and ^{13}C NMR spectra of **10**, corroborating the structure proposed for this linear oligocarbosiloxane with $-\text{OCH}_3$ end groups.

The ^{29}Si NMR signals also confirmed the arrangements of the three isolated ferrocenyl-oligocarbosiloxanes **7**, **8**, and **10**. Thus, two resonances can be seen at δ -0.2 and 7.7 ppm for **7**, and at δ 0.5 and 8.2 ppm for **8**, the formers assignable to $\text{Fc}-\text{Si}-\text{CH}_3$ and the latest to $\text{CH}_3-\text{Si}-\text{CH}_3$ silicon atoms. Regarding linear **10**, in addition to these peaks (δ 6.1 ppm for $\text{Fc}-\text{Si}-\text{CH}_3$ and 13.9 ppm for $\text{CH}_3-\text{Si}-\text{CH}_3$) an extra resonance at δ -6.4 ppm is observed. As it can be seen in its $\{^1\text{H}-^{29}\text{Si}\}$ HMBC spectrum, (see Figure S11, Supporting Information), this signal corresponds to the two Si atoms directly attached to the $-\text{OCH}_3$ terminal groups.

Mass spectrometry provided further evidence for the formation of the new ferrocenyl carbosilane species **7**, **8**, and **10**. The MALDI-TOF mass spectra of the purified macrocycles **7** and **8** are depicted in Figure 3, parts A and B, and show the corresponding molecular ions M^+ at m/z 660.2 and 1320.2, respectively. The insets in Figure 3 reveal that the agreement between the experimental and calculated isotopic patterns is excellent. In the same way a single peak can be seen in the MALDI-TOF mass spectrum shown in Figure 3C with m/z value 854.2, in excellent agreement with the calculated isotopic molecular mass for compound **10**.

As mentioned above, the hydrosilylation reaction of **6** and 1,1,3,3-tetramethyldisiloxane was repeated several times using different reactant concentrations, different temperatures (from 45 to 75 $^\circ\text{C}$) and several reaction times (see Table 1). Although in all cases, the experimental conditions were adopted for preparing polymers and involved no high dilution conditions, we have found that the cyclic hydrosilylation products **7**, **8**, and **9_n** as well as oligomers **10** and **11_n** were invariably obtained as the overwhelmingly major products. Fortunately, the more soluble component of the reaction mixture was isolable in pure form and X-ray crystallography fully identified this species as the novel 10-membered carbosiloxane macrocycle **7** (see below). In contrast, after several attempts, only poor quality crystals of **8** and **10** were obtained so far, from solutions of the compounds in hexane/ CH_2Cl_2 at -30 $^\circ\text{C}$. These yellow-orange crystals were small stacks of needles and diffracted weakly.

X-ray Structure of Cyclocarbosiloxane 7. In order to identify unambiguously the proposed cyclic structure, single-crystal X-ray diffraction studies of the ferrocenyl carbosiloxane **7** were undertaken. Suitable crystals of **7** for X-ray diffraction were obtained at -30 $^\circ\text{C}$ from a solution of the corresponding compound in hexane/ CH_2Cl_2 (10:2). A summary of crystallographic data and data collection parameters is included in Table 2. Table 3 contains a comparison of selected bond lengths and angles of **7**.

Macrocyclic compound **7** crystallizes in the monoclinic space group $\text{P}2_1/\text{n}$ with $Z = 8$. The molecular structure of **7** is illustrated in Figure 4. Two independent molecules are present in the unit cell. However, since the macrocyclic conformations are analogous, they differ slightly in a few bond lengths and bond angles, only one is shown in Figure 4. The two independent molecules in the asymmetric unit cell can be seen in Figure S23, Supporting Information, along with tables of their bond lengths and angles. The two ferrocenyl groups attached to the silicon atoms are disposed in a nearly parallel

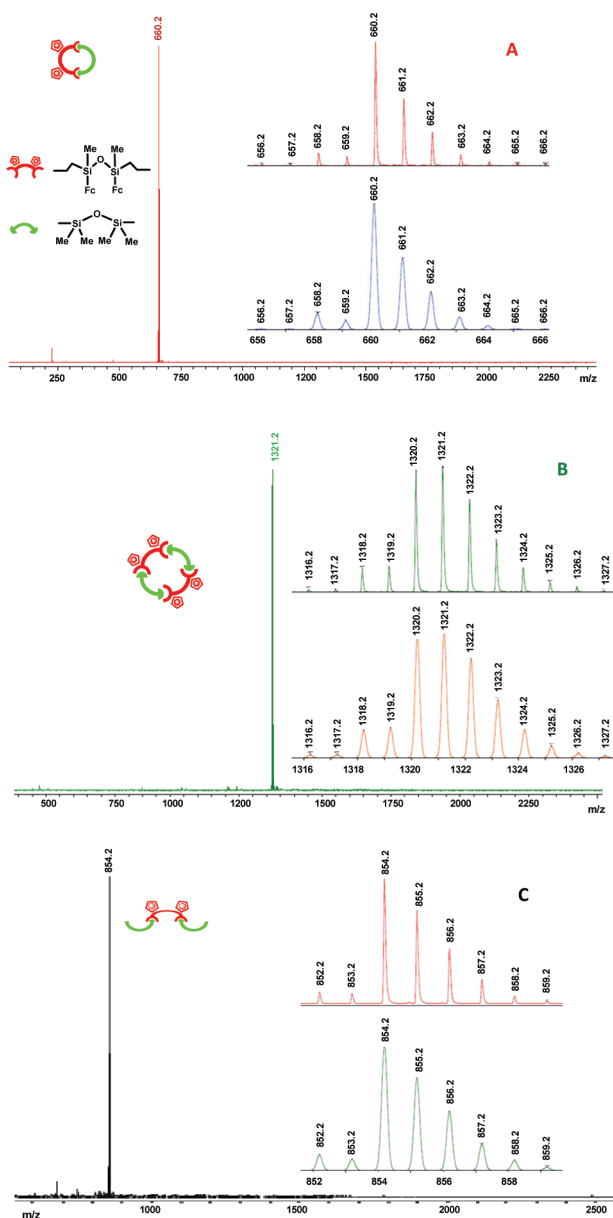


Figure 3. MALDI-TOF mass spectra: (A) purified macrocycle **7**; (B) purified macrocycle **8**; (C) purified oligoferrocenylcarbosiloxane **10**. The insets in the figures show the experimental (top) and calculated (bottom) isotopic patterns.

arrangement. The cyclopentadienyl rings are essentially parallel and essentially eclipsed in both ferrocenyl moieties, as occurred in its precursor **6**. The four silicon atoms are nearly tetrahedral with the entire C–Si–X bond angles (X = C or O) close to 109°. The intermolecular Fe–Fe distance in **6** was 7.597 Å,¹⁸ while in the cyclic oligomer **7** is shorter, 6.921 Å, probably due to its constrained ring structure. The Si–O–Si bond angle and the Si–O bond lengths of the ferrocenyl entity in **7**, 144.05(16)°, 1.634(2) and 1.636(2) Å, are approximately the same as the ones reported for its precursor **6**, 143.1(2)°, 1.641(3) and 1.627(3) Å. This indicates that the hydrosilylation reaction did not affect the nature of the Si–O–Si bridge in this compound. The value of the other Si–O–Si angle in the cyclic compound **7** is 150.75(17)° with Si–O distances 1.629 (2) and 1.631 (2) Å. The cavity size of this 10-membered ring can be defined by the transannular O1–O2, C2–C9, and C3–C8 distances, 4.67,

Table 2. Selected Crystallographic Data for Ferrocenyl Cyclosiloxane **7**

	7
empirical formula	C ₃₀ H ₄₄ Fe ₂ O ₂ Si ₄
fw	660.71
temp, K	100(2)
wavelength, Å	0.71073 Å
cryst syst	monoclinic
space group	P2 ₁ /n
a, Å	21.9636(11)
b, Å	12.4959(7)
c, Å	23.6723(16)
α, deg	90
β, deg	101.380(4)
γ, deg	90
V, Å ³	6369.2(6)
Z	8
density (calcd), mg m ^{−3}	1.378
F(000)	2784
no. of reflns collected	71 338
no. of indep reflns	12637 [R(int) = 0.0942]
completeness	99.4% (to θ = 26.14°)
no. of data/restraints/params	12637/0/697
goodness-of-fit on F ²	1.063
R ₁ , wR ₂ (I > 2σ(I))	0.0470, 0.1051
R ₁ , wR ₂ (all data)	0.0826, 0.1307
largest diff peak and hole, e Å ^{−3}	0.666 and −0.478

3.90, and 3.97 Å, respectively. The relatively large cavity within **7** makes this species a potential candidate for the encapsulation of metal ions. In addition, the two bulky ferrocene units and the CH₃ groups are all located outward the cycle in order to avoid steric congestion. The side view, Figure 4B, indicates that cyclic compound **7** adopts a chairlike conformation, having the two oxygen atoms in the opposite direction (*trans*). To the best of our knowledge, **7** is the first example of redox-active ferrocenyl cyclocarbosiloxane.

Electrochemical Studies of Cyclic and Linear Ferrocenyl–Oligocarbosiloxanes. The anodic electrochemistry of the cyclic carbosiloxanes **7** and **8**, and of their analogue linear oligomers **10** and **11**,_n was examined by cyclic voltammetry (CV) and square wave voltammetry (SWV) using dichloromethane as non-nucleophilic solvent. The half-wave potentials (*E*_{1/2}) of the electrochemical processes described below are summarized in Table 4, together with those of the vinylsilyl-functionalized disiloxane precursor **6**, measured in the same media.

As seen in Figure 5A the CV of cyclic **7** in dichloromethane solution with the traditional supporting electrolyte tetra-*n*-butylammonium hexafluorophosphate ([*n*-Bu₄N][PF₆]), shows two closely spaced voltammetric waves. A better resolution of the two redox processes was observed in the square wave voltammetric response of **7** measured in the same medium, which shows two redox waves at ¹*E*_{1/2} = +0.460 and ²*E*_{1/2} = +0.580 V (SCE) (see Figure S24, Supporting Information).

Our previous studies on the electrochemistry of disiloxane-bridged polyferrocenyl compounds, have showed that the use of tetra-*n*-butylammonium tetrakis(pentafluorophenyl)borate ([*n*-Bu₄N][B(C₆F₅)₄]) as supporting electrolyte provided improved solubility and enhanced peak separations, in cyclic and square wave voltammetries, than the conventional anions.¹⁸ The improved electrochemistry arises from the weakly

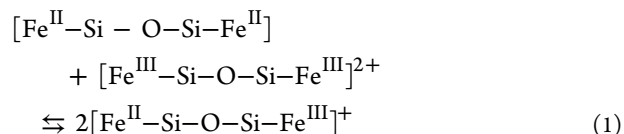
Table 3. Selected Bond Lengths (Å) and Angles (deg) for Cyclic Carbosiloxane 7

lengths/angles	7	lengths/angles	7
Si(1)–C(1)	1.845(4)	C(10)–Si(2)–C(21)	113.47(17)
Si(1)–C(2)	1.856(4)	C(9)–Si(2)–C(10)	110.90(18)
Si(1)–C(11)	1.839(4)	C(9)–Si(2)–O(1)	109.76(15)
Si(1)–O(1)	1.634(2)	C(21)–Si(2)–O(1)	108.76(15)
Si(2)–C(9)	1.852(4)	C(1)–Si(1)–O(1)	106.30(15)
Si(2)–C(10)	1.856(3)	C(10)–Si(2)–O(1)	104.71(14)
Si(2)–C(21)	1.840(4)	C(11)–Si(1)–C(2)	112.38(16)
Si(2)–O(1)	1.636(2)	C(21)–Si(2)–C(9)	109.12(16)
Si(3)–C(6)	1.848(4)	C(4)–Si(4)–C(5)	111.52(18)
Si(3)–C(7)	1.849(3)	C(4)–Si(4)–C(3)	112.24(19)
Si(3)–C(8)	1.854(4)	C(3)–Si(4)–O(2)	109.00(15)
Si(3)–O(2)	1.629(2)	C(5)–Si(4)–O(2)	111.32(17)
Si(4)–C(3)	1.860(4)	C(4)–Si(4)–O(2)	104.88(15)
Si(4)–C(4)	1.853(3)	C(5)–Si(4)–C(3)	107.87(17)
Si(4)–C(5)	1.852(4)	C(6)–Si(3)–C(7)	112.16(19)
Si(4)–O(2)	1.631(2)	C(7)–Si(3)–C(8)	111.66(18)
C(2)–C(3)	1.537(5)	C(8)–Si(3)–O(2)	108.33(15)
C(8)–C(9)	1.530(5)	C(6)–Si(3)–O(2)	110.10(16)
Fe(1)–Fe(2)	6.921	C(7)–Si(3)–O(2)	106.26(14)
O(1)–O(2)	4.667	C(6)–Si(3)–C(8)	108.28(17)
C(3)–C(8)	3.970	C(3)–C(2)–Si(1)	112.3(2)
C(2)–C(9)	3.896	C(2)–C(3)–Si(4)	115.9(2)
C(1)–Si(1)–C(11)	109.57(18)	C(8)–C(9)–Si(2)	113.4(2)
C(1)–Si(1)–C(2)	111.53(18)	C(9)–C(8)–Si(3)	115.6(2)
C(2)–Si(1)–O(1)	106.87(15)	Si(1)–O(1)–Si(2)	144.05(16)
C(11)–Si(1)–O(1)	109.96(15)	Si(3)–O(2)–Si(4)	150.75(17)

coordinating nature of the bulky $\text{B}(\text{C}_6\text{F}_5)_4^-$ anion. Geiger and co-workers have performed remarkable, extensive studies on this fluoroarylborate anion and ascribed the reported larger peak separation to its low ion-pairing strength and low nucleophilicity.²⁹

When $\text{B}(\text{C}_6\text{F}_5)_4^-$ is used as electrolyte anion, the CV of cyclic carbosiloxane **7** (Figure 5B) exhibits two perfectly resolved, reversible anodic waves. For both redox couples, the plot of peak current versus $\nu^{1/2}$ (ν = scan rate) is linear indicating that redox processes are diffusion controlled (Figures S25 and S26, Supporting Information). Likewise, the square wave voltammogram proceeds in two well-resolved oxidations steps at $^1E_{1/2} = +0.428$ and $^2E_{1/2} = +0.652$ V (vs SCE) (Figure 5C). Clearly, in agreement with the results reported by Geiger and co-workers,²⁹ the combination of CH_2Cl_2 and $[\text{n-Bu}_4\text{N}][\text{B}(\text{C}_6\text{F}_5)_4]$ as solvent/electrolyte medium, provides more favorable conditions for electrochemical studies of polyferrocenyl compounds, minimizing ion pairing interactions between the $[\text{B}(\text{C}_6\text{F}_5)_4]^-$ electrolyte anion and the cationic products generated in the oxidation processes. Consequently, as compared to the small inorganic $[\text{PF}_6]^-$ anion, the $[\text{B}(\text{C}_6\text{F}_5)_4]^-$ electrolyte anion has a lower coordinating power and restrains ion pairing, allowing development of interactions between the two metallocene units in **7**, which are electrostatic in nature, that is, mostly through-space interactions. This results in the observation of well-resolved one-electron oxidation waves, at different potentials, for each of the pendant ferrocenyl moieties. The presence of two separated oxidation processes for cyclic carbosiloxane **7**, with both $[\text{PF}_6]^-$ and $[\text{B}(\text{C}_6\text{F}_5)_4]^-$ electrolyte anions, suggests the existence of appreciable iron–iron electronic interactions between the two neighboring ferrocenyl units linked to different silicon atoms, in the disiloxane Si–O–Si moiety.

Despite of its greater number of electroactive ferrocenyl units, macrocycle **8**, having four pendant ferrocenes, also shows two well-resolved, reversible voltammetric waves in $\text{CH}_2\text{Cl}_2/[\text{n-Bu}_4\text{N}][\text{B}(\text{C}_6\text{F}_5)_4]$ medium at $^1E_{1/2} = +0.460$ and $^2E_{1/2} = +0.704$ V (vs SCE) (see Figure S27, Supporting Information), thus also suggesting communication between the pendant ferrocenyl centers connected by the Si–O–Si linkage. Likewise, linear oligomer **10** produced in the same solvent/electrolyte medium a CV showing two well-resolved waves of equal intensity, separated by 248 mV, suggesting two one-electron oxidations from interacting iron centers (Figure S27, Supporting Information). The straightforward determination of the two redox potentials for the ferrocenyl moieties for **7**, **8**, and **10** allowed the determination of the comproportionation constant, K_c , relative to the equilibrium among the three oxidation states of the two iron atoms, described by eq 1. The value of K_c can be obtained as $K_c = \exp[F\Delta E_{1/2}/RT]$.³⁰



The wave splitting ($\Delta E_{1/2} = ^2E_{1/2} - ^1E_{1/2}$) between the two successive redox events for **7**, **8** and **10**, and the comproportionation constant K_c , are both representative of the thermodynamic stability of the mixed valence state of these molecules relative to other redox systems. From the electrochemical viewpoint, based on the resulting values of $K_c = 6.11 \times 10^3$ (for **7**), 13.32×10^3 (for **8**) and 15.56×10^3 (for **10**), the partially oxidized molecules $[\text{7}]^+$, $[\text{8}]^{2+}$ and $[\text{10}]^+$ belong to the slightly delocalized class II mixed-valence species, according to the Robin–Day classification.³¹

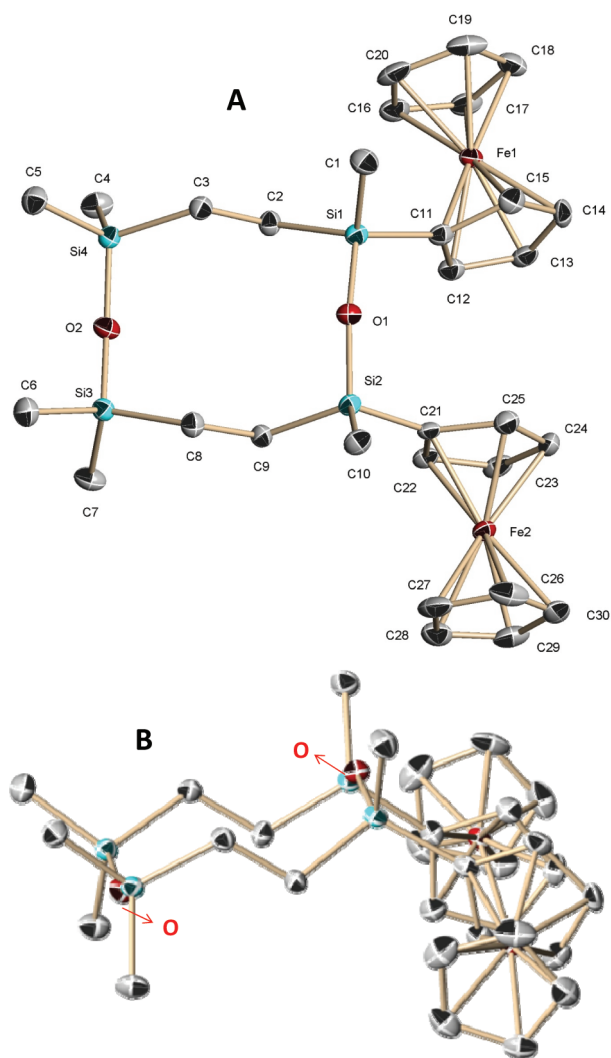


Figure 4. (A) Molecular structure of cyclic ferrocenyl-carbosiloxane 7. (B) Side view of 7. Thermal ellipsoids are drawn at the 50% probability level, and hydrogen atoms have been omitted for clarity.

Table 4. Electrochemical Data for Cyclic and Linear Ferrocenyl Carbosiloxanes^a

compound	¹ E _{1/2}	² E _{1/2}	ΔE (² E _{1/2} – ¹ E _{1/2}) ^b
7	0.428 (0.460)	0.652 (0.580)	224 (120)
8	0.460 (0.495)	0.704 (0.628)	244 (133)
10	0.508 (0.551)	0.756 (0.689)	248 (138)
11 _n	0.488 (0.348) ^c	0.708 (0.468) ^c	220 (120) ^c
	0.442 ^d	0.576 ^d	134 ^d
6	0.472 (0.484)	0.656 (0.592)	184 (108)

^aE_{1/2} in V vs SCE, determined by square wave voltammetry in CH₂Cl₂ solution (unless otherwise noted), with [n-Bu₄N][B(C₆F₅)₄] or [n-Bu₄N][PF₆] for values indicated in parentheses as supporting electrolytes. ^bThe peak potential separation values, ΔE, are given in mV. ^cIn CH₂Cl₂/CH₃CN (3:0.5) solution. ^dValues corresponding to a Pt disk electrode modified with a film of 11_n measured in CH₂Cl₂/ [n-Bu₄N][B(C₆F₅)₄].

Although the use of ΔE_{1/2} potential separation only provides a primary marker, with regard to electronic communication between redox-centers,²⁹ comparison of the ΔE_{1/2} values of carbosiloxanes 7, 8, and 10 with those shown by other related siloxane- or silicon-bridged polyferrocenyl derivatives in the

same solvent/electrolyte medium, provides a qualitative estimation of the electronic interaction extent between the ferrocenyl subunits. Thus, measured in CH₂Cl₂ with [B(C₆F₅)₄][–] as electrolyte anion, the wave splitting for the cyclic compounds 7 (ΔE_{1/2} = 224 mV) and 8 (ΔE_{1/2} = 244 mV), and linear 10 (ΔE_{1/2} = 248 mV), having pendant ferrocenyl units attached to the disiloxane bridge, are all slightly greater than the ΔE_{1/2} value for their divinylsiloxane precursor 6 (ΔE_{1/2} = 184 mV). These data suggest that the extent of the interaction between two adjacent ferrocenyl moieties linked to different silicon atoms in a Si–O–Si disiloxane bridge, appreciably depends on the nature of the substituents at the silicon. The results agree with those reported by Manners and co-workers in the study of a series of related polyferrocenylsilanes.³² On the other hand, the ΔE_{1/2} values for 7, 8, 10, and 6 (measured in CH₂Cl₂/[n-Bu₄N][PF₆]) are all appreciably greater than the observed by Pannell et al. for the oligoferrocenylsilane Fc(SiMe₂)₃Fc³³ containing a three-atom Si–Si–Si bridge, (ΔE_{1/2} = 80 mV in CH₂Cl₂/[n-Bu₄N][PF₆]). Clearly, these data indicate that the extent of iron–iron electronic interaction is somewhat higher when the two ferrocenyl moieties are linked by the three-atom oxygen-containing Si–O–Si bridging group than by the three-atom Si–Si–Si bridging group. Therefore, the degree of interaction is dependent on the nature of the bridge linking the adjacent ferrocenyl units. Our results are in agreement with the interesting studies on biferrrocenyl molecular wires FcCH=CHXCH=CHFc, recently reported by Tolbert et al.,³⁴ who have examined the role of the bridging heteroatoms X (X = O, P, S, Se), in supporting intramolecular electronic interactions between the two ferrocenyl units. They found that oxygen is a better electronic mediator and has superior transmission characteristics than sulfur (and than a double C=C bond), a phenomenon that was attributed to its readily accessible 2p electrons and superior molecular orbital overlap.³⁴

It is interesting to note that some significant differences can be observed when comparing the cyclic voltammetric behavior of 7 and 8 and 10 with that of ferrocenyl-containing oligocarbosiloxane 11_n in CH₂Cl₂/[n-Bu₄N][PF₆]. For cyclic molecules 7 and 8 (see for instance Figure 5A), oxidation and reduction did not appear to affect the solubility of the molecule, so, the voltammetric responses exhibited the wave shapes characteristic of a freely diffusing soluble species undergoing reversible charge transfer. As can be seen in Figure 5D, the features of the CV response in dichloromethane solution of ferrocenyl-oligocarbosiloxanes 11_n, having longest chain with greater number of pendant ferrocenyl units, are somewhat different, since, whereas the anodic waves have typical diffusional shape, a sharp cathodic wave was observed, which, in contrast, resembles more a surface wave. Consequently, for linear ferrocenyl oligocarbosiloxanes 11_n, the use of the small traditional PF₆[–] supporting electrolyte anion and low polarity dichloromethane solvent produces product surface interaction phenomena, probably due to precipitation of oxidized species [11_n⁺][PF₆[–]]_n on the electrode surface, giving rise to distortions from the wave shape expected for a reversible oxidation process. In addition, upon continuous scanning, there is a clear increase in the peak current with each successive scan (see Figure 5D and Figure S30) which indicates that formation of an electroactive film occurs on the electrode surface.

The ability of oligomer 11_n to undergo oxidative adsorption is remarkable and has allowed the preparation of ferrocenyl-carbosiloxane-modified electrode surfaces. The electrodeposi-

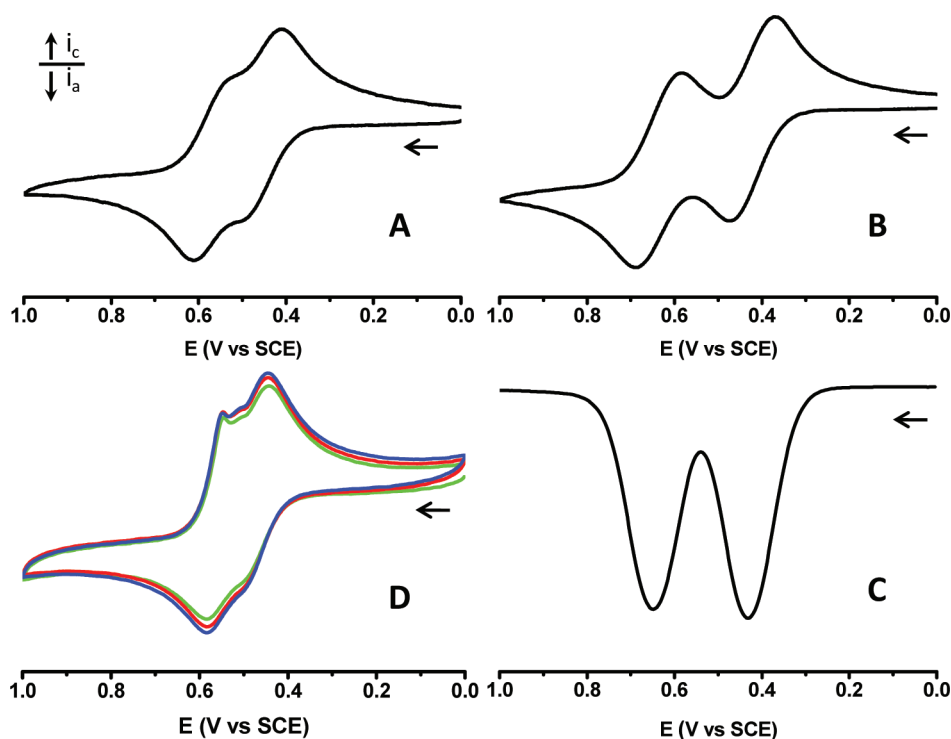


Figure 5. (A and B) Cyclic voltammograms at a scan rate of 0.1 V s^{-1} of dichloromethane solutions of cyclic 7 also containing: (A) $0.1 \text{ M } [n\text{-Bu}_4\text{N}][\text{PF}_6]$; (B) $0.1 \text{ M } [n\text{-Bu}_4\text{N}][\text{B}(\text{C}_6\text{F}_5)_4]$. (C) Square wave voltammetric response of 7 in $\text{CH}_2\text{Cl}_2/0.1 \text{ M } [n\text{-Bu}_4\text{N}][\text{B}(\text{C}_6\text{F}_5)_4]$. (D) CVs (successive scans) of linear oligomer 11_n measured in $\text{CH}_2\text{Cl}_2/0.1 \text{ M } [n\text{-Bu}_4\text{N}][\text{PF}_6]$.

tion of the oligomer was carried out on Pt electrodes, by repeated cycling (between +0.0 and +1.0 V vs SCE) in degassed CH_2Cl_2 solutions of the most insoluble fraction of 11_n . The electrochemical behavior of the films was studied by CV in ferrocenylcarbosiloxane-free CH_2Cl_2 solution containing only supporting electrolyte ($[n\text{-Bu}_4\text{N}][\text{PF}_6]$ or $[n\text{-Bu}_4\text{N}][\text{B}(\text{C}_6\text{F}_5)_4]$) to assess the extent of adsorption by cyclic voltammetry. Representative examples of the voltammetric responses obtained for different films of 11_n are shown in Figure 6. These electroactive films have been prepared by cyclically scanning the potential at different number of times (5, 15, or 50 scans) and consequently, they have different film thickness and different surface coverages Γ (mol/cm^2) of the ferrocenyl sites. Ferrocenyl carbosiloxane electroactive films are considerably stable as it was demonstrated by their nearly quantitative persistence after continuous CV scans in $\text{CH}_2\text{Cl}_2/[n\text{-Bu}_4\text{N}][\text{PF}_6]$ or $\text{CH}_2\text{Cl}_2/[n\text{-Bu}_4\text{N}][\text{B}(\text{C}_6\text{F}_5)_4]$ solutions. Likewise, after standing in air for several weeks, the redox responses were practically unchanged without loss of electroactive material.

Comparison of parts A and B of Figure 6 shows that the film thickness has a considerable effect on the electrochemical behavior of the films of 11_n , since the peak shapes of the polyferrocenyl-carbosiloxane films showed in the figure, are clearly different. At relatively low apparent coverage (Figure 6B, 15 scans, $\sim 2.0 \times 10^{-12} \text{ mol Fe}/\text{cm}^2$) the films in contact with $0.1 \text{ M } \text{CH}_2\text{Cl}_2/[n\text{-Bu}_4\text{N}][\text{PF}_6]$ exhibited two couples of well resolved oxidation–reduction waves, at $^1E_{1/2} = +0.450$ and $^2E_{1/2} = +0.515 \text{ V}$ (vs SCE), which are relatively similar to the CV waves of ferrocenyl-carbosiloxane 11_n in solution. For both waves, a linear relationship of peak current with potential sweep rate ν was observed, and the potential difference between the cathodic and anodic peak (ΔE_{peak}) is smaller than 25 mV at

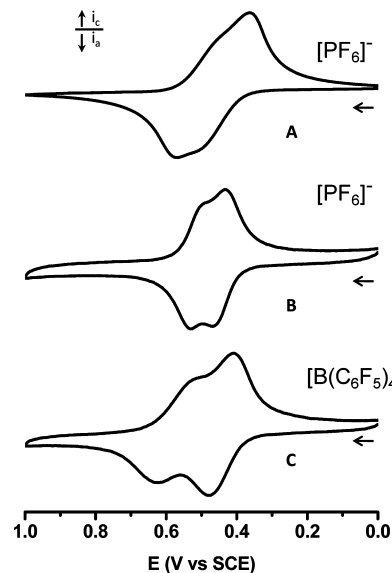


Figure 6. CV responses in CH_2Cl_2 solution of a platinum-disk electrode with a film of 11_n : (A) modified with 50 scans, measured in $0.1 \text{ M } [n\text{-Bu}_4\text{N}][\text{PF}_6]$; (B) modified with 15 scans, measured in $0.1 \text{ M } [n\text{-Bu}_4\text{N}][\text{PF}_6]$; (C) the same film as in part B measured in $0.1 \text{ M } [n\text{-Bu}_4\text{N}][\text{B}(\text{C}_6\text{F}_5)_4]/\text{CH}_2\text{Cl}_2$ solution. Scan rate $\nu = 0.025 \text{ V s}^{-1}$.

scan rates of 0.1 V s^{-1} or less (Figure S31, Supporting Information), which indicates that the rate of electron transfer is rapid on the time scale. These voltammetric features unequivocally indicate the surface-confined nature of the electroactive carbosiloxane film.^{35,36} As the film thickness increases (at high coverage, for example 50 scans, $\sim 1.2 \times 10^{-10} \text{ mol Fe}/\text{cm}^2$), significant differences in peaks shape, peak currents, and peak potentials appear (see Figures 6A and S33

(Supporting Information)). Specifically, the redox waves of the film in Figure 6A became asymmetrical, poorly resolved and show diffusional features. Both the oxidation and reduction peaks are sensitive to the scan rate, becoming more distorted at faster scan rates. The E_{pa} values are more sensitive to film thickness; they shifted to positive potentials quickly. This fact is consistent with the viewpoint that electrolyte permeability and diffusion control the oxidation process. In addition, the peak-to-peak separation of the film is larger (for instance, $\Delta E_{peak} = 140$ at scan rate of 0.025 V s^{-1}) and the peak currents are directly proportional to the square root of the scan rate, $v^{1/2}$ (see Figure S33, Supporting Information) (rather than to the scan rate, v , as experienced at low coverage) which suggests that in this case the charge transport through the film is limited by the electrolyte diffusion into the polymer film. These CV features indicate that increasing the film thickness hinders diffusion and electron transport and the film electrode process becomes quasi-reversible.

Finally, it is worth mentioning that the nature of the supporting electrolyte anion used also exerts a major effect on the electrochemical behavior of films of **11_n**. The cyclic voltammograms shown in Figure 6 are representative of the significant changes in $\Delta E_{1/2}$ values observed for the response of the same film of **11_n** measured in **11_n**-free electrolyte solution, first with PF_6^- (Figure 6B) and subsequently with $\text{B}(\text{C}_6\text{F}_5)_4^-$ (Figure 6C) as electrolyte anions. Clearly, in agreement with the results described for the solution redox behavior, the fluoroarylborate electrolyte anion improves the redox response of the film and gives wider peak separations ($\Delta E_{1/2} = 65 \text{ mV}$ with PF_6^- and $\Delta E_{1/2} = 134 \text{ mV}$ with $\text{B}(\text{C}_6\text{F}_5)_4^-$) for the films of **11_n**.

CONCLUSIONS

In summary, the vinylsilyl reactive groups in bifunctional disiloxane **6** have opened interesting possibilities to construct a series of novel precisely defined redox-active carbosiloxane macrocycles and short-chain linear co-oligomers by using hydrosilylation reactions. Although the original experimental conditions were adopted for preparing polymers and involved no high dilution conditions, macrocycles **7**, **8**, and **9_n** ($n = 3-6$) were invariably obtained as the major products. These results demonstrated that the formation of cyclic species is a favorable process in the followed reaction conditions. The combination of ^1H NMR spectrometry and MALDI-TOF mass spectrometry has proven to be the most definite characterization methods to confirm the macrocyclic and the linear structures for the hydrosilylation products obtained. Solution electrochemical studies indicated that macrocycles **7** and **8** as well as linear oligomers **10** and **11_n** ($n = 2-5$) are reversibly oxidized in two well-resolved oxidation steps which suggests significant electronic and electrostatic interactions among the ferrocenyl redox centers linked by the short three atom Si-O-Si bridge. A noteworthy aspect of the redox behavior of the linear oligo-ferrocenylcarbosiloxanes **11_n** is its ability to modify electrode surfaces, resulting in detectable electroactive films that remain persistently attached to the surface.

Further reactivity studies on the hydrosilylation reactions of divinylsilyl disiloxane **6** with other bis(silylhydrides) are underway along with its use aimed at the construction of branched dendritic structures. In addition, the fact that the new metallocene-containing carbosiloxane macrocycles present relatively large interior cavities decorated by disiloxane O atoms, coupled with the presence of pendant ferrocenyl units,

make these species potential candidates as hosts for binding metal ions in supramolecular chemistry. We are currently exploring this chemistry.

EXPERIMENTAL SECTION

Materials. Toluene was distilled over sodium/benzophenone under argon before use. Hexane, dichloromethane, and THF were dried by standard procedures over the appropriate drying agents and distilled immediately prior to use. Ferrocene (Aldrich) was purified by sublimation prior to use. 1,1,3,3-tetramethyldisiloxane (ABCR) and *tert*-butyllithium (1.7 M solution in pentane) (Aldrich) were used as received. Platinum-divinyltetramethyldisiloxane complex in xylene (3–3.5% Pt concentration) (Karstedt's catalyst) available from Aldrich was used as received. 1,3-Divinyl-1,3-dimethyl-1,3-dichlorodisiloxane (ABCR), was distilled prior to use. The vinyl-functionalized compound $[(\text{CH}_2=\text{CH})(\text{Fc})\text{MeSi}]_2\text{O}$ (**6**) was synthesized from monolithioferrocene (generated *in situ* from the reaction between ferrocene and *t*-BuLi, at low temperature) according to the procedure already described.¹⁸ Silica gel (70–230 mesh) (Merck) was used for column chromatographic purifications.

Hydrosilylation Reactions of 6 and 1,1,3,3-Tetramethyldisiloxane. All the hydrosilylation reactions were performed in all-glass apparatus, under oxygen and moisture-free atmosphere (Ar) using standard Schlenk techniques. Representative details of the hydrosilylations are summarized in Table 1. A typical experimental procedure was as follows and corresponds to the hydrosilylation of **6** with $[\text{Me}_2\text{SiH}]_2\text{O}$ under the conditions given in Table 1, no. 3.

In a 25 mL, three-necked, round-bottomed flask equipped with a gas inlet, a 25 mL pressure equalizing addition funnel, an Allihn condenser topped with gas inlet and bubbler, and a Teflon-covered magnetic stir bar, 0.2 g of monomer **6** (0.38 mmol) were dissolved in freshly distilled toluene (2.0 mL). To the resulting orange solution, 30 μL of Karstedt's catalyst were injected using a Hamilton precision syringe, under a flow of argon, and the mixture was aged at room temperature during 30 min. Subsequently, 69.26 μL (0.38 mmol) of 1,1,3,3-tetramethyldisiloxane were slowly added dropwise. The hydrosilylation reaction was allowed to proceed at 45–50 °C. The progress of the reaction was monitored by ^1H -NMR from the progressive disappearance of the Si-CH=CH₂ resonances of **6** at δ 5.8–6.4 ppm and Si-H of $[\text{Me}_2\text{SiH}]_2\text{O}$ at 4.7 ppm. This was done by the periodic removal of small aliquots from the reaction; toluene and other volatiles were removed under vacuum prior to obtaining the ^1H -NMR spectra. After 24 h, the ^1H NMR spectroscopy showed the complete disappearance of the Si-H and vinyl signals, in this moment the reaction was stopped. The mixture was allowed to cool to room temperature and the solvent was removed under vacuum. The orange oily residue was treated with methanol and purified by column chromatography on silica gel (3 cm \times 12 cm) using a mixture of hexane and CH_2Cl_2 as eluent. A first band containing a mixture of cyclic species was eluted with hexane/ CH_2Cl_2 (100:10). Then, on eluting with hexane/ CH_2Cl_2 (100:50) a second band was collected corresponding to a mixture of linear oligomers. A second column chromatography on silica gel (2 cm \times 15 cm) of the cyclic mixture was carried out. First, a major orange band was eluted (hexane/ CH_2Cl_2 100:5), and solvent removal afforded compound **7** as an air-stable orange crystalline solid. Subsequently a second orange band was separated (hexane/ CH_2Cl_2 100:15) affording, after solvent removal, compound **8** as an air-stable orange crystalline solid. The following bands, eluted with different mixtures of hexane/ CH_2Cl_2 , included mixtures of higher cyclic species **9_n**. Finally, a third column chromatography on silica gel (2 cm \times 15 cm) of the linear oligomers mixture was realized, eluting a first orange band with hexane/ CH_2Cl_2 (100:40). Solvent removal afforded compound **10** as an air-stable orange crystalline solid. As occurred before, the following bands, eluted with different mixtures of hexane/ CH_2Cl_2 , included mixtures of higher linear species **11_n**.

Cyclic 7. Yield: 50 mg (20%). Anal. Calcd for $\text{C}_{30}\text{H}_{44}\text{Fe}_2\text{O}_2\text{Si}_4$: C, 54.54; H, 6.72. Found: C, 54.77; H, 6.81. ^1H NMR (CDCl_3 , 300 MHz, ppm): δ 0.08, 0.09 (s, 12H, CH_3 -Si- CH_3), 0.22 (s, 6H, Fc-Si- CH_3),

0.55–0.90 (m, 8H, CH₂), 4.17 (s, 14 H, C₅H₅ and C₅H₄), 4.38 (s, 4H, C₅H₄). ¹³C{¹H} NMR (CDCl₃, 75 MHz, ppm): δ –0.8, 0.0, 0.1 (CH₃), 9.2, 9.9 (CH₂), 69.1 (C₅H₅), 70.1, 71.6, 72.4, 74.7 (C₅H₄). ²⁹Si{¹H} NMR (CDCl₃, 59 MHz, ppm): δ –0.2 (Fc–Si–CH₃), 7.7 (CH₃–Si–CH₃). IR (CsI): ν(Si–O–Si) 1032–1075 cm^{–1}, ν(Si–CH₃) 1251 cm^{–1}. MS (MALDI–TOF): *m/z* 660.2 [M⁺].

Cyclic 8. Yield: 45 mg (9%). Anal. Calcd for C₆₀H₈₈Fe₄O₄Si₈: C, 54.54; H, 6.72. Found: C, 54.82; H, 6.59. ¹H NMR (CDCl₃, 300 MHz, ppm): δ 0.08, 0.10 (s, 24H, CH₃–Si–CH₃), 0.29 (s, 12H, Fc–Si–CH₃), 0.50–0.80 (m, 16H, CH₂), 4.09 (s, 20H, C₅H₅), 4.11, 4.31 (m, 16H, C₅H₄). ¹³C{¹H} NMR (CDCl₃, 75 MHz, ppm): δ –0.9, –0.2, –0.1 (CH₃), 9.4, 9.9 (CH₂), 68.3 (C₅H₅), 70.6, 70.7, 73.0, 73.1 (C₅H₄). ²⁹Si{¹H} NMR (CDCl₃, 59 MHz, ppm): δ 0.5 (Fc–Si–CH₃), 8.2 (CH₃–Si–CH₃). IR (CsI): ν(Si–O–Si) 1032–1075 cm^{–1}, ν(Si–CH₃) 1251 cm^{–1}. MS (MALDI–TOF): *m/z* 1321.2 [M⁺].

Cyclic 9_n. ¹H NMR (CDCl₃, 300 MHz, ppm): δ 0.08, 0.11 (s, CH₃–Si–CH₃), 0.26–0.33 (m, Fc–Si–CH₃), 0.50–0.90 (m, CH₂), 4.05, 4.11, 4.12, 4.15, 4.29, 4.33 (m, C₅H₅ and C₅H₄). MS (MALDI–TOF): *m/z* 660.2 [M⁺, *n* = 1], 1321.2 [M⁺, *n* = 2], 1981.2 [M⁺, *n* = 3], 2642.2 [M⁺, *n* = 4], 3303.2 [M⁺, *n* = 5], 3964.2 [M⁺, *n* = 6]. IR (CsI): ν(Si–O–Si) 1039–1080 cm^{–1}, ν(Si–CH₃) 1251 cm^{–1}.

Linear 10. Yield: 19 mg (6%). Anal. Calcd for C₃₆H₆₂Fe₂O₅Si₆: C, 50.57; H, 7.32. Found: C, 50.91; H, 7.22. ¹H NMR (CDCl₃, 300 MHz, ppm): δ 0.08, 0.10 (s, 24H, CH₃–Si–CH₃ and (CH₃)₂Si(OCH₃)), 0.30 (s, 6H, Fc–Si–CH₃), 0.50–0.70 (m, 8H, CH₂), 3.46 (s, 6H, Si(OCH₃)), 4.09 (s, 14H, C₅H₅, C₅H₄), 4.32 (m, 4H, C₅H₄). ¹³C{¹H} NMR (CDCl₃, 75 MHz, ppm): δ –0.9, –0.4 (CH₃–Si–CH₃ and (CH₃)₂Si(OCH₃)), 9.3, 9.8 (CH₂), 49.7 (Si(OCH₃)), 68.3 (C₅H₅), 70.7, 73.1 (C₅H₄). ¹H–²⁹Si HMBC (CDCl₃, 59 MHz, ppm): δ –6.4 (Si(OCH₃)), 6.1 (Fc–Si–CH₃), 13.9 (CH₃–Si–CH₃). IR (CsI): ν(Si–O–Si) 1045–1066 cm^{–1}, ν(Si–CH₃) 1257 cm^{–1}. MS (MALDI–TOF): *m/z* 854.2 [M⁺].

Linear 11_n. ¹H NMR (CDCl₃, 300 MHz, ppm): δ 0.08–0.11 (br, CH₃–Si–CH₃ and (CH₃)₂Si(OCH₃)), 0.28, 0.30 (s, Fc–Si–CH₃), 0.50–0.70 (m, CH₂), 3.46 (s, Si(OCH₃)), 3.49 (s, Si(OH)), 4.11 (m, C₅H₅, C₅H₄), 4.33 (m, C₅H₄). ¹³C{¹H} NMR (CDCl₃, 75 MHz, ppm): δ –0.9 to 1.3 (CH₃–Si–CH₃ and (CH₃)₂Si(OCH₃)), 9.2–9.9 (CH₂), 49.7 (Si(OCH₃)), 68.3, 70.6, 70.7, 73.1 (C₅H₅ and C₅H₄). IR (CsI): ν(Si–O–Si) 1045–1066 cm^{–1}, ν(Si–CH₃) 1257 cm^{–1}. MS (MALDI–TOF): (OCH₃) × 2 terminated: *m/z* 855.2 [M⁺, *n* = 1], 1515.1 [M⁺, *n* = 2], 2175.1 [M⁺, *n* = 3], 2835.3 [M⁺, *n* = 4], 3495.7 [M⁺, *n* = 5]; (OCH₃)(OH) terminated: *m/z* 840.2 [M⁺, *n* = 1], 1500.1 [M⁺, *n* = 2], 2160.1 [M⁺, *n* = 3], 2820.3 [M⁺, *n* = 4], 3480.7 [M⁺, *n* = 5]; (OH) × 2 terminated: *m/z* 825.2 [M⁺, *n* = 1], 1485.1 [M⁺, *n* = 2], 2145.1 [M⁺, *n* = 3], 2805.3 [M⁺, *n* = 4], 3465.7 [M⁺, *n* = 5].

Characterization. Infrared spectra were recorded on Bomem MB-100 FT-IR and on Perkin-Elmer 100 FT-IR spectrometers. NMR spectra were recorded on Bruker-AMX-300 and Bruker DRX-500 spectrometers. Chemical shifts were reported in parts per million (δ) with reference to CDCl₃ residual solvent resonances for ¹H, δ 7.27 ppm and ¹³C, δ 77.0 ppm. ²⁹Si NMR spectra were recorded with inverse-gated proton decoupling in order to minimize nuclear Overhauser effects. Elemental analyses were performed in a LECO CHNS-932 elemental analyzer, equipped with a MX5METTLER TOLEDO microbalance. The Matrix-assisted laser desorption/ionization time-of-flight (MALDI–TOF) mass spectra were recorded using a Reflex III (Bruker) mass spectrometer equipped with a nitrogen laser emitting at 337 nm. Dichloromethane solutions of the matrix (dithranol, 10 mg/mL) and dichloromethane solutions of the corresponding compound (1 mg/mL) were mixed in the ratio 20:5. Then, 0.5–1 μL of the mixture were deposited on the target plate using the dried droplet method. The positive ion and the reflectron mode were used for these analyses.

Electrochemical Measurements. Cyclic voltammetric and square wave voltammetric experiments were recorded on a Bioanalytical Systems BASCV-50W potentiostat. CH₂Cl₂ and CH₃CN (SDS, spectrograde) for electrochemical measurements were freshly distilled from calcium hydride under argon. The supporting electrolytes used were tetra-*n*-butylammonium hexafluorophosphate (Fluka), which was purified by recrystallization from

ethanol and dried in vacuum at 60 °C, and tetra-*n*-butylammonium tetrakis(pentafluorophenyl)borate which was synthesized as described in the literature,³⁷ by metathesis of [NBu₄]Br with Li[B(C₆F₅)₄](*n*-OEt₂) (Aldrich) in methanol and recrystallized twice from CH₂Cl₂/hexane. The supporting electrolyte concentration was typically 0.1 M. A conventional three-electrode cell connected to an atmosphere of prepurified nitrogen was used. All cyclic voltammetric experiments were performed using either a platinum-disk working electrode (*A* = 0.020 cm²) or a glassy carbon-disk working electrode (*A* = 0.070 cm²) (both Bioanalytical Systems), each of which were polished on a Buehler polishing cloth with Metadi II diamond paste, rinsed thoroughly with purified water and acetone, and dried. All potentials were referenced to the saturated calomel electrode (SCE), which was separated from organic solutions by a fine frit. Under our conditions, the ferrocene redox couple [FeCp₂]^{0/+} is +0.462, and the decamethylferrocene redox couple [FeCp*₂]^{0/+} is –0.056 V vs SCE in CH₂Cl₂/0.1 M *n*-Bu₄NPF₆. A coiled platinum wire was used as a counter electrode. Solutions were, typically, 10^{–3} M or 10^{–4} in the redox active species. The solutions for the electrochemical experiments were purged with nitrogen and kept under an inert atmosphere throughout the measurements. From the CVs of the modified electrodes, the surface coverages, Γ (mol/cm²) of the ferrocenyl sites were calculated from the charge, *Q*, under the voltammetric current peaks, using Γ = *Q*/*nFA*. Square wave voltammetry (SWV) was performed using frequencies of 10 Hz.

X-ray Crystal Structure Determination. Cyclic compound 7 was structurally characterized by single-crystal X-ray diffraction. A suitable orange crystal of dimensions 0.25 × 0.12 × 0.10 mm, was located, coated with Paratone oil and mounted on a Mitegen MicroLoop. The crystal was frozen under a stream of nitrogen. The sample was transferred to a Bruker D8 KAPPA series II with APEX II area-detector system equipped with graphite monochromated Mo K_α radiation (λ = 0.71073 Å). A total of 12637 independent reflections (*R*_{int} = 0.0942) were collected in the range 1.16 < θ < 26.14°. X-ray data were collected at 100 K. ω and φ scans were employed to collect the data. The frame width for ω and φ was set to 0.5 deg for data collection with a crystal-to-detector distance of 5.0 cm. The substantial redundancy in data allows empirical absorption corrections (SADABS)³⁸ to be applied using multiple measurements of symmetry-equivalent reflections. The raw intensity data frames were integrated with the SAINT program,³⁹ which also applied corrections for Lorentz and polarization effects. The software package SHELXTL version 6.10 was used for space group determination, structure solution and refinement.⁴⁰ The space group determination was based on a check of the Laue symmetry and systematic absences and was confirmed using the structure solution. The structure was solved by direct methods (SHELXS-97), completed with different Fourier syntheses, and refined with full-matrix least-squares using SHELXL-97 minimizing ω(*F*_o² – *F*_c²).^{41,42} Weighted *R* factors (*R*_w) and all goodness of fit *S* are based on *F*²; conventional *R* factors (*R*) are based on *F*. All non-hydrogen atoms were refined with anisotropic displacement parameters. The hydrogen atom positions were calculated geometrically and were allowed to ride on their parent carbon atoms with fixed isotropic *U*. All scattering factors and anomalous dispersion factors are contained in the SHELXTL 6.10 program library. The crystal structure of 7 has been deposited at the Cambridge Crystallographic Data Centre and allocated the deposition number CCDC 853985.

■ ASSOCIATED CONTENT

Supporting Information

MALDI–TOF, NMR, and IR spectra, X-ray structure and bond lengths and angles for cyclic compound 7, and CV and SWV for 7–11_n, and crystallographic information files (CIF). This material is available free of charge via the Internet at <http://pubs.acs.org>.

■ AUTHOR INFORMATION

Corresponding Author

*E-mail: isabel.cuadrado@uam.es.

■ ACKNOWLEDGMENTS

We gratefully acknowledge financial support from the Spanish Ministerio de Ciencia e Innovación, Project CTQ2009-09125/BQU. S.B. acknowledges the Spanish Ministerio de Educación y Ciencia for a FPU grant. We thank Dr. M. Alonso and Dr. M. L. Gallego for their valuable assistance and helpful discussions on MALDI–TOF measurements.

■ REFERENCES

- (1) Manners, I. *Synthetic Metal-Containing Polymers*; Manners, I., Ed.; Wiley-VCH: Weinheim, Germany, 2004.
- (2) Peckham, T. J.; Gómez-Elipé, P.; Manners, I. In *Metalloenes. Synthesis, Reactivity, Applications*; Togni, A., Halterman, R. L., Eds.; Wiley-VCH: Weinheim, Germany, 1998; pp 723–771.
- (3) Long, N. J.; Kowalski, K. In *Ferrocenes. Ligands Materials and Biomolecules*; Stępnicka, P., Ed.; John Wiley & Sons: West Sussex, U.K., 2008; Chapter 10, pp 393–446.
- (4) *Frontiers in Transition Metal-Containing Polymers*; Abd-El-Aziz, A. S., Manners, I., Eds.; Wiley-Interscience: Hoboken, NJ, 2007.
- (5) For reviews on ferrocene-containing macromolecules and polymers, see for example: (a) Nguyen, P.; Gómez-Elipé, P.; Manners, I. *Chem. Rev.* **1999**, *99*, 1515–1548. (b) Pittman, C. U. J. *Inorg. Organomet. Polym.* **2005**, *15*, 33–55. (c) Bellas, V.; Rehahn, M. *Angew. Chem., Int. Ed.* **2007**, *46*, 5082–5104. (d) Abd-El-Aziz, A. S.; Manners, I. *J. Inorg. Organomet. Polym.* **2005**, *15*, 157–195. (e) Bellas, V.; Rehahn, M. *Angew. Chem., Int. Ed.* **2007**, *46*, 5082–5104. (f) Whittell, G. R.; Manners, I. *Adv. Mater.* **2007**, *19*, 3439–3468. (g) Casado, C. M.; Cuadrado, I.; Morán, M.; Alonso, B.; García, B.; González, B.; Losada, J. *Coord. Chem. Rev.* **1999**, *185*–186, 53–79. (h) Astruc, D.; Ornelas, C.; Ruiz, J. *Acc. Chem. Res.* **2008**, *41*, 841–856. (i) Cuadrado, I. In *Silicon-Containing Dendritic Polymers*; Dvornic, P., Owen, M. J., Eds.; Springer: Berlin, 2009; pp 141–196.
- (6) (a) Zamora, M.; Bruña, S.; Alonso, B.; Cuadrado, I. *Macromolecules* **2011**, *44*, 7994–8007. (b) Alonso, B.; González, B.; Ramírez, E.; Zamora, M.; Casado, C. M.; Cuadrado, I. *J. Organomet. Chem.* **2001**, *637*–639, 642. (c) Casado, C. M.; Cuadrado, I.; Morán, M.; Alonso, B.; Lobete, F.; Losada, J. *Organometallics* **1995**, *14*, 2618–2620. (d) Morán, M.; Casado, C. M.; Cuadrado, I.; Losada, J. *Organometallics* **1993**, *12*, 4327–4333. (e) Casado, C. M.; Cuadrado, I.; Morán, M.; Alonso, B.; Barranco, M.; Losada, J. *Appl. Organomet. Chem.* **1999**, *13*, 245–259.
- (7) (a) Zamora, M.; Alonso, B.; Pastor, C.; Cuadrado, I. *Organometallics* **2007**, *26*, 5153–5164. (b) Cuadrado, I.; Casado, C. M.; Alonso, B.; Morán, M.; Losada, J.; Belsky, V. *J. Am. Chem. Soc.* **1997**, *119*, 7613–7614. (c) García, B.; Casado, C. M.; Cuadrado, I.; Alonso, B.; Morán, M.; Losada, J. *Organometallics* **1999**, *18*, 2349–2356.
- (8) (a) Casado, C. M.; González, B.; Cuadrado, I.; Alonso, B.; Morán, M.; Losada, J. *Angew. Chem., Int. Ed.* **2000**, *39*, 2135–2138. (b) Alonso, B.; Cuadrado, I.; Morán, M.; Losada, J. *J. Chem. Soc., Chem. Commun.* **1994**, 2575–2576. (c) Alonso, B.; Morán, M.; Casado, C. M.; Lobete, F.; Losada, J.; Cuadrado, I. *Chem. Mater.* **1995**, *7*, 1440–1443. (d) Castro, R.; Cuadrado, I.; Alonso, B.; Casado, C. M.; Morán, M.; Kaifer, A. E. *J. Am. Chem. Soc.* **1997**, *119*, 5760–5761.
- (9) (a) *Hydrosilylation. A Comprehensive Review on Recent Advances. Advances in Silicon Science*; Marciniak, B., Ed.; Springer Science: Berlin, 2009; Vol. 1. (b) *Comprehensive Handbook on Hydrosilylation*; Marciniak, B., Ed.; Pergamon Press: Oxford, U.K., 1992. (c) Ojima, I. In *The Chemistry of Organic Silicon Compounds*; Patai, S., Rappoport, Z., Eds.; John Wiley & Sons: New York, 1989; Part 2, pp 1479–1526. (d) Roy, A. *Adv. Organomet. Chem.* **2008**, *55*, 1–59.
- (10) (a) Hilf, S.; Cyr, H.; Rider, D.; Manners, I.; Ishida, T.; Chujo, Y. *Macromol. Rapid Commun.* **2005**, *26*, 950–954. (b) McDowell, J. F.; Zacharia, N. S.; Puzzo, D.; Manners, I.; Ozin, G. A. *J. Am. Chem. Soc.* **2010**, *132*, 3236–3237.
- (11) (a) Kumar, M.; Metta-Magana, A. J.; Pannell, K. H. *Organometallics* **2008**, *27*, 6457–6463. (b) Kumar, M.; Pannell, K. H. *J. Inorg. Organomet. Polym.* **2008**, *18*, 131–142.
- (12) Jain, R.; Lalancette, R. A.; Sheridan, J. B. *Organometallics* **2005**, *24*, 1458–1467.
- (13) Wurm, F.; Hilf, S.; Frey, H. *Chem.—Eur. J.* **2009**, *15*, 9068–9077.
- (14) For an excellent recent review on silylative coupling of vinylsilanes, see: Pawluc, P.; Prukala, W.; Marciniak, B. *Eur. J. Org. Chem.* **2010**, 219–229.
- (15) Kong, J.; Schmalz, T.; Motz, G.; Müller, A. H. E. *Macromolecules* **2011**, *44*, 1280–1291.
- (16) Majchrzak, M.; Marciniak, B.; Kubicki, M.; Paweczyk, A. *Organometallics* **2005**, *24*, 3731–3736.
- (17) Bruña, S.; González-Vadillo, A. M.; Nieto, D.; Pastor, C.; Cuadrado, I. *Organometallics* **2010**, *29*, 2796–2807.
- (18) For remarkable examples silicon-containing ferrocenyl macrocycles, see: (a) Herbert, D. E.; Gilroy, J. B.; Chan, W. Y.; Chabanne, L.; Staibitz, A.; Lough, A. J.; Manners, I. *J. Am. Chem. Soc.* **2009**, *131*, 14958–14968. (b) Chan, W. Y.; Lough, A. J.; Manners, I. *Angew. Chem., Int. Ed.* **2007**, *46*, 9069–9072. (c) MacLachlan, M. J.; Zheng, J.; Lough, A. J.; Manners, I.; Mordas, C.; LeSuer, R. J.; Geiger, W. E.; Liable-Sands, L. M.; Rheingold, A. L. *Organometallics* **1999**, *18*, 1337–1345. (d) Grossmann, B.; Heinze, J.; Herdtweck, E.; Köhler, F. H.; Nöth, H.; Schwenk, H.; Spiegler, M.; Wachter, W.; Weber, B. *Angew. Chem., Int. Ed.* **1997**, *36*, 387–389. (e) Reyes-García, E. A.; Cervantes-Lee, F.; Pannell, K. H. *Organometallics* **2001**, *20*, 4734–4740.
- (19) For recent reviews on polycarbosiloxanes, see: (a) Pietrasanta, F. G.; Boutevin, B. *Adv. Polym. Sci.* **2005**, *179*, 1–27. (b) Putziena, S.; Nuyken, O.; Kühn, F. E. *Prog. Polym. Sci.* **2010**, *35*, 687–713.
- (20) Dvornic, P. R.; Gerov, V. V.; Govedarica, M. N. *Macromolecules* **1994**, *27*, 7575–7580.
- (21) Dvornic, P. R.; Gerov, V. V. *Macromolecules* **1994**, *27*, 1068–1070.
- (22) Antic, V. V.; Antic, M. P.; Govedarica, M. N.; Dvornic, P. R. *J. Polym. Sci. A: Polym. Chem.* **2007**, *45*, 2246–2258.
- (23) (a) Dvornic, P. R.; Lenz, R. W. *J. Polym. Sci., Polym. Chem. Ed.* **1982**, *20*, 951. (b) Dvornic, P. R. *J. Appl. Polym. Sci.* **1983**, *28*, 2729–2743.
- (24) (a) Hart-Smith, G.; Barner-Kowollik, C. *Macromol. Chem. Phys.* **2010**, *211*, 1507–1529. (b) Scrivens, J. H.; Jackson, A. T. *Int. J. Mass Spectrom.* **2000**, *200*, 261–276. (c) McEwen, C. N.; Peacock, P. M. *Anal. Chem.* **2002**, *74*, 2743–2748. (d) Peacock, P. M.; McEwen, C. N. *Anal. Chem.* **2006**, *78*, 3957–3964. (e) Montaudo, G.; Samperi, F.; Montaudo, M. S. *Prog. Polym. Sci.* **2006**, *31*, 277–357. (f) Gruendling, T.; Weidner, S.; Falkenhagen, J.; Barner-Kowollik, C. *Polym. Chem.* **2010**, *1*, 599–617.
- (25) Köhler, F. H.; Schell, A. *Rapid Commun. Mass Spectrom.* **1999**, *13*, 1088–1090.
- (26) Nielen, M. W. F. *Mass. Spec. Rev.* **1999**, *18*, 309–344.
- (27) The formation of cyclic structures has also observed in various hydrosilylation reactions. See, for example: (a) Perry, R. J.; Karageorgis, M.; Hensle, J. *Macromolecules* **2007**, *40*, 3929–3929. (b) Li, Y.; Kawakami, Y. *Macromolecules* **1998**, *31*, 5592–5597. (c) Tsumura, M.; Iwahara, T.; Hirose, T. *J. Polym. Sci., Part A* **1996**, *34*, 3155–3161.
- (28) For leading references on the dependence of $\Delta E_{1/2}$ values in organometallic compounds on different experimental conditions, see: (a) Geiger, W. E.; Barrière, F. *Acc. Chem. Res.* **2010**, *43*, 1030–1039. (b) Barrière, F.; Geiger, W. E. *J. Am. Chem. Soc.* **2006**, *128*, 3980–3989. (c) Nadafy, A.; Chin, T. T.; Geiger, W. E. *Organometallics* **2006**, *25*, 1654–1663. (d) Barrière, F.; Camire, N.; Geiger, W. E.; Mueller-Westerhoff, U. T.; Sanders, R. *J. Am. Chem. Soc.* **2002**, *124*, 7262–7263. (e) LeSuer, R. J.; Geiger, W. E. *Angew. Chem., Int. Ed.* **2000**, *39*, 248–250. (f) Camire, N.; Mueller-Westerhoff, U. T.; Geiger, W. E. *J. Organomet. Chem.* **2001**, *637*–639, 823–826.

- (30) Richardson, D. E.; Taube, H. *Inorg. Chem.* **1981**, *20*, 1278–1285.
- (31) (a) Robin, M. B.; Day, P. *Adv. Inorg. Chem. Radiochem.* **1968**, *10*, 247–422. (b) Creutz, C. *Prog. Inorg. Chem.* **1983**, *30*, 1–73.
- (32) Foucher, D. A.; Honeyman, C. H.; Nelson, J. M.; Tang, B. Z.; Manners, I. *Angew. Chem., Int. Ed. Engl.* **1993**, *32*, 1709–1711.
- (33) Dementiev, V. V.; Cervantes-Lee, F.; Parkanyi, L.; Sharma, H.; Pannell, K. H.; Nguyen, M. T.; Diaz, A. F. *Organometallics* **1993**, *12*, 1983–1987.
- (34) Li, Y.; Josowicz, M.; Tolbert, L. M. *J. Am. Chem. Soc.* **2010**, *132*, 10374–10382.
- (35) Murray, R. W. In *Molecular Design of Electrode Surfaces*; Murray, R. W., Ed.; Techniques of Chemistry, John Wiley and Sons: New York, 1992.
- (36) Abruña, H. D. In *Electroresponsive Molecular and Polymeric Systems*; Skotheim, T. A., Ed.; Dekker: New York, 1988; Vol. 1. p 97.
- (37) LeSuer, R. J.; Buttolph, C.; Geiger, W. E. *Anal. Chem.* **2004**, *76*, 6395–6401.
- (38) Sheldrick, G. M. SADABS Version 2.03, Program for Empirical Absorption Correction; University of Göttingen: Göttingen, Germany, 1997–2001.
- (39) SAINT+NT Version 6.04; SAX Area-Detector Integration Program; Bruker Analytical X-ray Instruments: Madison, WI, 1997–2001.
- (40) Bruker AXS SHELXTL Version 6.10, Structure Determination Package; Bruker Analytical X-ray Instruments: Madison, WI, 2000.
- (41) Sheldrick, G. M. *Acta Crystallogr. A* **1990**, *46*, 467.
- (42) Sheldrick, G. M. SHELXL97, Program for Crystal Structure Refinement, 1997.

Transformation of Living Cationic Polymerization of Vinyl Ethers to RAFT Polymerization Mediated by a Carboxylic RAFT Agent

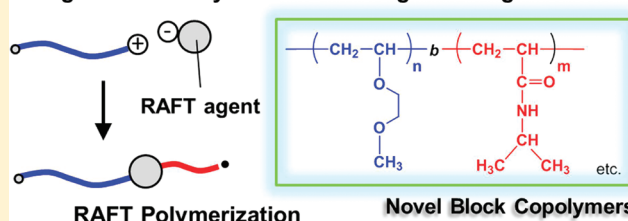
Shinji Sugihara,* Kenta Yamashita, Keiji Matsuzuka, Isao Ikeda, and Yasushi Maeda

Department of Applied Chemistry and Biotechnology, Graduate School of Engineering, University of Fukui, 3-9-1 Bunkyo, Fukui 910-8507, Japan

S Supporting Information

ABSTRACT: Novel block copolymers were synthesized by the transformation of living cationic polymerization of vinyl ethers into reversible addition–fragmentation chain transfer (RAFT) polymerization using two types of RAFT agents. Examples include cationically polymerizable monomer of either isobutyl vinyl ether or 2-methoxyethyl vinyl ether (MOVE) and radically polymerizable monomer such as ethyl acrylate, styrene, *tert*-butoxy styrene, and *N*-isopropylacrylamide (NIPAM). The key to success in the block copolymerization is to utilize a RAFT agent of the carboxylic trithiocarbonate/SnBr₄ initiation system in the presence of an additive such as ethyl acetate and dioxane for living cationic polymerization. The living cationic polymerization was initiated from a proton derived from the carboxylic RAFT agent. After a certain period, the polymerization was quenched and the RAFT group as a counteranion was concurrently recovered, followed by the RAFT process of radical polymerization using azobis(isobutyronitrile) at 70 °C. The first segments of the poly(vinyl ether) showed high number-average end functionality for the RAFT terminal group, 0.79 or more, and which were available as a macro-chain transfer agent for radical polymerization. Furthermore, using the transformation process, novel diblock copolymers were also prepared, containing two thermoresponsive segments possessing different lower critical solution temperatures (LCSTs), poly(2-methoxyethyl vinyl ether)–poly(*N*-isopropylacrylamide) (PMOVE–PNIPAM) block copolymers. The resulting block copolymers reversibly formed or deformed micellar assemblies during two LCSTs. The mean micellar sizes were controlled by the composition of PMOVE and PNIPAM, indicating the successful formation of the block copolymers.

Living Cationic Polymerization Using RAFT Agents



■ INTRODUCTION

Block copolymers by the covalent joining of segments with different chemical properties are promising molecules which have an affinity for two different types of environments in nanoscopic fields. Such block copolymers are generally synthesized by living or controlled polymerization via sequential addition technique of monomers through the same propagating species. Among these block copolymers, even for the block copolymers composed solely of vinyl ethers by living cationic polymerization,¹ various functional block copolymers such as polymer surfactants² involving glycopolymer, stimuli-responsive micelles and gels,^{3,4} and thermoplastic elastomers,⁵ have been reported. Thus, multimode polymerization capable of possessing various chain assortments by the transformation reaction between different propagating mechanisms proves to be further promising.

Over the past few decades a considerable number of studies have been conducted on the transformation reactions.⁶ For vinyl monomers, the transformation reactions are classified on the basis of interconversion of the propagating species such as cationic–radical, anionic–radical, anionic–cationic, and vice versa. Among them, we focus on the investigation of cationic–radical transformation using vinyl ethers because many monomers and materials generally undergo polymerization via a

radical process. However, the vinyl ethers and nonpolar olefins cannot be inherently polymerized via radical mechanism.^{6,7} In contrast, the vinyl ethers can be polymerized into high molecular weight products only by cationic polymerizations.^{1–5} Thus, efficient and versatile transformation reactions from living cationic to living radical polymerizations or vice versa should be required for block copolymers using vinyl ethers.

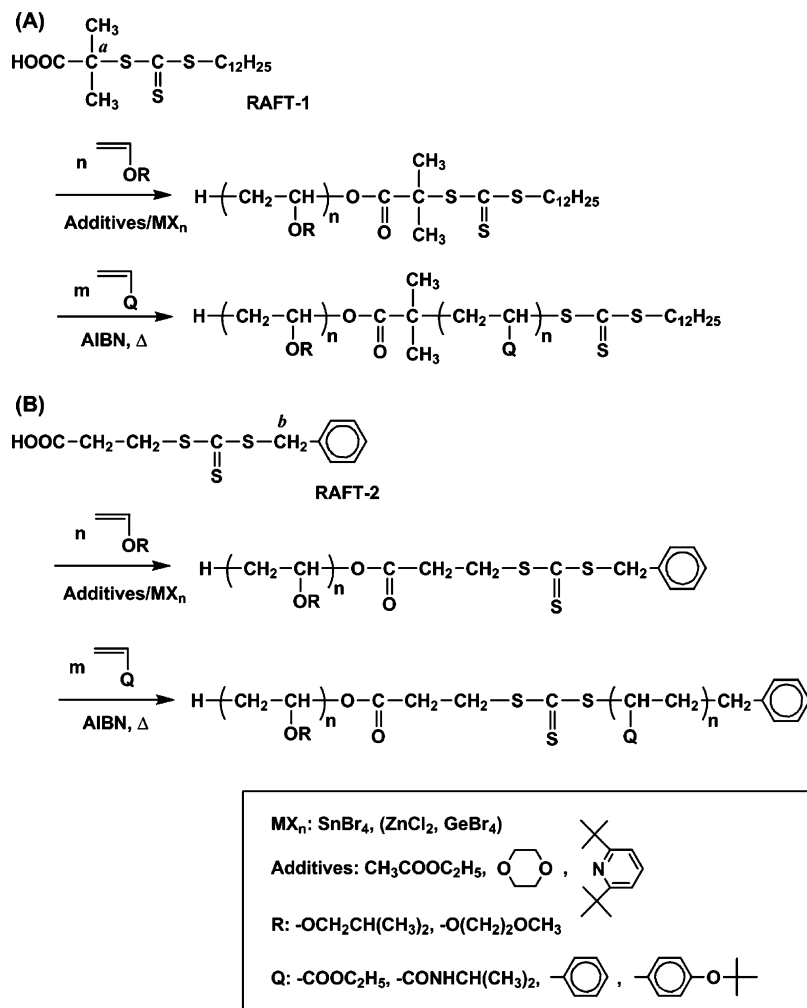
Such a transformation reaction of a propagating chain end has been applied to the synthesis of various block copolymers since the first mechanistic transformation from living anionic polymerization of styrene (St) to living cationic ring-opening polymerization of tetrahydrofuran.⁸ Then, the development of precision polymerization allowed the transformation reaction from living cationic to controlled radical polymerization using vinyl monomers, which was first reported by Matyjaszewski et al.⁹ They have reported the synthesis of block copolymers with polystyrene (PSt) and methyl acrylate by the transformation of living cationic polymerization into atom transfer radical polymerization (ATRP).^{10,11} Under such a strategy, synthesis of several block and graft copolymers has been subsequently

Received: August 31, 2011

Revised: November 15, 2011

Published: December 23, 2011

Scheme 1. Transformation of Living Cationic Polymerization of Vinyl Ether into RAFT Polymerization



achieved, e.g., poly(methyl vinyl ether)-*block*-polyacrylates, -poly(acrylic acid), or -PSt,¹² poly(β -pinene)-*block*-PSt,¹³ -poly(meth)acrylates,¹⁴ and graft copolymers from poly(isobutyl vinyl ether) (PIBVE) macromonomers.¹⁵ Moreover, quite recently, Yamago et al. reported the transformation of organotellurium-mediated living radical polymerization to cationic polymerization and precision synthesis of the related copolymers including vinyl ethers.¹⁶ Such transformation techniques are also promising and essential for the design of various copolymers.

As far as we aware, there has been only one example of block copolymers prepared by the combination of living cationic polymerization of vinyl ethers and reversible addition-fragmentation chain transfer (RAFT)^{17,18} polymerization, reported by Kamigaito et al. in 2010.¹⁹ They investigated *in situ* direct mechanistic transformation from RAFT to living cationic polymerization using a trithiocarbonate-type RAFT agent and an azo-initiator for RAFT polymerization of (meth)acrylates, followed by the addition of a Lewis acid catalyst for the sequential living cationic block polymerization of vinyl ethers. However, the reversed transformation, i.e., living cationic polymerization is first polymerization and the following is RAFT polymerization, has not been reported yet. In general, for being able to prepare the block copolymers from macro-chain transfer agent (macro-CTA) with RAFT process ultimately, a metal-free controlled polymerization techniques has been selected that leads to products which might be used in

optoelectronic materials²⁰ and biorelated applications.²¹ This is because there is no need to remove metal contaminants after polymerization. The design of RAFT agents makes available various monomers for polymerization. Thus, the transformation reactions from living cationic to living radical polymerizations in this order are required.

In this study, we report a novel method to prepare the block copolymers of poly(vinyl ether)s and radically polymerizable monomers such as acrylates, acrylamides, and styrenes with a well-defined structure and a controlled molecular weight by combination of two different polymerization mechanisms, living cationic polymerization and RAFT polymerization, as shown in Scheme 1. The process directly utilizes the counteranion mediated by living cationic polymerization initiated from a proton of a carboxyl group in the RAFT agent (RAFT-1 and RAFT-2) and has possibility for one-pot synthesis of the transformation of living cationic into RAFT polymerization. Moreover, in order to confirm the utility of this protocol, we prepared novel double thermoresponsive block copolymers using MOVE and NIPAM. The properties of the aqueous solutions of PMOVE-PNIPAM block copolymers were examined in detail, specifically focusing on the micelle formation behavior, because such block copolymers form the micellar assemblies in water between the LCSTs of each block⁴ (LCST for PMOVE is 66 °C,^{4,22,23} and for PNIPAM is 32 °C²⁴).

EXPERIMENTAL SECTION

Materials. Isobutyl vinyl ether (IBVE) (TCI; > 99.0%) and MOVE (donated by Maruzen Petrochemical; >99%) for cationic polymerization were washed with aqueous alkaline solution and then with water. These monomers were distilled twice over calcium hydride and were stored in a brown ampule under dry nitrogen in refrigerator. For solvent, toluene (Wako; >99.5%) were washed by the usual method and then was distilled over calcium hydride just before use. This solvent was also used for RAFT polymerization. Additives such as ethyl acetate (Wako; >99.5%) and dioxane (Wako; >99.0%) were distilled twice over calcium hydride and were stored in a brown ampule under dry nitrogen. 2,6-Di-*tert*-butylpyridine (DTBP) (Aldrich; >97%) was dissolved in dry toluene, and the solution was dried by 3A molecular sieves (Wako 3A 1/16) and filtered before use. Commercially available ZnCl_2 (Aldrich; 1.0 M solution in diethyl ether) and SnCl_4 (Aldrich; 1.0 M solution in dichloromethane) were used without further purification. For the SnBr_4 and GeBr_4 , 1.0 M stock solutions in toluene were prepared from anhydrous solid of SnBr_4 (Aldrich; >99%) and GeBr_4 (Wako; >99%), respectively. The stock solutions for these Lewis acids were further diluted to those at a desired concentration with dry toluene just before use.

For RAFT polymerization, the inhibitor of ethyl acrylate (EA) (TCI; > 99.0%) was removed by column chromatography using activated basic alumina. St monomer (Wako; >99.5%) and 4-*tert*-butoxy styrene (*t*BuSt) (donated by Maruzen Petrochemical; >99%) were washed with aqueous alkaline solution and then with water. These monomers were distilled under reduced pressure over calcium hydride and were stored in a brown ampule under dry nitrogen at -30°C . NIPAM monomer was recrystallized with benzene/hexane (3/7 v/v) and dried in vacuo. The initiator, azobis(isobutyronitrile) (AIBN) was recrystallized from diethyl ether and stored in refrigerator. RAFT agents, RAFT-1 and RAFT-2, were synthesized according to a well-known literature protocol.^{25,26}

Cationic Polymerization Procedures. Cationic polymerization was carried out at 0°C under a dry nitrogen atmosphere in a glass tube equipped with a three-way stopcock baked at 250°C for 10 min before use. First, carboxylic RAFT agent was added into the glass tube and was dried in vacuo. The carboxylic RAFT agent was diluted to 50 mM in toluene just before use. Toluene (3.0 mL), ethyl acetate (0.50 mL, 5.1 mmol), IBVE (0.50 mL, 3.8 mmol), and 50 mM of the RAFT agent in toluene (0.50 mL) were added into the glass tube using dry medical syringes, successively. The polymerization was initiated by the addition of a prechilled 5.0 mM SnBr_4 solution in toluene at 0°C . For the other conditions for cationic polymerization of IBVE, the same procedures were performed as follows: $[\text{IBVE}]_0 = 0.76\text{ M}$, $[\text{RAFT-1 or RAFT-2}]_0 = 5.0\text{ mM}$, $[\text{Lewis acid}]_0 = 0.5\text{ mM}$, $[\text{additive}] = 1.0\text{ M}$ for ethyl acetate, 1.25 vol % (0.146 M) for dioxane, or 0.15 mM for DTBT. For a thermoresponsive polymer, MOVE (0.44 mL, 3.8 mmol) was used instead of IBVE as follows: $[\text{MOVE}]_0 = 0.76\text{ M}$, $[\text{RAFT-1}]_0 = 5.0\text{ mM}$, $[\text{dioxane}] = 1.25\text{ vol \% (0.146 M)}$, $[\text{SnBr}_4]_0 = 0.5\text{ mM}$. After the desired time, the glass tube was cooled off under -40°C and the equilibrium of the reaction was displaced to dormant species. And then the reaction was terminated with prechilled methanol (0.5 mL) containing a small amount of aqueous ammonia solution (0.1 wt %). The quenched mixture (a) was diluted in either hexane or dichloromethane and was successively washed with 0.1 mol/L hydrochloric acid, water, 0.1 mol/L aqueous NaOH solution, and water to remove the initiator residues. The volatiles were then removed under reduced pressure over 50°C , and the residue was vacuum-dried for a day at room temperature. The monomer conversion was determined by gravimetry. In the case of the one-pot transformation, the quenched mixture (a) was used for the following RAFT polymerization, which was conducted by adding EA and AIBN only to the quenched mixture (a) at 70°C without further purification.

RAFT Polymerization Procedures. Either PIBVE or PMOVE macro-CTA obtained by living cationic polymerization was mixed with AIBN and varying amount of radically polymerizable monomer such as EA, St, *t*BuSt and NIPAM, and dried toluene for the desired concentration in Schlenk flask, which was equipped with a magnetic stir

bar. The typical contents for the polymerization of EA are as follows: Toluene (3.1 mL), EA (0.50 mL, 4.70 mmol), PIBVE macro-CTA using RAFT-2 (in the case of number-average degree of polymerization (DP) = 20, 0.054 g, 23.5 μmol), 1.0 wt % AIBN in toluene (0.117 g, 7.1 μmol); $[\text{EA}]_0/[\text{PIBVE macro-CTA}]_0/[\text{AIBN}]_0 = 200:1:0.3$ molar ratio. These solutions were stirred in an ice-bath until all reagents had dissolved. After sparging with nitrogen for approximately 30 min, each polymerization was allowed to proceed at 70°C and then quenched after the desired time via rapid cooling in -40°C and exposure to air. For block copolymers including a PIBVE block, the volatiles were then removed under reduced pressure over 40°C , and the residue was vacuum-dried for a day at room temperature. For PMOVE–PNIPAM block copolymer, the crude product was then purified by dialysis against deionized water using semi-permeable cellulose tubing (SPECTRA/POR, corresponding to a molecular weight cutoff of 1000 Da) with at least six changes of deionized water, followed by lyophilization.

Polymer Characterization. Molecular weight distributions (MWDs) excluding those of PMOVE–PNIPAM block copolymers were assessed by size exclusion chromatography (SEC) in tetrahydrofuran (THF) at 40°C using three polystyrene gel columns [TSK gel G-MHHR-MX3 (exclusion limit: 4×10^6 (PSt)); 7.8 mm i.d \times 300 mm each; flow rate 1.0 mL/min] connected to a Tosoh CCPM-II pump and a RI-8020 and UV-8020 for refractive index (RI) and ultraviolet (UV) detector, respectively. The RI detector was mainly used for determining of number-average molecular weight (M_n) and polydispersity (M_w/M_n). For PMOVE–PNIPAM, the MWDs were assessed by another SEC in *N,N*-dimethylformamide (DMF) with 10 mM LiBr at 40°C using a polystyrene gel columns [TSK gel G-MHHR-M; flow rate 1.0 mL/min] connected to a Tosoh CCPM-II pump and a RI-8012 and UV-8000 for refractive and UV detector, respectively. M_n and M_w/M_n was calculated from SEC curves on the basis of a PSt calibration. ^1H NMR spectra for the structure such as the number-average end functionality of the RAFT terminal (F_n) and the compositions of block copolymers were recorded on either JEOL JNM-EX300 (300 MHz) or JEOL JNM-EX500 spectrometer (500 MHz). Matrix-assisted laser desorption ionization time-of-flight mass (MALDI-TOF-MS) spectra were recorded using a Bruker Daltonics autoflex spectrometer (linear mode) using dithranol as the matrix and sodium trifluoroacetate as the ion source (polymer sample/dithranol/sodium trifluoroacetate = 1/8/1 weight ratio).²⁷

Characterization of Aqueous Block Copolymer Solutions. Aqueous solutions of the copolymers were prepared by dissolving the polymer in Mill-Q water and diluting the sample to those at a desired concentration. The thermoresponsive behavior of the solutions were measured by monitoring the transmittance of a 500 nm light beam through a 1.0 cm glass sample cell at a rate of $1.0^\circ\text{C}/\text{min}$ in heating and cooling scans between 15 and 85°C . The transmittance was recorded on a JASCO V-500 UV/vis spectrometer equipped with a Peltier-type thermostatic cell holder ETC-505. DSC measurements were performed using a Micro Calorimetry System (MicroCal) at a rate of $1.0^\circ\text{C}/\text{min}$ in heating and cooling scans between 20 and 80°C . The block copolymer sample dissolved in water (0.5 wt %) was degassed and transferred to the sample cell (cell volume: 1.22 mL) with a syringe. An identical volume of the solvent of the same composition was placed in the reference cell. Dynamic light scattering (DLS) studies were performed using a DLS-7000 (Photol, Otsuka Electronics) at various temperatures at scattering angle of 90° using 0.1–0.2 wt % aqueous solution of the thermoresponsive PMOVE–PNIPAM micelles. The light source was a He–Ne laser (10 mW, $\lambda = 632.8\text{ nm}$). The intensity-average hydrodynamic diameter (D_h) and polydispersity (PDI, μ_2/Γ^2) were calculated by cumulants analysis of the experimental correlation function using the attached software of the DLS-7000.

RESULTS AND DISCUSSION

Synthesis of Poly(vinyl ether) Macro-CTAs by Living Cationic Polymerization Using Carboxylic RAFT Agents. First, we synthesized two types of RAFT agents,

Table 1. Synthesis of PIBVE Macro-CTAs by Living Cationic Polymerization^a

entry	RAFT agent	Lewis acid	additive ^b	time (h)	convn (%)	$M_n \times 10^{-3}$ (calcd) ^c	$M_n \times 10^{-3d}$	M_w/M_n^d	F_n^e
1	1	ZnCl ₂	no	1	41.8	6.7	2.9	5.94	0.51 ^f
2	1	SnBr ₄	ethyl acetate	4	30.0	4.9	4.6	1.38	0.87
3	1	SnBr ₄	dioxane	3	50.3	8.0	7.7	1.30	0.86
4	2	ZnCl ₂	no	1	49.8	7.9	9.7	4.13	0.65 ^f
5	2	SnBr ₄	DTBP	3	17.3	2.9	2.2	1.44	0.79
6	2	SnBr ₄	DTBP	12	49.2	7.7	8.4	1.13	0.80
7	2	SnBr ₄	dioxane	3	24.7	4.0	4.1	1.14	0.88
8	2	SnBr ₄	ethyl acetate	3	13.0	2.3	2.2	1.11	0.88
9	2	SnCl ₄	ethyl acetate	1	42.4	6.7	7.4	1.16	0
10	2	GeBr ₄	ethyl acetate	67	11.1	2.0	1.7	1.39	0.60
11	2	GeBr ₄	dioxane	243	27.4	4.4	3.6	1.70	0.65

^aCationic polymerization conditions: [IBVE]₀ = 0.76 M, [RAFT agent]₀ = 5.0 mM, [Lewis acid]₀ = 0.5 mM, in toluene in the presence of an additive at 0 °C. ^bAdditives: [ethyl acetate] = 10.0% (1.0 M), [dioxane] = 1.25 vol % (0.146 M), [DTBP] = 0.15 mM. ^cMW_{RAFT agent} + (MW_{IBVE} × conversion × [IBVE]₀/[RAFT agent]₀). ^dDetermined by SEC (PSt calibration; THF eluent). ^eOn the basis of the peak intensity ratio of the methine proton on the hemiacetal ester to the α -end methyl protons. ^fOn the basis of the peak intensity ratio of the methine proton on the hemiacetal ester to the methine proton produced by methanol termination.

RAFT-1 and RAFT-2, which have a carboxylic group, a trithiocarbonate unit with a radical active moiety (free radical leaving group), and a radical stable moiety.^{17–20,25,26} However, quite recently, the RAFT agents are also commercially available. The trithio-type RAFT agents are estimated to be more stable than dithio-type ones against Lewis acid.²⁸ The radical active moieties are different between RAFT-1 and RAFT-2, which are **a** and **b** for RAFT-1 and RAFT-2, respectively, as shown in Scheme 1.

Some carboxylic acid/ZnCl₂/no additives or carboxylic acid/SnBr₄/additive-based initiation systems produce the poly-(vinyl ether) with the ester terminal group recovered from the counteranion even after quenching the polymerization with methanol.^{29,30} Hence, using one of the carboxylic RAFT agents as an initiator with a Lewis acid including ZnCl₂, SnBr₄, and its congener of GeBr₄, we examined the cationic polymerization of IBVE as a typical example. Table 1 summarizes the results for the various PIBVEs prepared at relatively low conversion (conversion ≤ 50%) by living cationic polymerization in this study, as calculated from the SEC and ¹H NMR data. All polymerization of IBVE was carried out in toluene in the presence of an additive (except for ZnCl₂) at 0 °C using carboxylic RAFT agent and Lewis acid with the following concentration: [IBVE]₀ = 0.76M; [carboxylic RAFT agent]₀ = 5.0 mM, [Lewis acid]₀ = 0.5 mM. Among them, SnBr₄, SnCl₄, and GeBr₄ induced a controlled reaction in the presence of an additive to produce polymers with relatively narrow MWDs even in the early stage (entries 2, 3, and 5–11 in Table 1). However, with ZnCl₂, PIBVE with broad MWDs were produced, indicating uncontrolled polymerization (entries 1 and 4 in Table 1). This is due to the slow interconversion between the dormant species and active species as previously reported for the CH₃COOH/ZnCl₂ initiation system.²⁹ With GeBr₄, very slow polymerization proceeded, regardless of the kind of additives. Thus, it appears to be hard to use the living cationic polymerization systems with GeBr₄ (entries 10 and 11 in Table 1). Compared with RAFT-1 and RAFT-2 for SnBr₄, the resulting MWDs of RAFT-1 were larger than those of RAFT-2 in the presence of any additives. This is because the initiation reaction of RAFT-2 is slightly quicker than that of RAFT-1 due to difference of the acidity of the carboxylic acid in the RAFT agent, that is, RAFT-2 has slightly more acidic than RAFT-1. For the additives such as ethyl acetate, dioxane, and DTBP, all are appropriate added

bases in this condition. Especially, with dioxane for RAFT-1 or RAFT-2 and with ethyl acetate for RAFT-2, the polymerizations were controlled well to produce polymers with very narrow MWDs ($M_w/M_n < 1.30$) in conjunction with SnBr₄. Furthermore, these living polymers obtained with SnBr₄ had a trithiocarbonate end group for either RAFT-1 or RAFT-2. The F_n s of the RAFT terminal were calculated by ¹H NMR spectroscopy, which were 0.79 or more. (The results of analysis are described later in detail by means of both ¹H NMR and MALDI-TOF-MS spectroscopies). The additives do not have any influence on the F_n . Instead, the F_n of RAFT-2 is slightly higher than that of RAFT-1 but within experimental errors. Thus, such an additive, i.e. an added base, is likely to be involved in the formation of a counteranion, which in turn interacts suitably with the propagation carbocation but does not affect the recovery of the RAFT terminal. These polymers are substantially available for a macro-chain transfer agent for next RAFT polymerization, prepared by living cationic polymerization. While with SnCl₄, no recovery of the RAFT terminal was observed. On the basis of these results, we next investigated the kinetics of the cationic polymerization of IBVE using either RAFT-1 or RAFT-2/SnBr₄/additive (either dioxane or ethyl acetate) initiation system in consideration of the MWD and F_n .

Figure 1A shows a typical example of the time–conversion curve for the polymerization of IBVE using either RAFT-1 or RAFT-2 in the presence of dioxane. Both polymerization occurred without an induction period and was almost completed in 30 h and ca. 50 h for RAFT-1 and RAFT-2, respectively, to afford soluble polymers in quantitative yield. The polymerization rate of RAFT-1 was faster than that of RAFT-2. This is due to the different structure of the counteranion derived from the corresponding RAFT agent which has both a ester and a trithioester group as a Lewis base. Figure 1B plots the M_n and M_w/M_n of PIBVE as a function of monomer conversion. The typical SEC curves are shown in Figure 1C. Irrespective of the kind of RAFT agents in this study, the M_n increased in direct proportion to the monomer conversion, and the values are very close to the calculated values assuming that one polymer chain is formed per one RAFT agent. The MWDs of the resulting polymers were relatively narrow for RAFT-2 ($M_w/M_n = 1.09–1.39$). The PIBVE obtained from RAFT-1 also had narrow M_w/M_n at high conversion region ($M_w/M_n = 1.19$ at 99.0% conversion). This is due to the rate of initiation as mentioned above. Furthermore, all SEC

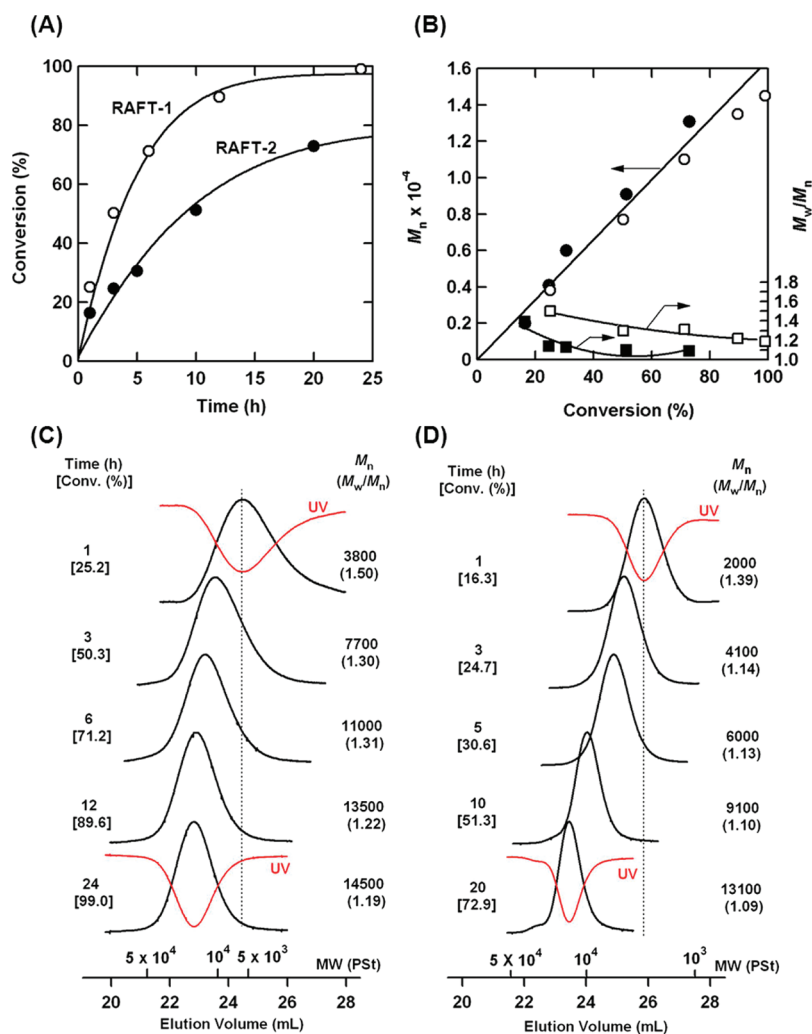


Figure 1. Cationic polymerization of IBVE using either RAFT-1 or RAFT-2 with SnBr_4 in toluene in the presence of dioxane at 0°C : $[\text{IBVE}]_0 = 0.76\text{ M}$, $[\text{dioxane}] = 146\text{ mM}$, $[\text{RAFT agent}]_0 = 5.0\text{ mM}$, $[\text{SnBr}_4]_0 = 5.0\text{ mM}$. (A) Kinetic plots for RAFT-1 (\circ) and RAFT-2 (\bullet) and (B) M_n and M_w/M_n as a function of monomer conversion (M_n and M_w/M_n are peaks (\circ) and (\square) for RAFT-1 or peaks (\bullet) and (\blacksquare) for RAFT-2, respectively). (C and D) Typical SEC curves for PIBVE using RAFT-1 and PIBVE using RAFT-2, respectively. Black curves are by refractive index and red curves (for the first and the final curves) are by UV at 308 nm.

chromatograms by UV at 308 nm were also detected at the same position as RI detection, indicating the existence of the RAFT terminal group. The 308 nm is around the maximum absorption wavelength of π - π^* absorption bands of the thiocarbonyl group in the RAFT agent.

Figures 2A and 3A show the ^1H NMR spectra of the PIBVE obtained from RAFT-1 and RAFT-2, respectively. Figure 2B and 3B show the ^1H NMR spectra of the corresponding RAFT agent (initiator). The typical polymers with relatively low molecular weights were prepared to evaluate the terminal polymer end structures under the same condition in Figure 1. All the polymers exhibited the signals ascribed to the methyl protons due to the initiator (*a*) (i.e., α -end), the methine proton of hemiacetal (*g*), the terminal RAFT group (*h*–*l* or *h*–*k* for RAFT-1 or RAFT-2, respectively) (i.e., ω -end), and protons due to IBVE repeating units (*b*–*f*), regardless of the RAFT structure. The peak intensity ratio of the methine proton of hemiacetal (*g*) and the protons of the terminal RAFT group (especially, *k* for RAFT-1 or *j* and *k* for RAFT-2, respectively) are relatively in good agreement with the calculated value expected by their structures.

In addition, a small peak *m* or *l* for RAFT-1 or RAFT-2, respectively, appeared around 4.6 ppm. This is assignable to the methine proton of the terminal acetate that arises on quenching the polymerization with methanol. These results show that the obtained PIBVE macro-CTA includes a small amount of different terminated polymer structures.

On the basis of the peak intensity ratio of the methine proton (*g*) to the α -end methyl protons (*a*), the F_n was calculated. It is significant because the F_n via living cationic polymerization corresponds to RAFT-CTA efficiency for the next RAFT polymerization. Here, F_n values were calculated to be 0.87 and 0.88 for RAFT-1 in Figure 2 and RAFT-2 in Figure 3, respectively (also see entries 2 and 8 in Table 1). The F_n is in good agreement with the F_n calculated by the peak intensity ratio of the methine proton (*g*) and the methine proton of the methoxy terminal (*m* or *l* for RAFT-1 or RAFT-2, respectively). All the values of F_n for the macro-CTAs prepared by living cationic polymerization are also listed in Table 1.

As an additional evidence for the retention of the RAFT end groups, MALDI-TOF-MS spectrometry analyses for the typical products were conducted as shown in Figure 4. The major peaks *a* in the spectrum correspond to: $\text{H}-(\text{IBVE})_n\text{-CH=CH(OiBu)}$;

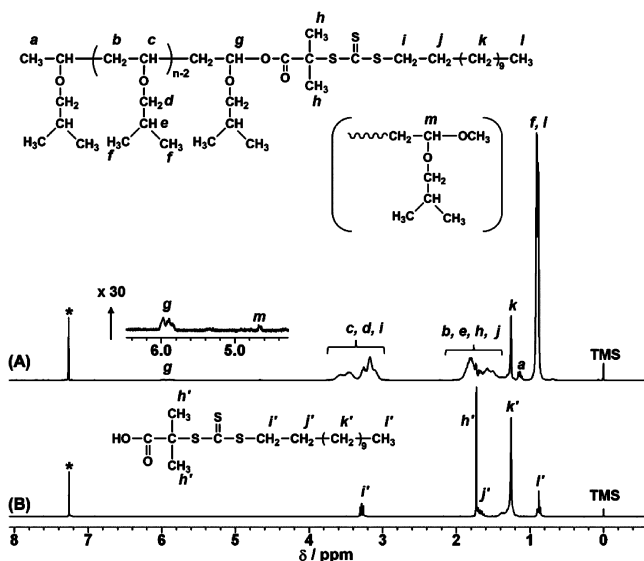


Figure 2. ^1H NMR spectra for (A) PIBVE macro-CTA prepared by living cationic polymerization from RAFT-1 and (B) RAFT-1 in CDCl_3 at 25°C . The inset shows the chemical structure of (A) the PIBVE macro-CTA (entry 2 in Table 1) and (B) RAFT-1 with full peak assignments (a – m and h' – l'). Asterisks denote CHCl_3 peaks (TMS: tetramethylsilane).

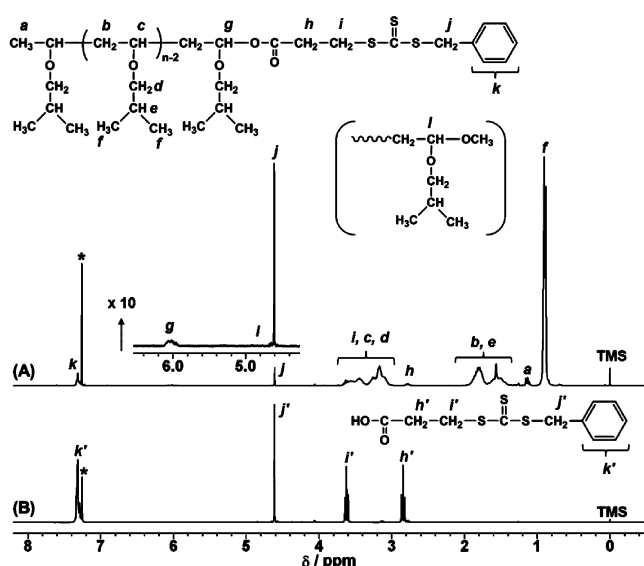


Figure 3. ^1H NMR spectra for (A) PIBVE macro-CTA prepared by living cationic polymerization from RAFT-2 and (B) RAFT-2 in CDCl_3 at 25°C . The inset shows the chemical structure of (A) the PIBVE macro-CTA (entry 8 in Table 1) and (B) RAFT-1 with full peak assignments (a – l and h' – k'). Asterisks denote CHCl_3 peaks.

consistent with the polymer being capped with the olefin (detailed structure: see “●” in Table 2). For $n = 14$ in the structure, one of the experimental signals (1525.4 g/mol, signal *a* in Figure 4A) fits the calculated molecular weight with Na^+ (1525.4 g/mol). The distance between individual peaks (e.g., difference between *a* and *b*) which is by 100 mass units is also corresponding to the molar mass of the IBVE repeating unit.

Our target PIBVE with RAFT-2 contains a hemiacetal ester as a relatively weak covalent bond between PIBVE and RAFT-2. Such weakly bonded end groups are often cleaved in the MALDI experimental process as well as RAFT end groups.³¹ If

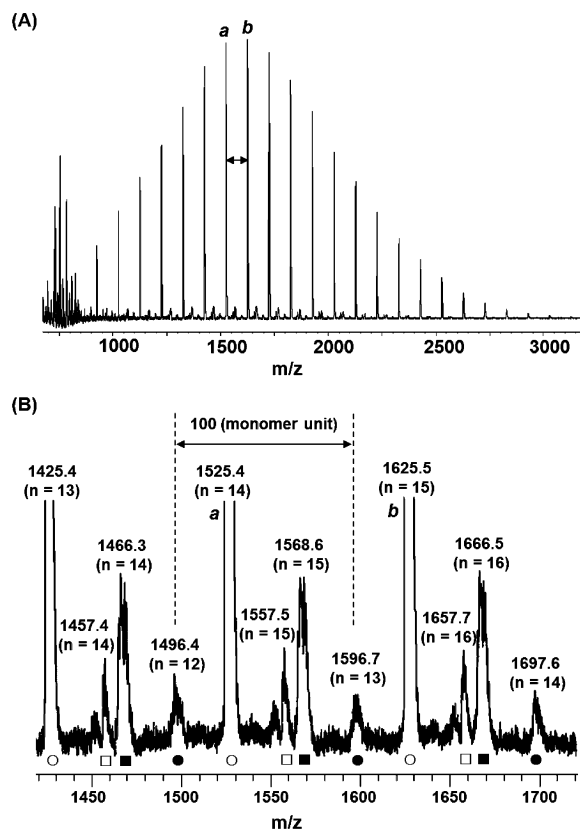


Figure 4. (A) MALDI-TOF-MS spectrum of PIBVE (entry 8 in Table 1). (B) Expanded region of the spectrum (A). The peaks are labeled with their measured molecular weights and the number of repeating units (n). The detailed structures (○, ●, □, and ■) are shown in Table 2. The interpeak distances between the same structures correspond to the mass of the IBVE repeating unit.

β -proton elimination from the growing cation is occurred and then the reaction generates a proton, the same structure $\text{H}-(\text{IBVE})_n-\text{CH}=\text{CH}(\text{OiBu})$ is also obtained.³² In such a case, experimental M_n becomes smaller than the calculated based on the amount of RAFT-2. However, the experimental M_n is in good agreement with the calculated (see Table 1 or Figure 1). Furthermore, ^1H NMR indicates that the signal due to methine proton derived from a RAFT end group was seen at a high functionality in Figure 3. Thus, the structure $\text{H}-(\text{IBVE})_n-\text{CH}=\text{CH}(\text{OiBu})$ is formed in the decomposition of hemiacetal esters due to MALDI experimental process.

Figure 4B shows the expanded region of the spectrum between mass/charge (m/z) = 1420 and 1720. Several series of peaks are observed in the spectrum. Fortunately, our target end group is still remained and the peak “●” values agreed with the calculated mass of our target PIBVE with RAFT-2; one of the experimental signals (1697.6 g/mol) fits the calculated molecular weight with Na^+ (1697.6 g/mol for $n = 14$) (detailed structure: “●” in Table 2). The distance between individual peaks is also corresponding to the molar mass of the IBVE repeating unit as shown in Figure 4B.

The other peaks are for quenching by methanol containing a small amount of aqueous ammonia solution (0.1 wt %). The peaks “□” correspond to the terminal quenched by methanol and the peaks “■” are ascribed to the terminal quenched by water and then dealcoholized of $i\text{Bu}-\text{OH}$ (detailed structures are also shown in Table 2).

Table 2. PIBVE with Various ω -End Groups Estimated by MALDI-TOF-MS in Figure 5

symbols in Figure 5	polymer structures	formula weight (+ Na)
○	$\begin{array}{c} 1.01 \quad 100.16 \times n \quad 99.15 \quad 22.99 \\ \text{H} - (\text{CH}_2 - \text{CH})_n - \text{CH} = \text{CH} \\ \quad \quad \quad \text{O}i\text{Bu} \quad \quad \quad \text{O}i\text{Bu} \end{array}$	$n = 14$ $\text{mass}(\text{exp}) = 1525.4$ $\text{mass}(\text{calcd}) = 1525.4$
●	$\begin{array}{c} 1.01 \quad 100.16 \times n \quad 271.40 \quad 22.99 \\ \text{H} - (\text{CH}_2 - \text{CH})_n - \text{O} - \text{C}(=\text{O}) - \text{CH}_2 - \text{CH}_2 - \text{S} - \text{C}(=\text{S}) - \text{S} - \text{CH}_2 - \text{C}_6\text{H}_5 \\ \quad \quad \quad \text{O}i\text{Bu} \end{array}$	$n = 14$ $\text{mass}(\text{exp}) = 1697.6$ $\text{mass}(\text{calcd}) = 1697.6$
□	$\begin{array}{c} 1.01 \quad 100.16 \times n \quad 31.03 \quad 22.99 \\ \text{H} - (\text{CH}_2 - \text{CH})_n - \text{OCH}_3 \\ \quad \quad \quad \text{O}i\text{Bu} \end{array}$	$n = 15$ $\text{mass}(\text{exp}) = 1557.5$ $\text{mass}(\text{calcd}) = 1557.4$
■	$\begin{array}{c} 1.01 \quad 100.16 \times n \quad 43.05 \quad 22.99 \\ \text{H} - (\text{CH}_2 - \text{CH})_n - \text{CH}_2 - \text{C}(=\text{O}) - \text{H} \\ \quad \quad \quad \text{O}i\text{Bu} \end{array}$	$n = 15$ $\text{mass}(\text{exp}) = 1568.6$ $\text{mass}(\text{calcd}) = 1569.4$

On the basis of these results, the apparent intensity area ratio of the peaks “○” and “●” derived from the RAFT end group to the whole peaks is calculated to be approximately 0.9, which is in good agreement with the end-functionality $F_n = 0.88$ calculated from ^1H NMR spectroscopy. For RAFT-1, the similar spectrum was observed. Unfortunately, all the RAFT end groups were cleaved in the MALDI experimental process to form the $\text{H}-(\text{IBVE})_n-\text{CH}=\text{CH}(\text{O}i\text{Bu})$, although the RAFT end-functionality determined by ^1H NMR spectrometry is sufficiently high ($F_n = 0.86$) (Figure S1 in the Supporting Information). As shown here, living cationic polymerization of vinyl ethers initiated from either RAFT-1 or RAFT-2 with SnBr_4 in the presence of added base, produced the poly(vinyl ether) possessing each RAFT end group recovered from the counteranion.

Synthesis of Various Block Copolymer by RAFT Polymerization. Once the CTA-functionalized PIBVE was obtained, RAFT polymerizations were conducted for the synthesis of various block copolymers between PIBVE macro-CTA and radically polymerizable monomer. For RAFT polymerization to function effectively, the proper choice of the structure of RAFT agents is extremely important. Since the guidelines for selection of RAFT agents for radically polymerizable monomers have been already shown by many researchers,^{17,18} the RAFT polymerization of appropriate monomers such as acrylates, acrylamides, and styrenes were next employed using PIBVE macro-CTA.

As a typical example, in order to check the livingness of this RAFT polymerization, the kinetic study of the polymerization of EA was carried out in toluene at 70 °C using PIBVE macro-CTA with molar ratio $[\text{EA}]_0/[\text{PIBVE}]_0/[\text{AIBN}]_0 = 200:1:0.3$, monitored by both ^1H NMR spectroscopy and SEC. That means the synthesis of PIBVE-poly(ethyl acrylate) (PIBVE-PEA) block copolymers. Figure 5A shows the time-conversion curve of the polymerization of EA using PIBVE macro-CTA of RAFT-2. The polymerization occurred smoothly and the RAFT polymerizations exhibited linear first-order plots, indicating an approximately constant number of growing species. As expected, the M_n was increased linearly with the monomer

conversion as shown in Figure 5B. The MWDs clearly shifted toward higher molecular weights from the M_n of PIBVE macro-CTA as shown in Figure 5C. As a typical example, the structure

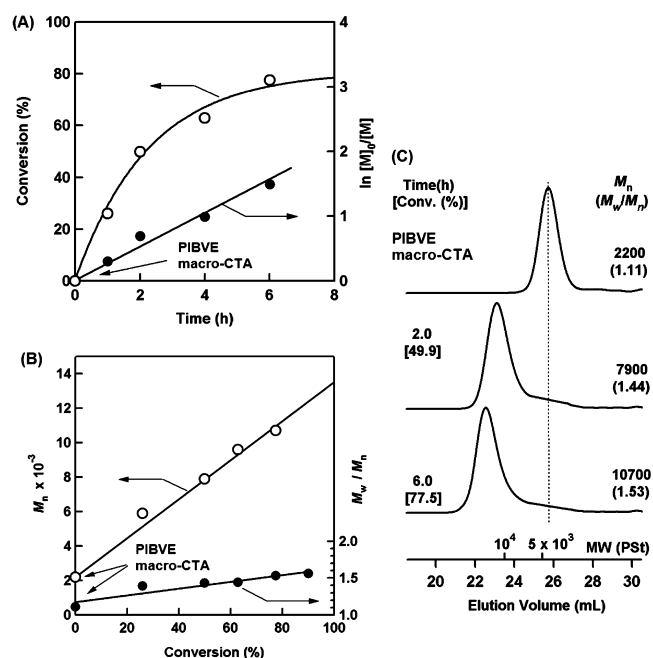


Figure 5. RAFT polymerization of EA using PIBVE macro-CTA of RAFT-2 (entry 8 in Table 1) in toluene at 70 °C: $[\text{EA}]_0/[\text{PIBVE}]_0/[\text{AIBN}]_0 = 200:1:0.3$. (A) Kinetic plots, (B) evaluation of M_n (○) and M_w/M_n (●) with conversion, and (C) the typical SEC curves for PIBVE macro-CTA, PIBVE-PEA at 2 and 6 h.

of the block copolymer obtained at 6.0 h was determined by ^1H NMR spectroscopy as shown in Figure 6. The composition was in agreement with the monomer feed ratio of EA to PIBVE macro-CTA at the conversion (77.5%), which was calculated from the characteristic peak intensities of the methyl protons of IBVE (peak e) and EA (peak i) assuming that $F_n = 1$ and the

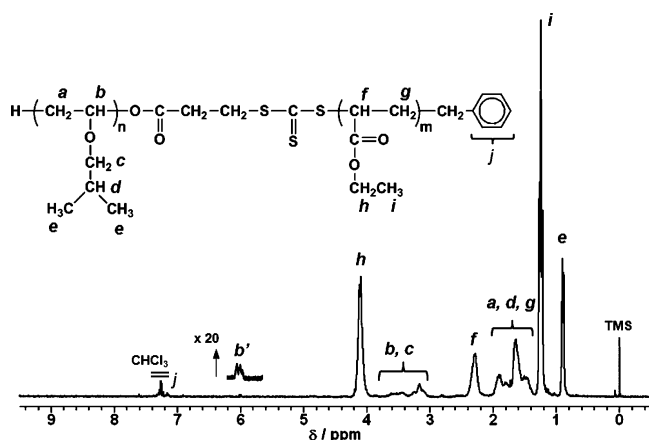


Figure 6. ^1H NMR spectrum recorded for the PIBVE-PEA block copolymer (conversion = 77.5%, $M_n = 10700$, $M_w/M_n = 1.53$, $n/m = 20:146$) in CDCl_3 . See Figure 5 for the polymerization conditions. The composition was determined from the area ratio of peaks (e and i) assuming that $F_n = 1$ and the degree of polymerization for the PIBVE macro-CTA (DP = 20). A magnified peak b' is the methine proton on the hemiacetal ester between PIBVE and PEA blocks.

degree of polymerization for the PIBVE macro-CTA (DP = 20). For the detailed polymer structure, the methine proton on the hemiacetal ester between PIBVE and PEA blocks remained in the block copolymer after RAFT polymerization (peak b'). While, there are no peaks around 4.6 ppm which correspond to the methylene protons of the terminal RAFT group (i.e., peak j in Figure 3) derived from PIBVE macro-CTA (RAFT-2). The peak was shifted to high magnetic fields after block copolymerization via RAFT polymerization. This indicates that the second RAFT polymerization virtually initiated from a benzyl moiety in inset chemical structure of Figure 6. However, there is small tailing in the lower molecular weight regions in SEC chromatograms, which may be due to end functionality of the RAFT terminal via living cationic polymerization because the apparent block efficiency is roughly correspond to the end functionality by SEC chromatograms.

The block copolymer, IBVE₇₆-EA₉₀, prepared from PIBVE macro-CTA using RAFT-1 (entry 3 in Table 1) were also obtained ($M_n = 16100$, $M_w/M_n = 1.33$; see Figure S2 for SEC and Figure S3 for the ^1H NMR spectrum in the Supporting Information). No differences were seen between PIBVE macro-CTAs using RAFT-1 or RAFT-2.

Figure 7 represents the SEC chromatograms on the results of the RAFT polymerization of the other monomers such as St and *t*BuSt. Both MWDs clearly shifted toward higher molecular weights from the M_n of the PIBVE macro-CTA as well as the MWDs of EA. The tailing of poly(*t*BuSt) (PtBuSt) was seen like a shoulder peak, indicating the lower end functionality ($F_n = 0.79$) as shown in Table 1. The compositions of the diblock copolymers were also determined by ^1H NMR spectroscopy assuming that $F_n = 1$ and were calculated from the characteristic peak intensities of the e and h for both in parts A and B of Figure 8. The observed ratio agreed well with the monomer feed ratio of PIBVE and St or *t*BuSt at the obtained conversion.

The Possibility for the One-Pot Transformation. This protocol has possibility for one-pot transformation of living cationic polymerization using vinyl ethers from a RAFT agent into RAFT polymerization using radically polymerizable monomers. For the one-pot method of PIBVE-PEA block copolymer prepared from RAFT-2, PIBVE was first polymerized by

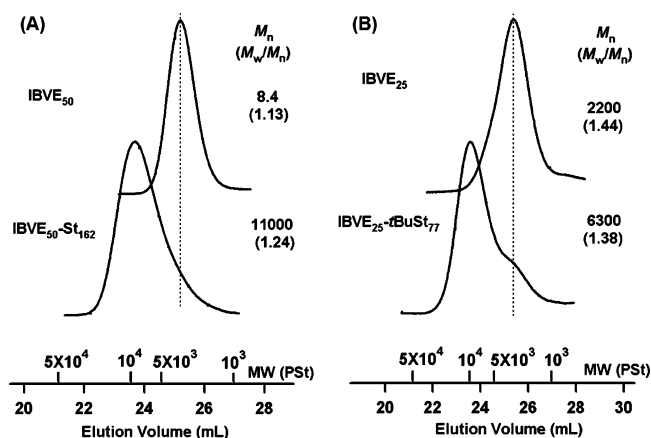


Figure 7. Typical SEC curves for (A) PIBVE-PSt and (B) PIBVE-PtBuSt block copolymers using PIBVE macro-CTA using RAFT-1 (entries 6 for part A and 5 for part B) in Table 1). The compositions were determined by calculation from the area ratio of characteristic peaks using ^1H NMR spectra shown in Figure 8 assuming that $F_n = 1$ and the degree of polymerization for the PIBVE macro-CTA.

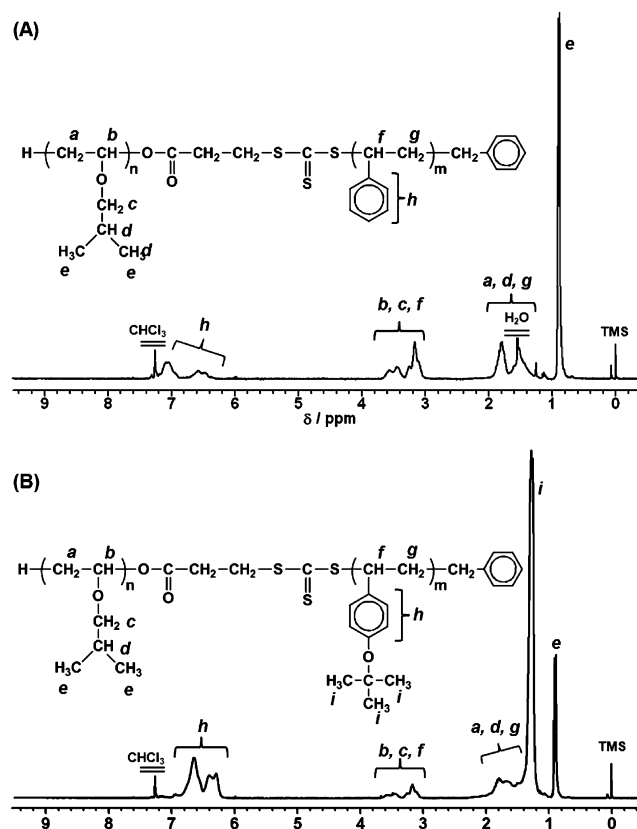


Figure 8. ^1H NMR spectra recorded for (A) PIBVE-PSt and (B) PIBVE-PtBuSt block copolymers in CDCl_3 . The block copolymers are the same as those in Figure 7.

living cationic polymerization and then EA using the sequential monomer addition method without purification. Unfortunately, in the presence of the residue derived from SnBr_4 and unreacted IBVE, RAFT polymerization was not controlled to show multimodal MWDs (Figure S4 in Supporting Information). Fortunately, after the perfect polymerization of IBVE (conversion > 95–99%) and passing the reaction mixture through silica column directly to remove the residue derived from SnBr_4

(without evaporation of the volatiles) and then RAFT polymerization of EA was conducted, well-defined PIBVE–PEA block copolymers were obtained as well as those by nonone-pot method in Figure 5. However, the protocol is substantially the same as nonone-pot method in Figure 5. Furthermore, if excess cationic polymerization proceed after IBVE monomers are consumed, aldehyde end groups instead of RAFT end groups would be observed due to β -proton elimination from the growing cation.³² Thus, it is necessary for purification of the poly(vinyl ether) macro-CTA to obtain well-defined block copolymers via the following RAFT polymerization.

Synthesis of Double Thermoresponsive Block Copolymer, PMOVE–PNIPAM. Using our protocol of this study above-mentioned, novel double thermoresponsive block copolymers, PMOVE–PNIPAM, were prepared. This is further confirmation of synthesis of novel block copolymer by the transformation of the living cationic polymerization to RAFT polymerization. As the first step, the living cationic polymerization of MOVE was conducted using RAFT-1 with SnBr_4 in

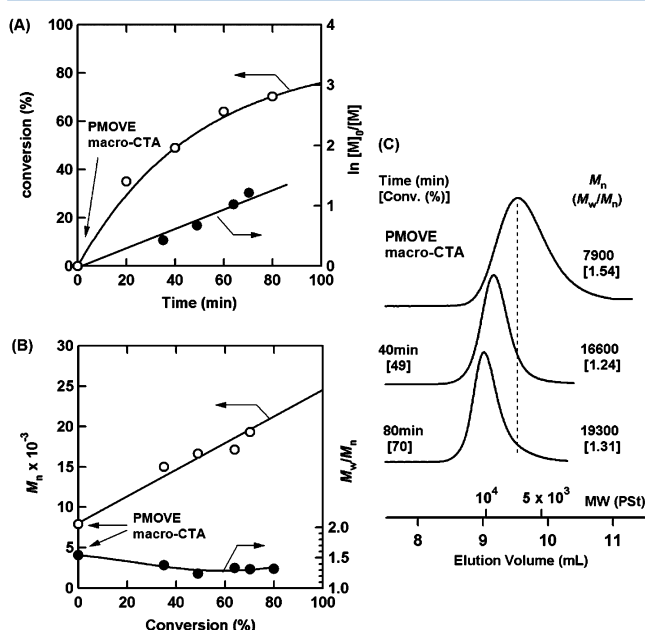


Figure 9. RAFT polymerization of NIPAM using PMOVE macro-CTA of RAFT-1 ($M_n = 7900$, $M_w/M_n = 1.54$) in toluene at 70 °C: $[\text{NIPAM}]_0:[\text{PMOVE}]_0:[\text{AIBN}]_0 = 200:1:0.3$. (A) Kinetic plots, (B) evaluation of M_n (○) and M_w/M_n (●) with conversion, and (C) the typical SEC curves for PMOVE macro-CTA, PMOVE–PNIPAM diblock copolymers at 40 and 80 min.

the presence of ethyl acetate. Irrespective of the different kind of vinyl ether, the values of M_n are close to the calculated values assuming that one polymer chain is formed per one RAFT agent (see the result of PMOVE macro-CTA in Figure 9). However, the obtained MWDs of PMOVE were somewhat broader than those of PIBVE; the values of M_w/M_n for MOVE₁₀₇ and MOVE₆₄ are 1.47 and 1.54, respectively (see Figure 9 and Table 3). The compositions were estimated by ^1H NMR spectroscopy at the conversion.

The obtained PMOVE was purified by dialysis against water and then dried. Then, it was used as a macro-CTA for next RAFT polymerization with NIPAM. The typical SEC chromatograms for the purified PMOVE macro-CTA and two PMOVE–PNIPAM block copolymers are shown in Figure 9C, monitored by both ^1H NMR spectroscopy and SEC. The MWDs clearly shifted toward higher molecular weights and the M_w/M_n becomes narrower in comparison to those of PMOVE. All the M_n and M_w/M_n of PMOVE–PNIPAM samples are summarized in Table 3.

^1H NMR spectroscopy in D_2O was used to examine the temperature dependence of phase-separation behavior. Figure 10 shows the ^1H NMR spectra of NIPAM₆₄–MOVE₁₆₅ (entry 15) as a typical example. At 10 °C which is temperature below LCST of both PNIPAM and PMOVE homopolymers, all peaks appeared at a high resolution (Figure 10A). At 45 °C which is temperature between LCSTs of PNIPAM and PMOVE homopolymers, all the copolymer signals were shifted downfield relative to H₂O at 4.7 ppm. Furthermore, all the signals assigned to the PNIPAM chains disappeared, whereas the peaks due to the PMOVE chains remained sharp (Figure 10B). This indicates that PNIPAM-core micelles are formed at 45 °C, above LCST of PNIPAM. The resulting micelle was reversibly formed or deformed, depending on the solution temperature over these temperature ranges.

The detailed phase separation behavior for PNIPAM–PMOVE in water as a function of temperature is shown in Figure 11. Below 32 °C, PNIPAM–PMOVE block copolymer is molecularly dissolved and shows a D_h of around 11–15 nm, relatively high PDI (μ_2/Γ^2), and a low scattering intensity (Figure 11A). Above 32 °C, the slightly opaque appearance was observed (transmittance at 500 nm decreased in Figure 11B) that is characteristic of micellar solutions. The diameter increased and the polydispersity decreased around this temperature. The transition temperature corresponds to the LCST values of the PNIPAM block, as indicated by the DSC thermogram in Figure 11B. On heating up to LCST of PMOVE block, the relationship between diameter and temperature shows a slightly convex curve in the range of 100–127 nm. On further heating to

Table 3. Synthesis of PMOVE–PNIPAM Block Copolymers by the Transformation of Living Cationic Polymerization Using RAFT-1 to RAFT polymerization^a

entry	polymer structure ^b	polymn time (h)		$M_n \times 10^{-3}$ ^c		M_w/M_n ^c		micellar D_h (nm) ^d	PDI (μ_2/Γ^2) ^d
		homo	diblock	homo	diblock	homo	diblock		
12	MOVE ₁₀₇ –NIPAM ₇₅	4.5	0.5	6.9	13.3	1.47	1.72	60	0.25
13	MOVE ₁₀₇ –NIPAM ₁₈₄	4.5	1	6.9	17.4	1.47	1.69	99	0.21
14	MOVE ₁₀₇ –NIPAM ₂₁₀	4.5	3	6.9	22.5	1.47	1.69	117	0.09
15	MOVE ₆₄ –NIPAM ₁₆₅	0.5	0.7	4.3	16.6	1.54	1.24	111	0.21
16	MOVE ₆₄ –NIPAM ₂₁₄	0.5	1.3	4.3	19.3	1.54	1.31	116	0.10

^aCationic polymerization conditions: $[\text{MOVE}]_0 = 0.76$ M, $[\text{RAFT-1}]_0 = 5.0$ mM, $[\text{dioxane}] = 146$ mM, $[\text{SnBr}_4]_0 = 0.5$ mM, in toluene at 0 °C. ^bThe degree of polymerization in the formula was determined by ^1H NMR spectroscopy in CDCl_3 on the basis of degree of polymerization of the PMOVE block assuming that $F_n = 1.0$. ^cDetermined by SEC (PSt calibration; DMF eluent with 10 mM LiBr). ^dDetermined by DLS at 45 °C.

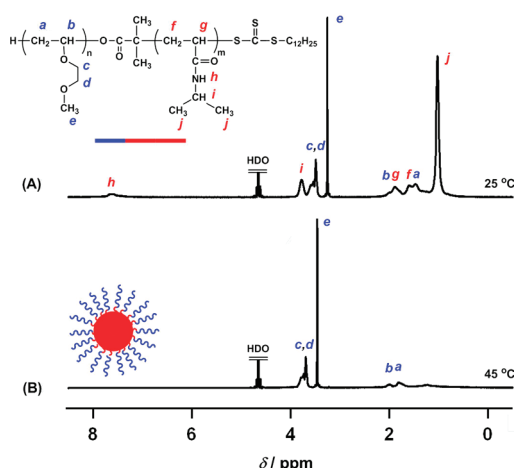


Figure 10. Typical ^1H NMR spectra recorded for $\text{MOVE}_{64}\text{-NIPAM}_{165}$ block copolymer (entry 15 in Table 3) in D_2O at (A) 25 °C and (B) 45 °C (polymer: 1.0 wt %). The inset shows the chemical structure of the diblock copolymer with full peak assignments.

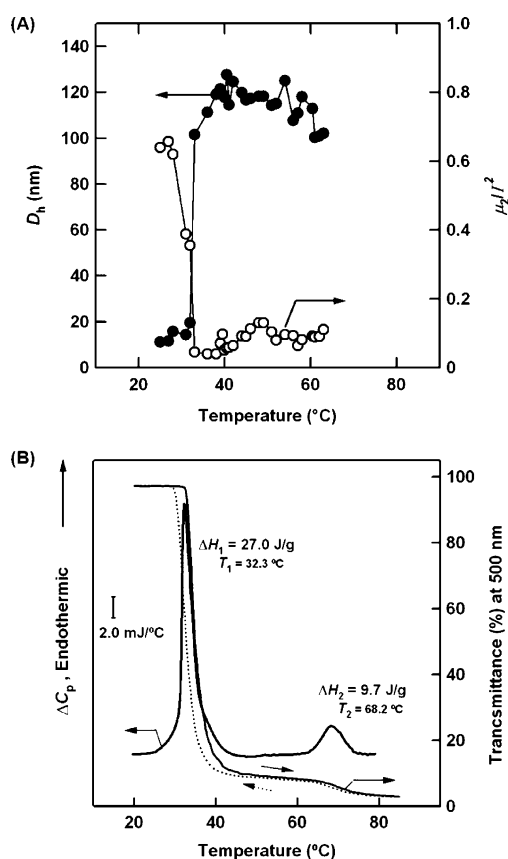


Figure 11. (A) Variation of hydrodynamic diameter (D_h) and PDI (μ_2/I^2) with temperature for a $\text{MOVE}_{107}\text{-NIPAM}_{210}$ diblock copolymer (entry 14 in Table 3) in water. (B) Temperature dependence of the transmittance at 500 nm (0.5 wt %) and DSC thermogram (1.0 wt %) of aqueous solution of the $\text{MOVE}_{107}\text{-NIPAM}_{210}$ diblock copolymer: heating and cooling rate 1.0 °C/min, heating (—) and cooling (---). The inset values are transition temperatures (T_1 and T_2) and their heats of transition (ΔH_1 and ΔH_2).

65–70 °C, higher than the LCSTs of all the blocks, the polymer was precipitated completely. Both the DSC thermogram and the temperature dependence of transmittance at 500 nm support that

two transitions occurred with increasing temperature, at 32 °C²³ and 66 °C,^{4,21,22} corresponding to the LCSTs of PNIPAM and PMOVE homopolymers, respectively. Furthermore, physical gelation was also occurred at the 20 wt % aqueous solution between 34 and 52 °C by visual observation (entry 14 in Table 3). The phase separation behavior is similar to that of double thermoresponsive poly(vinyl ether)s-based block copolymers such as PMOVE-poly(2-(2-ethoxy)ethoxyethyl vinyl ether) in water and the gelation is induced at concentrated solution due to macro-lattice of micelles.⁴ The different point is the first heat of transition ($\Delta H_1 = 27.0$ J/g) which was larger than that of poly(vinyl ether)s (Figure 11B). This is due to the different dehydration energy between poly(vinyl ether) such as poly(2-ethoxyethyl vinyl ether) and PNIPAM blocks.^{4,33} As a consequence, these results also indicate that the block copolymer was successfully obtained by the transformation of living cationic polymerization into RAFT polymerization.

In addition, the effect of varying the PNIPAM block length on the final micelle diameter was also examined. Table 3 also shows the intensity-average hydrodynamic diameter (D_h) and the PDI (μ_2/I^2) of the thermoresponsive micelles in water at 45 °C. Since all the block copolymers were molecularly dissolved at 10 °C, no or very low scattering intensities were observed. For the target DP = 107 of PMOVE block, as the target DP of the PNIPAM block (core) was varied from 75 to 210, the mean micelle diameter determined in water at 45 °C increased from 60 to 117 nm as judged by DLS (entries from 12 to 14 in Table 3). Moreover, in each case relatively lower PDIs were obtained as the PNIPAM length increased. Similarly, for the target DP = 64 of PMOVE block, the D_h of $\text{MOVE}_{64}\text{-NIPAM}_{214}$ is slightly larger than that of $\text{MOVE}_{64}\text{-NIPAM}_{165}$ (entries 15 and 16 in Table 3). It is well-documented that larger micelles are invariably obtained when the chain length of the core-forming block is increased.³⁴

CONCLUSION

In conclusion, novel block copolymers were synthesized by the transformation of living cationic polymerization of vinyl ethers into RAFT polymerization using two types of RAFT agents with a carboxylic group. The block copolymers consist of cationically polymerizable monomer such as IBVE and MOVE and radically polymerizable monomer such as EA, St, *t*BuSt, and NIPAM. The key to success in the block copolymerization is to utilize a RAFT agent of the carboxylic trithiocarbonate/ SnBr_4 initiation system in the presence of additives such as dioxane and ethyl acetate for living cationic polymerization. The living cationic polymerization was initiated from a proton derived from the carboxylic RAFT agent. After the cationic polymerization, the polymerization was quenched and the RAFT group as a counteranion was concurrently recovered, followed by the RAFT process of radical polymerization using AIBN at 70 °C. Using the transformation process, further novel double thermoresponsive diblock copolymers PMOVE–PNIPAM were also prepared, containing two thermoresponsive segments possessing different LCSTs. Since the resulting block copolymers reversibly formed or deformed micellar assemblies during two LCSTs, we concluded that the block copolymers were successfully obtained by the transformation of living cationic into RAFT polymerization. However, the obtained block copolymers have a hemiacetal ester bond. This is a weak bond for acidolysis.³⁵ In the forthcoming article, we will report another block copolymer having stronger junction than

hemiacetal ester prepared by different transformation from living cationic to RAFT polymerization.

■ ASSOCIATED CONTENT

■ Supporting Information

Further characterization for PIBVE macro-CTA and PIBVE-PEA using RAFT-1 by MALDI-TOF-MS and SEC, and results of the one-pot transformation reaction. This material is available free of charge via the Internet at <http://pubs.acs.org>.

■ AUTHOR INFORMATION

Corresponding Author

*Telephone: +81-776-27-9719. Fax: +81-776-27-8747. E-mail: sugihara@u-fukui.ac.jp.

■ ACKNOWLEDGMENTS

The authors are grateful to Maruzen Petrochemical Co., Ltd., for supplying MOVE and tBuSt monomers and for supporting this work.

■ REFERENCES

- (1) As a review for living cationic polymerization: (a) Sawamoto, M. *Prog. Polym. Sci.* **1991**, *16*, 111–172. (b) Kennedy, J. P. Iván, B. *Designed Polymers by Carbocationic Macromolecular Engineering: Theory and Practice*; Oxford University Press: New York, 1992. (c) Matyjaszewski, K., Ed. *Cationic Polymerizations: Mechanism, Synthesis, and Applications*; Marcel Dekker: New York, 1996. (d) Puskas, J. E.; Kaszas, G. *Prog. Polym. Sci.* **2000**, *25*, 403–452. (d) Aoshima, S.; Kanaoka, S. *Chem. Rev.* **2009**, *109*, 5245–5287.
- (2) Minoda, M.; Sawamoto, M.; Higashimura, T. *Macromolecules* **1987**, *20*, 2045–2049.
- (3) (a) Yamada, K.; Minoda, M.; Miyamoto, T. *Macromolecules* **1999**, *32*, 3553–3558. (b) Patrickios, C. S.; Forder, C.; Armes, S. P.; Billingham, N. C. *J. Polym. Sci., Part A: Polym. Chem.* **1998**, *36*, 2547–2554. (c) Sugihara, S.; Kanaoka, S.; Aoshima, S. *J. Polym. Sci., Part A: Polym. Chem.* **2004**, *42*, 2601–2611. (d) Sugihara, S.; Hashimoto, K.; Okabe, S.; Shibayama, M.; Kanaoka, S.; Aoshima, S. *Macromolecules* **2004**, *37*, 336–343. (e) Sugihara, S.; Ito, S.; Irie, S.; Ikeda, I. *Macromolecules* **2010**, *43*, 1753–1760.
- (4) Sugihara, S.; Kanaoka, S.; Aoshima, S. *Macromolecules* **2005**, *38*, 1919–1927.
- (5) Hashimoto, T.; Namikoshi, T.; Irie, S.; Urushisaki, M.; Sakaguchi, T.; Nemoto, T.; Isoda, S. *J. Polym. Sci., Part A: Polym. Chem.* **2008**, *46*, 1902–1906.
- (6) (a) Yagci, Y.; Tasdelen, M. A. *Prog. Polym. Sci.* **2006**, *31*, 1133–1170. (b) Hadjichristidis, N.; Pitsikalis, M.; Iatrou, H. *Adv. Polym. Sci.* **2005**, *189*, 1–124.
- (7) Kumagai, T.; Kagawa, C.; Aota, H.; Takeda, Y.; Kawasaki, H.; Arakawa, R.; Matsumoto, A. *Macromolecules* **2008**, *41*, 7347–7351.
- (8) Burgess, F. J.; Cunliffe, A. V.; MacCallum, J. R.; Richards, D. H. *Polymer* **1977**, *18*, 719–725.
- (9) (a) Coca, S.; Matyjaszewski, K. *Macromolecules* **1997**, *30*, 2808–2810. (b) Matyjaszewski, K. *Macromol. Symp.* **1998**, *132*, 85–101.
- (10) (a) Kamigaito, M.; Ando, T.; Sawamoto, M. *Chem. Rev.* **2001**, *101*, 3689–3746. (b) Kato, M.; Kamigaito, M.; Sawamoto, M.; Higashimura, T. *Macromolecules* **1995**, *28*, 1721–1723.
- (11) (a) Matyjaszewski, K.; Xia, J. *Chem. Rev.* **2001**, *101*, 2921–2990. (b) Wang, J.-S.; Matyjaszewski, K. *J. Am. Chem. Soc.* **1995**, *117*, 5614–5615. (c) Wang, J.-S.; Matyjaszewski, K. *Macromolecules* **1995**, *28*, 7901–7910.
- (12) Bernaerts, K. V.; Du Prez, F. E. *Polymer* **2005**, *46*, 8469–8482.
- (13) Lu, J.; Liang, H.; Li, A.; Cheng, Q. *Eur. Polym. J.* **2004**, *40*, 397–402.
- (14) Lu, J.; Liang, H.; Zhang, W.; Cheng, Q. *J. Polym. Sci., Part A: Polym. Chem.* **2003**, *41*, 1237–1242.
- (15) Yamada, K.; Miyazaki, M.; Ohno, K.; Fukuda, T.; Minoda, M. *Macromolecules* **1999**, *32*, 290–293.
- (16) (a) Mishima, E.; Yamada, T.; Watanabe, H.; Yamago, S. *Chem. Asian. J.* **2011**, *6*, 445–451. (b) Mishima, E.; Yamago, S. *Macromol. Rapid Commun.* **2011**, *32*, 893–898.
- (17) (a) Chiefari, J.; Chong, Y. K.; Ercole, F.; Krstina, J.; Jeffery, J.; Le, T. P. T.; Mayadunne, R. T. A.; Meijs, G. F.; Moad, C. L.; Moad, G.; Rizzardo, E.; Thang, S. H. *Macromolecules* **1998**, *31*, 5559–5562. (b) Moad, G.; Rizzardo, E.; Thang, S. H. *Aust. J. Chem.* **2005**, *58*, 379–410. (c) Moad, G.; Rizzardo, E.; Thang, S. H. *Polymer* **2008**, *49*, 1079–1131.
- (18) Barner-Kowollic, C., Ed. *Handbook of RAFT polymerization*; Wiley-VCH: Weinheim, Germany, 2008.
- (19) Kumagai, S.; Nagai, K.; Satoh, K.; Kamigaito, M. *Macromolecules* **2010**, *43*, 7523–7531.
- (20) Moad, G.; Chen, M.; Häussler, M.; Postma, A.; Rizzardo, E.; Thang, S. H. *Polym. Chem.* **2011**, *2*, 492–519.
- (21) Bulmus, V. *Polym. Chem.* **2011**, *2*, 1463–1472.
- (22) Aoshima, S.; Oda, H.; Kobayashi, E. *J. Polym. Sci., Part A: Polym. Chem.* **1992**, *30*, 2407–2413.
- (23) Maeda, Y.; Yamauchi, H.; Fujisawa, M.; Sugihara, S.; Ikeda, I.; Aoshima, S. *Langmuir* **2007**, *23*, 6561–6566.
- (24) (a) Schild, H. G. *Prog. Polym. Sci.* **1992**, *17*, 163–249. (b) Fujishige, S.; Kubota, K.; Ando, I. *J. Phys. Chem.* **1989**, *93*, 3311–3313. (c) Lai, J. T.; Filla, D.; Shea, R. *Macromolecules* **2002**, *35*, 6754–6756.
- (26) Stenzel, M. H.; Davis, T. P.; Fane, A. G. *J. Mater. Chem.* **2003**, *13*, 2090–2097.
- (27) Katayama, H.; Kitaguchi, H.; Kamigaito, M.; Sawamoto, M. *J. Polym. Sci., Part A: Polym. Chem.* **2000**, *38*, 4023–4031.
- (28) Chong, Y. K.; Moad, G.; Rizzardo, E.; Skidmore, M. A.; Thang, S. H. *Macromolecules* **2007**, *40*, 9262–9271.
- (29) Kamigaito, M.; Yamaoka, K.; Sawamoto, M.; Higashimura, T. *Macromolecules* **1992**, *25*, 6400–6406.
- (30) Hashimoto, T.; Iwata, T.; Minami, A.; Kodaira, T. *Polym. Sci. Part A: Polym. Chem.* **1998**, *36*, 3173–3185.
- (31) (a) Muscat, D.; Henderickx, H.; Kwakkenbos, G.; van Benthem, R.; de Koster, C. G.; Fokkens, R.; Nibbering, N. M. M. *J. Am. Soc. Mass Spectrom.* **2000**, *11*, 218–227. (b) Jiang, X.; Schoenmakers, P. J.; van Dongen, J. L. J.; Lou, X.; Lima, V.; Brokken-Zijp, J. *Anal. Chem.* **2003**, *75*, 5517–5524.
- (32) Katayama, H.; Kamigaito, M.; Sawamoto, M. *J. Polym. Sci., Part A: Polym. Chem.* **2001**, *39*, 1258–1267.
- (33) Sugihara, S.; Kanaoka, S.; Aoshima, S. *Macromolecules* **2004**, *37*, 1711–1719.
- (34) (a) Sugihara, S.; Sugihara, K.; Armes, S. P.; Ahmad, H.; Lewis, A. L. *Macromolecules* **2010**, *43*, 6321–6329. (b) Sugihara, S.; Armes, S. P.; Lewis, A. L. *Angew. Chem., Int. Ed.* **2010**, *49*, 3500–3503. (c) Büttin, V.; Armes, S. P.; Billingham, N. C. *Polymer* **2001**, *42*, 5993–6008.
- (35) Matsukawa, D.; Mukai, T.; Okamura, H.; Shirai, M. *Eur. Polym. J.* **2009**, *45*, 2087–2095.

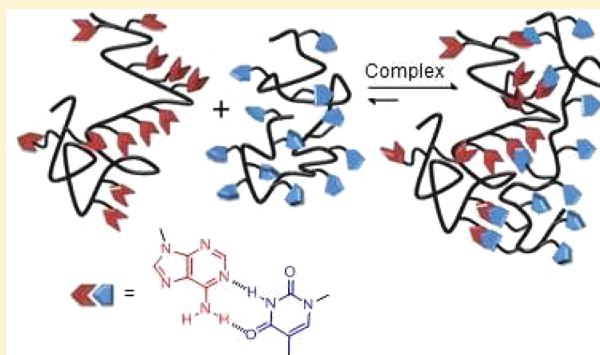
Nucleobase Self-Assembly in Supramolecular Adhesives

Shijing Cheng, Mingqiang Zhang, Ninad Dixit, Robert B. Moore, and Timothy E. Long*

Department of Chemistry, Macromolecules and Interfaces Institute, Virginia Tech, Blacksburg, Virginia 24061-0344, United States

S Supporting Information

ABSTRACT: Novel acrylic monomers functionalized with nucleobase-containing units (adenine and thymine) were prepared upon aza-Michael addition and successfully copolymerized with *n*-butyl acrylate. At a content of 7 mol %, adenine-containing units self-assembled into needle-like microstructures within amorphous polymer matrices as shown with atomic force microscopy (AFM), small-angle X-ray scattering (SAXS), and wide-angle X-ray diffraction (WAXD); thymine-containing units did not aggregate into distinct morphologies even to 30 mol %. Upon blending, thymine- and adenine-containing statistical copolymers associated into a thermodynamically stable complex, which was physically cross-linked through adenine–thymine base pairing. The molar fractions of the nucleobase monomer, nucleobase stacking interactions, and complementary hydrogen bonding principally influenced self-assembly. Additionally, the nucleobase-functionalized polyacrylates exhibited tunable adhesive and cohesive strength.



■ INTRODUCTION

The use of noncovalent interactions as a tool for the synthesis of well-defined supramolecular structures is paramount in current polymer science.^{1–5} Our motivation is to impart structural features of biomacromolecules with extension to emerging adhesive technologies, e.g., the unique molecular recognition of complementary nucleobases, the stimuli-responsiveness of multiple hydrogen bonding, and the self-assembly of cooperative multiple noncovalent interactions. Hydrogen-bonding based molecular recognition plays a crucial role in the functions of biopolymers. Recognition based upon nucleobase interactions, such as molecularly imprinted polymers^{6,7} and nucleobase-templated polymerization,⁸ also enables applications in catalysis, separations, biomedicine, chemo/biosensors, and information storage.

The design of synthetic polymers bearing nucleobase recognition sites is often challenging and requires multiple synthetic steps due to susceptibility of multiple substitutions. Nucleobase units were introduced using postpolymerization modification,^{9,10} and protection of the nucleobase monomers was necessary to obtain high conversions.^{11,12} Recent developments in controlled metathesis and radical polymerization techniques have expanded our ability to create well-defined polymers with high tolerance to hydrogen bonding and ionic functionalities. Sleiman et al. utilized ring-opening metathesis polymerization to synthesize adenine-containing block copolymers, which self-assembled into rod morphologies.¹³ van Hest et al. synthesized thymine-functionalized block copolymers using atom transfer radical polymerization (ATRP) of thymine methacrylate monomers from a poly(oxyethylene) macro-initiator.¹⁴ Lutz et al. polymerized styrenic nucleobase monomers using ATRP.^{15,16} Inaki et al. synthesized a wide

range of nucleobase-functionalized statistical and homopolymers and block copolymers using ring-opening cationic and anionic polymerization of acyclic derivatives of the nucleobases.¹⁷ Our group previously reported the high tolerance of nitroxide-mediated polymerization to nucleobase functionalities,¹⁸ and we prepared styrenic adenine- and thymine-containing ABA triblock copolymers using a novel difunctional alkoxyamine initiator.^{19,20} However, most bioreceptors and nucleobase-functionalized synthetic polymers for molecular recognition have either relatively rigid structures or sterically congested polymer backbones,²¹ such as vinyl,²² styrene,^{16,23} and methacrylate.^{14,15,24} Examples of receptors having relatively flexible structures and spacers are relatively very few.^{25,26} Meijer et al. recently reported the increase of the polymer backbone polarity significantly decreased the stability of benzene-1,3,5-tricarboxamides aggregates.²⁷ The molecular recognition process is highly dependent on both the recognition groups and the nature of these spacers.

In our present work, we constructed flexible alkyl chain spacers for recognition sites, which were compared with the styrene analogues to evaluate the influence of structural modifications on nucleobase self-assembly using AFM and SAXS. The novel acrylic nucleobase monomers were synthesized using a one-step aza-Michael addition without functional group protection. Michael addition is an efficient and mild reaction that is suitable for introducing highly functional groups, biopolymers (e.g., proteins), or bioactive species (e.g., drugs) into polymers.²⁸ The novel monomers were homopoly-

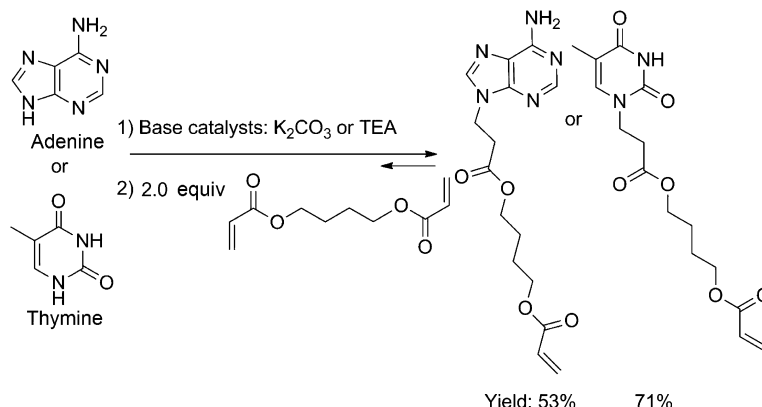
Received: September 19, 2011

Revised: December 21, 2011

Published: January 6, 2012



Scheme 1. Michael Addition of Adenine and Thymine with 1,4-Butanediol Diacrylate



merized or copolymerized with *n*-butyl acrylate using conventional free radical polymerization. The hydrogen-bonding polymers provided a reversible network with strongly temperature-dependent viscosity, and self-healing performance may impact industrial interest in coatings and hot melt adhesives. Peel strengths and shear strengths of nucleobase-containing polyacrylates were significantly higher than acrylic acid- and 4-vinylpyridine-based polyacrylate analogues at similar hydrogen-bonding molar concentrations.

EXPERIMENTAL SECTION

Materials. *n*-Butyl acrylate (*n*BA, 99+%), acrylic acid (AA, 99+%), and 4-vinylpyridine (VP, 99+%) were purchased from Aldrich and passed through neutral alumina columns before use. α,α' -Azobis(isobutyronitrile) (AIBN, Fluka, 99%) was recrystallized from methanol. 1,4-Butanediol diacrylate (Alfa Aesar, 99%) was used without further purification. Adenine (A, 99%), thymine (T, 99%), triethylamine (TEA, 99%), potassium carbonate (99%), and 2,6-di-*tert*-butyl-4-methylphenol (BHT, 99%) were purchased from Aldrich and used without further purification. Hexane (HPLC grade), chloroform (CHCl_3 , HPLC), tetrahydrofuran (THF, HPLC grade), *N,N*-dimethyl sulfoxide (DMSO, HPLC grade), and *N,N*-dimethylformamide (DMF, HPLC grade, anhydrous) were purchased from Fisher Scientific and used as received. 9-(4-Vinylbenzyl)adenine and 1-(4-vinylbenzyl)-thymine were synthesized according to the previous literature.²⁹

Synthesis of 4-((3-(Adenin-9-yl)propanoyl)oxy)butyl Acrylate. A suspension of adenine (1.0 g, 11.9 mmol), BHT (60 mg), and K_2CO_3 (40.0 mg, 0.29 mmol) in DMSO (20 mL) was stirred at 50 °C for 1 h and followed with adding 1,4-butanediol diacrylate (3 mL, 15.9 mmol). After the reaction mixture was stirred at 50 °C for 5 h, it was poured into water (150 mL) and washed with hexane to remove excess 1,4-butanediol diacrylate. Then, the water layer was extracted with dichloromethane (3×20 mL). The combined extracts were dried over MgSO_4 , filtered, and concentrated in a vacuum evaporator to remove all the solvents. The evaporation residue was separated using chromatography with CHCl_3 –MeOH (20:1) on silica gel. A trace amount of N-7 adduct were eluent first. Evaporation of the remained eluent gave a white solid of 1.30 g with an overall yield of 53%, melting at 117 °C. ^1H NMR (400 MHz, d_6 -DMSO): 1.45–1.64 (m, 4H, $\text{H}_{\text{b+b'}}$), 2.93 (t, 2H, $J = 6.8$ Hz, H_{c}), 3.95–4.10 (m, 4H, $\text{H}_{\text{a+a'}}$), 4.35 (t, 2H, $J = 6.8$ Hz, H_{d}), 5.91 (d, 1H, $J = 10.4$ Hz, H_{g1}), 6.13 (dd, 1H, $J_1 = 10.4$ Hz, $J_2 = 17.2$ Hz, H_{h}), 6.29 (d, 1H, $J = 17.2$ Hz, H_{g2}), 7.18 (bs, 2H, H_{i}), 8.07 (s, 1H, H_{e}), 8.11 (s, 1H, H_{f}). ^{13}C NMR (100 MHz, d_6 -DMSO): 25.1, 34.0, 64.0, 64.2, 128.7, 131.9, 141.3, 152.8, 156.4, 165.9, 171.1. HRMS (ES+): m/z calcd for $[\text{M} + \text{H}^+]$ 334.14 g/mol; found 334.15 g/mol.

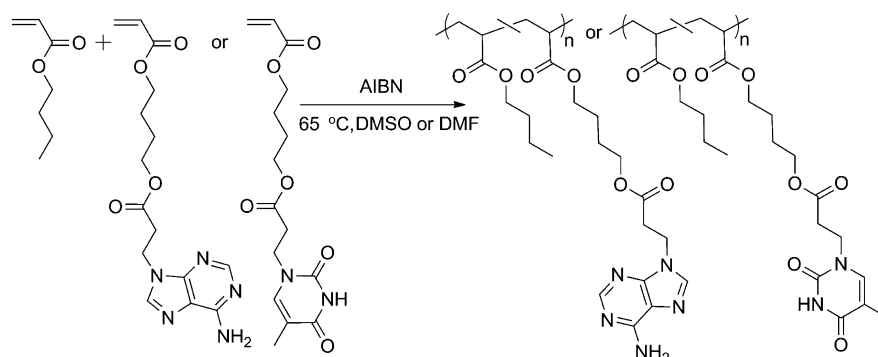
Synthesis of 4-((3-(Thymine-1-yl)propanoyl)oxy)butyl Acrylate. A suspension of thymine (1.00 g; 7.93 mmol) and BHT (60.0 mg) in DMF (20 mL) was treated with triethylamine (0.22 mL, 1.58 mmol) at room temperature. The reaction mixture was stirred under

an inert atmosphere (argon) for 1 h and then treated with 1,4-butanediol diacrylate (3.0 mL, 15.9 mmol). The reaction solution turned clear after stirring at room temperature for 24 h. Then, it was poured into water (150 mL) and washed with hexane to remove excess 1,4-butanediol diacrylate. The water layer was extracted with dichloromethane (3×20 mL). The combined extracts were dried over MgSO_4 , filtered, and concentrated in a vacuum evaporator to remove all the solvents. The evaporation residue was separated using flash column chromatography with CHCl_3 –MeOH (20:1) on silica gel. Evaporation of the total eluent resulted in a white solid of 1.82 g with an overall yield of 71%; melting at 70 °C. ^1H NMR (400 MHz, d_6 -DMSO): 1.54–1.68 (m, 4H, $\text{H}_{\text{b+b'}}$), 1.71 (s, 3H, H_{e}), 2.66 (t, 2H, $J = 6.0$ Hz, H_{c}), 3.83 (t, 2H, $J = 5.2$ Hz, H_{d}), 3.97–4.13 (m, 4H, $\text{H}_{\text{a+a'}}$), 5.91 (d, 1H, $J = 11.2$ Hz, H_{g1}), 6.14 (dd, 1H, $J_1 = 8.4$ Hz, $J_2 = 16.8$ Hz, H_{h}), 6.30 (d, 1H, $J = 6.8$ Hz, H_{g2}), 7.48 (s, 1H, H_{f}), 11.23 (br, 1H, H_{i}). ^{13}C NMR (100 MHz, d_6 -DMSO): 12.4, 25.1, 33.2, 44.2, 64.1, 64.2, 108.6, 128.8, 131.9, 142.2, 151.2, 164.7, 165.9, 171.2. HRMS (ES+): m/z calcd for $[\text{M} + \text{H}^+]$ 324.13 g/mol; found 324.14 g/mol.

Synthesis of Acrylic Nucleobase-Containing Copolymers and Hydrogen-Bonding Analogues. Poly(acrylic adenine-*co-n*BA), poly(acrylic thymine-*co-n*BA), and poly(AA-*co-n*BA) and poly(VP-*co-n*BA) were synthesized using solution free radical polymerization with AIBN as the initiator. A typical synthesis was carried out as follows. Acrylic adenine (1.0 g, 3.0 mmol) was weighed into a 100 mL round-bottomed flask containing a magnetic stir bar. The flask was sealed with a rubber septum and purged with N_2 for 20 min. Then anhydrous DMSO (35 mL, 10 wt % of solid) was added to the flask to dissolve acrylic adenine monomers. Purified *n*-butyl acrylate (4.0 mL, 28.0 mmol) was syringed into the reaction flask. Lastly, AIBN (10 mg, 0.15 mol %) was dissolved in 5 mL of anhydrous DMSO and flushed with dry nitrogen for 10 min and was then syringed into the reaction mixture. The reaction flask was placed in an oil bath at 60 °C for 24 h with constant stirring. After polymerization, DMSO was distilled off under reduced pressure. The product was redissolved in THF (25 mL) and precipitated into a methanol and water mixture (800 mL). The final products were dried at 30 °C under reduced pressure (0.5 mmHg) for 24 h. The product contained 10 mol % acrylic adenine and 90 mol % *n*BA, with a yield of 82%.

Synthesis of Styrenic and Acrylic Nucleobase-Containing Homopolymers. Styrenic and acrylic adenine- and thymine-containing homopolymers were synthesized using conventional free radical polymerization in DMF or DMSO solution with AIBN as the initiator. A representative example of the synthesis was conducted as follows. Acrylic adenine (4.0 g, 12.0 mmol), AIBN (10 mg, 0.6 mmol, 0.25 wt %), and anhydrous DMSO (30 mL) were placed into a 100 mL round-bottomed flask. After the flask was sealed and purged with N_2 for 20 min, it was placed in an oil bath at 60 °C for 24 h with constant stirring. After polymerization, the polymer solution was precipitated into diethyl ether (800 mL). The final products were dried at 30 °C under reduced pressure (0.5 mmHg) for 24 h. Yield: 90%

Scheme 2. Copolymerization of *n*-Butyl Acrylate and 4-(3-Adenine-9-yl-propanoyloxy)butyl Acrylate or 4-((3-(Thymine-1-yl)propanoyl)oxy)butyl Acrylate



Polymer Complexes Preparation. A 5 wt % solution of adenine-containing polyacrylate copolymer in CHCl_3 was mixed with a 5 wt % CHCl_3 solution of thymine-containing polyacrylate copolymer and stirred for 6–8 h. Then, CHCl_3 was left to evaporate slowly at room temperature for 48 h and annealed under reduced pressure at 100 °C for 2 days.

Instrumentation. See the Supporting Information.

RESULTS AND DISCUSSION

Synthesis of Nucleobase Functional Polyacrylates.

Synthesis of acrylic nucleobase-containing polymers involved acrylic monomer synthesis using Michael addition (Scheme 1) and direct radical polymerization of functional acrylic adenine and thymine monomers. Synthesis of nucleobase styrene²⁹ and methacrylate¹⁴ monomers has been reported in the literature. However, the corresponding homopolymers were glassy at room temperature and insoluble in polar aprotic organic solvents, which strongly disfavored molecular recognition.¹⁸ We targeted acrylic nucleobase monomers possessing alkyl chain spacers, which potentially promote the solubility in a variety of organic solvents. The introduction of nucleobases through regioselective substitution is crucial due to the presence of more than one nucleophilic sites on respective nucleobases. Previously, our group successfully attached nucleobases onto polystyrene¹⁰ and poly(D,L-lactide)³⁰ chain ends through Michael addition. The base-catalyzed Michael addition is thermodynamically controlled, which affords N1-substituted thymine and N9-substituted adenine as the major products.³¹ The reaction conditions, such as solvent, temperature, and the amount of base catalyst, were optimized and the regioselectivity was achieved in a satisfactory yield. The reaction was initially heterogeneous and became homogeneous with time due to enhanced solubility of the final products. In addition to product solubility, excess diacrylate suppressed undesirable difunctionalization.

Conventional free radical copolymerization of acrylic nucleobase monomers with *n*-butyl acrylate was performed homogeneously in DMF or DMSO, and the polymers were isolated in high yields (Scheme 2). The nucleobase concentration in the copolymer was calculated from the ratio of ^1H NMR resonances integration at 7.8–8.0 and 3.6–4.4 ppm (Figures S3(2) and S4(2)), which corresponded to the chemical shift of $-\text{CH}$ (H_β) in nucleobase and $-\text{O}-\text{CH}_2-$ ($\text{H}_{\text{a}+\text{a}'+\text{a}''}$) in both *n*-butyl acrylate and acrylic nucleobase monomers. Table 1 lists the monomer feed ratios and the corresponding copolymer compositions. The copolymer composition matched with the feed ratio well possibly due to the similar radical intermediate stability of *n*BA and acrylic

Table 1. Molecular Characterization of Adenine- and Thymine-Containing Poly(*n*-butyl acrylate) Copolymers and Complementary Hydrogen-Bonding Polymer Analogues^a

sample name	M_1	$[\text{M}_1]$ in feed (mol %)	$[\text{M}_1]$ in polymer ^b (mol %)	M_w^c (g/mol)	M_w/M_n^c	T_g (°C)
A-4	acrylic adenine	5	4	95K	2.09	−41
A-7	acrylic adenine	10	7	125K	1.64	−25
A-16	acrylic adenine	19	16	279K	2.39	0
A-100	acrylic adenine	100	100	NA	NA	65
T-10	acrylic thymine	10	10	122K	2.40	−30
T-20	acrylic thymine	20	20	155K	2.40	−14
T-25	acrylic thymine	29	25	164K	2.73	1
T-32	acrylic thymine	40	32	NA	NA	19
T-100	acrylic thymine	100	100	NA	NA	43
StA-100	styrenic adenine	100	100	—	—	204
StT-100	styrenic thymine	100	100	—	—	168
VP-10	[VP]	10	10	70.1K	2.33	−42
AA-4	[AA]	4	10	64.1K	1.85	−37

^aNA: polymers were difficult to filter; —: polymers were insoluble. ^b ^1H NMR. ^cSEC: 0.01 M LiBr/DMF.

nucleobase monomers. SEC results revealed relatively broad molecular weight distributions, which were attributed to conventional radical polymerization and strong hydrogen bonding.

Thermal Transitions. To understand the association of nucleobase-containing units, we studied the thermal and dynamic mechanical properties of adenine- and thymine-functionalized poly(*n*BA) and their complexes. DSC analysis of acrylic adenine- and thymine-containing copolymers all showed a single T_g (Figure S5), suggesting a statistical copolymerization of *n*-butyl acrylate and acrylic nucleobase monomers. Figure 1 shows the influence of nucleobase content on the T_g 's of the copolymers. A linear increase of T_g was observed with an increase of the mole fraction of adenine and thymine with positive deviation from the Fox equation. Such deviation was attributed to the incorporation of strong hydrogen-bond units.^{32–34} The more significant T_g deviation for adenine-

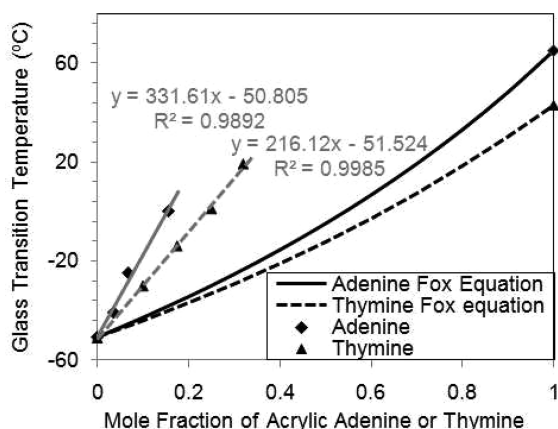


Figure 1. Relationship between acrylic adenine or thymine monomer contents and T_g .

containing polymers compared to thymine-containing polymers suggested stronger self-association of adenine units relative to thymine units at similar molar concentrations.

The thermodynamic mechanical properties of adenine- and thymine-containing acrylate copolymers at small deformations were studied using DMA in tension mode (Figure 2). The

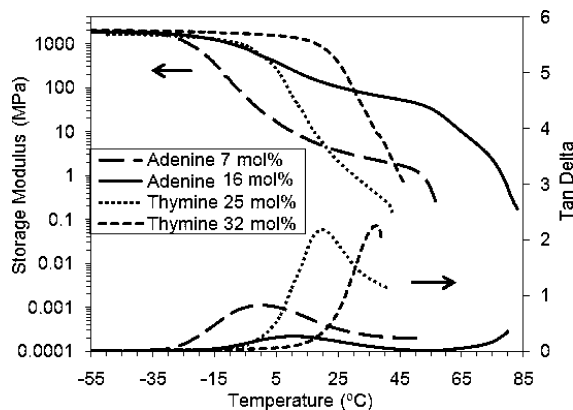


Figure 2. DMA traces of poly(*n*BA-*co*-acrylic adenine) with 7 and 16 mol % of acrylic adenine and poly(*n*BA-*co*-acrylic thymine) with 25 and 32 mol % of acrylic thymine.

storage modulus (G') of acrylic adenine-containing polymer with 7 mol % of adenine (A-7) exhibited a rubber plateau between 5 and 50 °C, followed with a subsequent sharp decrease of modulus and eventually flow at 57 °C. It was immediately obvious how the polymer properties significantly changed with low levels (mol %) of adenine units. With increasing adenine incorporation to 16 mol %, T_g increased; the plateau modulus was 2 orders of magnitude higher and the flow temperature increased to 85 °C. This change was attributed to the presence of associated adenine units, which reinforced the polymer matrices as physical cross-links. Additionally, the $\tan \delta$ curves in DMA thermograms revealed broad glass transitions spanning 80 °C for A-7 and 60 °C for A-16. This slow relaxation was presumably due to the dynamic bonds that restricted mobility of polymer backbone. In comparison to adenine, thymine-containing polymers only showed a short and less well-defined rubbery plateau at even higher nucleobase concentration, suggesting less pronounced self-association.

Infrared Spectroscopy. Infrared spectroscopy (IR) is well suited for monitoring supramolecular association and provides information on ordering processes.³⁵ Supramolecular assembly is temperature dependent, and reversibility is typically observed.^{25,36} Therefore, we performed variable temperature FT-IR on the adenine- and thymine-containing polymers in order to investigate the kinetics of supramolecular ordering. A slow heating and cooling rate of 1 °C/min was used to suppress kinetic (nonequilibrium) effects. Figure 3 shows the scale-

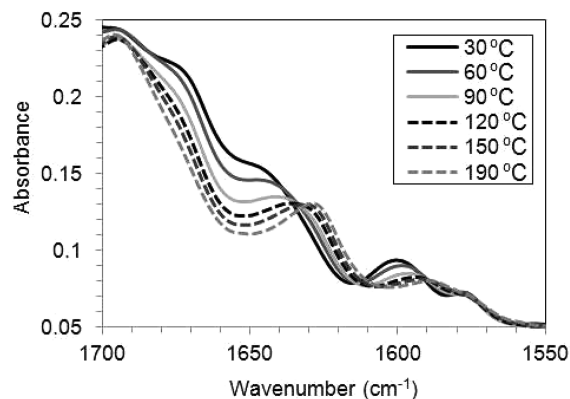


Figure 3. Variable temperature FT-IR spectra in the 1600–1700 cm^{-1} region for the complex of poly(*n*BA-*co*-acrylic adenine) and poly(*n*BA-*co*-acrylic thymine).

expanded FT-IR spectra of the adenine- and thymine-acrylate polymer complex with a stoichiometry ratio of $[A]:[T] = 1:1$ at various temperatures. The broad band with a peak maximum at 1672 cm^{-1} corresponded to the stretching vibration of hydrogen bonded C=O in thymine. The peaks at 1643 and 1600 cm^{-1} were attributed to the N–H bending/scissoring vibration of adenine. When temperature increased from 30 to 190 °C, the band at 1672 cm^{-1} disappeared, indicating the dissociation of hydrogen bonded C=O in thymine. Meanwhile, the absorbance of hydrogen-bonded N–H bending vibration of adenine at 1643 cm^{-1} also decreased upon heating, and a new peak emerged at lower wavenumber, suggesting the disruption of hydrogen bonds. The new peak shifted toward lower wavenumbers with temperature increase, and the peak maximum centered around 1627 cm^{-1} . In this case, the majority of complementary hydrogen bonds were disrupted. Variable temperature FT-IR study further confirmed hydrogen bonding at room temperature and its dissociation upon heating.

Morphology. AFM enables imaging of surface texture and morphology of microphase-separated structures and is frequently applied to polymer films.^{37,38} AFM micrographs of acrylic adenine-containing copolymers revealed intriguing surface morphologies as shown in Figure 4. Polymers with 7 mol % of adenine microphase separated into needle-like hard structures. These structures of approximately 100 nm in length and less than 10 nm in width were randomly oriented in the soft polymer matrix. SAXS results (Figure 5) also revealed a broad peak near 0.90 nm^{-1} with a d spacing of ca. 7.0 nm, which corresponded to the average distance between needle-like structures observed using AFM. These structures percolated as the adenine content increased from 7 to 16 mol %. The broadness of the SAXS peak also suggested the disparate distribution of length scales. To further understand the internal structure of the nanoneedles, wide-angle X-ray diffraction studies (WAXD) were performed on the annealed film samples

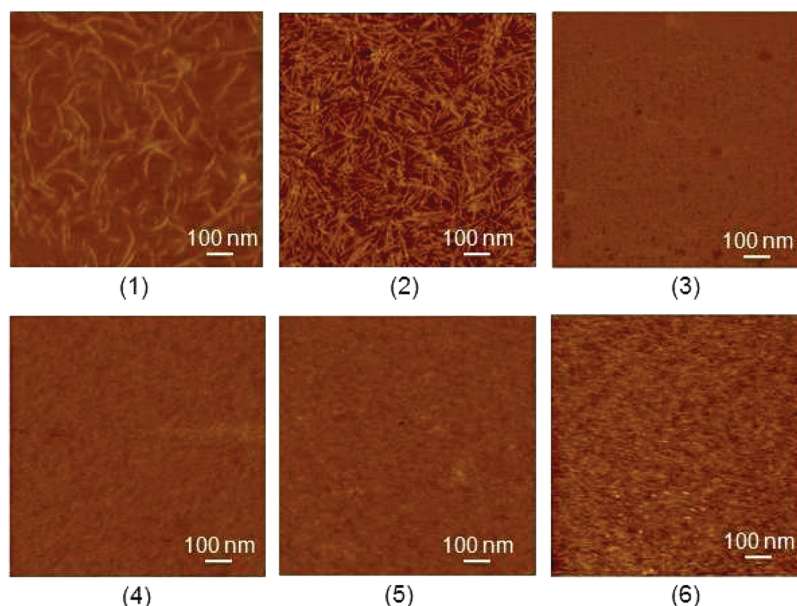


Figure 4. Tapping mode AFM phase images of thin films of poly(*n*BA-*co*-acrylic adenine) with (1) 7 mol % and (2) 16 mol % adenine, poly(*n*BA-*co*-acrylic thymine) with (3) 25 mol %, and (4) 32 mol % thymine. The polymer complexes of (2) and (4) at (5) $[A]/[T] = 2$ and (6) $[A]/[T] = 4$.

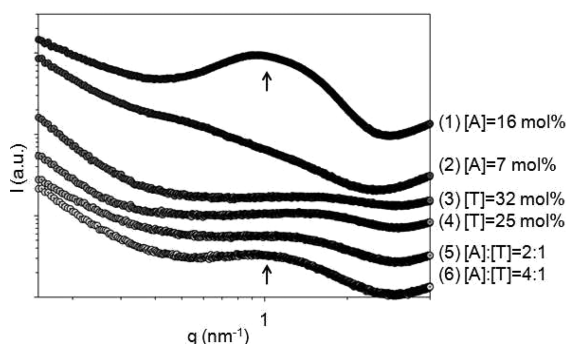


Figure 5. SAXS of poly(*n*BA-*co*-acrylic adenine) with (1) 7 mol % and (2) 16 mol % of adenine, poly(*n*BA-*co*-acrylic thymine) with (3) 25 mol % and (4) 32 mol % of thymine, and the polymer complexes of (1) and (4) at (5) $[A]/[T] = 2$ and (6) $[A]/[T] = 4$. For sake of clarity, data were shifted by arbitrary factors.

(Figure S6). The diffraction pattern of the adenine acrylate-containing copolymers displayed an intense diffraction peak located at $2\theta = 20^\circ$, which was assigned to the local chain packing (amorphous halo) of P*n*BA.³⁹ The reflection peak at $2\theta = 12.87^\circ$ ($d = 6.87 \text{ \AA}$) corresponded to the distance between nucleobase stacks,²⁵ which were held together with π – π interactions and, adenine–adenine hydrogen bonding from the FT-IR data. We interpreted these needle-like structures as one-dimensional ordered stacks of associated adenine units with a parallel arrangement of the rings.

The AFM micrograph of thymine acrylate copolymers did not show any obvious organized nanostructures even up to 32 mol % of thymine. Accordingly, the SAXS profiles of thymine-containing copolymers only showed broad peaks with very low intensity, implying less pronounced self-association of thymine than adenine. This observation was similar to the self-assembly behavior of adenine- and thymine-terminated telechelic poly-(tetrahydrofuran)s.²⁵ The weak hydrogen-bonding self-dimerization constant of adenine and thymine (both less than 10 M^{-1} in CDCl_3)⁴⁰ suggested that the unique higher order self-assembly of adenine-containing polymers was driven through

additional noncovalent interactions, such as π – π stacking, which was more pronounced for adenine than the other pyrimidine or purine derivatives.⁴¹ In general, the extent of stacking decreased as purine–purine > purine–pyrimidine > pyrimidine–pyrimidine.⁴² In addition, Hawker and Kramer et al. synthesized random copolymers consisting of *n*BA with quadruple hydrogen-bonding side chains based on 2-ureido-4[1*H*]-pyrimidinone (UPy).⁴³ Although the UPy groups strongly dimerized, they did not π – π stack into ordered structures and microphase separation was not observed in this case. Meijer et al. studied the self-assembly process of ureidotriazine functionalized oligo(*p*-phenylenevinylene), and they found that the π -conjugated structures were crucial in guiding hydrogen-bonded molecules to further assemble into supramolecular structures.⁴⁴

WAXD was performed on styrenic and acrylic nucleobase-containing homopolymers to further elucidate the significance of structural flexibility on supramolecular self-assembly (Figure

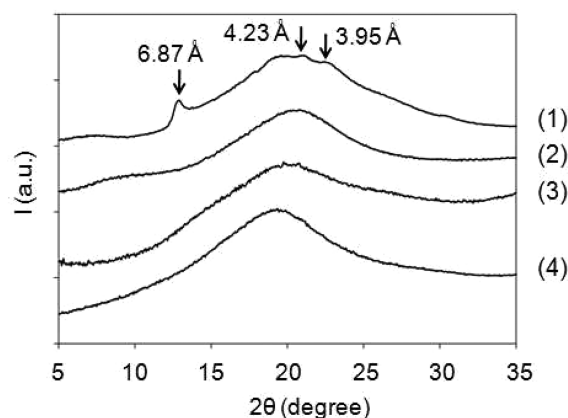


Figure 6. X-ray (radiation source Cu $K\alpha$) diffraction diagram of (1) acrylic adenine homopolymer, (2) acrylic thymine homopolymer, (3) styrenic adenine homopolymer, and (4) styrenic thymine homopolymer. For sake of clarity, data were shifted by arbitrary factors.

6). The diffraction pattern of acrylic adenine homopolymer displayed reflection peaks at $2\theta = 12.9^\circ$ ($d = 6.87 \text{ \AA}$) and 22.5° ($d = 3.95 \text{ \AA}$), which were assigned to associated adenine stacks.²⁵ In contrast, thymine did not π - π stack strongly and thymine-containing homopolymers did not show distinct reflection peaks. Interestingly, a styrenic adenine homopolymer did not reveal reflection peaks either. The bulky phenyl rings potentially hindered the well-defined position between adenine-adenine π - π stacks. Moreover, the spacing between functional groups along a polymer chain, and the presence of bulky pendant groups can also significantly reduce the associated hydrogen bonding per unit volume, as a result of a so-called functional group accessibility effect. This effect is also considered to be the origin of steric crowding and shielding.⁴⁵ Thus, the relatively strong π - π interactions of adenine as well as mobility and accessibility from alkyl chain spacers resulted in the unique well-defined nanostructures observed in acrylic adenine-containing copolymers.

Variable temperature SAXS and WAXD experiments were conducted on A-16 to further investigate the influence of temperature on adenine self-assembly (Figures S7 and S8). The intensity of the broad Bragg peak near $q = 0.90 \text{ nm}^{-1}$ decreased monotonically with temperature until the peak was barely visible at 80°C . The same trend was shown in WAXD profiles; i.e., the reflection of stacked adenine-adenine decreased in intensity with temperature increase and eventually disappeared above 80°C , implying the dissociation of the needle-like nanostructures upon heating. From DMA analysis (Figure 2), the polymer film lost mechanical integrity at 80°C and eventually flowed. These results were consistent with the proposed structural model of hard needle-like structures composed of π - π stacks of hydrogen-bonded adenine units, which reinforced the polymer matrix.

Blending acrylic adenine- and thymine-containing copolymers resulted in a polymer complex with weak microphase separation as shown in AFM (Figure 4). The absence of distinctive needle-like nanostructures was presumably due to the A-T base pairs that possessed weaker π - π interactions than A-A⁴² and the lack of stereoregularity in polymer backbone. For adenine-containing polymers, adenine intramolecularly π - π packed with neighboring adenine. This supposition was reinforced with SAXS results of the polymer complexes, which revealed averaged, intermediate Bragg spacings and no evidence of multiple interdomain spacings (Figure 5). As the ratio of [A]/[T] decreased from 4:1 to 2:1, the scattering peak intensity decreased and the polymer complexes became more uniform. Kuo et al. also reported a similar behavior for triazine- and thymine-containing PMMA copolymer mixtures, and the degree of homogeneity of the polymer complex was relatively higher than the precursors.⁴⁶ Hydrogen bonding suppressed the concentration fluctuations.

Rheology. Melt rheological characterization was conducted on adenine- and thymine-containing polyacrylates and their complexes ([A]:[T] = 1:1). Master curves of storage modulus versus frequency were referenced to 20°C , since the T_g 's of these polymers were lower than room temperature (Figure 7). It should also be noted that in the construction of the master curves vertical shift of the data was not needed, demonstrating that the plateau modulus G_N^0 was not a strong function of temperature. The master curve of the hydrogen-bonding complex exhibited an increased storage modulus and T_g with an extended terminal relaxation time by several orders of magnitude, which was attributed to complementary hydrogen

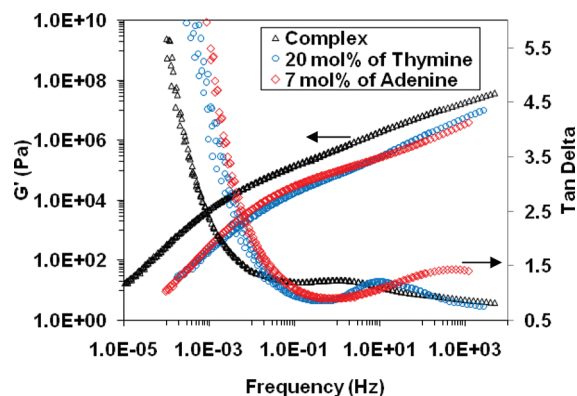


Figure 7. Storage and loss modulus master curves of polyacrylates containing 7 mol % of adenine and 25 mol % of thymine, respectively, and their complex ([A]:[T] = 1:1) referenced to 20°C showing the effect of complementary hydrogen bonding.

bonding and the formation of a higher apparent molar mass. Even at low frequencies (higher temperatures), the hydrogen bonding complex exhibited a G' 10 times higher than the precursors, indicating that a low level of A-T nucleobase pairs remained even at high temperatures; this was expected because of the higher association constant of A-T hydrogen bonding than A-A or T-T hydrogen bonding. In comparison with the precursors, the $\tan \delta$ peak of the polymer complex broadened and shifted to lower frequencies, and the corresponding plateau modulus was broader, suggesting weaker temperature dependence, possibly because the hydrogen-bonding nucleobase pair dissociates and re-forms in equilibrium prior to complete separation.⁴³ Although distinct microphase separation driven by π - π interactions occurred in A-7, time-temperature superposition was satisfied in all cases, indicating that all governing relaxation process had similar temperature dependences. In addition, plotting the shift factors (a_T) versus inverse temperature followed the Williams-Landel-Ferry (WLF) equation:

$$\log a_T = \frac{-c_1^0(T - T_0)}{c_2^0 + (T - T_0)} \quad (1)$$

where c_1^0 and c_2^0 are constants and T_0 is the reference temperature. Values of the constants c_1^0 and c_2^0 were determined from the plot of the $-(T - T_0)/\log a_T$ against $T - T_0$; the coefficient c_1^0 was obtained from the reciprocal of the slope and the coefficient c_2^0 from the intercept. The complexation of adenine and thymine led to an increase in c_1^0 and a significant decrease in c_2^0 (Table 2). Fractional free volume is an important

Table 2. Rheological Characterization of Adenine- and Thymine-Containing Poly(*n*-butyl acrylate) Copolymers and Their Complex ($T_0 = 20^\circ\text{C}$)

sample	G_N^0 (MPa)	c_1^0	c_2^0	f_0
adenine 7 mol %	74	8.1	110	0.054
thymine 20 mol %	49	7.5	103	0.058
complex	165	9.1	98	0.048

parameter that can be obtained from these fits.

$$f_0 = \frac{B}{2.303c_1^0} \quad (2)$$

where B is a constant usually assumed to be unity. The fractional free volume decreased for the polymer complex, which suggested strong complementary hydrogen bonding favored compact molecular packing. Hawker and Kramer et al. previously reported that TTS was satisfied for UPy-containing polyacrylates, but the shift factors followed an Arrhenius-type behavior since the dissociation of the polymer side-chain hydrogen bonding was a thermally activated process.⁴³ In our case, the kinetic restriction at $T_g < T < T_g + 100$ °C for molecular motions was free-volume availability.

Adhesion Measurements. Hydrogen-bonding associations provide strategies to increase polymer apparent molecular weight to inhibit creep and cohesive failure, while improving interfacial adhesion.⁴⁷ To demonstrate the effectiveness of complementary multiple hydrogen bonding on polymer adhesion, we measured the peel strength (the ability to resist removal upon peeling) and shear resistance (the ability to resist flow when shear forces are applied). Additionally, a comparative study was performed on acrylic acid (AA)- and 4-vinylpyridine (VP)-based polymer analogues with similar molecular weights and hydrogen-bonding contents in order to qualitatively describe the influence of bond strength on polymer peel strength (Table 1). An ASTM-D3300 standard 90° peel testing method was adopted, and the results are depicted in Figure 8.

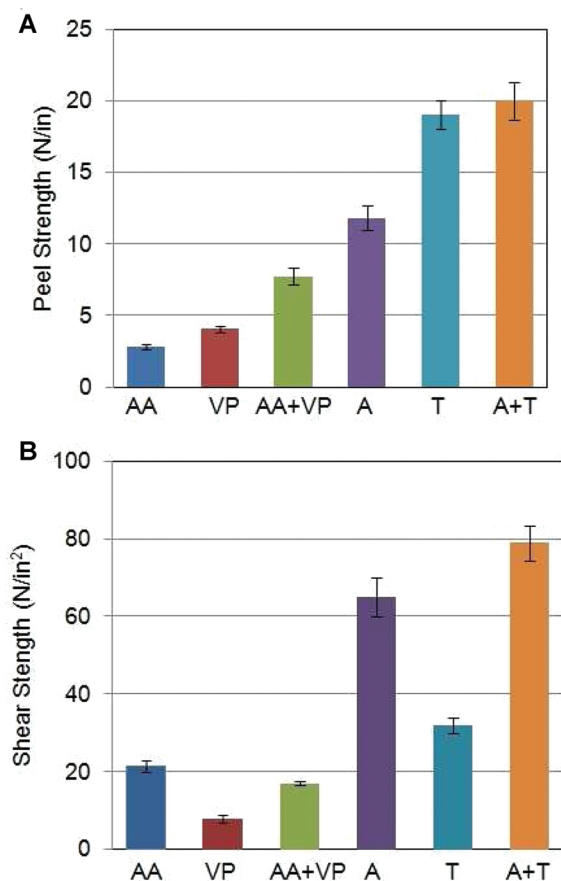


Figure 8. Peel strength and shear strength of poly(*n*BA-*co*-acrylic adenine) and poly(*n*BA-*co*-acrylic thymine) in comparison to AA- and VP-based complementary hydrogen-bonding polymer analogues.

All polymers with ≤ 10 mol % of hydrogen-bonding content failed cohesively. Peel strength of acrylic thymine- and adenine-containing copolymers with 10 mol % of thymine and 4 mol %

of adenine were 11.8 and 19.1 N/in., respectively, whereas poly(AA-*co*-*n*BA) and poly(VP-*co*-*n*BA) containing 4 mol % of AA and 10 mol % of VP, respectively, showed peel strength below 5 N/in., which was 3–4 times lower. The enhanced wettability was possibly due to strong nucleobase pairing as well as the strong association between nucleobases and the stainless steel surface in comparison to the association between carboxylic acid (AA) and vinylpyridine (VP). Additionally, peel strengths of the adenine and thymine-containing polymer complexes were higher than their precursors.

Dynamic shear measurement was performed on an Instron tensile tester to demonstrate the influence of complementary intermolecular hydrogen bonding, which potentially provided enhanced cohesion due to supramolecular structure. As shown in Figure 8, the shear strength of nucleobase-containing polymers is 3–4 times higher than the analogues, suggesting a significant improvement in adhesion at interface. The association of nucleobases led to an increase in apparent molecular weight and network structure with increased modulus and T_g . Because of stronger hydrogen bonding, blending adenine- and thymine-containing polymers further enhanced the shear strength. The optimum combination of cohesive and adhesive strengths was achieved, which contributed to high shear strength.

CONCLUSION

Novel acrylic adenine and thymine monomers were synthesized in decent yields through aza-Michael addition and then copolymerized with *n*BA using conventional radical polymerization. The resulted adenine-containing polyacrylate with only 7 mol % of adenine units self-assembled into ordered needle-like nanostructures. These needles approximately 100 nm in length and less than 10 nm in width were randomly oriented in the soft polymer matrix as shown from AFM. For thymine-containing polyacrylates possessing up to 32 mol % of thymine units, both AFM and SAXS images were featureless. In addition, compared to adenine-containing polyacrylates, thymine-containing analogues with similar hydrogen-bonding molar concentrations exhibited lower glass transition temperatures and storage moduli at room temperature. The different self-assembly behavior was ascribed to the pronounced π - π stacking of adenine than thymine. Time-temperature superposition (TTS) was successfully applied to adenine- and thymine-containing polyacrylates and their polymer complex. The shift factors and SAXS results demonstrated a decrease in free volume and an increase in homogeneity of the polymer complex in comparison to the precursors. Additionally, nucleobase-containing hydrogen-bonding polymers possessed peel and shear strengths 3–4 times higher than the AA- and VP-based complementary polymer analogues.

ASSOCIATED CONTENT

Supporting Information

Experimental details; Figures S1–S8. This material is available free of charge via the Internet at <http://pubs.acs.org>.

AUTHOR INFORMATION

Corresponding Author

*E-mail: telong@vt.edu; Tel (540) 231-2480; Fax (540) 231-8517.

■ ACKNOWLEDGMENTS

The authors acknowledge the financial support of the Petroleum Research Fund (ACS-PRF 35190-AC7), which is administered by the American Chemical Society. Parts of this work were carried out using instruments in the Nanoscale Characterization and Fabrication Laboratory, a Virginia Tech facility operated by the Institute for Critical Technology and Applied Science (ICTAS). We also acknowledge funding from NSF (CHE-0722638) for the acquisition of our Agilent 6220 LC-TOF-MS. This material is partially based upon work supported by the National Science Foundation under Grant DMR-0923107. Additionally, this research was supported in part by the U.S. Army Research Laboratory and the U.S. Army Research Office under Contract/Grant W911NF-07-1-0452, Ionic Liquids in Electro-Active Devices Multidisciplinary University Research Initiative (ILEAD MURI).

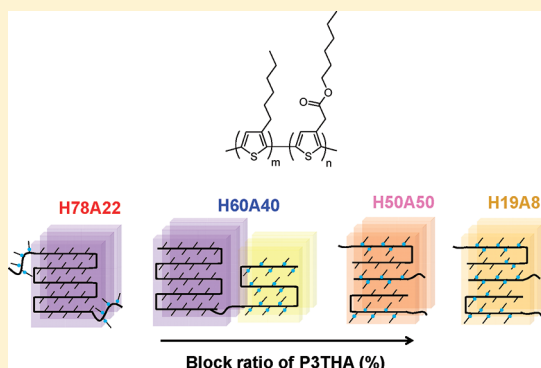
■ REFERENCES

- (1) Wojtecki, R. J.; Meador, M. A.; Rowan, S. J. *Nature Mater.* **2011**, *10* (1), 14–27.
- (2) Cordier, P.; Tournilhac, F.; Soulie-Ziakovic, C.; Leibler, L. *Nature* **2008**, *451* (7181), 977–980.
- (3) de Greef, T. F. A.; Meijer, E. W. *Nature* **2008**, *453* (7192), 171–173.
- (4) Sijbesma, R. P.; Beijer, F. H.; Brunsveld, L.; Folmer, B. J. B.; Hirschberg, J. H. K. K.; Lange, R. F. M.; Lowe, J. K. L.; Meijer, E. W. *Science* **1997**, *278* (5343), 1601–1604.
- (5) Nair, K. P.; Breedveld, V.; Weck, M. *Macromolecules* **2011**, *44*, 3346–3357.
- (6) Spivak, D.; Gilmore, M. A.; Shea, K. J. *J. Am. Chem. Soc.* **1997**, *119*, 4388–4393.
- (7) Duffy, D. J.; Das, K.; Hsu, S. L.; Penelle, J.; Rotello, V. M.; Stidham, H. D. *J. Am. Chem. Soc.* **2002**, *124*, 8290–8296.
- (8) Lo, P. K.; Sleiman, H. F. *J. Am. Chem. Soc.* **2009**, *131*, 4182–4183.
- (9) Lin, I. H.; Cheng, C.-C.; Yen, Y.-C.; Chang, F.-C. *Macromolecules* **2010**, *43* (3), 1245–1252.
- (10) Yamauchi, K.; Lizotte, J. R.; Long, T. E. *Macromolecules* **2002**, *35* (23), 8745–8750.
- (11) Khan, A.; Haddleton, D. M.; Hannon, M. J.; Kukulj, D.; Marsh, A. *Macromolecules* **1999**, *32*, 6560.
- (12) Marsh, A.; Khan, A.; Haddleton, D. M.; Hannon, M. J. *Macromolecules* **1999**, *32*, 8725.
- (13) Bazzi, H. S.; Sleiman, H. F. *Macromolecules* **2002**, *35* (26), 9617–9620.
- (14) Spijker, H. J.; van Delft, F. L.; van Hest, J. C. M. *Macromolecules* **2007**, *40* (1), 12–18.
- (15) Lutz, J.-F.; Thuenemann, A. F.; Rurack, K. *Macromolecules* **2005**, *38* (20), 8124–8126.
- (16) Lutz, J.-F.; Thuenemann, A. F.; Nehring, R. *J. Polym. Sci., Part A: Polym. Chem.* **2005**, *43* (20), 4805–4818.
- (17) Inaki, Y.; Futagawa, H.; Takemoto, K. *J. Polym. Sci., Polym. Chem. Ed* **1980**, *18*, 2959–2969.
- (18) Mather, B. D.; Lizotte, J. R.; Long, T. E. *Macromolecules* **2004**, *37* (25), 9331–9337.
- (19) Mather, B. D.; Baker, M. B.; Beyer, F. L.; Berg, M. A. G.; Green, M. D.; Long, T. E. *Macromolecules* **2007**, *40* (19), 6834–6845.
- (20) Mather, B. D.; Baker, M. B.; Beyer, F. L.; Green, M. D.; Berg, M. A. G.; Long, T. E. *Macromolecules* **2007**, *40* (13), 4396–4398.
- (21) Navacchia, M. L.; Favaretto, L.; Treossi, E.; Palermo, V.; Barbarella, G. *Macromol. Rapid Commun.* **2010**, *31* (4), 351–355.
- (22) Konodo, K.; Iwasaki, H.; Nakatani, K.; Ueda, N.; Takemoto, K.; Imoto, M. *Makromol. Chem.* **1969**, *125*, 42–47.
- (23) Hurduc, N.; Enea, R.; Scutaru, D.; Sacarescu, L.; Donose, B. C.; Nguyen, A. V. *J. Polym. Sci., Part A: Polym. Chem.* **2007**, *45* (18), 4240–4248.
- (24) Akashi, M.; Takada, H.; Inaki, Y.; Takemoto, K. *J. Polym. Sci., Part A: Polym. Chem.* **1979**, *17*, 747–757.
- (25) Sivakova, S.; Bohnsack, D. A.; Mackay, M. E.; Suwanmala, P.; Rowan Stuart, J. *J. Am. Chem. Soc.* **2005**, *127*, 182020–18211.
- (26) Binder, W. H.; Kunz, M. J.; Kluger, C.; Hayn, G.; Saf, R. *Macromolecules* **2004**, *37* (5), 1749–1759.
- (27) Mes, T.; Smulders, M. M. J.; Palmans, A. R. A.; Meijer, E. W. *Macromolecules* **2010**, *43*, 1981–1991.
- (28) Mather, B. D.; Viswanathan, K.; Miller, K. M.; Long, T. E. *Prog. Polym. Sci.* **2006**, *31* (5), 487–531.
- (29) Sedláč, M.; Šimůnek, P.; Antonietti, M. *J. Heterocycl. Chem.* **2003**, *40*, 671.
- (30) Karikari, A. S.; Mather, B. D.; Long, T. E. *Biomacromolecules* **2007**, *8*, 302–308.
- (31) Lira, E. P.; Huffman, C. W. *J. Org. Chem.* **1966**, *31* (7), 2188–2191.
- (32) Kuo, S.-W.; Liu, W.-P.; Chang, F.-C. *Macromolecules* **2003**, *36*, 5165–5173.
- (33) Kyeremateng, S. O.; Amado, E.; Kressler, J. *Eur. Polym. J.* **2007**, *43*, 3380–3391.
- (34) Elkins, C. L.; Park, T.; McKee, M. G.; Long, T. E. *J. Polym. Sci., Part A: Polym. Chem.* **2005**, *43*, 4618–4631.
- (35) Kuo, S. W.; Chang, F. C. *Macromolecules* **2001**, *34* (15), 5224–5228.
- (36) Sijbesma, R. P.; Beijer, F. H.; Brunsveld, L.; Folmer, B. J. B.; Hirschberg, J.; Lange, R. F. M.; Lowe, J. K. L.; Meijer, E. W. *Science* **1997**, *278* (5343), 1601–1604.
- (37) Kautz, H.; van Beek, D. J. M.; Sijbesma, R. P.; Meijer, E. W. *Macromolecules* **2006**, *39* (13), 4265–4267.
- (38) Aneja, A.; Wilkes, G. L. *Polymer* **2003**, *44*, 7221–7228.
- (39) Miller, R. L.; Boyer, R. F.; Heijboer, J. *J. Polym. Sci., Polym. Phys. Ed.* **1984**, *22* (12), 2021–2041.
- (40) Sartorius, J.; Schneider, H.-J. *Chem.—Eur. J.* **1996**, *2*, 1446 and references cited therein.
- (41) Sapper, H.; Lohmann, W. *Biophys. Struct. Mech.* **1978**, *4*, 327–335.
- (42) T'so, P. O. P.; Melvin, I. S.; Olson, A. C. *J. Am. Chem. Soc.* **1963**, *85*, 1289–1296.
- (43) Feldman, K. E.; Kade, M. J.; Meijer, E. W.; Hawker, C. J.; Kramer, E. J. *Macromolecules* **2009**, *42* (22), 9072.
- (44) Jonkheijm, P.; van der Schoot, P.; Schenning, A. P. H. J.; Meijer, E. W. *Science* **2006**, *313* (5783), 80–83.
- (45) Pehlert, G. J.; Painter, P. C.; Coleman, M. N. *Macromolecules* **1998**, *31*, 8423.
- (46) Kuo, S.-W.; Tsai, H.-T. *Macromolecules* **2009**, *42*, 4701–4711.
- (47) Cashion, M. P.; Park, T.; Long, T. E. *J. Adhes.* **2009**, *85*, 1–17.

Synthesis, Morphology, and Optical and Electrochemical Properties of Poly(3-hexylthiophene)-*b*-poly(3-thiophene hexylacetate)Chun-Chih Ho,[†] Yu-Cheng Liu,[‡] Shih-Hsiang Lin,[†] and Wei-Fang Su^{*,†,‡}[†]Department of Materials Science and Engineering, National Taiwan University, Taipei 10617, Taiwan[‡]Institute of Polymer Science and Engineering, National Taiwan University, Taipei 10617, Taiwan

S Supporting Information

ABSTRACT: A series of all-conjugated diblock copolythiophenes of poly(3-hexylthiophene)-*b*-poly(3-thiophene hexylacetate) (P3HT-*b*-P3THA) were synthesized via modified sequential Grignard metathesis polymerization. The living P3HT was formed first, then reacting with the monomer of P3THA. By using 2-bromo-3-hexyloxycarbonylmethylene-5-iodothiophene instead of dibromo monomer in metal exchange reaction and by controlling the polymerization temperature relatively low at 16–20 °C, the reaction between carboxylate group and Grignard reagent can be minimized and the polymerization can be controlled; low PDI (<1.3), high regioregularity (>95%), and well-controlled block ratios of block copolymer were obtained. The introduction of carboxylate group in the side chain of one of the monomers, and controlling the side-chain length difference by only three atoms between two monomers, there are profound effects on the optical and electrochemical properties and morphologies of the block copolymers. The electron-withdrawing carboxylate causes the absorption maximum of copolymer in solution to be blue-shifted from that of pristine P3HT, and the extent of blue shift is increased monotonically with increasing the molar ratio of P3THA. However, in thin film, the intermolecular π – π stacking plays a role in the absorption behavior of copolymer which decreases the extent of blue shift. The HOMO level of the copolymer is lowered by 0.38 eV from that of P3HT due to the presence of P3THA block. The crystalline structure of the copolymer can be controlled according to the molar ratio of each block. Crystalline–amorphous, crystalline–crystalline, and cocrystalline structures are observed in the bulk samples when the block molar percentage of P3THA is increased from 22, 40, to 50 and higher, respectively. Microphase separation is clearly present in the thin film fabricated from the copolymer containing crystalline–amorphous and crystalline–crystalline structures. The observation of various crystalline structures in a single type of all-conjugated diblock copolymer is very significant and provides a new approach to simultaneously manipulate the optical and electronic properties and nanostructures of conducting polymers by simply changing their compositions.



■ INTRODUCTION

All-conjugated polymers have received great attention in the past decade because of their high potential and promising applications in organic photovoltaic cells (OPVs),^{1,2} organic field-effect transistors (OFETs),^{3–5} organic chemical sensors,⁶ and organic light-emitting diodes (OLEDs).⁷ It is very important to control the morphologies of conducting polymers in nanoscale to achieve high performance in the application of optoelectronics.^{8–11} To precisely manipulate the nanostructures, one good strategy is to employ block copolymers (BCPs) composed of semiconducting polymer with exceptional electronic properties such as poly(3-alkylthiophene)s (P3AT). BCPs are well-known to have the capability to self-organize into a variety of nanostructures, driven by factors of immiscibility or the crystallinity difference between the two blocks.^{12,13} Synthesis and self-assembly of rod–coil BCPs containing a semiconducting block and an insulating block have been extensively investigated.^{14–16} We have demonstrated poly(3-hexylthiophene)-*b*-poly(2-vinylpyridine) (P3HT-*b*-P2VP)¹⁴

and poly(diethylhexyloxy-*p*-phenylenevinylene)-*b*-poly(methyl methacrylate) (DEH-PPV-*b*-PMMA)¹⁵ are able to self-assemble into lamellar, cylinder, and spherical structures as increasing the coil fraction. The insulating coil blocks indeed promote the self-assembly and mechanical properties of the copolymer. However, these insulating blocks deteriorate the electronic properties of polymer. McCullough et al. have shown the mobility of OFET fabricated from poly(3-hexylthiophene)-*b*-poly(methyl acrylate) (P3HT-*b*-PMA) decreases as increasing the content of PMA.^{17,18} Thus, there is a need to develop all-conjugated BCPs for polymer based high-performance optoelectronic and electronic devices.

Recently, P3ATs-based BCPs have been reported due to their high charge mobility, facile, and versatile synthesis.^{19–25} P3ATs-based BCPs exhibit three categories of crystalline

Received: September 25, 2011

Revised: December 19, 2011

Published: December 28, 2011

structures: crystalline–amorphous, crystalline–crystalline, and cocrystalline. Poly(3-hexylthiophene)-*b*-poly(3-phenoxyethylthiophene) (P3HT-*b*-P3PT)²⁶ and poly(3-hexylthiophene)-*b*-poly(3-(2-ethylhexyl)thiophene) (P3HT-*b*-P3EHT)²⁷ have been synthesized and show crystalline–amorphous structure. The formation of this structure is mostly caused by the large difference in crystallinity between two blocks. The crystalline–crystalline structure is revealed while the crystallization rate of two blocks is similar such as poly(3-butylthiophene)-*b*-poly(3-octylthiophene) (P3BT-*b*-P3OT),²⁸ poly(3-butylthiophene)-*b*-poly(3-dodecylthiophene) (P3BT-*b*-P3DDT),²⁹ poly(3-hexylthiophene)-*b*-poly(3-dodecylthiophene) (P3HT-*b*-P3DDT),²⁹ and poly(3-hexylthiophene)-*b*-poly(3-cyclohexylthiophene) (P3HT-*b*-P3CHT).²⁴ Ge et al. reported that by controlling the alkyl side-chain length different by two carbon atoms to improve the structure similarity, the cocrystalline structure can be observed in poly(3-butylthiophene)-*b*-poly(3-hexylthiophene) (P3BT-*b*-P3HT).²⁹ Nevertheless, none of these BCPs as above-mentioned have shown the effect of block ratio on the formation of various crystalline structures in one single type of all-conjugated diblock copolymer.

The long-term air stability of conducting polymer is a desired property for optoelectronic application. It can be improved by lowering the highest occupied molecular orbital (HOMO) of conducting polymer. The HOMO energy level of polythiophene derivatives can be lowered by diminishing the effective conjugation length from the constrained delocalization. Copolymers of thiophene with thieno[2,3-*b*]thiophene,³⁰ fluorene,³¹ and naphthalene³² have shown to have improved environmental stability but higher band gap. Another strategy to lower the HOMO energy level is the incorporation of electron-withdrawing substituents on the polymer backbone. Polythiophenes composed of electronegative carboxylate substituents can effectively increase their oxidative doping stability by lowering the HOMO energy level of conventional polythiophenes about 0.3–0.5 eV.^{33–36} Moreover, the carboxylate group can be easily converted into carboxylic acid via hydrolysis. The thus-obtained functionalized group enables the interface interaction between the polymer and inorganic substances and further enhances the interfacial charge-transfer efficiency.^{37–40}

Herein, we have synthesized a series of all-conjugated diblock copolythiophenes, poly(3-hexylthiophene)-*b*-poly(3-thiophene hexylacetate) (P3HT-*b*-P3THA), with well-controlled molecular weight and low PDI (<1.3) via modified sequential Grignard metathesis polymerization (GRIM).^{28,41} Their optical and electrochemical properties, crystalline behaviors, and nanoscale phase separation were investigated. Our study revealed that optical and electrochemical properties in solid state are attributed to the specific block. Crystalline–amorphous and crystalline–crystalline structures of these BCPs are observed at low 3THA molar fraction (<50%), whereas cocrystalline structures appeared as the 3THA fraction is larger than 50%. Distinct microphase separation is present for the copolymer with 3THA molar fraction is less than 50%.

■ EXPERIMENTAL SECTION

Materials. 3-Bromothiophene (98%), 3-thiopheneacetic acid (98%), magnesium, 1-bromohexane (98%), 1-hexanol (98%), *N*-bromosuccinimide (98%), iodine (98%), iodobenzene diacetate (98%), isopropylmagnesium chloride (2.0 M solution in THF) (*i*-PrMgCl), Ni(dppp)Cl₂ (99%), and Ni(dppe)Cl₂ (99%) were purchased from Acros and used without further purification. *N*-Butylammonium perchlorate

(Bu₄NClO₄) was recrystallized twice from ethanol. THF and ethyl ether for reaction were dried with Na/benzophenone before used. Acetonitrile was dried over CaH₂ and distilled prior to use. The monomers, 2,5-dibromo-3-hexylthiophene (DBHT) and 2-bromo-3-hexyloxycarbonylmethylene-5-iodothiophene (BHOCMIT), were prepared according to the literature.^{41,42}

Synthesis of Poly(3-hexylthiophene)-*b*-poly(3-thiophene hexylacetate) Block Copolymers (P3HT-*b*-P3THA). The synthetic conditions of the P3HT-*b*-P3THAs in this work were optimized according to the previous studies^{28,41} and also used to synthesize the P3HT and P3THA homopolymers. In general, two 250 mL round-bottom flasks were dried by heating under reduced pressure. When those flasks are cooled to room temperature, DBHT and BHOCMIT were respectively placed in these flasks. Both monomers were evacuated under reduced pressure to remove moisture and oxygen. After dried THF was added, these solutions were cooled down to 0 °C. 2 M *i*-PrMgCl in THF (1.1 equiv) was then added into the DBHT solution. Thirty minutes later, 2.0 mol % Ni(dppe)Cl₂ catalyst was added into the solution at 0 °C and then warmed up to 25 °C for 30 min. Meanwhile, BHOCMIT solution was also reacted with 1.1 equiv of *i*-PrMgCl at 0 °C for 30 min. This Grignard exchanged monomer was introduced via a cannula after the polymerization of the first block was complete. The polymerization of the block copolymer was allowed to proceed at 16–20 °C for another 5 h, and the reaction was then quenched with 5 M HCl solution. The copolymers were purified using Soxhlet extraction with following solvents: methanol, acetone, and hexane in sequence. In this study, the compositions of copolymers are controlled by the feed molar ratio of DBHT:BHOCMIT as follows: 70:30, 53:47, 47:53, and 35:65.

¹H Nuclear Magnetic Resonance (¹H NMR). The chemical structures and compositions of all synthesized polymers were determined by ¹H NMR spectra. These NMR spectra were recorded by a Bruker Avance 400 MHz and CDCl₃ was used as solvent.

Gel Permeation Chromatography (GPC). The molecular weight and molecular weight distribution of all synthesized polymers were determined using a Waters GPC (Breeze system). The system was equipped with two Waters Styragel columns (HR3 and HR4E), a refractive index detector (Waters 2414), and a dual-wavelength absorbance detector (Waters 2487). The apparatus was calibrated using polystyrene standards (Waters) and THF used as an eluent at 35 °C.

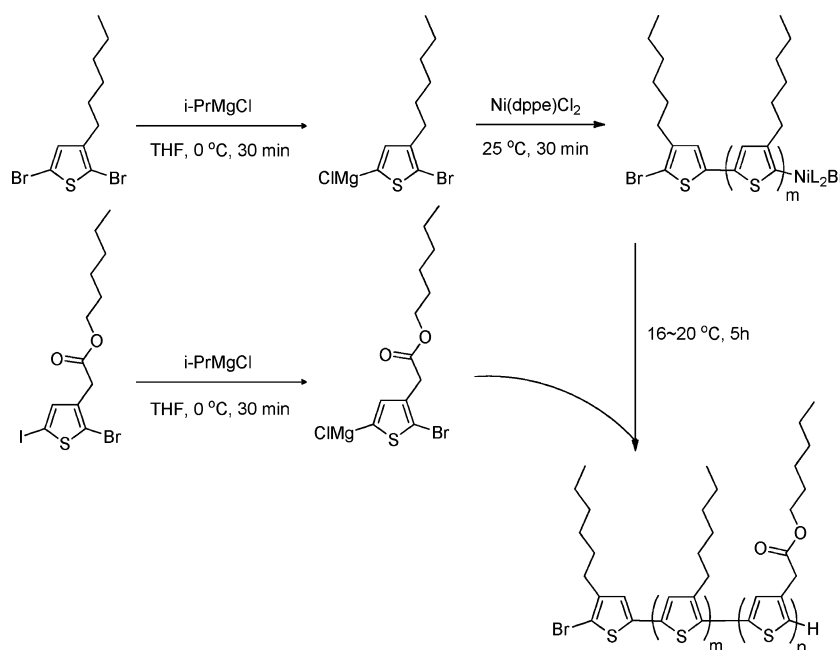
UV–vis Absorption Spectrometer. The optical properties of all synthesized polymers were characterized by UV–vis absorption spectrometer. UV–vis absorption spectra were recorded by a Perkin-Elmer Lambda 35 UV/vis spectrometer. For the solution state measurement, samples were dissolved in chlorobenzene with concentration of ~10^{−6} M. The samples for the solid state study were prepared by spin-coating on quartz substrate from 10 mg/mL chlorobenzene (CB) solution and subsequently annealed at 150 °C for 15 min.

Cyclic Voltammeter (CV). The highest occupied molecular orbital (HOMO) and the lowest unoccupied molecular orbital (LUMO) of all synthesized polymers were determined by cyclic voltammeter (CH Instrument 611B potentiostat/galvanostat system). Samples were spin-coated from 10 mg/mL CB solution onto ITO substrate and then annealed at 150 °C for 15 min. The substrate, platinum, and silver wire were used as working electrode, counter electrode, and reference electrode, respectively. The electrolyte was prepared by dissolving Bu₄NClO₄ in dried acetonitrile into a 0.1 M solution. All measurements were calibrated using ferrocene (Fc) as the standard, and each scan was proceeded at the scan rate of 100 mV/s.

Wide-Angle X-ray Scattering (WAXS). WAXS experiment was performed on the beamline 13A1 or 17A1 of the National Synchrotron Radiation Research Center (NSRRC), Taiwan. Samples were prepared from CB solution (10 mg/mL) and filled it into a thick washer attached with a kapton sheet. After the solvent was completely evaporated, the samples were annealed at 150 °C for 15 min.

Differential Scanning Calorimetry (DSC). A TA Instruments Q100 DSC was used to probe thermal transitions of polymers. Samples were prepared by CB solution casting directly into DSC pans and then allowing the solvent to evaporate slowly. The samples were

Scheme 1. Synthetic Routes of Poly(3-hexylthiophene)-*b*-poly(3-thiophene hexylacetate) Diblock Copolymer (P3HT-*b*-P3THA)



annealed at 150 °C for 15 min prior to DSC analysis. During DSC analysis, samples were reheated to 270 °C at a rate of 5 °C/min.

Atomic Force Microscopy (AFM). The microphase separation of the thin films was characterized by atomic force microscopy (DI Nanoscope III AFM instrument). The samples were prepared by spin-coating 10 mg/mL CB solution on silicon wafer, followed by annealing at 150 °C for 15 min.

RESULTS AND DISCUSSION

Synthesis of P3HT-*b*-P3THAs. Although the living character of GRIM polymerization for synthesizing diblock copolythiophenes with all alkyl side chain^{22,29} and functionalized side chain^{26,43} has been described, the synthesis of well-defined and carboxylate functionalized diblock copolythiophenes has not been reported. A series of P3HT-*b*-P3THA diblock copolymers with different compositions were synthesized using modified sequential GRIM method, as illustrated in Scheme 1. The type of the monomer, reaction sequence, and temperature are carefully designed and optimized.

Initially, we used dibrominated carboxylate functionalized monomers to obtain P3THA at room temperature, but the molecular weight and molecular weight distribution were uncontrollable. Instead, by replacing one reactive bromine of the carboxylated functionalized monomers with iodine, the side reaction of carboxylate group with the Grignard reagent was diminished during the magnesium–halogen exchange reaction.⁴¹ The activated monomers were dramatically deprotonated in a short period while the reaction temperature was raised above 20 °C. Hence, it is crucial to control temperature in both metal-exchange stage (0 °C) and polymerization stage (16–20 °C). Because of the lower reactivity of the carboxylate functionalized 3THA monomers⁴¹ as compared to 3HT monomers,⁴⁴ we grew P3HT block first in living state and then grew P3THA subsequently by reacting the living P3HT with 3HTA. The amount of 3HTA used was in excess in the feed molar ratio to compensate its lower reactivity. The extent of excess is increased with increasing P3THA ratio. GPC profiles of the first block of P3HT and P3HT-*b*-P3THA are shown in

Figure 1 (rest of compositions is shown in Figure S1 of the Supporting Information). The prepared P3HT is in unimodal

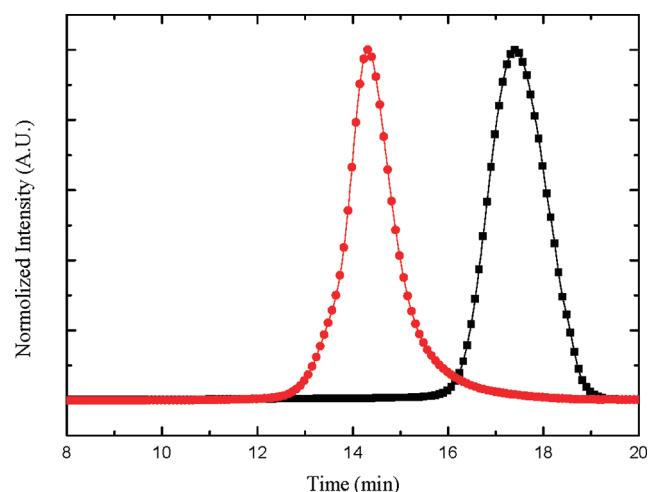


Figure 1. Representative GPC profiles of the first block of P3HT homopolymer (black square) synthesized via the modified GRIM method and P3HT-*b*-P3THA (H19A81) diblock copolymer (red circle) subsequently grown after introducing the activated 3THA monomers.

shape and narrow polydispersity. After adding the activated 3THA monomers, the peak shifts to higher molecular weight and remains unimodal shape, indicative of the formation of P3HT-*b*-P3THA diblock copolythiophene. Thus, well-controlled molecular weight ranged from 16 923 to 24 416, PDI below 1.3; four different molar ratios of diblock copolythiophenes were obtained, and their molecular characteristics are summarized in Table 1. We have used the symbol of HXXAYY to name the copolymer. H is P3HT segment and A is P3THA segment while XX and YY represent their molar ratio, respectively. For example, H78A22 is a block copolymer containing 78 mol % of P3HT and

Table 1. Summary of Molecular Properties of P3HT, P3THA, and P3HT-*b*-P3THA

polymer	denotation	feed molar ratio	3HT:3THA ^a	<i>M_w</i>	PDI
P3HT		100:0	100:0	23 369	1.17
P3THA		0:100	0:100	17 857	1.30
P3HT- <i>b</i> -P3THA	H78A22	70:30	78:22	16 847	1.14
	H60A40	53:47	60:40	24 416	1.18
	H50A50	47:53	50:50	16 923	1.21
	H19A81	35:65	19:81	18 677	1.28

^aMolar ratio determined by ¹H NMR.

22 mol % of P3THA. This symbol system is used throughout the study.

The compositions of these polymers were determined from their ¹H NMR spectra (Figure S2). Singlet peaks observed at 6.98 and 7.18 ppm are respectively attributed to the thiophene proton on P3HT segment and P3THA segment. Peaks at 3.81 and 4.16 ppm are belonging to the methylene protons neighboring to the thiophene rings and the oxygen atoms, respectively, of the side chains of P3THA. A methylene proton attributed to the side chain of P3HT segment is observed at 2.81 ppm. The regioregularity⁴⁵ and molar ratio of P3HT-*b*-P3THA diblock copolymers were estimated from the proton on thiophene ring and that adjacent to thiophene ring of each block. The regioregularity of each block is more than 95%, suggesting high regioselectivity is achieved for each block.

Optical and Electrochemical Properties. The optical and electrochemical properties of P3HT-*b*-P3THA diblock copolythiophenes were studied by using UV–vis absorption spectroscopy and electrochemical cyclic voltammetry (CV). In CB solution, the UV–vis spectra of these copolymers show a single absorption maxima which is placed in between that of P3HT (456 nm) and P3THA homopolymers (425 nm), as shown in Figure 2a. The peak is blue-shifted monotonically from 450 to 430 nm as increasing the P3THA fraction, which means the two blocks are miscible. However, very different features of UV–vis spectra are observed in the thin film samples due to the different crystalline behavior of each block, as shown in Figure 2b. Three characteristic peaks attributed to the intrachain π – π^* transition (525 nm), the increased conjugation length (560 nm), and the interchain π – π interaction (600 nm) for P3HT are observed, whereas only one peak at 425 nm is observed for P3THA. It is suggested that P3HT has better structural organization than the P3THA. In block copolymers, two characteristic peaks of 560 and 600 nm are belonging to the increased conjugation length and the interchain π – π interaction of polythiophene main chain. The interference effects on the structural organizations are increasing as increasing the P3THA fraction when we compared the normalized intensities of these two peaks among the copolymers. However, the absorption maximum of P3THA becomes dominate when the molar ratio of P3THA is larger than 50%. It is interesting to note that the absorption maximum of P3THA of copolymer is red-shifted from the pristine P3THA. We speculate that the synergistic effect from P3HT block increases the effective conjugation length of the P3THA block by increasing the P3HT molar ratio and induces cocrystallization between P3THA block and P3HT block. We will discuss these phenomena more in the section of crystalline behaviors.

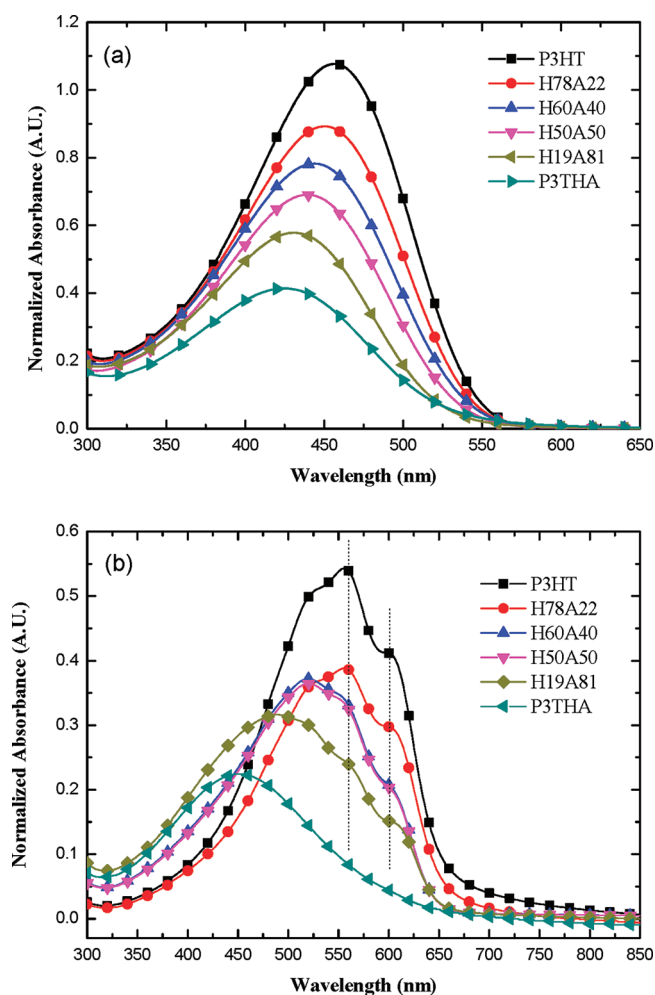


Figure 2. Normalized UV–vis absorption spectra of P3HT-*b*-P3THA diblock copolythiophenes and their homopolymers in (a) solution and (b) film. In film spectra, the dashed lines are assigned to the increased conjugation length peak (560 nm) and the π – π interaction peak (600 nm).

CV measurements were used to study redox behaviors of the P3HT-*b*-P3THA diblock copolythiophenes. The highest occupied molecular orbital (HOMO) and the lowest unoccupied molecular orbital (LUMO) energy levels from their onset oxidation and reduction potentials were determined, respectively. Figure 3 shows the cyclic voltammograms of P3HT, P3HT-*b*-P3THA, and P3THA. The onsets of oxidation potential (E_{ox}) and reduction potential (E_{red}) for P3THA are shown to be 0.949 and -1.043 V, respectively, while a distinguishable onset E_{ox} of 0.569 V is belonging to P3HT. Comparing to the P3HT, the oxidation potential of P3THA shows an increase of 0.38 V by placing the electron-deficient carboxylate group on the side chain. The HOMO and LUMO energy levels of the polymers were estimated according to the equations of $E_{LUMO} = -e(E_{red} + 4.8)$ (eV) and $E_{HOMO} = -e(E_{ox} + 4.8)$. The E_{LUMO} and the E_{HOMO} of the P3THA are positioned at -3.36 and -5.35 eV, respectively, while the E_{HOMO} of the P3HT is located at -4.97 eV. Interestingly, the E_{LUMO} and the E_{HOMO} of P3THA and P3HT blocks can be clearly identified in all copolythiophenes. The LUMO of P3THA block is lower than the LUMO of P3HT block by 0.3 eV, and the HOMO of P3THA block is lower than the HOMO of P3HT block by 0.38 eV. Herein, the enlargement of band gap in all

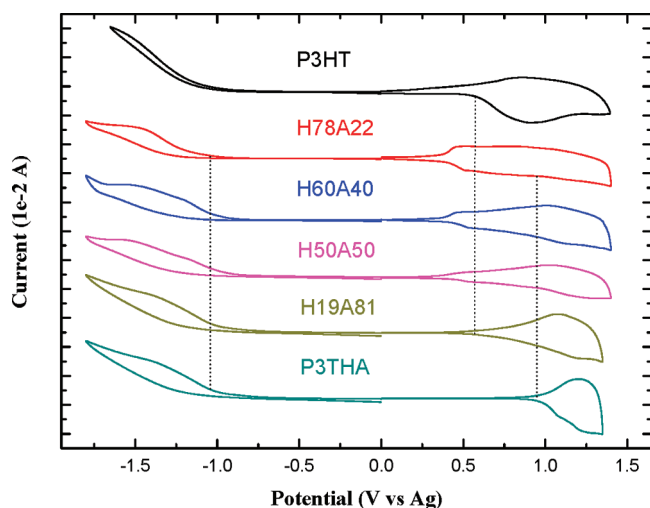


Figure 3. Cyclic voltammograms of P3HT-*b*-P3THA diblock copolythiophenes and their homopolymers. These samples were measured on ITO electrode in acetonitrile solution containing 0.1 M BuN₄ClO₄ at a scan rate of 100 mV/s. Dashed lines are represented as the onset of oxidation or reduction potentials. All curves are offset for clarity.

composition of P3HT-*b*-P3THAs as compared to that of P3HT is less than 0.17 eV calculated by optical band gap and 0.26 eV calculated by electrical band gap. These results suggest that the introduction of carboxylate group on the side chain is a very effective way to lower the E_{HOMO} of alkyl-substituted polythiophene for long-term air stability. For the copolymer having the molar ratio of P3THA ranged from 22 to 81%, the individual redox properties of each block is still remained which shows the characteristic of block copolymer.

Crystalline Behaviors. In order to investigate the crystalline behaviors of the P3HT-*b*-P3THA diblock copolythiophenes, WAXS and DSC measurements were performed. The study of crystalline behaviors of P3HT and P3THA was included for the purpose of comparison. Figure 4 reveals a lamellar structure for all polymer samples according to their characteristic peaks of WAXS. A peak associated with (100) reflection can be clearly observed for all of the samples, and the higher order reflections ($h00$) still can be recognized except for P3THA. Additionally, the peak at 15.8–16.6 nm⁻¹ is assigned to the (020) reflection, which corresponds to the π - π stacking distance of 0.378–0.398 nm and is accompanied by a broad halo resulting from the amorphous side chains. The interlayer d_{100} spacing of copolymers and their corresponding homopolymers are summarized in Table 2. The P3HT should be easier to form crystalline than P3THA because the hexyl side chain is less bulky and shorter than hexyl acetate side chain. Thus, the d_{100} spacing of P3HT is smaller than that of P3THA (16.11 vs 20.17 nm). The d_{100} spacing of the copolymers is in between the d_{100} spacing of P3HT and P3THA except the H19A81. The result again indicates the P3HT and P3THA are miscible. By following the simple mixing rule, the d_{100} spacing of the copolymers is expected to be larger than P3HT and smaller than P3THA. The d_{100} spacing of H19A81 is slight larger than that of pristine P3THA (20.27 vs 20.17 nm) which may be due to the competing crystallization between P3HT and P3THA and results in a less organized crystal. The (100) peak of H60A40 can be resolved into two peaks (see Figure S3) to have two d_{100} spacing values due to the presence of both P3HT crystalline

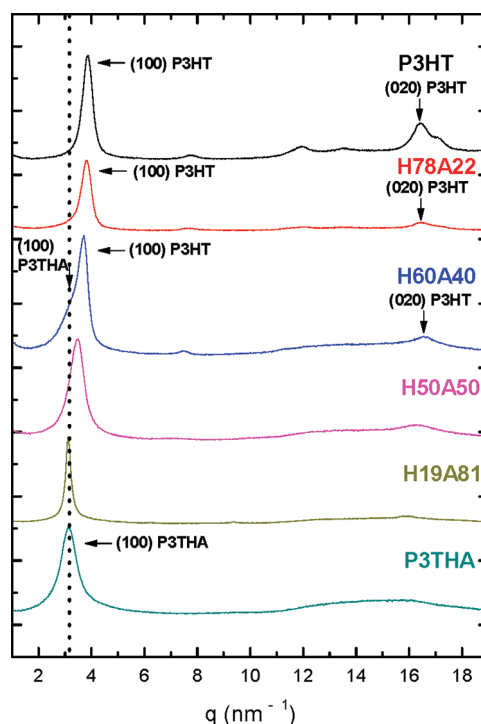


Figure 4. WAXS profiles of P3HT, P3THA, and P3HT-*b*-P3THA diblock copolythiophenes. Dashed line is presented as the (100) plane position of P3THA homopolymer to aid the comparison of the (100) planes of other polymers. All curves are offset for clarity.

Table 2. Summary of WAXS Measurements of P3HT, P3THA, and P3HT-*b*-P3THAs

polymer	d_{100}/nm (q/nm^{-1})	polymer	d_{100}/nm (q/nm^{-1})
P3HT	16.11 (0.39)	H50A50	17.95 (0.35)
H78A22	16.53 (0.38)	H19A81	20.27 (0.31)
H60A40	16.98 (0.37), 20.17 (0.29)	P3THA	20.17 (0.29)

and P3THA crystalline (demonstrate later by variable temperature WAXS study). However, a single (100) peak is observed for H50A50 and H19A81, which suggests the formation of a cocrystalline structure in the copolymer containing more than 50% molar ratio of P3THA (demonstrated later by variable temperature WAXS study).

Figure 5 shows the DSC thermograms of P3HT-*b*-P3THA diblock copolythiophenes and their homopolymers. The results are summarized in Table 3. For H78A22, only one transition is observed around 226 °C which is close to 235 °C of P3HT. This sample is likely to form microphase separation due to different crystalline behavior between P3HT and P3THA. The melting point of H78A22 is lower than that of P3HT because the P3THA segment is too short to form crystal and is dispersed randomly around P3HT crystal. For H60A40, two distinct transitions are observed at 138 and 216 °C for P3THA segment and P3HT segment, respectively. As the result, we can speculate that each segment of H60A40 is long enough to form its own crystalline domain with microphase separation. Thus, a crystalline–crystalline structure is formed. For H50A50 and H19A8, they show only a broad peak in the DSC thermograms which may exhibit a cocrystalline behavior. The results suggest that the crystalline structure of block copolymer is varied with changing the

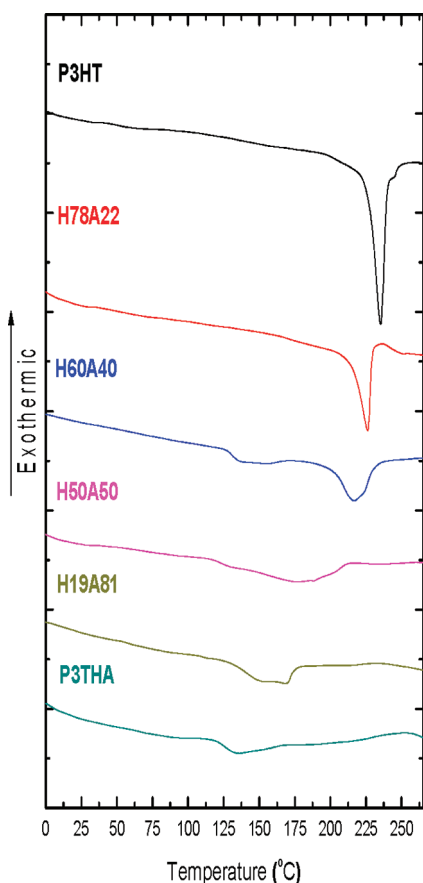


Figure 5. DSC thermograms of P3HT, P3THA, and P3HT-*b*-P3THAs.

Table 3. Results of DSC Measurements of P3HT, P3THA, and P3HT-*b*-P3THA

polymer	$T_m/^\circ\text{C}$	polymer	$T_m/^\circ\text{C}$
P3HT	235	H50A50	175
H78A22	226	H19A81	168
H60A40	138, 217	P3THA	135

molar ratio of two blocks as sketched in Figure 6. However, it is puzzled to see that two transitions are present in the DSC

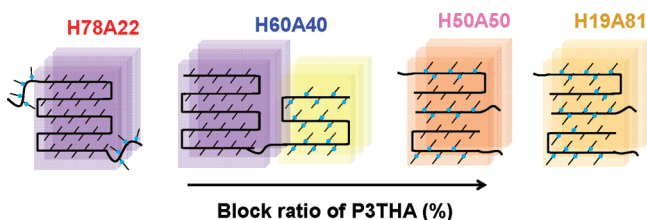


Figure 6. Schematic illustrations of crystalline structures in P3HT-*b*-P3THA diblock copolythiophenes. Blue spot is assigned as the carboxylate group on the P3THA side chain. The purple, yellow, and brown colors are assigned as P3HT crystalline structure, P3THA crystalline structure, and cocrystalline structure of P3HT and P3THA polymers. These copolythiophenes form various crystalline structures with increasing the block ratio of P3THA as follows: crystalline–amorphous, crystalline–crystalline, and cocrystalline structures.

thermogram of H60A40; only one peak with a slightly shoulder at lower- q region is observed in the WAXS scan. Thus, we performed variable temperature WAXS measurements to further

confirm the crystalline behavior which is affected by changing the molar ratio of the copolymer, as shown in Figure 7.

In Figure 7a, the (100) reflection of the H78A22 was completely disappeared while the temperature was raised above 240 °C. This transition temperature is close to that of P3HT at 235 °C in the DSC study. Together with the result of similar d_{100} spacing of H78A22 to that of P3HT, we can confirm the crystalline P3HT is present in H78A22. For H60A40 (Figure 7b), the intensity of the shoulder at low- q region, its location is similar to the (100) reflection of P3THA, decreases as increasing the temperature. Until heating to 150 °C, the shoulder completely disappeared with no reduction of the primary peak, indicative of this melted crystal is attributed to the P3THA block. Upon further heating to 190 °C, the intensity of the peak attributed to P3HT block starts to decrease, and finally the peak completely disappeared after heating above 230 °C. These two transition temperatures are in good agreement with the DSC study and are consistent with the deconvolution of the (100) peak (Figure S3). To deconvolute the (100) peak, the peak profile of P3HT block at 150 °C was used as the calculation basis; the peak position of P3THA was set, and thus the desired peak profile assumed to be the P3THA block can be extracted. The breadth of the calculated peak of P3THA block is similar to that of P3THA. Scrutinizing the results of transition temperatures, d_{100} spacing, and peak deconvolution, the crystalline–crystalline structure is deduced for H60A40. When the P3THA fraction is above 50%, the copolythiophenes show different crystalline behaviors. Both H50A50 and H19A81 exhibit only one peak until reaching their respective transition temperatures (Figure 7c,d). The H19A81 has a lower melting point (~ 170 °C) than that of H50A50 (~ 190 °C) because the higher P3THA fraction in H19A81. The results show similar trend in the DSC study. Note that d_{100} spacing of H50A50 is smaller than that of H19A81, indicative of closer packing and higher melting temperature. Summarizing the results from DSC and variable temperature WAXS measurements, the presence of cocrystalline structure in H50A50 and H19A81 is confirmed.

Microphase Separation. To further study the microphase separation behavior of P3HT-*b*-P3THA, their nanostructures were probed using AFM measurements. Although the height image of H78A22 shows a blurred pattern (Figure 8a), its phase image exhibits distinct nanopatterns with short lamellar-like structure (Figure 8b). The width of the short lamellae is irregular and is in the range of 15–25 nm. Since the P3THA segment of H78A22 is too short to form the crystalline structure, the high crystallinity of P3HT block dominates the nanostructure. When the P3HT fraction is decreased further, the influence from the profound crystallization ability of P3HT block is suppressed during the microphase separation process. A blur height image of H60A40 is also observed (Figure 8c) while its phase image appears clear nanopatterns with lamellar-like structure (Figure 8d). The lamellae are continuous and regular in size (~ 15 nm). The orientation of lamellae is correlated for 4–5 lamellae per bunch. The light region in the lamellae could be attributed to the crystalline area of the P3HT block, since the P3HT block has higher crystallinity than that of the P3THA block. The result suggests the morphology of H60A40 is dominated by the microphase separation due to the P3THA block is long enough to crystallize and thus prevents the substantially crystallization-driven from the P3HT block. As above-mentioned, when the P3THA fraction is higher than 50%, the copolymers show cocrystallization nature. Indeed, these copolythiophenes show smooth surface without

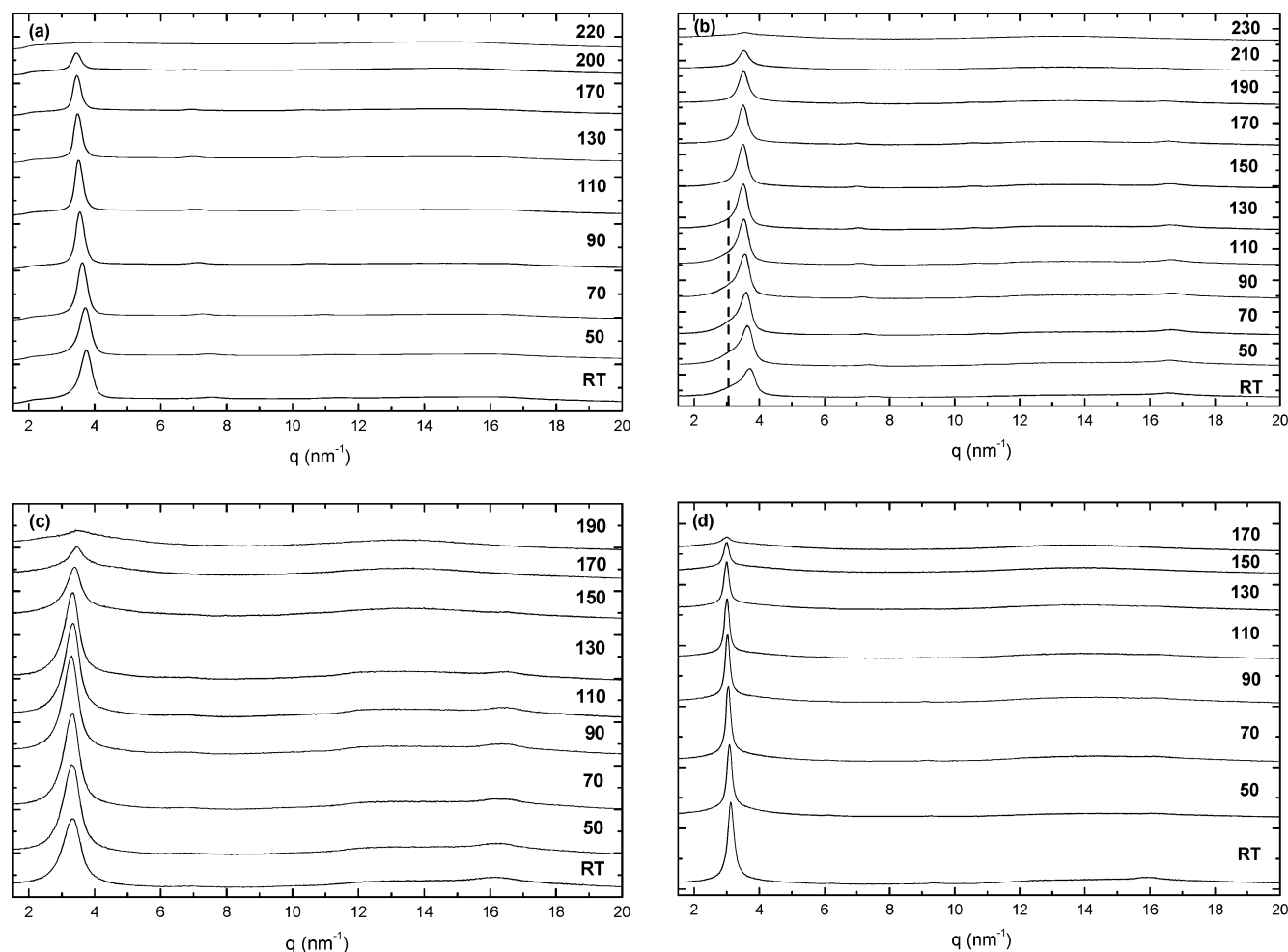


Figure 7. WAXS curves of P3HT-*b*-P3THA diblock copolythiophenes at different temperatures. The primary peaks are assigned as (100) plane in (a) H78A22, (b) H60A40, (c) H50A50, and (d) H19A81. Dashed line is used to locate the position of the (100) plane attributed to P3THA homopolymer. Curves are offset for clarity.

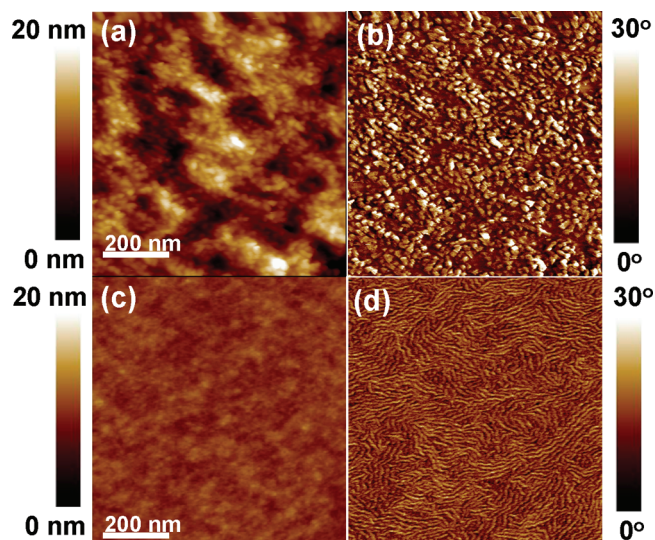


Figure 8. AFM height images and phase images of H78A22 and H60A40 diblock copolythiophenes. While H78A22 (a) and H60A40 (c) both show blur in height images, phase images of H78A22 (b) and H60A40 (d) reveal microphase separation morphologies in nanoscale.

phase contrast (Figure S4) which are similar to the previous reports.^{29,46}

CONCLUSION

We have successfully synthesized a series of all-conjugated diblock copolythiophenes P3HT-*b*-P3THA by the modified sequential GRIM method. Through the use of 2-bromo-3-hexyloxycarbonylmethylene-5-iodothiophene and the polymerization at low temperature (16–20 °C), the obtained copolythiophenes have high regioregularity (>95%), well-controlled block ratio, and molecular weight with narrow PDI (<1.3). By introducing the carboxylate group and controlling the blocks with side-chain length difference by only three atoms, profound effects on the optical and electrochemical properties and morphologies of the diblock copolythiophenes are observed. UV-vis absorption spectra show that the absorption maximum of copolymer in solution is blue-shifted monotonically as increasing the molar ratio of P3THA due to the presence of a carboxylate group. Whereas in thin film, the intermolecular π - π stacking reflected on the absorption behavior of copolymer; thus, the extent of blue shift is decreased. All four P3HT-*b*-P3THA copolymers exhibit lower HOMO level by 0.38 eV from that of P3HT because of the P3THA block. The WAXS and DSC measurements reveal that these block copolythiophenes possess a variety of crystalline structures: crystalline-amorphous, crystalline-crystalline, and cocrystalline with increasing the P3THA fraction. The microphase separation is occurred when the molar ratio of P3THA is less than 50%,

whereas no distinct nanopatterns are observed as the P3THA fraction is higher than 50%. The results of this study give a new insight of manipulating optical and electrochemical properties and nanostructures of conducting block polymer simultaneously by simply adjusting its compositions. Studies of photovoltaic devices and sensors using these block copolymer are in progress.

■ ASSOCIATED CONTENT

■ Supporting Information

GPC traces and ^1H NMR spectra of P3HT-*b*-P3THA diblock copolythiophenes; peak deconvolution of H60A40 in WAXS profile; AFM images of H50A50 and H19A81. This material is available free of charge via the Internet at <http://pubs.acs.org>.

■ AUTHOR INFORMATION

Corresponding Author

*E-mail: suwf@ntu.edu.tw.

■ ACKNOWLEDGMENTS

We gratefully acknowledge the financial support from the National Science Council of Taiwan (NSC 99-2221-E-002-020-MY3). We also thank the Department of Chemistry of National Taiwan University for the use of their NMR spectrometer. WAXS experimental help provided by Dr. Jey-Jau Lee and Dr. Ching-Yuan Cheng at 17A1 station and Dr. Ming-Tao Lee at 13A1 station of the National Synchrotron Radiation Research Center, Taiwan, is highly appreciated.

■ REFERENCES

- (1) Gunes, S.; Neugebauer, H.; Sariciftci, N. S. *Chem. Rev.* **2007**, *107* (4), 1324–1338.
- (2) Blom, P. W. M.; Mihailescu, V. D.; Koster, L. J. A.; Markov, D. E. *Adv. Mater.* **2007**, *19* (12), 1551–1566.
- (3) Di, C. A.; Yu, G.; Liu, Y.; Zhu, D. J. *Phys. Chem. B* **2007**, *111* (51), 14083–14096.
- (4) Muccini, M. *Nature Mater.* **2006**, *5* (8), 605–613.
- (5) Yamashita, Y. *Sci. Technol. Adv. Mater.* **2009**, *10* (2), 024313.
- (6) Thomas, S. W.; Joly, G. D.; Swager, T. M. *Chem. Rev.* **2007**, *107* (4), 1339–1386.
- (7) Kulkarni, A. P.; Tonzola, C. J.; Babel, A.; Jenekhe, S. A. *Chem. Mater.* **2004**, *16* (23), 4556–4573.
- (8) Berresheim, A. J.; Muller, M.; Mullen, K. *Chem. Rev.* **1999**, *99* (7), 1747–1785.
- (9) Carroll, D. L.; Reyes-Reyes, M.; Kim, K.; Dewald, J.; Lopez-Sandoval, R.; Avadhanula, A.; Curran, S. *Org. Lett.* **2005**, *7* (26), 5749–5752.
- (10) Tao, Y. F.; McCulloch, B.; Kim, S.; Segalman, R. A. *Soft Matter* **2009**, *5* (21), 4219–4230.
- (11) Yang, X. N.; Loos, J.; Veenstra, S. C.; Verhees, W. J. H.; Wienk, M. M.; Kroon, J. M.; Michels, M. A. J.; Janssen, R. A. J. *Nano Lett.* **2005**, *5* (4), 579–583.
- (12) Bates, F. S.; Fredrickson, G. H. *Phys. Today* **1999**, *52* (2), 32–38.
- (13) Lee, M.; Cho, B. K.; Zin, W. C. *Chem. Rev.* **2001**, *101* (12), 3869–3892.
- (14) Dai, C. A.; Yen, W. C.; Lee, Y. H.; Ho, C. C.; Su, W. F. *J. Am. Chem. Soc.* **2007**, *129* (36), 11036–11038.
- (15) Ho, C. C.; Lee, Y. H.; Dai, C. A.; Segalman, R. A.; Su, W. F. *Macromolecules* **2009**, *42* (12), 4208–4219.
- (16) Olsen, B. D.; Segalman, R. A. *Macromolecules* **2005**, *38* (24), 10127–10137.
- (17) Sauve, G.; McCulloch, R. D. *Adv. Mater.* **2007**, *19* (14), 1822–1825.
- (18) Iovu, M. C.; Zhang, R.; Cooper, J. R.; Smilgies, D. M.; Javier, A. E.; Sheina, E. E.; Kowalewski, T.; McCullough, R. D. *Macromol. Rapid Commun.* **2007**, *28* (17), 1816–1824.
- (19) Shrotriya, V.; Ouyang, J.; Tseng, R. J.; Li, G.; Yang, Y. *Chem. Phys. Lett.* **2005**, *411* (1–3), 138–143.
- (20) Sirringhaus, H.; Brown, P. J.; Friend, R. H.; Nielsen, M. M.; Bechgaard, K.; Langeveld-Voss, B. M. W.; Spiering, A. J. H.; Janssen, R. A. J.; Meijer, E. W.; Herwig, P.; de Leeuw, D. M. *Nature* **1999**, *401* (6754), 685–688.
- (21) Yang, H. C.; Shin, T. J.; Yang, L.; Cho, K.; Ryu, C. Y.; Bao, Z. N. *Adv. Funct. Mater.* **2005**, *15* (4), 671–676.
- (22) Zhang, Y.; Tajima, K.; Hirota, K.; Hashimoto, K. *J. Am. Chem. Soc.* **2008**, *130* (25), 7812–7813.
- (23) Ren, G. Q.; Wu, P. T.; Jenekhe, S. A. *Chem. Mater.* **2010**, *22* (6), 2020–2026.
- (24) Wu, P. T.; Ren, G. Q.; Kim, F. S.; Li, C. X.; Mezzenga, R.; Jenekhe, S. A. *J. Polym. Sci., Part A: Polym. Chem.* **2010**, *48* (3), 614–626.
- (25) Ren, G. Q.; Wu, P. T.; Jenekhe, S. A. *ACS Nano* **2011**, *5* (1), 376–384.
- (26) Ohshimizu, K.; Ueda, M. *Macromolecules* **2008**, *41* (14), 5289–5294.
- (27) Zhang, Y.; Tajima, K.; Hashimoto, K. *Macromolecules* **2009**, *42* (18), 7008–7015.
- (28) Wu, P. T.; Ren, G. Q.; Li, C. X.; Mezzenga, R.; Jenekhe, S. A. *Macromolecules* **2009**, *42* (7), 2317–2320.
- (29) Ge, J.; He, M.; Qiu, F.; Yang, Y. L. *Macromolecules* **2010**, *43* (15), 6422–6428.
- (30) Heeney, M.; Bailey, C.; Genevicius, K.; Shkunov, M.; Sparrowe, D.; Tierney, S.; McCulloch, I. J. *Am. Chem. Soc.* **2005**, *127* (4), 1078–1079.
- (31) Sirringhaus, H.; Wilson, R. J.; Friend, R. H.; Inbasekaran, M.; Wu, W.; Woo, E. P.; Grell, M.; Bradley, D. D. C. *Appl. Phys. Lett.* **2000**, *77* (3), 406–408.
- (32) McCulloch, I.; Bailey, C.; Giles, M.; Heeney, M.; Love, I.; Shkunov, M.; Sparrowe, D.; Tierney, S. *Chem. Mater.* **2005**, *17* (6), 1381–1385.
- (33) Hu, X. L.; Shi, M. M.; Chen, J. A.; Zuo, L. J.; Fu, L.; Liu, Y. J.; Chen, H. Z. *Macromol. Rapid Commun.* **2011**, *32* (6), 506–511.
- (34) Murphy, A. R.; Liu, J. S.; Luscombe, C.; Kavulak, D.; Frechet, J. M. J.; Kline, R. J.; McGehee, M. D. *Chem. Mater.* **2005**, *17* (20), 4892–4899.
- (35) Pomerantz, M.; Cheng, Y.; Kasim, R. K.; Elsenbaumer, R. L. *J. Mater. Chem.* **1999**, *9* (9), 2155–2163.
- (36) Wang, C.; Kim, F. S.; Ren, G. Q.; Xu, Y. Q.; Pang, Y.; Jenekhe, S. A.; Jia, L. J. *Polym. Sci., Part A: Polym. Chem.* **2010**, *48* (21), 4681–4690.
- (37) Kim, Y. G.; Walker, J.; Samuelson, L. A.; Kumar, J. *Nano Lett.* **2003**, *3* (4), 523–525.
- (38) Liu, J. S.; Kadnikova, E. N.; Liu, Y. X.; McGehee, M. D.; Frechet, J. M. J. *J. Am. Chem. Soc.* **2004**, *126* (31), 9486–9487.
- (39) Nazeeruddin, M. K.; Kay, A.; Rodicio, I.; Humphrybaker, R.; Muller, E.; Liska, P.; Vlachopoulos, N.; Gratzel, M. *J. Am. Chem. Soc.* **1993**, *115* (14), 6382–6390.
- (40) van Hal, P. A.; Wienk, M. M.; Kroon, J. M.; Janssen, R. A. J. *J. Mater. Chem.* **2003**, *13* (5), 1054–1057.
- (41) Vallat, P.; Lamps, J. P.; Schosseler, F.; Rawiso, M.; Catala, J. M. *Macromolecules* **2007**, *40* (7), 2600–2602.
- (42) Loewe, R. S.; Ewbank, P. C.; Liu, J. S.; Zhai, L.; McCullough, R. D. *Macromolecules* **2001**, *34* (13), 4324–4333.
- (43) Yokozawa, T.; Adachi, I.; Miyakoshi, R.; Yokoyama, A. *High Perform. Polym.* **2007**, *19* (5–6), 684–699.
- (44) Iovu, M. C.; Sheina, E. E.; Gil, R. R.; McCullough, R. D. *Macromolecules* **2005**, *38* (21), 8649–8656.
- (45) Trznadel, M.; Pron, A.; Zagorska, M. *Macromolecules* **1998**, *31* (15), 5051–5058.
- (46) Wu, P. T.; Ren, G. Q.; Jenekhe, S. A. *Macromolecules* **2010**, *43* (7), 3306–3313.

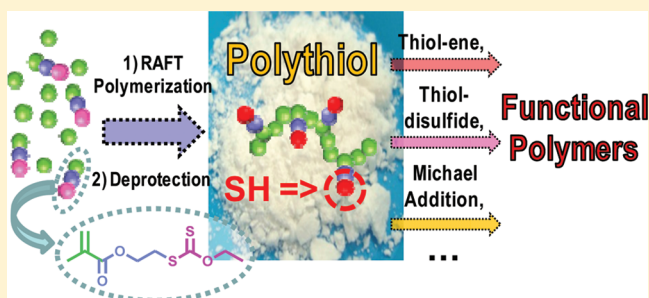
Synthesis of Well-Defined Polythiol Copolymers by RAFT Polymerization

Renaud Nicolai*

Matière Molle et Chimie (ESPCI-CNRS, UMR 7167), ESPCI ParisTech, 10 rue Vauquelin, 75005 Paris, France

Supporting Information

ABSTRACT: A simple methodology to prepare well-defined polythiol copolymers by RAFT polymerization was developed. A methacrylate monomer carrying a S-alkyl-O-ethyl xanthate moiety as thiol protecting group was prepared in two high yield steps. Polythiols were obtained by copolymerizing the functional methacrylate and subsequent aminolysis of the protecting groups. Model reactions and polymerizations showed that the S-alkyl-O-ethyl dithiocarbonate functionality is fully compatible with the RAFT polymerization of methacrylates and did not induce any side reactions. Functionalization of polythiol copolymers was done via thiol–ene addition, Michael addition and thiol–disulfide exchange. Thiol deprotection and functionalization were done in one pot for Michael addition and thiol–disulfide exchange. A complete conversion of thiol groups was observed for all three types of reactions, exemplifying the potential of polythiol copolymers for the preparation of functional materials.



INTRODUCTION

The recent and exponential development of click chemistry^{1–5} and other efficient functionalization methodologies^{6–10} has dramatically widened the scope of accessible functional polymers. Among these methodologies, thiol chemistry is of special interest since thiols are capable of reacting to high yields under benign conditions with numerous chemical species including alkyl halides, epoxides, enes, acrylates, ynes, and others.¹ As a result, thiol chemistry has been successfully employed for surface and (nano)particle patterning, bioorganic synthesis, polymer modification, imprint nanolithography, fabrication of optical components, hydrogel synthesis, curing of hard protective coatings, self-healing coatings, and many other applications.^{1,11–15} In addition, the specific interaction of thiols with soft Lewis acids such as gold, silver, cadmium, etc., has been widely used in different areas ranging from microelectronics to biochemistry.^{16–18}

Controlled radical polymerization (CRP) has emerged during the past decade as one of the most robust and powerful techniques for the synthesis of polymeric materials with various topologies (linear, star, comb, (hyper)branched, cyclic, network, etc.), compositions (homopolymer, statistical, gradient, alternating, block, multiblocks, etc.), and functionalities (with almost infinite possibilities regarding the number and nature of functions).^{19–22} Reversible addition–fragmentation chain transfer (RAFT)^{23–27} polymerization is one of the most efficient CRP methods, allowing the synthesis of novel (co)polymers with a predetermined degree of polymerization (DP) and low dispersity ($\bar{D} = M_w/M_n$, where M_w and M_n are the weight- and the number-average molecular weights, respectively), the incorporation of a wide range of functional

monomers, and the preparation of controllable macromolecular structures under mild reaction conditions.

Therefore, combining RAFT polymerization and thiol chemistry would allow preparing a variety of macromolecular architectures that could be used as building blocks for the synthesis of functional materials. Unfortunately, what makes thiols so reactive and efficient also makes them very difficult to directly incorporate into polymers. The thiol group is incompatible with most of the polymerization techniques and especially controlled/living polymerizations. Thiols induce side reactions with catalysts and monomers used in living alkene^{28,29} and living ring-opening metathesis polymerizations³⁰ as well as with monomers and/or active species employed in chain-growth polycondensation,³¹ living ring-opening polymerization of heterocyclic monomers,³² living anionic vinyl polymerization,³³ and controlled radical polymerization.²⁰ For instance, in the case of radical polymerizations, thiols can react with monomers through radical or Michael additions and will also induce irreversible transfer reactions with propagating radicals. As a result, the work dealing with thiol–ene functionalization almost exclusively relies on polyenes and monothiols.^{34–40} However, well-defined polythiols would much more versatile building blocks for macromolecular engineering,⁴¹ as such polymers would be reactive toward a wide range of functional (macro)molecules, including enes, acrylates, disulfides, alkyl halides, epoxides, and ynes.

Received: October 19, 2011

Revised: December 7, 2011

Published: December 20, 2011

Despite numerous reports on the synthesis of polymers containing thiol functional groups,^{42–57} the synthesis of well-controlled polymers with a defined number of mercapto groups remains challenging. The difficulty in preparing such polymers is that the typical polymerization and functionalization conditions give side reactions and/or moderate yields.^{14,51–57} Therefore, the search for a simple synthetic procedure that would allow synthesizing well-controlled polythiols is still an ongoing effort.

In the present work, a very simple and efficient methodology to prepare well-defined (block) copolymers incorporating thiol side groups is reported. Polythiol copolymers were prepared by copolymerizing a methacrylate monomer carrying a protected thiol, via RAFT polymerization, and then deprotecting the thiol functionality of the copolymers. The *S*-alkyl-*O*-ethyl xanthate moiety used as thiol protecting group proved to be fully compatible with the RAFT polymerization of methacrylates and did not induce any side reactions. In addition, thiol deprotection could be done under very mild conditions, e.g., aminolysis at room temperature, which allowed deprotection and functionalization to be performed in a one-pot process. To exemplify the versatility of polythiol copolymers as building blocks for macromolecular engineering, polythiol copolymers were quantitatively functionalized through thiol–ene addition, Michael addition, and thiol–disulfide exchange.

■ EXPERIMENTAL SECTION

Materials. Butyl methacrylate (BMA, 99%) and methyl methacrylate (MMA, 99%) were purified by passing through a column filled with basic alumina to remove the inhibitors or antioxidants. Unless otherwise noted, reagents were commercially available and used without further purification.

Analyses. Ultraviolet (UV) light irradiation was carried out with two UVGL-55 UV lamps at a wavelength of 365 nm. ¹H and ¹³C NMR spectra were recorded at 297 K on a Bruker AVANCE 400 spectrometer at 400 and 100 MHz, respectively, and referenced to the residual solvent peaks (¹H, δ 7.26 for CDCl₃; ¹³C, δ 77.16 for CDCl₃). Monomer conversions were determined by ¹H NMR. Molecular weights and dispersities were determined by size exclusion chromatography (SEC). SEC analyses were conducted with a Waters 590 pump and a Waters R410 refractive index detector using three thermostated styragel columns set (two HT6E and one HT2) in THF as eluent at 40 °C and at a flow rate of 1 mL min^{–1}. The apparent molecular weights ($M_{n,SEC}$ and $M_{w,SEC}$) and dispersities (M_w/M_n) were determined with a calibration based on polystyrene standards. The spectroscopic measurements were performed on a UV-2401PC (Shimadzu Corp.) UV/vis spectrometer.

Synthesis of *S*-2-Hydroxyethyl-*O*-ethyl Dithiocarbonate. A 500 mL round-bottomed flask equipped with a dropping funnel was charged with a magnetic stirring bar, potassium ethyl xanthogenate (53.8 g, 336 mmol), and acetone (210 mL). A solution of 2-bromoethanol (34.5 g, 276 mmol) in acetone (90 mL) was added dropwise at room temperature over a period of 60 min. Stirring was continued overnight at room temperature. Solids were removed by filtration to afford a clear pale yellow solution. The solids on the funnel were washed with acetone (total of 150 mL). The combined washings and filtrate were concentrated under vacuum to furnish a yellow solid that was dissolved in chloroform (500 mL). This solution was washed three times with brine (250 mL), dried over MgSO₄, and evaporated to dryness to afford 41.9 g (91.3%) of a yellow liquid. ¹H NMR (400 MHz, CDCl₃) δ : 4.59 (q, J = 7.12 Hz, 2H), 3.79 (t, J = 6.3 Hz, 2H), 3.27 (t, J = 6.3 Hz, 2H), 3.17–2.88 (broad peak, 1H, OH), 1.36 (t, J = 7.12 Hz, 3H); ¹³C NMR (100 MHz, CDCl₃) δ 214.4, 70.2, 60.4, 38.2, 13.7.

Synthesis of Monomer 1. *S*-2-Hydroxyethyl-*O*-ethyl dithiocarbonate (16.6 g, 100 mmol) and triethylamine (18.1 mL, 130 mmol) were dissolved in dry dichloromethane (125 mL). The reaction

mixture was cooled in an ice–water bath, and a solution of methacryloyl chloride (12.2 mL, 125 mmol) in dry dichloromethane (50 mL) was slowly added while stirring. The mixture was stirred in the cooling bath for 1 h and then at room temperature overnight. Excess of methacryloyl chloride was neutralized with 10 mL of water. The reaction mixture was then successively washed with water (2 \times 200 mL), a solution of hydrochloric acid (2 \times 200 mL, 0.5 M), a solution of sodium hydroxide (2 \times 200 mL, 0.5 M), and brine (200 mL). The organic phase was dried over MgSO₄, passed through a column filled with neutral alumina, and concentrated under vacuum to afford 19.4 g (yield = 82.8%) of a yellow liquid. ¹H NMR (400 MHz, CDCl₃) δ : 6.12 (apparent sextuplet, J = 1 Hz, 1H), 5.58 (quintuplet, J = 1.6 Hz, 1H), 4.65 (q, J = 7.12 Hz, 2H), 4.38 (t, J = 6.44 Hz, 2H), 3.44 (t, J = 6.44 Hz, 2H), 1.94 (dd, J = 1 Hz and J = 1 Hz, 3H), 1.42 (t, J = 7.12 Hz, 3H). ¹³C NMR (100 MHz, CDCl₃) δ : 213.8, 167.1, 136.1, 126.2, 70.4, 62.3, 34.5, 18.4, 13.9.

Synthesis of *S*-Propyl-*O*-ethyl Dithiocarbonate, 2. A 500 mL round-bottomed flask equipped with a dropping funnel was charged with a magnetic stirring bar, potassium ethyl xanthogenate (21 g, 131 mmol), and acetone (150 mL). A solution of 1-bromopropane (14.0 g, 114 mmol) in acetone (50 mL) was added dropwise at room temperature over a period of 60 min. Stirring was continued overnight at room temperature. Solids were removed by filtration to afford a clear pale yellow solution. The solids on the funnel were washed with acetone (total of 75 mL). The combined washing and filtrate solutions were concentrated under vacuum to furnish a yellow viscous liquid that was dissolved in dichloromethane (200 mL). This solution was washed twice with water (150 mL), and the organic phase was dried over MgSO₄ and evaporated to dryness to afford 17.2 g (91.7%) of a pale yellow liquid. ¹H NMR (400 MHz, CDCl₃) δ : 4.62 (q, J = 7.12 Hz, 2H), 3.08 (t, J = 7.3 Hz, 2H), 1.70 (apparent sextuplet, J = 7.32 Hz, 2H), 1.40 (t, J = 7.12 Hz, 3H), 1.00 (t, J = 7.38 Hz, 3H). ¹³C NMR (100 MHz, CDCl₃) δ : 215.3, 69.8, 37.8, 21.9, 13.9, 13.5.

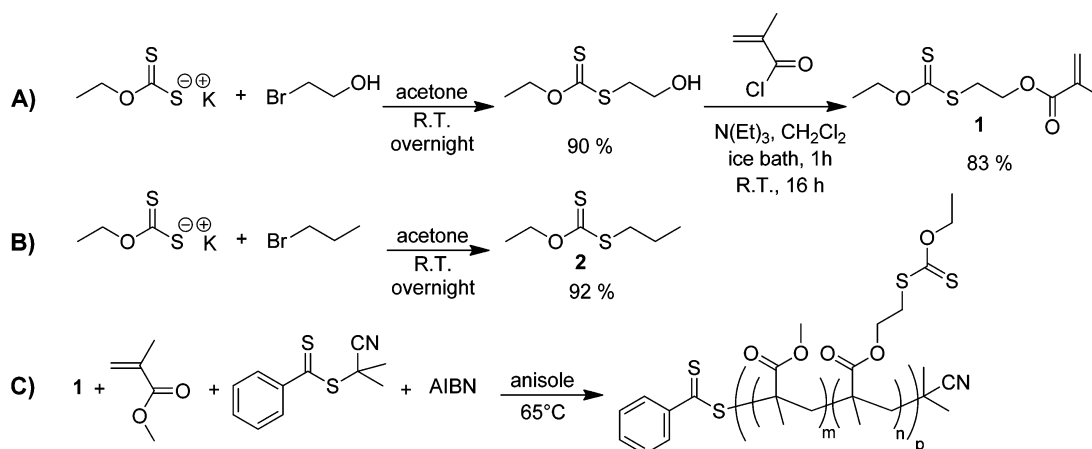
General Procedure for the RAFT Polymerization of Monomer 1. In a typical experiment, 2-cyano-2-propyl benzodithioate (CPBDT) (3.26 mg, 1.47×10^{-5} mol), 2,2'-azobis(2-methylpropionitrile) (AIBN) (2.42×10^{-1} mg, 1.47×10^{-6} mol), monomer 1 (622 mg, 2.65×10^{-3} mol), and anisole (0.175 mL) were charged in a flask. The flask was deoxygenated by bubbling N₂ for 30 min and placed in an oil bath thermostated at 65 °C for 15 h. The reaction was stopped by placing the flask in an ice–water bath, and the polymer was isolated by precipitation in diethyl ether.

General Procedure for RAFT Copolymerization of MMA, BMA, and Monomer 1. In a typical experiment, MMA was purified by passing through a basic alumina column and then bubbled with N₂ for 30 min. 2-Cyano-2-propyl benzodithioate (CPBDT) (25.9 mg, 1.17×10^{-4} mol), 2,2'-azobis(2-methylpropionitrile) (AIBN) (1.92 mg, 1.17×10^{-5} mol), monomer 1 (682 mg, 2.91×10^{-3} mol), and anisole (0.75 mL) were charged in a flask. The flask was deoxygenated by bubbling N₂ for 30 min. MMA (2 mL, 18.7×10^{-3} mol) was added, and the flask was placed in an oil bath thermostated at 65 °C for 24 h. Samples were withdrawn periodically under a N₂ atmosphere for monomer conversion and molecular weight determination. The reaction was stopped by placing the flask in an ice–water bath. A pink polymer was isolated by precipitation in methanol or diethyl ether.

General Procedure for Polythiol Copolymers Deprotection. In a typical experiment, the protected copolymer, P2 ($M_{n,th}$ = 21 000; 25 xanthate functions per chain) (420 mg, 0.5 mmol of thiocarbonyl moieties), was introduced in a flask placed under a nitrogen atmosphere. THF (3 mL) was added, and after complete dissolution of the polymer, butylamine (91.4 mg, 1.25 mmol, 2.5-fold molar excess with respect to the thiocarbonyl moiety) and traces of reducing agent, tributylphosphine, were added to the solution. The reaction mixture was stirred for 1.5 h at room temperature. During this period, the originally pink solution became pale yellow. A white polymer, P7 (M_n = 16 100; M_w/M_n = 1.18), was recovered by precipitation in diethyl ether.

General Procedure for Thiol–Ene Addition. In a typical experiment, the polythiol copolymer, P7 ($M_{n,th}$ = 18 700, 25 functions

Scheme 1. (A) Preparation of Functional Monomer 1; (B) Preparation of Model Xanthate 2; (C) RAFT Copolymerization of 1 with MMA



thiol per chain) (94 mg, 0.125 mmol of thiol moieties), and 2,2-dimethoxy-2-phenylacetophenone (DMPAP) (16 mg, 62.5×10^{-3} mmol) were introduced in a vial placed under a nitrogen atmosphere. Deoxygenated anisole (1 mL) was added, and after complete dissolution of the polymer, 4-allylanisole (92.6 mg, 0.625 mmol, 5-fold molar excess with respect to the thiol moiety) was added to the solution. UV irradiation at 365 nm was carried for 1 h at room temperature. A white polymer, **P11** ($M_n = 18\,800$; $M_w/M_n = 1.24$), was recovered by precipitation in diethyl ether.

General Procedure for Michael Addition. In a typical experiment, the protected copolymer, **P2** ($M_{n,th} = 21\,000$; 25 xanthate functions per chain) (210 mg, 0.25 mmol of thiocarbonyl moieties), was introduced in a flask placed under a nitrogen atmosphere. THF (2 mL) was added, and after complete dissolution of the polymer, butylamine (45.7 mg, 0.625 mmol, 2.5-fold molar excess with respect to the thiocarbonyl moiety) and traces of reducing agent, tributylphosphine, were added to the solution. The reaction mixture was stirred for 1.5 h at room temperature (under a nitrogen atmosphere). During this period, the originally pink solution became pale yellow. Benzyl acrylate (185 mg, 1.25 mmol, 5-fold molar excess with respect to the thiocarbonyl moiety) was added to the reaction mixture which was stirred overnight at room temperature. A yellow polymer, **P12** ($M_n = 28\,500$; $M_w/M_n = 1.15$), was recovered by precipitation in diethyl ether.

General Procedure for Thiol–Disulfide Exchange. In a typical experiment, the protected copolymer, **P2** ($M_{n,th} = 21\,000$; 25 xanthate functions per chain) (52.5 mg, 6.25×10^{-2} mmol of thiocarbonyl moieties), and 2,2'-dipyridyl disulfide (688 mg, 3.12 mmol, 50-fold molar excess with respect to the thiocarbonyl moiety) were dissolved in THF (1.5 mL). Butylamine (11.4 mg, 0.156 mmol, 2.5-fold molar excess with respect to the thiocarbonyl moiety) was added. The pink solution immediately turned to yellow. The reaction mixture was stirred overnight at room temperature. A white polymer, **P13** ($M_n = 24\,000$; $M_w/M_n = 1.22$), was recovered by precipitation in diethyl ether or methanol.

RESULTS AND DISCUSSION

Synthesis of Functional Monomer, 1. Dithiocarbonates, commonly called xanthates, are common chain transfer agents (CTAs) for the RAFT polymerization of nonconjugated monomers.^{25,26,58} However, it was recently demonstrated that xanthates can be designed to be inactive toward radical generated from conjugated monomers, such as methacrylates, styrenics, or even more reactive acrylates.^{59–62} In addition, thiols can easily be obtained by aminolysis of dithiocarbonyl moieties such as xanthates.^{48–50} Therefore, a methacrylate monomer containing a xanthate as thiol protecting group was

prepared in two simple steps with an overall yield of 76% (Scheme 1A).

In order to demonstrate that the xanthate moiety used as thiol protecting group does not induce transfer reactions during the polymerization of methacrylates, a model molecule, **2**, was synthesized (Scheme 1B). Methyl methacrylate (MMA) was then polymerized by RAFT in the presence of this model compound. The polymerization was conducted at 65 °C, using 2-cyano-2-propyl benzodithioate (CPBDT) as CTA and a ratio $[MMA]_0/[2]_0/[CPBDT]_0/[AIBN]_0$ of 200/200/1/0.2. The polymerization showed the typical features of a controlled radical polymerization (CRP), i.e., a constant concentration of propagating radicals with first-order kinetics in monomer and a linear evolution of molecular weight (MW) with conversion (Figure 1). After 22 h of reaction, a well-defined polymer, **P1**,

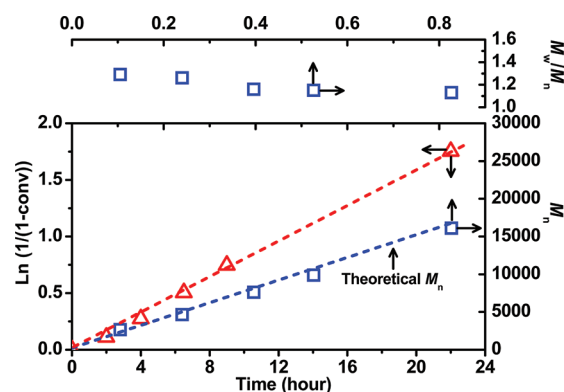


Figure 1. Kinetics, M_n , and M_w/M_n vs conversion plots for the RAFT polymerization of MMA in the presence of xanthate **2**. $[MMA]_0/[2]_0/[CPBDT]_0/[AIBN]_0 = 200:200:1:0.2$, MMA/anisole = 5:3 (v/v), 65 °C.

with $M_n = 16\,100$ ($M_{n,th} = 16\,800$) and $M_w/M_n = 1.13$, was obtained. The very good agreement between theoretical and experimental molecular weights is consistent with the absence of transfer reactions to model xanthate **2** during the polymerization. Transfer to model xanthate **2** would generate new polymer chains and would cause a discrepancy (toward lower mass) between experimental and theoretical molecular weights.

To further confirm that xanthate **2** did not induce transfer reactions during MMA polymerization, **P1** was analyzed by ^1H NMR and UV spectroscopy. The ^1H NMR spectrum of **P1** did not show any peak around 4.6 ppm that would be characteristic of protons in the α -position of the oxygen of the xanthate. On the other hand, three peaks at 7.82, 7.46, and 7.30 ppm confirmed the presence of the dithiobenzoate chain-end on **P1** (Figure 2).

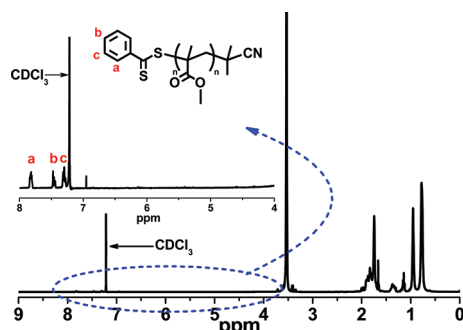


Figure 2. ^1H NMR spectrum in CDCl_3 of PMMA, **P1**, prepared in the presence of xanthate **2**. $[\text{MMA}]_0/[\text{2}]/[\text{CPBDT}]_0/[\text{AIBN}]_0 = 200:200:1:0.2$, MMA/anisole = 5:3 (v/v), 65 °C, 22 h. Polymer isolated by precipitation in diethyl ether.

UV/vis spectroscopy showed the presence of the dithiobenzoate chain-end (peak at 306 nm) and also confirmed the complete absence of xanthate group (no peak at 282 nm) on **P1** (Figure 3). All these results clearly demonstrate that the S-

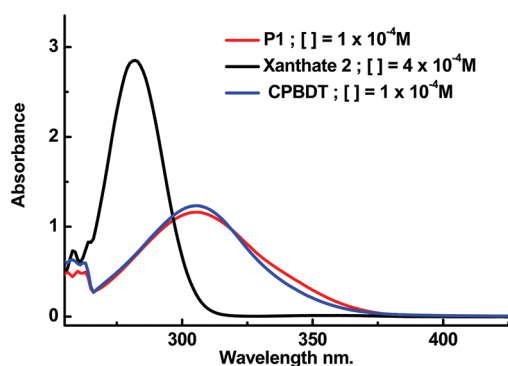


Figure 3. UV/vis spectra of **P1** (1×10^{-4} M in DMF), xanthate **2** (4×10^{-4} M in DMF), and CPBDT (1×10^{-4} M in DMF).

alkyl-O-ethyl dithiocarbonate functionality did not induce any side reactions during the RAFT polymerization of MMA.

The functional monomer **1** and MMA were copolymerized by RAFT using CPBDT as CTA (Scheme 1A). Different ratios of **1**/MMA were used, while keeping a targeted DP of ~ 180 (Table 1, **P2–P4**). First-order kinetics and linear evolutions of

MW with conversion were observed for all polymerizations, yielding well-defined copolymers with low dispersities (Figure

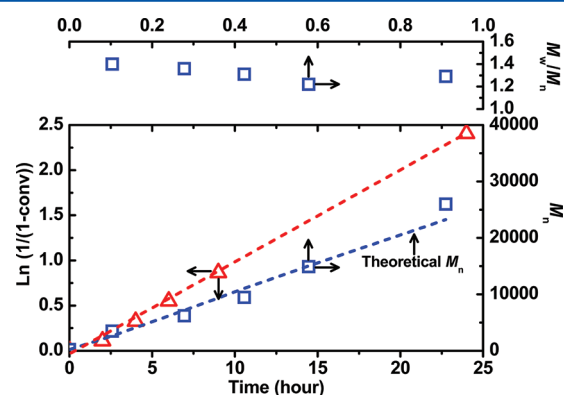


Figure 4. Kinetics, M_n and M_w/M_n vs conversion plots for the RAFT copolymerization of **1** and MMA, **P3**. $[\text{MMA}]_0/[\text{1}]_0/[\text{CPBDT}]_0/[\text{AIBN}]_0 = 120:55:1:0.1$, anisole 20% (in volume), 65 °C.

4). Moreover, a DP of 1000 was targeted to exemplify that high-MW functional copolymers can be prepared with monomer **1**. A well-defined copolymer with $M_n = 77\,600$ ($M_{n,\text{th}} = 72\,500$) and $M_w/M_n = 1.25$ was obtained. In every case, a drift of the composition in the final copolymer was observed, as compared to the initial ratio of monomers (Table 1). This drift of composition indicates that **1** was incorporated slightly faster than MMA into the polymer chains. Monomer **1** was also homopolymerized using a ratio $[\text{1}]_0/[\text{CPBDT}]_0/[\text{AIBN}]_0$ of 180/1/0.1. A well-defined polymer, with $M_n = 51\,000$ and $M_w/M_n = 1.08$ (monomer conversion of 97.4%; $M_{n,\text{th}} = 41\,400$), was obtained after 15 h of polymerization at 65 °C.

The retention of chain-end functionality is one of the key features of CRP. To confirm the presence of the dithiobenzoate chain-end on copolymers prepared with monomer **1**, a block copolymer was synthesized using **P2** as macroCTA and 2,2'-azobis(*N*-butyl-2-methylpropionamide) (VAm-110) as radical initiator. A well-defined high MW block copolymer, **P6**, with $M_n = 145\,000$ ($M_{n,\text{th}} = 165\,000$) and $M_w/M_n = 1.25$, was obtained by polymerizing 2000 equiv of butyl methacrylate (BMA) at 80 °C. No unreacted macroCTA could be detected by SEC, demonstrating very high chain-end functionality for copolymer **P2** (Figure 5).

Well-defined polythiols, **P7–P10**, were prepared by aminolysis at room temperature of the protected copolymers, **P2–P5** (Scheme 2A and Table 2). The quantitative deprotection of thiol groups was confirmed by ^1H NMR, ^{13}C NMR, and UV–vis spectroscopy. Before deprotection, peaks at 4.65 (a), 4.15 (b), and 3.40 (d) ppm corresponding to the protected thiols were observed by ^1H NMR (Figure 6). After deprotection, the peak (a) corresponding to the protons in α position of the oxygen of the xanthate completely disappeared.

Table 1. RAFT Copolymerization of **1** with MMA^a

	$[\text{MMA}]_0/[\text{1}]_0$	time (h)	conv (%) ^b	$M_{n,\text{SEC}}$	M_w/M_n	MMA/1 in polym ^c
P2	86.7/13.3	24	95.2; 96.6	18 800	1.15	85.5/14.5
P3	68.4/31.6	24	89.3; 94.4	26 800	1.29	65.9/34.1
P4	49.1/50.9	16	66.2; 77.9	31 100	1.30	44.2/55.8
P5	84.7/15.3	43	58.8; 62.0	77 600	1.25	81.2/18.8

^aAnisole 20% (in volume) at 65 °C; $[\text{CPBDT}]_0/[\text{AIBN}]_0 = 1:0.1$; targeted DP = $([\text{MMA}]_0 + [\text{1}]_0)/[\text{CPBDT}]_0$: **P2** = 185, **P3** = 175, **P4** = 200, **P5** = 1000. ^bConversion of MMA and **1**, respectively. ^cDetermined by ^1H NMR.

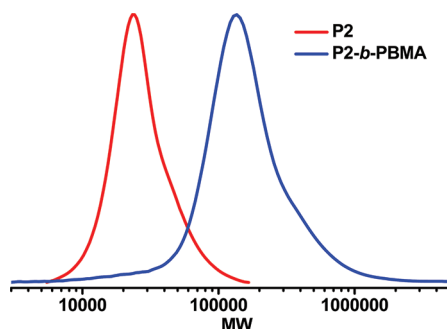


Figure 5. SEC trace of **P2-*b*-PBMA** block copolymer, **P6**, prepared by RAFT polymerization of BMA with **P2** as macroCTA. $[BMA]_0/[P2]_0/[VAm-110]_0 = 2000:1:1$, BMA/anisole = 1:3 (v/v), 73 h at 80 °C.

On the other hand, peaks (b' and d') from the ethyl linker could be observed and were shifted toward the high field region (Figure 6). The complete absence of thiocarbonyl (no peak at 214 ppm) and xanthate groups (no peak at 282 nm) on the deprotected polythiol copolymers was also confirmed by ^{13}C NMR and UV–vis spectroscopy, respectively (Figures S1–S9).

Table 2. Synthesis of Polythiol Copolymers^a

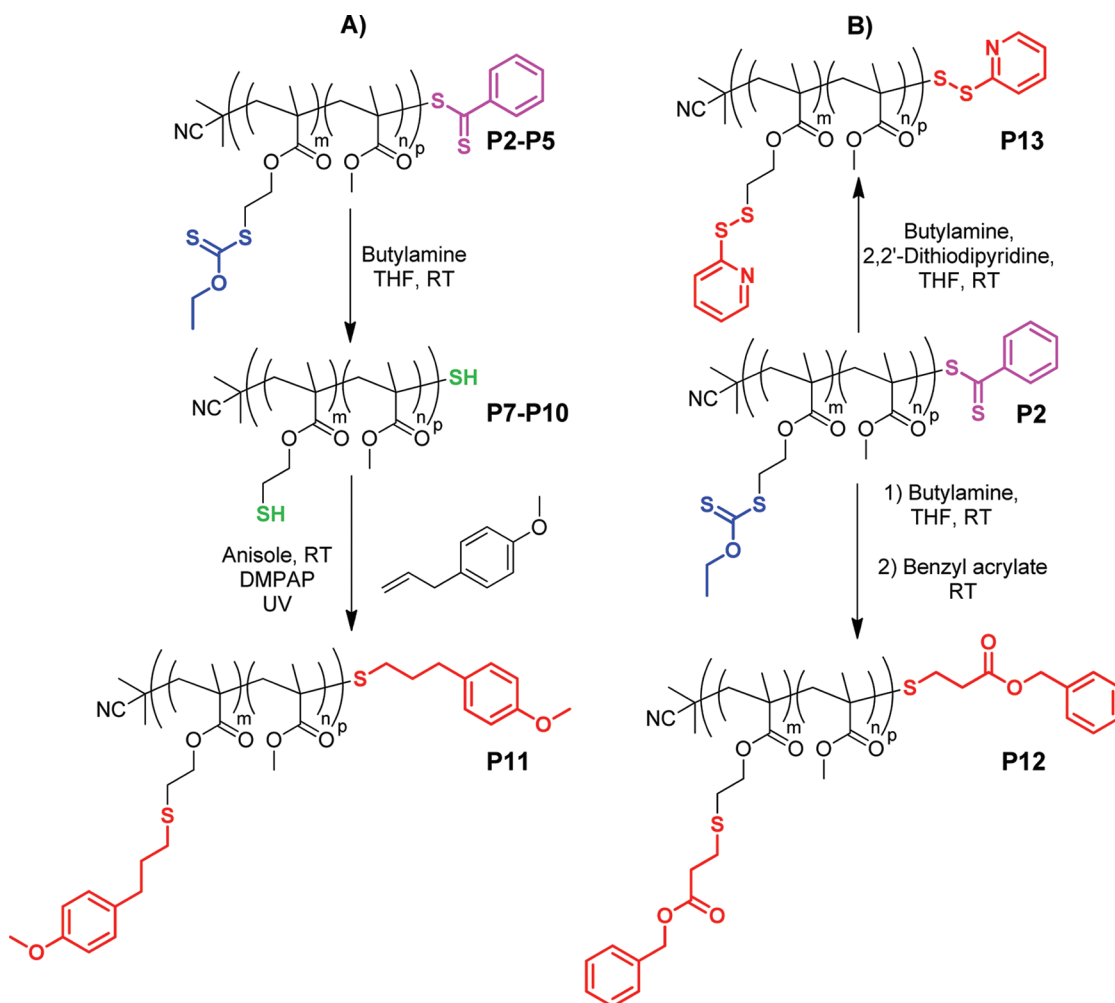
	precursor	$M_{n,SEC}$	M_w/M_n	thiol/chain ^b
P7	P2	16 100	1.18	26
P8	P3	28 400	1.27	53
P9	P4	25 100	1.35	82
P10	P5	66 900	1.33	96

^aThiol deprotection carried out in THF at RT for 1.5 h; 2.5 equiv of butylamine with respect to thiol groups, traces of tributylphosphine.

^bDetermined by 1H NMR.

Three model reactions relying on thiol–ene radical addition, thiol Michael addition, and thiol–disulfide exchange were performed on the polythiol copolymer **P7** and on the protected polythiol copolymer **P2** (Scheme 2 and Table 3). A complete functionalization of the thiol moieties was observed by 1H NMR for all three types of reactions (Figure 7 and Figures S10 and S11). The efficiency of the deprotection and functionalization reactions under these mild conditions is in good agreement with previous reports on thiol chemistry.^{14,63,64} For example, in the case of the thiol Michael addition, the peak (c) corresponding to the protons in α position of the oxygen of the xanthate protecting group completely disappeared after functionalization, while peaks corresponding to the benzyl moiety

Scheme 2. (A) Synthesis of Polythiol Copolymers and Their Subsequent Functionalization via Thiol–Ene Chemistry; (B) One-Pot Deprotection and Functionalization, through Michael Addition and Thiol–Disulfide Exchange, of Protected Polythiol Copolymers



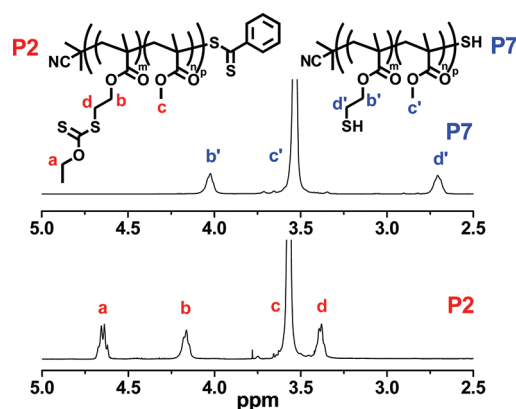


Figure 6. ^1H NMR spectra (zoomed in between 2.5 and 5 ppm) in CDCl_3 of protected copolymer **P2** and polythiol copolymer **P7**.

Table 3. Functionalization of Polythiol Copolymers

	precursor	reagent	$M_{n, \text{SEC}}$	M_w/M_n	conv (%) ^a
P11 ^b	P7	4-allylanisole	18 800	1.24	100
P12 ^c	P2	benzyl acrylate	28 500	1.15	100
P13 ^d	P2	2,2'-dithiodipyridine	24 000	1.22	100

^aConversion obtained from the disappearance of the thiol (or protected thiol) peak by ^1H NMR and the appearance of peaks corresponding to the product. ^bIrradiation at 365 nm for 1 h at RT in anisole; SH/4-allylanisole/DMAP = 1:5:0.5. ^cOvernight in THF at RT; benzyl acrylate added after 1.5 h; SH/butylamine/benzyl acrylate = 1/2.5/5. ^dOvernight in THF at RT; SH/butylamine/2,2'-dithiodipyridine = 1/2.5/50.

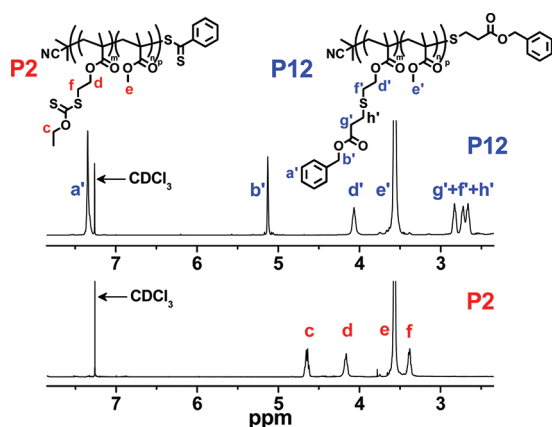


Figure 7. ^1H NMR spectra (zoomed in between 2.35 and 7.85 ppm) in CDCl_3 of protected copolymer **P2** and functional copolymer **P12**.

were observed by ^1H NMR (Figure 7). In addition, for the Michael addition and the thiol–disulfide exchange, deprotection and functionalization were done in one-pot directly from the protected copolymer **P2**. These results illustrate the versatility and potential of (protected) polythiol copolymers as precursors for the synthesis of functional polymers.

CONCLUSION

In summary, a very simple methodology to prepare well-defined polythiol copolymers by RAFT polymerization is reported. This approach relies on the use of S-alkyl-O-ethyl dithiocarbonate as thiol protecting group. Model reactions and polymerizations demonstrate that the xanthate protecting group does not induce any side reactions during the RAFT

polymerization of methacrylates. Well-defined protected polythiol copolymers and block copolymers were prepared. Polythiol copolymers were subsequently obtained by simple aminolysis of the xanthate protecting groups at room temperature. Functionalization of polythiol copolymers was done via thiol–ene addition, Michael addition, and thiol–disulfide exchange. A complete conversion of thiol groups was observed for all three types of reactions. Thanks to the mild conditions used for the removal of the xanthate protecting group, thiol deprotection and functionalization were done in one pot for Michael addition and thiol–disulfide exchange. The simplicity and efficiency of the reported procedure, coupled with the great potential of CRP and thiol chemistry, should allow using polythiol (co)polymers as versatile building blocks for the preparation of a wide range of functional materials.

ASSOCIATED CONTENT

Supporting Information

^1H NMR, ^{13}C NMR, and UV spectra. This material is available free of charge via the Internet at <http://pubs.acs.org>.

AUTHOR INFORMATION

Corresponding Author

*E-mail: renaud.nicolay@espci.fr.

ACKNOWLEDGMENTS

The author is grateful to ESPCI and CNRS for financial support. The author thanks the members of the Matière Molle et Chimie laboratory for their valuable help. Prof. Ludwik Leibler and Dr. Ilias Iliopoulos are especially acknowledged for many stimulating and extremely helpful discussions.

REFERENCES

- (1) Hoyle, C. E.; Lowe, A. B.; Bowman, C. N. *Chem. Soc. Rev.* **2010**, 39, 1355–1387.
- (2) Iha, R. K.; Wooley, K. L.; Nystrom, A. M.; Burke, D. J.; Kade, M. J.; Hawker, C. J. *Chem. Rev.* **2009**, 109, 5620–5686.
- (3) Hoyle, C. E.; Bowman, C. N. *Angew. Chem., Int. Ed.* **2010**, 49, 1540–1573.
- (4) Kade, M. J.; Burke, D. J.; Hawker, C. J. *J. Polym. Sci., Part A: Polym. Chem.* **2010**, 48, 743–750.
- (5) Hoogenboom, R. *Angew. Chem., Int. Ed.* **2010**, 49, 3415–3417.
- (6) Theato, P.; Kim, J.-U.; Lee, J.-C. *Macromolecules* **2004**, 37, 5475–5478.
- (7) Theato, P. *J. Polym. Sci., Part A: Polym. Chem.* **2008**, 46, 6677–6687.
- (8) Nicolay, R.; Marx, L.; Hemery, P.; Matyjaszewski, K. *Macromolecules* **2007**, 40, 9217–9223.
- (9) Fu, Q.; Lin, W.; Huang, J. *Macromolecules* **2008**, 41, 2381–2387.
- (10) Kulis, J.; Bell, C. A.; Micallef, A. S.; Jia, Z.; Monteiro, M. J. *Macromolecules* **2009**, 42, 8218–8227.
- (11) Ryu, J.-H.; Jiwanich, S.; Chacko, R.; Bickerton, S.; Thayumanavan, S. *J. Am. Chem. Soc.* **2010**, 132, 8246–8247.
- (12) Oh, J. K.; Siegwart, D. J.; Lee, H.-i.; Sherwood, G.; Peteanu, L.; Hollinger, J. O.; Kataoka, K.; Matyjaszewski, K. *J. Am. Chem. Soc.* **2007**, 129, 5939–5945.
- (13) Yuan, Y. C.; Rong, M. Z.; Zhang, M. Q.; Chen, J.; Yang, G. C.; Li, X. M. *Macromolecules* **2008**, 41, 5197–5202.
- (14) Ghosh, S.; Basu, S.; Thayumanavan, S. *Macromolecules* **2006**, 39, 5595–5597.
- (15) Wong, L.; Boyer, C.; Jia, Z.; Zareie, H. M.; Davis, T. P.; Bulmus, V. *Biomacromolecules* **2008**, 9, 1934–1944.
- (16) Trollss, M.; Hawker, C. J.; Hedrick, J. L.; Carrot, G.; Hilborn, J. *Macromolecules* **1998**, 31, 5960–5963.

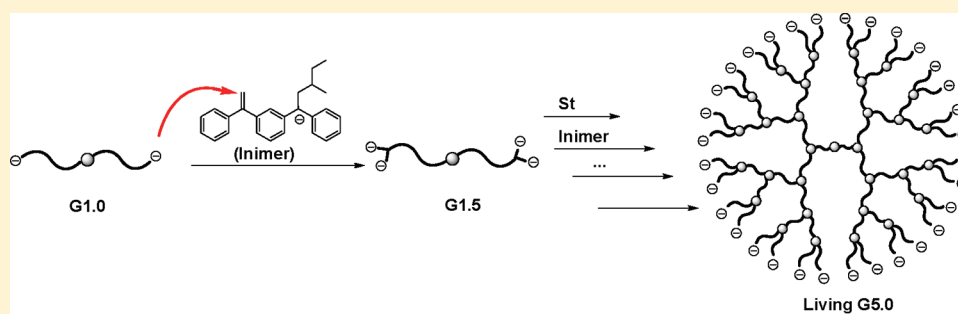
- (17) Lowe, A. B.; Sumerlin, B. S.; Donovan, M. S.; McCormick, C. L. *J. Am. Chem. Soc.* **2002**, *124*, 11562–11563.
- (18) Ryu, J.-H.; Park, S.; Kim, B.; Klaukherd, A.; Russell, T. P.; Thayumanavan, S. *J. Am. Chem. Soc.* **2009**, *131*, 9870–9871.
- (19) Moad, G.; Solomon, D. H. *The Chemistry of Radical Polymerization*, 2nd ed.; Elsevier Ltd.: Amsterdam, 2006; p 639.
- (20) Braunecker, W. A.; Matyjaszewski, K. *Prog. Polym. Sci.* **2007**, *32*, 93–146.
- (21) Matyjaszewski, K.; Tsarevsky, N. V. *Nature Chem.* **2009**, *1*, 276–288.
- (22) Beija, M.; Marty, J.-D.; Destarac, M. *Prog. Polym. Sci.* **2011**, *36*, 845–886.
- (23) Chiefari, J.; Chong, Y. K.; Ercole, F.; Krstina, J.; Jeffery, J.; Le, T. P. T.; Mayadunne, R. T. A.; Meijs, G. F.; Moad, C. L.; Moad, G.; Rizzardo, E.; Thang, S. H. *Macromolecules* **1998**, *31*, 5559–5562.
- (24) Destarac, M.; Brochon, C.; Catala, J.-M.; Wilczewska, A.; Zard, S. Z. *Macromol. Chem. Phys.* **2002**, *203*, 2281–2289.
- (25) Moad, G.; Rizzardo, E.; Thang, S. H. *Aust. J. Chem.* **2005**, *58*, 379–410.
- (26) Perrier, S.; Takolpuckdee, P. *J. Polym. Sci., Part A: Polym. Chem.* **2005**, *43*, 5347–5393.
- (27) Barner-Kowollik, C. *Handbook of RAFT Polymerization*; Wiley-VCH: Weinheim, 2008.
- (28) Coates, G. W.; Hustad, P. D.; Reinartz, S. *Angew. Chem., Int. Ed.* **2002**, *41*, 2236–2257.
- (29) Domski, G. J.; Rose, J. M.; Coates, G. W.; Bolig, A. D.; Brookhart, M. *Prog. Polym. Sci.* **2007**, *32*, 30–92.
- (30) Bielawski, C. W.; Grubbs, R. H. *Prog. Polym. Sci.* **2007**, *32*, 1–29.
- (31) Yokozawa, T.; Yokoyama, A. *Prog. Polym. Sci.* **2007**, *32*, 147–172.
- (32) Penczek, S.; Cypriak, M.; Duda, A.; Kubisa, P.; Slomkowski, S. *Prog. Polym. Sci.* **2007**, *32*, 247–282.
- (33) Baskaran, D.; Mueller, A. H. E. *Prog. Polym. Sci.* **2007**, *32*, 173–219.
- (34) Gress, A.; Voelkel, A.; Schlaad, H. *Macromolecules* **2007**, *40*, 7928–7933.
- (35) Killops, K. L.; Campos, L. M.; Hawker, C. J. *J. Am. Chem. Soc.* **2008**, *130*, 5062–5064.
- (36) ten Brummelhuis, N.; Diehl, C.; Schlaad, H. *Macromolecules* **2008**, *41*, 9946–9947.
- (37) Rissing, C.; Son, D. Y. *Organometallics* **2008**, *27*, 5394–5397.
- (38) Rissing, C.; Son, D. Y. *Organometallics* **2009**, *28*, 3167–3172.
- (39) Lotti, L.; Coiai, S.; Ciardelli, F.; Galimberti, M.; Passaglia, E. *Macromol. Chem. Phys.* **2009**, *210*, 1471–1483.
- (40) Chen, G.; Amajjahe, S.; Stenzel, M. H. *Chem. Commun.* **2009**, 1198–1200.
- (41) Sumerlin, B. S.; Vogt, A. P. *Macromolecules* **2010**, *43*, 1–13.
- (42) Tohyama, M.; Hirao, A.; Nakahama, S.; Takenaka, K. *Macromol. Chem. Phys.* **1996**, *197*, 3135–3148.
- (43) Sato, T.; Terada, K.; Yamauchi, J.; Okaya, T. *Makromol. Chem.* **1993**, *194*, 175–85.
- (44) Vidal, F.; Hamaide, T. *Polym. Bull.* **1995**, *35*, 1–7.
- (45) Kuang, L.; Wu, Q.; Yu, A.; Chen, Y. *Eur. Polym. J.* **1996**, *32*, 1371–1375.
- (46) Trollsas, M.; Hawker, C. J.; Hedrick, J. L.; Carrot, G.; Hilborn, J. *Macromolecules* **1998**, *31*, 5960–5963.
- (47) Carrot, G.; Hilborn, J.; Hedrick, J. L.; Trollsas, M. *Macromolecules* **1999**, *32*, 5171–5173.
- (48) Moad, G.; Rizzardo, E.; Thang, S. H. *Aust. J. Chem.* **2009**, *62*, 1402–1472.
- (49) Willcock, H.; O'Reilly, R. K. *Polym. Chem.* **2010**, *1*, 149–157.
- (50) Moad, G.; Rizzardo, E.; Thang, S. H. *Polym. Int.* **2011**, *60*, 9–25.
- (51) Wulff, G.; Schulze, I. *Angew. Chem., Int. Ed.* **1978**, *17*, 537–538.
- (52) Premachandran, R.; Banerjee, S.; John, V. T.; McPherson, G. L.; Akkara, J. A.; Kaplan, D. L. *Chem. Mater.* **1997**, *9*, 1342–1347.
- (53) Gozdz, A. S. *Makromol. Chem., Rapid Commun.* **1981**, *2*, 595–600.
- (54) Yamaguchi, K.; Kato, T.; Hirao, A.; Nakahama, S. *Makromol. Chem., Rapid Commun.* **1987**, *8*, 203–7.
- (55) Janout, V.; Hrudkova, H.; Cefelin, P. *Collect. Czech. Chem. Commun.* **1984**, *49*, 1563–8.
- (56) Kihara, N.; Tochigi, H.; Endo, T. *J. Polym. Sci., Part A: Polym. Chem.* **1995**, *33*, 1005–10.
- (57) Kihara, N.; Kanno, C.; Fukutomi, T. *J. Polym. Sci., Part A: Polym. Chem.* **1997**, *35*, 1443–1451.
- (58) Destarac, M.; Bzducha, W.; Taton, D.; Gauthier-Gillaizeau, I.; Zard, S. Z. *Macromol. Rapid Commun.* **2002**, *23*, 1049–1054.
- (59) Nicolay, R.; Kwak, Y.; Matyjaszewski, K. *Chem. Commun.* **2008**, 5336–5338.
- (60) Tong, Y.-Y.; Dong, Y.-Q.; Du, F.-S.; Li, Z.-C. *Macromolecules* **2008**, *41*, 7339–7346.
- (61) Kwak, Y.; Nicolay, R.; Matyjaszewski, K. *Aust. J. Chem.* **2009**, *62*, 1384–1401.
- (62) Huang, C.-F.; Nicolay, R.; Kwak, Y.; Chang, F.-C.; Matyjaszewski, K. *Macromolecules* **2009**, *42*, 8198–8210.
- (63) Qiu, X.-P.; Winnik, F. M. *Macromol. Rapid Commun.* **2006**, *27*, 1648–1653.
- (64) Campos, L. M.; Killops, K. L.; Sakai, R.; Paulusse, J. M. J.; Damiron, D.; Drockenmuller, E.; Messmore, B. W.; Hawker, C. J. *Macromolecules* **2008**, *41*, 7063–7070.

Continuous Process for the Synthesis of Dendrimer-Like Star Polymers by Anionic Polymerization

Hefeng Zhang, Junpo He,* Chao Zhang, Zhenhua Ju, Jia Li, and Yuliang Yang

The State Key Laboratory of Molecular Engineering of Polymers, Department of Macromolecular Science, Fudan University, Shanghai, 200433, China

Supporting Information



Continuous synthesis of dendrimer-like star polymer by anionic polymerization

ABSTRACT: A continuous anionic living process for the fast synthesis of dendrimer-like star polymers is described. The process is based on the selective addition of *sec*-butyllithium (*s*-BuLi) toward 1,3-bis(1-phenylethenyl)benzene (MDDPE), which gives stoichiometric monoadduct in tetrahydrofuran (THF). The monoadduct, an anionic inimer-like molecule, is then used as the branching agent in the synthesis of dendrimer-like star polymers. Thus, α,ω -bifunctional polystyryllithium (G1.0), initiated by a difunctional anionic initiator, undergoes addition reaction with the monoadduct to form a tetrafunctional species, which is able to initiate the polymerization of styrene to form a four-arm star with terminal polystyryl anions (G2.0). Repeating addition/polymerization in an alternate way leads to the formation of a dendrimer-like star polystyrene up to the fifth generation, G5.0. The process is performed in a continuous way without separation of the intermediate species. The synthetic procedure of dendritic polystyrene is greatly accelerated, e.g., G5.0 with 32 terminal groups being obtained within 12 h. Because the product is living, it is employed as a dendritic precursor to prepare dendrimer-like star block copolymers such as PS-*b*-PI, PS-*b*-PMMA, and dendrimer-like star polymer with a graft-on-graft periphery. The solution properties of the dendrimer-like star products, such as viscosity as a function of molecular weight and globular shape, are investigated using viscometry and laser light scattering. The morphology of the individual molecules is observed using AFM and TEM.

INTRODUCTION

Dendrimer-like star polymers are a new class of dendrimers, in which successive generations are interlinked by polymer chains emanating radially from a central core.¹ These polymers have not only precise numbers of branching points and periphery functionalities, but also polymer segments with controlled lengths. As such, their properties are endowed with both the “dendrimer effect,” which provides a multiplicity of reactive sites and a reduced intermolecular entanglement, and the chemistry of specific polymers. In addition, the size of dendrimer-like star polymers spans a wide range from several to hundreds of nanometers, which is quite different from regular dendrimers.

In analogy to conventional dendrimers,^{2,3} dendrimer-like star polymers are prepared through either divergent or convergent approaches.⁴ In both approaches the polymer segments are formed either by *in situ* polymerization, or by presynthesized polymer precursors with terminal functionalities. The synthesis

of dendrimer-like star polymers can be traced back to the seminal report on the synthesis of dendritic poly(ethylene oxide) (PEO) by Gnanou and co-workers using a divergent branching/polymerization approach.⁵ This strategy allows the syntheses of a series of dendrimer-like star PEOs,⁶ polystyrenes (PS),⁷ and dendrimer-like star block copolymers of EO/styrene,^{8–10} as well as styrene/*tert*-butyl acrylate (*t*BA)¹¹ with different block sequences, by employing living polymerization techniques such as atom transfer radical polymerization (ATRP) and anionic ring-opening polymerization (AROP). Incorporation of an ATRP initiating site at each branch point enables the preparation of dendrimer-like star PEO bearing pH responsive poly(acrylic acid) (PAA) segments.¹² The divergent polymer-

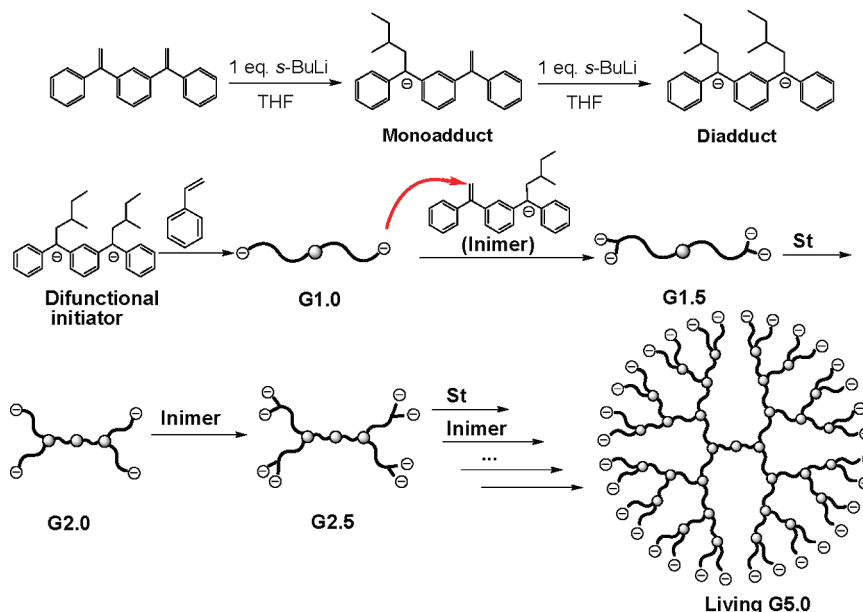
Received: October 29, 2011

Revised: December 14, 2011

Published: December 29, 2011



Scheme 1. Continuous Synthesis of Dendrimer-Like Star Living Polystyrene in a Divergent Process



ization approach has also been used to synthesize Janus-type dendrimer-like star PEOs, starting from a heterodifunctional initiator as the core.¹³ Recently, the same research group has explored a fast one-pot, two-step method to synthesize dendrimer-like star PEOs through a semicontinuous process, which does not require a protection/deprotection step, but only precipitation purification of the intermediate by using a commercially available glycidol as the branching agent.¹⁴ Hedrick is the first to give the name “dendrimer-like star polymers” to a series of dendritic poly(*ε*-caprolactone)s (PCLs) synthesized through ring-opening polymerization of caprolactone initiated by a multifunctional core, using protected 2,2-bis(phenyldioxymethyl)propionic acid (BMPA) as the branching agent.^{15–22} The terminal hydroxyl groups are further transformed into ATRP initiators, enabling the synthesis of dendrimer-like star block copolymers such as PCL-*b*-poly(methyl methacrylate) (PCL-*b*-PMMA),²³ and PHEMA-*g*-PEO.²⁴ In another elegant study, an array of constitutional isomers of dendrimer-like star PCLs are synthesized with varying placement of branching junctures, thus facilitating the relationship study of conformation and dendritic structure.¹⁹ Percec has developed a TERMINI (TERminator Multifunctional INitiator) strategy to synthesize dendrimer-like star PMMAs in which metal-catalyzed living radical polymerization (LRP) of MMA is quantitatively and irreversibly interrupted by TERMINI, such as (1,1-dimethylethyl)[[1-[3,5-bis(S-phenyl-4-*N,N'*-diethylthiocarbamate)phenyl]ethenyl]oxy]dimethylsilane, a masked difunctional initiator for the subsequent LRP of MMA.^{25,26} The synthesis is efficient, and the products possess perfect structure due to the quantitative masking and demasking reactions of TERMINI.²⁷ Therefore, the divergent branching/polymerization approach, such as TERMINI methodology and highly efficient group modification, has been proved an efficient way to synthesize dendrimer-like star polymers.²⁸ Divergent branching/*in situ* polymerization strategy has also been successfully used in the synthesis of dendrimer-like star copolymers of styrene and L-lactide or caprolactone by sequential ATRP and ROP.^{29–31} Combination of ATRP and azide–alkyne click chemistry as the branching reaction has led

to the synthesis of dendrimer-like star PS and PS-*b*-PtBA (*co*)polymers of third generation.³²

A notable strategy in the synthesis of dendrimer-like star polymers is the use of living anionic polymerization. The advantage lies in the fact that the reactions of anionic species, especially carbanions, are well-known robust, orthogonal, and efficient (ROE) reactions.^{33,34} Carbanionic polymerization enables the design of dendrimer-like star polymers not only through divergent branching, but also through convergent coupling using a polymeric precursor. For instance, Hirao and co-workers has developed an iterative divergent methodology in which the generation growth is fulfilled by the coupling reaction of premade living PMMA chains bearing two functional groups of *tert*-butyldimethylsilyloxymethylphenyl (SMP) in the α -end, which are subsequently transformed into benzyl bromide before the attachment of the next generation.^{35–40} The generation growth is similar to the synthesis of regular dendrimers, albeit using polymeric (mostly PMMA) AB_n-type building blocks, so that the dendritic products are of high perfection. For example, dendrimer-like star PMMAs have been synthesized up to the seventh generation with well-controlled branching densities.^{41–45} Modification of the method facilitates the syntheses of a number of dendrimer-like star copolymers such as PMMA-*b*-PHEMA,³⁷ PMMA-*b*-PtBMA, PMMA-*b*-P2VP, PMMA-*b*-PDDMMA (poly((2,2-dimethyl-1,3-dioxolan-4-yl)methyl methacrylate)),⁴⁶ and PMMA-*b*-PS,⁴⁷ as well as dendritic-linear block copolymers of styrene and MMA.^{48,49}

Anionic polymerization also affords the convergent process in which alternate coupling of living polymeric precursors and subsequent polymerization initiated by the residual living center is performed to form dendrimer-like star structures. This has been achieved in the pioneering work by Hadjichristidis in the synthesis of dendritic homopolymers and copolymers of styrene and dienes, through a coupling reaction of “living stars” with chlorosilane derivatives.^{50,51} Knauss has developed a one-pot process for the dendritic polystyrene through a multibatch, stoichiometric addition of styrene and chlorosilane functionalized styrene (the branching agent) into a solution of

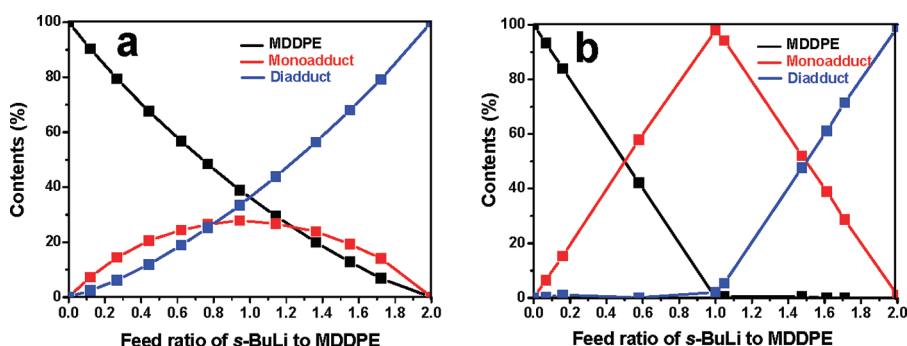
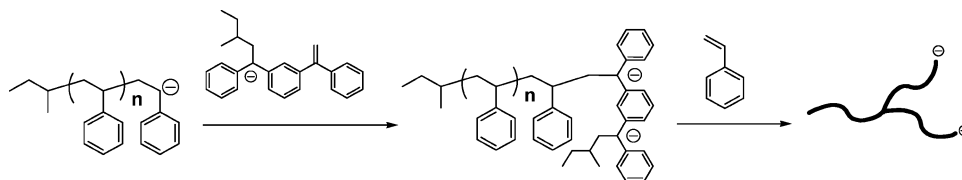


Figure 1. Variation of product distribution along with feed ratio of *s*-BuLi/MDDPE in the addition reaction in (a) cyclohexane at 45 °C and (b) in THF at ca. -80 °C.

Scheme 2. Model Reactions for the Branching Process



polystyryl anions.^{52–55} During the reaction, the chlorosilane moiety couples with living chains, while the vinyl group takes part in polymerization, thus forming a “T-shaped” branch juncture. Hutchings has synthesized dendrimer-like star polymers, such as the polystyrene DendriMacs, through convergent Williamson coupling of an AB₂-type polystyrene macromonomer prepared by anionic polymerization.⁵⁶ However, the coupling efficiency is influenced greatly by the solvent. Copper-catalyzed Huisgen dipolar cycloaddition, known as the “click” chemistry, affords higher coupling efficiency of corresponding polymer precursors with appropriate functionalities.^{57–61}

In both the divergent and convergent approaches, functionality transformations along with protection/deprotection processes are necessary to ensure a smooth switch between generations. These cascade processes are time-consuming. Although there have been a number of improved methods in the synthesis of regular dendrimers,^{33,34,62–64} to the best of our knowledge, the rapid synthesis dendrimer-like star polymers are limited to two cases. Dendrimer-like star PEOs was synthesized in a semicontinuous way by employing glycidol as the branching agent.¹⁴ Dendrimer-like star DNA up to fourth generation was synthesized through recognition-based divergent growth of Y-shaped DNA building blocks.^{65–67}

The chemistry of organolithium and 1, 3-bis(1'-phenylvinyl)-benzene (MDDPE) has long been used in macromolecular design through anionic polymerization. Depending on addition behavior of carbanions toward MDDPE, e.g., monoaddition or diaddition,^{68–82} a number of polymers with different architectures, such as ABA-type linear block,^{69,70} star-shaped,^{74–78} ring-shaped,^{79,80} and H/ π -shaped polymers⁸¹ have been synthesized. McGrath⁸² observed high yield of monoadduct from the reaction of equivalent *s*-BuLi and MDDPE, but the reaction was never used for the design of polymer structures. In a previous work, we developed a solvent-switching method in which the monoadduct was able to be stored in cyclohexane (as a stock solution), providing a reliable handle of an anionic inimer to prepare hyperbranched polymers.⁷³ In the present work, we use the anionic inimer

as a branching agent to synthesize more regular dendrimer-like star polymers through the divergent branching/polymerization approach. Since the intermediate species is living, the process can be performed in a continuous way, thus greatly promoting the synthetic efficiency of dendrimer-like star polymers.

RESULTS AND DISCUSSION

The overall route for continuous synthesis of dendrimer-like star polymers is outlined in Scheme 1. The synthesis starts with styrene polymerization initiated by a difunctional anionic initiator, e.g., the diadduct of *s*-BuLi with MDDPE. The resulting α,ω -difunctional polystyryllithium is coded **G1.0**, the first generation. **G1.0** is then reacted with an anionic inimer, e.g., the monoadduct of *s*-BuLi and MDDPE, yielding an $\alpha,\alpha',\omega,\omega'$ -tetrafunctional polystyryllithium, coded **G1.5**. Further polymerization of styrene initiated by **G1.5** results in the formation of **G2.0**. Repeating the process of inimer addition and initiation-polymerization will finally lead to dendrimer-like star polymers up to high generations.

There are two key steps in the synthesis: (i) the selective addition of *s*-BuLi toward MDDPE, which ensures the synthesis of pure anionic inimer and dilithium initiator; (ii) the branching reaction which is composed of stoichiometric addition reaction of polystyryllithium (PSLi) toward the anionic inimer, and the subsequent initiation of styrene polymerization by the resulting dianion. These reactions will be separately discussed in detail in the following sections.

Selective Addition of *s*-BuLi toward MDDPE. The addition reaction of *s*-BuLi toward MDDPE is well documented in the literature. The earlier reports show that the two vinyl groups are equivalent to anionic addition.^{82–85} Therefore, monoadduct was obtained usually by using excessive MDDPE in the reaction.^{85,86} Nevertheless, the addition behavior seems to be remarkably different between cyclohexane and THF as the solvent.⁸² As shown in Figure 1, in cyclohexane the product is always a mixture of monoadduct and diadduct. The monoadduct never exceeds 50% content, indicating comparable addition rate of the two double bonds. In THF the monoadduct is obtained in high yield (96% by HPLC and

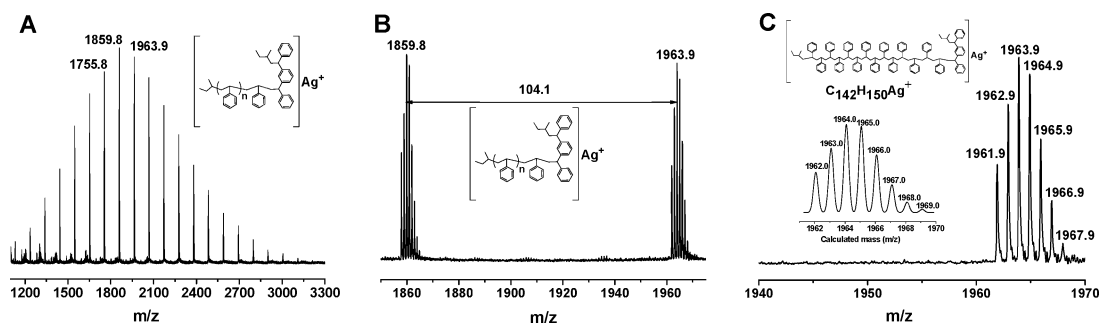


Figure 2. MALDI-TOF MS spectrum of the adduct of polystyryllithium and the inimer: (A) full spectrum, (B) enlarged part, and (C) calculated (inset) and observed isotope peaks.

GC) when the feed amounts of the reactants are equal in mole, while the diadduct is obtained in high yield from the double molar ratio of *s*-BuLi to MDDPE. This striking result stems from the electrostatic repulsion between the carbanion in the formed monoadduct and the approaching anion of *s*-BuLi, prohibiting the addition of the second molecule of *s*-BuLi.^{82,85–87} In THF, carbanions are more naked due to the solvation of the counterion, imparting larger electrostatic repulsive force than that in cyclohexane.

The addition reaction in THF is completed within 15 min at ca. -80°C . After the reaction, the solvent is switched from THF to cyclohexane by distillation. Both the monoadduct and the diadduct form a homogeneous solution in cyclohexane, which are used as stock solution of inimer and dilithium initiator, respectively. The characterization of the monoadduct has been performed as previously discussed.⁷³

The Branching Reaction. The efficiency of branching reaction is investigated through a model reaction (Scheme 2). First, the addition of polystyryllithium to the inimer is performed in cyclohexane using a linear polystyryllithium ($M_{n, \text{SEC}} = 1600 \text{ g/mol}$), resulting in a polystyryl α, α' -dianion ($M_{n, \text{SEC}} = 2000 \text{ g/mol}$). MALDI-TOF MS spectrum of the product is shown in Figure 2, in which the main series is assignable to the inimer-capped species. For instance, the peak at $m/z = 1963.9$ is assigned to species with a degree of polymerization, $\text{DP} = 14 (104.1 \times 14 + 57.1 \times 2 (\text{two butyl}) + 282.4 (\text{MDDPE}) + 107.8 (\text{Ag}) + 2.0 (\text{two hydrogens}) = 1963.8$.

Second, the dianionic adduct is used to initiate the polymerization of styrene to form a star-like product. SEC trace shifts clearly to larger molecular weight, as shown in Figure 3. The SEC measured molecular weight, 7800 g/mol , is notably smaller than that measured by multiangle laser light scattering (MALLS), 9600 g/mol , indicating a nonlinear architecture of the polymerization product after the cross-initiation. The initiation capability correlates well with previous successful access to MDDPE-derived dilithium initiators for the synthesis of SBS block copolymers^{68–70} and cyclic polymers.^{77,78}

Synthesis of Dendrimer-Like Star Polystyrene. The overall synthetic process of dendrimer-like star polystyrene involves essentially multistep of the two elementary reactions in the model branching process, performed by alternate charge of the stock solution of inimer and styrene without isolation of the intermediate species. This continuous approach, starting from the polymerization of styrene initiated by the diadduct, affords dendrimer-like star polystyrene up to the 5.0th generation within 12 h. Within each generation the molar ratio of monomer to organolithium is kept constant so as to obtain

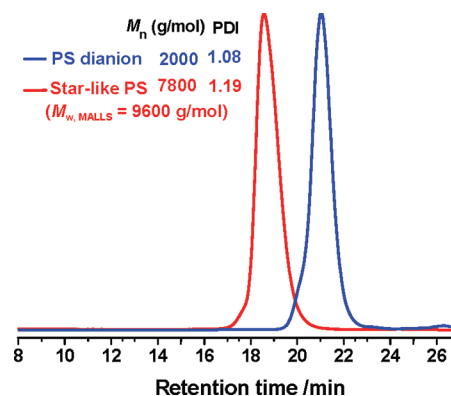


Figure 3. SEC chromatograms tracing the model branching reaction. Key: blue line, adduct of polystyryllithium with the inimer; red line, star-like polystyrene initiated by the adduct dianion.

identical chain length among generations, $M_{n, \text{arm}}$. The results of two polymerization systems with different $M_{n, \text{arm}}$ are listed in Table 1. Samples are taken for analysis after each step of the reaction. ^1H NMR is used to follow the alkyl diphenyl methine protons derived from the terminated MDDPE moieties. As shown in Figure 4, these protons give a multiplet at $\delta \sim 4.0 \text{ ppm}$ for the starting diadduct, but show broad signals at $\delta \sim 3.9 \text{ ppm}$ for those intermediate species with terminal MDDPE-derived moieties (G1.5–G3.5). The methine signal disappears in the spectra of samples after the subsequent polymerization (G1.0–G4.0), indicating rather efficient cross initiation. It is also noted that the intensity of methine signal becomes weaker along with the generation growth, and is undetectable for G4.5, due to decreasing content of the terminal MDDPE-derived moiety in the whole molecule. Backfolding of the periphery groups into the inner part of the dendritic structure may also reduce the intensity of methine signal.

Much attention should be paid to the formation of pseudogel during the process. The pseudogel is a physical network formed by the aggregation of polymeric anions, and is often encountered in the preparation of bi- and multifunctional organolithium species.^{28,73} Once it gels, the solution becomes heterogeneous with high viscosity, which impedes further stirring and reaction. It is observed that the pseudogel formation relates to two factors: the arm length, $M_{n, \text{arm}}$, and the structure of periphery anions. Longer arm length leads to earlier gelation. For instance, in the presence of small amount of THF, pseudogel appears at G4.5 when the arm length is 6000 g/mol , whereas earlier gelation at G3.5 is observed for the system with arm length of 12000 g/mol . Usually, the pseudogel formed with periphery polystyryl anions become fluidic upon

Table 1. Synthesis and Characterization of Dendrimer-Like Star Polystyrenes

samples	$M_{n,calc}$ (10^3 g/mol)	$M_{n,SEC}$ (10^3 g/mol)	$M_{w,MALLS}$ (10^3 g/mol)	PDI_{SEC}	$[\eta]_w^b$ (mL/g)	g'^c	$d\eta/dc$	R_h^d (nm)	R_g^e (nm)	R_g/R_h
G1.5-PS ₂₇₀₀ ^a	5.7	6.5	6.8	1.21	8.5	1.09	0.194	/	/	/
G2.5-PS ₂₇₀₀	16.5	15.6	16.9	1.26	12.4	0.84	0.197	/	/	/
G3.5-PS ₂₇₀₀	38.1	30.8	38.0	1.40	24.5	0.94	0.194	5.6	/	/
G4.5-PS ₂₇₀₀	81.3	42.7	73.3	1.46	31.0	0.75	0.198	6.7	/	/
G5.0-PS ₂₇₀₀	167.7	70.4	131.0	1.52	33.1	0.53	0.187	8.7	14.7	1.7
G1.5-PS ₄₃₀₀	8.9	10.6	11.0	1.21	13.7	1.26	0.181	3.3	/	/
G2.5-PS ₄₃₀₀	26.1	22.7	24.1	1.28	25.2	1.33	0.198	4.5	/	/
G3.5-PS ₄₃₀₀	60.5	42.6	52.2	1.26	37.8	1.16	0.205	6.5	/	/
G4.5-PS ₄₃₀₀	129.3	62.0	107.0	1.40	41.8	0.78	0.197	8.9	15.4	1.7
G5.5-PS ₄₃₀₀	266.9	103.0	223.2	1.50	40.9	0.45	0.198	18.9	26.7	1.4

^aG1.5-PS₂₇₀₀ refers to dendritic product of generation 1.5 with the molecular weight between successive generations, $M_{n,arm} = 2700$ g/mol. ^bWeight-average intrinsic viscosity measured by online viscometry detector, Viscostar (Wyatt). ^cContraction factor $g' = [\eta]_w$ (dendrimer-like)/ $[\eta]_{linear}$, where $[\eta]_{linear} = 1.62 \times 10^{-2} M_w^{0.70-0.73,91}$. ^dDetermined by dynamic light scattering at a scattering angle of 90° in THF at 30 °C. ^eDetermined by static light scattering in THF at 30 °C.

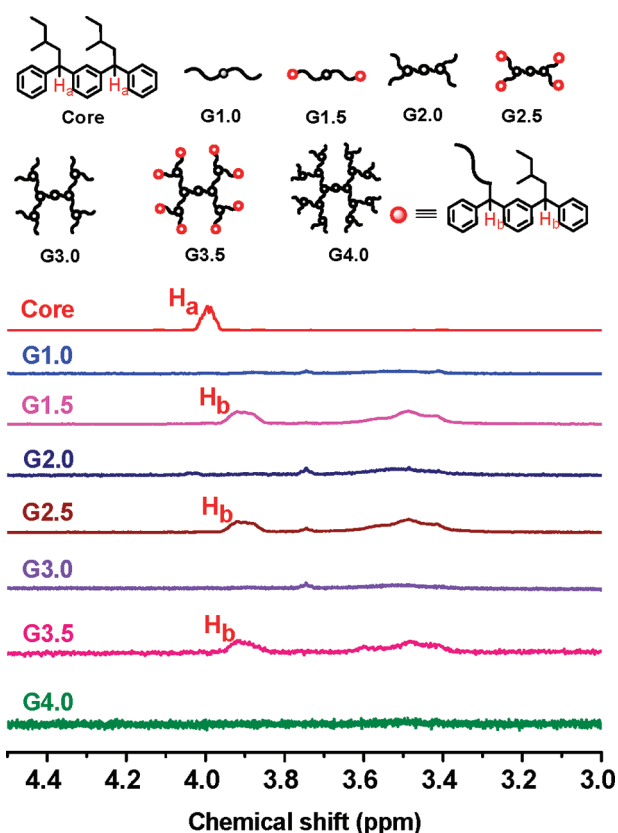


Figure 4. 1H NMR spectra monitoring the synthesis of dendrimer-like star polystyrene up to the fourth generation. The spectra are obtained in $CDCl_3$ with the same concentration, showing only the part between chemical shifts of 3.0–4.5 ppm.

addition of inimer. This phenomenon is most likely related to different aggregation number of the terminal groups. Polystyryl anions aggregate into dimers,⁸⁸ whereas MDDPE-derived dianions may exhibit a fractional aggregation number less than two.

In order to avoid the pseudogelation in the whole process, polar additives such as ether and TMEDA are employed without changing the main solvent, cyclohexane. The abilities of these additives to dissociate the gel are as follows (at 1.0–2.0 equiv of Li): TMEDA > THF > ethyl ether. In the presence of ether, the pseudogel appears in the second generation, while THF is able to keep the reaction mixture homogeneous up to

the fourth generation. TMEDA is the most effective, whereby the pseudogel does not appear in the whole procedure. However, the molecular weight distribution is broader possibly due to the slow initiation of MDDPE-derived dianion in the presence of TMEDA. Therefore, THF is used in lower generations, and TMEDA for the highest generation. The presence of trace amount of polar additives does not have a significant effect upon the addition reaction.

As the reaction proceeds in a proliferative manner, the feed amounts of inimer and monomer will be doubled in each follow-up step. This will cause difficulty in experimental manipulation. Therefore, the reaction mixture is divided into two parts of equal volume at each step, only one of which is subjected to the subsequent reaction after being diluted with equal volume of solvent.

Figure 5 shows the SEC traces of the fractionated polymerization products with increasing generations. The

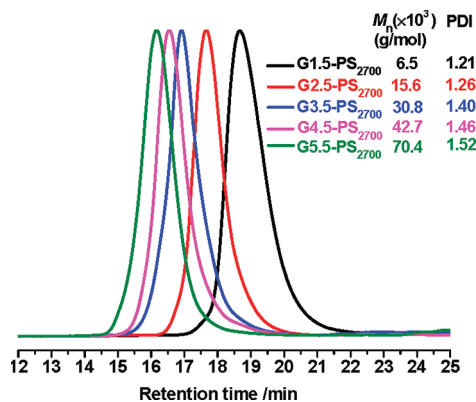
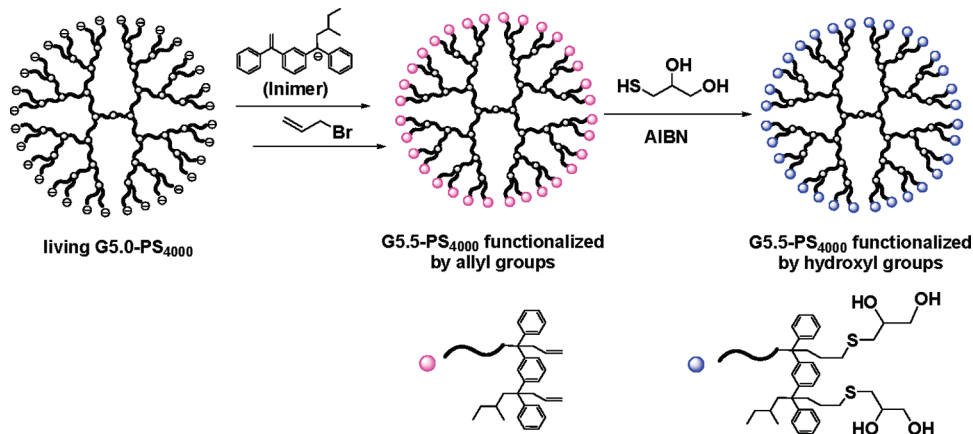


Figure 5. SEC traces monitoring the synthesis of dendrimer-like star polymers of G1.5 to G5.5 with the arm length of 2700 g/mol (samples are fractionated from toluene/methanol).

molecular weight shifts clearly to larger values while remaining monomodal distribution. The characterization data in Table 1 show that the molecular weights, $M_{n,SEC}$, are remarkably lower than the calculated, $M_{n,calc}$, due to smaller hydrodynamic volume of dendritic polymers. The latter is close to those measured by MALLS, $M_{w,MALLS}$. The polydispersity index measured by SEC varies from 1.2 for G1.5-PS₂₇₀₀, to 1.5 for G5.0-PS₂₇₀₀. These relatively broad values indicate the existence of defects in the dendrimer-like star structures. The

Scheme 3. Functionalization of Living G5.5-PS₄₀₀₀ with Allyl and Hydroxyl Peripheral Groups

degree of the perfection is therefore estimated in terms of the terminal or peripheral groups of the dendritic products after functionalization with allyl bromide. In order to avoid the potential lithium-halide exchange reaction, only inimer-capped living products are reacted with allyl bromide, as shown in Scheme 3.

The ¹H NMR spectrum of the functionalized product, G5.5-PS₄₀₀₀-vinyl with molecular weight of polystyrene between successive generations, $M_{n,arm} = 4000$ g/mol, is shown in Figure

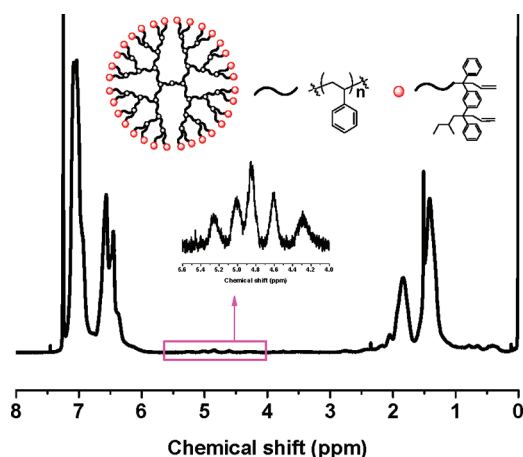


Figure 6. ¹H NMR spectrum of the G5.5-PS₄₀₀₀-vinyl with peripheral allyl functionality (in CDCl₃).

6. The peaks between $\delta = 4.0$ to 5.4 ppm are assigned to vinylic protons. Nevertheless, these signals are too weak to provide convincing information on the end functionality. Therefore, the content of the vinyl groups are analyzed via iodometric titration (IBr/KI/Na₂S₂O₃²⁻), and the results are listed in Table 2. It is

obvious that for samples of lower generations, a fair to good agreement between measured and anticipated number of peripheral vinyl functionalities is observed, but deviation is notable for higher generations. For instance, a number of 64 vinyl groups are expected for G5.5-PS₄₀₀₀-vinyl, whereas an average of 53.5 is measured. Thus, defects indeed exist in the dendrimer-like star products, possibly due to the incomplete addition and cross initiation. Furthermore, the experimental error in quantifying the reactants, such as the inimer, may also cause defects in the final products.

Solution Properties of Dendrimer-Like Star PS. One of the features that distinguish dendritic polymers from their linear counterparts is the dependence of intrinsic viscosity, $[\eta]$, on molecular weight. While the $[\eta]$ of linear polymers is expressed as a power law function of molecular weight, according to Mark–Houwink–Sakurada equation, the regular dendrimers usually show parabolic variations of $\log[\eta]$ as a function of generation or molecular weight, due to the gradual transition from open structure to compact globular form along with increasing generations. Dendrimer-like star polymers have a lower degree of branching compared to regular dendrimers, and thus have a less compact chain density in solution. Nonetheless, the same trend in viscosity variation with increasing generation should still hold for dendrimer-like star polymers. Gnanou and co-workers were the first to report similar behavior in the generation dependence of viscosity.^{7,28} They also pointed out that in some cases, a level-off of the curve $\log[\eta] \sim$ generation was observed because the maximum of viscosity may be shifted to generations higher than actually measured.⁶ Figure 7 shows the weight-average intrinsic viscosity, $[\eta]_w$, against molecular weight in double–logarithm scale for dendrimer-like star products possessing two different chain lengths between successive generations ($M_{n,arm}$). The intrinsic viscosity initially increases with molecular weight, but

Table 2. Results of Estimation of Number of Pheripheral Groups by Allylic Functionalization

samples	$M_{n,calc}$ (10 ³ g/mol)	$M_{n,SEC}$ (10 ³ g/mol)	$M_{w,MALLS}$ (10 ³ g/mol)	PDI _{SEC}	$N_{allyl,theor}^a$	$N_{allyl,obs}^b$
G1.5-PS ₄₀₀₀ -vinyl	8.4	9.0	8.8	1.19	4	3.8
G2.5-PS ₄₀₀₀ -vinyl	24.4	20.6	25.2	1.22	8	7.0
G3.5-PS ₄₀₀₀ -vinyl	56.4	30.8	54.0	1.30	16	14.2
G4.5-PS ₄₀₀₀ -vinyl	120.4	52.0	113.5	1.45	32	26.5
G5.5-PS ₄₀₀₀ -vinyl	248.4	79.0	255.0	1.52	64	53.5

^aTheoretical number of vinyl groups in the periphery was calculated by $N_{allyl,theor} = 2^{G+0.5}$, in which G is the number of generation. ^bObtained by iodometric titration using IBr.

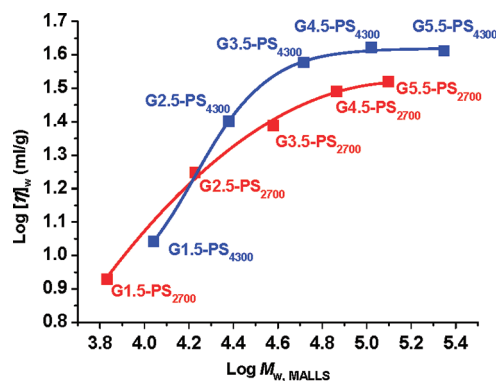


Figure 7. Dependence of intrinsic viscosity on molecular weight in double logarithmic style for dendrimer-like star polymers with various generations.

then reaches a level-off region, indicating a gradual transition from open structures of the first to third generations, to more compact globular conformation of the fourth and fifth generations.^{3,89} Nevertheless, we do not observe the inflection point on $[\eta]_w$ as a function of molecular weight, as is usually observed for regular dendrimers. This implies that the tightest compact form is not yet reached at the fifth generation. The samples with lower $M_{n,arm}$ show lower intrinsic viscosities due to the higher degrees of branching. In addition, the intrinsic viscosities measured for the dendritic samples are remarkably lower than those of linear polystyrene. The contraction factor, g' , defined the ratio of viscosities of dendritic samples to their linear counterparts of identical molecular weight, decreases from 1.09 to 0.53 along with the generation increase (Table 1).

The size and shape of the dendritic products in THF are investigated using static light scattering (SLS) and dynamic light scattering (DLS). SLS is performed either on MALLS in an off-line mode or on an ALV instrument. The radius of gyration, R_g , is measured to be 26.7 nm for the sample with the highest generation, **G5.5-PS₄₃₀₀**. For other samples, the signal-to-noise is too low to give accurate values of R_g s because of the small size. Hydrodynamic radius, R_h , is determined by DLS at the scattering angle of 90° (Table 1). As shown in Figure 8, the profiles show monomodal distribution from **G1.5** to **G4.5-PS₄₃₀₀**. The peak for **G5.5-PS₄₃₀₀** is broad, possibly because of the intermolecular coupling, which may occur easily due to the multiplicity of the peripheral anions. The measured R_h increases along with molecular weight and generation. Good linearity between $\log R_h$ and $\log M_w$ is observed from **G1.5** to **G4.5-**

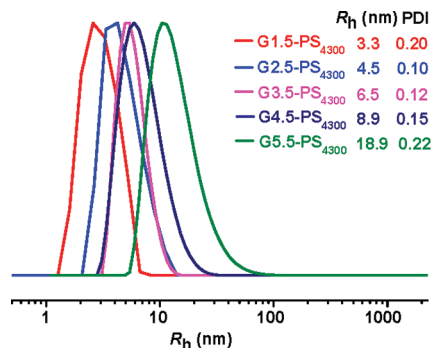


Figure 8. Profiles of DLS of dendrimer-like star polystyrenes from **G1.5-PS₄₃₀₀** to **G5.5-PS₄₃₀₀** (left), and the obtained R_h s as a function of $M_{w,MALLS}$ in double logarithmic style (right).

PS₄₃₀₀, but deviation in **G5.5-PS₄₃₀₀** is notable due to the presence of coupled species.

The globular shape of the dendrimer-like star polystyrene in THF is confirmed by DLS measurement on **G3.5-PS₄₃₀₀** at different scattering angles, a method used by Gnanou and co-workers.¹² As shown in Figure 9, CONTIN analysis gives

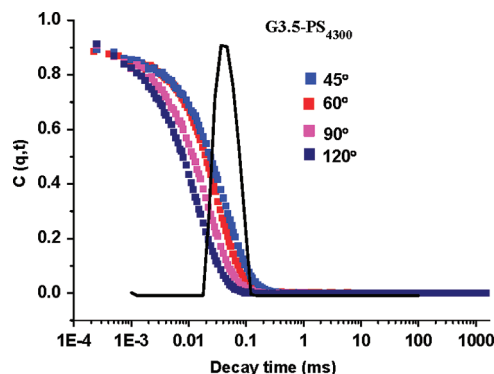
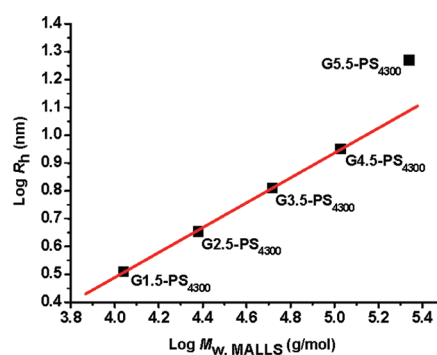


Figure 9. DLS results of dendrimer-like star polystyrenes of **G3.5-PS₄₃₀₀** at different angles (in THF, at 30 °C).

narrow, monomodal distribution which is independent of the scattering angles, indicating that the dendrimer-like star polystyrenes molecules adopt a globular conformation in solution. Nonetheless, the ratios of R_g/R_h for **G4.5-PS₄₃₀₀**, **G5.5-PS₄₃₀₀**, and **G5.0-PS₂₇₀₀** are 1.7, 1.4, and 1.7, respectively, which fall into the category for open structure,^{92,93} and are quite close to the result by Gnanou on dendrimer-like star PEOs.⁶

Microscopic Observation of Dendrimer-Like Star PS.

Single molecular morphology of dendrimer-like star polymers is investigated using AFM and TEM. AFM observations are performed by tapping mode for samples spin-coated on freshly cleaved mica from highly dilute solutions. Figure 10 shows the height image of **G5.5-PS₄₃₀₀**, in which single molecules are observed as scattered particles. The diameters and the heights of the particles are ca. 45 and 1.3 nm, respectively. The diameter is slightly larger than the R_h in solution (Table 1) while the height is strikingly small. This demonstrates that the dendrimer-like star products adopt a dome-like, flattened morphology on mica surface. Fine structures such as the branching points are invisible due to coiled conformation of polystyrene segments. The size of morphology observed by



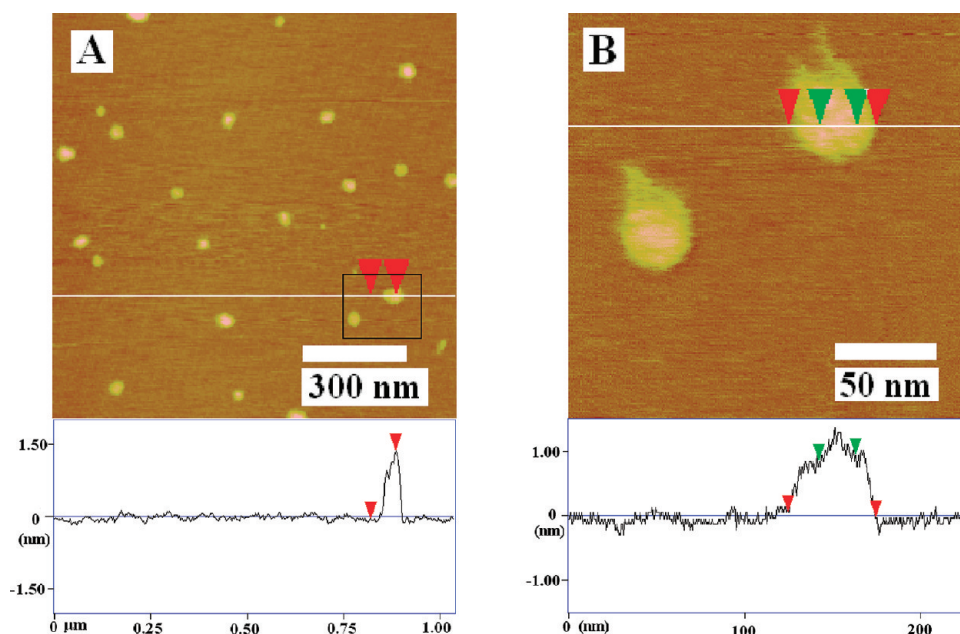


Figure 10. AFM images of G5.5-PS₄₃₀₀ obtained in tapping mode. The sample is spin-coated on mica from dilute CHCl₃ solution.

TEM (Figure 11) agrees well with AFM results, with a homogeneous circular profile after collapse on the copper grid.

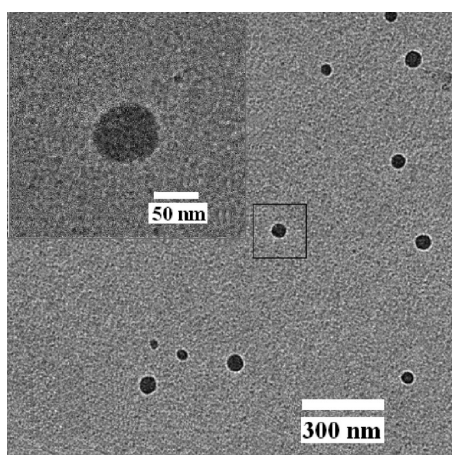


Figure 11. TEM image of G5.5-PS₄₃₀₀ deposited on a copper grid from dilute THF solution. The inset in red frame is the partial enlargement indicated in the figure.

The Application of Living Dendrimer-Like Star Polystyrene as the Precursor Building Block in Further Molecular Design. One of the attributes of the present method is that the product is living, and can be functionalized through anionic reaction or copolymerization. As an illustration, living dendrimer-like star polystyrene of the G5.5-PS₄₀₀₀ is functionalized with multiple periphery hydroxyl groups through sequential nucleophilic reaction with allyl bromide and thiol–ene reaction with 1-thioglycerol, as shown in Scheme 3.

Figure 12 shows the ¹H NMR result of the hydroxyl functionalized product. The protons of peripheral groups derived from 1-thioglycerol are clearly observed as signals at $\delta = 3.61$ (CH₂OH) and 3.74 (CHOH) ppm. From the integration the hydroxyl functionality is estimated to be 60.1, which is much lower than the anticipated hydroxyl functionality, 128, as

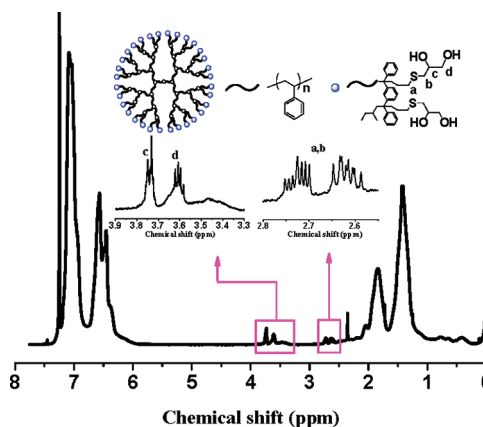


Figure 12. ¹H NMR spectrum (in CDCl₃) of G5.5-PS₄₀₀₀-vinyl after thiol–ene reaction.

well as the value determined by titration using a cyclohexane solution of 1, 1-diphenylhexyllithium (adduct of *s*-BuLi with 1,1-diphenylethylene), 92.7.

Dendrimer-like star block copolymers are synthesized via anionic polymerization of isoprene or methyl methacrylate (MMA) initiated by the dendritic polystyrene precursor end-capped with the inimer, e.g., G3.5-PS₃₃₀₀, as shown in Scheme 4. The polymerization of isoprene is performed in cyclohexane in the presence of trace amount of THF and TMEDA (polar additives used to destroy pseudogel as mentioned above), while MMA is polymerized in THF/cyclohexane (3:1) at low temperature. Both of the products, G4.0-PS-*b*-PI and G4.0-PS-*b*-PMMA, are easily fractionated from toluene/methanol to give monodisperse products (Figure 13).

Figure 14 shows the ¹H NMR spectra of the dendritic block copolymers after purification. It is obvious that the PI segment contains high percentage of 1,2- and 3,4-enchainment (69% and 11%, respectively) due to the presence of polar additives. The molecular weights and compositions of the dendritic block copolymers are listed in Table 3.

Scheme 4. Synthesis of Dendrimer-Like Star Block Copolymers

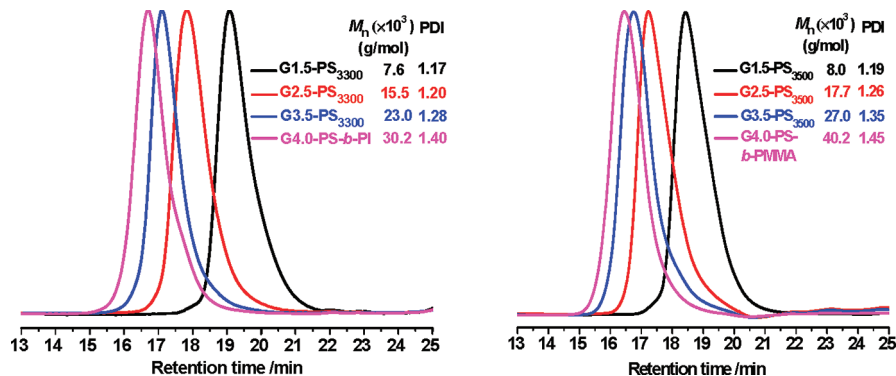
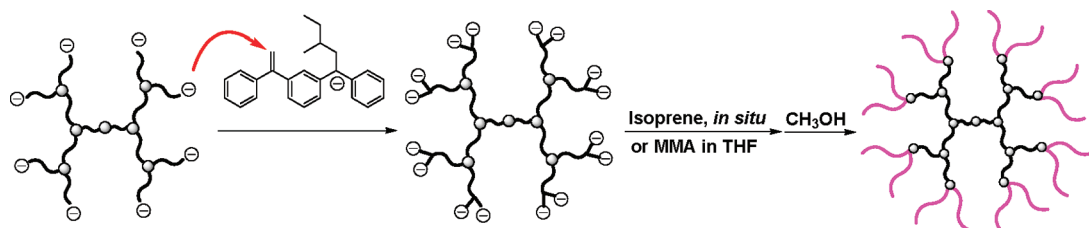


Figure 13. SEC curves tracing the synthesis of dendrimer-like star block copolymers, G4.0-PS-b-PI (left) and G4.0-PS-b-PMMA (right) (samples are fractionated from toluene/methanol).

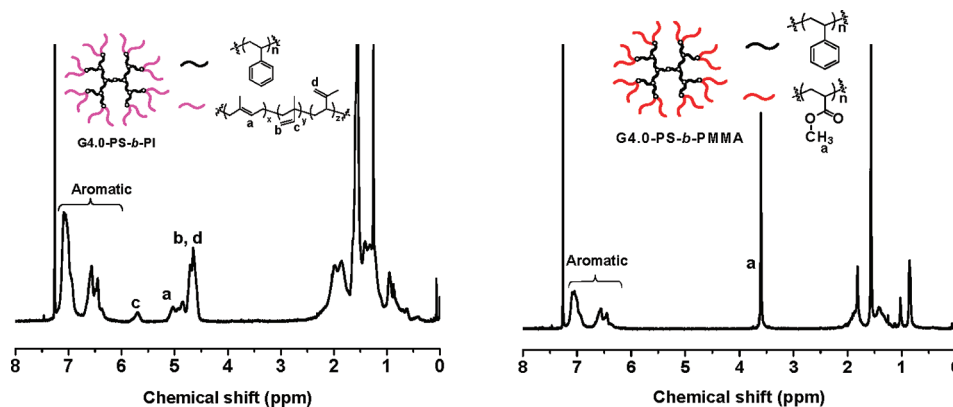


Figure 14. ^1H NMR spectra (in CDCl_3) of dendrimer-like star block copolymers, G4.0-PS-b-PI (left) and G4.0-PS-b-PMMA (right).

Table 3. Synthesis of Dendrimer-Like Star Block Copolymers and Dendrigrfts

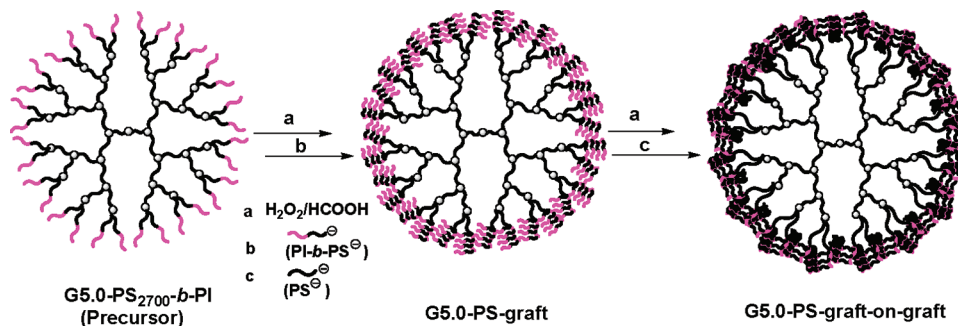
samples	$M_{n,\text{SEC}}$ (10^3 g/mol)	$M_{w,\text{MALLS}}$ (10^3 g/mol)	PDI_{SEC}	dn/dc	PS (%) _{theor} (in mol)	PS (%) from NMR (in mol)		
G3.5-PS ₃₃₀₀ (precursor)	23.0	45.0	1.28	0.190	/	/		
G4.0-PS- <i>b</i> -PI	30.2	71.2	1.47	0.136	54	55		
G3.5-PS ₃₅₀₀ (precursor)	27.0	55.3	1.35	0.190	/	/		
G4.0-PS- <i>b</i> -PMMA	40.2	96.8	1.52	0.112	67	60		
	$M_{n,\text{SEC}}$ (10^3 g/mol)	$M_{w,\text{MALLS}}$ (10^3 g/mol)	PDI_{SEC}	dn/dc	R_g (nm)	R_h (nm)	R_g/R_h	N_{arm}^d
G5.0-PS ₂₇₀₀ - <i>b</i> -PI ^a (precursor)	135	230	1.41	0.163	/	/	/	/
G5.0-PS-graft ^b	300	882	1.33	0.145	23.5	18.5	1.3	~300
G5.0-PS-graft-on-graft ^c	484	1840	1.21	0.173	25.2	24.5	1.1	850

^aG5.0-PS₂₇₀₀-b-PI is the product of isoprene polymerization initiated by living G5.0-PS₂₇₀₀ *in situ*. ^bPI₁₀-b-PS₁₀Li was used as the arm. ^cPSLi ($M_n = 1100 \text{ g/mol}$) was used as the arm. ^dNumber of arms in periphery calculated from $M_{w,\text{MALLS}}$.

Dendrimer-like star block copolymer, G4.0-PS-b-PI, is used to prepare dendrimer-like star polymers with a dendrigrft periphery, a structure resembling “dendritic box” as reported by Meijer and co-workers.⁹⁰ The dendrimer-like dendrigrfts are synthesized through polymer grafting to PI segments (Scheme 5). Thus, living G5.0-PS₂₇₀₀ is used as a dendritic initiator to

initiate the polymerization of isoprene to give G5.0-PS₂₇₀₀-b-PI ($M_{w,\text{MALLS}} = 2.3 \times 10^5 \text{ g/mol}$, molar percentage of isoprene units: 44%). The PI segment is then epoxidized by H_2O_2 /formic acid in toluene, followed by grafting of a living diblock copolymer, PI₁₀-b-PS₁₀Li (polyisoprene-*b*-polystyryllithium, total $M_n = 1700 \text{ g/mol}$, the subscripts refer to the individual

Scheme 5. Synthetic Route of Dendrimer-Like Star Polymer with a Graft-on-Graft Periphery



degree of polymerization), to prepare the first generation of dendrigrafts, **G5.0-PS-graft** ($M_{w, \text{MALLS}} = 8.82 \times 10^5$ g/mol, molar percentage of isoprene units: 35%). Further grafting of PSLi ($M_n = 1100$ g/mol) onto the PI segment of $\text{PI}_{10}\text{-b-PS}_{10}$ side chains in **G5.0-PS-graft** affords a graft-on-graft structure, **G5.0-PS-graft-on-graft** ($M_{w, \text{MALLS}} = 1.84 \times 10^6$ g/mol, molar percentage of isoprene units: 11%). The results are shown in Figure 15 and Table 3. The PDI becomes narrower after the

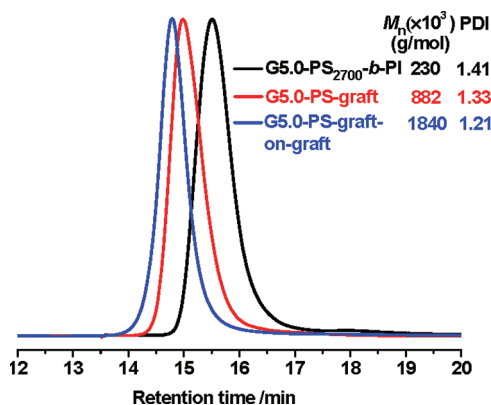


Figure 15. SEC results of dendrimer-like star polymer with graft-on-graft periphery after fractionation from toluene/methanol.

grafting reaction, decreasing from 1.41 in precursor to 1.33 and 1.21 after first and second grafting reactions, respectively. The grafting reaction is also confirmed by ^1H NMR (Figure S7, Supporting Information).

Light scattering measurement on **G5.0-PS-graft** and **G5.0-PS-graft-on-graft** gives $R_g/R_h = 1.3$ and 1.1, respectively. These lower values may indicate more condensed conformation than that of the precursor.

One purpose of the dendrimer-like dendrigrafts synthesis is to facilitate the AFM observation after densely grafting. The second generation dendrimer-like dendrigrafts (**G5.0-PS-graft-on-graft**) is visualized by AFM (Figure 16 and Figure S8, Supporting Information). The size of individual molecules increases from ~ 45 nm before grafting to ~ 75 nm after grafting; meanwhile, the height increases from 1.3 to 3.0 nm. The individual arms are visible due to the rigidity caused by densely grafted side chains. It is also clear that the central part is thicker than the periphery after collapse of the PS segments on mica. The properties of the functionalized dendrimer-like star polystyrene and copolymers with isoprene and MMA are currently under investigation.

CONCLUSIONS

The inimer-like monoadduct of stoichiometric reaction in THF between *s*-BuLi and MDDPE can be used as an efficient anionic chain branching agent. A continuous methodology is therefore developed for the synthesis of dendrimer-like star polymers using the monoadduct as the branching agent. The procedure involves alternate feeds of monomer and inimer into the reaction flask, with the aid of polar additives but without need for separation and purification of the intermediate generations. The synthetic efficiency is greatly promoted. To the best of our knowledge, this is the first truly continuous process in the synthesis of well-defined dendrimer-like star polymers.

Since the product is living, it is used as a precursor to synthesize dendrimer-like star polymers with peripheral functionalities and dendrigrafts, as well as dendrimer-like star block copolymers. We believe that this process can serve as a platform to synthesize a new class of dendrimer-like star polymers.

EXPERIMENTAL SECTION

Materials. Styrene (National Pharmaceutical, $\geq 99\%$), isoprene (TCI, $\geq 99\%$), methyl methacrylate (MMA) (TCI, $\geq 99\%$), and 1,1-diphenylethylene (DPE) (TCI, $\geq 99\%$) were distilled over CaH_2 and stored at -10°C . Styrene and isoprene were distilled over di-*n*-butylmagnesium (MgBu_2) (Aldrich, 1.0 M in heptane) on the vacuum line and MMA was distilled over tri-*n*-octylaluminum (Aldrich, 0.3 M solution in heptane) before use. Cyclohexane and tetrahydrofuran (THF) were refluxed over sodium with benzophenone as indicator, and distilled from 1, 1-diphenylhexyllithium (DPELi, adduct of *s*-BuLi with DPE) on the vacuum line before use. *N,N,N',N'*-Tetramethylethylenediamine (TMEDA) (Aldrich, $>99\%$) was purified by distilling from DPELi in a vacuum line and stored at -10°C . *n*-Butyllithium (*n*-BuLi) (Aldrich, 2.5 M solution in cyclohexane/heptane) and methylolithium (Acros, 1.6 M solution in diethyl ether) were used as received. *sec*-Butyllithium (*s*-BuLi) (Aldrich, 1.3 M solution in cyclohexane) was titrated before use. Methyltriphenylphosphonium bromide (Lancaster, $>98\%$) and 1, 3-dibenzoylbenzene (Aldrich, 98%) were vacuum-dried at 50°C for 24 h. MDDPE was synthesized according to previous method.⁹⁴

Measurements. High performance liquid chromatography (HPLC) was performed on an instrument composed of a Waters 515 pump, a C-18 column (Symmetry Shield RP-18, $5.0\ \mu\text{m}$, 4.6×250 mm), and a UV-detector (254 nm). Acetonitrile/water (83/17, v/v) was used as eluent (1.0 mL/min) at 40°C . ^1H NMR and ^{13}C NMR measurements were carried out on a Bruker (500 MHz) NMR instrument, using CDCl_3 as the solvent and tetramethylsilane as the interior reference. Gas chromatography/mass spectroscopy (GC-MS) was performed on a Finnigan Voyager instrument in electron impact mode (70 eV). Size exclusion chromatography (SEC) analysis was performed through three Waters Styragel columns (pore size 10^2 , 10^3 , and 10^4 Å), calibrated by narrow polystyrene standards, and equipped with three detectors: a DAWN HELEOS (14–154°) (Wyatt

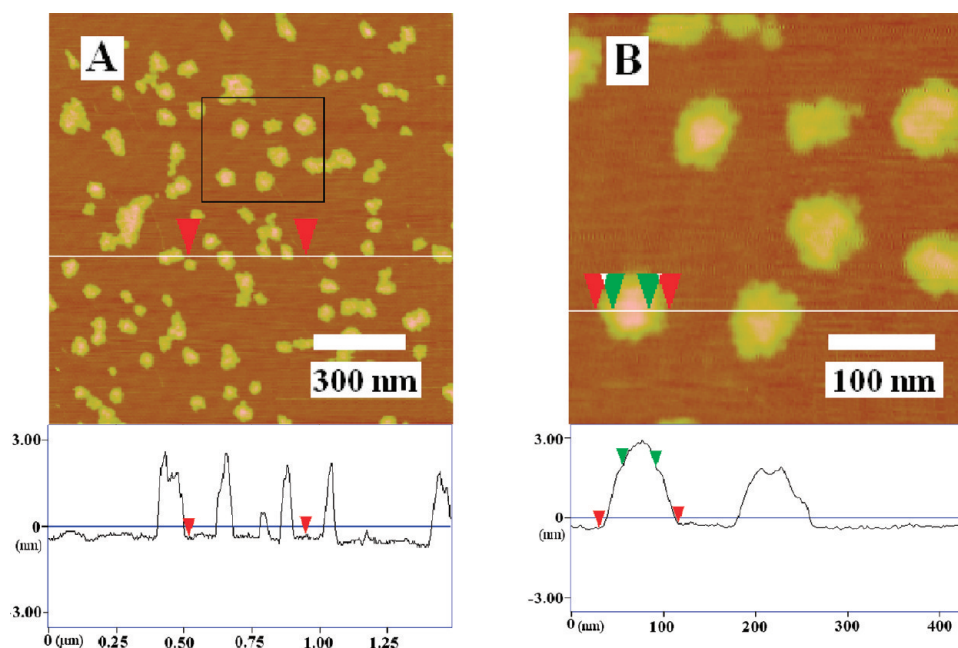


Figure 16. AFM images of G5.0-PS-graft-on-graft in a tapping mode by spin-coating on mica from CHCl_3 solution (0.05 mg/mL).

multiangle laser light scattering detector, He–Ne 658.0 nm), ViscoStar (Wyatt), and Optilab rEX (Wyatt). THF was used as the eluent at a flow rate of 1.0 mL/min at 35 °C. R_g was obtained by Zimm plot given by DAWN HELEOS in the off-line mode. dn/dc was determined in Optilab rEX in the off-line mode. AFM image was obtained in an instrument of NanoScope IV (Digital Instruments, Santa Barbara, CA) operated at tapping mode, using silicon tips of Model TESP (Digital Instruments) with radius of curvature of the tip less than 10 nm. Polymer solution (0.01–0.05 mg/mL) was spin-coated (1500 rpm for 5.0 s and then 2800 rpm for 1.0 min) on the surface of freshly cleaved mica. The MALDI–TOF mass spectrum was obtained from a Voyager DE-STR matrix-assisted laser desorption/ionization time-of-flight (MALDI–TOF) mass spectrometer equipped with a 337 nm nitrogen laser. A 10 μL sample solution (10 mg/mL in THF), 10 μL dithranol as the matrix (20 mg/mL in THF), and 2.0 μL silver trifluoroacetate (10 mg/mL in THF) were mixed, and then 0.50 μL of the mixed solution was dropped onto the plate and dried at ambient temperature. Mass spectra were given by a reflector mode using an acceleration voltage of 20 kV with an appropriate laser power and generally 1000 pulses were averaged. Transmission electron microscopy (TEM) images were recorded on a Tecnai G² 20 Twin TEM (FEI). The samples were prepared by placing one drop of CHCl_3 solution (0.01–0.05 mg/mL) on a copper grid coated with carbon. Before dynamic light scattering (DLS) measurements, all the sample solutions were filtered through 0.2 μm Millipore filters (Millipore Millex-FG, Phobic PTFE) to remove dust. The sample solutions were measured by an ALV-5000 Laser Light Scattering Spectrometer equipped with a multi- τ digital time correlation (ALV5000) and a He–Ne laser ($\lambda_0 = 632.8$ nm) light source at 30 °C and at a fixed scattering angle of 90°. The hydrodynamic radius (R_h) and polydispersity index (PDI) was obtained by the CONTIN program. R_g s of the samples were also determined on the ALV-5000. The sample solutions were carefully filtered through 0.2 μm Millipore filters (Millipore Millex-FG, Phobic PTFE) until there was not any dust found by DLS at 30°. After corrected by toluene and pure THF from 30° to 150° with a step of 5°, the static light scattering determination was performed on the same condition to give R_g . The dn/dc was obtained on Optilab rEX.

Preparation of Inimer and Difunctional Initiator. Glass apparatus were connected to the vacuum/argon line. The reactor with a magnetic stir bar inside was dried by five cycles of flaming/Ar-purging/evacuating. A volume of 6.0 mL cyclohexane solution of MDDPE (0.40 mmol/mL) was added, followed by distillation of cyclohexane to dryness. Then a volume of 70 mL of THF was distilled

into the flask, and the impurities was titrated by DPELi (adduct of *s*-BuLi and DPE) until red color appeared. THF was cooled to –80 °C by liquid nitrogen and acetone. *s*-BuLi (2 mL, 1.3 mmol/mL in cyclohexane) was slowly added and a dark red color appeared immediately. HPLC was used to trace the reaction until the MDDPE was consumed. The reaction proceeded for 15 min. THF was then completely distilled out and cyclohexane distilled into the flask at 0 °C. The inimer was obtained as stock solution in cyclohexane in volumetric ampoules (the concentration of organolithium is ca. 0.08 mol/mL) and stored at 0 °C. The content of monoadduct in the final product is 96% as determined by GC–MS.

The preparation of diadduct is similar to that of monoadduct except two equivalent of *s*-BuLi is used. The resulting diadduct was stored at 0 °C in cyclohexane solution (the concentration of organolithium is ca. 0.04 mol/mL).

Model Reaction for the Branching Process. A solution of PSLi in cyclohexane, prepared by *s*-BuLi (1.0 mL, 1.3 M in cyclohexane) initiated polymerization of styrene (1.90 g, 18.3 mmol) at 45 °C, was mixed with a cyclohexane solution of inimer (30 mL, 4.33×10^{-2} mol/mL) in the presence of THF (double equivalent of Li). The reaction proceeded for 1.0 h and an aliquot of the react mixture containing the product, polystyryl α , α' -dianion, was analyzed using MALDI–TOF mass spectrometry. The resulting dianion was used *in situ* to initiate the polymerization of styrene to give a star-like PS ($M_{n,SEC} = 7800$ g/mol, PDI = 1.19, $M_{w,MALLS} = 9600$ g/mol).

Continuous Synthesis of Living Dendrimer-Like Star Polystyrenes. Glass apparatus were connected to the vacuum/argon line. The polymerization was carried out in a volumetric ampoule with a magnetic stir bar inside which was dried by five cycles of flaming/Ar-purging/evacuating and rinsed sequentially with a dilute cyclohexane solution of *n*-BuLi and pure cyclohexane.

The preparation of dendrimer-like star polystyrene are described using the following reaction as an example. Cyclohexane (20 mL) was distilled into the reaction flask followed by adding 0.05 mL of THF as additive. A solution of diadduct of *s*-BuLi with MDDPE (as prepared above) (5.0 mL, 0.040 mmol/mL in cyclohexane), and styrene (1.72 g, 16.5 mmol, freshly distilled) were added to the flask at ~6 °C for 30 min, then raising the temperature to 45 °C for 60 min. After the polymerization, living G1.0-PS₄₃₀₀ was obtained and analyzed by SEC and NMR.

The living G1.0-PS₄₃₀₀ was mixed *in situ* with a solution of inimer (5.0 mL, 0.08 mmol/mL in cyclohexane). The addition reaction proceeded at 45 °C for 1.0 h to give living G1.5-PS₄₃₀₀. Half volume of

the reaction mixture was separated using a volumetric ampule, terminated with a solution of THF (20 mL) containing 1 mL of methanol and 0.10 mL of HCl (concentrated), and the intermediate product was precipitated into 300 mL of methanol. The residual reaction mixture was mixed with 15 mL dry cyclohexane containing 0.03 mL THF. Styrene (1.72 g, 16.5 mmol) was added to start the polymerization, followed by addition of inimer to the terminus of dendritic polymers. **G2.5-PS**₄₃₀₀ was obtained. Repeating the process gave dendritic products up to **G5.5**. TMEDA (~0.03 mL) was used in the preparation of highest generation. The characterization results are listed in Table 1.

Functionalization of Living Dendrimer-Like Star Polystyrene with Allylic and Hydroxyl Groups. The living dendrimer-like star polystyrenes with various generations as prepared above were reacted with dry allyl bromide *in situ* in cyclohexane at 10 °C for 2 min. Dendrimer-like star polymers of **G1.5-PS-vinyl** to **G5.5-PS-vinyl** were obtained. The final product was fractionated from toluene/methanol with a yield of ~60%. ($M_{n,SEC} = 79.0 \times 10^3$ g/mol, PDI = 1.52, $M_{w,MALLS} = 255.0 \times 10^3$ g/mol).

The allyl group functionalized dendrimer-like star PS with 5.fifth generation (0.50 g), **G5.5-PS-vinyl**, was dissolved in toluene followed by adding 1-thioglycerol (2.0 mL) and a small amount of AIBN (6.0 mg, ~30% in mole ratio to allyl group). The oxygen was removed by freezing-thawing-evacuating for 3 times. The reaction was carried out at 80 °C for 6 h. The product was precipitated from methanol, and washed 2 times with methanol with the aid of centrifuge ($M_{n,SEC} = 85.0 \times 10^3$ g/mol, PDI = 1.62, $M_{w,MALLS} = 243.0 \times 10^3$ g/mol).

Synthesis of Living Dendrimer-Like Star Copolymers. Living **G3.5-PS**₃₃₀₀ ($M_{n,SEC} = 23.0 \times 10^3$ g/mol, PDI = 1.28, $M_{w,MALLS} = 45.0 \times 10^3$ g/mol) was used as a dendritic initiator to initiate the polymerization of isoprene (1.32 mL, 13.2 mmol). Upon addition of isoprene, the reaction solution changed from orange to pale yellow in color, indicating the initiation of isoprene. **G4.0-PS-*b*-PI** was obtained and fractional purification by toluene/methanol ($M_{n,SEC} = 30.2 \times 10^3$ g/mol, PDI = 1.52, $M_{w,MALLS} = 71.2 \times 10^3$ g/mol).

Living **G3.5-PS**₃₅₀₀ was used as a dendritic initiator for the polymerization of MMA. Thus, the reaction solution of **G3.5-PS**₃₅₀₀ was mixed with 50 mL of dry THF followed by feeding the MMA monomer at -78 °C. The polymerization proceeded for 1 h to give dendrimer-like star copolymers of **G4.0-PS-*b*-PMMA** ($M_{n,SEC} = 40.2 \times 10^3$ g/mol, PDI = 1.52, $M_{w,MALLS} = 96.8 \times 10^3$ g/mol).

Synthesis of G5.0-PS-Graft-on-Graft Polymers. Dendrimer-like star copolymer, **G5.0-PS**_{2700-*b*-PI} (0.60 g, 0.0026 mmol), was dissolved in toluene and then mixed with 1 mL of HCOOH and 1.0 mL of H₂O₂ under stirring for 1.0 h at 35 °C. The reaction solution was washed by water two times. The product was precipitated in methanol and dried in vacuum for analysis. The epoxidized product was dissolved in THF followed by adding excessive presynthesized PI_{10-*b*-PS}₁₀Li in cyclohexane to accomplish the grafting reaction within 24 h at room temperature. The graft copolymer, **G5.0-PS-graft**, was obtained after precipitation in methanol and extraction by acetone to remove the excessive PS-*b*-PI arm polymers. The PI segments in **G5.0-PS-graft** were further epoxidized, and attacked by a presynthesized PSLi ($M_n = 1100$ g/mol) as arm. **G5.0-PS-graft-on-graft** was obtained. ($M_{n,SEC} = 484.0 \times 10^3$ g/mol, PDI = 1.21, $M_{w,MALLS} = 1.84 \times 10^6$ g/mol).

Titration of Vinyl Groups in Dendrimer-Like Star Polystyrenes Functionalized with Allylic Groups. The polymer of **G5.5-PS**_{4000-vinyl} (0.4038 g, 0.00158 mmol) was dissolved in cyclohexane (10 mL) followed by adding excessive IBr in cyclohexane solution (4.00 mL, 0.1010 mmol/mL) to react with the vinyl groups for 3.0 h at room temperature. The residual IBr was reduced by KI (2.0 mL, 1.0 mmol/mL in water) to I₂ in 30 min. The mixture was titrated by sodium thiosulfate solution (22.0 mL, 0.029 mmol/mL) using starch aqueous solution as the indicator. Number of vinyl groups in the periphery was calculated by $N_{vinyl, obs} = [N_{IBr} - V_{S_2O_3^{2-}} \times [S_2O_3^{2-}]/2]/N_{G5.0-PS-vinyl}$.

Titration of Hydroxyl Groups in Functionalized Dendrimer-Like Star Polymer, G5.0-PS-OH. Dry sample of **G5.0-PS-OH** (0.3045 g, 1.19×10^{-3} mmol) was dissolved in THF (10 mL) which

was titrated by a DPPELi in cyclohexane (2.83 mL, 0.0423 mmol/mL). The blank experiment was carried out in the absence of polymer under otherwise identical conditions. The number of hydroxyl groups in the periphery was estimated to be 92 ± 10 , according to the following equation:

$$N_{hydroxyl\ groups, obs} = (V_{DPPELi} \times [DPPELi])/N_{G5.0-PS-OH}$$

in which V_{DPPELi} is the consumed volume of DPPELi at the concentration of [DPPELi], and $N_{G5.0-PS-OH}$ represents a molar amount of polymer sample.

■ ASSOCIATED CONTENT

● Supporting Information

Results of SEC, ¹H NMR, and DLS, Tyndall phenomena, and AFM images of concerned dendrimer-like star (co)polymers. This material is available free of charge via the Internet at <http://pubs.acs.org>.

■ AUTHOR INFORMATION

Corresponding Author

*Fax: +86-21-6564-0293. E-mail: jphe@fudan.edu.cn.

■ ACKNOWLEDGMENTS

This work is financially supported by National Nature Science Foundation of China (NSFC 21074024). The authors are grateful to Professor You Wang and Doctor Jianghua Liu for their great help in AFM and DLS experiments, respectively. J. H. and H. Z. thank the Research Fund for the Doctoral Program of Higher Education of China (20100071110013).

■ REFERENCES

- (1) Daniel, T.; Feng, X.; Gnanou, Y. *New J. Chem.* **2007**, *31*, 1097–1110.
- (2) Fréchet, J. M.; Tomalia, D. A. *Dendrimers and Other Dendritic Polymers*; Wiley-VCH: Weinheim, Germany, 2001.
- (3) Vögtle, F.; Richardt, G.; Werner, N. *Dendrimer Chemistry: Concepts, Syntheses, Properties and Applications*; Wiley-VCH: Weinheim, Germany, 2009.
- (4) Konkolewicz, D.; Monteiro, M. J.; Perrier, S. *Macromolecules* **2011**, *44*, 7067–7087.
- (5) Six, J. L.; Gnanou, Y. *Macromol. Symp.* **1995**, *95*, 137–150.
- (6) Feng, X.; Taton, D.; Chaikof, E. L.; Gnanou, Y. *J. Am. Chem. Soc.* **2005**, *127*, 10956–10966.
- (7) Lepoittevin, B.; Matmour, R.; Francis, R.; Taton, D.; Gnanou, Y. *Macromolecules* **2005**, *38*, 3120–3128.
- (8) Angot, S.; Taton, D.; Gnanou, Y. *Macromolecules* **2000**, *33*, 5418–5426.
- (9) Taton, D.; Gnanou, Y. *Macromol. Symp.* **2001**, *174*, 333–341.
- (10) Francis, R.; Taton, D.; Logan, J. L.; Masse, P.; Gnanou, Y.; Duran, R. S. *Macromolecules* **2003**, *36*, 8253–8259.
- (11) Matmour, R.; Lepoittevin, B.; Joncheray, T. J.; El-khoury, R. J.; Taton, D.; Duran, R. S.; Gnanou, Y. *Macromolecules* **2005**, *38*, 5459–5467.
- (12) Feng, X.; Taton, D.; Borsali, R.; Chaikof, E. L.; Gnanou, Y. *J. Am. Chem. Soc.* **2006**, *128*, 11551–11562.
- (13) Feng, X.; Taton, D.; Ibarboure, E.; Chaikof, E. L.; Gnanou, Y. *J. Am. Chem. Soc.* **2008**, *130*, 11662–11676.
- (14) Feng, X.; Taton, D.; Chaikof, E. L.; Gnanou, Y. *Macromolecules* **2009**, *42*, 7292–7298.
- (15) Trollsås, M.; Hedrick, J. L. *J. Am. Chem. Soc.* **1998**, *120*, 4644–4651.
- (16) Würsch, A.; Möller, M.; Glauser, T.; Lim, L. S.; Voytek, S. B.; Hedrick, J. L. *Macromolecules* **2001**, *34*, 6601–6615.
- (17) Trollsås, M.; Claesson, H.; Atthof, B.; Hedrick, J. L. *Angew. Chem., Int. Ed.* **1998**, *37*, 3132–3136.

- (18) Hedenqvist, M. S.; Yousefi, H.; Malmström, E.; Johansson, M.; Hult, A.; Gedde, U. W.; Trollsås, M.; Hedrick, J. L. *Polymer* **2000**, *41*, 1827–1840.
- (19) Trollsås, M.; Atthof, B.; Würsch, A.; Hedrick, J. L. *Macromolecules* **2000**, *33*, 6423–6438.
- (20) Trollsås, M.; Atthof, B.; Claesson, H.; Hedrick, J. L. *J. Polym. Sci., Part A: Polym. Chem.* **2004**, *42*, 1174–1188.
- (21) Trollsås, M.; Claesson, H.; Atthof, B.; Hedrick, J. L. *Macromol. Symp.* **2000**, *153*, 87–108.
- (22) Trollsås, M.; Kelly, M. A.; Claesson, H.; Siemens, R.; Hedrick, J. L. *Macromolecules* **1999**, *32*, 4917–4924.
- (23) Stancik, C. M.; Pople, J. A.; Trollsås, M.; Lindner, P.; Hedrick, J. L.; Gast, A. P. *Macromolecules* **2003**, *36*, 5765–5775.
- (24) Hedrick, J. L.; Trollsås, M.; Hawker, C. J.; Atthof, B.; Claesson, H.; Heise, A.; Miller, R. D. *Macromolecules* **1998**, *31*, 8691–8705.
- (25) Percec, V.; Barboiu, B.; Grigoras, C.; Bera, T. K. *J. Am. Chem. Soc.* **2003**, *125*, 6503–6516.
- (26) Percec, V.; Grigoras, C.; Bera, T. K.; Barboiu, B.; Bissel, P. J. *J. Polym. Sci., Part A: Polym. Chem.* **2005**, *43*, 4894–4906.
- (27) Percec, V.; Grigoras, C.; Kim, H. J. *J. Polym. Sci., Part A: Polym. Chem.* **2004**, *42*, 505–513.
- (28) Matmour, R.; Gnanou, Y. *J. Am. Chem. Soc.* **2008**, *130*, 1350–1361.
- (29) Luan, B.; Pan, C. *Eur. Polym. J.* **2006**, *42*, 1467–1478.
- (30) Yuan, W.; Yuan, J.; Zhou, M.; Pan, C. *J. Polym. Sci., Part A: Polym. Chem.* **2008**, *46*, 2788–2798.
- (31) Kong, L.; Pan, C. *Polymer* **2008**, *49*, 200–210.
- (32) Liu, Q.; Zhao, P.; Chen, Y. *J. Polym. Sci., Part A: Polym. Chem.* **2007**, *45*, 3330–3341.
- (33) Killips, K. L.; Campos, L. M.; Hawker, C. J. *J. Am. Chem. Soc.* **2008**, *130*, 5062–5064.
- (34) Antoni, P.; Robb, M. J.; Campos, L.; Montanez, M.; Hult, A.; Malmström, E.; Malkoch, M.; Hawker, C. J. *Macromolecules* **2010**, *43*, 6625–6631.
- (35) Hirao, A.; Sugiyama, K.; Tsunoda, Y.; Matsuo, A.; Watanabe, T. *J. Polym. Sci., Part A: Polym. Chem.* **2006**, *44*, 6659–6687.
- (36) Higashihara, T.; Sugiyama, K.; Yoo, H. S.; Hayashi, M.; Hirao, A. *Macromol. Rapid Commun.* **2010**, *31*, 1031–1059.
- (37) Matsuo, A.; Watanabe, T.; Hirao, A. *Macromolecules* **2004**, *37*, 6283–6290.
- (38) Hirao, A.; Hayashi, M.; Loykulant, S.; Sugiyama, K.; Ryu, S. W.; Haraguchi, N.; Matsuo, A.; Higashihara, T. *Prog. Polym. Sci.* **2005**, *30*, 111–182.
- (39) Hirao, A.; Yoo, H. S. *Polym. J.* **2011**, *43*, 2–17.
- (40) Hirao, A.; Sugiyama, K.; Matsuo, A.; Tsunoda, Y.; Watanabe, T. *Polym. Int.* **2008**, *57*, 554–570.
- (41) Hirao, A.; Matsuo, A.; Watanabe, T. *Macromolecules* **2005**, *38*, 8701–8711.
- (42) Watanabe, T.; Tsunoda, Y.; Matsuo, A.; Sugiyama, K.; Hirao, A. *Macromol. Symp.* **2006**, *240*, 23–30.
- (43) Watanabe, T.; Hirao, A. *Macromol. Symp.* **2006**, *245/246*, 5–13.
- (44) Jin, S.; Jin, K. S.; Yoon, J.; Heo, K.; Kim, J.; Kim, K. W.; Ree, M.; Higashihara, T.; Watanabe, T.; Hirao, A. *Macromol. Res.* **2008**, *16*, 686–694.
- (45) Deffieux, A.; Schappacher, M.; Hirao, A.; Watanabe, T. *J. Am. Chem. Soc.* **2008**, *130*, 5670–5672.
- (46) Hirao, A.; Watanabe, T.; Ishizu, K.; Ree, M.; Jin, S.; Jin, K. S.; Deffieux, A.; Schappacher, M.; Carloti, S. *Macromolecules* **2009**, *42*, 682–693.
- (47) Yoo, H. S.; Watanabe, T.; Hirao, A. *Macromolecules* **2009**, *42*, 4558–4570.
- (48) Haraguchi, N.; Hirao, A. *Macromolecules* **2003**, *36*, 9364–9372.
- (49) Hirao, A.; Matsuo, A. *Macromolecules* **2003**, *36*, 9742–9751.
- (50) Chalari, I.; Hadjichristidis, N. *J. Polym. Sci., Part A: Polym. Chem.* **2002**, *40*, 1519–1526.
- (51) Orfanou, K.; Iatrou, H.; Lohse, D. J.; Hadjichristidis, N. *Macromolecules* **2006**, *39*, 4361–4365.
- (52) Knauss, D. M.; Al-Muallem, H. A.; Huang, T.; Wu, D. T. *Macromolecules* **2000**, *33*, 3557–3568.
- (53) Knauss, D. M.; Al-Muallem, H. A. *J. Polym. Sci., Part A: Polym. Chem.* **2000**, *38*, 4289–4298.
- (54) Asteriadi, A.; Sigel, R.; Vlassopoulos, D.; Meier, G.; Dorgan, J. R.; Knauss, D. M. *Macromolecules* **2003**, *36*, 6036–6042.
- (55) Bender, J. T.; Knauss, D. M. *Macromolecules* **2009**, *42*, 2411–2418.
- (56) Hutchings, L. R.; Roberts-Bleming, S. J. *Macromolecules* **2006**, *39*, 2144–2152.
- (57) Urbani, C. N.; Bell, C. A.; Whittaker, M. R.; Monteiro, M. J. *Macromolecules* **2008**, *41*, 1057–1060.
- (58) Lonsdale, D.; Whittaker, M. R.; Monteiro, M. J. *J. Polym. Sci., Part A: Polym. Chem.* **2009**, *47*, 6292–6303.
- (59) Wang, G.; Luo, X.; Zhang, Y.; Huang, J. *J. Polym. Sci., Part A: Polym. Chem.* **2009**, *47*, 4800–4810.
- (60) Altintas, O.; Demirel, A. L.; Hizal, G.; Tunca, U. *J. Polym. Sci., Part A: Polym. Chem.* **2008**, *46*, 5916–5928.
- (61) Whittaker, M. R.; Urbani, C. N.; Monteiro, M. J. *J. Am. Chem. Soc.* **2006**, *128*, 11360–11361.
- (62) Zeng, F.; Zimmerman, S. C. *J. Am. Chem. Soc.* **1996**, *118*, 5326–5327.
- (63) Maraval, V.; Caminade, A. M.; Majoral, J. P.; Blais, J. C. *Angew. Chem., Int. Ed.* **2003**, *42*, 1822–1826.
- (64) Brauge, L.; Magro, G.; Caminade, A. M.; Majoral, J. P. *J. Am. Chem. Soc.* **2001**, *123*, 6698–6699.
- (65) Li, Y.; Tseng, Y. D.; Kwon, S. Y.; d'Espaux, L.; Bunch, J. S.; McEuen, P. L.; Luo, D. *Nat. Mater.* **2004**, *3*, 38–42.
- (66) Bi, S.; Hao, S.; Li, L.; Zhang, S. *Chem. Commun.* **2010**, *46*, 6093–6095.
- (67) Freedman, K. O.; Lee, J.; Li, Y.; Luo, D.; Skobeleva, V. B.; Ke, P. C. *J. Phys. Chem. B.* **2005**, *109*, 9839–9842.
- (68) Bae, Y. C.; Faust, R. *Macromolecules* **1998**, *31*, 9379–9383.
- (69) Tung, L. H.; Lo, G. Y.-S. *Macromolecules* **1994**, *27*, 1680–1684.
- (70) Lo, G. Y.-S.; Otterbacher, E. W.; Gatzke, A. L.; Tung, L. H. *Macromolecules* **1994**, *27*, 2233–2240.
- (71) Lo, G. Y.-S.; Otterbacher, E. W.; Pews, R. G.; Tung, L. H. *Macromolecules* **1994**, *27*, 2241–2248.
- (72) Bredeweg, C. J.; Gatzke, A. L.; Lo, G. Y.-S.; Tung, L. H. *Macromolecules* **1994**, *27*, 2225–2232.
- (73) Sun, W.; He, J.; Wang, X.; Zhang, C.; Zhang, H.; Yang, Y. *Macromolecules* **2009**, *42*, 7309–7317.
- (74) Lee, J. S.; Quirk, R. P.; Foster, M. D. *Macromolecules* **2005**, *38*, 5381–5392.
- (75) Higashihara, T.; Nagura, M.; Inoue, K.; Haraguchi, N.; Hirao, A. *Macromolecules* **2005**, *38*, 4577–4587.
- (76) Wang, X.; Xia, J.; He, J.; Yu, F.; Li, A.; Xu, J.; Lu, H.; Yang, Y. *Macromolecules* **2006**, *39*, 6898–6904.
- (77) Wang, X.; He, J.; Yang, Y. *J. Polym. Sci., Part A: Polym. Chem.* **2007**, *45*, 4818–4828.
- (78) Quirk, R. P.; Yin, J.; Guo, S.; Hu, X.; Summers, G.; Kim, J.; Zhu, L.; Schock, L. E. *Chin. J. Polym. Sci.* **1990**, *8*, 97–107.
- (79) Lepoittevin, B.; Dourges, M. A.; Masure, M.; Hemery, P.; Baran, K.; Cramail, H. *Macromolecules* **2000**, *33*, 8218–8224.
- (80) Lepoittevin, B.; Hemery, P. *Polym. Adv. Technol.* **2002**, *13*, 771–776.
- (81) Pispas, S.; Hadjichristidis, N. *Macromolecules* **1996**, *29*, 7378–7385.
- (82) Broske, A. D.; Huang, T. L.; Allen, R. D.; Hoover, J. M.; McGrath, J. E. In *Recent Advances in Anionic Polymerization*; Hogen-Esch, T. E., Smid, J., Eds.; Elsevier: New York, 1987; pp 363–380.
- (83) Schulz, G.; Hocker, H. *Angew. Chem., Int. Ed. Engl.* **1980**, *19*, 219–220.
- (84) Leitz, E.; Hocker, H. *Makromol. Chem.* **1983**, *184*, 1893–1899.
- (85) Quirk, R. P.; Yoo, T.; Lee, Y.; Kim, J.; Lee, B. *Adv. Polym. Sci.* **2000**, *153*, 67–162.
- (86) Ikker, A.; Möller, M. *New Polym. Mater.* **1993**, *4*, 35–51.
- (87) Hsieh, H. L.; Quirk, R. P. *Anionic polymerization: Principles and Practical Applications*; Marcel Dekker: New York, 1996; p 357–366.
- (88) Worsfold, D. J.; Bywater, S. M. *Macromolecules* **1972**, *5*, 393–397.

- (89) Bosman, A. W.; Janssen, H. M.; Meijer, E. W. *Chem. Rev.* **1999**, *99*, 1665–1688.
- (90) Jansen, J. F. G. A.; Meijer, E. W.; de Brabander-van den Berg, E. M. M. *J. Am. Chem. Soc.* **1995**, *117*, 4417–4418.
- (91) Meyerhoff, G.; Appelt, B. *Macromolecules* **1979**, *12*, 968–971.
- (92) Burchard, W.; Schmidt, M.; Stockmayert, W. H. *Macromolecules* **1980**, *13*, 1265–1272.
- (93) Li, L.; He, C.; He, W.; Wu, C. *Macromolecules* **2011**, *44*, 8195–8206.
- (94) Schulz, G. G. H.; Höcker, H. *Makromol. Chem.* **1977**, *178*, 2589–2594.

■ NOTE ADDED AFTER ASAP PUBLICATION

This article posted ASAP on December 29, 2011. Figure 8 has been revised. The correct version posted on January 5, 2012.

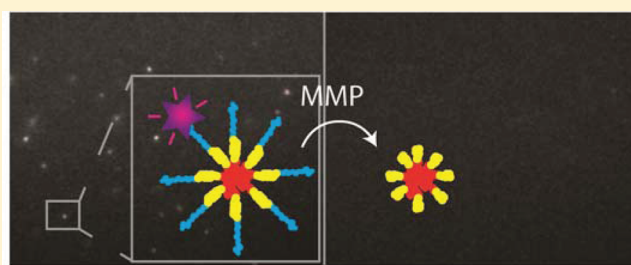
Thermosensitive Peptide-Hybrid ABC Block Copolymers Obtained by ATRP: Synthesis, Self-Assembly, and Enzymatic Degradation

Albert J. de Graaf,[†] Enrico Mastrobattista,[†] Tina Vermonden,[†] Cornelus F. van Nostrum,[†] Dirk T. S. Rijkers,[‡] Rob M. J. Liskamp,[‡] and Wim E. Hennink^{*,†}

[†]Utrecht Institute for Pharmaceutical Sciences, Pharmaceutics, Utrecht University, P.O. Box 80.082, 3508TB Utrecht, The Netherlands

[‡]Utrecht Institute for Pharmaceutical Sciences, Medicinal Chemistry & Chemical Biology, Utrecht University, P.O. Box 80.082, 3508TB Utrecht, The Netherlands

ABSTRACT: Peptide-hybrid ABC block copolymers were synthesized by growing two different polymer chains from a native peptide using atom transfer radical polymerization (ATRP). To this end, two different ATRP initiators were coupled via orthogonal methods to the N- and C-terminus of the peptide Ser-Gly-Pro-Gln-Gly-Ile-Phe-Gly-Gln-Met-Gly, a substrate for matrix metalloproteases 2 and 9. First, a hydrophilic block of poly(oligo(ethylene glycol) methyl ether methacrylate) (pOEGMA) was polymerized from the peptide's C-terminus. Before polymerization of the second block, the first living chain end was inactivated by substitution of its Cl-terminus with azide under mild conditions. Then, a thermosensitive block of poly(*N*-isopropylacrylamide) (pNIPAm) was polymerized from the peptide's N-terminus. Well-defined polymers were obtained with good control over both block sizes. The resulting polymers self-assembled into micelles above the cloud point of the pNIPAm block. As anticipated, it was shown that the peptide linkage between the polymer blocks can be cut by a metalloprotease, leading to "shedding" of the corona of the micelles which makes these systems potentially suitable for enzyme-triggered drug delivery.



INTRODUCTION

The field of biohybrid materials (materials that consist of synthetic materials together with biomolecules or even entire cells) has been rapidly expanding over the past decade. This is due to the promises it holds for pharmaceutical, medical, and bio- and nanotechnological applications.^{1,2} Among others, biohybrid materials are under investigation for use in targeted drug delivery and for the controlled release of therapeutic (bio)molecules. For example, biohybrid hydrogels can be used as depot formulations of drugs or as scaffolds for tissue engineering, whereas biohybrid micelles and vesicles are under investigation for targeted drug delivery to inflamed tissue, e.g., in cancer and rheumatoid arthritis.^{3–8} In these materials, the "bio" part may e.g. be a peptide containing a cell adhesion site or an enzymatic cleavage site or a pH-, redox-, or temperature-responsive peptide.^{4–6}

A number of techniques are presently available for the design of such peptide-hybrid polymers, including coupling a peptide to a premade polymer (the "grafting to" approach),^{9,10} polymerizing a peptide-functionalized monomer (the "grafting through" approach),^{11,12} or performing a polymerization using a peptide macroinitiator (the "grafting from" approach).^{13,14}

The advent of several controlled, "living" radical polymerization techniques has greatly expanded the scope of these "grafting" techniques. Techniques such as atom transfer radical polymerization (ATRP),^{15–17} reversible addition–fragmenta-

tion chain transfer (RAFT) polymerization,^{18–20} and nitroxide-mediated polymerization (NMP)^{21–23} allow for the synthesis of low-dispersity polymers with defined, reactive chain-ends.²⁴ A variety of monomers can be polymerized using these techniques, often under mild conditions. Furthermore, living radical polymerizations are compatible with many functional groups. Together, these properties render living radical polymerizations suitable for use in "grafting from" and "grafting through" strategies.²⁵

In the present work we aimed at incorporating a peptide into semisynthetic amphiphilic triblock copolymers, such that the peptide is positioned between a hydrophilic and a thermosensitive block. For the hydrophilic block of the final block copolymer, oligo(ethylene glycol) methyl ether methacrylate (OEGMA, $M_n = 300$ Da) was chosen as monomer. The thermosensitive block was prepared by polymerization of *N*-isopropylacrylamide (NIPAm). In aqueous solutions, these polymers likely self-assemble into micellar structures above the cloud point (CP) of the thermosensitive block as demonstrated for other thermosensitive block copolymers.^{26,27} The peptide, Ser-Gly-Pro-Gln-Gly-Ile-Phe-Gly-Gln-Met-Gly, was designed to be functionalizable by specific chemistries on both its N- and C-

Received: November 8, 2011

Revised: December 26, 2011

Published: January 12, 2012

terminus. Furthermore, this peptide is cleavable at the Gly–Ile bond by matrix metalloproteinases (MMPs) 2 and 9,²⁸ which are upregulated in inflamed tissues such as in cancer and rheumatoid arthritis.^{29–31} Micelles, formed by self-assembly of these amphiphilic block copolymers above the CP of the pNIPAM block, can be loaded with a drug and be administered intravenously. Because of the enhanced permeability and retention (EPR) effect, they will accumulate in the inflamed target tissue,³² where the hydrophilic stealth corona will subsequently be selectively shed off by action of the MMPs. The exposed micellar cores may then be taken up by the target cells or aggregate and release their payload over time.³³

In order to generate these thermosensitive block copolymers with a peptide connecting the hydrophilic and thermosensitive polymer blocks, in the present paper, two sequential polymerizations, each initiating on the other terminus of the same peptide, were carried out. Thereby, full benefit is taken from the advantages of the “grafting from” approach, mainly the high coupling efficiency and easy work-up. To the best of our knowledge, this is the first report of two sequential “grafting from” polymerizations, initiated from the C- and N-terminus of a peptide. Furthermore, we use the same polymerization technique, ATRP, for both blocks. At present, sequential “grafting from” has only been performed using a nonpeptide initiator carrying two initiating moieties each for a different polymerization chemistry.^{34,35} It is shown that well-defined amphiphilic polymers can indeed be synthesized in this way. These polymers self-assemble into micelles, having a corona which can be shed off by action of a metalloprotease.

EXPERIMENTAL PART

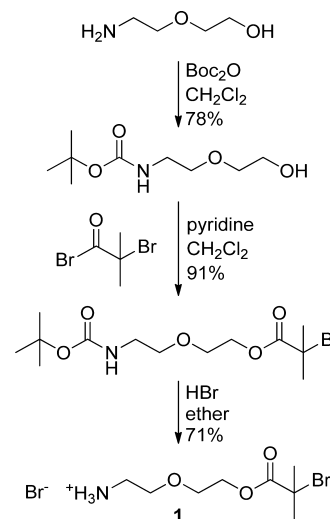
Chemicals. All solvents were obtained from Biosolve (Valkenswaard, The Netherlands). Unless otherwise noted, the chemicals were obtained from Sigma-Aldrich (Steinheim, Germany) and were used as received. Prior to use, *N,N*-dimethylacetamide (DMA) was dried on calcium hydride, distilled under reduced pressure, and stored over 4 Å molecular sieves. Triethylamine was dried on potassium hydroxide, distilled, and stored on 3 Å molecular sieves. Oligo(ethylene glycol) methyl ether methacrylate with average M_n of 300 Da (OEGMA₃₀₀) was passed over a column of basic alumina immediately prior to use. Tris[2-(dimethylamino)ethyl]amine (Me₆TREN) was prepared and purified according to a literature procedure.³⁶

Analytical Methods. HPLC was performed on a Waters 2695 system equipped with a dual wavelength UV absorption detector set to 210 and 254 nm. An Alltech ProSphere C18 column was used at 25 °C, employing a gradient of CH₃CN/H₂O/TFA 5/95/0.1 to 60/40/0.1 in 1 h. Unless noted otherwise, gel permeation chromatography (GPC) was performed on a Waters 2695 system equipped with a differential refractive index detector using a MixedD column (Polymer laboratories). The column temperature was 40 °C, 10 mM LiCl in DMF was used as the eluent at a flow rate of 1 mL/min, and linear PEG standards were used for calibration. Samples were allowed to dissolve for at least 16 h prior to analysis.

NMR spectra were recorded on a Varian Mercury spectrometer operating at 300 MHz (¹H) or 75.5 MHz (¹³C), and ESI-MS spectra were recorded on a Shimadzu QP8000 mass spectrometer. MALDI-TOF MS was performed on a Kratos Axima CFR apparatus using ACTH as external standard and α -cyano-4-hydroxycinnamic acid as matrix.

Synthesis of 2-(2-Aminoethoxy)ethyl-2-bromoisobutyrate Hydrobromide (Linker 1). The synthesis of linker 1 is shown in Scheme 1. In a round-bottom flask, 2-(2-aminoethoxy)ethanol (11.0 mL, 110 mmol) and di-*tert*-butyl dicarbonate (21.8 g, 100 mmol) were dissolved in CH₂Cl₂ (100 mL). The resulting mixture was stirred 16 h at room temperature. Then, the mixture was washed three times with 1 M NaHSO₄, three times with saturated NaHCO₃, and once with

Scheme 1. Synthesis Route of 2-(2-Aminoethoxy)ethyl-2-bromoisobutyrate Hydrobromide (Linker 1)

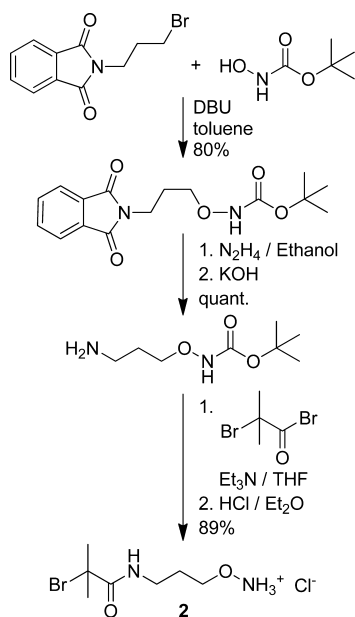


saturated NaCl. After drying on anhydrous MgSO₄, the CH₂Cl₂ layer was evaporated *in vacuo*, giving 2-(*N*-Boc-2-aminoethoxy)ethanol as a colorless oil in 78% yield (15.9 g, 78 mmol). ¹H NMR (300 MHz, CDCl₃): δ 5.28 (bs, 1H), 3.66 (t, 2H), 3.50 (t, 2H), 3.48 (t, 2H), 3.25 (m, 2H), 3.10 (bs, 1H), 1.37 (s, 9H). ¹³C NMR (75.5 MHz, CDCl₃): δ 156.3 (C=O), 79.4 (C(CH₃)₃), 72.3 (CH₂), 70.3 (CH₂), 61.5 (CH₂), 40.4 (CH₂), 28.4 (CH₃).

In the next reaction step, 2-(*N*-Boc-2-aminoethoxy)ethanol (14.3 g, 70 mmol) and pyridine (6.2 mL, 77 mmol) were dissolved in anhydrous CH₂Cl₂ (100 mL), and the solution was cooled on an ice bath. To this solution, 2-bromoisobutyryl bromide (9.5 mL, 77 mmol) was added dropwise while stirring. After addition, the mixture was allowed to reach room temperature and stirred for 30 min. The precipitated pyridinium bromide was filtered off. The filtrate was washed three times with 1 M NaHSO₄, three times with saturated NaHCO₃, and one time with saturated NaCl. After drying on anhydrous MgSO₄, the CH₂Cl₂ layer was evaporated *in vacuo*, giving 2-(*N*-Boc-2-aminoethoxy)ethyl-2-bromoisobutyrate in 91% yield (24.4 g, 69 mmol). The product was a colorless oil which slowly crystallized upon standing. ¹H NMR (300 MHz, CDCl₃): δ 4.93 (bs, 1H), 4.30 (t, 2H), 3.68 (t, 2H), 3.53 (t, 2H), 3.28 (m, 2H), 1.92 (s, 6H), 1.41 (s, 9H). ¹³C NMR (75.5 MHz, CDCl₃): δ 171.8 (C=O), 156.1 (C=O), 79.4 (C(CH₃)₃), 70.3 (CH₂), 68.6 (CH₂), 65.0 (CH₂), 55.7 (C–Br), 40.4 (CH₂), 30.9 (C(CH₃)₂), 28.5 (C(CH₃)₃).

In the last reaction step, 2-(*N*-Boc-2-aminoethoxy)ethyl-2-bromoisobutyrate (24 g, 68 mmol) was dissolved in diethyl ether (200 mL), and HBr (28 mL of a 33% solution in acetic acid) was added dropwise, after which the product precipitated out of solution. The reaction was left at room temperature for 16 h. The resulting white crystals of 2-(2-aminoethoxy)ethyl-2-bromoisobutyrate (1) were harvested by filtration, washed three times with a small volume of diethyl ether, and dried *in vacuo*. Yield: 16.1 g (48 mmol, 71%). ¹H NMR (300 MHz, CDCl₃): δ 7.93 (bs, 3H), 4.39 (t, 2H), 3.89 (t, 2H), 3.81 (t, 2H), 3.32 (m, 2H), 1.94 (s, 6H). ¹³C NMR (75.5 MHz, CDCl₃): δ 171.9 (C=O), 69.0 (CH₂), 66.5 (CH₂), 65.1 (CH₂), 56.0 (C–Br), 40.0 (CH₂), 30.9 (C(CH₃)₂). ESI-MS: calcd for C₈H₁₇NO₃Br [M]⁺ 254.04; found 254.25.

Synthesis of *N*-(3-Aminoxypropyl)-2-bromo-2-methylpropionylamide Hydrochloride (Linker 2). The synthesis of linker 2 is shown in Scheme 2. In a round-bottom flask, *N*-3-bromopropylphthalimide (24.5 g, 91 mmol) and *N*-Boc-hydroxylamine (13.3 g, 100 mmol) were dissolved in toluene (100 mL). The solution was boiled under reflux, and 1,8-diazabicyclo[5.4.0]undec-7-ene (DBU) (15 mL, 100 mmol) was added dropwise. During the addition of DBU the desired product separated as a yellow oil. After stirring for 1 h, the mixture was concentrated *in vacuo*. The residue was redissolved in

Scheme 2. Synthesis Route of *N*-(3-Aminoxypropyl)-2-bromo-2-methylpropionylamide Hydrochloride (Linker 2)

CH_2Cl_2 (200 mL) and washed with 10% citric acid (4×50 mL).³⁷ The organic phase was dried over MgSO_4 and concentrated *in vacuo* to give *N*-(3-(*N*-Boc-aminoxy)propyl)phthalimide as a pale yellow solid in 80% yield (23.5 g, 73 mmol). ^1H NMR (300 MHz, CDCl_3): δ 7.85 (t, 2H), 7.72 (t, 2H), 7.35 (s, 1H), 3.94 (t, 2H), 3.84 (t, 2H), 2.02 (m, 2H), 1.48 (s, 9H). ^{13}C NMR (75.5 MHz, CDCl_3): δ 168.5 (imide $\text{C}=\text{O}$), 157.0 (urethane $\text{C}=\text{O}$), 134.1 (CH), 132.2 (C), 123.3 (CH), 81.8 ($\text{C}(\text{CH}_3)_3$), 74.0 (CH_2), 35.1 (CH_2), 28.3 ($\text{C}(\text{CH}_3)_3$), 27.3 (CH_2).

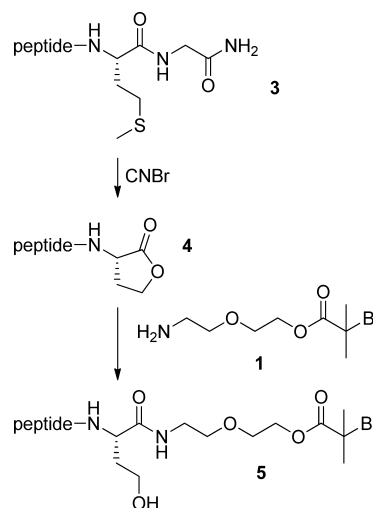
In the next step, *N*-(3-(*N*-Boc-aminoxy)propyl)phthalimide (13 g, 40 mmol) was dissolved in absolute ethanol (50 mL). Hydrazine hydrate (3 mL of an 85% aqueous solution) was added dropwise, and the mixture was boiled under reflux for 2 h. The product separated as its salt with phthalylhydrazide, from which it was liberated by adding KOH (2.5 g dissolved in 20 mL of absolute ethanol). After stirring vigorously for 1 h, the precipitate had turned into a fine white powder, the potassium salt of phthalylhydrazide. The mixture was concentrated *in vacuo*, resuspended in anhydrous CHCl_3 (100 mL) under vigorous stirring for 1 h, and filtered. The solids were washed three times with a small amount of CHCl_3 . The combined filtrates were dried on MgSO_4 and concentrated *in vacuo* to give 3-(*N*-Boc-aminoxy)propylamine as an oil in quantitative yield (8 g, 40 mmol). ^1H NMR (300 MHz, CDCl_3): δ 3.93 (t, 2H), 3.84 (t, 2H), 1.96 (bs, 2H), 1.75 (m, 2H), 1.46 (s, 9H). ^{13}C NMR (75.5 MHz, CDCl_3): δ 157.5 ($\text{C}=\text{O}$), 82.0 ($\text{C}(\text{CH}_3)_3$), 75.0 (CH_2), 39.1 (CH_2), 29.4 (CH_2), 28.4 ($\text{C}(\text{CH}_3)_3$). ESI-MS: calcd for $\text{C}_8\text{H}_{19}\text{N}_2\text{O}_3$ $[\text{M} + \text{H}]^+$: 191.14; found 190.90.

Subsequently, 3-(*N*-Boc-aminoxy)propylamine (6.9 g, 36 mmol) and triethylamine (7.5 mL, 54 mmol) were dissolved in anhydrous THF (70 mL). The mixture was purged with N_2 and cooled on an ice bath, after which 2-bromoisobutyl bromide (6.7 mL, 54 mmol) was added dropwise while stirring. Next, the ice bath was removed, and the mixture was stirred for 1 h at room temperature. The precipitated triethylammonium bromide was filtered off, and the filtrate was concentrated *in vacuo*. The residue was redissolved in EtOAc (300 mL), and this solution was washed with 1 M NaHSO_4 (3×50 mL), 1 M NaHCO_3 (3×50 mL), and saturated NaCl (2×50 mL). The organic layer was dried on MgSO_4 and concentrated *in vacuo* to give *N*-(3-(*N*-Boc-aminoxy)propyl)-2-bromo-2-methylpropionylamide as a yellow oil. A fraction (8 g) of this oil was dissolved in Et_2O (25 mL), and the solution was cooled on ice. HCl gas was bubbled through the solution, upon which a white precipitate of *N*-(3-aminoxypropyl)-2-bromo-2-methylpropionylamide hydrochloride (2) was formed. The product was purified twice by trituration with CH_2Cl_2 and Et_2O at

-20°C . Yield: 4.4 g (16 mmol, 89% over two steps). ^1H NMR (300 MHz, $\text{DMSO}-d_6$): δ 10.92 (bs, 3H), 8.18 (t, 1H), 4.01 (t, 2H), 3.17 (q, 2H), 1.87 (s, 6H), 1.75 (m, 2H). ^{13}C NMR (75.5 MHz, $\text{DMSO}-d_6$): δ 170.8 ($\text{C}=\text{O}$), 72.0 (CH_2), 60.7 ($\text{C}-\text{Br}$), 35.9 (CH_2), 31.1 ($\text{C}(\text{CH}_3)_2$), 27.2 (CH_2). ESI-MS: calcd for $\text{C}_7\text{H}_{16}\text{N}_2\text{O}_2\text{Br}$ $[\text{M}]^+$: 239.04; found 238.95.

Peptide Synthesis. The peptide H-Ser-Gly-Pro-Gln-Gly-Ile-Phe-Gly-Gln-Met-Gly- NH_2 was synthesized by standard Fmoc solid phase peptide synthesis.³⁸ 350 mg of peptide (TFA salt, 0.30 mmol) was obtained, with a purity of >95% (HPLC). MALDI-TOF MS: calcd 1077.23 $[\text{M} + \text{H}]^+$; found 1077.21. The product was used without further purification.

Functionalization of Peptide C-Terminus. To introduce a homoserine lactone functionality at the C-terminus (Scheme 3),^{39–41}

Scheme 3. Functionalization of the Peptide C-Terminus with Linker 1^a

^a"Peptide" indicates the sequence H-Ser-Gly-Pro-Gln-Gly-Ile-Phe-Gly-Gln-.

the peptide 3 (343 mg) was dissolved in 150 mL of N_2 -flushed $\text{CH}_3\text{CN}/\text{H}_2\text{O}/\text{TFA}$ (30/70/1). Under a nitrogen atmosphere, CNBr (12 mL of a 4 M solution in CH_3CN) was added, and the reaction mixture was stirred for 16 h in the dark. The mixture was evaporated to dryness *in vacuo* at 28°C . The lactone-functionalized peptide 4 was then redissolved in $\text{CH}_3\text{CN}/\text{H}_2\text{O}/\text{TFA}$ (30/70/0.1) and lyophilized. The yield after lyophilization was 383 mg. ESI-MS: calcd 973.47 $[\text{M} + \text{H}]^+$; found 973.47.

Linker 1 (3.0 g, 0.9 mmol) was dissolved in CH_2Cl_2 (50 mL) and converted into the free amine by shaking with an equimolar amount of aqueous NaOH (9.0 mL, 1.0 M). The organic layer was dried on MgSO_4 , followed by evaporation of the volatiles. Directly afterward, 1.2 mL of the resulting oil was added to the homoserine lactone-functionalized peptide 4 (325 mg, 0.30 mmol) together with 2-hydroxypyridine (200 μL of a 30 mg/mL solution in DMA). After vigorous stirring for 15 min, the reaction mixture became homogeneous, and it was then stirred for another 15 min. Excess linker and DMA were removed by precipitation of the product in MTBE (250 mL) containing 1% TFA. The resulting peptide macroinitiator 5 was purified by preparative HPLC (SunFire C18 preparative column, gradient: $\text{CH}_3\text{CN}/\text{H}_2\text{O}/\text{TFA}$ 30/70/0.1 to 50/50/0.1, over 15 min) and subsequently lyophilized yielding 294 mg (0.22 mmol) of the TFA salt of the pure peptide macroinitiator 5 as a white powder. ESI-MS: calcd 1226.51 $[\text{M} + \text{H}]^+$; found 1226.30.

ATRP of the C-Terminal Polymer Block. Prior to use, all solvents and liquid reagents were deoxygenated by flushing with nitrogen gas for 15 min. A catalyst stock was prepared by weighing CuCl (12.0 mg, 120 μmol), $\text{CuCl}_2 \cdot 2\text{H}_2\text{O}$ (13.6 mg, 80 μmol), and 2,2'-bipyridyl (bpy) (62.4 mg, 400 μmol) into a 7 mL glass screw-

capped vial equipped with a micro stirring bar. The vial was sealed with a septum and flushed with nitrogen gas for 15 min. Then, CH₃CN (0.6 mL) and H₂O (1.4 mL) were added through the septum, and the vial was held in an ultrasonic bath until all solids had dissolved forming the brown catalytic complex.

OEGMA₃₀₀ monomer (160, 320, or 640 μ L for the aimed pOEGMA block lengths of 4, 8, and 16 kDa, respectively) was charged into an N₂-filled 2 mL septum vial equipped with a stirring bar. Then, 500 μ L of the catalyst stock solution was added, followed by the peptide macroinitiator **5** (40 μ mol, dissolved in a minimal volume of DMSO). Conversion was monitored during the reaction by ¹H NMR of samples diluted in air-saturated D₂O, comparing the integral of the region between 6.3 and 5.6 ppm (2H, H₂C=C) with the integral of the region between 4.5 and 4.0 ppm (2H, C(=O)OCH₂). Furthermore, at several time points samples were taken, which were quenched by diluting in air-saturated DMF, and the evolution of molecular weight was analyzed by GPC.

Azide Substitution of the Living Chain End. When the monomer conversion was above 90%, NaN₃ (80 μ L of an N₂-purged 1 M aqueous solution) was added to the reaction mixture, causing the chloride chain end to be substituted by an azide by means of the copper–bipyridyl catalyst.⁴² Since the azide-functionalized chain end does not reinitiate, further OEGMA polymerization was prevented by this procedure. Azide functionalization also allows conjugation with a fluorescent probe.⁴² The reaction mixture was left for 16 h to ensure complete substitution, after which the polymer was purified by 3 \times 10-fold concentration using a Vivaspin concentrator (MWCO of 2, 5, or 10 kDa for pOEGMA block lengths of 4, 8, and 16 kDa, respectively), each time diluting with 10 mM phosphate buffer, pH 7.0. The molecular weight of the polymers was determined by ¹H NMR based upon the ratio of the integrals of the aromatic phenylalanine protons and methoxy protons from pOEGMA.

Chain Extension Experiment. A sample (10 μ L) of the peptide-pOEGMA₄ kDa polymer solution was taken before and after the substitution with NaN₃. The samples were diluted with CH₃CN (300 μ L) and H₂O (700 μ L) in a 2 mL septum vial. Subsequently, NIPAm (18 mg for target M_n = 32 kDa), CuBr (1.8 mg), and CuBr₂ (1.9 mg) were added. The vial was placed in an ice bath and purged with N₂ for 15 min. Then, the reaction was started by adding Me₆TREN (50 μ L of a 0.4 M N₂-purged aqueous solution).

Functionalization of the N-Terminus. To introduce an aldehyde functionality at the peptide's N-terminus (Scheme 4), 60 μ L of a 1 M

fluorescamine: 1 μ L of sample was diluted in 1 mL of 50 mM phosphate buffer of pH 8.9. Subsequently, to 150 μ L of this solution was added 50 μ L of a freshly prepared 0.3 mg/mL solution of fluorescamine in dry acetone. The fluorescence was recorded (λ_{ex} = 380 nm, λ_{em} = 460 nm) in a FluoStar Optima well plate reader (BMG Labtech), and it was verified that after reaction with NaIO₄ no fluorescence was observable. To test for the development of an aldehyde functionality, a drop of sample was placed on a TLC plate and allowed to dry. The plate was then sprayed with a solution of 2.0 g of 2,4-dinitrophenylhydrazine and 4.0 mL of concentrated sulfuric acid in 100 mL of methanol. The development of a yellow spot indicated the formation of an aldehyde **7**.

After reaction with NaIO₄, the solution was diluted to 10 mL in 50 mM anilinium acetate buffer, pH 4.6.⁴³ Linker **2** (110 mg, 0.4 mmol) was added, and the reaction was allowed to proceed for 16 h at room temperature under nitrogen.

The polymer solution was again concentrated (4 \times 10-fold) using a Vivaspin concentrator (MWCO 2, 5, and 10 kDa), exchanging the buffer solution for demineralized water. The efficiency of coupling was assessed by ¹H NMR spectroscopy, comparing the integral of the proton on the oxime carbon of **8**, at 7.7 ppm, with the integral of the aromatic phenylalanine protons.

ATRP of the N-Terminal Polymer Block. Following a published procedure,⁴⁴ CuBr (1.8 mg), CuBr₂ (1.9 mg), and *N*-isopropylacrylamide (NIPAm) (320 or 640 mg for a target M_n of 16 and 32 kDa, respectively) were weighed into a 2 mL septum vial. A stirring bar, CH₃CN (250 μ L) and the N-terminally functionalized peptide-pOEGMA **8** (1 mL of a 20 mM aqueous solution) were added. For the target M_n of 32 kDa, it was necessary to add 1 extra mL of H₂O and 250 μ L of CH₃CN to dissolve the NIPAm. The vial was placed in an ice bath, and the solution was purged with N₂ for 15 min. Then, the reaction was started by adding 50 μ L of a 0.4 M N₂-purged aqueous solution of Me₆TREN. During the reaction, the conversion was monitored by ¹H NMR of samples diluted in air-saturated D₂O. Furthermore, at several time points samples were taken, which were quenched by diluting in air-saturated DMF and analyzed by gel permeation chromatography (GPC). The final polymers were dialyzed against water and lyophilized.

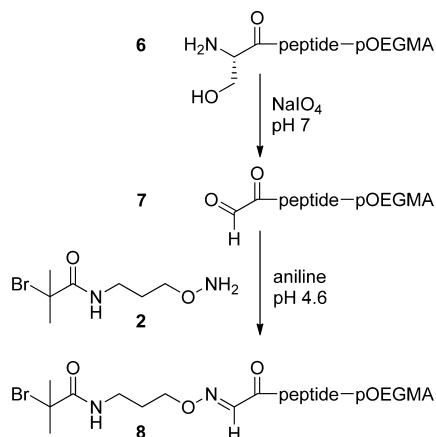
Polymer Characterization. CPs of the polymers were determined using a Shimadzu UV-2450 spectrophotometer with temperature control by a Peltier element. The temperature of polymer solutions (1 mg/mL) was raised from 20 to 50 at 1 $^{\circ}$ C/min, and the CP was defined as the onset of the curve of extinction at 650 nm vs temperature.

For the determination of the critical micelle concentration (cmc), the different block copolymers were dissolved in water in concentrations ranging from 1 μ g/mL to 1 mg/mL. Then, 5 μ L of a 1.8×10^{-4} M solution of pyrene in acetone was added to 1 mL of polymer solution. The micelles were formed by rapidly heating the solutions to 40 $^{\circ}$ C. After incubation for 16 h at this temperature, pyrene fluorescence was measured using a Horiba Fluorolog fluorometer at 37 $^{\circ}$ C. The emission was measured at 390 nm using excitation wavelengths of 333 and 338 nm. The ratio I_{338}/I_{333} was plotted against the logarithmic polymer concentration to determine the cmc.⁴⁵

Formation of Micelles. Micelles were formed using a heat shock procedure according to Neradovic et al.⁴⁶ by heating 900 μ L of 0.22 μ M-filtered water or phosphate buffered saline (PBS) to 40 $^{\circ}$ C and then adding 100 μ L of a 1 mg/mL solution (at room temperature) of the polymer. The mixture was kept at 40 $^{\circ}$ C for 5 min before being equilibrated at 37 $^{\circ}$ C. Particle size was measured at 37 $^{\circ}$ C by dynamic light scattering (DLS) on an ALV CGS-3 system at a 90 $^{\circ}$ scattering angle.

Fluorescent Labeling of the Polymer. To 1 mL of a 10 mg/mL aqueous solution of pNIPAm₃₂ kDa-peptide-pOEGMA₈ kDa was added 3 μ L of 0.1 mM copper(II) sulfate, 15 μ L of 1 mg/mL Alexa Fluor 555 functionalized with an alkyne moiety in DMSO (Invitrogen), and 30 μ L of 0.1 M ascorbic acid. The reaction mixture was purged with N₂ and stirred for 16 h in an N₂ atmosphere. The product was purified using a Vivaspin membrane with a molecular weight cutoff of 10 kDa

Scheme 4. Functionalization of the Peptide N-Terminus with Linker 2^a



^a“Peptide” indicates the sequence -Gly-Pro-Gln-Gly-Ile-Phe-Gly-Gln-.

aqueous solution of NaIO₄ was added to the solution of peptide-pOEGMA **6** (40 mM in 1 mL of 10 mM phosphate buffer pH 7.4). Before and 15 min after addition, samples were taken for analysis. Disappearance of the amino group was confirmed by reaction with

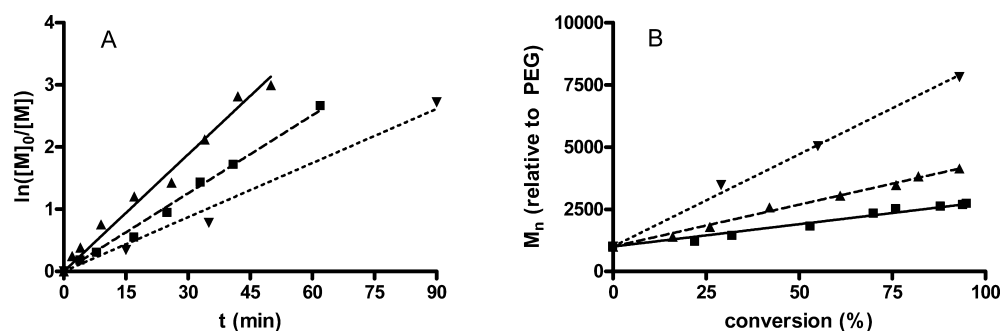


Figure 1. ATRP of OEGMA₃₀₀ using the synthesized peptide macroinitiator **5**: (A) semilogarithmic plot of monomer concentration $[M]$ (as $[M]_0/[M]$) in time; (B) number-averaged molecular weight M_n (determined by GPC) as a function of monomer conversion. (▲) target $M_n = 4$ kDa, (■) target $M_n = 8$ kDa, (▼) target $M_n = 16$ kDa.

(3×10 -fold concentration, each time diluting with H₂O). Labeling of the polymer was verified by GPC using a MesoPore column (Polymer Laboratories) at 40 °C, with DMF + 10 mM LiCl as the eluent and both refractive index (RI) and fluorescence detection.

Enzymatic Degradation. Metalloprotease (type IV collagenase) from *C. Histolyticum* was used as a model for MMP-2 and MMP-9. This enzyme has very similar substrate specificity and is commonly used as a readily available alternative to MMP-2 and MMP-9.^{3,4} The activity of the enzyme was determined colorimetrically by the *N*-(3-[2-furyl]acryloyl)-Leu-Gly-Pro-Ala (FALGPA) cleavage assay according to the manufacturer's protocol (Sigma-Aldrich) and was found to be 2300 units/mg (1 unit represents an activity of 1000 pmol substrate/min). The fluorescently labeled polymer was diluted to a final polymer concentration of 10 μ M in 0.22 μ M-filtered HEPES buffer of pH 7.4 containing 20 mM CaCl₂ and 100 mM NaCl at room temperature. Then, a solution (0.22 μ M-filtered) of 1000 units/mL of type IV collagenase in the same buffer was added to a final enzyme concentration of 10 units/mL, and the solution was incubated for 24 h at room temperature. GPC analysis with fluorescence detection was performed before and after the degradation (MesoPore column at 40 °C, DMF + 10 mM LiCl).

For the enzymatic degradation of intact micelles, micelles were formed by the above-mentioned heat shock procedure in HEPES buffer after which they were incubated with collagenase at 37 °C. At $t = 0$ and after 24 h a sample was diluted 10-fold in preheated buffer and injected into a Nanosight LM10-HS laser light scattering/fluorescence microscopy system, preheated to 37 °C. Using the Nanoparticle Tracking Analysis (NTA) software, images were taken to visualize the micelles and to determine whether their fluorescently labeled coronas had been cleaved off.

RESULTS AND DISCUSSION

Functionalization of the Peptide C-Terminus. To activate selectively the C-terminus of the peptide **3**, a reactive homoserine lactone was introduced by reaction of the penultimate methionine residue with CNBr (Scheme 3). This method, which is commonly used for the cleavage of recombinantly produced peptides from a carrier fusion protein,⁴¹ allows for rapid and selective modification of the C-terminus of any peptide having methionine as the penultimate residue on the C-terminus.^{39,40} The only requirement is the absence of internal methionine residues, which would lead to cleavage of the peptide. However, since methionine is one of the least occurring amino acids in proteins,⁴⁷ this requirement is often easy to meet, making methionine a favorable target for site-specific peptide conjugation. The main advantage over other methodologies that target the C-terminus, e.g., carbodiimide-based coupling,⁴⁸ is that CNBr functionalization is compatible with the presence of glutamate and aspartate residues. After reaction of the

peptide with excess cyanogen bromide, 95% of the peptide was converted into the lactone form **4** (HPLC). Apart from the small amount of unreacted peptide, there was also a trace impurity (<5%) of peptide in which the methionine residue had been oxidized to methionine sulfoxide, which renders it insensitive to lactonization with CNBr. The lactonized peptide was used without purification, as the main impurities are not reactive in the step of coupling the linker and could be removed after that step.

Linker **1**, which consists of a primary amine on one side and an efficient 2-bromoisobutyrate ATRP initiator on the other side, was synthesized in good yield and coupled to the peptide (Scheme 3). To catalyze aminolysis of the lactone, 10 mol % of 2-hydroxypyridine was added.⁴⁹ Nonreacted linker was easily removed after the reaction with the peptide, by selective precipitation, allowing the use of a large excess of linker. This yields a very short reaction time and negligible inter- and intramolecular reaction with the N-terminal amine. HPLC showed that after 15 min ~95% of the peptide lactone had reacted. After preparative HPLC, the peptide macroinitiator **5** was obtained in 73% yield.

ATRP of OEGMA₃₀₀ Starting from the C-Terminus. The polymerization of OEGMA₃₀₀ yields brush-shaped PEG-like polymers which are frequently used as hydrophilic polymers in the biomedical field since they possess several of the advantages over the well-known PEG, e.g., the fact that they are polymerizable by controlled radical polymerization.^{50–53} Furthermore, because of the hydrophilic oligo(ethylene glycol) side chains and the hydrophobic polymethacrylate backbone, pOEGMA's have thermosensitive properties, which can be tuned by the average length of the oligo(ethylene glycol) side chains.⁵³ By using a monomer with an average molar mass of 300 Da, it was ensured that the resulting polymer has a lower critical solution temperature (LCST) above 68 °C,⁵² meaning that the polymer is water-soluble at physiological temperature.

For the polymerization, a mild method compatible with the peptide was developed. Generally, ATRP of OEGMA is performed in alcohols at elevated temperatures,^{51,53} but it can also be performed in aqueous media at room temperature.⁵⁰ By addition of Cu(II) and a small amount of CH₃CN, a pseudoligand for Cu(I), the problem of disproportionation commonly faced in aqueous ATRP was eliminated.^{54,55} Furthermore, by varying the percentage CH₃CN (and consequently the polarity of the solvent), it is possible to adjust the rate of the reaction.⁵⁶ In the present study, a fast reaction with sufficient control at ambient temperature was obtained in a CH₃CN/H₂O 3/7 (v/v) solvent mixture, which is

a good solvent for the peptide used in the present study. As can be seen in Figure 1A, the residual monomer concentration decreased exponentially in time during the course of the reaction. This indicates a constant concentration of propagating radicals during the polymerization and thus effective and instantaneous initiation as well as negligible termination/combination; both are prerequisites for a controlled/living polymerization.⁵⁷ Furthermore, the number-averaged molecular weight (M_n) evolved linearly with conversion (Figure 1B), indicating a low rate of termination. These observations indicate that the polymerization was controlled.

¹H NMR spectroscopy of the polymers after purification showed that the pOEGMA blocks had M_n values of 3.2, 7.1, and 15.7 kDa, which are in good agreement with the expected molecular weights.

Inactivation of the Living Chain-End. One feature of ATRP is that the living chain end of the resulting polymers is able to reinitiate another polymerization, and this feature has been frequently used for the synthesis of block copolymers.^{58–61} To be able to grow a different polymer chain from the other (N-) terminus of the peptide, however, it must be ensured that the already existing polymer chain on the C-terminus will not reinitiate in a subsequent ATRP. Therefore, the chloride on the living chain end was substituted by azide using a recently developed copper-catalyzed azide substitution reaction.⁴² The introduced azide functionality also renders it possible to attach in a later stage a fluorescent probe or a targeting ligand using azide/alkyne “click” chemistry.^{42,62–68} Figure 2 shows that the substitution with NaN₃, as expected,

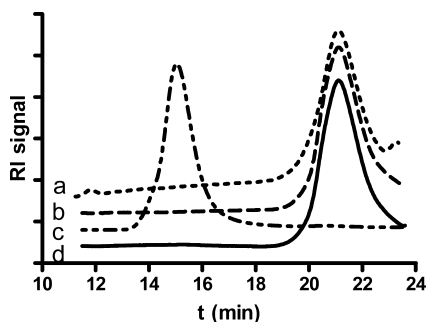


Figure 2. GPC chromatograms of peptide-pOEGMA₄ kDa hybrid polymer: (a) before substitution of the chloride chain end with azide, (b) after substitution with azide, (c) non-azidated polymer after chain extension with NIPAm, and (d) azidated polymer after chain extension.

did not alter the molecular weight (distribution) of the polymer as determined by GPC analysis. Furthermore, the non-substituted pOEGMA chain could be extended with a pNIPAm block, which provides indeed evidence for the living character of the ATRP of OEGMA on the peptide macroinitiator. On the other hand, after substitution with NaN₃, pOEGMA was not able to reinitiate an ATRP (Figure 2). This demonstrates quantitative substitution of the Cl end-group by azide.

Functionalization of the N-Terminus. Introduction of an aldehyde functionality into a peptide by mild periodate oxidation of an N-terminal serine residue followed by coupling of an O-substituted hydroxylamine is a highly selective, efficient, and well-known bioconjugation reaction.^{69–71} The formed oxime bonds are acid-sensitive but stable at physiological pH.⁷² The peptide-pOEGMA conjugates **6** were subjected to the above-mentioned oxidation with NaIO₄ in

phosphate buffer (pH 7.4) (Scheme 4). Reaction with fluorescamine indicated disappearance of the amine functionality of the N-terminal serine. Furthermore, a sample taken from the reaction mixture developed a yellow color after addition of 2,4-dinitrophenylhydrazine, indicating the formation of an aldehyde.

For further functionalization of the aldehyde-modified terminus of the peptide **7**, linker **2** was developed, carrying on one side a reactive aminooxy group and on the other side an ATRP initiator functionality. Linker **2** was synthesized as shown in Scheme 2. Subsequently, the aldehyde-functionalized peptide-pOEGMA conjugates **7** were incubated with linker **2** in 50 mM anilinium acetate buffer (pH 4.6) (Scheme 4), a known catalyst for the formation of oxime bonds.^{71,73,74} After coupling of linker **2**, the appearance of a peak at δ 7.7 ppm in ¹H NMR (in D₂O) indicated the formation of an oxime bond (Figure 3).

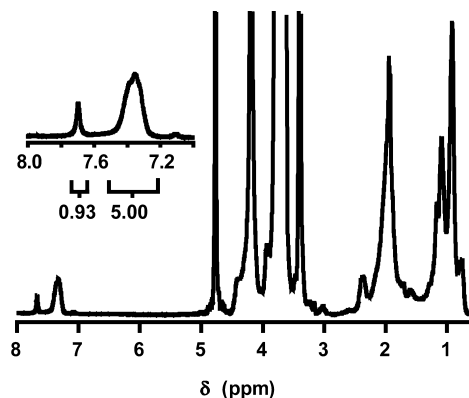


Figure 3. NMR spectrum of linker 2-peptide-pOEGMA₄ kDa showing the peak of the proton on the oxime carbon at δ 7.7 ppm and the aromatic phenylalanine protons at δ 7.3–7.4 ppm.

The degree of functionalization was >90% based on comparison of the integral of this peak with the integral of the peak of the phenyl protons of phenylalanine (δ 7.5–7.2 ppm).

ATRP of the N-Terminal Block. NIPAm was polymerized from the modified N-terminus of the peptide-pOEGMA conjugates **8** by ATRP in a CH₃CN/H₂O 3/7 (v/v) mixture at 0 °C.^{44,56,75} The reaction was well controlled as evidenced by an exponential decrease of the residual monomer concentration (Figure 4A) and a linear evolution of M_n with conversion, for both target molecular weights of the pNIPAm block (Figure 4B). This indicates successful growth of the pNIPAm block, starting from the peptide-pOEGMA macroinitiator **8**.

Characterization of the Polymers and Their Micelles. The structure of the final polymers is depicted in Figure 5. ¹H NMR analysis showed that the pNIPAm blocks had M_n values in good agreement with the expected molecular weight, based on the comparison of the integrals of the pOEGMA methoxy protons and pNIPAm methyl protons (Table 1). Furthermore, the dispersity of the synthesized polymers was low, with only polymers containing a pOEGMA₁₆ kDa block having a somewhat broader size distribution.

The cmc of the polymers dissolved in water was equal for all polymers. In general, a decrease in cmc with increasing hydrophobic block length would be expected, as well as an increase in cmc with increasing hydrophilic block length.^{76,77} Our observation of equal cmc's might be related to the fact that

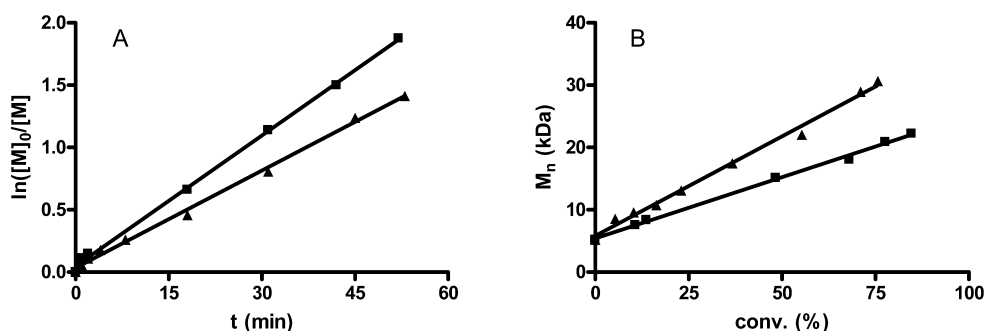


Figure 4. Kinetics of the polymerization of NIPAm onto peptide-pOEGMA₈ kDa: (A) semilogarithmic plot of monomer concentration $[M]$ (as $[M]_0/[M]$) in time; (B) number-averaged molecular weight M_n as a function of monomer conversion. (■) Target $M_n = 16$ kDa, (▲) target $M_n = 32$ kDa.

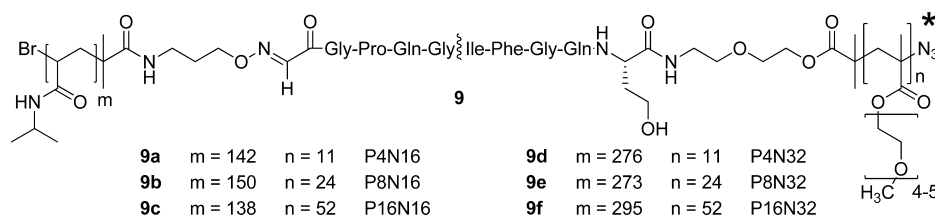


Figure 5. Structure of the final biohybrid triblock polymers. The wavy line indicates the bond that is cleavable by MMPs. The asterisk indicates the attachment point of the fluorescent probe in the P8N32 polymer.

Table 1. Properties of the Polymers and Their Micelles

abbrev ^a	polymers			micelles				
	M_n^b (kDa)		D^c	CP ^d (°C)		cmc ^e (mg/mL)	R_h^f (nm) (PDI)	
	pOEGMA	pNIPAm		H ₂ O	PBS		H ₂ O	PBS
P4	3.2		1.20					
P4N16	3.2	16.0	1.25	35.5 ± 0.1	33.0 ± 0.2	0.03 ± 0.01	29 ± 1 (0.1)	173 ± 2 (0.1)
P4N32	3.2	31.2	1.24	34.5 ± 0.1	32.0 ± 0.2	0.03 ± 0.01	28 ± 1 (0.1)	1756 ± 138 (0.5)
P8	7.1		1.32					
P8N16	7.1	17.0	1.24	35.6 ± 0.1	33.1 ± 0.1	0.03 ± 0.01	27 ± 1 (0.1)	35 ± 1 (0.1)
P8N32	7.1	30.8	1.26	34.8 ± 0.1	32.2 ± 0.1	0.03 ± 0.01	27 ± 1 (0.1)	123 ± 2 (0.1)
P16	15.7		1.45					
P16N16	15.7	15.6	1.52	36.0 ± 0.1	33.2 ± 0.1	0.03 ± 0.01	23 ± 1 (0.2)	24 ± 1 (0.1)
P16N32	15.7	33.3	1.64	34.7 ± 0.1	32.1 ± 0.1	0.03 ± 0.01	22 ± 1 (0.1)	33 ± 1 (0.1)

^aP denotes the aimed size of the pOEGMA block and N that of the pNIPAm block (both in kDa). ^bNumber-averaged molecular weight based on ¹H NMR. ^cDispersity from GPC. ^dCloud point. ^eCritical micelle concentration. ^fZ-averaged hydrodynamic radius (R_h) from DLS.

the found cmc values are very low, permitting an influence from the fluorescent probe (pyrene) itself.⁷⁸

The CPs of the polymers dissolved in water were slightly higher than the published value of 32 °C of pNIPAm homopolymer in water due to the presence of large hydrophilic polymer blocks.^{79,80}

Consequently, Table 1 shows that the CP in water increased from 35.5 to 36.0 °C with increasing the pOEGMA block length from 4 to 16 kDa (P4N16 vs P16N16) and decreased with increasing the pNIPAm length from 16 to 32 kDa. For self-assembly into micelles, a heat-shock protocol was used as it has been described that instantaneous heating of aqueous polymer solutions to above their CP leads to well-defined micelles.⁴⁶ Following this procedure, all polymers formed micelles with a size of 22–29 nm in water and narrow size distributions, which is favorable for drug delivery purposes.⁸¹

Increasing the pOEGMA length from 4 to 16 kDa leads to a larger surface area that is needed per polymer chain and thus to less polymer chains fitting in one micelle:⁴⁴ consequently, the size of the micelles decreased from 29 nm (P4N16) to 23 nm

(P16N16). Interestingly, increasing the pNIPAm block from 16 to 32 kDa did not lead to an increase of the micellar size, but to a small decrease, e.g., 29 nm (P4N16) vs 28 nm (P4N32). This effect has been observed before and has been attributed to greater hydrophobicity of the longer pNIPAm blocks, leading to more extensive dehydration of the micellar cores.^{46,82}

The difference in CP and size between micelles dispersed in water and PBS is also striking. The salting-out effect of PBS reduced the CPs by 2–3 °C, to values (32–33 °C) that are well below physiological temperature and thus compatible with drug delivery applications. Furthermore, PBS also led to a higher observed Z-averaged size. PEG is known to partially dehydrate upon addition of salt,^{46,83,84} and the same behavior may be expected for pOEGMA. This partial dehydration may lead to the formation of larger particles due to a change in the ratio between the hydrodynamic volumes of the hydrophilic and hydrophobic blocks. For large pOEGMA blocks and/or small pNIPAm blocks, the hydrophilic/hydrophobic ratio in buffer is still enough to form small micelles (P8N16, P16N16, and P16N32); for smaller pOEGMA blocks, the increase in size was

more pronounced. For the P4N32 polymer, the (decreased) hydrodynamic volume of the pOEGMA blocks in buffer was not enough anymore to support stable nanoparticles, and aggregation resulted.

Enzymatic Degradation. The peptide separating the hydrophilic micelle corona from the thermosensitive micelle core has been designed to be cleaved by MMP-2 and MMP-9, as these enzymes are upregulated in diseased tissues (e.g., in cancer and rheumatoid arthritis). For this reason, MMP-2/MMP-9 substrates have previously been utilized as building blocks of tissue-specific drug delivery systems.^{85–90}

To verify that the peptide could still be cleaved by metalloproteases after growing the two polymer blocks on its N- and C-termini, the P8N32 block copolymer was fluorescently labeled at the end of its hydrophilic block. Alkyne-functionalized Alexa Fluor 555 was coupled (“clicked”) to the azide-functionalized chain end by Cu(I)-catalyzed azide–alkyne cycloaddition. A label to polymer molar ratio of 1:10 was used in order to minimize any effects of the label on micelle formation. As shown in Figure 6, the polymer was successfully labeled with Alexa Fluor 555 by this procedure.

Subsequently, the polymer was incubated with collagenase for 24 h at room temperature. The cleaved polymer was then

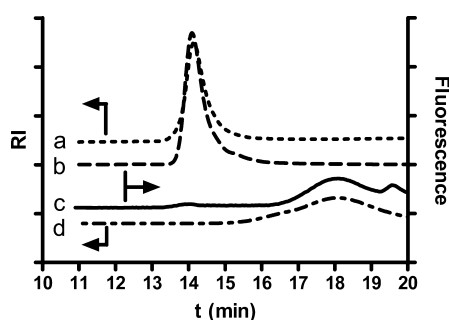


Figure 6. GPC traces of the fluorescently labeled polymer: (a) RI signal after labeling, (b) fluorescence signal ($\lambda_{\text{ex}} = 555$ nm, $\lambda_{\text{em}} = 585$ nm) after labeling, (c) fluorescence signal after enzymatic cleavage. For comparison, (d) shows the RI signal of peptide-pOEGMA₈ kDa.

analyzed by GPC with fluorescence detection. It is well-known that pNIPAm (co)polymers elute in GPC at retention times corresponding to much higher molecular weights than expected, probably due to very persistent interchain hydrogen bonds.^{91,92} This feature was exploited for the demonstration of cleavage of the peptide–polymer conjugate by collagenase. When a column with a narrow separation range was used, the fluorescently labeled intact polymer elutes in the void volume (at 14 min, Figure 6), whereas the fluorescently labeled pOEGMA that is cleaved off elutes much later (at 18 min, the same retention time as peptide-pOEGMA₈ kDa). Since the pNIPAm is unlabeled after cleavage, it is invisible using fluorescence detection. Thus, this method leads to a good separation of the uncleaved polymer and the cleaved-off hydrophilic blocks, while preventing interference from the cleaved thermosensitive blocks which coelute with the uncleaved polymer but are invisible using fluorescence detection.

To visualize the enzymatic degradation of the particles, micelles were formed by heat-shocking the fluorescently labeled polymer. Images of the solution were taken using a preheated Nanosight LM10-HS microscopy system which allows visualization of the nanoparticles by either their scattering of laser

light or by their fluorescence. Images were obtained in both laser scattering and fluorescence mode directly before addition of the enzyme and after 24 h incubation at 37 °C (Figure 7). As can be seen in Figure 7C, particles are still present after degradation, but their fluorescence has vanished into the

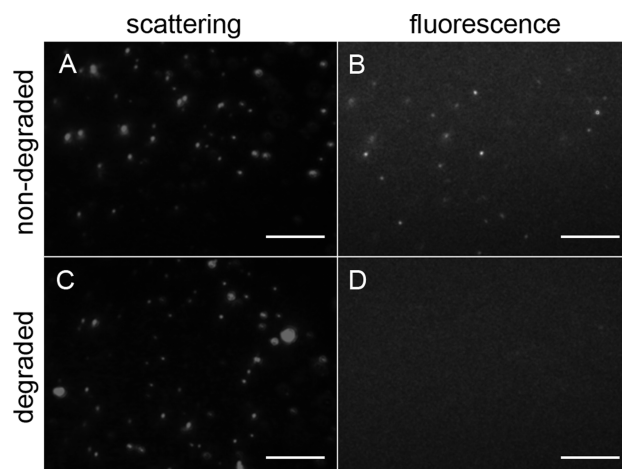


Figure 7. Images of the micellar dispersion of fluorescently labeled P8N32 polymer, taken using a Nanosight system before (A and B) and after (C and D) enzymatic cleavage in HEPES buffer. (A) and (C) were recorded in scattering mode and (B) and (D) in fluorescence mode ($\lambda_{\text{ex}} = 532$ nm, $\lambda_{\text{em}} > 565$ nm), keeping the camera gain settings constant. Scale bars correspond to 10 μm ; however, the apparent size of the micelles in these images reflects their scattering intensity rather than their actual size.

background noise (Figure 7D), indicating that the fluorescent and highly mobile hydrophilic pOEGMA chains have been cleaved off by the enzyme. On the basis of these findings, it can be expected that when these micelles are used for drug delivery to tumors or inflamed tissues, their “stealth” corona will be cleaved off at the target site of action. We hypothesize that this “shedding” of the corona will impede further circulation of the micelles and facilitate cellular uptake.

CONCLUSION

We have demonstrated a suitable approach to grow two different polymer chains from a native peptide by ATRP, using two orthogonal methods to couple ATRP initiators to the N- and C-terminus. Furthermore, in this work a mild method is presented to inactivate the first living ATRP chain end, allowing the same polymerization chemistry for both polymerizations. Both polymerizations were well controlled, leading to a well-defined end product with control over the desired polymer block lengths.

Above the cloud point of one of the blocks, the polymers self-assembled into micelles. The micelles have been shown to “shed” the hydrophilic polymer blocks on their outside by the action of collagenase, a model for diseased tissue-specific matrix metalloproteases. Thus, the technology presented herein offers new possibilities for enzyme-triggered drug delivery.

AUTHOR INFORMATION

Corresponding Author

*E-mail: w.e.hennink@uu.nl

■ REFERENCES

- (1) Ruiz-Hitzky, E.; Darder, M.; Aranda, P.; Ariga, K. *Adv. Mater.* **2010**, *3*, 323–336.
- (2) Venkatesh, S.; Byrne, M. E.; Peppas, N. A.; Hilt, J. Z. *Expert Opin. Drug Delivery* **2005**, *6*, 1085–1096.
- (3) Tsurkan, M. V.; Chwalek, K.; Levental, K. R.; Freudenberg, U.; Werner, C. *Macromol. Rapid Commun.* **2010**, *17*, 1529–1533.
- (4) Seliktar, D.; Zisch, A. H.; Lutolf, M. P.; Wrana, J. L.; Hubbell, J. A. *J. Biomed. Mater. Res., Part A* **2004**, *4*, 704–716.
- (5) Fuks, G.; Mayap Talom, R.; Gauffre, F. *Chem. Soc. Rev.* **2011**, *5*, 2475–2493.
- (6) Xun, W.; Wu, D. Q.; Li, Z. Y.; Wang, H. Y.; Huang, F. W.; Cheng, S. X.; Zhang, X. Z.; Zhuo, R. X. *Macromol. Biosci.* **2009**, *12*, 1219–1226.
- (7) Habraken, G. J.; Peeters, M.; Thornton, P. D.; Koning, C. E.; Heise, A. *Biomacromolecules* **2011**, *12*, 3761–3769.
- (8) Oerlemans, C.; Bult, W.; Bos, M.; Storm, G.; Nijssen, J. F. W.; Hennink, W. E. *Pharm. Res.* **2010**, *27*, 2569–2589.
- (9) Glinel, K.; Jonas, A. M.; Jouenne, T.; Leprince, J.; Galas, L.; Huck, W. T. *Bioconjugate Chem.* **2009**, *1*, 71–77.
- (10) Ku, T.; Chien, M.; Thompson, M. P.; Sinkovits, R. S.; Olson, N. H.; Baker, T. S.; Gianneschi, N. C. *J. Am. Chem. Soc.* **2011**, *22*, 8392–8395.
- (11) Bencherif, S. A.; Gao, H.; Srinivasan, A.; Siegwart, D. J.; Hollinger, J. O.; Washburn, N. R.; Matyjaszewski, K. *Biomacromolecules* **2009**, *7*, 1795–1803.
- (12) Katayama, Y.; Sonoda, T.; Maeda, M. *Macromolecules* **2001**, *24*, 8569–8573.
- (13) Zhu, B.; Lu, D.; Ge, J.; Liu, Z. *Acta Biomater.* **2011**, *5*, 2131–2138.
- (14) Broyer, R. M.; Quaker, G. M.; Maynard, H. D. *J. Am. Chem. Soc.* **2007**, *3*, 1041–1047.
- (15) Pintauer, T.; Matyjaszewski, K. *Chem. Soc. Rev.* **2008**, *6*, 1087–1097.
- (16) Fristrup, C. J.; Jankova, K.; Hvilsted, S. *Soft Matter* **2009**, *23*, 4623–4634.
- (17) Min, K.; Matyjaszewski, K. *Cent. Eur. J. Chem.* **2009**, *4*, 657–674.
- (18) Boyer, C.; Bulmus, V.; Davis, T. P.; Admiral, V.; Liu, J.; Perrier, S. *Chem. Rev.* **2009**, *11*, 5402–5436.
- (19) Gregory, A.; Stenzel, M. H. *Expert Opin. Drug Delivery* **2011**, *2*, 237–269.
- (20) Stenzel, M. H. *Chem. Commun. (Cambridge, U. K.)* **2008**, *30*, 3486–3503.
- (21) Studer, A.; Schulte, T. *Chem. Rec.* **2005**, *1*, 27–35.
- (22) Brinks, M. K.; Studer, A. *Macromol. Rapid Commun.* **2009**, *13*, 1043–1057.
- (23) Bertin, D.; Gimes, D.; Marque, S. R. A.; Tordo, P. *Chem. Soc. Rev.* **2011**, *5*, 2189–2198.
- (24) Braunecker, W. A.; Matyjaszewski, K. *Prog. Polym. Sci.* **2007**, *1*, 93–146.
- (25) Grover, G. N.; Maynard, H. D. *Curr. Opin. Chem. Biol.* **2010**, *6*, 818–827.
- (26) Topp, M. D. C.; Dijkstra, P. J.; Talsma, H.; Feijen, J. *Macromolecules* **1997**, *30*, 8518–8520.
- (27) Neradovic, D.; van Nostrum, C. F.; Hennink, W. E. *Macromolecules* **2001**, *34*, 7589–7591.
- (28) Netzel-Arnett, S.; Sang, Q. X.; Moore, W. G.; Navre, M.; Birkedal-Hansen, H.; Van Wart, H. E. *Biochemistry* **1993**, *25*, 6427–6432.
- (29) Benassi, M. S.; Gamberi, G.; Magagnoli, G.; Molendini, L.; Ragazzini, P.; Merli, M.; Chiesa, F.; Ballardelli, A.; Manfrini, M.; Bertoni, F.; Mercuri, M.; Picci, P. *Ann. Oncol.* **2001**, *1*, 75–80.
- (30) Raithatha, S. A.; Muzik, H.; Muzik, H.; Rewcastle, N. B.; Johnston, R. N.; Edwards, D. R.; Forsyth, P. A. *Neuro-Oncology (Cary, NC, U. S.)* **2000**, *3*, 145–150.
- (31) Kevorkian, L.; Young, D. A.; Darrah, C.; Donell, S. T.; Shepstone, L.; Porter, S.; Brockbank, S. M.; Edwards, D. R.; Parker, A. E.; Clark, I. M. *Arthritis Rheum.* **2004**, *1*, 131–141.
- (32) Maeda, H.; Wu, J.; Sawa, T.; Matsumura, Y.; Hori, K. *J. Controlled Release* **2000**, *1–2*, 271–284.
- (33) Khorsand Sourkahi, B.; Cunningham, A.; Zhang, Q.; Oh, J. K. *Biomacromolecules* **2011**.
- (34) Habraken, G. J. M.; Koning, C. E.; Heise, A. *J. Polym. Sci., Part A: Polym. Chem.* **2009**, *24*, 6883–6893.
- (35) Sun, P.; Zhang, Y.; Shi, L.; Gan, Z. *Macromol. Biosci.* **2010**, *6*, 621–631.
- (36) Ciampolini, M.; Nardi, N. *Inorg. Chem.* **1966**, *1*, 41–44.
- (37) Salisbury, C. M.; Maly, D. J.; Ellman, J. A. *J. Am. Chem. Soc.* **2002**, *50*, 14868–14870.
- (38) Chan, W. C.; White, P. D., Eds.; *Fmoc Solid Phase Peptide Synthesis: A Practical Approach*; Oxford University Press: New York, 2000.
- (39) Marcus, J. H. *Anal. Biochem.* **1975**, *2*, 583–589.
- (40) Horn, M. J.; Laursen, R. A. *FEBS Lett.* **1973**, *3*, 285–288.
- (41) LaVallie, E. R.; McCoy, J. M.; Smith, D. B.; Riggs, P. *Enzymatic and Chemical Cleavage of Fusion Proteins. In Current Protocols in Molecular Biology*; John Wiley & Sons, Inc.: New York, 2001.
- (42) de Graaf, A. J.; Mastrobattista, E.; Van Nostrum, C. F.; Rijkers, D. T. S.; Hennink, W. E.; Vermonden, T. *Chem. Commun. (Cambridge, U. K.)* **2011**, *24*, 6972–6974.
- (43) Dirksen, A.; Dirksen, S.; Hackeng, T. M.; Dawson, P. E. *J. Am. Chem. Soc.* **2006**, *49*, 15602–15603.
- (44) de Graaf, A. J.; Boere, K. W. M.; Kemmink, J.; Fokink, R. G.; van Nostrum, C. F.; Rijkers, D. T. S.; van, d. G.; Wienk, H.; Baldus, M.; Mastrobattista, E.; Vermonden, T.; Hennink, W. E. *Langmuir* **2011**, *16*, 9843–9848.
- (45) Wilhelm, M.; Zhao, C. L.; Wang, Y.; Xu, R.; Winnik, M. A.; Mura, J. L.; Riess, G.; Croucher, M. D. *Macromolecules* **1991**, *5*, 1033–1040.
- (46) Neradovic, D.; Soga, O.; Van Nostrum, C. F.; Hennink, W. E. *Biomaterials* **2004**, *12*, 2409–2418.
- (47) Wu, G.; Ott, T. L.; Knabe, D. A.; Bazer, F. W. *J. Nutr.* **1999**, *5*, 1031–1038.
- (48) Valeur, E.; Bradley, M. *Chem. Soc. Rev.* **2009**, *2*, 606–631.
- (49) Openshaw, H. T.; Whittaker, N. J. *Chem. Soc. C* **1969**, *1*, 89–91.
- (50) Wang, X.; Armes, S. P. *Macromolecules* **2000**, *18*, 6640–6647.
- (51) Lutz, J.-F.; Hoth, A. *Macromolecules* **2006**, *2*, 893–896.
- (52) Ishizone, T.; Seki, A.; Hagiwara, M.; Han, S.; Yokoyama, H.; Oyane, A.; Deffieux, A.; Carlotti, S. *Macromolecules* **2008**, *8*, 2963–2967.
- (53) Badi, N.; Lutz, J.-F. *J. Controlled Release* **2009**, *3*, 224–229.
- (54) Tsarevsky, N. V.; Braunecker, W. A.; Matyjaszewski, K. *J. Organomet. Chem.* **2007**, *15*, 3212–3222.
- (55) Tsarevsky, N. V.; Matyjaszewski, K. *Chem. Rev.* **2007**, *6*, 2270–2299.
- (56) Ye, J.; Narain, R. J. *Phys. Chem. B* **2009**, *3*, 676–681.
- (57) Matyjaszewski, K. *Curr. Opin. Solid State Mater. Sci.* **1996**, *6*, 769–776.
- (58) Shipp, D. A.; Wang, J.; Matyjaszewski, K. *Macromolecules* **1998**, *23*, 8005–8008.
- (59) Ma, Q.; Wooley, K. L. *J. Polym. Sci., Part A* **2000**, No. Suppl., 4805–4820.
- (60) Davis, K. A.; Matyjaszewski, K. *Macromolecules* **2000**, *11*, 4039–4047.
- (61) Liu, S.; Weaver, J. V. M.; Tang, Y.; Billingham, N. C.; Armes, S. P.; Tribe, K. *Macromolecules* **2002**, *16*, 6121–6131.
- (62) Tornøe, C. W.; Christensen, C.; Meldal, M. *J. Org. Chem.* **2002**, *9*, 3057–3064.
- (63) Rostovtsev, V. V.; Green, L. G.; Fokin, V. V.; Sharpless, K. B. *Angew. Chem., Int. Ed.* **2002**, *14*, 2596–2599.
- (64) Meldal, M.; Tornøe, C. W. *Chem. Rev.* **2008**, *8*, 2952–3015.
- (65) Lutz, J.-F. *Angew. Chem., Int. Ed.* **2007**, *7*, 1018–1025.
- (66) Binder, W. H.; Sachsenhofer, R. *Macromol. Rapid Commun.* **2007**, *1*, 15–54.
- (67) Lutz, J.-F.; Börner, H. G.; Weichenhan, K. *Macromol. Rapid Commun.* **2005**, *7*, 514–518.

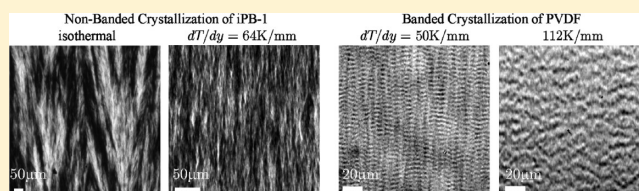
- (68) Lutz, J.-F.; Börner, H. G.; Weichenhan, K. *Macromolecules* **2006**, *19*, 6376–6383.
- (69) Gaertner, H. F.; Offord, R. E. *Bioconjugate Chem.* **1996**, *1*, 38–44.
- (70) Rose, K.; Chen, J.; Dragovic, M.; Zeng, W.; Jeannerat, D.; Kamalaprjia, P.; Burger, U. *Bioconjugate Chem.* **1999**, *6*, 1038–1043.
- (71) Dirksen, A.; Hackeng, T. M.; Dawson, P. E. *Angew. Chem., Int. Ed.* **2006**, *45*, 7581–7584.
- (72) Jin, Y.; Song, L.; Su, Y.; Zhu, L.; Pang, Y.; Qiu, F.; Tong, G.; Yan, D.; Zhu, B.; Zhu, X. *Biomacromolecules* **2011**, *10*, 3460–3468.
- (73) Dirksen, A.; Dawson, P. E. *Bioconjugate Chem.* **2008**, *12*, 2543–2548.
- (74) Thygesen, M. B.; Munch, H.; Sauer, J.; Cló, E.; Jørgensen, M. R.; Hindsgaul, O.; Jensen, K. J. *J. Org. Chem.* **2010**, *5*, 1752–1755.
- (75) Millard, P. E.; Mougin, N. C.; Böker, A.; Müller, A. H. E. *Polym. Prepr. (Am. Chem. Soc., Div. Polym. Chem.)* **2008**, *49*, 121–122.
- (76) van Hell, A. J.; Costa, C. I. C. A.; Flesch, F. M.; Sutter, M.; Jiskoot, W.; Crommelin, D. J. A.; Hennink, W. E.; Mastrobattista, E. *Biomacromolecules* **2007**, *9*, 2753–2761.
- (77) Carstens, M. G.; van Nostrum, C. F.; Ramzi, A.; Meeldijk, J. D.; Verrijk, R.; de Leede, L. L.; Crommelin, D. J.; Hennink, W. E. *Langmuir* **2005**, *24*, 11446–11454.
- (78) Jones, G.; Vullev, V. I. *Org. Lett.* **2001**, *16*, 2457–2460.
- (79) Teodorescu, M.; Negru, I.; Stanescu, P. O.; Drăghici, C.; Lungu, A.; Sârbu, A. *React. Funct. Polym.* **2010**, *10*, 790–797.
- (80) Xia, Y.; Yin, X.; Burke, N. A. D.; Stöver, H. D. H. *Macromolecules* **2005**, *14*, 5937–5943.
- (81) Saha, R. N.; Vasanthakumar, S.; Bende, G.; Snehathatha, M. *Mol. Membr. Biol.* **2010**, *7*, 215–231.
- (82) Soga, O.; van Nostrum, C. F.; Ramzi, A.; Visser, T.; Soulimani, F.; Frederik, P. M.; Bomans, P. H. H.; Hennink, W. E. *Langmuir* **2004**, *21*, 9388–9395.
- (83) Louai, A.; Sarazin, D.; Pollet, G.; François, J.; Moreaux, F. *Polymer* **1991**, *4*, 713–720.
- (84) Govender, T.; Stolnik, S.; Xiong, C.; Zhang, S.; Illum, L.; Davis, S. S. *J. Controlled Release* **2001**, *3*, 249–258.
- (85) Yamada, R.; Kostova, M. B.; Anchoori, R. K.; Xu, S.; Neamati, N.; Khan, S. R. *Cancer Biol. Ther.* **2010**, *3*, 192–203.
- (86) Wong, C.; Stylianopoulos, T.; Cui, J.; Martin, J.; Chauhan, V. P.; Jiang, W.; Popovic, Z.; Jain, R. K.; Bawendi, M. G.; Fukumura, D. *Proc. Natl. Acad. Sci. U. S. A.* **2011**, *6*, 2426–2431.
- (87) Garripelli, V. K.; Kim, J.; Son, S.; Kim, W. J.; Repka, M. A.; Jo, S. *Acta Biomater.* **2011**, *5*, 1984–1992.
- (88) Kratz, F.; Dreves, J.; Bing, G.; Stockmar, C.; Scheuermann, K.; Lazar, P.; Unger, C. *Bioorg. Med. Chem. Lett.* **2001**, *15*, 2001–2006.
- (89) Atkinson, J. M.; Siller, C. S.; Gill, J. H. *Br. J. Pharmacol.* **2008**, *7*, 1344–1352.
- (90) Vartak, D. G.; Gemeinhart, R. A. *J. Drug Targeting* **2007**, *1*, 1–20.
- (91) Ganachaud, F.; Monteiro, M. J.; Gilbert, R. G.; Dourges, M.; Thang, S. H.; Rizzardo, E. *Macromolecules* **2000**, *18*, 6738–6745.
- (92) Smithenry, D. W.; Kang, M.; Gupta, V. K. *Macromolecules* **2001**, *24*, 8503–8511.

Structure Evolution in Directional Crystallization of Polymers under Temperature Gradient

Akihiko Toda,* Ken Taguchi, and Hiroshi Kajioaka

Graduate School of Integrated Arts and Sciences, Hiroshima University, Higashi-Hiroshima 739-8521, Japan

ABSTRACT: In order to clarify the formation mechanism of polymer spherulites, we have experimentally examined the effect of externally applied gradient field of temperature on the structural evolution of polymer crystallization, especially on the characteristic length scales of the inner structures of nonbanded crystallization of isotactic poly(butene-1) and of banded crystallization of poly(vinylidene fluoride) and polyethylene. The inner structures were strongly influenced by the temperature gradient and suggested the important role of the gradient field of temperature, i.e., of chemical potential in general, at the growth front in the bulk melt. The results are in accordance with our proposal and experimental confirmation on the formation of polymer spherulites based on the instability-driven branching promoted by a self-induced gradient field in the bulk melt.



1. INTRODUCTION

Formation of polycrystalline aggregates of polymer crystals, so-called spherulites, requires a space-filling branching with noncrystallographic reorientation of lamellar crystals. In our prior experimental studies, a classical modeling^{1,2} based on the instability-driven branching has been experimentally examined for the banded spherulites of polyethylene (PE)^{3,4} and poly(vinylidene fluoride) (PVDF)⁵ and the nonbanded spherulites of isotactic poly(butene-1) (iPB-1)^{6,7} and isotactic polystyrene (iPS).⁸ In the original modeling of Keith and Padden,¹ the instability has been assumed to be caused by a self-induced gradient field of impurities, which are excluded from crystal growth front and form the gradient field with the highest concentration at the growth front. This gradient evolves the gradient in the driving force of crystallization with its minimum at the growth front and hence promotes the fingering instability of the growth front for branching. In our prior works, in addition to the possible effects of impurities, we noted the effect of a mechanical gradient field with negative pressure at the growth front, which is inevitably required for the steady-state growth of crystals with melt flow to compensate for the crystal–melt density gap.⁹ Though the direct experimental confirmation of the gradient field has been unsuccessful for many decades,^{1,2,10–14} the prediction of the instability-driven branching with the stabilizing effect of surface tension, γ , has been successfully confirmed for the above-mentioned polymers in our recent works.^{3–8} The critical lamellar width, λ , for branching is determined by the gradient of driving force at the growth front, a , and represented as

$$\lambda = 2\pi(\nu_s\gamma/a)^{1/2} \quad (1)$$

$$\lambda \propto (\gamma D/V)^{1/2} \quad \text{compositional} \quad (2)$$

$$\lambda \propto (\gamma/\eta V)^{1/2} \quad \text{mechanical} \quad (3)$$

where ν_s represents the specific volume of a segment in the crystal. In eqs 2 and 3, the effects of compositional and mechanical gradients are influenced by the crystal growth rate, V , the diffusion coefficient, D , and the viscosity, η . We have experimentally confirmed the temperature dependence of λ following the above prediction for PE,^{3,4} PVDF,⁵ iPB-1,^{6,7} and iPS.⁸ We have further tried to differentiate those effects of the compositional and mechanical gradients by means of the molecular weight dependences of those coefficients, D and η , for PE⁴ and iPB-1⁷ and of the decoupling of the related processes, i.e., translational and rotational diffusions of molecules, near the glass transition for iPS.⁸ The obtained results were in accordance with the mechanical gradient, not with the compositional gradient.

Those results were of the supporting evidence for the instability caused by a self-induced gradient field. In the present paper, we take an approach to this issue from different angles with the application of an external field to see the morphological change in the inner structure of polymer spherulites. As the external field, we can think of temperature, flow, and electric and magnetic fields. In the present approach, we apply temperature gradient for the steady-state crystallization with moving interface at a constant speed. Crystallization under temperature gradient has been often utilized for the purpose of directional solidification with oriented crystallites realized by moving of the sample along the temperature gradient at a constant speed.^{15–26} Under temperature gradient, the solidification spontaneously adjusts the position of the crystal–melt interface to choose the temperature at which crystal grows at the preset speed of moving. In other words, the gradient suppresses the fluctuations of the position of growth front.

Received: October 2, 2011

Revised: November 30, 2011

Published: December 23, 2011

Under temperature gradient, it is well-known that the growth of dendrites of organic and metallic alloys becomes directional and cellular with the formation of a periodic array of dendrites.^{27–32} Dendrites of alloys are generally formed by a fingering instability of Mullins–Sekerka type controlled by the gradient field of composition along the growth direction. Application of upward temperature gradient, i.e., higher temperature ahead of the growth front, imposes an additional gradient and brings the following systematic changes in the growth pattern of the dendrites^{28,29} (Figure 1). First, the upward temperature gradient stabilizes the

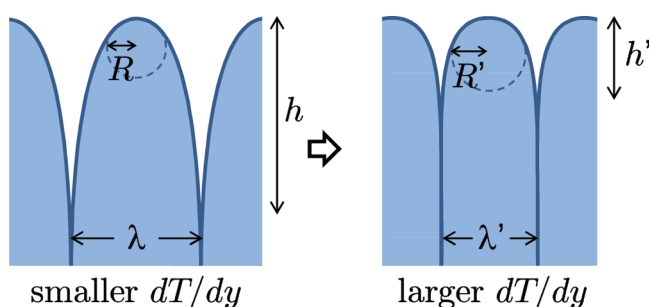


Figure 1. Schematic drawing of the effects of temperature gradient on the cellular growth in organic and metallic alloys: larger tip radius, $R' > R$, shorter cell groove, $h' < h$, and narrower cell width, $\lambda' < \lambda$.

fluctuations at the tips because the fingering tips experience higher temperature, i.e., lower driving force, and pull back. With this effect, the critical tip radius, R , increases for larger temperature gradient. Second, for the cellular structure, the depth of cell grooves, h , becomes shallower and the cell width, λ , becomes narrower because of the temperature decrease, i.e., higher driving force and faster growth, at the lower side of the grooves. The resultant effects on the cellular pattern are shown as Figure 1.

The morphological development of polymer spherulites in the directional solidification under temperature gradient has been studied by Lovinger et al.^{19,20,23} with the emphasis on the evolution of spherulites from nucleation to directional crystallization in the steady state along the temperature gradient. In the present study, we are concerned with the effects of the externally applied gradient of temperature on the inner structures, such as the spacing of banded crystallization and the patchy pattern in nonbanded crystallization, evolved by lamellar crystallites under temperature gradient in the steady state.

In our prior studies, we have experimentally confirmed the proportional relationship between the size of those inner structures, such as the band spacing, P , or the correlation length of the patchy pattern, L , and the size of their building blocks, namely, the width of lamellar crystals at the growth front, λ :

$$P, L \propto \lambda \quad (4)$$

The relationship indicates that the characteristic size of the inner structures is determined by the width of lamellar crystals, which is controlled by the frequency of instability-driven branching, as shown in eqs 1–3. Therefore, by examining the changes in the inner structures, which can be observed by optical microscopy, we can examine the changes on the lamellar branching at the growth front. If the lamellar width and consequently the inner structures are really determined by the self-induced gradient field, the addition of the external field should have an appreciable influence on the structures.

In the following, we introduce the equipment for the directional solidification under temperature gradient, which is specialized for the moving at relatively slow speed in accordance with slow polymer crystallization. Then, the experimental results of the observations are discussed for the nonbanded crystallization of iPB-1 and the banded crystallization of PVDF and PE.

2. EXPERIMENTAL SECTION

We used isotactic poly(butene-1), iPB-1, kindly supplied by Sun Allomer Ltd. ($M_w = 674\,000$, $M_w/M_n = 4.7$), poly(vinylidene fluoride), PVDF, of KF1000 ($M_w = 2.5 \times 10^5$ and $M_w/M_n = 2.1$, Kureha Chemical Industries, Co., Ltd.), and polyethylene, PE, of NIST SRM 1475 ($M_w = 52\,000$ and $M_w/M_n = 2.90$).

For the crystallization under temperature gradient, polymer samples between a pair of thin glass coverslips (150 μm in thickness, 25 mm in width, and 60 mm in length) were prepared by hot press at 180 $^\circ\text{C}$ (iPB-1), 220 $^\circ\text{C}$ (PVDF), and 180 $^\circ\text{C}$ (PE). The polymer film thickness prepared in this method was about 20 μm .

The temperature gradient was applied by two sets of a pair of temperature-controlled bars (9 mm wide). The two sets were placed next to each other and sandwiched the sample glass coverslips between the pair, as shown in Figure 2. The hot bars were heated by a ceramic

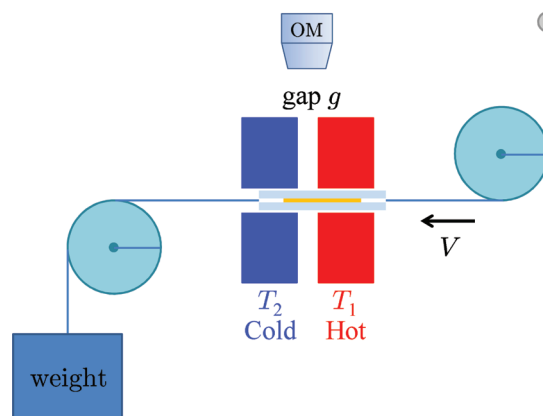


Figure 2. Schematic drawing of the equipment for the directional crystallization under temperature gradient determined by $T_1 - T_2$ and the gap length, g , by moving at a constant speed, V . OM represents an optical microscope.

heating plate placed in the bars, and the temperatures of the bars were monitored and controlled with the precision of ± 0.1 $^\circ\text{C}$. On the other hand, through the cold bars, temperature-controlled (± 0.1 $^\circ\text{C}$) water was circulated. The temperature ranges were 100–240 $^\circ\text{C}$ for the hot bars and 5–95 $^\circ\text{C}$ for the cold bars. The gap length, g , between the hot and cold bars was in the range 0.3–4.0 mm.

The speed of moving corresponds to the crystallization rate of polymers and was in the range 0.5 $\mu\text{m}/\text{min}$ to 2 mm/min. For the steady moving at slow speeds required for the slow crystallization of polymers, stick–slip moving was easily activated²¹ due to the elastic deformation of the system coupled with the friction at the bars and pulleys shown in Figure 2. In order to avoid the stick–slip motion, the steady moving was conducted under large tension by a weight of 3 kg, as shown in Figure 2. For the steady moving under large tension, the system was equipped with a testing machine (Autograph AG-IS, Shimadzu Corp.), with which we could apply the speed down to 0.05 $\mu\text{m}/\text{min}$ corresponding to the crystallization rates of majority of polymers.

The crystallization was *in situ* monitored from above the gap of the two hot cells (Figure 2) with a digital optical microscope (KH-7700, Hirox). For the determination of the actual temperature gradient, the relationship between the crystal growth rate of PVDF and temperature was utilized. The position of the growth front, y , along the gradient for

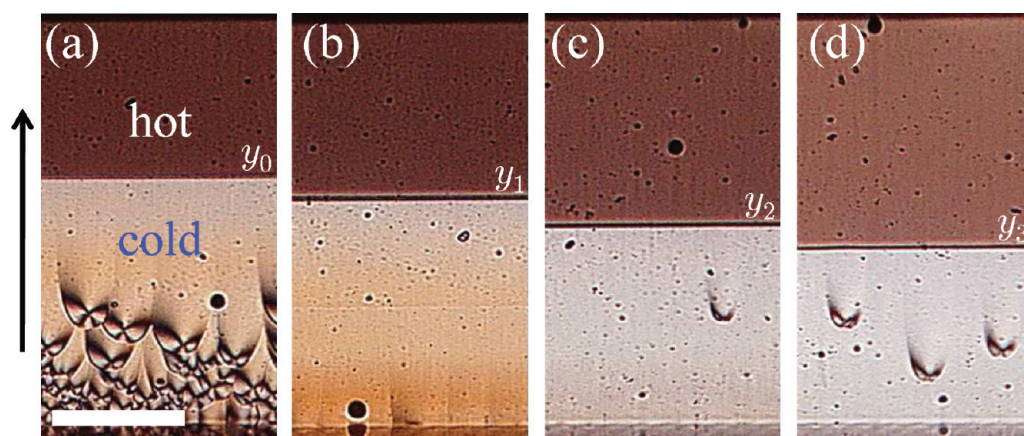


Figure 3. *In situ* OM images of PVDF during the directional crystallization under temperature gradient $T_1 - T_2 = 220 - 80$ °C and the gap length $g = 1.4$ mm. $V =$ (a) 3, (b) 7, (c) 25, and (d) 53 $\mu\text{m}/\text{min}$. The bar represents 400 μm . The arrow indicates the growth direction (the reverse direction of moving), and y_i represents the position of the growth front along the temperature gradient.

the respective moving speed gave the temperature corresponding to the rate of crystallization at the position, as shown in Figure 3. The relationship between the crystallization temperature and isothermal crystal growth rate was examined with a hot stage (THMS600 controlled by LK-600, Linkam), as shown in Figure 4a. From the

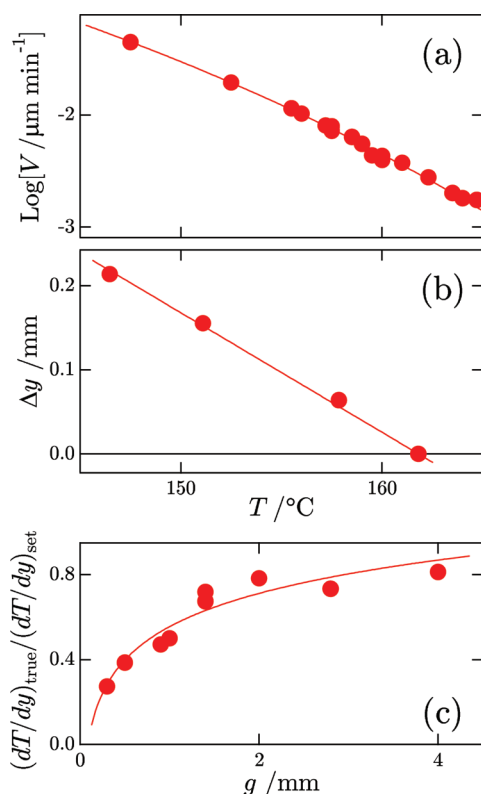


Figure 4. (a) Linear growth rate, V , of PVDF plotted against crystallization temperature. (b) The shift of the growth fronts, $\Delta y = |y_i - y_0|$, in Figure 3 plotted against crystallization temperature estimated from the V – T relation in (a). (c) The ratio $(dT/dy)_{\text{true}}/(dT/dy)_{\text{set}}$ plotted against the gap length, g , for various sets of T_1 and T_2 in the ranges of 100 °C $\leq T_1 \leq 240$ °C and 5 °C $\leq T_2 \leq 95$ °C.

position–temperature relation as in Figure 4b, the inverse of the slope gave the temperature gradient in the cell. It is noted that, as shown in Figure 4c, the true temperature gradient, $(dT/dy)_{\text{true}}$, determined by this method became much smaller than the preset temperature

gradient, which is defined by the preset temperature difference, $T_1 - T_2$, of the bars and the gap length between them, g , as $(dT/dy)_{\text{set}} \equiv (T_1 - T_2)/g$. This is due to the finite thickness, h , of the sample + cover glasses, in which temperature gradient along the thickness direction becomes effective and reduces the effective gradient along the moving direction, dT/dy , for the gap length, g , being close to or less than the thickness, $h \sim 320$ μm . The typical influence has been simulated, as shown in Figure 5, under the assumption that the hot

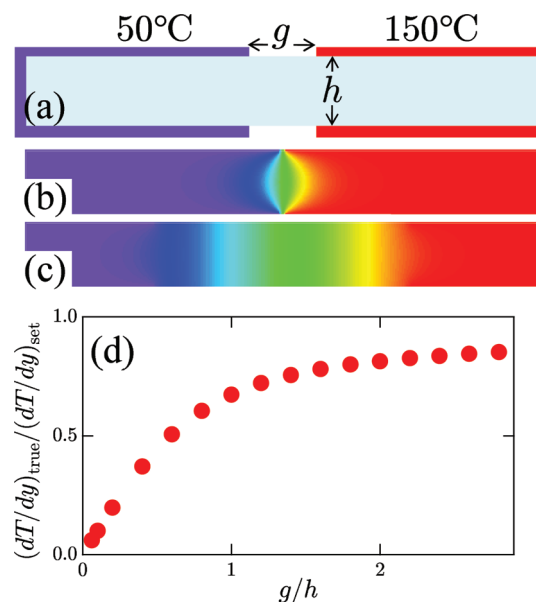


Figure 5. Numerical calculation of the temperature in a plate placed between the hot and cold bars kept at 150 and 50 °C, respectively, as in (a). The length/height ratio of the plate is 8. The ratio of the gap, g , and the height, h , is $g/h =$ (b) 0.2 and (c) 4. In (d), the results $(dT/dy)_{\text{true}}/(dT/dy)_{\text{set}}$ at the centers are plotted against the ratio g/h .

and cold bars were kept at the set temperatures isothermally, and the thermal contact between the bars and sample was perfect with negligible thermal contact resistance. The actual thermal contact of the sample to the hot and cold bars was maintained by the weight of the upper bars. The application of small amount of silicone oil was effective. The precise control of the contact was difficult especially for large dT/dy . The data scatter in Figure 4c (and in Figures 8, 11, and 14) is probably due to the variation of the contact.

After crystallization, the microstructure of the obtained crystals was subsequently examined by polarizing optical microscopy, POM (BX51,

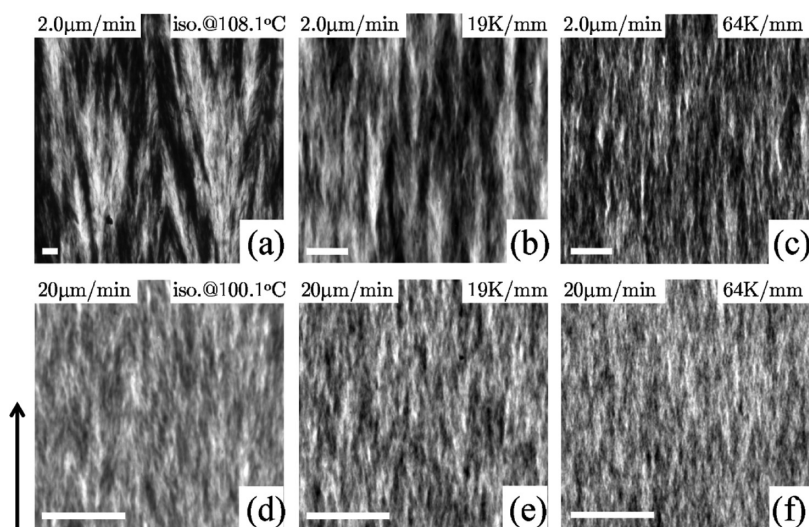


Figure 6. POM images of iPB-1 crystallized under isothermal conditions (a, d) or under temperature gradient (b, c, e, f) at the respective V and dT/dy shown at the upper left and right corners. The bars represent 50 μm . The arrow indicates the growth direction.

Olympus), and by atomic force microscopy, AFM (SPI3800N, Seiko Instruments Inc.), in a dynamic force mode in air at room temperature. Silicon cantilevers (SI-DF20, Seiko Instruments Inc.) with a resonance frequency of 110–150 kHz were used for the observations. For the AFM observations, samples with free surface were prepared by using spacers ($\sim 50 \mu\text{m}$) thicker than the samples and sandwiched between the pair of glass coverslips.

3. RESULTS AND DISCUSSION

3.1. Nonbanded Crystallization of iPB-1 in Form II

Figure 6 shows POM micrographs of iPB-1 crystals obtained isothermally or under temperature gradient. The textures of the nonbanded isothermal crystallization seen under POM in Figure 6a,d are characterized by the existence of a patchy pattern.⁶ The patterns represent the domains coherent in the orientations and are basically in the shape of inverted triangular shape elongated along the growth direction, i.e., along the radial axis of spherulites under isothermal conditions and the reverse direction of moving under temperature gradient, as schematically shown in Figure 7a. The appearance at the growth front will be clearly due to the competition among growing lamellar crystals. Namely, a growing lamellar crystal can lead to other crystals by fluctuations, which are promoted by the self-induced gradient field and occupy the lateral regions which are originally supposed to be for other lamellar crystals. The winner-take-all competition spontaneously generates the inverted triangular shape of the patchy pattern at the growth front. With the competition, the lamellar crystals in the triangular domains are the descendants of the mother lamella formed by successive branching, and hence the lamellar orientation will keep the correlation among them. This will be the reason why the triangular patchy region becomes evident in the POM images showing the crystal orientations.

As is seen in Figure 6, the application of temperature gradient strongly influences the basic pattern with the loss of the triangular domains. The change in the texture can be quantitatively analyzed by introducing the autocorrelation function of the image along the growth direction, i.e., along the long axis of the patchy pattern.⁶ The results of the correlation length of the autocorrelation function are shown in Figure 8 in the plots against moving speed for the respective dT/dy . Here, the correlation length, L , without the external

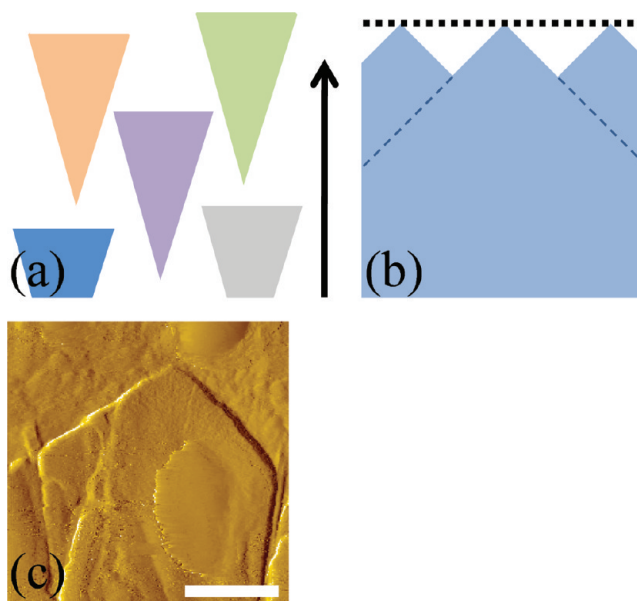


Figure 7. Schematic drawing of the growth domains: (a) inverted triangular domains formed by growth front fluctuations and (b) rectangular growth front forced to be aligned on an isothermal (dotted) line normal to the temperature gradient. (c) Typical lateral habit of the rectangular growth of iPB-1 crystal grown from the melt under isothermal condition (AFM amplitude image).⁶ The arrow in (a) and (b) indicates the growth direction. The bar in (c) represents 5 μm .

gradient of temperature became longer for slower crystallization speed (i.e., at higher temperatures). The trend is in accordance with the prediction of our modeling of eqs 1–4. Then, the correlation length became shorter with the application of temperature gradient, and the effect became stronger at slower speeds. It means that the patchy pattern became finer, i.e., thinner and shorter, with increasing the gradient, and the influence became more pronounced at slower speed.

The loss of triangular patchy pattern with temperature gradient must be a convincing evidence of the growth front fluctuations caused by a self-induced gradient under isothermal conditions and the suppression of the fluctuations by the

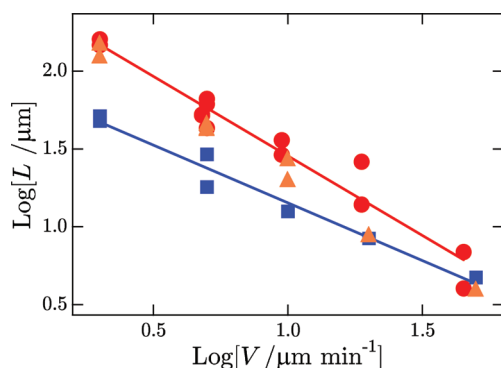


Figure 8. Plots of the correlation length, L , of the patchy pattern in nonbanded crystallization of iPB-1 against the moving speed, V , for iPB-1: isothermal (●) and $dT/dy = 20$ (▲) and 64 K/mm (■).

application of temperature gradient. Finer patchy pattern of nonbanded crystallization will be the consequence of the temperature gradient, which sets the growth interface being aligned on an isothermal plane normal to the gradient. Since the crystal habit of iPB-1 adheres to the rectangular shape, as shown in Figure 7c, the alignment means a subdivision of the growth front with branching into finer crystals, as shown in Figure 7b. Therefore, the finer patchy pattern corresponds to the cellular structures with narrower and shallower groove of organic and metallic alloys.^{28,29} In polymer crystallization, the formation of two-dimensional cellular pattern can be realized for the growth from ultrathin films, if the thickness is comparable with the lamellar thickness and the lamellar crystals are basically planar as in the case of iPB-1.³³ Figure 9 shows the

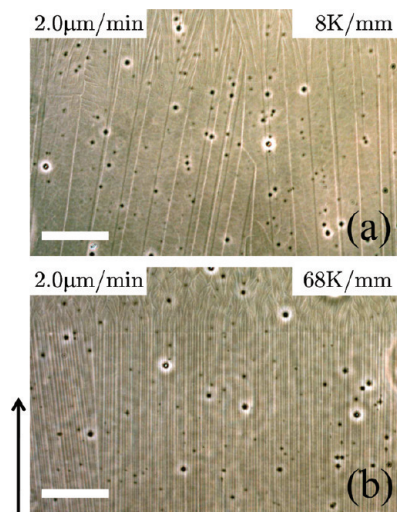


Figure 9. Phase-contrast OM images of the cellular growth of iPB-1 crystallized from thin films (68 nm thick) under temperature gradient at the respective V and dT/dy shown at the upper left and right corners. The bars represent $50 \mu\text{m}$. The arrow indicates the growth direction. The constant moving was terminated by a quick shift of samples, the boundaries of which are seen at the upper parts.

cellular structure of iPB-1 crystals grown from thin films (68 nm thick) under temperature gradient. The cell width indeed shows the expected change of narrower width under larger temperature gradient for the closely adjoined planar lamellar crystals of iPB-1.

3.2. Banded Crystallization of PVDF in the α Form and of PE

3.2.1. The Observation Results. Figure 10 shows the POM micrographs of PVDF crystals obtained under temperature gradients. As is clearly seen, the band spacing, P , became wider with increasing the gradient. The effect becomes more pronounced at slower speeds, which is more easily recognized in the plot of the band spacing against temperature gradient for the respective speeds in Figure 11a; the data are also replotted in Figure 11b against V for selected dT/dy . Figure 12 shows the AFM images of PVDF crystals on the free surface of the sample. The broader band spacing with higher temperature gradient can also be discernible at the higher magnification.

Similar results were obtained for PE crystallization, as shown in Figure 13. With PE, the bands became irregularly deteriorated as well as wider with increasing the gradient. As shown in the plot of the band spacing against speed in Figure 14b, the effects of the moving speed and the gradient were more pronounced with PE: i.e., negligible effects at faster speeds (Figure 13g–i) and broader band spacing at slower speeds with stronger gradient (Figure 13a–c). The data in Figure 14b are also replotted in Figure 14a against dT/dy for selected V . Here, it is noted that, for the irregularly deteriorated patterns (e.g., Figure 13b,c,f) under stronger gradient, the band spacing was determined by the spacing of patchy dark regions along the gradient (shown by double arrows in Figure 13), so that the spacing shown in Figure 14 may be representing the minimum value for the band spacing under high-temperature gradients.

3.2.2. Discussion on the Effects in Comparison with the Results of Nonbanded Crystallization of iPB-1. As the effects of externally applied temperature gradient, the above results of banded crystallization of PVDF and PE showed irregular deterioration of bands with longer spacing. On the other hand, nonbanded crystallization of iPB-1 suggested finer (thinner and shorter) patchy pattern. For the apparent difference in the influences of temperature gradient, we need careful examinations of the effects. First, the irregular deterioration of bands will be related to the disappearance of inverted triangular domains in nonbanded crystallization, the existence of which in banded crystallization is not obvious because of more distinct pattern of bands.³⁴ Since the correlation among descendants of mother lamella in the triangular domains is one of the mechanisms for the coordination of angular phase of twists, it will be reasonable that the loss of the domains results in the deterioration of bands with the application of temperature gradient, which brought shorter coherent region in the phase angle of twist along the tangential direction. From this evidence, we can confirm the strong influences of the external gradient of temperature on the formation of inner structures of both of banded and nonbanded crystallization.

Second, in terms of the longer band spacing of PVDF and PE with temperature gradient, we suggest that the correspondence of the proportional relationship of eq 4 between the band spacing and the lamellar width (i.e., wider lamellar width) will be the most probable cause of the change in the inner structure under temperature gradient by the following reasons. First, in our prior experiments on PVDF and PE under isothermal conditions,^{3–5} we have confirmed the proportional relationship. Second, under temperature gradient, the same trend has been confirmed in the nonbanded crystallization of iPB-1 in terms of the relation between the lamellar width and the characteristic length of the inner structure; i.e., shorter correlation length of patchy pattern, L , with stronger dT/dy was in accordance with

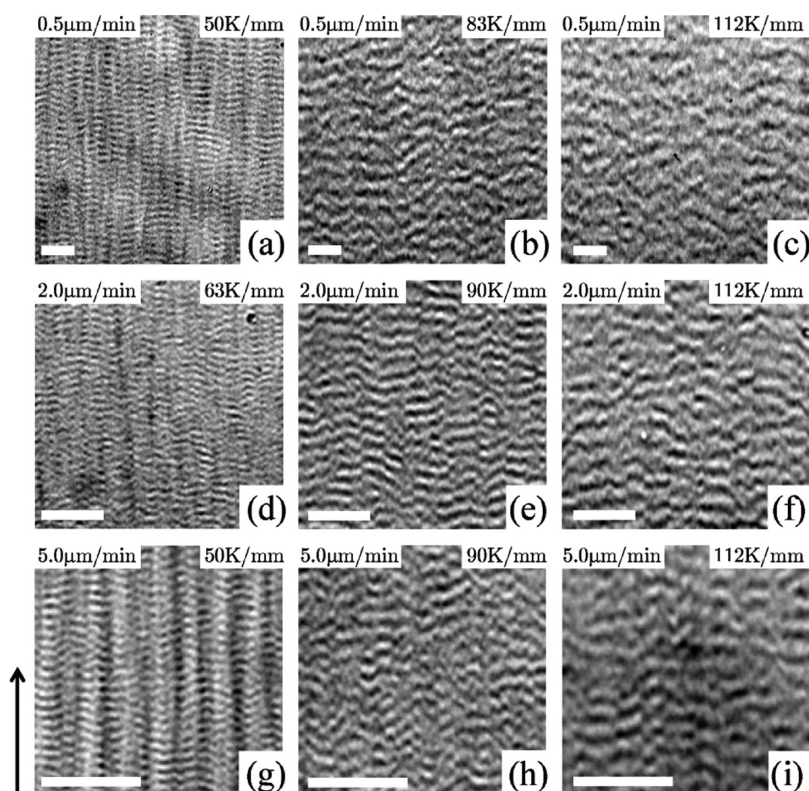


Figure 10. POM images of PVDF crystallized under temperature gradient at the respective V and dT/dy shown at the upper left and right corners, respectively. The bars represent $20\ \mu\text{m}$. The arrow indicates the growth direction.

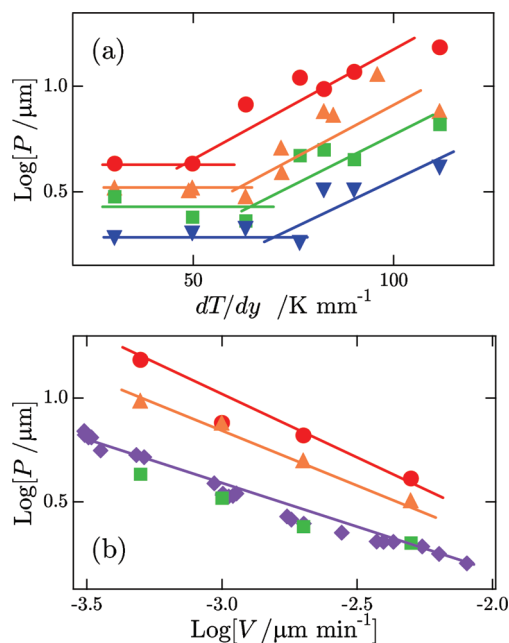


Figure 11. Plots of the band spacing, P , (a) against the temperature gradient for PVDF at the moving speeds of $V = 0.5$ (●), 1.0 (▲), 2.0 (■), and $5.0\ \mu\text{m}/\text{min}$ (▼) and (b) against the moving speed, V ; $dT/dy = 112$ (●), 83 (▲), and $50\ \text{K}/\text{mm}$ (■). The symbol ◆ in (b) is for isothermal crystallization.

narrower cell width, λ , in the growth from ultrathin film, as discussed above.

On the other hand, the difference between banded and nonbanded crystallization comes from the manner of twist; lamellar crystals in banded crystallization spontaneously twist

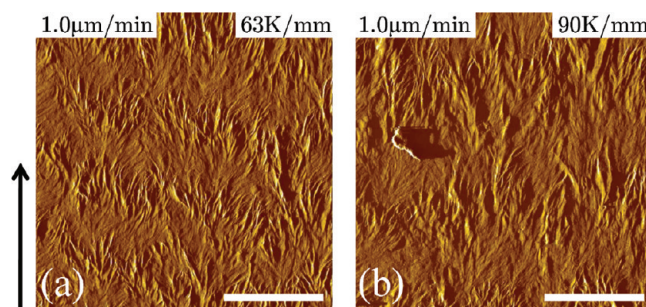


Figure 12. AFM amplitude images of PVDF crystallized under temperature gradient at the respective V and dT/dy shown at the upper left and right corners, respectively. The bars represent $5\ \mu\text{m}$. The arrow indicates the growth direction.

choosing one of the handedness, while in nonbanded crystallization those crystals basically keep their planarity and are supposed to be reoriented in a random direction on the occasion of branching.³⁵ The difference must be due to the nature of surface stresses caused by chain folding in those crystals.³⁶ Therefore, if we may think of the possibility of the violation of the proportional relationship only on banded crystallization under temperature gradient, the violation should suggest the effect of temperature gradient on the surface stresses; i.e., longer band spacing suggests less stresses, and *vice versa*. For the proportional relationship of eq 4, while the coefficient should be a function of the surface stresses, the constant coefficient has been confirmed experimentally at least for PVDF and PE at several different temperatures. It means that the stresses should be independent (or at least a weak function) of temperature and hence of the gradient. By this reason, the effects of temperature gradient on the stresses will

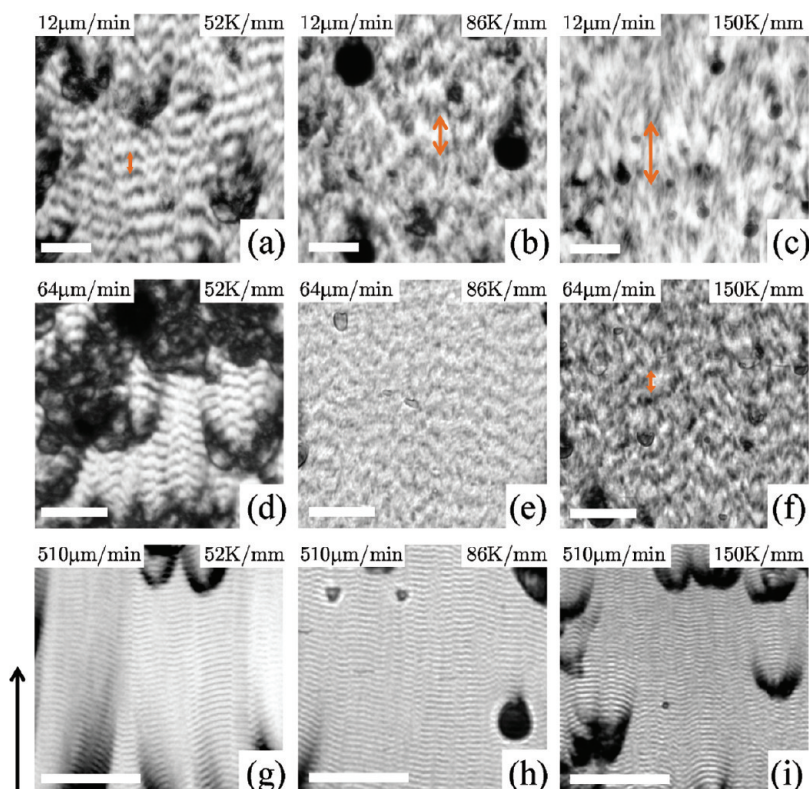


Figure 13. POM images of PE crystallized under temperature gradient at the respective V and dT/dy shown at the upper left and right corners, respectively. The double arrows in (b), (c), and (f) indicate the spacing read from the images. The bars represent $40\ \mu\text{m}$. The arrow indicates the growth direction.

be small enough when we discuss the proportionality between P and λ under temperature gradient. Lastly, the proportional relationship has also been theoretically suggested for both of the cases of continuous twist³⁷ and discontinuous reorientation on the occasion of branching.³ It is noted that the direct confirmation of wider lamellar width for the banded crystallization under temperature gradient was not possible because of the following fundamental reasons. First, the expected width ($\leq 1\ \mu\text{m}$) is too narrow to be directly observed by optical microscopy, and second, the temperature quench required for subsequent observation of the growth front by AFM or electron microscopy could not be fast enough with the present cells. Third, the examination of the growth from ultrathin films will not be meaningful because the nonplanar lamellar crystals of band-forming polymers inevitably come off from the film with twisting, as classical work suggested,³⁸ in contrast to the cellular growth of basically planar lamellar crystals of iPB-1.³³

The proportional relationship suggests wider lamellar width as the cause of the longer band spacing under temperature gradient. For the behavior, we need to recognize the essential difference in the three-dimensional shapes of lamellar crystals as the building blocks of the banded and nonbanded crystallization, i.e., twisting and basically planar lamellae, respectively. The spontaneous twist in banded crystallization means the renewal of geometric configuration surrounding the lamellar crystals all the time in the sense that the three-dimensional coordination of the array of stacked and twisted lamellae is practically impossible. Actually, it will be quite unlikely to expect lamellar platelets placed parallel to each other in a cellular arrangement and twisting in phase in each cell. During the growth from bulk melt, the reconfiguration will prevent the

sustainable structure formation similar to the cellular structure. The unattainable cell growth of band-forming polymers from ultrathin films³⁸ mentioned in the above also supports the argument. Because of this reason, it will not be appropriate to simply apply the existing models of cellular growth of alloys to the banded crystallization. Under temperature gradient, individual lamellar crystal in the banded crystallization probably adjusts the shape for its own sake without the formation of cellular structure.

In contrast with the rectangular edge of iPB-1 crystals (Figure 7c), the individual lamellar crystals of PVDF^{5,39–41} and PE^{42–45} are with curved edges at the growth front (Figure 15a,b), and the angle at the tips can be variable under different growth conditions.^{41,44} Then, as shown in Figure 15c, as a consequence of the stabilizing effect of temperature gradient increasing the critical width, wider lamellar width can be reasonably expected with the curved edges. The behavior has a similar corresponding change in the cellular growth of alloys under temperature gradient, where higher temperature gradient leads to larger tip radius of individual dendrites in the solidification of alloys^{28,29} (Figure 1). Without the constraint of cellular structure, larger tip radius will suggest wider width of individual lamellae.

As a possible stabilizing effect of temperature gradient, the following effect is also to be noted. The upward temperature gradient, namely higher temperature in the molten side, means higher diffusion coefficient and/or lower viscosity in the melt. Then, both of faster diffusion and lower viscosity will decrease the gradient and stabilize the interface, e.g., larger diffusion length, D/V , with higher diffusion coefficient. The process will not discriminate banded crystallization from nonbanded, so that the effect will not be considered in the following.

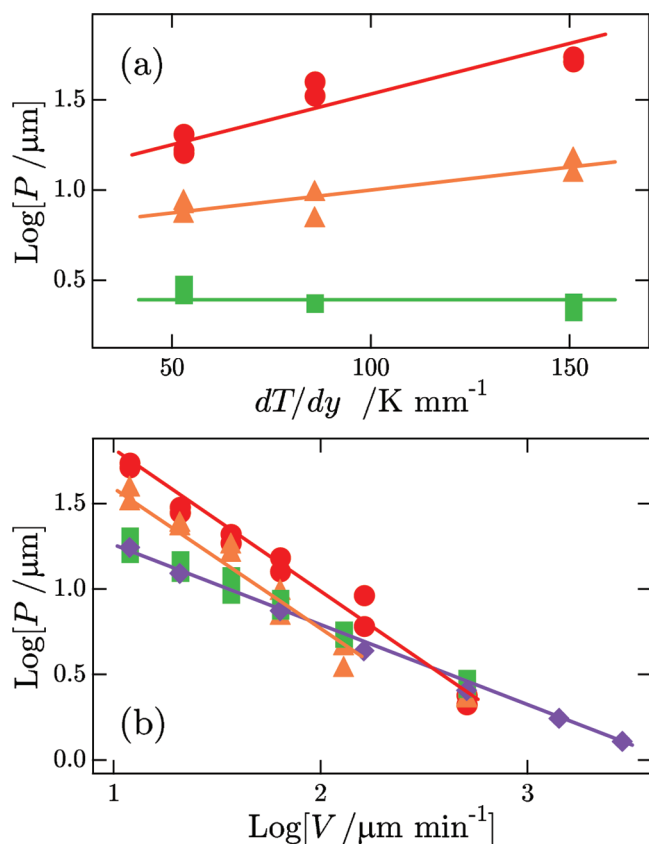


Figure 14. Plots of the band spacing, P , (a) against the temperature gradient for PE at the moving speeds of $V = 12$ (●), 64 (▲) and 510 μm/min (■) and (b) against the moving speed, V ; $dT/dy = 151$ (●), 86 (▲), and 53 K/mm (■). The symbol ◆ in (b) is for isothermal crystallization.

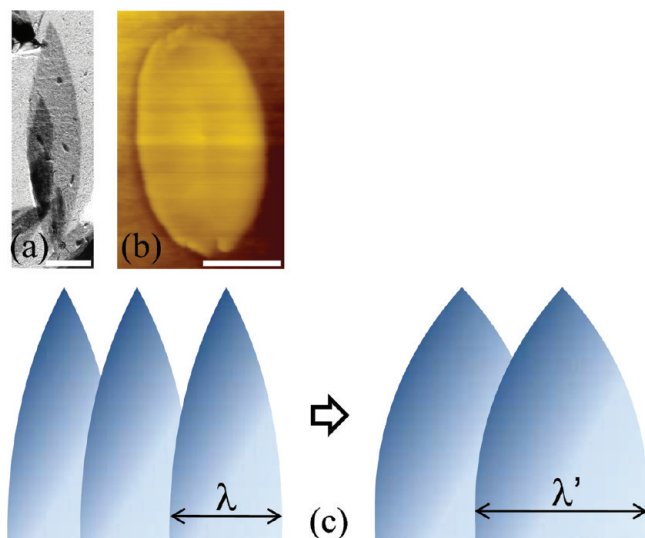


Figure 15. Typical lateral habits with curved edges of (a) PVDF (TEM image)⁴¹ and (b) PE (AFM height image)⁴⁵ single crystals grown from the melt isothermally. (c) Schematic drawing of the expected effects of temperature gradient on nonplanar lamellar crystals with curved edges: larger tip width, $\lambda' > \lambda$. The bars in (a) and (b) represent 1 μm.

3.2.3. A Possible Modeling of the Effect of Temperature Gradient. As an influence on individual lamellar crystal, the effects of temperature gradient and moving speed can be

explained by a simple modeling based on the branching driven by the instability, which is promoted by a self-induced gradient field, as shown in Figure 16a. The temperature gradient, $\partial T/\partial y$,

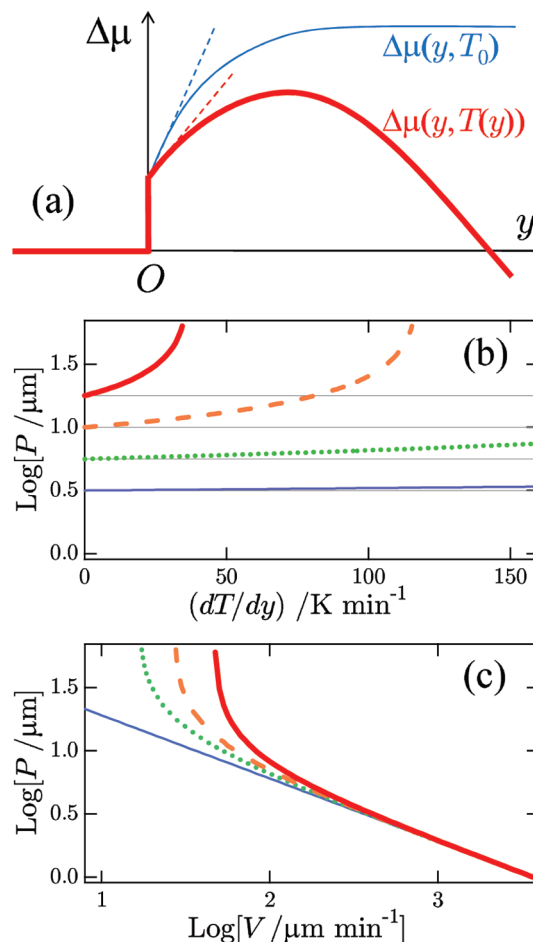


Figure 16. (a) Schematic diagram of the gradient in the driving force of the chemical potential for crystallization near the growth front denoted by O without and with the upward temperature gradient for the thin and thick lines, respectively. (b) Plots of P against dT/dy of eq 7 for $P_0(V) = 10^{0.5}$ (thin line), $10^{0.75}$ (dotted line), 10^1 (broken line), and $10^{1.25}$ μm (thick line). (c) Plots of P against V of eq 7 for $dT/dy = 0$ (thin line), 53 (dotted line), 86 (broken line), and 151 K/mm (thick line). It is noted that the coordinate system of (a) is moving with the growth front fixed at the origin, O . In (b) and (c), the data of $P_0(V)$ were taken from the experimental results in Figure 14.

corresponds to the gradient in chemical potential, a_T , as

$$a_T = \frac{\partial \Delta \mu}{\partial y} = - \frac{v_s \Delta h_f}{T_m} \frac{\partial T}{\partial y} \quad (5)$$

because the driving force of the chemical potential, $\Delta \mu$, is represented by the supercooling, $\Delta T \equiv T_m - T$, as $\Delta \mu = v_s \Delta h_f (\Delta T/T_m)$, where Δh_f represents the heat of fusion per unit volume and T_m the melting point.

As seen in eqs 2 and 3, the self-induced gradient field in the chemical potential, a , becomes stronger with increasing crystallization rate, V . On the other hand, the applied external gradient field of temperature weakens the self-induced gradient with the minus sign in eq 5 because of the upward shift of temperature ahead of the growth front, resulting in smaller driving force (Figure 16a). Then, the slope of driving force at

the growth front (at the origin, O , in Figure 16a) becomes smaller with the application of temperature gradient. The slope determines the critical lamellar width for branching, as shown in eq 1. The lamellar width is then expected to become wider with the effect, following the expression

$$\lambda = 2\pi \left(\frac{v_s \gamma}{a_0 + a_T} \right)^{1/2} \quad (6)$$

in which the slope only with the self-induced gradient, a_0 , under isothermal condition is replaced by that with the effect of temperature gradient, $a_0 + a_T$. It is noted that this approach to the stabilizing effect of temperature gradient is essentially the same as for larger tip radius in the directional solidification of alloys under temperature gradient in the regime of slow moving velocity, as suggested by Kurz and Fisher.²⁸

Here, based on the proportional relationship of eq 4, i.e., $P = k\lambda$, the expression of eq 6 predicts the effects on the band spacing, too, as was shown experimentally in the above. Equations 1, 5, and 6 then lead to the following:

$$\frac{1}{P^2} = \frac{1}{P_0(V)^2} - \frac{\Delta h_f}{4\pi^2 k^2 \gamma T_m} \frac{\partial T}{\partial y} \quad (7)$$

where $P_0(V)$ represents the band spacing for isothermal crystallization with the rate, V . Equation 7 only supposes the basic form of the critical width of eq 1 or 6 and the equivalence of the temperature gradient, $\partial T/\partial y$, and the gradient of chemical potential, a_T , represented as eq 5. Therefore, eq 7 is applicable without the knowledge of detailed mechanism of self-induced gradient field concerning the expression of a_0 in eq 6 and simply suggests a stronger effect of $\partial T/\partial y$ for longer P_0 (smaller P_0^{-2}) irrespective of V .

With the literature values of PE, i.e., $P = 4.5\lambda$,⁷ $\gamma \simeq 10$ erg/cm², $\Delta h_f = 2.8 \times 10^9$ erg/cm³, and $T_m \simeq 420$ K,⁴⁶ the coefficient in eq 7 is about 8.5×10^{-2} 1/(K μ m). Figures 16b,c show the plots of eq 7 with the coefficient and $P_0(V)$ of isothermal crystallization of PE in Figure 14. Therefore, Figures 16b,c should correspond to Figures 14a,b of PE. The simple modeling qualitatively reproduces the essential features of the experimental results, though the steep rise in P near the critical condition of $(a_0 + a_T) \rightarrow 0$ in eq 6 was not observed experimentally. This simple modeling may exceed the applicability limit near the condition or the deterioration of banding in PE may indicate the divergence of P . In terms of the PVDF results shown in Figure 11, we may also apply the literature values for PVDF, i.e., $P = 5.0\lambda$,⁵ $\Delta h_f = 2.0 \times 10^9$ erg/cm³, and $T_m \simeq 483$ K,⁴⁷ and an empirical relationship⁴⁶ of $\gamma \simeq 0.1\Delta h_f(ab)^{1/2} \simeq 10$ erg/cm² with $ab = 4.8 \times 10^{-15}$ cm² of the cross-sectional area of a stem. The coefficient of eq 7 for PVDF is then estimated to be about 4.2×10^{-2} 1/(K μ m), not much different from the value of PE. However, as seen in the comparison of the experimental results of Figures 11 and 16b,c with the coefficient of PE, the effect of $\partial T/\partial y$ in PVDF is stronger even at much shorter P_0 . It means that PVDF is more susceptible to temperature gradient. This behavior may be related to the anisotropic lateral shape of PVDF crystals with sharper curved tip along the growth direction (Figure 15a).^{5,39–41} Narrower tip means smaller tip radius and phenomenologically corresponds to smaller γ in eq 6. If γ in eq 7 becomes one-tenth of the evaluated value, the experimentally observed stronger effect of $\partial T/\partial y$ at shorter P_0 can be expected from eq 7.

In this way, the trend in the dependence of $P(\lambda)$ on V and $\partial T/\partial y$ can be qualitatively explained by this simple modeling. However, the agreement with the experimental results is not good enough. For the quantitative analysis of the growth patterns under gradient fields, we need to model the growth explicitly under the influence of the fields of compositional and/or pressure gradient with moving growth front; the variations of diffusion coefficient, viscosity, and thermal conductivity should also be taken into account. For the purpose, phase field modeling has been often utilized in the studies of cellular and dendritic crystallization in nonpolymeric systems.^{48,49} For the spherulitic growth of polymers, there have been remarkable developments in the application of phase field modeling recent years.^{50–52} Future work taking into account of those additional effects is awaited.

4. CONCLUSIONS

In the present paper, we have experimentally examined the effect of gradient field of temperature on the structural evolution of polymer crystallization from the bulk melt. Under temperature gradient, samples were moved at a constant speed, V , corresponding to the crystallization rate. The temperature gradient then fixes the growth interface at a position, y , of the crystallization temperature, $T(y)$, having $V(T(y))$. Therefore, the effect basically suppresses the fluctuations of the interface.

In our prior studies, we have proposed and experimentally examined the formation mechanism of polymer spherulites by the branching and reorientation of lamellar crystals. In the modeling, the branching is caused by the growth front instability driven by the self-induced gradient field of mass transport in the bulk melt. The temperature gradient is then supposed to suppress the instability and hence should have appreciable influence on the structural evolution of polymer crystallization. In the prior studies under isothermal conditions, we have also confirmed that the width of lamellar crystals, which is limited by the instability-driven branching, determines the band spacing of banded crystallization and the correlation length of patchy pattern of nonbanded crystallization, as the size of the building blocks of those structures.

On the basis of the relation, we have experimentally examined the effect of temperature gradient on the characteristic lengths of the inner structures. First, we have confirmed that the temperature gradient suppressed the formation of triangular domains, i.e., the unit of the patchy pattern, and the correlation of the pattern in nonbanded crystallization of iPB-1. The finer structure of patchy pattern corresponds to narrower cell width generally observed for the cellular growth of the array of dendrites of organic and metallic alloys in directional solidification. The cellular growth of iPB-1 from ultrathin films actually confirmed the behavior under temperature gradient.

Second, in banded crystallization of PVDF and PE, the bands are irregularly deteriorated with temperature gradient. The deterioration should be related to the loss of triangular domains, in which lamellar orientations of descendants of mother lamellae are correlated with each other. Temperature gradient also enlarged the band spacing. On the basis of the proportional relationship between the band spacing and the lamellar width, it has been suggested that the longer spacing of bands is most probably due to wider lamellar width. The behavior has been ascribed to the stabilizing effect of temperature gradient on the individual lamellae; the effect also has a similar correspondence in the cellular growth of

alloys as a larger tip radius. Those results of nonbanded and banded crystallization hence suggest the strong effects of externally applied gradient field of temperature and the essential role of gradient field in the structural evolution of polymer crystallization.

AUTHOR INFORMATION

Corresponding Author

*Tel +81-82-424-6558; Fax +81-82-424-0757; e-mail atoda@hiroshima-u.ac.jp.

ACKNOWLEDGMENTS

The authors thank Prof. T. Asano of Shizuoka University for the guidance on the directional solidification under temperature gradient. The authors also thank Prof. S. Tanaka of Hiroshima University and Prof. Y. Yamazaki of Waseda University for helpful discussions. This work was supported by KAKENHI (Grant-in-Aid for Scientific Research) on Priority Area "Soft Matter Physics" from the Ministry of Education, Culture, Sports, Science and Technology of Japan.

REFERENCES

- Keith, H. D.; Padden, F. J. Jr. *J. Appl. Phys.* **1963**, *34*, 2409.
- Keith, H. D. *J. Polym. Sci.* **1964**, *A2*, 4339.
- Toda, A.; Okamura, M.; Taguchi, K.; Hikosaka, M.; Kajioka, H. *Macromolecules* **2008**, *41*, 2484.
- Toda, A.; Taguchi, K.; Kajioka, H. *Macromolecules* **2008**, *41*, 7505.
- Toda, A.; Taguchi, K.; Hikosaka, M.; Kajioka, H. *Polym. J.* **2008**, *40*, 905.
- Kajioka, H.; Hikosaka, M.; Taguchi, K.; Toda, A. *Polymer* **2008**, *49*, 1685.
- Kajioka, H.; Yamada, K.; Taguchi, K.; Toda, A. *Polymer* **2011**, *52*, 2051.
- Kajioka, H.; Yoshimoto, S.; Taguchi, K.; Toda, A. *Macromolecules* **2010**, *43*, 3837.
- Schultz, J. M. *Polymer Crystallization*; Oxford University Press: Oxford, 2001; Chapter 10.
- Bassett, D. C.; Hodge, A. M. *Proc. R. Soc. London* **1981**, *A377*, 61.
- Bassett, D. C.; Olley, R. H. *Polymer* **1984**, *25*, 935.
- Bassett, D. C.; Vaughan, A. S. *Polymer* **1985**, *26*, 717.
- Keith, H. D.; Padden, F. J. Jr. *J. Polym. Sci., Part B: Polym. Phys.* **1987**, *25*, 2371.
- Vaughan, A. S.; Bassett, D. C. *Polymer* **1988**, *29*, 1397.
- Tanaka, K.; Seto, T.; Fujiwara, Y. *Rep. Prog. Polym. Phys. Jpn.* **1963**, *6*, 285.
- Fujiwara, Y. *Kolloid Z. Z. Polym.* **1968**, *226*, 135.
- Asano, T.; Fujiwara, Y. *Polymer* **1978**, *19*, 99.
- Asano, T. *Polym. Bull.* **1983**, *10*, 547.
- Lovinger, A. J.; Gryte, C. C. *J. Appl. Phys.* **1976**, *47*, 1999.
- Lovinger, A. J.; Gryte, C. C. *Macromolecules* **1976**, *9*, 247.
- Lovinger, A. J.; Gryte, C. C. *Eur. Polym. J.* **1977**, *13*, 391.
- Lovinger, A. J. *J. Appl. Phys.* **1978**, *49*, 5003.
- Lovinger, A. J.; Wang, T. T. *Polymer* **1979**, *20*, 725.
- Lovinger, A. J.; Chua, J. O.; Gryte, C. C. *J. Polym. Sci., Polym. Phys. Ed.* **1977**, *15*, 641.
- Laudise, A.; Bridenbaugh, P. M.; Siegrist, T.; Fleming, R. M.; Katz, H. E.; Lovinger, A. J. *J. Cryst. Growth* **1995**, *152*, 241.
- Pawlak, A.; Piorkowska, E. *Colloid Polym. Sci.* **2001**, *279*, 939.
- Tiller, W. A. *The Science of Crystallization: Macroscopic Phenomena and Defect Generation*; Cambridge University Press: New York, 1991; Chapters 5 and 6.
- Kurz, W.; Fisher, D. J. *Acta Metall.* **1981**, *29*, 11.
- Trivedi, R.; Somboonsuk, K. *Mater. Sci. Eng.* **1984**, *65*, 65.
- Bondarenko, Y. A.; Kablov, E. N.; Surova, V. A.; Echin, A. B. *Met. Sci. Heat Treat.* **2006**, *48*, 360.
- Bondarenko, Y. A.; Kablov, E. N. *Met. Sci. Heat Treat.* **2002**, *44*, 288.
- Üstün, E.; Çadrlı, E. C.; Kaya, H. *J. Phys.: Condens. Matter* **2006**, *18*, 7825.
- Kajioka, H.; Taguchi, K.; Toda, A. *Macromolecules* **2011**, *44*, 9239.
- Kajioka, H.; Hoshino, A.; Miyaji, H.; Miyamoto, Y.; Toda, A.; Hikosaka, M. *Polymer* **2005**, *46*, 8717.
- Kajioka, H.; Yoshimoto, S.; Gosh, R. C.; Taguchi, K.; Tanaka, S.; Toda, A. *Polymer* **2010**, *51*, 1837.
- Lotz, B.; Cheng, S. Z. D. *Polymer* **2005**, *46*, 577.
- Hatwalne, Y.; Muthukumar, M. *Phys. Rev. Lett.* **2010**, *105*, 107801.
- Keith, H. D.; Padden, F. J. Jr.; Lotz, B.; Wittmann, J. C. *Macromolecules* **1989**, *22*, 2230.
- Briber, R. M.; Khoury, F. J. *Polym. Sci., Part B: Polym. Phys.* **1993**, *31*, 1253.
- Lovinger, A. J.; Keith, H. D. *Macromolecules* **1996**, *29*, 8541.
- Toda, A.; Arita, T.; Hikosaka, M. *Polymer* **2001**, *42*, 2223.
- Organ, S. J.; Keller, A. J. *Mater. Sci.* **1985**, *20*, 1586.
- Patel, D.; Bassett, D. C. *Polymer* **2002**, *43*, 3795.
- Toda, A. *Colloid Polym. Sci.* **1992**, *270*, 667.
- Toda, A.; Okamura, M.; Hikosaka, M.; Nakagawa, Y. *Polymer* **2005**, *46*, 8708.
- Hoffman, J. D.; Davis, G. T.; Lauritzen Jr., J. I. *Treatise on Solid State Chemistry*; Plenum Press: New York, 1976; Vol. 3, Chapter 7.
- Wunderlich, B. *Macromolecular Physics*; Academic Press: New York, 1980; Vol. 3, p 72.
- Steinbach, I. *Acta Mater.* **2008**, *56*, 4965.
- Gurevich, S.; Karma, A.; Plapp, M.; Trivedi, R. *Phys. Rev. E* **2010**, *81*, 011603.
- Gránásy, L.; Pusztai, T.; Börzsönyi, T.; Warren, J. A.; Douglas, J. F. *Nature Mater.* **2004**, *3*, 645.
- Gránásy, L.; Pusztai, T.; Tegze, G.; Warren, J. A.; Douglas, J. F. *Phys. Rev. E* **2005**, *72*, 011605.
- Xu, H.; Chiu, H.-W.; Okabe, Y.; Kyu, T. *Phys. Rev. E* **2006**, *74*, 011801.

Frequency Response of Polymer Films Made from a Precursor Colloidal Monolayer on a Nanomechanical Cantilever

Ting Liu,[†] Sascha Pihan,[†] Marcel Roth,[†] Markus Retsch,^{†,‡} Ulrich Jonas,^{†,⊥} Jochen Stefan Gutmann,^{†,§,||} Kaloian Koynov,[†] Hans-Jürgen Butt,[†] and Rüdiger Berger*,[†]

[†]Max Planck Institute for Polymer Research, Ackermannweg 10, 55128 Mainz, Germany

[‡]Massachusetts Institute of Technology, 77 Massachusetts Avenue, Cambridge, Massachusetts 02139, United States

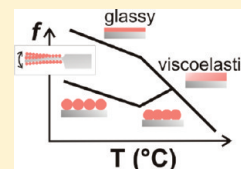
[§]Department of Chemistry and Center for Nanointegration Duisburg-Essen (CeNIDE), University Duisburg-Essen, Universitätsstr. 5, D-45117 Essen, Germany

^{||}Deutsches Textilforschungszentrum Nord-West e.V., Adlerstr. 1, D-47798 Krefeld, Germany

[⊥]Macromolecular Chemistry, Department Chemistry–Biology, University of Siegen, Adolf-Reichwein-Strasse 2, AR-G 213, D-57076 Siegen, Germany

S Supporting Information

ABSTRACT: Nanomechanical cantilevers (NMC) were used for the characterization of the film formation process and the mechanical properties of colloidal monolayers made from polystyrene (PS). Closely packed hexagonal monolayers of colloids with diameters ranging from 400 to 800 nm were prepared at the air–water interface and then transferred in a controlled way on the surface of NMC. The film formation process upon annealing of the monolayer was investigated by measuring the resonance frequency of the NMC (≈ 12 kHz). Upon heating of non-cross-linked PS colloids, we could identify two transition temperatures. The first transition resulted from the merging of polymer colloids into a film. This transition temperature at 147 ± 3 °C as measured at ≈ 12 kHz remained constant for subsequent heating cycles. We attributed this transition temperature to the glass transition temperature T_g of PS which was confirmed by dynamic mechanical thermal analysis (DMTA) and using the time temperature superposition principle. The second transition temperature (175 ± 3 °C) was associated with the end of the film formation process and was measured only for the first heating cycle. Furthermore, the transition of the colloidal monolayer into a homogeneous film preserved the mass loading on the NMC which allowed determination of the Young's modulus of PS (≈ 3 GPa) elegantly.



INTRODUCTION

During the past years nanomechanical cantilevers (NMC) have been used more and more for the analysis of polymer properties. The interaction of polymers with solvents,^{1–3} the response of polymers to pH changes,^{4,5} the wetting properties between different polymers,⁶ swelling and deswelling,^{7,8} interfacial tension of polymers,⁹ and thermal transition temperatures of hydrogels¹⁰ have been investigated by NMC. Typically, picograms to nanograms of materials are enough for the analysis,¹¹ and the method allows even screening of material properties.¹² Recently, Jung and co-workers probed the glass transition temperature (T_g) of polystyrene (PS) and poly(vinyl acetate) (PVAc) and block copolymers using NMCs.^{13–15} In their experiments, the NMCs were coated with a polymer solution by inkjet printing. After solvent evaporation, only polymer remained on the NMC. Then the deflection and the resonance frequency of the NMC were probed at different temperatures. Changes in volume and in elastic properties of the polymer during heating induced a deflection of the NMC, which allowed determining the T_g of the polymer. Furthermore, vibrating the polymer coated NMC at its resonance frequency enabled a qualitative investigation of the change of the Young's modulus of PVAc during heating.^{13,14} A better analysis was hampered by a nonuniform polymer coating. A quantitative

estimation of the Young's modulus requires a separation of mass and rigidity induced changes in the resonance frequency of NMC.¹⁶

Grüter and co-workers reported on a method to disentangle mechanical and mass effects of thin metal film on NMC by including measurements of the quality factor Q of the vibrating NMC.^{17,18} On the basis of this method, they found that ≈ 5 nm thick isolated islands of Cu did not contribute to the rigidity but only to the mass loading of NMC. In order to characterize metal coatings, a mass loading $<1\%$ of NMC mass was sufficient to separate rigidity from mass effects clearly. In contrast, polymers have lower densities and also lower Young's moduli compared to metals. Therefore, to be able to relate the shift of resonance frequency to mechanical properties of polymers, it is beneficial to deposit thicker polymer film onto NMC. Furthermore, the mechanical properties of polymers, e.g. the storage and loss moduli, exhibit strong frequency and temperature dependences, which can be described by the time–temperature superposition principle. Although polymer films are widely used for molecular sensing,^{19–27} not much

Received: October 27, 2011

Revised: November 29, 2011

Published: December 27, 2011

work was performed to explore the frequency-dependent response of the polymer layers. Furthermore, a direct relation to standard dynamic mechanical thermal analysis (DMTA) has, to our knowledge, not been carried out.

The deposition of homogeneous and thick polymer films on a NMC is in general not an easy task. NMC were coated by inkjet printing methods.^{14,28} However, the generated polymer films were usually not homogeneous due to coffee stain effects caused by the drying process.^{29–31} Alternatively, polymers were directly grafted onto or grafted from the NMC surface.³² With this method it was possible to make uniform polymer films, but their thickness was limited to several tens of nanometers. Further on, plasma deposition methods were used for depositing films from organic monomers onto NMCs.^{3,33} Plasma processes allowed depositing a variety of different materials with a controlled thickness.²⁶ Typically, plasma deposited films were smooth and homogeneous.³⁴ However, bulk properties of the deposited materials were difficult to measure since the amount of material is limited to a few nanograms. Thus, elastic properties determined by NMC were difficult to interpret, and a comparison with bulk material properties, e.g. measured by standard DMTA, was impossible.

In this paper, we introduce an elegant method to coat a NMC with homogeneous polymer films with thicknesses in range of a few hundred nanometers using closely packed polymeric colloidal monolayers as a precursor. The colloids inside the monolayers can be considered as noninteracting mass loadings, in analogy to the metal islands measured by Grütter et al.¹⁸ Upon thermal or organic vapor annealing, homogeneous polymer films can be formed from these colloidal monolayers^{35,36} without changing the mass of the coating film on NMC. Thus, homogeneous films with a defined thickness can be fabricated, since the film thickness scales with the diameter of the colloids. The latter allows a quantitative analysis of the mechanical properties, in particular Young's modulus E and the glass transition temperature T_g of the polymer films.

MATERIALS AND METHODS

Polystyrene Colloids. PS colloids were synthesized in house via surfactant-free emulsion polymerization. The colloids were charge stabilized with acrylic acid. The molecular weight of the non-cross-linked PS colloids used here was 20 000 g/mol with a polydispersity index of about 5. Cross-linked PS colloids were synthesized by adding divinylbenzene (DVB) in the polymerization mixture in ratios of 1 and 10 wt % to styrene.³⁷ Thus, these PS colloids are attributed to be 1% and 10% cross-linked PS colloids, respectively. The respective mean diameters were 400 ± 30 nm for the non-cross-linked particles, 780 ± 40 nm in diameter for 1%, and 620 ± 30 nm for 10% cross-linked particles, as determined from scanning electron microscope (SEM) images.

Nanomechanical Cantilevers. Silicon NMC (thickness $h_{\text{Si}} = 1.5\text{--}2.5$ μm , length $l_{\text{Si}} = 500$ μm , width $w_{\text{Si}} = 90$ μm , spring constant $0.1\text{--}0.4$ N/m, Octosensis, Micromotive GmbH, Germany) with a resonance frequency of 10 ± 3 kHz was used. The resonance frequencies of the NMC were measured with an EnviroScope scanning force microscope (SFM) (Instruments Inc., Plainview, NY). From the resonance frequencies the spring constant and the individual thickness of the NMC were calculated using eqs 2–4 (see Theoretical Background). For these calculations we used a Young's modulus of $E_{\text{Si}} = 170$ GPa and a density of $\rho_{\text{Si}} = 2330$ kg/m³. All the measurements were carried out in a vacuum chamber at 2 mbar in order to obtain a higher Q factor.

The NMC chip was mounted on a standard SFM holder. NMCs were vibrated by the built-in piezoelectric actuator. The temperature of the NMC was adjusted stepwise by a heating stage, which was

connected to a temperature controller (LakeShore 331, Westerville, OH). For instance, during the heating process, the temperature was first increased from ambient temperature to 30 °C. Typically about 30 s was required to reach the set temperature value. About 5 min after the desired temperature was reached, the resonance frequency of the NMC was constant and therefore recorded. For the next step the temperature was set up to 50 °C and so on. It took about 2 h to reach the end temperature of 220 °C, and therefore an average rate of the heating was about 2 K/min. In order to establish a good thermal heat transfer between the heating stage and the NMC, we placed the NMC 2–3 mm above the SFM heating stage. A temperature calibration using a thermistor (MultiMeter Ex505, EXTECH Instrument) revealed an offset of 5 K between the sample holder and the NMC position (Supporting Information, S1). NMCs and their coatings were imaged by a stereomicroscope (Leica Microsystems GmbH, Wetzlar, Germany, 10 \times magnification) and a SEM (LEO 1530 Gemini, Oberkochen, Germany) before and after annealing.

Mass Flow Controller. To adjust the toluene vapor pressure, a stream of nitrogen was split into a stream of pure nitrogen and one stream of nitrogen saturated with toluene vapor. For saturation with vapor the second stream of nitrogen was bubbled through toluene liquid. The flow of both streams was controlled by gauges. Both gas streams were mixed and led into the measuring cell. The temperature of the liquid toluene was kept at 20 °C, i.e. below room temperature at about 22–25 °C. The temperature of connecting tubes and the measuring cell was above 20 °C in order to prevent vapor condensation. The saturation vapor pressure of toluene at 20 °C was calculated to be 29 mbar. For the toluene exposure and the drying afterward, the flow of toluene vapor and N₂ was set to 0.5×10^{-6} m³/min. The volume of the fluid cell, in which the NMC chip was mounted, was 3×10^{-8} m³. Consequently, the fluid cell was approximately rinsed every 3 s.

Dynamic Mechanical Thermal Analysis. About 30 mg of the non-cross-linked PS particles were dried at 60 °C in vacuum overnight. The PS particles were then pressed to a pellet with a diameter of 6 mm and thickness of 1 mm and heated at 200 °C to form a continuous film that was studied using an ARES rheometer (Rheometric Scientific) equipped with a force-rebalanced transducer. Plate–plate geometry was used with plate diameters of 6 mm. The gap between plates was about 1 mm (sample thickness). Shear deformation was applied under conditions of controlled deformation amplitude, which was kept in the range of the linear viscoelastic response of the studied sample. Experiments were performed under a dry nitrogen atmosphere. Frequency dependencies of the storage G' and the loss G'' parts of the shear modulus were determined from frequency sweeps measured within the frequency range $10^{-1}\text{--}10^2$ rad/s ($1.6 \times 10^{-2}\text{--}16$ Hz) at various temperatures. Master curves for G' and G'' at a reference temperature were obtained using the time–temperature superposition, i.e., shifting the data recorded at various temperatures along the frequency coordinate. Furthermore, the temperature dependence of G' and G'' at constant frequency of 10 rad/s (1.6 Hz) was measured, too.

THEORETICAL BACKGROUND

The resonance frequency f_c of a rectangular blank NMC can be described by³⁸

$$f_c = \frac{1}{2\pi} \sqrt{\frac{k_c}{nm_c}} = \frac{1}{2\pi l_c^2} \sqrt{\frac{3E_c I_c}{nw_c \rho_c h_c}} \quad (1)$$

Here, m_c is the mass of the cantilever, $n = 0.2427$ is a factor converting a point mass to the real mass distribution of the NMC in the first vibration mode, and k_c is the spring constant. For a NMC with a rectangular cross section k_c can be calculated from the geometry by

$$k_c = \frac{E_c w_c h_c^3}{4l_c^3} = \frac{3E_c I_c}{l_c^3} \quad (2)$$

where E_c is the Young's modulus, ρ_c is the density of the NMC material (typically Si), w_c is the width, h_c is the thickness, l_c is the length, and $I_c = w_c h_c^3 / 12$ is the moment of inertia of the NMC.

In the case that the coating layer does not contribute to the Young's modulus and the loading is homogeneously distributed on both sides of the NMC (i.e., in the case for a polymer colloid monolayer), the resonance frequency f_{pc} can be calculated by

$$\begin{aligned} f_{pc} &= \frac{1}{2\pi} \sqrt{\frac{k_c}{n(m_c + m_{pc})}} \\ &= \frac{1}{2\pi l_c^2} \sqrt{\frac{3E_c I_c}{nw_c(\rho_c h_c + 2\rho_{pc} h_{pc})}} \end{aligned} \quad (3)$$

Here h_{pc} corresponds to the thickness and ρ_{pc} to the density of the polymer. The added mass m_{pc} can be determined by measuring the different resonance frequencies by combining eqs 1 and 3:

$$m_{pc} = \frac{k_c}{4n\pi^2} (f_{pc}^{-2} - f_c^{-2}) \quad (4)$$

Equations 3 and 4 are only valid under the condition that the spring constant k_c of the NMC does not change upon the additional mass loading m_{pc} . This assumption is justified when the product of thickness of the layer with its Young's modulus is much lower than the thickness of the cantilever multiplied with its Young's modulus, $h_{pc}^3 E_{pc} \ll h_c^3 E_c$.

In the cases where the Young's modulus of the coating layers has to be considered (i.e., in the case for a thick polymer film), the resonance frequency of the NMC f_{pf} can be described as follows:

$$\begin{aligned} f_{pf} &= \frac{1}{2\pi} \sqrt{\frac{k_c + 2k_{pf}}{n(m_c + m_{pf})}} \\ &= \frac{1}{2\pi l_c^2} \sqrt{\frac{3(E_c I_c + 2E_{pf} I_{pf})}{nw_c(\rho_c h_c + 2\rho_{pf} h_{pf})}} \end{aligned} \quad (5)$$

Here, E_{pf} is the Young's modulus of the polymer coating. The factor 2 in front of k_{pf} comes from a polymer coating being situated on both sides of the NMC. The moment of inertia I_{pf} can be calculated from the NMC geometry (see Supporting Information) using

$$I_{pf} = \frac{w_c h_p}{12} (3h_c^2 + 6h_c h_{pf} + 4h_{pf}^2) \quad (6)$$

Since in this paper all the investigated NMCs were coated on both sides with PS colloidal monolayers, eqs 3, 5, and 6 describe the resonance frequency for a both side coated NMC.

In order to estimate the order of magnitude at which the Young's modulus of the polymer plays a role for the measured resonance frequency of the NMC, we have performed a calculation of the normalized resonance frequency shift $(f_{pf} - f_c)/f_c$ for a polymer coating versus the Young's modulus (Figure 1a), which is based on eq 5.

For low Young's moduli ($<10^9$ Pa), the negative shift of the normalized resonance frequency shift corresponds to the additional mass loading on the NMC by the polymer. The increase in the normalized resonance frequency $>10^9$ Pa reflects

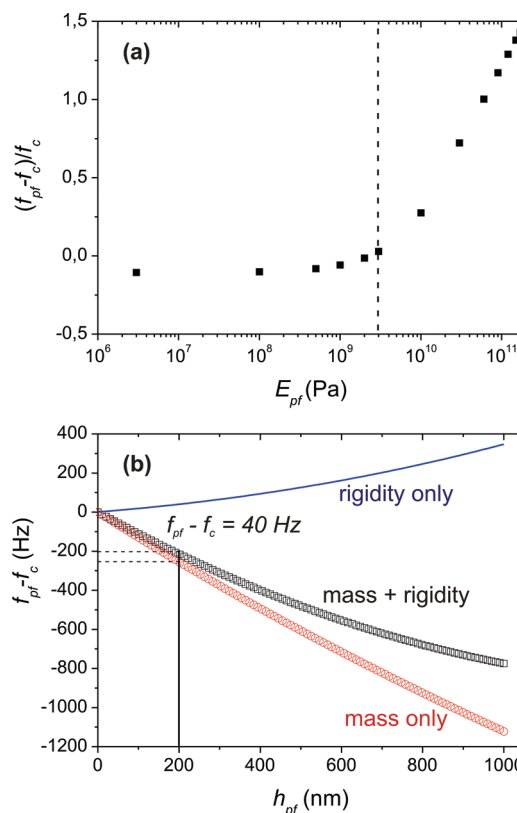


Figure 1. (a) Normalized resonance frequency shift upon increasing the Young's modulus E_{pf} of the coating material (based on eq 5). The mass of the coating material was kept constant. The thickness of the film was set constant at 400 nm. The dashed line indicates a Young's module of 3 GPa being a typical value of a polymer. (b) Resonance frequency shift of a NMC (500 μm long, 90 μm wide, and 2 μm thick, resonance frequency $f_c = 11\,023$ Hz) as a function of the coating film thickness h_{pf} . Effects of mass only (red circles), rigidity and mass (back squares), and rigidity only (blue solid line) are plotted.

the elastic contribution of the coated film to the spring constant of the NMC. Thus, at a Young's modulus $>10^9$ Pa, the elastic contribution of the coating layer needs to be considered.

In order to find the magnitude of the thickness of a polymer coating that is required to estimate its mechanical properties, we analyzed the resonance frequency f_{pf} of the NMC as a function of film thickness h_{pf} for a typical polymer material such as PS ($E_{pf} = E_{PS} = 3$ GPa). In one case we took eq 3 which is valid for mass changes only, and in the other case we took eq 5 where both mass and Young's modulus are considered. In both cases we took the difference to the initial resonance frequency of the uncoated cantilever f_c ; i.e., thickness of the PS corresponds to 0 nm (Figure 1b). From this plot we found that the thickness of polymer coatings, such as PS, must be >200 nm in order to obtain a contribution of 40 Hz to the resonance frequency change that is induced by the Young's modulus of the polymer film coating (error of measuring the resonance frequency corresponds to 2 Hz; thus, the error of a measurement would be in the order of 5%). Therefore, polymer film thickness >200 nm are beneficial for the analysis of polymeric layers on NMC.

RESULTS AND DISCUSSION

A. Coating NMC with Monolayers of Colloids. The first step in the coating procedure is based in a procedure reported

by Retsch and co-workers.³⁹ A layer of colloids was formed by spin-coating (4000 rpm) on a hydrophilic glass substrate ($2.5 \times 2.5 \text{ cm}^2$) using 90 μL of an aqueous dispersion containing 0.5–1.0 wt % colloids (Supporting Information S2). After drying, this process led to sparsely distributed colloids on the glass slide. Then the glass slide was taken by tweezers and was moved carefully by hand under a shallow angle into a trough of water containing $5 \times 10^{-4} \text{ M}$ sodium dodecyl sulfate (SDS) (pH 10.5 adjusted by ammonia). While moving the glass slide into the aqueous solution, the colloids floated off and remained at the air–water interface where they formed a close-packed monolayer on an area of $\approx 25 \text{ mm}^2$.

In the second step the monolayer was transferred onto NMC surfaces. Prior, the NMC were cleaned in an Ar plasma for 2 min. The NMC chip was taken with tweezers and was immersed in the water subphase by holding the chip. The NMC chip was then slowly withdrawn through the colloidal monolayer at an angle of about 30° in $\approx 3 \text{ s}$ (Figure 2a). Optical

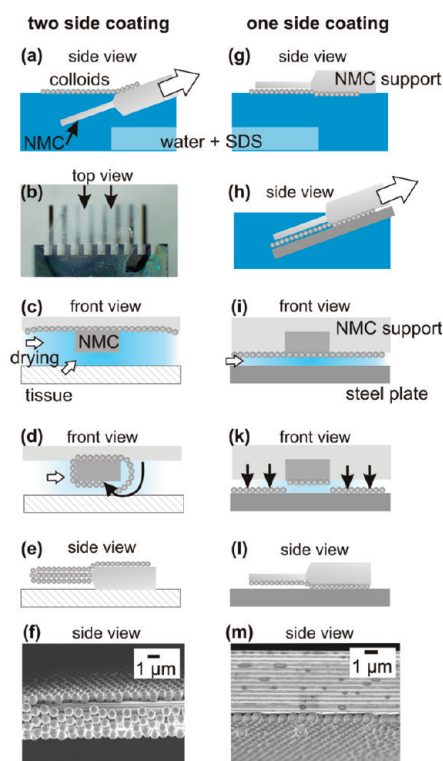


Figure 2. Transfer of the colloidal monolayer onto both sides (a–f) and onto only one side of a NMC array (g–m). (b) Microscope image of a NMC array with a large sheet of colloidal monolayer attached. The arrows indicate the free hanging colloidal monolayer between the NMC. (c, d, f) Illustration of the colloidal monolayer hanging between the NMCs and folding to the back sides of the NMC. (f) SEM image of NMC coated with PS colloidal monolayer on both sides. (i, k) Illustration of the deposition of the free hanging colloidal monolayer on the steel plate. (m) SEM image of NMC coated only on the “down” side with a PS colloidal monolayer. Details of the colloidal monolayer transfer steps are provided in the main text.

microscopy of the process showed that bridges of colloid films formed between individual NMC (Figure 2b,c). For drying, the support chip was placed on a sheet of tissue. The receding water led to the formation of colloidal monolayers on both sides of the NMCs (Figure 2d,e). The reason for the both sides coating was that the free hanging layer between the NMCs

folded back to the underside during the drying process. The SEM analysis of NMC showed that colloids were also coated the side walls (Figure 2f). The success of the coating can even be observed by the naked eye due to its colored appearance owing to interference of the scattered light from the colloids (Supporting Information S3a). Both side coated NMC can be readily used for dynamic measurements as will be explained later in part B.

For an operation of the NMC in the static mode, a one side coating, also called asymmetric coating, of the NMC surface is required. To obtain an asymmetric coating, NMCs were first hydrophobized by silanization with 1H,1H,2H,2H-perfluorodecyltrichlorosilane (liquid) by chemical vapor deposition (contact angle 113°) as reported by Hozumi et al.⁴⁰ In the present paper, the evaporation of the liquid silane was not induced by heating as described by Hozumi et al., but by reducing the pressure in a sealed desiccator with a vacuum pump. The hydrophobic NMC chip was placed horizontally on top of the floating monolayer of colloids (Figure 2g). A hydrophilic substrate, e.g. a metal plate, was placed underneath the NMC chip, and the whole assembly was removed from the water (Figure 2h). Then the assembly was dried in air for about 1 h (Figure 2i–l). During the drying process the colloids were kept on the NMC surfaces that faced the hydrophilic substrate. The optical microscope image of the substrate showed no colloidal monolayer at the areas where the NMC were placed. However, the colloids in the gaps between the NMC were all deposited on the substrate (Supporting Information S3b). Here the SEM images in side view of NMC coated with PS colloidal monolayers showed a one side coating and no coating of the sidewalls (Figure 1m).

B. Colloidal Monolayers before Annealing. Here we focused on the analysis of NMC coated with PS colloidal monolayers on both sides. Imaging the PS coated NMC by SEM showed a homogeneous coating of PS colloids on the entire cantilever surface (Figure 3a). At larger magnification we

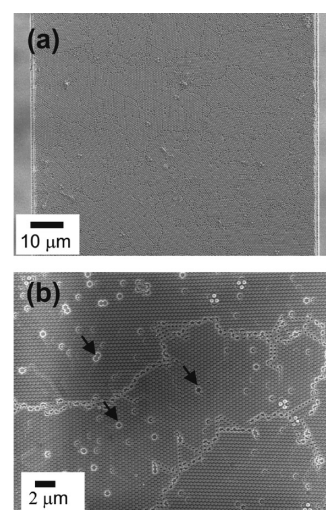


Figure 3. SEM images of colloidal monolayers deposited on NMC: (a) an area of $100 \times 90 \mu\text{m}^2$ of the colloidal monolayer; (b) an area of $36 \times 26 \mu\text{m}^2$ of the close-packed colloidal monolayer. In addition, two long line defects were observed which were caused by different orientations of colloidal domains.

determined only about 40 missing colloids in an area of $36 \times 26 \mu\text{m}^2$ corresponding to 2% of a closely packed monolayer with

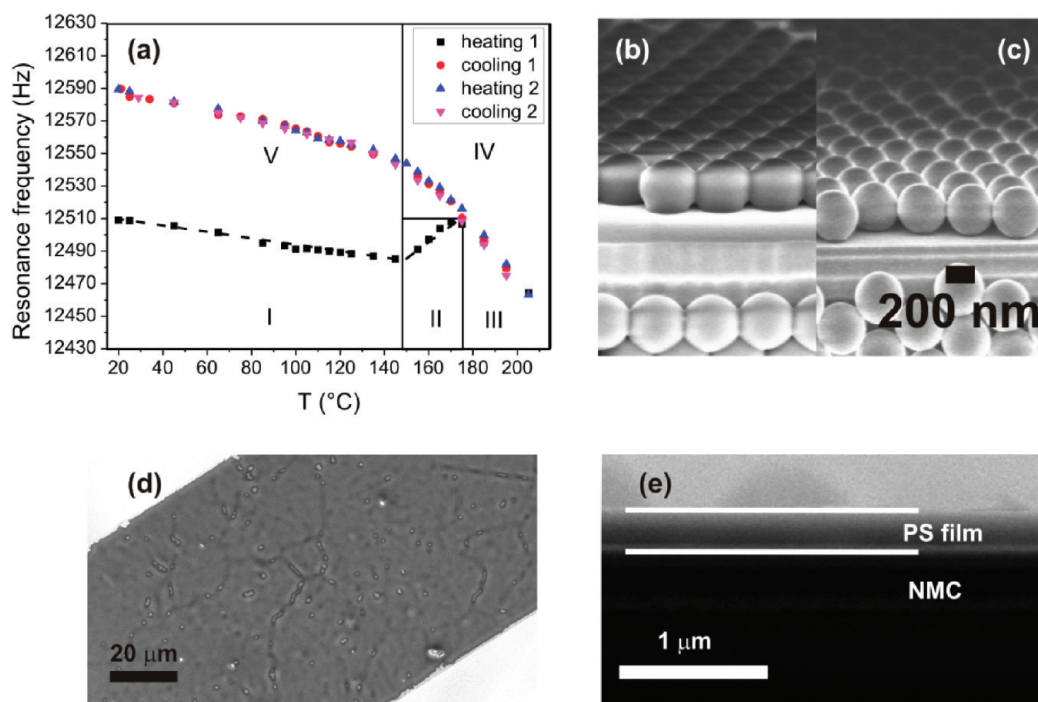


Figure 4. (a) Resonance frequency of NMC coated with non-cross-linked PS on both sides during the first and second heating and cooling process. Data of two more heating and cooling processes are provided in the Supporting Information S6. (b) SEM image of the onset of the merging of the colloids after heating to 155 °C as compared to colloids before heating (c). (d, e) SEM images of the homogeneous PS film after the colloids were heated to 220 °C (d: top view; e: side view).

about 2200 particles in total (Figure 3b, some of the vacancy defects are indicted by black arrows). On the basis of these SEM images, we determined the density of the PS colloids per area to be $2.24/\mu\text{m}^2$. This value is close to the theoretical value ($2.35/\mu\text{m}^2$) based on a hexagonal packing of the PS colloids having a radius of $r_{\text{pc}} = 200 \pm 15$ nm. Assuming a hexagonal close packing, the area per colloid particle is $(2r_{\text{pc}})^2 \sin 60^\circ$. Thus, the maximal number of colloid particles on both sides of the NMC is

$$N = \frac{w_c l_c}{2r_{\text{pc}}^2 \sin 60^\circ} \quad (7)$$

With the mass of one particle of $m_{\text{pc}} = 4\pi r_{\text{pc}}^3 \rho_{\text{pc}}/3$ (density of PS $\rho_{\text{pc}} = \rho_{\text{PS}} = 1050$ kg/m³), the mass of all PS colloids coated on NMC ($m_{\text{all pc}}$) is given by

$$m_{\text{all pc}} = \frac{2\pi w_c l_c \rho_{\text{pc}} r_{\text{pc}}}{3 \sin 60^\circ} = 2.42 w_c l_c \rho_{\text{PS}} r_{\text{pc}} \quad (8)$$

Thus, for the here used PS colloids ($r_{\text{pc}} = 200$ nm) and cantilevers ($w_c = 90$ μm, $l_c = 500$ μm), we obtain a mass loading $m_{\text{all pc}}$ of 22.9 ng.

In order to verify the homogeneous mass loading of NMCs ($h_c = 2.4$ μm and $k = 0.42$ N/m) with PS colloids, we measured the resonance frequency before ($f_c = 13018$ Hz) and after transferring the colloidal monolayers ($f_{\text{pc}} = 12509$ Hz). Using eq 4, which is valid for a negligible contribution of the added mass to the spring constant k_c of the NMC, we determined a mass loading of 21.8 ± 0.4 ng for the colloids. This agrees with the mass determined from the density of PS colloids based on SEM images (22.9 ng).

In total, we analyzed three PS colloidal coatings with different sizes on NMCs (double side coating, table of

measured frequencies and geometry of the NMCs see Supporting Information S4), and we did not find a systematic deviation toward higher or lower mass loadings. All measurements agreed within an error of 5% attributed to uncertainty in k_c . Therefore, we conclude that the deposition method results in homogeneous and reproducible monolayers of PS colloids. Furthermore, our assumption of a negligible contribution of the particle monolayer to the spring constant k is confirmed. This implies that the contribution of the PS colloidal monolayer to the elasticity of the coated NMC is negligible, despite of having a polymer layer thickness of 400 nm. We attribute this behavior to no or small contact areas and negligible friction between neighboring PS colloids. Thus, colloids do not significantly deform upon vibrating the NMC.

C. Thermomechanical Properties of Monolayers of Non-Cross-Linked Particles. C1. Increasing Temperature.

In order to study temperature-induced changes in non-cross-linked PS colloidal monolayers, we heated the NMC from room temperature up to 210 °C at a rate of 2 K/min (Figure 4). During the first heating process, the resonance frequency decreased linearly up to a temperature of ≈ 150 °C at a slope of -0.22 ± 0.01 Hz/K (Figure 4a, black squares, regime I). This change in frequency corresponded to the decrease of the Young's modulus of micromechanical cantilever sensor material (silicon) in this temperature range.⁴¹ In regime II, from ≈ 150 to 175 °C the resonance frequency increased with a slope of 0.67 ± 0.02 Hz/K. The increase in resonance frequency in this temperature interval indicated an increasing contribution of the PS colloids to the elastic properties of the vibrating NMC. We attribute the transition regime II to the onset of merging and softening of PS.^{42,43} Above ≈ 150 °C, mechanical bridges form between PS colloids. Increasing the temperature further led to filling of the voids between the PS colloids until a continuous PS film formed. In general, an increasing in resonance

frequency could also be caused by a decrease in mass of NMC loading.⁴⁴ However, a thermogravimetric analysis (TGA) of the PS colloids did not reveal a mass decrease up to a temperature of 380 °C (TGA provided in Supporting Information S5).

Above 175 °C, the resonance frequency of the NMC decreased again with a slope of -1.45 ± 0.04 Hz/K (regime III). The faster resonance frequency decrease in regime III as compared to regime I can be explained by the contribution of the temperature-dependent mechanical properties of the PS coating film which is characterized by significant decrease of the Young's modulus above T_g of PS from ≈ 3 GPa ($T < T_g$) to ≈ 0.002 GPa ($T > T_g$) in the rubbery plateau.⁴⁵ Thus, up to 175 °C the increase in elasticity of the particle layer due to the merging of neighboring particles dominated. From 175 °C on the softening of the polymer with increasing temperature dominated.

A fit of a linear dependence to all three regimes allowed us to estimate the transition temperatures between regime I \rightarrow II and II \rightarrow III to be 147 ± 3 and 175 ± 3 °C, respectively. The transition regime from colloids to films (regime II) was then studied by SEM (Figure 4b) recorded for the samples which were heated only to 155 °C (regime II). The contact area between colloids and between the colloids and NMC increased as compared to the sample before heating (Figure 4c). Complete film formation was obtained after heating the monolayer of PS particles to 210 °C (regime III, Figure 4d,e). Here the colloids merged completely into a continuous film having a thickness of 260 ± 30 nm (Figure 4e). In the top view image (Figure 4d) cracks can be seen which resemble line defects which were caused by different orientations of colloid domains (Figure 3). Additionally, the PS film thickness can be calculated from the particle radius and the densely packed hexagonal monolayer of PS colloids assuming that the total volume of the polymer does not change during film formation

$$h_{pf} = \frac{\pi r_{pc}^2}{3 \sin 60^\circ} = 1.21 r_{pc} \quad (9)$$

For our PS colloids having a radius of 200 nm we calculated a film thickness h_p of 242 nm, which is in agreement with the determined value from the SEM micrograph.

C2. Decreasing Temperature. After reaching 210 °C, the temperature was reduced at a constant rate of -2 K/min until room temperature. Hereby the measured resonance frequency increased, and only two different slopes were found (Figure 4a, red circles). The slope of the regime IV ($T > 150$ °C) was -1.45 ± 0.04 Hz/K, which is similar to the slope in regime III. At temperatures < 150 °C the slope decreased to -0.34 ± 0.02 Hz/K (regime V) being slightly lower than the slope in the regime I (-0.22 ± 0.01 Hz/K). The difference in slopes between regime I and V indicated an increase in the contribution of the temperature-dependent mechanical properties of the PS coating as an additional effect to the temperature-dependent Young's modulus of Si. Furthermore, no change in slope was recorded at a temperature of ≈ 175 °C, which was the transition temperature between regime II and III (Figure 3a). The fit of lines to both regimes indicated a transition temperature of 147 ± 4 °C being similar to the one between regime II and III.

A subsequent second temperature cycle (Figure 4a, blue triangles for heating and pink triangles for cooling) up to 210 °C for the PS-covered NMC exhibited identical frequency values as compared to the cooling curve (Figure 4a, red circles) of the first cycle. The measured resonance frequency changes

were fully reversible upon heating and cooling, and identical slopes in regime V (-0.34 ± 0.02 Hz/K) and regime IV (-1.45 ± 0.04 Hz/K) were observed. In addition, the change in slope at 147 ± 3 °C was confirmed for the heating and cooling measurements. This transition temperature might indicate the change of the mechanical properties of the PS layer, resulting from the transition from a viscoelastic regime of PS, IV, to the glassy regime V. Clearly, the temperature value of 147 °C is significantly higher than the glass transition temperature, T_g , of ≈ 100 °C commonly reported for bulk PS and measured using methods like differential scanning calorimetry (DSC) or DMTA.

To obtain a better insight into this issue, a series of DMTA measurements were performed using a classical plate–plate rheometer and a macroscopic sample prepared from the PS colloids as described in the Materials and Methods section. The temperature dependence of the real (open black squares) and imaginary (open red circles) part of the complex shear modulus and $\tan \delta = G''/G'$ (pink open triangles) measured at frequency of 1.6 Hz are shown in Figure 5. Using these data, a T_g can be

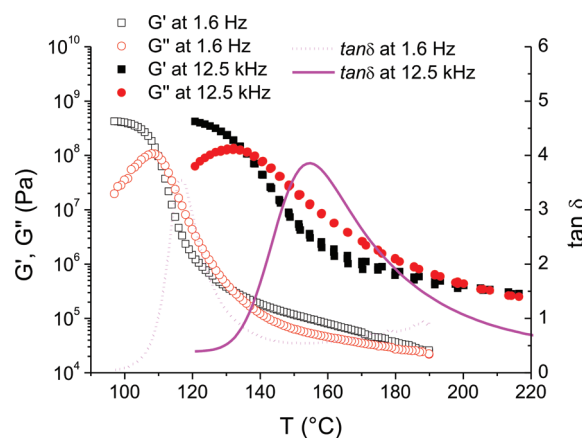


Figure 5. G' and G'' measured with classical rheology at shear frequency 1.6 Hz (open symbols). From the maximum in $\tan \delta$ (dashed line) a T_g of 115 ± 5 °C at this frequency was obtained. The G' and G'' calculated (filled symbols) for a reference frequency of 12.5 kHz are shifted toward higher temperature compared to the one at 1.6 Hz. A modified Gauss fit to the $\tan \delta$ values (solid line) yields an increase in the maximum of $\tan \delta$ corresponding to 155 ± 5 °C at 12.5 kHz.

obtained from the maximum of $\tan \delta$ at a temperature of $\approx 115 \pm 5$ °C. T_g given by this definition corresponds to the midpoint between the glassy and the rubbery states of a polymer.⁴⁶ Another possibility would be to use the maximum value of the loss module G'' which is also attributed to the glass transition in plastics and is associated with the onset of segmental motion. As a next step, a master curve, i.e. the frequency dependence of G' and G'' over broad frequency range at a reference temperature of 100 °C, was constructed using the time–temperature superposition principle (Supporting Information S7a) as suggested by Williams, Landel, and Ferry (WLF):⁴⁵

$$-\frac{C_1(T - T_{ref})}{C_2 + (T - T_{ref})} = \log \frac{f}{f_{ref}} \quad (10)$$

C_1 and C_2 are empirical constants, T and f are the temperature and frequency, and T_{ref} and f_{ref} are the corresponding reference temperature and frequency. The smooth master curve, the

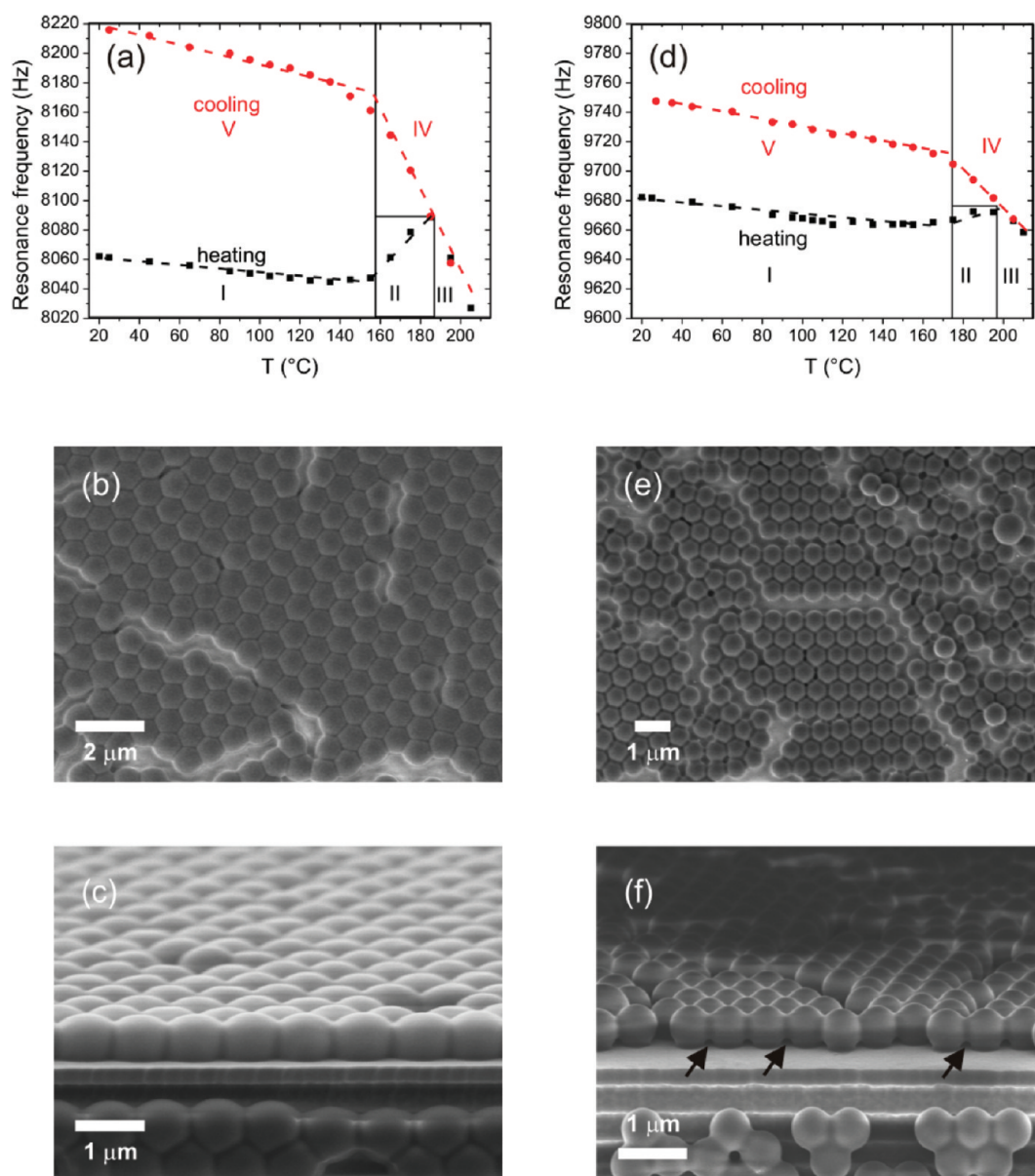


Figure 6. (a, d) Resonance frequency shift of NMC coated with of 1% and 10% cross-linked PS colloidal monolayer during thermal annealing. SEM images of 1% (b, c) and 10% (e, f) cross-linked colloids after annealing. In the case of 1% cross-linked colloids, the voids between the colloids were completely filled and the surface shows hilly structures. In the case of 10% cross-linked PS colloids, the voids between the colloids were only partially filled and empty areas remain (arrows in f).

good fit to the temperature dependence of the shift factors, and the reasonable values of the constants $C_1 = 10.78$ and $C_2 = 49.89$ estimated from the fit (Supporting Information S7b) indicated that the PS colloids have formed a continuous bulk sample with properties similar to the classical PS. Thus a mechanical contribution from other chemicals which were used during the synthesis of the colloids and might have contaminated the colloid samples were excluded. Based on WLF equation, the master curve can be translated into a temperature-dependent storage G' and loss modulus G'' at a given frequency. First, the results of such a conversion for a frequency of 1.6 Hz revealed an identical dependence of G' and G'' with temperature as measured at this frequency (data not shown). Second, the conversions for a reference frequency of 12.5 kHz are shown in Figure 5. The values for G' (filled black squares) and for G'' (filled red circles) are now shifted toward

higher temperatures. Furthermore, $\tan \delta$ (filled pink triangles) exhibits a maximum at a temperature of 155 ± 5 °C, which is in agreement with the measured temperature of 147 ± 3 °C at which the slope changes in the NMC studies. Upon remaining with the above definition for T_g being the maximum of $\tan \delta$, we associate the temperature of ≈ 150 °C to the glass transition temperature of PS measured at this high frequency. We conclude that the resonance frequency response of NMC allows one to measure T_g of polymers given by the midpoint of the change from the glassy to the rubbery state. It is worth to note that the determination of T_g at frequencies above 50 Hz is often not directly accessible by classical rheology.

C3. Calculation of Young's Modulus. Our experiment suggests that at the beginning the colloids did not interact strongly with each other and thus did not contribute to the measured resonance frequency, i.e. f_{pc} ($f_{pc} = 12509$ Hz), of the

NMC. After the first heating and cooling cycle, the resonance frequency of the coated cantilever increased by 80 Hz at room temperature, i.e., corresponds to f_{pf} ($f_{pf} = 12585$ Hz). Since the mass of the PS on the cantilever did not change during the film formation process, the ratio between f_{pc} and f_{pf} based on eqs 3 and 5 can be described as follows:

$$\left(\frac{f_{pf}}{f_{pc}}\right)^2 = \frac{E_c I_c + E_{pf} I_{pf}}{E_c I_c} \quad (11)$$

Now the Young's modulus of the coating can be directly calculated by

$$E_{pf} = E_c \frac{I_c}{I_{pf}} \left[\left(\frac{f_{pf}}{f_{pc}}\right)^2 - 1 \right] \quad (12)$$

where I_p is given by eq 6

$$I_{pf} = \frac{w_c h_{pf}}{12} (3h_c^2 + 6h_c h_{pf} + 4h_{pf}^2)$$

and by eq 9

$$h_{pf} = \frac{\pi r_{pc}}{3 \sin 60^\circ} = 1.21 r_{pc}$$

Please note that the film thickness h_p is determined by the radius of the PS colloids (eq 9). Thus, the film thickness does not need to be measured by SEM necessarily.

With the film thickness $h_{pf} = 242$ nm after the annealing experiment we obtain a Young's modulus of the PS film of 2.8 GPa at ambient temperature for the resonating NMC. This value is close to the Young's modulus of the bulk material of 3–4 GPa.^{47,48} Furthermore, it is possible to calculate the temperature dependence of the Young's modulus from the measured frequency dependence in regime I (corresponding to f_{pc}) and regime V (corresponding to f_{pf}) at each measured temperature. Our data inferred a linear decrease in Young's modulus of -4 ± 0.5 MPa/K up to a temperature of 140 °C.

C4. Thermal Annealing of Cross-Linked PS Particles. In order to apply the concept to different colloids, we measured the thermal behavior of PS colloids which were cross-linked by DVB. A NMC was coated with a monolayer of 1% cross-linked PS colloids having a radius of 390 nm and was heated up to 220 °C (Figure 6a). We found a similar dependence of the resonance frequency upon heating and cooling. All five regimes could be clearly identified. The temperatures marking the onset and end of the film formation shifted to higher temperatures, which were 158 ± 5 and 188 ± 5 °C for the 1% cross-linked colloids.

Using PS colloids which were cross-linked by 10% (radius 310 nm), even higher transition temperatures of 175 ± 5 and 198 ± 5 °C (Figure 6d) were revealed. Details of the used NMCs are provided in the Supporting Information S8. The increase in the glass transition temperature with the degree of cross-linking is in agreement with hindrance of the relaxation of the polymer chains by the cross-link agents.⁴⁹ SEM images of the PS coating layers after annealing revealed layers of particles exhibiting only partial merging (Figure 6b,c,e,f). The coating appears as a monolayer consisting of hexagonally arranged particles. In this case only an apparent Young's modulus can be calculated by eq 9 owing to the presence of residual colloidal

structures even after annealing. We associated an apparent Young's modulus of 1.3 GPa to the coating made by the 1% cross-linked PS colloids ($2r_{pc} = 780 \pm 40$ nm decreased in average to $h_p = 710 \pm 30$ nm) and to 0.8 GPa for the 10% cross-linked PS colloids ($2r_{pc} = 620 \pm 30$ nm decreased here to $h_p = 570 \pm 30$ nm). Polymer films which were formed from cross-linked colloids were studied by Zosel and Ley and were found to behave brittle.⁵⁰ They interpreted the data in a way that the interdiffusion of polymer chains between cross-linked colloids are limited compared to the non-cross-linked colloids. Therefore, the film generated from cross-linked colloids could not develop significant mechanical strength.

D. Organic Vapor Annealing of Non-Cross-Linked Particles. As an alternative to temperature annealing, we investigated the fabrication of thin films from colloidal monolayers via vapor annealing.⁵¹ In the case of PS colloids we have selected toluene solvent for the vapor annealing process. Upon exposure of PS to toluene vapor T_g decreases and even falls below room temperature.⁵¹ In order to probe film formation, we exposed a NMC, which is coated with non-cross-linked PS colloids (radius: 200 ± 15 nm) on both sides, to saturated toluene vapor at 2.9 kPa at 20 °C (Figure 7a).

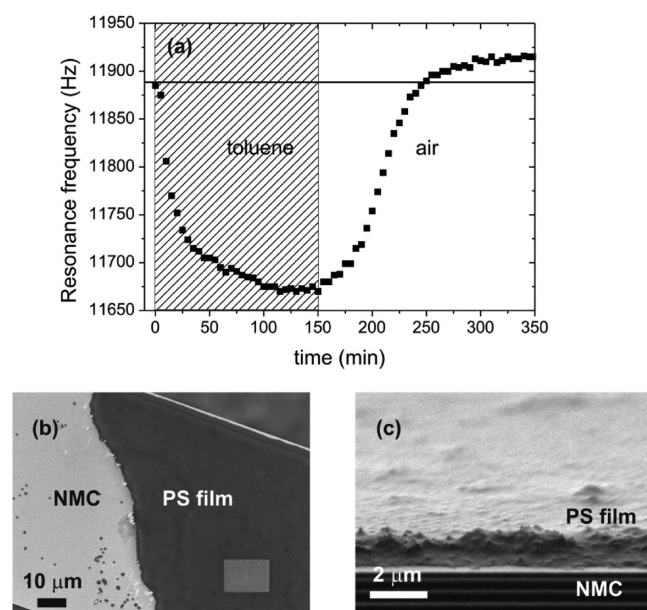


Figure 7. Resonance frequency shift of NMC coated with non-cross-linked PS colloidal monolayers on both sides during the toluene vapor annealing (a). SEM images of the PS film after toluene vapor annealing: (b) the top view; (c) the side view. The film thickness was 350 ± 29 nm. As compared to the PS film formed via thermal annealing, the PS film formed via organic vapor annealing is more homogeneous, which means the film is without cracks and voids. It is, however, more rough.

During the toluene exposure, the resonance frequency of the NMC decreased. After 160 min the toluene/ N_2 gas mixture was replaced by a stream of air in order to dry the film. During this process toluene was released from the coating film, and therefore the resonance frequency increased due to the decreased mass of the coating film. After an additional 90 min (or at 240 min total time) the measured resonance frequency crossed the initial resonance frequency ($f_{pc} = 11.89$ kHz) of the NMC. In analogy to the thermal annealing process, we associate the increase in resonance frequency to the

different types of films, i.e., at the beginning a monolayer of colloids and at the end a continuous film ($f_{\text{pf}} = 11.92$ kHz) which was proven by SEM (Figure 7b,c).

In order to determine the mechanical properties of the vapor phase annealed film, we have to consider two effects: First, resonance frequency changes are induced by mechanical properties changes of the colloids owing to the plasticizing effect of toluene. Second, the mass increase in PS colloids by toluene vapor has to be considered which is not constant during the toluene exposure step. Thus, a calculation of Young's modulus E of the homogeneous film based on eq 12 results in an underestimation of the Young's modulus (1.5 GPa) owing to remaining toluene in the PS colloids even after drying for several hours.⁵² The remaining mass of toluene was measured for the same PS sample (Supporting Information S9) as reported by Zhang and Kruger^{52,53} and can be compensated. Mass loading of toluene only would result in a decrease in resonance frequency by 40 Hz from 11.89 kHz to 11.85 kHz. Thus, reducing the final resonance frequency after toluene exposure by 40 Hz, we obtain a value of 11.85 kHz. On the basis of this compensation, a Young's modulus of 2.3 GPa was calculated for the PS film. This value is still lower than the one determined for thermal annealing (3.0 GPa). This difference is attributed to the plasticizing effect of the residual toluene in the film.

SUMMARY AND CONCLUSION

Here we have shown that PS colloidal monolayers can be transferred almost defect-free to nanomechanical cantilevers. The method can be tailored in a way to coat the NMC with the colloidal monolayer only on one side or on both sides. Although single side coatings of colloids do not play a role in our measurements that are presented here, they are essential for NMC bending measurements.^{54,55}

Colloidal monolayer coatings offer several advantages: first, the mass loading is given by the size of the colloids (eq 8). Second, the interaction between neighboring particles in a monolayer is negligible; therefore, the resonance frequency shift of the cantilever is only due to the added mass, which is crucial for a quantitative analysis of the homogeneous polymer film generated from a colloidal monolayer (combination of eq 3 and 5 to eq 11). Third, homogeneous polymer films can be generated from these colloidal monolayers by thermal and vapor annealing. Thus, polymer coating on NMC with thickness up to $1.0\ \mu\text{m}$ can be generated by using colloids with diameter of about $1.8\ \mu\text{m}$. This would allow even more precise measurements of mechanical properties as outlined in Figure 1b. The homogeneity of these polymer coating films simplifies the quantitative analysis of the NMC resonance frequency shifts; e.g., an additional thickness measurements (e.g., by SEM) can be omitted. Fourth, the use of a solvent free deposition process to make homogeneous films allows eliminating effects owing to residual solvent in the polymer.

The specialty of NMC is that the beam resonates at frequencies >1 kHz. Thus, mechanical properties of polymers can be investigated at high frequencies which are typically not accessible in a direct measurement of dynamic mechanical thermal analysis. NMC can be operated at a wide range of temperatures from -260 ⁵⁶ up to $700\ ^\circ\text{C}$.⁵⁷ In particular, we found that the slope in resonance frequency of the polymer coated NMC changes at a temperature which corresponds to the maximum of $\tan \delta$ obtained from the dynamic mechanical thermal analysis. Furthermore, arrays of NMC can be used that

feature different resonance frequencies (Figure 8). Using such arrays allows to study frequency-dependent characteristics of

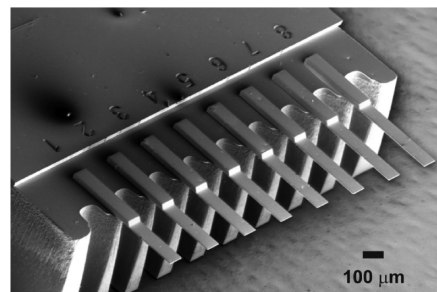


Figure 8. SEM image of a NMC with different length and thus different resonance frequency on one array.

the polymer coating. Thus, frequency-dependent degradation⁵⁸ and delamination effects could be studied as well. In summary, in our view the NMC method is a useful extension for mechanical spectroscopy of polymer films.

ASSOCIATED CONTENT

Supporting Information

Figures showing S1: temperature calibration curve of the heating stage; S2: formation of colloidal monolayer at air/water interface; S3: microscopic images of NMC coated with PS colloidal monolayer and the metal substrate with left over monolayer; S4: table of the mass of monolayer from colloids in different sizes calculated according to the geometry and from the resonance frequency shift; S5: TGA result of non-cross-linked PS colloids; S6: resonance frequency as a function of temperature of the NMC coated PS for a third and fourth thermal cycle; S7 master curve and the shift factor for non-cross-linked PS colloids; S8: details of NMCs used for the measurements shown in Figure 6; S9 coating cantilever with colloids only on the end and the toluene uptake of PS colloids; S10: origin of equation 6. This material is available free of charge via the Internet at <http://pubs.acs.org>.

AUTHOR INFORMATION

Corresponding Author

*Phone: +49-(0)6131-379-114; Fax: +49-(0)6131-379-100; e-mail: berger@mpip-mainz.mpg.de.

ACKNOWLEDGMENTS

We acknowledge partial financial support by the DFG through the priority program 1369 (Polymer solid contacts: interfaces and interphases; BE 3286/1; GU 771/3) and SFB 625 (From Single Molecules to Nanoscopically Structured Materials). We thank Maren Müller, Nikolas Vogel, Gabriele Schäfer, Gunnar Kircher, Uwe Rietzler, Sullivan Vianna, Günter Auernhammer, and Werner Steffen for discussions and technical support of the project.

REFERENCES

- (1) Baller, M. K.; Lang, H. P.; Fritz, J.; Gerber, C.; Gimzewski, J. K.; Drechsler, U.; Rothuizen, H.; Despont, M.; Vettiger, P.; Battiston, F. M.; Ramseyer, J. P.; Fornaro, P.; Meyer, E.; Guntherodt, H. J. *Ultramicroscopy* **2000**, *82*, 1.
- (2) Lei, H.; Payne, J. A.; McCormick, A. V.; Francis, L. F.; Gerberich, W. W.; Scriven, L. E. *J. Appl. Polym. Sci.* **2001**, *81*, 1000.

- (3) Igarashi, S.; Itakura, A. N.; Toda, M.; Kitajima, M.; Chu, L.; Chifene, A. N.; Forch, R.; Berger, R. *Sens. Actuators, B* **2006**, *117*, 43.
- (4) Zhou, F.; Shu, W. M.; Welland, M. E.; Huck, W. T. S. *J. Am. Chem. Soc.* **2006**, *128*, 5326.
- (5) Chen, T.; Chang, D. P.; Liu, T.; Desikan, R.; Datar, R.; Thundat, T.; Berger, R.; Zauscher, S. *J. Mater. Chem.* **2010**, *20*, 3391.
- (6) Lenz, S.; Nett, S. K.; Memesa, M.; Roskamp, R. F.; Timmann, A.; Roth, S. V.; Berger, R.; Gutmann, J. S. *Macromolecules* **2010**, *43*, 1108.
- (7) Snow, D.; Weeks, B. L.; Kim, D. J.; Loui, A.; Hart, B. R.; Hope-Weeks, L. J. *J. Colloid Interface Sci.* **2007**, *316*, 687.
- (8) Bradley, C.; Jalili, N.; Nett, S. K.; Chu, L. Q.; Forch, R.; Gutmann, J. S.; Berger, R. *Macromol. Chem. Phys.* **2009**, *210*, 1339.
- (9) Zhao, J.; Berger, R.; Gutmann, J. S. *Appl. Phys. Lett.* **2006**, 89.
- (10) Zauscher, S.; Abu-Lail, N. I.; Kaholek, M.; LaMattina, B.; Clark, R. L. *Sens. Actuators, B* **2006**, *114*, 371.
- (11) Chen, G. Y.; Thundat, T.; Wachter, E. A.; Warmack, R. J. *J. Appl. Phys.* **1995**, *77*, 3618.
- (12) Ludwig, A.; Cao, J.; Brugger, J.; Takeuchi, I. *Meas. Sci. Technol.* **2005**, *16*, 111.
- (13) Jung, N.; Jeon, S. *Macromolecules* **2008**, *41*, 9819.
- (14) Jung, N.; Seo, H.; Lee, D.; Ryu, C. Y.; Jeon, S. *Macromolecules* **2008**, *41*, 6873.
- (15) Yun, M.; Jung, N.; Yim, C.; Jeon, S. *Polymer* **2011**, *52*, 4136.
- (16) Ramos, D.; Tamayo, J.; Mertens, J.; Calleja, M.; Villanueva, L. G.; Zaballos, A. *Nanotechnology* **2008**, 19.
- (17) Tamayo, J.; Ramos, D.; Mertens, J.; Calleja, M. *Appl. Phys. Lett.* **2006**, 89.
- (18) Grueter, R. R.; Khan, Z.; Paxman, R.; Ndieyira, J. W.; Dueck, B.; Bircher, B. A.; Yang, J. L.; Drechsler, U.; Despont, M.; McKendry, R. A.; Hoogenboom, B. W. *Appl. Phys. Lett.* **2010**, 96.
- (19) Lang, H. P.; Berger, R.; Andreoli, C.; Brugger, J.; Despont, M.; Vettiger, P.; Gerber, C.; Gimzewski, J. K.; Ramseyer, J. P.; Meyer, E.; Guntherodt, H. J. *Appl. Phys. Lett.* **1998**, *72*, 383.
- (20) Jensenius, H.; Thaysen, J.; Rasmussen, A. A.; Veje, L. H.; Hansen, O.; Boisen, A. *Appl. Phys. Lett.* **2000**, *76*, 2615.
- (21) Battiston, F. M.; Ramseyer, J. P.; Lang, H. P.; Baller, M. K.; Gerber, C.; Gimzewski, J. K.; Meyer, E.; Guntherodt, H. J. *Sens. Actuators, B* **2001**, *77*, 122.
- (22) Vidic, A.; Then, D.; Ziegler, C. *Ultramicroscopy* **2003**, *97*, 407.
- (23) Pinnaduwage, L. A.; Thundat, T.; Hawk, J. E.; Hedden, D. L.; Britt, R.; Houser, E. J.; Stepnowski, S.; McGill, R. A.; Bubb, D. *Sens. Actuators, B* **2004**, *99*, 223.
- (24) Calleja, M.; Nordstrom, M.; Alvarez, M.; Tamayo, J.; Lechuga, L. M.; Boisen, A. *Ultramicroscopy* **2005**, *105*, 215.
- (25) Dohn, S.; Svendsen, W.; Boisen, A.; Hansen, O. *Rev. Sci. Instrum.* **2007**, 78.
- (26) Singamaneni, S.; LeMieux, M. C.; Lang, H. P.; Gerber, C.; Lam, Y.; Zauscher, S.; Datskos, P. G.; Lavrik, N. V.; Jiang, H.; Naik, R. R.; Bunning, T. J.; Tsukruk, V. V. *Adv. Mater.* **2008**, *20*, 653.
- (27) Yoshikawa, G.; Lang, H.-P.; Akiyama, T.; Aeschmann, L.; Staufer, U.; Vettiger, P.; Aono, M.; Sakurai, T.; Gerber, C. *Nanotechnology* **2009**, 20.
- (28) Bietsch, A.; Zhang, J. Y.; Hegner, M.; Lang, H. P.; Gerber, C. *Nanotechnology* **2004**, *15*, 873.
- (29) Deegan, R. D.; Bakajin, O.; Dupont, T. F.; Huber, G.; Nagel, S. R.; Witten, T. A. *Nature* **1997**, *389*, 827.
- (30) Shimoda, T.; Morii, K.; Seki, S.; Kiguchi, H. *MRS Bull.* **2003**, *28*, 821.
- (31) Bonaccorso, E.; Butt, H. J.; Hankeln, B.; Niesenhaus, B.; Graf, K. *Appl. Phys. Lett.* **2005**, 86.
- (32) Bumbu, G. G.; Kircher, G.; Wolkenhauer, M.; Berger, R.; Gutmann, J. S. *Macromol. Chem. Phys.* **2004**, *205*, 1713.
- (33) Igarashi, S.; Itakura, A. N.; Kitajima, M.; Chifene, A. N.; Forch, R.; Berger, R. *Appl. Phys. Lett.* **2006**, 88.
- (34) Zhang, Y.; Arfsten, J.; Pihan, S. A.; Kaule, T.; Foerch, R.; Berger, R. *J. Colloid Interface Sci.* **2010**, *351*, 532.
- (35) Steward, P. A.; Hearn, J.; Wilkinson, M. C. *Adv. Colloid Interface Sci.* **2000**, *86*, 195.
- (36) Arda, E.; Kara, S.; Sarac, A.; Pekcan, O. *J. Colloid Interface Sci.* **2006**, *297*, 520.
- (37) Eshuis, A.; Leendertse, H. J.; Thoenes, D. *Colloid Polym. Sci.* **1991**, *269*, 1086.
- (38) Butt, H.-J.; Cappella, B.; Kappl, M. *Surf. Sci. Rep.* **2005**, *59*, 1.
- (39) Retsch, M.; Zhou, Z. C.; Rivera, S.; Kappl, M.; Zhao, X. S.; Jonas, U.; Li, Q. *Macromol. Chem. Phys.* **2009**, *210*, 230.
- (40) Hozumi, A.; Ushiyama, K.; Sugimura, H.; Takai, O. *Langmuir* **1999**, *15*, 7600.
- (41) Cho, C. H. *Curr. Appl. Phys.* **2009**, *9*, 538.
- (42) Harel, E.; Meltzer, S. E.; Requicha, A. A. G.; Thompson, M. E.; Koel, B. E. *Nano Lett.* **2005**, *5*, 2624.
- (43) Yi, D. K.; Paik, U. *J. Nanosci. Nanotechnol.* **2010**, *10*, 4943.
- (44) Berger, R.; Lang, H. P.; Gerber, C.; Gimzewski, J. K.; Fabian, J. H.; Scandella, L.; Meyer, E.; Guntherodt, H. J. *Chem. Phys. Lett.* **1998**, *294*, 363.
- (45) Strobl, G. *The Physics of Polymers*; Springer-Verlag: Berlin, 2007.
- (46) Turi, E. A. *Thermal Characterization of Polymeric Materials*, 2nd ed.; Academic Press: San Diego, 1997; Vol. I.
- (47) Andrews, R. D.; Rudd, J. F. *J. Appl. Phys.* **1957**, *28*, 1091.
- (48) Rudd, J. F.; Gurnee, E. F. *J. Appl. Phys.* **1957**, *28*, 1096.
- (49) Kangwansupamonkon, W.; Damronglerd, S.; Kiatkamjornwong, S. *J. Appl. Polym. Sci.* **2002**, *85*, 654.
- (50) Zosel, A.; Ley, G. *Macromolecules* **1993**, *26*, 2222.
- (51) Juhue, D.; Lang, J. *Macromolecules* **1994**, *27*, 695.
- (52) Zhang, R.; Graf, K.; Berger, R. *Appl. Phys. Lett.* **2006**, *89*, 3.
- (53) Kruger, K. M.; Sadowski, G. *Macromolecules* **2005**, *38*, 8408.
- (54) Raiteri, R.; Butt, H. J.; Grattarola, M. *Electrochim. Acta* **2000**, *46*, 157.
- (55) Yoshikawa, G.; Akiyama, T.; Gautsch, S.; Vettiger, P.; Rohrer, H. *Nano Lett.* **2011**, *11*, 1044.
- (56) Park, J. S.; Lee, D. W.; Gysin, U.; Rast, S.; Meyer, E.; Despont, M.; Gerber, C. 2005 IEEE Sensors (IEEE Cat. No.05CH37665C), 2005.
- (57) Dai, Z.; King, W. P.; Park, K. *Nanotechnology* **2009**, 20.
- (58) Yun, M.; Yim, C.; Jung, N.; Kim, S.; Thundat, T.; Jeon, S. *Macromolecules* **2011**, DOI: dx.doi.org/10.1021/ma202194e.

Extensive Development of Precursory Helical Pairs Prior to Formation of Stereocomplex Crystals in Racemic Polylactide Melt Mixture

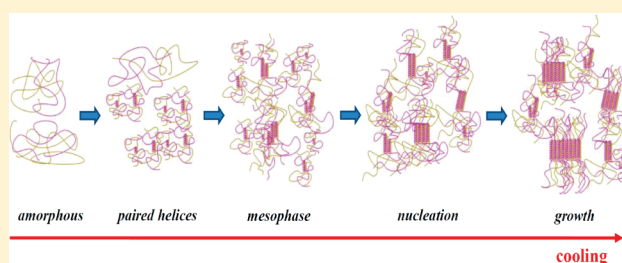
Ching-Feng Yang,[†] Yi-Fang Huang,^{†,‡} Jrjeng Ruan,^{*,‡} and An-Chung Su^{*,†}

[†]Department of Chemical Engineering, National Tsing Hua University, Hsinchu 300, Taiwan

[‡]Department of Materials Science and Engineering, National Cheng Kung University, Tainan 701, Taiwan

S Supporting Information

ABSTRACT: Melt crystallization of racemic polylactide (equimolar PLLA/PDLA) blend upon slow cooling (1 °C/min from 270 °C) was studied via a combination of wide-angle X-ray scattering (WAXS), differential scanning calorimetry (DSC), and Fourier-transform infrared spectroscopy (FTIR). Results indicated extensive development of racemic (3₂/3₁) helical pairs below 220 °C, followed by emergence of a broad mesomorphic peak in the WAXS profile below 190 °C; the intensity of this mesophase peak started to decrease at 150 °C, with concomitant emergence of WAXS- or DSC-discernible formation of stereocomplex (β_c) crystals. Isothermal measurements at 200 vs 170 °C revealed the presence of low vs high populations of helical pairs; β_c crystals were observed to develop only at 170 °C but not at 200 °C, indicating the need for adequate population of racemic helical pairs for formation of their mesomorphic clusters in the melt matrix as precursors of β_c nuclei. The clear change in the melt structure *well before* the formation of incipient β_c crystals reflects strong driving force under large supercooling toward transformation, but the transformation process is kinetically suppressed: only after extensive development of racemic helices and emergence of mesomorphic clusters in the melt matrix may nucleation occur. These observations suggest that the nucleation process proceeds in elementary units of preformed helical pairs in the melt matrix, with an intermediate stage of clustered helical pairs before incipience of β_c crystals.



INTRODUCTION

Stereocomplexation is an interesting phenomenon observed in organic polymers. It has been reported to occur in blends of stereoisomeric polymers of different tacticity/chirality such as stereoisomers of poly(methyl methacrylate),^{1,2} polythiirane,³ polylactone,^{4,5} polyoxirane,⁶ and polylactide.⁷ The common feature of the complex phase is that stereoisomeric chains are packed in pairs into a crystalline lattice of higher melting temperature (T_m) than that of the parent homopolymer crystals.

It was first reported⁸ in 1987 that racemic stereocomplex of poly(L-lactide) (PLLA) and poly(D-lactide) (PDLA) may crystallize specifically into the β_c form with T_m strongly increased to ca. 210 °C as compared to the case of $T_m \approx 160$ °C for the α crystalline form of enantiomeric components. Okihara et al.⁷ proposed that the β_c form is triclinic in structure (space group P1), with two chains per unit cell of parameters $a = b = 0.916$ nm, $c = 0.870$ nm, $\alpha = \beta = 109.2^\circ$, and $\gamma = 109.8^\circ$. On the basis of powder patterns from wide-angle X-ray scattering (WAXS) and results from molecular mechanics computations on the stereocomplex crystal, Brizzolara et al.⁹ refined the triclinic unit cell parameters as $a = 0.912$ nm, $b = 0.913$ nm, $c = 0.930$ nm, $\alpha = \beta = 110^\circ$, and $\gamma = 109^\circ$. Cartier et al.¹⁰ subsequently proposed a large trigonal cell that includes six

chains per unit cell with $a = b = 1.498$ nm, $c = 0.870$ nm, $\alpha = \beta = 90^\circ$, and $\gamma = 120^\circ$ (space group R3c) in order to explain the triangular shape of single crystals of the PLLA/PDLA stereocomplex in terms of frustrated packing of paired 3₁-helical chains of opposite handedness. Ozaki et al.¹¹ and Sarasua et al.¹² studied the interaction of stereocomplex chains of polylactides during crystallization by means of Fourier-transform infrared spectroscopy (FTIR), revealing a shift of the C=O stretching band in β_c crystals to a lower wavenumber lower than the corresponding band in α crystals of the chiral counterpart. This band shift is accompanied by similar displacements in the C–H spectral bands. These results were interpreted in terms of specific C–H \cdots O=C interactions between the paired stereoisomeric chains. More detailed assignments of conformation- or interaction-sensitive bands of polylactides were further made for both the chiral PLLA and the racemic PLLA/PDLA blend.^{13–18}

Although structural features of the β_c crystalline form have been extensively studied and specific interactions for stereocomplexation between PLLA and PDLA have been addressed,

Received: December 14, 2011

Revised: January 2, 2012

Published: January 12, 2012

the process of the stereocomplex formation was not thoroughly examined. Whether PLLA/PDLA stereocomplexation occurs in solution or melt states *prior* to the formation of β_c crystals or during crystallization where PLLA (3_2) and PDLA (3_1) helices develop through crystallographic clipping (i.e., recognition/selection) and extension at the crystal growth front is still an open question. Here we report our recent observations on the ordering process of racemic PLLA/PDLA blend during melt crystallization upon slow cooling (1 °C/min) from deeply equilibrated melt state (270 °C) via time-resolved FTIR and WAXS, with supplementary differential scanning calorimetric (DSC) results. We show that only after extensive formation and subsequent clustering of paired helices may nucleation of β_c phase occur.

EXPERIMENTAL SECTION

Samples of PLLA and PDLA, both of weight-average molecular mass $M_w \approx 120$ kDa, were purchased from Sigma-Aldrich. Circular dichroism/polarimetry measurements indicated molar ellipticity $[\theta] = \pm 185^\circ \text{ cm}^2 \text{ g}^{-1}$ at 228 nm and specific rotation $[\alpha]^{25} = \pm 155^\circ$ at 633 nm. From the reported¹⁹ value of $[\alpha]^{25} = 173^\circ$ at 589 nm for PLLA of perfect optical purity, the chiral purity may be estimated as ca. 95% for both samples. Racemic PLLA/PDLA blend were prepared by admixing component polymers at 1:1 weight ratio into chloroform and vigorous stirring overnight, followed by quick evaporation of chloroform under reduced pressure and further vacuum-drying for 24 h to remove residual solvent.

FTIR spectra were recorded by use of a Perkin-Elmer Spectrum RXI Fourier-transform infrared spectrophotometer equipped with a Thermo Spectra Tech HT-32 high-temperature cell. Spectra were taken at a resolution of 2 cm^{-1} and averaged over 16 scans. Films on KBr pellets were cast from chloroform solutions containing 1 wt % racemic PLLA/PDLA blend and were vacuum-dried for 0.5 h. Film specimens were first heated to 270 °C for 15 min to erase previous thermal history and then cooled to room temperature at a rate of 1 °C/min, during which FTIR spectra were continuously monitored. In the case isothermal crystallization, the film specimens were first heated to 270 °C for 15 min, followed by cooling at a rate of 5 °C/min to and maintaining at 200 or 170 °C for time-resolved measurements.

WAXS studies of racemic blend films cast on glass substrates were made by use of an in-house Rigaku Ultima IV instrument equipped with a Cu K α radiation source (with wavelength $\lambda = 1.542$ Å) operating at 40 kV and 20 mA and an INSTEC HCS302 high-temperature stage. DSC measurements for samples ca. 5 mg in weight were made by use of a Perkin-Elmer Diamond instrument routinely calibrated with high-purity indium and zinc standards and operated under a steady stream of protective nitrogen. In both WAXS and DSC studies, the same temperature programs as those in the FTIR studies were adopted for temperature- or time-resolved measurements.

RESULTS

Formation of Paired Helices in Melt. Given in Figure 1a–c are the temperature-resolved FTIR spectra of the racemic blend in respective ranges of 3100–2800, 1790–1720, and 1320–800 cm^{-1} upon cooling from 270 at 1 °C/min. It may be observed from Figure 1a that methyl C–H stretching (asymmetric vs symmetric, ca. 2990 vs 2940 cm^{-1}) and methine C_α –H stretching band (2880 cm^{-1}) all shift slightly to lower frequencies with decreasing temperature; concomitantly, the intensity of the CH_3 asymmetry stretching band increased whereas intensities of CH_3 symmetric stretching/ C_α –H stretching bands decreased. These are more clearly demonstrated by corresponding difference spectra given in the Supporting Information as Figure S1. The broad C=O stretching band around 1750 cm^{-1} (cf. Figure 1b) suggests a distribution of local surroundings for carbonyl groups. With

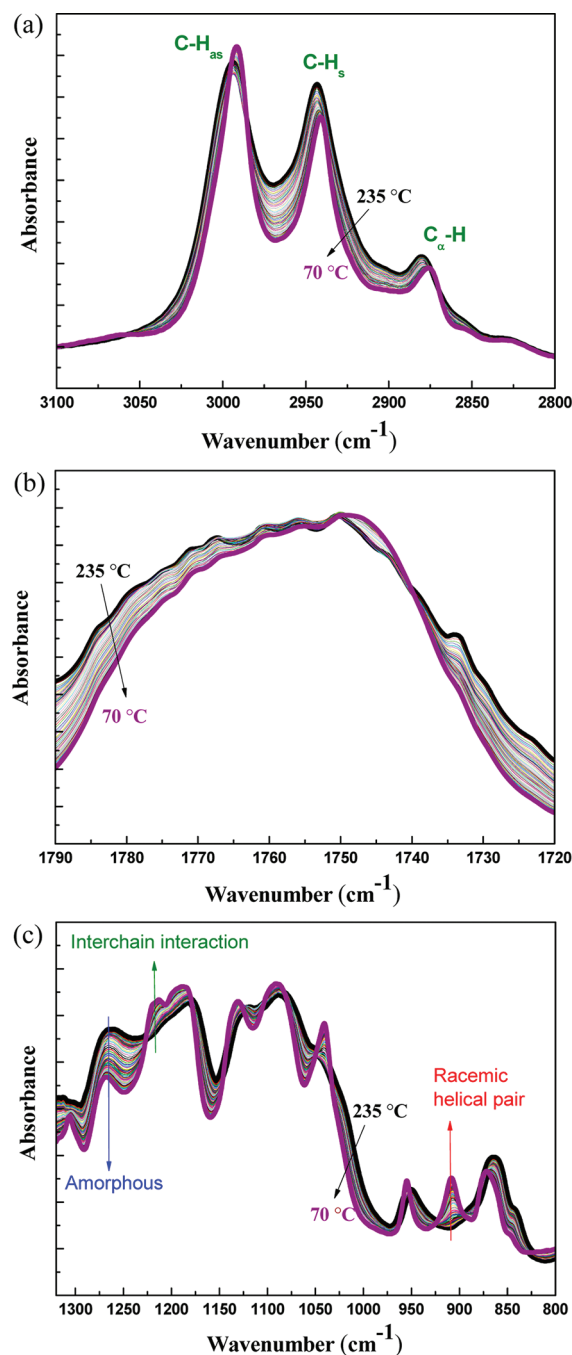


Figure 1. Temperature-resolved FTIR spectra in (a) the C–H stretching range of 3100–2800 cm^{-1} , (b) the C=O stretching range of 1790–1720 cm^{-1} , and (c) the fingerprint range of 1320–800 cm^{-1} collected during cooling of the racemic PLLA/PDLA blend at 1 °C/min from 270 °C. Note the decreased frequencies of the asymmetric vs symmetric C–H stretching peaks in (a), the general narrowing of the broad C=O stretching peak with delicate shifts of maximum position in (b), and the intensity changes of amorphous, interchain interaction, and $3_1/3_2$ helical peaks (around 1270, 1210, and 908 cm^{-1} , respectively) in (c).

decreasing temperature, there was a general narrowing of the C=O stretching band (signifying preference toward a specific molecular environment) with delicate shifts (as more clearly identifiable from the second-derivative curves in Figure S2) of maximum position toward lower wavenumbers. These observations suggest the development of weak interchain

CH \cdots O=C hydrogen bonding.^{11,12} Changes in peak positions of CH₃ asymmetry stretching and C=O stretching bands with temperature are given in Figure 2a, where significant changes in peak positions occur between 220 and 160 °C, beyond which the changes are more modest.

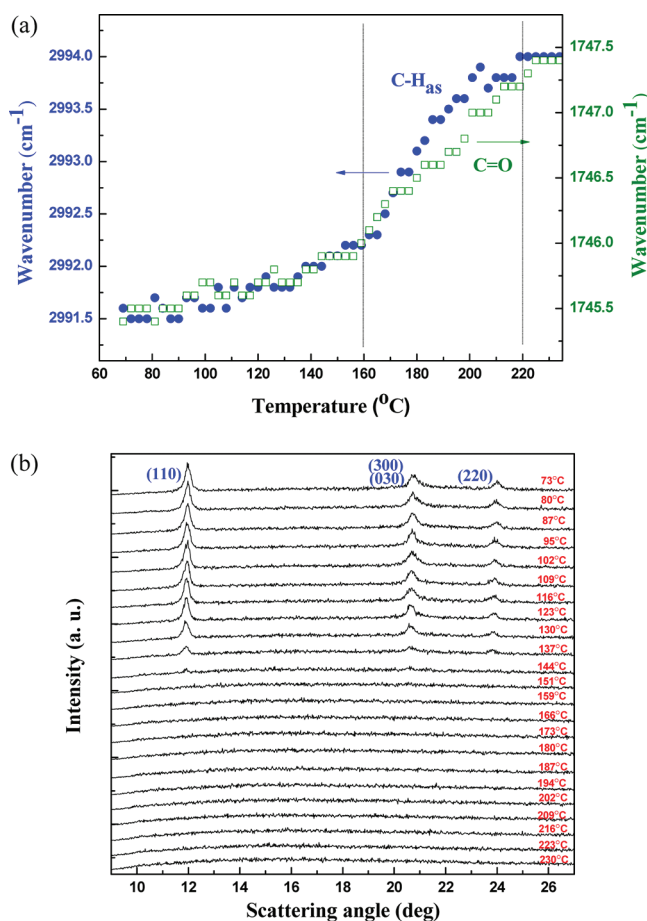


Figure 2. (a) Summary of variations of peak positions for C–H asymmetric stretching and C=O stretching bands in FTIR spectra shown in Figure 1a,b (as determined quantitatively from difference/derivative curves in Figure S1). (b) Corresponding WAXS profiles during cooling of the racemic blend at 1 °C/min from 270 °C.

Corresponding WAXS profiles shown in Figure 2b provide some clues to the molecular origins of spectral changes in Figure 1a,b. Upon cooling from 270 at 1 °C/min, the WAXS profiles remained featureless until reaching 150 °C where characteristic (110), (030)/(300), and (220) reflections of β_c crystals start to emerge at scattering angles $2\theta_B = 12.0^\circ$, 20.8° , and 24.1° , respectively. Intensities of these β_c reflections increased with further decreases in temperature below 150 °C. It hence appears that the development of interchain hydrogen bonding occurs well before crystallization.

This observation is further supported by intensity changes of the three key absorptions in the fingerprint region (cf. Figure 1c). The absorption at 908 cm⁻¹, assigned to the coupled C–C backbone stretching and CH₃ rocking mode, corresponds to racemic pair of 3₂/3₁ helices; the absorption in the vicinity of 1210 cm⁻¹ corresponds to coupled COC/CH₃ mode which is sensitive to interchain interactions, whereas the absorption around 1270 cm⁻¹, the coupled CH bending and COC stretching mode, is characteristic of the amorphous phase.¹⁸

Intensity changes of these three peaks with decreasing temperature are summarized in Figure 3. As may be observed

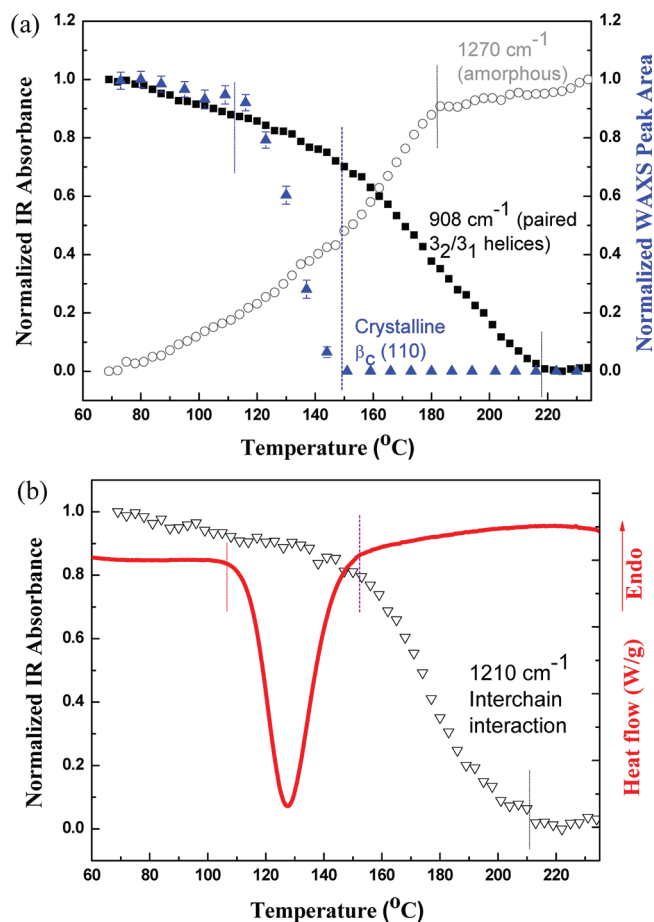


Figure 3. (a) Changes in normalized absorbance of helical peak at 908 cm⁻¹ and amorphous peak at 1270 cm⁻¹ (Figure 1c) and the WAXS (110) reflection of β_c crystals (Figure 2b) for racemic PLLA/PDLA blend during cooling (1 °C/min) from 270 °C. (b) Concomitant changes in normalized absorbance of interchain interaction peak at 1210 cm⁻¹ (Figure 1c) and the parallel DSC cooling trace (also at 1 °C/min).

in Figure 3a, the 908 cm⁻¹ band for paired helices was absent above 220 °C; the peak intensity rose quickly in the temperature range of 220 to 150 °C, beyond which the rate of increase slowed down significantly. This confirms unequivocally the extensive formation of coupled helices in the temperature range of 220 to 150 °C, well ahead of the emergence of β_c crystals below 150 °C as demonstrated by changes of the WAXS (110) reflection peak area (Figure 3a) and the parallel DSC cooling trace (Figure 3b). Also consistent with this picture is the gradual rise of the 1210 cm⁻¹ absorption (characteristic of interchain interaction) between 220 and 150 °C (Figure 3b).

Clusters of Helical Pairs as Mesomorphic Precursors of β_c Nuclei. It is then intriguing to note from Figure 3a that the temperature-resolved intensity of the amorphous band around 1270 cm⁻¹ exhibited a clear break at ca. 180 °C, with a lag of 40 °C behind the formation of paired helices at 220 °C yet ca. 30 °C ahead of the start of crystallization. This implies the existence of an intermediate state between the amorphous

phase (with or without isolated helical pairs) and the WAXS- or DSC-discernible β_c crystals.

As shown in Figure 4a, carefully deconvoluted WAXS profiles provide direct evidence for the existence of such a

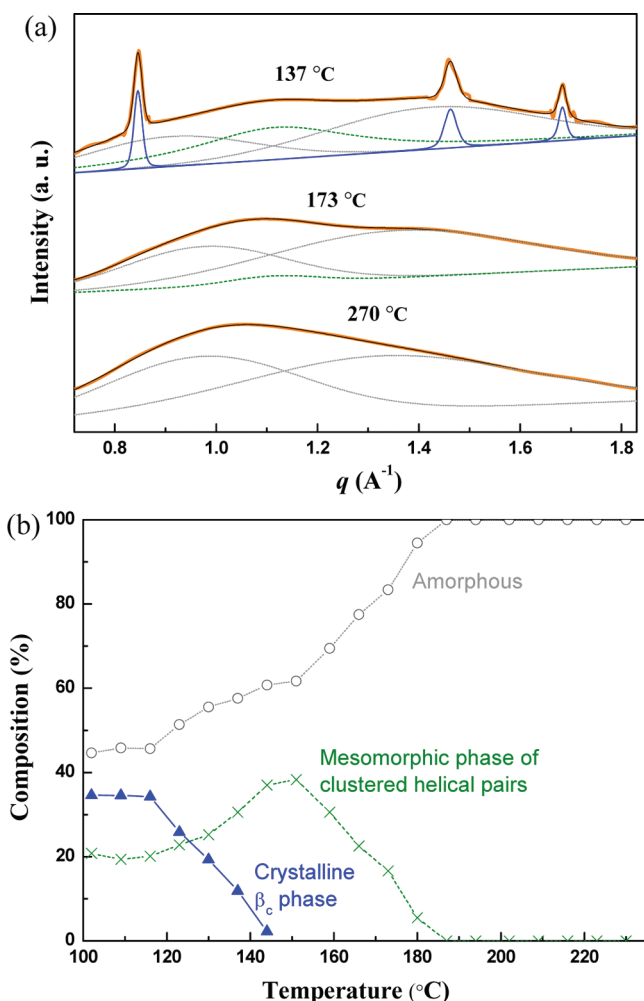


Figure 4. (a) Representative WAXS profiles obtained during cooling ($1\text{ }^{\circ}\text{C}/\text{min}$) of racemic PLLA/PDLA blend from $270\text{ }^{\circ}\text{C}$, fitted with two amorphous peaks (dotted lines), an intermediate halo for clustered helical pairs (dashed lines), and three crystalline peaks (solid thin lines). (b) Corresponding summary of the compositional changes.

mesomorphic phase of intermediate order. The WAXS profile at $270\text{ }^{\circ}\text{C}$ can be decomposed into two broad amorphous peaks which in combination give close description of the amorphous halo centered at scattering vector q ($\equiv 4\pi\lambda^{-1}\sin\theta_B$) $\approx 1.1\text{ }\text{\AA}^{-1}$. For temperatures below $180\text{ }^{\circ}\text{C}$ (the case of $173\text{ }^{\circ}\text{C}$ is selected for demonstration), a new (i.e., “mesomorphic”) component must be incorporated to provide proper description of the halo as continued from higher temperatures. For temperatures below $150\text{ }^{\circ}\text{C}$ (with the case of $137\text{ }^{\circ}\text{C}$ selected for demonstration), crystalline peaks representing (110), (300)/(030), and (220) reflections are further added. The fitted compositions (in terms of fractions of the corresponding peak areas) of amorphous, mesomorphic, and crystalline phases are summarized in Figure 4b. The amorphous fraction (f_a) started to decrease at $180\text{ }^{\circ}\text{C}$, with the mesomorphic fraction (f_m) increasing up to ca. 0.38 at $150\text{ }^{\circ}\text{C}$. Upon quick emergence of β_c crystals below $150\text{ }^{\circ}\text{C}$, f_a continues to decrease albeit at a

lower rate, whereas f_m also starts to decrease; both remain significant ($f_a \approx 0.46$ and $f_m \approx 0.20$) at $105\text{ }^{\circ}\text{C}$ where the crystallization process was completed (cf. DSC trace in Figure 3b), leaving a crystalline fraction $f_c \approx 0.34$. This means that nearly half of the pre-existing mesomorphic phase has eventually transformed into β_c crystals, whereas the rest half remains mesomorphic; nearly half of the final crystallinity is contributed by pre-existing mesomorphic phase, whereas the remaining half is contributed by conversion from the amorphous phase.

In view of the already extensive formation of paired helices at $180\text{ }^{\circ}\text{C}$ (cf. Figure 3a), the mesomorphic state is most likely related to clusters of helical pairs, which would be expected to serve subsequently as candidates for primary nucleation of β_c crystals. Figure 5a compares the time-resolved developments of

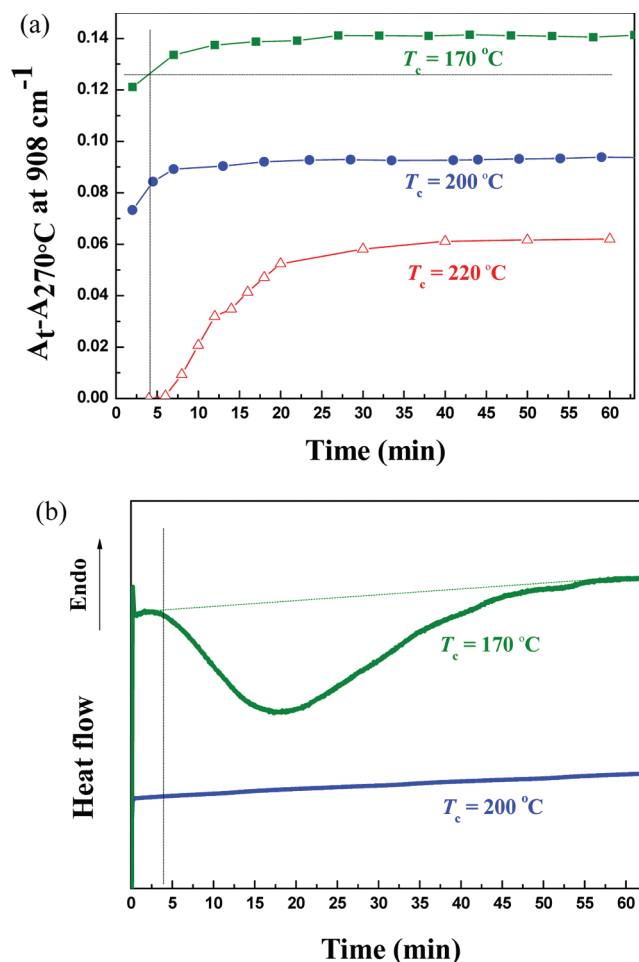


Figure 5. (a) Changes in absorbance of the 908 cm^{-1} band of paired helices as a function of time upon isothermal crystallization at 170, 200, and $220\text{ }^{\circ}\text{C}$. (b) Corresponding DSC traces, demonstrating progress of crystallization during the period of $t_c = 4\text{--}55\text{ min}$ at $170\text{ }^{\circ}\text{C}$ in contrast to the complete absence of crystallinity development at $200\text{ }^{\circ}\text{C}$ up to $t_c = 63\text{ min}$.

paired helices in supercooled melt at 170 and $200\text{ }^{\circ}\text{C}$, whereas Figures 5b and 6 show respectively the corresponding DSC traces and WAXS profiles. It may be observed that isothermal crystallization is well facilitated after a 4 min period of incubation at $170\text{ }^{\circ}\text{C}$ with significant development of paired helices. At a much lower population of paired helices,

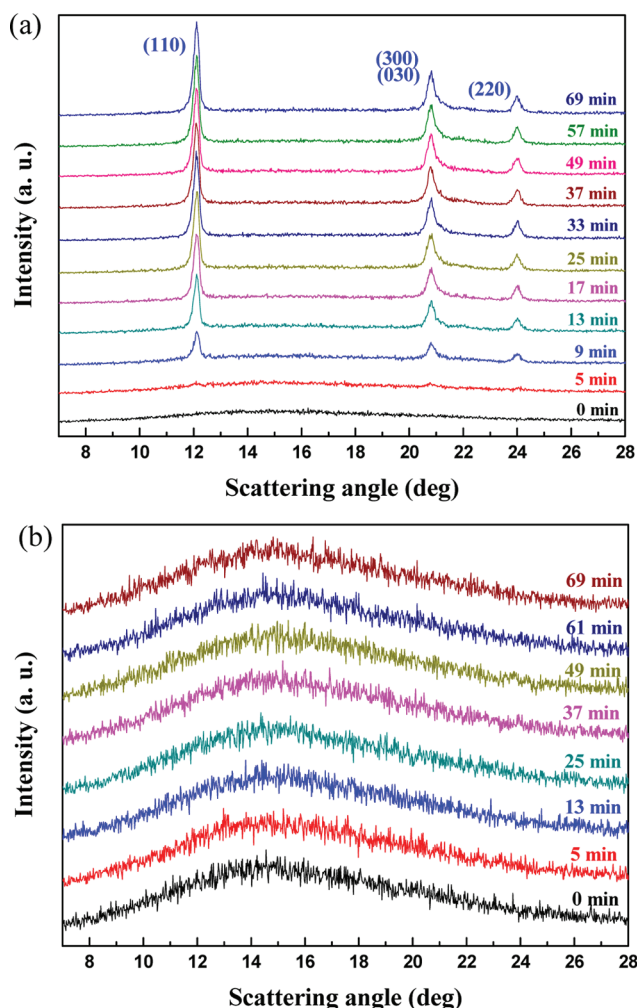


Figure 6. Representative WAXS profiles obtained during isothermal crystallization of the racemic PLLA/PDLA blend at (a) 170 and (b) 200 °C, reaffirming the absence of crystallinity development in the latter case.

isothermal crystallization at 200 °C remains inactivated even after prolonged incubation exceeding 1 h.

Summary of the Phase Transformation Process. To summarize our observations of melt-crystallization in the racemic PLLA/PDLA blend upon slow cooling at 1 °C/min from deeply equilibrated melt at 270 °C, a schematic illustration of the phase transformation process is given in Figure 7. The process begins with the formation of paired $3_2/3_1$ helices. With adequately developed population, clusters of

helical pairs are formed, which serve as nucleation sites upon further intracluster ordering. Growth of nuclei into crystals may then proceed.

DISCUSSION

Equilibrated Population of Helical Pairs. Some details in the phase transformation process depicted above deserve further discussion. First, in the absence of crystallization at high temperatures, the formation of paired helices at each temperature is fairly slow, reaching equilibrated population only after ca. 5 min at 200 °C or 20 min at 220 °C (cf. Figure 5a) with an identifiable incubation period of ca. 6 min in the latter case. The presence of an incubation period implies that the pairing process itself involves some fluctuation-induced nucleation-like process at the segmental level, most likely the local adjustment of rotational angles of backbone bonds for matched helical conformation. Nevertheless, as there is no discernible heat of transition, changes in the melt structure are essentially continuous in nature.

On the other hand, the equilibrated population of paired helices is clearly temperature-dependent. Extrapolation of the population (represented by the difference in absorbance) leads to zero population at ca. 260 °C, consistent with the value of equilibrium melting temperature $T_m^0 = 259 \pm 3$ °C determined via a combination of small-angle X-ray scattering (SAXS), WAXS, and DSC results.²⁰ The slow formation of such a limited quasi-equilibrium population without going further toward crystallization implies the presence of a balancing force, most likely the elastic force of entangled chains. With decreasing temperature, the energetic preference toward helical pairing is expected to increase while the opposing entropy-driven elasticity decreases, leading to increased population of helical pairs.

Clustering of Paired Helices. The clustering of paired helices is proposed in order to explain the emergence of the broad “mesomorphic” peak in the WAXS profile. This clustering can be a result of (1) induced generation of helical pairs around an existing helical pair or more likely (2) collision/attachment of neighboring pairs through thermally activated fluctuations or Brownian motion. Either of the two routes would be subjected to further balancing force of chain elasticity in the entangled melt. The process should again be continuous, as there is still no identifiable heat of transformation.

Nucleation/Growth of β_c Crystals and Nonvanishing f_m . A more careful examination of Figure 4b reveals that, in the temperature range of 150 to 130 °C, f_a decreased mildly from ca. 0.62 to 0.55; development of the crystalline fraction (up to $f_c \approx 0.20$) was mainly contributed by the decrease in f_m from 0.38

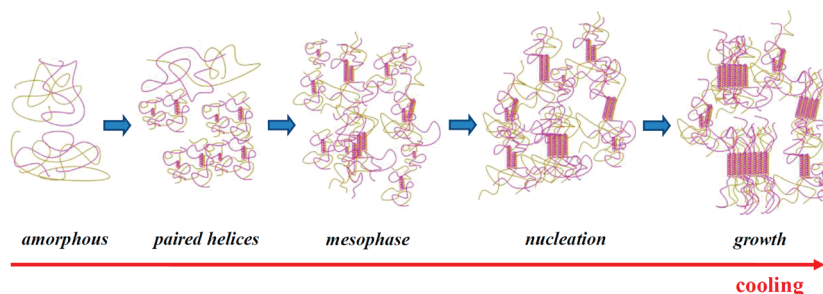


Figure 7. Schematic illustration of the proposed evolution of hierarchical structure during cooling of the racemic PLLA/PDLA blend from equilibrated melt state.

to 0.25. This signifies extensive formation of β_c crystals converted from mesomorphic phase and comparatively minor crystal growth in expense of the amorphous fraction. In the subsequent range of 130 to 105 °C, the increase in f_c from 0.20 to 0.34 was mainly contributed by the decrease in f_a (from 0.55 to 0.46) and a minor decrease in f_m (0.25 to 0.20).

Conversion of clusters of paired helices (i.e., the mesomorphic phase) into primary nuclei of β_c crystals is therefore progressive and incomplete. Mesomorphic clusters are envisioned to fluctuate in size and packing order with the balancing elastic forces or thermal fluctuations, similar to scenarios reported recently on the basis of molecular dynamic simulation for nucleation of polyethylene chains.²¹ It may be conceived that only those of highly improved packing order while exceeding the corresponding critical size may activate subsequent growth; this coincides with the classical picture of a discontinuous nucleation process. This critical barrier decreases with decreasing temperature yet remains nonvanishing, leaving significant mesomorphic phase fraction ($f_m \approx 0.20$) along with dominant amorphous fraction ($f_a \approx 0.46$) at the end the crystallization where crystallinity $f_c \approx 0.34$.

On the basis of Figure 4b, crystal growth is envisaged to proceed in two possible ways. Paired helices may be induced at the crystal growth front through surface nucleation (via crystallographic recognition/selection) as described by Hoffman's kinetic theory of crystal growth.^{22,23} Nevertheless, to be consistent with the strong decrease of the mesophase fraction in the first half of the crystallization process up to $f_c \approx 0.20$, an alternative route must also be allowed: when an existing mesomorphic cluster of helical pairs is brought into contact with a growing crystal front, the cluster may adsorb onto the growth front and reorient/coalesce with the crystal through layerwise epitaxial reorganization in a manner similar to the coalescence of nanograins during cold crystallization.^{24–26} By incorporating key features in both the epitaxial recognition asserted by Lotz^{10,27} and the mesomorphic nanoblock attachment advocated by Strobl^{28,29} at the crystal growth front, this picture serves to fully explain present observations on the transformation process from amorphous melt to β_c crystals in this particular case of racemic PLLA/PDLA blend.

Incomplete transformation of the mesomorphic phase after the apparent completion of crystallization process below 120 °C may also be taken to imply the presence of further constraints imposed on untransformed precursors. An apparent source of the constraints is the elastic balancing force from stretched chains in the remaining melt phase of highly concentrated entanglements and reduced mobility.²⁹ The presence of locked-in entanglements in the amorphous phase has been proposed to explain tensile responses and accompanying morphological evolution of semicrystalline polymers.³⁰

Suppressed Formation of α Crystals. As a final point, some comments are due on the absence of α crystals of either PLLA or PDLA (cf. Figure 4) in the present study. At a slow cooling rate of 1 °C/min, $3_2/3_1$ helical pairs were extensively developed above 150 °C, resulting in physically cross-linked network of chains which prohibits segregation of PLLA and PDLA chains for development of separate α crystals previously observed³¹ to compete with formation of β_c crystals in the temperature range of 150 to 90 °C. This prohibiting effect is certainly absent in the case of cold crystallization of quenched glass of racemic PLLA/PDLA blend; detailed kinetic analysis of this competition between α and β_c phases during cold

crystallization is currently ongoing; results will be presented in a separate occasion.

As a final remark, the present FTIR/WAXS evidences correspond mainly to high-resolution molecular processes; hence, we have restrained ourselves from discussing the shape/structure of the mesomorphic clusters of the helical pairs. This latter issue, however, will be addressed with proper analysis of low-resolution SAXS results in the near future.

CONCLUSION

Using FTIR, WAXS, and DSC, we have investigated the structure evolution of PLLA/PDLA stereocomplex during melt crystallization upon slow cooling (1 °C/min) from the equilibrated melt state at 270 °C. On the basis of the characteristic 908 cm⁻¹ peak for paired $3_2/3_1$ helices, we show that helical pairs started to emerge in the early stage of cooling below 220 °C. This is followed by the clustering of populated helical pairs into mesomorphic precursors (as indicated by a mesomorphic peak in the WAXS profile) below 190 °C, which subsequently serve as nucleation sites upon further cooling or isothermal standing. The observation that half of the mesomorphic clusters (extensively developed, i.e., $f_m \approx 0.38$, at 150 °C) transformed into crystalline β_c phase is explained by their participation in both the nucleation and the growth of β_c crystals; only half of the final crystalline fraction ($f_c \approx 0.34$ at the end of crystallization process) is attributed to crystal growth via the traditional route of surface nucleation of amorphous chains. We conclude that preformed helical pairs in the melt matrix play a dominant role in the crystallization process of the racemic PLLA/PDLA blend.

ASSOCIATED CONTENT

Supporting Information

Figures S1–S3, showing either difference or second-derivative curves of the FTIR spectra in Figure 1. This material is available free of charge via the Internet at <http://pubs.acs.org>.

ACKNOWLEDGMENTS

Financial support from the National Science Council (under Grant NSC98 2221 E 007 009 MY3) is gratefully acknowledged. Thanks are also due to Prof. Rong-Ming Ho and Mr. Chien-Wei Huang at NTHU for circular dichroism/polarimetry measurements.

REFERENCES

- (1) Bosscher, F.; ten Brinke, G.; Challa, G. *Macromolecules* **1982**, *15*, 1442–1444.
- (2) Koennecke, K.; Rehage, G. *Makromol. Chem.* **1983**, *184*, 2679–2691.
- (3) Matsubayashi, H.; Chatani, Y.; Tadokoro, H.; Dumas, P.; Spassky, N.; Gigwalt, P. *Macromolecules* **1977**, *10*, 996–1002.
- (4) Grenier, D.; Prud'homme, R. E.; Leborgne, A.; Spassky, N. *J. Polym. Sci., Polym. Phys.* **1984**, *22*, 577–587.
- (5) Lavallee, C.; Prud'homme, R. E. *Macromolecules* **1989**, *22*, 2438–2446.
- (6) Sakakihara, H.; Takakashi, Y.; Tadokoro, H.; Oguni, N.; Tani, H. *Macromolecules* **1973**, *6*, 205–212.
- (7) Okihara, T.; Tsuji, M.; Kawaguchi, A.; Katayama, K.; Tsuji, H.; Hyon, H.; Ikada, Y. *J. Macromol. Sci., Macromol. Phys.* **1991**, *B30*, 119–140.
- (8) Ikada, Y.; Jamshidi, K.; Tsuji, H.; Hyon, S. H. *Macromolecules* **1987**, *20*, 904–906.
- (9) Brizzolara, D.; Cantow, H. J.; Diederichs, K.; Keller, E.; Domb, A. *J. Macromolecules* **1996**, *29*, 191–197.

- (10) Cartier, L.; Okihara, T.; Lotz, B. *Macromolecules* **1997**, *30*, 6313–6322.
- (11) Zhang, J.; Sato, H.; Tsuji, H.; Noda, I.; Ozaki, Y. *Macromolecules* **2005**, *38*, 1822–1828.
- (12) Sarasua, J. R.; Rodriguez, N. L.; Arraiza, A. L.; Meaurio, E. *Macromolecules* **2005**, *38*, 8362–8371.
- (13) Kang, S.; Hsu, S. L.; Stidham, H. D.; Smith, P. B.; Leugers, M. A.; Yang, X. *Macromolecules* **2001**, *34*, 4542–4548.
- (14) Krikorian, V.; Pochan, D. J. *Macromolecules* **2005**, *38*, 6520–6527.
- (15) Zhang, J.; Duan, Y.; Sato, H.; Tsuji, H.; Noda, I.; Yan, S.; Ozaki, Y. *Macromolecules* **2005**, *38*, 8012–8021.
- (16) Meaurio, E.; Lopez-Rodriguez, N.; Sarasua, J. R. *Macromolecules* **2006**, *39*, 9291–9301.
- (17) Pan, P.; Kai, W.; Zhu, B.; Dong, T.; Inoue, Y. *Macromolecules* **2007**, *40*, 6898–6905.
- (18) Zhang, J.; Tashiro, K.; Tsuji, H.; Domb, A. J. *Macromolecules* **2007**, *40*, 1049–1054.
- (19) Huang, S. J.; Onyari, J. M. *J. Macromol. Sci., Part A: Pure Appl. Chem.* **1996**, *33*, 571–584.
- (20) Yang, C. F.; Su, A. C.; Su, C. H.; Jeng, U. Unpublished results.
- (21) Lan, Y. K.; Su, A. C. *Macromolecules* **2010**, *43*, 7908–7912.
- (22) Hoffman, J. D. *Polymer* **1983**, *24*, 3–26.
- (23) Hoffman, J. D.; Miller, R. L. *Polymer* **1997**, *38*, 3151–3212.
- (24) Chen, S. H.; Wu, Y. H.; Su, C. H.; Jeng, U.; Hsieh, C. C.; Su, A. C.; Chen, S. A. *Macromolecules* **2007**, *40*, 5353–5359.
- (25) Su, C. H.; Jeng, U.; Chen, S. H.; Lin, S. J.; Ou, Y. T.; Chuang, W. T.; Su, A. C. *Macromolecules* **2008**, *41*, 7630–7636.
- (26) Su, C. H.; Jeng, U.; Chen, S. H.; Lin, S. J.; Wu, W. R.; Chuang, W. T.; Tsai, J. C.; Su, A. C. *Macromolecules* **2009**, *42*, 6656–6664.
- (27) Lotz, B. *Eur. Phys. J. E* **2000**, *3*, 185–194 and references cited therein.
- (28) Strobl, G. *Eur. Phys. J. E* **2000**, *3*, 165–183 and references cited therein.
- (29) Strobl, G. *Rev. Mod. Phys.* **2009**, *81*, 1287–1300.
- (30) Men, M.; Rieger, J.; Strobl, G. *Phys. Rev. Lett.* **2003**, *91*, 095502.
- (31) Tsuji, H.; Hyon, S. H.; Ikada, Y. *Macromolecules* **1991**, *24*, 5651–5656.

Chain Dynamics in Antiplasticized and Annealed Poly(ethylene terephthalate) Determined by Solid-State NMR and Correlated with Enhanced Barrier Properties

Rudra Prosad Choudhury,[†] Jong Suk Lee,[‡] Robert M. Kriegel,[§] William J. Koros,[‡] and Haskell W. Beckham^{*,†}

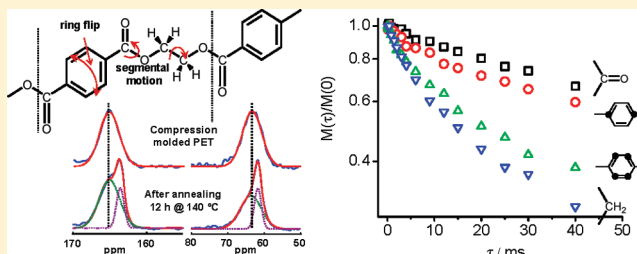
[†]School of Materials Science and Engineering, Georgia Institute of Technology, Atlanta, Georgia 30332, United States

[‡]School of Chemical & Biomolecular Engineering, Georgia Institute of Technology, Atlanta, Georgia 30332, United States

[§]The Coca-Cola Company, Atlanta, Georgia 30313, United States

S Supporting Information

ABSTRACT: Using solid-state NMR, site-specific chain dynamics from the hertz to mid-kilohertz regime were examined in compression-molded films of poly(ethylene terephthalate) (PET), PET filled with 2 wt % acetanilide or phenacetin, and PET annealed below and above the glass transition temperature (T_g). More specifically, ^{13}C relaxation time in the rotating frame, ^1H – ^{13}C cross-polarization times, and ^{13}C chemical-shift anisotropy exchange were measured at natural abundance. ^{13}C CP/MAS spectra revealed that PET annealed above T_g was 28% crystalline, and all other PET samples were completely amorphous. Relaxation times in these polymers were analyzed using stretched exponentials which yielded characteristic time constants. The filled PET and PET annealed above T_g exhibited suppressed chain dynamics across the entire hertz to mid-kilohertz regime that were correlated with reduced CO_2 and O_2 permeabilities. Using the centerband-only detection of exchange (CODEX) sequence, the fraction of flipping phenylene rings was observed to decrease in these polymers, with the decrease in the semicrystalline sample consistent with the crystalline fraction.



INTRODUCTION

Poly(ethylene terephthalate) (PET) is widely applied as a packaging material due to a useful combination of thermal, mechanical, and barrier properties.^{1–4} This thermoplastic polyester exhibits low permeabilities of O_2 and CO_2 that are related to its chemical structure, crystallinity, orientation, and molecular mobility.^{5,6} Permeabilities can be decreased by addition of low concentrations of certain low-molecular-weight diluents (LMWDs) that result in antiplasticization,^{7–9} leading also to increased stiffness and strength. Such property changes can be caused by suppression of chain dynamics and reduction of fractional free volume due to the presence of LMWDs.¹⁰ Computational studies on PET polyisomers have been conducted and suggest that chain dynamics, and not static free volumes, are primarily responsible for the differences in gas permeabilities observed for these polyesters.^{11–13} Specific interactions between oxygen and the aromatic rings of polymers^{14,15} have also been suggested as a potential mechanism for decreased O_2 permeability.¹⁶

Chain dynamics in pure PET films and fibers have been extensively investigated by solid-state NMR. Sefcik et al.¹⁷ studied quenched and annealed PET films with different crystallinities which were varied from 3 to 50%. They measured proton and carbon rotating-frame spin–lattice relaxation times, $T_{1\rho}(^1\text{H})$ and $T_{1\rho}(^{13}\text{C})$. They were mostly interested in the

$T_{1\rho}(^{13}\text{C})$ relaxation times which provide site-specific information about molecular motions in the mid-kilohertz regime. They observed multiexponential behavior of the ^{13}C magnetization decays which were attributed to the presence of multiple phases in the films, mainly amorphous and crystalline phases. In other PET samples, the presence of rigid and mobile amorphous phases has been observed;^{18–21} the rigid amorphous phase is typically associated with the interface between the rigid crystalline and the mobile amorphous phase and exhibits molecular mobilities that are intermediate between them.

In the present work, nuclear magnetic resonance (NMR) was used to identify changes in PET chain dynamics that occur upon addition of about 2 wt % acetanilide or phenacetin. In addition, changes in chain dynamics and gas permeabilities were also examined for PET samples annealed below and above the glass transition temperature (T_g). To study molecular motions over a broad range of time scales, three different types of NMR experiments were conducted: rotating-frame spin–lattice relaxation ($T_{1\rho}$), ^1H – ^{13}C cross-polarization (CP), and exchange. These three experiments provide information on

Received: September 2, 2011

Revised: December 21, 2011

Published: January 12, 2012

molecular motions from the mid-kilohertz to hertz regimes. At the experimental temperatures employed, and according to the well-known relaxation map for PET,²² with these NMR methods we are probing from the middle to the low-frequency side of the PET β relaxation, which has been associated with phenylene ring flips and low-angle oscillations.¹⁰ The information obtained from the NMR experiments are correlated with the gas permeabilities and compared with the fractional free volume of the same PET samples.

EXPERIMENTAL DETAILS

Samples. All samples were received from the Coca Cola Company as injection-molded bottle preforms (i.e., prior to blow molding) in which the diluent-loaded samples were prepared by melt blending. The preforms were cryogenically ground (Glen Mills, Inc.) after dipping in liquid nitrogen for 5 min. They were dried overnight at 120 °C under vacuum immediately prior to compression molding into dense films for permeability measurements. The compression molding was conducted on a Wabash vacuum chamber press using nonstick plates (Farberware) and a hard-temper aluminum foil (McMaster Carr, 1 or 3 mil thick) template into which two circles were cut. The Al template governed the film thickness, shape and dimensions. Small granular pieces were placed into the press onto a nonstick plate and heated to 270 °C for 1 min. After complete melting, it was pressed for 30 s at 270 °C and 30 tons under vacuum. After pressing, the samples were immediately quenched in water at room temperature. Care was taken to maintain uniform thickness while quenching the sample. After compression molding, the film samples were stored at room temperature for 1–3 weeks. Immediately prior to NMR and permeability measurements, the samples were further dried under vacuum at 35 °C for 48 h.

To investigate annealing effects, compression-molded sample films were sandwiched between two sheets of Al foil (Alufoil Products) and placed under a glass plate in a preheated oven (Sheldon Manufacturing 1415M) for 12 h at either 70 °C, which is below T_g , or 140 °C, which is above T_g .

The chemical structures of the phenacetin, acetanilide, and PET repeat unit are shown in Figure 1. These LMWDs are not used in current commercial PET bottles.

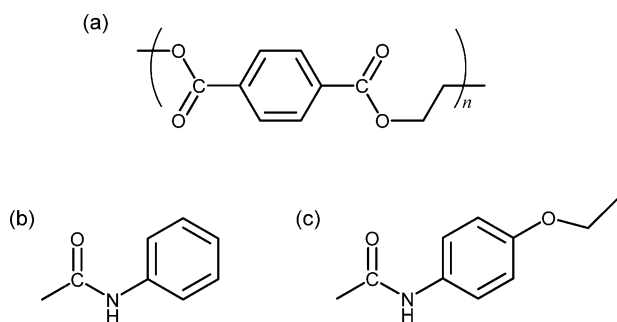


Figure 1. Chemical structures of (a) repeat unit of poly(ethylene terephthalate), (b) acetanilide, and (c) phenacetin.

While the samples were initially prepared with 3 wt % LMWD, compression molding at 270 °C causes some loss of the diluent. The amount of LMWD remaining in the films after compression molding was determined by thermal gravimetric analysis (TGA)²³ using a model Q5000 from TA Instruments to be 1.95 wt % acetanilide and 2.32 wt % phenacetin. The slightly greater loss for acetanilide is consistent with its lower boiling point (300 °C) as compared to the boiling point for phenacetin (350 °C).

Glass transition temperatures were determined under N_2 flow by differential scanning calorimetry (DSC) using a model Q200 from TA Instruments. Crystallinity was calculated using a heat of fusion value for 100% crystallized PET as 140 J/g.²⁴

Densities were determined using a density gradient column (Techne) which was filled with water–calcium nitrate solutions at 23 °C. Specific volumes were taken as the reciprocal densities. Occupied volumes were estimated by the Suggden method based on group contributions.²⁵ For the polymer–LMWD mixtures, a simple mixing rule was employed.²⁶ The fractional free volumes were calculated as the ratio of the difference between specific and occupied volumes to the specific volume.

The isochoric technique²⁷ was employed for single gas permeation measurements of O_2 and CO_2 at 1 atm and 35 °C. Details are provided elsewhere.²³

NMR Spectroscopy. NMR measurements were performed on a Bruker AV3-400 spectrometer operating at 400 MHz for 1H . In all measurements cross-polarization (CP) and proton decoupling were combined with magic-angle spinning (MAS) to obtain high-resolution ^{13}C spectra. A double-bearing CP/MAS probe was used with 4 mm rotor into which the films were cut into small pieces and packed tightly. All relaxation and contact-time variation measurements were performed with a 4 s recycle delay and at a spinning speed of 4.5 kHz at which frequency overlap of isotropic peaks with spinning sidebands did not occur. For the CODEX experiments, a 5 kHz spinning speed was used. Three ^{13}C radio-frequency field strengths of 50, 62, and 75 kHz were used for the ^{13}C rotating-frame spin–lattice relaxation experiment. For the 1H rotating-frame spin–lattice relaxation experiment, 50 kHz was used for the proton channel. Adamantane was used to optimize the Hartmann–Hahn condition for cross-polarization and as an external secondary chemical shift reference.

Rotating-frame spin–lattice relaxation times for both protons and carbons were obtained within the standard cross-polarization sequence. The $T_{1\rho}(^{13}C)$ was determined by varying the carbon spin-lock time from 0.1 to 40 ms in 16 steps without proton irradiation after cross-polarization (2 ms contact time). The $T_{1\rho}(^1H)$ was determined by varying the proton spin-lock time from 0.1 to 10 ms in 16 steps followed by cross-polarization (2 ms contact time) and detection through the carbons. The rotating-frame spin–lattice relaxation times were obtained by least-squares fitting on measured intensities, $M(\tau)$, to a single exponential for protons, and to a stretched exponential for carbons:

$$M(\tau) = M_0 e^{-(\tau/T_{1\rho})^\beta} \quad (1)$$

where M_0 is the initial magnetization, τ is the variable (in this case, spin-lock) time, and β is the nonexponentiality parameter or stretch exponent. $T_{1\rho}$ is the center of the decay constant distribution. The mean decay constant is related to $T_{1\rho}$ and β by $\langle T_{1\rho} \rangle = (T_{1\rho}/\beta)\Gamma(1/\beta)$.

1H – ^{13}C cross-polarization times, T_{CH} , were determined in a variable contact-time experiment where the contact time for cross-polarization was varied from 0.01 to 10.0 ms in 32 steps. T_{CH} values were obtained by fitting $M(\tau)$ to one or to a sum of different components:^{18,28,29}

$$M(\tau) = \sum_i M_{0i} \left[\frac{e^{-\tau/T_{1\rho i}(^1H)} - e^{-\tau/T_{CHi}}}{1 - T_{CHi}/T_{1\rho i}(^1H)} \right] \quad (2)$$

where τ in this case is the variable contact time. Equation 2 is composed of an ascending function describing the buildup of ^{13}C magnetization with time constant T_{CH} and a descending function describing the loss of magnetization as a result of 1H relaxation in the rotating-frame with time constant $T_{1\rho}(^1H)$. The $T_{1\rho}(^1H)$ was measured independently in a separate experiment so that fitting was accomplished by varying the T_{CH} value. In principle, the buildup of ^{13}C magnetization should also be affected by the $T_{1\rho}(^{13}C)$ parameter,²⁹ but fitting showed that the contribution of the known $T_{1\rho}(^{13}C)$ parameter was negligible. When deconvolution of spectra was needed, it was performed with the “dmfit” program.³⁰

The pulse sequence used in the CODEX experiment was identical to that introduced by deAzevedo et al., except there was no suppression of spinning sidebands by a TOSS sequence.^{31,32} The addition of a TOSS sequence causes a decrease in overall signal

Table 1. PET Samples: Results from Permeability, Thermal, and Density Measurements

sample	additive content (wt %)	permeability at 1 atm, 35 °C (barrer)		T_g (°C)	fractional free volume
		O ₂	CO ₂		
PET	0	0.12 ± 0.01	0.50 ± 0.03	81 ± 1	0.128 ± 0.001
PET–acetanilide	1.95	0.09 ± 0.01	0.35 ± 0.02	75 ± 1	0.126 ± 0.001
PET–phenacetin	2.32	0.10 ± 0.01	0.39 ± 0.02	75 ± 1	0.126 ± 0.001
PET-70 °C	0	0.12 ± 0.01	0.50 ± 0.03	79 ± 1	0.128 ± 0.001
PET-140 °C	0	0.06 ± 0.01	0.26 ± 0.01	87 ± 1	0.102 ± 0.001

intensity which is a major issue in these samples. The sum of the preparation and refocusing time used in the CODEX experiments was 1.6 ms.^{31,33} The mixing time (t_m) was varied from 20 ms to 1.2 s, and the loss of signal was minimized by using the smallest z -filter time (t_z) which is only one rotor period (200 μ s).³⁴ For each mixing time, a reference spectrum was measured by interchanging t_z and t_m in the pulse sequence. To increase the CP efficiency and the signal-to-noise ratio, all CODEX experiments were performed at −10 °C. A 4 s recycle delay was employed, and 4096 scans were accumulated. Before conducting CODEX on our samples, we confirmed the performance of the pulse sequence by measuring dimethyl sulfoxide and poly(methyl methacrylate) and compared the results to those published in the literature.³¹

RESULTS AND DISCUSSION

Important results from the permeability, thermal, and density measurements are summarized in Table 1 for films of PET, PET filled with 2.32 wt % phenacetin, PET filled with 1.95 wt % acetanilide, PET annealed at 70 °C, and PET annealed at 140 °C. The reductions in O₂ and CO₂ permeability due to the presence of 2.32 wt % phenacetin are 17 and 22%, respectively. The reductions in O₂ and CO₂ permeability due to the presence of 1.95 wt % acetanilide are 25 and 30%, respectively. Of the two additive-filled PET samples, the O₂ permeabilities are similar within experimental error, but the CO₂ permeability is lower for the acetanilide-filled PET. Acetanilide leads to greater improvements in CO₂ barrier properties even though it is present at a slightly lower concentration than phenacetin. As shown in Figure 1, the only structural difference between these two LMWDs is the presence of an ethoxy substituent in the phenacetin.

The fractional free volume for pristine PET is 0.128 (cf. Table 1). The fractional free volume for both additive-filled PET samples is 0.126. According to Table 1, these two additive-filled PET samples also exhibit exactly the same reductions in T_g compared to pristine PET, indicating the same overall reduction in segmental dynamics for both. The decreased fractional free volumes and reduced T_g s cannot explain the differences observed for CO₂ permeabilities. It is thus important to study the localized chain dynamics of the PET in these additive-filled PET samples.

Annealing the pure PET for 12 h at 70 °C, which is below T_g , caused no changes in the O₂ or CO₂ permeabilities. However, annealing for 12 h at 140 °C, which is above T_g , led to decreases in O₂ and CO₂ permeabilities of 50 and 48%, respectively. The reduced permeability, even in the absence of antiplasticizers, is related to the induction of crystalline regions in an otherwise glassy matrix. The presence of crystallites alone reduces sorption and diffusion; the accompanying reduced overall chain dynamics that propagate through the tie chains in the rigid amorphous regions augment the reduction in permeability. This is reflected in the significantly reduced fractional free volume from 0.128 to 0.102, and the increased

glass transition temperature from 81 to 87 °C upon annealing above T_g .

Figure 2 shows CP/MAS spectra of PET, PET filled with 2.32 wt % phenacetin, PET filled with 1.95 wt % acetanilide,

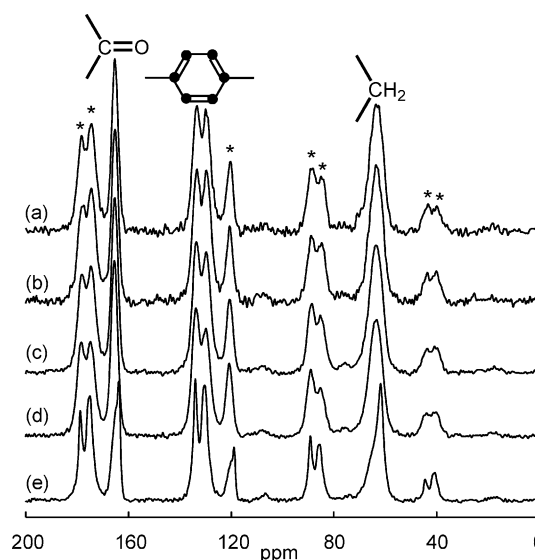


Figure 2. ¹³C CP/MAS spectra of compression-molded and quenched PET measured with a 2 ms contact time at 25 °C: (a) untreated and unfilled, (b) filled with 1.95 wt % acetanilide, (c) filled with 2.32 wt % phenacetin, (d) annealed at 70 °C for 12 h, and (e) annealed at 140 °C for 12 h. Spinning sidebands are marked with an asterisk.

PET annealed at 70 °C, and PET annealed at 140 °C. The ¹³C NMR spectrum of the quenched PET has four resonances arising from the carbonyl (165 ppm), nonprotonated aromatic (133 ppm), protonated aromatic (129 ppm), and ethylene (63 ppm) carbons. The protonated and nonprotonated aromatic carbon resonance lines overlap but were deconvoluted for analysis of the relaxation, contact-time variation, and CODEX experiments.

Upon adding LMWDs or annealing below T_g , no significant changes were observed in the chemical shifts or line widths of the resonance lines. However, the spectrum of the PET film annealed at 140 °C for 12 h (cf. Figure 2e) exhibits much sharper resonance lines than the other quenched films. The resonance lines for carbonyl and ethylene resonances are actually composed of two components, with the sharper line due to the crystalline phase appearing about 1 ppm upfield from a broader peak due to the amorphous phase. These kinds of distinctions between the crystalline and amorphous phase are well-known in PET films and yarns.^{18,21,35} Assuming similar cross-polarization efficiencies in the amorphous and crystalline regions, the amount of crystallinity can be quantified by deconvolution of the carbonyl or ethylene peaks (cf. Figure 3). The broad resonance lines in Figure 3b for the PET annealed at

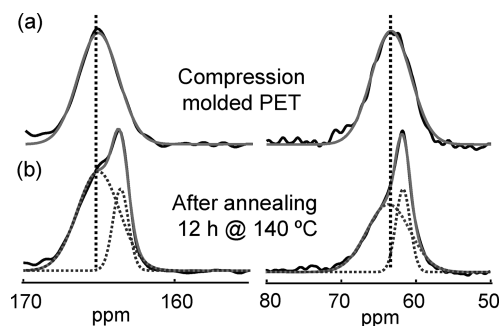


Figure 3. Ethylene (right) and carbonyl (left) resonances of (a) compression-molded and quenched PET and (b) PET annealed at 140 °C for 12 h. The sharp upfield peak for each carbon in the annealed sample is due to the crystalline regions, which after deconvolution yields a crystalline fraction of 28%.

140 °C correspond both in line width and in chemical shift with the resonance lines of the quenched compression-molded PET in Figure 3a, confirming the assignment of this peak to disordered amorphous regions. After deconvolution, the crystalline fraction was found to be 28%, which is consistent with the value determined by DSC (28%) and lower than the value determined from density measurements (38%). The sample annealed at 140 °C is the only sample to exhibit peaks due to crystalline regions. The other four samples examined in this study—compression-molded PET, PET filled with 2.32 wt % phenacetin, PET filled with 1.95 wt % acetanilide, and PET annealed at 70 °C—are fully amorphous.

Carbon spin–lattice relaxation times in the rotating-frame, $T_{1\rho}({}^{13}\text{C})$, were measured for all PET samples because they are not averaged by spin diffusion and can therefore provide site-specific information on dynamics.^{17,18,36} Figure 4 shows the ${}^{13}\text{C}$

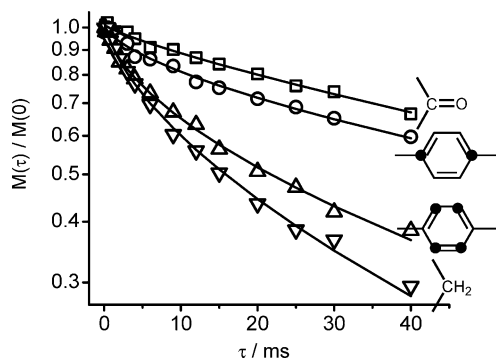


Figure 4. Normalized ${}^{13}\text{C}$ magnetization decay in the rotating frame ($\nu_1 = 75$ kHz) for each carbon of compression-molded PET. These data were fitted to a stretched exponential (solid lines) to yield $T_{1\rho}({}^{13}\text{C})$ values for each carbon.

magnetization decay of each carbon of the compression-molded PET as a function of spin-lock time (τ). Curvature in this semilogarithmic plot indicates that these carbons are not characterized by monoexponential relaxation. Least-squares fitting was conducted using a stretched exponential (cf. eq 1), and the results are summarized in Table 2 for three different spin-lock fields ($\nu_1 = 50, 62$, or 75 kHz). The $T_{1\rho}({}^{13}\text{C})$ values obtained from fitting, which represent the centers of the relaxation time distributions, were also used to calculate the mean relaxation decay times using $\langle T_{1\rho} \rangle = (T_{1\rho}/\beta)\Gamma(1/\beta)$. It was found that $T_{1\rho}({}^{13}\text{C})$ and $\langle T_{1\rho} \rangle$ follow the same trend so

Table 2. $T_{1\rho}({}^{13}\text{C})$ Relaxation Times and Stretch Exponents in Compression-Molded PET at 25 °C

ν_1 (kHz)	$T_{1\rho}({}^{13}\text{C})$ (ms)	β	$T_{1\rho}({}^{13}\text{C})$ (ms)	β
ethylene				
50	10.8 ± 0.8	0.59 ± 0.04	6.2 ± 1.2	0.37 ± 0.03
62	13.8 ± 0.8	0.54 ± 0.03	14.5 ± 1.3	0.55 ± 0.05
75	17.1 ± 0.4	0.60 ± 0.01	18.3 ± 1.1	0.55 ± 0.04
nonprotonated aromatic				
50	52.9 ± 4.6	0.53 ± 0.06	65.6 ± 3.0	0.69 ± 0.03
62	73.4 ± 9.6	0.57 ± 0.08	64.9 ± 4.8	0.89 ± 0.07
75	71.5 ± 3.2	0.61 ± 0.02	78.2 ± 7.3	0.81 ± 0.07
carbonyl				

that the $T_{1\rho}({}^{13}\text{C})$ values will be presented in the discussion below. In Table 2, longer $T_{1\rho}({}^{13}\text{C})$ values are observed for the nonprotonated aromatic and carbonyl carbons due to their lack of attached protons. For most of the carbons, the β parameters increase with increasing ν_1 , indicating the breadth of the measured $T_{1\rho}({}^{13}\text{C})$ distributions decrease at higher spin-lock fields.

Interpretation of $T_{1\rho}({}^{13}\text{C})$ as a motional parameter first requires establishment that ${}^{13}\text{C}$ relaxation occurs predominately by a motional mechanism, and then on what side of a $T_{1\rho}$ correlation time minimum the $T_{1\rho}({}^{13}\text{C})$ values reside.³⁷ In $T_{1\rho}({}^{13}\text{C})$ experiments ${}^{13}\text{C}$ spins are coupled to the lattice in two ways via fluctuating local magnetic fields due to protons. In one case the fluctuating fields arise from molecular motions that modulate the ${}^{13}\text{C}$ – ${}^1\text{H}$ dipolar interaction. This is the normal spin–lattice relaxation process characterized by a time constant $T_{1\rho}({}^{13}\text{C})$. In a second mechanism, strong ${}^1\text{H}$ – ${}^1\text{H}$ dipolar interactions give rise to fast proton–proton spin flip-flops, which also modulate the ${}^{13}\text{C}$ – ${}^1\text{H}$ dipolar coupling. This is a pure spin–spin relaxation process and can be described as a thermal contact with a characteristic time constant T_{CH}^{D} between the ${}^{13}\text{C}$ rotating-frame Zeeman reservoir and the ${}^1\text{H}$ dipolar reservoir, which in turn is coupled to the lattice with another time constant T_{ID}^{H} . So, spin–lattice relaxation can occur via a pathway involving motional spin–lattice processes and nonmotional spin–spin processes. It has been shown that under magic-angle spinning conditions $T_{\text{ID}}^{\text{H}} \ll T_{1\rho}({}^{13}\text{C})$, T_{CH}^{D} ,³⁷ so that the ${}^1\text{H}$ dipolar reservoir and the lattice can be considered as one reservoir to which the ${}^{13}\text{C}$ rotating-frame Zeeman reservoir relaxes with an effective relaxation time $T_{1\rho}^*({}^{13}\text{C})$:

$$\frac{1}{T_{1\rho}^*({}^{13}\text{C})} = \frac{1}{T_{1\rho}({}^{13}\text{C})} + \frac{1}{T_{\text{CH}}^{\text{D}}} \quad (3)$$

The relative contributions of T_{CH}^{D} and $T_{1\rho}({}^{13}\text{C})$ to measured spin–lattice relaxation times can be estimated by determining the spin–lattice relaxation times at different rotating-frame frequencies (ν_1). It was shown by VanderHart et al.³⁷ that if the spin–spin interactions dominate, then the spin–lattice relaxation time will show an exponential dependence on ν_1 , $T_{1\rho}({}^{13}\text{C}) \propto \exp(2\pi\nu_1\tau_{\text{D}})$, where τ_{D} represents the correlation time for proton dipolar fluctuations. Figure 5 shows a plot of the measured ${}^{13}\text{C}$ spin–lattice relaxation times versus the frequency of the spin-lock field. There is clearly no exponential dependence, especially for the higher field of 75 kHz, thus confirming that ${}^{13}\text{C}$ relaxation in the rotating frame occurs predominately by a motional mechanism in these samples.

To establish how differences in $T_{1\rho}({}^{13}\text{C})$ values may be interpreted in terms of average motional correlation times (τ_{C}),

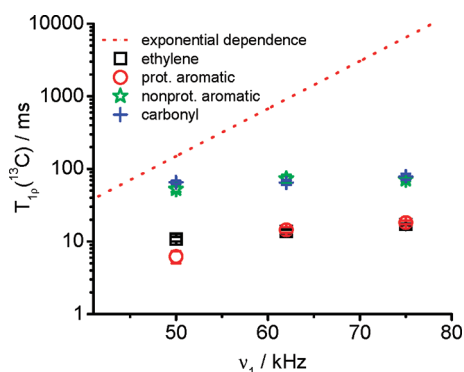


Figure 5. $T_{1\rho}(^{13}\text{C})$ relaxation times versus spin-lock field (ν_1) for each carbon of compression-molded PET. The dotted line represents exponential dependence of $T_{1\rho}(^{13}\text{C})$ on ν_1 .

$T_{1\rho}(^{13}\text{C})$ was determined as a function of τ_c by making measurements as a function of temperature. These data are summarized in Table 3 for each carbon of compression-molded

Table 3. $T_{1\rho}(^{13}\text{C})$ Relaxation Times and Stretch Exponents in Compression-Molded PET at a Rotating-Frame Frequency of 75 kHz

temp (°C)	$T_{1\rho}(^{13}\text{C})$ (ms)	β	$T_{1\rho}(^{13}\text{C})$ (ms)	β
ethylene				
−15	25.3 ± 0.7	0.61 ± 0.03	37.2 ± 1.0	0.57 ± 0.02
25	17.2 ± 0.4	0.60 ± 0.01	18.3 ± 1.0	0.55 ± 0.04
50	16.8 ± 0.5	0.61 ± 0.02	7.17 ± 0.7	0.44 ± 0.02
nonprotonated aromatic				
−15	106.5 ± 9.7	0.63 ± 0.04	118.8 ± 9.4	0.81 ± 0.04
25	71.5 ± 3.2	0.61 ± 0.03	78.2 ± 7.2	0.80 ± 0.07
50	74.7 ± 5.9	0.49 ± 0.04	64.7 ± 2.7	0.79 ± 0.03
carbonyl				

PET at $\nu_1 = 75$ kHz. The $T_{1\rho}(^{13}\text{C})$ times for the ethylene and carbonyl carbons decrease as temperature increases (i.e., τ_c decreases) from −15 to 50 °C. The $T_{1\rho}(^{13}\text{C})$ times for the aromatic carbons decrease from −15 to 25 °C and then do not change significantly from 25 to 50 °C. Thus, longer $T_{1\rho}(^{13}\text{C})$ values in these materials indicate increased average motional correlation times and slower segmental motions in the kilohertz regime. This is consistent with observations in other polymers, especially when the measurement temperature is below T_g .^{38–40}

From the observations described above, it was established that $T_{1\rho}(^{13}\text{C})$ relaxation times can be used as a motional parameter and longer times at room temperature mean slower

dynamics. Table 4 contains $T_{1\rho}(^{13}\text{C})$ relaxation times measured at 25 °C and 75 kHz for PET, PET filled with 2.32 wt % phenacetin, PET filled with 1.95 wt % acetanilide, PET annealed at 70 °C, and PET annealed at 140 °C. Addition of LMWDs or annealing above T_g leads to increased average $T_{1\rho}(^{13}\text{C})$ relaxation times for all carbons of PET, indicating slower chain dynamics. These results are in complete agreement with the gas permeability results in which these modified PET films showed better barrier properties than the untreated PET film (cf. Table 1). The PET film annealed at 70 °C for 12 h exhibits $T_{1\rho}(^{13}\text{C})$ relaxation times that are the most similar to those of the untreated PET film, suggesting the chain mobility is not seriously affected by annealing at this temperature. This is consistent with the similar gas permeabilities observed for these two films. The PET sample annealed above T_g is semicrystalline, which is reflected in the significantly longer average $T_{1\rho}(^{13}\text{C})$ times. For the ethylene and protonated aromatic carbons, the β parameter is unchanged for the purely amorphous samples but decreases for the semicrystalline PET (PET-140 °C), indicating a broader distribution of relaxation times.

The $T_{1\rho}(^{13}\text{C})$ data reported in Table 4 for the PET film annealed at 140 °C represent averages of the crystalline and amorphous regions as the total integrated intensity for each carbon was analyzed. The CP/MAS spectrum of this sample contains ethylene and carbonyl carbon peaks that can be deconvoluted into amorphous and crystalline contributions (cf. Figure 3). In the $T_{1\rho}(^{13}\text{C})$ data set, the ethylene carbon peak is the only one that can be deconvoluted across all spin-lock durations. By doing so, it is possible to extract separate $T_{1\rho}(^{13}\text{C})$ relaxation times for the amorphous and crystalline regions. The amorphous-phase ethylene peak was fitted with a stretched exponential decay to yield a $T_{1\rho}(^{13}\text{C})$ relaxation time of 24.5 ± 0.7 ms (with $\beta = 0.58 \pm 0.02$). This value is larger than the ethylene-carbon $T_{1\rho}(^{13}\text{C})$ relaxation times recorded for all of the purely amorphous polymers (cf. Table 4), which indicates that the presence of crystalline regions imparts some rigidity in the amorphous phase. The crystalline-phase ethylene peak exhibited a stretched exponential decay that was analyzed to yield a crystalline-phase $T_{1\rho}(^{13}\text{C})$ relaxation time of 240.9 ± 20.6 ms (with $\beta = 0.61 \pm 0.03$).

Site-specific $T_{1\rho}(^1\text{H})$ relaxation times were determined by varying the proton spin-lock duration followed by cross-polarization (2 ms) and detection through the carbons. Spin-diffusion averaging led to nearly identical $T_{1\rho}(^1\text{H})$ values for the different carbons in a given sample, which makes it difficult to

Table 4. $T_{1\rho}(^{13}\text{C})$ Relaxation Times and Stretch Exponents in PET Films Measured at 25 °C and 75 kHz

samples	$T_{1\rho}(^{13}\text{C})$ (ms)	β	$T_{1\rho}(^{13}\text{C})$ (ms)	β
ethylene				
PET	17.2 ± 0.4	0.60 ± 0.02	18.3 ± 1.8	0.55 ± 0.03
PET–acetanilide	22.9 ± 0.9	0.62 ± 0.03	22.9 ± 0.9	0.58 ± 0.03
PET–phenacetin	19.3 ± 0.6	0.59 ± 0.02	19.9 ± 0.7	0.51 ± 0.01
PET-70 °C	17.1 ± 0.5	0.59 ± 0.02	16.5 ± 0.9	0.53 ± 0.03
PET-140 °C	42.7 ± 1.1	0.53 ± 0.03	114.8 ± 6.2	0.44 ± 0.02
nonprotonated aromatic				
PET	71.5 ± 3.2	0.61 ± 0.02	78.2 ± 7.2	0.81 ± 0.07
PET–acetanilide	108.9 ± 9.5	0.68 ± 0.09	89.7 ± 15.8	0.81 ± 0.11
PET–phenacetin	93.5 ± 7.4	0.63 ± 0.04	91.7 ± 10.1	0.81 ± 0.06
PET-70 °C	86.3 ± 6.4	0.54 ± 0.03	73.9 ± 2.7	0.84 ± 0.03
PET-140 °C	201.3 ± 12.5	0.54 ± 0.05	127.9 ± 12.5	0.84 ± 0.05
carbonyl				

interpret such data in terms of localized motions.^{18,37} The spin-diffusion-averaged $T_{1\rho}(^1\text{H})$ relaxation times of the five PET films are given in Table 5. The highest value (11.5 ± 0.2 ms) is

Table 5. Spin-Diffusion-Averaged $T_{1\rho}(^1\text{H})$ Relaxation Times of PET at 50 kHz

samples	$T_{1\rho}(^1\text{H})$ (ms)	samples	$T_{1\rho}(^1\text{H})$ (ms)
PET	4.74 ± 0.04	PET-70 °C	4.91 ± 0.03
PET-acetanilide	5.28 ± 0.06	PET-140 °C	11.5 ± 0.2
PET-phenacetin	5.55 ± 0.07		

observed for the semicrystalline PET (PET-140 °C). As with the $T_{1\rho}(^{13}\text{C})$ data, the ethylene peak was deconvoluted into amorphous and crystalline components to yield $T_{1\rho}(^1\text{H})$ relaxation times of 7.41 ± 0.18 and 18.3 ± 0.7 ms, respectively. These values are larger than the $T_{1\rho}(^1\text{H})$ relaxation times for all of the purely amorphous polymers, consistent with the $T_{1\rho}(^{13}\text{C})$ data. Similarly, the $T_{1\rho}(^1\text{H})$ relaxation times are greater for the additive-filled PET (5.28 ± 0.06 and 5.55 ± 0.07 ms) than for the unfilled PET (4.74 ± 0.04 ms). Packer and co-workers^{41,42} found that if relaxation occurs in the presence of spin diffusion, then the relaxation times cannot be interpreted simply in terms of molecular dynamics. Thus, the spin-diffusion-averaged $T_{1\rho}(^1\text{H})$ relaxation times presented here will not be interpreted on their own as motional parameters.

Dynamics on shorter time scales than those probed by $T_{1\rho}$ relaxation times can be assessed from cross-polarization transfer times from ^1H to ^{13}C , T_{CH} . These T_{CH} times are determined from cross-polarization experiments by fitting variable contact-time curves using eq 2. Characteristic data are shown in Figure 6 for the ethylene, carbonyl, and nonprotonated aromatic carbon of the compression-molded PET. Figure 6a shows

variable contact-time curves for the carbonyl and ethylene carbons and illustrates the importance of bonded protons as the ethylene signal builds up much faster than the carbonyl signal. The initial buildup of magnetization intensity is primarily governed by T_{CH} and the subsequent decay by $T_{1\rho}(^1\text{H})$. The $T_{1\rho}(^1\text{H})$ values were measured independently (cf. Table 5) and used to fit the contact-time curves. Most of these curves could not be fit using single T_{CH} values, consistent with the presence of underlying distributions of ^1H – ^{13}C internuclear distances and motional correlation times. We employed a simple two-component fit to the data to yield short and long T_{CH} values.^{6,10} The short T_{CH} times are predominately influenced by local structure while the long times reflect more dynamics. Figure 6b–d shows variable contact-time curves for the ethylene, nonprotonated aromatic, and carbonyl carbons along with the overall and component fits. The results of the fitting for all samples are summarized in Table 6.

To a first approximation, the T_{CH} time depends on the number of attached protons or the number of adjacent protons. For example, the short T_{CH} times (T_{CH_A}) for the ethylene, protonated aromatic, nonprotonated aromatic, and carbonyl carbons in the untreated PET are 0.02, 0.03, 0.11, and 0.53 ms, respectively, and the longer T_{CH} times (T_{CH_B}) are 0.62, 1.03, 2.00, and 2.90 ms, respectively. While the nonprotonated aromatic and carbonyl carbons both contain no attached protons, the nonprotonated aromatic carbon is bonded to carbons with attached protons but the carbonyl carbon is not (cf. Figure 1), thus rendering its T_{CH} longest. This strong structural influence, r_{CH}^{-6} dependence where r_{CH} is the distance between ^{13}C and ^1H nuclei, makes it difficult to capture mobility differences in the short T_{CH} component caused by antiplasticizers or annealing. This is reflected in Table 6 as the T_{CH_A} values are essentially the same for a given carbon in all

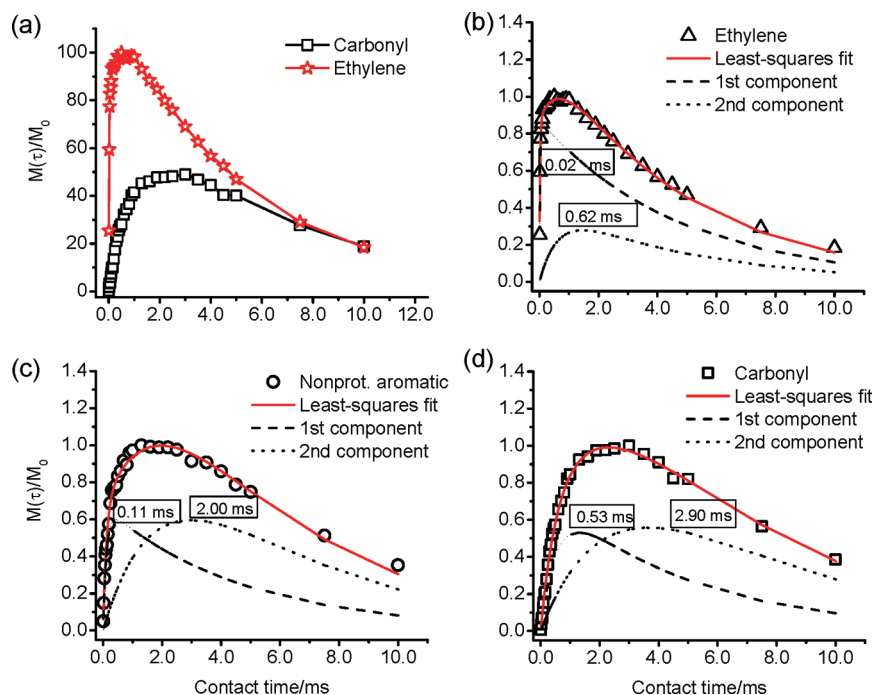


Figure 6. Evolution of ^{13}C magnetization in a cross-polarization variable contact-time experiment for compression-molded PET: (a) ethylene and carbonyl carbon, (b–d) ethylene, nonprotonated aromatic, and carbonyl carbons along with their respective overall (solid line) and component fits. Dashed line is the short T_{CH} (T_{CH_A}) and dotted line is the longer T_{CH} (T_{CH_B}) component. T_{CH} values for each component are shown in boxes on their respective fits.

Table 6. T_{CH} Transfer Times and Component Fractions in PET Films Measured at 25 °C

samples	T_{CH_A} (ms)	T_{CH_B} (ms)	I_A/I_B (%/%) ^a	T_{CH_A} (ms)	T_{CH_B} (ms)	I_A/I_B (%/%) ^a
		ethylene			protonated aromatic	
PET	0.022 ± 0.001	0.62 ± 0.06	69/31	0.033 ± 0.001	1.03 ± 0.07	59/41
PET–acetanilide	0.023 ± 0.001	0.56 ± 0.07	69/31	0.030 ± 0.001	0.97 ± 0.07	56/44
PET–phenacetin	0.020 ± 0.001	0.40 ± 0.05	70/30	0.031 ± 0.002	0.74 ± 0.07	61/39
PET-70 °C	0.022 ± 0.001	0.59 ± 0.06	69/31	0.031 ± 0.002	0.83 ± 0.07	59/41
PET-140 °C	0.021 ± 0.001	0.31 ± 0.06	75/25	0.029 ± 0.002	0.63 ± 0.07	59/41
		nonprotonated aromatic			carbonyl	
PET	0.11 ± 0.01	2.00 ± 0.18	36/64	0.53 ± 0.04	2.90 ± 0.29	37/63
PET–acetanilide	0.11 ± 0.02	1.80 ± 0.11	33/67	0.47 ± 0.04	2.69 ± 0.21	33/67
PET–phenacetin	0.12 ± 0.02	1.20 ± 0.11	37/63	0.96 ± 0.01		100
PET-70 °C	0.11 ± 0.02	1.18 ± 0.11	38/62	0.99 ± 0.01		100
PET-140 °C	0.16 ± 0.02	1.39 ± 0.11	39/61	0.40 ± 0.07	1.44 ± 0.11	25/75

^aError on I_A and I_B values typically ±1%.

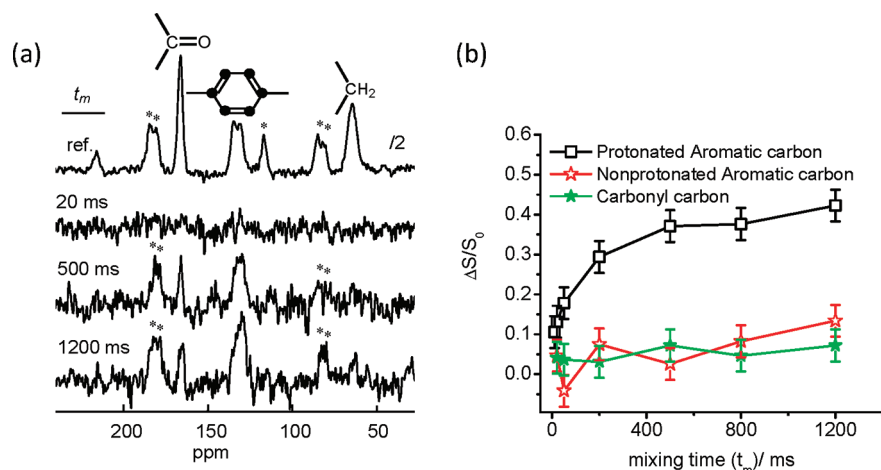


Figure 7. (a) Reference and pure-exchange CODEX spectra of compression-molded PET at −10 °C as a function of mixing time. For the reference spectrum shown, $t_m = 200 \mu s$ and $t_z = 20$ ms. (b) Normalized pure-exchange CODEX peak intensity $\Delta S/S_0$ as a function of mixing time for carbonyl, nonprotonated, and protonated aromatic carbons.

PET samples. The longer T_{CH} values do exhibit differences that can be attributed to dynamics that modulate the 1H – ^{13}C dipolar interactions necessary for magnetization transfer.⁴³ Addition of LMWDs or annealing above T_g results in a reduction of the longer T_{CH} values (T_{CH_B}) for all carbons, indicating slower dynamics in the hertz to kilohertz frequency range. This is consistent with the $T_{1\rho}$ and gas permeability measurements. Annealing below T_g also causes a decrease in the longer T_{CH_B} times for the protonated aromatic, nonprotonated aromatic, and carbonyl carbons, even though the ethylene T_{CH_B} remains unchanged.

Better measures of slow dynamics are offered by NMR exchange experiments.⁴⁴ Here we employed the CODEX pulse sequence³¹ to examine slow segmental reorientations (0.1/s to 1000/s). The reference spectrum of untreated PET is shown in Figure 7a along with three different pure-exchange CODEX spectra at mixing times (t_m) of 20 ms, 500 ms, and 1.2 s. From these spectra and after deconvolution of the overlapping aromatic carbon peaks (~129 ppm), peak intensities for the protonated aromatic, nonprotonated aromatic, and carbonyl carbons are plotted versus t_m in Figure 7b. The protonated aromatic carbons exhibit by far the greatest exchange intensity, approaching a $\Delta S/S_0$ value of 0.4 after 500 ms. The nonprotonated aromatic and carbonyl carbons exhibit much less exchange ($\Delta S/S_0 < 0.1$), and the ethylene carbon exhibits

none. These results indicate that the protonated aromatic carbons undergo large-amplitude motions in the hertz to kilohertz regime which are not present in the segment connecting the nonprotonated aromatic carbons. This is consistent with the widely reported rotation of the phenylene ring by 180° about its 1,4-axis, a phenylene ring flip, in which the chemical shift anisotropy of the protonated aromatic carbons is not completely refocused prior to CODEX detection.⁴⁵ We attribute the low exchange intensities exhibited by the nonprotonated aromatic and carbonyl carbons to small-angle oscillations that must also be contributing to the signal due to the protonated aromatic carbons.¹⁰

The growth of the pure-exchange CODEX intensity ($\Delta S/S_0$) shown in Figure 7b can be characterized by a stretched exponential:

$$\Delta S/S_0 = E_\infty \left(1 - e^{-(t_m/\tau_{\text{CODEX}})^\beta} \right) \quad (4)$$

where E_∞ is the final exchange intensity, τ_{CODEX} is the center of the correlation time distribution of the motion, and β is the nonexponentiality parameter or stretch exponent. The final exchange intensity (E_∞) is related to the fraction of mobile segments (f_m) and the number of orientational sites (M) accessed by a given carbon undergoing a given motion:³¹

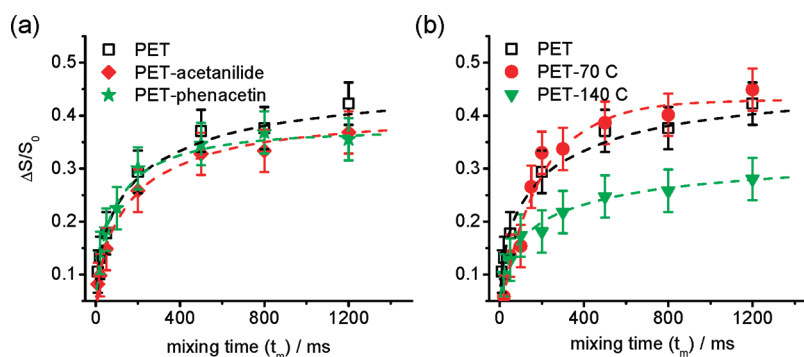


Figure 8. Pure-exchange CODEX signals as a function of mixing time for (a) untreated PET and PET with low-molecular-weight diluents, and (b) untreated PET and PET annealed below and above T_g . Dashed lines represent fits of experimental data to a stretched exponential.

Table 7. Stretched Exponential Fit Parameters of CODEX Signal of Protonated Aromatic Carbons in PET and Derived Mobile Fraction Assuming 180° Phenylene Ring Flip

samples	final exchange intensity (E_∞)	correlation time (τ_{CODEX} /ms)	nonexponentiality parameter (β)	mobile fraction (f_m)
PET	0.43 ± 0.04	196 ± 72	0.45 ± 0.04	0.86 ± 0.08
PET–acetanilide	0.39 ± 0.03	171 ± 62	0.54 ± 0.07	0.78 ± 0.06
PET–phenacetin	0.37 ± 0.03	92 ± 19	0.53 ± 0.07	0.74 ± 0.06
PET-70 °C	0.43 ± 0.02	171 ± 29	0.88 ± 0.14	0.86 ± 0.04
PET-140 °C	0.32 ± 0.02	205 ± 62	0.41 ± 0.06	0.64 ± 0.04

$$E_\infty = \frac{f_m(M-1)}{M} \quad (5)$$

For the 180° phenylene ring flip, $M = 2$ for the protonated aromatic carbons.

The pure-exchange CODEX intensity of the protonated aromatic carbons is plotted in Figure 8 for all five PET films. The growth of the exchange intensity was fitted to a stretched exponential and further analyzed using eq 5; results are summarized in Table 7. The low signal-to-noise ratios (cf. Figure 7) and limited numbers of mixing times result in fits to the exchange growth curves that are characterized by large errors. This is especially true for the correlation times, which are highly sensitive to the shapes of the curves so that single data points can have large effects on the outcome. Thus, we have not interpreted the correlation times in terms of differences in dynamics between the PET samples. That said, for the untreated PET, the extracted correlation time (τ_{CODEX}) gives a phenylene flip rate of 5.1 s^{-1} that is consistent with observations in other PET samples discussed in the literature.⁴⁵ In untreated pure PET films, $86 \pm 8\%$ of all phenylene rings undergo 180° flip motions, which does not change after annealing below T_g . Upon addition of acetanilide and phenacetin, the fraction of flipping phenylene rings decreases to $78 \pm 6\%$ and $74 \pm 6\%$, respectively. Annealing above T_g drops the mobile phenylene fraction to $64 \pm 4\%$; this is about 22% lower than the fraction observed in the untreated PET. Considering the error in the mobile phenylene fractions (± 6 to 8%), this drop is consistent with the 28% crystallinity in this semicrystalline sample, suggesting the phenylene flips are severely restricted in crystalline regions.

In summary, the slow phenylene ring flip motion in PET can be detected with CODEX. Addition of phenacetin and acetanilide or the formation of crystalline regions results in a decrease in the fraction of flipping phenylene rings. This affects chain dynamics in the hertz to kilohertz regime. Because of the connectivity and cooperative nature of motions in polymers,

the chain dynamics are also affected in the tens of kilohertz regime as evidenced by the rotating-frame spin–lattice relaxation results. For the semicrystalline sample, it is important to note that the reduced permeabilities (cf. Table 1) must also be related to the reduced sorption and diffusion caused simply by the presence of crystals.

Simple DFT and *ab initio* modeling of phenacetin and acetanilide with a methyl ester-terminated PET dimer shows a hydrogen bond interaction between the amide hydrogen of the low-molecular-weight additives and the carbonyl oxygens of the dimer. The hydrogen bond distance was consistently shorter for the acetanilide compared to the phenacetin, suggesting that PET interacts more closely with acetanilide than with phenacetin. As the only structural difference between these two LMWDs is the presence of an ethoxy group on phenacetin (cf. Figure 1), the longer hydrogen bond distance may be attributed to the additional steric bulk, inductive effects, or a combination of both. Hydrogen-bonded interactions enable the formation of local complexes that can impede the ring-flipping motion in PET, but π – π interactions between LMWDs and PET cannot be ruled out as a contributing factor. These modeling results are consistent with the observed greater efficacy of acetanilide as compared to phenacetin: lower concentrations of acetanilide in PET cause larger reductions in permeabilities (cf. Table 1).

Our observations are in good agreement with previous NMR experiments reported by Maxwell et al.¹⁰ on PET containing 10% tetrachlorophthalic dimethyl ester (TPDE). In their study, they observed that the low-molecular-weight TPDE additive acted as an antiplasticizer by reducing the molecular mobility of the phenylene rings associated with the β relaxation process. In our samples we also observed a reduction of phenylene ring motion due to the addition of acetanilide and phenacetin. In addition, we observed mobility reductions in the carbonyl and ethylene units due to the addition of these LMWDs.

CONCLUSIONS

Chain dynamics in PET were examined from hertz to mid-kilohertz time scales using solid-state NMR relaxation and exchange measurements. The addition of low-molecular-weight additives phenacetin (2.32 wt %) and acetanilide (1.95 wt %), and annealing-induced crystallite formation, resulted in a suppression of the chain dynamics across the time scales examined, which are correlated with the observed 25–50% reductions in CO₂ and O₂ permeabilities. Standard CP/MAS spectra showed that the untreated and additive-filled PET were purely amorphous while the PET annealed above T_g was about 28% crystalline. For all samples, distributions of correlation times could be clearly distinguished in the relaxation data, which were fitted with stretched exponentials. The antiplasticized samples exhibited identical glass transitions (75 °C) and fractional free volumes (0.126). Thus, the improved barrier properties are correlated with the NMR-determined suppression of local chain dynamics.

ASSOCIATED CONTENT

Supporting Information

Differential scanning calorimetry (DSC) thermograms for all samples, ¹³C magnetization decay curves in the rotating frame ($\nu_1 = 75$ kHz) for each carbon of the filled and annealed samples, and molecular modeling procedures and results. This material is available free of charge via the Internet at <http://pubs.acs.org>.

AUTHOR INFORMATION

Corresponding Author

*E-mail: beckham@gatech.edu.

ACKNOWLEDGMENTS

Samples and financial support were kindly provided by the Coca Cola Company. We are grateful to Dr. Jeffery L. White for providing assistance with implementation of the CODEX NMR experiment.

REFERENCES

- (1) Wu, G.; Jiang, J. D.; Tucker, P. A.; Cuculo, J. A. *J. Polym. Sci., Part B: Polym. Phys.* **1996**, *34* (12), 2035–2047.
- (2) Murthy, N. S.; Correale, S. T.; Minor, H. *Macromolecules* **1991**, *24* (5), 1185–1189.
- (3) Bove, L.; D'Aniello, C.; Gorrasi, G.; Guadagno, L.; Vittoria, V. *Polymer* **1996**, *37* (23), 5309–5311.
- (4) Karagiannidis, P. G.; Stergiou, A. C.; Karayannidis, G. P. *Eur. Polym. J.* **2008**, *44* (5), 1475–1486.
- (5) Auriemma, F.; Corradini, P.; Derosa, C.; Guerra, G.; Petraccone, V.; Bianchi, R.; Didino, G. *Macromolecules* **1992**, *25* (9), 2490–2497.
- (6) Fakirov, S.; Fischer, E. W.; Hoffmann, R.; Schmidt, G. F. *Polymer* **1977**, *18* (11), 1121–1129.
- (7) Jackson, W. J.; Caldwell, J. R. *J. Appl. Polym. Sci.* **1967**, *11* (2), 211.
- (8) Maeda, Y.; Paul, D. R. *J. Polym. Sci., Part B: Polym. Phys.* **1987**, *25* (5), 981–1003.
- (9) Vidotti, S. E.; Chinellato, A. C.; Pessan, L. A. *J. Appl. Polym. Sci.* **2007**, *103* (4), 2627–2633.
- (10) Maxwell, A. S.; Ward, I. M.; Laupretre, F.; Monnerie, L. *Polymer* **1998**, *39* (26), 6835–6849.
- (11) Karayiannis, N. C.; Mavrantzas, V. G.; Theodorou, D. N. *Macromolecules* **2004**, *37* (8), 2978–2995.
- (12) Tonelli, A. E. *J. Polym. Sci., Part B: Polym. Phys.* **2002**, *40* (12), 1254–1260.
- (13) Tonelli, A. E. *Polymer* **2002**, *43* (22), 6069–6072.
- (14) Capitani, D.; Segre, A. L.; Blicharski, J. S. *Macromolecules* **1995**, *28* (4), 1121–1128.
- (15) Gooding, E. A.; Serak, K. R.; Ogilby, P. R. *J. Phys. Chem.* **1991**, *95* (20), 7868–7871.
- (16) Litvinov, V. M.; Persyn, O.; Miri, V.; Lefebvre, J. M. *Macromolecules* **2010**, *43* (18), 7668–7679.
- (17) Sefcik, M. D.; Schaefer, J.; Stejskal, E. O.; McKay, R. A. *Macromolecules* **1980**, *13* (5), 1132–1137.
- (18) Gabrielse, W.; Gaur, H. A.; Feyen, F. C.; Veeman, W. S. *Macromolecules* **1994**, *27* (20), 5811–5820.
- (19) Havens, J. R.; Vanderhart, D. L. *Macromolecules* **1985**, *18* (9), 1663–1676.
- (20) Cheung, T. T. P.; Yaris, R. *J. Chem. Phys.* **1980**, *72* (6), 3604–3616.
- (21) Huang, J. M.; Chu, P. P.; Chang, F. C. *Polymer* **2000**, *41* (5), 1741–1748.
- (22) Halar, J.-L.; Laupretre, F.; Monnerie, L. *Polymer Materials: Macroscopic Properties and Molecular Interpretation*; John Wiley & Sons: Hoboken, NJ, 2011.
- (23) Lee, J. S.; Leisen, J.; Choudhury, R. P.; Kriegel, R. M.; Beckham, H. W.; Koros, W. J. *Polymer* **2012**, *53* (1), 213–222.
- (24) Arnoult, M.; Dargent, E.; Mano, J. F. *Polymer* **2007**, *48* (4), 1012–1019.
- (25) Krevelen, D. W. V. *Properties of Polymers-Correlation with Chemical Structure*, 3rd ed.; Elsevier: Amsterdam, 1990.
- (26) Maeda, Y.; Paul, D. R. *J. Polym. Sci., Part B: Polym. Phys.* **1987**, *25* (5), 1005–1016.
- (27) Pye, D. G.; Hoehn, H. H.; Panar, M. J. *J. Appl. Polym. Sci.* **1976**, *20* (7), 1921–1931.
- (28) Stejskal, E. O.; Schaefer, J.; Sefcik, M. D.; McKay, R. A. *Macromolecules* **1981**, *14* (2), 275–279.
- (29) Voelkel, R. *Angew. Chem., Int. Ed. Engl.* **1988**, *27* (11), 1468–1483.
- (30) Massiot, D.; Fayon, F.; Capron, M.; King, I.; Le Calve, S.; Alonso, B.; Durand, J. O.; Bujoli, B.; Gan, Z. H.; Hoatson, G. *Magn. Reson. Chem.* **2002**, *40* (1), 70–76.
- (31) deAzevedo, E. R.; Hu, W. G.; Bonagamba, T. J.; Schmidt-Rohr, K. *J. Am. Chem. Soc.* **1999**, *121* (36), 8411–8412.
- (32) deAzevedo, E. R.; Hu, W. G.; Bonagamba, T. J.; Schmidt-Rohr, K. *J. Chem. Phys.* **2000**, *112* (20), 8988–9001.
- (33) Wedeghiorghis, T. K.; Stueber, D.; Schaefer, J. *J. Polym. Sci., Part B: Polym. Phys.* **2008**, *46* (11), 1062–1066.
- (34) Hackel, C.; Franz, C.; Achilles, A.; Saalwachter, K.; Reichert, D. *Phys. Chem. Chem. Phys.* **2009**, *11* (32), 7022–7030.
- (35) Tang, P.; Reimer, J. A.; Denn, M. M. *Macromolecules* **1993**, *26* (16), 4269–4274.
- (36) Schaefer, J.; Stejskal, E. O.; Steger, T. R.; Sefcik, M. D.; McKay, R. A. *Macromolecules* **1980**, *13* (5), 1121–1126.
- (37) Vanderhart, D. L.; Garraway, A. N. *J. Chem. Phys.* **1979**, *71* (7), 2773–2787.
- (38) Xue, G.; Ji, G. D.; Yan, H.; Guo, M. M. *Macromolecules* **1998**, *31* (22), 7706–7711.
- (39) Percec, S.; Hammond, T. *Polymer* **1991**, *32* (7), 1252–1257.
- (40) Perez, E.; Vanderhart, D. L.; Crist, B.; Howard, P. R. *Macromolecules* **1987**, *20* (1), 78–87.
- (41) Packer, K. J.; Pope, J. M.; Yeung, R. R.; Cudby, M. E. A. *J. Polym. Sci., Part B: Polym. Phys.* **1984**, *22* (4), 589–616.
- (42) Kenwright, A. M.; Packer, K. J.; Say, B. J. *J. Magn. Reson.* **1986**, *69* (3), 426–439.
- (43) Demco, D. E.; Tegenfeldt, J.; Waugh, J. S. *Phys. Rev. B* **1975**, *11* (11), 4133–4151.
- (44) Beckham, H. W.; Spiess, H. W. *Two-Dimensional Exchange NMR Spectroscopy in Polymer Research*. In *NMR Basic Principles and Progress*; Blümich, B., Ed.; Springer: New York, 1994; Vol. 32, pp 163–209.
- (45) Wilhelm, M.; Spiess, H. W. *Macromolecules* **1996**, *29* (3), 1088–1090.

Nonlinear Rheology of Telechelic Associative Polymer Networks: Shear Thickening and Thinning Behavior of Hydrophobically Modified Ethoxylated Urethane (HEUR) in Aqueous Solution

Shinya Suzuki,^{†,‡} Takashi Uneyama,[†] Tadashi Inoue,[§] and Hiroshi Watanabe^{*,†}

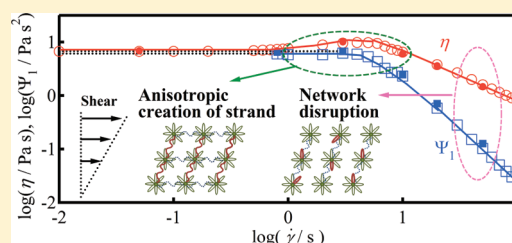
[†]Institute for Chemical Research, Kyoto University, Uji, Kyoto 611-0011, Japan

[‡]Lintec Corporation, 5-14-42 Nishikicho, Warabi, Saitama 335-0005, Japan

[§]Department of Macromolecular Science, Graduate School of Science, Osaka University, Toyonaka, Osaka 560-0043, Japan

ABSTRACT: Flow behavior was examined for a 1.0 wt % aqueous solution of hydrophobically modified ethoxylated urethane (HEUR; $M_w = 4.6 \times 10^4$). In the linear viscoelastic regime, the solution exhibited single-Maxwellian behavior attributable to thermal reorganization of the transient network composed of strings of HEUR flower micelles. Under shear flow at intermediate shear rates $\dot{\gamma}$ just above the equilibrium relaxation frequency $1/\tau$, the solution exhibited thickening characterized by monotonic increase of the viscosity growth function $\eta^+(t; \dot{\gamma})$ with time t above the linear $\eta^+(t)$ and by the steady-state viscosity $\eta(\dot{\gamma})$ larger than the zero-shear viscosity η_0 .

However, at those $\dot{\gamma}$, the first normal stress coefficient growth function $\Psi_1^+(t; \dot{\gamma})$ and its steady-state value $\Psi_1(\dot{\gamma})$ remained very close to the linear $\Psi_1^+(t)$ and $\Psi_{1,0}$ and exhibited no nonlinearity. In addition, the relaxation times of the viscosity and normal stress coefficient decay functions $\eta^-(t; \dot{\gamma})$ and $\Psi_1^-(t; \dot{\gamma})$ measured after cessation of steady flow agreed with those in the linear regime. All these results suggested that the network strands were just moderately stretched to show no significant finite extensible nonlinear elasticity (FENE) effect and that the number density ν of the network strands was negligibly affected by the shear at $\dot{\gamma}$ just above $1/\tau$. A simple transient Gaussian network model incorporating neither the FENE effect nor the increase of ν suggested that the thickening of $\eta^+(t; \dot{\gamma})$ and $\eta(\dot{\gamma})$ and the lack of nonlinearity for $\Psi_1^+(t; \dot{\gamma})$ and $\Psi_1(\dot{\gamma})$ could result from reassociation of the HEUR strands being in balance with the dissociation but *anisotropically enhanced* in the shear gradient direction. In contrast, at $\dot{\gamma} \gg 1/\tau$, $\eta^+(t; \dot{\gamma})$ exhibited overshoot above the linear $\eta^+(t)$ and then approached $\eta(\dot{\gamma}) < \eta_0$, whereas $\Psi_1^+(t; \dot{\gamma})$ stayed below the linear $\Psi_1^+(t)$ and approached $\Psi_1(\dot{\gamma}) \ll \Psi_{1,0}$ after exhibiting a peak. The relaxation of $\eta^-(t; \dot{\gamma})$ and $\Psi_1^-(t; \dot{\gamma})$ after cessation of flow was considerably faster than that in the linear regime. These nonlinear thinning features at $\dot{\gamma} \gg 1/\tau$ were attributable to the flow-induced disruption of the HEUR network (and decrease of ν).



1. INTRODUCTION

Telechelic polymers consisting of hydrophilic main chain and hydrophobic end groups are associated with each other in water to form various structures. Hydrophobically modified ethoxylated urethane (HEUR) is one of such telechelic polymers. The main chain of HEUR is poly(ethylene oxide) (PEO), and short hydrophobic groups such as aliphatic alcohol, alkylphenyl,¹ or fluorocarbons^{2–4} are attached to the chain ends through urethane groups. In aqueous solutions, the end groups of HEUR aggregate through the hydrophobic interaction and form micellar structures.^{5,6} At low concentration (that is still higher than the critical micellar concentration), the HEUR chains form so-called flower micelles. The core of this micelle is composed of hydrophobic end groups, and the corona is formed by hydrophilic PEO chains having the loop type conformation. As the concentration is increased, the number density of flower micelles increases, and the end groups of some chains are located in different cores to bridge the micelles. When the bridge fraction exceeds a percolation threshold, a huge network spread throughout the whole solution is formed. The hydrophobic end groups are thermally detached from a core and eventually

attached to the same and/or other core. Because of this dissociation/association processes, the HEUR network is a temporal network relaxing in a finite time scale.

Rheological properties of aqueous solutions of HEUR have been studied extensively.^{1–19} For example, Annable et al.^{5,6} found that concentrated HEUR solutions exhibit the single-Maxwellian relaxation in the linear viscoelastic regime. This behavior is attributed to the thermal reorganization (dissociation/association) of the HEUR network, and effects of temperature, concentration, and type of the end groups on the basic rheological parameters, the relaxation time, and zero-shear viscosity have been also investigated.^{7–10} Despite the simplicity in the linear regime, rheological properties of the HEUR solutions in the nonlinear regime are quite complicated. In particular, nontrivial behavior has been noted for the steady-state shear viscosity. Concentrated HEUR solutions often exhibit shear thickening at intermediate shear rates and shear thinning

Received: September 8, 2011

Revised: December 28, 2011

Published: January 10, 2012

at higher rates. The mechanism of this thickening/thinning behavior of HEUR solutions has been investigated,^{5,9,11} but uncertainty still remains.

The rheological properties of the concentrated HEUR solutions, the single-Maxwellian behavior in the linear regime, and the thickening/thinning under flow have been analyzed theoretically.^{20–34} One of the most frequently utilized models for telechelic polymers is the transient network model proposed by Tanaka and Edwards.^{20–23} (The transient network model was originally developed for polymeric systems by Green and Tobolsky²⁴ and by Yamamoto,²⁵ and it has been improved in later work.) Focusing on the association/dissociation process of a target chain in the solution, the Tanaka–Edwards transient network model naturally explains the single-Maxwellian relaxation. However, the original Tanaka–Edwards model does not explain the shear thickening behavior. Thus, several mechanisms such as shear-enhanced formation of the network strands and the finite extensible nonlinear elasticity (FENE) of the strands were introduced into the model to describe the thickening.^{26–37} Despite this improvement, it is still controversial if the thickening results from the FENE effect or the shear-enhanced strand formation, or other mechanism(s).

Thus, we have further examined the thickening behavior of a model HEUR solution through rheological tests at various shear rates, $\dot{\gamma}$. Specifically, we measured the viscosity and first normal stress coefficient growth functions $\eta^+(t;\dot{\gamma})$ and $\Psi_1^+(t;\dot{\gamma})$ after start-up of shear flow, $\eta(\dot{\gamma})$ ($=\eta^+(\infty;\dot{\gamma})$) and $\Psi_1(\dot{\gamma})$ ($=\Psi_1^+(\infty;\dot{\gamma})$) in the steady state and the viscosity, and first normal stress coefficient decay functions $\eta^-(t;\dot{\gamma})$ and $\Psi_1^-(t;\dot{\gamma})$ after cessation of steady flow. We found that the thickening seen for $\eta^+(t;\dot{\gamma})$ and $\eta(\dot{\gamma})$ at intermediate $\dot{\gamma}$ was associated with *no* nonlinearity of $\Psi_1^+(t;\dot{\gamma})$ and $\Psi_1(\dot{\gamma})$ and that the relaxation times of $\eta^-(t;\dot{\gamma})$ and $\Psi_1^-(t;\dot{\gamma})$ coincided with those in the linear regime. These features of $\Psi_1^+(t;\dot{\gamma})$, $\Psi_1(\dot{\gamma})$, $\eta^-(t;\dot{\gamma})$, and $\Psi_1^-(t;\dot{\gamma})$ suggest that the factors so far considered, the FENE effect and the shear-induced increase of the strand number density, are not important for the thickening of $\eta^+(t;\dot{\gamma})$ and $\eta(\dot{\gamma})$ observed for our model HEUR solution. Thus, we analyzed the behavior with the aid of a simple transient Gaussian network model without these factors. Irrespective of the model details, this analysis showed that the thickening of $\eta^+(t;\dot{\gamma})$ and $\eta(\dot{\gamma})$ and the lack of nonlinearity for $\Psi_1^+(t;\dot{\gamma})$ and $\Psi_1(\dot{\gamma})$ could result from reassociation of the HEUR strands being in balance with the dissociation but *anisotropically enhanced* in the shear gradient direction, suggesting that the thickening is not always due to the FENE effect and/or the shear-induced strand formation. Details of these results are presented in this paper together with the thinning feature of the solution at high $\dot{\gamma}$ and its mechanism (flow-induced disruption of the network).

2. EXPERIMENTAL SECTION

2.1. Materials. HEUR having hexadecyl groups at the chain ends was synthesized with a conventional method.¹² The structure of HEUR is shown in Figure 1. The chemicals utilized in the synthesis, poly(ethylene oxide) (PEO; $M_w = 1.9 \times 10^4$, $M_w/M_n = 1.1$), hexadecanol (HDOH), and methylene diphenyl-4,4'-diisocyanate

(MDPDI), were purchased from Wako Pure Chemical Industries Ltd. and used without further purification. The synthesis was conducted in dehydrated tetrahydrofuran (THF; Guaranteed grade, Wako) containing 25 wt % of PEO and given amounts of HDOH and MDPDI (molar ratio PEO:MDPDI:HDOH = 3:4:2). The PEO chains were first extended through the condensation reaction with MDPDI at 60 °C for 2 h, and then the end-capping reaction between HDOH and MDPDI (attached at the ends of the extended PEO chains) was conducted at 60 °C for 24 h. Then, the reaction mixture was cooled to room temperature, diluted with excess THF, and poured into a large volume of THF/hexane mixture of 1/3 (w/w) composition. The HEUR sample was recovered as a precipitant in this mixture. The sample thus recovered was thoroughly dried in a vacuum oven at 40 °C.

The HEUR sample was characterized with size-exclusion chromatography utilizing a column/pump system (HLC-8320 GPC EcoSEC, Tosoh) equipped with a refractive index monitor. The elution solvent was THF, and commercially available monodisperse PEO samples (Tosoh) were utilized as the elution standards. The weight-average molecular weight and polydispersity index of the HEUR sample, determined from the elution volume calibration with those standards, were $M_w = 4.6 \times 10^4$ and $M_w/M_n = 1.35$, respectively.

The material subjected to the rheological measurements was a 1.0 wt % aqueous solution of the HEUR sample in distilled water. Prescribed masses of water and HEUR were stirred for 24 h to prepare the solution.

2.2. Measurements. For the 1.0 wt % aqueous solution of HEUR, rheological measurements were conducted with laboratory rheometers, MCR-301 (Anton Paar) and ARES-G2 (TA Instruments). MCR-301 is a stress-controlled rheometer, whereas ARES-G2 is a strain-controlled rheometer.

Dynamic measurements in the linear viscoelastic regime were made with MCR-301 in a cone–plate (CP) geometry (diameter $d = 75$ mm, cone angle $\theta = 1.0^\circ$) at several temperatures between 5 and 25 °C. The measurement at 25 °C was made also with ARES-G2 in a CP geometry ($d = 25$ mm, $\theta = 2.3^\circ$). The storage and loss moduli, $G'(\omega)$ and $G''(\omega)$ measured as functions of the angular frequency ω , obeyed the time–temperature superposition at low ω where the HEUR network exhibited the terminal relaxation (through its thermal reorganization). Those data were reduced at 25 °C.

The viscosity and first normal stress coefficient growth functions after start-up of shear flow, $\eta^+(t;\dot{\gamma})$ and $\Psi_1^+(t;\dot{\gamma})$, the steady-state viscosity and the steady state first normal stress coefficient, $\eta(\dot{\gamma}) = \eta^+(\infty;\dot{\gamma})$ and $\Psi_1(\dot{\gamma}) = \Psi_1^+(\infty;\dot{\gamma})$, and the viscosity and first normal stress coefficient decay functions after cessation of steady shear, $\eta^-(t;\dot{\gamma})$ and $\Psi_1^-(t;\dot{\gamma})$, were measured at 25 °C with ARES-G2 in the CP geometry ($d = 25$ mm, $\theta = 2.3^\circ$) at several shear rates $\dot{\gamma}$ between 0.05 and 100 s^{-1} . $\eta(\dot{\gamma})$ and $\Psi_1(\dot{\gamma})$ were measured also with MCR-301 in the CP geometry ($d = 75$ mm, $\theta = 1.0^\circ$).

3. RESULTS

3.1. Linear Viscoelastic Behavior. For the 1.0 wt % aqueous solution of HEUR, the storage and loss moduli data, $G'(\omega)$ and $G''(\omega)$, measured at several temperatures (5–25 °C) obeyed the time–temperature superposition (tTS) at low ω . Figure 2 shows the master curves of those data reduced at $T_r = 25$ °C. (The data obtained with the stress- and strain-controlled rheometers, MCR-301 and ARES-G2, agreed with each other.)

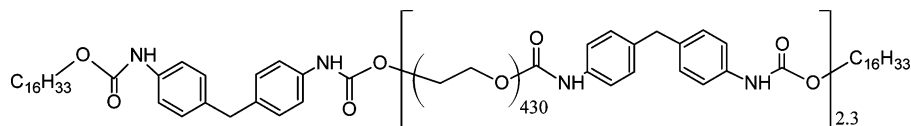


Figure 1. Chemical structure of HEUR chain.

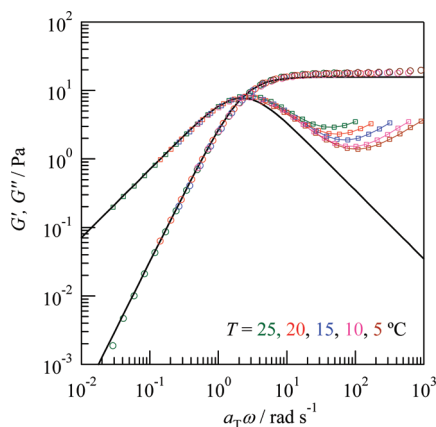


Figure 2. Storage and loss moduli, G' and G'' , measured for the 1.0 wt % aqueous solution of HEUR reduced at 25 °C. Symbols represent the experimental data (after time–temperature superposition), and the thick curves show the results of fitting with the single-Maxwellian model.

The thick curves indicate the result of fitting the G' and G'' data with the single-Maxwellian model:

$$G'(\omega) = G_0 \frac{\omega^2 \tau^2}{1 + \omega^2 \tau^2}, \quad G''(\omega) = G_0 \frac{\omega \tau}{1 + \omega^2 \tau^2} \quad (1)$$

Here, G_0 (= 15 Pa) and τ (= 0.45 s) are the high-frequency modulus and relaxation time, respectively. The fit is excellently achieved except at high ω (where tTS fails), as noted also in the previous studies.^{5,6} In fact, the G_0 and τ values of our HEUR solution are close to the values reported for a similar HEUR solution.¹³

The single-Maxwellian behavior of the HEUR solution is attributed to the thermal reorganization (dissociation/association) of the transient network occurring at the time τ ,^{20–23} and the deviation from this behavior seen at high ω reflects the motion within the network strand. (Since the activation process is different for the network reorganization and the intrastrand motion, tTS cannot be commonly achieved at low and high ω .) Consequently, G_0 is related to the entropy elasticity of the strands, and the number density ν of active strands can be estimated as

$$\nu = \frac{G_0}{k_B T} \cong 3.7 \times 10^{21} \text{ m}^{-3} \quad (2)$$

where k_B is the Boltzmann constant and T is the absolute temperature. This ν value is much smaller than the number density of the HEUR chains, $\nu_0 = 1.8 \times 10^{23} \text{ m}^{-3}$, evaluated from the HEUR concentration (0.01 g cm⁻³) and molecular weight ($M_n = 3.4 \times 10^4$): $\nu/\nu_0 = 0.021$, which is close to the ν/ν_0 ratio reported previously.¹³ Thus, the bridged sequence (string) of the flower micelles should behave as the active strand, although some fraction of those strings would be of loop type and not involved in the active strands.

Additional information for the HEUR network can be found in Figure 3 where the natural logarithm of the shift factor, $\ln a_T$, associating to the G' and G'' master curves is plotted against T^{-1} . The well-known Arrhenius behavior, $\ln a_T = E_a(T^{-1} - T_r^{-1})/R$ with R being the gas constant, is clearly noted, and the activation energy is evaluated to be $E_a \cong 88 \text{ kJ mol}^{-1}$. This E_a value, close to the data reported for similar HEUR solutions,^{5,8} can be assigned as the association energy of the hexadecyl

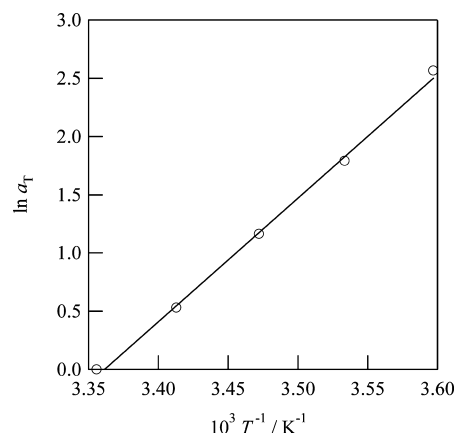


Figure 3. Time–temperature shift factor a_T for the 1.0 wt % aqueous solution of HEUR in the linear viscoelastic regime. The circles show the data, and the solid line represents the Arrhenius equation.

groups at the HEUR chain ends that stabilize the HEUR network.

3.2. Nonlinear Flow Behavior. For the 1.0 wt % HEUR solution at 25 °C, Figures 4 and 5 show the viscosity and first

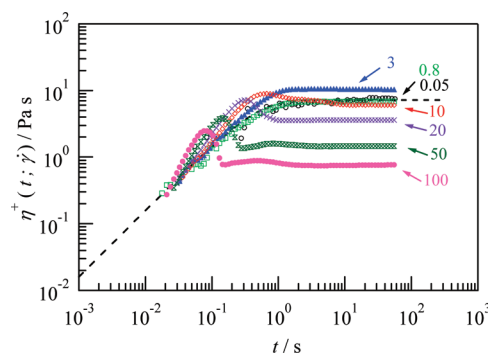


Figure 4. Shear viscosity growth function $\eta^+(t; \dot{\gamma})$ of the 1.0 wt % HEUR aqueous solution at 25 °C measured at various shear rates, $\dot{\gamma}/\text{s}^{-1} = 0.05, 0.8, 3, 10, 20, 50$, and 100. The dashed curve represents the growth function $\eta^+(t; \dot{\gamma})$ in the linear viscoelastic regime ($\dot{\gamma} \rightarrow 0$) evaluated from the G' and G'' data.

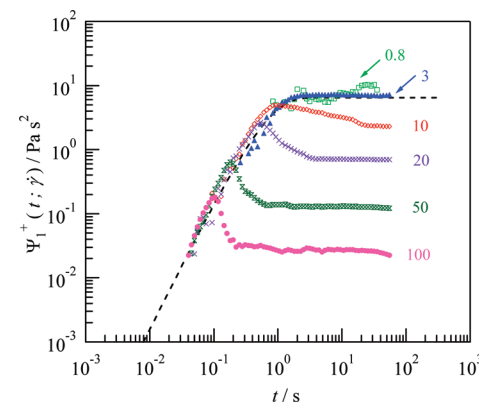


Figure 5. First normal stress coefficient growth function $\Psi_1^+(t; \dot{\gamma})$ of the 1.0 wt % HEUR aqueous solution at 25 °C measured at various shear rates, $\dot{\gamma}/\text{s}^{-1} = 0.8, 3, 10, 20, 50$, and 100. The dashed curve represents the growth function $\Psi_1^+(t; \dot{\gamma})$ in the linear viscoelastic regime ($\dot{\gamma} \rightarrow 0$) evaluated from the G' and G'' data.

normal stress coefficient growth functions after start-up of shear flow, $\eta^+(t; \dot{\gamma}) \equiv \sigma^+(t; \dot{\gamma})/\dot{\gamma}$ and $\Psi_1^+(t; \dot{\gamma}) \equiv N_1^+(t; \dot{\gamma})/\dot{\gamma}^2$ with σ^+ and

N_1^+ being the shear stress and first normal stress difference. These $\eta^+(t;\dot{\gamma})$ and $\Psi_1^+(t;\dot{\gamma})$ data were obtained with the strain-controlled rheometer, ARES-G2. The numbers indicate the shear rate $\dot{\gamma}$ (s^{-1}). For clarity of the plots, the data are shown only for representative $\dot{\gamma}$ values.

Figure 6 shows the corresponding steady-state viscosity and first normal stress coefficient, $\eta(\dot{\gamma})$ ($=\eta^+(\infty;\dot{\gamma})$) and $\Psi_1(\dot{\gamma})$ ($=\Psi_1^+(\infty;\dot{\gamma})$).

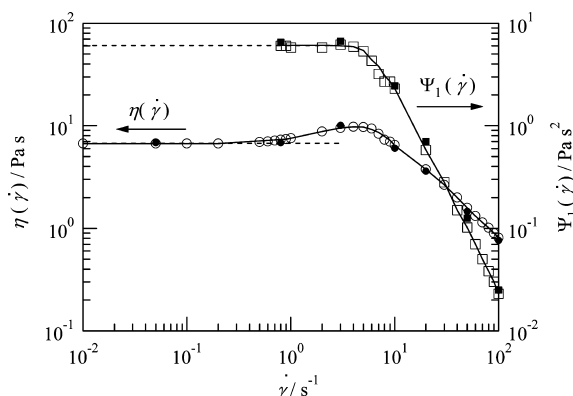


Figure 6. Steady-state shear viscosity $\eta(\dot{\gamma})$ and steady-state first normal stress coefficient $\Psi_1(\dot{\gamma})$ measured for the 1.0 wt % aqueous solution of HEUR at 25 °C. The unfilled and filled symbols indicate the data obtained with the stress- and strain-controlled rheometers, MCR-301 and ARES-G2, respectively. Horizontal dashed lines indicate η_0 and $\Psi_{1,0}$ in the linear viscoelastic regime ($\dot{\gamma} \rightarrow 0$) evaluated from the G' and G'' data.

The data shown with unfilled and filled symbols were obtained with the stress- and strain-controlled rheometers, MCR-301 and ARES-G2, respectively. The data obtained with these rheometers agree with each other.³⁸

Since the HEUR solution exhibits the single-Maxwellian G' and G'' data (cf. Figure 2), the growth functions in the linear viscoelastic regime, $\eta^+(t)$ and $\Psi_1^+(t)$, and the zero-shear viscosity and normal stress coefficient, η_0 ($=\eta^+(\infty)$) and $\Psi_{1,0}$ ($=\Psi_1^+(\infty)$), can be analytically calculated with the aid of the 3-dimensional Maxwell model as

$$\eta^+(t) = G_0\tau[1 - \exp(-t/\tau)], \quad \eta_0 = G_0\tau \quad (3)$$

$$\Psi_1^+(t) = 2G_0\tau^2[1 - \exp(-t/\tau) - (t/\tau)\exp(-t/\tau)], \quad \Psi_{1,0} = 2G_0\tau^2 \quad (4)$$

where G_0 ($= 15$ Pa) and τ ($= 0.45$ s) are the modulus and relaxation time determined for the G' and G'' data. These $\eta^+(t)$ and $\Psi_1^+(t)$ are shown with the dashed curves in Figures 4 and 5 and η_0 and $\Psi_{1,0}$ with the horizontal dashed lines in Figure 6.

At shear rates well below the equilibrium relaxation frequency $1/\tau$ ($= 2.2$ s^{-1}), the linear viscoelastic flow behavior is observed in Figures 4 and 5. Namely, the $\eta^+(t;\dot{\gamma})$ data for $\dot{\gamma} = 0.05$ and 0.8 s^{-1} agree with the linear $\eta^+(t)$ within experimental uncertainty, and the $\Psi_1^+(t;\dot{\gamma})$ data for $\dot{\gamma} = 0.8$ s^{-1} agree with $\Psi_1^+(t)$. (At $\dot{\gamma} = 0.05$ s^{-1} , N_1^+ was too small to give the $\Psi_1^+(t;\dot{\gamma})$ data accurately, and thus those data are not shown in Figure 5. However, $\Psi_1^+(t;\dot{\gamma})$ at such low $\dot{\gamma}$ should agree with $\Psi_1^+(t)$.) Correspondingly, the $\eta(\dot{\gamma})$ and $\Psi_1(\dot{\gamma})$ data at $\dot{\gamma} \ll 1/\tau$ agree with the linear η_0 and $\Psi_{1,0}$ (see Figure 6).

On an increase of $\dot{\gamma}$ from 1 s^{-1} ($= 0.45/\tau$) to 5 s^{-1} ($= 2.2/\tau$), the viscosity exhibits moderate thickening. For example, for $\dot{\gamma} = 3.0$ s^{-1} , the $\eta^+(t;\dot{\gamma})$ data monotonically grow, without exhibiting

overshoot, to a level above $\eta^+(t)$ (cf. Figure 4), and $\eta(\dot{\gamma})$ is larger than η_0 by $\cong 45\%$ (cf. Figure 6). However, the $\Psi_1^+(t;\dot{\gamma})$ and $\Psi_1(\dot{\gamma})$ data at $\dot{\gamma} < 5$ s^{-1} remain close to the linear $\Psi_1^+(t)$ and $\Psi_{1,0}$, as noted in Figures 5 and 6. Namely, the thickening of $\eta^+(t;\dot{\gamma})$ and $\eta(\dot{\gamma})$ is associated with no nonlinearity of $\Psi_1^+(t;\dot{\gamma})$ and $\Psi_1(\dot{\gamma})$.

Both $\eta(\dot{\gamma})$ and $\Psi_1(\dot{\gamma})$ begin to decrease on a further increase of $\dot{\gamma}$ above 5 s^{-1} , as seen in Figure 6. This thinning behavior is characterized by power-law relationships at high $\dot{\gamma}$

$$\eta(\dot{\gamma}) \propto \dot{\gamma}^{-0.97}, \quad \Psi_1(\dot{\gamma}) \propto \dot{\gamma}^{-1.98} \quad (\text{for } \dot{\gamma} \geq 30 \text{ s}^{-1}) \quad (5)$$

Thus, the thinning at high $\dot{\gamma}$ is characterized with $\dot{\gamma}$ -insensitive shear stress ($\sigma \propto \dot{\gamma}^{0.03}$) and first normal stress difference ($N_1 \propto \dot{\gamma}^{0.02}$). It should be also noted that the thinning behavior is qualitatively different for $\eta(\dot{\gamma})$ and $\Psi_1(\dot{\gamma})$. The thinning of $\eta(\dot{\gamma})$ is associated with a transient overshoot of $\eta^+(t;\dot{\gamma})$ well above the linear $\eta^+(t)$ (cf. Figure 4), while the thinning of $\Psi_1(\dot{\gamma})$ is associated with no significant overshoot of $\Psi_1^+(t;\dot{\gamma})$ (very weak overshoot, if any) above the linear $\Psi_1^+(t;\dot{\gamma})$ (cf. Figure 5).

As explained above, our 1.0 wt % HEUR solution exhibits characteristic thickening and thinning behavior commonly observed for solutions of telechelic polymers. The thickening and thinning obviously indicate that the HEUR network exhibits some structural change under shear. This change can be monitored through the stress decay after cessation of the steady shear. Thus, we examined the viscosity and normal stress coefficient decay functions, $\eta^-(t;\dot{\gamma})$ and $\Psi_1^-(t;\dot{\gamma})$, with the strain-controlled rheometer, ARES-G2. As representative examples, the data measured for $\dot{\gamma} = 3$ and 20 s^{-1} (in the thickening and thinning regimes for $\eta(\dot{\gamma})$) are shown in Figures 7 and 8,

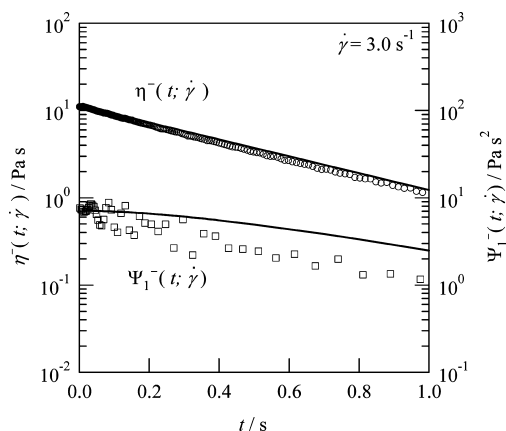


Figure 7. Shear viscosity and first normal stress coefficient decay functions, $\eta^-(t;\dot{\gamma})$ and $\Psi_1^-(t;\dot{\gamma})$, measured for the 1.0 wt % HEUR aqueous solution presheared at $\dot{\gamma} = 3.0$ s^{-1} (in the thickening regime for $\eta(\dot{\gamma})$) at 25 °C. The solid curves indicate the linear $\eta^-(t)$ and $\Psi_1^-(t)$ with adjustment made only for their initial values. For more details, see text.

respectively. The $\eta^-(t;\dot{\gamma})$ and $\Psi_1^-(t;\dot{\gamma})$ data at short t unequivocally reflect the HEUR network structure under steady shear (just before cessation of shear). The initial values, $\eta^-(0;\dot{\gamma})$ and $\Psi_1^-(0;\dot{\gamma})$, agreed with the steady-state values, $\eta(\dot{\gamma})$ and $\Psi_1(\dot{\gamma})$, which lends support to this argument for the data at short t .

In the linear regime, the decay functions are analytically expressed in terms of the time τ and modulus G_0 associated

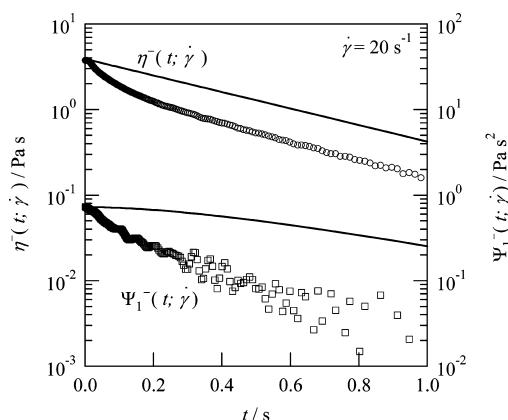


Figure 8. Shear viscosity and first normal stress coefficient decay functions, $\eta^-(t; \dot{\gamma})$ and $\Psi_1^-(t; \dot{\gamma})$, measured for the 1.0 wt % HEUR aqueous solution presheared at $\dot{\gamma} = 20 \text{ s}^{-1}$ (in the thinning regime for both $\eta(\dot{\gamma})$ and $\Psi_1(\dot{\gamma})$) at 25°C . The solid curves indicate the linear $\eta^-(t)$ and $\Psi_1^-(t)$ with adjustment made only for their initial values. For more details, see text.

with the single-Maxwellian relaxation:

$$\eta^-(t) = \eta_0 \exp(-t/\tau) \quad \text{with } \eta_0 = G_0\tau \quad (6a)$$

$$\Psi_1^-(t) = \Psi_{1,0} \left(1 + \frac{t}{\tau}\right) \exp(-t/\tau) \quad (6b)$$

with $\Psi_{1,0} = 2G_0\tau^2$

The solid curves in Figures 7 and 8 indicate these linear decay functions with the initial values being adjusted for the nonlinearity, $\{\eta_1(\dot{\gamma})/\eta_0\}\eta^-(t)$ and $\{\Psi_1(\dot{\gamma})/\Psi_{1,0}\}\Psi_1^-(t)$. In the thickening regime (Figure 7), these curves are close to the $\eta^-(t; \dot{\gamma})$ and $\Psi_1^-(t; \dot{\gamma})$ data in particular at short t where the data reflect the HEUR network structure just before cessation of shear. A rapid initial decay would be observed for both $\eta^-(t; \dot{\gamma})$ and $\Psi_1^-(t; \dot{\gamma})$ if the FENE-type nonlinear effect is significant in the steady shear state, and such a rapid decay, if any, can be detected with ARES-G2 (enabling the full cessation of flow within $\sim 0.025 \text{ s}$). In fact, the rapid initial decay (in the time scale of 0.2 s) is observed on cessation of fast shear, as explained later for Figure 8. However, no such rapid decay is observed on cessation of the steady shear flow at intermediate $\dot{\gamma}$ in the thickening regime for η (cf. Figure 7). This result strongly suggests that the dissociation time of the HEUR network under shear agrees with τ in the linear regime and that the network structure under shear is not too much different from that at equilibrium. (The scatter of the $\Psi_1^-(t; \dot{\gamma})$ data points at short t is mainly due to a mechanical noise in the shear-gradient direction on cessation of steady shear.)

In contrast, in the thinning regime for $\eta(\dot{\gamma})$ (Figure 8), the initial decay of the $\eta^-(t; \dot{\gamma})$ and $\Psi_1^-(t; \dot{\gamma})$ data in the time scale of 0.2 s is considerably faster than that in the linear regime (solid curves). This result suggests that the HEUR network is largely disrupted, and the fragmented network strands are considerably stretched by the shear in the thinning regime to exhibit fast contraction process of the strands at $t \ll \tau$. The decay of $\eta^-(t; \dot{\gamma})$ and $\Psi_1^-(t; \dot{\gamma})$ at longer t becomes as slow as that in the linear regime, possibly due to the thermal reorganization of the remaining network (that could also grow through association of the fragmented strands during the stress decay process).

The above decay behavior provides us with a clue for discussing the thickening and thinning behavior of the HEUR solution, as explained later. For this discussion, it is also informative to compare the behavior of wormlike micelles of surfactants formed in water with the behavior of the HEUR solution. Extensive studies^{35–37,39,40} revealed that the wormlike micelles of cetyltrimethylammonium bromide (CTAB) and sodium salicylate (NaSal) (1:1 molar ratio) exhibit the single-Maxwellian linear viscoelasticity very similar to that of the HEUR solution. Concentrated CTAB/NaSal (1/1) solutions under fast shear exhibit increases of both $\eta^+(t; \dot{\gamma})$ and $\Psi_1^+(t; \dot{\gamma})$ to levels well above the linear $\eta^+(t)$ and $\Psi_1^+(t)$, and this thickening behavior is attributable to the finite extensible nonlinear elasticity (FENE), i.e., stretch hardening of the wormlike micelles themselves, as reported by Inoue et al.³⁶ The thickening behavior of the HEUR solution (Figures 4–6) is quite different: The thickening of $\eta^+(t; \dot{\gamma})$ and $\eta(\dot{\gamma})$ of the HEUR solution is associated with the linear behavior of $\Psi_1^+(t; \dot{\gamma})$ and $\Psi_1(\dot{\gamma})$ and thus *not* attributable to the *simple* FENE effect of the HEUR strands.

Comparison of the thinning behavior of entangled polymers with that of the HEUR solution (at high $\dot{\gamma} > 5 \text{ s}^{-1}$) is also useful for elucidating the thinning mechanism in the HEUR solution. The thinning of entangled polymers due to strong shear orientation of the chains can be characterized by the power-law relationships:^{41,42}

$$\eta(\dot{\gamma}) \propto \dot{\gamma}^{-0.82} \quad \text{and} \quad \Psi_1(\dot{\gamma}) \propto \dot{\gamma}^{-1.5 \pm 0.05} \quad (7)$$

for monodisperse linear chains

In addition, empirical rules relating the nonlinear quantities of those polymers, $\eta(\dot{\gamma})$ and $\Psi_1(\dot{\gamma})$, to the linear quantities, $\Psi_1^+(t)$, $G'(\omega)$, and the complex viscosity, $\eta^*(\omega) \equiv \{G''(\omega) - iG'(\omega)\}/\omega$, have been proposed by Cox and Merz,⁴³ Gleissle,⁴⁴ and Osaki et al.⁴⁵

$$\text{Cox-Merz: } \eta(\dot{\gamma}) \cong |\eta^*(\omega)|_{\omega=\dot{\gamma}} \quad (8a)$$

$$\text{Gleissle: } \Psi_1(\dot{\gamma}) \cong [\Psi_1^+(t)]_{t=k/\dot{\gamma}} \quad (8b)$$

$$\text{Osaki: } \Psi_1(\dot{\gamma}) \cong \left[\frac{2G'(\omega)}{\omega^2} \right]_{\omega=\dot{\gamma}/k'} \quad (8c)$$

Here, k and k' are adjustable constants close to unity. These empirical rules hold for entangled polymers considerably well.^{43–46}

The $\dot{\gamma}$ dependence of $\eta(\dot{\gamma})$ and $\Psi_1(\dot{\gamma})$ of the HEUR solution (eq 5) is considerably stronger than that for entangled polymers specified by eq 7. Furthermore, the above three empirical rules severely fail for the HEUR solution, as demonstrated in Figure 9, where k and k' included in eqs 8b and 8c were set to be 1.55 and 1, respectively; compare large symbols. These results suggest that the thinning of the HEUR solution is *not* attributable to the simple shear orientation not associated with the network reorganization (dissociation and association under shear).

At the same time, we also note that $|\eta^*(\omega)|$ plotted against an adjusted (increased) angular frequency, $\omega = 4.6\dot{\gamma}$, agree with the $\eta(\dot{\gamma})$ data at high $\dot{\gamma}$; cf. small squares and large circles in top panel of Figure 9. Similarly, $\Psi_1^+(t)$ and $2G'(\omega)/\omega^2$ plotted against an increased reciprocal time ($\tau^{-1} = 2.7\dot{\gamma}/k = 1.7\dot{\gamma}$) and an increased angular frequency ($\omega = 2.6\dot{\gamma}/k' = 2.6\dot{\gamma}$), respectively, agree with the $\Psi_1(\dot{\gamma})$ data at high $\dot{\gamma}$; cf. small symbols and large circles in the bottom panel. These results could be

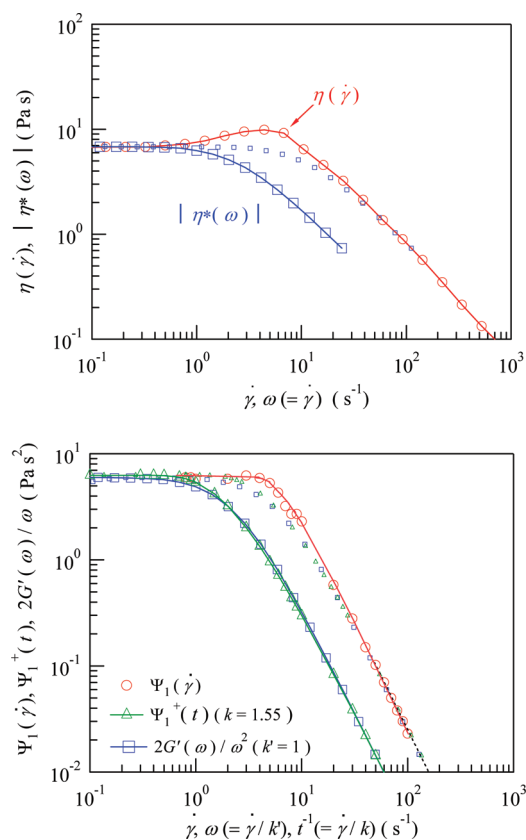


Figure 9. Test of validity of the empirical Cox–Merz, Gleissle, and Osaki rules for the 1.0 wt % HEUR solution at 25 °C.

related to the shear orientation of the fragmented (disrupted) network, as discussed later in more detail.

4. DISCUSSION

4.1. Test of Conventional Thickening Mechanisms for HEUR Solution. In the studies so far conducted for HEUR solutions, the shear thickening has been attributed to either the finite extensible nonlinear elasticity (FENE) of the shear-stretched HEUR strands or the increase of the effective strand number density on shear-induced reorganization of the network (shear-enhanced strand formation). In principle, both mechanisms could lead to the thickening, and the origin of the thickening is still controversial. We here make a brief summary of these mechanisms and then test the validity of those mechanisms for our 1 wt % HEUR solution.

The FENE concept, widely utilized for constitutive equations of polymers,⁴⁷ was first introduced into the transient network model by Marrucci and co-workers.^{27,28} The model was further elaborated by Koga and Tanaka,^{30–32} who improved the expression of the network dissociation rate in the transient FENE network model but assumed the network reformation to occur randomly/isotropically in space. Indei^{33,34} showed that the transient FENE network model does not always predict the thickening because of competition between the stress-enhancing FENE effect and the stress-suppressing dissociation effect. Nevertheless, in a considerably wide range of the shear rate $\dot{\gamma}$ where the former overwhelms the latter, Koga–Tanaka model predicts the thickening of *both* viscosity and first normal stress coefficient.³⁰ (Further details of this model are explained later.) Several experimental results were reported to be in favor of this FENE-induced thickening deduced from the Koga–

Tanaka model in that range of $\dot{\gamma}$. For example, Berret et al.^{3,14} conducted start-up flow experiments for HEUR solutions and attributed the thickening of the viscosity to the increase of the effective modulus due to the FENE effect. Pellens et al.^{11,15,16} reported that the stress-optical rule (SOR), being valid only in the absence of the FENE effect,⁴² fails for their HEUR solutions in the thickening regime, and thus the thickening is related to the FENE effect, although the reported increase of the η/η_0 ratio is only by 1–2% (and thus the reported thickening is much weaker than that observed for our HEUR solution). A much stronger FENE effect has been confirmed for both viscosity and first normal stress coefficient of the wormlike micelles.³⁶

However, our 1.0 wt % HEUR solution exhibits the thickening of the viscosity ($\eta^+(t;\dot{\gamma})$ and $\eta(\dot{\gamma})$) while allowing the first normal stress coefficient ($\Psi_1^+(t;\dot{\gamma})$ and $\Psi_1(\dot{\gamma})$) to stay in the linear regime (cf. Figures 4–6). In addition, the network strands being highly stretched (to a FENE level) under shear should exhibit fast contraction on cessation of shear, but no such fast process is observed for the $\eta^-(t;\dot{\gamma})$ and $\Psi_1^-(t;\dot{\gamma})$ data of our HEUR solution in the thickening regime (Figure 7). These results lead us to conclude that the thickening of our HEUR solution is *not primarily* due to the simple FENE effect.⁴⁹ In fact, this conclusion is in harmony with a simple but unambiguous analysis comparing the elastic energy of the HEUR strand and the association energy of the end groups of the HEUR chains, as explained in the Appendix.

Of course, we cannot fully rule out a possibility that the FENE effect is coupled with a structural change of the network (anisotropic creation of network strands explained later), thereby contributing, to some extent, to the behavior of our HEUR solution, the thickening of the viscosity associated with linear behavior of the first normal stress coefficient. However, it should be emphasized that all data in Figures 4–7 strongly suggest that the *simple* FENE effect alone cannot explain the behavior of our HEUR solution. The contribution of the FENE effect (coupled with the change of the network) to this behavior, *if any*, can be examined through a test of SOR. Unfortunately, at this moment, rheo-optical data useful for this test are not available for our HEUR solutions. The rheo-optical measurement is now being attempted, and the results will be reported in our future paper.

Concerning the above conclusion, we should note that the Koga–Tanaka model incorporates the FENE effect as one of the essential ingredients but does *not* always predicts thickening of both $\eta(\dot{\gamma})$ and $\Psi_1(\dot{\gamma})$:³⁰ The model includes two basic parameters A and g , with A representing the FENE contribution to the strand tension and g representing an effect of chain tension on the dissociation rate of the HEUR network. (The model reduces to a Gaussian transient network model if $A = 0$.) The nonlinear rheological behavior of the model including shear thinning and thickening are mainly determined by competition of the nonlinear elasticity (controlled by A) and the acceleration of the dissociation (controlled by g). The thickening of $\eta(\dot{\gamma})$ and thinning of $\Psi_1(\dot{\gamma})$ could be simultaneously deduced from the Koga–Tanaka model for a specific combination of the parameters. For example, slight thickening of the $\eta(\dot{\gamma})$ associated with slight thinning of $\Psi_1(\dot{\gamma})$ (both $\sim 10\%$ in magnitude) reported in ref 11 is fairly well described by the model, although some deviation is noted for the prediction of $\Psi_1(\dot{\gamma})$; see Figure 10 of ref 30. However, the parameters giving this description are $A = 5$ and $g = 0.16$, the former giving a significant FENE effect in a case of the strand stretching. The FENE effect is not important for our HEUR solution, as explained above. Thus, if we apply the Koga–Tanaka

model to our HEUR solution, the parameter A is to be set in a close vicinity of zero. Then, the other parameter g should be also set to be close to zero so as to reproduce the lack of thinning/thickening of $\Psi_1(\dot{\gamma})$ in the thickening zone of η , as clearly noted from Figure 4 of ref 30. For that case, the Koga–Tanaka model reduces to the Green–Tobolsky type transient network model considering no effect of chain tension on the strand dissociation rate. It may be still possible to seek for a set of Koga–Tanaka parameters A and g in the vicinity of zero that might qualitatively reproduce the behavior of our HEUR solution. However, it does not seem to be fruitful to seek for such parameters (if any) because the FENE effect, one of the essential ingredients in that model, is not important for our HEUR solution. An attempt of finding such parameters is nothing more than parameter fitting without physical basis. Thus, for our HEUR solution examined in this study, we simply attempt to make a general discussion within the context of the Gaussian transient network model allowing anisotropic formation of the HEUR network strands under shear. This discussion is given in the next section.

Now, we turn our attention to the conventionally considered second mechanism of thickening, the increase of the effective strand number density ν on shear-induced reorganization of the network. Some experimental data for HEUR solutions were reported to be not in accord to the FENE network model but support the model considering this increase of ν .^{17–19} For example, Tam et al.¹⁸ conducted shear experiments with parallel superposition of small-amplitude oscillation to find decrease and increase of the relaxation time and the characteristic modulus defined for the oscillation. This result led them to attribute the thickening to the increase of ν (due to incorporation of free micelles into the network). François et al.¹⁹ performed small-angle neutron scattering under shear and reported that the internal structure of the micellar core is not affected by flow in the thickening region. This shear insensitivity of the core structure is in harmony with the model considering the increase of ν . Nevertheless, this model results in simultaneous increases of the viscosity and normal stress coefficient, which does not match the behavior of our HEUR solution seen in Figures 4–6.

Thus, neither the transient FENE network model nor the model considering the flow-induced increase of ν can explain the thickening of η and lack of nonlinearity of Ψ_1 observed for our HEUR solution.⁴⁹ Thus, in the next section, we analyze the behavior of a simple, transient Gaussian network model (without FENE/increase of ν) to discuss the thickening behavior of our HEUR solution.

4.2. Simple Transient Gaussian Network Model for Shear Thickening. The thickening behavior of our 1.0 wt % HEUR solution is governed by neither the FENE effect (stretch hardening) nor the shear-induced increase of number density ν of the active strands, as explained in the previous section. Thus, we assume that the HEUR strands are in the Gaussian state (not stretch hardened) and have the constant ν even under the shear in the η thickening regime. With this assumption, we can simply express the steady-state viscosity and normal stress coefficient in terms of the end-to-end vector \mathbf{r} of the strands as^{47,48}

$$\eta(\dot{\gamma}) \cong \frac{3k_B T}{r_0^2} \frac{\nu}{\dot{\gamma}} \int d\mathbf{r} r_x r_y \psi_{ss}(\mathbf{r}, \dot{\gamma}) \quad (9)$$

$$\Psi_1(\dot{\gamma}) \cong \frac{3k_B T}{r_0^2} \frac{\nu}{\dot{\gamma}^2} \int d\mathbf{r} (r_x^2 - r_y^2) \psi_{ss}(\mathbf{r}, \dot{\gamma}) \quad (10)$$

Here, k_B and T are the Boltzmann constant and absolute temperature, respectively, and r_x and r_y indicate the components of \mathbf{r} in the shear and shear gradient directions. $\psi_{ss}(\mathbf{r}, \dot{\gamma})$ is the steady-state distribution function of \mathbf{r} under the shear at $\dot{\gamma}$. In eqs 9 and 10, all strands are approximated to have the same average size r_0 at equilibrium. These strands have the Gaussian spring constant, $3k_B T/r_0^2$, irrespective of their stretch ratio.

In eqs 9 and 10, all nonlinearities emerge from the deviation of $\psi_{ss}(\mathbf{r}, \dot{\gamma})$ from the equilibrium distribution function

$$\psi_{eq}(\mathbf{r}) = \left(\frac{3}{2\pi r_0^2} \right)^{3/2} \exp \left(- \frac{3\mathbf{r}^2}{2r_0^2} \right) \quad (11)$$

This deviation of $\psi_{ss}(\mathbf{r}, \dot{\gamma})$ is not trivial because the reorganization kinetics of the network should be affected by the shear flow. For description of this deviation in the thickening regime, we here adopt a simplified but analytically tractable version of the transient network model considering dissociation/association of the active, Gaussian strands having the constant number density ν in total. Namely, none of the thickening mechanisms explained in the previous section are incorporated in our model.

In this model, the dynamics of the system is simply described by the probability distribution function of the active strands. Specifically, we focus on the following birth-and-death type master equation⁵⁰ for those strands after start-up of shear at $\dot{\gamma}$:

$$\begin{aligned} \frac{\partial \psi(\mathbf{r}, t, \dot{\gamma})}{\partial t} = & -\dot{\gamma} r_y \frac{\partial \psi(\mathbf{r}, t, \dot{\gamma})}{\partial r_x} - \frac{1}{\tau_0} \psi(\mathbf{r}, t, \dot{\gamma}) \\ & + \frac{1}{\tau_0} \phi(\mathbf{r}, t, \dot{\gamma}) \end{aligned} \quad (12)$$

Here, $\psi(\mathbf{r}, t, \dot{\gamma})$ is the probability distribution function of \mathbf{r} of the strand at time t , τ_0 is the characteristic time for the dissociation and association, and $\phi(\mathbf{r}, t, \dot{\gamma})$ is the source function, i.e., probability distribution function of \mathbf{r} of the newly created (associated) network strands at t . At equilibrium, we have $\psi(\mathbf{r}, t, \dot{\gamma}=0) = \phi(\mathbf{r}, t, \dot{\gamma}=0) = \psi_{eq}(\mathbf{r})$, with $\psi_{eq}(\mathbf{r})$ being the equilibrium distribution function given by eq 11. Furthermore, τ_0 is equal to τ for the single-Maxwellian relaxation in the linear viscoelastic regime (cf. eq 1).

Here, a comment needs to be made for the source function, $\phi(\mathbf{r}, t, \dot{\gamma})$. A reviewer for this paper regarded eq 12 to be physically not sound unless the molecular mechanism of the strand creation is specified. As a hypothesis, we can list candidates of this mechanism, for example, recombination of the dangling chains, conversion of the loops into bridges, splitting of superbridges into shorter bridge (a mechanism not considered in the Koga–Tanaka model³⁰), and so on. However, an argument on the basis of such a specific mechanism is clearly dependent on the feature of the mechanism and is dependent *too much* on the assumption for the mechanism. In this study, we just focus on the anisotropy of the strand creation under shear flow, no matter what the underlying mechanism is. Under the shear flow, from the symmetry, all mechanisms listed above can lead to the strand creation process that is anisotropic and reasonably described by the $\dot{\gamma}$ -dependent anisotropic source function, $\phi(\mathbf{r}, t, \dot{\gamma})$. This approach allows us to make a general discussion free from the assumption for the mechanism.

To analyze the behavior of $\eta(\dot{\gamma})$ and $\Psi_1(\dot{\gamma})$, we need to obtain an explicit expression for the steady-state distribution function $\psi_{ss}(\mathbf{r}, \dot{\gamma})$; cf. eqs 9 and 10. This $\psi_{ss}(\mathbf{r}, \dot{\gamma})$, identical to $\psi(\mathbf{r}, t \rightarrow \infty, \dot{\gamma})$ determined by eq 12, is related to the source function in the steady state, $\phi_{ss}(\mathbf{r}, \dot{\gamma}) = \phi(\mathbf{r}, t \rightarrow \infty, \dot{\gamma})$, as

$$\dot{\gamma} r_y \frac{\partial \psi_{ss}(\mathbf{r}, \dot{\gamma})}{\partial r_x} + \frac{1}{\tau_0} \psi_{ss}(\mathbf{r}, \dot{\gamma}) = \frac{1}{\tau_0} \phi_{ss}(\mathbf{r}, \dot{\gamma}) \quad (13)$$

For relatively small $\dot{\gamma}$ (where the thickening is actually observed for the HEUR solution), we can expand $\psi_{ss}(\mathbf{r}, \dot{\gamma})$ and $\phi_{ss}(\mathbf{r}, \dot{\gamma})$ around their Gaussian forms at equilibrium, $\psi_{ss}(\mathbf{r}, \dot{\gamma}=0) = \phi_{ss}(\mathbf{r}, \dot{\gamma}=0) = \psi_{eq}(\mathbf{r})$. This expansion can be conveniently made by utilizing the Hermite polynomials as the basis:

$$\begin{aligned} \psi_{ss}(\mathbf{r}, \dot{\gamma}) &= \psi_{eq}(\mathbf{r}) \sum_{n,m,l=0}^{\infty} a_{n,m,l}(\dot{\gamma}) 2^{-(n+m+l)/2} \\ &\times H_n\left(\frac{\sqrt{3}r_x}{\sqrt{2}r_0}\right) H_m\left(\frac{\sqrt{3}r_y}{\sqrt{2}r_0}\right) H_l\left(\frac{\sqrt{3}r_z}{\sqrt{2}r_0}\right) \end{aligned} \quad (14)$$

$$\begin{aligned} \phi_{ss}(\mathbf{r}, \dot{\gamma}) &= \psi_{eq}(\mathbf{r}) \sum_{n,m,l=0}^{\infty} b_{n,m,l}(\dot{\gamma}) 2^{-(n+m+l)/2} \\ &\times H_n\left(\frac{\sqrt{3}r_x}{\sqrt{2}r_0}\right) H_m\left(\frac{\sqrt{3}r_y}{\sqrt{2}r_0}\right) H_l\left(\frac{\sqrt{3}r_z}{\sqrt{2}r_0}\right) \end{aligned} \quad (15)$$

Here, $a_{n,m,l}(\dot{\gamma})$ and $b_{n,m,l}(\dot{\gamma})$ are the expansion coefficients and $H_n(x)$ is the n th-order Hermite polynomial.⁵¹ From eqs 13–15 with the aid of the recurrence formula, $H_{n+1}(x) = 2xH_n(x) - 2nH_{n-1}(x)$ and $dH_n(x)/dx = 2nH_{n-1}(x)$, we can find relationships between the coefficients $a_{n,m,l}(\dot{\gamma})$ and $b_{n,m,l}(\dot{\gamma})$. For low-order coefficients necessary for calculating $\eta(\dot{\gamma})$ and $\Psi_1(\dot{\gamma})$ up to the order of $\dot{\gamma}^2$ (up to the lowest order of nonlinearity), the relationships are summarized as

$$a_{1,1,0}(\dot{\gamma}) = b_{1,1,0}(\dot{\gamma}) + (\tau_0 \dot{\gamma}) [1 + 2b_{0,2,0}(\dot{\gamma})] \quad (16)$$

$$a_{0,2,0}(\dot{\gamma}) = b_{0,2,0}(\dot{\gamma}) \quad (17)$$

$$\begin{aligned} a_{2,0,0}(\dot{\gamma}) &= b_{2,0,0}(\dot{\gamma}) + (\tau_0 \dot{\gamma}) b_{1,1,0}(\dot{\gamma}) \\ &+ (\tau_0 \dot{\gamma})^2 [1 + 2b_{0,2,0}(\dot{\gamma})] \end{aligned} \quad (18)$$

The $\dot{\gamma}$ dependence of these low-order coefficients can be found from simple consideration/analysis. First of all, the normalization condition for $\psi_{ss}(\mathbf{r}, \dot{\gamma})$ and $\phi_{ss}(\mathbf{r}, \dot{\gamma})$ gives $\dot{\gamma}$ -independent coefficients, $a_{0,0,0}(\dot{\gamma}) = b_{0,0,0}(\dot{\gamma}) = 1$. Furthermore, from the symmetry of $\psi_{ss}(\mathbf{r}, \dot{\gamma})$ and $\phi_{ss}(\mathbf{r}, \dot{\gamma})$ under simple shear field, $a_{n,m,l}(\dot{\gamma})$ and $b_{n,m,l}(\dot{\gamma})$ should be nonzero only when both $(n+m)$ and l are even integers. Finally, $\eta(\dot{\gamma})$ and $\Psi_1(\dot{\gamma})$ are required to be even functions of $\dot{\gamma}$ (to be invariant on reversal of the shear direction) and have finite nonzero values η_0 and $\Psi_{1,0}$ for the single-Maxwellian relaxation (cf. eqs 3 and 4) on a decrease of $\dot{\gamma}$ toward zero. This requirement forces the low-order coefficients $b_{n,m,l}(\dot{\gamma})$ appearing in eqs 16–18 to have the following form of expansion with respect to $\dot{\gamma}$ (unless $\dot{\gamma}$ is too large to disturb the convergence):

$$b_{1,1,0}(\dot{\gamma}) = b_{1,1,0}^{(3)} \{\tau_0 \dot{\gamma}\}^3 + O(\{\tau_0 \dot{\gamma}\}^5) \quad (19)$$

$$b_{2,0,0}(\dot{\gamma}) = b_{2,0,0}^{(2)} \{\tau_0 \dot{\gamma}\}^2 + b_{2,0,0}^{(4)} \{\tau_0 \dot{\gamma}\}^4 + O(\{\tau_0 \dot{\gamma}\}^6) \quad (20)$$

$$b_{0,2,0}(\dot{\gamma}) = b_{0,2,0}^{(2)} \{\tau_0 \dot{\gamma}\}^2 + b_{0,2,0}^{(4)} \{\tau_0 \dot{\gamma}\}^4 + O(\{\tau_0 \dot{\gamma}\}^6) \quad (21)$$

From eqs 9 and 10 combined with eq 14 and eqs 16–21, $\eta(\dot{\gamma})$ and $\Psi_1(\dot{\gamma})$ are calculated up to the lowest order of nonlinearity. The results are summarized as

$$\begin{aligned} \frac{\eta(\dot{\gamma})}{\eta_0} &= 1 + \{\tau_0 \dot{\gamma}\}^2 [b_{1,1,0}^{(3)} + 2b_{2,0,0}^{(2)}] \\ &+ O(\{\tau_0 \dot{\gamma}\}^4) \quad \text{with } \eta_0 = \nu k_B T \tau_0 \end{aligned} \quad (22)$$

$$\begin{aligned} \frac{\Psi_1(\dot{\gamma})}{\Psi_{1,0}} &= 1 + \{\tau_0 \dot{\gamma}\}^2 [b_{1,1,0}^{(3)} + 2b_{2,0,0}^{(2)} + b_{2,0,0}^{(4)} \\ &- b_{0,2,0}^{(4)}] + O(\{\tau_0 \dot{\gamma}\}^4) \quad \text{with } \Psi_{1,0} = 2\nu k_B T \tau_0^2 \end{aligned} \quad (23)$$

In the linear viscoelastic regime at low $\dot{\gamma}$, our model gives the single-Maxwellian behavior associated with η_0 and $\Psi_{1,0}$ ($= 2G_0\tau_0^2$ with $G_0 = \nu k_B T$) shown in eqs 22 and 23. In contrast, in the nonlinear regime, $\eta(\dot{\gamma})$ deduced from the model exhibits thickening while $\Psi_1(\dot{\gamma})$ remains close to the linear $\Psi_{1,0}$ if the coefficients satisfy the relationships $b_{1,1,0}^{(3)} + 2b_{2,0,0}^{(2)} > 0$ and $b_{2,0,0}^{(4)} - b_{0,2,0}^{(4)} \cong -(b_{1,1,0}^{(3)} + 2b_{2,0,0}^{(2)})$. Namely, the behavior of $\eta(\dot{\gamma})$ and $\Psi_1(\dot{\gamma})$ experimentally observed for the HEUR solution at intermediate $\dot{\gamma}$ can be qualitatively reproduced by the model that incorporates *neither* the FENE effect *nor* the shear-induced increase of ν .

Concerning this behavior of the model, we should note in eqs 22 and 23 that $\eta(\dot{\gamma})$ and $\Psi_1(\dot{\gamma})$ of our model are determined by the expansion coefficients b of the source function $\phi_{ss}(\mathbf{r}, \dot{\gamma})$. Namely, the strands are dissociated and associated under steady shear (to keep the constant ν), and the anisotropy of the orientation of the newly created (associated) strands, represented by $\phi_{ss}(\mathbf{r}, \dot{\gamma})$, determines the thickening/thinning behavior of $\eta(\dot{\gamma})$ and $\Psi_1(\dot{\gamma})$. Specifically, the coefficient $b_{n,m,l}$ for $\phi_{ss}(\mathbf{r}, \dot{\gamma})$ with $(n,m,l) = (1,1,0)$ corresponds to the mode of strand creation in the direction parallel to $\mathbf{e}_x + \mathbf{e}_y$, where \mathbf{e}_x and \mathbf{e}_y are the unit vectors in the shear and shear gradient direction, respectively. Similarly, the coefficients $b_{n,m,l}$ with $(n,m,l) = (2,0,0)$ and $(0,2,0)$ correspond to the mode of strand creation in the directions parallel to \mathbf{e}_x and \mathbf{e}_y , respectively. Thus, if the strands are preferentially created in the shear gradient direction rather than the shear direction and much less favorably in the direction in between (parallel to $\mathbf{e}_x + \mathbf{e}_y$), the coefficients *could* satisfy a relationship $b_{0,2,0}^{(4)} > b_{2,0,0}^{(2)} > b_{2,0,0}^{(4)} > b_{1,1,0}^{(3)} (>0)$, thereby simultaneously fulfilling the condition for thickening of $\eta(\dot{\gamma})$, $b_{1,1,0}^{(3)} + 2b_{2,0,0}^{(2)} > 0$, and the condition for the lack of nonlinearity of $\Psi_1(\dot{\gamma})$, $b_{2,0,0}^{(4)} - b_{0,2,0}^{(4)} = -(b_{1,1,0}^{(3)} + 2b_{2,0,0}^{(2)})$. (For $b_{2,0,0}^{(2)}$ and $b_{2,0,0}^{(4)}$ having the same (n,m,l) , the difference due to the expansion order ($b_{2,0,0}^{(2)} > b_{2,0,0}^{(4)}$) is considered in this relationship.) The preferential strand creation in the shear gradient direction appears to be reasonable because the HEUR micellar cores are distributed anisotropically under shear and the strand is rather stabilized (not significantly stretched) if it is created in this direction and also because the already existing strands tend to be oriented out of that direction. (It is also worth mentioning that the anisotropy of the molecular mobility has been considered in the constitutive equation⁵² and molecular model.⁵³ This anisotropy of mobility could also result in the preferential creation of the strands in the shear gradient direction.)

Of course, our model does not specify the mechanism of the strand creation and the dynamics of the source function $\phi(\mathbf{r}, t, \dot{\gamma})$, and it is too simple to reproduce the experimental

results quantitatively. In addition, it does not necessarily apply to all HEUR solutions so far examined in the literature: The FENE effect and shear-induced increase of ν could have been essential for some solutions.⁴⁹ In particular, the FENE effect might be coupled with the anisotropic creation of network strands, thereby contributing, to some extent, to the thickening behavior of our HEUR solution. (A rheo-optical measurement testing this contribution is now being attempted.) Nonetheless, it should be emphasized that the thickening of $\eta(\dot{\gamma})$ associated with no nonlinearity of $\Psi_1(\dot{\gamma})$ observed for our 1.0 wt % HEUR solution at relatively low $\dot{\gamma}$ can be qualitatively explained *without* considering the FENE effect and the increase of ν .

As far as the authors know, the anisotropy of the strand creation being balanced with the network disruption, the essence of our model, has not been considered explicitly in the transient network models. Our experimental results and the model analysis imply that the shear effect on the strand creation kinetics (anisotropic creation) can be an important factor for the nonlinearity in the thickening regime. A further study is desired for this anisotropic strand creation (and the coupling with the FENE effect discussed above) for full understanding of the thickening mechanism of HEUR solutions.

4.3. Mechanism of Shear Thinning. For our HEUR solution, both $\eta(\dot{\gamma})$ and $\Psi_1(\dot{\gamma})$ exhibit thinning at high $\dot{\gamma}$, as noted in Figures 4–6. The initial decay of $\eta^-(t;\dot{\gamma})$ and $\Psi_1^-(t;\dot{\gamma})$ at those $\dot{\gamma}$ is faster than that in the linear regime (Figure 8). In addition, the $\dot{\gamma}$ dependence of $\eta(\dot{\gamma})$ and $\Psi_1(\dot{\gamma})$ of the HEUR solution is stronger than that for entangled polymers (cf. eqs 5 and 7), and the empirical rules valid for those polymers (eq 8) do not hold for the HEUR solution (cf. Figure 9). These results suggest that the thinning of the HEUR solutions is attributable to the shear-induced disruption of the HEUR network, i.e., the decrease of the number density ν of the active strands.

At the same time, eq 8 still holds for $\eta(\dot{\gamma})$ and $\Psi_1(\dot{\gamma})$ in the power-law thinning region at high $\dot{\gamma}$ given that the angular frequency ω and time t for the linear viscoelastic quantities involved in eq 8 are increased and decreased, respectively, as explained for Figure 9. This result could mean that the HEUR network is not only disrupted/fragmented (to have a shorter relaxation time) but also oriented under fast steady shear to exhibit the thinning, and the orientation of those fragmented network is somewhat similar to that of the polymers satisfying the empirical eq 8.

Finally, we note that the thinning of $\eta(\dot{\gamma})$ is associated with the transient thickening of $\eta^+(t;\dot{\gamma})$ above the linear $\eta^+(t)$ while the thinning of $\Psi_1(\dot{\gamma})$ is associated with no significant overshoot of $\Psi_1^+(t;\dot{\gamma})$ (very weak overshoot, if any) above the linear $\Psi^+(t)$ (see Figures 4 and 5). These features of $\eta^+(t;\dot{\gamma})$ and $\Psi_1^+(t;\dot{\gamma})$ appear to correspond to the anisotropic creation of the strands in the transient state, as similar to the anisotropic creation in the steady state in the thickening regime discussed earlier (although the transient hardening of the stretched strand, which could occur in a short time scale before disruption of the HEUR core, might contribute a little to those features). However, the model developed in the previous section cannot be applied to those $\eta^+(t;\dot{\gamma})$ and $\Psi_1^+(t;\dot{\gamma})$ data because the dynamics of the source function, which can change with time in the transient state, is not specified in the model, and the expansion in the model is not valid (diverges) at high $\dot{\gamma}$. A more refined model explicitly incorporating the dynamics of the source function, requiring no expansion and allowing a shear-induced change of ν , is desired for further studying the transient thickening followed by the steady-state thinning. Formulation

of such a model is considered to be an important subject of future work.

5. CONCLUDING REMARKS

For the 1.0 wt % aqueous solution of HEUR containing the transient HEUR network and exhibiting the single-Maxwellian relaxation in the linear regime, we have examined the nonlinear thickening and thinning behavior under shear flow.

At intermediate shear rates $\dot{\gamma}$ just above the equilibrium relaxation frequency $1/\tau$, the solution exhibited thickening characterized by monotonic increase of the viscosity growth function $\eta^+(t;\dot{\gamma})$ above the linear $\eta^+(t)$ and by the steady-state viscosity $\eta(\dot{\gamma})$ larger than η_0 . However, at those $\dot{\gamma}$, the first normal stress coefficient growth function $\Psi_1^+(t;\dot{\gamma})$ and the steady-state coefficient $\Psi_1(\dot{\gamma})$ exhibited no nonlinearity. In addition, the relaxation times of the viscosity and normal stress coefficient decay functions $\eta^-(t;\dot{\gamma})$ and $\Psi_1^-(t;\dot{\gamma})$ obtained after cessation of steady flow agreed with those in the linear regime. These results, in particular the lack of nonlinearity of $\Psi_1^+(t;\dot{\gamma})$ and $\Psi_1(\dot{\gamma})$, suggested that our HEUR network strands were just moderately stretched to show no significant FENE effect and that the number density ν of the network strands was negligibly affected by the shear at $\dot{\gamma}$ just above $1/\tau$. A simple transient Gaussian network model incorporating neither the FENE effect nor the increase of ν suggested that the thickening of $\eta^+(t;\dot{\gamma})$ and $\eta(\dot{\gamma})$ and the lack of nonlinearity of $\Psi_1^+(t;\dot{\gamma})$ and $\Psi_1(\dot{\gamma})$ could result from anisotropy of creation of the HEUR strands attached to the network (although the FENE effect coupled with this anisotropic strand creation might contribute, to some extent, to the observed thickening behavior). The strand creation appeared to be enhanced in the shear gradient direction to result in both thickening of $\eta^+(t;\dot{\gamma})$ and $\eta(\dot{\gamma})$ and lack of nonlinearity of $\Psi_1^+(t;\dot{\gamma})$ and $\Psi_1(\dot{\gamma})$.

In contrast, at $\dot{\gamma} \gg 1/\tau$, $\eta^+(t;\dot{\gamma})$ exhibited overshoot well above the linear $\eta^+(t)$ and then approached $\eta(\dot{\gamma}) < \eta_0$, whereas $\Psi_1^+(t;\dot{\gamma})$ showed no significant overshoot (very weak overshoot, if any) to approach $\Psi_1(\dot{\gamma}) \ll \Psi_{1,0}$. In addition, the relaxation of $\eta^-(t;\dot{\gamma})$ and $\Psi_1^-(t;\dot{\gamma})$ after cessation of flow was considerably faster than that in the linear regime. These nonlinear thinning features at $\dot{\gamma} \gg 1/\tau$ can be mainly attributed to the flow-induced disruption/fragmentation of the HEUR network (decrease of ν) associated with the shear orientation of the fragmented network.

Finally, it should be emphasized that our HEUR chain is not unique in its structure (molecular weight and size of alkyl groups at the chain ends) and rather similar to the HEUR chains so far examined in the literature. However, the analysis of both viscosity and first normal stress coefficient data, not made in previous studies (except in ref 11 where the normal stress coefficient data were reported), led to the above conclusion. The results obtained in this study would contribute to better understanding of the behavior of HEUR solutions.

■ APPENDIX. ANALYSIS OF ELASTIC ENERGY

It is informative to compare the elastic energy of the HEUR network strands F_{el} and the association energy of the end groups of those strands, $E_a \cong 88 \text{ kJ mol}^{-1}$ (evaluated from the data in Figure 3), to test if the association is strong enough to allow the strands to be stretched into the FENE region. F_{el} increases with increasing end-to-end distance r of the strand. Thus, the end groups can sustain the strand stretching *only* in a region of r specified by

$$F_{el}(r) < E_a \quad (\text{A1})$$

The FENE effect emerges if r in this region can have a value reasonably close to the full-stretch length of the strand, and *vice versa*.

For this test, we can utilize the expression of $F_{el}(r)$ deduced from the standard FENE model³⁶

$$F_{el}(r) = -\frac{3n_K RT}{2} \ln \left[1 - \frac{r^2}{(n_K b_K)^2} \right] \quad \text{per 1 mole of strands} \quad (\text{A2})$$

Here, n_K is the number of Kuhn segments per strand, b_K is the Kuhn step length, and the product $n_K b_K$ corresponds to the full-stretch length of the strand. The ratio $\lambda_f = r/n_K b_K$ (a factor governing the r dependence of F_{el} in eq A2) specifies the relative stretch of the strand with respect to the full-stretch limit. Since $F_{el}(r)$ for a given λ_f value increases with increasing n_K , eq A1 can be satisfied in a wider range of λ_f to allow the FENE effect to emerge more easily for a smaller n_K value. Thus, we here test eq A1 for an unrealistically small n_K value, $n_K = 511$ for individual HEUR chains: This n_K value was obtained from the b_K data of PEO,⁵⁴ $b_K = 0.77$ nm, and $M_w (= 4.6 \times 10^4)$ of the HEUR chain. The actual HEUR network strand is a bridged sequence (string) of the HEUR micelles (as explained for eq 2), and the actual n_K value should be much larger than 511. Thus, the actual HEUR strand can exhibit the FENE effect *much less easily* compared to the extreme case examined below.

Utilizing $n_K = 511$, $b_K = 0.77$ nm, and $E_a = 88$ kJ mol⁻¹ in eq A2, we can specify the range of λ_f (range of r) where eq A1 is satisfied. The result is

$$\lambda_f < \left[1 - \exp \left(-\frac{2}{3n_K RT} E_a \right) \right]^{1/2} = 0.21 \quad (\text{at } 25^\circ \text{C}) \quad (\text{A3})$$

The maximum possible λ_f value, 0.21, is still too small to allow significant FENE effect to emerge for the elasticity of the HEUR chain, as can be clearly noted from comparison between $F_{el}(\lambda_f) = 85.6$ kJ mol⁻¹ (eq A2) and the elastic energy estimated for Gaussian chains, $F_{el,G}(\lambda_a) = \{3n_K RT/2\} \lambda_f^2 \cong 85.2$ kJ mol⁻¹.

The actual HEUR strands exhibit the FENE effect much less easily compared to individual HEUR chains examined above. Thus, this effect should have a negligible contribution to the actual HEUR solution, and the HEUR strands can be safely regarded as Gaussian strands.

ACKNOWLEDGMENTS

This work was supported by the Grant-in-Aid for Scientific Research (B) (grant 21350063) and by Grant-in-Aid for Young Scientists (B) (grant 22740273) from MEXT.

REFERENCES

- (1) Lundberg, D. J.; Glass, J. E.; Eley, R. R. *J. Rheol.* **1991**, *35*, 1255.
- (2) Xu, B.; Li, L.; Yekta, A.; Masoumi, Z.; Kanagalingam, S.; Winnik, M. A.; Zhang, K.; Macdonald, P. M. *Langmuir* **1997**, *13*, 2447.
- (3) Berret, J. F.; S  r  ro, Y.; Winkelman, B.; Calvet, D.; Collet, A.; Vigui  r, M. *J. Rheol.* **2001**, *45*, 477.
- (4) Calvet, D.; Collet, A.; Vigui  r, M.; Berret, J.; S  r  ro, Y. *Macromolecules* **2003**, *36*, 449.
- (5) Annable, T.; Buscall, R.; Ettelaie, R.; Whittlestone, D. *J. Rheol.* **1993**, *37*, 695.
- (6) Annable, T.; Buscall, R.; Ettelaie, R. *Colloids Surf., A* **1996**, *112*, 97.

- (7) May, R.; Kaczmariski, J. P.; Glass, J. E. *Macromolecules* **1996**, *29*, 4745.
- (8) Kaczmariski, J. P.; Tarng, M. R.; Ma, Z.; Glass, J. E. *Colloids Surf., A* **1999**, *147*, 39.
- (9) Ma, S. X.; Cooper, S. L. *Macromolecules* **2001**, *34*, 3294.
- (10) Barmar, M.; Ribitsch, V.; Kaffashi, B.; Barikani, M.; Sarreshtehdari, M.; Pfragner, J. *Colloid Polym. Sci.* **2004**, *282*, 454.
- (11) Pellens, L.; Corrales, R. G.; Mewis, J. J. *Rheol.* **2004**, *48*, 379.
- (12) Kaczmariski, J. P.; Glass, J. E. *Langmuir* **1994**, *10*, 3035.
- (13) Xu, B.; Yekta, A.; Li, L.; Masoumi, Z.; Winnik, M. A. *Colloid Polym. Sci., A* **1996**, *112*, 239.
- (14) Berret, J. F.; S  r  ro, Y. *Phys. Rev. Lett.* **2001**, *87*, 048303-1.
- (15) Pellens, L.; Vermant, J.; Mewis, J. *Macromolecules* **2005**, *38*, 1911.
- (16) Pellens, L.; Ahn, K. H.; Lee, S. J.; Mewis, J. J. *Non-Newtonian Fluid Mech.* **2004**, *121*, 87.
- (17) Tripathi, A.; Tam, K. C.; McKinley, G. H. *Macromolecules* **2006**, *39*, 1981.
- (18) Tam, K. C.; Jenkins, R. D.; Winnik, M. A.; Bassett, D. R. *Macromolecules* **1998**, *31*, 4149.
- (19) Fran  ois, J.; Maitre, S.; Rawiso, M.; Sarazin, D.; Beinert, G.; Isel, F. *Colloids Surf., A* **1996**, *112*, 251.
- (20) Tanaka, F.; Edwards, S. F. *J. Non-Newtonian Fluid Mech.* **1992**, *43*, 247.
- (21) Tanaka, F.; Edwards, S. F. *J. Non-Newtonian Fluid Mech.* **1992**, *43*, 273.
- (22) Tanaka, F.; Edwards, S. F. *J. Non-Newtonian Fluid Mech.* **1992**, *43*, 289.
- (23) Tanaka, F.; Edwards, S. F. *Macromolecules* **1992**, *25*, 1516.
- (24) Green, M. S.; Tobolsky, A. V. *J. Chem. Phys., A* **1946**, *14*, 80.
- (25) Yamamoto, M. *J. Phys. Soc. Jpn.* **1956**, *11*, 413.
- (26) Wang, S. Q. *Macromolecules* **1992**, *25*, 7003.
- (27) Vaccaro, A.; Marrucci, G. *J. Non-Newtonian Fluid Mech.* **2000**, *92*, 261.
- (28) Marrucci, G.; Bhargava, S.; Cooper, S. L. *Macromolecules* **1993**, *26*, 6483.
- (29) Inde, T.; Koga, T.; Tanaka, F. *Macromol. Rapid Commun.* **2005**, *26*, 701.
- (30) Koga, T.; Tanaka, F. *Macromolecules* **2010**, *43*, 3052.
- (31) Koga, T.; Tanaka, F.; Kaneda, I.; Winnik, F. M. *Langmuir* **2009**, *25*, 8626.
- (32) Koga, T.; Tanaka, F.; Kaneda, I. *Prog. Colloid Polym. Sci.* **2009**, *136*, 39.
- (33) Inde, T. *J. Non-Newtonian Fluid Mech.* **2007**, *141*, 18.
- (34) Inde, T. *Nihon Reoroji Gakkaishi (J. Soc. Rheol., Jpn.)* **2007**, *35*, 147.
- (35) Van Egmond, J. W. *Curr. Opin. Colloid Interface Sci.* **1998**, *3*, 385.
- (36) Inoue, T.; Inoue, Y.; Watanabe, H. *Langmuir* **2005**, *21*, 1201.
- (37) Tirtaatmadja, V.; Tam, K. C.; Jenkins, R. D. *Macromolecules* **1997**, *30*, 3271.
- (38) With the stress-controlled MCR-301, the constant-rate start-up of flow could not be accurately achieved at short times because of a delay in the built-in stress-strain rate feedback loop, but the steady flow measurements at long times were made without any problem (cf. Figure 6).
- (39) Shikata, T.; Hirata, H.; Kotaka, T. *Langmuir* **1987**, *3*, 1081.
- (40) Shikata, T.; Hirata, H.; Kotaka, T. *Langmuir* **1988**, *4*, 354.
- (41) Ferry, J. D. *Viscoelastic Properties of Polymers*, 3rd ed.; Wiley: New York, 1980.
- (42) Graessley, W. W. *Polymeric Liquids and Networks: Dynamics and Rheology*; Garland Science: New York, 2008.
- (43) Cox, W. P.; Merz, E. H. *J. Polym. Sci.* **1958**, *28*, 619.
- (44) Gleissle, W. Two time-shear rate relations combining viscosity and first normal stress coefficient in the linear and nonlinear flow range, 8th Int. Cong. Rheol., Naples, 1980.
- (45) Osaki, K.; Watanabe, H.; Inoue, T. *Nihon Reoroji Gakkaishi (J. Soc. Rheol., Jpn.)* **1998**, *26*, 49.

- (46) El-Kissi, N.; Piau, J. M.; Attané, R.; Turrel, G. *Rheol. Acta* **1993**, 32, 293.
- (47) Larson, R. G. *Constitutive Equations for Polymer Melts and Solutions*; Butterworth-Heinemann: Oxford, 1998.
- (48) Fuller, G. G. *Optical Rheometry of Complex Fluids*; Oxford University Press: New York, 1995.
- (49) No $\Psi_1^+(t;\dot{\gamma})$ and $\Psi_1(\dot{\gamma})$ data were shown in most of the previous reports for HEUR solutions, except in ref 11. Thus, we cannot rule out a possibility that the thickening of $\eta(\dot{\gamma})$ reported therein was actually *not* due to the FENE effect and the flow-enhanced strand creation. Pellens et al.¹¹ reported both $\eta(\dot{\gamma})$ and $\Psi_1(\dot{\gamma})$ data for their HEUR solution: Their $\eta(\dot{\gamma})$ data exhibited slight thickening ($\sim 10\%$ increase of η at the largest) and the $\Psi_1(\dot{\gamma})$ data exhibit slight thinning ($\sim 10\%$ decrease of Ψ_1 at the shear rate for the maximum of η); see Figure 4 of ref 11. This thickening behavior of η , less significant in magnitude but qualitatively similar compared to the behavior of our HEUR solution (Figure 6), might be attributed to the anisotropic creation of HEUR network strands under shear rather than the FENE effect and/or the flow-enhanced strand creation.
- (50) Van Kampen, N. G. *Stochastic Processes in Physics and Chemistry*, 3rd ed.; Elsevier: Amsterdam, 2007.
- (51) Abramowitz, M.; Stegun, I. A. *Handbook of Mathematical Functions with Formulas, Graphs, and Mathematical Tables*, 10th ed.; Dover: New York, 1972.
- (52) Beris, A. N.; Edwards, B. J. *Thermodynamics of Flowing Systems*; Oxford University Press: Oxford, 1994.
- (53) Uneyama, T.; Horio, K.; Watanabe, H. *Phys. Rev. E* **2011**, 83, 061802.
- (54) Aharoni, A. M. *Macromolecules* **1983**, 16, 1722.

Cross-Link Density Estimation of PDMS Networks with Precise Consideration of Networks Defects

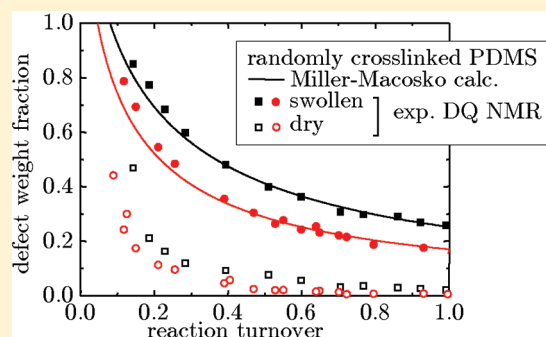
Walter Chassé,^{*,†} Michael Lang,[‡] Jens-Uwe Sommer,[‡] and Kay Saalwächter^{*,†}

[†]Institut für Physik — NMR, Martin-Luther-Universität Halle-Wittenberg, Betty-Heimann-Strasse 7, D-06120 Halle, Germany

[‡]Leibniz-Institut für Polymerforschung Dresden, e.V., Hohe Strasse 6, D-01069 Dresden, Germany

ABSTRACT: Two series of randomly cross-linked poly(dimethylsiloxane) (PDMS) networks with systematically varying and well-defined dangling chain and defect content were investigated by ¹H double-quantum low-field NMR (DQ NMR), equilibrium swelling, and high-resolution magic-angle spinning NMR (MAS NMR) experiments in order to obtain information about the absolute molecular weight of the polymer chains between two cross-links, M_c , and its distribution. A comparison of the experimental results from swelling and DQ NMR experiments with the results of Miller–Macosko calculations, based upon the reaction turnover determined by MAS NMR, clarifies the importance of a precise estimation of the defect fraction of the polymer network for a reliable determination of M_c . In order to properly account

for network defects in the evaluation of equilibrium swelling as well as DQ NMR experiments, we use the elastically effective polymer volume fraction $\phi_{p,el}$ (that can be obtained from DQ NMR or simple Hahn echo experiments on samples swollen in deuterated solvent) and the variable weight-averaged functionality f_{wa} of the cross-links taken from Miller–Macosko calculations. On the basis of the dependence of the so-obtained M_c on f_{wa} , we are able to confirm the validity of the phantom model of rubber elasticity, and find good agreement between the results from the different methods. Small deviations only pertain to a proportionality factor different from unity, which for the case of equilibrium swelling is attributed to the shortcomings of the Flory–Rehner theory. We further address the quantitative interpretation of the residual dipolar coupling constant as the central result of DQ NMR on dry samples, which is confirmed to be proportional to the inverse M_c , but is also subject to systematic errors.



INTRODUCTION

Permanent elastomers are commonly formed via connecting linear polymer chains by chemical cross-links, resulting in a three-dimensional polymer network. Their elastic properties are governed by the length of network strands, functionality of cross-links, (trapped) entanglements and defects. The precise characterization of these topological parameters, especially the molecular weight of polymer chains between two cross-links, M_c , and its influence on the physical properties of the elastomers has been a major task in polymer physics and chemistry for decades, with many open questions to-date.

For the determination of reliable structure–property relationships for elastomers, knowledge of the network structure is essential. A variety of different methodological approaches, e.g., dynamical mechanical analysis,¹ osmometry,² inverse gas chromatography,³ dielectric measurements, and neutron and X-ray scattering, has been applied for this purpose. The most often used experiments for the estimation of the cross-link density are equilibrium swelling, mechanical measurements, such as sulfur and NMR spectroscopy.

The network structure depends strongly on the formation process of the polymer network. Cross-linking techniques as sulfur vulcanization, peroxide curing, and electron or γ -irradiation^{4,5} lead to highly complex structures with broad

distributions of network strand lengths and substantial defect fractions due to the random insertion of cross-links.^{6–8} Therefore, well-defined model networks are commonly used to study theoretical models of rubber elasticity. An often used method is the controlled end-linking of polymers terminated with special reactive groups.^{9,10} Measurements to characterize the polymer chains are performed prior to their cross-linking to determine the number-average molecular weight M_n and the molecular-weight distribution. After the cross-linking with multifunctional cross-linkers, the molecular weight between two cross-links M_c and its distribution is predetermined by the given functionalized polymer chains.⁸ Additionally, the functionality of cross-links f is known and the amount of dangling-end defects is assumed to be negligible.¹¹ The quality of model networks is usually tested by investigating the unreacted amount of functional groups and the fraction of soluble polymer chains w_{sol} . We note, however, that even a well-defined local structure of polymer networks does not imply a simple network topology, and topological disorder and various kinds of topological defects occur.¹²

Received: September 12, 2011

Revised: November 21, 2011

Published: December 22, 2011



Equilibrium swelling is a basic and easily feasible experiment for the determination of M_c . The thermodynamic description is commonly based on the Flory–Rehner treatment^{13–15} of swollen polymer networks, which postulates the additivity of the free energy of mixing and the elastic free energy. A series of studies by Brotzman and Eichinger^{16–18} indicates serious concerns related with this assumption. The elastic contribution is estimated by a variety of different molecular theories of rubber-like elasticity generally assuming Gaussian statistics for the conformation of network strands between two cross-links. The classical and most often used theories are the affine model by Hermans, Flory, and Wall^{19,20} and the phantom model by James and Guth.^{21,22} These and other models of network elasticity²³ were put to a test in various extensive investigations of model polymer networks, especially of end-linked PDMS.^{1,6} Comparisons with mechanical experiments generally show a good coincidence in the qualitative description of network parameters and dependencies, but difficulties are encountered when a quantitative interpretation is sought. Especially the neglect of the influence of defects and distributions in the classical models of network elasticity, and the strong dependence on the rather empirical Flory–Huggins interaction parameter hampers the exact determination of M_c by equilibrium swelling.

Therefore, a precise analysis of the influence of elastically inactive network defects, i.e., dangling chains, loop structures, etc., is essential for a complete account of the network structure and with that, a more quantitative understanding of the mechanical and thermodynamical (swelling) properties of elastomers. For this purpose, networks with well-defined defect content were the subject of previous investigations. Commonly, such networks were prepared by controlled stoichiometrically imbalanced cross-link reactions²⁴ or by the addition of monofunctional polymer chains.^{25,26} Dangling chains, which are attached by only one end to the infinite gel, lead to a reduction of elastically effective polymer chains per unit volume.²⁷ In mechanical studies it was shown that the storage and loss moduli are quite sensitive to the fraction and molecular weight of pendant chains.^{25,28–31} Thereby, the exact defect fraction of the networks is estimated based on the chemical cross-linking mechanism¹⁰ or nonlinear polymerization (mean field) calculations,²⁶ since an independent quantitative determination on the basis of mechanical or equilibrium swelling experiments is not possible.

In the present work, we address the characterization of the network structure of randomly cross-linked poly(dimethylsiloxane) (PDMS) networks by ¹H double-quantum (DQ) low-field NMR and by equilibrium swelling experiments. The results of these readily available routine characterization methods, both of which rely on model assumptions, are compared with absolute-value results for the molecular weight between two cross-links M_c . The latter are taken from calculations based on the statistical theory of cross-linking published by Miller and Macosko,³² using as input the known molecular weight and polydispersity of the precursor polymers and the extracted sol content, as well as the turnover of the cross-linking reaction as taken from integrated signals in high-resolution ¹H magic-angle spinning (MAS) NMR spectra of the network samples. We demonstrate that the defect fraction of the investigated networks can be identified with high accuracy by decomposition of DQ NMR (alternatively Hahn-echo relaxation) data taken on samples swollen in deuterated solvent. The results are used to investigate different approaches to

considering network defects in the evaluation of equilibrium swelling experiments, and to assess the validity of M_c as calculated from residual dipolar coupling constants $D_{\text{res}} \propto M_c^{-1}$ measured on dry samples, where ambiguities arise from the specific model and the defect content of the network.

■ EXPERIMENTAL SECTION

Sample Preparation and Characterization. Two commercially available vinylmethylsiloxane-dimethylsiloxane trimethylsiloxy-terminated random precursor copolymers (rPDMS) with different vinylmethylsiloxane concentration, purchased from ABCR company and used as-received, were used to prepare the investigated silicone networks. Both prepolymers were characterized by gel permeation chromatography (GPC) to obtain information about the molecular weight and polydispersity. The ratio of dimethylsiloxane to vinylmethylsiloxane monomers was determined by ¹H solution NMR. For this purpose, the prepolymers were dissolved in deuterated toluene and ¹H spectra were recorded. The intensity of the measured signals is directly proportional to the amount of protons at the methyl and vinyl groups. Thus, a precise estimation of the average number of vinyl-functionalized monomers per dimethylsiloxane monomer, ρ_{vinyl} was possible by comparing the integrals of the different signals. The results of the GPC and NMR measurements are given in Table 1. The two

Table 1. Results of Sample Characterization by GPC and ¹H Solution NMR

polymer	M_n/kDa (GPC)	M_w/kDa (GPC)	M_w/M_n (GPC)	ρ_{vinyl} (NMR)
rPDMS-431	11.2	29.4	2.6	0.0426
rPDMS-731	12.5	32.2	2.6	0.0776

prepolymers differ slightly in their molecular weight and by about a factor of 2 in the density of vinylmethylsiloxane comonomers.

The vinyl-functionalized polymers were cross-linked by using a 2-functional cross-linker (1,1,3,3-tetradimethyldisiloxane, ABCR) and *cis*-dichlorobis(diethyl sulfide)platinum(II) as catalyst. Because of monofunctional impurities, its average functionality is 1.81, as again determined by solution NMR. The un-cross-linked polymer and the cross-linker were dissolved in 20 wt % of toluene with respect to the used amount of polymer to facilitate homogeneous mixing of the components. After adding the catalyst, the sample tube was sealed and stored for 7 days at room temperature. The details of the cross-link reaction are described in ref 33. After the cross-link reaction was completed, the toluene was evaporated carefully.

For the preparation of networks with different cross-link densities, the amount of cross-linker was chosen so as to react with a defined percentage of the vinyl groups. The used amounts of cross-linker are based upon the known density of vinylmethylsiloxane monomers ρ_{vinyl} from the solution NMR measurements. For the estimation of the actual fraction of reacted vinyl groups during cross-linking, henceforth referred to as the reaction turnover p_r , high-resolution ¹H spectra of all networks were measured by magic-angle spinning (MAS) NMR. In Figure 1, the MAS spectra of polymer networks made of rPDMS-431 are shown, demonstrating the good resolution of the spectra, almost matching solution-state conditions. By comparing the integral ratio of vinyl and methyl groups of the prepared polymer networks to the ratio of these in the un-cross-linked prepolymers, the reaction turnover could be determined with high precision. The intended and measured reaction turnovers p_r of the vinyl-groups for the rPDMS-431 samples are listed in Table 2.

NMR Spectroscopy. The ¹H DQ solid-state NMR experiments were carried out on a Bruker minispec mq20 spectrometer operating at a resonance frequency of 20 MHz with a 90° pulse length of 2.8 μs and a dead time of 13 μs. The experiments and the analysis of the measured raw data were performed following the previously published procedures.^{36–38} For the experiments on swollen networks, deuterated toluene was used as swelling solvent. The used sample amounts were

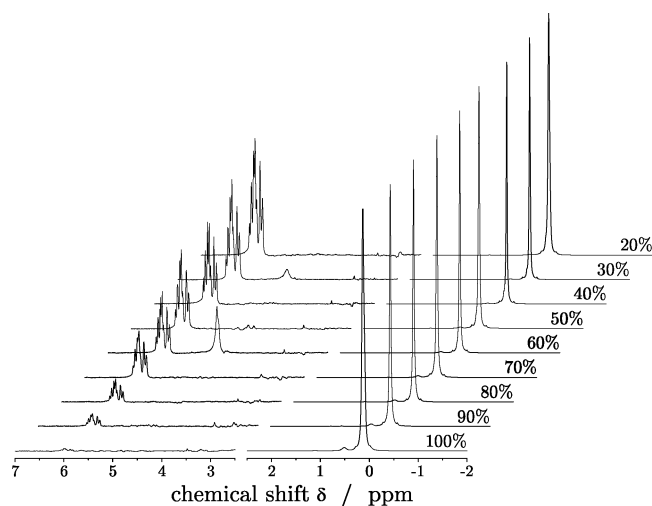


Figure 1. ^1H MAS spectra of rPDMS-431 networks cross-linked with different amounts of cross-linker, with the intended reaction turnover p_r indicated on the right. For clarity, the vinyl signal region (6.2–5.8 ppm) is amplified 100 times over the methyl signal (~ 0 ppm). The signal at 5 ppm is an unknown impurity, presumably water.

about 300 mg for measurements on dry networks and between 100 and 200 mg for measurements on swollen networks.

Equilibrium Swelling Experiments. The equilibrium swelling experiments were carried out at room temperature (21 °C) using toluene (molar volume $V_s = 106.2$ mL/mol, density $\rho_s = 0.87$ g/cm 3) as swelling solvent. The samples were weighed as-prepared (m_0) and swollen for 4 days to equilibrium. Swollen samples were blotted with tissue paper to remove the excess of toluene and weighed immediately (m_{sw}). Finally, the swelling solvent was evaporated carefully from the networks over a couple of days and the dry samples were weighed again (m_{dry}). For each sample, at least five pieces of different shape and weight of all prepared networks were investigated.

The sol content ω_{sol} is the fraction of polymer chains not coupled to the network after the cross-link reaction, and is was extracted from the samples during swelling. The sol fraction ω_{sol} was estimated by comparing the weight of the networks as-prepared m_0 and the weight of the dry networks m_{dry} corresponding to eq 1,

$$\omega_{sol} = \frac{m_{dry} - m_0}{m_0} \quad (1)$$

The equilibrium degree of swelling Q , and with that the volume fraction of polymer in the swollen network $\phi_p = 1/Q$ were calculated according to eq 2 using $\rho_p = 0.97$ g/cm 3 for PDMS.

$$Q = \frac{1}{\phi_p} = \frac{V_{sw}}{V_{dry}} = \frac{m_{dry}/\rho_p + (m_{sw} - m_{dry})/\rho_s}{m_{dry}/\rho_p} \quad (2)$$

All results of the swelling experiments with the rPDMS-431 networks are specified in Table 2. For their evaluation, we need the effective Flory–Huggins interaction parameter χ of the PDMS/toluene systems. It was investigated in several studies $^{4,39-43}$ by different experimental approaches, i.e., light scattering, osmometry and SANS. χ is generally not a constant and may attain different values in swollen networks vs solutions of linear polymers, highlighting the shortcomings of the Flory–Huggins mean-field theory as a basis for the calculation of the molecular weight between two cross-links, M_c . 44 See below for details. In this work, we use the volume-fraction dependent Flory–Huggins interaction parameter

$$\chi = 0.459 + 0.134\phi_p + 0.59\phi_p^2 \quad (3)$$

which was determined by osmotic deswelling experiments on different end-linked PDMS gels which were fitted to the Flory–Rehner model. 43

METHODOLOGICAL BACKGROUND

Determination of M_c and the Network Defect Fraction by ^1H DQ NMR Experiments. ^1H multiple-quantum solid state NMR spectroscopy 38,45 is a robust quantitative and versatile technique for the investigation of structure and dynamics in polymer networks and melts. In contrast to more traditional approaches such as Hahn-echo relaxometry, the essential advantage of this method is the measurement of two qualitatively different sets of data, the decaying reference intensity I_{ref} and the DQ build-up intensity I_{DQ} , both measured as a function of the DQ evolution time τ_{DQ} in subsequent experiments that only differ in the phase cycling of the receiver. See Figure 2 for sample data. On the basis of the data processing procedure described below, it is possible to reliably distinguish between (and characterize) the elastically active network chains that contribute to I_{DQ} and network defects, sol, and solvent, which contribute to I_{ref} in particular at long times.

Data Processing and Determination of the Defect Fraction. I_{DQ} is dominated by spin-pair DQ coherences 36,45

Table 2. Results of the Characterization of rPDMS-431 Network Samples, with the Intended Reaction Turnover in % as Part of the Sample Name (cXXX) a

sample	MAS NMR	DQ NMR					swelling		Miller–Macosko
	p_r	$\omega_{def,dry}$	$\omega_{def,sw}$	$D_{res}/2\pi$ [kHz]	$\sigma/2\pi$ [kHz]	$r_G = \sigma/D_{res}$	ω_{sol} [% of m_0]	$Q = V/V_0$	f_{wa}
c100	0.991	0.022	0.257	0.425	0.273	0.557	4.45	2.70	3.60
c090	0.921	0.027	0.270	0.413	0.231	0.560	5.36	2.70	3.58
c080	0.860	0.030	0.290	0.362	0.215	0.593	5.66	3.02	3.55
c075	0.768	0.036	0.297	0.309	0.177	0.571	6.23	3.29	3.51
c070	0.705	0.031	0.308	0.293	0.168	0.574	7.03	3.36	3.48
c060	0.598	0.056	0.363	0.241	0.144	0.597	8.26	3.71	3.41
c050	0.510	0.076	0.400	0.183	0.100	0.548	9.84	4.34	3.33
c040	0.394	0.092	0.481	0.138	0.084	0.609	13.77	5.08	3.21
c030	0.284	0.120	0.598	0.089	0.050	0.565	20.37	6.85	3.01
c025	0.229	0.163	0.683	0.069	0.040	0.580	25.47	9.20	2.87
c020	0.187	0.213	0.773	0.047	0.025	0.542	30.28	12.07	2.72
c015	0.142	0.469	0.850	0.034	0.023	0.681	42.51	21.89	2.51

$^aD_{res}$ is the average of the coupling constant distribution obtained by regularization of the normalized DQ build-up curves by using fast Thikonov regularization, 34,35 and the distribution width is characterized by the variance σ . Note that D_{res} and σ are obtained from measurements on dry network samples.

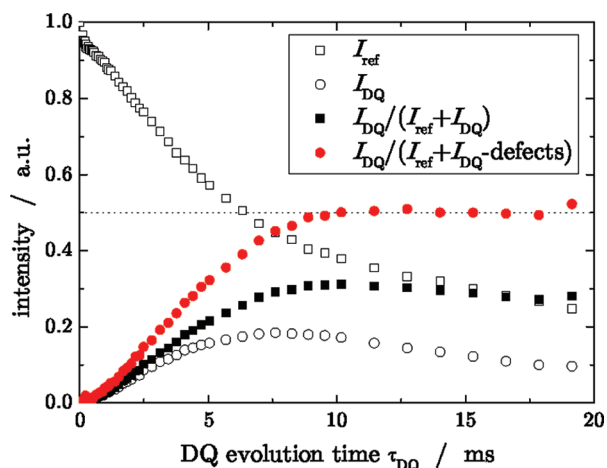


Figure 2. Experimental I_{DQ} and I_{ref} for the randomly cross-linked rPDMS-431 sample c020 and corresponding normalized I_{nDQ} data,

and comprises the structural information on the polymer chains, i.e., the residual dipolar coupling constant D_{res} and its distribution. Technically, I_{ref} contains signal from half of the quantum orders ($4n$) of the dipolar coupled network chains, as well as the signal from uncoupled components, i.e. isotropically mobile network defects like dangling chains and loops. The particular network fractions are characterized by a rather different relaxation behavior, as is apparent in Figure 3. The signals of

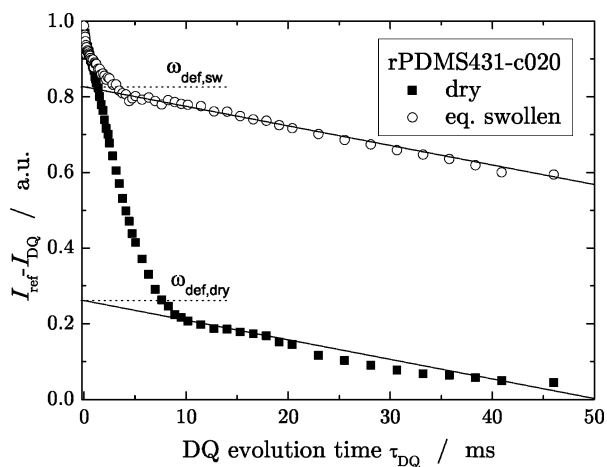


Figure 3. Experimental estimation of the defect weight fractions ω_{def} and $\omega_{def,sw}$ of the rPDMS-431 sample c020 from the difference of reference and DQ intensities ($I_{ref} - I_{DQ}$), measured in dry and equilibrium swollen state using deuterated solvent (closed and open symbols, respectively).

uncoupled, elastically ineffective defects show a slow exponential decay, while coupled network components relax much faster.⁴⁶ Plotting $I_{ref} - I_{DQ}$ amplifies this behavior and enables a quantitative identification and subtraction of the contribution of the network defects to the reference intensity I_{ref} see ref 38 for details. The structural information on the polymer network (build-up due to D_{res} , see below) is separated from the relaxation effects due to chain dynamics by a point-by-point division of the DQ build-up by the sum of the corrected relaxation function (eq 4). The obtained normalized DQ build-up I_{nDQ} is then independent of relaxation effects and has to reach a

long-time plateau value of 0.5, since I_{DQ} contains only half of the excited quantum orders ($4n + 2$).

$$I_{nDQ} = \frac{I_{DQ}}{I_{DQ} + I_{ref} - \text{defects}} \quad (4)$$

Note that both raw data intensities are, in the relevant data range of growing I_{DQ} , indeed dominated by spin dynamics among the quantum orders 0 (longitudinal magnetization) and 2, while higher-order coherences contribute only at later times and have a negligible effect.³⁶ We thus refer to the method as DQ NMR in the following.

The plateau of I_{nDQ} is only observed after a proper determination and subtraction of elastically ineffective defects (see Figure 2), providing a test for their precise quantification. Note that the apparent fraction of noncoupled network defects ω_{def} obtained by DQ NMR experiments can exhibit a significant dependence on cross-link density and in particular on temperature,⁴⁷ where the latter is related to the terminal relaxation of possibly large and branched structures being slow on the millisecond time scale of the DQ experiment (corresponding to slow mechanical relaxation processes in such imperfect networks). The defect fraction may thus be largely underestimated.

In dry networks, this problem can only be addressed by increasing the experimental temperature.⁴⁷ Another, more effective approach is the determination of defects in swollen networks by DQ NMR. Because of the network dilation by the solvent during the swelling process and the corresponding release of packing or topological constraints, the terminal relaxation of the defects is much accelerated. The solvent further acts as plasticizer, which also speeds up the chain dynamics. Motions of previously constrained defects thus become isotropic and the dipolar couplings ultimately average out. Figure 3 displays the change in the isotropically mobile fraction upon swelling. The detectable fraction of noncoupled and therefore elastically ineffective network defects in the equilibrium swollen sample $\omega_{def,sw}$ is considerably increased in comparison to the fraction in dry samples $\omega_{def,dry}$. Thus, the much decreased or even completely absent influence of restrictions on the relaxation time of defects in equilibrium-swollen samples allows for a reliable and precise quantitative estimation of the defect fraction in polymer networks. See below for an in-depth discussion of the observed drastic difference between $\omega_{def,sw}$ and $\omega_{def,dry}$ in the given samples.

The dependence of the detectable defect fraction and in particular of the residual coupling on the swelling degree below equilibrium will be discussed in more detail in an upcoming publication. Importantly, the observed defect fraction saturates already at solvent contents much below equilibrium swelling, which is equivalent to temperature variation, suggesting that the defect fraction is quantitatively determined under the given conditions. Note that the average residual coupling changes nontrivially upon addition of good solvent,⁴⁸ and its determination is further challenged by the appearance of swelling inhomogeneities, leading to broad D_{res} distributions.⁴⁹ Finally, it should be noted that simple Hahn-echo decay curves are in principle also suitable for a determination of the amount of slowly relaxing nonelastically active defects.³⁸

Determination of M_c . After a proper subtraction of the defect contribution to I_{ref} , the normalized DQ build-up curve I_{nDQ} solely reflects the residual dipolar interactions that are related to the network structure. These are proportional to the

dynamic segmental order parameter that is associated with the degree of anisotropy of rotational motion of the monomers (cf. Appendix), arising from the fact that the chain in question is fixed at its ends, at least on the time scale of the experiment itself (i.e., many milliseconds). Usually, residual dipolar interactions are evaluated by fitting a distribution function, eq 5, to the initial rise of I_{ndQ} assuming a Gaussian distribution of dipolar couplings.^{36,37}

$$I_{\text{ndQ}}(\tau_{\text{DQ}}, D_{\text{res}}, \sigma) = \frac{1}{2} \left(1 - \frac{\exp\left\{-\frac{\frac{2}{5}D_{\text{res}}^2\tau_{\text{DQ}}^2}{1+\frac{4}{5}\sigma^2\tau_{\text{DQ}}^2}\right\}}{\sqrt{1+\frac{4}{5}\sigma^2\tau_{\text{DQ}}^2}} \right) \quad (5)$$

The average apparent residual dipolar coupling constant D_{res} and its standard deviation σ , characterizing the width of the distribution, are obtained by this approach. In polymer networks with $M_c < M_e$, the experimental D_{res} is directly proportional to the cross-link density⁵⁰ and thus related to the molecular weight between two cross-links M_c . The proportionality factor depends on the investigated polymer, specifically, it involves a model accounting for chain stiffness (commonly characterized by Flory's characteristic ratio), and details on the spin dynamics among the protons in the monomer unit. On the basis of a fixed-junction model and explicit spin dynamics simulations, in ref 37 an approximate relation is derived for PDMS networks, eq 6, allowing for a direct determination of the average M_c from DQ NMR experiments:

$$M_c^{\text{PDMS}} = \frac{1266 \text{ Hz}}{D_{\text{res}}/2\pi} \frac{f-2}{f} \text{ kg/mol} \quad (6)$$

The factor $f-2/f$ depending on the (average) functionality f of the cross-links discussed below is newly introduced in this work, and arises when the phantom model is taken as the theoretical basis. Details can be found in the Appendix. One of the purposes of this work is the evaluation of the validity of this relation, for which systematic errors on the order of 40% can be expected.

Polymer networks with spatially inhomogeneously distributed cross-links show a distribution of coupling constants. For relative distribution widths $r_G = \sigma/D_{\text{res}} \geq 0.3$ the initial buildup of I_{ndQ} is not well described by the Gaussian fitting function. Therefore, eq 5 gives just a rough estimate of the average coupling constant.³⁷ In order to obtain a more quantitative picture of the actual residual dipolar coupling distribution, numerical inversion procedures based on fast Tikhonov regularization (*ftikreg*) can be applied.^{34,36} In a recent publication,³⁵ we have introduced a modified version of the fitting procedure using an improved Kernel function which provides precise and reliable results for the coupling constant distributions.

$$I_{\text{ndQ}}(\tau_{\text{DQ}}, D_{\text{res}}) = 0.5 \left(1 - \exp\left\{-(0.378D_{\text{res}}\tau_{\text{DQ}})^{1.5}\right\} \right) \times \cos(0.583D_{\text{res}}\tau_{\text{DQ}}) \quad (7)$$

In Figure 4, the coupling constant distributions obtained by regularization with *ftikreg* are shown for some networks

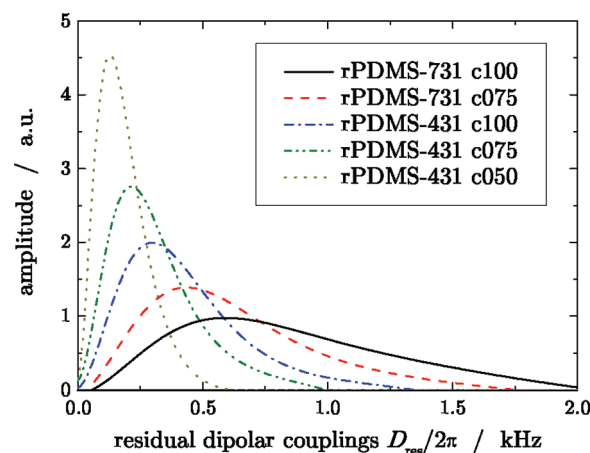


Figure 4. Residual dipolar coupling distributions of rPDMS samples obtained by analysis of the normalized build-up curve I_{ndQ} with the improved *ftikreg* fitting routine.³⁵

investigated in this study. The average residual dipolar coupling constant D_{res} and its variance σ are determined from the distributions. The results of this analysis are used for the characterization of the network structure and the calculation of the molecular weight between two cross-links according to eq 6.

Determination of M_c by Swelling Experiments: Flory–Rehner Theory. Bringing polymer networks in contact with appropriate solvents, the concentration difference causes an osmotic pressure, which is the driving force for the swelling process. The change of the total free energy ΔG^{tot} of the system depends thereby on the change due to the elastic deformation of the network ΔG^{el} and to the mixing of polymer and solvent ΔG^{mix} . The Flory–Rehner theory¹³ for the thermodynamics of swollen polymer networks postulates that the two contributions to the free energy are separable and additive. This assumption has been discussed extensively and controversially in the literature.^{16–18,51} According to Flory and Rehner, ΔG^{total} is expressed in terms of the change in the chemical potential of the swelling solvent, eq 8:

$$\frac{\Delta\mu_s^{\text{total}}}{RT} = \frac{\Delta\mu_s^{\text{mix}}}{RT} + \frac{\Delta\mu_s^{\text{el}}}{RT} \quad (8)$$

The mixing term, which considers the interaction between the polymer and the swelling solvent molecules, consist of an entropic and an enthalpic contribution. Commonly it is calculated according to eq 9, which is derived from the Flory–Huggins solution theory:^{52,53}

$$\frac{\Delta\mu_s^{\text{mix}}}{RT} = \ln(1 - \phi_p) + \phi_p + \chi\phi_p^2 \quad (9)$$

As mentioned above, this simplified mean-field theory is subject to limitations, meaning that the Flory–Huggins polymer–solvent interaction parameter χ is experimentally found to depend explicitly on the polymer volume fraction at swelling equilibrium ϕ_p and temperature T .⁵⁴

Furthermore, the estimate for the elastic contribution to the chemical potential depends the used network model. Classical approaches are the affine^{19,20} and the phantom^{21,22} models. In recent years, it was proposed that the phantom model should describe the behavior of swollen networks more appropriately.⁴⁴

For this case, the following expression for $\Delta\mu_s^{\text{el}}$ holds:

$$\frac{\Delta\mu_s^{\text{el}}}{RT} = \frac{\rho_p V_s}{M_c} \left(1 - \frac{2}{f} \right) \phi_p^{1/3} \quad (10)$$

where f represents the functionality of the cross-links, and M_c is the number-average molecular weight between two cross-links.

At swelling equilibrium, the gain in free energy upon mixing is exactly balanced by the free energy loss due to network deformation. Hence, the total change in the chemical potential vanishes. Combining eq 9 and eq 10 at equilibrium yields the well-known Flory–Rehner equation, eq 11:

$$\ln(1 - \phi_p) + \phi_p + \chi \phi_p^2 = - \frac{\rho_p V_s}{M_c} \left(1 - \frac{2}{f} \right) \phi_p^{1/3} \quad (11)$$

The difficulties in determining M_c by equilibrium swelling experiments are discussed in detail by Valentín et al.⁴⁴

In order to consider the effect of network defects for the estimation of M_c , the mixing (eq 9) and elastic (eq 10) terms of the Flory–Rehner equation must be treated differently. According to the Flory–Huggins theory, all monomer units belonging to the polymer network contribute equally to the mixing entropy and enthalpy in the calculation of the mixing term. Thus, a distinction between elastically effective and ineffective parts of the polymer network is not necessary, whereas the entropic elastic restoring forces only arise from elastically effective polymer chains. Therefore, just a certain fraction of polymer network ω_{el} is taken into consideration for the calculation of the elastic contribution, eq 10. The volume fraction of elastically effective polymer material in the equilibrium swollen sample $\phi_{\text{p,el}}$, eq 12, is estimated by using the results of the DQ NMR measurements of the defect fraction $\omega_{\text{def,sw}}$ in the polymer network.

$$\phi_{\text{p,el}} = \omega_{\text{el}} \phi_p = (1 - \omega_{\text{def,sw}}) \phi_p \quad (12)$$

The molecular weight between two cross-links M_c is thus calculated using the modified Flory–Rehner equation, eq 13:

$$M_c = - \frac{\rho_p V_s (1 - 2/f) \phi_{\text{p,el}}^{1/3}}{\ln(1 - \phi_p) + \phi_p + \chi \phi_p^2} \quad (13)$$

Furthermore, the functionality of cross-links f plays an important role in the determination of M_c by swelling experiments. The functionality depends on the number of chemically linked polymer chains at a cross-link, and $f = 4$ should be expected for the given system. For networks in which a significant fraction of cross-links does not have f active connections to the network, one has to replace the functionality f by the weight-average number of attached active strands per cross-link, f_{wa} .

For the consideration of this effect, calculations based on the Miller–Macosko theory of cross-linking³² are used to obtain information about the weight-averaged functionality f_{wa} of the investigated networks. Details of these calculations are given in the Appendix, and the results are given in Table 2. The actual computations are performed by a Fortran code that first reads in the precursor molecular weight distribution of the polymers. Then, equation eq A1 is computed numerically for all molecular weights of the sample. The following equations in the Appendix

are then evaluated step by step based on the numerical solutions of the distribution functions of previous steps. Note that the procedure was tested against exact solutions of the most probable and a uniform weight distribution. We note that the so-obtained f_{wa} is as low as 2.5 for the least cross-linked networks close the gel point, and reaches only values of about 3.6 at the highest conversions. The influence of $\phi_{\text{p,el}}$ and f_{wa} will be discussed in detail below.

RESULTS AND DISCUSSION

The main goal of this work is the determination of the molecular weight between two cross-links M_c in randomly cross-linked polymer networks with a precise consideration of defects. First, we will discuss the experimental results of the sample characterization by equilibrium swelling and DQ NMR experiments. The results are then compared with Miller–Macosko calculations based upon the experimentally determined sol fraction and the reaction turnovers from MAS NMR. Finally, M_c values obtained from the different approaches are correlated and the impact of network defects is demonstrated and discussed.

The desired reaction turnovers and the p_r determined by MAS NMR are in overall good agreement. In some cases, apparently more vinyl groups (2–6%) than expected were consumed during cross-linking (see Table 2), which appears counterintuitive. This can be attributed to the fact that the stoichiometric ratio of functionalized groups and cross-linking agent was adjusted to the average functionality 1.81 of the latter, due to an impurity fraction of monofunctional cross-linker. This latter fraction was probably slightly overestimated in the precharacterization. In any case, even samples with complete reaction turnover also contain some amount of consumed vinyl groups which do not lead to chemical cross-links.

Sol Fraction ω_{sol} . The fraction of polymer chains which were not connected to the infinite gel by permanent chemical cross-links during the network formation was obtained from the equilibrium swelling experiments. Figure 5 shows a continuous

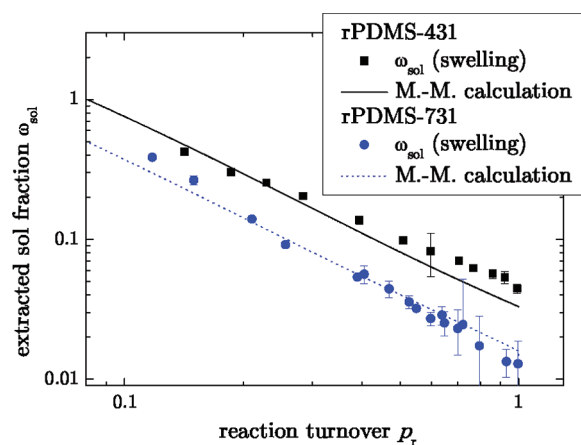


Figure 5. Variation of the extracted fraction of soluble network components ω_{sol} during equilibrium swelling as a function of the amount of reacted functional groups p_r during cross-linking along with results of Miller–Macosko calculations.

increase of extracted sol ω_{sol} from the networks with decreasing amount of used cross-link agent for sample preparation.

It is known for cross-linking reactions that a non-negligible fraction of cross-links is wasted in short dangling loops.⁵⁵

Additionally, about 19% of the added cross-links are monofunctional. In order to determine the fraction of cross-linked sites wasted in dangling loops or connected to monofunctional cross-links, and to restrict the analysis to actual cross-links which connect different chains, we computed the sol fraction as a function of p_r based on the known fraction of cross-linked sites. Next, we assumed that a constant fraction p_b (cf. Appendix) of these reacted sites does not lead to dangling loops and determined $p_b \approx 0.72$ and 0.66 for rPDMS-431 and rPDMS-731 samples, respectively, simply as a scaling factor (shift in logarithmic units, see Figure 5) between the data points and the original theoretical prediction. The theoretical lines in Figure 5 show the predictions for a branching fraction of $p_b p_r$ cross-links. The good agreement between data points and theory indicate that the assumption of constant fraction of cross-links is reasonable and that ignoring the weight fraction of dangling loops is of minor importance, as also shown previously.⁵⁵ Note that all later computations are based on the reduced fraction $p_b p_r$ of cross-links. The already considerable fraction of sol extracted from networks with a high degree of cross-linking can be attributed to the broad molecular weight distribution of the precursor polymers. Chains with low molecular weight show a reasonable probability of having no functionalized monomer. This assumption is supported by molecular weight distributions of the extracted sol obtained by GPC measurements. The percentage of polymer chains with a molecular weight lower than the average weight between two functionalized monomers in the melt is extracted nearly completely. This fraction stays roughly constant for decreasing reaction turnovers while the amount of high-molecular-weight sol increases notably.

Defect Fraction ω_{def} . The fraction of network defects was determined by ^1H DQ NMR experiments on sol-extracted networks, providing an absolute and precise measure. Results of the measurements in dry and equilibrium swollen samples are shown in Figure 6. The amount of defects identified in dry

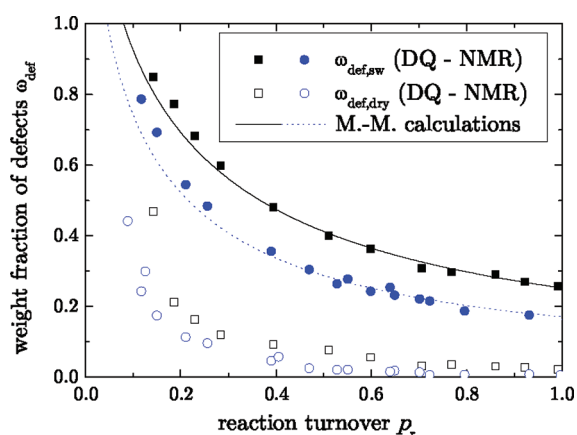


Figure 6. Fraction of network defects measured by DQ NMR in dry and equilibrium swollen rPDMS-431 (squares) and -731 (circles) samples, along with results of Miller–Macosko calculations in dependence of the reaction turnover p_r .

networks is of the order of a few percent and just slightly increases with decreasing reaction turnover. A significant increase of the measured defect fractions is observed only for reaction turnovers smaller than 50%. The accuracy of this low detected defect fraction is at least questionable, taking into account the way of cross-linking and the used prepolymers for

the studied samples. Because of the randomly distributed functionalized comonomers in the relatively short prepolymer backbones, even networks with 100% reaction turnover should have a nonzero amount of elastically inactive, dangling, and possibly branched material.

The fraction of defects depends primarily on the absolute number of possible cross-link sites along the polymer backbone and therefore, on the density of functionalized monomers ρ_{vinyl} and the length of the prepolymers. At low to moderate turnovers, at which the probability of simple chain extension reactions is higher, the molecular weight distribution of dangling chains is rather broad, and complex branched structures are present. An increase of the used amount of cross-linker primarily decreases the size of the dangling chain defects, and the defect fraction becomes dominated by linear dangling ends.⁵⁵ Because of the reasons discussed above, the used prepolymers with a broad molecular weight distribution generally causes an increase in the overall defect fraction.

The findings of a low fraction of nonelastic network defects measured in dry samples and the much increased fraction in swollen samples, see Figure 6, could be interpreted in different ways. Generally, if defects are present that are large or irregularly branched, their embedding in a dry cross-linked matrix renders them unobservable because the network constraints impede their terminal relaxation on the experimental time scale of the DQ NMR measurements. In this way, topological restrictions lead to similar nonisotropic motions of the associated chains on a time scale of ms as do chemical cross-links. A distinction between defects embedded in the network structure and elastically active polymer chains between two cross-links is thus not possible as they both contribute in a similar way (with similar apparent D_{res}) to the measured signal. Note that the slow relaxation of such defect structures contributes similarly to the mechanical properties, for instance, the stress relaxation modulus $G(t)$ or inversely, the time-dependent compliance $J(t)$, in defect-rich samples approach their rubber-elastic plateau values only very gradually.^{56,57}

However in the given samples and in particular at high conversion, the defect fraction is expected to be dominated by dangling ends of moderate molecular weight around or below the entanglement threshold ($M \leq M_e$), since rather short precursor polymers were used.⁵⁵ While it cannot be fully excluded that the topological structure of the defects in the given samples differs from the theoretical expectation, this nevertheless raises the question why a large part of the expected linear structures may not be able relax on the experimental time scale. The clarification of this issue is the subject of ongoing work, and we here sketch the starting point.

Our previous studies on polymer melts have approximately confirmed that the outer M_e portion of a highly entangled linear chain moves isotropically and is thus elastically inactive.⁵⁸ One may speculate that the isotropic fraction decreases if the chain is embedded in a highly cross-linked matrix (corresponding to an effectively narrower “tube”), and/or that intermolecular packing correlations have an effect on the motional anisotropy of the chains. The latter effect was previously addressed theoretically as a possible additional contribution to network elasticity and segmental orientation phenomena as detected by NMR.⁵⁹ In any way, the relatively narrow observed D_{res} distributions, see Figure 4, suggest that the defect fraction that is not relaxed on the time scale of the experiment exhibits a similar motional anisotropy as the network component, as it does not appear as a separate peak in the distribution.

Whatever the nature of the restrictions, network dilation due to swelling of the network samples leads to two opposing effects. On one hand, elastically active polymer chains are stretched, possibly amplifying the nonisotropic character of their motions. On the other hand, the topological or packing restrictions for defects are released for the most part, speeding up their terminal dynamics and enabling isotropic motion on the experimental time scale. The dynamics is of course further enhanced as a consequence of the plasticizer effect of the solvent. The different dynamic behavior of elastically effective and ineffective network fractions is thus amplified in swollen polymers and allows a precise distinction of their contribution to I_{ref} and I_{DQ} . It can therefore be assumed that results obtained by measurements on samples in swollen state give an accurate estimation of the actual defect fraction in polymer networks.

This assumption is proven by the near quantitative agreement of the experimental defect fraction $\omega_{\text{def,sw}}$ measured in equilibrium swollen samples by DQ NMR and the Miller–Macosko calculations, see Figure 6, reminding that the theoretical prediction is based upon p_b (see Appendix) as an independently determined single constant which results from fitting the experimental sol fraction of all samples of one series. The agreement shows the consistency of our analysis and strongly supports that we can achieve an accurate quantitative analysis of network structure. We note again that the residual coupling D_{res} taken from I_{NDQ} in *swollen* networks is subject to a wide distribution arising from swelling heterogeneities,⁴⁹ and is further strongly influenced by excluded-volume interactions in good solvent,⁴⁸ posing challenges to its determination and interpretation.

Residual Dipolar Coupling Constants and Their Distribution. Figure 7 shows the average residual dipolar

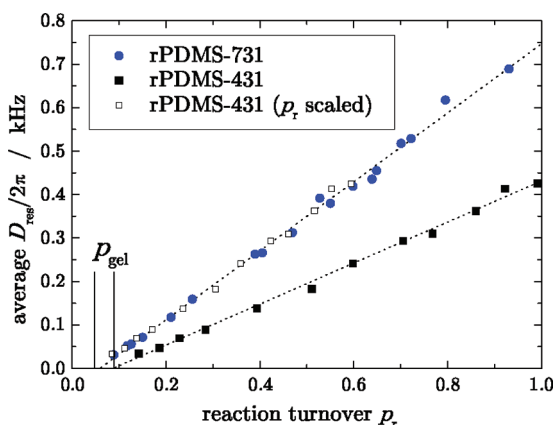


Figure 7. Relationship between the residual dipolar coupling constant D_{res} measured in dry rPDMS-431 (squares) and -731 (circles) samples, and reaction turnover p_r of vinyl-groups. D_{res} is the average of the coupling constant distribution obtained by regularization. The dashed lines represent linear fits of the data. The solid lines indicate the gel point obtained by the M.-M. calculations.

coupling constants D_{res} of the dry network samples in dependence of the reaction turnover p_r . The latter were obtained by using the numerical inversion procedure *ftikreg* for the evaluation of the normalized double-quantum build-up curves I_{NDQ} . For both series of polymer networks an apparent linear decrease of D_{res} with decreasing amount of cross-link agent is observed. In order to demonstrate the universality of the observation, the results of rPDMS-431 are scaled with respect to the ratio of the densities

of functionalized monomers ρ_{vinyl} in the two prepolymers. The near-perfect agreement of both prepared network series shows that the coupling constant mainly depends on the average number of monomer units between two chemical cross-links. We interpret the intercept of the linear fits of the data with the x -axis as an empirical measure of the minimum reaction turnover to obtain a network, in qualitative agreement with our previous observations.⁶⁰ These experimental estimations of the gel point, p_{gel} , are now again found to be in very good agreement to the results of Miller–Macosko calculations indicated by the vertical solid lines in Figure 7. It must be noted that this analysis is only possible because the used prepolymers are hardly entangled, meaning that the pure precursor melts do not exhibit measurable residual dipolar couplings arising from entanglements on the time scale of the DQ experiment at the given temperature. A detection of the gel point in terms of D_{res} would not be possible in systems of highly entangled, slowly reptating prepolymers.

In ideal monodisperse f -functional networks, the average residual dipolar coupling constant is related to the molecular weight between two cross-links, see eq 6. Since the measured coupling constant depends both on molecular weight between the cross-links and cross-link fluctuations,⁵⁰ a narrowing of the distribution of coupling constants as compared to the most probable weight distribution is expected and will be discussed in a forthcoming work. An important immediate consequence of this is that phantom-model considerations can be employed to provide a simple account of the cross-link fluctuations, as explained in the Appendix. This leads to the f -dependent correction factor for the DQ NMR results newly introduced in eq 6.

Since both, the average cross-link fluctuations and M_c , are roughly $\sim 1/p_r$, no significant changes in the width of the coupling constant distribution are expected as confirmed by Figure 8, which represents the ratio r_G between the variance σ

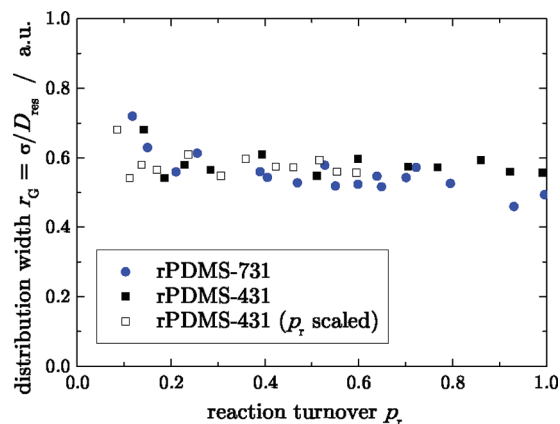


Figure 8. Variation of the relative width of the distribution of coupling constants as a function of reaction turnover p_r for samples rPDMS-431 and rPDMS-731. D_{res} represents the average and σ the variance of the coupling constant distribution obtained by regularization.

and the average D_{res} of the coupling constant distribution obtained by regularization of the normalized double-quantum build-up curve I_{NDQ} as a function of the reaction turnover p_r . The spatial distribution of cross-links has no significant dependence on the reaction turnover and ensures the comparability of the prepared networks. Additionally, this confirms a reasonably good mixing of the prepolymers and the cross-link agent prior to the cross-link reaction. We note again that even

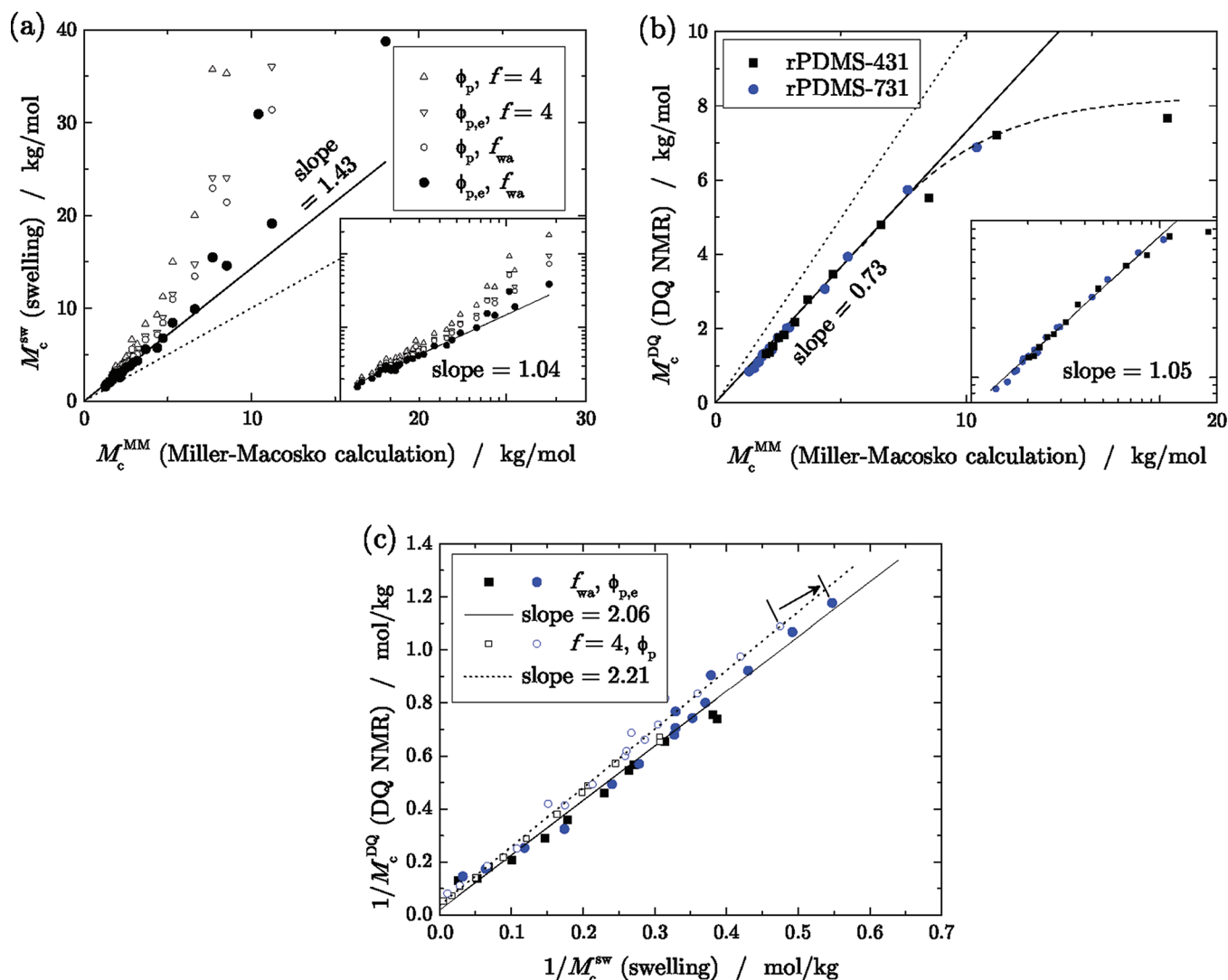


Figure 9. Comparison of the molecular weights between cross-links obtained by the different methods: (a) M_c for all samples from equilibrium swelling vs Miller–Macosko calculations, the former evaluated in different ways as discussed in the text, (b) M_c from DQ NMR using f_{wa} in eq 6 vs Miller–Macosko calculations, (c) cross-link density $1/M_c$ from DQ NMR vs swelling with or without consideration of defects in the analysis. The dotted lines in parts a and b have unity slope, and the insets show log–log representations of the data with fits allowing for a variable scaling exponent. The dashed line in (b) indicates the expected influence of entanglements. The arrow in part c connects two points from identical samples, demonstrating the magnitude of the f_{wa} - and $\phi_{p,e}$ -dependent correction.

though a considerable amount (>20%) of defects with potentially low residual coupling contributes to the total D_{res} measured on dry networks (see Figure 6), it is not possible to discern these as separate component in the D_{res} distributions.

The results in Figure 8 compare well with previous findings,³⁶ but it should be noted that the width of the observed D_{res} distributions is still larger than those observed, for example, for vulcanized natural rubber.^{37,47} In our recent paper concerned with the universality of I_{nDQ} curves for very homogeneous rubbers,³⁵ we have shown that even more homogeneous PDMS networks ($r_G \approx 0.1$) can in fact be prepared when the cross-linking is carried out at higher solvent content, facilitating mixing and diffusion of the reactants. This recent result demonstrates that the residual moderate inhomogeneity (distribution width) of the given samples is either due to spatial cross-linking inhomogeneities on a larger length scale (many mesh sizes), or to the mentioned defect fraction, or both.

Comparison of Molecular Weights between Cross-Links. Three completely different methods, DQ NMR, swelling experiments, and Miller–Macosko calculations based upon quantitative MAS NMR and the experimental sol content, were used to determine the molecular weight between two cross-links M_c . The D_{res} results of the DQ NMR measurements on dry network samples were evaluated according to eq 6, which takes into account the cross-link functionality-dependent correction arising from the phantom model (see Appendix). The Miller–Macosko approach, which we take as the standard for absolute (least model-dependent) M_c -determination, most directly yields the average number of monomers of an active network strand, cf. eq A2. The equilibrium swelling experiments were evaluated according to the Flory–Rehner treatment addressed above. For the calculation of the actual molecular weights, different values for the functionality of the cross-links, $f = 4$ vs variable f_{wa} , and the different volume fractions of the network component, ϕ_p vs $\phi_{p,e}$, were used.

We first focus on a comparison of the Miller–Macosko M_c^{MM} with the different swelling results, M_c^{sw} , plotted in Figure 9a. The functionality of cross-links in randomly cross-linked polymer networks is usually assumed to be four,⁴⁴ but the comparison shows that the relation to M_c^{MM} is then decisively nonlinear, see the triangles in the log–log inset. This can be attributed to an overestimation of the elastic contribution to the Flory–Rehner equation, related to an overestimation of the functionality of the networks. The results of the Miller–Macosko calculations for the weight-averaged cross-link functionality f_{wa} , see Table 2, confirm this assumption and reveal a distinct dependence of on the degree of cross-linking. For the polymers used in this study the number of possible cross-link sites is already defined before cross-linking by the number of functionalized monomers per polymer chain. The characterization of the prepolymers shows average numbers of 6 and 12 functionalized monomers per polymer chain for rPDMS-431 and rPDMS-731, respectively. The outer functional groups in the backbone of a single polymer chain have a functionality of at most $f = 3$ after cross-linking. If two outer functional groups are linked, the functionality reduces to $f = 2$, thus, with decreasing reaction turnovers less cross-links are established per chain, and the fraction of two- and three-functional cross-links increases drastically. This effect, in combination with the small number of functional groups per polymer chain leads to networks with average functionalities considerably smaller than four.

With the f_{wa} taken into account for the evaluation of the equilibrium swelling experiments, the correlation improves significantly, see the circles in the inset of Figure 9a. This clearly shows the importance of an approximately known functionality for a reliable determination of molecular weights by equilibrium swelling experiments.

In the previous section we introduced the elastically effective polymer volume fraction $\phi_{p,el}$ in equilibrium swollen samples. In this treatment it is assumed that the network defects do not contribute to the elastic term of the Flory–Rehner equation. Therefore, the volume fraction of polymer in an equilibrium swollen sample ϕ_p is reduced with respect to the defect fraction of the network. For this reason, the defect fraction obtained by DQ NMR experiments on the equilibrium swollen samples $\omega_{def,sw}$ was used to determine $\phi_{p,el}$ according to eq 12. Comparing the open and closed circles in the inset of Figure 9a, it is apparent that the neglect of this issue is again reflected in a significantly nonlinear relation between M_c^{sw} and M_c^{MM} .

With both quantities reflecting defects considered (f_{wa} and $\phi_{p,el}$), we obtain a log–log slope of 1.04, which is close to the expected linearity. Since the Flory–Rehner evaluation based on the affine model, see ref 44 for the corresponding formula, only depends very weakly on f , the evaluation using a constant $f = 4$ for all samples can be taken to represent the affine result up to a constant factor. We therefore interpret the near-linear correlation with variable f_{wa} considered (and the less linear correlation for constant $f = 4$) as a proof of the validity of the phantom model. Turning to the absolute values for M_c , we note that the swelling experiments yield results that are larger by a factor of 1.43. Considering the many potential shortcomings of the Flory–Rehner model, such as nonaffine swelling¹² and in particular the ambiguities related to the χ parameter and its potential dependence on concentration and cross-linking,⁴⁴ this deviation should be considered minor. One could of course use our absolute M_c^{MM} results for a recalibration of the used χ .

We now turn to gauging the M_c^{DQ} results from DQ NMR using the variable f_{wa} in eq 6 vs M_c^{MM} , see Figure 9b. The log–log inset demonstrates again a close-to linear relation, which also in this case can be taken as an additional and completely independent hint at the validity of the phantom network model, here without ambiguities related to the thermodynamic model. The direct comparison on the linear scale now indicates a deviation in the other direction, meaning that M_c^{DQ} appears to be underestimated by a factor of 0.73. A quick comparison with Figure 9a suggests that a factor of 2 can be expected in a direct comparison between M_c^{DQ} and M_c^{sw} , which will be addressed below. It is in any way clear that the omission of corrections due to f_{wa} and the elastically effective polymer volume fraction $\phi_{p,el}$ would only increase the deviation and increase the nonlinearity of the correlation at low M_c . Therefore, the absolute-value comparisons stress the importance of considering network defects.

A noticeable trend in Figure 9b is the apparent nonlinear behavior of M_c^{DQ} at higher molecular weights. This is the regime when M_c reaches the order of the entanglement molecular weight M_e , i.e. around 10–20 kg/mol for PDMS. Traditionally, the influence of entanglements was interpreted as being additive in the effective cross-link density ($1/M_c + 1/M_e$), which in turn determines the measured D_{res} . This interpretation was corroborated by a nonzero y intercept when plotting $D_{res} \propto 1/M_c^{DQ}$ vs $1/M_c^{sw}$ from swelling experiments.^{37,44} This means that in an inverse representation M_c^{DQ} should reach a plateau value. In contrast, more recent theoretical work has shown that D_{res} rather scales as $1/(M_c M_e)^{0.5}$ at low cross-linking when $M_c \gg M_e$.⁵⁰ However, this behavior is not easily observed experimentally, as the very slow terminal relaxation in lowly cross-linked networks formed by long entangled precursor chains leads to a finite D_{res} at finite temperature. If observable, M_c^{DQ} should thus scale as $M_c^{0.5}$ at high M_c^{DQ} . Since the accuracy of the D_{res} determination is challenged at low cross-linking degrees, it is not possible to distinguish the two scenarios with the given data. In any way, entanglement contributions can explain the bend at high M_c^{DQ} , and could also partially explain an underestimation of M_c^{DQ} (decreased slope).

As to entanglements, it should be stressed that the given samples, based upon nonentangled precursors, are not really dominated by entanglement effects at low cross-link conversions just above the gel point. In this regime, the elastically active network fraction consist of complex chain-extended and branched but weakly entangled structures that are embedded in a similarly complex mixture of isotropically mobile dangling material. At present, we do not have a sufficient theoretical understanding of the low NMR-determined D_{res} in such a system, reminding the reader that in Figure 7 it is shown that D_{res} reaches a near-zero value close to the gel point.

The overall good agreement of M_c^{DQ} and M_c^{MM} should be discussed in the context of the ambiguities related to the derivation of the constant of proportionality used in eq 6, which relies on spin dynamics simulations of the local spin system and a few model assumptions related to the geometry of local conformational fluctuations and the definition of the Kuhn segment.³⁷ It should be kept in mind the most highly cross-linked samples, with M_c of 5 kg/mol and less, still contain around 25–35% of defects (see Figure 6). These are part of the average D_{res} measured on the dry sample, so we can expect that D_{res} may be biased toward lower values, corresponding to higher M_c^{DQ} . Without the defects, M_c^{DQ} would be even lower, thus increasing the deviation. We therefore take this as another

hint that the defect contribution to D_{res} is minor and assign the lower slope of 0.73 mainly to shortcomings of the underlying model.

Last but not least, we address the direct correlation of DQ NMR and swelling results. This time, we choose the representation in terms of effective cross-link densities, $1/M_c^{\text{DQ}}$ vs $1/M_c^{\text{sw}}$, as already discussed above, see Figure 9c. As expected, the deviation in the linear representation is about a factor of 2. In this case, as opposed to our earlier work on vulcanized diene rubbers,^{37,44} the y intercept related to entanglements is hardly visible. This can be explained by the high M_c of PDMS and the correspondingly low y intercept, and the limited accuracy for networks with low D_{res} . In principle, this third correlation offers no new insights, and we just summarize that the factor of 2 deviation is, to roughly equal parts, due to inadequacies of the Flory–Rehner model and the DQ NMR calibration factor.

An issue of practical relevance is that the weight-average functionality f_{wa} is not routinely available, since the numerical Miller–Macosko calculations are not at everybody's disposal and are further based upon the molecular weight distribution and the density of functionalized monomers ρ_{vinyl} of the prepolymers, the exact extent of reaction from MAS NMR, and the experimental sol content. This poses the question to which extent the results are challenged when the swelling or DQ NMR experiments are evaluated without taking defects into account. Therefore, Figure 9c also contains data for which both M_c^{DQ} and M_c^{sw} were evaluated using a constant $f = 4$ and (for the latter) the as-determined polymer volume fraction ϕ_p . It is seen that, superficially, the corresponding data follow a similar trend as the data taking full account of the network defects. However, the agreement of the slopes is mainly due to the trivial fact that the phantom model introduces the very same f -dependence for the two results, see eq 6 and eq 13, which essentially cancels when just the quality of a linear correlation between the two quantities is discussed. The arrow in Figure 9c shows that data for one and the same sample do not deviate by more than 10–20% at high cross-link densities, which however is deceiving, as the relative deviation becomes very large (300–400%) for lowly cross-linked samples, an effect which is concealed close to the origin of this favorable representation. The main effect of the neglect of $\phi_{\text{p,e}}$ is an upward shift of the uncorrected data, implying an apparently higher entanglement contribution (y intercept).

Finally, it is noteworthy that the $1/M_c^{\text{DQ}}$ vs $1/M_c^{\text{sw}}$ correlation becomes almost perfect (unity slope) when the f -dependent correction factor for DQ NMR, which is 2 for when a constant $f = 4$ is used, is simply omitted from eq 6. This is of course not permissible as we have proven the validity of the Phantom model by reference to the unbiased Miller–Macosko calculations. However, the use of an analogue of eq 6 for natural rubber without the correction was exactly the state of knowledge at the time of publication of our earlier work, ref 44, where a slope of around 1 was observed when the swelling data was analyzed on the basis of the phantom model. Note that using a constant $f = 4$ is a good approximation for rubbers based on very long precursor chains over a wider range of cross-link densities. This means that the seemingly good previous correlation must be revised, suggesting that probably also for natural rubber, the same limitations of the Flory–Rehner model and the model-dependent DQ NMR calibration factor hold. In addition, it should be checked whether the omission of $\phi_{\text{p,e}}$ in swelling analyses is also responsible for systematic errors

related to the apparent entanglement contribution (y intercept) in such samples.

CONCLUSIONS

In this work, we have studied randomly cross-linked PDMS networks by ^1H double-quantum low field NMR, equilibrium swelling experiments, and Miller–Macosko calculations based upon a number of well-defined experimental input parameters, in order to assess their microstructure, with emphasis on network defects and the molecular weight between cross-links, M_c .

The defect fraction of the polymer networks has been investigated by double-quantum NMR. In the dry state, chain packing correlations or topological restrictions impede sufficiently fast isotropic motions of dangling structures and loops. Thus, a fraction of the defects is observed as elastically active chains on the experimental time scale of the double-quantum experiment, and the defect fraction is thus underestimated. The restrictions are released and the segmental dynamics is sped up by swelling of the networks with a suitable solvent, leading to fast isotropic motions, and the defect fraction determined in swollen networks is considerably higher as in the corresponding dry networks. The almost perfect agreement of the so-determined defect fraction with results of the Miller–Macosko calculations demonstrates that double-quantum NMR experiments on swollen samples provide a reliable measure of the elastically active and inactive fractions of polymer networks.

On the basis of the extracted sol known from the swelling experiments, the Miller–Macosko calculations yield the weight-averaged functionality of cross-links f_{wa} , which is found to be significantly smaller than the expected value of four, varying substantially between 3.6 and 2.5 depending on the degree of cross-linking. Another quantity related to network defects is the volume fraction of elastically active chains in the swollen state $\phi_{\text{p,el}}$, which is obtained from the polymer volume fraction at equilibrium swelling after correction using the correct defect fraction determined by NMR on swollen samples. Both quantities can be used for a proper evaluation of equilibrium swelling experiments, and a comparison of the resulting M_c with results from Miller–Macosko calculations clearly demonstrates the importance of the consideration of defects. A linear correlation between the M_c obtained from the two approaches is only observed when f_{wa} and $\phi_{\text{p,el}}$ are taken into account.

The absolute M_c values obtained by equilibrium swelling are 40% larger than the results from the Miller–Macosko calculations, and the deviations are assigned to the known inadequacies of the Flory–Rehner model. In comparison, double-quantum NMR experiments on dry samples, which also yield reliable results for M_c , underestimate it by 30%, which is assigned to minor inadequacies of the model underlying the determination of the calibration factor used to analyze such data. At high M_c , entanglement effects or slow dynamics in branched defect structures start to dominate the NMR results, and the correlation with the known M_c is no longer linear.

The fact that the network samples in this study exhibit different effective functionalities allowed for a rigorous test of the Phantom model of rubber elasticity. The assumption of phantom (rather than affine) behavior leads to strongly functionality-dependent results for both swelling as well as NMR experiments, as both methods are sensitive to fluctuations of the network chains. Since the results from the Miller–Macosko calculations are independent of such considerations,

we have demonstrated that the linear correlation of the M_c from either swelling or NMR with the Miller–Macosko results constitute a validity test of the phantom model.

■ APPENDIX

Miller–Macosko Calculations

In this section we describe the computations of the sol fraction, the dangling material, and the average lengths of active strands of the randomly cross-linked networks. Let us assume independence of all reactions, equal reactivity among all monomers, and that cross-linking occurs by a pairwise connection of arbitrary selected monomers out of the reaction bath. Under these assumptions, the distribution $P(f, N)$ of branches f per polymer of N monomers is given⁵⁵ by the binomial distribution

$$P(f, N) = \binom{N}{f} p^f (1-p)^{N-f} \quad (\text{A1})$$

based upon the probability p that an arbitrary selected monomer is reacted. Let n_N denote the mol fraction of molecules containing N monomers. For the polydisperse samples of our study with weight fractions w_N of molar masses, equation (A1) implicitly defines a weight distribution of polymer having f branches. The weight fraction of polymers with f branches is then given by

$$w_f = \sum_N P(f, N) M_N / \sum_N n_N M_N$$

whereby $M_N = N M_{\text{mon}}$ is the molar mass of the N -mer, M_{mon} the mass of a monomer. The number-average degree of polymerization of chains having f branches N_f is given by

$$N_f = \sum P(f, N) n_N N$$

The mol fractions of branches a_f on polymers of f branches is computed via

$$a_f = \frac{f \sum_N n_N P(f, N)}{\sum_f f \sum_N n_N P(f, N)}$$

Let Q denote the probability that a given branching monomer on a chain is the start of a *finite* chain.⁶¹ Q is computed recursively by numerically solving

$$Q = \sum_f a_f Q^{f-1}$$

If all f branches of a given polymer lead to a dangling end, then the chain is part of the sol. Thus, the weight fraction of sol is given by

$$w_{\text{sol}} = \sum_f w_f Q^f$$

The above treatment assumes no intra-molecular reactions in finite species, which is certainly not the case. Intra-molecular reactions in finite species lead to a fraction of non-branching reactions that increase the weight fraction of sol. Therefore, we introduce a fraction of reacted monomers p_b (out of the fraction of p reacted monomers) that lead to ideal branching reactions following mean field theory, while the remaining fraction $1 - p_b$ is involved in intra-molecular reactions in finite species. Since the molecular weight

distribution and the fraction of reacted monomers is known, we leave p_b as the only parameter to match the experimental sol content as a function of $p' = p_b p$ with our predictions above.

After p' is determined, we compute the length distribution of strands between these ideally branching monomers and the weight fraction of dangling material following refs 32 and 55 and the above results based on p' . Since Q denotes the probability that a given branch leads to a finite chain, we can compute the probability that a chain of f branches contains k connections which are not finite

$$P(X_{k,f}) = \binom{f}{k} Q^{f-k} (1-Q)^k$$

The weight fraction of dangling material is all polymer attached to gel $k \geq 1$ that is not between the first and last of these k active branches along the chain. Since k branches divide a chain into $k + 1$ sections, there is a fraction of $2/(k + 1)$ dangling material per chain. Thus, the weight fraction of dangling material is given by

$$w_{\text{dang}} = \sum_f 2N_f P(X_{2,f}) / (k + 1)$$

and the weight fraction of active material is then

$$w_{\text{act}} = 1 - w_{\text{sol}} - w_{\text{dang}}$$

The number fraction of branches that are active p_{act} is the number fraction of branches with at least three independent connections to the network

$$p_{\text{act}} = \sum_{f=3}^{\infty} (P(f, N) \sum_{k=3}^f P(X_{k,f}))$$

Thus, there is a number fraction of $p_{\text{act}} p'$ monomers inside the active material that is an active branch and the average active strand length is given by

$$N_{\text{act}} = \frac{w_{\text{act}}}{p_{\text{act}} p'} \quad (\text{A2})$$

with a molecular weight distribution that is quickly converging from the high molecular weight wing of the precursor weight distribution to a most probable weight distribution⁵⁵ of the above average and a polydispersity index of 2.

Let us introduce the active functionality f_a , which is given by the number of independent active connections of a junction to the network, and the weight fraction w_{f_a} of junctions with f_a active connections. The weight-average of the active functionality is then

$$f_{\text{wa}} = \sum_{i=3}^{\infty} i w_{f_a} / \sum_{i=3}^{\infty} w_{f_a}$$

If an active cross-link connects to a neighboring active cross-link, the connected cross-links are selected proportional to the number of active connections. Thus, the weight-average active functionality f_{wa} determines the average functionality of the surrounding network that is experienced by an active cross-link.

NMR Order Parameter and Phantom Model

The estimate for the average dynamic segmental order parameter will be performed in a pre-averaged manner by using the number-average length of an active strand \bar{N}_{act} and

following the phantom model as discussed in ref 50. To this end, we have to compute the length of the corresponding combined chain that allows to map the phantom model onto the affine model. Let us consider an active chain that is connected to two active junctions, each of average functionality f . Then, the average fluctuations of the cross-links without the chain in between can be modeled by attaching virtual chains of

$$K_a \approx \frac{\bar{N}_{\text{act}}}{f-2}$$

monomers to the non-fluctuating elastic background. The corresponding combined chain of the affine model consists of

$$N_{\text{comb}} \approx \bar{N}_{\text{act}} \frac{f}{f-2}$$

monomers. Below we denote ensemble averages by [...]. For the affine model using a large set of chains of N monomers with Gaussian end-to-end distribution and segments of length b it is known that in general the (ensemble average) vector order parameter $[m]$ is proportional to the tensor order parameter $[s]$

$$[m] = \frac{[R^2]}{b^2 N^2} = \frac{1}{N} = \frac{5}{3} [s]$$

using the Gaussian result $[R^2] = b^2 N$. Following the arguments of ref 50, we replace N by N_{comb} and use the average size of the combined chain to obtain the tensor order parameter as a function of the number-average active chain length and the weight-average active functionality

$$s \approx \frac{3}{5} \frac{f-2}{f} \frac{1}{\bar{N}_{\text{act}}}$$

The tensor order parameter s is directly proportional to the NMR-determined residual dipolar interaction, $D_{\text{res}} = s D_{\text{ref}}$ where D_{ref} is a pre-averaged dipolar coupling constant characterizing the spin arrangement and local motions within a statistical (Kuhn) segment.³⁷

AUTHOR INFORMATION

Corresponding Author

*E-mail: (W.C.) walter.chasse@physik.uni-halle.de; (K.S.) kay.saalwaechter@physik.uni-halle.de.

REFERENCES

- (1) Patel, S. K.; Malone, S.; Cohen, C.; Gillmor, J. R.; Colby, R. H. Elastic modulus and equilibrium swelling of poly(dimethylsiloxane) networks. *Macromolecules* **1992**, *25*, 5241–5251.
- (2) Arndt, K. F.; Schreck, J. Netzwerkcharakterisierung durch dampfdruckosmotische Messungen. *Acta Polym.* **1985**, *36*, 56–57.
- (3) Tan, Z.; Jaeger, R.; Vancso, G. Crosslinking studies of poly(dimethylsiloxane) networks: a comparison of inverse gas chromatography, swelling experiments and mechanical analysis. *Polymer* **1994**, *35*, 3230–3236.
- (4) Falcão, A. N.; Pedersen, J. S.; Mortensen, K. Structure of randomly crosslinked poly(dimethylsiloxane) networks produced by electron irradiation. *Macromolecules* **1993**, *26*, 5350–5364.
- (5) Folland, R.; Charlesby, A. Pulsed NMR studies of crosslinking and entanglements in high molecular weight linear polydimethylsiloxanes. *Radiat. Phys. Chem.* **1977**, *10*, 61–68.
- (6) Mark, J. E.; Sullivan, J. L. Model Networks Of End-Linked Polydimethylsiloxane Chains 0.1. Comparisons Between Experimental And Theoretical Values Of Elastic-Modulus And Equilibrium Degree Of Swelling. *J. Chem. Phys.* **1977**, *66*, 1006–1011.
- (7) Falender, J. R.; Yeh, G. S. Y.; Mark, J. E. The effect of chain length distribution on elastomeric properties. 1. Comparisons between random and highly nonrandom networks. *J. Am. Chem. Soc.* **1979**, *101*, 7353–7356.
- (8) Erman, B.; Mark, J. E. Rubber-Like Elasticity. *Annu. Rev. Phys. Chem.* **1989**, *40*, 351–374.
- (9) Mark, J. E.; Llorente, M. A. Model networks of end-linked polydimethylsiloxane chains. 5. Dependence of the elastomeric properties on the functionality of the network junctions. *J. Am. Chem. Soc.* **1980**, *102*, 632–636.
- (10) Llorente, M. A.; Andradý, A. L.; Mark, J. E. Chemical analysis of vinyl-crosslinked poly(dimethylsiloxane) model networks and use of the resulting structural information in the interpretation of their elastomeric properties. *J. Polym. Sci. Polym. Phys. Ed.* **1980**, *18*, 2263–2270.
- (11) Mark, J. E. Elastic Properties Of Model Polymer Networks. *Pure Appl. Chem.* **1981**, *53*, 1495–1503.
- (12) Sommer, J. U.; Lay, S. Topological Structure and Nonaffine Swelling of Bimodal Polymer Networks. *Macromolecules* **2002**, *35*, 9832–9843.
- (13) Flory, P.; Rehner, J. Statistical mechanics of cross-linked polymer networks. *J. Chem. Phys.* **1943**, *11*, 521–527.
- (14) Flory, P. Statistical Mechanics of Swelling of Network Structures. *J. Chem. Phys.* **1950**, *18*, 108–111.
- (15) Flory, P. *Principles of Polymer Chemistry*; Cornell University Press: New York, 1953.
- (16) Brotzman, R. W.; Eichinger, B. E. Volume dependence of the elastic equation of state. 2. Solution-cured poly(dimethylsiloxane). *Macromolecules* **1981**, *14*, 1445–1448.
- (17) Brotzman, R. W.; Eichinger, B. E. Volume dependence of the elastic equation of state. 3. Bulk-cured poly(dimethylsiloxane). *Macromolecules* **1982**, *15*, 531–535.
- (18) Brotzman, R. W.; Eichinger, B. E. Swelling of model poly(dimethylsiloxane) networks. *Macromolecules* **1983**, *16*, 1131–1136.
- (19) Hermans, J. Deformation and swelling of polymer networks containing comparatively long chains. *Trans. Faraday Soc.* **1947**, *43*, 591–600.
- (20) Wall, F. T.; Flory, P. J. Statistical Thermodynamics of Rubber Elasticity. *J. Chem. Phys.* **1951**, *19*, 1435–1439.
- (21) James, H. M.; Guth, E. Theory of the Elastic Properties of Rubber. *J. Chem. Phys.* **1943**, *11*, 455–481.
- (22) James, H. M.; Guth, E. Theory of the increase in rigidity of rubber during cure. *J. Chem. Phys.* **1947**, *15*, 669–683.
- (23) Gottlieb, M.; Gaylord, R. J. Experimental tests of entanglement models of rubber elasticity. 2. Swelling. *Macromolecules* **1984**, *17*, 2024–2030.
- (24) Andradý, A. L.; Llorente, M. A.; Sharaf, M. A.; Rahalkar, R. R.; Mark, J. E.; Sullivan, J. L.; Yu, C. U.; Falender, J. R. Model networks of end-linked polydimethylsiloxane chains. XII. Dependence of ultimate properties on dangling-chain irregularities. *J. Appl. Polym. Sci.* **1981**, *26*, 1829–1836.
- (25) Vega, D. A.; Villar, M. A.; Alessandrini, J. L.; Vallés, E. M. Terminal Relaxation of Model Poly(dimethylsiloxane) Networks with Pendant Chains. *Macromolecules* **2001**, *34*, 4591–4596.
- (26) Acosta, R. H.; Monti, G. A.; Villar, M. A.; Vallés, E. M.; Vega, D. A. Transiently Trapped Entanglements in Model Polymer Networks. *Macromolecules* **2009**, *42*, 4674–4680.
- (27) Bastide, J.; Picot, C.; Candau, S. The influence of pendent chains on the thermodynamic and viscoelastic properties of swollen networks. *J. Polym. Sci., Polym. Phys. Ed.* **1979**, *17*, 1441–1456.
- (28) Bibbó, M. A.; Vallés, E. M. Influence Of Pendant Chains On The Loss Modulus Of Model Networks. *Macromolecules* **1984**, *17*, 360–365.
- (29) Villar, M. A.; Bibbó, M. A.; Vallés, E. M. Influence of pendant chains on mechanical properties of model poly(dimethylsiloxane) networks 0.1. Analysis of the molecular structure of the network. *Macromolecules* **1996**, *29*, 4072–4080.

- (30) Villar, M. A.; Vallés, E. M. Influence of pendant chains on mechanical properties of model poly(dimethylsiloxane) networks 0.2. Viscoelastic properties. *Macromolecules* **1996**, *29*, 4081–4089.
- (31) Urayama, K.; Kawamura, T.; Kohjiya, S. Structure-mechanical property correlations of model siloxane elastomers with controlled network topology. *Polymer* **2009**, *50*, 347–356.
- (32) Macosko, C. W.; Miller, D. R. A New Derivation of Average Molecular Weights of Nonlinear Polymers. *Macromolecules* **1976**, *9*, 199–206.
- (33) Chalk, A. J.; Harrod, J. F. Homogeneous Catalysis. II. The Mechanism of the Hydrosilation of Olefins Catalyzed by Group VIII Metal Complexes. *J. Am. Chem. Soc.* **1965**, *87*, 16–21.
- (34) Weese, J. A. Reliable And Fast Method For The Solution Of Fredholm Integral-Equations Of The 1st Kind Based On Tikhonov Regularization. *Comput. Phys. Commun.* **1992**, *69*, 99–111.
- (35) Chassé, W.; Valentín, J. L.; Genesky, G. D.; Cohen, C.; Saalwächter, K. Precise dipolar coupling constant distribution analysis in proton multiple-quantum NMR of elastomers. *J. Chem. Phys.* **2011**, *134*, 044907.
- (36) Saalwächter, K.; Ziegler, P.; Spyckerelle, O.; Haidar, B.; Vidal, A.; Sommer, J. U. ¹H multiple-quantum nuclear magnetic resonance investigations of molecular order distributions in poly(dimethylsiloxane) networks: Evidence for a linear mixing law in bimodal systems. *J. Chem. Phys.* **2003**, *119*, 3468–3482.
- (37) Saalwächter, K.; Herrero, B.; Lopez-Manchado, M. A. Chain order and cross-link density of elastomers as investigated by proton multiple-quantum NMR. *Macromolecules* **2005**, *38*, 9650–9660.
- (38) Saalwächter, K. Proton multiple-quantum NMR for the study of chain dynamics and structural constraints in polymeric soft materials. *Prog. Nucl. Magn. Reson. Spectrosc.* **2007**, *51*, 1–35.
- (39) Bueche, A. M. Interaction of polydimethylsiloxanes with swelling agents. *J. Polym. Sci.* **1955**, *15*, 97–103.
- (40) Hecht, A. M.; Guillermo, A.; Horkay, F.; Mallam, S.; Legrand, J. F.; Geissler, E. Structure and dynamics of a poly(dimethylsiloxane) network: a comparative investigation of gel and solution. *Macromolecules* **1992**, *25*, 3677–3684.
- (41) Mallam, S.; Horkay, F.; Hecht, A. M.; Rennie, A. R.; Geissler, E. Microscopic and macroscopic thermodynamic observations in swollen poly(dimethylsiloxane) networks. *Macromolecules* **1991**, *24*, 543–548.
- (42) Soni, V. K.; Stein, R. S. Light-Scattering-Studies of Poly(dimethylsiloxane) Solutions and Swollen Networks. *Macromolecules* **1990**, *23*, 5257–5265.
- (43) Horkay, F.; Hecht, A. M.; Geissler, E. Thermodynamic Interaction Parameters In Polymer-Solutions And Gels. *J. Polym. Sci., Part B: Polym. Phys.* **1995**, *33*, 1641–1646.
- (44) Valentín, J. L.; Carretero-González, J.; Mora-Barrantes, I.; Chassé, W.; Saalwächter, K. Uncertainties in the Determination of Cross-Link Density by Equilibrium Swelling Experiments in Natural Rubber. *Macromolecules* **2008**, *41*, 4717–4729.
- (45) Graf, R.; Heuer, A.; Spiess, H. W. Chain-order effects in polymer melts probed by ¹H double-quantum NMR spectroscopy. *Phys. Rev. Lett.* **1998**, *80*, 5738–5741.
- (46) McLoughlin, K.; Szeto, C.; Duncan, T. M.; Cohen, C. End-Linked Poly(dimethylsiloxane) Elastomer Structure: 2H-NMR Transverse Dephasing Data Compared to Predictions of Statistical and Thermodynamic Models. *Macromolecules* **1996**, *29*, 5475–5483.
- (47) Valentín, J.; Posadas, P.; Fernández-Torres, A.; Malmierca, M. A.; González, L.; Chassé, W.; Saalwächter, K. Inhomogeneities and Chain Dynamics in Diene Rubbers Vulcanized with Different Cure Systems. *Macromolecules* **2010**, *43*, 4210–4222.
- (48) Sommer, J.-U.; Chassé, W.; Valentín, J. L.; Saalwächter, K. Effect of excluded volume on segmental orientation correlations in polymer chains. *Phys. Rev. E* **2008**, *78*, 051803.
- (49) Saalwächter, K.; Kleinschmidt, F.; Sommer, J.-U. Swelling Heterogeneities in End-Linked Model Networks: A Combined Proton Multiple-Quantum NMR and Computer Simulation Study. *Macromolecules* **2004**, *37*, 8556–8568.
- (50) Lang, M.; Sommer, J.-U. Analysis of Entanglement Length and Segmental Order Parameter in Polymer Networks. *Phys. Rev. Lett.* **2010**, *104*, 177801.
- (51) McKenna, G. B.; Flynn, K. M.; Chen, Y. Experiments on the elasticity of dry and swollen networks: implications for the Frenkel-Flory-Rehner hypothesis. *Macromolecules* **1989**, *22*, 4507–4512.
- (52) Flory, P. Thermodynamics of High Polymer Solutions. *J. Chem. Phys.* **1941**, *9*, 660–661.
- (53) Huggins, M. Solutions of Long Chain Compounds. *J. Chem. Phys.* **1941**, *9*, 440.
- (54) Schuld, N.; Wolf, B. A. Solvent quality as reflected in concentration- and temperature-dependent Flory-Huggins interaction parameters. *J. Polym. Sci., Part B: Polym. Phys.* **2001**, *39*, 651–662.
- (55) Lang, M.; Göritz, D.; Kreitmeier, S. Length of Subchains and Chain Ends in Cross-Linked Polymer Networks. *Macromolecules* **2003**, *36*, 4646–4658.
- (56) Plazek, D. J. Effect of Crosslink Density on the Creep Behavior of Natural Rubber Vulcanizates. *J. Polym. Sci., A-2: Polym. Phys.* **1966**, *4*, 745–763.
- (57) Curro, J. G.; Pearson, D. S.; Helfand, E. Viscoelasticity of Randomly Crosslinked Polymer Networks. Relaxation of Dangling Chains. *Macromolecules* **1985**, *18*, 1157–1162.
- (58) Vaca Chávez, F.; Saalwächter, K. Time-Domain NMR Observation of Entangled Polymer Dynamics: Universal Behavior of Flexible Homopolymers and Applicability of the Tube Model. *Macromolecules* **2011**, *44*, 1549–1559.
- (59) Oyerokun, F. T.; Schweizer, K. S. Microscopic theory of rubber elasticity. *J. Chem. Phys.* **2004**, *120*, 9359–9370.
- (60) Saalwächter, K.; Gottlieb, M.; Liu, R.; Oppermann, W. Gelation as Studied by Proton Multiple-Quantum NMR. *Macromolecules* **2007**, *40*, 1555–1561.
- (61) Rubinstein, M.; Colby, R. *Polymer Physics*; Oxford University Press: New York, 2003.

Modification of Melt-Spun Isotactic Polypropylene and Poly(lactic acid) Bicomponent Filaments with a Premade Block Copolymer

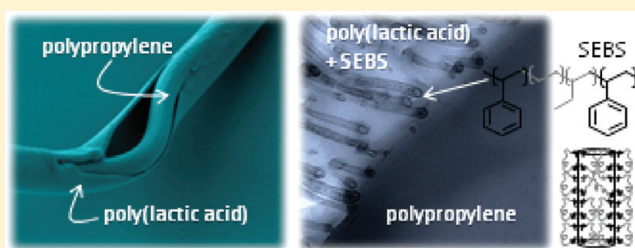
Sara A. Arvidson,[†] Kristen E. Roskov,[†] Jaimin J. Patel,[†] Richard J. Spontak,^{†,‡} Saad A. Khan,^{*,†} and Russell E. Gorga^{*,§}

[†]Department of Chemical & Biomolecular Engineering, North Carolina State University, Raleigh, North Carolina 27695, United States

[‡]Department of Materials Science & Engineering, North Carolina State University, Raleigh, North Carolina 27695, United States

[§]Department of Textiles Engineering, Chemistry & Science, North Carolina State University, Raleigh, North Carolina 27695, United States

ABSTRACT: While numerous studies have investigated the effect of adding a block copolymer as a macromolecular surfactant to immiscible polymer blends, no such efforts have sought to alter the properties of melt-spun bicomponent core–sheath filaments with a nonreactive compatibilizing agent. In this study, we examine the effect of adding poly[styrene-*b*-(ethylene-*co*-butylene)-*b*-styrene] (SEBS) triblock copolymer to core–sheath filaments consisting of isotactic polypropylene (iPP) and poly(lactic acid) (PLA). Incorporation of the copolymer into blends of iPP/PLA is observed to reduce the size scale of phase separation. Interfacial slip between molten iPP and PLA layers is evaluated by rheology under steady-shear conditions. Addition of SEBS to the PLA sheath during filament formation reduces the tendency of PLA sheaths to crack prior to iPP core failure during tensile testing. In reversed filament configurations, the copolymer does not hinder the development of molecular orientation, related to fiber strength, during fiber spinning. Electron microscopy reveals that the copolymer molecules form unique, highly nonequilibrium morphologies under the spinning conditions employed here.



INTRODUCTION

Polymers produced from sustainable resources are expected to become increasingly important as petroleum feedstocks become less secure. Polylactide, or poly(lactic acid), (PLA) is produced from lactide monomer, which is obtained from agricultural rather than petroleum raw materials and is especially interesting because it is also biocompatible and biodegradable. Currently PLA is used in sutures, medical devices, and food packaging films.¹ It is a fiber-forming polymer with high tensile strength² but suffers from brittleness and low ductility,³ poor gas barrier properties,⁴ and hydrolysis at temperatures suitable for melt processing, dyeing, or laundering.^{5–7} Cospinning PLA with a second polymer provides a route to overcome these challenges by producing bicomponent fiber with suitable mechanical properties.

Bicomponent filament spinning involves the coextrusion of two polymers (or polymer blends) from the same spinneret into a single filament that consists of both starting materials. This type of spinning can be configured in a variety of cross-sectional geometries such as core–sheath, side-by-side, segmented pie, islands-in-the sea, or tipped trilobal.^{8–10} In this study, we only consider further the core–sheath arrangement. The benefits of cospinning two polymers include a reduction in the cost associated with using less of a more expensive polymer to obtain the same desirable characteristics or adding an expensive additive to only the sheath polymer, exploiting the lower

melting point of a polymer spun in the sheath to promote bonding without a disruption in the morphology of the core component, improving the tactile quality of fabrics made from a spinnable polymer (sheath) with a polymer of poor spinnability (core), and suppression of an unfavorable rheological behavior (e.g., spinning a polymer behaving as a Newtonian liquid with a small fraction of a desirable polymer exhibiting Maxwell properties).¹¹ Moreover, since the viscoelasticity of the sheath polymer dictates the mechanics of melt flow during coaxial spinning even if its flow rate and viscosity are lower than those of the core polymer, core–sheath bicomponent fibers may be significantly thinner than would otherwise be achieved by spinning the polymers individually.¹¹ Lastly, while the bicomponent spinning of two polymers permits retention of component properties, comparable spinning of premixed polymer blends generally results in properties that lie intermediate between those of the individual components, thus compromising the net properties of the fibers.¹²

Isotactic polypropylene (iPP) constitutes an excellent choice for cospinning with PLA to impart improved mechanical properties; resistance to abrasion, solvents and biological agents (if iPP is the sheath component); and low cost. Furthermore,

Received: October 6, 2011

Revised: December 14, 2011

Published: January 3, 2012

iPP melts and can be processed at the same temperatures as PLA and can be viscosity-matched to PLA. Conversely, PLA provides a route to surface functionalize iPP, which is otherwise inert to many postspinning treatment processes available to other polymers, reduce fossil fuel consumption and greenhouse gas emission per mass of filament produced,¹³ impart hydrophilicity, and direct the development of molecular orientation within iPP during fiber formation.¹⁴

Depending on the thermodynamic compatibility of the polymers involved, bicomponent spinning can result in filaments or fibers (used interchangeably throughout text) that fail by splitting when subjected to an external mechanical force.¹⁵ While splittable fibers may be desired in the manufacture of synthetic suede and leather, technical wipes, and some filtration applications,^{16–18} good adhesion between the individual species comprising bicomponent fibers is required for maintaining mechanical integrity, developing sutures, or improving chemical or flammability resistance.^{19–22} At the interface separating immiscible polymers, a relatively low population of entanglements can lead to fiber delamination at temperatures below the melting temperatures (T_{ms}) of both components. Above the T_m of each component, subjecting immiscible polymers to external forces may result in “slip” of one molten polymer across the other. Evaluating the presence of slip and, by inference, the adequacy of interfacial chain entanglements in the melt remains a nontrivial task. Zhao and Macosko²³ have deduced that slip of multilayered samples occurs when a drop in viscosity accompanies an increase in the number of layers and, hence, interfacial contact area. Jiang²⁴ has similarly interpreted that a viscosity below the theoretical viscosity discerned from the reciprocal rule of mixtures (R-ROM) for layered high-density polyethylene/polystyrene (HDPE/PS) is indicative of slip. Slip has also been proposed as the cause for the viscosity discontinuity encountered while shearing layered HDPE/PS filled with tracer particles and observing the layers *in situ* with confocal microscopy.²⁵ Park et al.²⁶ have likewise investigated multilayer slip by using a sliding plate rheometer equipped with a camera.

Block copolymers, composed of two or more long, covalently linked sequences of chemically dissimilar repeat units, may be used to lower interfacial tension along polymer–polymer interfaces and thus improve adhesion by promoting chain entanglements. The apparent results of such compatibilization are net reductions in slip during extrusion and delamination in formed fibers.^{27,28} Generally speaking, compatibilization is considered to be effective if an added block copolymer reduces the size scale of phase domains and/or enhances the mechanical properties of a blend.^{12,29,30} The stabilizing efficacy and spatial segregation of premade block copolymer molecules along polymer–polymer interfaces have been previously addressed by Wei et al.³¹ and more recently by Gozen et al.³² Alternatively, reactive compatibilization of polymer blends can be induced through the use of species that react along the polymer–polymer interface to form block copolymers *in situ*.³³ In this spirit, blends of iPP and PLA have been modified with a maleic anhydride (MA)-grafted copolymer, which has been shown³⁴ to increase the impact strength of the resultant alloy. Similarly, iPP-g-MA has also been reported³⁵ to reactively cross-link core–sheath and side-by-side bicomponent fibers composed of nylon-6 and iPP. The concept of compatibilizing polymer–polymer interfaces that are not blended but rather contacted, such as those involved in core–sheath fibers or laminates, with premade block copolymers has largely been

ignored. To the best of our knowledge, no prior studies investigating the core–sheath compatibilization of bicomponent fibers by the addition of a block copolymer to one component have been reported.

During large-scale mechanical deformation, melt-spun bicomponent fibers composed of iPP and PLA are observed to possess interfacial voids that extend up to millimeters in length along the fiber axis. These voids are attributed to inherently poor interfacial adhesion between iPP and PLA.¹⁵ In this work, we endeavor to compatibilize and thus improve the mechanical properties of these two nonblended polymers by incorporating a triblock copolymer during melt spinning. In addition to filament property assessment, the morphology of the block copolymer in filaments is compared to that formed during melt mixing without extrusion to elucidate the effect of high-shear spinning on block copolymer structuration. Electron microscopy reveals that unique, nonequilibrium copolymer morphologies are generated during bicomponent filament spinning. We also discuss the application of steady-shear rheological methods to evaluate slip at layered iPP–PLA interfaces and the effect of adding the block copolymer.

■ EXPERIMENTAL SECTION

Materials and Specimen Preparation. The iPP and PLA were provided by Sunoco Chemicals (Pittsburgh, PA; CP360H) and NatureWorks (Minnetonka, MN; 6202D), respectively. A premixed compound containing a poly[styrene-*b*-(ethylene-*co*-butylene)-*b*-styrene] (SEBS) triblock copolymer with 18.6 wt % styrene (according to the manufacturer) and an overall molecular weight of 67 kDa (according to independent size exclusion chromatography) was supplied by Kraton Polymers (Houston, TX). While the identity of the compounding material is proprietary, it is midblock-selective, which indicates that it is more aliphatic than aromatic in nature. We do not, however, discount the possibility that the compounding species (hereafter referred to as the “midblock extender”) may be partially unsaturated, unlike the EB midblock of the copolymer. Reagent-grade dichloromethane (DCM) was purchased from Mallinckrodt Chemicals (Phillipsburg, NJ) and used as received.

Single and bicomponent filaments were melt-spun at various aspirator pressures on the Partners’ Pilot Spunbond line located in the Nonwovens Cooperative Research Center at North Carolina State University. All filaments examined here were spun with a total mass throughput of 0.4 g/(hole min) at a fiber composition of 50/50 (w/w) core/sheath. In select cases, 5 wt % of the PLA (2.5 wt % of the total mass) was replaced with the SEBS copolymer. In these instances, the PLA and copolymer were melt-compounded and coextruded. Confluence of the molten PLA (or PLA + SEBS) and iPP occurred in the spin pack. Below the spin pack, bicomponent filaments were directed through the quench zone to an attenuation zone, where the aspirator pressure controlled the air velocity around the fibers and effectively the fiber spinning velocity. Nonbonded fibers were collected immediately following extrusion so that the as-spun fiber morphology could be examined. Fiber diameters were used to calculate the “spinning velocity” (V) at the point where the fibers solidified according to

$$V = \frac{Q}{\rho A_c} \quad (1)$$

where Q is the mass flow rate of polymer per spinneret hole, ρ is the fiber mass density, and A_c is the cross-sectional area of the fiber. For comparison with the bicomponent fibers, corresponding polymer blends (50/50 wt % iPP/PLA; 50/47.5/2.5 wt % iPP/PLA/SEBS) were prepared using a Haake-Buchler HBI System 90 twin-screw melt mixer operated at 185 °C. iPP/PLA blends with and without SEBS were immersed in DCM for ~100 h under constant agitation at ambient temperature to selectively dissolve the PLA for morphological evaluation.

Specimen Characterization. X-ray diffraction (XRD) studies were conducted on a Bruker D-5000 diffractometer (Madison, WI) equipped with a Highstar area detector and using Cu K α radiation ($\lambda = 0.1542$ nm) at 40 kV and 30 mA. Resultant 2-dimensional XRD patterns were normalized with respect to an empty sample holder and analyzed with the Bruker General Area Detector Diffraction System (GADDS) software. Mechanical testing of fibers was conducted at ambient temperature on an Instron Model 5544 extensometer (Norwood, MA) fitted with a 5 N load cell. Single filaments with a gauge length of 28.6 mm were strained at a constant crosshead speed of 25.4 mm/min. Data were analyzed with the Bluehill v.2 software package, and a constant volume cylinder was assumed to calculate true stress. Representative stress–strain curves were obtained for specimens prepared at different fiber configurations and pressures after at least 10 trials. Optical microscopy of bicomponent fibers was performed on a Mach–Zehnder type interference microscope by Aus Jena (Jena, Germany) with polarized light ($\lambda = 546$ nm), and digital images were collected on a CCD camera for birefringence analysis. Both scanning and transmission electron microscopies (SEM and TEM, respectively) were employed to explore the morphologies of the fibers and blends prepared here. After using DCM to dissolve the PLA from melt-processed iPP/PLA blends, the remaining iPP matrix was sputter-coated with ~ 10 nm of Au and subsequently analyzed by SEM performed in an environmental FEI XL-30 microscope operated under high vacuum at 5 kV. The average size and standard deviation of the pores introduced by extracting PLA were discerned by measuring the diameter of 100 pores using the ImageJ software suite.

For complementary TEM examination of the block copolymer morphology, fibers were conformally sputter-coated with 30 nm of Au (as a barrier layer to avoid fiber contamination), embedded in epoxy, and microtomed at ambient temperature on a Leica UltraCut 7 with a diamond knife. Resultant sections were stained for 7 min with the vapor of 0.5% RuO $_4$ (aq), which is a selective stain for the phenyl groups on the S blocks of the SEBS copolymer. Cross-sectional TEM images were acquired on a field-emission Hitachi HF2000 microscope operated at an accelerating voltage of 200 kV. Average microdomain sizes and their corresponding standard deviations were determined by measuring 50–100 features of interest, unless otherwise noted, using ImageJ.

The zero-shear viscosities of the iPP and PLA homopolymers with and without copolymer, as well as multilayered samples thereof, were measured at 185 °C under nitrogen on a TA Instruments AR-G2 rheometer equipped with parallel plates measuring 25 or 40 mm in diameter. Multilayered specimens consisted of 1, 2, 4, or 8 alternating layers of iPP and PLA. Dynamic rheology was likewise performed on the same instrument operated at 185 °C with 25 mm plates and a 1 mm gap. Differential scanning calorimetry (DSC) was conducted on a TA Instruments Q2000 model calorimeter calibrated to an indium standard. Scans were carried out at heating rates of 10 °C/min under 50 mL/min N $_2$ purge with samples of ~ 10 mg in standard aluminum pans.

RESULTS AND DISCUSSION

Bicomponent iPP/PLA Fibers. Lipscomb³⁶ predicts that, for situations wherein the core polymer undergoes a greater increase in viscosity during cooling than the sheath polymer, the core polymer bears more of the spinline tension, which we hasten to add can serve to enhance crystallization and molecular orientation. Similarly, Kikutani¹⁹ reports that the solidification temperature and viscosity disparities in cospun polymers constitute the main factors influencing the “mutual interactions” of the constituent polymers. This conclusion is interpreted to relate to the ability of one polymer to direct or influence the crystallization and molecular orientation of the other polymer. On one hand, we find that the crystallization of PLA is not strongly influenced by its location (i.e., core or sheath) in bicomponent fibers, as seen in Figure 1. (Representative XRD reflections for iPP/PLA bicomponent fibers are available in our previous work.¹⁵) The iPP crystal morphology, on the other hand, is sensitively affected by the

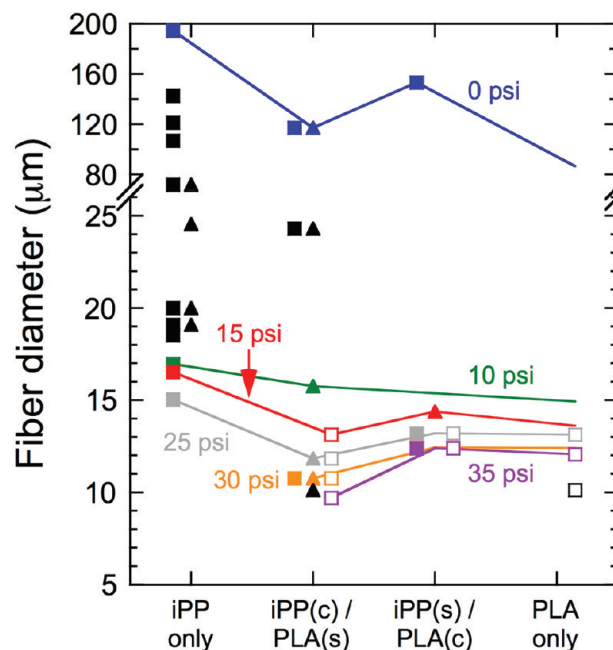


Figure 1. Filament diameter and polymer morphology as functions of aspirator pressure and fiber configuration, denoted by core (c) and sheath (s). While all filaments are at least partially amorphous, only crystalline or otherwise ordered morphologies are identified by symbols if present: α -crystalline iPP (filled squares), mesomorphic iPP (filled triangles), and α -crystalline PLA (open squares). Filaments spun at the same aspirator pressure with different configurations are connected by solid lines (color-coded and labeled).

fiber configuration. Our observation that iPP tends to crystallize in the sheath but not in the core, coupled with the results of Lipscomb³⁶ and our previous study³⁷ on the quiescent and stress-induced crystallization of iPP, suggests that iPP crystallization is due to exposure to the quench air while in the sheath and is not stress-induced while in the core. The presence of the iPP mesomorphic phase for most spinning velocities indicates an absence of high tension on the iPP core when cospun with a PLA sheath. (This may reflect the comparable melting temperatures and zero-shear viscosities of iPP and PLA, as listed in Table 1.) In marked contrast, Kikutani et al.¹⁹ have demonstrated that cospinning iPP with poly(ethylene terephthalate) (PET) into bicomponent iPP_{sheath}/PET_{core} fibers results in sheaths that do not solidify in the draw zone and fibers that could not be drawn as finely as either constituent polymer. The difference in melting points between iPP and PET is significantly greater (~ 100 °C) than

Table 1. Physical Properties of the Polymers Employed in This Study

polymer	T_m^{38} (°C)	zero-shear viscosity at 185 °C (Pa·s)	surface free energy ³⁹ at 20 °C (dyn/cm)	solubility parameter ^{40,41} (cal/cm ³) ^{1/2}
iPP	165 ^a	901 ^a	30.1	7.4
PLA	161 ^a	591 ^a	39.3	12.1
SEBS copolymer		6980 ^a		
atactic polystyrene			40.7	9.5
low-density polyethylene			35.3	8.0
polybutylene			33.6	7.8

^aProperty was measured in the present study.

that between iPP and PLA; this problem is not encountered here because the melt viscosities and thermal transitions of iPP and PLA are sufficiently similar so that neither polymer significantly influences the rheological properties or solidification behavior of the other compared to each polymer when spun individually.

According to the results displayed in Figure 1, an increase in aspirator pressure (and, correspondingly, spinning velocity) is generally accompanied by a reduction in fiber diameter that is significant from 0 to 10 psi for both single-component and bicomponent fibers. At a given aspirator pressure, the diameters of bicomponent fibers are often marginally lower than the fiber diameters of either polymer spun individually. This observation, along with the inherent thermodynamic incompatibility between iPP and PLA (discussed further in the next section), implies that the iPP/PLA interface may slip at high spin speeds, which occur at high shear rates. We return to address the occurrence of slip between molten iPP and PLA, as determined by rheology, later. Addition of the SEBS copolymer to PLA in bicomponent fibers is expected to influence the iPP/PLA interface and, by inference, the fiber morphology. Figure 2

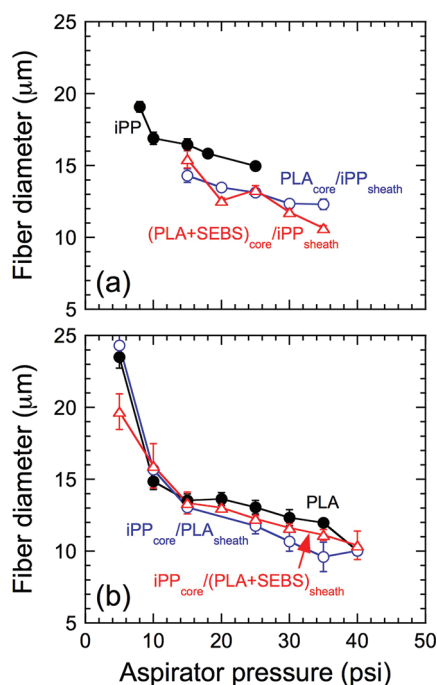


Figure 2. Filament diameter as a function of spinning pressure for different fiber configurations: (a) iPP only and iPP in the sheath (with PLA in the core) and (b) PLA only and PLA in the sheath (with iPP in the core). Homopolymers, bicomponent fibers without copolymer, and bicomponent filaments with copolymer are color-coded black, blue, and red and are correspondingly labeled. Error bars indicate the standard error in the data from ~10 trials, and the solid lines serve to connect the data.

shows the fiber diameters of bicomponent fibers cospun with and without copolymer. As is evident in Figures 1 and 2, an increase in aspirator pressure generally promotes a decrease in fiber diameter. Compared to iPP spun alone, finer fibers result from cospinning an iPP sheath around a PLA core (Figure 2a), but the addition of copolymer appears to have a nonsystematic effect on fiber diameter. With PLA as the

sheath (Figure 2b), bicomponent fibers are slightly smaller in diameter at moderate spin speeds, and the addition of copolymer has little statistical effect on fiber diameter over the conditions examined.

Compatibilized iPP/PLA Blends. The interfacial energy between iPP and PLA is related to the surface energy of each polymer according to Antonoff's rule:

$$\gamma_{\text{iPP-PLA}} = |\gamma_{\text{iPP}} - \gamma_{\text{PLA}}| \quad (2)$$

From eq 2, the interfacial energy between iPP and PLA is estimated to be about 9 dyn/cm.^{42,43} On the basis of the infinite-molecular-weight surface energies of the copolymer constituents (included in Table 1), addition of a SEBS block copolymer to an iPP/PLA blend lowers the interfacial tension at both the iPP-EB interface (3–5 dyn/cm) and the PS-PLA interface (~1 dyn/cm). Although Antonoff's rule is overly simplistic for many systems, it has been shown⁴⁴ to accurately describe the interfacial energy between PS and PLA. The interfacial energy provides a measure of thermodynamic incompatibility between two dissimilar species and contributes to the enthalpic portion of the system free energy. As such, it relates directly to the Flory-Huggins χ interaction parameter^{45–47} and, by extension, to the corresponding difference in solubility parameters between the two species. The solubility parameters of all polymer species of interest here are also listed for comparison in Table 1. Solubility parameters are often used to estimate the compatibility of two polymers insofar as the species are relatively nonpolar and mixing is endothermic. While there is no general guideline for predicting polymer-polymer miscibility from solubility parameters alone,³⁹ polymer pairs with nearly identical solubility parameters are more likely to be mutually miscible than those with even modestly different solubility parameters, regardless of their chemical constitution.⁴⁸ On the basis of their solubility parameters, the EB midblock of the copolymer should be compatible with iPP, whereas the S endblocks of the copolymer are not expected to show much preference for either iPP or PLA. We cannot comment much on the compatibility of the midblock extender in the copolymer, but it stands to reason that, since it is mixed with the EB midblock, it, too, will be compatible with iPP.

To discern if the SEBS copolymer compatibilizes iPP/PLA blends, we examine the morphologies of blends composed of 50 wt % iPP. Figure 3a displays a cross-sectional SEM image of a melt-mixed iPP/PLA blend after removal of the dispersed PLA phase upon selective-solvent exposure in DCM at ambient temperature. The diameter of the PLA domains (appearing as pores) is measured to be $5.0 \pm 2.9 \mu\text{m}$. Replacing 5 wt % of the PLA with SEBS is found to reduce the PLA domain diameter to $1.4 \pm 1.3 \mu\text{m}$ (cf. Figure 3b), which confirms that the copolymer effectively compatibilizes the iPP/PLA blends at this concentration, as anticipated from the thermodynamic considerations discussed above. It immediately follows that, if the copolymer molecules can locate along the interface between iPP and PLA, they should reduce slip (if it exists) during extrusion and improve the adhesion between iPP and PLA. Therefore, 2.5 wt % SEBS (5 wt % of the PLA phase) was also used for fiber-spinning experiments. It is of interest to note here that dissolution of the precompounded SEBS in DCM at a concentration of 5 wt % results in the formation of a cloudy solution that appears to remain stable to the unaided eye for several months at ambient temperature. We believe that the observed solution opacity arises from the self-organization of copolymer molecules into swollen micelles (spherical

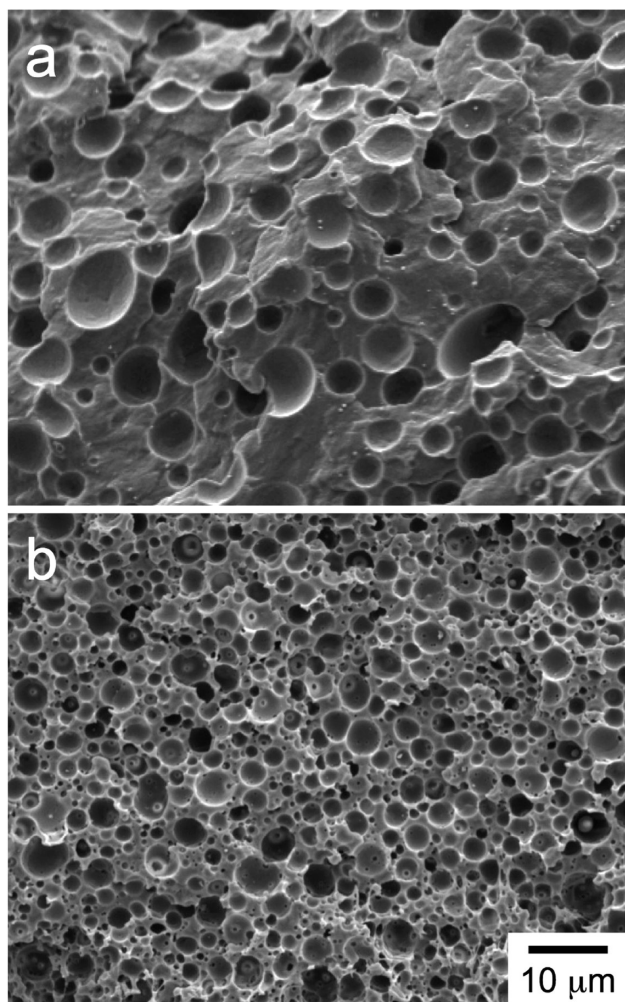


Figure 3. Cross-fracture SEM images of melt-mixed blends: (a) 50/50 w/w iPP/PLA and (b) 50/47.5/2.5 iPP/PLA/SEBS. The PLA is selectively removed upon immersion in DCM for ~100 h at ambient temperature.

microemulsions) or vesicles⁴⁹ that are sufficiently large to scatter light and encapsulate the midblock extender, which is most likely incompatible with DCM. A detailed account of this solution nanostructure is, however, beyond the scope of the present work.

Multilayer Melt Rheology. Various polymer pairs such as PS/poly(methyl methacrylate), PS/HDPE, PS/iPP, PE/fluoropolymer, and iPP/nylon-6 exhibit incompatibility-induced slip during rheological testing of layered specimens.^{23,24,26} Layered specimens are more representative of the present bicomponent fibers than are blends because the two polymer species are melt-contacted along an artificially introduced interface rather than along multiple interfaces that develop *in situ* due to thermodynamic instability. Generally speaking, “slip”, or negative viscosity deviation, tends to increase with increasing polymer–polymer incompatibility. To determine whether iPP and PLA undergo slip during extrusion, rheological testing has been conducted on alternating multilayers of iPP and PLA. As illustrated in Figure 4, these sandwich structures are first positioned on the bottom flat plate of the rheometer, and then the top plate of the rheometer is lowered until it contacts the top polymer layer. We have measured the shear viscosity of molten polymer multilayers as a function of

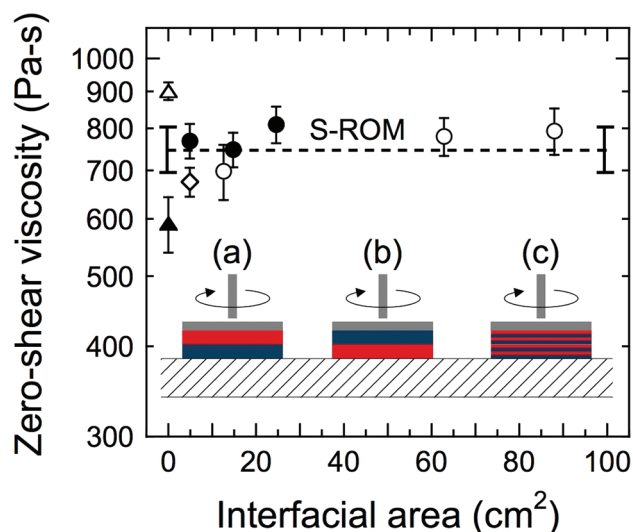


Figure 4. Zero-shear viscosities of iPP/PLA multilayers in different test configurations: PLA on the bottom with either 25 (●) or 40 (○) mm plates or iPP on the bottom with 25 mm plates (◇). Included are the individual viscosities of iPP (△) and PLA (▲). The error bars denote the standard error in the data, and the dashed line corresponds to the S-ROM prediction. The uncertainty of the prediction is based on the standard deviation of the neat iPP and PLA viscosities used to calculate the viscosity of the multilayers. Included are schematic illustrations of the iPP/PLA multilayers: (a) PLA (blue) on bottom, (b) iPP (red) on bottom, and (c) 8 alternating layers.

interfacial area, which is controllably manipulated by increasing the number of alternating layers, as well as the size of the plates. The zero-shear viscosities of these multilayers are presented as a function of interfacial area in Figure 4. To put these results into perspective, a melt-spun bicomponent fiber with an average inner diameter of 20 μm and measuring 1 m long would possess an interfacial area of $\sim 0.6 \text{ cm}^2$. Despite the greater incompatibility between iPP and PLA as compared to other polymer pairs, no significant decrease in viscosity is detected with increasing interfacial area up to an interfacial area of $\sim 90 \text{ cm}^2$, thereby indicating that slip between iPP and PLA is not detected by steady-shear rheology at stresses below $\sim 1 \text{ kPa}$.

One reason for the absence of slip in this work may be due to the low shear rates accessible with a parallel-plate rheometer relative to capillary rheometers or fiber extrusion. Slip first becomes apparent, for instance, at interfacial areas between 34 and 152 cm^2 at shear stresses above 1 kPa for multilayers composed of iPP and PS.²³ Inertial forces cause the polymer to flow from the plates at stresses above 1 kPa, thereby resulting in poor data quality. Smaller parallel plates exacerbate this problem. Alternatively, we consider the manner by which previous studies concluded the existence of slip. While viscosities are reported,^{23,24} the deviation from predicted “no-slip” conditions is often small. Because of the large variation in viscosity encountered in each sample, we have chosen to repeat each measurement seven times in this work. Jiang et al.²⁴ have reported the viscosity of a PS/HDPE bilayer with an interfacial area of about 5 cm^2 to be 11% lower than the reciprocal rule of mixtures (R-ROM). On the basis of this comparison, they conclude this deviation is representative of slip. To discern the validity of this criterion, we apply several rules of mixtures to the data in Figure 4. The first is the R-ROM, which has been used to predict the viscosity of multilayered specimens

composed of two polymers (indicated by subscripts 1 and 2). It is given by

$$\frac{1}{\eta} = \frac{\phi_1}{\eta_1} + \frac{\phi_2}{\eta_2} + \frac{\phi_i}{\eta_i} \quad (3)$$

where the subscripted i corresponds to the interfacial layer, which has few polymer entanglements and potentially lower viscosity.⁵⁰ In eq 3, η is the measured viscosity of the multilayer, ϕ_1 and ϕ_2 are the volume fractions of polymers 1 and 2, respectively, and η_1 and η_2 are the viscosities of polymers 1 and 2, respectively, measured individually. Since no difference in viscosity is evident in Figure 4 up to an interfacial area of $\sim 90 \text{ cm}^2$, this interfacial layer contribution is neglected.

Alternatively, other rules of mixtures should be considered. For example, the standard rule of mixtures (S-ROM) predicts viscosity according to

$$\eta = \phi_1 \eta_1 + \phi_2 \eta_2 \quad (4)$$

Moreover, a logarithmic rule of mixtures (L-ROM) has also been proposed for polymer blends, viz.⁵¹

$$\log \eta = \phi_1 \log \eta_1 + \phi_2 \log \eta_2 \quad (5)$$

Other rules include additional terms that attempt to explain deviations from the three provided in eqs 3–5 and are not considered here. The multilayer viscosity averaged over all the interfacial areas in Figure 4 is $754 \text{ Pa}\cdot\text{s}$, whereas those predicted by eqs 3–5 are 714 (R-ROM), 746 (S-ROM), and 729 $\text{Pa}\cdot\text{s}$ (L-ROM). Thus, the S-ROM most closely predicts the viscosity of our multilayered samples, while the R-ROM is found to give the poorest prediction of the three. The standard errors of the PLA and iPP viscosities used in the ROM predictions are 9 and 3%, respectively, which suggests that measured multilayer viscosities deviating modestly (by 11% according to Jiang et al.²⁴) from predicted values are not statistically significant in systems composed of iPP and PLA. The relatively large variation in measured multilayer and pure-component viscosities encountered here is indicative of the difficulty in confirming the existence of interfacial slip between iPP and PLA on a parallel-plate rheometer.

Fiber Mechanical Properties. The interface, which is largely responsible for the mechanical properties of bicomponent fibers (as well as fibers derived from polymer blends), is known¹⁵ to fail during the mechanical drawing of bicomponent fibers spun from iPP and PLA. To reduce the inherent incompatibility between iPP and PLA, the SEBS copolymer is compounded with PLA before iPP and PLA are cospun. When PLA with and without copolymer is spun as the core (Figure 5a), the tenacity of the bicomponent fibers increases with increasing aspirator pressure up to a level near 2 cN/dtex . Incorporation of the copolymer has no systematic effect, positive or negative, on these results. Recall from Figure 1 that the PLA and iPP are both semicrystalline in this fiber configuration. If the fibers are spun with an iPP core and PLA sheath, a similar dependence on aspirator pressure is seen (Figure 5b), but the maximum level attained is slightly lower for fibers with PLA only and lower still (but within experimental uncertainty) for fibers with a mixture of PLA + SEBS. In this configuration, the PLA is semicrystalline, but the iPP is, for the most part, mesomorphic. Recall that, while the EB midblock of the SEBS copolymer is compatible with iPP, the S endblocks are not expected, on the basis of solubility parameters alone, to be strongly iPP- or PLA-compatible.

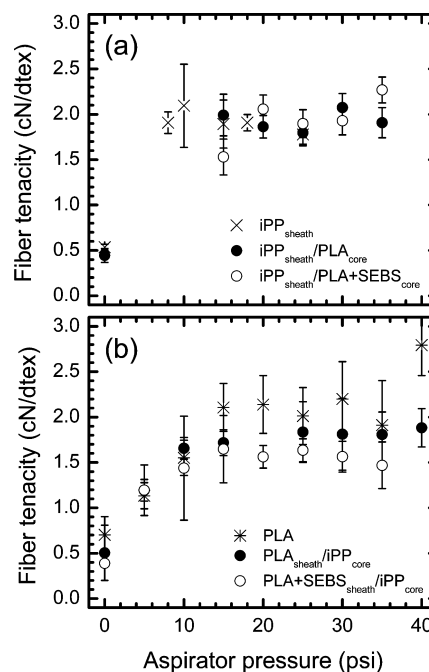


Figure 5. Dependence of tenacity of iPP, PLA, and bicomponent iPP/PLA filaments on aspirator pressure for two different fiber configurations identified by the location of the iPP: (a) sheath and (b) core. Open and filled symbols identify specimens with and without added SEBS copolymer, respectively. Error bars indicate the standard error in the data from ~ 10 trials.

Blending incompatible polymers into bicomponent fibers is expected to decrease fiber strength due to enlarged interfacial area and reduced interfacial strength. Yet, addition of the SEBS copolymer to PLA as the core (Figure 5a) or sheath (Figure 5b) does not compromise the mechanical properties of the fibers, indicating that the copolymer (with midblock extender) and PLA are not strongly incompatible.

At the lowest aspirator pressure (fiber spinning velocity) in Figure 6, addition of copolymer into the PLA sheath is

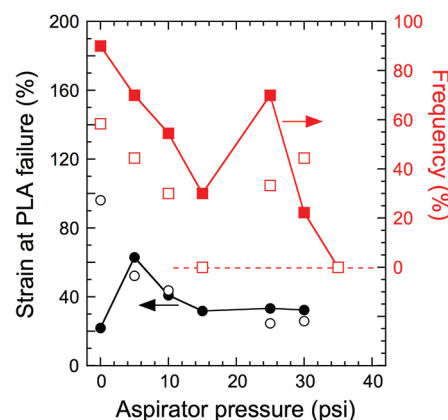


Figure 6. (left axis) True strain at which the sheath of $\text{iPP}_{\text{core}}/\text{PLA}_{\text{sheath}}$ bicomponent filaments with (○) and without (●) added SEBS copolymer fail as a function of aspirator pressure. (right axis, red) Frequency of PLA sheath failure prior to iPP core rupture with (□) and without (■) added copolymer. The solid lines serve to connect the data of systems without copolymer.

observed to increase substantially the strain at which rupture of the sheath occurs. As the aspirator pressure is increased,

however, the strain at which PLA ruptures does not appear to be dependent on copolymer addition. Note that not all fibers undergo failure of the PLA sheath at lower strains than the iPP core. Rather, in these cases, a single catastrophic failure signals nearly simultaneous rupture of both polymers. Such events are accompanied by an abrupt increase in the true strain at break of the fibers. By adding the SEBS copolymer to PLA, the frequency at which the PLA sheath ruptures prior to failure of the iPP core is reduced at most aspirator pressures (cf. Figure 6), which indicates that the SEBS-modified PLA is capable of undergoing greater extension prior to failure. In the event that the PLA sheath does not fail before the iPP core (i.e., the sheath and core corupture) in any of the tested specimen, the frequency in Figure 6 is shown as 0%. While the T_g (Figure 7) and melt viscoelasticity (Figure 8) of PLA are not greatly

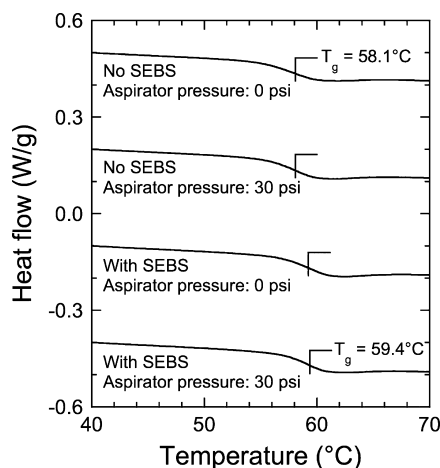


Figure 7. Series of DSC thermograms collected at a cooling rate of $10^\circ\text{C}/\text{min}$ from iPP_{core}/PLA_{sheath} bicomponent filaments with and without SEBS copolymer added to the PLA phase at two aspirator pressures (labeled). The location of the PLA T_g in each system is marked.

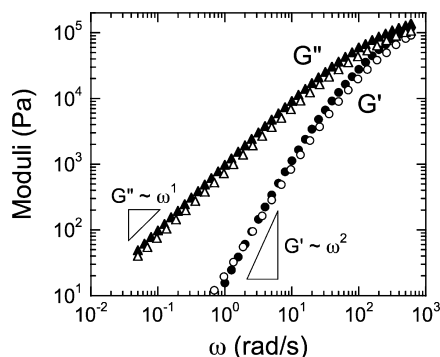


Figure 8. Frequency (ω) spectra of the dynamic moduli (G' , circles; G'' , triangles) measured from PLA (filled symbols) and PLA blended with 5 wt % SEBS (open symbols) at 185°C and a stress of 5 Pa (in the linear viscoelastic limit). Shown for comparison are the scaling relationships expected for G' and G'' in the low- ω (terminal) region for entangled homopolymers.

affected by the incorporation of SEBS, the elastomeric nature of the copolymer, coupled with its intrinsic ability to self-organize into nanostructural elements, may serve to improve the elasticity of the PLA sheath, which, in turn, promotes an increase in the strain at which the PLA sheath ruptures. In

Figure 7, addition of the SEBS copolymer alters the T_g of PLA by just over 1°C , which is considered to be within instrumental uncertainty. The melt frequency (ω) spectra displayed in Figure 8 show little variation upon addition of the SEBS copolymer to PLA. In both cases, the dynamic loss modulus (G'') scales as $\omega^{1.0}$ in the terminal region, which agrees with the behavior of entangled homopolymers (ω^1). The analogous scaling behavior of the dynamic storage modulus (G'), which is ω^2 for entangled homopolymers, changes upon copolymer addition from $\omega^{1.9}$ to $\omega^{1.6}$. While this subtle reduction in slope may signify a copolymer-induced change in the molten structure, it is reasonable to expect that such a change might be more apparent in the solid state (where the styrenic endblocks are glassy) than in the melt. The copolymer-induced reduction in the frequency of PLA rupture at low strains may also indicate improved adhesion along the iPP/PLA interface, which would promote greater stress transfer to the iPP core and permit the PLA to support a higher stress before rupturing.

Previously, some of us have introduced¹⁵ a facile optical method for estimating the molecular orientation of bicomponent core/sheath fibers from true stress–true strain curves when the refractive indices of the core and sheath polymers significantly differ. Figure 9 shows the progression of matching

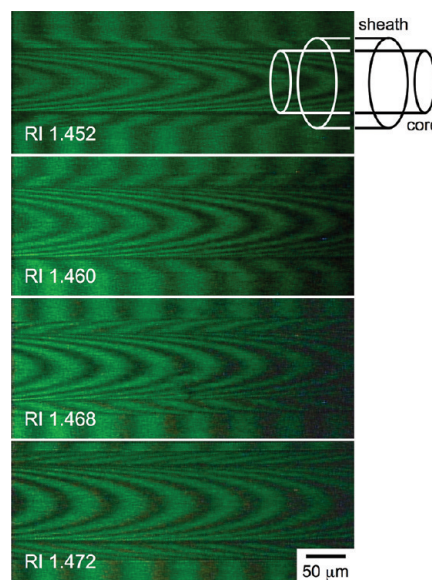


Figure 9. Optical micrographs of iPP_{core}/PLA_{sheath} bicomponent filaments (see schematic diagram) digitally recorded under polarized light to measure the birefringence according to ref 52. The measured birefringence can be related to molecular orientation and, thus, mechanical properties, as described elsewhere.^{53,54} The refractive index (RI) provided on each image corresponds to that of the liquid surrounding the filament.

a fiber with an iPP core and PLA sheath to liquids of known refractive index so that the birefringence of the sheath, which is related to molecular orientation and fiber strength, can be determined. These images confirm that the conformal PLA sheath completely wets the iPP core. The liquid surrounding the fiber must possess a refractive index (RI) that is similar to those of the two species in the fiber to yield clear fringes (dark bands) that can be followed through each interface. Because the refractive indices of the iPP core and PLA sheath are considerably different (1.504 and 1.542, respectively, at 20°C

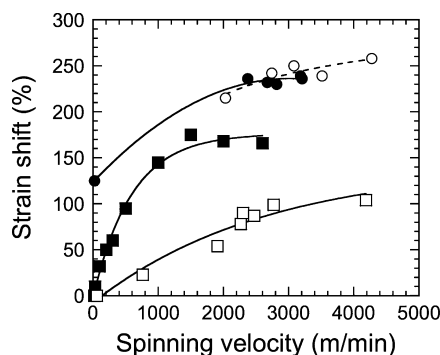


Figure 10. Dependence of the strain shift of iPP (■), PLA (□), $\text{PLA}_{\text{core}}/\text{iPP}_{\text{sheath}}$ (●), and $\text{PLA} + \text{SEBS}_{\text{core}}/\text{iPP}_{\text{sheath}}$ (○) filaments on spinning velocity. The lines serve as guides for the eye.

for unoriented samples), no single liquid can provide clear fringes for both the core and sheath simultaneously, which explains why the fringes blur at the core–sheath and/or sheath–liquid interface in each of the images in Figure 9. In addition, while the interface of unstrained fibers appears continuous for the fibers in this study, birefringence measurements would be difficult or altogether impossible for strained $\text{iPP}_{\text{core}}/\text{PLA}_{\text{sheath}}$ fibers exhibiting voids at the polymer–polymer interface. Therefore, using the method described elsewhere,¹⁵ we estimate the molecular orientation of $\text{PLA}_{\text{core}}/\text{iPP}_{\text{sheath}}$ fibers with and without added SEBS copolymer using stress–strain curves.

The strain shift of single-component and bicomponent fibers, which relates proportionally to molecular orientation, is presented as a function of spinning velocity in Figure 10. Here, spinning velocity, rather than aspirator pressure, is used to

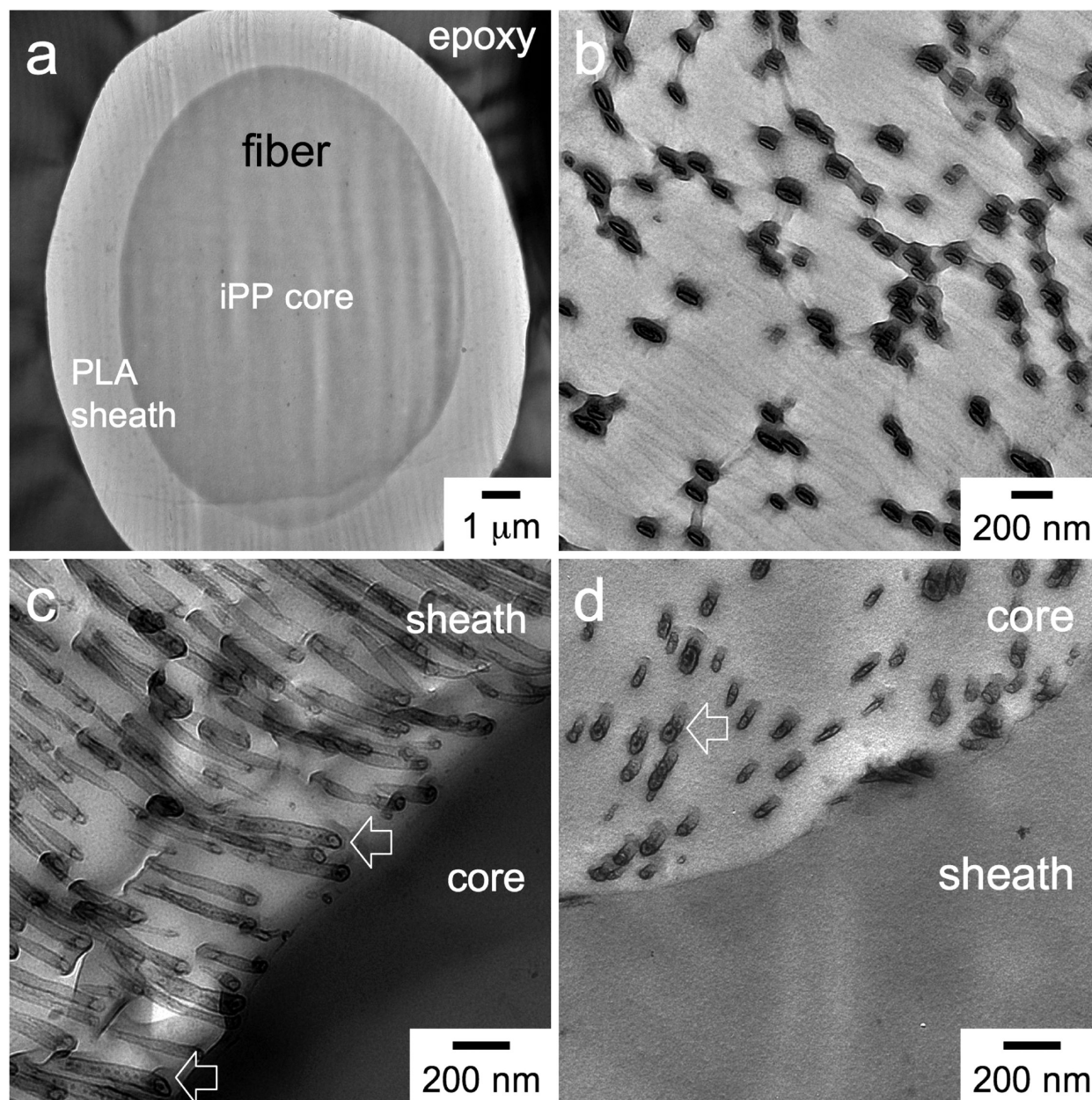


Figure 11. Cross-sectional TEM images of filaments in different configurations. In (a), an $\text{iPP}_{\text{core}}/\text{PLA}_{\text{sheath}}$ bicomponent filament coated in Au and embedded in epoxy (labeled) is shown. A PLA filament modified with 5 wt % SEBS copolymer is presented in (b). In (c) and (d), $\text{iPP}_{\text{core}}/(\text{PLA} + \text{SEBS})_{\text{sheath}}$ and $(\text{PLA} + \text{SEBS})_{\text{core}}/\text{iPP}_{\text{sheath}}$ bicomponent filaments are displayed. The styrene-rich copolymer nanostructures appear dark due to selective staining. In (c) and (d), the arrowheads identify a unique nanostructure: tubules with internal spheres (“peas in a pod”).

facilitate comparison of birefringence from fibers produced by other spinning methods, such as melt spinning or electrospinning, that do not require an aspirator pressure. Bicomponent fibers exhibit markedly increased strain shift relative to iPP and PLA alone, and addition of the SEBS copolymer to the PLA core does not inhibit molecular orientation in the iPP sheath. This observation is consistent with previous studies^{11,15} reporting that the sheath component dictates flow mechanics for core/sheath fiber extrusion, as well as the ultimate properties of bicomponent fibers, since the sheath component experiences the greatest stress in both the melt and solid phases. Spinning with an iPP sheath and a PLA (or PLA + SEBS) core serves to focus the spin-line stress over a smaller cross-sectional area, which results in higher molecular orientation in the iPP sheath. While the sheath component may control flow mechanics, the core polymer is crucial to achieve the synergistic effect of enhanced molecular orientation in the sheath polymer beyond that realized by spinning either polymer individually. The master stress-strain curve for PLA required in this methodology has been developed for PLA alone, not with SEBS copolymer. Therefore, we do not report strain shifts for iPP_{core}/PLA_{sheath} fibers with and without SEBS to avoid attributing effects introduced by SEBS to changes in PLA molecular orientation.

Nonequilibrium Copolymer Morphologies. The morphologies of triblock copolymers, such as the SEBS copolymer employed in this study, have been the subject of numerous studies. Most commercial triblock copolymers are designed as thermoplastic elastomers with dispersed glassy microdomains embedded in, and connected to, a continuous, rubbery matrix.⁵⁵ Addition of a midblock-selective oil,⁵⁶ tackifying resin,⁵⁷ or homopolymer⁵⁸ to a triblock copolymer can yield the same morphologies observed in diblock copolymer/homopolymer blends,^{59,60} in which case comparable design rules can be sensibly presumed. It immediately follows that, on the basis of the copolymer composition, the proprietary midblock extender added to the copolymer used here promotes a spherical or cylindrical morphology if the extender is largely or marginally miscible, respectively, with the EB midblock. Incorporation of the copolymer into PLA adds another level of complication, as the copolymer must now partition between the midblock extender and PLA as well as interact with iPP along the iPP-PLA interface. Under ideal equilibrium conditions of slow solvent evaporation or melt mixing, followed by extensive solvent or thermal annealing, the resultant copolymer morphology may be complex, depending on the individual strengths of six different binary interactions (assuming that the EB midblock and midblock extender can each be treated as a single species). If the rapid melt processing of the bicomponent fibers modified by the copolymer is now considered, highly nonequilibrium morphologies can be reasonably expected.

We begin with an overview of the morphologies of the SEBS copolymer in different fibers. Figure 11 shows a series of TEM images acquired from fibers varying in configuration, but spun at the same aspirator pressure (15 psi). In Figure 11a, a relatively low-magnification image of a bicomponent fiber composed of an iPP core and PLA sheath demonstrates that (i) the conformal Au coating around the edge of the fiber prevents swelling of the fiber with epoxy resin, which reacts with the vapor of RuO₄(aq), (ii) the iPP-PLA interface is clearly differentiated in cross section, and (iii) the iPP core is lightly stained. An image of a PLA fiber containing 5 wt % SEBS copolymer is provided in Figure 11b and reveals that the

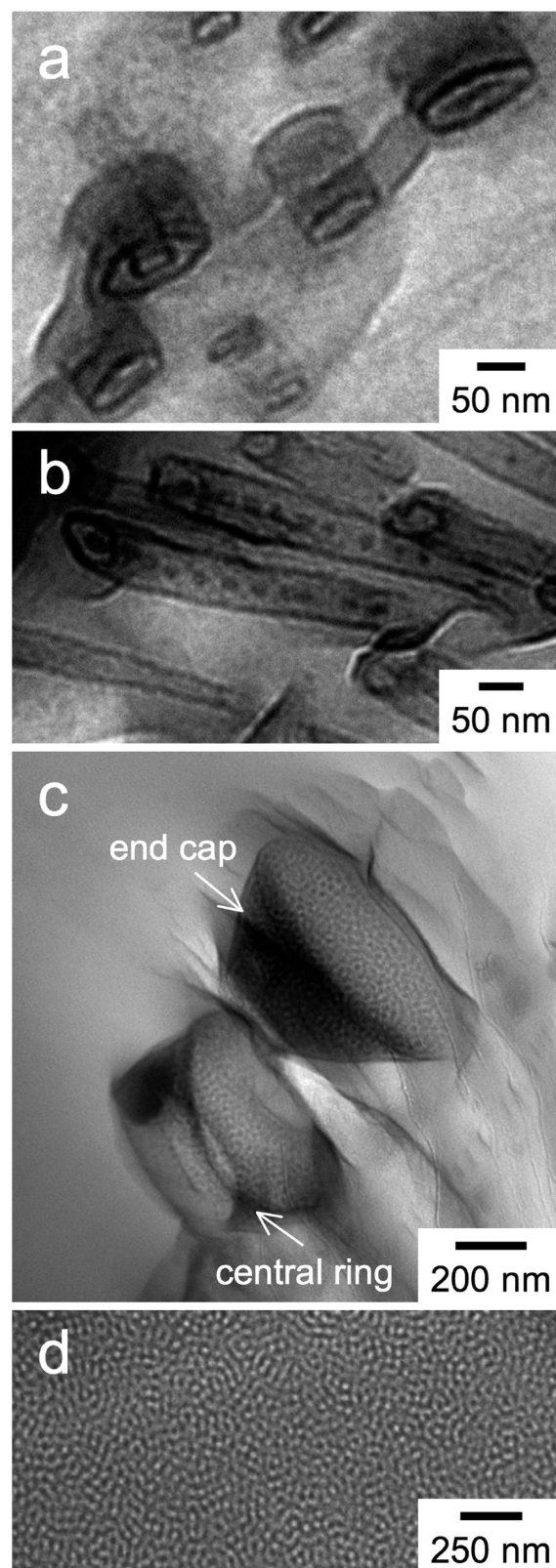


Figure 12. Series of TEM images showing unexpected morphologies of the SEBS copolymer after being compounded with PLA and melt-spun into bicomponent filaments. In (a), single tubules and concentric tubules are evident, whereas the “peas in a pod” morphology is clearly seen in (b). Large-scale structures that appear vesicular with ordered copolymer walls are visible in PLA melt-compounded with the SEBS copolymer prior to cospinning (c). The morphology of the as-received copolymer with midblock extender is provided for reference in (d).

copolymer molecules, selectively stained with the vapor of $\text{RuO}_4(\text{aq})$, are present in the form of discrete and aperiodic nanostructures that most closely resemble dispersed tubules. The existence of tubules suggests that the midblock extender is either not highly compatible with the EB midblock of the copolymer or present at sufficiently high concentration to preclude appreciable solubilization within the copolymer matrix. Moreover, assuming that the copolymer is uniformly dispersed in the PLA prior to melt spinning, the styrenic endblocks of the copolymer do not appear to be very compatible with PLA.

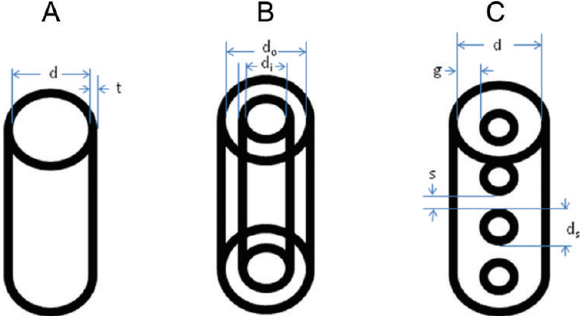
In the TEM images displayed in Figures 11c and 11d, the copolymer morphologies formed in bicomponent $\text{iPP}_{\text{core}}/(\text{PLA} + \text{SEBS})_{\text{sheath}}$ and $(\text{PLA} + \text{SEBS})_{\text{core}}/\text{iPP}_{\text{sheath}}$ fibers are evident. In both cases, copolymer molecules generate dispersed nanostructures that remain distributed throughout PLA rather than accumulating along the iPP–PLA interface. This tendency is consistent with the property measurements provided earlier and explains why the copolymer does not significantly alter the breaking strength of the bicomponent fibers investigated here. Although thermodynamic considerations indicate that the copolymer should migrate to the iPP–PLA interface, the time scale associated with fiber spinning is on par with or faster than that required for the diffusion of individual copolymer molecules from the PLA phase to the interface. To complicate matters further, the copolymer molecules are assembled into nanostructures that are less driven (due to a concentration gradient) and slower to diffuse to the interface where they are needed to compatibilize the core and sheath. Careful examination of the nanostructures observed in Figures 11c and 11d reveals that the copolymer nanostructures tend to orient along a common direction (which may be normal to the iPP–PLA interface) and, more importantly, that the copolymer molecules appear to self-organize into tubules, not cylinders, in PLA cospun with iPP. [Stained cylinders appear the most electron dense (darkest) along their centerline, whereas tubules are darkest along their periphery due to thickness considerations in projection.] While bicomponent block copolymers have been previously reported^{61,62} to form nanotubes, such morphologies normally require an additional driving force, such as crystallization, to do so. The orientation of the tubules relative to the fiber axis could not be unequivocally determined from TEM images because TEM provides a 2D representation

of a 3D object, wherein the orthogonal direction cannot be accurately determined. However, a series of images collected at different tilt angles have been carefully aligned as a precursor to transmission electron microtomography to qualitatively understand the relative orientation of the tubules with respect to neighboring tubules.

While it is intriguing that in all the core/sheath fiber configurations examined the copolymer molecules most often form tubules within PLA, more exotic morphologies, such as concentric tubules and spheres in tubules (what we term “peas in a pod”), are also observed, as evidenced by the TEM images provided in Figures 12a and 12b, respectively. Examples of the “peas in a pod” morphology are also highlighted in Figures 11c and 11d. A qualitatively similar sphere-in-cylinder morphology has been observed⁶³ in a thin film of an ABC triblock copolymer swollen with a good, neutral solvent. To the best of our knowledge, however, this morphology has not been previously reported for a blend of an ABA triblock copolymer dispersed in a C homopolymer. These highly nonclassical morphologies are schematically depicted in Table 2, and relevant dimensions identified in the illustrations and measured from TEM images are included. To put these dimensions into perspective, the unperturbed gyration diameter of the blocks comprising the SEBS copolymer are calculated from the freely jointed chain model⁶⁴ and the known block lengths. Since the EB midblock most likely adopts a looped or bridged conformation (which is rigorously true only at equilibrium), its molecular weight is halved so that it can be treated as a tail, a chain tethered at only one end, in similar fashion as the S endblocks. Block gyration diameters, estimated with the assumptions that (i) the statistical segment lengths of S and EB are comparable (~ 0.7 nm)^{65,66} and (ii) the EB midblock consists of equal fractions of E and B, are ~ 4 nm for the S block and ~ 15 nm for (half) the EB block. The number of unperturbed blocks (N) corresponding to the measured dimensions identified in the diagrams shown in Table 2 is included in the same table and reveals several important features.

Analysis of the tubule walls generally yields $N \approx 2$, which corresponds to an endblock bilayer. This finding is consistent with the EB midblocks extending into both the tubular core and the surrounding matrix. In the case of a single tubule (morphology A in Table 2), the measured internal diameter also results

Table 2. Dimensions (in nm) of the SEBS Copolymer Morphologies Observed in Melt-Spun Bicomponent Fibers



core/sheath fiber configuration ^a	morphology A		morphology B		morphology C			
	d (n)	t (n)	d_i (n)	d_0 (n)	d (n)	d_s (n)	s (n)	g (n)
PLA + SEBS in core	51 ± 31 (50)	8 ± 4 (50)	126 (1)	225 (1)	56 ± 16 (12)	16 ± 6 (32)	10 ± 4 (32)	17 ± 4 (32)
PLA + SEBS in sheath	30 ± 10 (50)	8 ± 2 (50)	70 (2)	100 (2)	42 ± 15 (13)	14 ± 4 (56)	13 ± 4 (56)	16 ± 5 (56)

^an denotes the number of features measured.

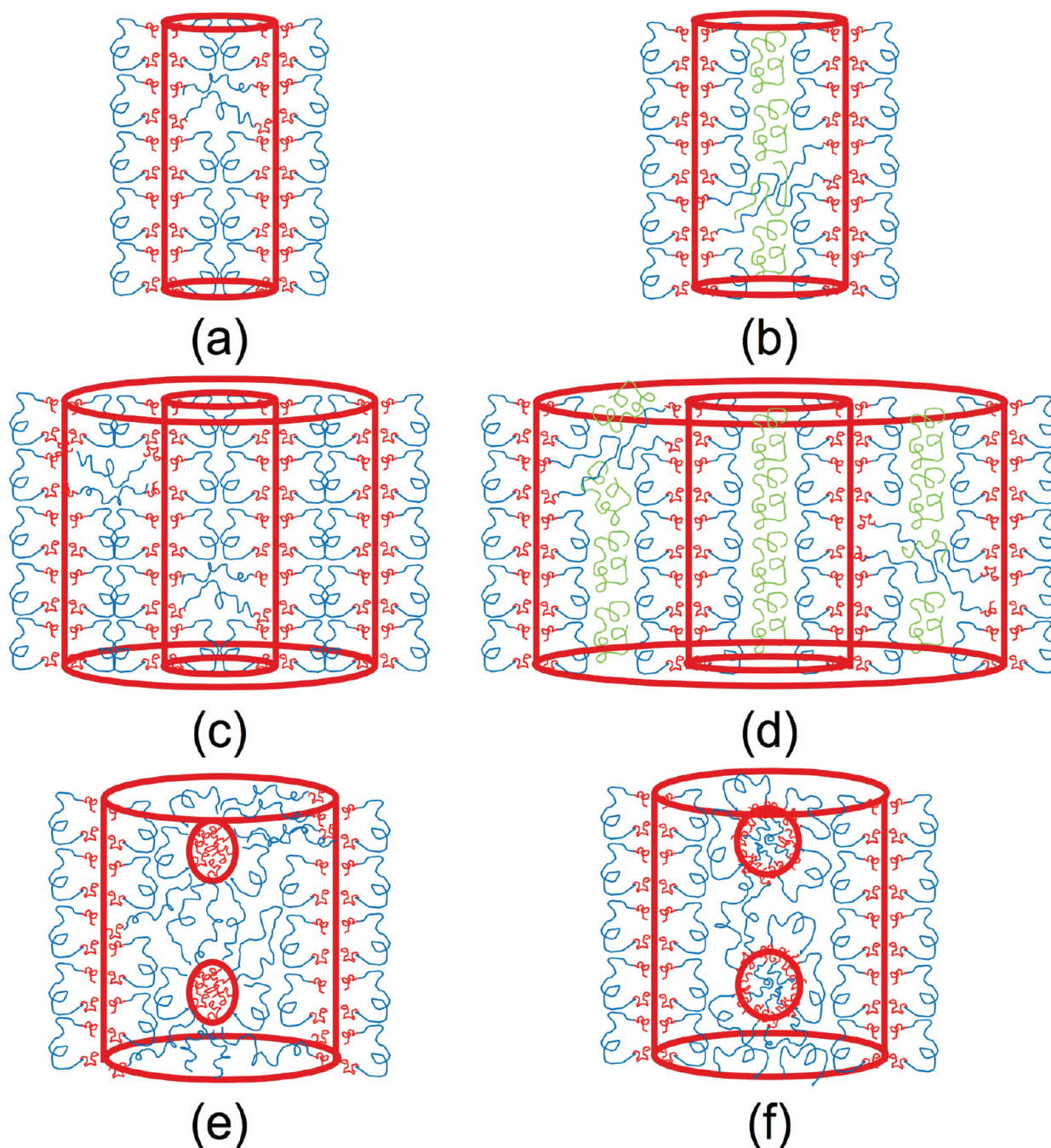


Figure 13. Schematic illustrations of the unexpected SEBS morphologies observed in melt-spun bicomponent filaments composed of iPP and PLA: (a) single tubules with bilayered S (red) walls, (b) tubules swollen with either the midblock extender or entrapped PLA (green), (c) concentric tubules that are connected by bridged EB midblocks (blue), (d) concentric tubules swollen with either the midblock extender or entrapped PLA, (e) equally sized and spaced S spheres in a single tubule (“peas in a pod”), and (f) equally sized and spaced core-shell S spheres in a single tubule.

in $N \approx 2$ (i.e., 2 EB blocks) for tubules formed in the (PLA + SEBS)_{sheath} configuration but varies considerably from about 1 to 3 in the (PLA + SEBS)_{core} configuration. This variation may reflect differences in the level of spin-line stress experienced by the copolymer molecules, as well as stochastic swelling of the EB midblock by the midblock extender or PLA. Similar variation is evident in the EB-rich regions of the concentric tubule morphology (morphology B in Table 2). Within the PLA + SEBS core, a single internal tubule appears highly swollen with $N \approx 8$, but the distance between the internal and external walls yields $N \approx 1$, which implies that the EB midblocks extending from the internal and external tubule

walls are interdigitated into a monolayer, rather than bilayered. Lastly, in the “peas in a pod” morphology (morphology C in Table 2), the diameter of the internal spheres (which appear circular but, in a few cases, as shells) is significantly larger than two S endblocks ($N \approx 4$). These enlarged spheres are presumed to be the result of partial PLA incorporation, although the possibility of other kinetically trapped species cannot be outright disregarded. The distances between neighboring spheres (which align along the direction of the tubule) and between the spheres and tubule wall in both the core and sheath fiber configurations yields $N \approx 1$, which strongly suggests that the spheres are most likely connected

together, as well as to the tubule walls, by bridged EB midblocks, as schematically depicted in Figure 13. Such molecular connectivity within the nanostructures present might serve to reinforce the PLA phase and improve its elasticity, as deduced from the flow and mechanical properties discussed earlier. It is comforting that these unique morphologies, although nonequilibrium in nature, tend to obey classical chain packing behavior.

In addition to establishing the presence of uncommon copolymer morphologies in bicomponent fibers, the images presented in Figures 11b, 11c, 12a, and 12b confirm that the S endblocks are not in direct contact with PLA. Rather, the EB midblock forms a contiguous coronal layer around the S-rich features. Such isolation helps to explain why the copolymer does not preferentially migrate to and accumulate along the iPP–PLA interface where it can promote compatibilization. To discern the extent to which the SEBS copolymer is dispersed within PLA prior to melt spinning, we have examined the melt-compounded PLA + SEBS mixture. Large structures such as those portrayed in Figure 12c are evident, indicating that the two materials are not thoroughly mixed. These macrostructures, measuring on the order of hundreds of nanometers across, also appear tubular (the figure displays a central “ring” and what appears to be an end-cap). Close examination of their walls reveals an organized copolymer nanostructure. Complementary inspection of the as-received copolymer with midblock extender (Figure 12d) confirms the existence of an irregular morphology that resembles the nanostructured walls of the macroscale tubules in Figure 12c. Thus, we conclude that the copolymer retains some of its as-received nanostructure after being melt-blended with PLA, indicating that the compounding temperature and mechanical mixing employed here were insufficient to molecularly disperse the copolymer within PLA.

On a side note, it is strangely curious, though, that the stainable, but minor, styrenic component in the as-received compound with the midblock extender appears as the matrix in Figure 12d, which suggests that the morphology may be more complicated than styrenic spheres or cylinders as previously anticipated. Although this figure is representative of entire sections of the as-received copolymer, it is likewise possible that the as-received copolymer is heterogeneous at macroscopic length scales. Such macroscale heterogeneity may be largely responsible for the unique nanoscale tubular morphologies reported here in Figures 11 and 12, as they could be the result of subjecting the parent morphologies in the heterogeneous PLA + SEBS mixture to very high shear and extensional flow through the spinneret during which time they became distorted and rearranged into lower-energy nanostructural elements. This nonequilibrium formation mechanism seems more plausible than conventional self-organization of the copolymer from a disordered state and would help to explain the variety of nanostructures observed on the basis of local copolymer composition and diffusion considerations.

CONCLUSIONS

The strategy of copolymer-induced blend compatibilization has been applied to melt-spun bicomponent fibers that bring together iPP and PLA in contact along a single interface separating the core from the sheath. Although the two polymers are incompatible, there is no evidence of measurable slip at the molten iPP–PLA interface according to steady-shear rheology. While the addition of a SEBS copolymer to a melt-mixed iPP/PLA blend serves as a compatibilizer by reducing the size of PLA domains arising from macrophase separation, incorpo-

ration of the copolymer into PLA prior to cospinning does not drastically improve the properties of bicomponent iPP/PLA fibers, which implies that the copolymer molecules are unable to concentrate along the iPP–PLA interface during spinning. Despite an absence of copolymer along the fiber interface, the strain at which PLA as the sheath ruptures increases sharply at low spinning pressure, and the number of fibers that undergo failure of the PLA sheath prior to failure of the iPP core is reduced by up to 30%, upon addition of copolymer. Thus, although the copolymer does not modify the iPP–PLA interface, it does affect the host PLA by improving its elasticity through the formation of unique copolymer nanostructures that include single tubular, concentric tubular, and “peas in a pod” morphologies. Careful analysis of such unexpected morphologies confirms the existence of nanostructural dimensions capable of accommodating local connectivity through midblock bridging, which consequently allows these highly elastic, EB-rich copolymer dispersions to rubber-toughen⁶⁷ the PLA.

ACKNOWLEDGMENTS

Financial support of this work has been provided by the Nonwovens Cooperative Research Center at North Carolina State University and the National Science Foundation through a Graduate Research Fellowship (K.E.R.). We thank Dr. Behnam Pourdeyhimi for insightful and fruitful discussions, as well as Christina Tang and Alina Higham for analytical assistance.

REFERENCES

- (1) Mutsuga, M.; Kawamura, Y.; Tanamoto, K. *Food Addit. Contam., Part A* **2008**, 25 (10), 1283–1290.
- (2) Mezghani, K.; Spruiell, J. J. *J. Appl. Polym. Sci.* **1998**, 36, 1005–1012.
- (3) Murariu, M.; Ferreira, A. D.; Alexandre, M.; Dubois, P. *Polym. Adv. Technol.* **2008**, 19 (6), 636–646.
- (4) Nyambo, C.; Mohanty, A. K.; Manjusri, M. *Biomacromolecules* **2010**, 11 (6), 1654–1660.
- (5) Agarwal, M.; Koelling, K. W.; Chalmers, J. J. *Biotechnol. Prog.* **1998**, 14 (3), 517–526.
- (6) Holm, V. K.; Ndoni, S.; Risbo, J. J. *Food Sci.* **2006**, 71 (2), E40–E44.
- (7) Mohd-Adnan, A. F.; Nishida, H.; Shirai, Y. *Polym. Degrad. Stab.* **2008**, 93 (6), 1053–1058.
- (8) Kabeel, M. A. *Rev. Sci. Instrum.* **1991**, 62, 2950–2954.
- (9) Sun, C.; Zhang, D.; Liu, Y.; Xiao, J. J. *Ind. Text.* **2004**, 34, 17–26.
- (10) Fedorova, N.; Pourdeyhimi, B. J. *J. Appl. Polym. Sci.* **2007**, 104, 3434–3442.
- (11) Park, C.-W. *AIChE J.* **1990**, 36 (2), 197–206.
- (12) Holsti-Miettinen, R.; Seppälä, J.; Ikkala, O. T. *Polym. Eng. Sci.* **1992**, 32, 868–877.
- (13) Cargill, Inc. <http://www.cargill.com/corporate-responsibility/environmental-innovation/pioneering-new-business/corn-plastic/index.jsp> (accessed 06/30/2010). Kimura, K. *Fujitsu Sci. Tech. J.* **2005**, 41 (2), 173–180.
- (14) Fuentes, C. A.; Tran, L. Q. N.; Dupont-Gillain, C.; Vanderlinden, W.; De Feyter, S.; Van Vuurea, A. W.; Verpoest, I. *Colloids Surf., A* **2011**, 380, 89–99.
- (15) Arvidson, S. A.; Wong, K. C.; Gorga, R. E.; Khan, S. A. *Polymer* (in revision).
- (16) Okamoto, M.; Mizuguchi, S.; Watanabe, K. U.S. Patent #3,705,226, Dec 5, 1972.
- (17) Dugan, J. *Critical factors in engineering segmented bicomponent fiber for specific end uses*, 1999 (<http://www.FITfibers.com/Publications.htm>).
- (18) Fruedenburg and Co kg. (<http://www.evolon.com>).

- (19) Kikutani, T.; Radhakrishnan, J.; Arikawa, S.; Takaku, A.; Okui, N.; Jin, X.; Niwa, F.; Kudo, Y. *J. Appl. Polym. Sci.* **1996**, *62*, 1913–1924.
- (20) Cho, H. H.; Kim, K. H.; Kang, Y. A.; Ito, H.; Kikutani, T. *J. Appl. Polym. Sci.* **2000**, *77*, 2254–2266.
- (21) Houis, S.; Schmid, M.; Lubben, J. *J. Appl. Polym. Sci.* **2007**, *106*, 1757–1767.
- (22) Im, J. N.; Kim, J. K.; Kim, H. K.; Lee, K. Y.; Park, W. H. *J. Biomed. Res., B* **2007**, *83B*, 499–504.
- (23) Zhao, R.; Macosko, C. W. *J. Rheol.* **2002**, *46*, 145–167.
- (24) Jiang, L.; Lam, Y. C.; Yue, C. Y.; Tam, K. C.; Li, L.; Hu, X. *J. Appl. Polym. Sci.* **2003**, *89*, 1464–1470.
- (25) Lam, Y. C.; Jiang, L.; Yue, C. Y.; Tam, K. C.; Li, L. *J. Rheol.* **2003**, *47*, 795–807.
- (26) Park, H. E.; Lee, P. C.; Macosko, C. W. *J. Rheol.* **2010**, *54*, 1207–1218.
- (27) Robeson, L. M. *Polymer Blends: A Comprehensive Review*; Hanser Gardner: Cincinnati, 2007.
- (28) Molau, G. E. *J. Polym. Sci., Part A* **1965**, *3*, 1267–1278.
- (29) Wang, D.; Li, Y.; Xie, X. M.; Guo, B. H. *Polymer* **2011**, *52*, 191–200.
- (30) Del Castillo-Castro, T.; Castillo-Ortega, M. M.; Herrera-Franco, P. J.; Rodriguez-Felix, D. E. *J. Appl. Polym. Sci.* **2010**, *119*, 2895–2901.
- (31) Wei, B.; Genzer, J.; Spontak, R. J. *Langmuir* **2004**, *20*, 8659–8667.
- (32) Gozen, A. O.; Zhou, J.; Roskov, K. E.; Shi, A. -C.; Genzer, J.; Spontak, R. J. *Soft Matter* **2011**, *7*, 3268–3272.
- (33) Pernot, H.; Baumert, M.; Court, F.; Leibler, L. *Nature Mater.* **2002**, *1*, 54–58.
- (34) Yoo, T. W.; Yoon, H. G.; Choi, S. J.; Kim, M. S.; Kim, Y. H.; Kim, W. N. *Macromol. Res.* **2010**, *18*, 583–588.
- (35) Godshall, D.; White, C.; Wilkes, G. L. *J. Appl. Polym. Sci.* **2001**, *80*, 130–141.
- (36) Lipscomb, G. G. *Polym. Adv. Technol.* **1994**, *5* (11), 745–758.
- (37) Arvidson, S. A.; Khan, S. A.; Gorga, R. E. *Macromolecules* **2010**, *43*, 2916–2924.
- (38) Mark, J. E., Ed.; *Polymer Data Handbook*; Oxford University Press: New York, 1999.
- (39) Sperling, L. H. *Polymeric Multicomponent Materials: An Introduction*; John Wiley & Sons: New York, 1998.
- (40) Small, P. A. *J. Appl. Chem.* **1953**, *3*, 71–80.
- (41) Hoy, K. L. *J. Paint Technol.* **1970**, *42*, 76–118.
- (42) Antonow, G. N. *J. Chim. Phys.* **1907**, *5*, 372–385.
- (43) Antonow, G. N. *J. Chim. Phys.* **1907**, *5*, 8.
- (44) Biresaw, G.; Carriere, C. J. *J. Polym. Sci. B: Polym. Phys.* **2002**, *40*, 2248–2258.
- (45) Helfand, E.; Tagami, Y. *J. Polym. Sci., Part B* **1971**, *9*, 741–746.
- (46) Helfand, E.; Tagami, Y. *J. Chem. Phys.* **1972**, *56* (7), 3592–3601.
- (47) Ermoshkin, A. V.; Semenov, A. N. *Macromolecules* **1996**, *29*, 6294–6300.
- (48) Gaylord, N. G. *CHEMTECH* **1976**, *6*, 392–395.
- (49) Discher, D.; Eisenberg, A. *Science* **2002**, *297*, 967–973.
- (50) Lyngaae-Jorgensen, J. K.; Thomsen, D. *Int. Polym. Proc.* **1988**, *3–4* (2), 123–130.
- (51) Utracki, L. A. *Polymer Alloys and Blends: Thermodynamics and Rheology*; Hanser: Munich, 1989.
- (52) Rangasamy, L.; Shim, E.; Pourdeyhimi, B. *J. Appl. Polym. Sci.* **2011**, *121*, 410–419.
- (53) Treloar, L. *Trans. Faraday Soc.* **1941**, *37*, 84–97.
- (54) Ward, I. *Proc. Phys. Soc.* **1962**, *80*, 1176–1188.
- (55) Holden, G.; Legge, N. R.; Quirk, R. P.; Schroeder, H. E., Eds.; *Thermoplastic Elastomers*, 2nd ed.; Hanser: Munich, 1996.
- (56) Krishnan, A. S.; Roskov, K. E.; Spontak, R. J. In *Advanced Nanomaterials*; Geckeler, K. E., Nishide, H., Eds.; Wiley-VCH: Weinheim, 2010; pp 791–834.
- (57) Krishnan, A. S.; Seifert, S.; Lee, B.; Khan, S. A.; Spontak, R. J. *Soft Matter* **2010**, *6*, 4331–4334.
- (58) Kane, L.; Norman, D. A.; White, S. A.; Matsen, M. W.; Satkowski, M. M.; Smith, S. D.; Spontak, R. J. *Macromol. Rapid Commun.* **2001**, *22*, 281–296.
- (59) Winey, K. I.; Thomas, E. L.; Fetters, L. J. *J. Chem. Phys.* **1991**, *95*, 9367–9375.
- (60) Matsen, M. W. *Macromolecules* **1995**, *28*, 5765–5773.
- (61) Raez, J.; Manners, I.; Winnik, M. A. *J. Am. Chem. Soc.* **2002**, *124* (35), 10381–10395.
- (62) Wang, X.; Wang, H.; Frankowski, D. J.; Lam, P. G.; Welch, P. M.; Winnik, M. A.; Hartmann, J.; Manners, I.; Spontak, R. J. *Adv. Mater.* **2007**, *19* (17), 2279–2285.
- (63) Elbs, H.; Drummer, C.; Abetz, V.; Krausch, G. *Macromolecules* **2002**, *35* (14), 5570–5577.
- (64) Dealy, J. M.; Larson, R. G. *Structure and Rheology of Molten Polymers: From Structure to Flow Behavior and Back Again*; Hanser: Munich, 2006.
- (65) Laurer, J. H.; Khan, S. A.; Spontak, R. J.; Satkowski, M. M.; Grothaus, J. T.; Smith, S. D.; Lin, J. S. *Langmuir* **1999**, *15* (23), 7947–7955.
- (66) O'Connor, K. M.; Pochan, J. M.; Thiagarajan, P. *Polymer* **1991**, *32* (2), 195–201.
- (67) Zhang, W.; Wei, F. Y.; Chen, L.; Zhang, Y. *Proc. 2009 Int. Conf. Adv. Fibers Polym. Mater.*; National Science Foundation of China: Shanghai, 2009; pp 207–209.

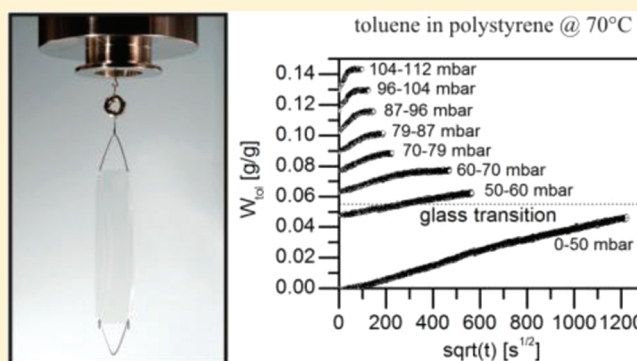
Non-Fickian Diffusion of Toluene in Polystyrene in the Vicinity of the Glass-Transition Temperature

Florian Mueller, Kai-Martin Krueger,[†] and Gabriele Sadowski*

Laboratory of Thermodynamics, Technische Universität Dortmund, Emil-Figge-Strasse 70, 44227 Dortmund, Germany

S Supporting Information

ABSTRACT: The diffusion process of toluene in polystyrene films is investigated in the vicinity and slightly above the glass-transition of the mixture. A detailed analysis investigates whether the diffusion follows Fick's law or other effects are superimposing the mass transport process. For that purpose, the diffusion of toluene in polystyrene films of different thicknesses at otherwise constant conditions was observed by gravimetric sorption measurements. Even slightly above the glass-transition of the toluene-loaded polymer a remaining influence of the polymer relaxation on the diffusion process (non-Fickian diffusion) is observed. The diffusion Deborah number concept was applied using an experimentally independent relaxation time for the polystyrene-toluene mixture. The results show quantitatively the same trend but finally deviate by about 1 order of magnitude.



INTRODUCTION

The knowledge of solubilities and of the diffusion processes in polymer/volatile organic compound (VOC) systems allows an optimal control of the polymer production processes in industrial applications. The information, how far and how much VOC dissolves in a polymer film provides the basis for the calculation of production or separation times, e.g. for polymer drying or in membrane separation processes.

In a previous work, a gravimetric-sorption apparatus was set up, and sorption isotherms as well as sorption curves (dynamic transport) for toluene in polystyrene were determined.¹ It was shown, that the dissolved VOC reduces the glass-transition temperature of the polymer dramatically and shifts the diffusion coefficient to higher values. On the basis of films of one selected thickness, diffusion coefficients above the glass-transition were determined as a function of VOC concentration and temperature. For that purpose, it was assumed that the diffusion process in this temperature region is always Fickian. In this work we now investigate to which extend this assumption can be considered to be true for the polystyrene/toluene system and whether the diffusion coefficients determined from the sorption curves at temperatures being slightly above the glass-transition are reliable.

The group of Kishimoto and Matsumoto² investigated this question already more than 40 years ago for other polymer/VOC systems. They showed, that non-Fickian sorption behavior can be observed at temperatures even above the glass-transition temperature of the neat polymer. Moreover, Odani³ identified non-Fickian sorption behavior for diffusion of a VOC in polystyrene slightly above the glass-transition temperature of the mixture. On the basis of their investigation and due to the fact that the experimental data for the region

slightly above the glass-transition of the mixture is very limited, a detailed study of the diffusion behavior of the polystyrene/toluene system is presented in this study. The results should give an idea of the broadness of the non-Fickian region above the glass-transition temperature of the mixture with respect to temperature and concentration.

According to Fujita,⁴ the shape of the sorption curves gives a first clue about the condition of the polymer and the diffusion type. However, the final answer whether the diffusion process is Fickian or not can only be given by comparing reduced sorption curves for different film thicknesses at otherwise identical conditions. The same information can also be obtained by assuming Fickian diffusion and comparing the diffusion coefficients obtained from the sorption curves at different film thicknesses. In case of Fickian diffusion, the reduced sorption curves as well as the derived diffusion coefficients should not depend on the film thickness and thus should be identical.

The concept of Deborah numbers proposed by Vrentas and Duda^{5,6} offers an alternative way to classify the diffusion type in polymers. This concept relates the characteristic relaxation time of the mixture to the characteristic time of the diffusion process.

In this work, the analysis of diffusion coefficients and of the sorption curves is being done for the polystyrene/toluene system for different film thicknesses of the polymer at temperatures of 30, 50, and 70 °C. Moreover the characteristic relaxation time of the considered polystyrene/toluene mixture

Received: October 19, 2011

Revised: December 14, 2011

Published: January 9, 2012



is estimated and the Deborah numbers for all temperatures and film thicknesses are determined. Finally, the results of the experimental sorption measurements are compared to Deborah-number calculations.

EXPERIMENTS

Experimental Setup. The main part of the gravimetric sorption equipment used in this work is a magnetic suspension balance measuring the weight increase of the polymer sample during an isothermal pressure step. The temperature of the cell is controlled by means of an air-bath thermostat. Depending on the viscosity of the mixture, the polymer sample is either hanging as a free film at the measuring hook or is lying horizontally attached to the bottom of a glass bucket. A more detailed description of the experimental procedure is given elsewhere.¹

Materials and Film Preparation. Polystyrene was obtained from Gefinex with $M_w = 240\,000$ g/mol, $M_w/M_n = 5.65$ and a glass-transition temperature of 105 °C. Toluene of 99.9% purity was obtained from Merck and was degassed by three successive freezing-evacuation-melting steps before being filled into the evacuated VOC vaporizer. The polymer films were prepared by casting from toluene/polystyrene solutions on a glass surface with subsequent flattening by means an applicator exhibiting a slit of defined height between glass and applicator surface. Afterward, the films were stored in a vacuum oven to enhance the toluene removal from the films with a temperature and pressure routine, as described earlier.¹ Using this procedure, the thickness of the polystyrene films varied at maximum by about ± 1 μm .

Sorption Measurements. As described earlier,¹ the polymer sample is positioned in the measurement cell and equilibrated at the measurement temperature. After evacuation of the cell, a certain VOC pressure is established in the cell and is kept constant. The weight of the polymer sample is observed by means of the magnetic suspension balance until no weight increase is observed for several hours.

For the next sorption step, the VOC pressure in the cell is increased also leading to an increasing amount of VOC absorbed. The VOC concentrations at different pressures and constant temperature yield the sorption isotherm (as, e.g., shown in Figure 1) whereas the time

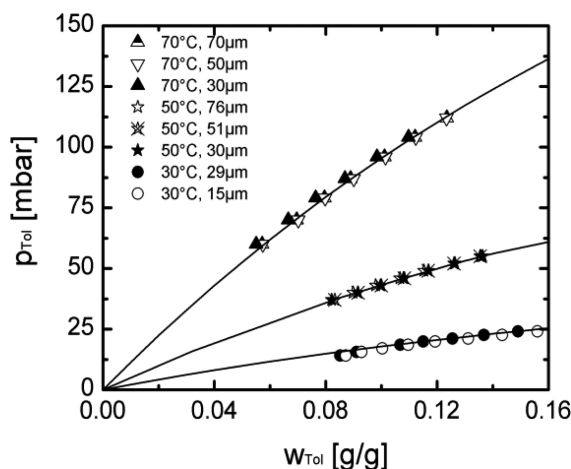


Figure 1. Experimental sorption data for the polystyrene/toluene system at 30, 50, and 70 °C as a function of the polymer-film thickness. Symbols are experimental data; lines are included for better visibility.

dependent weight increase for one pressure step is called sorption curve (as, e.g., shown in Figure 2 for several pressure steps).

Samples at 30 and 50 °C were measured as free-hanging films and films at 70 °C were attached to the bottom of a glass bucket, to be able to measure in the region above the glass-transition temperature at lower viscosities of the polymer/VOC mixture.

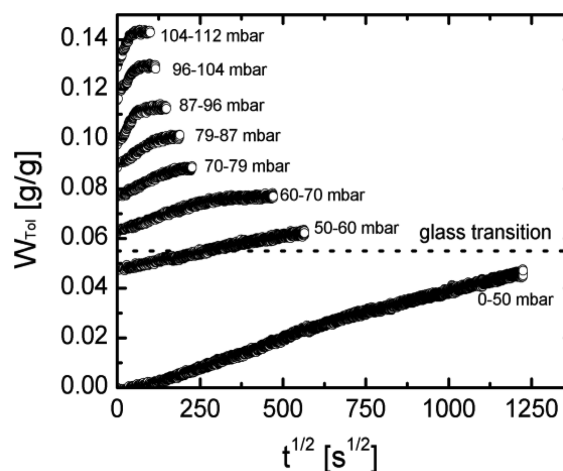


Figure 2. Experimental interval sorption curves for the polystyrene/toluene system at 70 °C and for a film thickness of 70 μm . The glass-transition was calculated using eq 1.

RESULTS

Sorption Isotherms. All experimental sorption data obtained within this and from our previous work⁷ are summarized in Table 1 of the Supporting Information. As an example, Figure 1 shows the sorption isotherms at 30, 50, and 70 °C for film thicknesses between 15 and 70 μm . For each of the three temperatures, the sorption isotherms at different film thicknesses cannot be distinguished within experimental accuracy.

Sorption Curves and Diffusion Behavior. Figure 2 shows the sorption curves for all isothermal pressure steps at 70 °C and a film thickness of 70 μm . The VOC-loading W_{Tol} (mass of absorbed toluene per mass of the dry polymer) is plotted versus the square root of time (\sqrt{t}). Each sorption step is starting at the final mass uptake of the previous step.

To distinguish whether the polymer/VOC mixture is in the rubbery or in the glassy state we use the approach of Mueller et al.⁸ who fitted the equation of Kelly and Bueche⁹ to describe the concentration dependence of the glass-transition temperature.

$$T_{g,\text{mixture}} = \frac{\alpha_2(1 - \phi_1)T_{g,2} + \alpha_1\phi_1T_{g,1}}{\alpha_2(1 - \phi_1) + \alpha_1\phi_1} \quad (1)$$

$T_{g,1}$ and $T_{g,2}$ are the glass-transition temperatures of the VOC and the neat polymer and α_1 and α_2 are the thermal expansion coefficients of the pure VOC and the polymer, respectively. These values can be found in Table 1. ϕ_1 is the VOC volume fraction, which is related to the VOC weight fraction w_1 as follows:

$$w_1 = \frac{v_{01}^{-1}(T, p)\phi_1}{v_{01}^{-1}(T, p) + \phi_1(v_{01}^{-1}(T, p) - v_{02}^{-1}(T, p))} \quad (2)$$

Table 1. Parameters for the Calculation of the Glass-Transition Temperature of the Polystyrene/Toluene Mixture Used in Equation 1

parameter	eq 1	ref
α_1	1.067×10^{-3} 1/K	12
α_2	5.73×10^{-4} 1/K	8
$T_{g,1}$	− 156.15 °C	11
$T_{g,2}$	105 °C	8

ν_{01} and ν_{02} are the specific volumes of pure VOC and polymer, respectively. They are calculated at the pressure p and temperature T of the mixture using an empirical correlation¹⁰ for ν_{01} and the Tait equation¹¹ for ν_{02} . More details as well as the used expressions and constants can be found elsewhere.¹

The VOC concentration which, according to eq 1, corresponds to a glass-transition of 70 °C is marked in Figure 2. The sorption curves below the calculated glass-transition show a different appearance than the curves above which look like Fickian sorption curves and which achieve the features of Fickian sorption given by Fujita⁴ and Crank.¹³ A typical representative for a sorption curve above the glass-transition is shown in more detail in Figure 3 for the pressure step from 79 to 87 mbar at 70 °C.

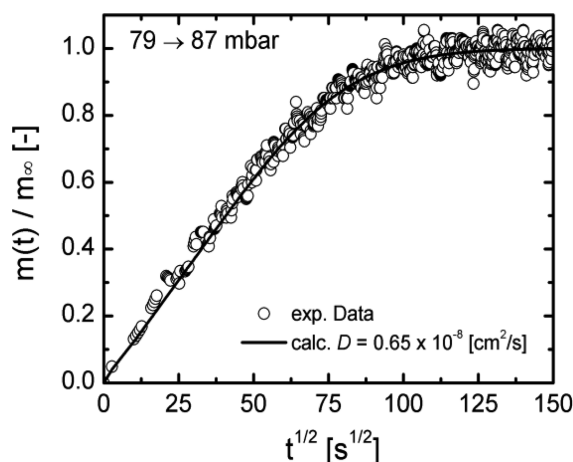


Figure 3. Experimental interval sorption curve of the polystyrene/toluene system at 70 °C and a film thickness of 70 μm (pressure step: 79–87 mbar). Symbols are experimental data; line is the calculation using eq 3.

According to the procedure used in our previous work,¹ the Crank equation¹³ (eq 3) was applied to determine the diffusion coefficient for a Fickian-type sorption curve.

$$\frac{m(t)}{m_\infty} = 1 - \sum_{n=0}^{\infty} \frac{8}{(2n+1)^2 \pi^2} \exp\left\{-\frac{D(2n+1)^2 \pi^2 t}{d^2}\right\} \quad (3)$$

In this equation d is the film thickness of a free hanging film at the beginning of this pressure step and D is the mean diffusion coefficient. d was calculated for each sorption interval individually based on the equilibrium volume increase of the previous sorption interval with no respect to excess volume and the assumption of one-dimensional swelling only in the direction of diffusion. As it can be seen from Figure 3, the Crank equation is able to describe the experimental data with satisfactory accuracy. All so-determined diffusion coefficients are summarized in Table 1 (Supporting Information)

Figure 4 shows a semilogarithmic plot of the diffusion coefficients versus the toluene weight fraction determined at three temperatures and for the different film thicknesses. Here, it was again assumed, that the diffusion above the glass-transition of the mixture can be described as Fickian diffusion. The data for 30 °C were taken from our previous work,^{1,7} and the data for the 50 °C measurements were taken from Heuwers.¹⁴

At 70 °C, the diffusion coefficients determined for different film thicknesses are close to each other, especially for higher

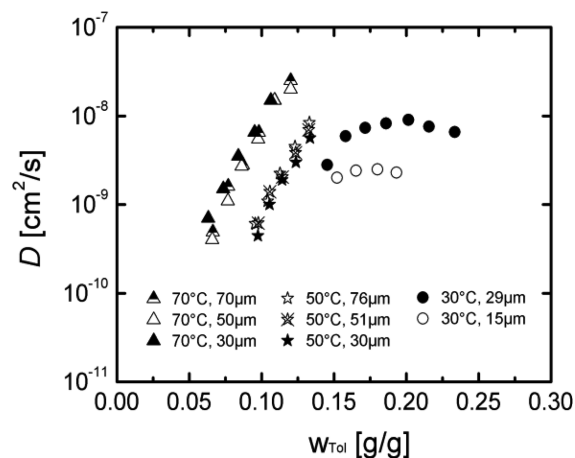


Figure 4. Diffusion coefficients for toluene in polystyrene at 30, 50, and 70 °C for films of different thicknesses. The data for 30 °C were taken from our previous work^{1,7} and the data for the 50 °C measurements were taken from Heuwers.¹⁴ All data were measured above the glass-transition of the mixture according to eq 1.

toluene concentrations. No systematic deviation of the data for different film thicknesses is observed. At 50 °C, the diffusion coefficients for different film thicknesses are also very similar. However, the diffusion coefficients at 30 °C obviously vary remarkably with film thickness. In particular, the sorption data for the thinner films lead to smaller diffusion coefficients up to toluene mass fractions of $w_{\text{Tol}} = 0.2$ and probably at even higher concentrations. These results indicate that the assumption of Fickian diffusion above the glass-transition of the mixture is valid for 50 and 70 °C but not for 30 °C. Although at this latter temperature only data points above the glass-transition of the polymer/VOC mixture were taken into account and the sorption curves look Fickian,^{4,13} the diffusion process is obviously still influenced by other effects (i.e., time-dependent swelling) and therefore non-Fickian.

Figure 5 shows a comparison of selected sorption curves as well as reduced sorption curves for different film thicknesses at 30 and 70 °C. As expected, the sorption curves for the 15 and 29 μm film at 30 °C (Figure 5a) and for the 30, 50, and 70 μm at 70 °C (Figure 5c) are different for different film thicknesses since for thicker films it takes longer to reach the equilibrium concentration throughout the film than for thinner films. This effect is eliminated for the reduced sorption curves which are obtained from the sorption curves by dividing the mass-uptake by the film thickness. Therefore, in case of Fickian diffusion the reduced sorption curves should coincide at given temperature and pressure step. Comparing the reduced sorption curves in Figure 5, parts b and d, at 30 and 70 °C, respectively, it can be seen, that the curves coincide more or less at 70 °C but do clearly separate from each other at 30 °C. This again supports the conclusion drawn from the comparison of the diffusion coefficients: in contrast to the diffusion at 70 °C, the diffusion process at 30 °C is non-Fickian although the system is above its glass-transition and the sorption curves have a Fickian-like shape. The reduced sorption curves for the 50 °C data (no example shown in Figure 5) behave similar than the 70 °C measurements, as can be expected from Figure 4.

A possible explanation for this behavior is the presence of swelling/relaxation effects which can delay the diffusion process in thinner films. The relaxation time of a polymer is independent of the film thickness and only depends on

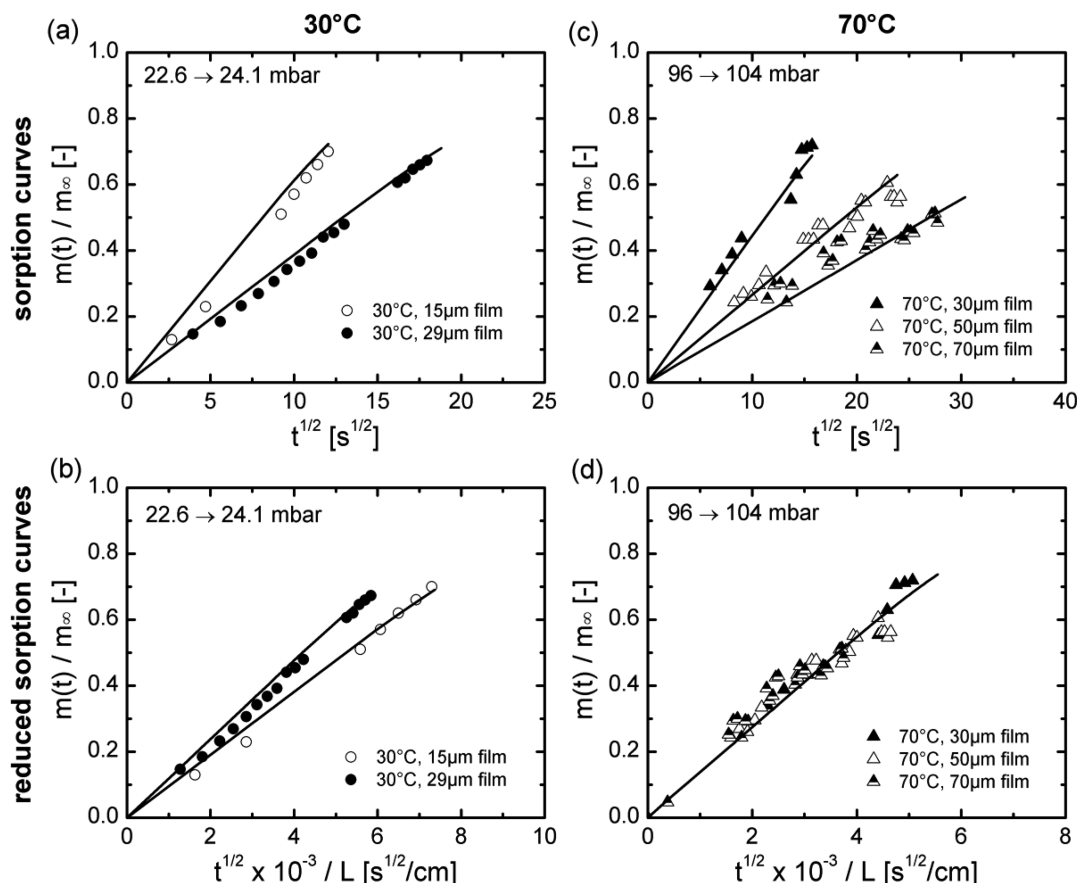


Figure 5. Sorption curves and reduced sorption curves of polystyrene/toluene systems for different film thicknesses at two different temperatures. (a) Sorption curves at 30 °C for films of 15 and 29 μm thickness. (b) Reduced sorption curves at 30 °C for films of 15 and 29 μm thickness. (c) Sorption curves at 70 °C for films of 30, 50, and 70 μm thickness. (d) Reduced sorption curves at 70 °C for films of 30, 50, and 70 μm thickness.

temperature and VOC concentration whereas the diffusion time increases proportionally with the film thickness squared (second Fick's law). For thicker films the relaxation of the polymer is fast compared to the diffusion time. Therefore, the relaxation does not influence the Fickian diffusion process. For thinner films with smaller diffusion times, the relaxation effects become more and more important for the transport process. Here, the time which the polymer molecules need to attain their new equilibrium conformation (e.g., density) and to absorb more VOC retards the transport process compared to pure Fickian diffusion. For the reduced sorption curves, where the film-thickness effect according to Fickian diffusion is eliminated, this effect should lead to flatter curves for thicker films. This is indeed what is observed in Figure 5b for the reduced sorption curves at 30 °C where the data points for the 15 μm film lie below those of the 29 μm film. At 70 °C no systematic variation of the reduced sorption curve data is observed (Figure 5d).

As already mentioned in the introduction, this influence of the polymer relaxation on the transport process is well-known for conditions below the glass-transition^{1,16} and slightly above the glass-transition temperature of the mixture.^{2,3} However, from this investigation it becomes clear that for the polystyrene/toluene system this effect can extend far into the rubbery region above the glass-transition of the mixture, especially for thin films and temperatures far below the glass-transition temperature of the neat polymer.

Those effects have been discussed by Vrentas¹⁵ for several systems. He used the Deborah-number concept to correlate and predict the presence of non-Fickian diffusion.

In the next chapter, the experimental results are therefore compared to the diffusion Deborah-number concept of Vrentas et al.^{5,17} which gives an estimate of whether Fickian or non-Fickian diffusion is to be expected. One advantage of this concept is that it combines all parameters which affect the sorption characteristics like temperature, concentration and film thickness.

Diffusion Deborah numbers. The diffusion Deborah number $(\text{Deb})_D$ is defined⁵ by the ratio of the characteristic relaxation time τ_m of the mixture and the mutual diffusion time θ_D according to eq 4:

$$(\text{Deb})_D = \frac{\tau_m}{\theta_D} \quad (4)$$

whereas the characteristic diffusion time θ_D is given by

$$\theta_D = \frac{L^2}{D^*} \quad (5)$$

L is the diffusion path length and D^* is given by the following expression

$$D^* = x_2 D_1 + x_1 D_2 \quad (6)$$

x_1 and x_2 are the mole fractions of the VOC and polymer, respectively. D_1 and D_2 are the corresponding self-diffusion coefficients. According to Billavits and Durning¹⁸ it is assumed

that D^* is in the order of magnitude of the binary mutual diffusion coefficient D .

As shown in the preceding section, the measured diffusion coefficients D at 50 and 70 °C comply the assumption of Fickian diffusion and can be directly used to calculate the diffusion Deborah numbers at those temperatures. In contrast, the diffusion coefficients estimated above for 30 °C are not real mutual diffusion coefficients, since the diffusion there is not only controlled by a purely Fickian diffusion mechanism and varies with film thickness. Therefore, the diffusion coefficients obtained at 30 °C were extrapolated to infinite film thickness as described by Kishimoto and Matsumoto² to yield the mutual diffusion coefficients at 30 °C. Figure 6 shows the typical

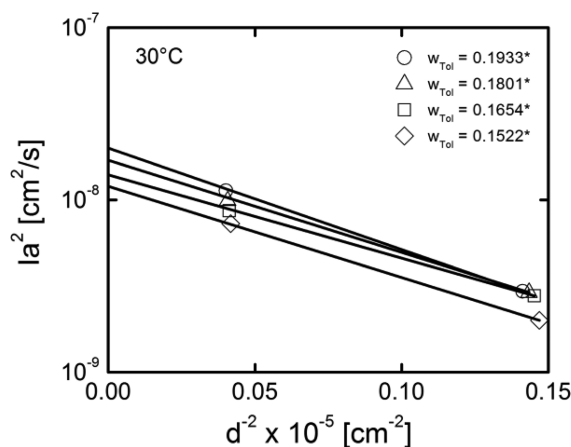


Figure 6. Plot of I_a^2 vs d^{-2} for the system polystyrene/toluene at 30 °C using the procedure of Kishimoto and Matsumoto.²

procedure: The initial slope I_a of sorption curves at 30 °C and different concentrations is plotted against the film thickness d . The increasing value of I_a with increasing film thickness implies that the absorption of toluene in polystyrene at 30 °C is not controlled by a purely Fickian diffusion mechanism. By assuming that the hypothetical sorption curve with the initial slope extrapolated to infinite film thickness is controlled by a purely Fickian diffusion mechanism, the mutual diffusion coefficient D was calculated. The results are listed in Table 1 (Supporting Information) with brackets.

As expected, the extrapolated diffusion coefficients were higher than the measured diffusion coefficients. The values are listed in Table 1 (Supporting Information) with brackets.

The concentration-dependent relaxation time $\tau_m(T, w)$ was calculated using the following equation proposed by Ferry:¹⁹

$$\tau_m(T, w) = a(T, T_0, w) \tau_m(T_0, w = 0) \quad (7)$$

Here $a(T, T_0, w)$ is a concentration-dependent shifting factor and $\tau_m(T_0, w = 0)$ is the reference relaxation time of the neat polymer at reference temperature $T_0 = T_g$. This shift-factor concept is based on the theory of William, Landel, and Ferry.²⁰ The shift factors for the temperature shift as well as for the concentration shift were taken from our previous work.⁸ The concentration dependence of the shift factor was introduced using the concentration dependence of the glass-transition temperature according to eq 1 from Kelly and Bueche⁹ which led to the following equation:⁸

$$\log a(T, T_0, w) = - \frac{c_1(T - T_{g,mixture})}{c_2 + (T - T_{g,mixture})} \quad (8)$$

Here c_1 and c_2 are the polymer-specific WLF-parameters, which have been already determined for the considered polystyrene, T is the measuring temperature in °C and $T_{g,mixture}$ is the glass-transition temperature of the polymer/VOC mixture in °C. At conditions, where $T_{g,mixture}$ is equal to the measuring temperature T , the shift factor $a(T, T_0, w)$ is equal to 1, which is equivalent to the relaxation time of the reference state: $\tau_m(T_{g,mixture}, w(T_{g,mixture})) = \tau_m(T_0, w = 0)$.

The reference relaxation time $\tau_m(T_0, w = 0)$ was estimated using a correlation given by Pipkin:¹⁷

$$\tau_m = \frac{1}{\eta_0} \cdot \int_0^\infty t(G(t) - G_e) dt \quad (9)$$

To apply this approach, the experimental creep-compliance data $F(t)$ of neat polystyrene published earlier⁸ was modeled by the following viscoelastic spring-dashpot model^{7,21}

$$F(t) = \frac{1}{E_0} + \sum_i \frac{1}{E_i} \left[1 - \exp\left\{-\frac{tE_i}{\eta_i}\right\} \right] + \frac{t}{\eta_0} \quad (10)$$

Afterward the creep compliance $F(t)$ was transferred into the shear modulus $G(t)$ using the following assumption:²¹

$$G(t) = \frac{1}{3F(t)} \quad (11)$$

The results of the creep-compliance modeling (eq 10) can be seen in Figure 7. Two different sets of parameters were used:

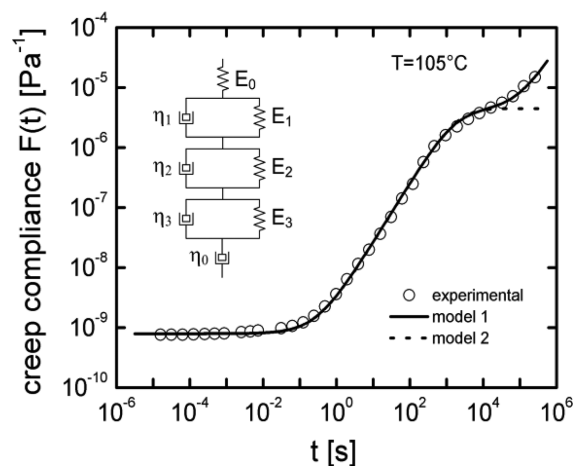


Figure 7. Creep-compliance curve of neat polystyrene at 105 °C. Experimental data were taken from Mueller et al.⁸ Lines are modeling results using eq 10. Model 1 describes the experimentally obtained data, and model 2 describes the theoretical behavior of the rubbery state without viscoelastic flow above the glass-transition.

parameter set one (model 1) was used to describe the true trend of the creep-compliance curve whereas parameter set two (model 2) was used to describe the theoretical trend of the creep-compliance curve without viscoelastic flow in the rubbery state. The assumption of no-viscoelastic flow in the rubbery state was necessary to allow for convergence of the integral in eq 9. All model parameters of eq 9 are listed in Table 2.

On the basis of that, we estimated a relaxation time of $\tau_m = 2.72 \times 10^4$ s at $T_0 = 105$ °C for the considered polystyrene. For comparison with literature, this value was converted to 129 °C using the WLF equation^{8,20} which led to a value of $\tau_m = 1.78 \times 10^2$ s.

Table 2. Model Parameters for the Spring–Dashpot Model (Eq 10) with Model Parameters for True Trend (Model 1) and for a Material Behavior without Viscous Flow (Model 2)¹⁴

parameter	model 1	model 2
E_0	4.2×10^8	4.2×10^8
E_1	1.0×10^4	1.0×10^4
E_2	1.4×10^5	1.4×10^5
E_3	2.0×10^5	2.0×10^5
η_0	8.0×10^9	8.0×10^{15}
η_1	6.0×10^{11}	6.0×10^{12}
η_2	1.5×10^8	1.5×10^8
η_3	1.0×10^9	1.0×10^9

Akovi²² published a value of $\tau_m = 8.40 \times 10^3$ s at 129 °C for a monodisperse polystyrene with the same molar mass of $M_w = 240\,000$ g/mol. The smaller value for the relaxation time obtained in this work could be caused by the fact, that the PDI of the investigated polystyrene is 5.65. For a given weight-average of a polymer, a broader molecular weight distribution (higher PDI value) causes smaller relaxation times due to the presence of the short polymer chains. Thus, monodisperse polystyrene with a molar mass of $M_w = 117\,000$ g/mol exhibits a relaxation time of $\tau_m = 5.2 \times 10^2$ s at 129 °C.²² This indicates that the order of magnitude of the estimated relaxation time is in good agreement with the values published in literature.

The finally obtained Deborah numbers for the investigated systems at 30, 50, and 70 °C are graphically shown in Figure 8

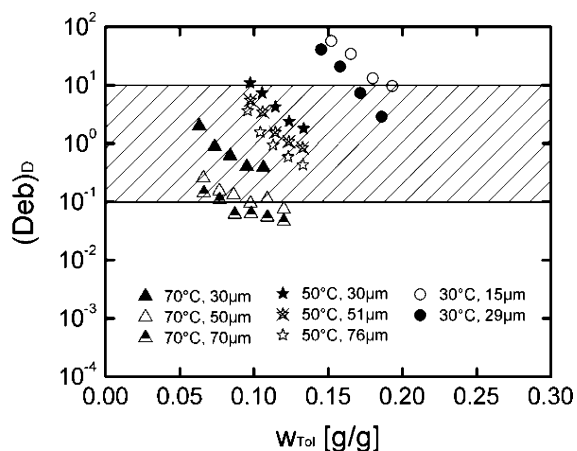


Figure 8. Calculated diffusion Deborah numbers for polystyrene/toluene mixtures at 30, 50, and 70 °C at different toluene concentrations. The hatching indicates a Deborah-number range between 0.1 and 10, which should indicate the region of non-Fickian diffusion.⁵

and summarized in Table 1 (Supporting Information). According to Vrentas et al.⁵ the value of the calculated Deborah number qualitatively indicates whether a diffusion is purely Fickian or not. They proposed that a Deborah number between approximately 0.1 and 10 indicates non-Fickian diffusion which means that the characteristic relaxation time τ_m of the mixture and the mutual diffusion time θ_D are in the same magnitude. The predicted diffusion regimes (Fickian or non-Fickian) are compared with the experimental observations for each individual sorption step in Table 1 (Supporting Information).

It can be seen in Figure 8 that all calculated Deborah numbers decrease with increasing toluene load. This is due to

the fact that increasing toluene load of the polymer/VOC mixture has the same effect as increasing temperature of a neat polymer, namely a decreasing relaxation time. Moreover, it can be seen, that the calculated Deborah numbers decrease with increasing film thickness for each temperature. This is due to the fact, that the diffusion coefficients as well as the relaxation times are independent of film thickness, whereas the Deborah number is a function of film thickness as it can be seen from eq 4 and eq 5.

Comparing the sorption measurements of this work to the diffusion regimes according to the Deborah number (see Table 1 (Supporting Information)), we find that all calculated Deborah numbers are in the order of one magnitude to high compared with the experimental findings. For the 30 °C measurements all experimental sorption curves were found to be non-Fickian whereas at least for the lower concentrations at 30 °C the calculated Deborah numbers are above 10 indicating Fickian diffusion behavior. The 50 °C and the 70 °C measurements all showed Fickian diffusion. In contrast to this the calculated diffusion regime for 50 °C is all non-Fickian with Deborah numbers between 0.1 and 10. For 70 °C only the calculated low concentration points still remain in the non-Fickian region whereas at higher solvent concentrations the calculated diffusion regime is again Fickian with Deborah numbers below 0.1.

It can be concluded that the findings in this paper are explainable with the diffusion Deborah number concept. The concept predicts the Fickian or non-Fickian diffusion for the polystyrene/toluene system qualitatively well, although there are some quantitative deviations since the calculated Deborah numbers are about 1 order of magnitude higher when compared with the experimental observations. The main reason for this discrepancy will probably be the determination of the relaxation time, which is burdened with some assumptions (e.g., concentration, temperature dependence, and shift to the experimental conditions, eq 7 and eq 8) as well as experimental uncertainties in the determination of the relaxation time. These can certainly account for an error of this magnitude.

A classification of the diffusion-type slightly above the glass-transition of the mixture only with the Deborah number concept based on literature data might not be accurate enough. A combination with the traditional analysis of reduced sorption curves for different film thicknesses at otherwise identical conditions promises to give the most reliable results.

CONCLUSIONS

The diffusion of toluene in polystyrene was investigated at different concentrations and temperatures in the vicinity of the glass-transition of the mixture. For this system, it was found that at lower temperatures, non-Fickian diffusion extends far more into the region above the calculated glass-transition of the mixture than at high temperatures. Here a determination of the diffusion coefficient from a single sorption curve alone can lead to wrong values although the sorption curve looks Fickian. A more thorough test at different polymer–film thicknesses and subsequent analyses of the reduced sorption curves and/or of the derived diffusion coefficients reveal the significance of the polymer relaxation for the diffusion process in the polystyrene/toluene system.

The Deborah number concept was applied using a relaxation time of the polystyrene/toluene mixture which was estimated using relaxation data measured in exactly the same system using a completely novel experimental setup which has recently been

published.⁸ The results show qualitatively the same trend but deviate by about 1 order of magnitude. The reason for this might be caused by the uncertainties of determination of the relaxation time.

■ ASSOCIATED CONTENT

■ Supporting Information

Table of experimental sorption data and calculated Fickian diffusion coefficients. This material is available free of charge via the Internet at <http://pubs.acs.org>.

■ AUTHOR INFORMATION

Corresponding Author

*E-mail: G.Sadowski@bci.tu-dortmund.de.

Present Address

†Evonik RohMax Additives GmbH, Innovation Management Oil Additives, Kirschenallee, 64293 Darmstadt, Germany, E-mail: Kai-Martin.Krueger@evonik.com

■ ACKNOWLEDGMENTS

The authors are grateful to the Deutsche Forschungsgemeinschaft for supporting this work with Grant SAD 700/13.

■ REFERENCES

- (1) Krueger, K.-M.; Sadowski, G. *Macromolecules* **2005**, *38* (20), 8408–8417.
- (2) Kishimoto, A.; Matsumoto, K. *J. Polym. Sci.: Part A* **1964**, *2* (2), 679–687.
- (3) Odani, H. *J. Polym. Sci., Part A-2* **1967**, *5* (6), 1189–1197.
- (4) Fujita, H. *Fortschr. Hochpolym.-Forsch.* **1961**, *3*, 1–47.
- (5) Vrentas, J. S.; Jarzebski, C. M.; Duda, J. L. *AIChE J.* **1975**, *21* (5), 894–901.
- (6) Vrentas, J. S.; Duda, J. L. *J. Polym. Sci., Part B: Polym. Phys.* **1977**, *15* (3), 441–453.
- (7) Krueger, K.-M. Sorption und Diffusion von Lösungsmitteln in glasartigen Polymeren. Dissertation, Dortmund, 2006.
- (8) Mueller, F.; Heuwers, B.; Katzenberg, F.; Tiller, J. C.; Sadowski, G. *Macromolecules* **2010**, *43* (21), 8997–9003.
- (9) Kelley, F. N.; Bueche, F. J. *J. Polym. Sci.* **1961**, *50* (154), 549–556.
- (10) Daubert, T. E.; Danner, R. P., *Data Compilation Tables of Properties of Pure Compounds*; American Institute of Chemical Engineers: New York, 1985.
- (11) Danner, R. P.; High, M. S., *Handbook of Polymer Solution Thermodynamics*; American Institute of Chemical Engineers: New York, 1993.
- (12) Riddick, J. A.; Bunger, W. B.; Sakano, T. K., *Organic Solvents Physical Properties*; Wiley-Interscience: New York, 1986; Vol. 4th.
- (13) Crank, J., *The Mathematics of Diffusion*; Clarendon Press: Oxford, U.K., 1975.
- (14) Heuwers, B. Diploma Thesis, TU Dortmund University 2009.
- (15) Vrentas, J. S.; Vrentas, C. M. *J. Polym. Sci., Part B: Polym. Phys.* **2001**, *39* (13), 1529–1547.
- (16) Sanopoulou, M.; Petropoulos, J. H. *Macromolecules* **2001**, *34* (5), 1400–1410.
- (17) Pipkin, A. C., *Lectures on Viscoelasticity Theory*; Springer-Verlag: New York, Heidelberg, Germany, Berlin, 1972; Vol. 7.
- (18) Billovits, G. F.; Durning, C. J. *Macromolecules* **1993**, *26* (25), 6927–6936.
- (19) Ferry, J. D. *Viscoelastic Properties of Polymers*, 2nd ed.; Wiley: New York, 1970.
- (20) Williams, M. L.; Landel, R. F.; Ferry, J. D. *Phys. Rev.* **1955**, *98* (5), 1549–1556.
- (21) Ferry, J. D. *Viscoelastic Properties of Polymers*; John Wiley & Sons Inc.: New York, 1980; Vol. 3.
- (22) Akovali, G. J. *J. Polym. Sci., Part A-2: Polym. Phys.* **1967**, *5* (5pa2), 875–889.

Positron Annihilation Spectroscopy of Polystyrene Filled with Carbon Nanomaterials

Somia Awad,[†] H. M. Chen,[†] Brian P. Grady,[§] Abhijit Paul,[‡] Warren T. Ford,[‡] L. James Lee,^{||} and Y. C. Jean^{†,*}

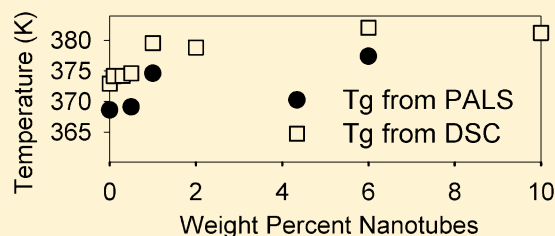
[†]Department of Chemistry, University of Missouri—Kansas City, 5009 Rockhill Rd., Kansas City, Missouri 64110, United States

[‡]Department of Chemistry, Oklahoma State University, Stillwater, Oklahoma 74078, United States

[§]Carbon Nanotube Technology Center (CaNTeC) and School of Chemical, Biological, and Materials Engineering, University of Oklahoma, Norman, Oklahoma 73019, United States

^{||}Department of Chemical and Biomolecular Engineering, The Ohio State University, Columbus, Ohio 43210, United States

ABSTRACT: Positron annihilation lifetime spectroscopy (PALS) was employed to study the free volume properties of polystyrene (PS) containing three different types of carbon nanoparticles: polystyrene-grafted single wall carbon nanotubes (SWCNTs-g-PS), single wall carbon nanotubes (SWCNTs), and carbon nanofibers (CNFs). The glass transition temperature measured via PALS was significantly lower than that from differential scanning calorimetry (DSC), although qualitatively the two methods agreed in that the T_g measured increased as nanotubes were added to the material. There were some specific differences between the two measurements which may have been related to the fact that DSC does not measure T_g of a portion of the material which is immobilized on the surface of the particle, while PALS measures all polymer, whether immobilized or not. PALS was also used to measure the thermal expansion coefficient and distributions of the free volume of the polystyrene.



1. INTRODUCTION

Polymer nanocomposites have been investigated extensively due to their advanced mechanical, thermal, and physical-chemical properties.^{1–5} The interaction between polymers and filler surface is much more important than with conventional fillers, because the interfacial area is much larger for the nanofillers. Glass transition temperature (T_g) is an important parameter and relates to the modulus, brittleness and permeability of polymers. In nanocomposites, the effect of the addition of filler on T_g is expected to depend on the interaction energy between the polymer chains and nanoparticle surfaces. Because of their high aspect ratio and specific surface area,⁶ high Young's modulus,⁷ high tensile strength, electrical conductivity and thermal conductivity,^{8,9} carbon nanotubes (diameter of 2–80 nm and typical length of 0.5–10 μm)^{10–12} and nanofibers (diameter of 70–200 nm and length 50–100 μm)^{10,13,14} are considered as excellent fillers for the development of advanced multifunctional polymer-based materials.

A single-wall carbon nanotube (SWCNT)^{15–17} can be treated as a conformal mapping of the two-dimensional hexagonal lattice of a single graphene sheet onto the surface of a cylinder. The graphite sheet may be 'rolled' in different orientations along any two-dimensional lattice vector (m,n) which then maps onto the circumference of the resulting cylinder; the orientation of the graphite lattice relative to the axis defines the *chirality* or *helicity* of the nanotube.⁸ Carbon nanofibers (CNFs)¹⁸ are mainly differentiated from nanotubes

by the orientation of the graphene planes: whereas the graphitic layers are parallel to the axis in nanotubes, nanofibers can show a wide range of orientations of the graphitic layers with respect to the fiber axis. CNFs can be visualized as stacked graphitic disks or (truncated) cones, and are intrinsically less perfect as they have graphitic edge terminations on their surface.

Because of the poor solubility of CNTs, chemical functionalization of its surface with suitable groups was proposed to enhance the solubility, to induce a better dispersion, and to improve bonding strength between nanotubes and the polymer matrix.¹⁹ Functionalizing nanotubes with a compatible polymer with the matrix²⁰ provides one of the best possible interfaces with a host polymer. Carboxylic acid groups created on the CNT surface by oxidation²¹ provide opportunity to synthesize many different functional groups on SWCNTs²² as well as polymers grafted to SWCNTs. Chemically modified carbon nanotubes are more dispersible than pristine nanotubes in most solvents²³ and are more easily incorporated into a polymer matrix.

Particle–matrix interactions play an increasingly important role as the filler size drops below 1 μm . It is not the absolute size but rather the specific surface area of the filler, and the resulting interfacial volumes, which significantly influence the properties of the final composite. Interfacial regions can have

Received: November 7, 2011

Revised: December 21, 2011

Published: January 6, 2012

distinctly different properties from the bulk polymer and can represent a substantial volume fraction of the matrix for nanoparticles with surface areas of the order of hundreds of m^2/g . The actual interphase volume depends on the dispersion and distribution of the filler particles, as well as their surface area. In traditional fiber composites, the interfacial region is defined as the volume in which the properties deviate from those of the bulk matrix or filler.²⁴ A straightforward calculation²⁵ of the interparticle distance s provides an estimate for the distance between particles:

$$s = d \times \left[\left(\frac{\pi}{6\phi_v} \right)^{1/3} - 1 \right] \quad (1)$$

where d is the diameter and ϕ_v is the volume fraction of uniformly sized, spherical particles on a lattice. When this distance is on the order of the radius of gyration of the polymer, then one would expect that the interfacial material would have a significant effect.

More common methods, such as NMR, FTIR, DMTA, neutron diffraction, X-ray diffraction, AFM, SEM, XPS, etc.,^{26–31} have been employed to investigate polymer nanocomposites. Only recently, a novel method, positron annihilation spectroscopy (PAS), has been used to investigate atomic and molecular defects and interfacial properties.^{32–61} One of the PAS techniques, positron annihilation lifetime spectroscopy (PALS), is capable of determining the free-volume and hole properties directly at the atomic and nanoscale.^{62,63} This capability arises from the fact that positronium (bound state of positron and electron; Ps) is preferentially localized in regions of low electron density sites, such as free volumes, holes, interfaces, and pores. The primary mechanism of annihilation of ortho positronium (o-Ps), the triplet state of Ps, is by pick-off with electrons of the polymeric materials under study. Thus, the intrinsic o-Ps lifetime (142 ns) is shortened to a few ns (1–10 ns) by two- γ annihilation processes. Generally, the lifetime of o-Ps is determined by an overlap integral between the positron and electron densities in the free volumes of molecular systems. Therefore, the o-Ps lifetime is expected to correlate directly with the dimensions where Ps is localized. A larger hole, which contains a lower mean electron density, results in a longer Ps lifetime. A simple quantum mechanical model, where o-Ps resides in a spherical well having an infinite potential barrier of radius R_0 with a homogeneous electron layer in the region $R < r < R_0$, ($R_0 = R + \Delta R$) was proposed to derive the relationship between size and o-Ps lifetime.⁶⁵ Such a model provides a simple relation between the o-Ps lifetime, usually denoted as τ_3 , the third mean lifetime as analyzed from experimental PALS data, and the mean free-volume radius (R). A semiempirical equation by fitting the measured o-Ps lifetime (τ_3) in a spherical infinitive potential model with known cavity sizes is established as:

$$1/\tau_3 = 2[1 - R/R_0 + (1/2\pi) \sin(2\pi R/R_0)] \quad (2)$$

where τ_3 and R are expressed in the units of ns and Å, respectively and ΔR was calibrated to be 1.656 Å.^{62,66}

PALS studies in polystyrene (PS) and carbon composite systems have been previously reported.⁶⁴ The main purpose of the present work is to understand how functionalizing the surface of the nanotubes and comparing results with untreated CNF affects the PAS determination of free volumes and the

glass transition temperature compared with those from DSC method.

2. EXPERIMENTAL SECTION

2.1. SWCNT/PS Material Preparation. SWCNT (HiPCo, Carbon Nanotechnologies Inc., Houston, TX) gently treated with nitric acid²¹ were used to prepare the SWCNT/PS composites^{67,68} and the SWCNT-g-PS/PS composites.^{67,69} SWCNT-g-PS (polystyrene-grafted single walled carbon nanotubes) was prepared by the free radical addition of TEMPO [(2,2,6,6-tetramethylpiperidin-1-yl)oxyl]-ended PS of $M_n = 15,000$ to the SWCNT. The SWCNT-g-PS/PS composites were prepared by coagulation of a PS solution in *N*-methylpyrrolidinone containing dispersed SWCNT into water.⁶⁹ AFM images of the SWCNT and TEM images of the SWCNT-g-PS showed individual SWCNT and bundles of SWCNT <10 nm in diameter.^{67,69} No high resolution images of the composites were obtained. The SWCNT/PS composites had a percolation threshold of electrical conductivity at 0.5 wt % SWCNT. The SWCNT-g-PS/PS composites had no percolation threshold up to 3 wt % SWCNT, which could be due to the insulating layer of PS grafted to the SWCNT or to poor dispersion. The polystyrene was an industrial grade having $M_n = 70,000$ and $M_w/M_n = 3.2$ and was the same material used previously.^{68,69}

Another type of industrial grade PS for CNF experiments was obtained from Atofina (Houston, TX, $M_n = 86,000$). The compositions of all composites are reported in wt % of carbon filler, irrespective of any grafted PS.

2.2. Preparation of CNF Composites. Polystyrene Fina (PS) ($M_n = 86,000$, Total Petrochemicals, formerly Atofina, Houston, Texas) was used as received. Vapor grown carbon nanofibers (CNF) (PR-24-PS, Applied Science Inc. Cedarville, Ohio) were pyrolytically stripped to remove surface organic contamination. The average diameter of these CNF was about 100 nm. CNF nanocomposites were prepared via melt blending which was performed using a DACA microcompounder.^{52,53} The compounding temperature, rotor speed and compounding time were set at 200 °C, 250 rpm and 5 min, respectively. The prepared composites samples have concentrations of 1, 3, 5, 7, and 9 wt % respectively of CNF in PS.⁵³

2.3. Positron Annihilation Lifetime Spectroscopy (PALS). A conventional fast-fast coincidence spectrometer with a time resolution 280 ps was used for PALS measurements.⁶² The samples of SWCNT, SWCNT-g-PS and CNF composites have thickness of about 100 μm and hence were stacked to obtain a suitable ~ 1 mm thickness. The positron source (10 μCi) ^{22}Na was deposited in an envelope of Kapton foils (6 μm thick) and then sandwiched in between eight identical pieces of the samples (for a total of approximately 1 mm thick, 1 cm \times 1 cm area). This sandwich was completely enclosed in a copper sample holder sealed in glass tube under vacuum. Each selected temperature was kept constant within 0.5 K during data acquisition. The entire source-sample assembly was placed under high vacuum. The following sequence of measurements was carried out: first, the sample temperature was raised to 433 K and the sample was annealed for 2 h to eliminate any temperature hysteresis. Second, the temperature was lowered in steps of 20 to 298 K and then increased at a temperature interval of 5–20 K per step to 433 K. Up to three cycles of this procedure were performed. One or two million counts were recorded at each temperature for a typical period of acquisition 3–4 h. In conventional analysis the PATFIT-88 program⁷⁰ was employed. The PALS spectra were analyzed into three components (τ_1 , τ_2 and τ_3) with their intensities (I_1 , I_2 , and I_3). Source correction terms were made from each spectrum in data analysis. We further used LT.9 program⁷¹ to obtain the lifetime distribution. Four-lifetime analyses were attempted and the results were not as systematic as from three-lifetime analysis and hence only three-lifetime analysis results are presented here.

2.4. Differential Scanning Calorimetry (DSC). DSC measurements for all composites were performed at 10 K/min on a TA Instruments Q-1000 as described previously for the SWCNT⁶⁸ and SWCNT-g-PS composites⁶⁹ and on a TA 2920 calorimeter for the CNF/PS composites.⁵³ In both cases, samples were heated above T_g to

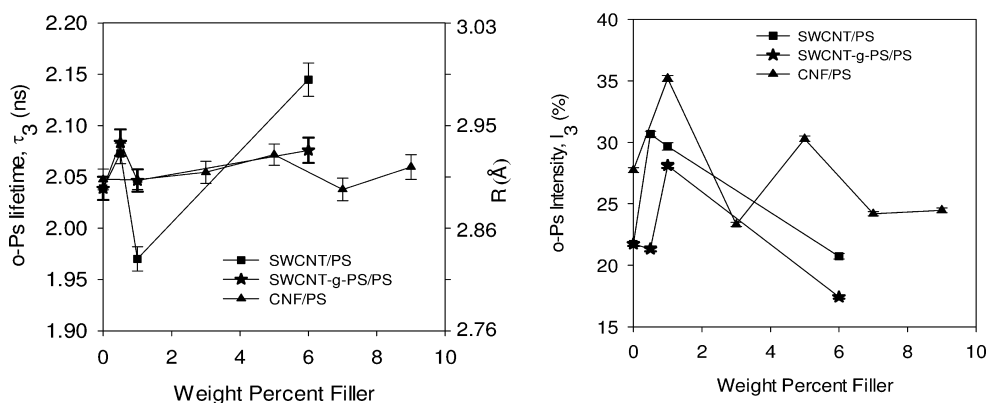


Figure 1. o-Ps lifetime and intensity as a function of filler concentration in PS. Error bars are smaller than the data points for the graph on the right.

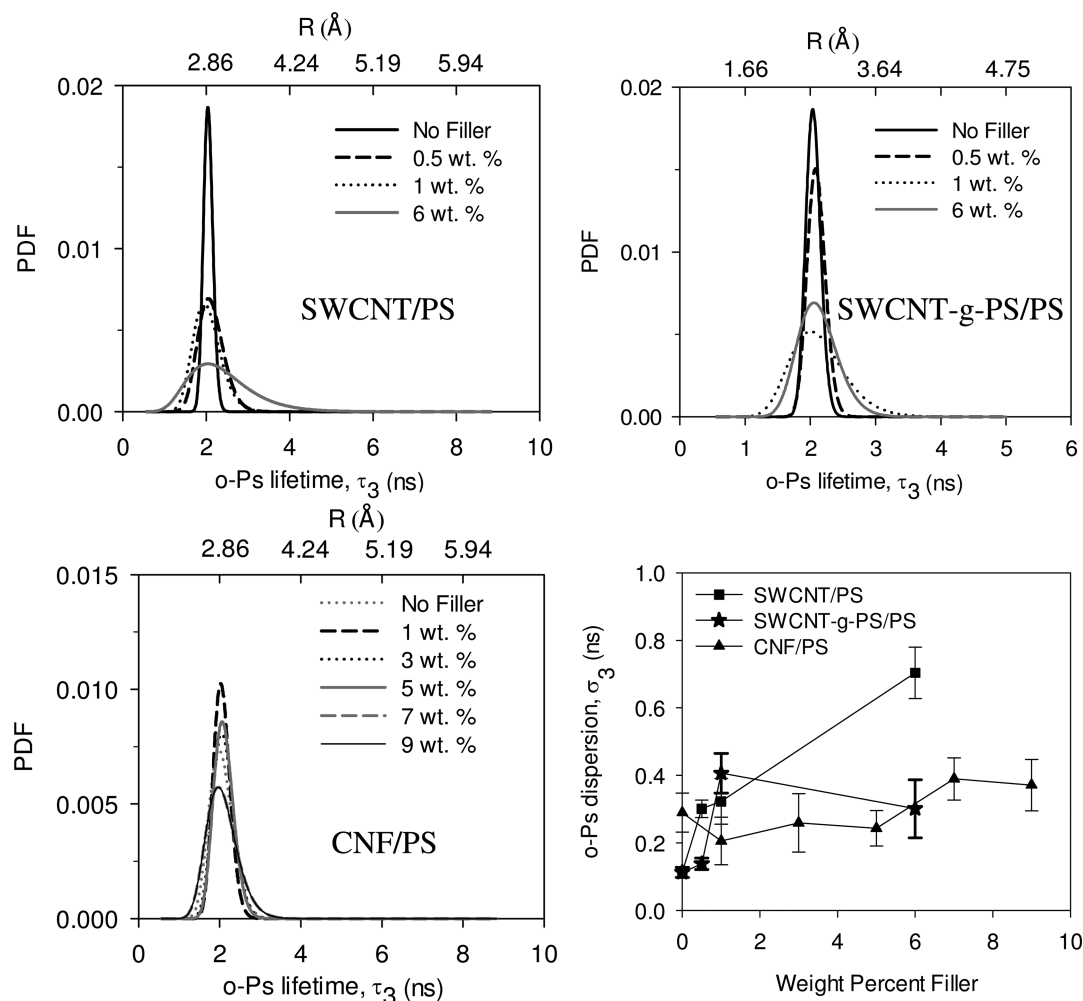


Figure 2. o-Ps lifetime distributions and its dispersion in different carbon nanoparticles concentrations in PS at 298 K.

erase any thermal history, quickly cooled to far below the T_g and then heated at 10 K/min and the heat capacity was measured. T_g s were defined as the midpoint of the change in the heat capacity ΔC_p .

3. RESULTS AND DISCUSSION

3.1. Dependence of o-Ps Lifetime on CNT Compositions in PS. Figure 1 shows the o-Ps lifetime, τ_3 , (also free-volume radius, R) and o-Ps formation intensity, I_3 , as a function of nanofiller concentration. The o-Ps lifetime does not have a systematic change with changing nanofiller concentration. On

the other hand, I_3 , the o-Ps probability formation, changes in the order SWCNT/PS-g-PS < SWCNT/PS < CNF/PS. While I_3 depends on chemical and physical properties, the trend of change may be related to whether or not PS chains are covalently bonded to the surface of the nanotubes.

PALS data were further fitted into lifetime distribution using the LT program. Figure 2 shows the results of o-Ps (τ_3 or free-volume radius) distributions and o-Ps lifetime dispersion σ_3 from LT analysis. It is interesting to observe a broadening of distributions for all systems with increasing SWCNT

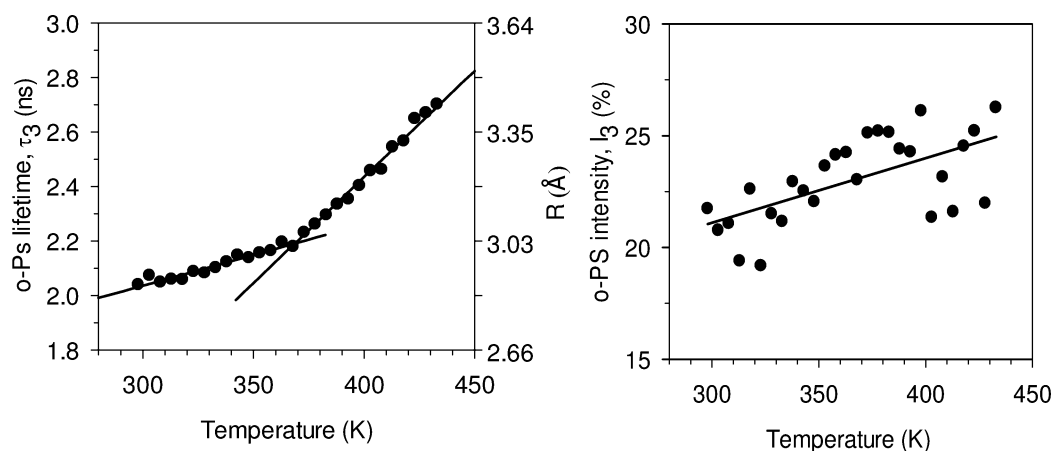


Figure 3. o-Ps lifetime vs temperature (left) and its intensity vs temperature (right) in the PS used for SWCNT composites. Lines were determined via linear regression. Error bars are within the sizes of data points shown.

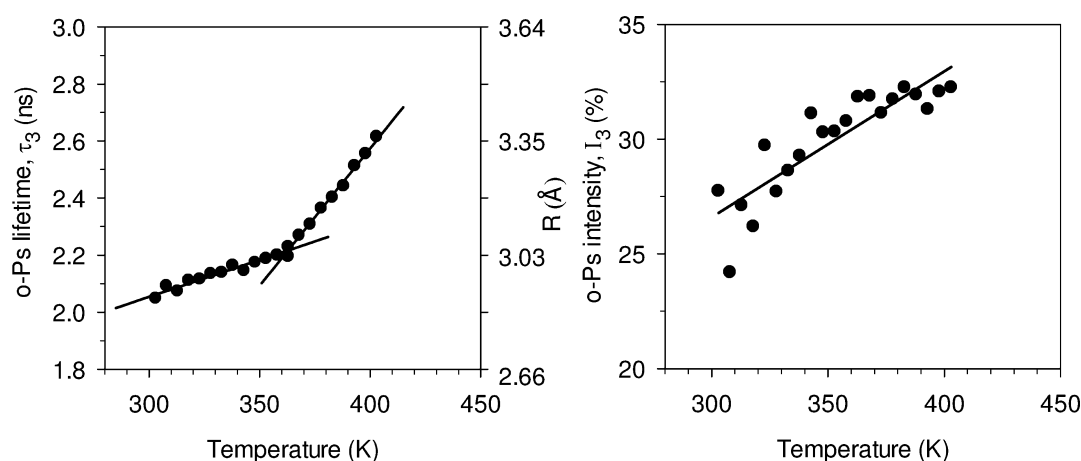


Figure 4. o-Ps lifetime vs temperature (left) and its intensity vs temperature (right) in the FINA PS used for CNF composites. Lines were determined via linear regression. Error bars are within the sizes of data points shown.

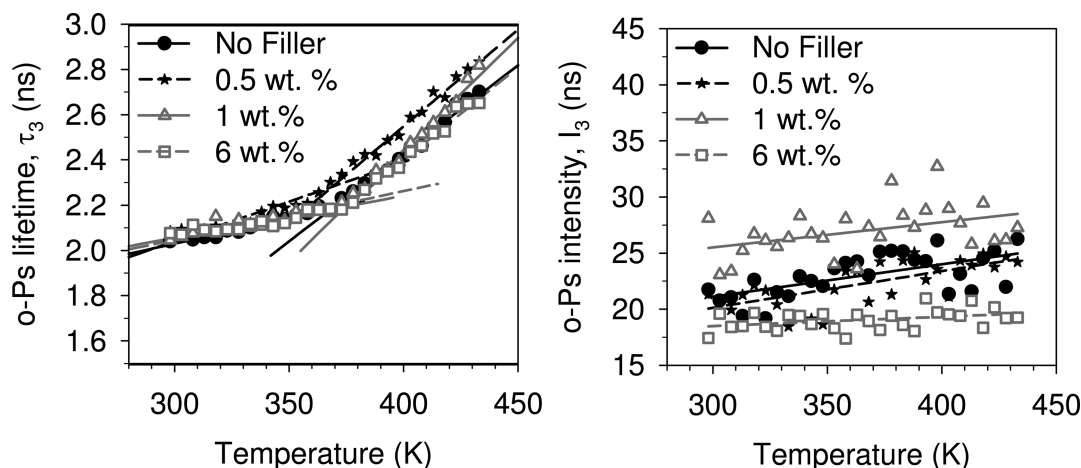


Figure 5. o-Ps lifetime vs temperature (left) and o-Ps intensity vs temperature (right) in SWCNT-g-PS/PS nanocomposites. Error bars are within the sizes of data points shown.

concentration. The broadening in free-volume distribution is likely a consequence of the broadening of free volumes from the changes in chain dimensions that occur with the introduction of nanotubes due to some chains being near the surface of the filler, and hence having smaller radii, and also

with some chains being further away and essentially having larger free-volume radii.

3.2. Temperature Dependence of Positron Annihilation Lifetime in PS. We have performed PALS experiments in well-annealed samples as a function of temperature under high vacuum (5×10^{-5} Torr). The temperature dependence of the

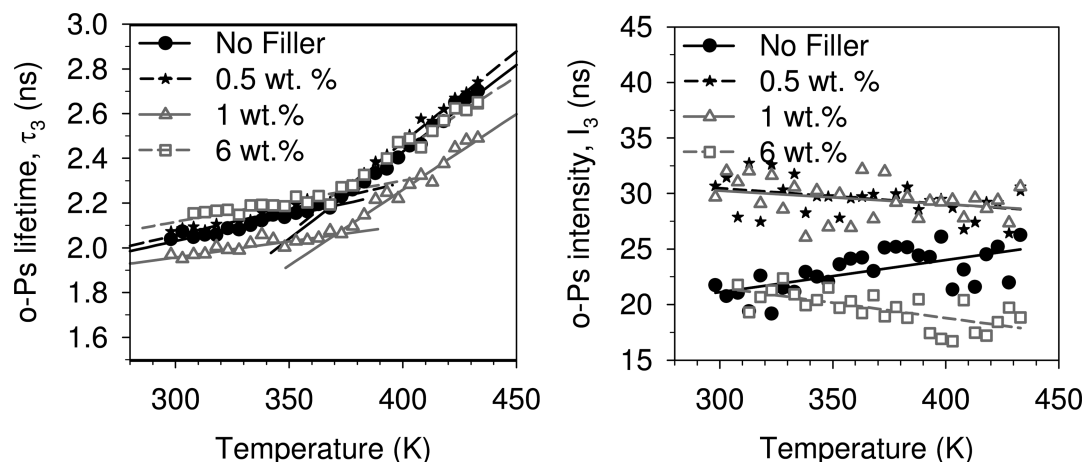


Figure 6. o-Ps lifetime vs temperature (left) and o-Ps intensity vs temperature (right) in SWCNT/PS nanocomposites.

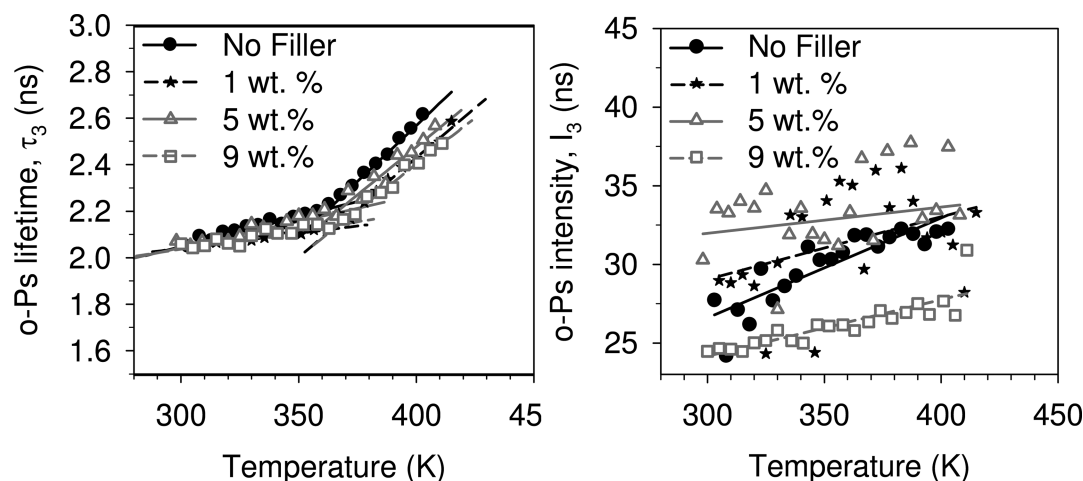


Figure 7. o-Ps lifetime vs temperature (left) and o-Ps intensity vs temperature (right) in CNF/PS nanocomposites. Error bars are within the sizes of data points shown.

o-Ps lifetime and its intensity for the matrix PS used for SWCNT-g-PS/PS and SWCNT/PS is shown in Figure 3. While the o-Ps lifetime increases with increasing temperature as observed in polymers as o-Ps localization in regions of low electron density, i.e., free volume holes.⁶² The o-Ps intensity increases slightly with temperature. The o-Ps lifetime variations compose of two regions: the low temperature ($T < 368$ K) and the high temperature $T > 368$ K, respectively. The variation from PALS in these two regions is consistent with the reported results obtained by different techniques in similar polystyrene systems.⁷³ We therefore fitted two regions data in two linear regressions and obtained two lines as shown in Figure 3. PALS results do not show hysteresis, which indicates that there is no physical or chemical aging in the temperatures between 300 and 433 K during a period of one month of the PALS experiments. Therefore, the increase of o-Ps lifetime or free-volume size is simply thermal expansion of free volume. In the low T region (< 368 K), the increase of free volume is dominated by molecular vibrations and local motions. The onset temperature (368.6 ± 0.6 K) where the free volume changes slope is assigned as T_g and is consistent with the literature T_g value measured using PALS.^{74–78} At temperatures above T_g , the polymer has increased segmental motions relative to that below T_g relating to a faster increase in hole size with increasing temperature.

For the PS used in CNF composites, results are shown in Figure 4. The o-Ps lifetime has similar behavior as pristine PS and $T_g = 362.1 \pm 2.4$ K. The fact that the T_g 's are that different is surprising, since the number-average molecular weights are comparable. We do not have a good explanation for this difference except that it is known that the absolute values of PALS results depend on the source of polymers, particularly for industrial grade samples. Furthermore, the o-Ps intensity is higher and increases more with increasing temperature than with the other PS.

The results of o-Ps lifetime vs temperature for SWCNT-g-PS/PS composites, SWCNT/PS composites, and CNF/PS composites with different nanoparticle loadings are shown in Figures 5–7. We observe: (1) o-Ps intensity increases slightly with temperature for all SWCNT-g-PS/PS samples with all concentrations, (2) two regions of o-Ps lifetime variations vs T are seen as in pristine PS, and (3) the intercept temperature can be obtained from linear regression as was done previously.

T_g determinations from PALS experiments are shown in Figure 8 and are compared to that from DSC measurement. The systematically lower T_g from PALS than from DSC is thought to be due to the rate difference between these two methods. One PALS experiment takes hours whereas a DSC experiment takes minutes.^{62,72–79} The most striking difference is that although all show an increase with an increase in filler

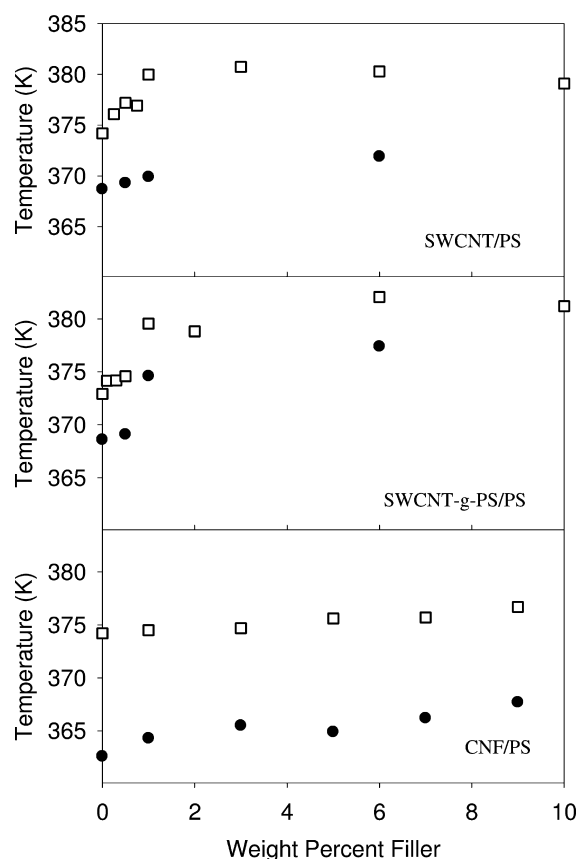


Figure 8. Comparison of glass transition temperatures as a function of carbon nanoparticle concentration in PS matrixes from PALS (solid symbols) and DSC (open symbols). Filled circles are PALS data while open squares are DSC data. Error bars are within the sizes of data points shown.

content, the qualitative nature of the increase is not consistent between the different fillers. In other words, for SWCNT/PS the increase in PALS T_g with nanotube content is linear, while that from DSC is not; conversely for CNF/PS the increases are both linear. There is a difference in the material that is being measured between the two measurements however. In nanocomposites, there is an interfacial region near the filler that can have a very different dynamic behavior which will not participate in the T_g of the bulk polymer. PALS will sample the interfacial and bulk material, while the T_g measured by DSC only reflects the bulk material.

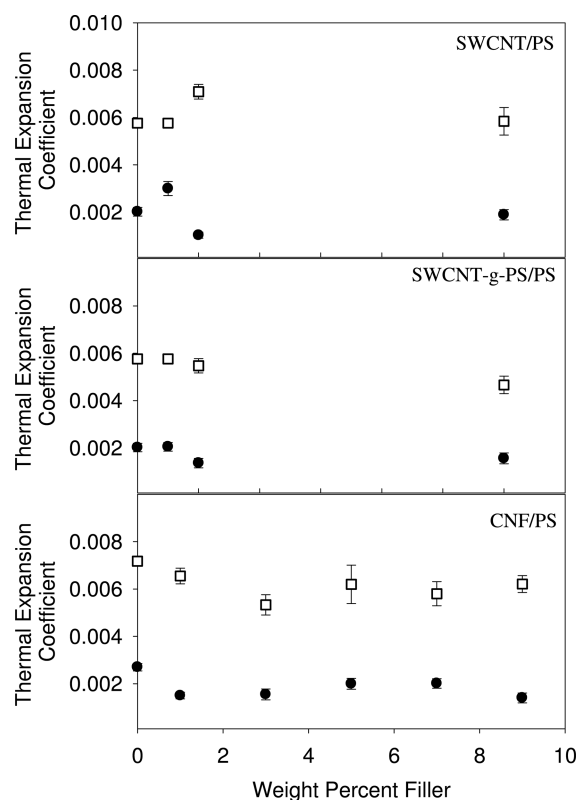


Figure 10. Comparison of free-volume thermal expansion coefficient as a function of carbon nanoparticle concentration in PS matrixes from PALS. Dark circles represent the value below T_g , while open squares represent the value above T_g .

Although the T_g of the interfacial material is not recorded during measurements over this temperature interval, the amount of interfacial material can be determined via the change in heat capacity (ΔC_p of pure polystyrene – ΔC_p of the nanocomposite) with the heat capacity normalized to the weight of polymer in the latter and not the weight of total material. The former is plotted in Figure 9 for the SWCNT/PS and SWCNT-g-PS and shows a significant qualitative difference between the two materials except at 10% where the SWCNT composition is high. However, there is no qualitative correspondence for the PALS data with ΔC_p either. The questions that this work raises are the following: (1) Does the free volume vs temperature behavior of the interfacial region change in some manner with the glass transition of the bulk

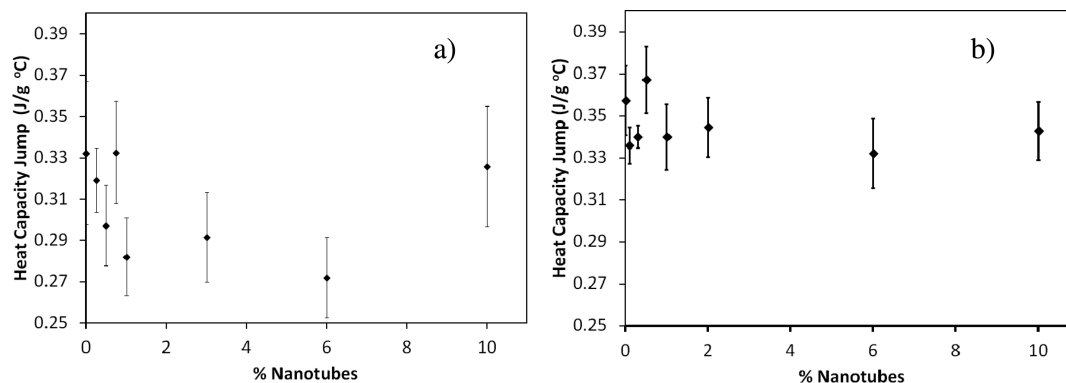


Figure 9. ΔC_p for (a) SWCNT/PS composites (b) and SWCNT-g-PS/PS composites.

polymer? (2) Does the C_p vs temperature behavior of the interfacial region change in some manner with the glass transition of the bulk polymer? To paraphrase the latter, is the C_p vs temperature behavior of the interfacial region above the glass transition of the polymer the same as the C_p vs temperature behavior of the glassy material? Both are very open questions.

The thermal expansion coefficient of the free volume is given by α_{fv} from the equation $\alpha_{fv} = (1/V_h)(\Delta V_h/\Delta T)^{62,63}$ where $V_h = 4\pi R^3/3$. The results of the free-volume thermal expansion coefficients in two regions α_{fv1} (glassy state), α_{fv2} (rubbery state) are found in Figure 10. PALS values (on the order of 10^{-3} K $^{-1}$), are significantly larger than the thermal expansion coefficient of bulk PS [$(1.7-2.18) \times 10^{-4}$ for $T < T_g$ and $(5.1-6) \times 10^{-4}$ K $^{-1}$ for $T > T_g$].⁸⁰ This large difference comes from the fact that PALS probes only the free volume while the bulk α_{bulk} is contributed from a fraction of free-volume expansion data.^{62,63} The SWCNT-g-PS/PS and CNF samples show a decrease in thermal expansion coefficient with added nanotubes, while the trend for the SWCNT/PS sample is not clear.

4. CONCLUSIONS

We have reported a systematic study of free volumes in a series of polystyrene/carbon nanoparticles composites as a function of temperature between 298 and 433 K using PALS. Overall, nanotubes shift the T_g to higher temperature, which is in agreement with DSC studies. The thermal expansion coefficient drops as expected since the carbon filler has a smaller thermal expansion coefficient than the polymer; however PALS measures just the free volume expansion in the polymer so this drop could not necessarily be predicted.

AUTHOR INFORMATION

Corresponding Author

*E-mail: jeany@umkc.edu. Telephone: 816-235-2295.

ACKNOWLEDGMENTS

S.A. wishes to thank the financial support of the channel system and mission department of Egypt. This research is supported by the NSF-sponsored Nanoscale Science and Engineering Center for Affordable Nanoengineering of Polymeric Biomedical Devices (NSEC-CANPBD), the National Institute of Standards, and Technology and Army Research Office (W911NF-10-1-0476), the Oklahoma State Regents for Higher Education (W.T.F.), and the Department of Energy (DE-FG02-06ER64239 to B.P.G.). We acknowledge Dr. Xiaohong Gu's involvement with this project.

REFERENCES

- (1) Moniruzzaman, M.; Winey, K. I. *Macromolecules* **2006**, *39*, 5194.
- (2) Ramanathan, T.; Abdala, A.; Stankovich, S.; Dikin, D.; Herrera-Alonso, M.; Piner, R.; Adamson, D.; Schniepp, H.; Chen, X.; Ruoff, R. *Nature Nanotechnol.* **2008**, *3*, 327.
- (3) Sahoo, N. G.; Rana, S.; Cho, J. W.; Li, L.; Chan, S. H. *Prog. Polym. Sci.* **2010**, *35*, 837.
- (4) Jordan, J.; Jacob, K. I.; Tannenbaum, R.; Sharaf, M. A.; Jasiuk, I. *Mater. Sci. Eng. A* **2005**, *393*, 1.
- (5) Hussain, F.; Hojjati, M.; Okamoto, M.; Gorga, R. E. *J. Compos. Mater.* **2006**, *40*, 1511.
- (6) Gojny, F. H.; Wichmann, M. H. G.; Fiedler, B.; Bauhofer, W.; Schulte, K. *Compos. Part A: Appl. Sci. Manuf.* **2005**, *36*, 1525.
- (7) Mitchell, C. A.; Bahr, J. L.; Arepalli, S.; James, M.; Krishnamoorti, R. *Macromolecules* **2002**, *35*, 8825.
- (8) Harris, P. J. F., Ed.; *Carbon Nanotubes and Related Structures-New Materials for the Twenty-First Century*; Cambridge University Press: Cambridge, U.K., 2001.
- (9) Terrones, M. *Annu. Rev. Mater. Res.* **2003**, *33*, 419.
- (10) Qian, D.; Dickey, E. C.; Andrews, R.; Rantell, T. *Appl. Phys. Lett.* **2000**, *76*, 2868.
- (11) Thostenson, E. T.; Ren, Z.; Chou, T.-W. *Compos. Sci. Technol.* **2001**, *61*, 18991.
- (12) Xie, X.-L.; Mai, Y.-W.; Zhou, X.-P. *Mater. Sci. Eng. R* **2005**, *49*, 89.
- (13) Tsubokawa, N. *Polym. J.* **2005**, *37*, 637.
- (14) Wu, G.; Asai, S.; Sumita, M.; Yui, H. *Macromolecules* **2002**, *35*, 945.
- (15) Iijima, S. *Nature* **1991**, *354*, 56.
- (16) Iijima, S.; Ichihashi, T. *Nature* **1993**, *363*, 603.
- (17) Ajayan, P. M. *Chem. Rev.* **1999**, *99*, 1787.
- (18) Gavrilenko, V. I., Eds.; *Optics of Nanomaterials*; Pan Stanford Publishing Pte. Ltd Temasek Boulevard: Singapore, 2011.
- (19) Niyogi, S.; Hamon, M. A.; Hu, H.; Zhao, B.; Bhowmik, P.; Sen, R.; Itkis, M. E.; Haddon, R. C. *Acc. Chem. Res.* **2002**, *35*, 1105.
- (20) Grady, B. P. *Macromol. Rapid Commun.* **2010**, *31*, 247.
- (21) Tchoul, M. N.; Ford, W. T.; Lolli, G.; Resasco, D. E.; Arepalli, S. *Chem. Mater.* **2007**, *19*, 5765.
- (22) Peng, X.; Wong, S. S. *Adv. Mater.* **2009**, *21*, 625.
- (23) Qin, S.; Qin, D.; Ford, W. T.; Resasco, D. E.; Herrera, J. E. *Macromolecules* **2004**, *37*, 752.
- (24) Drzal, L. T.; Rich, M. J.; Konig, M. F.; Lioyd, P. F. *J. Adhes.* **1983**, *16*, 133.
- (25) Wu, S. H. *J. Appl. Polym. Sci.* **1988**, *35*, 549.
- (26) Liaw, D. J. *J. Appl. Polym. Sci.* **1997**, *66*, 1251.
- (27) Koberstein, J. T.; Stein, R. S. *J. Polym. Sci., Polym. Phys. Ed.* **1983**, *21*, 1439.
- (28) Wang, C. B.; Cooper, S. L. *Macromolecules* **1983**, *16*, 775.
- (29) Hsieh, K. H.; Tsai, C. C.; Tseng, S. M. *J. Membr. Sci.* **1990**, *49*, 341.
- (30) Huang, S. L.; Lai, J. Y. *J. Membr. Sci.* **1995**, *105*, 137.
- (31) Ponangi, R.; Pintauro, P. N.; Dekee, D. J. *Membr. Sci.* **2000**, *178*, 151.
- (32) Merkel, T. C.; Freeman, B. D.; Spontak, R. J.; He, Z.; Pinnau, I.; Meakin, P.; Hill, A. J. *Science* **2002**, *296*, 519.
- (33) Forsyth, M.; MacFarlane, D. R.; Best, A.; Adebahr, J.; Jacobsson, P.; Hill, A. J. *Solid State Ionics* **2002**, *147*, 203.
- (34) Merkel, T. C.; Freeman, B. D.; Spontak, R. J.; He, Z.; Pinnau, I.; Meakin, P.; Hill, A. J. *Chem. Mater.* **2003**, *15*, 109.
- (35) Becker, O.; Cheng, Y. B.; Varley, R. J.; Simon, G. P. *Macromolecules* **2003**, *36*, 1616.
- (36) Garcia, M.; Barsema, J.; Galindo, R. E.; Cangialosi, D.; Garcia-Turiel, J.; Van Zyl, W. E.; Verweij, H.; Blank, D. H. A. *Polym. Eng. Sci.* **2004**, *44*, 1240.
- (37) Wang, S. J.; Zhang, M.; Liu, L. M.; Fang, P. F.; Zhang, S. P.; Wang, B. *Mater. Sci. Forum* **2004**, *445/446*, 355.
- (38) Winberg, P.; Eldrup, M.; Maurer, F. H. J. *Polymer* **2004**, *45*, 8253.
- (39) Winberg, P.; DeSitter, K.; Dotremont, C.; Mullens, S.; Vankelecom, I. F. J.; Maurer, F. H. *Macromolecules* **2005**, *38*, 3776.
- (40) Zheng, Y.; Ning, R.; Zheng, Y. J. *Reinf. Plast. Compos.* **2005**, *24*, 223.
- (41) Wang, Z. F.; Wang, B.; Qi, N.; Zhang, H. F.; Zhang, L. Q. *Polymer* **2005**, *46*, 719.
- (42) Knite, M.; Hill, A. J.; Pas, S. J.; Teteris, V.; Zavickis, J. *Mater. Sci. Eng.: C* **2006**, *26*, 771.
- (43) De Sitter, K.; Winberg, P.; D'Haen, J.; Dotremont, C.; Leysen, R.; A. Martens, J.; Mullens, S.; Maurer, F.; Vankelecom, I. *J. Membr. Sci.* **2006**, *278*, 83.
- (44) Park, I.; Peng, H. G.; Gidley, D. W.; Xue, S. Q.; Pinnavaia, T. J. *Chem. Mater.* **2006**, *18*, 650.
- (45) Kruse, J.; Kanzow, J.; Ratzke, K.; Faupel, F.; Sterescu, D. M.; Stamatiadis, D. F.; Wessling, M. *J. Phys. Chem. B* **2007**, *111*, 13914.

- (46) Peng, F.; Pan, F.; Sun, H.; Lu, L.; Jiang, Z. *J. Membr. Sci.* **2007**, *300*, 13.
- (47) Ladewig, B. P.; Knott, R. B.; Hill, A. J.; Riches, J. D.; White, J. W.; Martin, D. J.; Diniz da Costa, J. C.; Lu, G. Q. *Chem. Mater.* **2007**, *19*, 2372.
- (48) Kim, S. H.; Chung, J. W.; Kang, T. J.; Kwak, S. Y.; Suzuki, T. *Polymer* **2007**, *48*, 4271.
- (49) Anilkumar, S.; Kumaran, M. G.; Thomas, S. J. *Phys. Chem. B* **2008**, *112*, 4009.
- (50) Jessie Lue, S.; Lee, D. T.; Chen, J. Y.; Chiu, C. H.; Hu, C. C.; Jean, Y. C.; Lai, J. Y. *J. Membr. Sci.* **2008**, *325*, 831.
- (51) De Sitter, K.; Andersson, A.; D'Haen, J.; Leysen, R.; Mullens, S.; Maurer, F.; Vankelecom, I. *J. Membr. Sci.* **2008**, *321*, 284.
- (52) Chen, H. M.; Jean, Y. C.; James Lee, L.; Yang, J.; Huang, J. *Phys. Status Solidi* **2009**, *6*, 2397.
- (53) Chen, H. M.; James Lee, L.; Yang, J.; Gu, X.; Jean, Y. C. *Mater. Sci. Forum* **2009**, *607*, 177.
- (54) Ata, S.; Muramatsu, M.; Takeda, J.; Ohdaira, T.; Suzuki, R.; Ito, K.; Kobayashi, Y.; Ougizawa, T. *Polymer* **2009**, *50*, 3343.
- (55) Harms, S.; Rätzke, K.; Faupel, F.; Schneider, G. J.; Willner, L.; Richter, D. *Macromolecules* **2010**, *43*, 10505.
- (56) Claes, S.; Vandezande, P.; Mullens, S.; Leysen, R.; De Sitter, K.; Andersson, A.; Maurer, F. H. J.; Van den Rul, H.; Peeters, R.; Van Bael, M. K. *J. Membr. Sci.* **2010**, *351*, 160.
- (57) Zaleski, R.; Kierys, A.; Grochowicz, M.; Dziadosz, M.; Goworek, J. *J. Colloid Interface Sci.* **2011**, *358*, 268.
- (58)
- (59) Feldstein, M. M.; Bermesheva, E. V.; Jean, Y. C.; Misra, G. P.; Siegel, R. A. *J. Appl. Polym. Sci.* **2011**, *119*, 2408.
- (60) Chen, M.; Awad, S.; Jean, Y. C.; Yang, J.; Lee, L. J. *AIP Conf. Proc.* **2011**, *1336*, 444.
- (61) Harms, S.; Rätzke, K.; Zaporotchenko, V.; Faupel, F.; Egger, W.; Ravelli, L. *Polymer* **2011**, *52*, 505.
- (62) Jean, Y. C. *Microchem. J.* **1990**, *42*, 72.
- (63) Jean, Y. C.; Mallon, P. E.; Schrader, D. M., Eds.; *Principles and Applications of Positron and Positronium Chemistry*; World Scientific: Singapore, 2003.
- (64) Wang, Y. Q.; Wu, Y. P.; Zhang, H. F.; Zhang, L. Q.; Wang, B.; Wang, Z. F. *Macromol. Rapid Commun.* **2004**, *25*, 1973.
- (65) Tao, S. J. *J. Phys. Chem.* **1972**, *56*, 5499.
- (66) Eldrup, M.; Lightbody, D.; Sherwood, J. N. *Chem. Phys.* **1981**, *63*, 51.
- (67) Tchoul, M. N.; Ford, W. T.; Ha, M. L. P.; Chavez-Sumarriva, I.; Grady, B. P.; Lolli, G.; Resasco, D. E.; Arepalli, S. *Chem. Mater.* **2008**, *20*, 3120.
- (68) Grady, B. P.; Paul, A.; Peters, J. E.; Ford, W. T. *Macromolecules* **2009**, *42*, 6152.
- (69) Paul, A.; Grady, B. P.; Ford, W. T. Submitted for publication.
- (70) PATFIT package (1989) purchased from Riso National Laboratory, Denmark.
- (71) Kansy, J. *Nucl. Instrum. Methods Phys. Res., Sect. A* **1996**, *374*, 235.
- (72) Awad, S.; Chen, H.; Chen, G.; Gu, X.; Lee, J. L.; Abdel-Hady, E. E.; Jean, Y. C. *Macromolecules* **2011**, *44*, 29.
- (73) Kobayashi, H.; Takahashi, H.; Hiki, Y. *Mater. Sci. Eng. A* **2006**, *442*, 263.
- (74) Uedono, A.; Kawano, T.; Wei, L.; Tanigawa, S.; Ban, M.; Kyoto, M. *J. Phys. IV: Proc.* **1995**, *5*, 199.
- (75) Jean, Y. C.; Zhang, R.; Cao, H.; Yuan, J.-P.; Huang, C.-M.; Nielsen, B.; Asoka-Kumar, P. *Phys. Rev. B* **1997**, *56*, 56.
- (76) Jean, Y. C.; Chen, H.; Lee, L. J.; Yang, J.; Li, C. *Acta Phys. Polym. A* **2008**, *113*, 1385.
- (77) Zhang, J.; Chen, H.; Li, Y.; Suzuki, R.; Ohdaira, T.; Jean, Y. C. *Radiat. Phys. Chem.* **2007**, *76*, 172.
- (78) Bohlen, J.; Kirchheim, R. *Macromolecules* **2001**, *34*, 4210.
- (79) Yang, M.; Koutsos, V.; Zaiser, M. *J. Phys. Chem. B* **2005**, *109*, 10009.
- (80) *Polymer Handbook*; Brandrup, J., Immergut, E. H., Eds.; Wiley Interscience: New York, 1999.

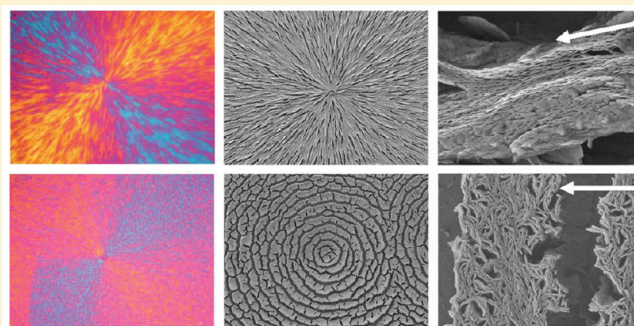
Lamellar Orientation Inversion under Dynamic Interplay between Crystallization and Phase Separation

Weichao Shi,^{†,‡} Jian Yang,[†] Yan Zhang,^{†,‡} Jun Luo,^{†,‡} Yongri Liang,[†] and Charles C. Han^{*,†}

[†]Beijing National Laboratory for Molecular Sciences, Joint Laboratory of Polymer Science and Materials, Institute of Chemistry, Chinese Academy of Sciences, Beijing 100190, China

[‡]Graduate School of the Chinese Academy of Sciences, Beijing 100190, China

ABSTRACT: Crystallization dynamics and lamellar orientation are affected under the dynamic interplay between crystallization and phase separation. We carried out the experiment in a dynamically asymmetric blend of amorphous poly(methyl methacrylate) (PMMA) and crystalline poly(ethylene oxide) (PEO). If phase separation is really weak, lamellae are normally grown in the radial direction within spherulites. Growth rate shows a bell-like curve with respect to temperature. However, when strong phase separation intervenes, the growth rate curve is characterized by double peaks, one of which is dominated by crystallization and the other by phase separation. Meanwhile, lamellae tend to orient in the tangential direction in concentric alternating structures, whose formation mechanism has been explained in previous studies. This lamellar orientation inversion is reflected by a negative to positive birefringence inversion under optical microscopy. Within lamellar stacks, more amorphous molecules tend to be pushed out under the effect of phase separation, leading to smaller long period.



INTRODUCTION

Blending and alloying are important in materials science, in order to meet the multifunctional need in industry.¹ But more than one kind of kinetic mechanisms may be involved mainly due to coupled phase transitions.² Both phase separation and crystallization are often encountered if at least one crystalline component is employed. The dynamics of each individual process has been well studied for many years.^{3–11} However, the mechanism is still a challenge when crystallization and phase separation take place simultaneously. Previously, we investigated phase separation behavior assisted at the growth interface and the concentric structures formed by alternating amorphous-rich and crystalline-rich domains.¹² As phase separation intervenes into the crystallization process, normal spherulitic shape and lamellar orientation may be affected at the same time, depending on the quench depth with respect to the phase boundaries of different transitions involved.

A crystal is always trying to grow after the primary nucleation by regularly arraying crystallizable molecules and rejecting the amorphous ones. In a fully miscible blend, crystalline component usually grows in a spherulitic shape, compact when the majority fraction is crystallizable molecules and loose on the contrary condition.¹³ In some cases, dendritic crystal appears when the crystalline fraction is small.^{14–17} The growth rate with respect to temperature usually show bell-like shape, which is nucleation limited in the high temperature region and diffusion limited in the low temperature region.

Spherulites can be further classified as negative or positive according to the birefringent character. A spherulite with the higher refractive index for light vibrating along the radial direction is called positive. If the higher refractive index is in the tangential direction, a spherulite is called negative. So, macroscopic birefringence may give qualitative information on crystal orientation. There have been a few reports on the presence of both positive and negative spherulites in syndiotactic polystyrene and its blends.^{18,19} Those results indicated that lamellae in spherulites may grow in radial as well as in tangential directions, which led to opposite birefringent properties.

When phase separation intervenes into a crystallization process, the dynamic interplay between these two transitions becomes more complicated. It has been noted in experimental observations^{20–24} that primary nucleation of crystallization can be assisted by concentration fluctuation, especially at the interface boundaries of phase separated domains. Simulation results^{25,26} support the preference of nucleation at the interface, however, without any specific information given on the orientational anisotropy of crystal arrangement.

If glass transition is introduced to mediate the phase transition dynamics, then phase separation is known as viscoelastic phase separation.^{27–29} Compared with normal phase separation, viscoelastic phase separation considers molecular

Received: September 8, 2011

Revised: December 14, 2011

Published: January 5, 2012

relaxation in addition. In this study, we consider the lamellar orientation under the interplay between a crystallization process and a slow viscoelastic phase separation process. One of the advantages of employing such a system is that we are able to mediate the dynamics of the two transitions on a much longer time scale, in contrast to the fast dynamic processes in polyolefin blends. Furthermore, the low mobility of the PMMA-rich phase may fix the regular concentric ring pattern so that lamellar orientation inversion can be observed on a macroscopic scale in alternating PEO-rich phase.

EXPERIMENTAL SECTION

Materials. PMMA was purchased from Aldrich Chemicals with a relative weight-average molecular weight of 15 000 g/mol and polydispersity of 1.73. PEO was purchased from Beijing Chemical Co. with a relative weight-average molecular weight of 20 000 g/mol and polydispersity of 1.08. The molecular weight was determined by gel permeation chromatography. The materials were used after purification. The glass transition temperatures of PMMA and PEO were found to be about +91 and −60 °C, respectively, using a differential scanning calorimeter (DSC, MettlerToledo-822e) at a heating rate of 10 °C/min.

Film Preparation. PMMA and PEO with a given weight fraction were dissolved in chloroform with 5% by weight. The solution was stirred at room temperature over 24 h. The film, with thickness of about 20 μm, was prepared by casting the solution onto a clean glass plate and evaporating the solvent until constant weight in vacuum oven at room temperature. Normally, this took about 24 h. The film sample was prepared independently for each observation. The samples were melted at 130 °C for 30 min for homogenization before each annealing.

Optical Microscopy. The experimental temperature is controlled by a Linkam (LTS350) hot stage. The phase contrast optical microscopy (PCOM) and polarized optical microscopy (POM) are carried out using an Olympus (BX51) optical microscope and Olympus (C-5050ZOOM) camera. The vector direction of the polarizer is kept vertical to the depolarizer. An optical compensating plate, with optical path difference 530 nm, is used to judge the positive or negative birefringence of the spherulites. The compensating plate is inserted in 45° with polarizing elements. The details of the POM instrument used in this study were schematically illustrated in Figure 1. Polarized light

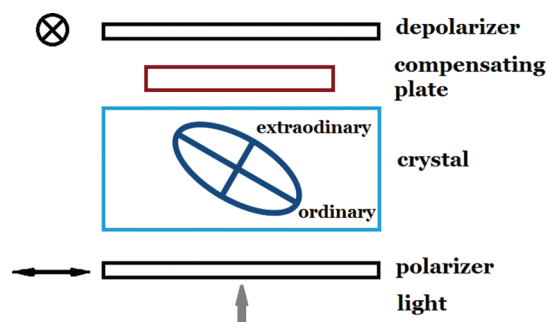


Figure 1. Schematic illustration of the POM instrument used in this study. The axis of the polarizer is parallel to the plane of the paper and the axis of the depolarizer is normal to the plane of the paper (indicated by the cross-in-circle).

with different wavelength have different intensity through the compensating plate. The light at 530 nm completely diminishes. For negative spherulites, the path difference in the I and III quadrants is decreased, showing a yellow color, while the path difference in the II and IV quadrants is enlarged, showing a blue color. The positive spherulites show the opposite property. The isotropic region shows red/purple color.

Scanning Electron Microscopy. Samples were coated by platinum before observation under SEM (JEOL JSM 6700F).

Small Angel X-ray Scattering. The small angel X-ray scattering (SAXS) experiments were performed on a 1.2KW MicroMAX-007HF rotating anode X-ray generator (Rigaku) equipped with a rotating anode Cu target. The X-ray source was operated at 40KV and 30 mA. The wavelength is 0.1545 nm. The diameter of the beam at the sample is about 1.5 mm. All the samples were preannealed on a Linkam (LTS350) hot stage at different temperatures. The SAXS experiments were carried out at room temperature. The transmitted X-ray was stopped by a beam stop and the scattered X-ray was collected by a 2D position sensitive detector.

SAXS Data Analysis. All SAXS scattering data were corrected before analysis by subtracting the background intensity associated with thermal density fluctuations. Following Ruland's approach, the high- q range intensity was fitted by $I(q)q^4 = K_p \exp(-\sigma^2 q^2) + I_B q^4$, where wave vector is $q = 4\pi \sin(\theta/2)/\lambda$ (θ is the scattering angle).^{30,31} K_p is the Porod constant, σ is related to the crystal/amorphous interface, and I_B is the scattering from thermal density fluctuation. The background intensity was subtracted all over the q -range to give corrected intensity $I_C(q)$.

Lorentz correction is generally used in X-ray scattering to correct the scattered intensities ($I_C(q)$) from crystalline materials to obtain correct structure factors, when there is a periodicity with consecutive lamellar structures ($I_S(q)$) in the crystalline systems, following the relationship $I_C(q) = A2\pi/q^2 I_S(q)$.³² So we gave all scattering curves by plotting $I(q)q^2$ versus q . The long periods were calculated directly from the equation $L = 2\pi/q_{\max}$ where q_{\max} is the wave vector corresponding to the peak maximum in the Lorentz-corrected plots.

The normalized 1D correlation function is defined as

$$g(r) = \int_0^\infty I_C(q)q^2 \cos(qr) dq / Q$$

where $Q = \int_0^\infty I_C(q)q^2 dq$ is the scattering invariant. The intensity at low q (near 0.20 nm^{−1}) and high q (1.3–1.6 nm^{−1}) regions were fitted by Guinier's law and Porod's law, respectively.³³ The thickness of the lamellar crystallites (or the amorphous layer) was obtained by the intersection between the slop of the triangle at $g(r) = 0$ and the horizontal line at the first minimum. The thickness of the lamellar crystal should be larger than that of the amorphous layer, due to the high crystallinity in neat PEO. Because of melting depression, the crystal thickness in the blend should be smaller than that in neat PEO. The crystal thickness in the blend is identified accordingly.

RESULTS AND DISCUSSION

Birefringence and Growth Dynamics. The phase and morphology diagram was given in the previous studies.^{12,34} The binodal line for phase separation locates below the crystal melting line. Accordingly, for a temperature quench, thermodynamic driving force is always larger for crystallization than for phase separation. A dynamic inversion line is also given, which locates deep within spinodal region, for two different reasons. On one hand, phase separation becomes dominant below this inversion line, leading to an inversion from spherulitic to concentric alternating structures.³⁴ On the other hand, lamellar orientation inverts from radial to tangential directions. At shallow quench (region 1 in Figure 2), crystallization dominates the process and negative birefringent spherulites form, with either compact or loose structures. As strong phase separation intervenes into the crystallization process (below the dynamic inversion line, region 2 in Figure 2), positive birefringent concentric ring patterns form.

When PEO weight fraction is over 0.7, compact spherulite always forms in the temperature range in this study. But there is a negative to positive birefringence transition as temperature lowers and PEO content decreases. We will give a detailed

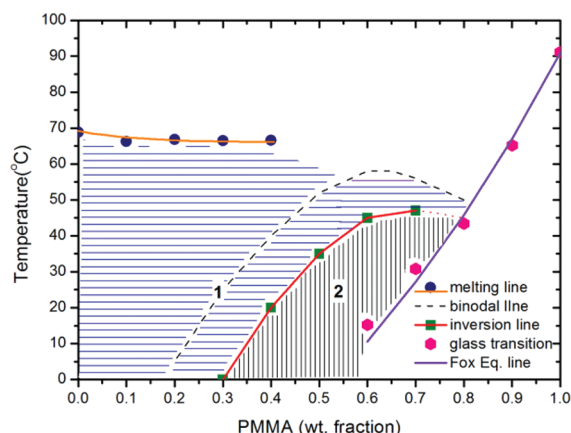


Figure 2. Phase and lamellar orientation diagram of PMMA/PEO blend.¹² Region 1 is crystallization dominated region and region 2 is phase separation dominated region. Lamellae grow in radial direction showing negative birefringence in region 1; lamellae orientation inverts to tangential direction showing positive birefringence in region 2.

discussion on this negative to positive inversion phenomenon below.

When PEO weight fraction is at 0.4, loose negative spherulites form in the temperature range between 45 and 50 °C. At higher temperatures, more compact spherulites grow quite slowly, usually via heterogeneous nucleation on impurities. Below 45 °C, loose spherulites cannot maintain the shape and changes into isolated stacks as phase separation becomes faster with decreasing temperature. Figure 2 shows the typical structure in each region. The characteristic morphologies were observed under PCOM and birefringence under POM.

Parts a and b of Figure 3 show typical spherulitic morphologies above 45 °C, characterized by long fibrillar crystals radiating from the center in the radial direction. The spherulites showed negative birefringent nature. However, Figure 3c shows that loose spherulite broke into short isolated lamellar stacks in phase separated PEO-rich domains, reflecting positive birefringent character macroscopically, when the sample was annealed at 42 °C. As reported in the previous paper,³⁴ the morphology lost the spherulitic shape but inverted to concentric alternating structure below 45 °C, because of effects from phase separation. Here we note that the negative to positive birefringence inversion also occurs near 45 °C. When the

sample was annealed at even lower temperature, lamellar stacks formed in the phase separated domains tended to lose their orientational preference, as shown in Figure 3d. We will give a detailed discussion on the lamellar orientation in the following sections.

As temperature approached glass transition temperature, long-range concentration fluctuation was sharply prohibited. However, after a long time annealing, small negative crystallites appeared again, as shown in Figure 4 where the sample was

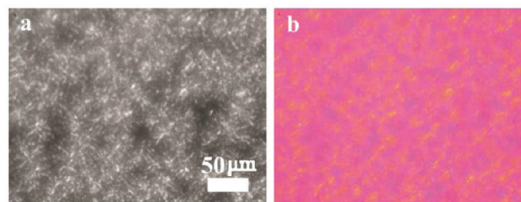


Figure 4. Sample PEO content at 0.4 annealed at 20 °C (near glass transition) observed under (a) POM and (b) POM coupled with a compensating plate.

annealed at 20 °C. To give a short summary, negative spherulites form when phase separation is weak at shallow quench, and invert to positive concentric patterns when phase separation dominates the deep quench region, but finally return to negative spherulites when long-range phase separation is dynamically depressed near glass transition. This also gives additional evidence that positive birefringence originates from phase separation.

As has been illustrated in the previous paper,³⁴ phase separation always grew faster than crystallization, especially below 40 °C. Accordingly, there was always size difference between pictures taken from PCOM and POM at nearly the same time. Measuring growth rate from these pictures taken from the two modes, we can obtain two typical growth rates for phase separated domains and for crystallized areas, respectively. As is shown in Figure 5, there is sharp acceleration of growth rate as temperature is decreasing to below 45 °C until 40 °C, then a mild increase between 40 and 25 °C, and a sharp drop as glass transition (15.2 °C) is approached. The optimum temperature near 40 °C corresponds to the largest growth rate of crystallization in a bell-like growth rate versus temperature curve. Deviations between 40 and 20 °C can be considered that crystallization was assisted in phase separated crystalline-rich domains. The growth peak of phase separation

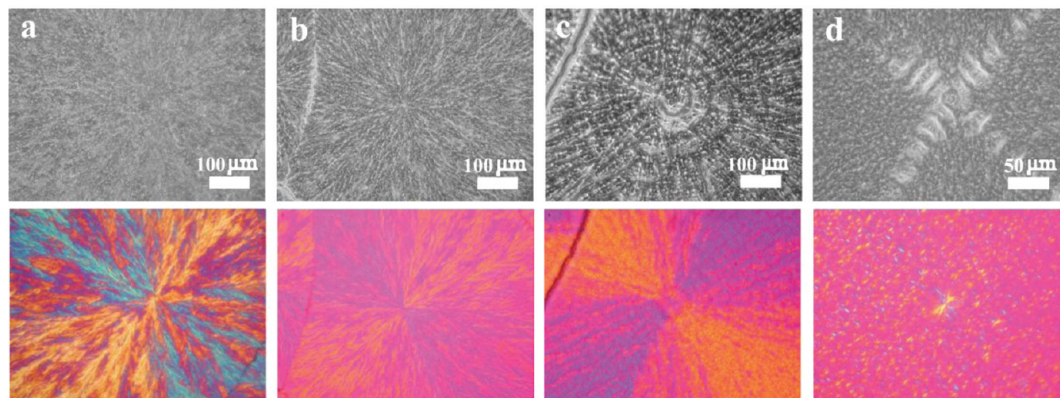


Figure 3. Typical morphology and birefringent character with PEO content at 0.4 annealed at (a) 53 °C, (b) 47 °C, (c) 42 °C, and (d) 30 °C. The pictures in the upper and lower rows were taken under PCOM and POM coupled with a compensating plate, respectively.

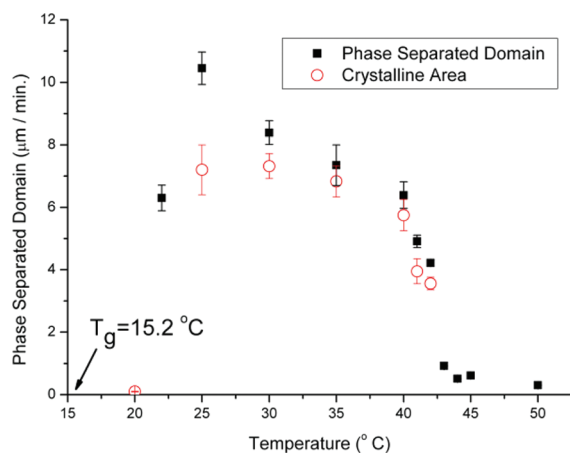


Figure 5. Growth rates of phase separated domains and crystallized areas versus temperature plot for the sample with PEO content at 0.4.

at the lower temperature (near 25 °C) was the result of phase separation with an upper critical solution temperature. So, enlarging quench depth gave larger thermodynamic driving force, and thus accelerated phase separation dynamics. On the other hand, the dynamics was also depressed by slow diffusion when approaching glass transition (below 25 °C).

When PEO weight fraction is at 0.5, compact negative spherulites form above 35 °C. The typical morphology changes to concentric alternating structure below 35 °C, usually with small compact spherulites initiating phase separation at the center. Figure 6 shows the characteristic birefringent pattern observed at different temperatures.

From Figure 6a, we see compact negative spherulites consist of long fibrillar structures. As a larger quench was applied, phase separation intervened. However, phase separation dynamics would not be enhanced significantly until a large enough concentration deviation was built up. This concentration deviation became intensified as the spherulite grew larger. So, as indicated in Figure 6, parts b–d, there were small compact spherulites at the center of the domains. It is interesting to note that the initial spherulites were negative, but the lateral crystallites showed positive nature under the effect of phase separation. This birefringence inversion temperature was measured to be near 35 °C. Also, as coupled with phase separation, short isolated lamellar stacks appeared instead of long fibrils.

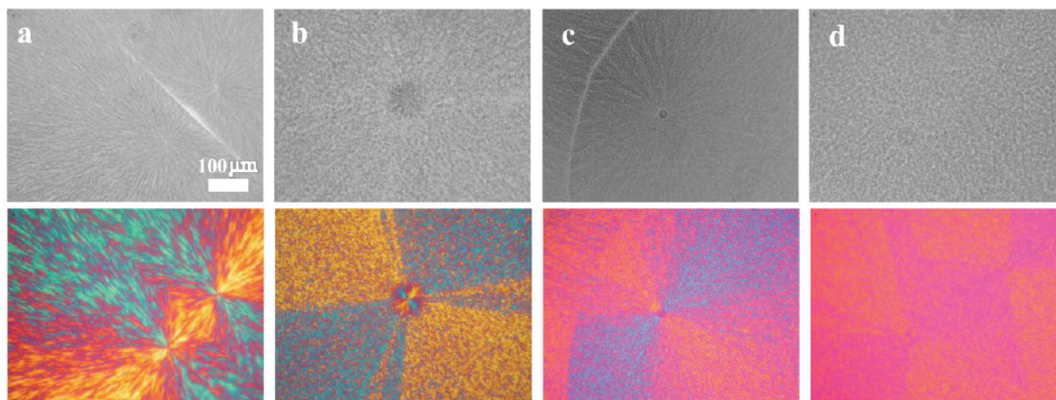


Figure 6. Typical morphology and birefringent character with PEO content at 0.5 annealed at (a) 40 °C, (b) 30 °C (c) 25 °C, and (d) 20 °C. The pictures in the upper and lower rows were taken under PCOM and POM coupled with a compensating plate, respectively.

The growth dynamics, shown in Figure 7a, is similar to the previously shown sample with PEO content at 0.4. But the

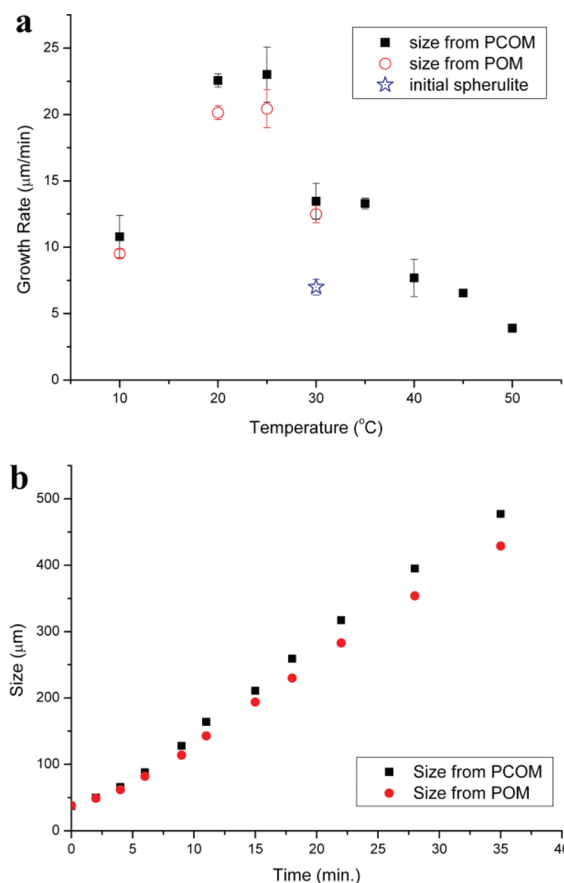


Figure 7. (a) Growth rates of phase separated domains and crystallized areas versus temperature plot for the sample with PEO content at 0.5. (b) Time evolution of the size increment of the sample annealed at 30 °C. Phase separation took place after 5 min.

double peak character (two separated peak temperatures) is more obvious. At higher temperatures between 50 and 35 °C, the growth rate of crystallization increases as temperature decreases. As phase separation intervenes near 35 °C, the growth rate continued to increase as temperature was reduced until near 10 °C. The glass transition temperature is estimated

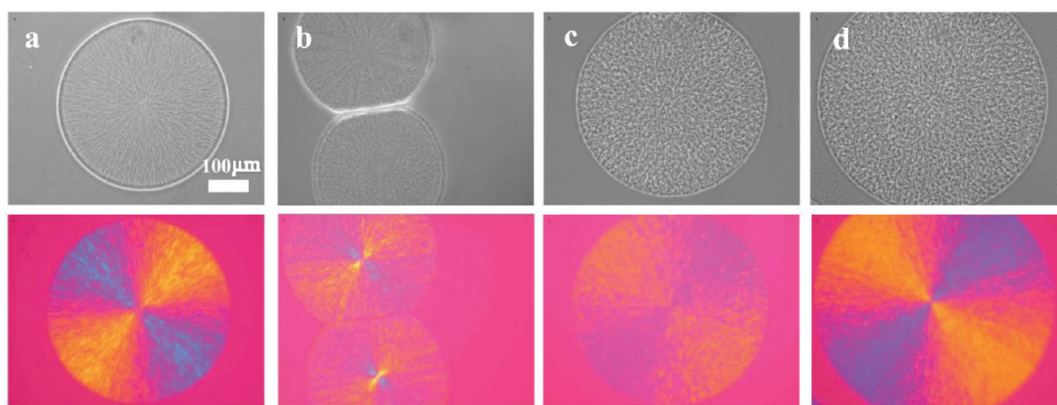


Figure 8. Typical morphology and birefringent character with PEO content at 0.6 annealed at (a) 25 °C, (b) 20 °C, (c) 15 °C, and (d) 10 °C. The pictures in the upper and lower rows were taken under PCOM and POM coupled with a compensating plate, respectively.

to be 0 °C via Fox equation. The melting point should be near 65 °C. So the maximum growth rate of crystallization, in the absence of phase separation, corresponds roughly near 35 °C. This estimation coincides with our experimental results.

As we reported before,^{12,34} crystallization took place first under deep quench, and phase separation occurred at the growth interface of the initial spherulites, and then led to concentric growth of alternating structures. The initial spherulites usually grew to large sizes before phase separation took place, especially shallowly below the inversion line. So we measured the growth rate of the initial spherulites at 30 °C (Figure 7 b), which gave a slow growth rate of about 7.0 μm/min, much slower than the lateral growth under the effect of phase separation. This confirms our estimation above and gives a conclusion, like before, that crystallization dynamics is enhanced by the phase separation at lower temperatures.

Similar birefringence inversion occurs near 20 °C when PEO content increases to 0.6. Compact spherulite showed regular Maltese cross and revealed negative birefringence at 25 °C, as shown in Figure 8a. The negative nature can be still kept at 20 °C. As temperature quench became larger, the structure showed a rough appearance under PCOM and the birefringence inverted to positive nature. The light intensity under POM mode became strong as temperature was decreased more, which reflected that lamellae were arranged more regularly when phase separation dominated the dynamics.

The growth dynamics becomes faster as PEO content increased to 0.6. The glass transition temperature is estimated to be −15 °C via the Fox equation. The melting point should be near 65 °C. So the maximum growth rate corresponds roughly near 25 °C. However, the maximum growth rate appears at a lower temperature near 15 °C. Because of the fast growth dynamics, crystallization occurs in phase separated domains as soon as phase separation takes place under deep quench. This gives the reason for a single peak in Figure 9 and the disappearance of the size difference between pictures under PCOM and POM (Figure 8).

Birefringence inversion occurs near 0 °C when PEO content increased to 0.7. Typical pictures are revealed in Figure 10. Because of the high PEO content, the growth dynamics was too fast (over 100 μm/min) to be precisely determined.

Lamellar Orientation. Birefringence is the consequence of the macroscopic refraction of the lamellae orientation. We will pursue the reason for the birefringence inversion on microscopic/mesoscopic level.

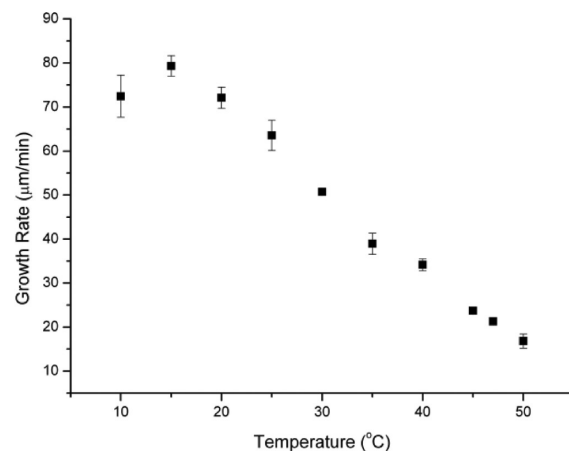


Figure 9. Growth rates of phase separated domains and crystallized areas versus temperature plot for the sample with PEO content at 0.6.

Figure 11a shows the crystal structure under SEM for PEO weight fraction at 0.4 annealed at 47 °C. The sample was etched by tetrahydrofuran (THF). We clearly see the long fibrillar crystals radiating from the center with many short branches, in accordance with Figure 3b. The magnified picture indicates that the lamellae grew in the radial direction, mostly edge-on with respect to the substrate.

Figure 11b shows the crystal morphology for the blend at 42 °C. The etched sample displayed a concentric alternating ring structure, with lamellar stacks oriented perpendicular to the radial direction, in contrast to the radial growth formed at 47 °C. Note that spherulites reflected positive birefringent character at 42 °C, compared with negative nature at 47 °C. Therefore, we may deduce that lamellar orientation inversion affected by phase separation was the origin of the macroscopic birefringence inversion. Unfortunately, it was difficult to observe lamellar structures at even lower temperatures using the etching method because of the isolated distribution of lamellae.

When PEO weight fraction is at 0.5, similar inversion of lamellar orientation can be observed under SEM. Figure 12 shows the typical structures formed at 40, 30, 25 and 10 °C. Above the inversion temperature (35 °C), a compact spherulite formed and long lamellar stripes grew in the radial direction trapping the amorphous domains into the interfibrillar regions. Below the inversion temperature, concentric alternating structures emerged. The lamellae in the crystalline-rich domains

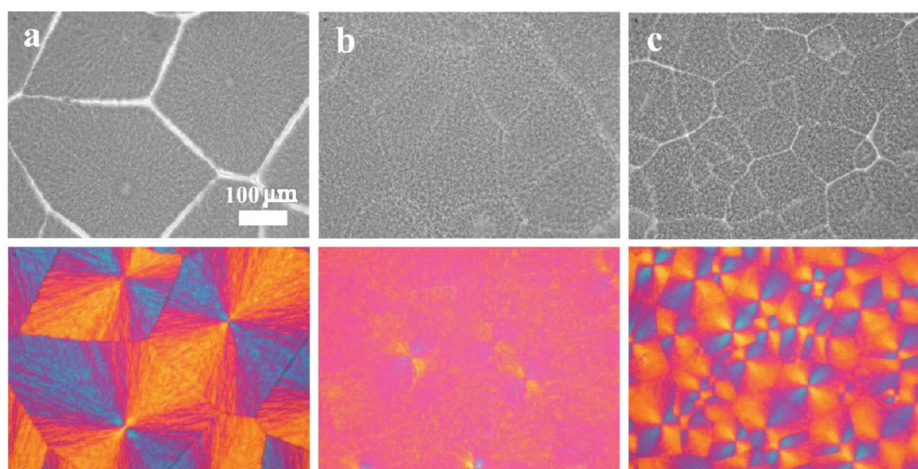


Figure 10. Typical morphology and birefringent character with PEO content at 0.7 annealed at (a) 10 °C, (b) 0 °C and (c) -5 °C.

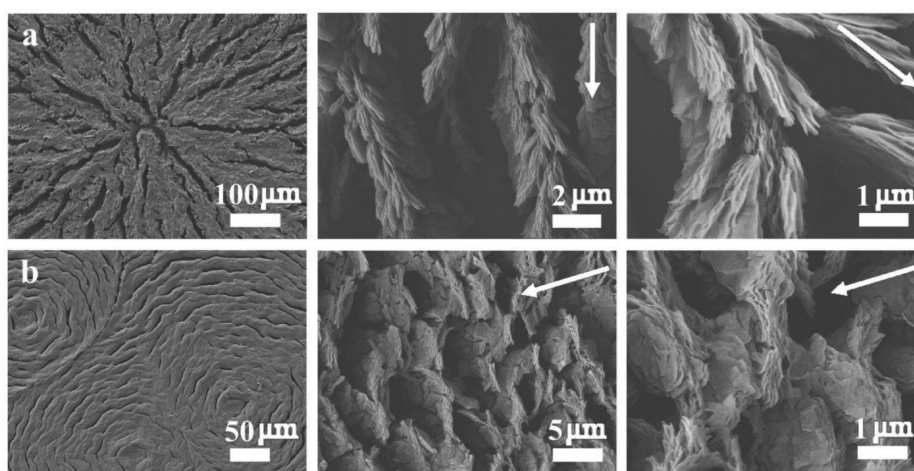


Figure 11. Structure of the sample with PEO content at 0.4 annealed at (a, upper row) 47 °C and (b, lower row) 42 °C observed under SEM after etching by THF. The arrow indicates the radial direction from the center.

tended to orient in the tangential direction. The lamellar arrayed more regularly as the quench depth was enlarged. However, if the regular concentric ring pattern broke up at even lower temperatures, the lamellae in the phase separated domains tended to orient randomly again.

As PEO content increased beyond 0.6, detecting lamellar orientation using etching method became very difficult, because of the compact internal structures formed. Figure 13 shows the typical structures at 25, 15 and 5 °C. Above the inversion temperature (20 °C), the spherulitic pattern was hardly destroyed and compact lamellae still oriented in the radial direction. Below the inversion temperature, in contrast, concentric structure appeared and long lamellar stripes tended to array tangentially.

Characteristic Length from SAXS Data. In this section, we will discuss information on even smaller scale, that is, within the lamellar stacks using SAXS. As a basic concept, thicker lamellae usually formed when crystalline polymer is annealed at shallower quench temperatures. The limiting case is that the thickness should approach infinity as the annealing temperature is approaching the equilibrium melting point. As temperature decreases, the lamellar thickness should decrease because of dynamic and thermodynamic reasons. The distance between

two nearest lamellae, characterized by the long period, reveals important microscopic information. It is known that the contribution to the long period comes from two parts: one is the thickness of lamellae; the other is the amorphous-rich domains in the interlamellar regions. In a fully miscible situation, as the temperature is decreasing or the amorphous component is increasing, the thickness of lamellae decreases but more amorphous molecules may be intercalated into the interlamellar regions.^{30,31} These two opposite factors compete to give the final characteristic length of the long period.

In the neat PEO, the characteristic wave vector, corresponding to the maximum intensity, became larger as temperature was decreased as shown in Figure 14a. The maxima at high wave vectors are the higher order reflections with respect to the low-*q* maximum. The characteristic long period of lamellar structure decreased from 22.4 nm at 50 °C to 17.6 nm at 10 °C. All samples were annealed for 48 h before scattering measurement. So, we can attribute the thinning trend of lamellae with decreasing temperature mainly to the thermodynamics. However, a similar trend is indicated in Figure 14b when PEO content is 0.6, but the mechanism is distinguishingly different as will be discussed later. From the 1D normalized correlation function, as shown in Figure 14c, the detailed lamellar information on

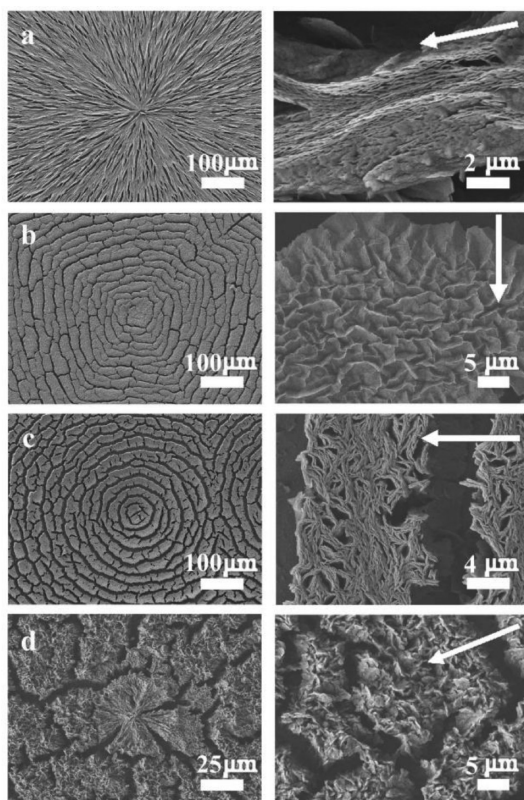


Figure 12. Structure of the sample with PEO content at 0.5 annealed at (a) 40 °C, (b) 30 °C, (c) 25 °C, and (d) 10 °C observed under SEM after etching by xylene (the 40 °C, 30 °C, and 25 °C samples) and THF (10 °C sample), respectively. The arrow indicates the radial direction from the center.

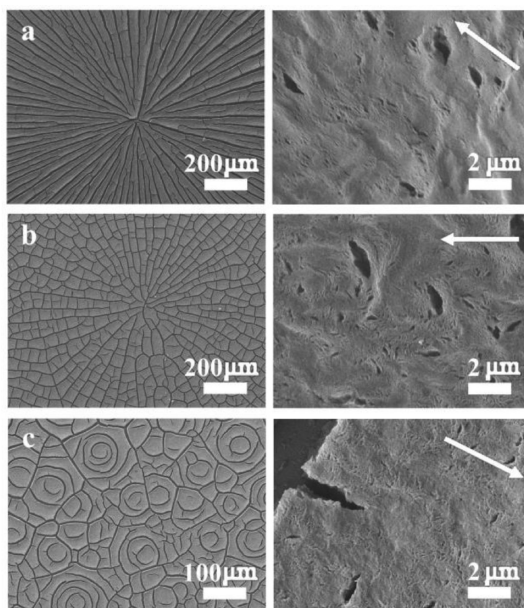


Figure 13. Structure of the sample with PEO content at 0.6 annealed at (a) 25 °C, (b) 15 °C, and (c) 5 °C observed under SEM after etching by xylene. The arrow indicated the radial direction from the center.

the thickness of the crystal and the amorphous layer can be obtained quantitatively.

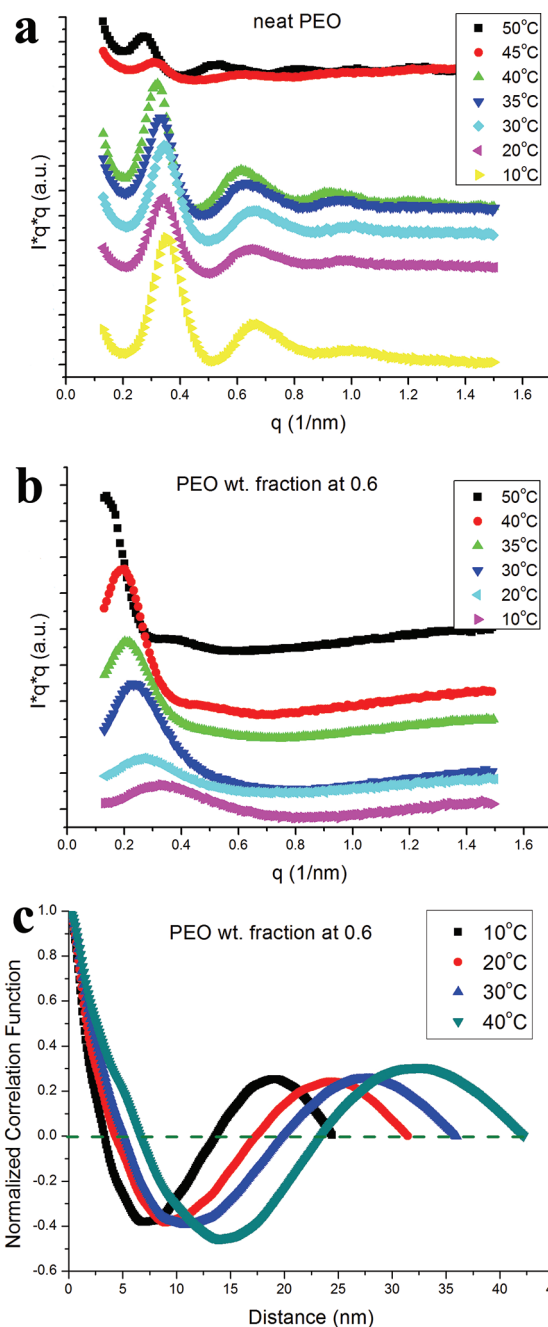


Figure 14. Lorentz-corrected SAXS curves obtained at different crystallization temperatures for (a) neat PEO and (b) PEO content at 0.6. The normalized correlation function for the blend with PEO content at 0.6 is shown in part c.

Figure 15a shows the temperature dependence of the long period for different PEO weight fractions. With respect to the decreasing temperature, the characteristic long period decreased for all compositions. But in the neat PEO, the decreasing trend was small. As the amorphous PMMA content increased, the decreasing trend became larger. Here we compare the lamellar structure in neat PEO and the blend with PEO content at 0.6. The mild dependence of crystal thickness on temperature is shown in Figure 15b. The thickness of the amorphous layer in neat PEO (Figure 15c) is almost unchanged with respect to temperature. For the blend with PEO content at 0.6, however, the thickness of the amorphous

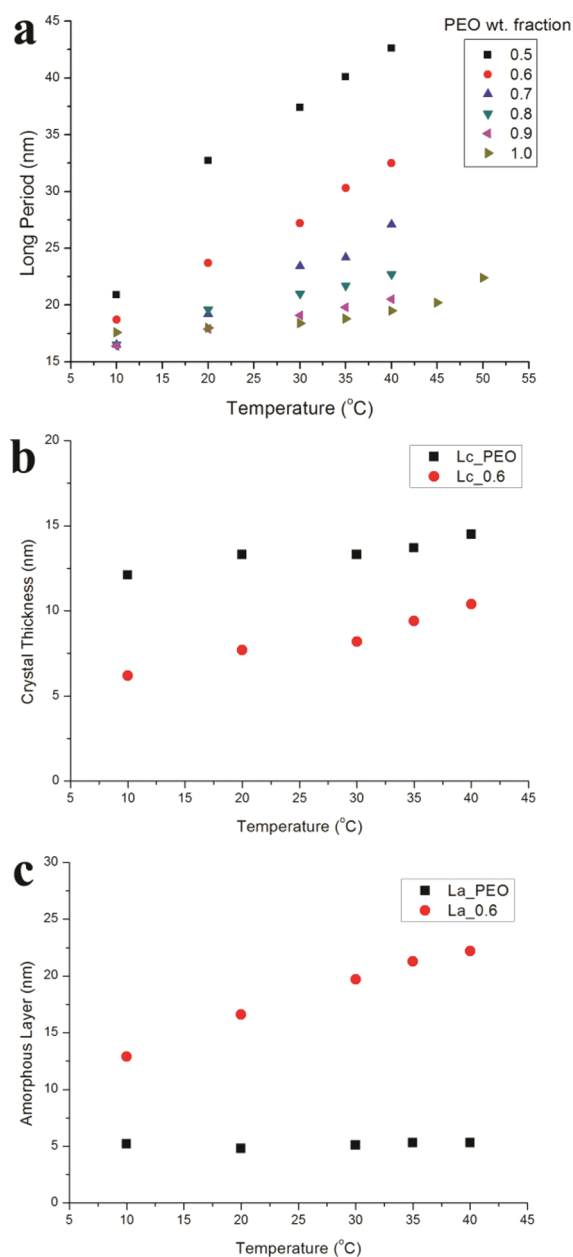


Figure 15. (a) Long period versus temperature plot for the blend. The thickness of the crystal (b) and the amorphous layer (c) with respect to temperature for neat PEO and the blend with PEO content at 0.6.

layer increases drastically as temperature increases. This led to a conclusion that more PMMA molecules were excluded out of the lamellar stacks, beyond the mild decrease of crystal thickness, as temperature decreased mainly due to phase separation.

Figure 16a shows the concentration dependence of the long period change. When samples with different compositions were annealed at the same temperature, the long period increased as more PMMA were involved at temperatures above 20 °C. But for temperatures below 20 °C, such as samples annealed at 10 °C, the long period first decreased slightly and then increased with the increase of PMMA. The monotonic tendency of increased long period at high temperatures indicated that more amorphous PMMA molecules were involved in the interlamellar regions as PEO content decreased. At low temperatures, the amorphous molecules tended to be repelled out by phase separation, accompanied by the decrease of lamellar

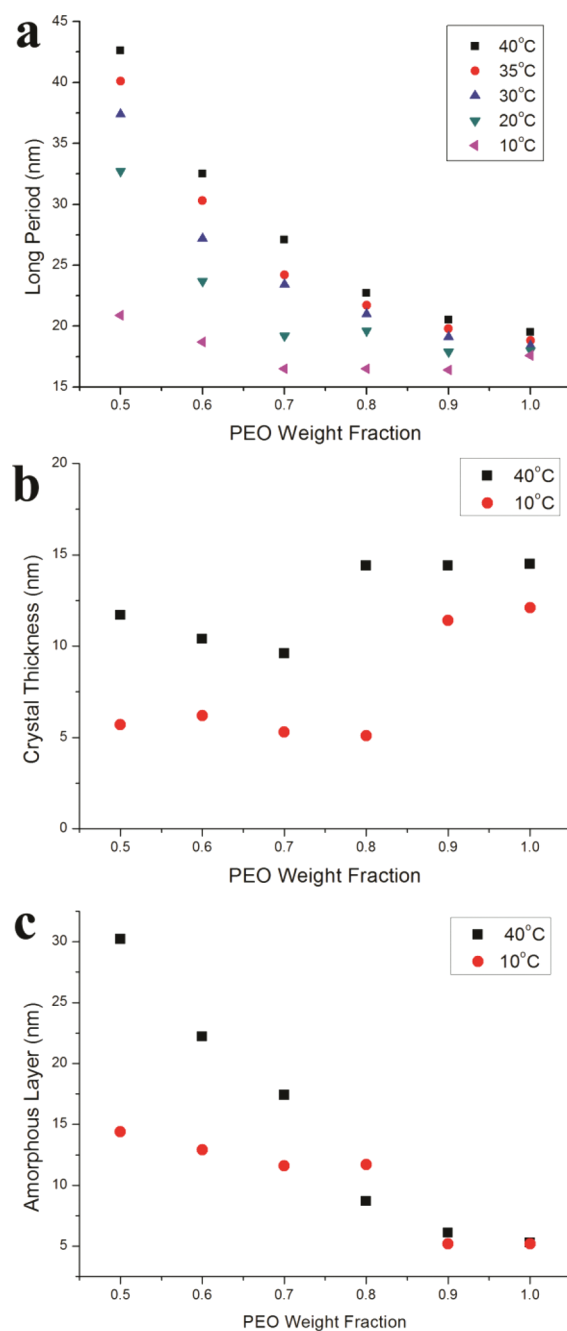


Figure 16. (a) Long period versus PEO weight fraction plot. The thickness of the crystal (b) and the amorphous layer (c) for the blend with different compositions at 40 and 10 °C, respectively.

thickness, when a small amount of PMMA was introduced. However, when PMMA content became larger, some amorphous molecules will be trapped in the interlamellar regions, and led to the further increasing of long period. This postulation can be confirmed by analyzing the thickness of the crystal and the amorphous layer obtained from the 1D correlation function, as revealed in Figure 16, parts b and c, respectively. There was minor decrease of the crystal thickness as a few PMMA was introduced. But the crystal thickness dropped drastically over a certain amount of PMMA content, and then increased mildly. The thickness of the amorphous layer increased as more PMMA were introduced into the blend. The increasing tendency was drastic at 40 °C but mild at 10 °C.

Phase separation tends to occur at lower temperatures below binodal line. On macroscopic scale, this leads to the concentric ring pattern and birefringence inversion. From the above analysis of SAXS results, we may conclude that phase separation may assist the formation of more compact lamellar stacks by pushing the amorphous molecules outward.

Analysis Using Dynamic Competition Model. In our previous papers,^{12,34} we proposed three characteristic times to describe a correlated crystallization and phase separation process. τ_i stands for the induction time for the formation of a new nucleus. τ_d indicates the deformation rate of phase separation. τ_o , the key parameter to correlate the dynamics of crystallization and phase separation, is the diffusion time for the crystallizable molecules crossing over the phase separated domain. Various morphologies are predicted and observed, based on the relative scales of τ_i , τ_o , and τ_d .

Furthermore, we would like to define two characteristic time intervals. The first interval, $I_1 = \tau_i - \tau_o$ indexes the relationship between the formation of new secondary nuclei and the original crystal growth. The second interval, $I_2 = \tau_i - \tau_d$, indexes the effect of phase separation on the crystal ordering.

If I_1 is positive, secondary nucleated crystal growth at the original growth front will be the dominant mechanism; the contrary case is, when I_1 is negative, then the crystalline molecules could begin nucleation before reaching the original crystal front and form new crystal, showing aloof tendency. The more negative I_1 is, the less effect was exerted on a new nucleus from the original crystal, which led to a more open structure on a macroscopic scale.

If I_2 is negative, crystallization dominates over phase separation, and crystal growth is hardly affected by phase separation. If I_2 is extremely positive, then crystallization takes place in the well phase separated crystalline-rich domains, like in a homogeneous phase. However, if I_2 is slightly positive, then phase separation could induce directional transport of crystalline molecules that may be fixed by the subsequent crystallization. As phase separation proceeds, molecules should diffuse from one phase, cross an interface and then reach the other phase. This transport process should be normal to the interface, then a coil may preferentially orient in this direction. The lateral crystallization could inherit this orientational preference, and led to lamellar growth parallel to the interface. However, this molecular orientation may be relaxed by thermal fluctuation before crystallization occurs, when I_2 tends to be more positive.

There has been long a debated question: How does phase separation affect crystal ordering? Although a phenomenological postulation was proposed that molecular chains may be deformed and more regularly aligned by mutual (or inter-) diffusion in a phase separation process,^{20,21,23} however, no direct experimental evidence was obtained before. Furthermore, recent simulations did not predict the orientation of lamellar growth under the coupled transitions of crystallization and phase separation.^{25,26} The lamellar orientation inversion reported in this study provides a first direct evidence to confirm that crystal ordering can be affected by phase separation. The failure to obtain a regular array of crystal lamellae in conventional studies (like polyolefin blends), we believe, lies in two factors. One is molecular orientation may be quickly relaxed in dynamically symmetric blends. The other is hydrodynamic coarsening may smear or randomize the possible patterns. But these limitations can be avoided in this dynamically asymmetric PEO/PMMA blend.

Combining the analysis above, we may conclude that the macroscopic birefringence inversion is the result of the microscopic lamellar orientation inversion. In a regular spherulite, negative birefringence means that the refractive index in the tangential direction is larger than that in the radial direction. When concentric ring patterns form, lamellae orient in the tangential directions. Larger refractive index is in the radial direction. Accordingly, concentric ring patterns will have a positive birefringent character. This birefringence inversion is schematically shown in Figure 17.

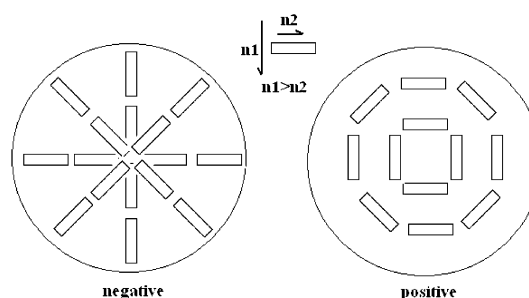


Figure 17. Schematic illustration of the negative birefringence of normal spherulite and the positive birefringence of concentric pattern.

CONCLUSIONS

In this study, a detailed investigation is made on the crystallization dynamics, as well as on the crystal structures at different length scales, under the dynamic interplay between crystallization and phase separation. The growth rate curve tends to show double peaks, in contrast to a bell-like growth rate curve in normal spherulitic growth. Coupled with strong phase separation under deep quench, lamellae prefer to array regularly in the tangential direction, instead of the growth in the radial direction within spherulites. The phase separation effect is also revealed by SAXS within lamellar stacks, reflected by drastic decrease of long period with respect to temperature.

AUTHOR INFORMATION

Corresponding Author

*E-mail: c.c.han@iccas.ac.cn. Telephone: +86 10 82618089. Fax: +86 10 62521519.

ACKNOWLEDGMENTS

This work is supported by National Natural Science Foundation of China (No. 50930003) and the Ministry of Science and Technology of China Special Funds for Innovation in 2009 (2009IM031000).

REFERENCES

- (1) Paul, D. R.; Newman, S. *Polymer blends*; Academic Press: New York, 1978.
- (2) Araki, T.; Qui, T.-C.; Shibayama, M. *Structure and properties of multiphase polymeric materials*; M. Dekker: New York, 1998.
- (3) Flory, P. J. *Principles of polymer chemistry*; Cornell University Press: Ithaca, NY, 1953.
- (4) Onuki, A. *Phase Transition Dynamics*; Cambridge University Press: New York, 2002.
- (5) Cheng, S. Z. D. *Phase transitions in polymers: the role of metastable states*; Elsevier: Boston, MA, 2008.
- (6) Keller, A.; Cheng, S. D. Z. *Polymer* **1998**, 39, 4461.
- (7) Hoffman, J. D.; Miller, R. *Polymer* **1997**, 38, 3151.
- (8) Strobl, G. *Rev. Mod. Phys.* **2009**, 81, 1287.

- (9) Balsara, N. P.; Lin, C. *Phys. Rev. Lett.* **1996**, *77*, 3847.
- (10) Hashimoto, T. *Phase Transitions* **1988**, *12*, 47.
- (11) Han, C. C.; Akcasu, A. Z. *Annu. Rev. Phys. Chem.* **1992**, *43*, 61.
- (12) Shi, W.; Cheng, H.; Chen, F.; Liang, Y.; Xie, X.; Han, C. C. *Macromol. Rapid Commun.* **2011**, *32*, 1886.
- (13) Liu, J.; Jungnickel, B.-J. *J. Polym. Sci., Part B: Polym. Phys.* **2007**, *45*, 1917.
- (14) Grozev, N.; Botiz, I.; Reiter, G. *Eur. Phys. J. E* **2008**, *27*, 63.
- (15) Ferreira, V.; Douglas, J. F.; Warren, J.; Karim, A. *Phys. Rev. E* **2002**, *65*, 051606.
- (16) Okerberg, B. C.; Marand, H. *J. Mater. Sci.* **2007**, *42*, 4521.
- (17) Lorenzo, M. L. D. *Prog. Polym. Sci.* **2003**, *28*, 663.
- (18) Wang, C.; Chen, C. C.; Cheng, Y. W.; Liao, W. P.; Wang, M. L. *Polymer* **2002**, *43*, 5271.
- (19) Cimmino, S.; Di Pace, E.; Martuscelli, E.; Silvertre, C. *Polymer* **1993**, *34*, 2799.
- (20) Zhang, X.; Wang, Z.; Zhang, R.; Han, C. C. *Macromolecules* **2006**, *39*, 9285.
- (21) Zhang, X.; Wang, Z.; Muthukumar, M.; Han, C. C. *Macromol. Rapid Commun.* **2005**, *26*, 1285.
- (22) Du, J.; Niu, H.; Dong, J. Y.; Dong, X.; Wang, D. J.; He, A.; Han, C. C. *Macromolecules* **2008**, *41*, 1421.
- (23) Zhang, X.; Wang, Z.; Dong, X.; Wang, D.; Han, C. C. *J. Chem. Phys.* **2006**, *125*, 024907.
- (24) Hong, S.; Zhang, X.; Zhang, R.; Wang, L.; Zhao, J.; Han, C. C. *Macromolecules* **2008**, *41*, 2311.
- (25) Mitra, M. K.; Muthukumar, M. *J. Chem. Phys.* **2010**, *132*, 184908.
- (26) Ma, Y.; Zha, L.; Hu, W.; Reiter, G.; Han, C. C. *Phys. Rev. E* **2008**, *77*, 061801.
- (27) Tanaka, H. *Macromolecules* **1992**, *25*, 6377.
- (28) Tanaka, H. *Phys. Rev. Lett.* **1996**, *76*, 787.
- (29) Tanaka, H. *J. Phys.: Condens. Matter* **2000**, *12*, R207.
- (30) Talibuddin, S.; Wu, L.; Runt, J. *Macromolecules* **1996**, *29*, 7527.
- (31) Chen, H. L.; Li, L. J.; Lin, T. L. *Macromolecules* **1998**, *31*, 2255.
- (32) Glatter, O.; Kratky, O. *Small Angle X-ray Scattering*; Academic Press: New York, 1982; p 35.
- (33) Strobl, G. *The Physics of Polymers*, 2nd ed.; Springer: New York, 1978; p 151.
- (34) Shi, W.; Han, C. C. *Macromolecules* **2011**, DOI: 10.1021/ma201940m.

Time-Resolved Synchrotron X-ray Scattering Study on Propylene–1-Butylene Random Copolymer Subjected to Uniaxial Stretching at High Temperatures

Yimin Mao, Christian Burger, Xiaowei Li, and Benjamin S. Hsiao*

Department of Chemistry, Stony Brook University, Stony Brook, New York 11794-3400, United States

Aspy K. Mehta

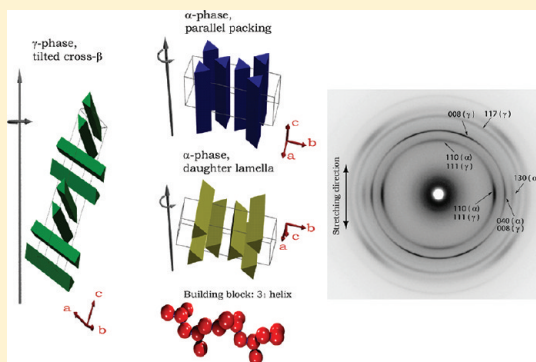
ExxonMobil Chemical Company, 5200 Bayway Drive, Baytown, Texas 77520, United States

Andy H. Tsou

ExxonMobil Research and Engineering Company, Annandale, New Jersey 08801, United States

Supporting Information

ABSTRACT: Synchrotron wide-angle X-ray diffraction (WAXD) and small-angle X-ray scattering (SAXS) were used to characterize the structure evolution of propylene–1-butylene (P–B) random copolymer subjected to uniaxial tensile deformation at 100 °C. Polymorphism and preferred orientation of the crystal phases were examined quantitatively by 2D WAXD. The results indicated that three ensembles of crystalline modifications with distinctive orientation modes coexisted during stretching. The orthorhombic γ -form adopted a tilted cross- β configuration, in which the c -axis had a tilt angle with respect to the fiber axis. The monoclinic α -form in the mother lamellae had a c -axis orientation with polymer chains parallel to the fiber axis. In the α -phase daughter lamellae, the unit cell assumed an a -axis orientation, where the c -axis had an 80° angle with respect to the fiber axis. Stretching transformed the γ -phase into the energetically more stable α -phase. In the late stage, the system was dominated by the α -phase with parallel chain packing. Complemented by qualitative SAXS analysis, simultaneous inter- and intralamellar chain slips were observed during the early stage of stretching. After yielding, a fibrillation process followed. The formation of fibril bundles together with a cross-linked network after yielding might account for the stress-hardening behavior in the late stage of stretching.



INTRODUCTION

Isotactic polypropylene (*i*-PP), one of the most widely used thermoplastic polymers, is valued by the industrial community because of its low cost, easy processability, and good mechanical performance in many applications. Furthermore, it exhibits rich experimental phenomena such as polymorphism, morphology, and preferred orientation under external fields during crystallization and is therefore frequently chosen by researchers as a model system to study the structure–property relationship of semicrystalline polymers. Recently, *i*-PP research has seen a revival due to attempts to further broaden its applications by copolymerization, creating a new family of propylene-based random copolymers varied in properties as a function of the comonomer type, content, and sequence distribution. In general, hybrid noncrystallizable segments in the polypropylene chain generate defects in the crystal lattice. If the comonomer concentration is low, noncrystallizable segments can be excluded from the *i*-PP homopolymer crystals during crystallization,

and accumulate in the amorphous lamellae.^{1–4} In other words, changing the primary structure of the polypropylene chain by adding only a small amount of comonomer will not alter its existing polymorphism. However, it does have influence on properties such as crystallinity, morphology, crystallization kinetics, etc.^{5–7} In addition, these defects may change the “habit” of chain motion, leading to a preference of forming certain types of crystal modifications over others.^{8–11} Only when the comonomer content exceeds a certain level can the hybrid segments be incorporated into the (more or less distorted) crystal lattice, forming new types of crystal modifications that are different from those of the *i*-PP homopolymer.

So far as the polymorphism of *i*-PP homopolymer is concerned, three crystal modifications— α -, β -, and γ -phases—have

Received: September 27, 2011

Revised: December 6, 2011

Published: December 23, 2011

been identified, depending on the crystallization conditions. Although these polymorphs share the same building block, i.e., the 3_1 chain helix, they have very different chain-packing geometries. The α -form was the first identified crystal form of *i*-PP.¹² It has a monoclinic unit cell with dimensions of $a = 6.65$ Å, $b = 20.96$ Å, $c = 6.5$ Å, and $\beta = 99.2^\circ$, where chains align in parallel to the c -axis. The γ -form crystal is favored in the presence of chain defects or special crystallization conditions such as high pressure. Brückner et al. in 1989^{13,14} solved the unique structure of the γ -form with an unusual nonparallel chain packing. In this case, eight chains are arranged perpendicularly to the c -axis in a cross-hatched style, forming a large orthorhombic unit cell ($a = 8.54$ Å, $b = 9.93$ Å, and $c = 42.41$ Å). The building block consists of two repeating units of 3_1 helices, being 13.0 Å in length. In one ab -plane, chains lay diagonally (the diagonal of an ab -plane is equal to twice the length of one pitch of a 3_1 helix). The β -phase is the third form of *i*-PP polymorphs, forming the least ordered thermodynamically metastable modification. While the β -form has been known for a long time, it was finally fully characterized by Brückner et al. in 1994¹⁵ and, independently, by Lotz.¹⁶ It has a trigonal or hexagonal unit cell ($a = b = 11.02$ Å and $c = 6.49$ Å) with three chains aligned parallel to the c -axis in a frustrated packing (e.g., two up and one down chain), typically also showing some rotational disorder.

In this study, we investigated a propylene–1-butylene (P–B) random copolymer with low comonomer content, aiming to understand the changes of polymorphism and preferred orientation when being subjected to strong uniaxial tensile deformation at high temperatures (i.e., 100 °C). The main experimental techniques were wide-angle X-ray diffraction (WAXD) and small-angle X-ray scattering (SAXS) using synchrotron X-rays. Data interpretation was based on the simulation of 2D WAXD patterns, complemented by qualitative 2D SAXS analysis. In addition to the present tensile stretching study, we have recently investigated this system under shear flow,¹⁷ hence completing the systematic studies of structure development under weak and strong flows.

■ THEORETICAL CONSIDERATION FOR SIMULATION OF 2D WAXD PATTERNS

A brief description of 2D WAXD fiber pattern calculation is given here, while the computational details have been demonstrated earlier.¹⁷ It should be pointed out that generation of a fiber diffraction pattern does not necessarily require the sample having a fiber shape but does require the microstructures inside the sample to possess a cylindrically rotational symmetry. This is the case here. A thin sheet specimen was used in the stretching experiment. The sample was prepared in such a way that minimum force was introduced before stretching (see Experimental Section for details). Consequently, a fiber axis was introduced by uniaxial tensile force, as will be shown later. In this study, different terms regarding different spatial directions are adopted to describe the measured intensity in real space and scattering geometry in reciprocal space. To avoid confusion, the system is further explained here. The sample was fixed by two clamps, which applied uniaxial tensile force; hence, the stretching direction (i.e., the machine direction) is the direction that the clamps move, and it is vertical. The fiber axis is the axis around which structures are rotationally symmetric: meridian and equatorial directions are thus defined accordingly to describe the fiber-symmetric system. The former is in parallel to the fiber axis, while the latter is perpendicular to the fiber axis.

In this paper, the directions of stretching, fiber, and meridian are defined in this manner, but this is not always the case. For example, in our earlier work dealing with the shear field-induced crystallization,¹⁷ the machine direction (i.e., the shear direction) was perpendicular to the fiber axis.

The essence of the calculation from preferentially oriented crystals is to redistribute the total scattering intensity of hkl nodes in reciprocal space controlled by an appropriate orientation distribution function. In spherical coordinates, the scattered intensity is a function of the azimuthal angle ψ , polar angle ϕ , and the absolute value of scattering vector $s = (2/\lambda) \sin(\theta/2)$, with θ being the scattering angle.^{18–20} In the presence of fiber symmetry, the fiber-averaged intensity distribution $\overline{J}(s, \phi)$ does not depend on the azimuthal angle, ψ . The volume integration of the fiber-averaged scattering intensity $\overline{J}(s, \phi)$ over the entire reciprocal space produces an invariant. For an individual hkl node, this means

$$\int_0^{2\pi} \int_0^\pi \int_0^\infty \overline{J}(s, \phi) s^2 \sin \phi \, d\psi \, d\phi \, ds = 2\pi \int_0^\pi \int_0^\infty \overline{J}(s, \phi) s^2 \sin \phi \, d\phi \, ds = I_{hkl} \quad (1)$$

where I_{hkl} represents the total intensity scattered by a given hkl node.

In order to confirm the presence of fiber symmetry in our stretching experiment, a P–B sample stretched at 60 °C (strain = 2.0) was cut into a small piece and irradiated by the X-ray beam using both face-on and edge-on geometries, having a 90° angle with respect to the fiber axis (i.e., the stretching direction). A comparison of the two patterns is shown in Figure 1a and the corresponding 1D averaged profiles (scaled by a constant due to different sample thickness) in Figure 1b. It is clear that despite slight differences in the relative intensity, the scattering patterns/curves are almost identical, verifying that fiber symmetry was an excellent approximation.

When the radial width of the scattering arcs is sufficiently narrow, which is the case here, the fiber-averaged intensity can be factorized into a radial and an angular component as follows^{18–20}

$$\overline{J}(s, \phi) = \overline{I_{hkl}}(s) F(\phi, \phi_{hkl}) \quad (2)$$

with $\overline{I_{hkl}}(s)$ being the powder scattering intensity of a given hkl node. $F(\phi, \phi_{hkl})$ determines how the intensity is distributed over ϕ , peaked at the hkl node's polar angle ϕ_{hkl} . It has the form

$$F(\phi, \phi_{hkl}) = \frac{p}{\sinh(p)} \cosh(p \cos \phi \cos \phi_{hkl}) \times I_0(p \sin \phi \sin \phi_{hkl}) \quad (3)$$

where Onsager's orientation distribution is used.²⁰ In eq 3, p is a parameter controlling the width of the Onsager distribution; I_0 is the modified Bessel function of the first kind of order zero. $F(\phi, \phi_{hkl})$ is normalized, and eq 1 is satisfied.

In the above procedure, powder intensities of all hkl nodes (within the range of detection in the actual experiment) have to be calculated as the first step. The approach is straightforward and can be found in many standard textbooks. The key is to have a complete set of coordinates of atomic groups in the unit cell, typically generated as the result of applying symmetry operations to an asymmetric unit. As described above, P–B copolymer with low comonomer content does not form new crystal modifications other than α -, β -, and γ -phases of the *i*-PP. Unit cells and space groups of crystal modifications used for

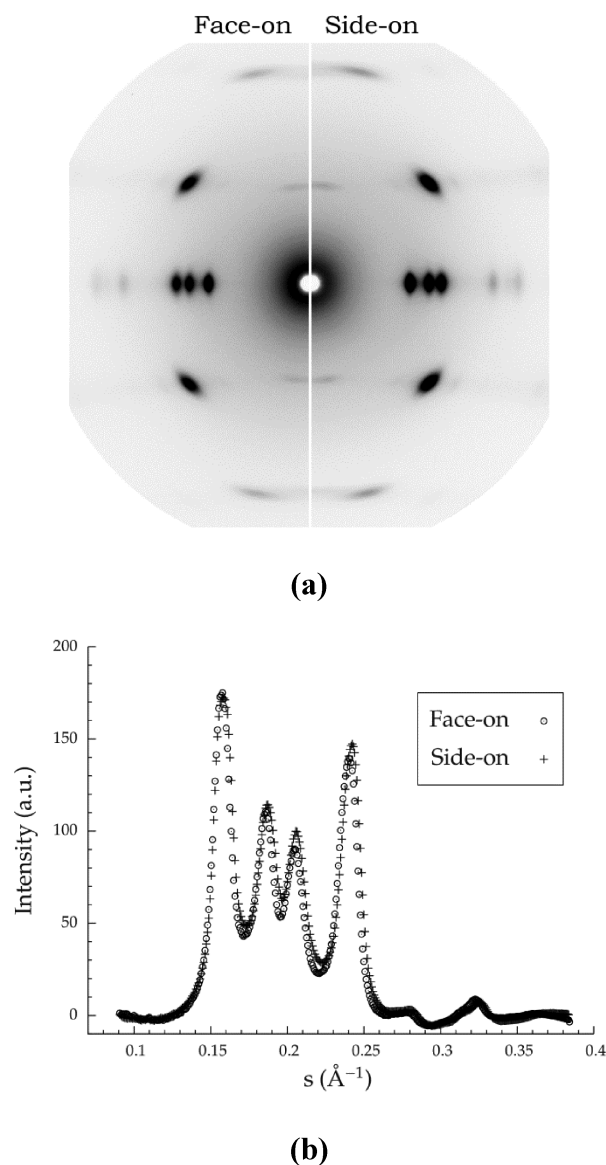


Figure 1. Comparison of scattering patterns of P-B copolymer subjected to uniaxial stretching, captured with X-ray beam in the direction of film's normal (face-on, left) and side (edge-on, right) (a); corresponding 1D profiles. The temperature during stretching was 60 °C, strain = 2.0 (b).

computation will be explained in relevant places in the following context. For random copolymers, polymer chains are often packed in unit cells in a relatively loose manner, causing variations in unit cell dimensions, i.e., lattice constants. Therefore, published lattice constants have to be treated as slightly adjustable parameters in order to fit the experimental data. Throughout this computation, only coordinates of carbon atoms are considered and hydrogen atoms are neglected, which introduces an error of less than 3% in the intensity calculations.

Crystal imperfection becomes important in copolymer crystallization because of the existence of noncrystallizable segments. We noticed that the experimental scattering intensity appears to be systematically attenuated at large angles compared with the calculated one. This phenomenon can be explained in terms of a lattice disorder of the first kind, where atomic groups are displaced statistically around their ideal positions. Defining ΔX as the average displacement of an atomic

group from its ideal position and assuming this displacement is isotropic in 3D, the corrected intensity after considering this type of disorder, $I_{hkl}^{(d)}$, can be expressed by multiplication with a Debye–Waller factor²¹

$$I_{hkl}^{(d)} = I_{hkl} \exp\left(-\frac{4\pi^2}{3}s^2\Delta X^2\right) \quad (4)$$

Equation 4 was originally derived for the treatment of thermal agitation. A generalization of eq 4 to anisotropic displacement disorder is straightforward. Other types of disorder, such as rotational disorder²² and up/down chain disorder,^{12,23,24} were not considered here for simplicity. In addition, lattice disorder of the second kind was found to be negligible, based on the observed radial peak width behavior as a function of s .

An orthogonal coordinate system with three axes, denoted as s_1 , s_2 , and s_3 , was adopted to define the intensity distribution in 3D reciprocal space (s_3 represents the fiber direction). In the presence of fiber symmetry, the intensity is only a function of s_3 and s_{12} where s_{12} equals $(s_1^2 + s_2^2)^{1/2}$. Unit cell dimensions could be deformed during stretching. We assume the presence of an affine deformation for our calculation. If the deformation ratio along s_3 is denoted as λ_d , then s_{12} is deformed by $1/\sqrt{\lambda_d}$, which guarantees that the total volume of the unit cell is unchanged. The absolute value of scattering vector, s , can thus be written as

$$s^2 = \frac{1}{\lambda_d}(s_1^2 + s_2^2) + \lambda_d^2 s_3^2 \quad (5)$$

Affine deformation causes diffraction patterns to become slightly elliptic, with the long axis of the ellipses perpendicular to the fiber axis²⁵ (reciprocal relationship). In our WAXD experiment, λ_d is about 1.01, i.e., about 1% deviation from ideal undeformed behavior.

Experimental WAXD fiber patterns are subject to a distortion as a result of the curvature of the Ewald sphere. This distortion can be corrected (often termed the “Fraser correction”), generating patterns showing undistorted sections through reciprocal space with missing regions around the meridian.^{26,27} In the present study, we kept the experimental WAXD fiber patterns uncorrected for this effect but distorted the calculated WAXD patterns (the “inverse Fraser correction”). Furthermore, a background due to density fluctuations and air scattering was added. This way, the original experimental data were kept intact and could be directly used to compare with the calculated patterns.

EXPERIMENTAL SECTION

Materials and Experimental Procedure. The P-B random copolymer was synthesized by ExxonMobil Chemical Company. The number-average molecular weight (M_n) was 56 000 g/mol, and the polydispersity index was 1.97. The mole fraction of the butylene component was 5.7%. The melting point of this polymer was 122 °C, as measured by DSC. An Instron machine was used to apply uniaxial stretching. The sample was first melted and kept at 150 °C in a mold with a thickness of 1.0 mm for 5 min and then naturally cooled to room temperature. The film was then cut into 30.0 mm long dumbbell-shaped specimens. The widths of the two ends and the central part of the dumbbell were 9.0 and 4.0 mm, respectively. The experimental protocol was as follows. The sample was held by two clamps of the Instron machine and was kept at desired temperatures for 2 min to reach thermal equilibrium and then uniaxially stretched with a constant speed of 6.0 mm/min at this temperature. At the same time, scattering patterns during stretching were captured by a MAR CCD detector in a time-resolved manner. All stretching experiments were performed at 100 °C.

Time-Resolved WAXD/SAXS Measurements. WAXD/SAXS measurements were carried out at the X27C Beamline in the National Synchrotron Light Source (NSLS), Brookhaven National Laboratory (BNL). The wavelength of the X-ray beam was 1.371 Å. All scattering images were captured *in situ* by a 2D MAR CCD detector. The exposure time for each image was 30 s. The diffraction/scattering angle was calibrated by Al₂O₃ for WAXD and by silver behenate for SAXS. When the stretching measurement was finished, an air background with equivalent exposure time was gathered. When correcting the experimental data, a coefficient of less than one was multiplied to the air background to account for the beam fluctuation and sample absorption. The background manipulation could be carried out in two equivalent ways; namely, it could be either subtracted from the experimental data or added to the simulated data (keeping experimental data as is), depending on how the data were presented. For 1D integrated intensity profile ($I(s)$ – s plot), the former method was adopted to abide by the convention. For 2D pattern comparison, we used the latter method to achieve the best visualization results.

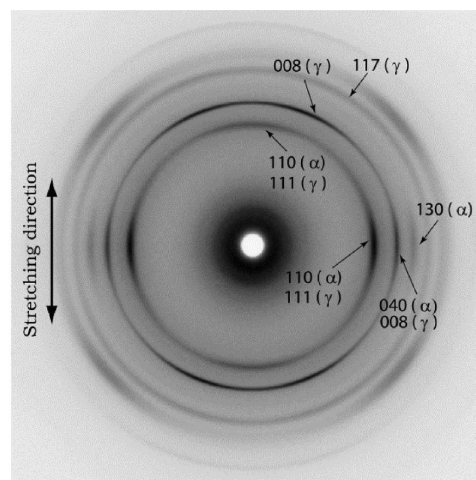
RESULTS

Polymorphism and Preferred Orientation Revealed by WAXD. The α -phase was considered as the first crystal modification of P–B copolymer stretched at 100 °C, since it is the most stable and the most common crystal form in *i*-PP homopolymer. Unit cell coordinates used for the α -phase calculation were obtained from ref 12, having the $C2/c$ space group. In a typical WAXD pattern/profile, the α -phase has the three most intense peaks at $s = 0.16$, 0.19, and 0.21 Å^{−1}, corresponding to (110), (040), and (130) reflection planes, respectively.^{12,28} In the stretching experiment, the polymer chains in the α -phase crystal (along the c -axis) are aligned parallel to the stretching direction, which would result in three strong arcs on the equator for these three ($hk0$) reflections. These features are clearly seen in Figure 2a. The γ -phase was naturally taken into account since it is frequently observed in propylene-based random copolymers. We adopted the unit cell coordinates given by Brückner et al.^{13,14} for the calculation of the γ -phase, using the $Fddd$ space group. We note that γ - and α -phases have very close chain packing energies. From the calculation, it was seen that many diffraction peaks overlapped in the WAXD pattern/profile, as shown in Figure 2b for the calculated powder diffraction profiles of both phases. The distinguishing signature feature of the γ -phase was the occurrence of the (117) peak.^{13,14,28} It could also be seen from Figure 2b that the (130) peak is unique for the α -phase, which was used to judge its presence in the following context.

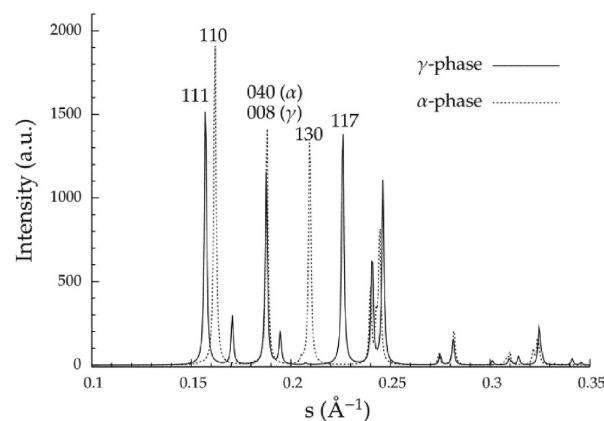
Without considering preferred orientation, one can calculate 1D powder intensity profiles representing the compositions of the γ - and α -phases and their fractions with respect to the amorphous matrix using the approach introduced above. Experimental 1D WAXD profiles corresponding to Figure 2a and the calculated profile are shown in Figure 3. 1D profiles were generated from 2D patterns using the following integration scheme:

$$I_{1D}(s) = \int_0^{\pi/2} I(s, \varphi) \sin \varphi \, d\varphi \quad (6)$$

All reflection peaks in the experimental profile were indexed using a mixture of γ - and α -phases. In Figure 3, the fraction of the α -form was about 32% in the crystalline portion. The change of relative ratio between these two phases will be discussed in detail later.



(a)



(b)

Figure 2. Typical experimental WAXD pattern of P–B copolymer stretched at 100 °C (strain = 0.5) (a). Calculated 1D powder diffraction profiles of γ - and α -form crystals (b).

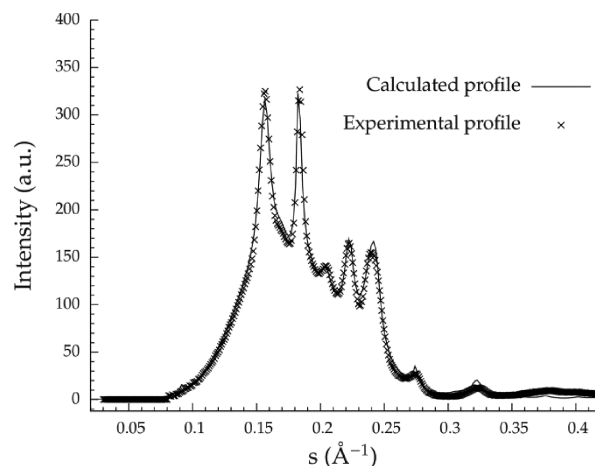


Figure 3. Experimental and calculated 1D WAXD profiles of P–B copolymer being stretched at 100 °C, strain = 0.5. The content of α -phase equals 70%.

To determine the orientation mode of each phase, a careful analysis of the polar distribution of the intensity is necessary.

As mentioned above, the three equatorial arcs of the α -phase represent a parallel chain packing with respect to the stretching direction. As for the γ -phase, two possible orientation modes have been reported. In the first case, the c -axis is perpendicular to the flow direction. Consequently, the polymer chains are somehow trying to align in “parallel” to the flow direction (we note that, in the γ -phase, the chain direction is perpendicular to the c -axis), but this parallelism is limited, since for the γ -phase crystal it is impossible to have two cross-hatched chains aligned parallel to a certain direction simultaneously. It only means that the polymer chains in this case tend to be aligned along the flow direction to a large extent.^{17,28} The other mode, with its name borrowed from protein structures, is called the “cross- β ” configuration.²⁸ In this case, the c -axis is parallel to the flow direction, indicating that all chains are perpendicular to the flow direction. The strong reflection peak of the (008) reflection plane in the γ -phase is a signature to judge the presence of this orientation mode. It is obvious that for the “parallel packing” mode, (008) should appear in the equatorial direction, while it must be located on the meridian if the “cross- β ” configuration is present.²⁸ However, our experimental results, as exhibited in Figure 2a, for example, clearly indicate that the (008) reflection arc was off the fiber axis. This means that the c^* -axis (the direction of which coincides with that of the c -axis for orthorhombic symmetry) had a tilt angle, which was denoted as φ_{008} , with respect to the fiber axis. To calculate 2D scattering patterns of this type, one needs to rotate the whole unit cell, including all the atomic coordinates of its contents accordingly beforehand. The coordinate rotation can be done in a standard way: the new coordinate \mathbf{x}' after rotation is related to the original one \mathbf{x} by²⁹

$$\mathbf{x}' = \mathbf{T}_r \cdot \mathbf{x} \quad (7)$$

where \mathbf{T}_r is a rotation tensor. For a fiber pattern, rotating about the a - or b -axis for a $\pm\varphi_{008}$ angle leads to the same tilting of the (008) plane. However, since other reflection planes will also be subjected to changes when rotated, it is required that the entire pattern generated after coordinate rotation must be consistent with the experimental one, not just the single (008) plane. With this consideration, a simple rotation about the b -axis for $\pm\varphi_{008}$ was adopted.

It was noticed that in Figure 2a the (110) arc from the α -phase also occurred in the direction close to the meridian. This has been reported to be a consequence of lamellar branching. The c -axis of the α -phase unit cell in the daughter lamellae had an 80° angle with respect to those in the mother lamellae. The same argument of the unit cell rotation as has been applied to the γ -crystal is also valid in this case. Since the (040) reflection arc remained in the same position, the rotation must be about the b -axis. This is the so-called b -axis orientation of the α -phase.³⁰ An example of a simulated 2D WAXD pattern corresponding to the experimental counterpart shown in Figure 2a generated under consideration of the discussion above is shown in Figure 4. Figure 4 consists of four quadrants representing both experimental data (upper left and lower right quadrant) and simulated patterns (upper right and lower left quadrant) for comparison purposes. Figure 5 gives a detailed comparison of polar scans of intensities in the selected regions between experimental data and simulated results. As seen from Figures 3–5, the current model explains the experimental 2D WAXD pattern very well. However, the molecular mechanism of the tilting of the cross- β configuration of the γ -phase is still not clear. Figure 6 illustrates the orientations of the γ - and α -phase

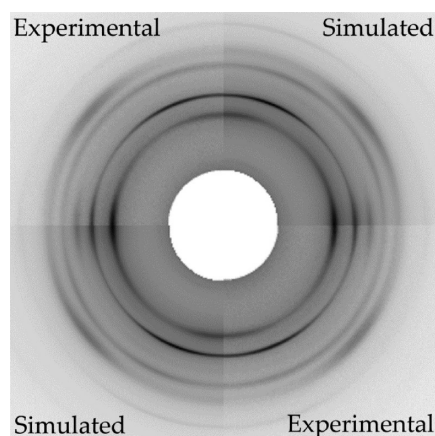


Figure 4. Comparison of experimental (upper left and lower right quadrants) and simulated (upper right and lower left quadrants) 2D WAXD pattern of P–B copolymer being stretched at 100 °C, strain = 0.5. The pattern is contributed by both γ - and α -phases with three orientation modes: 63% of parallel packed α -phase (the c -axis in parallel to the fiber axis), 7% of α -phase daughter lamellae (the c -axis has an 80° angle with respect to the fiber axis), and 30% of γ -phase with tilted cross- β configuration (the c -axis has a 22° tilt angle with respect to the fiber axis). Intensity is in linear scale.

crystals during stretching. Only crystals in the mother lamellae of the α -phase adopted parallel packing of the chains with respect to the fiber axis. The c -axis of the γ -phase and that of crystals in the daughter lamellae of the α -phase had a tilt angle with respect to the fiber axis. For the γ -phase, this tilt angle changed with the deformation ratio in the early stage of stretching, which will be discussed later. The angle between mother and daughter lamellae was fixed at about 80°. It should be pointed out that Figure 6 only demonstrates the orientation of the unit cells, not of the lamellae, which can be determined by SAXS.

Structural Development during Stretching. After a comprehensive examination of all features of one typical 2D WAXD pattern, it is now clear that the crystalline portion of the P–B copolymer stretched at high temperature (i.e., 100 °C) is a mixture of γ - and α -phase crystals. The complexity lies in the fact that several ensembles of scatterers with distinctive orientations contribute to the diffraction pattern. A coherent understanding of the relationships among the different phases requires decomposing and tracing the structure development during the stretching process. The time-resolved measurements enabled us to achieve this goal. To facilitate the discussion, we could divide the stretching process based on the critical points in the stress–strain curve into three stages, as shown in Figure 7.

Figure 7 is a typical stress–strain curve of a semicrystalline polymer. Point 1 represents the yield point. We refer to the interval from the very beginning of stretching until the end of yielding (point 2, strain ≈ 0.5) as the early stage. The interval from point 2 to point 3, during which stress remains almost unchanged as strain increases, is referred to as the intermediate stage. After point 3 until the end of stretching, stress increases monotonically with strain. We denote this period as the late stage. It should be mentioned that the division of a stress–strain curve is dependent on the procedure of the stretching experiment. Some authors^{31,32} found that for the real stress–strain curve (corrected for sample thickness variation) more regions could be distinguished. In our conventional “engineering stress–strain” curve, the division of three stages

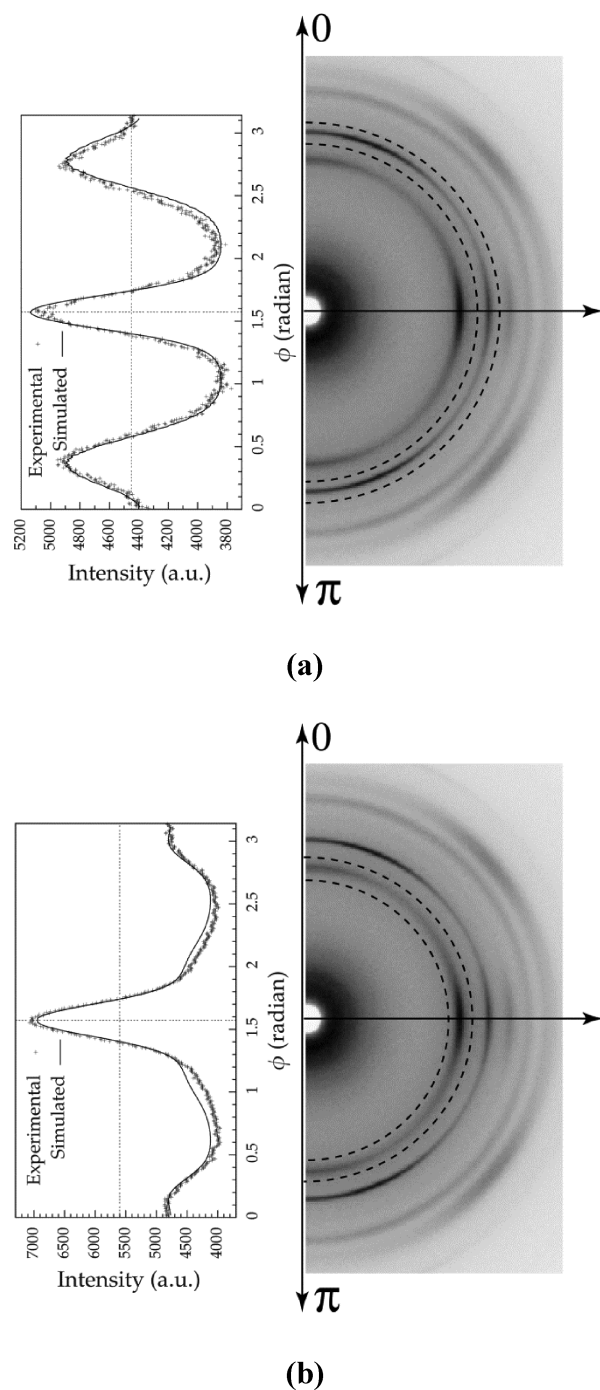


Figure 5. Comparison of experimental and simulated intensity profiles in the selected regions enclosed between dashed lines. Intensity is in linear scale.

was implemented based on the WAXD/SAXS patterns detected.

Figure 8 shows the overall crystallinity change during stretching. Crystallinity was obtained using the ratio of calculated intensity from all hkl planes and the total intensity. It decreased slightly in the very early stage (strain < 0.2) and then kept increasing. This decrease was related to yielding. The usual interpretation of the structure change before yielding of semi-crystalline polymers is due to the destruction of lamellar aggregates (spherulites) formed under quiescent conditions.³¹ Using eq 4, we could separate the portion of crystallinity due to

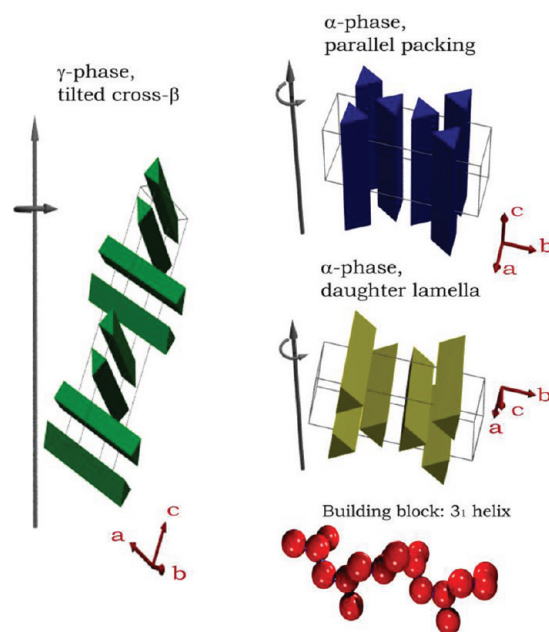


Figure 6. Illustration of two crystal modifications of *i*-PP and their possible orientation modes that occurred during stretching experiment at 100 °C.

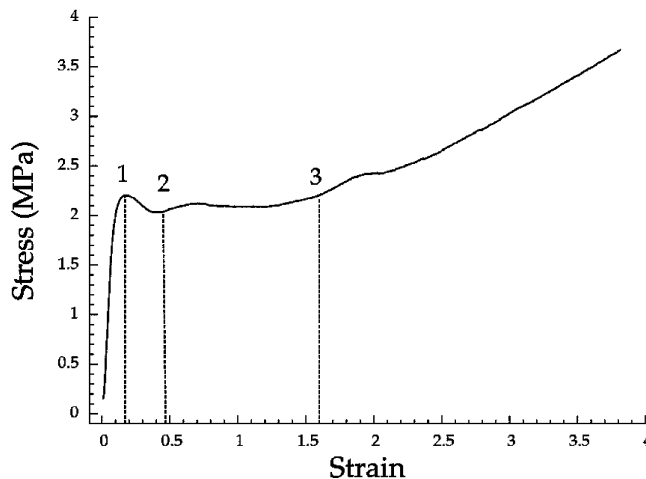


Figure 7. Stress-strain curve of P-B copolymer stretched at 100 °C.

disorder by calculating suppressed intensity caused by ΔX over the total intensity, as shown in the inset of Figure 8. This parameter was naturally used to evaluate the fraction of defects in the crystalline phase. Its monotonic increase could be attributed to stress being imposed on crystals, causing atomic groups to deviate from their ideal positions.

The crystallinity was further decomposed into fractions from the γ -phase and α -phase, respectively, as shown in Figure 9. An opposing trend of change of fractions from two phases was clearly seen. Given the fact that the γ -form crystals adopted a tilted cross- β configuration, in which the c -axis was close to the stretching direction, it is easy to rationalize that they are unstable if stretched, since chains are packed layer by layer along the c -axis in the unit cell. The stretching-induced destruction of this crystal resembles the melting process.³³ Because polymer chains are still quite mobile at this high temperature (100 °C), they tend to form a more stable crystal form (the α -phase in this case). Apparently, with parallel packing of polymer chains

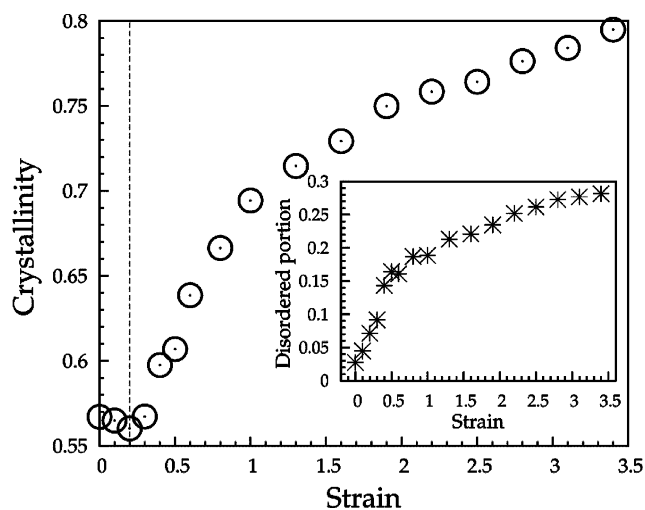


Figure 8. Crystallinity change as a function of strain during stretching. The inset shows the change of the portion due to disorder effect.

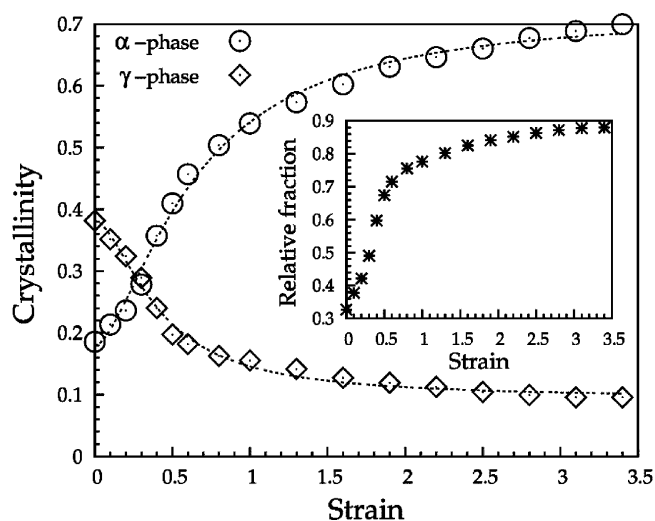


Figure 9. Change of crystallinity contributed by γ - and α -phases. The inset shows the relative fraction of the α -phase in crystalline part. It would equal 1 if the crystalline phase were completely composed of α -phase.

along the stretching direction, the unit cell of the α -form crystal is more durable as compared with that of the γ -phase. The inset of Figure 9 shows the relative percentage of α -phase in the crystalline portion. In the late stage, the composition was completely reversed. The α -phase became the dominant modification with a concentration of about 90%.

To quantify the degree of orientation, Hermans' orientation parameter $\langle P_2 \rangle$ was adopted. When using Onsager's function for the polar distribution of intensity, $\langle P_2 \rangle$ can be analytically written as²⁰

$$\langle P_2 \rangle = 1 - 3(\coth(p) - 1/p)/p \quad (8)$$

For perfect orientation parallel to the fiber axis, $\langle P_2 \rangle$ equals 1. It becomes zero when the scatterers are isotropically oriented. The changes of $\langle P_2 \rangle$ for the γ - and α -form crystal are exhibited in Figure 10a. For both phases, $\langle P_2 \rangle$ increased rapidly in the very early stage, followed by a slow increase, extending all the way through the intermediate to the late stage. Beyond the point where strain ≈ 0.5 , $\langle P_2 \rangle$ of the α -phase was always higher than that of the γ -phase. This is also a result of its parallel

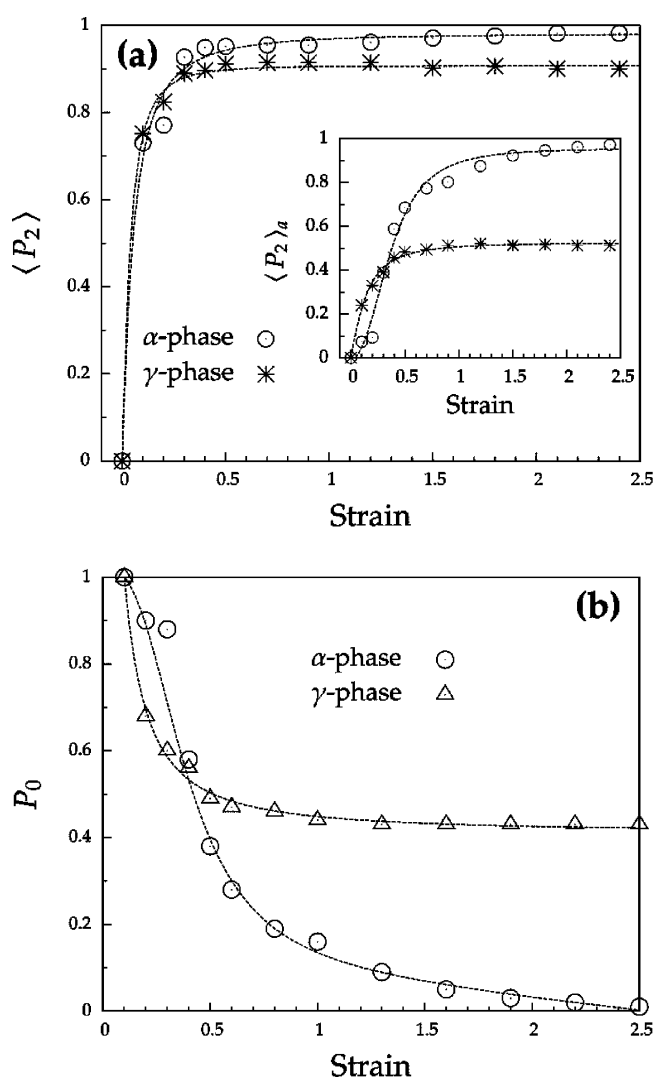


Figure 10. Changes of Hermans' orientation function $\langle P_2 \rangle$ (a) and unoriented portion P_0 (b) of γ - and α -phase during stretching. The inset in (a) is the same plot of apparent degree of orientation $\langle P_2 \rangle_a$ which is defined in the text.

packing nature. $\langle P_2 \rangle$ was only used to characterize the oriented portion of the crystals. The polar intensity scan showed a constant baseline, which corresponded to unoriented crystals forming a fraction, P_0 . The apparent degree of orientation, including oriented and unoriented portions, was $\langle P_2 \rangle(1 - P_0)$, which was denoted as $\langle P_2 \rangle_a$. The origin of P_0 can be explained as follows. Since the scattering pattern is an ensemble average of scattering from different scatterers, all crystals illuminated in the scattering volume are counted. Crystals are varied in size and in the degree that they are connected/entangled with their surroundings. The tensile force can also not be evenly transmitted to the entire polymer network. The consequence of these effects is that crystals that are well connected/entangled with their surroundings are more ready to be oriented. As stretching proceeds, tensile force can apply to more and more crystals, allowing P_0 to decrease continuously. The inset of Figure 10a shows its development. The change of P_0 could be found in Figure 10b. Again, strain ≈ 0.5 was a critical point beyond which P_0 turned to a slow decrease mode. The decrease of P_0 of the α -phase lasted until the very late stage of stretching where almost all crystals were oriented. In contrast to this

continuous decrease, P_0 of the γ -phase gradually reached a plateau value, which was about 40% higher than that of the α -phase in the late stage, while in the beginning, P_0 showed a reverse trend. This inversion was a consequence of the inversion of the ratio between the fractions of α - and γ -phases as discussed before. Since the γ -phase was the dominant crystal form in the early stage (Figure 9), stress was mainly withstood by the skeleton formed by the γ -phase rather than the α -phase, leading to a higher value of $\langle P_2 \rangle$ as well as P_0 . Once the α -phase became dominant, it took over the role of γ -phase, leading to the inversion.

Crystal Orientation versus Lamellar Orientation. So far the discussion on preferred orientation is at the crystal unit cell length scale. Complemented by the SAXS experiment, we could trace the lamellar orientation and the arrangement of crystals within the lamellae. Selected WAXD and SAXS patterns (the WAXD pattern consists of two quadrants of experimental images combined with two quadrants from simulation, similar to that shown in Figure 4) during stretching are shown in Figure 11. Before stretching, the WAXD pattern

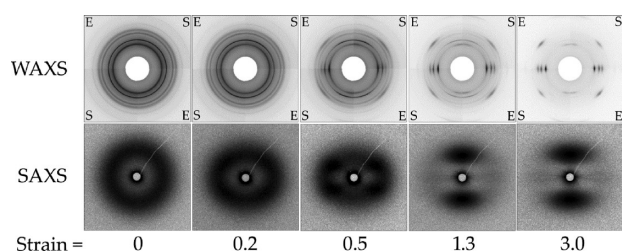


Figure 11. WAXD (top row) and SAXS (bottom row) patterns of P-B copolymer stretched at different strains. Each WAXD pattern shown in the top row is composed of four quadrants, with upper left and lower right quadrants being the experimental pattern (marked as “E”) and upper right and lower left quadrants being the simulated patterns (marked as “S”). Intensity is in linear scale.

exhibited a series of Debye–Scherrer rings that are typical in isotropic powder diffraction. The SAXS pattern showed a broad isotropic ring, which could be commonly interpreted as scattering from randomly oriented stacks of lamellae formed in quiescent crystallization conditions. A general trend for the development of WAXD patterns was that three equatorial arcs corresponding to the (110), (040), and (130) reflection planes of the α -phase crystals became more and more pronounced. The final pattern was almost completely dominated by the α -phase, with the c -axis parallel to the fiber axis. For the γ -phase, the strength of scattering continued to decrease, as evidenced by the weakening of scattering from the (008) and (117) reflection planes. Moreover, the (008) arc first moved gradually toward the meridian in the early stage and then maintained a constant tilt angle with respect to the fiber axis until the end of the experiment.

SAXS patterns are characterized by a four-point feature in the early stage, followed by a two-point feature along the meridian at the intermediate and late stages. When taking a close look, the change of the tilt angle of the (008) plane (denoted as φ_{008}) had a reverse trend when compared with the tilting of the four-point pattern observed in the SAXS measurements. If denoting the polar angle of the lobe position in the four-point SAXS pattern as φ_{SAXS} (see Figure 12a), it was seen that the complementary angle of φ_{SAXS} roughly equaled to φ_{008} . The change of the tilt angles obtained from both WAXD and SAXS

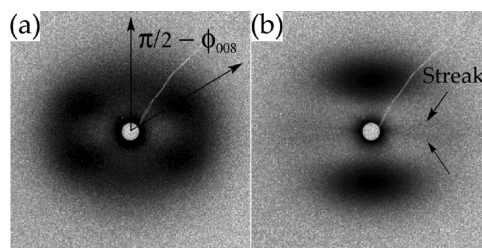


Figure 12. SAXS patterns of P-B copolymer during stretching, at strain of 0.5 (a) and 3.0 (b). Intensity is in linear scale.

experiments are shown in Figure 13. In this figure, φ_{SAXS} could only be measured at strain ≤ 0.6 , above which the maximum

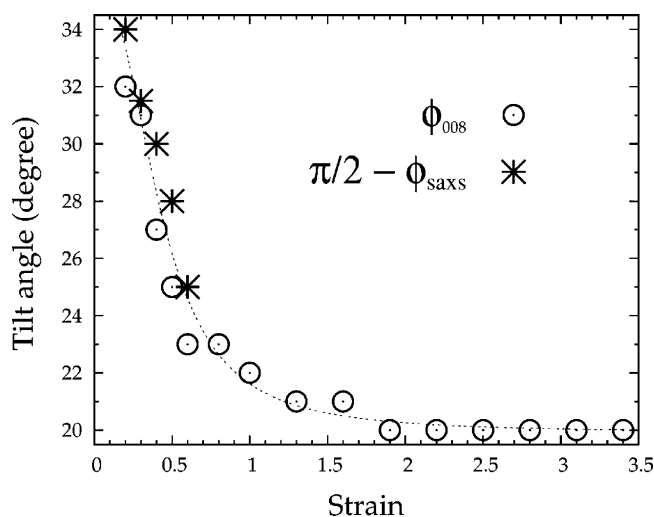


Figure 13. Changes of tilt angle of the (008) reflection plane (φ_{008}) obtained from WAXD pattern and tilt angle of lobes in four-point SAXS patterns ($\pi/2 - \varphi_{008}$) during stretching.

value in the polar scan was hard to distinguish and the pattern gradually transformed to the two-point feature along the meridian.

We note that $\varphi_{\text{SAXS}} \approx \pi/2 - \varphi_{008}$, where the lamella normal has a $\pi/2 - \varphi_{008}$ angle with respect to the fiber axis, equivalent to the lamella being tilted by φ_{008} with respect to the fiber axis. Therefore, combined with the WAXD pattern, the c -axis of the γ -phase unit cell must be parallel to the lamellae, or the polymer chains were parallel to the lamella normal. In contrast, for the α -phase, the polymer chains were always aligned in the stretching direction, as revealed by the WAXD patterns. Consequently, there was a shear angle being roughly equal to φ_{008} . The schematic diagram of the lamellar orientation and arrangement of the polymer chains within the lamellae in the early stage of the tensile deformation is illustrated in Figure 14a.

From the intermediate to the late stage of tensile deformation, SAXS patterns were featured with two points on the meridian, indicating that the lamellae were parallel to the equator (or the lamellae are perpendicular to the fiber axis). As discussed above, the α -phase was the dominant crystal form at the late stage. Therefore, it is reasonable to attribute the strong meridional intensity to the α -phase lamellae. A possible model describing the orientation of the lamellae and polymer chains in the late stage is shown in Figure 14b. However, besides the strong intensity on the meridian, additional features could be distinguished in these SAXS patterns; i.e., two tilted streaks, although weak, were clearly distinguished near the equator

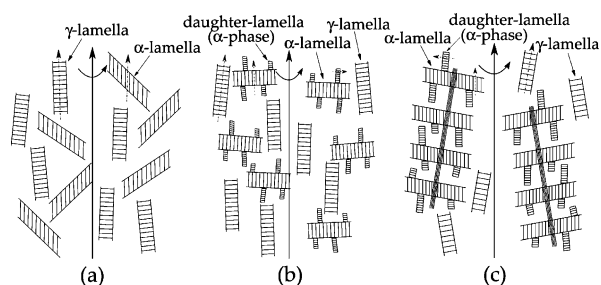


Figure 14. Schematics of three possible lamellar orientations and chain arrangements within the lamellae (derived from the WAXD/SAXS results): (a) shows lamellar and chain orientation in the early stage of stretching, where both γ - and α -phase lamellae are tilted. (b) and (c) represent the condition after yielding. Arrows drawn in lamellae represent the c -axis direction. Fibril structure is included in (c) as evidenced by the occurrence of streaks near equator in SAXS patterns. A detailed description can be found in the text.

(indicated by the arrows in Figure 12b). These equatorial streaks are due to the rodlike structures (or voids) oriented along an angle close to the fiber axis. For a stretched polymer sample, a likely explanation is the existence of fibril bundles. Once this concept is taken into account, a different model can be proposed. First of all, the equatorial streaks could not come from the γ -phase, although both had a tilt angle with respect to the fiber axis. This is because the tilt angle for the γ -phase crystal, φ_{008} , was eventually fixed at about 20° , while the tilt angle of the streaks with respect to the equator was below 10° , as seen from the SAXS pattern as well as the intensity profiles of the polar scan in Figure 15. If the α -lamellae were grown

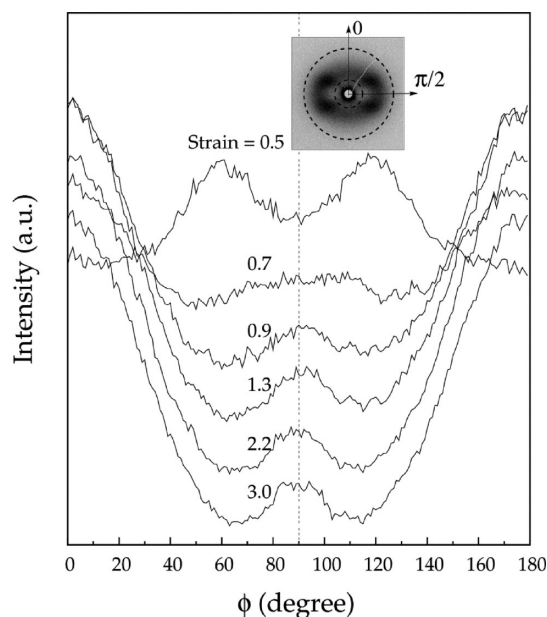


Figure 15. Polar angle dependence of intensity obtained from SAXS pattern at different strains. The scheme of polar scan is shown in the inset.

epitaxially on the fibril bundles, forming a “shish-kebab”-like structure, the meridional maxima would be the superposition of two maxima close to the fiber axis (the schematic diagram of this model is shown in Figure 14c). In this case, the polymer chains of the α -phase had a tilt angle with respect to the fibril bundles, since they were parallel to the fiber axis. However, the molecular

mechanism as to why these fibril bundles have a tilt angle with respect to the fiber axis instead of being parallel to it, as well as how the polymer chains in the lamellae are connected to the fibril bundles, is still not clear. Furthermore, as far as the fibril bundles are considered, the model shown in Figure 14b suggests that they are not coupled with the α -lamellae. On the basis of the current SAXS data, it is hard to judge which model represents the real situation. But it is at least possible to discern at which stage the fibrillation process was initiated. Figure 15 shows the dependence of the intensity with respect to the polar angle obtained from the SAXS patterns at different strains (the scheme of the polar scan is shown in the inset). It was seen that the intensity near the equator became more and more discernible when the strain went beyond 0.7. This indicates that the formation of fibril bundles started almost right after the accomplishment of yielding (strain = 0.5).

DISCUSSION

With the full sequence of the WAXD and SAXS data, we can correlate the structure development with the stress–strain curve. So far as the evolution of the scattering pattern is concerned, the early stage, i.e., from the beginning of stretching until the end of yielding, generates the most dramatic structure change. For semicrystalline polymers, yielding is closely related to destruction of pre-existing spherulites, which is accomplished by interlamellar and intralamellar chain slip.^{31,34} The former leads to the dissociation of lamellar aggregates, in which lamellae are connected by interlamellar chains, while the latter accounts for the tensile deformation of a single lamella. Interlamellar chain slip is believed to be easier to achieve as compared to intralamellar slip, since the former deals mainly with separation of chains in the intermediate amorphous layers between the crystalline lamellae. Therefore, a successive occurrence of these two processes can be expected.³⁵ Strobl et al.³¹ argued that for interlamellar slip polymer chains tend to be aligned parallel to the equator, whereas the chains will be parallel to the meridian for intrachain slip. On the basis of the WAXD results, in which the $(hk0)$ arcs were always located near the equator, they concluded that intralamellar slip took place in the very beginning of tensile deformation. In our experiment for P–B copolymer, we observed a simultaneous occurrence of inter and intralamellar slips in the early stage of deformation. On the one hand, the (008) arc from the γ -phase moved toward the meridian, indicating that the chains align parallel to the equator. On the other hand, all $(hk0)$ arcs from the α -phase were localized on the equator at the same time. The four-point feature becomes the main character in the SAXS pattern during this period, with four lobes gradually moving toward the equator. All these observations point to the coexistence of inter- and intralamellar slips, with the former dominated by the γ -phase and the latter by the α -phase.

The yield point is a critical step before which the slip takes place individually. After that point, a collective slip process occurs, resulting in a complete destruction of spherulites.^{31,36} This process proceeds all the way through the intermediate stage (the plateau region), by the end of which the system is transformed into a network consisting of cross-links based on residual crystals as well as chain entanglements within the amorphous matrix. Further tensile deformation of this network leads to stress-hardening, which can be described by the theory of rubber elasticity.^{31,36,37} The transformation to such a network structure is indirectly evidenced by the fact that the changes of parameters related to the orientation (P_0 , $\langle P_2 \rangle$) in

Figure 10 slowed down after point 1 (i.e., the yield point). This indicates that beyond point 1 the stress was mainly dispersed in the network structure rather than the crystal skeleton. Further evidence is that the dimensions of the unit cell in the γ -phase were prone to change in the early stage of deformation. Figure 16

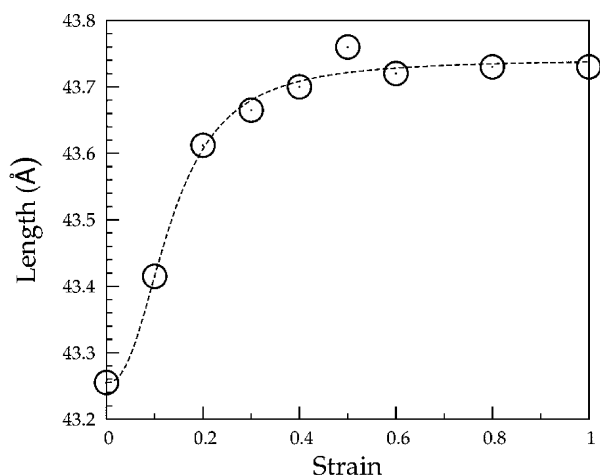


Figure 16. Change of dimension of the c -axis of the γ -phase crystal unit cell during stretching.

shows the change of the c -axis length of the unit cells in the γ -phase (the a - and b -axis change accordingly based on the affine deformation described in the simulation part). It was seen that the most significant change of this unit cell dimension occurred at the early stage, while after that, it converged to a constant value. The elongation of the c -axis is expected, since for tilted cross- β configuration, the stress is applied mostly in the packing direction of polymer chains (i.e., the c -axis). We did not observe such a dimensional change in the unit cell of the α -phase. The reason might lie in the fact that the polymer chains in this case are parallel to the stretching direction, before the deformation of the unit cell and intralamella chain slip took place, resulting in the shear angle in α -lamellae (see the schematic diagram in Figure 14a).

Another important feature of the structure formation during stretching was the fibrillation process which might also contribute to the stress-hardening behavior. As discussed earlier, this process occurred in the beginning of the intermediate stage of tensile deformation. Also, the consequences of fibrillation could only be seen in the SAXS patterns, as indicated by the two weak streaks near the equator. However, at this point, it is hard to provide the full details of its molecular nature. The composition in the fibril bundle as well as the molecular mechanism of its relationship to the lamellae is still not clear. It requires higher quality SAXS patterns to decipher, which will be one of the tasks of a future study.

CONCLUSIONS

The P-B random copolymer subjected to uniaxial stretching at 100 °C was studied using time-resolved synchrotron WAXD/SAXS measurements. Two crystal modifications, γ - and α -phase, with three distinctive orientation modes of the crystal unit cells were identified during stretching. The results indicated that the γ -phase adopted a tilted cross- β configuration, in which the c -axis had a tilt angle with respect to the fiber axis. Polymer chains were piled layer by layer in a cross-hatched manner along the c -axis direction. The α -phase had two orientation

modes, depending on the type of lamellae: the mother lamellae possessed a c -axis orientation in which the polymer chains were parallel to the fiber axis; the daughter lamellae possessed an a -axis orientation in which the c -axis had an 80° angle with respect to the fiber axis. The γ -phase was not stable under stretching; its fraction continued to decrease until the end of the experiment. In contrast, the α -phase became gradually dominant due to the enhanced parallel packing of polymer chains. The structure development could be correlated with the mechanical properties characterized by the stress-strain curve. It was found that the polymer exhibited the most dramatic changes in the WAXD/SAXS pattern near the region of yielding. Simultaneous inter- and intralamella slip processes were observed in the early stage. The SAXS patterns revealed a fibrillation process after the end of yielding. The fibril bundles, as well as the network formation as a consequence of continuous application of tensile force, might be responsible for the stress-hardening behavior in the late stage of tensile deformation.

ASSOCIATED CONTENT

Supporting Information

A demonstration of scattering geometry of specimens exhibiting fiber symmetry and a description of the fitting procedure. This material is available free of charge via the Internet at <http://pubs.acs.org>.

AUTHOR INFORMATION

Corresponding Author

*E-mail bhsiao@notes.cc.sunysb.edu; Tel 631-632-7793; Fax 631-632-6518.

ACKNOWLEDGMENTS

The authors thank the assistance of Lixia Rong and Jie Zhu for the synchrotron WAXD and SAXS experimental setup. The financial support of this work was provided by the National Science Foundation (DMR-0906512) and ExxonMobil Chemical Company.

REFERENCES

- (1) Poon, B.; Rogunova, M.; Hiltner, A.; Baer, E.; Chum, S.; Galeski, A.; Piorkowska, E. *Macromolecules* **2005**, *38*, 1232–1243.
- (2) De Rosa, C.; Dellolaccone, S.; Auriemma, F.; Ciaccia, E.; Resconi, L. *Macromolecules* **2006**, *39*, 6098–6109.
- (3) Lotz, B.; Ruan, J.; Thierry, A.; Alfonso, G. C.; Hiltner, A.; Baer, E.; Piorkowska, E.; Galeski, A. *Macromolecules* **2006**, *39*, 5777–5781.
- (4) De Rosa, C.; Auriemma, F.; De Ballesteros, O. R.; De Luca, D.; Resconi, L. *Macromolecules* **2008**, *41*, 2172–2177.
- (5) Crist, B.; Howard, P. *Macromolecules* **1999**, *32*, 3057–3067.
- (6) Crist, B.; Mirabella, F. *J. Polym. Sci., Part B: Polym. Phys.* **1999**, *37*, 3131–3140.
- (7) Jeona, K.; Palza, H.; Quijada, R.; Alamo, R. G. *Polymer* **2009**, *50*, 832–844.
- (8) Alamo, R.; Kim, M.; Galante, M.; Isasi, J.; Mandelkern, L. *Macromolecules* **1999**, *32*, 4050–4064.
- (9) Hosier, I.; Alamo, R.; Estes, P.; Isasi, J.; Mandelkern, L. *Macromolecules* **2003**, *36*, 5623–5636.
- (10) Gou, Q.; Li, H.; Yu, Z.; Chen, E.; Zhang, Y.; Yan, S. *Colloid Polym. Sci.* **2007**, *285*, 1149–1155.
- (11) De Rosa, C.; Auriemma, F.; de Ballesteros, O. R.; Resconi, L.; Camurati, I. *Macromolecules* **2007**, *40*, 6600–6616.
- (12) Natta, G.; Corradini, P. *Nuovo Cimento Suppl.* **1960**, *15*, 40–51.
- (13) Brückner, S.; Meille, S. V. *Nature* **1989**, *340*, 455–457.
- (14) Meille, S. V.; Brückner, S.; Porzio, W. *Macromolecules* **1990**, *23*, 4114–4121.

- (15) Meille, S.; Ferro, D.; Bruckner, S.; Lovinger, A.; Padden, F. *Macromolecules* **1994**, *27*, 2615–2622.
- (16) Lotz, B.; Kopp, S.; Dorset, D. C. R. *Acad. Sci., Ser. II* **1994**, 319, 187–192.
- (17) Mao, Y.; Burger, C.; Zuo, F.; Hsiao, B. S.; Tsou, A. H.; Thurman, D. W. *Macromolecules* **2011**, *44*, 558–565.
- (18) Ruland, W.; Tompa, H. *Acta Crystallogr., Sect. A: Cryst. Phys., Diffraction, Theor. Gen. Crystallogr.* **1968**, *A 24*, 93–99.
- (19) Ruland, W. *Colloid Polym. Sci.* **1977**, *255*, 833–836.
- (20) Burger, C.; Zhou, H.-W.; Sics, I.; Hsiao, B. S.; Chu, B.; Graham, L.; Glimcher, M. J. *J. Appl. Crystallogr.* **2008**, *41*, 252–261.
- (21) Guinier, A. *X-ray Diffraction in Crystals, Imperfect Crystals, and Amorphous Bodies*; Dover Publications: Mineola, NY, 1994.
- (22) Liu, X.; Ruland, W. *Macromolecules* **1993**, *26*, 3030–3036.
- (23) Auriemma, F.; de Ballesteros, O.; De Rosa, C.; Corradini, P. *Macromolecules* **2000**, *33*, 8764–8774.
- (24) Auriemma, F.; De Rosa, C.; Boscato, T.; Corradini, P. *Macromolecules* **2001**, *34*, 4815–4826.
- (25) Brandt, M.; Ruland, W. *Acta Polym.* **1996**, *47*, 498–506.
- (26) Fraser, R.; Macrae, T.; Miller, A.; Rowlands, R. *J. Appl. Crystallogr.* **1976**, *9*, 81–94.
- (27) Stribeck, N.; Noechel, U. *J. Appl. Crystallogr.* **2009**, *42*, 295–301.
- (28) Auriemma, F.; De Rosa, C. *Macromolecules* **2006**, *39*, 7635–7647.
- (29) Arfken, R.; Weber, H. *Mathematical Methods for Physicists*, 5th ed.; Academic Press: New York, 2000.
- (30) Lotz, B.; Wittmann, J.; Lovinger, A. *Polymer* **1996**, *37*, 4979–4992.
- (31) Hong, K.; Rastogi, A.; Strobl, G. *Macromolecules* **2004**, *37*, 10174–10179.
- (32) Gsell, C.; Hiver, J.; Dahoun, A.; Souahi, A. *J. Mater. Sci.* **1992**, *27*, 5031–5039.
- (33) Flory, P.; Yoon, D. *Nature* **1978**, *272*, 226–229.
- (34) Gaucher Miri, V.; Seguela, R. *Macromolecules* **1997**, *30*, 1158–1167.
- (35) Young, R.; Bowden, P.; Ritchie, J.; Rider, J. *J. Mater. Sci.* **1973**, *8*, 23–36.
- (36) Hong, K.; Rastogi, A.; Strobl, G. *Macromolecules* **2004**, *37*, 10165–10173.
- (37) Haward, R.; Thackray, G. *Proc. R. Soc. London, Ser. A* **1968**, *302*, 453–472.

Properties and Semicrystalline Structure Evolution of Polypropylene/Montmorillonite Nanocomposites under Mechanical Load

Norbert Stribeck,^{*,†} Ahmad Zeinolebadi,[†] Morteza Ganjaee Sari,[‡] Stephan Botta,[§] Katja Jankova,^{||} Søren Hvilsted,^{||} Aleksey Drozdov,[⊥] Rasmus Klitkou,[#] Catalina-Gabriela Potarniche,[#] Jesper deClaville Christiansen,[#] and Valentina Ermini[&]

[†]Institute TMC, Department of Chemistry, University of Hamburg, Bundesstr. 45, D-20146 Hamburg, Germany

[‡]Department of Polymer Engineering and Color Technology, Amirkabir University of Technology, P.O. 15875-4413, 424 Hafez Ave., Tehran, Iran

[§]HASYLAB at DESY, Notkestr. 85, D-22603 Hamburg, Germany

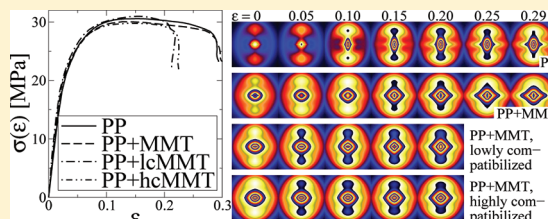
^{||}Danish Polymer Center, Department of Chemical and Biochemical Engineering, Technical University of Denmark, Building 227, DK-2800 Kgs. Lyngby, Denmark

[⊥]Danish Technological Institute, Gregersensvej 1, DK-2630 Taastrup, Denmark

[#]Department of Production, Aalborg University, Fibigerstræde 16, DK-9220 Aalborg, Denmark

[&]Laviosa Chimica Mineraria S.P.A., Via Galvani 20, I-57123 Livorno, Italy

ABSTRACT: Small-angle X-ray scattering (SAXS) monitors tensile and load-cycling tests of metallocene isotactic polypropylene (PP), a blend of PP and montmorillonite (MMT), and two block copolymer compatibilized PP/MMT nanocomposites. Mechanical properties of the materials are similar, but the semicrystalline nanostructure of the PP differs. This is explained by a nucleation effect of the MMT. Competitive crystal growth diminishes crystallite sizes. The reinforcing effect of the MMT filler appears consumed by weakening the PP matrix. Decays of mechanical and nanostructure response in dynamic load cycling indicate materials fatigue. Lifetimes describe the reinforcing and weakening effects. Addition of 3% MMT halves the fortifying effect of the PP nanostructure. A net gain of reinforcement (11%) is observed with the highly compatibilized composite in which the strength of the semicrystalline PP is reduced to 25%. Other results concern the evolution of Strobl's block structure and void formation during tensile loading.



1. INTRODUCTION

Polypropylene as Base Material of Composites. Polypropylene¹ (PP) is the material preferred² by automotive industry for replacement of metal by plastics for reduction of weight and fuel consumption. As it comes to weight reduction of load-bearing components, the materials properties of the polymer are insufficient. A solution of this problem is the use of hybrid modules from PP and metal. Such modules are expensive. One could reduce the cost if one would succeed to develop an easily processable, low-fatigue PP-based composite. Glass-fiber reinforced PP composites^{3,4} are well introduced and exhibit advanced properties. Nevertheless, the production of the molded parts is still elaborate because at least the rupture of the glass fibers must be minimized. Thus, layered silicates^{5–12} bonded with PP could become an economical alternative, as is pointed out in recent reviews on polymer nanocomposites.^{13,14}

Polypropylene as a Special Semicrystalline Material. Polypropylene^{1,15} is one of the many thermoplastics that are semicrystalline at service temperature. Their properties depend on the semicrystalline morphology. Joined crystallites form crystalline lamellae. Crystalline and amorphous lamellae pile up,

and these stacks are the building blocks of spherulites. This multiscale morphology is generated by crystallization from the melt. Whereas many polymers start to crystallize when the melt is moderately cooled below the melting temperature, pure PP only starts to crystallize when it is undercooled by more than 50 °C.^{5,16} Consequently, PP is strongly susceptible to additives that change the crystallization behavior. Particularly with polypropylene the crystallization has frequently been found to propagate via a blocky mesophase.^{17,18} Moreover, in contrast to most polymers, polypropylene tends to form cross-hatched crystalline lamellae^{19–21} that connect the main lamellae and thus may build a 3-dimensional scaffold that reinforces the material. Ultimately, the many possible crystal modifications¹ of PP can be used to optimize the grade with respect to application.

Nucleation of Technical Polypropylene. Delayed solidification is unacceptable for many manufacturing methods. Therefore, PP crystallization is accelerated by additives. Commercial

Received: September 2, 2011

Revised: November 6, 2011

Published: December 20, 2011

grades contain nucleators^{22–25} or clarifiers that nucleate the melt heterogeneously. During processing they support the creation of the required morphology. As such a grade and additional reinforcing components are bonded in a composite,²⁶ the solidification process may be altered.^{5–10} Effects on the semi-crystalline morphology cannot be excluded. Such effects may be investigated by small-angle X-ray scattering (SAXS). In particular, results from SAXS monitoring of structure evolution under load may advance the understanding of the relation between the composite's morphology and its practicality in a load-bearing application.

Monitoring Mechanical Tests. In service, materials are frequently subjected to strain or cyclic loading. Hence, resistance²⁷ to dynamic load (i.e., low fatigue^{28–30}) is required. There is abundant experimental literature on the relation between materials structure and mechanical load.³¹ Nevertheless, the number of papers in which scattering is studied simultaneously during fatigue tests is still small.^{32,33} Fortunately, recent progress at synchrotron X-ray radiation facilities makes it possible to follow the variation of anisotropic scattering patterns of polymers during mechanical tests with sufficient accuracy.

2. EXPERIMENTAL PART

Materials. Nanocomposites from metallocene polypropylene (HM562S, LyondellBasell) and nanoclay (hydrophilic montmorillonite, MMT) are studied. The MMT is obtained from Laviosa Chimica Mineraria, Italy, as a 3.8 wt % aqueous dispersion. A compatibilizer is added to two of the materials in order to intercalate the MMT. The compatibilizer is an amphiphilic block copolymer (AB) made by atom transfer radical polymerization (ATRP).^{34,35} It consists of a hydrophobic block of hydrogenated polybutadiene, i.e., poly(ethylene-co-1,2-butylene) monoalcohol (PEB) (trade name: Kraton L-1203 from Kuraray Co., Japan) with molecular weight 7000, PDI = 1.05, and a hydrophilic block of quaternized dimethylaminoethyl methacrylate (DMAEMA) with 35 DMAEMA units. Modified nanoclays with 4.7 and 8.0 wt % of the AB (PEB-*b*-PDMAEMA₃₅N⁺) have been prepared. For this reason 1660 mL (3.8 wt %) of MMT dispersion was diluted with 1320 mL of distilled water under stirring at 80 °C for 4 h. 4.5 g of AB in 450 mL of distilled water was added, and the mixture was stirred further at 40 °C. The modified clay dispersion was filtered off and washed with water until no more Na⁺ was detected (0.1 M AgNO₃), mixed with water, and then freeze-dried. Table 1 describes the composition

Table 1. PP/MMT Nanocomposites Based on Metallocene Polypropylene (PP)–HM562S (LyondellBasell) and Montmorillonite (MMT) (Laviosa)^a

sample	composition
PP	pure polypropylene
PP + MMT	PP + 3 wt % freeze-dried MMT
PP + lcMMT	PP + (3 wt % MMT + 4.7 wt % AB)
PP + hcMMT	PP + (3 wt % MMT + 8.0 wt % AB)

^aThe compatibilizer is an amphiphilic block copolymer (AB).

of the studied materials. Sample PP is the pure polypropylene. Sample PP + MMT is a blend of polypropylene and the freeze-dried hydrophilic MMT. The samples PP + lcMMT and PP + hcMMT are composites that contain MMT with low compatibilizer amounts and high compatibilizer amounts, respectively. In order to prepare the nanocomposites, modified lcMMT and hcMMT have first been freeze-dried and, second, blended with the PP.

Test bars S2 according to DIN 53504 are injection molded in a MiniJet II (Thermo Scientific) from a melt of 200 °C. Mold temperature: 30 °C, molding pressure: 650 bar, molding time: 45 s; holding pressure: 100 bar; holding time: 20 s. The cross section of the parallel central part is 4 mm × 2 mm.

Tensile Testing. Tensile testing is performed in a self-made³⁶ machine. A grid of fiducial marks is printed on the test bars.³⁷ The clamping distance is 45 mm. A 500 N load cell is used. Signals from load cell and transducer are recorded during the experiment. The sample is monitored by a TV camera. Video frames are grabbed every 10 s and stored together with the experimental data. The machine is operated at a cross-head speed of 0.5 mm/min. Using the fiducial marks, the local strain $\varepsilon = (l - l_0)/l_0$ is computed automatically³⁸ from the average initial distance, l_0 , of the fiducial marks and the respective actual distance, l . The true stress, $\sigma = F/A$, is computed from the force F measured by the load cell after subtracting the force exerted by the upper sample clamp, and $A = A_0/(1 + \varepsilon)$, the estimated actual sample cross section. A_0 is the initial cross section of the central zone of the test bar. The equation assumes conservation of sample volume.

In the continuous straining experiments necking starts after a draw path of ca. 3.5 mm. The experiment is stopped after the neck is fully developed. In the load-cycling experiments the samples are prestrained by 2 mm. After that the cycling starts. In each cycle the samples are strained by 1 mm and thereafter retracted by the same draw path.

SAXS Setup. Small-angle X-ray scattering (SAXS) is carried out in the synchrotron beamline A2 at HASYLAB, Hamburg, Germany. The wavelength of radiation is $\lambda = 0.15$ nm, and the sample–detector distance is 3031 mm. Scattering patterns are collected by a 2D marccd 165 detector (mar research, Norderstedt, Germany) in binned 1024 × 1024 pixel mode (pixel size: 158.2 μm × 158.2 μm). Scattering patterns are recorded every 30 s with an exposure of 20 s. The scattering patterns are normalized and background corrected.³⁹ This means intensity normalization for constant primary beam flux, zero absorption, and constant irradiated volume V_0 . Because the flat samples are wider than the primary beam, the correction has been carried out assuming $V(t)/V_0 = (1/(1 + \varepsilon(t)))^{0.5}$. The equation assumes constant sample volume.

SAXS Data Evaluation. The scattering patterns $I(s) = I(s_{12}, s_3)$ are transformed into a representation of the nanostructure in real space. The only assumption is presence of a multiphase topology. The result is a multidimensional chord distribution function (CDF), $z(r)$.⁴⁰ The method is exemplified in a textbook (ref 39, Sect. 8.5.5) and in the original paper⁴⁰ where figures show the change of the pattern from step to step. Here we do not dwell on the exposition of the evaluation method but summarize the steps and introduce the important quantities. The CDF with fiber symmetry in real space, $z(r_{12}, r_3)$, is computed from the fiber-symmetrical SAXS pattern, $I(s_{12}, s_3)$, of a multiphase material. $s = (s_{12}, s_3)$ is the scattering vector with its modulus defined by $|s| = s = (2/\lambda) \sin \theta$. 2θ is the scattering angle. In order to compute $z(r_{12}, r_3)$, $I(s_{12}, s_3)$ is projected on the representative fiber plane. Multiplication by s^2 applies the real-space Laplacian. The density fluctuation background is determined by low-pass filtering. It is eliminated by subtraction. The resulting interference function, $G(s_{12}, s_3)$, describes the ideal multiphase system. Its 2D Fourier transform is the sought CDF. In the historical context the CDF is an extension of Ruland's interface distribution function (IDF)⁴¹ to the multidimensional case or, in a different view, the Laplacian of Vonk's multidimensional correlation function.⁴² The CDF is an "edge-enhanced autocorrelation function"^{43–46}—the autocorrelation of the gradient field, $\nabla \rho(r)$. $\rho(r)$ is the electron density inside the sample that is constant within a domain (crystalline, amorphous). Thus, as a function of ghost displacement r , the multidimensional CDF $z(r)$ shows peaks wherever there are domain surface contacts between domains in $\rho(r')$ and in its displaced ghost $\rho(r' - r)$. Such peaks $h_i(r_{12}, r_3)$ are called⁴¹ distance distributions. Distance $r = (r_{12}, r_3)$ is the ghost displacement. Sometimes it is useful to replace the index i in $h_i(r_{12}, r_3)$ by a sequence of indices that indicate the sequence of domains that have been passed along the displacement path until the considered domain surface contact occurs. For example, $h_{ca}(r_{12}, r_3)$ indicates the passing of an amorphous and a crystalline domain. Thus, this peak is a long-period peak. h_{ca} will be used if the displacement is in the direction of strain. h_{ba} will be used if the displacement is in the lateral direction (i.e., transverse to strain), where b indicates the width of a block according to Strobl's block structure.^{17,18}

From the oriented scattering pattern we compute the scattering power Q of the ideal semicrystalline morphology (no density fluctuations within the domains, no density transition zone between the domains).³⁹ For this purpose we start from $G(s_{12}, s_3)$ and extract the scattering intensity $I_{id}(s)$ of the ideal semicrystalline morphology. Then $\{I_{id}\}(s_1, s_3) = \int I_{id}(s_1, s_2, s_3) ds_2$ is computed. The equation presents the definition of the projection operation. $\{I_{id}\}(s_1, s_3)$ is the scattering intensity of the ideal multiphase system projected on the representative s_{13} -plane of fiber symmetry.³⁹ From $\{I_{id}\}(s_1, s_3)$ the scattering power

$$Q = \iint \{I_{id}\}(s_1, s_3) ds_1 ds_3 \quad (1)$$

is directly computed. Q is normalized with respect to the irradiated volume because of the respective normalization of $I(s)$. In order to relate changing Q to structure evolution, it is helpful to know where the scattering intensity is changing. In general, the presentation of variations in *images* $\{I_{id}\}(s_1, s_3)$ is difficult, but if the intention is a discrimination between, e.g., void formation and change of the semicrystalline structure, an isotropic scattering curve $I(s)$ can be utilized. From $\{I_{id}\}(s_1, s_3) = \{I_{id}\}(s, \phi)$ an isotropic scattering curve

$$4\pi s^2 I(s) = \int_0^{2\pi} \{I_{id}\}(s, \phi) d\phi \quad (2)$$

is obtained by circular integration of $\{I_{id}\}(s, \phi) d\phi$ with respect to the polar angle ϕ in the s_{13} -plane. Of course, further integration with respect to s yields the scattering power. Thus, it appears reasonable to inspect the integrand $s^2 I(s)$ in order to determine which angular regime is responsible for observed changes in Q .

3. RESULTS

3.1. Tensile Tests. A self-made³⁶ tensile tester that performs symmetric drawing is used. Thus, the same spot of the sample is monitored by the X-ray, as long as the sample is homogeneously extended. If the tested material starts to neck, a peculiar problem is encountered that limits the interval in which data evaluation appears reasonable. This is demonstrated in Figure 1. In the inset images the irradiated spot is indicated by a cross. As the material begins to neck (Figure 1, inset c),

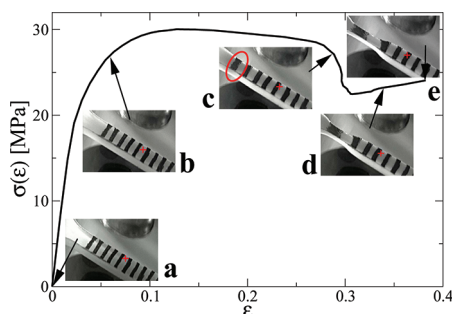


Figure 1. Stress relaxation and spot translation caused by necking. True stress $\sigma(\epsilon)$ as a function of local strain ϵ . (a) Start of test. The X-ray beam spot is indicated by a cross. (b) Homogeneous stretching. Spot does not move. (c) Necking has started (see ellipse). Material shows stress relaxation. (d) Spot moving toward neck. (e) End of experiment.

stress relaxation is observed and the irradiated spot starts to move along the sample toward its neck. Because the X-ray is no longer monitoring the same location of the material, the corresponding data are not discussed.

Figure 2 shows the mechanical data of the tensile tests in the synchrotron beam. The true stress σ is plotted as a function of the local strain ϵ measured at the point of irradiation by the

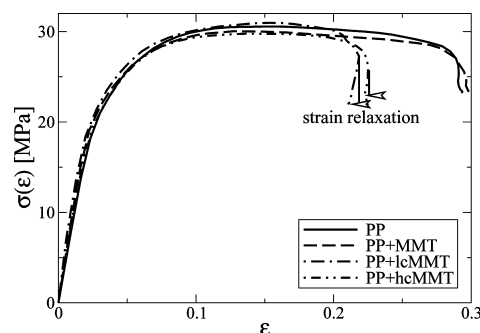


Figure 2. Tensile testing of PP/MMT materials in the synchrotron beam. True stress $\sigma(\epsilon)$ as a function of the local strain ϵ at the position of irradiation. Compatibilized nanocomposites exhibit even relaxation of local strain ϵ .

synchrotron beam. The spot-translation tail of the curves has been discarded. Obviously, the uncompatibilized materials (pure PP and PP + MMT) start necking at a higher elongation ($\epsilon \approx 0.29$) than the composites that contain compatibilized MMT. Moreover, these composites even show relaxation of the local strain while the neck is developing.

3.2. Discussion of Measured SAXS Patterns. Figure 3 presents central sections of selected SAXS patterns $I(s_{12}, s_3)$

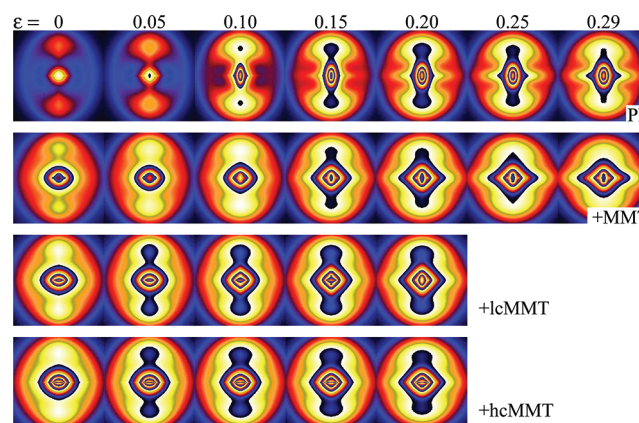


Figure 3. SAXS intensities $I(s_{12}, s_3)$ of PP, a blend (+MMT), and two composites (+lcMMT, +hcMMT) as a function of the local strain ϵ . Straining direction s_3 is vertical. The images are on the same logarithmic scale. They show the central region $-0.15 \text{ nm}^{-1} \leq s_{12} \leq 0.15 \text{ nm}^{-1}$ of the measured patterns in a repetitive pseudo-color presentation.

from the plain straining experiments as a function of the local strain ϵ . The measured images are larger and range to $s = 0.25 \text{ nm}^{-1}$. The logarithmic intensity scale is identical for all images.

Unstrained Materials. Before the start of the tests ($\epsilon = 0$) all the injection-molded materials exhibit discrete SAXS with high uniaxial orientation. Two-point patterns are observed. The peak maxima are on the vertical axis (s_3 , meridian, direction of the melt flow in the bar, straining direction). From top to bottom both the peak intensity and the lateral peak width are strongly increasing. The narrow reflections of the pure PP (top) and of the blend PP + MMT (below) are indicative for layer stacks made from crystalline lamellae in the PP that extend in the direction perpendicular to the direction of melt flow. Nevertheless, the blend already contains an additional background. It is a broad peak underneath the narrow reflection,

which indicates an additional microfibrillar component. In this component the shape of the crystalline domains is no longer an extended lamella, but only a granule of lower lateral extension. The blend and the composites exhibit strong central scattering of big scattering entities. These entities may either be crazes formed between the nanoparticles and the PP matrix or bigger particles of MMT that have not been exfoliated. Typical for craze scattering is diffuse central scattering showing an envelope of cross shape or of diamond shape.^{32,47–51}

Diffuse Central Scattering as a Function of Strain. At $\varepsilon = 0$ none of the samples exhibits diamond-shaped central scattering. From left to right in Figure 3 the local strain is increasing in steps of $\Delta\varepsilon = 0.05$. All samples that contain MMT develop diamond-shaped central scattering during the test. This observation can be explained by voids in the MMT materials at least for $\varepsilon > 0.15$. During the test even pure PP develops central scattering that is increasing up to $\varepsilon \approx 0.2$. Its envelope shows a different shape. It is an ellipse with its long axis in the direction of strain. This means that the corresponding scattering entities are oriented perpendicular to the straining direction. They could be explained by amorphous layers that are converted into crazes. In parallel, a rather well-defined equatorial streak is developing. Such streaks are typical for needle-shaped voids extended in the straining direction.⁵² In summary, the SAXS of all samples indicates void formation during tensile testing.

Pure Polypropylene. The top row of Figure 3 displays selected patterns taken during the tensile test of the pure PP material. The scale is identical for all pseudo-color images in the figure. With increasing local strain also the maximum peak intensity is increasing, and after the yield stress is reached (cf. Figure 2), i.e., $\varepsilon > 0.1$, the peak itself is broadening in lateral direction. The peak broadening after reaching the yield-stress level indicates a decrease of crystallite extension in the direction perpendicular to the “fiber” axis. This decrease can be explained⁵³ by disruption of crystalline lamellae. Such a morphological transition from a lamellar to a microfibrillar stack is generally observed whenever semicrystalline polymers are subjected to uniaxial strain.⁵⁴

PP/MMT Blend and Nanocomposites. The scattering patterns of the blend and the two nanocomposites are presented in rows 2–4 of Figure 3. All materials show the mentioned transition into a microfibrillar stack morphology, but their initial structure is different from the initial structure of the pure PP. The scattering patterns appear rather blurred, and a direct qualitative interpretation can only describe very general features. Thus, the scattering entities of the samples that contain MMT must be smaller, less homogeneous, and their arrangement less perfect than with the pure PP. A quantitative analysis will be based on the data after their transformation into the CDF that displays the morphological features more clearly.

3.3. Discussion of the CDF Patterns. Figure 4 shows the absolute values $|z(r_{12}, r_3)|$ of the CDFs for the four studied materials. The pseudo-color scale is identical for all images.

Nanostructure of the Unstrained Samples. The left column displays the CDFs of the samples at $\varepsilon = 0$. Most prominent are the layerlike peaks on the meridian of the CDFs. They describe the stacked crystalline and amorphous layers of the polypropylene matrix and their correlation in straining direction. Their lateral extension is a measure of the average lateral extension of the layers. These reflections are analyzed quantitatively in section 3.5.

The CDF in the top left corner shows the pure PP. Compared to the blend and the composites below, its peaks are wider in

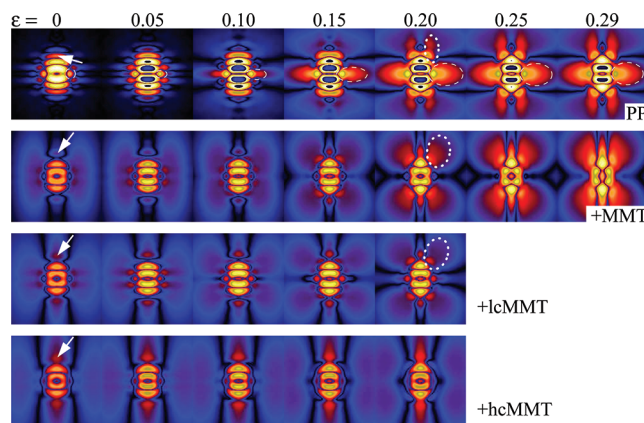


Figure 4. Absolute values $|z(r_{12}, r_3)|$ of chord distribution functions (CDF) of PP, a blend (+MMT), and two composites (+lcMMT, +hcMMT) as a function of the local strain ε . Straining direction r_3 is vertical. The images are on the same logarithmic scale. In a repetitive pseudo-color representation the images show the region $-60 \text{ nm} \leq r_{12}, r_3 \leq 60 \text{ nm}$ of the patterns computed from SAXS data by a special Fourier transform.

horizontal direction. Thus, the lamellae are wider than those of the samples that contain MMT. Moreover, several distinct reflections are piled up. This shows that the thickness variation of the layers is low, and at least three crystalline lamellae are correlated in each stack. In the samples containing MMT the correlation along the stack is even lower. There are only two crystalline layers in each stack (a “sandwich”). Arrows point at the shape distributions $h_{cac}(r_{12}, r_3)$ of such sandwiches. For the pure PP $h_{cac}(r_{12}, r_3)$ is narrow in the r_3 -direction. Thus, the heights of all sandwiches are almost the same. In the lateral r_{12} -direction the peak is extended. Thus, the sandwich is made from two crystalline lamellae that are well-aligned on top of each other.

In the materials that contain MMT the lateral width of $h_{cac}(r_{12}, r_3)$ is narrower than the lateral width of the inner peaks. Thus, there is some lateral disorder in the piling. Let us discuss the shape of the sandwich peak in Figure 4 from top to bottom. In the r_3 -direction the height distribution of the sandwiches becomes broader and more and more asymmetric. For the material with the high amount of compatibilizer (PP + hcMMT) the tail of the sandwich distribution even outreaches the limit of the image at $r_3 = 60 \text{ nm}$. From top to bottom a decrease of domain size, domain uniformity, and domain arrangement is observed. This fact is as well reflected in the decrease of the sharp off-meridional peaks. They characterize correlations among crystallites the connecting line of which is not in straining direction.

All the CDFs of the MMT samples show an off-meridional, vertically extended intensity region. This intensity characterizes the distance distribution between the left and the right edge of microfibrils that house the crystalline domains. For pure PP this peculiar arrangement of crystalline domains is not observed.

Nanostructure Evolution in the Tensile Tests. In Figure 4 proceeding from left to right, the evolution of the semicrystalline polypropylene structure as a function of ε is documented. For the pure PP (top row) the structure evolution is very much different from that of the other materials. Most peculiar is the development of a very strong equatorial long-period distribution $h_{pa}(r_{12}, r_3)$. In Figure 4, it is marked by a dashed-line ellipse. Already at $\varepsilon = 0$ a pointed precursor peak is found on the equator. As the yield-stress level is reached at $\varepsilon = 0.1$, the peak

starts to grow outward on the equator (i.e., in the r_{12} -direction) by combining with an outer satellite. At $\varepsilon = 0.2$ the peak widens in the r_3 -direction, and from $\varepsilon \approx 0.25$ the shape of the peak does not change anymore. h_{ba} describes a lateral correlation between adjacent crystallites that are no extended lamellae. Taking into account the satellite peaks that are visible at low strain, ensembles of three crystalline grains arranged along the r_{12} -direction are present. The corresponding scattering entity in the equatorial plane is readily identified as Strobl's block structure.^{17,18} In the patterns of samples containing MMT the block structure is much less distinct. Nevertheless, when the yield point is approached at $\varepsilon = 0.1$, all materials exhibit a block structure. At this strain the three top patterns even show many sharp block-correlation peaks surrounding the center of the pattern. This observation indicates that close to the yield point the blocks even arrange⁵⁵ in the third dimension. A three-dimensional macrolattice⁵⁶ of only short-range correlation has been formed.

Figure 5 presents results of a quantitative analysis of Strobl's block structure as a function of the local strain ε . The long

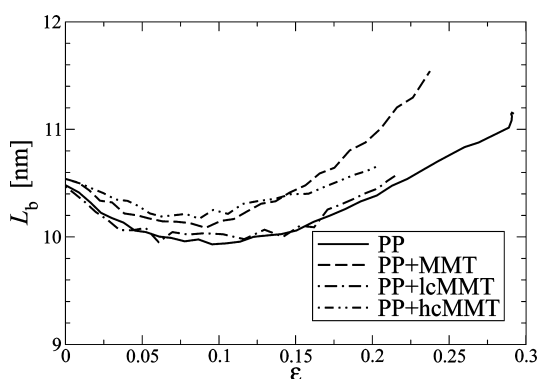


Figure 5. Evolution of the most-frequent long period L_b of Strobl's block structure during tensile testing of PP and PP/MMT materials. L_b is determined from the maximum position of the equatorial long period peak in the CDFs (cf. Figure 4).

period L_b is shown. L_b is the most-frequent distance between adjacent blocks in the equatorial r_{12} -plane as determined from the position of the maximum of $h_{ba}(r_{12}, r_3)$ in the CDF. For all samples L_b decreases slightly with increasing ε until yielding sets in. For $\varepsilon > 0.1$ a slight increase is observed. Thus, the block structure itself behaves identical in all samples. The only difference is that addition of MMT diminishes its fraction severely.

Only for the pure PP with its strong block structure a more involved peak shape analysis is possible. As described in previous work,^{38,57} a bivariate polynomial is fitted to the cap of the peak in order to determine its position and the standard deviations that describe the peak widths in equatorial and meridional direction, respectively. Figure 6 presents the result. L_b has already been discussed. ΔL_b is the breadth of $h_{ba}(r_{12}, r_3)$ in the equatorial r_{12} -direction. H_b is the height of $h_{ba}(r_{12}, r_3)$ in the meridional r_3 -direction. These two width parameters have been defined by 3 times the respective standard deviations. As has already been seen by inspection of the patterns, the breadth ΔL_b is increasing during the tensile test. The quantitative analysis shows that this increase is continuously slowed down with increasing ε . H_b reflects the average height of the blocks. For low strain H_b is constant at 5.5 nm. Just before the yield level is reached at $\varepsilon \approx 0.08$, H_b starts to increase linearly. The mechanism behind this growth of block height may be chain

extension caused by the increased local stress around the blocks. Such chain extension could make the blocks grow tending toward a formation of extended chain crystals.

Some peaks in Figure 4 are difficult to analyze. They are encircled by dotted lines. These peaks result from sandwich domain size distributions $h_{cac}(r_{12}, r_3)$ that overlap severely with the strong and narrow meridional distributions. Therefore, an analysis would require to separate these peaks from the meridional distributions by fitting the complete CDF patterns with a three-dimensional model of the semicrystalline PP nanostructure. The CDFs exhibit that such a model would have to be rather complex.

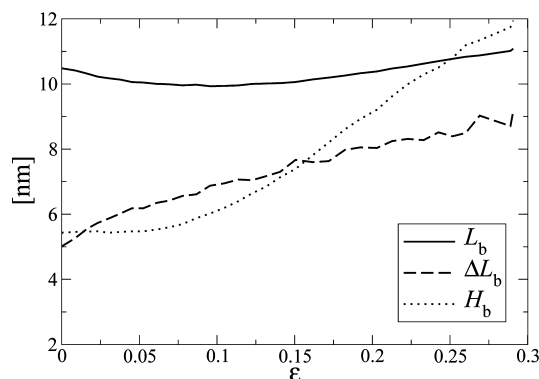


Figure 6. Nanostructure evolution of Strobl's block structure during tensile testing of the pure PP material from peak-shape analysis of the equatorial long-period peak $h_{ba}(r_{12}, r_3)$ in the CDF (encircled in Figure 4). L_b is the most frequent distance between adjacent blocks, ΔL_b is the breadth of $h_{ba}(r_{12}, r_3)$, and H_b is the height of $h_{ba}(r_{12}, r_3)$ in the straining direction.

3.4. Analysis of the Scattering Power. Figure 7 shows the evolution of the scattering power Q (cf. eq 1) of the semicrystalline

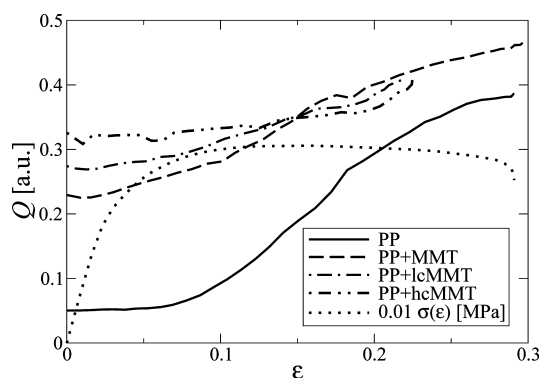


Figure 7. Evolution of the scattering power Q during tensile testing of PP nanocomposites as a function of the local macroscopic strain ε in the irradiated volume. Additionally, the stress–strain curve $\sigma(\varepsilon)$ of the pure PP material is shown.

PP as a function of strain. The curves are normalized to constant irradiated volume and constant flux. Thus

$$Qc = (\rho_c - \rho_a)^2 v(1 - v) + X \quad (3)$$

is valid with c being a calibration constant. The contrast factor is specified by the electron densities ρ_c and ρ_a of the crystalline and the amorphous domains, respectively. v is the volume crystallinity of the PP. Obviously, $v(1 - v) \approx 0.24$ remains

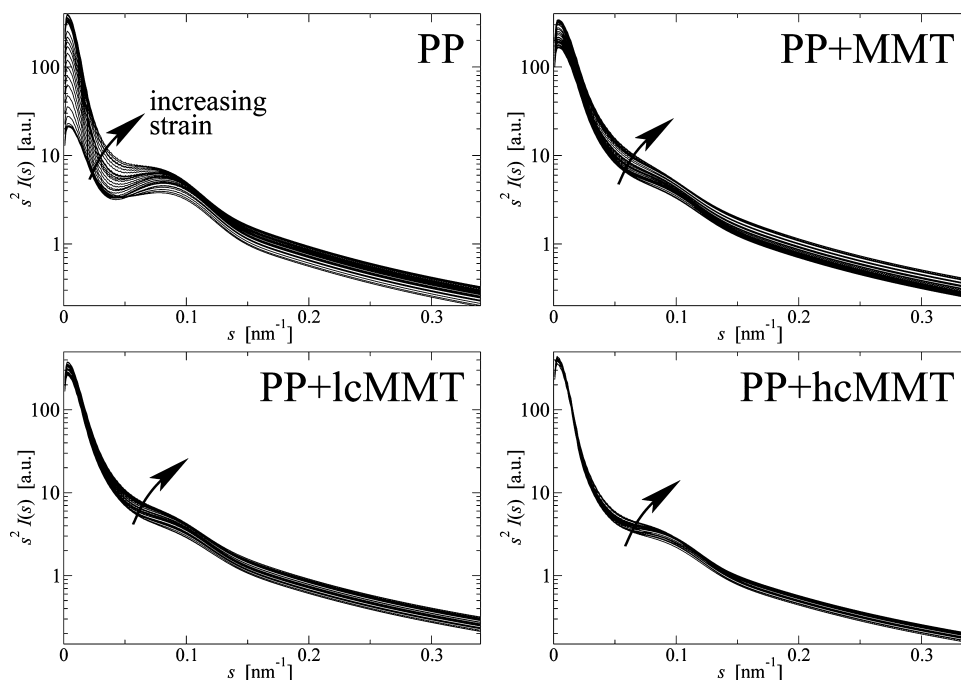


Figure 8. Evolution of the isotropic integrands $s^2 I(s)$ for the computation of Q during tensile testing of PP nanocomposites as a function of the local macroscopic strain ε on a logarithmic intensity scale.

almost constant for $0.3 < \nu < 0.7$. X is an unknown factor that describes both the scattering effects of MMT particles and of voids or crazes on Q . At $\varepsilon = 0$ the scattering power of PP is considerably smaller than that of the samples containing MMT. The reason is either the scattering tail of big MMT particles or the scattering of voids. Compatibilization of the MMT increases the scattering power even more. This result may be caused by MMT exfoliation in the nanocomposites.

For pure PP $Q(\varepsilon)$ remains constant until the onset of yielding. The constant value for low strain is readily explained by constant contrast. After yielding sets in, the sample starts to become white. Thus, the strong increase of $Q(\varepsilon)$ for $\varepsilon > 0.1$ can be related to void formation. It is well-known that voids mainly affect the scattering at low s . Because Q is only a number, the isotropic scattering $s^2 I(s)$ with $Q = 4\pi \int s^2 I(s) ds$ is prepared for angle-dependent inspection (Figure 8). For the sample PP Figure 8 shows a steep increase of scattering at very low angles ($s < 0.05 \text{ nm}^{-1}$). On the other hand, the change of the long period peak ($s \approx 0.09 \text{ nm}^{-1}$) is only moderate. Thus, it can be concluded that the steep increase of Q with sample PP indicates considerable formation of voids as the material is strained beyond the yield.

The blend PP + MMT exhibits high scattering at low s even in the unstrained state. Further increase of low- s scattering is moderate. This means that, in contrast to pure PP, straining of the blend does not induce an increase of voids that are small enough to be detected by SAXS.

For the nanocomposites PP + lcMMT and PP + hcMMT Figure 8 exhibits a similar response to strain, but the variation of the integrand with strain becomes even smaller. Thus, the effect of increasing compatibilization is an increased stability of the nanostructure of the polypropylene that has been formed during injection molding. Admittedly, this finding may simply mean that an already distorted structure cannot be destructed further. Another explanation would be based on a dynamic equilibrium that would not change the SAXS if the voids growing

out of the SAXS detection window would be dynamically replaced by new small voids while all voids are continuously growing. In Figure 7, the moderate increase of the total $Q(\varepsilon)$ is depicted. The increase is fastest for the uncompatibilized blend and slowest for the composite that contains the high amount of compatibilizer. Whitening during straining has not been detected with the samples containing MMT, but detection is difficult anyway because the samples look brownish from the MMT.

3.5. Quantitative Analysis of Meridional Peaks. Figure 9 presents the evolution of the long period $L(\varepsilon)$. This is the most

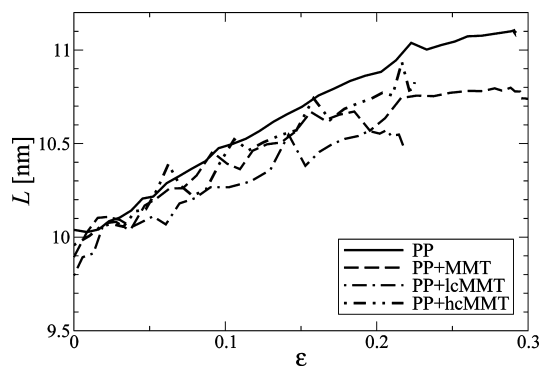


Figure 9. Nanostructure evolution during tensile testing of PP nanocomposites determined from the CDF long-period peak. Most-frequently long period $L(\varepsilon)$.

frequent distance between two crystalline domains measured in straining direction.

At $\varepsilon = 0$ the long periods of the four samples are identical. The increase of $L(\varepsilon)$ is much slower than expected from the macroscopic strain. At 30% strain ($\varepsilon = 0.3$) L has only grown by 10%. The increase is somewhat slower for the samples containing MMT. The evolution of the peak shape (Figure 4) shows that an asymmetric long-period distribution is nonaffinely strained.

Thus, the most probable L is no measure of the *average* nanoscopic strain⁵⁸ of the semicrystalline morphology (i.e., of the long period distribution $h_{ca}(r_{12}, r_3)$ that has its maximum at $(r_{12}, r_3) = (0, L)$).

The width ΔL of $h_{ca}(r_{12}, r_3)$ in the r_3 -direction describes the heterogeneity of the stacking of crystalline and amorphous domains. Let $\Delta L = 3\sigma_3(h_{ca})$ with $\sigma(h_{ca})$ the standard deviation h_{ca} . Data are presented in Figure 10. Addition of MMT increases

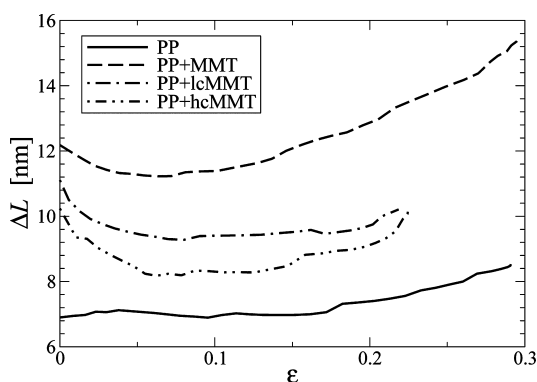


Figure 10. Nanostructure evolution during tensile testing of PP nanocomposites determined from the CDF long-period peak. Width $\Delta L(\epsilon)$ in straining direction r_3 of the long period distribution $h_{ca}(r_{12}, r_3)$.

the heterogeneity of h_{ca} considerably. Thus, the nanodomain stacking of PP is distorted by the MMT. Compatibilization leads to a relative reduction, indicating attenuation of the distorting effect of MMT on the semicrystalline structure.

With increasing strain the pure PP exhibits a moderate monotonous broadening. The MMT samples start with a slight homogenization of the stacks up to $\epsilon \approx 0.07$ that is followed by a distinct loss of uniformity when the materials are above the yield. At high strain compatibilization (PP + lcMMT, PP + hcMMT) even further attenuates the distortion introduced by MMT. The asymmetry of $h_{ca}(r_{12} = 0, r_3)$ is not considered and cannot be quantified from a peak fit that is based on a second-order polynomial only.

The lateral extension $e_{12}(\epsilon) = 3\sigma_{12}(h_{ca})$ (in the r_{12} -direction) of $h_{ca}(r_{12}, r_3)$ measures the size of the crystallites in the transverse direction. $\sigma_{12}(h_{ca})$ is the standard deviation of h_{ca} in the r_{12} -direction. Figure 11 presents the results. $e_{12}(\epsilon = 0)$ is

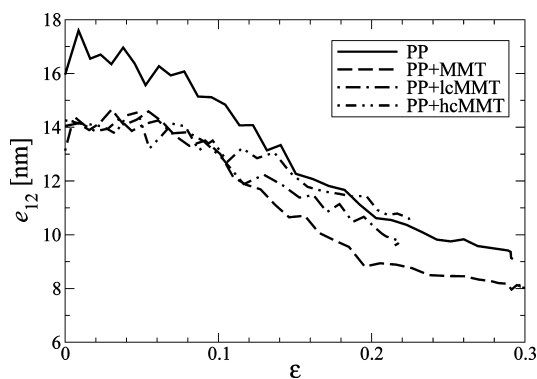


Figure 11. Nanostructure evolution during tensile testing of PP nanocomposites determined from the CDF long-period peak. Average lateral extension $e_{12}(\epsilon)$ of the crystalline PP domains.

highest for the pure PP. Addition of MMT leads to a decrease of $e_{12}(0)$ by 2 nm. The compatibilizer has no effect on the

initial lateral extension of the crystalline domains, but on its decrease in the addressed conversion from layer stacks to microfibrillar^{54,59,60} stacks. This decrease is generally observed^{55,61–66} during the straining of semicrystalline polymer materials. Compatibilization diminishes the degradation of the crystallite extension $e_{12}(\epsilon)$ for $\epsilon > 0.1$, i.e., above the yield point.

3.6. Discussion of Nucleation and Compatibilization in the PP/MMT Nanocomposites. Nucleation. The depicted effects of clay on the semicrystalline morphology (broadening of the crystallite thickness distribution, smaller crystallite extension) may be explained by a strong nucleating effect of the MMT on polypropylene crystallization. Consequently, the nuclei density must have been increased, and during processing many crystallites grow simultaneously, mutually inhibiting their growth. Finally, the altered morphology is described by a less ordered arrangement of undersized, weak crystalline domains. The crystallinity is not increased. This means that addition of MMT to the commercial PP reduces the reinforcing effect of the crystalline polypropylene phase. In summary, part of the intrinsic reinforcement of MMT is not added to the strength of PP. Instead, it only replaces lost self-reinforcement of the polypropylene. As observed with the studied materials, the desired macroscopic reinforcement is not achieved. In section 3.7 we try to assess loss of self-reinforcement and gain of foreign reinforcement.

Nevertheless, although the mechanical properties of the four materials are very similar, monitoring of the straining experiments by SAXS has shown that the semicrystalline nanostructure and its evolution vary considerably. The relative variations from material to material indicate that the dominant troublesome effect of blending MMT, and the studied metallocene polypropylene grade is not the interfacial incompatibility between filler and matrix, but the alteration of the adjusted nanostructure of the matrix grade by the filler.

The addressed strong nucleating effect of MMT has been reported in several papers.^{5–9,11,67,68} According to Deshmene et al.,¹⁰ the nucleating effect of MMT on polypropylene is high, whereas polyethylene remains almost unaffected. The addition of 4% MMT to polypropylene reduces the spherulite diameter from 210 to 14 μm , whereas the spherulite size of polyethylene remains unchanged. The different nucleating effect of MMT on polypropylene and polyethylene could explain why some of us have found⁶⁹ a strong reinforcing effect of MMT on polyethylene.

On the other hand, Deshmene et al.¹⁰ report an increase of crystallite size with respect to the pure PP, whereas we and others⁹ find a decrease. According to the Deshmene paper, the addition of MMT is not accompanied by a decrease of mechanical properties. In contrary, the authors report an increase of Young's modulus by 50% and a considerable increase of the impact strength. An indication for the reason for the different results is the different crystallite size. The small and imperfect crystallites in our composites may be weaker than the extended crystallites grown in the composite prepared by Deshmene et al.¹⁰ A comparative study has reported⁵ that the alteration of polypropylene nanostructure by clay is not only a function of the pretreatment but also of the geological origin of the clay. Thus, the reason for the different findings may probably be the sensitive response of different polypropylene grades on different nucleating agents, MMT, and compatibilization. Consequently, our results indicate that blending a nucleating additive into a polypropylene grade may require reoptimization of its

formulation. In a first step, one could try to reduce the supplier-provided nucleators^{22–25} of the grade.

A decrease of crystallite size may be considered a decrease of filler particle size in the amorphous matrix. Theories of particulate reinforcement predict no influence of the filler size on the mechanical properties, although frequently an increase is empirically found.⁷⁰ On the other hand, Sumita et al.⁷¹ report that for polypropylene also the opposite behavior can be observed. The reason may be that below a certain crystallite size further reduction will probably lead to weakening of the filler particle.

Compatibilization. The pathway to cure the shortcomings of a blend is compatibilization. The result is a nanocomposite. In our experiments the compatibilizer itself appears to inhibit crystal growth additionally (Figure 10 at $\varepsilon = 0$). On the other hand, addition of more compatibilizer makes the nanostructure more stable when subjected to mechanical loading (Figures 3, 4, and 8). Admittedly, this stability is the stability of an already degraded structure. As shown by the necking-induced local strain relaxation (Figure 2), the compatibilizer increases the elasticity of the material.

3.7. Load-Cycling Experiments. Figure 12 shows the evolution of the true stress in the load-cycling experiments. The

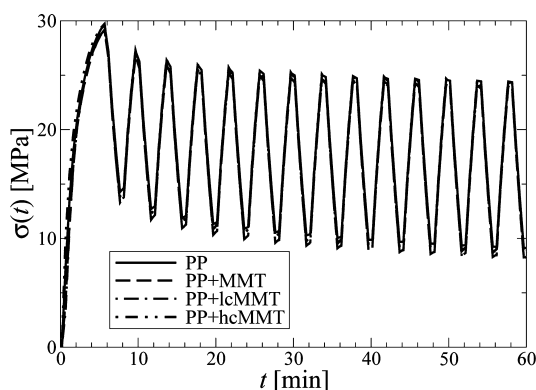


Figure 12. Slow load cycling of PP/MMT materials in the synchrotron beam. True stress $\sigma(t)$ as a function of the time t .

local strain $\varepsilon(t)$ is the dynamic stimulus. It is identical for all materials and presented in some of the following figures. Macroscopic fatigue of the materials is indicated by the decay of the peak stresses from cycle to cycle. Among the four materials the difference appears small. In order to quantify the macroscopic fatigue, the decay of the peak stresses has been evaluated quantitatively. Figure 13 shows the data in a semilogarithmic plot. In order to linearize the data, a residual stress σ_r has been subtracted. From the add-on decay the lifetime of macroscopic stress fatigue, τ_σ has been computed by logarithmic regression (results in Table 2).

The nanoscale response of the material is evaluated from the long-period peak of the CDFs that have been computed from the SAXS patterns. The evolution of the most-probable long periods L during load cycling is presented in Figure 14. The measured amplitudes are very low because the elongation of $h_{ca}(r_{12}, r_3)$ in the r_3 -direction is nonaffine (see section 3.5). For all materials the responses $L(t)$ are in phase with the stimulus $\varepsilon(t)$. This has been expected because of the low load-cycling frequency. Nanostructure fatigue is manifested in the underlying decay of $L(t)$. The fit of the peak L values with an exponential function (Figure 15) yields a quantitative assessment of

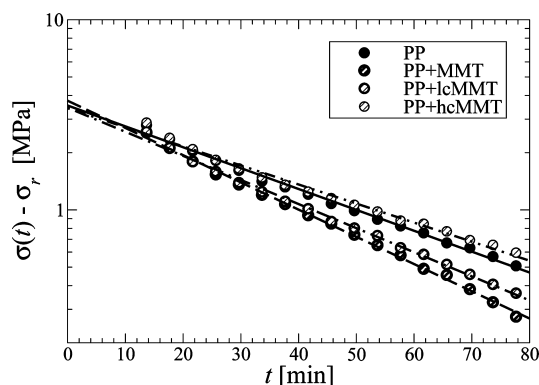


Figure 13. Slow load cycling of PP/MMT materials. Assessment of fatigue by exponential regression using the oscillation maxima of Figure 12. In order to linearize the plot $\sigma_r = 23.6$ MPa was subtracted for PP and PP + hCMMT. $\sigma_r = 23.4$ MPa linearizes the data of PP + MMT and PP + lCMMT.

Table 2. Fatigue in a Slow Load-Cycling Experiment (Cycle Time 4 min) Estimated from Exponential Fits^a

sample	τ_σ [min]	τ_L [days]	τ_ε [h]	$\tau_{\Delta L}$ [min]
PP	39	23.1	5.8	110
PP + MMT	30	12.4	0.9	43
PP + lCMMT	34	8.4	1.7	50
PP + hCMMT	43	6.1	[1.0]	[140]

^aThe lifetimes τ_σ , τ_L , τ_ε and $\tau_{\Delta L}$ characterize the macroscopic stress fatigue, the nanoscopic long-period fatigue, the nanoscopic lamella-extension fatigue, and the nanoscopic structure-heterogeneity fatigue, respectively. Data in brackets are only based on a part of the curve (cf. Figure 18).

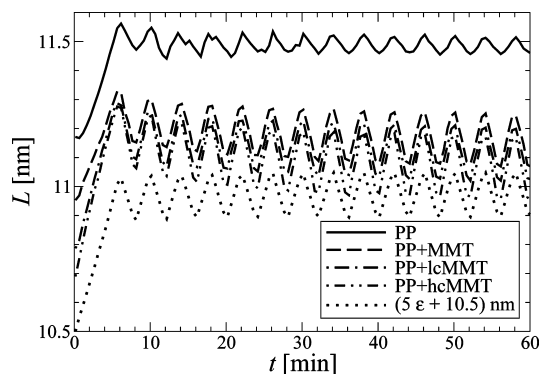


Figure 14. Nanostructure evolution during load cycling of PP nanocomposites determined from the CDF long-period peak. Most-frequently long period $L(t)$ as a function of the elapsed time t . Additionally, the local macroscopic strain $\varepsilon(t)$ is shown.

nanoscale fatigue (Table 2). Because the data are already linear in a semilogarithmic plot, a residual does not need to be subtracted here.

Table 2 shows that the lifetime τ_L of the long-period decay is halved as MMT is blended in. Addition of the full amount of compatibilizer weakens the semicrystalline nanostructure of the polypropylene even more. The decay is accelerated by another factor of 2. Thus, the introduction of MMT and compatibilizer reduce the polypropylene self-reinforcement to 25% of its initial performance. The effective performance of the materials can be estimated from the lifetime of the macroscopic stress decay, τ_σ . Table 2 shows that the blend has a reduced performance of

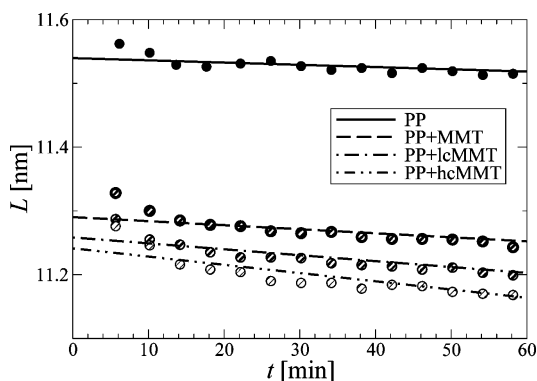


Figure 15. Assessment of nanostructure fatigue. Fit of the oscillation maxima from Figure 13 by an exponential for determination of the lifetime τ_L of long period decay.

$100 \times 21/27 \cong 77\%$ with respect to the commercial polypropylene grade. Only the compatibilization of the MMT with 8% amphiphilic block copolymer leads to a slight performance gain to 111%.

The dynamic variation of the lateral extension $e_{12}(t)$ of the layers during load cycling is presented in Figure 16. The initial

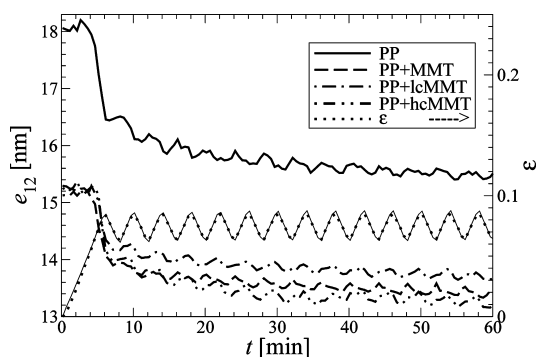


Figure 16. Nanostructure evolution during tensile testing of PP nanocomposites determined from the CDF long-period peak. Average lateral extension $e_{12}(t)$ of the crystalline PP domains as a function of the elapsed time t . Additionally the macroscopic strain $\varepsilon(t)$ is shown.

levels are somewhat higher than those reported from the plain tensile experiments, but this is only related to different data pre-evaluation. For this analysis we had to take out a step, namely an extrapolation of the scattering intensity to high angles. The extrapolation proved not to be stiff enough, and the noise introduced by extrapolation was higher than the weak variation of $e_{12}(t)$.

Layer-extension reduction starts after 4 min at $\varepsilon \approx 0.06$ and $\sigma \approx 27$ MPa for all studied materials. Thus, the lag time of lamellae disruption is not changed in the MMT-containing materials with respect to pure PP.

When the cycling starts, all materials respond with small oscillations about a monotonous decay. Thus, the fatigue of the nanostructure with respect to the breaking of crystalline layers can, again, be analyzed by exponential regression. Because the oscillations are not well-expressed but we know that we have eight SAXS patterns per cycle, this time the data are prepared for regression by sampling eight points in a running average. A residual layer extension, $e_r = 13.2$ nm, is subtracted in order to linearize the data sets in a semilogarithmic plot. An exception is the curve of PP + hcMMT. It cannot be linearized over the full

length of 85 min, and the data look strange for $t < 40$ min. The corresponding lifetimes τ_e of the lamellae extension are reported in Table 2. The blending with MMT reduces the lifetime of the lamellae extension to 15%, but in the composite PP + lcMMT the lifetime has recovered to 30% of the initial value. The determined value for PP + hcMMT is based on a short interval ($t > 40$ min). Thus, its significance is questionable, and in the table the value is enclosed in brackets.

Figure 16 exhibits a peculiar variation of the phase of the responses $e_{12}(t)$ on the dynamic strain $\varepsilon(t)$. For samples that are no composites (PP, PP + MMT) the layer extensions are low at the peak strains and vice versa. On the other hand, for the composites (PP + lcMMT, PP + hcMMT) the macroscopic stimulus $\varepsilon(t)$ and the nanoscopic response $e_{12}(t)$ are in phase. An explanation may be given that is based on a result of an earlier load cycling study of pure PP⁵³ combined with the notion that in a composite matrix and filler are well bonded. In the earlier study the transition from strain-induced crystallization to crystallite disruption was found at $\sigma \approx 20$ MPa. In the present load-cycling study, macroscopically the peak stress is well above the transition threshold. Thus, in pure PP and the blend many crystallites break. During the elongational branch of the cycles pieces of lamellae are moved apart. They recombine in the relaxational branch of the cycle. In the well-bonded composite the MMT bears part of the load, thus saving the polypropylene lamellae from breaking. On the other hand, the fraction of the load that is exerted on the polypropylene is low enough to guarantee a dominance of strain-induced crystallization over lamella disruption.

Figure 17 shows the breadth parameter $\Delta L = 3\sigma_3(h_{ca})$ of the long-period distribution h_{ca} as a function of time. It is related to

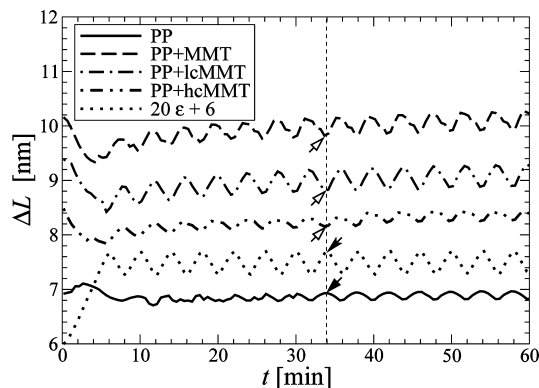


Figure 17. Nanostructure evolution during load cycling of PP nanocomposites determined from the CDF long-period peak. Breadth $\Delta L(t)$ of the long period distribution. Additionally, the local macroscopic strain $\varepsilon(t)$ is shown.

the variability of the distances in straining direction between two crystallites. During the first straining the MMT materials exhibit decreasing heterogeneity of the nanostructure in straining direction, whereas it almost remains constant for sample PP. This has already been found in tensile testing (cf. Figure 10).

As a function of time sample PP exhibits during the first seven cycles small variations about a constant level $\Delta L \approx 6.8$ nm. Thereafter, the material starts to respond to the macroscopic strain $\varepsilon(t)$ by a clear low-amplitude oscillation of $\Delta L(t)$. It is in phase with $\varepsilon(t)$. Thus, the arrangement of crystallites becomes more heterogeneous in each straining branch and returns to a more homogeneous state during relaxation. There is little fatigue

related to the arrangement of crystallites. This behavior is readily explained by nonaffine straining of layer stacks that contain durable crystallites in which the low long-period stacks are less extensible than the high ones.

Compared to sample PP, the behavior of the MMT materials is characterized by four features. First, they show higher heterogeneity. Second, they respond from the beginning by a high-amplitude oscillation. Third, the phase of the oscillation is inverted with respect to the stimulus $\varepsilon(t)$ (cf. arrows in Figure 17). Thus, the distances between the crystallites become more uniform in each straining branch and relax into a more inhomogeneous state. A possible explanation is based on the assumption of a considerable fraction of undersized, premature crystallites that are too weak to withstand even moderate strain. Disintegration by chain unfolding leads to a loss of long periods at small r_3 in $h_{ca}(r_{12}, r_3)$, and a carryover to greater r_3 . h_{ca} becomes more uniform. During the relaxation branch the corresponding chains fold again to form an undersized crystal, and the breadth of h_{ca} broadens again. Fourth, the heterogeneity of the MMT samples is increasing from cycle to cycle, exhibiting nanostructure fatigue. The reason for this nanostructure fatigue remains speculative. Let us assume that the premature state of the semicrystalline morphology itself is the reason. Then, under dynamic load it is easily worn down, leaving behind a broad spectrum of different long periods.

The corresponding lifetime analysis based on running averages $\overline{\Delta L}(t)$ of $\Delta L(t)$ is presented in Figure 18. It shows the

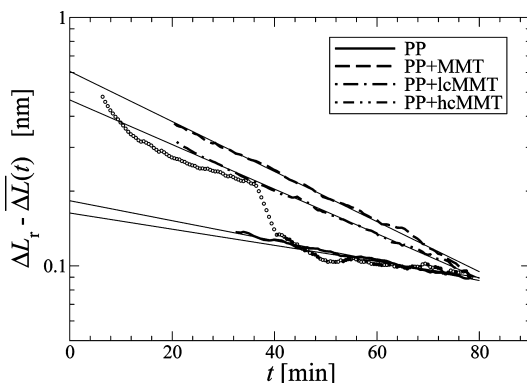


Figure 18. Nanostructure heterogeneity fatigue. Determination of lifetimes $\tau_{\Delta L}$. $\overline{\Delta L}(t)$ is the running average of the curves from Figure 17. Small circles show the complete set of PP + hcMMT containing the strange breakdown.

strange breakdown in the data from sample PP + hcMMT (full data set marked by circles), the running-average curves, and their fit by an exponential. The corresponding lifetimes $\tau_{\Delta L}$ are documented in Table 2. Obviously, the increase of nanostructure heterogeneity under dynamic load is doubled by addition of MMT to PP. The compatibilizer in the composites helps to reduce this fatigue.

The evolution of the scattering power Q under dynamical load is almost trivial. The curves do not change significantly during the cycling. This means at least that there is not much change of contrast or void content during the load cycling.

Finally, an oversimplified cartoon of the nanoscale morphology is presented in Figure 19. It shows a rather well-developed lamellar structure in the polypropylene and in the materials that contain MMT a distorted layer structure that is reinforced by the silicate layers depicted as thin vertical domains.

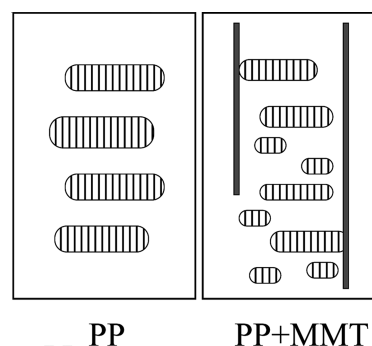


Figure 19. Simplified structural model for the semicrystalline structure of the pure polypropylene (left) and of the polypropylene phase in the nanocomposites (right). The thin vertical domains are drawn only to indicate that the composite contains MMT layers.

4. CONCLUSIONS

In general, the influences of the additives in a composite on the expression of the semicrystalline morphology of the matrix polymer are rarely taken into account. In-situ monitoring by means of small-angle X-ray scattering has shown that additives may vary the nanostructure at least of polypropylene considerably. On the one hand, this means that an improvement of mechanical properties in a composite may be hard to predict without having studied the interactions of the components. On the other hand, this shows that there is a considerable potential for tailoring the mechanical properties in the multidimensional parameter space. SAXS monitoring may be used as a tool to investigate this parameter space.

Here SAXS has been used to monitor slow mechanical tests of a set of nanocomposites from polypropylene (PP) and a layered silicate (montmorillonite, MMT). By comparing the extracted nanostructure evolution information to the mechanical data, it has been found that missing improvement of mechanical properties appears to result predominantly from the inhibition of a load-bearing semicrystalline morphology inside the PP by the MMT. Chemical compatibilization^{72–74} appears to be a secondary effect with the studied polypropylene grade. In fact, the predominant deterioration of mechanical properties of PP by nucleating mineral fillers has been reported in the literature.⁷⁵ Load cycling the materials below the yield exhibits macroscopic and nanoscopic fatigue detected from a decay of the peak stresses and peak nanostructure parameters, respectively. From the respective lifetimes we have for the first time assessed the reinforcement of the composite and the weakening of the PP by the MMT. It has been found that crystallite growth is obstructed even more when MMT is compatibilized. It remains to be clarified if this effect is caused by the compatibilizer itself or by improved exfoliation of the MMT.

With respect to application the results indicate that the optimization of a commercial PP grade undertaken by the manufacturer may be lost when it is bonded to a filler with nucleating capacity. If the optimization of the formulation has to be redone, one could start from a PP grade without nucleators.

It should be mentioned that crystallite growth in PP may not only be limited by a high nucleating capacity. Also, the confinement of PP by nanoclay layers⁷⁶ may lead to undersized crystallites. If there should be no way to control the nuclei density in MMT-extended polypropylene, then special processing, e.g., oscillating shear flow injection molding,⁷⁷ could be considered to enhance the properties of the nanocomposite, but this may become too expensive for general application.

■ ACKNOWLEDGMENTS

The authors thank the Hamburg Synchrotron Radiation Laboratory (HASYLAB) for beam time granted in the frame of projects II-2008-0015 and I-2011-0087. Kuraray Co., Ltd., Elastomer Division, Japan, is acknowledged for providing Kraton L-1203. This work has been supported by the seventh framework program of the European Union (Project NANO-TOUGH FP7-NMP-2007-LARGE).

■ REFERENCES

- (1) Varga, J. In *Karger-Kocsis, J., Ed.; Polypropylene: Structure, Blends and Composites*; Chapman & Hall: London, 1995; pp 51–106.
- (2) Edwards, K. L. *Mater. Des.* **2004**, *25*, 529–533.
- (3) Youssef, Y.; Denault, J. *Polym. Compos.* **1998**, *19*, 301–309.
- (4) Gupta, V. B.; Mittal, R. K.; Sharma, P. K.; Mennig, G.; Wolters, J. *Polym. Compos.* **1989**, *10*, 16–27.
- (5) Pozsgay, A.; Fráter, T.; Papp, L.; Sajó, I.; Pukánszky, B. *J. Macromol. Sci., Part B: Phys.* **2002**, *41*, 1249–1265.
- (6) Vu, Y. T.; Rajan, G. S.; Mark, J. E. *Polym. Int.* **2004**, *53*, 1071–1077.
- (7) Ma, J.; Zhang, S.; Qi, Z.; Li, G.; Hu, Y. *J. Appl. Polym. Sci.* **2001**, *83*, 1978–1985.
- (8) Li, J.; Zhou, C.; Gang, Wang. *Polym. Test.* **2003**, *22*, 217–223.
- (9) Xu, W.; Liang, Guodong; Zhai, H.; Tang, S.; Hang, G.; Pan, W.-P. *Eur. Polym. J.* **2003**, *39*, 1467–1474.
- (10) Deshmene, C.; Yuan, Q.; Perkins, R. S.; Misra, R. D. K. *Mater. Sci. Eng., A* **2007**, *458*, 150–157.
- (11) Smit, I.; Musil, V.; Švab, I. *J. Appl. Polym. Sci.* **2004**, *91*, 4072–4081.
- (12) Purohit, P. J.; Huacuja-Sánchez, J. E.; Wang, D.-Y.; Emmerling, F.; Thünemann, A.; Heinrich, G.; Schönhals, A. *Macromolecules* **2011**, *44*, 4342–4354.
- (13) Hussain, F.; Hojjati, M.; Okamoto, M.; Gorga, R. E. *J. Compos. Mater.* **2006**, *40*, 1511–1575.
- (14) Jancar, J.; Douglas, J. F.; Starr, F. W.; Kumar, S. K.; Cassagnau, P.; Lesser, A. J.; Sternstein, S. S.; Buehler, M. J. *Polymer* **2010**, *51*, 3321–3343.
- (15) Folkes, M. J. In *Karger-Kocsis, J., Ed.; Polypropylene: Structure, Blends and Composites*; Chapman & Hall: London, 1995; pp 340–370.
- (16) Xu, J.; Srinivas, S.; Marand, H.; Agarwal, P. *Macromolecules* **1998**, *31*, 8230–8242.
- (17) Hugel, T.; Strobl, G.; Thomann, R. *Acta Polym.* **1999**, *50*, 214–217.
- (18) Strobl, G. *Prog. Polym. Sci.* **2006**, *31*, 398–442.
- (19) Compostella, M.; Coen, A.; Bertinotti, F. *Angew. Chem.* **1962**, *74*, 618–624.
- (20) Norton, D. R.; Keller, A. *Polymer* **1985**, *26*, 704–716.
- (21) Olley, R. H.; Bassett, D. C. *Polymer* **1989**, *30*, 399–409.
- (22) Blumenhofer, M.; Ganzleben, S.; Hanft, D.; Schmidt, H.-W.; Kristiansen, M.; Smith, P.; Stoll, K.; Mäder, D.; Hoffmann, K. *Macromolecules* **2005**, *38*, 3688–3695.
- (23) Kristiansen, P. M.; Gress, A.; Hanft, D.; Schmidt, H.-W. *Polymer* **2006**, *47*, 249–253.
- (24) Libster, D.; Aserin, A.; Garti, N. *Polym. Adv. Technol.* **2007**, *18*, 685–695.
- (25) Lipp, J.; Shuster, M.; Terry, A. E.; Cohen, Y. *Polym. Eng. Sci.* **2008**, *48*, 705–710.
- (26) Li, J.; Ton-That, M.-T.; Leelapornpisit, W.; Utracki, L. A. *Polym. Eng. Sci.* **2007**, *47*, 1447–1458.
- (27) Thorby, D. *Structural Dynamics and Vibration in Practice*, 1st ed.; Butterworth-Heinemann: Amsterdam, 2008.
- (28) Peterlin, A. *Annu. Rev. Mater. Sci.* **1972**, *2*, 349–380.
- (29) Takemori, M. T. *Annu. Rev. Mater. Sci.* **1984**, *14*, 171–204.
- (30) Crist, B. *Annu. Rev. Mater. Sci.* **1995**, *25*, 295–323.
- (31) Pegoretti, A. In *Karger-Kocsis, J., Fakirov, S., Eds.; Nano- and Micro-Mechanics of Polymer Blends and Composites*; Hanser: Munich, 2009; pp 301–339.
- (32) Brown, H. R.; Kramer, E. J.; Bubeck, R. A. *J. Mater. Sci.* **1988**, *23*, 248–252.
- (33) Toki, S.; Sics, I.; Burger, C.; Fang, D.; Liu, L.; Hsiao, B. S.; Datta, S.; Tsou, A. H. *Macromolecules* **2006**, *39*, 3588–3597.
- (34) Jankova, K.; Chen, X.; Kops, J.; Batsberg, W. *Macromolecules* **1998**, *31*, 538–541.
- (35) Jankova, K.; Kops, J.; Chen, X.; Batsberg, W. *Macromol. Rapid Commun.* **1999**, *20*, 219–223.
- (36) Stribeck, N.; Nöchel, U.; Funari, S. S.; Schubert, T. *J. Polym. Sci., Polym. Phys.* **2008**, *46*, 721–726.
- (37) Stribeck, N. In *Karger-Kocsis, J., Fakirov, S., Eds.; Nano- and Micro-Mechanics of Polymer Blends and Composites*; Hanser Publisher: Munich, 2009; Vol. 1, pp 269–300.
- (38) Denchev, Z.; Dencheva, N.; Funari, S. S.; Motoviln, M.; Schubert, T.; Stribeck, N. *J. Polym. Sci., Part B: Polym. Phys.* **2010**, *48*, 237–250.
- (39) Stribeck, N. *X-Ray Scattering of Soft Matter*; Springer: Heidelberg, 2007.
- (40) Stribeck, N. *J. Appl. Crystallogr.* **2001**, *34*, 496–503.
- (41) Ruland, W. *Colloid Polym. Sci.* **1977**, *255*, 417–427.
- (42) Vonk, C. G. *Colloid Polym. Sci.* **1979**, *257*, 1021–1032.
- (43) Debye, P.; Bueche, A. M. *J. Appl. Phys.* **1949**, *20*, 518–525.
- (44) Porod, G. *Colloid Polym. Sci.* **1951**, *124*, 83–114.
- (45) Vonk, C. G. *J. Appl. Crystallogr.* **1973**, *6*, 81–86.
- (46) Baltá Calleja, F. J.; Vonk, C. G. *X-Ray Scattering of Synthetic Polymers*; Elsevier: Amsterdam, 1989.
- (47) Brown, H. R.; Kramer, E. J. *J. Macromol. Sci., Part B: Phys.* **1981**, *19*, 487–522.
- (48) Karl, A.; Cunis, S.; Gehrke, R.; Krosigk, G. v.; Lode, U.; Luzinov, I.; Minko, S.; Pomper, T.; Senkovsky, V.; Voronov, A.; Wilke, W. *J. Macromol. Sci., Part B: Phys.* **1999**, *38*, 901–912.
- (49) Pomper, T.; Lode, U.; Karl, A.; Krosigk, G. V.; Minko, S.; Luzinov, I.; Senkovsky, V.; Voronov, A.; Wilke, W. *J. Macromol. Sci., Phys.* **1999**, *B38*, 869–883.
- (50) Kobayashi, H.; Shioya, M.; Tanaka, T.; Irisawa, T. *Compos. Sci. Technol.* **2007**, *67*, 3209–3218.
- (51) Fischer, S.; Diesner, T.; Rieger, B.; Marti, O. *J. Appl. Crystallogr.* **2010**, *43*, 603–610.
- (52) Statton, W. O. *J. Polym. Sci.* **1962**, *58*, 205–220.
- (53) Stribeck, N.; Nöchel, U.; Funari, S. S.; Schubert, T.; Timmann, A. *Macromol. Chem. Phys.* **2008**, *209*, 1992–2002.
- (54) Peterlin, A. *Text. Res. J.* **1972**, *42*, 20–30.
- (55) Stribeck, N.; Androsch, R.; Funari, S. S. *Macromol. Chem. Phys.* **2003**, *204*, 1202–1216.
- (56) Fronk, W.; Wilke, W. *Colloid Polym. Sci.* **1985**, *263*, 97–108.
- (57) Stribeck, N. *J. Macromol. Sci., Part C: Polym. Rev.* **2010**, *50*, 40–58.
- (58) Stribeck, N.; Zeinolebadi, A.; Ganjaee Sari, M.; Frick, A.; Mikoszeg, M.; Botta, S. *Macromol. Chem. Phys.* **2011**, *212*, 2234–2248.
- (59) Peterlin, A. *J. Mater. Sci.* **1971**, *6*, 490–508.
- (60) Porod, G. *Fortschr. Hochpolym.-Forsch.* **1961**, *2*, 363–400.
- (61) Wilkes, G. L.; Zhou, H. *J. Mater. Sci.* **1998**, *33*, 287–303.
- (62) Butler, M. F.; Donald, A. M. *Macromolecules* **1998**, *31*, 6234–6249.
- (63) Wu, J.; Schultz, J. M.; Yeh, F.; Hsiao, B. S.; Chu, B. *Macromolecules* **2000**, *33*, 1765–1777.
- (64) Barbi, V.; Funari, S. S.; Gehrke, R.; Scharnagl, N.; Stribeck, N. *Macromolecules* **2003**, *38*, 749–758.
- (65) Kawakami, D.; Ran, S.; Burger, C.; Avila Orta, C.; Sics, I.; Chu, B.; Hsiao, B. S.; Kikutani, T. *Macromolecules* **2006**, *39*, 2909–2920.
- (66) Miyazaki, T.; Hoshiko, A.; Akasaka, M.; Shintani, T.; Sakurai, S. *Macromolecules* **2006**, *39*, 2921–2929.
- (67) Ibanes, C.; David, L.; de Boissieu, M.; Séguéla, R.; Epicier, T.; Robert, G. *J. Polym. Sci., Part B: Polym. Phys.* **2004**, *42*, 3876–3892.
- (68) Todorov, L. V.; Viana, J. C. *J. Appl. Polym. Sci.* **2007**, *106*, 1659–1669.
- (69) Drozdov, A. D.; Christiansen, J. d. *Eur. Polym. J.* **2007**, *43*, 10–25.
- (70) Ahmed, S.; Jones, F. R. *J. Mater. Sci.* **1990**, *25*, 4933–4942.

- (71) Sumita, M.; Tsukumo, Y.; Miyasaka, K.; Ishikawa, K. *J. Mater. Sci.* **1983**, *18*, 1758–1764.
- (72) Marchant, D.; Jayaraman, K. *Ind. Eng. Chem. Res.* **2002**, *41*, 6402–6408.
- (73) Rohlmann, C. O.; Horst, M. F.; Quinzani, L. M.; Failla, M. D. *Eur. Polym. J.* **2008**, *44*, 2749–2760.
- (74) Santos, K. S.; Liberman, S. A.; Oviedo, M. A. S.; Mauler, R. S. *Composites, Part A* **2009**, *40*, 1199–1209.
- (75) McGenity, P. M.; Hooper, J. J.; Paynter, C. D.; Riley, A. M.; Nutbeem, C.; Elton, N. J.; Adams, J. M. *Polymer* **1992**, *33*, 5215–5224.
- (76) Jin, Y.; Rogunova, M.; Hiltner, A.; Baer, E.; Nowacki, R.; Galeski, A.; Piorkowska, E. *J. Polym. Sci., Part B: Polym. Phys.* **2004**, *42*, 3380–3396.
- (77) Chen, Y. H.; Zhong, G. J.; Wang, Y.; Li, Z. M.; Li, L. *Macromolecules* **2009**, *42*, 4343–4348.

Thin Film Structure of Block Copolymer–Surfactant Complexes: Strongly Ionic Bonding Polymer Systems

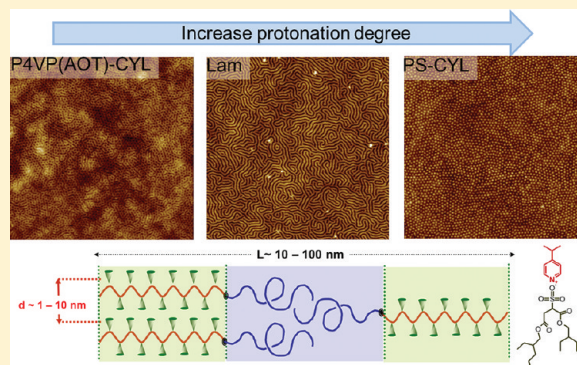
Jingbo Wang,[†] Wim H. de Jeu,[†] Paul Müller,[‡] Martin Möller,[†] and Ahmed Mourran^{†,*}

[†]DWI an der RWTH Aachen e.V. and Institut für Technische und Makromolekulare Chemie an der RWTH Aachen, Pauwelsstrasse 8, D-52056 Aachen, Germany

[‡]Institut für Anorganische Chemie der RWTH Aachen, Prof. Pirlet-Strasse 1, D-52056 Aachen, Germany

S Supporting Information

ABSTRACT: We present a structural investigation of thin films of diblock copolymers PS–P4VP in which 4VP forms an ionic bond with a sterically demanding surfactant, bis (2-ethylhexyl) sulfosuccinate acid (AOT). The results depend strongly on the interplay between microphase separation and surfactant ordering. Protonation of the P4VP homopolymer or diblock PS-*b*-P4VP with AOT leads to a multilayer structure in which the surfactant determines the layer thickness. In thin films of the protonated block copolymer, the segregation between the blocks generates nanostructures with an in-plane periodicity defined by the molecular mass of the copolymer and the stoichiometry of the complex. Variation of the composition of the blocks and the molar ratio AOT/pyridine leads to structural transitions: cylinders of (AOT/P4VP) → lamellae → cylinders of PS. Remarkably, regardless of the morphology, the bcp microdomain structure remains orthogonal to the air substrate interface. Finally, we show that hydrolysis of AOT results in the formation of pores with a variable geometry useful for templating two-dimensional inorganic structures.



INTRODUCTION

A distinctive feature of block copolymers (bcp) is their ability to self-assemble into mesophases whose structure and periodicity are defined by the Flory–Huggins parameter χ , the composition, and the molecular mass of individual blocks.^{1–3} This property has been extensively explored to tailor thin films, allowing to generate dense periodic arrays with sub-100 nm features.⁴ Such an attribute can be considered as an alternative to e-beam lithography, and has been successfully integrated in manufacturing processes of microelectronic devices such as high-density storage media, plasmonic devices, nanowire polarizer grids, silicon capacitors, etc.⁵ The thin films used for these applications require a certain degree of control of the orientational and positional order of the mesostructures.^{4,6} Because of the large interfacial area of thin films, the orientation of the domains depends largely upon the relative surface energies of the blocks as well as—in the case of incommensurability—upon the structural frustration between the intrinsic periodicity of the bulk structure and the film thickness.⁷ These confinement and surface effects can result in morphologies that are absent in the bulk.⁸

Morphologies of bcp's can be controlled rather well for solution-cast thin films. However, to obtain a uniform orientation of the microdomains normal to the film surface—as required in certain applications—remains a challenge.^{4,6} Strategies have been devised to overcome the surface interactions and induce perpendicular orientation of cylinders

or lamellae relative to the substrate.^{6,9} Some success has been achieved through techniques such as solvent annealing,¹⁰ zone casting,^{11,12} electric field alignment,¹³ optical alignment,¹⁴ topographical or chemical substrate patterning,¹⁵ and surfactant¹⁶ or nanoparticle-assisted orientational order.¹⁷

Hierarchical structures with more than one characteristic length scale have been found in copolymers whose macromolecules consist of more than two types of monomer units.^{18–22} A well-known example is a copolymer with side-chain liquid crystal (LC) units, wherein ordering of the mesogens moieties concur with microphase separation. In such a system, the LC field will affect mesophase formation and domain orientation, whereas in thin films thermally stable morphologies can be generated consisting of lamellae or cylinders oriented perpendicular to the surface.²²

An interesting example of a copolymer with mesogenic side chains is provided by specific interactions between an oligomer or a surfactant and a block of a diblock copolymer. These have been neatly used to generate a variety of mesomorphic structures characterized by two periodic scales (structure-within-structure).^{23–25} The copolymer self-assembles and sets a large period of about 100 nm, while the LC organization of the surfactant occurs at a much smaller scale of a few nanometers.

Received: September 15, 2011

Revised: November 2, 2011

Published: January 11, 2012

The obvious advantage of such bcp-complex systems is that the composition of one of the blocks can easily be adjusted by varying the amount of side chains. An additional peculiarity is that a noncovalent bond of the side groups can be used with a strength variable from very strong (ionic bond), to very weak (hydrogen bond).^{26–28} Complexes based on hydrogen bonding are particularly interesting since the binding is thermally reversible, selective and directional.^{23,24} Such interchangeable physical interactions can play a crucial role in the formation of mesophases and in the occurrence of an order–disorder transition.²⁹ Unlike hydrogen bonds, ionic interactions are stronger and the oligomers are tightly bound to the polymer backbone. Mesosstructure based on ionic interactions are thermally stable and in some cases the complex even decomposes before reaching the isotropic phase.^{29–33} Surfactants with sulfonic acid headgroup have been widely combined with polyvinylpyridines.^{27,28,31–35} In that case the nitrogen in the pyridine ring acts as a weak base and charge transfer takes place from acid to lone electron pairs. For diblock copolymers, incorporation of sulfonated oligomers such as dodecylbenzenesulfonic acid,^{28–30} eventually combined with a wedge-shaped mesogen,²⁷ resulted in the formation of mesophases with a hierarchical order at two different length scales.

Ionic bonding of a sterically demanding mesogen to a polymer backbone provides an additional degree of control over the macromolecular conformations and their subsequent self-assembly.^{27,32,33} Recently, we have complexed P2VP with a wedge-shaped ligand consisting of a sulfonated group at the tip and a large nonpolar body.^{32,33} In that situation the contour length of the homopolymer chain defines the shape of the complex (spheres or rods) while the degree of protonation sets the morphology (smectic or columnar). In addition, incorporation of such a ligand to a miscible diblock copolymer, P(EO-*b*-2VP),³⁴ greatly increases the segregation between blocks.²⁷ In thin films, smectic ordering of the ligand takes place with the layers that are orthogonal to the block interfaces. This allows effortless alignment of the bcp microstructure, e.g., cylinder or lamellae, perpendicular to the air/substrate interfaces.

In this work we extend the above ideas to ionic bonding of a widely studied surfactant, sodium bis (2-ethylhexyl) sulfosuccinate (AOT), with the diblock copolymer P(S-*b*-4VP). The solid state structure of pure AOT has been established only recently: it self-assembles in a hexagonal columnar phase with three molecules in a column cross-section.³⁵ Furthermore, unlike the ligands discussed so far,^{23,26–28,32,33} AOT has two branched aliphatic chains that prevents crystallization. The binding strength of the sulfonate head to the pyridine is still essential the same as described above. Furthermore, the bcp–AOT complex does not support uncomplexed ligands because AOT–H contains ester groups that are labile (easily cleaved). Consequently, the system bcp–AOT is appealing because it alleviates (1) any difficulties associated with crystallization of the side chains and (2) the presence of free ligands. Still, the truncated wedge-tail is appropriate to study the impact of steric hindrance on the organization of the bcp–AOT complex.

In the following, we show that protonation of the P4VP homopolymer or the diblock copolymer PS-*b*-P4VP with AOT leads to a mesomorphic multilayer structure in which the surfactant determines the layer thickness. In thin films the segregation between the blocks generates nanostructures with an in-plane periodicity defined by the molecular mass of the copolymer and by the stoichiometry of the complex. By varying the composition of the blocks and the molar ratio AOT/

pyridine, the following structural transitions are observed: cylinders of (AOT/P4VP) → lamellae → PS cylinders. Interestingly, in all morphologies, the bcp microdomain structure stays orthogonal to the air substrate interface. Finally, we show that hydrolysis of AOT results in pores with a variable geometry useful for templating a two-dimensional inorganic structure.

■ EXPERIMENTAL SECTION

Materials. Four PS–P4VP diblock copolymers were investigated: PS₃₉₀–P4VP₁₄₀ (PDI = 1.08), PS₃₅₀–P4VP₂₆₀ (PDI = 1.07), PS₁₉₀–P4VP₁₀₀ (PDI = 1.12), PS₁₂₀–P4VP₅₀ (PDI = 1.03), in which the subscript indicates the degree of polymerization of each block. They were synthesized via sequential anionic polymerization, as described elsewhere.³⁶ Sodium bis(2-ethylhexyl) sulfosuccinate (98%), iodine beads (>99.9), hydrazine hydrate (reagent grade, N₂H₄ 50–60%), diisopropyl ether (p.a.), chloroform (p.a.), benzene (p.a.), 2-propanol (p.a.), ion-exchange resin (Amberlyst 15, acid form), and gold(III) chloride hydrate (HAuCl₄, p.a., Au ≥ 49%), were purchased from Sigma-Aldrich. Silicon wafers (100) were supplied by Si-Mat GmbH. Copper grids, 200 mesh, with silicon oxide coating, and naked copper grids, 100 mesh, were supplied by Plano GmbH, Germany.

Polymer Complex and Thin Film Preparation. The procedures for preparation of polymer complex were similar as discussed in a previous paper.²⁷ 100 mg of AOT–Na was dissolved into 10 mL of diisopropyl ether and stirred with 1 g of Amberlyst 15 for 1 h; after this treatment, AOT–Na converted to its sulfonic acid form (denoted as AOT–H) with a yield of ~100%.^{31,33} The desired amounts of P4VP homopolymer or PS–P4VP block copolymer were dissolved into chloroform according to the desired degree of neutralization (DN, nominal ratio between AOT–H molecules versus 4-vinylpyridine repeat units). The solution of AOT–H was filtrated through a 1 μm PTFE syringe filter, and the ion-exchange resin was washed at least three times with 10 mL of diisopropyl ether. While stirring, the AOT–H solution was added to PS–P4VP solution. The total concentration of the mixed solution was controlled to within less than 1 mg/mL, and stirred overnight. Subsequently, the solvent was removed by a rotor evaporator at 60 °C. The complex was dissolved into chloroform again to make a stock solution of 30 mg/mL.

Silicon wafers or glass substrates were cleaned by sonication in 2-propanol for 5 min, dried in an air stream, and activated in UV/O₂ for 12 min. These treatments provided a clean silicon surface with a water contact angle of <5°. Before spin coating, the stock solution was diluted to the desired concentration and filtered through a 0.2 μm PTFE syringe filter. Thin films of the complexes were prepared by placing drop of 50 μL onto a cleaned silicon wafer and spin coated at a spinning rate of 2500 rpm for 30 s (Convac 1001S, Germany). The film thickness was controlled by the concentration of the solution. All films had approximately the same thickness (300 Å), as determined by ellipsometry (MM-SPEL-VIS, OMT GmbH, Germany). Vapor annealing was performed by exposing the films to saturated benzene vapor in a closed vessel at room temperature. After the solvent annealing, the solvent was allowed to evaporate slowly.

Fabrication of Nanoporous Film. Nanoporous film or nano-objects was prepared by washing of the polymer films in 0.33 mol/L NH₃ solution for 30 s. Subsequently, the films were rinsed with Milli-Q water and dried in an air stream. Free-standing films were prepared by floating thin film on 0.1 mol/L KOH solution, rinsing the film with Milli Q water, and then transferring onto a copper grid.

Gold Salts Deposition. To load the complex with gold salts, the polymer film were coated on a glass substrate and immersed into 1 g/L of aqueous HAuCl₄ solution for 3 h. Subsequently, the films were thoroughly rinsed with Milli Q water, and dried in an air stream. Reduction of the gold salt was performed by either exposing the film to hydrazine vapor in a closed vessel for 1 min, or in oxygen plasma (Plasma System 100, PVA Tepla AG). Typical conditions were as follows: 100 W, 0.89 mbar, and 30 min.

Thin Film Characterization. IR spectra (resolution 4 cm^{–1}) were recorded using a Nicolet NEXUS 670 Fourier Transform IR

spectrometer. Samples were prepared by drying several droplets of 30 g/L solution onto KBr plates at room temperature. For each spectrum more than 200 scans were averaged to enhance the signal-to-noise ratio. The morphology of the film was investigated by a tapping model SFM (NanoScope V, Digital Instruments Veeco Instruments Santa Barbara, CA) under ambient conditions. Commercial available standard silicon cantilevers (PPP-SEIH-W from Nanosensors) with a spring constant of 5–37 N/m and an oscillation frequency of ~ 125 kHz were used. The data were processed using NanoScope software Analysis, v-1.10. Transmission electron microscopy (TEM) images were acquired using a Zeiss Libra120 with an accelerating voltage of 120 kV. For TEM studies, a droplet of the polymer complex solution was put onto a copper grid. The excess of the solution was absorbed by a paper filter. Subsequently, grids plus sample were annealed in benzene. In order to enhance the contrast the films were stained in iodine vapor for about 2 h. Scanning electron microscope (SEM) experiments were performed using a Hitachi S4800 high-resolution field emission scanning electron microscope with an accelerating voltage of 1.5 kV. The optical properties of the gold patterns on glass support were measured with a JASCO V-610 UV-vis spectrometer.

Small and Wide Angle X-ray scattering was recorded by a powder diffractometer (STADI MP vertical from STOE, Darmstadt, Germany) with a focusing Ge-monochromator (Johansson-type) and a position-sensitive detector. The experiments were performed on flat samples in a transmission geometry. X-ray reflectivity (XRR) experiments were performed using a Bruker-Axs D8 Advance. The X-ray intensity was corrected for sample size effects at small incidence angles. The data were analyzed using an iterative matrix formalism derived from the Fresnel equations. During fitting to the multilayer model thickness, electron density, and interface roughness were allowed to vary for each layer.³⁷ The thickness, electron density, and roughness of the native SiO₂ layer were predetermined from a bare Si wafer and left fixed for the later fits.

RESULTS AND DISCUSSION

We first present the results of the FTIR, which substantiate complexation of the pyridine with the sulfonic acid (AOT-H). Second, on the basis of the X-ray scattering data, we discuss the impact of the degree of protonation on the bulk organization of the homopolymer and a copolymer. Subsequently, a structural characterization of the different thin films morphologies is presented based on scanning force microscopy and X-ray reflectivity. The discussion ends with a practical example in which the structure has been used to produce a template with pores of defined geometry.

Bulk Organization. FTIR. The transformation of AOT-Na to AOT-H, and the formation of the P4VP(AOT) complex have been characterized by FTIR. As shown before,^{27,31,33} ion-exchange resin is very effective for the preparation of molecules with sulfonic acid group. The yield is very high, close to 100%. Results of FTIR measurements (see Supporting Information, Figure S1) show that AOT-Na has two characteristic peaks at 1051 and 1247 cm⁻¹, corresponding to symmetric and asymmetric stretching vibrations of SO₃ in the sulfonic acid sodium salt. After stirring with ion-exchange resin for 1 h, these two peaks disappear, while two new peaks appear at 1038 and 1166 cm⁻¹. These are identified as the symmetric and asymmetric stretching vibration of SO₃ in sulfonic acid. Further increase of the treatment time does not change the spectra, which means that AOT-Na has completely transformed to AOT-H.³⁸ P4VP and PS-P4VP have an absorption band at ca. 1599 cm⁻¹, assigned to the aromatic carbon-carbon stretching vibration of the phenyl group (1600–1601 cm⁻¹), and a carbon-nitrogen stretching vibration of the unprotonated pyridine ring (1596–1597 cm⁻¹).³⁸ After incorporation of AOT-H, the intensity of the latter band decreases, and a

new distinct band corresponding to the protonated pyridine ring appears at 1637 cm⁻¹.³⁹ Increasing the DN increases the intensity of the later band and decreases the intensity of the one at 1599 cm⁻¹. In addition, a small shift of this band from 1599 cm⁻¹ to 1601 cm⁻¹ is observed. At DN = 1.0, only one band at 1601 cm⁻¹ is found corresponding to the aromatic carbon-carbon stretching vibration of phenyl group, indicating that at this condition all the free pyridine rings are protonated. (See Supporting Information, Figures S2–S5.) However, quantitative analysis of the FTIR spectra is difficult, because it requires curve fitting while the needed adsorption cross sections of pyridine before and after protonation are unknown. Moreover, for the band at about 1599 cm⁻¹, it is difficult to separate the contribution from the aromatic carbon-carbon stretching vibration of the phenyl group from that of the carbon-nitrogen stretching vibration of the unprotonated pyridine ring.

X-ray Scattering. The X-ray scattering of the fully neutralized homopolymer P4VP(AOT) (DN = 1.0) displays in the small-angle region a peak at scattering vector $q^* = 0.216$ Å⁻¹, corresponding to a periodicity of 29 Å, and a much weaker second-order one at $q = 0.43$ Å⁻¹. If the DN is reduced to 0.5, the q^* -value shifts to a slightly larger number. Further decreasing the DN does not change the position of the first-order peak, but the second-order one become weaker and vanishes at DN = 0.25. In all cases the scattering is rather weak and even at typical measurement times of a couple of hours the intensity is still quite small. This can be attributed to the limited contrast in electron density. The mass densities of AOT and P4VP are 1.13⁴⁰ and 1.11 g/cm³,⁴¹ respectively, and differ only little. In addition we note that the X-ray peak is broader at low DN values. We fitted the peaks to both a Gaussian and a Lorentzian line shape. In all cases—apart from DN = 1.0—the Lorentzian fit is significantly better. The corresponding correlation lengths are 22, 25, and 29 Å for DN = 0.5, 0.33 and 0.25, respectively. From these correlation, we can conclude that structure extends over a relatively small range. For DN = 1.0 a Gaussian fit is somewhat better than a Lorentzian one, which in principle indicates that the corresponding close packing leads to enhanced ordering.

As example of a complexed diblock copolymer the composition PS₃₉₀-P4VP₁₄₀ (DN = 1.0) has been selected. The organization of the P4VP₁₄₀(AOT)_{1.0} complex in the bcp is very similar as in the corresponding homopolymer, as shown in Figure 1a. The period is slightly larger than that of the

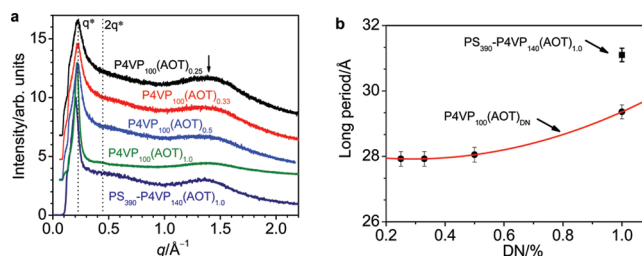


Figure 1. (a) Room temperature WAXS of P4VP₁₀₀(AOT)_{DN} complex and PS₃₉₀-P4VP₁₄₀(AOT)_{1.0}. (b) the long period depending on the degree of neutralization (see Supporting Information, Figure S7, for detail).

corresponding homopolymer-complex. Interestingly the X-ray peak of the block copolymer with DN = 1.0 is broader than for the homopolymer. The quality of the data does not allow a full

line shape analysis, but evidently introduction of the PS block leads to some interruption of the order.

The simplest interpretation compatible with the data is a lamellar (smectic) mesophase. However, due to the limited contrast only a faint second-order peak is observed. Hence we cannot fully exclude the presence of weak peaks at other positions like $q^*\sqrt{3}$, which would be evidence of a hexagonal (columnar) structure. Such structures have been observed in related surfactant–polymers complexes.⁴² From Figure 1b, the smectic mesophase has a lamellar period $L = 2\pi/q^*$ around 28–29 Å for the homopolymer and slightly larger for the block copolymer (around 31 Å). At large angles the scattering data show regardless of the DN a broad peak at $q = 1.6 \text{ Å}^{-1}$, indicative of liquid-like order inside the smectic layers. Evidently, the ligands do not display strong lateral positional correlations.

AOT has a small ionic headgroup with a diameter of about 5 Å and relatively short (about C6) but bulky hydrocarbon tails of fully stretched length 12 Å.⁴³ Hence the thickness of a bilayer of free AOT is about 35 Å, which is comparable, but somewhat larger, than the lamellar period of the homopolymer complex. Evidently the AOT self-assemble into layers with a partial interpenetration of side chains. Furthermore, Figure 1b shows that L increases slightly from 28.0 Å for DN = 0.25 to 29.3 Å at full protonation. This behavior differs from conventional LC side chain polymers.⁴⁴ In that situation the lateral smectic interactions are dominant and increasing the number of side groups leads to a decrease of the layer spacing due to stretching of the polymer backbone. We assume that in our situation at low degree of protonation the ligand is evenly distributed along a Gaussian conformation of P4VP chains. For high DN, further stretching of the side chains may reduce interpenetration and enhance the intersmectic order, leading to a slightly larger period. This would compensate for the reduction of L due to backbone stretching. The delicate balance of two interacting effects can be expected to depend on the overall morphology. Hence, one would not expect L to be exactly the same for bcp and homopolymer.

An alternative explanation³⁰ of the absence of a decreasing smectic period with increased DN—heterogeneity in the complex composition—cannot apply in our situation. As discussed above, in the present case a dynamic complexation equilibrium drives the system to an identical degree of complexation of all polymer chains.³³ Note that any entropic penalty associated with stretching of the P4VP backbone becomes significant only at saturation.³² Rigorous modeling would require knowledge of the bilayer thickness for ligands including the pyridine salt.

Thin Film Morphology. Thin films PS–P4VP(AOT)_{DN} (about 300 Å) with different degree of neutralization were deposited on silicon oxide from a chloroform solution, and annealed in benzene vapor for 24 h. The films were optically smooth and homogeneous before and after annealing, except for the low-molecular-weight sample, which started to dewet the SiO₂ support. Though we focus on thin films, for consistency also thicker films up to 3-fold the bcp periodicity were checked. No difference in morphology was found.

Depending on the composition of the bcp(AOT) complex, two morphologies are identified: cylinders of the P4VP(AOT) complex in a matrix of PS for weight fraction $f_{\text{comp}} = 0.45$ and the inverse for $f_{\text{comp}} = 0.8$, whereas a lamellar structure is observed for $0.55 \leq f_{\text{comp}} \leq 0.77$. Interestingly, the lamellae or cylinders are consistently orthogonal to the air/SiO₂ interface.

We shall proceed with a detailed account of the thin films morphology of bcp-complex, in dependence of the degree of protonation and molecular weight. Table 1 summarizes the

Table 1

bcp	DN	f_{comp} (%) ^a	morphology
PS ₃₉₀ –P4VP ₁₄₀	0	27	CYL
	0.25	44	mixed
	0.33	47	Comp-CYL
	0.5	54	LAM
	1	66	LAM
PS ₃₅₀ –P4VP ₂₆₀	0	51	LAM
	0.25	62	LAM
	0.33	65	LAM
	0.75	76	LAM
	1	80	PS-CYL
PS ₁₂₀ –P4VP ₅₀	0	30	CYL
	0.75	65	LAM/comp-CYL
	1	70	LAM
PS ₁₉₀ –P4VP ₁₀₀	0	36	LAM
	0.5	64	LAM/comp-CYL
	1	73	LAM

^a $f_{\text{comp}} = ((N_{\text{P4VP}}M_{\text{P4VP}} + \text{DN } N_{\text{P4VP}}M_{\text{AOT}})/(N_{\text{PS}}M_{\text{S}} + N_{\text{P4VP}}M_{\text{P4VP}} + \text{DN } N_{\text{P4VP}}M_{\text{AOT}}))$, where M_{P4VP} , M_{S} , M_{AOT} are molar masses of 4-vinylpyridine, styrene, and AOT–H, respectively.

composition of the studied copolymers: The subscript indicates the degree of polymerization of each block, DN is the degree of neutralization, f_{comp} the weight fraction of the P4VP(AOT), and the last column list the observed thin film morphologies.

PS₃₉₀–P4VP₁₄₀(AOT)_{DN}. Without AOT the bcp self-assembles into a structure with P4VP cylinders parallel to the SiO₂/air interface. The bcp-complex is different, Figure 2 depicts the film morphology depending on mass fraction of the P4VP–(AOT)_{DN}. For a weight ratio of 44% of the complex, three structures coexist: “sphere”-like or “cylinder”, lamellae, and a featureless domain in between (Figure 2a). Most likely, the low degree of protonation leads to structures with different orientations relative to the surface plane. For higher weight ratios, i.e., 47%, an hexagonally ordered structure evolves with a mean spacing of 420 Å (cf. Figure 2b). The mass ratio suggest cylinders of the P4VP(AOT) complex embedded in a PS matrix. Two observations support this assumption: the cylinders exhibit a well-defined depth of 25 Å, inferred to the organization of the AOT(P4VP)_{0.33} complex. The absence of steps with a height commensurate with the bcp periodicity suggests a perpendicular orientation of the cylinder relative to the substrate plane. Furthermore, increasing the weight fraction of the complex to 54% leads to interconnected lamellae with few P4VP(AOT) cylinders normal to the substrate plane. For this bcp, the highest weight fraction of the complex is 66% corresponding to DN = 1.0. In that case, the lamellar structure is preserved while contour length and branching are reduced. This is clearly seen by comparing the surface morphology of 54% in Figure 2c and 66% in Figure 2d. The average height distribution indicates that the lamellae or cylinders have a fairly well-defined surface profile of $24 \pm 5 \text{ Å}$ (cf. cross-section profile and Supporting Information, Figure S8).

WAXS data indicate for the 100% protonated copolymer a smectic structure with a period of about 31 Å. This bulk period is somewhat larger than the depth of the surface profile. The difference may be due to the indenting force of the SFM probe

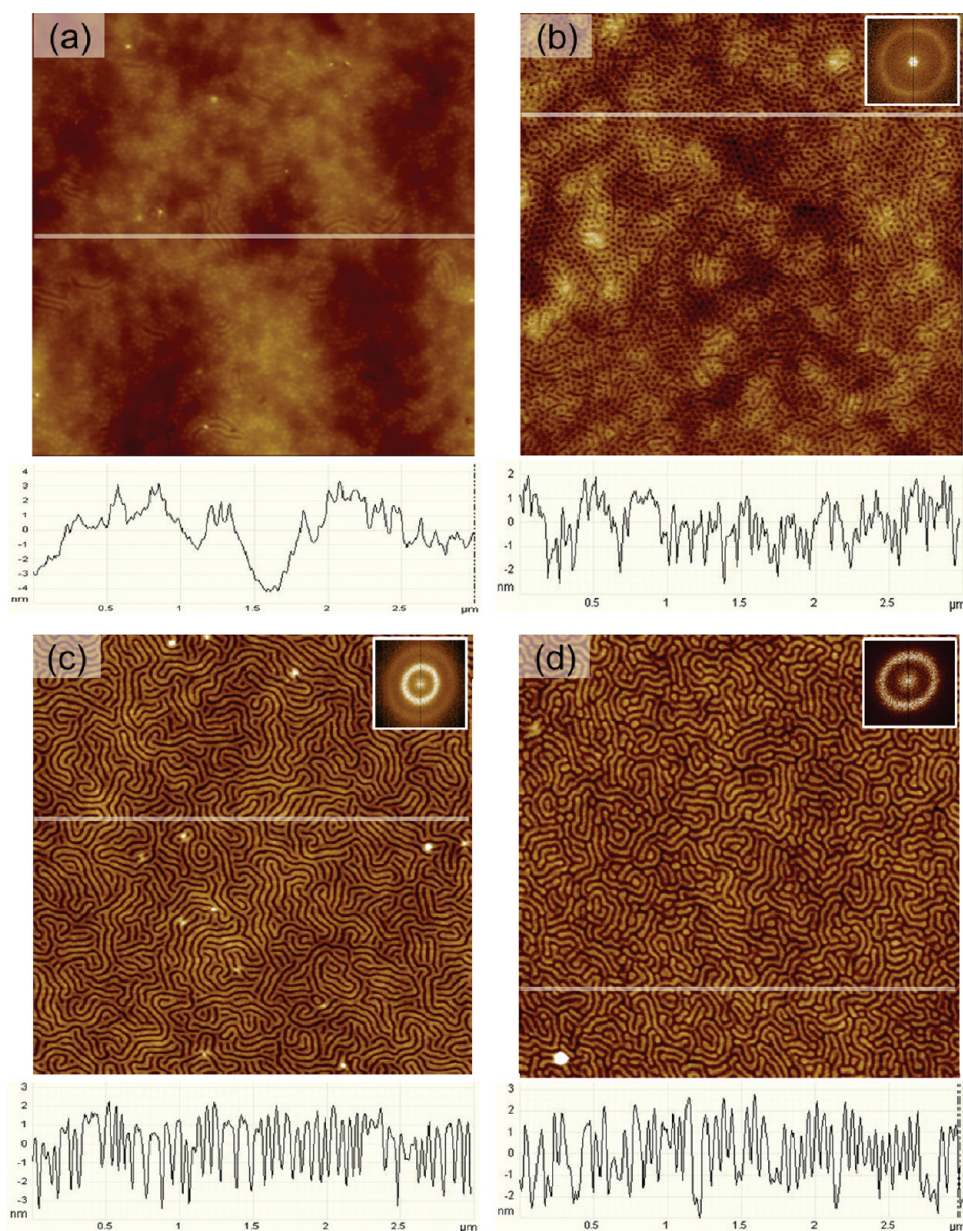


Figure 2. AFM height images of $PS_{390}\text{--}P4VP_{140}(\text{AOT})_{DN}$: (a) weight fraction of the $P4VP(\text{AOT})_{0.25}$ is $f_{\text{comp}} = 0.44$. In this case, each fourth 4VP monomer is protonated $DN = 0.25$. (b) Fraction corresponding to $f_{\text{comp}} = 0.47$ and $DN = 0.33$. (c) Fraction corresponding to $f_{\text{comp}} = 0.54$ and $DN = 0.5$. (d) Fraction corresponding to $f_{\text{comp}} = 0.66$ and $DN = 1.0$. The average periodicity assessed from the power spectral density over $3 \times 3 \mu\text{m}^2$ was 420, 470, and 500 Å, for $DN = 0.33, 0.5$, and 1.0 , respectively. The scan size is $3 \times 3 \mu\text{m}^2$, and the graph below each image is a cross section profile along the horizontal line as indicated.

which reduces the height. Thus, the surface profile is the result of a layer structure of P4VP (AOT) at the air/film.

$PS_{350}\text{--}P4VP_{260}(\text{AOT})_{DN}$. The bcp, without AOT forms lamellae parallel to the air/SiO₂ interface. The surface morphology of such films often shows islands or holes with a depth commensurate with the bcp periodicity.¹ This is not the case for the present bcp–AOT complex. SFM investigations summarized in Figure 3 show that, regardless of the fraction of the complex, the films display an in-plane periodicity without holes or islands. This suggests that the bcp microdomains are orthogonal to the air/SiO₂ interface. Increasing the weight fraction of the complex from 0.6 to 0.76 affects mainly the connectivity between the lamellae. This can be appreciated qualitatively by comparing Figure 3a or 3b to Figure 3c in which the numbers of junction between lamella and their

contour length are reduced. Further increasing of the complex weight fraction to 0.8 leads to hexagonally ordered isolated dots, which we assign to PS cylinder embedded in P4VP-(AOT)_{1.0} layer (Figure 3d). The common feature is the height distribution, which shows a well-defined depth of $24 \pm 5 \text{ Å}$ (cf. cross-section profile and Figure S8 (Supporting Information)). Interestingly, this value is somewhat smaller than L the bulk period. Thus, again this observation enforces the peculiar organization of $P4VP(\text{AOT})_{1.0}$ at the air/film surface (see X-ray Reflectivity section below).

$PS_{120}\text{--}P4VP_{50}(\text{AOT})_{DN}$. Irrespectively of the AOT composition, these films of low molecular mass are unstable and dewet upon vapor annealing (cf. Figure 4). Because the weight fraction of P4VP in the neat bcp is 30%, P4VP forms cylinders embedded in a PS matrix. In thin films, the surface structure

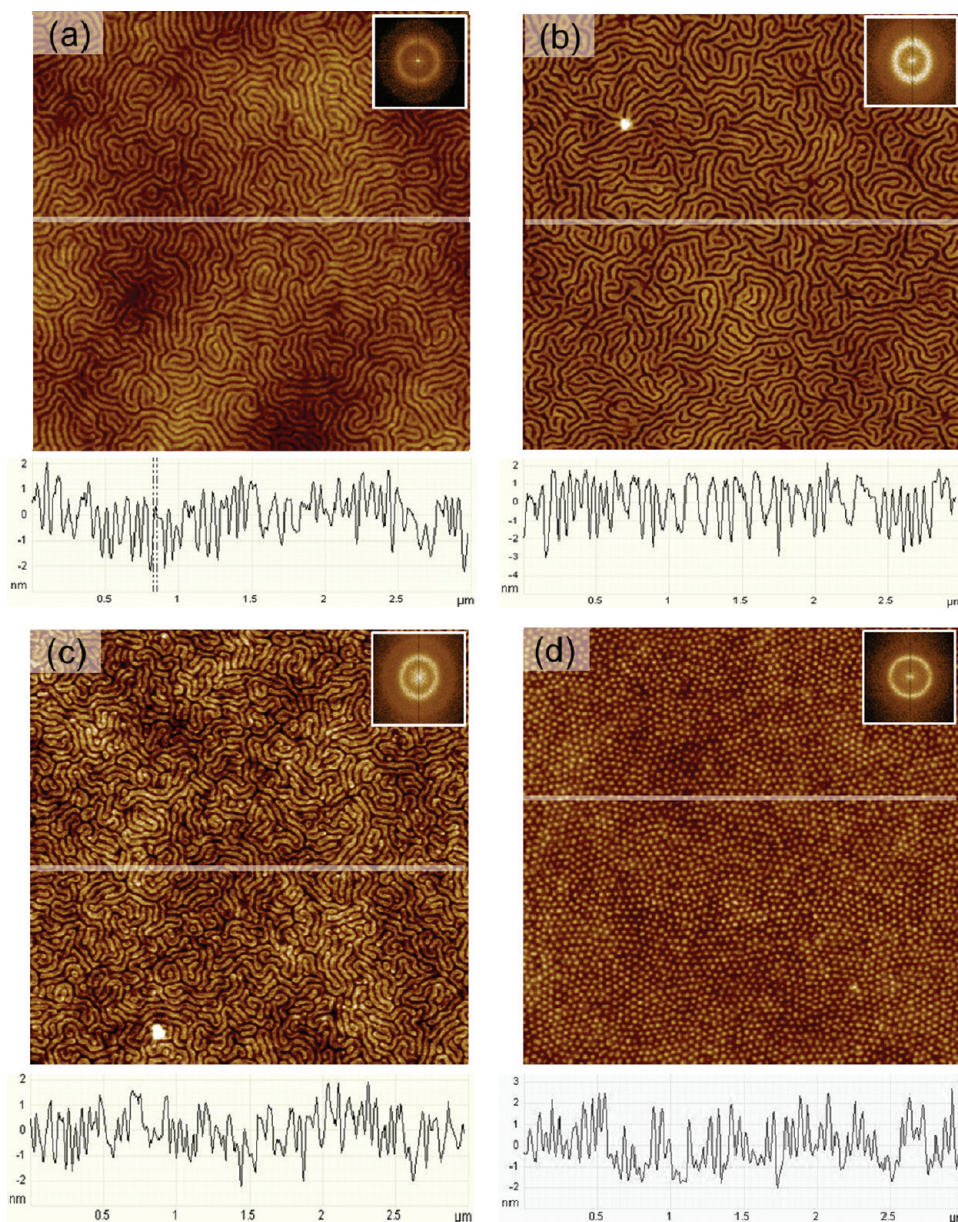


Figure 3. AFM height images of $\text{PS}_{350}\text{-P4VP}_{260}(\text{AOT})_{\text{DN}}$: (a) corresponds to $f_{\text{comp}} = 0.6$, where in this case each fourth 4VP monomer is protonated $\text{DN} = 0.25$; (b) corresponds to $f_{\text{comp}} = 0.65$ and $\text{DN} = 0.33$; (c) corresponds to $f_{\text{comp}} = 0.76$ and $\text{DN} = 0.75$; (d) corresponds to $f_{\text{comp}} = 0.8$ and $\text{DN} = 100\%$. The average periodicity assessed from the power spectral density over $3 \times 3 \mu\text{m}^2$ is 490, 510, 470, and 460 Å for $\text{DN} = 0.25, 0.33, 0.75$, and 1.0, respectively. The scan size is $3 \times 3 \mu\text{m}^2$, and the graph below each image is a cross section profile along the horizontal line as indicated.

starts to evolve only for weight fractions of the complex above 64%. Below this value the films exhibit a localized structure which might indicate mixed orientation (not shown). The bcp with 64% of the complex shows an ill-defined morphology, it might be coexisting lamellae and cylinder, but it is difficult to assign. The phase image indicates that the system is microphase separated with an average period of 290 Å. A higher weight fraction of the complex of ca. 70% leads to a lamellae structure orthogonal to the SiO_2/air interface. The structure has a mean periodicity of 250 Å.

$\text{PS}_{190}\text{-P4VP}_{100}(\text{AOT})_{\text{DN}}$. This composition shows a lamellae structure, but the total molecular weight is almost twice as low as the previous bcp $\text{PS}_{350}\text{-P4VP}_{260}$. If the weight fraction of the complex is smaller than 0.63, the surface morphology exhibit localized structures coexisting with a featureless layer. Most likely this indicates a mixed orientation. Ordered structures

evolve only at 63% weight fraction of P4VP(AOT), for which the dominant structure is lamellae coexisting with cylinders (cf. Figure 5a). Rather well-defined lamellae with improved ordering are observed for 73 wt % (cf. Figure 5b). In contrast to previous films, the surface profile is smooth, suggesting a specific organization of P4VP (AOT) complex. This observation will be discussed in more detail in the next section.

Intermediate Conclusions. To elucidate the influence of interfacial constraints on the surface structure, let us first consider the surface energy of each component in the system. Both pyridine and AOT have a high affinity for the silanol groups present at the surface of silicon oxide.^{45,46} On the other side, at the air interface, PS and AOT have a similar critical surface tension, $\gamma_{\text{PS}} = 33 \text{ mN/m}$;⁴⁷ $\gamma_{\text{AOT}} \sim 34 \text{ mN/m}$,⁴⁸ which ensures nonselective wetting of the air interface. To exclude any effect related to the confining interfaces,^{8,49} thicker films have

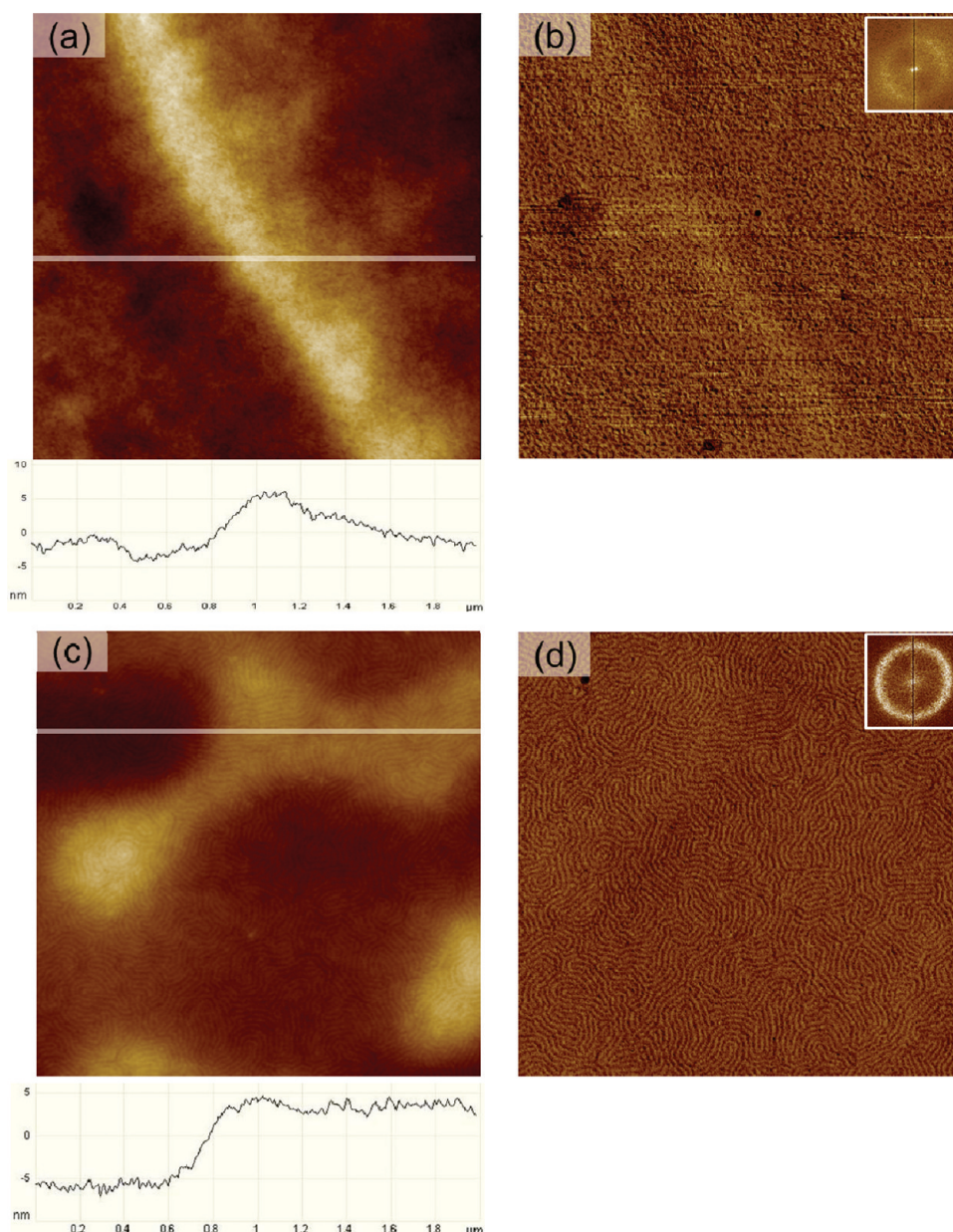


Figure 4. Height and phase SFM images of PS₁₂₀-P4VP₅₀(AOT) (a) topography and (b) phase for a bcp-complex with weight fraction of 0.64 equiv to protonation of three 4VP unit out of four, i.e., DN = 0.75; (c) topography and (d) phase for $f_{\text{comp}} = 0.7$ and DN = 1.0. The scan size is $2 \times 2 \mu\text{m}^2$, and the graph below each image is a cross section profile along the horizontal line as indicated.

also been studied. Up to 3-fold the block copolymer periodicity the surface structure turns out to be identical regardless of thickness (see Supporting Information, Figure S9). Second, WAXS provides clear evidence of bulk mesomorphic behavior of the P4VP(AOT) complex. Furthermore, the in-plan periodicity and the cross-section profile assessed by SFM imply smectic organization of the AOT-complex orthogonal to the PS interface. Finally, the question arises whether the layering persist over the film depth. This issue has been addressed by X-ray Reflectivity (see below).

Regarding the structural transition of the bcp complex, we note that, a comb architecture requires more space compared to a coil, which tends to curve the interface away from the comb region. For the present bcp-AOT complex, the comb blocks form cylinders at a nearly symmetric mass fraction, i.e., $f_{\text{comp}} = 0.45$. A cylindrical phase for such a composition is unusual. In

bulk, for a copolymer with a symmetric composition, curving of the interface requires a conformational asymmetry of the blocks.⁵⁰ In principle, steric stiffening due to complexation provides such a conformational asymmetry that may introduce spontaneous curvature.⁵¹ However, incorporation of AOT will also reduce the interfacial tension and thus the effective interaction parameter between PS/P4VP(AOT).^{52,53} In summary, steric stiffening may induce extra P4VP stretching which is partly compensated by lowering the interfacial tension at the coil/comb interface. In our experiments, the lamellae of the high-molecular-mass bcp complex show a remarkable connectivity and short contour lengths. This suggests that it is energetically favorable (less costly) to curve the interface to create junctions between the lamella. We attribute this behavior to a balance between interfacial tension reducing the interfacial

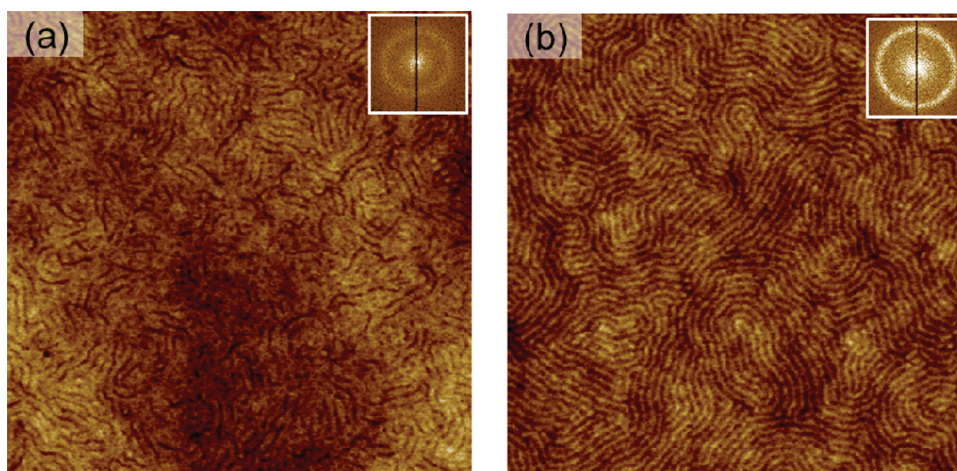


Figure 5. AFM height images of PS₁₉₀-P4VP₁₀₀(AOT)_{DN}: (a) corresponds to $f_{\text{comp}} = 0.63$ where in this case each second 4VP monomer is protonated DN = 0.5; (b) corresponds to $f_{\text{comp}} = 0.73$ and DN = 1.0. The average periodicity assessed from the power spectral density over $2 \times 2 \mu\text{m}^2$ is 380 and 300 Å, for DN = 0.5 and 1.0, respectively. The scan size is $2 \times 2 \mu\text{m}^2$.

area between the blocks and chain stretching favoring domains of uniform thickness in order to avoid packing frustration.

However, at present, it is neither clear how effectively the surfactant (AOT) reduces the incompatibility between the blocks, nor to what extent it affects the conformational asymmetry between P4VP(AOT) and PS. Furthermore, our observations were made for thin films, in which additional interfacial interactions come into play.

X-ray Reflectivity. The XRR intensities for two representative morphologies, PS cylinders and lamellae are shown in parts a and b of Figure 6, respectively, as a function of the

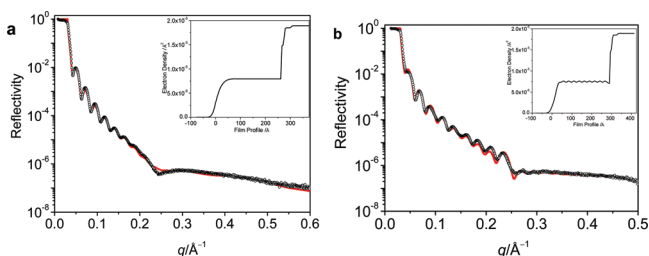


Figure 6. XRR intensity plotted as a function of the scattering vector q : (a) PS₃₅₀-P4VP₂₆₀(AOT)_{1.0} (PS cylinder) and (b) PS₁₉₀-P4VP₁₀₀(AOT)_{1.0} (lamellae). The solid red lines are fits to the data points using a three layer model for part a and a multilayer stack for part b. The inset gives the fitted density profiles normal to the substrate. The results of the fits are summarized below in Tables 2 and 3.

scattering vector q . The Kiessig fringes at low q -values correspond to the total film thickness which is similar for both samples: 299 Å for the cylindrical forming bcp-complex (a) and 276 Å for the lamellar forming one (b). For the first sample (Figure 6a), the solid line represents a fit to a three-layer model leading to the density profile shown in the inset. The essential elements are an ordered top and bottom layer of high density and a homogeneous middle layer. Two aspects are remarkable. First, inclusion of a separate bottom layer is essential to fit the change in slope of the reflectivity curve around $q = 0.2\text{--}0.3 \text{ Å}^{-1}$. The additional top layer has a minor influence on the quality of the fit and its incorporation hardly affects the conclusions from the model. Second, replacing the homogeneous middle layer by a stack of layers of alternating

density (smectic period), does hardly improve the quality of the fit. In fact the two densities converge to very close values with a small difference that cannot be considered to be significant within the given accuracy. Hence we conclude that no conclusive evidence for smectic layers parallel to the substrate is found. Given the small density contrast between P4VP and AOT (as also concluded from the bulk X-ray intensities), this cannot be considered as evidence of the *absence* of such a structure. The dense bottom layer with a thickness of ca. 12 Å is assigned to a monolayer of predominantly comb-like P4VP-(AOT). The comb polymer is forced (constrained) to be ordered on the substrate surface, with polar parts contacting SiO₂ and alkyl tails oriented toward the bulk of the sample. The thickness of the bottom and top layer are commensurate with the bulk smectic period and also in agreement with the height profile from SFM. Films of other compositions with a lower DN have been also measured by XRR. The results are very similar to Figure 6a, and the analysis shows that regardless the film morphology the data can be rationalized with the model described above for DN = 1.0.

Table 2. Structural Details Inferred from the Fit of XRR Data of Films of PS₃₅₀-P4VP₂₆₀(AOT)_{1.0}

model	thickness/Å	roughness/Å	electron density/ e Å^{-3}
top layer	26.5	12.4	0.19
middle layer	237	19.9	0.29
bottom layer	12.2	0.1	0.54
SiO ₂	29	2.6	0.66

We now come to Figure 6b, describing the block copolymer PS₁₉₀-P4VP₁₀₀(AOT)_{1.0} with a low molecular weight, which behaves somewhat differently. Similar to Figure 6a, the slope of the curve changes in the q range of $0.2\text{--}0.3 \text{ Å}^{-1}$, leading again to an adsorbed bottom layer in the model. However, in addition, irregular changes of the fringes occur in the same region. To fit this part of the curve now a stack of alternating layers is required, representing smectic ordering of the P4VP(AOT)_{1.0} complex parallel to the substrate. The full model requires an adsorbed bottom layer, 10 smectic layers parallel to the substrate, and a special “top stack” of two layers. The results are listed in Table 3. The smectic layer period is 25.9 Å, close to the bulk value, and the thickness of the

Table 3. Layered Structure Details of PS₁₉₀–P4VP₁₀₀(AOT)_{1.0} from Fitting the XRR Data

model		thickness/Å	roughness/Å	electron density/e Å ^{−3}
top layer		15.5	12.4	0.12
second layer		12.2	7.4	0.19
smectic layer stack	layer 1	7.8	7.9	0.30
	layer 2	18.1	7.5	0.25
bottom layer		11.9	0.1	0.52
SiO ₂		29	2.6	0.66

adsorbed bottom layer is again about half the smectic period. The top layer is clearly different from that of the previous block copolymer with high molecular weight. The resulting two separate top layers are somewhat ill defined, while each of the two layers has a thickness close to half the smectic period. They are needed to fit the rather gradual decrease of electron density upon approaching the air interface. The model agrees with the results of AFM that indicate a fuzzy morphology without well-defined height values of the smectic system.

Regarding the difference between Figure 6a and Figure 6b, we note that in general in smectic block copolymers the smectic layers have a tendency to be perpendicular to the block interfaces.²² Because of the comb geometry this situation leads to a natural continuity of the backbone polymer at the block interfaces. For films of PS₁₉₀–P4VP₁₀₀(AOT)_{1.0} (Figure 6b) this situation is realized with PS lamellae along the film normal. For the other case of Figure 6a, any orientation of smectic layer is unclear as discussed above.

Templating from PS–P4VP(AOT)_{DN}. The present complexes with low a molecular weight surfactant allow controlled orientation of microdomains structures, which may provide ideal templates. Indeed, the selective dissolution of AOT with NH₃ solution allows to generate porous polymer films. Three morphologies, PS cylinder, lamellae, and P4VP/AOT cylinder have been selected to demonstrate the process. Figure 7 shows the film structures after simple dipping the samples for 30s in a NH₃ solution.

For films in which the complex forms cylinders in a PS matrix, dissolution of the AOT lead to ca. 200 Å cylindrical pores connecting the two side of the film (cf. Figure 7a). Stripping the film from the Si support gives free-standing membranes that can be transferred on a bare TEM copper grid. Figure 7b shows the TEM image, in which the contrast is reversed compared to unwashed sample (Supporting Information, Figure S10). This indicates that the cylinder cores have a lower electron density compared to the situation before NH₃ treatment. Similarly for a lamellae morphology, dissolution of AOT leads to interconnected lamella or a labyrinth-like structure (cf. Figure 7c). The insert in Figure 7c confirms the orthogonal orientation of the lamellae relative to the SiO₂/air interface. For films in which the complex constitutes the continuous matrix, dissolution of AOT leads to PS pillars (cf. Figure 7d). The insert in Figure 7d shows an area where the film has been scratched mechanically to inspect the profile of pillar. Because polystyrene is glassy, the hydrolysis of AOT does not affect the periodicity of the structures. Therefore, any change in the interpolystyrene structure is exclusively associated with a contraction (collapse) of the P4VP chains. For a given

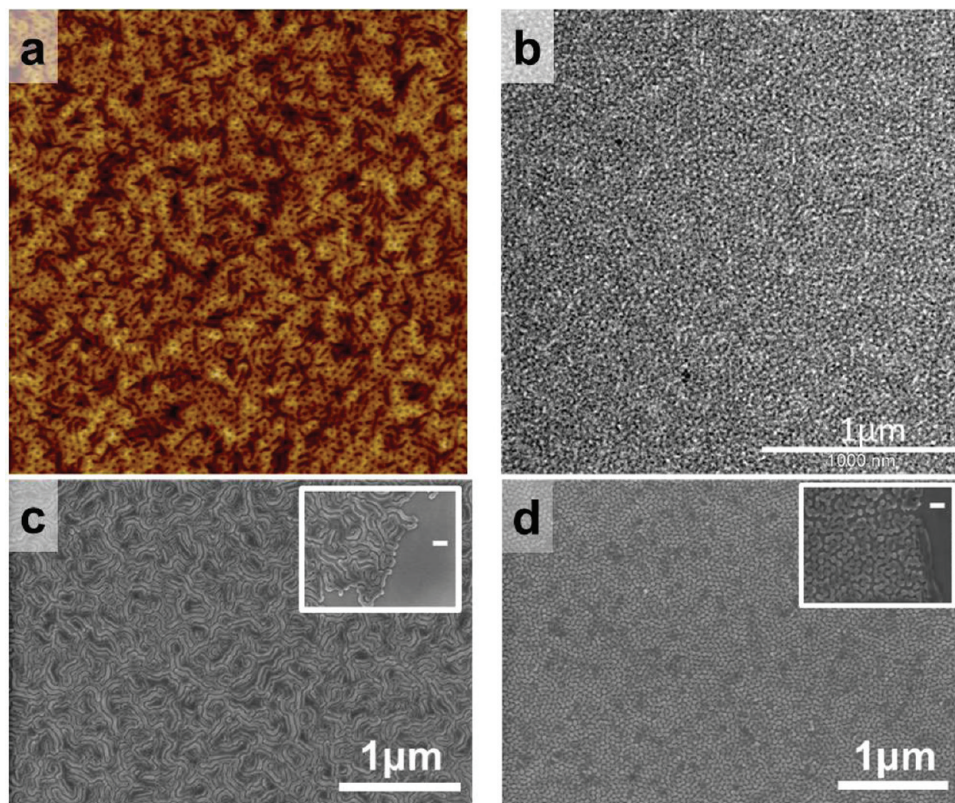


Figure 7. Morphology of PS–P4VP(AOT) complex thin films after NH₃ solution washing: (a) AFM topography the scan size is $3 \times 3 \mu\text{m}^2$ and (b) TEM images of PS₃₉₀–P4VP₁₄₀(AOT)_{0.33}; (c) FESEM image of PS₃₉₀–P4VP₁₄₀(AOT)_{0.5}; (d) FESEM image of PS₃₅₀–P4VP₂₆₀(AOT)_{1.0}. The inset is a magnified view with a scale bar representing 100 nm.

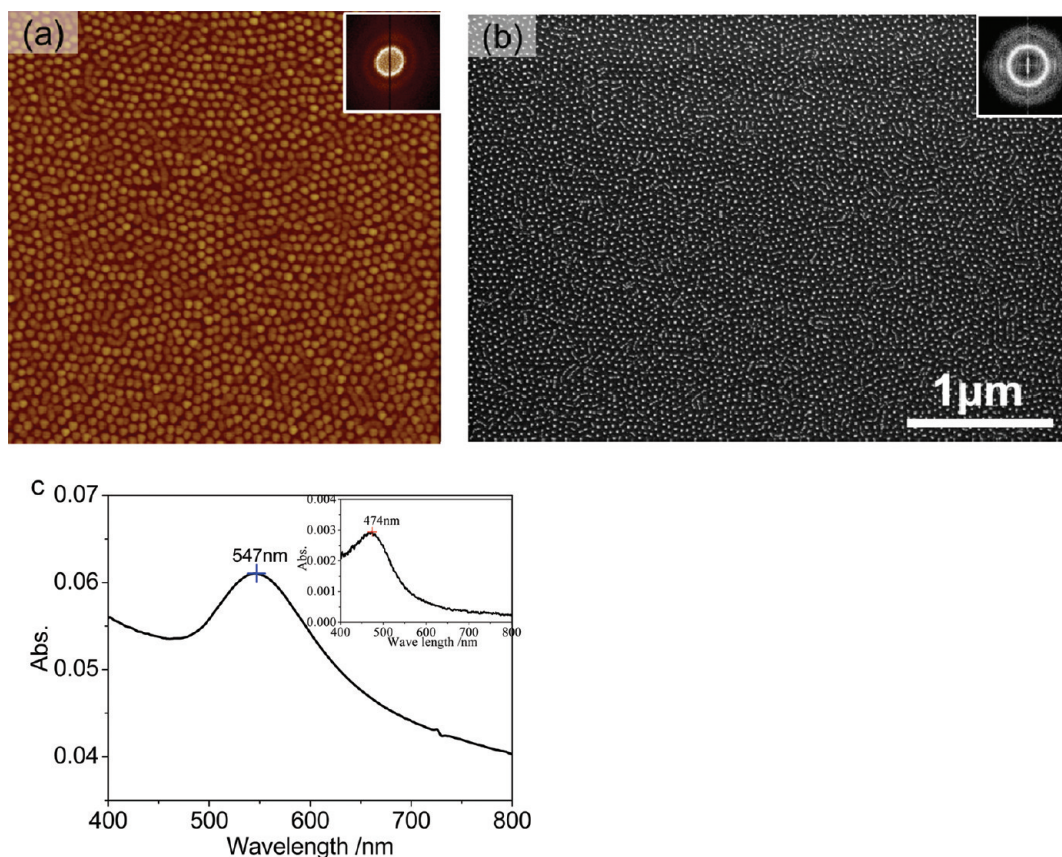


Figure 8. Morphology and optical properties of gold patterns from PS–P4VP(AOT) supramolecular template: (a) AFM and (b) SEM images of gold dots prepared by templating PS₃₉₀–P4VP₁₄₀(AOT)_{0.33}; (d) UV–vis spectra of the gold patterns, the inset shows the SPR peak of gold with a diameter of ca. 100 Å and a periodicity of ca. 800 Å prepared through solution loading of gold salt-block copolymer micelles.⁵⁷ The scan size of the AFM image is $2 \times 2 \mu\text{m}^2$.

morphology such as pillars, we can estimate a contraction of the chains of about 65%.

It is interesting to note that the P4VP chains are bounded to the glassy PS and the properties of the nanostructure is pH sensitive.⁵⁴ In addition, other functionalities can be easily introduced by incorporating other species, susceptible to specifically interact with P4VP chain such as, anionic dyes⁵⁵ or inorganic salts, as illustrated below.

If films of PS–P4VP(AOT)_{DN} are immersed in an aqueous solution of HAuCl₄, the P4VP is protonated and forms a complex with auric acid AuCl₄[–] ions through coordination and electrostatic interaction.⁵⁶ This allows a high amount of gold precursor to be incorporated. Subsequently, treatment of the sample with O₂-plasma converts the salt to gold while stripping-off the polymer templates. This results in a well-defined array of gold dots.

Figure 8 shows a two-dimensional pattern of gold dots obtained after plasma treatment. AFM and SEM micrographs (Figure 8a,b) allow to assess the regularity and uniformity of the pattern. The gold dots have an average periodicity of about 440 Å, with a mean diameter and height of about 200 Å and 300 Å, respectively. However, if one takes the radius of the AFM tip into account (~ 100 Å), the diameter of the gold dots is of the order of 100 Å, in agreement with the size inferred from SEM micrographs. Accordingly the pattern consists of gold pillars with an aspect ratio of ~ 3 . Additional information might be gained by recording the surface plasmon resonance (SPR) of such an array. Figure 8c shows the UV–vis spectra of

the gold dots prepared on a glass substrate. The pattern displays a pronounced SPR peak around 5470 Å. Spherical gold nanoparticles with a diameter of 100 Å made from PS₁₃₅₀–P2VP₄₀₀/HAuCl₄⁵⁷ on a glass substrate have an SPR peak at 4740 Å. The red shift of 700 Å is most likely due to the size increase of gold nanoparticles. If a lamella morphology is loaded, removal of the polymer and reduction of the gold yield interconnected gold nanoparticles (see Supporting Information, Figure S11).

CONCLUSIONS

In the solid state AOT–sodium salt is known to form a hexagonal columnar phase. Ionic bonding of AOT–acid and monomers of a P4VP backbone retains the mesomorphic properties. However, instead of a columnar phase, P4VP–(AOT)_{DN} complexes form a layered smectic structure. Formation and stability of the complex is provided by a large heat of protonation that overcomes the elasticity of the chain. The steric requirements of the complex impose a comb-like chain structure.

Incorporation of AOT in a diblock copolymer PS–P4VP has a minor effect on the smectic structure. However, incompatibility between the blocks drives the system to microphase separate. In such a situation, the degree of neutralization determines the morphology of the blocks and alleviates the interfacial constraints present in thin films. This allows to generate lamellar or cylindrical structures whose orientation is perpendicular to the air/substrate interface.

Thin films of the complex can be used as template for nanofabrication. Various structures like gold rods or nanowires can be made via simple post loading method and plasma treatment or gold-bcp hybrid films can be made via simple loading without any additional treatments.

■ ASSOCIATED CONTENT

■ Supporting Information

FTIR spectra of AOT and AOT-H, P4VP₁₀₀(AOT)_{DN}, PS₃₅₀-P4VP₂₆₀(AOT)_{DN}, PS₃₉₀-P4VP₁₄₀(AOT)_{DN}, PS₁₉₀-P4VP₁₀₀(AOT)_{DN}, PS₁₂₀-P4VP₅₀(AOT)_{DN}, WAXS spectra for each homopolymer and copolymer complex, selected height images and corresponding depth histogram (or height distributions), FESEM cross section of thin films of PS₃₉₀-P4VP₁₄₀(AOT)_{0.5}, TEM image of PS₃₉₀-P4VP₁₄₀(AOT)_{0.33}, SFM and FESEM images of gold nanowires from PS₃₉₀-P4VP₁₄₀(AOT)_{1.0}. This material is available free of charge via the Internet at <http://pubs.acs.org/>

■ AUTHOR INFORMATION

Corresponding Author

*E-mail: mourran@dw.rwth-aachen.de.

■ ACKNOWLEDGMENTS

We would like to thank Dr. Ulrich Rücker (Institut für Festkörperforschung Forschungszentrum Jülich) for help and assistance with the X-ray reflectivity measurements. Jingbo Wang acknowledges financial support from the Federal Ministry of Education and Research (Nanohybride Grant No. 13N9126).

■ REFERENCES

- (1) Hamley, I. W., *The Physics of Block Copolymers*; Oxford University Press: Oxford, U.K., 1998.
- (2) Leibler, L. *Macromolecules* **1980**, *13* (6), 1602–1617.
- (3) Bates, F. S.; Fredrickson, G. H. *Annu. Rev. Phys. Chem.* **1990**, *41* (1), 525–557.
- (4) Hamley, I. W. *Prog. Polym. Sci.* **2009**, *34* (11), 1161–1210.
- (5) Kim, H. C.; Park, S. M.; Hinsberg, W. D. *Chem. Rev.* **2010**, *110* (1), 146–177.
- (6) Marenic, A. P.; Register, R. A. *Annu. Rev. Chem. Biomol. Eng.* **2010**, *1* (1), 277–297.
- (7) Fasolka, M. J.; Mayes, A. M. *Annu. Rev. Mater. Res.* **2001**, *31* (1), 323–355.
- (8) Knoll, A.; Horvat, A.; Lyakhova, K. S.; Krausch, G.; Sevink, G. J. A.; Zvelindovsky, A. V.; Magerle, R. *Phys. Rev. Lett.* **2002**, *89* (3), 035501.
- (9) Sakurai, S. *Polymer* **2008**, *48*, 2781–2796.
- (10) Kim, S. H.; Misner, M. J.; Xu, T.; Kimura, M.; Russell, T. P. *Adv. Mater.* **2004**, *16* (3), 226–231.
- (11) Tang, C.; Tracz, A.; Kruk, M.; Zhang, R.; Smilgies, D.-M.; Matyjaszewski, K.; Kowalewski, T. *J. Am. Chem. Soc.* **2005**, *127* (19), 6918–6919.
- (12) Tang, C.; Wu, W.; Smilgies, D.-M.; Matyjaszewski, K.; Kowalewski, T. *J. Am. Chem. Soc.* **2011**, *133* (30), 11802–11809.
- (13) Thurn-Albrecht, T.; Schotter, J.; Kastle, G. A.; Emley, N.; Shibauchi, T.; Krusin-Elbaum, L.; Guarini, K.; Black, C. T.; Tuominen, M. T.; Russell, T. P. *Science* **2000**, *290*, 2126–2129.
- (14) Morikawa, Y.; Nagano, S.; Watanabe, K.; Kamata, K.; Iyoda, T.; Seki, T. *Adv. Mater.* **2006**, *18* (7), 883–886.
- (15) Kim, S. O.; Solak, H. H.; Stoykovich, M. P.; Ferrier, N. J.; de Pablo, J. J.; Nealey, P. F. *Nature* **2003**, *424*, 411–414.
- (16) Son, J. G.; Bulliard, X.; Kang, H.; Nealey, P. F.; Char, K. *Adv. Mater.* **2008**, *20*, 3643–3648.

- (17) Lin, Y.; Boker, A.; He, J.; Sill, K.; Xiang, H.; Abetz, C.; Li, X.; Wang, J.; Emrick, T.; Long, S.; Wang, Q.; Balazs, A.; Russell, T. P. *Nature* **2005**, *434* (7029), 55–59.
- (18) Osuji, C.; Zhang, Y.; Mao, G.; Obe, C. K.; Thomas, E. L. *Macromolecules* **1999**, *32* (22), 7703–7706.
- (19) Anthamatten, M.; Hammond, P. T. *J. Polym. Sci., Part B: Polym. Phys.* **2001**, *39*, 2671–2691.
- (20) Hamley, I. W.; Castelletto, V.; Lu, Z. B.; Imrie, C. T.; Itoh, T.; Al-Hussein, M. *Macromolecules* **2004**, *37*, 4798–4807.
- (21) Verploegen, E.; Zhang, T.; Jung, Y. S.; Ross, C.; Hammond, P. T. *Nano Lett.* **2008**, *8*, 3434–3440.
- (22) de Jeu, W.; Séréro, Y.; Al-Hussein, M. *Adv. Polym. Sci.* **2006**, *200*, 71–90.
- (23) Ikkala, O.; ten Brinke, G. *Science* **2002**, *295* (5564), 2407–2409.
- (24) Ruokolainen, J.; Mäkinen, R.; Torkkeli, M.; Mäkelä, T.; Serimaa, R.; Brinke, G. t.; Ikkala, O. *Science* **1998**, *280* (5363), 557–560.
- (25) van Zoelen, W.; Polushkin, E.; ten Brinke, G. *Macromolecules* **2008**, *41* (22), 8807–8814.
- (26) van Zoelen, W.; Asumaa, T.; Ruokolainen, J.; Ikkala, O.; ten Brinke, G. *Macromolecules* **2008**, *41* (9), 3199–3208.
- (27) Albrecht, K.; Mourran, A.; Zhu, X.; Markkula, T.; Groll, J.; Beginn, U.; de Jeu, W. H.; Moeller, M. *Macromolecules* **2008**, *41* (5), 1728–1738.
- (28) Chen, H.-L.; Lu, J.-S.; Yu, C.-H.; Yeh, C.-L.; Jeng, U.-S.; Chen, W.-C. *Macromolecules* **2007**, *40*, 3271–3276.
- (29) Gopinadhan, M.; Beach, E. S.; Anastas, P. T.; Osuji, C. O. *Macromolecules* **2010**, *43* (16), 6646–6654.
- (30) Ikkala, O.; Ruokolainen, J.; ten Brinke, G.; Torkkeli, M.; Serimaa, R. *Macromolecules* **1995**, *28* (21), 7088–7094.
- (31) Zhu, X.; Tartsch, B.; Beginn, U.; Möller, M. *Chem.—Eur. J.* **2004**, *10* (16), 3871–3878.
- (32) Albrecht, K.; Gallyamov, M.; Zhu, X.; Moeller, M. *Macromol. Chem. Phys.* **2007**, *208* (13), 1409–1415.
- (33) Zhu, X.; Beginn, U.; Möller, M.; Gearba, R. I.; Anokhin, D. V.; Ivanov, D. A. *J. Am. Chem. Soc.* **2006**, *128* (51), 16928–16937.
- (34) Yeh, C.-L.; Hou, T.; Chen, H.-L.; Yeh, L.-Y.; Chiu, F.-C.; Müller, A. J.; Hadjichristidis, N. *Macromolecules* **2011**, *44* (3), 440–443.
- (35) Ungar, G.; Tomašić, V.; Xie, F.; Zeng, X.-b. *Langmuir* **2009**, *25* (18), 11067–11072.
- (36) Eibeck, P. Surface Induced nano patterns formed by amphiphilic block copolymers. University of Ulm: Ulm, Germany, 1999.
- (37) Tolan, M., *X-Ray Scattering from Soft-Matter Thin Films*. Springer: Berlin and Heidelberg, Germany, 1999.
- (38) Socrates, G., *Infrared and Raman Characteristic Group Frequencies*. John Wiley & Sons: New York, 2004.
- (39) Kosonen, H.; Valkama, S.; Ruokolainen, J.; Torkkeli, M.; Serimaa, R.; Brinke, G. t.; Ikkala, O. *Eur. Phys. J. E* **2003**, *10* (1), 69–75.
- (40) Ghosh, O.; Miller, C. A. *J. Phys. Chem.* **1987**, *91* (17), 4528–4535.
- (41) Mark, J. E., *Polymer Data Handbook*; Oxford University Press: 1999.
- (42) Starodubtsev, S. G.; Laptinskaya, T. V.; Yesakova, A. S.; Khokhlov, A. R.; Shtykova, E. V.; Dembo, K. A.; Volkov, V. V. *Polymer* **2010**, *51* (1), 122–128.
- (43) Sheu, E. Y.; Chen, S. H.; Huang, J. S. *J. Phys. Chem.* **1987**, *91* (12), 3306–3310.
- (44) Diele, S.; Oekiner, S.; Kuschel, F.; Hisgen, B.; Ringsdorf, H.; Zentel, R. *Makromol. Chem.* **1987**, *188*, 1993–2000.
- (45) Birch, W. R.; Knewton, M. A.; Garoff, S.; Suter, R. M.; Satija, S. *Colloid Surf. A: Physicochem. Eng. Asp.* **1994**, *89* (2–3), 145–155.
- (46) Spatz, J. P.; Möller, M.; Noeske, M.; Behm, R. J.; Pietralla, M. *Macromolecules* **1997**, *30* (13), 3874–3880.
- (47) Zisman W. A. Relation of the Equilibrium Contact Angle to Liquid and Solid Constitution. In *Contact Angle, Wettability, and Adhesion*; American Chemical Society: Washington, DC, 1964; Vol. 43, pp 1–51.

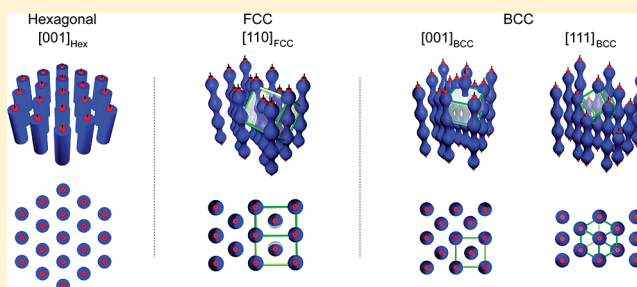
- (48) Hare, E. F.; Zisman, W. A. *J. Phys. Chem.* **1955**, *59* (4), 335–340.
- (49) Tsori, Y.; Andelman, D. *Eur. Phys. J. E* **2001**, *5* (5), 605–614.
- (50) Bates, F. S.; Fredrickson, G. H. *Macromolecules* **1994**, *27* (4), 1065–1067.
- (51) Bates, F. S.; Schulz, M. F.; Khandpur, A. K.; Forster, S.; Rosedale, J. H.; Almdal, K.; Mortensen, K. *Faraday Discuss.* **1994**, *98*, 7–18.
- (52) Polushkin, E.; Alberda van Ekenstein, G. O. R.; Knaapila, M.; Ruokolainen, J.; Torkkeli, M.; Serimaa, R.; Bras, W.; Dolbnya, I.; Ikkala, O.; ten Brinke, G. *Macromolecules* **2001**, *34* (14), 4917–4922.
- (53) Vukovic, I.; Punzhin, S.; Vukovic, Z.; Onck, P.; De Hosson, J. T. M.; ten Brinke, G.; Loos, K. *ACS Nano* **2011**, *5* (8), 6339–6348.
- (54) Nunes, S. P.; Sougrat, R.; Hooghan, B.; Anjum, D. H.; Behzad, A. R.; Zhao, L.; Pradeep, N.; Pinnau, I.; Vainio, U.; Peinemann, K. V. *Macromolecules* **2010**, *43* (19), 8079–8085.
- (55) Křenek, R.; Cimrová, V.; Stamm, M. *Macromol. Symp.* **2008**, *268* (1), 86–90.
- (56) Spatz, J. P.; Roescher, A.; Sheiko, S.; Krausch, G.; Möller, M. *Adv. Mater.* **1995**, *7* (8), 731–735.
- (57) Glass, R.; Arnold, M.; Blümmel, J.; Küller, A.; Möller, M.; Spatz, J. P. *Adv. Fun. Mater.* **2003**, *13* (7), 569–575.

Single-Walled Carbon Nanotube-Induced Lyotropic Phase Behavior of a Polymeric System

Hyung-Sik Jang,[†] Changwoo Do,[†] Tae-Hwan Kim,^{†,‡} and Sung-Min Choi^{*,†}[†]Department of Nuclear and Quantum Engineering, Korea Advanced Institute of Science and Technology, Daejeon 305-701, Republic of Korea[‡]Neutron Science Division, Department of Reactor Utilization and Development, Korea Atomic Energy Research Institute, Daejeon 305-353, Republic of Korea

S Supporting Information

ABSTRACT: We report for the first time a new single-walled carbon nanotube (SWNT)-induced lyotropic phase behavior of a F108 block copolymer/water system. As the concentration is increased by evaporation, the F108-SWNT/water system exhibits isotropic–hexagonal–FCC–BCC–lamellar transitions. This is in clear contrast with the F108/water system (isotropic–BCC–lamellar transitions), indicating that the hexagonal and the FCC phases are newly induced by the presence of one-dimensional SWNTs. The SWNTs maintain their individuality or very small bundle state in all the phases except the lamellar phase. In the hexagonal phase, the SWNTs are located in the hydrophobic core of F108 cylinders oriented parallel to the [001] direction. The epitaxial transitions between the phases allowed us to identify the possible orientation of SWNTs in each phase: [110] in the FCC and either <100> or <111> in the BCC. In the lamellar phase, the SWNTs exist most likely in the hydrophobic layers forming aggregations among them. This new SWNT-induced lyotropic phase behavior in a block copolymer system may provide a new scalable route to fabricate SWNT superstructures with well-defined architecture and new functionalities.



■ INTRODUCTION

For many practical applications of single-walled carbon nanotubes (SWNTs),¹ the fabrication of SWNT superstructures with well-defined morphology, density, and direction are highly required to enhance the physical properties of SWNTs collectively or to make new functionalities. Although many efforts have been made for this purpose using methods such as solvent evaporation,^{2,3} electric,^{4,5} magnetic,^{6,7} or flow field,^{8–11} an easy and simple method is yet to be developed. Amphiphilic molecules, such as block copolymers, exhibit rich phase behavior and have been extensively used as excellent templates for nanostructured materials.^{12–14} Recently, there have been many efforts to incorporate nanoparticles,¹⁵ such as spherical gold nanoparticles,^{16,17} CdS nanoparticles,¹⁸ and CdSe nanoparticles,¹⁴ into self-assembled block copolymers to efficiently fabricate patterned nanoparticle–polymer composites. Theoretical studies and computer simulations predict that the cooperative self-assembly of functionalized nanoparticles and block copolymers can provide a wide variety of nanoparticle–polymer composites with well-controlled particle arrangements.^{19–21} It is, therefore, highly desirable to use the rich phase behavior of block copolymers to fabricate well-controlled SWNT superstructures, which may provide an easy and scalable fabrication method. However, this approach is in its very early stage,^{22,23} and to make this approach successful, it is essential to understand the phase behavior of polymeric

systems when SWNTs are incorporated into the systems, which is the key information to design self-assembled SWNT superstructures using polymeric systems.

Here, we report a SWNT-induced lyotropic phase behavior in a Pluronic block copolymer system, which exhibits isotropic, hexagonal, face-centered cubic (FCC), body-centered cubic (BCC), and lamellar phases as concentration is increased. It should be noted that the hexagonal and FCC phases, which were not present in the block copolymer system, are newly induced by the presence of SWNTs. The expected location and orientation of SWNTs (which maintain their individuality or very small bundle state without aggregations) within the ordered phases are identified utilizing the epitaxial transitions between the phases.

■ EXPERIMENTAL SECTION

Materials. Purified HiPCO SWNTs (high-pressure CO conversion type, purity >90 wt %) were purchased from Unidym. Pluronic F108 (poly(ethylene oxide)₁₃₀–poly(propylene oxide)₆₀–poly(ethylene oxide)₁₃₀, PEO₁₃₀–PPO₆₀–PEO₁₃₀) was kindly provided by BASF Corporation and used without further purification. D₂O (99.9 mol % deuterium enriched) was purchased from Cambridge Isotope

Received: September 18, 2011

Revised: November 3, 2011

Published: December 22, 2011

Laboratory. H₂O was purified with a Millipore Direct Q system (electrical resistivity 18.2 MΩ cm) immediately before use.

Dispersion of SWNT and Sample Preparation. SWNTs of 0.09 g were added into 3 wt % Pluronic F108 in D₂O (0.9 g/30 g). To make the exfoliated SWNTs (individually isolated or very small bundles) adsorbed with Pluronic F108 (F108-SWNT), the mixtures were ultrasonicated for 1 h, followed by ultracentrifugation (ca. 110000g) for 4 h. After centrifugation, the upper ca. 70% of the dispersion was decanted to remove large bundled SWNTs at the bottom and freeze-dried. To prepare 5 wt % samples, the freeze-dried F108-SWNT powders were redispersed in distilled H₂O by mild shaking. This stock solution of F108-SWNT was divided into 20 tubes which were evaporated into different concentrations (5–100 wt % in 5 wt % steps). The F108 in H₂O samples at different concentration were prepared by the same manner, i.e., by evaporating 5 wt % samples of F108 in H₂O.

UV–vis–NIR Spectra. All the UV–vis–NIR spectra were measured by using a PerkinElmer L-750 UV–vis–NIR spectrometer. For the F108-SWNT samples with low viscosity, standard quartz cells of 2 mm beam path length were used, and for the F108-SWNT samples with high viscosity, two quartz plates (between which samples were placed) were used.

Small-Angle Neutron Scattering Measurements. Small-angle neutron scattering (SANS) measurements were performed using the 40 m SANS instrument at the HANARO, the Korea Atomic Energy Research Institute (KAERI) in Daejeon, Republic of Korea. Neutrons of wavelength $\lambda = 6 \text{ \AA}$ with a full width half-maximum $\Delta\lambda/\lambda = 12\%$ were used. Three configurations of sample-to-detector distance of 1.16, 7.78, and 17.9 m were used to cover the q range of $0.003 \text{ \AA}^{-1} < q < 0.6 \text{ \AA}^{-1}$, where $q = (4\pi/\lambda) \sin(\theta/2)$ is the magnitude of the scattering vector and θ is the scattering angle. Sample scattering was corrected for background and empty cell scattering and the sensitivity of individual detector pixels. The corrected data sets were placed on an absolute scale through the secondary standard method. All the SANS measurements were carried out at 25 °C using quartz cells of 2 mm path length.

Atomic Force Microscopy Measurement. Atomic force microscopy (AFM) images were taken in tapping mode by using a VEECO AFM instrument (Digital Instrument). For the AFM measurements, the as-prepared F108-SWNT dispersion was spin-coated (at 4000 rpm for 2 min) onto silicon wafers. To prepare the samples for bare SWNTs, the F108-SWNT dispersion deposited onto a silicon wafer was burned at 650 °C for 6 h in an argon atmosphere to remove the Pluronic F108 adsorbed on SWNTs.

Small-Angle X-ray Scattering Measurements. Small-angle X-ray scattering (SAXS) measurements were performed on the 4C1 beamline at Pohang Accelerator Laboratory (PAL), Republic of Korea, where a W/B4C double multilayer monochromator delivered monochromatic X-rays with a wavelength of 0.1608 nm and a wavelength spread $\Delta\lambda/\lambda$ of 0.01. A two-dimensional CCD camera (Mar CCD, Mar USA, Inc., CCD165) was used to collect scattered X-rays. Sample cells with a path length of 0.8 mm enclosed by two thin Kapton windows were used. The sample-to-detector distance was 1 m, covering the q range of $0.2 \text{ nm}^{-1} < q < 3.2 \text{ nm}^{-1}$. The q values were calibrated using silver behenate ($\text{AgO}_2\text{C}(\text{CH}_2)_{20}\text{CH}_3$). All measurements were performed at room temperature.

RESULTS AND DISCUSSION

Pluronic F108 ($\text{PEO}_{130}\text{--PPO}_{60}\text{--PEO}_{130}$) is a triblock copolymer which shows various phases in water depending on concentration at room temperature.^{24,25} The F108-SWNT was prepared by sonicating the mixture of SWNTs and F108 in water for 1 h, followed by ultracentrifugation and freeze-drying of supernatant. To enhance the ultracentrifugation efficiency, D₂O was used. The decanted dispersion was stable for more than 2 months without any precipitation (Figure 1a). The UV–vis–NIR spectrum of as-prepared F108-SWNT dispersion shows sharp van Hove transition peaks (Figure 1b), indicating

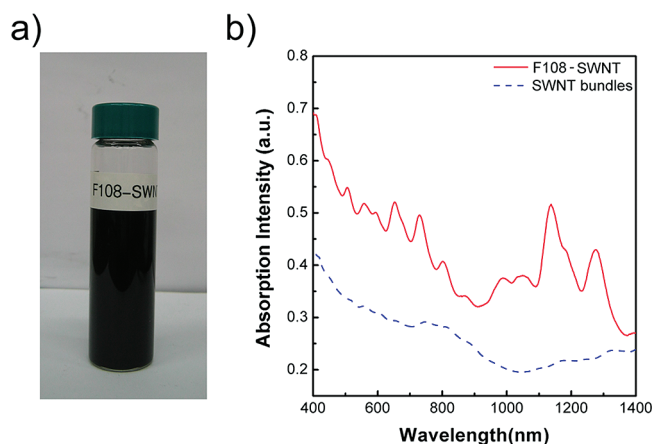


Figure 1. (a) F108-SWNT dispersion after ultracentrifugation. (b) UV–vis–NIR spectra of F108-SWNT dispersed in water and bundled SWNTs.

that SWNTs exist in an isolated form or in a very small bundle. The concentrations of SWNT and F108 in the decanted solution determined by using Beer's law,^{26,27} and the dried mass of the decanted dispersion is 0.011 and 2.1 wt %, respectively.

To further characterize the dispersion quality of the decanted F108-SWNT in D₂O, the SANS measurements were performed at 25 °C using the 40 m SANS instrument at the HANARO neutron facility, Korea Atomic Energy Research Institute (KAERI), Korea. As a comparison, an F108 only sample in D₂O prepared at the same concentration as that of the decanted dispersion was also measured. The SANS intensities are shown in Figure 2. Since F108 at 2.1 wt % in water does not

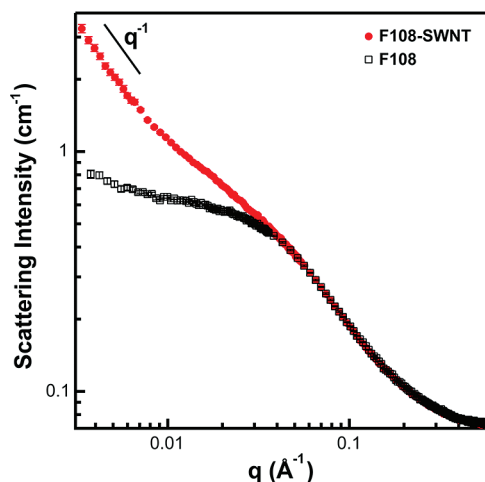


Figure 2. SANS intensities of as-prepared F108-SWNT and F108 only in D₂O at 25 °C. The concentration of both samples was 2.1 wt %.

make micelles at 25 °C (Supporting Information), the scattering intensity of F108 only shows a pattern typical for fully dissolved Gaussian polymer chains in the solution.^{28,29} On the other hand, the scattering intensity of F108-SWNT in D₂O shows at a clear q^{-1} behavior in the low- q region (where $q = (4\pi/\lambda) \sin(\theta/2)$ is the magnitude of scattering vector, λ is neutron wavelength, and θ is scattering angle), which is typical for long, thin, cylindrical nanoparticles dispersed in solu-

tion.^{30,31} This clearly indicates that SWNTs are well dispersed without forming aggregations or networks.

The diameter and length distribution of bare SWNTs (obtained by burning F108-SWNT on silicon wafer in Ar atmosphere) were determined from the AFM measurements (Figure 3).^{30,32} The diameter distribution of bare SWNTs is

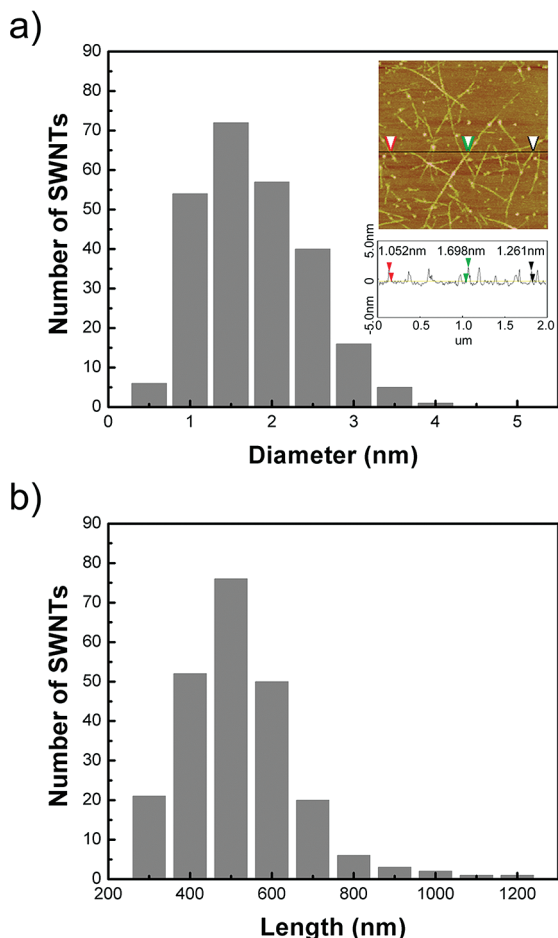


Figure 3. (a) Diameter and (b) length distributions of bare SWNTs after burning F108-SWNTs at 650 °C for 6 h in an Ar atmosphere. The inset shows a representative AFM image.

peaked at 1.5 ± 0.25 nm, and the diameter less than 2.5 nm occupies 84% of the distribution, which indicates that F108-SWNT are dispersed in an isolated form or in a very small bundle. The length distribution is peaked at 500 ± 50 nm with a mean length of ca. 500 nm.

The F108-SWNT samples in H₂O with different concentrations (5–100 wt % in 5 wt % steps) were prepared by evaporating 5 wt % samples (which were prepared by redispersing freeze-dried F108-SWNT in H₂O by mild shaking). The UV–vis–NIR spectra of F108-SWNT at various concentrations (up to 70 wt %) show sharp van Hove transition peaks which are essentially identical with that of as-prepared F108-SWNT dispersion (Figure 4). This clearly indicates that the exfoliated SWNTs are well maintained even at high concentrations without aggregations. However, when the concentration is 80 wt % or higher, the sharp peaks become flattened, indicating aggregation of SWNTs. This is directly related with the lamellar phase of F108 which appears at 80 wt %. This will be discussed more in detail later.

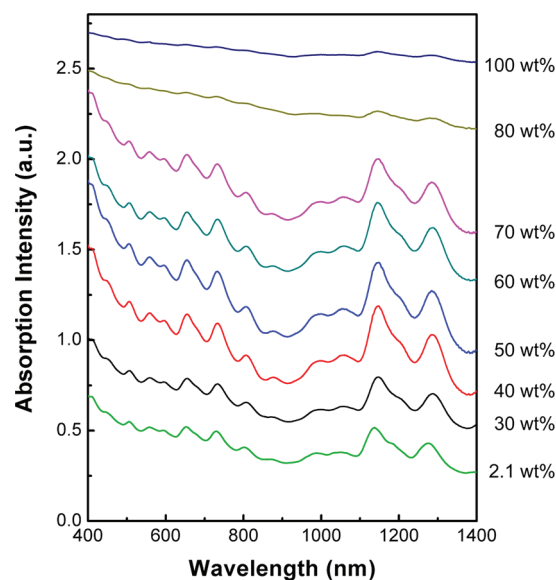


Figure 4. UV–vis–NIR spectra of F108-SWNT in water at different concentration. The spectra are shifted vertically for visual clarity.

To characterize the difference in phase behavior depending on the existence of SWNTs, SAXS measurements of F108 only and F108-SWNT dispersions at different concentrations were performed at room temperature using the 4C1 beamline at the Pohang Accelerator Laboratory, Korea. The SAXS intensities of F108 only and F108-SWNT in water at different concentrations are shown in Figure 5. The SAXS intensities show that the F108 only in water (without SWNTs) goes through isotropic, BCC, and lamellar phases as the concentration is increased. At 5 wt %, F108 polymers are fully dissolved and micelles are not formed. As the concentration is increased, the F108 only forms isotropic micellar phase as shown by the SAXS intensity at 15 wt %. At 25 wt %, the SAXS intensity shows a broad peak near 0.67 nm^{-1} , indicating that F108 solution starts to form an ordered structure. In the concentration range from 30 to 65 wt %, the SAXS intensities show sharp peaks with the peak position ratio of $1:\sqrt{2}:\sqrt{3}:\sqrt{4}:\sqrt{5}:\sqrt{6}:\sqrt{7}$, indicating the BCC phase. At 70 and 75 wt %, the SAXS intensities show peaks relevant to BCC and lamellar structures, indicating a mixed phase. When the concentration is higher than 80 wt %, the F108 solution forms a lamellar phase as indicated by the peak position ratio of 1:2:3.

The SAXS intensities of F108-SWNT samples show a sequence of changes with concentration, which is clearly different from that of F108 only samples. The SAXS intensities of F108-SWNT samples at 5 and 15 wt % show an upturn in the low- q region which is induced by the presence of long and thin SWNTs. This scattering pattern is clearly different from that of the isotropic spherical micellar phase which was observed in the F108 only sample at 15 wt %. When the concentration is increased to 20 wt %, a few small peaks start to build up (not shown), and at 25 wt %, a scattering pattern with a peak position ratio of $1:\sqrt{3}:\sqrt{4}:\sqrt{7}:\sqrt{9}:\sqrt{12}$ (with a lattice parameter of 23.8 nm) becomes apparent, indicating the formation of hexagonal phase. This scattering pattern is maintained up to 30 wt %. It should be noted that the hexagonal phase was not observed in the F108 only samples at any concentration. It is clear, therefore, that the hexagonal phase is induced by the long one-dimensional shape of SWNTs (adsorbed by F108), forming hexagonal arrays of SWNTs

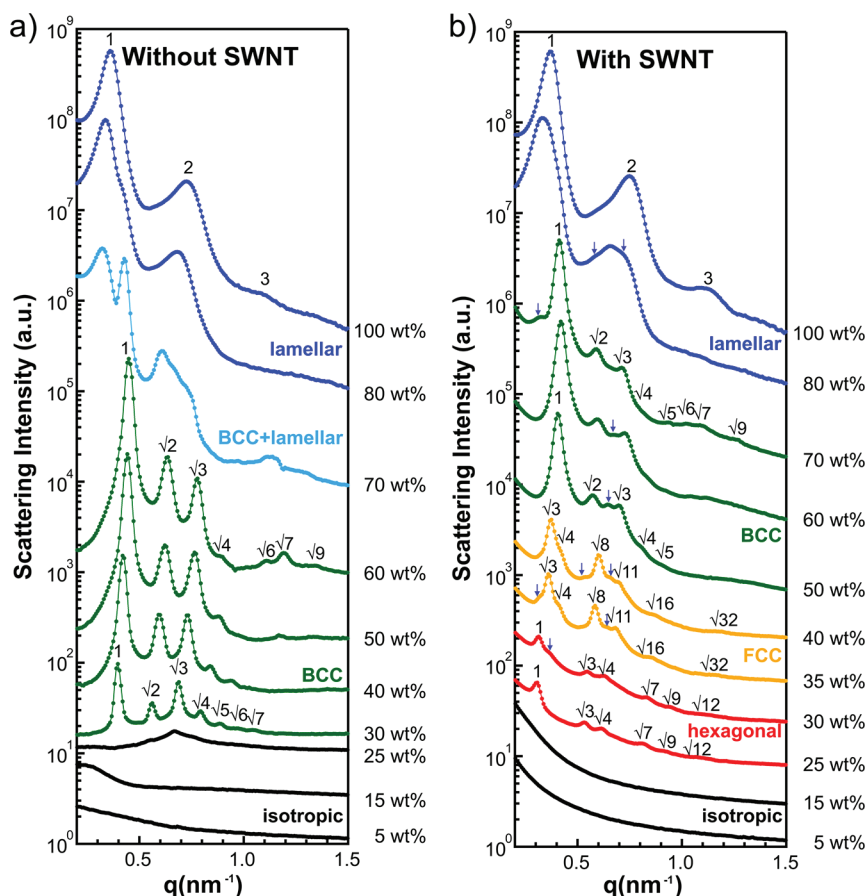


Figure 5. SAXS intensities of (a) F108 and (b) F108-SWNT in H₂O at different concentration at room temperature. The relative peak position ratios relevant to each phase are presented. The peaks indicated by arrows show some mixture of phases. Scattering intensities are shifted vertically for visual clarity. The peak positions (except those indicated by arrows) of each scattering pattern are given in the Supporting Information, Tables S1 and S2.

which are centered at the cylindrical hydrophobic core of F108. It should be noted that no other peaks, which do not correspond to the hexagonal phase, were observed in the scattering intensity of the 25 wt % sample. This indicates that the hexagonal phase at 25 wt % is homogeneous without forming any phase separation or a mixed phase. This may indicate that majority of F108 are adsorbed on the surface of SWNTs. When the concentration is increased to 35 wt %, the F108-SWNT system makes a topological transition to the FCC phase, as indicated by the peak position ratio of $\sqrt{3}:\sqrt{4}:\sqrt{8}:\sqrt{11}:\sqrt{16}:\sqrt{32}$. The FCC phase is maintained up to 40 wt %. It should be also noted that the FCC phase was not observed in the F108 only samples at any concentrations measured in this study. Therefore, it is clear that the FCC phase is induced by the existence of SWNTs, although the physical mechanism for the formation of FCC phase in the F108-SWNT solution is not clear. As the concentration is increased to 45 wt %, the SAXS intensity shows a mixed phase of the FCC and the BCC. At 50 wt %, the BCC peaks become dominant with a peak position ratio of $1:\sqrt{2}:\sqrt{3}:\sqrt{4}:\sqrt{5}:\sqrt{6}:\sqrt{7}$. The BCC phase is maintained up to 75 wt %. The SAXS intensities at 80 wt % or higher show that the F108-SWNT systems finally transform into the lamellar phase as it was seen in the F108 only samples.

Summarizing the phase behaviors, the F108-SWNT system makes a sequence of phase transitions, isotropic–hexagonal–FCC–BCC–lamellar phases, as the concentration is increased

from 5 to 100 wt %, which is in clear contrast with the sequence of phase transitions of the F108 only system, isotropic–BCC–lamellar phases. The hexagonal and FCC phases are newly induced by the presence of SWNTs. It should be noted that while the hexagonal phase in polymeric systems is typically observed between the cubic and lamellar phases, the hexagonal phase in the F108-SWNT system was observed before the cubic phase due to the presence of long one-dimensional objects, SWNTs. To the best of our knowledge, this is the first observation of hexagonal phase in polymeric system induced by SWNTs.

The lattice parameter of each phase was calculated from the first-order Bragg peaks q_1 using $a_{\text{hex}} = 4\pi/\sqrt{3}q_1$ for the hexagonal, $a_{\text{fcc}} = \sqrt{3}\cdot 2\pi/q_1$ for the FCC, $a_{\text{bcc}} = \sqrt{2}\cdot 2\pi/q_1$ for the BCC, and $a_{\text{lam}} = 2\pi/q_1$ for the lamellar phase. The results are summarized in Figure 6. While the SAXS intensities show some signatures of mixed phases (as indicated by arrows in Figure 5), for simplicity, only the dominant phases are presented, except the cases where the weightings of two constituting phases are similar.

Since F108 works as a dispersion agent of SWNTs in water (with its hydrophobic PPO segment adsorbed on the surface of SWNT and its hydrophilic PEO segments facing water^{33–35}), it is naturally expected that the SWNTs in the hexagonal phase are located at the center of cylindrical hydrophobic core of F108 with their long axes oriented along the [001] direction. Since the hexagonal phase is transformed into the FCC phase

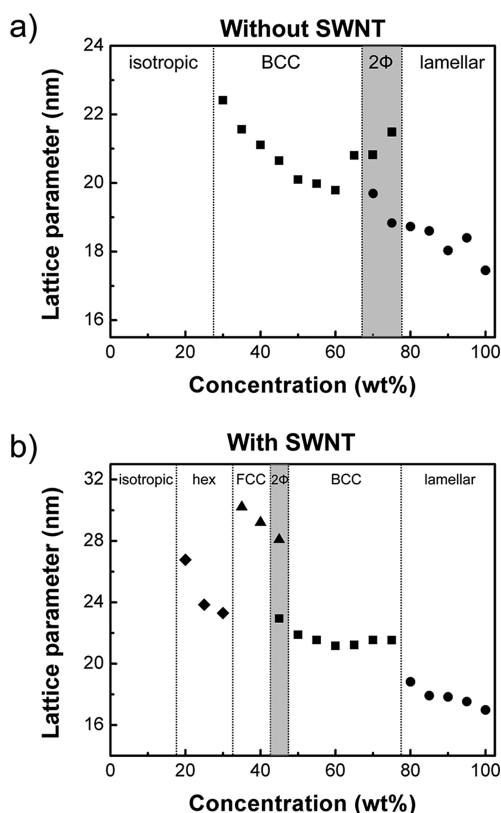


Figure 6. Lattice parameter of (a) F108 and (b) F108-SWNT in water at different concentration corresponding to each phase.

with the dispersion quality of SWNTs fully maintained (as clearly indicated by the UV–vis–NIR spectra in Figure 4), it is also expected that spherulike micelles of F108 are formed on SWNTs with the hydrophobic cores of the micelles pierced through by the SWNTs. If this is not the case, the good dispersion quality of SWNTs as shown by the UV–vis–NIR spectra cannot be maintained. Similar structures are expected for the BCC phase as well. In the lamellar phase, the SWNTs should be present in the PPO domains. While the PPO domains of the FCC and BCC phases are enclosed by the PEO domains (maintaining the isolation of SWNTs), the PPO domains of the lamellar phase are fully open in the transverse direction. Therefore, the SWNTs in each two-dimensional PPO

domain can aggregate easily. In fact, this should be the reason why the UV–vis–NIR spectra at 80 wt % or higher concentration are flattened.

Since all the samples that formed the FCC and the BCC phases were prepared by evaporating 5 wt % samples, they went through the hexagonal phase at which the SWNTs are oriented along the [001] direction (Figure 7a). Therefore, it is expected that there should be a preferred direction of SWNTs in the FCC and the BCC phase. Recently, it was shown that the hexagonal to FCC phase transition in block copolymer solution occurs epitaxially and the cylindrical axis (the [001] direction of hexagonal phase) coincides with the [110] direction of FCC structure.³⁶ Therefore, it is expected that the SWNTs in the FCC phase are oriented along the [110] direction (Figure 7b). The FCC to BCC transition in block copolymer solution is also epitaxial and commonly described by the well-known Bain distortion in which a distorted BCC unit cell imbedded in two FCC unit cells transforms to a BCC unit cell by compressing along one $\langle 100 \rangle$ direction and expanding along two $\langle 110 \rangle$ directions of the FCC unit cell. In this FCC to BCC transition, the {111} planes of the FCC structure are parallel with the {110} planes of the BCC structure^{37,38} and the [110] direction of FCC structure coincides with either the $\langle 100 \rangle$ or $\langle 111 \rangle$ direction of BCC structure. Therefore, it is expected that the SWNTs in the BCC phase are oriented along the $\langle 100 \rangle$ or $\langle 111 \rangle$ direction (Figure 7c). Finally, the {110} planes in the BCC phase, where the areal number density of micelle is the highest and both of $\langle 100 \rangle$ and $\langle 111 \rangle$ vectors are present, are expected to form the hydrophobic layers of lamellar structure, resulting in the aggregation of SWNTs possibly with a preferred orientation parallel to their orientation in the BCC phase.

To support the epitaxial phase transitions in the F108-SWNT system which we used to identify the orientations of SWNTs in the ordered phases, the areal number densities of SWNTs at the hexagonal, FCC, and BCC phases are calculated using the measured lattice parameters. Here, the areal number density of SWNTs is defined as the number of SWNTs per unit area in the plane perpendicular to the orientation of SWNTs. In this calculation, it was assumed that all the hydrophobic cores of cylinders in the hexagonal phases are filled with SWNTs and all the spherulike micelles in the FCC and BCC phases are pierced through by SWNTs. If the F108-SWNT system makes epitaxial transitions as described above, the areal number density of SWNTs should change smoothly across the phase

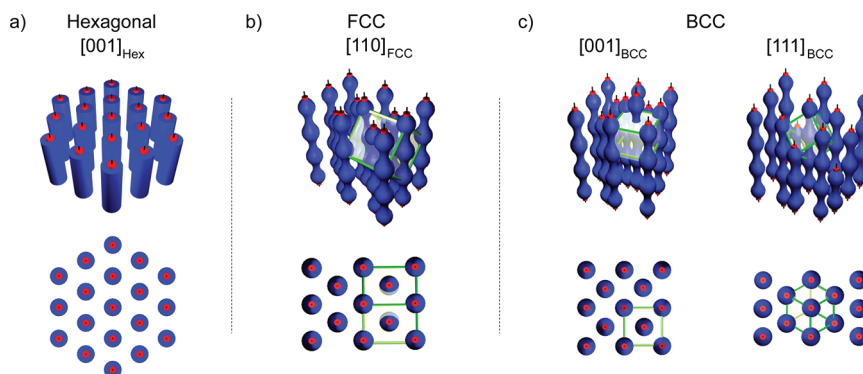


Figure 7. Schematics for the structures of F108-SWNT in water at different phases: (a) hexagonal, (b) FCC, and (c) BCC phases. The boxes in green color represent unit cells. The orientation of SWNTs in each phase is specified in each figure and the views from the directions of SWNTs are given on the bottom side of each figure. Here, for the BCC phase, [001] and [111] directions were used as representative directions for $\langle 100 \rangle$ and $\langle 111 \rangle$, respectively. Colors represent PPO (red), PEO (blue), and SWNT (black).

transitions. Also, since all the samples were prepared by evaporating 5 wt % samples, the areal number density of SWNTs should increase smoothly with concentration. The areal number densities of SWNTs, which were calculated for the SWNTs orientations identified based on the epitaxial transitions (the [001] direction in the hexagonal phase, the [110] direction in the FCC phase, and either the $\langle 100 \rangle$ or $\langle 111 \rangle$ direction in the BCC phase), change smoothly across the phase transitions (Figure 8). For all other orientations, the areal

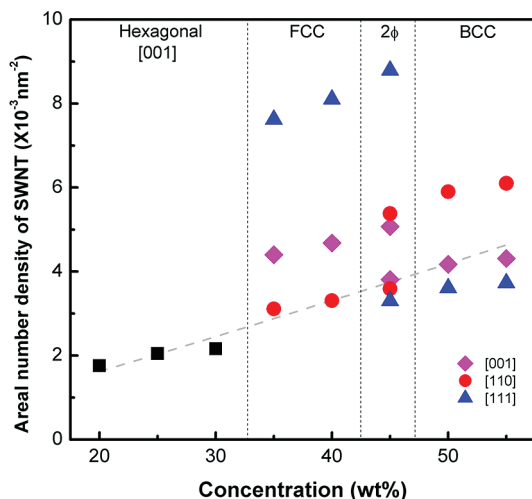


Figure 8. Areal number density of SWNTs at different concentrations calculated using the measured lattice parameters. The dotted line is a guide for eyes, showing that the areal number density of SWNTs changes smoothly across the phase transitions when the directions of SWNTs are [001] in hexagonal, [110] in FCC, and either $\langle 100 \rangle$ or $\langle 111 \rangle$ in BCC phases. Here, for the BCC phase, [001] and [111] directions were used as representative directions for $\langle 100 \rangle$ and $\langle 111 \rangle$, respectively.

number density of SWNTs clearly deviates from the smooth linear change across the phase transitions. This results support the epitaxial transitions in the F108-SWNT system from which the directions of SWNTs in the FCC and BCC phases are identified.

CONCLUSION

We report for the first time a new SWNT-induced lyotropic phase behavior of Pluronic F108 block copolymer system. As the concentration increases from 5 to 100 wt %, the F108-SWNT in water exhibit a sequence of phase transitions, isotropic–hexagonal–FCC–BCC–lamellar transitions, which is in clear contrast with that of the F108 only samples, isotropic–BCC–lamellar transitions. This clearly indicates that the hexagonal and the FCC phases are newly induced by the presence of long one-dimensional SWNTs. The SWNTs maintain their individuality or very small bundle state up to 80 wt % before the lamellar phase is formed. These suggest that, in the hexagonal phase, the SWNTs are located in the hydrophobic core of F108 cylinders. The epitaxial transitions between the hexagonal and the FCC phases and between the FCC and the BCC phases allowed us to identify the possible orientations of SWNTs in the FCC and the BCC phases: [110] in the FCC and either $\langle 100 \rangle$ or $\langle 111 \rangle$ in the BCC. In the lamellar phase, the SWNTs exist most likely in the hydrophobic layers, forming aggregations among them. This new SWNT-induced lyotropic phase behavior in a block copolymer system

may provide a new scalable route to fabricate SWNT superstructures with well-defined architecture and new functionalities. Furthermore, this may provide new possibilities for self-assembling other one-dimensional nanoparticles into highly ordered superstructures using the phase behavior of block copolymer systems.

ASSOCIATED CONTENT

Supporting Information

Measurements of micellization of F108 in water and a summary of scattering peak positions of F108 and F108-SWNT in water. This material is available free of charge via the Internet at <http://pubs.acs.org>.

AUTHOR INFORMATION

Corresponding Author

*E-mail: sungmin@kaist.ac.kr.

ACKNOWLEDGMENTS

This work was supported by the National Research Foundation grants funded by the Ministry of Education, Science and Technology of the Korean government (Nos. 2011-0000383 and 2011-0018680) and a grant from the Construction Technology Innovation Program funded by the Ministry of Land, Transportation and Maritime Affairs of the Korean government. The authors acknowledge the Pohang Accelerator Laboratory for providing access to the beamline 4C1 and the HANARO Center of the Korea Atomic Energy Research Institute for providing access to the 40 m SANS instrument used in this work.

REFERENCES

- Baughman, R. H.; Zakhidov, A. A.; de Heer, W. A. *Science* **2002**, 297, 787–792.
- Simmons, T. J.; Hashim, D.; Vajtai, R.; Ajayan, P. M. *J. Am. Chem. Soc.* **2007**, 129, 10088–10089.
- Shimoda, H.; Oh, S. J.; Geng, H. Z.; Walker, R. J.; Zhang, X. B.; McNeil, L. E.; Zhou, O. *Adv. Mater.* **2002**, 14, 899–901.
- Kamat, P. V.; Thomas, K. G.; Barazzouk, S.; Girishkumar, G.; Vinodgopal, K.; Meisel, D. *J. Am. Chem. Soc.* **2004**, 126, 10757–10762.
- Park, C.; Wilkinson, J.; Banda, S.; Ounaies, Z.; Wise, K. E.; Sauti, G.; Lillehei, P. T.; Harrison, J. S. *J. Polym. Sci., Part B: Polym. Phys.* **2006**, 44, 1751–1762.
- Tumpane, J.; Karousis, N.; Tagmatarchis, N.; Norden, B. *Angew. Chem., Int. Ed.* **2008**, 47, 5148–5152.
- Sano, N.; Naito, M.; Kikuchi, T. *Carbon* **2007**, 45, 78–82.
- Geblinger, N.; Ismach, A.; Joselevich, E. *Nature Nanotechnol.* **2008**, 3, 195–200.
- Xin, H.; Woolley, A. T. *Nano Lett.* **2004**, 4, 1481–1484.
- Huang, Y.; Duan, X.; Wei, Q.; Lieber, C. M. *Science* **2001**, 291, 630–633.
- Lay, M. D.; Novak, J. P.; Snow, E. S. *Nano Lett.* **2004**, 4, 603–606.
- Ruzette, A.-V.; Leibler, L. *Nature Mater.* **2005**, 4, 19–31.
- Bates, F. S.; Fredrickson, G. H. *Phys. Today* **1999**, 52, 32–38.
- Lin, Y.; Boker, A.; He, J.; Sill, K.; Xiang, H.; Abetz, C.; Li, X.; Wang, J.; Emrick, T.; Long, S.; Wang, Q.; Balazs, A.; Russell, T. P. *Nature* **2005**, 434, 55–59.
- Vaia, R. A.; Maguire, J. F. *Chem. Mater.* **2007**, 19, 2736–2751.
- Bockstaller, M. R.; Lapetnikov, Y.; Margel, S.; Thomas, E. L. *J. Am. Chem. Soc.* **2003**, 125, 5276–5277.
- Chiu, J. J.; Kim, B. J.; Kramer, E. J.; Pine, D. J. *J. Am. Chem. Soc.* **2005**, 127, 5036–5037.
- Yeh, S. W.; Wei, K. H.; Sun, Y. S.; Jeng, U. S.; Liang, K. S. *Macromolecules* **2005**, 38, 6559–6565.

- (19) Thompson, R. B.; Ginzburg, V. V.; Matsen, M. W.; Balazs, A. C. *Science* **2001**, *292*, 2469–2472.
- (20) Kang, H.; Detcheverry, F. A.; Mangham, A. N.; Stoykovich, M. P.; Daoulas, K. C.; Hamers, R. J.; Muller, M.; de Pablo, J. J.; Nealey, P. F. *Phys. Rev. Lett.* **2008**, *100*, 148303.
- (21) Sknepnek, R.; Anderson, J. A.; Lamm, M. H.; Schmalian, J.; Travesset, A. *ACS Nano* **2008**, *2*, 1259–1265.
- (22) Doe, C.; Jang, H.-S.; Kim, T.-H.; Kline, S. R.; Choi, S.-M. *J. Am. Chem. Soc.* **2009**, *131*, 16568–16572.
- (23) Doe, C.; Jang, H.-S.; Kline, S. R.; Choi, S.-M. *Macromolecules* **2010**, *43*, 5411–5416.
- (24) Yardimci, H.; Chung, B.; Harden, J. L.; Leheny, R. L. *J. Chem. Phys.* **2005**, 123.
- (25) Mohan, P. H.; Bandyopadhyay, R. *Phys. Rev. E* **2008**, *77*, 041803.
- (26) Wenseleers, W.; Vlasov, I. I.; Goovaerts, E.; Obratsova, E. D.; Lobach, A. S.; Bouwen, A. *Adv. Funct. Mater.* **2004**, *14*, 1105–1112.
- (27) Matarredona, O.; Rhoads, H.; Li, Z.; Harwell, J. H.; Balzano, L.; Resasco, D. E. *J. Phys. Chem. B* **2003**, *107*, 13357–13367.
- (28) Mortensen, K. *J. Phys.: Condens. Matter* **1996**, *8*, A103–A124.
- (29) Jain, N. J.; Aswal, V. K.; Goyal, P. S.; Bahadur, P. *J. Phys. Chem. B* **1998**, *102*, 8452–8458.
- (30) Kim, T.-H.; Doe, C.; Kline, S. R.; Choi, S.-M. *Adv. Mater.* **2007**, *19*, 929–933.
- (31) Kim, T.-H.; Doe, C.; Kline, S. R.; Choi, S.-M. *Macromolecules* **2008**, *41*, 3261–3266.
- (32) Islam, M. F.; Rojas, E.; Bergey, D. M.; Johnson, A. T.; Yodh, A. G. *Nano Lett.* **2003**, *3*, 269–273.
- (33) Florent, M.; Shvartzman-Cohen, R.; Goldfarb, D.; Yerushalmi-Rozen, R. *Langmuir* **2008**, *24*, 3773–3779.
- (34) Nativ-Roth, E.; Shvartzman-Cohen, R.; Bounioux, C.; Florent, M.; Zhang, D.; Szleifer, I.; Yerushalmi-Rozen, R. *Macromolecules* **2007**, *40*, 3676–3685.
- (35) Shvartzman-Cohen, R.; Florent, M.; Goldfarb, D.; Szleifer, I.; Yerushalmi-Rozen, R. *Langmuir* **2008**, *24*, 4625–4632.
- (36) Park, M. J.; Char, K.; Bang, J.; Lodge, T. P. *Langmuir* **2005**, *21*, 1403–1411.
- (37) Bang, J.; Lodge, T. P.; Wang, X.; Brinker, K. L.; Burghardt, W. R. *Phys. Rev. Lett.* **2002**, *89*, 215505.
- (38) Bang, J.; Lodge, T. P. *J. Phys. Chem. B* **2003**, *107*, 12071–12081.

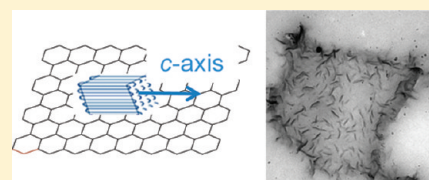
Reduced Graphene Oxide-Induced Polyethylene Crystallization in Solution and Nanocomposites

Shan Cheng,[†] Xi Chen,[†] Y. Grace Hsuan,[‡] and Christopher Y. Li^{*,†}

[†]Department of Materials Science and Engineering, Drexel University, Philadelphia, Pennsylvania 19104, United States

[‡]Department of Civil, Architectural and Environmental Engineering, Drexel University, Philadelphia, Pennsylvania 19104, United States

ABSTRACT: We report epitaxial crystallization of polyethylene (PE) on reduced graphene oxide (RGO) nanosheets via a controlled solution crystallization method. Polarized light microscopy, scanning electron microscopy, transmission electron microscopy, and atomic force microscopy were used to investigate morphology of RGO-induced PE crystals. The PE edge-on crystals formed from randomly distributed rodlike nuclei on the basal plane of RGO nanosheets and further grew into larger lamellae with an average dimension of a few hundreds of nanometers. Selected area electron diffraction (SAED) pattern revealed that the *c*-axis of polymer chain is parallel to the basal plane of the RGO nanosheets. PE/RGO nanocomposites (PGNs) with different RGO loadings were fabricated through solution crystallization/precipitation using the PE-decorated RGO hybrid as the precursor. Both nonisothermal and isothermal crystallization behaviors of PGNs were studied using differential scanning calorimetry (DSC). Crystallization kinetics of PGNs was substantially accelerated in the presence of 2D RGO nanosheets. Dramatic improvement of thermal stability was found for PE in the presence of a small amount of RGO nanosheets.



INTRODUCTION

Since the discovery in 2004 by Novoselov et al.,¹ graphene has drawn a great deal of interests in various applications due to its unique electrical,^{1–3} thermal,^{4,5} and mechanical^{6,7} properties. One of the most attractive applications of graphene is polymer nanocomposites, where graphene is often employed in different forms such as graphene oxide (GO) and chemically or thermally reduced graphene oxide (RGO).⁸ The pioneer work on polystyrene/graphene nanocomposites by Ruoff et al. showed extraordinary electrical properties with percolation occurring at 0.1 vol % of graphene loading.⁹ Extensive research on different polymer/graphene nanocomposites systems with enhanced properties has been conducted afterward; polymers that have been used include thermoplastics such as poly(vinyl alcohol),^{10–12} polyamide 6,¹³ poly(L-lactide),¹⁴ thermosets such as epoxy,^{15,16} elastomers such as polyurethanes,^{17,18} amorphous glassy polymers such as polystyrene,^{9,19} poly(methyl methacrylate),²⁰ and functional polymers such as polyaniline^{21,22} and poly(3-hexylthiophene).²³

Semicrystalline polymer is one of the most important matrices that used in polymer nanocomposites. Study of the crystallization behavior of semicrystalline polymer nanocomposites is of both scientific and practical importance because crystal structure and morphology are directly related to the properties of the material such as mechanical strength. Nanosized fillers such as 1D carbon nanotubes (CNTs)^{24–30} and 2D nanoclay^{31–34} are known to enhance the heterogeneous crystallization of the crystalline polymer matrix. Graphene, which exhibits a 2D geometry as nanoclay, and has sp² carbon atoms arranged in a hexagonal lattice as CNT, has also been considered to have great impact on the crystallization behavior

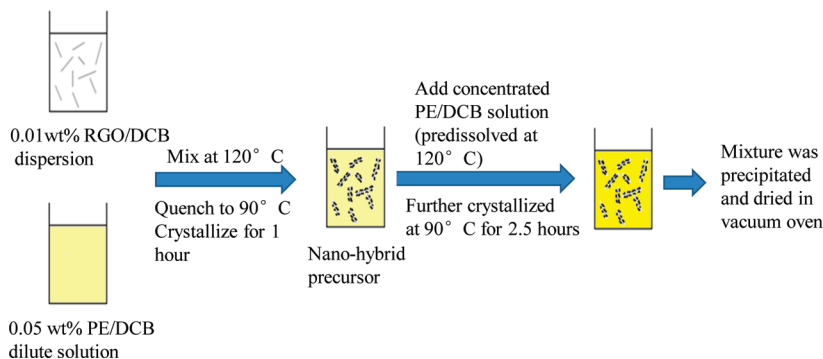
of polymer nanocomposites. Xu et al. compared the geometric effects of both CNT and graphene nanosheets (GNS) on the crystallization kinetics of poly(L-lactide) (PLLA). In general, the half-crystallization time ($t_{1/2}$) was significantly shortened for PLLA/CNT and PLLA/GNS nanocomposites compared with neat PLLA. However, the induction time was shortened when the CNT loading increased from 0.05 to 0.1 wt %, whereas the inverse trend is found in GNS system.¹⁴ Their further work on isotactic polypropylene (iPP)/GNS nanocomposites showed that the $t_{1/2}$ was reduced to more than 50% for 0.05 wt % iPP/GNS nanocomposites compared to neat iPP under quiescent condition. Crystallization kinetics become even faster under shear flow.³⁵ A few studies on poly(vinyl alcohol) (PVA)/RGO nanocomposites have shown an increased glass-transition temperature (T_g) due to the restriction of polymer chain motion by the H-bonding interaction between PVA chains and the filler.^{10–12} Both Yang et al.¹¹ and Salavagione¹² report a significant reduction of crystallinity from around 50% of neat PVA to almost amorphous phase at high graphene content, which compromises the mechanical properties of the nanocomposites. However, Liang et al.¹⁰ report no obvious change in crystallinity and melting temperature but a 76% increase in tensile strength and a 62% increase in Young's modulus for 0.7 wt % nanocomposites. They ascribe this improvement to the molecular level dispersion of graphene in the polymer matrix and the efficient load transfer due to strong interfacial interactions.

Received: September 22, 2011

Revised: November 18, 2011

Published: December 22, 2011

Scheme 1. Fabrication Process of PE/RGO Nanocomposites



Polyethylene (PE)/graphene nanocomposites have been studied very recently by Kim et al., and they found that linear low-density polyethylene samples modified with different polar functional groups such as $-\text{NH}_2$, $-\text{NHEt}$, $-\text{CN}$, and $-\text{NCO}$ are more compatible with graphene and have higher tensile modulus compared with the unmodified PE.³⁶ At the same time, molecular dynamics (MD) simulations of PE nanocomposites system with different nanofillers (buckyball, graphene, single wall carbon nanotubes) showed that graphene sheets have the strongest interaction with PE matrix among all the nano inclusions.³⁷

In this article, we report the study of crystallization behavior of a PE/RGO system. First, epitaxial crystallization of PE crystals on the basal plane of RGO sheets was observed from controlled solution crystallization. The morphology of PE lamellae was clearly revealed by transmission electron microscopy (TEM) and atomic force microscopy (AFM), and the orientation of the polymer chain was determined by selected area electron diffraction (SAED). PE/RGO nanocomposites (PGNs) with different RGO loadings were further prepared through a coprecipitation method. Crystallization behaviors from the melts of nanocomposites as well as the thermal stability were investigated and discussed. This study will shed light on better understanding of the influence of 2D graphene sheets on the crystallization behavior of semicrystalline polymer nanocomposites and on fabricating advanced hybrid materials with improved mechanical properties as well as other functionalities.

EXPERIMENTAL SECTION

Materials and Methods. Natural flake graphite with an average lateral size of $\sim 44 \mu\text{m}$ was kindly provided by Asbury Carbons, Inc. High-density PE pellets ($M_w = 125\,000$, $\rho = 0.95 \text{ g/cm}^3$, melt flow index = 0.3 g/10 min) were purchased from Scientific Polymer Products. Hydrochloric acid (HCl) (37%), sulfuric acid (H_2SO_4) (95–98%), potassium permanganate (KMnO_4) ($\geq 99.0\%$), sodium nitrate (NaNO_3) ($\geq 99.0\%$), hydrogen peroxide (H_2O_2) (35%), hydrazine hydrate ($\text{N}_2\text{H}_4\cdot\text{H}_2\text{O}$) (50–60%), 1,2-dichlorobenzene (DCB) (spectrophotometric grade, 99%), and N,N' -dimethylformamide (DMF) were purchased from Sigma-Aldrich and used as received.

RGO was prepared using a chemical oxidation–reduction process. First, graphite oxide was synthesized by the modified Hummers method.^{13,38} Graphite (1.0 g), NaNO_3 (0.5 g), and KMnO_4 (3.0 g) were loaded into a 50 mL flask and cooled in an ice bath, followed by slow addition of 25 mL of H_2SO_4 under stirring. The mixture was then heated to 35°C in an oil bath with continued stirring for 2 h. The product was poured into excess deionized (DI) water and cooled in an ice bath. H_2O_2 was slowly added until no gas evolution was observed. The product was then filtered, washed with 5% HCl solution, and DI water, and subsequently dried in a vacuum oven at room temperature

over 1 week. RGO nanosheets were then obtained by chemical reduction of GO using hydrazine hydrate as the reductant.^{39,40} GO (75 mg) was first dispersed in 80 mL of DMF/water (volume ratio 9:1) mixed solution via sonication, followed by reacting with 3 mL of hydrazine hydrate at 100°C for 24 h under stirring to yield a homogeneous suspension of RGO sheets.

Epitaxial crystallization of PE on RGO nanosheets was achieved via a controlled solution crystallization procedure.²⁶ RGO (1 mg) was dispersed in 10 mg of DCB by sonication for 1–2 h to form a uniform dispersion of single-layer or a few-layer RGO sheets, which was then mixed with 10 mg of 0.05 wt % predissolved PE/DCB solution at 120°C . The mixture was quenched to 90°C and crystallized for 1 h, followed by isothermal filtration at 90°C to remove excess free polymer. This resulted in a nanohybrid structure with RGO nanosheets decorated with PE single crystals on both surfaces that are ideal for morphological and structural study. PE/RGO nanocomposites (PGNs) can be further fabricated using this nanohybrid structure as the precursor. Instead of isothermal filtration, concentrated PE/DCB solutions with desired weight percentages were added into the precursor and further crystallized for 2.5 h at 90°C . The mixture was then coprecipitated in excessive methanol dropwise, filtered, washed with methanol to remove residual solvent, and dried in vacuum oven at room temperature for 1 week (Scheme 1).

Characterization. Differential scanning calorimetry (DSC) experiments were carried out using a Perkin-Elmer DSC 7. The samples with an average weight of 2–4 mg were heated from 30 to 200°C at a scanning rate of 10°C/min under a nitrogen atmosphere and were cooled and reheated using the same rate. 100% crystallized PE with an enthalpy of fusion of 293.6 J/g was used as a reference to calculate the crystallinity of the nanocomposites samples. Isothermal crystallization was conducted by quenching samples from 200°C to the preset crystallization temperatures at 400°C/min . Thermogravimetric analysis (TGA) tests were performed using a Perkin-Elmer TGA 7 under nitrogen atmosphere with 20 mL/min flow rate. Approximately 3–5 mg of sample was heated from 30 to 650°C at a heating rate of 10°C/min . Tapping mode AFM experiments were conducted using a Nanoscope IIIa (Digital Instruments/Veeco). Sample was spin-coated on a clean glass slide and dried in a vacuum oven before test. TEM characterization was conducted by a JEOL JEM2100 microscope with an accelerating voltage of 200 kV. Samples were spin-coated on carbon-coated copper grids and dried in a vacuum overnight. Scanning electron microscopy (SEM) experiments were performed using a Zeiss Supra 50VP scanning electron microscope. Samples were spin-coated onto a glass slide, vacuum-dried to remove solvent, and sputtered with platinum for 25 s before testing. Wide-angle X-ray diffraction (WAXD) experiments were conducted using a Siemens D500 diffractometer with a $\text{Cu K}\alpha$ wavelength of 1.54 \AA . Samples were scanned from 5° to 40° at a rate of $0.03^\circ/\text{s}$. Morphology of PGN was also investigated using a polarized light microscope (PLM) (Olympus BX51) equipped with a Mettler Toledo hot stage (MTFP82HT). Elemental analysis and Karl Fischer coulometric titration were conducted in Robertson Microlit Laboratories (Ledgewood, NJ).

RESULTS AND DISCUSSION

Characterization of RGO Nanosheets. The chemical oxidation–reduction reaction of graphite provides an easy and feasible way to obtain single- or few-layer graphene nanosheets at a large scale. Figure 1a shows a typical TEM micrograph of

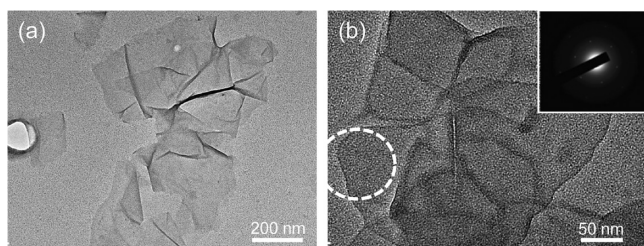


Figure 1. TEM micrographs of RGO sheets. (a) RGO deposited on carbon-coated Cu grid. (b) Higher magnification of one layer of RGO and the corresponding SAED pattern of the circled region.

RGO sheets made by sonication of reduced graphite oxide in DCB for 1 h. These sheets have an average lateral size of 0.2–1 μm and partially overlap with each other. Buckling of the sheets is evident, particularly in the overlapped regions. The SAED pattern from the dotted circle area (Figure 1b) shows a typical hexagonal symmetry, which is representative for graphene layers. Thermal stability tested by TGA (Figure 2) shows the

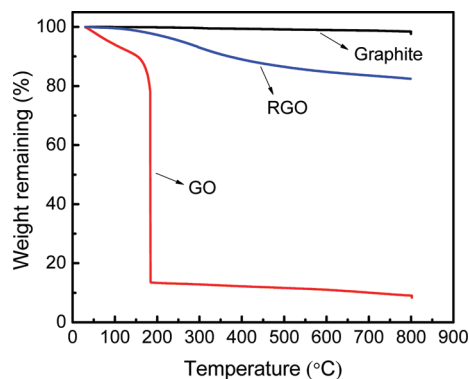


Figure 2. TGA of pristine graphite, GO, and RGO.

synthesized RGO retained 83% in weight after being heated to 800 $^{\circ}\text{C}$, while GO lost more than 80% weight near 200 $^{\circ}\text{C}$. These results are comparable with literature values.³⁹ Elemental analysis together with Karl Fischer coulometric titration shows that the C/O molar ratio increases from 1.3 for GO to around 6 for RGO, indicating the removal of the functional groups and recovery of sp^2 carbon bond of GO after chemical reduction.

RGO-Induced PE Crystallization in Dilute Solution. It has been demonstrated that graphite can induce polymer epitaxial crystallization. Balik et al. observed epitaxial growth of polyoxymethylene (POM) from 0.5% iodobenzene solution onto the basal plane of graphite substrate to form a rodlike structure well oriented in three directions.⁴¹ Early work of epitaxial growth of polyamide on graphite revealed that the polymer chain adopted an all-trans conformation and interacted with adjacent chains through hydrogen bonding.⁴² The first study of PE crystallization on graphite was conducted in the 1970s, when the epitaxial relation $(0001)\langle 2-1-10 \rangle_{\text{graphite}} // (110)\langle 001 \rangle_{\text{PE}}$ was reported.⁴³ More recent research by Takenaka et al. confirmed the crystallization of PE on highly

oriented pyrolytic graphite (HOPG) to be indeed epitaxial, and they further found that the monoclinic phase instead of orthorhombic phase was formed at the interface.⁴⁴

In the present work, controlled solution crystallization²⁶ has been used to study the crystallization of PE on RGO nanosheets. Epitaxial growth of PE crystals on RGO occurs over a broad range of temperatures. Figure 3a shows PE

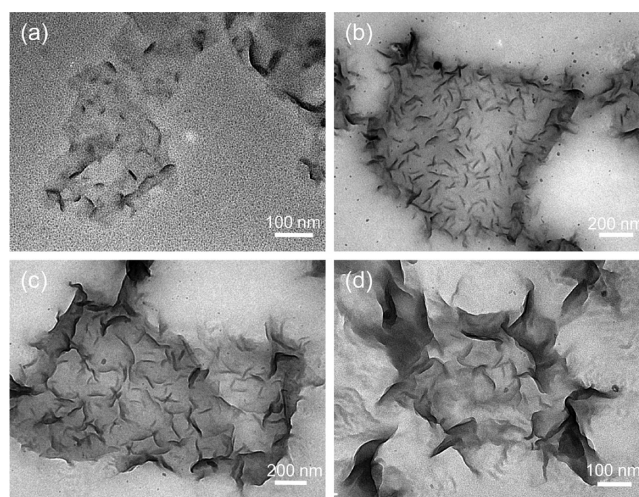


Figure 3. Bright-field TEM images of RGO nanosheets induced PE crystallization at different conditions. (a) PE was crystallized at 90 $^{\circ}\text{C}$ for 1 h with a PE/RGO concentration ratio of 1:2. (b–d) PE was crystallized at 100 $^{\circ}\text{C}$ overnight with PE/RGO ratio 1:1, 2:1, and 5:1, respectively.

crystallized at 90 $^{\circ}\text{C}$ for 1 h with a PE/RGO concentration ratio of 1:2. Discrete nuclei and small rodlike crystals can be observed on the surface of RGO nanosheets, which represents the early stage of PE crystallization. Figure 3b–d shows PE crystallization at 100 $^{\circ}\text{C}$ overnight with PE/RGO ratio of 1:1, 2:1, and 5:1, respectively. Small nuclei and crystals of PE continue grow into larger lamellae with an average size of 100 nm when increasing the crystallization time. And as the PE/RGO concentration ratio increases, these edge-on lamellae can further grow, and above a certain degree, the lamellae start to bend and orientation of the lamellae at the crystal/RGO interface becomes less clear (Figure 3c,d). Tapping mode AFM experiments were conducted on PE/RGO hybrids crystallized at 100 $^{\circ}\text{C}$ overnight with PE/RGO ratio of 1:1. RGO is covered with PE crystals (Figure 4a). The height of PE edge-on crystals ranges from several nanometers to a few tens of nanometers (Figure 4b, green arrows). The vertical distance between the RGO flake surface and the substrate (red arrows in Figure 4b) is around 13 nm, which suggests that PE crystals are grown on both sides of the RGO sheets.

The orientation of polymer chains is determined by SAED. Figure 5a shows PE crystal-decorated RGO while Figure 5b shows the corresponding SAED pattern with the correct orientation. In the diffraction pattern, the bright spots are diffractions from RGO, and the arcs with weaker intensity are diffractions from PE. Six symmetric PE (002) reflection arcs are superimposed with RGO (2–1–10) reflections, and the (310) PE diffraction can be found close to (10–10) RGO diffractions. These indicate the c -axis of polymer is parallel to the basal plane of RGO sheets, and the PE crystals are preferentially growing at three directions that are 120 $^{\circ}$ apart from each other. The overlapped PE and RGO diffraction patterns are consistent

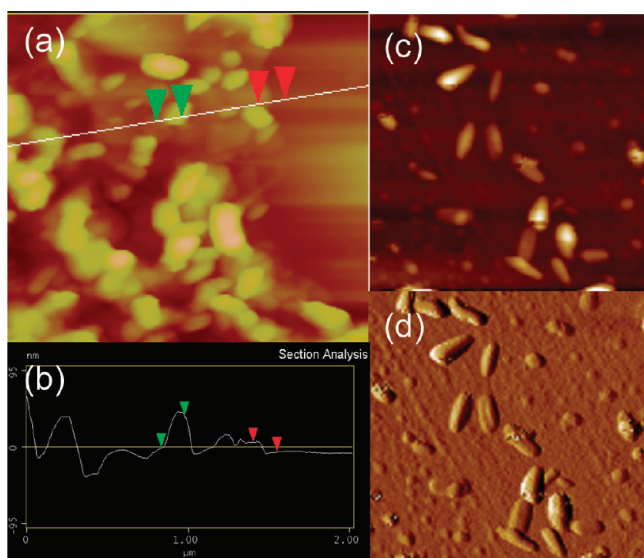


Figure 4. Tapping mode AFM images of PE crystals on RGO sheets. (a) is the height image of a 2 μm scan, and (b) is the corresponding height profile along the white line in (a). (c) and (d) are height and amplitude images, respectively, at a higher magnification (0.8 μm scan). Sample was taken from the same batch in Figure 3b.

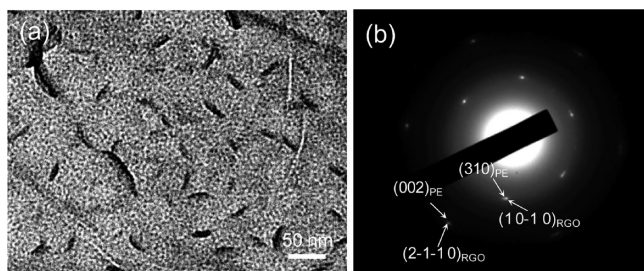


Figure 5. (a) High-magnification TEM image of PE single crystal epitaxially grown on RGO sheets; PE/RGO concentration ratio 1:1. (b) The corresponding SAED pattern.

with earlier work,^{43,44} suggesting an epitaxial relation of $(0001)\langle 2-1-10 \rangle_{\text{RGO}} // (110)\langle 001 \rangle_{\text{PE}}$.

As a control experiment, PE was also crystallized on the pristine graphite flakes in the same way as PE/RGO system. Figure 6a reveals that PE lamellae have densely grown on the

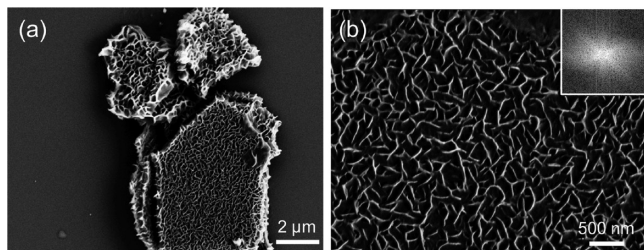


Figure 6. SEM image of (a) PE crystallization on graphite flake surface, graphite/PE concentration ratio 1:5, crystallized for 1 h at 90 $^{\circ}\text{C}$. (b) Higher magnification image of (a). Inset shows a fast Fourier transform of the image.

(001) surface of the pristine graphite with edge-on orientation, and the lamellae size is ~ 200 nm. The PE crystals appear to be more uniform with a larger crystal size on pristine graphite compared with RGO, which is probably due to the larger lateral

size (2–10 μm) and less defect sites of graphite flakes compared with RGO. Fast Fourier transform (FFT) shows stronger scattering in two directions while relatively weak scattering in the third direction, which may be because of local preferred orientation of PE lamellae along two directions.

Crystalline Morphology of PGNs. PGNs with seven different RGO loadings ranging from 0.04 to 4.4 vol % were prepared according to the method discussed in the Experimental Section. The volume fraction was converted from weight fraction using the density of 0.95 and 2.2 g/cm^3 for PE and RGO, respectively. WAXD was used to study the crystalline structure of these PGNs (Figure 7). Two peaks at

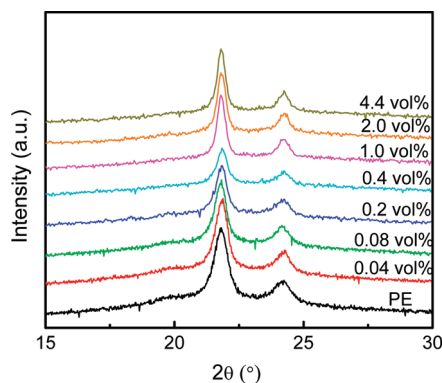


Figure 7. WAXD patterns of PE/RGO nanocomposites.

$2\theta = 21.78^{\circ}$ and 24.23° were observed for all PGNs, which correspond to the (110) and (200) Bragg reflections of PE, respectively. The intensity ratio of (110) and (200) peaks remains unchanged for all the PGNs, indicating that the addition of RGO nanosheets does not significantly modify the crystalline morphology of PE.

PGN films were melted at 160 $^{\circ}\text{C}$ and quenched to 115 $^{\circ}\text{C}$ crystallization temperature for polarized light microscopy (PLM) evaluation. Figure 8 shows that large agglomerates are absent in the PGN samples, indicating good dispersion of RGO sheets in the polymer matrix. In contrast with neat PE, which consists of large spherulites, all the PGN samples show a reduced crystalline size. This is common in most polymer nanocomposites systems since the presence of RGO network significantly restricts the 3D growth of polymer spherulites.⁴⁵

Crystallization Behavior of PGNs. The influence of 2D RGO sheets on the crystallization behavior of PGNs is of interest. Both nonisothermal and isothermal crystallization behaviors of PGNs were studied by DSC. Figure 9 shows the nonisothermal crystallization/melting behavior of PGNs with different RGO loadings. The first heating curve represents the thermal history of PGNs and is strongly influenced by the fabrication process, while the second heating curve reveals the crystallization of PGNs from melts. An intriguing observation is that two distinct melting peaks are observed on the first heating curves of 0.04 and 0.08 vol % PGNs, while PE only has a single melting peak (Figure 9a). The relative intensity of the peak with higher T_m increased as the RGO content increased, whereas the peak with lower T_m diminished and broadened with the increase of RGO content. The melting peak with higher T_m can be explained as a result of the heterogeneous nucleated, better formed PE crystals templated by the RGO sheets during solution crystallization. The increase of RGO concentration provides more sites for polymer to nucleate and

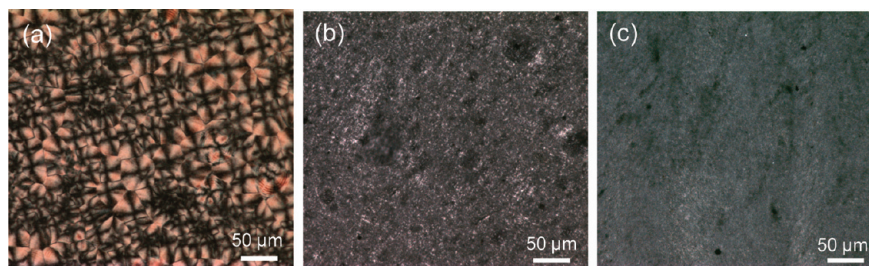


Figure 8. PLM micrographs of (a) neat PE and nanocomposites containing (b) 0.04 vol % and (c) 0.2 vol % of RGO.

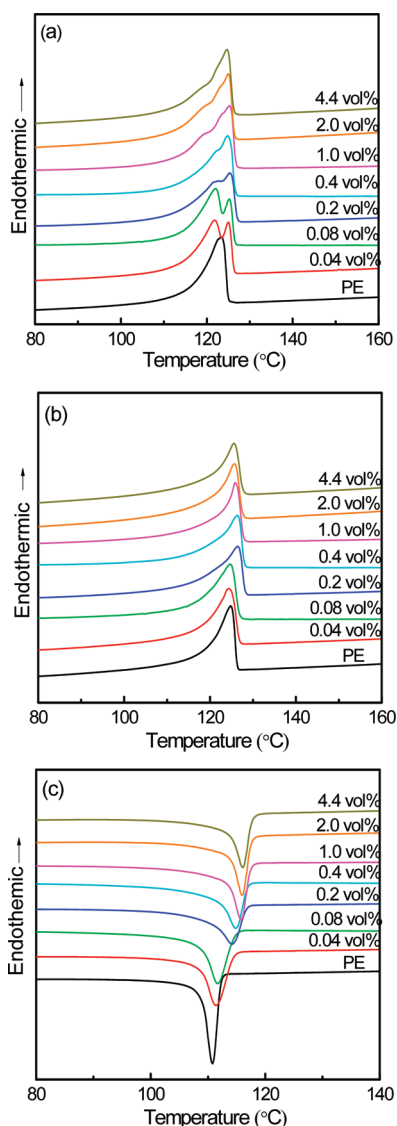


Figure 9. Nonisothermal DSC scans of PGNs at a constant scanning rate of 10 °C/min: (a) first heating, (b) second heating, and (c) cooling.

grow and thus contributes to higher intensity of the melting peak. During the second heating process in DSC, the crystallization became more uniform in melt, and all PGNs exhibited only one single melting peak (Figure 9b).

The melting temperature T_m determined by the second heating is summarized in Table 1. There is 1–1.5 °C variation of T_m for different samples, but in general the addition of RGO does not significantly alter the T_m of PGNs. The crystallization

Table 1. Crystallization Characteristics of PGNs with Different RGO Contents

RGO (vol %)	T_c (°C)	first heating		second heating	
		T_m (°C)	crystallinity (%)	T_m (°C)	crystallinity (%)
PE	110.8	123.3	53.7	124.9	58.9
0.04	111.5	121.9/125.0	57.8	124.4	58.5
0.08	111.6	122.0/125.3	59.4	124.7	59.5
0.2	114.3	125.4	56.7	126.4	57.2
0.4	114.8	124.8	60.2	126.4	58.6
1.0	115.8	125.2	70.1	125.9	60.7
2.0	116.0	125.0	70.4	125.7	60.4
4.4	116.1	124.7	72.4	125.5	61.6

temperature (T_c) which obtained from the exothermic peak on the DSC cooling curve (Figure 9c) increased from 110.8 °C of pure PE to 116.1 °C of 4.4 vol % PGN (Table 1). This dramatic increase of T_c was attributed to the heterogeneous nucleation induced by the 2D RGO nanosheets.

Crystallinity data determined from the heat of fusion under the area of melting peaks for PGNs are shown in Table 1. All the crystallinity calculation for PGNs was normalized by PE weight. According to the second heating data, the addition of RGO does not change much of the crystallinity (from 58.9% to 61.6%). However, most of the PGN crystallinity calculated from first heating data is higher than that from second heating, and this trend becomes more prominent at higher RGO loadings (above 0.4 vol %). This further confirms that PE crystals induced by RGO are better ordered so that as the RGO contents increase, the percentage of RGO-induced PE crystal increases, leading to a higher crystallinity. A similar phenomenon was observed for PE/CNT system using the nanohybrid shish kebab as template.²⁴

Isothermal crystallization of PGNs at low RGO loadings was also investigated by DSC. Figure 10a shows the results of PGNs up to 0.4 vol % that crystallized at 117 °C. $t_{1/2}$, which is defined as the time taken to complete 50% of the crystallization process, is plotted in Figure 10b. At higher RGO loading, the crystallization of PGNs becomes even faster than the isothermal peaks are no longer distinguishable under present crystallization conditions and therefore was not discussed here. A broad exothermic peak was observed for PE while the peak becomes much narrower for all the PGN samples. The $t_{1/2}$ decreases to ~27% of pure PE at 0.04 vol % of RGO loading and ~11% of pure PE at 0.4 vol % of RGO loading, indicating the efficient nucleation ability of RGO nanosheets. This acceleration effect of the nanofiller on the crystallization kinetics of polymers is common in most of the PE/CNTs,^{24,28} PE/nanoclay systems,³² and iPP/graphene systems.³⁵ However, contradictory results were observed in some nylon/MWNT²⁵ as well as PLLA/

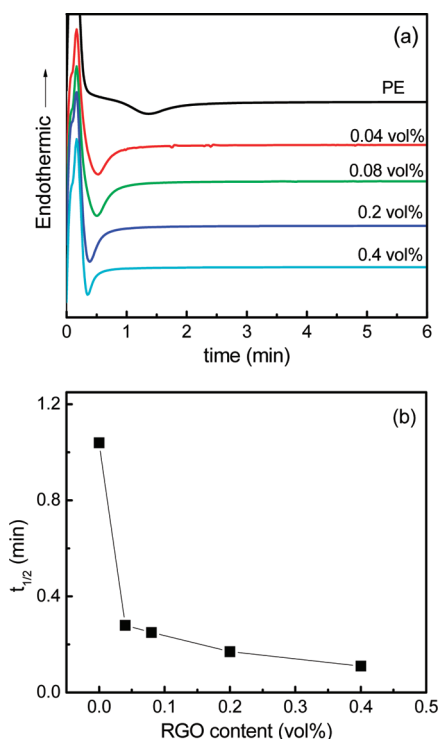


Figure 10. Isothermal crystallization behavior of PGNs. (a) DSC curves of PGNs crystallized at 117 °C. (b) Plot of $t_{1/2}$ against RGO contents.

graphene nanosheets system,¹⁴ in which the crystallization was initially accelerated and then hindered as further increasing the nanofiller loading. The latter results suggest complex effects of CNT or graphene on the crystallization of polymer: a small amount of nanofiller is sufficient to provide nucleation sites for polymer crystallization, whereas the nanoconfinement becomes the overwhelming factor when further increase the nanofiller concentration. In the present PE/RGO system, within the range of RGO loading studied, the crystallization rate of PE increases continuously with increasing the RGO content, which can be ascribed as the nucleation ability induced by the 2D sheets overcomes the nanoconfinement effects.

The Avrami equation⁴⁶ was employed to study the crystallization kinetics of PGNs as follows.

$$1 - X(t) = \exp(-Kt^n)$$

where $X(t)$ is the relative crystallinity calculated as the ratio of the heat of fusion at time t and the total heat of fusion of the whole crystallization process; n is the Avrami exponent and K is crystallization rate parameter. Twenty points were collected between 0% and 100% of the relative crystallinity $X(t)$. Figure 11a shows a representative Avrami plot of 0.2 vol % PGN. Values of n and K are determined using the initial linear part of the Avrami plot. The kinetics parameter K for PGNs at different isothermal crystallization temperatures are plotted in Figure 11b. Results of PGNs with high RGO loadings were not included in Figure 11 since the crystallization occurs so fast that no well-defined isothermal peaks can be obtained. It can be seen that for all PGNs in the temperature region studied K decreases with increasing crystallization temperature, which indicates the crystallization rate decreases at higher crystallization temperature. At the same crystallization temperature, K increases substantially with the increase of RGO contents and is

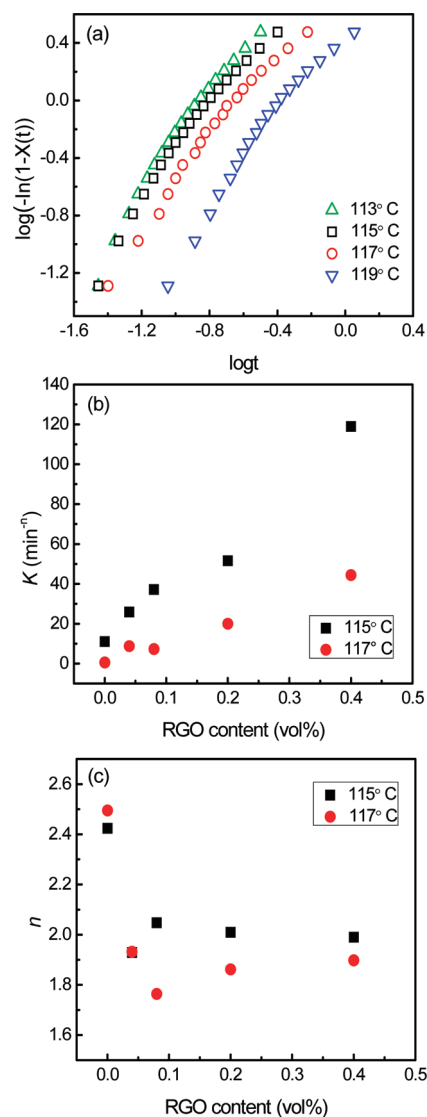


Figure 11. Avrami analysis of PGNs. (a) Avrami plot of isothermally crystallized 0.2 vol % PGN at different temperatures. (b) Effect of RGO contents on the crystallization rate parameter K at different isothermal crystallization temperatures. (c) Plot of Avrami exponent n as a function of RGO contents at different isothermal crystallization temperatures.

1–2 orders of magnitude higher at 0.4 vol % RGO loading compared with neat PE.

The Avrami exponent n typically indicates the growth dimension of the polymer. However, it should be noted that, in addition to growth dimensionality, the exponent also depends on many other factors. For example, 3D growth of athermal nucleation leads to an exponent of 3 while similar 3D growth of thermal nucleation has an exponent of 4. Other factors complicate the situation include volume change during crystallization, changing growth rate during crystal growth, changing of nucleation mechanism during crystallization due to exhaustion of the heterogeneous nuclei, etc.⁴⁷ Crystallization of PE melting may have an exponent of 1–4.⁴⁷ Therefore, caution should be taken when applying Avrami analysis in polymer crystallization. Nevertheless, general trends can normally be obtained when comparing the Avrami exponent of polymer nanocomposites with pristine polymers. For example, it has been reported that addition of 1 wt % CNT changes the n value

of PE ~ 2.5 to 1.6 .²⁸ A similar result is found for the PE/clay system, where the Avrami exponent is between 1 and 2 for nanocomposites samples.³² In the present case, the Avrami exponent decreases from 2.5 to 1.93 at 0.04 vol % of RGO loading and remains constant between 1.8 and 2 when further increasing the RGO content (Figure 11). Considering PE spherulite growth from a RGO surface, the growth dimensionality of individual spherulites may remain unchanged. However, such numerous spherulites would grow at or near the RGO surface, impinge with each other at a relatively early stage of crystallization, and form a quasi-2D layer of spherulites. Therefore, the observed Avrami exponent is decreased. Note that this decreased Avrami exponent should not suggest the change of growth behavior of individual crystals, but rather the dimensionality change of the overall growth (or solidification) process. This is consistent with PLM observation that the PE spherulite size is significantly reduced due to the impingement of adjacent spherulites at a relatively early stage of crystallization.

Thermal Stability of PGNs. The thermal stability of PGNs was evaluated by TGA under a nitrogen atmosphere (Figure

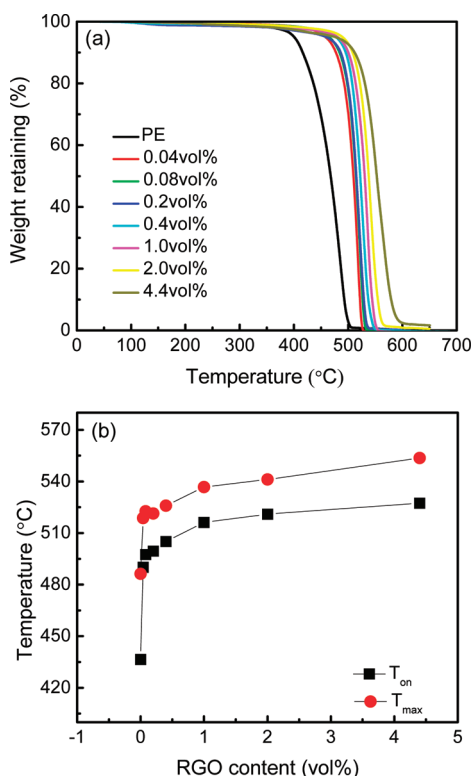


Figure 12. (a) TGA of PGNs. (b) Plot of degradation temperature vs RGO contents.

12). The temperature of the onset of degradation (T_{on}) and the temperature of maximum weight loss (T_{max}) for neat PE were recorded as 436.46 and 486.35 °C, respectively. Inclusion of as low as 0.04 vol % RGO sheets led to a 53.66 °C increase of T_{on} and a 32.38 °C increase of T_{max} . Further increasing RGO content gradually shifted the degradation temperature of the polymer to higher temperature. A 90.97 °C increase of T_{on} and a 67.33 °C increase of T_{max} were observed for 4.4 vol % PGN. This substantial enhancement of thermal stability can be ascribed to the high efficiency of the RGO to capture free radicals generated by polymer chain scission during the

degradation process at high temperature. The result is comparable with the PE/CNT system, where 65–115 °C increase of the degradation temperature was found at low CNT loading.²⁴ The observation suggests that although there are numerous defect sites on RGO, it is efficient in catching free radicals and improve the thermal stability of PE.

CONCLUSIONS

Solution crystallization was used to clearly reveal RGO-induced PE epitaxial crystallization. Small rodlike PE nuclei are randomly distributed on the basal plane of the RGO nanosheets at the initial crystallization stage and further grow into larger lamellae with average length of hundreds of nanometers. SAED shows that the polymer chain is parallel to the basal plane of the RGO sheets with an epitaxial relation $(0001)\langle 2-1-10 \rangle_{RGO} // (110)\langle 001 \rangle_{PE}$. A series of PGNs were fabricated via the solution crystallization/precipitation method. RGO was found to be uniformly dispersed in PE matrix, and the crystallization behavior of PE was significantly altered by addition of RGO. Crystallization shifts to higher temperature during cooling and the crystallization kinetics are much faster for all PGNs compared with neat PE, indicating the superb capability of RGO nanosheets to induce heterogeneous crystallization of PE. Decrease of Avrami exponent n was observed for PGNs, which was attributed to the RGO templating effect and relatively early impingement of PE crystals in the nanocomposite systems. Thermal stability of PGNs is also dramatically enhanced compared with neat PE due to the efficient charge transfer of the free radical generated by polymer chain scission to RGO.

AUTHOR INFORMATION

Corresponding Author

*E-mail: chrisli@drexel.edu; Tel 215-895-2083; Fax 215-895-6760.

ACKNOWLEDGMENTS

This work was supported by the National Science Foundation Grants DMR-0804838 (C.Y.L.), CMMI-1100166 (C.Y.L.), and CMMI-0825195 (Y.G.H.).

REFERENCES

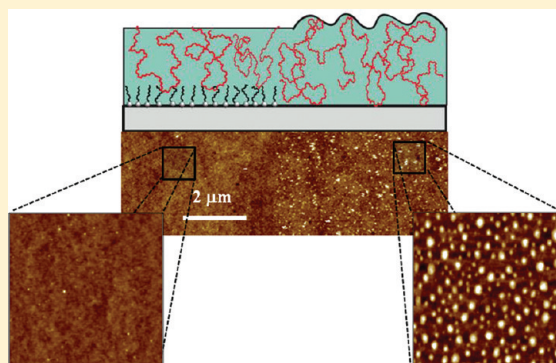
- (1) Novoselov, K. S.; Geim, A. K.; Morozov, S. V.; Jiang, D.; Zhang, Y.; Dubonos, S. V.; Grigorieva, I. V.; Firsov, A. A. *Science* **2004**, 306, 666–669.
- (2) Du, X.; Skachko, I.; Barker, A.; Andrei, E. Y. *Nature Nanotechnol.* **2008**, 3, 491–495.
- (3) Peres, N. M. R.; Guinea, F.; Neto, A. H. C. *Phys. Rev. B* **2006**, 73, 125411.
- (4) Balandin, A. A.; Ghosh, S.; Bao, W. Z.; Calizo, I.; Teweldebrhan, D.; Miao, F.; Lau, C. N. *Nano Lett.* **2008**, 8, 902–907.
- (5) Ghosh, S.; Calizo, I.; Teweldebrhan, D.; Pokatilov, E. P.; Nika, D. L.; Balandin, A. A.; Bao, W.; Miao, F.; Lau, C. N. *Appl. Phys. Lett.* **2008**, 92, 151911.
- (6) Lee, C.; Wei, X. D.; Kysar, J. W.; Hone, J. *Science* **2008**, 321, 385–388.
- (7) Dikin, D. A.; Stankovich, S.; Zimney, E. J.; Piner, R. D.; Dommett, G. H. B.; Evmenenko, G.; Nguyen, S. T.; Ruoff, R. S. *Nature* **2007**, 448, 457–460.
- (8) Kim, H.; Abdala, A. A.; Macosko, C. W. *Macromolecules* **2010**, 43, 6515–6530.
- (9) Stankovich, S.; Dikin, D. A.; Dommett, G. H. B.; Kohlhaas, K. M.; Zimney, E. J.; Stach, E. A.; Piner, R. D.; Nguyen, S. T.; Ruoff, R. S. *Nature* **2006**, 442, 282–286.

- (10) Liang, J.; Huang, Y.; Zhang, L.; Wang, Y.; Ma, Y.; Guo, T.; Chen, Y. *Adv. Funct. Mater.* **2009**, *19*, 2297–2302.
- (11) Yang, X.; Li, L.; Shang, S.; Tao, X.-m. *Polymer* **2010**, *51*, 3431–3435.
- (12) Salavagione, H. J.; Martinez, G.; Gomez, M. A. *J. Mater. Chem.* **2009**, *19*, 5027–5032.
- (13) Steurer, P.; Wissert, R.; Thomann, R.; Mulhaupt, R. *Macromol. Rapid Commun.* **2009**, *30*, 316–327.
- (14) Xu, J. Z.; Chen, T.; Yang, C. L.; Li, Z. M.; Mao, Y. M.; Zeng, B. Q.; Hsiao, B. S. *Macromolecules* **2010**, *43*, 5000–5008.
- (15) Rafiee, M. A.; Rafiee, J.; Wang, Z.; Song, H. H.; Yu, Z. Z.; Koratkar, N. *ACS Nano* **2009**, *3*, 3884–3890.
- (16) Wang, S. R.; Tambraparni, M.; Qiu, J. J.; Tipton, J.; Dean, D. *Macromolecules* **2009**, *42*, 5251–5255.
- (17) Kim, H.; Miura, Y.; Macosko, C. W. *Chem. Mater.* **2010**, *22*, 3441–3450.
- (18) Khan, U.; May, P.; O'Neill, A.; Coleman, J. N. *Carbon* **2010**, *48*, 4035–4041.
- (19) Vickery, J. L.; Patil, A. J.; Mann, S. *Adv. Mater.* **2009**, *21*, 2180–2184.
- (20) Ramanathan, T.; Abdala, A. A.; Stankovich, S.; Dikin, D. A.; Herrera-Alonso, M.; Piner, R. D.; Adamson, D. H.; Schniepp, H. C.; Chen, X.; Ruoff, R. S.; Nguyen, S. T.; Aksay, I. A.; Prud'homme, R. K.; Brinson, L. C. *Nature Nanotechnol.* **2008**, *3*, 327–331.
- (21) Yan, J.; Wei, T.; Shao, B.; Fan, Z. J.; Qian, W. Z.; Zhang, M. L.; Wei, F. *Carbon* **2010**, *48*, 487–493.
- (22) Wang, D. W.; Li, F.; Zhao, J. P.; Ren, W. C.; Chen, Z. G.; Tan, J.; Wu, Z. S.; Gentle, I.; Lu, G. Q.; Cheng, H. M. *ACS Nano* **2009**, *3*, 1745–1752.
- (23) Li, G. L.; Liu, G.; Li, M.; Wan, D.; Neoh, K. G.; Kang, E. T. *J. Phys. Chem. C* **2010**, *114*, 12742–12748.
- (24) Kodjie, S. L.; Li, L. Y.; Li, B.; Cai, W. W.; Li, C. Y.; Keating, M. J. *Macromol. Sci., Phys.* **2006**, *45*, 231–245.
- (25) Li, L. Y.; Li, C. Y.; Ni, C. Y.; Rong, L. X.; Hsiao, B. *Polymer* **2007**, *48*, 3452–3460.
- (26) Li, C. Y.; Li, L. Y.; Cai, W. W.; Kodjie, S. L.; Tenneti, K. K. *Adv. Mater.* **2005**, *17*, 1198–1202.
- (27) Czerw, R.; Guo, Z. X.; Ajayan, P. M.; Sun, Y. P.; Carroll, D. L. *Nano Lett.* **2001**, *1*, 423–427.
- (28) Haggenueller, R.; Fischer, J. E.; Winey, K. I. *Macromolecules* **2006**, *39*, 2964–2971.
- (29) Cadek, M.; Coleman, J. N.; Barron, V.; Hedicke, K.; Blau, W. J. *Appl. Phys. Lett.* **2002**, *81*, 5123–5125.
- (30) Liu, T. X.; Phang, I. Y.; Shen, L.; Chow, S. Y.; Zhang, W. D. *Macromolecules* **2004**, *37*, 7214–7222.
- (31) Fornes, T. D.; Paul, D. R. *Polymer* **2003**, *44*, 3945–3961.
- (32) Gopakumar, T. G.; Lee, J. A.; Kontopoulou, M.; Parent, J. S. *Polymer* **2002**, *43*, 5483–5491.
- (33) Ke, Y. C.; Long, C. F.; Qi, Z. N. *J. Appl. Polym. Sci.* **1999**, *71*, 1139–1146.
- (34) Priya, L.; Jog, J. P. *J. Polym. Sci., Part B: Polym. Phys.* **2002**, *40*, 1682–1689.
- (35) Xu, J. Z.; Chen, C.; Wang, Y.; Tang, H.; Li, Z. M.; Hsiao, B. S. *Macromolecules* **2011**, *44*, 2808–2818.
- (36) Kim, H.; Kobayashi, S.; AbdurRahim, M. A.; Zhang, M. L. J.; Khushainova, A.; Hillmyer, M. A.; Abdala, A. A.; Macosko, C. W. *Polymer* **2011**, *52*, 1837–1846.
- (37) Li, Y. *Polymer* **2011**, *52*, 2310–2318.
- (38) Hummers, W. S.; Offerman, R. E. *J. Am. Chem. Soc.* **1958**, *80*, 1339.
- (39) Stankovich, S.; Dikin, D. A.; Piner, R. D.; Kohlhaas, K. A.; Kleinhammes, A.; Jia, Y.; Wu, Y.; Nguyen, S. T.; Ruoff, R. S. *Carbon* **2007**, *45*, 1558–1565.
- (40) Park, S.; An, J. H.; Jung, I. W.; Piner, R. D.; An, S. J.; Li, X. S.; Velamakanni, A.; Ruoff, R. S. *Nano Lett.* **2009**, *9*, 1593–1597.
- (41) Balik, C. M.; Tripathy, S. K.; Hopfinger, A. J. *J. Polym. Sci., Part B: Polym. Phys. Ed.* **1982**, *20*, 2003–2016.
- (42) Sano, M.; Sasaki, D. Y.; Kunitake, T. *Science* **1992**, *258*, 441–443.
- (43) Tuinstra, F.; Baer, E. *J. Polym. Sci., Part B: Polym. Lett.* **1970**, *8*, 861–865.
- (44) Takenaka, Y.; Miyaji, H.; Hoshino, A.; Tracz, A.; Jeszka, J. K.; Kucinska, I. *Macromolecules* **2004**, *37*, 9667–9669.
- (45) Dillon, D. R.; Tenneti, K. K.; Li, C. Y.; Ko, F. K.; Sics, I.; Hsiao, B. S. *Polymer* **2006**, *47*, 1678–1688.
- (46) Avrami, M. *J. Chem. Phys.* **1939**, *7*, 1103–1112.
- (47) Wunderlich, B. *Macromolecular Physics*; Academic Press: New York, 1976; Vol. II.

Substrate Remote Control of Polymer Film Surface Mobility

Igor Siretanu,^{†,‡} Jean Paul Chapel,[†] and Carlos Drummond^{*,†}[†]Centre de Recherche Paul Pascal, UPR8641, CNRS, Université de Bordeaux, Avenue Schweitzer, 33600 Pessac Cedex, France[‡]Laboratoire de Chimie des Polymères Organiques, CNRS, Université Bordeaux 1, 33607 Pessac Cedex, France

ABSTRACT: Polymer segments at the surface of glassy polymer films remain mobile at temperatures below the glass transition temperature, T_g . This mobility, which is usually attributed to the access to a larger free volume by segments at the surface, opens pathways for polymer surface structuration by the effect of a destabilizing force. By studying the destabilization of polystyrene films under the influence of ions dissolved in degassed water at temperatures well below T_g , we have observed that this mobility can be strongly affected by a substrate buried down distances of the order of the chain size below the film surface. This effect is particularly important if there is a strong interaction between the polymer and the substrate or in the presence of pinning points for the polymer chains. These results can be qualitatively interpreted in terms of the sliding model for T_g reduction in thin polymer films. This effect allows remotely controlling the structuration of the polymer surface.



■ INTRODUCTION

A large number of studies have addressed the properties of polymer thin films and their relationship to their bulk counterparts. In particular, the glass transition of polymer thin films has been extensively investigated. Since the seminal paper by Keddie et al.¹ showing the influence of film thickness on the glass transition temperature T_g was published, many studies dealing with chain mobility under confinement have been reported.² An aspect investigated in great detail has been the influence of the boundary conditions on the glass transition. A majority of the experimental results show that attractive walls tend to reduce the mobility of the polymer and increase the glass transition temperature, T_g . On the contrary, less attractive or free boundaries enhance the mobility and hence reduce T_g . In fact, as suggested by de Gennes³ and later experimentally demonstrated by Ellison and Torkelson⁴ by studying the fluorescence of selectively marked PS layers at different depths, thin films' behavior can be better understood in terms of a depth-dependent distribution of the actual polymer mobility (or T_g). The "globally" measured T_g value will then depend on the way the average is performed through the entire specimen. Other studies support the idea of a heterogeneous dynamic of thin glassy polymer films.^{5,6} In particular, the existence of a mobile layer several nanometers thick on top of glass-forming polymer films is gaining general acceptance in the polymer physics community:⁷ polymer segments near the surface are obviously less constrained than segments inside the bulk of the film. It is reasonable to expect that this excess mobility will persist if the film is in contact with a low-viscosity nonswelling media. As an example of this mobile surface layer, we have recently shown that when polystyrene films are put in contact with degassed water solutions of acidic or basic pH for a few minutes, a long-lasting nanostructuration spontaneously forms

on the solid surface.⁸ This only happens in the presence of certain ions if dissolved gases are removed from the aqueous phase; otherwise, no modification of the polymer film is observed. Atomic force microscopy micrographs illustrating this novel phenomenon are presented in Figure 1. The typical size of the self-assembled patterns depends on pH, temperature, and the amount of dissolved gas in the aqueous phase. This patterning process is a consequence of an electrohydrodynamic instability at the nanoscale⁹ due to the adsorption of the water-ions at the polymer-water interface. Regardless of its unexpected origin, this process clearly reveals the mobility of the upmost surface layer of otherwise glassy polymer films. In this work we report on how this phenomenon is modified by the molecular weight of the polymer and the polymer-substrate interaction.

■ MATERIALS AND METHODS

Polystyrene (PS) of four different molecular weights (7, 160, 250, and 500 kDa) were investigated. PS of 500 kg/mol (T_g 103 °C) and 59 kg/mol (T_g 99 °C) were obtained from Sigma-Aldrich. PS of 250 kg/mol (T_g 103 °C) was obtained from ACROS Organics. PS of 7 kg/mol (T_g 90 °C), synthesized by ATRP, was a gracious gift from Dr. Antoine Bousquet.

Film Preparation. We prepared films of PS on four different substrates by spin-coating. First, hydrophilic surfaces of freshly cleaved molecularly smooth mica and thoroughly cleaned oxide-coated silicon wafers were used. A second set of films were prepared on surfaces of the same materials which were modified with an adhesion primer layer in order to modify the interaction of the polymer layer with the substrate. Mica surfaces were coated with a monolayer of 10 nm

Received: September 28, 2011

Revised: December 5, 2011

Published: December 22, 2011



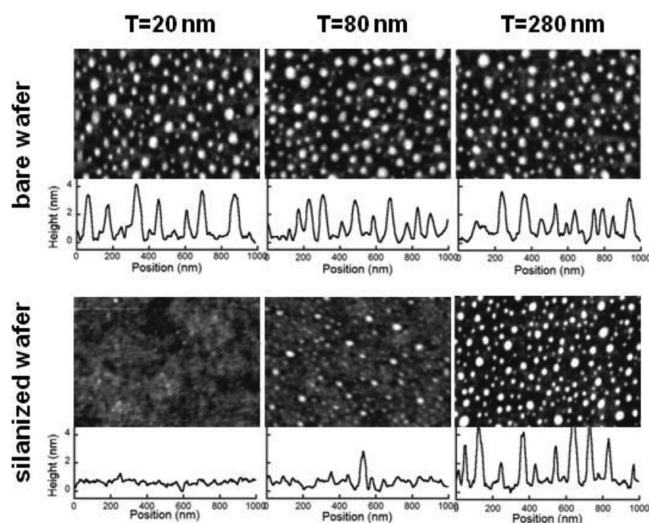


Figure 1. Height AFM micrographs of films of 250 kDa polystyrene films measured in tapping mode in air. The films of indicated thickness were spun-coated on bare and silanized silicon wafers (fractional OTS surface coverage 0.7) and then exposed to a degassed solution of nitric acid in double distilled water at pH 1.5 at room temperature. A typical height profile for each image is presented. The presence of asperities of regular nanometric size is clearly observed on some of the films exposed to the degassed solution for 5 min. On the contrary, no modification was detected when identical films were exposed to the same solution under identical conditions (or much longer times) before removing the dissolved gases. All the films were featureless before treatment.

diameter ceria nanoparticles by dip-coating. A close-packed monolayer of ceria nanoparticles get adsorbed on mica by this procedure, which strongly increases the adhesion between the subsequently deposited polymer layer and the substrate.¹⁰ SiO₂-coated silicon wafers were hydrophobized at different degrees by the Langmuir–Blodgett coating technique¹¹ with octadecyltrichlorosilane (OTS) by varying the imposed surface pressure while film transfer. It has been reported that slipping of PS is modified in silane-modified silicon wafers and depends on silane grafting density.¹² After spin-coating, the films were annealed at 95 °C for 12 h, unless indicated otherwise. They were subsequently exposed to degassed double distilled water at pH 1.5 as described below.

Film Characterization. The thickness of the films was determined by ellipsometry (Nanofilm); roughness and morphology were assessed by atomic force microscopy in tapping mode in air (multimode and Icon, Veeco) before and after treatment with degassed water. Extremely smooth films, with rms roughness smaller than 0.5 nm were typically obtained after spin-coating. After degassed water treatment the generated structures were characterized by the average size and height of the observed self-assembled polymer bumps. The films were also characterized by water contact angle (IDC Concept). The contact angle of water on the films was around 90° before and after structuration, with very small hysteresis.

Water Degassing and Film Treatment. Millipore water with a conductivity of 18 MΩ cm⁻¹ was used for preparing the acid solutions. The pH of the aqueous phase was adjusted to 1.5 by adding small amounts of nitric acid (Aldrich) as necessary. Carefully cleaned Teflon bar stirrers were introduced in the solutions to be degassed to induce the nucleation of gas bubbles. The solutions were subjected to agitation under pressure of 0.2 mbar for 2 h. The appearance of macroscopic bubbles in the aqueous phase was observed only during the first 30 min of degassing. After degassing was finished, the air pressure on the flask was gently increased back to atmospheric pressure. The degassed solutions were put right away in contact with the polymer surfaces for few minutes after stopping the pumping, unless otherwise indicated. The PS films were then dried with a gentle

flow of nitrogen gas. In some rare cases water penetrated between the polymer film and the substrate. These tests were not further considered.

RESULTS AND DISCUSSION

As mentioned before, the exposure of the PS films to degassed acid water during few minutes provokes the formation of bumps several nanometers tall and several tens of nanometers wide. As can be observed in Figures 1 and 2, the self-assembled

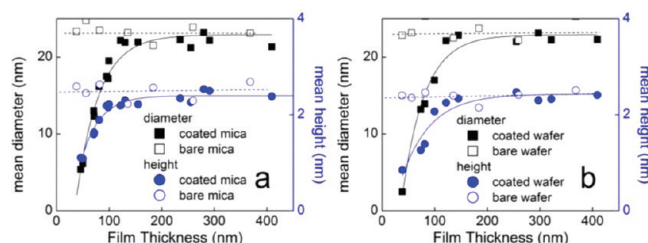


Figure 2. Average height (circles) and diameter (squares) of self-assembled bumps observed on the surface of thin polymer films of PS 250 kDa of different thickness treated with degassed water at pH 1.5. The films were deposited on (a) bare and ceria-coated mica and (b) silicon wafers and silanized silicon wafers (fractional OTS surface coverage 0.7). Closed symbols: coated substrates; open symbols: bare substrates.

surface pattern depends on the type of substrate used. The typical radii and heights of the observed bumps are similar in bare mica or oxidized Si wafers and are independent of polymer film thickness down to 10 nm. On the contrary, the characteristic size of the bumps is substantially reduced—or they are not present—for films spun on ceria-coated mica or hydrophobized wafers for polymer films thinner than a certain thickness. The same results were observed after longer times (few hours) of exposure of the polymer films to degassed water (kept out of contact with air). Although we cannot discard the possibility of a very slow evolution of the surface which would lead to surface structuration at longer times, this would not challenge the fact that there is a dramatic deceleration of the structuration process due to the presence of the primer layers.

As mentioned above, the idea that polymer segments close to the surface are more mobile than bulk segments is now broadly accepted, although the properties of the mobile layer (thickness, variation with temperature, and molecular weight) are still debated. On the contrary, it is not obvious why this excess mobility should be impaired by the influence of the underlying substrate buried down several tens of nanometers below the polymer film surface. It is noteworthy (cf. Figure 2) that above certain film thickness the size of the formed bumps seems to achieve a terminal value which is independent of PS molecular weight. On the contrary, the threshold thickness for surface structuration is determined by polymer size, as can be observed in Figure 3a,b. The larger the molecular weight, the longer the range of the effect of the substrate on the structuration of the polymer layer. In all cases the observed effect has a range too large—up to 100 nm for the largest polymer investigated—to be interpreted in terms of the dispersion interaction between the solid substrate and water through the polymer film. The reason for the long-range effect of the substrate on the polymer structuration must be related to the connectivity of the polymer chains. It is remarkable that by normalizing the film thickness by the mean-square end-to-end

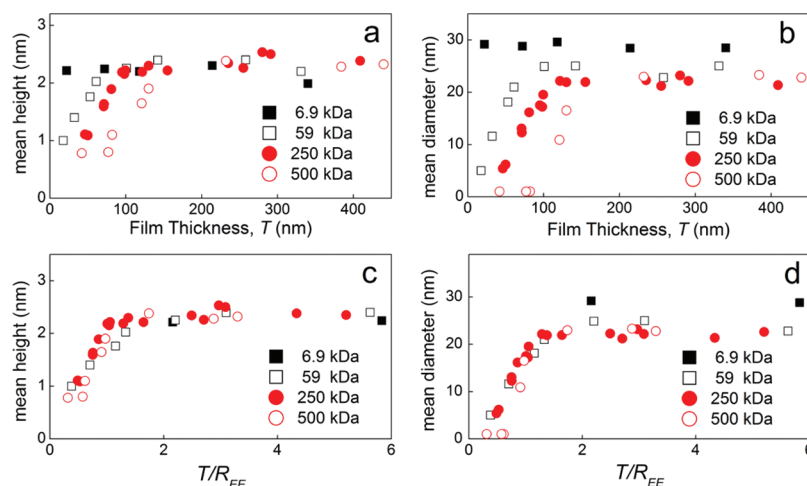


Figure 3. Effect of polymer molecular weight on the self-assembled structure. Average height (a) and diameter (b) of self-assembled bumps of thin polymer films deposited on silanized silicon wafers (fractional surface coverage 0.7) treated with degassed water at pH 1.5. The results for the different polymer sizes collapse on a single curve if the film thickness is normalized by the polymer end-to-end distance, R_{EE} (c, d).

distance of the polymer, R_{EE} , the results for the different molecular weights tested collapse on a single master curve, as can be observed in Figure 3c,d. This collapse indicates that a mechanism related to the polymer size is responsible for the observed drop of polymer surface mobility.

By exploring different annealing conditions, we observed that the effect of the two primer layers investigated is not completely equivalent, but rather process dependent. While ceria-coated mica suppressed the pattern formation in thin films regardless of the annealing process, silanized silicon wafers were effective structuration inhibitors only after annealing of the films. Otherwise, the modification of the supported film resembled the one observed for the case of bare silicon wafers. In addition, we observed that varying the grafting density of OTS on the Si wafer has a strong influence on the inhibitor effect of the primer silane layer, as can be observed in Figure 4.

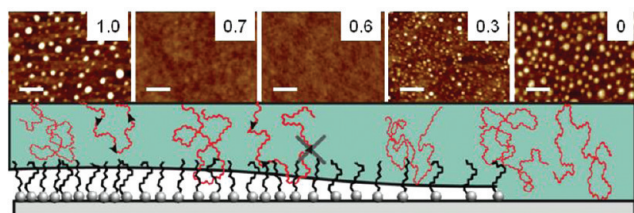


Figure 4. Height tapping mode AFM micrographs measured in air of 50 nm thick 250 kDa polystyrene films after exposure to a degassed solution of nitric acid in double distilled water for 5 min. pH 1.5; T 25 °C. The films were deposited on silanized silicon wafers with OTS surface coverage indicated on each micrograph. Scale bars correspond to 200 nm. The propagation of a kink (indicated by the black arrows) is slowed by the pinning effect of the OTS layer at intermediated grafting densities, stopping the structuration of the polymer surface.

Very high or very low silane grafting densities produced no effect on the structuration: in these cases the self-assembled structures were observed on polymer films down to 10 nm thick. On the contrary, intermediate grafting densities effectively diminished the surface structuration of thin polymer films, provided that the film has been annealed before treatment with degassed acid water.

The more puzzling question emerging from the results reported in this work is how the effect of the solid substrate can extend over tens of nanometers up to the polymer surface. We can attempt to rationalize our results at a qualitative level with the help of the sliding mechanism sketched by de Gennes,³ formulated to explain the reduction of T_g in free-standing or supported polymer thin films. This model proposes that the reduced density at the polymer surface confers a greater mobility to the polymer segments: monomers at the polymer surface are less sterically constrained to move. This is probably also valid for the case of contact of the polymer film with a low-viscosity poor solvent, the scenario studied in this work. de Gennes proposed that this enhanced free volume then propagates at a certain speed through the polymer chain to depths of the order of the size of the polymer molecules, effectively fluidizing the polymer layer several nanometers inside the film. The free surface will then act as source and sink of “free volume”. The idea behind the model is that the energy barrier for kink (free volume) transport is lower than for segmental motion; polymer loops that start and end at the free surface can then be effectively fluidized, with the chains moving along their own paths. This process is not to be mistaken with the reptation of entangled polymer chains in a melt, which is obviously not possible at temperatures below T_g .¹³ This motion is not available for chains with only one “contact” with the free surface: sliding motion would imply entering into volume occupied by other chains. Milner and Lipson ML¹⁴ have built on this idea to develop their “delayed glassification model”, to quantitatively explain how the effect of a free surface can then fluidize a polymer layer, and have looked into the issue of how deep the influence of the free surface propagates into the sample. They labeled a certain loop (starting and ending at the surface) as “fast” when the time necessary to cover the distance between the source and the sink of free volume is shorter than a reasonable experimental time. ML studied in detail the probability for a chain segment at a given depth in the film to be part of a fast loop in order to quantify the plasticizing effect of the free surface.¹⁴ Here we are interested in the analogous problem of an otherwise fast loop being in contact or not with the supporting substrate. If the polymer–substrate interaction is sufficiently strong, the presence of the wall can slow down or stop the free volume propagation through the

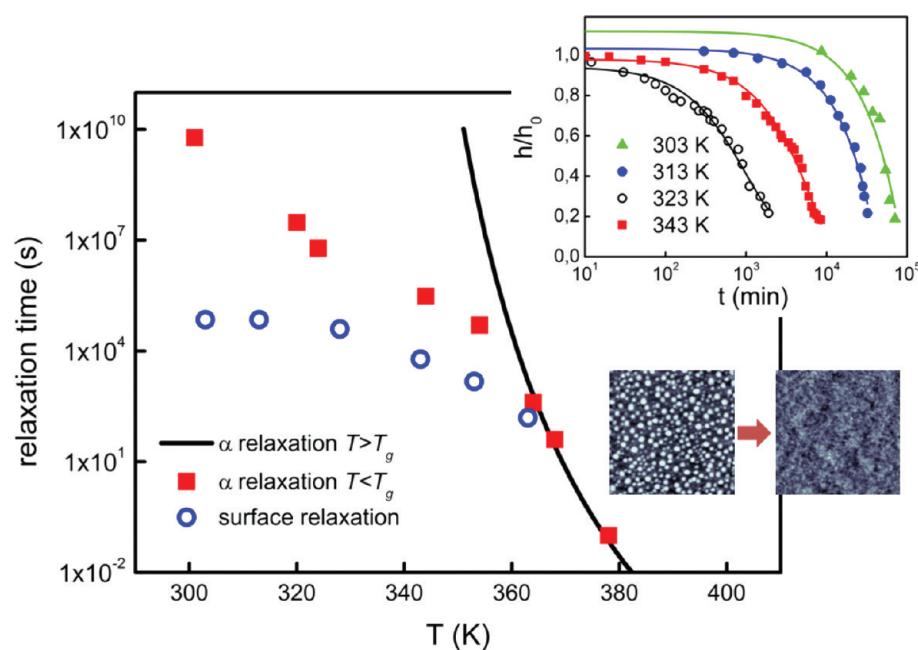


Figure 5. Characteristic relaxation times. PS relaxation at the surface (this work, blue circles) increases more slowly with decreasing temperatures than reported bulk α -relaxation (red squares, ref 16) or extrapolated values from polymer behavior at temperatures above T_g (black line, ref 17). Inset: time dependence of the bump height at selected temperatures and typical $1 \times 1 \mu\text{m}^2$ AFM height micrographs measured in air before and after relaxation of the structure.

chain, effectively freezing a given loop. If this probability is negligible, the polymer chains at the free surface should not be affected by the presence of the wall. It is obvious that for polymer films substantially thicker than R_{EE} the effect of the free surface will not be modified by the presence of the solid boundary. On the contrary, for films thinner than R_{EE} the presence of the boundary might affect the propagation of a kink along a polymer chain, as sketched in Figure 4. The penetrating effect of the substrate will be less pronounced in samples of lower molecular weight. For the two substrate modification methods discussed in this work (ceria-coated mica and silanized Si wafer) the friction coefficient for the monomers in contact with the modified surface is higher than with the bare substrate, slowing down the polymers movement near the substrate and reducing the structuration. The origin of the slow dynamic seems to be different for each case: for the ceria-coated mica it is due to the enhanced dispersion interaction between polymer chains and the ceria nanoparticles. On the contrary, for the silanized wafers the enhanced friction is probably due to the interpenetration between the polymer molecules and the silane layer, which is enhanced upon annealing, but it is more difficult at very high OTS coverage (or absent at low coverage). In that sense, the defects on the OTS layer acts as “pinning points” that avoid the sliding of the polymer chains. Even though both effects are short-ranged (a fraction of a nanometer) their influence propagates to the polymer surface due to the long-range effects of chain connectivity.

Although conceptually appealing, the sliding model of de Gennes in the ML formulation¹⁴ predicts a probability of polymer segments belonging to a fast loop that decays very quickly with depth at room temperature. If that is true, polymer films thicker than a few nanometers should not be sensitive to the presence of the solid boundary, which is clearly inconsistent with our results. At least two reasons can be evoked to rationalize this discrepancy. First, it is possible that the ML model overestimates the temperature decay of the length of the

longest fast loop allowed, which they modeled by using a temperature dependence of the WLF form¹⁵ by extrapolating from the behavior of bulk PS above T_g . However, it has been experimentally shown that the dynamic of near-surface polymer chains in glassy PS is substantially faster than the one predicted by extrapolation from the behavior of liquid PS or the one measured in bulk glassy PS.⁷ To further investigate this point, we have conducted an extensive study of PS surface relaxation using the structuration technique discussed in this work. As we have reported in a previous publication,⁸ the bump size decreases with time (and eventually disappears) following a thermally activated relaxation process well described by single-exponential time decay, as illustrated in the inset of Figure 5. The measured characteristic relaxation times of the surface modification indicate that the dynamic of the polymer surface slows down with decreasing temperature at a lesser pace than the polymer bulk in a glassy state. Similarly, it is clear that extrapolating the molten state behavior to temperatures below T_g —the method chosen by ML—grossly underestimates the mobility of polymer chains close to the surface of the film. The characteristic relaxation times of the polymer near to the surface would be between the ones measured at the surface and at the bulk of the film, both much shorter than the values extrapolated from the behavior at $T > T_g$. Significantly longer fast loops close to the surface than the ones considered in ref 14 should then be anticipated.

A second reason can be evoked to explain the long spatial range of fast loops mentioned above: the cooling of the polymer films after annealing might have been carried out too quickly (in terms of the relaxation time of the system). A very long time may be necessary to reach thermodynamic equilibrium of the films at room temperature. Upon cooling, the polymer chains might effectively be frozen in conformations that would correspond to a higher temperature (an effective or “structural” temperature). Indeed, it has been recently reported that the relaxation times of spin-coated polymer films,

measured from dewetting experiments, strongly depends on the processing history of the sample.^{18,19} It has also been reported that an extremely long time (of the order of weeks) may be necessary to reach final equilibrium in thin viscous polymer films, even at temperatures above T_g .^{20,21} This could also explain the weak temperature dependence of the relaxation at low temperatures (Figure 5). A more detailed report of thermal aspects related to the process described here will be published elsewhere.

The effect described in this work can be used to direct the structuration of thin polymer films by controlled patterning of the supporting substrate. As an example, Figure 6 shows how a

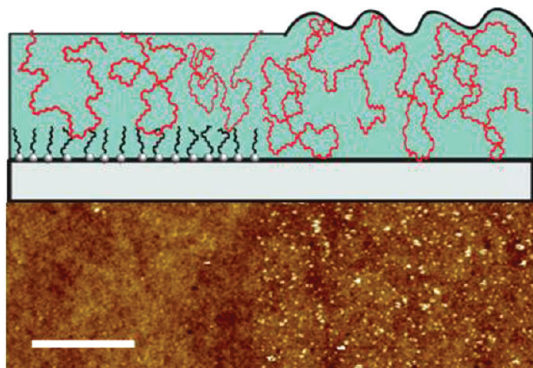


Figure 6. Height tapping mode AFM micrograph measured in air of 50 nm thick 250 kDa polystyrene films after exposure to a degassed solution of nitric acid in double distilled water for 5 min. pH 1.5; T 25 °C. The film was spin-coated on a half-silanized silicon wafer. Scale bar corresponds to 2 μ m. The presence of asperities of regular nanometric size bumps is clearly observed on the bare silicon wafer. On the contrary, no modification was detected in the region which was coated with OTS.

polymer film coating a half-silanized silicon wafer gets partially structured after treated with degassed water at pH 1.5. Only the region of the film above the bare silicon wafer gets structured; more complicated surface morphologies can be conceived by following this strategy. In conclusion, we have shown that the structuration of the surface of glassy PS films by contact with degassed water can be affected by the presence of a solid boundary (up to film thickness of the order of R_{EE}) which may slow down or even prevent the polymer film restructuring if there is a strong interaction between the polymer chains and the substrate.

REFERENCES

- (1) Keddie, J.; Jones, R.; Cory, R. *Europhys. Lett.* **1994**, *27*, 59–64.
- (2) Alcoutlabi, M.; McKenna, G. B. *J. Phys.: Condens. Matter* **2005**, *17*, R461–S24.
- (3) de Gennes, P. G. *C. R. Acad. Sci. Paris, Ser. IV* **2000**, *1*, 1179–1186; *Eur. Phys. J. E* **2000**, *2*, 201–203.
- (4) Ellison, C. J.; Torkelson, J. M. *Nature Mater.* **2003**, *2*, 695–700.
- (5) Rotella, C.; Napolitano, S.; De Cremer, L.; Koeckelberghs, G.; Wübbenhorst, M. *Macromolecules* **2010**, *43*, 8686–8691.
- (6) Inoue, R.; Kawashima, K.; Matsui, K.; Kanaya, T.; Nishida, K.; Matsuba, G.; Hino, M. *Phys. Rev. E* **2011**, *83*, 02180.
- (7) Fakhraei, Z.; Forrest, J. A. *Science* **2008**, *319*, 600–604.
- (8) Siretanu, I.; Chapel, J.-P.; Drummond, C. *ACS Nano* **2011**, *5*, 2939–2947.
- (9) Schaffer, E.; Thurn-Albrecht, T.; Russell, T. P.; Steiner, U. *Nature* **2000**, *403*, 874–877.
- (10) Chapel, J.-P.; Morvan, M. *PCT Int. Appl. WO* 2007126925 A2 20071108, 2007.
- (11) Peterson, I. R. *J. Phys. D* **1990**, *23*, 379–395.
- (12) Xu, L.; Sharma, A.; Joo, S. W. *Macromolecules* **2010**, *43*, 7759–7762.
- (13) de Gennes, P. G. *Scaling Concepts in Polymer Physics*; Cornell University Press: Ithaca, NY, 1979.
- (14) Milner, S. T.; Lipson, J. E. G. *Macromolecules* **2010**, *43*, 9865–9873. Lipson, J. E. G.; Milner, S. T. *Macromolecules* **2010**, *43*, 9874–9880.
- (15) Williams, M. L.; Landel, R. F.; Ferry, J. D. *J. Am. Chem. Soc.* **1955**, *77*, 3701–3707.
- (16) Dhinojwala, A.; Wong, G. K.; Torkelson, J. M. *J. Chem. Phys.* **1994**, *100*, 6046–6054.
- (17) Ferry, J. D. *Viscoelastic Properties of Polymers*, 3rd ed.; John Wiley and Sons: New York, 1980.
- (18) Raegen, A.; Chowdhury, M.; Calers, C.; Schmatulla, A.; Steiner, U.; Reiter, G. *Phys. Rev. Lett.* **2010**, *105*, 227801.
- (19) Reiter, G.; Hamieh, M.; Damman, P.; Slavovs, S.; Gabriele, S.; Vilmin, T.; Raphaël, E. *Nature Mater.* **2005**, *4*, 754–758.
- (20) Barbero, D. R.; Steiner, U. *Phys. Rev. Lett.* **2009**, *102*, 248303.
- (21) Thomas, K. R.; Chenneviere, A.; Reiter, G.; Steiner, U. *Phys. Rev. E* **2011**, *83*, 021804.

Liquid Crystalline Ionic Dendrimers Containing Luminescent Oxadiazole Moieties

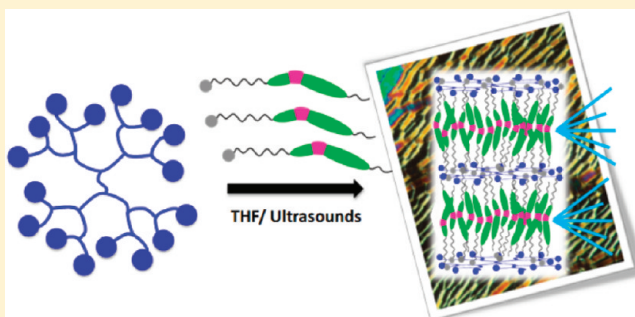
Silvia Hernández-Ainsa,[†] Joaquín Barberá,^{*,†} Mercedes Marcos,^{*,†} and José Luis Serrano[‡]

[†]Departamento de Química Orgánica, Facultad de Ciencias-Instituto de Ciencia de Materiales de Aragón, Universidad de Zaragoza-CSIC, C/Pedro Cerbuna 12, 50009 Zaragoza, Spain

[‡]Instituto de Nanociencia de Aragón, Mariano Esquillor edif. I+D, 50018 Zaragoza, Spain

S Supporting Information

ABSTRACT: Two novel series of dendrimers constituted by the ionic grafting of poly(propyleneimine) PPI-(NH₂)_x ($x = 4, 8, 16, 32, 64$) and poly(amidoamine) PAMAM-(NH₂)_x ($x = 64$) with carboxylic acids bearing an oxadiazole ring have been synthesized, and their liquid crystalline properties have been investigated. Series I is generated by the ionic attachment between the dendrimers and 1,3,4-oxadiazole-containing acids. Series II results from the ionic junction of the dendrimers to 1,2,4-oxadiazole-containing acids. The liquid crystalline behavior has been investigated by means of differential scanning calorimetry (DSC), polarizing optical microscopy (POM), and X-ray diffractometry (XRD). The liquid crystal properties are significantly improved in the dendrimers compared to the mesogenic precursors. The structural parameters determined by X-ray diffraction reflect the different supramolecular organization built by each kind of oxadiazole-containing acid introduced. On the basis of these experimental results, a packing model is proposed based on a microsegregation phenomenon and a variable degree of interdigitation between the mesogenic units. The absorption and emission properties of the compounds have also been studied. To our knowledge, these are the first dendrimers reported up to date combining oxadiazole units and liquid crystal properties.



INTRODUCTION

Dendrimers are highly branched macromolecules that have attracted significant interest in material science and biomedicine fields.¹ Their unique architecture originates novel properties, such as better solubility and lower viscosity than their analogous linear polymers. Moreover, the high density of functional groups contained in their structure allows the introduction of a higher number of active units with specific properties.

The 1,3,4- and 1,2,4-oxadiazole moieties have been incorporated to many series of organic compounds due to their interest as electron transporting materials or their application in emission layers for OLEDs² and in biology.³ These molecules have also been investigated in the liquid crystal field. As a general term, they tend to generate mesophases typical of rodlike mesogens such as the smectic or the nematic phase,⁴ but some columnar mesophases⁵ have also been described when these molecules are conveniently designed to possess a disk shape.

More interesting is the occurrence of the biaxial nematic mesophase for some of these derivatives.⁶ This mesophase, of great interest in liquid-crystal electro-optical display technology, has also been investigated in dendrimers. Thus, the side-on attachment of the mesogen as a side group to siloxane dendrimers hinders the rotation about the molecular long axis,

and this has been demonstrated to be a good strategy to avoid the rotational symmetry in the molecule and to give a biaxial nematic mesophase.⁷

Oxadiazole units have been extensively incorporated in dendrons⁸ and dendrimers⁹ to study their luminescent properties in nonmesomorphic materials. The highly branched structure of the dendrimer may improve the luminescence efficiency of the materials in films since their globular shape reduces intermolecular interactions.¹⁰ Interestingly, light harvesting effects have also been observed in luminescent dendrimers.¹¹ However, no works concerning the liquid crystalline behavior of dendrimers bearing oxadiazole have been reported. The well-defined architecture of dendrimers enables for the specific and controlled location of the oxadiazole moieties in the dendritic scaffold, and this feature favors the supramolecular organization required to obtain mesomorphic properties.

A simple method to obtain mesomorphic dendrimers is the incorporation of appropriate molecules to the periphery of a dendrimer.¹² Although most of the works collected up to now deal with covalent attachment, the ionic junction of molecules

Received: September 8, 2011

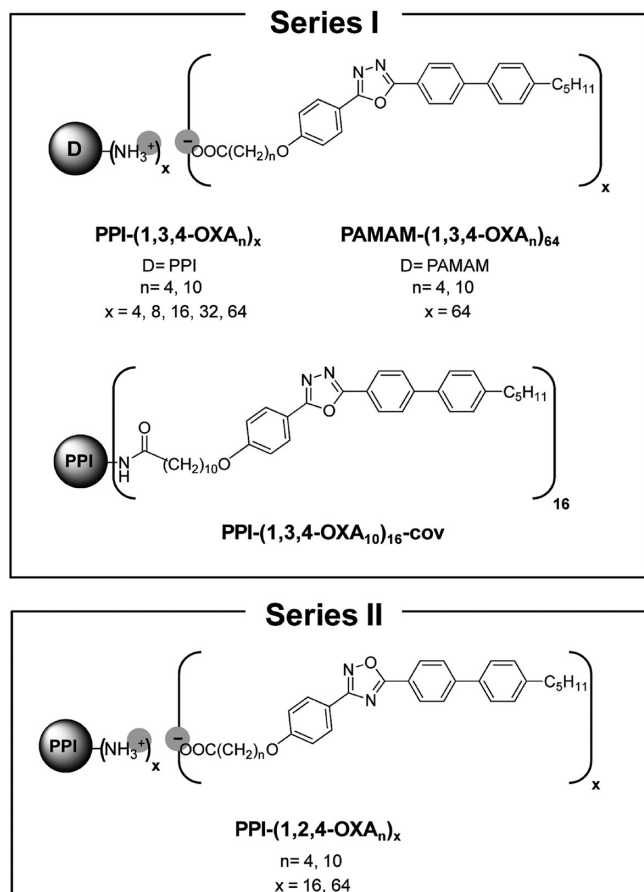
Revised: December 14, 2011

Published: December 28, 2011

bearing a carboxylic group to the amine terminal groups of the poly(propyleneimine) (PPI) and poly(amidoamine) (PAMAM) dendrimers has demonstrated to be an easy and versatile strategy to produce mesomorphic materials.¹³

Following this approach, we have prepared the two series of dendrimers shown in Scheme 1. Series I is constituted by

Scheme 1. Schematic Representation and Nomenclature of the Reported Dendrimers



dendrimers coming from the ionic functionalization of PPI ($x = 4, 8, 16, 32$, and 64) and PAMAM ($x = 64$) with carboxylic acids (1,3,4-OXA_n) bearing the 1,3,4-oxadiazole moiety with different spacer lengths ($n = 4$ and 10). One dendrimer coming from the covalent attachment of the 1,3,4-OXA₁₀ unit to the third-generation PPI ($x = 16$) is also included in this series. Series II is formed by ionic dendrimers constituted by the functionalization of PPI ($x = 16$ and 64) with carboxylic acids (1,2,4-OXA_n) containing the 1,2,4-oxadiazole ring with different spacer length ($n = 4$ and 10). Both dendritic scaffolds have been chosen because of their easy functionalization by means of the transfer proton reaction between their peripheral amine groups and the carboxylic acid. Besides, most of the compounds have been prepared by using the PPI dendrimer because this dendrimer presents higher fluidity and thermal stability when compared with the PAMAM core. These two properties are of great importance for future applications of these materials.

The aim of this work is to study the liquid crystalline behavior, looking for the nematic biaxial mesophase, and to evaluate the luminescent properties in these dendrimers.

EXPERIMENTAL SECTION

1. Materials and Methods. PPI-(NH₂)_x ($x = 4, 8, 16, 32$, and 64) dendrimers were purchased from SyMO-Chem BV (Eindhoven, The Netherlands), and Starburst-PAMAM-(NH₂)₆₄ dendrimer was manufactured by Dendritech. The rest of reagents were purchased from Aldrich, and all of them were used as received. Anhydrous THF used for dendrimer preparation was purchased from Scharlau and dried using a solvent purification system.

The infrared spectra of all the compounds were obtained with a Nicolet Avatar 360 FTIR spectrophotometer in the 400–4000 cm^{−1} spectral range using KBr pellets and NaCl cells. ¹H NMR was performed on a Bruker AVANCE 400 spectrometer and on a Bruker AVANCE 300 spectrometer. ¹³C NMR was performed on a Bruker AVANCE 400 spectrometer operating at 100 MHz and on a Bruker AVANCE 300 spectrometer operating at 75 MHz. Elemental analyses were performed using a Perkin-Elmer 240C microanalyzer.

Mesogenic behavior and transition temperatures were determined using an Olympus DP12 polarizing optical microscope equipped with a Linkam TMS91 hot stage and a CS196 central processor.

Differential scanning calorimetry (DSC) experiments were performed in DSC TA Instruments Q-20 and Q-2000 equipments. Samples were sealed in aluminum pans, and a scanning rate of 10 °C min^{−1} under a nitrogen atmosphere was used. The equipment was calibrated with indium (156.6 °C, 28.4 J g^{−1}) as the standard. Three thermal cycles were carried out. The mesophase transition temperatures were read at the maximum of the corresponding peaks. Thermogravimetric analysis (TGA) was performed using a TA Instruments TGA Q5000 at a rate of 10 °C min^{−1} under an argon atmosphere.

The XRD experiments were performed in a pinhole camera (Anton-Paar) operating with a point-focused Ni-filtered Cu Kα beam. Lindemann glass capillaries with 0.9 mm diameter were used to contain the sample, and when necessary, a variable-temperature attachment was used to heat the sample. The patterns were collected on flat photographic film perpendicular to the X-ray beam. Bragg's law was used to obtain the spacing.

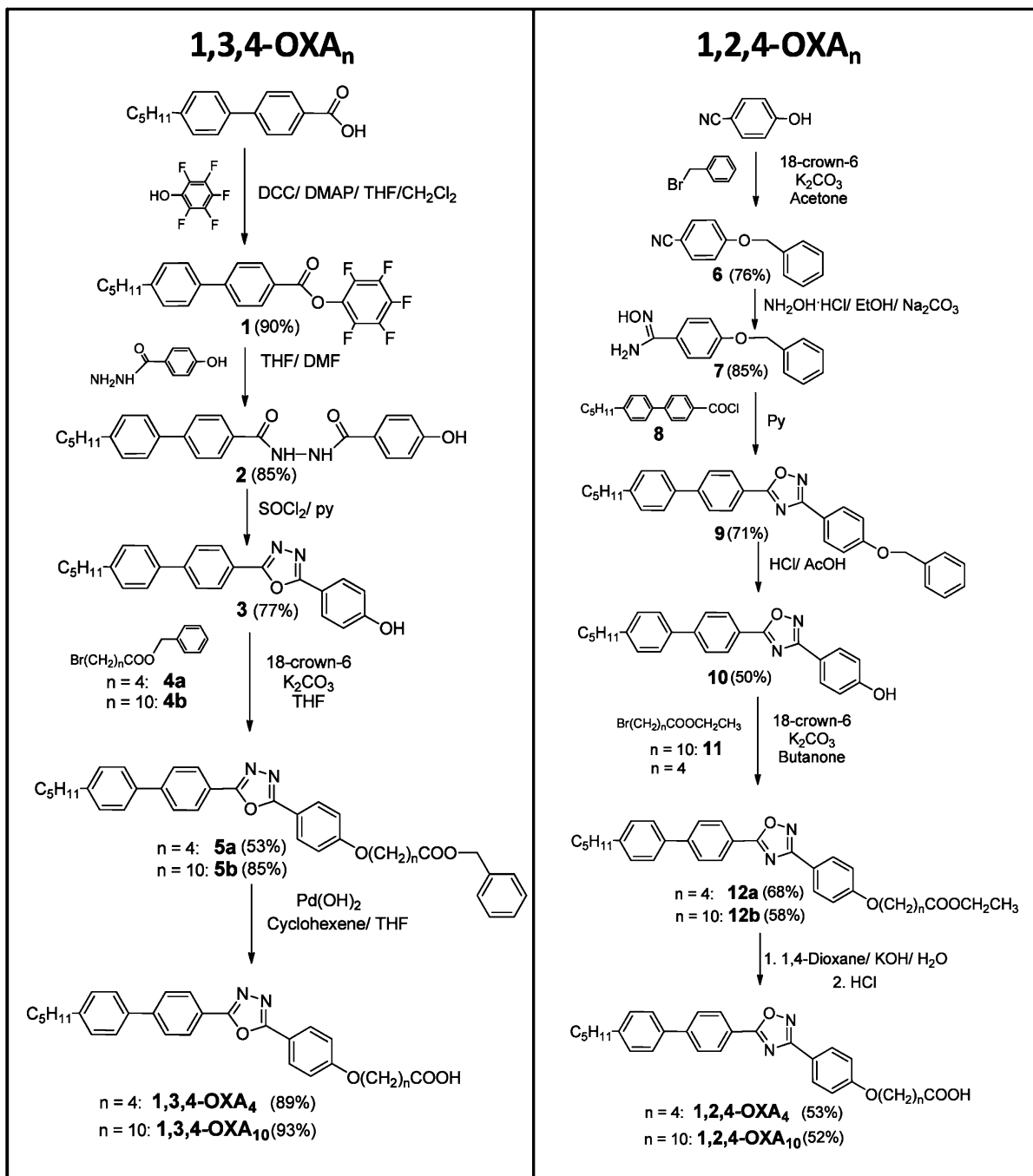
UV–vis absorption spectra were measured with a UV4–200 from ATI-Unicam using 10^{−5}–10^{−6} M solutions in CHCl₃ (HPLC grade). Fluorescence spectra were measured with a Perkin-Elmer LS50B fluorescence spectrometer using solutions in CHCl₃ of ca. 0.01 absorbance (about 10^{−8}–10^{−9} M) under excitation at the absorption maximum. Films were prepared by casting of a solution of ~1 mg/mL in CHCl₃ on a quartz plate.

2. Synthesis and Nomenclature.

2.1. Oxadiazole Acids. Carboxylic acids based on two oxadiazole isomers (1,3,4- and 1,2,4-) have been used to prepare the dendrimers. They are denoted 1,3,4-OXA_n and 1,2,4-OXA_n. The subscript “n” indicates the length of the spacer between the rigid moiety and the carboxyl group, namely $n = 4$ and 10 . The synthesis of 1,3,4-OXA_n and 1,2,4-OXA_n was performed following previously described methods (Scheme 2).^{6d,14}

2.2. Ionic Dendrimers. Ionic dendrimers were synthesized by a procedure previously described by us,^{13c} following the method of Crooks¹⁵ as schematically represented in Scheme 3a. Namely, x equiv of the OXA_n acid was dissolved in anhydrous THF. The mixture was added to a solution of 1 equiv of PPI or PAMAM dendrimer of the corresponding generation (PPI-(NH₂)_x or PAMAM-(NH₂)_x) in anhydrous tetrahydrofuran (THF) and sonicated for 10 min. The mixture was then slowly evaporated at room temperature and dried in vacuum until the weight remains constant for ca. 12 h at 40 °C. These compounds are named D-(1,3,4-OXA_n)_x or D-(1,2,4-OXA_n)_x, where D denotes the type of dendrimer matrix (PPI or PAMAM), n the spacer length of the acid, and x the number of terminal amine groups of the dendrimers (related to the generation). The terminal chain of the oxadiazole-based carboxylic acids is pentyl in all cases.

2.3. Covalent Dendrimer. Covalent dendrimer (PPI-(1,3,4-OXA₁₀)_{16-cov}) belonging to series I was synthesized following a method previously described,¹⁶ as schematically represented in Scheme 3b. 1.03 equiv of 1,3,4-OXA₁₀ acid was dissolved in THF

Scheme 2. Synthetic Route and Nomenclature of Intermediates for 1,3,4-OXA_n and 1,2,4-OXA_n Acids

(10 mL), and a solution of carbonyldiimidazole (CDI) (1 equiv) in THF (10 mL) was slowly added to the acid solution. The reaction mixture was stirred for 1 h at room temperature under a stream of argon to remove the CO₂ formed. The mixture was transferred to a Schlenk flask containing the PPI (1 equiv of terminal amino groups). The mixture was heated to 40 °C for 72 h. The solvent was half reduced in vacuum, and then 50 mL of water was added to yield a precipitate, which was isolated by filtration. The product obtained was purified by further washing with water and hot methanol to give a white powder after drying in vacuum (51% yield).

RESULTS AND DISCUSSION

1. Characterization of the Dendrimers. IR and NMR spectroscopy, together with elemental analysis, reveal the correct formation of the dendrimers (series I and II) and

their purity. MALDI-TOF spectrometry was also employed to characterize the covalent dendrimer, but the ionic nature of the rest of the dendrimers prevents the use of this technique.

1.1. FT-IR Characterization. As observed in Figure 1a, the stretching absorption at 1707–1699 cm⁻¹ corresponding to the carbonyl groups of 1,3,4-OXA_n acids is replaced by a new band corresponding to the asymmetric stretching absorption of the carboxylate group at 1560–1550 cm⁻¹ in ionic dendrimers of series I. In the case of dendrimers of series II, the band of the carbonyl group shifts from 1707 to 1705 cm⁻¹ in the 1,2,4-OXA_n acids to 1567–1561 cm⁻¹ in the carboxylate of the ionic dendrimers (see Figure 1a).¹⁷ For PPI-(1,3,4-OXA₁₀)₁₆-cov a band at 1641 cm⁻¹ corresponding to the symmetric stretching of the carbonyl group in the amide bond replaces the band of

Scheme 3. Schematic Representation of the (a) Ionic Synthetic Route and (b) Covalent Synthetic Route of the Dendrimers

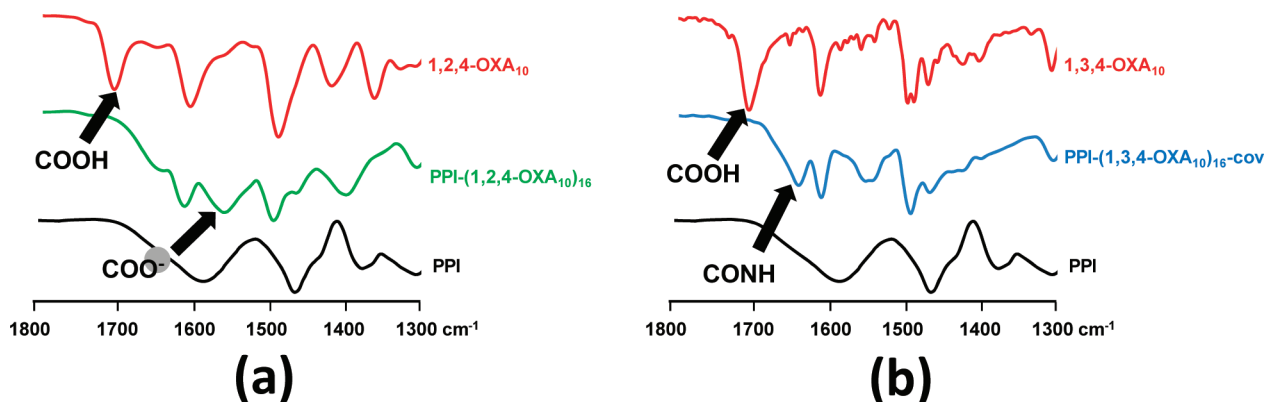
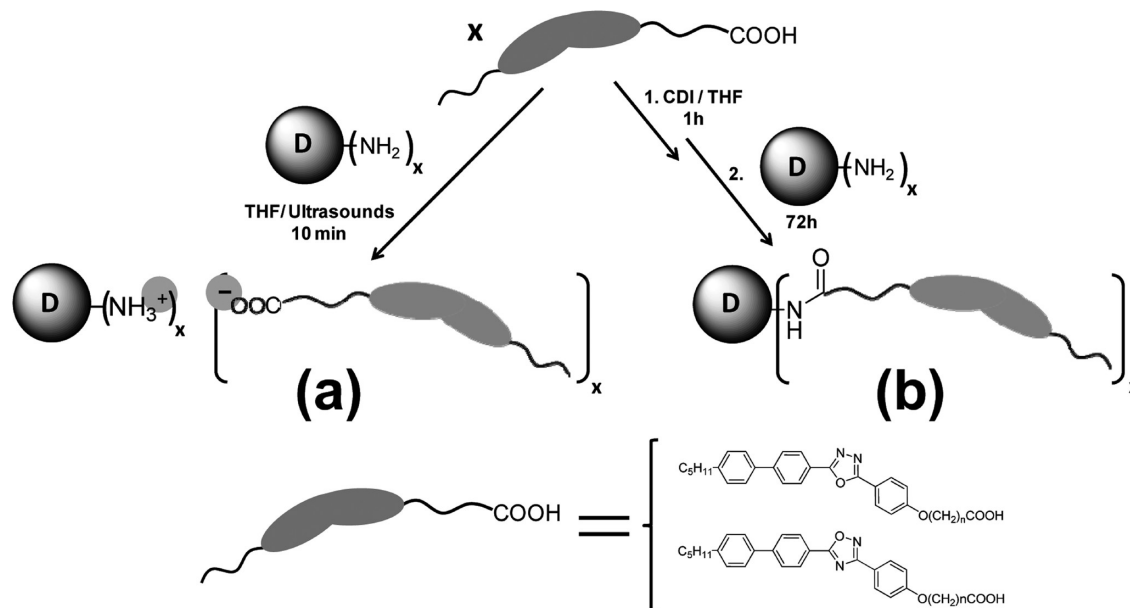


Figure 1. FT-IR spectra: (a) PPI-(1,2,4-OXA₁₀)₁₆ (green), 1,2,4-OXA₁₀ (red), PPI₁₆ (black); (b) PPI-(1,3,4-OXA₁₀)₁₆-cov (blue), 1,3,4-OXA₁₀ (red), PPI₁₆ (black).

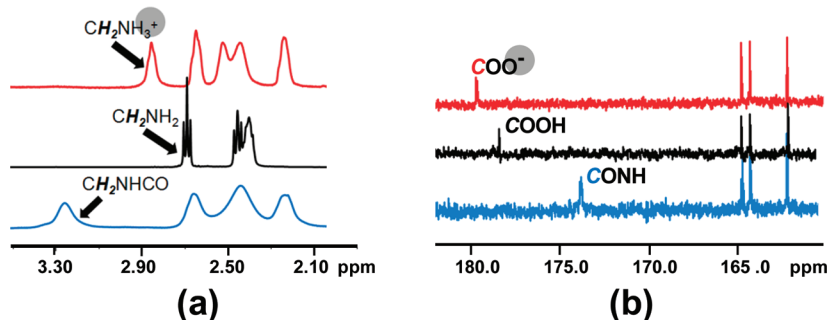


Figure 2. (a) ¹H NMR spectra of PPI-(1,3,4-OXA₁₀)₁₆-cov (blue), PPI₁₆ (black), and PPI-(1,3,4-OXA₁₀)₁₆ (red). (b) ¹³C NMR spectra of PPI-(1,3,4-OXA₁₀)₁₆-cov (blue), 1,3,4-OXA₁₀ (black), and PPI-(1,3,4-OXA₁₀)₁₆ (red).

the carboxyl group in the 1,3,4-OXA₁₀ acid at 1707 cm⁻¹ (see Figure 1b). Moreover, a band at 3295 cm⁻¹ corroborates the presence of the amide NH group.

1.2. NMR Experiments. Dendrimers were studied by ¹H NMR and ¹³C NMR spectroscopy. In ¹H NMR experiments (Figure 2a) the absence of signal at 2.70 ppm related to [−CH₂−NH₂] of PPI and the appearance of another signal at ca. 2.90 ppm corresponding to [−CH₂−NH₃⁺] for ionic PPI-

[1,3,4-OXA_n]_x and PPI-[1,2,4-OXA_n]_x compounds (series I and II) reveals the complete formation of the salts in the ionic compounds. In the same way, the shift of the signal from 3.30 ppm [−NHCH₂CH₂NH₂] to ca. 3.45 ppm [−NHCH₂CH₂NH₃⁺] and the displacement from 2.70 ppm [NHCH₂CH₂NH₂] to ca. 3.05 ppm [NHCH₂CH₂NH₃⁺] indicates the salt formation in PAMAM derivatives (not shown). In the covalent compound (PPI-[1,3,4-OXA₁₀]₁₆-

cov) the signal is shifted from 2.70 to 3.30 ppm, which indicates the formation of the amide bond [$-\text{CH}_2-\text{NHCO}$] (Figure 2a).

In the ^{13}C NMR spectra (Figure 2b) the signal of the carbon atom of the carboxyl group (COOH) of the acid shifts from 178.2 ppm ($1,3,4\text{-OXA}_{10}$) to 179.2 ppm ($\text{PPI-}(1,3,4\text{-OXA}_{10})_{16}$), which indicates the formation of the carboxylate (COO^-). Likewise, the deprotonation of the carboxylic acid is corroborated by the displacement of the signal corresponding to the C_α to the carbonyl group (CH_2-COOH) from 33.8 ppm in the acid to 36.9 ppm in the dendrimer (CH_2-COO^-). Carboxylate is also formed in the case of PAMAM dendrimers, as denoted by the signal shift from 178.2 ppm (in case of the $1,3,4\text{-OXA}_{10}$ acid) to 179.5 ppm (assigned to the carboxylate group in $\text{PAMAM-}(1,3,4\text{-OXA}_{10})_{64}$) (not shown). The formation of the amide group in the case of $\text{PPI-}(1,3,4\text{-OXA}_{10})_{16}\text{-cov}$ is confirmed by the appearance of the signal at 173.6 ppm, assigned to the carbon of the amide group (CH_2NHCO) (see Figure 2b).

1.3. MALDI-TOF Analysis. The complete functionalization of $\text{PPI-}(1,3,4\text{-OXA}_{10})_{16}\text{-cov}$ was checked by MALDI-TOF mass spectrometry. The MALDI-TOF MS spectrum reveals the presence of an intense peak corresponding to the fully functionalized dendrimer (see Figure S1, Supporting Information). Except for the peak appearing at 9925 that could correspond to the dendrimer with one nonfunctionalized amino group, the rest of the peaks must be associated with statistical defects present in the original PPI dendrimer.¹⁸

2. Thermal Stability of the Dendrimers. The thermal stability of the dendrimers was studied by TGA experiments (see Table S1, Supporting Information).

The type of OXA moiety ($1,3,4\text{-}$ or $1,2,4\text{-}$) and the length of the spacer in the OXA_n moiety ($n = 4, 10$) exercise a marked influence in the onset temperature of decomposition of these dendrimers. Thus, dendrimers bearing the $1,3,4\text{-OXA}_n$ moiety possess the onset temperature of decomposition above 340°C , whereas those containing the $1,2,4\text{-OXA}_n$ moiety exhibit lower temperatures (between 275 and 305°C). Likewise, when comparing dendrimers with the same OXA_n moiety, it is observed that temperatures of decomposition for the longer spacer ($n = 10$) compounds are at least 15°C higher than those bearing the shorter spacer ($n = 4$).

The type of bond affects the thermal stability of the compounds. Hence, the temperature at which 5% of initial mass is lost ($T_{5\%}$) is higher for the covalent compound ($\text{PPI-}(1,3,4\text{-OXA}_{10})_{16}\text{-cov}$) when compared with its homologous ionic compound ($\text{PPI-}(1,3,4\text{-OXA}_{10})_{16}$) and the rest of the compounds (see Table S1).

Also, the dendrimer scaffold exerts influence in the $T_{5\%}$, this temperature being considerably higher for PPI than for PAMAM derivatives. In fact, PAMAM dendrimers are well-known to be less thermally stable than PPI dendrimers.¹⁹

3. Liquid Crystal Properties. The mesomorphic behavior of the compounds was analyzed by POM, DSC, and X-ray diffraction. Three cycles were carried out in DSC experiments, and data were taken from the second cycle. In some cases, the isotropization temperatures were taken from POM observations because no transition peaks were detected in the DSC curves.

3.1. Liquid Crystal Properties of the Precursors. The type of oxadiazole moiety plays a determinant role in the liquid crystal behavior of the precursors. Indeed, precursors of series I containing the $1,3,4\text{-oxadiazole}$ ring are not mesomorphic or the mesomorphism is only monotropic, whereas those

belonging to series II (precursors of $1,2,4\text{-OXA}_n$) exhibit enantiotropic mesomorphism (see Table 1 and Table S2).

Table 1. Temperatures and Enthalpies of Selected Precursors^a

series	compound	thermal data
I	3	C 197 C' 205 [20.1] I
I	$1,3,4\text{-OXA}_4$	C 186 [54.0] I; I 166 ^b N 162 [50.4] C
I	$1,3,4\text{-OXA}_{10}$	C 175 [47.9] I
II	10	C 120 [0.6] C' 154 [20.8] SmA ^c N 217 [0.6] I
II	$1,2,4\text{-OXA}_4$	C 153 [26.7] SmA 190 [0.5] N 217 [1.0] I
II	$1,2,4\text{-OXA}_{10}$	C 142 [35.3] SmA 181 [0.7] N 193 [0.8] I

^aTemperatures ($^\circ\text{C}$) at the maximum of the peak and enthalpy values (kJ mol^{-1} in brackets) of the transitions obtained by DSC in the second heating process, or in the second cooling process in the case of the monotropic mesophases, performed at 10°C/min . C, C' = crystalline phases, SmA = smectic A mesophase, N = nematic mesophase, I = isotropic liquid. ^bThermal transition observed only by POM. ^cThe SmA-N transition is hidden in the C'-SmA transition.

3.2. Liquid Crystal Properties of the Dendrimers. In spite of the absence of mesomorphism or the occurrence of only monotropic behavior in some OXA_n acids, all dendrimers exhibit liquid crystalline properties in addition to a number of crystal-to-crystal transitions (Table 2).

The liquid crystalline temperature ranges oscillate between 30 and 50°C , being slightly higher for PAMAM derivatives when compared with their PPI homologues. This fact may be connected with the different nature of the dendrimer scaffolds because of the existence of hydrogen bonds in the structure of the PAMAM core.

The covalent dendrimer ($\text{PPI-}(1,3,4\text{-OXA}_{10})_{16}\text{-cov}$) presents a shorter mesomorphic range than its homologous ionic compound ($\text{PPI-}(1,3,4\text{-OXA}_{10})_{16}$). Thus, the ionic attachment enhances the tendency of these compounds to display liquid crystal properties, a feature that is in good agreement with other reported works.²⁰

Dendrimers belonging to series I display higher melting and isotropization temperatures when bearing the shorter spacer ($n = 4$). This is probably due to the increase in the interactions between the promesogenic moieties compared to the longer spacer ($n = 10$).

Compounds of series II exhibit lower melting but higher isotropization temperatures than their homologues belonging to series I, thus presenting broader mesomorphic temperature range (between 145 and 180°C).

On the other hand, the generation of the dendrimer does not produce remarkable influence in the melting and isotropization temperatures of the compounds belonging to both series.

All of the compounds present smectic A mesomorphism as revealed by the textures observed by POM (see Figure 3) and confirmed by the patterns obtained by XRD (vide infra). A hexagonal columnar mesophase has also been detected by XRD for $\text{PPI-}(1,3,4\text{-OXA}_{10})_{64}$ and $\text{PPI-}(1,3,4\text{-OXA}_4)_{64}$ at lower temperatures. The occurrence of this type of mesomorphism can be explained by the sterical hindrance at the periphery of the fifth generation of the PPI dendrimer. In contrast, PAMAM dendrimers show no columnar mesomorphism due to the larger volume of the PAMAM dendritic architecture with respect to the PPI one, which prevents this congestion.^{13c,21}

4. X-ray Studies of the Compounds. The mesomorphic behavior of the dendrimers and precursors has been confirmed

Table 2. Temperatures and Enthalpies of the Phase Transition of the Dendrimers^a

series	compound	thermal data				
I	PPI-(1,3,4-OXA ₁₀) ₄	C 110 [4.7]	C' 130	C'' 137 [27.4] ^c	SmA 164 [9.4]	I
I	PPI-(1,3,4-OXA ₁₀) ₈	C 98 [18.2]	C' 122	C'' 130 [46.1] ^c	SmA 163 [37.0]	I
I	PPI-(1,3,4-OXA ₁₀) ₁₆	C 92 [31.2]	C' 128 [162.2]		SmA 176 [55.2]	I
I	PPI-(1,3,4-OXA ₁₀) _{16-cov}	C 109 [37.3]	C' 146 [248.8]		SmA 189 [59.5]	I
I	PPI-(1,3,4-OXA ₁₀) ₃₂	C 91 [66.6]	C' 131 [343.3]		SmA 185 [117.5]	I
I	PPI-(1,3,4-OXA ₁₀) ₆₄	C 91 [114.9]	C' 124	C'' 133 [45.2] ^c	Col _h 140 ^c	I
I	PAMAM-(1,3,4-OXA ₁₀) ₆₄	C 83 [87.3]	C' 125 [429.2]		SmA 176 [390.6]	I
I	PPI-(1,3,4-OXA ₄) ₄	C 121 [12.6]	C' 140 [0.2]	C'' 156 [1.3]	SmA 183 [6.3]	I
I	PPI-(1,3,4-OXA ₄) ₈	C 111 [9.0]	C' 148 [17.6]		SmA 184 [15.7]	I
I	PPI-(1,3,4-OXA ₄) ₁₆	C 110 [15.7]	C' 151 [29.0]		SmA 190 [27.5]	I
I	PPI-(1,3,4-OXA ₄) ₃₂	C 94 [60.7]	C' 149 [88.7]		SmA 183 [60.4]	I
I	PPI-(1,3,4-OXA ₄) ₆₄	C 123 [76.8]			Col _h 170 ^c	I
I	PAMAM-(1,3,4-OXA ₄) ₆₄	C 121 [187.6]			SmA 191 [103.4]	I
II	PPI-(1,2,4-OXA ₁₀) ₁₆	C 43 [57.7]	C' 67	C'' 83 [69.2] ^c	SmA 234 ^d	I
II	PPI-(1,2,4-OXA ₁₀) ₆₄	C 65 [9.1]	C' 95 [365.1]		SmA 240 ^d	I
II	PPI-(1,2,4-OXA ₄) ₁₆	C 65 [108.9]			SmA 237 ^d	I
II	PPI-(1,2,4-OXA ₄) ₆₄	C 59 [386.7]			SmA 240 ^d	I

^aTemperatures (°C) read at the maximum of the corresponding peaks and enthalpy values (kJ mol⁻¹, in brackets) of the transitions obtained by DSC corresponding to the second heating process performed at 10° C/min. The peaks are broad and transitions span several degrees below and above the peak maximum. ^bTwo peaks are observed for this transition that probably correspond to overlapped melting of two crystalline phases (C' and C''). ^cMesophase and transition temperature identified by XRD. ^dTemperature determined by POM. C, C', C''= crystalline phases, SmA = smectic A mesophase, Col_h = hexagonal columnar mesophase, I = isotropic liquid.

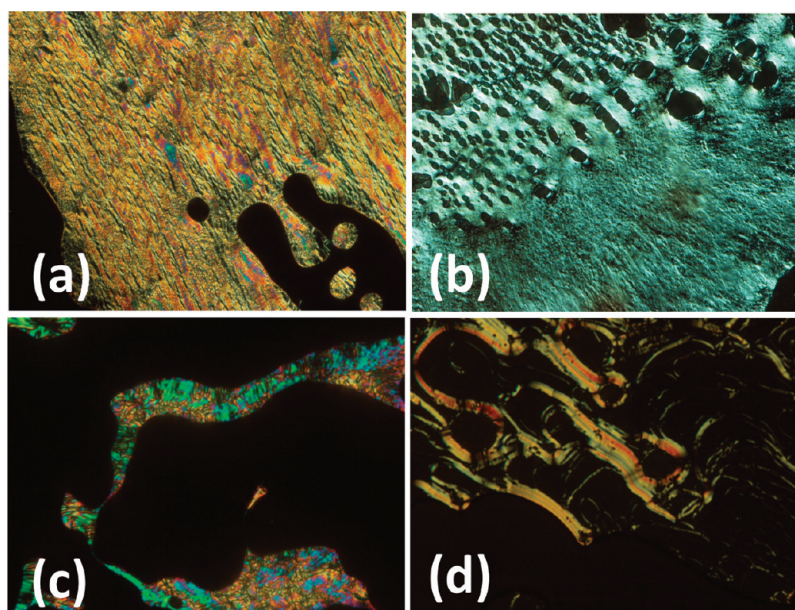


Figure 3. POM textures of (a) PPI-(1,3,4-OXA₁₀)₃₂ at 150 °C in the second heating process in the SmA phase, (b) PPI-(1,3,4-OXA₁₀)_{16-cov} at 140 °C in the first cooling process in the SmA phase, (c) PPI-(1,3,4-OXA₄)₄ at 165 °C in the second heating process in the SmA phase, and (d) PPI-(1,2,4-OXA₄)₆₄ at 170 °C in the first cooling process in the SmA phase.

by X-ray diffraction. Precursors exhibiting nematic mesomorphism contain a diffuse scattering maximum at low angles and a diffuse halo at high angles corresponding to the intermolecular short-range interactions between molecules. The high-angle scattering corresponds to a mean distance of 4.5–4.6 Å and is related to the mean distance between the conformationally disordered alkyl chains and between aromatic segments. The low-angle scattering arises from the short-range interaction along the main molecular axes. In the SmA mesophase (precursors of series II), this low angle scattering is replaced by a sharp, strong peak corresponding to the layer periodicity.

All of the dendrimers display SmA mesomorphism. In this case, X-ray diffraction patterns are constituted by a diffuse halo in the wide angle region, corresponding to the short-range correlations between the mesogenic units and the conformationally disordered terminal chains coming from the oxadiazole moieties and from the dendrimer branches, and by one or two sharp maxima in the small angle region (see Figure S4a,b). These sharp maxima evidence a long-range lamellar packing of molecules, and when there are two small-angle maxima, they correspond to the first and second layer orders. The layer spacing of the SmA mesophase of each dendrimer was obtained by applying Bragg's law, and they are collected in Table 3.

Table 3. X-ray Structural Parameters Data of Dendrimers and 1,2,4-OXA_n Acids

series	compound	T/°C	phase ^a	structural parameters ^b
I	PPI-(1,3,4-OXA ₁₀) ₄	170	SmA	<i>d</i> = 42.9
I	PPI-(1,3,4-OXA ₁₀) ₈	165	SmA	<i>d</i> = 43.9
I	PPI-(1,3,4-OXA ₁₀) ₁₆	163	SmA	<i>d</i> = 44.8
I	PPI-(1,3,4-OXA ₁₀) _{16-cov}	160	SmA	<i>d</i> = 47.4
I	PPI-(1,3,4-OXA ₁₀) ₃₂	161	SmA	<i>d</i> = 45.9
I	PPI-(1,3,4-OXA ₁₀) ₆₄	130	Colh	<i>a</i> = 49.4
I	PPI-(1,3,4-OXA ₄) ₆₄	150	SmA	<i>d</i> = 49.3
I	PAMAM-(1,3,4-OXA ₁₀) ₆₄	148	SmA	<i>d</i> = 56.0
I	PPI-(1,3,4-OXA ₄) ₄	175	SmA	<i>d</i> = 56.0
I	PPI-(1,3,4-OXA ₄) ₈	168	SmA	<i>d</i> = 54.1
I	PPI-(1,3,4-OXA ₄) ₁₆	168	SmA	<i>d</i> = 55.4
I	PPI-(1,3,4-OXA ₄) ₃₂	168	SmA	<i>d</i> = 56.1
I	PPI-(1,3,4-OXA ₄) ₆₄	168	Colh	<i>a</i> = 67.3
	PPI-(1,3,4-OXA ₄) ₆₄	180	SmA	<i>d</i> = 53.6
I	PAMAM-(1,3,4-OXA ₄) ₆₄	168	SmA	<i>d</i> = 61.6
II	1,2,4-OXA ₁₀	175	SmA	<i>d</i> = 38.5
II	1,2,4-OXA ₄	175	SmA	<i>d</i> = 30.8
II	PPI-(1,2,4-OXA ₁₀) ₁₆	165	SmA	<i>d</i> = 47.4
II	PPI-(1,2,4-OXA ₁₀) ₆₄	165	SmA	<i>d</i> = 49.4
II	PPI-(1,2,4-OXA ₄) ₁₆	170	SmA	<i>d</i> = 40.4
II	PPI-(1,2,4-OXA ₄) ₆₄	170	SmA	<i>d</i> = 41.1

^aMesophases exhibited by the compounds at the given temperature.

^b*d* = layer spacing (Å) of the smectic phase. *a* = lattice constant of the hexagonal columnar mesophase.

The length of the low-molecular-weight molecules obtained by molecular modeling are 35.8 Å (1,3,4-OXA₁₀), 28.7 Å (1,3,4-OXA₄), 35.0 Å (1,2,4-OXA₁₀), and 28.2 Å (1,2,4-OXA₄). These data are in accordance with the experimental values obtained by XRD for the mesomorphic 1,2,4-OXA acids (38.5 Å for 1,2,4-OXA₁₀ and 30.8 Å for 1,2,4-OXA₄).

It has been previously described that this kind of ionic and covalent dendrimers self-assembling in a smectic A layer adopt a cylindrical shape, in which the substituents are statistically located upward and downward with respect to the dendrimeric core.^{13c,22} The assumption of this location of the oxadiazole moieties in the dendrimers here described should lead to layer spacing being higher than twice the oxadiazole moieties length. However, the XRD experimental layer spacing values are significantly lower, suggesting some peculiarities in the distribution of the oxadiazole units in the cylindrical model. Furthermore, dendrimers of series I bearing the 1,3,4-OXA₄ unit exhibit a layer spacing of 53.6–56.1 Å, whereas dendrimers containing the same oxadiazole ring but a longer spacer (1,3,4-OXA₁₀) possess a shorter layer spacing (42.9–49.3 Å).

The most plausible explanation to justify these unexpected experimental features is that some interdigitation of the oxadiazole moieties belonging to adjacent layers takes place (see Figure 4). In fact, the longer spacer present in the structure of 1,3,4-OXA₁₀ favors a more efficient interaction with molecules of the neighboring layers. This packing is based on a side-by-side arrangement of the aromatic moieties of adjacent molecules in a head-to-tail fashion, and this arrangement allows the electrostatic interactions between the carboxylate groups and the ammonium groups of the dendrimer (Figure 4a). On the other hand, interdigitation of 1,3,4-OXA₄ with a side-by-side arrangement of the aromatic moieties would preclude the ionic interactions between the carboxylate groups and the

ammonium as a consequence of the mismatch between the length of the different segments of the mesogenic units.

Therefore, the 1,3,4-OXA₄ units do not interdigitate to such a large extent, and the side-by-side arrangement of this aromatic units is probably replaced by a side-by-side arrangement of the hydrocarbon chains (Figure 4b). In both models there is segregation of the aromatic units and the hydrocarbon chains in different sublayers.

The layer thickness is also dependent on the nature of the dendrimer matrix. Greater values are obtained for the two PAMAM derivatives as it was expected due to its larger size when compared to PPI, and the same relationship as for the PPI derivatives is observed between the spacer length and the layer periodicity.

The layer thickness of the ionic PPI-(1,3,4-OXA₁₀)₁₆ dendrimer (44.8 Å) and that of its analogous covalent PPI-(1,3,4-OXA₁₀)_{16-cov} (47.4 Å) dendrimer do not significantly differ from each other. The slightly higher spacing layer value obtained for the covalent one gives evidence of a higher mobility present in the case of the ionic compounds, where the moieties can fluctuate in position and slightly penetrate in the dendrimer. By contrast, in the covalent compound moieties occupy fixed positions. The same tendency has been previously described in other similar dendrimers.^{13a} This enhanced mobility may allow the ionic compound to reach the mesomorphic state at lower temperatures than the covalent analogue.

It is important to highlight how a subtle change in the structure of the oxadiazole heterocycle, namely the 1,3,4- or 1,2,4-oxadiazole ring, produces great differences not only in the mesomorphic behavior, as described before, but also in the supramolecular packing of the dendrimers. Thus, dendrimers bearing the 1,2,4-OXA_n unit (series II) also exhibit layer spacings consistent with interdigitation of the oxadiazole moieties. However, in this case, no influence of the spacer length is observed, and full interdigitation between molecules of adjacent layers occurs in all of the dendrimers, as deduced from the X-ray results. This fact clearly indicates that more effective intermolecular side-by-side interactions are taking place in case of the 1,2,4-OXA moieties, favoring their interdigitation independently of the spacer length.

The hexagonal columnar phase exhibited by PPI-(1,3,4-OXA₁₀)₆₄ and PPI-(1,3,4-OXA₄)₆₄ is identified by the existence of two sharp reflections in the reciprocal ratio 1:√3 in the low angle region of the patterns (see Figure S4c). In this case the molecules adopt a disk shape where the dendrimer matrix is located in the central part and the oxadiazole moieties are disposed radially.

As observed in Table 3, the structural parameters of this columnar hexagonal mesophase considerably change in an unexpected way when going from the longer spacer moiety dendrimer (*a* = 49.4 Å) to the shorter one (*a* = 67.3 Å). This fact is mainly connected to the elongation of the dendrimer matrix along the vertical axis of the discs. By applying geometrical calculations taking into account the XRD experimental data,^{13c} we have estimated the height (*h*) of the disks that constitute the columnar arrangement, being *h* = 34 Å for PPI-(1,3,4-OXA₁₀)₆₄ and *h* = 16 Å for PPI-(1,3,4-OXA₄)₆₄. These height values indicate that the dendrimer with the longer spacer elongates twice along the vertical axis of the disk compared to the dendrimer with the smaller spacer. Hence, neighboring columns interpenetrate in a large extent in the case of the PPI-(1,3,4-OXA₄)₆₄ (Figure 5a) compared to PPI-(1,3,4-

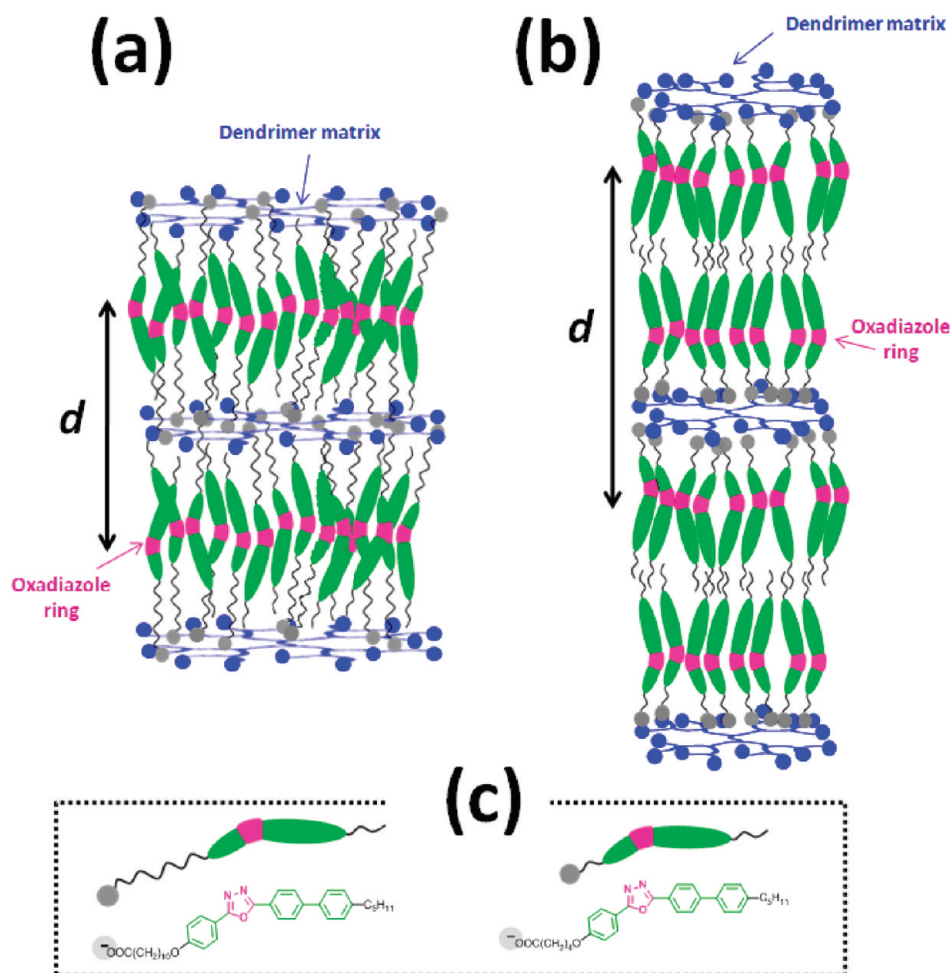


Figure 4. Schematic representation of the molecular packing model of the ionic dendrimers in the SmA mesophase. (a) Interdigitated 1,3,4-OXA₁₀ moieties. (b) Partially interdigitated 1,3,4-OXA₄ moieties. (c) Schematic representation of the 1,3,4-OXA₁₀ and 1,3,4-OXA₄ acids. The thickness of each sublayer, and hence the space filled by each molecule region, is approximately proportional to its mass.

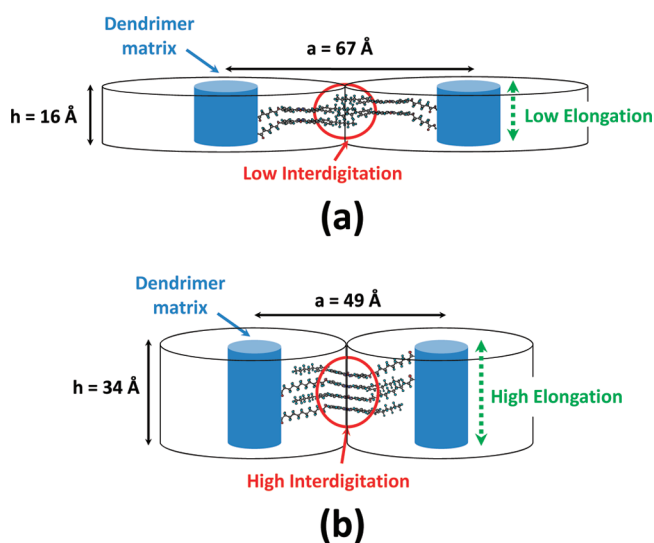


Figure 5. Schematic representation of the disk packing, values of the diameter a , and the height h of the dendrimer disks for (a) PPI-(1,3,4-OXA₄)₆₄ and (b) PPI-(1,3,4-OXA₁₀)₆₄ in the hexagonal columnar mesophase.

OXA₁₀)₆₄ (Figure 5b), and both situations fulfill the requirements for an efficient packing and space filling. It is interesting

to note that the interdigitation phenomenon between molecules in neighboring columns follows the same trend described for the low generation derivatives in the SmA phase. Both effects (dendrimer matrix elongation and interdigitation) are connected to each other and simultaneously contribute to account for the difference in the hexagonal lattice constant a .

5. Optical Properties. The UV–vis absorption and emission spectroscopic data of the OXA_{*n*} acids and dendrimers of series I and series II in CHCl₃ and in casted films are summarized in Table S3 (Supporting Information). All compounds containing the same oxadiazole ring yielded identical absorption and emission spectra. No remarkable influence of the length of the spacer, the generation, or the type of dendrimer has been found. Thus, dendrimers with the 1,3,4-OXA_{*n*} unit present the absorption maximum at 315–316 nm and dendrimers with the 1,2,4-OXA_{*n*} moiety exhibit the absorption maximum at 295 nm (Figure 6). These absorption bands are assigned to $\pi \rightarrow \pi^*$ transitions produced in the conjugated oxadiazole framework due to their high molar absorption coefficients ($(4.7\text{--}3.3) \times 10^4$).^{4c}

All of the compounds present emission in the UV region. The emission spectra of the compounds are only dependent on the type of oxadiazole ring. Compounds belonging to series I exhibit the strongest emission maxima at 377–379 nm. Two less intense maxima are found at ~ 360 and ~ 390 nm.

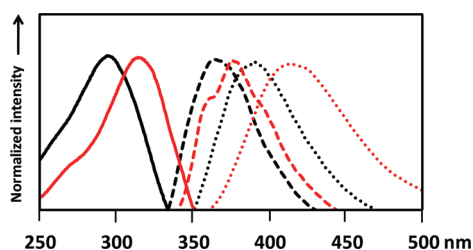


Figure 6. UV absorption spectra in solution (CHCl_3) (full line), emission spectra in solution (CHCl_3) (dashed line), and emission spectra in film (dotted line). Red lines correspond to PPI-(1,3,4-OXA₄)₃₂, and black lines correspond to PPI-(1,2,4-OXA₁₀)₆₄.

Compounds in series II present only one maximum at 365–366 nm (see Figure 6).

The quantum yields of luminescence have been measured taking the 2-phenyl-5-(4-biphenyl)-1,3,4-oxadiazole as standard ($\Phi = 0.80$, benzene),²³ and they fluctuate between 0.46 and 0.74. Lower quantum yields are observed for series II, as it was expected because 1,2,4-oxadiazole molecules have been previously reported to produce lower quantum yield values compared with their 1,3,4-isomers.^{4e} In general, in series I the quantum yields decrease as the generation increases. However, in series II, efficiency is not dependent on the generation. The covalent compound (PPI-(1,3,4-OXA₁₀)_{16-cov}) presents a lower value than the analogous ionic compound (PPI-(1,3,4-OXA₁₀)₁₆).

The emission in solid film has also been analyzed for these compounds by casting of a solution of ~ 1 mg/mL in CHCl_3 on a quartz plate. Interestingly, as observed in Figure 6, emission bands appear broader respect to those in solution because of the stronger intermolecular interactions produced in the solid state. The Stokes shifts are remarkably higher in film than in solution.

CONCLUSIONS

We have successfully synthesized liquid crystal dendrimers containing the oxadiazole heterocycle in their structure (series I (1,3,4-OXA_n) and series II (1,2,4-OXA_n)) using an easy and versatile method via ionic bonding of commercial amino-terminated PPI and PAMAM dendrimers with oxadiazole-containing carboxylic acids.

As far as we know, this is the first time that liquid crystalline properties have been described in dendrimers containing oxadiazole moieties in their structure. All of them present smectic A mesomorphism, although a hexagonal columnar mesophase has also been observed in some of the higher generation PPI dendrimers belonging to series I. No nematic mesomorphism has been achieved in any case. Dendrimers containing 1,2,4-OXA_n (series II) exhibit lower melting points and broader mesomorphic temperature ranges than those of the 1,3,4-OXA_n derivatives (series I) although they present lower thermal stability. Moreover, the liquid crystal properties are significantly improved in the dendrimers compared to the mesogenic precursors.

XRD studies reveal interesting structural details concerning the packing of these compounds in their mesophases. On the basis of the experimental results, some supramolecular models have been proposed. In particular, interdigitation between neighboring layers or columns is observed, the extent of which depends on the spacer length and the oxadiazole isomer.

Regarding the luminescent properties, all the dendrimers display emission in solution and in the solid state. Derivatives bearing the 1,3,4-OXA_n moiety present higher quantum yield values compared to their homologous containing the 1,2,4-OXA_n unit.

It has been shown how the change in the oxadiazole heterocycle isomer leads to remarkable differences in the mesomorphism, structural parameters of the supramolecular organization, and luminescent properties of these dendrimers.

ASSOCIATED CONTENT

Supporting Information

More details about the synthesis, characterization, thermal stability data, POM textures, XRD patterns, and optical data of the materials. This material is available free of charge via the Internet at <http://pubs.acs.org>.

AUTHOR INFORMATION

Corresponding Author

*E-mail: jbarbera@unizar.es (J.B.); mmarcos@unizar.es (M.M.).

ACKNOWLEDGMENTS

This work was supported by the MICINN, Spain, under Project CTQ2009-09030, and FEDER funding, EU, by the seventh FP-THE PEOPLE PROGRAMME, The Marie Curie Actions; ITN, No. 215884-2, and by the Gobierno de Aragón (Project PI109/09, Research Group E04). S.H.-A. thanks the MICINN (Spain) for a FPU grant.

REFERENCES

- (1) (a) Vögtle, F.; Richardt, G.; Werner, N. *Dendrimer Chemistry*; Wiley-VCH: Weinheim, 2009. (b) Majoros, J.; Baker Jr., J. R. *Dendrimer-Based Nanomedicine*; Pan Stanford Publishing Pte. Ltd.: Singapore, 2008. (c) Fréchet, J. M.; Tomalia, D. A. *Dendrimers and Other Dendritic Polymers*; Wiley and Sons, Ltd.: New York, 2001.
- (2) (a) Lee, T.; Landis, C. A.; Dhar, B. M.; Jung, B. J.; Sun, J.; Sarjeant, A.; Lee, H. J.; Katz, H. E. *J. Am. Chem. Soc.* **2009**, *131*, 1692–1705. (b) Bolton, O.; Kim, J. *J. Mater. Chem.* **2007**, *17*, 1981–1988. (c) Huces, G.; Bryce, M. R. *J. Mater. Chem.* **2005**, *15*, 94–107. (d) Cha, S. W.; Choi, S. H.; Kim, K.; Jin, J. I. *J. Mater. Chem.* **2003**, *13*, 1900–1904. (e) Chien, Y. Y.; Wong, K. T.; Chou, P. T.; Cheng, Y. M. *Chem. Commun.* **2002**, 2874–2875.
- (3) (a) Sharma, S.; Sharma, P. K.; Kumar, N.; Dudhe, R. *Pharma Chem.* **2010**, *4*, 253–263. (b) dos Anjosa, J. V.; Sinoua, D.; de Meloc, S. J.; Srivastava, R. M. *Carbohydr. Res.* **2007**, *342*, 2440–2449. (c) Park, Y. D.; Kim, J. J.; Chung, H. A.; Kweon, D. H.; Cho, S. D.; Lee, S. G.; Yoon, Y. J. *Synthesis* **2003**, 560–564. (d) Shi, W.; Qian, X.; Zhang, R.; Song, G. *J. Agric. Food Chem.* **2001**, *49*, 124–130.
- (4) (a) Parra, M.; Hidalgo, P.; Elgueta, E. Y. *Liq. Cryst.* **2008**, *35*, 823–832. (b) Zafiropoulos, N. A.; Choi, E.-J.; Dingemans, T.; Lin, W.; Samulski, E. T. *Chem. Mater.* **2008**, *20*, 3821–3831. (c) Han, J.; Zang, F. Y.; Chen, Z.; Wang, J. Y.; Zhu, L. R.; Pang, M. L.; Meng, J. B. *Liq. Cryst.* **2008**, *35*, 1359–1365. (c) Gallardo, H.; Cristiano, R.; Vieira, A. A.; Filho, R. A. W. N.; Srivastava, R. M.; Bechtold, I. H. *Liq. Cryst.* **2008**, *35*, 857–863. (d) Cristiano, R.; Vieira, A. A.; Ely, F.; Gallardo, H. *Liq. Cryst.* **2006**, *33*, 381–390. (e) Parra, M.; Hidalgo, P.; Carrasco, E.; Barberá, J.; Silvino, L. *Liq. Cryst.* **2006**, *33*, 875–882. (f) Cristiano, R.; Ely, F.; Gallardo, H. *Liq. Cryst.* **2005**, *32*, 15–25. (g) Sung, H. H.; Lin, H. C. *Liq. Cryst.* **2004**, *31*, 831–841. (h) Torgova, S. I.; Karamysheva, L.; Strigazzi, A. *Braz. J. Phys.* **2002**, *32*, 593–601.
- (5) (a) Westphal, E.; Bechtold, I. H.; Gallardo, H. *Macromolecules* **2010**, *43*, 1319–1328. (b) Yelamaggad, C. V.; Achalkumar, A. S.; Rao, D. S. S.; Prasad, S. K. *J. Org. Chem.* **2009**, *74*, 3168–3171. (c) He, C. F.; Richards, G. J.; Kelly, S. M.; Contoret, A. E. A.; O'Neill, M. Liq.

- Cryst.* **2007**, *34*, 1249–1267. (d) Qu, S.; Lin, M. *Tetrahedron* **2007**, *63*, 12419–12436. (e) Barberá, J.; Godoy, M. A.; Hidalgo, P. I.; Parra, M. L.; Ulloa, J. A.; Vergara, J. M. *Liq. Cryst.* **2011**, *38*, 679–688.
- (6) (a) Luckhurst, G. R. *Angew. Chem., Int. Ed.* **2005**, *44*, 2834–2836. (b) Görtz, V.; Southern, C.; Roberts, N. W.; Gleeson, H. F.; Goodby, J. W. *Soft Matter* **2009**, *5*, 463–471. (c) Apreutesei, D.; Mehl, G. H. *J. Mater. Chem.* **2007**, *17*, 4711–4715. (d) Görtz, V.; Goodby, J. W. *Chem. Commun.* **2005**, 3262–3264. (e) Madsen, L. A.; Dingemans, T. J.; Nakata, M.; Samulski, E. T. *Phys. Rev. Lett.* **2004**, *92*, 145505.
- (7) (a) Neupane, K.; Kang, S. W.; Sharma, S.; Carney, D.; Meyer, T.; Mehl, G. H.; Allender, D. W.; Kumar, S.; Sprunt, S. *Phys. Rev. Lett.* **2006**, *97*, 207802. (b) Figueirinhas, J. L.; Cruz, C.; Filip, D.; Feio, G.; Ribeiro, A. C.; Frère, Y.; Meyer, T.; Mehl, G. H. *Phys. Rev. Lett.* **2005**, *94*, 107802. (c) Merkel, K.; Kocot, A.; Vij, J. K.; Korlacki, R.; Mehl, G. H.; Meyer, T. *Phys. Rev. Lett.* **2004**, *93*, 237801.
- (8) (a) Peng, Q.; Xu, J.; Li, M.; Zheng, W. *Macromolecules* **2009**, *42*, 5478–5485. (b) Li, B. L.; Liu, Z. T.; He, Y. M.; Pan, J.; Fan, Q. H. *Polymer* **2008**, *49*, 1527–1537. (c) Yang, P. J.; Wu, C. W.; Sahu, D.; Lin, H. C. *Macromolecules* **2008**, *41*, 9692–9703.
- (9) (a) Natera, J.; Otero, L.; D'Eramo, F.; Sereno, L.; Fungo, F.; Sen, N.; Min, Y.; Wong, K. T. *Macromolecules* **2009**, *42*, 626–635. (b) Li, Y. H.; Wu, H. H.; Wong, K. T.; Hsieh, C. C.; Lin, Y. C.; Chou, P. T. *Org. Lett.* **2008**, *10*, 3211–3214. (c) Chen, S.; Xu, X.; Liu, Y.; Qiu, W.; Yu, G.; Sun, X.; Zhang, H.; Qi, T.; Lu, K.; Gao, X.; Liu, Y.; Zhu, D. *J. Mater. Chem.* **2007**, *17*, 3788–3795. (d) Wu, C. W.; Lin, H. C. *Macromolecules* **2006**, *39*, 7985–7997. (e) Xin, Y.; Wen, G. A.; Zeng, W. J.; Zhao, L.; Zhu, X. R.; Fan, Q.-L.; Feng, J. C.; Wang, L. H.; Peng, W. B.; Cao, Y.; Huang, W. W. *Macromolecules* **2005**, *38*, 6755–6758. (f) Cha, S. W.; Choi, S. H.; Kim, K.; Jin, J. I. *J. Mater. Chem.* **2003**, *13*, 1900–1904.
- (10) (a) Frein, S.; Camerel, F.; Ziessel, R.; Barberá, J.; Deschenaux, R. *Chem. Mater.* **2009**, *21*, 3950–3959. (b) Peng, Q.; Xu, J.; Li, M.; Zheng, W. *Macromolecules* **2009**, *42*, 5478–5485. (c) Wu, C. W.; Tsai, C. M.; Lin, H. C. *Macromolecules* **2006**, *39*, 4298–4305. (d) Wu, C. W.; Lin, H. C. *Macromolecules* **2006**, *39*, 7985–7997.
- (11) (a) Li, Y. H.; Wu, H. H.; Wong, K. T.; Hsieh, C. C.; Lin, Y. C.; Chou, P. T. *Org. Lett.* **2008**, *10*, 3211–3214. (b) Du, P.; Zhu, W. H.; Xie, Y. Q.; Zhao, F.; Ku, C. F.; Cao, Y.; Chang, C. P.; Tiana, H. *Macromolecules* **2004**, *37*, 4387–4398.
- (12) (a) Rosen, B. M.; Wilson, C. J.; Wilson, D. A.; Peterca, M.; Imam, M. R.; Percec, V. *Chem. Rev.* **2009**, *109*, 6275–6540. (b) Marcos, M.; Martín-Rapún, R.; Omenat, A.; Serrano, J. L. *Chem. Soc. Rev.* **2007**, *36*, 1889–1901. (c) Donnio, B.; Buathong, S.; Bury, L.; Guillon, D. *Chem. Soc. Rev.* **2007**, *36*, 1495–1513. (d) Deschenaux, R.; Donnio, B.; Guillon, D. *New J. Chem.* **2007**, *31*, 1064–1073. (e) Donnio, B.; Guillon, D. *Adv. Polym. Sci.* **2006**, *201*, 45–155.
- (13) (a) Hernández-Ainsa, S.; Barberá, J.; Marcos, M.; Serrano, J. L. *Angew. Chem., Int. Ed.* **2010**, *49*, 1990–1994. (b) Fitié, C. F. C.; Tomatsu, I.; Byelov, D.; de Jeu, W. H.; Sijbesma, R. P. *Chem. Mater.* **2008**, *20*, 2394–2404. (c) Martín-Rapún, R.; Marcos, M.; Omenat, A.; Barberá, J.; Romero, P.; Serrano, J. L. *J. Am. Chem. Soc.* **2005**, *127*, 7397–7403. (d) Ujiie, S.; Yano, Y.; Mori, A. *Mol. Cryst. Liq. Cryst.* **2004**, *411*, 483–489. (e) Faul, C. F. J.; Antonietti, M.; Henzle, H. P.; Smarsly, B. *Colloids Surf., A* **2003**, *212*, 115–121. (f) Hernández-Ainsa, S.; Barberá, J.; Marcos, M.; Serrano, J. L. *Chem. Mater.* **2010**, *22*, 4762–4768.
- (14) dos Santos, D. R.; de Oliveira, A. G. S.; Coelho, R. L.; Begnini, I. M.; Magnago, R. F.; da Silva, L. *ARKIVOC* **2008**, *xvii*, 157–166.
- (15) Chechik, V.; Zhao, M.; Crooks, R. M. *J. Am. Chem. Soc.* **1999**, *121*, 4910–4911.
- (16) Martínez, V.; Mecking, S.; Tassaing, T.; Besnard, M.; Moisan, S.; Cansell, F.; Aymonier, C. *Macromolecules* **2006**, *39*, 3978–3979.
- (17) Tsiourvas, D.; Felekis, T.; Sideratou, Z.; Paleos, C. *Liq. Cryst.* **2004**, *31*, 739–744.
- (18) Hummelen, J. C.; van Dongen, J. L. J.; Meijer, E. W. *Chem.—Eur. J.* **1997**, *3*, 1489–1493.
- (19) (a) Balogh, L.; Leuze-Jallouli, A.; Dvornic, P.; Kunugi, Y.; Blumstein, A.; Tomalia, D. A. *Macromolecules* **1999**, *32*, 1036–1042. (b) Dvornic, P. R.; Tomalia, D. A. *Starburst Dendrimers, Technology Review*; Dendritech, Inc.: Midland, MI, 1995.
- (20) (a) Cameron, J. H.; Facher, A.; Stebani, G.; Latterman, G. *Adv. Mater.* **1995**, *7*, 578–581. (b) Tsiourvas, D.; Stathopoulou, K.; Sideratou, Z.; Paleos, C. M. *Macromolecules* **2002**, *35*, 1746–1750.
- (21) Martín-Rapún, R.; Marcos, M.; Omenat, A.; Serrano, J. L.; Taffin de Givenchy, E.; Guittard, F. *Liq. Cryst.* **2007**, *34*, 395–400.
- (22) (a) Baars, M. W. P. L.; Söntjens, S. H. M.; Fischer, H. M.; Peerlings, H. W. I.; Meijer, E. W. *Chem.—Eur. J.* **1998**, *4*, 2456–2466. (b) Barberá, J.; Marcos, M.; Serrano, J. L. *Chem.—Eur. J.* **1999**, *5*, 1834–1840.
- (23) Zhou, J. X.; Wong, F. F.; Chen, C. Y.; Yeh, M. Y. *Bull. Chem. Soc. Jpn.* **2006**, *79*, 644–648.

A Small-Angle Neutron Scattering Study of the Equilibrium Conformation of Polyelectrolytes in Stoichiometric Saloplastic Polyelectrolyte Complexes

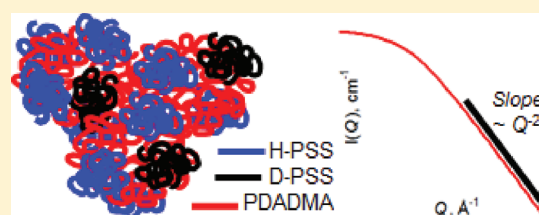
Marie Z. Markarian,^{†,§} Haifa H. Hariri,[†] Andreas Reisch,^{†,⊥} Volker S. Urban,[‡] and Joseph B. Schlenoff^{*,†}

[†]Department of Chemistry and Biochemistry, The Florida State University, Tallahassee, Florida 32306, United States

[‡]Center for Structural Molecular Biology, Oak Ridge National Laboratory, Oak Ridge, Tennessee 37831, United States

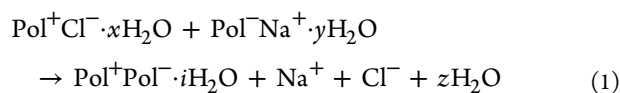
S Supporting Information

ABSTRACT: Stoichiometric polyelectrolyte complexes, PECs, from fully sulfonated poly(styrenesulfonate), PSS, as polyanion and poly-(diallyldimethylammonium chloride), PDADMA, as polycation, were prepared by mixing them at optimized polyelectrolyte and NaCl concentrations. The complexes were compacted by ultracentrifugation and then annealed in NaCl solutions at elevated temperatures to allow the polymers to fully intermix and relax. Small-angle neutron scattering, SANS, with contrast matching, was used to study single polyelectrolyte chain dimensions in PECs made from a mixture of deuterated and protonated PSS chains. Two PSS molecular weights in PECs were investigated at various ionic strengths. SANS curves, form factor fits, and corresponding Kratky plots indicate the Gaussian nature of the polyelectrolyte chains in the complexes regardless of molecular weight. PSS coils were slightly larger than the unperturbed dimension, more so for the higher molecular weight material, which was attributed to an effective stiffening of the chain due to ladderlike interactions between polyelectrolytes.



INTRODUCTION

Polyelectrolyte complexes, PECs, are held together by ion pairing interactions, Pol^+Pol^- , between oppositely charged units on (bio)macromolecules. The driving force for these polyvalent interactions is mainly the entropic release of counterions and water molecules.^{1–3}



PECs exist in a range of morphologies, largely differentiated by the way charge is balanced within the complex, and the water content. The counterion content of PECs also controls their physical and mechanical properties.^{4,5} Charges on polyelectrolytes are balanced either by the complementary polyelectrolyte (intrinsic charge compensation) or by counterions (extrinsic charge compensation).⁶ Nonstoichiometric PECs require extrinsic charge, whereas stoichiometric PECs may or may not contain ions.

Solution-precipitated PECs are prepared by mixing roughly stoichiometric (based on the charged repeat units) quantities of polyelectrolytes to yield diffuse precipitates that are close to stoichiometric.⁷ Michaels³ showed that these precipitates may be dissolved in ternary solvents and recast as dense films. Alternatively, they may be plasticized by the addition of salt and then re-formed into compact shapes (saloplastics).⁵ Under certain conditions, such as an excess of one polyelectrolyte, dilute solution, and a strong mismatch of molecular weight, a stable colloidal dispersion of nanoparticles (quasi-soluble PECs,

q-PECs) may be obtained.^{8,9} Q-PECs rely on a shell of extrinsic charge to keep them dispersed.¹⁰ Polyelectrolyte multilayers, PEMUs, a third example of complex, are formed by the alternating adsorption of polyelectrolytes at a surface.^{11,12} PEMUs remain nonstoichiometric, with plenty of extrinsic charge throughout, and grow exponentially layer after layer,^{13–15} or they reach a stoichiometric composition within the bulk but maintain nonstoichiometry at the surface, wherein they grow linearly.^{16,17} The final morphology of PEC is known as a coacervate.^{18,19} Coacervates contain the highest proportion of water and are diffuse liquidlike networks of polyelectrolytes which may or may not be at equilibrium.

Despite decades of intensive work on all morphologies of PEC, very little is known about the conformation of their polyelectrolyte components. Kabanov described one experiment where the single chain conformation of poly-(methacrylate), PMA, in PMA/chitosan complexes was characterized by neutron scattering.²⁰ Recently, the Saclay group has started to address the question of polyelectrolyte conformation in biopolymer PECs using small-angle neutron scattering, SANS.^{21–24} They investigated the conformation of polyanions and proteins in complexes from mixtures of deuterated and protonated PSS, D- and H-forms, respectively, and lysozyme at various mole ratios resulting in different levels of complexation and organization. These studies reinforce the

Received: October 9, 2011

Revised: December 5, 2011

Published: December 20, 2011

notion that PEC morphology is controlled by sample preparation techniques, including mixing stoichiometry.

Complexes of biopolymers such as proteins may include interactions stemming from the heterogeneity of the biomolecule. The central goal of our work was to establish the conformation of a polyelectrolyte inside a stoichiometric, synthetic complex at equilibrium. This goal required the synthesis of fully sulfonated deuterated polystyrene, followed by the precipitation of stoichiometric complexes and densification using saloplastic processing. Stoichiometry was verified by chemical composition and by analysis of the response of the poly(4-styrenesulfonate), PSS, poly(diallyldimethylammonium), PDADMA, complex to salt. The equilibrium conformation was promoted by extensive exposure to salt, which has been shown to “melt” structure locked in by nonequilibrium processing, such as multilayer formation.²⁵ Interpretation of the neutron scattering results was simplified through the use of contrast matching conditions and diluting deuterated with undeuterated polymer.

■ EXPERIMENTAL SECTION

Materials. H-polystyrene, H-PS, C_8H_8 ($M_w = 8000$ g/mol, $M_w/M_n = 1.06$ and $M_w = 55\,500$ g/mol, $M_w/M_n = 1.07$), and D-polystyrene, D-PS, C_8D_8 ($M_w = 7400$ g/mol, $M_w/M_n = 1.06$ and $M_w = 56\,700$ g/mol, $M_w/M_n = 1.09$), were from Polymer Source, Inc. PDADMA, 20 wt % in H_2O (average $M_w = 200\,000$ – $350\,000$), sodium chloride, sulfuric acid- D_2 , D_2SO_4 (96–98 wt % and 99.5 atom % D), and methanol were from Sigma-Aldrich; dichloroethane, $C_2H_4Cl_2$, from Fisher Scientific; sulfuric acid- H_2 , H_2SO_4 (96–98 wt %), from EMD; deuterium oxide, D_2O , from Cambridge Isotope Laboratories, Inc. All chemicals were used as received.

Sulfonation of H- and D-Polystyrenes. A previously reported method^{26,27} with slight modifications was used for the sulfonation of polystyrene. 1.0 g of H-PS was dissolved in 60 mL of dichloroethane which was gradually added, under vigorous stirring, to 200 mL of methanol to form a fine precipitate. The precipitate was collected and dried under vacuum for 12 h. The dried polystyrene was then sorted through a 106 μm sonic sifter sieve (ATM Corp.). 0.8 g of the H-PS powder (particle size <106 μm) was transferred to a round-bottom flask, and 80 mL of H_2SO_4 was added. The solution was stirred at 90 °C for 6 h in an oil bath. The sulfonation of D-PS was carried out similarly, except D_2SO_4 was used to avoid exchange of the PS deuteriums with protons. The reaction was quenched by placing the round-bottom flask in an ice bath. The product was slowly added to 1.5 L of ice-cold water and then dialyzed against water in 3500 MWCO dialysis tubing (SpectraPor) for 5 days. The PSSH solution was neutralized using NaOH, and the product was collected by lyophilization. Titrations, NMR characterization, and GPC coupled to light scattering showed full sulfonation for PSSH and PSSNa chains. Elemental analysis (Atlantic Microlab, Inc.) on the PSSNa samples indicated 98.4% sulfonation for the 104K and 102% for the 14K PSSNa chains (theoretical C:S by weight = 3.00; found C:S = 3.05 for 104K and 2.95 for 14K).

Light Scattering from D-PSSNa Solutions. D-PSSNa solutions were prepared at various concentrations in 4.17 M NaCl and 27:73 D_2O/H_2O and were left at room temperature for 24 h to completely dissolve. The solutions were filtered through 0.1 μm Supor-100 membrane filters, Pall Corp., and introduced into a temperature controlled cell from a 1.0 mL injection loop immersed in a water bath at 20 °C at 0.1 mL/min. Static and dynamic light scattering were performed with a DAWN-EOS (Wyatt Technologies) equipped with a Ga-As laser at 690 nm, a temperature controlled cell, 18 photodiode detectors, Wyatt QELS autocorrelator, and an Optilab-DSP interferometric refractometer. All data analysis was done using ASTRA (v 5.3.4) for Windows provided by Wyatt Technologies. The viscosity and the refractive index of the solvent were determined offline and were $\eta = 1.704$ cP and $n = 1.37$.

Preparation of PSS/PDADMA Complexes. Compact PSS/PDADMA complexes, CoPECs, were prepared with different molecular weight PSSNa and varying compositions, either 100% H-PSSNa or 20:80 by mole D- to H-PSSNa. Polyelectrolyte solutions were 0.125 M with respect to the monomer units at pH 7.0 in 0.25 M NaCl. To 25.0 mL PSS solution in centrifuge tubes, 25.0 mL of PDADMA solution was added followed by 25.0 mL of 0.25 M NaCl. The tubes were shaken on a vortex mixer for 5 min. Once the precipitates settled, the tubes were placed in a water bath at 50 °C for 2 h. The complexes were then compacted with a spatula and transferred along with the supernate to polycarbonate thick wall Beckman centrifuge tubes and centrifuged in a Beckman Optima XL-90 ultracentrifuge equipped with a type 90Ti rotor (fixed tube angle, Beckman) at 155000g for 4 h at 20 °C. To ensure complete intrinsic charge compensation, the centrifuged complexes were placed in 1.0 M NaCl and heated at 70 °C for 6 h. Next they were placed in 2.5 M NaCl and centrifuged at the conditions mentioned above and left in the centrifuge tubes to anneal in the supernate for 8 h. White, compact, and tough complexes were obtained.

Stoichiometry of Complexes by NMR Spectroscopy. Pieces of complexes, weighing 100 mg each, were soaked in 100% D_2O to remove H_2O . The exchange was performed twice, 1 h each, to ensure complete exchange of H_2O with D_2O . Next, they were dissolved in 2.5 M KBr in D_2O . NMR spectra were collected with a Bruker Avance 600 MHz operated by TopSpin 2.1 software. The peak area of aromatic protons from PSS and the cumulative peak areas of aliphatic protons from the PSS backbone and the PDADMA units were recorded, and their ratios were compared to a standard curve constructed from known ratios of PSS to PDADMA dissolved in similar conditions.

Neutron Scattering of CoPECs and D-PSSNa Solutions. Complexes were cut into $0.8 \times 10 \times 12$ mm³ slices and placed in 0.1, 0.25, 0.5, 1.0, and 1.5 M NaCl in 27:73 D_2O/H_2O by mole for solvent exchange. The NaCl/ D_2O/H_2O solutions were exchanged twice. After 48 h of soaking in the salt solutions, the samples were placed in 1 mm path length Spectrosil quartz cuvettes (VWR) with their corresponding salt solutions to avoid sample drying over the data acquisition time period. D-PSSNa solutions, from 14K and 104K polyelectrolytes, were prepared at a concentration of 80 mg/mL in 4.17 M NaCl in 27:73 D_2O/H_2O to determine the coil dimension of the PSS chains at theta conditions.²⁸ 4.17 M NaCl in 27:73 D_2O/H_2O was used as background.

Neutron scattering measurements were performed at the High Flux Isotope Reactor facility's Bio-SANS CG-3 beamline at the Oak Ridge National Laboratory.²⁹ The detector Ordela 2100N (Ordela, Inc.) was a position-sensitive 3He 1×1 m² with a resolution of 5.1×5.1 mm² per pixel and was offset from the direct beam axis. The scattering vector Q , defined by $Q = (4\pi/\lambda)(\sin(\theta/2))$ where λ ($6 \text{ \AA} \pm 15\%$) is the wavelength of the neutrons and θ is the scattering angle, was varied between $0.003 < Q < 0.4 \text{ \AA}^{-1}$ by performing scattering measurements at two detector distances: 14.5 m for $0.003 < Q < 0.07 \text{ \AA}^{-1}$ and 1.7 m for $0.01 < Q < 0.4 \text{ \AA}^{-1}$. The temperature of the sample holder was set at 20 °C for the complexes and either 20 or 16.4 °C for the solutions. 2-D scattering data were acquired using the SPICE data acquisition system, and the $I(Q)$ vs Q profiles were generated by azimuthally averaging the 2-D scattering profiles using the SPICE Package for IgorPro, provided by ORNL, which were then normalized to the incident beam transmission and sample thickness and corrected for the detector dark current. See Supporting Information for data treatment.

Microscopy Imaging of CoPECs. Complexes, prepared and stored in 0.25 M NaCl, were sliced into 10 μm thick slices by cryosectioning (Leica CM1850). The samples were rinsed, immersed, and then imaged in 0.1, 0.25, 0.5, 1.0, and 1.5 M NaCl solutions. Imaging was carried out on a Nikon Eclipse Ti inverted microscope equipped with a photometrics CoolSNAP HQ2 camera and NIS-Elements AR 3.0 imaging software.

Time lapse imaging was carried out on a Nikon SMZ1000 with NIS-Elements BR 3.1 imaging software to study the effect of NaCl on the swelling or shrinking of the complexes. Complexes were cut into $1 \times 1 \times 15$ mm³ pieces and fixed at one end in a sample holder containing the appropriate salt concentration. Frames were captured

every 30 s for the first 10 min, every 1 min for the following 50 min, and every 15 min for 23 h.

RESULTS AND DISCUSSION

The conformation of individual polyelectrolytes depends on the ionic nature and strength of their environment.³⁰ With increasing salt concentration polyelectrolytes transition from extended to coiled and then to globular structures.^{30–32} The response of PECs to increasing salt is highly dependent on their morphology and stoichiometry. For example, well-matched, intrinsically compensated complexes prepared as multilayers swell with added salt³³ due to doping by the salt (the reverse of eq 1). Expansion of polyelectrolytes in added salt is often termed “antipolyelectrolyte” behavior and is commonly seen with polymeric zwitterions, another system which has well-matched positive and negative units.³⁴ An early example of swelling of intrinsic PECs in salt are “snake cage resins” made by polymerizing acrylic counterions inside conventional ion exchange resins.³⁵

One interpretation of antipolyelectrolyte response in PECs is that charges on repeat units are already heavily screened by oppositely charged monomer units, as they would be in concentrated salt solution, and therefore adopt a compact coil conformation. For polyelectrolytes, long-range interactions include electrostatic repulsions between like-charged segments, which are eliminated, at the θ -condition,³⁶ by screening with sufficient salt concentration. The θ -solvent and temperature for dilute H-PSSNa solutions are known:^{28,37} 4.17 M NaCl at 16.4 °C where the second virial coefficient is zero and the coil dimension is given by

$$R_{g\theta}^2 = 3 \times 10^{-4} M_w \quad (2)$$

where R_g is the radius of gyration in nm and M_w is the molecular weight of the PSSNa chain.^{28,38} The ideality theory often extends to polymer melts where the chains adopt unperturbed Gaussian conformations.^{39–41} It is of interest to ascertain whether individual polymer chains in polyelectrolyte complexes are close to their θ (unperturbed) dimensions and would, in this respect, resemble a polymer melt.

Sulfonated Polystyrene. Preparing fully charged poly(styrenesulfonate) has been a challenge.^{42–47} There are two main synthetic methods: the Vink's (or “soft”) and the “hard” sulfonation methods.^{27,44} Drawbacks of these methods are the incomplete sulfonation of the polystyrene units, sulfone bridge formation, and chain degradation by oxidation of the polymer backbone. In this work, an improved sulfonation procedure was employed where 100% sulfonation of polystyrene was observed with no detectable backbone degradation or bridging. The products were characterized by gel permeation chromatography (Figure S1 and Table S1 in the Supporting Information) titration and elemental analysis. ¹H NMR of deuterated PS sulfonated by 96% H₂SO₄ revealed exchange of ~17% deuteriums for protons on the sulfonated product. Therefore, to maintain full deuteration of the D-PSS, D₂SO₄ was required for sulfonation.

Stoichiometric, Compact Complexes at Equilibrium.

In recent works by our group compact complexes, CoPECs, from PSS and PDADMA, described as saloplastic, were prepared by mixing polyelectrolytes under high salt concentration and characterized by mechanical testing.^{4,5} A key finding was that under the conditions employed the CoPECs, although prepared from equimolar polyelectrolyte solutions, were highly

porous nonstoichiometric complexes exhibiting viscoelastic properties depending on the salt concentrations of the storing medium. As prepared, these PECs were shown to contain excess polyelectrolyte trapped in pores. Extrinsic charge present on as-made PECs leads to a “polyelectrolyte” response to added salt (i.e., shrinkage), as observed in these CoPECs and in some multilayers.²⁷ For as-made PEMUs, we have shown that “annealing” in salt helps to expel extrinsic charge by promoting polyelectrolyte intermixing.^{25,33}

The variety in morphology, and thus response to salt concentration, is often a result of kinetic limitations in polyelectrolyte mixing: the number of polyelectrolyte ion pairs formed is not necessarily all of those mixed. It was essential in this work to ensure full intrinsic mixing of components. Thus, the polyelectrolyte solution mixing method was modified to prepare complexes with maximum intrinsic compensation. Relative to our prior work, polyelectrolyte solutions were prepared at lower concentration, 0.125 M with respect to the monomer units, and in lower ionic strength, 0.25 M NaCl, where the polymer chains adopt a less compact conformation.^{48,49} These conditions provide high contact area at initial complexation and therefore a higher probability of pairing between PSS and PDADMA units relative to those prepared at high polyelectrolyte and salt concentrations where the chains are compacted due to charge screening by salt ions.

On mixing solutions, a white fibrous precipitate was formed which settled within 10 min but dispersed upon shaking. In order to maximize the homogeneity of the samples, the nascent complexes were annealed in 1.0 M NaCl at 50 °C. The annealing conditions increase the diffusion of the polyelectrolyte chains, optimizing charge pairing in the networks.²⁵ This procedure induced fusing of the fibrous material and within 2 h a highly porous blob was obtained which was compacted to a white and tough material by centrifugation, but the porosity of the sample remained even under ultracentrifugation and annealing in 2.5 M NaCl, as shown in Figure 1.

The expansion of polyelectrolyte complexes with decreasing salt concentration is a signature of nonstoichiometric composition. Pores played a major role in controlling the mechanical properties of nonstoichiometric CoPECs studied by Hariri et al.⁴ The phenomenon was attributed to excess polyanions trapped within them contributing to the bulk elastic modulus through osmotic stressing which caused swelling of the complexes in solutions of decreasing NaCl concentration. In this study, the stoichiometry of the CoPECs was investigated by NMR where pieces of complexes were dissolved in 2.5 M KBr in D₂O (Figure S2). The peak area of aromatic protons from PSS and the cumulative peak areas of aliphatic protons from the PSS backbone and the PDADMA units were recorded, and their ratio was determined. The equimolarity in the bulk complex was thus confirmed. In addition, 1:1 stoichiometry within the bulk of the PEC was investigated by testing the response of the saloplastic complexes to salts. The complexes were placed in different NaCl solutions and time lapse imaging was performed, followed by microscopy imaging of 10 μ m sections. The complexes prepared from high molecular weight PSSNa yield more compact materials than those prepared from the low molecular weight PSSNa, which are softer.

Doping of PEMUs and polyelectrolyte complexes is accompanied by swelling.^{3,33} Michaels reported the volumetric increase of PSS and poly(vinylbenzyltrimethylammonium) complexes by 25% in 1.0 M bromide salts and up to 5% in 1.0 M chloride salts; the difference was attributed to the

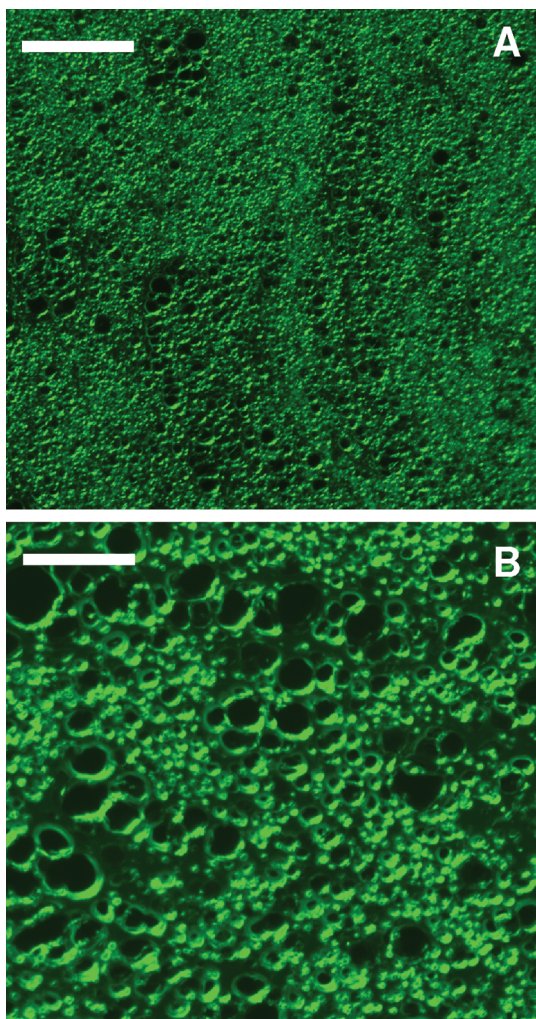


Figure 1. Micrographs of 10 μm thick sections of PSS/PDADMA complexes made from 104K D-PSSNa (A) and 14K D-PSSNa (B) immersed in 0.25 M NaCl. The scale bar in both panels is 100 μm . Though porous, the complex is fully stoichiometric and intrinsic (i.e., no counterions) in the undoped state. Since pores are much larger than the characteristic size of the chains, they do not contribute structure to the scattering data over the angles recorded.

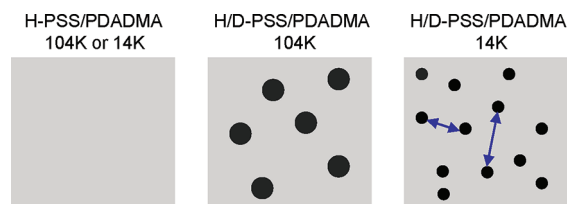
hydrating force of the different ionic species.³ In the case of PEMUs built from PSS/PDADMA, an increase in thickness by 6% was reported for multilayers immersed in 1.0 M NaCl.³³ The doping and hydration of PEMUs were investigated by ATR-FTIR which revealed 35% doping by NaNO_3 at 1.0 M and the incorporation of 15 water molecules per doping ion pair, causing the increase in thickness of the multilayers.⁵⁰

In this study, minimal swelling was observed in both the bulk material and the pores of complexes. PECs made with 104K PSS increased by 5% in length and those prepared with 14K PSS increased by 10%, when immersed in solutions from 0.1 to 1.5 M NaCl, consistent with doping only. Qualitatively, the CoPECs placed in increasing salt concentration became softer as a result of doping, and in 1.5 M NaCl they turned translucent due to refractive index matching of the polymeric material and the NaCl solution (see Figure S3). No change in pore size (Figure S4) indicates the absence of excess polyelectrolyte trapped in the pores eliminating osmotic swelling with decreasing NaCl concentration. Therefore, the

bulk PEC is concluded to be 1:1 charge matched, i.e., fully intrinsic, in the undoped state.

Minimizing Polymer/Polymer Correlations by Dilution. The neutron scattering length densities of the H- and D-forms of poly(styrenesulfonate) vary greatly; yet, it was shown this isotopic substitution did not change complexation with proteins.^{22–24,51} By diluting the deuterated polymer with the nondeuterated one, chain overlap and interchain correlations are minimized, which simplifies the data treatment for the investigation of single polyelectrolyte chain conformation, as shown in Scheme 1. Such a strategy was used by Gummel et al.

Scheme 1. Cartoon Depicting the Neutron Contrast^a



^aLight gray corresponds to contrast matched components. Black circles are the coils of deuterated PSS. Blue arrows correspond to possible long-range correlations observed in the 14K samples.

to investigate the conformation of D-PSS in PSS/lysozyme complexes: polyelectrolyte correlation peaks disappeared from the SANS profiles as the content of D-PSS was decreased from 100% to 25% in a mix of H- and D-forms.²⁴

In our studies two molecular weights of PSSNa were used, labeled as 104K and 14K, with degrees of polymerization $N = 506$ and $N = 66$, respectively. To determine the D- to H-PSS ratio needed, the overlap concentration, C^* , of 104K PSS in the complexes was calculated based on the PSS persistence length at θ -conditions $l_p = 6.9 \text{ \AA}$ ^{49,52} (see Supporting Information). The calculated C^* is 0.341 M. To minimize interchain scattering signal correlations in the SANS profiles, complexes were prepared using 20 mol % D-PSS and 80 mol % H-PSS since the calculated C^* is 43% of the concentration of PSS in the CoPECs, 0.782 M, which is calculated assuming all of the starting material, 3.125 mmol, occupies 4 cm^3 as complex; i.e., the D-PSS concentration was about half of the calculated C^* .

Contrast Matching. Further data treatment simplification was achieved through SLD contrast matching of sample components and appropriate solvent mixtures.²¹ The method allows background corrections and eliminates mathematical complications arising from multiple scattering components (see Scheme 1). Accuracy of contrast matching increases with the homogeneity of the samples; PSS/PDADMA stoichiometry and porosity are important factors controlling the validity of the method. Although our samples are highly porous, the CoPECs are homogeneous in the Q -range covered in this study, 1.5–209 nm. In addition, the annealing steps introduced during sample preparation maximize uniformity at the monomer unit scale. Therefore, samples may be assumed to be a homogeneous blend of H-PSS/PDADMA and D-PSS/PDADMA.

Contrast matching was required for any component that was not D-PSS/PDADMA, i.e., electrolyte, water, and H-PSS/PDADMA. SLDs were determined using the SLD calculator available online from NIST.⁵³ First, at different $\text{NaCl}:\text{D}_2\text{O}:\text{H}_2\text{O}$ conditions, the atomic composition and SLDs of the complexes, $\text{C}_{16}\text{H}_{23}\text{O}_3\text{NS}(\text{NaCl})_x(\text{H}_2\text{O})_y(\text{D}_2\text{O})_z$, were determined, where the extent of salt doping and hydration of the

complexes were estimated from spectroscopic studies on PSS/PDADMA multilayers.⁵⁰ Next, the SLDs of NaCl:D₂O:H₂O were established at different NaCl molarities and H₂O/D₂O ratios.⁵⁴ Finally, the results were compared (Figure 2), where

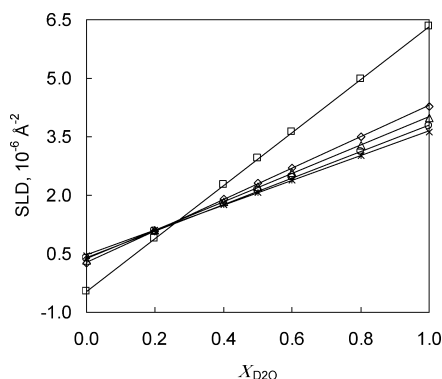


Figure 2. Scattering length densities of NaCl:H₂O:D₂O (□) and of H-PSS/PDADMA complexes at different NaCl concentrations [1.5 M (◇), 1.0 M (△), 0.5 M (○), and 0.1 M (×)] as a function of solvent D₂O mole fraction.

the intersecting lines indicated the contrast matching conditions; 27:73 by mole D₂O/H₂O regardless of NaCl concentration.

Neutron Scattering Results. Four sets of complexes were prepared: two from 104K PSS and PDADMA at either 20%:80% D-PSS:H-PSS, as sample, or 100% H-PSS, as background, and two from 14K PSS and PDADMA at the same D- to H-PSS conditions. SANS measurements were performed on samples that were solvent exchanged with 27:73 by mole D₂O/H₂O and stored in different ionic strengths in the same solvent for 48 h. From prior work on porous CoPECs, it takes about an hour for samples of similar dimensions to those employed here to equilibrate.⁴ Scattering and transmission data were collected for each set at different NaCl concentrations at 20 °C. Offline data analysis and form factor fittings were carried out (Supporting Information).

The SANS intensity depends on three components: contributions from the intrachain and interchain correlations and background scattering.⁵⁵ The background contribution is compensated by subtracting the profiles of 100% H-PSS/PDADMA CoPECs from those of the mixed 20%:80% D-PSS:H-PSS/PDADMA CoPECs. SANS features from interchain correlations are minimized as the concentration of the deuterium labeled polyelectrolyte is decreased;²⁴ the concentration of D-PSS is 10 mol % of the complex. Hence, the Debye formula for flexible polymers with Gaussian statistics was used to perform the form factor fits, $P(Q)$.⁵⁶

$$P(Q) = \frac{2[\exp(-u) + u - 1]}{u^2}, \quad u = \langle R_g^2 \rangle Q^2 \quad (3)$$

The fits for the different molecular weight PSS chains were performed at varying Q -ranges; for the 14K PSS, $0.02 < Q < 0.25 \text{ Å}^{-1}$, and for the 104K PSS, $0.004 < Q < 0.25 \text{ Å}^{-1}$ (see solid lines in Figure 3). The fit ranges excluded the low Q scattering signal contribution.

To validate the fits, Kratky plots, $I(Q) \times Q^2$ versus Q , were constructed where plateaus are observed as scatterings scale with Q^{-2} . For clarity, in Figure 4, the scattering curves and Kratky plots of the complexes in 1.0 M NaCl in 27:73 D₂O/

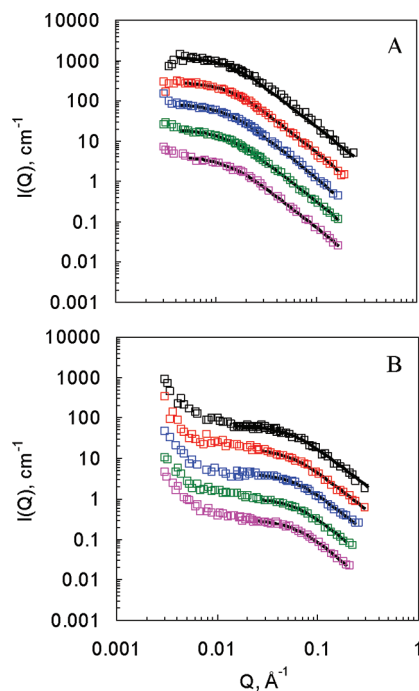


Figure 3. Small-angle neutron scattering data of PSS/PDADMA complexes made from different molecular weight PSSNa, 104K (A) and 14K (B), and immersed in different NaCl concentrations in 27:73 D₂O/H₂O; 0.1 M in magenta, 0.25 M in green, 0.5 M in blue, 1.0 M in red, and 1.5 M in black. The full lines show the Debye function fits for Gaussian polymers. The scattering curves and the form factor fits are offset vertically for clarity with increasing salt concentration.

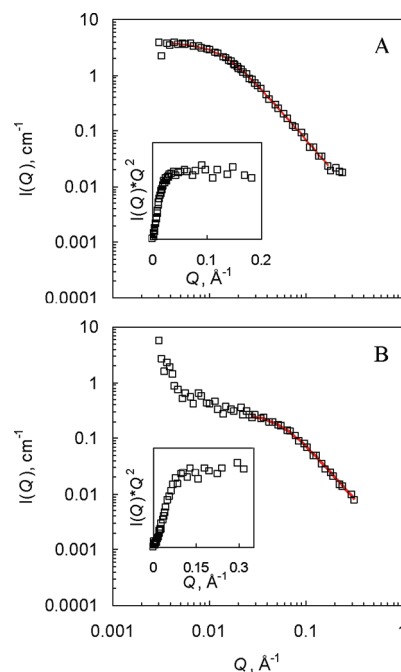


Figure 4. SANS of D-PSS/PDADMA in complexes made from 104K PSSNa (A) and 14K PSSNa (B) immersed in 1.0 M NaCl in 27:73 D₂O/H₂O. The solid lines are the Debye function fits for Gaussian polymers with R_g values of 105 ± 2 and $26.7 \pm 0.5 \text{ Å}$, respectively. The insets in both panels correspond to the Kratky plots indicating the Q^{-2} dependence of the scatterings at $0.05 < Q < 0.5 \text{ Å}^{-1}$ for the 104K complexes and $0.1 < Q < 0.35 \text{ Å}^{-1}$ for the 14K complexes.

H₂O are shown with their corresponding Kratky plots which clearly level off. The Kratky plots of all the SANS results are presented in Figure S7, and the R_g values determined are shown in Figure 5. The radii of 14K D-PSS chains in the complexes are

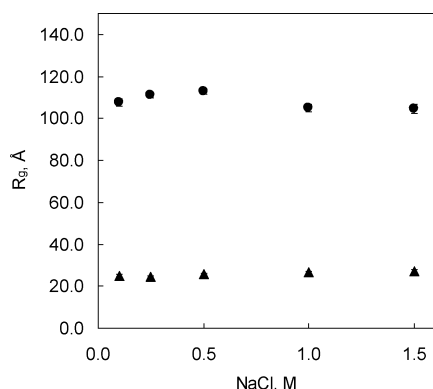


Figure 5. Radii of gyration from the Debye function fits for Gaussian polymers of D-PSS/PDADMA single chains in complexes immersed in different NaCl solutions: circles for 104K D-PSS and triangles for 14K D-PSS.

between 25.0 ± 0.6 and 27.2 ± 0.9 Å, while those of the 104 K chains vary between 105 ± 2 and 113 ± 1 Å.

Using eq 2, which is derived from dilute solutions, the R_g of D-PSSNa chains at θ -conditions was estimated: for the 14K D-PSSNa with a degree of polymerization $N = 66$ ($M_w = 14\,000$ g/mol) the R_g predicted is 20.5 Å, while the value for the 104K sample with a degree of polymerization $N = 506$ ($M_w = 108\,000$ g/mol) is 56.9 Å. To compare the conformation of PSS in complexes and in solution, scattering measurements were performed on D-PSSNa solutions at 80 mg/mL 4.17 M NaCl in 27:73 D₂O/H₂O and at 16.4 and 20 °C—conditions initially thought to be close to the θ -solvent.

Figure 6 presents the SANS profiles, the Kratky plots, and the form factor fits of the D-PSSNa chains in solution. The scattering profiles and the corresponding Kratky plots indicate deviations from Gaussian behavior. The SANS profiles of all solutions show a correlation peak at $Q \sim 0.28$ Å⁻¹ corresponding, roughly, to a 22 Å mesh structure, and at the low Q range no plateau is observed. In addition, the radii of gyration obtained from form factor fits and by Guinier analysis⁵⁷ are much larger than those predicted for D-PSSNa in dilute solutions, suggesting the presence of aggregates, although no precipitation was observed in solutions except for the 104K at 16.4 °C (Figure S8). The Kratky plots for the 104K D-PSSNa solutions show a peak at low Q followed by a gradual increase with increasing Q , regardless of temperature. In addition, the peak from the SANS at 16.4 °C is narrower than the peak at 20 °C (Figure 6A). On the other hand, the plots for the 14K D-PSSNa solutions show a slow increase with increasing Q with a broad peak formed at intermediate Q values (Figure 6B and Figure S9).

The presence of a peak in Kratky plots is a signature of globular structure. Semisotnov et al.^{58,59} studied the coil globule transition of certain proteins and the peak position dependence on molecular weight by small-angle X-ray scattering. In this study, the peak in the Kratky plots of the 104K D-PSSNa suggests the existence of globular polyelectrolytes. In fact, the globular structure of PSSNa at θ -conditions has been observed.⁶⁰ Pavlov et al. compared the hydrodynamic

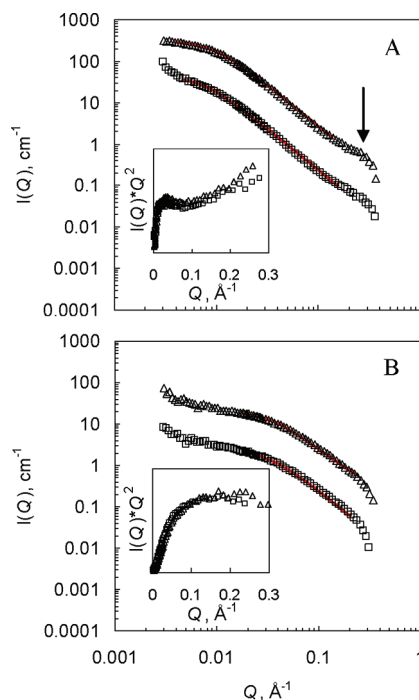


Figure 6. SANS profiles of 80 mg/mL D-PSSNa in 4.17 M NaCl in 27:73 D₂O/H₂O: 104K panel A; 14K panel B. The triangles correspond to scattering profiles collected at 20 °C and the squares at 16.4 °C. The data points at 20 °C are offset vertically for clarity. The arrow in panel A highlights the presence of a correlation peak. Red lines are Debye function fits for Gaussian polymers. Insets correspond to the Kratky plots of the SANS profiles.

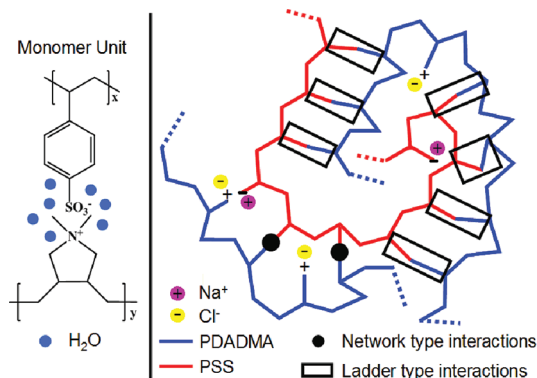
volume of PSSNa chains under various ionic conditions to the volumes of polystyrene at θ -conditions and to those of globular proteins; for PSSNa chains at θ -conditions the results agree with the volumes of globular structures. Here, for the 104K D-PSSNa chains based on the peak position in the Kratky plots, values of M_w are assigned to the samples in solutions using the calibration plot reported by Semisotnov et al.,⁵⁹ and the values are 400 and 220 kDa at 16.4 and 20.0 °C, respectively, which correspond to aggregates of the D-PSSNa and are consistent with the R_g values obtained by SANS (Figure S8).

To test the solvent quality, in particular for the 104K D-PSSNa, we performed dynamic and static light scattering experiments on D-PSSNa at various concentrations in 4.17 M NaCl in 27:73 D₂O/H₂O at 20 °C (Figures S10 and S11). The solvent and temperature conditions employed are not the θ -conditions, since the second virial coefficient, A_2 , is negative, $A_2 = -3.23 \times 10^{-4}$ mol mL/g², which indicates unfavorable solvent conditions for the 104K; i.e., the solvent is actually slightly “worse” than a θ -solvent. The observation is attributed to the D₂O in the solvent which alters the mixing thermodynamics of the polymer solutions. Isotope effects of solvents have been shown to increase the θ -temperature and the χ_p solvent–polymer interaction parameter of polymer solutions.⁶¹

Because the conditions (4.17 M NaCl in 27:73 D₂O/H₂O) employed for individual PSS chains were not the θ -conditions, eq 2 was used to estimate unperturbed dimensions within the PEC, which yielded 20.5 and 56.9 Å respectively for the low- and high-MW PSS. Various chain expansion effects can be considered to explain the fact that the observed R_g 's are higher than unperturbed. For example, eq 2 predicts the coil dimension of H-PSS chains where Na⁺ ions compensate the

negative sulfonate groups of the polyelectrolyte, while in the complexes charge is balanced by PDADMA units. To account for the additional bulk of the PDADMA unit in expanding the PSS chain, the PDADMA unit is added to the M_w of the D-PSS chain (see Scheme 2 for a representation of the monomer unit).

Scheme 2. Chemical Representation of a PSS/PDADMA Monomer Unit (left); Cartoon Depicting Network versus Ladder Type Interactions in a Polyelectrolyte Complex (right)^a



^aThe water molecules and the polyelectrolyte charges have been omitted for clarity.

The calculated R_g value for the 14K, $M_w = 21\,000$ g/mol, becomes 25.0 Å, comparable to the values observed in complexes (Table 1).

Table 1. Radii of Gyration of D-PSS Chains under Different Conditions (All Values in Å)

	D-PSSNa from eq 2	D-PSS/PDADMA from eq 2	D-PSS/PDADMA in complex at 0.1 M NaCl
104K	56.9	69.3	105 ± 2
14K	20.5	25.0	25.0 ± 0.6

Recent theoretical investigations of polymer melts predict deviations from ideality, in particular for polymers with high degree of polymerization, manifested as a dip in the Kratky plots.^{62–64} The behavior is attributed to long-range interactions due to the connectivity and incompressibility of the chains which swell the coil.⁶³ The work by Beckrich et al.⁶² on such melts provides some interesting comparisons: for a volume fraction of 0.5, similar to PSS in PECs, R_g was calculated to be 20 Å for 66 repeat units (i.e., 14K PSS) of length 2.63 Å and 53 Å for 506 repeat units (104K PSS), similar to eq 2. The Kratky plots in Figure S7 show plateaus in the interval $0.05 < Q < 0.31$ Å^{−1}, but no evidence for incompressibility is seen in the limited Q-range presented.

In the higher MW PSS, experimental R_g s are significantly larger than calculated for unperturbed coils, even adding an expansion for the bulky “counterpolyelectrolyte” segment (Table 1). Therefore, a scaling effect indicating chain expansion of the type one might observe for a good solvent could be invoked. Prior work by Jaber et al., who performed mechanical testing on microscale complexes of PSS/PDADMA prepared by multilayering,⁶⁵ provides some possible insight on the observed deviations. Mechanical testing on the PEMUs suggested a combination of 70% ladder type interactions where PSS and

PDADMA repeat units interact consecutively and 30% network type creating cross-links within the material.⁶⁵

The network type interactions introduce toughness in the saloplastic complexes translating into an increase of elastic modulus, whereas the ladder type interactions increase the stiffness of the polyelectrolytes on a local, i.e. the monomer, scale. Thus, the cooperative interactions between polyelectrolytes may also be responsible for an expansion of the chain if sequential ladder type interactions occur, causing R_g to scale greater than $N^{0.5}$. It should be noted that PDADMA has a positive charge for every four backbone carbons, whereas PSS has a negative charge for every 2 carbons. Thus, PDADMA is likely to cause more stiffening than polycations which have better backbone charge matching with PSS (i.e., 1 charge per 2 backbone C).

Conformations of PSS in doped PEC were evaluated. For the 14K samples the radius of gyration increases from 25.0 to 27.2 Å going from 0.1 to 1.5 M NaCl which corresponds to 9% expansion, similar to the swelling observed by time lapse microscopy in this work and by AFM.³³ An increase in R_g is expected as the counterions dope the complex. In contrast, for the 104K samples an increase of 4.5% is observed in R_g from 0.1 to 0.5 M NaCl followed by a slight decrease in 1.0 and 1.5 M NaCl. The macroscopic complex in turn swells up to 5% in 1.0 M NaCl, and no further swelling is observed at 1.5 M. We speculate that at 0.1 – 0.5 M NaCl not enough salt ions are incorporated into the CoPECs to break up the ladder type monomer pairs, whereas at 1.0 and 1.5 M enough counterions, 35% and more, dope the material, breaking the ladder type interactions which causes a slight decrease in the stiffness of the chain.

While only slight deviations at low Q from the fit to a Gaussian coil are observed for the 104K samples (Figures 3A and 4A) the 14K samples exhibited an increase in scattering at $Q < 0.01$ Å^{−1} (Figures 3B and 4B). An increase in scattering at low Q due to counterion SLD mismatch was observed by Prabhu et al. while studying the association of various counterions from a mixture to PSS chains.⁶⁶ SLD mismatch is not expected to be significant here, given the good coincidence of SLDs shown in Figure 2. It is possible that the minor deviations for the 104K sample at low Q are due to slight mismatch which alleviates at higher salt concentration. The low Q signals of complexes from 14K are larger and do not disappear with increasing salt concentration. Cousin et al. attributed the low Q “tails” to large scale heterogeneities due to aggregates.²² Annealing of the 14K complexes is expected to be more efficient than those prepared from high molecular weight polymers and therefore a better PSS PDADMA pairing which eliminates the possibility of aggregates and heterogeneities, as seen in the low R_g values presented in Figure 5. The increase in scattering at $Q < 0.01$ Å^{−1} is believed to be the result of long-range signal correlations due to the distribution of the D-PSS chains in the complexes (blue arrows in Scheme 1), which do not change with increasing salt concentrations.

Comparison of PEMU and PEC Properties. Convergence in properties of complexes prepared by multilayering and solution precipitation has been emphasized recently⁶⁷ and in the discussions above. For example, it is assumed that salt promotes interdiffusion and chain relaxation in bulk stoichiometric PECs and PEMUs. Because we are comparing identical compositions, we are confident such an assumption can be made. However, polymers within as-made (unannealed) PEMUs, especially those that grow “linearly”, are in kinetically

trapped conformations, or at least in layers, as demonstrated by neutron reflectivity.^{11,68–71} To what extent the kinetic trapping impacts the molecular conformation in PEMUs is unknown, but the Saclay group has demonstrated a rich phase behavior for protein/PSS PECs, depending on preparation conditions.^{21–24} In PEMUs it may well be that polyelectrolytes have anisotropic dimensions due to flattening at the surface on adsorption.

Finally, there is growing interest in the changing properties of films with decreasing film thickness. For example, the crystallization kinetics of poly(3-hydroxybutyrate) in thin films is greatly inhibited with decreasing thickness due to the reduced mobility of the polymers.^{72,73} To observe film thickness effects, it is generally understood that critical dimensions are of the order of the polymer coil. In the present case, for a polymer of molecular weight ca. 10^5 ; this size is about 10 nm, which is less than the thickness of almost all multilayers. On the other hand, it should be emphasized that the polymer dimensions presented herein are for intrinsically charged, equilibrated (by extensive annealing in salt) conditions. Extrinsically compensated regions of polyelectrolyte complexes, such as those at the surface of a PEMU, will contain more expanded chains.

CONCLUSIONS

In conclusion, stoichiometric PSS/PDADMA complexes were prepared by solution mixing of polyelectrolytes at low concentration and ionic strength for the study of the polyelectrolyte chain conformation in the complexes. Ultra-centrifugation followed by temperature and salt annealing provided porous yet homogeneous samples for small-angle neutron scattering characterization. Mixtures of H- and D-forms of PSS coupled with solvent/sample SLD contrast matching proved useful for the investigation of the polyanion conformation in the complexes. The single chain dimensions of deuterated PSS were determined by form factor fittings of scattering profiles from complexes prepared with different molecular weights polyanion and stored in ionic strengths ranging from 0.1 to 1.5 M NaCl in H₂O/D₂O.

Deviations from the θ -state of PSSNa were observed for both degrees of polymerization attributed to the presence of the intrinsically compensating PDADMA units. The ladder type interactions between consecutive repeat units of the PSS and PDADMA polyelectrolytes introduce chain stiffening which at low salt concentrations contribute to the expansion of the chains. At high salt concentrations two competing factors are observed: chain swelling due to the hydrating effects of doping ions and chain collapse due to the decoupling of PSS from PDADMA units, which especially influence ladder type interactions. The results present a first insight into the conformation of single polyelectrolyte chains in synthetic complexes at the macroscopic scale prepared by polyelectrolyte solution mixing or at the micro- to nanoscale for PEMUs built via the layer-by-layer assembly technique.

ASSOCIATED CONTENT

Supporting Information

GPC chromatograms, NMR of complexes, microscopy images, calculation of overlap concentration, SANS 2-D plots and data analysis, Kratky plots, dynamic light scattering, and concentrated D-PSSNa solutions at θ -conditions. This material is available free of charge via the Internet at <http://pubs.acs.org>.

AUTHOR INFORMATION

Corresponding Authors

*Tel 850-644-3001; Fax 850-644-8281; e-mail schlen@chem.fsu.edu.

§Current address: Intel Corporation, Hillsboro, Oregon 97124, United States.

†Current address: Faculté de Pharmacie, Université de Strasbourg 67401 Illkirch Cedex, France.

ACKNOWLEDGMENTS

The work was supported through NSF, Grant DMR 0939850. The Research at Oak Ridge National Laboratory's High Flux Isotope Reactor was sponsored by the Scientific User Facilities Division, Office of Basic Energy Sciences, U.S. Department of Energy.

REFERENCES

- (1) Ball, V.; Winterhalter, M.; Schwinte, P.; Lavalle, P.; Voegel, J. C.; Schaaf, P. *J. Phys. Chem. B* **2002**, *106*, 2357.
- (2) Bucur, C. B.; Sui, Z.; Schlenoff, J. B. *J. Am. Chem. Soc.* **2006**, *128*, 13690.
- (3) Michaels, A. S.; Bixler, H. J. *Kirk-Othmer Encycl. Chem. Technol.*, 2nd Ed. **1968**, *16*, 117.
- (4) Hariri, H. H.; Schlenoff, J. B. *Macromolecules* **2010**, *43*, 8656.
- (5) Porcel, C. H.; Schlenoff, J. B. *Biomacromolecules* **2009**, *10*, 2968.
- (6) Schlenoff, J. B.; Ly, H.; Li, M. *J. Am. Chem. Soc.* **1998**, *120*, 7626.
- (7) Michaels, A. S. *Ind. Eng. Chem.* **1965**, *57*, 32.
- (8) Karibyan, N.; Dautzenberg, H. *Langmuir* **1998**, *14*, 4427.
- (9) Kabanov, V. A.; Zevin, A. B. *Macromol. Chem. Suppl.* **1984**, *6*, 259.
- (10) Zintchenko, A.; Rother, G.; Dautzenberg, H. *Langmuir* **2003**, *19*, 2507.
- (11) Decher, G. *Science* **1997**, *277*, 1232.
- (12) Decher, G.; Schlenoff, J. B. *Multilayer Thin Films: Sequential Assembly of Nanocomposite Materials*; Wiley-VCH: Weinheim, 2003.
- (13) Picart, C.; Lavalle, P.; Hubert, P.; Cuisinier, F. J. G.; Decher, G.; Schaaf, P.; Voegel, J. C. *Langmuir* **2001**, *17*, 7414.
- (14) Porcel, C.; Lavalle, P.; Ball, V.; Decher, G.; Senger, B.; Voegel, J. C.; Schaaf, P. *Langmuir* **2006**, *22*, 4376.
- (15) Porcel, C.; Lavalle, P.; Decher, G.; Senger, B.; Voegel, J. C.; Schaaf, P. *Langmuir* **2007**, *23*, 1898.
- (16) Ladam, G.; Schaad, P.; Voegel, J. C.; Schaaf, P.; Decher, G.; Cuisinier, F. *Langmuir* **1999**, *16*, 1249.
- (17) Schlenoff, J. B.; Dubas, S. T. *Macromolecules* **2001**, *34*, 592.
- (18) Li, Y. J.; Dubin, P. L.; Havel, H. A.; Edwards, S. L.; Dautzenberg, H. *Langmuir* **1995**, *11*, 2486.
- (19) Dubin, P. L.; Li, Y. J.; Jaeger, W. *Langmuir* **2008**, *24*, 4544.
- (20) Kabanov, V. A. In *Multilayer Thin Films: Sequential Assembly of Nanocomposite Materials*; Decher, G., Schlenoff, J. B., Eds.; Wiley-VCH: Weinheim, 2003; p 47.
- (21) Boué, F.; Cousin, F.; Gummel, J.; Oberdisse, J.; Carrot, G.; El Harrak, A. C. R. *Phys.* **2007**, *8*, 821.
- (22) Cousin, F.; Gummel, J.; Ung, D.; Boué, F. *Langmuir* **2005**, *21*, 9675.
- (23) Gummel, J.; Boué, F.; Deme, B.; Cousin, F. *J. Phys. Chem. B* **2006**, *110*, 24837.
- (24) Gummel, J.; Cousin, F.; Boué, F. *Macromolecules* **2008**, *41*, 2898.
- (25) Jomaa, H. W.; Schlenoff, J. B. *Macromolecules* **2005**, *38*, 8473.
- (26) Li, M.; Schlenoff, J. B. *Anal. Chem.* **1994**, *66*, 824.
- (27) Schlenoff, J. B.; Li, M. *Ber. Bunsen. Phys. Chem.* **1996**, *100*, 943.
- (28) Hirose, E.; Iwamoto, Y.; Norisuye, T. *Macromolecules* **1999**, *32*, 8629.
- (29) Lynn, G. W.; Heller, W.; Urban, V.; Wignall, G. D.; Weiss, K.; Myles, D. A. *Physica B: Condens. Matter* **2006**, *385–86*, 880.
- (30) Netz, R. R.; Andelman, D. *Phys. Rep.: Rev. Sect. Phys. Lett.* **2003**, *380*, 1.
- (31) Beer, M.; Schmidt, M.; Muthukumar, M. *Macromolecules* **1997**, *30*, 8375.

- (32) Volk, N.; Vollmer, D.; Schmidt, M.; Opperman, W.; Huber, K. *Adv. Polym. Sci.* **2004**, *166*, 29.
- (33) Dubas, S. T.; Schlenoff, J. B. *Langmuir* **2001**, *17*, 7725.
- (34) Schulz, D. N.; Peiffer, D. G.; Agarwal, P. K.; Larabee, J.; Kaladas, J. J.; Soni, L.; Handwerker, B.; Garner, R. T. *Polymer* **1986**, *27*, 1734.
- (35) Hatch, M.; Dillon, J.; Smith, H. *Ind. Eng. Chem.* **1957**, *49*, 1812.
- (36) Flory, P. J. *Statistical Mechanics of Chain Molecules*; Interscience Publishers: New York, 1969.
- (37) Iwamoto, Y.; Hirose, E.; Norisuye, T. *Polym. J.* **2000**, *32*, 428.
- (38) Serhatli, E.; Serhatli, M.; Baysal, B. M.; Karasz, F. E. *Polymer* **2002**, *43*, 5439.
- (39) Edwards, S. F. *J. Phys. A: Math. Gen.* **1975**, *8*, 1670.
- (40) de Gennes, P. G. *Scaling Concepts in Polymer Physics*; Cornell University Press: Ithaca, NY, 1979.
- (41) Oono, Y. *J. Phys. Soc. Jpn.* **1976**, *41*, 228.
- (42) Sulkowski, W. W.; Wolinska, A.; Pentak, D.; Maslanka, S.; Turanek, J.; Neca, J.; Sulkowska, A. *Macromol. Symp.* **2007**, *247*, 420.
- (43) Sulkowski, W. W.; Nowak, K.; Sulkowska, A.; Wolinska, A.; Bajdur, W. M.; Pentak, D.; Mikula, B. *Mol. Cryst. Liq. Cryst.* **2010**, *523*, 218.
- (44) Pepper, K. W. *J. Appl. Chem.* **1951**, *1*, 124.
- (45) Vink, H. *Macromol. Chem. Phys.* **1981**, *182*, 279.
- (46) Akovali, G.; Ozkan, A. *Polymer* **1986**, *27*, 1277.
- (47) Sutherland, J. E. *Abstr. Pap. Am. Chem. Soc.* **1976**, *172*, 90.
- (48) Borochov, N.; Eisenberg, H. *Macromolecules* **1994**, *27*, 1440.
- (49) Spiteri, M. N.; Boué, F.; Lapp, A.; Cotton, J. P. *Phys. Rev. Lett.* **1996**, *77*, 5218.
- (50) Schlenoff, J. B.; Rmaile, A. H.; Bucur, C. B. *J. Am. Chem. Soc.* **2008**, *130*, 13589.
- (51) Cousin, F.; Gummel, J.; Clemens, D.; Grillo, I.; Boué, F. *Langmuir* **2010**, *26*, 7078.
- (52) Yashiro, J.; Norisuye, T. *J. Polym. Sci., Part B: Polym. Phys.* **2002**, *40*, 2728.
- (53) <http://www.ncnr.nist.gov/resources/sldcalc.html>.
- (54) Bonnete, F.; Zaccai, G. *Biophys. Chem.* **1994**, *53*, 69.
- (55) Gabrys, B. J., Ed. *Applications of Neutron Scattering to Soft Condensed Matter*; Gordon & Breach: Amsterdam, 2000.
- (56) Pedersen, J. S. *Adv. Colloid Interface Sci.* **1997**, *70*, 171.
- (57) Guinier, A.; Fournet, G. *Small-Angle Scattering of X-rays*; Wiley: New York, 1955.
- (58) Semisotnov, G. V.; Kihara, H.; Kotova, N. V.; Kimura, K.; Amemiya, Y.; Wakabayashi, K.; Serdyuk, I. N.; Timchenko, A. A.; Chiba, K.; Nikaido, K.; Ikura, T.; Kuwajima, K. *J. Mol. Biol.* **1996**, *262*, 559.
- (59) Semisotnov, G. V.; Timchenko, A. A.; Melnik, B. S.; Kimura, K.; Kihara, H. *Photon Factory Activity Report 2002 #20 Part B 2003*; p 256.
- (60) Pavlov, G. M.; Zaitseva, I. I.; Gubarev, A. S.; Korneeva, E. V.; Gavrilova, I. I.; Panarin, E. F. *Dokl. Chem.* **2008**, *419*, 111.
- (61) Strazielle, C.; Benoit, H. *Macromolecules* **1975**, *8*, 203.
- (62) Beckrich, P.; Johnner, A.; Semenov, A. N.; Obukhov, S. P.; Benoit, H.; Wittmer, J. P. *Macromolecules* **2007**, *40*, 3805.
- (63) Wittmer, J. P.; Beckrich, P.; Crevel, F.; Huang, C. C.; Cavallo, A.; Kreer, T.; Meyer, H. *Comput. Phys. Commun.* **2007**, *177*, 146.
- (64) Wittmer, J. P.; Beckrich, P.; Johnner, A.; Semenov, A. N.; Obukhov, S. P.; Meyer, H.; Baschnagel, J. *Europhys. Lett.* **2007**, *77*, 56003 p1.
- (65) Jaber, J. A.; Schlenoff, J. B. *J. Am. Chem. Soc.* **2006**, *128*, 2940.
- (66) Prabhu, V. M.; Amis, E. J.; Bossev, D. P.; Rosov, N. J. *Chem. Phys.* **2004**, *121*, 4424.
- (67) Sukhishvili, S. A.; Kharlampieva, E.; Izumrudov, V. *Macromolecules* **2006**, *39*, 8873.
- (68) Kellogg, G. J.; Mayes, A. M.; Stockton, W. B.; Ferreira, M.; Rubner, M. F.; Satija, S. K. *Langmuir* **1996**, *12*, 5109.
- (69) Korneev, D.; Lvov, Y.; Decher, G.; Schmitt, J.; Yaradaikin, S. *Physica B* **1995**, *213*, 954.
- (70) Kharlampieva, E.; Kozlovskaya, V.; Ankner, J. F.; Sukhishvili, S. A. *Langmuir* **2008**, *24*, 11346.
- (71) Lösche, M.; Schmitt, J.; Decher, G.; Bouwman, W. G.; Kjaer, K. *Macromolecules* **1998**, *31*, 8893.
- (72) Capitán, M. J.; Rueda, D. R.; Ezquerro, T. A. *Macromolecules* **2004**, *37*, 5653.
- (73) Napolitano, S.; Wübbenhorst, M. *Macromolecules* **2006**, *39*, 5967.

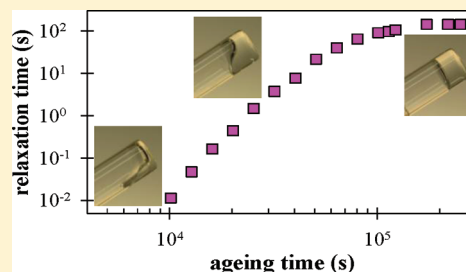
Progressive Freezing-in of the Junctions in Self-Assembled Triblock Copolymer Hydrogels during Aging

Céline Charbonneau, Christophe Chassenieux,* Olivier Colombani,* and Taco Nicolai

LUNAM Université, Laboratoire Polymères, Colloïdes et Interfaces, UMR CNRS 6120, Université du Maine, av. O. Messiaen, 72085 Le Mans cedex 9, France

Supporting Information

ABSTRACT: The evolution with time was investigated for self-assembled networks formed by triblock copolymers in aqueous solution. The polymers consisted of a central hydrophilic poly(acrylic acid) block and two hydrophobic end-blocks formed by random copolymers of 50% acrylic acid and 50% *n*-butyl acrylate units. The rheological properties of the systems at steady state were strongly influenced by the degree of ionization (α) and thus by the pH. This allows one to obtain systems ranging from low viscosity solutions to hydrogels just by varying α . However, steady state was not reached instantaneously when α was changed, but proceeded through a slow progressive increase of the viscosity. The rate at which the systems aged was independent of α and of the polymer concentration and is attributed to slow reorganization of the cores formed by the self-assembled hydrophobic blocks.



I. INTRODUCTION

Triblock copolymers (BAB) self-assemble when dissolved in a selective solvent for the block A. In dilute solutions, flower-like multiplets are formed with a dense core containing the B-blocks and a corona of back looping solvated A-blocks. When the concentration is increased, B blocks of the same chain increasingly enter different cores and bridge two multiplets.^{1–4} As a consequence, the multiplets connect into aggregates with increasing size until at a critical percolation concentration (C_p) a system spanning network is formed. The rheological properties of the network depend on the concentration and the lifetime of the bridges.^{5,6}

Dynamic self-assembly with fast exchange rates of B-blocks between multiplets is found when the B-blocks are very short^{3,7,8} or not very solvophobic.^{9–11} However, for many systems the exchange rate is extremely slow and may be considered kinetically frozen.^{12–15} Often the properties of these systems depend on the preparation method.^{16–18} The frozen character of block copolymers is related to the high activation energy that the B-block needs to overcome in order to escape from the core: $E_a \propto N^{2/3}\gamma$, where N is the polymerization degree of the B block and γ is the interfacial tension between the B block and the solvent.^{9,19} Consequently, in aqueous solution the high value of γ for typical hydrophobic blocks such as polystyrene or poly(*n*-butyl acrylate) inhibits exchange even for small values of N .^{18,20,21}

One way to decrease γ is to incorporate hydrophilic units into the hydrophobic blocks. This was done for diblock copolymers with an acrylic acid (AA) A-block and an *n*-butyl acrylate (*n*BA) B-block into which AA monomers were incorporated randomly. It was shown that dynamic polymer micelles were formed when the B-block contains 50% AA units,²² whereas particles formed with pure *n*-butyl acrylate (*n*BA) B-block were kinetically frozen.^{12,21} Recently, we reported an investigation of the equivalent triblock copolymer: P(*n*BA_{50%}-stat-AA_{50%})₁₀₁-*b*-PAA₂₀₄-*b*-P(*n*BA_{50%}-stat-AA_{50%})₁₀₁.²³ We demonstrated that by incorporating hydrophilic units into the hydrophobic blocks dynamic networks could be generated. The introduction of acidic monomers allowed control of the dynamics by varying the pH and thus the degree of ionization of the AA units (α). We note that a

similar effect has been observed recently for triblock copolymers²⁴ based on styrene and acrylic acid. However, in this case the incorporation of the hydrophilic units within the hydrophobic blocks was not random.

The critical percolation concentration of P(*n*BA_{50%}-stat-AA_{50%})₁₀₁-*b*-PAA₂₀₄-*b*-P(*n*BA_{50%}-stat-AA_{50%})₁₀₁ was low (about 3 g/L) at low ionization degrees, but increased for $\alpha > 0.30$. For $C > C_p$ a transition from frozen to dynamic networks was observed as a function of α . At $\alpha > 0.30$ the systems behaved as viscoelastic fluids with a terminal relaxation time (τ) that strongly decreased with increasing α or increasing temperature. At $\alpha < 0.30$, the systems behaved as soft solids on the time scale of the experiment.

Remarkably, direct dissolution of the polymer in the presence of NaOH led to homogeneous transparent gels within 1 day even for $\alpha < 0.30$, although the terminal relaxation time was immeasurably long. Similar observations have been earlier reported for frozen triblock copolymer systems.^{10,16,25–27} The objective of the present study was to investigate in more detail the formation of networks in particular for systems where the exchange rate is extremely slow in order to understand how the polymer can form transparent and homogeneous gels in spite of an almost complete lack of exchange. We have studied the dynamic mechanical properties of the systems during the formation of the networks by decreasing α in situ. The effects of the final ionization degree, the concentration and the temperature were investigated systematically. The results show that, when α is decreased, the exchange time of the B-blocks increases progressively with time after the network is formed. The increase continues long after the target value of α is reached until finally steady state is attained. Even for low final values of α , the network is initially highly dynamic and then locks-in progressively. These results explain why homogeneous transparent gels could be formed even if the system is ultimately kinetically frozen at steady state. Aging of networks formed by triblock

Received: October 17, 2011

Revised: December 2, 2011

Published: December 20, 2011

copolymers in selective solvents has been observed earlier for poly(methyl methacrylate)-*block*-poly(*tert*butyl acrylate)-*block*-poly(methyl methacrylate) dissolved in alcohols.²⁸ We believe that investigating the network formation *in situ* will improve understanding of the behavior of amphiphilic triblock copolymers in solution.

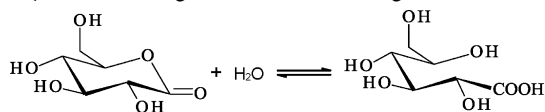
II. MATERIALS AND METHODS

1. Materials. The $P(nBA_{50\%}\text{-stat-AA}_{50\%})_{101}\text{-}b\text{-PAA}_{204}\text{-}b\text{-P}(nBA_{50\%}\text{-stat-AA}_{50\%})_{101}$ (BAB) triblock copolymer, noted henceforth TH50, was synthesized by ATRP (atom transfer radical polymerization) as described previously.²³ TH50 is narrowly distributed in terms of molecular weight ($M_n = 3.3 \times 10^4$ g/mol, $M_w/M_n = 1.10$) and chemical composition. Furthermore, the copolymerization of *t*BA, which is the precursor of AA units, and *n*BA units was purely statistical, leading to a random distribution of these units in the B blocks. Sodium hydroxide 1 M (Lab-online) and D-glucono- δ -lactone (GDL) (Fluka, ~99%) were used as received.

2. Sample Preparation. Samples were initially prepared at an ionization degree of the AA units (α) close to unity. The quantity of NaOH required to reach $\alpha = 1$ was calculated from the chemical structure of the polymer considering that all AA units could be ionized, which was verified by potentiometric titration.²³ The amount of excess NaOH was kept close to zero (pH = 9) in order to avoid hydrolysis of *n*BA units. The polymer was first dissolved in demineralized water (Millipore) containing 50–70% of the required amount of NaOH while stirring overnight. Then, the remaining quantity of NaOH was added in order to completely ionize the AA units and the solution was stirred for several hours. This procedure led to homogeneous transparent solutions. The degree of ionization was decreased *in situ* to the desired value by adding the required amount of D-glucono- δ -lactone (GDL) powder to the solutions while vigorously stirring. The samples were degassed under vacuum for 2–3 min prior to loading on the rheometer.

3. Hydrolysis of D-Glucono- δ -lactone. GDL is used in the food industry as an additive and in biological systems as sequestering agent. In water, GDL hydrolyses to D-gluconic acid following the equilibrium shown below.

Hydrolysis of the D-glucono- δ -acid in D-gluconic acid.



The hydrolysis of GDL leads to progressive release of protons and therefore to a reduction of the pH. Figure 1 shows the evolution of pH as a function of time for GDL solutions at 0.01, 0.1, and 1 M. These concentrations correspond to the range used here. Complete

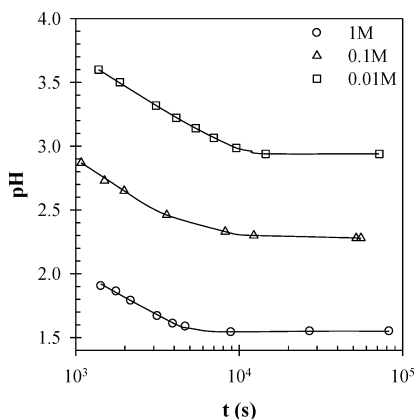


Figure 1. Evolution of the pH as a function of time for solutions of GDL at different concentrations at 20 °C. The solid lines are guides to the eye.

hydrolysis requires around 10⁴ s at 20 °C independently of the GDL concentration. The rate of the hydrolysis can be accelerated by heating from 10⁴ to 300 s between 20 and 70 °C and is characterized by an activation energy of 58 kJ/mol.²⁹ GDL has $pK_a = 3.6$ at 20 °C,²⁹ which is low enough to consider that all AA units become neutralized in the range of ionization degree used in this study. The ionization degree of the AA units (α) depends on the molar concentration of GDL ([GDL]) and the total amount of AA ($[AA]_{tot.}$): $\alpha = 1 - [GDL]/[AA]_{tot.}$

4. Methods. Dynamic Mechanical Measurements. Measurements were carried out with a controlled-strain rheometer equipped with a plate–plate geometry (gap = 0.25 mm, diameter = 20 mm): ARES (Rheometric Scientific). To prevent water evaporation, the geometry was covered with silicon oil. The temperature was controlled with a thermostatic bath. Oscillatory shear measurements were done in the linear response regime. The isochronal frequency dependence of the storage (G') and loss (G'') moduli at different observation times was obtained by interpolation of the time dependence of G' and G'' at different frequencies.

Gels that were formed separately in glass vials and carefully loaded onto the rheometer gave the same results as *in situ* prepared gels for all α . However, at low α values where the systems exhibit very slow dynamics, breakup of the gel into small pieces by stirring before loading onto the rheometer led to a decrease of G' by an order of magnitude. At larger α where the systems are highly dynamic, the gels self-healed rapidly when treated similarly.

III. RESULTS

Fully ionized TH50 at $\alpha = 1$ does not self-assemble in aqueous solution except perhaps at very high concentrations. Reducing α leads to association of the B-blocks and the formation of a system spanning network. If a strong acid such as HCl is used, the solution becomes turbid and large flocs are formed that are visible to the naked eye, probably due to the excessive local drop of the pH. Therefore, the pH was decreased progressively using GDL as described in the Materials and Methods, which led to transparent and homogeneous solutions.

1. Aging. In Figure 2a, the frequency dependence of G' and G'' at different times (t) after the addition of GDL are represented for a solution at $C = 32$ g/L, $\alpha = 0.38$ and $T = 20$ °C. Reliable measurements could be obtained after 10⁴ s, i.e., when the GDL was fully hydrolyzed (see Figure 1) and α had reached the steady state value of 0.38. At all times, the system behaved as a viscoelastic fluid, demonstrating that the B-blocks exchanged spontaneously between multiplets. However, the terminal relaxation time of the system increased with time indicating that the exchange slowed down progressively although the ionization degree does not change anymore after 10⁴ s. The increase of the relaxation time after 10⁴ s is thus solely due to an aging of the system and is not related to any change of α .

The results at different times could be superimposed using horizontal and vertical shifts, see Figure 2b. The horizontal shift factors were important, but the vertical shifts were small for all systems (less than a factor of 3).

The relaxation of the shear modulus is characterized by a broad distribution of relaxation times, which has also been observed for systems with longer and less mobile hydrophobic blocks.^{2,6,30} In our case, we explain the origin of the broad relaxation process by the fact that even a weak polydispersity of the hydrophobic blocks both in length and composition can lead to a broad relaxation time distribution.^{31,32} A polydispersity of the number of associated blocks within the cores may also contribute to the broadening of the relaxation. The fact that a master curve could be obtained implies that even though

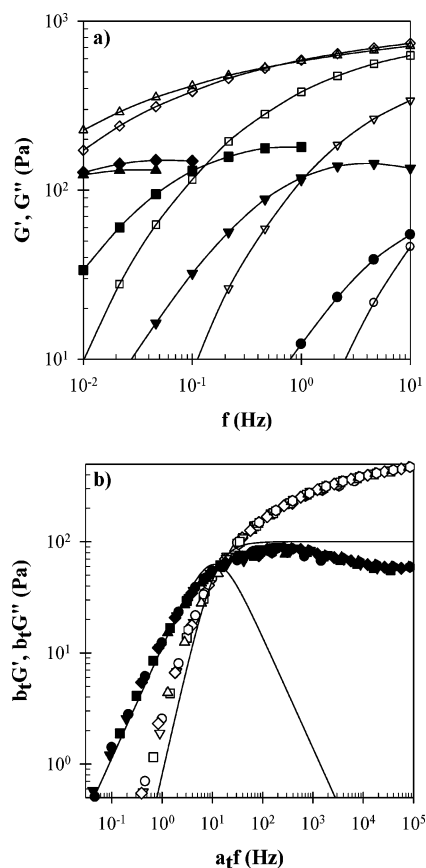


Figure 2. (a) Frequency dependence of the storage (open symbols) and loss (filled symbols) shear moduli at different times of observation for $C = 32$ g/L and $\alpha = 0.38$ (\circ , $t = 1.0 \times 10^4$ s; ∇ , $t = 1.6 \times 10^4$ s; \square , $t = 2.5 \times 10^4$ s; \diamond , $t = 6.4 \times 10^4$ s; Δ , $t = 1.1 \times 10^5$ s). The solid lines are guides to the eye. (b) Master curve obtained by frequency-time superposition at $t_{\text{ref}} = 1.0 \times 10^4$ s of results obtained at a range of aging times including those shown in part a. The solid line represents a single exponential relaxation process (Maxwell model).

the relaxation systematically slows down with aging, the distribution remains the same, because the polydispersity remains the same.

We defined the characteristic average relaxation time (τ) as the inverse of the radial frequency ($\omega = 2\pi f$) where G' and G'' cross. The elastic modulus (G_e) was estimated from G' at high frequencies (100 times the crossover frequency). From the frequency-time superposition, the evolution of τ could be obtained as a function of the observation time even at times when the crossover could not be measured directly. We found that τ increased by 4 orders of magnitude between $t = 10^4$ and 10^5 s and then stabilized at a value of $\tau_{\infty} = 144$ s, see Figure 3. We may conclude that the system aged for more than a day and then reached steady state.

2. Effect of the Ionization Degree. Aging at different values of α was studied at $C = 30$ g/L. Figure 4 shows the evolution of τ as a function of time after reducing α from unity to different values between 0.10 and 0.57 at $T = 20$ °C. Systems at $\alpha > 0.57$ were not investigated because they did not form a system spanning network at $C = 30$ g/L as was shown in ref 23. τ_{∞} increased strongly with decreasing α from 3×10^{-2} s at $\alpha = 0.57$ to 2×10^8 s at $\alpha = 0.10$. However, surprisingly, the steady state was reached after about the same time ($t_{\text{st}} = 10^5$ s) independently of α .

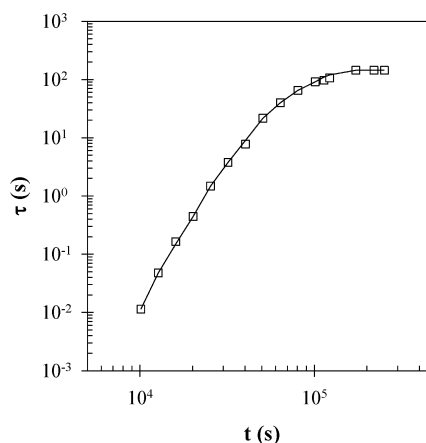


Figure 3. Evolution of the average relaxation time (τ) during aging for $C = 32$ g/L $\alpha = 0.38$.

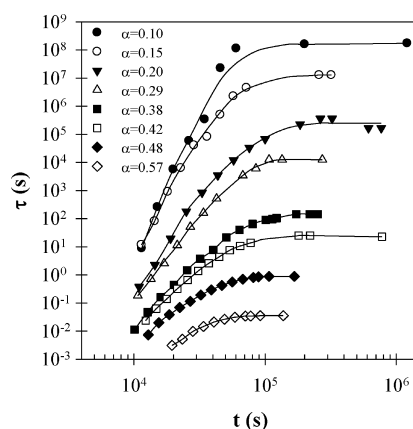


Figure 4. Evolution of τ as a function of time at $C = 30$ g/L and $T = 20$ °C for different α as indicated in the figure. The solid lines are guides to the eye.

We also looked at the aging process when starting from different values of α . The aging time was the same when α was decreased from 1 to 0.57, from 0.57 to 0.38 or directly from 1 to 0.38, see Figure 5. This implies that the aging time does not depend on the initial and final values of α when α is decreased. However, when α was increased from 0.38 back to 0.57, steady state was reached very rapidly, see Figure 5. We note that the viscosity at steady state at $\alpha = 0.57$ was larger after the passage to $\alpha = 0.38$, because the adjustment of α leads to an increase of the ionic strength, which has an influence on the viscosity.

The evolution of τ_{∞} as a function of α is plotted in the Figure 6 at different concentrations (filled symbols) and compared to the average results obtained from our previous study²³ (open symbols). For our previous study the samples were prepared directly at different α by dissolving the polymers in water containing the required amount of NaOH.

For $\alpha > 0.30$, both preparation methods lead to the same value of the relaxation time at steady-state. This is consistent with the formation of a dynamic system able to reach thermodynamic equilibrium independently of the preparation pathway. However, solutions formed by direct dissolution of the polymer in the presence of NaOH at 20 °C got trapped in steady states with immeasurably long relaxation times for $\alpha < 0.30$. Interestingly, the method presented in this paper allowed us to extend the measurement of the terminal relaxation time to

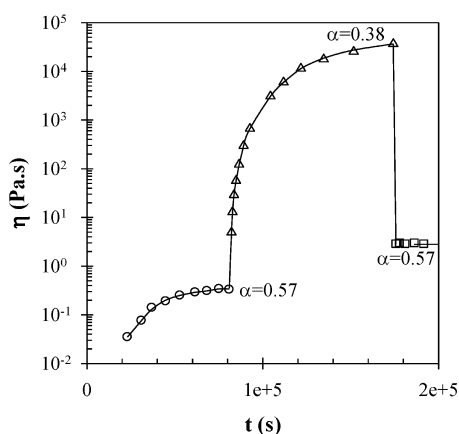


Figure 5. Evolution of η as a function of time at $C = 20$ g/L and $T = 20$ °C after α was decreased from 1 to 0.57 at $t = 0$, then to 0.38 at $t = 8 \times 10^4$ s and finally increased back to 0.57 at $t = 1.7 \times 10^5$ s. The solid lines are guides to the eye.

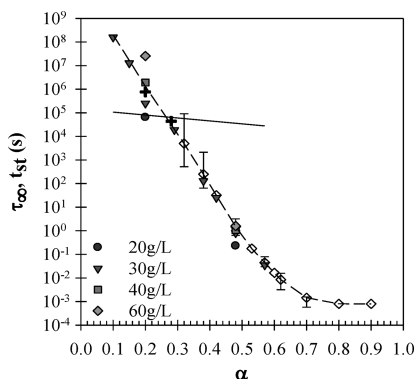


Figure 6. Evolution of τ_∞ measured after in situ decreasing of the ionization degree as a function of α at $T = 20$ °C (filled symbols) for different concentrations as indicated in the figure. The open symbols correspond to the average results obtained in our previous study²³ after direct dissolution of the polymer in water containing NaOH at 20 °C. The error bars indicate the variation of the results obtained at different concentrations. The crosses represent τ_∞ of systems obtained by direct dissolution of the polymer in water containing NaOH and kept for several days at 70 °C. The dotted line is a guide to the eye while the solid line represents the dependence of t_{st} on α .

values of α down to 0.2. For this ionization range, the same values of τ_∞ were obtained by directly dissolving the polymer in water containing NaOH if the solutions were kept at 70 °C for several days (see crosses in Figure 6) which indicate that an equilibrium state was reached.

τ_∞ decreased exponentially with increasing α from about 10^8 s at $\alpha = 0.10$ to 10^{-3} s at $\alpha = 0.70$. At $\alpha \geq 0.70$, τ_∞ became almost independent of α suggesting that further increase of the charge density of the B-block no longer influenced the exchange rate. Remarkably, the time needed to reach steady state was almost independent of α and thus was not correlated to the terminal relaxation time at steady state. τ_∞ could even be orders of magnitude larger than the aging time (see solid line in Figure 6). The aging process observed when GDL is used to decrease α explains why transparent and homogeneous gels are formed at low values of α in a much shorter time than the terminal relaxation time of the gel. Initially, the exchange dynamics is fast which allows for the formation of a

homogeneous transient network that subsequently progressively locks-in over time.

3. Effect of the Temperature. As was mentioned in the Materials and Methods, GDL hydrolyses faster at higher temperatures, which means that the required ionization degree is reached sooner at higher temperatures. Figure 7 shows τ as a function of time at different temperatures for a solution at $C =$

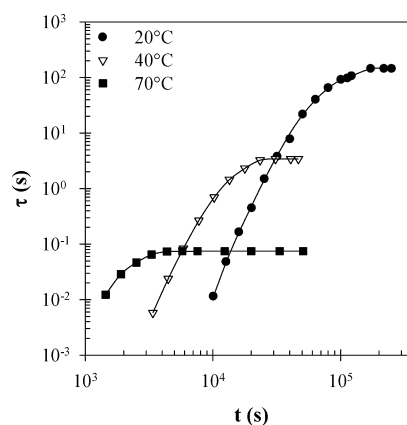


Figure 7. Evolution of the average relaxation time as a function of time at different temperatures for a solution at $C = 32$ g/L and $\alpha = 0.38$. The solid lines are guides to the eye.

32 g/L after α had reached the target value of 0.38. Clearly, the subsequent aging process is also faster at higher temperatures. The temperature dependence of the time needed to reach t_{st} is plotted in an Arrhenius representation in Figure 8, showing that

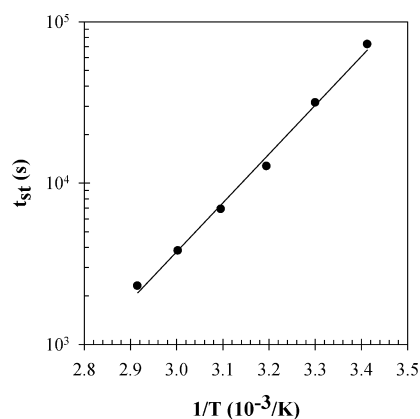


Figure 8. Arrhenius representation of the temperature dependence of t_{st} . The solid line represents a linear least-squares fit.

aging of the system investigated here is a thermally activated process with an activation energy of about 60 kJ/mol.

Interestingly, once steady state was reached at a given temperature the system no longer aged after subsequent modification of the temperature. Moreover, the same steady state was found at a given temperature independently of the temperature at which the system was aged. Thus, steady state at low temperatures can be obtained more rapidly by aging at elevated temperatures and subsequently cooling.

4. Effect of the Concentration. The effect of the polymer concentration on aging was studied at $T = 20$ °C for $\alpha = 0.48$, see Figure 9. The time needed to reach steady state was almost

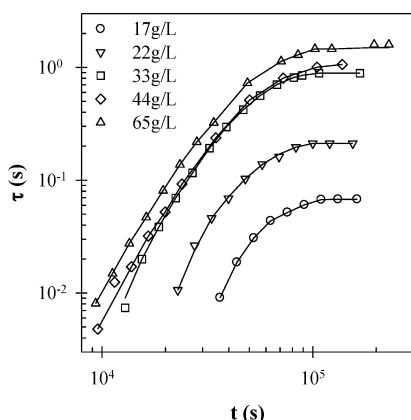


Figure 9. Evolution of the average relaxation time as a function of time for solutions at $\alpha = 0.48$ and $T = 20\text{ }^{\circ}\text{C}$ at different concentrations as indicated in the figure. The solid lines are guides to the eye.

independent of the polymer concentration, which strongly suggests that the aging is related to restructuring of individual multiplets as will be discussed below. The terminal relaxation time at steady state increases with increasing concentration, but stabilizes for $C > 30\text{ g/L}$ at $\alpha = 0.48$. A similar observation was already reported at other values of α in reference²³ and was related to defects in the network (loops and superbridges) close to C_p .

IV. DISCUSSION

Oscillatory shear measurements revealed that, at $C > C_p$, TH50 forms a system spanning network that ages after in situ decrease of the ionization degree before reaching a steady state. The time needed to reach steady state was independent of α and the concentration, but could be accelerated by heating. In the following we focus on the phenomenon of aging during which the terminal relaxation time increases progressively while α remains constant. The dynamic mechanical properties at steady state and their dependence on α , T , and C were already discussed elsewhere.²³ We only mention that the present results obtained at steady state with a different preparation method confirm and extend our earlier results. In particular, we showed here that the relaxation time continues to increase exponentially with decreasing α down to $\alpha = 0.10$.

In order to relax the shear stress the B-blocks must exchange between multiplets. The escape of a B-block from the core is a localized process and therefore the exchange rate is expected to be independent of the polymer concentration. Schematically the escape of a B-block involves two steps: (1) retraction of the hydrophobic chain to the interface with the hydrophilic corona and (2) entering and diffusion through the corona.^{19,32,33} The first step is controlled by the mobility of the B-blocks in the core. The second step involves the formation of an interface with the hydrated corona and thus depends on the length of the B-block and its interfacial tension with water.

Depending on the system, either step 1 or step 2 can be rate limiting. If step 1 is the rate-limiting step one would expect that the viscosity of bulk B-blocks depends as strongly on α as τ_{∞} . In order to test this hypothesis we have measured the viscosity of neat B-blocks at different values of α , see Supporting Information. The viscosity increased with decreasing α , but the dependence was much smaller than for τ_{∞} . We conclude that step 1 is probably not the rate-limiting step.

If we consider that step 2 is the rate-limiting step, then the progressive slow down of the exchange during aging corresponds to an increasing difficulty for the B-block to enter the water phase. We speculate that this is caused by a progressive local decrease of the degree of ionization of the B-blocks and a concomitant dehydration of the cores. We found that neat B-blocks are significantly hydrated and that the equilibrium water content of neat B-block melts increased with increasing α , see Supporting Information. The reorganization of the structure of the core leads to a decrease of the mobility of B-blocks in the cores (step 1), but more importantly, it leads to an increase of the energy barrier to enter the water phase (step 2). The reorganization does not depend on the exchange dynamics and therefore on the exchange rate, which explains why aging is independent of α but is faster at higher temperatures. No aging was observed upon increase of α , which means that hydration of the cores is much faster than dehydration. We did not observe a systematic change of the elastic modulus during aging even close to C_p . This implies that during the reorganization of the cores the aggregation number of the multiplets does not change much, which is corroborated by the observation that the aggregation number of micelles formed by the equivalent diblocks stabilized within minutes when α was decreased (data not shown).

V. CONCLUSIONS

The triblock copolymer TH50 forms a system spanning network by self-assembly above a critical percolation concentration. It was already reported²³ that its shear rheology is characterized by a broad distribution of relaxation times with a terminal relaxation time that increases exponentially with decreasing degree of ionization. The present article focuses on the time-evolution of the rheological properties of the system upon a change of the ionization degree. It was observed that the terminal relaxation time continues to increase with time well after the ionization degree has reached its target value, until a steady state is reached. The time needed to reach the steady state is almost independent of the ionization degree and the polymer concentration. It took more than a day at room temperature, but decreased with increasing temperature. Remarkably, the time needed to reach the steady state is not related to the terminal relaxation time of the system, which was up until 3 orders of magnitude slower at $\alpha = 0.1$. Aging in these systems is probably caused by slow reorganization of the hydrophobic cores involving dehydration and local reduction of the ionization degree of the associated B-blocks.

At low ionization degrees the average relaxation time was extremely long so that the systems no longer flowed when tilted and behaved as irreversibly cross-linked hydrogels. Nevertheless homogeneous transparent gels could be formed, because the systems were initially dynamic and became kinetically frozen only after the network was formed. These findings may explain why many BAB triblock copolymers studied in the literature can form homogeneous gels while their exchange dynamics is immeasurably slow. It would be interesting to apply the strategy described in this article to study in situ the time-evolution of the rheological properties of other pH-sensitive amphiphilic block copolymer networks described in the literature.

■ ASSOCIATED CONTENT

Supporting Information

This material is available free of charge via the Internet at <http://pubs.acs.org>.

AUTHOR INFORMATION

Corresponding Author

*E-mail: (Ch.C.) christophe.chassenieux@univ-lemans.fr;
(O.C.) olivier.colombani@univ-lemans.fr.

ACKNOWLEDGMENTS

This work has been funded by the Agence Nationale de la Recherche in the framework ANR-09-BLAN-0174-01. The authors thank Jean-Luc Monéger for the TGA analysis.

REFERENCES

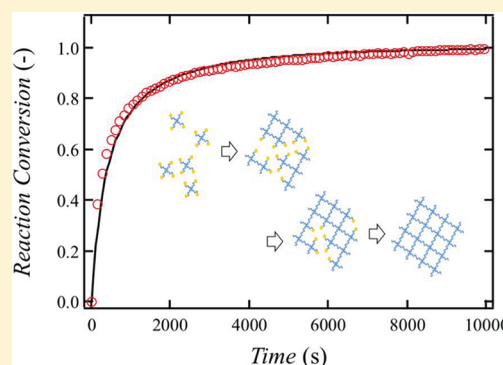
- (1) Bossard, F.; Aubry, T.; Gotzamanis, G.; Tsitsilianis, C. *Soft Matter* **2006**, *2*, 510–516.
- (2) Seitz, M. E.; Burghardt, W. R.; Faber, K. T.; Shull, K. R. *Macromolecules* **2007**, *40*, 1218–1226.
- (3) Pham, Q. T.; Russel, W. B.; Thibault, J. C.; Lau, W. *Macromolecules* **1999**, *32*, 5139–5146.
- (4) Séréro, Y.; Aznar, R.; Porte, G.; Berret, J. F. *Phys. Rev. Lett.* **1998**, *81*, 5584–5587.
- (5) Annable, T.; Buscall, R.; Ettelaie, R.; Shepherd, P.; Whittlestone, D. *Langmuir* **1994**, *10*, 1060–1070.
- (6) Chassenieux, C.; Nicolai, T.; Benyahia, L. *Curr. Opin. Colloid Interface Sci.* **2011**, *16*, 18–26.
- (7) Berret, J. F.; Calvet, D.; Collet, A.; Viguier, M. *Curr. Opin. Colloid Interface Sci.* **2003**, *8*, 296–306.
- (8) Renou, F.; Nicolai, T.; Nicol, E.; Benyahia, L. *Langmuir* **2009**, *25*, 515–521.
- (9) Nicolai, T.; Colombani, O.; Chassenieux, C. *Soft Matter* **2010**, *6*, 3111–3118.
- (10) Popescu, M.-T.; Athanasoulis, I.; Tsitsilianis, C.; Hadjiantoniou, N. A.; Patrickios, C. S. *Soft Matter* **2010**, *6*, 5417–5424.
- (11) Tsitsilianis, C. *Soft Matter* **2010**, *6*, 2372–2388.
- (12) Colombani, O.; Ruppel, M.; Burkhardt, M.; Drechsler, M.; Schumacher, M.; Gradzielski, M.; Schweins, R.; Müller, A. H. E. *Macromolecules* **2007**, *40*, 4351–4362.
- (13) Bendejacq, D.; Joanicot, M.; Ponsinet, V. *Eur. Phys. J. E.* **2005**, *17*, 83–92.
- (14) Meli, M.; Lodge, T. P. *Macromolecules* **2009**, *42*, 580–583.
- (15) Théodoly, O.; Jacquin, M.; Muller, P.; Chhun, S. *Langmuir* **2009**, *25*, 781–793.
- (16) Tsitsilianis, C.; Iliopoulos, I. *Macromolecules* **2002**, *35*, 3662–3667.
- (17) Stavrouli, N.; Aubry, T.; Tsitsilianis, C. *Polymer* **2008**, *49*, 1249–1256.
- (18) Tsitsilianis, C.; Iliopoulos, I.; Ducouret, G. *Macromolecules* **2000**, *33*, 2936–2643.
- (19) Halperin, A.; Alexander, S. *Macromolecules* **1989**, *22*, 2403–2412.
- (20) Stam, J. V.; Creutz, S.; De Schryver, F. C.; Jérôme, R. *Macromolecules* **2000**, *33*, 6388–6395.
- (21) Jacquin, M.; Muller, P.; Talingting-Pabalan, R.; Cottet, H.; Berret, J. F.; Futterer, T.; Théodoly, O. *J. Colloid Interface Sci.* **2007**, *316*, 897–911.
- (22) Lejeune, E.; Drechsler, M.; Jestin, J.; Muller, A. H. E.; Chassenieux, C.; Colombani, O. *Macromolecules* **2010**, *43*, 2667–2671.
- (23) Charbonneau, C.; Chassenieux, C.; Colombani, O.; Nicolai, T. *Macromolecules* **2011**, *44*, 4487–4495.
- (24) Borisova, O.; Billon, L.; Zaremski, M.; Grassl, B.; Bakaeva, Z.; Lapp, A.; Stepanek, P.; Borisov, O. *Soft Matter* **2011**, *7*, 10824–10833.
- (25) Castelletto, V.; Hamley, I. W.; Ma, Y.; Bories-Azeau, X.; Armes, S. P. *Langmuir* **2004**, *20*, 4306–4309.
- (26) Katsampas, I.; Tsitsilianis, C. *Macromolecules* **2005**, *38*, 1307–1314.
- (27) Tsitsilianis, C.; Katsampas, I.; Sfika, V. *Macromolecules* **2000**, *33*, 9054–9059.
- (28) Drzal, P. L.; Shull, K. R. *Macromolecules* **2003**, *36*, 2000–2008.
- (29) Pocker, Y.; Green, E. *J. Am. Chem. Soc.* **1973**, *95*, 113–119.
- (30) Lund, R.; Willner, L.; Richter, D.; Iatrou, H.; Hadjichristidis, N.; Lindner, P. *J. Appl. Crystallogr.* **2007**, *40*, s327–s331.
- (31) Choi, S. H.; Lodge, T. P.; Bates, F. S. *Phys. Rev. Lett.* **2010**, *104*, 047802.
- (32) Choi, S. H.; Bates, F. S.; Lodge, T. P. *Macromolecules* **2011**, *44*, 3594–3604.
- (33) Lund, R.; Willner, L.; Richter, D. *Macromolecules* **2006**, *39*, 4566–4575.

Kinetic Study for AB-Type Coupling Reaction of Tetra-Arm Polymers

Kengo Nishi,[†] Kenta Fujii,^{*,†} Masashi Chijiishi,[‡] Yukiteru Katsumoto,[§] Ung-il Chung,[‡] Takamasa Sakai,^{*,‡} and Mitsuhiro Shibayama[†][†]Institute for Solid State Physics, The University of Tokyo, 5-1-5 Kashiwanoha, Kashiwa, Chiba 277-8581, Japan[‡]Department of Bioengineering, School of Engineering, The University of Tokyo, 7-3-1 Hongo, Bunkyo-ku, Tokyo 113-8656, Japan[§]Department of Chemistry, Graduate School of Science, Hiroshima University, 1-3-1 Kagamiyama, Higashihiroshima, Hiroshima 739-8526, Japan

S Supporting Information

ABSTRACT: The reaction rate for the polycondensation in the Tetra-PEG gel system, i.e., A–B type coupling reaction between mutually reactive two four-arm polymers, has been studied by ATR-IR spectroscopy. It was found that (1) the polycondensation kinetics of Tetra-PEG gel can be simply treated as a chemical reaction between mutually reactive end-groups in solution, (2) the reaction undergoes as a simple second-order reaction from beginning to end regardless of gelation threshold, and (3) the gelation mechanism was predicted from the thermodynamic enthalpy and entropy at the transition state estimated by temperature dependence of rate constants. The reason of smooth second-order kinetics is suspected to be that the mean-field approximation can be applied to the reactivity of terminal groups on Tetra-PEGs; i.e., the reactivity of terminal groups on Tetra-PEGs is not affected by the steric hindrance, substitution effect, and gelation threshold.



■ INTRODUCTION

Gelation or cross-linking is one of the fundamental but key reactions in the production of polymeric materials. A variety of commercial products, namely rubbers, gels, paints, and adhesives, are made by way of gelation threshold, i.e., the onset of formation of infinitely large clusters. Hence, the understanding of the kinetics of network formation is of particular importance not only from basic science but also from industrial points of view.

One of the simplest ways describing the cross-linking kinetics is to treat as a series of branching reactions.^{1,2} Let us consider the AB-type polycondensation. When the mean-field approximation is applied to the reactivity of terminal functional group, the reaction rate equation is described as a simple diffusion-controlled reaction rate equation.

$$\frac{dC_A(t)}{dt} = \frac{dC_B(t)}{dt} = -kC_A(t)C_B(t) \quad (1)$$

Here, $C_A(t)$, $C_B(t)$, and k are the concentrations of species A and B and reaction rate constant. It should be noted that k is constant from initiation to completion regardless of the gelation threshold because the mean-field approximation is applied to the reactivity of terminal functional group. The validity of this equation was tested and partly confirmed. For example, Yokoyama and Dusek et al. investigated the time variation of the number of cross-links on the polyurethane network formation. However, the reaction kinetics was not discussed in detail.^{3,4} Rozenberg, Kambe, and Dusek et al. reported that the reaction rate constant fell down at the later

stage of reaction between epoxides and amines.^{5–8} These studies were on the polymer melt systems. As for the network formation of conventional chemical gels, Bates and Howard calculated the reaction rate constants for gelation reaction under assumption of third-order kinetics.⁹ This reaction obeyed a third-order kinetics only at the early stage of gelation. In addition, Stepto et al. reported polycondensation reaction of low-molecular-weight precursors around the gel point.^{10,11} However, the reaction exponent or reaction rate constant was not predicted.

As mentioned above, there are only a few experimental data fully supporting the eq 1. There are two possible reasons preventing experimental validation. The first reason is the substitution effect. The substitution effect is an effect on a reaction probability of one terminal group to other terminal groups. This effect can be either positive or negative depending on the electron state. This effect is pronounced in a reaction using low-molecular-weight precursors. Hence, for most researches dealing with low-molecular-weight precursors, the reactivity of terminal groups cannot be assumed to be constant. The second reason is the steric hindrance. When we use the low-molecular-weight precursors, reactive sites are expected to be buried in the polymer chain in the course of reaction. In this case, the contact probability of reaction site is expected to decrease during the network formation process.

Received: October 26, 2011

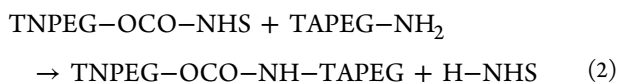
Revised: December 6, 2011

Published: December 22, 2011

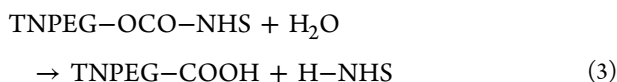
In this study, we focused on the polycondensation kinetics of Tetra-PEG gel, which is fabricated from AB-type cross-end coupling of two mutually reactive tetra-arm polymers of the same size.^{12–20} Each tetra-arm polymer has four amine groups (TAPEG) or activated ester groups (TNPEG). The Tetra-PEG gel system is different from conventional cross-linking systems in the way that the cross-linking point is preformed in the precursor; all of the reaction occurs between the arm-ends of precursors. Therefore, the substitution effect and the steric hindrance are expected to be insignificant on the Tetra-PEG gel system. The polycondensation process of Tetra-PEG gel was investigated in the viewpoint of the chemical reaction kinetics between mutually reactive terminal groups of Tetra-PEGs by using FT-IR spectroscopy. We, for the first time, report the rate constant, k , and activation thermodynamic quantities (ΔG^\ddagger , ΔH^\ddagger , and ΔS^\ddagger) for the gelling polycondensation system through the Tetra-PEG gel.

REACTION KINETICS

The main reaction of the Tetra-PEG gel system is aminolysis reaction between the amine group within TAPEG and activated ester (*N*-hydroxy succinimidyl (NHS) ester) group within TNPEG.



Here two points should be noted. First, the activated ester group within TNPEG gradually dissociates in aqueous solution due to hydrolysis reaction as follows:



In addition, the terminal NH_2 group within TAPEG coexists with the protonated NH_3^+ in equilibrium, as follows:



$$K_a = [-\text{NH}_2][\text{H}^+]/[-\text{NH}_3^+] \quad (5)$$

$$[-\text{NH}_2]_{\text{total}} = [-\text{NH}_2] + [-\text{NH}_3^+] \quad (6)$$

where $[-\text{NH}_2]_{\text{total}}$ corresponds to the total concentration of amine group within TAPEG. Only the un-ionized amine group reacts with the activated ester group because the ionized amine group does not have an unshared electron pair. Therefore, the rate equation for the gelation is described as follows:

$$\begin{aligned} -d[-\text{NH}_2]_{\text{total}}/dt &= k_{\text{gel}}[-\text{NH}_2][- \text{NHS}] \\ &= k_{\text{gel}}f[-\text{NH}_2]_{\text{total}}[- \text{NHS}] \end{aligned} \quad (7)$$

$$\begin{aligned} -d[- \text{NHS}]/dt &= k_{\text{gel}}f[-\text{NH}_2]_{\text{total}}[- \text{NHS}] + k_{\text{deg}}[- \text{NHS}] \end{aligned} \quad (8)$$

where k_{gel} and f denote the rate constant for the gelation and the fraction of un-ionized amine to total amine, i.e., $f = [-\text{NH}_2]/[-\text{NH}_2]_{\text{total}} = K_a/(K_a + [\text{H}^+])$, respectively. Here f is determined by K_a in eq 5 and pH. The $\text{p}K_a$ in eq 5 was separately determined by potentiometric titration for TAPEG solution, and the value was estimated to be 9.27 from the

potentiometric titration in our previous work.¹⁴ On the other hand, though pH was almost controlled by using phosphate buffer, pH was slightly varied along with $[-\text{NH}_2]_{\text{total}}$ in solution. In this work, the values of pH were experimentally determined by pH measurement, which is described in detail in the Supporting Information (Figure S1).

EXPERIMENTAL SECTION

Materials. Tetra-amine-terminated PEG (TAPEG) and tetra-NHS-glutarate-terminated PEG (TNPEG) were prepared from tetrahydroxyl-terminated PEG (THPEG) having equal arm lengths. The details of TAPEG and TNPEG preparation are reported elsewhere.²⁰ The molecular weights (M_w) of TAPEG and TNPEG were matched to be 10 kg/mol. Here NHS represents *N*-hydroxysuccinimide. The activity of the functional groups was estimated using NMR. TNPEG ^1H NMR (CDCl_3 , δ): 2.07 (m, 2H, $\text{CH}_2\text{CH}_2\text{CH}_2$), 2.49 (t, 2H, $\text{CH}_2\text{CH}_2\text{CH}_2$), 2.72 (t, 2H, $\text{CH}_2\text{CH}_2\text{CH}_2$), 2.83 (s, 4H, $\text{NCOCH}_2\text{CH}_2\text{CON}$), 3.4 (s, 2H, CH_2O), 3.63 (m, (4m-2)H, $(\text{CH}_2\text{CH}_2\text{O})_m - 1\text{CH}_2$), 4.24 (t, 2H, $\text{CH}_2\text{CH}_2\text{O}$). TAPEG ^1H NMR (CDCl_3 , δ): 1.91 (br, 2H, NH_2), 3.18 (t, 2H, CH_2CH_2), 3.42 (s, 2H, CH_2O), 3.63 (m, (4m-2)H, $(\text{CH}_2\text{CH}_2\text{O})_m - 1\text{CH}_2$).

IR Spectroscopy. IR spectra were measured at a resolution of 2 cm^{-1} with a coaddition of 128 scans using a Nicolet 6700 Fourier-transform IR spectrometer equipped with a liquid-nitrogen-cooled MCT detector. The attenuated total reflection (ATR) technique was employed to obtain IR spectra of the polymer solution. The solution was filled in an ATR cell, which was made of a horizontal ZnSe crystal (R.I. 2.403) with an incident angle of 45° . The ATR cell was kept at $10\text{--}50^\circ\text{C}$ with an accuracy of 0.1°C throughout the entire experiment by using a homemade thermoelectric device. The ATR cell was sealed by a toggle-clamp-type cover to prevent the evaporation of solvent.

The reaction rate for degradation of TNPEG was estimated by ATR-IR spectrometry. A constant amount of TNPEG (240 mg) was dissolved in 3.0 mL of 0.2 M phosphate D-buffer (pH 7.0) at $10\text{--}50^\circ\text{C}$, and the solutions were added into an ATR cell. The time course of the degradation was investigated by ATR-IR spectra. In gelation system, constant amounts of TAPEG and TNPEG (240 mg) were dissolved in 3 mL of phosphate D-buffer solution (PB; 0.2 M, pH 7). The two solutions thus obtained were mixed in a 50 mL Falcon tube for 30 s at $10\text{--}40^\circ\text{C}$ and poured into the ATR cell.

IR spectra obtained were deconvoluted to extract single bands. A single band is assumed to be represented as a pseudo-Voigt function, $f_V(\nu) = \gamma f_L(\nu) + (1 - \gamma)f_G(\nu)$, where $f_L(\nu)$ and $f_G(\nu)$ stand for Lorentzian and Gaussian components, respectively, and the parameter γ ($0 < \gamma < 1$) is the Lorentzian component. A nonlinear least-squares curve fitting procedure was employed for the analyses. The integrated intensity A of a single band is evaluated according to $A = \gamma A_L + (1 - \gamma)A_G$, where A_L and A_G denote integrated intensities of the Lorentzian and Gaussian components, respectively. Total intensity $A_{\text{calc}}(\nu)$ calculated were compared with observed one $A_{\text{obs}}(\nu)$ in terms of the Hamilton R factor, $R = (\sum(A_{\text{obs}}(\nu) - A_{\text{calc}}(\nu))^2 / \sum A_{\text{obs}}(\nu)^2)^{1/2}$. Observed intensities were indeed reproduced with $R < 0.01$.

DFT Calculations. Evaluation of the full geometry optimization followed by normal frequency analyses was carried out on the basis of the density functional theory taking into account an electron correlation effect with Becke's three parameter and Lee–Yang–Parr correlation function (B3LYP), coupled with 6-311+G(d,p) basis set.^{21,22} All calculations were carried out using the Gaussian 03 program package.²³ The $\text{C}_2\text{H}_5\text{--CO--NHS}$, NHS ion, and $\text{C}_2\text{H}_5\text{COO}$ ion were examined as a model molecule for terminal NHS ester of TNPEG, dissociated NHS, and hydrolyzed terminal end of TNPEG in this gelation system; i.e., main PEG chain within Tetra-PEG is replaced by ethyl group to calculate easily. In this calculation, their molecules were hydrated stepwise from mono- to trihydrated ones to obtain the optimized structure and theoretical IR band in all the molecules. Among them, the theoretical bands for the hydrated molecules were well consistent with the experimental IR bands. Typical optimized structures are shown in Figure S2.

RESULTS AND DISCUSSION

Degradation Kinetics of TNPEG in Solution. In order to estimate the rate constant for gelation in the Tetra-PEG system, the rate for the degradation of TNPEG was evaluated by ATR-IR measurements. Figure 1 shows IR spectra in the range of

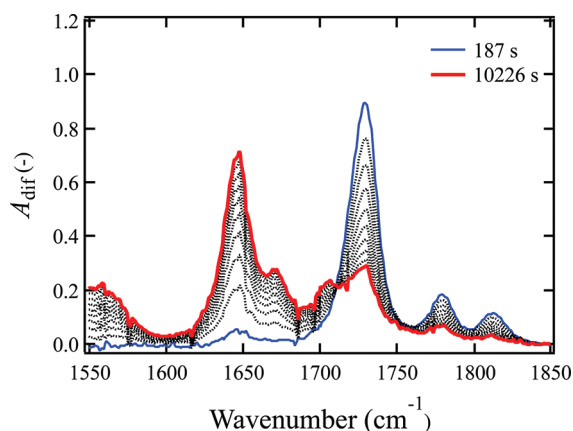


Figure 1. Time dependence of IR spectra for TNPEG solution, $C = 80$ mg/mL, containing 0.2 M phosphate D-buffer (pH 7.0) at 30°C .

$1550\text{--}1850\text{ cm}^{-1}$ obtained for TNPEG solution ($C = 80$ mg/mL) at various t . In this wavenumber range, IR bands originated from TNPEG or dissociated NHS were seriously overlapped with an intense and wide band from water. Therefore, IR spectra examined here were subtracted by those for aqueous buffer solution measured separately to extract TNPEG and dissociated NHS components as shown in Figure 1. As seen in Figure 1, the peak intensities at 1728, 1778, and 1812 cm^{-1} decreased with increasing t and those at 1555, 1646, 1670, and 1704 cm^{-1} increased. It was found that an isosbestic point is clearly seen at 1720 cm^{-1} , implying that dissociation reaction quantitatively occurs in this system.

Figure 2 shows typical IR bands of TNPEG solution after 1205 s, together with theoretical IR bands for the hydrated $\text{C}_2\text{H}_5\text{--CONHS}$, NHS ion, and $\text{C}_2\text{H}_5\text{COO}^-$ ion as a model molecules calculated by DFT calculations. The theoretical IR bands of a given molecule are predicted by full geometry optimizations followed by normal frequency analyses, and the optimized structures are shown in Figure S2. On the basis of theoretical IR bands, the observed IR spectrum can be satisfactorily deconvoluted into seven bands. Three bands at 1728, 1778, and 1812 cm^{-1} are assigned to the terminal NHS group within TNPEG and three bands at 1646, 1670, and 1704 cm^{-1} to dissociated NHS ion. The weak and broad band at 1555 cm^{-1} is ascribed to the terminal ionized carboxyl group. With regard to the dissociated NHS and TNPEG, we examined to calculate theoretical bands for neutral NHS and TNPEG-COOH. However, their band positions did not represent the observed ones, and we thus concluded that NHS and TNPEG after the degradation exist as ionic species.

The kinetic trace of $[\text{NHS}^-]$ at various temperatures, i.e., dissociated NHS ion concentration based on the integrated IR band at 1646 cm^{-1} assigned to stretching $\nu(\text{C--O})$ vibration plotted against t , is shown in Figure 3a. Figure 3b shows $\ln([-\text{NHS}]/[-\text{NHS}]_0)$ vs t , where $[-\text{NHS}]_0$ denotes the initial concentration of terminal NHS. As can be seen in these figures, the degradation rate became fast with increasing temperature. The apparent rate constant, k_{deg} , was estimated

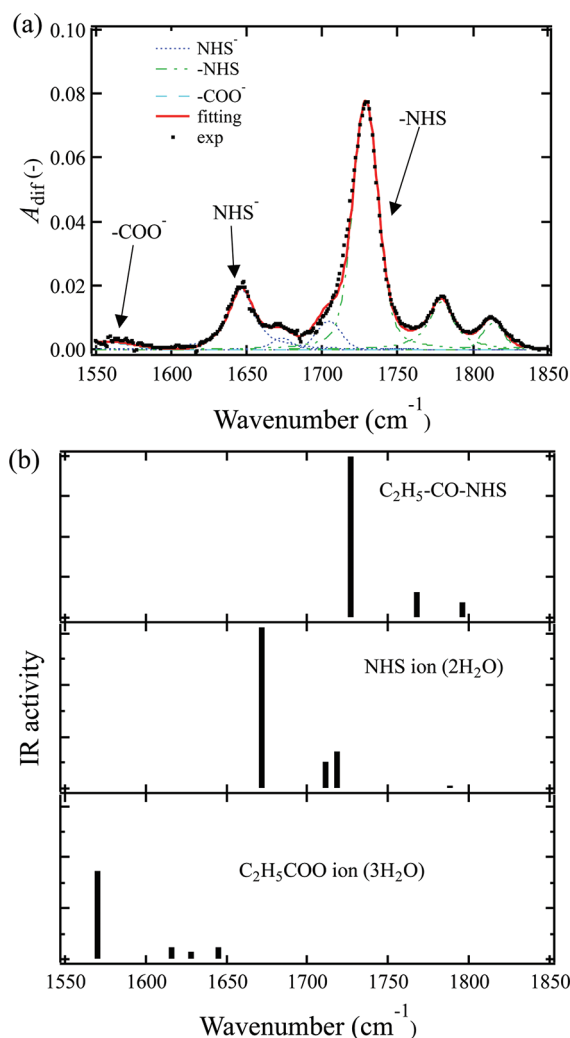


Figure 2. (a) Typical deconvoluted IR bands for TNPEG solution, $C = 80$ mg/mL at 1205 s (30°C). Dotted black and red lines show the observed and calculated IR spectra. Blue, green, and light blue lines correspond to the dissociated NHS, terminal NHS, and ionized carboxylic acid components, respectively. (b) Theoretical IR bands for hydrated $\text{C}_2\text{H}_5\text{--NHS}$ (neutral), NHS (ion), and $\text{C}_2\text{H}_5\text{COO}^-$ (ion) groups as a simple model, obtained from DFT calculations.

by least-squares-fit analysis on the basis of the following rate equation: $-\text{d}[-\text{NHS}]/\text{d}t = \text{d}[\text{NHS}^-]/\text{d}t = k_{\text{deg}}[-\text{NHS}]$. The observed variation (open symbols) was well represented with the fitting curve (solid line). Furthermore, Figure 3b clearly indicates the linear relationship between $\ln([-\text{NHS}]/[-\text{NHS}]_0)$ and time. These results suggest that the TNPEG in solution dissociates under a pseudo-first-order kinetics reaction to give NHS and TNPEG-COO ions. By assuming a second-order reaction kinetics including $[-\text{NHS}]$ and $[\text{OH}^-]$ terms to this dissociation, i.e., $-\text{d}[-\text{NHS}]/\text{d}t = k'_{\text{deg}}[\text{OH}^-][-\text{NHS}]$, we can obtain k'_{deg} independent of $[\text{H}^+]$ and/or pH. The values were estimated to be $k'_{\text{deg}} = 427, 723, 2060, 3010$, and $4730\text{ mol dm}^{-3}\text{ s}^{-1}$ at 283, 293, 303, 313, and 323 K, respectively. The rate constants obtained here are almost the same as those reported for the corresponding reactions of anisoyl-NHS in the literature, which supports the validity of our experiments.²⁴ These values will be used as fitting parameters in the following section. The estimated rate constants plotted against reciprocal temperature give the

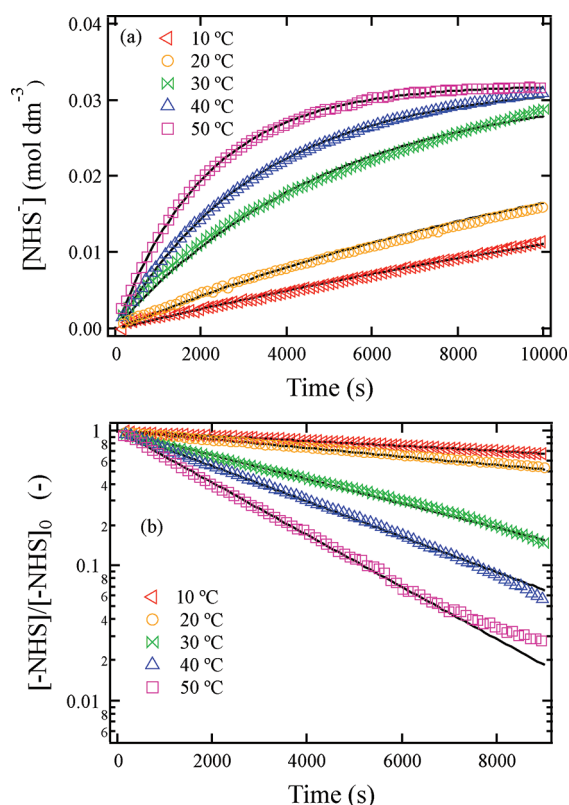


Figure 3. (a) Kinetic trace obtained for the degradation of TNPEG at 1646 cm⁻¹ (C–O stretching vibration) as a function of t . the concentration of the dissociated NHS is defined as $C_t = (A_t/A_\infty)C_\infty$ where C_t , C_∞ , A_t , and A_∞ denote the concentration of dissociated NHS at time t , that at infinitive time, the peak intensity of 1646 cm⁻¹ band at t , and that at infinitive time, respectively. (b) Pseudo-first-order plots of the degradation of TNPEG.

activation enthalpy and entropy according to the Eyring equation for the theory of transition state. The $\ln(k_{deg}T^{-1})$ vs T^{-1} plot is shown in Figure S3, and the activation ΔH^\ddagger and ΔS^\ddagger are obtained from the slope and intercept of the plot on the basis of the equation $\ln(k_{deg}T^{-1}) = -\Delta H^\ddagger/(RT)^{-1} + \Delta S^\ddagger/R + \ln(\kappa k_B h^{-1})$. The ΔH^\ddagger , $T\Delta S^\ddagger$, and ΔG^\ddagger values were estimated to be 47(4) kJ mol⁻¹, -9(5) kJ mol⁻¹ (at $T = 298$ K), and 56(9) kJ mol⁻¹, respectively. The activation energy are consistent with the corresponding energies for the hydrolysis reaction of 11,11'-dithiobis (*N*-hydroxysuccinimidylundecanoate) in self-assembled monolayers on gold, which also supports the validity of our experiments.²⁵ The estimated activation entropy $\Delta S^\ddagger \leq 0$ indicates that the TNPEG does not completely dissociate to remain TNPEG–CO⋯NHS bond at the transition state on the hydrolysis reaction.

Polycondensation Kinetics and Reaction Mechanism of Tetra-PEG Gel. Figure 4 shows the time dependence of IR spectra for Tetra-PEG components at 20 °C obtained by subtracting those for buffer solutions. The peak intensities at 1728, 1778, and 1812 cm⁻¹ decreased and those at 1614, 1646, 1670, and 1704 cm⁻¹ increased with progressing reaction. The IR spectra showed an isosbestic point at around 1720 cm⁻¹, implying that the polycondensation process in the Tetra-PEG gel system is successfully observed by our IR technique examined here. Figure 5 shows a typical IR spectrum observed at 1400 s, together with theoretical IR bands calculated by DFT calculations. According to theoretical IR bands calculated for the hydrated three simple molecules as a model of terminal

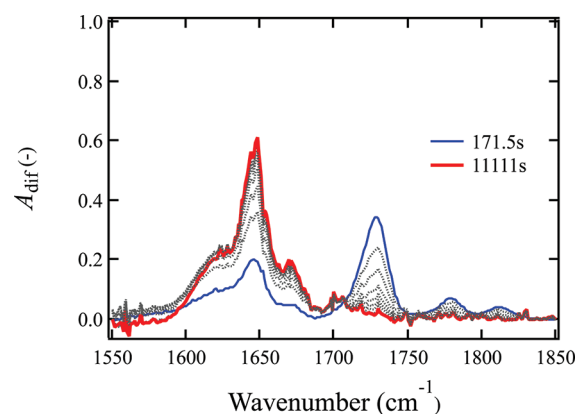


Figure 4. Time dependence of IR spectra for the gelation of Tetra-PEG macromers (TNPEG: 80 mg/mL; TAPEG: 80 mg/mL) in solution containing 0.2 M phosphate D-buffer (pH 7.0) at 20 °C.

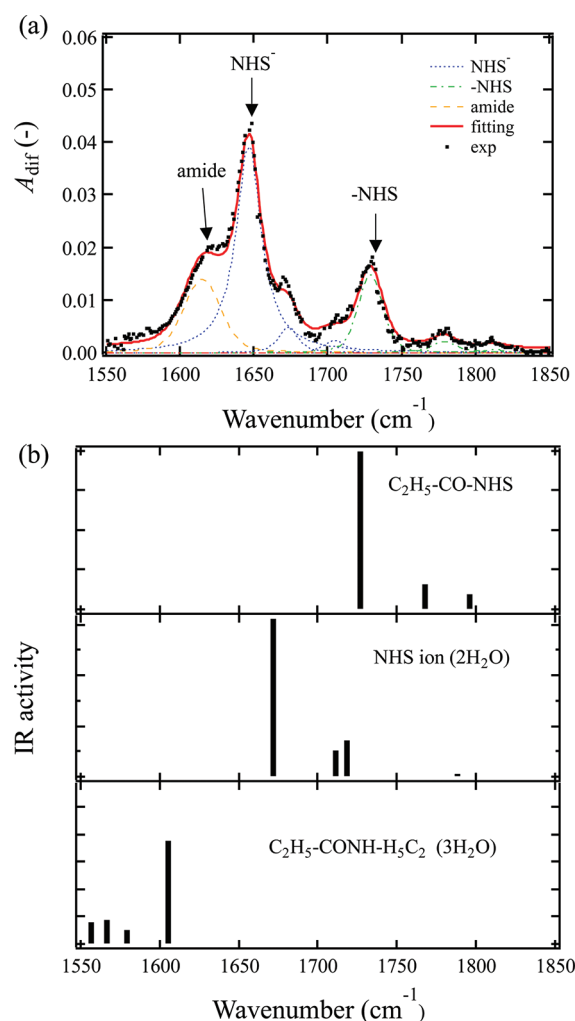


Figure 5. (a) Typical deconvoluted IR bands on a gelation process, $C = 80$ mg/mL at 1400 s (20 °C). Dotted black and red lines show the observed and calculated IR spectra. Blue, green, and orange lines correspond to the dissociated NHS, terminal NHS, and amide bond components, respectively. (b) Theoretical IR bands for hydrated C₂H₅-NHS (neutral), NHS (ion), and C₂H₅COO⁻ (ion) groups as a simple model, obtained from DFT calculations.

groups of Tetra-PEGs, the IR spectrum can be deconvoluted into eight bands, i.e., three bands at 1728, 1778, and 1812 cm⁻¹

originated from $\text{C}_2\text{H}_5\text{CO-NHS}$, three at 1646, 1670, and 1704 cm^{-1} from dissociated NHS ion, and the 1624 cm^{-1} band from a newly formed amide bond. It is found that there is no peak at 1555 cm^{-1} assigned to the ionized carbonyl group, which is clearly seen in Figure 3. This indicates that the formation of amide bond ($-\text{CONH}-$) on the polycondensation successfully proceeds, while hydration of terminal NHS group does not proceed practically.

Parts a and b of Figure 6 show the kinetic traces for the dissociated NHS ion, $[\text{NHS}^-]$, and second-order plots at

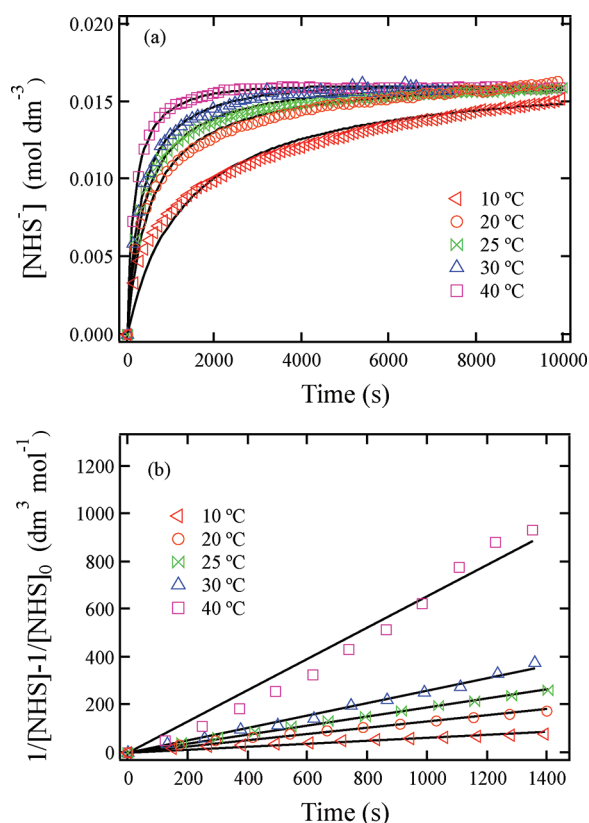


Figure 6. (a) Kinetic trace obtained for the gelation at 1646 cm^{-1} (C–O stretching vibration of dissociated NHS) as a function of t . (b) Pseudo-second-order plots of the gelation of Tetra-PEG gel.

various temperatures, respectively, based on the integrated IR intensities of the stretching $\nu(\text{C}-\text{O}, \text{NHS})$ band. It was found that the gelation rate increases with increasing temperature. The fit results using eqs 7 and 8 are also shown in Figure 6a. Here, we set k_{deg} as a fixed parameter obtained by the degradation analysis. The fit worked well from the initiation to nearly completion of reaction. Moreover, the second-order plot gives a straight line passing through the origin in Figure 6b. It should be noted that the gelation occurred at 1187, 496, 194, and 100 s after initiation at 283, 293, 303, and 313 K, respectively. These results suggest that this polycondensation reaction obeys a simple second-order kinetics from the initiation to end regardless of gelation threshold. This reason is suspected to be that the polycondensation kinetics of Tetra-PEG gel is not affected by the substitution effect and steric hindrance.

Figure 7 shows the rate constant, k_{gel} , plotted against reciprocal temperature as a form of Eyring plot. It is proved that Eyring plot for gelation reaction can be made, and this result

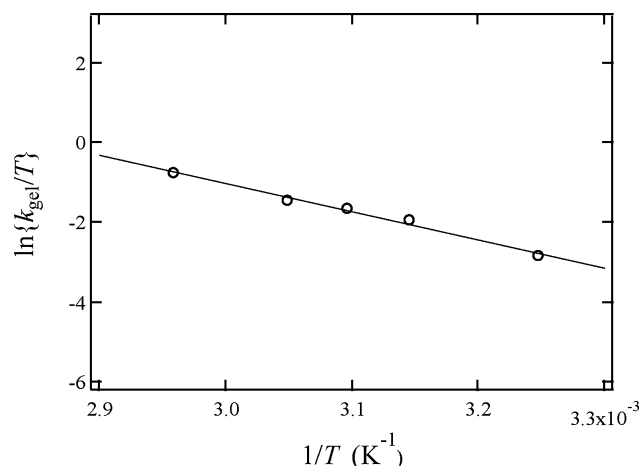


Figure 7. $\ln\{k_{\text{gel}}/T\}$ plotted against $1/T$ as a form of Eyring plot.

suggests that k_{gel} is thermodynamically meaningful. The activation enthalpy ΔH^\ddagger , entropy $T\Delta S^\ddagger$, and Gibbs free energy ΔG^\ddagger obtained from the slope and intercept in this figure were estimated to be 59(4) kJ mol^{-1} , $-9(3)$ kJ mol^{-1} (at $T = 298$ K), and 68(7) kJ mol^{-1} , respectively. Though small, the negative entropy implies the amide bond ($\text{NH}-\text{CO}$) between TNPEG and TAPEG is formed as the intermediate product on the polycondensation process; i.e., an associative mechanism operates at the transition state. The activation thermodynamic quantities involve a solvation effect at the transition state. However, it is difficult to discuss the hydration effect at the present stage. We need to accumulate the experimental activation energy in various solvent systems, which is now going on for alcohols or room-temperature ionic liquids.

Conclusion. The polycondensation reaction forming Tetra-PEG gel was investigated by ATR-IR spectroscopy in the viewpoint of reaction kinetics. We showed here that (1) the gelation kinetics of Tetra-PEG gel could be simply treated as a chemical reaction between mutually reactive end-groups in solution, (2) the gelation underwent as a simple second-order reaction from beginning to end regardless of gelation threshold, and (3) the gelation mechanism was predicted from the thermodynamic enthalpy and entropy at the transition state estimated by temperature dependence of rate constants. The reason of smooth second-order kinetics is suspected to be that the mean-field approximation can be applied to the reactivity of terminal groups on Tetra-PEGs; i.e., the reactivity of terminal groups on Tetra-PEGs is not affected by the steric hindrance, substitution effect, and gelation threshold, contributing to the homogeneous network structure of Tetra-PEG gel.

■ ASSOCIATED CONTENT

Supporting Information

Experimentally obtained function of unimerized amine, f (Figure S1), optimized geometries of model molecules in this study (Figure S2), and Eyring plot for TNPEG degradation (Figure S3). This material is available free of charge via the Internet at <http://pubs.acs.org>.

■ AUTHOR INFORMATION

Corresponding Author

*E-mail: sakai@tetrapod.t.u-tokyo.ac.jp (T.S.); k-fujii@issp.u-tokyo.ac.jp (K.F.).

■ ACKNOWLEDGMENTS

This work has been financially supported by Grant-in-Aids for Scientific Research from the Ministry of Education, Culture, Sports, Science and Technology (No. 23700555 to T.S., No. 22850002 to K.F., and No. 22245018 to M.S.).

■ REFERENCES

- (1) Rolfes, H.; Stepto, R. F. T. *Makromol. Chem. Theory Simul.* **1992**, *1*, 245–260.
- (2) Stockmayer, W. H. *J. Chem. Phys.* **1943**, *11*, 45–55.
- (3) Spirkova, M.; Dusek, K. *Polym. Bull.* **1989**, *22*, 191–198.
- (4) Furukawa, M.; Yokoyama, T. *Makromol. Chem.* **1981**, *182*, 2201–2207.
- (5) Nakonechnyi, V. P.; Rend'kina, N. K.; Dzhavadyan, E. A.; Irzhak, V. I.; Rozenberg, B. A. *Polym. Sci. U.S.S.R.* **1986**, *28*, 1682–1689.
- (6) Horie, K.; Hiura, H.; Sawada, M.; Mita, I.; Kambe, H. *J. Polym. Sci., Part A-1* **1970**, *8*, 1357–1372.
- (7) Dusek, K. *Polym. Gels Networks* **1996**, *4*, 383–404.
- (8) Dusek, K.; Duskova-Smrckova, M. *Prog. Polym. Sci.* **2000**, *25*, 1215–1260.
- (9) Bates, R. F.; Howard, G. J. *J. Polym. Sci., Part C* **1967**, *16*, 921–934.
- (10) Hopkins, W.; Peters, R. H.; Stepto, R. F. T. *Polymer* **1974**, *15*, 315–318.
- (11) Smith, R. S.; Stepto, R. F. T. *Makromol. Chem.* **1974**, *175*, 2365–2373.
- (12) Akagi, Y.; Katashima, T.; Fujii, K.; Matsunaga, T.; Shibayama, M.; Chung, U.; Sakai, T. *Macromolecules* **2011**, *44*, 5817–5821.
- (13) Akagi, Y.; Matsunaga, T.; Shibayama, M.; Chung, U.; Sakai, T. *Macromolecules* **2010**, *43*, 488–493.
- (14) Kurakazu, M.; Katashima, T.; Chijiishi, M.; Nishi, N.; Akagi, Y.; Matsunaga, T.; Shibayama, M.; Chung, U.; Sakai, T. *Macromolecules* **2010**, *43*, 3935–3940.
- (15) Li, X.; Tsutsui, Y.; Matsunaga, T.; Shibayama, M.; Chung, U.; Sakai, T. *Macromolecules* **2011**, *44*, 3567–3571.
- (16) Matsunaga, T.; Asai, H.; Akagi, Y.; Sakai, T.; Chung, U.; Shibayama, M. *Macromolecules* **2011**, *44*, 1203–1210.
- (17) Matsunaga, T.; Sakai, T.; Akagi, Y.; Chung, U.; Shibayama, M. *Macromolecules* **2009**, *42*, 1344–1351.
- (18) Matsunaga, T.; Sakai, T.; Akagi, Y.; Chung, U.; Shibayama, M. *Macromolecules* **2009**, *42*, 6245–6252.
- (19) Sakai, T.; Matsunaga, T.; Akagi, Y.; Kurakazu, M.; Chung, U.; Shibayama, M. *Macromol. Rapid Commun.* **2010**, *31*, 1954–1959.
- (20) Sakai, T.; Matsunaga, T.; Yamamoto, Y.; Ito, C.; Yoshida, R.; Suzuki, S.; Sasaki, N.; Shibayama, M.; Chung, U. *Macromolecules* **2008**, *41*, 5379–5384.
- (21) Becke, A. D. *J. Chem. Phys.* **1993**, *98*, 5648.
- (22) Lee, K. Y.; Mooney, D. J. *Chem. Rev.* **2001**, *101*, 1869.
- (23) Frisch, M. J.; Trucks, G. W.; Schlegel, H. B.; Scuseria, G. E.; Robb, M. A.; Cheeseman, J. R.; Montgomery, J., J. A.; Vreven, T.; Kudin, K. N.; Burant, J. C.; Millam, J. M.; Iyengar, S. S.; Tomasi, J.; Barone, V.; Mennucci, B.; Cossi, M.; Scalmani, G.; Rega, N.; Petersson, G. A.; Nakatsuji, H.; Hada, M.; Ehara, M.; Toyota, K.; Fukuda, R.; Hasegawa, J.; Ishida, M.; Nakajima, T.; Honda, Y.; Kitao, O.; Nakai, H.; Klene, M.; Li, X.; Knox, J. E.; Hratchian, H. P.; Cross, J. B.; Adamo, C.; Jaramillo, J.; Gomperts, R.; Stratmann, R. E.; Yazyev, O.; Austin, A. J.; Cammi, R.; Pomelli, C.; Ochterski, J. W.; Ayala, P. Y.; Morokuma, K.; Voth, G. A.; Salvador, P.; Dannenberg, J. J.; Zakrzewski, V. G.; Dapprich, S.; Daniels, A. D.; Strain, M. C.; Farkas, O.; Malick, D. K.; Rabuck, A. D.; Raghavachari, K.; Foresman, J. B.; Ortiz, J. V.; Cui, Q.; Baboul, A. G.; Clifford, S.; Cioslowski, J.; Stefanov, B. B.; Liu, G.; Liashenko, A.; Piskorz, P.; Komaromi, I.; Martin, R. L.; Fox, D. J.; Keith, T.; Al-Laham, M. A.; Peng, C. Y.; Nanayakkara, A.; Challacombe, M.; Gill, P. M. W.; Johnson, B.; Chen, W.; Wong, M. W.; Gonzalez, C.; Pople, J. A. *Gaussian 03, Rev. B.04*; Gaussian, Inc.: Pittsburgh, PA, 2003.
- (24) Cline, G. W.; Hanna, S. B. *J. Org. Chem.* **1988**, *53*, 3583–3586.

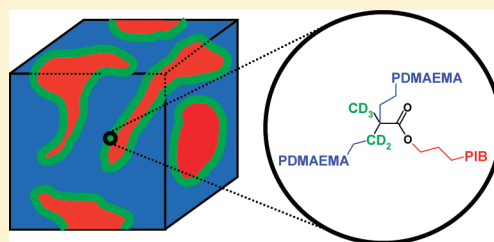
(25) Schönherr, H.; Feng, C.; Shovsky, A. *Langmuir* **2003**, *19*, 10843–10851.

Behavior of the Interphase Region of an Amphiphilic Polymer Conetwork Swollen in Polar and Nonpolar Solvent

Attila Domján,^{*,†} Péter Mezey,[‡] and Jenő Varga[§][†]Institute of Structural Chemistry, [‡]Institute of Materials and Environmental Chemistry, [§]Institute of Biomolecular Chemistry, Chemical Research Center, Hungarian Academy of Sciences, H-1025 Budapest, Pusztaszeri út 59-67, Hungary

S Supporting Information

ABSTRACT: The most attractive property of amphiphilic polymer conetworks (APCNs) is their ability to swell in both polar and nonpolar solvents. Depending on the composition, their structure is phase separated on the nanometer scale possessing highly different morphologies. This special nanophase-separated structure provides numerous possible applications for heterogeneous chemical and biological processes. Although the interphase region can fundamentally influence the material transport between the different polarity phases, there has been no specific information regarding its nature. Recent work demonstrates that by selective labeling of the cross-linking molecules by deuterium, information on the mobility of the interphase region can be obtained by solid-state NMR techniques. The first results show that this interphase region behaves differently in dry state as well as when swollen in polar or nonpolar solvents. Although the cross-linker is a polar molecule, its mobility hardly changes upon swelling in water; however, its mobility increases drastically by swelling in heptane. Additionally, the amount of nonreacted, thus non-cross-linked, chain ends could be quantified by solid-state NMR methodologies.



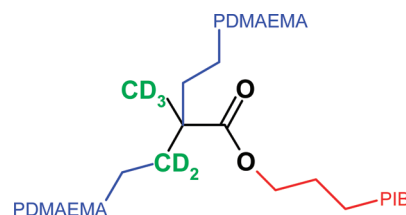
■ INTRODUCTION

Since the first successful synthesis of amphiphilic polymer conetworks (APCNs),^{1,2} a broad interest has risen from both synthetic and application points of view. Generally, APCNs are composed of covalently connected hydrophilic and hydrophobic chains with phase-separated structure. The size of the separated domains lies on the nanometer scale with diverse morphology. Because of their special chemical composition and morphology, they are able to swell in both polar and nonpolar solvents, keeping their superior mechanical properties as opposed to homopolymer gels. APCNs have been synthesized with various chemical and molecular structure in the past.^{3–6} Extensive research has been carried out to describe the structure and morphology of these materials by AFM,^{7,8} TEM,^{7,9} SEM,¹⁰ SAXS,^{7,11} SANS,⁹ and solid-state NMR¹¹ methods. All these studies have confirmed the phase-separated structure, but only the ¹H spin-diffusion study¹¹ suggested that an interphase region exists between the phases, with a size not exceeding 1 nm. Because of its small size, neither the macroscopic properties can be observed nor its existence can be proved by microscopic or scattering methods. The special properties of APCNs in combination with their large chemical and structural variety have inspired an array of different application-oriented studies in chemical, biological, and medical fields, such as nano-reactors,^{7,12} catalysis,¹³ solid-phase extractions,¹⁴ pervaporation matrices,¹⁵ promoted release hosts,¹⁶ medical implants and immunoisolators,¹⁷ cell culture¹⁸ and antifouling surfaces,¹⁹ drug delivery matrices,²⁰ contact lenses,¹⁵ tissue engineering scaffolds,^{18,19b} enzymatic catalysis supports,¹² sensors, etc.

To directly observe and study the interphase region and to gain information on its properties, poly[2-(*N,N*-dimethylamino)ethyl

methacrylate]-*l*-polyisobutylene (PDMAEMA-*l*-PIB) samples of different compositions (31, 49, 65 wt % of PIB) were synthesized. The conetwork samples were prepared by the macro-monomer method, using deuterium-labeled telechelic α,ω -dimethacrylate(*d*₅)-polyisobutylene (Scheme 1). Static deuterium

Scheme 1. Chemical Structure of the Cross-Link Point of the Poly[2-(*N,N*-dimethylamino)ethyl methacrylate]-*l*-polyisobutylene Amphiphilic Polymer Conetwork^a



^aThe cross-linker molecules are labeled by deuterium.

NMR spectra were recorded, deconvoluted, and analyzed in dry state as well as swollen in polar (water) and nonpolar (*n*-heptane) solvent.

■ EXPERIMENTAL SECTION

Static solid-state NMR spectra of the samples were recorded on a Varian NMR System operating at a ¹H frequency of 600 MHz (92.1 MHz for ²H)

Received: October 26, 2011

Revised: December 15, 2011

Published: January 9, 2012



with a Chemagnetics 6.0 mm narrow-bore triple-resonance T3 probe in double-resonance mode. Spectra were recorded by single pulse technique with 12 μ s delay between the $\pi/2$ pulse (8 μ s) and acquisition (20 ms). The relaxation delay was 2 s, and 40 000 transients were collected for each spectrum. The samples were kept in vacuum oven on 50 °C for 3 days before measurement. The swollen samples were measured after 2 days of soaking in water and *n*-heptane. The equilibrium swelling degree ($Q_{eq} = m_{swollen}/m_{dry}$) of the samples was determined gravimetrically (Table 1).

Table 1. Equilibrium Swelling Degree of Samples in Water and *n*-Heptane

wt % of PIB	Q_{eq} in water	Q_{eq} in <i>n</i> -heptane
31	1.75	1.95
49	1.51	2.55
65	1.24	3.19

RESULTS AND DISCUSSION

The shape of deuterium solid-state NMR spectra shows a large variety depending on the rate and symmetry of the molecular motions.²² Changes in the molecular motions as well as in the thermomechanic behavior of polymers (glass transition, melting, and crystallization, etc.) cause clearly detectable changes in the spectrum. Using the single pulse method instead of quadrupole echo causes overestimating of contribution of the narrow signals in the center of spectra. On the other hand, if motions are present in the intermediate regime, the echo line shape and intensity depend strongly on the delay time.²³ Because there are not any previous investigations on the molecular motions of these kinds of materials, in the present study a single pulse technique was used. In our experiments, spectra were recorded above the glass transition temperature (T_g) of both components, i.e., 90 °C above the T_g of PIB and 10 °C above the T_g of the PDMAEMA homopolymer. According to the deuterium spectra of dry APCN (Figure 1a), it consists of two different

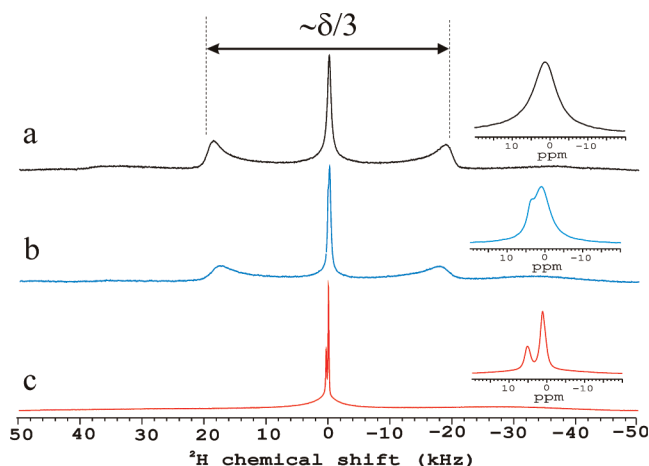


Figure 1. Static solid-state deuterium (^2H) spectra of (a) dry, (b) swollen in water, and (c) swollen in *n*-heptane PDMAEMA-*l*-PIB amphiphilic polymer conetworks containing 49 wt % of PIB. The middle regions are enlarged on the right side of the spectra.

types of components. There is a narrow signal in the middle of the spectra which can be attributed to fast molecular motions as well as a signal reminiscent of a Pake doublet with a

quadrupolar coupling constant of $\sim\delta/3$. Appearance of a Pake doublet shows that both nanophases are in a rubbery state, the interphase region; i.e., the cross-linker molecules are only capable of hindered motions. The CD_3 methyl groups can rotate freely, and the CD_2 methylene groups make crankshaft motion.²⁴ For the relatively rigid chains revealing a kink motion was not detectable. This phenomenon shows that for the dynamics of the cross-link points both phases have crucial role. At room temperature the PDMAEMA homopolymer is a solid, while the PIB is a viscous liquid. The mobility of the cross-linking points is much closer to the hydrophobic than to the hydrophilic component.

Swelling of the conetwork sample in water increases the mobility of the hydrophilic PDMAEMA chains, but astonishingly the deuterium spectra do not change dramatically (Figure 1b). On the contrary, swelling in *n*-heptane results in drastic changes (Figure 1c). The molecular motions are becoming very fast, and the quadrupolar interactions are averaging out almost completely. Two signals can be observed in the spectrum with approximately the same shape. The lower chemical shift signal at 1 ppm can be assigned to CD_3 , while the higher shift at 3.5 ppm can be attributed to the CD_2 groups. Detailed analysis of the deuterium spectra provides more information. Therefore, the spectra of dry samples and samples swollen in water were deconvoluted into a Pake doublet and two or three Gaussian peaks by the DMFIT²⁵ software. Because of the complexity of the motions and hereby the ways of averaging of the quadrupolar tensor, no physical meaning was attached to the Gaussian signals. The determined quadrupolar coupling constants were assigned to crankshaft motion and/or to methyl rotation. In samples swollen in water an additional narrow signal emerges around 3.5 ppm, which can be attributed to the CD_2 group of non-cross-linked PIB-MA chain ends. The CD_3 signal of these non-cross-linked chain ends cannot be differentiated from cross-linked CD_3 signals because their shape is mostly determined by the fast rotation. No signal belonging to double bonds can be detected; thus, all the PIB-MA chain ends were reacted with DMAEMA, but part of them are not connected to the network structure. The intensity of this additional peak is about 1–2% relative to the central line; thus, the amount of non-cross-linked chain ends can be estimated to be 2–3%. This observation opens up the possibility of quantification and direct determination of the ratio of “free” chain ends not only in the given conetwork but for APCN samples in general.

As shown in Figure 2, the quadrupolar coupling constant decreases in the dry samples and increases in the water swollen samples with increasing PIB content. When interpreting this information, it is important to take into account that with increasing PIB content the main chain length of the hydrophilic PDMAEMA chains decreases, whereas the macromonomer MA-PIB-MA chain length remains constant with a very narrow distribution. This feature arises from the basic properties of the macromonomer method we used for the synthesis of the investigated APCN samples.

A smaller coupling constant indicates that the mobility of the cross-link points, that is, the rate of the crankshaft motion, increases with decreasing of the PDMAEMA chain length. The faster cross-link motion suggests that at least a portion of the DMAEMA units in the vicinity of the cross-link points are more mobile. This finding is in a good agreement with the observation that the glass transition temperature of the PDMAEMA

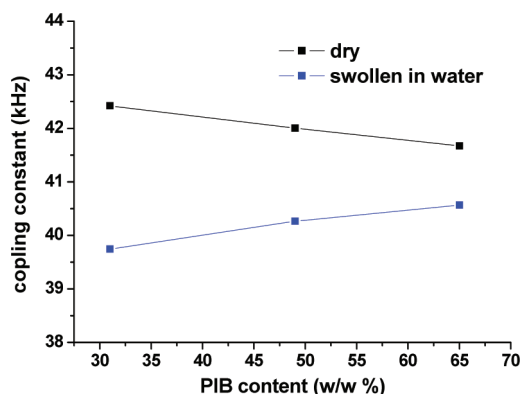


Figure 2. Quadrupolar coupling constants of dry and in water swollen APCN samples as a function of the composition. Coupling constants were determined by deconvolution of the recorded static deuterium NMR spectra.

component decreases with decreasing its chain length in the conetwork.

Swelling of the conetwork sample in water has only a small influence on the basic characteristics of the deuterium spectra, but as a result of the higher mobility of the swollen PDMAEMA nanophases the quadrupolar constant decreases. This decreasing effect is larger for longer chains. It appears that PIB chains influence stronger the mobility of the cross-link points. Swelling in *n*-hexane supports this observation because no Pake-like doublet can be perceived on the resulting spectra. The methyl rotation and the crankshaft motion are becoming very fast, and probably their axes can wriggle, too.

The broadening of the quadrupolar doublet depends on the composition in both dry and water swollen samples (Figure 3).

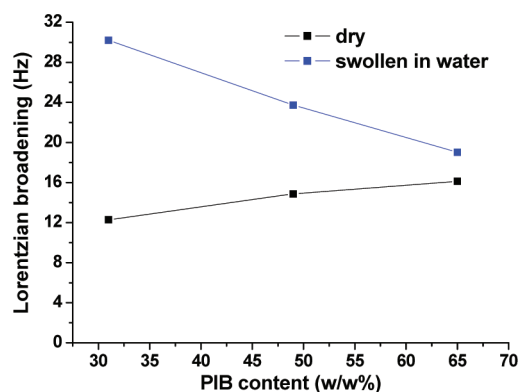


Figure 3. Lorentzian broadening of the quadrupolar doublet in dry and in water swollen APCN samples.

Increase in the broadening arises from different modes of motion of the cross-link points. Since the PIB chains are of narrow molecular weight distribution, the different modes may originate from the distribution of the PDMAEMA chain length. This suggests that less PDMAEMA content, thus shorter PDMAEMA chain length, results in a broader chain length distribution. Similar to the coupling constants, the effect on the broadening is different in samples swollen in water. In the water swollen samples the increase of the broadening is much larger at high PDMAEMA content. This broadening cannot be explained exclusively by differences in chain length distribution. Most likely

the nonuniform swelling of the hydrophilic nanophases plays a significant role.

In conclusion, the behavior of cross-link points in the investigated amphiphilic polymer conetwork samples differs significantly from both hydrophilic and hydrophobic nanophases. The interphase region of amphiphilic polymer conetwork plays an important role in heterogeneous processes. Because of the small size of the phases, there is an incredibly large interface region between the hydrophilic and the hydrophobic phases. The molecular motion of the interphase region is similar to the less mobile hydrophobic nanophases, and its mobility increases only a little by swelling in a polar solvent. On the contrary, its mobility increases dramatically if the conetwork is swollen in a nonpolar solvent, although the cross-linker is a polar molecule. This peculiar behavior has to be taken into account not only at the interpretation of heterogeneous processes but also at the thermodynamic description of APCNs. Additionally, we have shown that the amount of non-cross-linked chain ends can be quantified by solid-state NMR methodology.

■ ASSOCIATED CONTENT

§ Supporting Information

Description of the synthesis procedure of the deuterium-labeled APCN samples. This material is available free of charge via the Internet at <http://pubs.acs.org>.

■ AUTHOR INFORMATION

Corresponding Author

*E-mail: domjan@chemres.hu.

■ ACKNOWLEDGMENTS

We gratefully acknowledge the financial support from the Hungarian project GVOP-3.2.1-2004-04-0210/3.0 for the NMR equipment. We thank Prof. Béla Iván for the helpful discussions on APCNs.

■ REFERENCES

- (1) Chen, D.; Kennedy, J. P.; Allen, A. J. *J. Macromol. Sci., Part A: Pure Appl. Chem.* **1988**, *25*, 389–401.
- (2) Weber, M.; Stadler, R. *Polymer* **1988**, *29*, 1064–1070.
- (3) Patrickios, C. S.; Georgiou, T. K. *Curr. Opin. Colloid Interface Sci* **2003**, *8*, 76–85.
- (4) Erdődi, G.; Kennedy, J. P. *Prog. Polym. Sci.* **2006**, *31*, 1–18.
- (5) Mespouille, L.; Hendrick, J. L.; Dubois, P. *Soft Matter* **2009**, *5*, 4878–4892.
- (6) Patrickios, C. S., Ed. *Macromol. Symp.* **2010**, 291–292.
- (7) Scherble, J.; Thomann, R.; Iván, B.; Mülhaupt, R. *J. Polym. Sci., Part B: Polym. Phys.* **2001**, *39*, 1429–1436.
- (8) (a) Iván, B.; Haraszi, M.; Erdődi, G.; Scherble, J.; Thomann, R.; Mülhaupt, R. *Macromol. Symp.* **2005**, *227*, 265–273. (b) Bruns, N.; Scherble, J.; Hartmann, L.; Thomann, R.; Iván, B.; Mülhaupt, R.; Tiller, J. C. *Macromolecules* **2005**, *38*, 2431.
- (9) Iván, B.; Almdal, K.; Mortensen, K.; Johannsen, I.; Kops, J. *Macromolecules* **2001**, *34* (6), 1579–1585.
- (10) Sun, Y.; Rimmer, S. *Ind. Eng. Chem. Res.* **2005**, *44* (23), 8621–8625.
- (11) Domján, A.; Erdődi, G.; Wilhelm, M.; Neidhöfer, M.; Iván, B.; Spiess, H. W. *Macromolecules* **2003**, *36*, 9107–9114.
- (12) Bruns, N.; Tiller, J. C. *Nano Lett.* **2005**, *5*, 45–48.
- (13) (a) Savin, G.; Bruns, N.; Thomann, Y.; Tiller, J. C. *Macromolecules* **2005**, *38*, 7536–7539. (b) Hensle, E. M.; Tobis, J.; Tiller, J. C.; Bannwarth, W. *J. Fluorine Chem.* **2008**, *129*, 968–973.
- (14) Reyntjens, W. G.; Jonckheere, L. E.; Goethals, E. J. *Macromol. Rapid Commun.* **2002**, *23*, 282–285.

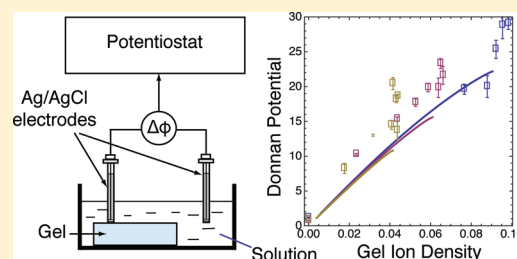
- (15) Künzler, J.; Ozark, R. *J. Appl. Polym. Sci.* **1997**, *65*, 1081–1089.
- (16) Brown, G. O.; Berquist, C.; Ferm, P.; Wooley, K. L. *J. Am. Chem. Soc.* **2005**, *127*, 11238–11239.
- (17) (a) Isayeva, I. S.; Gent, A. N.; Kennedy, J. P. *J. Polym. Sci., Part A: Polym. Chem.* **2002**, *40*, 2075–2084. (b) Kennedy, J. P.; Rosenthal, K. S.; Kashibhatla, B. *Des. Monomers Polym.* **2004**, *7*, 485–494.
- (18) (a) Haigh, R.; Fullwood, N.; Rimmer, S. *Biomaterials* **2002**, *23*, 3509–3516. (b) Rimmer, S.; German, M. J.; Maughan, J.; Sun, Y.; Fullwood, N.; Ebdon, J.; MacNeil, S. *Biomaterials* **2005**, *26*, 2219–2230.
- (19) (a) Gudipati, C. S.; Finlay, J. A.; Callow, J. A.; Callow, M. E.; Wooley, K. L. *Langmuir* **2005**, *21*, 3044–3053. (b) Behraves, E.; Jo, S.; Zygorakis, K.; Mikos, A. G. *Biomacromolecules* **2002**, *3*, 374–381. (c) Hu, Z.; Chen, L.; Betts, D. E.; Pandya, A.; Hillmyer, M. A.; DeSimone, J. M. *J. Am. Chem. Soc.* **2008**, *130*, 14244–14252.
- (20) (a) Bromberg, L.; Temchenko, M.; Hatton, T. A. *Langmuir* **2002**, *18*, 4944–4952. (b) Iván, B.; Kennedy, J. P.; Mackey, P. W. U.S. Patent 5,070,381, Dec 17, 1991. (c) Lin, C.; Gitsov, I. *Macromolecules* **2010**, *43*, 10017–10030. (d) Kennedy, J. P. *Macromol. Symp.* **2001**, *175*, 127–131. (e) Iván, B.; Kennedy, J. P.; Mackey, P. W. *ACS Symp. Ser.* **1991**, *469*, 194–202. (f) Iván, B.; Kennedy, J. P.; Mackey, P. W. *ACS Symp. Ser.* **1991**, *469*, 203–212. (g) Scherble, J.; Iván, B.; Müllhaupt, R. *Macromol. Chem. Phys.* **2002**, *203*, 1866–1871.
- (21) (a) Hanco, M.; Bruns, N.; Tiller, J. C.; Heinze, J. *Anal. Bioanal. Chem.* **2006**, *386*, 1273–1283. (b) Hanco, M.; Bruns, N.; Rentmeister, S.; Tiller, J. C.; Heinze, J. *Anal. Chem.* **2006**, *78* (18), 6376–6383.
- (22) Schmidt-Rohr, K.; Spiess, H. W. *Multidimensional Solid-State NMR and Polymers*, 3rd ed.; Academic Press: San Diego, CA, 1999.
- (23) *Solid State NMR of Polymers*; Ando, I., Asakura, T., Eds.; Elsevier Science B.V.: Amsterdam, 1998.
- (24) (a) Thomsen, T.; Zachmann, H. G.; Korte, S. *Macromolecules* **1992**, *25*, 6934–6937. (b) Moro, G. T. *J. Phys. Chem.* **1996**, *100*, 16419–16422. (c) Khuong, T. A. V.; Zepeda, G.; Sanrame, C. N.; Dang, H.; Bartberger, M. D.; Houk, K. N.; Garcia-Garibay, M. A. *J. Am. Chem. Soc.* **2004**, *126*, 14778–14786.
- (25) Massiot, D.; Fayon, F.; Capron, M.; King, I.; Le Calvé, S.; Alonso, B.; Durand, J. O.; Bujoli, B.; Gan, Z. H.; Hoatson, G. *Magn. Reson. Chem.* **2002**, *40*, 70–76.

Electromechanical Equilibrium Properties of Poly(acrylic acid/acrylamide) Hydrogels

Katsiaryna Prudnikova^{†,‡,§} and Marcel Utz^{*,†,‡,⊥}

[†]Center for Microsystems for the Life Sciences, [‡]Department of Mechanical and Aerospace Engineering, and [⊥]Department of Chemistry, University of Virginia, Charlottesville, Virginia 22904, United States

ABSTRACT: Thermomechanical properties of poly(acrylic acid-co-acrylamide) hydrogels have been measured for a range of gels while systematically varying the acrylamide/acrylic acid ratio. The gels have been equilibrated with a buffer solution at constant pH and salinity. The gels were characterized in terms of their equilibrium swelling ratio, elastic modulus, and electrochemical potential. The results are in quantitative agreement with the predictions from a recently published thermodynamic field theory.



INTRODUCTION

Polyelectrolyte hydrogels (PHG) consist of cross-linked macromolecules that carry dissociable electric charges along the polymer backbone. In a polar solvent such as water, the ionizable groups dissociate, providing a powerful entropic driving force that leads to substantial swelling. Because of this unique structure, dry PHG can absorb many times their own weight in water. They are therefore widely used as super-absorbers in diapers and cleaning products. In the swollen state, PHG exhibit rubber elasticity, i.e., solid-like behavior, in spite of water contents in excess of 90%. The equilibrium swelling ratio is sensitive to small changes in outside conditions, such as temperature, pH, and salinity of the surrounding solution. Consequently, PHGs have been studied widely as chemically, thermally, and electrically controlled actuators.^{1–9}

Several authors have provided theoretical approaches toward understanding the electrical and mechanical behavior of PHG.^{2,8,10–15} Much of this work has focused on the kinetics of the electrically induced swelling processes either analytically^{2,9} or by finite element simulation.¹³ Rubinstein et al. have developed a scaling theory of polyelectrolyte gels, and applied it to predict gel elastic modulus as a function of solvent salinity.¹¹ De Gennes has sketched a theory based on nonequilibrium thermodynamics coupling solvent flux and electrical fields,¹² which has recently been shown to quantitatively predict the bulk streaming potentials observed in PHG exposed to gradients in solvent pressure.¹⁶

On the other hand, a comprehensive field theory of the thermodynamic equilibrium state of PHG in the presence of solvent, electrical fields, and mechanical stress has only been reported recently by Hong et al.^{17,18} It differs from scaling-theory approaches in that it attempts to make absolute predictions on the gel properties, rather than merely their scaling. Like other theoretical approaches, it is based on a combination of Donnan equilibrium with the Flory–Rehner theory of polymer gels.^{19,20} This approach is widely used to rationalize the equilibrium swelling behavior of PHG.^{21–26} The

particular merit of the theory by Hong et al. lies in its rigorous incorporation of the effects of electric fields and mechanical stress and strain tensors.

In this contribution, we compare the results of an experimental study on poly(acrylic-co-acrylamide) gels with its predictions. The composition of the gels (acrylic acid versus acrylamide) as well as their cross-link density was varied, and the equilibrium swelling degree, electrical (Donnan) potential, and the elastic modulus were measured. As discussed in the remainder of this paper, the agreement between the theory and the experimental results is excellent for the swelling degree and modulus across the entire range of compositions and cross-link densities studied. At the same time, while the scaling of the Donnan potential with gel composition is captured correctly, its magnitude is underestimated consistently by about 20%.

THEORY

Following Hong et al.^{17,18} the free energy of a gel is separated into contributions due to the entropy elasticity of the polymer chains W_{el} , the free energy of mixing of the polymer W_{mix} and free ions W_{ion} with the solvent, and the free energy due to the electrical displacement polarization W_{pol} . Using the Flory–Huggins expression for W_{mix} , the ideal mixing law for W_{ion} , and the Flory–Rehner model for the elasticity of the polymer chains, Hong et al. obtained for the stress field

$$\sigma_{ij} = \frac{NkT}{\det \mathbf{F}} (F_{iK} F_{jK} - \delta_{ij}) + \frac{1}{\epsilon} \left(D_i D_j - \frac{1}{2} D_m D_m \delta_{ij} \right) - \Pi \delta_{ij} \quad (1)$$

where N is the concentration of polymer chains (per dry volume of polymer), \mathbf{F} is the deformation gradient, ϵ the

Received: November 10, 2011

Revised: December 19, 2011

Published: January 13, 2012

electrical permittivity of the gel, \mathbf{D} the electrical displacement field, and Π represents the osmotic pressure

$$\Pi = \frac{kT}{v_s} \left[\frac{C_+ + C_-}{C_s} - 2v_s c_0 - \log \frac{v_s C_s}{1 + v_s C_s} - \frac{1}{1 + v_s C_s} - \frac{\chi}{(1 + v_s C_s)^2} \right] \quad (2)$$

with the molecular volume of the solvent v_s (18 cm³/mol for water), the solvent concentration (per unit volume of dry polymer) C_s , the concentration of positive and negative free ions in the gel C_{\pm} , and the salt concentration in the solvent c_0 . Inside the gel, away from the Debye layer at the gel/solution interface, both the stress and the electric displacement field vanish. Assuming isotropic swelling $F_{ij} = \delta_{ij}\lambda_0$, on finds from (eq 1) for the equilibrium osmotic pressure

$$\Pi_0 = NkT(\lambda_0^{-1} - \lambda_0^{-3}) \quad (3)$$

Since the polymer molecules and the solvent can be regarded as incompressible, and the contribution of the free ions to the total volume of the system is negligible, the equilibrium swelling ratio λ_0^3 satisfies

$$\lambda_0^3 = 1 + v_s C_s \quad (4)$$

The concentrations of positive and negative free ions in the gel are given by the Boltzmann distribution

$$C_{\pm} = c_0 \phi C_s \exp \frac{\mp e \phi}{kT} \quad (5)$$

where c_0 is the salt concentration in the solution, and v_{\pm} are the molar volumes of positive and negative ions, respectively, ϕ denotes the Donnan potential within the gel, and the ions are assumed to have a valency of 1. Finally, due to charge neutrality deep inside the gel, we have

$$C_0 + C_- = C_+ \quad (6)$$

where C_0 denotes the concentration of fixed negative charges inside the gel. As detailed in ref 17, eqs 2–6 represent a nonlinear system of six independent equations, which can be solved numerically to yield the six unknowns λ_0^3 , ϕ , C_{\pm} , Π , and C_s , given the input parameters χ , N , v_s , v_{\pm} , c_0 , and C_0 . In the present work, gels with varying composition and cross-link density were synthesized, and their swelling ratio λ_0^3 , the Donnan potential ϕ , and the elastic modulus were measured. While λ_0^3 and ϕ emerge directly from solving the above equations, the elastic modulus can be obtained from eq 1 by assuming the strain to be of the form

$$F_{ik} = \lambda_0(\delta_{ik} + u_{ik}) \quad (7)$$

where $u_{ik} = \partial u_i / \partial x_k \ll 1$ represents the infinitesimal strain applied to the swollen network. Inserting this into (eq 1), assuming the electrical displacement to vanish, one finds to first order in the infinitesimal strains

$$\sigma_{ik} = 2G \frac{u_{ik} + u_{ki}}{2} + \delta_{ik} \Lambda u_{jj} \quad (8)$$

with the Lamé constants

$$G = \frac{NkT}{\lambda_0}, \Lambda = kT \left(\frac{C_- + C_+}{\lambda_0^3} + \frac{1 - 2\chi}{v_s \lambda_0^6} - \frac{N}{\lambda_0} \right) \quad (9)$$

(see Appendix for derivation). In the present work, the elastic properties of the samples were measured by a uniaxial compression experiment. This yields Young's modulus Y , which is obtained from the Lamé constants as

$$Y = \frac{NkT}{\lambda_0} \left[3 - \frac{Nv_s \lambda_0^5}{1 - 2\chi + (C_+ + C_-)v_s \lambda_0^3} \right] \quad (10)$$

■ EXPERIMENTAL SECTION

The details of the gel synthesis have been published elsewhere,²⁷ and are only summarized briefly here. Acrylic acid (AA) and acrylamide (AM) were used as comonomers. *N,N'*-methylenebis(acrylamide) (nBisA) and 2,2-dimethyl-2-phenylacetophenone (DMPA) were used as received as cross-linker and photoinitiator, respectively. The polymerization was carried out in a potassium phthalate/methyl alcohol buffer solution pH 4.00 (Fisher) with a small amount of added dimethyl sulfoxide (DMSO); the resulting gels were then equilibrated in a potassium acid phthalate/sodium hydroxide buffer solution at pH 5.00. The salt concentration of both buffer solutions was $c_0 = 0.05$ M.

All copolymerizations were performed at an overall monomer concentration of 3.8 M, while the mol fraction of AA x_{AA} was varied between 0 and 1. In this way, three sequences of copolymers were created using different initial concentrations of nBisA = 22 mM, 43 mM, and 86 mM. The photoinitiator DMPA concentration was equal to 6.78 mM and was kept constant during all copolymerizations. Samples were polymerized in a square mold made of two microscope slides (Fisher) separated with PDMS spacers of 2.2 mm thickness. Polymerization was initiated by exposure to an UV lamp ($\lambda = 365$ nm) at room temperature for 10 min. The samples were then carefully removed from the mold and equilibrated in a buffer solution at pH 5.00 for 7 days, at which point the sample mass reached a constant value. Sample mass was monitored as a function of time on an analytical balance after gentle drying with paper towels.

The elastic modulus of the same gels was measured by a quasi-static uniaxial compression measurement using a TA Instruments QA 800 dynamic mechanical analyzer. A sample of 15 mm diameter was exposed to a preload of 1 mN, which was then gradually increased to 7 N at a rate of 2 N/min. Sample thickness ranged from 2.5 mm to 3 mm, depending on the swelling degree. Experimental error was estimated from running three independent samples per data point.

The Donnan potential in each sample was measured by gentle indentation of the sample surface with a Ag/AgCl electrode, as described in detail in ref 27. A reference Ag/AgCl electrode was kept in solution, while the surface of the gel sample was gently pressed with the working Ag/AgCl electrode. The resulting potential difference was recorded with a GAMRY Reference 600 Potentiostat.

■ RESULTS AND DISCUSSION

Parts A and B of Figure 1 show the experimental results for the swelling degree and Young's modulus of the gels, respectively (closed symbols). The least-squares fit of the theory laid out above to the data is represented by solid lines; the bands indicate the 95% confidence regions of fit, as discussed in more detail below. The swelling degree (Figure 1A) increases with the acrylic acid content, and decreases with the density of cross-links. Pure acrylamide gels ($x_{AA} = 0$) exhibit swelling ratios between 3 and 10, whereas acrylic acid gels ($x_{AA} = 1$) reach values of up to 35 at the lowest cross-link density.²⁷ These swelling degrees are consistent with values reported by other groups; e.g., Vashaghani-Farahani et al. have obtained swelling degrees between 5 and 10 for a gel very similar to our sample with intermediate cross-link density at $x_{AA} = 0.1$ around neutral pH.²⁸

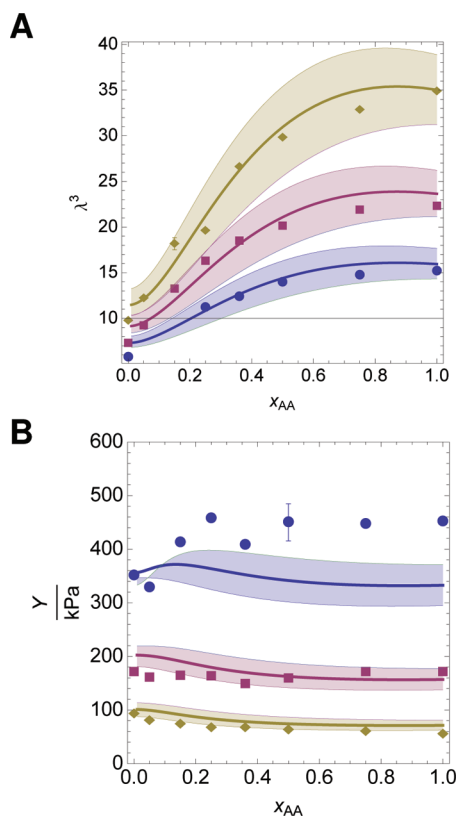


Figure 1. (A) Swelling degree of poly(acrylic acid-co-acrylamide) gels prepared with cross-linker concentrations of 22 mM (green diamonds), 43 mM (red squares), and 86 mM (blue circles) in equilibrium with buffer solution at pH = 5. (B) Elastic moduli of the same samples. Solid lines represent the best fit of the model to the experimental data (cf. text); the bands indicate 95% confidence intervals of fit.

Three separate samples of each composition were made; the error bar shown in Figure 1A represents ± 3 standard deviations. Error bars for the other data points are of similar or smaller size, and have been omitted from the figure for clarity.

The Young's moduli of the gels, as obtained from uniaxial compression, are shown in Figure 1B. The samples with the lowest cross-link density exhibit the lowest modulus, as expected. For a given cross-link density, the modulus appears to be almost constant as the acrylic acid content is increased. This may seem surprising, since the swelling degree of the gels is a very strong function of acrylic acid content.

The data in Figure 1 were used to fit the model, with the Flory interaction parameter χ , the density of cross-linked chains N and the density of dissociated charges on the polymer backbone C_0 as adjustable parameters. The remaining quantities appearing in the model, the solvent salt concentration c_0 , and the molar volumes of the solvent and salt, are well-known. Even for the free parameters, there are quite narrow physical bounds. χ is known to be in the vicinity of 0.5 for aqueous acrylate gels.^{29–31} The experiments described here were designed to control the density of chains and the polymer charge density through the composition of the gels. The concentration of chains N is proportional to the concentration of cross-linker. However, not every cross-linker molecule that is incorporated into the polymer network leads to an active branching point; many are lost due to the formation of short loops or chain

termination. In order to fit the experimental data, the chain density was therefore taken to be proportional to the concentration of cross-linker: $N = \eta_c C_{\text{nBisA}}$, where the cross-linker efficiency η_c was used as a fit parameter. Several authors have explored the efficiency of cross-linkers in the formation of polymer networks;^{30,32,33} typical values for η_c range from 1% to 50%.

At pH 5, acrylic acid groups in the copolymers dissociate partially, whereas the acrylamide groups do not. Therefore, changing the ratio of AA vs AM monomers in the gel provides control over the concentration of fixed charges in the gel. However, this is complicated by the fact that the pK_a value, and therefore the degree of acrylic acid dissociation at fixed pH, varies with the concentration of acrylic acid.³⁴ In the present work, this effect was captured by assuming the concentration of fixed negative charges C_0 to grow with the acrylic acid fraction x_{AA} as

$$C_0 = \frac{\alpha x_{AA}}{v_m} \exp(-\beta x_{AA}) \quad (11)$$

where α and β were fit constants, and v_m denotes the molecular volume of the monomers (which is almost the same for acrylic acid and acrylamide).

The four adjustable parameters are listed in Table 1, along with their physically meaningful range, and the best fit value

Table 1. Adjustable Model Parameters with Their Meaningful Physical Range

parameter		physical range	fitted value
Flory interaction	χ	0.45–0.55	0.505 ± 0.01
cross-linker efficiency	η_c	0–0.3	0.05 ± 0.005
dissociation degree	α	0.1–0.5	0.32 ± 0.05
dissociation exponent	β	0–2	1.14 ± 0.05

obtained from the data shown in Figure 1. A normalized overall mean square deviation of fit was computed as

$$\sigma^2 = \sum_{k=1}^3 \sum_{j=1}^M \left(\frac{(\lambda_{kj}^3 - \lambda'_{kj})^2}{\lambda_{kj}^3} + \frac{(Y_{kj} - Y'_{kj})^2}{Y_{kj}} \right) \quad (12)$$

where k runs over the three different cross-link densities and j over the acrylic acid concentrations. Primed quantities are calculated from the fit parameters by numerically solving the system of equations (eq 1–eq 6), whereas their unprimed counterparts λ^3 and Y denote the experimental values. The fitted parameter values given in Table 1 were obtained by minimizing σ^2 . The error bars represent estimated 95% confidence contours based on the 95% quantile of the F distribution with $p = 4$ fit parameters and $n = 46$ independent data points.³⁵

As shown in parts A and B of Figure 1, the overall agreement of the theory with the experimental swelling and modulus data is remarkably good. At the lowest cross-link density, however, the fit overestimates the saturation of the swelling degree with acrylic acid content; the experimental data seems to exhibit a finite slope as $x_{AA} = 1$ is approached, whereas the fit clearly saturates. Also, the swelling degree of pure acrylamide gels ($x_{AA} = 0$) is overestimated somewhat. The experimental data suggest a finite slope of the swelling degree at this point, which is not represented by the model. The moduli of the gels with the lower two cross-link densities are very well represented by the

model, even including a slight downward trend as the acrylic acid content increases. The most highly cross-linked gels, however, exhibit a modulus that increases from 350 to 450 kPa as the acrylic acid content increases from 0 to 0.3, and then stays level. The model, by contrast, fits the value at $x_{AA} = 0$, but shows a much smaller increase, which is followed by a slight decline. It therefore underestimates the moduli of the most highly cross-linked gels at large acrylic acid content by about 25%. The fact that this deviation surfaces at the most swollen gels at the highest cross-link density suggests that it may be due to finite extensibility of the polymer chains, which is neglected in the Flory–Rehner approach, which underlies the model.

In addition to the swelling degree and the elastic modulus, the Donnan potential of the gels has been measured using the approach shown in Figure 2A; Figure 2B shows the results.

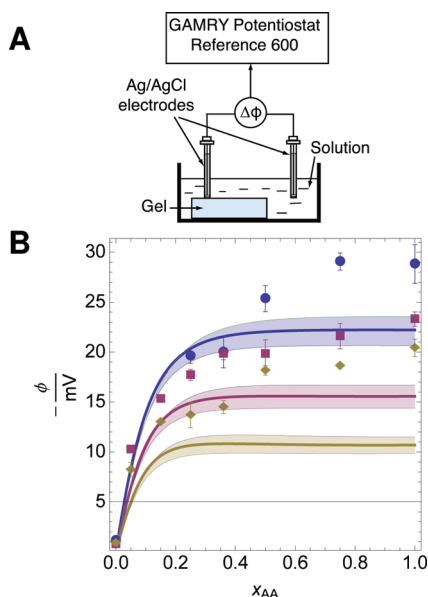


Figure 2. (A) Setup for measuring the Donnan potential; (B) Donnan Potential values (closed symbols), and predicted values from the model (solid lines), using the best fit parameters given in Table 1.

Measurements were repeated for three independent samples per data point; the error bars represent $\pm \sigma$. Because of the negatively charged polymer backbone, the Donnan potential values are negative; i.e., the electrical potential inside the gel is less than in the surrounding solution. As expected, the values obtained are zero within experimental error for pure acrylamide gels, and then increase in magnitude with increasing acrylic acid content. More highly cross-linked samples exhibit higher Donnan potential. The values increase rapidly at low acrylic acid content, and then start to saturate around $x_{AA} = 0.5$.

The solid lines in Figure 2 show the predicted Donnan potential ϕ , using the fit parameter values obtained from the swelling and modulus data (Table 1). The predicted values show the same scaling and trends as the experimental data: gradual increase with x_{AA} and saturation around $x_{AA} = 0.5$. The scaling with cross-link density is also similar to the experimental data. However, the predicted values underestimate the measured data by a factor of 1.5 to 2, particularly at high acrylic acid concentrations. These discrepancies notwithstanding, the agreement in overall behavior and scaling is remarkable. It should be noted that an even better agreement could have been obtained by incorporating the Donnan data into the data

fitting procedure, albeit at the expense of somewhat worse fit of the swelling and modulus data.

It has been noted previously that the Donnan potential data fall onto a single curve if they are plotted against the actual concentration (spatial density) of ionizable groups in the gel.²⁷ In fact, in simplified terms, the Donnan potential can be seen as a potential difference that arises due to the charge imbalance at the Debye layer at the gel surface, and should therefore be proportional to the number density of (dissociated) negative charges on the polymer backbone in the swollen gel.

Using (eq 11) and the values obtained from the fit in Table 1, Figure 3 plots the Donnan potential ϕ versus the spatial

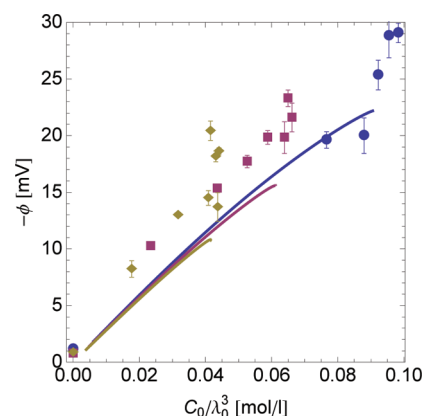


Figure 3. Donnan potential data plotted as a function of true spatial density of dissociated charges on the polymer backbone C_0/λ_0^3 , determined from eq 11 and the parameters given in Table 1.

concentration of negative backbone charges C_0/λ_0^3 . Indeed, the points do seem to fall onto a straight line, even though there is some scatter, including two outlying data points around $C_0/\lambda_0^3 = 0.08$ mol/L.

The model predictions for the three cross-link densities (solid lines in Figure 3) almost collapse on a single curve, which very closely approximates a straight line. However, they are consistently below the experimental data by a few millivolts. Nonetheless, the fact that both the experimental and model data essentially fall onto a straight line provides an independent consistency check and suggests that eq 11, combined with the values of Table 1, correctly captures the dissociation behavior.

CONCLUSIONS

A thermodynamic field theory for the electromechanical behavior of polyelectrolyte gels has been applied to the case of acrylamide/acrylic acid copolymer gels. Samples have been made at different cross-link densities, and with monomer compositions ranging from pure acrylamide to pure acrylic acid. The swelling degree and elastic moduli of the gel have been used to determine four free parameters of the model, for which physically plausible values were obtained. The fit of the swelling data is excellent, and the moduli are well represented, except at the highest cross-link densities in combination with high acrylic acid content. The model, in combination with the fitting parameters obtained in this manner, predicts the correct scaling of Donnan potentials with gel composition but underestimates the experimental values systematically by about 30%.

Nonetheless, the model comes very close to quantitatively capturing the electromechanical behavior of the gels over a wide range of cross-link densities and gel compositions, in spite

of being based on very simple treatments of solvent–polymer interactions (Flory–Huggins), polymer network entropy (Flory–Rehner), and osmotic pressure (ideal solution theory).

■ APPENDIX: ELASTIC CONSTANTS

The linear elastic properties for a swollen gel can be derived from (eq 1). We assume that the gel is in equilibrium with a solvent, and has swollen to an isotropic state with $F_{ij} = \delta_{ij}\lambda_0$. An additional (small) displacement u_i produces the strain

$$F_{ij}' = \frac{\partial x_i}{\partial X_j} + \frac{\partial u_i}{\partial X_j} = F_{ij} + \frac{\partial u_i}{\partial x_k} \frac{\partial x_k}{\partial X_j} \quad (13)$$

Since F_{ij} is isotropic, we find

$$F_{ij}' = \lambda_0(\delta_{ij} + u_{ij}) \quad (14)$$

where $u_{ij} = \partial u_i / \partial x_j$ is the infinitesimal strain. The stress given in (eq 1) depends on the strain through the determinant $\det F'$, the explicit expression $F_{ik}F_{jk}$ and through the osmotic pressure Π . In the following, the first order variations of these terms in the infinitesimal strain u_{ij} are derived.

Making use of the identity $\det(I + A) = \exp(\text{tr} \log(I + A))$, and expanding the matrix logarithm and exponential to first order in u_{ij} we find

$$1/\det(F_{ij}') \approx \lambda_0^{-3}(1 - u_{kk}) \quad (15)$$

Equation (eq 4) expresses the swelling ratio λ_0^3 in terms of the solvent concentration C_s . In the presence of an additional infinitesimal strain, (eq 4) becomes

$$\lambda_0^3(1 + u_{kk}) = 1 + v_s C_s \quad (16)$$

Using this to substitute C_s in (eq 2) and expanding to first order in u_{kk} one finds

$$\Pi \approx \Pi_0 - \frac{kT}{v_s} \left[\frac{v_s(C_+ + C_-)}{\lambda_0^3} + \frac{1 - 2\chi}{\lambda_0^6} \right] u_{kk} \quad (17)$$

with the equilibrium osmotic pressure Π_0 given by eq 3. By definition, the stress vanishes for $u_{ij} = 0$. Together with this, the expressions in eqs 14, eq 15, and eq 17 can be introduced into eq 1. Retaining only terms of first order, we obtain the Lamé formulation of isotropic linear elasticity (eq 8), with the Lamé constants given by eq 9.

■ AUTHOR INFORMATION

Corresponding Author

*E-mail: mu3q@virginia.edu.

Present Address

[§]Department of Materials Science and Engineering, Drexel University, Philadelphia PA.

■ ACKNOWLEDGMENTS

This work has been supported by the US National Science Foundation under Grant Number DMR 0647790. We gratefully acknowledge helpful discussions with Prof. Zhigang Suo, School of Engineering and Applied Science, Harvard University.

■ REFERENCES

(1) Tanaka, T.; Nishio, I.; Sun..., S. *Science* **1982**, *218*, 467–469.

- (2) Doi, M.; Matsumoto, M.; Hirose, Y. *Macromolecules* **1992**, *25*, 5504–5511.
- (3) Beebe, D.; Moore, J.; Bauer, J.; Yu, Q.; Liu, R.; Devadoss, C.; Jo, B. *Nature* **2000**, *404*, 588–590.
- (4) Shahinpoor, M.; Kim, K. *Smart Mater. Struct.* **2001**, *10*, 819–833.
- (5) Kaneko, D.; Gong, J. P.; Osada, Y. *J. Mater. Chem.* **2002**, *12*, 2169–2177.
- (6) Murdan, S. J. *Controlled Release* **2003**, *92*, 1–17.
- (7) Lutolf, M.; Raeber, G.; Zisch, A.; Tirelli, N.; Hubbell, J. *Adv. Mater.* **2003**, *15*, 888–892.
- (8) Bassetti, M.; Chatterjee, A.; Aluru, N.; Beebe, D. *J. Microelectromech. Syst.* **2005**, *14*, 1198–1207.
- (9) Yamaue, T.; Mukai, H.; Asaka, K.; Doi, M. *Macromolecules* **2005**, *38*, 1349–1356.
- (10) Bleijser, J. D.; Hollander, J.; Leyte, J. J. *Phys.: Condens. Matter* **1994**, *6*, A311–A315.
- (11) Rubinstein, M.; Colby, R.; Dobrynin, A.; Joanny, J. *Macromolecules* **1996**, *29*, 398–406.
- (12) Gennes, P. D.; Okumura, K.; Shahinpoor, M.; Kim, K. *Europhys. Lett.* **2000**, *50*, 513–518.
- (13) Wallmersperger, T.; Kröplin, B.; Gülch, R. *Mech. Mater.* **2004**, *36*, 411–420.
- (14) Darwish, M.; van der Maarel, J.; Zitha, P. *Macromolecules* **2004**, *37*, 2307–2312.
- (15) Hong, W.; Zhao, X.; Suo, Z. *J. Mech. Phys. Solids* **2010**, *58*, 558–577.
- (16) Fiumefreddo, A.; Utz, M. *Macromolecules* **2010**, *43*, 5814–5819.
- (17) Hong, W.; Liu, Z.; Suo, Z. *Int. J. Solids Struct.* **2009**, *46*, 3282–3289.
- (18) Hong, W.; Zhao, X.; Zhou, J.; Suo, Z. *J. Mech. Phys. Solids* **2008**, *56*, 1779–1793.
- (19) Flory, P.; Rehner, J. *J. Chem. Phys.* **1943**, *11*, 512.
- (20) Flory, P.; Rehner, J. *J. Chem. Phys.* **1943**, *11*, 521.
- (21) Ricka, J.; Tanaka, T. *Macromolecules* **1984**, *17*, 2916–2921.
- (22) Brannon-Peppas, L.; Peppas, N. *Chem. Eng. Sci.* **1991**, *46*, 715–722.
- (23) Baker, J.; Hong, L.; Blanch, H.; Prausnitz, J. *Macromolecules* **1994**, *27*, 1446–1454.
- (24) Okay, O.; Sariisik, S. *Eur. Polym. J.* **2000**, *36*, 393–399.
- (25) Victorov, A.; Radke, C.; Prausnitz, J. *Phys. Chem. Chem. Phys.* **2006**, *8*, 264–278.
- (26) Plotnikov, N.; Victorov, A. *Fluid Phase Equilib.* **2007**, *261*, 26–34.
- (27) Prudnikova, K.; Utz, M. *Macromolecules* **2010**, *43*, 511–517.
- (28) Vasheghani-Farahani, E.; Vera, J.; Cooper, D.; Weber, M. *Ind. Eng. Chem. Res.* **1990**, *29*, 554–560.
- (29) Horkay, F.; Tasaki, I.; Basser, P. *Biomacromolecules* **2000**, *1*, 84–90.
- (30) Hooper, H.; Baker, J.; Blanch, H.; Prausnitz, J. *Macromolecules* **1990**, *23*, 1096–1104.
- (31) Gudeman, L.; Peppas, N. *J. Appl. Polym. Sci.* **1995**, *55*, 919–928.
- (32) Gundogan, N.; Melekaslan, D.; Okay, O. *Macromolecules* **2002**, *35*, 5616–5622.
- (33) Kizilay, M.; Okay, O. *Polymer* **2003**, *44*, 5239–5250.
- (34) Tamura, T.; Uehara, H.; Ogawara, K.; Kawauchi, S.; Satoh, M.; Komiyama, J. *J. Polym. Sci., Part B: Polym. Phys.* **1999**, *37*.
- (35) Draper, N. R.; Smith, H. *Applied Regression Analysis*; Wiley: New York, 1981.

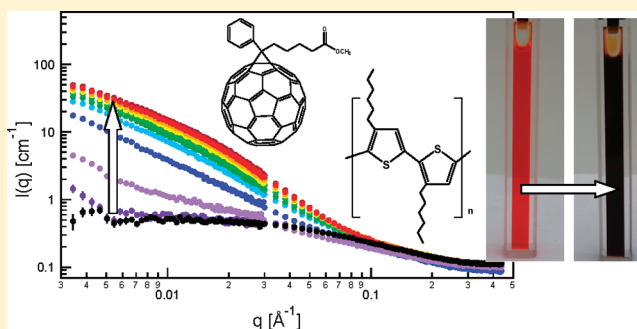
Effect of Fullerenes on Crystallization-Induced Aggregation in Polymer Photovoltaics Casting Solutions

Margaret J. Sobkowicz, Ronald L. Jones, R. Joseph Kline, and Dean M. DeLongchamp*

Polymers Division, National Institute of Standards and Technology (NIST), Gaithersburg, Maryland 20899, United States

S Supporting Information

ABSTRACT: We measure the time- and temperature-dependent aggregation of the organic photovoltaic polymer poly(3-hexylthiophene) in *o*-dichlorobenzene solution using small-angle neutron scattering and rheometry. Results from this study provide guidance for formulation stability assessment and process-dependent morphology optimization. The aggregates are similar to the supramolecular crystalline structures found in annealed films and poor solvents. The addition of phenyl-C₆₁-butyric acid methyl ester (PCBM) molecules to the polymer solution slows the aggregation rate by about 10-fold. PCBM addition also appears to reduce the overall extent of crystallization in solution. Dynamic rheological measurements show thermoreversible mechanical stiffening of the solutions into gel-like solids with a physical cross-link density that depends on temperature and oscillation frequency.



INTRODUCTION

A great advantage of organic photovoltaics (OPV) is that device layers such as the bulk heterojunction (BHJ) can be coated from solution, allowing for easier, faster, and less expensive device manufacture.¹ Solution coating, however, affords little control over the final BHJ morphology, and the morphological requirements for a high-efficiency BHJ are complex. Current BHJ processing strategies rely on the solidification of a solution containing both polymer and fullerene; the ultimate morphology will depend on the relative rates of solidification of the two components. Because the polymer and fullerene are not extremely soluble in commonly used solvents, it is expected that solidification will commence while significant solvent remains in the applied coating. To understand and ultimately control the development of BHJ morphology, it can therefore be valuable to evaluate the structure of the BHJ coating in the semisolid states that it passes through during solidification. The characteristics of these states are also relevant to the coating process itself because the coating viscosity will depend on the structure that forms. The shear rate the solution experiences depends on the coating technique. In inkjet printing and slot die coating, for instance, the shear rate can be as high as 10 000 s^{-1} .^{2–4} The BHJ film smoothness and thickness will depend on the interaction of applied shear forces with the changing coating viscosity,^{5,6} regardless of whether the BHJ is coated using spin-casting, inkjet printing, blade coating, slot-die, or gravure methods.

Here we study structure formation in solutions of poly(3-hexylthiophene) (P3HT) and phenyl-C₆₁-butyric acid methyl ester (PCBM). Under certain processing conditions, these two components solidify from the same solution into a nanoscale

morphology that produces reasonable photovoltaic performance with devices up to 5% efficiency.⁷ Because solvent evaporation is challenging to control, we instead use solution temperature to mimic the effect of solvent removal. In effect, we lower the solution temperature to lower the solubility of the components. In drawing an analogy between structure formation in cooled solutions and in drying coatings, we assume that the solubility of one component changes proportionally to the other with temperature. This assumption may not be valid, but we believe that the analysis still provides a starting point for understanding important aspects of morphology development in drying BHJ films. Validation of the analogy would require extrapolation to thermodynamic equilibrium in the solutions at different degrees of undercooling and different concentrations to map out the temperature–concentration phase diagram. Here we examine several polymer concentrations, starting at a value near typical casting solutions (20 mg/mL) and moving higher, to observe the kinetic difference at a constant undercooling and to mimic the beginning of the drying process.

The use of temperature as a variable to induce structure formation in BHJ solutions also yields practical information about BHJ solution stability. Many semiconducting polymers have been shown to aggregate in solution, forming gel-like assemblies at a range of concentrations and temperatures, due to their stiff backbones and attractive interactions between conjugated monomers. Room-temperature aggregation is

Received: September 13, 2011

Revised: November 16, 2011

Published: December 28, 2011



problematic from a processing standpoint because ink formulations will change over time, compromising reproducibility and potentially leading to a short shelf life. Aging and aggregation in solutions of polyfluorenes,⁸ poly(phenylenevinylene)s^{9,10} and poly(3-alkylthiophenes)^{11–14} have been investigated before. Studies on the poly(3-alkylthiophenes) have focused on the formation of high aspect ratio nanowires of poly(3-alkylthiophenes) by addition of a nonsolvent^{11,12} or dissolution and aging in a marginal solvent.^{13,14} Early studies of fundamental dilute solution properties of P3ATs using light and neutron scattering and viscometry^{15,16} found that the polymers exhibit typical random coil behavior, with crossover concentrations from 7 to 30 mg/mL depending on molecular mass, and a rather large persistence length of 2.4 nm (6 monomer units) due to the main chain rigidity. Observations of regioregular P3HT solutions in tetrahydrofuran or xylene indicate a red shift in the absorption spectrum associated with increasing conjugation length as the polymer crystallizes. It has been suggested that the network formation takes place in a two-step process: first the polymers undergo a coil-to-rod transformation, and then rods aggregate into fibrillar crystals.¹⁷ It is known that the crystal morphology of P3HT tends toward high aspect ratio wires with width of tens of nanometers, thickness several nanometers, and length—depending on crystallization conditions—of up to a micrometer or more.^{18,19,13,20}

Physical aggregation and gelation in polymers are due to complex enthalpic and entropic interactions between monomers and solvent molecules. Two mechanisms have been proposed for physical association in polymer solutions: solvent induction and polymer crystallization.²¹ Solvent induction can occur in amorphous or semicrystalline polymers, but it requires a specific interaction such as ionic or hydrogen bonding between the polymer and solvent molecules that induces physical connectivity among polymer molecules. P3HT aggregation is more likely driven by crystallization because the stiff backbone of the polymer favors an ordered conformation. P3HT gelation is therefore likely to be less sensitive to solvent type, as indeed it has been found to occur in several different solvents. Throughout this article, we will refer to P3HT aggregation in solution as “crystallization”, without direct evidence from diffraction of the solutions. This assertion, however, is supported by optical measurements of backbone conformational order and ubiquitous reports by others of P3HT crystallinity in solid films.

The polymer–fullerene solutions measured in this work are uniquely matched to small-angle neutron scattering (SANS) as a structure evaluation tool. SANS has lately gained attention as a tool for investigating morphology and phase behavior in polymer–fullerene BHJ blends because it probes length scales relevant to exciton diffusion. Furthermore, contrast in SANS is naturally present due to the large difference in proton content between the proton-poor fullerene and the proton-rich P3HT. By exploiting this natural contrast, other researchers have used SANS^{22,23} and neutron reflectivity²⁴ to describe coarsening of the domains in OPV thin solid films. Our work extends this strategy by exploiting contrast between a solvent–fullerene phase and pure P3HT. Using SANS and rheological measurements, we investigate the time- and temperature-dependent crystallization of P3HT in the common casting solvent *o*-dichlorobenzene, and we characterize the effect of PCBM presence on the rate of solidification and its extent.

■ EXPERIMENTAL METHODS

Solution Preparation. P3HT used in this study was purchased from Plextronics²⁵ ($M_w = 120\,000$ g/mol, PDI = 1.9, and regioregularity >98%). PCBM was purchased from NanoC. Solvents used were deuterated *o*-dichlorobenzene (dDCB) from Cambridge Isotopes and reagent-grade anhydrous *o*-DCB from Sigma-Aldrich. Solutions of P3HT and/or PCBM in dDCB were prepared in an oxygen- and moisture-free environment in amber vials. Solutions were heated to 80 °C and held at least 12 h for complete dissolution.

Ultraviolet–Visible Spectrometry. Absorption spectra in the ultraviolet–visible (UV–vis) range were collected on a Perkin-Elmer Lambda 950 instrument in transmission mode. Corrections were made for blocked beam and 100% transmission. Solutions of P3HT in *o*-DCB (25 mg/mL) were dispensed onto a quartz slide and covered with another quartz slide and then cooled over desiccant (to avoid moisture accumulation) at 5 °C for 24 h prior to initial measurement. Samples were equilibrated for 2 min at each temperature before the spectrum was then collected at room temperature. The dry film sample was spin-cast at $2000 \times 2\pi$ rad/min (2000 rpm) for 2 min onto quartz from a 40 mg/mL solution.

Small-Angle Neutron Scattering. SANS measurements were performed at the National Institute of Standards and Technology (NIST) Center for Neutron Research on both NG3 and NG7 30 m SANS instruments. Solutions were measured in titanium cells with 1 mm path length and quartz windows 2 cm in diameter (total sample volume = 0.3 mL). A sample holder block cooled with a circulating bath was used to hold the sample temperature during measurement. A light flow of dry nitrogen around the sample chamber prevented ambient humidity from condensing. Measurements were performed at two detector distances for a q range spanning almost 3 decades ($0.006 \text{ \AA}^{-1} < q < 0.4 \text{ \AA}^{-1}$, where $q = (4\pi/\lambda) \sin(\theta/2)$). The neutron wavelength was 6 Å. The scattered intensity was adjusted to an absolute scale by correcting for background scattering, detector sensitivity, empty cell scattering and transmission, and sample transmission.²⁶ Igor Pro software developed at NIST (version 4.20) was used to reduce data following protocols detailed in ref 26. Prior to each crystallization kinetic study, samples were equilibrated for 20 min at 80 °C. They were then placed in the cooling block, and the SANS measurement was started. Three P3HT concentrations (80, 40, and 20 mg/mL) and three P3HT:PCBM ratios (1:0.5, 1:1, and 1:2 by mass) were investigated. All crystallizations were run at 5 °C; however, for the pure P3HT solution at 80 mg/mL, measurements were also made at 15 °C in order to observe the change in kinetics with temperature. Scattering collection time was 10 min per curve.

Rheometry. Rheological measurements were made using a TA AR-G2 rheometer with a cone and plate geometry. The cone angle and diameter were 2° and 20 mm, respectively, for a total sample volume of 0.07 mL. Cooling experiments were performed using a Peltier plate assembly for temperature control (± 0.2 °C) and a solvent reservoir and trap in place over the cone to limit solvent evaporation. The instrument was kept in a nitrogen-purged environment to avoid condensation. For time-dependent modulus measurements the sample was quenched from 70 °C to the required gelation temperature (quench time was always less than 5 min), and then oscillatory shear with 1% strain amplitude at a variety of frequencies was applied to the sample. For temperature scans the sample was placed in the rheometer and pregelled at quiescent conditions for 2 h prior to measurement. Then the temperature was ramped at 1 °C/min, while measuring the modulus at 1% strain, 0.1 Hz (0.628 rad/s). For frequency-dependent measurements, samples were quenched from 70 °C to the gelation temperature, and the frequency was ramped from 0.1 to 100 rad/s at 1% strain. The measurements were repeated until minimal change in the sample was observed. Each frequency scan was 17 min.

■ RESULTS AND DISCUSSION

The ultraviolet–visible absorption of P3HT solutions is sensitive to the backbone conformation, which in turn offers insight into the degree of aggregation. These characteristics can be evaluated qualitatively by eye, as shown in Figure 1. Typical

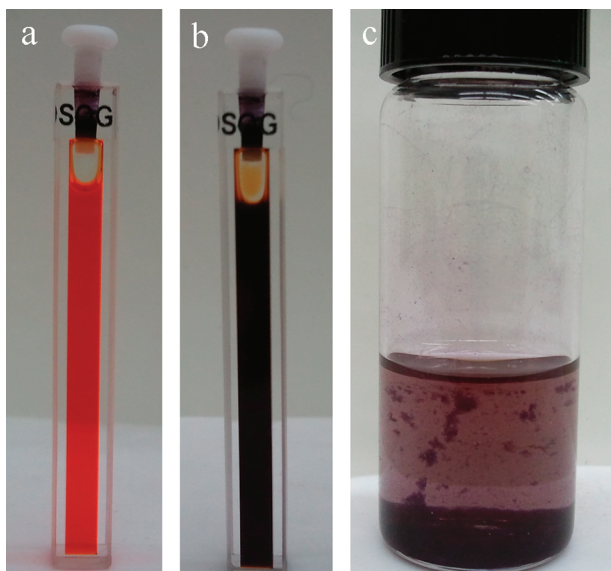


Figure 1. Photographs of P3HT solutions: (a) 7 mg/mL in *o*-DCB after dissolution at 80 °C; (b) 7 mg/mL in *o*-DCB after 66 h aging at 4 °C; (c) 1 mg/mL in tetrahydrofuran after several weeks aging at room temperature.

polymer solutions for device fabrication consist of 10–50 mg/mL of P3HT in chloroform, chlorobenzene (CB), or *o*-DCB. These solutions have previously been presumed stable at these concentrations. Figure 1 shows, however, that aggregation can occur when these typical casting solutions are modestly cooled. There is a color change (increased blue transmittance, increased diffuse scatter) but no observable phase separation, as exemplified in Figure 1b, for solutions prepared from *o*-DCB, CB, or chloroform. Separated solidlike aggregates precipitate from the P3HT–THF solution shown in Figure 1c, even when it is aged at room temperature.

The color changes in P3HT solutions are quantitatively measured using UV–vis absorption spectroscopy. Under good solvent conditions over a range of concentrations, P3HT shows a single peak centered around 450 nm.²⁷ Additional peaks at 560 and 610 nm are attributed to vibronic coupling upon organization of the molecules into crystals, and the ratio of the two is diagnostic of the conjugation length.^{27,28} The red shift of the main peak from 450 to 520 nm is due to both H aggregation and an increase in conjugation length as the polymer backbone stiffens and ordered aggregates form in films.²⁹ The UV–vis spectra shown in Figure 2 for a 25 mg/mL solution provide evidence of this crystallization-induced aggregation. The single peak at 456 nm in the spectrum of the fully dissolved high-temperature solution has identical breadth and location to those collected from lower concentration solutions down to 0.1 mg/mL (not shown). The peak location after 24 h of aging at 5 °C is shifted to slightly longer wavelengths, but the emergence of peaks at 560 and 610 nm indicates that the intermolecular coupling is stronger and the conjugation length is longer than in the fully dissolved solution. This spectroscopic evidence strongly suggests that molecular aggregation occurring in the P3HT solutions is due to the crystallization of the polymer chains.

Small-Angle Neutron Scattering. Small-angle neutron scattering (SANS) is an ideal technique for investigating the structure of the physically associating solutions because it probes length scales characteristic of P3HT chains and typical

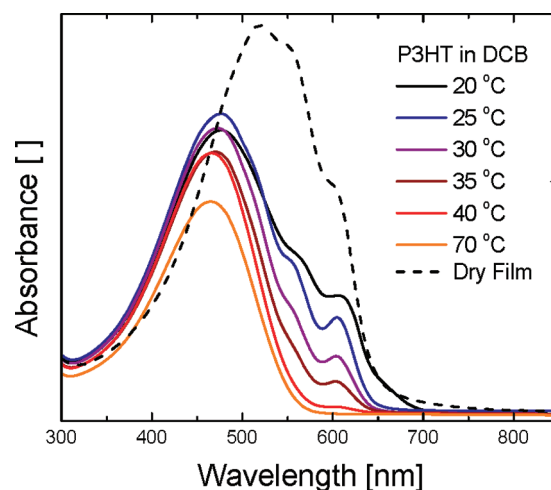


Figure 2. UV–vis absorbance spectra for P3HT dry film and 25 mg/mL P3HT–DCB solution after gelation and through the dissolution transition. Wavelength resolution is 2 nm.

P3HT solid aggregates. Although isotopic labeling is often required to achieve contrast in SANS, there exists a strong natural contrast between relatively hydrogen-rich P3HT and the relatively hydrogen-poor PCBM in a deuterated solvent. The calculated scattering length density of PCBM ($4.51 \times 10^{-6} \text{ Å}^{-2}$) is very close to that of dDCB ($4.58 \times 10^{-6} \text{ Å}^{-2}$), and the packed spacing of the fullerene spheres ($\approx 10 \text{ Å}$) is too small to be observed in the measured q -range. Consequently, the PCBM molecules are not observed in the SANS experiment; instead, the structure of the polymer and its evolution can be observed with and without PCBM present.

The variation of absolute scattered intensity $I(q)$ with the magnitude of the wave vector q for solutions of pure P3HT and solutions with PCBM is shown in Figure 3. Solutions at $T = 80 \text{ °C}$ have scattering characteristic of random coil polymers, with a plateau at low q . The scattering intensity at $q < 0.12 \text{ Å}^{-1}$ increases significantly for the cooled solutions as aggregation occurs. The curves shown were collected in a time sequence with repeated measurements every 30 min. After the first measurement, aggregation is virtually complete in the pure P3HT solution, whereas the solutions with PCBM aggregate over a much longer time scale. Although the scattering curves still appear to be changing slightly at long times, the majority of the crystallization is complete by the highest curve presented in each plot of Figure 3. If we estimate an asymptote for the low- q scattered intensity at infinite time, it is lower for the P3HT:PCBM solutions, indicating less aggregated material. All curves collapse to an incoherent scattering baseline of near 0.1 cm^{-1} at $q > 0.3 \text{ Å}^{-1}$. Figure 3d shows the final scattering patterns (e.g., at the end of the time sequence) for pure P3HT and 1:1 P3HT:PCBM solutions, along with fits to the two-exponential Guinier–Porod model. This model has been used to describe other aggregating polymer solutions when there are the two length scales present.^{30–32} Detailed explanation of the fitting technique can be found in the Supporting Information. The Porod slope is higher for the pure polymer solutions than for the BHJ solutions (Table 1), which suggests that the PCBM interferes with the organization of polymer chains into highly ordered, smooth-surfaced domains. The dimension exponent lies between the values expected for rods and platelets (1 and 2, respectively) for pure P3HT solutions, and it is lower (more rodlike) with PCBM present. The radius of gyration (R_g) of the

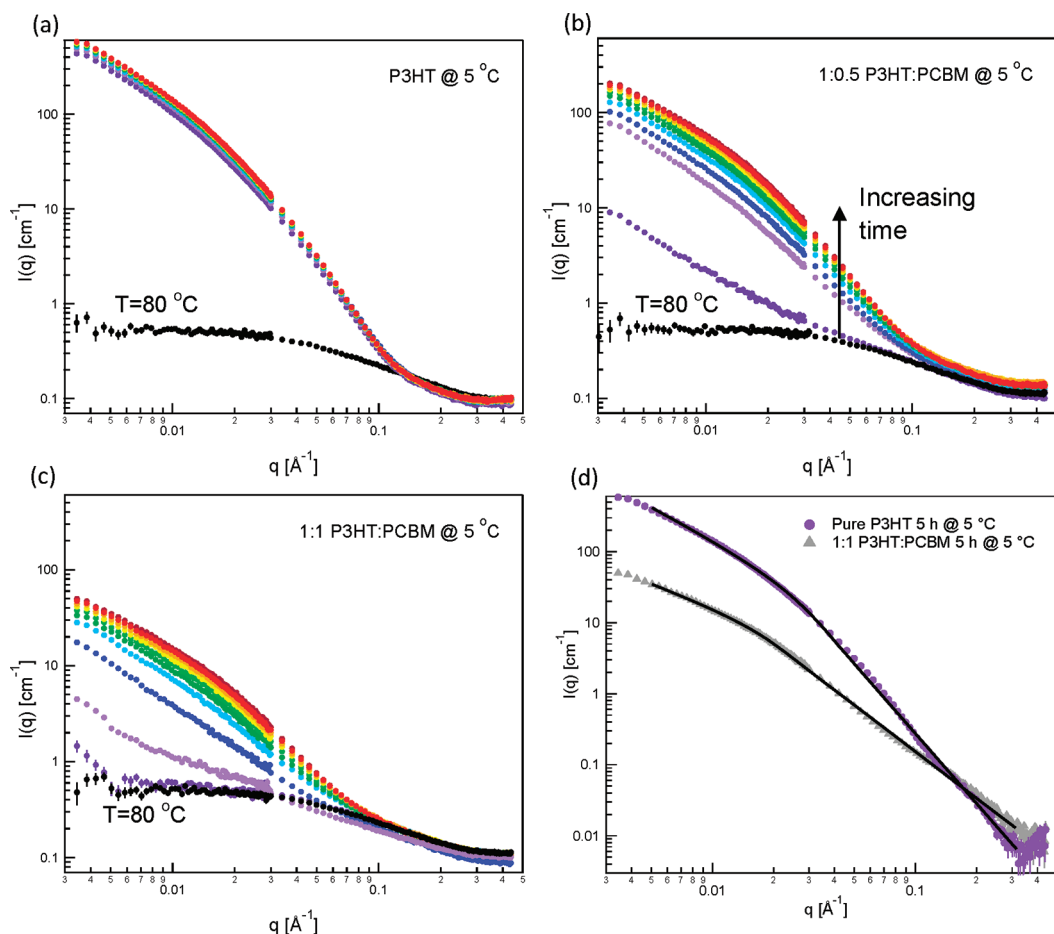


Figure 3. SANS intensity vs q for three solutions crystallized at 5 °C: (top left) 80 mg/mL P3HT in dDCB, (top right) 80 mg/mL P3HT with 1:0.5 P3HT:PCBM, (bottom left) 80 mg/mL P3HT:PCBM, and (bottom right) crystallized P3HT and P3HT:PCBM solutions with Guinier–Porod fit. Resolution in q is 0.0004 Å^{−1}; statistical error bars in intensity are shown.

Table 1. Fitted Parameters to the Guinier–Porod Model for the Longest Aggregation Times for Each Sample

	dimension	R_g [Å]	Porod slope
80 mg/mL Solutions			
1:0	1.5 ± 0.01	33.8 ± 0.2	3.3 ± 0.01
1:0.5	1.2 ± 0.01	41.5 ± 0.4	2.7 ± 0.01
1:1	1.1 ± 0.01	47.1 ± 0.9	2.2 ± 0.01
40 mg/mL Solutions			
1:0	1.9 ± 0.01	20.8 ± 0.2	3.5 ± 0.01
1:0.5	1.5 ± 0.01	29.6 ± 0.5	2.8 ± 0.01
1:1	1.5 ± 0.01	28.9 ± 0.6	2.7 ± 0.01

aggregates is also larger with the PCBM present, which may be due to the difference in aspect ratio. A slight secondary feature also appears in the background-subtracted data from around 0.1 Å^{−1} < q < 0.2 Å^{−1} that may be attributed to the nanofibril thickness, which is usually found to be 3–6 nm.²⁰ While the uncertainty of the data at highest q is large, the faint peak in the background-subtracted scattering curve of pure P3HT may originate in a P3HT (100) Bragg peak at 0.39 Å^{−1}.³³ The nonzero slope at the largest length scale probed indicates that structures are present that are too large to be resolved within the measured q range (>1570 Å).

When the scattering curves are plotted in the Kratky representation, Iq^2 vs q , as shown in Figure 4, a peak emerges which does not shift with time. A peak in the Kratky plot is

characteristic of anisotropic structures³⁴ and has also been observed for thermoreversible gels of PVC, polystyrene, and several biopolymers.^{21,35} The peak q value corresponds to a length scale of the forming network ($d = 2\pi/q$ from Bragg's law). Because the peak does not shift significantly with time, it is dominated by the characteristic fibril width. The d -spacing from our Kratky plots is 30–45 nm, which is close to reported values measured with microscopy for the P3HT fibril width.³⁶ Interestingly, the peak is at higher q for both increasing concentration and increasing PCBM content, with the PCBM concentration having a stronger effect. Both trends are logical: impingement of the crystals may limit their size in high concentration solutions, and increasing PCBM content appears to have a solubilizing effect resulting in a limitation on the scale of P3HT crystal growth.

The Avrami equation is a simple model describing the kinetics of material phase transformation that assumes random nucleation (in space) and a constant growth rate independent of fractional conversion. It is often used to describe crystallization of polymer melts, solutions, and composites, but its application can be problematic at early times, when there may be an induction period, and at late times, when secondary crystallization events can occur.³⁷ The double logarithm of the untransformed fraction of the material ($1 - X(t)$, where $X(t)$ is the normalized peak intensity) in the Kratky plots is shown vs log time in Figure 4 along with linear fits to the Avrami crystallization kinetic model, given by eq 1.^{38,39} Figure 4 also

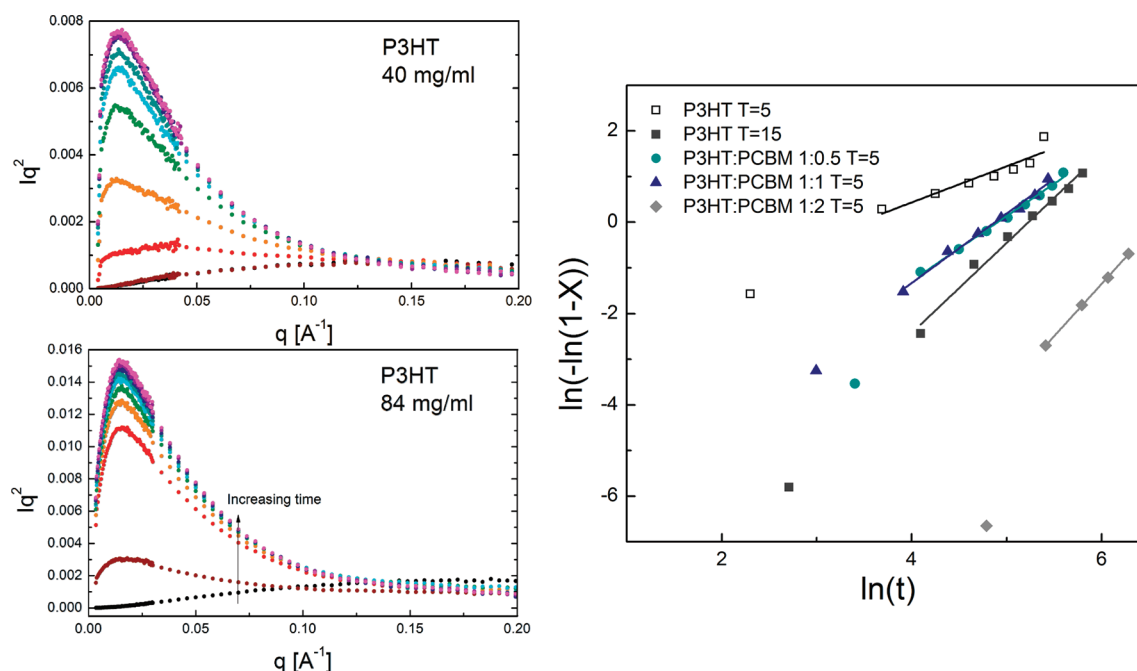


Figure 4. (left) Representative Kratky plots from P3HT solutions at two concentrations throughout crystallization. (right) Avrami plots for 80 mg/mL solution series.

Table 2. Solution Compositions (Experimental Error for Concentrations Is ± 0.3 mg/mL), Kratky Peak q Values (q Resolution for SANS Measurement Is 0.0004 \AA^{-1}), and Avrami Fit Parameters for SANS Gelation Kinetics^a

sample	c_{P3HT} [mg/mL]	c_{PCBM} [mg/mL]	q (peak) [Å ⁻¹]	d [nm]	n	$t_{1/2}$ [min]
P3HT Solutions						
20 mg/mL	19.6		0.014	45 ± 2		
40 mg/mL	40.1		0.015	43 ± 2	1.0 ± 0.10	113
80 mg/mL	83.5		0.016	40 ± 2	0.80 ± 0.13	19.7
P3HT:PCBM Solutions						
1:0.5 40 mg/mL	38.8	19.7	0.018	35 ± 2		
1:1 40 mg/mL	37.9	38.3	0.022	29 ± 2		
1:2 40 mg/mL	35.8	71.8	0.028	22 ± 2		
1:0.5 80 mg/mL	81.1	40.2	0.018	34 ± 2	1.4 ± 0.04	103
1:1 80 mg/mL	78.8	76.4	0.021	30 ± 2	1.5 ± 0.07	105
1:2 80 mg/mL	77.8	155.1	0.021	30 ± 2	2.3 ± 0.02	623

^aStated uncertainties are standard deviations from the linear fit.

includes the crystallization of the 80 mg/mL P3HT solution at 15 °C for comparison to the deeper quench temperature. The fits shown in Figure 4 exclude the first data point because for all samples the early time conversion of the crystalline fraction was lower than expected. This deviation is likely due to an induction period before the steady-state crystallization rate is reached. Exponents (n) extracted from the fits and crystallization half-times are shown in Table 2. The Avrami exponent near 1 for the 5 °C crystallization of both 40 and 80 mg/mL P3HT solutions indicates predetermined nucleation (all nuclei are formed at $t = 0$) and linear crystal growth, as can be expected given the crystal morphology shown in previous works.⁴⁰ At quench temperature 15 °C the Avrami exponent of the 80 mg/mL P3HT solution (fit not shown) is close to 2, indicating either continuous nucleation or a more disklike growth habit. The exponent is close to 1.5 for the solutions with PCBM present, which suggests sporadic nucleation occurring during crystal growth and rodlike crystal growth. The Avrami exponent over 2 for the 1:2 P3HT:PCBM sample indicates that both nucleation rate and growth geometry may be responsible for

the increased exponent with increasing PCBM loading.⁴¹ Experiments on the samples for which Avrami analysis is missing were not carried to high enough conversion to estimate the peak intensity for the fully aggregated polymer.

$$X(t) = 1 - \exp(Kt^n) \quad (1)$$

PCBM can be said to have a stabilizing effect on the P3HT solutions because the polymer aggregation slows and appears to approach a lower value at long times. To extract quantitative information about the solution stabilizing quality of PCBM, fits to the random phase approximation (RPA) model for polymer solutions were made on the dissolved solutions at 80 °C. The RPA model is used to describe correlations in dense interacting polymer blends, solutions, and copolymers.^{42,43} Here, component 1 is taken to be the polymer chains and component 2 is either the dDCB solvent molecules or the dDCB + PCBM phase. Since the PCBM molecules do not scatter coherently in the investigated q range^{44,45} (see Supporting Information), they can be considered part of the background component, which can be eliminated from the equations for the case of an

incompressible mixture. To construct the two component RPA model, the form factor for a Gaussian chain, $P_1(q)$, is combined with the volume fraction, ϕ_1 , the segment volume, ν_1 , and the degree of polymerization, N , to calculate the noninteracting structure factor, $S_{11}^0(q)$. The interaction parameter χ_{12} scaled by a reference volume ν_0 is introduced to calculate the interacting structure factor, $S_{11}(q)$. Inclusion of the contrast term $\Delta\rho^2$ and an incoherent background contribution allows calculation of the scattered intensity.

$$P_1(q) = \frac{2}{(q\xi)^4}(\exp(-q^2\xi^2) - 1 + q^2\xi^2)$$

$$S_{11}^0(q) = N\phi_1\nu_1P_1(q)$$

$$\nu_{11}(q) = \frac{1}{S_{11}^0(q)} - \frac{2\chi_{12}}{\nu_0}$$

$$S_{11}(q) = \frac{S_{11}^0(q)}{1 + \nu_{11}(q)S_{11}^0(q)}$$

$$I(q) = \Delta\rho^2 S_{11}(q) + \text{background} \quad (2)$$

Equation 2 was used to fit the random coil polymer solution data simultaneously for three concentrations at 80 °C, and the results for pure polymer solutions are shown in Figure 5 and

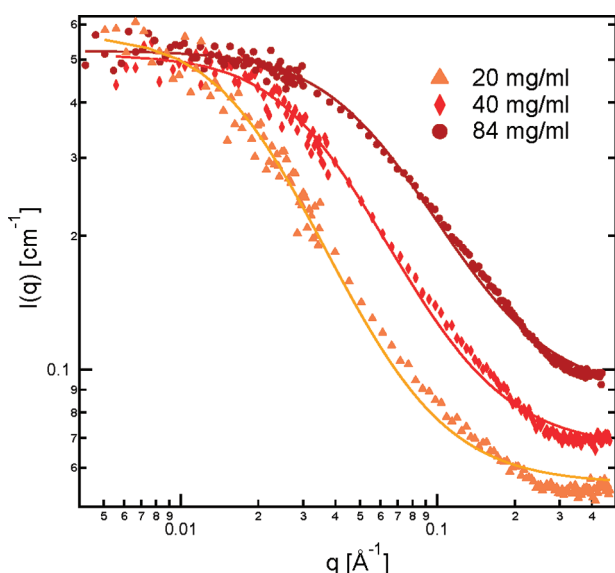


Figure 5. RPA fits to three pure P3HT solutions (q resolution: 0.0004 Å⁻¹).

Table 3. The BHJ solution data were also fit to eq 2, adjusting the contrast factor and volume fractions to reflect the presence of the PCBM in the background (component 2). For the fits, the background was taken as the flat baseline intensity at high q and the contrast factor was calculated as the difference between the scattering length density of pure P3HT (6.76×10^{-7} Å⁻²) and the solvent–PCBM mixture ($\rho_{\text{dDCB}} = 4.58 \times 10^{-6}$ Å⁻² and $\rho_{\text{PCBM}} = 4.51 \times 10^{-6}$ Å⁻²). The χ_{12} in this fitting procedure is the interaction parameter between the P3HT and the “effective” solvent (either pure dDCB or the dDCB–PCBM mixture). It should be noted that the interaction parameter extracted from SANS data is not identical to the thermodynamic χ when the parameter depends on concentration. The

Table 3. Fitted Parameters to the Two-Component RPA Model for All Solutions^a

concentration		fit parameters		
P3HT [mg/mL]	PCBM [mg/mL]	ξ [Å]	χ_{12}	bkgd [cm ⁻¹]
83.5		108 ± 2	−0.421 ± 0.003	0.088 ± 0.002
40.1		120 ± 2	−0.390 ± 0.004	0.067 ± 0.002
19.6		147 ± 2	−0.291 ± 0.005	0.055 ± 0.002
81.1	40.2	102 ± 2	−0.422 ± 0.003	0.100 ± 0.002
78.8	76.4	105 ± 2	−0.456 ± 0.003	0.101 ± 0.002
38.8	19.7	133 ± 2	−0.366 ± 0.004	0.069 ± 0.002
37.9	38.3	120 ± 2	−0.386 ± 0.002	0.074 ± 0.002
35.8	71.8	137 ± 2	−0.378 ± 0.004	0.072 ± 0.002

^aExperimental error for concentrations is ±0.3 mg/mL; stated uncertainties are standard deviations from the nonlinear least-squares fit.

experimental χ is the second derivative of the excess free energy of mixing with respect to volume fraction.^{46,47} The negative interaction parameter is indicative of a strong polar attraction between polymer and solvent.⁴⁸ For the pure polymer solutions χ_{12} becomes more negative with increased concentration, so values of χ_{12} for BHJ solutions can only be compared for similar polymer concentrations. The χ_{12} for solutions with PCBM decreases slightly compared with the values for pure polymer solutions, which reflects the solubilizing effect of the PCBM. The 1:2 ratio 35 mg/mL P3HT solution does not have as high a background level or as negative a χ_{12} as expected; hence, it is likely that there was some precipitation of the PCBM during measurement due to saturation of the solution. It should be noted that the mesh size, ξ , was allowed to vary in these fits, whereas the degree of polymerization was fixed at the manufacturer-reported mass-average value, 723. This choice was made because the assumption of a Gaussian polymer conformation is not realistic for this stiff chain system. The fits shown in Figure 5 could likely be improved using a wormlike chain form factor,⁴⁹ but the Gaussian model was chosen for simplicity. The ξ value provides an approximate size scale from the low- q plateau in the fit. The radius of gyration given by eq 3, assuming a Gaussian chain, is 44 Å for the P3HT monomer size, a , and degree of polymerization, N ($a = 4$ Å, $N = 723$). The polymers are 2–3 times larger than the expected value which is a reflection of the good solvent quality (excluded volume interactions) and the long persistence length of the stiff chains. Notably, the presence of PCBM does not appear to have a significant effect on ξ at the concentrations studied.

$$R_g = \sqrt{\frac{a^2 N}{6}} \quad (3)$$

Rheology. Modulus measurements of polymers undergoing gelation can provide information on the kinetics of the solidification process and the structure of the aggregates. Gelation of a polymer solution is defined as the point when the aggregates percolate and establish connectivity throughout the whole sample. It is accompanied by divergence of the viscosity and development of a finite modulus. When the junctions are purely physical, as in the crystalline aggregates of P3HT, they are more easily disrupted by shear forces or temperature change than are chemically cross-linked gels. By inducing oscillatory shear at small strain, the mechanical properties of the aggregated solutions can be investigated without inducing

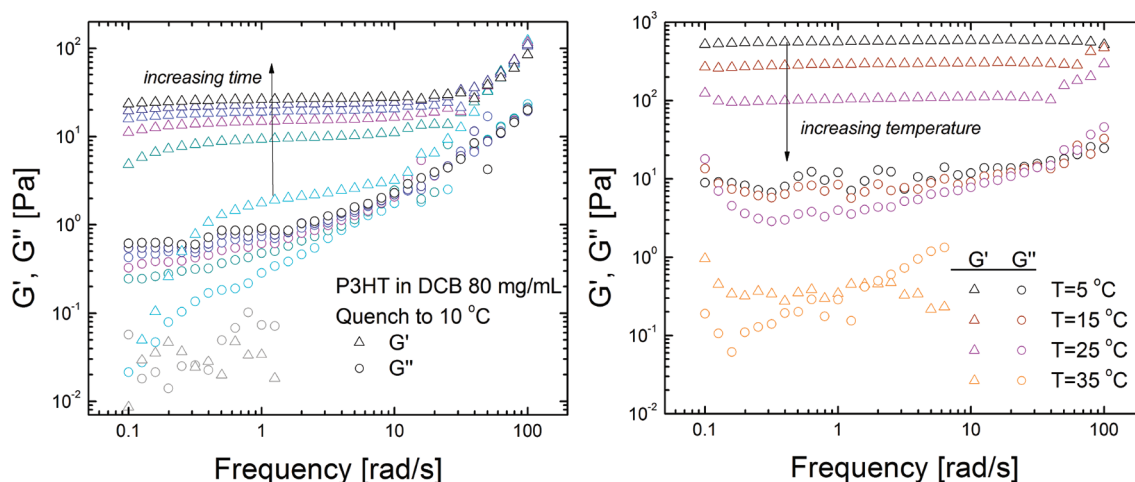


Figure 6. Frequency scans of 80 mg/mL P3HT solutions. Left: storage (G') and loss (G'') moduli during gelation at 10 °C. Lowest modulus data sets at 70 °C prior to quench. Right: storage and loss modulus measured at several temperatures after gelation at 5 °C for 1 h.

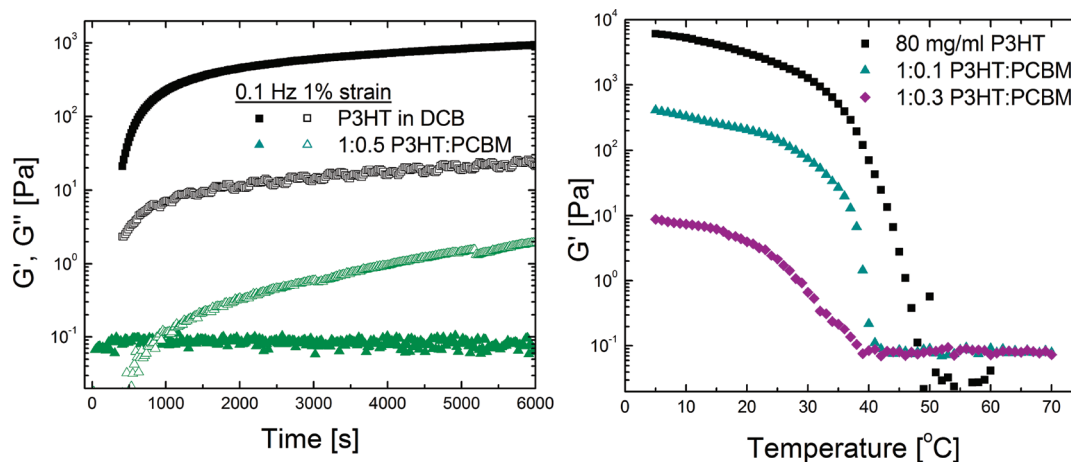


Figure 7. (left) Storage and loss moduli for pure P3HT solution and 1:0.5 P3HT:PCBM solution during crystallization at 5 °C. Open symbols are loss modulus, and filled symbols are storage modulus. (right) Storage modulus of precrystallized solutions while heating (0.1 Hz, 1% strain, 1 °C/min).

fracture of the material. No independent measurement was made to verify infinite connectivity, but the solution-state aggregates examined in this study did not flow upon tipping of the vials and so their rheological behavior will be discussed in the framework of physical gels. The steady-shear viscosity of the well-dissolved P3HT solutions was found to be independent of shear rate, or Newtonian, up to a shear rate of 1000/s in the concentration range examined here (see Supporting Information).

The complex rheological behavior of solutions without PCBM is shown in Figure 6. The plot on the left shows repeated frequency sweeps over 3 decades of frequency at a fixed strain of 1% (within the linear viscoelastic response regime) after quenching to 10 °C. As the pure polymer goes through the gel transition, the storage modulus becomes frequency-independent, characteristic of a cross-linked material rather than a viscoelastic fluid.⁵⁰ The gel point, often defined as the point at which the storage and loss moduli are equal,⁵¹ is only observable in the early curves right after the quench to 10 °C. The plot on the right of Figure 6 shows the deaggregation, heating the solution in isothermal steps through the transition. The moduli gradually decrease but have not completely recovered to the liquidlike state by 35 °C, beyond which the

data become noisy due to low transducer signal. It is clear that around typical casting temperatures the behavior can vary significantly depending on thermal history. The modulus of a physical gel is also highly dependent on concentration, and the values obtained for the 80 mg/mL solution shown here approaching 1000 Pa are similar to other polymer physical gels.^{52,53}

The physical cross-links in the P3HT gels can be envisaged as rigid bundles of crystalline material that enforce cooperative motion of the amorphous tie chains. There could be branching of the fibrillar crystal structures as well as entanglements of tie chains contributing to the network formation and accompanying modulus increase. Results from time-dependent storage and loss modulus measurements for solutions with and without PCBM are shown in Figure 7. During aggregation the modulus rises rapidly for both samples shown, but the increase occurs slightly later for the solution with PCBM. The plateau modulus is also lower for the solutions with PCBM, an indication that the physical cross-link density is lower for these systems. The classical theory of rubbery elasticity, usually employed for chemically networked systems, relates the modulus to the cross-link density following eq 4, where n is the cross-link density in moles per volume, R is the universal gas constant, and T is

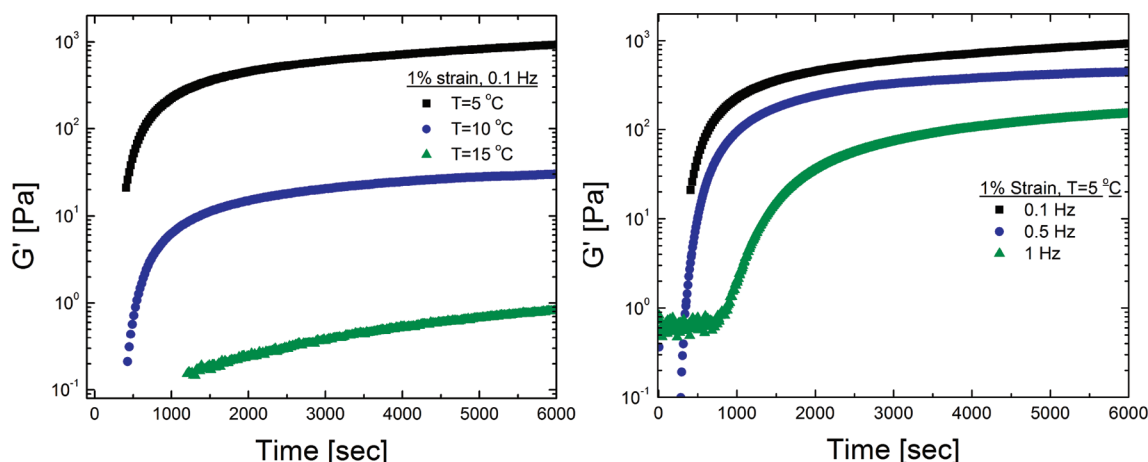


Figure 8. Storage modulus vs time for 80 mg/mL pure P3HT solutions (left) gelled at different temperatures and (right) gelled at 5 °C and measured at different frequencies.

temperature in kelvin.³⁷ Equation 4 is a valid approximation for affine deformation and low strain, with no disruption of cross-links due to applied stress.

$$G = nRT \quad (4)$$

Using this definition, the pure P3HT cross-link density is roughly 0.4 mol/m³, corresponding to a distance between cross-links of 16 nm. For the 1:0.5 P3HT:PCBM gel the cross-link density attained during the experiment is 0.0009 mol/m³ or 120 nm between cross-links. A denser population of aggregates in the pure polymer solution restricts chain motion and leads to a higher modulus. This description of the gels is oversimplified because it takes into account neither the aggregate size nor the solution viscosity difference due to the presence of PCBM.⁵⁴ Figure 7 also shows a scan through the transition temperature for the aggregated solutions after a quiescent period of 2 h at 5 °C. The system displays hysteresis as is typical for polymer crystallization: the transition occurs at higher temperature when melting than when forming crystallites. The melting transition appears to occur over a broader temperature range with increasing PCBM content; this may be indicative of a broader aggregate size distribution.

Temperature and frequency dependence of the aggregation process of pure P3HT are shown in Figure 8. The pure P3HT solution still aggregates to some extent when cooled to 15 °C; however, the 1:0.5 P3HT:PCBM solution does not aggregate at 10 °C over a measurement period of 3 h (not shown). The significant decrease in plateau modulus when aggregated at a lower temperature corresponds to a lower number of junction points forming the network. Dependence of the plateau modulus on frequency is less significant. The faster oscillation results in a lower final modulus and slows the onset of aggregation. This finding may be significant for process design considerations because of the wide range of shear rates encountered in printing processes. Spin-casting induces relatively low radial and axial shear rates in the solution, the first of which decreases to zero once the liquid film stops flowing outward,⁵ whereas inkjet printing induces extremely high shear rates, often on the order of 10⁵ s⁻¹.⁶ Significant questions remain about both the equilibrium structure and mechanism of thermoreversible gelation in polymer solutions in general; this is a topic of current theoretical consideration.⁵⁵

Scattering and rheometry are often employed as complementary techniques to explore structure–property relationships

in polymers. In this study, scattering shows that the rate of P3HT aggregate growth is slowed when PCBM is present, whereas rheometry shows that the rate of stiffening from network formation is less affected. Differences in the rate of P3HT aggregation observed using either technique can be ascribed to both the features to which each measurement technique is sensitive and the conditions under which the solutions were solidified. SANS describes overall size and shape of the aggregate structures and was performed under quiescent conditions. Rheometry was performed under dynamic conditions. Both SANS and rheometry reveal less participation of the polymer chains in the network when PCBM is present. Because P3HT aggregation from solution is crystallization-driven, structural evolution is likely similar to that of a drying film. It can therefore be expected that the presence of PCBM will slow the solidification rate of P3HT during solvent evaporation, while also maintaining a lower coating viscosity. Further investigation of the consequences of organic photovoltaic solution gelation is the subject of ongoing work.

CONCLUSIONS

Structural and kinetic observations were made of organic photovoltaic casting solutions using neutron scattering and rheometry in this work. The observable length scale and shape of polymer aggregates were identified to be tens of nanometers and rodlike, respectively, in agreement with previous works that relied on imaging of dried aggregated solutions. It was found that the presence of PCBM dramatically slows the aggregation of P3HT in solution. Concentration and temperature dependencies were identified, with the latter being the more sensitive parameter. RPA analysis shows a strong affinity between P3HT and DCB; the interaction parameter becomes more negative with increasing concentration, and elevated temperature dissolution suggests UCST behavior in this polymer–solvent system. Modest cooling of P3HT solutions even in “good” solvents such as DCB results in rapid aggregation. The aggregated solutions do not completely phase separate, but rather form physical gels consisting of anisotropic structures. An increase in solution modulus of several orders of magnitude accompanies the aggregation and the pure polymer solution modulus becomes frequency-independent. Although the percent crystallinity in the aggregated solutions cannot be calculated directly from these results, it appears that the

crystalline fraction is lower in the solutions with PCBM present. These results also lend insight into the film drying process and will lead to improved processing procedures in pursuit of an optimized morphology for bulk heterojunction devices.

■ ASSOCIATED CONTENT

■ Supporting Information

Incoherent scattering of PCBM solutions, additional fits to the Guinier Porod model and fitting equation details, steady-shear viscosity of P3HT solutions. This material is available free of charge via the Internet at <http://pubs.acs.org>.

■ AUTHOR INFORMATION

Corresponding Author

*E-mail: deand@nist.gov.

■ ACKNOWLEDGMENTS

M.J.S. thanks the National Research Council Postdoctoral Associateship Program for funding. We acknowledge the support of the National Institute of Standards and Technology, U.S. Department of Commerce, in providing the neutron research facilities used in this work. This work utilized facilities supported in part by the National Science Foundation under Agreement DMR-0944772. We also thank Paul Butler and Wen-Li Wu for helpful discussions.

■ REFERENCES

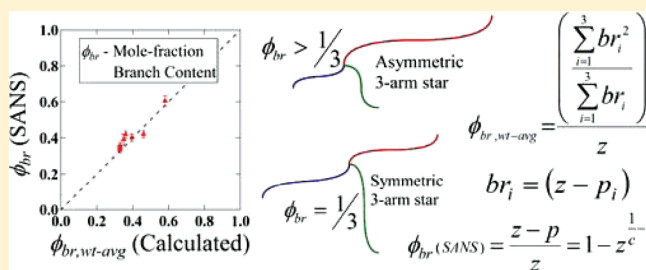
- (1) Krebs, F. C. Fabrication and processing of polymer solar cells: A review of printing and coating techniques. *Sol. Energy Mater. Sol. Cells* **2009**, *93*, 394–412.
- (2) de Gans, B.; Duineveld, P. C.; Schubert, U. S. Ink jet printing of polymers: State of the art and future developments. *Adv. Mater.* **2004**, *16* (3), 203–213.
- (3) Krebs, F. C.; Gevorgyan, S. A.; Alstrup, J. A roll-to-roll process to flexible polymer solar cells: model studies, manufacture and operational stability studies. *J. Mater. Chem.* **2009**, *19* (30), 5442–5451.
- (4) Krebs, F. C.; Fyenbo, J.; Tenenbaum, D. M.; Gevorgyan, S. A.; Andriessen, R.; vanRemoortere, B.; Galagan, Y.; Jorgensen, M. The OE-A OPV demonstrator anno domini 2011. *Energy Environ. Sci.* **2011**, *4* (10), 4116–4123.
- (5) Yonkoski, R. K.; Soane, D. S. Model for spin coating in microelectronic applications. *J. Appl. Phys.* **1992**, *72* (2), 725–740.
- (6) Vaddillo, D.; Tuladhar, T.; Mulji, A.; Mackley, M. The rheological characterization of linear viscoelasticity for ink jet fluids using piezo axial vibrator and torsion resonator rheometers. *J. Rheol.* **2010**, *54*, 781–795.
- (7) Li, G.; Shrotriya, V.; Huang, J.; Yao, Y.; Moriarty, T.; Emery, K.; Yang, Y. High-efficiency solution processable polymer photovoltaic cells by self-organization of polymer blends. *Nature Mater.* **2005**, *4*, 864–868.
- (8) Knaapila, M.; Garamus, V.; Dias, F.; Almasy, L.; Galbrecht, F.; Charas, A.; Morgado, J.; Burrows, H.; Scherf, U.; Monkman, A. Influence of solvent quality on the self-organization of archetypical hairy rods - Branched and linear side chain polyfluorenes: Rodlike chains versus "beta-sheets" in solution. *Macromolecules* **2006**, *39*, 6505–6512.
- (9) Li, Y.; Chen, K.; Chen, H.; Hsu, C.; Tsao, C.; Chen, J.; Chen, S. Fractal aggregates of conjugated polymer in solution state. *Langmuir* **2006**, *22*, 11009–11015.
- (10) Li, Y.; Chen, C.; Chang, Y.; Chuang, P.; Chen, J.; Chen, H.; Hsu, C.; Ivanov, V.; Khalatur, P.; Chen, S. Scattering Study of the Conformational Structure and Aggregation Behavior of a Conjugated Polymer Solution. *Langmuir* **2009**, *25*, 4668–4677.
- (11) Park, Y.; Lee, H.; Choi, Y.; Kwak, D.; Cho, J.; Lee, S.; Cho, K. Solubility-Induced Ordered Polythiophene Precursors for High-Performance Organic Thin-Film Transistors. *Adv. Funct. Mater.* **2009**, *19*, 1200–1206.
- (12) Li, L.; Lu, G.; Yang, X. Improving performance of polymer photovoltaic devices using an annealing-free approach via construction of ordered aggregates in solution. *J. Mater. Chem.* **2008**, *18*, 1984–1990.
- (13) Malik, S.; Nandi, A. Influence of alkyl chain length on the gelation mechanism of thermoreversible gels of regioregular poly(3-alkyl thiophenes) in xylene. *J. Appl. Polym. Sci.* **2007**, *103*, 2528–2537.
- (14) Koppe, M.; Brabec, C.; Heiml, S.; Schausberger, A.; Duffy, W.; Heeney, M.; McCulloch, I. Influence of Molecular Weight Distribution on the Gelation of P3HT and Its Impact on the Photovoltaic Performance. *Macromolecules* **2009**, *42*, 4661–4666.
- (15) Heffner, G. W.; Pearson, D. S. Molecular Characterization of Poly(3-hexylthiophene). *Macromolecules* **1991**, *24* (23), 6295–6299. Heffner, G.; Pearson, D.; Gettinger, C. Characterization of poly(3-octylthiophene). 1. Molecular characterization in dilute solution. *Polym. Eng. Sci.* **1995**, *35*, 860–867.
- (16) Aime, J.; Bargain, F.; Schott, M.; Eckhardt, H.; Miller, G.; Elsenbaumer, R. Structural study of doped and undoped polythiophene in solution by small-angle neutron scattering. *Phys. Rev. Lett.* **1989**, *62*, 55–58.
- (17) Malik, S.; Jana, T.; Nandi, A. Thermoreversible gelation of regioregular poly(3-hexylthiophene) in xylene. *Macromolecules* **2001**, *34*, 275–282.
- (18) Kiriya, N.; Jahne, E.; Adler, H.; Schneider, M.; Kiriya, A.; Gorodyska, G.; Minko, S.; Jehnichen, D.; Simon, P.; Fokin, A.; Stamm, M. One-dimensional aggregation of regioregular polyalkylthiophenes. *Nano Lett.* **2003**, *3*, 707–712.
- (19) Liu, J.; Arif, M.; Zou, J.; Khondaker, S.; Zhai, L. Controlling Poly(3-hexylthiophene) Crystal Dimension: Nanowhiskers and Nanoribbons. *Macromolecules* **2009**, *42*, 9390–9393.
- (20) Samitsu, S.; Shimomura, T.; Heike, S.; Hashizume, T.; Ito, K. Effective Production of Poly(3-alkylthiophene) Nanofibers by means of Whisker Method using Anisole Solvent: Structural, Optical, and Electrical Properties. *Macromolecules* **2008**, *41*, 8000–8010.
- (21) Guenet, J.-M. *Thermoreversible Gelation of Polymers and Biopolymers*; Academic Press: London, 1992; p xi, 280 pp.
- (22) Chen, D.; Nakahara, A.; Wei, D.; Nordlund, D.; Russell, T. P. P3HT/PCBM Bulk Heterojunction Organic Photovoltaics: Correlating Efficiency and Morphology. *Nano Lett.* **2010**, *11* (2), 561–567.
- (23) Kiel, J.; Eberle, A.; Mackay, M. Nanoparticle Agglomeration in Polymer-Based Solar Cells. *Phys. Rev. Lett.* **2010**, *105*, 168701.
- (24) Kiel, J. W.; Kirby, B. J.; Majkrzak, C. F.; B., M. B.; Mackay, M. E. Nanoparticle concentration profile in polymer-based solar cells. *Soft Matter* **2010**, *6*, 641–646.
- (25) Certain commercial equipment, instruments, or materials are identified in this paper in order to specify the experimental procedure adequately. Such identification is not intended to imply recommendation or endorsement by the National Institute of Standards and Technology, nor is it intended to imply that the materials or equipment identified are necessarily the best available for the purpose.
- (26) Kline, S. Reduction and analysis of SANS and USANS data using IGOR Pro. *J. Appl. Crystallogr.* **2006**, *39*, 895–900.
- (27) Clark, J.; Silva, C.; Friend, R.; Spano, F. Role of intermolecular coupling in the photophysics of disordered organic semiconductors: Aggregate emission in regioregular polythiophene. *Phys. Rev. Lett.* **2007**, *98*, 206406.
- (28) Yamamoto, T.; Komarudin, D.; Arai, M.; Lee, B.; Suganuma, H.; Asakawa, N.; Inoue, Y.; Kubota, K.; Sasaki, S.; Fukuda, T.; Matsuda, H. Extensive studies on pi-stacking of poly(3-alkylthiophene-2,5-diyl)s and poly(4-alkylthiazole-2,5-diyl)s by optical spectroscopy, NMR analysis, light scattering analysis, and X-ray crystallography. *J. Am. Chem. Soc.* **1998**, *120*, 2047–2058.
- (29) Yang, C.; Orfino, F.; Holdcroft, S. A phenomenological model for predicting thermochromism of regioregular and nonregioregular poly(3-alkylthiophenes). *Macromolecules* **1996**, *29*, 6510–6517.
- (30) Hammouda, B.; Ho, D.; Kline, S. SANS from poly(ethylene oxide)/water systems. *Macromolecules* **2002**, *35*, 8578–8585.

- (31) Hammouda, B.; Ho, D.; Kline, S. Insight into clustering in poly(ethylene oxide) solutions. *Macromolecules* **2004**, *37*, 6932–6937.
- (32) Hammouda, B. A new Guinier-Porod model. *J. Appl. Crystallogr.* **2010**, *43*, 716–719.
- (33) Kline, R.; McGehee, M.; Kadnikova, E.; Liu, J.; Frechet, J.; Toney, M. Dependence of regioregular poly(3-hexylthiophene) film morphology and field-effect mobility on molecular weight. *Macromolecules* **2005**, *38*, 3312–3319.
- (34) Higgins, J. S.; Benoit, H. C. *Polymers and Neutron Scattering*; Clarendon Press: Oxford, 1997; p 456.
- (35) Reinecke, H.; Mijangos, C.; Brulet, A.; Guenet, J. Molecular structures in poly(vinyl chloride) thermoreversible gels: Effect of tacticity and of solvent type. *Macromolecules* **1997**, *30*, 959–965.
- (36) Zhang, R.; Li, B.; Iovu, M.; Jeffries-EL, M.; Sauve, G.; Cooper, J.; Jia, S.; Tristram-Nagle, S.; Smilgies, D.; Lambeth, D.; McCullough, R.; Kowalewski, T. Nanostructure dependence of field-effect mobility in regioregular poly(3-hexylthiophene) thin film field effect transistors. *J. Am. Chem. Soc.* **2006**, *128*, 3480–3481.
- (37) Sperling, L. H. *Introduction to Physical Polymer Science*, 4th ed.; John Wiley and Sons, Inc.: Hoboken, NJ, 2006; p 845.
- (38) Avrami, M. Kinetics of Phase Change I: General Theory. *J. Chem. Phys.* **1939**, *7*, 1103–1112.
- (39) Mandelkern, L. *Crystallization of Polymers*, 2nd ed.; Cambridge University Press: Cambridge, UK, 2002; p 424.
- (40) Hay, J. Application of the modified avrami equations to polymer crystallisation kinetics. *Br. Polym. J.* **1971**, *3* (2), 74–82.
- (41) Matsuba, G.; Kaji, K.; Kanaya, T.; Nishida, K. Detailed analysis of the induction period of polymer crystallization by depolarized light scattering. *Phys. Rev. E* **2002**, *65* (6), 061801.
- (42) De Gennes, P.-G. *Scaling Concepts in Polymer Physics*; Cornell University Press: Ithaca, NY, 1979; 324 pp.
- (43) Akcasu, A.; Tombakoglu, M. Dynamics of copolymer and homopolymer mixtures in bulk and in solution via the random phase approximation. *Macromolecules* **1990**, *23*, 607–612.
- (44) Affholter, K.; Henderson, S.; Wignall, G.; Bunick, G.; Haufler, R.; Compton, R. Structural characterization of C-60 and C-70 fullerenes by small-angle neutron scattering. *J. Chem. Phys.* **1993**, *99*, 9224–9229.
- (45) Melnichenko, Y.; Wignall, G.; Compton, R.; Bakale, G. Characterization of fullerenes and fullerene derivatives by small-angle neutron scattering and transmission measurements. *J. Chem. Phys.* **1999**, *111*, 4724–4728.
- (46) Gundert, F.; Wolf, B. Polymer-Solvent Interaction Parameters. In *Polymer Handbook*, 3rd ed.; Brandrup, I., Immergut, E., Eds.; John Wiley and Sons: New York, 1989; pp VII/173–VII/182.
- (47) Sanchez, I. C. Relationships between polymer interaction parameters. *Polymer* **1989**, *30*, 471–475.
- (48) Orwoll, R. A.; Arnold, P. A. Polymer–Solvent Interaction Parameter χ . In *Physical Properties of Polymers Handbook*, 2nd ed.; Mark, J. E., Ed.; Springer: Cincinnati, OH, 2007; pp 233–258.
- (49) Pedersen, J.; Schurtenberger, P. Scattering functions of semidilute solutions of polymers in a good solvent. *J. Polym. Sci., Part B: Polym. Phys.* **2004**, *42*, 3081–3094.
- (50) Ferry, J. *Viscoelastic Properties of Polymers*, 3rd ed.; Wiley: New York, 1980; p xxiv, 641 pp.
- (51) Winter, H.; Mours, M. Rheology of polymers near liquid-solid transitions. *Adv. Polym. Sci.* **1997**, *134*, 165–234.
- (52) Kobayashi, K.; Huang, C.; Lodge, T. Thermoreversible gelation of aqueous methylcellulose solutions. *Macromolecules* **1999**, *32*, 7070–7077.
- (53) Aoki, Y.; Hirayama, K.; Kikuchi, K.; Sugimoto, M.; Koyama, K. Uniaxial elongational behavior of poly(vinyl chloride) physical gel. *Rheol. Acta* **2010**, *49*, 1071–1076.
- (54) Erman, B.; Mark, J. E. *Structures and Properties of Rubberlike Networks*; Oxford University Press: New York, 1997; p xiii, 370 pp.
- (55) Chou, C.-M.; Hong, P.-D. Spatiotemporal evolution in morphogenesis of thermoreversible polymer gels with fibrillar network. *Macromolecules* **2010**, *43* (24), 10621–10627.

Quantification of Branching in Model Three-Arm Star Polyethylene

Ramnath Ramachandran,[†] Gregory Beaucage,^{*,†} Durgesh K. Rai,[†] David J. Lohse,[‡] Thomas Sun,[‡] Andy H. Tsou,[‡] Alexander Norman,^{‡,§} and Nikos Hadjichristidis^{†,||}[†]Department of Chemical and Materials Engineering, University of Cincinnati, Cincinnati, Ohio 45221, United States[‡]Corporate Strategic Research Laboratories, ExxonMobil Research & Engineering Company, Annandale, New Jersey 08801, United States[§]Department of Chemistry, University of Athens, Panepistimiopolis, Zografou, 157 84 Athens, Greece^{||}Chemical and Life Sciences and Engineering Division, King Abdullah University of Science and Technology, Thuwal 23955-6900, Kingdom of Saudi Arabia

ABSTRACT: The versatility of a novel scaling approach in quantifying the structure of model well-defined 3-arm star polyethylene molecules is presented. Many commercial polyethylenes have long side branches, and the nature and quantity of these branches varies widely among the various forms. For instance, low-density polyethylene (LDPE) is typically a highly branched structure with broad distributions in branch content, branch lengths and branch generation (in hyperbranched structures). This makes it difficult to accurately quantify the structure and the inherent structure–property relationships. To overcome this drawback, model well-defined hydrogenated polybutadiene (HPB) structures have been synthesized via anionic polymerization and hydrogenation to serve as model analogues to long-chain branched polyethylene. In this article, model 3-arm star polyethylene molecules are quantified using the scaling approach. Along with the long-chain branch content in polyethylene, the approach also provides unique measurements of long-chain branch length and hyperbranch content. Such detailed description facilitates better understanding of the effect of branching on the physical properties of polyethylene.



■ INTRODUCTION

The molecular structure of commercial polyethylenes varies widely among the several forms that have proven useful in the marketplace. In particular, the levels and types of long chain branching vary greatly. One finds nearly linear structures to low levels of long-chain branching in linear-low density polyethylene (LLDPE) and high density polyethylene (HDPE). Higher levels of long-chain branching are seen in low density polyethylene (LDPE). Long-chain branching in polyethylene is known to have significant effects on its chain dimensions and physical properties.^{1–3} For instance, the presence of long-chain branches in low-density polyethylene (LDPE) significantly improves its processability. In order to quantify the branch content in polyethylene, techniques such as size exclusion chromatography (SEC), nuclear magnetic resonance (NMR) spectroscopy, light scattering, and rheological measurements are frequently employed. Essentially, these techniques measure the number-average long-chain branches per chain, which is not sufficient to provide a detailed description of the structure of polyethylene.^{4–6} Moreover, the limitations of these techniques lead to incomplete quantification of branching. For instance, while SEC is ineffective in measuring low levels of branching,⁴ NMR is unable to distinguish between branches exceeding six carbon atoms in length.⁷ A novel scaling approach has been developed recently to quantify the branch content in ramified structures such as polyethylene.⁸ The scaling model,^{4,8}

when applied to small-angle neutron scattering (SANS) data, can quantify both short-chain branching⁹ and long-chain branching in polyethylene.⁵ Results obtained from this approach can complement analysis performed by other techniques such as those mentioned above.^{5,6} The scaling approach has been used previously to characterize other ramified materials such as ceramic aggregates,⁸ proteins,¹⁰ hyper-branched polymers,¹¹ and cyclic polymers.¹²

LDPE is an industrially important polyethylene and typically displays broad distributions in molecular weight, branch content and branch length. Hence, it is difficult to get an accurate quantification of the nature of the long-chain branching and its effect on physical properties. To better understand the structure–property relationships due to the presence of long-chain branches, it is desirable to have model structures with a low polydispersity index as well as controlled levels of branch content and branch length. Anionic polymerization is one of the most useful techniques in synthesizing polymers having precisely controlled structures.^{13–15} This form of living polymerization is characterized by its rapid initiation step and elimination of chain transfer and termination reactions that results in nearly monodisperse polymers. While it is not

Received: September 15, 2011

Revised: November 8, 2011

Published: January 10, 2012

possible to synthesize polyethylene directly by this technique, it is possible to synthesize model polybutadiene that can be hydrogenated to eliminate unsaturation and form analogues of polyethylene.^{1,16} Polybutadiene synthesized by anionic polymerization have cis, trans and vinyl double bonds incorporated in the structure. Upon hydrogenation, the cis and trans double bonds are removed while the vinyl double bonds result in ethyl short-chain branches.¹⁴ Long-chain branched polybutadiene can be prepared using chlorosilane condensation chemistry.^{1,16,17} Hadjichristidis et al. have synthesized¹ a variety of model branched polyethylene analogues by hydrogenating branched polybutadienes. These include polyethylene with 3-arm star, comb, H, and pom-pom as well as dendritic¹⁸ architectures. In this article, the aforementioned scaling approach^{4,5,8} is applied to quantify the structure of model 3-arm star polyethylene synthesized by Hadjichristidis et al.¹ The versatility of the scaling approach is highlighted here by presenting the detailed quantification of such model branched polyethylene resins.

Scaling Model. Polyolefins like polyethylene (PE) in dilute solution display two structural levels: the average chain size R with mass-fractal dimension d_f and an average substructural rod-like persistence unit of length l_p or Kuhn length $l_k \approx 2l_p$.¹⁹ [Additionally, a dynamic size close to l_p called the packing length³ can be defined which is not discussed here.] These structural levels are observed in small-angle scattering patterns from polyethylene. The Unified Function^{5,6,8,9,20,21} used in this article is useful in quantifying these structural levels in terms of their size and associated mass-fractal dimensions. A branched polymer like polyethylene can be described in terms of two distinct features. One is a short circuit path through the branched structure that displays an average tortuosity linked to the thermodynamic conditions and steric constraints. The other is an average connectivity based on the branch content, which is invariant to changes in thermodynamic conditions. These two average features of branched polymers can be described using a universal scaling model.⁸ The scaling model has been used previously in describing the structure and quantifying the topology of a variety of mass-fractals.^{4,5,8–12}

Considering a polyethylene chain of end-to-end distance R and mass-fractal dimension d_f composed of z Kuhn steps of size l_k (see Figure 1), the scaling model describes an average short-circuit path or minimum path p with mass-fractal dimension d_{\min} . The tortuosity in the polyethylene chain is described by p and d_{\min} . The connectivity of the polyethylene chain can be described by a connecting path s with an associated connectivity dimension, c , that is obtained by joining chain ends and branch points with straight lines. z , p and s can be related to the chain size R/l_k by

$$z = \left(\frac{R}{l_k}\right)^{d_f}, \quad p = \left(\frac{R}{l_k}\right)^{d_{\min}} \quad \text{and} \quad s = \left(\frac{R}{l_k}\right)^c \quad (1)$$

A scaling relationship between z , p and s can then be derived as^{5,8}

$$z = p^c = s^{d_{\min}} \quad (2)$$

From eqs 1 and 2, a simple relationship is obtained, $d_f = cd_{\min}$, that shows how chain scaling is described via contributions from tortuosity and connectivity. For regular objects like rods and discs that are completely connected and have no tortuosity through the structure, $d_f = c$ and $d_{\min} = 1$.

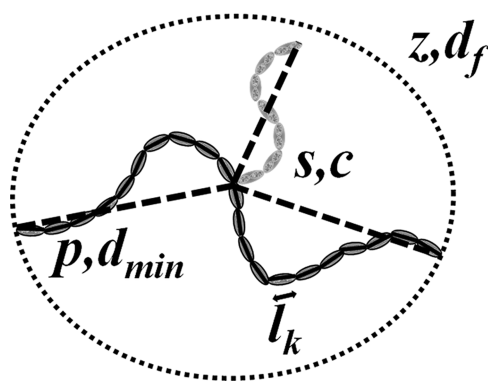


Figure 1. Schematic of a 3-arm star polymer in the scaling model. Each Kuhn step is represented by a bead. The polymer of mass-fractal dimension d_f is composed of z Kuhn steps of size l_k . The dark beads represent a minimum path p of dimension d_{\min} , composed of 2 arms. The lighter Kuhn steps depict the long-chain branch which is the third arm. The dotted lines represent the connective path of length s and dimension c . The chains are depicted in a nonoverlapping extended conformation in order to distinguish the arms.

d_{\min} increases with tortuosity, c increases with increased connectivity. Thus, for linear polyethylene in a good solvent, $d_f = d_{\min} \approx 5/3$ and $c = 1$. For branched polyethylene in a good solvent, $d_f > d_{\min}$, $1 < c \leq d_f$, and $1 \leq d_{\min} \leq 5/3$.

In the scaling approach,^{4–6,8} to describe a branched polymer chain of molecular weight z , we define a minimum path, p , which is the molecular weight of the short-circuit path taken through the polymer chain from one end to another. The part of the molecule outside of the minimum path, $z - p$, is then considered to be as branches. Thereby, the mole fraction long-chain branch content, ϕ_{br} , is obtained by,

$$\phi_{br} = \frac{z - p}{z} = 1 - z^{(1/c)-1} \quad (3)$$

The calculation of branch fraction for symmetric stars is trivial and can be calculated by,⁸ $\phi_{br} = (f - 2)/f$, where f is the functionality of the symmetric star. For asymmetric stars, three different minimum paths (short circuits) are possible through the structure. The average minimum path can then be calculated as a weight-average moment of this path. For the model star polyethylene in this paper, where information about number of arms and arm lengths is available (see Table 2), an expression to obtain weight-average branch content is given by,

$$\phi_{br, wt-avg} = \frac{\sum_{i=1}^3 (z - p_i)^2}{\sum_{i=1}^3 (z - p_i)} \quad (3a)$$

The Unified Function^{5,9,20,21} along with the scaling model⁸ when applied to scattering data from polyethylene provides substantial information to describe the topology of branched polyethylene. For example, the Unified Function in eq 4 gives R_g^2 , G_2 , B_2 , G_1 , B_1 , and d_f .

$$I(q) = \{G_2 e^{-(q^2 R_g^2)^{2/3}} + B_2 e^{-(q^2 R_g^2)^{2/3}} (q_2^*)^{-d_{f2}}\} + \{G_1 e^{-(q^2 R_g^2)^{2/3}} + B_1 (q_1^*)^{-1}\} \quad (4)$$

where $q_i^* = [q / \{\text{erf}(qkR_g / \sqrt{6})\}^3]$ and $k \approx 1.06$.

The terms in the first bracket with subscript “2” represent the overall chain size and the second bracket with subscript “1” represent the rod-like persistent scaling regime. The minimum

Table 1. SANS Characterization of Model 3-Arm Star Polyethylene Resins

sample	M_w (kg/mol) ^a	PDI (M_w/M_n) ^a	M_w (kg/mol) ^b	ϕ_{br}	n_{br}	z_{br} (kg/mol)	n_i	ϕ_{si}
PES(50) ₂ (5)	130	1.03	135 ± 10	0.42 ± 0.02	1.21 ± 0.05	47 ± 5	0.23 ± 0.09	0.033 ± 0.005
PES(50) ₂ (15)	138	1.04	135 ± 8	0.40 ± 0.02	0.93 ± 0.04	54 ± 5	0.22 ± 0.08	0.026 ± 0.005
PES(50) ₂ (25)	131	1.06	134 ± 9	0.42 ± 0.02	0.97 ± 0.04	49 ± 5	0.26 ± 0.08	0.027 ± 0.005
PES(43) ₃	133	1.13	135 ± 9	0.34 ± 0.01	0.76 ± 0.03	44 ± 4	0.10 ± 0.05	0.026 ± 0.006
PES(15) ₂ (85)	129	1.17	128 ± 13	0.61 ± 0.03	1.88 ± 0.07	66 ± 6	1.00 ± 0.12	0.034 ± 0.005
PES(40) ₂ (60)	125	1.08	137 ± 8	0.39 ± 0.03	0.87 ± 0.06	59 ± 7	0.20 ± 0.10	0.024 ± 0.004
PES(27) ₃	82	1.04	103 ± 5	0.36 ± 0.02	0.90 ± 0.06	33 ± 4	0.10 ± 0.08	0.032 ± 0.005
PES(53) ₃	139	1.12	132 ± 7	0.34 ± 0.02	0.81 ± 0.05	49 ± 6	0.08 ± 0.06	0.025 ± 0.005
PES(48) ₃	138	1.21	146 ± 7	0.35 ± 0.01	0.80 ± 0.06	51 ± 4	0.11 ± 0.08	0.024 ± 0.004

^aMeasured by SEC–MALLS. ^bMeasured by SANS.

dimension, d_{min} , is calculated from these parameters and is given by^{5,8}

$$d_{min} = \frac{B_2 R_{g,2}^{d_f}}{C_p \Gamma\left(\frac{d_f}{2}\right) G_2} \quad (5)$$

where C_p is the polydispersity factor^{5,9,22} and Γ is the gamma function. The weight-average number of Kuhn steps, z , is given by the ratio of G_2 over G_1 .^{8,9,21} The connectivity dimension, c , is obtained from d_f/d_{min} as described in the scaling model. From the topological parameters obtained, an expression is derived⁵ for the weight-average number of branch sites per chain, n_{br} , which is given by⁵

$$n_{br} = \left(\frac{z^{(5/2d_f - 3/2c) + (1 - 1/c)} - 1}{2} \right) \quad (6)$$

The weight-average n_{br} is comparable to the number of long-chain branches per chain that is obtained from NMR^{5,23} for trifunctional branch points except that the NMR measurement is a number-average. The weight-average long-chain branch length, z_{br} , is determined by,

$$z_{br} = \frac{z \phi_{br} M_{Kuhn}}{n_{br,p}} \quad (7)$$

where M_{Kuhn} is the mass of one Kuhn step and assuming $f = 3$ (branch site functionality). For polyethylene, $M_{Kuhn} = 13.4 l_k$, where M_{Kuhn} has units of g/mol and l_k has units of Å.⁵ $n_{br,p}$ represents the average number of branches per minimum path. Using n_{br} and $n_{br,p}$, an expression for the hyperbranch content in terms of the average number of inner segments per chain, $n_i = n_{br} - n_{br,p}$ is obtained.⁵ Inner segments refer to segments in a polymer that have branch points at both ends.

MATERIALS AND METHODS

The well-controlled, model, 3-arm star polyethylene resins analyzed in this article were derived by saturation of anionically synthesized polydienes^{1,16} and were the same resins used in an earlier work.¹ The polymers were stored under conditions appropriate to avoid degradation by DJL. The resins included both symmetric (A_3 type) and asymmetric 3-arm (A_2B) stars, where A and B represent the individual arms in the 3-arm star polyethylene. A detailed description of the synthesis of the polybutadiene precursors and the subsequent hydrogenation to obtain the polyethylene analogues are given elsewhere.¹ These model polymers have been well studied and characterized in the literature.^{1,2} SANS was performed on dilute solutions of model 3-arm star hydrogenated polybutadiene in deuterated *p*-xylene which is a good solvent for polyethylene at 125

°C. 500 ppm of butylhydroxytoluene (BHT) was used as a stabilizer and dissolved in the solvent during sample preparation. BHT and deuterated *p*-xylene were purchased from Fisher Scientific. The samples were equilibrated at 125 °C for 2 h prior to the measurements to ensure complete dissolution of the polymer. The polymer solution was stirred by means of micromagnetic stir bars to homogenize the solution prior to the measurement. One wt % solutions were used which is well below the overlap concentration²⁴ for all fractions. SANS experiments were carried out at NG-7 SANS²⁵ at the National Institute of Standards and Technology (NIST) Center for Neutron Research (NCNR), Gaithersburg. Standard data correction procedures for transmission and incoherent scattering along with secondary standards were used to obtain $I(q)$ vs q in absolute units.²⁶ Experimental runs took approximately 2 h per sample.

RESULTS AND DISCUSSIONS

The corrected SANS data for the 3-arm star polyethylenes were plotted in log–log plots of $I(q)$ vs q and fit to the Unified Function in eq 4 followed by the application of the scaling model. Table 1 lists the sample names along with weight-average molar mass, M_w , and polydispersity index, PDI, measured from SEC–MALLS.¹ Table 1 also lists the quantities estimated from SANS and the scaling model that include weight-average molar mass, mole-fraction long-chain branch content, ϕ_{br} , from eq 3, number of long-chain branch sites per chain, n_{br} , from eq 6, average long-chain branch length, z_{br} , from eq 7 and number of inner segments per chain, n_i , that was estimated as described in ref 5. n_i is a measure of the hyperbranch content in a polymer chain.⁵ The last column in Table 1 lists the measured steric interaction in the 3-arm star polymers, ϕ_{si} , which is described later in this article. The errors reported were propagated from the data.

Scattering techniques like light, X-ray, and neutron scattering measure the weight-average molar mass, M_w , of polymers. In this paper, a number of quantities including M_w are measured from SANS. The analysis of model 3-arm star polyethylene can allow us to verify if these quantities are weight-average. The molar mass of 3-arm star polyethylene resins were estimated from SANS using a method described by Boothroyd et al.²⁷ Figure 2 plots the weight-average molar mass, M_w , obtained from SANS against weight-average molar mass, M_w , from SEC–MALLS. The data shows reasonable agreement between the molar mass measured from the two techniques (error bars are not available for SEC–MALLS values).

Figure 3 plots the mole-fraction branch content, ϕ_{br} , from eq 3, obtained from SANS against $\phi_{br,wt-avg}$ obtained from eq 3a. In a previous study⁶ conducted on commercial linear low-density polyethylene fractions, mole-fraction branch content measured for the parent resin using the SANS-scaling approach was found to be in good agreement with corresponding weight-

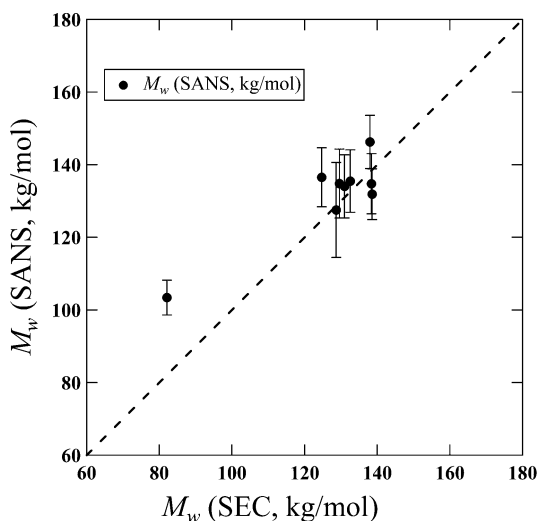


Figure 2. Plot of weight-average molar mass, M_w , obtained from SANS and weight-average molar mass, M_w , obtained from SEC-MALLS for 3-arm star polyethylenes.

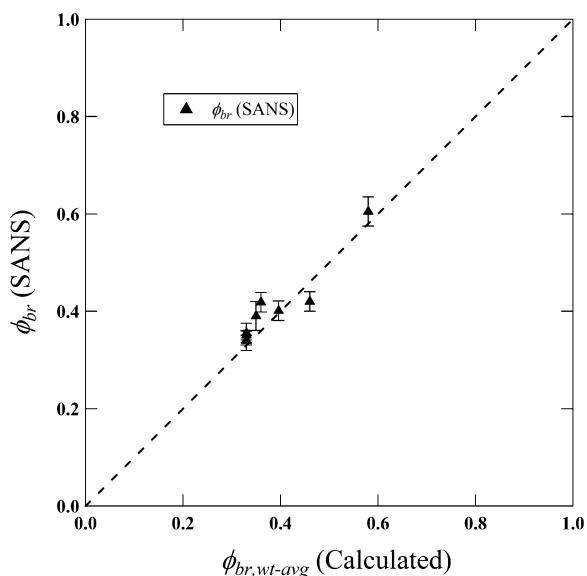


Figure 3. Plot of mole-fraction branch content, ϕ_{br} , from eq 3, obtained from SANS versus the calculated weight-average branch content, $\phi_{br,wt-avg}$, from eq 3a for 3-arm star polyethylenes.

average values calculated by summing the contribution from individual fractions. In the current study, the good correlation between ϕ_{br} and $\phi_{br,wt-avg}$ seen in Figure 3 for the model long-chain branched polyethylene is compelling evidence that the branch fraction measured from the SANS-scaling approach is a weight-average quantity.

Using the individual arm-lengths available in Table 2, it is possible to calculate the weight-average arm length, $z_{br,wt-avg}$, for the model 3-arm star resins by

$$z_{br,wt-avg} = \frac{\sum_{i=1}^3 (arm)_i^2}{\sum_{i=1}^3 (arm)_i} \quad (8)$$

Figure 4 plots the average branch length, z_{br} , from eq 7, obtained from SANS versus weight-average arm length, $z_{br,wt-avg}$, from eq 8. The good correlation seen in Figure 4 substantiates

Table 2. Arm Lengths for 3-Arm Star Polyethylenes

sample	arm 1 (kg/mol)	arm 2 (kg/mol)	arm 3 (kg/mol)	$z_{br,wt-avg}$ (kg/mol)
PES(50) ₂ (5)	52	52	5.2	49.8
PES(50) ₂ (15)	52	52	15.5	47.3
PES(50) ₂ (25)	52	52	26	46.8
PES(43) ₃	44.5	44.5	44.5	44.5
PES(15) ₂ (85)	15.5	15.5	88.5	69.6
PES(40) ₂ (60)	42	42	62	50.5
PES(27) ₃	28	28	28	28
PES(53) ₃	55	55	55	55
PES(48) ₃	48	48	48	48

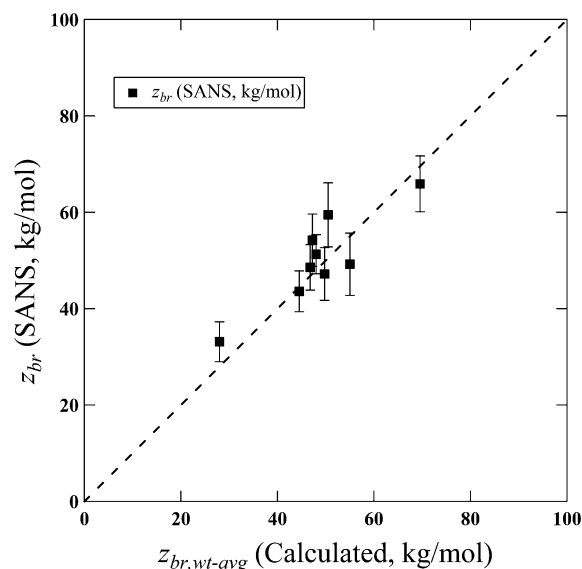


Figure 4. Plot of average branch length, z_{br} , obtained from SANS using eq 7 versus the calculated weight-average arm length, $z_{br,wt-avg}$, from eq 8 for 3-arm star polyethylenes.

that the average branch length measured from the SANS-scaling approach is a weight-average quantity.

The SANS-scaling approach uniquely quantifies the average hyperbranch content in terms of the average number of inner segments, n_i , in a hyperbranched polymer. Previously it was seen that n_i has significant impact on rheological properties such as the zero-shear rate viscosity enhancement in branched polyethylene.⁵ Table 3 lists the zero-shear rate viscosity and the

Table 3. Zero-Shear Rate Viscosity Enhancement for 3-Arm Star Polyethylenes^a

sample	η_0 (Pa·S)	$\eta_0/\eta_{0,L}$
PES(50) ₂ (5)	9.25×10^5	141
PES(50) ₂ (15)	8.56×10^6	1300
PES(50) ₂ (25)	2.28×10^6	347
PES(43) ₃	5.70×10^6	866
PES(15) ₂ (85)	4.60×10^7	6990
PES(40) ₂ (60)	6.42×10^6	976

^aFrom ref 2

zero-shear rate viscosity enhancement for certain 3-arm star polyethylenes where data was available in the literature.² A linear polyethylene with similar weight-average molecular weight was chosen to determine the enhancement for the branched polymers. Figure 5 plots the hyperbranch content, n_i ,

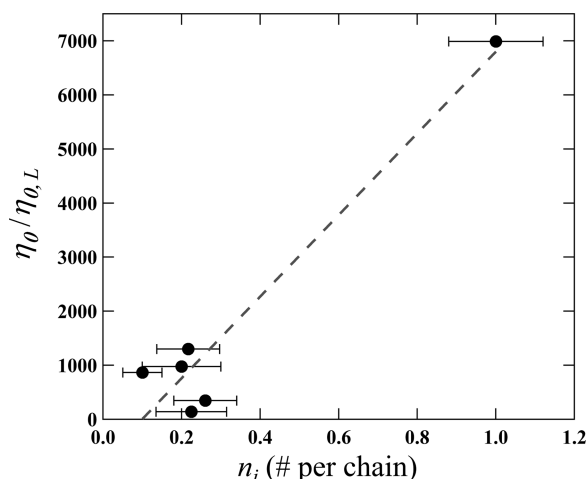


Figure 5. Plot of the zero-shear rate viscosity enhancement, $\eta_0/\eta_{0,L}$, versus the hyperbranch content, n_i , measured from SANS for 3-arm star polyethylenes. A linear behavior is expected based on results shown in ref 5.

measured from SANS versus the zero-shear rate viscosity enhancement, $\eta_0/\eta_{0,L}$. Almost all the resins show very low hyperbranch content and it can be concluded that the viscosity enhancement is primarily due to the presence of a branch. In the case of PES(15)₂(85), it is seen that the viscosity enhancement is much higher when compared to the other resins. Correspondingly, high hyperbranch content is also measured for this resin. While it is not expected that hydrogenated 3-arm star polybutadienes prepared using chlorosilane linking chemistry¹ have any hyperbranching, the distinctively high viscosity enhancement (along with a measured $n_{br} = 1.88 \pm 0.07$) for PES(15)₂(85) seems to indicate the presence of an additional hyperbranched arm (leading to an inner segment) in this resin. Additionally, considering the measured average branch length, z_{br} , for PES(15)₂(85), it can be inferred that the additional arm is the smaller arm (15.5 kg/mol) of the asymmetric star. The results here suggest that hyperbranched chains may be present even in polymers synthesized using anionic chemistry and SEC-based characterization may not be sufficient to discern these branched structures. Recently, chromatographic techniques such as temperature gradient interaction chromatography (TGIC) have shown great potential in characterizing such complex structures.^{28,29} The scaling approach in this article can complement analysis from such specialized chromatographic techniques.

The enhancement of viscosity due to the presence of branches is multifaceted where the number, size and type of branch can affect the rheological behavior. However, at low levels of hyperbranching, there seems to be a linear relationship between zero-shear rate viscosity enhancement and the hyperbranch content (n_i) as observed previously.⁵ The data plotted in Figure 5 can be treated analogous to Figure 4b in ref 5. We can consider the polyethylene melt as a dilute solution of hyperbranched segments in a melt of nonhyperbranched 3-arm star polyethylene. A linear functionality of $\eta_0/\eta_{0,L}$ in n_i is then comparable to a dilute suspension of particulates. The Einstein solution viscosity equation³⁰ for a dilute particulate suspension, $\eta_0 = \eta_{0,L}(1 + n_i[\eta_0])$, can be used as an approximation, except that there is a shift of 0.1 on the n_i axis. We obtain a slope of 7,550 chains/inner segment corresponding to a type of intrinsic

viscosity for hyperbranched structures in a suspension of nonhyperbranched chains. This slope is much higher than the 278 chains/inner segment observed previously for certain metallocene polyethylenes.⁵ The higher slope can be explained due to the presence of the hyperbranched segments among pure branched 3-arm star chains rather than mostly linear chain as in the case of the metallocene polyethylene.⁵ The 3-arm stars dynamically interact to a greater extent than their linear analogues thereby amplifying the effect of inner segments.

In general, for star polymers, the crowding of the arms can lead to steric interactions. Such steric effects are expected to be lowest for 3-arm stars and increase with higher number of arms. There are two effects of branching in star polymers. The mass fractal dimension d_f and topological dimension c increase since the structure contains more mass in the same volume and it achieves this through addition of topological complexity. At the same time, the arms are forced to become less convoluted (decrease in d_{min}) to accommodate this increased topological complexity and increase in mass per volume. An analogy can be found in chains tethered to a surface where the chains tend to straighten out at high packing densities.³¹ There are limits to this behavior in star polymers as described in the Daoud–Cotton model³² where the macromolecule forms a 3-d core due to the high degree of topological constraint at high functionality. For low functionality we observe a steric interaction that serves to diminish d_{min} .

In the scaling approach, for a linear polymer chain in a good solvent, $d_{min} = 5/3$. For a theoretical star polymer with a large number of arms, the steric interaction will be at a maximum. At such a state, the polymer chains could be fully extended (rod like) with $d_{min} = 1$. Using the limits of a linear chain and infinite-arm star, an expression can be obtained to quantify the steric interaction factor in a star polymer, ϕ_{si} that is given by,

$$\phi_{si} = \frac{s_{observed} - s_{unperturbed}}{s_{extended} - s_{unperturbed}} = \frac{z^{1/d_{min}} - z^{3/5}}{z^1 - z^{3/5}} \quad (10)$$

Table 1 lists the ϕ_{si} measured for dilute solutions of the 3-arm star polymers in a good solvent. As expected, the steric interaction is very low for these polymers. For the symmetric 3-arm star polymers, while the measured ϕ_{si} values do not show much variation, the data seems to suggest that the steric interaction increases with increasing average number of arms per chain, n_{br} (see Table 1). Additionally, Figure 6 shows a possible dependence of the steric interaction factor on the geometric mean arm length. Generally, intrachain interactions in a good solvent are described through the interaction parameter and crowding of arms also involves an enthalpic interaction. However, the structural transformation observed by changes in d_{min} and quantified in ϕ_{si} , reflect entropic changes in chain conformation associated with this enthalpic interaction. We have only observed the steric interaction in good solvent for dilute solutions. If we follow the tethered chain analogy then we would expect this steric effect to almost vanish at the theta temperature or in a melt.³¹ We plan to investigate the steric interaction factor in the future using model star polymers with variable arm length, functionality and solvent quality.

CONCLUSION

A novel scaling approach to quantify the topology of complex macromolecular structures has been presented in this article. The usefulness of the scaling approach in quantifying the branch content of model polyethylene resins was illustrated.

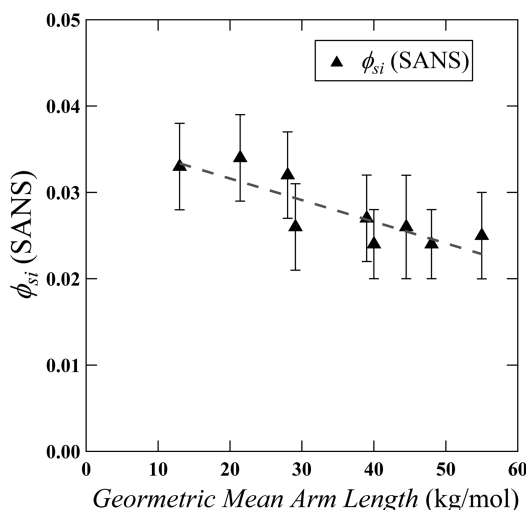


Figure 6. Plot of the steric interaction factor, ϕ_{st} , versus the calculated geometric mean arm length for 3-arm star polyethylenes. The dotted line is a trend line.

Along with estimating the average number of long-chain branches per polymer chain, n_{br} , the approach provides unique measurements of mole-fraction branch content, ϕ_{br} , average long-chain branch length, z_{br} , hyperbranch content, n_v , and steric interaction due to branching, ϕ_{st} . The measurements of ϕ_{br} and z_{br} made via the SANS-scaling approach show good correlation with the calculated averages for these model 3-arm star resins. Additionally, the high viscosity enhancement in a particular 3-arm star resin was attributed to the presence of hyperbranched segments that was measured using the SANS-scaling approach. The examples discussed in this article demonstrate how the detailed quantification available using the scaling approach can lead to better understanding of the effects of polymer structure on physical properties. The scaling approach can also be employed to quantify branching in other complex structures such as ceramic aggregates,⁸ cyclic polymers¹² and to quantify the degree of folding in proteins and RNA.¹⁰

AUTHOR INFORMATION

Corresponding Author

*E-mail: gbeaucage@gmail.com.

Present Address

[§]United Technologies Research Center, 411 Silver Lane, Mail Stop 129-22, East Hartford, CT 0610

ACKNOWLEDGMENTS

This work was funded by ExxonMobil Research & Engineering Co. and the University of Cincinnati Graduate School Distinguished Dissertation Completion Fellowship. This work utilized facilities supported in part by the National Science Foundation under Agreement No. DMR-0454672. We acknowledge the support of the National Institute of Standards and Technology (NIST), U.S. Department of Commerce, for providing the neutron research facilities used in this work. Research at Oak Ridge National Laboratory's High Flux Isotope Reactor was sponsored by the Scientific User Facilities Division, Office of Basic Energy Sciences, U.S. Department of Energy. We thank B. Hammouda and S. Kline at NIST and Y. Melnichenko at ORNL for their valuable support during the beamtime.

REFERENCES

- (1) Hadjichristidis, N.; Xenidou, M.; Iatrou, H.; Pitsikalis, M.; Poulos, Y.; Avgeropoulos, A.; Sioula, S.; Paraskeva, S.; Velis, G.; Lohse, D. J.; Schulz, D. N.; Fetters, L. J.; Wright, P. J.; Mendelson, R. A.; Garcia-Franco, C. A.; Sun, T.; Ruff, C. J. *Macromolecules* **2000**, *33* (7), 2424–2436.
- (2) Lohse, D. J.; Milner, S. T.; Fetters, L. J.; Xenidou, M.; Hadjichristidis, N.; Mendelson, R. A.; Garcia-Franco, C. A.; Lyon, M. K. *Macromolecules* **2002**, *35* (8), 3066–3075.
- (3) Garcia-Franco, C. A.; Harrington, B. A.; Lohse, D. J. *Macromolecules* **2006**, *39* (7), 2710–2717.
- (4) Kulkarni, A. S.; Beaucage, G. *J. Polym. Sci., Part B: Polym. Phys.* **2006**, *44* (10), 1395–1405.
- (5) Ramachandran, R.; Beaucage, G.; Kulkarni, A. S.; McFaddin, D.; Merrick-Mack, J.; Galiatsatos, V. *Macromolecules* **2009**, *42* (13), 4746–4750.
- (6) Ramachandran, R.; Beaucage, G.; McFaddin, D.; Merrick-Mack, J.; Galiatsatos, V.; Mirabella, F. *Polymer* **2011**, *52* (12), 2661–2666.
- (7) Bovey, F. A. *Pure Appl. Chem.* **1982**, *54* (3), 559–568.
- (8) Beaucage, G. *Phys. Rev. E* **2004**, *70*, 3.
- (9) Ramachandran, R.; Beaucage, G.; Kulkarni, A. S.; McFaddin, D.; Merrick-Mack, J.; Galiatsatos, V. *Macromolecules* **2008**, *41* (24), 9802–9806.
- (10) Beaucage, G. *Biophys. J.* **2008**, *95* (2), 503–509.
- (11) Kulkarni, A. S.; Beaucage, G. *Macromol. Rapid Commun.* **2007**, *28* (12), 1312–1316.
- (12) Beaucage, G.; Kulkarni, A. S. *Macromolecules* **2010**, *43* (1), 532–537.
- (13) Hsieh, H. L.; Quirk, R. P. *Anionic polymerization: Principles and Practical Application*; Marcel Dekker: New York, 1996.
- (14) Morton, M. *Anionic Polymerization: Principles and Practice*; Academic Press: New York, 1983.
- (15) Hadjichristidis, N.; Iatrou, H.; Pispas, S.; Pitsikalis, M. *J. Polym. Sci., Part A: Polym. Chem.* **2000**, *38* (18), 3211–3234.
- (16) Rachapudy, H.; Smith, G. G.; Raju, V. R.; Graessley, W. W. *J. Polym. Sci., Part B: Polym. Phys.* **1979**, *17* (7), 1211–1222.
- (17) Rochefort, W. E.; Smith, G. G.; Rachapudy, H.; Raju, V. R.; Graessley, W. W. *J. Polym. Sci., Part B: Polym. Phys.* **1979**, *17* (7), 1197–1210.
- (18) Orfanou, K.; Iatrou, H.; Lohse, D. J.; Hadjichristidis, N. *Macromolecules* **2006**, *39* (13), 4361–4365.
- (19) Doi, M.; See, H. *Introduction to polymer physics*; Clarendon Press: London, 1996.
- (20) Beaucage, G. *J. Appl. Crystallogr.* **1995**, *28*, 717–728.
- (21) Beaucage, G. *J. Appl. Crystallogr.* **1996**, *29*, 134–146.
- (22) Sorensen, C. M.; Wang, G. M. *Phys. Rev. E* **1999**, *60* (6), 7143–7148.
- (23) Costeux, S.; Wood-Adams, P.; Beigzadeh, D. *Macromolecules* **2002**, *35* (7), 2514–2528.
- (24) Murase, H.; Kume, T.; Hashimoto, T.; Ohta, Y.; Mizukami, T. *Macromolecules* **1995**, *28* (23), 7724–7729.
- (25) Glinka, C. J.; Barker, J. G.; Hammouda, B.; Krueger, S.; Moyer, J. J.; Orts, W. J. *J. Appl. Crystallogr.* **1998**, *31*, 430–445.
- (26) Kline, S. R. *J. Appl. Crystallogr.* **2006**, *39*, 895–900.
- (27) Boothroyd, A. T.; Squires, G. L.; Fetters, L. J.; Rennie, A. R.; Horton, J. C.; Devallera, A. *Macromolecules* **1989**, *22* (7), 3130–3137.
- (28) Chang, T. Y.; Lee, H. C.; Lee, W.; Park, S.; Ko, C. H. *Macromol. Chem. Phys.* **1999**, *200* (10), 2188–2204.
- (29) Chen, X.; Rahman, M. S.; Lee, H.; Mays, J.; Chang, T.; Larson, R. *Macromolecules* **2011**, *44* (19), 7799–7809.
- (30) Einstein, A. *Ann. Phys.* **1906**, *19*, 289–306.
- (31) Kent, M. S.; Majewski, J.; Smith, G. S.; Lee, L. T.; Satija, S. J. *Chem. Phys.* **1998**, *108* (13), 5635–5645.
- (32) Daoud, M.; Cotton, J. P. *J. Phys.* **1982**, *43* (3), 531–538.

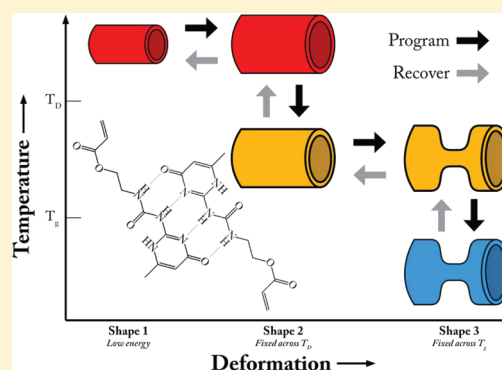
Triple-Shape Memory Polymers Based on Self-Complementary Hydrogen Bonding

Taylor Ware,[†] Keith Hearon,[‡] Alexander Lonnecker,[§] Karen L. Wooley,^{§,⊥} Duncan J. Maitland,[‡] and Walter Voit^{*,†}

[†]Department of Materials Science and Engineering, The University of Texas at Dallas, 800 West Campbell Road, Mailstop RL 10, Richardson, Texas 75080, United States

[‡]Department of Biomedical Engineering, [§]Department of Chemistry, and [⊥]Department of Chemical Engineering, Texas A&M University, College Station, Texas 77843, United States

ABSTRACT: Triple shape memory polymers (TSMPs) are a growing subset of a class of smart materials known as shape memory polymers, which are capable of changing shape and stiffness in response to a stimulus. A TSMP can change shapes twice and can fix two metastable shapes in addition to its permanent shape. In this work, a novel TSMP system comprised of both permanent covalent cross-links and supramolecular hydrogen bonding cross-links has been synthesized via a one-pot method. Triple shape properties arise from the combination of the glass transition of (meth)acrylate copolymers and the dissociation of self-complementary hydrogen bonding moieties, enabling broad and independent control of both glass transition temperature (T_g) and cross-link density. Specifically, ureidopyrimidone methacrylate and a novel monomer, ureidopyrimidone acrylate, were copolymerized with various alkyl acrylates and bisphenol A ethoxylate diacrylate. Control of T_g from 0 to 60 °C is demonstrated: concentration of hydrogen bonding moieties is varied from 0 to 40 wt %; concentration of the diacrylate is varied from 0 to 30 wt %. Toughness ranges from 0.06 to 0.14 MPa and is found to peak near 20 wt % of the supramolecular cross-linker. A widely tunable class of amorphous triple-shape memory polymers has been developed and characterized through dynamic and quasi-static thermomechanical testing to gain insights into the dynamics of supramolecular networks.



INTRODUCTION

Shape memory materials are a widely investigated class of smart materials capable of changing from one predetermined shape to another in response to a stimulus.¹ This macro-scale phenomenon has been demonstrated in ceramics, metals and a range of polymeric systems, but results from very different mechanics in each material.² Shape memory polymers (SMPs) can “remember” a metastable shape and upon application of a stimulus, such as heat or light, recover a globally stable shape.^{3,4} This memory phenomenon is referred to as dual-shape memory and is enabled by the presence of a switching phase and a cross-linking phase in a polymer network. The switching phase can be deformed under certain temporary conditions, such as high temperature, to program a metastable shape. Switching phases maintain this deformation through chain immobilization by reversible crystallization, vitrification or supramolecular interactions^{5,6} to hold this metastable shape until requisite activation energy facilitates a return to the original shape. The cross-linking phases serve as net points, which allow the deformation of chains, but maintain the relative positions of the chains. Cross-linking phases include covalent cross-links and physical cross-links, such as crystalline or glassy domains in phase separated polymers or strong supramolecular interactions.⁷ Cross-links can be incorporated during initial polymerization or

through new alternative methods, including, for instance, the use of ionizing radiation to selectively cross-link SMPs after thermoplastic processing.^{8–10}

The combined effect of a thermally activated switching phase and a cross-linking phase yields a polymer with the capability of deformation at high temperatures, fixation of the induced deformation when cooled below the transition temperature of the switching phase, and recovery of the deformation when heated above the transition temperature. This thermomechanical cycle describes the shape memory phenomenon in polymers. This effect is inherently different from the behavior exhibited by shape memory alloys, as it permits one-time large scale shape recovery. Deformation up to 800% has been shown to be fully recoverable in optimized acrylic SMPs as compared to roughly 8% for shape memory alloys.¹¹ Shape memory has been demonstrated in a large number of polymer systems and has been investigated for use in biomedical and commodity applications.^{12–15} One inherent limitation of SMPs is that SMP-based devices will, when actuated, always recover toward a

Received: September 19, 2011

Revised: December 20, 2011

Published: January 6, 2012

single predetermined shape that must be set at the time of molding or cross-linking.

Triple-shape memory polymers (TSMPs) are an emerging class of polymers that have the capability of storing two metastable shapes in addition to a globally stable shape.¹⁶ These polymers contain a cross-linking phase, and two independent switching phases associated with two different transitions. Figure 1 is a schematic representing the

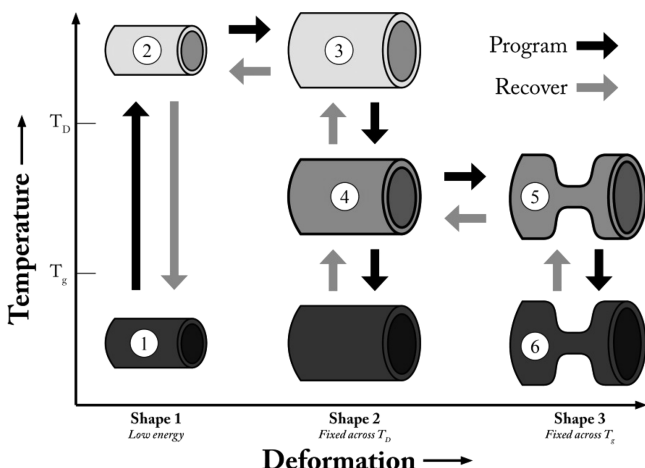


Figure 1. Schematic of a triple shape memory polymer programming and recovery cycles. The triple shape cycle consists of heating (1 \rightarrow 2) and programming a shape above both transitions (2 \rightarrow 3); cooling to a temperature between the two transitions to fix this shape (3 \rightarrow 4); further deforming the polymer (4 \rightarrow 5); cooling to a temperature below both transitions to fix the third shape (5 \rightarrow 6).

programming and recovery cycles of a generic TSMP. Programming the TSMP consists of (1) heating the polymer above both transitions and inducing deformation, (2) maintaining the deformation while cooling the polymer to fix shape 2 at a temperature between the two transitions, (3) further deforming the polymer, and (4) maintaining the second deformation while cooling below both transitions, fixing shape 3. Upon heating without any applied load, the polymer will first recover shape 2 and, upon reaching the second transition, then recover shape 1. Bellin et al. have demonstrated the triple-shape memory effect in systems containing two crystalline switching phases, while others have combined an amorphous phase with a crystalline switching phase.^{17,18} Recently Xie has shown quadruple-shape memory utilizing the broad transition of

perfluorosulfonic acid ionomers.¹⁹ Luo et al. have also demonstrated a system of composites capable of demonstrating the triple-shape memory effect.²⁰ TSMPs stand to increase the complexity of devices utilizing the shape memory effect by enabling multistage complex recovery profiles. Recent work has elucidated the benefits of this approach and also certain limitations, especially a strong sensitivity to the specific conditions of the programming step.²¹

Supramolecular polymers are materials containing directional, intermolecular and highly reversible noncovalent interactions.²² There are many examples of the interactions that can be used for supramolecular engineering including hydrogen bonding, metal ion coordination and electrostatics. These interactions can be used to assemble monomers to form polymeric chains or assemble covalently linked chains into polymer networks through the formation of cross-links. Meijer et al. have demonstrated the unique ability of self-complementary arrays of hydrogen bonds in the formation of supramolecular polymers, specifically utilizing 2-ureido-4[1H]-pyrimidone (UPy) units.²³ UPy has been proposed for a number of advanced applications due to its extremely high tendency to dimerize, with a dimerization constant greater than 10^6 M^{-1} in CHCl_3 .²³ Specific areas of research include self-healing materials, biomimetic modular polymers, thermoplastic elastomers and SMPs.^{6,24–27} UPy functionalities have been included into thermoplastic segmented polyurethanes and thermoset acrylic elastomers (with T_g 's well below the intended use temperature) and used as the switching phase.^{6,28} Acrylic elastomers containing UPy show shape recovery approaching 100%, but show lower shape fixity, $\sim 90\%$, as compared to switching segments based on vitrification or crystallization.⁶ To the knowledge of the authors, UPy has not previously been incorporated into acrylic systems with a glass transition near the intended use temperature or used in TSMPs.

This work seeks to combine the properties of supramolecular and covalent cross-links in an acrylic system to demonstrate amorphous TSMPs with tunable glass transitions and supramolecular and covalent cross-link density. Specifically, UPy functionalized (meth)acrylate monomers were synthesized and polymerized with *n*-alkyl acrylates and a diacrylate cross-linker in a one-pot method. Thermomechanical properties of the synthesized system were evaluated by dynamic mechanical analysis, differential scanning calorimetry, and quasi-static tensile testing. The ability to serve as a TSMP was also evaluated for several samples.

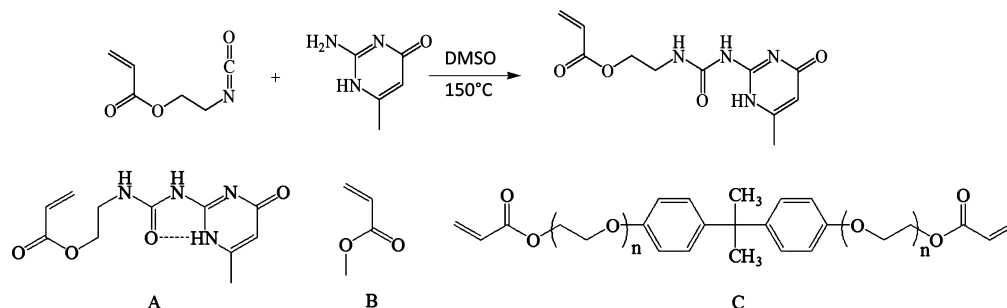


Figure 2. Schematic of the synthesis procedure. Top: Reaction utilized to synthesize ureidopyrimidine functionalized acrylate monomer (UPyA). 2-Isocyanatoethyl acrylate is allowed to react with 6-methylisocytosine in DMSO. Bottom: The synthesized UPy(M)A, “A”, (UPyA shown) was mixed with an *n*-alkyl acrylate, “B” (methyl acrylate shown), and “C” bisphenol A ethoxylate diacrylate and photopolymerized using a photoinitiator in DMSO.

Table 1. Gel Fraction with Increased UPy(M)A Concentration

sample	10% UPyA	20% UPyA	30% UPyA	10% UPyMA	20% UPyMA	30% UPyMA
gel fraction	0.920 ± 0.004	0.934 ± 0.006	0.977 ± 0.005	0.882 ± 0.002	0.907 ± 0.011	0.935 ± 0.007

MATERIALS AND METHODS

Methyl acrylate (MA), ethyl acrylate (EA), butyl acrylate (BA), bisphenol A ethoxylate diacrylate (BPAEDA) ($M_w \sim 512$ g/mol), anhydrous dimethyl sulfoxide (DMSO), 6-methylisocytosine, and 2,2-dimethoxy-2-phenyl acetophenone (DMPA) were purchased from Sigma-Aldrich. Propyl acrylate was purchased from Alfa Aesar. 2-isocyanatoethyl acrylate was purchased from Wako Chemicals. 2-Isocyanatoethyl methacrylate was purchased from TCI America. All chemicals were used as received without further purification.

One-Pot Synthesis of UPy Functionalized (Meth)acrylate Monomer and Polymer Films. Synthesis of (meth)acrylate functionalized monomer was adapted from Yamauchi et al. and is depicted in Figure 2.²⁹ 6-Methylisocytosine and 2-isocyanatoethyl (meth)acrylate were added to DMSO in concentrations appropriate for the subsequent polymerization and heated to 150 °C until the isocytosine had completely dissolved. The solutions were held at 150 °C for 15 min and subsequently removed and quenched to room temperature, precipitating a white solid confirmed to be UPy(M)A by IR and 1D and 2D NMR spectroscopy. ¹H NMR (300 MHz, CDCl₃, 25 °C): δ (ppm) 11.95 (s, 1H), 10.50 (t, 1H, $J = 4.7$ Hz), 6.18–6.17 (m, 1H), 5.78 (t, 1H, $J = 1.0$ Hz), 5.54 (q, 1H, $J = 1.6$, $J = 1.5$ Hz), 4.27 (t, 2H, $J = 5.6$ Hz), 3.60–3.54 (q, 2H, $J = 5.67$ Hz), 2.23 (s, 3H), 1.93 (s, 3H). ¹³C NMR (300 MHz, CDCl₃, 25 °C): δ (ppm) 172.8, 167.3, 156.8, 154.5, 148.2, 136.1, 125.8, 106.7, 63.1, 38.7, 18.9, 18.3. FTR-IR (ATR): $\nu = 2939$ (broad), 1697, 1651, 1581, 1519, 1450, 1411, 1327, 1249, 1165, 1011, 941, 763, 740. ESI-TOF-MS (m/z) calcd, 280.12; observed, 281.1024 ($M + H^+$). The appropriate n -alkyl acrylates, BPAEDA and DMPA were added and dissolved in the DMSO. 1.5 wt % (by monomer weight) DMPA was used as the initiator concentration for all samples. Total monomer concentration was fixed at 30 wt % for all samples. The monomer solution was then heated to 120 °C until UPy(M)A was completely solubilized, and the warm monomer mixture was injected between two glass slides (75 × 50 mm) separated by a glass spacer, 1.2 mm thick. Polymerization was performed using a cross-linking chamber with five overhead 365 nm UV bulbs (UVP via Cole-Parmer) for 120 min. The resulting gel was dried under vacuum at 110 °C until a constant weight was reached (approximately 12 h). Shrinkage of approximately 70% during drying was observed. Samples were dried on PTFE sheets to allow shrinkage without tearing during solvent removal. Upon removal from the vacuum oven, the samples were stored in a desiccated container and removed only for testing. It is expected all DMSO as well as any unreacted n -alkyl acrylates are removed by drying. Gel fractions were determined ($n = 3$) for samples containing 10, 20, and 30 wt % of both UPyA and UPyMA by repeated (3×) swelling and deswelling in chloroform for 1 week. After the third swelling, samples were dried for 12 h in ambient conditions and 24 h under vacuum at 70 °C to remove chloroform.

Differential Scanning Calorimetry. DSC was performed on a Mettler Toledo DSC 1 with an intracooler option. Samples were heated from room temperature to 100 °C, cooled to −50 °C, and subsequently heated to 200 °C. Data shown are of only the second heating ramp. All heating and cooling rates were fixed at 10 °C/min. Tests were conducted in a nitrogen atmosphere.

Dynamic Mechanical Analysis. DMA was performed on a Mettler Toledo DMA 861e/SDTA. Samples were cut into squares approximately ~0.4 mm thick and ~2 mm in dimension. The mode of deformation was shear, and strain was limited to a maximum of 0.29%. Samples were tested between −50 and +150 °C at a heating rate of 2 °C/min. A multiplexed frequency mode was run on all samples in which 1, 2, 5, and 10 Hz deformation occurs simultaneously; the frequency of deformation shown is 5 Hz, unless otherwise stated. For higher frequency measurements, a second multiplexed frequency test

was run, where the frequencies probed were 10, 20, 50, and 100 Hz. Tests were conducted in a nitrogen atmosphere.

Uniaxial Tensile Testing. Tensile testing was conducted to failure on select samples ($n \geq 3$) using a Lloyd-Ametek LR5KPlus with a 100 N load cell. The grips used were TG-22 self-tightening roller grips also supplied by Lloyd-Ametek. Tests were conducted at 10 mm/min inside a Eurotherm Thermal Chamber at the peak of loss modulus (G'') as determined by DMA at 1 Hz. Strain was measured using a long-travel laser extensometer. All stresses and strains reported are engineering stresses and strains, and toughness was measured as the integrated area under the stress–strain curve.

Shape Memory Testing. Shape memory testing consisted of free-strain recovery and constrained recovery. All samples were programmed using the same temperature-strain profile. All samples were programmed by (1) heating the polymer to the second peak of $\tan \delta$ (determined by DMA at 1 Hz) and straining the sample to 20% in compression, (2) maintaining the deformation while cooling the polymer to the first peak of $\tan \delta$, fixing shape 2, (3) further deforming the polymer to 40% in compression, and (4) maintaining the second deformation while cooling below both transitions, fixing shape 3. For free-strain recovery, samples were unloaded at this temperature and then heated at 2 °C/min. For constrained recovery, 40% deformation was maintained and heated at 2 °C/min. All shape memory testing was performed on a TA Instruments Q800 DMA in DMA Strain Rate mode on 5 mm-diameter, 2 mm-thick cylindrical samples.

RESULTS

The gel fractions of samples containing 10, 20, and 30 wt % of both UPyA and UPyMA are reported in Table 1. All networks tested showed gel fractions greater than 88%. UPyA containing samples possessed higher gel fractions than samples containing UPyMA at equal UPy(M)A concentration.

The thermomechanical properties of each synthesized network were characterized through DMA and DSC. Select samples were then further characterized through uniaxial tensile testing and shape memory testing. In Figures 3a,b, a 1:1 ratio of the linear monomers MA and BA was maintained in order to elucidate the effect of increased supramolecular cross-links at constant covalent cross-link density on the dynamic mechanical properties of the polymer system. Shear storage modulus from DMA is presented for samples containing UPyA or UPyMA. In all compositions tested, two transitions are present; the first transition is accompanied by a drastic decrease in modulus, from approximately 700 to 1 MPa. The second transition is accompanied by a much smaller decrease in modulus, approximately 0.9 MPa, near 80 °C. The first transition is strongly dependent in both breadth and temperature on the composition of UPy(M)A. The second transition, however, is nearly constant in peak temperature. From Figure 3, three modulus “regions” can be defined. The first region occurs below the low temperature transition, and represents the glassy modulus; the second occurs between the two transitions and will be denoted the “middle modulus” (G_M); the third plateau occurs above both transitions and the rubbery modulus (G_R).

The effect of increasing covalent cross-linking at constant UPyMA concentration is evaluated in Figure 3c. In these samples, increasing BPAEDA is matched by an increasing BA:MA ratio in order to maintain the separation of the two transitions. It can be seen that increasing the covalent or supramolecular cross-linker concentration leads to an increase

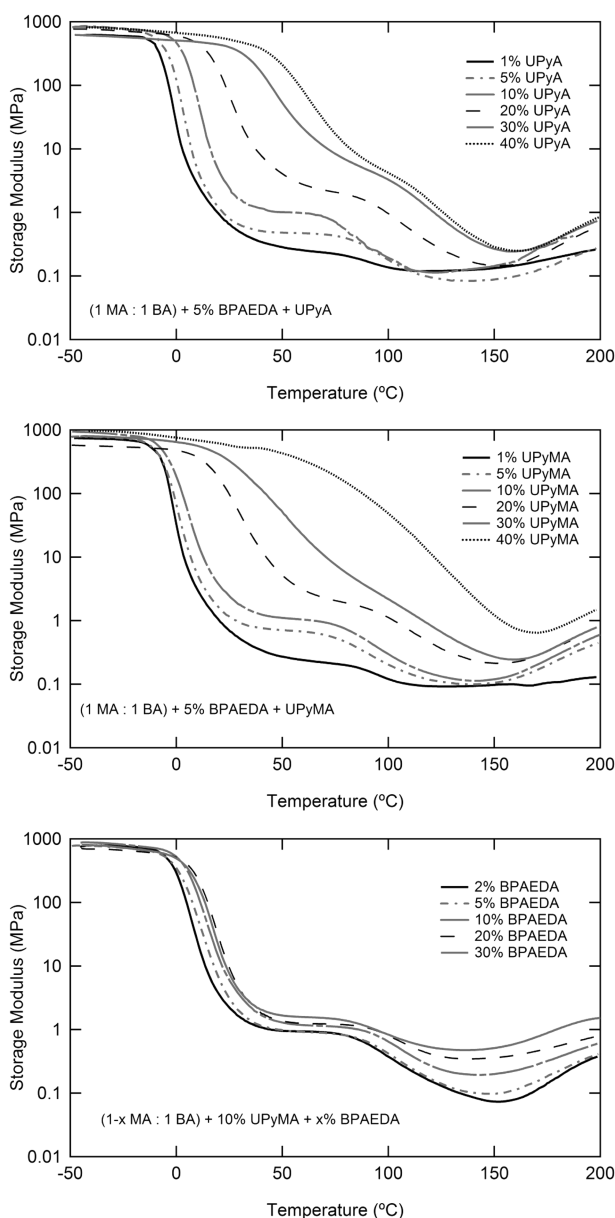


Figure 3. Dynamic mechanical analysis demonstrates the effects of (a) increasing supramolecular cross-links via UPyA concentration (upper), (b) increasing supramolecular cross-links via UPyMA concentration (middle), and (c) increasing covalent cross-links via BPAEDA concentration (lower). The glass transition increases strongly with added supramolecular cross-links. The plateau modulus increases with both supramolecular and covalent cross-link. Rubbery modulus increases with covalent cross-linking.

in G_M and G_r . G_r increases from 0.07 to 0.47 MPa with an increase in BPAEDA concentration from 2 to 30 wt %.

Figure 4 serves as a comparison between samples made with UPyA and UPyMA. Figure 4a shows the difference in properties associated with the acrylate and methacrylate functionalized analogues of UPy. For low concentrations of UPy, it should be noted that two transitions are present for both UPyA and UPyMA. As the concentration of supramolecular cross-linker increases, UPyA maintains to a large degree the separation of the two transitions, but UPyMA does not. Figure 4b shows DSC thermograms of representative samples containing UPy. It should be noted that a glass

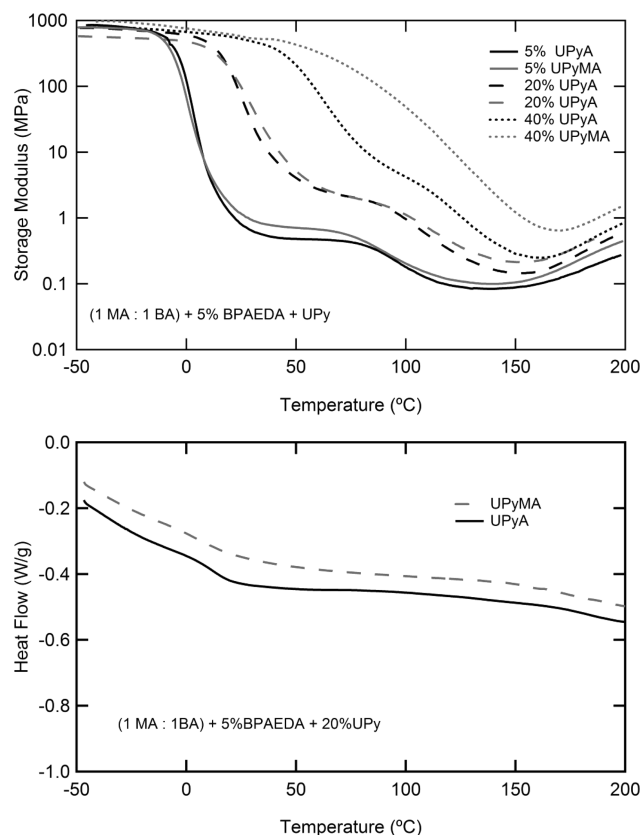


Figure 4. Comparison of the thermomechanical properties of samples containing the methacrylated and acrylated analogues of UPy by dynamic mechanical analysis of samples containing 5, 20, and 40% UPy (upper, a) and differential scanning calorimetry (Exo up) of samples containing 20% UPy (lower, b). The glass transition for high UPy concentrations is lower for UPyA, causing it to be more easily distinguished from the UPy dissociation.

transition can be distinguished for the 20% UPyA sample but not for the UPyMA sample. There are no other apparent thermal events present in the thermograms over the temperature range studied.

The tunability of T_g of the studied system is presented in Figure 5. Figure 5a shows the storage modulus as a function of temperature for polymers containing different *n*-alkyl acrylates. It should be noted that G_M and G_r are largely unaffected by the change of linear comonomers. Increasing the length of the alkyl side chain on the acrylate decreases the glass transition from 60 to 0 °C as can be seen in Figure 5b. The shape of the loss factor ($\tan \delta$) curve is common among samples with the methyl acrylate sample showing a larger area under the first peak and less area under the second peak than other samples tested.

Figure 6 contains loss factor curves for a single representative sample, tested over two decades of frequency between -50 and $+200$ °C. The peaks associated with both transitions are shown to be frequency dependent. It should be noted that while the first peak varies with frequency by approximately 7 °C/decade of frequency, the second varies by 27 °C/decade of frequency. The quasi-static tensile response of the samples as a function of increased supramolecular cross-linker (UPyMA) concentration is shown in Figure 7a. Samples were tested at the lower temperature peak of loss modulus as determined by DMA at 1 Hz; the testing temperature for each sample is shown in Figure 7c. Strain-to-failure decreases with increased UPyMA while

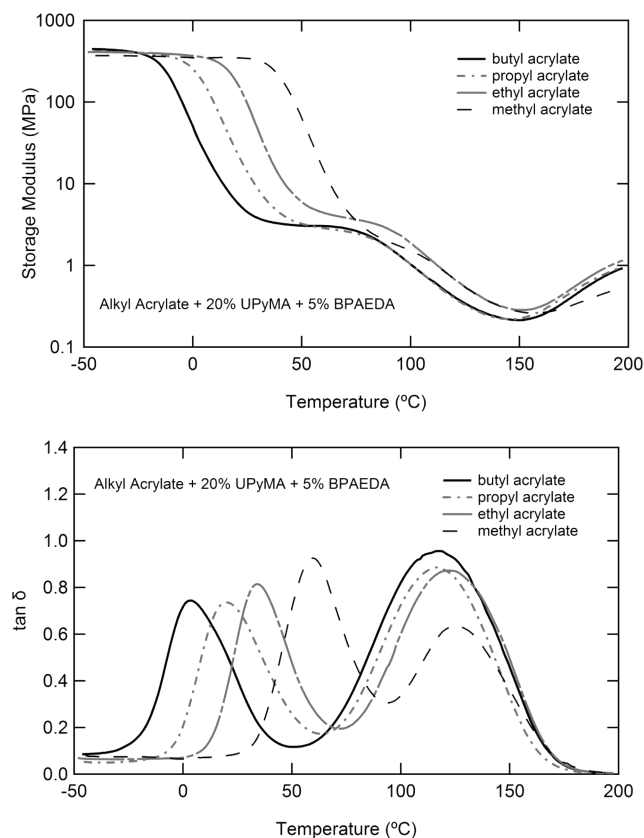


Figure 5. Dynamic mechanical analysis showing the effect of different *n*-alkyl acrylate comonomers on the (a) storage modulus and (b) loss factor ($\tan \delta$) as a function of temperature. The glass transition is lowered with increasing alkyl side group length.

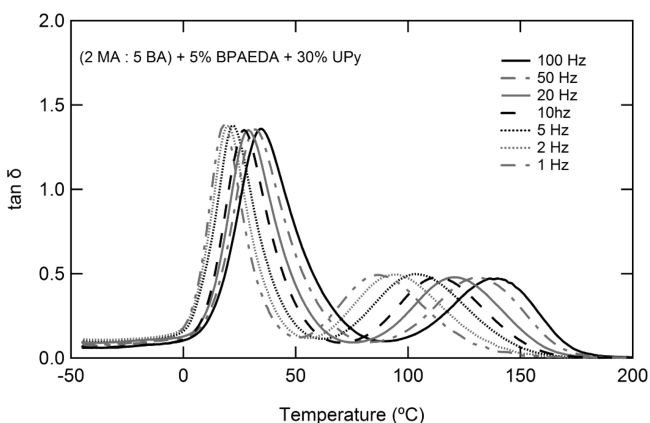


Figure 6. Dynamic mechanical analysis showing the effect of deformation frequency on the loss factor peaks associated with the two transitions. While both transitions are frequency dependent, the dissociation of UPy shows a much larger frequency response than does the glass transition.

stress-at-failure increases. The toughness of the samples, measured as the integrated area under the engineering stress–strain curve is shown for each sample in Figure 7b. A peak in toughness is seen around 15% UPyMA.

Figure 8 presents shape recovery behavior of samples containing UPyMA in both free-strain and constrained recovery conditions. All samples were programmed by (1) heating the polymer to the second peak of $\tan \delta$ (determined by DMA at 1 Hz) and straining the sample to 20% in compression, (2)

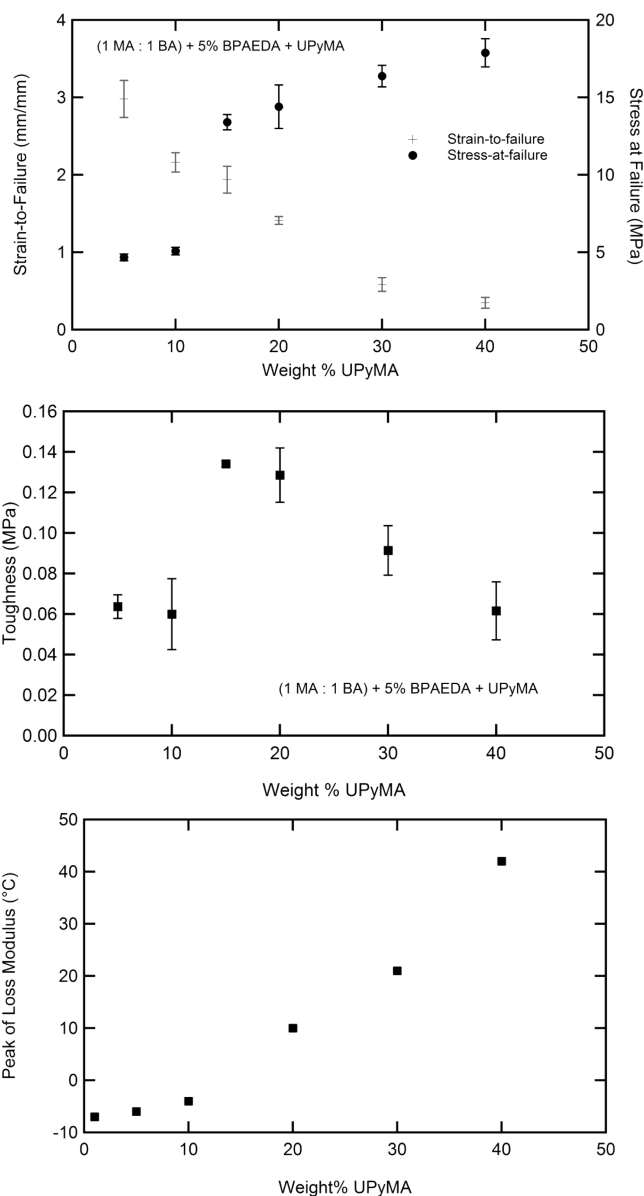


Figure 7. Quasi-static tensile testing-to-failure results for samples with increased supramolecular cross-linking. Failure strain decreases while failure stress increases with increased UPy content (upper, a). Toughness peaks around 15 wt % UPy. All tests were conducted at the peak of loss modulus from DMA (1 Hz) (middle, b). Peak of loss modulus as determined by DMA at 1 Hz for samples that were subsequently quasi-statically strained to failure (lower, c).

maintaining the deformation while cooling the polymer to the first peak of $\tan \delta$, fixing shape 2, (3) further deforming the polymer to 40% in compression and (4) maintaining the second deformation while cooling below both transitions, fixing shape 3. In Figure 8a, each sample was released and allowed to recover without an applied load while heating. With increased UPyMA concentration, the onset of recovery occurs at higher temperatures and the separation of the two recovery events decreases. Final recovery exceeded 95% of the induced deformation for all samples tested. Figure 8b shows the stress generated through sample recovery for a sample containing 10% UPyMA. The peak stress generated is 0.81 MPa and occurs near physiological temperature for the selected system. An effort was made to demonstrate the versatility of the

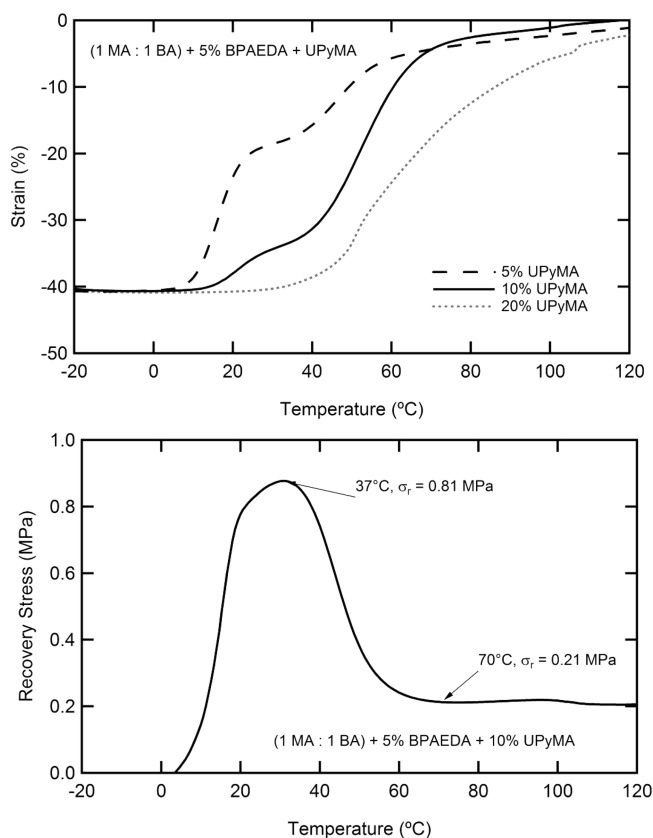


Figure 8. Recovery behavior of samples with between 5 and 20 wt % UPyMA: (a) free-strain recovery and (b) constrained recovery of a sample with 10% UPyMA. Samples were heated to 130 °C, strained to 20% in compression, cooled to T_g , further strained to 40% of the original length, and cooled to -20 °C while maintaining the applied deformation.

fabricated TSMP system for fixing arbitrary deformations, as compared to the uniaxial triple-shape memory effect that was quantitatively described in Figure 8, Figure 9 shows the recovery of a sample that was twisted and textured on half the sample with a clamp at 90 °C, cooled to 37 °C untwisted and bent and subsequently cooled to 20 °C,

DISCUSSION

Demonstration of a tunable SMP (or TSMP) system requires wide and, where possible, independent control of several key

properties, namely the activation temperature(s), determined by the temperature of the transition(s), and recovery characteristics, determined by the cross-link density(ies). This work attempts to demonstrate wide and independent control of the glass transition and covalent cross-link density in a system where a supramolecular network is formed by self-complementary hydrogen bonding. The specific effects of supramolecular cross-links on the thermomechanical properties of a covalently cross-linked system are investigated in quasi-static and dynamic regimes to understand the interplay between covalent and supramolecular network phenomena.

Figure 3 demonstrates control over the supramolecular and covalent cross-link densities in a system where the glass transition and UPy dissociation occur between 0 and 100 °C, which is across the useful range for many applications. The acrylated and methacrylated analogues of UPy introduce thermoreversible cross-links into the covalent network. As shown in Table 1, Gel fraction was above 88% for all measured samples, indicating a high level of network formation. Reactivity of the *n*-alkyl acrylates is likely to be closer to UPyA than to UPyMA leading to slightly better network incorporation for UPyA. Increasing UPy content also led to more complete network formation. The effect of the presence of UPy on polymerization and termination events is beyond the scope of this work, but should be considered in future work. This is demonstrated by the presence of a transition above the glass transition. Figure 4b and Figure 6 demonstrate that this UPy-mediated transition is both frequency dependent and not associated with a distinct enthalpic event, indicating the second transition is not crystalline in nature. Increasing UPy(M)A or BPAEDA concentration increases G_M , due to the increase of total cross-link density. Quantifying the increase in G_M proves difficult beyond 10 wt % UPy(M)A, as the glass transition increases in temperature and broadens significantly, causing the two transitions to overlap.

In order to study independent glass and UPy dissociation transitions, UPyA was synthesized and characterized. The temperature at which the UPy dissociation transition occurs is unaffected by the change from methacrylate to acrylate, but the T_g does not increase as rapidly with UPyA, thereby allowing for the two transitions to remain separated for compositions with less than 20 wt % UPyA. Figure 4 directly compares samples made with UPyA and UPyMA. The glass transition associated with UPyA-containing samples is consistently lower than that for equivalent concentrations of UPyMA, which allows the two transitions to be distinguished by DMA. The cost and lack of

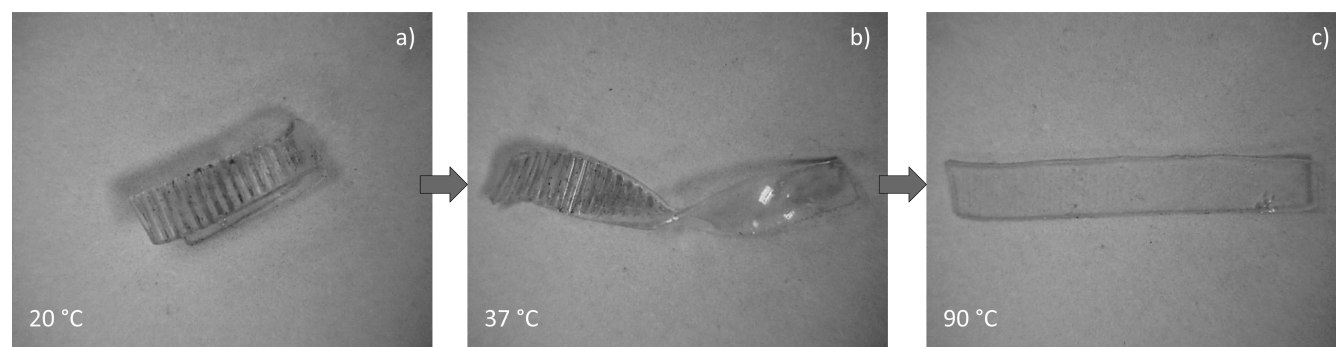


Figure 9. Sequential photographs taken of the recovery of a sample containing 10% UPyMA demonstrating the triple-shape memory effect. Recovery proceeded from the first temporary shape (bent and textured) (a) to the second temporary shape (twisted and textured) (b) and to the permanent shape (flat and smooth) (c).

commercial availability of 2-isocyanatoethyl acrylate as compared to 2-isocyanatoethyl methacrylate, however, led to the selection of UPyMA for further synthesis and thermo-mechanical testing. The 10 wt % UPyMA sample was selected as a test composition to study the effect of covalent cross-link density. Increasing the covalent cross-link density at constant supramolecular cross-link density and approximately constant T_g was achieved by varying the MA:BA ratio, to decrease proportionally with the increase in BPAEDA concentration (Figure 3c).

Figure 5 demonstrates the utility of the selected *n*-alkyl acrylate system for changing the first activation temperature of the TSMP. By varying the length of the alkyl side group from 1 to 4 carbons, the glass transition is tuned over a range of 60 °C at an approximately constant G_M and G_R . While this study was limited to 4 commercial alkyl acrylate comonomers, the authors recognize the potential of this system for further tuning, by utilizing the plethora of available (meth)acrylate monomers. The same MA-BA system characterized in Figure 3b was selected for quasi-static tensile testing at the first peak of loss modulus from DMA at 1 Hz (Figure 7). As the UPyMA concentration increases, stress-at-failure increases while strain-to-failure decreases. This behavior is consistent with the view of the supramolecular hydrogen bonding serving as cross-links. A peak in toughness is seen around 15 wt % UPyMA. It is proposed that this sharp increase in toughness is due to the increasing likelihood of the hydrogen bonds to break and reform, thus dissipating energy as the temperature increases and the concentration of the hydrogen bonding moiety increases. This effect is difficult to isolate, as testing was carried out at a relative temperature to the first transition, but the testing temperature increased relative to the second transition, with increasing UPyMA. The peak of loss modulus increases dramatically between 10 and 20 wt %, as shown in Figure 7c, thus allowing for significant toughening from the hydrogen bonding. Beyond 20 wt % the toughness decreases as strain-to-failure is severely limited by the increased supramolecular interactions without a concomitant increase in stress-at-failure.

The dynamic nature of the supramolecular networks is probed further in Figure 6 by DMA at frequencies between 1 and 100 Hz. The UPy dissociation transition shifts $\sim 4\times$ further along the temperature scale than does the glass transition, as a function of frequency. This can be attributed to the constant breaking and reforming of the hydrogen bonds along the UPy moieties. This strong frequency dependence elucidates the truly dynamic nature of the supramolecular network, which must persist in order to serve as a cross-linking phase. It is important to consider that shape recovery exists in the quasi-static domain and that the persistence of a cross-link must be evaluated under similar deformation conditions. The free-strain recovery of selected systems shown in Figure 8a demonstrates the importance of the differences between quasi-static shape recovery and dynamic mechanical deformation. Samples containing more than 10 wt % UPyMA do not show two distinct transitions but instead undergo a single broad recovery. Interestingly, this transition in properties occurs in the same composition range as the abrupt change in toughness shown in Figure 7b. Since both changes in properties can be attributed to the dynamic nature of the supramolecular cross-links, we propose a common mechanism for both properties. Segmental motion begins at a much higher temperature with increasing UPy, and the likelihood of a UPy molecule being able to

disassociate and find a different UPy moiety to bond with increases with increasing UPy. The supramolecular network does not persist under quasi-static conditions for compositions of UPy beyond 10 wt % for the studied system. Despite this lack of an effective supramolecular network for high compositions of UPy, triple shape properties can be clearly distinguished for the 5% and 10% samples. Stress recovery for the 10% UPyMA sample under constraint shows a single recovery peak, as is commonly seen for SMPs strained near the T_g .

The described material system has several characteristics that are expected to influence future work in this area. The highly dynamic nature of the supramolecular network is the most defining of these characteristics. This leads to poor shape fidelity above the glass transition, which at high UPy concentrations can lead to a loss in high quality triple shape properties. Despite these limitations, enabling large-scale shape recovery while maintaining a deformation that was induced postpolymerization, such as a surface texturing, is demonstrated Figure 9. This supramolecular network may also show interesting cyclic properties, due to its ability to sustain nonpermanent damage, and should be investigated in future work. Another major hurdle this system must face is a current lack of processability. Although a one-pot synthetic procedure was developed for this work, any device would be subjected to the constraints of the polymers' thermoset nature and the fact that the materials must be made as a gel. This significantly hinders processing for geometries that are not sheets or films, as the materials cannot be melt-processed and large cross sections complicate the removal of solvent and lead to warping. Although challenges and further investigation remain, a systematic approach of optimizing thermomechanical programming and creative synthetic approaches would enable a highly tunable TSMP system based on widely available (meth)acrylate monomers and synthetically available supramolecular cross-links.

CONCLUSIONS

A system of acrylic triple shape memory polymers that utilizes the glass transition and the dissociation of self-complementary hydrogen bonding moieties has been synthesized and characterized. A one-pot synthetic procedure was developed in which a (meth)acrylated 2-ureido-4[1H]pyrimidone monomer was first synthesized and then subsequently copolymerized with desired ratios of *n*-alkyl acrylates and a bisphenol A-based diacrylate cross-linker. The resulting samples had both supramolecular and covalent network properties. The glass transition was varied between 0 and 60 °C, and covalent cross-link density was varied quasi-independently from the glass transition. The effect of increased supramolecular cross-linking on the thermomechanical properties of the polymer networks was also demonstrated, with results providing insights into the dynamics of UPy supramolecular cross-linking. Finally, triple-shape capability was shown in an amorphous monophasic polymer system. Accurate control of the transitions and thermomechanics of TSMPs make them candidate materials for specialty applications that demand multiple high-strain shape changes after deployment without intermediate mechanical retraining.

AUTHOR INFORMATION

Corresponding Author

*E-mail: walter.voit@utdallas.edu.

■ ACKNOWLEDGMENTS

The Welch Foundation is gratefully acknowledged for support through the W. T. Doherty-Welch Chair in Chemistry (K.L.W.), Grant No. A-0001. This work was partially supported by the National Institutes of Health/National Institute of Biomedical Imaging and Bioengineering, Grant R01EB000462. This material is based also partially based upon work supported by a National Science Foundation Graduate Research Fellowship under Grant 2011113646.

■ REFERENCES

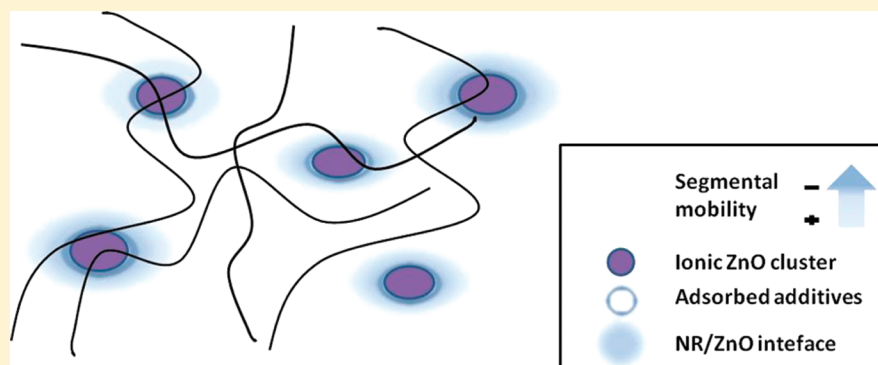
- (1) Lendlein, A.; Langer, R. *Science* **2002**, 296 (5573), 1673–1676.
- (2) Feninat, F. E.; Laroche, G.; Fiset, M.; Mantovani, D. *Adv. Eng. Mater.* **2002**, 4 (3), 91–104.
- (3) Mather, P.; Luo, X.; Rousseau, I. *Annu. Rev. Mater. Res.* **2009**, 39, 445–471.
- (4) Lendlein, A.; Jiang, H.; Junger, O.; Langer, R. *Nature* **2005**, 434 (7035), 879–882.
- (5) Liu, C.; Qin, H.; Mather, P. T. *J. Mater. Chem.* **2007**, 17, 1543–1558.
- (6) Li, J.; Viveros, J.; Wrue, M.; Anthamatten, M. *Adv. Mater.* **2007**, 19 (19), 2851.
- (7) Tobushi, H.; Hara, H.; Yamada, E.; Hayashi, S. *Smart Mater. Struct.* **1996**, 5, 483–491.
- (8) Voit, W.; Ware, T.; Gall, K. *Polymer* **2010**, 51 (15), 3551–3559.
- (9) Ware, T.; Voit, W.; Gall, K. *Radiat. Phys. Chem.* **2010**, 79 (4), 446–453.
- (10) Hearon, K.; Gall, K.; Ware, T.; Maitland, D. J.; Bearinger, J. P.; Wilson, T. S. *J. Appl. Polym. Sci.* **2011**, 121 (1), 144–153.
- (11) Voit, W.; Ware, T.; Dasari, R. R.; Smith, P.; Danz, L.; Simon, D.; Barlow, S.; Marder, S. R.; Gall, K. *Adv. Funct. Mater.* **2010**, 20 (1), 162–171.
- (12) Gall, K.; Yakacki, C. M.; Liu, Y.; Shandas, R.; Willett, N.; Anseth, K. S. *J. Biomed. Mater. Res., Part A* **2005**, 73A (3), 339–348.
- (13) Baer, G.; Wilson, T. S.; Matthews, D. L.; Maitland, D. J. *J. Appl. Polym. Sci.* **2007**, 103 (6), 3882–3892.
- (14) Yakacki, C. M.; Shandas, R.; Lanning, C.; Rech, B.; Eckstein, A.; Gall, K. *Biomaterials* **2007**, 28 (14), 2255–2263.
- (15) Small, I. V. W.; Singhal, P.; Wilson, T. S.; Maitland, D. J. *J. Mater. Chem.* **2010**, 20 (17), 3356–3366.
- (16) Behl, M.; Lendlein, A. *J. Mater. Chem.* **2010**, 20 (17), 3335–3345.
- (17) Bellin, I.; Kelch, S.; Langer, R.; Lendlein, A. *Proc. Natl. Acad. Sci. U.S.A.* **2006**, 103 (48), 18043–18047.
- (18) Liu, G.; Ding, X.; Cao, Y.; Zheng, Z.; Peng, Y. *Macromol. Rapid Commun.* **2005**, 26 (8), 649–652.
- (19) Xie, T. *Nature* **2010**, 464 (7286), 267–270.
- (20) Luo, X.; Mather, P. T. *Adv. Funct. Mater.* **2010**, 20 (16), 2649–2656.
- (21) Li, J.; Xie, T. *Macromolecules* **2010**, 44 (1), 175–180.
- (22) Lehn, J.-M. *Polym. Int.* **2002**, 51 (10), 825–839.
- (23) Sijbesma, R. P.; Beijer, F. H.; Brunsveld, L.; Folmer, B. J. B.; Hirschberg, J. H. K. K.; Lange, R. F. M.; Lowe, J. K. L.; Meijer, E. W. *Science* **1997**, 278 (5343), 1601–1604.
- (24) Bergman, S.; Wudl, F. *J. Mater. Chem.* **2008**, 18 (1), 41–62.
- (25) Wietor, J.-L.; Dimopoulos, A.; Govaert, L. E.; van Benthem, R. A. T. M.; de With, G.; Sijbesma, R. P. *Macromolecules* **2009**, 42 (17), 6640–6646.
- (26) Berl, V.; Schmutz, M.; Krische, M. J.; Khoury, R. G.; Lehn, J.-M. *Chem.—Eur. J.* **2002**, 8 (5), 1227–1244.
- (27) Kushner, A.; Gabuchian, V.; Johnson, E.; Guan, Z. *J. Am. Chem. Soc.* **2007**, 129 (46), 14110–14111.
- (28) Zhu, Y.; Hu, J.; Liu, Y. *Eur. Phys. J. E: Soft Matter Biol. Phys.* **2009**, 28 (1), 3–10.
- (29) Yamauchi, K.; Lizotte, J.; Long, T. *Macromolecules* **2003**, 36 (4), 1083–1088.

Role of Vulcanizing Additives on the Segmental Dynamics of Natural Rubber

Marianella Hernández,^{*,†} Tiberio A. Ezquerro,[§] Raquel Verdejo,[†] and Miguel A. López-Manchado^{*,†}

[†]Instituto de Ciencia y Tecnología de Polímeros, ICTP-CSIC, Juan de la Cierva 3, Madrid 28006, Spain

[§]Instituto de Estructura de la Materia, IEM-CSIC, Serrano 119, Madrid 28006, Spain



ABSTRACT: The influence of the addition of vulcanizing additives on the molecular dynamics of unvulcanized natural rubber (NR) has been studied by broadband dielectric spectroscopy. Results reveal a slowdown of the segmental dynamics of NR, restricting the motion of the chains tightly bounded to the additive surfaces. In general, when zinc oxide is present a second dynamic process is detected, ascribed to strong interfacial interactions between the zinc ionic clusters and the NR polymer segments. The study of such interactions prior to vulcanization is a very useful strategy to control the vulcanization process, maximizing its benefits and, hence, improving the final products. Here, we demonstrate that broadband dielectric spectroscopy is a good experimental alternative in order to obtain a deeper insight into the vulcanization mechanisms. Furthermore, our results support one previously proposed sulfur vulcanization mechanism, in which molecules of accelerators, sulfur, and fatty acids are adsorbed on the zinc oxide surface.

INTRODUCTION

Natural rubber (NR) holds a unique place in rubber technology due to its outstanding tack and strength in the unvulcanized state; and high tensile strength and crack growth resistance once vulcanized.¹ For most applications, it is necessary to convert the rubbery linear polymer into a three-dimensional network in order to ensure a complete recovery after deformation. Such a network is the result of cross-linking, covalent bonding among some chain segments, by means of temperature and pressure in which an essentially fluid material is transformed into a fully elastic one. This process is commonly known as vulcanization.¹ The sulfur vulcanization is the traditional method for polydiene rubbers, including NR; however, although sulfur vulcanization is a very old large-scale industrial process, and has been considerably studied over the last several decades, a complete fundamental understanding of this complex chemical process remains a significant scientific challenge. A rigorous research effort continues today to unravel the mechanisms of the individual steps in the sulfur vulcanization process.^{2,3} The difficulties encountered in this research field must be accredited to a combination of diversity and complexity. This process usually involves several chemicals such as a vulcanizing agent (sulfur (S)), an accelerator, and an

activator complex formed by a fatty acid (stearic acid (SA)) and zinc oxide (ZnO). The situation is further complicated by the interaction of the accelerators and activators, each component influencing the reactivity of the other, and the way these interactions affect the vulcanization mechanism.

Plenty of literature^{1,4–9} reveals that the addition of these chemicals in small quantities with respect to raw rubber affects the processability and the final properties of the vulcanized compounds. In general, the use of accelerators in combination with zinc activators has a pronounced effect on the speed of vulcanization and on the distribution of cross-links formed. Besides these, the durability of rubber articles as well as the physical properties, in particular the tensile strength, are very much improved by organic accelerators.

Nonetheless, the authors are struck by the fact that despite the enormous practical knowledge developed so far, a detailed description on how these constituents affect the molecular dynamics and related properties of unvulcanized NR is unknown and has not been reported until now. Moreover,

Received: October 17, 2011

Revised: November 29, 2011

Published: December 20, 2011



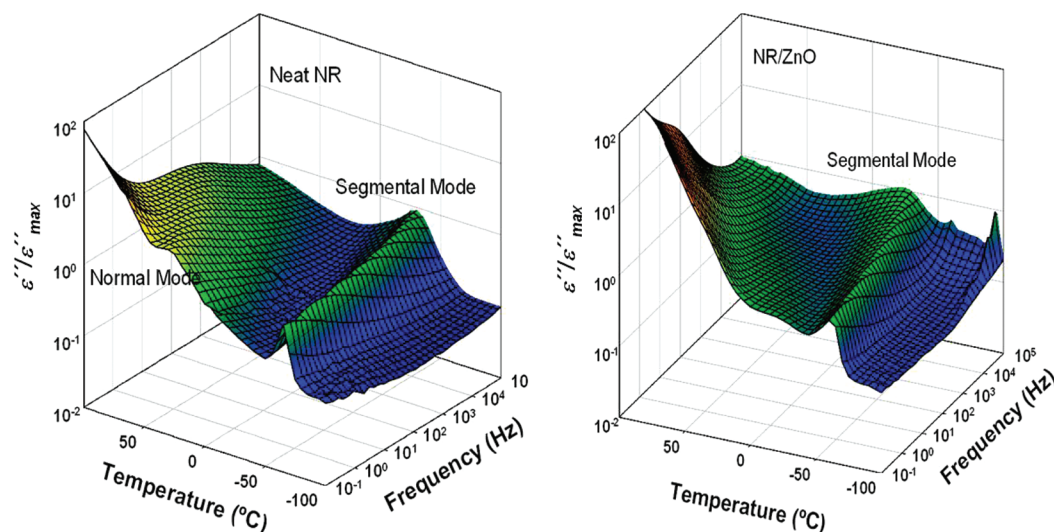


Figure 1. 3D representation of the frequency and temperature dependence of the dielectric loss ϵ'' for neat NR and NR/ZnO compound.

most vulcanization systems have been developed by skillful and elaborated techniques based on the trial-and-error method.¹⁰ So, a detailed discussion on the relationship between molecular dynamics and the effect of each of the additives in the vulcanization system, prior to vulcanization, will be of great interest not only for technological developments but also for academic interests. In this manuscript, we present experimental evidence, using broadband dielectric spectroscopy (BDS),^{11–14} of the changes on the segmental dynamics of NR when every vulcanizing additive has been added, and how the interactions between such additives and NR chains can help to elucidate the reactions involved in the sulfur vulcanization mechanism.

EXPERIMENTAL SECTION

NR used was kindly supplied by Malaysian Rubber (Berhad, Malaysia) under the trade name SMR CV60 (Mooney viscosity: ML(1 + 4) 100 °C = 60). The compound formulation given on the basis of a total of 100 parts of rubber by weight (phr) is as follows: S (2.5 phr), ZnO (5 phr), SA (1 phr), and MBTS (mercapto benzothiazyl disulfide) (1 phr). All compounds were mixed in an open two-roll laboratory mill at room temperature, starting with the mastication of the rubber and then followed by the incorporation of the rest of ingredients. The prepared samples are referred to as NR/*x*/*y*/*z*, where “*x*”, “*y*”, and “*z*” correspond to the additives present in the compound. It should be emphasized that in this study we are dealing with unvulcanized samples.

BDS measurements were performed on an ALPHA high resolution dielectric analyzer (Novocontrol Technologies GmbH, Hundsangen, Germany). The complex dielectric permittivity ($\epsilon^* = \epsilon' - i\epsilon''$) of the NR compounds was measured over a frequency window of $10^{-1} < F/\text{Hz} < 10^7$ ($F = \omega/2\pi$ is the frequency of the applied electric field) in the temperature range from -100 to $+100$ °C in 5 °C steps. Samples of masticated neat NR and NR compounds as disk-shaped films were prepared by compression molding at room temperature. The disk samples were then mounted in the dielectric cell between two parallel gold-plated electrodes. Kapton spacers of 0.074 mm of thickness were used to prevent short circuits.¹⁵ Because of the use of spacers, the measured values have to be considered as relative ones.

RESULTS AND DISCUSSION

Similar to synthetic 1,4-*cis*-poly(isoprene) (PI),^{16–19} two distinct regions of dielectric dispersion are present in NR:¹¹ a low temperature process (the segmental mode) related to the segmental motions of the polymer chain which has its origin in

local motions of the perpendicular dipole moment and a more intense process assigned to the normal mode, which corresponds to motions of the entire chain caused by dipole components parallel to the chain backbone. In this research, we only analyze the segmental mode since the contribution of conductivity and interfacial polarization at low frequencies interfere in the analysis of the normal mode, as it can be seen in Figure 1. In this figure, a 3D representation of the frequency and temperature dependence of the dielectric loss ϵ'' for neat NR and NR/ZnO compound is shown, for comparative purposes.

Figure 2 shows selected dielectric loss ϵ'' spectra at $T = -50$ °C for neat NR and NR/additives compounds measured in the

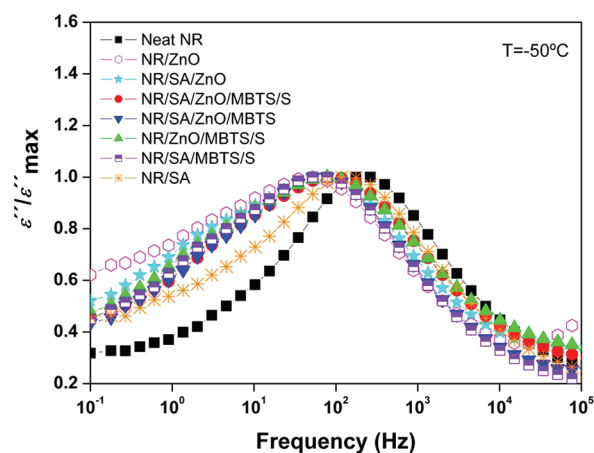


Figure 2. Normalized dielectric loss ϵ'' versus frequency of NR and its compounds in the region of the segmental mode.

available frequency range. From the spectra hereby presented, we can notice that the segmental mode process (α -relaxation) is well resolved in the frequency domain and manifests itself in all systems by a maximum in $\epsilon''(F)$. We can also see that the presence of additives shifts the maximum of the loss peak to slightly lower frequencies, suggesting a restricted dynamics for the NR/additive compounds. For the sake of comparison and in order to avoid the effect of the nonabsolute character of the measured ϵ'' , the data have been normalized to the

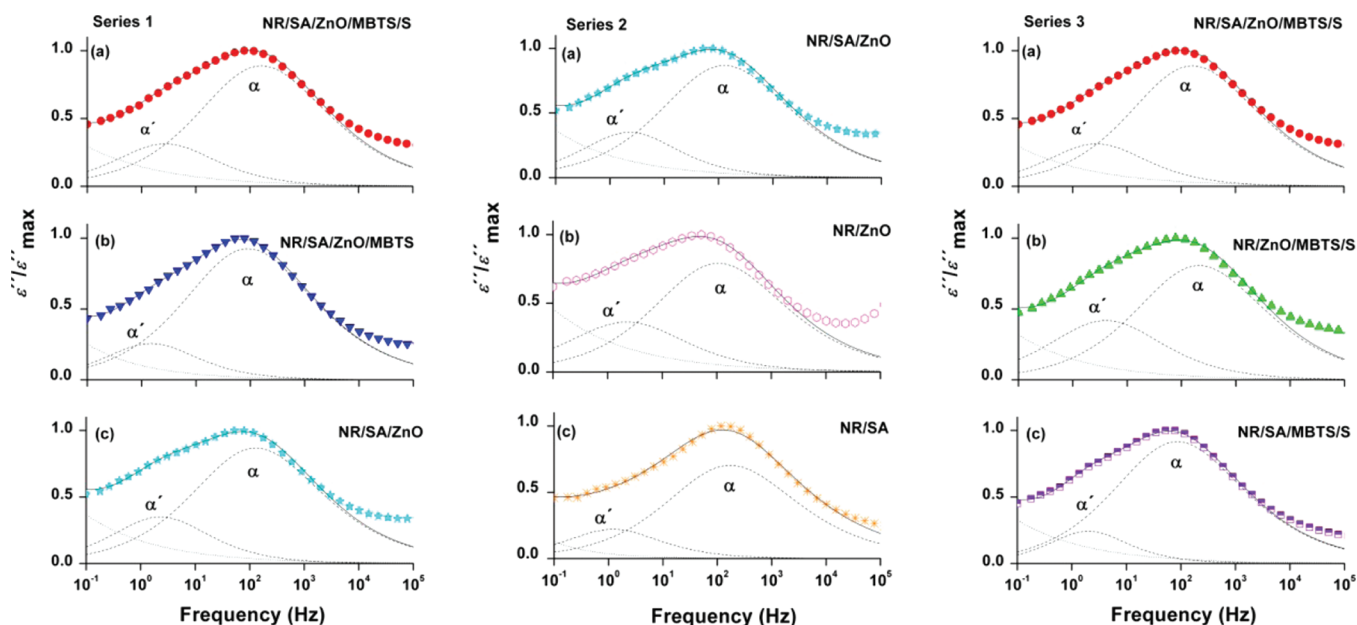


Figure 3. Deconvolution results for the normalized dielectric loss ε'' of NR compounds. Solid lines represent the HN fitting curve, dashed lines the individual processes, and dotted lines the conductivity contribution.

Table 1. Representative Values of the Fitting Parameters of the HN Function for All Tested Compounds at $T = -50\text{ }^{\circ}\text{C}$

compound	$\Delta\varepsilon_{\alpha}$	$\Delta\varepsilon_{\alpha'}$	$\tau_{\text{HN}\alpha}$	$\tau_{\text{HN}\alpha'}$
neat NR	1.431×10^{-1}	—	1.045×10^{-3}	—
NR/ZnO	6.699×10^{-2}	2.763×10^{-2}	2.062×10^{-3}	7.112×10^{-2}
NR/SA/ZnO	6.514×10^{-2}	2.232×10^{-2}	1.599×10^{-3}	6.463×10^{-2}
NR/SA/ZnO/MBTS/S	1.169×10^{-1}	3.211×10^{-2}	1.370×10^{-3}	5.799×10^{-2}
NR/SA/ZnO/MBTS	3.119×10^{-2}	8.782×10^{-3}	2.403×10^{-3}	1.115×10^{-1}
NR/ZnO/MBTS/S	6.355×10^{-2}	2.865×10^{-2}	1.048×10^{-3}	3.900×10^{-2}
NR/SA/MBTS/S	7.785×10^{-2}	1.279×10^{-2}	2.556×10^{-3}	7.941×10^{-2}
NR/SA	4.975×10^{-2}	7.061×10^{-3}	1.328×10^{-3}	1.341×10^{-1}

corresponding $\varepsilon''_{\text{max}}$ of every curve. Here, we can notice a clear asymmetric broadening toward the low-frequency side of the dielectric loss curves.

Such a behavior suggests the existence of a second dynamic process slower but close to the segmental mode of NR appearing when additives are present. In one hand, it is worth to notice that the relaxation behavior of the NR/SA compound is the closest to the neat NR. On the other hand, the rest of the NR/additives compounds present a more pronounced broadening at the low frequency side of the dielectric loss curves.

In order to estimate the contribution of each additive in the relaxation process, every dielectric spectrum was analyzed and the experimental data of ε'' versus frequency was fitted in terms of the phenomenological Havriliak–Negami (HN) function^{20,21} described by

$$\varepsilon^*(\omega) = \varepsilon_{\infty} + \frac{\Delta\varepsilon}{[1 + (i\omega\tau_{\text{HN}})^b]^c} \quad (1)$$

where $\Delta\varepsilon = \varepsilon_s - \varepsilon_{\infty}$, ε_{∞} and ε_s are the unrelaxed and relaxed values of the dielectric constant and b and c are shape parameters ($0 < b, c \leq 1$) describing the symmetric and the asymmetric broadening of the equivalent relaxation time distribution function, respectively. τ_{HN} is the Havriliak–Negami relaxation time, representing the most probable relaxation time of the relaxation time distribution function.²² The HN relaxation time is related to the frequency of maximum loss,

$F_{\text{max}} = 1/(2\pi\tau_{\text{max}})$, by the following equation:²³

$$\tau_{\text{max}} = \frac{1}{2\pi F_{\text{max}}} = \tau_{\text{HN}} \left[\sin \frac{b\pi}{2 + 2c} \right]^{-1/b} \left[\sin \frac{bc\pi}{2 + 2c} \right]^{1/b} \quad (2)$$

Both characteristic relaxation times coincide when the relaxation spectrum is symmetric, $c = 1$.

The dielectric loss data were fitted by the superposition of two HN relaxation processes (named α' and α in order of increasing frequency) corresponding to each one of the experimentally determined relaxations, plus a conductivity contribution (Figure 3).

The relaxation parameters ($\Delta\varepsilon$, b , c , and τ_{HN}) representative of each fitting were calculated (Table 1). This fitting protocol was chosen in order to ensure physical coherence. In a first approach, we assumed that the main relaxation process (α) was not significantly affected by the additives. Accordingly, we have considered a similar shape than that of the α -relaxation of neat NR. Thus, the shape parameters b and c were kept constant and similar to those obtained for neat NR ($b = 0.527$; $c = 0.833$). While for the α' -relaxation, the parameter c was set to a value of 1 in order to force a symmetric shape and thus, a narrower distribution of relaxation times. Considering asymmetric shape for the α' process rendered no reasonable fitting for the overall

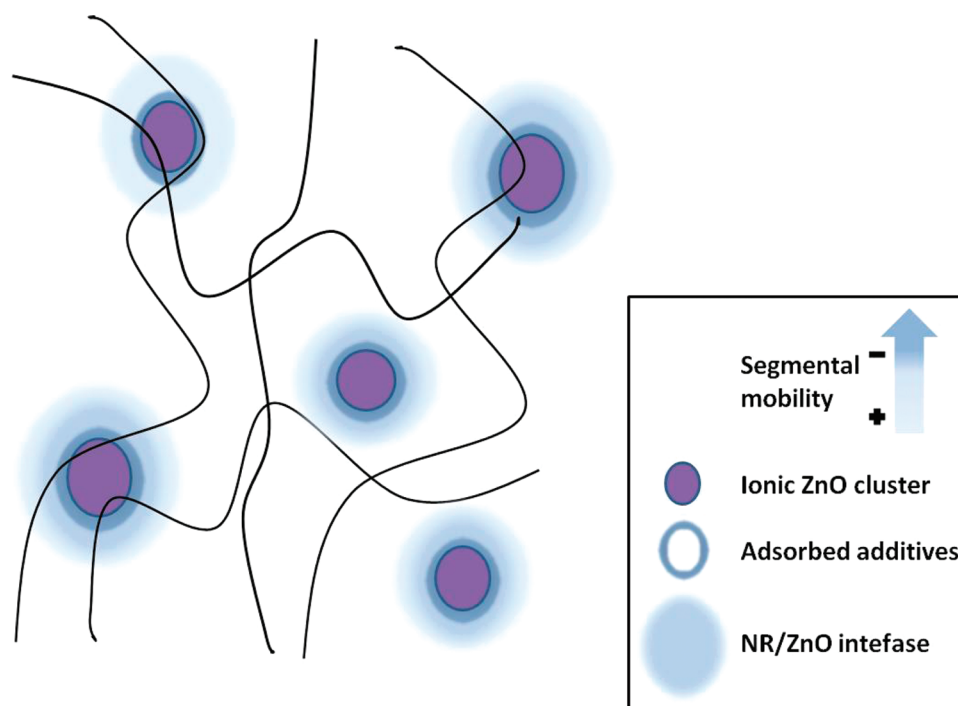


Figure 4. Proposed schematic representation of morphological structure of NR/additives compound.

process. As expected, the strength relaxation intensity ($\Delta\epsilon$) is higher for the α -relaxation than for the α' -relaxation for all compounds.

The dielectric loss spectra of the NR compounds have been grouped in Figure 3 as three different series, in order to analyze separately the effect of each of the additives on both relaxations (α and α'). With series 1 we intend to study the effect of sulfur (S) and accelerator (MBTS), while series 2 and series 3 results serve to elucidate the effect of the activator complex (SA/ZnO) with and without other additives present. Some of the figures shown in the series are duplicated for the sake of clarity and better understanding of the systematic removal of the different vulcanizing additives.

From Figure 3 series 1 results, we can infer that sulfur (S) and accelerator (MBTS) are not likely to be responsible for the appearance of the slower process represented by α' . In this case, we can clearly see that after removing MBTS and S from the compound (series 1c), the shoulder at low frequencies is still present.

Next, we evaluate the effect of the activator complex (SA/ZnO) (Figure 3 series 2). Several authors^{6,24–26} have studied the influence of the activator complex on the cross-linking reaction of NR. Recently, Ikeda et al.⁵ have proposed that the combination of ZnO with the other reagents is crucial to control the quality of the vulcanization. Here we corroborate by BDS that ZnO is the element with the strongest effect on the segmental dynamics of NR. In this sense, the low frequency shoulder characterized by α' appears when the complex, SA/ZnO, is present (Figure 3 series 2a). However, the elimination of SA from the formulation leaves α' almost unaffected (Figure 3 series 2b). The origin of this slow relaxation in NR has been discussed in the literature. In a previous study, Ortiz-Serna et al.²⁷ attributed this slower relaxation to the dynamics of SA linked to the polymer chains. Our measurements indicate that this slower relaxation is mainly attributed to the presence of ZnO.

The influence of ZnO on the dielectric behavior of polymer matrices has been discussed. Psarras et al.^{28,29} found an additional relaxation mode related to the presence of ZnO in epoxy resin–ZnO composites, in the same frequency and temperature range as the α -relaxation, leading to a mutual superposition. They attributed this behavior to polarization effects taking place in parts of the ZnO, which are relaxing under the influence of the AC electric field. Also, Smaoui et al.³⁰ found that the presence of ZnO in epoxy nanocomposites increases the interactions at the interface, so decreasing the orientation capabilities of dipoles under the effect of an AC electric field.

ZnO is known as the best activator for sulfur vulcanization. There is nowadays, however, an increasing concern regarding the potential environmental and health effects of releasing zinc compounds into the environment from rubber products or rubber production.³¹ Thus, it is desirable to keep the ZnO content in rubber compounds as low as possible, not only for environmental but also for economical reasons. Nonetheless, the exact role of ZnO on the network structure has not been well understood. Several theories have been postulated, and the complexity of the vulcanization process has given rise to many uncertainties and contradictions in the literature about the influence of ZnO during the different stages of the process and its exact mechanisms.^{2,3,32} One of the proposed mechanisms^{2,7,33} suggest that ZnO plays the role of a catalyst and promotes the initial response by activating and bringing together reactants. It is assumed that ZnO is distributed in the form of crystal particles in the rubber compounds. Molecules of accelerators, sulfur, and fatty acid are adsorbed on the surface of the ZnO, forming intermediate complexes (benzothiazole–zinc complex). The reactant of the benzothiazole–zinc complex does not have appreciable solubility in rubber, but the solubility and reactivity can be enhanced by the presence of SA, forming zinc stearate.^{5,25} Some authors⁴ suggest that the ionic nature of zinc stearate is responsible for

the appearance of a second relaxation process in vulcanized NR, which may be attributed to rubber chains of lower mobility tightly bounded to zinc stearate surface. It is known that in the case of ion-containing polymers, ion pairs segregate to form ion aggregates, which restrict the mobility of adjacent segments of the polymer chains and form a separate rigid phase.^{34,35} These immobile segments of the rubber chains undergo relaxation at lower frequencies. In other words, this means that, there are some restrictions on the molecular dynamics of this process limiting the motion of NR chains in their surrounding environment. Thus, these BDS results are strong evidence of the activator effect that ZnO has on the vulcanization process of NR, since the α' -relaxation could be attributed to the ionic clusters of ZnO that could form initial physical entanglements within the rubber chains, acting as cross-link precursors, as schematically represented in Figure 4. Results from Figure 3 series 3 confirm that the absence of ZnO in the formulation gives an α' -relaxation of very low intensity.

In Figure 5, we present an intensity relation chart between the dielectric strength values of both relaxation processes

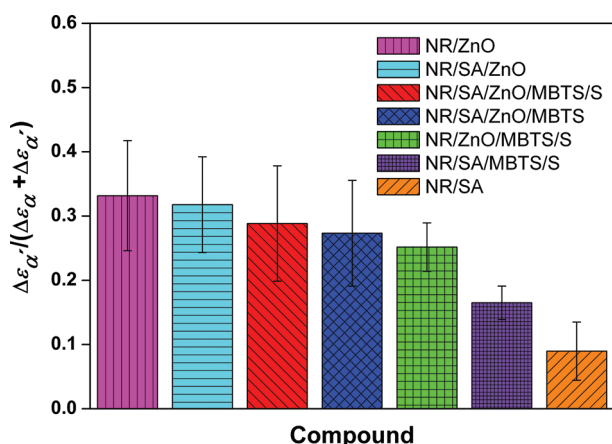


Figure 5. Dielectric strength intensity relation of the α - and α' -relaxations of NR compounds. Bars correspond to average values representative of different possible HN fittings.

applying different fitting protocols in order to establish the merits of our previous fitting assumptions. It should be noted that the error bars presented in the graph do not correspond to the experimental error but arise from the spread of the fitting parameters applied. It is clear that the origin of the slower process present in the NR compounds is directly associated with the presence of the different additives. However, two interesting results can be extracted from the analysis of this chart. First of all, the NR/SA compound has the lower intensity relation value, so we can presume that the contribution of the SA to the α' -relaxation is insignificant. This fact is in agreement with the results shown in Figure 2, where, as previously mentioned, there is certain similarity between the normalized loss curves of neat NR and NR/SA compound.

The second interesting result extracted from Figure 5 is the higher intensity relation value obtained for all compounds where ZnO is present. Thus, it clearly implies that the origin of the slower process present in the NR compounds is directly associated with the presence of ZnO.

CONCLUSIONS

In summary, we have made an experimental study of the influence of the addition of vulcanizing components on the molecular dynamics of NR. Our results reveal a slowdown of the segmental dynamics of NR restricting the motion of rubber chains tightly bounded to additive surfaces. In general, when ZnO is present a visible second dynamic process is detected. Systematic removal of the different vulcanizing additives leads us to ascribe this slow process to strong interfacial interactions formed at the interfaces between the ZnO ionic clusters and the NR polymer segments, forming initial physical entanglements between both components, which may act as cross-linking precursors. We believe that these results can help to understand basic issues related to the network structure and molecular mobility of NR, essentials for the optimization of the vulcanization process, the role of additives and their interactions with the NR matrix. Moreover, the better understanding of the role of ZnO in the vulcanization reaction is a key issue for the ongoing efforts to reduce zinc content of vulcanization mixtures without reducing the overall quality of the products.

AUTHOR INFORMATION

Corresponding Author

*E-mail: (M.H.) marherna@ictp.csic.es; (M.A.L.-M.) lmachado@ictp.csic.es.

ACKNOWLEDGMENTS

The authors gratefully acknowledge the financial support of the MCINN (Grants MAT2009-07789 and MAT2010-18749). M.H. thanks the Venezuelan Ministry of Science and Technology for the concession of a "Mision Ciencia" grant.

REFERENCES

- (1) Brydson, J. A. *Rubbery Materials and Their Compounds*; Elsevier Science Publishers Ltd.: London, 1988; p 469.
- (2) Heideman, G.; Datta, R. N.; Noordermeer, J. W. M.; Van Baarle, B. *Rubber Chem. Technol.* **2004**, 77 (3), 512–541.
- (3) Steudel, R.; Steudel, Y. *Chem.—Eur. J.* **2006**, 12 (33), 8589–8602.
- (4) Ward, A. A.; El-Sabbagh, S.; El-Aal, N. S. A. *KGK-Kautsch. Gummi Kunstst.* **2008**, 61 (9), 429–437.
- (5) Ikeda, Y.; Higashitani, N.; Hijikata, K.; Kokubo, Y.; Morita, Y.; Shibayama, M.; Osaka, N.; Suzuki, T.; Endo, H.; Kohjiya, S. *Macromolecules* **2009**, 42 (7), 2741–2748.
- (6) Poh, B. T.; Tang, W. L. *J. Appl. Polym. Sci.* **1995**, 55 (3), 537–542.
- (7) Kim, I. J.; Kim, W. S.; Lee, D. H.; Kim, W.; Bae, J. W. *J. Appl. Polym. Sci.* **2010**, 117 (3), 1535–1543.
- (8) Cavdar, S.; Ozdemir, T.; Usanmaz, A. *Plast. Rubber Compos.* **2010**, 39 (6), 277–282.
- (9) Kohjiya, S.; Tosaka, M.; Masahiro, F.; Ikeda, Y.; Toki, S.; Hsiao, B. S. *Polymer* **2007**, 48, 3801–3808.
- (10) Hofmann, W. *Vulcanization and Vulcanizing Agents*. Maclaren: 1967; p 371.
- (11) Hernandez, M.; Carretero-Gonzalez, J.; Verdejo, R.; Ezquerra, T. A.; Lopez-Manchado, M. A. *Macromolecules* **2010**, 43 (2), 643–651.
- (12) Carretero-Gonzalez, J.; Ezquerra, T. A.; Amnuaypornsi, S.; Toki, S.; Verdejo, R.; Sanz, A.; Sakdapipanch, J.; Hsiao, B. S.; Lopez-Manchado, M. A. *Soft Matter* **2010**, 6 (15), 3636–3642.
- (13) Boese, D.; Kremer, F. *Macromolecules* **1990**, 23 (3), 829–835.
- (14) Hernandez, M.; Lopez-Manchado, M.; Sanz, A.; Nogales, A.; Ezquerra, T. A. *Macromolecules* **2011**.
- (15) Sics, I.; Ezquerra, T. A.; Nogales, A.; Balta-Calleja, F. J.; Kalnins, M.; Tupureina, V. *Biomacromolecules* **2001**, 2 (2), 581–587.

- (16) Mijovic, J.; Lee, H. K.; Kenny, J.; Mays, J. *Macromolecules* **2006**, *39* (6), 2172–2182.
- (17) Boese, D.; Kremer, F. *Macromolecules* **1990**, *23* (3), 829–835.
- (18) Boese, D.; Kremer, F.; Fetters, L. J. *Macromolecules* **1990**, *23* (6), 1826–1830.
- (19) Page, K. A.; Adachi, K. *Polymer* **2006**, *47* (18), 6406–6413.
- (20) Havriliak, S.; Negami, S. *Polymer* **1967**, *8* (4), 161–210.
- (21) Kremer, F.; Schönhals, A. *Broadband Dielectric Spectroscopy*; Springer: New York, 2003; p 721.
- (22) Böttcher, C. J. F.; Bordewijk, P., *Theory of Electric Polarization*; Elsevier: 1978; Vol. II.
- (23) Richert, R.; Angell, C. A. *J. Chem. Phys.* **1998**, *108* (21), 9016–9026.
- (24) Allan, J. R.; Geddes, W. C.; Hindle, C. S.; Lowe, A. J. *Plast. Rubber Compos. Process. Appl.* **1991**, *16* (2), 91–94.
- (25) Zhao, F.; Zhang, P.; Zhao, S. G.; Yu, J.; Kuhn, W. *KGK, Kautsch. Gummi Kunstst.* **2008**, *61* (5), 224–229.
- (26) Helaly, F. M.; El Sabbagh, S. H.; El Kinawy, O. S.; El Sawy, S. M. *Mater. Des.* **2011**, *32* (5), 2835–2843.
- (27) Ortiz-Serna, P.; Diaz-Calleja, R.; Sanchis, M. J.; Floudas, G.; Nunes, R. C.; Martins, A. F.; Visconte, L. L. *Macromolecules* **2010**, *43* (11), 5094–5102.
- (28) Soultzidis, A.; Kontos, G.; Karahaliou, P.; Psarras, G. C.; Georga, S. N.; Krontiras, C. A. *J. Polym. Sci., Part B: Polym. Phys.* **2009**, *47* (4), 445–454.
- (29) Ioannou, G.; Patsidis, A.; Psarras, G. C. *Compos./Part A: Appl. Sci. Manuf.* **2011**, *42* (1), 104–110.
- (30) Smaoui, H.; Mir, L. E. L.; Guermazi, H.; Agnel, S.; Toureille, A. *J. Alloys Compd.* **2009**, *477* (1–2), 316–321.
- (31) Chapman, A. V. *Safe Rubber Chemicals: Reduction of Zinc Levels in Rubber Compounds*; TARRC/MRPRA: Brickendonbury, Hertford, UK, 1997.
- (32) Heideman, G.; Datta, R. N.; Noordermeer, J. W. M.; van Baarle, B. *J. Appl. Polym. Sci.* **2005**, *95* (6), 1388–1404.
- (33) Nieuwenhuizen, P. J.; Timal, S.; Van Veen, J. M.; Haasnoot, J. G.; Reedijk, J. *Rubber Chem. Technol.* **1998**, *71* (4), 750–765.
- (34) Antony, P.; Bandyopadhyay, S.; De, S. K. *Polym. Eng. Sci.* **1999**, *39* (5), 963–974.
- (35) Hird, B.; Eisenberg, A. *Macromolecules* **1992**, *25* (24), 6466–6474.

New Correlations in Polymer Blend Miscibility

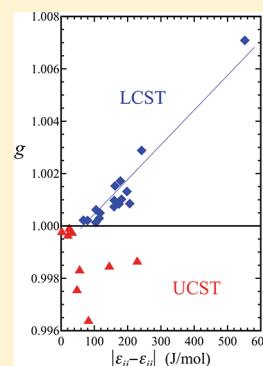
Ronald P. White and Jane E. G. Lipson*

Department of Chemistry, Dartmouth College, Hanover, New Hampshire 03755, United States

Julia S. Higgins

Department of Chemical Engineering and Chemical Technology, Imperial College, London SW7 2AZ, U.K.

ABSTRACT: We present new correlations revealed by our study of polymer mixture miscibility. Applying our simple lattice-based equation of state, we search for patterns in a large sample of experimental blends and uncover some intriguing relationships. One such correlation connects the value of the difference in pure component energetic parameters with that of the mixed segment interactions, suggesting new possibilities for predictive modeling that would require only pure component data. Our work reveals different patterns for UCST-type and LCST-type blends which we connect with physical underpinnings reflected in the microscopic parameters. Throughout we emphasize the importance of modeling protocol, most notably, the importance of carefully and consistently applying a fitting procedure to the same temperature range for the two pure components. The reasons for this are demonstrated and discussed in terms of a careful analysis of the model behavior which includes a look at the sensitivity to pure component fitting. We provide details (applicable to other equations of state as well) on the methodology needed in order to obtain the most robust and consistent results.



I. INTRODUCTION

The history of experimental and theoretical work on polymer blends dates back over a relatively small number of decades, but during this time perceptions of miscibility have undergone several shifts. In earlier literature one finds reference to expectations that, in general, polymer mixtures would be immiscible or that they would exhibit phase separation only upon lowering of temperature (yielding an upper critical solution temperature, or UCST). Subsequently, it has become apparent that many experimental examples can be found of partially miscible blends of both UCST and LCST type, the latter becoming immiscible upon an increase in temperature (thus having a lower critical solution temperature, or LCST).

On the theoretical front there have been numerous developments as well. Some important examples include equation of state approaches for pure polymer fluids, solutions, and blends.^{1–14} Among the equation of state theories capable of describing the range of miscibility behavior, we have focused on a simple analytic lattice-based model (developed by one of us) which we have successfully applied to a range of blend problems including such effects as pressure, molecular weight, and recently an investigation of the effect of deuteration on miscibility.^{15–20}

Over the course of many studies we have collected and analyzed data on many blends, solutions, and melts. As our applications of the model have broadened, we have increasingly stretched the abilities of the theory toward the goal of being predictive. The main thrust of this paper is now to explore the correlations between mixture energetics and blend behavior that have been both revealed and strengthened as our database of mixtures has increased. An additional goal of the paper is to share in detail our analysis of the full library of blends studied.

This collection numbers 25 blends, including both UCST and LCST mixtures, and we hope that making our results available may save other investigators a significant amount of analysis as well as spur interest in the abilities of our model.

The remainder of the paper is organized as follows. In section II we give a brief theoretical background describing the equation of state and its associated microscopic parameters, along with some of the important aspects of the implementation. In section III, we present an initial analysis of some of the tabulated results, including an examination of the effect of the fitted data range on the best fit parameters, and suggestions on how to obtain a consistent and meaningful parametrization. The key patterns and correlations observed in the model blend parametrizations are discussed in section IV, and we then conclude in section V.

II. THEORETICAL BACKGROUND AND IMPLEMENTATION

In this section we describe the equation of state that is used here to model polymeric melts and blends. It is based on a lattice model designed for chain molecule fluids and mixtures. The theory accounts for both the effects of compressibility and nonrandom mixing, thereby moving several steps beyond Flory–Huggins theory.²¹ The derivations, described in detail elsewhere,^{15,16,22,23} follow an integral equation formalism in which site–site (pair) probabilities are calculated for all possible neighboring pairs of segments in the chain fluid. These temperature-dependent probabilities are used to calculate the

Received: October 26, 2011

Revised: December 15, 2011

Published: January 5, 2012



system's internal energy, which can be integrated over temperature (starting from an athermal reference state) to give a closed-form expression for the Helmholtz free energy (A), thereby leading to all of the other thermodynamic quantities.

The analytic result for A is shown in eq 1 for the case of a binary mixture comprised of components i and j

$$\begin{aligned} \frac{A}{k_B T} = & N_i \ln \phi_i + N_j \ln \phi_j + N_h \ln \phi_h \\ & + \frac{N_i q_i z}{2} \ln \left(\frac{\xi_i}{\phi_i} \right) + \frac{N_j q_j z}{2} \ln \left(\frac{\xi_j}{\phi_j} \right) + \frac{N_h z}{2} \ln \left(\frac{\xi_h}{\phi_h} \right) \\ & - \frac{N_i q_i z}{2} \ln \left[\xi_i \exp \left(\frac{-\varepsilon_{ii}}{k_B T} \right) + \xi_j \exp \left(\frac{-\varepsilon_{ij}}{k_B T} \right) + \xi_h \right] \\ & - \frac{N_j q_j z}{2} \ln \left[\xi_i \exp \left(\frac{-\varepsilon_{ij}}{k_B T} \right) + \xi_j \exp \left(\frac{-\varepsilon_{jj}}{k_B T} \right) + \xi_h \right] \end{aligned} \quad (1)$$

with definitions

$$N_h = (V/v) - N_i r_i - N_j r_j$$

$$\phi_\alpha = N_\alpha r_\alpha v / V$$

$$\xi_\alpha = N_\alpha q_\alpha / (N_i q_i + N_j q_j + N_h)$$

$$q_\alpha z = r_\alpha z - 2r_\alpha + 2$$

where α can be i, j , or h , and $q_h = r_h = 1$. In eq 1, A is expressed as a function of independent variables N_i, N_j, V , and T which are respectively the numbers of molecules of components i and j , the total volume, and the absolute temperature. z is the lattice coordination number which is fixed at a value of 6,²⁴ and k_B is the Boltzmann constant. The key microscopic lattice parameters are v , the volume per lattice site, r_i (r_j), the number of segments per chain molecule of component i (j), ε_{ii} (ε_{jj}), the pure component nonbonded segment–segment interaction energy between near-neighbor segments of types i – i (j – j), and g , which defines the mixed interaction energy according to $\varepsilon_{ij} = g(\varepsilon_{ii}\varepsilon_{jj})^{1/2}$. (g characterizes ε_{ij} relative to the geometric mean value.) As mentioned above, the model is compressible, so the total volume, V , is comprised of filled and empty lattice sites. Therefore, N_h is the total number of vacant sites (h stands for “holes”); this value increases with V for any given N_i, N_j . The remaining definitions in eq 1 are as follows: ϕ_α is the volume fraction of sites of type α ($\alpha \in \{i, j, h\}$), and ξ_α is a concentration variable defining the fraction of nonbonded contacts ascribed to component α out of the total number of nonbonded contacts in the fluid, where, due to its bonded connections, a chain molecule has $q_\alpha z$ nonbonded contacts.

We now briefly summarize some of the more important points regarding the implementation of the theory. As mentioned above, the expression for the Helmholtz free energy, A (eq 1), leads to all of the other thermodynamic properties. Though explicit expressions will not be listed here, the pressure ($P = -(\partial A / \partial V)_{N_i, N_j, T}$), Gibbs free energy ($G = A + PV$), and the chemical potentials ($\mu_i = (\partial A / \partial N_i)_{N_j, V, T}$) can all be obtained by straightforward differentiation of $A[N_i, N_j, V, T]$. As with many theoretical equations of state, note that while P is expressed as a function of V , V cannot be directly expressed as a function of P , and thus numerical root finding is commonly used to obtain V and other properties for cases where P is the

known (input) variable. Note that it is often convenient to work entirely in terms of intensive variables by defining $N = N_i + N_j$, and $x_i = x = N_i / (N_i + N_j)$, and thus switching from the four independent variables [N_i, N_j, V, T] in eq 1 down to three, where (A/N) , P , (G/N) , μ_i , etc., are all expressed as a function of [$x, (V/N), T$].

Important characterizations arising in blend modeling include the conditions for phase equilibrium, which are commonly posed for the case of two phases, I and II, at a given T and given P (e.g., 1 atm). Because we are working with functions of [$x, (V/N), T$] and not [x, P, T], this leads to four equations, $\mu_i^I = \mu_i^{II}$, $\mu_j^I = \mu_j^{II}$, $P^I = 1$ atm, and $P^{II} = 1$ atm (all for some given T), which can then be solved for the four unknowns, $x^I, x^{II}, (V/N)^I$, and $(V/N)^{II}$. The compositions in each phase (x^I, x^{II}) obtained over a range of T thus provide the information necessary to map out the theoretical phase diagram. Another important phase boundary, the spinodal, marks the metastability limit. This is described by two equations: $(\partial^2(G/N) / \partial x^2)_{T,P} = 0$ and $P = 1$ atm, which can be solved for the two unknowns, x and (V/N) , thus giving a spinodal point for a given T . The critical point is found by solving the three equations, $(\partial^3(G/N) / \partial x^3)_{T,P} = 0$, $(\partial^2(G/N) / \partial x^2)_{T,P} = 0$, and $P = 1$ atm, for the three unknowns T , x , and (V/N) , these thus being, the critical temperature (UCST or LCST), critical composition, and critical volume.

In order to model a blend, one needs to obtain a full set of characteristic parameters. We focus first on the parameters that characterize the pure components, keeping in mind that the ultimate goal is to model a mixture. The one remaining parameter, g , that characterizes the mixture is discussed further below.

The five parameters $r_i, r_j, v, \varepsilon_{ii}$, and ε_{jj} are most commonly obtained by fitting the model pure component equation of state to experimental pressure–volume–temperature (PVT) data.²⁵ For each pure component, there will thus be a resulting set of optimal values, $r_i^{\text{pure}}, v^{\text{pure}}$, and $\varepsilon_{ii}^{\text{pure}}$. Note, however, that, while each component has its own optimal value for v , we use a single v to model the mixture. (Often we take a compromise value, such as the average of the two optimal pure component v values.) To compensate for the change in v , we then rescale the r value in a way that keeps the hard-core volume of a molecule the same. In other words, the r value that is used in the mixture, r_i , is given by $r_i = (r_i^{\text{pure}} v_i^{\text{pure}}) / v$, where v is the value chosen for modeling the mixture, and r_i^{pure} and v_i^{pure} were the optimal values obtained from the original pure component fitting. (The ε parameter remains the same on going from pure melt to mixture, $\varepsilon_{ii} = \varepsilon_{ii}^{\text{pure}}$.) It is also common to scale r in order to account for changes in component molecular weights (M), where for any particular v , $r_i = M_i(r_i^{\text{old}} / M_i^{\text{old}})$, where r_i^{old} and M_i^{old} are the original values. Altogether, these scalings follow $rv/M = \text{constant}$. This constant, along with ε , are the two key pieces of information obtained from the pure component fitting and will be discussed further below.

Changing from the component's optimal v to a compromise value used for the blend means that some of the agreement with the corresponding pure component physical properties will be sacrificed. However, scaling the r value as described above preserves agreement at low pressure. This follows from the fact that (over a very wide range of r, v) the $V(T)$ curve at zero pressure depends only on ε , and on the product rv , not on r and v separately. Conversely, it follows that fitting only to zero pressure data will produce a unique value for ε and a unique value for rv , but not r and v . In view of the fact that the v value

is changed on going to the model blend, the above observations have led us to believe that it is important in our fitting to weight for best agreement with low-pressure data because this is the agreement that is still guaranteed to be preserved following the above simple scaling at fixed hard-core molecular volume. Furthermore, the relevant experimental predictions and comparisons for the blend are most often for the low-pressure behavior anyway.

The fitting protocol is as follows. The model equation of state is first fit to only the zero pressure $V(T)$ (or lowest single P available), and from this, optimal values for ε and the product rv are determined. This fit can be done, for example, by allowing the ε and the r to vary (ε and r are optimized) while holding the v value fixed at any typical value (e.g., 8, 9, 10 mL/mol, etc.); the optimal r multiplied by this v will give the characteristic optimal value for the product rv , which, as noted above, is the relevant/unique result (because this same rv (and ε) would have been obtained if we had chosen to optimize at some other fixed v). Then, in a second stage of fitting, we obtain separate optimal values for r and v by fitting against the full set of PVT data (incorporating higher pressures, say, up to about 100 MPa). Here, we fix ε and the product rv at the values determined from the above low- P fit and perform a one-parameter optimization, for example, optimizing v (i.e., viewing v as the free parameter) with r always being the corresponding value from the fixed rv .

Note that by using the procedure outlined here, the pure component ε values are not influenced by higher pressure data. If both blend components are fit this way, the two ε values in the blend will be the most comparable, one relative to the other. If higher pressure data were allowed to influence the ε value, then there would be the potential for inconsistency in the fit depending, for example, on how much high-pressure data were incorporated, and further, as stressed above, the blend parameters would not necessarily map back to good agreement with the corresponding low-pressure pure component behavior (or, possibly even worse, perhaps one component would, but not the other). We argue below that consistency in how the pure components are fit is absolutely crucial to obtaining results that are predictive. In addition, since most experimental blend data are collected at atmospheric pressure, optimizing in this range makes sense.

Moving to the mixed interaction parameter, g , we note first that there is in general no way to determine its value (and thus the value of ε_{ij}) *a priori* using only pure component data. To obtain g , we require at least a single datum point on the mixture, such as a critical temperature (UCST or LCST). With the first five parameters (r_v , r_p , v , ε_{iv} , ε_{ij}) from the pure component fitting held fixed, the g parameter is then tuned (fit) to a value that brings the theoretical critical solution temperature into agreement with that found from experiment. The fact that g cannot be obtained *a priori* brings this quantity to the forefront. The situation is analogous for other theories, which means that this is an outstanding issue in mixture modeling. A main focus in this article will be to study the trends in this mixture parameter as it relates to the other pure component parameters (the ones which are determined without requiring data on the mixture).

III. ANALYSIS

As mentioned in the Introduction, a goal of the present work is to explore the patterns and correlations that have arisen in modeling pure component and mixture energetics for the present theory applied to a sizable collection of blend systems. These

blends systems cover 23 different polymer species, and for convenience all polymer acronyms have been listed in Table 1 along with corresponding experimental references for PVT data.

Table 1. Table of Polymer Acronyms^a

acronym	full name	ref PVT data
PS	polystyrene	26 ^b
dPS	deuterated polystyrene	20, 27 ^c
PB	polybutadiene	26 ^d
PE	polyethylene	28
PIB	polyisobutylene	28
PEP	poly(ethylene-co-propylene) alternating copolymer	28
hhPP	head-to-head polypropylene	28
PP	head-to-tail polypropylene	28
PMS	poly(α -methylstyrene)	29
PI	polyisoprene	30
PMPS	poly(methylphenylsiloxane)	31 ^e
PMMA	poly(methyl methacrylate)	26 ^f
iPMMA	isotactic poly(methyl methacrylate)	32
PMA	poly(methyl acrylate)	26
PEA	poly(ethyl acrylate)	26
PEMA	poly(ethyl methacrylate)	26
PCHMA	poly(cyclohexyl methacrylate)	32
PVME	poly(vinyl methyl ether)	33
PEO	poly(ethylene oxide)	26
PES	poly(ether sulfone)	26
TMPC	tetramethyl bisphenol A polycarbonate	34
PECH	polyepichlorohydrin	1
PVC	poly(vinyl chloride)	26

^aThe table contains the acronyms used in this article and the corresponding full polymer names. The column on the right contains the corresponding experimental references for PVT data which were used to obtain pure component parameters for each species. ^bSeparate parametrizations were performed for three different molecular weights, $M = 110\,000$, 9000 , and 910 g/mol. ^cSANS data in ref 27 for the dPS/PVME blend were used to obtain pure component parameters for dPS, which were then used to predict PVT data in ref 20. ^dSeparate parametrizations were performed for $M = 233\,000$ and 3000 g/mol. ^ePVT data for the PS/PMPS blend were used to obtain pure component parameters for PMPS. ^fSeparate parametrizations were performed for $M = 100\,000$ and $10\,000$ g/mol.

Twenty-five blend systems have been studied. We divide them into two categories based on the nature of their partial miscibility behavior: those which are miscible at high T and phase separate on cooling (exhibiting an upper critical solution temperature, UCST) and those which are miscible at low T and phase separate on heating (exhibiting a lower critical solution temperature, LCST). As outlined above, for most of these systems we have first obtained the pure component parameters by fitting to pure component PVT data and then obtained the mixed interaction energy (as characterized by the parameter g) by fitting to a single datum point for the blend, viz., its critical temperature (UCST or LCST). All of the characteristic parameters along with other experimental information on these blends are listed in Tables 2 and 3 for UCST-type and LCST-type blends, respectively. (Further detailed information related to the fitting of the corresponding pure components is available in Table 4 and in the Appendix.)

One general observation across the set of experimental blends is that, very commonly, UCST-type blends have low

Table 2. UCST-Type Blends

blend: <i>i/j</i>	ref ^a	M_i/M_j^b (g/mol)	UCST (K)	r_i/r_j	v (mL/mol)	$-\epsilon_{ii}/-\epsilon_{jj}$ (J/mol)	$ \epsilon_{ii} - \epsilon_{jj} $ (J/mol)	<i>g</i>
PS/PB	35	1344/2585	360	151.31/335.42	8.0000	2042.5/1960.3	82.2	0.996415
PS/PMPS	36	6324/1977	391	693.73/208.98	8.0000	2104.1/2056.4	47.7	0.997590
PS/PMMA	29	9200/4250	522	1124.8/450.46	7.2538	2200.7/2145.1	55.6	0.998350
PB/PMS	37	3600/5300	464	414.76/482.93	9.2713	2187.1/2331.7	144.6	0.998493
PS/PI	36	2286/2802	391	233.22/315.59	8.8280	2042.5/1813.7	228.8	0.998684
PEP/PE	38	29450/23560	421	3281.6/2624.3	9.8121	2032.9/2012.5	20.4	0.999678
PEP/aPP ^c	39, 40	58000/58700	>300	5701.9/5862.5	11.122	2032.9/2065.9	33.0	0.999781
PS/PMS	37	49000/56400	469	4561.3/4973.9	9.6573	2405.1/2403.4	1.7	0.999809
PEP/hhPP	40	59850/171780	340	6343.0/17771	10.317	2032.9/2057.5	24.6	0.999943

^aThe column lists the experimental references for the blend. Experimental references for the corresponding pure component PVT data used to obtain the pure component parameters are given in Table 1 and in the pure component fitting information in Table 4. ^bMolecular weights (*M*) are given as weight-averaged molecular weights (M_w). ^cThe *g* value is the average obtained ($0.999646 < g < 0.999916$) from experimental bounds on miscibility reported for miscible and immiscible systems given in refs 39 and 40.

Table 3. LCST-Type Blends

blend: <i>i/j</i>	ref ^a	M_i/M_j^b (g/mol)	LCST (K)	r_i/r_j	v (mL/mol)	$-\epsilon_{ii}/-\epsilon_{jj}$ (J/mol)	$ \epsilon_{ii} - \epsilon_{jj} $ (J/mol)	<i>g</i>
iPMMA/PVC	41	17500/75000	435	2238.2/8211.6	5.9481	2156.9/2053.0	103.9	1.000139
PECH/PCHMA	42	555000/492000	430	46725/49725	8.0827	2128.3/2048.9	79.4	1.000216
PEO/PMA	43	300000/576000	448	42140/75398	5.7447	1880.5/1947.4	66.9	1.000219
PMMA/PVC	44	60000/55000	461	7755.7/6021.9	5.9481	2167.1/2053.0	114.1	1.000364
PS/PCHMA	36	255300/143640	522	23380/12309	9.7368	2334.6/2218.0	116.6	1.000434
PECH/PMA	43	555000/576000	523	55755/64498	6.7155	2052.0/1947.4	104.6	1.000625
PS/TMPC	45	300000/40000	521	27733/3384.0	9.7248	2405.1/2246.0	159.1	1.000741
PMMA/PMS	46	4250/6700	438	11136/21578	7.8863	2221.0/2394.6	173.7	1.000838
PIB/PEP	47	38600/59900	313	3925.6/6460.6	10.137	2239.1/2032.9	206.1	1.000860
dPS/PVME ^c	48	119000/99000	439	12567/11419	7.6670	2106.0/1946.4	159.6	1.000980
PIB/hhPP	49	137000/73077	422	13968/7713.4	10.112	2239.1/2057.5	181.6	1.001022
PS/PVME	50	120000/99000	394	13652/11419	7.6670	2144.3/1946.4	197.9	1.001317
PECH/PEA	43	555000/137000	500	49478/14732	7.5674	2052.0/1890.0	162.1	1.001529
PECH/PEMA	42	555000/438000	485	54667/51023	6.8740	2083.8/1905.4	178.3	1.001724
PMMA/PEO	42	130000/300000	502	15674/38290	6.3996	2199.1/1957.2	241.9	1.002886
PEO/PES	51	200000/20000	350	27101/2187.2	6.0503	1977.0/2529.1	552.1	1.007095

^aThe column lists the experimental references for the blend. Experimental references for the corresponding pure component PVT data used to obtain the pure component parameters are given in Table 1 and in the pure component information in Table 4. ^bMolecular weights (*M*) are given as weight-averaged molecular weights (M_w). ^cThis system was parametrized in using SANS data in ref 27 for a system with $M = 255000/99000$ where $r = 26929/11419$ (details in ref 20).

molecular weights in the oligomeric size regime (exceptions being only when the two components become very similar), while on the other hand, most LCST-type blends have high molecular weights. This means that, typically, the magnitude of the combinatorial contribution to the entropy of mixing is higher for UCST-type blends compared to LCST-type blends. This observation appears to be connected to the fact that UCST-type blends rely on this combinatorial contribution to the entropy of mixing to obtain miscibility, and thus, moving to higher molecular weights will always bring about total immiscibility. Conversely, for LCST-type blends, which already have a favorable enthalpy of mixing, moving to lower molecular weights will only bring about total miscibility.

Before discussing the key correlations, it should be noted that there appear a multiplicity of pure component parameter values (particularly, ϵ) for the same polymer. For example, PS appears in three blends in Table 3, with $|\epsilon|$ values of 2335, 2405, and 2144 J/mol, and three other values are observed in Table 2 (2043, 2104, and 2201 J/mol). One reason for this is that some blends are comprised of components in the oligomeric size regime, and in these cases we try to use PVT data for oligomeric samples in nearby sizes when it is available because PVT data often depend on molecular weight in the oligomeric

regime. However, the most common reason for differences in ϵ values is the fact that the best fit ϵ value is dependent on the temperature range chosen for the fitted data. This effect, traceable to an overly strong T dependence in the coefficient of thermal expansion, is common in other theoretical equations of state as well, and it has been noted at times in the literature.^{29,30,52} The issue of best-fit parameters and the question of how to choose the data range for fitting is an important consideration and thus requires some more commentary.

In Figure 1, we take a systematic look at the dependence of the best fit ϵ value on the (midpoint of the) fitted temperature range of the PVT data for 11 different polymers, all of which are components in the blends presently studied. It should first be recalled that the exact values that one obtains will depend to a degree on the details of the chosen fitting protocol. As discussed above, we find the most consistent results by weighting for best agreement at low pressure, and all of the polymers in Figure 1 have been treated in this same way providing for the best comparison. The results in the figure show that the best fit ϵ 's of all 11 polymers exhibit the same qualitative behavior, with an increase in the magnitude of the best fit ϵ as the midpoint temperature of the fitting range increases. Though the rate of this increase differs somewhat from polymer to polymer, a

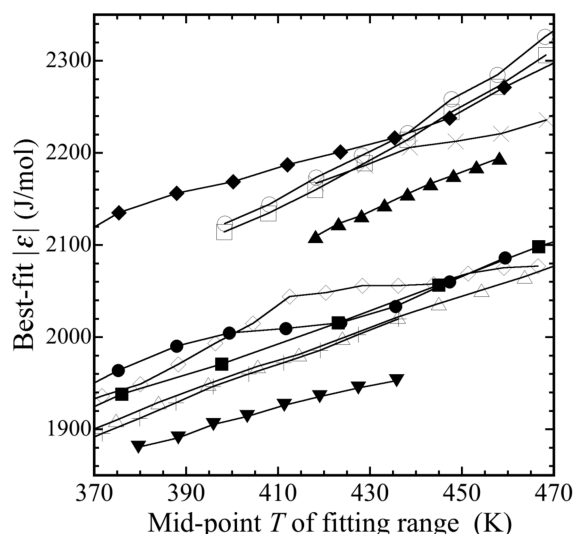


Figure 1. Best fit pure component ε value as it varies with the fitted temperature range of the PVT data. Each point represents the best fit ε for a given temperature range. In all cases the temperature range covered a span of 70 deg, and the T values given on the x -axis correspond to the midpoint of the temperature range. Results are given for 11 different polymers: PS with $M_w = 110\,000$ g/mol (open circles), PS with $M_w = 9000$ g/mol (open squares), PMMA with $M_w = 100\,000$ g/mol (crisscross), PB with $M_w = 233\,000$ g/mol (solid circles), PIB (solid diamonds), PCHMA (solid triangles), PMA (open diamonds), PVME (plus signs), PEP (open triangles), hhPP (solid squares), PEO (down-pointing solid triangles). Experimental references for the data are given in Tables 1 and 4, and more details are available in the Appendix.

typical effect is roughly an increase in the best fit $|\varepsilon|$ of about 200 J/mol for an increase in 100 K in the midpoint T of the data range. More specifically, applying simple linear fits to extract the slope for each polymer, we find that the average for the 11 polymers is an increase in best fit $|\varepsilon|$ of 1.87 J/mol per degree. The variability (standard deviation) within this sample is 0.6 J/mol per degree. The values for the best fit ε are not as sensitive to the size (width) of the chosen temperature range as they are to the midpoint of that range; the results here are for widths of 70 deg.

From a practical point of view, the most relevant insight to be drawn from the above results is based on the fact that all polymers are exhibiting the same qualitative behavior. So, while the best fit $|\varepsilon|$ value for any one component may increase as the midpoint temperature of the fitting range increases, the *difference* between the best fit $|\varepsilon|$ values for any two components in a blend ($|\varepsilon_{ii} - \varepsilon_{jj}|$) will remain somewhat stable by comparison. In order to obtain the most meaningful value for $|\varepsilon_{ii} - \varepsilon_{jj}|$, it then follows that it is important to match (as best as possible) the fitted temperature ranges of the two pure components. This will give the most appropriately matched pair of ε values. Furthermore, we note that the coefficient of thermal expansion, $\alpha = (1/V)(\partial V/\partial T)_p$, is almost exclusively sensitive to the ε parameter (r and v have only a very small effect) where, at any particular T , the larger the magnitude of ε , the smaller is the resulting α . Therefore, fitting both components over the same temperature range leads to ε values that not only give the correct individual pure component α 's for that temperature range, but further, the corresponding value for $|\varepsilon_{ii} - \varepsilon_{jj}|$ will maintain the correct *difference* in α even outside of that range. Accounting properly for differences in pure component α

values may be key, as they are known to have a very strong effect on the corresponding miscibility behavior for mixtures.

Following the arguments above, our ordering of importance for pure component fitting is thus to first make sure that each component in the blend is fit over the same temperature range (within the limits of the data); then, if sufficient data are available, the temperature range is chosen such that it also covers the vicinity of the important blend behavior, i.e., near phase separation temperatures, etc.

One caveat is the case of oligomeric components; we always try to use PVT data that is the best possible match for the molecular weights in the blend being considered. As mentioned above, the ε values for polymeric and oligomeric samples are often different. Generally, we find that $|\varepsilon|$ decreases upon going from polymer to oligomer, with stronger decreases as the oligomers become smaller. For example, for PS, comparing fits covering the same midpoint $T \approx 410$ K, we obtain $|\varepsilon| = 2144$, 2134, and 2061 J/mol respectively for $M_w = 110\,000$, 9000, and 910 g/mol. Similarly for PB (midpoint $T \approx 400$ K), $|\varepsilon| = 2005$, 1960, and 1921 J/mol respectively for $M_w = 233\,000$, 3000, and 1000 g/mol.

We will have more to say about these considerations in modeling protocol, especially the importance of matching the fitted temperature ranges, when we discuss some of the results further below.

IV. DISCUSSION

Having laid out a framework of the important considerations in implementing a meaningful and consistent model parametrization, we now move to a discussion and comparison of some key trends in these resulting parameters when applied to a large collection of experimental polymer blends. In particular, we will be focusing on a comparison of results for the mixed model energetic parameter, g , and the *difference* in the pure component energetic parameters, $|\varepsilon_{ii} - \varepsilon_{jj}|$, the former being a characteristic property of a blend and the latter being derived from independent characterization of the two pure components.

Shown in Figure 2 are the spread of results for the g parameter over the full set of 25 experimental blends (values

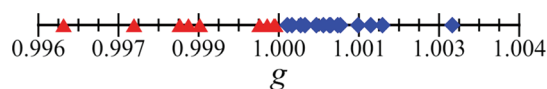


Figure 2. Distribution of the mixed interaction parameter (g) values for the 25 polymer blends systems. UCST-type blends are given by triangles and LCST-type blends by diamonds.

also given in Tables 2 and 3). There is a clear delineation showing that UCST-type blends in all cases have $g < 1$, and LCST-type blends have $g > 1$; this is a pattern that we have noted before with the present theory, but now verify with a much larger number of systems. The observation that g is always less than unity for UCST-type blends appears to follow from the fact that, with the geometric mean approximation for ε_{ij} ($g = 1$), we have never observed the theory to give a positive enthalpy change on mixing at constant pressure, a requirement for UCST-type phase separation.

The trends in the $|\varepsilon_{ii} - \varepsilon_{jj}|$ values are shown in Figure 3 (see also Tables 2 and 3.) Here again there are some clear correlations, though not as stark as for the case of g . The general trend is that the UCST-type blends typically have

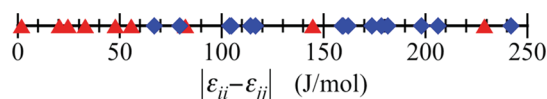


Figure 3. Distribution of values for the difference in the pure component interaction parameters ($|\epsilon_{ii} - \epsilon_{jj}|$) for the 25 polymer blends systems. UCST-type blends are given by triangles and LCST-type blends by diamonds.

smaller $|\epsilon_{ii} - \epsilon_{jj}|$ values than LCST-type blends, though there is clear overlap of the two types of systems. Very roughly, the typical UCST-type blend has an $|\epsilon_{ii} - \epsilon_{jj}|$ value of around 50 J/mol, while the typical LCST-type blend will often have a $|\epsilon_{ii} - \epsilon_{jj}|$ of 150 J/mol or more. Specifically, for our present samples, the UCST-type blends had an average $|\epsilon_{ii} - \epsilon_{jj}|$ of 71.0 J/mol with a standard deviation of 72.6 J/mol. (Two UCST blends in particular are “outliers” in the overall correlation: PB/PMS with $|\epsilon_{ii} - \epsilon_{jj}| = 144$ J/mol and PS/PI with a value of 228 J/mol.) The LCST-type blends had an average $|\epsilon_{ii} - \epsilon_{jj}|$ of 174.9 J/mol with a standard deviation of 111.6 J/mol.

One important point related to the trends in $|\epsilon_{ii} - \epsilon_{jj}|$ is the following: It is known that for polymer blends LCST-type phase separation is typically driven by equation-of-state-type effects, situations where there is a difference in the volumetric response of the two components to change in temperature, i.e., substantial differences in the two pure component α values ($\alpha = (\partial \ln V / \partial T)_p$). As noted above, for the present theory, though there are three pure component parameters (r , v , and ϵ), the model α values are sensitive almost exclusively to ϵ . So, with ϵ speaking for α , large differences in the ϵ values will indicate large differences in α for the blend components and thus a tendency for LCST-type phase separation. As noted in Figure 3, it is indeed the blends with large pure component model ϵ differences that generally give LCST-type phase separation.

So far, we have considered trends in g and $|\epsilon_{ii} - \epsilon_{jj}|$ separately, but particularly provocative are the results shown in Figure 4 where we see the relationship between the pure component fitted $|\epsilon_{ii} - \epsilon_{jj}|$ values and the corresponding g values. For LCST-type blends (diamonds) there appears to be a clear correlation where g increases as $|\epsilon_{ii} - \epsilon_{jj}|$ increases; that is, g tends to be larger for blends where the pure component $|\epsilon_{ii} - \epsilon_{jj}|$ is larger. (This will be commented on further below.) For UCST-type blends, on the other hand, the points are fairly scattered, and there appears to be no such correlation, with one possibly very interesting exception.

There is a cluster of four UCST-type points that appear to be in line with the trend for the LCST blends (as g extends downward into values slightly less than unity at very small $|\epsilon_{ii} - \epsilon_{jj}|$). It is important to note that these four blends are distinct from the remainder of the UCST-type systems; they are all composed of pairs of very similar components. Three are polyolefin blends, PEP/PE, PEP/hhPP, and PEP/aPP, and the other is PS/PMS; in all of these cases the paired components differ by only a single methyl group on the backbone. Similarities such as this suggest that the pure component properties of the two components are expected to be fairly close in value, and this is indeed reflected in the relatively small differences in the pure component ϵ values (the $|\epsilon_{ii} - \epsilon_{jj}|$'s). Note as well that isotopic blends are also likely to fall into this category.

Before considering further the apparent difference between UCST and LCST blends in Figure 4, it is relevant to ask the following questions: (1) Does one lose or distort the g vs $|\epsilon_{ii} - \epsilon_{jj}|$ correlation (for the LCST blends) if one uses ϵ values

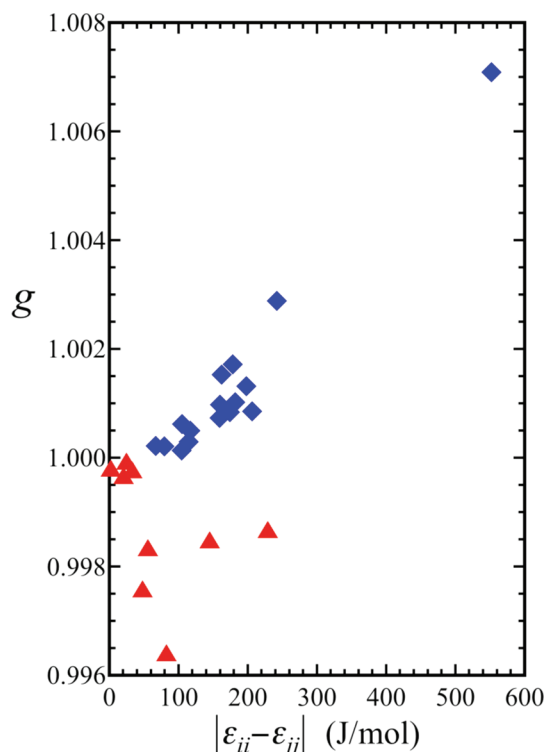


Figure 4. Correlations in the mixture interaction parameter, g , with the difference in the pure component interaction parameters ($|\epsilon_{ii} - \epsilon_{jj}|$) for the 25 blend systems. UCST-type blends are given by triangles and LCST-type blends by diamonds.

that were best-fit in mismatched temperature ranges? (2) If one uses ϵ values for both components such that their T ranges do match each other, but are not a good match for the experimental range of interest (e.g., for the blend miscibility behavior), does one lose this g vs $|\epsilon_{ii} - \epsilon_{jj}|$ correlation?

In order to answer, consider changing the ϵ value of one or both components by an amount that reflects a sizable (but feasible) shift in the midpoint T of the fitted range. A shift of about 100 deg, for example, would translate to a change in the ϵ value by about 150 J/mol.

It turns out that situation 1, where the fitted T ranges are not matched, could be quite destructive. If we set up an example where we take the component with the lower magnitude ϵ and imagine that we fit it over a T range that is roughly 100 deg higher than the other component, this, as noted, would have the effect of increasing the magnitude of its ϵ value by 150 J/mol. For most of the LCST-type blends in Table 2, this severely lowers the magnitude of the $|\epsilon_{ii} - \epsilon_{jj}|$, so much so that 10 of our 15 LCST-type blends cannot be fit to an LCST-type phase diagram. They become too miscible, and if we reduce g , we only obtain phase separation of the UCST type. Thus, the importance of our protocol of matching the fitted T range of the PVT data in the two components of a blend is strongly reinforced.

Situation 2 turns out to be far less damaging. We test this assertion for LCST-type blends by increasing the magnitude of both pure component ϵ 's (i.e., simulating the situation of having fit both components over the same T range, but one that is roughly 100 deg higher). Here the g changes systematically by a small amount (it gets lower), but there is no problem refitting all 15 LCST-type blends. Furthermore, given the systematic change to g , there is still a clear g vs $|\epsilon_{ii} - \epsilon_{jj}|$ correlation, being shifted somewhat.

Table 4. Pure Component Fitted Parameters Associated with Each Blend

		M^a (g/mol)	r/M (g/mol) ⁻¹	ν (mL/mol)	ν/M (mL/g)	$-\epsilon$ (J/mol)	T range (K)	PVT data
PS/PB	PS	910	0.122188	7.3709	0.900629	2042.5	364–433	26
	PB	3000	0.120415	8.6207	1.038058	1960.3	359–431	26
PS/PMPS	PS	9000	0.122657	7.1548	0.877578	2104.1	363–423	26
	PMPS ^b	2347	0.105732	8.0000	0.845859	2056.4	361–422	31
PS/PMMA	PS	9000	0.108789	8.1520	0.886848	2200.7	383–482	26
	PMMA	10000	0.120972	6.3555	0.768841	2145.1	383–484	26
PB/PMS	PB	233000	0.099686	10.715	1.068148	2187.1	472–495	26
	PMS	55000	0.107926	7.8275	0.844784	2331.7	463–503	29
PS/PI	PS	910	0.122188	7.3709	0.900629	2042.5	364–433	26
	PI	2800	0.120009	8.2851	0.994285	1813.7	359–436	30
PEP/PE	PEP	N/A	0.105718	10.3422	1.093357	2032.9	401–502	28
	PE	N/A	0.117747	9.2821	1.092934	2012.5	434–493	28
PS/PMS	PS	110000	0.084306	10.6634	0.898986	2405.1	474–524	26
	PMS	55000	0.098447	8.6512	0.851681	2403.4	463–534	29
PEP/aPP	PEP	N/A	0.105718	10.3422	1.093357	2032.9	401–502	28
	aPP	N/A	0.093332	11.9011	1.110752	2065.9	435–495	28
PEP/hhPP	PEP	N/A	0.105718	10.3422	1.093357	2032.9	401–502	28
	hhPP	N/A	0.103712	10.2908	1.067279	2057.5	402–503	28
iPMMA/PVC	iPMMA	N/A	0.113711	6.6902	0.760745	2156.9	383–453	32
	PVC	N/A	0.125094	5.2061	0.651249	2053.0	385–456	26
PECH/PCHMA	PECH	N/A	0.084191	8.0827	0.680482	2128.3	373–413	1
	PCHMA ^c	N/A	0.101068	8.0827 ^c	0.816897	2048.9	383–408	32
PEO/PMA	PEO	100000	0.149436	5.3999	0.806941	1880.5	343–416	26
	PMA	N/A	0.123488	6.0894	0.751969	1947.4	334–417	26
PMMA/PVC	PMMA	100000	0.114924	6.6902	0.768860	2167.1	384–452	26
	PVC	N/A	0.125094	5.2061	0.651249	2053.0	385–456	26
PS/PCHMA	PS	110000	0.091579	9.7368	0.891685	2334.6	443–493	26
	PCHMA ^c	N/A	0.085696	9.7368 ^c	0.834404	2218.0	443–493	32
PECH/PMA	PECH	N/A	0.091891	7.3416	0.674631	2052.0	333–413	1
	PMA	N/A	0.123488	6.0894	0.751969	1947.4	334–417	26
PS/TMPC	PS	110000	0.084306	10.6634	0.898986	2405.1	474–524	26
	TMPC	33000	0.093638	8.7862	0.822718	2246.0	490–540	34
PMMA/PMS	PMMA	40000	0.107006	7.2630	0.777185	2221.0	454–505	26
	PMS	55000	0.099989	8.5095	0.850860	2394.6	463–513	29
PIB/PEP	PIB	N/A	0.103797	9.9323	1.030941	2239.1	400–507	28
	PEP	N/A	0.105718	10.3422	1.093357	2032.9	401–502	28
dPS/PVME	dPS ^d	255000	0.105605	7.6667	0.809676	2106.0	note ^d	20
	PVME	99000	0.111006	7.9666	0.884338	1946.4	375–423	33
PIB/hhPP	PIB	N/A	0.103797	9.9323	1.030941	2239.1	400–507	28
	hhPP	N/A	0.103712	10.2908	1.067279	2057.5	402–503	28
PS/PVME	PS	110000	0.115786	7.5333	0.872252	2144.3	373–443	26
	PVME	99000	0.111006	7.9666	0.884338	1946.4	375–423	33
PECH/PEA	PECH	N/A	0.091891	7.3416	0.674631	2052.0	333–413	1
	PEA	N/A	0.104414	7.7933	0.813725	1890.0	331–417	26
PECH/PEMA	PECH	N/A	0.089085	7.6004	0.677082	2083.8	353–413	1
	PEMA	N/A	0.130253	6.1477	0.800751	1905.4	343–428	26
PMMA/PEO	PMMA	100000	0.110744	6.9674	0.771602	2199.1	394–484	26
	PEO	100000	0.140061	5.8318	0.816812	1957.2	407–472	26
PEO/PES	PEO	100000	0.137128	5.9788	0.819855	1977.0	439–472	26
	PES	N/A	0.108080	6.1218	0.661646	2529.1	484–533	26

^aMolecular weights (M), if available, are given as weight-averaged molecular weights (M_w). ^bPure component parameters for PMPS were determined by fitting to PVT data for a PS/PMPS blend as described in ref 31. ^cHigh- P data for PCHMA were not available; fitting of low- P data allowed for the determination of ϵ and the product ν/M ; the ν value was assigned, taking that of the intended blend partner. ^dPure component parameters obtained by fitting to SANS data for a dPS/PVME blend in ref 20.

Now we return to the puzzle of the lack of any apparent correlation for the UCST blends in Figure 4. It is well-known that the major differences between UCST and LCST blends are the sign of the enthalpy of mixing (positive for UCST blends and negative for LCST ones) and the difference in the typical

magnitude of the combinatorial entropy, being generally smaller for LCST-type blending partners because of the very high molecular weights (noted above). A consequence of the negative enthalpy in the LCST blends is that there has to be a negative contribution to the entropy of mixing—usually termed

noncombinatorial—in order to drive partial miscibility. If there is no entropy term to oppose the favorable enthalpy, then the system would be completely miscible (the combinatorial entropy is always positive). For the UCST blends the combinatorial entropy and unfavorable enthalpy act in opposition so that at some temperature phase separation is inevitable. However, it has been reported in the literature⁵³ that some UCST blends also have a relatively important noncombinatorial entropy contribution. This may reinforce the combinatorial term or diminish it, i.e., increase miscibility or reduce it (lowering or raising the UCST, respectively). It is thus the case that the behavior of the LCST blends in Figure 4 is a consequence of the balance of just two key thermodynamic contributions, while the UCST blends may involve three contributions playing a more complex balancing game. We have already shown in a previous paper that with our equation of state in hand we can successfully calculate the enthalpy of mixing for an LCST blend where experimental data were available. If we can demonstrate the same confidence for UCST blends, we may be able to extract the entropy term and explore the combinatorial and noncombinatorial contributions. We intend to extend our investigations in this direction in our next publication.

V. SUMMARY AND CONCLUSIONS

In this paper we have discovered new correlations between the microscopic character of blend components and their bulk miscibility. We have been guided in this by the extensive library of results we have developed on blends exhibiting both upper and lower critical solution temperatures (UCSTs and LCSTs). Our ability to draw connections between a set of pure components, on the one hand, and blend behavior, on the other, depends crucially upon a consistent method of characterization. We would like to emphasize that, although no single step in the method is new, the implementation is key. Therefore, in this paper we describe in detail our sequential route to determining the characteristic parameters for each component; we also explore the ramifications of a somewhat more careless approach.

One intriguing pattern to emerge is that the averaged difference between pure component energy parameters, $|\varepsilon_{ii} - \varepsilon_{jj}|$, is significantly greater for LCST blends than for UCST blends—by a factor of close to 3. Further, in the case of LCST blends there is a strong, linear correlation between g , which defines the mixed-segment interaction, and $|\varepsilon_{ii} - \varepsilon_{jj}|$. Our discussion of the reasons for this trend in LCST, but not UCST, blends leads us to conclude that there is potential for a deeper thermodynamic understanding of how the chemical nature of the blend components controls the entropic and enthalpic contributions to the free energy of mixing. We expect to delve further into this subject in future work.

As a final general remark, we note that while truly predictive blend modeling is a goal, knowledge of $|\varepsilon_{ii} - \varepsilon_{jj}|$ is a starting point that can provide at least a rough form of predictive guidance. We note, for example, that the larger the difference, the greater the tendency of the system toward immiscibility; this appears connected with an unfavorable contribution to the noncombinatorial entropy of mixing (details related to work in progress). As the pure component energy difference grows, it may first lead to an LCST-containing system while, with a large enough $|\varepsilon_{ii} - \varepsilon_{jj}|$ difference, mixing would likely be altogether prevented. Where this difference is overcome, one might look to some specific source of enthalpic compensation. Thus, some coarse-grained predictions (miscible or not?) may be accessible through pure component parameters alone. All that is required

to obtain $|\varepsilon_{ii} - \varepsilon_{jj}|$ are the respective pure component PVT data; it is possible that $V(T)$ data at atmospheric pressure may suffice. In any case, we believe that continued collection of these data will be important in extending future modeling opportunities and insight.

■ APPENDIX

In Table 4 we provide our pure component parametrizations which are organized such that each pure component is paired with its corresponding blend partner. Also included is the temperature range utilized for the fitted data.

The two-stage fitting procedure is described in section II. There it was noted that in the first stage the lowest pressure $V(T)$ curve (usually corresponding to $P = 0$ or 10 MPa) is fitted to obtain a unique value for ε and the product rv . In Table 4 the latter is tabulated as rv/M . The M and v typically change on going from the pure component PVT fit to the model blend, and thus the new r for the blend is obtained from the tabulated rv/M values by multiplying by the new M and dividing by the new v . It can also be verified from Tables 2 and 3 that the v values used for each blend were chosen to be similar to the optimal pure component values given in Table 4 (very often being the average of the values obtained for the two blend components).

Note that in some cases the molecular weight of the sample associated with the experimental PVT data was unavailable. Because the data are for the *specific* volume anyway (e.g., per gram), we simply assume the model molecular weight is 100 000 g/mol, which in the calculations simply allows us to work in terms of an explicit model r value, and then we report the optimized r in the form of r/M (and rv/M) which would be the relevant quantity, not knowing the actual molecular weight. The utility of the quantity r/M (or rv/M) assumes that r can be scaled proportional to any desired molecular weight. This is justified for any range of M in the polymeric size regime, but not as justified in the oligomeric size regime as PVT data can depend on M in this latter case. For oligomeric sizes we still do employ r - M scalings, but we try as best as possible not to scale too far away from the M of the fitted system; i.e., we fit to oligomeric data of the nearest possible M to those that are in the blends of interest.

■ ACKNOWLEDGMENTS

We appreciate the financial support provided by the National Science Foundation (J.E.G.L. and R.P.W., Grants DMR-0804593 and DMR-1104658) and EPSRC (J.S.H. and J.E.G.L.). J.E.G.L. also benefited from the hospitality of those in the Chemical Engineering Department at Imperial College, where some of this work was carried out.

■ REFERENCES

- (1) Rodgers, P. A. *J. Appl. Polym. Sci.* **1993**, *48*, 1061.
- (2) Sanchez, I. C.; Lacombe, R. H. *J. Phys. Chem.* **1976**, *80*, 2352.
- (3) Sanchez, I. C.; Lacombe, R. H. *J. Phys. Chem.* **1976**, *80*, 2368.
- (4) Sanchez, I. C.; Lacombe, R. H. *Macromolecules* **1978**, *11*, 1145.
- (5) Panayiotou, C.; Vera, J. H. *Polym. J.* **1982**, *14*, 681.
- (6) Kleintjens, L. A.; Koningsveld, R. *Colloid Polym. Sci.* **1980**, *258*, 711.
- (7) Bawendi, M. G.; Freed, K. F. *J. Chem. Phys.* **1988**, *88*, 2741.
- (8) Dudowicz, J.; Freed, K. F.; Madden, W. G. *Macromolecules* **1990**, *23*, 4803.
- (9) Dudowicz, J.; Freed, K. F. *Macromolecules* **1991**, *24*, 5076.
- (10) Prigogine, I.; Trappeniens, N.; Mathot, V. *Discuss. Faraday Soc.* **1953**, *15*, 93.

- (11) Prigogine, I.; Bellemans, A.; Mathot, V. *The Molecular Theory of Solutions*; North-Holland: Amsterdam, 1957.
- (12) Flory, P. J.; Orwoll, R. A.; Vrij, A. *J. Am. Chem. Soc.* **1964**, *86*, 3507.
- (13) Dee, G. T.; Walsh, D. J. *Macromolecules* **1988**, *21*, 811.
- (14) Dee, G. T.; Walsh, D. J. *Macromolecules* **1988**, *21*, 815.
- (15) Lipson, J. E. G. *J. Chem. Phys.* **1992**, *96*, 1418.
- (16) Lipson, J. E. G.; Andrews, S. S. *J. Chem. Phys.* **1992**, *96*, 1426.
- (17) Luettmmer-Strathmann, J.; Lipson, J. E. G. *Macromolecules* **1999**, *32*, 1093.
- (18) Lipson, J. E. G.; Tambasco, M.; Willets, K. A.; Higgins, J. S. *Macromolecules* **2003**, *36*, 2977.
- (19) Higgins, J. S.; Lipson, J. E. G.; White, R. P. *Philos. Trans. R. Soc., A* **2010**, *368*, 1009.
- (20) White, R. P.; Lipson, J. E. G.; Higgins, J. S. *Macromolecules* **2010**, *43*, 4287.
- (21) Flory, P. J. *Principles of Polymer Chemistry*; Cornell University Press: Ithaca, NY, 1953.
- (22) White, R. P.; Lipson, J. E. G. *J. Chem. Phys.* **2009**, *131*, 074109.
- (23) White, R. P.; Lipson, J. E. G. *J. Chem. Phys.* **2009**, *131*, 074110.
- (24) Using other values of z (e.g., $z = 8$ or 10) will cause the optimal values of the other parameters to change but will not appreciably change the overall quality of the fitted properties.
- (25) Another option is to fit to SANS data, which was done here in one case for the dPS/PVME blend. Details are available in ref 20.
- (26) Zoller, P.; Walsh, D. *Standard Pressure-Vol.-Temperature Data for Polymers*; Technomic Pub Co.: Lancaster, PA, 1995.
- (27) Shibayama, M.; Yang, H.; Stein, R. S.; Han, C. C. *Macromolecules* **1985**, *18*, 2179.
- (28) Krishnamoorti, R.; Graessley, W. W.; Dee, G. T.; Walsh, D. J.; Fetters, L. J.; Lohse, D. J. *Macromolecules* **1996**, *29*, 367. Tabulated values for these data were made available to us by D. J. Lohse.
- (29) Callaghan, T. A.; Paul, D. R. *Macromolecules* **1993**, *26*, 2439.
- (30) Rudolf, B.; Kressler, J.; Shimomai, K.; Ougizawa, T.; Inoue, T. *Acta Polym.* **1995**, *46*, 312.
- (31) Gitsas, A.; Floudas, G.; White, R. P.; Lipson, J. E. G. *Macromolecules* **2009**, *42*, 5709.
- (32) Wilson, P. S.; Simha, R. *Macromolecules* **1973**, *6*, 902.
- (33) Ougizawa, T.; Dee, G. T.; Walsh, D. J. *Macromolecules* **1991**, *24*, 3834.
- (34) Kim, C. K.; Paul, D. R. *Polymer* **1992**, *33*, 1630.
- (35) Rostami, S.; Walsh, D. J. *Macromolecules* **1985**, *18*, 1228.
- (36) Rudolf, B.; Cantow, H.-J. *Macromolecules* **1995**, *28*, 6586.
- (37) Lin, J.-L.; Roe, R.-J. *Macromolecules* **1987**, *20*, 2168.
- (38) Bates, F. S.; Schulz, M. F.; Rosedale, J. H. *Macromolecules* **1992**, *25*, 5547.
- (39) Lohse, D. J.; Fetters, L. J.; Doyle, M. J.; Wang, H.-C.; Kow, C. *Macromolecules* **1993**, *26*, 3444.
- (40) Graessley, W. W.; Krishnamoorti, R.; Reichart, G. C.; Balsara, N. P.; Fetters, L. J.; Lohse, D. J. *Macromolecules* **1995**, *28*, 1260.
- (41) Vorenkamp, E. J.; ten Brinke, G.; Meijer, J. G.; Jager, H.; Challa, G. *Polymer* **1985**, *26*, 1725.
- (42) Fernandes, A. C.; Barlow, J. W.; Paul, D. R. *J. Appl. Polym. Sci.* **1986**, *32*, 5481.
- (43) Fernandes, A. C.; Barlow, J. W.; Paul, D. R. *J. Appl. Polym. Sci.* **1986**, *32*, 6073.
- (44) Jager, H.; Vorenkamp, E. J.; Challa, G. *Polym. Commun.* **1983**, *24*, 290.
- (45) Casper, R.; Morbitzer, L. *Makromol. Chem.* **1977**, *58/59*, 1.
- (46) Cowie, J. M. G.; Miachon, S. *Macromolecules* **1992**, *25*, 3295.
- (47) Krishnamoorti, R.; Graessley, W. W.; Fetters, L. J.; Garner, R. T.; Lohse, D. J. *Macromolecules* **1995**, *28*, 1252.
- (48) Yang, H.; Shibayama, M.; Stein, R. S.; Shimizu, N.; Hashimoto, T. *Macromolecules* **1986**, *19*, 1667.
- (49) Unpublished values for spinodal temperatures for PIB/hhPP were made available to us by M. Rabeony.
- (50) Beaucage, G.; Stein, R. S.; Hashimoto, T.; Hasegawa, H. *Macromolecules* **1991**, *24*, 3443.
- (51) Voutsas, E. C.; Pappa, G. D.; Boukouvalas, C. J.; Magoulas, K.; Tassios, D. P. *Ind. Eng. Chem. Res.* **2004**, *43*, 1312.
- (52) Patterson, D. *Macromolecules* **1969**, *2*, 672.
- (53) Higgins, J. S.; Tomlins, P. E. *Macromolecules* **1988**, *21*, 425.

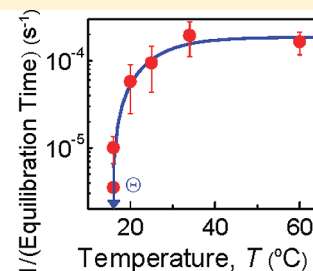
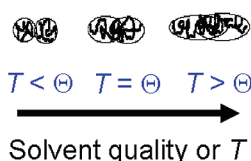
Equilibration of Polymer Films Cast from Solutions with Different Solvent Qualities

Ranxing Nancy Li, Andrew Clough, Zhaohui Yang,[†] and Ophelia K. C. Tsui*

Department of Physics, Boston University, Boston, Massachusetts 02215, United States

ABSTRACT: We study the effect of film preparation on the equilibration and viscoelastic properties of polymer films. Polystyrene films with a thickness of 14 nm are spun-cast from decalin solutions at different temperatures near the theta temperature to produce films with different chain conformations. We find that the equilibration time of the films increases significantly near the theta temperature. We attribute this to the onset of a rapid collapse in the polymer coil size at the theta condition, along with an increase in the solvent concentration in the films and thereby interchain separation at the time of vitrification. We find that these effects also cause the plateau modulus and equilibrium viscosity of the films to decrease.

Chain Conformation in As-cast Films:



INTRODUCTION

The conformation of polymer chains in a solution is a strong function of the solvent quality. In a good solvent, the interaction between the chain segments and solvent molecules is more favorable than that between the chain segments. This causes the chains to swell. In a bad solvent, the converse is true and that causes the chains to collapse. In between is the theta solvent, in which the two kinds of interactions have the same strength so the polymer chains assume the same conformation as in a melt.

When a polymer solution is subject to rapid drying, as in spin-coating, the polymer chains in the solution may not have enough time to attain equilibrium before vitrifying. As a result, some memory of the chains' conformation in the solution can get carried over to the resultant, dried film. Such an effect has been speculated to be the cause for some of the more bizarre properties found of spin-coated polymer films, including negative thermal expansion and visible aging well below the glass transition temperature, T_g .^{1–9} When a polymer solution is dried, the sample volume decreases; thereby, the interpenetration between neighboring chains increases. Rapid drying can, however, preclude the chains from achieving full interpenetration before vitrification, resulting in the final, dried film having a smaller degree of entanglement than equilibrium. The notion that spin-coated polymer films possess less entanglement than equilibrium has been confirmed in recent experiments studying the viscosity of freshly spin-coated polystyrene films supported by silicon.^{6,7} By using solvents with different qualities, the degree of entanglement can be further fine-tuned. Specifically, when solvents with poorer quality are used, individual polymer chains would be more compact, and so the interchain entanglement further reduced. In addition, the vertical shrinkage of the films upon drying may force the chains into an oblate conformation, creating a residual in-plane stress in the films. Such a residual stress has been suggested⁸ to be at least in part responsible for the occurrence of physical aging in

spin-coated polymer films well below the T_g .^{2,3,8} Recently, Raegen et al.⁸ measured the aging rate of polystyrene (PS) films spin-coated on poly(dimethylsiloxane) from solutions made of good to near-theta solvents. They found that the aging rate increased abruptly as the theta condition was approached. Since the entanglement reduction should be bigger while the residual stress smaller on approaching the theta condition, this result shows that the effect of entanglement reduction dominates that of the in-plane residual stress.

In this experiment, we study whether polymer films prepared from solutions with different solvent qualities equilibrate differently upon annealing above the T_g . On the one hand, reduced entanglement may speed up the polymer dynamics and hence the equilibration process. On the other hand, a more compact conformation the chains may inherit from a poor solution can on the contrary render the chains a longer time to re-entangle to the full equilibrium state. Besides studying how the films equilibrate, we shall also examine whether upon equilibration the films will settle on the same dynamic properties. Recently, Fujii et al.¹⁰ found that the polymer chains in the films can bind irreversibly to the supporting substrate. If the binding occurs before equilibration completes, part of the initial, out-of-equilibrium conformation can get locked in and affect the final equilibrium state.

EXPERIMENTAL SECTION

Polystyrene (PS) with $M_w = 212$ kg/mol and polydispersity index = 1.08 was purchased from Scientific Polymer Products (Ontario, NY). Silicon (100) wafers covered with a 102 ± 5 nm thick thermal oxide layer and cut into 1×1 cm² slides were used for the substrates. Prior to use, the slides were cleaned in a piranha solution ($\text{H}_2\text{SO}_4\text{:H}_2\text{O}_2$ in 7:3 volume ratio) at 140 °C for 20 min followed by thorough rinsing

Received: December 1, 2011

Revised: December 28, 2011

Published: January 11, 2012

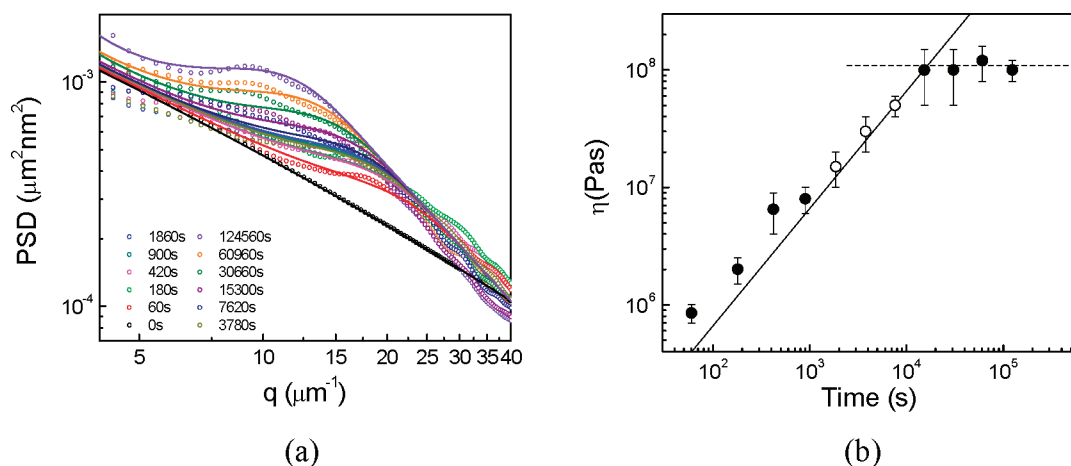


Figure 1. (a) Power spectral density of a PS/decalin film prepared at 20 °C upon annealing at 130 °C for different times (from bottom to top): 0, 60, 180, 420, 900, 1860, 7620, 15 300, 30 660, 60 960, 124 560, and 219 240 s. (b) Fitted value of η plotted versus time for the data shown in (a). The open symbols denote the values obtained when the film was in the rubbery state or the PSDs made negligible evolution.^{13,14} The solid line is a fit of the data to the relation $\eta = 2\mu_0 t$ valid in the rubbery state prior to the saturation in η as seen in the data.^{13,14} The dashed line is the best fit of the data in the saturated region to a constant value.

with deionized water and then drying with 99.99% nitrogen. Afterward, the substrates were further cleaned in an oxygen plasma for 25 min.

Polystyrene films were spin-coated from solutions of toluene (a good solvent) and decalin (a PS solvent with a theta temperature, Θ , of ca. 16 °C) with concentrations of 0.4–0.7 wt % polymer. The quality of the solvent can be characterized by the coil size of the polymer in the solution, commonly expressed in terms of the expansion factor, α , by

$$\alpha = \sqrt{\frac{\langle R^2 \rangle}{\langle R_0^2 \rangle}} \quad (1)$$

where R and R_0 are the radius of gyration of the polymer in the solution and melt, respectively. Typically, the solvent quality and hence α decrease as the solution temperature, T , is decreased. It has been shown that α and T are related by¹¹

$$\frac{1}{\sigma} \left[\frac{14}{3N\alpha_{\min}^3} (\alpha^3 - \alpha^5) + \frac{2}{3} \frac{\alpha_{\min}^3}{\alpha^3} \right] = \frac{\Theta}{T} - 1 \quad (2)$$

where α_{\min} is the amount of swelling in the totally collapsed state and $\sigma = 1 - \Delta S/k_B$, with k_B being the Boltzmann constant and ΔS the entropic change associated with segment–segment interactions. For PS in decalin, α varies between 1.0 and 1.2 when the solution temperature is varied from 16 °C ($= \Theta$) to 60 °C; while for PS in toluene at room temperature, $\alpha = 1.4$. Prior to spin-coating, the solution was placed in a water bath with the temperature controlled at the desired temperature for at least 12 h. To bring the core temperature of the spin-coater to the desired temperature, we adjusted the position of an incandescent lamp from the spin-coater chuck if the desired temperature was above ambience; otherwise, we adjusted the time dry ice was placed in the proximity of the spin-coater before spin-coating. All films were prepared with a thickness of 14 nm as determined by ellipsometry.

Ex-situ measurements of the surface topographic image of the films were made using tapping-mode atomic force microscopy (AFM) at different times, t , as the films were annealed at 130 °C (cf. $T_g = 100$ °C). To prepare the AFM data for analysis, each topographic image was multiplied by a Welch function before Fourier transformed. The resultant two-dimensional image was radially averaged to give the power spectral density (PSD). We have previously shown that in the initial stage of annealing when the height fluctuations in the film were small compared to the film thickness the temporal evolution of the PSD ($A_q^2(t)$) could be described by^{6,12,13}

$$A_q^2(t) = A_q^2(0) \exp(2\omega_q t) + \left[\frac{k_B T_a}{d^2 G(h)/dh^2 + \gamma q^2} \right] \times (1 - \exp(2\omega_q t)) \quad (3)$$

where T_a is the annealing temperature, ω_q is the relaxation rate of the surface capillary mode with wavevector q , and $G(h)$ and γ are respectively the van der Waals (vdW) potential and surface tension of the film. For (viscoelastic) entangled polymer films that exhibit elastic behavior (while in the rubbery state) at short times, but viscous behavior after time, τ_{rep} , where the film enters the terminal flow regime, we have shown^{13,14} that ω_q can be expressed by

$$\omega_q = \frac{\omega_{\text{liq}}}{1 - \omega_{\text{liq}} \tau_{\text{rep}}} \quad (4)$$

In eq 4, $\omega_{\text{liq}} = -(h^3/3\eta)[(d^2 G(h)/dh^2)q^2 + \gamma q^4]$ and η is a parameter identifiable with the effective or average film viscosity upon equilibration. To analyze the PSDs, we first fitted the high- q segment of the data to $k_B T_a/\gamma q^2$ ¹⁵ using γ as the fitting parameter while setting T_a equal to 403 K (130 °C). This allows the value of γ to be determined.¹⁵ We find that the values of γ found this way typically lie between 0.029 and 0.032 J/m², consistent with the literature value of 0.03 J/m².^{6,16} Next, we fitted the full PSDs to eq 3 with η being treated as the only fitting parameter and h and $d^2 G(h)/dh^2$ set equal to respectively the film thickness measured by ellipsometry and a value obtained in a previous calculation.¹⁷ It should be emphasized that while the present method measures the viscoelastic properties of the films (see below and refs 13 and 14 for further details), it differs notably from the typical AFM-based techniques for similar purposes.^{18–20} In particular, the AFM in those techniques acts actively to produce a mechanical perturbation to the film and thereafter monitors the overarching response. But in here, the AFM acts as a passive monitor of the surface topography of the film as the film roughens with time.

RESULTS AND DISCUSSION

Figure 1a shows a typical sequence of PSDs we obtained in experiment (symbols) and the corresponding best fits to eq 3 (solid lines), where good agreement between the two is clearly evident. The values of η used to produce the fitted lines in Figure 1a are shown in Figure 1b. As seen, η increases with t from $t = 0$ to $\sim 10^4$ s. It has been shown^{13,14} that the value of η acquired when a film is in the rubbery state (denoted by the

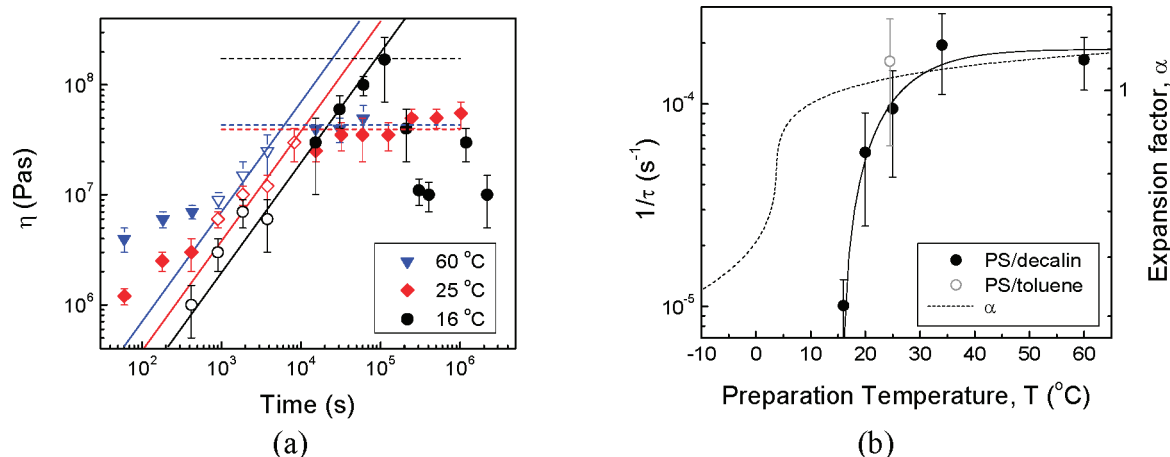


Figure 2. (a) Fitted value of η plotted versus time for the PS/decalin film prepared at 60, 25, and 16 °C on annealing at 130 °C. (b) Reciprocal of the equilibration time ($1/\tau$) plotted as a function of the preparation temperature (solid and open symbols). The solid line is a guide to the eye. The dashed line denotes the expansion factor, namely, the ratio of the coil size of PS in decalin to that in a melt, calculated by using the model described in ref 11.

open symbols) is related to the plateau modulus of the film, μ_0 , by $\eta = 2\mu_0 t$. This prediction is validated by the good agreement between the measurement (open symbols) and the best fit to this equation as seen by the solid line in Figure 1b.

Figure 2a shows the fitted value of η plotted versus annealing time, t , for PS/decalin films prepared at various temperatures, T , of 60, 25, and 16 °C. It is apparent from the data taken in the rubbery state (open symbols) that μ_0 varies systematically with T . Beyond the rubbery state (solid symbols), η is seen to increase with time in all the films, suggesting a progressive increase in the entanglement density as reported before.^{7,14} After sufficiently long times, η either reaches a saturation steadily or shows a dramatic decrease at one point before coming to a steady state. The latter behavior was only found in the films prepared at 16 °C (Θ) and was reproducible in another similarly prepared film. We determined the equilibration time, τ , from the intercept between the asymptotic behaviors of the data in the rubbery state and that representing the maximum level reached by η as illustrated by the solid and dashed lines in Figure 2a. The result is plotted in Figure 2b as $1/\tau$ vs T (symbols). We first notice that all values of τ found here are bigger than the reptation time of the bulk polymer (≈ 1600 s, as determined from η/μ_0 of the bulk polymer). This is in keeping with the above observation that the equilibration process probably involves rearrangement of the chain conformation to increase the entanglement density. In addition, the data also show that $1/\tau$ decreases continuously with decreasing temperature and starts to plummet near 16 °C.

To gain some insight about what causes the equilibration time, τ , to increase (or $1/\tau$ to decrease) with decreasing T , we plot $2\mu_0$ and η_{\max} , the maximum level attained by η , as a function of T in parts a and b of Figure 3, respectively. These plots show that with decreasing T , μ_0 decreases but η_{\max} increases. The former signifies a slowing down in the temporal growth of η with decreasing T ; the latter shows that a higher maximum η is attainable by the films prepared at lower T . Either tendency has the effect of increasing τ . The slowing down in the temporal growth of η is likely caused by the increasing difficulty for the chains to interpenetrate as the polymer chains in the as-cast films become more compact as T is lowered toward Θ . Another factor to consider is the solvent concentration, ϕ_s , at which the film solution vitrifies during

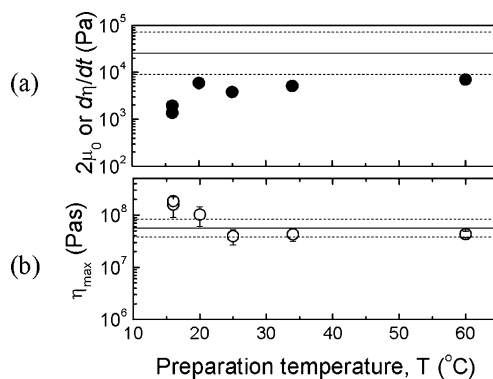


Figure 3. Upper panel: $2\mu_0$ or $d\eta/dt$ obtained from the data before the onset of saturation or maximum in η plotted versus the preparation temperature. Lower panel: maximum or saturation value of η plotted as a function of preparation temperature. The solid and dashed lines in the upper and lower panel denote the values of $2\mu_0$ and η_{\max} obtained from the PS/toluene films, respectively.¹⁴

spin-coating, which can also affect the amount of interpenetration between neighboring chains in the films. It has been established that ϕ_s is a function of T , obtainable by substituting T for the vitrification temperature, T_v , in the following modified Fox equation:⁸

$$\frac{1}{T_v} = \frac{\phi_s}{T_m} + \frac{1 - \phi_s}{T_g} \quad (5)$$

where T_m is the melting temperature of the solvent and all temperatures are in kelvin. For decalin, $T_m = -30$ °C (manufacturer's data) with which eq 5 predicts that ϕ_s increases monotonically with decreasing T and is 0.22 and 0.54 at $T = 60$ and 16 °C, respectively. Taken together, the degree of entanglement decreases with decreasing T not only because the coil size of the polymer in the solution is smaller but also because the solvent content in the film, and thereby interchain separation is bigger at the time of vitrification. The reason for the increase in η_{\max} with decreasing T (Figure 3b) may not be as readily perceivable, however. Fujii et al.¹⁰ observed that PS adsorbed irreversibly on silicon (with or without an oxide cover layer). The presence of strong pinning

between the polymer and substrate can prevent the polymer chains from attaining the equilibrium conformation. As T is decreased, the coil size and hence the surface area per chain in contact with the substrate get smaller. Correspondingly, the number of pinning sites per chain would also get smaller whereby the chains may be able to re-entangle more and reach a higher η_{\max} .

To determine whether the polymer–substrate pinning may differ between films prepared at different preparation temperatures, T , we measured the thickness of the residual (or adsorbed) films as a function of T . To make the residual films, PS/decalin films were prepared as described in the Experimental Section and then annealed at 130 °C for several days. Afterward, the films were thoroughly rinsed with toluene before being soaked in a fresh toluene bath three times for over 30 min to remove any polymer chains that were not adsorbed to the substrate. The thickness of the residual film that remained was measured with ellipsometry. The result is shown in Figure 4.

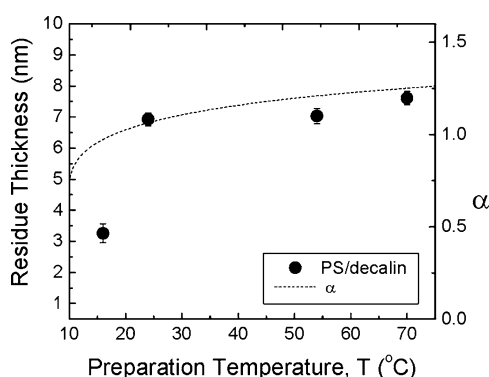


Figure 4. Thickness of the residual film as a function of preparation temperature for the PS/decalin films (symbols). The dashed line represents the expansion factor, α .

The data clearly show that the pinning strength plummets as T approaches Θ , consistent with the picture surmised above.

We notice that while the η_{\max} of the $T = 16$ °C film is bigger than the other films, its steady-state viscosity is actually smaller, attributable to the distinctive collapse exhibited by its η vs t plot just before equilibrium (Figure 2a). We do not have a good explanation for this result. We speculate that it may be due to the onset of slip in the film. As noted above, the coil size in this film is smaller than the other films, and so the grafting density of the pinned layer should be bigger initially. As the chains equilibrate and re-entangle, at one point the pinned layer may get overcrowded, and the strain that builds up may be big enough to cause some of the pinned chains to break off from the substrate and slip atop the remaining pinned layer. With the onset of slip, the apparent viscosity can be smaller than that demonstrated by the other films that do not slip (or slip less).²¹

It is interesting to see from Figure 3a that even at a high preparation temperature of 60 °C, the plateau modulus and hence density of entanglement of the PS/decalin(60 °C) films (i.e., PS films cast from a decalin solution at 60 °C) are lower than those of the PS/toluene films. We examine whether this discrepancy can be accounted for by the different expansion factors— $\alpha_{\text{tol}} = 1.4$ and $\alpha_{\text{decalin,60 °C}} = 1.2$ —of the PS chains in the two solutions. Because the radius of gyration of the polymer (~ 12 nm) is comparable to the film thickness ($= 14$ nm), the ratio of the pervaded volume of the chains in the two films just before complete drying is $\approx (\alpha_{\text{tol}}/\alpha_{\text{decalin,60 °C}})^2 = 1.36$. Because

$\phi_s = 0.22$ and 0.25 for the PS/decalin(60 °C) and PS/toluene films, respectively, the ratio of pervaded volume in the two kinds of films upon complete drying is $\approx 1.36 \times (0.75/0.78) = 1.31$. This ratio can be related to the ratio of the plateau moduli in the films. Studies had been performed to examine the relation between the plateau modulus and chain conformation in bulk polymer.^{22,23} More recently, Si et al.²⁴ addressed the issue for polymer under confinement in thin films. According to their result, the effective interchain entanglement density in ultrathin films is

$$\nu_{\text{inter}} = \nu(1 - PV_p/V_{p,i}) \quad (6)$$

where ν is the unperturbed, total entanglement density, P is a constant, V_p is the average volume pervaded by an unperturbed chain, and $V_{p,i}$ is the volume pervaded by a chain in solution i . By eq 6, we can write $PV_p/V_{p,i} = 1 - \nu_{\text{inter},i}/\nu$ ($i = t$ and d denotes toluene at room temperature and decalin at 60 °C, respectively). To proceed further, we need to know the value of P for each system. To get some idea, we adopt the simple assumption that $P = 0$ (i.e., all the entanglements are interchain) in the bulk but is nonzero and about the same in the PS/toluene and PS/decalin(60 °C) films. With this and the additional assumptions that the rubbery plateau modulus μ_0 is $\sim \nu_{\text{inter},i}$ and the μ_0 value of entangled PS in bulk, PS/toluene films, and PS/decalin(60 °C) films is 1×10^5 ,²⁵ 1.2×10^4 ,¹⁴ and 4366 Pa (Figure 3b) as found in experiment, respectively, we estimate that $1 - \nu_{\text{inter},i}/\nu = 0.87$ and 0.956 for $i = t$ and d , respectively. These give $V_{p,t}/V_{p,d} = 0.956/0.87 = 1.1$. This is $\sim 16\%$ smaller than that estimated above by using the expansion factors. Given the crudeness of the estimates, the agreement found here is not bad indeed. This may help show that the variation in the plateau modulus of the films is caused by the variation in the chain conformation that gets frozen in the films upon spin-coating.

CONCLUSION

We have shown that the time required for spin-coated polymer films supported by a substrate to reach equilibrium on heating above the T_g is significantly affected by the quality of the solvent the film is cast from. In particular, as the temperature the films are cast at is reduced toward Θ resulting in a worsening solvent quality, the equilibration time increases drastically. We found that this increase near Θ is due to both a decrease in μ_0 and an increase in η_{\max} with decreasing T . The decrease in μ_0 is attributed to a reduced entanglement in the cast film due to a more compact chain size and higher solvent volume fraction at vitrification. The increase in η_{\max} may be associated with the reduced amount of pinning between the polymer chains and substrate allowing the chains to re-entangle more and thereby reach a higher η_{\max} .

AUTHOR INFORMATION

Corresponding Author

*E-mail: okctsui@bu.edu.

Present Address

[†]Center for Soft Condensed Matter Physics & Interdisciplinary Research, Soochow University, Suzhou 215123, P. R. China.

ACKNOWLEDGMENTS

We thank Dongdong Peng for useful discussions. We are grateful to the support of the National Science Foundation through the projects DMR-0908651 and DMR-1004648.

■ REFERENCES

- (1) Kanaya, T.; Miyazaki, T.; Watanabe, H.; Nishida, K.; Yamano, H.; Tasaki, S.; Bucknall, B. *Polymer* **2003**, *44*, 3769–3773.
- (2) Reiter, G.; Hamieh, M.; Damman, P.; Slavovs, S.; Gabriele, S.; Vilmin, T.; Raphael, E. *Nature Mater.* **2005**, *4*, 754–758.
- (3) Priestley, R. D.; Ellison, C. J.; Broadbelt, L. J.; Torkelson, J. M. *Science* **2005**, *309*, 456–459.
- (4) Bodiguel, H.; Fretigny, C. *Eur. Phys. J. E* **2006**, *19*, 185–193.
- (5) Tsui, O. K. C.; Russell, T. P.; Hawker, C. J. *Macromolecules* **2001**, *34*, 5535–5539.
- (6) Tsui, O. K. C.; Wang, Y. J.; Lee, F. K.; Lam, C.-H.; Yang, Z. *Macromolecules* **2008**, *41*, 1465–1468.
- (7) Barbero, D. R.; Steiner, U. *Phys. Rev. Lett.* **2009**, *102*, 248303.
- (8) Raegen, A.; Chowdhury, M.; Calers, C.; Schmatulla, A.; Steiner, U.; Reiter, G. *Phys. Rev. Lett.* **2010**, *105*, 227801.
- (9) Napolitano, S.; Wubbenhorst, M. *Nature Commun.* **2011**, *2*, 260–266.
- (10) Fujii, Y.; Yang, Z.; Leach, J.; Atarashi, H.; Tanaka, K.; Tsui, O. K. C. *Macromolecules* **2009**, *42*, 7418–7422.
- (11) Sun, S.-T.; Nishio, I.; Swislow, G.; Tanaka, K. *J. Chem. Phys.* **1980**, *73*, 5971–5975.
- (12) Yang, Z.; Fujii, Y.; Lee, F. K.; Lam, C.-H.; Tsui, O. K. C. *Science* **2010**, *328*, 1676–1679.
- (13) Peng, D.; Yang, Z.; Tsui, O. K. C. *Macromolecules* **2011**, *44*, 7460–7464.
- (14) Yang, Z.; Clough, A.; Lam, C.-H.; Tsui, O. K. C. *Macromolecules* **2011**, *44*, 8294–8300.
- (15) Yang, Z. H.; Wang, Y.; Todorova, L.; Tsui, O. K. C. *Macromolecules* **2008**, *41*, 8785–8788.
- (16) Brandrup, J.; Immergut, E. H. *Polymer Handbook*, 3rd ed.; Wiley: New York, 1989.
- (17) Zhao, H.; Wang, Y. J.; Tsui, O. K. C. *Langmuir* **2005**, *21*, 5817–5824.
- (18) Tsui, O. K. C.; Wang, X. P.; Ho, J. Y. L.; Ng, T. K.; Xiao, X. *Macromolecules* **2000**, *33*, 4198–4204.
- (19) Wang, X. P.; Xiao, X.; Tsui, O. K. C. *Macromolecules* **2001**, *34*, 4180–4185.
- (20) Du, B.; Zhang, J.; Zhang, Q.; Yang, D.; He, T.; Tsui, O. K. C. *Macromolecules* **2000**, *33*, 7521–7528.
- (21) Clough, A.; Peng, D.; Yang, Z.; Tsui, O. K. C. *Macromolecules* **2011**, *44*, 1649–1653.
- (22) Fetters, L. J.; Lohse, D. J.; Graessley, W. W. *J. Polym. Sci., Part B: Polym. Phys.* **1999**, *37*, 1023–1033.
- (23) Sukumaran, S. K.; Grest, G. S.; Kremer, K.; Everaers, R. *J. Polym. Sci., Part B: Polym. Phys.* **2005**, *43*, 917–933.
- (24) Si, L.; Massa, M. V.; Dalnoki-Veress, K.; Brown, H. R.; Jones, R. A. L. *Phys. Rev. Lett.* **2005**, *94*, 127801.
- (25) Strobl, G. R. *The Physics of Polymers*; Springer-Verlag: Berlin, Germany, 1996.

Self-Assembly of Bifunctional Patchy Particles with Anisotropic Shape into Polymers Chains: Theory, Simulations, and Experiments

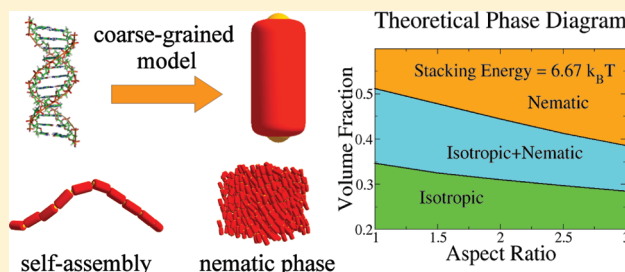
Cristiano De Michele,^{*,†} Tommaso Bellini,[‡] and Francesco Sciortino[§]

[†]Dipartimento di Fisica, Sapienza - Università di Roma, P. le A. Moro 2, 00185 Roma, Italy

[‡]Dipartimento di Chimica, Biochimica e Biotecnologie per la Medicina, Università di Milano, I-20122 Milano, Italy

[§]Dipartimento di Fisica and CNR-ISC, Sapienza - Università di Roma, P. le A. Moro 2, 00185 Roma, Italy

ABSTRACT: Concentrated solutions of short blunt-ended DNA duplexes, as short as 6 base pairs, are known to order into the nematic liquid crystal phases. This self-assembly is due to the stacking interactions between duplex terminals that promotes their aggregation into polydisperse chains with a significant persistence length. Experiments show that liquid crystal phases form above a critical volume fraction depending on the duplex length. We introduce and investigate via numerical simulations, a coarse-grained model of DNA double-helical duplexes. Each duplex is represented as an hard quasi-cylinder whose bases are decorated with two identical reactive sites. The stacking interaction between terminal sites is modeled via a short-range square-well potential. We compare the numerical results with predictions based on a free energy functional and find satisfactory quantitative matching of the isotropic–nematic phase boundary and of the system structure. Comparison of numerical and theoretical results with experimental findings confirm that the DNA duplex self-assembly can be properly modeled via equilibrium polymerization of cylindrical particles. This insight enables us to estimate the stacking energy.



I. INTRODUCTION

Self-assembly is the spontaneous organization of matter into reversibly bound aggregates. In contrast to chemical synthesis, where molecular complexity is achieved through covalent bonds, supramolecular aggregates spontaneously form in a self-assembly process due to free energy minimization. Self-assembly is ubiquitous in nature and can involve the structuring of elementary building blocks of various sizes, ranging from simple molecules (e.g., surfactants) to the mesoscopic units (e.g., colloidal particles). This ability to assemble complicated entities from relatively simple building blocks has made self-assembly interesting to several fields, including soft matter and biophysics.^{1–3} Understanding and thus controlling self-assembly is important for devising new materials whose physical properties are controlled by tuning the interactions of the various components.^{4–7,7–12}

A particular but very interesting case of self-assembly occurs when the anisotropy of attractive interactions between the monomers favors the formation of linear or filamentous aggregates, i.e., linear chains. A longstanding example is provided by the formation of worm-like micelles of amphiphilic molecules in water or microemulsions of water and oil which are stabilized by amphiphilic molecules. If supramolecular aggregates possess a sufficient rigidity the system may exhibit liquid crystal (LC) ordering even if the self-assembling components do not have the required shape anisotropy to guarantee the formation of nematic phases. Intense experimental activity has been dedicated to the study of nematic transitions in micellar systems.^{13–15} Another prominent case is

the formation of fibers and fibrils of peptides and proteins.^{16–19} Over the last 50 years LC phases have been also observed in solutions of long duplex B-form DNA composed of 10^2 to 10^6 base pairs,^{20–23} and in the analogous case of filamentous viruses.^{24–28} More recently, a series of experiments^{29–31} have provided evidence that a solution of short DNA duplexes (DNAD), 6 to 20 base pairs in length, can also form liquid crystals above a critical concentration, giving rise to nematic and columnar LC phases.²⁹

However, this behavior was found when the terminals of the duplexes interact attractively. This condition is verified either when duplexes terminate bluntly, as in the case of fully complementary strands shown in Figure 1a, or when the strands arrange in shifted double-helices whose overhangs are mutually interacting. This behavior is not restricted to B-form DNA oligomers, as it has also been observed in solutions of blunt-ended A-form RNA oligomeric duplexes.³² As the terminal groups are modified to disrupt attraction, the LC long-range ordering is lost. Overall, the whole body of experimental evidence supports the notion that LC formation is due to the formation of reversible linear aggregates of duplexes, in turn promoting the onset of long-ranged orientational LC ordering. According to this picture, the LC ordering of oligomeric DNA is analogous to the LC ordering of chromonic liquid crystals.³³ Both in chromonics and in blunt-

Received: August 27, 2011

Revised: December 12, 2011

Published: December 29, 2011

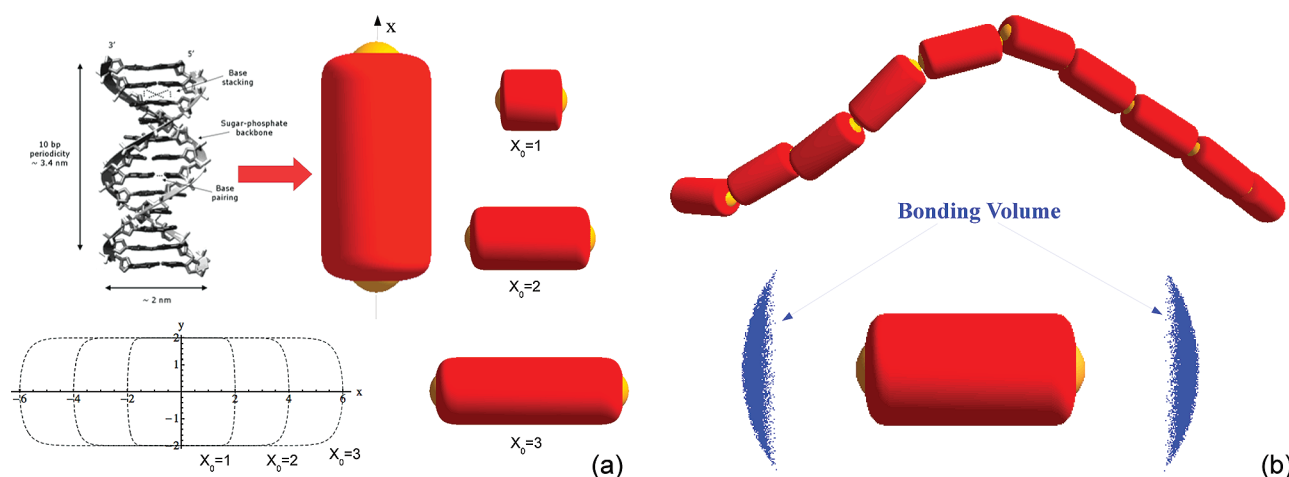


Figure 1. Coarse-grained model of DNA duplexes. (a) DNA duplex and a 3D graphical representation of its corresponding coarse-grained model comprising a SQ symmetric around the x axis, decorated with two sticky spots located on its bases. The figure also shows SQs of different aspect ratios ($X_0 = 1, 2, 3$) and the projection of their surfaces onto the xy -plane. Note that the base roundness increases on increasing X_0 . (b) Random chain of 10 monomers and a representation (blue clouds) of the points where the center of mass of a different monomer can be located in a bonding volume.

ended DNA duplexes, the aggregation takes place because of stacking interactions, generally understood as hydrophobic forces acting between the flat hydrocarbon surfaces provided by the core of chromonic molecules and by the paired nucleobases at the duplex terminals.^{34,35}

The LC ordering of nucleic acids is relevant for various reasons. First, it provides a new model of reversible aggregation leading to macroscopic ordering in which the strength of the intermonomer attraction can be modified by changing the duplex terminals (blunt-end stacking or pairing of overhangs). Second, it provides new access to DNA–DNA interactions, and in particular to stacking interactions, whose nature is still being investigated and debated.^{34,35} In this vein, self-assembly acts as an amplifier of the intermonomeric interactions, enabling study of the effects of minor molecular modification (e.g., oligomer terminations) on base stacking. Finally, stacking and self-assembly are often invoked as the prebiotic route to explaining the gap between the random synthesis of elementary carbon-based molecules and the first complex molecules, possibly RNA oligomers, which are capable of catalyzing their own synthesis.³⁶ To proceed in any of these directions, it is necessary to rely on models which allow us to quantitatively connect the collective behavior of nucleic acids oligomers to their molecular properties and, in particular, to the duplex size and to the strength and range of the interduplex attractions.

While the isotropic–nematic transition in rigid and semi-flexible polymers has been investigated in details in the past and rather accurate thermodynamic descriptions have been proposed,^{37–45} much less is known for the case in which the nematic transition takes place in reversibly assembling polymers, i.e., when the average length of the chains depends on the state point explored. Recent theoretical and numerical works^{46,47} has renewed the interest in this topic.⁴⁸ Reference 47 investigates the self-assembly and nematization of spheres, while ref 46 focuses on the polymerization of interacting cylinders. In this article, we propose a coarse-grained model similar to the one introduced in ref 46 devised to capture the essential physical features of equilibrium polymerization of DNA duplexes. We study this model numerically via Monte Carlo simulations in the constant temperature and pressure ensembles, applying special biasing techniques^{49,50} to speed up

the equilibration process. We then develop a free-energy functional, building on Wertheim^{51–53} and Onsager⁵⁴ theories, which provides a satisfactory description of the system in the isotropic and nematic phases. A comparison of the calculated phase boundaries for different aspect ratios and different interaction strengths with experimental results allow us to confirm that (i) the DNAD aggregation and LC ordering processes can be properly modeled via equilibrium polymerization of cylindrical particles and (ii) to provide an estimate of the stacking energy.

In section II, we introduce the coarse-grained model of DNADs and provide some details of the computer simulations. Section III gives a summary of the analytic theory which we developed to describe the system in the isotropic and nematic phases. A comparison of our analytical approach with numerical results is presented in section V, while in section VI we provide an estimate of the stacking energy by comparing our theoretical results with experimental data. Section VII represents our conclusions.

II. MODEL AND NUMERICAL DETAILS

In this section we introduce a coarse-grained model devised to capture the essential physical features of end-to-end stacking (equilibrium polymerization) of DNA duplexes which is well suited to being investigated both theoretically and numerically. In the model, particles (DNADs) are assimilated to super-quadratics (SQ) with a quasi-cylindrical shape decorated with two reactive sites on their bases determining their interactions. SQs are a straightforward generalization of hard ellipsoids (HE), their surface is in fact defined as follows:

$$f(x, y, z) = \left| \frac{x}{a} \right|^p + \left| \frac{y}{b} \right|^m + \left| \frac{z}{c} \right|^n - 1 = 0 \quad (1)$$

where the parameters p, m, n are real numbers and a, b, c are the SQ semiaxes.

In our case we set $m = n = 2$, $p = 16$, and $b = c$, so that the SQ resembles a cylinder with rounded edges (see Figure 1). The absence of surface gradient discontinuities makes this model also suitable for investigating its dynamics via event-driven molecular dynamics.⁵⁵

Such SQs can be fully characterized by the aspect ratio $X_0 = a/b$ and by the parameter p , that determines the sharpness of the edges (see Figure 1). As for the case of HEs SQs of aspect ratio $X_0 < 1$ are called “oblate”, while SQs of aspect ratio $X_0 > 1$ are called “prolate”. As unit of length in our simulations we use the length of the short semiaxes b . In the present study we investigated only prolate SQs with aspect ratio $X_0 = 1, 2$ and 3. We chose such aspect ratios because DNADs used in experiments²⁹ have a diameter $D = 2$ nm and are composed of 6 to 20 base pairs (BP) each 0.3 nm long. Hence their aspect ratio X_0 ranges approximately from 1 to 3.

Each particle is decorated with two attractive sites, located along the symmetry axis (x -axis in Figure 1) at a distance $d/b = X_0 - 0.46$ from the DNAD center of mass, in order to model hydrophobic (stacking) forces between DNADs. Sites belonging to distinct particles interact via the following square-well (SW) potential:

$$\beta u_{SW} = \begin{cases} -\beta \Delta E_S & r < \delta \\ 0 & r > \delta \end{cases} \quad (2)$$

Here r is the distance between the interacting sites, $\delta/b = 1.22$ is the range of interaction (i.e., the diameter of the attractive sites), $\beta = 1/k_B T$, and k_B is the Boltzmann constant. Therefore, in the present model the anisotropic hard-core interaction is complemented with an anisotropic attractive potential in a fashion similar to past work on water,⁵⁶ silica,⁵⁷ and the stepwise polymerization of bifunctional diglycidyl ether of bisphenol A with pentafunctional diethylenetriamine.^{58,59}

The location and diameter of the attractive sites have been chosen to best mimic the stacking interactions between blunt-ended DNAD, and in particular, they ensure the following points.

- 1 The maximum interaction range between two DNADs bases is of the order of the typical range for hydrophobic interactions (i.e., 2 Å, see ref 60), i.e., comparable to the dimensions of the water molecule.
- 2 The extent of the attractive surface of the DNADs bases is compatible with the surface of aromatic groups present in DNADs, which are responsible for hydrophobic interactions.

We note that in the present model each DNAD is symmetric around the x -axis (see Figure 1), and hence, we are neglecting rotations around it.

We performed Monte Carlo (MC) simulations in the canonical and isobaric ensembles. We implemented the aggregation biased MC technique (AVBMC) developed by Chen and Siepmann^{49,50} in order to speedup (up to a factor of 2 compared to standard MC) the formation of linear aggregates.

To detect the overlap of two DNADs we calculated the distance using the algorithm described in ref 55. In all simulations we adopted periodic boundary conditions in a cubic simulation box.

We studied a system of $N = 1000$ particles in a wide range of volume fractions ϕ and pressure P , respectively. Initially, we prepared configurations at high temperature with all DNADs being bonded, and then we quenched the system to the final temperature (i.e., to the final value of $\beta \Delta E_S$) before letting it equilibrate. We checked equilibration by inspecting the behavior of the potential energy and the nematic order parameter (see section VB) in the system.

III. THEORY

Following the work of van der Schoot and Cates^{14,48} and its extension to higher volume fractions with the use of the Parsons–Lee approximation^{61,62} as suggested by Kuriabova et al.,⁴⁶ we assume the following expression for the free energy of our system:

$$\frac{\beta F}{V} = \sum_{l=1}^{\infty} \nu(l) \{ \ln[\nu_d \nu(l)] - 1 \} + \frac{\eta(\phi)}{2} \sum_{l=1}^{\infty} \sum_{l'=1}^{\infty} \nu(l) \nu(l') v_{excl}(l, l') - (\beta \Delta E_S + \sigma_b) \sum_{l=1}^{\infty} (l-1) \nu(l) + \sum_{l=1}^{\infty} \nu(l) \sigma_o(l) \quad (3)$$

where $\nu(l)$ is the number density of chains of length l , normalized such that $\sum_{l=1}^{\infty} l \nu(l) = \rho$, ν_d is the volume of a monomer, $\beta \Delta E_S$ is the (positive) stacking energy, $v_{excl}(l, l')$ is the excluded volume of two chains of length l and l' and σ_b is the entropic free energy penalty for bonding (i.e., is the contribution to free energy due to the entropy which is lost by forming a single bond). $\eta(\phi)$ is the Parsons–Lee factor⁶¹

$$\eta(\phi) = \frac{1}{4} \frac{4 - 3\phi}{(1 - \phi)^2} \quad (4)$$

and σ_o ⁴⁵ accounts for the orientational entropy that a chain of length l loses in the nematic phase (including possible contribution due to its flexibility). Different from refs 46 and 48 but as in ref 47, we explicitly account for the polydispersity inherent in the equilibrium polymerization using a discrete chain length distribution. We explicitly separate the bonding free energy in an energetic ($\beta \Delta E_S$) and an entropic (σ_b) contribution. Different from ref 47 and 48 but as in ref 46, we include the Parsons–Lee factor. Indeed, the Parsons decoupling approximation satisfactory models the phase diagram of uniaxial hard ellipsoids,⁶³ hard cylinders,⁶⁴ linear fused hard spheres chains,⁶⁵ mixtures of hard platelets,⁶⁶ hard spherocylinders,^{67–69} rod–plate mixtures,⁷⁰ mixtures of rod-like particles^{71,72} and mixtures of hard rods and hard spheres.⁷³ On the other hand, ref 74 finds that the Parsons theory is not satisfactory in the case of rigid linear chains of spheres.

A justification of the use of Parsons–Lee factor in eq 3 for the present case of aggregating cylinders is provided in Appendix A. Here we only note that the present system, in the limit of high T where polymerization is not effective, reduces to a fluid of hard quasi-cylinders, where the use of Parsons–Lee factor is justifiable.^{64,68,69} Moreover, in the dilute limit ($\eta(\phi) \rightarrow 1$) the excluded volume term in eq 3 reduces to the excluded volume of a polydisperse set of aggregates with length distribution $\nu(l)$, which conforms to Onsager’s original theory.⁵⁴ In other words, the form chosen in eq 3 for the excluded volume contribution to the free energy reduces to the correct expressions in the limit of high temperatures and of low volume fractions.

Following van der Schoot and Cates,^{14,48} $v_{excl}(l, l')$ can be assumed to be as a second order polynomial in l and l'

$$v_{\text{excl}}[l, l'; f(\mathbf{u})] = 2 \int f(\mathbf{u})f(\mathbf{u}')D^3[\Psi_1(\gamma, X_0) + \frac{l+l'}{2}\Psi_2(\gamma, X_0)X_0 + \Psi_3(\gamma, X_0)X_0^2ll'] d\Omega d\Omega' \quad (5)$$

where $f(\mathbf{u})$ is the probability for a given monomer having an orientation \mathbf{u} within the solid angle Ω and $\Omega + d\Omega$ and Ψ_α describes the angular dependence of the excluded volume. The orientational probability $f(\mathbf{u})$ is normalized as

$$\int f(\mathbf{u}) d\Omega = 1 \quad (6)$$

In particular, for two rigid chains of length l and l' which are composed of hard cylinders (HC) of diameter D and length X_0D , $v_{\text{excl}}(l, l')$ has been calculated by Onsager in 1949

$$v_{\text{excl}}(l, l') = \int f(\mathbf{u})f(\mathbf{u}')D^3 \left[\frac{\pi}{2} \sin \gamma + \frac{\pi}{2} X_0(1 + |\cos \gamma|) + \frac{4}{\pi} E(\sin \gamma) \frac{l+l'}{2} + 2X_0^2 \sin \gamma ll' \right] d\Omega d\Omega' \quad (7)$$

where $\cos \gamma = \mathbf{u} \cdot \mathbf{u}'$ and $E(\sin \gamma)$ is the complete elliptical integral

$$E(\sin \gamma) = \frac{1}{4} \int_0^{2\pi} (1 - \sin^2 \gamma \sin^2 \psi)^{1/2} d\psi \quad (8)$$

In passing, we observe that the integrals in eq 7 can be calculated exactly in the isotropic phase while in the nematic phase the calculation can be done analytically only with suitable choices of the angular distribution $f(\mathbf{u})$. Comparing eqs 7 and 5 for HC one has:

$$\begin{aligned} \Psi_1(\gamma, X_0) &= \frac{\pi}{4} \sin \gamma \\ \Psi_2(\gamma, X_0) &= \frac{\pi}{4} \left(1 + |\cos \gamma| + \frac{4}{\pi} E(\sin \gamma) \right) \\ \Psi_3(\gamma, X_0) &= \sin \gamma \end{aligned} \quad (9)$$

In view of eqs 9 we note that for HCs the functions $\Psi_1(\gamma)$, $\Psi_2(\gamma)$, and $\Psi_3(\gamma)$ accounts for the orientational dependence of the excluded volume of two monomers having orientations \mathbf{u} and \mathbf{u}' with $\mathbf{u} \cdot \mathbf{u}' = \cos \gamma$. It is also worth observing that the first term of the integrand in eq 7 is independent of l and hence accounts for the excluded volume interaction between two HCs ends. The second term is linear in l and l' and accounts for the excluded volume between the end of a chain and all midsections of a second one. The third term, proportional to ll' , models the interaction between all ll' pairs of midsections of the two chains.^{14,48} In summary, eq 5 is exact for two rigid chains of HCs but, to lowest order of approximation,^{14,39} it is justifiable even for two semiflexible chains. We then assume that v_{excl} remains additive with respect to end-end, end-midsection and midsection-midsection excluded volume contributions even if the chain is semiflexible. Finally, our further ansatz is that eq 5 is also a good functional form for the excluded volume of two superquadrics having quasi-cylindrical

shape: we will check the validity of this hypothesis using our simulations data.

It is worth noting that in the present case eq 7 is not appropriate for evaluating the excluded volume between two linear aggregates of SQs, for at least two reasons: (i) a superquadric and a cylinder with same diameter and aspect ratio have different volumes. (ii) Equation 7 holds if linear aggregates of SQs retain a “tube-like” shape. In the present model instead, two bonded SQs may have their symmetry axes parallel but not coaxial. Despite the general inadequacy of eq 7 for our SQ model, one can expect that the scaling with respect to l and l' is still valid and for this reason we assume the functional form in eq 5 for the excluded volume between two chains of SQs.

An exact expression for σ_o is not available. The two following limits have been calculated by Khokhlov and Semenov:^{37,40,45}

$$\begin{aligned} \sigma_o(l) &= \frac{l}{8l_p} \int \left(\frac{\partial f}{\partial \theta} \right)^2 f^{-1} d\Omega - 2 \ln \int f^{1/2} d\Omega \\ &\quad + \ln(4\pi) \quad (l_p \ll l) \\ \sigma_o(l) &= \int f \ln(4\pi f) d\Omega + \frac{l}{12l_p} \int \left(\frac{\partial f}{\partial \theta} \right)^2 f^{-1} d\Omega \\ &\quad (l_p \gg l) \end{aligned} \quad (10)$$

Finally, we note that, in the limit of rigid rods with $f_l(\mathbf{u}) = f(\mathbf{u})\nu(l)$, (the same limit selected in ref 46), the free energy in eq 3 reduces to:

$$\begin{aligned} \frac{\beta F}{V} &= \frac{2}{3l_p} \sum_{l=1}^{\infty} l \int [f_l(\mathbf{u})]^{1/2} \nabla^2 [f_l(\mathbf{u})]^{1/2} d\Omega + \\ &\quad \sum_{l=1}^{\infty} \int f_l(\mathbf{u}) \{ \ln[4\pi \nu_d f_l(\mathbf{u})] - 1 \} \\ &\quad + \frac{\eta(\varphi)}{2} \sum_{l=1, l'=1}^{\infty} \int f_l(\mathbf{u}) f_{l'}(\mathbf{u}') v_{\text{excl}}(l, l') \\ &\quad d\Omega d\Omega' - (\beta \Delta E_S + \sigma_b) \\ &\quad \sum_{l=1}^{\infty} \int (l-1) f_l(\mathbf{u}) d\Omega \end{aligned} \quad (11)$$

which is analogous to the free energy expression used by Kuriabova et al.⁴⁶

A. Isotropic Phase. In the isotropic phase all orientations are equiprobable, and hence

$$f(\mathbf{u}) = \frac{1}{4\pi} \quad (12)$$

Plugging eq 12 into eq 3 and calculating the integrals one obtains:

$$\begin{aligned} \frac{\beta F}{V} &= \sum_{l=1}^{\infty} \nu(l) \{ \ln[\nu_d \nu(l)] - 1 \} + \frac{\eta(\varphi)}{2} \\ &\quad \sum_{l=1, l'=1}^{\infty} \nu(l) \nu(l') v_{\text{excl}}(l, l') - (\beta \Delta E_S + \sigma_b) \\ &\quad \sum_{l=1}^{\infty} (l-1) \nu(l) \end{aligned} \quad (13)$$

For hard cylinders the excluded volume can be calculated explicitly:

$$v_{\text{excl}}(l, l') = \frac{\pi^2}{8} D^3 + \left(\frac{3\pi}{8} + \frac{\pi^2}{8} \right) [l + l'] X_0 D^3 + \frac{\pi}{2} l l' X_0^2 D^3 \quad (14)$$

Building on eq 14, the generic expression for the excluded volume $v_{\text{excl}}(l, l')$ reported in eq 5 in the isotropic phase takes the form:

$$v_{\text{excl}}(l, l') = 2 \left[A_I(X_0) + k_I(X_0) v_d \frac{l + l'}{2} + B_I(X_0) X_0^2 l l' \right] \quad (15)$$

We assume that the chain length distribution $\nu(l)$ is exponential with an average chain length M

$$\begin{aligned} \nu(l) &= \rho M^{-(l+1)} (M-1)^{l-1} \\ &= \frac{\rho}{M(M-1)} e^{-l[\ln M - \ln(M-1)]} \end{aligned} \quad (16)$$

where

$$M = \frac{\sum_1^\infty l \nu(l)}{\sum_1^\infty \nu(l)} \quad (17)$$

With this choice for $\nu(l)$ the free energy in eq 13 becomes:

$$\begin{aligned} \frac{\beta F}{V} &= -\rho(\beta \Delta E_S + \sigma_b)(1 - M^{-1}) \\ &+ \eta(\varphi) \left[B_I X_0^2 + \frac{v_d k_I}{M} + \frac{A_I}{M^2} \right] \rho^2 \\ &+ \frac{\rho}{M} \left[\ln \left(\frac{v_d \rho}{M} \right) - 1 \right] + \rho \frac{M-1}{M} \ln(M-1) - \rho \ln M \end{aligned} \quad (18)$$

Note that, in general, k_I , B_I and A_I depend on X_0 .

The minimization of the free energy with respect to M yields, after dropping terms in $O(1/M^2)$

$$M = \frac{1}{2} \left(1 + \sqrt{1 + 4\omega \varphi e^{k_I \varphi \eta(\varphi) + \beta \Delta E_S}} \right) \quad (19)$$

where $\omega \equiv e^{\sigma_b}$. This formula for M differs from the one reported by Kindt⁴⁷ by the presence of the Parsons-Lee factor, which will play a role at high volume fractions.

The expression for M in eq 19 coincides with the parameter-free expression for the average chain length M_w obtained within Wertheim's theory (e.g., see refs 51–53, 75, and 76), when ϕ is small and $e^{k\phi\eta(\phi)} \approx 1$. Indeed, in Wertheim theory

$$M_w = \frac{1}{2} + \frac{1}{2} \sqrt{1 + 8 \frac{\Phi}{v_d} \Delta} \quad (20)$$

where $\Delta = V_b(e^{\beta \Delta E_S} - 1)$ and V_b is the bonding volume.⁷⁵ In the limit $e^{\beta \Delta E_S} \gg 1$, which is always valid in the T -region where chaining takes place

$$M_w = \frac{1}{2} + \frac{1}{2} \sqrt{1 + 8 \frac{V_b}{v_d} \varphi e^{\beta \Delta E_S}} \quad (21)$$

The equivalence between the two expressions provides an exact definition of ω as

$$\omega = 2 \frac{V_b}{v_d} \quad (22)$$

Although eq 19 has been derived ignoring $O(1/M^2)$ terms in the free energy, the average chain length M can be always calculated, and this is what we do in this work, numerically locating the zero of $\partial(\beta F/V)/\partial M = 0$.

B. Nematic Phase. In the nematic phase the function $f(\mathbf{u})$ depends explicitly on the angle between a given particle direction and the nematic axis, i.e., on the axis \mathbf{u} . The orientational distribution function $f(\mathbf{u})$ generally depends on a set of parameters that have to be obtained through the minimization of the free energy. Also in the nematic phase we assume an exponential distribution for $\nu(l)$. In addition, we consider an angular distribution function $f(\mathbf{u})$ with the form proposed by Onsager,⁵⁴ i.e.:

$$f(\mathbf{u}) = f_O(\mathbf{u}) = \frac{\alpha}{4\pi \sinh \alpha} \cosh(\alpha \cos \theta) \quad (23)$$

where θ is the angle between the particle and the nematic axis and the system is supposed to have azimuthal symmetry around such axis.

In view of the analytical expression for the excluded volume v_{excl} for cylinders, we assume the following form for the v_{excl} of two DNADs averaged over the solid angle using the one parameter (α) dependent orientational distribution function $f_O(\mathbf{u})$ defined in eq 23:

$$\begin{aligned} v_{\text{excl}}(l, l', \alpha) &= 2 \left[A_N(\alpha) + v_d k_N(\alpha) \frac{l + l'}{2} \right. \\ &\quad \left. + B_N(\alpha) X_0^2 l l' \right] \end{aligned} \quad (24)$$

If we insert eqs 24 and 16 into eq 3, we obtain after some algebra:

$$\begin{aligned} \frac{\beta F}{V} &= \hat{\sigma}_0 - \rho(\beta \Delta E_S + \sigma_b)(1 - M^{-1}) \\ &+ \eta(\varphi) \left[B_N(\alpha) X_0^2 + \frac{k_N(\alpha)}{M} v_d \right. \\ &\quad \left. + \frac{A_N(\alpha)}{M^2} \right] \rho^2 + \frac{\rho}{M} \left(\ln \left[\frac{v_d \rho}{M} \right] - 1 \right) \\ &- \rho \ln M + \rho \ln(M-1) \frac{M-1}{M} \end{aligned} \quad (25)$$

where $\hat{\sigma}_0 \equiv \sum_l \sigma_0(l) \nu(l)$.

C. Phase Coexistence. Using the free energy functionals in eqs 18 and 25 the phase boundaries, i.e. $\phi_N = v_d \rho_N$ and $\phi_I = v_d \rho_I$ of the isotropic–nematic transition can be straightforwardly calculated by minimizing the free energy with respect to the average chain lengths in the isotropic and nematic phases, i.e. M_I and M_N , and α . We also require that the isotropic and nematic phases have the same pressure, i.e., $P_I = P_N$ and the same chemical potential $\mu_I = \mu_N$. These conditions require numerically solving the following set of equations:

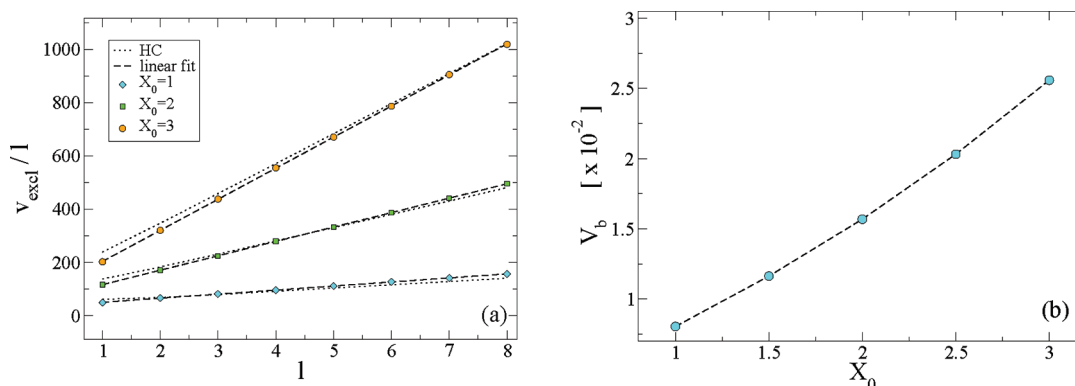


Figure 2. (a) Excluded volume of two chains of length l calculated numerically as a function of l for $X_0 = 1, 2, 3$. Dashed lines are fits to eq 27. Dotted lines are excluded volumes for chains of HCs calculated using eq 7. (b) Bonding volume as a function of aspect ratio X_0 .

$$\begin{aligned}
 \frac{\partial}{\partial M_I} F_{\text{iso}}(\rho_I, M_I) &= 0 \\
 \frac{\partial}{\partial M_N} F_{\text{nem}}(\rho_N, M_N, \alpha) &= 0 \\
 \frac{\partial}{\partial \alpha} F_{\text{nem}}(\rho_I, M_I, \alpha) &= 0 \\
 P_I(\rho_I, M_I) &= P_N(\rho_N, M_N, \alpha) \\
 \mu_I(\rho_I, M_I) &= \mu_N(\rho_N, M_N, \alpha)
 \end{aligned} \quad (26)$$

IV. CALCULATION OF FREE ENERGY PARAMETERS

The theory illustrated in the previous section requires the calculation of several parameters, V_b , k_I , A_I , B_I , k_N , A_N , B_N , and l_p . Since an explicit calculation of these parameters is very unlikely for superquadrics in the following we describe simple methods to calculate them numerically. For example, the calculation of the excluded volume between aggregates and the calculation of the bonding volume require the evaluation of complicated integrals, which can be estimated with a Monte Carlo method.^{77–79} The general idea behind Monte Carlo is that such complicated integrals can be calculated by generating a suitable distribution of points in the domain of integration.

A. Excluded Volume in the Isotropic Phase. In the isotropic phase, $v_{\text{excl}}(l, l')$ can be written as reported in eq 15. If $l = l'$

$$v_{\text{excl}}(l, l) = 2A_I + 2k_I v_d l + 2B_I X_0^2 l^2 \quad (27)$$

Hence, from a numerical evaluation of $v_{\text{excl}}(l, l)$ for several l values (whose detailed procedure is described in Appendix X) it is possible to estimate A_I , k_I , and B_I . Figure 2a shows $v_{\text{excl}}(l, l)/l$ vs l . A straight line properly describes the data for all X_0 values, suggesting that $A_I \approx 0$. From a linear fit one obtains $2B_I X_0^2$ (slope) and $2k_I v_d$ (intercept). We also show in Figure 2a, the excluded volume of chains of HCs calculated using the Onsager expression reported in eq 7. Although Onsager formula is a good approximation, eq 27 provides a better representation of the “exact” (i.e., numerically estimated) excluded volume for SQs.

B. Calculation of the Bonding Volume. The bonding volume V_b can be calculated numerically by performing a Monte Carlo calculation of

$$V_b = \int \theta(-\Delta E_S - u_{\text{SW}} - V_{\text{HC}}) \, \text{d}\mathbf{r} \, \text{d}\Omega_1 \, \text{d}\Omega_2 \quad (28)$$

where $V_{\text{HC}} = V_{\text{HC}}(\mathbf{r}, \Omega_1, \Omega_2)$ is the hard core part of the interaction potential and $\theta(x)$ is the Heaviside step function; i.e., $\theta(x) = 1$ if $x \geq 0$ or 0 otherwise. The details of the numerical integration are reported in Appendix X. The resulting values of V_b for different X_0 are shown in Figure 2b. V_b grows with X_0 , an effect introduced by the different rounding of the SQ surface close to the bases. Indeed, as shown in Figure 1, on increasing X_0 the base surface is more rounded and such different rounding offers a different angular width over which bonds can form. This effect will also reflect in the X_0 dependence of the persistence length of the self-assembled chains, as it will be discussed in details in subsection IVE. For HCs, the aspect ratio X_0 does not impact the bonding angle and so the bonding volume would be constant.

The values of $\sigma_b(V_b)$ (the loss in entropy of forming a bond) calculated using eq 22 are around -6 and thus they are comparable with the studied values of $\beta \Delta E_S$ ($\Delta E_S = 5.56, 6.67$, and 8.33).

C. Excluded volume in the nematic phase. The excluded volume $v_{\text{excl}}(l, l, \alpha)$ between two aggregates of equal length l can be calculated using the procedure illustrated previously for the isotropic case with the only difference that now monomers are inserted with an orientation extracted from the Onsager angular distribution defined in eq 23.

To numerically estimate $A_N(\alpha)$, $k_N(\alpha)$, and $B_N(\alpha)$ we specialize eq 24 to the case of $l = l' = 2$, $l = l' = 3$, $l = l' = 4$, and numerically evaluate $v_{\text{excl}}(2, 2, \alpha)$, $v_{\text{excl}}(3, 3, \alpha)$ and $v_{\text{excl}}(4, 4, \alpha)$ for several values of α . Inverting eq 24 allows us to express $A_N(\alpha)$, $k_N(\alpha)$ and $B_N(\alpha)$ as a function of $v_{\text{excl}}(2, 2, \alpha)$, $v_{\text{excl}}(3, 3, \alpha)$ and $v_{\text{excl}}(4, 4, \alpha)$ as explained in detail in Appendix C.

D. Estimate of the Orientational Entropy in the Nematic Phase. We propose to model the orientational entropy in the nematic phase using the following approximate expression proposed by Odijk⁴⁵ (other possibilities can be found in refs 80 and 81)

$$\begin{aligned}
 \hat{\sigma}_o^{\text{od}} = \sum_{l=1}^{l=\infty} v(l) \left\{ \ln \alpha + \frac{(\alpha - 1)l}{6l_p} \right. \\
 \left. + \frac{5}{12} \ln \left[\cosh \left(\frac{(\alpha - 1)l}{5l_p} \right) \right] - \frac{19}{12} \ln 2 \right\} \quad (29)
 \end{aligned}$$

Unfortunately, eq 29 is hardly tractable in the minimization procedure required to evaluate the equilibrium free energy and hence the two following expressions are often preferred

$$\begin{aligned}\sigma_o^{RC}(l) &= \ln(\alpha) - 1 + \frac{\alpha - 1}{6l_p}l \quad \alpha l \ll l_p \\ \sigma_o^{FC}(l) &= \ln(\alpha/4) + \frac{\alpha - 1}{4l_p}l \quad \alpha l \gg l_p\end{aligned}\quad (30)$$

which can be obtained by inserting the Onsager orientational function $f_o(\mathbf{u})$ in eq 10 and which are highly accurate in the limit of “rigid chains” (RC) and “flexible chains” (FC).

While in the case of fixed length polymers, the knowledge of the persistence length selects one of the two expressions, in the case of equilibrium polymers, different chain lengths will contribute differently to the orientational entropy. In particular, when the chain length distribution is rather wide, it is difficult to assess if the RC (chosen in ref 46) or the FC (chosen in ref 47) limits should be used. To overcome the numerical problem, still retaining both the RC and the FC behaviors, we use the following expression for $\hat{\sigma}_o$:

$$\begin{aligned}\hat{\sigma}_o &= \sum_{l=1}^{l_0-1} \nu(l) \left\{ [\ln(\alpha) - 1] + \frac{\alpha - 1}{6l_p}l \right\} + \\ &\quad \sum_{l=l_0}^{\infty} \nu(l) \left\{ \ln(\alpha/4) + \frac{\alpha - 1}{4l_p}l \right\}\end{aligned}\quad (31)$$

in which the contribution of chains of size l_0 is treated with the RC expression while the contribution of longer chains enters with the FC expression. We pick l_0 by requiring the maximum likelihood between eq 31 and eq 29 in the relevant M - α domain. The procedure is quite straightforward: given an appropriate domain in the (M, α) plane (e.g., $5 < M < 150$ and $5 < \alpha < 50$), we chose a grid G within this domain and we determined the value of l_0 which minimizes the following function $T(l_0)$:

$$T(l_0) \equiv \min_G |\hat{\sigma}_o^{od} - \hat{\sigma}_o| \quad (32)$$

Although l_0 weakly depends on l_p (i.e., $l_0 = l_0(l_p)$), we find that the value $l_0 \approx 9$ is appropriate for most studied cases.

E. Estimate of Persistence Length. In order to estimate the persistence length, entering in eq 31, we randomly build chains according to the procedure described in Appendix B. We estimate the “chain persistence length” l_p by evaluating following spatial correlation function:

$$C_O(li - jl) \equiv \sum_{i,j} \langle \hat{\mathbf{x}}(i) \cdot \hat{\mathbf{x}}(j) \rangle \quad (33)$$

where i, j label two monomers along the chain ($i = 0$ is the first monomer at chain end) and $\hat{\mathbf{x}}(i)$ is a unit vector directed along x -axis of the monomer (i.e., their axis of symmetry, see Figure 1), that coincides with the direction along which the two attractive sites lie. $\langle \dots \rangle$ denotes an average over the whole set of independent chains which has been generated.

In Figure 3 we plot $C_O(li - jl)$ for all aspect ratios studied. All correlations decay following an exponential law, whose characteristic scale is identified as the persistence length (in unit of monomer). In the X_0 range explored, $10 < l_p < 25$. The more elongated monomers have a smaller persistence length.

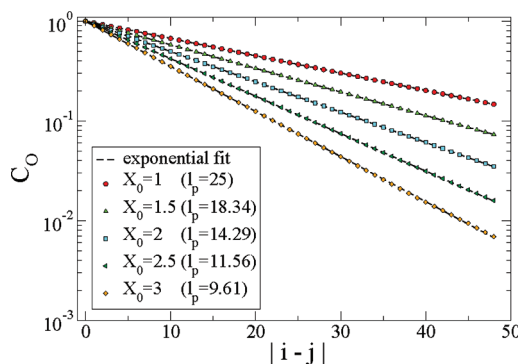


Figure 3. Spatial correlation function $C_O(li - jl)$ (see text for its definition) calculated by generating random chains of 50 monomers for aspect ratios $X_0 = 1, 1.5, 2, 2.5, 3$. Dashed lines are fits to the functional form $C_O(li - jl) = \exp[-li - jl/l_p]$. From these fits, the chain persistence length l_p can be estimated (see legend).

The X_0 dependence of l_p arises from the different roundness of the bases (implicit in the use of SQ), as discussed in the context of the bonding volume and in Figure 1.

V. RESULTS AND DISCUSSION

In this section we compare results from simulations with theoretical calculations based on the theory discussed in section III

A. Isotropic Phase. Parts a–c of Figure 4 show the packing fraction dependence of M for $X_0 = 1, 2, 3$ for all temperatures investigated. The dashed curves are calculated by minimizing the isotropic free energy in eq 18 with respect to M using the values of V_b , k_b , and B_t obtained in subsection IVA without any fitting. Up to volume fractions around $\phi \approx 0.20$ the agreement between theoretical and numerical results is quite good for all cases considered. Above this volume fraction the theoretical predictions start deviating appreciably, a discrepancy that we attribute at moderate and high ϕ to the inaccuracy of the Parsons decoupling approximation. We also plot in Figure 4, parts a–c, as dotted lines the predictions based on a Onsager-like theory, i.e. setting the Parsons-Lee factor $\eta(\phi)$ equal to 1 in eq 3. At low volume fractions the approximation $\eta(\phi) = 1$ does not affect the quality of the results but above $\phi \approx 0.20$ the use of Parsons decoupling approximation seems to better capture the behavior of $M(\phi)$. In Figure 4d, we report the aggregate size distribution $\nu(l)$ as obtained from both simulation and theory, the latter calculated according to eq 18 with M obtained by minimization of the isotropic free energy. As expected, the aggregate size in the isotropic phase is exponential. These results suggest that a reasonable first principles description of the isotropic phase is provided by the free energy of eq 18, when the parameters of the model are properly evaluated.

B. Nematic Phase. On increasing ϕ the system transforms into a LC phase. We estimate the degree of nematic ordering by evaluating the largest eigenvalue S of the order tensor \mathbf{Q} , whose components are:

$$Q_{\alpha\beta} = \frac{1}{N} \sum_i \frac{3}{2} \langle (\mathbf{u}_i)_\alpha (\mathbf{u}_i)_\beta \rangle - \frac{1}{2} \delta_{\alpha\beta} \quad (34)$$

where $\alpha\beta \in \{x, y, z\}$, and the unit vector $(\mathbf{u}_i(t))_\alpha$ is the component α of the orientation (i.e., the symmetry axis) of particle i at time t . A nonzero value of S signals the presence of orientational order in the system and it can be found not only

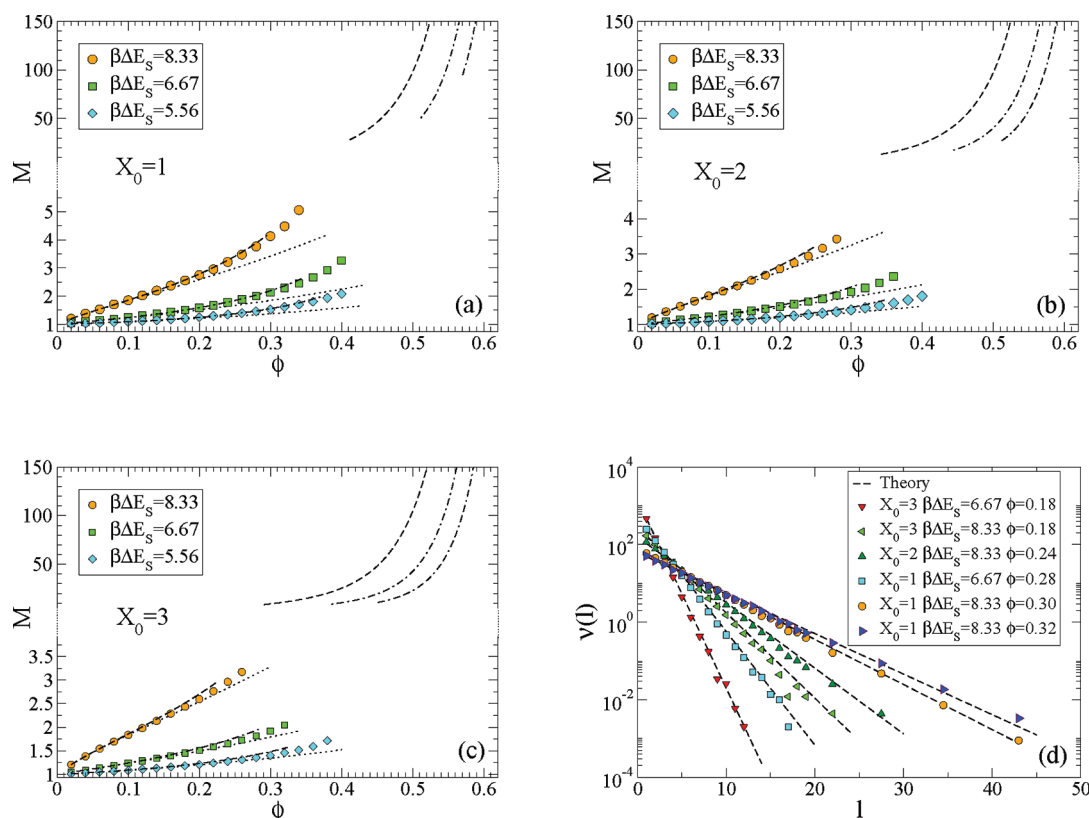


Figure 4. (a–c) Average chain length M against ϕ for $X_0 = 1, 2, 3$ for the three studied $\beta\Delta E_s$ values. Symbols are MC results in the isotropic phase. Dashed lines are theoretical predictions, obtained by minimizing the free energy in eqs 18 (isotropic phase, bottom part of the figures) and 25 (nematic phase, upper part of the figures). Different types of dashed lines refer to different stacking energies. The dashed lines are limited by the region of stability of the isotropic and nematic phases. Dotted lines are theoretical predictions according to Onsager second virial approximation, i.e. setting $\eta(\phi) = 1$. Please note the change of scale along y-axis. (d) MC results for the aggregate size distributions (colored symbols) for several state points in the isotropic phase and corresponding theoretical predictions (dashed lines).

in the nematic phase but also in partially ordered phases as columnar and smectic phases. Since in this article we focus only on the nematic phase, to verify that the simulated state points are not partially ordered we calculate, following ref 46, the three-dimensional pair distribution function $g(\mathbf{r})$ defined as

$$g(\mathbf{r}) = \frac{1}{\rho N} \left\langle \sum_{i=1}^N \sum_{j \neq i}^N \delta(\mathbf{r} - (\mathbf{r}_i - \mathbf{r}_j)) \right\rangle \quad (35)$$

where $\delta(\mathbf{x})$ is the Dirac delta function. We calculate the $g(\mathbf{r})$ in a reference system with the z -axis parallel to the nematic director. Figure 5 shows $g(x, y, 0)$ and $g(0, y, z)$, which correspond, respectively, to the correlations in a plane perpendicular to the nematic director and in a plane containing it for a given nematic state point ($X_0 = 2$, $\phi = 0.38$, $\beta\Delta E_s = 8.33$). The $g(x, y, 0)$ is found to be isotropic, ruling out the possibility of a columnar or crystal phase (no hexagonal symmetry is indeed present). The $g(0, y, z)$ reflects the orientational ordering along the nematic direction and rules out the possibility of a smectic phase (no aligned sequence of peaks are present⁴⁶). Figure 5c also shows a snapshot of the simulated system at the same state point.

In what follows, we have systematically calculated and inspected $g(\mathbf{r})$ to verify that all state points having a value of S large enough to be considered nematic are indeed translationally isotropic, i.e. with no translational order.

Figure 6 shows the nematic order parameter and the average chain length M calculated from simulations as well as with the

theoretical methodology described previously for two different aspect ratios at $\beta\Delta E_s = 8.33$. The theoretical value for S is obtained according to:

$$S(\alpha) = \int 2\pi \frac{3 \cos^2 \theta - 1}{2} f_0(\theta; \alpha) \sin \theta d\theta \quad (36)$$

Figure 6a shows that the nematic order parameter is very well captured by the theory, while the average chain length shows a clear disagreement between theory and simulations, again suggesting that the error introduced by the Parsons decoupling approximation, previously discussed in the case of the isotropic phase at large packing fractions, is enhanced by the further increase in ϕ . Another possible source of error could arise from the hypothesis that the aggregate size distribution is also exponential in the nematic phase. To test this hypothesis Figure 6b shows the aggregate size distributions at two different state points. In all cases, the distributions are not a single exponential. This phenomenon has been already observed and discussed by Lu and Kindt,⁴⁷ who described the distribution with two exponential decays of $v(l)$ with the exponential decay of short chains extending up to $l \approx 50$. They took into account such a biexponential nature of the distribution to better reproduce the isotropic–nematic phase boundaries⁸² in their theoretical approach. In the present case, only very short chains (not to say only the monomers), fall out of the single exponential decay. To test if the different decay reflects a different orientational ordering of the small aggregates compared to long chains, we

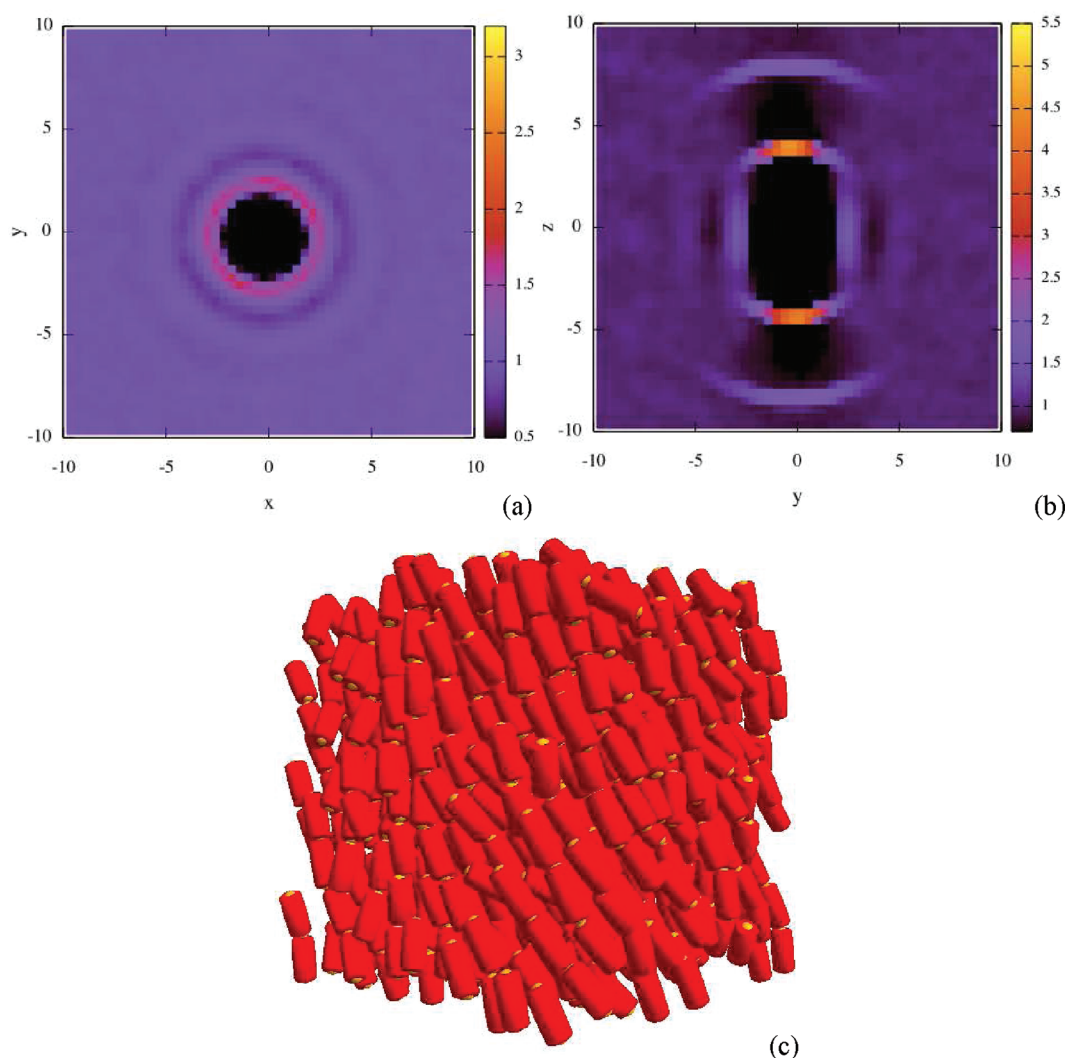


Figure 5. Plot of $g(x,y,0)$ (a) and $g(0,y,z)$ (b) where the z -axis is chosen parallel to the nematic director for $X_0 = 2$, $\phi = 0.38$, and $\beta\Delta E_S = 8.33$. (c) Example of nematic configurations at the same state point.

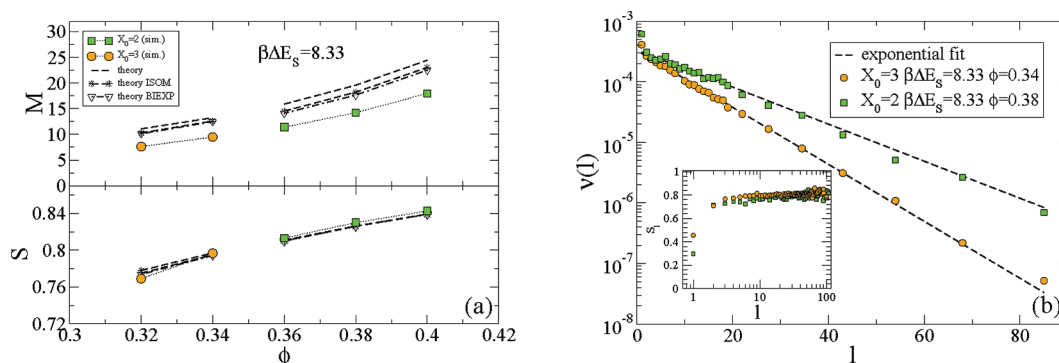


Figure 6. (a) Average chain length and nematic order parameter S for several nematic state points. Dashed lines with stars (theory ISOM) and down triangles (theory BIEXP) are improved theoretical predictions (see text for details). (b) Aggregate size distribution for two state points ($X_0 = 2$, $\phi = 0.38$, $\beta\Delta E_S = 8.33$) and ($X_0 = 3$, $\phi = 0.34$, $\beta\Delta E_S = 8.33$). Circles are numerical results and dashed lines are exponential fits. The inset shows the chain length dependent nematic order parameter S_l for the same state points.

follow ref 82 and evaluate the length-dependent nematic order parameter S_l , that is the nematic order parameter calculated for each population of aggregates of size l . The results, reported in the inset of Figure 6b, show that S_l is around 0.7–0.8 for all aggregates sizes except for $l = 1$, i.e., except for monomers.

To assess how much the theoretical predictions are affected by the assumption of a single exponential decay (and of the associated identity of S for all chains), we evaluate the correction of the free energy functional in eq 25 for the two following cases:

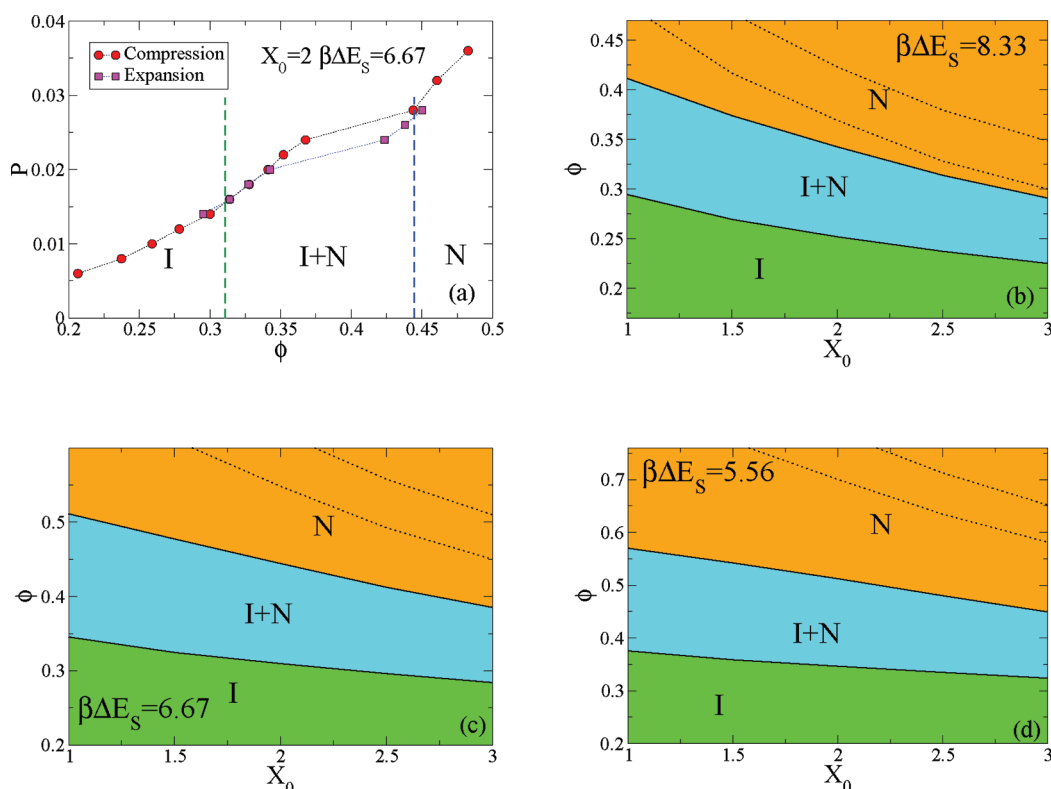


Figure 7. (a) Equation of state (P vs ϕ) calculated compressing an isotropic initial configuration (squares) or expanding an initial nematic configurations (circles). Vertical dashed lines show the theoretical predictions for the phase boundaries. (b–d) Coexistence regions predicted from theoretical calculations for the three stacking energies values $\beta\Delta E_s$ investigated. Dotted lines are phase boundaries calculated within Onsager (second virial) approximation. For each X_0 , the appropriate persistence length (see Figure 3), has been selected.

- We retain a single exponential distribution $\nu(l)$ but monomers are assumed to be isotropic, while all other chains are nematic.
- Monomers are assumed to be isotropic but we also assume a bimodal chain length distribution $\nu(l)$, i.e.

$$\nu(l) = \begin{cases} \rho_I & l = 1 \\ \nu_N(l, \rho - \rho_I, M_N) & l > 1 \end{cases} \quad (37)$$

where ρ_I is the number density of monomers, which is calculated by free energy minimization, and

$$\nu_N(l, \rho - \rho_I, M_N) = \frac{(M_N - 1)^{l-2} M_N^{1-l}}{M_N + 1} (\rho - \rho_I) \quad (38)$$

Note also that the average chain length for the above choice of $\nu(l)$ is

$$M = \frac{\rho}{\rho_I + \frac{\rho - \rho_I}{M_N + 1}} \quad (39)$$

In case i, we exclude from the calculation of the orientational entropy the monomers and take into account the fact that monomers are isotropic in the excluded volume calculation. The revised free energy can be thus written as

$$\begin{aligned} \frac{\beta F}{V} = & \hat{\sigma}_0^* - \rho(\beta\Delta E_s + \sigma_b)(1 - M^{-1}) \\ & + \eta(\phi) \left[B_N(\alpha) X_0^2 + \frac{k_N(\alpha)}{M} v_d \right. \\ & \left. + \frac{A_N(\alpha)}{M^2} \right] \rho^2 - \beta\Delta f_N + \frac{\rho}{M} \\ & \left(\ln \left[\frac{v_d \rho}{M} \right] - 1 \right) - \rho \ln M + \rho \\ & \ln(M - 1) \frac{M - 1}{M} \end{aligned} \quad (40)$$

where

$$\begin{aligned} \sigma_o^* = & \sum_{l=2}^{l=l_0-1} \nu(l) \left\{ [\ln(\alpha) - 1] + \frac{\alpha - 1}{6l_p} l \right\} + \\ & \sum_{l=l_0}^{\infty} \nu(l) \left\{ \ln(\alpha/4) + \frac{\alpha - 1}{4l_p} l \right\} \end{aligned} \quad (41)$$

and

$$\begin{aligned} \beta\Delta f_N = & \eta(\phi) \left\{ v_d [k_N(\alpha) - k_I] \left(\frac{1}{M^2} + \frac{1}{M^3} \right) \right. \\ & \left. + 2X_0^2 [B_N(\alpha) - B_I] \frac{1}{M^2} + 2 \frac{A_N(\alpha)}{M^3} \right\} \rho^2 \end{aligned} \quad (42)$$

In case ii, after some more cumbersome calculations, one obtains the following expression for the free energy:

$$\begin{aligned} \frac{\beta F}{V} = & \hat{\sigma}_0^* - (\rho - \rho_I)(\beta \Delta E_S + \sigma_b) \\ & \left(1 - \frac{1}{M_N + 1}\right) + \eta(\varphi) \left[B_N(\alpha) X_0^2 \right. \\ & + \frac{k_N(\alpha)}{M_N + 1} v_d + \frac{A_N(\alpha)}{(M_N + 1)^2} \left. \right] (\rho - \rho_I)^2 \\ & + \eta(\varphi) \left\{ k_I v_d \left[\rho_I^2 + \rho_I(\rho - \rho_I) \right] \right. \\ & \left. \left(1 + \frac{1}{M_N + 1}\right) \right\} + X_0^2 B_I \\ & \left[\rho_I^2 + 2\rho_I(\rho - \rho_I) \right] \left\{ + \frac{M_N - 1}{M_N + 1} (\rho - \rho_I) \right. \\ & \ln(M_N - 1) - M_N \frac{\rho - \rho_I}{M_N + 1} \ln(M_N) \\ & - \frac{\rho - \rho_I}{M_N + 1} \ln(M_N + 1) \\ & + \rho_I [\ln(v_d \rho_I) - 1] + \frac{\rho - \rho_I}{M_N + 1} \\ & \left. \left. \left\{ \ln[v_d(\rho - \rho_I)] - 1 \right\} \right\} \right. \end{aligned} \quad (43)$$

In passing, we note that eq 43 reduces to eq 40 if we assume a single exponential distribution, i.e., if we set $\rho_I = \rho/M^2$ and $M_N = M$, and if we neglect terms $O(1/M^4)$.

Minimizing the free energy expressions in eqs 43 and 40 results in an improved estimate for the average chain length and nematic order parameter (Figure 6, see curves labeled by (i) ISOM and (ii) BIEXP). The new estimates slightly improve over the previous ones, suggesting once more that the leading source of error in the present approach, as well in all previous ones, has to be found in the difficulty of properly handling the higher order terms in the virial expansion.

C. Phase Coexistence. *NPT*–MC simulations only provide a rough estimate of the location of phase boundaries, since these simulations can be affected by the hysteresis associated with the metastability of the coexisting phases. It is thus only possible to bracket the region of coexistence, by selecting the first isotropic state point on expansion runs which started from a nematic configuration and the first nematic state point on compression runs started from an isotropic configuration. We performed *NPT*–MC simulations for $X_0 = 2$ and $\beta \Delta E_S = 6.67$ over a wide range of pressures P for a system of 1000 SQs. The resulting equation of state is shown in Figure 7a. As expected, a clear hysteresis is observed, which allows us to detect only some overestimated boundaries for the isotropic–nematic transition. The same figure also reports the theoretical estimates of the transition. The theoretical critical pressure is smaller than the numerical one, resulting in a more extended region of coexistence than observed numerically. Comparing the values of the pressure predicted by the theory with the simulation values, we notice that the main error arises from the pressure of the nematic phase, which is underestimated. Parts b–d of

Figure 7 show the predicted phase diagram for several values of $\beta \Delta E_S$ as a function of the aspect ratio. On increasing $\beta \Delta E_S$ (i.e., decreasing T or increasing the stacking energy), there is a small decrease of ϕ_I and a significant decrease of ϕ_N , resulting in an overall decrease of the I–N coexistence region. Such trends can be understood in terms of the increase of the average chain length resulting from the increase of $\beta \Delta E_S$. The theoretical values for the average chain length at the nematic–isotropic coexistence are shown in Figure 4, parts a–c. Along the ϕ_I transition line, M ranges from 2 to 4. On the contrary, along the ϕ_N transition line, the M values are larger and depend on aspect ratio and stacking energy.

As expected, both ϕ_I and ϕ_N decrease on increasing X_0 . In parts b–d of Figure 7, we also plot the phase boundaries calculated within the Onsager (second virial) approximation, i.e., by setting $\eta(\phi) = 1$ in our free energy functional. It is clear from these plots that neglecting higher order terms in the virial expansion results in a significant overestimate of the isotropic–nematic transition volume fraction. Hence the Parsons–Lee approximation captures, albeit approximatively, the contribution of higher order virial coefficients on increasing the volume fraction, which are neglected in the Onsager approximation.

Finally, we recall that in our model the persistence length l_p depends on the aspect ratio as discussed in subsection IVE.

VI. COMPARISON WITH EXPERIMENTS

References 29 and 31 report the critical concentrations (c), in mg/mL, for the I–N transition of blunt-ended DNAD. These experimental data can be transformed into volume fractions once the relevant properties of DNAD are known (DNAD molecular weight $m_D = 660N_b$ Da, diameter $D \approx 2$ nm, and length $L = N_b/3$ nm, where N_b is the number of bases in the sequence). The number density ρ of DNADs is related to the mass concentration

$$\rho = \frac{c}{m_D} \quad (44)$$

Since $v_d = LD^2\pi/4$ is the volume of a DNAD, the volume fraction can be expressed as:

$$\varphi = \rho v_d = \frac{cLD^2\pi}{4m_D} \quad (45)$$

Data in refs 29 and 31 suggest that blunt-end duplexes of equal length but different sequences may have different transition concentrations. As discussed in refs 31 and 83, this phenomenon can be attributed to the slight differences in B-DNA helical conformation resulting from the difference in sequences. These differences induce some curvature in the DNAD aggregates, in turn enhancing the transition concentration. Indeed, sequences that are known to form straight double helices order into the N phase at lower concentrations. Therefore, for each oligomer length in the range 8–16 bases, we selected the lowest transition concentration among the ones experimentally determined, since these would be closest to the symmetric monomers considered in the model. Such values have been reported in Figure 8 as a function of base number N_b (top axis) and as a function of X_0 (bottom axis). Apart for $N_b = 12$, for which a large number of sequences have been studied, the transition concentrations for the other N_b values would probably be corrected to lower values if a larger number of sequences were experimentally explored. We would expect this to be particularly true for the shortest sequences, in which the effect of bent helices could be more relevant.

In the experiments, DNADs are in a water solution with counterions resulting from the dissociation of the ionic groups

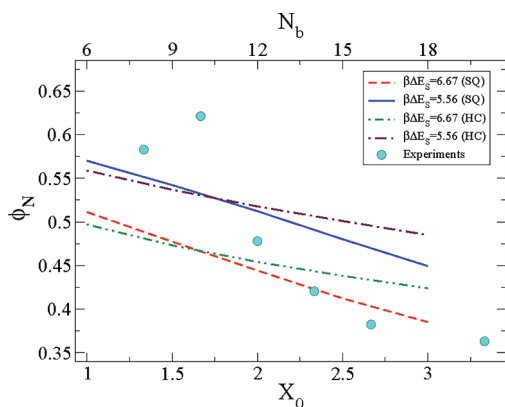


Figure 8. Critical volume fractions Φ_N as a function of aspect ratio X_0 (or equivalently N_b) from theoretical calculations for SQs and HCs (for $\beta\Delta E_S = 6.67$ and $\beta\Delta E_S = 5.56$) and for experiments²⁹ (circles).

of the phosphate-sugar chain. Given the high DNA concentration necessary for the formation of the N phase, corresponding to concentration of nucleobases in the 1 M range, the ionic strength simply provided by the natural counterions is large enough to effectively screen electrostatic interactions between DNADs. This becomes less true for the longest studied sequences, for which the transition concentration is lower. We hence decided to perform a small number of test experiments on the $N_b = 20$ oligomers with a double purpose: (i) determine more accurately the transition concentration value for this compound and (ii) test the effect of varying the ionic strength predicted by the model here described. With respect to a fully screened DNAD, where electrostatic repulsion can be neglected, a partly screened DNAD has a larger effective volume, thus filling a larger volume fraction of the solution, and a smaller axial ratio X_0 , since electrostatic repulsion is equal in all directions. Therefore, adding salt would bring about two competing effects: the reduction in particle volume, which enhances the concentration needed to reach the I–N phase boundary, and the growth of X_0 , which could favor the nematic ordering even at lower concentrations.

The behavior expected upon increasing the salt concentration can be obtained combining two elements: (i) From eq 45, we can deduce the following relation between the critical concentration c_N and the critical volume fraction ϕ_N :

$$c_N = \phi_N(X_0) \frac{4m_D}{LD^2\pi} \quad (46)$$

(ii) The phase diagrams of Figure 7b–d indicates that $\phi_N(X_0)$ depends weakly on $X_0 = L/D$, i.e. $\phi_N(X_0) = \phi_N^0$, where ϕ_N^0 is constant.

Hence the theory introduced in the present paper predicts that a reduction of DNAD effective volume due to the addition of salt (i.e., a decrease of LD^2 in eq 46 leads to an overall increase of the concentration required for N ordering.

We have measured the transition concentration of the self-complementary 20mer CGCGAAAATTTTCGCG, a sequence whose I–N transition at room temperature was previously measured and determined to be $c_N \approx 200$ mg/mL.²⁹ With the same method, based on the measurement of the refractive index of the solution, we determined the I–N transition concentration at room temperature at three different ionic strengths. The values we obtained are $c_N \approx 215$ mg/mL (no added salt), $c_N \approx 320$ mg/mL (0.8 M NaCl), and $c_N \approx 380$ mg/mL (1.2 M NaCl). The data indicate that the onset of the nematic ordering in solutions of 20mers is indeed sensitive to the ionic strength, and that the

transition concentration grows upon increasing the amount of salt, as expected on the basis of our theoretical calculations for the present model. In Figure 8, we display the transition volume fraction derived by the transition concentration measured for 1.2 M NaCl. At this ionic strength, the total concentration of Na^+ ions (from the assumed fully dissociated oligomers + added with the salt) is about the same as the one resulting from counterions dissociated oligomers in the more concentrated solutions of shorter (8–12 mers) oligomers.

Figure 8 compares the experimentally determined transition volume fractions with the values calculated from the SQ model for $\beta\Delta E_S = 6.67$ and $\beta\Delta E_S = 5.56$. Although the experimental data are noisy, they fall in the range $\Delta E_S \approx 5$ –7 (in units of $k_B T$). Despite all the simplifying assumptions and despite the experimental uncertainty, the results in Figure 8 provide a reasonable description of the X_0 dependence of ϕ_N . In this figure we also reported the theoretical volume fractions calculated for HCs with a fixed bonding value equal to $V_b(X_0 = 2) \approx 0.0157$. Chains of HCs have a persistence length which does not depend on X_0 . It is clear that the estimated ΔE_S for HCs is unchanged with respect to SQ, i.e., the phase diagram of our model is not significantly affected by the X_0 dependence of the persistence length (at least in the investigated windows).

In comparing the model with the experimental results, it is necessary to take note of the fact that the stacking energy between nucleobases, and thus the interaction energy ΔE_S between DNAD, is temperature dependent, i.e., its entropic component is relevant.³⁵ This is a general property of solvation energies and thus it is in line with the notion that stacking forces are mainly of a hydrophobic nature. Therefore, the range of values for ΔE_S determined in Figure 8 should be compared to the values of ΔG for the stacking interactions at the temperature at which the experiments were performed. Overall, the estimate of ΔE_S here obtained appears as in reasonable agreement with the free energies involved in the thermodynamic stability of the DNA double helices and confirms the rough estimate that was given before (see the supporting online material associated with ref 29).

Experimental data are often compared to the original Onsager theory for monodisperse thin hard rods, approximating the polydispersity created by the aggregation process as an average aspect ratio MX_0 .^{16,29} As a guide to the interpretation of such data, we compare in Figure 9 the theoretically estimated

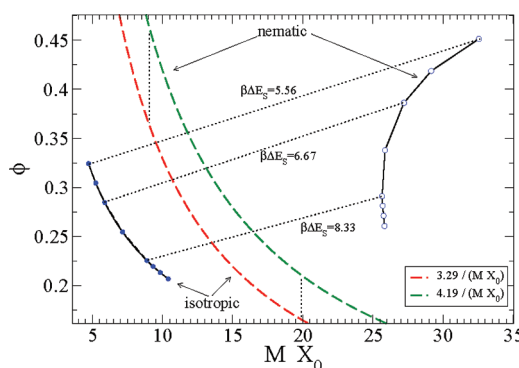


Figure 9. Isotropic–nematic coexistence lines in the average aspect ratio MX_0 and packing ϕ plane. Solid lines with symbols indicate theoretical predictions for $X_0 = 3$. Symbols along the isotropic and nematic phases at coexistence are joined by dotted lines, to indicate the change in packing and average chain length at the transition. Dashed lines indicate the Onsager original predictions, as re-evaluated in ref 37 for ϕ_I and ϕ_N . In this case, the tie lines (dotted) are vertical.

isotropic–nematic coexistence lines in the $MX_0 - \phi$ plane, parametrized by the stacking energy. The figure shows also the Onsager original predictions, as re-evaluated in ref 37, in which no change of aspect ratio takes place at coexistence. Including polydispersity as a result of reversible assembling (and higher order excluded volume contributions) significantly alters the coexisting values of ϕ .

VII. CONCLUSIONS

In this study we have developed a free energy functional to calculate the isotropic–nematic phase diagram of bifunctional quasi-cylindrical monomers, aggregating into equilibrium chains. The model has been inspired by experiments on the aggregation of short DNA, which exhibits nematic phases at sufficiently high concentrations. The comparison between the theoretical predictions and the experimental results allows us to provide an estimate of the stacking energy, consistent with previous propositions.

Our approach is quite general, parameter free and not restricted to particular shapes. Once the shape of the monomer and geometry of the sticky sites are defined, the model dependent quantities, like bonding volume, persistence length and excluded volume can be calculated either theoretically, as for HCs, or numerically, as done in the present case resorting to a MC integration technique. Using these quantities the phase diagram can be evaluated without any fit or adjustment of the parameters and we do not need to perform any simulation to calculate these quantities.

We provide techniques to evaluate the bonding volume and the excluded volume, which enters into our formalism via the Parsons–Lee decoupling approximation. We build on previous work, retaining the discrete aggregate size description of ref 47 and the Parsons–Lee factor for the excluded volume contribution proposed in ref 46. With respect to previous approaches, we (i) explicitly account for the entropic and energetic contributions associated with bond formation, and (ii) we do not retain any adjustable fit parameter.

The resulting description of the isotropic phase is rather satisfactory and quantitative up to $\phi \approx 0.2$. The description of the nematic phase partially suffers from some of the approximations made in deriving the free energy functional. More specifically, several signatures point toward the failure of the Parsons decoupling approximation in the ϕ range typical of the nematic phase. While there is a sufficient understanding of the quality of such approximation for monodisperse objects,^{63,64,66,68,69,73} work needs to be done to assess the origin of the failure of this approximation in the equilibrium polymer case and to propose improvements.

We finally note that the model introduced here does not consider the azimuthal rotations of each monomer around its axis. This neglect is adequate when the aggregation does not entail constraints in the azimuthal freedom of the monomers. This is the case of base stacking, in which the angular dependence of the stacking energy is arguably rather small. However, this is not the case of DNAD interacting through the pairing of overhangs and of the LC ordering of RNA duplexes. Because of its A-DNA-type structure, the terminal paired bases of RNA duplexes are significantly tilted with respect to the duplex axis, thus establishing a link between the azimuthal angle of the aggregating duplexes and the straightness of the aggregate even in the case of blunt ended duplexes. However, with minor modifications the model here introduced could become suitable to include these additional situations. The

limiting factor in developing such extensions is the lack of knowledge to quantify the azimuthal constraints implied by these interactions. This situation, as well as the effects of off-axis components of the end-to-end interduplex interactions, will be explored in a future work.

■ APPENDIX A

Here we provide a justification for the use of Parsons decoupling approximation in the case of linear chains poly disperse in length (with distribution $\nu(l)$), based on the extension of Onsager's second-virial theory to mixtures of nonspherical hard bodies proposed in ref 84. The contribution F_{excl} to the free energy due to excluded volume interactions between chains can be written if we neglect intrachain interactions:^{84,85}

$$\frac{\beta F_{\text{excl}}}{V} = \frac{\rho}{6} \int_0^P d\rho' \int d\mathbf{r} \int d\Omega_1 d\Omega_2 \sum_{ll'} \frac{\nu(l)\nu(l')}{\rho^2} g_{ll'}(\mathbf{r}, \Omega_1, \Omega_2) f(\Omega_1) f(\Omega_2) \mathbf{r} \cdot \nabla_{\mathbf{r}} V_{\text{HC}}(\mathbf{r}, \Omega_1, \Omega_2) \quad (47)$$

where \mathbf{r} is the distance between the centers of mass of the two chains 1 and 2, $\Omega_1 = \{\mathbf{u}_1^1, \dots, \mathbf{u}_1^l\}$ and $\Omega_2 = \{\mathbf{u}_2^1, \dots, \mathbf{u}_2^{l'}\}$ are the orientations of the two chains, where \mathbf{u}_i^α is the orientation of monomer i belonging to chain $\alpha = 1, 2$, $g_{ll'}(\mathbf{r}, \Omega_1, \Omega_2)$ is the molecular radial distribution function of the mixture, which represents the correlations between two chains of length l and l' , whose relative distance is \mathbf{r} and which have orientations Ω_1 and Ω_2 respectively, $V_{\text{HC}}(\mathbf{r}, \Omega_1, \Omega_2)$ is the hard-core part of the interaction potential and $f(\Omega_\alpha)$ is the angular distribution function of chain α . We note that in eq 47 the integration in ρ' is performed keeping fixed all the parameters related to $f(\Omega_\alpha)$. Neglecting intrachain interactions is equivalent to ignore self-overlaps of chains, an assumption which is appropriate if chain length is not much greater than its persistence length and the chains can be considered nonextensible.

Parsons decoupling approximations in this case accounts to putting:

$$g_{ll'}(\mathbf{r}, \Omega_1, \Omega_2) = g_{ll'}^{\text{HS}}[r/\sigma_{ll'}(\hat{\mathbf{r}}, \Omega_1, \Omega_2)] \quad (48)$$

where $g_{ll'}^{\text{HS}}$ is the radial distribution function of a mixture of hard spheres and $\sigma_{ll'}(\hat{\mathbf{r}}, \Omega_1, \Omega_2)$ is an angle-dependent range parameter which depends on chain lengths l and l' . If the pair interaction is of the special form

$$V_{\text{HC}}(\mathbf{r}, \Omega_1, \Omega_2) = V_{\text{HC}}[r/\sigma_{ll'}(\hat{\mathbf{r}}, \Omega_1, \Omega_2)] \quad (49)$$

noting that $\mathbf{r} \cdot \nabla_{\mathbf{r}} = r(\partial)/(\partial r)$, eq 47 becomes

$$\frac{\beta F_{\text{excl}}}{V} = \frac{\rho}{6} \int_0^P d\rho' \int d\hat{\mathbf{r}} d\Omega_1 d\Omega_2 \sum_{ll'} \frac{\nu(l)\nu(l')}{\rho^2} \int dr r^3 g_{ll'}^{\text{HS}}(r/\sigma_{ll'}) f(\Omega_1) f(\Omega_2) \frac{\partial V_{\text{HC}}(r/\sigma_{ll'})}{\partial r} \quad (50)$$

With the substitution $y = r/\sigma_{ll'}$ from eq 50 one obtains:

$$\frac{\beta F_{\text{excl}}}{V} = \frac{\rho}{2} \sum_{ll'} \frac{1}{3} \frac{\nu(l)\nu(l')}{\rho^2} \int_0^{\rho} d\rho' \int d\hat{r} d\Omega_1 d\Omega_2 \int dy y^3 \frac{\partial V_{\text{HC}}(y)}{\partial y} g_{ll'}^{\text{HS}}(y) f(\Omega_1) f(\Omega_2) \sigma_{ll'}^3 \quad (51)$$

The derivative of V_{HC} is a delta function hence we need only to evaluate the value of $g_{ll'}^{\text{HS}}(y)$ at contact (i.e., $y = 1^+$) and eq 51 becomes:

$$\frac{\beta F_{\text{excl}}}{V} = \frac{\rho}{2} \sum_{ll'} \frac{\nu(l)\nu(l')}{\rho^2} \int d\rho' g_{ll'}^{\text{HS}}(1^+) \int d\hat{r} d\Omega_1 d\Omega_2 f(\Omega_1) f(\Omega_2) \frac{\sigma_{ll'}^3}{3}$$

This expression tends to Parsons–Lee's expression when the system is monodisperse ($\nu(l) = \rho\delta_{l,1}$). In the specific case of spherical particles $\sigma_{ll'}(\hat{r}, \Omega_1, \Omega_2) = \sigma(\hat{r}, \Omega_1, \Omega_2)$ and

$$\sum_{ll'} \nu(l)\nu(l') f(\Omega_1) f(\Omega_2) \int d\hat{r} d\Omega_1 d\Omega_2 \frac{1}{3} \sigma(\hat{r}, \Omega_1, \Omega_2) = \frac{4\pi}{3} \sigma^3 \quad (52)$$

i.e., the excluded volume of two spheres of diameter σ . Hence we are allowed to make the identification:

$$v_{\text{excl}}(l, l') = \int d\hat{r} d\Omega_1 d\Omega_2 \frac{1}{3} f(\Omega_1) f(\Omega_2) \sigma_{ll'}^3(\hat{r}, \Omega_1, \Omega_2) \quad (53)$$

and write:

$$\frac{\beta F_{\text{excl}}}{V} = \frac{\rho}{2} \sum_{ll'} \frac{\nu(l)\nu(l')}{\rho^2} \left[\int d\rho' g_{ll'}^{\text{HS}}(1^+) \right] v_{\text{excl}}(l, l') \quad (54)$$

We note that the identification made in eq 53 can be also further justified using the same reasonings given in section III. As discussed in ref 84, a possible expression for $g_{ll'}^{\text{HS}}$ is the one derived by Boublik,⁸⁶ which generalizes the Carnahan–Starling relation⁸⁷ for pure hard spheres to the case of mixtures, i.e.

$$g_{ll'}^{\text{HS}}(1^+) = \frac{1}{1 - \zeta_3} + \frac{3\zeta_2}{(1 - \zeta_3)^2} \frac{\hat{\sigma}_{ll'} \hat{\sigma}_{l'l'}}{\hat{\sigma}_{ll} + \hat{\sigma}_{l'l'}} + \frac{2\zeta_2^2}{(1 - \zeta_3)^3} \frac{(\hat{\sigma}_{ll} \hat{\sigma}_{l'l'})^2}{(\hat{\sigma}_{ll} + \hat{\sigma}_{l'l'})^2} \quad (55)$$

where $\hat{\sigma}_{ll}$ is the diameter of an hard sphere corresponding to a chain of length l and $\zeta_n = (\pi/6) \sum \nu(l) \hat{\sigma}_{ll}^n$. To map the system of polydisperse chains onto the equivalent mixture of hard spheres we need an expression for $\hat{\sigma}_{ll}$. According to ref 84, the simplest choice is to consider spheres having the same volume of the corresponding linear chain of length l , i.e.

$$v_d = \frac{\pi}{6l} \hat{\sigma}_{ll}^3 \quad (56)$$

where we recall that v_d is the volume of a monomer. Although in principle we could use eq 54 together with eqs 55 and 56 to calculate the free energy contribution due to the excluded volume between particles, if we make the further assumption that

$$g_{ll'}^{\text{HS}}(1^+) \approx g^{\text{HS}}(1^+) \quad (57)$$

i.e., if we approximate the radial distribution function of the hard spheres mixture at contact with that of a monodisperse system of hard spheres having the same total volume fraction (i.e., setting in eq 55 $\hat{\sigma}_{ll'} = \hat{\sigma}$ with $Mv_d = (\pi/6)\sigma^3$), we finally obtain

$$\frac{\beta F_{\text{excl}}}{V} = \frac{\eta(\varphi)}{2} \sum_{ll'} \nu(l)\nu(l') v_{\text{excl}}(l, l') \quad (58)$$

where we used the Carnahan–Starling expression for $g^{\text{HS}}(1^+; \rho')$ and we performed the integration in ρ' . Equation 58 is exactly the expression for the contribution to the free energy due to steric repulsion which we used in section III. In summary according to the above derivation we argue that eq 58 can be not accurate at high volume fractions due to the approximations made in eqs 48 (i.e., the Parsons decoupling approximation) and 57. Within the present treatment, eq 58 is also not appropriate for chains with $l \gg l_p$ because, as already noted, chain self-overlaps can be significant and the hard body pair potential V_{HC} does not have the special form assumed in eq 49.

We finally note that the approximation made in eq 57 can be avoided if one resorts to eq 54 instead of eq 58, although the required free energy calculations would become much more complicated. Anyway we verified for the isotropic phase that employing eq 54 instead of eq 58 does not provide any appreciable improvement in the present case.

APPENDIX B

The procedure, which we adopted to calculate the excluded volume v_{excl} , recalls the one described in ref 77, except that we generate new configurations without any bias technique and by assuming an angular distribution for monomer orientations, which is uniform in the isotropic phase and the Onsager orientational distribution function in the nematic phase. Our procedure in the isotropic phase consists in fact in performing N_{att} attempts of inserting two chains of length l in a box of volume V as described in the following list:

- 1 Set the counter $N_{\text{ov}} = 0$
- 2 Build first chain of length l randomly, according to the following procedure:
 - (a) Insert a first randomly oriented monomer.
 - (b) Insert a monomer M bonded to a free site S on chain ends (S can be chosen randomly among the two free sites of the partial chain). The orientation of M will be random and its position will be chosen randomly within the available bonding volume between M and S . The bonding volume between M and S is defined as the volume corresponding to all possible center of mass positions of M with M bonded to S .
 - (c) If the number of monomer inserted is l terminate otherwise go to point 1
 - (d) where the first monomer inserted is placed in the center of the box and it is oriented with its attractive sites parallel to the x -axis.
- 3 Build a second chain of length l , where the first monomer inserted is placed randomly within the simulation box with a random orientation.

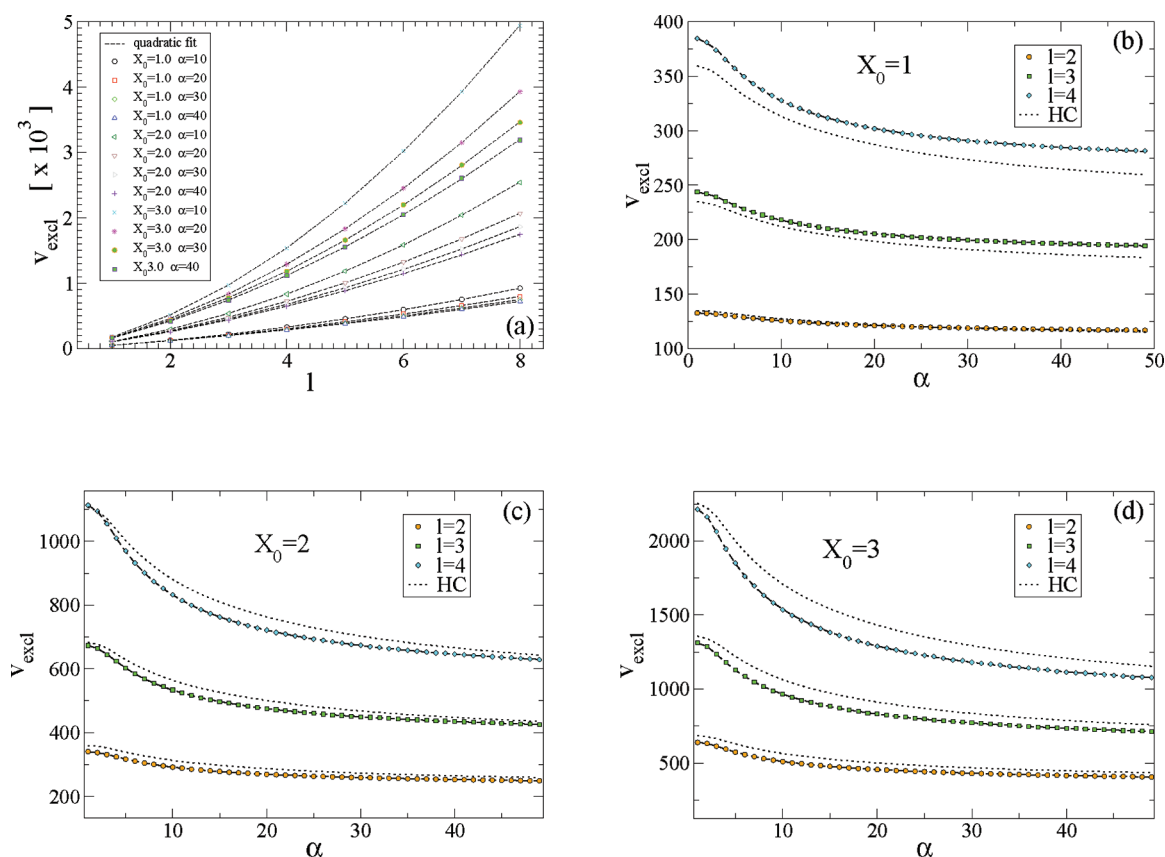


Figure 10. (a) Excluded volume of two chains of length l as a function of chain length for the nematic cases $\alpha = 10, 20, 30, 40$ and three different aspect ratios $X_0 = 1, 2, 3$. (b–d) Excluded volume in the nematic phase calculated numerically as a function of α for two chains of equal length l , where $l = 2, 3, 4$, composed of monomers with $X_0 = 1, 2, 3$. Dotted lines represent the excluded volume calculated with Onsager formula reported in eq 7.

- 4 Increase N_{ov} by 1 if two monomers belonging to different chains overlap and the two chains are either not self-overlapping or forming a closed loop.
- 5 If the number of attempts is less than N_{att} go to point 2; otherwise, terminate.

Then v_{excl} can be calculated as follows:

$$v_{\text{excl}} = \frac{N_{ov}}{N_{att}} V \quad (59)$$

A reasonable choice for the total number of attempts is $N_{att} = 10^6$. In a similar fashion one can also calculate the bonding volume⁷⁵ between two monomers. In this case one monomer is kept fixed in the center of the simulation box and the other one is inserted with random position and orientation for a total of N_{att} attempts. The bonding volume will be:

$$V_b = \frac{N_{bond}}{4N_{att}} V \quad (60)$$

where the factor 4 accounts for the fact that two particles can form 4 different possible bonds and N_{bond} is the number of times that the two monomers were bonded after a random insertion. Finally with the same procedure used to calculate the excluded volume in the isotropic phase we can evaluate the excluded volume in the nematic phase. The only difference is that now monomers have to be inserted with an orientation extracted from the Onsager angular distribution defined in eq 23, so that the excluded volume depends also on the parameter

α . Again if N_{ov} is the number of times that two monomers belonging to different aggregates overlap and N_{att} is the total number of attempts then we have:

$$v_{\text{excl}}(l, l, \alpha) = \frac{N_{ov}}{N_{att}} V \quad (61)$$

■ APPENDIX C

In this appendix, we explain how to calculate the parameters $A_N(\alpha)$, $k_N(\alpha)$, and $B_N(\alpha)$ of the nematic free energy functional. As a preliminary step we check that $v_{\text{excl}}(l, l', \alpha)$ for a fixed value of α is a second order polynomial of l and l' as assumed in eq 5. In Figure 10a, we plot $v_{\text{excl}}(l, l, \alpha)$ as a function of l for different values of α and X_0 . $v_{\text{excl}}(l, l, \alpha)$ can be well represented by a parabolic function, in agreement with eq 5.

We start by observing that the α dependence of $A_N(\alpha)$, $k_N(\alpha)$, and $B_N(\alpha)$ in the case of hard cylinders following the Onsager distribution can be expanded in powers of $\alpha^{-1/2}$ as

$$\begin{aligned} A_N(\alpha) &= c_{00} + \frac{c_{01}}{\alpha^{1/2}} + \frac{c_{02}}{\alpha} + \frac{c_{03}}{\alpha^{3/2}} + \frac{c_{04}}{\alpha^2} \\ k_N(\alpha) &= c_{10} + \frac{c_{11}}{\alpha^{1/2}} + \frac{c_{12}}{\alpha} + \frac{c_{13}}{\alpha^{3/2}} + \frac{c_{14}}{\alpha^2} \\ B_N(\alpha) &= c_{20} + \frac{c_{21}}{\alpha^{1/2}} + \frac{c_{22}}{\alpha} + \frac{c_{23}}{\alpha^{3/2}} + \frac{c_{24}}{\alpha^2} \end{aligned} \quad (62)$$

where c_{ij} are the elements of the 3×4 matrix \mathbf{C} . In the case of cylinders, some of the c_{ij} vanishes.⁴⁵ We assume here that the same α dependence holds for SQs.

In view of this result the covolume as a function of l and α can be expressed as

$$v_{\text{excl}}^{(\text{fit})}(\alpha; X_0, l) = d_{l0} + \frac{d_{l1}}{\alpha^{1/2}} + \frac{d_{l2}}{\alpha} + \frac{d_{l3}}{\alpha^{3/2}} + \frac{d_{l4}}{\alpha^2} \quad (63)$$

where d_{lp} , for $p = 0 \dots 4$ are fitting parameters. Parts b–d of Figure 10 show the numerical calculation of the covolume varying α for three particular aspect ratios ($X_0 = 1, 2, 3$), together with fits to the functional form of eq 63 and the excluded volume calculated using the Onsager expression for HC (see eq 7). Onsager formula as in the isotropic case provides only an approximate description of SQs “exact” (i.e., numerically estimated) excluded volume.

The good quality of the fits (reduced χ^2 is always much less than 1 for all fits) suggests that retaining terms up to $O(1/\alpha^2)$ is to the present level of accuracy of our calculations absolutely appropriate.

From these fits we can estimate the matrix \mathbf{C} needed to evaluate the free energy in the nematic phase for each X_0 . If we define in fact the following matrix \mathbf{P} and the vectors \mathbf{q}_p , with $p = 0 \dots 4$ as follows:

$$\mathbf{P} = \begin{pmatrix} 1 & l_a & l_a^2 \\ 1 & l_b & l_b^2 \\ 1 & l_c & l_c^2 \end{pmatrix} \mathbf{q}_p = \begin{pmatrix} d_{lap} \\ d_{lbp} \\ d_{lcp} \end{pmatrix} \quad (64)$$

where l_a , l_b , and l_c are three different chain lengths for which we calculated the v_{excl} as a function of α , then we can calculate the matrix elements of \mathbf{C} in the following way:

$$2 \begin{pmatrix} c_{0p} \\ v_d c_{1p} \\ X_0^2 c_{2p} \end{pmatrix} = \mathbf{P}^{-1} \mathbf{q}_p \quad (65)$$

ACKNOWLEDGMENTS

C.D.M. and F.S. acknowledge support from ERC (226207-PATCHYCOLLOIDS). T.B. acknowledges support from the Italian MIUR Ministry (grant PRIN-2008F3734A). The authors thank Prof. S. Kumar for his careful reading of the manuscript and G. Zanchetta for the support in the experimental tests.

REFERENCES

- (1) Hamley, I., *Introduction to Soft Matter*; Wiley & Sons: New York, 2007.
- (2) Glotzer, S. C. *Science* **2004**, 306, 419.
- (3) Whitesides, G. M.; Boncheva, M. *Proc. Natl. Acad. Sci. U.S.A.* **2002**, 99, 4769.
- (4) Workum, V.; Douglas, J. *Phys. Rev. E* **2006**, 73, 031502.
- (5) Mirkin, C.; Letsinger, R.; Mucic, R.; Storhoff, J. *Nature* **1996**, 382, 607.
- (6) Manoharan, V. N.; Elssesser, M. T.; Pine, D. J. *Science* **2003**, 301, 483.

- (7) Cho, Y.-S.; Yi, G.-R.; Lim, J.-M.; Kim, S.-H.; Manoharan, V. N.; Pine, D. J.; Yang, S.-M. *J. Am. Chem. Soc.* **2005**, 127, 15968.
- (8) Yi, G.; Manoharan, V. N.; Michel, E.; Elssesser, M. T.; Yang, S.; Pine, D. J. *Adv. Mater.* **2004**, 16, 1204.
- (9) Starr, F. W.; Douglas, J. F.; Glotzer, S. C. *J. Chem. Phys.* **2003**, 119, 1777.
- (10) Starr, F. W.; Sciortino, F. *J. Phys.: Condens. Matter* **2006**, 18, L347.
- (11) Stupp, S. I.; Son, S.; Lin, H. C.; Li, L. S. *Science* **1993**, 259, 59.
- (12) Doye, J. P. K.; Louis, A. A.; Lin, I.-C.; Allen, L. R.; Noya, E. G.; Wilber, A. W.; Kok, H. C.; Lyus, R. *Phys. Chem. Chem. Phys.* **2007**, 9, 2197.
- (13) Khan, A. *Curr. Opin. Colloid Interface Sci.* **1996**, 1, 614.
- (14) van der Schoot, P.; Cates, M. *Langmuir* **1994**, 10, 670.
- (15) Kuntz, D. M.; Walker, L. M. *Soft Matter* **2008**, 4, 286.
- (16) Jung, J.-M.; Mezzenga, R. *Langmuir* **2010**, 26, 504.
- (17) Lee, C. F. *Phys. Rev. E* **2009**, 80, 031902.
- (18) Ciferri, A. *Liq. Cryst.* **2007**, 34, 693.
- (19) Aggeli, A.; Bell, M.; Carrick, L. M.; Fishwick, C. W. G.; Harding, R.; Mawer, P. J.; Radford, S. E.; Strong, A. E.; Boden, N. *J. Am. Chem. Soc.* **2003**, 125, 9619.
- (20) Robinson, C. *Tetrahedron* **1961**, 13, 219.
- (21) Livolant, F.; Levelut, A. M.; Doucet, J.; Benoit, J. P. *Nature* **1989**, 339, 724.
- (22) Merchant, K.; Rill, R. L. *Biophys. J.* **1997**, 73, 3154.
- (23) Tombolato, F.; Ferrarini, A. *J. Chem. Phys.* **2005**, 122, 054908.
- (24) Tombolato, F.; Ferrarini, A.; Grelet, E. *Phys. Rev. Lett.* **2006**, 96, 258302.
- (25) Barry, E.; Beller, D.; Dogic, Z. *Soft Matter* **2009**, 5, 2563.
- (26) Grelet, E.; Fraden, S. *Phys. Rev. Lett.* **2003**, 90, 198302.
- (27) Tomar, S.; Green, M. M.; Day, L. A. *J. Am. Chem. Soc.* **2007**, 129, 3367.
- (28) Minsky, A.; Shimoni, E.; Frenkel-Krispin, D. *Nat. Rev. Mol. Cell. Biol.* **2002**, 3, 50.
- (29) Nakata, M.; Zanchetta, G.; Chapman, B. D.; Jones, C. D.; Cross, J. O.; Pindak, R.; Bellini, T.; Clark, N. A. *Science* **2007**, 318, 1276.
- (30) Zanchetta, G.; Nakata, M.; Buscaglia, M.; Clark, N. A.; Bellini, T. *J. Phys.: Condens. Matter* **2008**, 20, 494214.
- (31) Zanchetta, G.; Giavazzi, F.; Nakata, M.; Buscaglia, M.; Cerbino, R.; Clark, N. A.; Bellini, T. *Proc. Natl. Acad. Sci. U.S.A.* **2010**, 107, 17497.
- (32) Zanchetta, G.; Bellini, T.; Nakata, M.; Clark, N. A. *J. Am. Chem. Soc.* **2008**, 130, 12864.
- (33) Lydon, J. J. *Mater. Chem.* **2010**, 20, 10071.
- (34) Guckian, K. M.; Schweitzer, B. A.; Ren, R. X.-F.; Sheils, C. J.; Tahmassebi, D. C.; Kool, E. T. *J. Am. Chem. Soc.* **2000**, 122, 2213.
- (35) Bellini, T.; Cerbino, R.; Zanchetta, G. *Top. Curr. Chem.* **2011**, 1–55.
- (36) Budin, I.; Szostak, J. W. *Annu. Rev. Biophys.* **2010**, 39, 245.
- (37) Vroege, G. J.; Lekkerkerker, H. N. W. *Rep. Prog. Phys.* **1992**, 55, 1241.
- (38) Dijkstra, M.; Frenkel, D. *Phys. Rev. E* **1995**, 51, 5891.
- (39) Khokhlov, A.; Semenov, A. *Physica* **1981**, 108A, 546.
- (40) Khokhlov, A.; Semenov, A. *Physica* **1982**, 112A, 605.
- (41) Wessels, P. P. F.; Mulder, B. M. *J. Phys.: Condens. Matter* **2006**, 18, 9335.
- (42) Dennison, M.; Dijkstra, M.; van Roij, R. *Phys. Rev. Lett.* **2011**, 106, 208302.
- (43) Wang, Z.; Kuckling, D.; Johannsmann, D. *Soft Mater.* **2003**, 1, 353.
- (44) Chen, Z. Y. *Macromolecules* **1993**, 26, 3419.
- (45) Odijk, T. *Macromolecules* **1986**, 19, 2313.
- (46) Kouriabova, T.; Betterton, M.; Glaser, M. *J. Mat. Chem.* **2010**, 20, 10366.
- (47) Lü, X.; Kindt, J. J. *J. Chem. Phys.* **2004**, 120, 10328.
- (48) van der Schoot, P.; Cates, M. *Europhys. Lett.* **1994**, 25, 515.
- (49) Chen, B.; Siepmann, J. J. *Phys. Chem. B* **2000**, 104, 8725.
- (50) Chen, B.; Siepmann, J. J. *Phys. Chem. B* **2001**, 105, 11275.
- (51) Wertheim, M. J. *Stat. Phys.* **1984**, 35, 19.

- (52) Wertheim, M. J. *Stat. Phys.* **1984**, 35, 35.
- (53) Wertheim, M. J. *Stat. Phys.* **1986**, 42, 459.
- (54) Onsager, L.; Ann., N. Y. *Acad. Sci.* **1949**, 627.
- (55) De Michele, C. J. *Comput. Phys.* **2010**, 229, 3276.
- (56) De Michele, C.; Gabrielli, S.; Tartaglia, P.; Sciortino, F. J. *Phys. Chem. B* **2006**, 110, 8064.
- (57) De Michele, C.; Tartaglia, P.; Sciortino, F. J. *Chem. Phys.* **2006**, 125, 204710.
- (58) Corezzi, S.; De Michele, C.; Zaccarelli, E.; Fioretto, D.; Sciortino, F. *Soft Matter* **2008**, 4, 1173.
- (59) Corezzi, S.; De Michele, C.; Zaccarelli, E.; Tartaglia, P.; Sciortino, F. J. *Phys. Chem. B* **2009**, 113, 1233.
- (60) Lee, C.; Cammon, J. M.; Rossky, P. J. *Chem. Phys.* **1984**, 80, 4448.
- (61) Parsons, J. *Phys. Rev. A* **1979**, 19, 1225.
- (62) Lee, S. J. *Chem. Phys.* **1987**, 87, 4972.
- (63) Camp, P. J.; Mason, C. P.; Allen, M. P.; Khare, A. A.; Kofke, D. A. *J. Chem. Phys.* **1996**, 105, 2837.
- (64) Wensink, H.; Lekkerkerker, H. *Mol. Phys.* **2009**, 107, 2111.
- (65) Varga, S.; Szalai, I. *Mol. Phys.* **2000**, 98, 693.
- (66) Wensink, H.; Vroege, G.; Lekkerkerker, H. J. *Phys. Chem. B* **2001**, 105, 10610.
- (67) Gámez, F.; Merklings, P.; Lago, S. *Chem. Phys. Lett.* **2010**, 494, 45.
- (68) Cinacchi, G.; Mederos, L.; Velasco, E. J. *Chem. Phys.* **2004**, 121, 3854.
- (69) McGrother, S. C.; Williamson, D. C.; Jackson, G. J. *Chem. Phys.* **1996**, 104, 6755.
- (70) Wensink, H. H.; Vroege, G. J.; Lekkerkerker, H. N. W. *J. Chem. Phys.* **2001**, 115, 7319.
- (71) Szabolcs, V.; Galindo, A.; Jackson, G. *Mol. Phys.* **2003**, 101, 817.
- (72) Galindo, A.; Haslam, A. J.; Varga, S.; Jackson, G.; Vanakaras, A. G.; Photinos, D. J.; Dunmur, D. A. *J. Chem. Phys.* **2003**, 119, 5216.
- (73) Cuertos, A.; Martnez-Haya, B.; Lago, S.; Rull, L. *Phys. Rev. E* **2007**, 75, 061701.
- (74) Williamson, D.; Jackson, G. J. *Chem. Phys.* **1998**, 108, 10294.
- (75) Sciortino, F.; Bianchi, E.; Douglas, J. F.; Tartaglia, P. J. *Chem. Phys.* **2007**, 126, 194903.
- (76) Jackson, G.; Chapman, W. G.; Gubbins, K. E. *Mol. Phys.* **1988**, 65, 1.
- (77) Fynewever, H.; Yethiraj, A. J. *Chem. Phys.* **1998**, 108, 1636.
- (78) Movahed, H. B.; Hidalgo, R. C.; Sullivan, D. E. *Phys. Rev. E* **2006**, 73, 032701.
- (79) Ibarra-Avalos, N.; Gil-Villegas, A.; Richa, A. M. *Mol. Simul.* **2007**, 33, 505.
- (80) DuPré, D. B.; Yang, S.-J. *J. Chem. Phys.* **1991**, 94, 7466.
- (81) Hentschke, R. *Macromolecules* **1990**, 23, 1192.
- (82) Lü, X.; Kindt, J. J. *Chem. Phys.* **2006**, 125, 054909.
- (83) Frezza, E.; Tombolato, F.; Ferrarini, A. *Soft Matter* **2011**, 7, 9291.
- (84) Malijevski, A.; Jackson, G.; Varga, S. J. *Chem. Phys.* **2008**, 129, 144504.
- (85) Honnell, K. G.; Hall, C. K.; Dickman, R. J. *Chem. Phys.* **1987**, 87, 664.
- (86) Boublík, T. J. *Chem. Phys.* **1970**, 53, 471.
- (87) Carnahan, N. F.; Starling, K. E. *J. Chem. Phys.* **1969**, 51, 635.

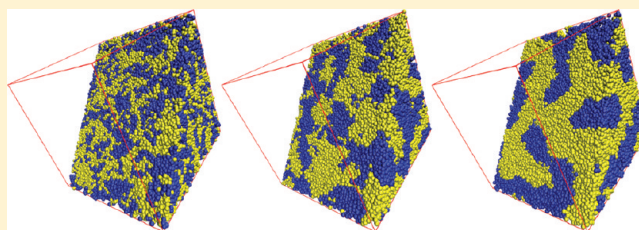
Properties of Random Block Copolymer Morphologies: Molecular Dynamics and Single-Chain-in-Mean-Field Simulations

Birger Steinmüller,[†] Marcus Müller,^{*,†} Keith R. Hambrecht,[‡] Grant D. Smith,[‡] and Dmitry Bedrov^{*,‡}

[†]Institut für Theoretische Physik, Georg-August Universität, 37077 Göttingen, Germany

[‡]Department of Materials Science and Engineering, University of Utah, Salt Lake City, Utah 84112, United States

ABSTRACT: The equilibrium structure and ordering kinetics of random AB block copolymers is investigated using a Lennard-Jones bead–spring model and a soft, coarse-grained model. Upon increasing the incompatibility a disordered microemulsion-like structure is formed, whose length scale slightly increases with segregation. The structure factor of composition fluctuations, molecular conformations, single-chain dynamics and collective ordering kinetics are investigated as a function of the segregation between A and B blocks. The harsh repulsion of the Lennard-Jones potential gives rise to pronounced fluid-like packing effects that affect the liquid structure on the length scale of the bead size and, upon cooling and increase of the local density, result in an additional slowing down of the dynamics. The soft, coarse-grained model does not exhibit pronounced packing effects and the softness of the potential allows for a faster equilibration in computer simulation. The structure and dynamics of the two different models are quantitatively compared. The parameters of the soft, coarse-grained model are adjusted as to match the long-range structure of the bead–spring model, and it is demonstrated that the soft, coarse grained model can be utilized to generate starting configurations for the Lennard-Jones bead–spring model.



INTRODUCTION

The structural properties of multicomponent polymer melts have attracted abiding interest in the field of polymer science. Experiments^{1–3} and theoretical models^{4–6} have been very successful in discovering different phases of block copolymer melts and their mixtures with homopolymers. The intricate prediction of the phase diagram of diblock copolymers and its experimental vindication gives testament to the possibilities of theoretical models and computer simulations in this field. For random block copolymers, however, theoretical, simulational, and experimental investigations are not as prevalent as for the simpler systems. Mean field calculations^{7–9} and integral equation theory^{10–12} predict a complex phase behavior encompassing macrophase-separated states and periodically ordered microstructures. The aforementioned theoretical works and experiments by Ryan et al.¹³ and by Eitouni et al.¹⁴ indicate that there is an order–disorder transition and that the structures formed become smaller when advancing further into the ordered region. More recent approaches have highlighted the role of fractionation between spatially homogeneous phases and microphase separated morphologies.^{15,16} The role of fluctuations has been considered within the Brazovskii theory^{17,18} and by computer simulations.^{19–21} The latter reveal that fluctuation effects are large and, unlike other dense polymer systems, their importance increases as the number of blocks per molecules grows large. Fluctuations prevent the formation of well-ordered, spatially periodic microphases, and the random copolymer melt adopts for a wide parameter range a disordered, microemulsion-like morphology.

At the time and length scales interesting for the dynamics of a polymer melt, which are its end-to-end radius and the time a polymer chain needs to diffuse this distance, atomic models are still too slow for such simulations. Moreover, in models with a harsh segmental repulsion (excluded volume), only very small invariant degrees of polymerization, \bar{N} , are accessible and, consequently, fluctuation effects are large.²² Therefore, we resort to coarse-grained models, which grant access to the relevant time and length scales. For the structural properties of the melt, a coarse-grained model with soft interactions is sufficient. The softness of the interactions allows us to model experimentally relevant values of \bar{N} and permits an efficient equilibration of the system. The soft, coarse-grained model, however, does not capture the effect of noncrossability²³ and, more important for the present study, local packing effects of the segments that may lead to a glassy arrest of the dense polymer melt at low temperatures.^{24,25} Therefore, we additionally employ a model, which utilizes a harder interaction, i.e., a Lennard-Jones bead–spring model, and we compare the results of the two models quantitatively. This comparison of static and dynamic properties is performed at high temperatures, where we can equilibrate both model systems. Then we explore how to utilize the equilibrated configurations of the soft, coarse-grained model as starting configurations of the Lennard-Jones

Received: October 19, 2011

Revised: December 6, 2011

Published: December 21, 2011

bead–spring model so as to benefit from the advantages of both inherently different models.

In this article, we will first introduce the two coarse-grained models used, the soft coarse-grained model, which we study by a Single-Chain-in-Mean-Field simulations,^{22,26} and a Lennard-Jones bead–spring model²⁷ that we use in conjunction with molecular dynamics (MD) simulations.²⁸ In the following section, we use several static quantities, e.g., the structure factor and the radial pair correlation function, to characterize the morphology and single-chain conformation. We identify a correspondence between the parameters of the soft, coarse-grained model and the Lennard-Jones bead–spring model.

Subsequently, we estimate the equilibration time of the system in two different ways. First, we characterize the single-chain dynamics like the diffusivity of the polymers and the end-to-end vector correlation function. Second, we investigate the time the melt needs to establish a morphology in response to a quench from the disordered structure. The kinetics of structure formation is compared between the two simulation methods. Additionally, we quantify the time required for the Lennard-Jones bead–spring model to establish the equilibrium structure when starting from equilibrated configurations of the soft, coarse-grained model which already exhibit the equilibrium structure on intermediate and large scales. The manuscript ends with a brief summary and an outlook.

MODELS AND TECHNIQUES

System. We use Single-Chain-in-Mean-Field (SCMF) simulations of a soft, coarse-grained model and molecular dynamics (MD) simulations of a Lennard-Jones bead–spring model to study the thermodynamic equilibrium properties of random block copolymers. Random block copolymers are linear, flexible polymers that are comprised of $Q = 6$ blocks. Each block, in turn, consists of a sequence of M A segments or B segments, respectively. Thus, a melt of these random block copolymers contains $2^Q = 64$ different species of chains where we do not account for the head–tail symmetry. The total number, $n = 4160$, of chains in the system is much larger than the number of molecular sequences. Thus, a melt of random block copolymers can be conceived as a mixture of many (2^Q) components. The probability or concentration of a specific sequence is fixed during a Markovian polymerization process.⁷ In this manuscript, we restrict ourselves to a symmetric sequence distribution, i.e., a sequence (e.g., AABABA) and its counterpart (e.g., BBABAB), in which all A segments are replaced by B segments and *vice versa*, have identical probability. Moreover, we consider the case that the blocks along a random copolymer are completely uncorrelated, i.e., an A-block is followed by another A block or a B block with equal probability. Thus, we conceive the system as a mixture of 2^Q components, each fixed sequence being one component. In the bulk, all different sequences occur with equal concentration.

The segment species A and B repel each other, and this interaction leads to a local unmixing. Mean-field calculations predict that, upon increasing the incompatibility, χ , between the segment species, the system will first macroscopically phase-separate into macroscopic domains. One domain will be enriched in sequences that are characterized by a large excess of A segments and the other, coexisting phase will be predominantly comprised of B-rich sequences. The segregation between the two coexisting phases, however, is small because the typical excess of A segments is only on the order of \sqrt{Q} along a polymer comprised of Q blocks.⁷ At larger

incompatibility, a three-phase coexistence occurs, where the A-rich and B-rich homogeneous phases coexist with a microphase-separated, lamellar phase.^{15,16,20} The polymer sequences partition between the coexisting phases (fractionation); the A-rich sequences are enriched in the A-rich homogeneous phase, the B-rich sequences are preferentially located in the B-rich homogeneous phase, and polymers with a small excess of A or B mainly constitute the microphase-separated morphology. Upon increasing the incompatibility, the volume fraction of the two homogeneous phases shrinks and the characteristic length scale of the microphase-separated morphology decreases in marked contrast to the behavior of diblock copolymers.^{8,16}

Previous simulations indicate that for uncorrelated random block copolymers with symmetric composition and many blocks, thermal fluctuations are very important and result in important deviations from the mean-field predictions.²⁰ Rather than observing the sequence of disordered phase, macrophase separation, three-phase coexistence with fractionation, and microphase separation, one only observes a completely gradual formation of local domains; i.e., the systems remain disordered and adopt a microemulsion-like structure.

SOFT COARSE-GRAINED MODEL AND SCMF SIMULATION TECHNIQUE

We consider n random copolymers in a volume V . In the framework of the soft, coarse-grained model, we describe the molecular architecture of linear, flexible polymers by a simple bead–spring model with N effective segments per polymer. The bonded interactions along the chain molecule, that define the macromolecular architecture, are harmonic,

$$\frac{\mathcal{H}_b(\{\vec{r}_i(s)\})}{k_B T} = \sum_{i=1}^n \sum_{s=1}^{N-1} \frac{3(N-1)}{2R_{eo}^2} |\vec{r}_i(s) - \vec{r}_i(s+1)|^2 \quad (1)$$

where k_B is Boltzmann's constant and T stands for the temperature. $\vec{r}_i(s)$ denotes the coordinate of the s th segment on the polymer with index i . In the soft, coarse-grained model, we discretize the chain contour into $N = 120$ segments. The strength of the harmonic bond potential is chosen such that the mean squared end-to-end distance of the Gaussian chain conformations in the absence of nonbonded interactions is $R_{eo}^2 = \langle (\vec{r}_1(s) - \vec{r}_N(s))^2 \rangle$.

The nonbonded interactions cater for the near-incompressibility of the dense polymer liquid, that arises from the harsh excluded volume interactions on the atomistic scale, and the repulsion between segments of unlike species, that gives rise to structure formation. The nonbonded interaction takes the form of a density functional and only second-order virial coefficients are retained.^{22,29,30}

$$\frac{\mathcal{H}_{nb}}{k_B T} = \frac{\rho_o}{N} \int d^3r \left[\frac{\kappa_o N}{2} ([1 - \alpha]\hat{\phi}_A + [1 + \alpha]\hat{\phi}_B - 1)^2 - \frac{\chi_o N}{4} (\hat{\phi}_A - \hat{\phi}_B)^2 \right] \quad (2)$$

where $\rho_o = nN/V$ denotes the segment number density.

The coefficient κ_o is inversely proportional to the isothermal compressibility of the melt. The prefactor $1 \pm \alpha$ is the relative normalized volume of an A segment or a B segment, respectively. For $\alpha = 0$, the system is completely symmetric with respect to exchanging $A \rightleftharpoons B$ while for $\alpha > 0$ the A segments have a smaller segmental volume than B segments.

χ_o is the bare Flory–Huggins parameter that quantifies the repulsion between A and B segments.

Equation 2 expresses the nonbonded interactions in terms of the local normalized densities, $\hat{\phi}_A(\vec{r})$ and $\hat{\phi}_B(\vec{r})$. In order to employ this form of nonbonded interactions in a particle-based simulation, we express the local densities via the particle coordinates, $\{\vec{r}_i(s)\}$. To this end, we use a cubic collocation grid to define the local densities of a grid vertex, $\{\vec{c}_k\}$,³¹ by assigning particle coordinates to a vertex according to

$$\hat{\phi}_A(\vec{c}_k|\{\vec{r}_i(s)\}) = \sum_{i=1}^n \sum_{s=1}^N \frac{\gamma_i(s)}{\rho_o \Delta L^3} \Pi(\vec{c}_k, \vec{r}_i(s)) \quad (3)$$

where ΔL denotes the linear extent of a grid cell. $\gamma_i(s) = 1$ if the s th segment of polymer i is an A segment and $\gamma_i(s) = 0$ otherwise. The local normalized density of B segments is calculated by a similar relation. The assignment function $\Pi(\vec{c}_k, \vec{r}_i(s))$ obeys the normalization conditions

$$\sum_{\vec{c}} \Pi(\vec{c}, \vec{r}) = 1 \quad \forall \vec{r} \quad \text{and} \quad \int d^3r \Pi(\vec{c}, \vec{r}) = \Delta L^3 \quad \forall \vec{c} \quad (4)$$

which state that the contributions of a particle to all cells add up to unity irrespectively of its position and that the volume assigned to each grid cell is ΔL^3 . Similar particle-mesh techniques have been used for calculating electrostatic interactions^{32,33} and in plasma physics.³⁴ They are particularly advantageous for calculating interactions in dense systems. In the following, we utilize a linear assignment function of the form

$$\Pi(\vec{c}, \vec{r}) = \prod_{\alpha \in \{x,y,z\}} \pi(|\vec{r}_\alpha - \vec{c}_\alpha|) \quad \text{with} \quad \pi(d) = \begin{cases} 1 - \frac{|d|}{\Delta L} & \text{for } |d| \leq \Delta L \\ 0 & \text{otherwise} \end{cases} \quad (5)$$

i.e., a segment influences the density of the eight vertices of the grid cell in which it is contained. One advantage of this assignment function is that the densities change continuously with the segment coordinate and nonbonded forces can be defined. Using this grid-based assignment, we can rewrite eq 2 in the form

$$\frac{\mathcal{H}_{\text{nb}}(\{\vec{r}_i(s)\})}{k_B T} = \frac{\rho_o \Delta L^3}{N} \sum_{\vec{c}} \left[\frac{\kappa_o N}{2} ([1 - \alpha] \hat{\phi}_A + [1 + \alpha] \hat{\phi}_B - 1)^2 - \frac{\chi_o N}{4} (\hat{\phi}_A - \hat{\phi}_B)^2 \right] \quad (6)$$

This form of the interactions is suitable for Monte Carlo simulations. The interactions of the model depend on the parameters, R_{eo} , which sets the length scale, $\chi_o N$, which parameterizes the incompatibility between polymers, α , which describes the asymmetry of segmental volumes, the polymer number density, ρ_o/N , and the inverse compressibility, $\kappa_o N$. The architecture of the random copolymers are defined by the number of blocks, Q , and the symmetric Markov process that fixes the sequence distribution. Note that neither the number M of segments per block nor the total number N of segments along the macromolecular contour is a physically significant parameter of the model; only the ratio $Q = N/M$ has a physical meaning as the number of blocks per molecule.

In Single-Chain-in-Mean-Field (SCMF) simulations, we replace the pairwise interactions, eq 6, of a segment with its

surroundings by the interaction of a segment with an external field, i.e.,^{22,26}

$$\frac{\mathcal{H}_{\text{nb}}^{\text{SCMF}}(\{\vec{r}_i(s)\})}{k_B T} = \frac{\rho_o \Delta L^3}{N} \sum_{\vec{c}} [w_A \hat{\phi}_A + w_B \hat{\phi}_B] \quad (7)$$

where the external fields w_A/N and w_B/N that act on A and B segments, respectively, are frequently calculated from the local fluctuating densities according to

$$w_A(\vec{c}) = \frac{N}{\rho_o \Delta L^3} \frac{\partial \mathcal{H}_{\text{nb}}}{\partial \phi_A(\vec{c})} \quad (8)$$

and a similar equation holds for $w_B(\vec{c})$. This computational scheme exploits the separation between the strong, rapidly fluctuating, bonded interactions, which dictate the size of a segmental movement in one Monte Carlo step, and the weak, nonbonded interactions, which only very slowly evolve in time.

A SCMF simulation cycle is comprised of two parts: First, one evolves the polymer conformations in the external fields w_A and w_B for a small, fixed amount of Monte Carlo steps. During this Monte Carlo simulations the molecules do not interact with each other and the simulation of independent chain molecules can be straightforwardly implemented on parallel computers. In the second step, one recalculates the external fields from the instantaneous densities according to eq 8. Then the simulation cycle commences again. In the second step, fluctuations and correlations are partially restored. The quasi-instantaneous field approximation that consists in replacing the interactions via frequently updated fluctuating fields is accurate if the change of the local composition, ϕ_A and ϕ_B , between successive updates of the external fields is small.²² This property is controlled by the parameter

$$\varepsilon = \frac{V}{n N^2 \Delta L^3} \quad (9)$$

which plays a similar role as the Ginzburg parameter in a mean-field calculation. In contrast to the Ginzburg parameter, ε depends on the discretization of space, ΔL , and the molecular contour, N , and these parameters are chosen such that the quasi-instantaneous field approximation is accurate. In the present simulations, the control parameter adopts the values $\varepsilon = 1.8 \times 10^{-3}$. For selected parameter combinations we have explicitly verified that the results of the SCMF simulations are very close to the data obtained by Monte Carlo simulations using eq 6.

In order to propagate the chain conformations in the SCMF simulations, we use smart Monte Carlo moves,^{23,35} where the forces that act on a segment influence its trial displacement. The single-chain dynamics closely mimics the Rouse-like motion of short macromolecules in a melt for all but the first 10 SMC steps. The ‘time’ scale of the structural relaxation of the single-chain conformations and the morphology is measured in units of the time τ_{melt} that it takes a homopolymer, $\chi_o N = 0$, comprised of N segments to diffuse a distance on the order of R_{melt}^2 , i.e., $\tau_{\text{melt}} = R_{\text{melt}}^2/D$, where D denotes the self-diffusion coefficient in a homopolymer melt and $R_{\text{melt}}^2 = R_e^2(\chi_o N = 0, \alpha = 0)$ is the measured mean squared end-to-end distance of polymers in a homopolymer melt, i.e., we apply the bonded interactions, eq 1, and the nonbonded interactions, eq 2, with $\chi_o N = 0$ and $\alpha = 0$. We will use R_{melt} as the relevant length scale for the rest of this article. In the SCMF simulations

we obtain $\tau_{\text{melt}} = 274500$ SMC steps, where each segment on average had the chance of one trial displacement in a SMC step.

The softness of the interactions allows for an efficient equilibration of the morphology and the description of dense polymer melts that are characterized by experimentally relevant, large values of the invariant degree of polymerization, $\bar{N} = (\rho_o R_e^3 / N)^2$. Here, R_e denotes the measured end-to-end distance using the full Hamiltonian.

Lennard-Jones Bead–Spring Model. The absence of harsh excluded-volume interactions in the soft, coarse-grained model prevents us from studying the interplay between morphology and liquid-like structure. As we reduce the temperature or increase the incompatibility, both the segregation between A- and B-rich domains becomes more pronounced and, simultaneously, the density increases and one species arrests in a glassy state. While the former effect can be described by soft interactions the latter cannot. Therefore, we turn to the Lennard-Jones bead–spring model for additional studies of the properties of random copolymers.

In a model with harsh excluded-volume interactions, however, it is difficult to achieve experimentally large values of \bar{N} . Therefore, we use in both, the soft, coarse-grained model and the model with harsh excluded-volume interactions, small values of the invariant degree of polymerization, ranging from $\bar{N} = 175$ for a homopolymer melt ($\chi_o N = 0, \alpha = 0$) to $\bar{N} = 320$ for a high incompatibility of the two types of monomers. These values are orders of magnitude smaller than in experiments; therefore, we expect that fluctuation effects are significantly larger than in experimental systems.

In our model with harsh excluded-volume interactions, the nonbonded pairwise interactions act between all segments with a cutoff at a distance $r = r_c = 2.5\sigma$ and truncated such that the potential and the force are continuous at the cutoff distance, r_c .³⁶

$$\frac{\mathcal{H}_{\text{nb}}(\{\vec{r}_i(s)\})}{k_B T} = \frac{1}{2} \sum_{i,j=1}^n \sum_{s,t=1}^N {}'U_{\text{LJ}}(r) - U_{\text{LJ}}(r_c) - (r - r_c) \left. \frac{dU_{\text{LJ}}(r)}{dr} \right|_{r=r_c} \quad (10)$$

where the prime indicates that the sum runs only over pairs of particles. $r = |\vec{r}_i(s) - \vec{r}_j(t)|$ is the distance between the interacting particles, and $U_{\text{LJ}}(r)$ denotes the Lennard-Jones potential

$$U_{\text{LJ}}(r) = 4\epsilon_{\text{IJ}} \left(\frac{\sigma^{12}}{r^{12}} - \frac{\sigma^6}{r^6} \right) \quad (11)$$

σ characterizes the spatial range of the potential, and the depth of the potential, ϵ_{IJ} with IJ being A or B, depends on the segment species. The repulsive part of the Lennard-Jones interaction limits the compressibility of the dense polymer melt and dictates the liquid-like packing of the Lennard-Jones segments, while the attractive part of the Lennard-Jones interaction results in a realistic equation of state and a densification of the liquid upon cooling. The difference in the attractive interactions gives rise to the incompatibility between A and B segments and drives the structure formation in the random copolymer melt. In the following, we set $\epsilon_{\text{AB}} = \epsilon_{\text{BB}} \equiv \epsilon$, which defines the energy scale; ϵ_{AA} is varied to control the incompatibility between A and B segments. In the following,

we measure the length scale of the Lennard-Jones bead–spring model in units of σ and the energy scale in units ϵ . The value $\epsilon_{\text{AA}} = 1$ corresponds to a melt, where A and B segments are identical. Larger values of ϵ_{AA} give rise to local demixing of A and B segments and, additionally, to an increase of the density of A-rich domains relative to that of B clusters.

The bonded interactions are modeled as finitely extensible, nonlinear elastic (FENE) interactions

$$\frac{\mathcal{H}_{\text{b}}(\{\vec{r}_i(s)\})}{k_B T} = -\frac{k r_0^2}{2} \sum_{i=1}^n \sum_{s=1}^{N-1} \ln \left(1 - \frac{|\vec{r}_i(s) - \vec{r}_i(s+1)|^2}{r_0^2} \right) \quad (12)$$

with the maximal bond lengths, $r_0 = 1.5\sigma$, and the spring constant, $k = 16$. The parameters are chosen such that the combination of bonded and nonbonded interactions prevents the chain molecules from crossing through each other in the course of their motion in molecular dynamics simulations. The repulsive part of the Lennard-Jones potential also imparts a local stiffness on the chain conformations. Since the nonbonded interactions differ for A and B species, the equilibrium bond length slightly differs for A and B blocks and changes with segregation. Each molecule is comprised of $N = 60$ Lennard-Jones interaction centers.

We studied the properties of the Lennard-Jones bead–spring model by molecular dynamics simulations using the program package LAMMPS.³⁷ The equations of motions were integrated using the velocity-Verlet^{38,39} algorithm with an integration step of $\Delta t = 0.005\tau$ in units of the Lennard-Jones time scale τ . The temperature was fixed at $T = 1$ in Lennard-Jones units using a Nosé–Hoover thermostat^{40,41} with a damping parameter of 0.7 in Lennard-Jones units. Simulations in the isobaric ensemble (NPT) at $P = 0$ employed a Nosé–Hoover barostat^{41,42} with a pressure damping of 5 in Lennard-Jones units.

In analogy to the SCMF simulations, the “time” scale of the molecular dynamics simulations is calculated from the number of integration steps that it takes a homopolymer in a pure homopolymer melt to diffuse a distance on the order of R_{melt}^2 , i.e., $\tau_{\text{melt}} = R_{\text{melt}}^2/D$, where D denotes the self-diffusion coefficient in a homopolymer melt and R_{melt}^2 is the measured mean squared end-to-end distance of polymers in a homopolymer melt, which we will use as the relevant length scale in the following text. In the MD simulations we obtain $\tau_{\text{melt}} = 21000000$ integration steps, i.e., $\tau_{\text{melt}} = 105000\tau$.

RESULTS

Static Properties. The snapshots shown in Figure 1 illustrate how the morphology of the melt changes with growing incompatibility of the two different monomeric repeat units. Already for small incompatibility, see Figure 1a and Figure 1d, A and B segments are not randomly mixed but they show a preference to form clusters, albeit with small differences in composition. The internal “interfaces” of these clusters of high concentration of one type of segments are rather broad.

For the next set of parameters, $\epsilon_{\text{AA}} = 1.3$ and $\chi_o N = 100$, a microemulsion-like structure has formed, cf. Figure 1, parts b and e, where the domains are segregated more strongly and the interfaces can now be clearly determined.

In the final set of parameters, depicted in parts c and f of Figure 1, the microemulsion-like structure has fully formed, and therefore the internal interfaces between the domains are rather sharp. The morphology is characterized by a well-defined, finite, characteristic length scale but no long-range order like in

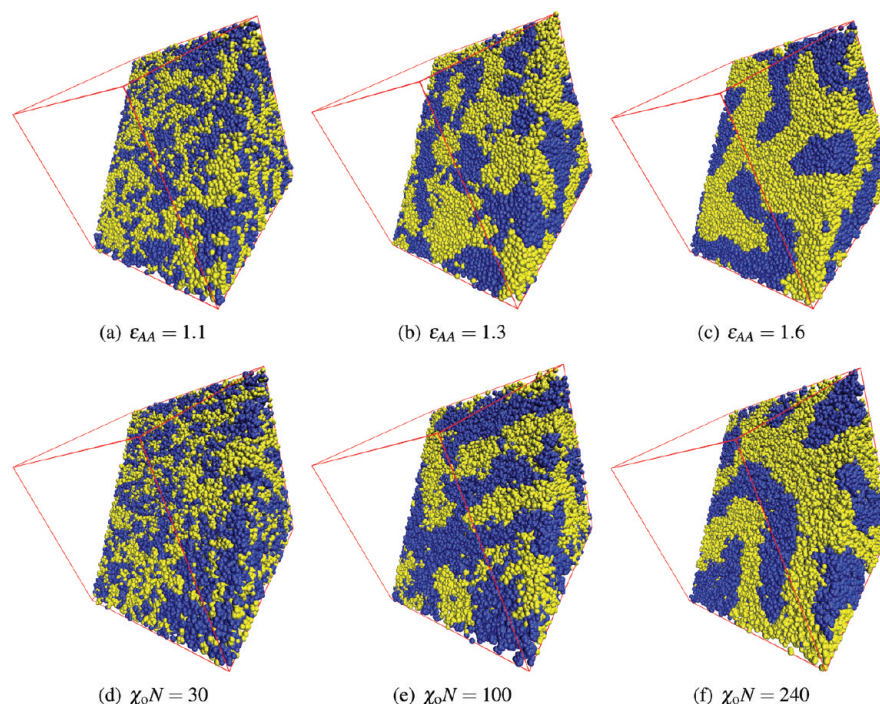


Figure 1. Snapshots for different values of the interaction parameter as indicated below each figure. On the top, the snapshots are from the Lennard-Jones bead-spring model while the bottom figures show snapshots obtained with the soft, coarse-grained model. These figures were produced using VMD.⁴³

a lamellar phase is established on the time scale of our simulations.⁴⁵

Although these snapshots are generated by simulating different models, where there is no analytical expression to identify matching parameters, they show a striking similarity in their mesoscopic structure in a statistical sense. The first goal of our study is to identify parameters of the two different models to produce this structural similarity.

We chose R_{melt} as the length scale, which allows us to compare the results of these two models. The values are $R_{\text{melt}} = 1.2R_{\text{eo}}$ in the soft, coarse-grained model used in the SCMF simulations and $R_{\text{melt}} = 10.0\sigma$ in the Lennard-Jones bead-spring model used in MD simulations, respectively. The quantities, which we used to characterize the static structure, are the radial pair correlation function of A and B segments, $g_{AB}(r)$, as well as the structure factor, $S(q)$. The structure factor is defined as

$$S(q) = \frac{1}{nN} \left\langle \left| \sum_{i=1}^n \sum_{s=1}^N (2\gamma_i(s) - 1) \exp(i\vec{q} \cdot \vec{r}_i(s)) \right|^2 \right\rangle \quad (13)$$

with $\gamma_i(s)$ used as in eq 3. It measures fluctuations of the A-density on different length scales. Since the fluctuations of the A-density chiefly arise from composition fluctuations, we can compare the data of the soft, coarse-grained model and the strongly repulsive Lennard-Jones bead-spring model although their isothermal compressibilities differ. The choice of values for q is constrained by our finite simulation box. Since it is cubic, we can only calculate $S(q)$ for values of $q = (2\pi)/(L)((k_x^2 + k_y^2 + k_z^2)^{1/2})$ where all k_i are integers. The A-B pair correlation function is defined as

$$g_{AB}(r) = \frac{\int d^3r_1 \int d^3r_2 \langle \rho_A(\vec{r}_1) \rho_B(\vec{r}_2) \rangle \delta(r - |\vec{r}_1 - \vec{r}_2|)}{\int d^3r_1 \int d^3r_2 \langle \rho_A(\vec{r}_1) \rangle \langle \rho_B(\vec{r}_2) \rangle \frac{4\pi r^2}{V}} \quad (14)$$

where $\rho_{A,B}(\vec{r})$ denote the local densities.

In order to match the equilibrium structure of the soft, coarse-grained model to the Lennard-Jones bead-spring model, we have adjusted the parameters incompatibility, χ_oN , and the segmental asymmetry, α , keeping the inverse compressibility, $\kappa_oN = 600$ fixed.

Varying α does not strongly influence the AB pair correlation function, but chiefly affects the AA and BB pair correlation functions. We have adjusted the value of α to match the behavior of the total correlation functions, g_A and g_B at large distances to the results of the Lennard-Jones bead-spring model. Increasing α , we increase the difference of local densities in A- and B-rich domains, i.e., the density of A increases and the density of B decreases. The density difference becomes notable in the Lennard-Jones bead-spring model for large values of the incompatibility. In the inset of Figure 2c, we highlight the behavior of g_A and g_B at large distances in the Lennard-Jones bead-spring model and compare the data with the results of the soft, coarse-grained model for two values of α .

When one changes the value of χ_oN , it results in a shift of position and change of magnitude of the peak in the pair correlation function. A greater value of χ_oN shifts this peak to larger length scales and increases its height.

In Figure 3 the pair correlation functions are plotted for three sets of parameters, which show similar structure behavior on a mesoscopic length scale. The analogue data for the structure factor are displayed in the insets.

Because of the harsh repulsion (excluded volume) of the Lennard-Jones bead-spring model, as compared to the soft interactions of the soft, coarse-grained model, which allow segments to overlap, the two structural properties of both models cannot be reconciled on short length scales for the pair correlation function and large q -values for the structure factor, respectively. This difference manifests itself as a peak of the structure factor for MD simulations around $(qR_{\text{melt}})^2 = 5000$, which corresponds to $(q\sigma)^2 = 50$, and the packing structure of the pair correlation function. At intermediate to large length

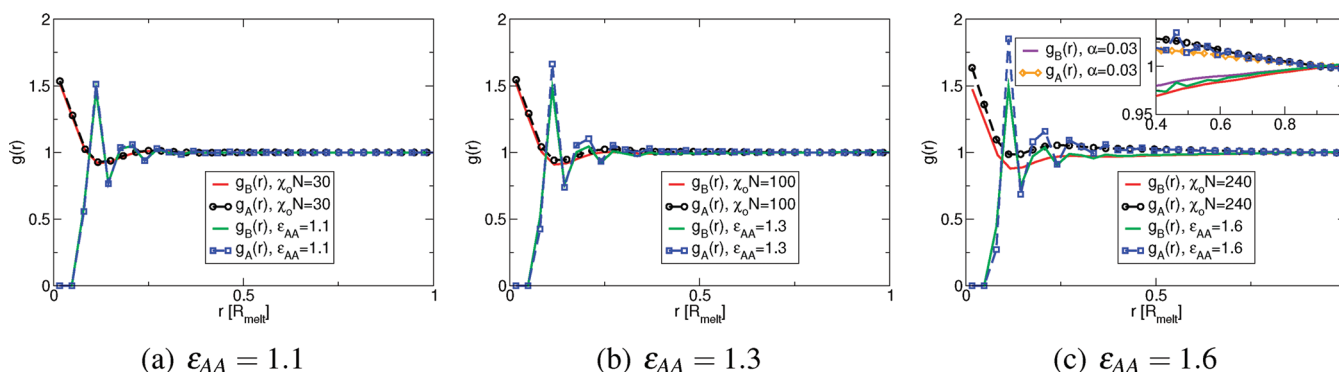


Figure 2. Comparison of the radial pair correlation function of A ($g_A = (g_{AA} + g_{AB})/2$) and B ($g_B = (g_{BB} + g_{AB})/2$) monomers for three different sets of parameters between the two different models. The density of A-rich domains becomes larger than that of B-rich domains at higher incompatibility. In the soft, coarse-grained model, χ_oN was always set to 600, α and χ_oN are as follows: (a) $\alpha = 0.01$, $\chi_oN = 30$; (b) $\alpha = 0.02$, $\chi_oN = 100$; (c) $\alpha = 0.05$, $\chi_oN = 240$.

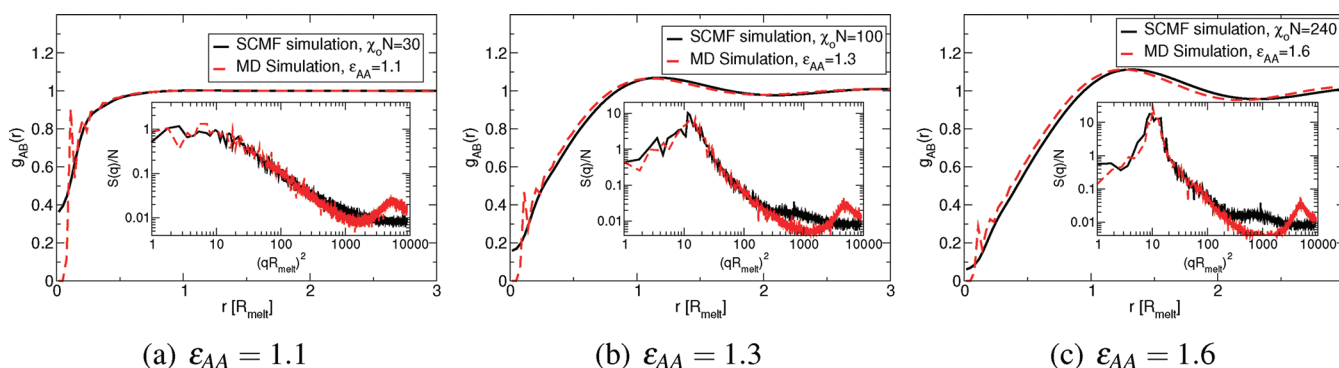


Figure 3. Comparison of the radial A–B pair correlation function and the structure factor for three different sets of parameters. In the soft, coarse-grained model, χ_oN was always set to 600, α and χ_oN are as follows: (a) $\alpha = 0.01$, $\chi_oN = 30$; (b) $\alpha = 0.02$, $\chi_oN = 100$; (c) $\alpha = 0.05$, $\chi_oN = 240$.

scales, however, the equilibrium structure agrees very well for each set of parameters. Let us discuss the three different sets in turn. For the smallest incompatibilities, $\chi_oN = 30$ and $\epsilon_{AA} = 1.1$, we observe a correlation hole in the AB pair correlation function, Figure 3a, but no peak appears, neither in the pair correlation function, nor in the structure factor, which is displayed in the inset. As the snapshots already suggested, this value of interaction strength fails to impose a strong segregation onto the system. When we increase the interaction strength to $\chi_oN = 100$ and $\epsilon_{AA} = 1.3$, see Figure 3b, we observe a formation of a structure on a scale of $1.2R_{\text{melt}}$ in the pair correlation function and a peak in the structure factor at $(qR_{\text{melt}})^2 \approx 14$, which corresponds to a wavelength of $1.7R_{\text{melt}}$. The position of this peak of the structure factor corresponds to a point of inflection in the pair correlation function. Increasing the interaction strength further to $\chi_oN = 240$ and $\epsilon_{AA} = 1.6$, cf. Figure 3c, the peak of the pair correlation function shifts to $1.3R_{\text{melt}}$ and the peak in the structure factor to $(qR_{\text{melt}})^2 \approx 11$. Again, the position of this peak in the structure factor, with a wavelength of $1.9R_{\text{melt}}$ and the point of inflection of the pair correlation function coincide.

Mean-field theory predicts that at intermediate segregation, random block copolymers form a microphase separated morphology with a characteristic wavelength that decreases with increasing incompatibility.⁷ This prediction differs from our simulation results. First, the morphology, which we observe in the simulations, lacks long-range order. Second, the characteristic length scale increases as we increase the incompatibility

between unlike segments. The reason are the strong fluctuation effects due to the small value of \bar{N} .

We summarize the results of this section in Figure 4, plotting the pairs of χ_oN and ϵ_{AA} for which we found good agreement of the static structure at mesoscopic length scales.

Conformations. In the previous section, we have demonstrated that one can identify parameters such that the morphology of the soft, coarse-grained model and the Lennard-Jones bead–spring model at intermediate and long length scales coincide. In this section we investigate to what extent this structural agreement also holds for conformational properties of individual molecules.

Chain conformations have been analyzed by examining the mean square radius of gyration, R_g^2 , and the mean squared end-to-end distance, R_e^2 . In this analysis we have sorted all chains based on the overall chain composition. Since all chains consist of 6 blocks there are 7 different types of chains with 0, 1, 2, 3, 4, 5, or 6 blocks of type B. Conformational properties were averaged for each chain composition. Figure 5 shows the change of conformations as a function of the interaction parameter, ϵ_{AA} and χ_oN , respectively, for different chain composition. As the interaction strength increases, the conformations of chains with different composition show dissimilarities. With the formation of a microemulsion-like structure, homopolymer chains become more compact as is evident from the reduced values of R_g^2 in Figure 5(a), compared to the homopolymer melt with $\epsilon_{AA} = 1.0$ and $\chi_oN = 0$, respectively. The shrinking of the molecular extension is likely a consequence of the confinement into corresponding A or B domains.

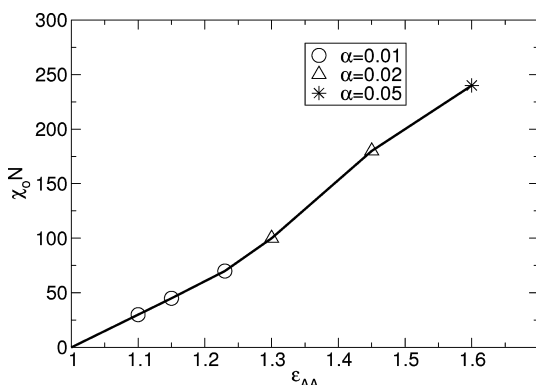


Figure 4. Model parameters for similar equilibrium morphologies of the two different models. In the soft, coarse-grained model, κN was always set to 600, $\alpha = 0.01$ for $30 \leq \chi_o N \leq 75$, $\alpha = 0.02$ for $100 \leq \chi_o N \leq 180$, and $\alpha = 0.05$ for $\chi_o N = 240$.

Interestingly, after a well-segregated morphology forms, $\varepsilon_{AA} \geq 1.3$ and $\chi_o N \geq 100$, the conformations of homopolymer chains are almost independent of the strength of the interaction and the corresponding changes in structure observed in Figure 3.

Chains that contain both A and B blocks become more extended, compared to a homopolymer melt, as the interaction strength increases. This molecular stretching is the strongest for chains with 50–50 composition. We also calculated the ratio of $\langle R_e^2 \rangle / \langle R_g^2 \rangle$ to examine if the stretching/shrinking of chains will affect their Gaussianity. For Gaussian chains, this ratio is 6. Figure 5b shows that chains with 50–50 A/B compositions noticeably deviate from the Gaussian behavior with their ratio being larger than 6.0 as a sign characteristic for extended conformations. Chains with 33 or 67% of A segments have ratios very close to 6 indicating that, on average, their conformations are similar to a Gaussian chain. Finally, homopolymer chains (A or B) and chains with large composition asymmetry have $\langle R_e^2 \rangle / \langle R_g^2 \rangle$ ratio smaller than 6.0 indicating a more coiled conformations compared to Gaussian chains.

We emphasize that the same parameters that result in an agreement of the morphology between the Lennard-Jones bead–spring model and the soft, coarse-grained model additionally give rise to excellent agreement of the conformation properties.

Dynamic Properties. In this section, we compare the single-chain dynamics of the soft, coarse-grained model and the Lennard-Jones bead–spring model. In Figure 6, we present the mean square displacement (MSD), and the end-to-end vector autocorrelation, $C(t)$, as a function of time. The analysis of the static properties in Figure 2 revealed structural differences on the length scales $\leq 0.25R_{\text{melt}}$. The differences in the local, fluid-like structure on the segment scale give rise to different local friction coefficients in the soft, coarse-grained model and the Lennard-Jones bead–spring model. The latter exhibits a local, glass-like dynamics at high segregation. To account for these differences, the time scale is adjusted by the diffusion coefficient, D , see Table 1 and Table 2. The diffusion coefficient is calculated from the MSD of the polymers' centers of mass, $g_3(t)$,⁴⁴ by $D = \lim_{t \rightarrow \infty} (g_3(t)) / (6t)$. The vertical dashed line in the figure indicates the time scale, on which the segments have diffused several segment sizes. Beyond this time and length scale the static structure agrees and the single-chain dynamics can be compared. The diffusion coefficient decreases by a factor of 2 when we compare the disordered melt, $\chi_o N = 0$, 30, with the microemulsion like, $\chi_o N = 100$, 240, systems. We can deduce that the formed structure severely restricts the mobility of the chains. When we compare the segmental MSD, the A segments show a slightly smaller value for large length scales, see parts a and b of Figure 6. Using this matching of time scales, the dynamics of the slower A-segments nicely agrees between the soft, coarse-grained model and the Lennard-Jones bead–spring model, while there are some differences in the dynamics of B-segments and the center-of-mass at small and intermediate times.

The end-to-end vector autocorrelation function in Figure 6d shows that the time needed for the end-to-end vector to decorrelate undergoes a larger change than the diffusion coefficient. This decoupling of translational and rotational dynamics due to domain formation in the Lennard-Jones bead–spring model is quantitatively captured by the soft, coarse-grained model. This time grows by a factor of 5 when we compare $\chi_o N = 30$ to $\chi_o N = 100$, and a factor of 10 when we compare $\chi_o N = 30$ to $\chi_o N = 240$. The influence of the formation of domains and their boundaries becomes more pronounced in this quantity, while also being noticeable in the MSD.

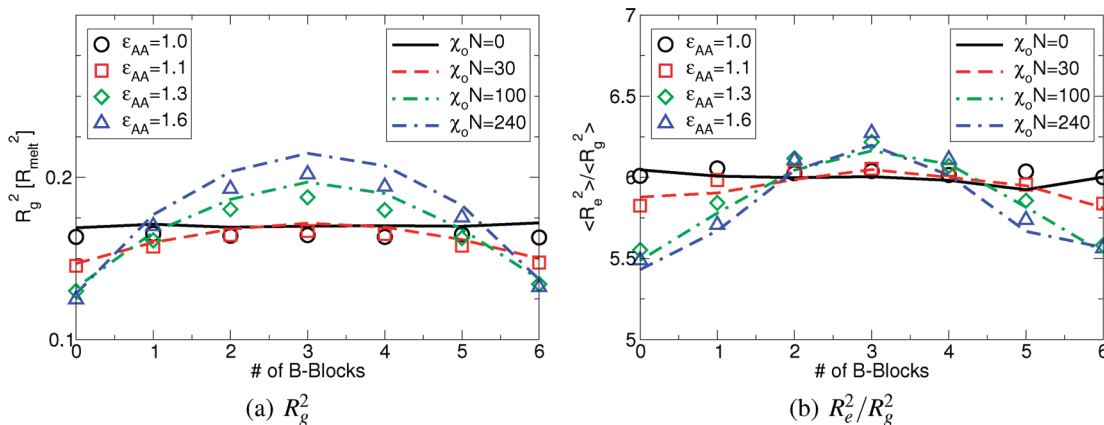


Figure 5. Conformational properties of the two different models as a function of interaction strength and the number of B blocks of the chains. The mean squared radius of gyration, R_g^2 , normalized by the mean squared end-to-end distance of the homopolymer melt, is shown in the left figure (a) to investigate the extension of the polymers. The figure to the right (b) is used to examine the Gaussianity of the chains by plotting $\langle R_e^2 \rangle / \langle R_g^2 \rangle$. Both figures show these results for the soft, coarse-grained and the Lennard-Jones bead–spring models.

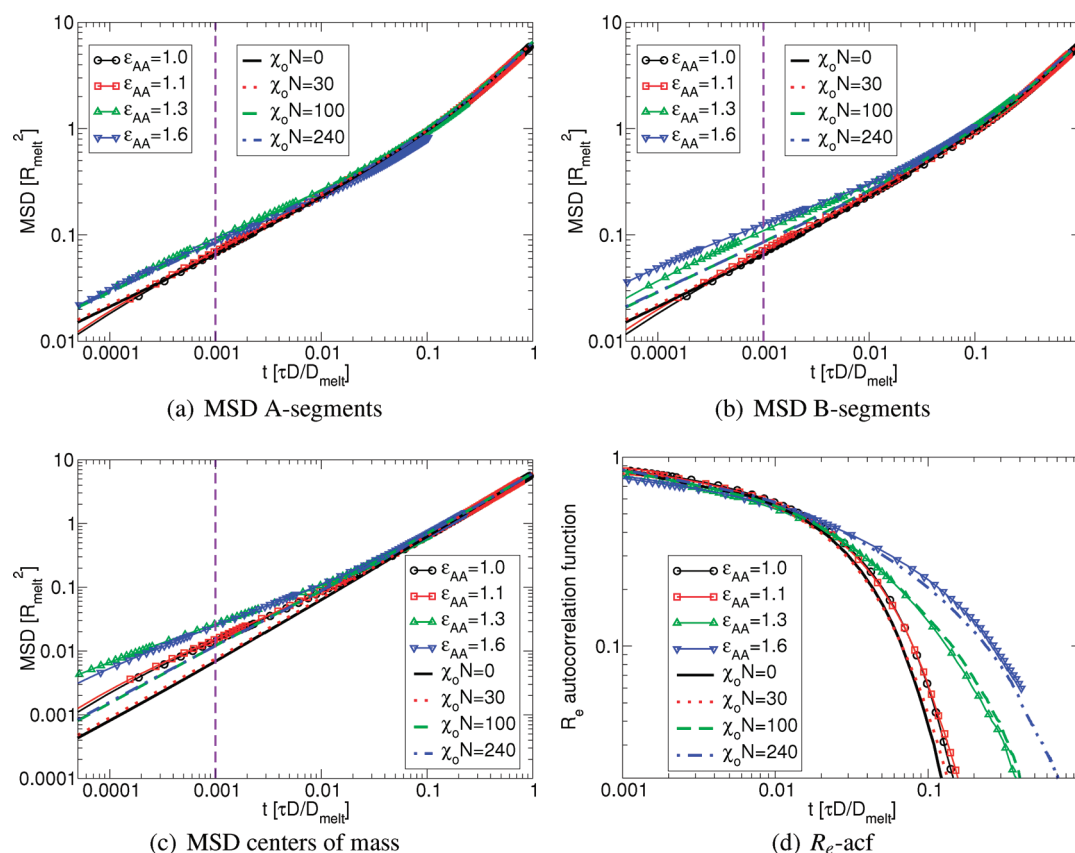


Figure 6. Dynamic properties of both models. The MSD of A-segments, B-segments and the center of mass is depicted in panels a, b, and c. Panel d displays the end-to-end vector autocorrelation function. The time is multiplied by the diffusion coefficient of the random block copolymer melt and divided by the diffusion coefficient of the homopolymer melt. The different dynamics for short time scales of the two models are clearly visible. The end-to-end vector autocorrelation function decorrelates on the same time scale for MD and SCMF simulations for each set of parameters.

Table 1. Diffusion Coefficient of the Polymer Chains in SCMF Simulations, Calculated for Different Parameters of the Soft, Coarse-Grained Model

$\chi_o N$	0	30	100	240
D/D_{melt}	1.0	0.88	0.49	0.46

Table 2. Diffusion Coefficient of the Polymer Chains in MD Simulations, Calculated for Different Parameters of the Lennard-Jones Bead–Spring Model

ϵ_{AA}	1.0	1.1	1.3	1.6
D/D_{melt}	1.0	0.83	0.25	0.11

When looking at the same quantities, MSD and the end-to-end vector autocorrelation function in the MD simulations, see Figure 6, the dynamic quantities show a significantly different behavior as a function of the interaction strength. The diffusion coefficients in Table 2, calculated from the mean-squared displacement of the polymers' centers of mass, Figure 6(c), decrease faster in the MD simulations with increasing interaction strength. We examine the MSD of single segments in parts a and b of Figure 6 for A and B segments, respectively. For short times, an increase of the interaction strength does not affect the movement of B segments; their freedom becomes constricted only at larger time scales, when the collective motion of the entire chains dominates. For A segments, a larger interaction strength also gives rise to a reduction of mobility at

short time scales. The difference in the MSD of single segments decreases with longer time scales. In Figure 6d, we investigate the autocorrelation function of the polymers' end-to-end vector. As in the case of the MSD, this dynamic quantity implies the same slower dynamics of the LJ melt when compared to the soft, coarse-grained model.

Equilibration Times after Quench. We investigate the structure formation in response to a quench from the disordered phase in SCMF simulations. For each set of parameters, we take an equilibrated homopolymer melt as the starting configuration, then distribute the polymer types randomly, and let the system equilibrate, now with a different α and $\chi_o N$.

In Figure 7, the time evolution of the pair correlation function is presented for three different values of $\chi_o N$ and, in the inset, the time evolution is presented for the structure factor. For the smallest interaction strength, $\chi_o N = 30$, see Figure 7a, the pair correlation function and the structure factor show that the system equilibrates very fast; within $0.18\tau_{\text{melt}}$ its structure has reached an equilibrated state. When we look at the structure formation at the intermediate interaction strength, $\chi_o N = 100$, we estimate from the pair correlation function, Figure 7a, that it takes $0.36\tau_{\text{melt}}$ to equilibrate the system. This equilibration time is compatible with the time evolution of the structure factor in Figure 7b, but it is more difficult to extract a time scale from $S(q)$. In case of the highest interaction strength, $\chi_o N = 240$, it takes even longer to achieve an equilibrated

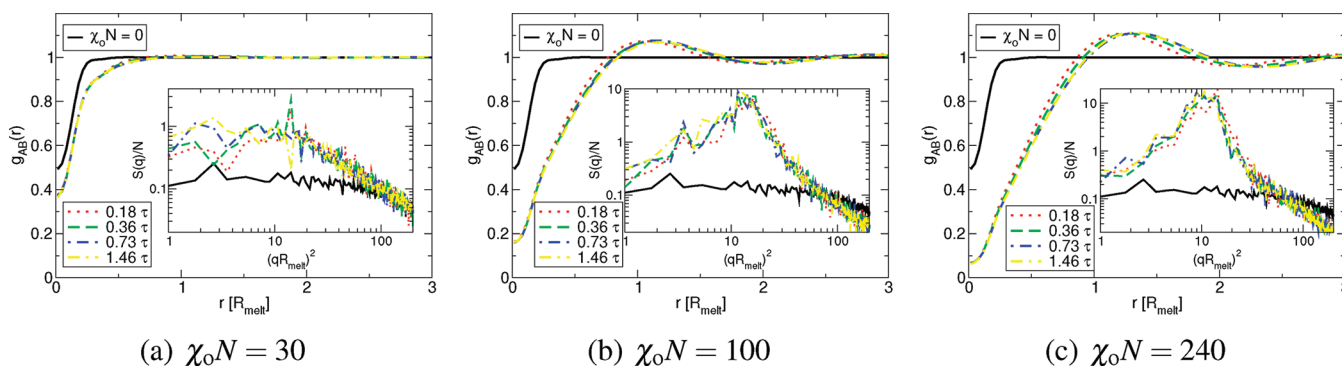


Figure 7. Time evolution of the radial A–B pair correlation function and the structure factor for three different sets of parameters in the soft, coarse-grained model. κN was always set to 600, α and $\chi_o N$ are as follows: (a) $\alpha = 0.01$, $\chi_o N = 30$; (b) $\alpha = 0.02$, $\chi_o N = 100$; (c) $\alpha = 0.05$, $\chi_o N = 240$.

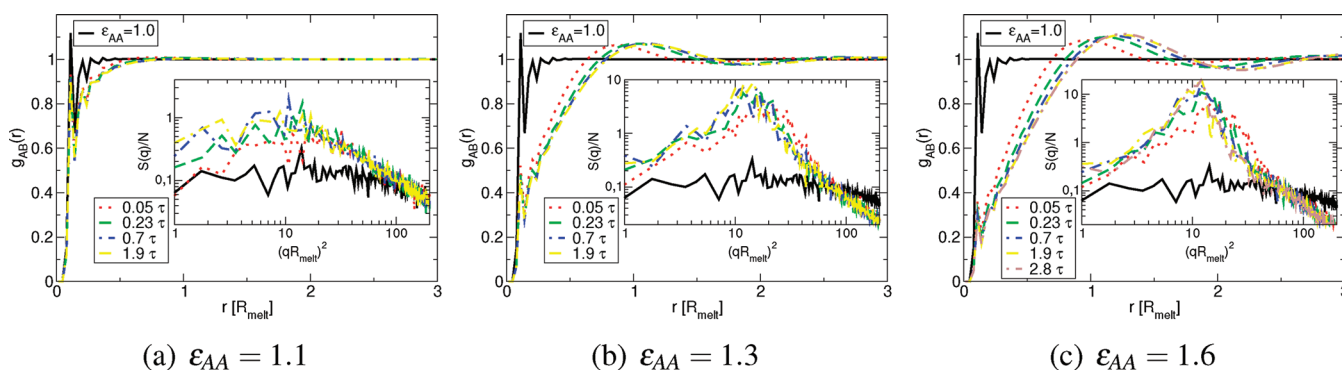


Figure 8. Time evolution of the radial A–B pair correlation function and the structure factor for three different sets of parameters in the MD simulations. The parameter ϵ_{AA} was set as follows: (a) $\epsilon_{AA} = 1.1$; (b) $\epsilon_{AA} = 1.3$; (c) $\epsilon_{AA} = 1.6$.

structure. From the evolution of the pair correlation function, see Figure 7c, we estimate that the system takes about $0.73\tau_{\text{melt}}$ to equilibrate. The failure to reach equilibrium at $0.36\tau_{\text{melt}}$ can, for this large incompatibility, also be inferred from the structure factor, cf. Figure 7c.

In the MD simulations, we adhered to the following simulation setup. We equilibrated a melt at $\epsilon_{AA} = 1.0$ and then quenched the system to the desired value of ϵ_{AA} . After the quench, we continued the simulation of the system in the NPT ensemble. We studied the time evolution for the three different values of $\epsilon_{AA} = 1.1, 1.3$, and 1.6 , which we investigated in the last section. In Figure 8, the time evolution of the pair correlation function is shown for these three different values of ϵ_{AA} , and the insets present the corresponding data for the structure factor. In qualitative agreement with the SCMF simulations, the time to form the equilibrium morphology increases with incompatibility, $\chi_o N$. At $\epsilon_{AA} = 1.1$, both measures of structure formation show an equilibration within $0.23\tau_{\text{melt}}$ see Figure 8a. For the intermediate incompatibility, $\epsilon_{AA} = 1.3$, the equilibration takes $0.7\tau_{\text{melt}}$ as depicted in Figure 8b, and for the highest incompatibility, $\epsilon_{AA} = 1.6$, there is a further increase in the equilibration time to $1.7\tau_{\text{melt}}$.

Quantitatively, the soft, coarse-grained model attains the equilibrium morphology faster than the Lennard-Jones bead–spring model when measured in units of the relaxation time of a single molecule in the disordered state. Moreover, the ratio of time scales $[\tau_{\text{eq,MD}}/\tau_{\text{melt,MD}}]/[\tau_{\text{eq,SCMF}}/\tau_{\text{melt,SCMF}}]$ increases from 1.28 at low incompatibilities to 2.33 at high incompatibility. The relative slowing-down of the Lennard-Jones model is partially explained by the increase of the density in the segregated A-rich clusters. Upon further increase of ϵ_{AA} , the density

inside the well-segregated A-domains will increase and eventually lead to a vitrification. Note that the glass transition occurs in similar Lennard-Jones bead–spring models around $1/\epsilon_{AA} \approx 0.42$. Since the slowing-down and the glass transition are related to the local, fluid-like packing, which is not captured by the soft, coarse-grained model, packing effects do not contribute to an increase of the equilibration time in the SCMF simulations.

Equilibration after Mapping the Soft, Coarse-Grained Model onto the Lennard-Jones Bead–Spring Model.

Since the Lennard-Jones bead–spring model and the soft, coarse-grained model agree in their equilibrium structure at intermediate and large length scales, and the SCMF simulations are computationally more efficient because the interactions are softer and the time scale is not affected by the liquid-like packing of segments, it is tempting to use equilibrated configurations of the SCMF simulations for generating starting configurations for the Lennard-Jones bead–spring model.

It is important to note that the configurations obtained by Single-Chain-in-Mean-Field simulations capture intermolecular correlations on the scale of the molecule's extension, e.g., the correlation hole in the intermolecular pair correlation function. Otherwise, a full single-chain relaxation time, τ_{melt} would be required to establish those correlations.^{46,47}

Given an equilibrated soft, coarse-grained configuration with chain length $N = 120$, we construct a starting configuration of the Lennard-Jones model with $N = 60$ by representing the center of mass of two neighboring soft beads by a Lennard-Jones particle. Since the soft beads may overlap, also the Lennard-Jones particles will overlap resulting in excessively large forces, and we cannot simply switch on the harsh

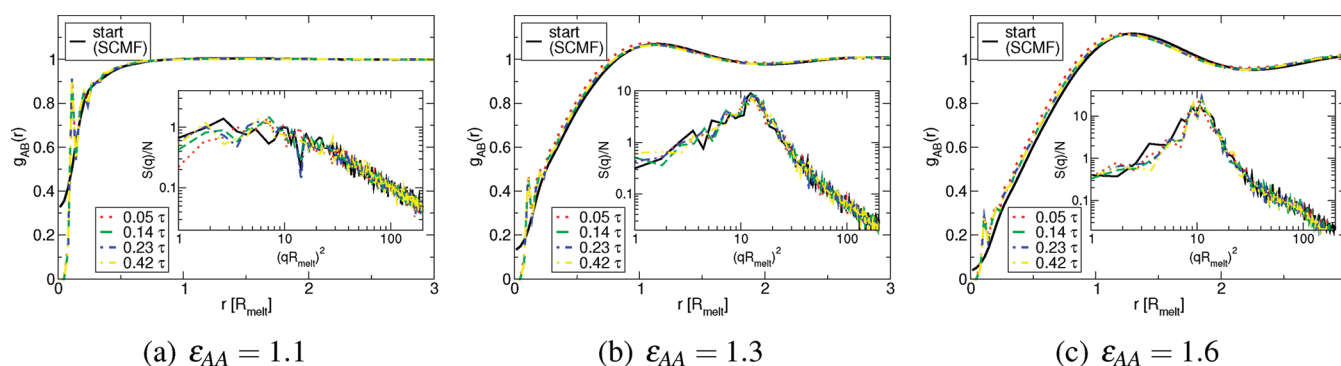


Figure 9. Time evolution of the A–B pair correlation function and structure factor in MD simulations. This simulation used equilibrated configurations of the soft, coarse-grained model as starting configurations. In the soft, coarse-grained model, $\kappa_o N$ was always set to 600, α and $\chi_o N$ are as follows: (a) $\alpha = 0.01$, $\chi_o N = 30$; (b) $\alpha = 0.02$, $\chi_o N = 100$; (c) $\alpha = 0.05$, $\chi_o N = 240$.

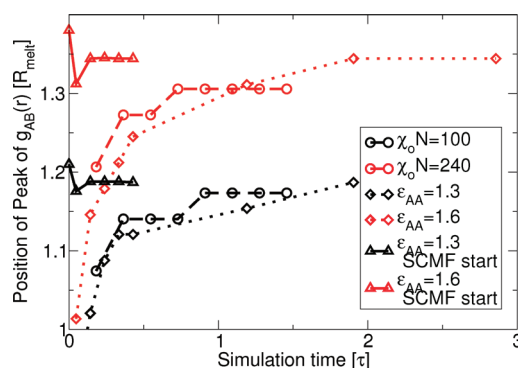


Figure 10. Position of the first maximum of the A–B pair correlation function. This quantity is used to gauge the time needed to equilibrate the system in SCMF simulations, the MD simulations with a random starting configuration and the MD simulations with the equilibrated SCMF configuration used as starting configurations.

repulsion of the Lennard-Jones potential. Therefore, we first relax the system in the microcanonical ensemble and restrict the maximum movement per bead and integration step to 0.05σ . At the same time, we rescale the velocities to put the temperature to $k_B T / \epsilon_{BB} = 1$ at the end of this simulation part. After 100 integration steps with $\Delta t = 0.005\tau$, we switch on the thermostat and equilibrate the system for $t = 0.05\tau_{\text{melt}}$. Finally, we simulate the system in the NPT-ensemble at vanishing pressure, $P = 0$. The time evolution of the pair correlation function and the structure factor, cf. Figure 9, show that the structural equilibration of the system is very fast. Only the local fluid-like packing has to be established by the equilibration procedure. Both the morphology of A and B domains and the conformations on intermediate and large length scales as well as the correlation hole in the intermolecular pair correlation function are already captured by the SCMF simulations. For all three incompatibilities the desired structure is safely attained within three million integration steps which is equivalent to $0.14\tau_{\text{melt}}$. The results of the last two sections can be summed up by Figure 10. It depicts the position of the first peak of the AB pair correlation function as a function of the simulation time. We can deduce from this figure that the equilibration of the Lennard-Jones bead–spring model with the help of an equilibrated starting configuration takes only a small fraction of the time compared to using a random starting configuration. To put this graph and the time scales into perspective, on a single CPU of the type Intel XEON X5570 at 2.93 GHz, $1 \tau_{\text{melt}}$ takes roughly 3600 h of computing time when using LAMMPS

with a system of this size, but only 36 h when we use the SCMF method.

SUMMARY AND OUTLOOK

We have investigated the structure and dynamics of random block copolymer melts as a function of the incompatibility using a soft, coarse-grained model and a Lennard-Jones bead–spring model. Upon increasing the incompatibility, both models gradually form a microemulsion-like structure. When we compare our results for a higher incompatibility to mean-field predictions^{7,8} for random block copolymer melts, we find a significant difference in the structure formed. (i) we do not observe well-ordered, periodic microphases and (ii) the characteristic length scale of the morphology does not decrease with growing incompatibility. These discrepancies are rooted in fluctuation effects, which are particularly strong in our system because the Lennard-Jones model can only describe systems with a modest value of \bar{N} .

We have characterized the molecular conformations and morphology and the single-chain dynamics and identified a mapping between the parameters of the two different models such that they exhibit similar structure on intermediate and large length scales. On short length scales, the Lennard-Jones model is characterized by strong liquid-like packing effects that are absent in the soft coarse-grained model and give rise to a pronounced slowing down of the dynamics in the Lennard-Jones bead–spring model at low temperatures.

Although the short-ranged structural properties of the two systems are inherently different, we can use the quickly equilibrated SCMF simulations to create starting configuration for the Lennard-Jones bead–spring model, which reduces the equilibration time needed as compared to a random starting configuration by at least 1 order of magnitude.

When comparing the dynamic properties of the models, we see that the dynamics, as exemplified by the mean-squared displacement and the end-to-end vector correlation function, are significantly different for the two models. In the simulations of the soft, coarse-grained model the slowing-down of the dynamics is less pronounced for higher incompatibilities than for the harder Lennard-Jones bead–spring model because the local fluid structure is independent from the incompatibility.

This method for acquiring equilibrated configurations for a Lennard-Jones bead–spring model grants better access to equilibrium properties of random block copolymer melts. For example, one can use these results to probe mechanical properties of random block copolymer melts. Thereby, creating

independent equilibrated configurations in order to perform statistically relevant measurements of said properties has become more efficient computationally.

AUTHOR INFORMATION

Corresponding Author

*E-mail: (M.M.) mmueller@theorie.physik.uni-goettingen.de; (D.B.) d.bedrov@utah.edu.

ACKNOWLEDGMENTS

Financial support by the DFG priority program “polymer-solid contacts: interfaces and interphases” under Grant MU 1674/9-1 and computing time at the GWDG Göttingen, the HLRN Hannover/Berlin, and Jülich Supercomputing Centre are gratefully acknowledged. The support of the National Science Foundation through NSF MRSEC grant DMR-1536145 and allocation of computing time at the University of Utah Center for High Performance Computing are gratefully acknowledged.

REFERENCES

- (1) Sakamoto, N.; Hashimoto, T. *Macromolecules* **1995**, *28*, 6825–6834.
- (2) Ogawa, T.; Sakamoto, N.; Hashimoto, T.; Han, C. D.; Baek, D. M. *Macromolecules* **1996**, *29*, 2113–2123.
- (3) Bates, F. S.; Fredrickson, G. H. *Phys. Today* **1999**, *52*, 32–38.
- (4) Leibler, L. *Macromolecules* **1980**, *13*, 1602–1617.
- (5) Ohta, T.; Kawasaki, K. *Macromolecules* **1986**, *19*, 2621–2632.
- (6) Matsen, M. W.; Schick, M. *Phys. Rev. Lett.* **1994**, *72*, 2660–2663.
- (7) Fredrickson, G. H.; Milner, S. T. *Phys. Rev. Lett.* **1991**, *67*, 835–838.
- (8) Fredrickson, G. H.; Milner, S. T.; Leibler, L. *Macromolecules* **1992**, *25*, 6341–6354.
- (9) Subbotin, A. V.; Semenov, A. N. *Eur. Phys. J. E: Soft Matter Biol. Phys.* **2002**, *7*, 49–64.
- (10) Sung, B. J.; Yethiraj, A. *J. Chem. Phys.* **2005**, *122*, 234904.
- (11) Sung, B. J.; Yethiraj, A. *J. Chem. Phys.* **2005**, *123*, 214901.
- (12) Sung, B. J.; Yethiraj, A. *Macromolecules* **2005**, *38*, 2000–2008.
- (13) Ryan, A. J.; Macosko, C. W.; Bras, W. *Macromolecules* **1992**, *25*, 6277–6283.
- (14) Eitouni, H. B.; Rappl, T. J.; Gomez, E. D.; Balsara, N. P.; Qi, S.; Chakraborty, A. K.; Fréchet, J. M. J.; Pople, J. A. *Macromolecules* **2004**, *37*, 8487–8490.
- (15) von der Heydt, A.; Müller, M.; Zippelius, A. *Macromolecules* **2010**, *43*, 3161–3164.
- (16) von der Heydt, A.; Müller, M.; Zippelius, A. *Phys. Rev. E* **2011**, *83*, 051131.
- (17) Fredrickson, G. H.; Helfand, E. *J. Chem. Phys.* **1987**, *87*, 697–705.
- (18) Panyukov, S.; Potemkin, I. *Phys. A: Stat. Mech. Appl.* **1998**, *249*, 321–326.
- (19) Houdayer, J.; Müller, M. *Europhys. Lett.* **2002**, *58*, 660.
- (20) Houdayer, J.; Müller, M. *Macromolecules* **2004**, *37*, 4283–4295.
- (21) Gavrilov, A. A.; Kudryavtsev, J. V.; Khalatur, P. G.; Chertovich, A. V. *Chem. Phys. Lett.* **2011**, *503*, 277–282.
- (22) Daoulas, K. C.; Müller, M. *J. Chem. Phys.* **2006**, *125*, 184904.
- (23) Müller, M.; Daoulas, K. C. *J. Chem. Phys.* **2008**, *129*, 164906.
- (24) Barrat, J. L.; Baschnagel, J.; Lyulin, A. *Soft Matter* **2010**, *6*, 3430–3446.
- (25) Baschnagel, J.; Varnik, F. *J. Phys.: Condens. Matter* **2005**, *17*, R851–R953.
- (26) Müller, M.; Smith, G. D. *J. Polym. Sci., B: Polym. Phys.* **2005**, *43*, 934–958.
- (27) Grest, G. S.; Kremer, K. *Phys. Rev. A* **1986**, *33*, 3628–3631.
- (28) Allen, M. P.; Tildesley, D. J., *Computer simulation of liquids*; Clarendon Press: Oxford, U.K., 1990.
- (29) Detcheverry, F. A.; Kang, H. M.; Daoulas, K. C.; Müller, M.; Nealey, P. F.; de Pablo, J. J. *Macromolecules* **2008**, *41*, 4989–5001.
- (30) Daoulas, K. C.; Müller, M. *Adv. Polym. Sci.* **2010**, *224*, 197–233.
- (31) Müller, M.; Daoulas, K. C. *J. Chem. Phys.* **2008**, *128*, 024903.
- (32) Eastwood, J. W.; Hockney, R. W.; Lawrence, D. N. *Comput. Phys. Commun.* **1980**, *19*, 215–261.
- (33) Deserno, M.; Holm, C. *J. Chem. Phys.* **1998**, *109*, 7678–7693.
- (34) Dawson, K. A.; March, N. H. *Phys. Lett. A* **1983**, *96*, 460–462.
- (35) Rossky, P. J.; Doll, J. D.; Friedman, H. L. *J. Chem. Phys.* **1978**, *69*, 4628–4633.
- (36) Sewell, T. D.; Rasmussen, K. O.; Bedrov, D.; Smith, G. D.; Thompson, R. B. *J. Chem. Phys.* **2007**, *127*, 144901.
- (37) Plimpton, S. J. *Comput. Phys.* **1995**, *117*, 1–19.
- (38) Verlet, L. *Phys. Rev.* **1967**, *159*, 98.
- (39) Verlet, L. *Phys. Rev.* **1968**, *165*, 201–214.
- (40) Hoover, W. G. *Phys. Rev. A* **1985**, *31*, 1695–1697.
- (41) Melchionna, S.; Ciccotti, G.; Holian, B. L. *Mol. Phys.* **1993**, *78*, 533–544.
- (42) Hoover, W. G. *Phys. Rev. A* **1986**, *34*, 2499–2500.
- (43) Humphrey, W.; Dalke, A.; Schulten, K. *J. Mol. Graphics* **1996**, *14*, 33–38.
- (44) Paul, W.; Binder, K.; Heermann, D. W.; Kremer, K. *J. Chem. Phys.* **1991**, *95*, 7726–7740.
- (45) In very long simulation runs of the soft, coarse-grained model, $t > 50\tau_{\text{melt}}$ we observe a gradual change of the morphology to a defected lamellar structure without a change of the characteristic spacing.
- (46) Hömberg, M.; Müller, M. *J. Chem. Phys.* **2008**, *128*, 224911.
- (47) Local packing and density fluctuations have to be re-equilibrated. Since the length scale of local packing effects as well as the correlation length of density fluctuations in a dense melt is on the order of the segment size, these local effects can be equilibrated on a time scale that is much shorter than the single-molecule relaxation time. The compressibility of the soft, coarse-grained model is sufficiently small for a correlation hole to develop in the intramolecular chain correlations function,²² thus intermolecular chain conformations and the large-scale molecular structure are correctly captured by the soft, coarse-grained model. Long wavelength density fluctuations, however, differ in the Lennard-Jones model and the soft, coarse-grained model, which are characterized by different isothermal compressibilities, and large scale diffusion is required to equilibrate these long wavelength fluctuations of the total density. Since fluctuations of the total density and the composition approximately decouple in dense multicomponent polymer melts and fluctuations of the total density are much smaller than composition fluctuations even in the soft, coarse-grained model, density fluctuations will not affect the morphology.

Lactide Cyclopolymerization by an Alumatrane-Inspired Catalyst

Jonathan Weil,[†] Robert T. Mathers,[‡] and Yutan D. Y. L. Getzler^{*,†}[†]Department of Chemistry, Kenyon College, Gambier, Ohio 43022, United States[‡]Department of Chemistry, The Pennsylvania State University, New Kensington, Pennsylvania 15068, United States

S Supporting Information

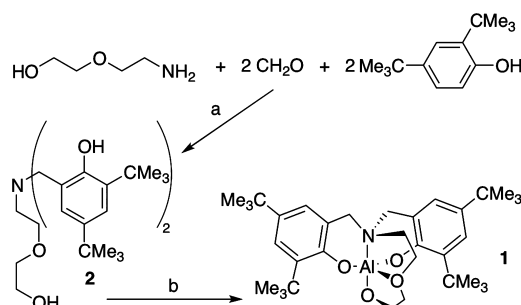
■ INTRODUCTION

Control of molecular structure is an enduring motivation for chemists. From total synthesis¹ to self-assembly² to crystal growth,³ the pursuit continues unabated. Polymer synthesis, in particular, has seen a revolution in control. It is now possible to precisely predetermine chain length, extent of cross-linking, comonomer incorporation, block length, stereochemistry and topology.⁴ There has even been success in sequence control,⁵ previously achieved only in biological systems. The difficulties inherent in the synthesis of pure macrocycle⁶ have limited their availability, despite their compelling predicted properties. A variety of strategies have been employed but only two avoid linear material at all stages: catalyst-free ring equilibration and ring-expansion polymerizations (REP).⁷ Our general catalyst design has been influenced by a recent example of the latter strategy wherein Grubbs used a ring-opening metathesis polymerization (ROMP) catalyst modified with a permanently tethered initiating group to polymerize cyclooctene yielding high-molecular-weight rings free of any linear contaminants.^{8,9} Taking a cyclic catalyst and a cyclic monomer as our design criteria, we focused on cyclic poly(lactic acid) (cPLA) as a target. PLA architectures are interesting due to their degradation profiles and because they can be renewably sourced, and the cyclic architecture of cPLA in particular may be advantageous in drug delivery.¹⁰ Whereas cyclic lactide oligomer have been synthesized,^{11–13} we sought to produce high-molecular-weight cPLA.¹⁰ *N*-Heterocyclic carbenes,^{14,15} organotin compounds¹⁶ and imidazoles¹⁷ have previously been reported as effective catalysts for lactide REP to form cPLA. Herein we report an alumatrane-inspired catalyst, (*N,N*-bis(3,5-di-*tert*-butyl-2-benzyloxy)-2-(2-aminoethoxy)ethoxy)aluminum [(*t*-Bu-SalAmEE)Al, **1**], that is active for controlled cPLA synthesis by lactide REP.

Metallatranes, the trigonal bipyramidal complexes of tripodal tetradentate ligands,¹⁸ have been widely used^{19–21} and continue to be an area of active research.^{22–28} Of particular relevance to this work are recent examples of monomeric alumatranes.^{29–31} Alumatranes are most commonly dimeric, and the alumatrane dimers which have been examined for lactide polymerization are inactive.^{32,33} However, a monomeric alumatrane-isopropanol adduct capable of lactide polymerization in the melt has been reported.³² Further inspiration was drawn from ligand hemilability where changes in hapticity³⁴ or denticity³⁵ can stabilize reactive catalytic intermediates or allow substrate coordination.

■ RESULTS AND DISCUSSION

Catalyst Synthesis. The synthesis of catalyst **1** is straightforward and uses inexpensive materials (Scheme 1).

Scheme 1. Ligand and Catalyst Synthesis^a

^aKey: (a) C₇H₈, reflux. (b) 0.01 M **2**, AlMe₃, THF, reflux, N₂, 5 days.

Ligand **2** was produced via Mannich condensation of the relevant phenol and aminoalcohol in toluene under Dean–Stark conditions. Although related ligand syntheses are frequently driven by precipitation of the product,^{36,37} **2** remained soluble, limiting yields. Despite this, **2** has been isolated on >15 g scale. Metalation was more challenging as initial attempts using known procedures^{29–33} yielded an intractable and complex mixture of products that, remarkably, included unreacted aluminum alkyls. Success required dilution in THF and an extended (five day) reflux. The necessity of both the relatively high dilution and lengthy reaction time were verified separately. Characterization by ¹H and ¹³C NMR spectroscopies revealed a highly symmetric compound. However, given the frequent dimerization of alumatranes noted above, our representation of **1** as monomeric must be taken as tentative. Detailed characterization of **1** is underway and will be reported elsewhere.

Polymerization Activity and Polymer Characterization. Catalyst **1** was active for the polymerization of lactide in the melt and in solution and produced polymers with high molecular weights and narrow polydispersities (Table 1). At constant concentration of monomer and catalyst with increasing reaction time, the conversion of monomer to polymer steadily increased, consistent with a well-defined catalyst (Table 1, entries 1–3). The system also clearly

Received: August 26, 2011

Revised: December 13, 2011

Published: January 9, 2012

Table 1. Solution and Melt Polymerizations of Lactide with Catalyst 1^a

entry	solvent	[monomer]/[catalyst]	time (h)	convn (%) ^b	M_w (g/mol) ^c	M_w/M_n ^c	$[\eta]$ (mL/g) ^d	MHS values ^d	
								α	K (mL/g)
1	toluene	62	2	24	4080	1.8	4.1	0.29	0.383
2	toluene	62	4	39	6130	1.2	5.8	0.37	0.243
3	toluene	62	8	64	7380	1.2	8.7	0.81	0.006 74
4	toluene	52	12	79	9200	1.2	9.5	0.39	0.290
5	toluene	250	12	34	12 680	1.1	10.6	0.71	0.0135
6	toluene	416	12	21	16 320	1.1	9.7	0.91	0.002 47
7	melt	104	2	79	31 880	1.2	21.8	0.44	0.239
8	melt	165	2	66	33 760	1.4	22.9	0.46	0.201
9	melt	407	2	39	38 820	1.2	26.1	0.53	0.109

^aMelt polymerizations were conducted under nitrogen at 130 °C using monomer and catalyst (3.5 mg). Solutions polymerizations were conducted under nitrogen at 130 °C using monomer (106 mg), catalyst, and toluene (1.1 mL). ^bConversion was calculated from the ¹H NMR spectrum of the crude reaction mixture. ^cWeight-average (M_w) molecular weights and molecular weight distributions (M_w/M_n) were calculated by gel-permeation chromatography using light scattering in tetrahydrofuran (THF). ^dMark–Houwink–Sakurada (MHS) values and intrinsic viscosity ($[\eta]$) were measured in THF at 35 °C using a gel-permeation chromatography system with light scattering and viscometer detectors.

displayed the expected time-dependent increases in both molecular weight and intrinsic viscosity (Table 1, entries 1–3). If reaction time was instead held constant, but catalyst loading decreased, percent conversion displayed a concomitant decline, consistent with fewer active polymerization sites (Table 1, entries 4–6). Fewer active sites should also produce material with higher molecular weights, a trend which was observed in the same data (Table 1, entries 4–6). Melt polymerizations by catalyst 1 responded to decreasing catalyst loadings in an analogous fashion (Table 1, entries 7–9), with decreased conversion of monomer and increased molecular weights.

The polymerization activity of compound 1 was consistent with a well-defined catalyst (Figure 1). Melt polymerizations

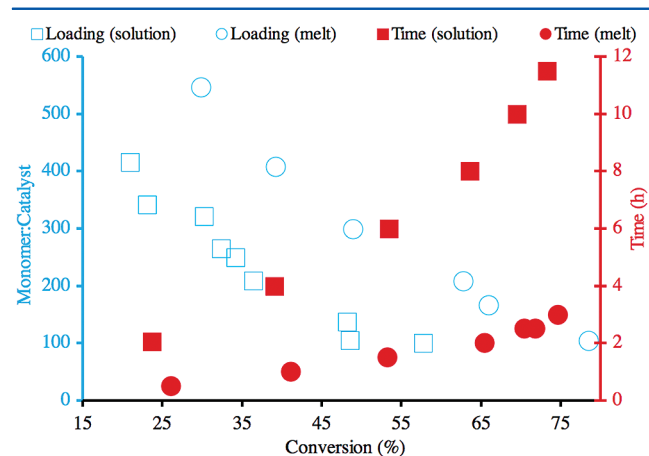


Figure 1. Conversion of lactide monomer in solution and melt polymerizations as a function of catalyst loading and time. Conversion was calculated from the ¹H NMR spectrum of the crude reaction mixture. Key: (blue □) 0.7 mmol of lactide, 1.1 mL of toluene, 12 h, 130 °C; (blue ○) 6 μmol of 1, 2 h, 130 °C; (red ■) 60:1 monomer:1, 5 μmol of 1, 0.55 mL of toluene, 130 °C; (red ●) 190:1 monomer:1, 6 μmol of 1, 130 °C.

gave higher conversion with decreasing monomer-to-catalyst ratio as did solution polymerizations. When concentrations were instead held constant but reaction time was varied, conversion increased with time as expected. Unsurprisingly, the much higher concentrations of catalyst in the melt polymerizations resulted in much higher conversions at a given time than the comparable solution polymerizations.

The proposed cyclic structure of 1 means that the polymer formed from enchainment of lactide by 1 could also be cyclic. We investigated this possibility by comparing the polymer to authentic linear PLA, synthesized with a bis(2-ethylhexanoate)-tin catalyst. When the absolute molecular weights and elution volumes of linear PLA and the polymer produced by 1 were compared, the latter eluted at higher volumes, consistent with the smaller hydrodynamic volume of a cyclic topology

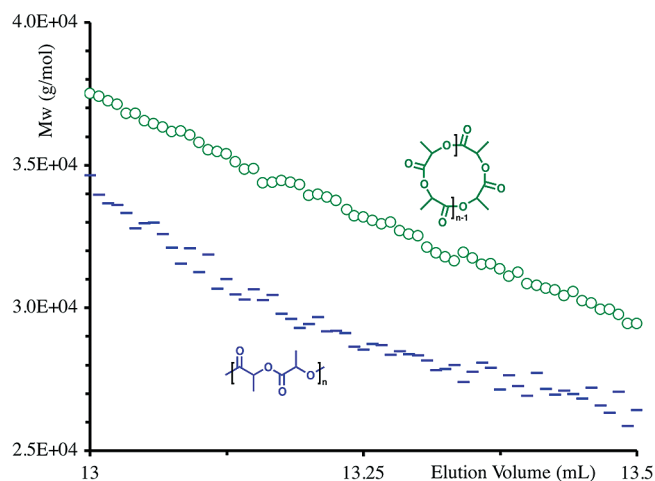


Figure 2. Molecular weight as a function of elution volume for linear PLA (blue —) and the PLA produced by 1 (green ○).

(Figure 2). Further evidence for a cyclic topology was found in overlaid Mark–Houwink–Sakurada plots of linear material and the polymer formed by 1 (Figure 3). As expected, for a given molecular weight, the linear material displayed a higher intrinsic viscosity. Cyclic polymer topology is also supported by MALDI–TOF MS data, where the dominant peaks are integer multiples of the monomer (Supporting Information).

A plausible polymerization mechanism for the formation of cPLA by 1 is shown in Scheme 2. Enchainment of lactide could proceed through a coordination–insertion mechanism³⁸ to generate macrometallacycle 3, which would eventually undergo an intramolecular chain transfer⁹ to liberate cPLA (4) and regenerate free catalyst (1). We are interested in more closely examining the kinetics of the system, particularly whether molecular weight and molecular weight distribution can be

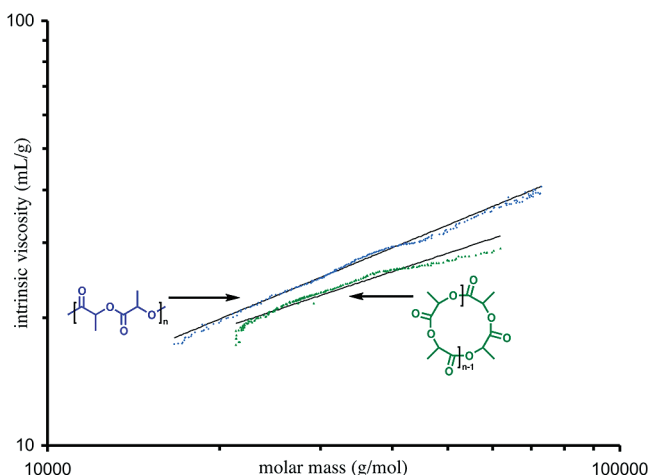
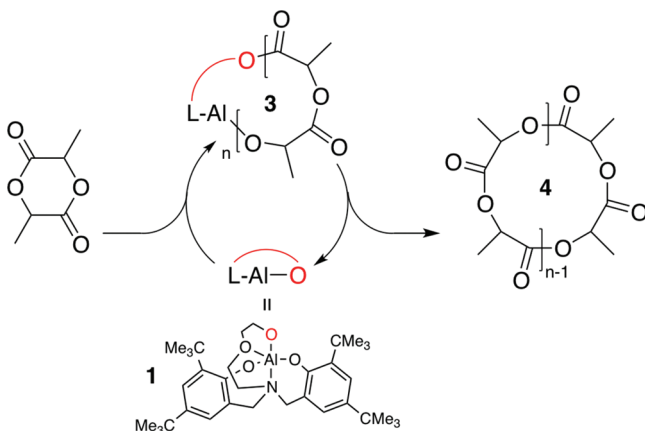


Figure 3. Mark-Houwink-Sakurada plot of linear PLA (blue) and PLA produced by **1** (green), each overlaid with their respective linear regressions.

Scheme 2. Proposed Mechanism for the Ring-Expansion Polymerization of Lactide by **1**



influenced by reaction temperature, as might be expected from the proposed mechanism.

CONCLUSION

We presented a new catalyst for the ring-expansion polymerization of lactide to cyclic poly(lactic acid). The pseudoalumatrane complex contains a putative initiating group tethered to a permanently bound ligand, analogous to Grubbs' catalyst for ring-expansion polymerization of cyclooctene. Our catalyst is active for polymerization of lactide in solution and in the melt and shows a linear increase in conversion with either catalyst loading or polymerization time under either polymerization condition, consistent with a well-defined active site. The expected trends are also observed for molecular weight and intrinsic viscosity. The polymer produced displays physical characteristics consistent with a cyclic architecture when compared to linear material of equivalent molecular weights including longer elution times when subjected to size exclusion chromatography and lower intrinsic viscosity. This catalyst is a valuable addition to an ever-expanding body of methods for the control of macromolecular structure.

ASSOCIATED CONTENT

Supporting Information

Detailed experimental procedures and characterization of new compounds including MALDI-TOF and NMR spectra (two files). This material is available free of charge via the Internet at <http://pubs.acs.org>.

AUTHOR INFORMATION

Corresponding Author

*E-mail: getzlery@kenyon.edu.

ACKNOWLEDGMENTS

This work was generously supported by Kenyon College Summer Science Scholars Program (J.W.), Kenyon College Startup Funds, the American Chemical Society's Petroleum Research Fund (42880-GB 7)(YDYL). R.T.M. thanks the donors of the American Chemical Society's Petroleum Research Fund and the Alcoa Foundation for support.

REFERENCES

- (1) Corey, E. J.; Cheng, X. *The Logic of Chemical Synthesis*; John Wiley & Sons: New York, 1995.
- (2) Whitesides, G. M.; Grzybowski, B. *Science* **2002**, 295, 2418–2421.
- (3) Qiu, S. R.; Orme, C. A. *Chem. Rev.* **2008**, 108, 4784–4822.
- (4) Mueller, A. H. E.; Matyjaszewski, K. *Controlled And Living Polymerizations: Methods And Materials*; Wiley-VCH: Weinheim, Germany, 2009.
- (5) Kramer, J. W.; Treitler, D. S.; Dunn, E. W.; Castro, P. M.; Roisnel, T.; Thomas, C. M.; Coates, G. W. *J. Am. Chem. Soc.* **2009**, 131, 16042–16044.
- (6) Semlyen, J. A., In *Cyclic polymers*, 2nd ed.; Kluwer Academic Publishers: Dordrecht, The Netherlands, 2000.
- (7) Kricheldorf, H. R. *J. Polym. Sci., Part A: Polym. Chem.* **2010**, 48, 251–284.
- (8) Boydston, A. J.; Xia, Y.; Kornfield, J. A.; Gorodetskaya, I. A.; Grubbs, R. H. *J. Am. Chem. Soc.* **2008**, 130, 12775–12782.
- (9) Bielawski, C. W.; Benitez, D.; Grubbs, R. H. *Science* **2002**, 297, 2041–2044.
- (10) Hoskins, J. N.; Grayson, S. M. *Polym. Chem.* **2011**, 2, 289–299.
- (11) Chisholm, M. H.; Gallucci, J. C.; Yin, H. *Proc. Natl. Acad. Sci. U.S.A.* **2006**, 103, 15315–15320.
- (12) Chisholm, M. H.; Gallucci, J. C.; Yin, H. *Dalton Trans.* **2007**, 4811–4821.
- (13) Chisholm, M. H. *J. Organomet. Chem.* **2008**, 693, 808–818.
- (14) Culkin, D. A.; Jeong, W.; Cshony, S.; Gomez, E. D.; Balsara, N. P.; Hedrick, J. L.; Waymouth, R. M. *Angew. Chem., Int. Ed.* **2007**, 46, 2627–2630.
- (15) Jeong, W.; Shin, E. J.; Culkin, D. A.; Hedrick, J. L.; Waymouth, R. M. *J. Am. Chem. Soc.* **2009**, 131, 4884–4891.
- (16) Kricheldorf, H. R. *J. Polym. Sci., Part A: Polym. Chem.* **2004**, 42, 4723–4742.
- (17) Kricheldorf, H. R.; Lomadze, N.; Schwarz, G. *Macromolecules* **2008**, 41, 7812–7816.
- (18) Voronkov, M. G.; Baryshok, V. P. *J. Organomet. Chem.* **1982**, 239, 199–249.
- (19) Verkade, J. G. *Acc. Chem. Res.* **1993**, 26, 483–489.
- (20) Verkade, J. G. *Coord. Chem. Rev.* **1994**, 137, 233–295.
- (21) Schrock, R. R. *Acc. Chem. Res.* **1997**, 30, 9–16.
- (22) Kim, J. H.; Yoon, S.; Mun, S. D.; Kim, S. H.; Lee, J.; Chung, Y.; Kwon, S. H.; Lee, K. S.; Lee, C.; Kim, Y. *J. Org. Chem.* **2011**, 696, 1729–1735.
- (23) Jyothish, K.; Zhang, W. *Angew. Chem., Int. Ed.* **2011**, 50, 3435–3438.
- (24) Jevric, M.; Zheng, T.; Meher, N. K.; Fettingner, J. C.; Mascal, M. *Angew. Chem., Int. Ed.* **2011**, 50, 717–719.
- (25) Phukan, A. K.; Guha, A. K. *Inorg. Chem.* **2011**, 50, 1361–1367.

- (26) Martinez, A.; Guy, L.; Dutasta, J. P. *J. Am. Chem. Soc.* **2010**, *132*, 16733–16734.
- (27) Schwarz, A. D.; Herbert, K. R.; Paniagua, C.; Mountford, P. *Organometallics* **2010**, *29*, 4171–4188.
- (28) Mun, S. D.; Kim, S. H.; Lee, J.; Kim, H. J.; Do, Y.; Kim, Y. *Polyhedron* **2010**, *29*, 379–383.
- (29) Su, W.; Kobayashi, J.; Ellern, A.; Kawashima, T.; Verkade, J. G. *Inorg. Chem.* **2007**, *46*, 7953–7959.
- (30) Su, W.; Kim, Y.; Ellern, A.; Guzei, I. A.; Verkade, J. G. *J. Am. Chem. Soc.* **2006**, *128*, 13727–13735.
- (31) Kim, Y.; Verkade, J. G. *Inorg. Chem.* **2003**, *42*, 4804–4806.
- (32) Johnson, A. L.; Davidson, M. G.; Perez, Y.; Jones, M. D.; Merle, N.; Raithby, P. R.; Richards, S. P. *Dalton Trans.* **2009**, 5551–5558.
- (33) Hemmingson, S. L.; Stevens, A. J.; Tanski, J. M.; Getzler, Y. D. Y. L. *Acta Crystallogr. E* **2010**, *66*, m937.
- (34) Alt, H. G.; Samuel, E. *Chem. Soc. Rev.* **1998**, *27*, 323–329.
- (35) Slone, C. S.; Weinberger, D. A.; Mirkin, C. A. *Prog. Inorg. Chem.* **1999**, *48*, 233–350.
- (36) Chandrasekaran, A.; Day, R. O.; Holmes, R. R. *J. Am. Chem. Soc.* **2000**, *122*, 1066–1072.
- (37) Tshuva, E. Y.; Goldberg, I.; Kol, M.; Goldschmidt, Z. *Organometallics* **2001**, *20*, 3017–3028.
- (38) Kiesewetter, M. K.; Shin, E. J.; Hedrick, J. L.; Waymouth, R. M. *Macromolecules* **2010**, *43*, 2093–2107.

Cyclodextrin-Centered Polyesters: Controlled Ring-Opening Polymerization of Cyclic Esters from β -Cyclodextrin-Diol

Mickael Normand, Evgueni Kirillov, Jean-François Carpentier, and Sophie M. Guillaume*

Sciences Chimiques de Rennes (UMR 6226), CNRS, Université de Rennes 1, Campus de Beaulieu, 35042 Rennes Cedex, France

S Supporting Information

■ INTRODUCTION

Cyclodextrins (CDs) are currently being widely used in pharmaceuticals, cosmetics and food industries.¹ In particular, CD host–guest inclusion complexes may be applied as drug-carrier systems via oral, parenteral, or other administration routes, providing solubility to lipophilic drugs thereby enhancing their bioavailability and/or reducing adverse effects. CD-polymers find further applications as gels or DNA transfection vectors.² Aliphatic polyesters, including polycarbonates and polyhydroxyalkanoates form biocompatible, bio- and hydrolytically degradable (co)polymers that exhibit good thermo-mechanical properties. These (co)polymers are highly valuable as various biomaterials including controlled/sustained release drug-delivery systems and tissue engineering devices.³ The conjugation of CDs to polyesters thus appears highly promising in the biomedical/pharmaceutical sciences.

Among the different types of CD-polymers reported, one can distinguish between those including linear polymers either end-capped by CD unit(s),⁴ or incorporating CDs into their backbone,⁵ with pending CDs,⁶ forming inclusion complexes with CD,⁷ centered on CD,⁸ or leading to self-assembled supramolecular architectures.⁹ Most of the reported work on CD-polyesters is dealing with polylactides, polylactones (ϵ -caprolactone, δ -valerolactone) and poly(ethylene glycol), the former two types of polymers being commonly prepared upon ring-opening polymerization (ROP) of the corresponding monomer using CD as initiator in water or in bulk,^{4a–c,7} possibly in the presence of tin octanoate ($\text{Sn}(\text{Oct})_2$).^{8a–c} In such a procedure, the monomer is included and activated within the CD; the assumed mechanism is similar to that of an enzymatic-mediated ROP in that the monomer is not covalently bound to the active CD site, and the polymers are eventually released from the active site.^{4a–c} In the presence of $\text{Sn}(\text{Oct})_2$ as ROP catalyst, the seven primary hydroxyl groups located at the smaller side of the CD or the fourteen secondary hydroxyl groups at the periphery of the largest side of the CD cone, can act as a multifunctional initiator.^{8a–c} Thus, one, seven, or fourteen polymer arms per CD have been claimed in these CD-centered polymers. The resulting polymer chains are end-capped by a CD. The molar mass generally remained below $7\,800\text{ g}\cdot\text{mol}^{-1}$ for 1-arm CDs and up to $36\,300\text{ g}\cdot\text{mol}^{-1}$ for a 14-arms CD, with molar mass distribution values in the 1.1–2.5 range.^{4–8}

In the general approach to design conjugated polyesters aimed at biomedical/pharmaceutical applications and to develop polymers within environmentally friendly considerations, we preferentially select monomers such as lactides (LA), β -butyrolactone (BL), and trimethylene carbonate (TMC) and coreagents (diol or triol co-initiators such as 1,3-propanediol and glycerol) that

are derived from biomass. We also favor “green” polymerization procedures such as the bulk (i.e., solvent-free), controlled “immortal” ring-opening polymerization (iROP) promoted by a biofriendly metal or an organic catalyst.^{10,11}

Herein we report the iROP of LA, BL, and TMC, under mild operating conditions, with the binary system composed of the amido zinc catalyst $[(\text{BDI}^{\text{IPr}})\text{Zn}(\text{N}(\text{SiMe}_3)_2)]$ ($\text{BDI}^{\text{IPr}} = 2-((2,6\text{-diisopropylphenyl})\text{amido})-4-((2,6\text{-diisopropylphenyl})\text{-imino})-2\text{-pentene}$) initially developed by Coates,¹² and β -CD-(OBn)₁₉(OH)₂ acting as a diol co-initiator and chain transfer agent. The controlled growth of two macromolecular chains per β -CD allowed the synthesis of well-defined β -CD-centered polymers. The limitation of the hydroxyl groups on CD available as polymerization site to two was anticipated to enable better control and understanding of the polymerization, while the benzyloxy moieties impart lipophilicity (and hence solubility) to this reagent. The resulting β -CD-(OBn)₁₉(O-polyester/polycarbonate)₂ were thoroughly characterized by NMR, FT-IR, SEC, DSC, and MALDI–ToF MS techniques. This work provides an in-depth complementary approach to the recent communication by Zinck and co-workers who briefly reported the ROP of LA in the presence of β -CD-(OBn)₁₉(OH)₂ (among other carbohydrates) and 4-*N,N*-dimethylaminopyridine (DMAP) as catalyst.¹³ Also, mass spectrometry insights of polyester- β -CD conjugates is provided in light of the work reported by Kowalczyk and co-workers on the ROP of BL from β -cyclodextrintriol (β -CD(OH)₃).¹⁴

■ EXPERIMENTAL SECTION

Materials. All manipulations involving air-sensitive compounds (i.e., polymerizations mediated by the Zn catalyst) were performed under inert atmosphere (argon, <3 ppm of O₂) using standard Schlenk, vacuum line and glovebox techniques. Solvents were thoroughly dried and deoxygenated by standard methods and distilled before use. CDCl_3 was dried over a mixture of 3 and 4 Å molecular sieves. Native β -cyclodextrin (β -CD, Aldrich) was dried *in vacuo* for 24 h at 40 °C before use. Perbenzylated β -cyclodextrin (β -CD-(OBn)₂₁),¹⁵ ¹H NMR, Figure S1 in the Supporting Information) and β -cyclodextrin-diol (β -CD-(OBn)₁₉(OH)₂),¹⁶ hereafter abbreviated as β -CD(OH)₂; ¹H NMR, Figure S2; ¹³C NMR, Figure S3; MALDI–ToF MS, Figure S4 in the Supporting Information) were prepared as previously described. Yet, the purification of β -CD(OH)₂ from other *n*-ol side-products was optimized by column chromatography on neutral alumina using a 1:3 (*v/v*) mixture of EtOAc/heptane. *rac*-Lactide (*rac*-LA) was received from Acros, and L-lactide (L-LA) was kindly provided by Total

Received: October 28, 2011

Revised: December 15, 2011

Published: January 11, 2012

Table 1. iROP of LA, TMC and BL Initiated by the Catalytic System $[(\text{BDI}^{\text{IPr}})\text{Zn}(\text{N}(\text{SiMe}_3)_2)]/(\beta\text{-CD}(\text{OH})_2)$ at 60 °C

entry	monomer	$[\text{monomer}]_0/[(\text{BDI})\text{Zn}]_0/[(\beta\text{-CD}(\text{OH})_2)_2]_0$	solvent	reaction time ^a (min)	convn ^b (%)	$\bar{M}_{\text{theo}}^c \times 10^3$ (g mol ⁻¹)	$\bar{M}_{\text{NMR}}^d \times 10^3$ (g mol ⁻¹)	$\bar{M}_{\text{SEC}}^e \times 10^3$ (g mol ⁻¹)	\bar{M}_w/\bar{M}_n^f
1	rac-LA	40:2:1	toluene	10	100	8.6	11.5	5.4	1.45
2	rac-LA	100:2:1	toluene	10	87	15.4	nd	5.2	1.49
3	rac-LA	250:2:1	toluene	15	98	38.1	44.4	20.6	1.36
4	rac-LA	400:2:10	toluene	10	96	8.6	nd	9.7	1.28
5	rac-LA	500:2:1	toluene	20	98	73.5	83.4	37.4	1.41
6	rac-LA	1 000:2:1	toluene	15	98	147.0	57.4	61.6	1.42
7	rac-LA	1 000:2:4	toluene	10	98	38.1	41.3	28.3	1.36
8	rac-LA	1 000:2:4	DMF	10	0	-	-	-	-
9	rac-LA	1 000:2:10	toluene	10	84	17.2	nd	18.5	1.27
10	L-LA	1 000:1:5	toluene	30	65	21.6	28.7	25.8	1.31
11	L-LA	1 000:2:4	toluene	10	94	36.7	38.4	29.8	1.35
12	L-LA	5 000:1:5	toluene	30	59	88.9	nd	72.0	1.34
13 ^g	rac-BL	1 000:2:4	toluene	20	0	-	-	-	-
14	rac-BL	250:2:4	-	12 × 60	46	5.3	nd	8.3	1.08
15	rac-BL	500:2:4	-	18 × 60	67	10.0	14.0	12.2	1.08
16	rac-BL	1 000:2:4	-	2 × 60	0	-	-	-	-
17	rac-BL	1 000:2:4	-	19 × 60	71	15.2	17.8	14.1	1.14
18	rac-BL	1 000:2:4	-	26 × 60	98	21.1	nd	22.0	1.11
19	TMC	200:1:5	toluene	10	100	6.9	nd	8.4	1.67
20	TMC	500:2:4	toluene	10	100	15.6	nd	26.1	1.96
21 ^g	TMC	500:2/4	toluene	15	40	5.1	19.7	10.1	1.30
22 ^g	TMC	1 000:2:4	toluene	10	100	28.4	66.0	34.0	1.80
23	TMC	3 000:2:4	toluene	15	100	79.4	87.1	49.6	2.13
24 ^g	TMC	3 000:2:4	toluene	30	35	26.8	nd	33.0	1.79
25	TMC	5 000:2:4	toluene	15	100	130.0	145.2	56.9	2.13

^aReaction times were not necessarily optimized; results are representative of at least duplicated experiments. ^bMonomer conversion determined by ¹H NMR. ^cCalculated from $[\text{monomer}]_0/[\beta\text{-CD}(\text{OH})_2]_0 \times \text{monomer conversion} \times M_{\text{monomer}} + M_{\beta\text{-CD}(\text{OH})_2}$, with $M_{\text{LA}} = 114 \text{ g mol}^{-1}$, $M_{\text{TMC}} = 102 \text{ g mol}^{-1}$, $M_{\text{BL}} = 86 \text{ g mol}^{-1}$, and $M_{\beta\text{-CD}(\text{OH})_2} = 2847 \text{ g mol}^{-1}$. ^dDetermined from the relative intensity ratios of the $\beta\text{-CD}-\text{OCH}_2\text{C}_6\text{H}_5$ and main chain polyesters groups ¹H NMR signals +2800 g mol⁻¹ for $M_{\beta\text{-CD}(\text{OBN})_{19}}$; refer to Experimental Section. ^eDetermined by SEC vs. polystyrene standards and corrected by a factor of 0.58 for PLA¹⁷ and 0.73 for PTMC.¹⁸ ^fMolar mass distribution determined from SEC traces. ^gExperiment run at 23 °C.

Petrochemicals. Purification of either rac-LA or L-LA required a three-step procedure involving first a recrystallization from a hot, concentrated iPrOH solution (80 °C), followed by two subsequent recrystallizations in hot toluene (100 °C). After purification, rac-LA was stored at a temperature of -30 °C in the glovebox. Trimethylene carbonate (TMC, 1,3-dioxane-2-one, kindly provided by Labso Chimie Fine, Blanquefort, France) was first dissolved in THF and stirred over CaH₂ for 2 days, before being filtered and dried; TMC was then recrystallized from cold THF. Racemic β -butyrolactone (rac-BL, TCI Europe) was dried three times over CaH₂ and then distilled before use. Benzyl alcohol (Acros) was distilled over Mg turnings under argon atmosphere and kept over activated 4 Å molecular sieves. $[(\text{BDI}^{\text{IPr}})\text{Zn}(\text{N}(\text{SiMe}_3)_2)]$ was synthesized following the literature procedure.¹²

Instrumentation and Measurements. ¹H (500 or 400 MHz) and ¹³C (125 or 100 MHz) NMR spectra were recorded in CDCl₃ on Bruker Avance AM 500 and AM-400 spectrometers at 23 °C. Chemical shifts (δ) are reported in ppm and were referenced internally relative to tetramethylsilane (δ 0 ppm) using the residual ¹H and ¹³C solvent resonance.

Average molar mass (\bar{M}_{SEC}) and molar mass distribution (\bar{M}_w/\bar{M}_n) values were determined by SEC in THF at 30 °C (flow rate = 1.0 mL·min⁻¹) on a Polymer Laboratories PL50 apparatus equipped with a refractive index detector and two ResiPore 300 × 7.5 mm columns. The polymer samples were dissolved in THF (2 mg·mL⁻¹). Reported experimental SEC molar mass values (\bar{M}_{SEC}) for PLA and PTMC samples were corrected by a factor of 0.58¹⁷ and 0.73,¹⁸ respectively, as previously established. The SEC traces of the polymers all exhibited a unimodal and symmetrical peak.

Monomer conversions were calculated from ¹H NMR spectra of the crude reaction mixtures in CDCl₃, from the integration (Int.) ratio

$\text{Int}_{\text{polymer}}/[\text{Int}_{\text{polymer}} + \text{Int}_{\text{monomer}}]$, using the methyl hydrogen resonances for PLA at δ 1.49 ppm and for LA at δ 1.16 ppm, the methine hydrogen resonances for PHB at δ 5.25 ppm and for rac-BL at δ 4.66 ppm, and the methine hydrogen resonances for PTMC at δ 4.47 ppm and for TMC at δ 4.25 ppm.

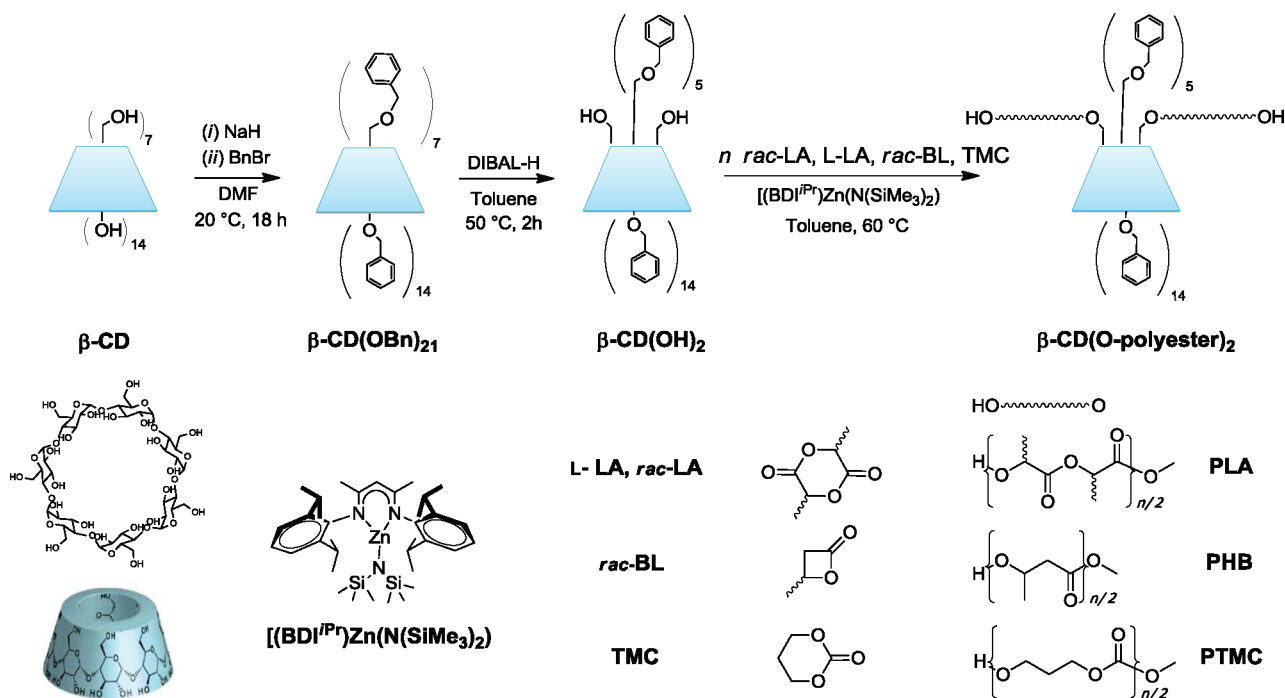
Molar masses of $\beta\text{-CD}(\text{OBN})_{19}(\text{O-polyester/polycarbonate})_2$ samples, hereafter abbreviated as $\beta\text{-CD}(\text{O-polyester})_2$, were determined by ¹H NMR spectroscopy in THF-*d*₆, taking into account the relative intensities of signals for the benzyloxy and the main chain ester units. For $\beta\text{-CD}(\text{OPLA})_2$: $\bar{M}_{\text{NMR}} = [\text{Int}(\text{CH}_2\text{LA})/2]/[\text{Int}(\text{CH}_2\text{C}_6\text{H}_5)/(5 \times 19)] \times 114 (=M_{\text{LA}}) + 2800 (=M_{\beta\text{-CD}(\text{OBN})_{19}}) \text{ g mol}^{-1}$ using the methine hydrogens of PLA at δ 5.15 and 5.21 ppm. For $\beta\text{-CD}(\text{OPHB})_2$ and $\beta\text{-CD}(\text{OPTMC})_2$ samples, the methine hydrogens of PHB at δ 5.25 ppm and the methylene hydrogens of PTMC at δ 4.47 ppm were used, correspondingly.

MALDI-ToF mass spectra were recorded with an AutoFlex LT high-resolution spectrometer (Bruker) equipped with a pulsed N₂ laser source (337 nm, 4 ns pulse width) and time-delayed extracted ion source. Spectra were recorded in the positive-ion mode using the reflectron mode and an accelerating voltage of 20 kV. The polymer sample was dissolved in THF (HPLC grade, 10 mg·mL⁻¹) and a saturated solution of α -cyano-4-hydroxycinnamic acid (10 mg·mL⁻¹) in acetonitrile (HPLC grade) was prepared. Then this latter solution was mixed in a 3:2 volume ratio with a 0.1% TFA solution in water. Both solutions were deposited sequentially on the sample target and then air-dried. Bruker Care Peptide Calibration and Protein Calibration 1 Standards were used for external calibration.

FTIR spectra of the polymers were acquired on a Shimadzu IRAffinity-1 equipped with an ATR.

Differential scanning calorimetry (DSC) analyses were performed on a Setaram DSC 131 apparatus calibrated with indium at a rate of

Scheme 1. Synthesis of β -CD(O-polyester/polycarbonate)₂ upon (i)ROP of LA, BL, or TMC from the Catalytic System $[(\text{BDI}^{\text{IPr}})\text{Zn}(\text{N}(\text{SiMe}_3)_2)]/\beta\text{-CD}(\text{OH})_2$



10 °C·min⁻¹, under continuous flow of helium (25 mL·min⁻¹), using aluminum capsules. The thermograms were recorded according to the following cycles: 50 to 220 °C at 10 °C·min⁻¹; 220 to 50 °C at 50 °C·min⁻¹; 50 °C for 17 min.

Typical Polymerization Procedure. In a typical experiment (Table 1, entry 7), $[(\text{BDI}^{\text{IPr}})\text{Zn}(\text{N}(\text{SiMe}_3)_2)]$ (2.3 mg, 3.5 μmol) and $\beta\text{-CD}(\text{OH})_2$ (2 equiv vs Zn, 20 mg, 7.0 μmol) were charged in a Schlenk flask in the glovebox. Toluene (880 μL) was then added and the solution stirred for 2 min. *rac*-LA (254 mg, 1760 μmol) was then added to the solution, and the flask was immersed in an oil bath preset at the desired temperature. The reaction mixture was stirred over the appropriate time (10 min; note that reaction times have not been systematically optimized). The reaction was quenched by addition of an excess of H₂O (ca. 2 mL of a 10% H₂O solution in THF). The resulting mixture was then concentrated under vacuum and the conversion determined by ¹H NMR analysis of the residue. Finally, the crude polymer was dissolved in CH₂Cl₂ and purified upon precipitation in pentane (ca. 15 mL), filtered and dried under vacuum. The recovered polymer was then analyzed by NMR, IR, SEC, DSC, and MALDI-ToF MS.

RESULTS AND DISCUSSION

β -Cyclodextrindiol ($\beta\text{-CD}(\text{OH})_2$) bearing two primary hydroxyl groups on the narrow side of the CD cone (Figures S2 and S3, Supporting Information) was first synthesized in a two-step procedure starting from native $\beta\text{-CD}$ via the perbenzylated analogue ($\beta\text{-CD}(\text{OBn})_{21}$) (Scheme 1), as previously described.^{15,16} The protecting benzyl groups provided lipophilicity to the CD, thus allowing to perform the polymerization in organic solvents.¹⁹ The iROP of LAs, BL or TMC from the catalytic system composed of $[(\text{BDI}^{\text{IPr}})\text{Zn}(\text{N}(\text{SiMe}_3)_2)]$ associated with $\beta\text{-CD}(\text{OH})_2$ in a ratio of at least 2:1 (each zinc center undergoes a protonolysis reaction with one of the two OH groups of $\beta\text{-CD}(\text{OH})_2$; the loading in $\beta\text{-CD}(\text{OH})_2$ chain transfer agent could also be increased) was carried out under mild operating conditions (toluene,¹⁹ 60 °C, Scheme 1).²⁰ The most significant results are reported in Table 1.

The iROP of both *rac*-LA and L-LA could be achieved within 10–20 min with almost quantitative monomer conversion and

similar reactivity, thereby highlighting a quite good activity ($120 < \text{TOF}^{21} (\text{h}^{-1}) < 5\,900$) of the $[(\text{BDI}^{\text{IPr}})\text{Zn}(\text{N}(\text{SiMe}_3)_2)]/\beta\text{-CD}(\text{OH})_2$ catalytic system (Table 1, entries 1–12). Increasing the initial loading of *rac*-LA from 40 to 1 000 equiv allowed the synthesis of PLAs of high molar mass (up to 72 000 and 83 400 g·mol⁻¹ as determined by SEC and NMR, respectively). A fairly good control over the polymerization was achieved as evaluated from the global agreement of the molar mass values determined by SEC (\bar{M}_{nSEC}) and NMR (\bar{M}_{nNMR}) and the expected ones (\bar{M}_{ntheo}), as well as regarding the molar mass distribution values which remained below 1.5. However, although the SEC traces were not that broad and remained always unimodal, these results are indicative of the occurrence of some side-reactions (which are commonly encountered in ROP of cyclic esters, e.g., transesterification). Increasing the initial loading of $\beta\text{-CD}(\text{OH})_2$ from 1 to 10 proportionally decreased the molar mass of PLA (compare entries 6, 7 and 9).^{10a} These results demonstrated an overall efficiency of the chain transfer between growing PLA chains and dormant (macro)alcohols. Attempts to ring-open polymerize *rac*-LA in DMF, a more polar solvent that better solubilizes the native $\beta\text{-CD}$, did not allow the formation of any polymer (entry 8). This behavior results most likely from the competition between DMF and *rac*-LA for coordination to the zinc center in favor of the solvent, as often observed in such ROP reactions promoted by oxophilic metallic initiators.

¹H NMR and ¹³C{¹H} NMR analyses of the precipitated polymers demonstrated the formation of $\beta\text{-CD}(\text{OPLA})_2$ consistent with the role of $\beta\text{-CD}(\text{OH})_2$ as co-initiator and chain transfer agent (Figures 1, 2; Figure S6, Supporting Information). A typical 500 MHz ¹H NMR spectrum (CDCl₃) of a $\beta\text{-CD}(\text{OPLA})_2$ sample ($\bar{M}_{\text{ntheo}} = 8\,600 \text{ g}\cdot\text{mol}^{-1}$; $\bar{M}_{\text{nSEC}} = 5\,400 \text{ g}\cdot\text{mol}^{-1}$, $\bar{M}_{\text{nNMR}} = \text{ca. } 11\,500 \text{ g}\cdot\text{mol}^{-1}$; Table 1, entry 1) is depicted in Figure 1. The $\beta\text{-CD}$ moiety was clearly evidenced by the typical set of low intensity broad resonances at δ 3.45, 3.96, 4.35, 4.41, and 4.69 ppm and of the benzyloxy groups at δ 7.13 ppm. The PLA signals

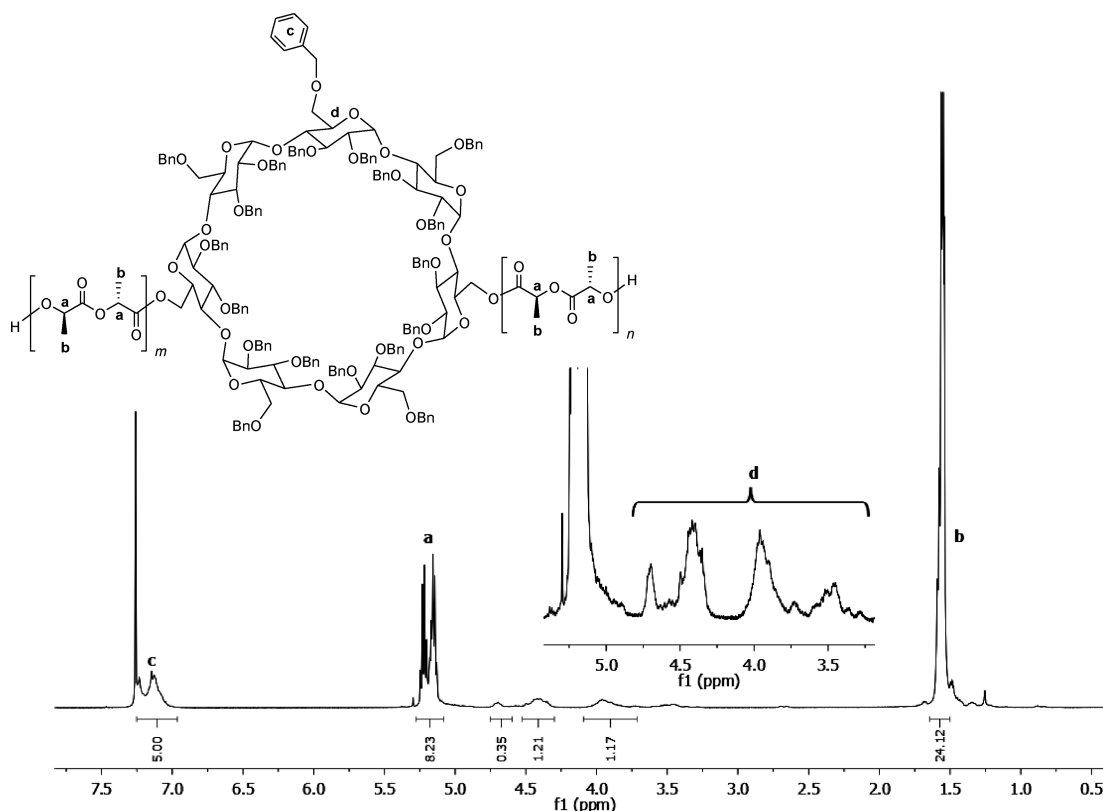


Figure 1. ^1H NMR spectrum (500 MHz, CDCl_3 , 23 $^\circ\text{C}$) of a $\beta\text{-CD}(\text{OBn})_{19}(\text{OPLA})_2$ sample prepared upon iROP of *rac*-LA from the $[(\text{BDI}^{\text{Pr}})\text{Zn}(\text{N}(\text{SiMe}_3)_2)]/\beta\text{-CD}(\text{OH})_2$ system (Table 1, entry 1).

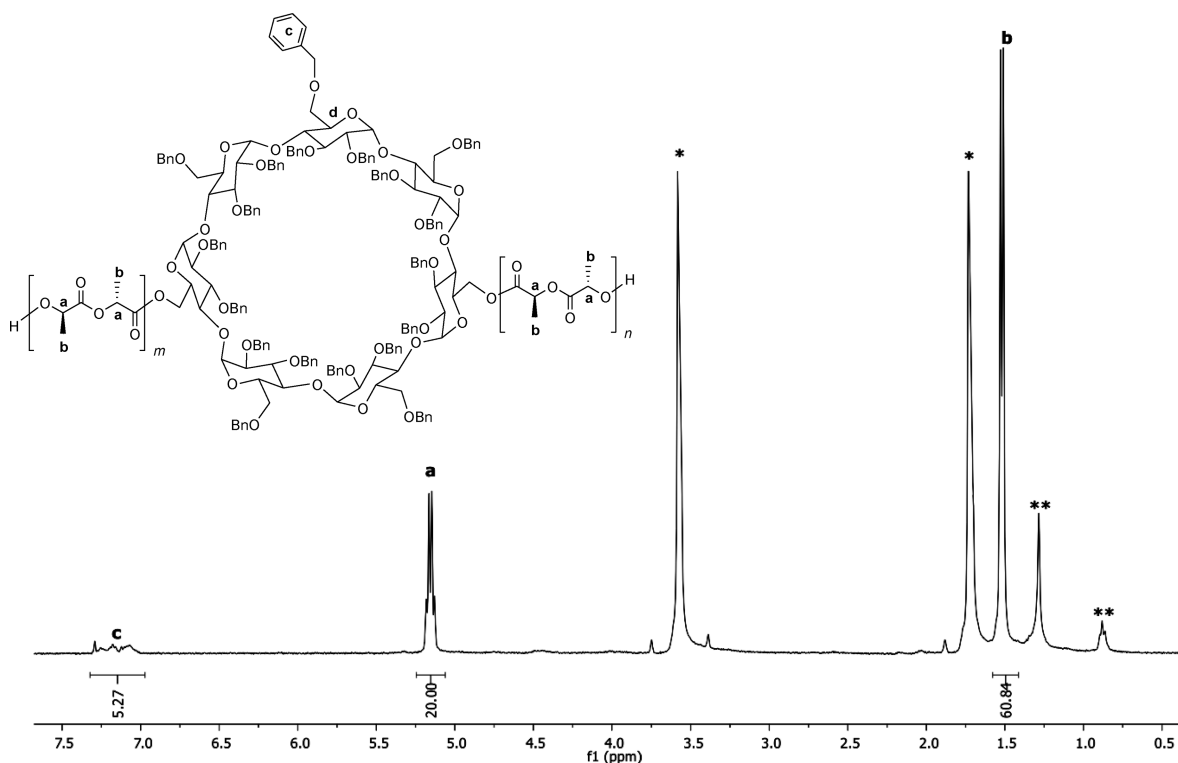


Figure 2. ^1H NMR spectrum (400 MHz, $\text{THF-}d_8$, 23 $^\circ\text{C}$) of a $\beta\text{-CD}(\text{OBn})_{19}(\text{OPLLA})_2$ sample prepared upon ROP of *L*-LA from the $[(\text{BDI}^{\text{Pr}})\text{Zn}(\text{N}(\text{SiMe}_3)_2)]/\beta\text{-CD}(\text{OH})_2$ system (Table 1, entry 10). Markers * and ** stand for residual signals from $\text{THF-}d_8$ and pentane, respectively (the intensity of these residual signals stem from the poor solubility of these isotactic polymers, even in THF).

were clearly observed in the ^1H NMR spectrum in CDCl_3 at δ 5.15 and 5.21 ($\text{OC}(\text{O})\text{CHMe}$) and 1.55 ($\text{OC}(\text{O})\text{CHMe}$) ppm.

The two former strong signals for the PLA methine hydrogens are indicative of a heterotactic-enriched microstructure, which was

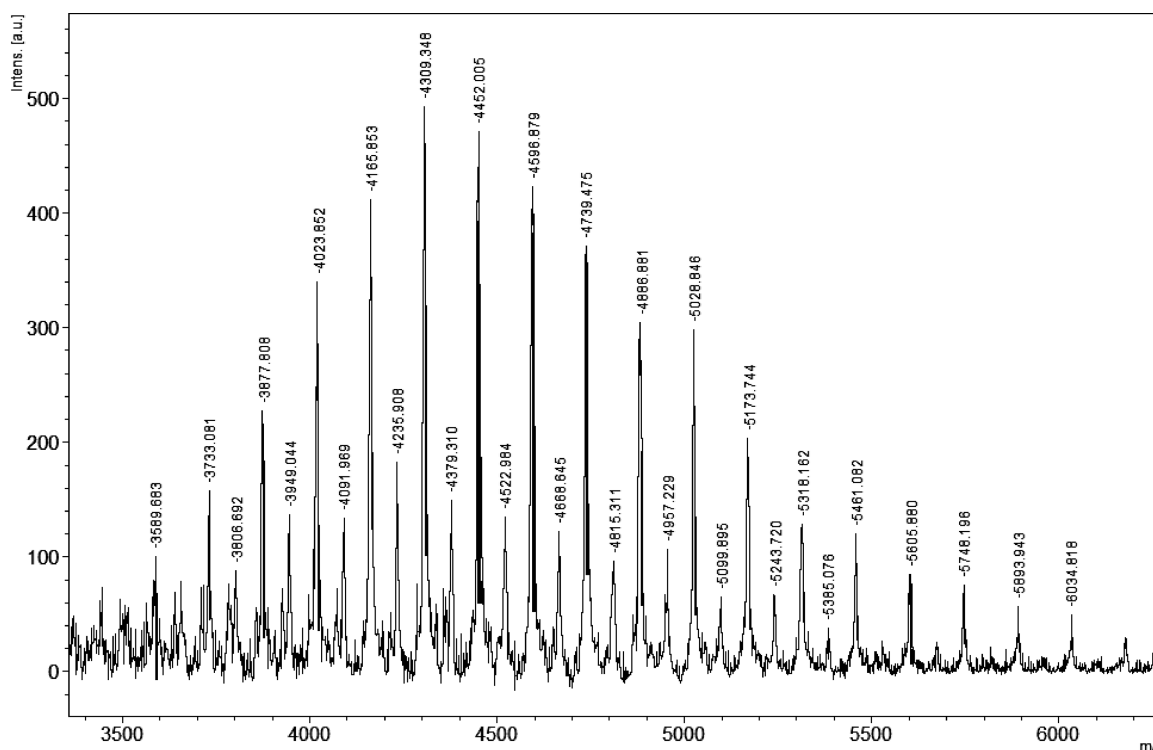


Figure 3. MALDI–ToF mass spectrum of a low molar mass β -CD(OBn)₁₉{H[(OCHMeC(O)OCHMeC(O))₅]₂Na⁺ sample prepared upon iROP of *rac*-LA from the [(BDI^{iPr})Zn(N(SiMe₃)₂)]/ β -CD(OH)₂ system (Table 1, entry 1).

unambiguously confirmed by homodecoupling ¹H NMR experiments ($P_r = 0.81$; see Figure S5 in the Supporting Information). The formation of heterotactic-enriched PLA segments in those β -CD(OPLA)₂ synthesized from *rac*-LA (entries 1–9) is clearly ascribed to the use of the [(BDI^{iPr})Zn(N(SiMe₃)₂)] catalyst;¹² apparently, the presence of β -CD(OH)₂ did not affect significantly the stereoselectivity of the growing polymer chain [as observed also for the iROP of *rac*-BL; vide infra]. On the other hand, polymers prepared from L-LA resulted in perfectly isotactic β -CD(OPLLA)₂ ($P_m > 0.99$), as indicated by a sharp quartet at δ 5.17 ppm (Figure 2),²² revealing no epimerization under the conditions used.

These ¹H NMR spectra allowed to determine the molar masses of β -CD(OPLA)₂ samples, taking into account the relative intensities of signals for benzyloxy and main chain lactic units. This was best done in THF-*d*₈ in which the above signals do not overlap with residual solvent resonances (Figure 2), in contrast to other usual solvents (i.e., C₆D₆, CD₂Cl₂ or CDCl₃, Figure 1). As mentioned above, the \bar{M}_{nNMR} values thus determined ($\bar{M}_{\text{nNMR}} = [\text{Int}(\text{CH}_{\text{LA}})/2]/[\text{Int}(\text{CH}_2\text{C}_6\text{H}_5)/(5 \times 19)] \times 114 (M_{\text{LA}}) + 2\,800 (=M_{\beta\text{-CD}(\text{OBn})_{19}}) \text{ g mol}^{-1}$) were generally in quite good agreement with the theoretical ones calculated from the conversion and the [LA]₀/[β -CD(OH)₂]₀ ratio. On the other hand, the molar masses determined by SEC (\bar{M}_{nSEC}) were in several cases significantly lower than \bar{M}_{nNMR} and \bar{M}_{ntheo} values. This suggests that the factor used for correcting the \bar{M}_{nSEC} values (established for regular PLA samples made from L-LA)¹⁷ of these β -CD(OPLLA)₂ materials might not be appropriate and/or that inclusion phenomena (i.e., of the PLA chains in the β -CDs cavities)^{4,7} may affect the hydrodynamic volumes of such materials. Similar observations were made for β -CD-(OPTMC)₂ materials (vide infra).

The ROP of the four-membered ring lactone, *racemic* β -butyrolactone (*rac*-BL), a monomer more reluctant to undergo polymerization,²³ was first attempted under similar operating conditions in solution within a similar reaction time, yet without success (Table 1, entry 13). The ROP was then carried out in bulk conditions to improve the kinetics (Table 1, entries 14–18), but still required prolonged reaction times (18–26 h, TOF_{BL} up to 37 h^{−1}) to form the β -CD(OPHB)₂. The operating conditions used in the present work for the iROP of *rac*-BL were, however, milder than those previously reported in the presence of native β -CD alone, which proceeded in bulk at 100 °C.^{4b,c} In fact, the activity was greatly improved upon using the zinc catalyst in combination to β -CD(OH)₂: up to 113 turnovers could be reached within 26 h (Table 1, entry 18), whereas less than 15 turnovers were obtained in 96 h without the zinc catalyst.^{4b,c} The activity and productivity were thus significantly improved without any detrimental effect on the PHBs molecular features. The atactic PHB chains thus produced featured also larger molar mass ($\bar{M}_{\text{nNMR}} \approx \bar{M}_{\text{nSEC}}$ up to 22 000 g·mol^{−1}) and narrower molar mass distribution values ($\bar{M}_w/\bar{M}_n = 1.08\text{--}1.14$) in comparison to the ones previously reported ($\bar{M}_n < 5\,700 \text{ g mol}^{-1}$, $\bar{M}_w/\bar{M}_n = 2.3\text{--}2.5$).^{4b,c} The iROP of *rac*-BL thus afforded β -CD(OPHB)₂ in a quite well controlled process. The ¹H NMR spectra of these β -CD(OPHB)₂ displayed the signals of the β -CD moiety along with the typical resonances corresponding to the methine, methylene or methyl groups of the polyester main chain (Figures S7–S9, Supporting Information). The ¹³C{¹H} NMR spectrum of β -CD(OPHB)₂ (Figure S9, Supporting Information) confirmed these features and revealed atactic PHB segments [as observed with the same Zn catalyst used as initiator].^{12b}

The same strategy was successfully applied to the synthesis of β -CD(O-polycarbonate)₂ samples from the iROP of TMC (Table 1, entries 19–25). Under these conditions, the PTMC molar mass increased monotonously with the [TMC]₀/

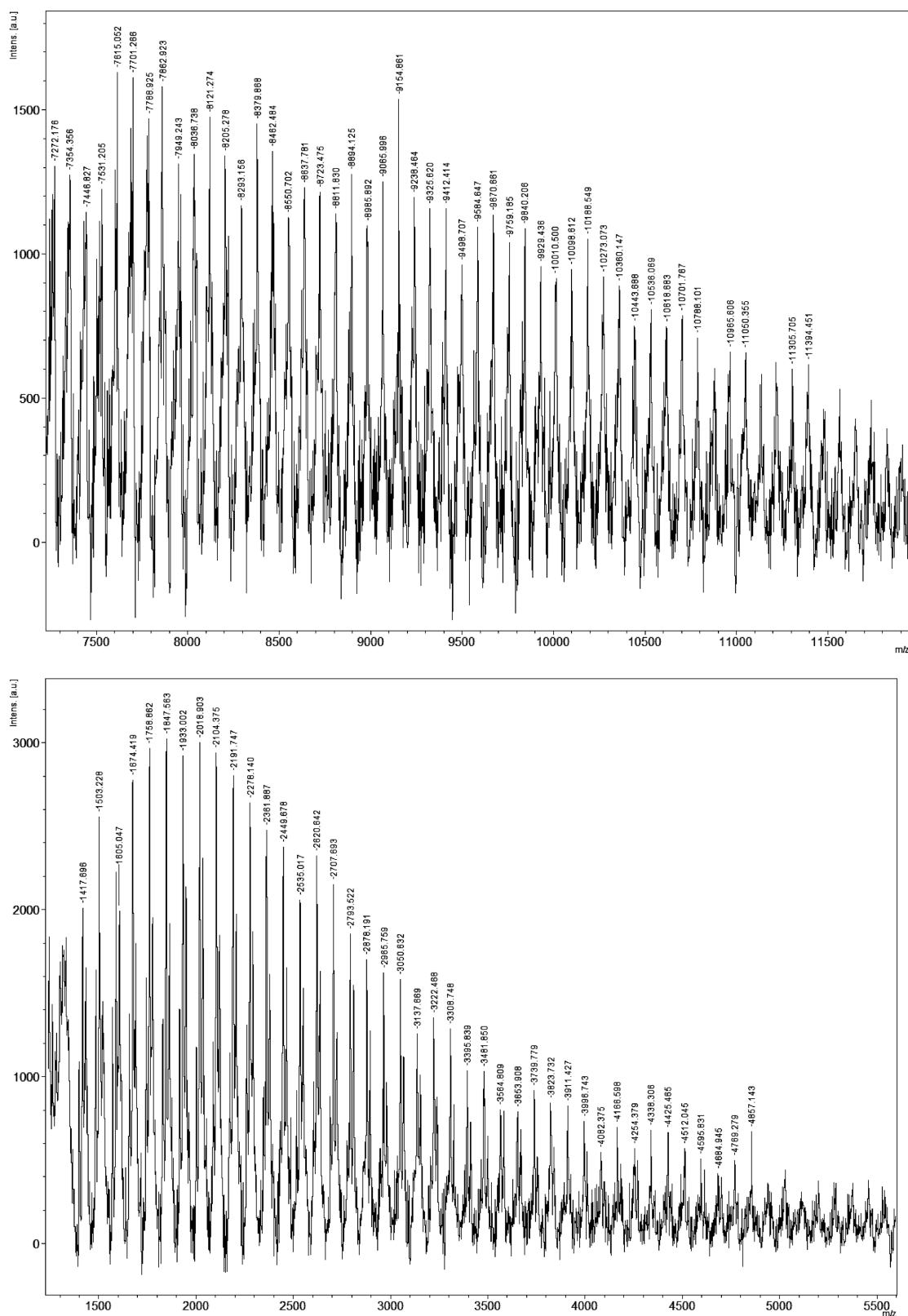


Figure 4. High (top) and low (bottom) molar mass region of the MALDI-ToF mass spectrum of a PHB sample prepared upon iROP of *rac*-BL from the $[(\text{BDI}^{\text{iPr}})\text{Zn}(\text{N}(\text{SiMe}_3)_2)]/\beta\text{-CD}(\text{OH})_2$ system (Table 1, entry 14). The high molar mass species correspond to $\beta\text{-CD}(\text{OBn})_{19}[\text{H}[(\text{OCHMeCH}_2\text{C}(\text{O}))_n]_2\text{Na}^+$ and the low molar mass species correspond to $[\text{H}[(\text{OCHMeCH}_2\text{C}(\text{O}))_n\text{OH}]\text{Na}^+$.

$[\beta\text{-CD}(\text{OH})_2]_0$ ratio. Up to 5 000 TMC units were converted quite rapidly (within 30 min), affording well-defined $\beta\text{-CD}(\text{OPTMC})_2$ (Figure S10, Supporting Information) with $\bar{M}_{\text{D-NMR}}$ up to 145 000 $\text{g}\cdot\text{mol}^{-1}$. When the polymerizations were carried

out at 23 °C (entries 21, 22, 24), the $\bar{M}_{\text{D-NMR}}$ values were much larger than the theoretical ones. This observation suggests moderate initiation efficiency (30–45%) at this temperature. On the other hand, the $\bar{M}_{\text{D-NMR}}$ and \bar{M}_{theo} values matched quite well for

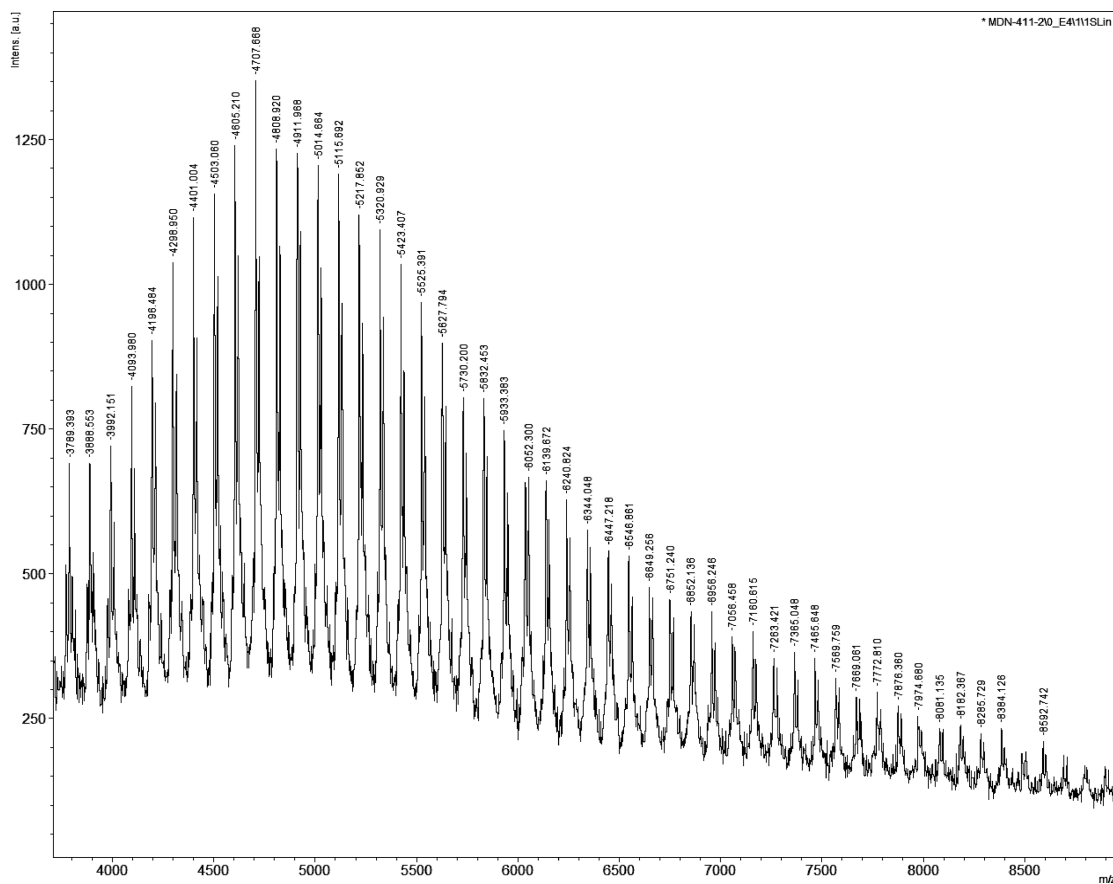


Figure 5. MALDI–ToF mass spectrum of a low molar mass β -CD(OBn)₁₉{H-[(O(CH₂)₃OC(O))₉]₂ sample cationized by Na⁺/K⁺ prepared upon iROP of TMC from the [(BDI^{IPr})Zn(N(SiMe₃)₂)]/ β -CD(OH)₂ system (Table 1, entry 19).

β -CD(OPTMC)₂ prepared at 60 °C (entries 23, 25). As observed for β -CD(OPLA)₂, the $\bar{M}_{n,SEC}$ values of the β -CD(OPTMC)₂ were always significantly lower than the $\bar{M}_{n,NMR}$ values.

Evidence for the formation of α,ω -hydroxy β -cyclodextrin-(polyester)₂ materials was further confirmed through MALDI–ToF MS investigations. The MALDI–ToF mass spectrum of an heterotactic β -CD(OPLA)₂ sample is depicted in Figure 3. It features one major distribution of peaks unambiguously assignable to β -CD(OBn)₁₉(OPLA-H)₂ macromolecules cationized by Na⁺ ions with a repeat unit of 144 g·mol^{−1} (i.e., the molar mass of LA). The most intense signal detected at m/z = 4 309 g·mol^{−1} corresponds to the species β -CD(OCH₂Ph)₁₉-{H[(OCHMeC(O)OCHMeC(O))₅]₂Na⁺ (calculated isotopic mass for ¹²C₂₃₅¹H₂₆₄³Na₁¹⁶O₇₅: 4 309 g·mol^{−1}). The other minor population observed at m/z + 72 corresponds to the analogous series depleted from one lactic fragment of the LA diester (O₂C₃H₄), consistent with the occurrence of minor transesterification side-reactions, as hinted by the molar mass distribution value of 1.4 determined by SEC (*vide supra*).

Similarly, the MALDI–ToF mass spectrum of a low molar mass PHB sample (Table 1, entry 14) precipitated in cold pentane (see Figure S8, Supporting Information for ¹H NMR spectrum)²⁴ displayed one major distribution of peaks unambiguously assignable to β -CD(OBn)₁₉(OPHB-H)₂ macromolecules cationized by Na⁺ ions, with a repeat unit of 86 g·mol^{−1} (i.e., the molar mass of BL) (Figure 4). For instance, one of the most intense signals detected at m/z = 8 380 g·mol^{−1} corresponds to the species β -CD(OCH₂Ph)₁₉{H[(OCHMeCH₂C(O))₃₂]₂Na⁺ (calculated isotopic mass for ¹²C₄₃₁¹H₅₆₈²³Na₁¹⁶O₁₆₃: 8 380

g·mol^{−1}). The other population observed at lower molar mass (centered at m/z = ca. 2 000 g·mol^{−1}) apparently corresponds to β -CD-free homopolymers, i.e. {H[(OCHMeCH₂C(O))_{*n*}OH]Na⁺ (*n*, obsvd and calcd m/z : 21, 1 848, 1 847; 22, 5 000, 1 933). This observation was unexpected since the SEC analyses of these β -CD-PHBs displayed a single monomodal trace at relatively high molar masses (Figure S10, Supporting Information), with no lower molar mass signal assignable to β -CD-free PHB homopolymers or free β -CD(OH)₂. It is possible that this second set of macromolecules is produced by hydrolysis of the former population β -CD(OBn)₁₉(OPHB-H)₂ under ionization conditions,²⁵ rather than during the polymerization process. In comparison, such β -CD-free PHB homopolymers were recovered in much larger amounts in the sparteine-catalyzed ROP of BL carried out at 50 °C in the presence of β -CD(OH)₃.¹⁴

Finally, the MALDI–ToF MS analysis of a low molar mass β -CD(OPTMC)₂ sample prepared (Table 1, entry 19) depicted in Figure 5, displayed one major distribution of peaks unambiguously assignable to β -CD(OBn)₁₉(OPTMC-H)₂ macromolecules cationized by Na⁺ ions, with a repeat unit of 102 g·mol^{−1} (i.e., the molar mass of TMC). The most intense signal detected at m/z = 4 707 g·mol^{−1} corresponds to the species β -CD(OCH₂Ph)₁₉{H[(O(CH₂)₃OC(O))₉]₂Na⁺ (calculated isotopic mass for ¹²C₂₄₇¹H₂₉₂²³Na₁¹⁶O₈₉: 4 705 g·mol^{−1}). The other minor population observed at m/z + 16 corresponds to the analogous β -CD(OCH₂Ph)₁₉{H[(OCHMeC(O)-OCHMeC(O))₉]₂K⁺ series.

FTIR analysis of a β -CD(OPLA)₂ sample prepared upon iROP of *rac*-LA (Table 1, entry 4; Figure S12, Supporting Information) confirmed the presence of both the β -CD and PLA segments. In particular, the typical stretching modes of the β -CD symmetric and antisymmetric O–H at 3 028 cm^{−1} were no longer observed in the spectrum of the conjugated polyester, as compared to the spectrum of β -CD(OH)₂ (Figure S13, Supporting Information), and the characteristic carbonyl stretching absorption of the carbonyl polyester segment was recorded at 1 747 cm^{−1}.

The thermal behavior of a β -CD(OPLLA)₂ sample prepared upon iROP of *L*-LA (Table 1, entry 11) was compared to that of β -CD(OH)₂ and of a PLLA sample (Figures S16, S14, S15, respectively; see Supporting Information). The new material featured the typical glass transition (T_g = 52 °C) and melting (T_m = 173 °C) temperatures of isotactic PLLA segments. Interestingly, a crystallization peak (T_c = 99 °C) was observed during the heating phase of the second and third cycles, indicating a lower crystallization rate of this material as compared to native PLLA. This may be correlated with the somewhat lower crystalline character of the conjugated β -CD-polyester (ΔH_m = 54 J·g^{−1}; ΔH_c = −25 J·g^{−1}) as compared to native PLLA (ΔH_m = 73 J·g^{−1}; ΔH_c = −53 J·g^{−1}).

All these analyses supported the covalent linking of β -CD to the PLA, PHB, or PTMC segments. This demonstrated in turn that β -CD(OH)₂ indeed acted as an effective co-initiator and chain transfer agent in the iROP of LAs, BL, and TMC. In the present case, the polymerization is assumed to proceed through a typical coordination–insertion mechanism, involving incorporation of monomer units into covalently bonded [Zn]–(O-polymer), eventually resulting in β -CD end-capped polymer chains.^{10a}

CONCLUSION

The controlled immortal ring-opening polymerization of *rac*-LA, *L*-LA, *rac*-BL, and TMC was achieved successfully by using the [(BDI^{IPr})Zn(N(SiMe₃)₂)]/[β -CD(OH)₂] catalytic system, under mild conditions. This survey of different monomers including lactides, lactone and carbonate, showed that the order of reactivity of the various monomers (TMC > *rac*-LA \approx *L*-LA > *rac*-BL) reflects the one commonly observed in (i)ROP of these cyclic esters for a given catalytic system, including [(BDI^{IPr})Zn(N(SiMe₃)₂)].¹⁰ Well-defined β -CD(OBn)₁₀(O-polyester/polycarbonate)₂ of molar mass ranging from 11 500 up to 145 200 g·mol^{−1} were prepared and thoroughly characterized by ¹H and ¹³C NMR and FT-IR spectroscopies, MALDI–ToF mass spectrometry, SEC and DSC analyses. These investigations at the molecular and thermal level supported the linking of β -CD to the PLA, PHB, or PTMC segments. Such an approach is prone to the general elaboration of polyester/polycarbonate–cyclodextrin conjugates for further valuable applications in the vectorization of drugs.

ASSOCIATED CONTENT

Supporting Information

Additional NMR, IR, and MALDI–ToF spectra, and SEC profile, and DSC traces of monomer and polymers. This material is available free of charge via the Internet at <http://pubs.acs.org>.

ACKNOWLEDGMENTS

M.N. is thankful to the French Ministry of Higher Education (MESR) for a PhD grant. S.M.G. gratefully acknowledges the

Region Bretagne ACOMB research program and Rennes Métropole for equipment support.

REFERENCES

- (1) (a) van de Manacker, F.; Vermoden, T.; van Nostrum, C. F.; Hennik, W. E. *Biomacromolecules* **2009**, *10*, 3157–3175. (b) Szejtli, J. *Chem. Rev.* **1998**, *98*, 1743–1753.
- (2) Selected recent reviews: (a) Davis, M. E. *Mol. Pharmaceutics* **2009**, *6*, 659–668. (b) Zhang, J. J.; Sun, H.; Ma, P. X. *ACS Nano* **2010**, *4*, 1049–1059. (c) Zhou, J.; Ritter, H. *Polym. Chem.* **2010**, *1*, 1552–1559. (e) Li, J. J.; Zhao, F.; Li, J. *Appl. Microbiol. Biotechnol.* **2011**, *90*, 427–443.
- (3) (a) Ulery, B. D.; Nair, L. S.; Laurencin, C. T. *J. Polym. Sci. B, Polym. Phys.* **2011**, *11* (49), 832–864. (b) Cameron, D. J. A.; Shaver, M. P. *Chem. Soc. Rev.* **2011**, *40*, 1761–1776. (c) Dove, A. P. *Chem. Commun.* **2008**, 6446–6470. (d) Nair, L. S.; Laurencin, C. T. *Prog. Polym. Sci.* **2007**, *32*, 762–798. (e) Slomkowski, S. *Macromol. Symp.* **2007**, *253*, 47–58. (f) Albertsson, A.-C.; Varma, I. K. *Biomacromolecules* **2003**, *4*, 1466–1486. (g) Ajellal, N.; Thomas, C. M.; Aubry, T.; Grohens, Y.; Carpentier, J.-F. *New J. Chem.* **2011**, *35*, 876–880.
- (4) Selected examples: (a) Harada, A.; Osaki, M.; Takashima, Y.; Yamaguchi, H. *Acc. Chem. Res.* **2008**, *41*, 1143–1152. (b) Osaki, M.; Takashima, Y.; Yamaguchi, H.; Harada, A. *Macromolecules* **2007**, *40*, 3154–3158. (c) Takashima, Y.; Osaki, M.; Harada, A. *J. Am. Chem. Soc.* **2004**, *126*, 13588–13589. (d) Setijadi, E.; Tao, L.; Lui, J.; Jian, Z.; Boyer, C.; Davis, T. P. *Biomacromolecules* **2009**, *10*, 2699–2707.
- (5) Selected examples: Gonzales, H.; Hwang, S. J.; Davis, M. E. *Bioconjugate Chem.* **1999**, *10*, 1068–1074.
- (6) Selected examples: Jazkewitch, O.; Mondrzyk, A.; Staffel, R.; Ritter, H. *Macromolecules* **2011**, *4*, 1365–1371. (b) Tian, W.; Fan, X.-D.; Kong, J.; Liu, Y.-Y.; Zhang, W.-H.; Cheng, G.-W.; Jiang, M. *Macromol. Chem. Phys.* **2009**, *210*, 2107–2117.
- (7) Selected examples: Ohya, Y.; Takamido, S.; Nagahama, K.; Ouchi, T.; Ooya, T.; Katoono, R.; Yui, N. *Macromolecules* **2007**, *18*, 6441–6444. (b) Harada, A.; Okada, M.; Li, J.; Kamachi, M. *Macromolecules* **1995**, *28*, 8406–8411. (c) Kawaguchi, Y.; Nishiyama, T.; Okada, M.; Kamachi, M.; Harada, A. *Macromolecules* **2000**, *33*, 4472–4477. (d) Williamson, B. R.; Krishnaswamy, R.; Tonelli, A. E. *Polymer* **2011**, *52*, 4517–4527.
- (8) Selected examples: (a) Gou, P.-F.; Zhu, W.-P.; Shen, Z.-Q. *Biomacromolecules* **2010**, *11*, 934–943. (b) Gou, P.-F.; Zhu, W.-P.; Xu, N.; Shen, Z.-Q. *J. Polym. Sci.* **2008**, *46*, 6455–6465. (c) Gou, P.-F.; Zhu, W.-P.; Xu, N.; Shen, Z.-Q. *J. Polym. Sci.* **2010**, *48*, 2961–2974. (d) Adeli, M.; Zarnegar, Z.; Kabiri, R. *Eur. Polym. J.* **2008**, *44*, 1921–1930. (e) Mellet, C. O.; Benito, M. J.; Fernandez, J. M. G. *Chem.—Eur. J.* **2010**, *16*, 6728–6742. (f) Nagahama, K.; Shimizu, K.; Ouchi, T.; Ohya, Y. *React. Funct. Polym.* **2009**, *69*, 891–897.
- (9) Stademann, J.; Komber, H.; Erber, M.; Däbritz, F.; Ritter, H.; Voit, B. *Macromolecules* **2011**, *44*, 3250–3259.
- (10) (a) Ajellal, N.; Carpentier, J.-F.; Guillaume, C.; Guillaume, S.; Helou, M.; Poirier, V.; Sarazin, Y.; Trifonov, A. *Dalton Trans.* **2010**, 39, 8363–8376. (b) Guillaume, C.; Carpentier, J.-F.; Guillaume, S. M. *J. Polym. Sci., Polym. Chem.* **2011**, *49*, 907–917. (c) Helou, M.; Miserque, O.; Brusson, J.-M.; Carpentier, J.-F.; Guillaume, S. M. *Chem.—Eur. J.* **2008**, *14*, 8772–8775. (d) Helou, M.; Miserque, O.; Brusson, J.-M.; Carpentier, J.-F.; Guillaume, S. M. *Adv. Synth. Catal.* **2009**, *351*, 1312–1324. (e) Helou, M.; Miserque, O.; Brusson, J.-M.; Carpentier, J.-F.; Guillaume, S. M. *Macromol. Rapid Commun.* **2009**, *30*, 2128–2135. (f) Brignou, P.; Priebe Gil, M.; Casagrande, O. Jr; Carpentier, J.-F.; Guillaume, S. M. *Macromolecules* **2010**, *43*, 8007–8017. (g) Brignou, P.; Carpentier, J.-F.; Guillaume, S. M. *Macromolecules* **2011**, *44*, 5127–5135.
- (11) The main advantages of successful iROPs using active species such as metal-alkoxide derivatives are that (1) both solution and solvent-free (bulk) procedures are efficient, (2) the initial catalyst loading can be lowered down to a few (10) ppm, thereby minimizing residual metallic traces in the isolated polymer, (3) the number of growing polymer chains per metal center can be largely increased upon raising the alcohol content (as much as 1 000 equiv successfully

added), thereby making the process truly “catalytic” with respect to both the monomer and the polymer chains, (4) the molar mass of the polymer can be tuned according to the initial [monomer]/[chain transfer agent] ratio, and (5) the process still allows one to prepare high molar mass polymers upon increasing the initial monomer amount (evaluated up to 100 000 monomer units), without altering neither the control of the ROP, nor the activity or productivity of the catalytic system, nor the macromolecular features (molar mass measured in agreement with the predicted ones, relatively narrow molar mass distribution values, chain-end fidelity relative to the nature of the alcohol introduced, control of the microstructure) of the polymers thus prepared.¹⁰

(12) (a) Chamberlain, B. M.; Cheng, M.; Moore, D. R.; Ovitt, T. M.; Lobkovsky, E.; Coates, G. W. *J. Am. Chem. Soc.* **2001**, *123*, 3229–3238.

(b) Rieth, L. R.; Moore, D. R.; Lobkovsky, E. B.; Coates, G. W. *J. Am. Chem. Soc.* **2002**, *124*, 15239–15248.

(13) Miao, Y.; Rousseau, C.; Mortreux, A.; Martin, P.; Zinck, P. *Polymer* **2011**, *52*, 5018–5026.

(14) Peptu, C.; Nicolescu, A.; Peptu, C. A.; Harabagiu, V.; Simionescu, B. C.; Kowalczyk, M. *J. Polym. Sci., Part A: Polym. Chem.* **2010**, *48*, 5581–5592.

(15) Lecours, T.; Herault, A.; Pearce, A. J.; Sollogoub, M.; Sinaÿ, P. *Chem. – Eur. J.* **2004**, *10*, 2960–2971.

(16) Pearce, A. J.; Sinaÿ, P. *Angew. Chem., Int. Ed.* **2000**, *39*, 3610–3612.

(17) Kowalski, A.; Duda, A.; Penczek, S. *Macromolecules* **1998**, *31*, 2114–2122.

(18) Palard, I.; Schappacher, M.; Belloncle, B.; Soum, A.; Guillaume, S. M. *Chem. – Eur. J.* **2007**, *13*, 1511–1521.

(19) Note that the iROP of LA was run in solution (rather than in bulk) to enable solubilization of the monomer. For comparison purposes, the ROP of TMC was similarly run in solution, whereas the ROP of BL, initially carried out in solution, was next studied in bulk so as to improve the kinetics of the reaction.

(20) Note that, as demonstrated in our previous work (see refs 10 and 22b), the presence of an alcohol (either monoalcohol, diol, or triol) acting as a co-initiator and chain transfer agent is required for the (i)ROP of LA, BL and TMC catalyzed by the $[(\text{BDI}^{\text{IPr}})\text{Zn}(\text{N}(\text{SiMe}_3)_2)]$ to be controlled. Indeed, in absence of any added alcohol, the zinc amido complex cannot provide polyesters with expected molar mass values and with narrow molar mass distribution values.

(21) Turnover frequency values expressed in $\text{mol}_{\text{Monomer}} \cdot \text{mol}_{\text{Catalyst}}^{-1} \cdot \text{h}^{-1}$; these values are derived from high conversion values and reaction times that were not necessarily optimized, and are therefore lower estimates.

(22) ¹H NMR analysis of the β -CD(OPLLA)₂ sample was also recorded in THF-*d*₈ (Figure 2), in which solvent the β -CD benzyl groups do not overlap with other resonance (in contrast to CDCl₃), thus allowing to determine accurately the molar mass.

(23) (a) Carpentier, J.-F. *Macromol. Rapid Commun.* **2010**, *31*, 1696–1705. (b) Guillaume, C.; Carpentier, J.-F.; Guillaume, S. M. *Polymer* **2009**, *50*, 5909–5917. (c) Thomas, C. M. *Chem. Soc. Rev.* **2010**, *39*, 165.

(24) Note that the precipitation filtrate was not analyzed since high BL conversion (refer to Table 1) and high yields (gravimetrically determined at $\approx 85\%$) were always reached.

(25) For a similar hydrolysis of terminal groups in a polyester under MALDI–ToF MS conditions, see for instance: Koller, J.; Bergman, R. G. *Organometallics* **2011**, *30*, 3217.

Glass Transitions in Highly Attractive Highly Filled Polymer Nanocomposites

Joseph Moll[†] and Sanat K. Kumar^{*,‡}

[†]Department of Chemistry and [‡]Department of Chemical Engineering, Columbia University, New York, New York 10027, United States

The influence of geometric confinement on the glass transition temperature (T_g) of small molecules and high polymers has been thoroughly investigated in recent years. Starting with the benchmark experiments of Jackson and McKenna^{1,2} and Keddie et al.,^{3,4} changes in the T_g of polymers in thin films and in pores and nanocomposites (PNC) have been related to the interactions at the polymer/substrate or polymer/nanoparticle interface.^{5–20} The dominant belief now is that strong, favorable interactions increase T_g , while weak or unfavorable interactions decrease T_g . Clear support for this picture comes from the simulations of de Pablo and co-workers

bonding surfaces can give the appearance of a change in T_g . Prolonged annealing of these samples causes these T_g shifts to disappear, bolstering this argument. Therefore, dilatometric methods (i.e., methods that measure volume change) could be strongly influenced by these strains at high filler loadings. The role of confinement on the glass transition temperatures of polymers thus appears to be quite unresolved at this time.

In our previous work we had contributed to this discussion by examining the glass transition temperature of poly-(2-vinylpyridine) when it is loaded with silica nanoparticles (14 nm in diameter).³² We studied this system since it is well accepted

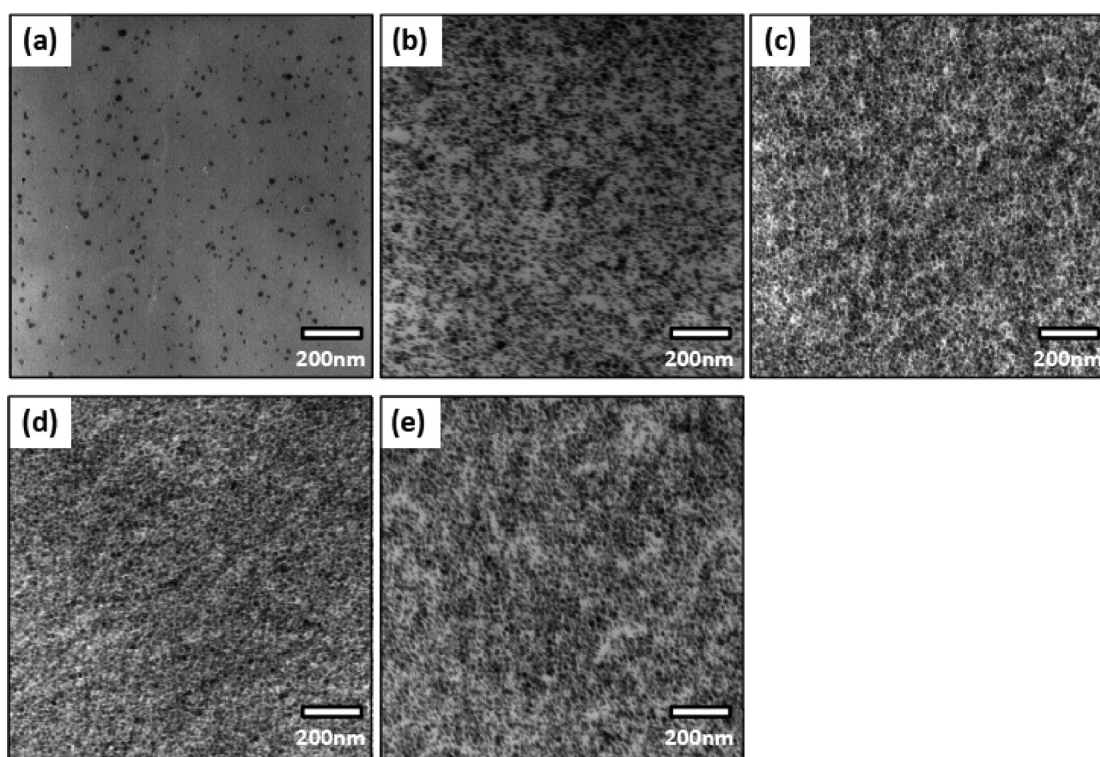


Figure 1. TEM images for PMMA nanocomposites with (a) 1, (b) 20, (c) 40, (d) 50, and (e) 62.5 wt % silica.

(among others) which have shown that T_g should increase in direct proportion to the attractive polymer–surface interactions.^{13,21,22} However, numerous recent experimental investigations have shown negligible changes in T_g under confinement in thin films and PNCs, regardless of interactions at the surfaces.^{23–31} Recent work of Russell et al. and Kremer et al. propose one potential reason for this discrepancy:^{26,27} in thin films, for example, nonequilibrium strains quenched in due to

that there are strongly favorable interactions between the polymer chains and the nanoparticles (primarily through hydrogen bonding). Consequently, on the basis of simulations on thin polymer films, we expected a large change in the T_g of these

Received: October 3, 2011

Revised: November 12, 2011

Published: January 12, 2012



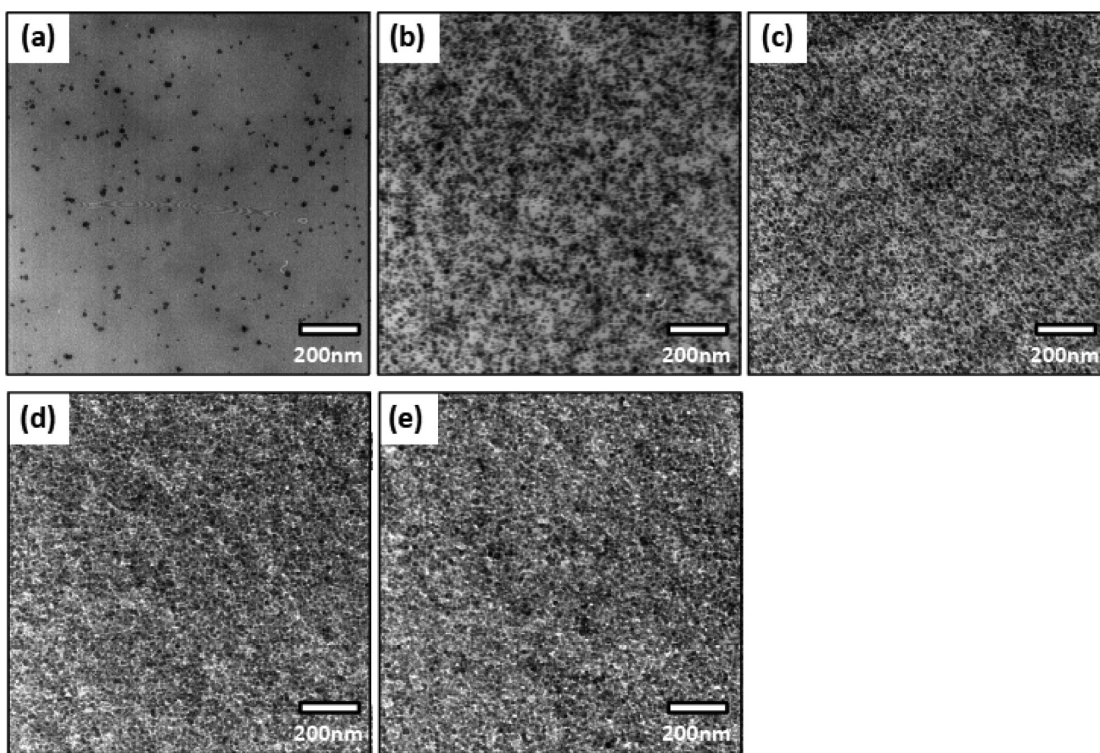


Figure 2. TEM images for PEMA nanocomposites with (a) 1, (b) 20, (c) 40, (d) 50, and (e) 62.5 wt % silica.

systems with increased nanoparticle loading. In fact, we found the contrary result—the T_g increased by less than 10 K even for particle loadings as large as 62.5 wt % silica, where the face-to-face separation between the particles, which is the analogue of film thickness, is ≈ 5 nm! To examine whether this system (P2VP–silica) was simply an outlier, here we present results from two other polymer–nanoparticle pairs, namely poly(methyl methacrylate)–silica²³ and poly(ethyl methacrylate)–silica, where strong hydrogen-bonding interactions between the nanoparticles and the polymers facilitate miscibility. We examined nanoparticle dispersion through transmission electron microscopy (which we have validated previously with ultrasmall-angle X-ray scattering)³² and the polymer glass transition temperatures through the use of differential scanning calorimetry. For these mixtures, with intimate mixing of the nanoparticles and polymers, the polymer T_g does show a dependence on nanoparticle loading, but the magnitude of the shifts is less than 10 K for all nanoparticle loadings. Our results agree with the picture that there are negligible shifts in glass transition temperature on confinement, and we offer a potential explanation for these findings.

To probe the influence of confinement and measuring technique on T_g of PNCs, we have chosen three polymers, namely poly(2-vinylpyridine) ($M_w \sim 100$ kDa, $T_g \approx 100$ °C), poly(methyl methacrylate) (PMMA, $M_w \sim 75$ kDa, $T_g \approx 110$ °C), and poly(ethyl methacrylate) (PEMA, $M_w \sim 250$ kDa, $T_g \approx 70$ °C), with colloidal silica nanoparticles (14 ± 4 nm in diameter) at loadings of 1–62.5 wt %. All polymers were purchased from Scientific Polymer Products and used as received. They have been synthesized using free radical techniques and therefore have polydispersity indices of ~ 2 . Irganox 1010 (an antioxidant) was donated by Ciba, and colloidal silica in MEK (30% w/w) was donated by Nissan Chemicals.

The nanocomposites were prepared by dissolving the polymer and Irganox 1010 (0.1% w/w relative to polymer only) in MEK. In a separate vial, the silica suspension was diluted with pyridine

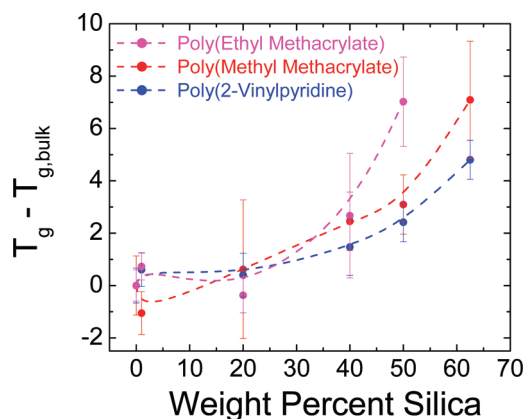


Figure 3. DSC determined results for the shift in apparent glass transition temperature as a function of the wt % silica loading. The data for three different polymers are shown as discussed in the text.

(33% v/v, only in the case of P2VP), and the solution was sonicated with a probe sonicator for 5 min. Pyridine plays a crucial role in properly dispersing the particles within the P2VP melt: in the absence of pyridine, P2VP strongly binds to the silica surfaces, even in the presence of MEK, and causes the P2VP to reversibly “cross-link” the silica. A silica–P2VP gel then precipitates out, causing poor particle dispersion in the resulting nanocomposite. Addition of the pyridine, which competitively hydrogen bonds with the silica surface, prevents silica–P2VP gelation and precipitation and alleviates this problem. The PMMA and PEMA nanocomposites were prepared in an identical manner except that no pyridine was added. Various concentrations of the silica suspension were added to the polymer solutions, and the polymer/silica suspensions were vigorously shaken for 2 h followed by 1 min of ultrasonication, poured into PTFE drying dishes, and allowed to sit overnight in a fume hood. The cast films

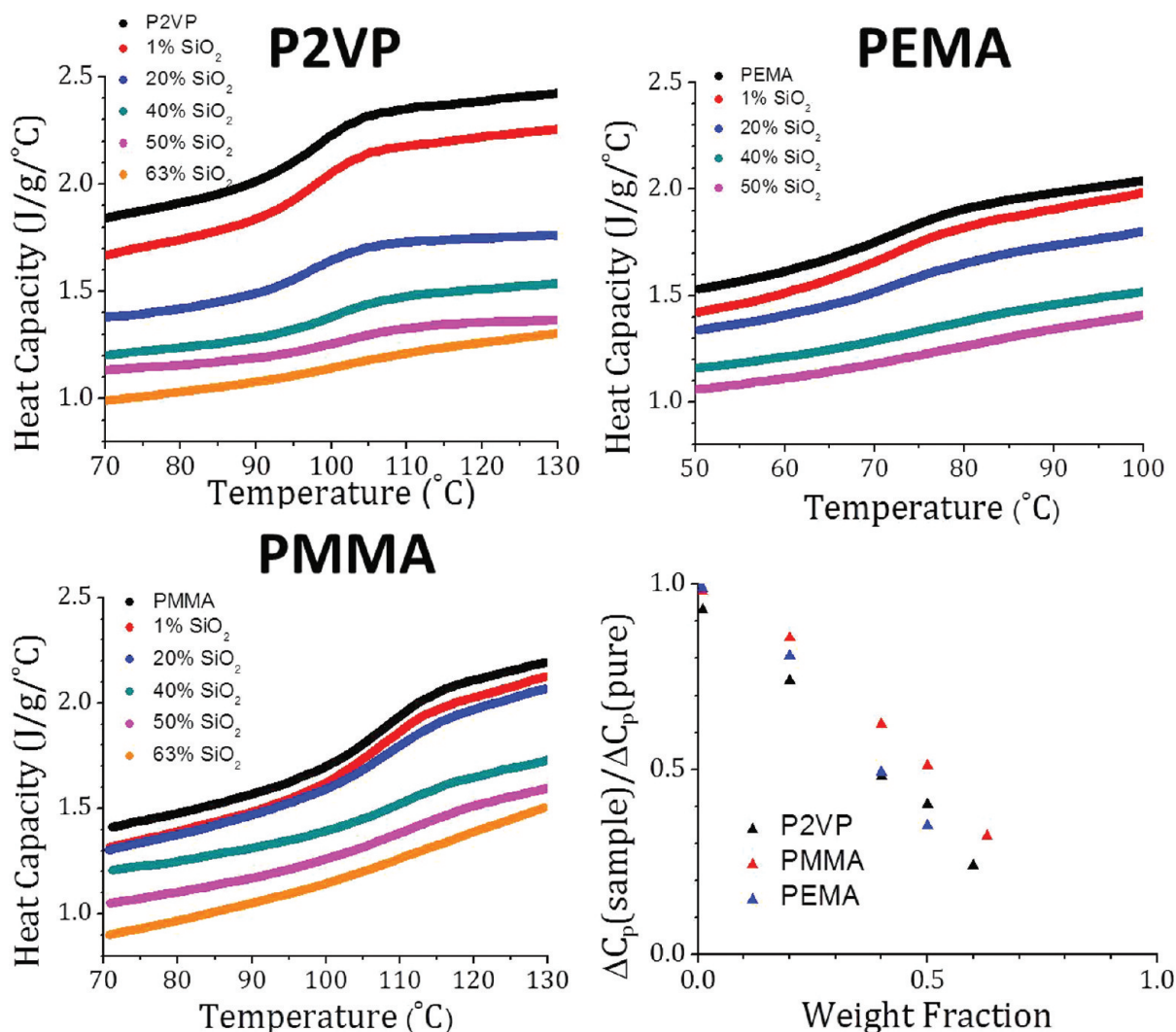


Figure 4. DSC traces for the P2VP, PMMA, and PEMA samples. The last plot sketches the ΔC_p scaled by the value for the pure polymer plotted as a function of the volume fraction of silica. The plot should scale linearly if there is no bound layer and go to zero for 100% silica.

were annealed *in vacuo* ($\sim 10^{-3}$ mmHg) at 150 °C for 48 h and then compression-molded at 180 °C for 5 min into 12.7 mm diameter \times 0.8 mm thick disks. The disks were subsequently annealed at 110–120 °C (depending on filler loading) *in vacuo* for 2 h to remove any stresses from compression molding.

Fourier transform infrared spectroscopy (FTIR) was performed on a Digilab/Biorad 7000 spectrometer with 2 cm^{-1} resolution and 64 scans. Samples were placed on 25 mm diameter \times 2 mm thick NaCl windows for processing and analysis. Modulated DSC³³ was performed using an indium (temperature) and sapphire (heat capacity) calibrated TA Instruments Q100 in a nitrogen atmosphere. Approximately 10 mg of sample was placed in an aluminum sample pan and held at 190 °C for 5 min. These samples were then cooled at a rate of 2 °C/min, with a modulation amplitude of 1 °C and a modulation period of 60 s, to a final temperature of 30 °C. The TA Instruments software package, Universal Analysis 2000, was used to quantify the glass transition temperature, T_g . The inflection point in the transition of the heat capacity from the rubbery state to the glassy state was interpreted as the T_g , and at least three samples were averaged at each state point. For TEM, samples were cut into ~ 50 nm slices using ultramicrotomy. For analysis of the interparticle spacings, ultrasmall angle X-ray

scattering (USAXS) was performed at beamline X10A at the National Synchrotron Light Source. The silica primary particle radius ($R_p = 7.5 \pm 2.2$ nm) was also determined using SAXS at X10A with a fit to a Gaussian-convoluted form factor.

FTIR was used to (i) confirm complete removal of the solvents during nanocomposite annealing, through the use of isotopically labeling to distinguish it from the polymer spectrum and to (ii) quantify the strong hydrogen-bonding interactions between the polymers and the silica. FTIR was also used to confirm no measurable polymer degradation under any conditions implemented here. Please note that this does not mean that the samples are absolutely dry—rather that we cannot find any solvent within the resolution of the IR instrument (which is at least 0.1%).

FTIR revealed ~ 1.5 hydrogen bonds/nm² for P2VP/silica³² and ~ 2.0 hydrogen bonds/nm² for PMMA/silica and PEMA/silica. The hydrogen bonding energy associated with a 2VP/silanol bond is ~ 10 kT, while that of MMA/silanol and EMA/silanol bonds are ~ 5 kT. Therefore, these polymer/nanoparticle interfaces have an attractive interaction ~ 10 – 15 kT/nm², resulting in strong physisorption, which indicates a strongly favorable interface in all cases.

Figures 1 and 2 and data from our previous work on P2VP³² suggest that all three systems have comparable nanoparticle dispersion states. We have also performed USAXS experiments on the P2VP nanocomposite samples³² and a select number of the PMMA specimens. These results, in conjunction, support the view that the strongly favorable interactions between the polymers and the silica ensures good nanoparticle dispersions in all cases, up to the highest nanoparticle loading of 62.5 wt %.

We now focus on the primary result of this paper, namely the T_g shift obtained on the addition of nanoparticles to the three polymers. Figure 3 shows the shifts in the T_g values as obtained from DSC for the three polymers in question. (Figure 4 shows the raw data). Two things are apparent. First, there is a definite increase of the T_g with the addition of the nanoparticles. However, the magnitude of these increases is small and typically smaller by about an order of magnitude than many reports in the current literature. However, they are consistent with recent findings for PMMA–silica nanocomposites²³ and also PS–silica nanocomposites^{34,35} with favorable interfacial interactions, which suggest only small changes of T_g for PNC systems.

Our results support a suite of recent findings on thin films and polymer nanocomposites which suggest that annealing thin polymer films can lead to an almost complete absence of a T_g shift even when the interactions between the polymer and surface are attractive. As noted in the introduction, this finding conflicts with simulation results that predict a monotonic dependence of thin film T_g 's with interfacial interaction strength. To resolve this apparent contradiction, we examine Figure 4d, which shows that the strength of the DSC transition (i.e., ΔC_p) with increasing silica content. While this dependence is linear, the slope of this line is larger than unity, suggesting that the heat capacity goes to zero for finite polymer concentration. This implies that there is a bound layer of polymer on each particle, and we estimate based on the slopes of the lines that the thicknesses are 0.8 nm, to within relatively large error bars (± 0.6 nm). We therefore propose a picture that is inspired by our previous work on the phase transitions in thin polymer films.^{36,37} In the presence of strong polymer–surface interactions it is now well accepted that a “bound”, essentially irreversibly adsorbed, polymer layer forms at the particle interface. Because of the essentially irreversible nature of polymer adsorption, this bound layer is dynamically decoupled from the “free” polymer on top of it, with this free polymer having essentially no interactions with the attractive surface. We postulate that the bound layer does not relax in the time frame of our DSC experiments, and hence only the bulk of the sample (i.e., the free chains) shows a glass-like relaxation—since this layer is unaffected by the surface it essentially has the same T_g as the bulk polymer. Additional credence for this assessment is provided by recent experiments on polystyrene spheres³⁸ and for PMMA–silica composites²³ where the heat capacity change in traversing the glass transition region was found to decrease monotonically with increasing surface content. In fact, this reduction in ΔC_p on confinement has previously been used to determine the effective thickness of the bound polymer layer, giving more credence to our picture. It must be emphasized here that we only propose one possible picture, and other alternative possibilities also need to be considered in this context.

ACKNOWLEDGMENTS

The authors thank the National Science Foundation (DMR-1006659) for partial support for this research. This paper is

based on data taken by Shane Harton when he was a postdoc at Columbia.

REFERENCES

- (1) Jackson, C. L.; McKenna, G. B. *J. Non-Cryst. Solids* **1991**, *131*, 221–224.
- (2) Jackson, C. L.; McKenna, G. B. *Chem. Mater.* **1996**, *8* (8), 2128–2137.
- (3) Keddie, J. L.; Jones, R. A. L.; Cory, R. A. *Faraday Discuss.* **1994**, *98*, 219–230.
- (4) Keddie, J. L.; Jones, R. A. L.; Cory, R. A. *Europhys. Lett.* **1994**, *27* (1), 59–64.
- (5) de Gennes, P. G. *Eur. Phys. J. E* **2000**, *2* (3), 201–203.
- (6) Rittigstein, P.; Torkelson, J. M. *J. Polym. Sci., Part B: Polym. Phys.* **2006**, *44* (20), 2935–2943.
- (7) Rittigstein, P.; Priestley, R. D.; Broadbelt, L. J.; Torkelson, J. M. *Nature Mater.* **2007**, *6* (4), 278–282.
- (8) Kim, S.; Hewlett, S. A.; Roth, C. B.; Torkelson, J. M. *Eur. Phys. J. E* **2009**, *30* (1), 83–92.
- (9) Forrest, J. A.; Dalnoki-Veress, K.; Stevens, J. R.; Dutcher, J. R. *Phys. Rev. Lett.* **1996**, *77* (10), 2002–2005.
- (10) Forrest, J. A.; Dalnoki-Veress, K.; Dutcher, J. R. *Phys. Rev. E* **1997**, *56* (5), 5705–5716.
- (11) Forrest, J. A.; Mattsson, J. *Phys. Rev. E* **2000**, *61* (1), R53–R56.
- (12) Mattsson, J.; Forrest, J. A.; Borjesson, L. *Phys. Rev. E* **2000**, *62* (4), 5187–5200.
- (13) Torres, J. A.; Nealey, P. F.; de Pablo, J. J. *Phys. Rev. Lett.* **2000**, *85* (15), 3221–3224.
- (14) Fryer, D. S.; Peters, R. D.; Kim, E. J.; Tomaszewski, J. E.; de Pablo, J. J.; Nealey, P. F.; White, C. C.; Wu, W. L. *Macromolecules* **2001**, *34* (16), 5627–5634.
- (15) Frank, B.; Gast, A. P.; Russell, T. P.; Brown, H. R.; Hawker, C. J. *Macromolecules* **1996**, *29* (20), 6531–6534.
- (16) van Zanten, J. H.; Wallace, W. E.; Wu, W. L. *Phys. Rev. E* **1996**, *53* (3), R2053–R2056.
- (17) Kajiyama, T.; Tanaka, K.; Takahara, A. *Macromolecules* **1997**, *30* (2), 280–285.
- (18) Long, D.; Lequeux, F. *Eur. Phys. J. E* **2001**, *4* (3), 371–387.
- (19) Alcoutlabi, M.; McKenna, G. B. *J. Phys.: Condens. Matter* **2005**, *17* (15), R461–R524.
- (20) Bansal, A.; Yang, H. C.; Li, C. Z.; Cho, K. W.; Benicewicz, B. C.; Kumar, S. K.; Schadler, L. S. *Nature Mater.* **2005**, *4* (9), 693–698.
- (21) Starr, F. W.; Schroder, T. B.; Glotzer, S. C. *Phys. Rev. E* **2001**, *64* (2), xxxx.
- (22) Starr, F. W.; Schroder, T. B.; Glotzer, S. C. *Macromolecules* **2002**, *35* (11), 4481–4492.
- (23) Sargsyan, A.; Tonoyan, A.; Davtyan, S.; Schick, C. *Eur. Polym. J.* **2007**, *43* (8), 3113–3127.
- (24) Lupascu, V.; Picken, S. J.; Wubbenhorst, M. *J. Non-Cryst. Solids* **2006**, *352* (52–54), 5594–5600.
- (25) Napolitano, S.; Prevosto, D.; Lucchesi, M.; Pingue, P.; D'Acunto, M.; Rolla, P. *Langmuir* **2007**, *23* (4), 2103–2109.
- (26) Lu, H. Y.; Chen, W.; Russell, T. P. *Macromolecules* **2009**, *42* (22), 9111–9117.
- (27) Erber, M.; Tress, M.; Mapesa, E. U.; Serghei, A.; Eichhorn, K. J.; Voit, B.; Kremer, F. *Macromolecules* **2010**, *43* (18), 7729–7733.
- (28) Mapesa, E. U.; Erber, M.; Tress, M.; Eichhorn, K. J.; Serghei, A.; Voit, B.; Kremer, F. *Eur. Phys. J.: Spec. Top.* **2010**, *189* (1), 173–180.
- (29) Tress, M.; Erber, M.; Mapesa, E. U.; Huth, H.; Muller, J.; Serghei, A.; Schick, C.; Eichhorn, K. J.; Volt, B.; Kremer, F. *Macromolecules* **2010**, *43* (23), 9937–9944.
- (30) Serghei, A.; Kremer, F. *Fractals, Diffus. Relax. Disord. Complex Syst., Part B* **2006**, *133*, 595–632.
- (31) Serghei, A.; Tress, M.; Kremer, F. *J. Chem. Phys.* **2009**, *131* (15), xxxx.
- (32) Harton, S. E.; Kumar, S. K.; Yang, H. C.; Koga, T.; Hicks, K.; Lee, E.; Mijovic, J.; Liu, M.; Vallery, R. S.; Gidley, D. W. *Macromolecules* **2010**, *43* (7), 3415–3421.

- (33) Wunderlich, B.; Jin, Y. M.; Boller, A. *Thermochim. Acta* **1994**, 238, 277–293.
- (34) Bansal, A.; Yang, H. C.; Li, C. Z.; Benicewicz, R. C.; Kumar, S. K.; Schadler, L. S. *J. Polym. Sci., Part B: Polym. Phys.* **2006**, 44 (20), 2944–2950.
- (35) Sen, S.; Xie, Y.; Bansal, A.; Yang, H.; Cho, K.; Schadler, L. S.; Kumar, S. K. *Eur. Phys. J.: Spec. Top.* **2007**, 141, 161–165.
- (36) Indrakanti, A.; Jones, R. L.; Kumar, S. K. *Macromolecules* **2004**, 37 (1), 9–12.
- (37) Jones, R. L.; Indrakanti, A.; Briber, R. M.; Muller, M.; Kumar, S. K. *Macromolecules* **2004**, 37 (18), 6676–6679.
- (38) Sasaki, T.; Shimizu, A.; Mourey, T. H.; Thureau, C. T.; Ediger, M. D. *J. Chem. Phys.* **2003**, 119 (16), 8730–8735.